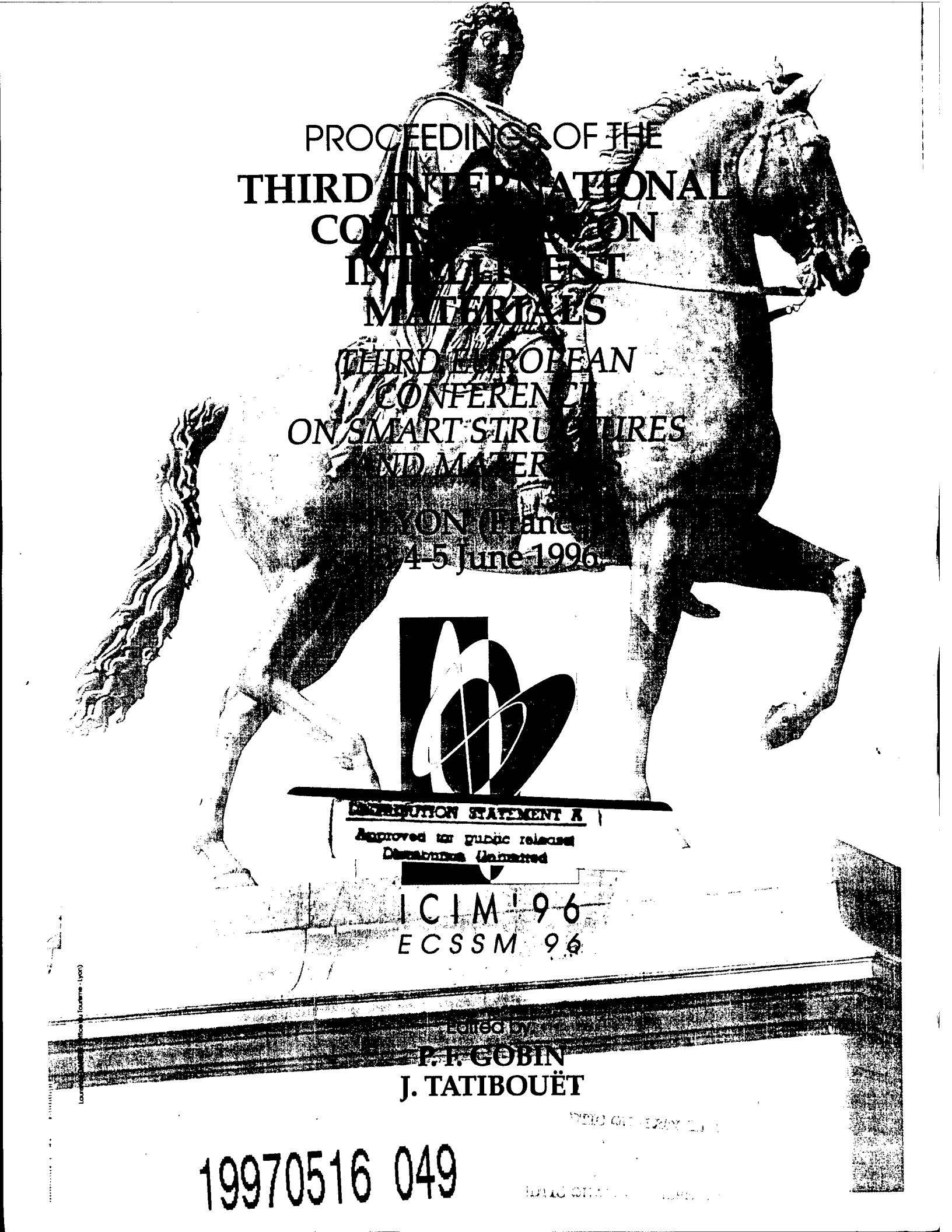


PROCEEDINGS OF THE

THIRD INTERNATIONAL CONFERENCE ON INTELLIGENT MATERIALS

(THIRD EUROPEAN CONFERENCE ON SMART STRUCTURES AND MATERIALS)

LYON (France)
3-5 June 1996

DISTRIBUTION STATEMENT A
Approved for public release;
Distribution Unlimited

ICIM 96
ECSSM 96

Edited by
P.F. GOBIN
J. TATIBOUËT

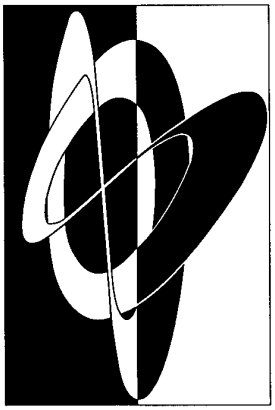
19970516 049

THIRD INTERNATIONAL CONFERENCE ON INTELLIGENT MATERIALS

THIRD EUROPEAN CONFERENCE ON SMART STRUCTURES AND MATERIALS

LYON / 3-4-5 June 1996

CENTER OF CONGRESS "L'ESPACE TETE D'OR"
103, boulevard Staligrad - Lyon Villeurbanne (Rhône)



DISTRIBUTION STATEMENT A
Approved for public release
Distribution Unlimited

General Chair:
P. F. GOBIN

INSA LYON

Chair:
B. CULSHAW

UNIVERSITY OF STRATHCLYDE

Edited by: **P. F. GOBIN and J. TATIBOUËT**

SPIE Volume 2779

DTIC QUALITY INSPECTED 1



The papers appearing in this book comprise the proceedings of the meeting mentioned on the cover and title page. They reflect the authors' opinions and are published as presented and without change, in the interests of timely dissemination. Their inclusion in this publication does not necessarily constitute endorsement by the editors or by SPIE.

Please use the following format to cite material from this book:
Author(s), "Title of paper," in *Third International Conference on Intelligent Materials and Third European Conference on Smart Structures and Materials,* Pierre F. Gobin, Jacques Tatibouët, Editors, Proc. SPIE 2779, page numbers (1996).

Library of Congress Catalog Card No. 96-67474
ISBN 0-8194-2165-0

Published by
SPIE—The International Society for Optical Engineering
P.O. Box 10, Bellingham, Washington 98227-0010 USA
Telephone 360/676-3290 (Pacific Time) • Fax 360/647-1445

Copyright ©1996, The Society of Photo-Optical Instrumentation Engineers.

Copying of material in this book for internal or personal use, or for the internal or personal use of specific clients, beyond the fair use provisions granted by the U.S. Copyright Law is Bauthorized by SPIE subject to payment of copying fees. The Transactional Reporting Service base fee for this volume is $6.00 per article (or portion thereof), which should be paid directly to the Copyright Clearance Center (CCC), 222 Rosewood Drive, Danvers, MA 01923. Payment may also be made electronically through CCC Online at http://www.directory.net/copyright/. Other copying for republication, resale, advertising or promotion, or any form of systematic or multiple reproduction of any material in this book is prohibited except with permission in writing from the publisher. The CCC fee code is 0-8194-2165-0/96/$6.00.

Printed in the United States of America.

Contents

xv *Acknowledgments*
xvii *Preface*

PLENARY LECTURES

2 **Concept of and recent research on intelligent materials**
T. Takagi, Ion Engineering Research Institute Corp. (Japan)

16 **Intelligent materials and systems as a basis for innovative technologies in transportation vehicles**
C. Boller, Daimler-Benz AG (FRG)

28 **Biomimetic materials and structures**
D. De Rossi, Univ. di Pisa (Italy)

34 **Intelligent biointerface: remote control for hydrophilic-hydrophobic property of material surfaces by temperature**
T. Okano, A. Kikuchi, Tokyo Women's Medical College (Japan)

42 **Materials and their uses**
P. Richard, Bouygues SA (France)

48 **Research and commercialization obstacles and opportunities for intelligent material systems (Title Only)**
C. A. Rogers, Virginia Polytechnic Institute and State Univ. (USA)

BIOLOGICAL MATERIALS

50 **Design of intelligent biomolecular materials with engineered protein assemblies (Invited Paper)**
M. Aizawa, N. Damrongchai, T. Haruyama, E. Kobatake, Tokyo Institute of Technology (Japan)

53 **Design of conductive nanospace interfaces for smooth electrochemical communication between redox enzyme proteins and electrodes**
H. Shinohara, M. Sisido, Okayama Univ. (Japan)

58 **Intelligent molecules: examples from biological charge transport**
L. N. Christophorov, Bogoliubov Institute for Theoretical Physics (Ukraine)

66 **Control of the activity of an enzyme immobilized into thermoreversible hydrogel**
L. V. Sigolaeva, N. L. Eremeev, N. F. Kazanskaya, Moscow State Univ. (Russia)

72 **Metallization of bacterial surface layer by cross-beam pulsed laser deposition**
W. Pompe, M. Mertig, R. Kirsch, A. A. Gorbunov, A. Sewing, Max-Planck AG (FRG); H. Engelhardt, Max-Planck-Institut für Biochemie (FRG); A. Mensch, Technische Univ. Dresden (FRG)

78 **Collagen assembly from acid solution to networks on solid surfaces and to fibrils**
J.-H. Bradt, M. Mertig, B. Winzer, U. Thiele, W. Pompe, Max-Planck AG (FRG)

83 **Blubber and compliant coatings for drag reduction in fluids III: viscoelastic properties of dolphin blubber matched by a gel-foam composite**
E. R. Fitzgerald, Johns Hopkins Univ. (USA); J. W. Fitzgerald, Kildare Corp. (USA)

INTELLIGENT COMPOSITES AND HEALTH MONITORING

90 **Some aspects of health monitoring in composite materials (Invited Paper)**
K. Schulte, Technical Univ. Hamburg-Harburg (FRG)

100 **Proposal for a new maintenance inspection**
K. Egawa, Niigata Institute of Technology (Japan)

106 **Qualitative nondestructive evaluation research at CIMSS**
F. Lalande, C. A. Rogers, Virginia Polytechnic Institute and State Univ. (USA)

112 **Use of in-situ dielectric sensing for intelligent processing and health monitoring**
D. Kranbuehl, H. Aandahl, N. Haralampus, W. Newby, D. Hood, College of William and Mary (USA); G. Boiteux, G. Seytre, J. P. Pascault, A. Maazouz, J. F. Gerard, H. Sautereau, J. F. Chailan, Univ. Lyon I (France); A. C. Loos, J. D. MacRae, Virginia Polytechnic Institute and State Univ. (USA)

118 **Impact damage diagnostics for composite structures using built-in sensors and actuators**
M. Tracy, Y.-S. Roh, F.-K. Chang, Stanford Univ. (USA)

124 **Sensor technology for structural integrity monitoring**
R. Jones, W. K. Chiu, Monash Univ. (Australia); S. Pitt, Melbourne Univ. (Australia)

130 **Evaluation of Lamb wave performance for health monitoring of composites using bonded piezoelectric transducers**
H. Kaczmarek, C. Simon, ONERA (France); C. Delebarre, Univ. de Valenciennes (France)

136 **Carbon fibres: sensor components for smart materials**
O. Ceysson, T. Risson, M. Salvia, Ecole Centrale de Lyon/CNRS (France)

142 **Application of a laser Raman sensor for stress monitoring in composites**
B. Arjyal, C. Galiotis, Queen Mary and Westfield College (UK)

146 **Comparison between flat multi-element array device and oblique incidence transducers for Lamb waves generation: application for embedding in composite material**
T. Demol, P. Blanquet, C. Delebarre, Univ. de Valenciennes (France); H. Kaczmarek, ONERA (France)

152 **Piezoelectric implant method: theoretical and experimental study of the influence of inherent geometric and bonding defects**
N. Saint-Pierre, Y. Jayet, J. C. Baboux, Institut National des Sciences Appliquées de Lyon (France)

158 **Piezoelectric implant: monitoring the water degradation in polymer-based composites**
D. Zellouf, N. Saint-Pierre, Y. Jayet, J. Tatibouët, Institut National des Sciences Appliquées de Lyon (France)

164 **Two intelligent materials: both are self-forming and self-repairing, one also self-senses and self-recycles**
C. M. Dry, Univ. of Illinois/Urbana-Champaign (USA).

SMART COMPOSITES AND OPTICAL FIBRES

174 **Ultrasonic condition monitoring of CFRP and GRP plates using a surface-mounted source and an embedded optical fibre sensor (Invited Paper)**
W. R. Philp, S. G. Pierce, A. Gachagan, A. McNab, G. Hayward, B. Culshaw, Univ. of Strathclyde (UK)

180 **Integration of optical fibers and piezoelectric ceramics in composite materials**
S. Bourasseau, M. Dupont, M. Pernice, A. Thiriot, ONERA (France); P. Blanquet, T. Demol, C. Delebarre, D. Coutellier, Univ. de Valenciennes (France)

186 **Interferometric optical strain gauge: production, use, and comparison to conventional techniques**
M. Tatti, Institute for System Engineering and Informatics (Italy); G. Sala, P. Mantegazza, Politecnico di Milano (Italy)

192 **Dual-wavelength operation of digital spatial domain multiplexed fibre sensor arrays for dynamic strain monitoring**
Y. Hu, S. Chen, South Bank Univ. (UK)

198 **Optical fiber sensor for temperature measuring**
M. Baran, Lviv Polytechnic State Univ. (Ukraine)

203 **Development of embedded sapphire optical waveguides for intelligent ceramic composites**
M. A. El-Sherif, J. Radhakrishnan, J. Yuan, Drexel Univ. (USA)

209 **Practical terminations for optical fibres embedded in composite materials**
A. K. Green, S. Darvish, Israel Aircraft Industries; E. Shafir, Soreq Nuclear Research Ctr. (Israel)

213 **Strain and failure sensing with a fiber optic Michelson sensor embedded in a composite beam**
C. S. Hong, I. B. Kwon, C. G. Kim, Korea Advanced Institute of Science and Technology

217 **Fatigue strength of glass reinforced polyester (GRP) laminates with embedded optical fibers**
A. Güemes, J. M. Menéndez, Univ. Politécnica de Madrid (Spain)

222 **Examination of reliability of fibre optic sensors embedded in carbon/epoxy composites**
K. Levin, S. Nilsson, Aeronautical Research Institute of Sweden

230 **Impact detection and vibration sensing for material composite structures by integrated optic fibre sensors**
L. Michel, M. Labarrère, ENSICA (France); R. Gafsi, A. R. Malki, P. Lecoy, Ecole Centrale Paris (France)

235 **Using optical sensors to understand core crush in composite panels during processing**
N. Zahlan, G. T. Emmerson, ICI Research and Technology Ctr. (UK)

SMART SENSORS AND SYSTEMS

240 **Smart materials and sensors: a reality or a dream for tomorrow? (Invited Paper)**
J.-C. Andre, ENSIC/INPL and INRS (France)

255 **Magnetic studies of persistent photoconductivity in compensated PbTe:Ga**
A. N. Vasil'ev, T. N. Voloshok, S. V. Kuvshinnikov, Moscow State Univ. (Russia)

260 **Photosensitive tetragonal germanium nanostructures deposited by cluster-beam evaporation**
S. Nozaki, S. Sato, H. Ono, H. Morisaki, Univ. of Electro-Communications (Japan); M. Iwase, Tokai Univ. (Japan); K. Takahashi, Nishi-Tokyo Univ. (Japan)

266 **Semiconductor light detector with optical control of the photosensitive region for intelligent systems**
P. G. Kasherininov, A. V. Kichaev, A.F. Ioffe Physical-Technical Institute (Russia)

269 **From intelligent materials to smart sensors**
E. Fortunato, G. Lavareda, R. Martins, New Univ. of Lisbon (Portugal); F. Soares, L. Fernandes, CEMOP-UNINOVA (Portugal)

275 **Investigations of porous silicon layers with regard to chemical microsensor applications**
M. J. Schöning, M. Crott, Forschungszentrum Jülich GmbH (FRG); F. Ronkel, Heinrich-Heine-Univ. Düsseldorf (FRG); M. Thust, Forschungszentrum Jülich GmbH (FRG); J. W. Schultze, Heinrich-Heine-Univ. Düsseldorf (FRG); P. Kordos, H. Lüth, Forschungszentrum Jülich GmbH (FRG)

281 **Use of intelligent ceramic materials as a strategy for the development of chemical sensors**
E. Traversa, Univ. di Roma Tor Vergata (Italy)

289 **Micro-Hall magnetic sensors with high magnetic sensitivity based on III-V heterostructures**
S. Del Medico, T. Benyattou, G. Guillot, Institut National des Sciences Appliquées de Lyon (France); T. Venet, M. Gendry, J. Tardy, Ecole Centrale de Lyon/CNRS (France); A. Chovet, ENSERG (France)

294 **Ultrasonic carbon-fiber gyrosensor**
Y. Tomikawa, K. Kimura, Yamagata Univ. (Japan); S. Sugawara, Ishinomaki Sensyu Univ. (Japan)

298 **Optoelectronic logical system with thin film photoconducting and electroluminescent devices**
Z. W. Porada, Kraków Polytechnic (Poland)

ELECTRO- AND MAGNETORHEOLOGIC FLUIDS

306 **Adaptative fluids: rheology and light transmission control (Invited Paper)**
G. Bossis, S. Cutillas, E. Lemaire, A. Meunier, O. Volkova, Univ. de Nice (France)

310 **Engineering with ER fluids: a design methodology based upon generalised fluid data**
D. J. Peel, R. Stanway, W. A. Bullough, Univ. of Sheffield (UK)

317 **Chemical preparation of new magnetic fluids based on spinnel ferrite nanoparticles**
F. A. Tourinho, P. C. Morais, M. H. Sousa, L. G. Macedo, Univ. de Brasília (Brazil)

322 **Magnetic particle-particle interaction in single-particle systems and agglomerates**
M. C. F. L. Lara, P. C. Morais, F. A. Tourinho, Univ. de Brasília (Brazil)

328 **Investigation of magnetic anisotropy in frozen magnetic fields**
P. C. Morais, A. F. Bakuzis, F. A. Tourinho, Univ. de Brasília (Brazil)

331 **Damping control of a CFRP cantilevered beam with electrorheological fluids actuator**
T. Fukuda, N. Oshima, Osaka City Univ. (Japan)

337 **Nontraditional application of electrorheological effect**
E. V. Korobko, A.V. Luikov Heat and Mass Transfer Institute (Belarus)

POLYMERS AND POLYMERIC GELS FOR SMART SYSTEMS

344 **Polymer gel: soft and wet intelligent material (Invited Paper)**
Y. Osada, Y. Ueoka, J. P. Gong, Hokkaido Univ. (Japan)

349 **Spontaneous motion of polymer gels on water**
S. Matsumoto, J. P. Gong, Y. Osada, Hokkaido Univ. (Japan)

353 **Lumped parameter modeling of polymer gel for real-time control**
W. Lee, D. Brock, Massachusetts Institute of Technology (USA)

359 **Ion-exchange polymer artificial muscle and actuating system**
D. Vial, B. Tondu, P. Lopez, Y. Aurelle, Institut National des Sciences Appliquées Complexe Scientifique de Rangueil (France); A. Ricard, Ecole Nationale Supérieure d'Ingénieurs de Génie Chimique (France)

365 **Artificial muscles: influence of electrolyte concentration on bilayer movement**
T. F. Otero, J. M. Sansiñena, Univ. del País Vasco (Spain)

371 **Conducting polymer electromechanics: a continuum model of passive mechanical properties**
A. Della Santa, A. Mazzoldi, C. Tonci, Univ. di Pisa (Italy); P. Chiarelli, CNR Institute of Clinical Institute Physiology (Italy); D. De Rossi, Univ. di Pisa (Italy)

377 **Polymer composites for temperature and current sensors**
R. G. Strümpler, ABB Corporate Research (Switzerland)

383 **Interpolyelectrolyte complexes as smart binders with controllable stability in water-salt solutions**
D. V. Pergushov, V. A. Izumrudov, A. B. Zezin, V. A. Kabanov, Moscow State Univ. (Russia)

389 **Superparamagnetic composite material based on polyaniline and magnetite**
V. D. Pokhodenko, O. Yu. Posudievsky, L.V. Pisarzhevsky Institute of Physical Chemistry (Ukraine)

393 **Supramolecular polymers for optical resolution**
N. Ogata, Sophia Univ. (Japan)

401 **Opaque-transparent transition in polymeric hydrogel systems (Abstract Only)**
H. Goering, H.-R. Holzbauer, A. Schönhals, H.-E. Carius, A. Seeboth, Institut für Angewandte Chemie Berlin-Adlershof (FRG)

402 **Adaptable and adaptive materials for light flux control**
P. Sixou, A. Magnaldo, J. Nourry, C. Laye, CNRS (France)

408 **Some functional macromolecules as exciton converters**
V. G. Syromyatnikov, V. Yashchuk, T. Ogul'chanski, A. Kolendo, I. Savchenko, V. Kudrya, Kiev Taras Shevchenko Univ. (Ukraine)

414 **Memory elements based on an inducted strain in polycarbonate**
J. Golobič, D. M. Vasiljević, VTI-VJ (Yugoslavia)

418 **Thermomechanical properties of shape memory polymer of polyurethane series and their applications**
H. Tobushi, H. Hara, E. Yamada, Aichi Institute of Technology (Japan); S. Hayashi, Mitsubishi Heavy Industries, Ltd. (Japan)

424 **Dependence of the molecular dynamics of comblike polyacrylates and polymethacrylates on the mesophase structure studied by dielectric spectroscopy**
A. Schönhals, Institut für Angewandte Chemie Berlin-Adlershof eV (FRG); D. Wolff, J. Springer, Technische Univ. Berlin (FRG)

430 **Gel-dispersed liquid crystals: a new material for displays**
A. Seeboth, Institut für Angewandte Chemie Berlin-Adlershof eV (FRG)

435 **Polymer-dispersed liquid crystals: liquid crystal/polymer composites as electro-active materials**
H. M. Siddiqi, M. Dumon, J. P. Pascault, Institut National des Sciences Appliquées de Lyon (France)

SHAPE MEMORY ALLOYS AND ADAPTIVE MATERIALS

442 **Adaptivity of shape memory alloys for use in adaptive materials (Invited Paper)**
J. Van Humbeeck, Katholieke Univ. Leuven (Belgium)

452 **Cyclic deformation properties of TiNi shape memory alloy under thermomechanical loading**
H. Tobushi, S. Yamada, T. Hachisuka, Aichi Institute of Technology (Japan); K. Tanaka, Tokyo Metropolitan Institute of Technology (Japan)

458 **Hysteretic behavior of NiTi shape memory alloy as a function of deformation, temperature, and rate of deformation**
M. C. Piedboeuf, R. Gauvin, F. Trochu, Ecole Polytechnique de Montréal (Canada)

463 **Investigation of deformation and damping mechanisms in Ti-50.6% Ni alloy**
A. A. Ilyin, I. S. Golovin, M. U. Kollerov, A. A. Shinaev, Moscow State Aircraft Technology Univ. (Russia)

469 **Thermomechanical properties in CuAlNi shape memory alloys processed by powder metallurgy**
J. San Juan, R. B. Pérez-Sáez, V. Recarte, I. Sáez-Ocáriz, M. L. Nó, Univ. del País Vasco (Spain); O. Ruano, Ctr. Nacional de Investigaciones Metalúrgicas (Spain)

475 **Solder paste/shape memory alloy composite for adaptive solder joint**
S. Trombert, J. Chazelas, P. Bonniau, Thomson-CSF (France); W. Van Moorleghem, M. Chandrasekaran, AMT nv (Belgium); J. F. Silvain, ICMCB/CNRS (France)

481 **Comparison of the fatigue of two shape memory alloys (CuZnAl and TiNiCu) during shape memory effect cycles**
M. J. Bigeon, M. Morin, Institut National des Sciences Appliquées de Lyon (France)

487 **Shape memory alloy superelastic behavior: 3D finite-element simulations**
F. Auricchio, Univ. di Roma Tor Vergata (Italy); R. L. Taylor, Univ. of California/Berkeley (USA)

493 **Use of shape memory alloys in actuators**
G. Guénin, P. Gaudez, Institut National des Sciences Appliquées de Lyon (France)

499 **Stress-optimised shape memory microactuator**
K. D. Skrobanek, M. Kohl, Forschungszentrum Karlsruhe/IMT (FRG); S. Miyazaki, Univ. of Tsukuba (Japan)

505 **Large-stroke and high-strength actuator materials for adaptive structures**
K. Ullakko, Massachusetts Institute of Technology (USA)

511 **Modelling of the thermomechanical behaviour of shape memory wires embedded in matrix materials**
R. Stalmans, J. Van Humbeeck, L. Delaey, Katholieke Univ. Leuven (Belgium)

517 **Active modification of the vibration frequencies of a polymer beam using shape memory alloy fibres**
J.-E. Bidaux, J.-A. E. Månson, R. Gotthardt, Ecole Polytechnique Fédérale de Lausanne (Switzerland)

523 **Responses and responsive shape control of environmentally responsive composites with embedded TiNi alloy as effector**
H. Yoshida, National Institute of Materials and Chemical Research (Japan); A. Funaki, Mie Industrial Research Institute (Japan); S. Yano, National Institute of Materials and Chemical Research (Japan)

530 **Influence of processing conditions on actuation properties of adaptive hybrid composites**
J. Grando, M. Salvia, Ecole Centrale de Lyon/CNRS (France)

535 **Smart material thermal characterization: NiTi shape memory alloy embedded in a resin epoxy matrix**
F. Thiebaud, Lab. de Mécanique Appliquée R. Chaléat (France); B. Zeghmati, Lab. de Métrologie des Interfaces Techniques (France); J. F. Charmoillaux, C. Lexcellent, Lab. de Mécanique Appliquée R. Chaléat (France)

541 **Mathematical modelling of the incomplete transformations in pseudoelastic processes in binary alloys**
D. Vokoun, V. Kafka, Institute of Theoretical and Applied Mechanics (Czech Republic)

SMART SYSTEMS USING PIEZOELECTRIC SENSORS AND APPLICATIONS

548 **Sensor and actuator applications of piezocomposite materials in large smart structures (Invited Paper)**
R. Y. Ting, Naval Undersea Warfare Ctr. (USA)

560 **Fluoridated piezoelectric ceramics for power transducer (Invited Paper)**
L. Eyraud, P. Eyraud, P. Gonnard, D. Audigier, Institut National des Sciences Appliquées de Lyon (France)

564 **Elaboration of PZT thick films by screen printing**
V. Tajan, P. Gonnard, M. Troccaz, Institut National des Sciences Appliquées de Lyon (France)

570 **Co-formed accelerometer-actuator composites using injection-molded PZT**
R. D. Corsaro, J. D. Klunder, Naval Research Lab. (USA); R. Gentilman, D. Fiore, Materials Systems Inc. (USA)

575 **Oxygen diffusion and defect structure in PTCR-barium titanate**
H. Haneda, J. Tanaka, T. Ishigaki, National Institute for Research in Inorganic Materials (Japan)

580 **Composite transducer for shear stress measurement**
D. Roche, C. Richard, L. Eyraud, Institut National des Sciences Appliquées de Lyon (France); C. D. Audoly, DCN Ingenierie Sud/LSM (France)

586 **Application of nonlinear dynamics in the study of ferroelectric materials**
S. Blochwitz, R. Habel, M. Diestelhorst, H. Beige, Univ. Halle-Wittenberg (FRG)

592 **Power limitations in acoustic transducers due to PZT material nonlinearities**
N. Aurelle, D. Guyomar, L. Eyraud, Institut National des Sciences Appliquées de Lyon (France)

598 **Sensor-actuator panels for underwater acoustic control**
R. D. Corsaro, B. H. Houston, Naval Research Lab. (USA)

603 **Smart actuators with piezoelectric materials**
H. Janocha, D. J. Jendritza, P. Scheer, Univ. of Saarland (FRG)

610 **Piezoelectric and electrostrictive bimorph actuators and sensors for smart microsystems**
P. Gaucher, Thomson-CSF (France)

616 **Micromechanical ultrasonic transducer for liquid nebulization**
R. Paneva, Univ. Erlangen-Nürnberg (FRG)

622 **Two-dimensional (x-y) actuator using multimode degeneration of a piezoelectric ring vibrator**
T. Takano, Tohoko Institute of Technology (Japan); Y. Tomikawa, H. Hata, S. Hirose, Yamagata Univ. (Japan)

628 **Estimation of available performances of ultrasonic motors**
L. Petit, L. Lebrun, R. Briot, P. Gonnard, Institut National des Sciences Appliquées de Lyon (France)

634 **New multimode piezoelectric motor**
F. Claeyssen, R. LeLetty, L. Chouteau, N. Lhermet, ZIRST (France); L. Petit, R. Briot, P. Gonnard, Institut National des Sciences Appliquées de Lyon (France)

638 **Model for the nonlinear response of a Terfenol-D-type magnetostrictive actuator**
A. DeSimone, Univ. di Roma Tor Vergata (Italy)

642 **Dynamic interaction between piezoelectric bonded actuators and an axial beam**
S. Accettella, P. Gaudenzi, Univ. di Roma La Sapienza (Italy)

648 **Performance optimisation of active control with piezoceramics**
D. Lang, L. Reithler, C. Rousset, Aérospatiale (France)

VIBRATION AND SOUND CONTROL

656 **Overview of active/passive damping techniques employing viscoelastic materials (Invited Paper)**
G. R. Tomlinson, Univ. of Sheffield (UK)

670 **Smart composite cylindrical shells without vibration (Invited Paper)**
J. Tani, J. Qiu, Tohoku Univ. (Japan)

682 **High-precision form measurements through the use of adaptive structures technology**
L. Campanile, R. Lammering, J. Melcher, DLR (FRG)

688 **Multimodal vibration control of laminated composite plates using piezoceramic materials**
Y. K. Kang, M. H. Kim, H. C. Park, W. Hwang, K. S. Han, POSTECH (Korea)

694 **Piezodamping: a low-power-consumption technique for semi-active damping of light structures**
D. Bondoux, Metravib RDS (France)

700 **Control of high-frequency smart structures through embedded NiTiNOL fibers**
A. V. Srinivasan, Worcester Polytechnic Institute (USA); D. M. McFarland, H. A. Canistraro, E. K. Begg, Univ. of Connecticut (USA)

706 **Active vibration control by piezoceramic actuators on a jet aircraft partial frame structure**
L. Lecce, M. Viscardi, S. Cantoni, Univ. di Napoli Federico II (Italy)

712 **Reduction of the sound power radiation of a typical helicopter panel by use of piezoceramic actuators**
L. De Vivo, A. Concilio, Italian Aerospace Research Ctr.

718 **Piezoceramics/CFRP composites for active vibration control and shape control of aerospace structures**
U. Herold-Schmidt, W. Schäfer, H. W. Zaglauer, Daimler-Benz Dornier Research Ctr. (FRG)

724 **Magnetic-field requirements for an active-control flap on a rotorcraft**
G. P. Carman, M. Mitrovic, Univ. of California/Los Angeles (USA)

729 **Active-control headset protector using piezoceramic material actuator**
M. Brissaud, P. Gonnard, Institut National des Sciences Appliquées de Lyon (France); J. C. Béra, M. Sunyach, Ecole Centrale de Lyon/CNRS (France)

734 **Actively enhanced porous layers for free-field acoustic absorption**
M. Furstoss, D. Thenail, M.-A. Galland, Ecole Centrale de Lyon/CNRS (France)

INTELLIGENT PROCESSING

742 **Fabrication of polymers and composites containing embedded sensors (Invited Paper)**
H. Denham, Arizona Materials Lab. (USA); G. George, L. Rintoul, Queensland Univ. of Technology (Australia); P. Calvert, Arizona Materials Labs. (USA)

748 **Self-controlled material processing (Invited Paper)**
Y. Aoyagi, RIKEN—The Institute of Physical and Chemical Research (Japan)

753 **Research project on nanospace laboratory and related topics (Invited Paper)**
I. Yamada, Kyoto Univ. (Japan)

759 **Nanoscale processing by gas-cluster ion beams: novel technique in ion-beam processing**
I. Yamada, J. Matsuo, Kyoto Univ. (Japan)

765 **Cluster-assembled materials: a new class of nanostructured materials with original structures and properties**
A. Perez, P. Melinon, V. Dupuis, J. Tuaillon, B. Prevel, M. Pellarin, J. L. Vialle, M. Broyer, Univ. Lyon I (France)

772 **Application of ionized cluster beam (ICB) deposition**
A. S. Zolkin, Novosibirsk State Univ. (Russia)

777 **Exciton confinement effect in semiconductor quantum wells studied by resonant second harmonic generation**
H. Ito, F. Minami, Tokyo Institute of Technology (Japan); K. Yoshida, K. Inoue, Hokkaido Univ. (Japan); K. Watanabe, National Institute for Research in Inorganic Mater (Japan)

783 **Direct formation of GaAs quantum dot structure by droplet epitaxy**
N. Koguchi, K. Ishige, National Research Institute for Metals (Japan)

788 **Optoelectronic functions in organic-inorganic hetero nanosystems**
J. Takada, M. Hoshi, Hiroshima Univ. (Japan); T. Yamamoto, M. Watanabe, T. Takagi, Ion Engineering Research Institute Corp. (Japan)

794 **Morphology of thin film growth of gallium nitride by atmospheric pressure organometallic vapor phase epitaxy**
S. M. Liao, J. H. Wen, Chung Yuan Christian Univ. (Taiwan); H. F. Hung, S. M. Lan, Institute of Nuclear Energy Research (Taiwan)

802 **Pinning-controlled metal/semiconductor interfaces**
S. Hara, Electrotechnical Lab. (Japan); T. Teraji, Electrotechnical Lab. and Univ. of Tsukuba (Japan); H. Okushi, Electrotechnical Lab. (Japan); K. Kajimura, Electrotechnical Lab. and Univ. of Tsukuba (Japan)

807 **Two-dimensional design of intelligent materials: introduction of frontier ceramics (Froc) project**
H. Yanagida, Univ. of Tokyo (Japan)

813 **Sol-gel route to functional and hierarchical ceramic matrix composites**
P. Colomban, ONERA and CNRS (France)

819 **Thermodynamic considerations on mass transfer along and across grain boundaries in ceramic materials**
H. Yokokawa, N. Sakai, T. Horita, M. Dokiya, National Institute of Materials and Chemical Research (Japan)

823 **Defect control in crystal growth of photorefractive materials**
K. Kitamura, N. Iyi, J. Tanaka, National Institute for Research in Inorganic Materials (Japan)

828 **Self-organization of phthalocyanine molecules along the atomic step arrays on sapphire**
T. Hayashi, A. Yamashita, T. Maruno, S. Fölsch, S. Matsumoto, NTT Interdisciplinary Research Labs. (Japan); H. Konami, M. Hatano, Tohoku Univ. (Japan)

833 **Growth and tubule formation of boron filament by electron-beam heating in an electron microscope**
M. Tomita, T. Hayashi, S. Suzuki, NTT Interdisciplinary Research Labs. (Japan); J. Tanaka, National Institute for Research in Inorganic Materials (Japan)

838 **Modified aerosol pyrolysis as a preparation route of hexaferrite particles for magnetic media**
V. Pankov, A. Henis, D. Dubanevich, A. Malashevich, A. Shablovski, Institute of Solid State Physics and Semiconductors (Belarus)

842 **Formation method of particle arrangement on substrate and its analysis**
M. Kobayashi, H. Fudoji, M. Egashira, N. Shinya, National Research Institute for Metals (Japan)

848 **Effects of double Schottky barrier on the electric properties of ceramic semiconductors**
K. Mukae, K. Tsuda, A. Tanaka, Fuji Electric Corporate R&D Ltd. (Japan)

MATHEMATICS FOR SMART MATERIALS AND STRUCTURES

856 **Design and manufacturing of material microstructures and micromechanisms (Invited Paper)**
O. Sigmund, Technical Univ. of Denmark

867 **Dynamic controller which insures a given exponential decay rate: application to the stabilization of plate vibrations with piezoelectric actuators**
M. Lenczner, Univ. de Franche Comté (France)

872 **Optimal placement of piezoelectric actuators in intelligent structures using genetic algorithms**
I. Lee, J.-H. Han, Korea Advanced Institute of Science and Technology

876 **Smart system model: thin plate with distributed sensors and actuators**
M. Rahmoune, CNAM (France); D. Osmont, ONERA (France)

883 **Dynamic analysis of peizoelectric actuator bonded on beam**
X. Wang, Xian Jiaotong Univ. (China); C. Ehlers, M. Neitzel, Institut für Verbundwerkstoffe GmbH/Univ. of Kaiserslautern (FRG)

891 **Bodies with controllable constitutive laws: some mathematical issues for active optimisation**
M. Brocato, Univ. di Genova (Italy)

897 **Use of artificial neural networks as estimators and controllers**
A. Concilio, A. Sorrentino, Italian Aerospace Research Ctr.

903 **Active control of blade-vortex interactions using a neuro-fuzzy controller**
R. Swaminathan, J. V. R. Prasad, L. N. Sankar, Georgia Institute of Technology (USA)

907 **Controlling a chaotic response**
M. Battaini, F. Casciati, Univ. di Pavia (Italy)

913 **Finite-element modeling of PMN electrostrictive materials**
J. C. Debus, B. Dubus, Univ. de Valenciennes (France); M. D. McCollum, S. Black, Naval Undersea Warfare Ctr. (USA)

919 **Bifurcation diagrams and dissipative structure formation in noncrystalline materials**
A. Shatalov, M. Maryan, A. A. Kikineshy, Uzhgorod State Univ. (Ukraine)

925 **Thermal protection memory capacity**
A. K. Alekseev, RSC Energia (Russia)

SMART TECHNOLOGY APPLICATIONS

932 **Distributed sensing for intelligent civil engineering structures (Invited Paper)**
W. C. Michie, Univ. of Strathclyde (UK)

947 **Synthesis of science and art: creating a new domestic world of sensual products**
C. Thorpe, C. M. Friend, Cranfield Univ. (UK)

953 **Smart materials in construction**
A. Sheehan, Ove Arup & Partners (UK)

958 **Smart earthquake-resistant materials: using time-released adhesives for damping, stiffening, and deflection control**
C. M. Dry, Univ. of Illinois/Urbana-Champaign (USA)

968 **Active materials for application in room acoustics**
X. Meynial, Ctr. Scientifique et Technique du Bâtiment (France)

974 **Concept of functional materials use in unconventional means for nuclear plants**
R. R. Ionaitis, Research and Development Institute of Power Engineering and Moscow State Technical Univ. of Bauman (Russia)

986 **Elaboration of the first experience of application of nitinol extravessel corrector with the shape memory effect**
S. D. Prokoshkin, A. C. Butckevitch, A. P. Chadaev, E. P. Ryklina, I. Yu. Khmelevskaya, Moscow Steel and Alloys Institute (Russia) and Russian State Medical Univ.

991 **Biomedical engineering in design and application of nitinol stents with shape memory effect**
E. P. Ryklina, I. Yu. Khmelevskaya, T. V. Morozova, S. D. Prokoshkin, Moscow Steel and Alloys Institute (Russia)

994 **Temperature measurement of the human body**
B. Stadnyk, M. Stepanyak, E. Dziuban, Lviv Polytechnic State Univ. (Ukraine)

ADDITIONAL PAPERS

1000 **Multifingered grabbers as smart structures for robotic applications**
M. Shahinpoor, Univ. of New Mexico (USA)

1006 **Ionic flexogelectric effect in polymeric gels**
M. Shahinpoor, Univ. of New Mexico (USA)

1012 **Ion exchange membrane-platinum composites as electrically controllable artificial muscles**
M. Mojarrad, M. Shahinpoor, Univ. of New Mexico (USA)

1019 *Author Index*

Acknowledgments

SPONSORS

European Commission DG XII C—Industrial and Materials Technology
Society of Non Traditional Technology—Intelligent Materials Forum (Japan)
Centre National de la Recherche Scientifique—DIMAT (France)
Direction de la Recherche et de la Technologie—DGA (France)
U.S. Army European Research Office
Region Rhône Alpes
Conseil Général du Rhône
Ville de Lyon
Ville de Villeurbanne
Société Aérospatiale
Compagnie de St. Gobain
Société Thomson CSF
CIBA Composites—Brochier

PARTICIPATING PROFESSIONAL SOCIETIES

AMAC—Association pour les Matériaux Composites
ASM—The Materials Information Society
EMRS—European Materials Research Society
GFP—Groupe Français d'Etudes et d'Application des Polymères
IEE—Institution of Electrical Engineers
IMC—Institute of Measurement and Control
IMechE—Institution of Mechanical Engineers
RAeS—The Royal Aeronautical Society
SFP—Société Française de Physique
SF2M—Société Française de Métallurgie et des Matériaux
SNTT—Society of Non Traditional Technology
SPIE—The International Society for Optical Engineering

PARTICIPATING ORGANIZATIONS

INSA de Lyon
University of Strathclyde

Preface

Nobody really knows where the term originated, far less does anyone really know what it means. However, the idea of the smart structure evolved in the United States in the early 1980s as the potentially viable solution to the problems posed by the next generation of—particularly military—aircraft. In parallel, the concept of intelligent materials was pioneered in Japan with the purpose of establishing a new area in material science to take into account the interrelations between materials, the natural environment, and society. It was probably in the late 1980s when the term crept into European vernacular, and over the past decade the meaning of the words has been discussed, frequently very philosophically and very late at night, resulting in an accepted interpretation which is quite accurately reflected in the diversity of topics and approaches mirrored in the contents of this conference.

The common aim is in the frame of a "biomimetic" inspiration to engender materials and structures with the ability to respond adaptively to their environmental constraints and their own condition. A central theme to this is clearly in the necessary ability to measure the condition of the structural material. The early protagonists postulated that, out of necessity, this implied the evolution of new sensing and measurement techniques, and fibre optics, in particular, was identified as a potentially ideal enabling technology. Fibre optics remains a potentially important enabling technology for sensor systems, but a lot of new sensors, with a tendency toward miniaturization, multi-information, and integration, have become more and more available in many fields (for optical, chemical, and mechanical applications). Nevertheless, the smart structures which have been realized in practice to date all use traditional instrumentation technologies.

Perhaps it is at the actuation end of the equation that smart materials and structures present the greatest challenge. It is here, in particular, that improved and even new materials have a leading role to play, and piezoelectrics, electrostrictives, photostrictives, magnetostrictives, shape memory alloys, and rheological fluids all have their important contributions to make. This is the reason why we note strenuous efforts in the innovative field of intelligent processing of biological, organic, and inorganic materials, and their combination as composite systems to improve their primitive functions or to develop new ones. Concerning the actuation problems for structural parts, we are gradually changing our approach to the concept of actuation from a response at a point to a distributed low-energy-density concept. This is particularly evident in some of the emerging designs for aircraft wings, but is a concept that can be applied to many situations ranging from vibration damping to the adaptive control of building stiffness for earthquake compensation.

Since it was stimulated within the aerospace industry some 15 or 20 years ago, much of the initial interest in smart structures and materials has changed. Aerospace is a famously conservative discipline—and correctly so—and the potential offered those years ago still remains. However, the real current potential lies in what are perhaps viewed by many as more modest applications, predominantly in civil engineering, ground transportation sectors, and even domestic goods, but neither the technological demands nor the intellectual challenge inherent with these applications must be underestimated. All have reliability, materials compatibility, and environmental specification problems to be overcome. All address potentially very significant economic benefits if only the systems could really work. All have highlighted deficiencies in current technologies

and current approaches and all have stimulated research in sensing, processing, and actuation specific to their particular environments.

New technologies in the major areas of data processing and signal analysis have made enormous contributions to promote the health monitoring concept for complex technological structures. This is thanks primarily to ever-increasing computer power available at ever-decreasing prices, coupled to the continually advancing ingenuity of the computer scientist. Words like neural network and genetic algorithm were known only to specialists a few years ago but can now be implemented on every PC.

Moreover, new fields are emerging: adaptive biomaterials, drug delivery systems, cellular- and molecular-level measurements, controlled nanofabrication techniques, and self-replicating molecules. So where do we go from here? Better understanding of current or new sensors and actuators, and research into applications-oriented new ones, must figure in the future budgets for our collective activities. Many sensing technologies are available, but appreciating which technology to apply and/or refine to a particular situation is a rare art, especially in the context of the diversity of environments within which our smart material and structures must operate. Finally, how do we respond to the signals? Sending someone to fix the ailing structure is naive but effective; adapting the structure to respond to the need is more elegant and infinitely more difficult. The techniques for configuring appropriate response functions have barely been addressed, and most actuator technology remains based on traditional approaches. There is much to be done; hopefully our conference will give at least some hints about where we are, and about where this intriguing amalgam of fundamental knowledge, technologies, techniques, and applications may lead us in the future.

P.F. Gobin
B. Culshaw

Plenary Lectures

The Concept and the Recent Research on Intelligent Materials

Toshinori Takagi

Ion Engineering Research Institute Corporation
4547-15, Tsuda, Hirakata
Oaka 573-01, Japan

ABSTRACT

Intelligent materials are the materials possessing the following functions in themselves such as the sensing function which detect the enviromental change or their inner anomaly, the processor function which can judge the situation to lead the conclusion, and actuating function that the materials themselves can take action or give instruction.

The structural and functional materials simply utilize the native properties and functions of their own. On the other hand, the intelligent materials are based on a new concept where the information science will be united with their own properties and functions. The intelligent materials can be very important and useful in many fields and their interdisciplinary fields such as the medicine, phermacy, bioengineering, polymer, metalugy, semiconductor, ceramics, electronics, machinery. It is also extremely important in the human engineering, safty engineering, enviromental study and study on the resources.

In this report, the category of the Intelligent material and the recent activities of researches on the intelligent materials are dsiscussed.

2. INTRODUCTION

The intelligent material is a newly created concept. It is a complex science which is based on the contemporary material science and the information science. This concept aims to create an artificially designed material, so-called "Tailored Material", having several functions in itself as a sensor, a processor, an actuator and feedback/feedforward functions in combination with the properties and the functions of the material. The purpose of establishing this new scientific field is to assemble smarter structure and achieve higher performance and more complete systems with potential of recognition, discrimination, adjustability, etc. by using the intelligent material. The intelligent material is related to a wide area of researches, i.e., interdisciplinary field of such technology as medicine, pharmacy, biomaterial, polymer, metal, semiconductor, ceramics, mechanical engineering and electronic engineering.

By conceptional prediction it is expected in the future that the material will be combined with software to achieve firmware. This idea is consistent with the concept of intelligent material. In a sense, this corresponds to many forms of living creature, and it will be able to control itself according to the environmental changes. Intelligent materials may be defined as the materials which respond to environmental changes and adjust themselves toward the optimum conditions and manifest their functions according to the changes.

In Japan, from July 1987 to November 1989, the pioneer study of the intelligent material has been initiated under the official organization in Council for Aeronautics, Electronics and Other Advanced Technologies, Science and Technology Agency of the Japanese Government[1]. This was the first occasion for argument that clarified the concept of intelligent materials through discussions by the specialists from wide area mentioned above. These activities stimulated "the First International Workshop "[2] in Tsukuba on March 15-17th, 1989 and "the First International Conference on Intelligent Materials" [3] in Oiso Japan, on March 1992. The 2nd Conf. [4], also, was held at Williamsburg, U.S.A, on June, 1994, successfully and the 3rd Conf. will be held at Lyon, France, on June 3rd-5th, 1996. In this paper, the recent situation of the Intelligent Material is reported by introducing the activities on them in Japan.

0-8194-2165-0/96/$6.00

3. A CONCEPT OF INTELLIGENT MATERIALS

3.1 A Concept of Intelligent Materials

Figure 1 shows a concept of intelligent materials in comparison with structural and functional materials. The structural and functional materials simply utilize the native property and function of their own. On the other hand, intelligent materials are based on a new concept where the information science are introduced in the material.. The information science has several functions including those as sensor, processor, actuator (effector) and feedback/feedforward function. The intelligent materials achieve their functions within the materials themselves by systematic combination of the property and function of the materials.

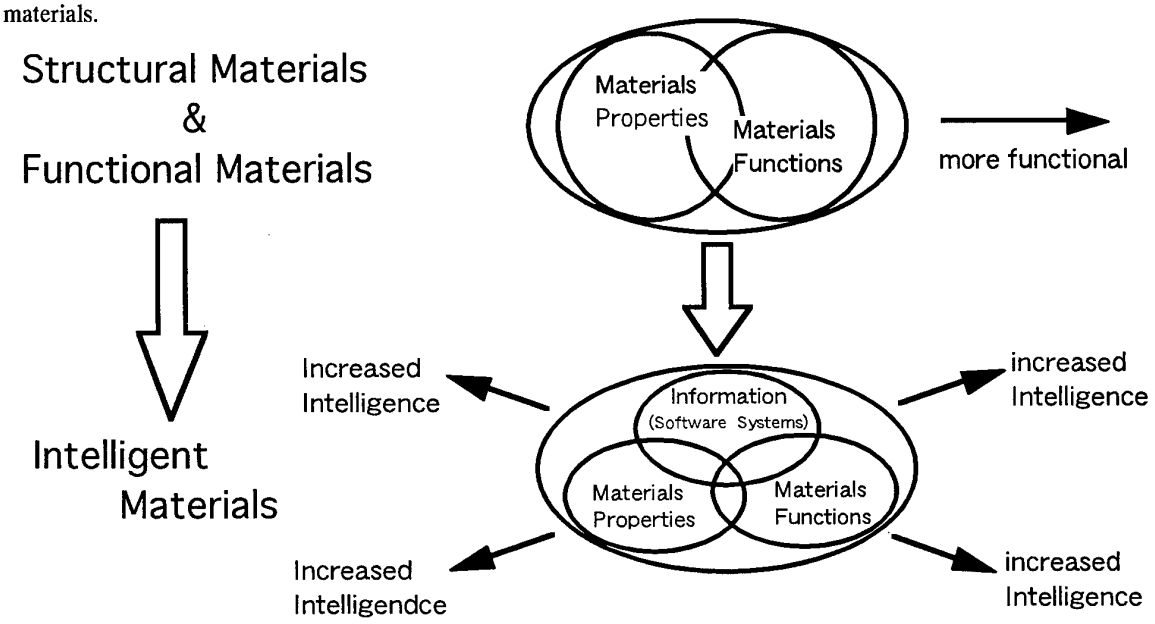


Fig.1 A Concept of intelligent materials to be compared withstructual and functional materials.

Various kind s of materials, not only inorganic materials, but also organic materials and their composite materials are related to the object of study to create intelligent materials. The typical characteristics of the materials are the followings; whose properties, structure/composition, function and/or systematized function can adapt the changes in environment and/or operating conditions. They may be realized if the materials have some built-in intelligence such as self-diagnosis, self-learning, self-repair, prediction/notification, ability of backup, stimulus-reactiveness and ability to recognize/discriminate.

Another important and large reseach field is concerned with biomaterials with self-adjusting function. For example, biostructural (artificial bone, etc.), biofunctional (artificial human skin, liver, kidney, pancreas, etc.) materials have attracted much interest.

The science and technology of today has reached a level where materials design and structure control can be developed on atomic or molecular scales. Therefore, we have a possibility of creating materials with built-in software systems by using process as systematization and integration. In addition, the systematization and integration of functions such as the sensor, processor, and actuator functions are important in the achievement of information transmission.

3.2 "Smart" and "Intelligent"

Smart structure and intelligent materials will be discussed here,giving some examples. To prevent aircraft,building, bridge etc. from a sudden crash due to a crack generated and grown in a part of body, surface acoustic wave or optical fiber network can be constructed on the inner surface of body and wing, just like the "nervous system", and all data are delivered to a central processor. When a crack of unusual phenomenon occurs in the structure, real time damage assesment and computer

decision are carried out with quick response. This approach is one of the development from the standpoint of smart structures [5, 6]. They are now going to include a capability of repair in the system.

The smart structure (structur and/or system which possesses functions of diagnoses and self adjustability to its enviroment) was originated in the researches and developements of the adaptive structure and the sensory structure[7, 8]. Those were supposed to be initiated with the necessities to cope with many technological problems emerged in the aero and space industries.

For example, the concept of "Health Monitoring Aircraft" was developed in the safety industry in order to protect human life from accident and defect of an aeroplane in the flight[9]. The similar concepts were spread and applied widely in the structures of constructions such bridges and buildings as Civil Engineering, and concequently the researches on the smart structure have been attracting attention[10,11]. The smart structure is a high performance system, which has a hybrid structure consisting of the materials or devices possessing sensing function and of that having actuating function impregnated itself in connecting with a computor separated outside for the processing function.

The smart material may be defined as a material which has potential to embody the function of a smart structure. Therefore, the materials such as an optical fiber, a surface acoustic wave device (SAW) etc. may be defined as smart materials because they embody the sensing function, and piezoelectronic devices and shape memory alloys etc. are considered to belong to the categoly of the smart material in the cases where they embody the actuating function.

On the otherhand, the intelligent material may be defined by introducing the concept of the information science as follows, the material possesses sensor, processor, actuator and feedback/feedforward functions internally in the material itself. In the intelligent materials, when a crack occurs in the material by shock and/or static or dynamic stress, the state of material changes according to the cracking speed and the strength of stimulation, impact, etc.. For example, color or electron emission vary according to the internal damage due to fatigue, thus giving a warning. In addition, cracking is prohibited from proceeding due to the change of strength and the volume expansion in the cracked part. For example, tip becomes round or stiff. Cracking spacing is occupied by the component material dissolved due to a phase transition by stress. The behavior of the intelligent material is desirable to have the capability of self (internal)-diagnosis, prediction/notification, and self-repair, etc.. These approaches may be said to be the research from the stand point of intelligent materials.

Therefore, a material which has even two or three functions still does not satisfy the condition to be an intelligent material. The important condition to be an intelligent material is that the multifunctions of the material should relate each other by making feedback and feedforward their information to embody the desired intelligence.It is, of course, supposed to be difficult to fabricate the material with a high level intelligence from the begining. However,if materials with some useful functions as the intelligent materials are found, by combining or hybridizing them we can expect to obtain a smarter system and a smarter structure or we can simplify the smart structure with the same level of the function.

"Intelligence" is an intuition which can cope with unpredicted processes, that is to say the ability to manage to survive in any unexpected circumstances which can not be expressed by any programm[12]. This definition just satisfies the ability which we expect for the intelligent material. This is the ability which promptly responds to an enviromental change and an anormaly, and repares itself or regenerates to adjust itself to the change and the anormaly in a more suitable shape or the better way, those abilities are just nothing but the required conditions for the intelligent material.

Similar to the regeneration process of living creatures to make their species survive, the intelligent material can adapt itself to the enviroment by changing its nature drastically in order to attain the best suitable response.

On the other hand, "Smart" means a way of respond to the predicted condition following a certain programm faithfully and promptly.

3.3 Three Viewpoints of Intelligent Materias as a Hierarchy [1]

When considering the concept of intelligent materials, it is natural to evaluate their functions in connection with the natural environment and society. Since intelligent materials are those which respond to environmental conditions intelligently and manifest their functions, it is particulary important that the concept should take more careful consideration of the relationship between materials and their environment and people than in the case of common materials. Therefore, "Intelligence from the Human Standpoint" will be discussed and evaluated as a level of "Social Utility" .

As the macroscopic function inherent in the material itself, the intelligent function is defined as "Intelligence Inherent in the Materials" , which is independent of its evaluation and utilization by man. However, it is important to understand the intelligent functions after taking the environment, place and occasion in which the materials are used, into account.

The "Intelligence Inherent in Materials" is based on primitive functions and fundamental properties in a material, that is, "Primitive Functions of Intelligence" .

In order to develop the primitive function in materials, a new research project named "New Material Development by Nano - space Lab." has been started in 1994, as a national project in Japan. The nanospace is defined as an ultimate material space of nanometer size which has possibility to create unique material characteristics utlizing quantum effects, electronic states, chemical reactions and material transport in nanospace[13].

As the information science are introduced in the material, the internal processor and feedback/feedforward functions become important in the intelligent material. In other words, information transfer through hetero - contact or hetero - junction between metal - ceramics, or ceramics - organic material etc. and verious kinds of combinations among exatic materials have to be investigated physically, chemically and/or three dimentronally in atomic or molecular scale. From this standpoint, another national project named "Research on Fundamental Science of Frontier Ceramics" has been started in 1995 in Japan [14].

By understanding these three viewpoints as a hierarchy, we can organize the concept of intelligent materials as shown in Fig.2. [1]

The main international conferences on the Intelligent Material and the Smart Structure /Material are listed chronologically in the Table 1.

Table 1. List of International Conferences on Intelligent Materials, Smart Structures and Smart Materials.

(1) Mar.15-17, 1989, Tsukuba, Japan International Workshop on Intelligent Materials
(2) Mar.19-23, 1990, Honolulu, Hawaii, U.S.A. U.S.-Japan Workshop on Smart/Intelligent Materials and Systems
(3) Nov.13-15, 1990, Maui, Hawaii, U.S.A. First U.S.-Japan Conference on Adaptive Structures
(4) Nov.4-8, 1991, Alexandria, Virginia, U.S.A. Active Materials & Adaptive Structures Conference (ADPA/AIAA/ASME/SPIE)
(5) Nov.12-14, 1991, Nagoya, Japan 2nd Japan-U.S. Conference on Adaptive Structures
(6) Mar.23-25, 1992, Oiso, Kanagawa, Japan First International Conference on Intelligent Materials -ICIM'92-
(7) May.12-14, 1992, Glasgow, Scotland, U.K. First European Conference on Smart Structures & Materials
(8) Nov.9-11, 1992, San Diego, California, U.S.A. 3rd International Conference on Adaptive Structures
(9) Feb.1-4, 1993, Albuquerque, New Mexico, U.S.A. SPIE's 1993 North American Conference on Smart Structures & Materials
(10) Nov.2-4, 1993, Cologne, Germany 4th International Conference on Adaptive Structures
(11) Feb.13-18, 1994, Orlando, Florida, U.S.A. SPIE's 1994 North American Conference on Smart Structures & Materials
(12) Jun.5-8, 1994, Williamsburg, Virginia, U.S.A. 2nd International Conference on Intelligent Materials-ICIM'94-
(13) Oct.12-14, 1994, Glasgow, Scotland, U.K. 2nd European Conference on Smart Structures & Materials
(14) Dec.5-7, 1994, Sendai, Japan 5th International Conference on Adaptive Structures
(15) Feb.26-Mar.3, 1995, San Diego, California, U.S.A. SPIE's 1995 North American Conference on Smart Structutres & Materials
(16) Nov.13-15, 1995, Key West, Frolida, U.S.A. 6th International Conference on Adaptive Structures
(17) Feb.25-29, 1996, San Diego, California, U.S.A. SPIE's 1996 Symposium on Smart Structures & Materials
(18) June 3-5, 1996, Lyon, France 3rd International Conference on Intelligent Materials-ICIM'96- & 3rd European Conference on Smart Structures and Materials

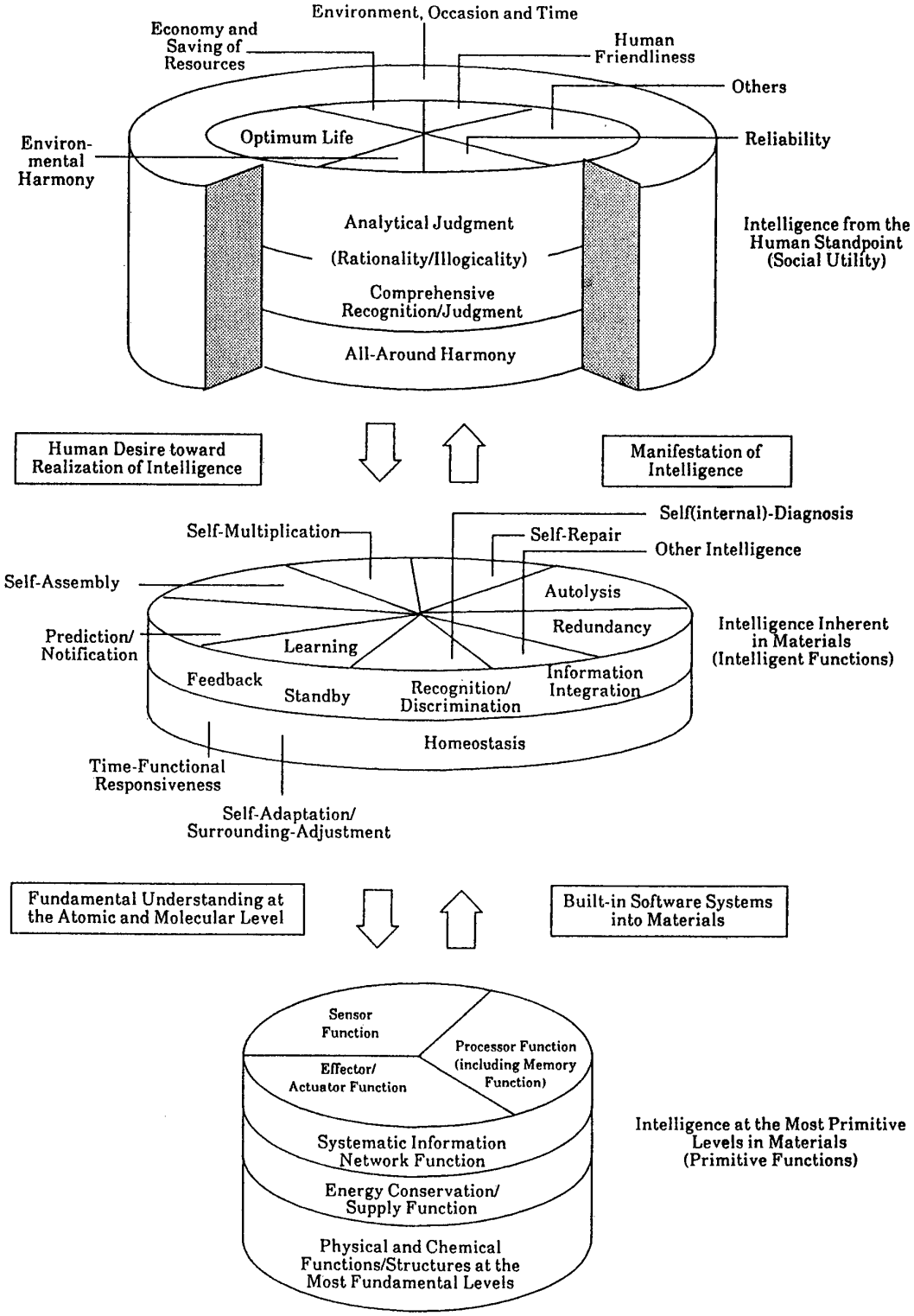


Figure 2 Schematic Representation of Intelligent Materials [1]

4. ADVANCED TECHNOLOGIES FOR INTELLIGENT MATERIALS

The technological barriers to creation of intelligent materials are rapidly diminishing by many new advances in advanced techniques for materials synthesis, characterization and modification. Chemical synthesis methods, such as sol-gel and Langmuir-Blodgett techniques, and physical methods for film formation, such as ion beam deposition, ionized cluster Beam (ICB) deposition & epitaxy, implantation, laser ablation, CVD,PVD, plasma etching etc., have been developed and joined by new classes of techniques which hold the promise of materials manipulation on an atomic scale, such as the scanning tunneling microprobe (STM).

As a typical example of advanced technologies, the ionized-cluster-beam (ICB) technique will be discussed here. This technique has been developed by Takagi et al. at Kyoto University [15,16,17]. In the ICB source,clusters are created by condensation of supersaturated vapor atoms produced by an adiabatic expansion process, and some of the clusters are ionized by electron impact. Kinetic energy can be added to the ionized clusters by applying an acceleration voltage.

The clusters (macroaggregates) consist of hundreds to thousands of atoms by pure vapor expansion, although it has been regarded as difficult to form such clusters from vaporized solidstate-materials, such as, metal, ceramics, insulator, organic materials [18,19]. Figure 3 shows the high resolution micrographs of individual Ag clusters deposited on a carbon substrate under a condition of almost zero incident energy on to the substrate cooled by liquid nitrogen [20]. Because of the small cluster size, the particles in the as-recorded film image are barely discernible [Fig.3(a)]. However, by digitizing and processing, the image of the metal cluster can be signficantly enhanced relative to that of the substrate as seen in the examples of Fig.3(b),(c), and (d). A variation in the cluster size and shape is found and the substructure varies from being single crystalline(b) to more complex particles with a preferred orientation (c),(d).

The metal clusters, whose constituent atoms are loosely coupled together, are ionized and accelerated to a few kV. By this means, extremely low energy ion beams of the order of a few eV to a few hundred eV/atom with equivalently high intensity which is suitable for film deposition, can be produced. The effect of ionic charge of the cluster is sufficient to influence film formation, even when the number of ionized clusters in the total flux is small. Since the ionized cluster is characterized by very small charge-to-mass ratio, space-charge problems in beam transport can be solved and deposition on semiconductors and insulators becomes possible without charging problems. When the ionized clusters with acceleration energy attack onto a substrate, they are suddenly broken up into the atomic state and migrate on the substrate. That means the surface diffusion energy is enhanced and contolled keeping the substrate temperature relatively low. It is expected that amorphous, polycrystalline and crystalline states can be controlled by changing the acceleration voltage of ionized cluster and/or contents of ionized particles in total flux.

Recently, many works related to computer simulation on migration behaivier on the surface substrate, as shown in Figure 4 have been done [21,22].

5. SOME EXAMPLES OF INTELLIGENT MATERIALS UNDER DEVELOPING

5.1 CFGFRP (Carbon Fiber-Glass Fiber Reinforced Plastic) Composites with Self Diagnostic Function [23]

These composites are materials with self-diagnostic function for preventing fatal fracture and detecting damage. When the carbon fiber bundles fractured, changes in the electrical resistance of the CFGFRP composites increased greatly, and afterwards, the CFGFRP composites were able to resist the load due to the presence of the glass fiber bundles. A large change in the electrical resistance can be conveniently used to prevent a fatal fracture by monitoring changes in the electrical resistance of the CFGFRP composites during loading. The point where a great change in the electrical resistance occurred can be controlled through suitable selection of the type of carbon fiber bundles based on its value of ultimate elongation. Changes in the residual electrical resistance are observed after unloading, and these changes are dependent on the maximum strain applied in the past for the CFGFRP composites as shown in Figure 5. These characteristics will be effective to check the case

history of buildings and make decision to exchange period. The method of monitoring changes in the electrical resistance of the CFGFRP composites during and after loading is simple in terms of technique and manageable in terms of cost for diagnosing latent damage and preventing fatal fracture. The CFGFRP composites used as concrete reinforcement are promising materials which have self-diagnostic for preventing the concrete from the fatal fracture.

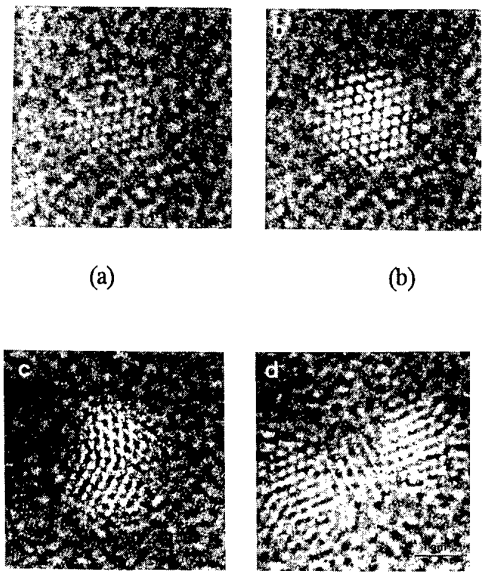


Fig.3 High resolution micrographs of individual Ag clusters. (a): an as-recorded image, (b),(c), and (d): computer-enhanced images.

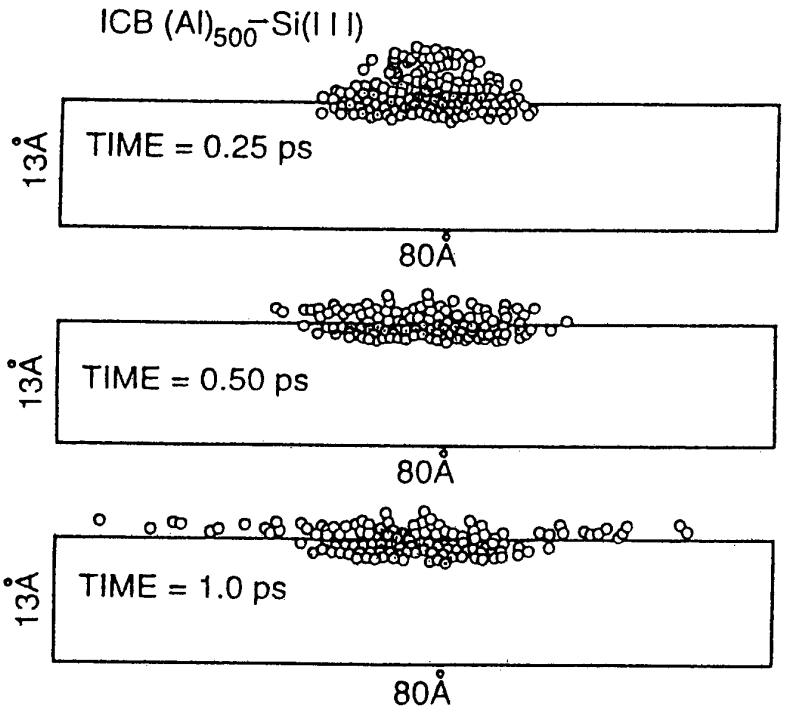


Fig.4 Simulation of ICB bombardment at t=0.25,0.5 and 1.0 ps, where a 5keV Al cluster consisting of 500 atoms impinges on a Si(111) surface.

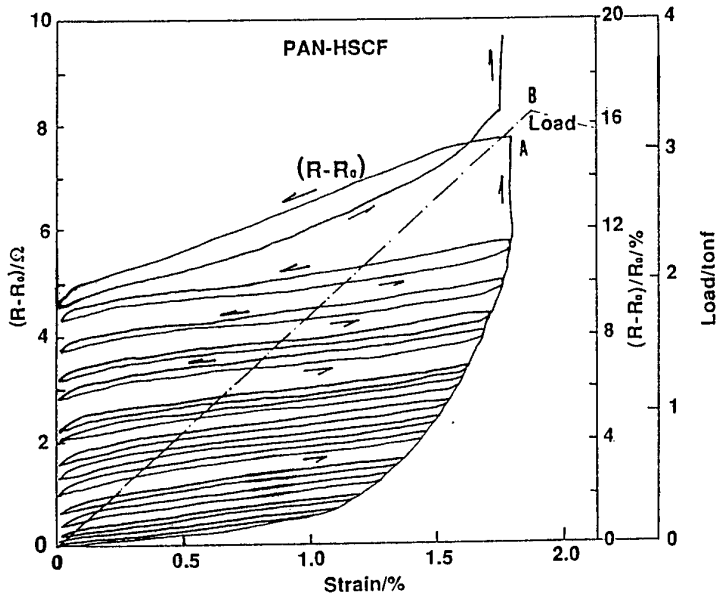


Fig.5 Change in electrical resistance, relative change in the electrical resistance and load as a function of strain for CFGFRP composites containing 0.36 vol% PAN-HSCF (polyacrylonitrile - based high-strength carbon fibers). [23]

5.2 Organic (CuPc)-Inorganic (TiOx) Hetero Multilayer for Opto-electronics Devices [24,25]

By utilizing the Characteristics of ICB as shown in chapter 4, Cupc (48 Å thickness) - TiOx (48 Å thickness) hetero multilayer (20 multilayer × 2) was formed with abrupt junction at the interface of the ceramics and organic layers.

This organic-inorganic hetero multilayer as shown in Figure 6, has been proposed as an approach to intelligent materials. The organic layer has a role of sensing light in this system. Photogenerated electrons in organic layers of copper phthalocyanine (CuPc) transfer to the conduction band of inorganic layers of titanium oxide (TiOx) through the interfaces, due to the difference in electron affinities, and then the electrons and holes are spatially separated. The electronic conductivity of the inorganic layer is increased drastically by free electrons donation. The values of photoconductivity for the multilayers are found to be remarkably larger than those of the single layer of CuPc. Light-intensity dependence for the multilayers is much stronger than one for the single layer. These indicate significantly less recombination in the multilayers suggesting charge spatial separation at the interfaces. In this system, it may be said that the organic, the inorganic layers and the interface have roles of a sensor, an actuator and a prosessor respectively.

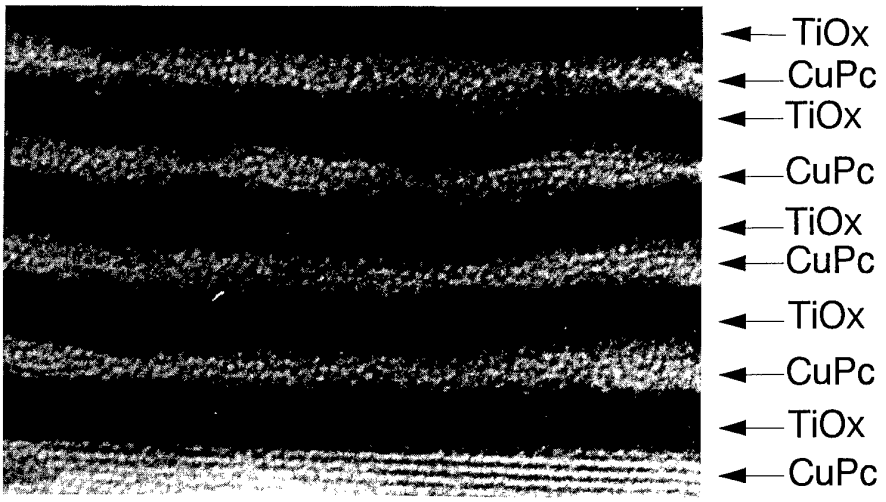


Fig.6 Cross-sectional TEM image of a [CuPc(48 Å)/TiOx(48 Å)] 20 multillayer

5.3 Intelligent Separation Systems by Temperature-responsive Polymers [26]

Stimuli-responsive polymers such as temperature-responsive polymers have been extensively studied with a common names as "Intelligent Polymers". For instance, poly (N-isopropylacrylamide) (PIPAAm) is a water-soluble polymer having remarkable hydration-dehydration changes in an aqueous solution in response to temperature changes, owing to a transition behavior between hydrophilic and hydrophobic characters of PIPAAm which is caused by temperature. The transition temperature called as a lower critical solution temperature can be controlled from lower to higher temperature by changing composition of copolymers of IPAAm and other comonomers.

When the temperature sensitive PIAAm is combined with biomaterials such as protein or enzyme, novel polymers of "Intelligent Bioconjugates" may be obtained so that recycling systems of these bioconjugate materials would be established by using the phase transition phenomena. The intelligent bioconjugate systems to combine biomolecules with the temperature-responsive polymers have a high potentiality to make novel separation methods. Novel polymeric adsorbents based on the temperature-responsive polymers for optical resolution were successfully prepared to separate one-side optical isomers by specific adsorption onto the polymeric adsorbents.

5.4 Synthesis and Characterization of Optical Intelligent Polymers Carrying Super-Cage Molecular Pendants [27]

The super-cage molecules (fulleroide) are well known to have large optical nonlinearity and high photo-sensitivity. The object of this research is to develop the photo-responsive polymers which possess the multi-functional properties such as the photo-conductivity and the second-order optical nonlinearity. The starting super-cage molecules 4,4 ´ -difluorodiphenyl fulleroide $(FPh)_2C_{61}$ was synthesized and polycondensed with aromatic diamine sulfone to give poly (4,4 ´ -diphenyl C_{61} ethers). Polycondensation was carried out in different solvents with and without catalyst. Molecular structural characterization of super-cage monomer and the polymers was carried out by NMR, infrared and UV-visiblespectroscopies, mass spectrometry, and the thermal analysis. The third-order nonlinear optical susceptibilities $\chi^{(3)}$ was found to be 1.4×10^{-14} esu by degenerate four wave mixing. Optical switching or deflection device using photo refractive effect which conbines the functions of photo-conductivity and optical nonlinearity is shown in Figure 7.

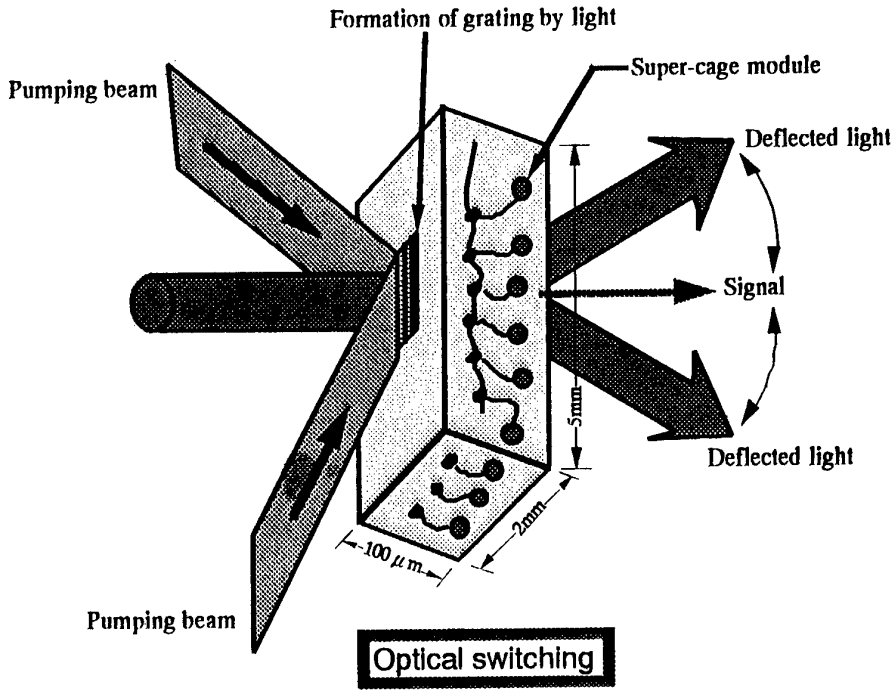


Fig.7 Development of optical intelligent polymers

5.5 Stimuli-responsive Protein Assemblies [28,29]

In a cell of life, calcium - binding protein , calmodulin(CaM), recognizes calcium ions selectively and responds to calcium ion bound with a resulting change in its conformation. By the conformational change of calmodulin, it can conjugate with such a protein as phosphodiesterase(PDE). This combination is followed by a conformational change of phosphodisterase from the inactive form to the active form. Therefore, the sensing and actuating functions are portioned out in the calmodulin and enzyme parts of the phosphodisterase. The information process is carried out by the conformational change between calmodulin and phosphodisterase through a stimulation of calcium ions.

Recently, by a biochemical technique, calmodulin has covalently been conjugated with phosphodisterase retaining both binding affinity and enzyme activity and the two different parts of molecular functions have successfully been coordinated in a single protein assembly as shown in Fig 8.

This stimuli-responsive protein assembly has also been fabricated in monolayer membrane form on the water surface. The membrane was prepared by developing calmodulin and bovine serum albumin (BSA) at the air-water interface and by conjugating them with a bifunctional agent. In the case of the BSA monolayer, complex formation with Mg^{2+} generated a larger change in surface pressure than that with Ca^{2+}. On the other hand, a drastic change in surface pressure was observed for the conjugated thin membrane associated with Ca^{2+} than that associated with Mg^{2+}. Due to a drastic change in the conformation of calmodulin, the conjugated protein film changes its morphology (STM image), depending on Ca^{2+}. The largest surface pressure change was detected when calmodulin was mixed with an equimolar amount of BSA.

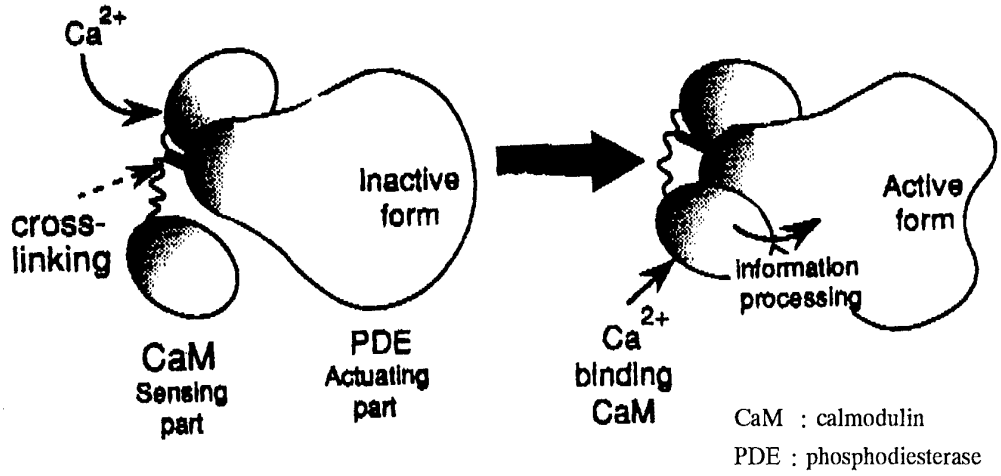


Figure 8. A postulated scheme of stimuli - response of CaM - PDE hybrid.

5.6 Intelligent Drug Delivery System [30,31,32]

In recent years, temporal control of drug delivery has been of interest to achieve improved drug therapies. Intelligent drug delivery systems are one of the expected results, demonstrating an ability to sense external environmental changes, judge the degree of external signal, and release appropriate amounts of drug. Intelligent DDS may be achieved using stimuli-responsive polymeric hydrogels which alter their structure and physical properties in response to external stimuli. Pulsatile drug release has the advantages of avoiding drug tolerance or matching the body's release of specific peptides or hormones.

Temporal Control of drug release has been attempted using stimuli - responsive polymers in response to special chemical agents, pH, and physical signals such as temperature change, electric field, supersonic wave, etc. Studies on intelligent DDS having auto - feedback mechanisms to release drug only during a disease state and to stop release when a bady recovers from disease have been recently initiated. A schematic diagram of Intelligent DDS having auto - feedback mechanism is shown in Fig 9. Also, a concept of glucose sensitive insulin release system using "Intelligent Material" poly Vinyle Alcohole/poly (N-Vinyle Pyrrolidone - copolymer - phenylboronic Acide) complex material, in comparison with a concept of glucose sensitive insulin release system using "Smart Structure" are shown in Fig 10(a),(b).

The method for the molecular design of temperature-responsive polymers exhibiting remarkable swelling change in response to temperature are discussed. Achievement of pulsatile drug release from stimuli-responsive polymeric hydrogels as on-off switches and its mechanism are investigated in terms of control for stimuli-responsive swelling.

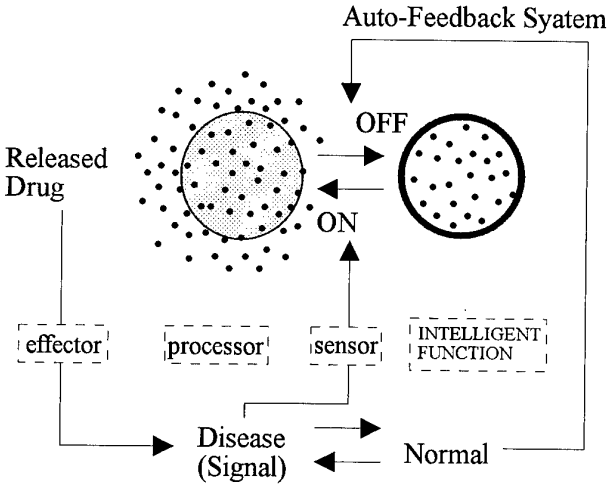


Fig.9 Intelligent DDS having auto - feedback mechanism

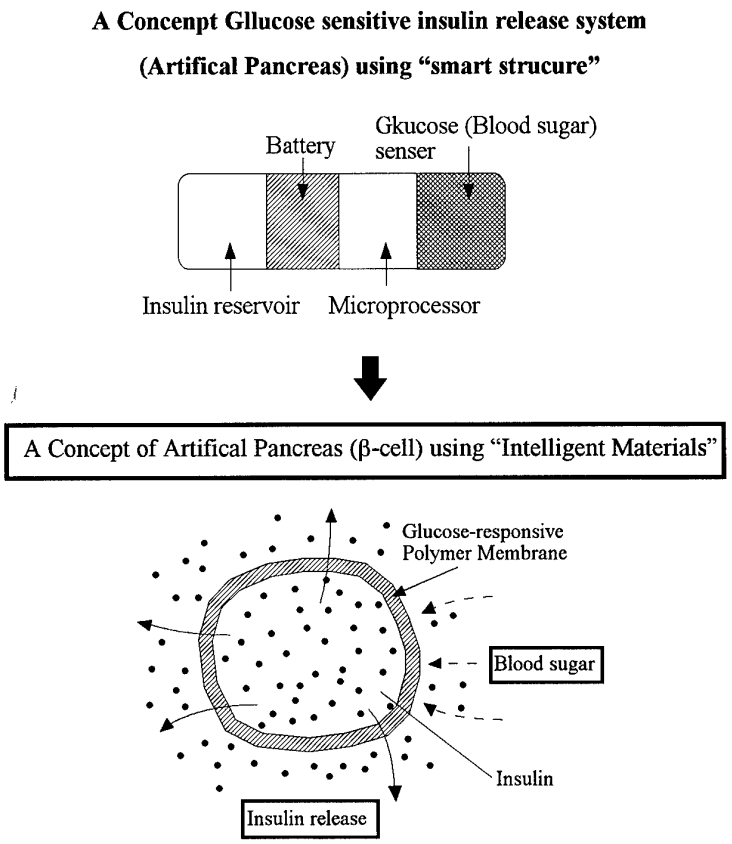


Fig 10(a). A Concept of Glucose Sensitive Insulin Release System (Artificial Pancreas) using "Smart Structure" and "Intelligent Materials"

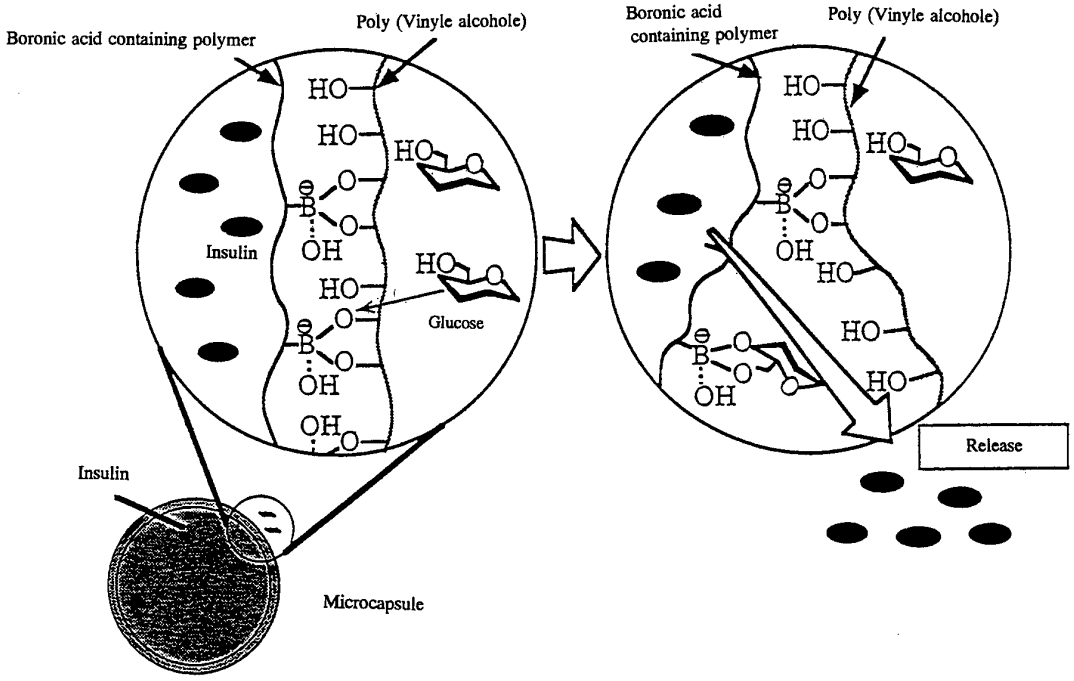


Fig 10(b). A Concept of Glucose sensitive insulin release system using PVA/poly (NVP-co-PBA) [32]

6. REFERENCES

1. The Concept of Intelligent Materials and Guidelines on Their R&D Promotion, Science and Technology Agency in Japan, Nov. 30, 1989 (published in English in Jan. 1990).
2. Proceedings of the International Workshop on Intelligent Materials, Tsukuba Science City, Japan, March 15-17, 1989 , The Society of Non-Traditional Technology, Tokyo, Japan. Technomic Publishing Co., Inc., Pennsylvania U.S.A., 1989.
3. Proceedings of the First International Conference on Intelligent Materials-ICIM'92-, ed. T.Takagi et. al, Oiso, Kanagawa, Japan, March 23-25, 1992, The Society of Non-Traditional Technology, Tokyo, Japan. Technomic Publishing Co., Inc., Pennsylvania U.S.A., 1992.
4. Proceedings of the Second International Conference on Intelligent Materials -ICIM'94-, ed. C.A.Rogers et. al, Williamsburg, U.S.A. June 5-8, 1994, Technomic Publishing Co., Inc., PA, 1994.
5. US-Japan Workshop on Smart/Intelligent Materials and Systems, Honolulu, Hawaii, March 19-23, 1990, Technomic Publishing Co., Inc., Pensylvania, U.S.A.
6. Proceedings of the First European Conference on Smart Structures and Muterials, ed. B.Culshaw et. al., Glasgow, May 12-14, 1992, Institute of Physics Publishing, Bristol and Philadelphia, 1992.
7. Proceeding of the First U.S.-Japan Conference On Adaptive Structure, Maui, Hawaii, Nov. 13-15, 1990. Technomic Publishing Co.,Inc., Pennsylvania, U. S. A..
8. Proceeding of Active Materials and Adaptive Structures Conference, Alexandria, Virginia, Nov. 4-8, 1991. Institute of Physics Publishing, London.
9. T. G. Geradi, "Health Monitoring Aircraft", reference [5], p.82, 1990.
10. W. B. Spillman. Jr, "The Evolution of Smart Structure/Materials", reference [5], p.97, 1990 .
11. R. Wolef and H.Miesseler, "Monitoring of Prestressed Concrete Structure with optical fiber sensors", reference [6], pp.23-29, 1992,.
12. G. Beck, "Current Status of Reseaches on Intelligent Materials in France", translator, H.Usui, Non-Traditional Technology, Mar./Apr. pp.5-26, 1992, The Society of No-Traditional Technology, Tokyo, Japan.
13. I.Yamada; "Research Project on Nano - space Laboratry and Related Topics" , to be published in the Proceedings of the 3rd International Conference on Intelligent Materials & the 3rd European Conference on Smart Structure and Materials, Lyon , France, June 3-5, 1996.
14. H.Yanagida; "Two Dimentional Design of Intelligent Materials - Introduction of Froc - Project -" , to be published in the Proceedings of the 3rd International Conference on Intelligent Materias & the 3rd European Conference on Smart Structures and Materials, Lyon, France, June 3-5, 1996.
15. T.Takagi, I.Yamada, M.Kunori, and S.Kobiyama; Proceedings of the 2nd International Conference on Ion Sources, Austria, Sep.11-15, 1972, pp790-795, Vienna SGAE, Vienna.
16. T.Takagi, Ionized Cluster Beam Deposition and Epitaxy, Noyes Publishers, Park Ridge, Now Jersey, U.S.A. 1988.
17. I.Yamada and G.H.Takaoka ,"Ionized Cluster Beams : Physics and Tecnology",Jpn.J.Applide Physics, Vol.32,part 1, No.5A, pp.2121-2141, May 1993
18. I.Yamada, H.Usui, and T.Takagi; J. Phys. Chem. 91, p.2463, 1987.
19. T.Takagi and I.Yamada; Ion Beam Assisted Film Growth, ed. T.Itoh, Elsevier, Amsterdam, p.253, 1989.
20. K.H.Westmacott and U.Dahmen; Proceedings of the 12th Symposium on Ion Sources and Ion-Assisted Technology, Tokyo (The Research Group of Ion Engineering, Kyoto), p.255, 1989.
21. Y.Yamamura, I.Yamada and T.Takagi; Nucl. Instrum. & Methods Phys. Res. B 37/38 , p.902, 1989 .
22. K. H. Muller; J. Appl. Phys, 61, p. 2516, 1987.
23. N.Muto, H.Yanagida, T.Nakatsuji, M.Sugita, Y.Ohtsuka, Y.Arai and C.Saito; Sensors and Materials, Vol.6 No.1 , pp.045-062, 1994.
24. J.Takada, H.Awaji M.Koshioka, A.Nakajima W.A.Nevin, M.Imanishi, N.Fukada and M.Tarumoto; Advanced Materials '93/A: Biomaterials, Organic and Intelligent Materials, ed. H.Aoki et al., Trans. Mat. Res. Soc. Jpn, 15A, p.667, 1994.

25. J.Takada; Jpn.J.Appl.Phys., Vol.34, p3864, 1995.
26. N.Ogata; reference[4], pp.13-22, 1994.
27. M.Berrada, Y.Hashimoto, S.MIiyata; Chem. Mater., 6 , p.2023, 1994.
28. T.Miwa, N.Damrongchai, H.Shinohara, Y.Ikariyama and M.Aizawa; Journal of Biotechnology, 20, p.141, 1991.
29. T.Miwa, N.Damrongchai, E.Kobatake, Y.Ikariyama and M.Aizawa; reference[3], pp.476-479, 1992.
30. T.Okano, N.Yui, M.Yokoyama, R.Yoshida; Japanese Technology Reviews E, Gordon Science, Switzerland, 4, 1993.
31. R.Yoshida, K.Uchida, Y.Kaneko, K.Sakai, A.Kikuchi, Y.Sakurai and T.Okano; Nature, Vol. 374, No.6519, pp.240-242, March 1995
32. R.Yoshida, K.Sakai, T.Okano and Y.Sakurai; Advanced Drug Delivery Reviews, Vol.11, pp85-108, 1993.

Paper presented at the Third ICIM/ECSSM '96, Lyon '96

Intelligent Materials and Systems as a Basis for Innovative Technologies in Transportation Vehicles

Christian Boller
Daimler-Benz AG, Research and Technology, D-70546 Stuttgart, Germany

Introduction

Engineering structures and systems such as transportation vehicles are made of structural materials which generally only have a passive function. All sensing, control and actuation required to make these vehicles move has originated from biological creatures. Human beings have always kept the major role of sensing and control while animals have initially been mainly selected to take over the actuation part. This fundamental fact, which is based on the nature to survive, has been the driver for all following technological development.

The initial step has been the introduction of mechanical engineering. Systems have been developed and improved, such as by increasing the allowable transportation mass through the introduction of wheels, the control of transportation masses through the introduction of brakes or the increase of transportation speed, distance and reliability through development of various kinds of engines. This development has been pursued until today, where we actually deal with optimizing the use of energy by improving structural, thermodynamic and aerodynamic design by use of advanced materials and design methodologies.

The second step which originated much later, has been the introduction of electrical and especially electronics into engineering systems including control. This step, which has either improved the human being's safety and/or comfort, allowed to get rid of a lot of tiresome, repetitive and thus unattractive activities. It started with introducing simple control lamps, various kinds of meters or secondary electrical motors and has recently resulted in systems such as anti-blocking-systems (ABS), airbags or navigation systems (GPS) with respect to safety or an automatic transmission, an air-condition system or an adaptive undercarriage with respect to comfort.

There is finally a third step which is related to computer science and data processing. This step actually booming in our scientific and engineering world has allowed to make engineering systems to work adaptive. It is a new dimension in a way, that a part of human logic can be stored and repeated, allowing the human being to concentrate on core functions or to control systems of even higher complexity. It can also lead to more comfort in a way that systems are controlled by a sidestick or even by voice recognition, reducing the required physical actuation of the human being close to zero.

Beside the technological potential in these three steps lasting until some non definable time in the future, interrelationships between those have appeared during the last years and decades, which can be well seen for example with respect to micromechanics. Materials and manufacturing techniques have been developed, which have significantly improved the potential of electronics, sensors, actuators and even computers. After decades of analysis we are now continuously generating the synthesis between various technologies and disciplines, which is also the basis for all work related to intelligent materials and systems.

The Way to Intelligent Materials and Systems

It is now more than a decade ago since people have started to talk about intelligent materials and systems. Various definitions have been given (e.g. Ahmad 1988, Takagi 1989, Measures 1989) and various expressions such as smart, multifunctional or adaptive are used, which sometimes need to be clarified. There is however some common sense in the way that an intelligent material or system incorporates sensors and actuators with both being linked via a controller. Trying to summarize the various definitions and expressions can result in a view as shown in fig. 1.

0-8194-2165-0/96/$6.00

	Sen-sor	Actu-ator	Con-troller	Pro-cessor
Intelligent Material & System	●	●	●	●
Adaptive Material & System	●	●	●	
Active Material & System	●	●		
Sensory Material & System	●			
Passive Material & System				

Fig. 1

A key question leading to intelligent materials and systems is: *Why cannot materials and systems with structural functions take over additional functions?* Their basic/traditional use is mainly related to passive functionality. It is therefore termed to be a *passive material or system*. Adding sensors to the material or system leads to what can be called a *sensory material or system*. The term *active material or system* can be used if the material or system also includes actuators. Sophistication is improved if sensors and actuators are linked via a controller allowing the material or system to adapt itself to various prescribed conditions which can be called an *adaptive material or system*. The highest level that can be actually thought of is achieved if the adaptive material or system also includes a processor allowing itself to adapt to various conditions by self-learning. It can be specified to be the real *intelligent material or system* and is in many cases a vision which still requires to be achieved.

A look into specific books, journals and conference proceedings shows that the wide range from sensory to intelligent materials and systems is covered under the expression of smart, adaptive or intelligent materials and systems. Technologies considered are not limited very much although there are some materials and technologies being actually favoured. These include optical fibers and piezoelectric materials with respect to sensors, piezoelectric and electrostrictive materials, shape memory alloys (SMAs) or electro-rheological (ER) fluids with respect to actuators and microprocessors, neural networks, fuzzy logic and various types of signal analysis with respect to control.

Activities in the world of smart/intelligent materials and systems has mainly originated from applications in aerospace (e.g. Wada and Garba 1992, Fanson 1993). In the meantime applications are also considered with respect to military and civil transportation, starting with those for military aircraft and recently followed by those for automobiles and railway systems. This development becomes especially obvious when considering a wider range of sensor, actuator and control types than those just mentioned above. Other types of sensors can be those based on the change of electrical properties such as resistivity or capacity, thermal imaging or pressure. Actuators mainly used today are electrical motors, hydraulic or pneumatic actuators. These different types of sensors and actuators linked via control algorithms are the basis of advanced engineering systems actually available in products which easily fall into the range of smart/intelligent systems.

The sensing and actuation materials considered and just mentioned before cannot be specified to be new anymore. Nor can this be said with respect to phototropic or electrochromatic glasses. It is more the challenge to combine these materials with conventional structural materials such as can be well done with polymerbased composites (Varadan and Varadan, 1993) or by introducing these materials into a wider industrial application. Another significant area being still exclusively related to research is the implementation of sensing and actuation functions on a microstructural or even molecular basis into a material (Shinya 1994; Hirukawa 1994; Takeuchi 1994).

Whenever the application of intelligent materials in engineering systems is considered, the following question has to be answered:

What is the cost-effectiveness when a material becomes multifunctional and how has a system to be designed under these conditions?

This can be done by using cost evaluation procedures on the one hand and analytic approaches easily determining the boundary conditions of intelligent materials on the other. Some hints how to achieve this will be given throughout the following.

Examples of Available Systems and Materials

When comparing the definition given above for a sensory, active, adaptive and intelligent or briefly a smart material or system with materials and systems used today in transportation vehicles, it becomes obvious that smart systems have already been implemented somehow. Automobiles, trains and aircraft nowadays all contain a large number of sensors such as for sensing temperature, speed, acceleration, brightness, humidity or volume flow or actuators allowing to move components, to exert forces, to inject a fluid or a gas or to reduce light intensity. All actuation is done by either human or electronic control, the latter requiring the type of sensors mentioned before. The smart systems available today are based on the fact that structural components are fully made out of passive materials with sensors and actuators being added to the system. They can be classified in the range from sensory to adaptive systems, while intelligent systems are still the vision to be followed in future research and development. It is far beyond the scope of this paper to present all available systems containing sensors, actuators and controllers in transportation vehicles, but a few will be mentioned which have a relationship to what is discussed with respect to smart or intelligent materials and structures. These systems, which are either used in production or at least demonstrated in a prototype, will include systems

- allowing to monitor the condition of structural components or systems
- using materials with sensing and actuation capabilities such as piezoelectrics, SMAs, ER fluids or electrochromatic glasses
- incorporating structural components made of passive materials being driven by individual actuators.

Regarding the kind of materials considered to be smart/intelligent, piezoelectrics, SMAs and electrochromatic glasses are the ones already being used today. Their application is so far limited to the traditional use of these materials such as sensors and often not controlled actuators within the systems described below.

Sensory Systems

It has become common in a variety of cars today, that incidents for inspections are not anymore related to fixed intervals of kilometers but instead due to the way the car is driven. This results from the possibility of using various sensors for monitoring parameters such as rpm, speed, distance, temperature and acceleration. Another system discussed with automobiles is recognition of road conditions. Furthermore ultrasonic or electromagnetic sensors or even video cameras are used to determine the distance between a car and foreign objects.

Sensory systems monitoring acoustic signals have been implemented into railway systems for mainly determining the condition of moving and especially rotating components. The information retrieved from the monitoring system is sent in advance to the train's maintenance depot allowing to make preparations for provision of spare parts or specific tools thus reducing depot times as well as manpower-related inspection effort and enhancing operational availability.

In aerospace condition monitoring is widely used in jet engines. A network of sensors monitors temperature and gas flow within the engine and thus informs if critical engine parameters are within the operational range. Recently an integrated health and usage monitoring system (IHUMS) has been made commercially available for helicopters (Bristow, 1992). The system has been made to monitor gears and is based on sensors monitoring acoustic signals being generated from the various rotating parts of the gear. Other systems include the use of video cameras for monitoring flaps and landing gears positions of widebody aircraft or the ones used for monitoring operational loads of military and civil aircraft based on either strain or flight parameters, where a broad selection of systems has been described (AGARD, 1991).

Active Systems

A variety of active systems has been developed for automobiles. One of them is a spring made of SMAs used for a control slide in the automatic gear of diesel engines (Krämer, 1994). Due to the hydraulic oil's higher viscosity at low temperatures the control slide did not work smoothly enough. Implementing a SMA-spring which only exerts an additional force at low temperatures helped to solve the problem and allowed smooth operation. Another application of SMAs is by using them as grips for drills (Krämer and Renz, 1993) or as clamps for tubes, where the latter has mainly used in aerospace applications.

Piezoelectric motors have been proposed as an alternative to electromagnetic motors (Schöner, 1992). Prototypes have been developed allowing to be used to position seats or flaps, drive wipers or open and shut electrical windows.

Electrochromatic windows allowing to change light transmissivity is another active system widely considered for windows of automobiles, train or aircraft cockpits (Daimler-Benz High Tech Report, 3/1994). The window has a sandwiched cross-section including two transparent electrodes, two electrochromatic layers and an electrolytical polymer layer. A small current of 1 to 2 volts imposed by the electrodes on the system allows to change the colour of the electrochromatic layers as a result of a chemical process initiated by the electrical current.

Adaptive Systems

An adaptive system quite wellknown in automotive applications is the adaptive undercarriage. Developed and used for racing cars this system allows to adapt itself to various road and driving conditions using a network of different sensors, actuators and dampers with variable characteristics and a controller allowing to permanently adapt the system to varying conditions. On a similar basis the suspension of a baby rescue car has been developed and successfully applied which smoothly allows to transport the baby independent of road and driving conditions (Trimboli et al., 1994).

Another widely known type of adaptive system are autopilot systems used for navigation of aircraft and ships. Within the European project Prometheus prototypes have even been shown to be applicable even for automobiles (Daimler-Benz High Tech Report, 4/1994). The system consists of small video cameras used as sensors. Pictures observed with these cameras are analysed and processed by a computer. The computer either informs the driver about the actual situation or even initiates all operations required for driving by itself.

Noise cancellation in aircraft fuselages is a major issue with turboprop aircraft. Noise is monitored at the locations where it should be cancelled using conventional microphones. The signals are analysed and processed for actively generating an anti-noise which is either emitted using conventional loudspeakers or recently by adapting some small piezoelectric plates to the inside panel of the fuselage (Fuller et al., 1992).

Finally an adaptive structure operating successfully and worth to be mentioned even though it is not directly related to transport vehicles is the Articulating Fold Mirror (AFM) which forms part of the optical scheme for correcting the spherical aberration of the Hubble Space Telescope (Fanson, 1993). Each AFM utilizes six electrostrictive multilayer ceramic actuators which also contain the required sensor unit while control is performed for the six actuators in a central unit.

Future Trends

A trial to summarize state-of-the-art technological development in intelligent materials and systems and to determine possible future trends in smart and intelligent materials and systems is shown in fig. 2.

The following three main areas are seen to actually drive the technological development:

1. Engineering systems made of passive materials with sensors, actuators, and controllers being added (attached) to the system in the way described before.
2. Data processing and control which mainly involves high performance computing, neural networks, fuzzy logic and genetic algorithms as well as microelectronics related to it.

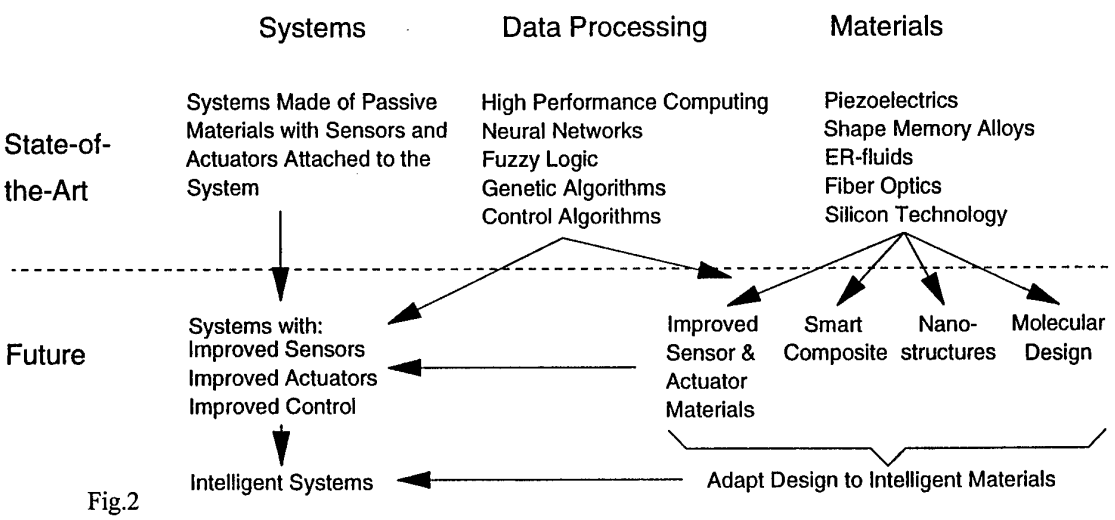


Fig.2

3. Materials and micromechanics which includes all kinds of materials and components such as fibre optics, piezoelectrics, SMAs and polymers, ER-fluids, nanostructures, composite materials, liga and silicon technology.

With respect to the first area improvement can be expected through improvement of the sensors, actuators, and control algorithms used. Improvements achieved in the second area are applied for increase of the performance and/or the number of sensors and actuators used in the smart/intelligent system. Sensors and actuators can still be monofunctional and just attached to the system considered.

The third area can again be split into three sections. The first section is related to improvement and possible development of materials with sensing and actuation functions. This includes topics such as improved ductility of piezoceramics, increase of piezoelectric induced strain as well as development of means for stroke amplification, higher Curie temperatures with piezoelectric polymers, better understanding of the constitutive behaviour of SMAs with respect to control of SMA actuation, extension of the range of possible transformation temperatures in SMAs, and much more.

The use of composite materials, which is related to the second section, has opened a wide field of integrating functional elements into these materials. This includes the integration of sensing or actuation elements such as fibre optics, piezoelectrics or SMAs. Studies recently performed involve determination of the effectiveness of these composite materials with respect to strength and performance. A lot of ideas have been generated in that area by integrating various types of sensors and actuators using technologies such as applied for printing electric circuit boards or other types of surface coating, thus leading to what is called a conformal smart skin (Varadan and Varadan, 1993) or generally a smart composite (Gardiner et al., 1993). Since such a type of composite will be able to take over sensing and actuation functions on a macroscopic and microscopic level, significant changes in design philosophies can be expected. However these new structural components have to meet the requirements set with respect to strength, environmental stability, cost, and reliability, the latter being achieved through redundancy in sensing and actuation elements allowing graceful degradation during operation. Activities similar to what is performed with smart composites is starting on a microscopic level in metallic and polymerbased materials through implementation of particles with sensing and/or actuating functions in a way as having been initiated with the development of nanostructures. Finally it is worth mentioning that work in progress with polymers on trying to implement sensing and actuation functions on a molecular basis.

The third section can be related to work performed with respect to micromechanics including micromachines. Work performed here is mainly related to electronic, medical and surgical applications and has still not gained significance for being directly applied in transportation vehicles.

Analysing specific scientific papers leads to the conclusion, that intelligent materials and systems are mainly considered to be used in transportation vehicles for the following:

- monitoring the condition of a system
- exerting strokes
- influencing dynamic behaviour.

Condition monitoring has become a major issue with composite materials where major concern exists with respect to barely visible impact damage (BVID) which occurs inside the structural material and can often not be seen from the outside. To minimize the effort required for inspecting the material or component with conventional Non Destructive Testing (NDT) technology, the NDT-technology is considered to become an integral part of the structure by implementing a network of appropriate sensors (Boller and Dilger, 1992). The types of sensors mainly considered are fibre optics (Measures, 1992; Tutton and Underwood, 1992) and piezoelectrics (Boller, 1994). Such structure health monitoring systems are actually mainly discussed for aircraft applications but could even gain interest when especially carbon fibre reinforced polymers will be more applied in railway systems and automobiles. Other issues include monitoring any condition which is required as an input for an adaptive or intelligent system (e.g. monitoring the pressure profile for an adaptive wing).

Exerting strokes is done to statically change the position of a component. A lot of effort is actually placed to adapt the shape of aerodynamic profiles according varying service conditions. When deformation speed is relatively low but strokes quite high, the use SMAs is a solution to be considered (e.g. Misra et al., 1992). However this requires a precise control of temperature, which can become highly challenging when thinking of operational temperatures ranging between -50 and + 120°C for aircraft applications. If deformation speed is a major requirement, piezoelectric actuators seem to be a solution to be considered. A lot of studies have been performed with respect to active control of helicopter rotor blades using induced strain actuators where overviews have been given by Strehlow and Rapp, 1992 and Giurgiutiu et al., 1995. It turns out that a hinged flap activated by a bimorph PZT actuator such as proposed by Spangler and Hall, 1989 is the most promising solution so far, especially since improvement has been gained with that system during the last years. Comparing this to conventional helicopter rotorblade design shows that the potential of active, adaptive and intelligent materials can only be taken full advantage of if design is adapted to the potential of these materials, which has been especially done here. Looking to applications in the automotive industry, control of valves in engines using piezoelectric stack actuators seems to be an interesting field from a technological point of view. Cost is however a major aspect which prevents this solution to become actually competitive.

Reducing dynamic loads in any kind of engineering structures is a major field for considering intelligent materials and systems. Solutions have been proposed such as using piezoelectric stack actuators as part of an active acoustic noise control system between a jet engine and the fuselage (Sumali and Cudney, 1994). Similar actuators can also be considered to be applied for reducing vibrations by increasing damping characteristics in chassis or engine mounts of automobiles or to reduce vibrations in bogies or pantographs of highspeed railway systems. To achieve however the large displacements required to reduce vibrations of these relatively low frequencies, much effort has to be placed into the activities of amplifying the low displacements generated by the piezoelectric actuators. Alternatives for these applications may exist by using actuators based on ER-fluids (Naem et al., 1994). Much effort is actually also going on in aeroelastic research using piezoelectric actuators for flutter and buffeting suppression and vibration damping (Heeg et al., 1994). Solutions here consider piezoelectric patches integrated into the aerodynamic profile, allowing to globally as well as locally influencing the aeroelastic and aerodynamic behaviour. Finally the noise cancellation methods based on integrating piezoelectric patches into panels such as mentioned above is another activity in the field of reducing dynamic loads which is actually related to aircraft but might become of interest even to other transportation vehicles.

Summarizing state-of-the-art and future trends in intelligent systems for transportation vehicles leads to the conclusion that first applications start by adding sensors, actuators and controllers to a conventionally designed system based on passive materials. Progress in data processing technology provided today can be made use of at this stage, which mainly allows to increase the number of sensors or sensor information as well as to improve the performance of controllers applied. Parallel to this a large amount of development has to be done in the area of intelligent materials. As long as their potential is not sufficiently described it is difficult to say if they can be used in reality. A look at three different R&D-programmes on adaptive aircraft wings in the USA, Germany and the UK respectively proves the conclusion made here to be realistic since they are all based on the following strategy: (1) Take a wing with its conventional sensors and actuators and improve control and data processing which allows to extend the use of existing flaps; (2) Implement sensors and actuators based on appropriate materials with known characteristics (e.g. piezoelectrics, SMAs, ER-fluids) and start to adapt the structural design according to these materials; (3) Use a smart composite system for design of the wing. It is the latter two

steps which strongly require much more knowledge about active, adaptive and intelligent materials than we have today.

This knowledge will be the basis for deciding if these active, adaptive and intelligent materials can be finally applied due to the various requirements they will have to fulfil with respect to strength, environmental stability and compatibility and especially cost. It is difficult for a material scientist to be aware of these requirements and it might be difficult for a designer in engineering vehicle to clearly understand the potential of new materials developed so far. To overcome this problem, to briefly determine the solution of best technological and economical potential and to always be on the track of minimum development time, means for validating the technological and economic potential have to be established, where an example is given for validating a structure health monitoring system in the following paragraph.

Validating the Potential of Structure Health Monitoring - An Example

The variety of numerical tools available today allows to determine and validate the potential of technologies before starting an experiment. Even though the numbers calculated may not completely reflect reality, it is the relative numbers between different technological alternatives which are the key to decide which is the most promising to be followed. A large number of excellent studies have been performed for active and adaptive structures (e.g. Crawley and Anderson, 1989; Barrett, 1995) while comparatively less has been done for structure health monitoring.

Structure Health Monitoring Systems (SHMS) are used to monitor the condition of a material or a structure. A change in its condition and especially 'health' is therefore directly related to a change in its state of damage. A key aspect with SHMS is the problem of damage accumulation, which has now been especially discussed for metals for nearly 70 years (Palmgren, 1929; Miner, 1945). It is therefore imperative to know the behaviour of damage accumulation of the material applied whenever considering the implementation of a SHMS. Damage accumulation - as far as considered for metals - is assumed to occur linear. Drawing this in a plot of damage D versus normalized fatigue life (N_r/N_f) as shown in fig. 3 and using the following equation

$$D = 1 - \left(\frac{N_r}{N_f} \right)^a \qquad (1)$$

where N_r is the residual fatigue life and N_f the total fatigue life respectively, the case of linear damage accumulation is achieved when the exponent a is equal to one. However from a variety of experiments with metals it is known that damage does not accumulate linearly and thus the exponent a is mainly not equal to one.

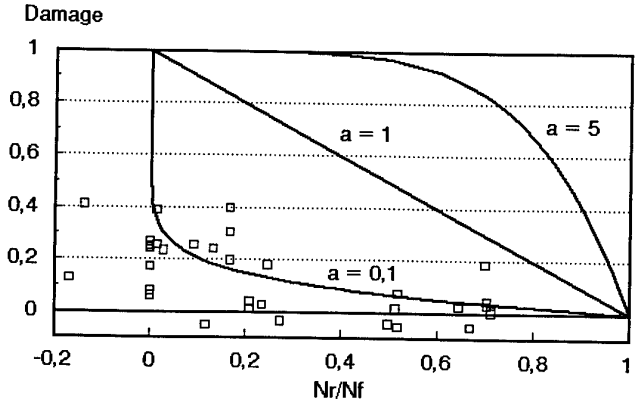


Fig. 3

Damage accumulation in composite materials is quite different when compared to metals. Since the approach mentioned above is however more of a phenomenological nature and fatigue properties of composites are described similar to metals this approach will even be applied here for characterizing the damage behaviour of composite materials.

Fig. 3 contains some data for a graphite composite laminate $[0_2/+45/0_2/-45/0/90]_S$ which Prinz, 1983 tested on flat unnotched specimens under reversed fatigue loading (R = -1). 64 specimens were tested until complete buckling under compression loading and used to determine the fatigue life curve which can be well described in a semi-log scale using the following equation

$$log\left(\frac{N_i}{N_{ref}}\right) = k \times \left(1 - \frac{\sigma_i}{\sigma_{ref}}\right) \qquad (2)$$

with N being the number of cycles, k the slope, and σ the applied stress while i and *ref* denote the actual and an arbitrary reference value respectively. Additionally 33 specimens were tested the same way but removed unfailed after N_i cycles and finally tested under a static compression test. The ratio of their compression strength $\sigma_{i,comp}$ compared to the mean compression strength $\sigma_{0,comp}$ of a virgin specimen has been taken as the basis to determine their degree of damage according to the following equation:

$$D_i = 1 - \frac{\sigma_{i,comp}}{\sigma_{0,comp}} \qquad (3)$$

Since neither the virgin compressive strength nor the total fatigue life could be determined for these 33 specimens, the mean values of the fatigue life curve described with eq. (2) have been taken to convert the damage determined under eq. (3) to a damage being related to the number of cycles as described with eq. (1) with N_r being

$$N_r = N_f - N_i \qquad (4)$$

This explains the large scatter of the experimental data in fig. 3 and why some of the data fall below a value of 0 for the damage and ratio of residual life respectively.

Composite components nowadays are often designed such that they do not require to be inspected during their whole life. This requires to always consider the most severe case which depends on how damage accumulates or in terms of eq. (1) if a is < 1 or > 1.

The most severe condition for a material/component without a SHMS and with a<1 is when the material/component is hit by an impact inducing a damage of D_{im} initially. The residual life of the material/component can be calculated using eq. (1) which leads to

$$\frac{N_{r,i}}{N_f} = (1 - D_{im})^{1/a} \qquad (5)$$

Since the material/component has to survive at least the first mission (time between maintenance) of N_m cycles during which the impact can occur, the normalized residual life becomes

$$\frac{N_r}{N_f} = \frac{N_{r,i}}{N_f} + \frac{N_m}{N_f} \qquad (6)$$

Including eq. (6) into eq. (2) and having cycles and stresses based on the reference values N_{ref} and σ_{ref} respectively, leads to the relationship

$$\frac{\sigma_i}{\sigma_{ref}} = 1 + \frac{1}{k}\left[log\left\{(1 - D_{im})^{1/a} - \frac{N_m}{N_f}\right\} - log\left(\frac{N_i}{N_{ref}}\right)\right] \qquad (7)$$

which describes a fatigue life curve for fatigue lives including impact damage D_{im}.

Considering a material/component with a SHMS, which allows the material's/component's inspection at arbitrary intervals, the most critical condition is when the impact damage D_{im} is included just at the beginning of the last mission. Following eq. (1) the residual damage after the impact is

$$D_{r,m} = 1 - \left(\frac{N_m}{N_f} \right)^a \qquad (8)$$

and the equivalent before the impact is

$$D_{r,i} = D_{r,m} - D_{im} = 1 - \left(\frac{N_m}{N_f} \right)^a - D_{im} \qquad (9)$$

The residual life thus becomes

$$\frac{N_r}{N_f} = 1 - \left[\left(\frac{N_m}{N_f} \right)^a + D_{im} \right]^{1/a} \qquad (10)$$

Including eq. (10) into eq. (2) leads to

$$\frac{\sigma_{i,SHM}}{\sigma_{ref}} = 1 + \frac{1}{k} \left[log\left\{ 1 - \left[\left(\frac{N_m}{N_f} \right)^a + D_{im} \right]^{1/a} \right\} - log\left(\frac{N_i}{N_{ref}} \right) \right] \qquad (11)$$

with $\sigma_{i,SHM}$ being the allowable stress when using a SHMS.

When using an SHMS compared to a conventional design the ratio of allowable stresses can now be determined using eq.s (7) and (11) which leads to the following for $N_i/N_{ref}=1$:

$$\frac{\sigma_{i,SHM}}{\sigma_i} = \frac{k + log\left\{ 1 - \left[\left(\frac{N_m}{N_f} \right)^a + D_{im} \right]^{1/a} \right\}}{k + log\left\{ (1 - D_{im})^{1/a} - \frac{N_m}{N_f} \right\}} \qquad (12)$$

With $a > 1$ in eq. (1) the most critical situation is for both, the material/component with and without a SHMS, when the impact occurs at the very end of the component's life. Thus no gain in allowable stress can be achieved by using a SHMS for a material accumulating damage with $a > 1$.

For $a < 1$ the gain in allowable stress can now be determined for a material/component with an SHMS using eq. (12). This has been done based on the experimental data mentioned above, where the following standard values have been used:

$$k = 4,617 \qquad \sigma_{ref} = 600\,MPa \qquad a = 0,1 \qquad D_{im} = 0,3 \qquad \frac{N_m}{N_f} = 10^{-3}$$

The fatigue life curve used and some variations in its slope k is shown in fig. 4 while the resulting gain in allowable stress determined from eq. (12) and resulting from these different slopes can be seen in fig. 5. It becomes

obvious that the gain in allowable stress decreases with increase in k. A significant gain in using a SHMS is seen with very steep fatigue life curves (e.g. $k = 2$).

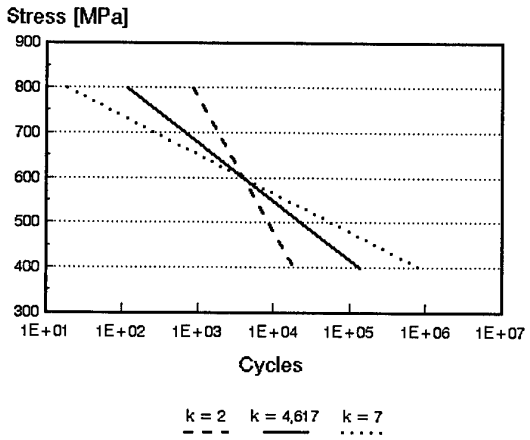


Fig. 4

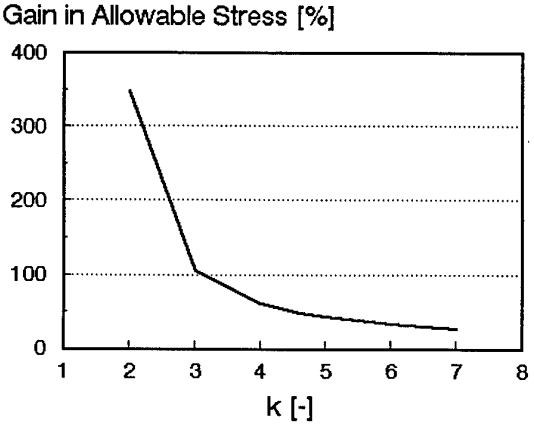


Fig. 5

The relationship between the gain in allowable stress and the induced impact damage D_{im} is shown for different values of the exponent a on fig. 6. Generally the gain in allowable stress increases with an increase in allowed induced impact damage and reaches an infinite value when the induced damage reaches its maximum allowable value. The reason for infinity here comes from the fact that a component without a SHMS and the equivalent impact damage is not able to withstand any stress for that condition anymore. It also becomes apparent that the exponent a - and thus the way how damage accumulates - has a strong influence on the gain in allowable stress.

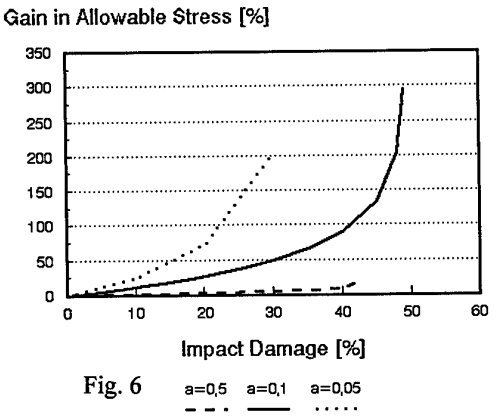


Fig. 6

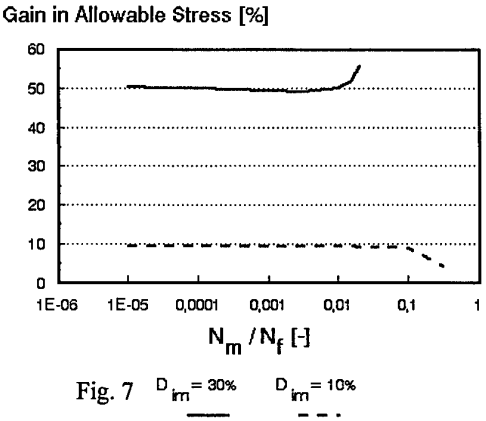


Fig. 7

Finally fig. 7 shows the influence of the length N_m of a mission which is considered to be here the time between the possibilities of maintenance, where no significant influence can be seen for the two standard examples shown.

Beside this possibility of increasing allowable stress and thus reducing structural weight a major advantage of using a SHMS is the reduction in inspection effort, which is mainly related to the manpower required. Quantifying this generally is quite difficult since every type of component mainly follows its specific inspection guidelines. However it can be said for a component designed to require no inspection, that implementing a SHMS has to be carefully considered. Reasons include that:

- the possible increase in allowable stress through use of a SHMS will increase the effort required for repair
- that the SHMS might require maintenance or
- the SHMS's mass might absorb the structural mass gained through the increase in allowable stress if the SHMS's mass cannot be used multifunctionally to also carrying loads.

The aspects to be considered can therefore just be summarized as follows:

Aspect	*Gain*	*Loss*
Saving in Structural Material	x	
Increase in Payload	x	
Reduced Manpower Effort for Inspection	x	
Higher Availability Due to Less Inspection Time	x	
Cost of SHMS		x
Maintenance of SHMS		x
Increased Structural Mass through SHMS		(x)
Increased Structural Repair		x
Less Availability Due to Increased Repair		x

Based on these aspects and possibly others a quantitative balance has to be performed, allowing finally to determine if the SHMS is a cost-effective solution.

Similar analyses can be performed for any other type of intelligent material and structure. This is highly beneficial for determining the potential of application and giving guidance to the designer with respect to finding the appropriate solution at the very beginning.

Conclusions

The conclusions drawn from what has been said above can be summarized as follows:

- Actual intelligent systems design is based on adding various types of sensors and actuators to existing systems and taking much advantage of advanced computation and electronics for control purposes.
- Available materials with sensing and/or actuation functions are actually mainly limited to piezoelectric materials, shape memory alloys, electro-rheological fluids or special glasses. Even for these materials a lot has to be explored and done with respect to better understanding their mechanical behaviour as well as their processing and use in manufacturing and operation.
- There is a significant need to explore the potential of composites with sensing and actuation functions, with functions working on a macroscopic and even microscopic level. Such types of composites can significantly change design principles whenever shown to be cost-effective. Related to structural health monitoring such changes could be to significantly increase the allowance of impact damage in composites or to develop materials with a very special damage accumulation characteristic.
- The few available systems aiming at an intelligent system for transportation vehicles prove that they have achieved a good performance. This has been shown for vibration damping, noise reduction, static deformation as well as for sensor networks and control.
- To determine the areas of the most promising technological and cost-effective performance, means for validating the potential and determining optimum solutions have to be established initially. These are mainly simple analytic tools allowing to quickly determine the boundary conditions of the technology considered and thus guide development on the right track.
- A lot of analytic work has been done and a lot of analytic models developed. More experimental verification of that analytic work is timely, which has to be performed on laboratory models and even full scale structures depending on the complexity of the system.

It is advanced data processing, electronics, control, sensing and actuation which will help to let transportation systems of today to become somehow 'intelligent' tomorrow. It is however the introduction of intelligent materials which can significantly lead to a change in our engineering design philosophies towards intelligent structures. But none of all this can become reality if cost-effectiveness has not been proven.

References

AGARD, 1991; Fatigue Management; AGARD-CP-506
Ahmad I., 1988; "Smart" Structures and Materials; in:C.A. Rogers (Ed.); Smart Materials, Structures, and Mathematical Issues; Technomic, pp. 13 - 16
Barrett R., 1995; All-moving Active Aerodynamic Surface Research; Smart Mater. Struct. 4, pp. 65-74

Boller Chr. and R. Dilger, 1992; In-Flight Aircraft Structure Health Monitoring Based on Smart Structures Technology; AGARD-CP-531; Paper 17
Boller Chr., 1994; Parameters and Techniques Based on Piezoelectric Sensing for Monitoring the Integrity of Composite Structures; Proc. of the 5th Internat. Conf. on Adaptive Structures; Technomic Publ. Comp.
Bristow, 1992; Integrated Health and Usage Monitoring System (IHUMS); Aircraft Engineering, February 1992, pp. 12-13
Crawley E.F. and E.H. Anderson, 1989; Detailed Models of Piezoceramic Actuation of Beams; AIAA 89-1388-CP, pp. 2000-2010
Daimler-Benz High Tech Report, 3/1994; pp. 44-45
Daimler-Benz High Tech Report, 4/1994; pp. 8-16
Fanson J., 1993; Articulating Fold Mirror for the Wide Field and Planetary Camera; Proc. of the 4th Internat. Conf. on Adaptive Structures, Technomic, pp. 278-302
Fuller C.R., S.D. Snyder, C.H. Hansen and R.J. Silcox, 1992; Active Control of Interior Noise in Model Aircraft Fuselages Using Piezoceramic Actuators; AIAA Journal, Vol. 30, No. 11, pp. 2613-2617
Gardiner P., A. Kelly and A.R. Bunsell (Eds.), 1993; ECCM Smart Composites Workshop; Bordeaux/France; Woodhead Publ. Ltd.
Giurgiutiu V, Z. Chaudhry and C.A. Rogers, 1995;Engineering Feasibility of Induced Strain Actuators for Rotor Blade Active Vibration Control; J. of Intell. Mat. Syst. and Struct., Vol. 6, pp. 583-597
Heeg J., R.C. Scott and A.-M. R. McGowan, 1994; Aeroelastic Research: Using Smart Structures Concepts; in AD-Vol. 44, Aeroelasticity and Fluid Structure Interaction Problems, ASME, pp. 161-173
Hirukawa H., S. Matsuoka, E. Takeuchi, K. Miyahara and Y. Muramatsu, 1994; Arrest Function of Fatigue Crack Growth by Phase-Transformed Oxide Particles; Proc. of the 3rd National Intelligent Materials Symposium, pp. 25-27 (in Japanese)
Krämer J., 1994; Federn aus Formgedächtnis-Legierungen; DVM Report, pp. 109-120
Krämer J. and R. Renz, 1993; Neues Werkzeug-Präzisionsspannsystem; VDI-Z-Special Werkzeuge, p. 6 - 17
Measures R., 1989; Smart Structures with Nerves of Glass; Progress in Aerospace Sci. vol. 26, pp. 289 - 351
Measures R., 1992; Fibre Optic Sensing for Composite Smart Structures; AGARD CP-531, Paper 11
Miner M.A., 1945; Cumulative Damage in Fatigue; Trans. ASME, J. Appl. Mech. 12, pp. 159-164
Naem A.S.H., R. Stanway, J.L. Sproston and W.A. Bullough, 1994; A Strategy for Adaptive Damping in Vehicle Primary Suspension Systems; AD-Vol. 45/MD-Vol. 54, Adaptive Structures and Composite Materials: Analysis and Application, ASME; pp. 395-404
Palmgren A., 1929; Die Lebensdauer von Kugellagern; VDI-Z 69; pp. 337-341
Prinz R., 1983; Growth of Delaminations under Fatigue Loading; AGARD-CP-335; Paper 5
Schöner H.-P., 1992; Piezo-Electric Motors and their Applications; Ferroelectrics, vol. 133, pp. 27-34
Shinya N., M. Egashira and H. Fudouzi, 1994; Powder Particles Assembly Using Electron Beam for Creation of Multi-Functional Materials (manuscript prepared for publication)
Spangler R.L. Jr. and S.R. Hall, 1989; Piezoelectric Actuators for Helicopter Rotor Control; Report #SSL 1-89, SERC 14-90, MIT Cambridge/USA
Strehlow H. and H. Rapp, 1992; Smart Materials for Helicopter Rotor Active Control; AGARD CP-531; Paper 5
Sumali H. and H.H. Cudney, 1994; Electro-Mechanical Analysis of an Active Engine Mount Incorporating Piezoelectric Stack Actuators; AD-Vol. 45/MD-Vol. 54, Adaptive Structures and Composite Materials: Analysis and Application, ASME; pp. 211-218
Takagi T. et al., 1989; The Concept of Intelligent Materials and the Guidelines on R&D Promotion; Science and Technology Agency, Tokyo/Japan
Takeuchi E., S. Matsuoka, K. Miyahara, H. Hirukawa, Y. Ikeda, 1994; Arrest Function of Elevated Temperature Fatigue Crack by Metallic Dispersed Particle of Low Melting Point; Proc. of the 3rd National Intelligent Materials Symposium, pp. 31-33 (in Japanese)
Trimboli M.S., R. Wimmel and E. Breitbach, 1994; Quasi-active Approach to Vibration Isolation Using Magnetic Springs; SPIE Vol. 2193, pp. 73ff
Tutton P.A. and F.M. Underwood, 1992; Structural Health Monitoring Using Embedded Fibre Optic Sensors; AGARD CP-531, Paper 18
Varadan Vi. and Va. Varadan, 1993; Smart Materials, Smart Skins, and Composites for Aerospace Applications; in Proc. of the ECCM Smart Composites Workshop, Bordeaux, pp. 17-22
Wada B.K. and J.A. Garba, 1992; Advances in Adaptive Structures at Jet Propulsion Laboratory; AGARD-CP-531, Paper 28

BIOMIMETIC MATERIALS AND STRUCTURES

Danilo De Rossi

Centro "E. Piaggio", School of Engineering

University of Pisa, Italy

An old-rooted endeavour of man, i.e. fabrication of material and structures taking inspiration from nature, is again actively pursued under a renewed name: biomimesis.
This approach, once belonging to the realm of biological sciences, is based on the observation that, when one tries to embody our recognition criteria for biological organisms in an explicit list, nothing can be found on that list that cannot be mimicked by some inorganic system (1). Hence, a large variety of artifacts can be made, all possessing, to some extent, life-like features.
Biomimetic arguments are today common reasoning in experimental studies about "origin-of-life" and in "advanced robotics"; a relatively new entry pertains to the area of "material science".

The "magic" and the "economic" as engineering factors

The development of embryonic technical areas very much depends upon the value recognized to them by the leading social components of the time; those values should not be only identified with utility or economicity. The self-perception of their own role of operators involved in the development of the area has also an influence on the selection of style and subject of the study, as we may recognize through a few, scattered historical remarks (2).
In the greek world the machine had a magic character since it opposes to nature, it permits to operate against nature and so, the mechanician, the engineer, the "mekanopoiós", for his being a creator of machines, is a wizard, a demon.
It is still true that in the ellenistic period the engineer is an ambigous character, even difficult to define: he doesn't care, although he knows geometry and mathematics, of theory; neither he operates as an artisan or a technician. Unable to place himself between "tékne" and "epistéme", since the radicality of the contraddiction makes a mediation impossible, he becomes a pivot in the struggle with nature which he forces, through his knowledge, to produce wonders.
The motivation behind new technologies at the beginning of modern era doesn't consist in conceiving, inventing and constructing machines because of their utility or economic value: this will only happen in a later moment, it will occur with the onset of industrial revolution. The aim instead, consists, in accordance to the program of ascertainment of the true possibility of controlling and dominating nature, in constructing all possible machines, that is, all machines which can be conceived on the lines of the defined new physics, in verifiyng the possibility of making something from every other thing.
Nowadays, industrial society is a mass society, characterized by huge industrial enterprises and gigantic public administrations, standardized mass production methods and diffused conformism in mass media and life-styles. In this society utility/economicity is the engineering factor.
The oncoming information society seems to present the connotation of a society of individuals in which new technologies will cope with the already manifested tendency of our young generations to escape from conformistic life and to express individuality. All this will occur only through the emergency of a social and economic order based on decentralized power and responsibility of the individual (3).
I have no difficulty to foresee in the information society a role of the playful/magic engineering factor in the design of man-machine interfaces and of small, individually supervised facilities for the computer-controlled generation of artifacts.

Soft and hard biomimesis

There is little doubt that in the area of biomimetic engineering the two characters (useful/economic and playful/magic) described above coexist either in terms of personal motivation of operators and in the foreseeable results of ongoing research.
Biomimicking as a respectable branch of material engineering has been questioned on the basis of its predicted inadequacy to fulfill industrial process requirements, particularly in terms of "time-to-make" (4).

Stereolithography and related rapid prototyping techniques (5), exploiting the moving front biomimetic principle (6), with the potential capacity to operate as home-based production facilities may well vanify the prediction above.
Beside this debate on time and economics, we have to underline the fact that this line of research looks at the materials to be prepared and the structures to be fabricated along the classical mechanistic/reductionistic attitude of physics. Analysis and synthesis of isolated parts, studied and prepared under the highest possible level of operator control, will eventually make available useful biomimetic materials and structures at a viable price. This we may call "soft biomimesis". Any student of biological science would realize soft biomimesis being so far from biology as Newtonian mechanics is.
Different by the practitioners of "hard biomimesis" find the pioneers of their discipline in the founders of "synthetic biology".
Synthetic biology was most lucidly defined and clearly reported in its first attemps by Stephan Leduc (7), but it only had approximately fourty years (from 1870 to 1910) of stunted life before falling into oblivion. Artificial cells, osmotic creatures and membraneous precipitations, all made of inorganic compounds, were prepared showing almost all the observable attributes of living creatures at an astonishing degree of resemblance.
It is worth mentioning, however, that the very large majority of today students of hard biomimesis don't use chemisty glassware, they operate with a computer keyboard to animate "Artificial Life".
Artificial Life, as it is cultivated today, has its roots in computer programming and, beside using serial machines of Von Neumann type, it attempts to generate life-like behaviours in their parallel, emergent nature. More than dealing with life-as-we-know-it, it deals with life-as-it-could-be or it-will-be (8).
We may say that Artificial Life has taken from contemporary science and technology mostly the computational aspects, with a minimum attention to other major advances such as the analysis of dynamic patterns, dissipative structures, self-assembly phenomena and other offsprings of non-linear effects in physical chemistry.

The material breeder

As remarked before, a truly peculiar characteristic of living systems resides in the emergent nature of their behaviour, which de-facto prevent any a-priori deterministic reasoning about the structure and function of the entity to be generated.
If we attempt to adopt an hard biomimesis approach we definitely proceeds along the lines indicated by D. Parisi (10) and K. Kelly (11).
"A form of engineering truly inspired to biology should aim to construct artifacts which, when they leave the hands of the engineer, are not yet what they have to be, they will become so after a process of development. The engineer does not create the artifact anymore, he just sets the suitable conditions for an artifact to develop and learn" (D. Parisi).
"Yet as we unleash living forces into our created machines,we loose control of them. They acquire wildness and some of the surprises that the wild entails. This, then, is the dilemma all gods must accept: that they can no longer be completely sovereign over their finest creations. The world of the made will soon be like the world of the born: autonomous, adaptable,and creative but, consequently, out of control". (K. Kelly).
Biology tells us that the emergent nature of the living systems originates from the distinction genotype/phenotype. The genotype is the complete set of genetic instructions. The phenotype is the physical organism, the structure emerging in space and time as a result of interpretation of the genotype code in a specific environment.
The process through which the phenotype develops in time, following genotype instructions, is called morphogenesis. The non-linear interactions between the objects specified by the genotype set the ground for a very rich variety of possible phenotypes. The price for this wealth of creatures resides in the impredictability about which phenotypes will finally emerge. Impredictability of genotype/phenotype systems prevents determination, by mere inspection, of which kind of phenotype will be produced by an arbitrary genotype. If we want to know the phenotype, we forcely have to test the genotype in a specific environment and let the things go.
Now, in the context of biomimetic systems, how can we look for suitable artificial genotypes capable of generating life-like phenotypes?

The artificial genotypes

The search for the appropriate artificial genotype and the optimum conditions for the development of the living phenotype was pursued by man in the time of Alchemy recurring to a proper state of spirit and the help of God.

Since the times the of fierce attack of Boyle in "The sceptical chemist" in 1661 and after the Royal Society's investigation (1783) of Dr. Pierce claim of transmutation of mercury into gold, Alchemy has no links with science (12).
Instead, the search for artificial genotypes is actively pursued in the field of Artificial Life with the aim of generating immaterial creatures throug computer programming or, as it is called, "life-in silico" (13).
With this aims, at present, Artificial Life is not involved in any activity related to material science and engineering and so, the connections with the area of biomimetic materials and structures are virtually non existent. All the equipment needed by Artificial Life practitioners resides in computers and peripherals requiring nowadays little investment to buy and short time to run.
The search for artificial genotypes and appropriate "growing" conditions of life-like phenotype in hard biomimesis, on the other side, appears to be an extremely laborious and expensive operation with limited change of success,at least in a near future. Such an enterprise would appear a sort of a dream (you may even say a nightmare) in an historical period in which dreams are valuable depending on their stock market value.

New tools

If a resuscitation of synthetic biology will prove to be possible, the worlds of Sthephane Leduc may be worth to remember: "The synthesis of life is not going to be the sensational discovery evoqued by the expression. If evolution occured as we presently believe, the synthesis of life can only originate through productions being intermediate between the mineral and the life kingdoms, having no more than a few rudimentary attributes of life, to whom, laboriously, other ones will add who, we may say, will lead to a progressive evolution of the first productions of synthetic biology".
The physicochemical tools and phenomena of biomimetic nature have much increased in terms of quality and understanding from the times of Leduc; even higher is our acquired knowledge in physics and chemistry, in the analysis of the characteristics of living systems and in some form of mathematics useful to describe them (14).
According to a materialistic vision, a biomimetic organism, as much as a living creature, may be described as a spatially-confined entity of limited duration in time in which space-and time-resolved chemical processes operate purposefully (teleonomy); the entity has the capability of autonomous morphogenesis and invariant reproductibility (15). If we look at material details we realize that an organism, as a functional necessity, needs to be structured.
As underlined by Rowland and Blumenthal (16): "An annoying ambiguity attaches to the word <<structure>>. It traditionally refers to static spatial patterns that are near or at thermodinamical equilibrium. But the word has been extensively adapted in the temporal domain and in thermodinamics to apply to systems with recognizable patterns mantained for finite period, however brief or enduring. These patterns differ significantly, however, from the old space structure in their requirement of energy for their manteinance. Thus, the classical structure-function dichotomy in biology is blurred by the introduction of dissipative structures (dynamic patterns)".
Dissipative structures (17) and related far-from-equilibrium phenomena (18) all refer to the onset of anisotropic dynamic effects spontaneously generated by isotropic causes.
This is the key issue of morphogenesis and structure formation in hard biomimesis.
We may be in front, here, to governing or enabling phenomena which, in analogy to the prepattern concept in biological morphogenesis, may consent to "froze-in" structures (static patterns) being the permanent record of the originating dynamic patterns (19). The generated static patterns will then form an influential skeleton for the development of newly operating dynamic patterns.
Oscillating chemical reactions and chemical waves (20), spatially periodic precipitations and other forms of patterning tools will operate in the support medium purposefully structured as a chemical (wave) guide, through appropriate local changes of material coefficients.
I will try to clarify this procedure through a possible implementation in my talk where a repertoire of potential artificial genotypes and an environment for phenotypes development will be illustrated.
At this early evolutionary stage of hard biomimesis we limit our selection criteria of emerging phenotypes to the ascertaiment of a purposefull action.
Although I am aware that invariant reproduction (21) and autonomous morphogenesis (9) have been both demonstrated in inorganic material systems, I do not believe the implementation of these life-like features, when combined with the requirement of purposefulness, belongs to the domain of predictable operations. Easier is the converse.

Rings in a brick

One attempt to exploit dinamic patterns for an engineering realization deals with the preparation of anisotropic ceramics using Liesegang rings (LR) (22). LR are forms of periodic precipitations that manifest themselves in a great variety of diffusive media permeated by suitable reactants (23). This form of patterns are known from a long time (24), although a detailed comprehension of their complex origin is still elusive (25).
It is worth mentioning that also Leduc made extensive study on these phenomena and reported about interesting realizations of optical diffraction gratings made by silver arseniate LR into gelatine blocks (9).
Leduc also reported evidence of guided chemistry with LR, proposing a close analogy between refraction, diffraction, dispersion and interference in optics and LR propagation in structured diffusive media.
The state of scientific understanding at that time was not developed enough to inhibit the analogy to be pushed too far; however the "spherical horse" we may call "optochemistry" could proove to be dense of theoretical and practical implications.

The toymaker and the butterfly wing

Hard biomimesis today is an activity of the mekanopoios more than the one of the economy-concerned engineer.
This consideration doesn't prevent the conception and eventual implementation of biomimetic structures endowed with the beauty and fascination of like-life behaviours, which are in-se valuable characteristics.
To be more specific, I refer to one of the most spectacular chromatic effects exploited by living creatures, i.e. submicron diffraction gratings (26). The hypotesis of Liesegang precipitation being responsible, though their diffractive properties, for the stripes of butterfly wings has been proposed a long time ago (27). Without being firmly disprooved, this hypothesis belongs to the inventory of rejected ideas. Many other models based on periodic solutions of reaction-diffusion equations have been proposed in time to account for patternig phenomena in morphogenesis (28). Most recently the possibility of a Turing mechanism (29) being responsible for stripes formation in sea angelfish has been convincingly supported (30).
However, it is not matter here to enquire about the biological role of these phenomena, but of conceiving methods and techniques for generating hard biomimesis creations, as it has been attempted by using Belousov-Zabotinsky reaction-based genotypes to originate classes of phenotypes capable to restore blurred visual images (31).
Ainfin, space in the Proceedings is gone and it is time to tell you "a viva voce" about my new toy: a patterning tool, a growing medium and the butterfly-wing analogs emerging out of them.

References

1) R. Rosen, "Life Itself. A comprensive inquiry into the nature, origin, and fabrication of life". Columbia Univ. Press, New York, 1991.

2) R. Rinaldi in a Introduction to: J. Cohen "I robot nel mito e nella scienza", De Donato, Bari, 1981.

3) K. Seitz, "Europe: a technological colony?", Community Editions, Bruxelles, 1995.

4) I. Amato, "Meeting the call of the wild". Science, vol. 253, pp. 966-968, Aug. 1991.

5) P.J. Jacobs, "Fundamentals of stereolithography", Society of Manufacturing Engineers, Deaborn (MI), 1992.

6) A.H. Hener et al., "Innovative materials processing strategies: a biomimetic approach", Science, vol. 255, pp. 1098-1105, 1992.

7) see M. Zeleny, G.J. Klir, K.D. Hufford," Precipitation membranes, osmotic growths, and synthetic biology" in Artificial Life, C.G. Langton (ed), Addison-Wesley Publ. Co, 1988.

8) C.G. Langton, "Artificial life" in - as 7).

9) S. Leduc, "Theorie physico-chimique de la vie et generation spontanèes", A. Poinat Ed., Paris, 1910.

10) D. Parisi, "Il controllo perduto", Virtual, vol I, n. 3, 1993.

11) K. Kelly, "Out of control: The new biology of machines", Fourth Estate, London., 1994.

12) E.J. Holmyard, "Alchemy", Dover Publ. Inc, New York, 1990.

13) see the volumes of the serie of Proceedings of the Santa Fe Institute Studies in the Sciences of Complexity published by Addison-Wesley Pub. Inc. as Artificial Life I, II and III.

14) V.I. Arnold, "Catastrophe theory", Springer Verlag, Berlin, 1992.

15) J. Monod, "Il caso e la necessità" EST Mondadori, Milano, 1970.

16) in "Dynamic patterns of brain cell assemblies" Neurosciences Res. Prog. Bull, vol 12 (1), pg. 54, March 1974.

17) I. Prigogine, G. Nicolis "Self-organization in nonequilibrium systems", J. Wiley & Sons, New York 1977.

18) J.A.S. Kelso, M. Ding and G. Schoner: "Dynamic pattern formation: a primer" in "Principles of organization in organism" SFI Studies in the Science of Complexity, Proc. Vol. XIII, J. Mittenthal and A. Baskin (Eds), Addison Wesley, 1992.

19) L.E. Scriven in 16) at pg 17.

20) A.T. Winfree, "The geometry of biological time", Springer Verlag, Berlin, 1990.

21) M. Kuckuck, "L'Univers, etre vivent", Librairie Kundig, Geneve, 1911.

22) J. Adair, S.A. Touse and P.J. Melling, American Ceramic Society Bulletin, 66, 1490, 1987.

23) H.K. Henish, "Crystals in gels and Liesegang rings", Cambridge University Press, Cambridge, 1988.

24) G. Runge, "Der Bildungstrieb der Stoffe, Oranejburg, 1855.

25) G. Venzi, J. Ross, "Nucleation and colloidal growth in concentration gradients (Liesegang rings)," J. Chem. Phys., 77 (3), pp. 1302-1307, 1982.

26) M. Gale, "Diffraction, beauty and commerce", Physics World, pp. 24-28, Oct. 1989.

27) W. Gebhardst, Verk. d.d. Zool. Ges., 22, 175, 1912.

28) H. Meinhardt, "Models of biological pattern formation", Academic Press, London, 1982.

29) A.M. Turing, "The chemical basis of morphogenesis" Phil Trans. R. Soc., B 237, pp. 37-72, 1952.

30) S. Kondo, R. Asai, "A reaction-diffusion wave on the skin of the marine angelfish Pomachantus", Nature, vol. 376, pp. 765-768, 1995.

31) N.G. Rambidi, A.V. Maximychev, "Molecular image processing devices based on chemical reaction systems, 4: Image processing operations performed by active media functioning in the oscillating mode". Advanced Materials for Optics and Electronics, vol 5, pp. 233-241, 1995.

Intelligent biointerface: remote control for hydrophilic-hydrophobic property of the material surfaces by temperature

Teruo Okano and Akihiko Kikuchi

Institute of Biomedical Engineering, Tokyo Women's Medical College,
8-1 Kawada, Shinjuku, Tokyo 162, JAPAN
Phone: +81-3-3353-8111, FAX: +81-3-3359-604

ABSTRACT

Considerable research attention has been focused recently on materials which change their structure and properties in response to external stimuli. These materials, termed "intelligent materials", sense a stimulus as a signal (sensor function), judge the magnitude of this signal (processor function), and then alter their function in direct response (effector function). Introduction of stimuli-responsive polymers as switching sequences into both artificial materials and bioactive molecules would permit external, stimuli-induced modulation of their structures and "on-off" switching of their respective functions at molecular levels [1-3].

Intelligent materials embodying these concepts would contribute to the establishment of basic principles for fabricating novel systems which modulate their structural changes and functional changes in response to external stimuli. These materials are attractive not only as new, sophisticated biomaterials but also for utilization in protein biotechnology, medical diagnosis and advanced site-specific drug delivery systems.

1. BIOMEDICAL INTELLIGENT SYSTEMS

The research described in this paper is directed toward development and fundamental studies of biomedically relevant modulation systems using the temperature-responsive polymer, poly(*N*-isopropylacrylamide) (PIPAAm) with a carboxyl end group, as switching sequence. This polymer was attached to solid surfaces, crosslinked hydrogels and biomolecules to create new grafted surfaces, graft type gels and modified bioconjugates, respectively. PIPAAm was used to introduce a reversible switching function correlated to hydration–dehydration changes of polymer chains in response to changes in temperature, shown in Figure 1.

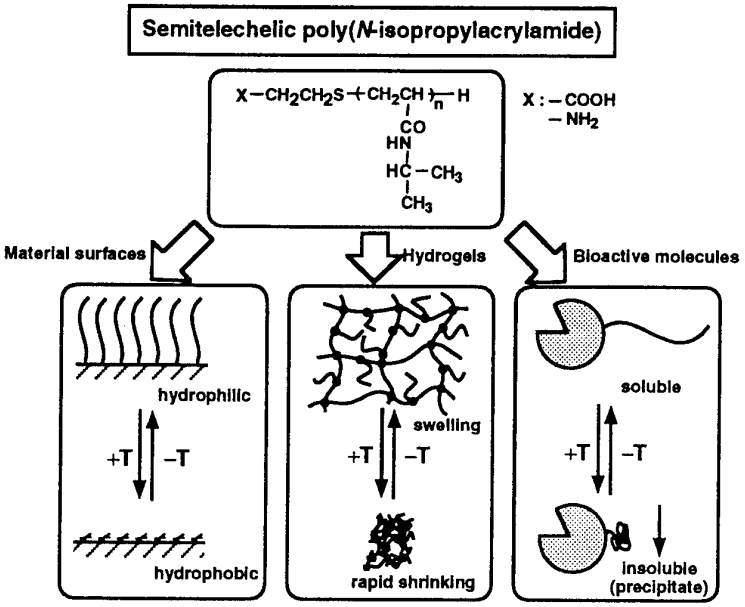


Figure 1. Basic concept for biomedical modulation systems using temperature-responsive polymers.

0-8194-2165-0/96/$6.00

2. INTELLIGENT SURFACES

Soluble–insoluble changes of PIPAAm in response to external temperature could be utilized for temperature-responsive hydrophilic–hydrophobic surface property alterations. We have reported hydrophilic–hydrophobic surface property alterations in response to temperature changes using solid surfaces grafted with PIPAAm molecules [4-7]. These surfaces demonstrate hydrophobic properties above the LCST where PIPAAm chains have collapsed.

We have utilized the surface hydrophilic–hydrophobic property alterations for cell culture system. PIPAAm molecules are introduced to polystyrene culture dishes by electron-beam irradiation. Briefly, N-isopropylacrylamide (IPAAm) solution in isopropyl alcohol was added to polystyrene dishes, and these dishes were allowed to irradiate electron beam to introduce PIPAAm on the surface. Used cells for cell culture and recovery experiments are bovine aortic endothelial cells and rat hepatocytes and cultured in a humidified atmosphere of 5% CO_2 at 37°C. Lower temperature treatment was carried out as follows: Cells were plated on PIPAAm-grafted dishes at 4 x 10^4 cells/cm^2 and inoculated for 2 days in a humidified atmosphere of 5% CO_2 at 37 °C. Temperature was then lowered to a predetermined degree for 30 min without changing medium. The detached cells were collected with minimal pipetting and counted to determine %-recovery. Morphological changes of cultured cells were observed directly under phase-contrast microscope or scanning electron microscope after fixation and lyophilization of cells. Sodium azide was used to examine the effect of cellular metabolism on cultured cell detachment by lowering temperature. Cultured hepatocytes were incubated with various concentration of sodium azide at 37 °C for 60 min, then low temperature treatment was to detach cells. It was found that cells adhered and proliferated on PIPAAm-grafted surface at 37 °C where surface of temperature as well as cell metabolism. showed hydrophobic property, and these cultured cells can easily be recovered from the surfaces by simple temperature decreases as shown in Figure 2. In particular, mechanism of cell detachment from the PIPAAm-grafted surfaces was investigated in terms of temperature as well as cell metabolism.

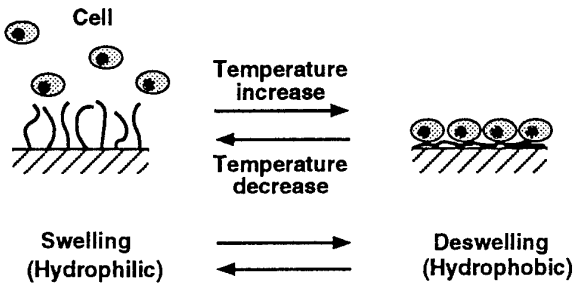


Figure 2. Temperature–modulated hydrophilic/hydrophobic surfaces utilized as cell culture substrates.

The effect of temperature on recovery of cultured cells from PIPAAm-grafted dish was investigated with respect to both degree of surface hydrophilic–hydrophobic change and cell metabolism change. Although minimal detachment of cells cultured on PIPAAm-grafted dishes was observed by incubation for 30 min at lower temperature (4-25°C), greater recovery of cells was achieved by additional incubation at 25 °C for 5 min after 30 min incubation at each temperature. As temperature decreases, surface grafted PIPAAm chains are assumed to be extended conformation due to high hydration, resulting in reduced cell-materials interaction. From the above mentioned results, hydration of PIPAAm at cell–materials interface is not considered as only the factor to govern cell detachment from the PIPAAm-grafted dishes. Recovery of cells by temperature treatment was decreased by treating cultured cells with sodium azide, implying that cellular metabolism is involved in the detachment process of

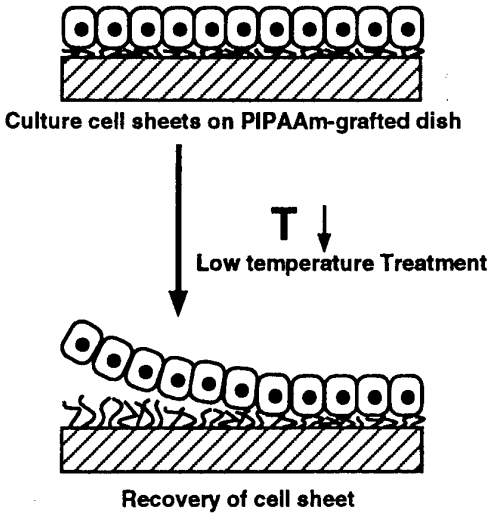


Figure 3. Tissue Recovery by Low Temperature Treatment

cultured cells. Recovered cells by lower temperature treatment well proliferated on tissue culture dishes and retained high functionality as judged by secretion of albumin from hepatocytes compared with cells recovered by conventional trypsin treatment. Confluent culture of cells was also recovered by temperature treatment, as schematically shown in Figure 3, indicating that PIPAAm-grafted surfaces might be useful for construction of artificial tissues such as artificial skin and artificial cornea. Consequently, feasibility of thermo-responsive hydrophilic/hydrophobic alterations of PIPAAm-grafted dishes was indicated as novel cell recovery system.

3. INTELLIGENT HYDROGELS

3.1. Intelligent hydrogels for drug delivery systems

In the case of oral doses, the drug concentration in blood first rises rapidly to a maximum. The level then falls slowly as drug is metabolized, excreted or degraded. Intravenous injection results in an exponential decrease from the maximum blood concentration. Drug concentration must be maintained within a certain therapeutic range to act properly. It becomes toxic above the upper level and ineffective under the lower level. In the conventional dosage form, drug concentration in blood cannot be kept in an effective range for a long period. Further, all dosed drug is not always delivered to the target disease site. A large excess of drug must be systemically dosed to deliver small amount of drug to the target site. Drug not delivered to the target site can result in a deleterious influence on normal sites (side effects). Since drug typically acts through multiple interactions with the body, drug doses must consider physiological side effects independent of the targeting site, particularly with drugs of high toxicity. Such problems in conventional drug therapy have prompted the development of new delivery systems to keep drug concentrations in effective ranges for longer periods, or deliver drugs only to target sites. Achievement of such a system would enable use of many kinds of drugs which cannot now be effectively utilized due to high toxicity.

With this perspective, the concept of a novel "drug delivery system (DDS)" has been developed in order to maintain effective drug concentrations in blood over longer periods, maximize efficacy and minimize side effects of drugs. Studies on DDS were initiated to achieve slow release (sustained release) to obtain longer lasting drug effects. Recently, biologically active therapeutic peptides have been artificially synthesized using genetic engineering techniques. These peptides are easily degraded under physiological conditions and also encounter absorption problems due to their high molecular weight. Hence, they cannot be utilized effectively in conventional dosage forms. For such active agents, new types of DDS must be developed to deliver drug effectively to the targeting site (targeted, site-specific delivery) and release drug when drug is required (temporal control) in addition to conventional rate-controlling systems. The achievement of such DDS is becoming an increasingly important technological subject. To realize the new DDS, it is important to construct a system where the drug device itself senses an environmental stimulus and responds to appropriately control drug release as shown in Figure 4. The system is called as "intelligent DDS" [1,8-10], which is distinguished from the conventional DDS as shown in Figure 5.

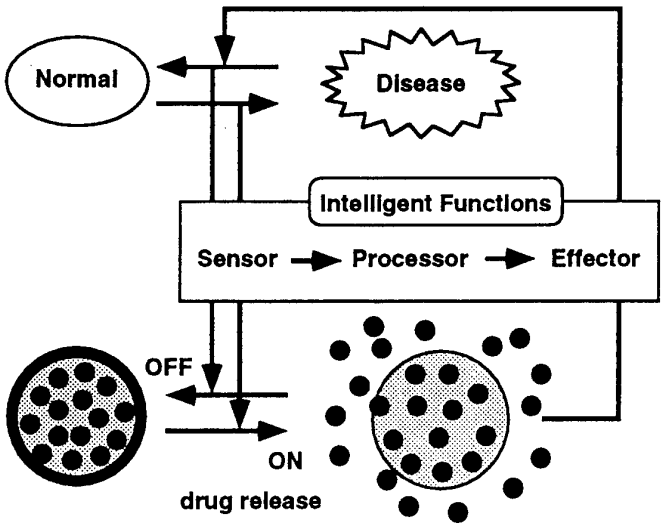


Figure 4. Auto feed-back drug delivery

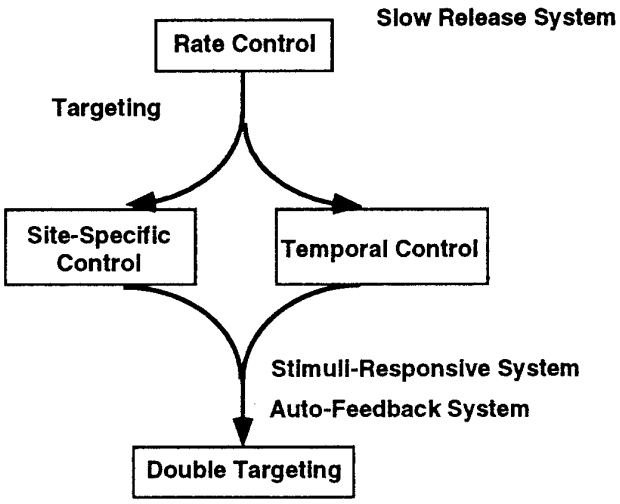


Figure 5. Strategy of new drug delivery systems.

3.2. On-off switching mechanism of drug release and permeation using PIPAAm hydrogels

Polymer chains of IPAAm hydrate to form expanded structures in water at lower temperature. At higher temperature, however, the chains form compact structures due to dehydration. Crosslinked poly(IPAAm) gel exhibits remarkable swelling changes in aqueous media in the vicinity of 32°C due to the rapid hydration and dehydration changes of the polymer chain. According to free volume theory, solute diffusivity in a gel increases with an increase in the swelling of the gel. Thermo-responsive polymer hydrogels would be capable of controlling drug release rate by temperature change to achieve a possible intelligent DDS. Pulsatile drug delivery in response to temperature using thermo-responsive IPAAm gels has been studied [11-18].

In designing a pulsatile release device, it is desirable to modulate the release rates to provide an effective amount of drug during the 'on' state and have no effect on a body during the 'off' state. If the system does not give a complete 'off' state and only increases or decreases the release rate in response to external stimuli (1-2 control), drug released during the 'off' state cannot be ignored. Consequently, it is very important to establish an effective design for the 0-1 control system for complete 'on-off' regulation of drug release.

We have studied 'on-off' regulation of drug permeation and release using poly(IPAAm-co-alkyl methacrylate) (P(IPAAm-co-RMA) gels [18-20]. In this system, the gel surface acts as an 'on-off' switch. Drug permeation through the gel or drug release from the gel is stopped by the dense skin layer formed on the surface immediately after increasing temperature (Figure 6). This surface-regulating mechanism results in a quick 'on-off' response as well as achieving complete 0-1 control, although more than 1 month is needed to reach the equilibrium shrunken state from the swollen state. The effects of the surface skin as an 'on-off' switch on pulsatile drug release have been investigated in detail [10].

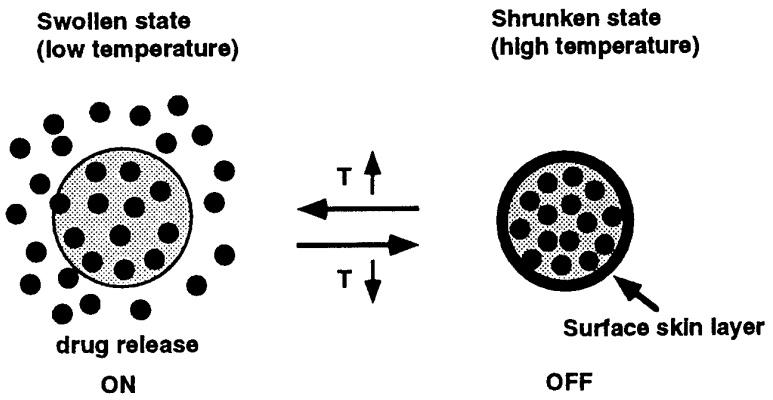


Figure 6. On–off switching mechanism of drug release.

3.3. Graft type PIPAAm hydrogels

The rate of volume change in the stimuli-responsive hydrogels directly affected the efficiency of energy transfer, mass separation and releasing solutes. Due to the crosslinking incorporated into the hydrogels, gel swelling–deswelling kinetics are governed by diffusion–mass transfer into and out of the network [21]. Furthermore, the gel swelling kinetics (based on collective diffusion properties) is inversely proportional to the square of the gel dimension. Thus, crosslinked gels have limited utility in applying swelling–deswelling kinetics for practical application due to size dependency. To overcome these constraints, many groups have incorporated hydrophilic components [22] or introducing porosity [23,24] in an attempt to enhance the swelling–deswelling kinetics.

An another approach, polymer networks are being synthesized containing comb-type grafts (Figure 7). The change in molecular structure accompanied by graft chain may create new functions and properties compared to normal crosslinked gels. The increased mobility of grafted chains may enhance thermo-responsiveness due to elastic and diffusional properties of the new gels, thus increasing the kinetics of volume change. We have synthesized comb-type grafted gels composed of thermo-responsive PIPAAm to control responsive rate and reversibility of the gel by utilization of freely mobile nature of graft PIPAAm chains [25]. PIPAAm macromonomer was prepared by radical telomerization reaction using aminoethanethiol as telogen, followed by condensation reaction of end-amino group with *N*-acryloxysuccinimide to introduce polymerizable group at chain end. The comb-type PIPAAm gels were then synthesized using IPAAm monomer (70wt%) and PIPAAm macromonomer (30wt%) dissolved in distilled water. *N,N'*-methylenebisacrylamide (1.7wt% with respect to the total monomer) and *N,N,N'N'*-tetramethylenediamine were used as a crosslinker and an accelerator, respectively. After nitrogen was bubbled in the solution, ammonium persulfate was added as an initiator. The solutions were allowed to polymerize at 15°C for 24 h between two glass plates covered with Mylar sheets, separated by a Teflon gasket (2.0 mm). Comb-type grafted gels having grafts with molecular weight 2900, 4000, and 9000 were abbreviated as GG2900, GG4000 and GG9000 respectively.

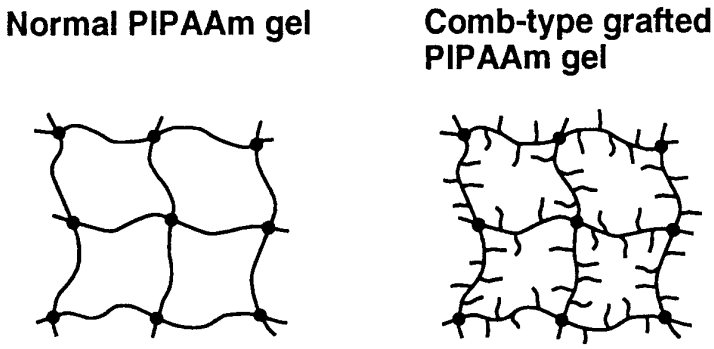


Figure 7 Schematic illustration of structure of normal-type crosslinked gel and comb-type grafted gels.

Deswelling kinetics for both comb-type and normal PIPAAm gels, from equilibrium-swelling (10°C) to equilibrium-shrunken (40°C) gels, are demonstrated in Figure 8. The normal PIPAAm gel shrank slowly, taking more than a month to reach its equilibrium deswelling state at 40°C. In contrast, comb-type hydrogels shrank rapidly (within minutes) as a function of chain length. The gels became opaque immediately after the temperature was increased above their phase transition temperatures, indicating the polymer networks became heterogeneous. At the molecular level, the polymers were phase-separated from water molecules.

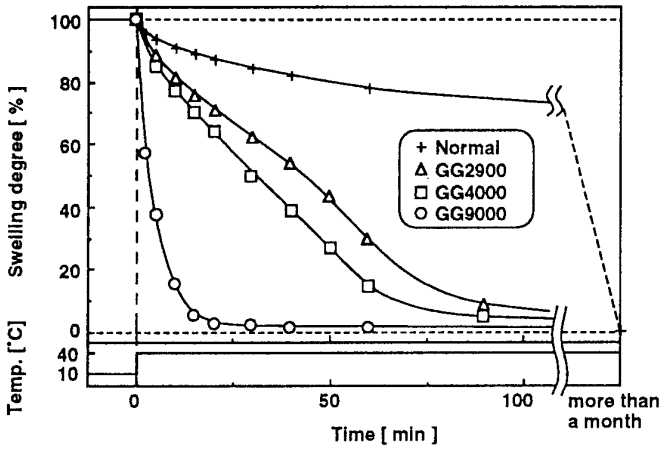


Figure 8 Time course of deswelling for hydrogels undergoing shrinking at 40°C in response to stepwise temperature change from 10°C.

The surface structure of deswelling polymers was observed. Deswelling processes of two types of gels were schematically shown in Figure 9. The normal PIPAAm gel formed "surface skin" layers upon deswelling, entrapping water inside the gel [8,18,21,26-28]. The impermeable skin formation lead to the building of hydrostatic pressure within the gels [21,27,28]. When the shrinking force in the network bulk became large, the surface portion of the gel exhibits a bubble-like structure, and the entrapped water is squeezed from the interior through bubble formation [21,28]. The comb-type PIPAAm gels, GG2900 and GG4000, also showed bubble formation at the surface immediately after temperature increase during shrinkage processes. Larger bubbles were seen on GG2900 compared to GG4000, due to observed denser surface layer. Stronger aggregation forces in the network bulk occurred in GG4000 and GG9000, which may influence formation of skin structures on the gel collapse. In particular, GG9000 showed no skin layer formation (no bubbles), yet this gel did exhibit mechanical buckling, due to the strong chain aggregation forces inside the hydrogel. The strong aggregation in the interior of polymers creates large hydrostatic pressures within the gel, leading to rapid expulsion of water from the gel to external medium.

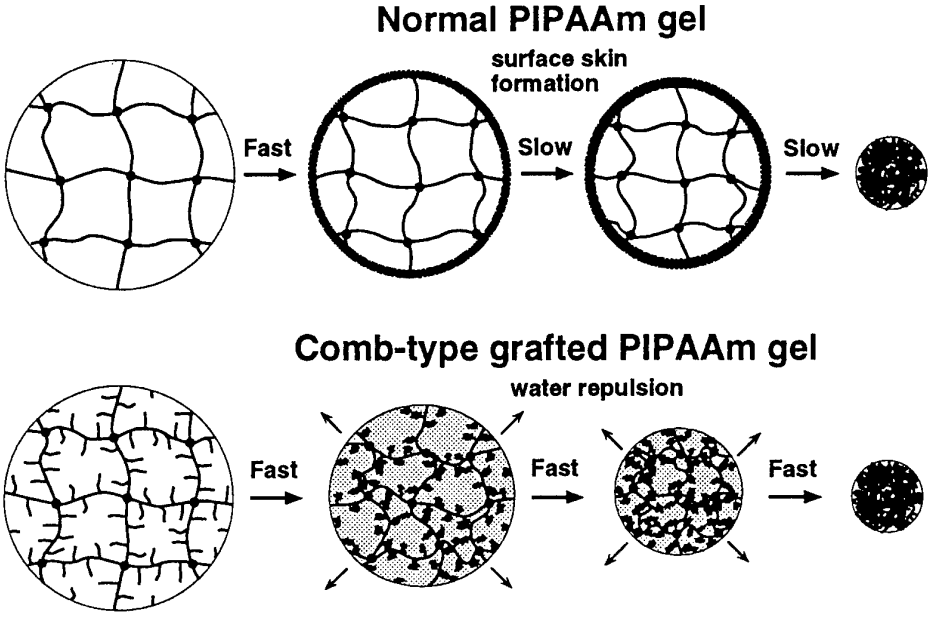


Figure 9 Schematic illustration of deswelling mechanism for two types of gels.

4. INTELLIGENT PROTEIN-POLYMER CONJUGATES

Chemical modification of biomolecules with synthetic and natural polymers has allowed new applications of protein conjugates in the fields of medicine, bio-engineering and bioreactors. Poly(ethylene glycol)-modification of proteins, for example, has broadened the applications of many proteins. Decreased immunoreactivity and/or immunogeneity [29], increased stability *in vivo* [30] and use in organic synthesis [31] have been described for PEG-modified proteins. Using these techniques, functional polymers are capable of integrating new functions into biomolecules without destroying the original protein function.

We have been studying temperature-responsive bioconjugates using poly(N-isopropylacrylamide) (PIPAAm) and proteins connected with a single-end attachment [32-35]. Previously, we reported preparation of PIPAAm-lipase in which PIPAAm chains were attached to the enzyme by single chain ends [34]. The bioconjugate exhibited an LCST and retained its native activity. Recovery of conjugates was possible by changing temperature, with multiple cycles achieved without denaturation. Although PIPAAm has been introduced to various proteins to date [36,37], there was no report which discussed its molecular architecture comparing single-end attachment chemistry with multiple attachment chemistry in the same system.

We have investigated the molecular architecture of PIPAAm–enzyme conjugates by preparing two types of PIPAAm–trypsin conjugates, wherein PIPAAm chains are attached by either single-end or multipoint chemistry [38]. A semitelechelic co-oligomer (IDc) was attached to trypsin by single-point conjugation (IDc–trypsin). A copolymer (PIDAAc) consisting of acrylic acid and IPAAm randomly linked in polymer chains was attached to trypsin using multipoint conjugation (PIDAAc–

trypsin) (Figure 10). Both conjugates exhibited reversible temperature-responsive phase separation. The IDc–trypsin conjugate exhibited phase separation at the same temperature as pure IDc, due to the highly mobile free polymer end group which remains sensitive to small temperature changes. The PIDAAc–trypsin conjugate precipitated at higher temperatures than pure PIDAAc, whose movement was restricted by multiple binding points. Enzyme stability in solution was improved after introducing PIPAAm chains, which prevented autolysis attributed to conjugate steric hindrance. Stability under repeated temperature cycling was also dependent on the architecture of conjugates; the IDc–trypsin conjugate was more stable than the PIDAAc–trypsin. As a consequence, single-end conjugation of polymer to enzyme provides novel bioconjugate with novel functionality attributed from attached polymer while retaining native biological function with high stability.

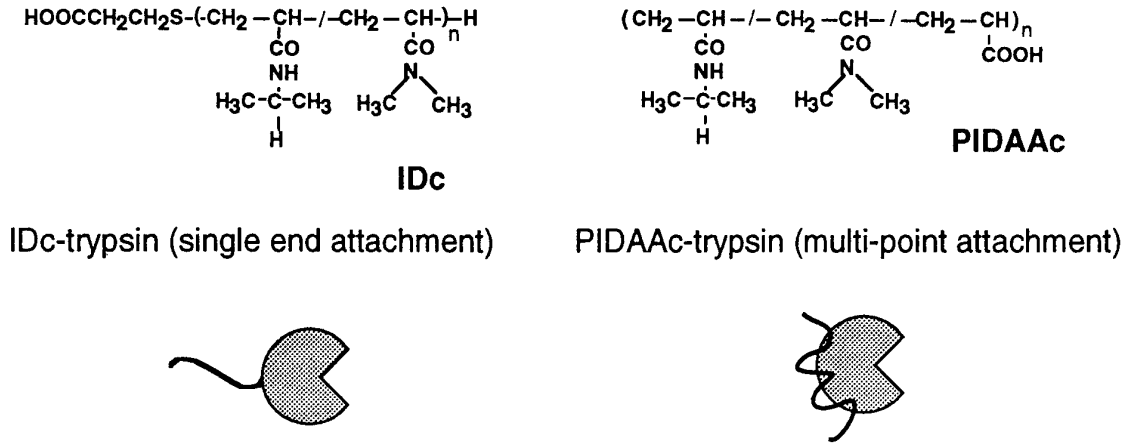


Figure 10. Structural formulae of temperature-responsive polymers and schematic illustration of temperature-responsive biomolecules.

REFERENCES

1. T. Okano and R. Yoshida, "Intelligent Polymeric Materials for Drug Delivery" in Biomedical Applications of Polymeric Materials, Eds. by T. Tsuruta, T. Hayashi, K. Kataoka, K. Ishihara and Y. Kimura, pp.407-428, CRC Press, Boca Raton, FL., 1993.
2. T. Okano, "Molecular design of temperature-responsive polymers as intelligent materials", in Advances in Polymer Science, Responsive Gels: Volume Transition II, Eds. by K. Dusek, Vol.110, pp.179-197, Springer-Verlag, Berlin, 1993.
3. T. Okano and R. Yoshida, "Thermo-responsive property of poly(*N*-isopropylacrylamide-co-alkyl methacrylate)", in New Functionality Materials, Volume B, Synthesis and Function Control of Biofunctionality Materials, Eds. by T. Tsuruta, M. Doyama, M. Seno and Y. Imanishi, pp.189-196, Elsevier, Amsterdam, The Netherlands, (1993).
4. N. Yamada, T. Okano, H. Sakai, F. Karikusa, Y. Sawasaki and Y. Sakurai, "Thermo-responsive polymeric surfaces; control of attachment and detachment of cultured cells", Makromol. Chem., Rapid Commun., **11**, 571-576 (1990).
5. T. Okano, N. Yamada, H. Sakai and Y. Sakurai, "A novel recovery system for cultured cells using plasma-treated polystyrene dishes grafted with poly(N-isopropylacrylamide)", J. Biomed. Mater. Res., **27**, 1243-1251 (1993).
6. Y. G. Takei, T. Aoki, K. Sanui, N. Ogata, Y. Sakurai, and T. Okano, "Temperature-modulated platelet and lymphocyte interactions with poly(*N*-isopropylacrylamide)-grafted surfaces", Biomaterials, **16**, 667-673 (1995).
7. Y. G. Takei, T. Aoki, K. Sanui, N. Ogata, T. Okano and Y. Sakurai, "Dynamic contact angle measurement of temperature-responsive surface properties of poly(*N*-isopropylacrylamide) grafted surfaces", Macromolecules, **27**, 6163-6166 (1994).
8. T. Okano, Y. H. Bae and S. W. Kim, "Temperature responsive controlled drug delivery", in Pulsed and Self-Regulated Drug Delivery, Eds. by J. Kost, pp.17-46 , CRC Press, Boca Raton, FL., 1990.
9. T. Okano, "Stimuli-sensitive Polymers", Proc. 17th Intern. Symp. Control. Rel. Bioact. Mater., **17**, 19 (1990).
10. R. Yoshida, K. Sakai, T. Okano and Y. Sakurai, "Pulsatile drug delivery systems using hydrogels", Advanced Drug Delivery Reviews, **11**, 85-108 (1993) and references therein.
11. Y. Okahata, H. Noguchi and T. Seki, "Thermo-selective permeation from a polymer grafted capsule membrane", Macromolecules, **19**, 493 (1986).
12. Y. Okahata, H. J. Lim, G. Nakamura and S. Hachiya, J. Am. Chem. Soc., **105**, 4855 (1983).

13. Y. H. Bae, T. Okano and S. W. Kim, "Temperature dependence of swelling of crosslinked poly(*N,N*-alkyl substituted acrylamides) in water", J. Polym. Sci., Polym. Phys. Ed., **28**, 923-936 (1990).
14. H. Yasuda, C. E. Lamaze and L. D. Ikenberry, Permeability of solutes through hydrated polymer membranes. Part I. Diffusion of sodium chloride", Makromol. Chem., **118**, 19 (1968).
15. Y. H. Bae, T. Okano, R. Hsu and S. W. Kim., "Thermo-sensitive polymers as on-off switches for drug release", Makromol. Chem., Rapid Commun., **8**, 481-485 (1987).
16. T. Okano, Y. H. Bae, H. Jacobs and S. W. Kim, "Thermally on-off switching polymers for drug permeation and release", J. Controlled Release, **11**, 255-265 (1990).
17. Y. H. Bae, T, Okano and S. W. Kim, "On-off thermocontrol of solute transport. I. Temperature dependence of swelling of *N*-isopropylacrylamide networks modified with hydrophobic components in water.", Pharm. Res., **8**, 531-537 (1991).
18. R. Yoshida, K. Sakai, T. Okano and Y. Sakurai, Surface-modulated skin Layers of thermal responsive hydrogels as on-off switches. II. Drug permeation. J. Biomater. Sci., Polym. Ed., **3**, 243-252 (1992).
19. R. Yoshida, K. Sakai, T. Okano and Y. Sakurai, Surface-modulated skin Layers of thermal responsive hydrogels as on-off switches. I. Drug release. J. Biomater. Sci., Polym. Ed., **3**, 155-162 (1991).
20. T. Okano, R. Yoshida, K. Sakai and Y. Sakurai, "Thermo-responsive polymeric hydrogels and their application to pulsatile drug release", in Polymer Gels, Eds. by D. DeRossi, pp.299-308, Plenum Press, New York, 1991.
21. E. Sato Matsuo, T. Tanaka, "Kinetics of discontinuous volume-phase transition of gels", J. Chem. Phys., **89**, 1695-1703 (1988)
22. A. Gutowska, Y. H. Bae, S. W. Kim, "Heparin release from thermosensitive hydrogels", J. Control. Rel., **22**, 95-104 (1992)
23. B. G. Kabra, S. H. Gehrke, "Synthesis of fast response, temperature-sensitive poly(*N*-isopropylacrylamide) gel", Polym. Commun., **32**, 322-323 (1991)
24. X. S. Wu, A. S. Hoffman, P. Yager, "Synthesis and characterization of thermally reversible macroporous poly(*N*-isopropylacrylamide) hydrogels", J. Polym. Sci. Part A, **30**, 2121-2129 (1992)
25. R. Yoshida, K. Uchida, Y. Kaneko, K. Sakai, A. Kikuchi, Y. Sakurai, T. Okano, "Comb-type grafted hydrogels with rapid de-swelling response to temperature changes", Nature, **374**, 240-242 (1995)
26. T. Okano, N. Yui, M. Yokoyama, R. Yoshida, in Advances in Polymeric Systems for Drug Delivery, pp. 67-105, Gordon and Science Publishers, Switzerland 1993.
27. R. Yoshida, K. Sakai, T. Okano, Y. Sakurai, "Modulating the phase transition temperature and thermosensitivity in *N*-isopropylacrylamide copolymer gels", J. Biomater. Sci. Polym. Edn., **6**, 585-598 (1994)
28. Y. Kaneko, R. Yoshida, K. Sakai, Y. Sakurai, T. Okano "Temperature-responsive shrinking kinetics of poly(*N*-isopropylacrylamide) copolymer gels with hydrophilic and hydrophobic comonomers", J. Memb. Sci., **101**, 13-22 (1995)
29. W. Y. Lee, and H. Sehon, "Abrogation of reaginic antibodies with modified allergens", Nature, **267**, 618-619 (1977).
30. A. Abchowski, T. van Es, N. C. Palczuk and F. F. Davis, "Alteration of immunological properties of bovine serum albumin by covalent attachment of polyethylene glycol", J. Biol. Chem., **252**, 3578-3581 (1977).
31. T. Yoshimoto, K. Takahashi, H. Nishimura, A. Ajima, Y. Tamaura and Y. Inada, "Modified lipase having high stability and various enzymatic activities in benzene, and its re-use by recovering from benzene solution", Biotechnol. Lett., **6**, 337-340 (1984).
32. Y. G. Takei, T. Aoki, K. Sanui, N. Ogata, T. Okano, and Y. Sakurai, "Temperature-responsive bioconjugates I. Synthesis of temperature responsive oligomers with reactive end groups and their coupling to biomolecules", Bioconjugate Chem., **4**, 42-46 (1993).
33. Y. G. Takei, T. Aoki, K. Sanui, N. Ogata, T. Okano and Y. Sakurai, "Temperature-responsive bioconjugates 2. Molecular design for temperature-modulated bioseparations", Bioconjugate Chem., **4**, 341-346 (1993).
34. M. Matsukata, Y. G. Takei, T. Aoki, K. Sanui, N. Ogata, Y. Sakurai and T. Okano, "Temperature modulated solubility-activity alterations for poly(*N*-isopropylacrylamide)-lipase conjugates", J. Biochem., **116**, 682-686 (1994).
35. Y. G. Takei, M. Matsukata, T. Aoki, K. Sanui, N. Ogata, A. Kikuchi, Y. Sakurai and T. Okano, "Temperature-responsive bioconjugates. 3. Antibody-poly(*N*-isopropylacrylamide) conjugates for temperature-modulated precipitation and affinity bioseparations", Bioconjugate Chem., **5**, 577-582 (1994).
36. G. T. Park and A. S. Hoffman, "Synthesis and characterization of a soluble temperature-sensitive polymer-conjugated enzyme", J. Biomater. Sci., Polymer Edn., **4**, 483-504 (1993).
37. G. Chen and A. Hoffman, "Preparation and properties of termoreversible, phase-separating enzyme-oligo(*N*-isopropylacrylamide) conjugates", Bioconjugate Chem., **4**, 509-514 (1993).
38. M. Matsukata, T. Aoki, K. Sanui, N. Ogata, A. Kikuchi, Y. Sakurai and T. Okano, "Effect of molecular architecture of poly(*N*-isopropylacrylamide)–trypsin conjugates on their solution and enzymatic properties", Bioconjugate Chem., in press (1996).

Materials and their uses

Pierre Richard

Research Director Senior Vice-President Group - Bouygues SA, France

ABSTRACT

New materials have been emerging in the industry for several decades.

Recently, the research into materials has spread ; the development of university and industrial laboratories, the use of physic and chemistry for their design give a new impetus to this research.

A material apparently as common as concrete is no exception to this general trend. However, the economic aspect of research must always be kept in mind and performance objectives selected with discernment.

The initial attitude of engineers and builders was to use a given material in the best possible way. It was on this basis for example that structures in wood, cast iron, reinforced concrete, non-reinforced concrete and prestressed concrete were gradually defined.

Later on, engineers and researchers began to examine the question as to whether it was possible to design a material which met the need of this or that problem in a more specific way. This led initially to simple enhancement of the characteristics of existing materials, frequently employing simple means, in some cases merely by improving the care with which the materials were prepared, so as to make them more efficient for their intended application. During the same period, new qualities were achieved in many cases by association with other materials, a classic example of this approach being reinforced concrete.

The emergence of prestressed concrete was associated with two improvements: firstly the incorporation of forces generating stresses, compressions or tensions in a structure, working in directions opposite to those corresponding to gravitational loads, using stressed steel, and secondly the development of steels with high elastic strength, without which the prestressing effect would have disappeared as a result of the shrinkage and/or creep of the concrete. It was Eugène Freyssinet who understood the phenomena of concrete shrinkage and creep, from which he realised that the concept of prestressing could only become a reality through the introduction of new grades of steel with high elastic strength.

Obviously there are other examples.

Finally, and this was not genuinely new, a number of synthetic materials were conceived and designed to cater for this or that problem, the long list of such materials including nylon, PTFE, etc. It was at this point that physico-chemistry made its appearance in laboratories and industry.

However it was probably ambition on the one hand, and the appearance of initially astonishing new characteristics on the other, which led to these materials being called "intelligent" - materials with shape-recovery memory, materials sensitive to magnetic fields or immune to changes in temperature, etc.

Concrete in its common form has not escaped this process, as we have already seen. I therefore propose to recapitulate what has already happened, and look ahead to potential future applications.

The concrete research field is relatively recent, with work only commencing in the early 1980s. However results appeared very quickly, and the related industrial applications have been numerous, and in many cases rich in new information.

0-8194-2165-0/96/$6.00

We must not forget that the relation between a sophisticated, ambitious material and the applications for this material should lead to a high-performance result. Examples of astonishing materials for which there are no valid applications, are frequently explained in terms of economic realities. Likewise, no error is permissible in the definition of a new material project. Remember the exaggerated expectations associated with ceramics. Although the new performance offered by these materials (hardness, compressive strength and resistance to wear) place them ahead of their competitors, applications remain limited as their natural defect (fragility) has remained. Despite marginal improvements, the progress achieved in this area was not in line with that obtained for the basic qualities of ceramic materials.

We shall therefore consider this general process in the case of concretes, looking at a number of interesting phenomena and leading to the notion of powder concretes. We shall then examine possible lines of development for this new material, which for example, could modify structural design and be used in other sectors than the civil engineering field.

Thus well before 1980, civil engineers interested in the principal material used in their profession knew, and were able to explain that a reduction in the quantity of mixing water produced concretes with enhanced mechanical characteristics, and better resistance to the forms of chemical aggression to which structures are subjected. They also observed the difficulty in placing these concretes, the risk of improper filling of the formwork. This led to cost levels which were frequently considered unjustified. This was also a time when the appearance of jobsite chemistry was feared, simply due to lack of understanding of this discipline. The use of additives in concretes was prohibited for many years, despite the fact that many were familiar with plasticizers, at least in terms of their effect on the rheology of cement pastes.

We therefore decided to analyse the industrial advantage offered by these concrete plasticizer products.

We quickly observed that the water/cement ratio could be shifted from the customary range of 0.40 to 0.50 to values below 0.35, while at the same time achieving marked gains in strength, moving without difficulty, and using standard equipment, from a compression strength of 40MPa to at least 60MPa.

The special properties of amorphous silica, a bi-product from the manufacture of silicon, considered as a pollutant at the time, were also used and took compression strength values up to 80MPa and more, since a value of 120MPa can be achieved combining these two means.

The economic advantage of these solutions remained to be checked. It was then demonstrated, at a time when regulations authorised the use of 60MPa concrete, that this advantage was indeed genuine, though not strictly revolutionary. Authorisation of using 80MPa concrete further increased the difference with respect to earlier solutions. The first large structure for which these concretes were used was the Ile de Ré bridge, confirming the trend despite the higher production costs for this material.

However at the same time we observed that , beyond these values, prices tended towards an asymptote , despite the definition of design alternatives for the structures concerned. Indeed the defect of concretes, namely fragility, still remained: as before, prestressing, passive steel elements used to enhance the ductility or compensate the lack of tensile strength of the concrete, continued to be necessary. Apart from the decision to place all or part of the prestressing cables outside the concrete, we have to respect the whole geometry such that we could prepare and install reinforcing elements under cover, so as to ensure adequate protection.

Concomitant enhancement of the resistance of these concretes to chemical aggressions, although recognised, was not sufficient justification on its own for going much beyond 80MPa.

The results of this research work, although interesting in technical and economic terms, were thus strictly limited by the fragility of the material.

This work also made it possible to identify more clearly, and obtain a better understanding of the operating mechanisms for binder pastes, as also the combination of paste and aggregate, which appeared at the time as an economic necessity in terms of production cost reduction, and frequently as a technical necessity to reduce shrinkage.

This work demonstrated that shrinkage reduction was achieved through initial micro-cracking, basically unattractive for obvious reasons of reduced mechanical strength, and the creation of favourable conditions for the action of aggressive agents.

On completion of this work, or at the final stage, these aggregates appeared increasingly as defects in the solid mechanics sense, whereas reduced shrinkage could be obtained by reducing the quantity of mixing water.

We were a little disappointed, but we would have been wrong to neglect the considerable improvement in quality, economic savings and new openings for concretes in other areas of activity, a good example being the N'Kossa barge, provided by high-performance concretes.

Many engineers shared these thoughts on ductility, with less emphasis on the negative aspect of the utilisation of heavy aggregates, and the research work conducted at the same time on fibre concretes, demonstrated their relevance. Unfortunately this line of approach turned out to be relatively disappointing, in view of the limited technical advantages compared with preparation difficulties and cost. It became evident that a number of key questions had to be faced, in particular as to whether concrete was condemned to miss out on tensile strength, and remain a fragile material or not. Our answer on both these points was in the negative, accepting the elimination of aggregate particles with a dimension exceeding a fraction of 1mm.

This choice enabled us to imagine proper mechanical behavior with small-dimension fibres, with a length of one centimetre and a diameter of 150 to 200 microns, perfectly scaled for good operating conditions, and easily mixable with this new concrete. The composition of this material resulted, relatively simply, from our earlier observations made during the study of high-performance concretes.

The results fully meet our expectations, from the simplest processes at ambient temperature, with no compression during setting, to the most sophisticated forms of processing, with pressure applied during setting, and thermal treatment suited to the set goal. All intermediate preparation conditions provided intermediate results in terms of mechanical strength, and in certain cases, optimum results, such as porosity dimensions for example.

We can quote a few facts and figures for mixes not incorporating fine metal aggregates:

- Compressive strength rises between 80 and 100MPa, to values between 180 and 700MPa.
- Tensile-bending strength increases from a few MPa to between 40 and 140MPa.
- Ductility is enhanced, and ultimate elongation approaches a figure of 1cm/m.
- The elongation/stress curve is that of a ductile material.
- Fracture energy is between 30,000 and 50,000J/m², compared with a figure of 100,000J/m² for a semi-hard steel, and barely 100J/m² for H.P. and conventional concretes under optimum conditions.

We thus had a new material, more suitable for our requirements, and it was then a question of determining whether the obviously higher price of this material did not outweigh the advantages obtained.

In fact the reality of the situation was quite different. Simulations have demonstrated that the new material is in fact a powerful construction cost reduction tool. This is not really very surprising when we know, for example, that bottom of the range reactive powder concretes, prepared at ambient temperature, can be obtained with the conventional equipment of the profession, while those obtained using more intellectually sophisticated processes, although extremely simple to produce, can find applications in other industries far outside the civil engineering sector. Examples include shielding and a wide range of mechanical parts, such as sheet steel stamping tools. There are many other examples. A quick think on the subject will convince you.

In simple terms, we can now say that a cubic metre of high-performance concrete straight from the batching plant costs FF400, compared with a price of FF40,000 for a cubic metre of steel ex foundry.

Now we know that concrete technology with the required reinforcement does not always win out in competition with steel for civil engineering applications. However, with its mid-range price and performance, reactive powder concrete

will take a substantial share of the design and construction markets, when the resulting cultural revolution has taken place.

It should be possible to improve still further the results already obtained with existing cements and commercial aggregates. Reactive powder concrete has taught us to approach the question in terms of microstructure, using the most sophisticated observation tools, such as the electron microscope, NMR, etc. Microstructural analysis is already leading us towards improved quality and lower cost.

I am not sure whether this new material can be classified as an intelligent material, or whether it will enable us to build intelligent structures. However, I believe that we can regard it as an example of what we can achieve today, when we extend our thinking beyond the confines of mechanics into the areas of solid physics and chemistry, applying modern resources which enable us to observe the microstructures, and thus understand what we can do to improve them.

BPR

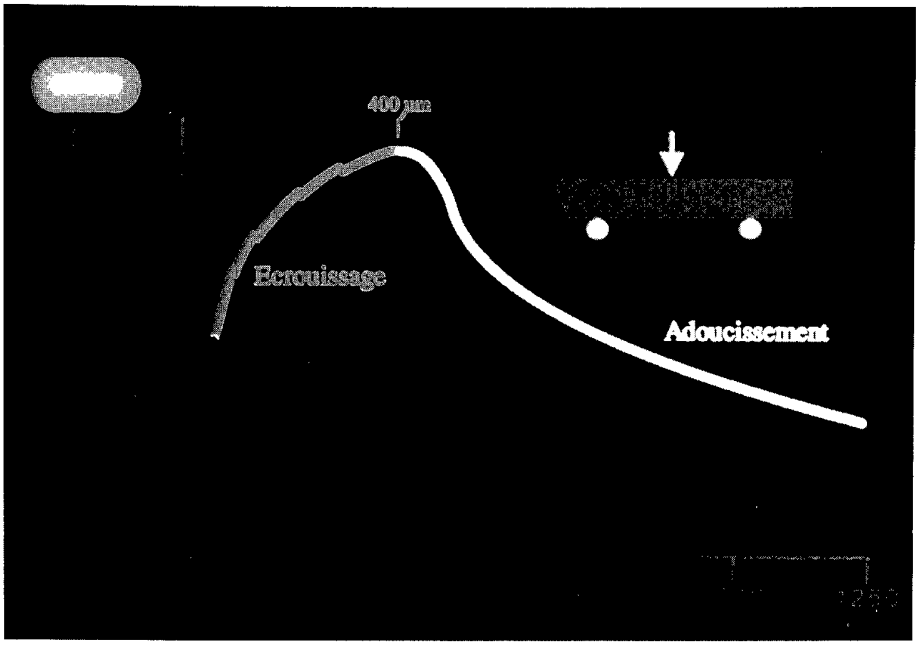
Résistances à la compression en MPa

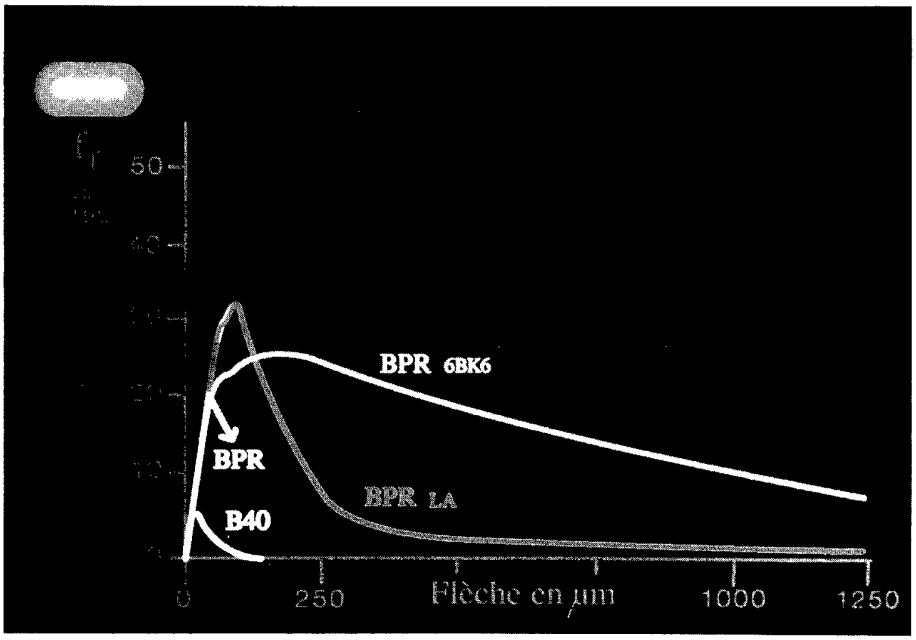
	Températures de cure		
	20 °C	90 °C	250 °C
Sans pression	200	280	550
Avec pression	250	400	810

BPR

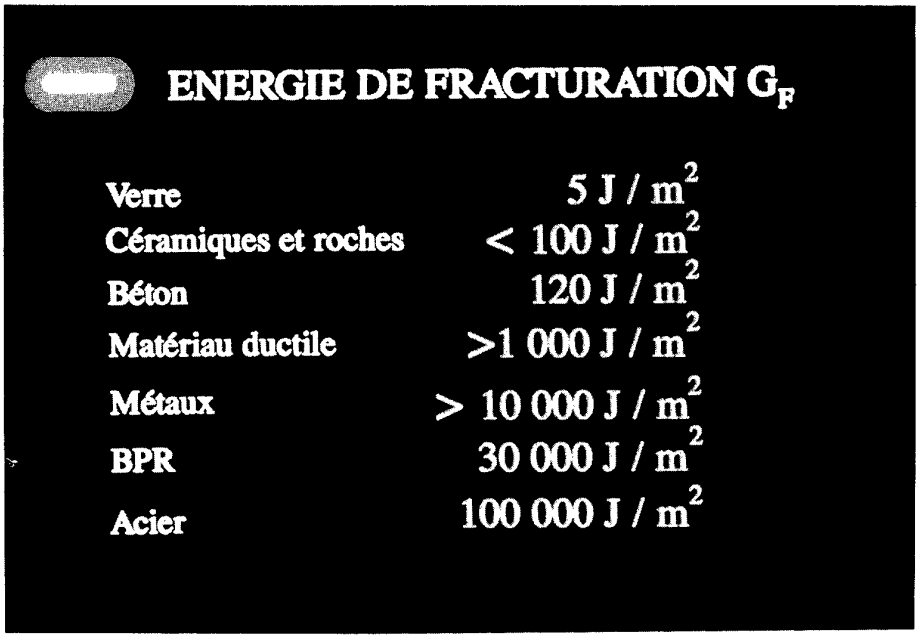
Résistances à la flexion en MPa

	Température de cure		
	20°C	90°C	250°C
Sans fibres	30	35	40
Avec fibres	70	80	141





Comparison of deflection stresses curves


ENERGIE DE FRACTURATION G_F
Verre 5 J / m²
Céramiques et roches < 100 J / m²
Béton 120 J / m²
Matériau ductile >1 000 J / m²
Métaux > 10 000 J / m²
BPR 30 000 J / m²
Acier 100 000 J / m²

Research and Commercialization Obstacles and Opportunities for Intelligent Material Systems

Rogers C.A.

Center for Intelligent Material Systems and Structures
Virginia Polytechnic Institute and State University
Blacksburg, VA 24061-0261

0-8194-2165-0/96/$6.00

Biological Materials

Invited Paper

DESIGN OF INTELLIGENT BIOMOLECULAR MATERIALS WITH ENGINEERED PROTEIN ASSEMBLIES

M.Aizawa, N.Damrongchai, T. Haruyama, and E.Kobatake

Department of Bioengineering, Tokyo Institute of Technology
Nagatsuta, Midori-ku, Yokohama 226

1. INTRODUCTION

Intelligent materials may simply feature structural integration of sensing, information processing and actuating capabilities, although they have been described in various manners from different viewpoints [1]. The conventional design concept of focused on the structure-function correlation to realize unit-function. Several material designs have been aimed at multi-functionality by hybridizing and compositing elemental materials. Built-in functions, however, have never been coordinated within the material. In contrast, the concept of intelligent materials is to install software capability for coordinating or to integrate such unit-functions as sensing and actuating.

The intelligent material could be programmed by material design to adapt in a controlled manner to various levels of exterior stiumlus. Several successful examples of intelligent biomaterials are described in this paper to demonstrate the effectiveness of design concept.

One of intelligent biomaterials can be modeled on receptor molecular assemblies embedded in cellular membranes which recognize selectively a specific molecule and transduce the molecular information into another type of information. The stimuli-responsive protein molecular assemblies have been organized in such a manner as intermolecular communication undergoes through the conformational change of the individual protein molecules.

Calmodulin (CaM) undergoes drastic conformational change when it binds to Ca^{2+} and amphiphilic peptides such as mastropran and endorphin, which results in the modulation of many important biochemical reactions. The N-terminal and C-terminal of rigid structureed globular domains are bridged with a long flexible peptide of α -helical structure. Each domain binds two Ca^{2+} ions to its hydrophobic sites. Phosphodiesterase (PDE) is one of enzymes that are modulated in the activity by binding the Ca^{2+}-bound state of CaM. The enzyme remains inactive in a Ca^{2+}-free state and is activated by Ca^{2+} in conjugation with CaM. Such a supramolecular assembly as CaM/PDE leads us to design an intrinsically inteligent molecular assembly which comprises of a sensing part, information processing part, and actuating part.

Our effort has been focused on synthesizing a molecular system of CaM and PDE which retains its

0-8194-2165-0/96/$6.00

information procesing function in native form . Such a molecular system has been accomplished by two different design principles. One is to covalently hybridizes CaM with PDE and to assemble the hybridized protein on the solid matrix . The other is to geneticaly engineer CaM to be endowed with self-assembling on the solid matrix. CaM was genetically fused with glutathione S-transferase (GST). The fused protein was assembled on glutathione which was self-assembled on the gold surface. These two molecular systems demonstrated environmental responses in such a manner as modulating PDE activity depending on calcium concentration in solution phase.

2. EXPERIMENTAL

The GST-CaM gene fusion vector, pGEX-CaM, was constructed as follows. The coding region of human CaM (19) was amplified by polymerase chain reaction using synthetic of oligonucleotides, 5'-AGGGAAGGATTTCAGCTGACCAACTGACTGAAG abd 5'-CAGGTCGACTCACTTTGCTGTGTC-ATCATTTG, The amplified fragment was digested with *Xmn*I and *Sal*I, subsequently, both terminal ends were blunted with T4DNA polymerase. The isolating gene fragment of CaM was ligated to the *Sma*I site of the pGEX3X with T4DNA ligase. In the resulting plasmid, the gene of CaM was fused to the gene of GST in frame.

The *E.coli* strain JM105 cells transformed with plasmid, pGEX-CaM, were cultured in 400 ml of LB medium containing amplicillin (50 mg mL^{-1}) at 37 °C with shaking. In the mid-exponential phase, isopropylthio-b-D-galactoside (IPTG) was added to the final concentration of 0.1 mM and cultured for another 3 h. The bacterial cells were harvested by centrifugation at 4000 g for 10 min at 4°C, and the cell pellet was washed twice with cold STE buffer (0.1 M NaCl. 10 mM Tris-HCl, 1 mM EDTA, pH 7.8) and resuspended in 10 ml of the same buffer containing 1 % of Triton-X100. The cell suspension was sonicated for 30 min, and centrifugated at 5000 g for 10 min to remove the cell debris. The fusion protein was purified through the use of Glutathione-Sepharose beads and incubated for 30 min at room tempareture. The beads were washed three times with PBS (150 mM NaCl, 16 mM Na_2HPO_4, 4 mM NaH_2PO_4, pH 7.3) and then mixed with elution buffer (50 mM Tris-HCl, pH8.0 containing 50 mM glutathione). The protein bound to the beads were released competitively from the beads with the elution buffer. The solution containing the fusion protein was obtained from the supernatant by centrifugation.

The fusion protein was immobilized on Glutathione-Sepharose beads which were used in purification process. Cell lysate containing the fusion protein was mixed with Glutathione-Sepharose, and incubated for 30 min. The beads were washed well with PBS to remove proteins which adsorbed nonspecifically on a matrix. The resulting beads were directly used as the fusion protein-immobilized solid-phase matrix.

3. RESULTS AND DISCUSSION

The constructing plasmid, pGEX-CaM, was possessing the fusion gene of GST and CaM under the control of the tac promoter. The resulting fusion protein was designed by forming a site-to-site biding, that is, the C-terminal site of GST fused to the N-terminal site of CaN. The fused gene encodes a single

polypeptide of GST and CaM. The fusion protein deduced from the DNA sequence has a molecular weight of ca. 43 kDa.

The cell extracts obtained from *E.coli* JM 105 harboring pGEX-CaM were analyzed by a 10 % SDS-PAGE. The protein was produced large amounts in soluble form from only the transformed cells induced with IPTG.

PDE is activated in the presence of Ca^{2+}-binding CaM, and catalyzes the hydrolysis of cAMP to AMP. CaM-deficient PDE will catalyze this reaction at low rate, and CaM activates PDE only in the presence of Ca^{2+}. Thus, the rate of reaction of PDE can be used to estimate the amount of CaM present in the reaction mixture.

PDE activity with the fusion protein was determined in the absence and presence of Ca^{2+}. The activity of PDE in the presence of Ca^{2+} is about 4-fold higher than the activity in the absence of Ca^{2+}. Moreover, the PDE activity with CaM (not fusing with GST) which separated from the fusion protein by factor Xa was almost the same as the activity by the fusion protein. These resluts indicate that CaM moiety in the fusion protein functioned as an activator of PDE without loosing its activity by fusing with GST.

In order to confirm the possibility for on-off switching of enzymatic activity by CaM with or without Ca^{2+}, the fusion protein was immobilized on a solid-phase matrix. The Gluthathione-Sepharose beads were used as matrix for immobilizing of the fusion protein through the use of GST moiety. Then the PDE activity which is modulated by immobilized CaM was investigated. Fifty micro liter of a solution of the glutathione beads which immobilized the fusion protien was used instead of CaM solution in assay mixture. After incubation for 10 min at 30 °C, cAMP was added to a final concentration of 87 mM. The change in absorbance for 10 min at 265 nm was measured and PDE activity was almost same as that activated by free CaM. Then, the beads were washed three times with 100 mM glycilglycine buffer (pH 7.5) containing 3 mM EGTA for chelating Ca^{2+}. After centrifugation, the beads were resuspended in 970 mL of the reaction buffer containing EGTA instead of $CaCl_2$, following a solution of cAMP was added. In this case, PDE activity was restricted at lower level. Then the beads were washed again with 100 mM glycilglycine buffer (pH 7.5) and suspended in a reaction buffer containing 2 mM $CaCl_2$. The PDE activity was recovered to the initial level. These experiments were repeated three times. Almost the same PDE activity could be obtained in each stage of the experiment. These results suggest that the fusion protein could be used repeatedly by immobilizing on a solid-phase matrix.

REFERENCES

1.T.Miwa, E.Kobatake, Y.Ikariyama, M.Aizawa, Bioconjugate Chem., 2, 270-274 (1991).

2 T.Miwa. N.Damrongchai, H.Shinohara, Y.Ikariyama, M.Aizawa, J.Biotechnol., 20, 141-150 (1991).

3.N.Damrongchai, E.Kobatake, T.Haruyama, Y.Ikariyama, M.Aizawa, Bioconjugate Chem., 6, 264-268 (1991).

Design of conductive nanospace interfaces for the smooth electrochemical communication between redox enzyme proteins and electrodes

Hiroaki Shinohara, Masahiko Sisido

Department of Bioengineering Science, Faculty of Engineering, Okayama University, Tsushima-Naka, Okayama 700, Japan

ABSTRACT

Nanoscale layers of conducting polymers were prepared around redox enzyme molecules on electrode surfaces and were applied to electric interfaces to perform the smooth electron transfer between the redox proteins and electrodes. The interface design might be useful to bind the functions of both biocatalysts and electronic materials and to develop intelligent devices.

1.INTRODUCTION

How to perform the smooth electrochemical communication between redox enzyme proteins and electrodes has been studied very actively to design the bioelectronics devices such as intelligent enzyme sensors and reactors. However, direct electron transfer between redox enzymes and electrodes is not performed so easily, because the redox site of the enzyme is usually embedded into the polypeptide shell which keeps the redox site away from electrode surface. In this study, two types of conductive nanospace interfaces were designed to perform smooth direct electron transfer between redox enzyme proteins and electrodes. At the first strategy, a conducting polymer as a nanospace electric wire was electrochemically synthesized around the enzyme molecules adsorbed on an electrode surface. At the second strategy, redox enzyme molecules were immobilized on an electrode surface with a water-soluble self-doped polymer as a conductive nanospace interface.

2.EXPERIMENTAL

D-fructose dehydrogenase (FDH) , which possesses a pyrrolo-quinoline quinone (PQQ) as a coenzyme was employed. FDH (EC 1.1.99.11) from *Gluconobacter industrius* was obtained from TOYOBO Co. and was used without further purification. Nanospace conductive interfaces between the enzyme molecules and electrode substrates were prepared by the following two methods.

Experiment 1. FDH molecules were adsorbed onto gold or highly oriented pyrolytic graphite (HOPG) electrodes by incubation method or electrochemically assisted adsorption method. Natural adsorption was carried out for 1 hour in 0.1M MES buffer solution (pH 5.7) containing FDH (1mg/mL). Electrochemically assisted adsorption was performed under the

0-8194-2165-0/96/$6.00

potential application on the electrode substrates at 0.5V vs.Ag/AgCl for 5 min. in the enzyme solution. After these adsorption processes, the electrode was next set into the 0.1M KCl solution containing 0.1M pyrrole monomer. About 10 nm thickness of polypyrrole layer was formed around the enzyme molecules adsorbed on the electrode by electro-oxidative polymerization of pyrrole at a potential of 0.7V vs.Ag/AgCl as reported previously[1]. The polypyrrole layer was grown until the enzyme molecules were completely covered by the control of polymerization charge. Enzymatic activity of the electrodes was measured by colorimetry. using reactions (1), (2) before and after polypyrrole formation. Interfacial electron

$$\text{D-Fructose} + 2\,K_3Fe(CN)_6 \xrightarrow{\text{FDH}} \text{5-Keto-D-fructose} + 2\,K_4Fe(CN)_6 \qquad (1)$$

$$2\,K_4Fe(CN)_6 + Fe_2(SO_4)_3 \longrightarrow 2\,KFe_{III}[Fe_{II}(CN)_6] + 3\,K_2SO_4 \qquad (2)$$

(Prussian blue, 660nm)

transfer between the immobilized enzyme and the gold electrode was characterized by the measurement of current change upon D-fructose addition at an oxidation potential with a three electrodes system.

Experiment 2. Poly-{3-(3-thenyl)propanesulphonate} was employed as a self-doped polymer (SDP). This polymer was produced by Showa Denko K.K.[2,3] and used without further purification. The chemical structure is shown in Fig.1. FDH (0.5mg/mL) and SDP (0.09mg/mL) were mixed in McIlvain buffer solution (pH4.5) and coated on the F-doped SnO_2 deposited glass (SnO_2) electrodes. When necessary, 50mM potassium ferricyanide was further added into the coating solution. After drying under the air, the electrodes were rinsed thoroughly with buffer solution. The electron transfer between FDH and SnO_2 electrode was characterized by the similar method described in experiment 1.

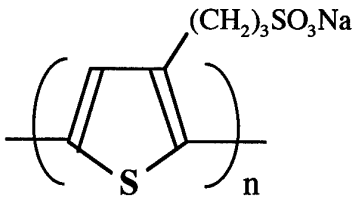


Fig.1 Structure of SDP Na salt.

3.RESULTS AND DISCUSSION

Electrochemical communication between fructose dehydrogenase and gold electrode through the polypyrrole interface.

The activities of enzyme-adsorbed on gold plates and HOPG plates were measured as shown in Table 1. The amounts of adsorbed enzyme molecules were estimated from the activities with the postulation that the enzyme activity was not affected by adsorption. It was shown that the enzyme amount adsorbed on HOPG surface was less than monolayer adsorption and that the enzyme amount adsorbed on gold was 10 times more than monolayer adsorption. From this result, it was suggested that hydrophilic gold surface is advantageous to immobilize much enzyme molecules as compared with hydrophobic HOPG surface. Then gold was chosen

as the electrode materials to proceed to next step. The effect of potential application to adsorb more enzyme molecules was next investigated with gold electrodes. It was demonstrated that potential application at around 0.5V vs.Ag/AgCl was effective to promote enzyme adsorption at about 4 times. Therefore polypyrrole nanospace interface layers were prepared on the gold electrodes on which FDH was adsorbed by the potential application at 0.5V.

Table 1 Adsorption characteristics of FDH on gold and HOPG substrates.

Substrate materials	Activity of adsorbed enzyme (U/cm^2)	Enzyme amount estimated from the activity (mol/cm^2)
Au	$3.1x10^{-2}$	$1.7x10^{-11}$
HOPG	$1.2x10^{-3}$	$6.5x10^{-13}$

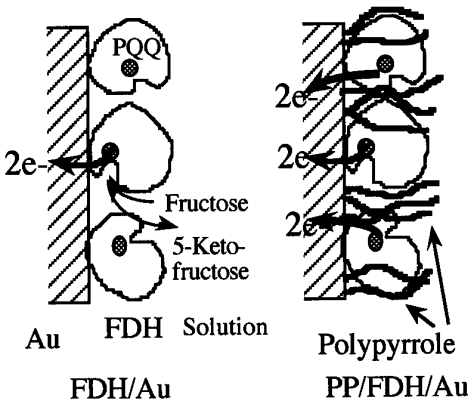


Fig.2 Schematic illustration of polypyrrole interface.

Figure 2 shows the imaginable location and the working concept of the polypyrrole interface as a nanospace electric wire. After the preparation of polypyrrole matrix, the enzymatic activity of the electrode decreased to about 60% as before the preparation. This activity decrease might be due to the diffusion interference by the polypyrrole matrix for the enzymatic reactants including the substrate. On the other hand, electron transfer between FDH molecules and the gold electrode was certainly improved as expected. Figure 3 shows the typical response curves with a FDH/Au electrode and a PP/FDH/Au electrode at the constant potential of 0.4V vs.Ag/ AgCl upon the addition of D-fructose and other saccharides.

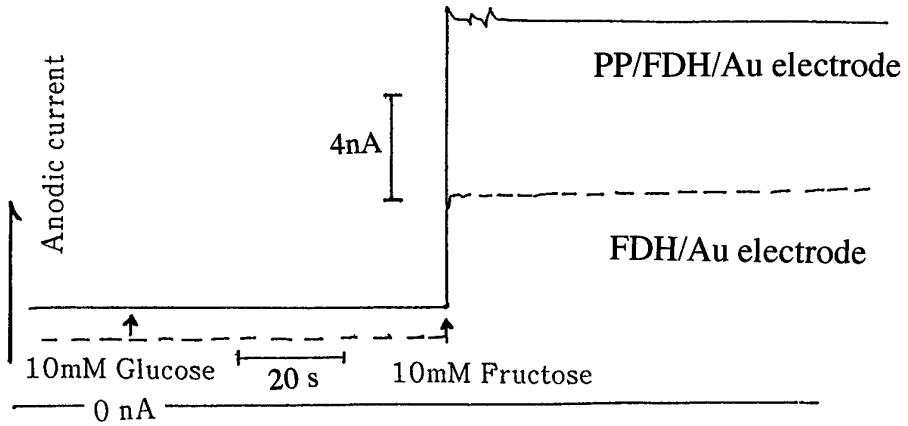


Fig.3 Fructose response with the FDH/Au and the PP/FDH/Au electrodes.

The PP/FDH/Au electrode showed about 2 times greater response for the same concentration of fructose as compared with the FDH/Pt electrode. Figure 4 shows the fructose concentration dependencies of current response with the PP/FDH/Au electrode and the FDH/Au electrode.

These results strongly support that the nanospace layer of electrochemically synthesized polypyrrole around redox enzyme molecules is powerful to promote the facile electron transfer between redox enzymes and electrodes.

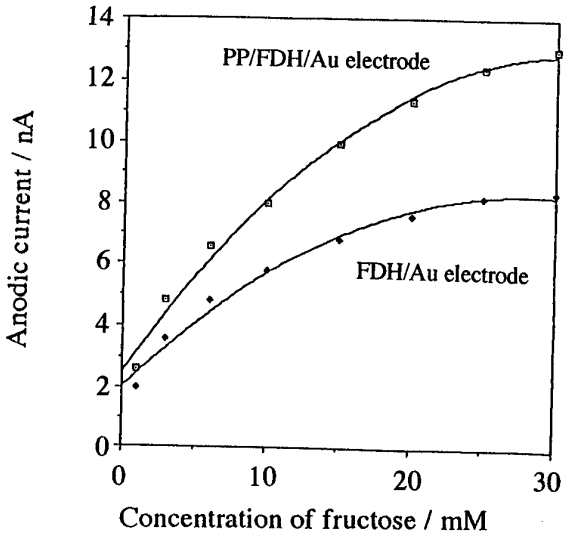


Fig.4 Fructose concentration dependencies of current response with each electrode.

Smooth electron transfer between FDH molecules and SnO_2 electrode through a self-doped polymer interface[4].

The absorption spectra of poly-{3-(3-thenyl)propanesulphonate} were observed in various buffer solutions (pH 3 - 9). The absorption peak was observed at around 430nm and was attributed to the $\pi-\pi^*$ transition of the polymer. As pH decreased, the absorption at 430nm decreased and the absorption at around 800nm increased. But it was demonstrated that the conductivity of poly-{3-(3-thenyl)propanesulphonate} might be not enough to be used as an electric wire even at pH 3. Therefore chemical doping on the polymer was examined by the addition of ferricyanide . The absorption spectra of the SDP in the absence and presence of potassium ferricyanide are shown in Fig.5. The addition of 50mM ferricyanide caused the significant decrease of $\pi-\pi^*$ transition absorption and the clear increase of absorption around 800nm. From these spectra, it was suggested that the SDP oxidized with ferricyanide may be available as an conductive molecular wire.

FDH-coated SnO_2, (FDH + SDP)-coated SnO_2, (FDH + $K_3Fe(CN)_6$)-coated SnO_2 and (FDH + SDP + $K_3Fe(CN)_6$) -coated SnO_2 electrodes were prepared and the fructose responses on these electrodes were measured in McIlvain buffer solution (pH 4.5) at a constant potential of 0.5V vs.Ag/AgCl with a potentiostat. Typical responses were shown in Fig.6. Significant increase of the catalytic oxidation current upon the fructose injection was observed on the (FDH + SDP + $K_3Fe(CN)_6$) -coated SnO_2 electrode, whereas the increase of response current with (FDH + SDP)- coated electrode was small as compared with the response current with the FDH- coated electrode. We consider from these data that SDP-ferricyanide complex works as a conductive interface between FDH molecules and SnO_2 electrode. By the way, co-adsorption of FDH and ferricyanide also induced the noticeable increase of fructose response current. It is expected that the surface of SnO_2 electrode and FDH molecules are positively charged in this pH

condition. So we considered that negatively charged SDP-ferricyanide complex and ferricyanide itself might act as not only electron mediator but also adhesion interface between enzyme molecules and electrode substrate. On the other hand, the fructose response of the (FDH + SDP + $K_3Fe(CN)_6$) -coated gold electrode was very small. This result further indicated that surface charge of the electrode materials is important to immobilize the enzyme and SDP complex. It was suggested that electrostatic interaction should be considered well for the design of nanospace interface with SDP.

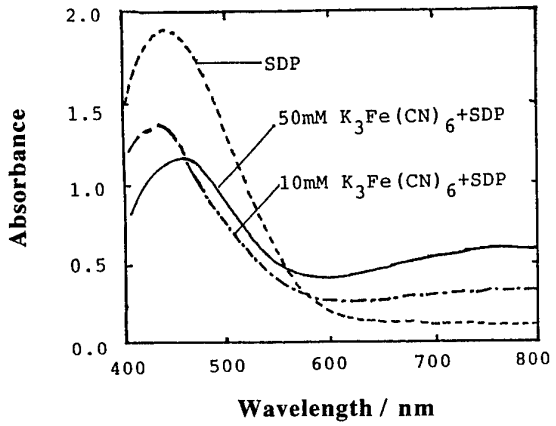


Fig.5 Absorption spectra of SDP in the absence and presence of ferricyanide.

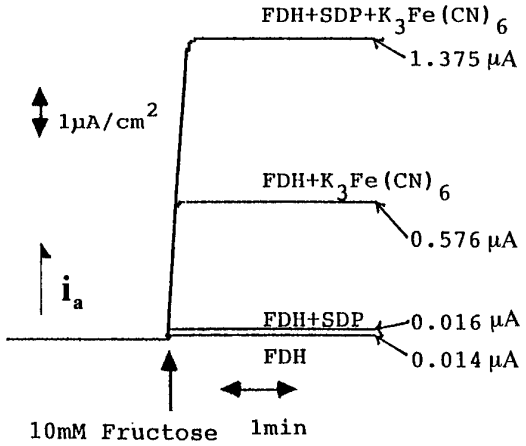


Fig.6 Response currents for fructose on (FDH+SDP+$K_3Fe(CN)_6$)-coated SnO_2 electrode etc.

4.ACKNOWLEDGMENTS

We thank Showa Denko K.K for the kind supply of SDP solution. This study has been partially supported by Special Coordination Funds for Promoting Science and Technology entitled "Research on New Materials Development by Nanospace Lab.".

5.REFERENCES

1.G.F.Khan, E.Kobatake, H.Shinohara, Y.Ikariyama and M.Aizawa, "Molecular interface for an activity controlled enzyme electrode and its application for the determination of fructose," Anal.Chem., **64**, 1254-1258, 1992.

2.Y.Ikenoue, Y.Saida, M.Kira, H.Tomozawa, H.Yashima and M.Kobayashi, "A facile preparation of a self-doped conducting polymer," J.Chem.Soc., Chem.Commun., **1990**, 1694-1695, 1995.

3.Y.Ikenoue, H.Tomozawa, Y.Saida, M.Kira and H.Yashima, "Evaluation of electrochromic fast-switching behavior of self-doped conducting polymer," Synthetic Metals, **40**, 333-340, 1991.

4.H.Shinohara, S.Oota and M.Sisido, "Polymer interface for the promotion of facile electron transfer between redox enzymes and electrodes," Polymer Preprints, Japan, **44** (10), 2208-2209, 1995.

Paper presented at the Third ICIM/ECSSM '96, Lyon '96

Intelligent molecules: examples from biological charge transport

Leonid N. Christophorov

Bogoliubov Institute for Theoretical Physics
of the Ukrainian National Academy of Sciences, SRC 'Vidhuk',
Metrologichna str. 14b, Kiev 252143 Ukraine;
E-mail: lchrist@gluk.apc.org

Abstract

A nonequilibrium version of the charge-conformational interactions is presented in order to substantiate the synergetic modes of the functioning of biological charge transport systems as molecular switches, processing fluxes of charges.

1 INTRODUCTION

The concept of intelligent materials implies substances or materials which are able to appropriately respond to changes of external factors by changing their structure and functions. The necessity of continuing miniaturization of base elements integrating several functions have brought the problem of designing them to a (macro)molecular level.

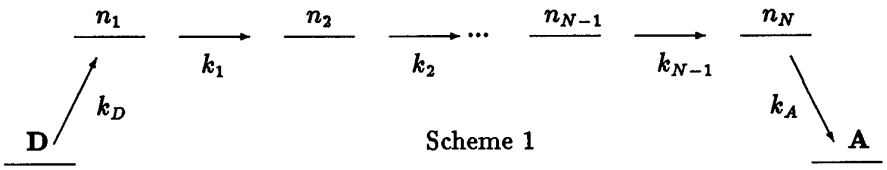
It is obvious that most effectively this problem has been solved by the very nature. However, there is a rather long distance between this commonplace and applications of natural biomolecular systems and principles of their functioning to creating novel molecular devices and systems of information processing. This concerns even such a promising and well-studied biomolecular object as bacteriorhodopsin. Seemingly, further progress is retarted by not only the complexity of biomolecules and corresponding nanotechnology, or irreproducibility of *in vivo* conditions, etc, but also the incompleteness of theoretical concepts of the biomolecules' functioning. In this report we outline a new approach to the description of the well-known biomolecular

0-8194-2165-0/96/$6.00

charge transport systems which seems fruitful for the concept of intelligent materials and present some evidences in its favor.

2 MOVABLE STRUCTURE OF THE TRANSPORT CHAIN AS A SOURCE OF ITS SELF-ORGANIZATION UNDER FLUX CONDITIONS

The charge transfer through macromolecular structures is frequently treated as a donor-acceptor process via some mediators. The latter can be rather extended on the molecular scale (molecular chains, biopolymers, hydrogen-bonded networks, etc).



Scheme 1

The problem may be sketched with a set of states for the transferred charged particle at different links (molecular groups) of the transport chain, with given interactions (exchange integrals, relaxation or diffusion constants, etc) between them. The total transfer pattern is then determined by solving the corresponding equations for the density matrix (see e.g. Ref.1). In case the classical description can be applied, instead of Scheme 1 one can use a picture of the system's potential profile, with its minima at the binding sites and barriers between them. Whatever description we choose, the problem involves the calculation of the transition probabilities between links and the total effective rate of the donor-acceptor transfer is determined by the parameters of the transport system and environment (often modelled with a set of vibrations). As a rule, these parameters, though it were tunnel or thermally activated transitions, are assumed to be fixed, thereby assuming unchangeable (or fast-recovering just after the pass of the transferred charge) structure.

It is obvious, however, that, passing in close proximity to polar or charged groups of the macromolecule-mediator and generating the local electrical fields up to 10^{7-9} V/cm, the transferred particles can significantly affect the very transport system. Of movements of its nuclei, there are fast-relaxing modes, like phonons, which 'forget' the charge passage right away; but there

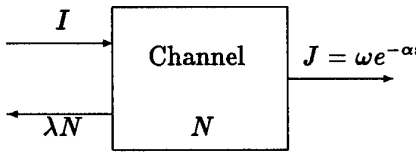
also are the modes with characteristic times from 10^{-4}s to seconds and more, reflecting the system's conformational lability. Due to the latter, the transport system meets the *next* charged particle in a changed, even slightly, state (e.g. with changed potential profiles), and the indirect interaction emerges between the transported charges even if there occurs no more than one of them in the system at any moment. This is a typical nonlinear feedback situation, having something in common with synergetic effects in the laser. The nonlinearity is rather strong, since the changes of the potential profiles, such as barrier heights and widths, etc, enter the corresponding elementary rate constants (based on Gamov's and Marcus' formulae) as exponentials. Allowing for the influence of the transferred charge upon the next ones spells an essentially *nonequilibrium* description (flux conditions). Within such a framework, the 'slow' transport system integrates the action of the more fast (charges flux) one, and their self-consistency by means of the charge-conformational interaction leads to formation of dynamical bound states of the flux and the macromolecule-mediator. In particular, depending on the incident flux intensity (pumping), the system can go over in a threshold way to bistable functional regimes, so on. Such dynamical self-organization within one macromolecule or even its fragment may turn out to be very important both for molecular electronics, intelligent materials, etc, and the functioning of biological transport chains or proteins-enzymes.

It is in the first place bioobjects in which we can expect to observe the effects of functional structural rearrangements of the kind. Biomolecules posess a high conformational lability and many slow-relaxing degrees of freedom (spatio-temporal hierarchy), providing a profound nonlinear feedback of the mentioned type; also, nonequilibrium flux conditions are inherent in practically all biosystems. These features sound trivial; nevertheless, consistent considering them as a natural base of molecular synergetics phenomena has started rather recently[2, 3, 4]. The creative role of the flux in generating new states in the functioning of a molecular object was often underrated, and self-organization was usually treated as free-energy-driven self-assembly.

3 MODELS AND EXPERIMENTAL EVIDENCES

Typical biological charge transport systems, such as transmembrane ionic channels or reaction centres (RC) of photosynthetizing systems, are specialized protein complexes embedded in the membrane and having intermediate binding sites for transferred ions or electrons. To illustrate our concept, it

is not necessary to consider the total trasport chain like shown in Scheme 1, since, even experimentally, one can often study its separate fragment only (as, for example, in studying the primary photosynthetic reactions). Similarly, being rather complex formations, ionic channels are frequently modelled by a fixed potential profile with one or several binding sites. Along these lines, it is reasonable to assume that, for example, the height of one of the potential barriers aruond the binding site minimum depends on the conformational coordinate x related to some polar group of the channel-forming protein. The position of this group, in its turn, is affected by the presence of the ion. Then even within an oversimplified scheme



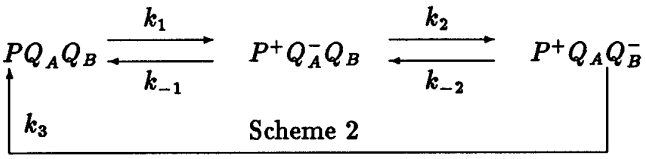
$$J = \omega e^{-\alpha x} N \qquad \dot{N} = I - (\lambda + \omega e^{-\alpha x})N \qquad (1)$$

$$\dot{x} = -kx + \chi N$$

where the conformational motion is represented by an overdamped oscillator affected by the *mean* ionic population N of the channel, and the barrier mobility is introduced by the exponential dependence on x of the ion passage constant (I is the 'pumping' depending on the difference of the outer and inner ionic concentrations), we can easily see that the stationary solutions of Eqs.(1) have a bistability domain within a certain interval of I. Consequently, the quantity J of the passing flux is strongly different in those two nonequilibrium states. This can be related to the well-known open and closed channels states (discrete levels of conductivity). As shown in Refs. 2,3,5,6, where such a sketch has been developed in more complicated and specific models (several binding sites, ensembles of channels, allowing for noises, etc), it is a scheme within which many peculiarities of the potential-dependent kinetics of the channel (dependence on the ion type or ionic concentrations, etc) can be explained. For a collection of experimental data indicating appearance and disappearance of the channel functional states in a threshold way, starting from certain ionic current values, see also these Refs.

Of course, the balance equations like (1) are phenomenological, and the validity of considering the ion action in terms of the *mean* valies (populations) is far from obvious. Nevertheless, the exact stochastic theory[7] we have developed for studying the electron transport in the RC leads to similar results. The primary photochemical reactions in the bacterial RC

performing the charge separation act under the actinic illumination are usually sketched as



Scheme 2

where P is the bacteriochlorophyll dimer (electron donor), Q_A and Q_B are the primary and secondary acceptors (ubiquinones). The electron tramsition kinetics is studied quite thoroughly. Under standard conditions, the rate constant k_1 induced by the actinic light (pumping) is the greatest, $\sim 10^{10}s^{-1}$; $k_{-1} \sim 10$, $k_2 \sim 10^4 s^{-1}$, $k_{-2} \ll k_2$, and k_3 less than $1s^{-1}$. These values ensure the efficient vectorial electron transport. However, it is well-established that affecting the conformational state of the RC-forming protein by various factors can essentially change the RC kinetics, indicating the crucial role of the electron-conformational interactions. We are especially interested in changing the kinetics behavior by varying the duration and intensity of actinic illumination (k_1). At one time, the notion of the light ('contact') and dark ('non-contact') RC conformations was introduced; the latter was notable for the absence of the secondary electron transport ($k_2 \simeq 0$). We can try to seek for the emergence of discrete functional RC states within a minimal chain fragment, e.g. the stage $PQ_A \underset{k_{-1}}{\overset{k_1}{\rightleftharpoons}} P^+Q_A^-$ (such a restriction of the chain is easily and often performed in experiment), assumind k_1 as pumping intensity and $k_{-1}(x)$ as conformation-dependent recombination constant, sensitive to the presence of the electron near the movable group (e.g. in the locus of the primary acceptor Q_A). Then in the stochastic equation

$$\dot{X}_t = h(X_t) + g(X_t)I_t^{(x)} \qquad (2)$$

the dichotomous noise $I_t^{(x)}$ which symbolizes the force affecting the conformation in the presence only of the electron at Q_A depends itself on the conformational state via $k_{-1}(x)$ entering the noise master equation. The stochastic problem with this modified noise can be solved exactly; in particular, even in the simplest case of the overdamped oscillator ($h = -\mu x$, $g(x) = 1$) and the standard dependence $k_{-1} = ae^{-cx}$ (which can be related to the change of the distance of the electron tunneling between P and Q_A due to the replacement of the movable group) there exist the bistability windows under varying the light intensity (k_1).

By the way, the adiabatic approximation similar to that exploited in (1) and related to substitution I_t for the *mean* population N_{Q_A} in (2) has turned out to be valid when $\mu \gg k_1$, that is under slow conformational relaxation. This make it possible to describe the electron-conformational self-organization effects within the total Scheme 2 by means of simple balance equations. With the available from literature kinetic data on RCs adapted to light and darkness, theoretical estimations show that the electron-conformational coupling at the stage PQ_A is not strong enough to give rise to the kinetics bistability, whereas the latter can be expected for the electron transfer from Q_A to Q_B owing to more conformationally sensitive rate constant $k_2 \sim \exp(-x^2)$ (here x is the dimensionless reorganization energy). In this connection, measurements of the optical absorption at characteristic wavelengths under different prehistory of photoexcitation (increasing excitation intensity from zero to 10^{12-13} quanta/cm^{2}s and then decreasing back to zero) were conducted on bacterial RCs. At each excitation level quasi-equilibrium conditions were held. The hysteresis of the absorption coefficient was revealed with the first bifurcation at 10^{10-11}quanta/cm^{2}s. In another type of experiments the pronounced hysteresis of the kinetics of the photodonor recovery after saturating optical pulses was revealed under varying the pulses frequency[8, 9].

4 CONCLUDING REMARKS

We may conclude that discrete functional states of biological charge transport systems (such as different conductivity levels of the ionic channel or contact and non-contact states of the photosynthetic RC) can be described by not postulating additional conformations as it was being done previously for both these objects[10, 11, 12] but generating them in a threshold fashion due to charge-conformational self-organization under flux conditions, i.e. by flux-induced rearrangement of the transport system. Biological significance of just this mode of the RC functioning should be discussed separately. As regards the outlined concept of a molecular object which adjust its structure to process passing fluxes, it seems to be very important in the realm of intelligent materials or even intelligent molecules. Perhaps, native ionic channels or RCs are not the best candidates for molecular computing devices, etc. Nevertheless, the concept needs no biological specificity of macromolecules except their pronounced conformational lability. The latter provides very convenient and natural conditions for manifesting nonlinear

and synergetic effects. With this, we are in hopes that such dynamical charge-conformational self-organization in macromolecular objects can be successfully exploited on systems of artificial channels and on many known photochemical complexes not yet tested to changing actinic light intensity and other nonequilibrium parameters.

REFERENCES

[1] L.N.Christophorov, V.N.Kharkyanen, "Theory of interimpurity transitions in condensed medium", *phys.stat.sol.(b)*, Vol.116, pp. 415-425, 1983.

[2] V.A.Chinarov, Yu.B.Gaididei, V.N.Kharkyanen, S.P.Sitko, "Ion pores in biological membranes as self-organized bistable systems", *Phys. Rev. A*, Vol.46, pp. 5232-5241, 1992.

[3] L.N.Christophorov, V.N.Kharkyanen, S.P.Sitko, "On the concept of nonequilibrium conformon", *J. Biol. Phys.*, Vol. 18, pp. 191-202, 1992

[4] L.N. Christophorov, "Dynamical self-organization in biomolecular systems of charge transport", *BioSystems*, Vol. 35, pp. 171-174, 1995.

[5] Yu.B. Gaididei, "Ionic-conformational interactions in transmembrane ionic channels", *J. Biol. Phys.*, Vol. 19, pp. 19-38, 1993

[6] V.N. Kharkyanen, A.S.Panchouk, G.E. Weinreb, "Self-organization effects induced by ion-conformational interactions in biomembrane channels", *J. Biol. Phys.*, Vol.19, pp.259-272, 1994.

[7] L.N.Christophorov, "Conformation-dependent charge transport: a new stochastic approach", *Phys. Lett. A*, Vol. 205, pp. 14-17, 1995

[8] A.O.Gushcha *et al.*, "New physical phenomenon of dynamical self-organization in molecular electron transfer systems", *Phys. Lett.A*, Vol. 191, pp.393-397, 1994.

[9] A.O.Gushcha *et al*, "Experimental evidence of dynamic self-organization in the electron transfer system (example of reaction centres of purple bacteria)", *J. Biol. Phys.*, Vol. 19, pp. 285-293, 1994.

[10] P.Läuger, "Ionic channels with conformational substrates", *Biophys. J.*, Vol. 47, pp. 585-595, 1985.

[11] V.N.Kharkyanen, L.N.Christophorov, P.P.Knox, A.A.Kononenko, "Low-temperature fixation of states as a method of investigating into electron-conformational transitions in photosynthetic reaction centres", *Molek. Biologiya (Moscow)*, Vol. 20, pp. 994-1001, 1986.

[12] E.G.Petrov, V.N.Kharkaynen, P.P.Knox, A.A.Kononenko, A.B.Rubin, "A kinetic model of electronic and conformational transitions in photosynthetic reaction centres", *Transact. Acad. Sci. USSR (Izvestiya)*, Vol. 1, pp. 28-43, 1983.

What is matter of control for activity of enzyme immobilized into thermoreversible hydrogel.

Larisa V. Sigolaeva*, Nicolay L. Eremeev, and Novella F. Kazanskaya

Department of Chemical Enzymology, Faculty of Chemistry, Moscow State University
Moscow 119899, Russia

ABSTRACT

The effect of phase transition of a thermosensitive matrix on temperature dependencies of observed activity, equilibrium, and kinetic constants of the enzymatic reaction was studied using α-chymotrypsin immobilized into thremosensitive poly-N-isopropylacrylamide gel as a model system. The behaviour of the system is determined by the properties of the enzyme at temperatures less then critical temperature corresponding to phase transition of the polymeric gel but by the properties of the thermosensitive polymeric matrix at temperatures higher than that critical temperature. The phase transition of the thermosensitive gel was shown to affect weakly temperature dependencies of equilibrium parameters of enzymatic reactions. All reversible effects of the reduction of the enzymatic activity at high temperature are exclusively due to the changes in temperature behaviour of kinetic parameters of the enzymatic reaction.

1. INTRODUCTION

The problem of the regulation of the enzymatic activity occupies a central place in biochemistry. Thermoregulation is known to be an effective way of the control of the enzymatic activity. For example, the activity of some phospholipid membrane enzymes drastically changes when the thermoinduced phase transition gel-liquid crystal of such membranes takes place[1]. Obviously, complex mechanism of the regulation of the enzymatic activity in biosystems can be understood by the investigation of proper artificial imitation. Enzymes immobilized into thermoreversible polymeric hydrogels are quite suitable models of thermoregulated enzymatic systems.

Thermoreversible (or thermosensitive) polymeric hydrogels undergo a phase transition from swollen to collapsed state when temperature increases above the certain critical value. This transition is accompanied by hydrophobization and significant shrinking of polymeric matrix[2]. The activity of the enzymes immobilized in such hydrogels strongly decreases if polymeric matrix collapses[3,4]. Arrhenius plot for the immobilized enzymes shows the break point and region with the negative activation energy[4,5]. It is remarkable that this phenomenon is quite reversible. All samples of enzymes immobilized into thermoreversible hydrogels are able to operate in cyclic regime with the reproduction of the level of the initial enzymatic activity at least for 5 cycles[4,5].

Thus, thermoreversible polymeric hydrogels containing immobilized enzymes can be considered as intelligent materials because the temperature behaviour of the polymeric matrix regulates the temperature behaviour of the enzymatic activity.

What is the matter of the lost in the enzymatic activity induced by the hydrogel phase transition? This important question arises when such enzymatic systems are considered. To make clear this problem, we carried out a systematical study of the anomalous temperature behaviour of the activity of α-chymotrypsin immobilized into the thermosensitive poly-NIPAA gel, which is characterised by the critical temperature of dehydratation equal to 32^0C.

2. EXPERIMENTAL SECTION

2.1 Materials

α-Chymotrypsin of B grade was used as received from Biokhimreactiv (Latvia). N,N'-Methylenebicacrylamide (MBA), N,N,N',N'- tetramethylethylenediamine (TEMED), and ammonium persulfate were obtained from Reanal (Hungary). N-Acetyl-L-tyrosine ethyl ester (ATEE) and phenylmethylsulfonyl fluoride were received from BDH (England) and from Sigma (USA), respectively. All other reagents were obtained from Reakhim (Russia) and used without additional purification.

The syntheses of acryloyl chloride and N-isopropylacrylamide (NIPAA) were carried out according to[6,7], respectively.

0-8194-2165-0/96/$6.00

2.2 Synthesis of preparations of immobilized enzyme

200 mg of monomer (NIPAA), crosslinking agent (MBA), and initiators (0.02 ml of aqueous 0.78 M ammonium persulfate solution and 0.01 ml of TEMED) were added to 1 ml solution of α-chymotrypsin modified with acrylic acid residues at 10^0C and continuous stirring. The concentration of the acryloylated enzyme in the initial mixtures varied from $1.2*10^{-5}$ M to $4.8*10^{-5}$ M. The molar ratio NIPAA/MBA changed from 75/1 to 7500/1. The obtained by such a way block copolymers were used both for activity and for swelling measurements. For activity measurements, samples of block copolymers were suspended in a homohenizer to get the particle size equal to 20-100 microns. For swelling experiments, samples of NIPAA - α-chymotrypsin preparations were cut into 10mm*5mm*2mm pieces. The suspension or gel particles was washed by the salt solution with ionic strength varied from 0.2 M NaCl+0.02 M $CaCl_2$ to 0.002 M NaCl+0.0002 M $CaCl_2$ until the absence of activity in washing waters.

The modification of α-chymotrypsin by acryloylcloride was carried out according to[8].

2.3 Enzyme activity assay

Activities of native and immobilized α-chymotrypsin with respect to ATEE were determined by measurements of initial rates of the substrate hydrolysis with a RTS822 pH-State (Radiometer, Denmark) equipped with a thermostatic vessel. The substrate concentration, temperature, pH, and ionic strength varied from $5*10^{-3}$ M to 10^{-2} M, from 20 to 45^0C, from 6.5 to 9.5, from 0.2 M NaCl+0.02 M $CaCl_2$ to 0.002 M NaCl+0.0002 M $CaCl_2$, respectively.

2.4 Determination of constants

Parameters of Michaelis-Menten equation for α-chymotrypsin were defined using dependencies of initial rates of the ATEE hydrolysis on the substrate concentration in double reciprocal Lineweaver-Burk coordinates. Equilibrium ionization constants K_a and K_b of an enzyme-substrate complex were evaluated from dependencies of $\log(V_{max})$ on pH.

2.5 Inhibition of immobilized enzyme

500-fold excess of phenylmethylsulfonyl fluoride (inhibitor) as compared with a total amount of immobilized α-chymotrypsin was added to the hydrogel suspension at 45^0C and continuous stirring. The addition of the inhibitor was carried out by a successive introduction of 0.01 ml portions of the solution of phenylmethylsulfonyl fluoride in dimethyl sulfoxyde with an interval 30 sec. Complete inhibition was followed by a separation of the hydrogel suspension by decanting. The decanted precipitate was washed thoroughly with the salt solution (0.2 M NaCl+0.02 M $CaCl_2$) preheated to 45^0C. The residual activity of immobilized α-chymotrypsin was assayed at room temperature.

2.6 Determination of hydrogel swelling

Pieces of the hydrogel were blotted gently by filter paper, weighed, immersed in the salt solution (0.2 M NaCl+0.02 M $CaCl_2$) reheated to the corresponding temperature, and incubated during 3 hours. Then they were taken out, blotted by filter paper, and weighed again. The relative weight of gel β at corresponding temperature was calculated according to the formula:

$$\beta = \frac{W_{20^\circ C} - W_t}{W_{20^\circ C}},$$

were $W_{20^\circ C}$ and W_t are the hydrogel weights at 20^0C and temperature t, respectively.

3. RESULTS AND DISCUSSION

Does the region with apparent negative activation energy observed in Arrhenius plots of immobilized into thermoreversible hydrogels enzyme really connect with the perturbation of the polymeric matrix during thermoinduced phase transition? This is the first question that arises when the temperature behaviour of such enzymatic systems is investigated. To make clear this problem, we studied how the factors affecting hydrogel swelling influence on the activity of immobilized enzyme. First, we studied the effects of the concentration of crosslinks in the polymeric gel and ionic strength of the solution on the activity of immobilized α-chymotrypsin

because they are well known to be the factors[9,10] that strongly determine the swelling properties of poly-NIPAA gel.

The enhancement in the content of crosslinks increases temperature corresponding to the phase transition of the polymeric gel and makes the gel dehydratation smoother. As can be seen in Fig.1, the same picture is observed for the activity of the immobilized α-chymotrypsin. Indeed, the break point shifts to higher temperatures and the thermoinduced lost of the enzymatic activity becomes to be not so sharp as the concentration of crosslinks increases.

With increasing ionic strength of the solution, the lost of the activity of the immobilized enzyme also becomes less pronounced but temperature corresponding to the break point in Arrhenius plot decreases (Fig.2).

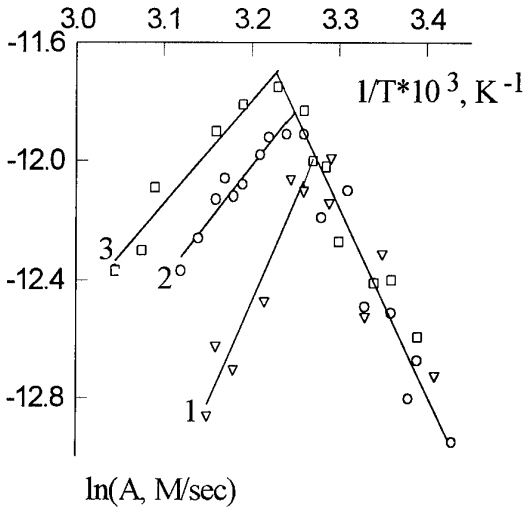


Fig.1. Arrhenius plots for preparations of immobilized α-chymotrypsin for different molar ratios crosslink/monomer unit of poly-NIPAA gel: 1/7500 (1), 1/750 (2), and 1/75 (3) (conditions: 0.2 M NaCl + 0.02 M $CaCl_2$, pH 8.0).

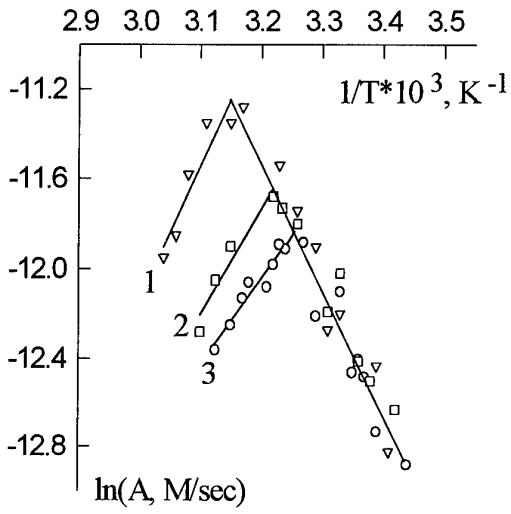


Fig.2. Arrhenius plots for preparations of immobilized α-chymotrypsin for different ionic strengths of solutions: 0.002 M NaCl + 0.0002 M $CaCl_2$ (1), 0.02 M NaCl + 0.002 M $CaCl_2$ (2), 0.2 M NaCl + 0.02 M $CaCl_2$ (3) (conditions: molar ratio crosslink/monomer unit of poly-NIPAA gel 1/750, pH 8.0).

It is remarkable that all presented in Fig.1 and 2 dependencies obtained for various conditions coincide within an experimental error at the temperatures below break points. This fact indicates that all differences in the behaviour of immobilized α-chymotrypsin are displayed only under conditions when poly-NIPAA gel collapses.

The interconnection between temperature dependent properties of the hydrogel and catalytic properties of the immobilized enzyme is also confirmed by the data given in Fig.3 that shows the temperature dependencies of poly-NIPAA gel swelling and the residual activity of α-chymotrypsin. As is evident, there is a good correlation between parameters that characterize the properties of the polymeric matrix and the immobilized enzyme.

Thus, one can conclude that the factors that affect hydrogel swelling influence on the activity of enzymes immobilized into the thermoreversible polymeric network in a similar manner. The behaviour of the system is determined by the properties of the enzyme at temperatures less then critical temperature corresponding to phase transition of the polymeric gel but by the properties of the thermosensitive polymeric matrix at temperatures higher than that critical temperature.

The possible ways to explain such an influence may be (i) internal diffusion limitations emerged during dehydration of the polymeric gel, (ii) conformational changes of protein globule that result from

shrinking of the polymeric matrix, and (iii) sterical limitations for the enzymatic catalysis. Let us consider these explanations on the basis of the experimental results obtained in our research.

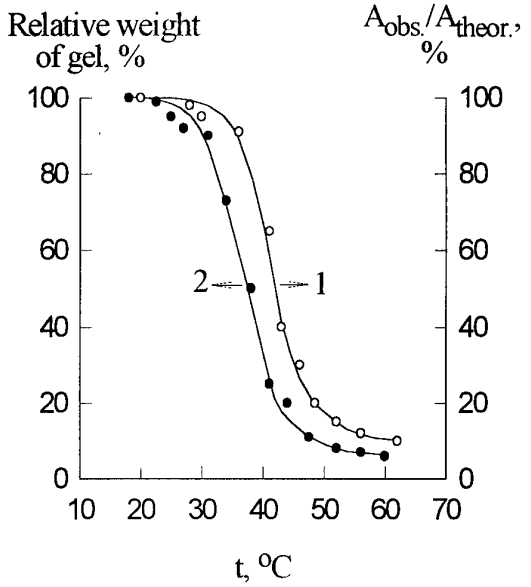


Fig.3. Fraction of observed activity of immobilized α-chymotrypsin (1) and swelling degree of poly-NIPAA gel (2) versus temperature (conditions: 0.2 M NaCl + 0.02 M $CaCl_2$, pH 8.0). $A_{obs.}$ is observable enzymatic activity, $A_{theor.}$ is theoretical enzymatic activity obtained by extrapolation of low temperature part of Arrhenius plot to high temperature region.

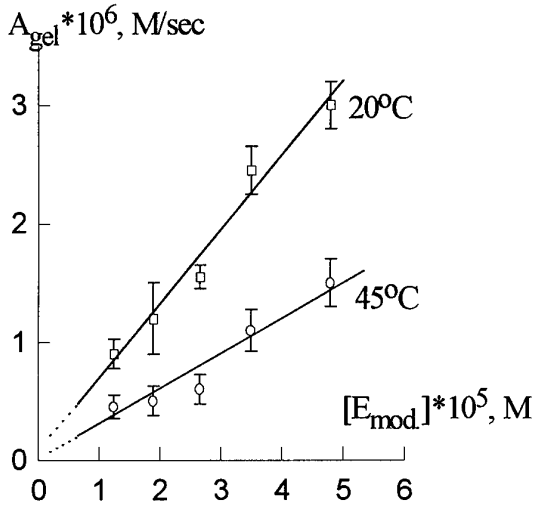


Fig.4. Observed activity of the preparations of immobilized α-chymotrypsin versus the enzyme concentration in the solution during polymerization at 20 and 45°C. Activity was determined using initial rates of ATEE hydrolysis (conditions: 0.2 M NaCl + 0.02 M $CaCl_2$, pH 8.0, [ATEE]=0.01 M).

3.1 Internal diffusion limitations

To evaluate possible internal diffusion limitations, we carried out an experiment to clarify an influence of the concentration of α-chymotrypsin in the preparations of the immobilized enzyme on the activity observed at saturating substrate concentrations. Fig.4 demonstrates that these dependencies obtained at temperatures both less (20°C) and higher (45°C) the break point observed in Arrhenius plot are linear and tends to the origin of coordinates over the whole studied range of concentrations of the enzyme. This fact clearly indicates the absence of internal diffusion limitations for the preparations of immobilized α-chymotrypsin.

3.2 Conformational changes in protein globule

To verify the role of conformational changes in the protein globule, we have passed from the analysis of observable enzymatic activities to the analysis of kinetic and equilibrium constants of the reaction catalyzed by the enzyme. In the case of α-chymotrypsin, the hydrolytic reaction is described by three-step mechanism:

$$E + S \underset{}{\overset{K_s}{\rightleftharpoons}} ES \overset{k_2}{\underset{P_1}{\rightleftharpoons}} EA \xrightarrow{k_3} E + P_2 \qquad (1),$$

where can be written as $k_3=k_4*[H_2O]$. The constants determined experimentally, K_m and $k_{cat.}$, are complex functions of the constants of the individual steps:

$$K_m = (K_s*k_3)/(k_2+k_3) \qquad (2),$$

$$k_{cat.} = k_2*k_3/(k_2+k_3) \qquad (3).$$

However the difference between k_2 and k_3 values for ATEE hydrolysis is well known to be rather significant[11] (k_2= 5000 sec^{-1} and k_3=200 sec^{-1}) that allows us to substantially simplify the equations.

$$K_m = K_s*(k_3/k_2) \quad (4),$$

$$k_{cat} = k_3 \quad (5).$$

Thus, V_{max} determined in the experiment is directly proportional to the k_3 whereas K_m remains a function of three parameters and the analysis of its temperature dependence gives no useful information. It is noteworthy that the pH optimum of α-chymotrypsin is too narrow and shifts to the acidic region when temperature increases. Besides, the pH optimum of the immobilized enzyme shifts to the basic region as compared with that of native α-chymotrypsin. For these two reasons, it is necessary to analyze three-dimensional surfaces V_{max}-pH-temperature. The obtained from such surfaces dependencies of V_{max} on pH at constant temperatures enable to evaluate the V_{max} values corresponding to the pH optima and the values of equilibrium ionization constants K_a and K_b for complexes of the substrate with both native and immobilized enzymes.

The obtained by such a way temperature dependencies of equilibrium and kinetic parameters for native and immobilized α-chymotrypsin are presented in Fig.5. As is seen in Fig.5(a), the temperature dependencies of equilibrium constants are linear within the studied temperature interval. It is remarkable that the inclinations of these linear dependencies appear to be close both for native and for immobilized enzymes. On the contrary, the temperature behaviours of V_{max} obtained for native and immobilized α-chymotrypsin significantly differ each other (Fig.5(b)).

It is noteworthy that the sign of the apparent activation energy of the hydrolytic reaction (1) catalyzed by the immobilized α-chymotrypsin changes at the gel critical temperature. The analogous results were obtained for alkaline phosphotase that was physically entrapped into poly-NIPAA gel[5].

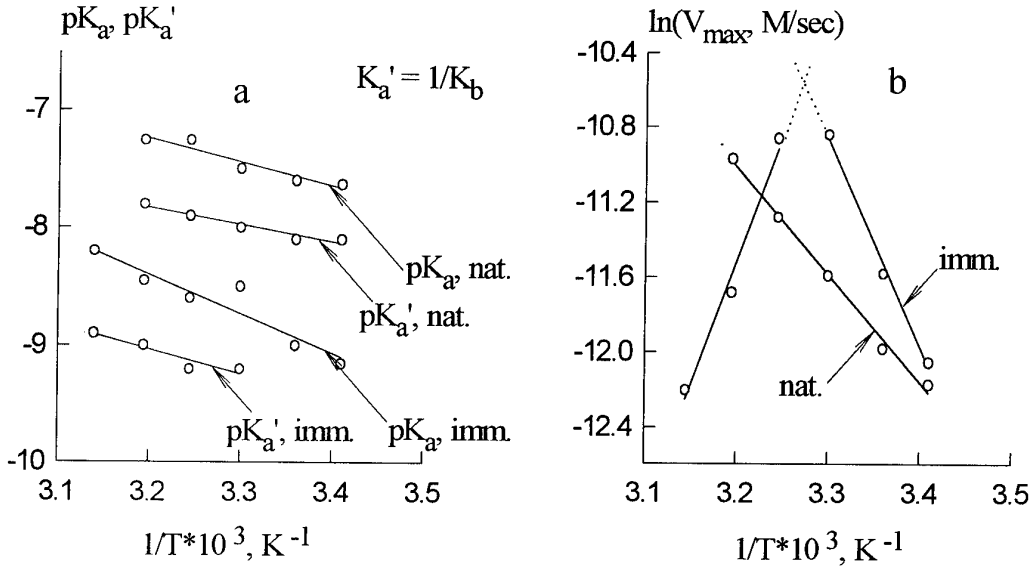


Fig.5. K_a, K_a '=1/K_b (a) and V_{max}, (b) for hydrolysis of ATEE by native and immobilized α-chymotrypsin versus temperature. V_{max} values correspond to pH optima.

Obviously, the temperature behaviour of equilibrium parameters would vary if the conformational changes in protein globule take place when the polymeric gel collapses. However experimental data obtained in this work do not confirm this assumption (Fig.5). Thus, we conclude that the unusual temperature behaviour of the activity of immobilized into thermoreversible hydrogels enzymes can not be explained by the conformational changes in the protein globule.

3.3 Sterical limitations

The observed decrease in V_{max} could be also explained either by the decreasing number of active sites of α-chymotrypsin. which can effectively participate in the catalysis, that results from hydrogel shrinking or by

the decrease in k_{cat}. We found that the incubation of preparations of α-chymotrypsin immobilized into poly-NIPAA gel with the irreversible proteinase inactivator phenylmethylsulfonyl fluoride, whose size is close to the size of ATEE, for 10-15 min. leads to the complete and irreversible inhibition the α-chymotrypsin catalytic activity at temperatures higher than the value of temperature corresponding to the break point in Arrhenius plot, i.e., at conditions of maximum shrinking of the polymeric network and consequently minimum availability of active sites of the enzyme. Thus, this fact points out that virtually all active sites of α-chymotrypsin are available for the substrates even at high temperatures when effects of sterical limitations could take place.

4. CONCLUDING REMARKS

Hence, the results of our experiments clearly demonstrate the impossibility to explain the unusual temperature behaviour of the enzyme immobilized into the thermosensitive hydrogel on the basis of well known effects that are internal diffusion limitation emerged as a result of the gel dehydration, conformational changes in protein globule, and sterical limitations for enzymatic catalysis. We suppose that the decrease in k_{cat} but not in the number of active centres of the enzyme plays the main role in the V_{max} reduction. The possible reason for that is the change of microenvironment of the immobilized enzyme that results from the structural reorganization of the polymeric network under its collapse and leads to the sufficient decrease in the concentration of "free" or "active" water inside the hydrogel. According to mechanism considered above, water takes an active part in the hydrolytic process (1) and consequently significantly affects V_{max}.

The experimental results obtained in this work can be useful for the construction of artificial thermoregulated biocatalitic systems. The study of such systems is very important both for understanding of complex regulation of biochemical processes that take place in living cells and for the creation of a new generation of intelligent devices that are able to transfer an information by the same principle as is observed in living organisms.

5. REFERENCES

1. M.D. Houslay and R.W. Palmer, Changes in the form of Arrhenius plots of the activity of glucagon-stimulated adenilate cyclase and other hamster liver plasma-membrane enzymes occurring on hibernation, *Biochem J.*, Vol. 174, pp. 909-919, 1978.

2. Y. Li and T. Tanaka, Phase transition of gels, *Annu. Rev. Mater. Sci.*, Vol. 22, pp. 243-277, 1992.

3. T.G. Park and A.S. Hoffman, Immobilization and characterization of β-galactosidase in thermally reversible hydrogel beads, *J. Biomed. Mat. Res.*, Vol. 24, pp. 21-38, 1990.

4. E. Kokufuta, O.Ogane, H. Iehijo, S. Watanabe and O. Hirasa, Poly(vinyl metyl ester) gel for the construction of a thermosensitive immobilized enzyme system exhibiting controllable reaction initiation and termination, *J. Chem. Soc., Chem. Commun.*, N 5, pp. 416-418, 1992.

5. N.L. Eremeev, L.V. Sigolaeva, P.A. Simakov and N.F. Kazanskaya, Temperature dependencies of equilibrium and kinetic constants of enzymatic reactions during a phase transition in a thermosensitive matrix, *Biokhimiya*, Vol. 60, N 8, pp. 1307-1317, 1995 (Russian).

6. K. Veigand and G. Hilgetag, *Experimental Methods in Organic Chemistry*, p.387, Khimiya, Moscow, 1968 (Russian translation)

7. H. Plaut and J.J. Ritter, A new reaction of nitriles. VI. Unsaturated amides, *J. Am. Chem. Soc.*, Vol. 74, pp. 4076-4077, 1951.

8. E.V. Lukashova, R.B. Aisina, N.F. Kazanskaya and N.L. Eremeev, A properties of α-chymotrypsin covalently entrapped in a spherical polyacrylamide microgranules, *Biokhimiya*, Vol. 45, N 3, pp. 449-454, 1980.

9. O. Chiantore, M. Guaita and L. Trossarelli, Solution properties of poly(N-isopropylacrylamide), *Macromol. Chem.*, Vol. 180, pp. 969-973, 1979.

10. M. Ilavsky and J. Hrouz, Phase transition in swollen gels. 4. Effect of concentration of the crosslinking agent at network formation on the collapse and mechanical behaviour of polyacrylamide gels, *Polym. Bull.*, Vol. 8, pp. 387-394, 1982.

11. A.A. Klesov and I.V. Berezin, *Enzyme Catalysis*, p. 115, MGU Publishers, Moscow, Vol. 1, 1980 (Russian).

Metallization of bacterial surface layer by cross-beam pulsed laser deposition

Wolfgang Pompe, Michael Mertig, Remo Kirsch, Andre A. Gorbunov, and Andreas Sewing

Max–Planck–Arbeitsgruppe "Mechanik heterogener Festkörper", Hallwachsstr. 3, D–01069 Dresden, Germany

Harald Engelhardt

Max–Planck–Institut für Biochemie, D–82152 Martinsried, Germany

Axel Mensch

Institut für Werkstoffwissenschaft, Technische Universität Dresden, D–01062 Dresden, Germany

ABSTRACT

We present first results on thin film metal deposition on the regular bacterial surface layer of Sporsarcina urea by pulsed laser deposition. To prevent structural damage of the biological specimen a recently developed cross beam technique is applied providing an effective filtering of the most energetic plasma particles. The deposited films are examined by low voltage scanning electron microscopy. The surface profile of the S-layer adsorbed onto mica substrate was investigated by atomic force microscopy. A lattice constant of 13.2 nm has been measured. The lattice parameters and the structural appearence of the protein layer is in reasonable agreement with the results of an electron microscopical 3d structural analysis.

1. INTRODUCTION

There is a currently growing interest in the development of fabrication techniques for structures in the 10 nm region where the application of conventional electron-beam lithography is limited by the proximity effect. A novel, promising direction of this development is biological templating. Here, biological specimens with structural features typically on the 10 nm length scale and below are employed as templates for the build-up of solid state nanostructures. In addition to the small lateral dimension, the high reproducibility of self-assembled biological templates over larger areas is especially promising for the achievement of a high density of precision devices. First composite biomolecular - solid state nanostructures have been produced by Douglas et al.[1] and Sleytr et al.[2] Apart from microelectronic applications, novel concepts are under development for the biological template-based fabrication of micromachines and -robots.[3]

Two-dimensional bacterial surface layer proteins (S-layer) are the outermost cell envelope components of many bacteria in almost all branches of eu- and archaeobacteria.[4,5] They exhibit different kinds of lattice symmetry with spacings of the morphological units in the 10 nm range and possess pores of identical size in the range below 6 nm. Isolated S-layer subunits from numerous bacteria have shown the ability to reconstitute into 2d arrays with perfect uniformity over large areas in suspension or on solid supports.[6,7] That makes them almost ideal patterning templates for supra–molecular engineering.

We have investigated the surface geometry of the S-layer of *Sporsarcina urea* adsorbed onto mica substrates

0-8194-2165-0/96/$6.00

by atomic force microscopy (AFM). The 2d protein crystal structure could be imaged reproducibly. We have deposited thin nickel films by cross-beam laser deposition onto protein crystals immobilized on mica, silicon and highly oriented pyrolytic graphite (HOPG). Structural features of the metal films have been investigated by low energy scanning electron microscopy (SEM) and scanning tunneling microscopy (STM). The motivation for this study is the search for nanostructured templates for ultra thin layer growth.

2. MATERIALS AND METHODS

2.1. Preparation of the biological template

The S-layer sheets were isolated from *Sporsarcina urea*. The cell cultivation and preparation of the S-layer is described elsewhere.[8] The S-layer preparation is stored at 4 °C in a buffer solution (50 mM sodium phosphate, pH 7.8, 1 mM $MgCl_2$) containing 0.02 % NaN_3. Before the transfer to the substrate surface the S-layer preparation was diluted with destilled water. The adsorption of the S-layer to mica, silicon and HOPG was accomplished by placing a drop of S-layer suspension on the substrate for about one minute. Excess water was removed with filter paper and the preparation was air-dried.

2.2. Cross–beam pulsed laser deposition

The adsorbed S-layers were metallized by means of cross–beam pulsed laser deposition (CBPLD).[9] PLD is a speciality among physical vapor deposition techniques.[10] It is effective there, where special requirements are applied on the composition and film thickness in the nanometer scale or unusual or advanced physical properties are expected.[11,12] It is a pulsed non-stationary method that is characterized by a relatively high content of charged particles in the plasma plume (up to 30%), having kinetic energies of up to 1 keV (the mean energy is 3–30 eV at relevant laser parameters) and extremely high pulse deposition rates, several orders of magnitude higher than those obtained, for instance, by resistive or e–beam evaporation. These peculiarities of PLD strongly control the properties of the deposited films. It is possible to choose the process parameters in a way, that the formation of a highly randomized nanocrystal or amorphous film structure is favored. Thus surface migration of atomic species, segregation and island growth of the film are suppressed, so that the film starts being continuous already at thicknesses that are comparable to a single monolayer. The absence of an eigentexture or pronounced crystallinity, and the continuity of the ultrathin films make PLD an ideal technique for coverage and replication of nanometer structures for the purposes of structure characterization and templating.

CBPLD allows the effective refinement of the deposited species from the most energetic plasma ions ($E \simeq 1$ keV) that can damage the nanostructure of biological objects and the slowest portions of the plasma ($E \simeq 1$ eV) that provide thermalized particles migrating along the surface and causing island coalescence and coarsening of the films. Also it rejects droplets of the molten material that might be ejected from the target during the laser ablation and deteriorate the uniformity of the films. This refinement is accomplished in the intersection region of two independent laser plums produced by simultaneous ablation of two targets by two synchronized laser beams (Fig.1). The system is tuned in a way that the most dense medium energy part of the laser plasma is deflected towards the substrate, whereas the less dense front (high energy ions) and the rear portions of the plasma cloud (low energy neutrals, droplets) will not interact in the intersection region and will pass it unaffected thus missing the substrate. A diaphragm positioned at the symmetry axis of the system prevents the substrate from the direct deposition from the targets. Computerized control allows the deposition of continuous ultrathin metal single and compound films and multilayers with a thickness control within 0.01 nm and r.m.s. roughness of 0.1–0.6 nm.

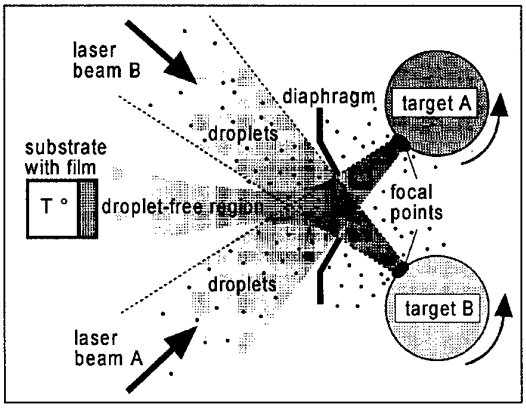


Figure 1: Schematic diagram of the cross-beam pulsed laser deposition.

2.3. Electron and atomic force microscopy

SEM of uncovered and metallized specimen was carried out with a DSM 982 Gemini (Carl Zeiss, Oberkochen). The micrographs were taken at beam voltages below 2 kV with a magnification up to 100,000 x.

AFM was performed with a commercial multimode microscope (Nanoscope IIIa, Digital Instruments, Santa Barbara) operated in the tapping mode in air. Tapping mode provides a 'gently' imaging of the soft biological sample, since lateral forces to the specimen are circumvented. Silicon tips have been used for imaging. The resonance frequency of the cantilevers was about 300 kHz.

3. PRELIMINARY RESULTS

The AFM image in Fig.2 displays S-layer sheets adsorbed on mica with different crystal orientations of the individual sheets. Fig.2 shows the untreated amplitude signal of the tapping mode in air, simultaneously recorded with the height signal (not shown). The amplitude signal is analogous to the deflection signal in the conventional error signal mode.[13] It allows to resolve very small corrugations of the sample and has been therefore successfuly applied to protein imaging.[14] Fig.2 shows that the protein crystals exhibit a tetragonal symmetry. A 2d Fourier analysis yields a lattice constant of 13.2 nm which is in good agreement with the values of 12.8 nm[15] and 12.9 nm[8] determined by electron microscopy. The protein crystals are smoothly adsorbed onto the substrate. This is a necessary prerequisite for the large area formation of a protein crystal monolayer on the substrate. The S-layer sheets have a thickness of about 6 nm, which is close to the value determined by 3d reconstruction,[8] thus air–drying did not deteriorate dramatically the structure of the protein layer. The observed surface corrugations have an amplitude of 1-1.5 nm.

Uncovered S-layer adsorbed on conducting substrates such as silicon and HOPG have been examined in the SEM. Although it is not possible to resolve the 2d crystal structure, S-layer sheets can be visualized at beam voltages below 2 kV. Typically the sheets exhibit a more rectangular shape with a width of about 250 nm and a lenght up to 1 μm. Furthermore, the images allow to assess the degree of surface coverage of the substrate by S-layer sheets.

In first experiments nickel films with a thickness of about 3 nm have been deposited onto the specimen by CBPLD. The deposition is performed in vacuum of $3{\cdot}10^{-8}$ mbar with a deposition rate of about 0.004 nm/pulse. The pulse duration is about 10 μs. At a repetition rate of 0.5 Hz the incoming energy can be dissipated in

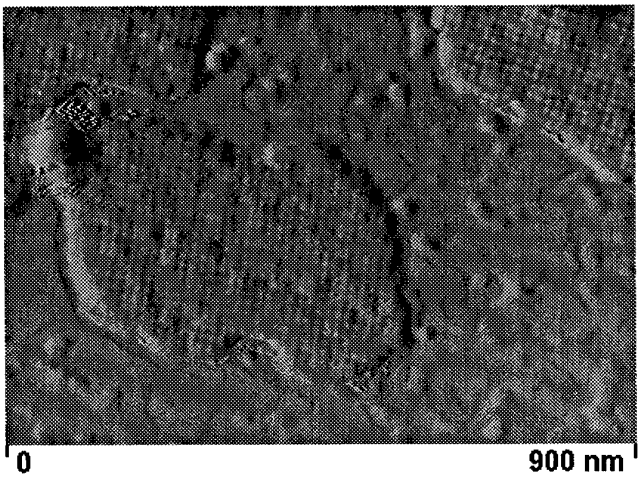


Figure 2: S-layer sheets from *Sporosarcina ureae* adsorbed on mica and imaged by AFM in tapping mode. The amplitude signal is shown. It corresponds to a derivative of the height signal and accentuates small corrugations of the sample.

the substrate before the beginning of the next pulse. The overheating of the sample above room temperature is estimated to be smaller than 3 K. Fig.3 shows a SEM micrograph of a nickel covered sample. The S-layer sheets adsorbed on HOPG show the typical rectangular-like shape. It can be seen, that the structure of the metal film is different on the substrate and on the protein crystal. The characteristic 'grain' size of the film covering the S-layer is larger than that on the substrate. This observation is true for all substrates used and has also been found by imaging freshly prepared samples by STM in air. The metal film on the S-layer sheets shows a preferential 'grain' orientation of 45° with respect to the longer edges of the sheets, which occurs typically along the (1,1,0) direction of the protein crystals as observed in transmission electron microscopy investigations. This suggests that the 'grains' of the deposited nickel film are oriented along the crystallographic axes of the S-layer.

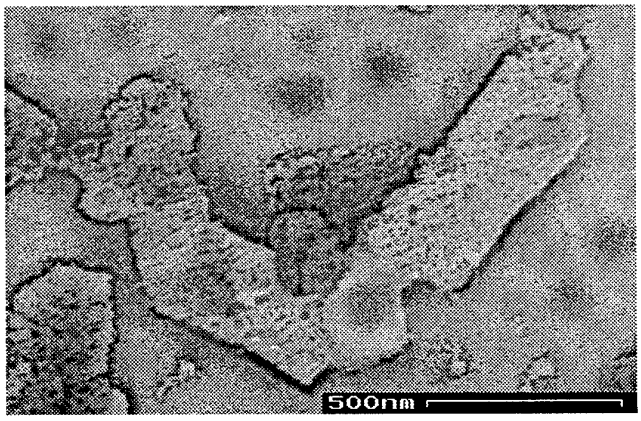


Figure 3: SEM micrograph of nickel covered S-layer sheets adsorbed on HOPG taken at a beam voltage of 1 kV. The thickness of the nickel film is about 3 nm.

Fig.4 shows a SEM micrograph of nickel covered S-layer adsorbed on silicon. This micrograph presents a selected region of the sample, where a 100% coverage of the substrate with protein crystals is achieved. The size

of this area is 3.3 x 2.0 μm^2.

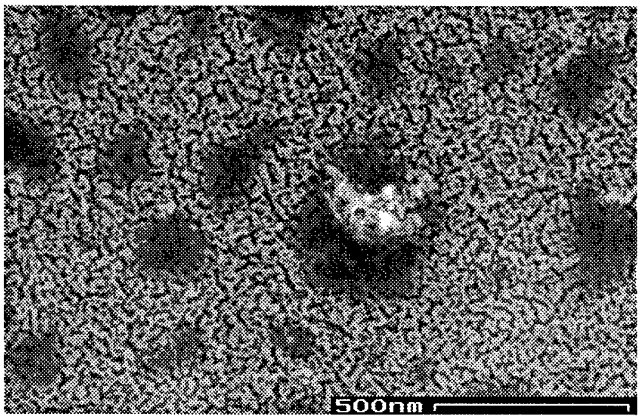


Figure 4: SEM micrograph of nickel covered S-layer sheets adsorbed on silicon. The presented area of 6.6 μm^2 is completely covered by S-layers. The micrograph was recorded at a beam voltage of 1 kV.

4. CONCLUSIONS AND FUTURE INVESTIGATIONS

S-layer from *Sporocarsina urea* adsorbed on different solid state surfaces and air-dried form a monolayer of a two-dimensional protein crystal. The observed large scale reconstitution of nearly continuous films formed from smaller sheets demonstrates that S-layer from *Sporocarsina urea* can be used as templates for the preparation of microstructures larger than 10 μm in size. The surface structure of the S-layer could be imaged stably by AFM in tapping mode. Although the resolution is currently not high enough to detect the pores of the protein crystal, the lattice constant could be resolved. The crystal surface exhibits corrugations with a height of about 1.5 nm and a lateral periodicity of 13.2 nm. The intrinsic spatial inhomogeniety of the surface of the protein monolayer may serve as a template, which patterns an overlayer. The first results on metal deposition onto S-layer by pulsed laser ablation show evidence for the transfer of the crystal pattern to the metal film structure. We have not yet established in detail the mechanism responsible for the film pattern formation. It can be concluded from the observed difference in the 'grain' size of metal films deposited on the protein and on the anorganic substrate that the film growth mechanisms are different. Two major differences should be considered: first, enhanced stress relaxation in the metal film due to relaxation processes in the compliant protein template, and second, different types of nucleation centres in the protein film and on the substrate. We assume that due to the kinetic energy of the laser plasma particles there is a higher probability of 'implantation' in the protein crystal than in the anorganic substrate. For the softer protein template this would result in a higher sticking probability for the atoms at the place of impact. Thus the S-layer nanostructure can be replicated. The presented experiments open the way to the fabrication of nanostructured metal films with interesting physical and chemical properties.

Future investigations will focus on the metallization of S-layer with thinner metal films, which exhibit very small grain structure. Investigation with Pt/C and Ta/W films are under way. Transmission electron microscopy will be employed and the resolution of the used scanning probe microscopy methods will be improved to get more detailed structural information.

5. ACKNOWLEDGEMENTS

This work is supported by the Bundesministerium für Bildung, Wissenschaft, Forschung und Technologie (Contracts No: 0310812 and 13N6149/9).

6. REFERENCES

[1] K.Douglas, N.A.Clark and K.J.Rothschild, "Composite biomolecular/solid state nanostructures", Mat. Res. Soc. Symp. **174**, 151–156, 1990.

[2] U.B.Sleytr, M.Sara and D.Pum, "Application potential of two-dimensional protein crystals", Microelectronic Engineering **9**, 13–20, 1989.

[3] K.E.Drexler, Nanosystems, molecular machinery, manifacturing and computation, J.Wiley and Sons, Inc., New York, 1992.

[4] U.B.Sleytr and P.Messner, "Crystalline surface layers in prokaryotes", Journal of Bacteriology **170**, 2891–2897, 1988.

[5] W.Baumeister and H.Engelhardt, "Three-dimensional structure of bacterial surface layers", Electron microscopy of proteins, Vol. 6, Membranous structures, ed. by J.R.Harris and R.W.Horne, 109–154, Acad.Press, London, 1987.

[6] H.Engelhardt, "Electron microscopy of microbial cell wall proteins. Surface topography, three-dimensional reconstruction, and strategies for two-dimensional crystallization", Fungal cell wall and immune responce, ed. by J.P.Latge and D.Boucias, NATO ASI Series, Vol. H53, 11–25, Springer-Verlag, Berlin, 1991.

[7] D.Pum and U.B.Sleytr, "Large–scale reconstitution of crystalline bacterial surface layer proteins at the air–water interface and on lipid films", Thin Solid Films **244**, 882–886, 1994.

[8] H.Engelhardt, W.O.Saxton and W.Baumeister, "Three-dimensional structure of the tetragonal surface layer of Sporosarcina urea", Journal of Bacteriology **168**, 309–317, 1986.

[9] A.A.Gorbunov, W.Pompe, A.Sewing, S.V.Gaponov, A.D.Akhsakhalyan, I.G.Zabrodin, I.A.Kaskov, E.B.Klyenkov, A.P.Morozov and N.N.Salaschenko, "Ultrathin film deposition by pulsed laser ablation using crossed beams", Appl. Surface. Sci., accepted.

[10] K.Reichelt and X.Jiang, "The preparation of thin films by physical vapour deposition methods", Thin Solid Films **191**, 91–126, 1990.

[11] Laser ablation of electronic materials. Basic mechanisms and applications, ed. by E.Fogarassy and S.Lasare, Elsevier Science Publishers, 1992.

[12] Pulsed deposition of thin films, ed. by D.B.Chrisey and G.K.Hubler, J. Wiley and Sons, New York, 1994.

[13] C.A.J.Putman, K.O.van der Werf, B.G.de Grooth, N.F.van Hulst, J.Greve and P.K.Hansma, "A new imaging mode in atomic force microscopy based on the error signal", Proc. SPIE **1639**, 198–204, 1992.

[14] M. Fritz, M.Radmacher, M.W.Allersma, J.P.Cleveland, R.J.Stewart, P.K.Hansma and C.F.Schmidt, "Imaging microtubules in buffer solution using tapping mode atomic force microscopy", Proc. SPIE **2384**, 150–157, 1995.

[15] M.Stewart and T.J.Beveridge, "Structure of the regular surface layer of Sporosarcina urea", Journal of Bacteriology **142**, 302–309, 1980.

Collagen assembly from acid solution to networks on solid surfaces and to fibrils

Jens–Hilmar Bradt, Michael Mertig, Bettina Winzer, Uwe Thiele, Wolfgang Pompe

Max–Planck–Arbeitsgruppe "Mechanik heterogener Festkörper"
Hallwachsstr. 3, 01069 Dresden, Germany

ABSTRACT

Two different kinds of collagen assembly have been studied: The reconstitution of type I collagen to fibrils and the formation of two dimensional networks on surfaces. The kinetics of fibril assembly are influenced by polyaspartate, as measured turbidimetrically. Addition of polyaspartate increases the fibril diameter. The reconstituted fibrils are imaged by atomic force microscopy and scanning electron microscopy. The preparation of thin collagen films on highly oriented pyrolytic graphite leads to networks or tree like structures depending on the collagen concentration in the precursor. The results presented are of interest for the development of new bone–like implant materials and the covering of bone grafts with a biocompatible layer.

1. INTRODUCTION

The repair of bone defects acquired by accident or degradation is a frequent application in medicine. As graft materials mainly metals are used currently. They have excellent mechanical properties but there are problems with the bone metal interface. Therefore, investigations have been initiated to fill bone defects with a more bone–like material.[1] A biocomposite made from collagen I and hydroxyapatite (HAP), the major components of bone, could be gradually resorbed by the body and replaced with new bone.

The first step in the development of bone *in vivo* is the production of the collagen matrix. Collagen I assembles to fibrils under physiologic conditions. The mineralization of the organic matrix leads to a hierarchically structured material with imposing properties. Until now it is not possible to imitate this process *in vitro* sufficiently. Bone and other mineralizing materials contain a remarkable amount of polyanionic proteins, which are thought to play an important role in biomineralization. Our aim is to reconstitute collagen fibrils under addition of polyanionic compounds. In a second step this collagen matrix should be mineralized. The following investigation are based on the hypothesis that polyanionic compunds (i) control the collagen assembly process, and (ii) can be used as HAP nucleation centers. In a first step we examined the effect of polyanions, especially polyaspartate on the collagen assembly process. Collagen fibrils from young animals can be dissolved in acid and they reassemble *in vitro* after neutralization.[2,3]

In this study two different kinds of collagen assembly have been investigated, the reconstitution to fibrils in a 3d gel, and the formation of 2d collagen structures on surfaces.

Since currently composite materials from hydroxyapatite and collagen do not reach the mechanical properties required for bone implants, another attempt is to cover conventional graft matrials with collagen to improve the bone-implant interface. To understand the basic mechanisms of collagen adsorption, we study the characteristics of thin collagen films on solid surfaces. Because carbon is a widely used biomaterial, highly oriented pyrolytic

0-8194-2165-0/96/$6.00

graphite (HOPG) was chosen as model substrate. Thin collagen films can be deposited on HOPG substrates by well–known liquid precursor technology.

2. EXPERIMENTAL

2.1. Turbidimetric measurement

Acid soluble collagen I from calf skin (Fluka, Neu–Ulm) was dissolved at a concentration of 4 mg/ml in 10 mM HCl under stirring for several hours at 4°C. The assembly process was initiated by mixing the collagen solution with an equal amount of a double strength fibril formation buffer containing 40 mM KH_2PO_4/K_2HPO_4 pH 7.4, 260 mM NaCl and an appropriate amount of poly-L-aspartate (Sigma, Deisenhofen, average molecular weight 10700). The final concentration was: 2 mg/ml collagen, 20 mM PO_4^{3-}, 130 mM NaCl. The solution was transferred to a cuvette, and the aggregation process was measured turbidimetrically at a wavelength of 400 nm with a photometer (Spekol 10, Carl Zeiss, Jena).

2.2. AFM and SEM imaging of reconstituted fibrils

The collagen solution was prepared as described in 2.1, however with a collagen concentration of 0.5 mg/ml. Immediately after mixing, the solution was spread out as a thin film on a glass (AFM) or silicon (SEM) substrate. It was incubated in a Petri dish at 35°C for 3 h, dried in an exsiccator, washed with distilled water and dried again.

Atomic force microscopic (AFM) investigations were carried out with a commercial AFM (Nanoscope IIIa, Digital Instruments, Santa Barbara, CA). Tapping mode in air was applied. Scanning electron microscopy (SEM) was performed with a DSM 982 Gemini (Carl Zeiss, Oberkochen) at a beam voltage of 1 kV.

2.3. Preparation of collagen networks on HOPG

A thin film of an acid collagen solution is made by spin-coating. Since the collagen is not neutralized, it does not assemble to fibrils but builds up 2d networks or tree-like structures after drying. Collagen was dissolved in 0.1 M acetic acid under stirring at 4°C at a concentration of 0.2 mg/ml, where not otherwise stated. A 30 μl droplet of this solution was set on a freshly cleaved HOPG substrate. By spin coating a thin film of this solution was generated. The formed structures were imaged by AFM.

3. FIBRIL ASSEMBLY

3.1. Turbidimetric measurement

Collagen fibrils have dimensions of some microns in length and about 100 nm in diameter, therefore it is possible to study the fibril assembly turbidimetrically.[4] Figure 1 shows the turbidity-time plots for different concentrations of polyaspartate. The absorbance was plotted versus time in minutes. A tangent to the steepest slope of the curve can be drawn. Its intersection with the x-axis defines the end of the lag phase, the intersection of this tangent with a horizontal line drawn at the turbidity after 120 min defines the end of the growth phase. Low concentrations of polyaspartate accelerate primarily the growth phase, while they have no significant influence

on the lag phase. Higher concentrations of polyaspartate increase both lag and growth phase. The fastest fibril assembly was observed at a polyaspartate concentration of 10 μg/ml. The turbidity at the end of the fibril forming process (defined as 120 min) increases with rising polyaspartate concentration. This is explained by a larger fibril diameter.

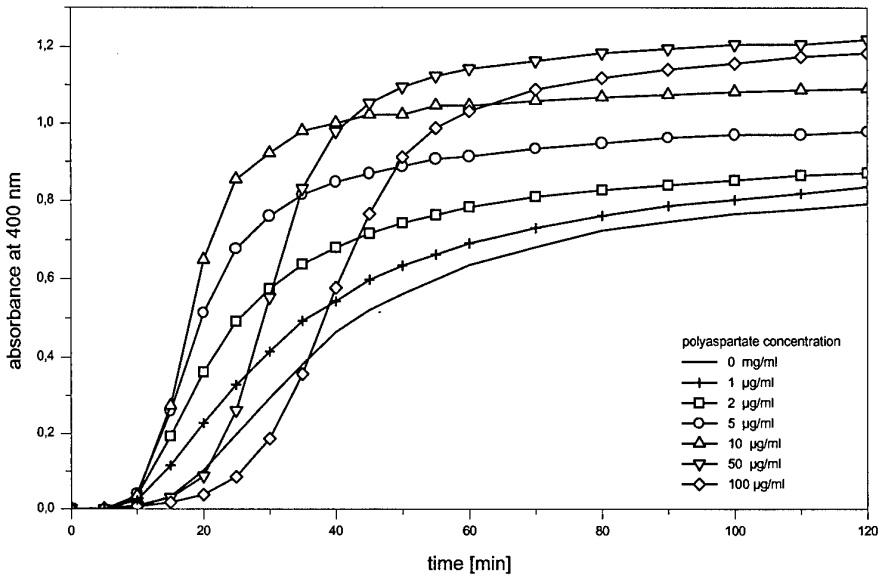


Figure 1: The effect of polyaspartate on the collagen fibril formation. Low concentrations accelerate the fibrillogenesis whereas high concentrations delay it.

3.2. AFM and SEM imaging

The fibrils formed were imaged by AFM and SEM. An AFM image is shown in Figure 2. Under all conditions examined, the fibrils showed the 67 nm periodicity of native Type I collagen fibrils. Frequently several fibrils were twisted to bundles in form of a righthanded helix. The twist angle was about 7°.

The influence of polyaspartate on the fibril diameter has been studied by evaluation of electron micrographs. The average diameter for the polyaspartate containing sample (0.1 mg/ml) was apparently wider (250 nm) than for the control sample without polyaspartate (190 nm). This is in accordance with the turbidimetric data.

3.3. Discussion

It is known that polyanionic compounds can influence the kinetics of fibril assembly.[5] Both acceleration and delay have been reported. The addition of polyaspartate at low concentrations increases the fibril diameter and accelerates the formation of fibrils. This could be explained by electrostatic effects, because collagen (pI = 9.0) is slightly positive charged at physiologic pH. At higher concentrations, polyaspartate increases the fibril diameter further, while the fibril assembly is delayed. This is possibly due to binding of polyaspartate to sites, which are responsible for attractive forces between collagen molecules. The location of the binding sites of polyaspartate is not known so far.

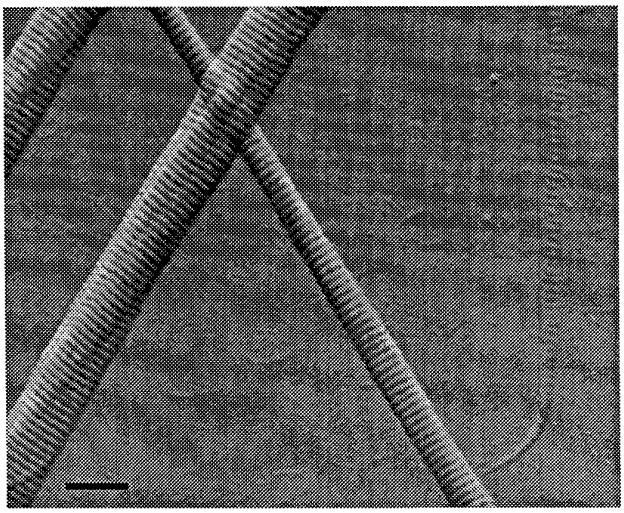


Figure 2: AFM image of collagen fibrils (amplitude signal). Scalebar is 500 nm

4. COLLAGEN NETWORKS ON HOPG

The collagen layers obtained by spin-coating were imaged by AFM. The structure of these layers is observed to be concentration dependent (Figure 3). Under standard conditions (0.2 mg/ml) collagen networks were formed. They have a typical mesh size of some 100 nm. Decreasing the collagen concentration to a value of 0.05 mg/ml leads to a morphological change (tree-like structure).

To examine the influence of the substrate on the structure formation process, experiments were repeated on other substrates. Collagen networks were only obtained on the strongly hydrophobic surface of HOPG. When hydrophilic substrates such as mica and silicon were used, a complete covering of the surface was observed. A HOPG substrate made hydrophilic by glow discharge was also completly covered.

The topological and metrical properties of the observed collagen networks are under investigation. In mathematics such networks are known as random cellular structures. This makes it possible to analyse the networks with established methods and compare them with similar structures like 2d soap foams or sections of grain structures in metals.

In contrast to soap foams there are not only vertices with a coordination of 3, but also with a coordination of 4, i.e. the mean value of the edge number distribution is less then 6 (this is the exact value for networks which have only vertices with a coordination of 3). The second moment of this distribution ranges from 2.5 to 3.5 and is so comparable to values for an aged soap foam.[6] In the case of soap foams the building blocks of the networks are molecules with typical size significantly smaller than the network edges, and the driving force is the minimization of surface energy. However in our case the dimension of the molecules is comparable to the dimension of the network edges. Therefore, it is not possible to assume that a vertex with a coordination of 3 is the only possible equilibrium configuration. The networks are found with typical edge length of about 60 nm and 300 nm. The question in what respect these lengths of the network are related to the biochemical properties of the collagen I molecule is under further investigation.

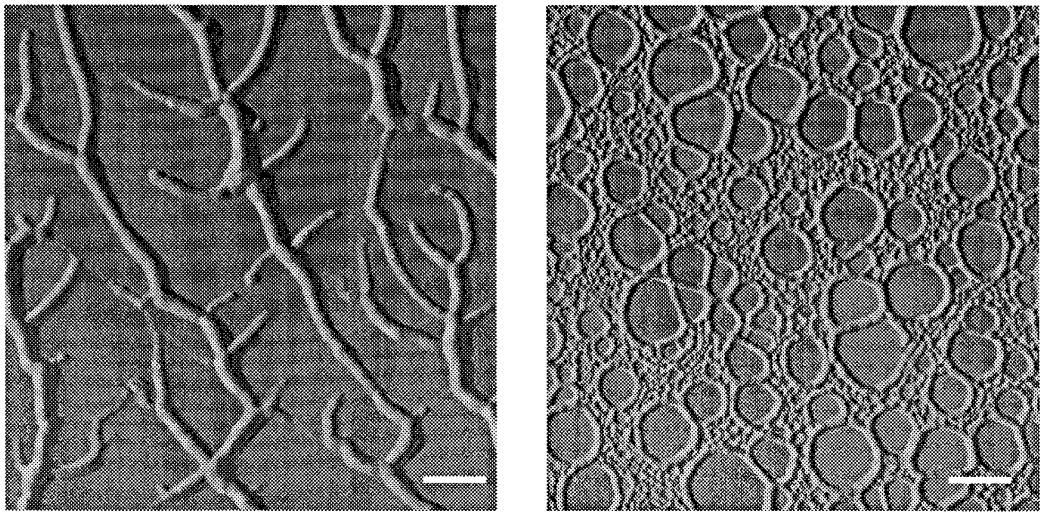


Figure 3: AFM images (amplitude signal) of collagen structures formed on HOPG by spin-coating. At a concentration of 0.05 mg/ml tree-like structures are formed (left), whereas at 0.2 mg/ml networks are observed (right). Scalebars are 500 nm

5. ACKNOWLEDGMENTS

We wish to thank Gudrun Keßler and Mechthild Fischer for many suggestions, and Sophie Richter and Axel Mensch of the Institut für Werkstoffwissenschaft, Technische Universität Dresden, for taking the SEM images.

6. REFERENCES

[1] B. R. Constantz et al., "Skeletal repair by in situ formation of the mineral phase of bone", Science **267**, 1796–1799 (1995)

[2] A. Veis, K. Payne, "Collagen fibrillogenesis", Collagen, Vol. I Biochemistry, ed. by M. E. Nimni, CRC Press, Boca Raton, 1988, 113–137

[3] G. C. Wood, M. K. Keech, "The formation of fibrils from collagen solutions 1. The effect of experimental conditions: Kinetic and electron-microscope studies", Biochem. J. **75**, 588–598 (1960)

[4] F. H. Silver, D. E. Birk, "Kinetic analysis of collagen fibrillogenesis: I. Use of turbidity–time data", Collagen Rel. Res. **3**, 393–405 (1983)

[5] J. R. E. MacBeath, D. R. Shackleton, D. J. S. Hulmes, "Tyrosine–rich acidic matrix protein (TRAMP) accelerates collagen fibril formation *in vitro*", J. Biol. Chem. **268**, 19826–19832 (1993)

[6] D. Weaire, N. Rivier, "Soap, cells and statistics – Random patterns in two dimensions", Contemp. Phys. **25**, 59–99 (1984)

Blubber and compliant coatings for drag reduction in fluids III: Viscoelastic properties of dolphin blubber matched by a gel-foam composite

Edwin R. Fitzgerald
The Johns Hopkins University
3400 N. Charles St. Baltimore, MD 21218

James W. Fitzgerald
The Kildare Corporation
95 Trumbull St. New London, CT 06320

ABSTRACT

In contrast to the unsuccessful efforts of many investigators to reduce underwater drag by the use of thin compliant coatings designed to simulate dolphin skin, it was suggested in prior publications in this series that the dolphin's delay in the onset of boundary layer turbulence and reduced drag results from the "intelligent" properties of the thick blubber underlying its skin. The blubber is supposed to have viscoelastic properties such that the dolphin acts as a compliant layer load of mechanical shear impedance, Z_L, which matches the impedance, Z_G, of incipient boundary layer turbulence acting as an equivalent shear force generator. Under this matched condition maximum power transfer and energy absorption in the blubber then quenches continued boundary layer turbulence and restores laminar flow. A gel-foam composite with frequency variations of complex shear compliance and shear modulus close to those of dolphin blubber is described, and suggested as a composite system for use in thick compliant material coatings for drag reduction.

1. INTRODUCTION

It has long been noted that dolphins are able to swim on and under water at high speeds[1], and to cruise for long distances at speeds of 10 to 15 knots (11.5 to 17.2 mph). This ability has been attributed to reduced drag[2] resulting from a delay in the onset of turbulence with increasing Reynold's number[3]. In 1957 Kramer suggested that the exterior skin, acting as thin biomaterial compliant coating on the dolphin, was responsible for its drag reduction[2], and later reported drag reduction for towed underwater bodies covered with thin compliant coatings to simulate the dolphin's skin[4]. Attempts to reproduce Kramer's results have been unsuccessful, and reports on the effects of thin coatings in drag are contradictory as noted, for example, by Gad-El-Hak in an extensive review article[5], and as pointed out in preceeding articles on blubber and compliant coatings for drag reduction[6,7]. Most previous investigators have concentrated on thin compliant coatings, about 0.2 cm thick, which are supposed to deflect so as to interact with the boundary layer waves to reduce their stability, and thus delay the transition to turbulent flow with increasing speed. Adequate quantitative information on the viscoelastic properties of the compliant coatings used, and of the dolphin's skin, is not given by any of these investigators. By contrast the frequency dependences in the range from 2 to 1000 Hz of viscoelastic properties of both dolphin blubber and of a suggested thick compliant coating material are presented here. Delay in the onset of boundary layer turbulence and reduced drag is attributed to the particular "intelligent" viscoelastic properties of 2 to 3 cm thick dolphin blubber, and the key to reduced drag is said to be a thick coating with viscoelastic properties matching those of blubber; such a gel-foam composite is described here and its measured viscoelastic properties compared to the measured viscoelastic properties of blubber.

0-8194-2165-0/96/$6.00

2. MATCHED SHEAR IMPEDANCE FOR DRAG REDUCTION

The matched shear impedance hypothesis of boundary layer turbulence control has been described in detail in previous publications[3,7] together with an equivalent mechanical circuit representation of incipient turbulent flow over compliant surfaces, but is summarized briefly.

a) The turbulent boundary layer (TBL) is considered to be a fluctuating shear force generator with mechanical impedance (force/velocity), Z_G, coupled to a compliant layer load (CLL) with impedance, Z_L, through a viscous inner boundary layer with mechanical resistance, R_S.
b) In order to transfer energy at an appreciable rate (power) from the TBL generator to the compliant layer load, the generator impedance, Z_G , must match the load impedance, Z_L , according to the maximum power transfer theorem of (electrical) circuit theory. That is, Z_L must be the complex conjugate of Z_G; $R_L = R_G$, $X_L = -X_G$. If the phase angle of the load is fixed, then the absolute values of load and generator impedance must be equal.
c) Under matched mechanical impedance conditions the incipient turbulence dies out as its energy is transferred/absorbed rapidly by the (blubber) load, and laminar flow persists with reduced drag and flow noise.
d) Dolphin blubber somehow acts to provide just such a matched load for Reynold's numbers up to about $Re = 2 \times 10^7$.

The actual situation, of course, is more complicated; the load impedance is dependent not only on the mechanical impedance of the blubber , but also on a terminal impedance at the inner surface of the blubber. However if this terminal impedance is large, the load impedance will depend largely on the blubber impedance. For incipient turbulence, the equivalent rotational inertia will be small and provide only a small inductive reactive component, ωI_V , of the TBL generator impedance which can then be considered chiefly resistive. In the absence of any exact knowledge of these terms, the dolphin blubber remains the best guide for a synthetic compliant coating to reduce drag.

3. VISCOELASTIC MEASUREMENTS OF COMPLIANT MATERIALS

3.1 Viscoelastic properties from dynamic mechanical measurements

Viscoelastic properties of a material can be measured by its response to an alternating sinusoidal stress in terms of the instantaneous (elastic) part of the response, and the delayed (viscous) part. For a very weak, compliant material this can be done with the material confined between rigid, parallel surfaces so as to be vibrated in simple shear. Then for an alternating stress, s, of frequency, f, at any time, t, the shear stress is $s = s_1 \sin 2\pi ft$, and a delayed shear strain, a, of the same frequency results so that, $a = a_1 \sin (2\pi ft - \delta)$. This retarded/delayed strain can be divided into an in-phase elastic component, of amplitude a′, and a viscous component, with a 90° phase lag, of amplitude a″ to provide the necessary two parameters needed to characterize a viscoelastic material at any vibration frequency. The ratio of the in-phase, elastic strain amplitude to the stress amplitude is called the elastic compliance, $J' = a'/s_1$, and the ratio of the 90° phase lag strain amplitude to the stress amplitude is the viscous compliance, $J'' = a''/s_1$, where $a''/a' = J''/J' = \tan \delta$. These component shear strain/shear stress ratios lead also to the definition of a complex shear compliance, $J^* = J' - iJ''$, and the complex reciprocal defines a complex shear modulus, $G^* = G' + iG''$. Values of J* and G* for viscoelastic materials very greatly over some ranges of frequency and temperature; values at one temperature and one frequency are insufficient, and may be misleading.

3.2 Measurement method

In order to determine values of complex compliance and modulus as functions of vibration frequency, an automated forced vibration measurement system, described in detail in many previous places[6,8] , was used; only its essential features are given here. An electromagnetic transducer is employed in which an alternating electrical current, $\mathbf{I}_1$, through a flat coil with wire length, l_1, embedded in a rigid plate suspended by fine wires to place the coil transverse to a permanent magnetic field, B_1, produces a vibrating force, $\mathbf{F}_1 = B_1 l_1 \mathbf{I}_1$, on the plate. A second coil with winding length, l_2, embedded in the plate and transverse to a second magnetic field, B_2, then generates an alternating Emf, $\mathbf{E}_2 = B_2 l_2 \mathbf{v}_2$, where $\mathbf{v}_2$ is the velocity of the embedded coil 2 (and plate) resulting from the vibrating force, $\mathbf{F}_1$, on coil 1 (and the plate). The suspended plate with coils because of its mass, M_P , and the suspension wires elastance, S_W, has a mechanical impedance (force/velocity), $\mathbf{Z}_P$, which is measured in terms of the electrical transfer admittance, $\mathbf{Y}_{12} = \mathbf{I}_1/\mathbf{E}_2$. When two small sample disks with combined mechanical impedance, $\mathbf{Z}_S$, are pressed against opposite faces of the driving plate, with their outer faces fixed, then the total impedance of the driving plate and samples is the vector sum, $\mathbf{Z}_T = \mathbf{Z}_P + \mathbf{Z}_S$, and a corresponding value, $\mathbf{Y'}_{12}$, of the electrical transfer admittance results. Hence,

$$\mathbf{Z}_S = \underset{\text{(with samples)}}{B_1 l_1 B_2 l_2 \mathbf{Y'}_{12}} - \underset{\text{(without samples)}}{B_1 l_1 B_2 l \mathbf{Y}_{12}} \quad \ldots\ldots\ldots\ldots\ldots \quad (1)$$

From the cross sectional areas and thicknesses of the disks, the complex shear compliance and its inverse, the complex shear modulus, are thus found in terms of the differences of two complex electrical admittances. Values of complex shear compliance, shear modulus, and shear wave velocity and attenuation are obtained at any frequency between 2 and 10,000 Hz in about 4 seconds. Values are usually found to a precision of 3 to 5%, but, because of the increasing driving plate inertial mass reactance at high frequencies, the difference in mechanical impedances with and without samples becomes very small for soft, compliant samples; this limits the upper frequency range of measurements. Thin samples of large cross sectional areas are necessary for reliable high frequency measurements of compliant materials like gels and many animal tissues.

3.3 Results for some compliant materials

Room temperature frequency variations of elastic compliance, J', and viscous compliance, J", for two polydimethyl siloxane (PDMS) gels with polymer: curing agent ratios of 10:1 and 5:1 are adduced in Figure 1. The results shown are for curing times at 20°C of 24 and 36 hours respectively. The gels continued to cure at 20°C, with decreasing compliances, and a shift in the retardation dispersion toward high frequencies as the gel junction points increased, and the polymer chain lengths between junctions decreased. To support thick coatings of weak gels, a matrix framework is needed, and therefore the frequency variations of compliance for an open cell rubber foam, an open cell poyurethane foam, and an open/closed cell polyurethane foam are shown also in Figure 1. As mentioned in section 3.2 above, measurements on these samples were limited to the range from 2 to 1000 Hz or less because of their low compliances; cross sectional areas were about 1.0 to 1.5 in^2, but the thickness varied from 1/4 to 1/32 in for samples of different materials, and this accounts for the variation in the reliable measurement high frequency cutoffs from 200 to 1000 Hz. In addition to a supporting matrix, a thin, flexible protective cover will be necessary for a practical thick compliant coating, but because it will be thin, such a cover will not contribute much to the "load" mechanical impedance.

4. DOLPHIN BLUBBER AND A GEL-FOAM COMPOSITE

The automated measurement system mentioned in section 3.2 was used to determine the viscoelastic properties of excised samples of blubber and skin from an injured young female Atlantic bottlenose dolphin found stranded at Virginia Beach, VA in September, 1995. Because of its severe injuries, rescue efforts failed one day after the dolphin was flown to the National Aquarium in Baltimore. Immediately after death iced samples were transferred to the measurement laboratory and were surrounded with saline solution for room temperature measurements at 21°C from 3.08 to 10 hours after death. Small amplitude dynamic mechanical measurements on blubber at 25 frequencies from 2 to 2500 Hz, requiring 2.5 minutes for each frequency scan, were carried out at intervals after death. As for many animal tissues, a linear plot of decreasing compliance vs time after death showed a "life to death" transition at 5.4 hours; extrapolation of compliance values, from the pre-transition slope, to 0 hours yielded the "live" tissue values of shear compliance and shear modulus indicated by the dashed lines in Figure 2 where values at 4.5 and 6.5 hours are shown also.

A gel-foam composite was formed from the rubber cushioning foam and the 10:1 polydimethyl siloxane (PDMS) gel whose frequency variations of compliance are shown in Figure 1. A piece of foam was immersed in the PDMS gel just after mixing the polymer and curing agent at 20°C. The foam-uncured polymer mix was put under decreasing vacuum from -26 to -15 cm Hg over a period of 15 minutes, and the foam-gel was cured for 2 hours at 150°F and then at room temperatures of 20 to 23°C for 25 days before the dynamic mechanical measurements from 2 to 400 Hz shown in Figure 2. Measurements at 57, 70, and 153 days after the sample preparation showed no compliance changes. While not an exact fit, the gel-foam frequency variations of compliance and modulus are close to those for the dolphin blubber.

5. CONCLUSIONS

The similarity of viscoelastic properties shown here for dolphin blubber and a gel-foam composite indicates that it will be possible to get a close viscoelastic property match. Variations in polymer gel cure, and in the foam matrix material should lead to a very close match. Of course much remains to be learned about the range of viscoelastic property changes in dolphin blubber with location, age, season, etc., but these initial results are encouraging. Rotating disk drag measurements using compliant coating materials of measured viscoelastic properties are underway to determine the validity of the matched shear impedance explanation of the dolphin's reduced drag.

6. ACKNOWLEDGEMENTS

This work was supported, in part, by the Advanced Research Projects Agency, and by the Office of Naval Research. The excised dolphin samples were provided by Brent R. Whitaker.

7. REFERENCES

1. J. Cousteau and P. Diole, Dolphins, Doubleday and Co., New York, N.Y. (1975).
2. M.O, Kramer, J. Aero Sci.,**24**, 459-460 (1957).
3. J.W. Fitzgerald et al, Am. Chem. Soc. Mtg., Chicago, Ill. (Sept. 5, 1985).
4. M.O. Kramer, J. Am. Naval Engr.,**72**, 25-33 (1960); **73**, 103-107 (1961); **74**, 341-348 (1962).
5. M. Gad-El-Hak, Appl. Mech. Rev., **39**, 511-523 (1986); J. Fluids & Struct., **1**, 55-70, (1987).
6. E.R. Fitzgerald and J.W. Fitzgerald, Proc. 2nd Int'l. Conf. Intel. Mt'ls., 510-522 (1994).
7. J.W. Fitzgerald, E.R. Fitzgerald et al, Proc. 2nd Int'l. Conf. Intel. Mt'ls., 523-533 (1994).
8. E.R. Fitzgerald, Proc. Am. Chem. Soc., **60**, 573-578 (1989); U.S. Patent 5,081,872 (1992).

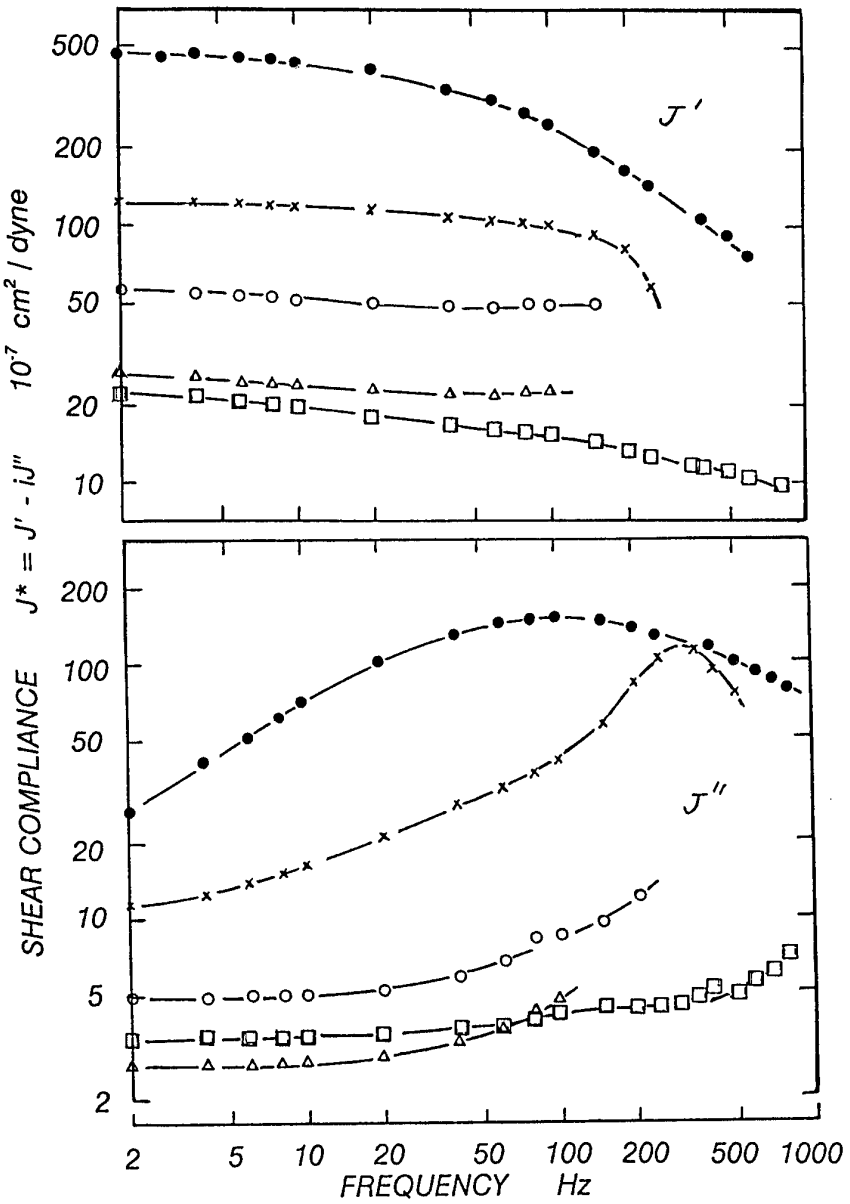


Figure 1 Frequency variation of elastic compliance, J', (top) and viscous compliance, J", (bottom) components of the complex shear compliance, J* = J' - iJ", at 20°C for a 10:1 polymer:curing agent polydimethyl siloxane gel (filled circles), cured 20 hours at 20°C; a 5:1 polydimethyl siloxane gel (x's) at 20°C, cured 36 hours at 20°C, an open cell rubber foam (open circles) at 21°C; an open cell polyurethane foam (triangles) at 22°C; an open/closed cell polyurethane foam (squares) at 20.5°C. After 5 days at 20°C the low frequency 10:1 polydimethyl siloxane values of J' and J" decreased 45%, and the retardation dispersion shifted to higher frequencies; e.g.,the maximum value of J" shifted from 100 to 200 Hz, and dropped from 150 to 83 10^{-7}cm^2/dyne .

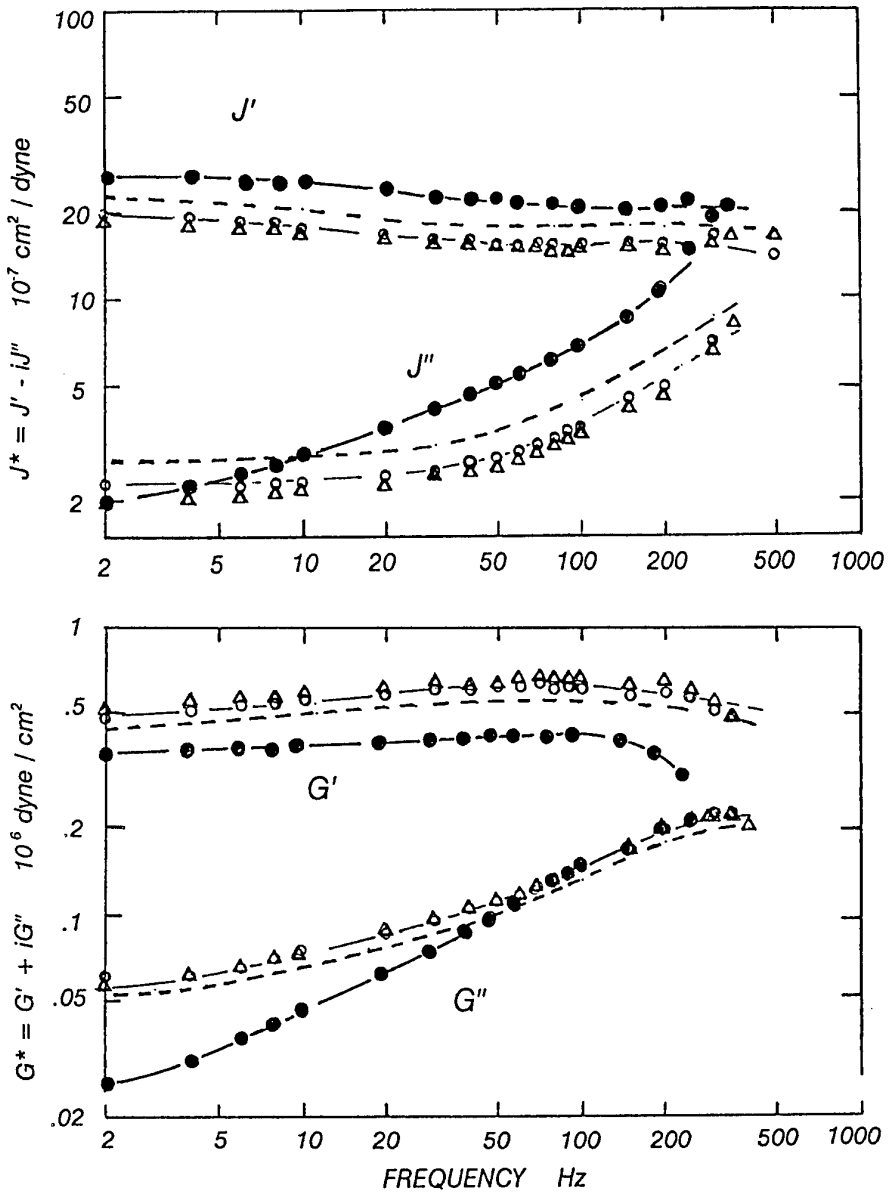


Figure 2 Frequency variation of complex shear compliance, J* = J' - iJ", (top), and complex shear modulus, G* = G' + iG", (bottom) for a gel-filled open cell rubber foam composite (filled circles) at 20°C compared to the corresponding shear compliance (top) and shear modulus (bottom) frequency variations for dolphin blubber at 21°C , 4.5 hours after death (open circles) and 6.5 hours after death (open triangles). The dashed lines represent compliance and modulus values for "live" blubber obtained from extrapolation of compliance and modulus vs time after death plots to 0 hours from measurements taken before the "life to death" transition occured at 5.4 hours as explained in the text. The composite was formed from an open cell rubber foam and 10:1 polymer:curing agent polydimethyl siloxane gel like those of Figure 1.

Intelligent Composites and Health Monitoring

Invited Paper

Some aspects on health monitoring in composite materials

Karl Schulte

Technical University Hamburg-Harburg
Polymer/Composites Section
21073 Hamburg, Germany

ABSTRACT

Health monitoring of composite materials would give improved durability and safety of composite structures. Much effort has been performed in the past to obtain information on the health of e.g. aircraft structures. However, it can yet not been foreseen which monitoring technology will once be used. This paper will give an overview on same selected technologies available, with a special emphasis on electrical methods.

1. INTRODUCTION

Carbon, glass and aramide fibre reinforced composite materials with polymer matrix systems have been in use for several decades. However, there still remain uncertanties concerning the actual mechanical loads which the structure can withstand and towards the effects of damage, as delamination and fibre fracture, due to cyclic loading and impact.

The instrumentation of a structure with strain gauges to ascertain its mechanical performance is not new. Bridges, air frames or automotive structures have been studied and the resulting strains monitored. However, the continuous monitoring of the mechanical condition of a structure during its operating lifetime has usually been precluded, because of the complexity involved in accomodating the very considerable interconnects to all strain gauges.[1]

In order to get inhanced safety and a more effective use of the basic material, there is a need of structural health monitoring during operational life.

On-line health monitoring systems must meet the followig requirements[2]:
1. They must be small and offer the possibility of being located in inaccessible remote areas of the structure and they must be able to transmit information to a central processor.
2. They must compete in sensivity with conventional NDE-techniques.
3. They must be able to on-line monitor a certain area of structure.

2. MONITORING TECHNOLOGIES

2. 1 Load monitoring

In composite laminates the fatigue process is characterized by the initiation and multiplication rather than propagation of cracks. Crack initiation in composites takes place very early in fatigue life and coincides with the first ply failure, i.e., the first cracking of the weakest ply. While in metals, crack growth accelarates during fatigue, the crack multiplication in composites decelerates, resulting in the uncontrolled final rupture of the composite, also called the "sudden death".[3]

Based on strain gauges the damage related variation in stiffness can continuously be monitored. During fatigue cycling, stiffness reduction can be used as an analogue to monitor damage development. Its change can be related directly to stress redistributions which can be expected, if internal damage occurs in composite laminates.[4-6] A typical stiffness reduction curve for the cross-ply laminate with continuous fibres is shown in Fig. 1a. The shape of the curve suggests three regions of interest: an initiation region (stage I) with a rapid stiffness reduction of 2-5 per cent, an intermediate region (stage II), in which additional 1-5 per cent stiffness reduction occurs in an approximately linear fashion, and a final region (stage III), in which stiffness reduction occurs in abrupt steps ending in specimen fracture. [7]

0-8194-2165-0/96/$6.00

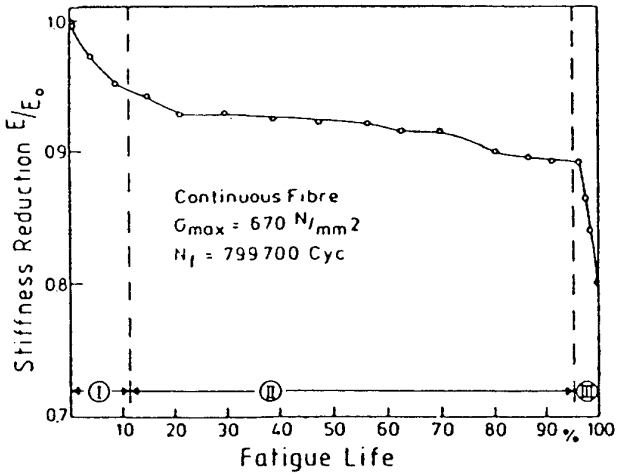


Fig. 1: Normalized stiffness reduction (E/E_0) versus fatigue life. Cross-ply laminate with continuous fibres

2. 2 Temperature monotoring

Under cyclic loading conditions, when performed at high frequences of about 10 Hz, an internal generation of heat leads to an increase in specimen temperature. Polymer materials show an internal heating due to cyclic loading. Therefore a temperature variation can as well be used to monitor damage[8]. During fatigue loading of a composite material the heat generation can mainly be related to the matrix material used, its viscoelastic behaviour, internal friction and the amount of crosslinking. The type of fibre, its volume fraction and orientation and the stacking sequence in a composite laminate additionally effect matrix loading and therefore heat generation. In addition to the materials aspects, conditions as shape of sample, test frequency and load level influence the amount of heating.

However, also under static loading conditions a temperature variation of a material can occur. In 1851 Thomson (Lord Kelvin)[9] showed the proportionality between the load change applied and the resulting temperature variation for an isotropic material under adiabatic elastic deformation and uniaxial stress where

$$\Delta T = -\alpha_1 \, T_0 \, \Delta\sigma / c \, \rho$$

α_1	K^{-1}	= linear coefficient of thermal expansion
T_0	K	= ambient temperature
c	$kJ\ K^{-1}\ m^{-3}$	= specific heat capacity
ρ	g/cm^3	= specific density
$\Delta\sigma$	N/mm^{-2}	= stress change
ΔT	K	= temperature change

The above equation describes, the so called "Thermoelastic Effect". The amount of temperature change of a certain volume element depends on the change of the sum of principal stresses, on its material factors and on the ambient temperature. For an isotropic material with a positive coefficient of thermal expansion uniaxial tensile stresses lead to a decrease in temperature.

In Fig. 2 are shown the results from a cross-ply laminate, containing 0°- and 90°-plies. The fibres in the 90°-plies hinder transverse deformation. They are under compressive load and their temperature change is negative. In addition, the matrix in the 90°-plies is under tensile loading, leading for the matrix, which has a positive thermal expansion coefficient, to a cooling down.

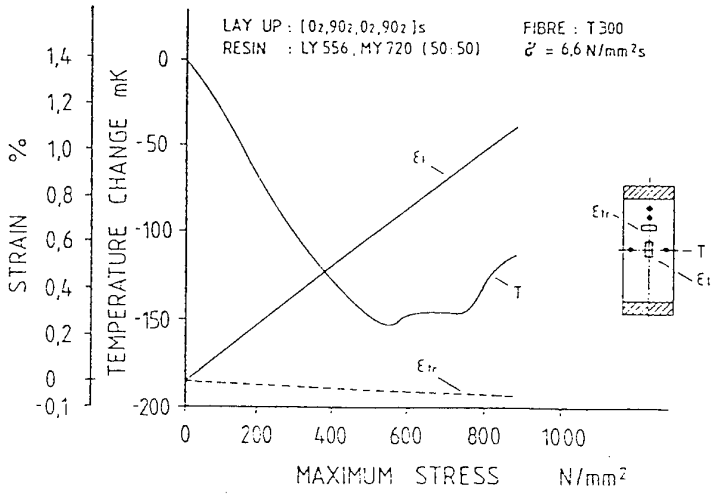


Fig. 2: Tensile test of a cross-ply laminate. Variation of strain and specimen temperature.

Both these effects superimpose the temperature increase in the 0°-plies, and the result is a cooling down of the entire specimen. At higher stresses, with the initiation of transverse cracks in the 90°-plies, the stresses in the 90°-plies are locally released and a load transfer from the 90°-plies into the neighbouring 0°-plies occurs. With increasing number of cracks the temperature increase due to loading of the 0°-plies becomes more and more dominant (the curve of temperature change goes through a minimum) and at high stresses the temperature increase can be measured. Viscoelastic deformations at the transverse crack tips possibly contribute to the temperature increase.

In Fig. 3 is shown the temperature development in a cross-ply test piece. A temperature increase due to dissipation can be observed at the beginning of the test. Later the temperature remains constant. This has two reasons:

- Each specimen has, depending on load level, frequency, stacking sequence and constituents a stable temperature level.[8]
- A damaged specimen has, if a constant damage state is reached, a higher stable temperature level as an undamaged one.[8]

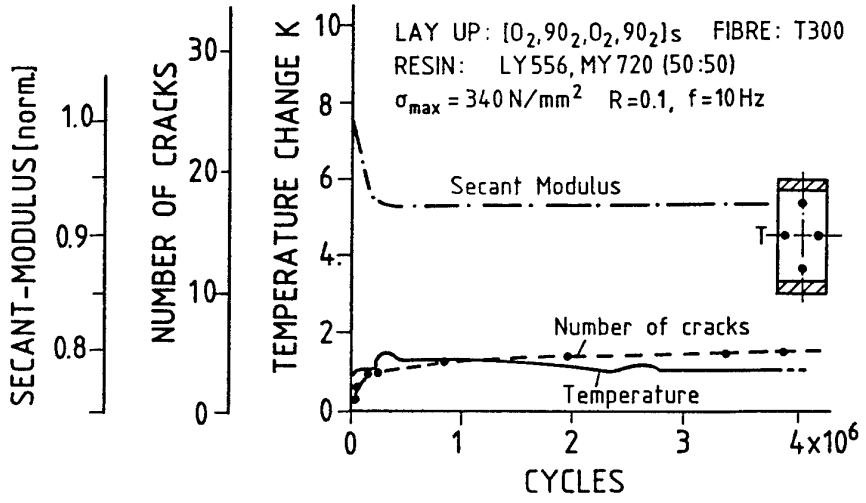


Fig. 3: Fatigue test of a cross-ply laminate at a low load level. Stiffness reduction, development of transverse cracks and temperature change are plotted versus the number of load cycles. Specimen did not fail. Number of transverse cracks taken from x-ray radiographs.

For the present test, where the result is shown in Fig. 3, a constant damage state means, that in early load history (during the first load cycles) transverse cracks initiate in the 90°-plies, which are also responsible for the slight stiffness reduction observed at the beginning of the test. Later the number of transverse cracks, the stiffness reduction and the specimen temperature remain constant.

In the case of continuous damage growth, which will be observed at higher fatigue load levels, also a continuous increase in specimen temperature is measured. Fig. 4a shows the temperature change for four different tests. All tests were performed until specimen rupture occurred. A continuous temperature increase can be observed throughout the tests. This corresponds with the parallel observation of the transverse crack development (Fig. 4b), where the number of cracks increases with increeasing load cycles, and, the higher the cyclic load level the more transverse cracks are formed.

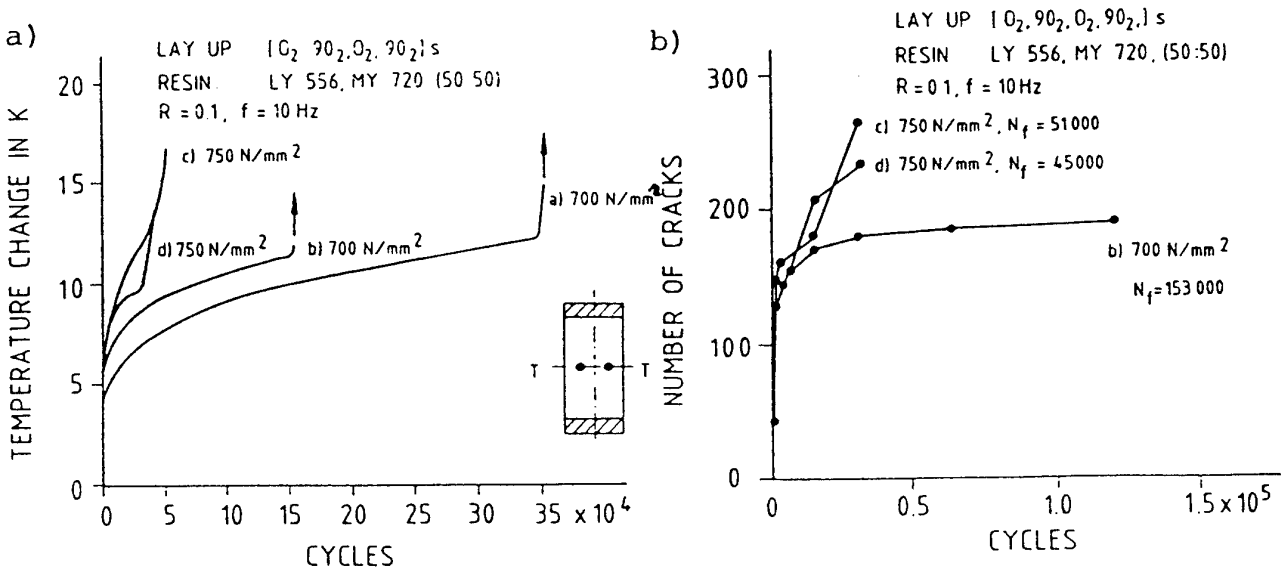


Fig. 4: Fatigue test of cross-ply laminates at high load levels. All specimens run to failure.
a) Temperature change versus number of load cycles.
b) development of transverse cracks versus number of load cycles. Number of transverse cracks taken from x-ray radiographs.

The variation of specimen temperature can be used, as well, as a damage analogue for composite materials. Increasing specimen temperature is a result of increasing (matrix) damage.

2. 3 Fibre optics

Much efforts have been spent in the past to use fibre optics. To obtain reliable sensor signals optical fibres have been integated into the composite structure. They can then be used to produce valuable data regarding the structures current load state as well supply information about the structure´s health.

However, the compatibility of the sensors with the composite is one important problem which has to be solved. Mainly the levels of temperature and pressure used to fabricate a composite laminate have to be such, that melting of the fibre optic coating is avoided, the shift from acrylate coatings to e.g. polyimide coatings is necessary.

Typically optical fibres have a diameter which is between 10 to 100 times larger than most reinforcing fibres. It represents therefore a structural discontinuity and causes a mechanical degragdation:

- Residual stresses arise during processing due to the thermal mismatch between the optical fibre and the host composite.

- The fibre acts as a stress concentrator due to the differing stiffness between the fibre, coating and composite.
- For (transverse) optical fibres the physical size of the fibre and coating do effect the stress concentration in the composite The greater the separation between plies around the fibre the greater are the bending moments experienced by the plies from longitudinal loads. The shape of the resin rich region also effects the results.[10]

Its presence reduces slightly the tensile properties of a composite laminate but severely degrades the compressiv properties.[11] Knowing and solving the above mentioned problems strain maesurements can be performed with satisfactor results, as shown in Fig. 5.[12]

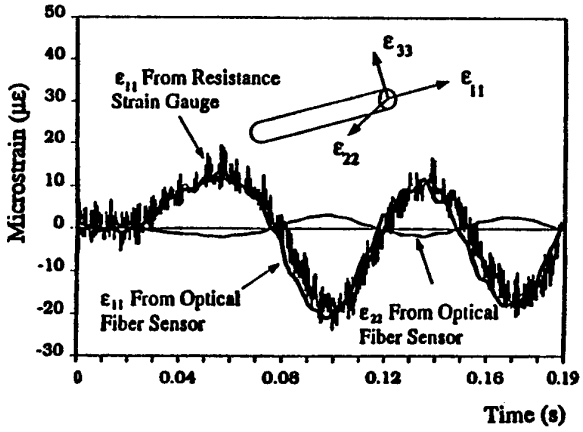


Fig. 5: Comparison of the longitudinal and transverse strain obtained from optical fibre sensors and strain gauges.

2. 4 Electrical response

2. 4. 1 Electrical resistivity (DC-tests)

The DC-technique records fibre breakage in form of an increase in electrical resistivity.[13] The observation of fibre fracture within CFRP specimens is in general, not possible during a load test, except when fibres split off the specimen surface and can be seen with the bare eye, or from accustic attenuation signals. However, the variation in electrical resistivity during static loading is a clear indicator of fibre fracture. Fig. 6 shows the stress/strain curve of a unidirectional specimen together with the variation of electrical resistivity with laminate strain.

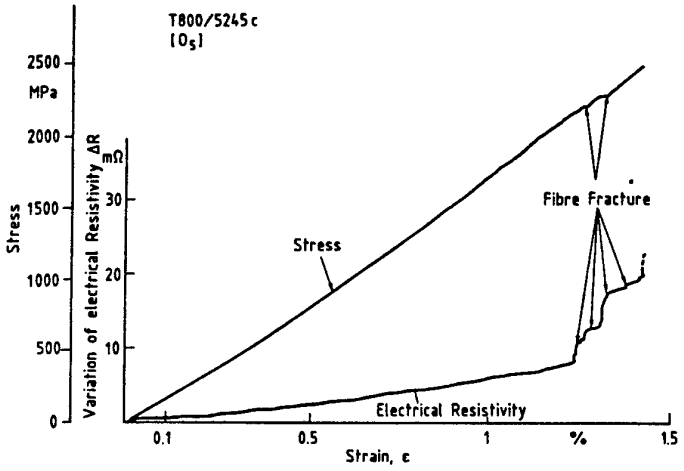


Fig. 6: Tensile test of a unidirectional laminate, showing the stress/strain curve and dependent electrical resistivity variationof a CFRP specimen

The electrical resistivity first increases approximately linearly with increasing fibre strain. This increase in resistivity (R) is expected because

$R = \rho\, l/A,$

with ρ: specific electrical resistivity, l: current path length and A: conductor section. The length l increases under tensile load and A decreases. After about 1.25% strain the electrical resistivity no longer varies linearly. The electrical resistivity rises in stepwise fashion to higher values. This can be directly related to increase fibre fracture. The fibre fracture is partly indicated - but with a much lower resolution - in the stress/strain curve.

The electrical resistivity method, however, cannot only indicate strain and fibre fracture, but also delaminations, one of the most pronounced damage mechanism. In Fig. 7 is shown the result of a tensile test on a unidirectional specimen consisting of 5 plies. The third ply (center ply) was cut through. During initial loading linear elastic deformation occurs, following Hook's law, with a linear increase in electrical resistivity. In the cutted third ply shear stresses transfer the loads from one ply end to the other through the matrix and neighbouring intact plies. When the shear stress exceeds the matrix properties a delamination (under Mode II) initiates, and a plateau is formed in the stress-strain curve. Subsequently the electrical resistivity increases. Only when the delamination growth has come to an end, that is when the third (center)ply is completely separated from the neighbouring plies, a further increase in the stress-strain curve and electrical resistivity can be observed. The reasons are first: During delamination fibres bridging the matrix crack will break and second: An electrical conductivity transverse to the fibre direction is possible at high fibre volume fraction.[14] A delamination will separate touching fibres, this contributes to an increase in electrical resistivity.

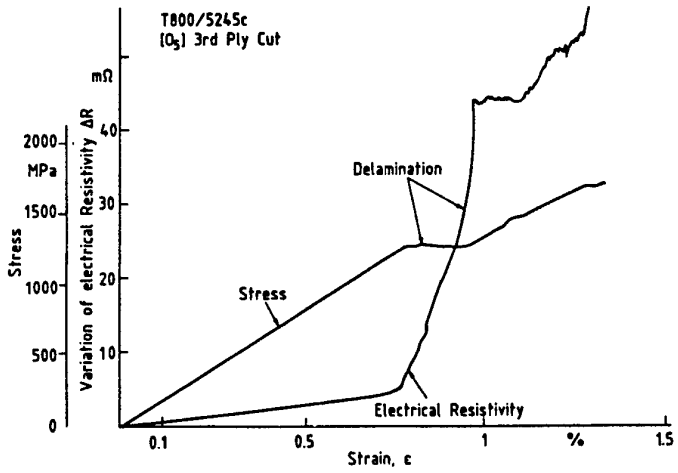


Fig. 7: Tensile test of a unidirectional laminate. Center ply was cut through. Stress-strain curve and dependent variation of electrical resistivity; both indicating delamination growth.[15]

In Fig. 8 is shown the result of a fatigue test on a $[0_2, \pm 45, 0_2, \pm 45, 90]_S$ quasi isotropic laminate. Specimen temperature, electrical resistivity and stiffness reduction (normalized secant modulus) were simultaneously measured and correlated with fatigue life.

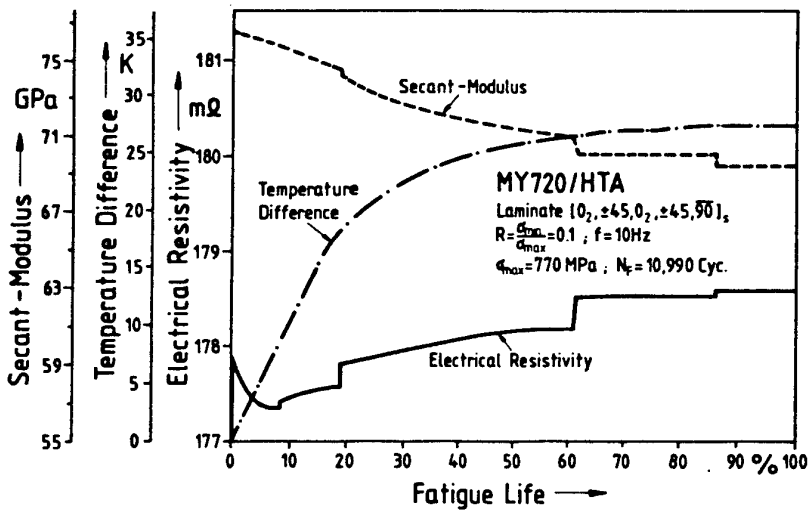


Fig. 8: Variation of secant modulus, temperature and electrical resistivity during cyclic loading (% of fatigue life) quasi-isotropic laminate.

Under fatigue loading, the temperature in a test coupon cannot be regarded as constant; at test frequencies of 10 Hz for example, significant increases in temperature were observed.[13] The variation of the specimen temperature can also be used as a means of detecting damage in a composite. Increasing specimen temperature is a result of increasing (matrix) damage. A good correlation between specimen temperature and stiffness reduction was found in reference[13].

Fig. 8 suggests the following:

(1) During the test a continuous increase in temperature, dependent on frequency, maximum load level and fatigue life, can be seen.

(2) The secant-modulus decreases. The reduction in stiffness can mainly be related to edge delamination growth and the development of transverse cracks in the 90°-ply.[5] However, the stepwise reduction in stiffness has to be related to rupture of the load bearing 0°-fibres.

(3) The variation in electrical resistivity reflects this situation; with increasing damage (reduction in secant modulus) also the electrical resistivity increases. Due to the stepwise reduction in stiffness also the elctrical resistivity responds with a jump in its curve.

(4) At the initial fatigue loading the elctrical resistivity decreases. This is due to the fact, that incarbon fibres the resistivity is temperature dependent and decreases with increasing temperature. Only when the damage growth (delamination, transverse cracks and fibre rupture) accelerates, the electrical resistivity increases again and superposes the temperature dependent resistivity reduction.

2. 4. 2 Dielectrical properties

The observed effect of an increasing load and strain on the capacitance and dielectric dissipation of a CFRP cross-ply laminate is shown in Fig. 9.

While generally the capacitance decreases, the dissipation increases with increasind load and strain. In Fig. 10 the condition in a CFRP specimen is schematically demonstrated. The high resistivity of the matrix causes a capacitance between the fibres. Close or touching fibres cause current flow between fibres which results in a resistivity. Considering the total specimen thickness between the electrodes we have thus a total capacitance (C_{tot}) and a parallel total resistivity (R_{tot}).

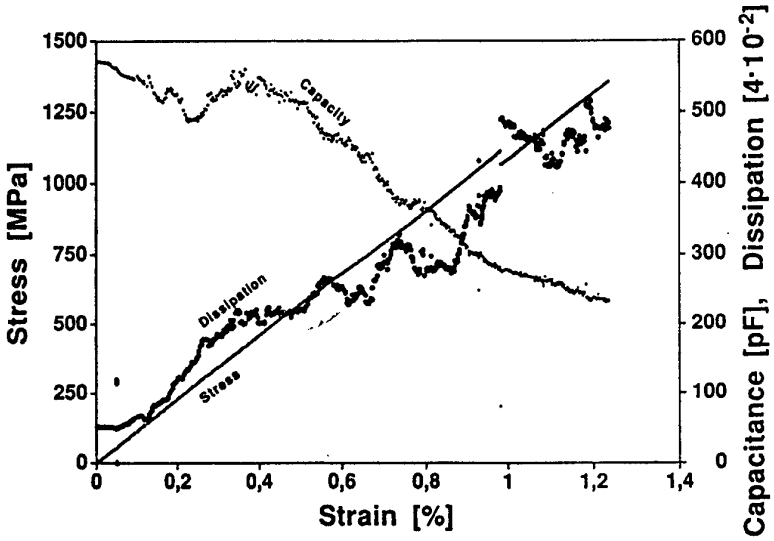


Fig. 9: Tensile test of a cross-ply laminate, showing the stress/strain curve and dependent capacitance and dielectric dissipation (at 1 MHz and 100 mV) of a CFRP specimen

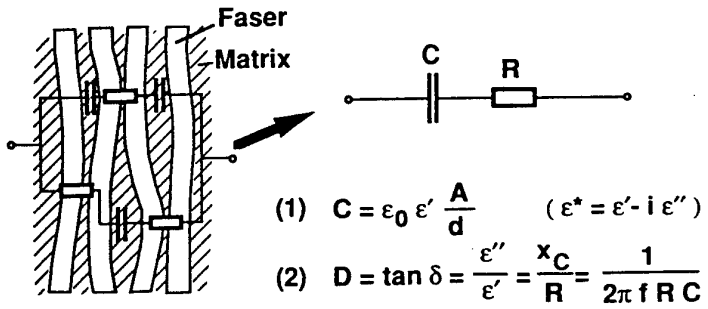


Fig. 10: Condition in a CFRP laminate, electrical equivalent circuit and fundamental relations of AC-properties (C: capacitance, R: resistivity (transvers), A: electrode area, d: electrode distance, ε_0: vacuum permittivity, ε^*: relative permittivity, ε': dielectric constant, ε'': loss-factor, D: dissipation, X_C: reactance, f: frequency)

From fundamental equation 1 (Fig. 10) one can derive that the capacitance decreases because the dielectric constant (ε') of the CFRP material decreaes too. A reason for this effect may be that the conductive, load bearing fibres, get closer during loading due to the high poisson ratio of the epoxy matrix. Other perameters such as the vacuum permittivity and the electrode area remain constant during loading. The elctrode distance (= specimen thickness) decreases, causing an opposite effect, an increase in capacitance. Also matrix cracks lead to an increase in ε' and thus in capacitance due to the formation of new surfaces within the material. These effects may be the reason for the observed unregularities and slope changes in the capacitance curve especially at lower loads where transverse matrrix cracks in the 90°-plies occur. From equation 2 (Fig. 10) it can be seen that the dissipation behaves inverse to the capacitance and laminate transverse resistivity. Like the capacitance, the resistivity decreases because the insulating matrix becomes thinner during loading, enabling a current flow between fibres.

Thus the dissipation reflects two different physical properties (C and R) which are affected by load and strain with the sam tendency.

At about 1% strain of this tensile test fibre breakage occured in the specimen right between the electrodes. This failure of loa bearing fibres leads to a stiffness loss and thus to a drop in load in a displacement controlled test. Locally the former stress o the broken fibres is transferred in neighbouring fibres, resulting in stress concentration and thus in an increasing local stress Because the fibre breakage was observed to be in the electrode area, the dissipation reacts very sensitive by jumping to higher level.

- Measurement of the DC-electrical resistivity, AC-capacitance and dielectric dissipation can be used in situ to detect damage in a carbon/epoxy specimen or component under load.
- Dependent on the load applied to a carbon/epoxy part or specimen, the DC-electrical resistivity, AC-capacitance and dielectric dissipation varies directly as a result of the actual strain or load.
- The conclusion to be drawn is therefore that the measurement of DC-electrical resistivity, AC-capacitance and dielectric dissipation in a CFRP component is a non-destructive evaluation (NDE) technique, with which composite parts can be inspected even when they are in use.
- While the response of the DC-resistivity due to load or strain and fibre breakage is quite well understood, further fundamental investigations will be needed for fully understanding the response of AC-capacitance and dielectric dissipation due to load, strain and different damage mechanisms

2. 4. 3 Piezo electrics

Piezoelectric fibres are currently under development.[16] They provide the possibility of actively measuring the actual load (o vibration) induced strain variations. Piezoelectric fibres with an electric resitant coating are introduced e.g. in a fibr reinforced composite. Mechanical stress applied on the component is converted by the piezoelectric fibre into electrica energie which reflects the strain variation. The fibres can be produced with diameters between 10 and 100 µm. They wil therefore perfectly fit between the reinforcement glass or carbon fibres. However, their mechenical properties are still poor with low tensile strength and fracture strain. They need further development.

2. 5 Modal analysis

The analysis of vibration modes seems to be promising for structural health monitoring. The incorporation of piezoelectri sensors (fibres) as discribed in the above section, can provide the vibrational data. It was already shown, that higher harmoni frequences are highly affected by size and location of delaminations. Modal analysis on a frequency based approach can us the piezoelectric fibre sensors for health monitoring.[17]

3. REFERENCES

1. B. Culshaw,"Strain and temperature measurements in composites". ECCM Smart Composites Workshop, Sept. 21-2 1993, Bordeaux (F).Editors: P. Gardiner et al., Woodhead Publisher Limited, Cambridge (UK). pp. 25-39.

2. C. A. Rogers,"Solid-state actuators for in -situ monitoring". Proc. 4th Japan Int. Symposium, Sept. 25-29, 1995, Toky (J). Editors: Z. Maekawa et al., pp. 1066-1069.

3. Chou P.C. and Croman R., Degradation and sudden-death models of fatigue of graphite/epoxy components. ASTM-ST 674 (1979) pp. 431-454.

4. Hahn H.T. and Kim R.Y., "Fatigue behaviour of composite laminate", J. of Comp. Materials 10 (1976) pp. 156-180.

5. Reifsnider K.L., Schulte K. and Duke J.C.,"Long-term fatigue behaviour of composite materials", ASTM-STP 813 (198 pp. 136-159.

6. Schulte K.,"Stiffness reduction and development of longitudinal cracks during fatigue loading of composite laminates Proc. European Mechanics Collocquium 182, "Mechanical characterisation of load bearing fibre composite laminates", 29-31 Aug. 1984, Elsevier Science Publisher, London (1985) pp. 36-54.

7. Schulte K.,"Damage development under cyclic loading", Proc. European Symposium on Damage Development and Failure Processes in Composite Materials, 4.-6. May 1987, Leuven Belgium (1987) pp. 39-54.

8. Neubert H., Schulte K., Harig H.,"Evaluation of the fatigue behaviour by monitoring continuously temperature development in cfrp-laminates", ASTM-STP 1059 (1990) pp. 435-453.

9. Thomson W., Mathematical and Physical Papers 1 (1882), Collected Works, Cambridge University Press, Cambridge (1882) pp. 174-332.

10. R. Davidson and S. S. J. Roberts,"Finite element analysis of composite laminates containing transversely embedded optical fibre sensors", 1st European Conf. on Smaet Structures and Materials, Glasgow (UK) 1992, pp. 115-122.

11. D. W. Jensen et al.,"Performance of graphite/BMI laminates with embeded optical fibres", Smart Materials Structures, 1 (1992) pp.24-35.

12. H. Singh, Y. L. Lo and J. S. Sirkis,"Meaningful damage evolution tracking in composites using structurally embeded optical fiber sensors", Smart Structures workshop, Arlington ,TX, Sept. 1993.

13. K. Schulte, Ch. Baron,"Load and failure analysis of cfrp laminates by means of electri resistivity measurements", Composites Science and Technology 36 (1989) pp.63-76.

14. W.J. Gajda," A fundamental study of the electromagnetic properties of advanced compo materials", RADC-TR-78-158 AO59029, (1978).

15. K. Schulte and H. Wittich,"The electrical response of strained and/or damaged polymer matrix composites", Proc. of ICCM-10, Whistler (Canada), Vol. V, 1995, pp. 349-356.

16. H. Scholz et al.,"Processing and properties of PZT-fibres for 1-3 composites", Proc. of ICCM-10, Whistler (Canada), Vol. IV, 1995, pp. 481-488.

17. L. F. Campanile,"A modal method for structural health monitoring", 4th Int. Conf. on Adaptive Structures, Editors: E. J. Breitbach et al., Nov. 2-4, Cologne (Germany) 1993, PP. 205-219.

A proposal for a new maintenance inspection

Koichi EGAWA

Niigata Institute of Technology, Department of Mechnical & Control Engineering
Fujihashi 1719, Kashiwazaki, Niigata, Japan 945-11

ABSTRUCT

Thinking about intellectualization of nondestructive inspection, the author found that maintenance inspection was the most beneficial one of applying health-monitoring concept. The goal of this new smart maintenance inspection is; continual monitoring and self-, automatic-inspection and warning, instead of inspectionp eriodical and by many hands and slow-results obtaining today. On this new, smartm aintenance inspection, the author presents a method and its problems.

1. PRESENT STATUS OF NONDESTRUCTIVE INSPECTION

Nondestructive inspection is a different technology from that of production, and its aims are to guarantee the quality of industrial production and to reduce inspection cost.

It is used for the purpose of;

(1)quality control;
selecting condemned goods out in each production line.

(2)quality assuarance;
checking performance of ordered production and guarantee safety using at delivering time.

(3)maintenance inspection;
the inspection done by users for long time up to the end of the life of objective structures.

Table 1 Major techniques of NDI

1.	Radiographic testing	(RT)
2.	Ultrasonic testing	(UT)
3.	Magnetic particle inspection	(MT)
4.	Leakage flux inspection	(MT)
5.	Eddy current inspection	(ET)
6.	Penetrant inspection	(PT)
7.	Leakage testing	(LT)
8.	Potential drop method	
9.	Thermography	
10.	Optical method	
11.	AE testing	
12.	Visual inspection	

At early time, manupulation of inspection devices, observation and judgement of inspection results were done by hands in every techniques of nondestructive inspection(NDI) shown in Table 1. But automatization of NDI were gradually developed by the demands for reduction of inspection cost and the shortage of qualified inspectors. In this process UT, MT, ET and other techniques using electronic instruments were automated more easily than RT, PT and others which require man's hands. In factories, that is, in quality control, automation of NDI were developed greatly.

In quality guarantee, progress of automation of NDI depended upon the size and number of inspective objects; it is easier to apply automated NDI for small size

0-8194-2165-0/96/$6.00

and large number one, but, on the contraly, for small number and large size one it is not. Even today they are inspected mostly by hands except by using robot for welded tanks and building walls as rare examples.

In mainatenance inspection most of the objects are checked by man even now with stopping operation of these objects. Comparison of these three category of NDI relating with inspection term, frequency and means is shown in Table 2.

Table 2 A classification of NDI

	Classification	Inspector	Period	Frequency	Time	Means
1	Quality control	Maker	Each production process	One	Short	Fairly A
2	Quality assurance	Maker	Delivering time	One	Short	A or H
3	Maintenance inspection	User	Periodical	Many	Long	Mainly H
	Classification	Inspective object				
1	Quality control	Factory procuction (Mass-production)				
2	Quality assurance	Production by assembling (Large and middle size)				
3	Maintenance inspection	Production by assembling (Ultra large and large size)				

notes, A:automatic inspection, H:Inspection by hands

2. A PROPOSAL FOR NEW MAINTENANCE INSPECTION

2.1 Intellectulization of maintenance inspection

Here, the author try to construct a thought of future NDI by using concept of smart structures which is a revolutional idea to make structures having capacity of living things. According to this concept the fuction of nerves, muscles and brains being put into structures, and that means one must put sensors, actuators, neural networks and computor chips into structures. In Fig. 1 this concept is shown by the example of intellectulization of composite laminate[3].

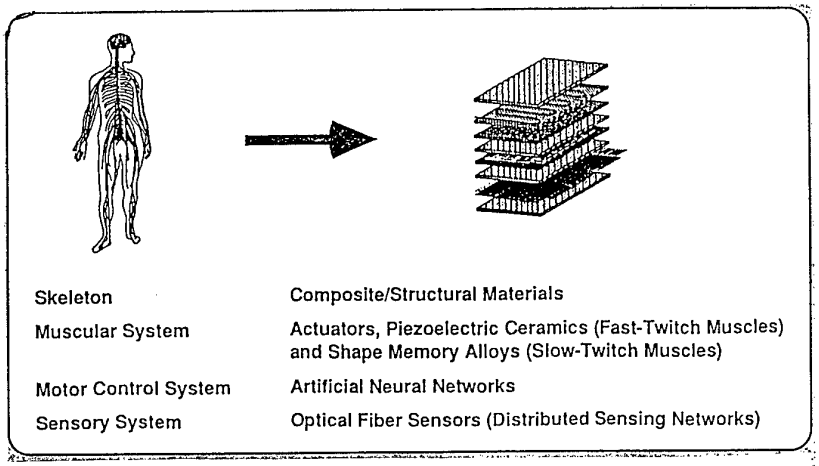


Fig. 1 Prevailing concepts of smart structure (C. A. Rogers, 1992)

Then the idea of NDI in near future get closer to automatization of NDI. Thus one can easily find that the magnitude of expected advantages when NDI will be intellectualized depends inversely upon the degree of automatization, and so the maintenance inspection is the most advantageous one. This will be explained by using Table 2, concerning the term and frequecy and the requirement of labour of maintenance inspection. They are long, many and much, and so the inspection cost becomes high. However, there are many objects, like oil and gas strage tanks, to be inspected pepriodically, and when it would broken the damage given to surroundings will be huge and sometimes human lives will be lost. Thus maintenance inspection can not be avoided even it requires works, time and spendings greatly. Moreover, we have a big problem that one can not cope with the accidents during periodical inspection even if we use the knowledge of reliability. When we want to ensure more safety, we need the system which will allow us to monitor inspective objects all the time.

Now backing to the concept of smart structures, the author try to get an idea of such monitoring systems. Following the definition shown in Fig. 2[4], there are five steps of intellectulization, and the first step, sensory structures, which have distributed sensor network in its body like nerves in a creature, is very useful concept for reforming maintenance inspection. When one can make this concept real on the structures, which are inspected periodically by hands now, we can expect to moniotor those structures ceaselessly and to obtain self-and quick-warning from themselves. These are the ideal property of maiantenance inspection we have been waiting for long time.

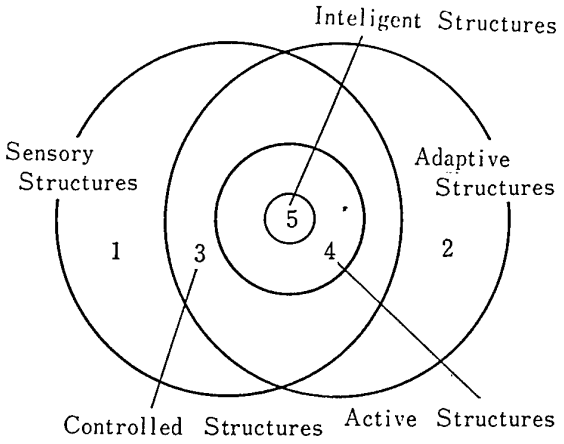


Fig. 2 Definition of intelligent structure (Wada et al, 1990)

2.2 Sensors

The required qualities of the sensor for this new maintenance inspection are;

(1)checking damaged and/or cracking location not by point by point system, but by the system covering large area and even three dimensional space.
(2)prompt responce for quick warniing.
(3)duarability.
(4)capability for continual monitoring.
(5)low cost--including measuring system.
(6)insensitive of electric, magnetic, thermal, humid, radiate, vibrate, noisy circumstances.
(7)small size, light weight.

Optical-fiber sensor(OFS) are chosen as a sensor satisfied these requirements in some extent. Comparing with electric resistance strain gauge(ERSG) which is the most popular strain sensor using in the field, OFS has four advantages as follows;

(1)only one lead wire required, instead of two for ERSG
(2)with breaking off of OFS, one can estimate the location where large deformation, crack or droping out of bolts, some parts, tiles, a part of walls or something others of inspective structures occurs.
(3)covering much longer distance and larger area
(4)a great possibility of becoming line-sensor which can measure or detect along the wire line

As intellectualization of structure began in aeronautical and space engineering, so the sensor attachment was decided to be embedding from the first, and luckily fiber-reinforced plastic laminate was becoming one of the major materials from that time. The study of embedding OFS in FRP laminate began from the begining, and it includs ingress and egress issue, connection and interaction of sensor and material.

On the other hand, for concrete structures like buildings, bridges, high-ways, one can embed OFS, but we will face the repairing problem after breaking of OFS. Because these structures will be used for long time after OFS broken and crack or other damage of the structure being repaired. We can not easily replace large concrete columns or girders even if several cracks occure in them. So we must attach OFS and other sensors on the outside for these structures. Choice of adhesives, research of attachment method will be required for these purpose.

2.3 A smart mainatenance inspection

There are many studies of making an airplane a sensory structure[5]. Summerizing these studies for obtaining a thought of new smart maintenance inspection, the result becomes as follows;

(1)large scale development researches are going on.
(2)study is developing considerably.
(3)OFS is adopted mainly; it is used as a sensor of measuring strains, and also as a sensor of point detection where large deformation or crack or other damage occurs.
(4)it is planned to used other sensors like AE and ERSG etc.
(5)embeddment of OFS is a must. Distribution of OFS is done mainly in the form of bented line or lattice.
(6)OFS being embedded only in FRP laminate.

From this summery, a thought of smart maintenance inspection is constructed.

(1)OFS is distributed all the part of structures or attached to the special points as jointed, welded part and to the place of large deformation expected.
(2)building up measuring system including computor and warning device as shown in Fig. 3[5].

(3)sensing mainly by OFS broken, and by this fact the location where the deformation being over the threshold value being found

(4)for the location where the magnitude of measuring quantity being necessary, OFS, AE, ERSG and other sensors being used.

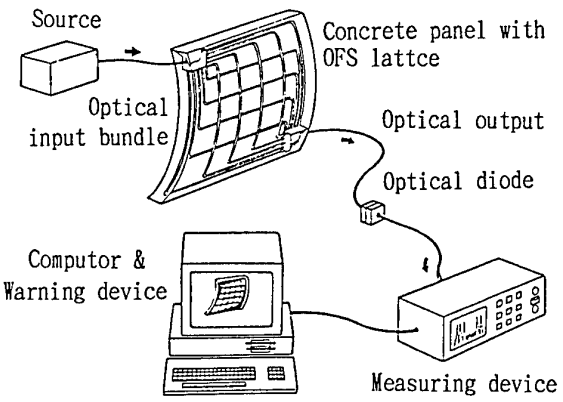


Fig. 3 Distributed OFS and its measuring, warning system

A final thought of sensroy structure is the health monitoring concept introduced by T. G. Geraldi as health monitoring aircraft[6]. The main structural parts of health monitoring aircraft was made by composite laminate with distributed OFS. This OFS is used at first as a sensor for monitoring temperature and pressure of curing process of composite laminate. When the aircraft was assembled, the OFS measured residual strains caused by assemblage. During operation strains and accelerations of the aircraft were monitored, including emergency cases like gusts, fires, thunderbolt falls, being shot, maneuvering miss etc. Finally these strains/stresses were accumulated for estimating residuallife of the aircraft comparing its calculated one, and when time being come its retirement was declared by this monitoring system in the aircraft itself.

It is difficult to resist to put this wonderful idea to monitoring many large civil-and infra-structures like bridges, highways, tunnels, dam walls, building, strage tanks etc. The main difference between health monitoring of aircraft and of these large structures is material; concrete and welded steel are main material in the latter case. As attaching method of OFS and other sensors on concrete and welded steel one must think about adhering or welding adding to embedding. And the structures are large and heavy, there is possibility to choose other sensors like composite strand, electric wires, shape memory alloy wires/tubes/bars etc which are strong enough to endure severe construction work process.

3. DISCUSSION

Thinking about NDI at present day, importance of maintenance inspection is gradually increased, because there occured many accidents like bridge falls, leakage of crude oil from storage tanks all over the world. As the nature of human beings we use these infra-and civil-structures more and more severely and adding this tendency these structures are getting older and older. Thus new maintenance inspection to which many new technologies are introduced is demanded strongly. The author checked the present status of NDI technology and found that it is one of the most important and advantageous thing to introduce health monitoring concept into maintenance inspection and bring forth new maintenance inspection which can meet this expectation. For realizing this thought, the author checked out several problems to be solved;

(1)how to use OFS and other sensors.
  a)measuring physical quantities like strainor temperature, or assessing the location of these quantities over the threshold value and/or crack or some damages occured.
  b)embedding method.
  c)attaching method (assessment of endurance being required).
  d)ways of distribution (line, plane, three dimensional).
  e)measuring system including self-and automatic-warning system.
(2)development of new sensors.
  a)strong enough to endure severe construction process.
  b)SMA wire, pipe, bar----cost, endurance.
  c)carbon fiber strand, metal wire/rope----cost, corrosion resistance, endurance.
(3)materials(concrete, welded steel) of structures to be measured.
  a)threshold measurement or quantitative measurement.
  b)requiring sensitivity (minimum quantity of measurement).
  c)area of measurement for one unit part (length, area, depth).
(4)interaction and endurance
  a)sensitivity change of sensors during long time using and/or embedding.
  b)influence of lead wire to the sensitivity of sensors.
  c)degradation of strength(especially fatigue strenght) of the material by embedding or attaching sensor and lead wires.
  d)influence of coating or painting to the sensitivity of the sensors.
(5)repairing.
  a)repairing of sensors.
  b)repairing of structures.
  c)design of assembling units or parts of the structures which can be replaced easily when damages occured.

The goals coming from the idea of applying health monitoring concept to maintenance inspection are, I would like to say, continual-, automatic- monitoring and automatic-, self-warning by the inspective structures themselves.

4. REFERENCES

1. Y. Ishii, New Nondestructive Inspection Engineering, Sampo Press, Tokyo, 1993.
2. K. Egawa, "A proposal of intellectualization of Nondestructive inspection", Machine Science, Vol. 46-4, pp. 407-414, April 1994.
3. C. A. Rogers, Note of One-day Seminar by J. Sirkis, Japanese Society for Nondestructive Inspection, 1993.
4. B. K. Wada et al, "Adaptive structures", J. of Intell. Mater. Syst. & Struc., Vol. 1-1, pp. 157-174, April 1990.
5. R. M. Measures, "Smart structures with nerves of glass", Prog. Aerospace Science, No. 26, pp. 289-351, 1989.
6. T. G. Geraldi, "Health monitoring aircraft", J. of Intell. Matr. Syst. & Struc., Vol. 1-2, pp. 375-385, July 1990.

Paper presented at the Third ICIM/ECSSM '96, Lyon '96

Qualitative Nondestructive Evaluation Research at CIMSS

Frederic Lalande and Craig A. Rogers
Center for Intelligent Material Systems and Structures
Virginia Polytechnic Institute and State University
Blacksburg, VA 24061-0261

ABSTRACT

A brief overview of the qualitative nondestructive evaluation techniques developed at the Center for Intelligent Material Systems and Structures (CIMSS) is presented. The principal goal of the three techniques (impedance-based, laser Doppler vibrometer-based, and particle tagging) is to detect, on-line, incipient damage before the structural integrity is affected. By providing a better assessment of the structure, these real-time health monitoring will significantly reduce maintenance costs.

INTRODUCTION

The engineering community has great interest in the development of new real-time, in-service health monitoring techniques to reduce cost and improve safety. The current health monitoring of complex structures is often based on a preventive inspection schedule, inspecting the critical areas of the structure at pre-set time intervals. With the current health monitoring techniques, the complex mechanical systems needs to be taken out of service for an extended period of time for the inspection. The inspection becomes even more lengthy and expensive for inaccessible locations. Also, on the same preventive basis, structures are often withdrawn from service early, even if the structure is still capable of performing its task.

Currently, various NDE techniques capable of detecting microscopic cracks and incipient damage are used to inspect critical sections of structures. One common NDE method is ultrasonic (A, B, and C scans), which monitors the transducer echoes of the specimen as a function of time to detect the presence of defects. This technique is very useful but usually has the inconvenience of requiring a liquid couplant between the ultrasonic transducer and the structure to give accurate results. This method can be difficult and tedious for in-service NDE. Another type of NDE is based on a variation of the structural vibrational properties. The coin-tap test, the mechanical impedance method, and the membrane resonance method are among this second sonic vibration family. Most of the techniques do not need the liquid coupling, but still require a physical contact between the transducer and the structure. The sensitivity to small defects of sonic vibration methods is usually reduced due to the typical operation frequencies limited to 30 kHz. Other NDE techniques include X-radiography and passive thermography. However, an important drawback of these techniques is that they often require access to the structure to be inspected and involve bulky equipment.

There is a need of developing new health monitoring techniques that would reduce the off-service time and the inspection, maintenance, and operating costs; as well as increase the reliability of the NDE method. One way to fulfill this need is the development of a qualitative real-time health monitoring technique, which would provide a warning when incipient damage occurs that can be fixed easily, rather then when serious damage requiring extensive repairs occurs. The warning would obviously be most useful when damage is initiated rather than when serious damage has occurred and the structure's functions are compromised.

In the development of new qualitative NDE techniques, various features should be included in order to distinguish them from the currently used NDE techniques. The first feature is the possibility of performing real-time monitoring, which can give a better assessment of the structural health status at all times. This increased knowledge of the current status of the structure can reduce greatly the maintenance costs because thorough inspection of the structure would be done only when necessary. The second positive feature would be qualitative NDE as opposed to quantitative NDE. A quantitative NDE technique gives more information than a qualitative NDE technique by alerting the operator not only of the presence of damage, but also the extent of the damage. On the other hand, a qualitative NDE techniqueallows a real-time structural assessment, which can be easily implemented on-line, throughout the life of the structure. The third positive feature would be a non-model NDE technique. A non-model technique can be applied easily to complex structures since no theoretical or numerical modelization is necessary. Finally, the new NDE technique should be inexpensive to implement and to operate to insure its competitiveness against other traditional NDE techniques. The possibility of retrofit application of the NDE technique is another advantage. An ideal NDE technique would have all the features discussed, but this would be difficult to achieve in a realistic world. By reconciling of some of the features, new NDE techniques can be tailored to given applications.

0-8194-2165-0/96/$6.00

REAL-TIME IMPEDANCE-BASED TECHNIQUE

The impedance-based health monitoring technique utilizes the changes in the dynamic response (due to damage) to qualitatively identify damage. But, it is different from modal analysis-based methods. The fundamental difference lies in the frequency used to interrogate the structure, i.e., excite and sense the resulting vibration magnitude and phase. The frequencies used in this technique are much higher than those typically used in modal analysis-based methods. To sense incipient-type damage which does not result in any measurable change in the structure's global stiffness properties, it is necessary for the wave-length of excitation to be smaller than the characteristic length of the damage to be detected. Finding damage when it is at an incipient level and before the global structural integrity is compromised, is most useful. This is because it can provide us with a warning before actual failure occurs. The modal analysis-based techniques, since they typically rely on lower-order global modes, are not sensitive to incipient-type damage. The damage, generally, must be of a global scale for it to cause an experimentally measurable change in the lower-order global frequencies and modes. The other serious limitation of the modal analysis methods is the extreme sensitivity of the frequencies and modes to the boundary conditions. For aircraft structures, changes in the mass and stiffness are a part of the normal operation of the aircraft, e.g., consumption of fuel from the wing fuel cells, retraction and extension of landing gears, release of external stores, movement of control surfaces and flaps, etc. Simulation of all possible normal usage changes and their effect on the modal parameters is impossible to store so as to distinguish them from damage. Even under very controlled conditions, it would be extremely difficult to reproduce the aircraft for modal testing in the same configuration in which the original data was acquired.

The electrical impedance approach to local damage identification:

The impedance-based technique utilizes small PZT patches to provide high-frequency excitation, typically in the high kHz range, to the structure being monitored. By using the direct and the converse electromechanical properties of piezoelectric (PZT) materials, the simultaneous actuation and sensing of the structural response is possible. The variation in the electrical impedance of a PZT bonded to the structure of interest, while driven by a fixed alternating electric field over a frequency range, is analogous to the frequency response but has much higher resolution and is more easily obtained. The size of the PZT patch-sensor is typically small (less than 0.5 sq. in., .01 in. thick), allowing for non-intrusive installation. Electrical high-frequency excitation at low power is another benefit of the solid-state PZT actuator-sensor. High-frequency excitation provides two benefits: the response is dominated by local modes and incipient damage like small cracks, loose connections, and delaminations, producing measurable changes in the impedance characteristics. The high frequencies also limit the actuation/sensing area. Thus, it is possible to say with certainty that the change in impedance is due to damage in the sensing area and not due to a change in far-field boundary conditions, such as mass loading, etc., which may be part of the normal usage of the structure. Localization is the unique feature which makes this vibration signature-based technique practical for implementation on real complex structures. Another very significant advantage of this technique is that it relies on well-developed high-frequency electrical impedance instrumentation.

Proof-of-concept demonstrations of the impedance-based technique:

The impedance-based NDE technique has been successfully tested on critical sections of three complex structures: the bolted joint between the fuselage and the vertical tail of a light aircraft (Figure 1)[1]; the bolted joint of a bridge structure [2]; and the connections between members of a four-bay space truss [3]. In all of the demonstrators, the localization of the sensing area was observed as well as the sensitivity to incipient damage in the structure. The impedance-based technique has also been used to monitor a high-strength composite repair patch bonded on an aluminum plate [4]. The crack growth and the debonding of the composite patch were successfully monitored. Finally, cracks and abrasive wear were monitored in high-precision gears [5]. For large structures that require several collocated actuator/sensors, the

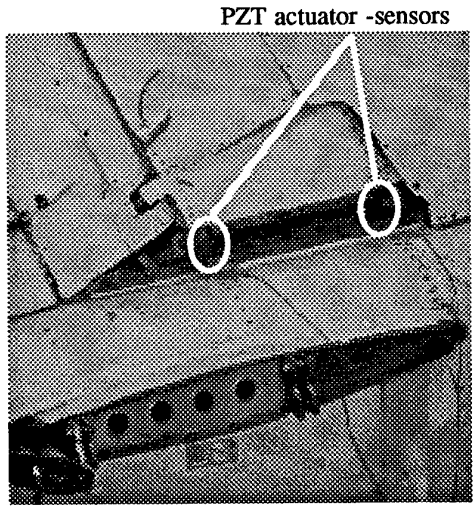


Figure 1. *The integrity of the two main brackets which connect the rear fuselage to the vertical tail of a Piper Model 601P airplane was monitored in a proof-of-concept demonstrator.*

technique has been automated where a computer is used to control a single impedance analyzer to monitor several sensors in sequence [3].

The experimental results for the bolted aircraft joint are presented below. The two graphs in Figure 2 show the real admittance measurements of the actuator/sensor with local damage and global damage, respectively. The change in the electrical admittance measurements with a small defect (smallest possible turn of the connecting bolt) is significant while the measurements are unaffected by distant damage. The principal conclusions drawn from this work were that: i) the technique, because of the high-frequency, is very sensitive to minor change; ii) the actuation-sensing area is limited to a small area. The localization of the sensing area provides a practical means of utilizing vibration/impedance measurements to monitor critical sections of structure.

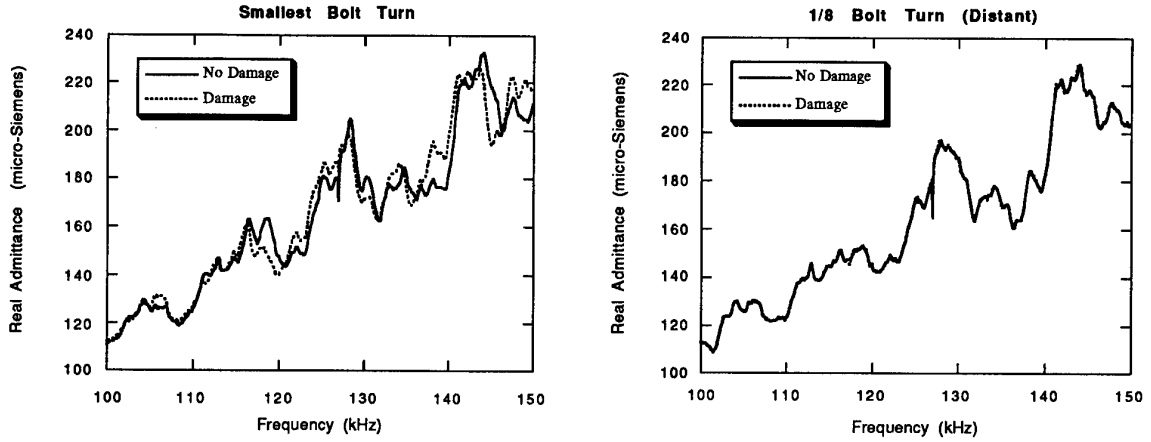


Figure 2. *Graph on the real electrical admittance of the PZT actuator-sensor. Note the large variations in the local bolt while the values for the distant bolt values remain unchanged.*

A scalar damage index used to simplify the interpretation of the impedance changes is shown in Figure 3 for the aircraft bolted joint, with five different types of damage, both local and far-field. The damage index is defined as the sum of the differences of the real admittance change, squared at each frequency step. This damage index is then normalized to 100% with respect to the local smallest bolt turn to which all other damage is then relatively compared. A larger damage index than 100% means more structural damage than the reference smallest bolt turn. The principal advantage of this damage index is the facilitation of the result interpretation. Based on the damage index, damage can be reported to the operator automatically when a threshold value is reached, in a green/red light form.

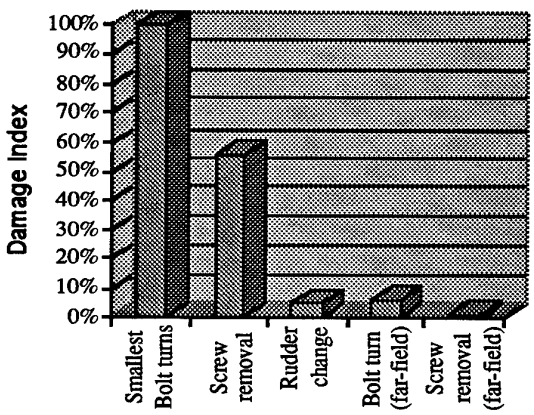


Figure 3 *Damage index of a bolted joint between the fuselage and the vertical tail of an aircraft subjected to various local and far-field alterations.*

Advantages of the impedance-based technique:

The impedance-based health monitoring technique has been shown to be very efficient for the detection of incipient damage in complex structures. In summary, this new qualitative NDE technique has the following principal advantages:

- The technique is not based on any model, and thus can be easily applied to complex structures;
- The technique uses non-intrusive and small-size actuators to monitor inaccessible locations;
- The technique is unaffected by changes in boundary conditions, loading, or operational vibrations;
- The technique can be implemented for real-time health monitoring;
- The continuous monitoring provides a better assessment of the current status of the structure, which can eliminate the scheduled base inspections.
- The added weight of the actuator/sensor is negligible.

NON-CONTACTING LASER-DOPPLER VIBROMETER TECHNIQUE

A new NDE technique based on membrane resonance and using a laser Doppler vibrometer system is currently being researched at CIMSS. This NDE technique has the principal advantage of being non-contacting, covering large areas, and operating over a high-frequency bandwidth. This laser-based technique differs from the membrane resonance method currently used in which the instrumentation to excite and read the structural response requires a physical contact with the structure to be monitored. The contacting transducer, the maximum operating frequency of 30 kHz, and the multipoint excitation are all undesirable properties that need to be resolved. By replacing the transmitting and receiving transducer probe with a laser Doppler vibrometer system to read the structural velocities and with a single piezoceramic actuator bonded to the structure to excite the system over a high-frequency bandwidth, a more performant NDE technique is obtained. The non-contacting laser can be automated to scan large areas quickly and accurately and can operate at frequencies up to 100 kHz, which allows the technique to detect smaller defects.

The membrane resonance technique is based on the dynamic characteristics of the structure, which will be modified by structural defects. The principal concept is to consider a debond or a delamination as a membrane with clamped edges. This membrane will have added resonant frequencies to the base structure resonant frequencies, which will induce higher velocity amplitudes in the debonded or delaminated than in the neighboring intact structure. By measuring the surface velocity amplitude, one will be able to locate precisely the damaged areas.

Various factors need to be considered for this novel damage detection method to be reliable. First, the technique works better if the stiffness of the debonded/delaminated area is smaller than the stiffness of the base structure. When the stiffnesses are similar, the base structure and the damaged area will have similar velocity response amplitudes. This implies that the sensitivity of the NDE technique will decrease with increasing depth of the delamination in a composite. Second, the method will be more precise if more than one membrane mode is included in the excitation frequency range. An excitation of numerous modes will produce a higher RMS value of the transverse velocity of the structure.

Proof-of-concept demonstrations of the laser Doppler vibrometer technique:

The laser Doppler vibrometer NDE procedure has been successfully applied to detect debonds of glass/epoxy repair patches bonded to aluminum plates [6] and debonds of graphite/epoxy repair patches bonded to a concrete block [7]. The technique was shown to be very sensitive, detecting the shape of the defect very accurately. The detection of delaminations in composites was also successfully demonstrated [8].

The aluminum plate with the bonded glass/epoxy composite repair patch is shown in Figure 4, with a corner debond created by the incorporation of Teflon tape. A piezoceramic actuator is bonded on the aluminum plate to induced the high-frequency broad-band excitation. The surface velocity response was read with the laser Doppler vibrometer. An RMS meter averages the velocity response over the excited frequency range to a scalar value for an easier output. The resulting surface velocities from a 25 - 50 kHz excitation is presented in Figure 5. The corner debond area of the glass/epoxy repair patch has an RMS velocity 70% larger than in the well-bonded area. Scanning the debonded area with a finer mesh (not shown) proved this NDE technique capable of mapping the debonded area accurately.

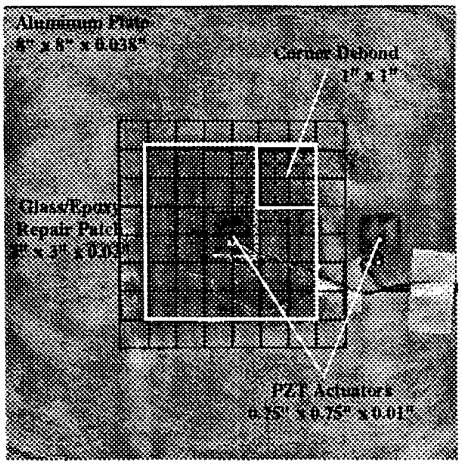


Figure 4 *Experimental aluminum plate with debonded composite repair patch.*

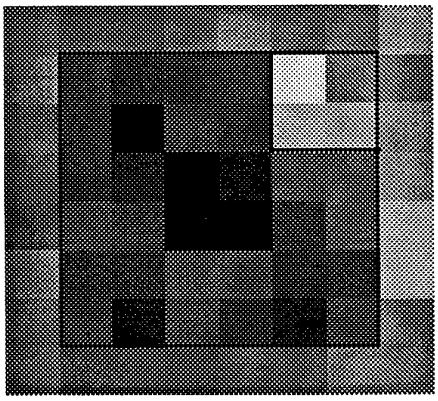


Figure 5 *The higher (lighter shade of gray) transverse surface velocity amplitudes of the glass/epoxy repair patch applied to an aluminum plate precisely locate the corner debond.*

Advantages of the laser Doppler vibrometer technique:

This non-destructive evaluation technique provides a new tool to locate debonds and delamination, or any other kind of parallel damage to the structure surface. The principal advantages of this laser Doppler vibrometer technique are:

- The technique is not based on any model, and thus can be easily applied to complex structures;
- The technique is non-contacting and non-intrusive (with laser ultrasound);
- The scanning laser enables rapid damage detection over large areas;
- The high-frequency excitation provides the capability of detecting very small defects.

PARTICLE TAGGING

Deterioration of reinforced concrete structures due to corrosion of the reinforcing steel is one of the greatest contributors to the billions of dollars spent on infrastructure decay annually. Advanced composites, such as fiber-reinforced plastics (FRP), can eliminate many problems associated with the corrosion of metals because of their excellent fatigue and corrosion resistance as well as their very high specific strength. Acceptance of the composites in both retrofit applications and new construction necessitates quality control and quality assurance and in-service monitoring techniques to ensure the performance and serviceability of the composites. However, the diverse properties of the epoxy matrix and the reinforcing fibers in the composite prevent the use of conventional non-destructive evaluation methods that utilize signal differentiation to reveal defects in the material.

Particle tagging is a technology that enhances the inspectability of advanced composites. Tagging involves embedding micron-size particles into materials, such as composites, concrete, or adhesive layers, to make them an integral part of the host material. The tagging particls will render the composite either amiable to conventional NDE techniques, or will permit the development of new NDE techniques specific to composite materials. The weight ratio of the tagging particles is usually small enough (3-5%w/w) not to affect the mechanical properties of the material. The particle tagging techniques can be separated into two categories: active tagging and passive tagging. The active tagging technique requires an external energy source to energize the embedded tagging particles, while passive tagging directly uses conventional techniques to inspect the presence and distribution of particles. When interrogated by suitable instrumentation, the embedded particle sensors interact with their host structures and generate certain types of measurable signatures. The signatures can then be correlated with the material and structural conditions, such as defects.

The research performed at CIMSS investigated the fundamental physics and mechanisms involved in using the tagging method for in-situ NDE of composite materials for infrastructure applications. This research led to the development of a dynamic model of active tagging with ferromagnetic particles that estimate the dynamic response of the particles, and to a model relating the response of the tagging particles and the tagged system to external excitation and host material conditions. A modeling method to evaluate the properties of the tagged material, such as the complex Young's modulus, based upon the frequency response function of the tagged material, has also been investigated.

Proof-of-concept demonstrations of particle tagging:

Experimental research with various specimens using different tagging particles was performed to increase knowledge in this new NDE field. For the active tagging, the interrogation of the specimens was made in an AC-biased magnetic field with a force gage. The variation in frequency response with the presence of defects was found to vary with the type and method of tagging. For the passive tagging, defects in the composite decreased the response amplitude of the standard eddy current when a minimum tagging particle concentration was present in the composite.

The particle tagging techniques have also been used in other applications: detection of defects (voids, inclusions, etc.), monitoring of the state-of-cure of epoxy matrices, and inspection of damage (delamination, cracks, etc.) during manufacturing or service. Potential applications include the inspection of coatings, quality control of powder bleeding processes in industry, and in-process quality assurance of the manufacturing process of composites.

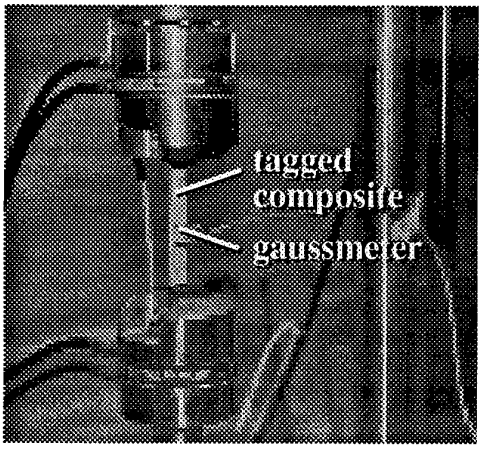


Figure 6 *The monitoring of stress concentration locations with magnetostrictive particles was successfully demonstrated.*

Advantages of particle tagging:

Particle tagging offers many advantages over the conventional sensing techniques which are not always very effective for in-field inspection of advanced composites:

- Provides cost-effective distributed sensing of composites;
- Enhances the inspectability of composites and provides a new technology for improved material diagnostics;
- Can be implemented for real-time in-service health monitoring or for in-production quality control.

CONCLUSIONS

In this paper, a brief overview of the research on qualitative nondestructive evaluation methods done at CIMSS was presented. The three different NDE techniques offer different features that can be more easily matched with the needs of a particular application. The impedance-based technique can offer real-time localized inspection of critical sections; the laser Doppler vibrometer-based technique is appropriate for the inspection of debonds and delaminations on large areas; while the particle tagging technique offers a novel approach to the monitoring of adhesives and composites.

REFERENCES

[1] Chaudhry, Z., Joseph, T., Sun, F., and Rogers, C.A., 1995, "Localized Health Monitoring of Aircraft via Piezoelectric Actuator/Sensor Patches", *Proceedings, SPIE Conference on Smart Structures and Materials,* San Diego, CA, 26 February - 3 March, SPIE Publishing, Bellingham, WA; in press.

[2] Ayres, J., Chaudhry, Z., and Rogers, C.A., 1996, "Localized Health Monitoring of Civil Infrastructure via Piezoelectric Actuator/Sensor Patches," *Proceedings, SPIE Conference on Smart Structures and Materials,* San Diego, CA, 25-29 February, SPIE Publishing, Bellingham, WA; in press.

[3] Sun, F., Liang, C., Rogers, C.A., and Majmundar, M., 1995, "Automated Real-Time Structure Health Monitoring Through Signature Pattern Recognition", *Proceedings, SPIE Conference on Smart Structures and Materials,* San Diego, CA, 26 February - 3 March, SPIE Publishing, Bellingham, WA; in press.

[4] Chaudhry, Z., Sun, F., Lalande, F., and Rogers, C.A., 1995, "Monitoring the Integrity of Composite Patch Structural Repair via Piezoelectric Actuators/Sensors", *Proceedings, AIAA/ASME/ASCE/AHS/ASC 36th Structures, Structural Dynamics and Materials Conference, Adaptive Structures Forum,* New Orleans, LA, 10-14 April, AIAA Publishing, Washington, DC, pp. 2243-2248.

[5] Lalande, F., Childs, B., Chaudhry, Z., and Rogers, C.A., 1996, "Utilization of High-Frequency Vibration Pattern Recognition for NDE of Complex Precision Parts," *Proceedings, SPIE Conference on Smart Structures and Materials,* San Diego, CA, 25-29 February, SPIE Publishing, Bellingham, WA; in press.

[6] Lalande, F., Chaudhry, Z., Sun, F., and Rogers, C.A., 1995, "Debond Detection using Broad-Band High-Frequency Excitation and Non-Contacting Laser Vibrometer System," *Proceedings, 6th International Conference on Adaptive Structures,* Key West, FL, 13-15 November, Technomic Publishing, Lancaster, PA; in press.

[7] Sun, F., Chaudhry, Z., and Rogers, C.A., 1996, "Debonding Detection of Composite Patch on Concrete Structure with Laser Dopler Vibrometer," *Proceedings, SPIE Conference on Smart Structures and Materials,* San Diego, CA, 25-29 February, SPIE Publishing, Bellingham, WA; in press.

[8] Sun, F., Chaudhry, Z., Lalande, F., and Rogers, C.A., 1996, "Debonding Detection of Composite Patch with Laser Dopler Vibrometer," *Proceedings, 8th International Congress on Experimental Mechanics,* Nashville, TN, 10-13 June, in press.

[9] Zhou, S.W., Chaudhry, Z., and Rogers, C.A., 1995a, "Review of Embedded Particle Tagging Methods for NDE of Composite Materials and Structures," *Proceedings, SPIE Conference on Smart Structures and Materials,* San Diego, CA, 25-29 February, SPIE Publishing, Bellingham, WA; in press.

[10] Zhou, S.W., Chaudhry, Z., and Rogers, C.A., 1995b, "An Active Particle Tagging Method Using Magnetic Excitation for Material Diagnostics," *Proceedings, AIAA/ASME/ASCE/AHS/ASC 36th Structures, Structural Dynamics and Materials Conference, Adaptive Structures Forum,* New Orleans, LA, 10-14 April, AIAA Publishing, Washington, DC, pp. 3260-3268.

[11] Giurgiutiu, V., Chen, Z., Lalande, F., Rogers, C.A., and Quattrone, R., 1996, "Passive and Active Tagging of Reinforced Composites for In-Process and In-Field Non-Destructive Evaluation", *Proceedings, SPIE Conference on Smart Structures and Materials,* San Diego, CA, 25-29 February, SPIE Publishing, Bellingham, WA; in press.

Use of Insitu Dielectric Sensing for Intelligent Processing and Health Monitoring*

D. Kranbuehl, H. Aandahl, N. Haralampus, W. Newby and David Hood

Chemistry Department
College of William and Mary
Williamsburg, VA 23187-8795 USA

G. Boiteux, G. Seytre,. P. Pascault, A. Maazouz, J.F. Gerard, H. Sautereau, J.F. Chailan

Laboratory d'Etudes des Matériaux Plastiques & Biomatériaux
URA CNRS 507, Université Lyon I. 69622
Villeurbane Cedex, France

A. C. Loos and J. D. MacRae

Department of Engineering Science and Mechanics
Virginia Polytechnic Institute and State University
Blacksburg, Virginia 24061-0619

ABSTRACT

Frequency dependent dielectric measurements (FDEMS) provide a sensitive, automated insitu sensor for intelligent processing and an insitu means for monitoring durability, that is degradation of polymers during use. FDEMS in situ sensors can be designed and calibrated to monitor changes in processing properties during fabrication and changes in mechanical or electrical service life properties of polymer materials during use. With a proper understanding of the type of polymer and the use environment, the sensor output can be related to changes in modulus, maximum load and elongation at break. The FDEMS technique has advantages over other monitoring techniques: nondestructive; accuracy/reproductivity; sensitivity; insitu capability; remote sensing; automated.

INTRODUCTION

With the future expanded use of polymers as adhesives, rubbers and composites in extended use structures, such as pipelines, bridges and aircraft with life times of 20 to 40 years, there is a need to develop both an insitu intelligent processing and a health monitoring sensor capability. These areas are already acute in industry as it strives for lower cost, higher performance solutions. For the industry the use of polymer materials in various composite structures is an enabling technology making reduced weight and lower cost solutions possible. In the area of intelligent processing, frequency dependent electromagnetic or dielectric sensing (FDEMS) are needed to monitor resin position, viscosity and degree of cure insitu in the mold during fabrication. As such the sensor output can be used as the input for knowledge based software to intelligently control the cure process.

Polymer health sensing techniques need to involve small scale, short time test methods capable of monitoring large scale long time aging of polymer performance properties. A critical need in using polymers in load bearing structures is a sensor method that can verify the suitability of polymer materials under realistic aging conditions. Even more important is the ability to monitor the change in the polymer materials performance properties insitu in the field under variable, unpredictable, degradation use conditions. One of the already existing uses of polymer materials is as the fluid gas barrier in flexible pipes for transport of oil and gas from the ocean floor to the surface on offshore platforms.

The ultimate objective is to develop effective sensing methods both for insitu intelligent process control and for monitoring the remaining life, rate of aging and projected replacement of the polymer structure insitu during use in the variable, field environment. First, this paper discusses the use of frequency dependent electromagnetic sensors, FDEMS, to monitor resin position, and viscosity during cure. Second the paper addresses the ability of dielectric sensing to monitor degradation-aging and changes in mechanical stress-strain performance properties such as elongation at break in two thermoplastics and in insulating properties of cables.

* This work was supported inpart by EDF, PIRELLI for materials and the NSF Center of Excellence at VPI DMR9120004.

0-8194-2165-0/96/$6.00

INSTRUMENTATION

Frequency dependent complex dielectric measurements are made using an Impedance Analyzer controlled by a microcomputer.[1,2] Measurements at frequencies form Hz to MHZ were taken and converted to the complex permittivity, $\epsilon'=\epsilon''-i\epsilon''$. Measurements were made with a geometry independent DekDyne micro sensor which has been patented and is now commercially available. The sensor is planar, 1 x ½ inch in area and 5 mm thick. This single sensor-bridge microcomputer assembly is able to make continuous uninterrupted measurements of both ϵ' and ϵ'' over 10 decades in magnitude at all frequencies. The sensor is inert and has been used at temperatures exceeding 400°C and over 1000 psi pressure. Laboratory measurements used a Hewlett Packard 4284A Impedance Analyzer and insitu testing of LOCA cables.

THEORY

Frequency dependent measurements of the material's dielectric impedance as characterized by its equivalent capacitance, C, and conductance, G, are used to calculate the complex permittivity, $\epsilon''=\epsilon'-i\epsilon''$, where $\omega=2\pi f$, f is the measurement frequency and C° is the air replacement capacitance of the sensor. $\epsilon'(\omega) = \frac{C(\omega)material}{C_o}$ $\epsilon''(\omega) = \frac{G(\omega)\ material}{\omega C_o}$

This calculation is possible when using the sensor whose geometry is invariant over all measurement conditions. Both the real and the imaginary parts of ϵ'' have an ionic and dipolar component. $\epsilon' = \epsilon'_d + \epsilon'_i$ $\epsilon'' = \epsilon''_d + \epsilon''_i$

Plots of the product of frequency (ω) multiplied by the imaginary component of the component of the complex permittivity $\epsilon''(\omega)$ make it relatively easy to visually determine when the low frequency magnitude of ϵ'' is dominated by the mobility of ions in the resin and when at higher frequencies the rotational mobility of bound charge dominates ϵ''. Generally, the magnitude of the low frequency overlapping values of $\omega\epsilon''(\omega)$ can be used to measure the change with time of the ionic mobility through the conductivity parameter σ where

$$\sigma(ohm^{-1}cm^{-1}) = \epsilon_o\omega\epsilon''_i(\omega) \qquad \epsilon_o = 8{,}854 \times 10^{-14}C^2J^{-1}cm^{-1}$$

The changing value of the ionic mobility as measured by σ is a molecular probe which can be used to quantitatively monitor changes in the structure and morphology of the resin during cure and during aging. The dipolar component of the loss at higher frequencies can then be determined by subtracting the ionic component. $\epsilon''(\omega)\ dipolar = \epsilon''(\omega) - \frac{\sigma}{\omega\epsilon_o}$

During cure, the peaks in ϵ'' dipolar (which are usually close to the peaks in ϵ'') can be used to determine the "mean" dipolar relaxation time. The dipolar mobility as measured by the mean relaxation time τ can be used as a molecular probe of the buildup in Tg during processing and changes in structure during aging. The magnitude of the dipolar relaxation time can be quantitatively related to the attainment of a specific value of the resin's glass transition temperature during processing or to changes in morphology or structure and thereby mechanical or electrical properties during use in the field.

CURE MONITORING

Experiment

The experimental set-up for the mold filling experiments consisted of a 0.36m x 0.36m picture frame mold. This size frame allowed for a 0.30m x 0.30m preform which was placed within the frame. A shim was then placed on top of the preform to ensure that the desired fiber volume fraction was achieved. A top plate with a venting port connected to a vacuum pump was then placed on top of the shim. The positive displacement injection pump was connected to the mold by high temperature plastic tubing. Resin enters the cavity through two side ports and flows along a 0.64 cm channel around the perimeter of the preform. A diagram detailing the mold assembly is given in Fig. 1. The entire mold assembly was then placed into a press and heated. Both the injection pump and plastic tubing were heated. After a vacuum had been pulled on the mold to remove entrapped air, the injection was started with a constant flow rate.

Sensors were placed in the bottom of the mold to monitor the flow front position, viscosity and degree of cure as a function of time during the injection process. Six sensors were used to monitor the infiltration patterns, with three located on the perimeter of the preform and

three located in the interior of the preform.(Fig. 1) The preform used in these experiments consisted of 16 plies of 1M7/7HS compacted to a nominal fiber volume fraction of 60%. Two different epoxy resins 3M's PR-500 epoxy resin and Shell 1895/Curing Agent W, mixed in a 3:1 ratio were used and injected at a constant flow rate of 10 cc/min.

Results

The purpose of the experiment was to use the FDEMS technology to monitor resin position as a function of time during the filling process and compare the recorded times with the model predicted values. The resin flow patterns during mold filling are shown in Fig. 2. The locations of the six FDEMS sensors and the corresponding wet-out times are denoted on the figure. The wet-out of sensor #1 was used to approximate the beginning of the mold filling process. There is excellent agreement between the measured wet-out times and model predictions for both the internal (sensors #2, #3, and #5) and perimeter (sensors #4 and #6) sensor locations. Note the skewed flow pattern due to the shifting of the preform during mold closing.

Similar experiments were conducted using 3M's PR-500, solid resin at room temperature, PR-500 must be heated to above 150° at which temperatures it both reacts and attains a low enough viscosity for resin transfer molding. This feature makes it both very desirable in terms of room temperature stability and a challenge to use for resin transfer molding since it is slowly increasing its viscosity at the temperatures required to decrease its viscosity for resin injection. Figure 3 shows the sensor output monitoring arrival of the resin front at the center location and thereafter, the resin's viscosity and degree of cure. Figure 4 displays the value of the viscosity as monitored by the FDEMS sensor. A discussion of the laboratory characterization work which is used to predict viscosity and degree of cure for PR-500 from the sensor output has been previously described.[3]

LIFE MONITORING OF ETHYLENE, PROPYLENE, HEXADIENE TERPOLYMER

First a neat polymer and its industrial compound were examined. The pure polymer was an uncross linked, unfilled and unstablized ethylene propylene hexadiene 1-4 terpolymer supplied by Dupont de Nemours under the trade name NORDEL 2722. From this polymer an industrial rubber was supplied by PIRELLI under the trade name EPR 1321. This material was cross linked, filled and stabilized. For all experiments exposure to thermal ageing was carried out in ventilated ovens regulated at ±1°C. Measurements were made on polymer sheets for laboratory tests and directly on cables as shown in Figure 5

Discussion

As demonstrated by dielectric measurements and corresponding FTIR spectra Fig. 6 and 7, aging of ethylene-propylene-hexadiene terpolymer sample A is a gradual oxidation of the macromolecular main chain. Other authors have studied these processes in detail[4]. The originality of our work is to show such effects by a non-conventional dielectrical measurement. Dielectric sensing involves the detection of changes in molecular dynamics and structure with cure or degraedation-aging. In the particular case of non polar polymers, such as polyethylene or polypropylene, the very low value of tan $\delta = \epsilon''/\epsilon'$ is difficult to measure, except for slightly oxidated polymers[5,6]. This is the case for our aged material. The gradual appearance of oxidized functions induces an increase in the α dielectric relaxation[7], in relation to the number and the mobility of dipoles. In the case of the cross linked industrial material, the vulcanizing process and especially the processing of samples, induce oxidation which allows the detection of dielectric relaxation, even on unaged materials. As in the case of the pure polymer (Fig. 6), this relaxation in the cross linked material increases with aging.(Fig.8} As seen from the sheet results, the aging time is too short (85 days, -125°C) to induce large changes on a dielectric relaxation of insulation EPR cables. However we can note that on the most aged cable, dielectric loss tangent spectrum is a bit above the unaged sample Fig. 9. Due to complex geometry of the cable, the diffusion of oxygen is limited and degradation of insulation is essentially an anaerobic phenomenon. This *insitu* life monitoring results demonstrate that for the same temperature aging the insulation degradation is slower than for polymer sheets.

LIFE MONITORING OF NYLON 11

Experimental

A series of accelerated aging tests have been carried out on Nylon 11, Rilsan BESNO P40 by Atochem to investigate the ability of FDEMS sensors to detect degradation. The test we report here was carried out in a mixture of 95% water and 5% volume ASTM grade 3 oil saturated with CO_2. The oil, water, CO_2 mixture was kept at a temperature of 105°C in a closed container producing an equilibrium pressure of about 1.2 bar. The high temperature was to create aging over a reasonably short time.

Samples were instrumented with embedded FDEMS sensors. The samples were approximately 6mm thick and 40 mm square and the sensors were embedded well inside the material typically around the center in the plane of the square. A large number of premachined "dog-

bone" samples for mechanical testing were included together with the instrumented samples. At pre-determined intervals the aging bath was opened to carry out FDEMS measurements on all sensors and to retrieve in triplicate samples for mechanical testing. The mechanical testing was carried out according to an ASTM D638 standard and average values reported. The test reported here was completed after 150 days of aging.

Results

In Figure 10, we present the results from the mechanical aging studies. Each value is the average of 3 samples. Measurements of elongation and load at yield were also made but are not reported here. The scatter of the mechanical measurements for 3 nominally identical samples indicated a significant variance demonstrating the uncertainties for this kind of tests. After 60 days the elongation at break has dropped to approximately 45% compared to 350% for the virgin material. The rate of drop is also large. Significant degradation has taken place. The material would no longer, from the point of ductility be suitable for use in a flexible pipe.

Measurements of the complex permittivity of the FDEMS sensor embedded in the Rilsan and left in a CO_2 saturated water oil tank at 105°C were also made over a frequency range of 100 Hz to 100 kHz. Both the value of ϵ' and ϵ'' showed a rapid rise over the initial 20 day period as water diffused into the Rilsan and plasticizer diffused out. These conclusions are supported by weight loss studies on the Rilsan specimens. Figure 11 shows the FDEMS sensor output for ϵ' measured at 1 kHz. Similar results are observed at other frequencies and for the loss component ϵ''. For this report we focus only on ϵ' measured at 1 kHz.

The FDEMS sensor output, can be correlated with the mechanical aging results. The FDEMS sensor samples and the mechanical test specimens age at different rates because of differences in sample volume-surface area and the role of diffusion in affecting the extent of aging. In order to make the correlation, the molecular weight of both the mechanical and the FDEMS sensor specimens was made. The correlation is based on samples which have been aged to the point of equivalent molecular weight. Other techniques including FTIR, T; Tg and H (crystallinity) were used. These support the result that the molecular weight is decreasing. This results in increased crystallinity. The result is a less ductile lower strength material with age.

The FDEMS sensor output was normalized relative to its maximum value on day 20, when the water and plasticizer diffusion process has reached the Rilsan on the sensor. Then it was correlated with the mechanical property degradation data in Fig.10. The resulting normalized sensor output monitoring elongation at break is shown in Figure 12. Similarly the FDEMS sensor output can be correlated with other mechanical test criteria for thermosets as well as thermoplastics such as load at break or yield as well as with any other information and used to monitor degradation in the polymer.

CONCLUSIONS

The RTM fabrication experiments show that frequency dependent dielectric sensing can be used to monitor resin position and viscosity and thereby to provide the online input for intelligent process control.

The aging experiments on polyethylene terpolymers show that dielectric sensing can be used to monitor thermoxidative degradation of this relatively nonpolar polymer.

The nylon 11 aging studies show that dielectric measurements using an insitu DekDyne sensor can be used to health monitor this thermoplastic as it hydrolyses during use in an oil-water environment.

REFERENCES

1. Kranbuehl, D. "Cure Monitoring", Int. Encyclopedia of Composites, ed. S. Lee, 531-543 (1990).
2. Kranbuehl, D., P. Kingsley, S. Hart, G. Hasko, B. Dexter, A. C. Loos, "Sensor-Model Insitu Monitoring and Intelligent Control of the Resin Transfer Molding Composite Cure Process," Polymer Composites, 15 (4) 297-305 (1994).
3. J. D. MacRae, Development and verification of a resin film infusion/resin transfer molding simulation model for fabrication of advanced textile composites. M.S. Thesis, Virginia Polytechnic Institute and State University, Blacksburg, VA, December 1994.
4. K. T. Gillen, R.L. Clough, in R.L. Clough and S.W. Shalaby (ed), Radiation Effects of Polymers, ACS Symposium Series 475. American Chemical Society, Washington, D.C.
5. G. Seythe, G. Boiteiux, J. F. Chailon, J. Chaunchand, Polym. Deg. Stab., in the press, 46 and 47.
6. G. Seythe, G. Boiteiux, J. F. Chailon, J. Chaunchand, Jicable 95, 4th Int. Conf., June 1995.
7. K. Benhabiles, Thesis ENSAM, Paris, 1994.

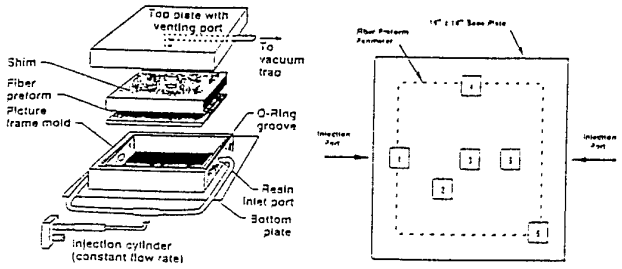


Figure 1. Sketch of RTM mold assembly (left) and location of FDEMS sensor array in bottom plate of RTM mold

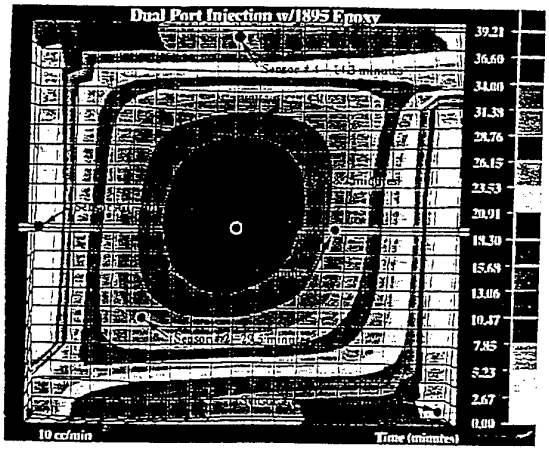


Figure 2. Model predicted flow patterns during mold filling for a flow rate of 10 cc/min.

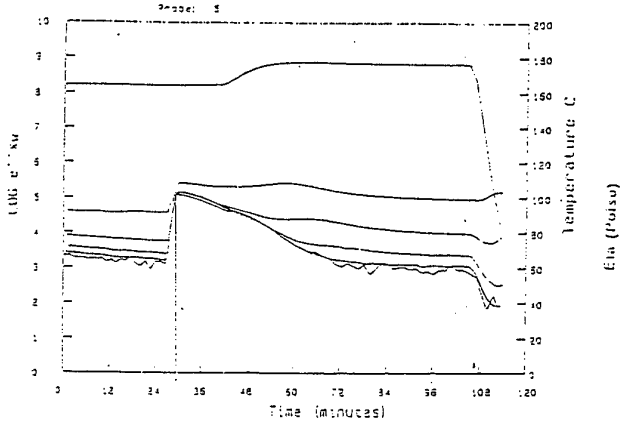


Figure 3. FDEMS sensor monitoring wetout and cure.

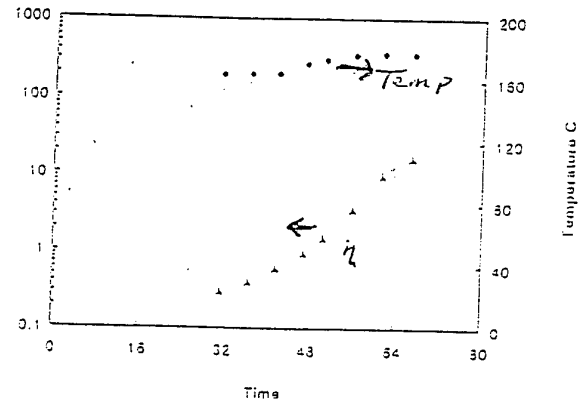


Figure 4. FDEMS sensor monitoring viscosity.

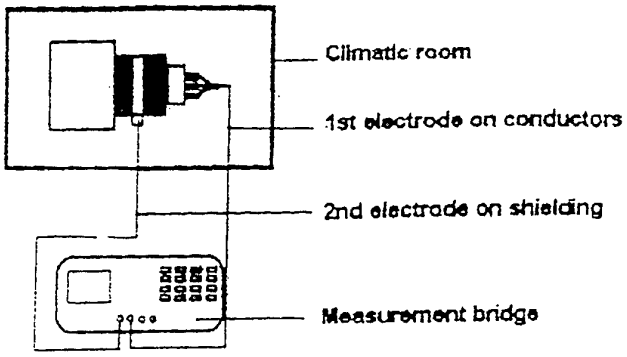


Figure 5. Schematic representation of dielectric measurements on cables.

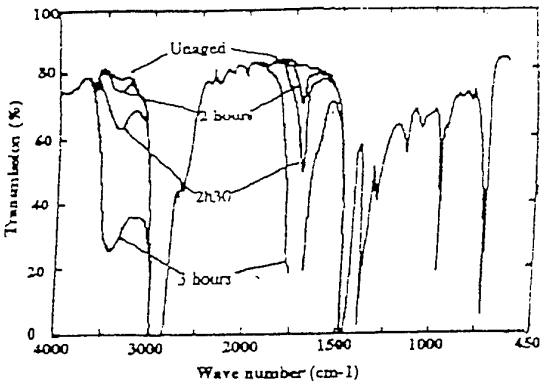


Figure 6. FTIR spectra of neat polymer film before and after thermal exposure (180°C).

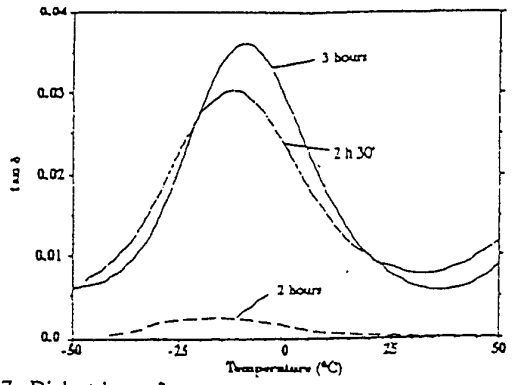


Figure 7. Dielectric tan δ versus temperature for neat polymer thermally aged at 180°C. Frequency 1000 Hz - Heating rate 2°C min^{-1}.

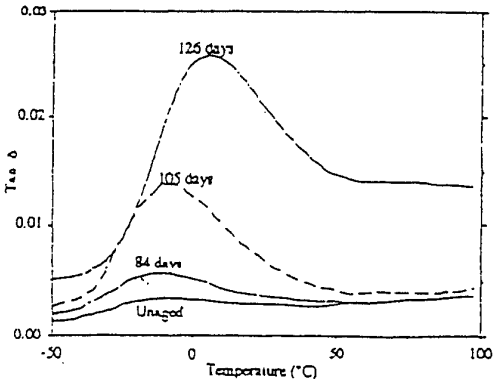


Figure 8. Effects of thermal aging at 135°C on dielectric tan δ for industrial rubber - Frequency 1000 Hz - Heating rate 2°C min^{-1}.

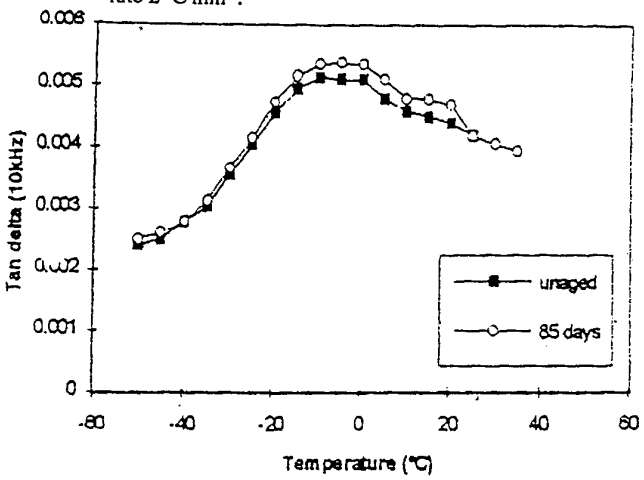


Figure 9. Experimental results on EPR isolated conductor aged at 125°C.

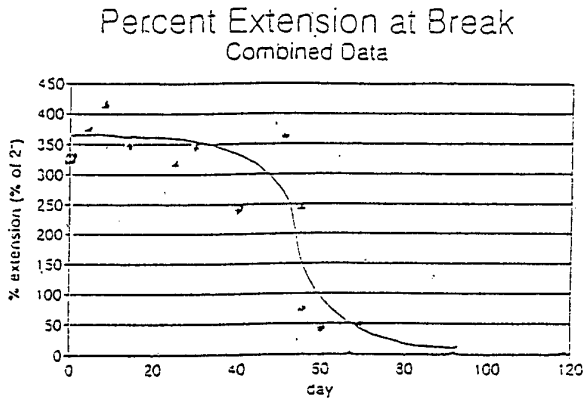


Figure 10. Aging, % extension versus days 105° oil, water, CO_2

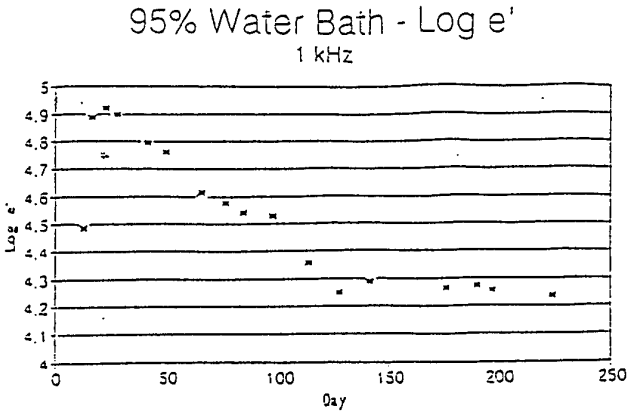


Figure 11. Aging, log ϵ′ versus days.

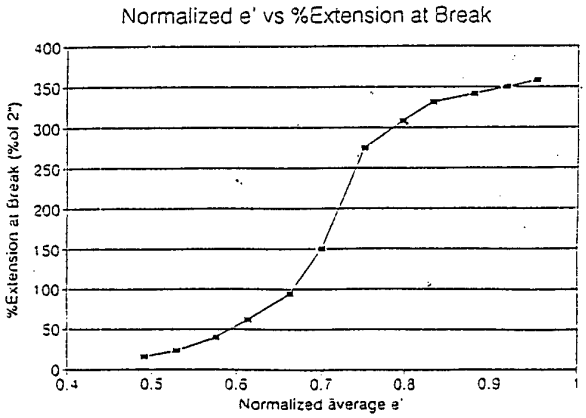


Figure 12. Normalized sensor output ϵ′ at 1 kHz monitoring degradation in % extension.

Impact Damage Diagnostics for Composite Structures Using Built-In Sensors and Actuators

Michael Tracy, Youn-Seo Roh, and Fu-Kuo Chang
Department of Aeronautics and Astronautics
Stanford University, Stanford, CA 94305

ABSTRACT

This paper presents a concept for a built-in diagnostic system for detecting impact damage in in-service composite structures. The proposed system consists of two major diagnostic processes: passive sensing diagnosis (PSD) and active sensing diagnosis (ASD). The PSD utilizes the sensor measurements to determine the impact force and predict the location of the impact. The ASD generates diagnostic signals from the actuators to estimate the size of the impact damage resulting from the impact.

In PSD, a computer code,"IDIMPACT," has been developed for identifying impact force and location using distributed sensor measurements for both metallic and composite plates. For active sensing diagnosis (ASD), current work is focused on developing diagnostic methods based on the propagating waves. A key development for this work is to construct appropriate diagnostic waves for effectively detecting impact damage.

I. INTRODUCTION

Due to recent advances in sensor technology, a new concept of damage diagnostics for monitoring the integrity of in-service structures has been proposed [1-8]. Because these sensors could be built into composites as an integral part of the structures during manufacture, the built-in damage diagnostics become especially attractive for composite structures design. Optical fibers and piezoelectrics are being considered as potential candidates for this application.

In general, all the built-in structural damage detection systems can be classified into two types [8]: Passive Sensing Diagnosis (PSD) - a sensor-only based system and Active Sensing Diagnosis (ASD)- a sensor/actuator based system.

A PSD system relies solely on passive sensor measurements to determine any changes in the condition or environment of the structures. Because a sensor could only measure a parameter at a given location such as a strain or displacement, it is very difficult to practically interpret the local measurements in terms of the overall damage state and the integrity of a structure.

Using built-in actuators to interact with the sensors, an ASD system can generate essentially unlimited diagnostic signals for the sensors to further examine the integrity of the structures and to detect damage in the structures.

Accordingly, both systems are needed and should be integrated in order to develop a real-time structural health monitoring system for advanced structures. This presentation will primarily focus on developing a technique for detecting impact damage in composite structures with built-in piezoelectrics as shown in Figure 1. Both PSD and ASD processes will be discussed for developing such a technique.

II. PASSIVE SENSING DIAGNOSIS

For given distributed sensor measurements, a PSD process is to determine the impact force and the location of the impact. Mathematically, this process becomes a nonlinear, inverse problem. Choi and Chang [9] developed a PSD diagnostic method using an array of sensor mea-

0-8194-2165-0/96/$6.00

surements for identifying the impact force (energy) and the impact location for beams. The diagnostic method consists of a structural model and a response comparator. The structural model calculates the sensor measurements for a given impact force and location. The comparator compares the sensor measurements with the simulations generated from the structural model to estimate the impact energy and location.

The model was further extended and considerably modified recently by Tracy and Chang [10] to apply to two dimensional plate problems. Based on the model, an interactive computer code,"IDIMPACT," was developed. The code, which serves as the controller, can be directly linked with distributed sensor measurements for identifying impact force and location for both metallic and composite plates.

Extensive experiments were also performed to verify the model and the computer code. Figure 2 shows typical measurements of six piezo-sensors attached to a 36" by 30" composite plate subjected to an instrumented hammer impact. A schematic description of the test setup is shown in Figure 3. All the sensors were separated by 7 inches from each other. Due to limited recording channels available from the data acquisition board, six sensors were used. Impact was introduced by an instrumented hammer which could record the force-time history during each impact. The physical impact test area of the plate was located within the domain encompassed by the sensors.

Based on the sensor measurements, the code ran automatically and predicted the impact force-time history and the location of the impact. Figure 4 shows the percentage of the success rate of the predicted location falling within the neighborhood of the actual impact points over fifty tests. Overall, the predicted locations falling within a 0.25 inch radius from the actual impact locations were about 70 percent. All the predicted locations fell within a 0.75 inch radius from the actual locations. Figure 4 also shows the comparison of a force-time history between a measurement and the corresponding prediction.

III. ACTIVE SENSING DIAGNOSIS

To estimate the extent of the impact damage, appropriate diagnostic signals must be selected which could strongly interact with the impact damage and be transmitted to neighboring sensors at a minimal distance from the actuator. One of the major difficulties in selecting the appropriate propagating waves is the dispersion of the elastic waves in solids.

However, with built-in piezoceramics, various types of propagating waves could be generated. A sine-bursted waveform with a narrow-band frequency spectrum was selected as the input signal for the actuators as shown in Figure 5. The piezoelectric-generated diagnostic waveform was well preserved in composites during transmission from the actuators to the neighboring sensors before the impact. With the selection of the diagnostic waves, the waves reflected from the boundary could be clearly detected, and, as a consequence, the possibility of the sensor signals being corrupted by the reflected waves could be minimized.

However, significant change in the waveform and phase was observed after the impact. Figure 6 presents the measured correlation between the impact damage size and phase delay in transmitted diagnostic waves measured from a piezo-sensor. A linear relationship between the phase delay and the impact damage size could be concluded from the test results. Such a relationship is crucial for identifying impact damage size in composites based on an ASD method.

Currently, based on the propagating wave approach, work is being conducted to develop an appropriate ASD technique using a distributed network of sensors and actuators for detecting impact damage. It is believed that both the PSD and ASD techniques are essential for the development of a built-in impact damage diagnostic system.

IV. CONCLUSIONS

For passive sensing diagnosis, a computer code, "IDIMPACT", was developed for identifying impact force and location in both metallic and composite plates using the outputs of piezoelectric sensors that were distributed on the surface of the plates. Comparison with experiments showed that the predicted impact location and force-time history agreed quite well with the test data.

For active sensing diagnosis, appropriate diagnostic waves have been selected and generated using built-in piezoceramics for detecting impact damage in composites. Experiments showed that impact damage could significantly affect the transmitted diagnostic waves. Work is being performed to characterize the effect of impact damage on diagnostic waves and to develop a technique for assessing impact damage.

V. ACKNOWLEDGEMENT

The financial support of the Air Force Office of Scientific Research and the National Science Foundation for this program is gratefully appreciated.

VI. REFERENCES

1) G. Hickman et al, "Application of Smart Structures to Aircraft Health Monitoring," *J. of Intelligent Material Systems and Structures,* pp. 411-430, 1990.

2) J.N. Kudva, C. Marantidis, and J. Gentry, "Smart Structures Concepts for Aircraft Structural Health Monitoring," *Proceedings of SPIE on Smart Structures and Intelligent Systems,* Vol. 1917, pp. 974-971, 1993.

3) R.M. Measures et al, "Structurally Integrated Fiber Optic Damage Assessment System for Composites," *SPIE: Fiber Optic Smart Structures and Skins,* Vol. 968, pp. 120-129, 1988.

4) C.-C. Chang and J. Sirkis, "Metal Coated Optical Fiber Damage Sensors," *Proceedings of SPIE on Smart Sensing, Processing, and Instrumentation,* Vol. 1918, pp. 138-144, 1993.

5) C.A. Paul and G.P. Sendeckyj, "Detection of the Onset of Damage Using an Extrinsic Fabry-Perot Interferometric Strain Sensor," *Proceedings of SPIE on Smart Structures and Intelligent Systems,* Vol. 1918, pp. 154-164, 1993.

6) C.H. Keilers, Jr. and F. K. Chang, "Damage detection and diagnosis of composites using built-in piezoceramics," *Proceedings of SPIE on Smart Structures and Material Systems,* Vol. 1917, pp. 1009-1019, 1993.

7) K. Choi, C. Keilers Jr. and F. K. Chang, "Impact Damage Detection in Composite Structures Using Distributed Piezoceramics," *Proceedings of the 35th AIAA/ASME/ASCE/AHS/ASC Structures, Structural Dynamics, and Materials Conference,* Part I, 94-1322, Hilton Head, SC, April 18-20, 1994, pp. 118-124.

8) F.K. Chang, "Built-In Damage Diagnostics for Composite Structures," *Proceedings of the Tenth International Conference on Composite Materials (ICCM-10),* Whistler, B.C., Canada, August, 14-18, 1995, Vol. V, pp. 283-289.

9) K. Choi and F.K. Chang, "Identification of Impact Force and Location Using Distributed Sensors," *J. of AIAA* (to appear).

10) M. Tracy and F.K. Chang, "Identifying Impact Load in Composite Plates Based on Distributed Piezoelectric Sensor Measurements," *Proceedings of SPIE on Smart Structures and Material Systems,* February, 1996.

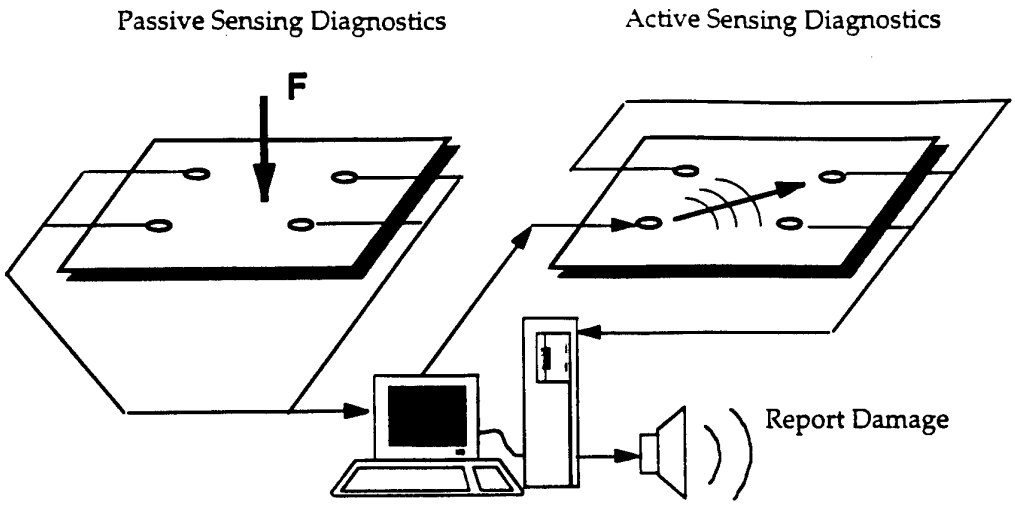


Figure 1. Description of a proposed impact damage diagnostic system.

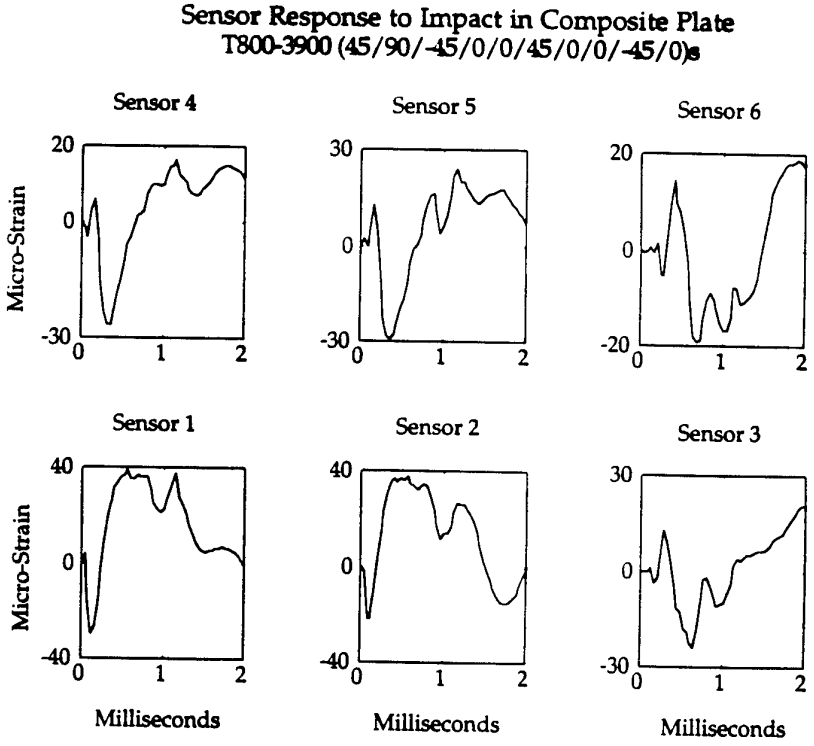


Figure 2. Six measurements of piezoelectric sensors mounted on a composite plate corresponding to an instrumented impact.

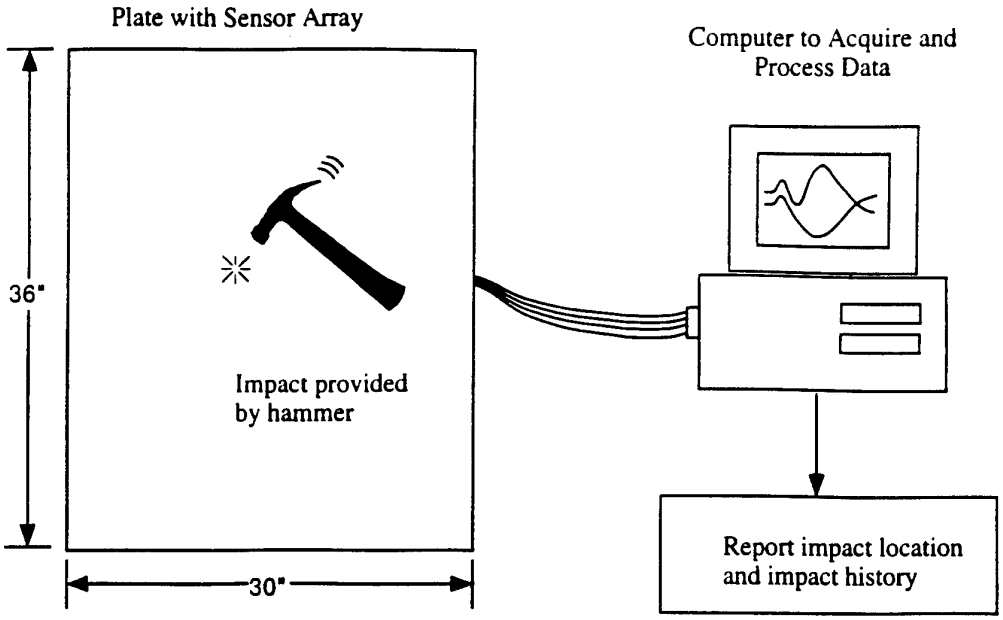


Figure 3. Schematic description of the test setup.

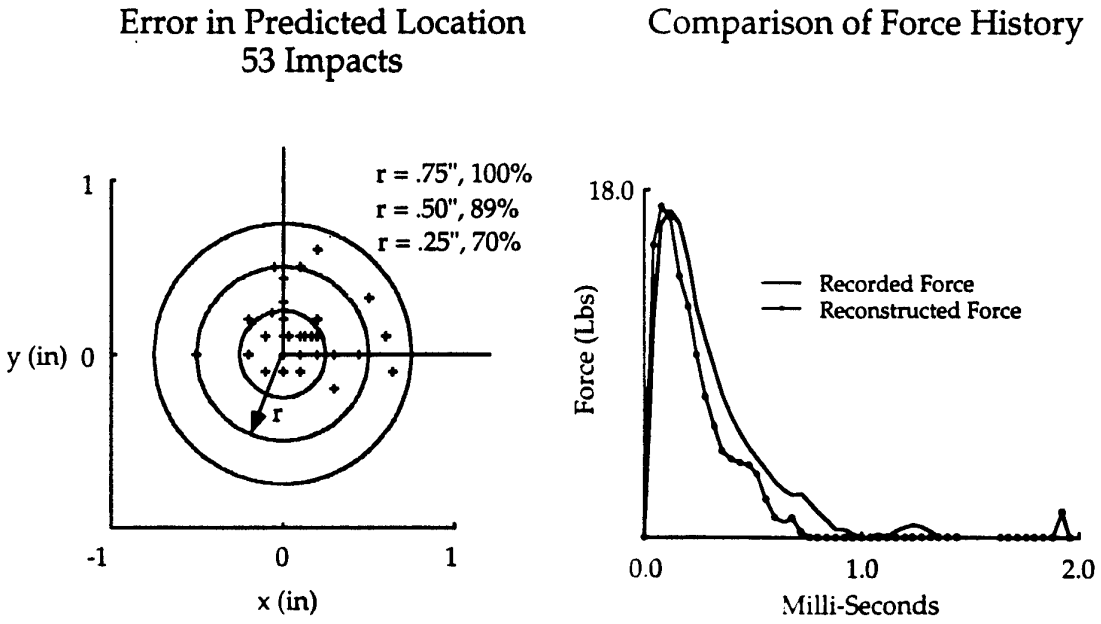


Figure 4. **(Left)** Precentage of success rate of the predicted locations falling within the neighborhood of the actual impact points over fifty impact tests. **(Right)** Comparison of the impact force history between a measurement and the corresponding prediction.

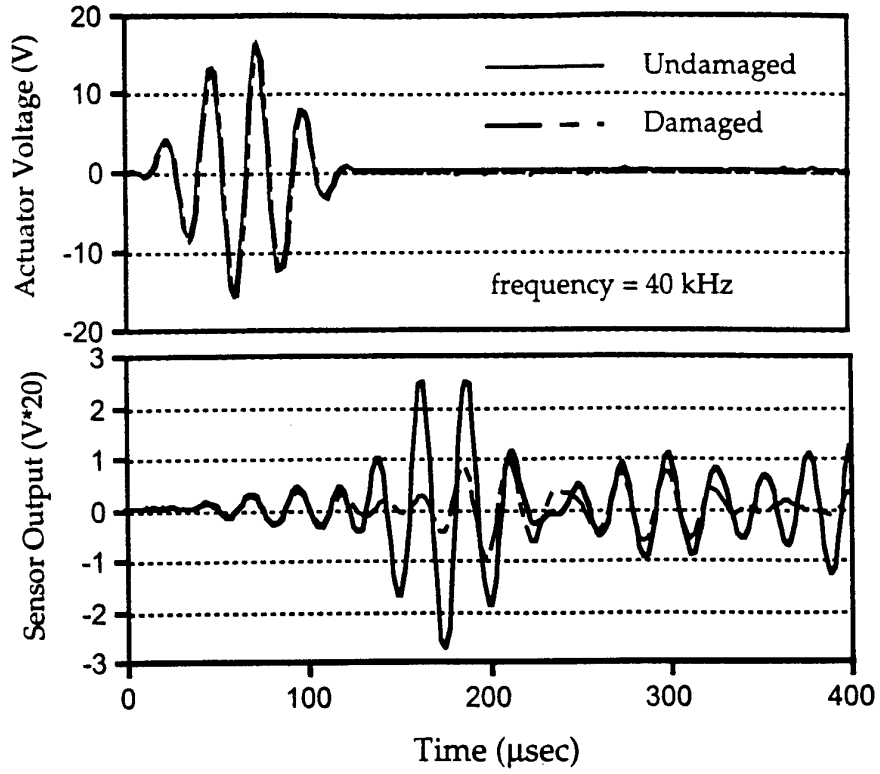


Figure 5. Comparison of sensor measurements to a controlled diagnostic wave generated by piezo-electrics for a composite plate before and after an impact.

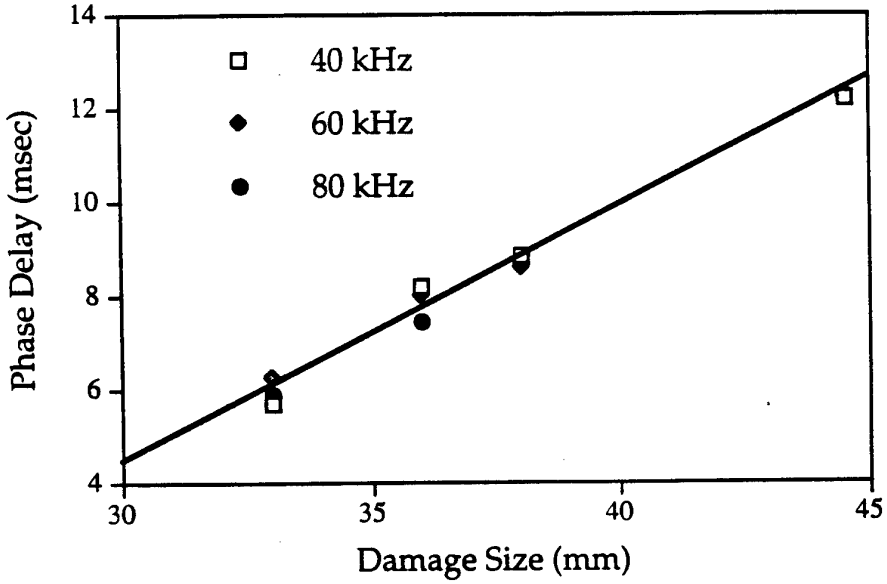


Figure 6. The relationship between impact damage size and phase delay in transmitted diagnostic waves measured from a piezo-sensor.

Sensor technology for structural integrity monitoring

R. Jones[1] , W.K. Chiu[1] and S. Pitt (Hammond)[2]

[1] Department of Mechanical Engineering, Monash University, Clayton, 3168, Victoria, Australia
[2] Department of Mechanical and Manufacturing Enging, Melbourne University, Parkville, Victoria.

ABSTRACT

Recent high visibility aviation accidents have led to increased research into the use of sensor technology for monitoring aircraft structural integrity. To this end this paper describes applications to crack growth, multiple interacting flaws, and composite repairs.

1. INTRODUCTION

The down turn in the global economy coupled with the high acquisition costs associated with the purchase of modern military and civilian aircraft has resulted in greater utilisation of existing aircraft fleets. This trend, in operating existing aircraft approaching or beyond their intended design life, has been reflected in an increasing number of structurally significant defects and increases the possibility of a reduction, or loss, of structural integrity due to fatigue. In the civilian arena the importance of understanding and managing ageing structures was highlighted by the failure of the Aloha 737 on April 28, 1988 [1]. This failure was essentially due to the linking, into one large crack, of numerous small cracks at a number of fastener holes. This phenomenon has subsequently been termed "multi-site damage" (MSD). In the Australian scene the importance of maintaining continued airworthiness was further highlighted by the November 1990 failure of a Royal Australian Air Force (RAAF) Macchi aircraft which suffered a port wing failure whilst in an estimated 6g manoeuvre[2]. As a result of this event a Macchi Recovery Program was initiated to determine the structural condition of the fleet and to reassess the fatigue lives and management philosophies of the main structural components. A tear down inspection program involving two fuselages, two fins and five horizontal tail planes was then undertaken. Six of the wings showed significant cracking indications and of approximately 1000 holes which were examined 100 revealed fatigue cracks, including major cracking in the D series rivet holes. This failure event subsequently led to a major change in the RAAF approach to Air Structural Integrity Management.

Although the phenomenon of MSD was first observed in civilian aircraft recent Australian work[3] has found that MSD plays a major role in determining the fatigue life of the F/A-18 aft bulk head, ie. bulk head FS-488[3]. In this case fractographic evaluation of the "failure location" revealed a population of several hundred cracks. As a result of this test it was concluded [3], that existing NDI techniques could not be relied upon to find the critical crack. This conclusion further highlighted the need to develop both advanced NDI techniques as well as new analysis and measurement tools for the assessment of structural integrity, particularly when the critical component contains large numbers of interacting flaws.

With these recent events in mind it is apparent that to optimise the operational life of RAAF assets new tools are needed to assist in assessing structural integrity. To this end this paper describes the application of sensor technology to a range of problems involving crack growth, multiple interacting flaws , and composite repairs.

2. INTEGRITY MONITORING OF CRACKED METALLIC STRUCTURES

Adequate condition monitoring is an essential part of an efficient structural maintenance program and is widely used throughout the field of mechanical engineering. The challenge is to extend the methodologies and philosophies

0-8194-2165-0/96/$6.00

currently used for plant and machine condition monitoring to the assessment of the integrity of aircraft structural components. To address this challenge the present paper evaluates the feasibility of using piezoelectric sensors to monitor crack growth in metallic structural components and composite repairs. The specimen used in this study, see Figure 1, was a 12.5 mm thick centre-cracked aluminium alloy (US alloy 2214) subjected to constant amplitude-tension cyclic loading, with a mean load of 40 kN, a cyclic amplitude of 20 kN, at a frequency of 5 Hz. The crack growth resulting from this cyclic loading was periodically measured with a travelling vernier microscope. A number of NiCr sputtered 28 μm thick piezoelectric sensors, of dimension is 4 x 20 mm, were located on the specimen as shown in Figure 1. The signal from sensor C, which was located away from the "damage" area, was used as a reference signal and is denoted as the "far-field" signal. The "near-field" signals were obtained from sensors A and B. In addition to the experimental results, the change in the piezoelectric sensor reading with crack growth was predicted numerically using Finite Element Analysis. Figures 2(a) and (b) show the comparison between the predicted signal and the measured signal with increasing crack length. The agreement between the two results confirms the ability of piezo sensors to monitor the crack growth. The change in gradient observed in curve (b) of Figure 2 is attributed to the change in the stress state in the piezoelectric sensor when the crack propagates under the sensor. From these figures it is clear that the piezo signal can be directly related to crack length and to structural integrity.

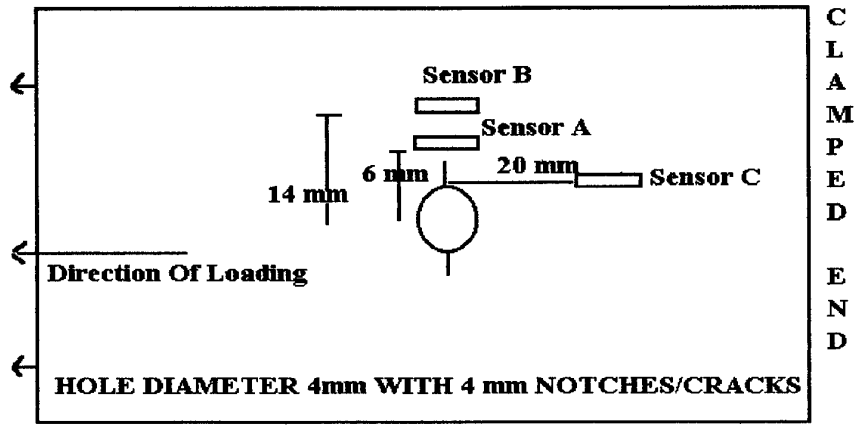


Figure 1. Schematic representation of test specimen

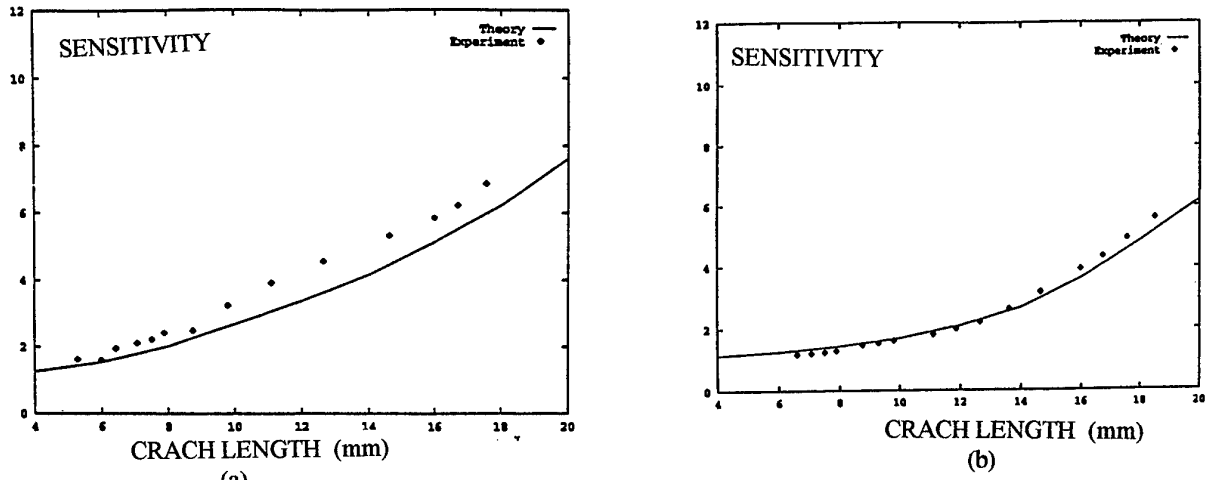


Figure 2. Comparison between predicted and measured sensitivities
a) At sensor A; b) at sensor B

3. MULTIPLE INTERACTING CRACKS.

As mentioned in Section 1, although the phenomena of multi-site damage was first seen in civilian aircraft, recent full scale testing in Australia and the US in support of the F/A-18 revealed that the fatigue critical location contained several hundreds of small cracks. To understand this phenomenon, i.e. the effect of multiple interacting cracks, a simpler test problem was considered. This problem involved an array of sixteen identical cracks placed in a symmetrical fashion around the origin of the coordinate system, see Figure 3. In this investigation the length of each crack was defined as 2a, the horizontal distance between the crack centres was defined as 2b and the vertical spacing between the rows was defined as c, see Figure 3. The maximum value(s) of the stress intensity factors thus calculated, using the finite element alternating method[4], are shown in Figure 4. The advantage of this technique is that it does not require the crack(s) to be explicitly modelled.

For cases where the a/b ratio was less than 0.75 the K_I/K_0 value lay within the range 0.8 to 1.2. It thus appears that, as a first approximation, for these crack configurations the maximum stress intensity factor behaves as though it is being produced by a single (ie. "just one") crack. It is only when the cracks become very closely spaced that the full impact of MSD becomes apparent. (This begins to occur when the a/b ratio reaches 0.75. As a result it appears that, in any row, around 80% of the region must be cracked before an appreciable difference in the stress intensity factor occurs.) Consequently, monitoring of the near tip stresses and strains may not be particularly sensitive.

Structural integrity considerations, for MSD in the F/A-18 aft bulk head, mandate the development of adequate inspection intervals. This means that, prior to "link up", it is desirable (indeed essential) to detect these very small flaws (cracks). The challenge is therefore to develop fracture mechanics based tools, which will allow accurate and rapid assessment of the structural integrity. In this investigation attention is focused on the use of compliance measurements, with the hope that they may provide a useful tool for assessing the structural integrity of the F/A-18 488 bulkhead. In service aircraft this can be achieved using either extensometers or piezo-electric sensors. With this in mind the test case was used to evaluate the effect of these interacting cracks on the compliance, at various points on the y-axis, of the specimen. To then simulate typical sensor output signals the difference in displacements at the end points, $u_1 - u_2$, divided by the length (L) of the sensor (or extensometer), was evaluated for a range of different (sensor) lengths. A graph of the resulting displacement per unit length versus the "measurement" length (L), over which the displacement was computed, is shown in Figure 5. In all cases the vertical spacing between the rows of cracks has been kept constant. Each curve represents a different horizontal spacing between the cracks. For the cases where the cracks were closely spaced it would appear that, for the present problem, there is an optimal measurement length, of approximately 12mm, after which the signal becomes relatively constant. (This length is thought to be a function of the particular problem.) It thus appears that this approach has potential for monitoring the cracking process. Furthermore, if as in the 488 aft bulk head, a prior knowledge of the size and location of the critical region exists then there may exist an optimal sensor size.

4 INTEGRITY ASSESSMENT OF COMPOSITE REPAIRS

The recent RAAF requirement that repairs be assessed for their effect on damage tolerance means that tools for assessing their in-service performance need to be developed. The present paper focuses on composite repairs[5] and a detailed discussion on failure mechanisms and the requirements for maintaining continued airworthiness is presented in[6]. As an illustration of the ability of piezo-electric sensors to address this requirement let us consider the case when an externally bonded 7 ply unidirectional boron/epoxy patch is bonded over a centrally located through crack in an aluminium alloy plate, see Figure 6. The alloy, adhesive and patch were modelled using twenty noded isoparametric brick elements and fifteen noded isoparametric wedge elements. A uniform tensile stress was assumed to be acting on the ends of the plate in the x-direction and for simplicity the lower surface of the plate was restrained in the z-direction to eliminate bending effects.

In this study a strip of piezoelectric film (sensor) was assumed to be placed, perpendicular to the crack, on the upper surface of the patch. The ability of a piezoelectric film to detect damage was then evaluated using a sensitivity parameter, S, which we define in terms of the voltage output from a sensor located over the damage, V_{damage}, and the output from a sensor located in the far field, $V_{farfield}$, namely: $S = 100.\ X\ (V_{damage} - V_{farfield})/\ V_{farfield}$. The change in the sensitivity parameter S with length was then calculated for a number of crack lengths and the results are shown in Figure 7 (the width of the sensor is taken to be 10 mm). Maximum sensitivity was achieved with a strip length of approximately 8 mm (i.e., extending to $x = \pm 4$mm). Assuming that the measurement of the piezoelectric signal involves a 15% error then, for a strip length of 8mm, the minimum detectable crack length was approximately 11 mm. Note that a strip of length 40 mm would not be able to detect cracks smaller than 50 mm. The size of crack that can readily be detected is also determined by the width of the strip. In this case an 8 mm long and 10 mm wide strip was able to detect an 11 mm long crack. In contrast an 8 mm long and 5 mm wide strip was able to detect a 7 mm long crack. It is evident from Figure 7 that there is an optimum length of the strip for crack detection. This length is related to distance from the crack to the peak fibre strain. This distance appears to be essentially independent of both crack length and patch thickness.

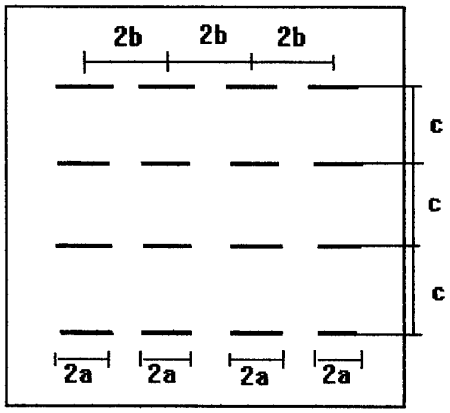


Figure 3 - Nomenclature used for an array of 16 identical cracks.

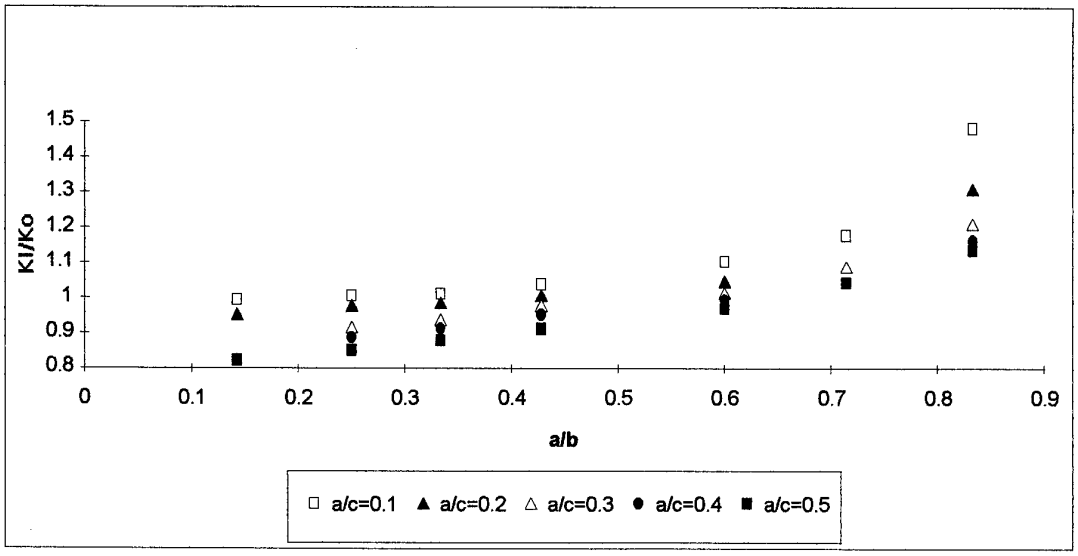


Figure 4 - Variation of Maximum Stress Intensity Factor with Crack Spacing

On the upper surface of the patch the optimum size of the sensor is determined by the location(s) of the peak fibre strain, which is independent of both crack length and patch thickness. However, the magnitude of the sensitivity parameter S is determined by the thickness of the patch. Maximum sensitivity was achieved by placing a small piezoelectric film on the lower surface of the patch directly over the centre of the crack. Locating an optimal size sensor on the upper surface results in a 35% reduction in sensitivity when compared with the same sized sensor on the lower surface. However, bonding the sensor at the patch-adhesive interface, which is often a critical failure location[6] in the patch/repair, may cause premature delamination of the patch.

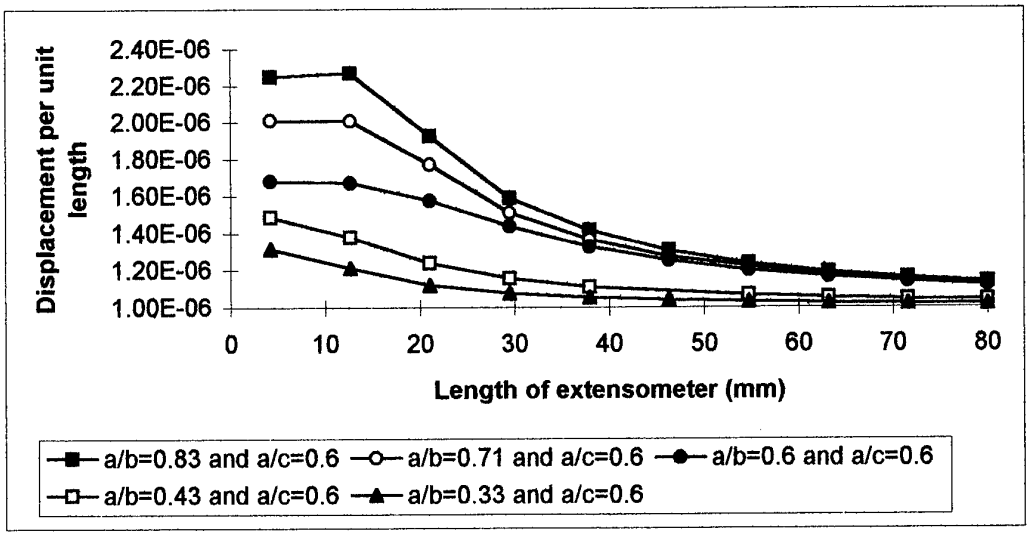


Figure 5 - Comparison of Output Signals for Different Horizontal Crack Spacings.

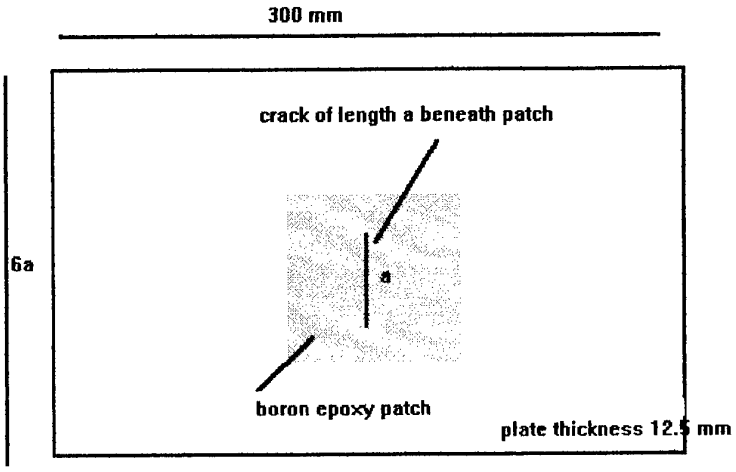


Figure 6. General outline of the repaired structure

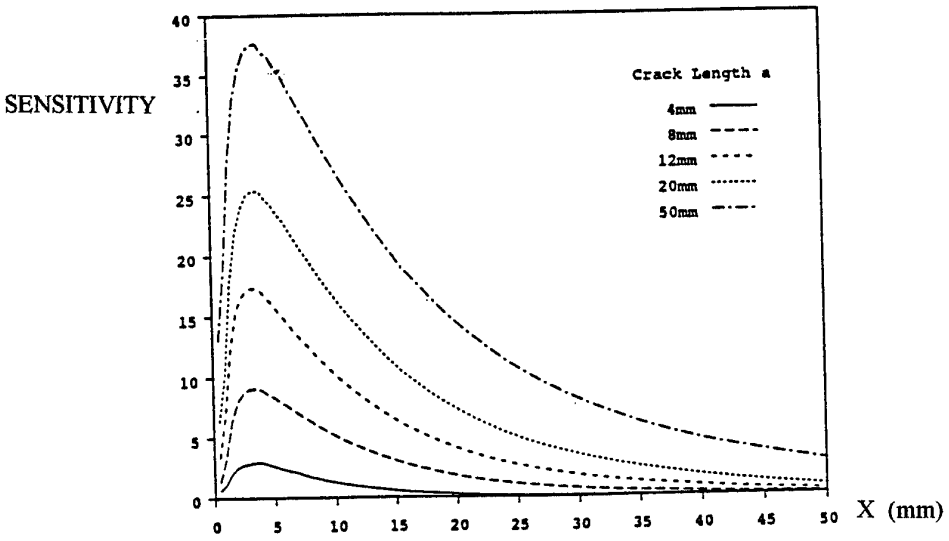


Figure 7. Sensor readings

5. CONCLUSION

The work outlined above summarises recent work at Monash University aimed at the development of "active" sensor technology for structural integrity monitoring using piezoelectric sensors. The work presented shows the viability of using piezoelectric sensors for crack growth monitoring in both metallic structures and composite repairs.

6. REFERENCES

1. W. R. Hendricks, "The Aloha Airlines Accident - A New Era for Aging Aircraft", *Structural Integrity Of Aging Airplanes*, pp 152-165, Springer-Verlag (1991).

2. G. D. Young, "Macchi MB326H Aircraft Structural Integrity Management Plan", Issue 1, *RAAF Logistics Systems Agency*, Logistics Command, Melbourne, Australia, December 1994.

3. S. Barter and G. Clark, "Fatigue and fracture control in components from modern military aircraft", *Proceedings International Aerospace Congress 1991*, Melbourne, Australia, 12-16th May, 1991, Vol 1, pp35-43, 1991.

4. R. Jones, S. Hammond (Pitt), J. F. Williams and M. Heller, "A numerical study of MSD in aluminium alloys", *Journal of Computers and Structures*, vol 55, No 1, ppl 177-183, 1995.

5. A. A. Baker and R. Jones, Bonded Repair of Aircraft Structures, Martinus Nijhoff, The Netherlands, 1988.

6. R. Jones and R. Smith, "Continued Airworthiness Of Composite Repairs To Primary Structures For Military Aircraft", *Proceedings 6th Australian Aeronautical Conference*, pp 311-316, 20-23 March, 1995, published by The Institution of Engineers Australia, NCP 95/1, ISBN (Book) 0 85825 624 X, also in *Journal of Composite Structures (in press).*

EVALUATION OF LAMB WAVE PERFORMANCES FOR THE HEALTH MONITORING OF COMPOSITES USING BONDED PIEZOELECTRIC TRANSDUCERS

H. Kaczmarek, C. Simon.
ONERA, L3C LAb, BP 72, 92322 Chatillon cedex-France.

C. Delebarre.
Université de Valenciennes, IEMN, département OAE (UMR CNRS 9929)
Le mont Houy, BP 311, 59304 Valenciennes cedex-France.

ABSTRACT

Specific characteristics of Lamb waves, and more particularly their ability to propagate over long distances, make them a promising technique for health monitoring of composite structures using piezoelectric transducers bonded on the surface or embedded inside the material. In order to evaluate the possibilities of the technique, a theoretical dispersion model for the Lamb waves propagation has been realized for a carbon-epoxy composite material, and the control parameters, incidence angle, emission mode and frequency, have been fixed. The technique has then been experimented in a transmission mode with contact conversion mode transducers. The propagation over long distance and the detection of delaminations have been put in evidence.
Then, optimized transducers have been manufactured in order to instrument, first, monolithic composite structures using surface bonding, and second, sandwich structures with embedded elements in the bulk.
Experimental results show that a large network could be envisaged. This technique presents serious interests compared to conventional ultrasonic techniques, testing at a point, or passive measurements of local stress and strain modifications due to the delamination.

ACKNOWLEDGEMENTS

The authors would like to tank M[r] THIRIOT, M[r] GODEFROY and M[r] THOBOIS of ONERA 's Physics Department for manufacturing of miniaturized transducers.

0-8194-2165-0/96/$6.00

I - INTRODUCTION.

In order to increase security, to reduce delays of airplane maintenance and to lower the repairing costs, integrated health monitoring could be envisaged in a permanent or semi-permanent way, for the evaluation of the degradation state of composite structures. This could allow the material to furnish information about his damage state.
The choice of the monitoring system must be guided by the respect of the material integrity through his ability to receive sensible sensors. In particular, the loss of mechanical properties and/or failure strength due to the presence of the insert must be minimized. An other selection criterion of the system is the reduction of the number of sensors for different imperatives : cost, connectors reduction and complexity of the electronic.
The research of such a system leads us to use Lamb waves, as they can propagate over long distances and are totally adapted to the inspection of large, thin plates with a very small amount of sensors. We propose in this study to evaluate the performances of Lamb waves in propagation and detection of delaminations due to impacts. The technique has been tested along a line in a transmitting mode using commercial mode conversion transducers. The selected excitation mode is the symmetrical and nondispersive one, S_0. The control parameter used is the attenuation of the ultrasonic signal due to the delamination. After the validation of the technique, optimized transducers have been realized. The incidence angle and the excitation frequency have been fixed by a theoretical model of the dispersion of Lamb waves. Miniaturized sensors could be bonded on the surface of monolithic structures or embedded inside sandwich one.

II - LAMB WAVES GENERATION AND PROPAGATION IN COMPOSITE PLATES.

Longitudinal and transverse waves are the solution of the waves propagation equation in infinite solid elastic media. Lamb waves are the solutions of this equation for limited media, and they must verify the limit conditions fixed by the medium dimensions. A basic work on the subject can be found in Victorov [1], Saulie and Auld [2], Dieulesaint et Royer [3], Nayfeh and Chimenti [4].
These waves may propagate in plates with a thickness value nearby the wavelength, and are generated under oblique incidence using a conversion mode transducer (see figure 1). There are mainly two kind of waves, asymmetrical and symmetrical, with a propagation direction parallel to the surface of the plate. Their associated displacement presents a longitudinal and transverse components. Two zero modes, A_0 and S_0, exist at all frequencies, but higher modes have cut-off frequencies f_c given by the following formula :
for symmetrical modes :

$f_c = n\, V_L / 2\, e$ where $n = 1, 3, 5....$
and $f_c = n\, V_T / 2\, e$ $n = 2, 4, 6....$

for asymmetrical modes :

$f_c = n\, V_L / 2\, e$ $n = 2, 4, 6....$
and $f_c = n\, V_T / 2\, e$ $n = 1, 3, 5....$

V_L is the longitudinal velocity, V_T the transverse velocity and e the sample thickness. As the velocity of the different modes depends on frequency, Lamb waves have a dispersive feature.

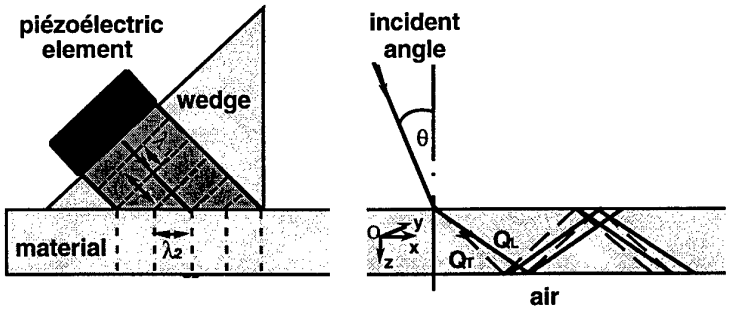


fig 1 : Generation and propagation of Lamb waves

- Control parameters selection.

Non Destructive Evaluation using Lamb waves involves the selection of different parameters like : incidence angle, frequency and excitation mode [5]. So, a dispersion model for homogeneous anisotropic layered material, taking into account of the mechanical properties of each layer has been developed and applied to Carbon-Epoxy cross-ply laminate.

Dispersion curves obtained for a T300-914 material and a $[0_4 \setminus 90_4]_S$ lay-up are given in figure 2, where the phase velocity is represented as a function of the frequency half-thickness product. One may see on this curve that the asymmetrical zero mode A_0 is dispersive for very low frequencies but it becomes nondispersive for higher frequencies and tends to the Rayleigh velocity.

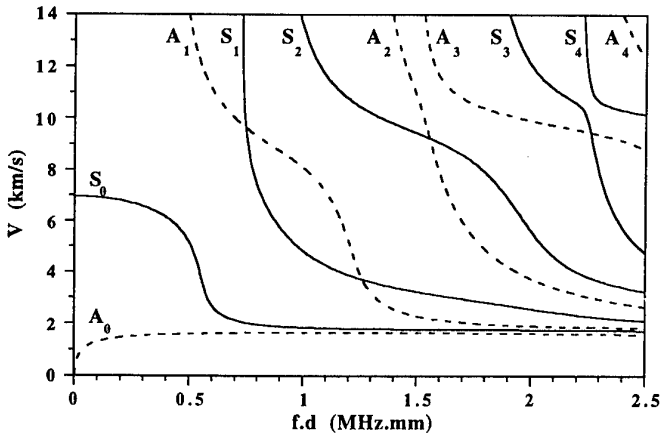


fig 2 : Lamb wave dispersion curves.
Symmetrical modes S_i and asymmetrical modes A_i
Lay-up: $(0_4 \setminus 90_4)_S$

The symmetrical zero mode S_0 is not very dispersive at low frequencies in a wide frequency range, then, its velocity decreases rapidly and tends to the Rayleigh velocity. The S_1 mode presents also a nondispersive region but for higher frequencies whereas other modes are all rather dispersive. Due to its nondispersive nature for low frequencies, the S_0 mode could be used for Non Destructive Evaluation of high thickness plates ($e = \lambda$) over long distance propagation. To generate this mode, the angle of incidence is given by the following relation :

$$\sin\varphi = V_L / V_P$$

where V_L is the longitudinal incident wave velocity and V_P is the Lamb wave velocity.

III - EXPERIMENTAL CONFIGURATION.

- Experimental set-up.

The main characteristics of the experimental set-up are the following :

- conversion mode wedge transducers with a variable angle of incidence. The coupling medium with the material is an oil film.
- 5 or 10 cycles "tone burst" excitation type.
- signal acquisition using a digital oscilloscope with data storage on "floppy disk" for offline treatment.
- ultrasonic transmission mode, using attenuation as control parameter.

- Material and damages studied.

The studied material is a Carbon-Epoxy T300-914 composite laminate with a $[0_4 \setminus 90_4]_S$ lay-up. Each ply has a 0.125 millimeter thickness and the total thickness of the laminate composite is 2 mm . The composite plate has a 150 x 100 mm square surface.

The different plates have been loaded under static indentation and the generated damages are comparable to the low velocity impact ones. Damage morphology has been characterized by a classical C-Scan ultrasonic technique, and an example of delamination is given in figure 3. The loading levels applied to the plates and the corresponding delaminations are summerized in table 1. The delamination area increases as a function of the applied loading.

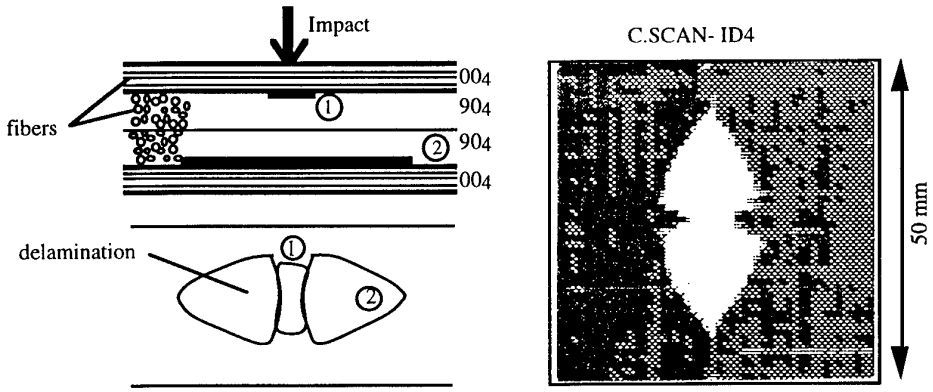


fig 3 : Morphology of damage - Lay-up : $(0_4 \setminus 90_4)_S$

- Ultrasonic technique.

The selected propagation mode of Lamb waves is the asymmetrical zero one, S_0 and the excitation frequency is 500 kHz corresponding to a frequency half-thickness product of 0.5 MHz.mm for the studied plate. The evaluation parameter is the signal attenuation due to the presence of the delaminations on the ultrasonic beam path.

The detection of the delaminations is evaluated by the comparison of the maximum signal amplitude between a sane plate (reference) and a delaminated one. The reference signal may also be measured on the sane part of the damaged plate (see figure 4). Amplitude measurements may be done whether in voltage or using the Power Spectrum Density of the ultrasonic signal performed by a Fast Fourier Transform algorithm [6].

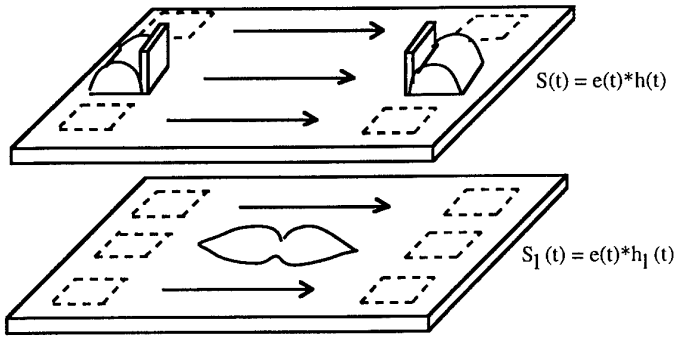


fig 4 : Delamination control procedure

IV - EXPERIMENTAL RESULTS.

Received temporal waveforms are shown in figure 5. The reference signal obtained on the sane plate for a distance between the sensors of 67 millimeters is named IDO.67. The peak to peak amplitudes of the different signals, measured for each loading level, are reported in table 1. The attenuation due to the delaminations is given by the following formula :

$$A\ dB = 20 \log V_d / V_e$$

where V_d is the voltage furnished by the receiving sensor on the damaged plate and v_e is the amplitude given by the receiver on the reference plate. Then we obtain the transfer function in maximum amplitude for the delaminations. The results show that this technique may be applied in health monitoring of composite structures.

Plate	ID0-67	ID2	ID3	ID4	ID5
Peak to peak amplitude (mv)	10.5	6.5	4.3	3.25	1.35
Attenuation (dB)		4.1	7.7	10.1	17
Delamination area (cm2)		0.2	1.9	4.41	7.67

Table 1

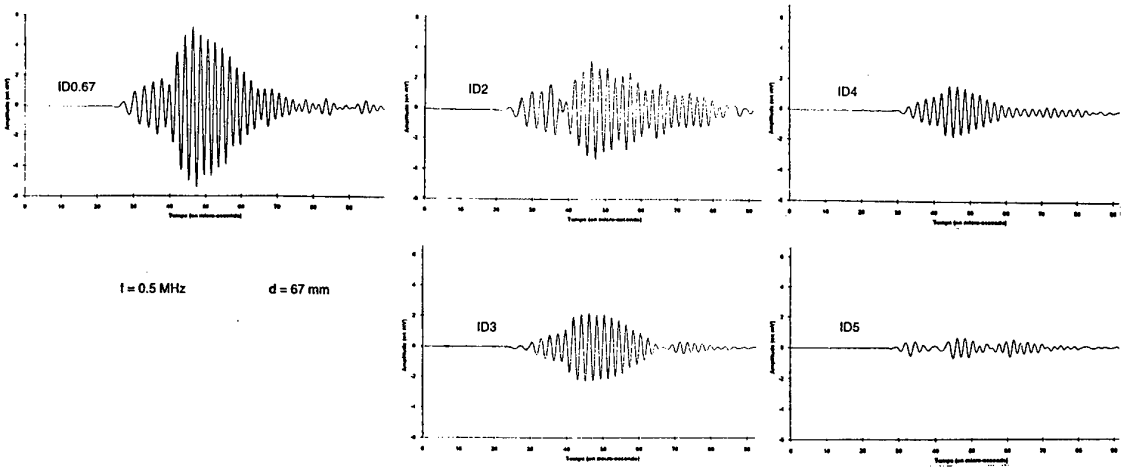


fig 5 : Delamination temporal responses

Validation of the Lamb wave propagations over long distances has been realized on a 500 x 500 mm square surface plate. The attenuation curve has been taken for a $[0_2 / 90_2 / 0_2 / 90_2]_S$ composite (see figure 6). A very low attenuation (10 dB) is obtained for a 400 mm distance, which allows to expect propagation over much larger distances.

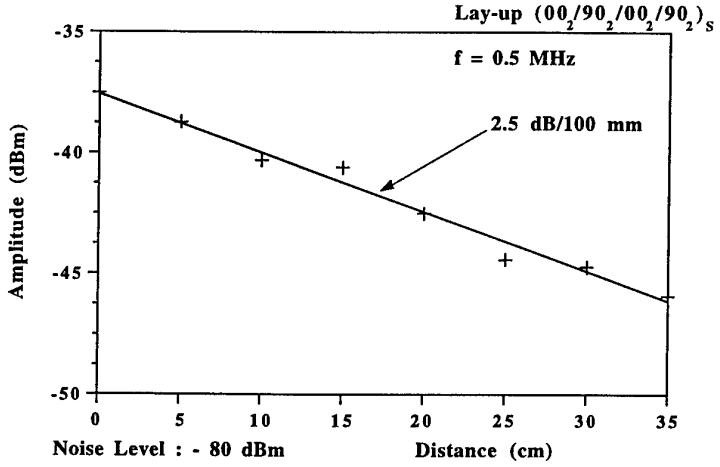


fig 6 : Long distance propagation

- Manufacturing of optimized and miniaturized transducers.

The conception of instrumented structures able to furnish information on their damage state, requires the realization of miniaturized transducers and optimized for the generation and the propagation of Lamb waves. Objectives of this first approach in the conception of Smart Materials are the bonding of sensors on the surface of composite monolithic structures and the embedment of these sensors in the bulk of some sandwich structures, by testing the damage level of the skins. The study of the Lamb wave performances previously presented leads to the fabrication of mode conversion piezoelectric sensors, bonded on a plexyglass wedge with a fixed angle. In this case, the structure is excited by a nondispersive symmetrical zero mode S_0.

The dimensions of the transducers are given in figure 7. The first evaluations of the performances of these transducers compared to that of commercial sensors show that similar results may be obtained. Experimental results for the sensibility and the detection of delaminations for the miniaturized transducers are given in figure 8. Amplitude levels measured on the frequency spectrum (FFT) are respectively of - 32 dBm in the sane part and - 39 dBm in the damaged one. So, attenuation due to the delamination is of 7 dB.

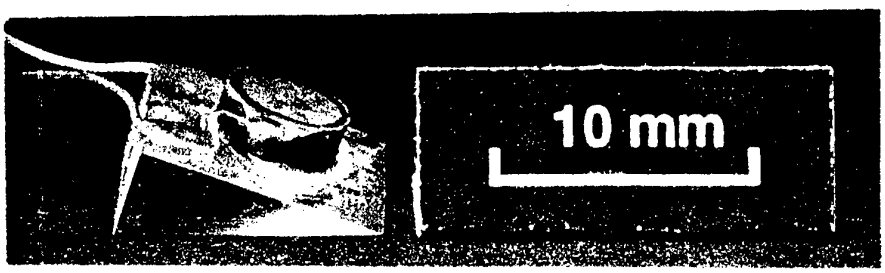


fig 7 : Miniaturized conversion mode transducer

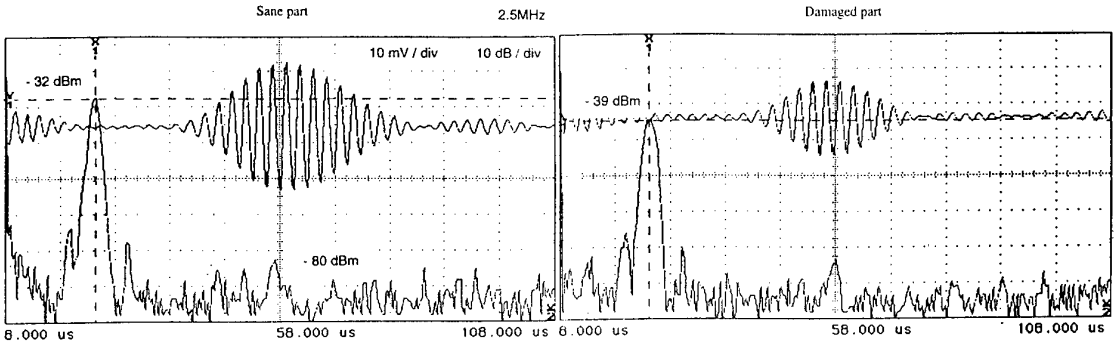


fig 8 : Delamination control using miniaturized transducers

V - CONCLUSION.

An ultrasonic technique has been experimented, consisting in the generation of ultrasonic waves inside the composite structure and in the evaluation of the modification due to the presence of delaminations of the transmitted signal. The evaluation of Lamb wave performances, for the health monitoring of composite structures requires several steps. A model for Lamb waves dispersion has first been developed, allowing the definition of experimental parameters for the generation and the propagation of efficient modes. Based on this model, the angle of incidence and the excitation frequency have been defined. Then, the technique has been experimented using commercial transducers. The capability of Lamb waves to propagate over long distances and to detect delaminations have been put in evidence. Finally, the use of the fundamental study results has leaded to the realization of miniaturized piezoelectric transducers susceptible to be bonded on the surface of monolithic structures or embedded in the bulk of sandwich structures.

Experimental results obtained show the feasibility of the technique for the detection of delaminations and the diagnostic of the damage state using attenuation measurement. The experimental model shows that attenuation is a function of the delamination area. The development of theoretical models describing the interaction of the Lamb waves and the defects is envisaged. Considering results obtained, a large spacing network of transducers might be realized but it remains some technical problems to be solved. For instance, a good knowledge of the surface covered by the ultrasonic beam and a better knowledge of the transducer performances will be very useful.

VI - REFERENCES

[1] : I.A. Victorov, "Rayleigh and Lamb Wave", Plenium, New York (1967)

[2] : L.P. Saulie and B.A. Auld, "Elastic waves in free anisotropic plates"
The Journal of the Acoustical Society of America, Vol. 54, N° 1 (1973)

[3] : E. Dieulesaint et D. Royer, "Ondes élastiques dans les solides", Massson et C^{ie}

[4] : A.H. Nayfeh and D.E.Chimenti, "Ultrasonic Wave Reflection From Liquid-Coupled Orthotropic Plates With Application to Fibrous Composites", Journal of applied Mechanics (1988)

[5] : N. Guo and P. Cawley, "The interaction of Lamb waves with delaminations in composite laminates", The Journal of the Acoustical Society of America, Vol. 94 N° 4 (1993)

[6] : D.A. Hutchins, D.P. Jansen and C. Edwards, "Lamb-wave tomography using non-contact transduction" Ultrasonics, Vol. 31, N° 2 (1993)

Carbon Fibres : Sensor components for smart materials

Olivier Ceysson, Tania Risson, Michelle Salvia

Ecole Centrale de Lyon, Département Matériaux Mécanique Physique
BP 163, 69131 Ecully Cedex, France

ABSTRACT

Recently, smart composites have appeared as new materials. But, these materials require the integration of functional elements within the composite structure which generates some problems.
This paper demonstrates how carbon fibres are not only the reinforcement but also the sensor to detect in-situ damages in CFRP laminates.
(±45°) laminates were subjected to monotonic and creep tests under three-point bending conditions. The in-situ monitoring of electrical resistance variation and AE activity allowed the detection and the identification, at different stages, of various types of damage mechanisms (not only fibre fractures but also matrix cracks, debondings and delaminations).

1. INTRODUCTION

Carbon fibre reinforced plastics (CFRP) offer high specific mechanical properties (performance vs weight ratio). Thus during the last decade, they have been increasingly used as components of structures having essentially mechanical functions, particularly in aeronautical applications. It is therefore imperative to detect, evaluate, and analyse the various types of damage propagation caused by both static or cyclic loads and also by environmental effects.
Although traditional non-destructive techniques (Ultrasonics (A-SCAN or C-SCAN), X-ray radiography, Infrared thermography, Holographic interferometry, Eddy currents,...) enable the a posteriori detection of damage at successive stages of the life of these materials, it seems more difficult to monitor in-situ the evolution of internal damage nucleation and growth, especially in CFRP (opaque materials).
Currently, the integration of functional elements in CFRP laminates allow in-situ damage detection and in-service health monitoring[1]. Some of the sensing materials used for this purpose include optical fibres, piezoelectric materials or "tagging" particules. These sensors must be externally attached or embedded within the composite structure during manufacturing. But these techniques present some drawbacks. For example, the incorporating of optical fibres within the structure leading to ply deviation and inhomogeneous stress and strain distributions within the composite (because they have large diameter compared to the reinforcing carbon fibres).
So, we have contributed to the development of a new technique based on the measurement of the electrical resistance of the carbon fibres.
In this case, carbon fibres are not only the reinforcement but also the sensor to detect damages in CFRP laminates.
Since carbon fibres are electrical conductors ($\rho = 2.10^{-5}$ Ω.m), the measurement of the variations of electrical resistance appears to be a valuable technique for the in-situ detection of various types of damages in CFRP laminates.

In the case of CFRP samples, conductivity is not isotropic but depends on the orientation of the carbon fibres.
The electrical conduction of (0°) unidirectional (UD) CFRP parallel to the fibres is due to the current flow along the fibres.
The resistance of the composite R, may be written as follows :

$$R = \frac{\rho_f L}{b\,d\,V_f} + R_c$$

where ρ_f : the fibre resistivity; V_f : volume fraction of unbroken fibres; L : length between the electrodes; b and d : specimen width and thickness respectively; and R_c : the contact resistance between the sample and the electrodes.

Fibre fractures will cause V_f to decrease hence increasing suddenly the sample electrical resistance R.

Recently, the electrical resistance measurements was used on one hand to detect fibre breakage in longitudinal unidirectional CFRP laminates caused by monotonic and cyclic tensile loading[2-6] or bending loading[7], and on the other hand to record the strain[8] or to measure the crack length during delamination test of CFRP samples[9-10]. But up to now, no study has used the electrical resistance measurements to detect damages in transverse UD or (±45°) laminates.

0-8194-2165-0/96/$6.00

In the case of transverse unidirectional CFRP, the conduction behaviour depends only on fibre-to-fibre contacts between neighbouring fibres (Epoxy matrix is electrically insulating : $\rho = 10^{13}$ to 10^{15} Ω.m).
The same phenomenon appears in (±45°) laminates in such a way that conduction occurs through continuous paths between carbon fibres along and between the plies of the laminates. Below some critical values of fibre volume fraction (V_f), there are insufficient fibre-to-fibre contact paths and conductivity is insufficiently large. But with current V_f values in engineering composites (50-60%), contact between fibres is always achieved.

Hence conductivity variations also allow the detection of transverse and longitudinal intraply matrix cracking and delamination by modifications to the fibre-fibre conduction paths and the gradual cutting of the resistive tracks.
Figure 1 illustrates how matrix cracks and delaminations can cause changes in transverse conduction.

In conclusion, the conduction paths are formed in 3 directions. The current flow in all the volume of the sample.
* In longitudinal direction, mainly by carbon fibres.
* In transverse direction, by fibre-to-fibre contact paths between neighbouring fibres.
* In the thickness of the sample, by contacts between plies of the laminates.

Consequently, the variation of the electrical conductivity can be taken as an indicator of the evolution of various types of damage in CFRP laminates (not only fibre fractures but also matrix cracks and delaminations).

On the other hand, the Acoustic Emission (AE) technique is now used to detect and possibly to identify damage mechanisms in CFRP.
This is achieved by analysis of AE parameters like the amplitude event, and, to a lesser degree, the energy and the duration of the event. But comparison between amplitude values found during different tests and with different samples is sometimes difficult. Beside, it is critical to achieve a relationship between amplitudes and rupture mechanisms.
In spite of this, several authors[11-15] agree that low amplitudes are correlated with matrix cracking, medium amplitudes with delamination and high amplitudes with fibre breakage.

Following these preliminary remarks, the monitoring of both the variations of electrical resistance and the Acoustic Emissions will allow the in-situ detection and identification of various types of damage mechanisms in CFRP.

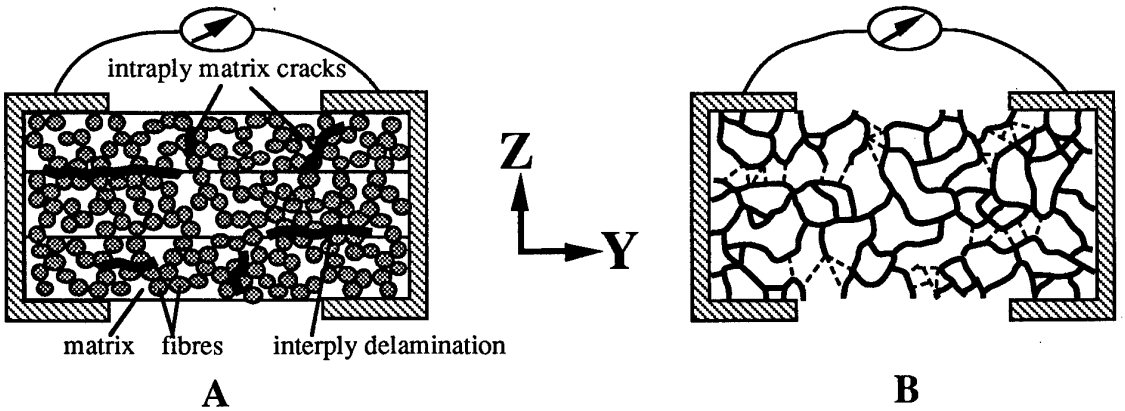


Fig. 1. (A) Various types of damage mechanisms and (B) its electrical analogue

2. EXPERIMENTALS

2.1 Materials

The material used was a 24-ply carbon fibre/epoxy laminate with a $[(\pm 45°)_6]_S$ lay-up. The fibre volume fraction V_f was about 60%. The CFRP sample had a width of 25 mm, a length of 100 mm and a thickness of about 4 mm.The span length to thickness ratio (L/h) was kept at 20.
These samples were subjected to monotonic and creep tests. Monotonic tests were performed with a constant cross-head speed of 2 mm/min. These tests allow the determination of the ultimate stress. Then, CFRP samples were subjected to creep tests at different load levels (x % of ultimate stress).

2.2 Electrical resistance measurement system

Figure 2 shows schematically the assembly used for the measurement of the electrical resistance.
The electrical resistance was measured by a HP 3458A multimeter. A constant electric current of about 50mA was introduced into the specimen by electrical cables soldered to U-shape copper plates. The value of current intensity was deliberately kept very low to avoid heating the specimen. Electrical contact between carbon fibres and the copper plates was ensured with a silver adhesive. To increase this contact and therefore allow better current transfer, locally, the specimen ends and side surfaces were polished (suppression of insulator epoxy matrix which are softer than carbon fibre).

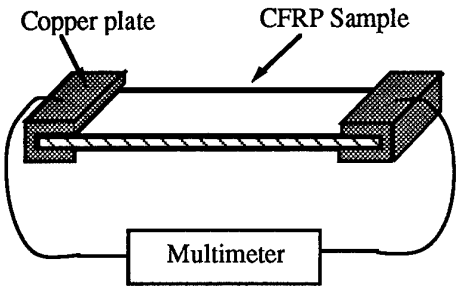


Fig. 2. Schematic illustration of assembly used to monitor in-situ the electrical resistance

2.3 Acoustic Emission system

Acoustic emissions signals were acquired and processed with an AE acquisition and analysing system LOCAN Jr of Physical Acoustics Corp. The AE signals during the tests were detected by a piezo-electric sensor (type R15) attached to the sample by a silicon grease and an adhesive tape. Its operating frequency range is between 50 and 200 KHz, and its resonant frequency is 150 KHz. This transducer was particularly recommended to detect matrix cracking and delamination. The signals were amplified by a pre and a post-amplifier with a total gain of 70dB. The threshold of AE system is 45dB, therefore events with an amplitude of lower than 45 dB were not detected.

3. RESULTS AND DISCUSSION

3.1 (±45°) laminates subjected to monotonic tests in three point bending condition

Figure 3 shows the evolution of bending stress, electrical resistance and cumulative Acoustic Emission events counts versus strain. Three zones can be identified. They correspond to various types of damage mechanisms.

1. Zone I : (0% < Strain < 1.5%) : Transverse intraply matrix crack nucleation.
This damage appears as soon as the load is applied, in the outer tensile layers and mainly at the free surfaces of the samples. In this case, the electrical resistance increases slowly due to gradual nucleation of matrix cracking and the subsequent reduction in the number of fibre-to-fibre conduction paths.
The activity of acoustic emission appears as soon as the load is applied and increases consistently. Energy, event duration and amplitude values are low. For the amplitude, one distribution is centred around 50 dB (Fig.4).
Initially during this first stage, the stress vs strain curve is non-linear. This non linearity can be explained by the nucleation of damages (matrix cracks).

2. Zone II : (1.5% < Strain < 2.5%) : Percolation of these matrix cracks led to delaminations.
At the beginning of the second zone, transverse matrix cracks propagated and multiplied rapidly.These cracks collapsed and caused delaminations (inter-ply cracks) particularly in the middle of the loaded beam (where shear stresses are maximum). There is an effect of mutual induction between various types of damage: intraply matrix cracks induce delamination which induces other intraply cracks.
The mutual coupling of matrix cracking with delamination led to damage growth throughout the whole depth of the sample. Coupling of damage mechanisms arises rapidly and only during the second zone.The presence of intraply matrix cracks modify the conduction paths and the current flow in all the plies of the sample. So, when delaminations occur, contacts between plies are not achieved and the area available for current flow decreases. Therefore, the electrical resistance increases suddenly.
In the same time, the AE activity increases greatly. Amplitude values are higher than those of zone I. There are two distributions centred around 50 dB and 62 dB corresponding respectively to intraply matrix cracking and delamination (Fig.4).

3. Zone III : (2.5% < Strain < 7.5%) : Opening of delamination and slip between plies
This result is linked to friction between plies (fibre/fibre and fibre/matrix). Friction between existing fracture surfaces does serve as a continuous source of AE.

The electrical resistance fluctuates but the mean value remains unchanged. The bending stress reaches a maximum value and becomes constant. Fracture of (±45°) laminates subjected to three point bending tests is never achieved.

All of these assumptions were confirmed by microscopic examination of tested samples.

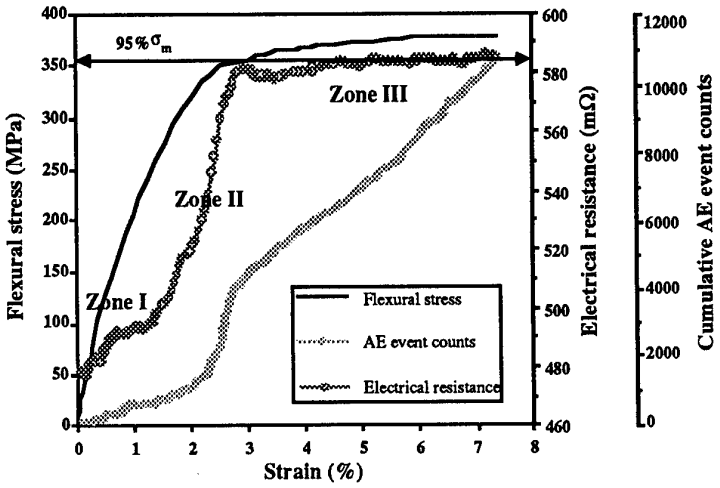


Fig. 3. Flexural test of a (±45°) laminate, showing the stress/strain curve and dependent electrical resistance and cumulative AE event counts

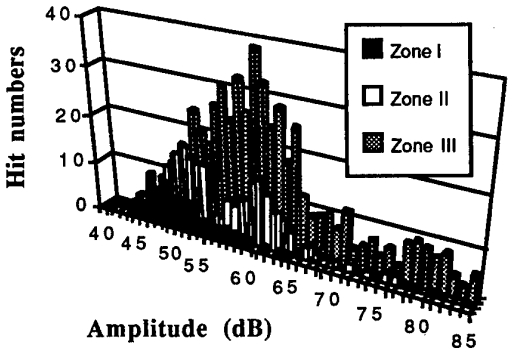


Fig. 4. Acoustic emission amplitude distributions for the three zones

3.2 (±45°) laminates subjected to creep tests in three point bending condition

Creep tests were conducted at high load levels (95% of the ultimate stress), at a temperature of 23°C and under a controled relative humidity of 50%. Figure 5 shows the evolution of creep strain, electrical resistance variations, and cumulative acoustic emission event counts versus time. Three zones can be identified. They correspond to various types of damage mechanisms.

1. Zone A (20 s.< t <45 s.) : Emergence of transverse intraply matrix cracks and delaminations.

This first zone corresponds to the loading of the sample. Considering the high load level at which creep tests were conducted (Figure 3), it is easily understandable that both intraply matrix cracks and delaminations appear during this loading zone.
In this case, the electrical resistance quickly increases due to sudden nucleation of matrix cracks and subsequent reduction in the number of fibre-to-fibre conduction paths.
The acoustic emission activity increases too. Three distributions are observed for the amplitude. The first one is centred around 50 dB : this corresponds to intraply matrix cracks. The second one is centred around 62 dB : during loading, delaminations are created. Friction between existing fracture surfaces may explain the third distribution for amplitudes higher than 75 dB (Figure 6).

2. Zone B (45 s.< t <80 s.) : Multiplication of transverse intraply matrix cracks.
In this zone, the rate of matrix crack apparition decreases. The nucleation and propagation rates of these damages, as well as the creep rate, finally reach a minimum limit value and remain constant : the evolution of strain with time is then linear. At the end of this zone, the number of intraply matrix cracks reaches a maximum limit value.
A slight increase of the electrical resistance is observed due to the modification of the conduction paths.
Concerning the acoustic emission event counts, a similar evolution is obtained. One distribution is centred around 55 dB (characteristic value for intraply cracking - Figure 6).

3. Zone C (80 s. < t < 100 s.) : Mutual coupling of the two types of damage mechanisms.
Due to the great amount of transverse intraply matrix cracks in the sample tested at the end of the second zone, the probability for such cracks to meet delaminations is significant. This implies coupling of these two types of damage mechanisms which led to damage growth throughout the whole depth of the sample. As a consequence, the creep rate quickly increases.
Moreover, the presence of numerous intraply matrix cracks modifies the conduction paths : the current flows in all the plies of the sample, and consequently allows the detection of delaminations. We indeed observed a sudden increase of the electrical resistance, which is similar to that observed for the creep rate.
Concerning the amplitude of acoustic emission events, one distribution is centred around 70 dB, and an other, around amplitude values greater than 80 dB (Figure 6) : this can be explained considering the growth and the opening of delaminations, and the subsequent friction between plies respectively.

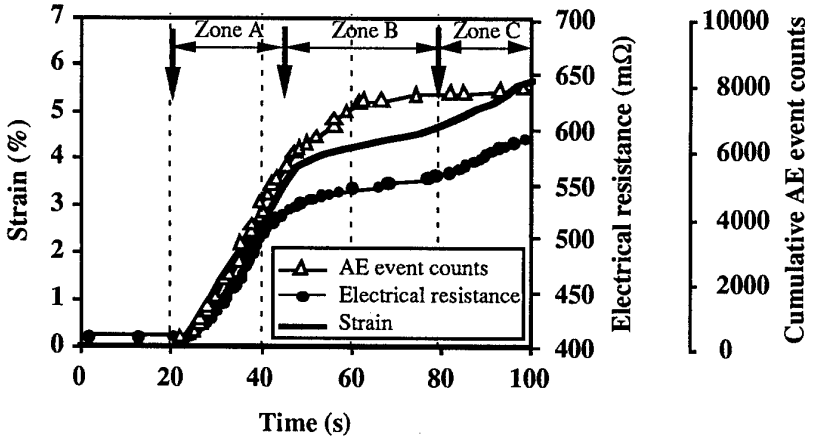


Fig. 5. Flexural creep test of a (±45°) laminate, showing the stress/strain curve and relative electrical resistance and cumulative AE event counts

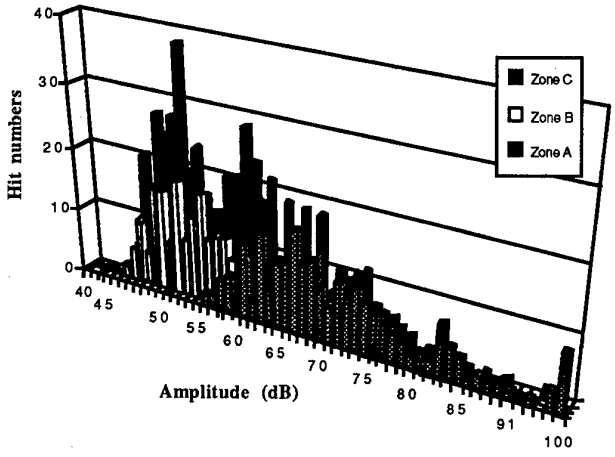


Fig. 6 : Acoustic emission amplitude distributions for the three zones

4. CONCLUSION

Measurement of the electrical resistance and the analysis of Acoustic Emission parameters provide accurate means to monitor the in-situ evolution of damage nucleation and growth in CFRP laminates particularly for internal damage.
These methods enable the detection as well as the identification of various damage mechanisms : fibre fractures but also intraply matrix cracks and interply delaminations. These types of damage appear at different stages for (±45°) CFRP laminates subjected to monotonic and creep tests.

5. REFERENCES

1. C.A. Rogers, "Intelligent material systems - The dawn of a new materials age". J. of Intelligent Material Systems and Structures, Vol. 4, pp 4-12, 1993.

2. R. Prabhakaran, "Damage assessment through electrical resistance measurements in graphite fiber-reinforced composites". Experimental Techniques, Vol. 14, pp 16-20, 1990.

3. K. Schulte and Ch. Baron, "Load and failure analyses of CFRP laminates by means of electrical resistivity measurements". Composites Science and Technology, Vol. 36, pp 63-76, 1989.

4. K. Schulte, "Damage monitoring in polymer matrix structures". J. physique IV-supplément de J. physique III, Vol. 3, pp 1629-1636, 1993.

5. C. Thiagarajan, I. Sturland, D. Tunnicliffe and P. E. Irving, "Electrical potential techniques for damage sensing in composite structures". 2nd Eur. Conf. on Smart Structures and Materials, Session 3, pp 128-131, Glasgow, 1994.

6. P. T. Curtis, N. J. Williamson and R. M. J. Kemp, "Development of self sensing smart composites using electrical resistance properties". 6th Int. Conf. on Fibre Reinforced Composites (FRC 94), Paper 17, Newcastle, 1994.

7. O. Ceysson, M. Salvia and L. Vincent, "In-situ detection and identification of damage mechanisms in CFRP by both electrical resistance measurements and acoustic emission analysis". 10th Int. Conf. on Composite Materials, Vol. 5, pp 381-390, Vancouver, 1995.

8. K. Schulte and H. Wittich, "The electrical response of strained and/or damaged polymer matrix composites". 10th Int. Conf. on Composite Materials, Vol. 5, pp 349-357, Vancouver, 1995.

9. K.Moriya and T.Endo, "A study on flaw detection method for CFRP composite laminates (1st report) The measurement of crack extension in CFRP composites by electrical potential method". Transactions of Japan Society for Aeronautical and Space Science, Vol. 32, pp 184-196, 1990.

10. C.Fischer and F.J.Arendts, "Electrical crack length measurement and the temperature dependence of the mode I fracture toughness of carbon fibre reinforced plastics". Composites Science and Technology, Vol. 46, pp 319-323, 1993.

11. S. Barré and M. L. Benzeggagh, "On the use of acoustic emission to investigate damage mechanisms of glass fiber-reinforced polypropylene". Composites Science and Technology, Vol. 52, pp 369-376, 1994.

12. J. M. Berthelot, "Relation between amplitudes and rupture mechanisms in composite materials". J. of Reinforced Plastics and Composites, Vol. 7, pp 284-299, 1988.

13. J. M. Berthelot and J. Rhazi, "Acoustic emission in carbon fibre composites". Composites Science and Technology, Vol. 37, pp 411-428, 1990.

14. K. Komai, K. Minoshima and T. Shibutani, "Investigations of the fracture mechanism of Carbon/Epoxy composites by AE signal analyses". JSME Int. J., Serie I, Vol. 34, pp 381-388, 1991.

15 N. Takeda, O. Chen, T. Kishi, W. Tredway and K. Prewo, "AE characterisation of the fracture mechanisms of a high compliant glass matrix composite". Engineering fracture mechanisms, Vol. 40, pp 791-799, 1991.

Application of a laser Raman sensor for stress monitoring in composites

B. Arjyal and C. Galiotis
Materials Department, Queen Mary & Westfield College,
Mile End Road, London E1 4NS, U.K.

ABSTRACT

Localised stress/ strain measurements in polymer based composites can now be made using a laser Raman sensor. In this case the stress sensor is the reinforcing fibre of the composite and the detector is the Raman spectrometer. Measurements can be conducted in reinforcing fibres near the surface of laminates. For measurements in the bulk of composites, the exciting laser light has to be transported to the reinforcing fibres via an embedded fibre optic cable. The backscattered light is transmitted through the same fibre optic and is sent to the Raman spectrometer for analysis. The effect of the direction of the fibre optic cable with respect to the axis of the reinforcing fibres is examined. Finally, the relationships between the local fibre stress or strain obtained from the Raman sensor and the far field stress or strain measured conventionally, are established.
Keywords: Laser Raman Spectroscopy, Fibre Optics, Composites, Stress/ Strain Sensors

1. INTRODUCTION

'Smart' materials and the structures fabricated from them, are defined as materials which incorporate the functions of sensing, actuation and control. These features are integrated in all biological systems and impart to them intelligence, efficiency and superior functionality. Advanced fibrous composites already have many desirable characteristics of natural materials. By adding the biological features of sensing, actuation and control, they can taken a step further and given true life features and 'intelligence'[1]. One of the most critical functions of a 'smart' material such as a composite, is accurate sensing. Sensing capabilities can be given to structures by externally attaching sensors or by incorporating them within the structure during manufacturing. Over the last few years a new spectroscopic technique for non-destructive stress/ strain measurements in composites has been under development. This technique is based on the fact that most Raman backbone vibrational modes of crystalline fibres, shift to lower values in tension and to higher values in compression[2]. In short, bond extension or contraction changes the bond stiffness and hence the atomic vibrational frequencies. The magnitude of this Raman frequency shift can be related to external stress or strain, hence, making stress/ strain measurements in composites, possible[2]. The superiority of the Raman sensor over other existing sensors is its ability to provide independently values of fibre stress and strain from composite sample volumes as small as 1 mm^3. In addition, this is the only technique that can directly measure stress in composites as most of the currently available non-destructive methods can only provide strain measurements[1].

In this work, various methods for retrieving the fibre stress or strain using ReRaM is reported. Attention is given to techniques that allow measurements in the bulk of a composite laminate. Stress within angle ply laminates is also measured. Finally, Kevlar 49® fibres have been used as stress/ strain sensors within carbon / epoxy resin system.

2. EXPERIMENTAL

2.1 Materials/ Specimen Preparation

Kevlar 49® / epoxy resin pre-impregnated tapes were manufactured by Ciba-Geigy (type 914k-49-54.8%). Carbon / epoxy resin pre-impregnated tapes were manufactured at QMW. 8-ply laminates were produced from the prepreg tape by curing them in an autoclave according to manufacturer's instructions. After curing the volume fraction of fibres was found to be 65% in the bulk.

2.1.1 Fibre-optic cable embedded perpendicular to reinforcing fibres (Fig. 1a)

0-8194-2165-0/96/$6.00

In this work, advances in the instrumentation allowed us to obtain high quality Raman response from the reinforcing fibres. The prepreg tapes were cut to strips of 203 mm in length and 12.7 mm in width. The 8-plies were laid on top of each other with a cleaved fibre-optic embedded in the centre. Multimode fibre optic cables were made by Newport Co. (model F-MLD) of nominal core diameter of 100 mm and a numerical aperture of of 0.29, were used. The laminates were cured in an autoclave as above.

2.1.2 Fibre-optic cable embedded perpendicular to reinforcing fibres of angle ply laminates

The laminates were cut to the dimension and cured as in the case of section 2.1.1. But this time the laminates were placed in $[0_2, -45, +45]_s$ order. A cleaved fibre optic cable was placed in the centre of angle ply laminates in a direction perpendicular to the axis of the reinforcing fibres of the laminate.

2.1.3 Kevlar® fibres placed in the centre of unidirectional carbon / epoxy laminates (Fig. 1b)

The laminates were cut to the dimension as in the case of section 2.1.1. Strand of Kevlar® fibres were placed in the centre in a direction parallel to the reinforcing carbon fibres. A cleaved fibre optic is then placed perpendicular to the Kevlar® fibres. The laminates were cured in an autoclave as above.

2.2 Mechanical testing

The Raman sensor was calibrated by loading single Kevlar® fibres in air and by plotting the shift of Raman frequency as a function of axial stress or strain. The composites were tested in tension following the ASTM D3039-76 standard procedure. All specimens were loaded on to fracture on a 20 kN screw-driven Hounsfield mechanical tester at a strain rate of approximately 0.002 min^{-1}.

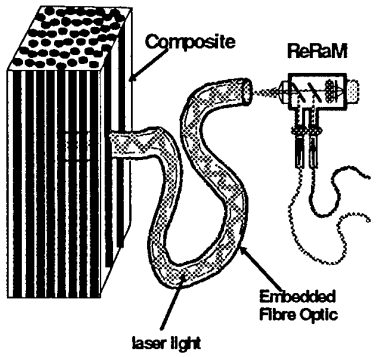


Fig. 2- Schematic of bulk-measurements. The items are not shown in scale.

2.3 Laser Raman Experiments

The input laser light of an argon-ion laser excited at 514.5 nm, was directed to the objective of the ReRaM and then was focused onto the free tip of the embedded fibre optic. For moderate levels of laser power the 514.5 nm wavelength was not found to cause any damage to the fibre. The light emitted by the fibre optic was non-polarised and, therefore, the calibration of the stress sensor in air was also carried through using non-polarised laser light. The 180^0 scattered light from the bulk or the surface of the composite was collected via the same embedded fibre optic and, by means of the ReRaM, was directed to the single monochromator for analysis and Raman light detection. The laser power was maintained constant throughout each test. 3.8 mW of incident laser radiation was directed to the embedded fibre optic and measurements were taken at 4 sec exposure intervals during the mechanical loading of the composite. Both the strain in the laminate- measured by means of the attached strain gauge- and the corresponding applied load, were independently recorded.

3. RESULTS AND DISCUSSION

As mentioned earlier, the basis of the laser Raman sensing technique is the stress or strain dependence of the Raman vibrational frequencies of almost all reinforcing fibres. In Figs. 2a and 2b the Raman frequency shift as a function of tensile stress and of tensile strain for fibres free standing in air, are presented, respectively. Both relationships can be considered linear within experimental error. The slope of the least-squares-fitted straight lines (Fig. 2) represent the sensitivity of the stress or strain sensors and can be used to convert Raman frequency into values of fibre stress or strain in composites[3].

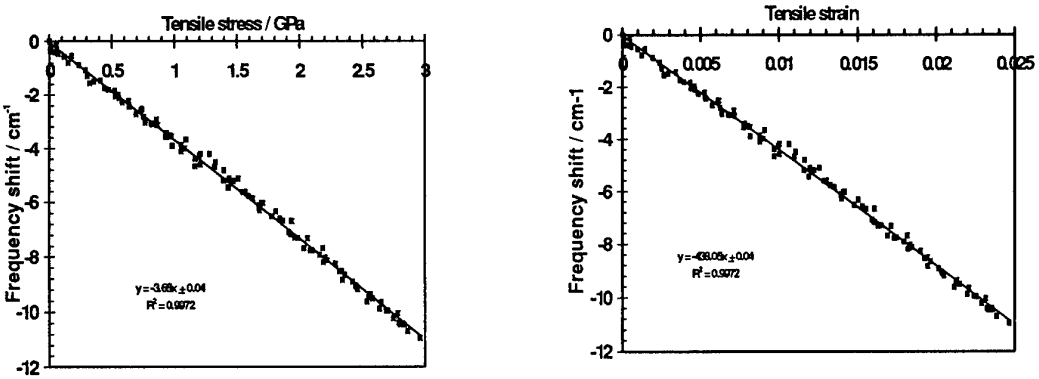


Fig. 2- Raman frequency shift as a function of tensile stress (left) and tensile strain (right) for the Kevlar 49® fibres (Raman sensor) in air. These curves are used as calibration curves for the conversion of the Raman frequency values into values of fibre stress or strain in composites.

The strain sensor measurements shown in Fig. 3 and 6 clearly indicate that a 1:1 relationship between composite strain, as measured by the attached strain gauge, and fibre strain, as measured by the ReRaM is attained for both Kevlar 49® / epoxy resin and carbon / epoxy resin (with a strand of Kevlar 49® fibres as sensors) systems. This is because for composites loaded along the reinforcing fibre axis, an equal-strain situation prevails. The stress sensor measurements shown in Fig. 4 indicates a 1:1 relationship between applied stress on individual fibres of the composite and the fibres stress measured by ReRaM. The composite stress, σ_c is related to the fibre stress sf via the rule-of-mixtures relationship:

$$\sigma_c = \sigma_f V_f + \sigma_m (1- V_f) \qquad (1)$$

where σ_m is the matrix stress and V_f the fibre volume fraction.

Fig. 5 shows the measured stress by ReRaM on fibres of +45 ply in relation to applied composite. As mentioned earlier the composite geometry is $[0_2, -45, +45\}_s$. As expected, the axial fibre stress is only a fraction of the applied composite stress. However, a closer inspection of the data points reveals that the relationship is not linear and therefore one may be able to extract useful information upon the deformation mechanisms in these geometries based on the relationship of the fibre stress at an angle θ to that of the applied stress in the axial direction.

Finally, the possibility of using the Kevlar fibre stress sensor in composites which incorporate reinforcing fibres that exhibit a weak Raman signal has been investigated. Fig. 6 shows the relationship between the Kevlar fibre strain to that of the applied composite strain. The data points lie on a least-square-fitted straight line the slope of which is unity. Thus, a small amount of Kevlar fibres can be used to assess the fibre strain in carbon fibre composites and indeed any composite, such as glass fibre reinforced polymers, for which the Raman signal cannot be obtained directly from the reinforcing fibres. The fibre stress can also be obtained but, in this case, the ratio of the tensile moduli of the Kevlar fibre to that of the reinforcing fibre of the composite must be known.

4. CONCLUSIONS

A new stress/ strain sensor has been built and tested. The technique is based on the stress or strain sensitivity of the Raman frequencies of the reinforcing fibres which are the load supporting elements of all the high performance composites. Measurements can be conducted on the near-surface of the laminate and also in the bulk. The latter are performed by employing fibre optic cables to transport the exciting laser radiation to the embedded reinforcing fibres in the composite. It has been demonstrated that the Raman stress/ strain sensor can be employed for unidirectional, as well as, multidirectional composites. In all cases the axial stress/ strain in the fibre at a given ply can be measured. The Kevlar 49® sensor can also be incorporated in composites that contain fibres whose Raman signal is considered too weak for accurate measurements.

6. REFERENCES

1. C. A. Rogers, Smart Composites, ECCM-6, ed. by P. Gardiner, A. Kelly, A. R. Bunsell, Woodhead Pub. (Cambridge), 1993, 3-9

2. C.Galiotis, Materials Technology, 8 (1993), 9/10, 203-209

3. C. Vlattas and C. Galiotis, Polymer, 35/ 11 (1994), pp. 2335-2347

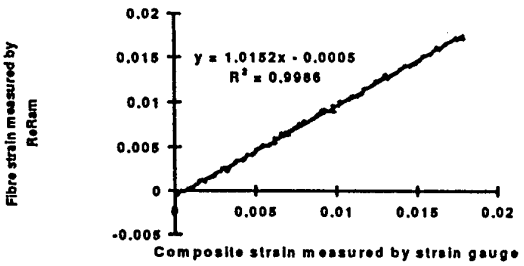


Fig. 3- Fibre strain measured by the remote Raman microprobe using an embedded fibre optic in a direction perpendicular to the reinforcing fibres of Kevlar 49® / epoxy composite, as a function of the strain in the composite measured by means of an attached strain gauge. The solid line is a least-squares-fit to the experimental data.

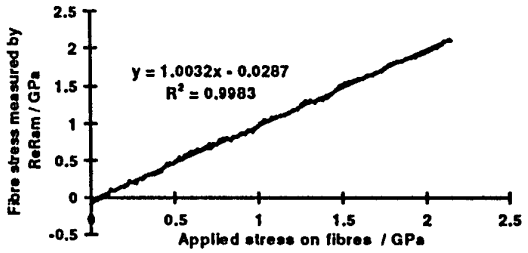


Fig. 4- Fibre stress measured by the remote Raman microprobe using an embedded fibre optic in a direction perpendicular to the reinforcing fibres of Kevlar 49® / epoxy composite, as a function of the applied stress over the whole composite coupon. The solid line is a least-squares-fit to the experimental data.

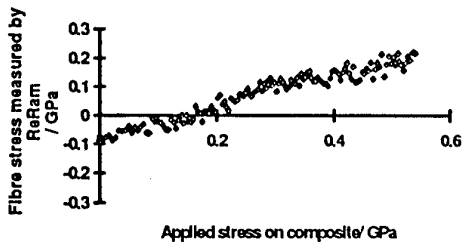


Fig. 5- Fibre stress measured by the remote Raman microprobe using an embedded fibre optic in a direction perpendicular to the +45 ply, as a function of the applied stress over the whole composite coupon.

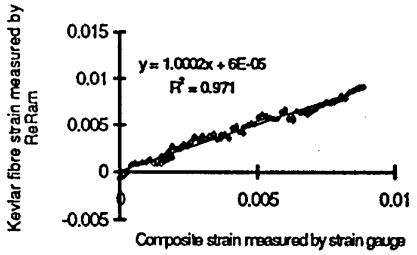


Fig. 6- Fibre strain measured by the remote Raman microprobe using an embedded fibre optic in a direction perpendicular Kevlar 49® fibres which are incorporated between 8-ply carbon / epoxy composite, as a function of the strain in the composite measured by means of an attached strain gauge. The solid line is a least-squares-fit to the experimental data.

COMPARISON BETWEEN FLAT MULTI-ELEMENTARRAY DEVICE AND OBLIC INCIDENCE TRANSDUCERS FOR LAMB WAVES GENERATION. APPLICATION FOR EMBEDMENT IN COMPOSITE MATERIAL.

T.Demol, P.Blanquet, C.Delebarre
Université de Valenciennes, IEMN, département OAE (UMR CNRS 9929)
Le Mont Houy, BP 311, 59304 Valenciennes Cédex. France

H.Kaczmarek.
ONERA, Direction de la Physique, BP 72, 92322 Chatillon cedex- France.

ABSTRACT

Lamb waves are used in the non destructive evaluation (NDE) of composite materials as they can propagate over long distances. The usual method of generation relying on a transducer that can not be reduced to a low thickness (oblic incidence transducer), the development of a thin transducer using a comb-like array of piezoelectric elements has been investigated. It requires a deep understanding of the dispersion relations in the material, in order to determine its geometrical parameters for a set of frequencies. Then, a prototype designed to work on surface is presented and Lamb waves generation is compared with classical oblic incidence sensors.

I - INTRODUCTION

Because they can propagate over long distances, Lamb waves are totally adapted to the inspection of large, thin plates with a very small number of transducers. These waves are usually generated by mode conversion at the interface using an angled transducer. This method of excitation, generally known as the wedge method, requires a transducer with a plastic or perspex body providing the suitable angle of incidence. This body makes it impossible to significantly reduce the height of the transducer. The interest in Smart Materials, especially health monitoring and impact damage detection on composite laminates using Lamb waves, justifies the development of a thin transducer which may be stuck on the surface or integrated into the structure. Hence, the priority is to reduce the height of the transducer, and the use of a comb-like array of piezoelectric elements makes it feasible.[1]

II - THEORETICAL STUDY

The first method of excitation, already described by Viktorov [2] as the comb structure method, consists in generating a set of normal perturbations, distributed periodically over the surface of the plate with a spatial period equal to the excited Lamb wavelength. To determine the geometrical parameters of the array, the first task to complete is to calculate the appropriate wavelength, corresponding to the less dispersive mode in the material at the working frequency.
The carbon-epoxy composite plates used in this study have 16 and 32 layers. The ply lay-ups for these laminates are $[0_{32}]$, $[0_2/90_2/0_2/90_2]_S$, $[45_2/0_2/-45_2/90_2]_{2s}$ and $[45/0/-45/90]_{4s}$.
An extensive literature on methods to calculate the dispersion relations in anisotropic media is available (Nayfeh [3], Nayfeh and Chimenti [4], Datta, Shah, Bratton and Chakraborty [5], Lowe [6],...). But few papers take the disparities in mechanical properties between layers into account and develop the calculations for every lay-up.
This study relies on the classical method, i.e. the resolution of a matrix equation which describes stresses and displacements in each layer of the laminate and the transfer relations between them. This equation leads to characteristic functions whose roots bring the results. Discussions of the different methods may be found in [6].
With those calculations, we obtained the wavelength dispersion curves plotted as a function of the frequency for the different plates. Figure 1 shows the curves in the case of a cross-ply laminate ($[0_2/90_2/0_2/90_2]_s$).
The classical dispersion curves (phase velocities as a function of the frequency-thickness product) show the less dispersive mode that can be generated in a frequency domain. Figure 2 shows these curves for the same sample.

0-8194-2165-0/96/$6.00

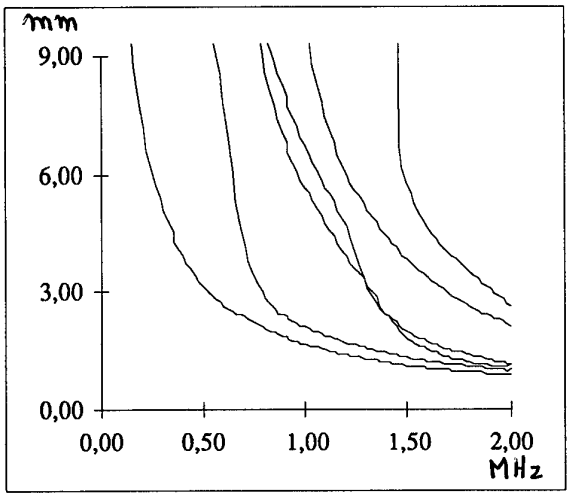


Figure 1 : wavelength as a function of frequency for a cross-ply laminate.

These curves allow the determination of the transducer's geometrical parameters for the generation of Lamb waves in a specific plate, using the same signal applied to each element of the array, similar to the comb structure method. The frequency range is imposed by the piezoelectric elements. Once the working mode has been selected (the less dispersive one at this frequency), the element spacing is fixed by its wavelength, as it must be a multiple of it.

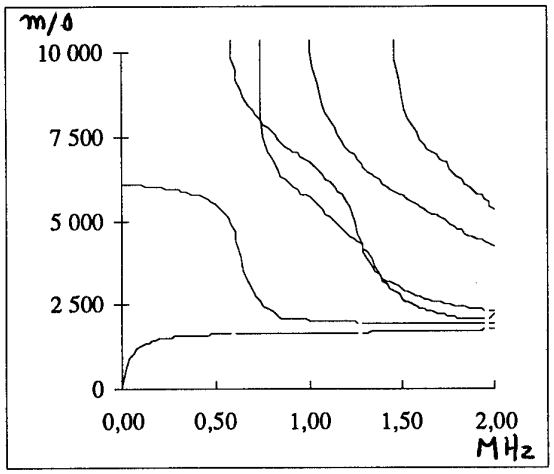


Figure 2: phase velocity as a function of frequency for a cross-ply laminate

Taking into account the different plates to inspect and their dispersion relations as calculated above, a 3 mm element spacing was retained for the technological part of this study.

3 - TECHNOLOGICAL APPROACH

The prototypes are designed to work on surface. The piezoelectric material is a plate of PZT (P1-60 from Quartz et Silice) whose resonance frequency is 1 MHz. In order to move the transducer easily, this plate is bonded on a glass slide previously coated with gold. The plate is cut out into 1.2 mm strips with a 0.3 mm cutting width. It allows element spacing equal to 1.5 mm (but this distance between active elements is too small), 3 mm, 4.5 mm and other multiples. Each transducer is equipped with 16 independent elements. A perspex layer protects the connections. The total height of the transducer is 3 mm , its width is 25 mm and its length is 45 mm.
Figure 3 shows the diagrams of the prototype.

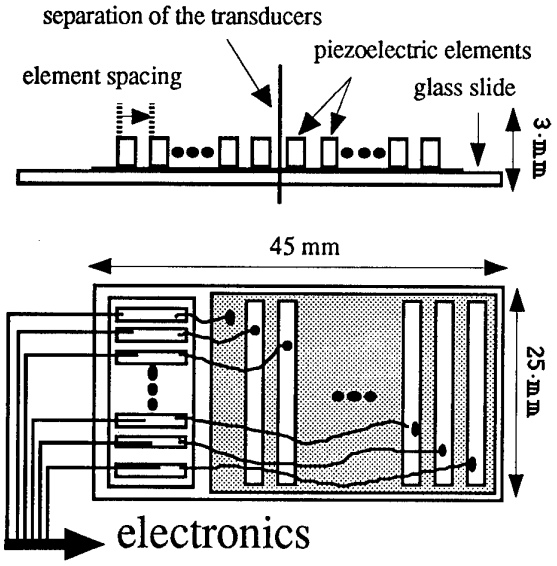


Figure 3 : description of the prototype.

4 - EXPERIMENTAL RESULTS

For each measurement, only one element of the receiving transducer was connected to the oscilloscope. The received signals were then transferred to a computer via the GPIB bus. The function generator delivered a 5-cycle tone burst of 20 volts peak to peak. Seven elements of the transmitting transducer were connected to it. All the results presented in this study are for the $[0_2/90_2/0_2/90_2]_s$ laminate (the same as for the previous figures).
Figure 4 presents the variation of the response as a function of the frequency. The distance between the transducers was 15 cm. Even if the resonance frequency of the piezoelectric elements is 1 MHz, this curve shows that the amplitude of the signal decreases beyond 600 kHz. The reason is the importance of the attenuation factor for high frequencies, and working with dispersive modes.
The other variations are due to the transition from one mode to another.

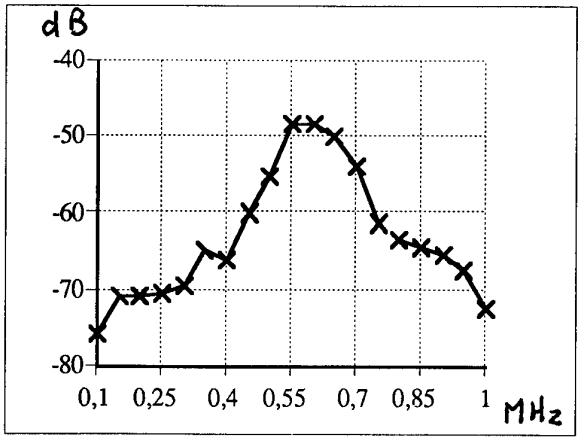


Figure 4: Variation of the response as a function of frequency.

Figure 5 presents a typical signal obtained with the multi-element array devices. The working frequency was 550 kHz. The distance between the transducers was 15 cm. Velocity measurements allowed the identification of the main mode in the response as the lowest symmetrical mode (S_0). The wavelength of this mode at this frequency

is 12 mm. According to the above theorical study, the predominant mode should have been the lowest antisymmetrical (A_0) whose wavelength at this frequency is 3 mm (exactly the element spacing). Nevertheless, it is present in the response, certainly in a higher proportion than with the classical Lamb wave generation. This is due to the comb structure effect. But this result is not interesting as a single mode excitation is more desirable for NDE applications, as described in [7].

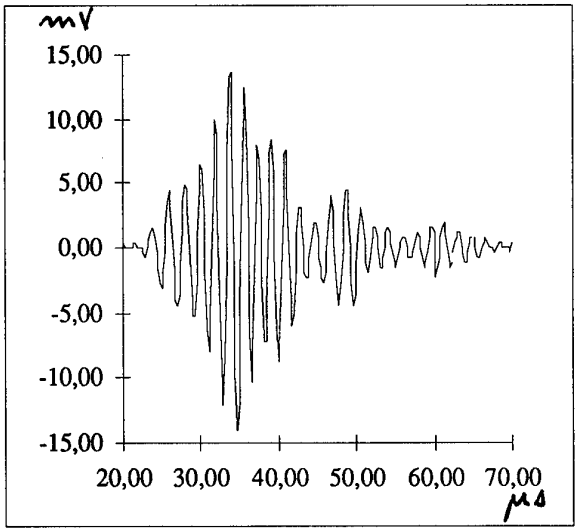


Figure 5: response of the transducer.

5 - EXPERIMENTAL COMPARATIVE STUDY

In this study we have used Lamb waves sensors from Panametrics (V 413 SB) with a 0.5 Mhz center frequency and an incidence angle of 20°. In the frequency range from 250 kHz to 740 kHz, transmission measurements have been performed, first with a couple of array sensors, and second, with a couple of wedge ones.
The distance between emitting and receiving sensors has been fixed at 15 centimeters and the sample used is a $[O_{32}]$ composite with a 200 x 200 millimeters square area. The emitting signal is a pulse with 5 cycles sinusoide and a 10 peak to peak volts. The amplitude detection is performed in the frequency domain, after a windowing and a Fast Fourier Transform computing.
The following figure 6 gives the comparaison between the two techniques, and shows that the 370 kHz frequency is not interesting for this kind of sample. For a given frequency, the two techniques give comparable amplitude levels.

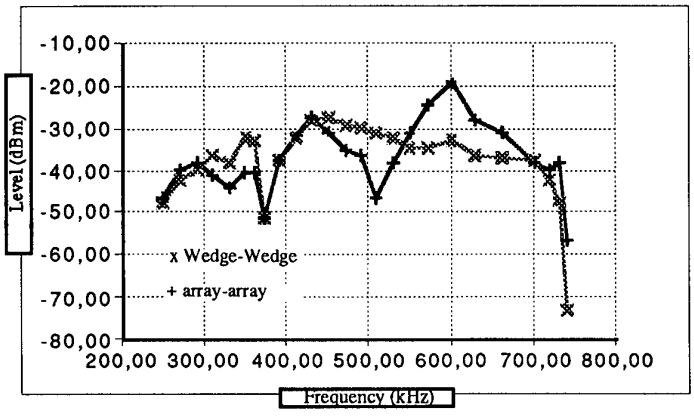


Figure 6 : Comparaison between the two techniques.

In the following study, we have fixed the working frequency at 450 kHz.
Figures 7-a and 7-b show the different waveforms obtained for each couple of transducers. The efficiency of the array devices is slightly better than the wedge sensors one.

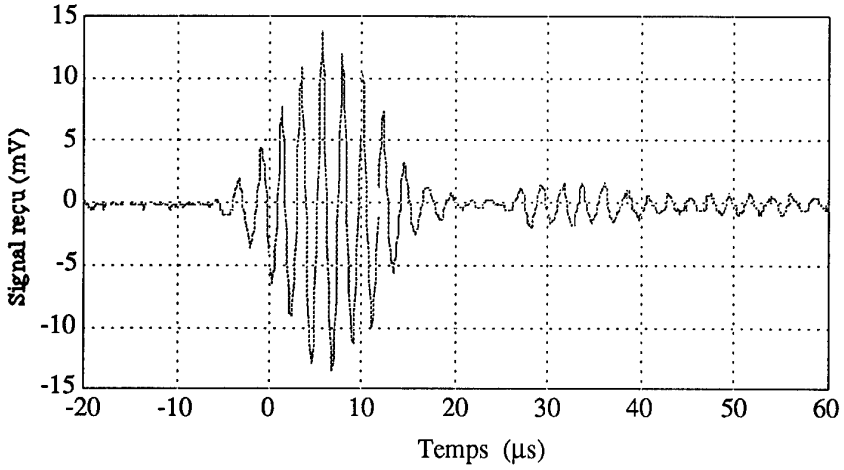


Figure 7-a: Waveform obtained with the wedge method.

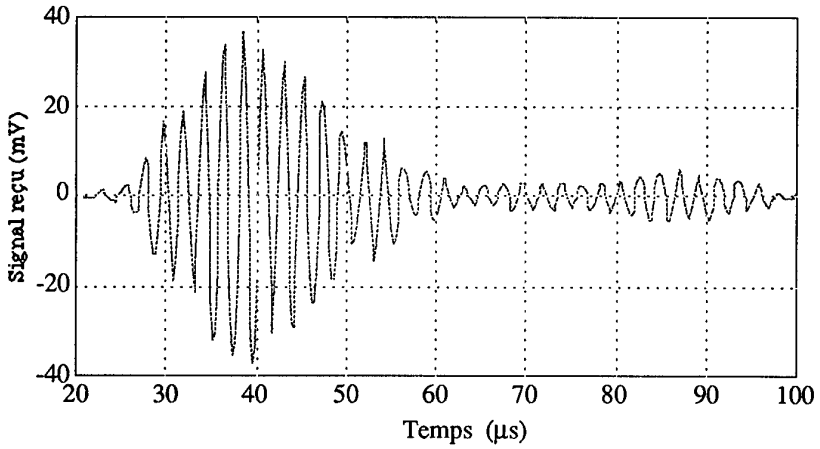


Figure 7-b: Waveform obtained with the array devices.

However, the duration of the waveform is longer for the array sensors, and is due to the presence of the glass plate under the piezoelectric elements.

Then, we have performed attenuation measurements using a $[O_4/90_4]_s$ sample with a 500 x 500 millimeters square area. Figure 8 gives the attenuation curves as a function of the distance between emitting and receiving sensors for the two couples.

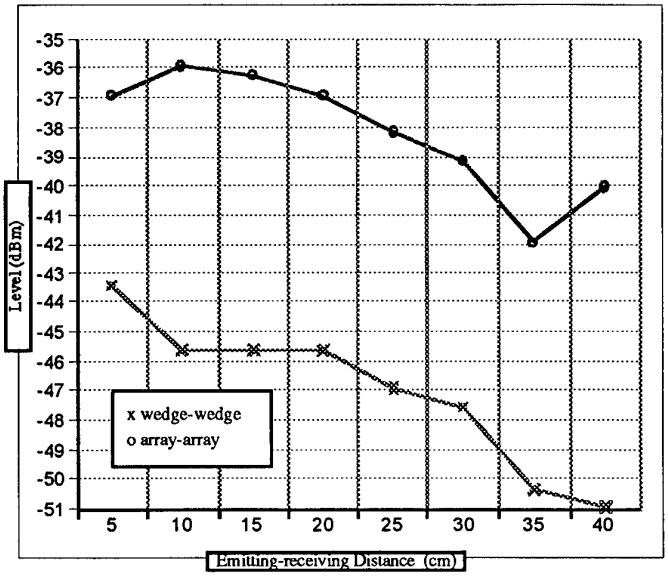


Figure 8: attenuation curves as a function of the distance.

6 - CONCLUSION

Even if it is not yet possible to select an arbitrary working mode, the array transducer makes it possible to improve the mode generally obtained with classical methods. Furthermore, the array transducers are likely to be reduced to a very low thickness.
Different kinds of velocity measurements have shown that array devices generate Lamb waves, and with a very satisfactory level.
The main problem with these sensors is the duration of the waveform which could reduce the resolution of the technique.

7 - ACKNOWLEDGEMENTS

This work has been sponsored by the ONERA (Contract n°22.630/DA0A1/CDC) and the CNRS.

8 - REFERENCES

[1] T.Demol, P.Blanquet and C.Delebarre, « Lamb waves generation using a flat multi-element array device ». 1995 IEEE International Ultrasonics symposium, 7-10 Nov 95, Seattle.
[2] I.A. Viktorov, Rayleigh an Lamb Waves, New-York: Plenum Press, 1967
[3] A.H. Nayfeh, "The propagation of horizontally polarized shear waves in multilayered media", J. Acoust. Soc. Am., vol. 89, pp. 2007-2012, November 1989
[4] A.H. Nayfeh and D.E. Chimenti, "Free Wave Propagation in Plates of General Anisotropic Media", Journal of Applied Mechanics, vol. 56, pp. 881-886, December 1989
[5] S.K. Datta, A.H. Shah, R.L. Bratton and T. Chakraborty, "Wave propagation in laminated composite plates", J. Acoust. Soc. Am., vol. 83, pp. 2020-2026, June 1988
[6] M.J.S. Lowe, "Matrix Techniques for Modeling Ultrasonic Waves in Multilayered Media", IEEE Transactions on Ultrasonics, Ferroelectics, and Frequency Control, vol. 42, pp. 525-542, July 1995
[7] D.N. Alleyne and P. Cawley, "Optimization of Lamb wave inspection techniques", NDT&E International, vol. 25, pp. 11-22, 1992

The piezoelectric implant method : theoretical and experimental study of the influence of inherent geometrical and bonding defects.

SAINT-PIERRE N., JAYET Y., BABOUX J.C.

Institut National des Sciences Appliquées de LYON,
GEMPPM, URA CNRS 341
69621 Villeurbanne cedex- FRANCE

ABSTRACT

The piezoelectric implant method has demonstrated its efficiency to monitor the mechanical properties of polymer based materials and in particular to follow in situ curing and ageing phenomena. From the electrical impedance of a piezoelectric plate inserted in the material to be tested and using an optimization algorithm, we have shown previously that it is possible to determine two acoustical parameters of the material : the attenuation and the velocity of the ultrasonic waves. This paper deals with the influence of different defects (non parallelism and debonding) on the validity of these results. Thanks to a model, and using the Kramers-Krönig relations, the defects that does not disturb the correct use of the identification process were evaluated.

1. INTRODUCTION

In classical ultrasonic methods, a piezoelectric element is usually used to generate ultrasounds in the material to be evaluated. Theses methods are well adapted to the characterization of the viscoelastic properties of polymers [1,2]: Ultrasonic velocity is directly linked to the elastic constant of the propagating medium and the ultrasonic attenuation to the viscosity of these materials. Theses techniques need a good acoustical coupling, which is often not easy to keep constant when operating during a long period of control. This is the case when ultrasonic techniques are used to monitor the mechanical properties of the material during the manufacturing process or to follow ageing phenomena.

We have developed an original method to overcome these limitations. This method is based on a piezoelectric element inserted directly in the composite as soon as the structure is manufactured. The electrical impedance of this element is significant of its deformations ; thus, it depends on the geometric, acoustic, piezoelectric and dielectric properties of the element and is also connected to the geometric and acoustic properties of the surrounding media. A one-dimension theoretical model has been developed and has been experimentally validated in the case of the curing of polymer matrix composites [3]. By application of a non-linear algorithm, the values of ultrasonic velocity and attenuation of the surrounding medium can be derived from the convergence of experimental and simulated electrical impedance media [4]. This identification procedure provides the two parameters (velocity and attenuation) independently, and it has been shown that the resulting values of velocity and attenuation satisfy the Kramers-Krönig relations [5].

In this theoretical approach, the one dimensional model assumes that the boundaries between the different media are parallel planes and that the acoustic coupling is perfect. Practically, it is difficult to assume a true parallelism between the faces of the material to be characterized. It is also possible that optimal coupling conditions are not obtained between the piezoelectric element and the material. Indeed, if such defects occur, the numerical treatment applied to the electric impedance of the ceramic will yield erroneous values for the velocity and the attenuation. The aim of the present investigations is then to show that these defects can be detected and do not restrict the application of the method.

In this paper, the modelling is modified to take into account these defects. The validity is obtained by confrontation of experimental and simulated impedance considering defects of different sizes. Then the modelling is used to study the influence of these defects on the results given by the identification algorithm and a method to detect such defects is proposed.

0-8194-2165-0/96/$6.00

2. PARALLELISM DEFECT

2-1/ Theoretical work:

Let us consider a piezoelectric element with one face in contact with the material to be characterized. This material has a finite thickness and the whole set is surrounded by semi-infinite media. The finite thickness material perfectly bonded with the active element exhibits a parallelism defect between its two faces characterized by angle α (Fig 1). The Oz axis is normal to the piezoelectric element faces and parallel to the polarization direction. Because α is small, we consider the longitudinal vibrations without mode conversion. So, we can replace the system composed by the piezoelectric element and the material by a set of elementary devices. Each elementary device is composed of a piezoelectric element coupled with a parallel-faced plate of thickness e(x) function of x. The small value of the angle enables us to make the assumption that each elementary device vibrates essentially in the Oz direction independently of the other neighbouring elementary devices. Assuming that the charge density remains uniform on the surfaces of the piezoelectric element, it is possible to calculate the global electrical impedance by applying the one-dimensional model to each elementary device.

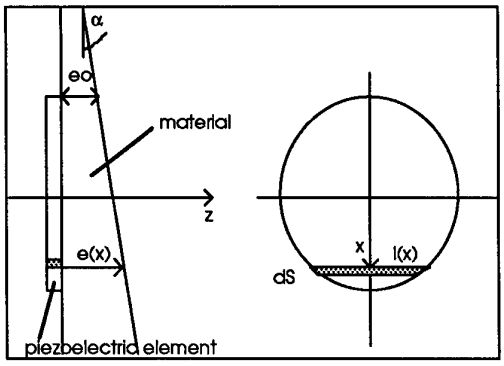


Figure 1: Used model

2-2/ Experimental and simulated results:

The piezoelectric element used in this study are PZT discs with diameter D=10 mm and thickness e=0.4 mm (resonance frequency 5 MHz). The mechanical and dielectrical properties are determined by a pulsed technique developed in the laboratory [6]. The front face of this element is perfectly bonded to the material to be studied, a PMMA plate. This element of initial thickness e_0=9,6 mm is machined to obtain different parallelism defects characterized by the angle α.

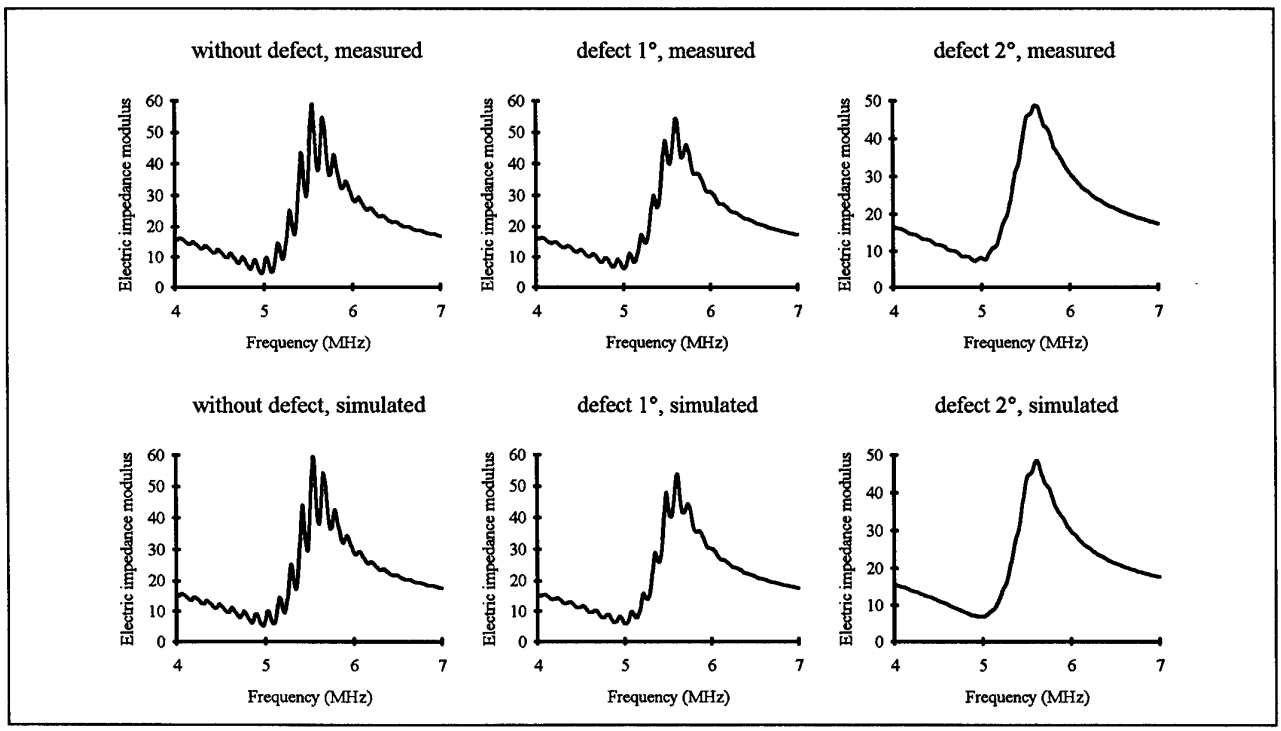


Figure 2: Measured and simulated electric impedances with parallelism defects (α=0°, α=1° and α=2°).

The modulus of electrical impedance of such a device is measured by an impedancemeter linked to a personal computer. The experimental and simulated results are presented on fig 2, corresponding respectively to $\alpha=0°$, $\alpha=1°$ and $\alpha=2°$. A parallelism defect between the faces of the material leads to a decrease of the amplitude of the frequency modulations due to the resonance of the PMMA plate. When $\alpha>2°$, we obtain the electric impedance of the piezoelectric element coupled with the same material of infinite thickness.

It must be noted that there is a good agreement between the experiments and the simulations derived from our model.

2-3/ Influence of parallelism defect on the validity of the method:

We now use this model as a tool to determine, when parallelism defects are present, the conditions of using the optimization algorithm that was previously developed to determine the acoustical velocity and attenuation of the material coupled to the piezoelectric element [4]. So, we simulate electrical impedance for materials where opposites faces are not parallel and we apply the optimization algorithm. Because this algorithm assumes a perfect parallelism between the faces of the material, the two extracted parameters, velocity and attenuation, will not be intresintic characteristics of the material and there are called "apparent" values. In the results of figure 3, we can see the apparent attenuation spectra exhibits an important dependence on the frequency and becomes very large when the α angle increase.

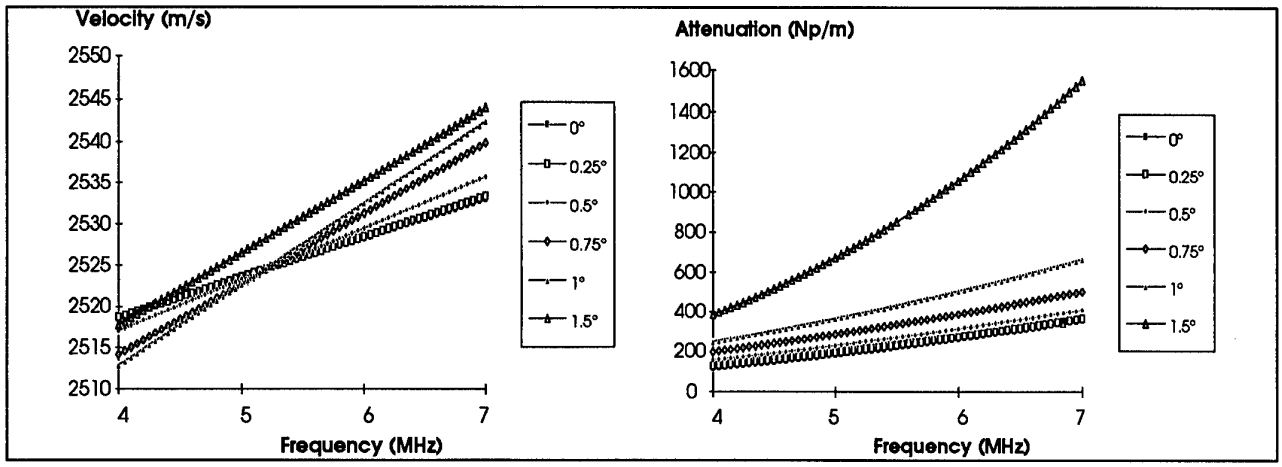
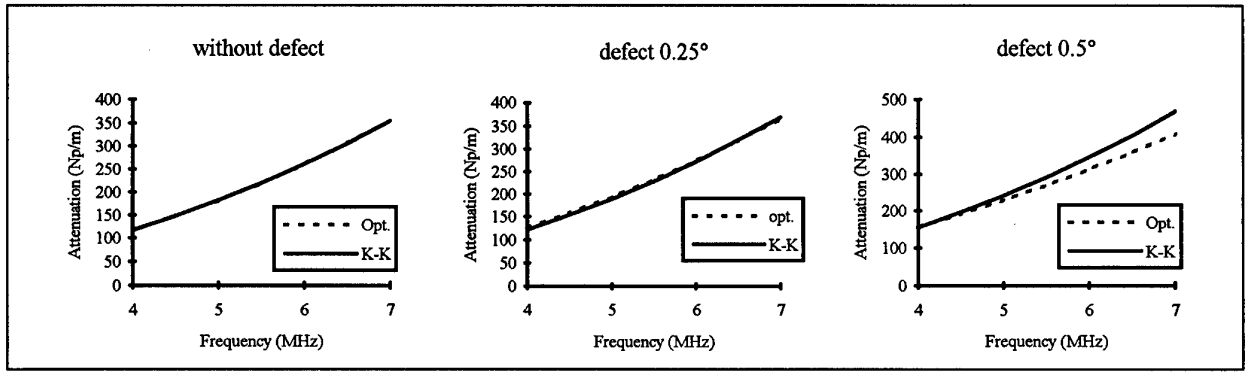


Figure 3: Apparent velocity and attenuation values obtained for different parallelism defects.

The two acoustical parameters are determined independently from each other by the optimization algorithm. In fact, to respect the causality principle, they are linked by the analytical Kramers-Krönig relations [7]. By application of these relations to the apparent velocity curves, we can deduce the attenuation law in this frequency range. In figure 4, the attenuation spectra derived from optimization algorithm is compared to that obtained by Kramers-Krönig relations.



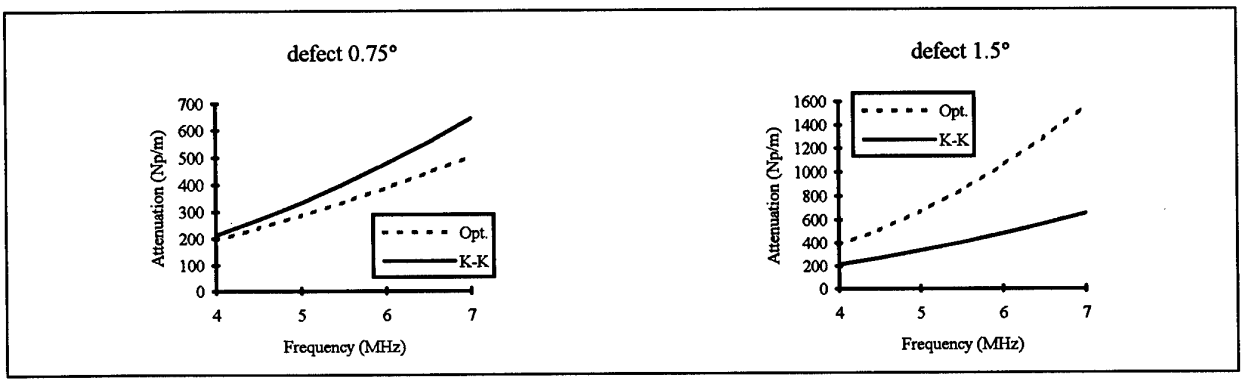


Figure 4: Comparison between attenuation obtained by Kramers-Kroning relation and attenuation obtained by optimization.

A good correlation is found for α less than 0.5°. For α>0.5°, the frequency dependence of the velocity and attenuation does not satisfy the Kramers-Krönig relations and consequently these parameters cannot be considered as physical characteristics of the material.

3. BONDING DEFECT

3-2/ Theoretical work :

We consider a piezoelectric element in contact on one face with the material to be characterized. This material with perfectly parallel faces presents a bonding defect with the plane face of the piezoelectric element.

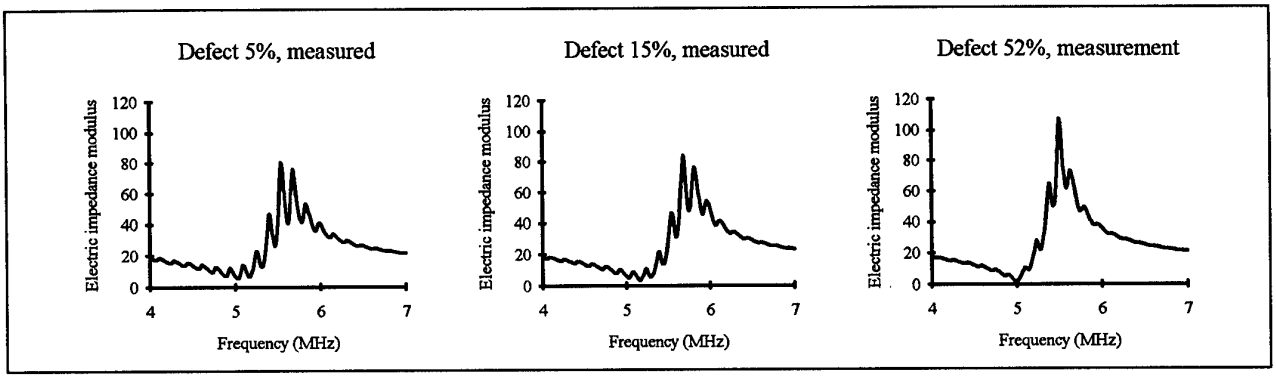
In these conditions, the piezoelectric ceramic may be considered as formed of numerous constituent piezoelectric elements ; either well bonded or non-bonded with the material to be characterized. Then, for modelling the ceramic electric impedance we assume that:

- the two different parts of the piezoelectric ceramic, the bonded and the non-bonded areas, vibrate independently.
- these two parts are electrically connected in parallel.

We can apply the one-dimensional model for each part of the ceramic. So, it is easy to determine the global electrical impedance value of the complete ceramic considering two independent electric admittance connected in parallel.

3-2/ Experimental and simulated results :

The piezoelectric element used in this study are the same as that described in §2-2. Bonding defects of different sizes were obtained by introducing between the ceramic and the PMMA plate a thin film. The size of these defects was defined by the relative area of the non-bonded part (5%, 15% and 52%). The experimental and simulated electrical impedance are presented in figure 5.



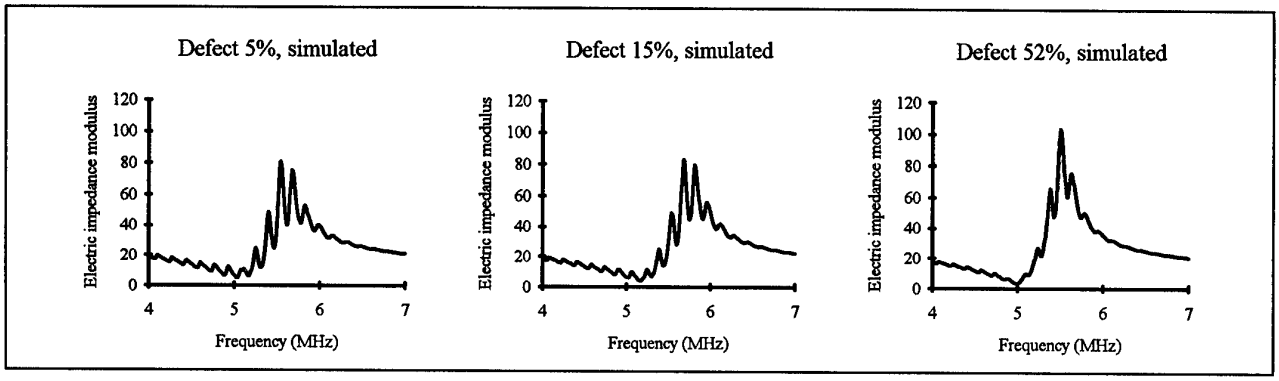


Figure 5: Measured and simulated electric impedances with bonding defects (5%, 15% and 52%).

The presence of bonding defects modifies the ceramic electrical impedance. In particular, the magnitude of the low frequency modulation associated with the resonance of the PMMA plates is as lower as the size of the defect is large. Furthermore, the magnitude of the high frequency resonance due to the piezoelectric element increases with the bonding defect size. The comparison of the experimental and simulated curves shows a good agreement, whatever the size of the bonding defect.

3.3 Influence of bonding defect on the validity of the method :

As it was done to study the parallelism defect, this modelling has also been used to determine the limits of the application of the optimization algorithm. We simulate the electrical impedance for materials with bonding defects and we apply the optimization algorithm considering a well-bonded interface. Apparent velocity and attenuation spectra are compared in figure 6. When the defect increases, the apparent attenuation tends to decrease with frequency, a situation without physical reality.

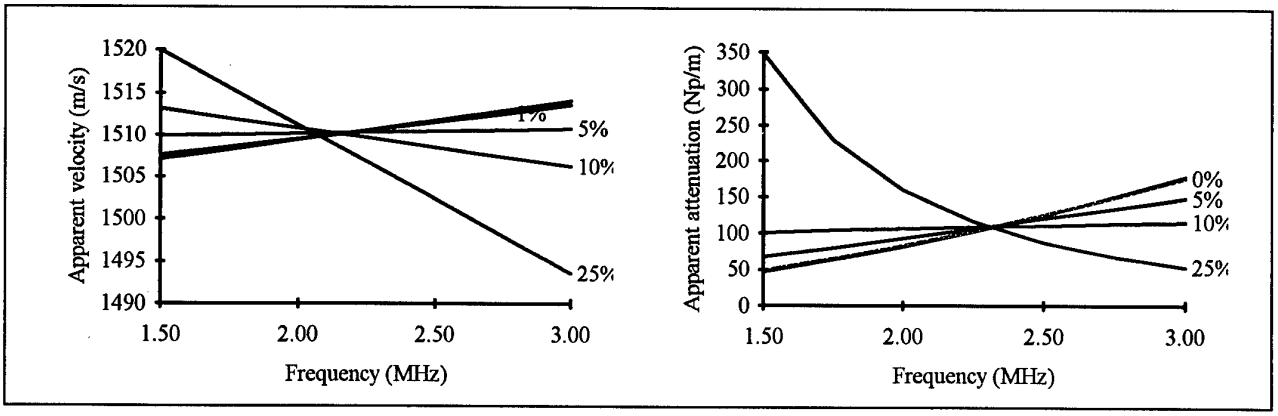


Figure 6: Apparent velocity and attenuation values obtained for different values of bonding defect.

The validity of these results were also tested by comparing the attenuation law predicted by the Kramers-Krönig relations with the apparent value obtained from the optimization algorithm (Figure 7). Discrepancies appear for bonding defect greater than 1%.

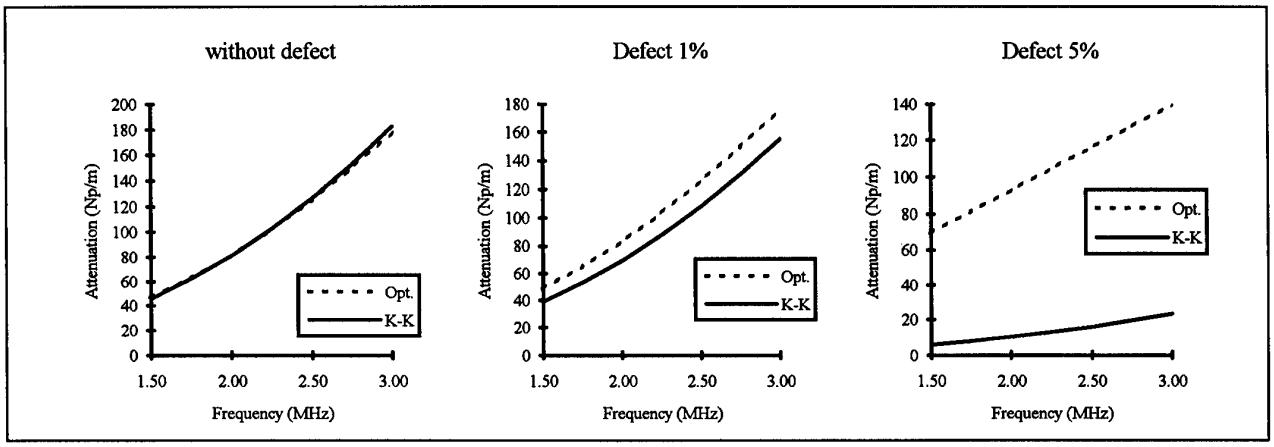


Figure 7: comparison between attenuation from optimization and those from Kramers-Krönig relations.

4. CONCLUSION

From an original model, we have studied the influence of parallelism or bonding defects on the results given by the piezoelectric insert. Such defects change the resonance of the ceramic plate. In fact, a parallelism defect reduces the surimposed modulation due to the resonance of the material to be characterized ; as for the bonding defect, this leads to an increase of the proper resonance of the piezoelectric element. The effects of these defects were correctly modelled.

Thanks to this model, and by means of the Kramers-Krönig relations for testing the validity of the acoustical parameters obtained by the optimization algorithm, it has been possible to determine, with a good sensitivity, the domain where these defects have a negligible influence on the results.

At present, a work based on the use of the Kramers-Krönig relations is in progress in order to evaluate the importance of these defects. Then, we plan to adapt the optimization algorithm in order to be able to give correctly the two acoustical parameters of the material to be characterized, even when rather large defects are present.

5.ACKNOWLEDGEMENTS

The authors wish to thanks Electricité de France, Elf-Atochem, Prodemat and Groupement de la plasturgie Industrielle et des Composites for their financial support.

6. REFERENCES

[1] PICHE L. "Phenomena related to the propagation of ultrasound in polymers." IEEE Ultrasonics Symposium, 599-608, 1989

[2] PETHRICK R.A. "Ultrasonics studies of polymeric solids and solutions." Adv. in Sonochemistry, 2, 65-133, 1992.

[3] PERRISSIN-FABERT I., JAYET Y. "Simulated and experimental study of the electric impedance of a piezoelectric element in a viscoelastic medium." Ultrasonics, 1994, vol. 32, n° 2, p. 107-112.

[4] PERRISSIN-FABERT I., JAYET Y. "Polymer evaluation by using the thickness longitudinal and shear vibrations of piezoelectric ceramics: Application to the monitoring of thermosetting resins' polymerisation" J. Phys. D: Appl. Phys., 1995, n° 28, p. 1-7.

[5] ZELLOUF D., JAYET Y. SAINT-PIERRE N., TATIBOUET J., BABOUX J.C. "Measurements of attenuation and phase velocity in polymeric materials by ultrasonic spectroscopy. Application of the Kramers-Kronig relations." Submitted for publication in Journal of applied Physic.

[6] LAKESTANI F., BABOUX J.C., PERDRIX M., FLEISCHMANN P., "Mesure par une méthode impulsionnelle de certaines constantes élastiques, piézoélectrique et diélectrique d'un transducteur." J. Phys. D. Appl. Phys., vol.8, 1869-1872, 1975.

[7] MANGULIS V. "Kramers-Krönig or dispersion relations in acoustics." J. Acoust. Soc; Am., 36,221,1964.

Piezoelectric Implant: Monitoring the Water Degradation in Polymer based Composites

D.ZELLOUF, N.SAINT-PIERRE, Y.JAYET, J.TATIBOUET

Institut National des Sciences Appliquées de Lyon
Goupes d'Etudes de Métallurgie Physique et de Physique des Matériaux
URA CNRS 341
69621 Villeurbanne, France

ABSTRACT

Theoretical considerations show that the electrical impedance of a piezoelectric element depends on the physical and geometrical properties of the element and also on the viscoelastic characteristics of the different media surrounding it. According to a dynamic model, an original technique has been developed by inserting a piezoelectric ceramic in the composite structure when processed. The electric signal, after signal processing and numerical treatments, gives access to the viscoelastic properties of the external medium. This method is an excellent indicator to display the curing kinetics of the resin as well as the post-curing phase of the composite structure process. Moreover, a further application of this non destructive method is the monitoring of the hydrolitic degradation of the composite structure. The evolution of the electrical impedance of the piezoelectric sensor is presented here as a function of water exposition time for different polymer-based composites and compared to classical ultrasonic and rheological measurements.

1.INTRODUCTION

A previous original study[1] has shown that it is possible to monitor the polymerization process of a thermoset resin by measuring the electrical impedance of a piezoelectric element inserted in the composite structure. Principally based on the study of the damping of the resonances of this element by the viscoelastic properties of the surrounding medium, this work pointed out the sensitivity of the method to the detection of structural evolution of the material (gel point, glass transition). However, at the end of the curing process, these parameters are not very sensitive to the weak evolution of the mechanical properties of the thermoset which are clearly shown by classical ultrasonic methods. So, we have developed a physical model to simulate the electrical impedance of the piezoelectric element inserted in a viscoelastic medium. This model gives access to ultrasonic propagation characteristics (sound velocity, attenuation) which are directly related to viscoelastic properties of the thermoset resin. Simulations obtained from this approach were compared to experimental measurements and to results deduced from classical ultrasonic measurements. We shown the validity of these technique by comparing our results with those obtained by Barcol hardness measurement which is a classical test to monitor the curing process.

As the piezoelectric element remains inserted in the structure, its resonance properties will be related to the evolutions of the mechanical properties of the composite with time or under the action of the external environment. In particular, water immersion may be an important factor of degradation which is known to decrease the mechanical properties.

2.MODEL FOR THE ELECTRICAL IMPEDANCE

The piezoelectric element in this work is a classical PZT thin disc. When submitted to electric excitation, two types of mechanical deformation occur: radial and axial modes. As the thickness of the element is small compared to its radius, axial and radial vibrations appear in very different domains of frequencies and

0-8194-2165-0/96/$6.00

are considered to be independent. They can be studied separately and in the present study only the axial modes will be considered.

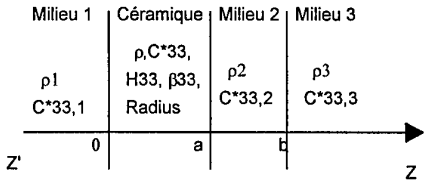


Figure 1. Schematic description of the theoretical model

To describe the axial comportment of the piezoelectric element inserted in the composite structure, we use a multilayered structure as described in figure 1. Each medium is characterized by its viscoelastic modulus (C^*_{ij}) and density (ρ_i). The opposite faces of the piezoelectric disc are in contact respectively with semi-infinite medium 1 and with the medium 2 (thickness e) which is the medium to monitor. The medium 3 can be either air or liquid medium. All this assembly can represented for example the wall of a storage tank. Characteristics of the ceramic element are also needed to describe the whole system. In particular, piezoelectric (h_{33}) and dielectric (β_{33}) characteristics of the disc as well as its modulus, density and geometry are involved in the calculation of the resulting electric impedance. The analytical expression of the electric impedance is obtained by developing the general equations of piezoelectricity and of ultrasonic waves propagation in the different media[2]. Acoustical parameters of the media surrounding the ceramic are functions of their mechanical properties and the velocity of the longitudinal ultrasonic waves is directly related to the viscoelasticity constant C^*_{33} of the media whereas the ultrasonic attenuation $\alpha(v)$ is a function of the viscosity and of the heterogeneity of the propagating media.

An optimization method has been developed[3] to deduced from the electrical impedance sound velocity and attenuation which can be related to the dynamic modulus of the composite material.

3.MONITORING HYDROLITIC DEGRADATION

Water ageing of polymer-based composites is an important factor when investigating the durability of this type of materials. Two main points are to be considered: i) the sorption and the diffusion of water molecules through the material. This phenomenon is generally reversible and has been extensively studied in the case of the more common composites[4]. ii) the chemical reactions between water and matrix or fibres that lead to the nonreversible degradation of the composite structure. In that case, important effects on both the dynamic modulus and the damping are expected. These effects are generally attributed to microcraze phenomenon.

Considering now the acoustical characteristics of the material, sound velocity and attenuation will be the pertinent parameters to monitor the water ageing and for that reason, classical ultrasonic spectroscopy measurements will be done to compare with the piezoelectric implant method. In addition, dynamic mechanical spectroscopy experiments at low frequencies (1Hz) will be performed on the same specimen as the study of secondary mechanical has demonstrated a good sensitivity to water ageing [5].

3.1 Materials

In order to simplifly the problem, experiments were done on the polymer matrix. Two types of polymer matrix were selected for this study: an isophtalic polyester resin which is known to have a weak resistance to water and a vinylester resin (Derakane, Dow Chemicals) which is considered to be chemically very stable.

3.2 Experimental procedure

Polymerization of the two resins occurs through classical formulation (1%MEK peroxide +0.1% cobalt naphtenate) at room temperature. Specimens (plates 3mm thick) with piezoelectric implant were post-cured 7 days at 70°C. Piezoelectric elements are PZT discs 1mm thick leading to axial vibration frequency close to 2MHz. Water ageing is performed by immersion of the specimens in distilled water at 70°C. Electrical impedance and ultrasonic spectroscopy measurements[6] are done simultaneously after a vacuum drying period of 5 days to minimize the effect of water sorption-desorption. Small parallelepipedic specimens (1x2x40 mm^3) are then cutted from the plates for dynamic mechanical measurements[7]. Specimens densities were also measured at this moment to be sure that the observed variations in sound velocity are only related to alterations in the elastic modulus.

3.3 Isophtalic resin

Variations of acoustic characteristics obtained respectively by the piezoelectric implant method and by ultrasonic spectroscopy are shown on figures 2 and 3. Comparisons between the two techniques exhibit a very good agreement. Concerning sound velocity, the decrease after one week immersion is very important. As the density remains almost constant (variation from 1.22 to 1.21) this result can be attributed only to the evolution of the elastic modulus. The evolution of the attenuation shows that the material becomes more dispersive (i.e. the attenuation is more frequency dependent) probably due to the development of micro-heterogeneities (microcrazes).

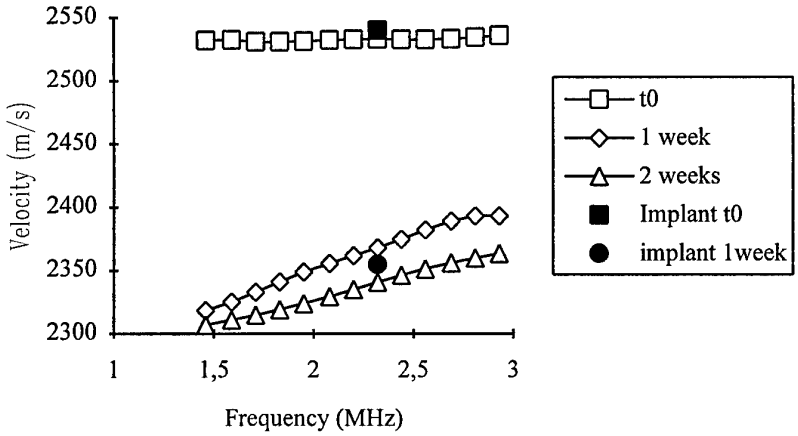


Figure 2. Isophtalic polyester resin. Evolution of sound velocity

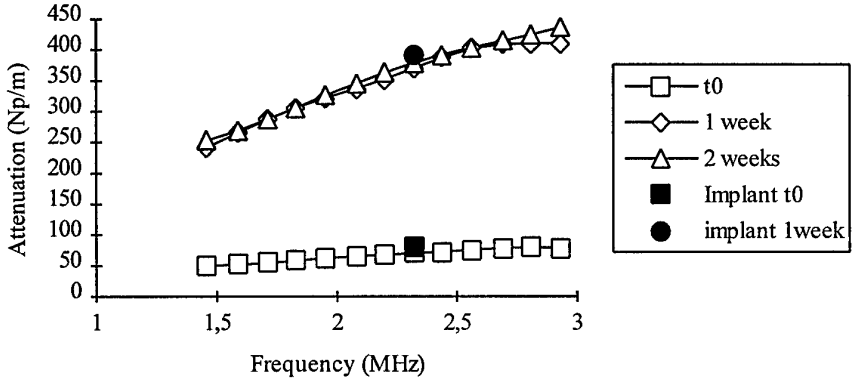


Figure 3. Isophtalic polyester resin. Evolution of attenuation

The degradation of the material is confirmed by the dynamic mechanical spectroscopy experiments as shown on figure 4 where log G''/G' is plotted against temperature. Modifications occuring in the material is clearly exhibited by the changes in shape and in temperature of the sub-vitreous relaxation peak.

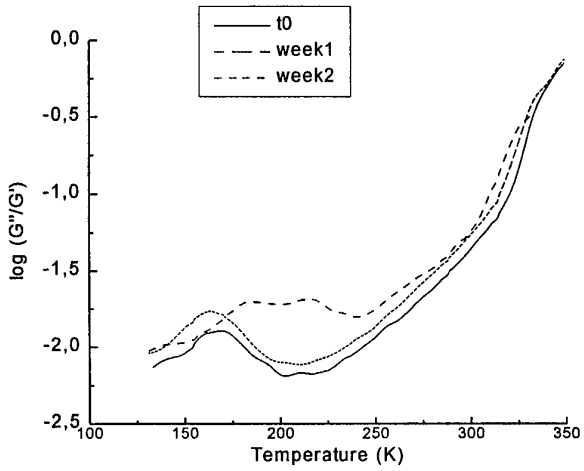


Figure 4. Isophtalic polyester resin. Evolution of log (G''/G') during water ageing

3.4.Vinylester resin

In that case, a very weak variation on velocity is observed as shown on figure 5. The relative change in velocity is about 1 % whereas density remains almost constant (d=1.13). Values of sound velocity deduced from the implant method present a small shift compared to values issued from ultrasonic spectroscopy but within the experimental error. However, variations are coherent between the two methods.

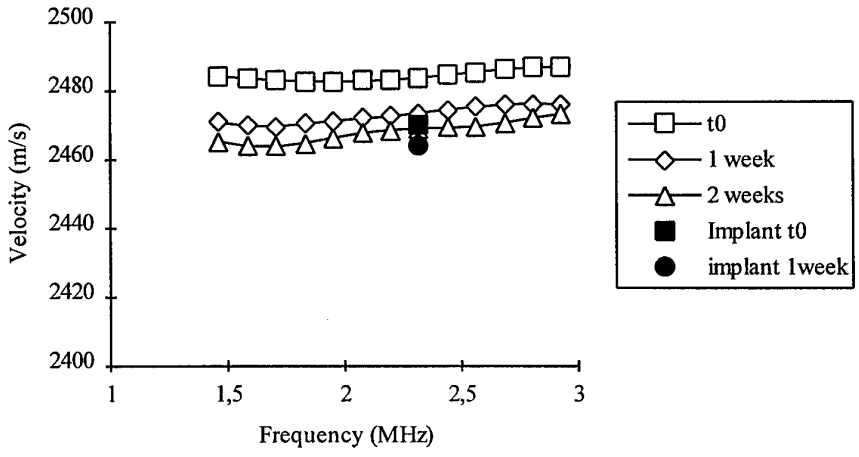


Figure 5. Vinylester resin. Evolution of the sound velocity

On figure 6, variations of attenuation are presented with comparisons between the two methods. As for velocity, changes are small. Results deduced from the implant are also in agreement with those obtained by ultrasonic spectroscopy.

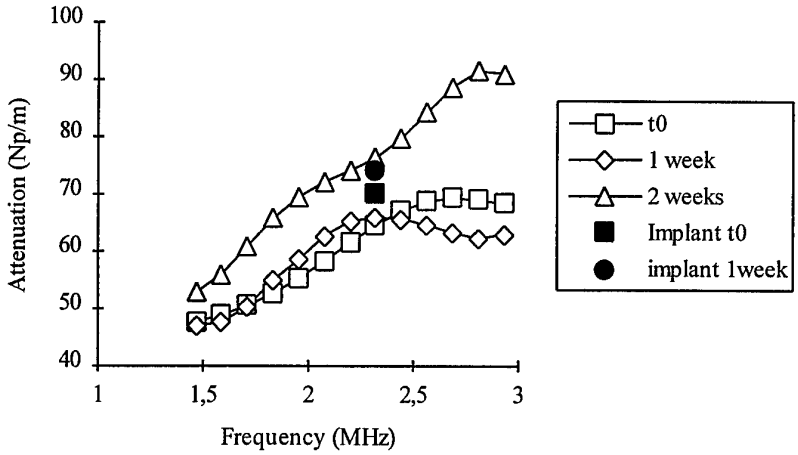


Figure 6. Vinylester resin. Evolution of attenuation

Non degradation of the vinylester resin is confirmed by dynamic mechanical spectroscopy (figure 7) where evolutions can be observed only after 6 weeks of immersion.

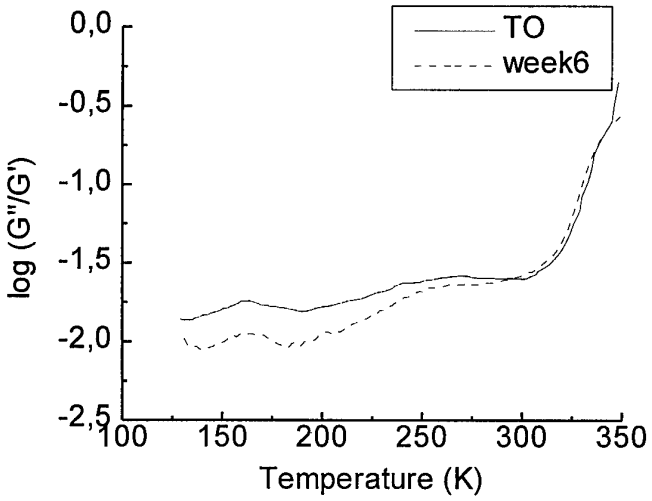


Figure 7. Vinylester resin. Variations of log (G''/G') during water ageing

4.CONCLUSION

An original method, which has been developed previously to monitor polymer-based composite processing through the measurements of the electrical impedance of a piezoelectric element inserted in the structure, is found to be also sensitive to the alterations of the polymer matrix when water ageing occurs.

This technique which takes into account the ultrasonic propagation in the medium in contact with the piezoelectric element presents two major advantages compared to the classical ultrasonic method of non destructive evaluation. On one hand, problems related to coupling reproducibility are avoided by direct insertion of the implant in the structure as soon as the material is processed. On another hand, this method may be applied to very dispersive media such as strongly filled polymers in which attenuation is large.

Further works are now in progress to detect and monitor the hydrolitic degradation in its different stages (sorption-desorption of water, modification of interfaces matrix-fibre). Different degradation modes in composite materials are also planned to be monitor by the piezoelectric implant method. Among classical degradation mechanisms, thermal cycling and small strain-induced fatigue are expected to be detected by this method. In the first case, thermal cycling leads essentially to the modification of the matrix-fibre interfaces by the mismatch of the different expansion coefficients and the resulting attenuation increase may be used as a damage indicator. The second case is more difficult to monitor as fatigue often induces localized cracks and delaminations which appear uneasy to detect by a classical piezoelectric element able to monitor only a small volume of the material. Nevertheless, one can imagine either piezoelectric implants located at critical points of the structure, or piezoelectric shear plates able to generate shear or Rayleigh waves propagating in the interfacial zones. Preliminary work is in progress in these two research axis.

5. ACKNOWLEDGEMENTS

The authors wish to thank Electricité de France, Elf-Atochem and Groupement de la Plasturgie Industrielle et des Composites for their financial support.

6.REFERENCES

1. I.Perrissin-Fabert,Y.Jayet, G.Merle, ''Monitoring thermoset polymerization by using piezoelectric measurements'',*J.Appl.Polym.Sci.*,vol.46, pp.1087-1093,1992.

2. I.Perrissin-Fabert, Y.Jayet, ''Simulated and experimental study of the electric impedance of a piezoelectric element in a viscoelastic medium'',*Ultrasonics,*, vol.32, n°2,pp.107-112, 1994.

3. N.Saint-Pierre,Y.Jayet,S-H.Lee, I.Perrissin-Fabert,J.Tatibouet, ''Application de la méthode piézoélectrique à la caractérisation du durcissement final des thermodurcissables'',*Composites*, n°5,pp.30-35,1994.

4. V.Denis, M.Fontanille, P.Spiteri, J-J.Villenave, ''Influence de la structure moléculaire sur l'hydrolysabilité des résines polyester insaturé'',*Annales des composites-AMAC*, 1992/1-2, pp.43-51, 1992.

5. E.Leguay,''Etude d'un matériau composite verre-epoxy et de son endommagement: mesures mécaniques, acoustiques et physiques'',*Ph.D.Thesis,*INSA Lyon, 1992.

6. A.S.Lakestani, J-C.Baboux, M.Perdrix, P.Fleischmann, ''Mesure par une méthode impulsionnelle de certaines constantes élastiques, piézoélectriques et diélectriques d'un transducteur'', *J.Phys.D:Appl.Phys.*,vol.8,pp.1869-1872,1975.

7. S.Etienne, J-Y.Cavaille,J.Perez, R.Point and M.Salvia,Rev.Sci.Instrum., 53,n°8, pp.1261,1982

TWO INTELLIGENT MATERIALS BOTH OF WHICH ARE SELF-FORMING AND SELF-REPAIRING, ONE ALSO SELF SENSES AND RECYCLES

Carolyn Dry, Associate Professor

School of Architecture-Building Research Council
University of Illinois @ Urbana-Champaign
Champaign, Illinois

ABSTRACT:

Two self-forming and repair polymer cementitious composites were developed over a decade apart by the author. Both relied on a nature based paradigm as a model for building, in particular bone formation, repair, and degradation. For the first composite, the proposed material accreted from the ocean, made from a fluids based chemistry, that of seawater. The land based system was not built in-situ but relied on a man made supply of materials which were self-forming, self-repairing and dissolving. But in both cases a fluid based chemistry was necessary for self-building, repair and recycling of a bone-like composite material.

1. INTRODUCTION

Building with natural processes is to build like a natural system does. It accomplishes this by: (1) using only the most common and abundant resources, and (2) putting these into an organization by means of technologies which are indigenous to the environment, (3) self-regulation through a process which is integral to the system's material and organizing system. The self-regulating process entails a way of sensing a need for change, re-organizing, re-collecting material and re-distributing it according to the new organization. Thus there is material, ways of distributing the material, organizing principles, ways of sensing, and means of reclaiming material.

Design with natural processes draws from the "experience" of evolution and integrates those principles into technology. It is an examination of properties of entire systems and elements, their effects on each other and their performances based on interactions of a complex system. Ultimately their capacity to organize material in a complex way and reorganize it depends upon the interrelationships among elements, not upon the number of elements added.

The advantages for building in this way are potentially enormous. The savings are in the energy normally used for prefabrication, the imported material required, installation time, repair time and costs of replacement and obsolescence. Insufficient attention has been paid to the possibility of using reversible natural processes as building construction technologies which are

0-8194-2165-0/96/$6.00

economical, energy-efficient and ecologically sound. Such processes are especially applicable to military port design where time requirements are fluid and space needs are stringent. They may require speedy use of indigenous materials in a variety of available settings.

Natural processes design applied tobuilding materials is comprised of the following:
1) available materials, which are
2) put into organization or constructed by natural process means, with an
3) indigenous energy source
4) have self-sensing repair and regulation through a process integral to the systems material (1) and organizing system (2)
5) a way of sensing exterior environmental changes and communicating that information.
6) ability to disorganize and recycle itself.

A concept for self-forming/self-repairing military ports using the material processes available in the chemistry of seawater was developed by the author with Office of Naval Research funding from 1980-1983.

2. DESIGN OF A SELF-FORMING, REPAIRING, AND SENSING PORT WITH NATURAL PROCESSES OF THE OCEAN

Seawater which contains vast quantities of minerals and elements has the ability to dissolve most substances. It acts to corrode and dissolve most structures placed in it, and covers them with encrustations of its minerals and organic matter. This study emphasizes building with the natural physical, chemical, biological, and climatic processes of the ocean and suggests how to build and protect ports. The ocean and climatic environment are opportunities for new ways of building with natural processes.

2.1. Use of Available Indigenous Material: Mineral Accretion

The ability of seawater to dissolve and corrode many substances in it and to cover them with encrustations of minerals and organic matter can be harnessed. These natural accretions have been found to have the bearing strength of concrete. Sea corals and seashells make their shells by excreting minerals through use of an electric potential. (see Figure 1)

Metals in seawater are subject to such electrolytic processes and ions can be precipitated onto their surfaces. A metal armature can be hooked to electrodes with a charge and submerged in seawater, the electrical current produces an electrolytic deposition on minerals onto the armature frame-work. The cathode gives off hydrogen; the anode, oxygen. The electrochemical reactions are seen in Figure 2. For this system developed by Hilbertz [1], a power supply from a battery charger of about 4.8U at 200mA to hardware cloth, anode of carbon about 10cm x 2cm in an aquarium 3 x 1 ½ x 2 for a period of 500 hours produces an accretion of 10mm (as seen in Figure 3).[1]

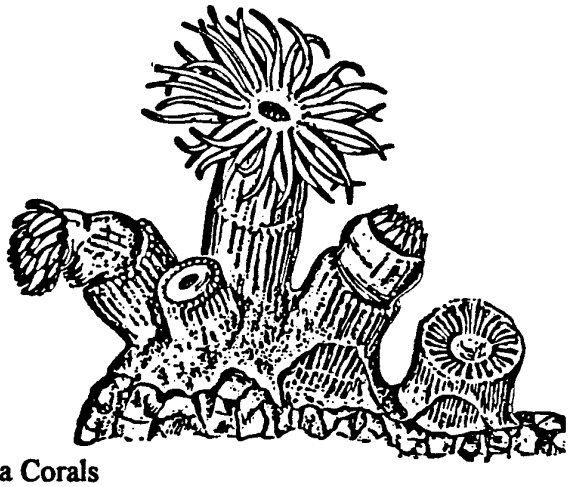


Figure 1. Sea Corals

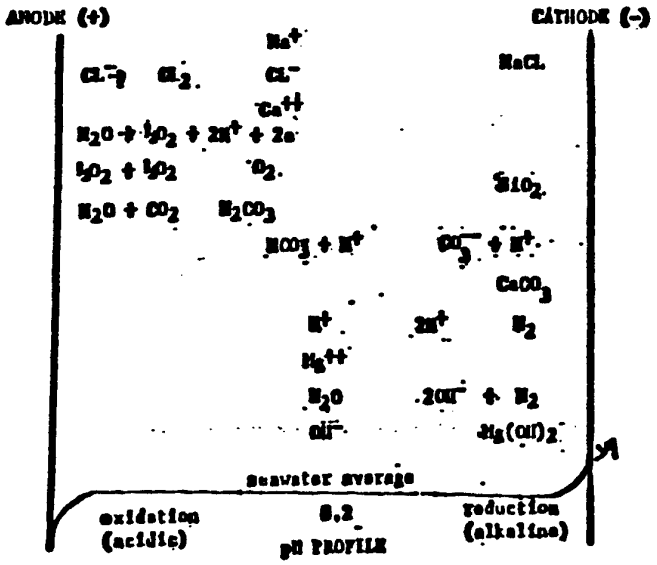


Figure 2. Electrochemical reactions for accretion [1].

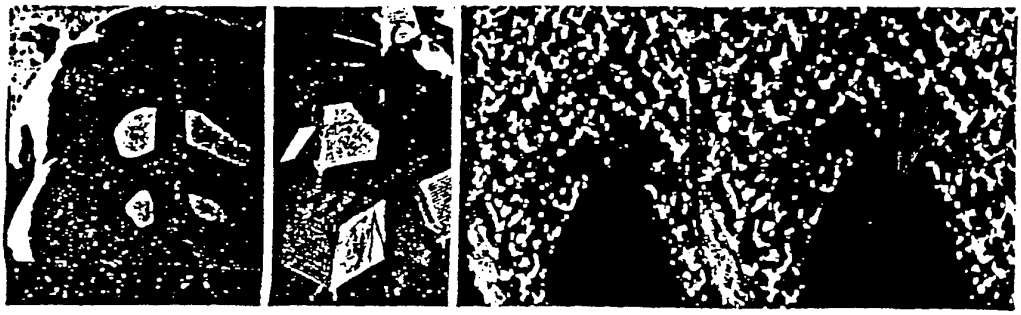


Figure 3. Photo of accretion material [1].

2.2. Use of Piezoelectric Effect for Self-Repair and Regulation

An automatic reclamation and redeposition system of accreted materials to enhance the structural properties could use the piezoelectric effect of transforming mechanical energy into electrical and vice versa if a piezoelectric polymer component is added. An electrical potential develops when the material is strained. It could be used to sense deformation and stress in the accreted structure and accomplish self-reorganizing repair through the migration of electrically charged minerals.

2.3. Sensing the Environment

Ions moving across an osmotic membrane can create an electrical impulse. This ionic impulse is the natural way of generating a current in seawater. An electrical cable in seawater is like a nerve in lymph, in that lymph fluid has nearly the same composition as seawater. In the human body, ionic leakage across a membrane from the potassium rich "seawater" of the nerve to normal "seawater" of the blood, can propagate a nervous impulse. It is interesting to note that the original research on nerves by A. L. Hodgkin was done by studying cables in seawater for the equations which apply to nerves in blood.

Within the cell and the axon, however, there is a little sodium and a lot of potassium. The natural law of equilibrium would make the sodium tend to diffuse from the external environment into the axon and the potassium in the opposite direction. The neuron is polarized with respect to the external environment. (see Figure 4) The membrane leaks ions in an effort to reach concentration and charge equilibrium of the ions. A sudden large flow of ions in an attempt to reach equilibrium causes a pulse, and this propagates a signal along the nerve.

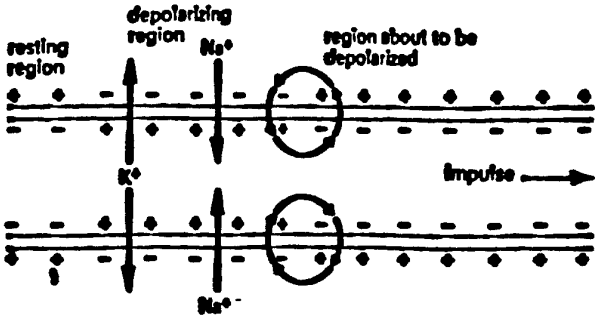


Figure 4. The neuron [2].

The conclusion is that electrical signals can be generated by the membrane without the direct intervention of metabolism. Selectively changing the ionic permeabilities allows ions to flow downhill along their electrochemical gradients. With each action the cell gains sodium and loses potassium, but for a single impulse the amounts are small enough for the resultant concentration changes to be ignored.

The poorly insulated nerves use the leakage problems in the system to building up a large charge by the change in ionic and electrical potential across a membrane.[3,4] This situation is an

example of using materials available and using their defects, i.e. leakage, to tremendous advantage.

Use of natural processes in this system is an example of complex self-organizing interrelationships among elements that is found in natural processes. The system uses material and energy indigenous to the area. It (the process) has its own inseparable installation, repair, sensing, and reclamation processes integrated into one organization. The capacity to organize material and reorganize it in a complex way depends upon interrelationships among elements.

3. A BIOMIMETIC BONE-LIKE POLYMER CEMENTITIOUS COMPOSITE

The second design is a material that is a biomimetic, prefabricated synthetic material designed to have the superior properties of bone. In this work done in 1995, accomplished and sponsored by Natural Process Design, a company, the goal was to make a polymer/ceramic created at low temperature which resembles bone and is an organic/inorganic composite. Bones and shells have been found to have greater toughness and strength than conventional ceramics alone, because of the presence of organic bonding materials. Also, the intimate connection between material phases is due to careful growth sequences, i.e. the fibers are made first and the matrix grown around them as opposed to the case of conventional ceramics in which any fibers are usually added to the matrix later. We attempt to follow the rules under which bone material forms naturally as spelled out by researchers in biological materials, and not use indigenous natural materials themselves.

3.1 Rules of Bone Formation

The goal is to mimic bone material formation to obtain superior performance properties. The rules of natural bone formation are as follows:

"Bone is made up of an oriented matrix which is secreted by bone-forming cells: the osteoblasts. This organic matrix is first made of structural molecules which serve as a scaffolding and which are laid down in a very precise, oriented pattern of fibrils into and onto which the inorganic crystalline phase forms. The formation of the first crystals of inorganic salt of calcium phosphate is referred to as the initiation or nucleation site which appear at regular intervals along this complex organic scaffolding of collagen laid down by osteoblast. Once nucleation has occurred, the next major process involves the continuation of crystalline growth from the nucleation sites outward along the fabric of the organic matrix and eventually between the molecules which serve as scaffolding. As crystal growth continues and forms a dense, inorganic matrix, there is a loss of organic components which are designed to reserve space in this matrix for the ever-expanding inorganic phase." [5]

> "The important landmarks of the organizational rules that can be deduced are as follows:
>
> 1. Oriented multi component organic matrix of fibrils as secreted by osteoblasts.
> 2. The formation of these oriented structural molecules serve as scaffolding

(fibrils) and nucleation sites.
3. Initiation or nucleation of this inorganic, calcium phosphate crystalline phase on the sites.
4. The continuation of crystal growth with simultaneous rearrangement or elimination of components from the organic matrix."[5]

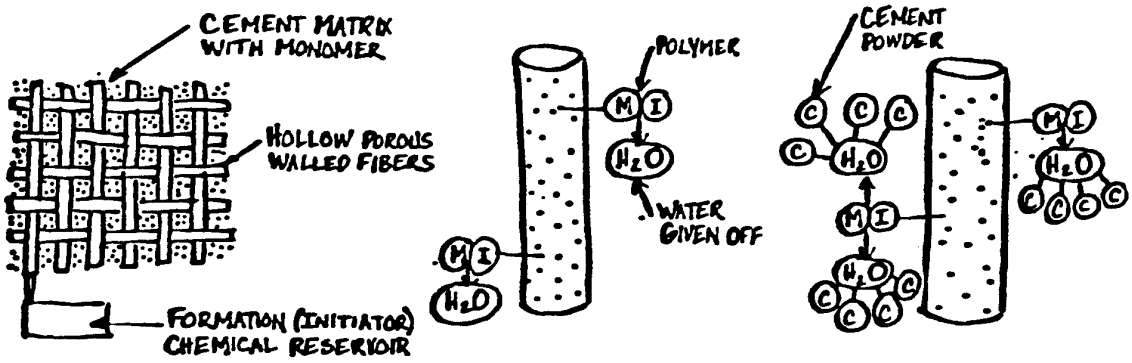
3.2 The Biomimetic Processes

Following the above rules in the self-growing structure and shown in Figure 5: porous walled hollow polymer fibers would release organic polymer chemicals into an inorganic matrix. The fibers would act as the organic template of fibrils onto which forms the strong structural bone-like composite, calcium phosphate from the matrix. The chemicals released from the fibers are designed to form a linked organic/inorganic matrix The chemicals are monomers which release water when polymerizing. The released water hydrates the cement. The hollow polymer tubes or fibers concentrate the polymer and bone-like inorganic substances on their surface. Reactions in which the water released (as they crosslink) hydrates the calcium phosphate cement. The structural design of the matrix organization to resist particular stresses can be built into the formation process by the application of prestressing. More particularly, these generated lines of force can cause the charged cementitious ions to migrate along them. The prestressing forces on the composite would thus generate the appropriate microstructure, metal fibers could be used as the fibers which carry an electrical change.

Ongoing self-healing over the life of the structure would be accomplished by reuse of the original void fibers. These porous walled hollow fibers would deliver repair chemicals if and when damage to the matrix occurs, such as cracking. In other research we have shown this type of repair improves strength, toughness and ductility.

Referring back to the organization of rules, then the 1) organic scaffolding of fibrils is mimicked by the hollow porous polymer fibers. 2) Structural molecules that are scaffolding and nucleation sites are the polymers which are created near the fiber release points by crosslinking from the monomer in the matrix and the catalyst released from the fiber. 3) Initiation of the inorganic crystallizing phase in the polymer is caused by the released water which hydrates in the cement, and 4) continuation of crystal growth and simultaneous rearrangement of the organic matrix is mimicked by the ions which migrate along stress lines generated by electricity from metal fibers.

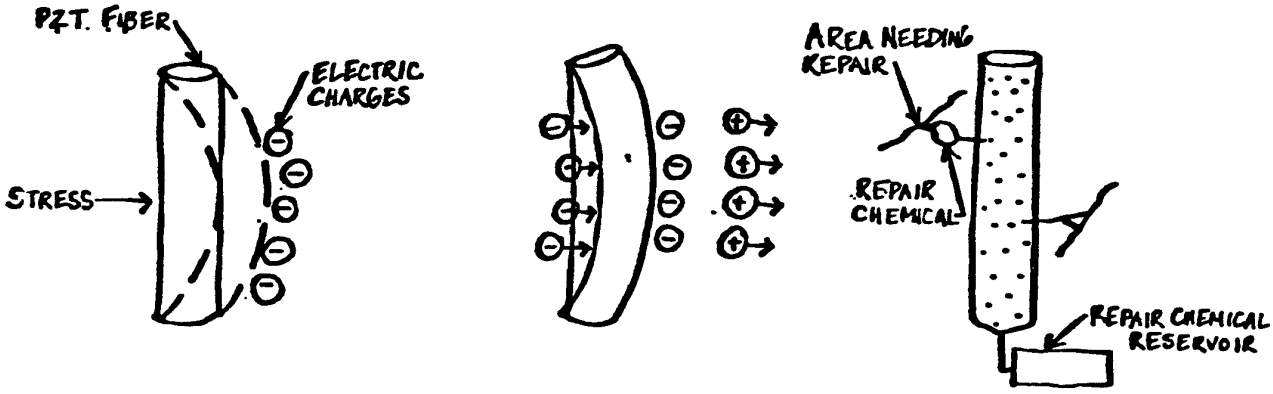
The significance of this work is 1) that brittle cement materials will have ductile fibers bonded in the matrix and a polymer/cement inherently bonded and therefore the composite will have superior strength properties, 2) the morphology and controlled reaction between phases in the matrix will impart superior properties, 3) the material will be formed under the actual stress environment and therefore perform in a superior way in the field and, 4) the material will be self-repairing.



Initiator is pumped or released through the fibers. It crosslinks with the monomer in the matrix.

Polymer is formed by reaction between monomer and initiator, giving off water.

Water from polymer condensation reaction hydrates cement powder.



Some fibers are piezo-electric and give off a charge when stressed (in a prestressing mode).

Charged ions in the cement polymer matrix are migrated away from the fiber bend and charged ions are attracted, e.g. the negative ions fill (beef up) a stressed member.

Some of the hollow fibers are used to deliver repair chemicals to change the matrix' interior microstructure.

Figure 5. The sequence of forming the biomimetic bone-like polymer cementitious composite.

4 COMPARISONS OF TWO SELF-FORMING AND SELF-REPAIRING MATERIAL SYSTEMS

In comparing the two systems it is first noted that, 1) one is ocean based and the other land based, 2) the ocean based system uses indigenous material while the land based system uses materials which are provided by the manufacture, 3) the ocean structures are grown in-situ and the land based materials are prefabricated, 4)A self-formation from a water based chemistry in the ocean is possible while for the land based system the chemical start must be accomplished by the addition of flowable materials, 5) in the land based material in the in-service environment is simulated by prestressing whereas from the ocean the material is always located in the in-service environment, 6) both systems self-repair, but again the land based one needs the addition of repair materials, 7)the ocean structures dissolve back into a material sink with disuse, the land based materials do not.

4.1 Design Improvement as a Result of Comparisons

Natural processing methods in the ocean or on land are largely based on a solution chemistry which interacts with and draws from a large sink of chemicals. In the ocean, seawater provides the material for both coral or seaport formation. The biomimetic formation of bone-like composite perhaps needs a self-replenishing sink of chemicals to supply the solution chemistry reactions for self-formation and self-repair. The hollow fibers, could have a liquid chemical reservoir to release into each fiber for either formation or repair. The hollow porous fibers would provide the delivery system for such a supply of chemicals from the reservoirs.

5. REFERENCES

[1] Hilbertz, Wolf, "Electro Depositions of Minerals in Seawater", Extended Abstracts, May 6-11, 1979, Spring Meeting, IEEE, Boston Mass.

[2] Ailley, D.J., The Physiology of Excitable Cells, London, England, Cambridge University Press, 1978.

[3] Kuffler, S. W. & J. G. Nichols, From Neuron to Brain, Sunderland, Mass., Sinauer Assoc., Publishes, 1976.

[4] R. N. Swamy, *J. Materials Sci.*, 14, 1521-1553 (1979).

[5] Arnold Caplan, Bone Foundation, The Rules for Fabricating a Composite Ceramic. Mat. Res. Soc. Symp. Proc. Vol. 174, pp. 9, 10 (1990).

Smart Composites and Optical Fibres

Invited Paper

ULTRASONIC CONDITION MONITORING OF CFRP AND GRP PLATES USING A SURFACE MOUNTED SOURCE AND AN EMBEDDED OPTICAL FIBRE SENSOR

W.R. Philp†, S.G. Pierce†, A. Gachagan*, A. McNab*, G. Hayward* and B. Culshaw†
Department of Electronic and Electrical Engineering, University of Strathclyde, Glasgow, UK., G1 1XW
† Optoelectronics Research Group * Ultrasonics Research Group

INTRODUCTION

Glass reinforced plastic (GRP) and carbon fibre reinforced plastic (CFRP) laminates are durable, versatile and light-weight materials which are progressively replacing metals traditionally used in aerospace, automobile, rail, gas-storage and many other industries. If these composite structures were to debond, fracture or seriously degrade whilst in-service, public injury or catastrophic failure could result. Therefore, in-service condition monitoring techniques for composite structures are most significant and are of immediate importance.

This paper reports preliminary ultrasonic non-destructive testing studies conducted for the BRITE-EURAM programme "**S**tructurally **I**ntegrated **S**ystem for comprehensive evaluation of **CO**mposites (SISCO)", conducted in conjunction with EPSRC grant GR/J/12260. Members of the European Community aerospace, automobile, rail and gas-storage industries are collaborative partners in this research programme. The project seeks to embed ultrasonic sources and sensors in plate-like CFRP, GRP and CFRP/GFP hybrid structures for in-situ defect interrogation and condition monitoring. Integrity assessment of a composite structure on a "pass/fail" basis may be determined by comparing the time-signature gained from in-situ ultrasonic interrogation of a test-structure with that obtained when the structure was known to be undamaged. If the amplitude of a difference signal were to exceed a given tolerance threshold, early warning of structural failure may be indicated. The concept of a structurally integrated source and optical fibre sensor is illustrated in figure 1.

A wafer-thin (about 1 mm thick) interdigital ultrasonic transducer has recently been developed by the authors, and this is presently undergoing characterisation and embedding trials in composite panels. This transducer may either be embedded within the structure or permanently bonded to the surface. The work presented in this paper used a conventional surface-coupled piezocomposite transducer, which was rigidly fixed in position on 2-3 mm thick CFRP and GRP plates via an angled perspex shoe. Fundamental symmetric mode (S_0) Lamb waves [1] were generated at the perspex-composite interface, and these insonified the plate. Other than the obvious difference in surface profile, there is little practical difference between the piezocomposite and interdigital sources, since both simply insonify the test-structure. However, the latter is structurally integrated and should therefore detract less from the structure's appearance or function.

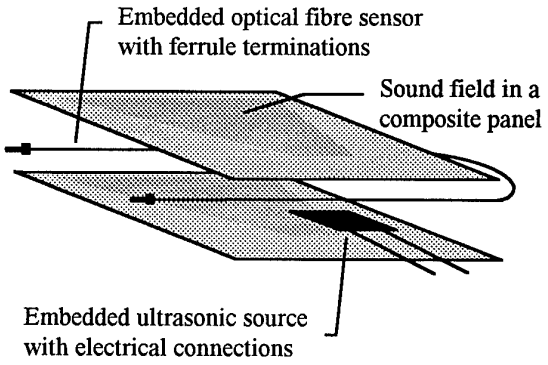


Figure 1. Conceptual illustration of a structurally integrated ultrasonic transducer and sensor

Ultrasonic wave propagation in thin composite plates is mostly determined by the plate frequency-thickness product, the dispersion characteristics and the boundary conditions of the plate. In-service flexing or vibration of an insonified plate at frequencies much lower than the ultrasonic excitation frequency cause little change in the sound field. However, changes in the externally applied stresses or internal defects such as holes, impact damage or delaminations may result in regional refraction, reflection, diffraction, scatter or mode conversion of the ultrasonic wavefronts and thereby significantly alter the sound field within the plate. [2] Hence, a structurally integrated ultrasonic interrogation system may be used for in-situ non-destructive inspection or in-service condition monitoring of composite panels.

The S_0 Lamb waves were selectively generated for defect interrogation because of their high speed and low attenuation (about -0.2 dB/cm in CFRP at 285kHz), which was much better than for the fundamental antisymmetric mode (typically -3 dB/cm). The S_0 mode

0-8194-2165-0/96/$6.00

travelled faster than all other modes (about 5.5 mm/μs in CFRP and 3 mm/μs in GRP) and so arrived at the detector first, making feature identification simple. Moreover, a pulse centre-frequency of about 300 kHz provided a frequency-thickness product of approximately 1 MHz.mm which ensured that in the materials used, the S_0 Lamb waves were essentially non-dispersive.

A structurally integrated optical fibre ultrasonic sensor [3] was simply achieved using the signal arm of an actively stabilised 633 nm (visible red) homodyne Mach-Zehnder fibre interferometer, which was spliced to 4/125 μm optical fibres embedded within a composite plate during manufacture. Generally, standard acrylate buffered optical fibre was used however, when embedded fibres were required to withstand temperatures above 150 °C during plate manufacture, the acrylate buffered fibre was replaced with a 5-10 μm thick polyimide coated fibre.

EXPERIMENTAL ARRANGEMENT

Selected A_0 or S_0 mode ultrasonic Lamb waves were generated by a piezocomposite transducer fitted with an angled perspex shoe to efficiently couple the acoustic energy into the plate and excited every 10 ms by a single-cycle or a 5-cycle tone burst at the transducer centre frequency from a function/arbitrary waveform generator via a 50 dB linear power amplifier. The launch angle of the transducer was adjusted once the propagation velocities within the materials had been determined, so as to best match the spatial character of the compressional wave to the desired plate wave.

Unlike homogeneous metals, laminated composite plastics are highly anisotropic and so the microstructure of the plate will partially scatter ultrasonic wavefronts and cause background "noise" at a frequency close to, or below, that of the interrogating wave-train. Any change in the launch conditions may alter the overall affect of the microstructure on the sound field and cause significant change in substructure of the detected signal response. Therefore, the pespex shoe was rigidly fixed to the plate using an external clamping arrangement to eliminate any possible shift or movement which might alter the sound field within the plate. Such concerns are irrelevant for structurally integrated or embedded sources.

When an acoustic wave modulates the optical phase of light in an acoustically coupled optical fibre, the phase shift may be demodulated to a change in optical intensity in an optical fibre interferometer [4]. Preliminary study of the optical phase shift in such an interferometric sensing fibre revealed that modulation was most likely caused by pressure on the fibre core; this pressure being translated by mechanical coupling of shear and normal stresses in the plate [3]. A high-speed photodetector with a low noise/high-gain amplifier was used to provide a transient signal to a digitising oscilloscope, from where the data could be transferred to a personal computer for storage and signal processing. A schematic diagram of the complete embedded fibre system is shown in figure 2.

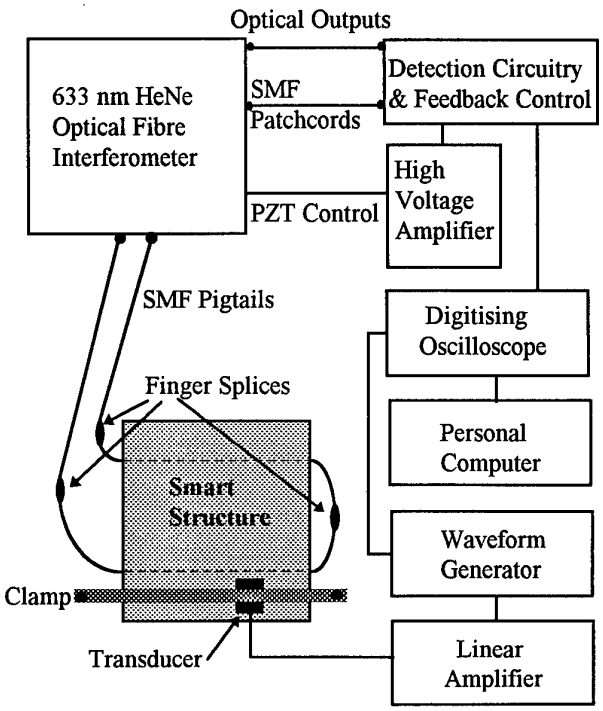


Figure 2. Schematic diagram of the experimental set-up

A portable, fibre-connector terminated Mach-Zehnder interferometer was purpose built so that a length of optical fibre, which formed the sensing arm of the interferometer, could be either bonded to the surface of a test-structure or spliced to an embedded fibres in that structure. Both the surface-bonded and embedded optical fibres performed well as ultrasonic receivers and gave very good temporal resolution. The optical fibre interferometer operated in an actively stabilised homodyne configuration using electrical feedback to a phase modulator formed by wrapping reference arm optical fibre around a PZT cylinder. The sensing arm was essentially a long length of optical fibre external to the housing and this made the interferometer particularly prone to local thermal variations and consequent unpredictable fading of the output signal. To counter fading, the PZT cylinder stretched the reference arm fibre which phase biased the system at the quadrature condition; the point of maximum sensitivity. The sensor had high-sensitivity (maximum sensitivity value of 2.5 ± 0.1 mrad/nm for 100mm gauge length) and a flat bandwidth response from 1 kHz to 20 MHz. The amplitude response of the surface bonded fibre was found to be linear as a function of gauge length, to a maximum when the gauge length equalled or exceeded the source width, and was equally sensitive to in and out-of-plane motions. The effectiveness and sensitivity

of the sensor was not lessened by the presence of an external acrylate or polyimide buffer coat. For both CFRP and GRP plate types, an electrical signal gain of about 26 dB (×20) over the surface-bonded case, was achieved in the detection of S_0 Lamb waves when the optical fibre was embedded.

DISCUSSION

The gain in detector sensitivity and a likely improvement in the efficiency of Lamb wave generation, argue well for embedding the acoustic source and detection system. Moreover, embedding the optical fibre sensor, and indeed the proposed ultrasonic source, within the composite panel offers total protection from minor surface damage and allows integration with the structure regardless of external corrugations, fixtures or appendages. There are also several simple advantages in using a surface mounted system which should be considered. Embedding the optical fibre sensor requires that the fibre terminations protrude from the side of the structure, leaving the fibre prone to fracture. For a surface mounted sensor, if the fibre is broken, it can be replaced. The surface mounted source and sensor can be retrospectively fitted after manufacture of the structure and so do not unduly complicate the production process or require special coatings or adhesives to withstand high temperatures.

Initial manufacturing trials involving resin transfer methods, had difficulty in maintaining uniform acoustic coupling between the external coating of the optical fibre and the resin/fibre mat, along the length of the embedded fibre. This caused the sensitivity of the fibre sensor to vary along its length. Careful attention to cleanliness and pre-wetting agents should resolve this problem, however for condition monitoring applications the sound field along the optical fibre is integrated and so spatial sensitivity variations are unimportant.

LAMB WAVE INTERACTION WITH DEFECTS

A single-cycle pulse, at a centre frequency of 285 kHz, was used to excite a Lamb wavefront of approximately 50 mm in width and 15° beam divergence either side of the source transducer. Figure 3 shows a representative averaged signal (128 averages) acquired with two embedded fibres which have been spliced together so as to pass twice through a CFRP/GRP hybrid (1:2) plate, as illustrated in Figure 4.

The representative signal shows four distinct peaks, corresponding to the outward travel of the acoustic wave incident on fibre 1 (A), then incident on fibre 2 (B), the subsequent detection of the reflected wave, from the back face of the plate, on fibre 2 (C) and finally on fibre 1 (D). The background "noise" due to scatter from the composite microstructure is visible between the peaks. The acoustic wave travelled a total distance of 560mm (between pulses A and D), where the separation between the fibres was 205mm. The acoustic attenuation of the wave is illustrated through the reduction in signal level between the pulses A and D on the first optical-fibre. The effect of beam spreading and dispersion within the plate is evident from the difference in wave shape between these pulses.

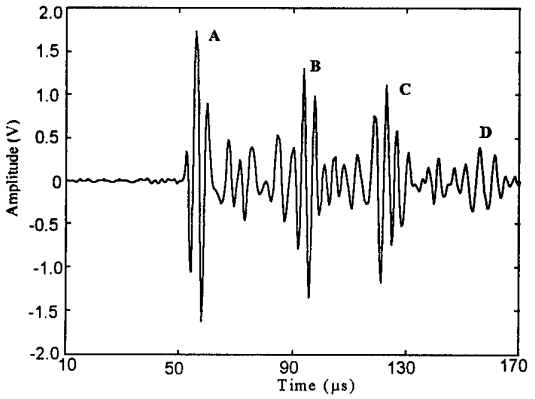


Figure 3 Representative signal response of a dual embedded fibre sensor during Lamb wave interrogation.

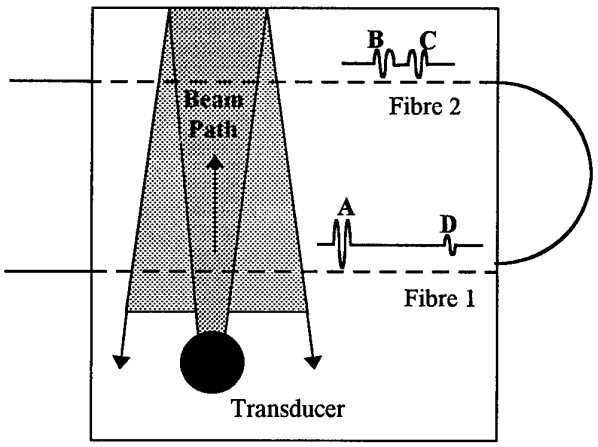


Figure 4. Diagram of the source and fibre configuration

Detection of Penetrating Defects.

The experimental arrangement used to investigate the interaction of the S_0 mode Lamb wave with holes was as illustrated in Figure 4. By drilling a hole in the beam path between fibre 1 and fibre 2, the change in signal features, both in reflection and in transmission from the defect, could be examined. Typical averaged signal responses including peaks A and B (figure 3) are shown in figure 5, where the upper trace was acquired in the sample prior to the introduction of a hole, the centre trace after a 5 mm diameter hole had been drilled and the lower trace is from the same plate containing a 10 mm diameter hole.

The presence of a hole can most clearly be indicated by considering the difference signal. After the averaged

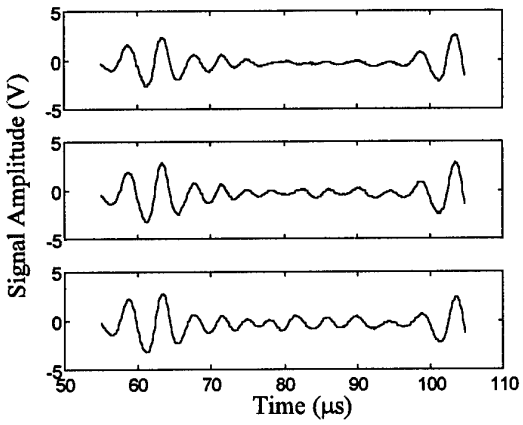


Figure 5. Comparison between the signals received from a composite sample with no holes (upper), a 5 mm dia. hole (centre) and a 10 mm dia. hole (lower).

signal responses for the no-hole and 5 mm diameter hole had been normalised, the two traces were subtracted and the difference amplitude plotted as shown in figure 6. Reflections and scatter from the 5mm hole have clearly altered the detected sound field between about 80 - 90 μs. There is also evident change in the outgoing pulse arrival at the second fibre after passing over the defect.

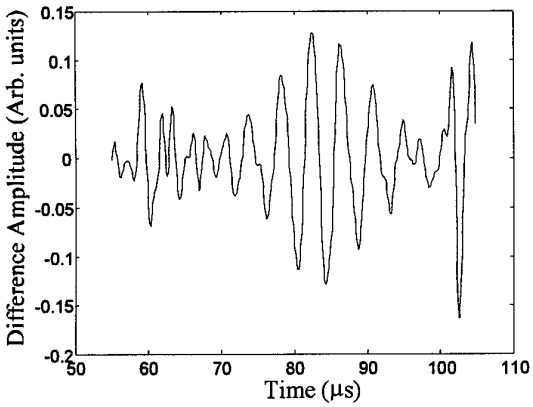


Figure 6. Difference signal for the no-hole and 5 mm diameter hole traces, clearly indicating the presence of the hole at about time 80 μs.

This difference method was used to detect the presence of a series of holes, diameter 1 mm to 10mm, which were drilled in steps of 0.5 mm. The influence of the increasing hole size has been plotted and is shown in Figure 7. The data is presented as the percentage reflection coefficient from each hole, whereby the peak-to-peak value from the difference signal has been normalised to the magnitude of the outgoing S_0 wave. Figure 7 illustrates both single cycle and 5-cycle excitation of the composite transducer, with an approximately linear relationship between reflection coefficient and hole diameter.

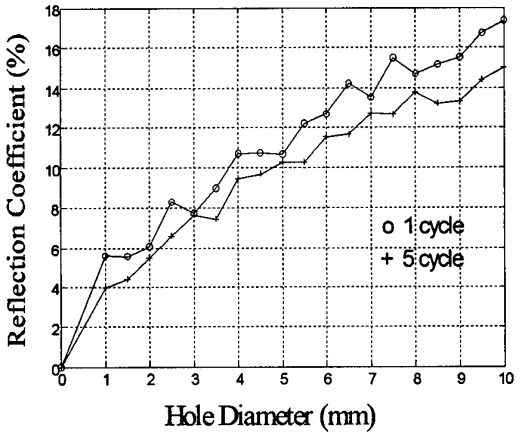


Figure 7. S_0 Lamb wave reflection from holes drilled in a composite plate

Detection of Impact Damage.

A similar arrangement to that shown in figure 4 was used to investigate impact damage to a CFRP plate. This CFRP plate contained only one fibre sensor and so only the outgoing Lamb wave pulse and its reflection from the rear wall of the plate are evident in the sensor response. A guided impacting tool of selected mass (0.85, 1.70 and 2.55 kg) was dropped from a fixed height onto the surface of the plate at three different sites located midway between the optical fibre and the rear edge of the plate. On completion of each trial, the transducer was moved behind the next impact site and reclamped to the plate. Figure 8 shows the normalised sensor responses before and after an impact to the plate of 30 J over a diameter of 7 mm. The difference signal, produced by subtracting the before and after traces, is also shown.

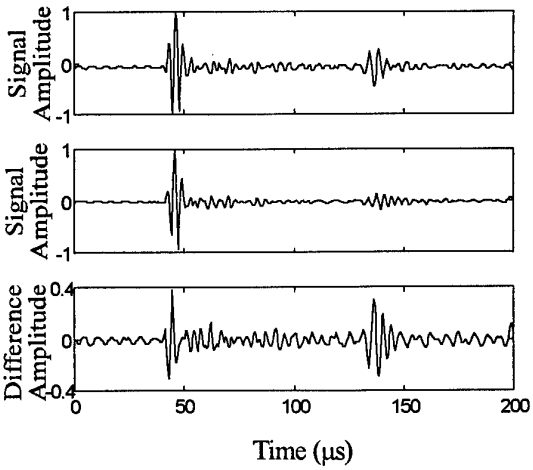


Figure 8. Normalised optical fibre sensor response before impact damage (upper) and after an impact of 30 J over 5 mm diameter (centre). The lower trace shows the difference signal.

A reduction in the amplitude of the pulse reflected from the rear edge of the plate is evident by both direct

comparison of the before and after traces and in the difference signal. The reduced rear-wall echo amplitude was most likely due to omnidirectional scatter of the wavefront by localised delamination or fracture of the composite plys, caused by the impact. There is no evidence of direct reflection. Figure 9 shows the difference signals for lesser impacts of 20 J and 10 J. In the 10 J case, the difference in rear-wall echo amplitude was less evident, but still discernible.

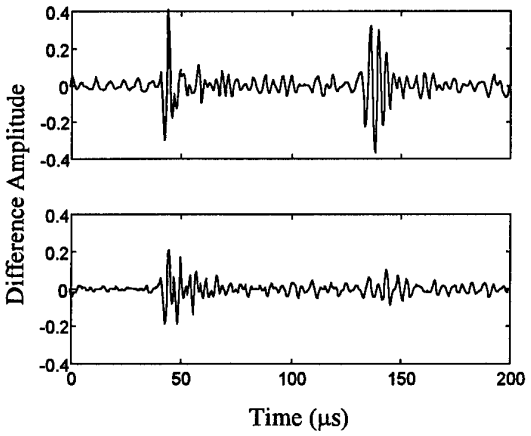


Figure 9. Normalised difference signal (before and after impact) for 20 J (upper) and 10 J (lower) over 7 mm dia. impacts.

Detection of Delaminations.

The position of a delamination through the thickness of a composite plate is critical as the shear stress distribution is non-uniform for the S_0 Lamb wave propagation [1]. The stress profile through the thickness of a composite plate contains positions of zero shear stress, which correspond to locations at which a delamination will be transparent to the S_0 Lamb wave propagation. Furthermore, when the length of the delamination is significantly greater than the wavelength and the Lamb wave velocity in approximately half the plate thickness is much the same as in the whole thickness, the wavetrains travelling above and below the delamination will recombine after transit of the delamination. In such a case, the transmitted pulse will be essentially unchanged, but may experience some phase delay. A small reflection is expected from the boundaries of the delamination which are parallel to the interrogating wavefronts.

A delamination was introduced into the rear face of a 470 × 430 × 2 mm CFRP plate at approximately 1/3rd of the thickness, via incision of a thin steel shim. The 'defect' measured approximately 40 × 100 mm, the narrower aspect being presented parallel to the interrogating wavefront. Again the plate contained a single optical fibre sensor and the plate was interrogated with a single-cycle pulse at 285 kHz. In this experiment it was not possible to cause the delamination without removing the ultrasonic source and this process significantly altered the acoustic launch conditions. Consequently, a plate scan was conducted to indicate the effect of the damage, moving the transducer from on side of the defect to the other, covering 10 cm in 1 cm increments. Figure 10 shows the normalised sensor response with no delamination, with the delamination and the difference signal of these at a position (22 cm from the LHS of the plate) immediately behind the delamination site.

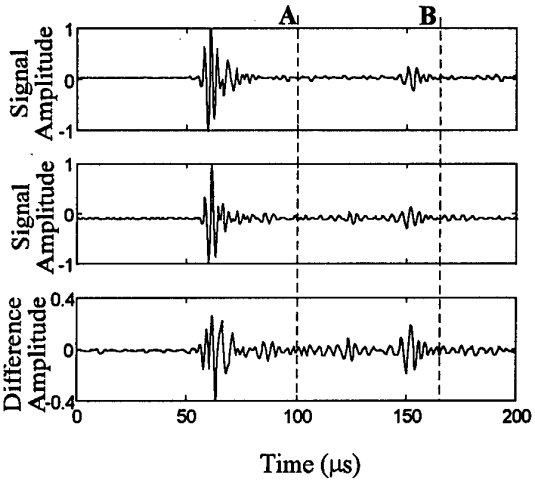


Figure 10. Signal responses acquired prior to (upper) and after (centre) the introduction of a delamination. The lower trace shows the difference amplitude.

The arrival of a small reflection is evident at about 120 μs in figure 10 (centre & lower traces), but there is no significant change to the rear-wall echo. This was further investigated by scanning the source from the left to right in the vicinity of the defect. With reference to Figure 10 (upper), the outgoing S_0 wave was used as a reference signal and correlated with each acquired sensor response thereafter to improve the SNR of S_0 reflections, within the time frame A-B as shown.

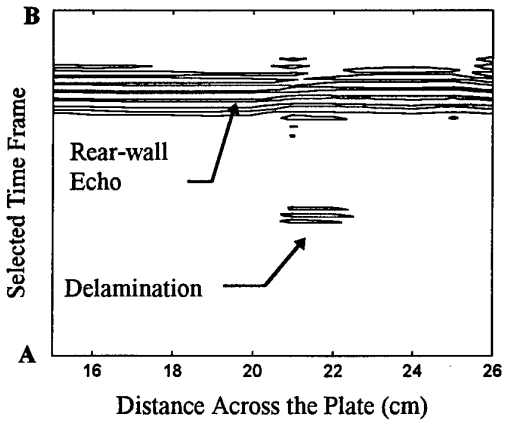


Figure 11. B-Scan of the CFRP plate in the vicinity of a delamination defect.

Figure 11 illustrates the B-scan from the resultant processed data and is presented as a contour map of the amplitude peaks in the correlated data. The two main

features illustrated in this figure are the echo from the rear face of the plate and an echo from the delamination centred at approximately 21 cm. A secondary feature is a phase shift in rear-wall echo close to the area of the delamination, which supplements the direct reflection signal to enhance the detection capacity of this hybrid system.

CONCLUSIONS

This paper has demonstrated the fundamental basis for a condition monitoring system using a high-temporal resolution fibre-optic sensor to detect acoustically generated S_0 Lamb waves within thin carbon-glass fibre reinforced composite plates. The implantation of optical fibres within the composite plates provides a sensitivity enhancement of approximately 26dB, when compared to the performance of surface bonded fibres. This semi-integrated system has readily demonstrated the detection of holes, impact damage and delaminations introduced into CRFP and CFRP/GRP hybrid composite plates. With the successful integration of a thin acoustic source, the described system may be totally integrated with a composite structure.

ACKNOWLEDGEMENTS

The authors would like to acknowledge funding for this work through BRITE-EURAM contract BRE2.CT94-0990 and EPSRC contract GR/J/12260 and specifically, to INCA (Ireland) for analytical theoretical development and British Gas plc (UK), Construcciones Aeronáuticas SA (Spain), GEC-Alsthom plc (UK) and Vetrotex International SA (France) for manufacture and supply of the composite plates. Also, thanks to Bertin (France) for dispersion curve analysis on the composite plates and management of this project.

REFERENCES

1. Rayleigh And Lamb Waves: Physical Theory and Applications
   I.A. Viktorov
   Plenum, 1967.

2. Detection of Ultrasonic Lamb Waves in Composite Plates using Optical Fibres.
   A. Gachagan, S.G. Pierce, W.R. Philp, A. McNab, G. Hayward and B. Culshaw.
   Proceedings of the UFFC, IEEE International Ultrasonics Symposium, Seattle, Washington, November 1995

3. Ultrasonic Sensors from Surface Bonded or Embedded Optical Fibres
   W.R. Philp, S.G. Pierce, A. Gachagan, A. McNab, G. Hayward and B. Culshaw
   Submitted to OFS-11, 11th Conference on Optical Fibre Sensors, Sapporo, Japan, May 1996.

4. Interferometers
   D.A. Jackson, J.D.C. Jones
   Chapter 10, Optical Fibre Sensors, Vol 2, editors B. Culshaw, J. Dakin, Artech House, pp 329-380, 1989.

INTEGRATION OF OPTICAL FIBERS AND PIEZOELECTRIC CERAMICS IN COMPOSITE MATERIALS

S. Bourasseau, M. Dupont, M. Pernice, A. Thiriot
ONERA, Direction de la Physique, B.P. n°72, 92322 Chatillon cedex - FRANCE

P. Blanquet, T. Demol, C. Delebarre
Université de Valenciennes, IEMN, Département O.A.E. (UMR CNRS 9929)
B.P. 311- Le Mont Houy, 59034 Valenciennes cedex - France

D. Coutellier
Université de Valenciennes, LAMIH (URA CNRS 1175)
B.P. 311- Le Mont Houy, 59034 Valenciennes cedex - France

1. INTRODUCTION

The concept of intelligent material/structure, largely debated for a few years, is generally applied to systems able to react to internal *stimuli* (selfcontrol) and external ones (adaptation to environmental conditions) in order to realize in the best way the function for which they have been designed. These systems include, in the most general case, sensors, actuators, bonded to the surface or integrated in the bulk of the structure, and a control unit.

ONERA (Office National d'Études et de Recherches Aérospatiales), as other research institutes for aeronautics and aerospace, has undertaken for years important studies on intelligent vibration control of structures, at the Structures Department. More recently, at the Physics Department, we started investigations on the smart non destructive evaluation of composite aeronautical structures, typical materials being laminates carbon/epoxy, a few millimeters thick. As the sensors we intend to use are either optical fibers or piezoelectric ceramics, we have had to study their integration in the material. If the incorporation of optical fibers has been the object of numerous investigations, on the contrary, the integration of piezoelectric elements has been rarely tackled.

The objective of this paper is to present the study we have started in this field, which we consider to be a critical one, and on which depends the future development of intelligent/smart structures.

After a short bibliography, we give first a brief description of the integration of optical fibers, carried out at our laboratory and, second, a more detailed study of the embedment of piezoelectric elements in a stratified composite, including a technological part and a theoretical part.

2. STATE OF THE ART : A SUMMARY

For optical fibers, a numerous literature describes the embedment conditions, the preparation and properties of the mechanical coating, the location of the fibers in the materials, their spacing, density, etc. and, most important, the modification of the mechanical properties of the structures containing the inserts (see, for example, [1-4]).

Very roughly, all these studies lead to the conclusion that the performances of the stratified composites with integrated optical fibers are only slightly weakened (except for the compressive strength) if the maximum fiber diameter is no more than the thickness of a ply (125 μm) and if their density in the material is not too high.

Concerning the embedment of piezoelectric ceramics, we have only found four papers[5-8]. In reference[5], Paradies et al. describe the manufacturing process for carbon fiber stratified thermoplastic materials in which is embedded a piezoelectric element (PZT), as an actuator. To avoid the electrical short-circuiting of the actuator, an insulating layer is placed between the surrounding laminate, and to secure a strong bond between the host structure and the piezoelectric element, a glass fiber reinforced thermoplastic fabric film or a 10 μm thick Upilex® film is bonded to the actuator with a thermoplastic film (Litrex TK®). Moreover, in order for the

0-8194-2165-0/96/$6.00

stratified material not to contain any internal "bump", a hole, having the same diameter as the PZT's one, is cut in the plies that are to receive it. This solution has also been retained by Hagood et al.[6] to insert piezoelectrics in glass/epoxy and graphite/epoxy composites. In an other work, Elspass et al.[7] propose a neighbouring solution, the integration of the ceramic being done with an internal interruption of a few plies. Finally Vizzini[8] mentions, as a first result, the incorporation of a PZT in a stratified plate to validate an analytical study of an integrated acousto-ultrasonics technique.

In our opinion, the principle of the method used in references[5-8] is in itself a potential source of important defects for the material in so far as it includes a carbon fiber breakage (internal discontinuity through several plies), and consequently an initial important damage.

To avoid this difficulty, we propose an other solution, where all the plies maintain their integrity, although some of them are somewhat distorted.

3. EXPERIMENTAL RESULTS

Optical fibers

In order to get some experience in the integration processes, we began to incorporate optical fibers in stratified composites fabricated in a mould with movable walls. A first 8-plies stratified material, of T300/914 type, incorporating near its symmetry axis an optical fiber with a polyimide coating, was manufactured by pressing between two stainless steel plates, leaving the fiber undamaged. In the same manner, an optical fiber was successfully incorporated in a second 16-plies stratified composite, avoiding fracture at the outlet of the material. Later on, this fabrication process, which involves some difficulties for the fiber outlet, has been replaced by a system with mobile wedges (figure 1).

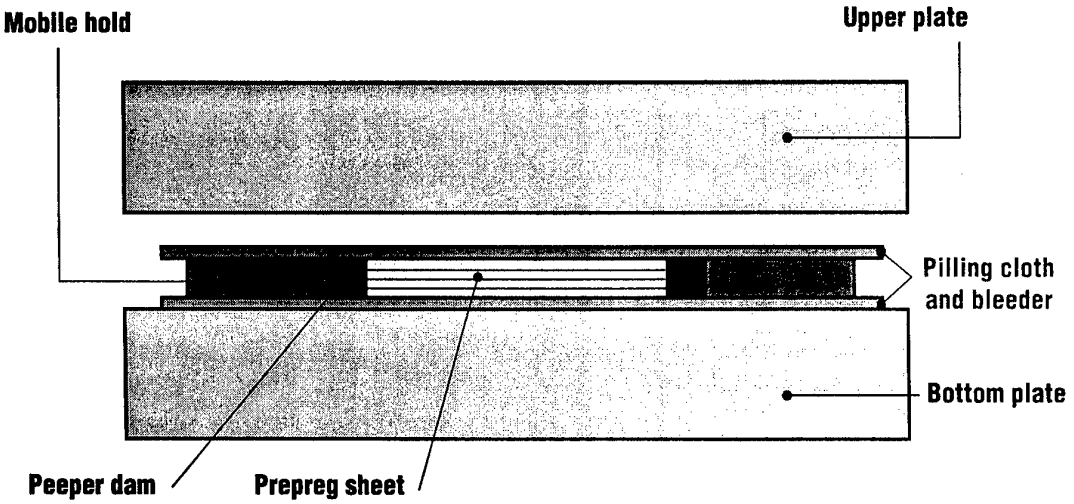


Figure 1

Piezoelectric ceramics

Our objective is to integrate a piece of lithium niobate, with a typical thickness of about 100 µm, in a composite plate, minimizing the intrusiveness of the insert (figure 2). Two Kapton® films, 12 µm thick, maintain the electrical insulation between the piece of ceramic and the composite, and are also used as an holder for connectics. Electrical contact between the connectics tapes and the metallized parts of the ceramic is obtained

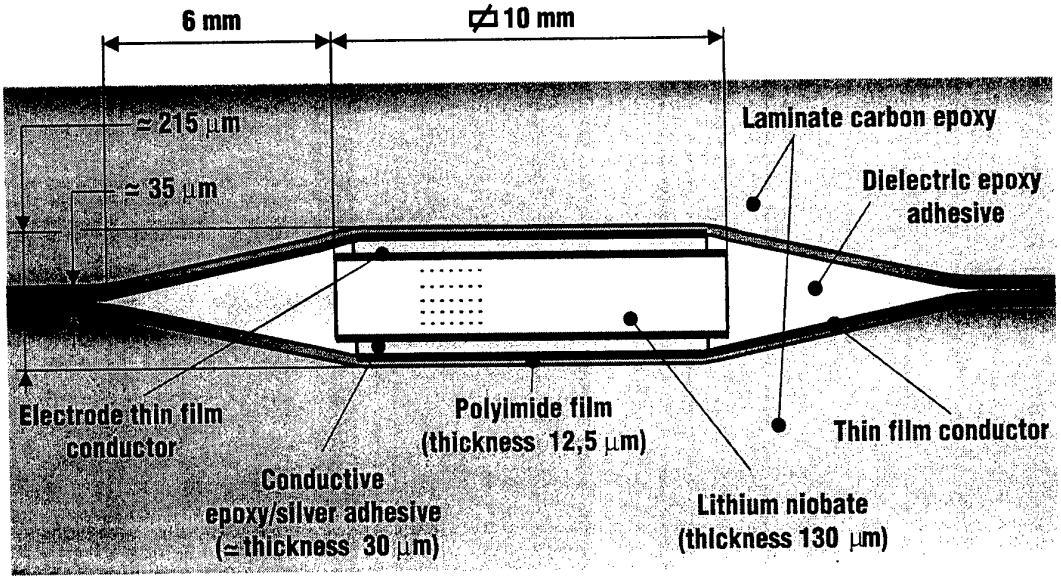


Figure 2

with a thin layer of conducting epoxy. The insert thickness being a maximum at the ceramic location, we have to get a progressive decrease of the thickness from the ceramic to the contact zone between the two Kapton® films, so as to minimize the probability of breakage. With these guidelines in mind, we developed a manufacturing technique which permitted at the same time to give the insert a lens shape and to deal with ceramic fragility.

At present, following this technique, an insert, manufactured with a piece of glass, having the same dimensions as those of lithium niobate, was integrated in the middle of a 32 plies composite, of the T300/914 type. The presence of the insert has not induced any visible deformation of the composite.

As the embedment of the ceramic and Kapton® films may lead to delaminations and other damages, we have started a series of tests in order to study the behaviour of the material containing the insert.

So, in a first experiment, two Kapton® tapes were cross-embedded between the 8th and 9th ply in a unidirectional composite of 16 plies. No starting delamination was observed by ultrasonic non destructive evaluation.

Then, Kapton® tapes, 35 µm thick and of dimensions 100 mm x 150 mm, were incorporated during the manufacturing of carbon/epoxy composites of T300/914 type, to study their behaviour when submitted to a static indentation, simulating the damage induced by a low velocity (0 to 5 m/s) impact. In effect, it has been shown that static indentation is a mechanical action which induces damages similar to those obtained by impact, for the same energy levels.[9]

To carry out this study, we did an ultrasonic non destructive evaluation (C-scan) of indented plates with and without inserts. The images we got show delaminations starting from the upper plies of the plate on the indentation side to the lower face of the coupon. These delaminations appear as star-shaped surfaces growing in a continuous way from the indentation point to the lowest ply, as well as for plates without inserts as for plates with inserts. On the contrary, for the latest, the presence of Kapton® brings about a growing delaminated surface at the insert level. But under the insert, delaminated surfaces are no more modified. These results are represented in a schematic way on figure 3, where the limit cone of delamination is given in both cases.

Summing up, the first tests of incorporation of Kapton® films in a quasi-isotropic carbon/epoxy composite show that the insert does not modify the maximum delaminated surface (a criterion used in industry) but only its distribution among the plies.

After this series of experiments, the next step will be a full mechanical characterization of the composite with the glass insert. The last step, currently in progress, is aimed at fabricating and characterizing a composite material containing a lithium niobate insert.

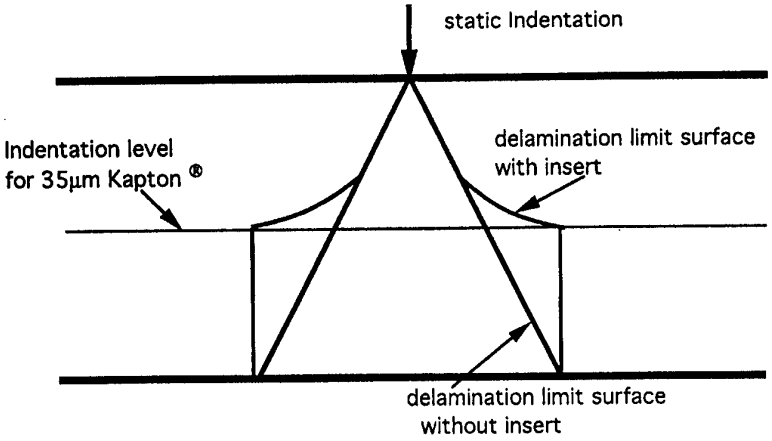


Figure 3

4. THEORETICAL RESULTS

In order to get a better understanding of the damage which may be induced by the embedment of a piezoelectric element in a composite material, we developed a finite element numerical model, based on ANSYS® code. With this model, we calculated the deformation of a carbon/epoxy plate submitted either to a three-point bending or to a uniform loading, first without insert, and second with insert (figure 4). The results obtained show that the instrumented plates are slightly less deformed than the non instrumented ones. Consequently the integration of the ceramic gives a higher rigidity to the plates.

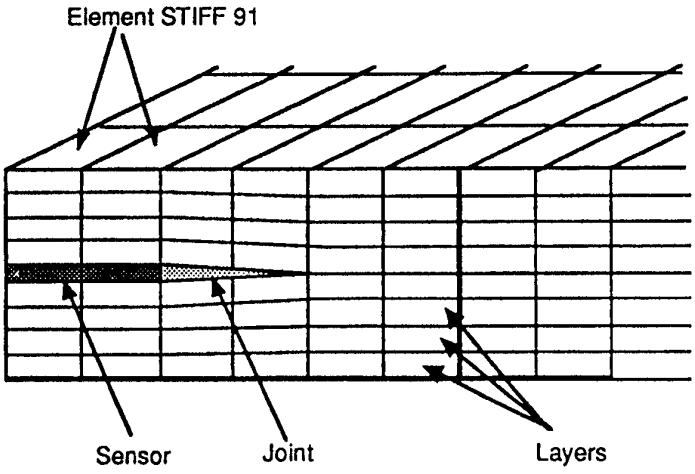


Figure 4

Then we studied the influence of the integrated sensor on the local stresses at the interface between the carbon fibers and the insert. On figure 5, it appears clearly that the stresses are growing inside the material, what could bring about delaminations or other defects in the structure.

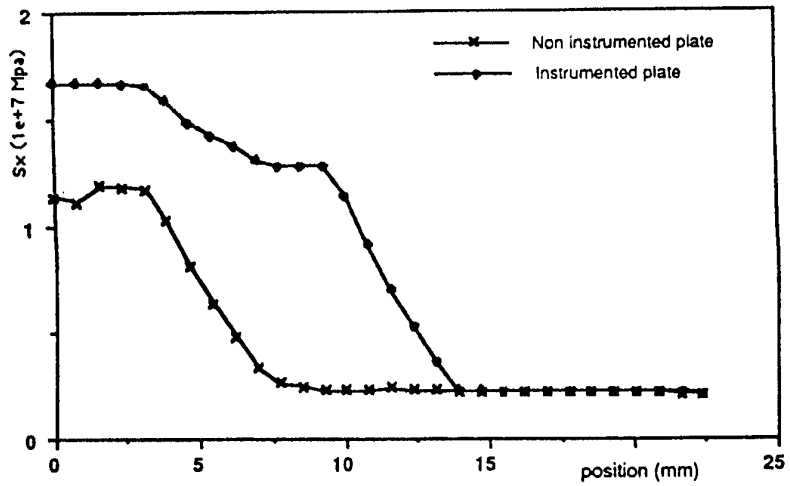


Figure 5

5. CONCLUSION

The problem of integrating piezoelectric ceramics, sensors and actuators, in intelligent structures, without inducing any damage and without strongly modifying the mechanical properties of these structures has not been completely solved today. The first results we obtained with glass, as a mechanical substitute for a piezoceramic, show that the integration may be done without too much damage. However these results must be confirmed by numerous supplementary tests before getting a satisfying level of confidence.

6. ACKNOWLEDGEMENTS

This study has been partially funded by D.R.E.T. (Direction des Recherches, Études et Techniques) of French Ministry of Defence, under contract n° 94-001-00-043.

7. REFERENCES

1. D.W. Jensen, J. Pascual, and J.A. August, "Performance of graphite/bismaleimide laminates with embedded optical fibres. Part I : uniaxial tension", Smart Mater. Struct. **1**, 24-30 (1992).

2. D.W. Jensen, J. Pascual, and J.A. August, "Performance of graphite/bismaleimide laminates with embedded optical fibres. Part II : uniaxial compression", Smart Mater. Struct. **1**, 31-35 (1992).

3. S.S.J. Roberts and R. Davidson, "Mechanical properties of composite materials containing embedded fiber optic sensors", SPIE **1588**, 326-341 (1991).

4. A. Dasgupta and J.S. Sirkis, "Importance of coatings to optical fiber sensors embedded in "smart" structures", AIAA J. **30**, 1337-1343 (1992).

5. R. Paradies, W.J. Elspass, K. Schindler, "Shape control of an adaptive composite reflector panel", Second Europ. Conf. Smart Struct. Mater., 121-126 (Glasgow, 1994).

6. N.W. Hagood, E.F. Crawley, J. de Luis and E.H. Anderson, "Development of integrated components for control of intelligent structures", Selected Papers presented at U.S. Army Research Office Workshop on Smart Mater., Struct. and Mathematical Issues, p. 80, Virginia Polytechnic Institute and State University, Blacksburg, Virginia, Sept. 15-16 (1988).

7. W.J. Elspass, J. Kunzmann, M. Flemming, D. Baumann, "Design, manufacturing and verification of piezoceramics embedded in fiber-reinforced thermoplastics", SPIE **2443**, 327-333 (1995).

8. A.J. Vizzini, "Damage detection, mitigation and repair", Projects and Progress in the University Research Initiative, Research Initiation Program, Interdisciplinary Research in Smart Structural Systems, U.S. Army Research Office, 7 November 1994.

9. H. Kaczmarek, "Impact basse vitesse et indentation statique", La Rev. des Lab. d'Essais, n° 39, 7 (mai - juin 1994).

Interferometric optical strain gauge: production, use and comparison to conventional techniques

M. Tatti

European Commission - Joint Research Centre
Institute for System Engineering and Informatics, TP 210
via Fermi 40 - 21016 Ispra (Va) - Italy

G. Sala, P. Mantegazza

Politecnico di Milano
Aerospace Engineering Department
V.le Golgi 40 - 20133 Milano - Italy

ABSTRACT

A technique for easy installation and usage of optical fibre strain sensors is presented. This technique allows reliable and accurate fibre positioning by means of a resin support in which optical sensing leads are embedded. Static and dynamic behaviour of the optical strain gauge is investigated and its performance is compared to similar optical sensing systems either directly surface mounted on the structure or embedded into composite laminates. Comparisons to values derived from a semiconductor electrical strain gauges are also made.

1. INTRODUCTION

The need of structures having increased efficiency and reliability has boosted the research in the field of smart materials, structures and sensors. Within the latter field the development of systems capable of detecting stresses and strains with high precision is of great interest as strain sensors must often work in hostile environments characterised by strong electromagnetic (EM) fields, high temperatures or corrosive chemicals. Immunity to these factors coupled to a highly reliability, accuracy and ease of installation procedures are often further mandatory requirements. Two main approaches can be used to detect strain: the first develops systems which disregard EM noise, the other leads to systems that are electromagnetically immune but often show drawbacks due to installation difficulties. Belong to the first category electrical strain gauges, the most conventional and widespread method of strain detection, which are able to operate in a reliable and accurate way. They are easy to use and strains as small as 1 $\mu\varepsilon$ can be detected. They may become ineffective when strain has to be measured in environments characterised by strong EM fields where they require accurate calibration and can guarantee only a marginal reliability. Also in corrosive chemical environments, electrical strain gauges do not retain their accuracy over long period of time.

To avoid all these problems many alternatives have been proposed. They are generally based on optical fibres as light propagation is insensitive to EM effects and the glass quartz by which they are often made makes them capable of sustaining high temperatures and corrosive chemical environments. For those reasons their use is increasing, particularly in the field of strain detection where easily installable and easily-handled fibre optic transducers still do not exist. The device introduced and presented in this work represents a possible technique to simultaneously solve harsh environment and installation problems with a straightforward solution originating from simple considerations related to the necessity of an electromagnetically immune, highly-sensitive and easily-handled transducer.

2. SURFACE MOUNTED AND EMBEDDED OPTICAL FIBRE SENSOR

By using a Michelson based interferometric scheme with active homodyne phase recovery (Fig.1) [1,2,3], some preliminary tests were carried out by both bonding the optical sensing leads directly to the specimen surface and by embedding them into a composite laminate. The difficulties that immediately appeared when bonding the sensing fibres were related to their circular cross section which generally does not match the surface of the specimen (Fig.2a). Also the reduced diameters of the fibres as well as their brittleness further complicate their mounting.

0-8194-2165-0/96/$6.00

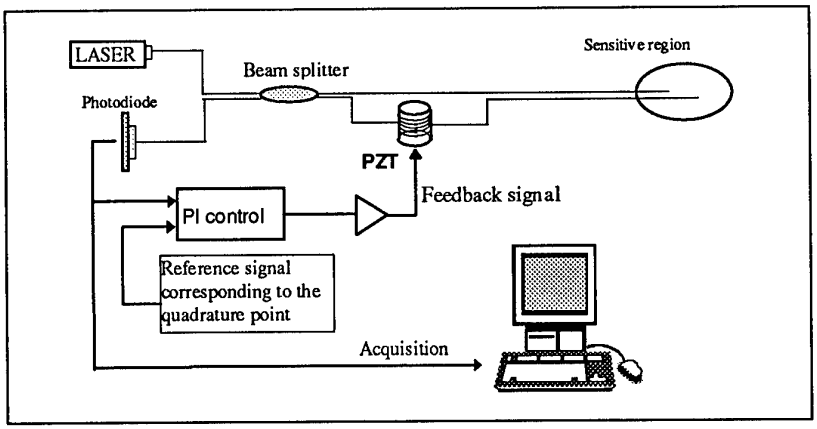


Fig.1: Optical set-up

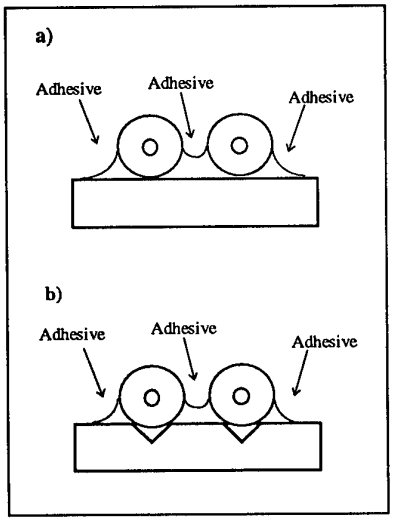


Fig.2

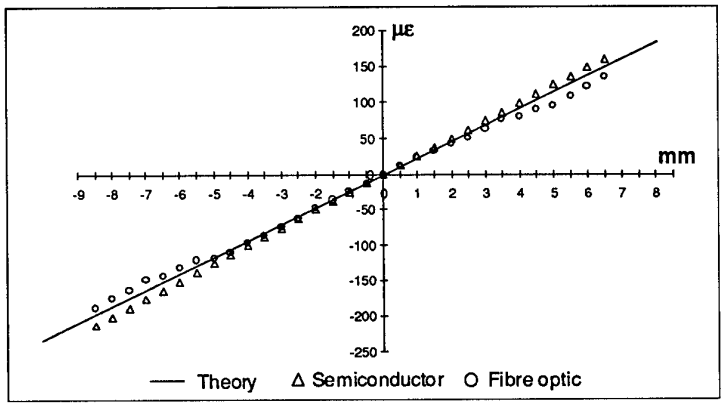


Fig.3: Static behaviour of the bonded sensor.

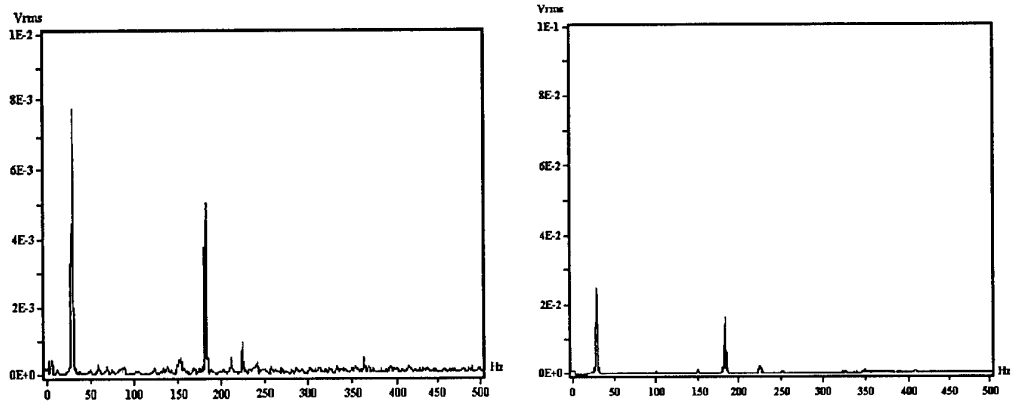


Fig.4: Dynamic behaviour of the optical sensor bonded to the specimen (left) and of the semiconductor electrical strain gauge (right). Vertical scales are different.

The bonding tests were performed on an aluminium alloy cantilever beam with two longitudinal grooves (0.1 mm wide and 0.1 mm deep; their inter-axis was 1 mm) on its upper surface produced by means of a jewellery circular cutter. The grooves had to guarantee the correct mutual orientation of the transducer axis and the direction of strain detection, as well as the correct relative position between the two optical sensing leads (Fig.2b). Grooves dimensions were narrower than the sensing fibres to avoid them *sinking* under the surface of the specimen. Single mode fibres (125 μm external cladding diameter) were used for the tests and the bonding was made with epoxy resin cured for two hours at 0.02 Kg/cm^2 pressure and 50 °C temperature.

Static and dynamic tests were performed, by statically deflecting the cantilever beam and by applying an impulsive load respectively. The results were compared to the predictions of the elementary beam theory, as well as to the experimental strain values detected by a semiconductor electrical strain gauge (gauge factor: 120) located close to the optical transducer; both optical and electrical transducers having a 5 mm gauge length. In fig.3 a comparison is shown between the imposed beam edge displacement and the experimental values as detected by the two transducers. The values of strains predicted by theory in the same beam section to which sensors are bonded, are also shown. The mismatch between the percent average deviation of the theoretical predictions and that of the optical data is 7.75% while between theory and values derived from the semiconductor transducer 7.43%. The results are in good agreement, even if the data scatter is higher for the optical sensor (4.51 percent standard deviation), than for the electrical one (2.09%). These discrepancies were likely to be due to the fluctuation of environmental parameters during the tests, as the optical device is more sensitive to temperature changes than the electrical one, well compensated through a half-bridge installation. The dynamic tests aimed at the determination of the eigen-frequencies by exciting the beam specimen through impulsive loads in order to simultaneously excite many of its bending modes. The results obtained are in excellent agreement with those predicted by the theory and no significant difference can be noted from those coming from the semiconductor strain gauge. Only the reduced band-pass imposed by the adopted *active-homodyne* electronic circuit limited the possibility to detect frequencies higher than that of the second bending mode. The results are shown in fig.4 where a spectral analysis of the signals coming from the two sensors is given.

The same Michelson based interferometric system was modified to make similar tests on a composite laminate cantilever beam produced by 24 *prepreg* graphite/epoxy plies. Its dimensions are equal to those of the aluminium alloy specimen and four fibre optic transducers were embedded between the second and the third unidirectional ply. This allows an easy detection of strain imposed by beam deflections without a relevant increase of the notch factor [4,5]. The resulting static deflections were compared with theoretical predictions and with data measured by conventional electrical strain gauges bonded to the surface of the specimen (gauge factor: 2.1); all the transducers had a 5 mm sensitive length. To take into account the different locations of

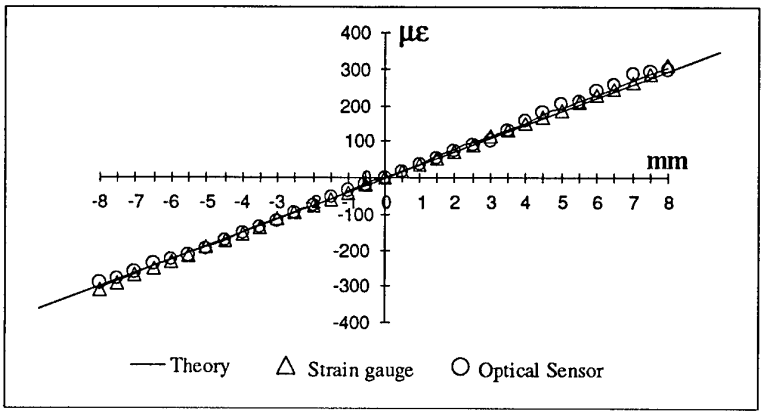


Fig 5: Static behaviour of one of the embedded sensors.

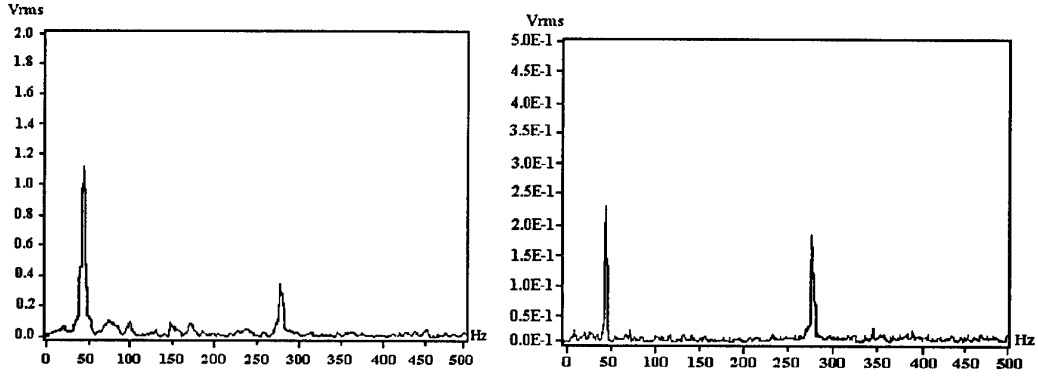


Fig.6: Dynamic behaviour of one of the optical sensor embedded into the composite laminate (left) and of the electrical strain gauge (right). Vertical scales are different.

optical and electrical sensors, the results were related assuming a perfect linear behaviour of the host material and takes into account the elasto-optic change effects due to embedding[6]. As reported in fig.5, the data measured by the optical sensors agree well with both the theoretical solution and the data measured by the electrical strain gauges. The percent average deviation from the theory is 4.57 for the optical sensor and 3.57 for the electrical strain gauge (average value on tree optical sensors), while the standard percent deviation is 4.22 (optical sensor) and 3.66 (electrical strain gauge). These values indicate that embedding is affective in reducing the environmental influence on the measures as the host material offers a good protection against both temperature changes and slowly fluctuating environmental noise.

The values reported are an average calculated only on tree of the four embedded transducers as the fourth seemed not to work correctly as the deviation from theory was 19.5%. It is difficult to give an explanation of that even if a local delamination can be reasonably supposed considering that the corresponding electrical strain gauge gives the same result. The method adopted in fibre optic positioning, not the presence of the embedded fibre, was probably the cause of the damage since that was the first transducer put into position and the tools used in the operation were not probably used in the correct manner. To approximately evaluate the dimension of damaged area, four electrical strain gauges were bonded to the specimen surface around the optical sensor. With them it was possible to verify that at the distance of 10 mm no significant difference with the theory could be detected, while at 5 mm a 5% difference was evaluated.

The composite beam was also tested under dynamic loads through a pulse excitation and the eigen-frequencies transduced again agreed well, see fig.6, with both electrical strain gauges values and theoretical predictions.

4. OPTICAL STRAIN GAUGE

4.1. Production

As mentioned above, several problems may arise during the installation of any fibre optic sensor; in particular, due to their high sensitivity, interferometric scheme based sensors need great accuracy in fibre positioning and a suitable support can certainly contribute to overcome difficulties by assuring the correct positioning of the optical sensing leads and allowing a reduction in the installation time. In a Michelson interferometric scheme based sensor (Fig.1), the support also contributes to ensure correct relative positioning of the two fibres at the sensitive regions. The aim is to develop an optical strain detector easy to install and offering all the advantages of conventional optical techniques: EM noise immunity, high sensitivity and high resolution.

A prototype of such a strain gauge was set up by using commercial components and adopting a sensor based on a true fibre optic Michelson interferometer. After a mirror preparation of their ends by aluminium deposition trough vacuum evaporation, two optical sensing leads were embedded into the support (Fig.7) which was made with a high performance two component epoxy resin cured for 6 hours at 20 °C; it allows approximately 6% elongation capability and essentially creep-free performance[7]. The device is relatively oversized if compared with conventional electrical strain gauges, but it shall be made smaller in the future; it is 15 mm long, 8 mm wide and 0.5 mm thick. The transducer has a 5 mm gauge length. In fig.8 a close up view of the optical strain gauge is presented. To embed the fibres into the support as desired, a special mould (Fig.9) was machined in a PTPE block which allows an easy extraction and is further improved by a four part disassembling of the mould itself. The top face of the mould is not sealed allowing an easy removal of the gas generated in the curing process. Two grooves (0.3 mm wide and 0.5 mm high) locate the sensing optical fibre leads in the correct position in a cavity while the desired gauge length is assured by the accurate relative positioning of the fibres edge. The optical strain gauge is made by pouring the resin into the residual volume.

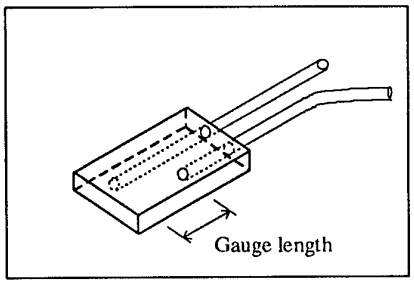
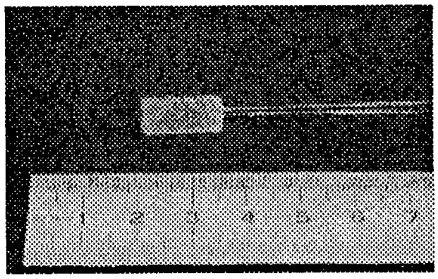


Fig 7


Fig.8

4.2. Usage and comparisons with bonded and embedded sensors

To evaluate the performance of the optical strain gauge in practical application it was bonded to a specimen with a resin commonly used for electrical strain gauges. The specimen adopted is the same aluminium cantilever beam previously described to which were bonded both the unsupported optical strain sensor and the semiconductor strain gauge. This offered the possibility of comparing strains detected by the new optical strain gauge and by the semiconductor electrical transducer approach. The optical strain gauge was bonded to the opposite beam surface and at the same beam section to which the semiconductor transducer was placed. Static deflections were imposed and their measured values compared to the strain values detected by the semiconductor strain gauge and theoretical predictions. Fig.10 shows a comparison of the experimental results.

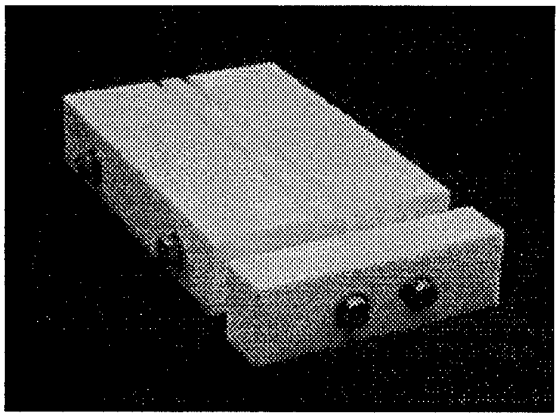


Fig.9: PTPE mould used to produce the optical strain gauge

The mismatch between optical strain gauge and theory is 9.7% while that between semiconductor measures and theory is 6.9%. These values point out a worse behaviour of the true optical strain gauge with respect to both that embedded within (4.57%) and that surface mounted (7.75%). Even the scatter is higher: 4.95% standard deviation against 4.51% of the unsupported transducer and 4.22% of the embedded one. This behaviour was expected because, unlike in the case of the full embedding, the support alters the sensed. However, the low discrepancies between results presented indicates that the support does not effect the reliability and the high sensitivity of the interferometric sensor. Fig.11 reports a brief summary of the static response as obtained from the tests described before.

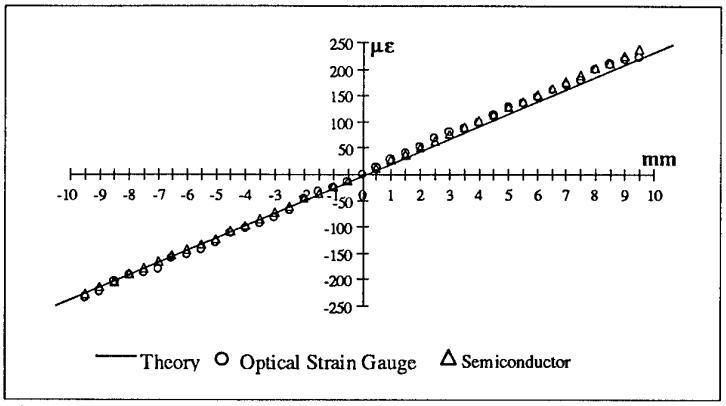


Fig 10: Static behaviour of the true optical strain gauge.

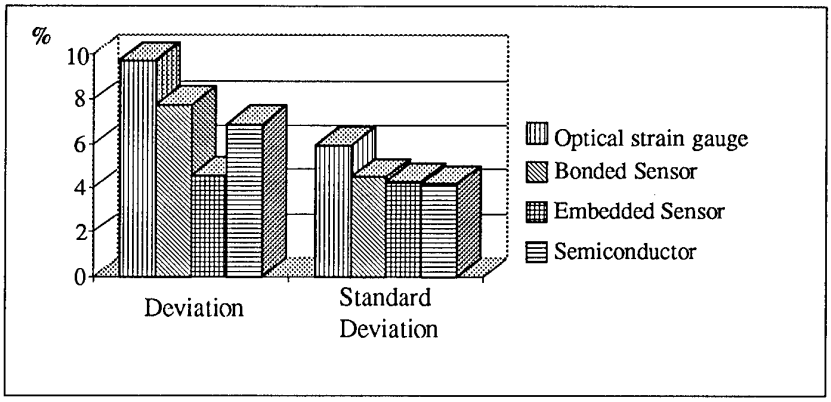


Fig 12

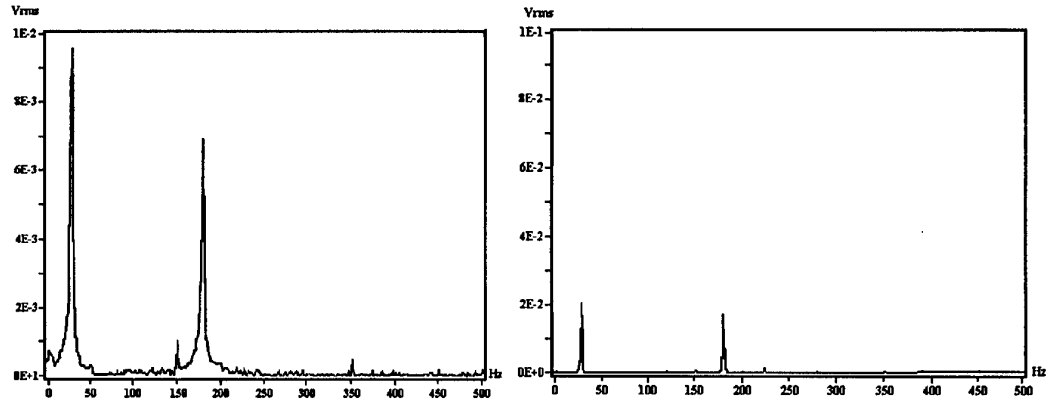


Fig.11: Dynamic behaviour of the true optical strain gauge (left) and of the semiconductor electrical strain gauge (right). Vertical scales are different.

Dynamic tests were also carried out by applying impulsive loads to the beam edge. Both spectra of data detected by the optical and semiconductor strain gauge are reported in Fig.12. No significant discrepancy can be noted which infers that the dynamic behaviour of the optical strain gauge does not differ from that of all the other transducers here considered. This is an expected result as the *active homodyne Michelson* scheme does not interfere with rapidly changing measures.

5. CONCLUSIONS

A resin supported optical fibre sensor employing a Michelson interferometer was developed, built and used to detect strains under static and dynamic conditions. The results were compared to the values derived from sensors based on the same optical scheme either directly bonded to the specimen or embedded in it. The approach adopted does not compromise significantly the high sensitivity of the interferometric sensor and provides a working baseline in view of the development of new optical strain gauges. The device allows an easy installation and usage guaranteeing the proper fibre positioning even in 2 fibre optic installation schemes. With adequate support materials, it will be possible to produce high performance strain sensors suitable for high temperature and corrosive environments, but as easy to handle as the most conventional and widespread electrical strain gauges.

6. REFERENCES

1. T. Valis, E. Tapanes, R. M. Measures, "Localized fiber optic strain sensor embedded in composite materials", SPIE Fiber Optic Smart Structures and Skins, Vol. 1170, pp. 495-504, 1989.
2. K. Liu, R. Measures, "Signal processing techniques for interferometric fibre-optic strain sensors", J. of Intell. Mater. and Struct., Vol. 3, No. 7, pp. 432-461, July 1992.
3. M. Tatti, "Estensimetria in fibra ottica: sviluppo di un trasduttore di deformazione ed inglobamento in laminati compositi", Joint Research Centre - Tech. Note No. I.95.70 ISEI/IE 2971/95, June 1995.
4. R. M. Measures, "Smart composite structures with embedded sensors", Composites Engineering, Vol. 2, Nos. 5-7, pp. 597-618, 1992.
5. A. Dasgupta, Y. Wan, J. S. Sirkis, H. Singh, "Micro-mechanical investigation of an optical fiber embedded in a fiber reinforced composite, SPIE Fiber Optic Smart Structure and Skins, Vol. 986, pp. 43-48, Boston, 1988.
6. J. S. Sirkis, H. W. Haslach, "Complete phase-strain model for structurally embedded interferometric optical fibre sensors", J. of Intell. Mater. and Struct, Vol. 2, No. 3, pp. 3-24, 1991.
7. M-Line Accessories, Instrumentation Bulletin No. B-137-11 (adhesive M-Bond AE-10 ©), Measurement Group Inc.

Dual-wavelength operation of digital spatial domain multiplexed fibre sensor arrays for dynamic strain monitoring

Y Hu and S Chen

School of Electronic, Electrical and Information Engineering, South Bank University, 103 Borough Road, London SE1 0AA, UK.

Abstract A new dual wavelength digital spatial domain multiplexing technique for optical fibre sensor array is reported. It can integrate a large number of sensing fibres and as well as dual-wavelength method into a simple, robust and low cost system. It greatly enhances the capacity of tracing fast varying measurands and the absolute measuring range of strain with the digital spatial domain multiplexed sensor system. Preliminary experiments have shown the feasibility of the technique.

Introduction

Smart Structures and Materials are a fast developing subject area and has a wide range of applications[1]. Because of the unique characteristics of an optical fibre, i.e. extremely small and light weight, resistant to corrosion and fatigue, immune to electrical interference, safe and practically incapable to initiating fires and explosions, and compatible with composites, materials embedded with optical fibres as optical nerves have been extensively researched. In such applications, it is essential to have an efficient and low cost multiplexing scheme to interrogate an array of fibre sensors. Although the existing time [2], wavelength [3], frequency [4] and coherence [5] multiplexing techniques have made some progress in reduction of the number of required optical sources and electrical processing units in a multiplexed system, they are not very successful in reducing the number of fibre optical devices and total architecture complexity in the network, especially for interferometric type sensors. This greatly restricted the ability of fibre based sensor systems to be embedded into a structure because fibre devices, such as couplers and modulators, are comparatively heavy, rigid and bulky.

The authors have developed a digital spatial domain multiplexing technique for the integration of large scale interferometric sensor arrays which is suitable for applications in smart structure and material [6]. It makes use of digital image processing technique to significantly reduce the number of optical fibre devices in the network and greatly simplify the system architecture. It is very robust with no mechanical moving parts throughout the system. Phase signals in such a system are retrieved from a far-field fringe pattern using digital processing techniques. The time taken to retrieve all the phase signals in each sensing fibre is defined as a period of one frame. Due to the periodical nature of the fringes, the algorithm has an unambiguous measurement range of $-\pi$ to $+\pi$. If the phase changes more than $\pm\pi$ during such a period, the change can not be registered correctly. A lot of structure monitoring applications, for example, bridge monitoring, requires the measurement of long term trend as well as dynamic strain such as vibration of the structures. To enable the system to monitor fast varying measurands, we have to either increase the frame rate or expand the unambiguous range of the measurement. The former approach demands a greater computation resources, hence is not very cost effective. The later can be achieved using phase signals of two slightly separated wavelength carriers[7] and can be easily integrated into a digital spatial domain multiplexing system.

In the existing dual-wavelength interferometric fibre sensor systems, discrete band pass filters to separate wavelength carriers have been reported[7, 8]. Such a technique, however, is not suitable for sensor systems with a large number of sensing channels because the system will be just too complicated. With the new dual-wavelength digital spatial domain multiplexing technique a large number of sensors can be addressed with simple and robust overall system structure. Therefore it has a huge potential to be used in the Smart Structures and Materials. The theoretical analysis and preliminary experimental results are presented.

Operating principles

A dual-wavelength interferometric optical fibre sensor array multiplexed in digital spatial domain is shown schematically in Figure 1. The light from a compound light source, which contains two narrow band wavelength components centred at λ_1, λ_2, is coupled into N-1 sensing fibres and a reference fibre via a 1xN star coupler. The end-faces of the fibres are arranged in a line parallel to the linear CCD array at some distance away. The far-field interferometric fringe pattern of the fibre array are sampled by the CCD camera and sent to the computer for processing.

0-8194-2165-0/96/$6.00

With only one sensing fibre, k, and a source of a single wavelength at λ_i, the above described system will be reduced to a standard optical fibre Young's interferometer investigated before[9] with its Young's fringe pattern sampled by the linear CCD pixels presented as

$$I_i^k[m] = \bar{I}_i^k \cos(2\pi \frac{d^k a}{\lambda_i L} m + \phi_i^k) \quad (1)$$

where $\bar{I}_i^k$ and I_i^k are two constants, d^k the spatial separation between the sensing fibre k and reference fibre in the plane where all fibres terminate, L is the distance between the fibre end-face plane and the CCD array, m = 0, 1, ...,

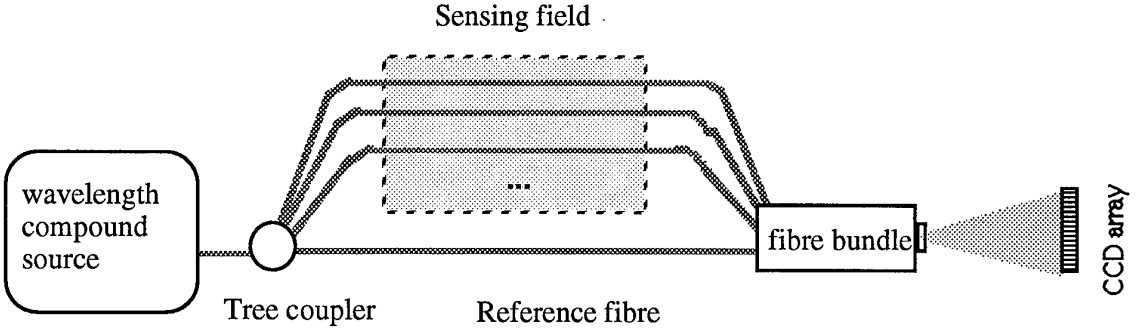


FIGURE 1 The schematic set-up of wavelength-coded interferometric sensor array multiplexed in digital spatial domain

M-1 is the pixel number along the CCD array with M the total number of pixels in the array, a is the pixel spacing and finally, ϕ_i^k is the relative phase between the light in fibre k and that in the reference fibre at wavelength λ_i. A digital Fourier transform on the digitised Young's fringe converts it into a digital spatial domain array presented as

$$P_i^k[n] = \bar{I}_i^k \delta(n) + I_i^k[\delta(n - n_i^k)\exp(j\phi_i^k) + \delta(n + n_i^k)\exp(-j\phi_i^k)] \quad (2)$$

where n = 0, 1, ..., M-1 is data pixel number in the digital spatial domain, δ is a Dirac function and n_i^k, expressed as

$$n_i^k = \frac{M d^k a}{\lambda_i L} \quad (3)$$

is the digital spatial frequency of the fringe, which is clearly a function of the fibre end-face separation, d^k, and the wavelength, λ_i and is known as soon as the system is set up. Now, if a compound source with two narrow band wavelengths is used, the fringe pattern is the superimposition of all Young's fringe sets produced by each individual wavelength. The digitised signal after Fourier transform can be expressed as

$$P^k[n] = \bar{I}^k \delta(n) + \sum_{i=1}^{2} I_i^k[\delta(n - n_i^k)\exp(j\phi_i^k) + \delta(n + n_i^k)\exp(-j\phi_i^k)] \quad (4)$$

where the subscript, i, denotes a wavelength component, and the superscript k, denotes a particular sensing fibre channel . P[n] can be separated into an intensity and a phase spectrum. From Equation (3), different wavelength components have different spatial frequencies and can be discriminated in the digital spatial domain. The phase signal ϕ_i^k, which is uniquely associated with, or in another word coded by, its wavelength, λ_i, can be read directly from the phase spectrum at the pixel position $n = n_i^k$. Finally in the full system configuration with N-1 sensing fibres, every combination of two fibres will generate two sets of Young's fringe associated with two wavelength components producing a total of N(N-1)+1 peaks in the intensity spectrum. The fringe set generated by the interference between a sensing fibre and the reference has a digital spatial frequency as expressed in Equation (3) and a useful phase signal ϕ_i^k can be obtained from such a frequency position. On the other hand, a fringe set generated by the interference between two sensing fibres, k and l, has a digital spatial frequency, n_i^{kl}, expressed as

$$n_i^{kl} = \frac{M(d^k - d^l)a}{\lambda_i L} \tag{5}$$

Phase values at these frequency positions are normally not used. From Equation (5), it is possible to separate these phases from useful phase signals in the digital spatial domain by arranging positions of the fibre end-faces in such a way so that

$$n_1^{(N-1)l} < n_2^1 \tag{6}$$

In addition, in order that all useful phase signals can be discriminated from each other in the digital spatial domain, additional constrain has to be applied to the positioning of the fibre end-faces, which can be expressed as

$$n_1^p < n_2^{p+1} \quad (p=1,2,...N-2) \tag{7}$$

Now all phase delays between the light in sensing and reference fibres can be obtained directly from the phase spectrum. Bringing Equation (3) and (5) into (6) and assuming $\lambda_1 < \lambda_2$, $d^1 < d^2 < ... < d^N$, we get

$$d^N < \frac{\lambda_1}{\lambda_1 + \lambda_2} d^1 \text{ and } \frac{d^p}{\lambda_1} < \frac{d^{p+1}}{\lambda_2} \quad (p=1,2,...N-2) \tag{8}$$

The positioning of fibre end-faces and the corresponding intensity spectrum are illustrated in Figure 2a and 2b, respectively.

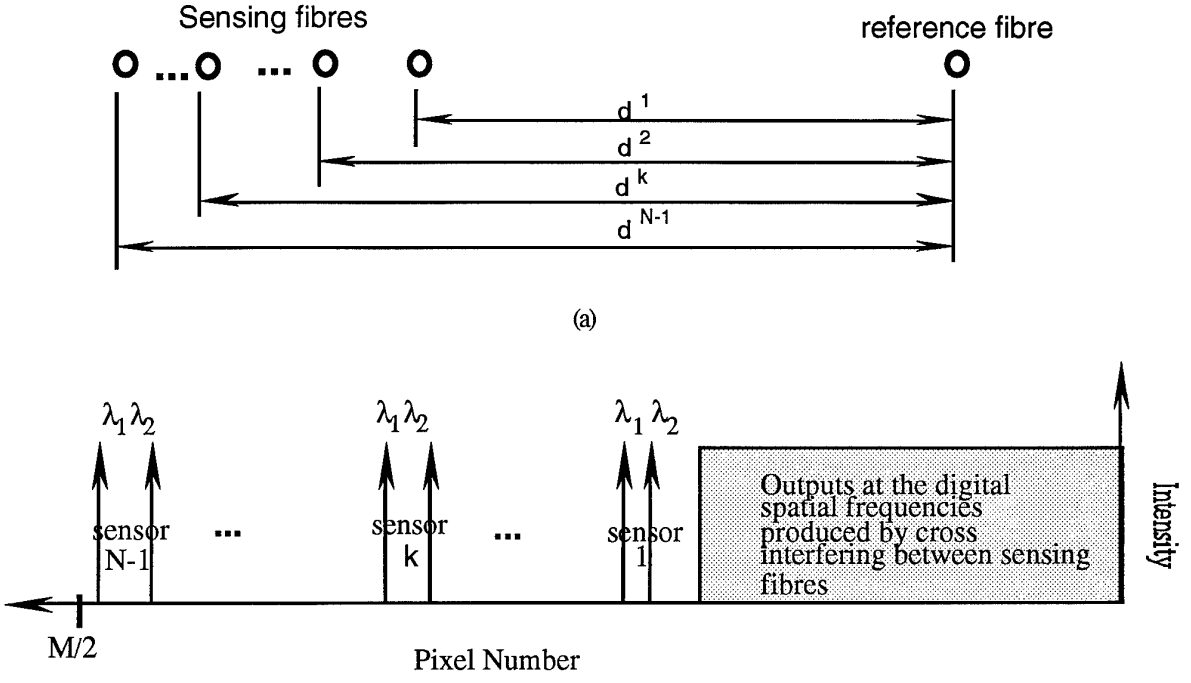


FIGURE 2 The positioning arrangement of fibre end-faces (a) and its corresponding digital spatial frequency distribution (b)

By differentiating both sides of Equation (3), the resolution of wavelength discrimination of the proposed system, $\partial\lambda$, can be written as

$$\partial\lambda = \frac{L\lambda_2^2}{Md^1 a} \tag{9}$$

In normal situations where $(\lambda_2 - \lambda_1)/(\lambda_2 + \lambda_1) << 1$, Equation (8) became $d^N < 2d^1$. Under this condition and according to Figure 2b, in theory, a maximum of M/16 sensor channels can be interrogated in optical fibre interferometric sensor array.

Preliminary experiments

As described above, the directly retrieved phase changes in sensing fibre k are ϕ_i^k coded by wavelength λ_i. However, because of the ambiguity problem, the real phase change, $\bar{\phi}_i^k$ is actually written as

$$\bar{\phi}_i^k = 2X\pi + \phi_i^k \qquad i = 1, 2; k=1, 2, N-1 \tag{10}$$

where X is an unknown integer. However, if $\left|\bar{\phi}_{12}^k\right| = \left|\bar{\phi}_1^k - \bar{\phi}_2^k\right| < \pi$, then [3]

$$\bar{\phi}_{12}^k = \phi_1^k - \phi_2^k = \frac{\lambda_2 - \lambda_1}{\lambda_1}\bar{\phi}_2^k \tag{11}$$

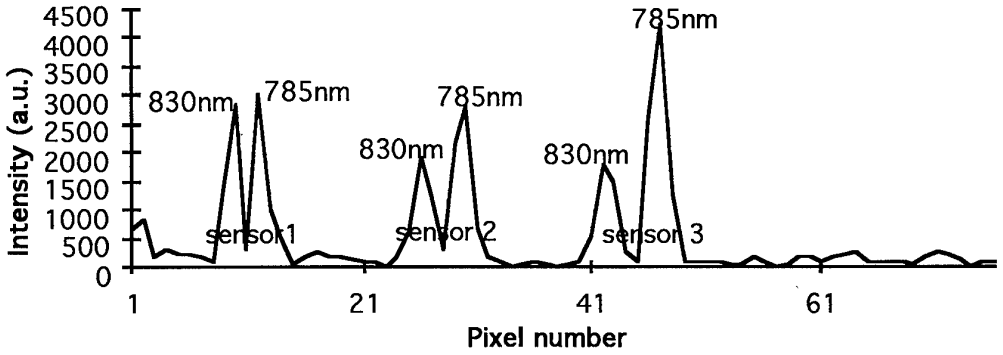


FIGURE 3 Part of the digital spatial domain intensity spectrum of the fringe pattern generated in a system shown in Figure 1 with three sensors and two wavelength carriers

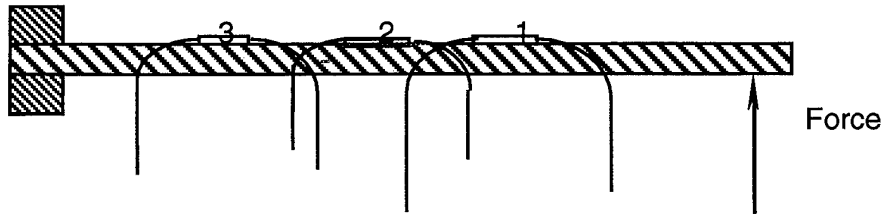


FIGURE 4 Arrangement of optical fibre sensors along a cantilever beam

Bringing Equation (11) into (10), the real phase change in fibre k is calculated indirectly as

$$\bar{\phi}_2^k = 2\pi \bullet \mathrm{Trunc}\left\langle \left[\lambda_1\left(\phi_1^k - \phi_2^k\right)/(\lambda_2 - \lambda_1) - \phi_2^k\right]/2\pi \right\rangle + \phi_2^k \tag{12}$$

where Trunc<> stands for truncate to nearest integer. The unambiguous measurement range is enhanced by a factor of $\lambda_1/(\lambda_2-\lambda_1)$ without sacrificing the phase resolution.

In the experimental set-up, the compound source was constructed with two laser diodes centred at λ_1= 785 nm and λ_2= 830 nm launching into a 1x2 star coupler. The sensor system had three sensing fibres (N=4). Other system parameters are: L= 200 mm, d_1= 5 mm, d_2= 5.6 mm, d_3= 6.2 mm, M=512 and a= 10 μm. This gave the system a wavelength interrogation resolution of 5.3 nm and its unambiguous range was enhanced by factor of 17.4. The processing was performed by a 486-DX2/66 PC which achieved a frame rate of 24 frames per second. Part of the digital spatial domain intensity spectrum of the experimental system is shown in Figure 3. A 30 mm section of each fibres were bound to a cantilever beam at different positions with an adhesive, as shown in Figure 4. When the cantilever beam is deflected, the phase signals in different sensing fibres represent the strain variations at different positions along the beam. At first, a slow deflection was applied by pushing and releasing the free end of the beam.

The phase changes from all sensing fibres can be traced from the directly retrieved values at any one of the two wavelengths. Directly retrieved phase signals at λ_2= 830 nm is shown in Figure 5. However, when a pulse force was applied at the free end and generated a damped vibration, the phase changes cannot be correctly followed by the

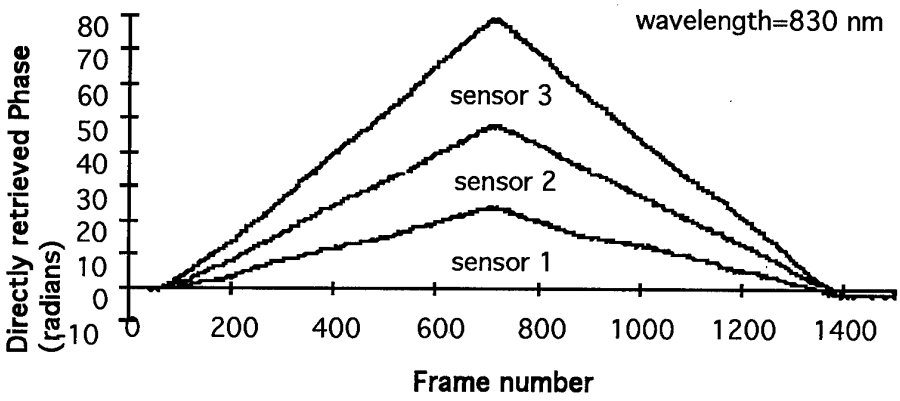
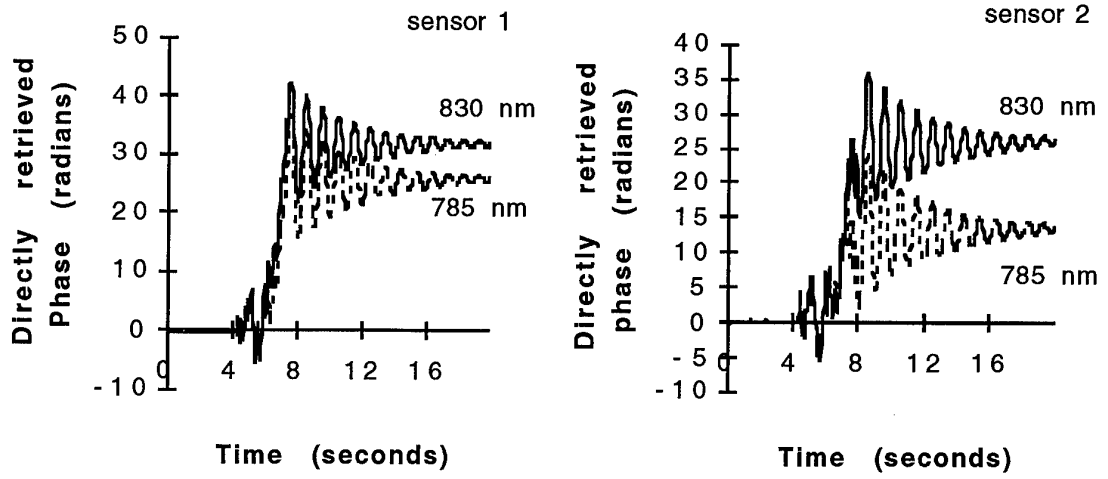


Figure 5 Phase changes associated with λ_2=830 nm at different sensing fibres as directly retrieved from the phase spectrum in the slow loading condition



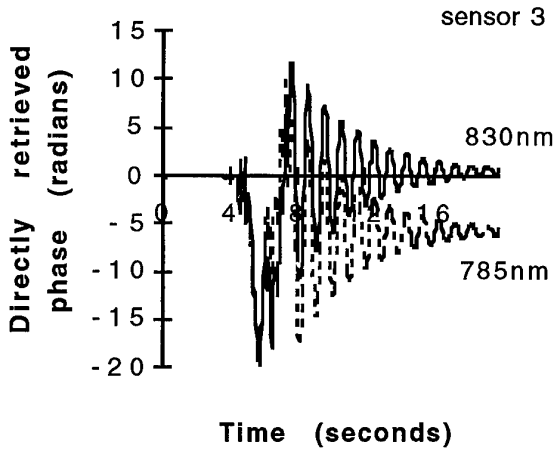


FIGURE 6 Incorrectly traced phase changes associated with λ_2=830 nm at different sensing fibres as directly retrieved from the phase spectrum in the pulse loading condition

directly retrieved phase values as shown in Figure 6 because the phases changed more than $\pm\pi$ during a period of one frame. By making use of additional phase information from a second wavelength carrier as presented in Equation (12), the real phase changes can be recovered as shown in Figure 7.

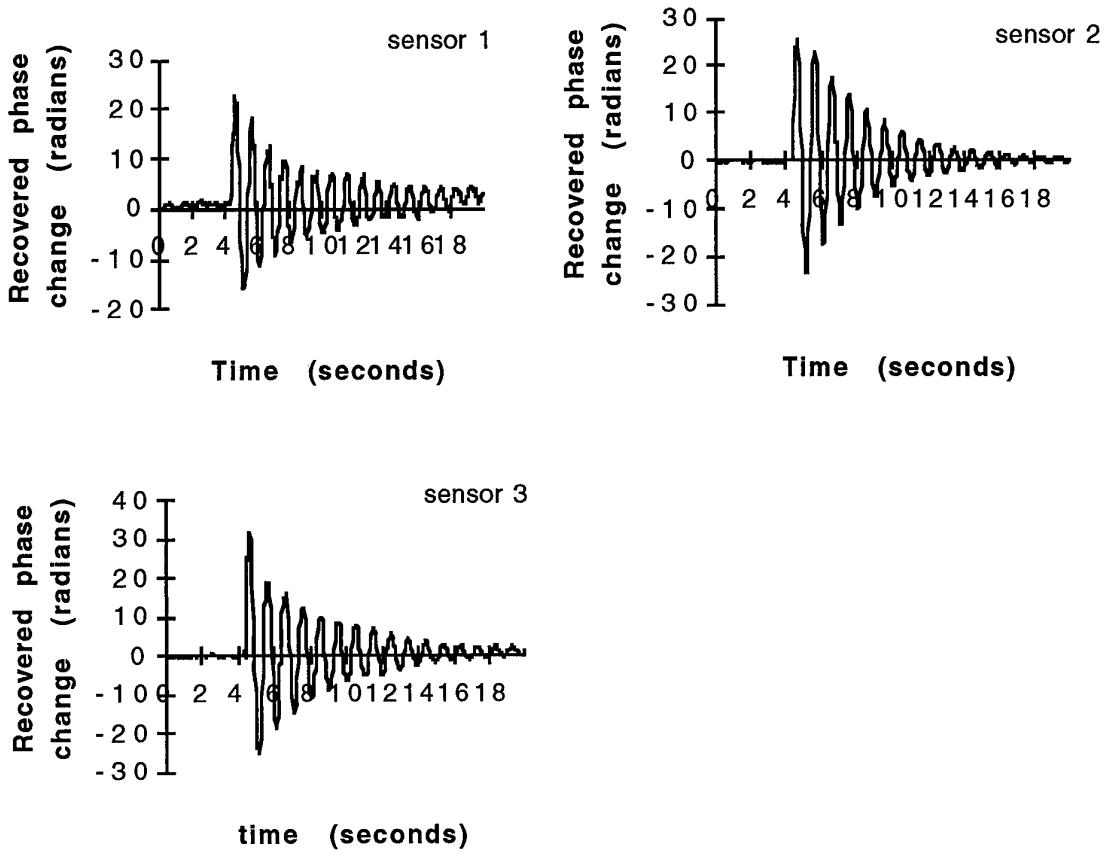


FIGURE 7 Real phase changes recovered in the same experiment as that of Figure 6 using dual wavelength-coded phase signals

Conclusion

The interrogation of phase signals can be easily implemented in a dual wavelength digital spatial domain multiplexed fibre sensor array without additional hardware provisions. Potentially a large number of sensing fibres can be integrated into a simple, robust and low cost system. The results of experimental demonstrations have shown that the capability of an optical fibre sensor array to trace fast varying strains has been greatly enhanced. This sensing system is specially suitable to the subject area of smart Structures and Materials. The study is carrying on to develop its further applications.

Mr Y. Hu is supported by the Overseas Research Scholarship.

Reference

1. Robert S. Rogowski, Proc. SPIE, **1370**, Fibre Optic Smart Structures and Skins, III, pp2-5,1990.
2. A. D. Kersey , K. L. Dorsey and A. Dandridge, Electron. Lett., 1988, **24,** pp. 689-690.
3. R. Duratians, G. Anglaret, C. J. Hugues And G. W. Fehrebach , Springer Proceedings in Physics, Optical fibre sensors, Spring-Verlag Berlin Heidelberg, 1989), **44**, pp504-512.
4. J. L. Santos, F. Farahi, T. Newson, A. P. Teite and D. A. Jackson, IEEE J. Lightwave Technol., 1992, **10**, pp853-863.
5.J. L. Brooks, R. H. Wentworth, C. R. Youngquist, M. Tur, B. Y. Kim, and H. J. Show , IEEE J. Lightwave Technol., 1985, **3**, pp.1062-1070.
6. Y. Hu and S. Chen , Photon. Technol. Lett., 7 (1995) 673.
7. D. J. Webb , J. D. C. Jones , R. M. Taylor and D. A. Jackson , International J. Optoelectron., 3 (1988) 213 .
8. A. D. Kersey and T. A. Berkoff , Electron. Lett., 28 (1992) 1215.
9. S. Chen, B. T. Meggitt and A. J. Rogers, Electron. Lett., 27 (1991) 1032.

Optical fiber sensor for temperature measuring.

Markijan Baran

State University "Lviv Polytechnic", Department of Data Measuring Technique,
Bandera street 12, Lviv-13, 290646 Ukraine
Email: adrian@sigma.icmp.lviv.ua

ABSTRACT

Simple fiber-optic sensor for temperature measuring, based upon the temperature-dependent bend losses in plastic clad silica optical fibers, is being proposed. The quantity of light energy transmitted along the fiber depends on the numerical aperture of the fiber, i.e. the refractive index difference between the silica core (n_1) and the plastic cladding (n_0). On the one hand, the refractive index of polymer cladding n_0 for plastic clad silica optical fibers exhibits considerable temperature dependence. On the other hand, local aperture in fiber bend region also changes at strong curvature, which reduces the number of guided modes and respectively decreases the transmitted light power. Interaction of these two effects produces great dependence of light output energy on temperature. High sensitivity over a wide temperature range (at least from -20°C to +60°C) can be obtained.

1. INTRODUCTION

In recent years, research and development into optical fiber sensors has made rapid progress. Accordingly, many studies of application of optical fibers for industrial measurements utilizing their excellent properties have been carried out.

We propose an optical fiber sensor for temperature measuring. The sensor consists of several closely wounded turns of sharp bend plastic clad silica (PCS) fiber. The light output intensity is sharply reduced at small bend radius of the fiber because of the decreasing of local aperture in bend region. On the other hand, the transmission losses along a curved fiber are decreasing, when the temperature and consequently, the core-cladding refractive index difference n_1--n_0, are increasing. Thus the output light energy is modulated by temperature.

Our sensor has the following features: the sensor and transmission line are united in one body, it is capable of remote sensing, it is easy to manufacture and it is cheap.

In this paper we describe the fundamental principles and characteristics of the sensor. Experimental investigation results of sensor constructions parameters and some application spheres of this sensor are also being discussed.

2. PRINCIPLES

To achieve high temperature sensitivity in the proposed sensor two effects are applied: fiber aperture change as a result of strong temperature dependence on the refractive index difference between silica core and the plastic claddind in the PCS fibers and local aperture change as a result of sharp fiber bend. Let us discuss each of them separately:

Practically the temperature dependence of transmission loss in PCS optical fiber is greatly influenced by the organic fiber materials, especially the coating materials. In general we can write the refractive index n as a function of the temperature T:

$$n(T)=n(T_0)+\frac{dn}{dT}(T-T_0), \tag{1}$$

The amount of power which can be guided in a fiber is proportional to the square of the numerical aperture (NA). With the change of temperature a numerical aperture is expressed by the following expression:

$$NA_T = \sqrt{n_1^2(T) - n_0^2(T)} = \sqrt{\left[n_1(T_0) + \frac{dn_1}{dT}T\right]^2 - \left[n_0(T_0) + \frac{dn_0}{dT}T\right]^2} \tag{2}$$

0-8194-2165-0/96/$6.00

The temperature gradient of the cladding refractive index, dn_0/dT, is represented by the cladding coefficient of expansion. As a rule, the density of plastic materials decreases with temperature increasing and that is why refractive index decreases too. Usually, n_1 as well as n_0 change with temperature variation, but the refractive index (n_0) of the cladding (plastic) is more than a single-order greater than the temperature gradient (absolute value) of the refractive index (n_1) of the core (silica).However in silica glasses, electron polarizability dominantes and so the refractive index increases with temperature increasing[1]. That is fibers NA increases with the temperature because of the n_0 decreasing as well as n_1. increasing. So temperature coefficient of refractive index for fused silica[2] is $dn_1/dT=1.02\times10^{-5}$ C^{-1}. As for polymers it is not easy to find temperature coefficients because the materials used by manufactures are never pure and perfectly defined, and also the exact composition of each one is a manufacturing secret. Temperature coefficient of refractive index for some polymers[3] (for example Polystyrene and Polymethylmethacrylate (PMMA)) is $dn_0/dT=-14\times10^{-5}$ $°C^{-1}$.

To use this normally unwanted effect with efficiency, we induce bend-losses under a strong curvature; radiation losses in bent region are a sharp decreasing function of the refractive index difference, and hence of the temperature at this point. When the multimode optical fiber is bent, because of the change of total internal reflection condition, part of guided modes reflected into the cladding, reduces the number of guided modes which continue to propagate in the fiber core, and, respectively, output light intensity.

The number of guided modes in straight fiber (N_0) depends upon the physical parameters (i.e. relative refractive index difference, core radius(a)) of the fiber and the wavelengths (λ) of the transmitted light and can be expressed by[4]:

$$N_0 = \frac{\alpha}{\alpha+2}\cdot\frac{V^2}{2}, \tag{3}$$

where $= \dfrac{2a\pi\cdot NA}{\lambda}$ - is the normalized frequency, which describes the propagation properties of a fiber, and a is the index profile. For straight stepindex fiber $\alpha=\infty$, and then $N_0=V^2/2$. When the optical fiber is bent, the profile of refractive index changes as a result of appearance of mechanic strengths, and then the number of propagated modes decreases and can be expressed as[5]:

$$N = \left\{\frac{\alpha(R)}{\alpha(R)+2}\cdot\frac{V^2(R)}{2}\right\} < N_0, \tag{4}$$

High order modes, the propagation conditions of which in the curved fiber do not satisfy the total internal reflection condition, are refracted into the cladding and are not involved in the light energy transmission. In bend section of the fiber the propagation angle at the outer side of optical fiber increases and the inner side it decreases. At each reflection point an the outer side the part of light power is refracted into the cladding. The curvature involves the loss which is expressed by

$$L(R)=10\log(N/N_0)=10\log\{\alpha(R)/[\alpha(R)+2]\}+20\log[NA_R/NA_F] \tag{5}$$

according to (3) and (4), where NA_R is the local numerical aperture (bent region) and NA_F is the numerical aperture of the straight fiber. The variation of the core and cladding refractive index under the curvature effect modifies the local numerical aperture of the fiber. That is, with the decreasing of bend radius, NA_R decreases too, and as a result those of high order modes which do not satisfy total internal reflection condition come out into cladding and propagate for some time in it. However, with temperature increasing, because of the change of total internal reflection condition and aperture increasing, the cladding modes return into the core, strengthening the general light intensity. Radiation emitted in a bend fiber is submitted to a modification which is the function of the temperature T, the bending radius R, the wavelength λ and the fiber materials. The resulting loss is independent of the fiber length.

3. EXPERIMENTAL RESULTS AND DISCUSSION

For a trial manufacture of the sensor, we chose the step index multimode HCN/H fibers produced by English-Bickford Optics Company (EBOC). These fibers are classified as hard-plastic clad silica fibers (H-PCF), which contrary to traditional PCS fibers, nave thin enough cladding made of special hard polymer. Unfortunately, authentic PCS-fibers are generally not available. Hard cladding polymer of HCN/H fibers has somewhat lower temperature coefficient of refractive index than standard polymers for PCS fibers, and therefore it is less sensitive to temperature and strength deformation. However it does not influence the function principles of our sensor.

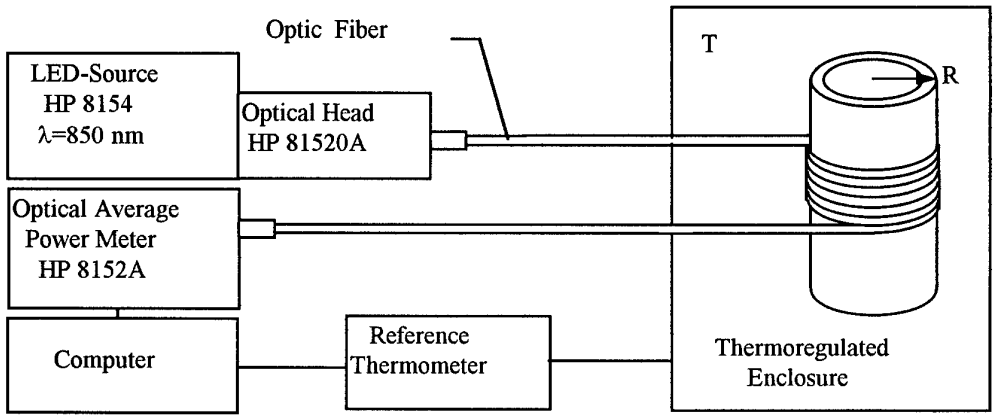


Figure 1. Experimental setup configuration.

As test sample we used a HCN/H 110/125/250 fiber with the following characteristics:
Core -Silica, 110 μm,
Cladding -Proprietary Bonded Hard Polymer (BHP), 125 μm,
Buffer -Tefzel®, 250 μm.
The fibers numerical aperture at 20°C was NA=0.37. This corresponds to acceptance angle ca. 43°. Refractive index for fused silica at 20°C at wavelength λ=852mm is n_1=1.452. Hence, it is easy to obtain n_0=1.404. Preference of applying HCN/H fibers in this case is that the less fiber diameter allows to have the less bend radius and, respectively, less sensor dimensions.

The experimental arrangement is shown schematically in fig.1. The fiber was wrapped around a hollow cylinder placed in thermoregulated enclosure, in which the temperature was varied from -30°C to +100°C. The sensing part is the bent section of the fiber. The source is a light-emitting diode (LED), emitting at λ=850 nm. The light modulated by the temperature is transmitted at the output of the fiber to an optical powermeter. The data from a

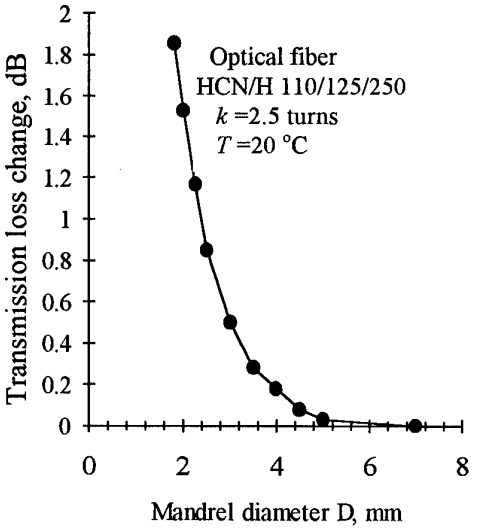


Figure 2. The pure bend loss dependence on the different bend radii.

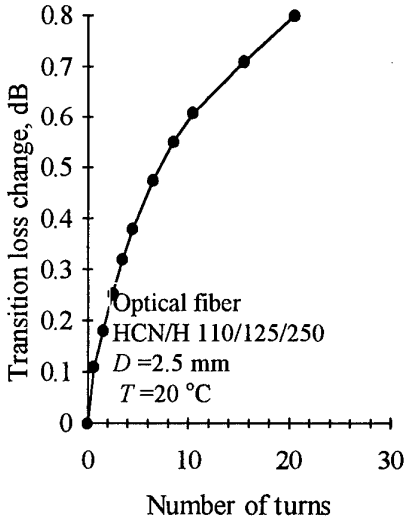


Figure 3. The pure bend loss dependence on number of fiber turns.

powermeter as well as temperature values from reference thermometer are received by the computer. The length of the fibers in our experiment was 2.5-3m, but for remote measuring it can be increased.

First we have investigated pure bend loss versus the bend radius R and number of turns k at constant temperature T=20°C. The results of some experiments are given in fig.2 and fig.3.The growth of relative loss at bend radius decreasing for 2.5 fiber turns at room temperature is shown in fig.2. Fig.3 shows the same in dependence on the number of fiber turns k, with mandrel diameter D=2.5mm. The relation between D and bend radius R is as follows: $R=0.5(D+d)$, where d is the outer diameter of the fiber. As is seen from the diagrams, increasing of k as well as decreasing of D influence similarly on relative transmission loss increase.

The experimental results of investigation sensor temperature sensitivity in dependence on bend radius (more exactly on mandrel diameter D) and number of turns k are shown on fig.4 and fig.5 respectively. Fig.4 shows the

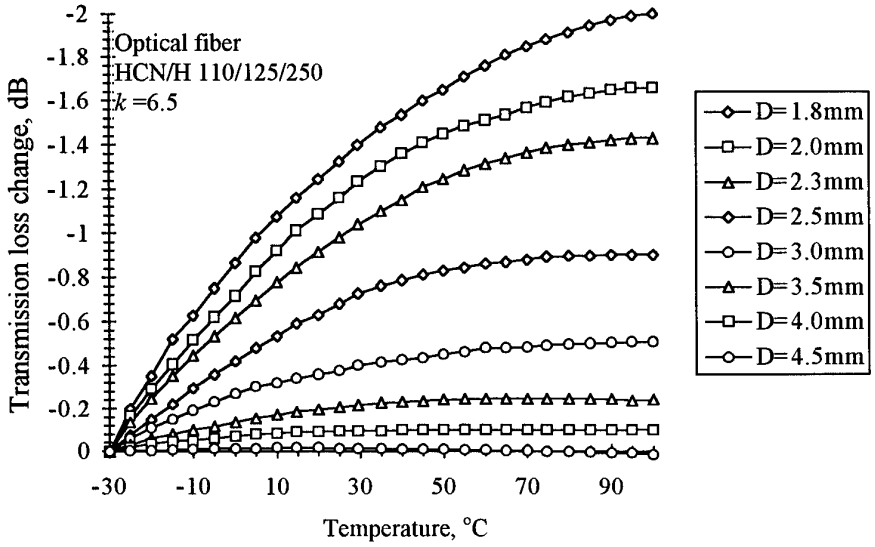


Figure 4. Temperature dependence on transmission loss for the HCN/H fiber versus different mandrel diameters.

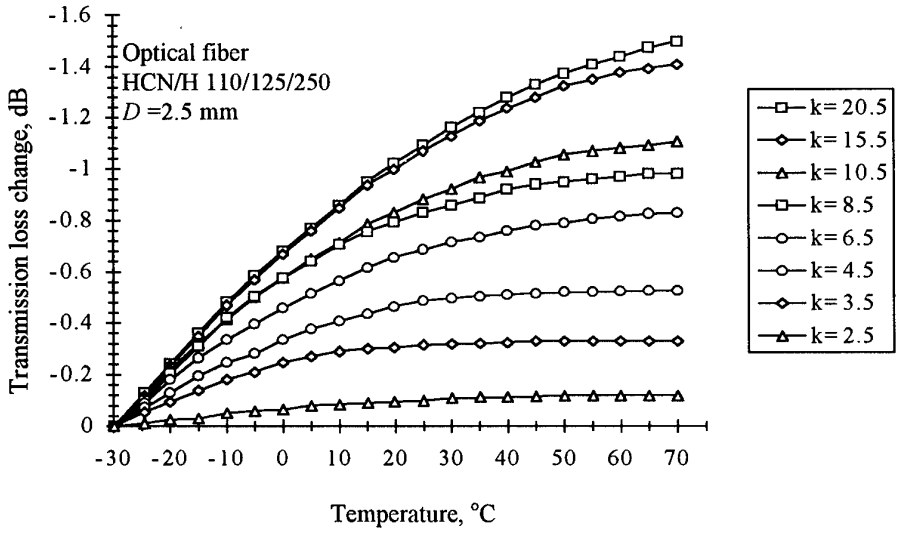


Figure 5. The temperature dependence of HCN/H fiber transmission loss with different number of fiber turns.

temperature dependence on transmission loss for the HCN/H 110/125/250 fiber wound up to 6.5 turns on mandrel with different diameters. Fig.5 shows the same dependence in case the fiber is wound up on mandrel with 2.5 mm diameter for different number of turns.

As is seen from the diagrams, the greater is the number of fiber turns, and the smaller is the bending radius, the larger is the relative loss change and the faster is the increase of the transmitted light intensity with temperature increasing. It should be taken into consideration that the resulting light intensity not only compensates but exceeds the level of bend losses. As can be seen the sensitivity decreases at 50-60°C (as is theoretically predicted), but it is possible to shift the maximum sensitivity region by changing the radius of curvature, or/and number of turns. The sensor sensitivity grows some what more slowly with increasing of the number of turns than with decreasing of the bend radius. Although the number of turns may be increased deliberately, it is obvious that the decreasing of bend radius is limited by the fiber strength.

However the main problem is the reliability of the fiber under the very strong curvature. Because of the high Young modulus of the silica, very high constraints occur in the fiber and it can break. Experimentally determined limit of reability in the case of the HCN/H 110/125/250 fibers amounts to D=1.6mm, that is R_{min}=0.9mm. We assume that optimum parameters (for the given type of fiber) are as follows k=6÷10 and D=1.8÷2.5 mm. Dimensions of such sensor (for example at k=10.5 turns and diameter D=2.0mm) amount to not more than 3 mm × ∅2.5 mm.

In general, in this experiment a sensitivity to a ~0.02 dB/°C in the temperature range from -30°C to +70°C was found. Besides, principles described above can be applied in distributed sensor by means of the optical time domain reflectometry (OTDR) technique[6].

4. CONCLUSIONS

Investigation of transmission losses at the fiber bend during temperature change has shown stable and definite relation between the refractive index variations and bend radius of multimode step index PCS optical fibers. This sensitive effect allows to measure successfully the temperature in the wide range. Change of sensor sensitivity is possible at the selection of the bend radius, number of turns and fiber type (namely dn_0/dT). Choosing the fibers with considerably higher dn_0/dT, than the one used in our experiment, it is possible to achieve sensitivity[6] of 0.1 dB/°C.

Sensor functioning according to the described principles may be applied in industry for temperature processes control and for biomedical measurements.

5. ACKNOWLEDGMENT

The author would like to thank Prof. E.Gerhard and research associates of the department of Electromechanical constructions of Gerhard-Mercator University of Duisburg for the possibility of carrying out experiments.

6. REFERENCES

1.L.G.Cohen, J.W.Flemming, "Effect of Temperature on Transmission in Lightguides," *Bell System Technical Journal*, Vol.68, No.4, April, 1979.

2.Vogel, Werner, *Glas Chemie*. 3.Auflage, Springer Verlag, 1992, p.247.

3.G.W.C.Kaye & T.H.Laby, *Tables of Physical and Chemical Constants*, Logman Group Limited, London and New York, 1972, p.251.

4.Wolf, Helmut F., *Handbook of Fiber Optics: Theory and Applications,* Garland SPTM Press, New York & London 1979, p. 62.

5.Semenkoff, M., "Bending effect on light propagation in an optical fiber: application to a temperature sensor," *Optics and Lasers in Engineering*, vol.17, iss.3-5, 1992, p.183.

6.P.Lecoy, M.Groos, L.Guenadez, "New fiber optic distributed temperature sensor," *SPIE* Vol.798, fiber optic sensors II (1987), pp.131-136.

Development of embedded sapphire optical waveguides for intelligent ceramic composites

Mahmoud A. El-Sherif, Jay Radhakrishnan and Jianming Yuan

Drexel University, Department of Materials Engineering
Philadelphia, PA 19104, USA

ABSTRACT

Embedded fiber-optic sensors offer an attractive method for real-time in-situ characterization of composite materials. The present work is directed toward the development of an appropriate optical waveguide and sensing technique for high temperature ceramic applications. The waveguide consists of a sapphire optical fiber core and polycrystalline alumina cladding. The sensing technique is based on spatial intensity modulation induced within multimode optical fibers. This paper presents a brief description of the optical waveguide fabrication, a theoretical model for spatial intensity modulation (SIM) and experimental verification of SIM in sapphire fibers.

1. INTRODUCTION

Embedded fiber-optic sensors offer significant potential for application in composite materials. Optical fibers made of silica or polymer based materials are proposed as sensing elements for testing composite materials at low temperatures. However, at high temperatures (over 1000° C), silica and polymer optical fibers cannot be used as waveguides. For these high temperature environments, optical grade sapphire (aluminum oxide) fibers offer an alternative[1]. Unlike silica or polymer fibers that are available commercially, optical grade sapphire fibers are uncladded single crystal fibers. In order to be able to use these fibers as embedded optical waveguides, two coatings are necessary (a cladding layer and a protective jacket). The cladding layer is required to confine the optical signal propagating within the fiber core and limit attenuation and losses. The external protective coating is needed to protect the fiber from its surrounding environment. For thermal durability of the sapphire optical waveguide, alumina is the preferred cladding material. For the protective layer, silicon carbide was chosen due to its superior mechanical and thermal properties. The second section of the paper describes a methodology that has been developed for coating sapphire optical fibers.

Sapphire fibers possess reasonably good optical properties, but are difficult to be fabricated into single mode fibers. Most conventional high sensitive techniques are either based on phase modulation or polarization modulation and, therefore, require single mode fibers for propagation of coherent light. Since available sapphire fibers are multimode fibers, as opposed to single mode, these techniques are not suitable. For multimode fibers, an inexpensive and reasonably sensitive technique was developed recently[2]. The technique is based on spatial intensity modulation (SIM) induced within multimode optical fibers. The feasibility of using this technique with conventional optical fibers to characterize composite materials was demonstrated successfully[3]. In the present communication, a theoretical model for spatial intensity modulation in multimode optical fibers and simulation results are presented in section 3. Section 4 provides experimental evidence of spatial intensity modulation in sapphire optical waveguides when lateral compression loads are applied to the fiber.

0-8194-2165-0/96/$6.00

2. FABRICATION OF SAPPHIRE OPTICAL WAVEGUIDES

The developed technique is based on using a polymerizable monomer as the carrier for very fine alumina particles. A solution of acrylic acid in water with benzoyl peroxide (BPO) as the initiator and N,N-dimethyl para toluidine (DMPT) as the accelerator is used to dissolve alumina particles and form a suspension. The fiber to be coated is immersed in the suspension, and the polymerization reaction is allowed to proceed. The BPO in the solution forms free radicals and reacts with the acrylic acid monomer. Before the end of complete polymerization, the fiber is pulled out of the suspension. The coated fibers are left to dry at room temperature for 24 hours, and then heated for evaporation of the polymer. This is followed by sintering of the fiber coating to obtain a uniform cladding of polycrystalline alumina.

The concentration of alumina, acrylic acid, BPO and DMPT and the length of time for which the polymerization reaction is allowed to proceed are important parameters that determine the uniformity and thickness of the cladding. These parameters depend on the diameter of the fiber that needs to be coated. By successfully adjusting these conditions, a uniform coating with a good interface between the core and the cladding can be achieved. Complete details of the coating process and results obtained from the process were reported in an earlier communication[4].

3. SPATIAL MODULATION IN MULTIMODE OPTICAL FIBERS

Propagation of electromagnetic waves in multimode fibers is known to be in the form of a finite number of guided modes that are responsible for a stable light pattern within the optical fiber[5]. The presence of any mechanical stresses or other forms of perturbation that changes the boundary conditions in the fiber will lead to energy exchange between the modes, resulting in modal power redistribution. This energy exchange or coupling is referred to as spatial modulation, since it results in spatial variation of the light pattern within the fiber.

Comparative measurements of the distribution and subsequent redistribution of the modal power can be accomplished by scanning the far field pattern at the fiber end using a CCD camera or array of photodetectors. This technique can be employed as a sensitive mechanism for measuring perturbations induced by external mechanical stresses. The sensitivity of this type of fiber-optic sensor is related to the modal structure of the fiber and to the medium surrounding it. In order to improve the sensitivity of the device, it is preferred to excite higher order modes within the fiber. This is done by launching an optical beam slightly off-axis to the fiber. In this way, the far field pattern becomes totally dark at the center, and any induced power coupling from higher to lower order modes i.e.., from the periphery to the center, can be detected easily. The quality of the fiber end faces and the fiber coating are additional factors that influence the level of sensitivity.

The possible changes in boundary conditions induced by mechanical stresses that leads to spatial modulation can be listed as, changes in refractive indices of the core and/or cladding, the geometry of the waveguide and the interaction length of the fiber with the mechanical stress. In principle, the coupled mode theory[6] can be employed for accurate analysis of the spatial modulation induced by the stress. In practice however, the coupled mode theory is too complicated to be used for multimode fibers supporting a large number of guided modes.

For the special case of modal perturbation where an external load is applied along the length of the fiber for a known distance 'd', the device can be treated as a waveguide consisting of discontinuities at $z = 0$ and $z = d$, as shown in Fig. 1. The effect of the changes in boundary conditions is to redistribute the power between the various guided modes in region II of the fiber. The output modal power distribution (region III) can be solved in terms of the input modal power distribution (region I) and changes in the boundary conditions in region II, by applying continuity equations at $z = 0$ and $z = d$,

$$\sum_{n=1}^{N} b_n \mathbf{e}_n - \sum_{n=1}^{N} c_n \mathbf{e}_n = \sum_{s=1}^{S} f_s \mathbf{E}_s - \sum_{s=1}^{S} g_s \mathbf{E}_s \qquad \text{at } z = 0 \text{ and} \qquad (1)$$

$$\sum_{s=1}^{S} f_s \mathbf{E}_s \exp(-j\alpha_s d) - \sum_{s=1}^{S} g_s \mathbf{E}_s \exp(+j\alpha_s d) = \sum_{m=1}^{N} a_m \mathbf{e}_m \exp(-j\beta_m d) \qquad \text{at } z = d \qquad (2)$$

b_n and c_n are the complex amplitude of the nth mode of the incident and reflected fields in region I, f_s and g_s are the complex amplitude of the sth mode of incident and reflected fields in region II and a_m is the complex amplitude of the mth mode in region III. β_n, α_s and β_m are the respective propagation constants. **e** represents the eigen functions of the electric field in regions I and III, and **E** the eigen functions in region II. N denotes the total number of guided modes in regions I and III and S the total number of guided modes in region II. The expressions for the magnetic fields are similar to the above equations. The simultaneous solution of these sets of equations yields the expression for the output modal amplitudes, a_m, in terms of the input modal amplitudes, b_n and c_n, and changes in boundary conditions in region II. The details of this theoretical analysis will be published soon.

Simulation results obtained from the theoretical analysis are shown in figures 2 and 3. Figure 2 is a 3-D plot of the intensity distribution in the absence of stress. When a stress is applied to the fiber, light from the higher order modes is coupled to the lower modes; this is shown in the form of a 3-D plot in figure 3. In figure 3, the total power remains the same, but the intensity in the center has increased with a corresponding decrease in power in the periphery.

4. EXPERIMENTAL INVESTIGATION AND RESULTS

The testing set-up designed for the detection of modal power, coupled with a computerized data acquisition system has been described elsewhere[7]. The light launching angle used during the present experimental investigation was about 8° off-axis, and the fiber used was an optical grade sapphire fiber of approximate core diameter 300 μm. This launching condition was used to excite higher order modes which are more sensitive to external perturbations than lower order modes. Results obtained by using the spatial modulation technique on an optical grade sapphire fiber, are shown in figures 4 and 5. The figures show the 2-D far-field pattern recorded at the fiber output. In addition, the figures also show the normalized output intensity profile of the far-field pattern as a function of the scanning angle. Figure 4 shows the 2-D image and the horizontal intensity profile before any stress was applied. This figure illustrates that the optical intensity for the lowest order modes (on axis modes) is almost zero, and that most of the power is concentrated at an angle equal to the excitation angle.

When a transverse compression load was applied to a centimeter length of the optical fiber, there was a change in the far-field pattern at the exit of the fiber. The applied stress caused an intermodal coupling, leading to transfer of power from higher to lower order modes, thus broadening the light intensity toward smaller angles. As the applied load was increased, more power was shifted from the periphery to the center. Figure 5 shows a typical far field pattern for an applied load. A significant increase in power is seen at the center. Increasing the load further will result in more power transfer to the center. This process can be continued until most of the power is shifted to the center of the optical fiber. Thus, the increase in intensity at the center of the fiber can be correlated to the compression load applied to the fiber.

This work was directed toward the experimental investigation of modal power variation in optical grade sapphire fibers under various loading conditions. Based on the results obtained from far-field

patterns such as in figures 4 and 5, a simple relation can be drawn for the on-axis intensity of the far-field pattern as a function of the applied load. The result is a smooth variation in optical intensity at the center of the fiber as a function of the applied stress. A direct and cost effective method of applying this technique in practice would be to replace the CCD camera by a single photodetector positioned on the fiber axis, to collect power from the lower order modes alone.

5. CONCLUSION

The combination of spatial modulation with multimode sapphire fibers appears to be an attractive methodology for the development of optical sensors for very high temperature applications. The results presented in this paper show that the spatial modulation technique is a sensitive and cost effective methodology that can be exploited for using multimode sapphire optical fibers in sensor applications. Multimode sapphire fibers can be employed as intrinsic or extrinsic sensors for on-line monitoring of ceramic composites and other materials in high temperature environment.

6. REFERENCES

1. E. D. Jungbluth, "Sapphire Fiber Sensors Survive 1600° C," Laser Focus World, Vol. 28, 18-19 June 1992.
2. M. A. El-Sherif, "Spatial light modulators in multimode fibers," Spatial light modulators and applications, Technical Digest Series, OSA, Vol. 8, 200-203, 1988.
3. M. A. El-Sherif, "Spatial modulation within embedded fiber optic sensors for smart structures characterization," First European Conference on Smart Structures and Materials, B. Culshaw, P. T. Gardiner and A. McDonach, Ed., Vol. 1777, 85-88, SPIE, Bellingham, 1992.
4. M. A. El-Sherif, I. L. Kamel, F. K. Ko, M. Shaker, D. J. Roth, B. Lerch and S. Swickard, "A Novel Sapphire Fiber-optic Sensor for Testing Advanced Ceramics," Ceramic Engineering and Science Proceedings, Vol. 14, No. 7-8, 437-444, 1993.
5. A. W. Snyder and J. D. Love, Optical waveguide Theory, Chapman and Hall Ltd., London, 1983.
6. D. Marcuse, "Coupled mode theory of round optical fibers," The Bell System Technical Journal, Vol. 52, No. 6, 817 - 842, 1973.
7. M. A. El-Sherif, "Smart composites with embedded sensors for in situ monitoring and diagnostic systems," Materials Technology, Vol. 9, Nos. 7/8, 141-143, 1994.

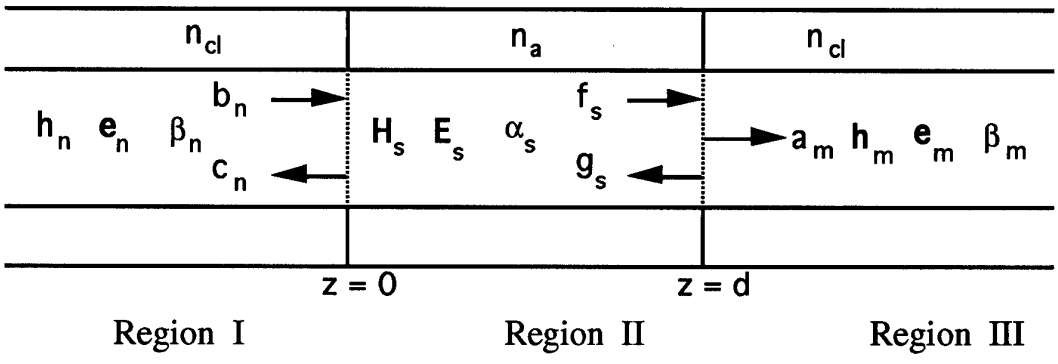


Figure 1. The geometry of a multimode fiber under perturbation in region II, showing the fields ($\mathbf{e}_n$, $\mathbf{h}_n$, $\mathbf{E}_S$, $\mathbf{H}_S$, $\mathbf{e}_m$ and $\mathbf{h}_m$), the complex amplitudes (b_n, c_n, f_S, g_S and a_m) and the propagation constants (β_n, α_S and β_m) for each of the three regions.

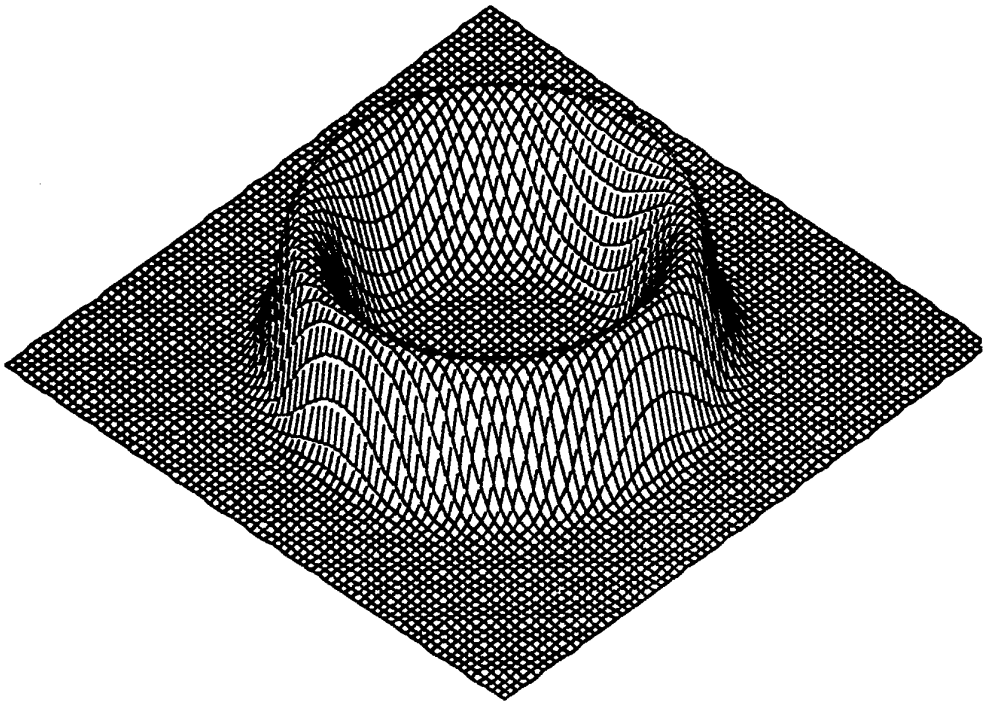


Figure 2 3-D plot obtained from simulation when no stress is applied

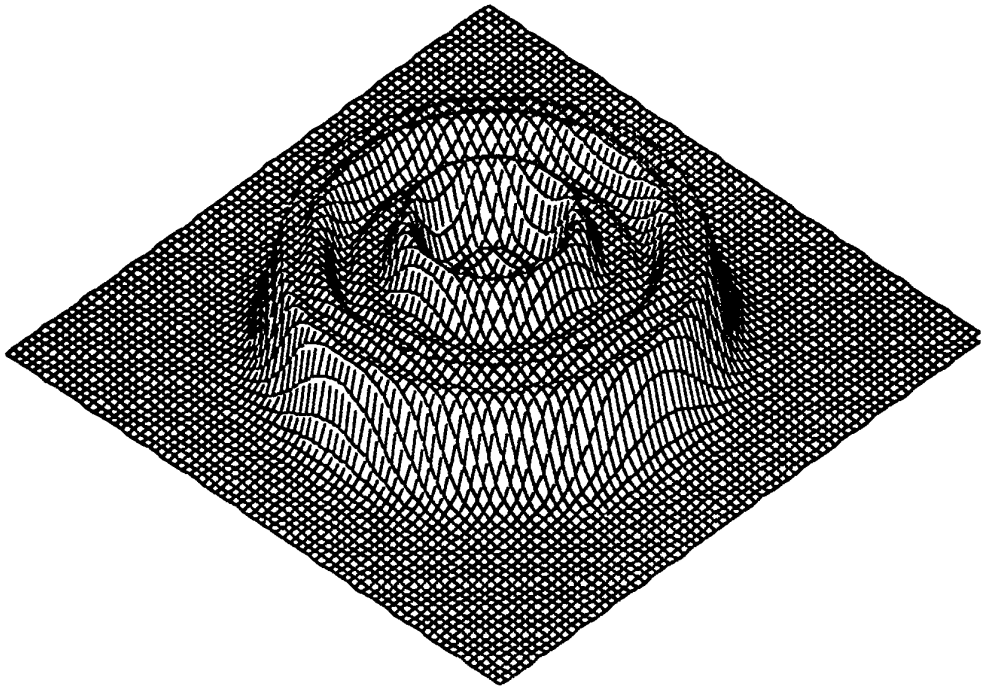


Figure 3 3-D plot obtained from simulation when a stress is applied.

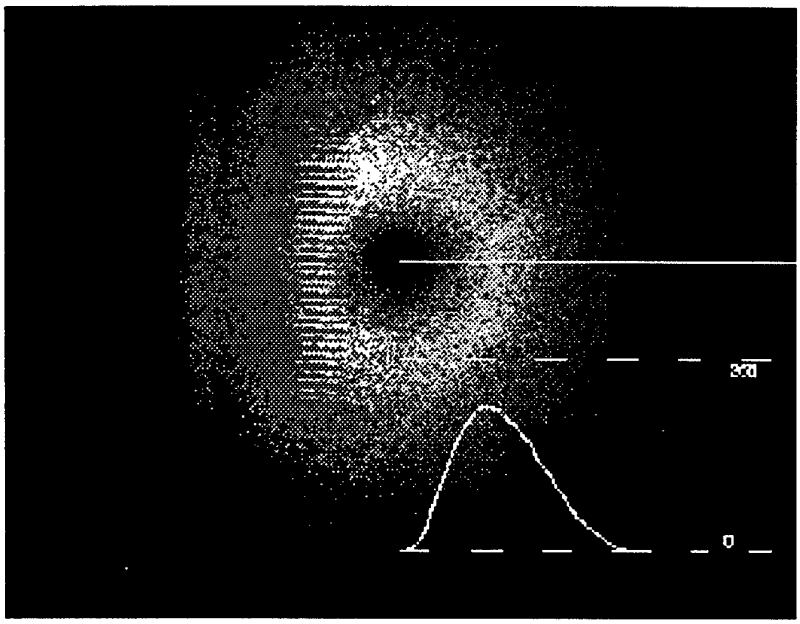


Figure 4 The 2-D image and the optical intensity profile of the fiber far-field pattern for scanning angles from -20° to +20°, before the load was applied.

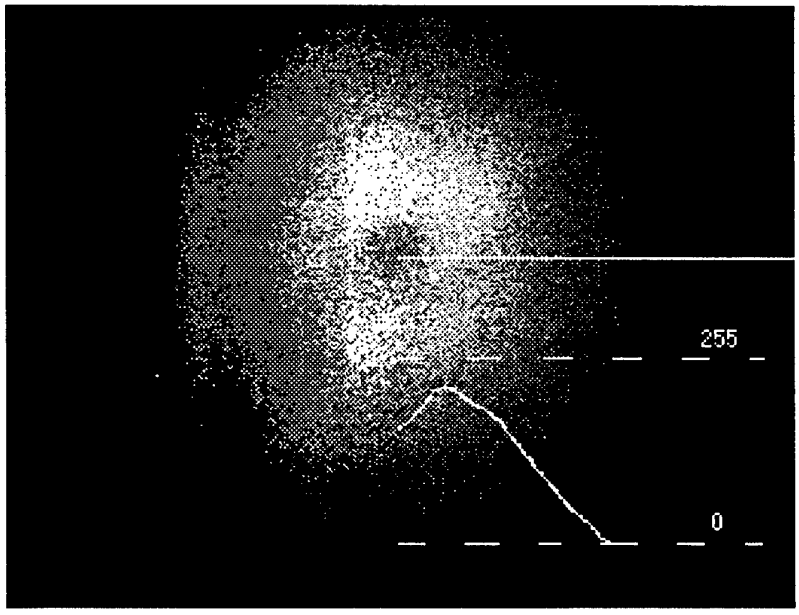


Figure 5 The 2-D image and the optical intensity profile of the fiber far-field pattern for scanning angles from -20° to +20°, under a normal applied load.

PRACTICAL TERMINATIONS FOR OPTICAL FIBRES EMBEDDED IN COMPOSITE MATERIALS

A.K. GREEN[1], S. DARVISH[1], AND E. SHAFIR[2]

[1] MATERIALS ENGINEERING AND TECHNOLOGY DEVELOPMENT DEPARTMENT, ENGINEERING DIVISION, ISRAEL AIRCRAFT INDUSTRIES, LOD, ISRAEL, 70100.

[2] SOREQ, N.R.C., YAVNE, ISRAEL, 81800.

BACKGROUND

The concept of using embedded sensors based on optical fibre technology for condition monitoring in fibre reinforced composites is no longer novel. Extensive literature is available on the topic, and several development programmes have demonstrated concept feasibility. No routine service application has yet been reported.

An interdisciplinary team in Israel, comprising industry and academic partners, has been developing various aspects of the technology, with the ultimate aim of real time monitoring of aircraft structural components during flight. Aspects studied have included optical signal processing and analysis, optical signal correlation with mechanical loading, micromechanical modelling of composites containing optical fibres, optical fibre to composite matrix stress transfer and techniques for embedding optical fibres during conventional composite manufacturing processes.

The development reported herein used autoclave-cured, prepreg lay-ups incorporating carbon fibres, the 'industry standard' for high performance aircraft components. The curing process for these parts involves elevated temperatures and pressures, typically 180°C and 6 bar. The conventional acrylic jacket applied during manufacture to standard optical fibres is not stable under these conditions. It was found necessary to use polyimide jacketed fibres, that resisted the process conditions. With these fibres, embeddment was a comparatively simple process. Various types of carbon fiber prepreg configuration were studied, with multi-fibre arrays incorporating sharp curvatures and optical fibre crossovers. In all cases the fibres were incorporated undamaged, with minimal disturbance to the parent composite structure, and fibre optical performance was maintained. However, a major problem exists at the edge of a composite part at the entry and exit points of the optical fibres. Conventional composite manufacturing results in a vulnerable and fragile optical fibre at these points, which frequently breaks during separation of the composite part from the tool.

This present study developed methods to prevent this fibre fragility. Additionally, efforts were directed towards developing fibre termination methods that would be practical for a part requiring assembly to and disassembly from aircraft structure.

EXPERIMENTAL STUDIES

The primary cause of the optical fibre fragility is the accretion of the composite matrix resin on the fibre during the cure process. Even though a 'net' resin prepreg system was used, some resin flow is involved in the cure process as an aid to eliminating entrained vapours that cause porosity. Some of this resin flow is out of the laminate, and in conventional composite manufacturing procedures is absorbed in the bleeder and breather layers of the vacuum bagging system. Matrix resins are often brittle, and their cure onto the optical fibre causes its fragility, particularly at the vulnerable entry and exit points at the laminate edge.

Excess matrix resin cured onto the fibres is apparent in Fig. 1, as a yellow deposit on the fibres. Fig.1 also illustrates some of the protection methods developed for fibre entry and exit points. Initial efforts were directed towards the use of a structural film adhesive laid into the composite panel edge at the fibre entry and exit points. Adhesives of this type have minimum viscosities several orders of magnitude higher than composite matrix resins during the cure process, and were expected not to flow onto the fibre. Additionally, after cure, adhesives are flexible and tough, and should not embrittle the fiber entry and exit points. However,

0-8194-2165-0/96/$6.00

as can be seen in Fig. 1, the matrix resin flowed around the adhesive and cured onto the fibre, causing embrittlement distant from the entry and exit points. The use of sealed bags of FEP release film around the fibres during the curing process provided protection to the fibres from resin flow, and a clean fibre of this type is apparent in Fig. 2, emerging from an adhesive fillet at the edge of a composite face sheet of a honeycomb cored beam undergoing mechanical test.

Additionally, various trials were made using polymeric sleeves and tubes for local protection of the fibre entry and exit points. These were usually combined with the use of film adhesive, since it was found that, even with close fitting shrunk-on tubing, the low viscosity matrix resin flowed between the sleeve and the fibre, embrittling the fibre. Embedded sleeves of this type are apparent in Fig. 1, and it is clear that resin has flowed around them, embrittling the fibres. Accordingly this solution also required the use of protective FEP film bags during the composite cure process.

These solutions to the problem of entry and exit point embrittlement were adequate for manufacture of test elements by laboratory personnel, but are totally unsuitable for the manufacture of flight components in a production environment. Accordingly, efforts were directed to developing a robust termination method at the laminate edge that would both eliminate the fibre fragility problem, and provide a practical connection method to standard optical fibre cable systems.

A conventional optical fibre plug incorporates a precision ferrule, usually ceramic, into which the fibre is bonded. Following bonding, the ferrule end is polished together with the fibre to provide the required smooth contact surface for low-loss and low-reflection optical signal transmission. The plug housing incorporates a spring for maintaining positive and controlled contact forces between opposing ferrules, and standard fittings are available for plug-to-plug contact. It was decided to attempt to embed fibres within composites following bonding to ferrules and polishing. There were two concerns with this approach, (1) that matrix resin would flow onto the polished ferrule face degrading optical performance, and (2) stresses during the cure process could damage the fibre exit point from the ferrule within the laminate.

The second problem was coped with by a specially designed composite ply build-up at the laminate edge incorporating the ferrule and attached fibre. This build-up also accommodated two embedded stainless steel studs for positive attachment of a conventional fibre optic adaptor to the ferrule. The first problem was coped with by using a precision drilled tooling block during cure to protect the polished ferrule end and to locate and align the studs relative to the ferrule. This tooling block is shown in Fig. 3, together with the cured laminate and the embedded ferrule and studs, and the lack of resin contamination on the ferrule and studs is apparent. The plug adaptor is shown assembled to the ferrule and studs in Fig. 4, ready for connection to a standard optical fibre FC-PC type connector.

X-radiography of the laminate showed that no damage had occurred at the fibre exit points from the embedded ferrules within the ply build-up at the laminate edge. This was confirmed by measurements of optical signal transmission via the embedded fibre.

SUMMARY AND CONCLUSIONS

The developments described herein have led to a practical concept for monitoring instrument attachment to optical fibres embedded in composite materials. The system developed for laboratory use, while satisfactory for test purposes, is impractical for real aircraft parts. The principle of using a standard plug adaptor for connection to an embedded ferrule demonstrated the practicality of a system that is sufficiently robust for use in a production environment. This development is continuing with the aim of developing a multi-point connector that enables one-shot connection to an embedded optical fibre array within a laminate.

ACKNOWLEDGMENTS

The authors acknowledge the financial support of the Directorate of Defense R&D, Israel Ministry of Defense, and the technical input to the overall program of Prof. M. Tur of Tel-Aviv University, Dr. S. Gali, Dr. D. Shalev and Mrs. G. Gilai of the Advanced Structures Group of the IAI Engineering Division and Mr. T. Inbar of Soreq NRC.

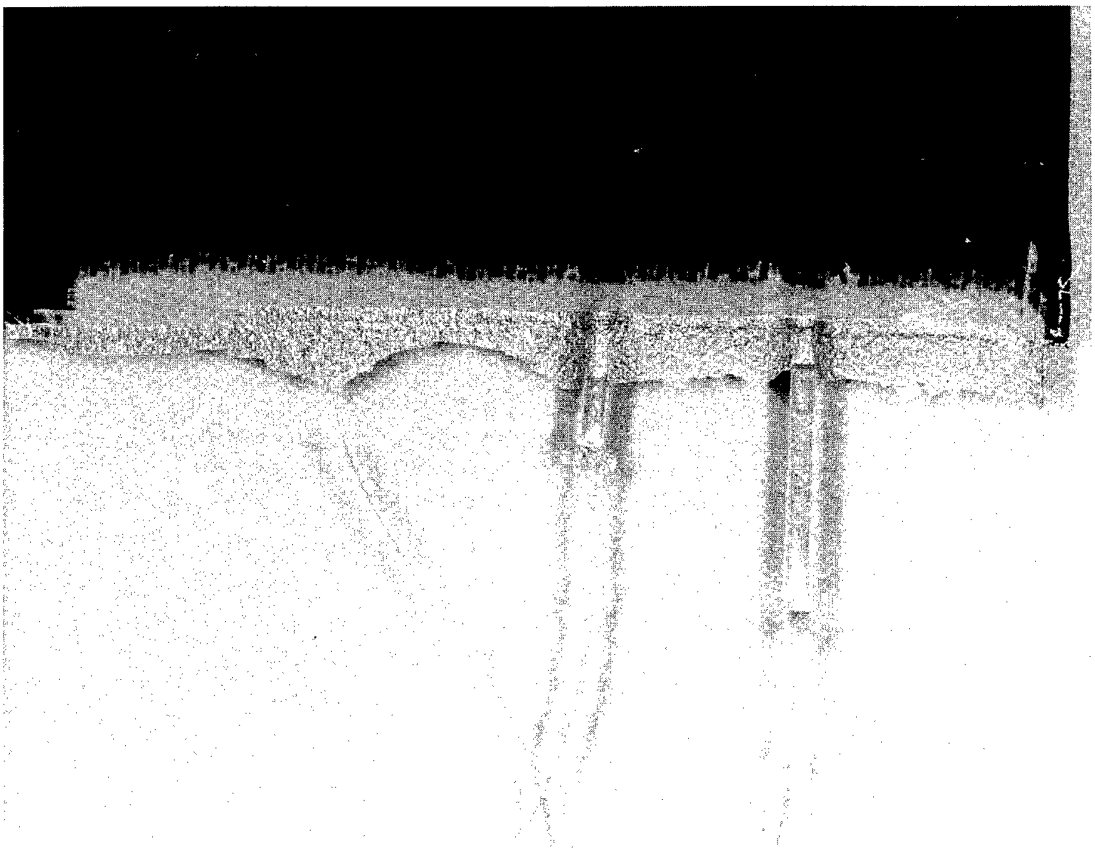


Fig. 1 Optical fibre protection methods at laminate entry and exit points. Note excess resin flow onto fibers

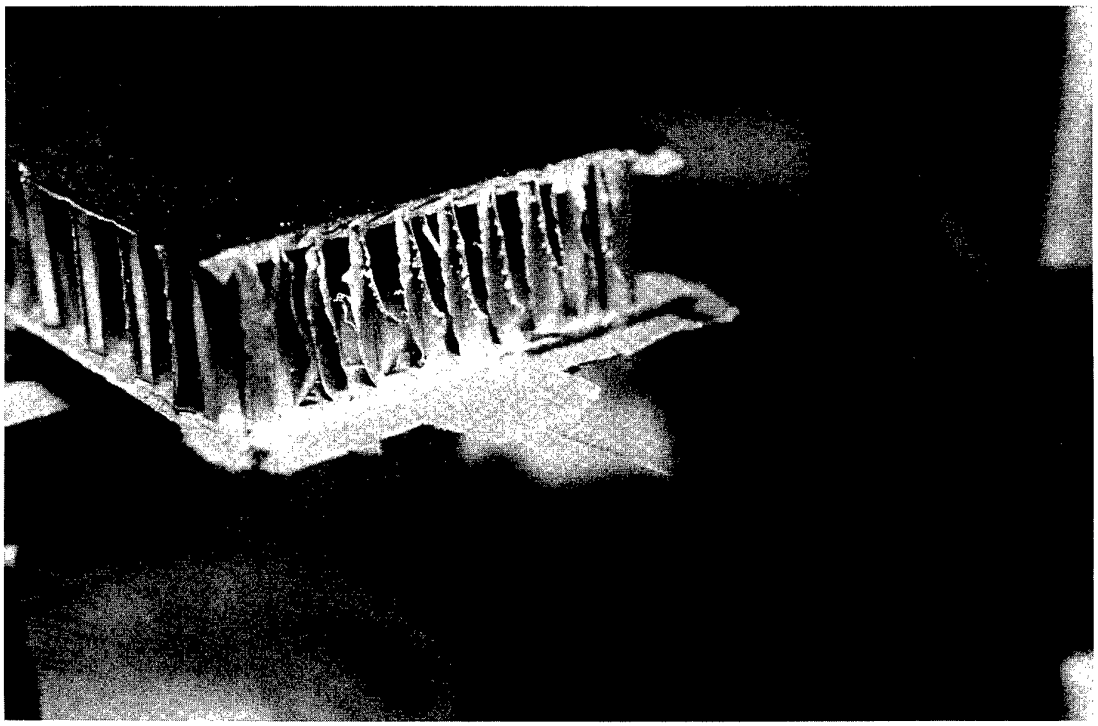


Fig. 2 Beam Test Element incorporating optical fibres into face skin

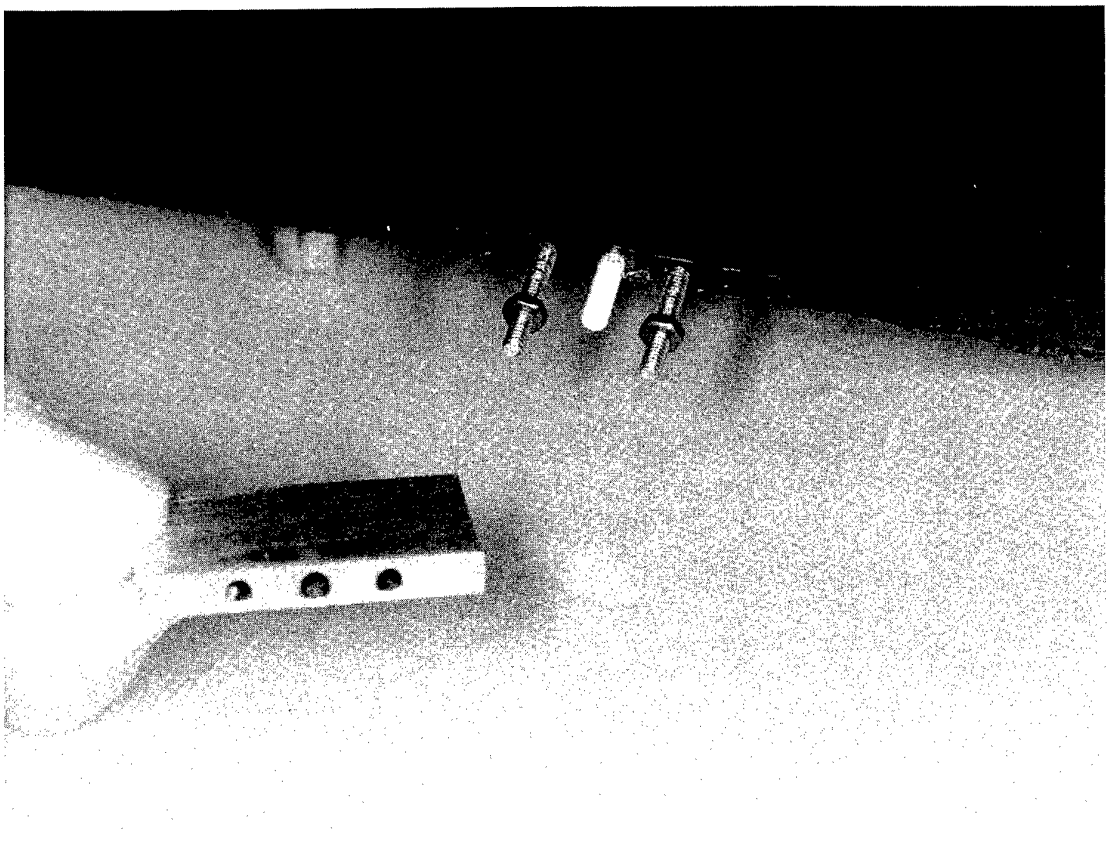


Fig. 3 Tooling block and embedded ferrule

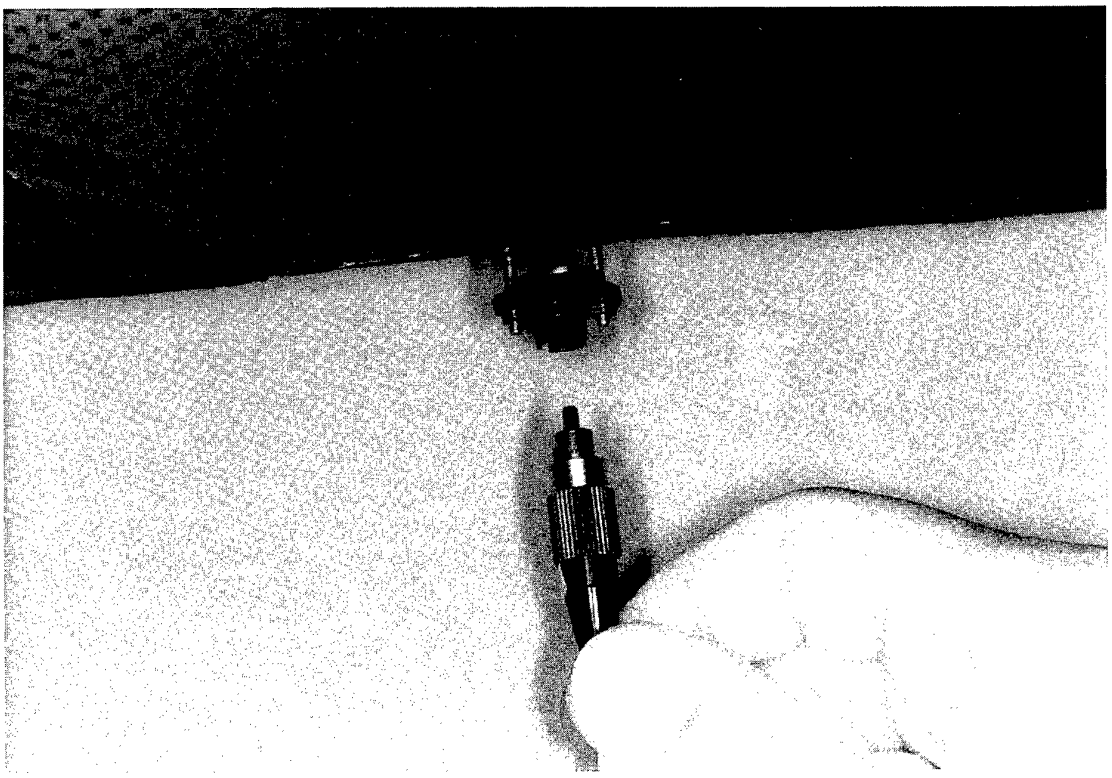


Fig. 4 Optical plug connector assembled onto laminate

Strain and Failure Sensing by the Fiber Optic Michelson Sensor Embedded in Composite Beam

C. S. Hong, I. B. Kwon, C. G. Kim

ABSTRACT

The bending deformation and matrix cracking were investigated by conducting a four-point bending test for a cross-ply composite beam with an embedded fiber optic Michelson sensor. The fiber optic Michelson interferometric sensor was constructed and embedded in the composite beam. The failure of composite beam, due to the matrix cracking, was successfully detected by the fiber optic sensor and the matrix crack in the composite beam was confirmed by an edge replica method. The characteristics of the failure signals from the fiber optic sensor were studied. The strain and failure signals of the composite beam were separated by digital filtering of the signal from the fiber optic sensor. The failure was obviously detectable by the failure signal filtered from the optical signal.

INTRODUCTION

Aerospace composite structures are damaged by external effects such as excessive design load, impact load and fatigue load, etc. These defects degrade the integrity of the composite structures. For assuring the structural integrity, it is desirable to do the real-time health monitoring of composite structures[1]. Fiber optic sensors have many advantages in that they are easy to embed in composites, they are very sensitive[2], and they can give several informations from one probe. The matrix cracking failure of composites is the initial failure mode and it decreases the stiffness and strength of composite structures[3]. Therefore it is very important to sense simultaneously the internal strain and matrix cracking failure of composite structures in order to evaluate the structural integrity.

In this paper, the failure and internal strain of a cross ply laminated composite beam with an embedded fiber optic Michelson sensor were sensed by conducting a four point flexural beam test. The characteristics of the failure signal from the fiber optic sensor were investigated. The internal strain and failure strain of the composite beam were obtained by digital filtering from one fiber optic sensor signal.

PRINCIPLE OF FIBER OPTIC MICHELSON SENSOR

If single mode optical fiber is deformed, the phase is shifted for the light propagating in optical fiber. The phase shift $\Delta\phi$ of the light propagating in optical fiber which is in 3-dimensional strain field under the fiber axial loading is as follows[4].

$$\frac{\Delta\phi}{(\Delta L+\delta)}=\frac{4\pi n}{\lambda_0}\left\{1-\frac{n^2}{2}[P_{12}-\nu(P_{11}+P_{12})]\right\} \tag{1}$$

where n is the refractive index of optical fiber and λ_0 is the wavelength of the light in vacuum condition. P_{ij} is the strain-optic tensor of optical fiber. In the case of the homogeneous optical fiber, non-zero components in strain-optic tensor are only P_{11} and P_{12}. In this study, the light source of the fiber optic sensor system is He-Ne laser with a wavelength in vacuum of 632.8nm. The refractive index n of 3M single mode optical fiber is 1.456. Poisson's ratio ν of the optical fiber is 0.17. The values of P_{11} and P_{12} are 0.121 and 0.270, respectively. Putting these values in Eq. (1), the right hand side of Eq. (1) is 2.309×10^7. But the right hand side of Eq. (1) was determined to be 2.319×10^7 from the tensile test of composite embedded with fiber optic Michelson sensor[5].

$$\frac{\Delta\phi}{(\Delta L+\delta)}=2.319\times10^7\,(rad/m) \tag{2}$$

In the above Eq. (2), ΔL is the length change of the embedded optical fiber according to the static structural deformation and δ is the length change of the optical fiber according to the rapid deformation propagation when the structures are failed. If m is the number of the half wave of optical fiber sensor signal then the phase shift $\Delta\phi$ can be written with $m\pi$. Also, when the gage length of optical fiber sensor is L, the strain ε of optical fiber is $\Delta L/L$, therefore the Eq. (2) is as follows.

Dept. of Aerospace Engineering, Korea Advanced Institute of Science and Technology, Taejon, Korea

0-8194-2165-0/96/$6.00

$$\varepsilon = \frac{m\pi}{2.319 \times 10^{7} L} = 1.355 \times 10^{-7} \frac{m}{L} \quad (3)$$

In Eq. (3), when L is 1cm and m is 1, the strain of optical fiber ε is 13.6 x 10^{-6}. Therefore the fiber optic Michelson sensor is very sensitive to detect the strain and failure of composites even by counting the number of half wave of the signal.

EXPERIMENTS

1. Fabrication of the composite beam embedded with the fiber optic sensor

The cross section of the optical fiber was coated with pure gold using a vacuum evaporation method in order to reflect the light propagating in the optical fiber. The gage length of the optical fiber, which was the length difference of the two optical fibers, was measured by PIKA microscope having a resolution of 1/100mm. After manufacturing the fiber optic sensor, this sensor was embedded in the composite beam as shown in Fig. 1. The dimensions of the flexural beam specimen made of CU-125NS (Hankook Carbon Co.) graphite/epoxy prepreg are shown in Table 1. The laminate stacking sequence was chosen as $[90_4/0_4]_s$ to accelerate the matrix cracking failure of composites. The specimen dimensions were determined according to ASTM D790M : 100mm specimen length, 80mm span length and 40mm load span. The optical fiber sensor was embedded either above the neutral plane or bellow the neutral plane of the composite beam as shown in Table 1. The electric strain gage was attached on the top surface of the composite beam to compare with the internal strain from the fiber optic sensor as shown in Fig. 2. Also the side of composite beams was polished to acquire the failure image of the composite beam by the edge replica method.

2. Experimental device and procedure

In this experiment, we used a 10mW Meles-Griot He-Ne laser, a Newport F-506B coupler and 3M FS-SN-3224 single mode optical fiber. 20X microscope and micro-translator were used to transmit the laser light into the optical fiber. The received fiber optic signal by Newport model 818SL photodetector in fiber optic sensor system was amplified by a DANTEC 56N20 amplifier and was transmitted to a Tektronix TDS-420 digital storage oscilloscope as shown in Fig. 3. The electric strain gage signal and load transducer signal were acquired by a digital storage oscilloscope and all signals were stored in a PC through GPIB. A four point bending test was performed using a 10 ton INSTRON model 1350 static test machine. When the failure of the composite beam occurred, the failure signal was always triggered by the digital storage oscilloscope and was stored in a PC after holding a INSTRON machine in order to investigate the characteristics of the failure signal. To confirm the failure mode in composite beam, the image of the side of composite beam was taken by the edge replica method with holding a INSTRON machine when the failure of composite beam was saturated. The digital filtering of the fiber optic sensor signal was performed by MATLAB to detect the failure instant and measure the internal strain of composite beam.

EXPERIMENTAL RESULTS AND DISCUSSION

The edge replica of specimen is matrix cracked shown in Fig. 4. The obtained failure signals that was triggered by the matrix cracking in an oscilloscope directly when the failure happened are shown in Fig. 5. The amplitude of the initial failure signal was usually bigger than the other failure signals and the time span of the failure signals were about 100mili-seconds. The frequency spectra of typical failure signals are shown in Fig. 6. The frequency range of the failure signals was 0-450Hz. The characteristics of failure signals of the other specimens were just similar to those shown in Fig. 5 and 6. Therefore the signal from the fiber optic sensor digitally recorded in the time interval of 10 mili-seconds to get the strain and failure signals by digital filtering from this signal. The signals from the fiber optic sensor and the strain from the electric strain gage were shown in Fig. 7. The signal has drift, noise and beating which was the disadvantages of fiber optic Michelson sensor. However, the signal was still possibly used to determne the internal strain and failure signal by digital filtering. Low pass digital filtering was performed with 1 Hz cut-off frequency to get the signal to convert the internal strain of composite beam and high pass digital filtering was performed with 7 Hz cut-off frequency to separate the failure signal from fiber optic sensor signal in Fig. 7. The internal strain was converted from the signal after low pass filtering and the failure signal was obtained after high pass filtering. The strain of electric strain gage and digitally filtered signals with the internal strain from the fiber optic sensor signal are compared in Fig. 8. Fig. 8 shows that the failure instant and internal strain of the composite beam could be sensed by digital filtering from one fiber optic Michelson sensor. The initial failure strain of composite beam was determined

when the high passed failure signal of the fiber optic sensor showed abruptly large intensity, and summarized in Table 2.

CONCLUSION

The internal strain and matrix cracking failure were investigated by a four point bending test of the composite laminated beam with an embedded fiber optic Michelson sensor. The characteristics of the failure signal were studied for the fiber optic Michelson sensor. The fiber optic signal was processed to yield an internal strain signal by low pass filtering, and to give a failure signal by high pass filtering. The initial matrix cracking was identified by an abrupt change in intensity of the high passed signal, i.e. failure signal. The amplitude of the first failure signal was bigger than that of the later failure signals. The time interval was 100mili-seconds and the frequency ranged up to 450Hz. The internal strain and failure instant of the composite beam were sensed by digital filtering from one fiber optic Michelson sensor signal.

ACKNOWLEDGMENT

This work has been supported by Korea Science and Engineering Foundation (KOSEF). The authors gratefully acknowledge this support.

REFERENCES

1. T. G. Geradi, "Health Monitoring Aircraft." US-Japan Workshop on Smart/Intelligent Materials and Systems, Honolulu, Hawaii, March, 1990 pp. 82-93.

2. R. O. Claus, "Optical Fiber Sensors for Smart Materials Characterization." Proc. of the Second International Conference on Intelligent Materials, Colonial Williamsburg, Virginia, USA, June, 1994, pp 384-390.

3. S. G. Lim and C. S. Hong, "Prediction of Transverse Cracking and Stiffness Reduction in Cross - ply Laminated Composites." Journal of Composite Materials, Vol. 23, July 1989, pp. 695-713.

4. J. S. Sirkis and H. W. Haslach, "Complete Phase-strain model for structurally embedded optical fiber sensors." J. of Intelligent Material Systems and Structures, Vol. 2, Jan. 1991, pp. 3-24.

5. J. W. Park, "Strain Measurement in Composite Laminate Using a Fiber Optic Sensor." MS Thesis, Dept. of Aerospace Engineering, Korea Advanced Institute of Science and Technology, 1994.

Table 1. Specimens of composite beam with embedded fiber optic Michelson sensor

Specimen / Lay-up	Thickness / Width (mm)	Gage length (mm)
T1/ $[90_4/0_2/\{0\}/0_6/90_4]_T$	1.77 / 20.60	15.06
T2 / $[90_4/0_2/\{0\}/0_6/90_4]_T$	1.76 / 20.70	15.22
B1 / $[90_4/0_6/\{0\}/0_2/90_4]_T$	1.78 / 23.28	18.02
B2 / $[90_4/0_6/\{0\}/0_2/90_4]_T$	1.78 / 21.95	13.58

Table 2. Initial failure strain of composite beam

Specimen	Initial failure strain by strain gage, ε_{SG} (%)	Initial failure strain by optical fiber, ε_{OF} (%)
T1	0.41	0.065
T2	0.43	0.061
B1	0.41	0.075

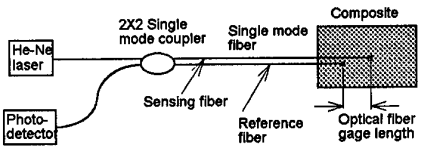


Fig. 1 Fiber optic Michelson interferometric sensor.

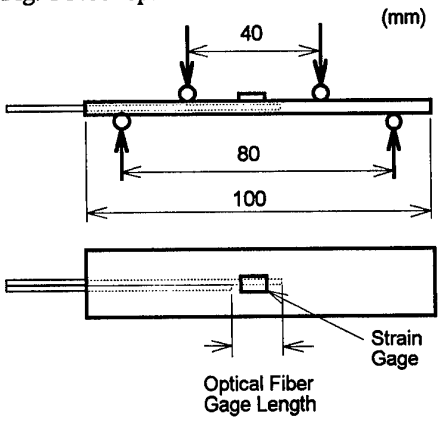
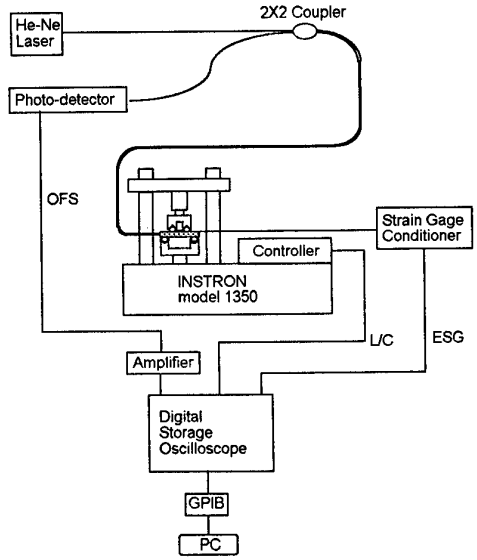


Fig. 2 Specimen configuration of Gr/Ep composite beam embedded with fiber optic Michelson sensor.



OFS : Optical fiber sensor signal
ESG : Electric strain gage signal
L/C : Load cell signal

Fig. 3 Experimental setup for 4 point bending test of smart composite beam.

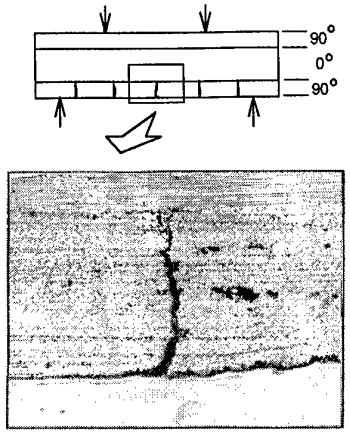


Fig. 4 Matrix cracking failure of $[90_4/0_4]_s$ Gr/Ep composite beam (T1).

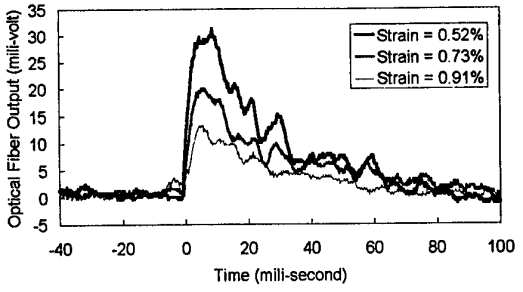


Fig. 5 Failure signal of $[90_4/0_6/\{0\}/0_2/90_4]_T$ Gr/Ep composite beam (B2).

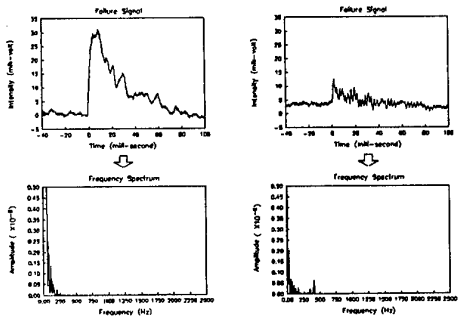


Fig. 6 Frequency spectrum of matrix cracking failure signal of $[90_4/0_6/\{0\}/0_2/90_4]_T$ Gr/Ep composite beam (B2).

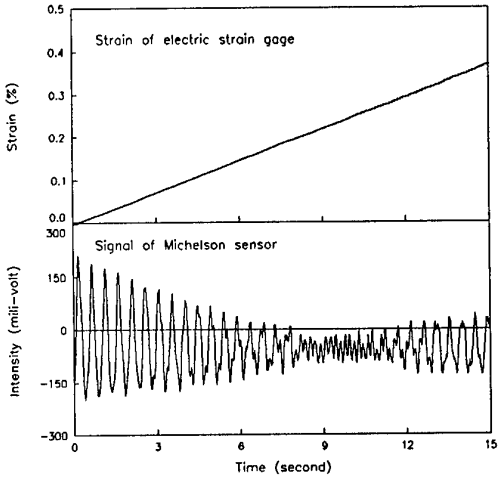


Fig. 7 Fiber optic Michelson sensor signal of $[90_4/0_2/\{0\}/0_6/90_4]_T$ Gr/Ep composite beam (T1).

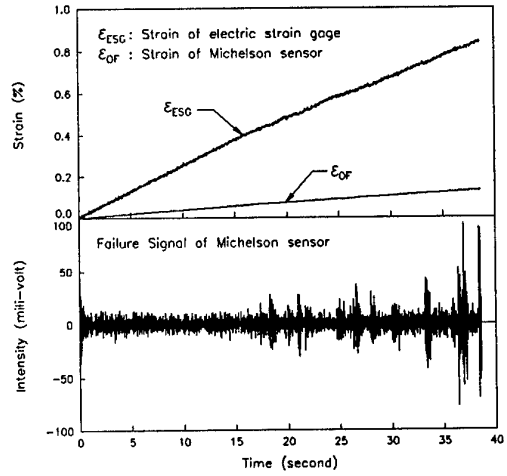


Fig. 8 Failure signal of fiber optic Michelson sensor of $[90_4/0_2/\{0\}/0_6/90_4]_T$ Gr/Ep composite beam (T1).

Fatigue strength of glass reinforced polyester (GRP) laminates with embedded optical fibers

Alfredo Güemes and José M. Menéndez

Universidad Politécnica de Madrid
E.T.S. Ingenieros Aeronáuticos, 28040 Madrid, Spain.

ABSTRACT

The effect of embedded optical fibers on the static and fatigue interlaminar shear strength of a glass reinforced polyester laminate is evaluated. Seventy identical specimens with and without embedded optical fibers were tested reaching more than 500,000 cycles in some cases; It was found that the optical fiber does not have a negative influence on the laminate, neither static nor in fatigue. These tests were included into a project to develop smart wind turbine blades.

1. INTRODUCTION

This work is included into a larger project attempting to develop smart wind turbine blades (WTB). WTBs are a kind of severely stressed, hardly inspectable structures, so they would greatly benefit from a permanent damage monitoring system.

Blade failure use to be really catastrophic, flying away part of the blade, and use to happen by fatigue growth of undetected damages produced by overloading. Design need to be conservative; if feasibility of the blade is increased, costs of the whole system could be cut significantly.

The proposed system would make use of white light interferometry, with the aim of measuring the loss of stiffness that usually precedes to the blade failure. White light interferometry has many advantages for this application: it is a cheap procedure, because only standard single mode optical fibre is needed; sensing region is distributed along the fiber length; contrary to intensity based sensors, the signal does not suffer from drifting with time or aging of the fiber. The procedure has been suggested for long term monitoring of civil structures[1].

Our scheme (Fig. 1) is essentially the same as those proposed, a Michelson interferometer, but differs in two concepts: First, we can control the external load of the structure during the test; by rotating the blade, the sign of the load is changed. Second, we are no interested into absolute measurement of displacement, but in stiffness, that is, changes in the difference of the length of two opposing fibers consequently to a change of loading. In this sense, the problem is much easier.

Optical fibers are easily embedded into the laminate during its manufacturing. Its typical diameter of 250 μm, coating included, is in the order of magnitude of the laminate thickness, so they create a local perturbation, whose severity depends on the relative orientation between the optical fibre and the fibers of the adjacent layers. Static tests on composites with embedded optical fibers[2] reflect a minimal effect when optical fibers are collinear. Only two references were found concerning fatigue behavior[3,6] and the results were rather disappointing; fatigue life of the composite specimen was halved by the presence of an optical fiber, and the optical fiber itself breaks very early under cycling loads. If this behavior where confirmed, the system would be ineffective.

Failure in composites is closely related to the nature of the fiber and the matrix. A qualification program has been started on E-glass/polyester resin, the materials commonly employed in wind turbine blades. The program includes tension, compression and interlaminar shear tests, in specimens with and without embedded optical fibers, under static and fatigue loading.

At the time of writing this paper, the interlaminar shear strength tests were completed, and contrary to the results previously reported, they showed a very benign behavior by the presence of optical fibers.

0-8194-2165-0/96/$6.00

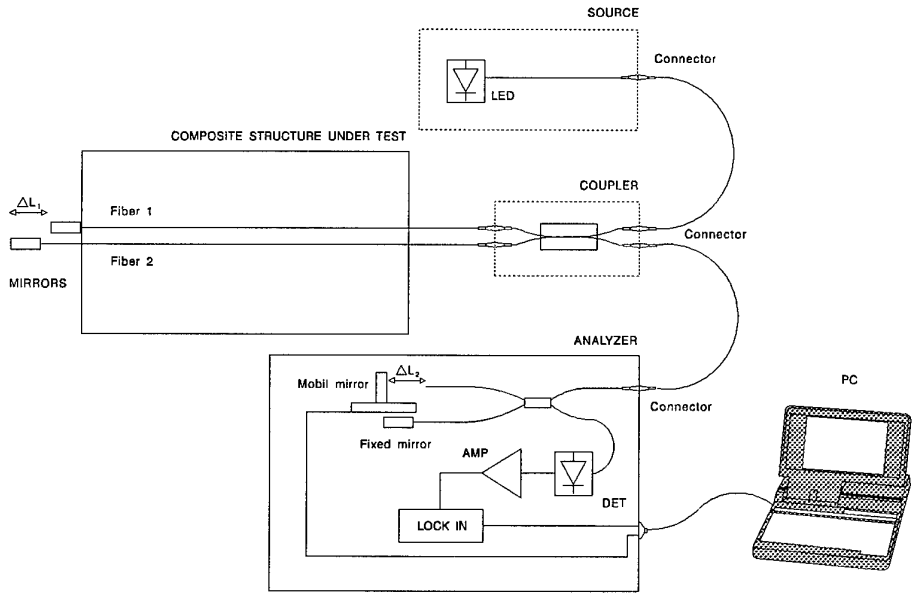


Fig. 1. Scheme of permanent monitoring system.

2. MATERIALS AND EXPERIMENTAL METHODS

The specimens tested were short beams cut from a flat laminate manufactured by wet lay-up. Materials used were E-glass unidirectional cloths (Vetrotex 420 gr/m^2) and a conventional isoftalic polyester resin (Cronolite 1112) catalyzed with benzoyl peroxide (0.5% by weight), for curing at 100 Celsius degrees and 3 KPa. The stacking sequence of all the specimens is $[0]_{16}$ (16 unidirectional plies oriented at 0). Newport single mode optical fibers, with and without the acrylate coating, were included at the midplane of the laminate, perpendicular to the reinforcing fibers. Fiber volume was quite uniform, with an average value of 58.28% (standard deviation of 1.87). Porosity was low (an average value of 1.41% and a deviation of 1.41). General configuration of specimens and location of optic fiber is shown in Fig. 2.

Tree different kind of test were run, all of them on a MTS 810 servo-hydraulic test machine. First, static tests were carried out on 15 specimens according ASTM-D-2344 standard test method for apparent interlaminar shear strength of parallel fiber composites, getting apparent horizontal shear strength and stiffness curve of each specimen.

Second, 20 specimens were tested for loss of stiffness and residual strength after fatigue loading during 200,000 and 300,000 cycles respectively under a sinusoidal load (with a frequency of 3Hz, stress ratio, R, was 0, and a maximum stress 50% of average static strength).

The remaining 35 specimens were tested for fatigue life, with load levels between 60% and 82% of the static strength, R=0 and a frequency of 15 Hz (up to 25 Hz, frequency has shown not to be an important factor). In each group, for every 5 specimens, 3 were plain, one with a coated optical fiber, and the other with an uncoated optical fiber. The specimens were quite uniform in every other sense.

Stiffness was measured regularly and specimens were considered to fail if stiffness drops by more than 20%.

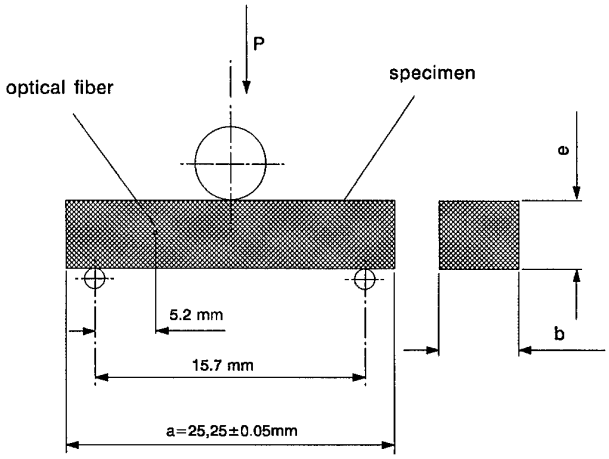


Fig. 2. General configuration of specimens

3. RESULTS AND DISCUSSION

Static strength results are shown in Table 1. Contrary to what could be thought, although the optical fibers were embedded in a configuration that was assumed to represent the most harmful case, the presence of the optical fiber does not reduce the interlaminar shear strength of laminate, but even these specimens seems to have improved behavior. This results could be considered surprising, but similar results were previously reported by Measures et al.[4], showing a slight improvement in the mechanical properties of Kevlar-epoxy laminates.

GROUP	SPECIMEN	e (mm)	b (mm)	P (KN)	S_H (MPa)
1	SF1	4.13	5.89	-0.767	23.7
	SF2	4.10	5.93	-0.774	23.9
	SF3	4.01	5.96	-0.700	22.0
	FC	4.26	5.99	-0.943	27.7
	FS	4.20	5.85	-0.853	26.0
2	SF1	4.13	5.90	-0.889	27.4
	SF2	4.12	5.77	-0.764	24.1
	SF3	4.01	5.74	-0.794	25.9
	FC	4.28	5.98	-0.943	27.6
	FS	4.26	5.90	-0.853	25.5
3	SF1	4.15	5.89	-0.839	25.7
	SF2	4.07	5.93	-0.788	24.5
	SF3	4.03	5.96	-0.773	24.1
	FC	4.28	5.85	-0.931	27.9
	FS	4.26	5.84	-0.868	26.2

Table 1. Dimensions and Interlaminar Shear Strength of specimens statically tested.

In agreement with well-known behavior of composite laminates under fatigue loading[5], called sudden death, the residual strength and stiffness after cycling were found not to differ significantly from the static values, even after cycling near failure, and the optical fiber does not make any difference.

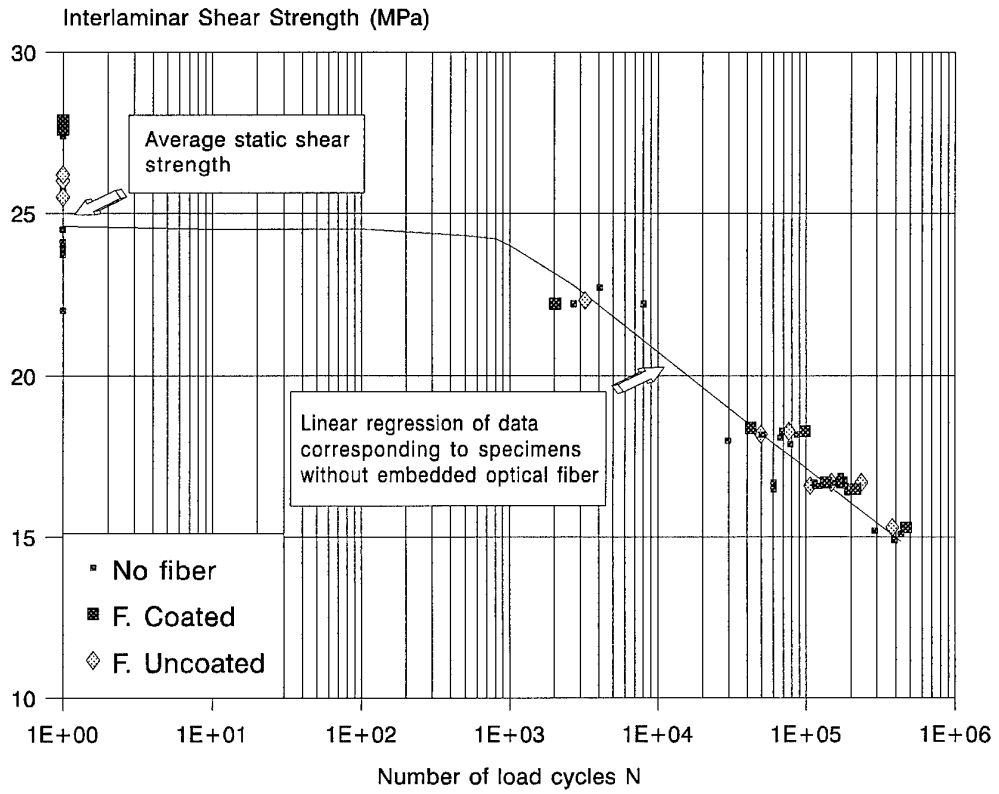


Fig. 3. S/N curves of specimens with and without optical fiber.

Results obtained from the last group of tests where more revealing. The logarithm of the number of cycles to failure increase linearly when decreasing the maximum stress level, a behavior that agress with many others published results. Not significant differences in life under fatigue stress has been revealed after this tests, as shown in Fig. 3. It is easily observable that the deviation of the data corresponding to specimens with optical fiber embedded with regard to the estimated linear regression of data calculated for the specimens without optical fiber is negligible. Even a slightly improvement could be denoted, mainly for low level loads, but the small amount of specimens tested and the characteristic scatter of fatigue life data not allow to reach any decisive conclusion in the matter.

Fig. 4 shows a negative of a micrograph of a broken specimen after fatigue, using rear illumination. Shear bands failures are observed at the opposite site of the position of the optical fiber, also illuminated.

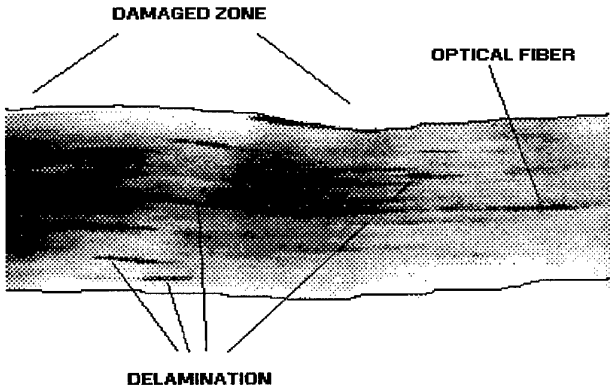


Fig. 4. Negative of a micrograph of a broken specimen after cycling.

4. CONCLUSIONS

Literature search indicated that embedding optical fibers into composites promoted a significant decrease in the fatigue strength of the composite and in the life of the optical fiber itself. This would be a serious handicap for the industrial applications of optical fiber smart structures.

Our first results show that those conclusions were far from being universally valid for every kind of composites and test conditions. For glass reinforced polyester, tested for interlaminar shear strength, the optical fiber does not show any deleterious influence.

Tests are on progress for tensile and compressive properties under fatigue loading.

5. REFERENCES

1. A. Elamari, J. Breguet, N. Ggisin, "Low Coherence Fiber Optic Sensors for Structural Monitoring", *Structural Engineering International*, Vol. 5, N° 1, Feb. 1995.
2. D. W. Jensen, J. S. Sirkis, "Integrity of Composite Structures with Embedded Optical Fibers", *Fiber Optic Smart Structures*, Chp. 5, Eric Udd, Wiley Interscience, New York, 1994.
3. D. C. Lee, J. J. Lee, "Fatigue Behavior of Composite Structures with Embedded Optical Fiber Sensors", *10th International Conference on Composite Material*, Vol. 5, pp. 307-314, Vancouver, 1995.
4. R. M. Measures, N. D. W. Glossop, J. Lymer, M. LeBlanc, J. West, S. Dubois, W. Tsaw, and R. C. Tennyson, "Structurally Integrated Fiber Optic Damage Asessment System for Composite Materials", *Appl. Opt.* 28, 2626-2633, 1989.
5. H. W. Bergmann, R. Prinz, "Fatigue Life Estimation of Graphite/Epoxy Laminates under Consideration of Delamination Growth", *International Journal for Numerical Methods in Engineering*, Vol. 27, 323-341, 1989.
6. D. W. Jensen, D. Brzenchek, "Fatigue of a Composite Laminate with Embedded Optical Fibers". *Proc. Int. Congr. Exp. Mech. Soc. Exp. Mech. 7th*, 1992, Vol. 2, pp. 1319-1325, 1992.

Examination of reliability of fibre optic sensors embedded in carbon/epoxy composites

K. Levin & S. Nilsson
FFA (The Aeronautical Research Institute of Sweden), Box 11021, S-161 11, Sweden

ABSTRACT

One of the most important tasks in achieving a reliable performance of embedded optical fibre sensors in aircraft health monitoring and usage systems is to clarify the their function reliability. In this study the limit of reliable sensor function is addressed for a number of loading conditions at room temperature.

For static tensile loading the function strain limit for EFPI-sensors was approximately 0.20%, whereas the function limit of embedded Bragg grating sensors was above the strain level (0.4-0.5%) for initiation of matrix cracking in the laminate. In compression the function of the EFPI-sensor was unimpaired to a strain level which was about four times larger than that in tension. In constant amplitude fatigue loading the function strain limit of the EFPI-sensor was similar to that in static tensile loading, i.e. 0.20% at 10^5 cycles. The silica glass/polyimide coating interface in the EFPI-sensor was identified as the sites where failure was initiated. The finite element analysis showed that the effects of curing stresses and moisture in laminates have significant influence on the function reliability of sensors. The stress concentrations on the interface caused by the cavity in the EFPI-sensor are the main reason for the lower reliability obtained for the EFPI-sensor than for embedded Bragg grating sensors.

1. INTRODUCTION

Of large concern is the function reliability of fibre optic sensors embedded in composite materials. A number of different loading and environmental conditions is expected to affect the limit of sensor function[1,2]. To have a reliable sensor system the transference of stresses from the composite to the fibre optic sensor through the interface are crucial, in addition to the strength of the fibre optics. Therefore, the reliability is closely connected to the interfacial adhesion between the optical fibre and composite material system. However the sensor performance is affected not only by the strength of the adhesion but it is also governed by the local stress state in the composite.

Two sensors are candidates for use in aircraft health monitoring and usage systems. These are the Bragg grating sensor [3,4] and the extrinsic Fabry-Perot interferometer, EFPI, sensor[5]. The Bragg grating sensor, used as an interferometer, consisted of two periodic modulations which were wavelength selective in the fibre core. The EFPI-sensor consists of an air gap between the two reflective optical fibre ends. An improved EFPI-sensor has been developed [6] which is tailored to reduce the effect of the geometrical mismatch between the sensor and the composite material.

There are a great interest to both experimentally determine the function limits for fibre optic sensors and in refining the methodology of predicting thermo-mechanical stresses and failure in the sensor region. In this study the sensor function reliability is addressed for loading condition typical for aircraft structure. Laminates with a centrally or a surface embedded EFPI- and Bragg grating sensors were evaluated. In order to quantitatively determine the failure strain, the failure mechanisms and locations in the finite element analysis, different failure criteria have been applied in conjunction to the calculated three-dimensional stress field. To further improve the numerical analyses additional stresses from temperature and moisture have been included in the analysis.

2. EXPERIMENTS

2.1 Specimen manufacturing and geometry

Laminates were fabricated from Ciba-Geigy carbon fibre epoxy prepreg HTA/6376C with embedded fibre optic sensors and cured in autoclave at 180°C and 0.6 MPa for 2 hours. The prepreg stacks were laminated as 20-plies $(0_2/90_2/0_2/90_2/0_2)_S$ panels. Each ply was 0.127 mm thick for the nominal fibre volume content of 65 %. The EFPI-sensors were embedded at two different depths, either at the centre of the thickness or at the surface, whereas the Bragg grating sensors only were embedded in the centre. The embedded sensors did in all cases coincide with the fibre direction of the 0°-plies.

The specimens had the dimensions of 200 by 24 mm. The specimens length between the grips was 120 mm with the optical

0-8194-2165-0/96/$6.00

sensor embedded at the centre. At the ends of the specimen, tabs were attached. Subsequently, axial strain gauges with 2 mm gauge length were mounted on the centre section of the specimens to measure the strain level at the sensor position. At the specimens with surface-embedded sensors two strain gauges were mounted at both sides of the sensor and one directly at the opposite side of the specimen. Two strain gauges were attached at each surface of the specimens with the centre-embedded sensors.

2.2 Sensor geometry

The geometry of the EFPI-sensor is shown in Fig. 1 including a 3 μm thick polyimide coating. The sensor is fused in both ends, the thickness of the sensor is the same as of the optical fibre and the end of the sensor is tapered. The design and manufacturing of the improved sensor are further presented in [6]. The geometry of Bragg grating sensor is identical to the geometry of the optical fibre. The gauge length was approximately 80 mm.

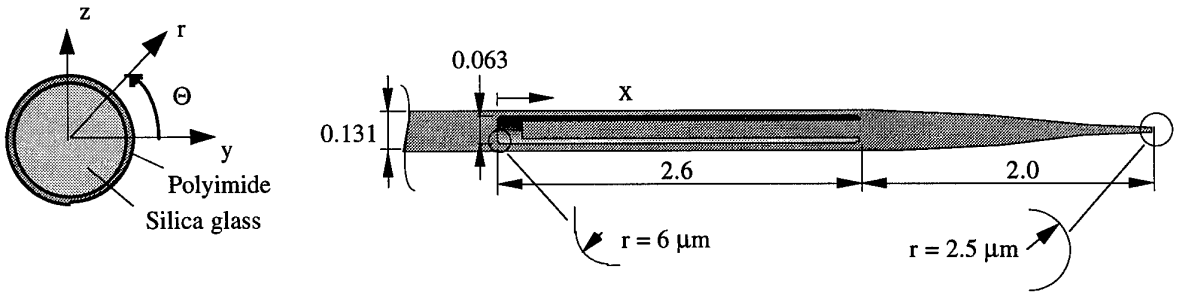


Fig. 1 Geometry of the sensor. including the coating Dimensions in mm.

2.3 Experimental procedure

In the test matrix both the effect of static tensile, compressive loading and fatigue loading at room temperature/laboratory condition on the fibre optic sensor are included. In the static compression tests, the specimens were supported using a pair of anti-buckling plates with a 40mm by 20mm cut-out. The constant amplitude fatigue testing was running at the stress ratio R=0.02 excluding compression loads and at a frequency of 1Hz. After 100000 cycles the fatigue testing was interrupted. During static testing the output from the load cell, the strain gauges and the separated DC/low-frequency (<10kHz) signal from fibre optic sensor support system, FiberMetrics Phase Demodulation Unit, were collected.
For the data acquisition during the fatigue loading a 300MHz digital oscilloscope was used to collect the data with a sample rate of 1MHz from the load cell and, the DC-output from the fibre optic sensor support system. During the first 1000 cycles data for each second cycle was collected. At number of cycles larger than 1000, typically the data for each hundredth cycle were collected. The data from the oscilloscope were successively transferred during the fatigue testing to a computer for further data processing.

3 FINITE ELEMENT MODELS

The finite element program used, called STRIPE, is based on the *p*-version of the finite element method [7] The polynomial order of the basis functions can be increased to achieve a solution with the desired accuracy with respect to discretization errors. Two FE-meshes of the specimens were created to permit the stresses in the sensor and the surrounding materials to be analysed. The load was applied as a uniform displacement in the length direction. The stress state for the Bragg grating sensors was analysed in the same model as that for the EFPI-sensors, determining the stress field at a location several fibre diameters from the EFPI-sensor. The stress field was checked at a number of positions along the optical fibre to ensure that the stress/strength ratios were the same at these positions. Perfect bonding between the sensor, the coating and the composite material was assumed. Material data used in the analyses were: for the composite material;E_{11}=145 GPa, $E_{22}=E_{33}$= 10.5 GPa, $G_{12}=G_{13}$=5.25 GPa, G_{23}=3.3 GPa, $\nu_{12}=\nu_{13}$=0.3, ν_{32}=0.6, $\alpha_{1,comp}=-0.2\cdot10^{-7}$ C^{-1}, $\alpha_{2,comp}=\alpha_{3,comp}=28\cdot10^{-6}$ C^{-1}, $\beta_{1,comp}$=0 $\%^{-1}$, $\beta_{2,comp}=\beta_{3,comp}$ =0.343 $\%^{-1}$[8] and for the silica glass and polyimide coating; E_{glass}=70 GPa, ν_{glass}=0.16, $\alpha_{glass}=3.9\cdot10^{-7}$ C^{-1}, β_{glass}=0 $\%^{-1}$ and E_{pi}=3 GPa, ν_{pi}=0.3, $\alpha_{pi}=40\cdot10^{-6}$ C^{-1}, β_{pi}=0.143 $\%^{-1}$[8].

4. FAILURE CRITERIA

The stress/strength ratios in the silica glass and polyimide coating were determined using the failure strengths for silica glass σglass=6000 MPa[9] and polyimide σpi=131 MPa[10]. From the consideration that the load direction corresponded

to the fibre direction in the ply with the embedded sensor, the tensile fibre failure criterion,

$$R^2 = \left(\sigma_{xx}{}^2 / X^2\right) + (\sigma_{xy}{}^2 + \sigma_{xz}{}^2) / S^2, \quad (1)$$

and the tensile and compressive matrix failure criteria,

$$R^2 = (\sigma_{yy} + \sigma_{zz})^2 / Y^2 + (\sigma_{yz}{}^2 - \sigma_{yy} \cdot \sigma_{zz}) / S^2 + (\sigma_{xy}{}^2 + \sigma_{xz})^2 / S^2 \quad (2)$$

and

$$(\frac{(\sigma_{22} + \sigma_{33})^2}{4S^2} + \frac{(\sigma_{23}{}^2 - \sigma_{22}\sigma_{33})}{S^2} + \frac{(\sigma_{12}{}^2 - \sigma_{13}{}^2)}{S^2})(1/R)^2 + (\frac{(\sigma_{22} + \sigma_{33})}{Y'}((\frac{Y'}{2S})^2 - 1)(1/R) = 1 \quad (3)$$

respectively, given by Hashin [11] were applied where R, X, Y, Y' and S denote the stress/strength ratio, tensile strength parallel and perpendicular to the fibre direction, compressive strength perpendicular to the fibre direction and shear strength respectively. The stress/strength ratio indicates the margin to failure for the predicted failure mode. Failure occurs when R = 1. In this analysis, the strength values were X = 2090 MPa, Y=112 MPa, Y'=346 MPa and S = 131 MPa [12].

The average values of the continuous stresses across the interfaces were calculated at points close to the interfaces. These average values were used in the failure criterion:

$$R_{int}{}^2 = \left(\sigma_{rr} / Y_{int}\right)^2 + \left(\sigma_{r\theta}{}^2 + \sigma_{xr}{}^2\right) / S_{int}{}^2 \quad (4)$$

where R_{int}, Y_{int} and S_{int} are the stress/strength ratio in the interface, the interface tensile and shear strength respectively.

5. RESULTS-EXPERIMENT

5.1 Static loading

Experiments were conducted on specimens without embedded fibre optic sensors to determine the first failure in the composite. In the experiments a number of specimens was loaded and unloaded in incrementally increasing tensile loads. After each load step the specimens were removed, and the presence of damage was determined by careful examination of the polished edges of the specimen and using X-ray radiographic technique. After the examination the specimen was refitted in the test machine and loaded to the next load level unless damage was detected. The first failure mechanism appeared as matrix cracks in the 90°-plies appeared at a strain level of approximately 0.4 %. Exceeding this strain level the local strain field is altered. As a result the strain state in the sensor will be changed and consequently the signal obtained from the sensor is affected. Therefore the interpretation of the sensor signal is ambiguous above 0.4 %. In compression the transverse failure strain is typically threefold larger [12]. No matrix cracking was observed in the compressive loaded specimens.

Uni-axial tests were used to characterize the limit of sensor function of EFPI- and Bragg grating sensors in tensile and compressive loading. The geometry of the specimens was identical to those in the experiments of specimens without sensors. The condition in the laboratory was approximately 20°C and 40-50% RH. The specimens were kept in this environment for a couple of months allowing the specimens to absorb 0.55 % moisture.

A typical phase-strain response of an embedded EFPI-sensor and strain gauges are plotted in Fig. 2a-b in static tensile loading. The output from the EFPI-sensor in terms of number of fringes was linear in the first regime up to 0.30 %. The output of the same sensor plotted as function of the axial strain in Fig. 2b shows that a clear anomaly occurs at approximately 0.29 %. At this point a sudden drop is shown. This first indication of malfunction of the sensor is considered as the function limit of the sensor. Although interpretation of the non-linearity is by no means unambiguous, this anomaly in the response indicates failure in the sensor or the sensor region. In a later stage during the loading a complete loss of signal occurred due to final failure of the optical fibre in the tab area.

Different failure modes can result in changes in output signal from the sensor. An optical fibre failure can result either in a complete loss of the signal or creation of new reflective surfaces which provide an apparent change of the gauge length. Another feasible failure mode is debonding in the sensor/coating or coating/composite interfaces resulting in loss of interference fringes due to improper transfer of stresses from the composite material to the sensor. This type of behaviour in the sensor output can also be related to fracture in the composite material as matrix cracking and fibre failure.

Table 1 summarizes the strain levels where the anomaly is observed. Experiments indicated that the function limit for tensile loaded specimens with embedded EFPI-sensor occurred at the average strain levels of 0.19-0.25% dependent on the position of the EFPI-sensor and in compression at approximately 0.8%. The result also indicated that the centre embedded sensors have slightly lower function strain limit than those embedded in the surface layer.

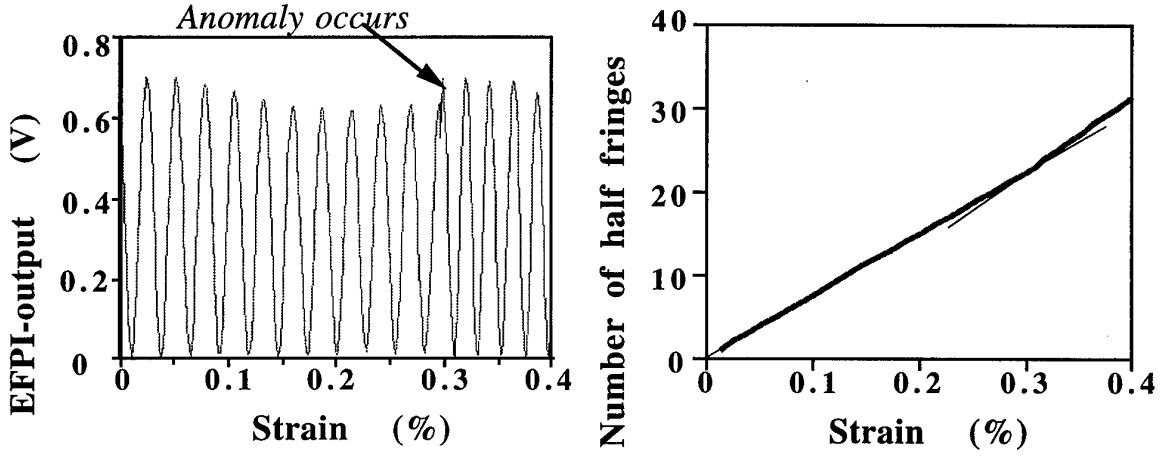


Fig. 2 (a) Example of an output from a surface embedded EFPI-sensor in tensile loading.
(b) Number of half fringes as a function of strain.

Test condition/Sensor	Sensor location	Average strain level (%)
Tension/EFPI	centre embedded	0.19
	surface embedded	0.25
Compression/EFPI	centre embedded	0.79
	surface embedded	0.78
Tension/Bragg grating	centre embedded	0.47

Table 1 Static experiments -EFPI and Bragg grating sensor

Another observation was that the Bragg grating sensor appeared to generate linear response at substantial higher strain levels than the EFPI-sensor. The function limit of the Bragg sensor was in the order of the strain level of the first ply failure in the specimen, 0.4 %, as indicated in the experiments with specimen without embedded fibre optic sensor. The matrix cracking could have changed the local strain field, consequently, the signal obtained from the sensor was affected.

5.2 Fatigue testing

In the fatigue loading only specimens with an EFPI-sensor embedded in the centre were evaluated. The maximum number of cycles was 100000. However in one case the testing was interrupted after approximately 11500 cycles because of failure of the lead in optical fibre in the tab area.

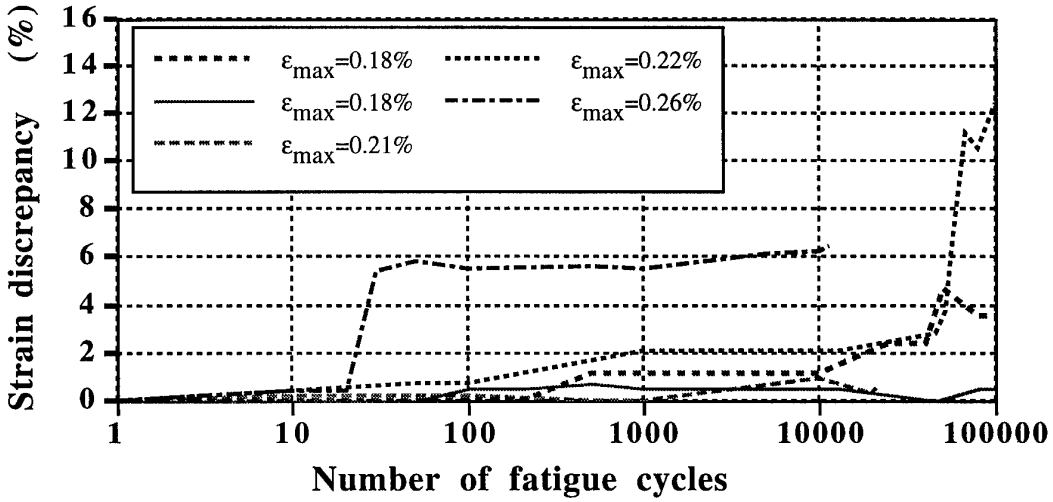


Fig. 3 The error in the measured strain from the EFPI-sensor as function of number of fatigue cycles

The fatigue results are shown in Fig. 3. The strain discrepancy is defined as the change of the strain output relative the first cycle. Keeping in mind that the first anomaly with centrally embedded EFPI-sensor occurred for tensile static loaded specimens at strain levels of 0.17-0.21% in room temperature. The results indicates that within this range of the maximum strain levels the reliability of the sensor in fatigue loaded specimens is not significantly affected. At a number of fatigue cycles less than 10000 the discrepancy in the sensor output did not exceed 1 % within these strain levels. For one of the specimen loaded with the maximum strain 0.18 % an increasing strain discrepancy appeared after 10000 cycles. For the two other specimens within the maximum strain range of 0.17-0.21%, the change in strain output was confined within 1 %. For larger maximum strain levels the strain discrepancy appeared in several order of cycles earlier. For the specimens loaded at maximum strain levels larger than 0.21 % the reliability of the sensor function is degraded from the beginning of loading.

5.3 Failure modes

To determine the failure mode which is related to the anomalies in the signal from the fibre optic sensor, samples from the specimens were carefully ground keeping the cut parallel to the sensor. As a final step the samples were polished with diamond particles on a hard cloth to remove the surface scratches from the grinding. Optical microscopy was used to examine the failure modes. A failure in the sensor is easily observed by slight defocusing whereas debonding appears in the microscope as a fine line between two constituents in the samples. Large care has to be taken not to confuse debonding with the relief of the sample surface which can appear from the polishing.

Matrix cracking was observed in all the tensile loaded specimens. In the tensile loaded specimen with embedded EFPI-sensor two failure locations in the silica glass were observed. The failure locations were in conjunction to the ends of the sensor cavity. Also debonding was identified in all samples examined. The first failure mode affecting the sensor response can have been blurred of subsequent failures since the loading was not directly interrupted. The strain level at which the experiments were interrupted was in level with the failure strain of the sensor, approximately 1 %[6]. Examination of failure modes in conjunction with the detected anomalies in the sensor output, indicates that the first actual failure in the sensor region is debonding for the tensile loaded conditions. In the specimen with Bragg grating sensor neither failures in the sensor nor coating including debonding were detected. The result indicates that matrix cracking in the composite resulted in the detected signal anomaly from the Bragg grating sensor. In the compression loaded specimens with the EFPI-sensor no clear indication of fully debonded interfaces could be found. Debonding appeared partially along the interface in the sensor's gauge length. Neither failure of silica glass was possible to observe in the samples. The failure mechanism in the region of the embedded sensor was not finally determined in compression, but the examination indicates that debonding can have affected the sensor reliability. In the specimens tested in fatigue the only failure mode observed was debonding between the silica glass and the polyimide. The failure mode was observed in the samples where an anomaly in sensor output had been detected.

The detected signal will not be affected whether the sensor is completely constrained axially. The behaviour after debonding is attributed to frictional sliding between the interface of the sensor and the surrounding material. The stresses must be sufficient to counteract, in addition to the frictional stresses, also the initial residual strains due to the difference in thermal and swelling expansions of the sensor, coating and composite materials.

6. RESULTS -ANALYSIS

The first step was to determine the tensile and shear strengths of the interfaces by using the experimental values at room temperature in conjunction with the calculated stresses acting on the interfaces of the EFPI-sensor. The effects of the differences in thermal and moisture expansion coefficients of the materials on the stress field have been included in the stress analysis. The environmental effects considered were the temperature change relative the stress free temperature $T = 180°C$[13] to room temperature, $\Delta T = -160°C$, and the moisture absorption $\Delta M = 0.55$ % that take place when the specimens are exposed to humidity in the laboratory. The mechanical loads were either a tensile or a compressive load corresponding to the uniform strain $\varepsilon_{\infty} = 0.19$ % or $\varepsilon_{\infty} = -0.79$ %, respectively. The strain levels coincided with those in the experiments where an anomaly in the DC-output was recorded. On the assumption that debonding was initiated in the interface between the sensor and the coating at these strain levels, the stresses calculated from mechanical loading and environmental effects at room temperature were superimposed and finally the interfacial failure criterion was applied. In the case of tensile loading the location of the failure initiation, i.e. where the highest stresses were calculated, was located at the fused connection of the lead in optical fibre to the hollow core at the circumferential location $\Theta = 0°$. In compression the maximum stresses occurred in the same location at the interface in the length direction as in tension. As the compressive radial stresses were significant smaller and the shear stresses higher at $\Theta = 0°$ compared to $\Theta = 90°$ the failure was assumed to be initiated at $\Theta = 0°$.

The maximum stresses in tension and compression were used in the failure criterion for interfacial strength and the interface strength parameters Y_{int} and S_{int} were calculated. The interface shear strength S_{int} was determined to be 13 MPa for the silica glass/polyimide coating interface, whereas the interface tensile strength Y_{int} was determined to be 28 MPa. By assuming same strength values as for the EFPI-sensor, the criticality of embedded Bragg grating sensors for premature failure was determined.

During the analysis, the order of approximation p in each element was increased up to a given maximum value. By studying the stresses at each p-level, it was possible to evaluate the convergence of the solution. Although the FE-mesh was rather coarse where some of the elements had a high geometrical aspect ratio a good convergence of the solution was obtained when the analysis was performed with $p = 6$. The difference in the numbers between the iterations $p = 5$ and $p = 6$ was less than 3 %. The number of degrees of freedom was 78 770 and 94 337 at the highest order of approximation for the centrally and surface embedded sensor respectively.

6.1.1 Centrally embedded EFPI-sensor

In the region of the EFPI-sensor there are two stress concentrations extending only a few tens of microns as seen in Fig. 4. These coincide with the locations of the ends of the cavity in the sensor as a result of the abrupt change in local stiffness in the sensor[1]. The longitudinal stress in the sensor has to be transferred from the solid glass to the part of the sensor with a cavity. At the silica glass/coating interface, the stress/strength ratio is at its maximum. The stress/strength ratio for the polyimide/composite interface showed similar behaviour, although the peaks were slightly lower when applying the same strength data as for the silica glass/polyimide interface. An important observation was that, in tensile loading, the radial stress across the interface is tensile, on the contrary compressive loads create compressive radial stresses and consequently the stress/strength ratio is lower as shown in Fig. 4.

The largest stress/strength ratios are 0.45 and 0.155 for tensile matrix failure and tensile fibre failure respectively, which are 1.61 and 1.13 times greater than the stress/strength ratio far from the sensor. Despite the complex sensor geometry, the margin to failure at the stress peaks is of the order of 6-7 in the coating and 30 in the silica glass, although it should be noted that the failure strength in the sensor is locally reduced due to the heat-induced stresses in the fused zones. Further greater margins were determined in compression loaded specimen. Therefore, these failure modes in the composite, silica glass and polyimide coating are not significant for the reliability of a system with EFPI-sensors.

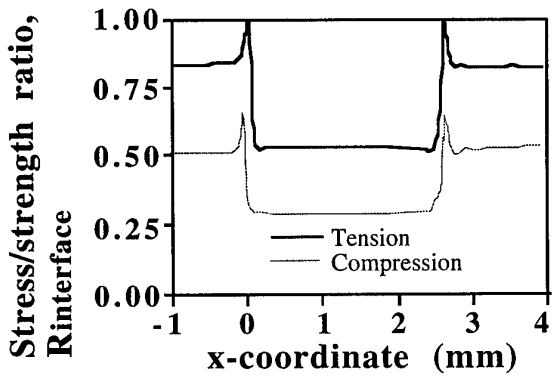


Fig. 4 Comparison of stress/strength ratio in tension and compression for the sensor/coating interface of a centrally embedded sensor. $\varepsilon_\infty = 0.19\%$, $\varepsilon_\infty = -0.19\%$

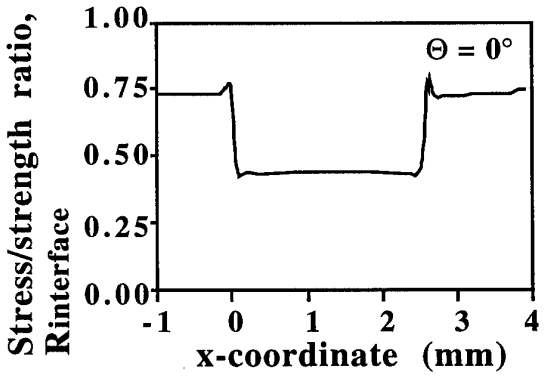


Fig. 5 The effect of moisture and curing stresses on the stress/strength ratio at room temperature along the sensor/coating interface for a centrally embedded sensor.

In Fig. 5 the calculated stress/strength ratio at the silica glass/coating interface for the additional effect of environmental condition is separately presented. The analysis showed that the curing stresses have a significant contribution on the criticality for failure in the interface. Despite that the absorbed moisture has a reverse effect to the curing stresses the calculated stress is 75 % of the failure strength as a result of the additional environmental stresses. These stresses, mainly due to the ply stiffness mismatch in laminates, are present in a laminate during service life. Moreover the slight additional effect of the cavity in a embedded EFPI-sensor is indicated.

6.1.2 Surface embedded EFPI-sensor

The calculated stress/strength ratios for the surface embedded EFPI- sensor showed that the margins to failure for a surface embedded sensor are similar in the polymer coating, silica glass and the composite as those for a centrally embedded sensor. There is a significant margin for failure in the materials.

Also for the surface embedded sensor, the analysis indicates that the strength of the interface is critical for failure initiation in the sensor/coating interface. Two stress concentrations are present in the same regions as for the centrally embedded sensors. However, an effect of the composite surface on the stress field is present. The stress/strength ratio at the interface varies with the circumferential location. Close to the surface of the specimen, $\theta = 90°$, the stress/strength ratio is negligible for an axial strain $\varepsilon_{\infty} = 0.19\%$. The stress/strength ratio at $\theta = -90°$ is also small compared to the maximum value 1.04 that was obtained at $\theta = 0°$. This value is 4 % higher than the value obtained for the centrally embedded sensor at the same strain level. However, in this analysis the region with low fibre content between the sensor and the surface was not modelled. This region affect the stress state. A region of low fibre volume content around an optical fibre can slightly decrease the stress/strength ratio[1]. This can explain that higher failure strain was obtained in the experiments with surface embedded sensors.

6.2 Bragg grating sensor

Stress/strength ratios at the silica glass/polyimide coating interface were evaluated for the Bragg grating sensor. The sensor has no cavity, therefore the stress peaks which are characteristic for the EFPI-sensor are not present. The stress/strength ratios at the interface were reduced to 0.83 and 0.51 for tensile and compressive loading respectively, compared to 1.0 and 0.64 at the interface of the EFPI-sensor.

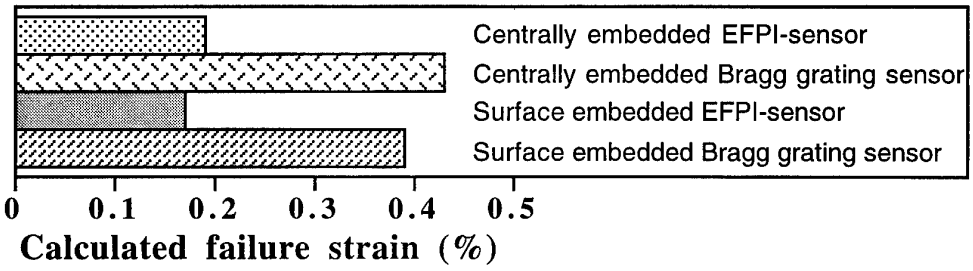


Fig. 6 Comparison of calculated failure strain at the silica/glass/ coating interface for tensile loaded specimens

The calculated stress/strength ratios were used to predict the failure strain with respect to stresses acting on the interface. Comparisons between the EFPI- and Bragg grating sensor are shown in Figs. 6-7. The predicted failure strains for tensile and compressive loaded specimens demonstrate the advantage of Bragg grating sensors. In tensile loaded laminates the failure strain for the embedded Bragg grating sensors are twice as large as for embedded EFPI-sensors. The predicted failure strain exceeds the strain level for the experimentally observed matrix failure in the 90°-plies. The function strain limit is then not determined by the strength of the silica glass/polyimide coating interface but the tensile matrix failure strength in the composite.

The difference in failure strain for EFPI- and Bragg grating sensors is smaller in compression than in tension as seen in Fig. 7. However the failure strain exceeds well typical design value for composites.

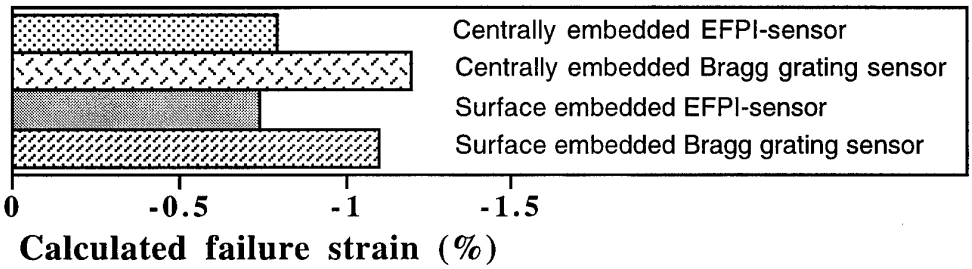


Fig. 7 Comparison of calculated failure strain at the silica/glass/ coating interface for compressive loaded specimens

7. CONCLUSIONS

During static and fatigue loading the sensor function was determined by constantly measuring the sensor response. Laminates with a centrally or a surface embedded EFPI- and Bragg grating sensors were evaluated. It was observed that for static tensile loading in room temperature the function limit for EFPI-sensors was approximately 0.20%. Constant amplitude fatigue loading did not affect the function reliability of the EFPI-sensors at maximum faigue strain 0.20 % for 10^5 cycles. Typical design values for composite aircraft structures are 0.30%. On the other hand in compression the EFPI-sensor functioned to a strain level which was more than twice than those in aircraft. The silica glass/polyimide coating interface was identified as the site where failure was initiated. In tensile loaded laminates the function limit of embedded Bragg grating sensors was above the strain level for initiation of matrix cracking in the laminate. When the interface has failed, the accuracy of the measured signal declines, resulting in a loss of function of the sensor. The stress analyses have identified that the cavity in an EFPI-sensor creates large stress concentrations. The narrowly extended stress peaks are a source to failure in the interface between the sensor and the polyimide coating. To further improve the mechanical performance of embedded EFPI-sensors in a composite material it is necessary to increase the strength of the interfaces, or use sensors without a cavity. The use of Bragg gratings instead of EFPI-sensors improves the function reliability for damage initiation at the interface. Then the reliable sensor function is limited by the initiation of matrix cracking in laminates.

8. ACKNOWLEDGEMENTS

A. Henriksson, F. Brandt and B. Thörnqvist are acknowledged for their contribution to the experiments. The reported work is a part of joint project on Smart Composite Structures sponsored by the FMV- Defence Materiel Administration, Sweden. The joint group consists of; FFA-The Aeronautical Research Institute of Sweden, and IOF-Institute of Optical Research, Sweden.

9 REFERENCES

[1] Levin, K. and Nilsson, S.,"Analysis of the local stress field in a composite material with an embedded extrinsic Fabry-Perot interferometer sensor," Second European Conference on Smart Structures and Materials, Proc SPIE 2361, pp. 379-383, Glasgow, Scotland, Oct 1994

[2] Levin K., Jarlås R.,"Vulnerability of Embedded EFPI-sensors to Low-Energy Impacts, " FFA TN 1994-52, Bromma, Sweden, 1995

[3] W.W. Morey, G.A. Ball, G. Meltz, Photo induced bragg gratings in optical fibers, Optics and Photonics News, pp. 8-14, Feb. 1994

[4] Wosinski, L., Breidne, M., Stubbe; R., Sahlgren, B., and Betend-Bon, J-P., "Experimental system considerations for distributed sensing with grating Fabry-Perot interferometers," Tenth International Conference on Optical Fibre Sensors, Proc. SPIE 2360, Glasgow, Scotland, Oct. 1994, pp.146-149

[5] K.A. Murphy, M. F. Gunther, A.M. Vengsarker and R.O. Claus, Quadrature phase-shift, extrinsic Fabry-Perot optical fiber sensors, Opt. Letter, Vol. 16 p.273, 1991

[6] Henriksson, A & Brandt, F., "Design and manufacturing of an EFPI-sensor for embedding in carbon/epoxy composites," 10th Optical Fibre Sensors Conference, Proc. SPIE 2360, pp.473-476, Glasgow, Scotland, Oct. 1994,

[7] Andersson, B.& Falk, U., "Self-adaptive analysis of three-dimensional structures using a p-version of finite element method," FFA TN 1987-31, Bromma, Sweden, 1987

[8] Levin, K., Nilsson, S.,"Adverse Effect of Fibre Optic Sensors Embedded in Carbon/Epoxy Composites," FFA TN 1994-49, Bromma, Sweden, 1995

[9] Handbook of composites, vol. 1, Strong fibers, Editor. W.Watt & B.V. Perov Elsevier Science Publishers B.V. 1985

[10] DuPont material data sheet

[11 Hashin, Z., "Failure criteria for unidirectional fiber composites," Journal of Applied Mechanics, Vol. 47, p239, June 1980

[12] Finn, S.R. & Springer, G., "Delaminations in composite plates under transverse static or impact loads -a model," Composite Structures, Vol. 23, p177, 1993

[13] G. Fernlund, Theoretical and experimental investigation of thermal stresses and strains in CFRP, FFA TN 1989-27, Bromma, Sweden, 1989

Impact detection and vibration sensing for material composite structures by integrated optic fibre sensors

L Michel*, M Labarrère*, R Gafsi**, A Malki**, P Lecoy**

*Département de Génie Mécanique
Ecole Nationale Supérieure d'Ingénieurs de Construction Aéronautique
49 avenue Léon Blum
31056 Toulouse cédex
**Département d'Electronique. Ecole Centrale Paris
Grande voie des vignes
92295 Chatenay-Malabry cédex

ABSTRACT

An optic fibre sensor based on the intermodal interference principle was integrated in a composite material structure to detect impacts and vibrations. Six fibres were integrated at the top of a carbon/epoxy composite panel and arranged to form a regular network on the structure. A series of impacts at various positions on the plate were performed using an instrumented hammer. The spectral responses of the optic sensors were compared to a reference piezoelectric accelerometer. Moreover a determination of the impacts position was performed with the arrival times measure of the generated acoustic wave front to the optic sensors. These tests proved the great sensitivity of this type of sensor, its integration easiness and the possibility to localize an impact on composite structures with a very simple device.

1.INTRODUCTION

During the last twenty-five years, there was a considerable increase in the use of composite materials for aeronautical structures. In spite of their various qualities: weight saving, properties optimization and in-service behaviour which has contributed to generalize their use, composite materials present some inconvenients and particularly their very low damage tolerance [1]. This point is really critical for the maintenance costs and induced an over-sizing of the structure which means a lower weight saving than it could be expected. So today there is a considerable interest in monitoring of the composite structures health. One of the proposed solutions is the integration of optical fibre sensors in the material itself [2].
Optical fibre use is very interesting. It offers intrinsic safety, galvanic insulation and it can operate under intense electromagnetic fields. Moreover in this study the fibre is used as a sensitive element (intrinsic sensor), so the integration is facilitated because of the low weight and dimensions of the fibre sensor.
This work was conducted in order to prove the viability of impact detection and vibration sensing on composite structures by built-in optic fibre sensors.

2.OPTICAL PRINCIPLES OF THE SENSOR

This sensor is a distributed fibre optic sensor using the principle of modal interferometry in multimode fibres [3]. When a coherent light, coming from a laser diode, is guided in a multimode fibre, a phase shift between the guided modes can occur when an external mechanical stress induces a refraction index change by the phenomenon of photoelasticity. The phase shift can easily be converted in intensity variation by using a spatial filtering, achieved by splicing the multimode fibre to a second fiber, which can be monomode or multimode but guiding less modes (Fig. 1). In our experiences standard 62.5/125 and 50/125 multimode fibres, spliced outside of the structure, were used as sensitive and filtering fibres.
So the sensor is the fibre itself. This principle is very efficient to measure low-frequency vibrations of structures. If the fibre is embedded in materials, it can be used as a wide-band transducer of vibrations and high frequency acoustic waves, generated for example by impacts. However a very good mechanical coupling between the material and the optical fibre has to be achieved first.

0-8194-2165-0/96/$6.00

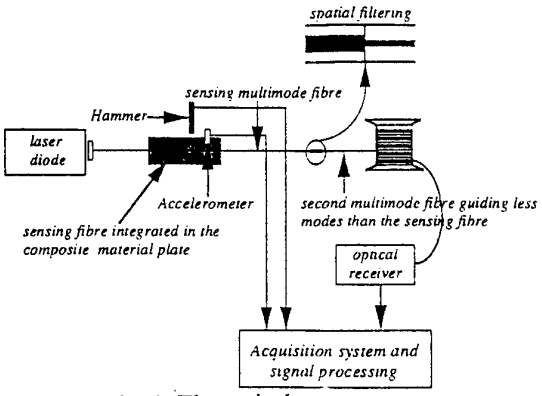


Fig. 1. The optical sensor set-up

3.SENSOR INTEGRATION IN COMPOSITE PLATES

3.1.Materials

The composite plate was manufactured with carbon fibre-epoxy resin (T300/M10) prepegs supplied by *BROCHIER*. The stacking sequence of the panel is as follows: $[0_3, 90_3, +45, -45]_s$. After fibre integration this cross-ply laminate was moulded according to the recommended curing process: 4 hours at 90 °C under a 5 10^5 Pa pressure. Its final dimensions were 2*275*275 mm^3.

The optic fibres used in this study are two multimode graded-index fibres supplied by *OPTICAL FIBRES* with diameters of core/cladding/coating equals to 50/125/250 μm and 62.5/125/250 μm.

3.2 Fibres integration

Six optical fibres were integrated in the laminate before the curing process and positionned at the top of the plate.Three of them were placed between the second and third layers along the carbon fibres direction and 100mm away from each other as indicated in Fig. 2. Three others were inserted between the fourth and fifth layers like in the previous disposition.

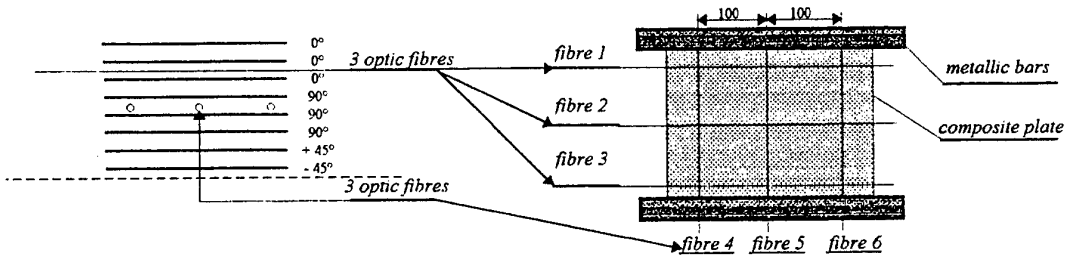


Fig. 2. Disposition of the optic fibres in the composite plate

A plastic cladding was used to protect from break at the plate edges during and after the manufacturing. This fibre integration procedure was already used in a former study and its quality was assessed by a microscopic observation of a sample cut [3].

4.EXPERIMENTAL DEVICES

4.1.Sensing device

The inputs of the fibre sensors were connected through an 1 to 8 optical coupler to a laser diode (λ=850nm, MG 9002 A) supplied by *ANRITSU*. After their way out from the panel the 62.5/125/250 fibres were spliced to the 50/125/250 fibres in order to realize the spatial filtering (Fig. 1). Then the end of each fibre was connected to a photodiode and the photoelectric outputs amplified. These signals were recorded by a performing acquisition device (*NICOLET* Multipro II).

All the fibre to fibre connections were realized by fusion-splicing. Standard connectors ST were used for the other connections.

4.2 Impact device

The test equipment was made of a massive support on which the sensing panel was built-in along two opposite sides. This is achieved by pinching the plate between metallic bars bolted to the support.

The impacts were obtained by a hammer equipped with a force transducer. These impacts generated free vibrations of the plate which permitted to evaluate the vibration sensitivity of the optical fibre sensors. In this case an accelerometer transducer was stuck to the panel as a reference vibration sensor.

4.3 Testing conditions

Concerning the tests which have been realized , the six fibres on the top of the plate were connected at the same time. For the vibrations measure a sampling frequency of 10 Khz was estimated to be sufficient to measure the first modes of vibration of the plate. The recording duration was fixed to 500 ns. For the impact localization the sampling frequency was fixed to 1Mhz in order to obtain a good precision for the measure of the arrival times of the acoustic waves to the fibre sensors. The recording duration was 50 ns. The electrical output of the hammer was used as a trigger signal for the different outputs monitoring with a pre-trigger to record the rising front of the impact.

5.RESULTS and DISCUSSION

5.1.Vibration sensing

This part of the study dealed with the detection of plate vibrations by the optic fibre sensors. The test consisted in impacting at several spots the panel with the hammer. Then the response of the optic fibre sensors was recorded and compared to the response of an accelerometer placed on the structure as a reference sensor.
Many impacts were done and the different comparisons show a good correlation between the optical sensor and the accelerometer.As an example the frequency responses of an optical sensor and of the accelerometer are reported on Fig. 3. The impact was done upon the fibre n°4 very close to the clamped part of the plate.The accelerometer was placed upon the fibre n°4 midway between the clamped parts of the plate. These spectra show the low frequency free vibration modes of the plate. The principal and first flexural mode appears around 206Hz. Other secondary modes are located at upper frequencies.

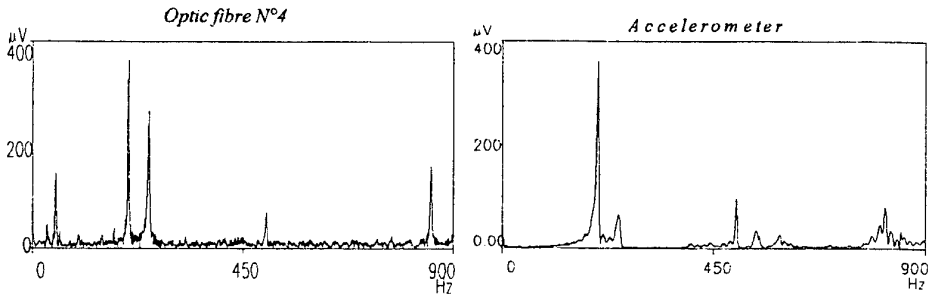


Fig. 3. Frequency responses of the optic fibre n°4 and of the reference accelerometer

Other impacts were realized at many points on the plate, in order to stimulate various vibration modes. The optic fibre sensors responses show clearly the evolution of the frequency spectra according to the impact location (Fig. 4). Indeed the important point to be noted is that the impact position determines the spectral information detected by the sensor. This is particularly true in the low frequencies domain corresponding to the free flexural vibration modes.

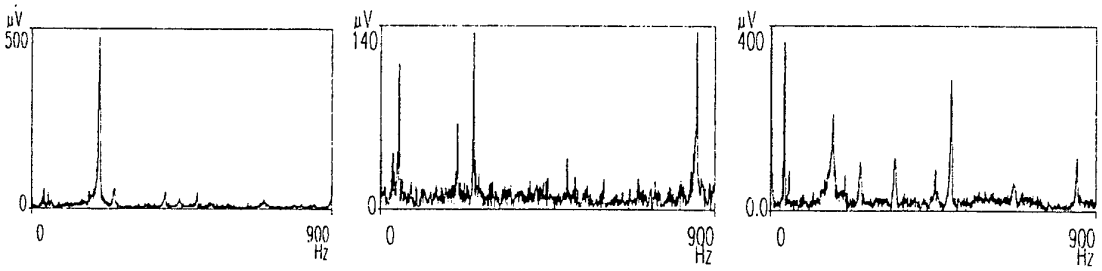


Fig. 4. Frequency responses of optic fibres for various impact locations

5.2.Impact location

The principle of this location is based upon the detection of the impact generated acoustic waves by the embedded optic fibre sensors. In order to cover the structure, the fibres were arranged to form a regular grid into the panel. In this study the size of the grid has been chosen arbitrarily. However for an industrial application, this dimension may be chosen as the distance at which an impact, generating the minimal damage to the structure, can no more be detected by the surrounding sensors.

Another question concerns the acoustic wave speeds which are dependant on the direction of propagation, on the wave frequency and on the type of waves [4,5]. To avoid this problem, the detection of the (x,y) position of the impact was only based on the difference of arrival times of the wave front to the fibres. These times were calculated after the tests with the different temporal recorded signals.

For these tests only four fibres were used : fibre n°1, 3, 4 and 6. They formed a 200mm side (« a » in Fig. 5) square at the top of the panel. For each of the 24 impact positions reported in Fig. 5, three impacts were realized in order to obtain four mean values of the wave arrival time to the fibres. Assuming that in the direction x and y the wave velocities may be different, these times ($t_{i\ fibre}$) permitted to calculate the (x,y) position of the impact, and the velocities (v_x ,v_y):

$$x = \frac{a}{\left(1+\frac{t3}{t1}\right)} \qquad y = \frac{a}{\left(1+\frac{t6}{t4}\right)}$$

$$v_x = \frac{a}{(t1+t3)} \qquad v_y = \frac{a}{(t4+t6)}$$

The real position and calculated position of impact are presented for many impacts in Fig. 5. The mean deviation on the measurement of the impact position is equal to 11.83mm and the standard deviation is equal to 6.61mm. These results seem to be very encouraging and confirm the possibility to determine the position of an impact on a composite structure by a very simple method.

Concerning the waves velocity the results present a rather big dispersion. The mean values in both directions x and y are close to 800ms^{-1} . This value is quite reasonnable comparing to other values of the litterature (400 à 2000ms^{-1}) but difficult to assess because of the wave velocity dependance upon various factors [4,5,6].

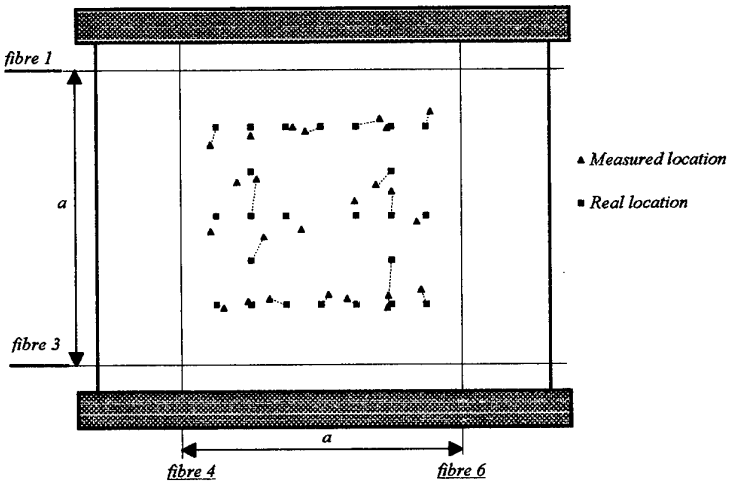


Fig. 5. Real and measured positions for various impact

These results may be improved. First there was several noise problems related to the inputs and outputs leads which are free of vibrations. This may be eliminated by the fixation of the source/detector system to the structure itself [7]. Elsewhere, the method do not include the fact that the faster way of the acoustic wave, between the impact source and the fibre, may not be the normal direction to the optic fibre.

6.CONCLUSION

The different results show the possibility to localize impacts on a composite structure with an optic fibre sensors network embedded in the structure. They prove too the good vibration sensitivity of the optic sensor used in this study.

However there is still a lot of questions to be adressed. It is necessary to study the possibility to measure the energy of the impacts. Thus in order to better understand the sensitivity of this optic sensor and to improve the accuracy of the impact localization, it has to be taken into account the real nature of the acoustic waves generated by the impact. And the position of the fibres in the plate through the thickness or in regard to the plate edges has to be optimized.
These are the necessary steps before to deal with the current realization of this technique: calibration, fibre network and device optimization...

7.REFERENCES

1. U. G. Goranson and J. F. McGuire, « Airworthiness challenge », *Aerospace engineering*, pp28-34, March 1994.
2. R. M. Measures, « Fiber optic sensing for composite smart structures », *75th meeting of the AGARD Structures and materials panel CP-531*, pp 11-1/42, Lindau (Ger.), 5th-7th October 1992.
3. P. Lecoy, A. Malki, R Gafsi, M. Labarrère, L. Michel, « Capteur de vibration et d'impacts basé sur l'interférence intermodale, dans les fibres optiques multimodes », *14ème Journées Nationales d'Optique Guidée*, pp100-102, Besançon (F), 1994.
4. R.A. Kline, *Nondestructive characterization of composite media*, Technomic Publishing Company, Lancaster (USA), 1992.
5. W. Goldsmith, *Impact*, Edward Arnold Publishers Ltd, London, 1960.
6. Y. Ousset, H. Fagot, B. Dischli, « Etude par holographie du comportement dynamique de plaques composites sous l'effet de chocs », *Institut franco-allemand de Saint-Louis rapport CO 203/91*, March 1991.
7. P. L. Fuhr, « Single-fiber simultaneous vibration sensing and impact detection for large space structures », *Smart materials structures*, Vol 3, pp 124-128, 1994.

Using optical sensors to understand core crush in composite panels during processing

Nabil Zahlan & Gordon T Emmerson

ICI Fiberite
at
ICI Research & Technology Centre
Wilton, Middlesbrough, England, TS90 8JE, UK

ABSTRACT

The phenomenon of core crush encountered in the aerospace industry during manufacture of co-cured composite panels has been explained. An experimental programme which relied on direct measurement of pressure within the honeycomb core using an optical sensing technique has been used in conjunction with experimental observation and numerical modelling to determine the sequence of events which lead to this costly problem. Having understood the issue, it is now possible to take steps to reduce or eliminate the occurrence of core crush.

INTRODUCTION

Many papers have been published which introduce developments of sensing techniques and demonstrator components containing sensor systems. Of the technology options available, fibre optic based sensors appear to be the best established and most developed. In this paper we present work which utilises rather than develops optical sensing techniques. We employ a proprietary sensing system to understand a long standing issue encountered during the processing of composite sandwich panels, namely, the core crush phenomenon.

Composite honeycomb sandwich panels are used extensively within the aerospace industry because they utilise composite pre-pregs most efficiently in producing structures with high specific stiffness. Such panels can be manufactured in a multi-step procedure where each skin is cured separately and then these are joined to the core; a costly process. Alternatively, the panel can be co-cured, such that the whole panel is assembled and then cured in one step; this is the preferred option. However, co-curing sandwich panels presents a number of difficulties. Often a high level of porosity is found in the composite skins adjacent to the honeycomb core due to the lower consolidation pressures experienced in these areas. The resulting porosity provides easy routes for moisture to diffuse into the core causing weight gain in service. Another problem encountered during co-curing of sandwich panels is a tendency of the core to crush laterally resulting in a distorted panel and leading to costly rejection of defective parts. It is due to this core crush phenomenon that co-cured honeycomb sandwich panels are moulded at reduced autoclave pressures; typically 300 KPag. Steps can to be taken to prevent core crush from occurring; this usually involves the use of tie down plies which secure the core to the tool surface. These stabilisation methods become increasingly difficult to implement when moulding complex shapes.

There is much debate and mythology within the aerospace industry around the factors which cause core crush, yet very little has been published on the subject. A fundamental understanding of the core crush phenomenon is necessary in an area which is of great concern to aircraft manufacturers.

In order to gain this fundamental understanding of the core crush phenomenon, the problem was approached on two fronts, in conjunction. A detailed experimental approach lead to a thorough identification of how various resin and pre-preg characteristics influenced core crush performance, while numerical modelling was used to bring together the findings from the experimental investigation yielding a more holistic understanding of the core crush phenomenon and the mechanisms by which the resin and pre-preg characteristics influence the crushing process.

0-8194-2165-0/96/$6.00

THE CORE CRUSH PANEL AND CO-CURE PROCESS

The core crush panel specified in the Boeing specification BMS 8-256 measures 508 mm by 610 mm. For the purpose of this work, a scaled down version of the panel measuring 203 mm by 254 mm was used. The panels consisted of two skins sandwiching a core of honeycomb core, 12.5 mm thick with chamfered edges. Each skin comprised several plies of Fiberite 970 carbon fibre epoxy composite pre-preg. In addition, 'doubler' pre-preg pieces where inserted in specific areas to reinforce the panel, in-particular around the edge band

The procedure followed to manufacture the panel begins with lay-up of the lower skin on a flat tool; on to this a film adhesive is placed. The core and doubler edge band plies are placed next and finally this is covered with the upper skin separated from the core by another adhesive film. The assembly is then enclosed within a bag which is sealed to the flat tool.

The assembly is placed in an autoclave and vacuum is applied to the bag; this removes excess air from within the bag and serves to stabilise the panel components. A consolidation pressure of 0.3 MPa is applied to the assembly while temperature is increased at a rate of 2°C/min to a maximum of 180°C which is held for two hours. Cooling follows at a rate of 2-5°C/min to room temperature, at which instant, the pressure is removed. The vacuum is released when the consolidation pressure is first applied and the vacuum port is vented to atmosphere during the process cycle.

The above paragraphs describe standard material system and process conditions used for this investigation. Two alternative procedures where employed in separate experiments in order to influence the magnitude of vacuum developed within the honeycomb core cells. In the first instance the compaction procedure which pre-preg usually undergoes was not performed, thus, altering its surface characteristics, in another the adhesive film was omitted from the system providing a more direct path between the core cells and the vacuum port.

INTERNAL PRESSURE MEASUREMENT TECHNIQUE

An experimental technique was sought to measure the pressure and temperature within the cells of the honeycomb core during the co-cure process. To this end, a Photonetics Fiberoptic MultiSensor System[1] model Metricor 1450 was used. Sensors are available for measurement of pressure, temperature and refractive index and rely on the ColorOptic™ measurement approach in which the colour or spectral makeup of the light reflected by the sensor is modified in proportion to the parameter being measured. The light is supplied from a spectrum-stabilized LED source and modified at the sensor tip which is connected to the instrument through a multi-mode optic fibre. Both the pressure and temperature sensors were used in the present work. The first sensor consists of a shallow recess and a reflective diaphragm which flexes inward in response to external pressure; the second contains, between two reflecting materials, a material whose refractive index is sensitive to temperature.

Four sensor probes, 0.8 mm in diameter and 10 mm long, connected via 100μm/140μm optic fibres where routed through the composite panel lay-up into the cells of the honeycomb core. One temperature and one pressure probe where positions in the centre of the core, an area which does not experience much distortion, while a second set was located in the chamfer region which suffers most of the crush. The signals from all four sensors were monitored and recorded throughout the co-cure process cycle.

EXPERIMENTAL OBSERVATION TECHNIQUE

In addition to the direct measurement of pressure and temperature, direct observation of the panels during processing, as well as, the resulting components was very beneficial. An autoclave had been modified previously to allow direct observation of a composite panel during processing using a camera and necessary lighting. The camera functions including zoom, pan and iris could be controlled from the autoclave control panel. This capability allowed identification of the stage in the process cycle when the core distortion took place.

Subsequent to processing, the extent of core crush was measured as the percentage of area of the crushed core relative to its initial area. Finally, some panels were cut for microscopic examination of the crushed core and the surrounding composite plies.

MODELLING

To enable isolation and investigation of the many parameters which play a part in controlling the core crush mechanism, a model was implemented using the Finite Element Analysis technique. A structural model was created in which the skins and the core were represented. The interface between these was described as a viscous layer whose behaviour was time dependant. Finally, the pressure acting to crush the core was applied to the model. Consideration of engineering mechanics indicates that the magnitude of the acting pressure was the externally applied consolidation pressure less the internal core cell pressure. The model was able to simulate the core crush process indicating in relative terms the influence of changes in external pressure, internal vacuum, resin rheology and the collapse strength of the honeycomb core. Further details of the modelling work are presented in reference 2.

RESULTS AND DISCUSSION

Values of the internal pressure recorded at room temperature and at 180°C have been extracted from the collected data and are listed in the table below for each of the three panel configurations considered. The resultant pressure acting to crush the honeycomb core is also listed in the table. Together with these data, the extent of core crush measured in each case is noted.

Panel	Internal P @ RT [KPa]	Resultant P @ RT [KPa]	Internal P @ 180°C [KPa]	Resultant P @ 180°C [KPa]	Core Crush [%]
Standard	-7	283	269	7	24
Uncompacted	-14	290	228	48	38
No adhesive	-48	324	110	166	51

For any one of the cases above, the internal pressure increases during the cycle, albeit from a negative start point, as the temperature rises, this is due to expansion of the air remaining in the honeycomb cells after application of the vacuum and due to evaporation of moisture contained within the cell wall material. A corresponding decrease in the resultant pressure driving the crush mechanism is noted. This trend suggests that the cells would be expected to collapse at the start of the cycle. However, microscopic examination of the manufactured panel indicates that the movement of the core occurs at a resin interface between the plies of the composite skins. This resin movement would be expected to be easier at higher temperatures when the viscosity of the resin in low. Therefore, there is a point in the cycle where the resultant pressure is sufficiently high and the core is sufficiently mobile such that movement commences. The video recording of the process confirms that core crush does occur early in the process and progresses gradually; this observation is contrary to previous assumptions that the movement did not occur until the resin reached its minimum viscosity at about 130°C . Furthermore, results of the modelling simulation corroborate the sequence of events suggested above.

Having established the nature of core crush, we can now compare the performance of the different panels tested. The data presented in the table above confirm once again that reduced internal cell pressure, leading to increased resultant pressure, corresponds to more core crush being observed.

CONCLUSION

The results obtained from the experimental procedures and the numerical modelling are consistent in indicating that core crush, at least for the particular material system under investigation, is controlled by the magnitude of resultant pressure acting on the panel. For a fixed applied consolidation pressure, the extent of vacuum developed within the cells of the honeycomb core is key. Consideration of the process of core crush does suggest that parameters other than vacuum could become more significant for other material systems, however, the sequence of events should remain the same.

REFERENCES

1. E. Saaski, "Fiberoptic sensors measure in adverse conditions using a new fiberoptic technology", Measurement & Control, February 1989.

2. N. Zahlan and G. T. Emmerson, "Understanding core crush during processing of composite panels", Proceedings of the Ninth Worldwide ABAQUS Users' Conference, Newport, Rhode Island, USA, 29 - 31 May, 1996.

Smart Sensors and Systems

Invited Paper

Smart materials and sensors : a reality or a dream for tomorrow ?

by J.C. ANDRE

GdR 1080 CNRS "Procédés optiques ; applications aux microtechniques"
ENSIC-INPL, B.P. 451 - F 54001 NANCY CEDEX
and
INRS - avenue de Bourgogne - F 54501 VANDOEUVRE

Summary

Society's demand for the development of new types of information gathering systems is very strong, and corresponds in part to intelligent sensors, containing systems for the numerical treatment of information using sensitive elements composed of intelligent materials. The relational difficulties that exist between fundamental research and different socio-economic environments on the one hand, and those existing between scientific disciplines on the other hand significantly limit creativity in this extremely promising area.
The implementation of a science of structural relations favouring interdisciplinarity is the only possible guarantee of the establish of dynamic research in this field, which is at the interface between fundamental science, engineering sciences and technology.

One the tasks of fundamental research in the different countries of the European Union is to maintain a level of scientific knowledge - a knowledge reservoir - capable of responding to the future needs of European society. Existing knowledge in natural science, e.g. physics and chemistry, has been obtained through the use of both deductive and inductive approaches. And portions of this knowledge have been used in the engineering sciences, one of the goals of which is to harness fundamental science to the needs of society. In France, the engineering sciences are directly concerned with the creation and control of the information, mass, and energy fluxes used to satisfy human needs. Technical knowledge almost always implies transformation that leads to man-made systems. The objective of engineering sciences is thus to satisfy the present and future needs of society through the application of fundamental science and multidisciplinarity.

0-8194-2165-0/96/$6.00

For some years now the "knowledge reservoir" has been emptying, and, in my opinion, the motivation (and funding) of research at a national level has been insufficient if we want to replenish it. If one searches for a better system (!), for example by adapting a "just-in-time" approach (highly unusual in research activities), then it is absolutely necessary to strongly associate the present and future needs of society on the one hand, and the research community whose results are needed for this on the other. Engineering sciences have naturally strong links with industry and society, and they are willing and able to develop new actions in co-operation with other scientific disciplines - their basic objective is to integrate the "know-how" of different sciences in truly multi-disciplinary projects.

Such partnerships should lead to creative breakthroughs, a better use of human talent and energy and of funding and resources through increased mobilisation, and a renewed flexibility in relations between science and technology. Also, the training and education of research workers in all fields should definitely be improved if research is to be carried out in a unified environment with fewer frontiers and dogmas.

In order to help bridge the gap that exists between researchers in the fundamental sciences and society, and to replenish the knowledge reservoir at a rate which industry can obtain the "just-in-time" knowledge that it needs, the Department of Engineering Sciences of the CNRS has proposed the development of eight themes in co-operation with their homologues from the natural sciences. Several of these themes are concerned by information systems and technology, and one of the major fields of interest deals with the areas of intelligent materials in microtechnologies and microsystems.

One of the major technical achievements of the second half of the twentieth century is most certainly in the area of electronics leading to the development of microsystems and microtechnologies which are now used in myriad different applications (military, professional, medical, and domestic). The miniaturisation and integration techniques that have been developed for the electronics industry will diffuse into other areas, and will themselves become generic disciplines. It will thus be possible to integrate a single piece of mechanical, optical, chemical, biochemical, acoustic, etc., equipment with electronic ones. Note that the latter are now in charge of the treatment and control of information.

There already exists a number of initial applications of such combined applications in different areas, including components of micro-mechanical structural and mobility, micro optical, and micro acoustical components. The principle uses of these tools are in sensors, electromagnetic compatibility, encapsulation, etc. Another promising area of application is in robotics.

A "mixing" of disciplines is required in all of the research operations in this area, e.g. research on micro-sensors, integrated microsystems, and in medical applications that rely on the key fields of smart structures and materials. The last point includes adaptive and intelligent materials.

This objectives of this conference are primarily a brief presentation of some of the problems that must be solved, a global introduction of some of the needs that must be satisfied for certain applications, and some "biased" comments on means for promoting intelligent materials for the creation of smart sensors.

1 - THE SENSOR

A sensor can be defined as an element of a system that uses a physical, or physico-chemincal principle in order to transform a measurable quantity into an exploitable quantity by means of an appropriate method of treatment. In the majority of cases we are dealing with an electrical signal.
The transducer shown in the schema in Figure 1 is the element that transforms the measured quantity into another quantity according to a known law. Within this framework, the definition of the information gathering system consists of drawing a boundary around one possible representation in order to include certain elements and exclude others. Any such system selects information in terms of what it can transcribe, and either rejects and does not treat the rest, or does not treat it directly. The development of a sensor is a complex task, and, as shown schematically in Figure 2, depends in part on the filtering and communication of information. Different physical, or physico-chemical elements of the process can be measured, with the resultant value having a wide range of theoretical applications as shown in Figure 3.
These three Figures are intended to clarify an important difficulty, one associated essentially with the complexity of the original information gathering system which is based on an understanding of the physical phenomena in question in order that they can be used as an exploitable measurement. There are thus different schools of thought, different habits and conventions, and even mental blocks that make this area of study even more complex. Furthermore, a large number of the firms that manufacture sensors and probes are small and medium-sized industries that are often subject to temporal constraints that can different significantly from those commonly found in the research domain.
One can therefore naturally ask the question is fundamental research, globally speaking, capable of providing new information gathering systems to society, or should (must ?) it simply content itself with adapting tried and true techniques without any technological or scientific perturbations?

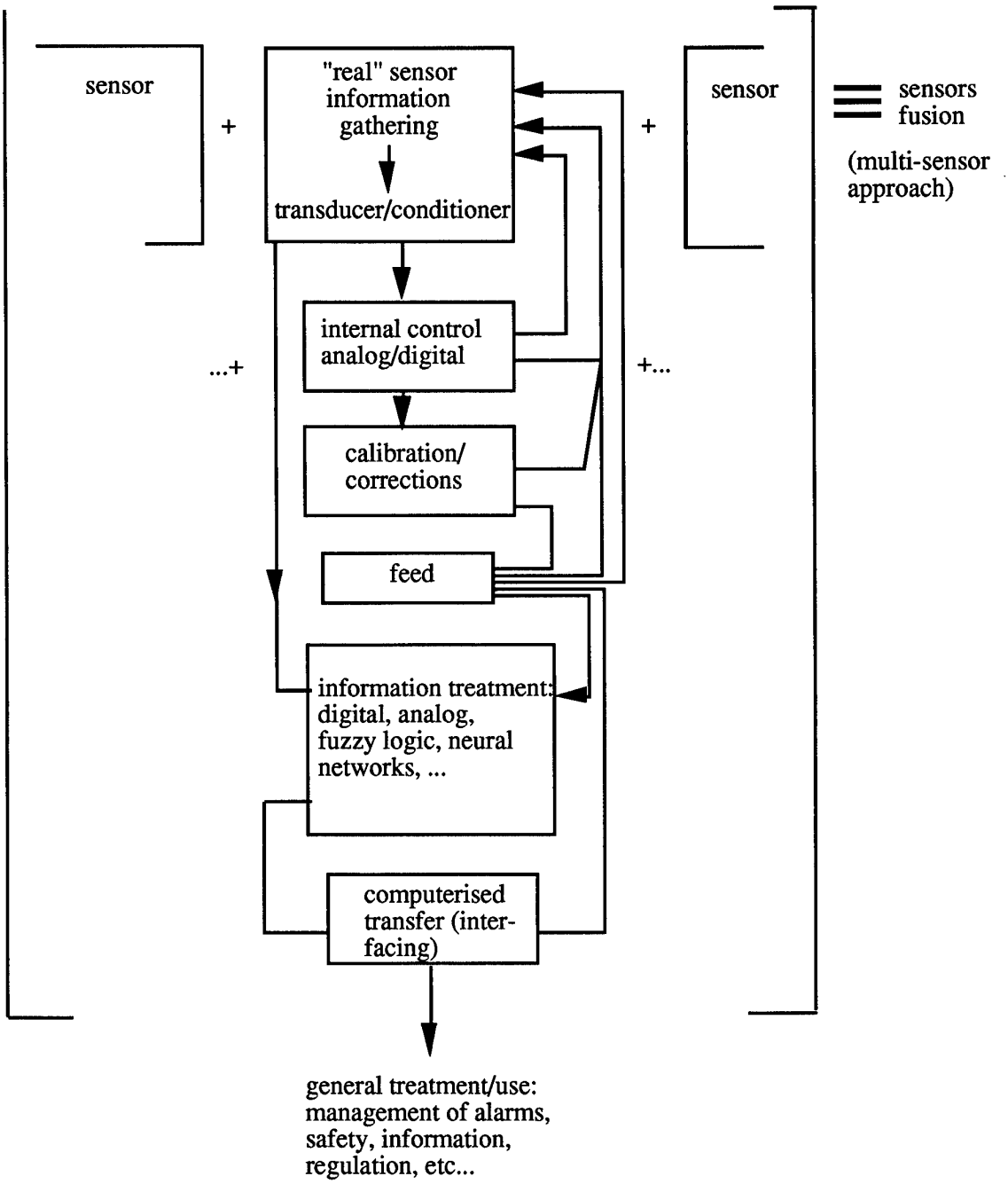


Figure 1. Use of information provided by sensors

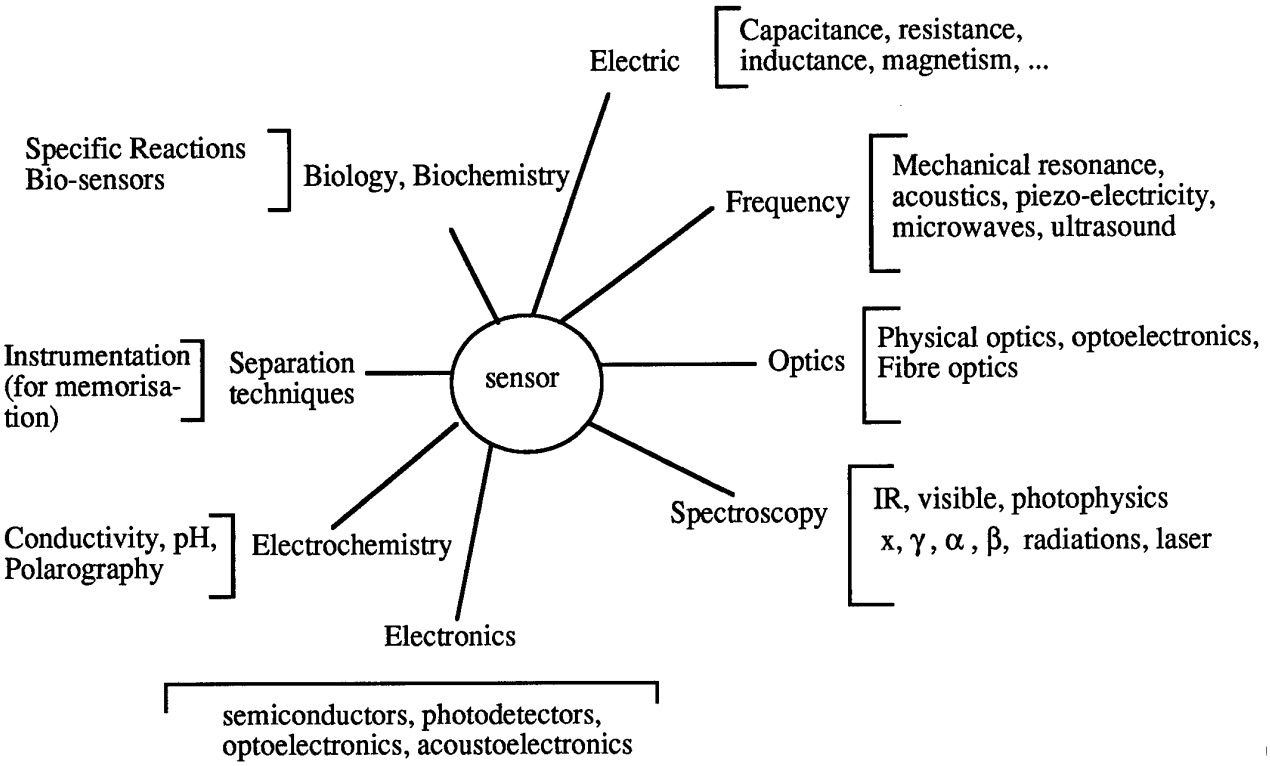


Figure 2. Possibilities for the use of physical phenomena in the development of an information gathering system

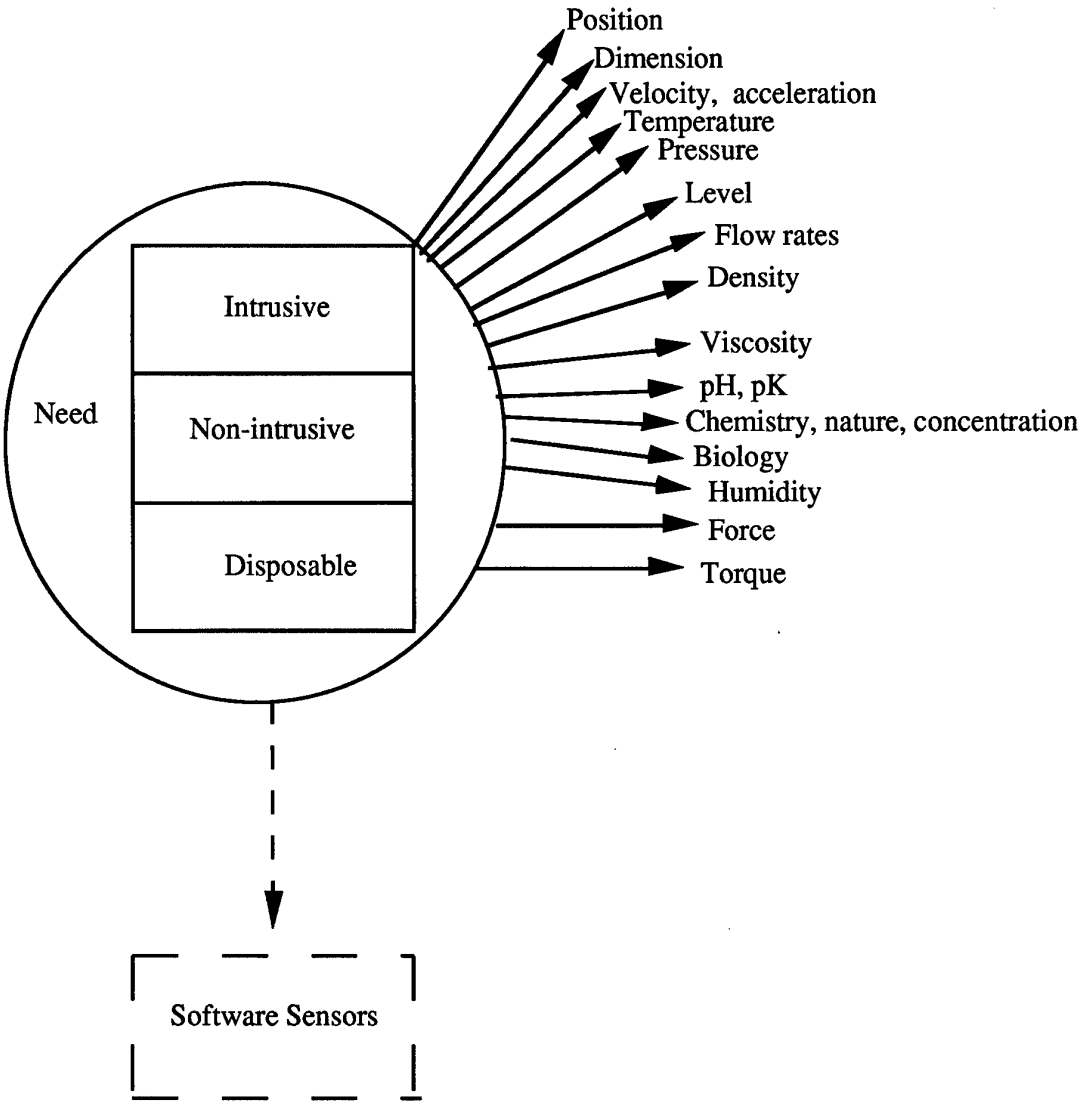


Figure 3. Range of needs for sensors, for both industry and research

1.1 - Intelligent Sensors

The specificity of an intelligent sensor can be summarised by its internal capacity for calculation and treatment of information. Including such an intelligent element in the electronic circuitry of a sensor was made possible due to technological progress in the area of micro-electronics.
The term "intelligent", which could have been replaced by interactive numerical calculation, is widely used in the profession. It generally refers to the following qualities:
- capacity for understanding (transduction, collection of information),
- possibility of auto-adaptation to different situations due to its internal software,
- capacity for communication.

In this context, intelligence is essential localised in that part of the sensor responsible for transmission, which generally delivers a digital signal after internal treatment.

1.2 - Intelligent Materials

Another incorrectly phrased term is that of intelligent materials. In the context of the current exposé, intelligent materials are used for the creation of useful information. In this sense, any sensor composed of at least one specific, sensitive element contains some intelligent materials that produce information (see Figure 2). Of course, the form in which the material is found has an influence on the quality of the measurement.
The level of "intelligence" varies as a function of the complexity of the information gathering system. The more the systems contains different elements (e.g. sensitive deposited films, integrated electronic circuitry, transducers, etc.), the more it will be qualified as "intelligent". As such, the intelligence of a sensor is more and more associated with the intelligence of the materials of which it is composed. Another concept linked to defining these concepts is the easy with which these products are machined or manufactured - a quality which only becomes apparent once the sensitive element has been developed.
The above discussion points out some of the semantic difficulties encountered in defining just what constitute intelligent materials for sensors. Nevertheless, it can safely be said that regardless of the exact context, this term refers more and more to multi-material pieces, miniaturisation, multi-information, and, naturally, integration.

2 - AN EXAMPLE OF A SOCIETAL NEED

Contacts have been made with industrial groups in the area of materials processing in order to ascertain their future needs in terms of specific sensors. Their requirements correspond more or less to the following four families:

- optical sensors (opto-electronics)
    - spectroscopy and use of lasers
    - fibre optic sensors and optodes
- electro-chemical sensors
- sensors made from semi-conductors
    - micro-sensors
    - surface wave sensors
- enzymatic sensors.

Simultaneously, the new systems approach is associated with a need for systems better adapted to satisfying the needs of the "client" (see Figure 4). However, as we will see further on, the production of an industrial sensor is long and delicate. It is useful to note here that a given unit operation in the chemical industry contains on the order of 400 sensors, and again as many actuators. This would tend to indicate a certain number of things, especially if one accounts for the overall costs and safety of the work force:

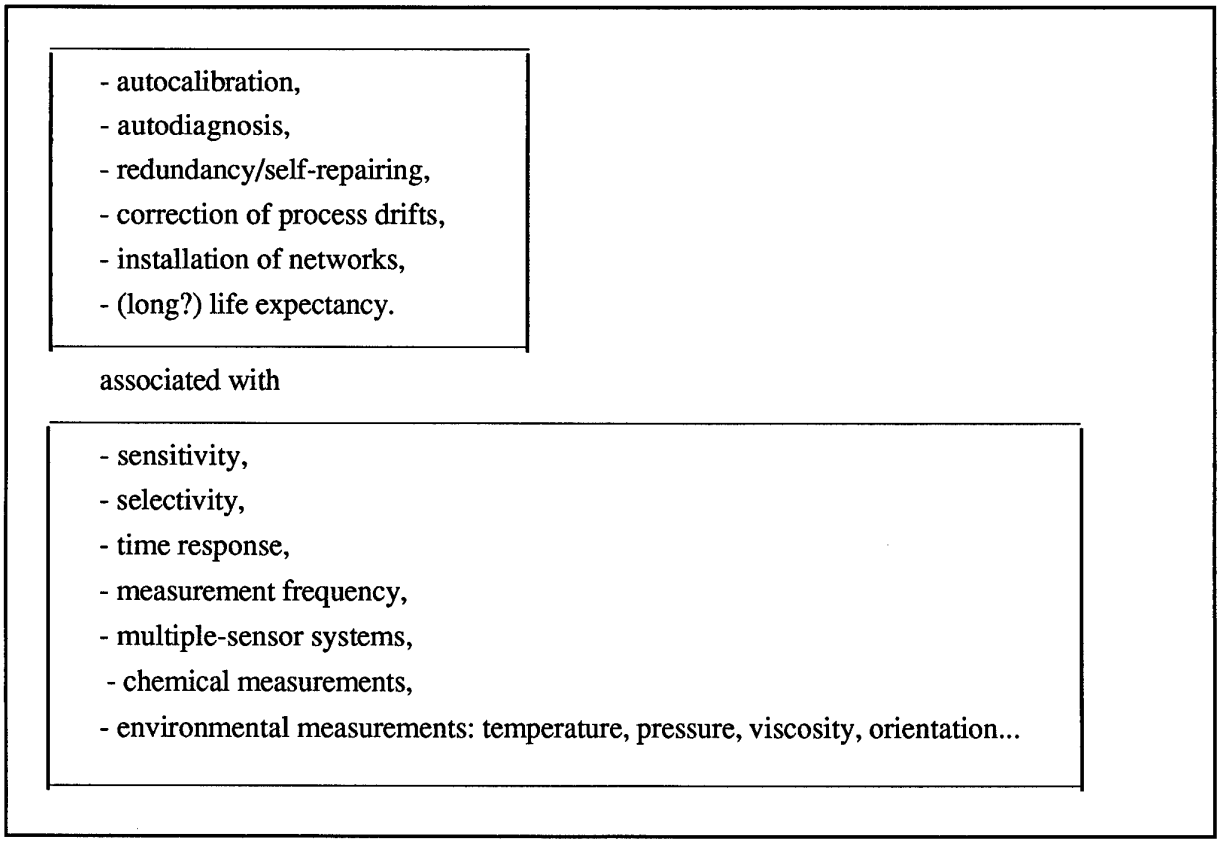


Figure 4. Industrial needs for on-line sensors

Tables I to VII outline those aspects of "intelligent" materials that must be mastered. It can be seen from this that there is a vast field of research that needs to be investigated in order to satisfy such a strong demand. The different stages of this type of research are outlined schematically in Figure 5.

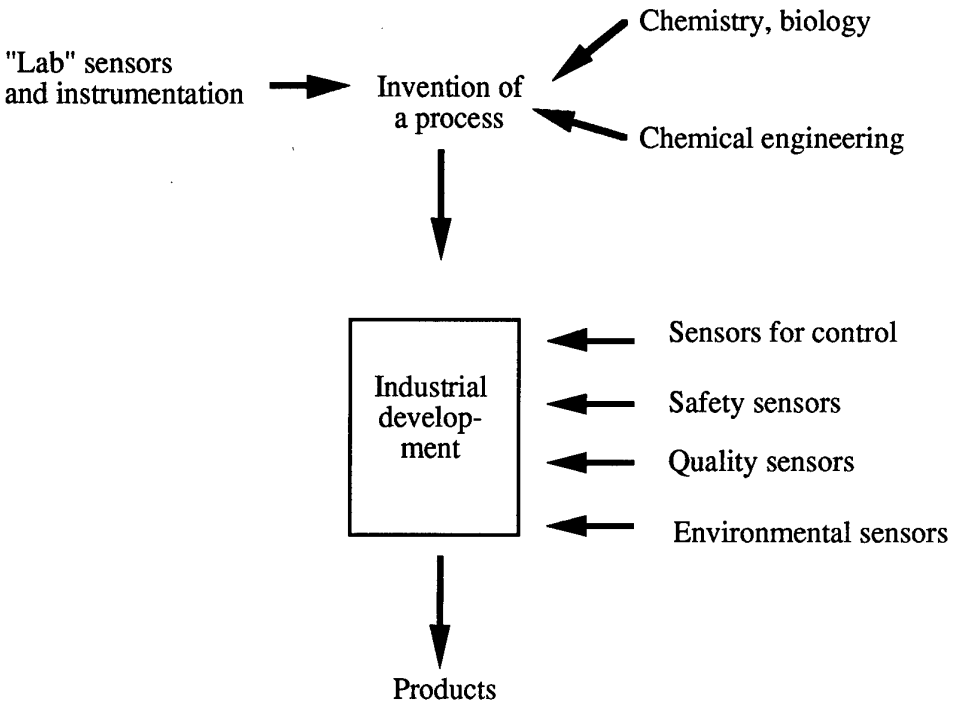


Figure 5. Steps in development from concept to industrial sensor

3 - HOW TO SATISFY THE NEED FOR SENSORS

For scientists developing their research activities in the area of the gathering of information, it would seem to me that they should answer the questions outlined in Figure 6 (or even better, to not even have to think of them) before beginning their activities. It is well known that, in the area of sensors, the scientific activity involved consists of assembling a wide diversity of elements in order to attain a given goal, and that such an "assembly" is not the result of habits and know-how that are not continually questioned. Rather, research in this area is a pluri-disciplinary activity that requires an understanding and enriching of the activities of each researchers by those of his or her colleagues (separate technologies and materials research that already exist that might be exploited with an eye to improving on the totality of the scientific knowledge).

Because of the incompatibilities that can exist between research that is useful to society as a whole, and research that is useful to the career of an individual scientist (usually judged by the number of publications), we run the danger of being conceptually stifled by the repetition of ideas and the rarity of real innovations in this area. Without a strong demand for interdisciplinary co-operation - useful because it stimulates innovation - it can be imagined that one's creative and intellectual capacity is proportional to one's capacity to create and be responsible to retroactive effects coming from society. In this context, the individual disciplines clearly show their limitations and constraints.

• Principles:	communication of optical information, use of fibres sensitive to external constraints.
• Objectives:	control of constraints, analysis of light signals, one-line control, possibility of working in polluted or contaminated environments.
and	
Results:	chemical analysis, measurement of pH, velocity, viscosity, constraints.
• Sectors concerned:	chemical analysis, measurement of pH, velocity, viscosity, mechanical and thermal, safety, industrial hygiene.

• Problems to be resolved:

- adaptation of optical systems to fibres,
- feasibility studies,
- optical multiplexing,
- production of special fibres for perfectionning of distributed sensors,
- integrated optics,
- optodes,
- new fibres
- behaviour of fibres in industrial environments (e.g. biotechnology, nuclear, ...),
- multi-sensor approach.

Table I. Fibre optic sensors (underscored text refers to those elements dealing with the material portions)

• Definition:	end of a fibre optic cable where the interaction between the limit and the milieu to evaluated occurs.
• Principles:	modification of the optical characteristics of certain materials as a function of the environment.
• Objectives and results:	in situ study of chemical and biochemical compositions.
• Sectors concerned:	biotechnology, chemistry, safety, industrial hygiene, biological and medical engineering (BME).
• Problems to be resolved:	- grafting of the reactive components, - feasibility, - nature of information, - elimination of parasitic effects of chemical or physical (e.g. bubbles) nature, - sterilisation, - temporal resolution, - multi-sensor approach.

Table II. Optodes

• Principles:	micro-ionic (solid electrolytes in thin films produced by techniques derived from the electronic industry). A concentration gradient (0_2, H_20 ...) in the ionic conductor leads to the generation of a voltage.
• Objectives:	environmental studies, on-line control.
• Sectors concerned:	industry, pollution, industrial hygiene, artificial noses.
• Problems to be resolved:	miniaturisation, deposition techniques, search for reactive systems.

Table III. Solid phase electrochemical sensors

• Principles:	use of phenomena at the conductor/electrolyte interface.
• Objectives:	measurement of equilibrium potentials, polarisation, current, chemical concentrations, temperature.
• Sectors concerned:	chemistry, biotechnology, BME, fluid mechanics (flowrate sensors for pulp and paper).
• Problems to be resolved:	integrated measurement heads, new specific electrodes.

Table IV. Electrochemical sensors (liquid phase)

• Principles:	semi-conductors used in integrated electronic circuits used in development of micro-sensors.
• Objectives:	industrial micro-sensors: temperature, pressure, magnetic fields, gas compositions.
• Sectors concerned:	automotive industry, engineering sciences, environment, safety, industrial hygiene, industrial control, artificial noses.
• Problems to be resolved:	miniaturisation, cost reduction, sensors with integrated electronic, sensitive surfaces.

Table V : Micro-sensors

• Principles:	mechanical modification of acoustic surface waves using surface wave oscillators on piezo-electric crystals (frequency modified by pressure or temperature).
• Objectives:	gas sensors, pressure, temperature.
• Sectors concerned:	automotive industry, engineering sciences, environment, safety, industrial hygiene, industrial control, artificial noses
• Problems to be resolved:	miniaturisation, cost reduction, sensors with integrated electronic, sensitive surfaces.

Table VI. Surface wave sensors

• Principles:	coupling of enzymatic and other reactions: electrochemical, optical, ...
• Objectives:	chemistry, biology, biotechnologies.
• Sectors concerned:	biotechnology, medical and biological engineering, chemical and biological analysis, industrial hygiene.
• Problems to be resolved:	development of new reactions, multiple enzyme systems, feasibility, fouling, membranes, integrated measurement heads, immobilisation of enzymes, optodes, grafting on micro-sensors.

Table VII. Enzymatic sensors

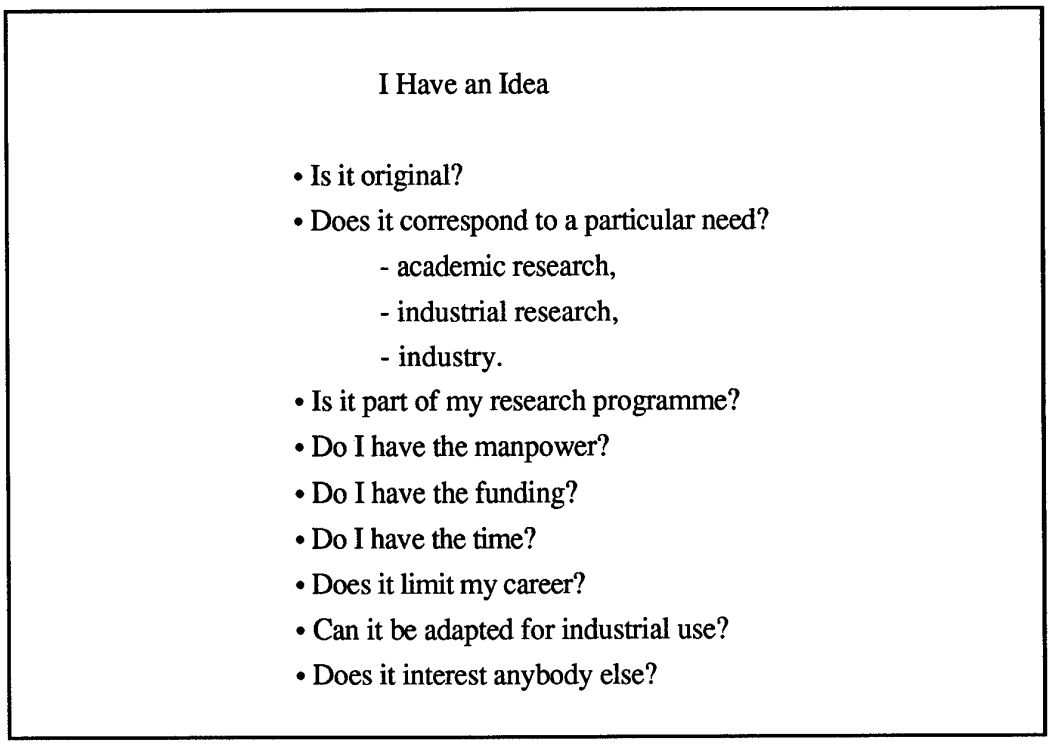


Figure 6. The ten commandments for research

Working on intelligent sensors using intelligent materials allows us in principle to look for new formal areas of research in order to explore subjects, which, until now, have remained in the dark. This will also allow us to go beyond looking at the actual devices and equipment, and to (more or less) freely explore new formal combinations. In this manner, our objectives can be satisfied, even if the weight of old structures and habits continues to be brought to bear. In this manner, it is human attitudes and behaviour that must change with respect to the production of information. It is not really a question of trying to manipulate people or things, but rather of manipulating information as if it were a "thing", to build unified environments, which, when examined in their entirety, can be explored to reveal their maximum potential, and thus to lead to the design of information gathering systems having highly original capacities and qualities.

This paradigm is defined in terms of complex information. In this area, the system is the whole set of separate entities that can be brought together, using different relationships, to form much larger structures. In this sense, the idea is to transform external information in response to a given need, or into an action. It can be stored, compared, treated, used in decision making... The reception of messages depends on a chemical, physical, or biological support, and the action it provokes can be of a macroscopic, mesoscopic, microscopic, or quantum nature. However, the nature of the substrate is of much less importance than its capability of handling a wide diversity of organised forms at the same time as it exercices its basic functions (transformation, treatment, alteration, combination, digitalisation,...).

Because of the dependance on different phenomena that occur very rapidly, the current trend of self-imitation still aims too high. A coherent development that depends on an engineering science of structural relations is needed in order to pass from the current self-limiting stage of compartmentalised relations to another more inventive stage of information gathering using new structures, and associated with the use of new, and thus intelligent, materials.

This path will be difficult to follow for that part of the French research establishment that I believe I know well, and which is strewn with structural and relational pitfalls, more than with conceptual ones. However, in a market worth on the order of 20 million U.S. dollars, it is the price to pay if France is to play a small role in a world where information supports (or controls?) human activity.

Magnetic studies of persistent photoconductivity in compensated PbTe:Ga

A.N. Vasil'ev, T.N. Voloshok, and S.V. Kuvshinnikov

Low Temperature Physics and Superconductivity Department, Physics Faculty, Moscow State University, Moscow 119899, Russia

ABSTRACT

The solid state memory effect, known as persistent photoconductivity is described in terms of electronic configurations of impurity centers in narrow-gap semiconductors. The studies of resistivity and magnetic susceptibility of compensated bulk single crystal PbTe:Ga present strong evidence that the dopant centers produce two types of electronic states: a shallow and delocalized paramagnetic level associated with the normal substitutional site configuration and a more localized non-magnetic level arizing from a lattice distortion at or near the donor. The metastable properties of the impurity centers suggest a redistribution of electrons, $2Ga^0 \Leftrightarrow Ga^+ + Ga^-$, where, rather than all donors being neutral, half the Ga atoms have two electrons and become negatively charged whereas the other half have none and are positively charged. The potential areas of application of these intelligent materials are discussed.

1. INTRODUCTION

The ability of some semiconducting compounds to memorize the action of visible or infrared light allows to consider them as a kind of intelligent or adaptive materials[1]. The term "persistent photoconductivity" used to describe this property means that the conductivity of these semiconductors is greatly enhanced at low temperatures by illuminating the sample with light of a mimimum quantum energy and that the low resistance state is maintained for a long period of time (usually hours or days) after turning off the illumination, provided the sample is kept at low temperatures. The observation of persistent photoconductivity has been reported for a number of binary and ternary compounds belonging practically to every major semiconducting family. It was found to exist in CdTe [2], and $Cd_{1-X}Mn_XTe$ [3] (A_2B_6-type compounds), $Ga_{1-X}Al_XAs$ [4] (A_3B_5-type compounds), PbTe [5], and $Pb_{1-X}Sn_XTe$ [6] (A_4B_6-type compounds), doped with various impurities. It has been observed also, in unintentionally doped semiconducting films and quantum wells [7]. Since these semiconductors and heterojunctions are potentially useful for high-speed digital applications, light-emitting devices and memory cells for infrared radiation there has been a considerable amount of experimental and theoretical attention directed towards the understanding of the phenomena of persistent photoconductivity. It has been focused mainly on electronic properties of substitutional donor dopants in binary and ternary compounds and has led to many interesting hypotheses concerning complexities exhibited by these impurities.

2. MICROSCOPIC MODEL

Most theoretical approaches explaining this solid state memory effect deal with microscopic models for the structure of defect produced by a dopant in the lattice of host compounds. These models include large and small lattice relaxation [8,9], and the exchange-site model [10]. In addition, there are more general models like the model of a Jahn-Teller instability [11], and the charge separation model [12]. Of all the models quoted the large lattice relaxation model combined with idea of charge separation, it seems, is the best corresponding to experimental findings. One of the most important outcomes of recent studies is the realization that in many cases independent of alloy composition and for various dopants each donor produces two types of electronic states: a shallow and delocalized effective mass level associated with the normal substitutional site configuration and a more localized level arizing from a lattice distorsion at or near the donor.

The dual nature of donors is usually treated from two different points of view, a localized description or effective mass approach. The localized description is valid in principle for deep states whose spatial extension is fairly limited so that only that the short-range part of the defect potential reveals itself. On the other hand, an effective mass approach is applied to cases of a smooth long-range potential. Each conduction band minimum, when treated independently, gives rise to a series of hydrogenic states. Those connected with lowest conduction band will be truly localized, while the others will form resonant states with a short lifetime. The synthesis of these approaches can be reached in a calculation of donor states when the full potential seen by the electrons

0-8194-2165-0/96/$6.00

reduces to short-range potential in the vicinity of the defect and to long-range potential in the outer region. The net conclusion is that the deep state and the shallow hydrogenic states will coexist but with some modified features.

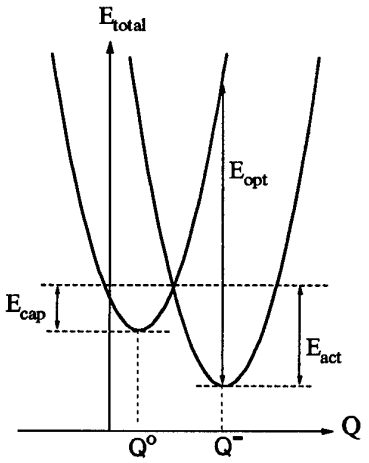


Fig. 1. Configuration-coordinate diagram for Ga donor center PbTe. The upper parabola corresponds to a neutral electronic state Ga^0, the lower one corresponds to a negatively charged state Ga^-.

The relative stability of the two types of states depends on many parameters, including pressure, temperature, and alloy composition. The general feature, however, is the existence of a repulsive barrier for the transformation between deep and shallow states. The total energy of the donor-host system has, therefore, two minima as a function of the local atomic environment of the donor. That is why the persistent conductivity can be observed in a number of doped semiconducting compounds. Using a simple configuration-coordinate diagram of the type presented in Fig. 1, one can show that the barriers for electron capture from a shallow state into a deep state and for emission from a deep state into a shallow state led to a large optical gap typically order-of-magnitude larger then a thermal ionization energy. Which one of these diagrams correspond to the chosen semiconductor can be derived from experimental data.

To understand the physical nature of the donor states one can use the tight binding description, i.e. the defect molecule model, which we illustrate for Pb vacancy substituted by Ga atom. For this we first remove the Pb atom, creating at its place a vacancy. We then replace it by the Ga impurity. In this view the s and p atomic states of the dopant interact with the appropriate symmetry combinations of the Pb vacancy dangling bond states. Each pair of states of the same symmetry will lead to one bonding (σ, or π) and one antibonding combination (σ^*, or π^*). This leads to the level structure of Fig. 2. For attractive donor potential the bonding level fall in the valence band and is filled. Among antibonding combinations lower can possibly fall into the gap, while upper will be resonant in the conducting band. The half-occupied antibonding level should possess a magnetic momentum, which can be revealed by direct magnetic measurements.

3. EXPERIMENTAL

Gallium-doped lead telluride is one of the numerous materials which exhibit, at low temperature, a persistent photoconductivity. The solubility of Ga in PbTe is only slight. No more than 1 at.% of Ga can enter the lead sublattice as a substitutional impurity. Even in this narrow interval, the dopant presents an unusual behaviour [13]. With increasing Ga content in p-type PbTe sample, the hole density falls off linearly, putting the crystal in a compensated state at $N_{Ga} \approx 0.1$ at.%. Further doping,however, does not take PbTe:Ga out of the insulating phase, the latter persists up to $N_{Ga} \approx 0.3$ at.%. Only when we leave this interval do we find the p-n conversion and a rapid increase in the density of electrons in n-type samples.

The measurements of resistivity and magnetic susceptibility were carried out on bulk single crystals of PbTe:Ga. The Ga content was chosen to be 0.3 at.%, which roughly corresponds to the region of the highest photosensitivity of this compound. The samples were spark-cut in the shape of rectangular parallelepiped and were chemically etched to remove the damaged surface layer. The ohmic contacts for Hall-effect and resistivity measurements were made by soldering of copper wire with gold-doped indium. The magnetic susceptibility was measured by Faraday balance technique. Both resistivity, and susceptibility studies were carried out over the temperature range 4-150 K. A miniature incandescent lamp adjacent to sample was used either to briefly illuminate the crystal at liquid-helium temperature, or to keep it under the permanent illumination while changing temperature.

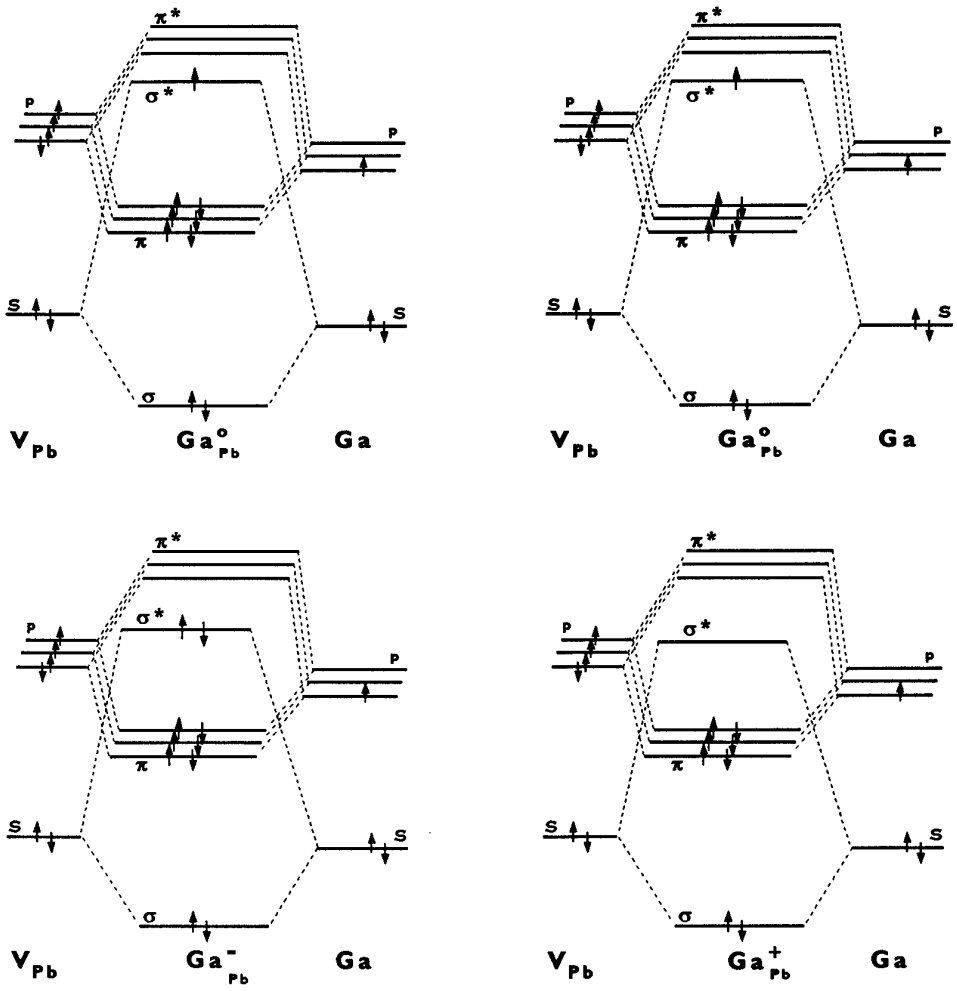


Fig. 2. Electronic configurations of Ga substituting Pb in the lattice of PbTe in neutral Ga^0, negatively charged Ga^-, and positively charged Ga^+ states. The transitions to deep electronic level are accompanied by the redistribution of electrons, $2Ga^0 \Leftrightarrow Ga^+ + Ga^-$.

3.1. Resistivity

At room temperature the resistivity of the PbTe:Ga single crystal has a value $\rho \sim 10^{-1}$ Ω·cm. At cooling in light-shielded metal chamber, it rapidly increases reaching values $\rho \geq 10^5$ Ω·cm in dark state at low temperatures. The slope of the resistivity vs. temperature curve corresponds to the activation energy of carriers $E_a = 66$ meV, which significantly differs from the value of gap in PbTe $E_g = 220$ meV. Upon illumination at liquid-helium temperature, the resistivity of the sample once again decreases to $\rho \sim 10^{-1}$ Ω·cm, comparable with high temperature value. It does not change significantly with time, except for the very fast recovery of minor part of resistivity just after illumination turn-off.

As shown in Fig. 3, at heating the resistivity remains essentially constant over a broad temperature range (to be more precise, it slightly increases with temperature), then a sharp increase in ρ up to few hundreds in Ω·cm units takes place, which gives way to an exponential decay at high temperatures. When the illumination of sample is kept permanent during heating the magnitute of resistivity peak diminishes and it shifts to higher temperature.

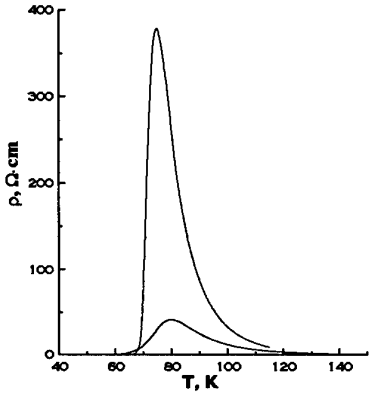


Fig. 3. Temperature dependences of the resistivity of PbTe:Ga after brief illumination at T = 4.2 K (upper curve) and under permanent illumination (lower curve) at heating.

3.2. Susceptibility

Analogous to resistivity studies the magnetic susceptibility measurements were performed in two ways, i.e. under either brief, or permanent illumination. In dark state its diamagnetic, being of the same magnitude, $\chi \sim 4 \cdot 10^{-7}$ cm^3/g, as those of the undoped lead telluride[14]. As shown in Fig. 4, under permanent illumination the diamagnetic susceptibility of PbTe:Ga slightly reduces at heating, however, small increase of diamagnetic susceptibility is evident at ~ 50 K. Quite different picture appears when the magnetic susceptibility of PbTe:Ga is measured at heating after brief illumination of the sample at low temperatures. The diamagnetic susceptibility appears to be somewhat smaller after illumination turn-off. The initial increase of diamagnetic susceptibility precedes a broad temperature range, where χ reaches temperature independent value, then a decrease in diamagnetic susceptibility takes place, which gives way in turn to the sharp increase to the same level. It should be admitted that the temperatures of singularities on temperature dependences of resistivity and magnetic susceptibility do not coincide, the latter takes place at lower temperature.

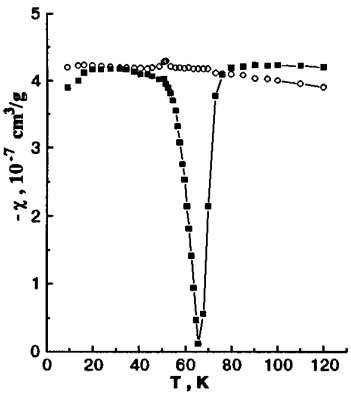


Fig. 4. Temperature dependences of magnetic susceptibility of PbTe:Ga after brief illumination at T = 4.2 K (squares) and under permanent illumination (circles) at heating.

4. DISCUSSION

The results obtained lead to the following picture of the processes, responsible for persistent photoconductivity in PbTe:Ga. The shallow electronic level produced by Ga in the gap of PbTe corresponds to the state with a small lattice distortion, which nevertheless gives rise to a thermal barrier preventing recapture of electrons at low temperatures. An order of magnitude bigger thermal barrier separates it from deep electronic level associated with large lattice distorsion. An optically induced transition from the thermodynamically stable deep state to unrelaxed metastable shallow state, or conduction band cannot be reversed at low temperatures. In accordance with Fig. 1, there exists the large Stokes shift between the thermal and optical ionization energies of the deep state due to the large lattice relaxation. The shallow electronic level produced by Ga in the gap of PbTe can be considered as a hydrogenic donor. The dopant atoms in a neutral electronic configuration, Ga^0, represent this shallow level and possess one electron on antibonding orbital σ^*. The transitions from the conduction band to metastable shallow level produce paramagnetic centers in the compound revealed by the sharp decrease of diamagnetic susceptibility. At further cooling the transitions to deep electronic level are accompanied by the redistribution of electrons, $2Ga^0 \Leftrightarrow Ga^+ + Ga^-$, where, rather than all donors being neutral, half the donors have two electrons and become negatively charged whereas the other half have none and are positively charged. When both electrons are in the singlet state of the same Ga atom due to the Pauli exclusion principle they have opposite spins resulting in all donors being diamagnetic. This explains the diamagnetic susceptibility of PbTe:Ga both in the dark, and illuminated state at low temperatures.

5. SUMMARY

In conclusion, we have perfomed direct resistivity and magnetic susceptibility measurements on a narrow-gap semiconductor, PbTe:Ga, characterized by well defined property of persistent photoconductivity. The data obtained provide strong evidence to the hypotheses of dual nature of gallium donors in lead telluride. They produce two types of electronic levels in host compound: a paramagnetic one, associated with small lattice relaxation, and a diamagnetic one, accompanied by large lattice relaxation. The transitions between these states

need a redistribution of the electrons between Ga atoms, where negatively charged donors possess two electrons per site, and those positively charged possess none electrons on antibonding orbital.

6. ACKNOWLEDGMENTS

The authors express their deep gratitute to L.A. Ponomarenko for assistance in measurements, stimulatung discussions and critical reading of the manuscript.

7. REFERENCES

1. C.A. Rogers, " Intelligent materials", Scientific American, pp. 154-157, Sept. 1995.

2. S. Scholl, J. Gerschultz, H. Schafer, F. Fischer, A. Waag, and G. Landwehr, "Persistent photoconductivity in CdTe-based II-VI semiconductors", Sol. St. Comm., Vol. 91, No. 6, pp. 491-495, 1994.

3. J. Stankiewicz and V.M. Yartsev, "Photoionization of electron traps in Ga-doped $Cd_{1-X}Mn_XTe$", Sol. St. Comm., Vol. 95, No. 2, pp. 78-78, 1995.

4. K.A. Khachaturyan, D.D. Awschalom, J.R. Rozen, and E.R. Weber, "Magnetic studies of persistent photoconductivity in n-$Al_XGa_{1-X}As$", Phys. Rev. Lett., Vol. 63, No. 12, pp. 1311-1314, 1989.

5. A.N. Vasil'ev, T.N. Voloshok. Yu.P. Gaidukov, and N.P. Danilova, "Nature of the delayed photoconductivity in PbTe(Ga)", JETP Lett., Vol. 58, No. 12, pp. 907-911, 1993.

6. B.A. Akimov, N.B. Brandt, S.A. Bogoslovskii, L.I. Ryabova, and S.M. Chudinov, "Non-equilibrium metallic state in alloys $Pb_{1-X}Sn_XTe$(In), JETP Lett., Vol. 29, No. 1, pp. 11-14, 1980.

7. S. Elhamri, M. Ahoujja, K. Ravindran, D.B. Mast, R.S. Newrock, W.C. Mitchel, G.J. Brown, I. Lo, M. Razeghi, and X. He, 'Persistent photoconductivity in thin undoped GaInP/GaAs quantum wells", Appl. Phys. Lett., Vol. 66, No. 2, pp. 171-173, 1995.

8. D.J. Chadi and K.J. Chang,"Theory of the atomic and electronic structure of DX centers in GaAs and $Al_XGa_{1-X}As$ alloys", Phys. Rev. Lett., Vol. 61, No. 7, pp. 873-876, 1988.

9. D.J. Chadi and K.J. Chang, "Energetics of DX center formation in GaAs and $Al_XGa_{1-X}As$ alloys", Phys. Rev. B, Vol. 39, No. 14, pp. 10063-10074, 1989.

10. T.N. Morgan, "The DX centre", Semicond. Sci. Technol., Vol. 6, pp. B23-B26, 1991.

11. O.B. Maksimenko and A.S. Mishchenko, "On the pseudo Jahn-Teller nature of the IV-VI compounds phonon spectra anomalies", Sol. St. Comm., Vol. 92, No. 10, pp. 797-802, 1994.

12. M. Lannoo, "Theoretical treatment of DX and EL2", ", Semicond. Sci. Technol., Vol. 6, pp. B16-B22, 1991.

13. F.F. Sizov, S.V. Platzko, and V.M. Lakeenkov, "Deep levels in PbTe", Sov. Phys. Semocond., Vol. 19, pp. 53-55, 1985.

14. M.Matyas, "Magnic susceptibility of PbTe", Czech. J. Phys., Vol.8, pp. 301-304, 1958.

Photo-sensitive tetragonal germanium nanostructures deposited by the cluster-beam evaporation

Shinji Nozaki, Seiichi Sato, Hiroshi Ono, Hiroshi Morisaki,
Mitsuo Iwase*, and Kiyoshi Takahashi**

Department of Communications and Systems,
The University of Electro-Communications
1-5-1 Chofugaoka, Chofu-shi, Tokyo 182, Japan
*Department of Electrical Engineering, Tokai University
1117 Kitakaname, Hiratsuka-shi, Kanagawa, 259-12, Japan
**Department of Electronics and Information Science
The Nishi-Tokyo University
Uenohara-cho, Kitatsuru-gun, Yamanashi 409-01, Japan

ABSTRACT

The germanium (Ge) films of nanostructures deposited at 300 and 77 K by the cluster-beam evaporation technique are found to consist of small nanostructures. The crystal structure of the films is not the ordinary diamond but tetragonal structure. The Ge film deposited at 77 K exhibits photo-oxidation and blue-light emission when it is exposed to UV light. It may be said that the material possesses an ability to sense the environment and change in response to a change in the environment, which is one of functions of intelligent materials. It, however, never restores itself even if an external stimulus (UV light in this case) is removed. Nevertheless, because of the unique crystal structure and optical properties of the Ge films, there is a possibility that further study may reveal their potential for intelligent materials.

1. INTRODUCTION

Since the 1st International Conference on Intelligent Materials in Oiso, Japan in 1992,[1] the concept of intelligent materials has spread worldwide. What distinguishes intelligent materials from conventional materials are functions as follows: the environment-judge/adjust function, the self-restorative function. the self-diagnostic function, and the time-dependent function. Such materials are in great demand in many fields of industry. Because of absence of intelligent materials in nature, most research activities focus on creation of intelligent materials.

As described by Nozaki and Takahashi,[2] scientists and engineers in Japan launched out into the project called the "Nanospace Lab" in 1993 with an assist of the Science and Technology Agency. The Nanospace Lab is an experimental and theoretical approach to physically understanding of the behavior of the nanospace when an external stimuli such as a light beam is applied to the nanospace and is expected to lead to creation of intelligent materials. Through the Nanospace Lab, we have established the cluster-beam evaporation technique to deposit thin films consisting of germanium (Ge) nanostructures, which exhibit optical and electrical properties distinct from those of bulk Ge. In this paper, we show unique properties of the Ge nanostructures and discuss their potential for intelligent materials.

2. EXPERIMENTAL

Figure 1 shows an apparatus of the cluster-beam evaporation technique, which is equipped with a crucible machined from a carbon rod. The cap of the crucible is 1 mm thick and has a nozzle hole with a diameter of 1 mm. The crucible loaded with small pieces of undoped Ge ($\sim$40 Ωcm) was heated by electron bombardment. During the deposition, the temperature of the crucible was kept at 2000 K, and the pressure in the chamber was fixed at 5×10^{-6} torr. The substrate temperature was either room or liquid nitrogen temperature. The typical film thickness was 100 nm after 60 min deposition. The classical nucleation theory[3] predicts that the sizes of Ge nanostructures formed by the cluster-beam evaporation technique would be much smaller than those by the gas-evaporation technique, which is conventionally used to deposit metal or semiconductor

0-8194-2165-0/96/$6.00

nanostructures.

P-type (100) Si substrates were used for Raman spectroscopy, electron spectroscopy for chemical analysis (ESCA) and photoluminescence (PL) measurements, while quartz substrates were used for optical absorption measurements. The Raman study was made by using the 514.5 nm line of argon (Ar) ion laser with an intensity of 400 mW. The 313 nm line of a mercury lamp selected with an maximum (FWHM) was 10 nm, was used as an irradiation light and an excitation source for PL measurements. PL and Raman measurements were carried out in the air at room temperature.

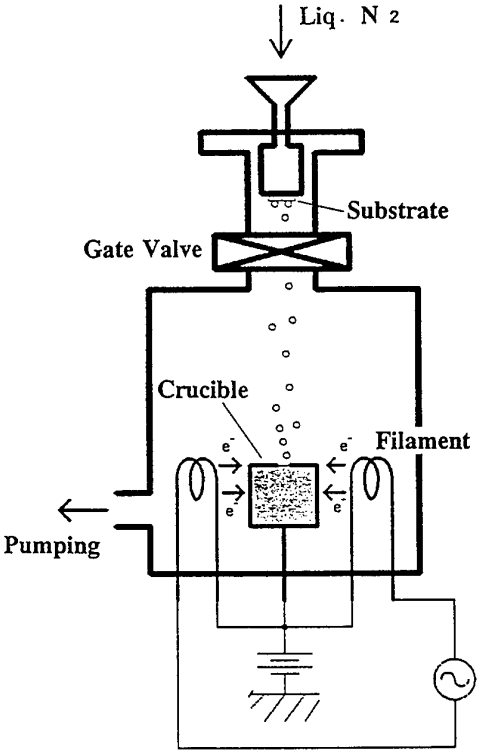


Fig. 1. Apparatus of the cluster-beam evaporation technique.

3.RESULTS AND DISCUSSION

Typical Raman spectra of the Ge films deposited at 77 and 300 K are shown in Fig. 2, where the

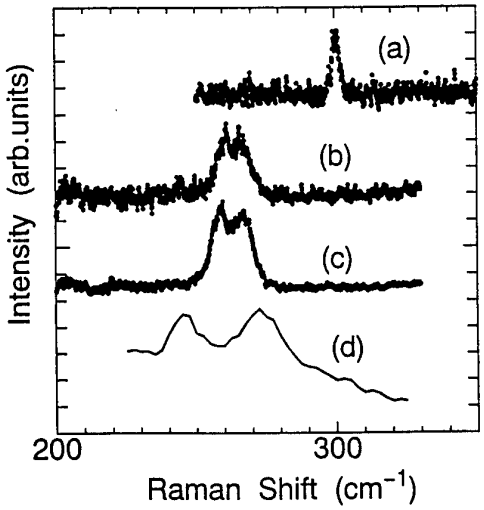


Fig. 2. Raman spectra of the Ge films deposited at (b) 300 K and (c) 77 K. The Raman spectra of (a) bulk Ge and (d) a high-pressure form of Ge are also shown for comparison.

Raman spectra of an undoped Ge wafer (c-Ge) and a high-pressure form of Ge (ST-12)[4] are also shown for comparison. The Raman spectra of both Ge films deposited at 77 and 300 K indicate that their structure is not the ordinary diamond structure but the tetragonal structure, for which Kobliska et al. reported peaks at 273±3 (Γ_5) and 246±3 cm^{-1} (Γ_3). The double peak observed for both Ge films by the cluster-beam evaporation technique resembles that obtained by Kobliska et al. Maeda et al. also observed a structure other than the diamond structure in the transmission electron microscope (TEM) image of Ge nanostructures embeddedin SiO_2 for sizes less than 4 nm. Since the structure of a crystallite may change from the diamond to a more close-packed structure so as to reduce the surface energy for sizes smaller than a critical size. Tomanek and Schluter estimated that the phase transition of Si nanostructures from the diamond to the bcc structure, a high-pressure form of Si occurred when the number of atoms in a nanostructure becomes $10^2 \sim 10^{3.6}$ In TEM micrographs, the Ge film deposited at 300 K appears smooth and uniform, while that deposited at 77 K consists of nanostructures with diameters from 4 to 40 nm.[7] However, the Ge film deposited at 300 K may consists of much smaller nanostructures.

The optical bandgap of the Ge film deposited at 300 K estimated by a simple extrapolation from its absorption spectrum in Fig. 3. is 1.4±0.2 eV, which is considerably greater than that of bulk Ge (0.66 eV, indirect gap) and agrees with a theoretical calculation of the direct bandgap of a high-pressure form of Ge.[8] It is, however, difficult to estimate the optical bandgap of the Ge film deposited at 77 K, because of a gradual increase of the optical absorption coefficient. It appears to be higher than that of the Ge film deposited at 300 K.

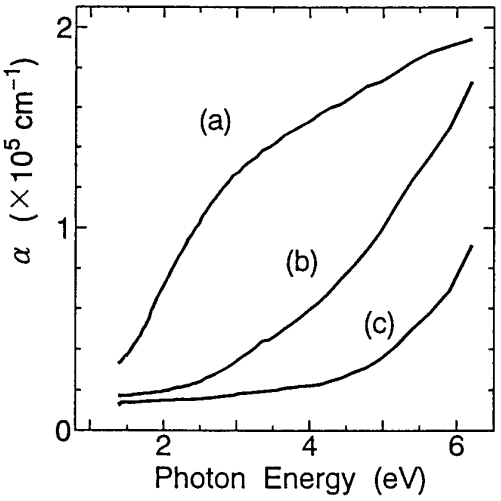


Fig. 3. Optical absorption spectra of the Ge films deposited at (a) 300 K and (b) 77 K. Curve (c) is the optical absorption spectra of the Ge film deposited at 77 K after being exposed to 20 μW/mm^2 UV light with a wavelength the of 313 nm for 30 min.

Figure 4 shows the ESCA spectra of the surfaces of the Ge films deposited at 300 and 77 K. The solid and broken curves are the spectra of the as-deposited samples and those of the samples after exposure to the 313 nm line of UV light with a power of 20 μW/mm^2 for 30 min, respectively. It is found that the Ge film deposited at 300 K is hardly oxidized as expected, while the Ge film deposited at 77 K, which is partially oxidized even before exposure to the UV light, is photo-oxidized rapidly. The photo-oxidation is found to proceed to the deeper inside of the Ge nanostructure for a prolonged exposure. With decreasing the size of a Ge core, the apparent bandgap of a Ge nanostructure increases due to the quantum-size effect. An increase in the optical bandgap of the Ge film deposited at 77 K after photo-oxidation, as seen in Fig. 3, evidences the quantum-size effect. The photo-oxidation of Ge nanostructures was first reported by Harshavardhan and Hegde.[9] They observed photo-oxidation of highly porous low-density microstructures in the obliquely deposited Ge film when it is irradiated with photons whose energy is higher than its bandgap. The photo-oxidation is unique to Ge nanostructures.

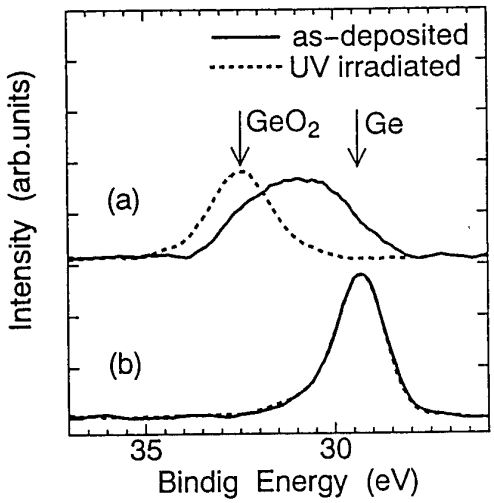


Fig. 4. Ge3d ESCA spectra of the surfaces of (a) the Ge film deposited at 77 K and (b) that deposited at 300 K. Solid and broken curves are those for before and after UV irradiation, respectively. The samples were exposed to 20 μ W/mm^2 UV light with a wavelength of 313 nm for 30 min.

The PL spectra of the Ge film deposited at 77 K after 0, 15, and 30 min-exposure to the UV light are shown in Fig. 5. The solid curve is a Gaussian curve which is fitted to the experimental data. The PL peak

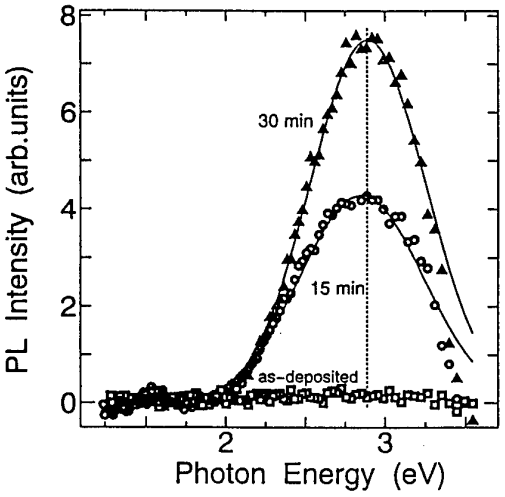


Fig. 5. Typical PL spectra of the as-deposited and UV-irradiated Ge films. Solid curves are the Gaussian curves fitted to experimental data. The sample was exposed to 20 μ W/mm^2 UV light with a wavelength of 313 nm. The irradiation periods were shown in the figure.

energy is 2.9 eV, independent of the exposure time. The blue light emission is strong enough to be recognized with the naked eye even under room light. It should be noted that the Ge film deposited at 77 K shows no detectable luminescence before exposure to the UV light, and that the Ge film deposited at 300 K is not luminescent either before or after exposure to the UV light. As seen in Fig. 6, there is a positive correlation between the degree of the photo-oxidation and the PL peak intensity. The degree of the photo-oxidation is monitored as the GeO_x content measured by a ratio of an amount of GeO_x to a sum of amounts of Ge and GeO_x. Since the PL peak energy is independent of the degree of photo-oxidation, and its intensity correlates with

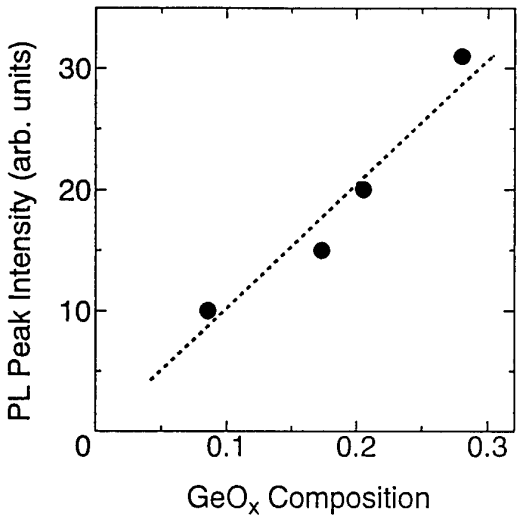


Fig. 6. Correlation between the PL peak intensity and the GeO_x composition. The GeO_x composition is defined as a ratio of the GeO_x content to a sum of the GeO_x and Ge contents (GeO_x/(GeO_x+Ge)).

the degree of photo-oxidation, we attribute the blue-light PL to defects in GeO_x.

As discussed above, both Ge films deposited at 77 and 300 K by the cluster-beam evaporation technique are distinct from bulk Ge. In particular, the Ge film deposited at 77 K is photo-sensitive and is made luminescent by UV irradiation. Because of its ability to respond to an external stimulus, the Ge film deposited at 77 K may possess an ability to sense the environment and change in response to a change in the environment. It is, however, unable to restore itself, because the Ge film remains oxidized even if the UV irradiation is ceased. Although the photo-oxidation modifies the optical properties such as optical absorption and PL characteristics, these modifications are permanent. Therefore, the Ge films deposited at 77 by the cluster-beam evaporation technique is still far from ideal intelligent materials unless we are able to find an external stimulus which can cause a restorable modification. It is not clear why the Ge film deposited at 300 K exhibits neither photo-oxidation nor blue-light emission when it is exposed to the UV light. Nevertheless, the Ge films deposited by the cluster-beam evaporation technique are distinct from bulk Ge in the crystal structure, and further study on their material properties may reveal a potential for intelligent materials.

4.CONCLUSIONS

Ge films were deposited on substrates whose temperatures were kept at room and liquid nitrogen temperatures by the cluster-beam evaporation technique. The Ge film deposited at 77 K is found to consist of nanostructures with diameters from 4 to 40 nm, while that deposited at 300 K appeases to consist of much smaller nanostructures. Even a larger-size nanostructure in the Ge film deposited at 77 K may be an agglomeration of smaller-size nanostructures. Both Ge films are found to consist of the tetragonal crystalline structure, not the ordinary diamond one. Such a phase transition to a close-packed structure was theoretically predicted in order to reduce the surface energy when the size becomes smaller than a critical size.

It is also interesting to find that the Ge film deposited at 77 K becomes oxidized by the UV exposure and exhibits blue light emission. The material manifests an ability to sense the environment and change in response to a change in the environment, which is one of functions of intelligent materials. It, however, never restores itself. Nevertheless, both Ge films deposited by the cluster-beam evaporation technique are unique in the crystal structure, and further studies on their material properties may lead to creation of intelligent materials.

This study was partially supported by a research grant from the Yazaki Science Promotion Foundation and Special Coordination Funds for Promoting Science and Technology entitled "Research on New Material Development by Nanospace Lab."

5. REFERENCES

1. T. Takagi et al. (ed.), Proceedings of the First International Conference on Intelligent Materials, Technomic Publishing Co., Inc., Lancaster, PA, USA, 1993.

2. S. Nozaki and K. Takahashi, "Research activities on intelligent materials in Japan," Proceedings of the Second International Conference on Intelligent Materials, C.A. Rogers and G. G. Wallance (ed.), Technomic Publishing Co., Inc., Lancaster, PA, USA, pp. 1230-1241, 1994.

3. T. Takagi, Ionized-Cluster Beam Deposition and Epitaxy, Chapter 3, Noyes Publications, Park Ridge, NJ, USA, 1988.

4. R. J. Kobliska et al., "Raman scattering from phonons in polymorphs of Si and Ge," Phys. Rev. Lett. **29**(11), pp. 725-728, 1972.

5. Y. Maeda et al., "Mechanism of visible photoluminescence from μc-Ge embedded in SiO_2 glassy matrics," Extended Abstracts of the 1992 International Conference on Solid State Devices and Materials, Yokohama, Japan, pp. 379-381, 1992.

6. D. Tamanek and M. A. Schluter, "Structure and bonding of small semiconductor clusters," Phys. Rev. B, **36** (2), pp. 1208-1217, 1987.

7. S. Sato et al., "Tetragonal germanium films deposited by the cluster-beam evaporation technique," Appl. Phys. Lett. **66**(23), pp. 3176-3178, 1995.

8. J. D. Joannopoulos and M. L. Cohen, "Electronic properties of complex crystalline and amorphous phases of Ge and Si. I. Density of States and band structures," Phys. Rev. B 7(6), pp. 2644-2657, 1973.

9. K. S. Harshavardhan and M. S. Hegde, "On photooxidation of Ge in obliquely deposited Ge and $Ge_{25}X_{75}$(X=S, Se, Fe) thin films," Solid State Commun. **69**(1), pp. 117-120, 1989.

SEMICONDUCTOR LIGHT DETECTOR WITH OPTICAL CONTROL OF THE PHOTOSENSITIVE REGION FOR INTELLIGENT SYSTEMS

P.G.Kasherininov, A.V.Kichaev

A.F.Ioffe Physical-technical Institute,
Russian Academy of Sciences, St.Petersburg

A new type of photodetector is proposed in which the size and configuration of its photosensitive surface, as well as its sensitivity to the detected optical signal, are controlled by a special sensitizing light flux.

This kind of detector can be used for various purposes:

(1) identification of images,
(2) recording information from one of several spatially separated light fluxes simultaneously incident on its surface,
(3) determining the location of the centers of light spots on the surface of the photodetector in two coordinates,
(4) formation of two-dimensional image signals, etc.

The detector functions through a reversible photoinduced spatial readjustment of the electric field in structures based on high-resistivity (semi-insulating) crystals and caused by the charges of free photocarriers [1]. On the surface of this kind of crystal there are potential barriers in the form of tunnel-thin insulating (oxide) layers (TI). Passage of currents (photocurrents) through them has been shown [2,3] to be accompanied by a buildup, near the interface, of charge from free photocarriers, which cause an effective readjustment of the electric field in the crystal. When the surface of these structures is illuminated, a readjustment of the field takes place only at the irradiated portions [4].

A change in the distribution of the electric field in a crystal is accompanied in turn by a change in the sensitivity of the crystal to another (the detected) optical signal incident on its surface.

The main idea behind the new photodetector is the use of a sensitizing light flux to specify the size and configuration of the photosensitive area on the detector surface and also to control its sensitivity by varying the intensity of the sensitizing flux. A detector of this type has been realized in the form of an n-p-(TI)-metal metal structure on a semi-insulating p-CdTe crystal ($\rho=10^8$ $\Omega\cdot$cm, $\mu_p=50$ cm^2/V$\cdot$s, $\mu_n=5\cdot10^2$ cm^2/V$\cdot$s, $\tau_p\cong\tau_n=0.15$-0.2 μs). A thin n-p junction was created on the surface of a plane-parallel slab of p-CdTe (7×8×2.5 mm) by thermal diffusion of indium ions from an optically transparent low-resistance layer of In_2O_3 deposited on the crystal surface by the reactive magnetron sputtering in an Ar, O_2, H_2 atmosphere. On the other surface a transparent gold electrode was deposited by chemical depositions. A dc-voltage V=200-400 V was applied to the structure in reverse bias polarity for the n-p junction.

The structure was illuminated on the side of the n-p junction by sensitizing light at the characteristic wavelength ($\lambda=0.82$ μm) with an intensity $I_0=1$-20 mW/cm^2 and on the side of the gold electrode by a low intensity modulated light flux, also in the fundamental absorption region, which was to be detected (Fig.1a).

0-8194-2165-0/96/$6.00

The distribution of the electric field in the interior of the photoconductor was measured from the magnitude of the transverse electrooptical effect when the crystal was probed by a narrow transmitted beam of polarized light (λ=1.3 μm) perpendicular to the direction of the electric field [5]. It was found that when the sensitizing light is absent the electric field tn this type of structure is concentrated in the space-charge region of the n-p junction (Fig. 1b), whose width (W) is substantially less than the thickness of the crystal (L) (W<L). The electric field in the base region is almost zero. The diffusion length for the carriers (L_D) is much less than the thickness of the base region of the crystal (L_D<<L-W); hence the effect of the detected light at the gold electrode does not produce a response in the external circuit because the photocarriers produced in this light are not separated by the electric field and recombine near the irradiated electrode (Fig. 1b).

Turning on the sensitizing light (I_0) causes a change in the spatial distribution of the electric field in the structure [4]. The high-field region is shifted in the base towards the gold electrode (Fig. 1c). When the field is redistributed in this way, a photoresponse to the modulated flux (I_1) begins to show up the external circuit since now the electron-hole pairs produced by this light are separated by the electric field and contribute to the photocurrent. This signal can be picked out against the dc background current given by the sum of the dark current of the photodetector and the dc current created by the sensitizing light.

The magnitude of the detected signal will vary when the field distribution in the structure is changed by the sensitizing light and, therefore, when the intensity of this light is changed. Figure 2 shows plots of the response as function of the intensity of the sensitizing light, I_0, for different applied voltages V. It is clear that the response increases with I_0 and saturates at a certain level I_S=f(V). For example, for V=50 V, we have I_S=25 mW/cm^2. The sensitivity of this type of detector depends on the power of the sensitizing light flux (the size of the irradiated area) and the applied voltage. For V=100 V the sensitivity of the detector was $D > 10^7 \text{ cm} \cdot \text{Hz}^{1/2}/\text{W}$.

The spatial resolution of the detector was determined from the variation in the response with position during simultaneous irradiation of the n-p junction by a strip of sensitizing light through the spatial transparency (MIR) and scanning the surface of the detector on the side of the gold electrode with a focused modulated light beam. The measured spatial resolution of the detector was 5-10 lines/mm with a response rate $\nu \sim 10^0$ cycles/s.

These detectors can be used for identification images using masks. The kind of mask is determined by the size and configuration of the photosensitive surface.

When these detectors are used for recording information from one of several spatially separated light fluxes that are simultaneously incident on its surface, the sensitizing light should be directed on to the area of the n-p junction surface opposite that portion of the surface of the gold electrode that is being illuminated by the chosen data flax and the signal from that flux will be picked up in the external circuit.

When the detector is used to create signals from a two-dimensional image, a two-dimensional pattern is projected onto the

detector surface on the side with the gold electrode. Then the surface of the n-p junction is scanned in two dimensions by a narrow intense beam of sensitizing light. This beam causes a local redistribution of the electric field and at any given time the external circuit picks up a data signal from a portion of a projected image. The reconstructed image can be projected on a CRT screen.

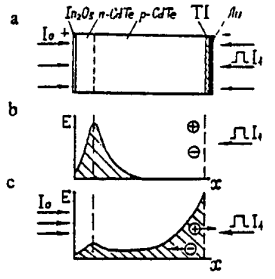


Fig.1. A photodetector with optically controlled photosensitivity: (a) a diagram of the experiment, (b) distribution of the electric field in the structure when the sensitizing light is absent (I_0=0), and (c) distribution of the electric field in the structure when the sensitizing light is turned on (I_0>0).

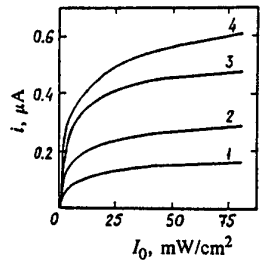


Fig.2. The photoresponce as a function of the intensity of the sensitizing light (I_0) for a fixed intensity of the signal to be detected (I_1=5 mW/cm^2) and for detector voltages V=30 (1), 50 (2), 100 (3) and 150 (4) V.

REFERENCES

1. P.G.Kasherininov, D.G.Matyukhin and V.A.Sladkova *Sov.Phys. Semicond.* 14, 763, (1980)
2. A.A.Gutkin and V.E.Sedov *Sov.Phys.Semicond.* 10, 1589, (1976)
3. H.C.Card and F.S.Yang *Appl.Phys.Lett.* 29, 51, (1976)
4. P.G.Kasherininov, A.V.Kichaev, S.L.Kuzmin and I.D.Yaroshetskii *Tech.Phys.Lett.* 19(5), 278, (1993)
5. P.G.Kasherininov, A.V.Kichaev and A.A.Tomasov *Semiconductors* 29(11), 1092, (1995).

FROM INTELLIGENT MATERIALS TO SMART SENSORS

Elvira Fortunato, Guilherme Lavareda and Rodrigo Martins

Materials Science Dep., Faculty of Science and Technology of New University of Lisbon
Quinta da Torre, P-2825 Monte de Caparica, Portugal

Fernando Soares and Luís Fernandes

Centre of Excellence for Microelectronics and Optoelectronic Processes - CEMOP-UNINOVA
Quinta da Torre, P-2825 Monte de Caparica, Portugal

ABSTRACT

A Linear array Thin Film Position Sensitive Detector (LTFPSD) based on hydrogenated amorphous silicon (a-Si:H) is proposed for the first time, taking advantage of the optical properties presented by a-Si:H devices we have developed a LTFPSD with 128 integrated elements able to be used in 3-D inspections/measurements. Each element consists on an one-dimensional LTFPSD, based on a p.i.n diode produced in a conventional PECVD system, where the doped layers are coated with thin resistive layers to establish the required device equipotentials. By proper incorporation of the LTFPSD into an optical inspection camera it will be possible to acquire information about an object/surface, through the optical cross-section method[1]. The main advantages of this system, when compared with the conventional CCDs, are the low complexity of hardware and software used and that the information can be continuously processed (analogue detection).

1. INTRODUCTION AND MOTIVATION

In 1992 the authors began working into a new idea for making direct measurements of an incident light pattern. This idea was stimulated by the desire to perform high-speed 3-D profile measurements, for industrial applications.

Traditionally, 3-D profile measurement systems are based on laser triangulation techniques, where a laser line is projected on the object under analysis and the reflected image captured (through optical lenses) by a Charged Coupled Device detector (CCD) and from it, processed through a conversion circuit to deliver the information to a computer. Usually, the CCD detector is incorporated in a standard TV camera positioned with a certain angle relative to the laser line projection plane. However, the use of TV cameras delivering standard video signals limit the measurement rate to the number of frames per second of a standard TV signal (25 frames per second), even if the processing is performed in hardware. When the application requires high resolution and/or high speed 3-D profile inspection, a different sensor system should be used.

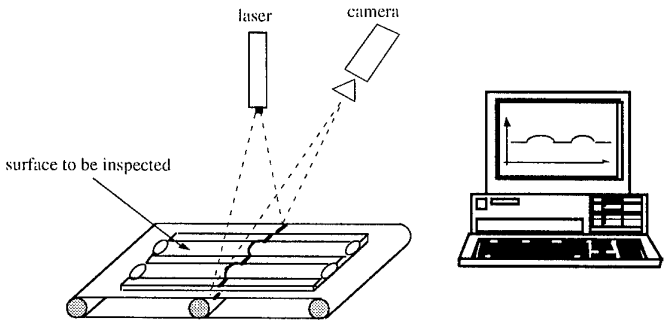


Figure 1 - Illustration of the 3-D measurement performed by the LTFPSD.

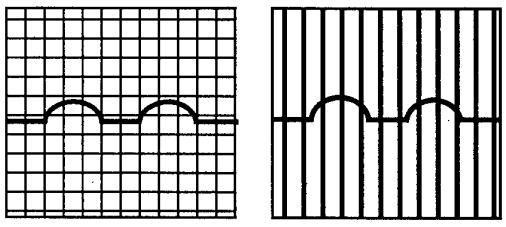


Figure 2 - Comparison of profile detection by a conventional CCD and the LTFPSD.

The development and the application of an array of linear thin film position sensitive detectors constituting a linear-camera-like device enables the inspection at a rate up to 1000 measurements per second. The output of this new sensor system

0-8194-2165-0/96/$6.00

delivers directly the position of the laser line in each sensor element of the array while the output of a standard TV camera has to be pre-processed to determine the position of the laser line in each column (see figures 1 and 2). This linear camera-like-device enables the interface to standard processing boards already developed for linear cameras and minimise the integration efforts and costs. The developed 3-D profile inspection system based in arrays of 1-D LTFPSD can be used directly to inspect 3-D production pieces or finished articles, in a non contact manner, where the main limitation is the specifications of the mechanical tools and not the ones related to the detector (such as conveyors where quality control of each product or piece can be performed item by item, in real time).

2. OPERATION PRINCIPLE

Each elemental 1D-LTFPSD of the array has the end-terminals connected to an analogue shift register (SR - MX4 circuit) to process the information recorded in both end-contacts as shown in figure 3. Per stripe, we get the information concerning the "point" of the line projected on the array as:

$$P_n(y_n) = \frac{L(I_{0,n} - I_{1,n})}{2(I_{0,n} + I_{1,n})} \quad (1)$$

where L is the length of each stripe, the subscripts 0 and 1 refer to the position of each end-contact, n is an integer that varies from 1 to 128 and the reference is considered to be the centre of the gravity of each elemental 1-D LTFPSD.

The recorded values are processed in sequential series ($[I_{0,1}...I_{0,n}]$ and $[I_{1,1}...I_{1,n}]$) by the SR whose output correspond to a voltage signal that is fed to the SENSIT^2 card. From that card, a sequential voltage information is obtained concerning P_n as given by equation (1). After that, the information is supplied to an A/D card to digitise the analogue signal (P_n) prior to be received by the computer. The SR's and the A/D converters (12 bits) are commanded by a controller box that determines the required time delays and the number of scans allowed per second, between information pockets, using the same clock command at frequencies up to 1 MHz.

The position of an image line projected in the plane z-y is determined by the y_n data obtained by the 128 stripes and related to the currents detected by both SR, as above explained. The third variable (x) is the angle between the light source (laser) and/or the detector (TFPSD array) with the object plane to be inspected and by so, the determination of the depth profile related to the image received by the TFPSD array.

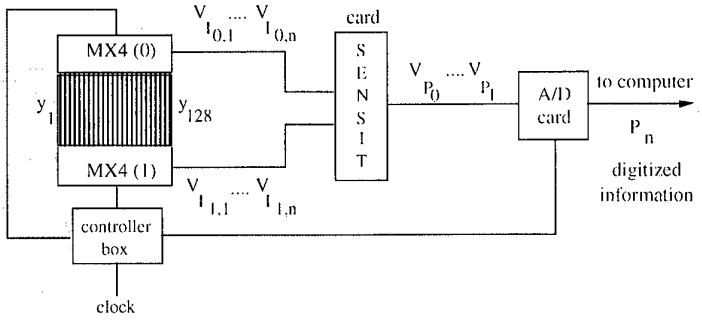


Figure 3 – Schematic diagram of the sensor electronics.

3. EXPERIMENTAL DETAILS

3.1. Device fabrication steps

The structure of the LTFPSD is presented in figure 4, which illustrates the plane (top) and cross-sectional views. The fabrication process has the following steps (see Table I):

1- deposition of an Indium Tin Oxide (ITO) onto a glass substrate (front equipotential) by reactive thermal evaporation and patterned using standard photolithography processes;

2- deposition of the p-i-n a-Si:H structure by PECVD techniques, using the procedure described elsewhere[3]. To prevent lateral leakage currents,[4] the p-i-n structure was also patterned;

3- finally an Aluminium metalization was performed by electron gun technique, followed by a reactive plasma etching to define the metal contacts and the thin resistive layer (back equipotential).

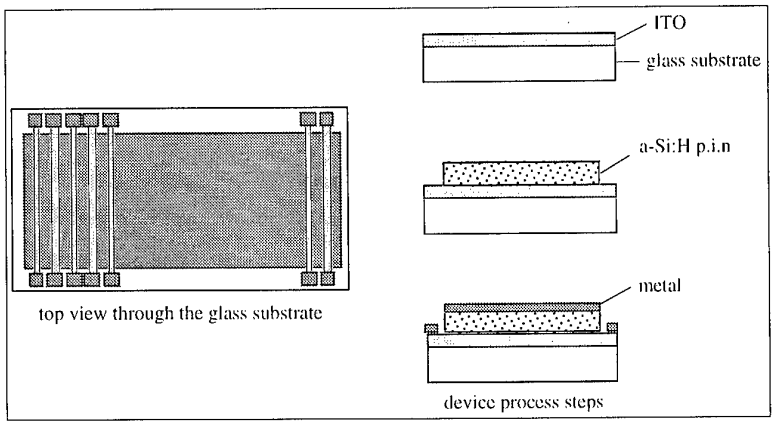


Figure 4 – Fabrication process of an LTFPSD.

Table I - Main process conditions for the fabrication of an Linear array Thin Film Position Sensitive Detector.

N°	Process step	Conditions
1	Glass substrate	Cleaning
2	ITO deposition (reactive thermal evaporation)	T = 200 °C d = 1000 Å
3	ITO patterning	mask #1
4	p-i-n semiconductor deposition (PECVD system)	*p-layer:* d = 200 Å 0.6% doping (B_2H_6/SiH_4) p = 15 W *i-layer:* d = 5000 Å pure SiH_4 p = 10 W *n-layer:* d = 600 Å 1.6% doping (PH_3/SiH_4) p = 12 W
5	p-i-n patterning	mask #2
6	Metalization (electron gun)	Aluminium d = 3000 Å
7	Patterning of thin resistive layer and contacts	mask #3

3.2. Device characterization

To evaluate the main device characteristics, a detailed electrical and optical characterization measurements was performed on singular 1-D LTFPSD that constitute the final array. This also allow us to determine the offset of the centre of gravity of the complete array.

The device current-voltage (I-V) characteristics in the dark and under illumination were measured to determine the device sensitivity and sensibility. These measurements were performed using two electrometers (a power supply and a picoameter, Keithley 236 and 486, respectively) computer controlled and a monochromatic radiation with a wavelength (λ) of 632.8 nm with a light intensity of 2.6×10^{-4} W/cm^2. To determine the light intensity detection level of the device, the light intensity (I_{LH}) was varied using neutral density filters (03FSG017).

The device response time was measured using a HeNe laser (λ = 632.8 nm with 10 mW) light chopped where the load resistance (R) was varied from 10 Ω to 10 MΩ by means of a calibrated resistance box (Lionmount, model RD16) at a chopper frequency of 500 Hz and the output signal detected through an oscilloscope (LeCroy, model 9400A).

The linearity and spatial resolution measurements were carried out using the system shown in figure 5. A HeNe laser (λ = 632.8 nm with 10 mW) was focused on the TFPSD, which was set on a computer-controlled X-Y table, with a spatial resolution better than 10 μm/step. The laser beam scanned the sensing area of the TFPSD using the X-Y table in a step by step method. For each step, the output data were obtained by an electrometer/power supply (Keithley 236) and compiled by a PC computer using a specific developed hardware and software tool (SENSIT)[2].

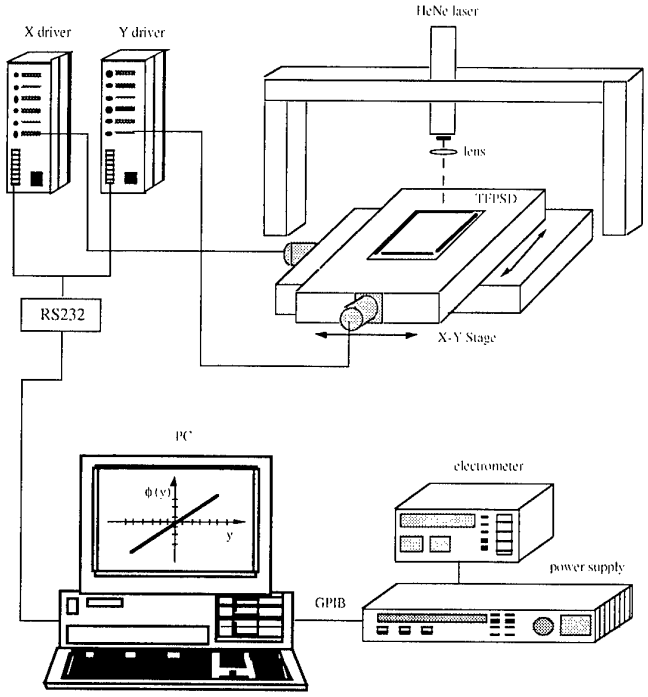


Figure 5. Experimental set-up used for nonlinearity and resolution measurements.

4. PERFORMANCE CHARACTERISTICS

4.1. Basic optoelectronic characteristics

The photo-to-dark characteristics are depicted on figure 6. There, we observe a photo-to-dark ratio higher than 10^4.for I_{LH} = 2.6×10^{-4} Wcm^{-2}. We have obtained a relatively high signal to noise ratio (S/N) even for light intensities below 1×10^{-6} W/cm^2 meaning that good device resolutions are obtained in the range of 10 dB. The slightly increase observed in the dark saturation current density is related to the lateral leakage currents[4].

A typical spectral response curve of 1-D TFPSD of the array is depicted in figure 7, for λ in the range of 400 nm to 800 nm. The spectral response peak is around 610 nm. The cut-of wavelength is located around 730 nm and a good bandwidth response is obtained in the range from 525 nm to 685 nm. These data show that several types of solid state lasers can be used as light source for the present application. The curve shape is related to the performances of the i-layer and the interfaces involved[3].

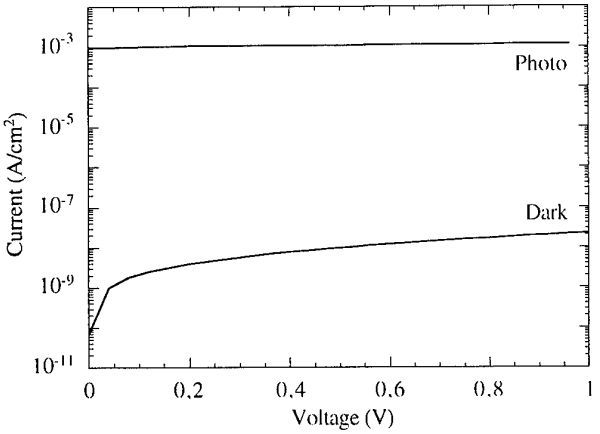


Figure 6 – Reverse bias characteristics of a singular 1-D TFPSD in the dark and under illumination (2.6×10^{-4} W/cm^2).

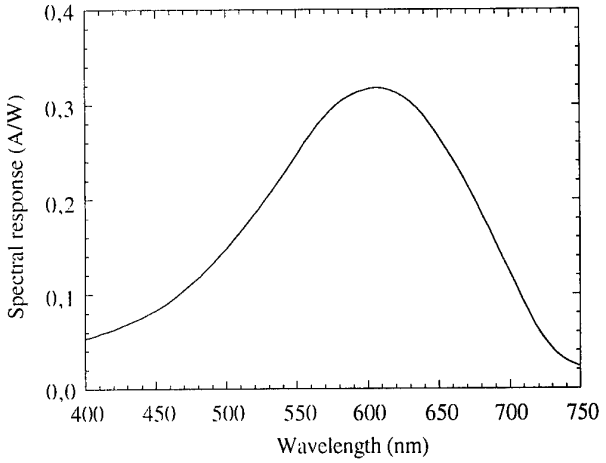


Figure 7 – Spectral sensitivity of a typical 1-D TFPSD.

4.2. Response time

The device response time measures the TFPSD speed response to a step function incident light. If the sensor is instantaneously illuminated, it takes a certain time for the photogenerated current to flow in the external circuit. This is called rise time (t_r). If the light beam is instantaneously turned off, it takes a certain time for the photogenerated current to stop flowing which is function of the used load resistance and the device size that determines the total device capacitance. This is called decay time (t_d) to a light pulse.

The data (see figure 8) show similar t_r either when the reverse bias is applied or not ($\approx$ 10 µs). The same does not happen with t_d since the capacitance associated with the depletion layer decreases when the reverse bias is applied, for the same R. The data show that t_d decreases from 3×10^{-5} s to 1.3×10^{-5} s and the steady state output signal is enhanced by almost 4% when V_R changes from 0 V to -1 V.

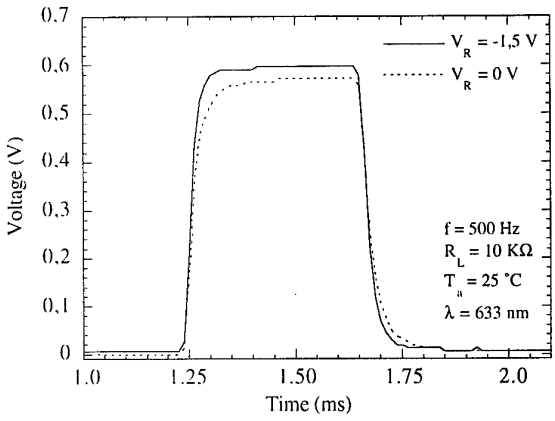


Figure 8. Photoresponse speed of an p.i.n TFPSD (dashed line without polarisation, solid line with reverse bias applied).

To improve the response time, either the load resistance or the device area have to decrease. By using a R = 1KΩ and an amplifier with a low input resistance, the elemental 1-D LTFPSD is readable in about 1µs, meaning that at most the required delay time between measurements is in the range of 2-5 µs, for sets of information pockets interconnected in parallel (see figure 3).

4.2. Position detection characteristics

Figure 9 shows the device linearity measurements performed in a singular 1-D LTFPSD with the back metal either floating or reversed biased. The data reveal a good fitting between the recorded data and the spatial position of the light spot on the scanned surface. The position detection error (∂), is obtained taking into account that[5]: $\delta = 2\sigma / F$ (where σ is the root mean square deviation from the regression line data and F is the measured full scale). The data recorded also show that the position detection error is in the range of ± 1% mainly ascribed to the end terminals of the 1-D TFPSD related to edge effects[3]. The experimental data are well fitted by the equation: y=-0.067251 + 11.708x, with a correlation better than 0.999.

4.3. Position resolution

The position resolution is the minimum light spot displacement that can be detected, i.e., the limit of detection expressed by the distance on the sensitive surface. To determine the resolution of the singular 1-D LTFPSD's, we use the set-up shown in figure 5 using very short steps and scanned distances. Table IV shows the results obtained concerning the device nonlinearity. The data reveal that below 10 μm the nonlinearity increases which can be attributed either to device limitations or to the noise introduced by the hardware used in the measuring system[2]. However, as the clearance between stripes in the array is about 30 μm, this will not influence the final system resolution.

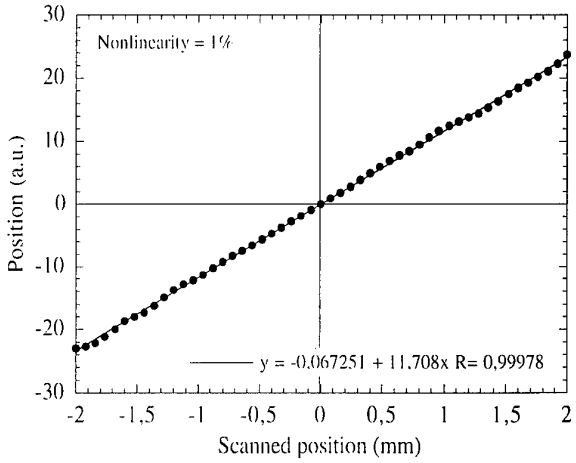


Figure 9 – Results of a singular 1-D TFPSD nonlinearity, using a HeNe laser beam with a diameter of 1 mm.

Table IV. Position detection resolution.

Step (μm)	Distance scanned (μm)	Standard Deviation (σ)	Nonlinearity (%)
80 μm	4000	0.297	0.98
40 μm	2000	0.173	0.98
20 μm	1000	0.144	2.6
10 μm	500	1.249	15.0

6. SUMMARY AND FUTURE OUTLOOK

We have developed a TFPSD array with a detection active area of 4 mm × 3 mm, able to be incorporated in a standard TV camera for processing image information recorded in a continuos manner. The device spatial resolution is better than 10 μm, and the position detection error is below 1% mainly influenced by the hardware used to process the information recorded.

The overall device response time can be as low as 2-5 μs which makes the array detector (when the detector information pocket is driven by a parallel input SR) suitable to laser 3-D triangulation applications. The proposed sensor array shows to be an effective substitute of the conventional digital like detectors and can be used in automated inspection systems improving the quality and the reliability of manufacturing products, for a wide range of industries.

In conclusion, we are extremely encouraged by the promising 1-D TFPSD array associated to a low cost technology due to its positive impact in real time control processes. However a sustained research effort is still required for further development of the complete system.

7. ACKNOWLEDGEMENTS

This work is supported by NATO-Science for Stability Programme (Phase III) under project PO-THINFILM.

8. REFERENCES

1. A. Kawasaki, M. Goto, H. Yashiro and H. Ozaki, "An array-type PSD (Position-sensitive Detector) for light pattern measurement", Sensors and Actuators, **A21-A23**, 529-533, 1990.
2. F. Soares and R. Martins, internal report (in Portuguese).
3. E. Fortunato, M. Vieira, G. Lavareda, L. Ferreira and R. Martins," Material properties, project design rules and performances of single and dual-axis a-Si:H large area position sensitive detectors", J. of Non-Cryst. Solids **164-166**, 797-800, 1993.
4. R. Martins and E. Fortunato, "Dark current voltage characteristics in transverse asymmetric hydrogenated amorphous silicon diodes", J. Appl. Phys.**75(5)**, 3481-3486, 1995.
5. A. Kawasaki and M. Goto, "On the position response of a position sensitive detector (PSD) irradiated with multiple light beams", Sensors and Actuators, **A21-A23**, 534-537, 1990.

Investigations on porous silicon layers with regard to chemical microsensor applications

M. J. Schöning, M. Crott, F. Ronkel[a], M. Thust, J. W. Schultze[a], P. Kordos, H. Lüth

Institut für Schicht- und Ionentechnik, Forschungszentrum Jülich GmbH, D-52425 Jülich, Germany
[a]Institut für Physikalische Chemie und Elektrochemie, Heinrich-Heine-Universität Düsseldorf, Universitätsstr. 1, D-40225 Düsseldorf, Germany

ABSTRACT

A new concept for silicon microsensors based on porous EIS (Electrolyte-Insulator-Semiconductor) structures is presented. The porous sensor was prepared by anodic etching of n-doped silicon and subsequent deposition of a dielectric layer of SiO_2. Experimental conditions were investigated to realize a well-defined macroporous formation of the porous silicon. To compare the chemical sensor properties with similar built-up planar Si/SiO_2 structures, C/V (Capacitance-Voltage) measurements have been performed. The porous EIS structures have been characterized by SEM (Scanning Electron Microscopy), XPS (X-ray Photoelectron Spectroscopy) and cyclic voltammetry. This solid-state technology allows the preparation of transducer materials for pH microsensors.

1. INTRODUCTION

Since the invention of the ISFET (Ion Sensitive Field Effect Transistor[1]) in 1970 the main effort in the development of chemical sensors is the combination of the advantages of silicon microelectronic technology with the properties of conventional ion selective electrodes. Hence, in most sensor applications the chemically sensitive layer is deposited directly on top of the semiconductor transducer. However, this configuration offers some crucial drawbacks, like the insufficient mechanical stability and poor adhesion of the sensitive layer on the silicon substrate as well as the fast leaching out of the sensitive component during sensor operation[2]. In the case of the EIS (Electrolyte-Insulator-Semiconductor) structures described in literature[3,4] a miniaturization as chemical microsensor is very difficult, since the scaling down of the active sensor area is accompanied by a proportional decrease of the measured capacitance to small absolute signal values[5].

To solve these problems a new concept for silicon microsensors has been developed using porous silicon layers as transducer material for biochemical sensing. Porous silicon is obtained by anodic etching in concentrated hydrofluoric acid (HF) and has been applied in different fields[6-8]. The porous structure is highly influenced by different process parameters, like doping type and level of the silicon substrate, the anodization current densitiy, the HF concentration and the illumination[9]. Due to the surface enlargement of the porous layer structure the measured capacitance value is increased[10]. Furthermore, the sensitive components are protected against leaching out due to an anchoring effect which is discussed in detail[11].

The purpose of this work is to tailor the porous silicon layer structure for chemical microsensor applications. Therefore oxidized porous EIS sensors have been manufactured by anodic etching and subsequent PECVD (Plasma Enhanced Chemical Vapor Deposition) processing of SiO_2. Dependent on the experimental conditions a formation of macropores could be adjusted and characterized by SEM. XPS sputter profiling and cyclic voltammetry were used to monitor the indepth silicon dioxide content. In order to study the pH sensitivity and stability, C/V (Capacitance-Voltage) measurements have been carried out to compare porous and planar EIS structures.

2. EXPERIMENTAL

2.1 Materials and processing

The EIS structures were prepared from n-type phosphorus-doped (10-15 Ωcm, (100)-orientation) silicon substrates with a thickness of 380 µm. Before processing, the substrates were cleaned by successively immersing in acetone, propanol and de-ionized water. As an ohmic contact a layer sequence of 5 nm Cr, 150 nm AuSb and 20 nm Au was deposited on the rear side of the silicon wafers by means of vacuum evaporation. A porous silicon layer was formed by anodic etching in an 1:1 mixture of 50% HF solution and pure ethanol with a current density of 6.4 mA/cm^2 and an anodization time of 600 seconds.

0-8194-2165-0/96/$6.00

The etching process was assisted by illumination with a halogen lamp (12 V). The resulting microporous layer on top of the macroporous layer was removed with 1 M NaOH. Subsequently the samples were rinsed in de-ionized water and dried in nitrogen gas atmosphere. SiO_2 as a pH sensitive gate insulator material with a layer thickness of about 50 nm was deposited by PECVD technique ($p=10^5$ Pa, T=300°C) into the pores. A cross section of the resulting porous EIS sensor is schematically shown in Fig. 1. In the case of the planar EIS structure the SiO_2 layer (50 nm) was deposited by PECVD onto the silicon substrate material. The corresponding cross section of the planar EIS sensor is given in Fig. 2.

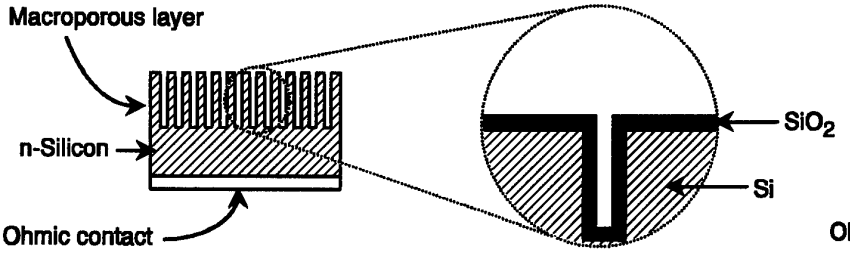


Fig. 1: Schematic of the porous EIS structure.

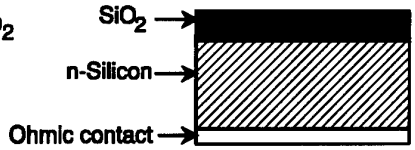


Fig. 2: Schematic of the planar EIS structure.

2.2 C/V measurement principle and sensor characterization

After processing, the planar samples as well as the porous samples were cut into single sensor chips of 10 mm * 10 mm and mounted in a measuring cell sealed by an o-ring as shown in Fig. 3. The sensor chip was contacted on its front side by the analytical solution using a conventional Ag/AgCl reference electrode and on its rear side by a gold-plated pin. To investigate the sensor properties, C/V measurements were performed with an impedance analyzer (Zahner elektrik) at a frequency of 120 Hz. The measurements were carried out at a d.c. voltage V_b, sweeping from 0.8 V to -1 V in 100 mV steps, with a superposed a.c. voltage amplitude of 20 mV. This principle is described in detail[12]. In order to determine the pH sensitivity of the EIS structures technical buffer solutions (Titrisol, Merck) in the concentration range pH=4 to pH=8 were used.

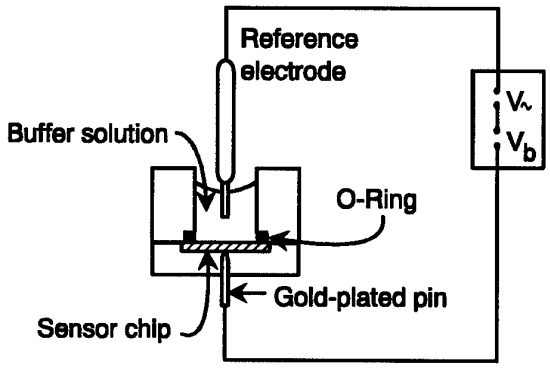


Fig. 3: Schematic of the C/V (Capacitance-Voltage) measurement set-up.

To characterize the Si/SiO_2 interface and determine the indepth SiO_2 content on the porewalls of the porous samples XPS sputter depth profiles were recorded for the planar as well as for the porous EIS structures. XPS measurements were performed on an ESCALAB 5 (VG Instruments) with Mg K_α radiation. Si 2p spectra were deconvoluted with the chemical shift data for silicon suboxides[13].The layers were sputtered with 4 keV Ar^+ from a AG 21 cold ion source (VG Instruments). The sputtering rate was estimated to be about 3 nm/min for the planar structures and 5 nm/min for the porous structures.

Cyclic voltammograms were recorded in 0.5 M sulfuric acid with a $Hg/Hg_2SO_4/H_2SO_4$ reference electrode. Potentials are reported versus an SHE (Standard Hydrogen Electrode). This method was used to examine the insulating behavior of the SiO_2 layer on the porewalls.

3. RESULTS AND DISCUSSION

3.1 Study of the structure of the porous silicon layer

Fig. 4 presents the SEM photographs of the topview (a) and cross section (b) of the porous morphology. Dependent on the etching parameters a formation of the macropores with a layer thickness of about 2 µm could be achieved. In the topview the homogeneous distribution of the circular pores across the complete etch area is found. The mean pore diameter varies

from about 1 µm at the surface of the silicon substrate to about 2 µm at the bottom of the grown pores. The distance between the middle of the single pores amounts approximately 2 µm. The macroporous layer exhibits a grape-like shape of the pores. Due to this shape a stable und protected deposition of different sensitive components, e.g. biomolecules or ionophores is suggested.

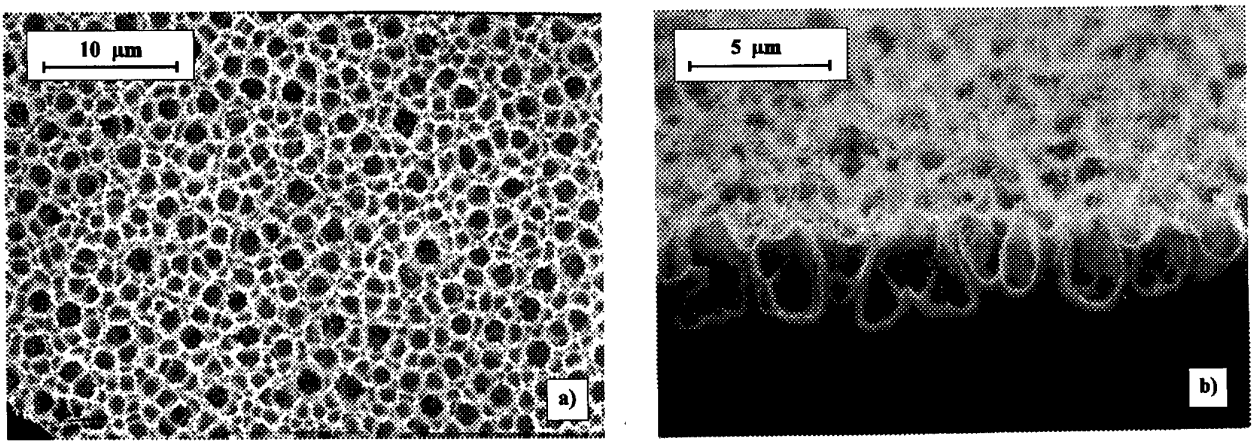


Fig. 4: SEM photographs of the porous layer structure: a) topview (open areas are dark), b) cross section (angle of 10°).

3.2 Physical characterization of the porous and planar Si/SiO_2 structures

Fig. 5 shows the sputter depth profiles for PECVD SiO_2 layers on planar as well as on porous EIS structures. The figure is corrected for the different sputter rates of the samples (see experimental). Both samples have the same compositon in the near surface region, but after 50 nm the oxygen content of the planar sample begins to decrease and reaches zero after 55 nm. In contrast the oxygen content of the porous sample exhibits an exponentional decay after 60 nm and reaches a lower limit of 13% after 300 nm. This indicates that the porewalls are covered with SiO_2. Detailed Si 2p spectra (Fig. 6) reveal that the deposited PECVD silicon oxide is indead SiO_2 and no indication for suboxides is found. The Si 2p XP spectrum without sputtering is shifted to higher binding energies because of sample charging.

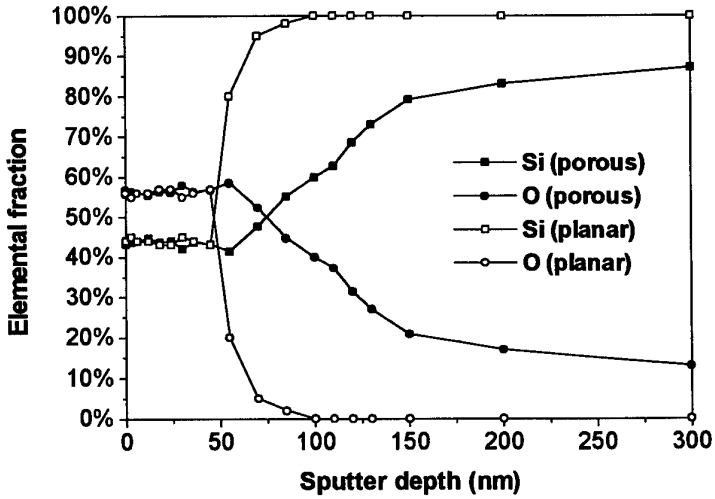


Fig. 5: Sputter depth profile of 50 nm PECVD SiO_2 on planar and porous silicon.

Comparison of the cyclic voltammograms of planar and porous EIS structures covered with PECVD SiO_2 (Fig. 7) show that current densities are much higher in case of the porous sample. This can have two reasons: 1. The surface area is much higher for the porous sample but the current density is calculated for the geometric surface. 2. The probability for cracks or pinholes in the oxide layer is much higher in the rough and porous structure. On the other hand the cyclic voltammogram has no similarity to a cyclic voltammogram of an n-type untreated silicon surface[14], as one would expect if large uncovered areas would exist. This suggests that even the pore tips are covered with insulating oxide. The increase in conductivity (slope in Fig. 7) by a factor of 30 of the porous sample compared to the planar one can be explained by an increasing surface area. This means that the quality of the passivating oxide layer is the same for the planar and the porous structure.

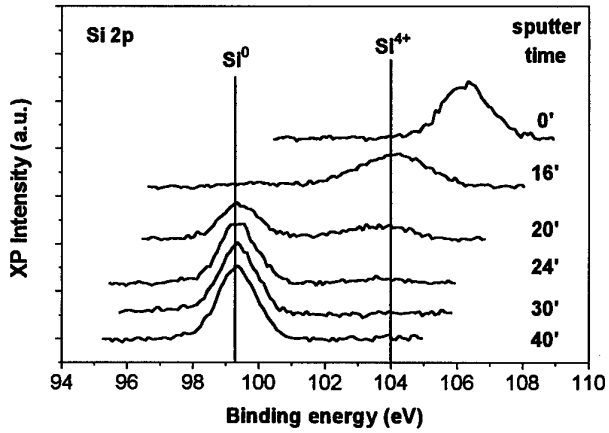


Fig. 6: Detailed Si 2p XP spectra for the sputter depth profile of PECVD SiO_2 on porous silicon.

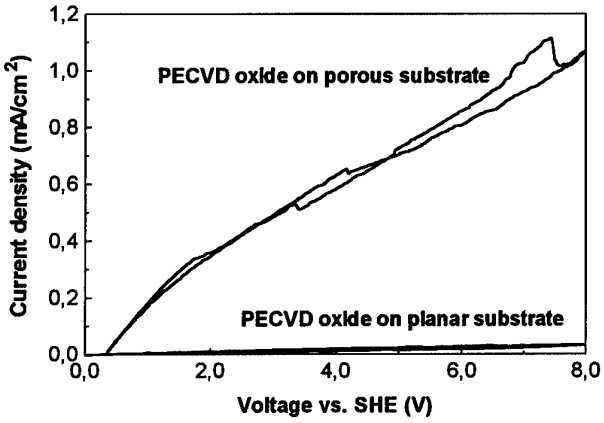


Fig. 7: Cyclic voltammogram of 50 nm PECVD SiO_2 on planar and porous silicon in 0.5 M sulfuric acid (dV/dt=20 mV/s).

3.3 Chemical sensor properties

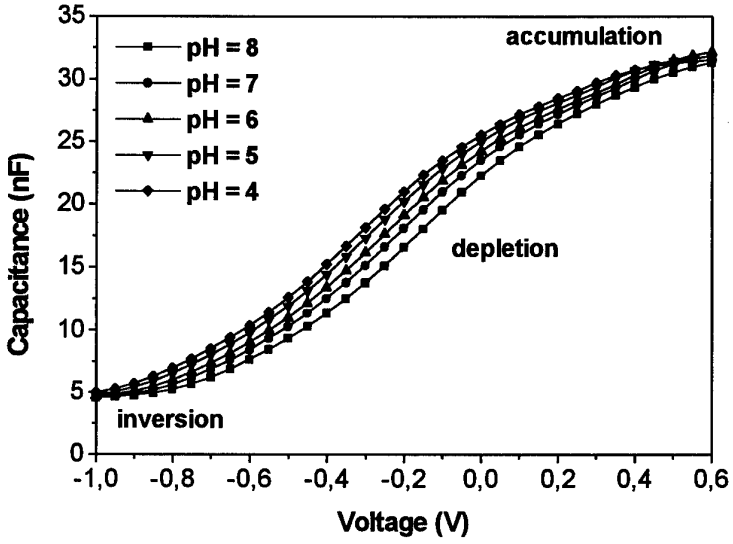


Fig. 8: Typical set of C/V curves of the pH-sensitive planar EIS structure at different pH values.

Fig. 8 shows a typical set of C/V curves of a planar EIS structure in the concentration range between pH=4 and pH=8. The shape of the C/V curve can be explained by the three distinct regions: accumulation, depletion and inversion[5]. Electrochemical interaction between the electrolyte and the SiO_2 surface modifies the space charge in the semiconductor by a field effect through the oxide layer. With increasing pH value the C/V curve shifts along the voltage axis towards positive voltage values. The voltage shift is due to the surface potential at the interface SiO_2/electrolyte which varies depending on the H^+-ion concentration of the buffer solution[15]. As an electrical signal output of the sensor system, this voltage shift was evaluated at 60% of the maximum capacitance. An average pH sensitivity calculated from linear regression of about 40 mV per decade exists. The accumulation capacitance of 34 nF corresponds very well to the estimated value for SiO_2, assuming a dielectric constant of 3.9.

In contrast a set of C/V curves of the porous EIS structure is presented in Fig. 9. The maximum capacitance value is obtained to be about 900 nF. This corresponds to an approximately 30-fold increase with respect to the planar EIS structure. Since XPS and cyclic voltammetry measurements have shown an equivalent geometric factor the homogeneous deposition of SiO_2 into the pores can be assumed. The increased capacitance value is caused by the enlargement of the sensor surface. Furthermore in the case of the porous sensor device a higher slope of the C/V curve was found, whereas the voltage range for both systems is nearly identical. This involves a higher accuracy of measurement of the detected sensor output signal.

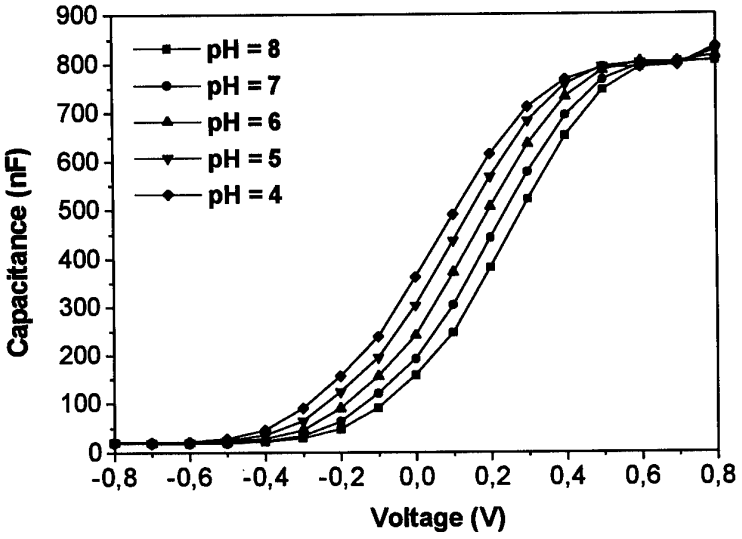


Fig. 9: Typical set of C/V curves of the pH-sensitive porous EIS structure at different pH values.

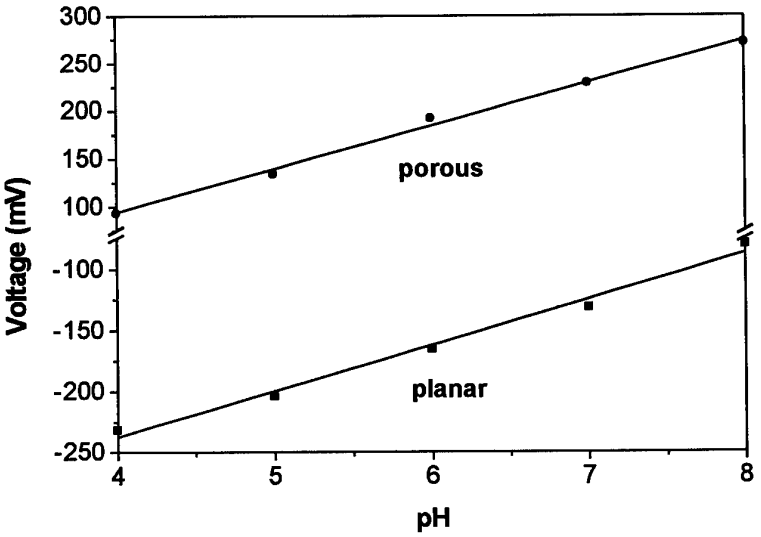


Fig. 10: Calibration curve of the porous and the planar pH sensor.

The porous EIS sensor shows an average pH sensitivity of 45 mV per decade. This result is similar to that of the planar EIS structure. For both sensors a deviation from the theoretical Nernst sensitivity exists. Ideally the Nernstian law predicts a voltage difference of 59 mV per pH decade under standard conditions. However, this deviation is well-known for SiO_2 and described in literature[15,16].

For comparison the two calibration curves of the planar and porous sensor device are shown in Fig. 10. The voltage shift is plotted as a function of the respective pH value. The measurement cycles were performed from pH=4 to pH=8. For both sensor types a linear shape of the calibration curve results, where the porous samples possess a slightly higher slope. The pH sensitivity of the planar EIS structure fluctuates between 38 and 45 mV per decade with an average sensitivity of 40 mV/pH, whereas the pH sensitivity of the porous EIS structure varies between 43 and 47 mV per decade with an average sensitivity of 45 mV/pH. Both sensor systems possess a long-term stability of more than 4 weeks during permanent electrolyte exposure.

4. CONCLUSIONS

Porous EIS sensors as a novel concept for pH-sensitive potentiometric microsensors have been developed using conventional preparation methods of semiconductor processing. In order to proof the SiO_2 growth into the pores XPS and cyclic voltammetry have been performed. The scaling up of the surface due to the porous layer structure raises the capacitance value. In our experiment a macroporous layer thickness of about 2 µm and a mean pore diameter of 1-2 µm results in an enlargement by a factor 30. Thus a simple miniaturization as microsensor is possible. The porous sensor shows a pH sensitivity of about 45 mV per decade in the concentration range pH=4 to pH=8.

Further studies are required in order to improve both, the pH sensitivity and the electrochemical stability of the porous sensor. Therefore we suggest the application of alternative dielectrics discussed in literature[17], e.g. Si_3N_4 or Al_2O_3. First

attempts have already proven the successful deposition of Si_3N_4 by means of the PECVD technique into the porous layer structure. Moreover, dependent on the different echting parameters the porous layer structure should be tailored with regard to the stable and protected embedment of different sensitive components for biochemical sensing.

5. ACKNOWLEDGEMENTS

The authors thank A. Steffen and H. P. Bochem for technical support and M. Thönissen for valuable discussions.

6. REFERENCES

[1] P. Bergveld, „Development of an ion-sensitive solid-state device for neurophysiological measurements", *IEEE Trans. Biomed. Eng.*, BME-17, 70-71, 1970.
[2] M. J. Schöning, M. Sauke, A. Steffen, M. Marso, P. Kordos, H. Lüth, F. Kauffmann, R. Erbach, B. Hoffmann, „Ion sensitive field effect transistors with ultrathin Langmuir-Blodgett membranes", *Sensors and Actuators*, B, 26-27, 325-328, 1995.
[3] P. Fabry, L. Laurant-Yvonneau, „The C-V method for characterizing ISFET or EOS devices with ion-sensitive membranes", *J. Electroanal. Chem.*, 286, 23-40, 1990.
[4] M. Beyer, C. Menzel, R. Quack, T. Scheper, K. Schügerl, W. Treichel, H. Voigt, M. Ullrich, R. Ferretti, „Development and application of a new enzyme sensor type based on the EIS-capacitance structure for bioprocess control", *Biosensors and Bioelectronics*, 9, 17-21, 1994.
[5] B. J. Gordon, „C-V plotting: Myths and methods", *Solid State Techn.*, 57, 57-61, 1993.
[6] R. C. Anderson, R. S. Muller, C. W. Tobias, „Investigations of porous silicon for vapor sensing", *Sensors and Actuators*, A, 23, 835-839, 1990.
[7] S. Barret, F. Gaspard, R. Herino, M. Ligeon, F. Muller, I. Ronga, „Porous silicon as a material in microsensor technology", *Sensors and Actuators*, A, 33, 19-24, 1992.
[8] R. L. Smith, S. F. Chuang, S. D. Collins, „A theoretical model of the formation morphologies at porous silicon", *J. Electron. Mater.*, 17, 533-541, 1988.
[9] Y. Arita, „Formation and oxidation of porous silicon by anodic reaction", *J. Cryst. Growth*, 45, 383-392, 1978.
[10] V. Lehmann, W. Hönlein, H. Reisinger, A. Spitzer, H. Wendt, J. Willer, „A novel capacitor technology based on porous silicon", to be published in *Thin Solid Films*.
[11] M. Thust, M. J. Schöning, S. Frohnhoff, R. Arens-Fischer, P. Kordos, H. Lüth, „Porous silicon as a substrate material for potentiometric biosensors", *Meas. Sci. Technol.* in press.
[12] M. J. Schöning, A. Steffen, M. Sauke, P. Kordos, H. Lüth, A. Zundel, M. Müller-Veggian, „Improved pH-sensitivity of PECVD silicon nitride as gate material for ion sensitive field-effect transistors (ISFETs)", *Proc. of 3rd European Conf. Sensors for the environment*, Grenoble 30-31 March, 55-59, 1995.
[13] H. Münder, M. G. Berger, S. Frohnhoff, M. Thönissen, H. Lüth, M. Jeske, J. W. Schultze, „Investigations of different oxidation processes for porous Si by XPS", *J. of Luminescence*, 57, 223-226, 1993.
[14] O. V. Romanov, „Nature cristallo-physico-chemique de l'interface entre un semiconducteur et son oxide propre", *Revue Phys. Appl.*, 19, 379-388, 1984.
[15] C. D. Fung, P. W. Cheung, W. H. Ko, „A generalized theory of an electrolyte-insulator-semiconductor field-effect transistor", *IEEE Trans. Electron. Dev.*, 33, 1, 8-18, 1986.
[16] T. Matsuo, M. Esashi, „Methods of ISFET fabrication", *Sensors and Actuators*, 1, 77-96, 1981.
[17] L. Bousse, S. Mostarshed, B. van der Schoot, N. F. de Rooij, „Comparison of the hysteresis of Ta_2O_5 and Si_3N_4 pH-sensing insulators", *Sensors and Actuators* B, 17, 157-164, 1994.

The use of intelligent ceramic materials as a strategy for the development of chemical sensors

Enrico Traversa

Dipartimento di Scienze e Tecnologie Chimiche, Universita' di Roma "Tor Vergata",
Via della Ricerca Scientifica, 00133 Rome, Italy

ABSTRACT

The practical applications of chemical sensors based on ceramic sensing elements is strongly limited by the problems inherent to their sensing mechanisms. For gas sensors, the main problems of semiconducting oxides are the insufficient gas selectivity, the inability to detect very low gas concentrations, and changes in sensing properties caused by surface contamination. For humidity sensors, the factor which limits the market diffusion of porous ceramics is the progressive drift in sensor resistance, which makes a heat-cleaning treatment of the sensing elements necessary for the recovery of sensor performance. The problems encountered in using the conventional ceramic materials as chemical sensors are strictly related to their sensing mechanisms. Given that, the strategy to eradicate the problems is the exploitation of innovative sensing mechanisms. Novel detection principals for chemical sensors can be obtained by materials having intelligent properties. Examples of multiphase systems for humidity and gas sensors are reviewed.

1. INTRODUCTION

The problems related to a clean and safe environment are continuously arising and are of primary concern for the future development of technologies. One of the aspects which is relevant to these problems is the control and monitoring of pollutants, with the easy and accurate detection of the minor components in the gas phase. At present, only very expensive and bulky analytical instruments are available for this purpose, which are not always suitable for continuous on-site monitoring and feed-back control. Moreover, their cost do not allow the installation of a capillary network of instruments, for the picture of the real situation in big towns. As an example, in Rome the monitoring of atmospheric pollutants takes place in less than 20 locations, and this does not give the possibility to represent correctly the real state of air pollution in the whole town. The reduction of the cost of monitoring equipments will lead to the possibility of a wider distribution of monitoring locations, resulting in a more precise picture of air quality.

The use of devices based on solid-state sensors for the detection of gases would be dramatically cheaper than the use of analytical techniques. Recently, much attention is thus paid to the study of solid-state sensors based on ceramics, which are inexpensive devices able to detect gas concentration practically in real time.[1] Although sensors based on conductivity changes of semiconducting oxides, caused by the reaction of gases with the oxygen adsorbed on the oxide surface, have been studied since 30 years,[2] they are not in practical use with reliable results for environmental monitoring. The main problems which limit their use are the insufficient gas selectivity, the inability to detect very low gas concentrations, and changes in sensing properties caused by surface contamination. These limits are strictly due to the sensing mechanisms of the semiconducting oxides, the materials conventionally used for gas sensors.

Humidity sensors based on ceramic materials are another type of chemical sensors which has limited practical applications. In fact, ceramic humidity sensors show better chemical resistance and mechanical strength with respect to polymeric sensors.[3] Nevertheless, at present, commercial humidity sensors are mainly based on polymeric films. The market for ceramic humidity sensors, which are based on porous sintered oxides,[4] is shrinking because the polymer film fabrication technology is far cheaper than the conventional ceramic technology used for porous oxide production. Moreover, the fabrication of integrated sensors is the present trend in sensor research, which needs the miniaturization of sensing elements in thin-film form.[5]

Another factor which limits the market diffusion of ceramic humidity sensors is surface contamination, which affects their stability and reliability.[6] Humidity sensors made of porous ceramics are based on impedance changes with increasing humidity, related to water adsorption on the oxide surface. The sensing mechanism generally accepted for porous oxides at room temperature is of the ionic-type, which can be summarized as follows.[7] At low humidities, conduction is due to proton hopping between hydroxyl ions on the first layer of chemisorbed water, while at higher humidities, protons hop between physisorbed molecules, with a Grotthuss chain reaction mechanism. The presence of pores is effective in increasing the specific surface area, but also in permitting capillary condensation of water within the pores, which results in electrolytic conduction, added to protonic conduction.

0-8194-2165-0/96/$6.00

For these sensors, a progressive drift in sensor resistance is observed, which is caused by the gradual formation of stable hydroxyl ions on the oxide surface during prolonged exposure to humid environments.[8] Given the ionic-type humidity sensing mechanism, proton hopping is adversed by the surface presence of hydroxyl ions instead of water molecules, thereby resulting in a decrease in surface conductivity over time. The sensor properties can be recovered through a so-called heat-cleaning treatment: the sensor is heated to a high temperature (about 400°C) to remove the adsorbed molecules.[3] Thus, it is needed to expend energy for the recovery of sensitivity of porous ceramics, and during the cleaning operation the sensor is unable to give information about humidity.[9] Also in this case, the problems encountered in using the conventional ceramic materials as humidity sensors are strictly related to their sensing mechanisms.

Given that the actual limits of chemical sensors are intrinsic to their sensing mechanisms, the strategy to eradicate the problems is the exploitation of innovative sensing mechanisms. Novel detection principals for chemical sensors can be obtained by materials having intelligent properties.[10] The development of materials with smart functions, such as selectivity, self-diagnosis, self-repair, self-recovery, self-tuning, stand-by capabilities for detecting non-linear onset, etc., is a key point for the development of novel technologies.

The design of intelligent materials can be achieved by the hybridization and/or the integration in simple structures of materials with differing properties (i.e. functional/structural, conductor/insulator, interfaces between p- and n-type semiconductors).[11] The interaction in the multiphase structures may lead to the development of intelligent functions and innovative properties which are not possessed by the single phase materials.[12] The materials in the ceramics class may have completely different properties, and thus offer outstanding potential for the development of intelligent functions. In fact, interfaces between p- and n-type semiconducting oxides, expected to have novel functions different from those of each individual material, have been tested for gas[13] and humidity[14] sensors.

The aforesaid strategy has been applied by the author to the study of some multiphase systems for humidity and gas sensors. In this paper, together with a review of the most interesting results reported in the literature, examples are presented of the gas and humidity sensitivity of La_2CuO_4/ZnO p-n heterocontacts, and of the humidity sensitivity of Au/ZnO Schottky barriers and of sol-gel processed thin films of TiO_2 with 10 at% of K, discussed in terms of their functions as intelligent materials. The intelligent functions of the systems are based on the multiphase interaction of p-type/n-type semiconducting oxides, metal/ceramic, and conductor/insulator materials.

2. GAS SENSORS

Recently, different approaches have been attempted in order to improve the performance of gas sensors. The control of the microstructure of the semiconducting oxides for gas sensors is one of the key factors for improving their sensitivity.[15] A clear understanding of the real state of surfaces and interfaces in sensor materials is also very important for the control of their geometric and electronic structures at the atomic scale.[16] In fact, many of the most interesting results about gas selectivity and sensitivity of materials for gas sensors have been reported in the relevant literature for multiphase materials. The occurrence of metal/oxide or oxide/oxide interfaces at molecular or atomic level is of primary concern for the achievement of gas selectivity.[15]

A sensor selective to ethanol based on an In_2O_3 thick film doped with Pd and La_2O_3 has been developed by the group of Yamazoe.[17] Loading SnO_2 with CuO particles produced a selective sensor for the detection of H_2S, explained by the formation of p-n junctions at the contact sites between the two oxides. CuO is easily converted to CuS when exposed to H_2S, with the disruption of the p-n junctions, and the formation and disruption of p-n junctions is responsible for the high sensitivity and selectivity of the element.[18] Mixing different oxides has been found to improve the sensitivity and selectivity of semiconducting oxide gas sensors.[19]

Very promising results in terms of gas selectivity have been obtained with p-n heterocontacts, which have been studied as intelligent materials for the detection of various gases.[20] Ceramic heterocontacts between CuO and ZnO have shown interesting properties of selectivity toward CO.[21] However, it was recently clarified that the ability to distinguish CO from hydrogen is given by the presence of small amounts of Na_2O in CuO.[22] This is explained by the electron donation from the alkali metal to the transition metal, which may catalyze the dissociation of CO. Oxidizing gases can be detected at room temperature by SiC/ZnO heterocontacts.[23,24]

The author studied the sensitivity to reducing gases of p-n heterocontacts prepared by mechanically pressing sintered discs of La_2CuO_4 and ZnO. The preparation of the materials and the measurements performed are described elsewhere.[25] The substitution of the CuO element was dictated by its chemical instability, which do not allow its practical use in commercial devices.

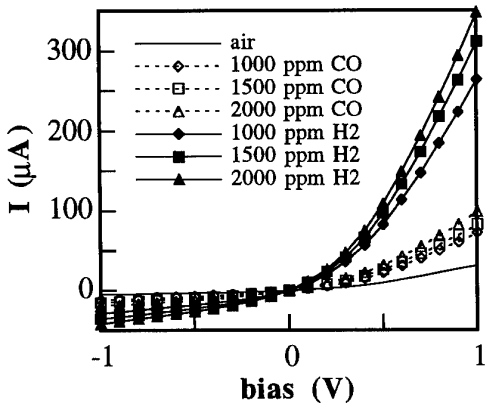


Fig. 1. Dark I-V curves of La_2CuO_4/ZnO heterocontacts at 400°C in environments at various gas concentrations.

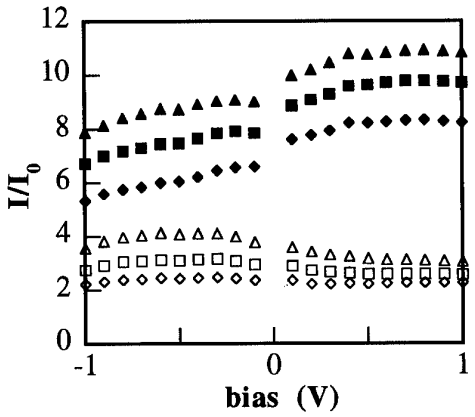


Fig. 2. The voltage dependence of the gas sensitivity of La_2CuO_4/ZnO heterocontacts at various gas concentrations, evaluated from the data in fig.1. The symbols are the same as in fig. 1.

Fig. 1 shows the I-V characteristics of La_2CuO_4/ZnO heterocontacts at 400°C in environments at various concentrations of CO and H_2. The curve measured in dry air shows typical p-n diode behaviour, with rectifying current under forward direction ($La_2CuO_4^+$/ZnO^-). The rectifying character of I-V curves was enhanced upon contact with increasing gas concentrations (both CO and H_2). The highest sensitivities, expressed as I/I_0, where I is the current flowing with gases and I_0 the current flowing in air, were measured at 400°C. For the La_2CuO_4/ZnO heterocontacts, no distinctive selectivity to CO was observed, as is the case for the CuO/ZnO system. Much higher gas sensitivities were however measured. The gas sensitivity was bias-dependent, as shown in Fig. 2. For bias values higher than 0.5 V, the greatest hydrogen sensitivity (above 10 for 2000 ppm) was observed. For CO, a different trend for sensitivity with bias was observed. At 0.5 V and 2000 ppm CO the sensitivity was about 3.5.

The predictable reactions between gas molecules and the oxygen originally adsorbed at the interface are the basis of the gas sensing mechanism of these heterocontacts. CO and hydrogen are ionized by electron holes injected from the p-type oxide and react with negatively charged oxygen ion adsorbates to form CO_2 or vapour. This results in an increase of the forward current across the p-n junction. These chemical reactions are enhanced when the forward bias is greater than 0.5 V, for hydrogen. The external electric field may control the chemical reactions, and thus the gas sensitivity, giving rise to the possibility of tuning the gas sensitivity of the heterocontacts by externally applied bias.

3. HUMIDITY SENSORS

3.1. Heterocontacts

The use of p-n heterocontacts has been first proposed for humidity detection by Kawakami and Yanagida in 1979.[14] The CuO/ZnO contacts showed a humidity sensing mechanism different from those known for single-phase oxides.[26] Heterocontacts with ZnO and NiO doped with Li have also been studied.[27] Recently, given their sensing mechanism which involves self-recovery, the study of humidity-sensitive p-n contacts has gained wider attention with a view to the development of commercial humidity sensors.[28-30]

Fig. 3 shows the I-V curve of La_2CuO_4/ZnO heterocontacts at room temperature in a nearly dry environment. The curve shows a typical p-n diode behaviour, with a rectifying current under forward direction ($La_2CuO_4^+$/ZnO^-). Under high humidity, the forward current increased markedly, while reverse current remained at low levels, showing thus a highly rectifying character, as shown in Fig. 4. The response to relative humidity (RH) was bias-dependent, as shown in Fig. 5, and thus externally tunable by changing the applied voltage. RH-response, expressed as I_{wet}/I_{dry}, where I_{dry} is the current recorded in a nearly dry environment, up to about 4 orders of magnitude at 2.5 V d.c. and 95% RH was measured for the contacts. The RH-sensitivity of the heterocontacts was due to phenomena occurring at the p-n interfaces. Measurements carried out on the single pellets of La_2CuO_4 and ZnO confirmed that single oxides were insensitive to RH.[31] Dense pellets were used for the heterocontacts in order to hinder the ionic-type humidity-sensitive conduction mechanism of the ceramic materials.

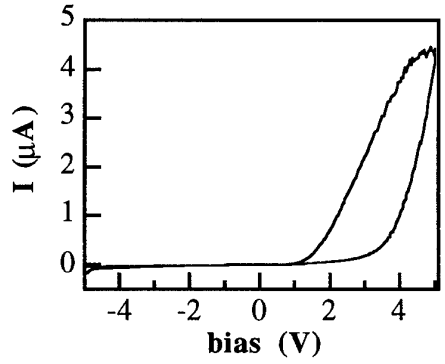


Fig. 3. Dark I-V curve of La_2CuO_4/ZnO heterocontacts at room temperature and 0% RH.

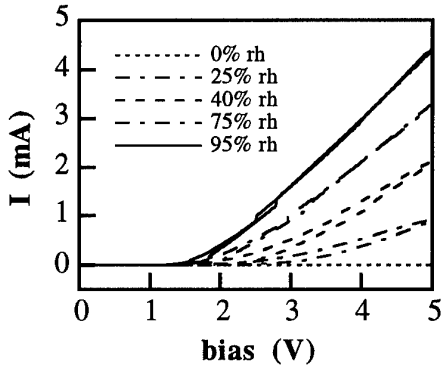


Fig. 4. Dark I-V curves of La_2CuO_4/ZnO heterocontacts at room temperature, at various RH values.

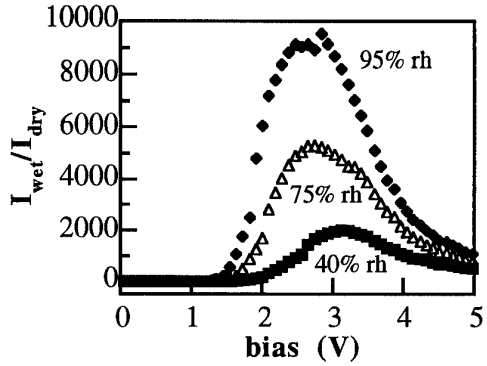


Fig. 5. The voltage dependence of the RH-sensitivity of La_2CuO_4/ZnO heterocontacts at various RH values, evaluated from the data in fig. 4.

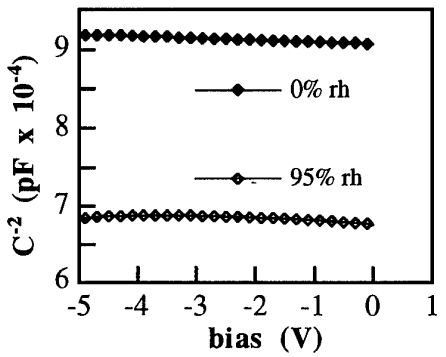


Fig. 6. The voltage dependence in the reverse bias region of $1/C^2$ for La_2CuO_4/ZnO heterocontacts at 0% and 95% RH, at room temperature.

The humidity detection mechanism of the heterocontacts is thus different from that of single-phase porous ceramics, and can be described as follows. In the proximity of the p-n junction sites electron holes are injected from the p-type semiconductor into the adsorbed water molecules, giving rise to protons in the adsorbed water phase. The positive charge is liberated at the surface of the n-type semiconductor, resulting in electrolysis of adsorbed water, with current increases only in the forward bias. The amount of hydrolysis increases at higher RH, because the higher the humidity, the higher the amount of water adsorbed. Electrolysis provides cleaning during working with a self-cleaning/self-recovery mechanism.[32] In this respect, p-n junctions can be regarded as intelligent materials; heat-cleaning is not needed, because the sensing mechanism itself is the cleaning treatment.

Fig. 6 shows the the bias-dependence in the reverse bias region of $1/C^2$, measured at high-frequency (100 kHz), in a nearly dry environment and at 95% RH. The intersection of the extrapolated line of $1/C^2$, evaluated in the reverse bias region, with the bias axis usually indicates the diffusion potential at the p-n junction interface. However, in this case, the diffusion potential value obtained would be unrealistically large both with and without moisture. The interface barrier at the La_2CuO_4/ZnO heterocontacts is, thus, not a physical diffusion barrier, but a chemical-like barrier, due to the presence of a high density of interface states derived from chemical adsorbates. These adsorbates are likely to be derived from oxygen and/or water adsorption. The importance of original interface states for the sensitivity of thin-film CuO/ZnO heterojunctions has also been reported.[33]

The high RH-sensitivity can thus be explained in terms of the saturation of the original interface states by physisorbed water, which, with increasing RH, leads to the release of trapped electrons, resulting in an increase in the forward current.[34] This mechanism explains the influence of the external electric field on the reactions with water. The presence of interface states modifies the potential barrier at the p-n junction, and an applied electric field can control the barrier height, and thereby the RH-sensitivity of the device.[35] This is another function of p-n heterocontacts as intelligent materials for chemical sensors.

3.2. Au/ZnO Schottky Barriers

The humidity sensitivity of Au/ZnO Schottky barriers was also studied.[36] The dense ZnO pellets had an ohmic contact on one side, made of fired Al paste. On the other side, a gold electrode was mechanically pressed by a spring to the ZnO surface in a home-made test cell. Open metal/oxide interfaces were obtained, accessible to moisture. Fig. 7 shows the I-V curves of the Au/ZnO samples at 2% and 85% RH, at room temperature. As for the p-n heterocontacts, a diode behaviour was observed, enhanced in wet environments, due to the formation of Schottky barriers at the chemically abrupt interfaces between Au (a metal with a high work function) and ZnO, at contact points between the mechanically pressed ZnO disc and the Au sheet. The RH-sensitivity of the Au/ZnO Schottky barriers was bias-dependent (Fig. 8). With forward bias (Au^+/Al^-) the specimens responded to RH, with a maximum sensitivity of 2.6, at 85% RH upon application of 10 V. The humidity sensitive electrical properties are given by the Au/ZnO interface. In fact, as already stated above, the use of dense ZnO samples hindered the ionic-type conduction mechanism in the presence of humidity. Dense ZnO pellets with two Al contacts showed linear I-V curves which were independent of the RH level.[37]

The bias-dependent, RH-sensitive resistivity of Au/ZnO interfaces may be determined by variations of the Schottky barrier height, with a mechanism similar to that shown by Schottky barrier gas sensors.[38] Semiconducting oxides usually possess surface states associated with adsorbed oxygen or water-decomposed species. At low RH, the barrier height is affected by the presence of extrinsic surface states which can be formed by water chemisorption. The shape of the I-V curves in the forward-bias region is due to the band-bending at the ZnO surface, which is in turn due to the charge of the intrinsic states and the charge of the extrinsic states by chemisorbed hydroxyl ions. At high RH, layers of water molecules physisorb on the chemisorbed layer. Therefore, exposure of the specimen to humidity leads to the complete saturation of hydroxyl ions through hydrogen bonds, resulting in the neutralization of the charge due to the extrinsic surface states. The result is a further decrease in the height of the barrier at high RH, resulting in an increase in forward current.

These results show that the RH-sensitivity of dense ZnO pellets with one Au electrode is due to a sensing mechanism which is close to that of p-n heterocontacts. The presence of a Schottky barrier gives a rectifying character, which in the case of heterocontacts is given by p-n junctions. The RH-sensitivity is related to the variation of the barrier height due to the presence of surface/interface states. The neutralization of these states by physisorbed water causes the current enhancement with RH in the forward-bias region. This mechanism is different from those already proposed for ceramics.[37] Water electrolysis may assist the humidity sensing mechanism, but further investigation are needed to clarify this point. The possibility to tune with an external electric field their RH-response and their stand-by capability are intelligent properties of the Au/ZnO Schottky barriers.

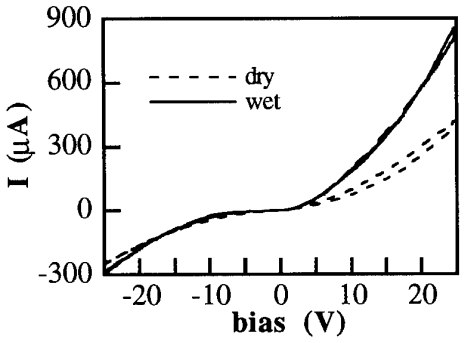


Fig. 7. Dark I-V curves of ZnO discs with one Al and one Au electrode, in dry (2% RH) and wet (85% RH) environments, at room temperature.

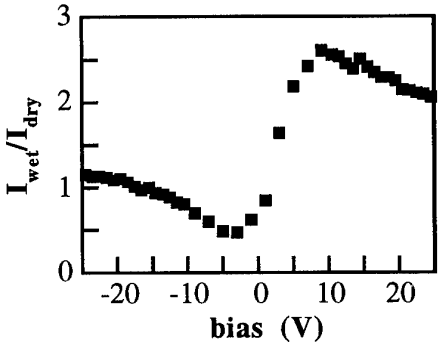


Fig. 8. The voltage dependence of the RH-sensitivity of Au/ZnO Schottky barriers at 85% RH and room temperature, evaluated from the data in fig. 7.

3.3. Sol-Gel Processed TiO_2 Films with 10 at% of K

TiO_2-based films with 10 at% of K (with respect to Ti) were deposited on Al_2O_3 substrates with comb-type Au electrodes by means of a sol-gel method.[39] Fig. 9 shows the RH-dependence of the resistance of the films measured at different frequencies. The RH-sensitivity depends on the frequency at which the resistance was measured. At 50 Hz, a linear variation of the logarithm of the resistance with RH, of 4 orders of magnitude was observed over the entire RH range tested (4-85% RH). At the lowest RH values, a noticeable RH-sensitivity of about 3 orders of magnitude in the RH range from 4% to 10% was measured only at frequencies $\leq$ 1 Hz, as shown in fig. 10 for resistance measured at 100 mHz. Another interesting feature of these films is their stability over time: for this material very little drift was observed even after a long time of testing.[40]

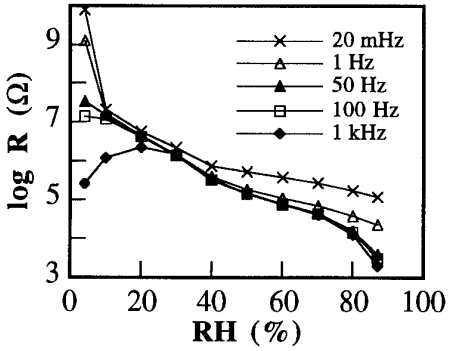


Fig. 9. The RH dependence of the resistance of sol-gel processed 10 at% K-doped TiO_2 films at 40°C, measured at various frequencies.

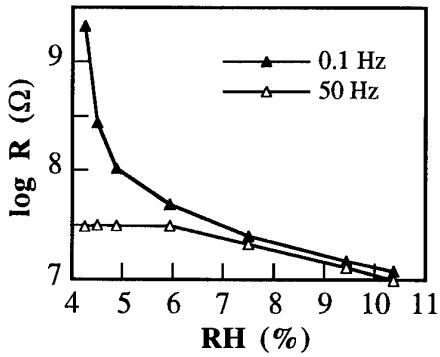


Fig. 10. Log resistance versus low values of RH curves for sol-gel processed 10 at% K-doped TiO_2 films at 40 °C, measured at various frequencies.

These results show that the 10 at% K-doped TiO_2 films possess some unique properties. For ceramic materials, it has been reported that a large pore volume is needed for high RH-sensitivity.[41] The sol-gel processed K-doped TiO_2 films, although they were free of capillary pores, showed very high RH-sensitivity, seldom observed even for porous sintered ceramics. The undoped TiO_2 films, prepared in the same way by sol-gel, showed very limited humidity-sensitivity.[42] The addition of alkali ions has been found to be effective in increasing the RH-sensitivity of several ceramic oxides.[7] The increase in sensitivity observed for doped-TiO_2 films with respect to the undoped films is explained by a humidity sensing mechanism which is different from that generally accepted for porous ceramic oxides. The impedance spectroscopy measurements led us to show that this mechanism involves the direct participation of alkali ions in conduction in wet environments.[43]

Another interesting feature is the possibility of measuring very low RH values with great sensitivity using 10 at% K-doped TiO_2 films, by measuring the resistance in a.c. at low frequencies. Moreover, the high RH-sensitivity is stable over time, and heat-cleaning is probably not necessary for practical applications. Both these characteristics are extremely interesting for practical application. The new humidity sensing mechanism explains the limited drift observed for these materials.

By choosing the frequency at which the resistance is measured, it is possible to modify the response of the alkali-doped films. Therefore, the RH sensing properties of the films are tunable with the frequency. This property is among those of intelligent materials. The structure of the materials may explain their intelligent properties: with the sol-gel process, very homogeneous and uniform materials can be obtained, with intimate mixing at the atomic scale. The resulting material has integrated functions of insulator (titania) and ionic conductor (K-containing phase). Also in this case the integration of materials with different functions (insulator/conductor) led to an improved material with novel characteristics, which are not possessed by the single phases.

4. ACKNOWLEDGMENTS

This work was supported partly by the National Research Council of Italy (CNR), under the auspices of the Targeted Project "Special Materials for Advanced Technologies".

5. REFERENCES

1. N. Yamazoe and N. Miura, "Environmental gas sensing," *Techn. Digest of the 7th Intern. Conf. on Solid-State Sensors and Actuators (Transducers 93)*, Yokohama, Japan, 1993, pp. 340-345.

2. T. Seiyama, A. Kato, K. Fujiishi, and M. Nagatani, "A new detector for gaseous components using semiconductive thin films," *Anal. Chem.*, Vol. 34, pp. 1502-1503, 1962.

3. B.M. Kulwicki, "Humidity sensors," *J. Am. Ceram. Soc.*, Vol. 74, pp. 697-708, 1991.

4. N. Yamazoe and Y. Shimizu, "Humidity sensors: principles and applications," *Sensors and Actuators*, Vol. 10, pp. 379-398, 1986.

5. Q. Wu, K.M. Lee, and C.C. Liu, "Development of chemical sensors using microfabrication and micromachining techniques," *Sensors and Actuators B*, Vol. 13, pp. 1-6, 1993.

6. J.G. Fagan and V.R.W. Amarakoon, "Reliability and reproducibility of ceramic sensors: part III, humidity sensors," *Am. Ceram. Soc. Bull.*, Vol. 72, n. 3, pp. 119-130, March 1993.

7. E. Traversa, "Ceramic sensors for humidity detection: the state-of-the-art and future developments," *Sensors and Actuators B*, Vol. 23, pp. 135-156, 1995.

8. T. Nitta, Z. Terada, and S. Hayakawa, "Humidity-sensitive electrical conduction of $MgCr_2O_4$-TiO_2 porous ceramics," *J. Am. Ceram. Soc.*, Vol. 63, pp. 295-300, 1980.

9. H. Yanagida, "Intelligent materials - a new frontier," *Angew. Chem.*, Vol. 100, pp. 1443-1446, 1988.

10. E. Traversa, "Intelligent ceramic materials for chemical sensors," *J. Intelligent Mater. Systems and Structures*, Vol. 6, in press, 1995.

11. H. Yanagida, "Intelligent ceramics," *Ferroelectrics*, Vol. 102, pp. 251-257, 1990.

12. E. Traversa, "Design of ceramic materials for chemical sensors with novel properties," *J. Am. Ceram. Soc.*, Vol. 78, pp. 2625-2632, 1995.

13. Y. Nakamura, T. Tsurutani, M. Miyayama, O. Okada, K. Koumoto, and H. Yanagida, "The detection of carbon monoxide by the oxide-semiconductor heterocontacts," *J. Chem. Soc. Jpn.*, pp. 477-483, 1987.

14. K. Kawakami and H. Yanagida, "Effects of water vapor on the electrical conductivity of the interface of semiconductor ceramic-ceramic contacts," *J. Ceram. Soc. Jpn.*, Vol. 87, pp. 112-115, 1979.

15. N. Yamazoe, "New approaches for improving semiconductor gas sensors," *Sensors and Actuators B*, Vol. 5, pp. 7-19, 1991.

16. K.D. Schierbaum, "Engineering of oxide surfaces and metal/oxide interfaces for chemical sensors: recent trends," *Sensors and Actuators B*, Vol. 24, pp. 239-247, 1995.

17. J. Tamaki, T. Maekawa, S. Matsushima, N. Miura, and N. Yamazoe, "Ethanol gas sensing properties of Pd-La_2O_3-In_2O_3 thick films," *Chem. Lett.*, pp. 477-480, 1990.

18. J. Tamaki, T. Maekawa, N. Miura, and N. Yamazoe, "CuO-SnO_2 element for highly sensitive and selective detection of H_2S," *Sensors and Actuators B*, Vol. 9, pp. 197-203, 1992.

19. T. Ishihara, K. Shiokawa, K. Eguchi, and H. Arai, "The mixed oxide Al_2O_3-V_2O_5 as a semiconductor gas sensor for NO and NO_2," *Sensors and Actuators*, Vol. 19, pp. 259-265, 1989.

20. H. Yanagida, "Design of intelligence in materials," in *Fourth Euroceramics, Vol. 5: Electroceramics*, ed. by G. Gusmano and E. Traversa, Faenza Editrice, Faenza, Italy, pp. 3-8, 1995.

21. Y. Nakamura, H. Yoshioka, M. Miyayama, H. Yanagida, T. Tsurutani, and Y. Nakamura, "Selective CO gas sensing mechanism with CuO/ZnO heterocontact," *J. Electrochem. Soc.*, Vol. 137, pp. 940-943, 1990.

22. S.J. Jung, H. Ohsawa, Y. Nakamura, H. Yanagida, K. Hasumi, and O. Okada, "Effects of Na_2CO_3 addition on the gas sensing characteristics of CuO/ZnO heterocontact," *J. Electrochem. Soc.*, Vol. 141, pp. L53-L55, 1994.

23. M. Miyayama, H. Yatabe, Y. Nakamura, and H. Yanagida, "Chlorine gas sensing using ZnO/SiC hetero-contact," *J. Ceram. Soc. Jpn.*, Vol. 95, pp. 1145-1147, 1987.

24. Y. Nakamura, R. Koyama, K. Koumoto, and H. Yanagida, "Oxidizing gas sensing by SiC/ZnO heterocontact - NO_x sensing," *J. Ceram. Soc. Jpn.*, Vol. 99, pp. 823-825, 1991.

25. E. Traversa, M. Miyayama, and H. Yanagida, "Gas sensitivity of ZnO/La_2CuO_4 heterocontacts," *Sensors and Actuators B*, Vol. 17, pp. 257-261, 1994.

26. Y. Nakamura, M. Ikejiri, M. Miyayama, K. Koumoto, and H. Yanagida, "The current-voltage characteristics of CuO/ZnO heterojunctions," *J. Chem. Soc. Jpn.*, pp. 1154-1159, 1985.

27. R.A. Marra, Y. Nakamura, S. Fujitsu, and H. Yanagida, "Humidity sensitive electrical conduction of ZnO-$Ni_{1-x}Li_xO$ heterocontacts," *J. Am. Ceram. Soc.*, Vol. 69, pp. C143-C145, 1986.

28. H. Yagi and H. Yanagida, "Humidity sensor using ceramic hetero-contact," *Jpn. Sensors Newsletter*, Vol. 5, n. 3, pp. 23-31, 1991.

29. Y. Ushio, M. Miyayama, and H. Yanagida, "Fabrication of thin film CuO/ZnO heterojunction and its humidity sensing properties," *Sensors and Actuators B*, Vol. 12, pp. 135-139, 1993.

30. N. Ichinose, "R & D trends in chemical sensors," *Chem. Sensors*, Vol. 9, Suppl. A, pp. 41-44, 1993.

31. E. Traversa, A. Bianco, G. Montesperelli, G. Gusmano, A. Bearzotti, M. Miyayama, and H. Yanagida, "ZnO/La_2CuO_4 hetero-contacts as humidity sensors," in *Ferroic Materials: Design, Preparation, and Characteristics*, ed. by A.S. Bhalla, K.M. Nair, I.K. Lloyd, H. Yanagida, and D.A. Payne, Am. Ceram. Soc., Westerville, pp. 375-384, 1994.

32. E. Traversa, M. Miyayama and H. Yanagida, "The application of La_2CuO_4/ZnO hetero-contacts as intelligent chemical sensors," in *Intelligent Materials and Systems*, ed. by P. Vincenzini, Techna, Faenza, pp. 39-46, 1995.

33. Y. Ushio, M. Miyayama, and H. Yanagida, "Effects of interface states on gas sensing properties of a CuO/ZnO thin film heterojunction," *Sensors and Actuators B*, Vol. 17, pp. 221-226, 1994.

34. E. Traversa, A. Bearzotti, M. Miyayama, and H. Yanagida, "Study of the conduction mechanism of La_2CuO_4/ZnO heterocontacts at different relative humidities," *Sensors and Actuators B*, Vol. 25, pp. 714-718, 1995.

35. E. Traversa, A. Bearzotti, M. Miyayama, and H. Yanagida, "The electrical properties of La_2CuO_4/ZnO heterocontacts at different relative humidities," *J. Mater. Res.*, Vol. 10, pp. 2286-2294, 1995.

36. E. Traversa and A. Bearzotti, "Humidity sensitive electrical properties of dense ZnO with non-ohmic electrode," *J. Ceram. Soc. Jpn.*, Vol. 103, pp. 11-15, 1995.

37. E. Traversa and A. Bearzotti, "A novel humidity detection mechanism for ZnO dense pellets," *Sensors and Actuators B*, Vol. 23, pp. 181-186, 1995.

38. K.D. Schierbaum, U.K. Kirner, J.F. Geiger, and W. Göpel, "Schottky-barrier and conductivity gas sensors based upon Pd/SnO_2 and Pt/TiO_2," *Sensors and Actuators B*, Vol. 4, pp. 87-94, 1991.

39. G. Montesperelli, A. Pumo, E. Traversa, G. Gusmano, A. Bearzotti, A. Montenero, and G. Gnappi, "Sol-gel processed TiO_2-based thin film as innovative humidity sensors," *Sensors and Actuators B*, Vol. 25, pp. 705-709, 1995.

40. E. Traversa, G. Gusmano, and A. Montenero, "Innovative humidity sensitive electrical properties of sol-gel processed ceramic thin films," *Eur. J. Solid State Inorg. Chem.*, Vol. 32, pp. 719-729, 1995.

41. Y. Shimizu, H. Arai, and T. Seiyama, "Theoretical studies on the impedance-humidity characteristics of ceramic humidity sensors," *Sensors and Actuators*, Vol. 7, pp. 11-22, 1985.

42. G. Gusmano, G. Montesperelli, P. Nunziante, E. Traversa, A. Montenero, M. Braghini, G. Mattogno, and A. Bearzotti, "Humidity-sensitive properties of titania films prepared using the sol-gel process," *J. Ceram. Soc. Jpn.*, Vol. 101, pp. 1095-1100, 1993.

43. G. Gusmano, A. Bianco, G. Montesperelli, and E. Traversa, "An EIS study of the humidity sensitive electrical conduction of alkali-doped TiO_2 films," *Electrochim. Acta*, in press.

Micro-Hall magnetic sensors with high magnetic sensitivity based on III-V heterostructures

S. Del Medico*, T. Benyattou*, G.Guillot*, T. Venet°, M. Gendry°, J. Tardy°, A. Chovet•

*LPM (URA CNRS n°358), INSA de Lyon Bât 502, 69621 Villeurbanne cedex, France
°LEAME (URA CNRS n°848), Ecole Centrale de Lyon, BP 163, 69131 Ecully cedex, France
•LPCS (URA CNRS n°840), ENSERG, BP 257, 38016 Grenoble cedex, France

ABSTRACT

In this work, we propose solutions based on engineering of III-V heterostructures to develop new types of semiconductor magnetic sensors. These micro-Hall sensors use the properties of a two-dimensional electron gas and the benefit of pseudomorphic material, in which both the alloy composition and the built-in strain offer additional degrees of freedom for band structure tailoring, to exhibit high magnetic sensitivity, good linearity, low temperature coefficient and high resolution. With the growth optimization which is described, two pseudomorphic $In_{0.75}Ga_{0.25}As/In_{0.52}Al_{0.48}As$ heterostructures were grown on a semi-insulating InPsubstrate by molecular beam epitaxy. To understand better the influence of the heterostructure design on its electronic properties, a model involving the self-consistent solution of the Poisson and Schrödinger equations using the Fermi-Dirac statistics has been developed. These results have been used to optimize the structure design.
A magnetic sensitivity of 346 V/AT with a temperature coefficient of -230 ppm/°C between -80°C and 85°C has been obtained. The device show good linearity against magnetic field and also against the supply current. High signal-to-noise ratios corresponding to minimal magnetic field of 350 $nT/Hz^{1/2}$ at 100 Hz and 120$nT/Hz^{1/2}$ at 1 kHz have been measured.

1. INTRODUCTION

Electronic devices capable of sensing magnetic field such as Hall devices, are under consideration because of the development of semiconductor technology and the lot of practical applications of these sensors. The annual industrial market of Hall effect magnetic sensors totalizes at present time a billion of devices. There are two types of applications :
- direct when the sensor consists of a part of the magnetometer : earth magnetic field measurement, reading of magnetic tapes and disks.
- indirect when the sensor is associated to a magnet : contactless switches, linear or angular displacement detection, contactless current sensors.[1,2]

Lots of studies are being carried out to produce low cost and easily reproducible devices with conventional microelectronic technology and with the aim of making smart sensors (i.e. detection and processing signal on the same chip). However, in these "3D" classical sensors, it is impossible to obtain both a high sensitivity and a low thermal drift. The sensitivity of InSb devices is highly dependent upon temperature because of its narrow band gap and Si has a larger band gap but a rather low mobility as well as thermal drift problems. This sort of devices requires therefore the use of compensation electronic circuits, which involves an increase of the cost price.
With the development of sophisticated growth techniques, it is now possible to fabricate high quality III-V 2D heterostructures. The use of a III-V two-dimensional electron gas (2DEG) seems to be an effective method of producing simultaneously a high electron mobility, a low sheet carrier density, which is essential to obtain a high magnetic sensitivity, and a reduced temperature sensitivity. The high electron mobility of the 2DEG confined at the heterointerface has a beneficial effect on the reduction of equivalent offset fields and on power dissipation [3]. The use of a pseudomorphic strained InGaAs layer as the 2DEG channel has been demonstrated to be best because of its efficient charge transfer and confinement of the electrons in the channel, due to the larger conduction band offset. Moreover, owing to the composition effect, the decrease of the electron effective mass leads to a higher mobility.
Furthermore, these magnetic sensors can be integrated with high electron mobility transistor (HEMT) on the same chip.
We report here on the use of pseudomorphic InAlAs/InGaAs/InP heterostructures for the fabrication of Hall micro-sensors with high sensitivity, low temperature coefficient, good linearity and high magnetic resolution.
After the description of the device structure and fabrication, the design of the heterostructure using the self-consistent description of the quantum well channel is given. Then the characteristics of the InGaAs-2DEG Hall device are described.

0-8194-2165-0/96/$6.00

2. DEVICE STRUCTURE AND FABRICATION

The present samples were grown using a Riber 2300 MBE system. The substrates were semi-insulating (001) oriented "epi-ready" InP wafers from Crismatec-Inpact. An optimized procedure with indium stabilization of the InP surface for a few seconds at 565°C is used for the oxide desorption [4]. Two pseudomorphic $In_{0.52}Al_{0.48}As/In_{0.75}Ga_{0.25}As$ heterostructures, E508 and E750, were realized with different layer thicknesses and Si doping in the barrier. A cross-sectional view of the structures is shown in Fig. 1. The growth conditions were as follow : the V/III beam equivalent pressure ratio was 25 and the growth rate was ~1µm/h for each material. The growth temperature was 500°C for the two pseudomorphic heterostructures. The substrate temperature was measured with an infrared pyrometer, calibrated at the melting point (525°C) of a sliver InSb mounted near the substrate wafer. For the InGaAs and InAlAs lattice matched compositions, the In/Ga or In/Al pressure ratios were defined by a Bayard Alpert gauge. Compositions were then verified by double-crystal X ray diffraction measurements. The nominal composition of $In_{0.75}Ga_{0.25}As$ was defined by extrapoling In/Ga pressure ratio values used for growing lattice matched InGaAs and assuming the same cation incorporation coefficients. A growth interruption procedure previously reported [5] to obtain a smooth channel interface and a low impurity incorporation was achieved by closing the main shutter for 5 seconds allowing surface reconstruction from a (2x1) As-stabilized surface to a (4x1) cation stabilized surface.

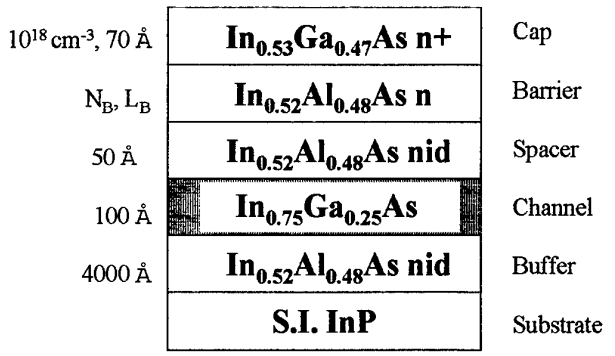


Fig. 1 : Cross-sectionnal view of the structure (L_B : barrier thickness, N_B : doping level)

The growth of an InAlAs buffer on the semi-insulating InP substrate is necessary to produce good quality materials and interfaces. An $In_{0.75}Ga_{0.25}As$ channel was then inserted. This layer contains the high mobility electron gas at the InAlAs barrier/InGaAs hetero-interface. The spacer increases the spatial separation between donors and electrons. The InAlAs barrier layer is doped with Si so as to provide electrons in the channel. The InGaAs lattice matched cap layer is highly doped to make good ohmic contacts.

Hall measurements were carried out on square samples using the Van der Pauw technique to measure electron concentration and mobility. The characteristics of the structures are listed in Table 1.

Structure	L_B (Å)	N_B (cm^{-3})	μ_H (300K) ($cm^2V^{-1}s^{-1}$)	n_s (300K) (cm^{-2})	n_sth (300K) (cm^{-2})
E508	580	$8x10^{17}$	13100	$1.76x10^{12}$	$1.89x10^{12}$
E750	400	$6x10^{17}$	9380	$9.84x10^{11}$	$9.35x10^{11}$

Table 1 : Characteristics of the structures

Two types of conventional cross Hall devices were fabricated. The Hall elements were 600 µm in length by 200 µm in width (L_1) and 1000 µm by 200 µm (L_2) respectively. The shapes of the Hall devices were not optimized to reduce the offset voltage. Hall devices were processed in a two step procedure. First, a mesa etching was performed in a phosphoric solution H_3PO_4, H_2O_2, H_2O (1 : 1 : 38). Then ohmic contacts were delimited by optical lithography and reversal image processing. AuGe/Ni/Au metallisation was then evaporated and lifted off. Alloying was carried out onto hot plate under N_2 atmosphere at 420°C for 1 mn. No passivation was carried out.

3. HETEROSTRUCTURE MODELLING

To understand better the influence of the heterostructure design on its electronic properties, a model involving the self-consistent solution of Schrödinger and Poisson equations using Fermi-Dirac statistics has been developed. The Fermi level pinning at the GaInAs surface was considered as a boundary condition and was estimated at 0.3 eV from the bottom of the conduction band. This model allows us to determine the conduction band structure and the energy levels in the channel, as well as their wave functions and their population (Fig. 2). We can thus visualize the localization of the electrons and check for possible parasitic parallel conduction in the barrier. This conduction occurs when, for example, the barrier is not depleted because it is too wide. Then

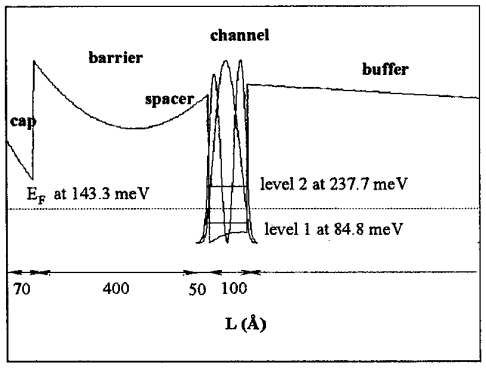


Fig. 2 : Band diagram of the InGaAs/InAlAs structure (E750) at 300K

spacer and channel thicknesses. In this structure the first electron level is located at 60 meV below the Fermi level, which corresponds to an electron population of 8.97×10^{11} cm^{-2}. The second level is situated at 106 meV above the Fermi level and is nearly empty. The calculated sheet carrier density is equal to 9.08×10^{11} cm^{-2}. Hall effect measurement gives 9.8×10^{11} cm^{-2}, in good agreement. This structure presents a lower barrier thickness and a lower doping level (see table 1) than E508 and therefore has a lower sheet carrier density. Theoretically, it should present a better magnetic sensitivity.

there are two conduction paths : the 2DEG of the well and the non-depleted zone of the barrier. We have also studied the inflence of several factors on the sheet carrier density (doping level of barrier, spacer and channel thicknesses). The E508 structure was fabricated before the physical modelling was done and so is not optimized. In fact, the value of the sheet carrier density of this structure is much too high to obtain a very high magnetic sensitivity We therefore simulated the E750 structure in order to reduce n_S and parallel conduction and to maximise carrier confinement in the channel. Figure 3, which shows the theoretical sheet carrier density plotted against the doping level of barrier, allowed us to determine the doping level of barrier requisite to obtain a sheet carrier density around 9×10^{11} cm^{-2} for given

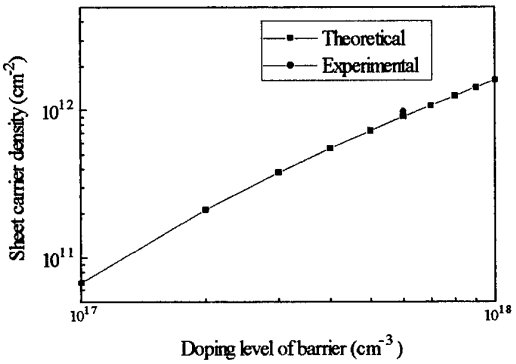


Fig. 3 : Simulated behaviour of the sheet carrier density against barrier doping level
L_B = 400 Å, L_{sp} = 50 Å

RESULTS

5.1. Magnetic sensitivity, temperature coefficient

One of the most important characteristics of a Hall effect sensor is the "supply-current-related sensitivity" or magnetic sensitivity K_H, expressed in $VA^{-1}T^{-1}$ and defined by the following expression [3] :

$$K_H = \left(\frac{\partial V_H}{I \partial B}\right) = G\frac{r_H}{q n_s} \qquad (1)$$

where I is the supply current, V_H the Hall voltage produced by the magnetic field B, G the geometrical

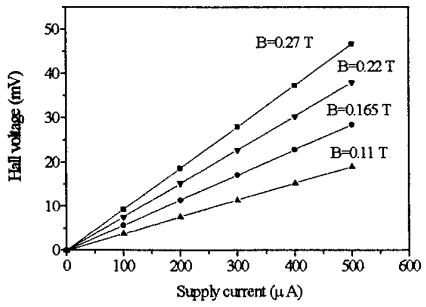


Fig.4 : Hall voltage as a function of magnetic field for different values of the bias current for the E508-L_1 device

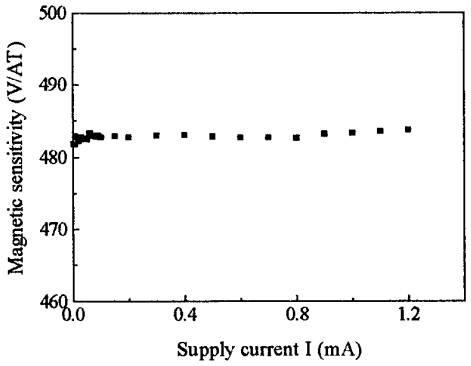


Fig. 5 : Magnetic senstivity versus supply current for a E750-L1 Hall device at a magnetic field of 0.11 T

correction factor, n_S the sheet electron density and r_H the Hall scattering factor of the majority carriers. In III-V 2D heterostructures the Hall scattering factor has a value of approximately unity.

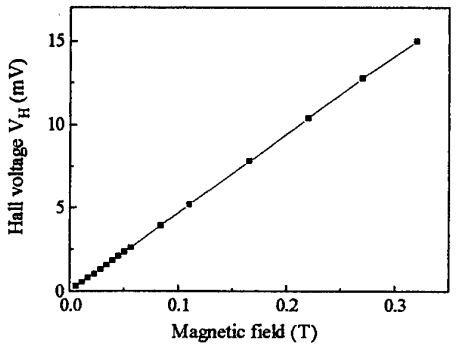


Fig. 6 : Dependence of the Hall voltage on the magnetic field for a E750-L_1 device at a supply current of 100 μA

The output Hall voltage for the E750 device with the L_2 shape is shown in Figure 4. All the devices show good linearity against magnetic field in the investigation range ± 0.3 T and also against the supply current. Figure 5 shows that the magnetic sensitivity is not dependent on the supply current. Therefore, there is no backgating effect in the structures, i.e. the sheet carrier density does not depend on the bias current, contrary to what was observed for the AlGaAs/GaAs Hall sensors[6] where it has recently been reported that there is an important backgating effect due to the semi-insulating GaAs substrate. The dependence of the Hall voltage on the magnetic field B is shown Figure 6 for values of B in the range 5 mT to 0.3 T. The coefficient of linear regression is 0.99997, so taking experimental errors into account, no non-linearity can be detected. Our best magnetic sensitivity K_H is 580 $VA^{-1}T^{-1}$. All the results are summarized in Table 2. As expected, the E750 devices have better magnetic sensitivities than the E508 devices. K_H was also calculated at various temperatures between -80°C and 85°C. The values of the temperature coefficent are situated between -230 to -550 ppm/K for the different devices. At low magnetic fields, the geometrical correction factor G depends only on the device shape and not on temperature. For strongly degenerate structures r_H is practically equal to unity and does not depend on temperature. Consequently the temperature coefficient can be expressed as :

Structure	E508 L_1	E508 L_2	E750 L_1	E750 L_2
K_H ($VA^{-1}T^{-1}$)	346	325	550	580
$\frac{1}{K_H}\frac{dK_H}{dT}$ (ppm/°C)	-230	-360	-500	-550

Table 2 : Values of magnetic sensitivity at 300K and of the temperature coefficient obtained on the two materials and for different geometries between -80 and 85°C

$$TC = n_S \frac{\partial(n_S^{-1})}{\partial T} \qquad (2)$$

Although the E750 structure has been optimized following the physical modelling, its temperature coefficient is not as good as that of E508. This means that its sheet carrier density is more temperature dependent. The electron mobility of the E750 structure is also lower than in E508 (see table 1). We suppose that in this structure there may have been growth problems, such as partial relaxation, which would explain the lower mobility.

4.2. Noise spectrum

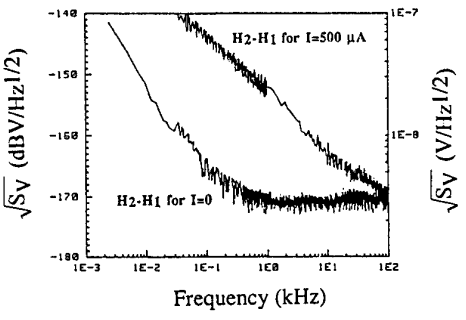


Fig. 7 : Hall-voltage noise spectrum for the L_1 device of E508 sample. H_2-H_1 represents the voltage fluctuations between the two Hall contacts H_1 and H_2

Voltage fluctuations across the Hall electrodes H_1 and H_2 have been measured at zero magnetic field as a function of frequency. This noise is expected to be the same in the low B range (i.e. $\mu^2B^2 << 1$). Figure 9 shows the noise power spectral density S_V of the Hall voltage for the sample E508 on a L_1

Structure	E508	E750
B_{min} at 1 kHz	120 $nT/Hz^{1/2}$	900 $nT/Hz^{1/2}$
B_{min} at 100 Hz	350 $nT/Hz^{1/2}$	2.5 $\mu T/Hz^{1/2}$

Table 3 : Values of the minimum magnetic fields of the sensors

device. A 1/f behaviour is clearly observed. For frequencies above ~80 kHz, the noise spectrum reaches the thermal noise floor which is 3×10^{-9} $V/Hz^{1/2}$. The theoretical value for thermal noise (given by Nyquist relation) is 4kTR. For this device R=395 Ω, so what the

calculated thermal noise is 2.5×10^{-9} $V/Hz^{1/2}$ which is in good agreement with the observed value. The minimum magnetic field B_{min} which can be detected by the sensors were calculated and are resumed in table 3.

5. CONCLUSION

Highly sensitive InGaAs-2DEG Hall devices have been fabricated from high mobility $In_{0.75}Ga_{0.25}As/In_{0.52}Al_{0.48}As$ pseudomorphic heterostructures grown by MBE. Hall devices show a magnetic sensitivity of 346 V/AT with a temperature coefficient of -230 ppm/K and good magnetic resolutions of 350 $nT/Hz^{1/2}$ at 100 Hz and 120 $nT/Hz^{1/2}$ at 1kHz. These devices also show excellent linearity and a magnetic sensitivity independent of the supply current. These characteristics are at the state of the art of the InGaAs-2DEG Hall sensors[7].

6. REFERENCES

1. J. Heremans, D. L. Partin, C. M. Thrush and L. Green, "Narrow-gap semiconductor magnetic field sensor and applications", Semicond. Sci. Technol., 8, pp. 424-430, 1993.
2. Y. Sugiyama, "Trends on recent development of semiconductor magnetic sensors", Bull. Electrotech. Laboratory, n°54, pp. 65-95, 1990.
3. R. S. Popovic. Hall effect devices, Ch. 3, pp. 90-118, Adam Hilger, Bristol, 1991.
4. A. Overs, G. Jacob, M. P. Besland, V. Drouot, G. Hollinger, M. Gauneau, D. Lecrosnier and J. L. Benchimol, "Evaluation of InP epi-ready wafers for epitaxial growth", Proceedings of the 5th International Conference on InP and Related Materials, pp. 267-270, Paris France, 1993.
5. V. Drouot, M. Gendry, C. Santinelli, P. Viktorovitch, G. Hollinger, S. Elleuch and J. L. Pelouard, "High electron mobility in pseudomorphic modulation-doped $In_{0.75}Ga_{0.25}As/InAlAs$ heterostructures achieved with growth interruptions", J. Appl. Phys., 77, pp. 1810-1812, 1995.
6. V. Mosser, S. Aboulhouda, J. Denis, S. Contreras, Ph. Lorenzini, F. Kobbi and J.L. Robert, "High-performance Hall sensors based on III-V heterostructures", Sens. and Act. A, 41-42, pp. 450-454, 1994.
7. Y. Sugiyama, "Recent progress on magnetic sensors with nanostructures and applications", J. Vac. Sci. Technol. B, 13, pp. 1075-1083, 1995.

Ultrasonic carbon-fiber gyro-sensor

Yoshiro Tomikawa[1], Kazuhiro Kimura[1] and Sumio Sugawara[2]

[1]Yamagata University, Dept. of Electrical Engineering and Information Science, Jonan 4-3-16, Yonezawa, Yamagata 992 Japan
[2]Ishinomaki Sensyu University, Faculty of Science and Technology, Minami-Sakai, Shinmizuto1, Ishinomaki, Miyagi 986 Japan

ABSTRACT

We constructed an ultrasonic carbon-fiber and investigated its characteristics for its application to electronic devices. That is, in the first part of this paper, are dealt with the construction of ultrasonic carbon-fiber and such ultrasound transmission characteristics as propagation speed, attenuation characteristics and phase. The second part contains the carbon-fiber gyro-sensor and its experimental results. It is found that judgement of revolution direction can be made possible by the prototype gyro-sensor, with relatively high sensitivity.

1.INTRODUCTION

A carbon-fiber as a new material has atracted special interest recently, in the field of its application to electronic devices, too. This is because the carbon-fiber is very light, stout and flexible, and moreover it can be used in a high temperature. Therefore, the carbon-fiber is applied as a reinforeced material in metal, resin and ceramics etc. Of course, it is known that the carbon-fiber is less susceptible to chemical corrosion. In addition to these facts, now, the carbon-fiber material becomes to be easily supplied to researchers and be effectively applied to electronic devices. From such back-ground as mentioned above, we have inventend to construct the ultrasonic carbon-fiber and apply it to a gyro-sensor for detect of an angular velocity.

That is, this paper deals with the construction of an ultrasonic carbon-fiber and measurement of its propagation characteristics along the fiber, and then the construction of a gyro-sensor using such a carbon-fiber and experimental results on it are described herein. As for propagation of ultrasound through a fiber, we first constructed the ultrasonic fiber using an ordinal optical fiber and investigated its characteristics. However, the ultrasonic fiber using an optical fiber seemed not to be easily treated because of its easiness to break without coating with resin, large attenuation by the coating and non-easiness to bonding piezo-electric ceramic pieces on the fiber. On the other hand, the ultrasonic carbon-fiber also has such specific merits as :

- the material is made of carbon; therefore it is essentially safe to a human body.
- the carbon-fiber needs no-coating.
- the carbon-fiber can be fabricated as a belt-form, and then this is easy to bond the piezo-ceramic chips to the fiber

On ultrasound propagation through the flexible fiber, many researches have been published until now and their application to electronic devices have also been investigated by research groups of C.K.Jen (Canada)[1], S.Ueha (Japan)[2], and so on[3]. Therefore construction of the ultrasonic fiber dealt with herein is not so much original, but the report on the ultrasonic carbon-fiber might not be found yet.

2.ULTRASONIC CARBON-FIBER

2.1 Construction

Basic construction of an ultrasonic carbon-fiber proposed herein is shown in Fig.1, where two pieces of piezo-ceramics are bonded at both-ends of it for excitation and detection of ultrasound. Using such an ultrasonic carbon-fiber with a fine characteristic of flexiblity, some ultrasonic sensors can easily be fabricated[4].

0-8194-2165-0/96/$6.00

2.2 Characteristics of ultrasound propagation

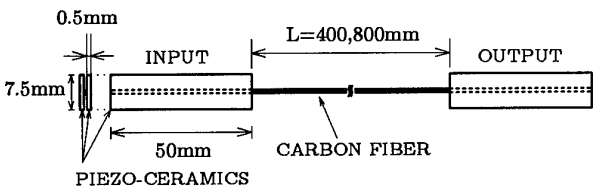
We measured the carbon-fiber characteristics on ultrasound propagation. Figures 2(a) and (b) show one example of attenuation vs. frequency characteristics in case of fiber length L=400(mm) and its input admittance characteristics; that is, it was found that the ultrasound could effectively be transmitted at slightly higher frequency than the resonance frequency of both-end piezo-ceramics, with not so much attenuation of 38.5(dB/m)(f=34.0 kHz).

We obtained the ultrasound propagation speed, using such two ultrasonic carbon-fibers of L=400(mm) and L=800(mm), as shown in Fig.1. The results were as follows:

$$\left.\begin{array}{l} \cdot L = 400(mm) \\ \quad f = 34.1(kHz) \quad t_1 = 174(\mu sec.) \\ \cdot L = 800(mm) \\ \quad f = 34.4(kHz) \quad t_2 = 216(\mu sec.) \end{array}\right\} \quad (1)$$

Therefore, ultrasound propagation speed v_g was calculated as*:

$$v_g = \frac{(800-400)\times 10^{-3}}{(216-174)\times 10^{-6}} = 9523.8$$
$$= 9500(m/sec.) \quad (2)$$

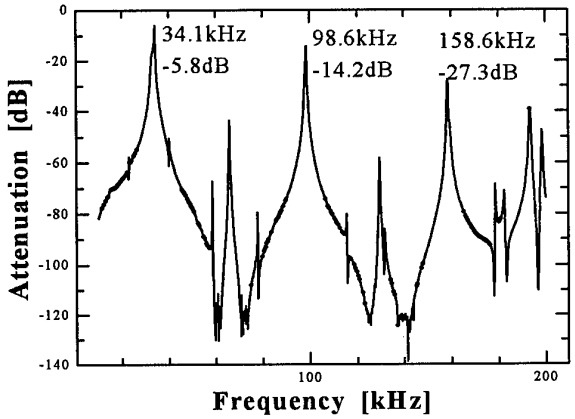


CROSS-SECTION : 1.0×0.15(mm^2) (BELT SHAPE)

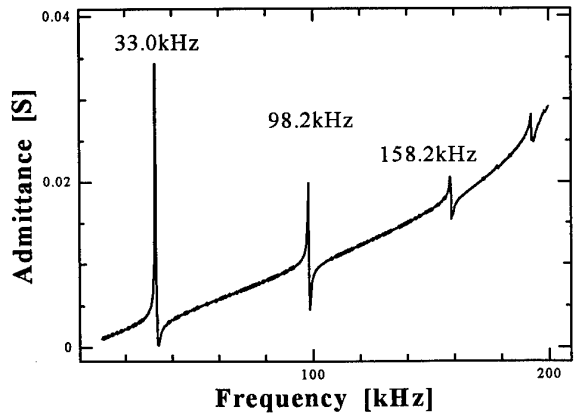
FIBER NUMBERS : STRANDED WIRES OF 0.15μm^{ϕ}

PRODUCTION : JAPAN CARBON FIBER CO. LTD.

Fig.1 Basic construction of an ultrasonic carbon-fiber



(a)Attenuation (input/output voltage ratio) vs. frequency characteristics (L=400mm)



(b)Input admittance characteristics of the fiber shown in Fig.1(L=400mm)

Fig.2 Measured ultrasonic transmission characteristics of the fiber shown in Fig.1

3.ULTRASONIC CARBON-FIBER GYRO-SENSOR

3.1 Basic construction and principle of detection

A gyro-sensor as an electronic device is indispensably used for prevention of hand-deflection in a camera work and control of a robot-posture etc.. In order to achieve such a gyro-sensor, we have invented to construct an ultrasonic carbon-fiber gyro-sensor by applying its ultrasound propagation characteristics. Basic construction of the gyro-sensor proposed by us is shown in Fig.3, where it is constructed by winding two lines of CH1 and CH2 on an acryle bobin in opposite direction. In the construction in Fig.3, an ultrasonic signal S_0 is input through the left-side piezo-ceramic chip and is divided to two signals S_1, S_2 through CH1 and CH2, and more-

*Foot-note: Using Young's modules $E = 26.8 \times 10^{11}(dyn/cm^2)$, and density $\rho = 2.71(g/cm^3)$ of carbon-fiber material, the longitudinal wave velocity $v = \sqrt{\frac{E}{\rho}}$ was calculated as v=9940(m/sec.).

over they are detected by two piezo-ceramic chips. In this case, when the carbon-fiber ring constructed at the center-portion in Fig.3 is rotated as a rate of $\pm\Omega$ (angular velocity: deg./sec.), it is expected that difference of the signals between CH1 and CH2 ($S_2 - S_1$) might be changed in its amplitude and phase; that is, detection of the angular velocity of $\pm\Omega$ can be made possible if change of the amplitude and phase is measured.

3.2 Measurement

We measured the characteristics of proto-type ultrasonic carbon-fiber gyro-sensor, applying the syncronous detection method. In the measurement, two proto-type gyro-sensors were prepared.

(Proto-type 1) First we constructed the gyro-sensor of proto-type 1 as:

- Largeness of piezo-ceramic chips used: $^{\ell}$ 50.0 $\times^{b}$ 7.5 $\times^{t}$ 0.5 (mm^3)
- Resonance frequencies of the piezo-ceramics: $f_{01st} = 32.6$ (kHz) $f_{11st} = 32.8$ (kHz) $f_{21st} = 32.4$ (kHz)
- Carbon-fiber: winded belt-form of 1.0×0.15(mm^2) constituting of an original slender fiber of diameter 0.15 μm^{ϕ}
- Carbon-fiber ring: diameter 40.0(mm$^{\phi}$), number of turn 1 in each channel 1 and 2
- Interval between input-ceramics and output-ceramics: 63.0(mm)
- Total length of the fiber: 20(mm)

Whole construction of the proto-type 1 is shown in Photo.1. Measured gyro-sensor characteristics of voltage E_{out} and phase θ are plotted as shown in Figs.4(a) and (b), and moreover judgement of revolution direction by syncronous detection is presented in Fig.5, where revolution speed of a turn-table was constantly set as 20(deg./sec.) and its direction was switched at the rate of 1.0 sec. interval. From these results, it was made clear that the construction in Fig.2 and Photo.1 could surely operate as a gyro-sensor, although the characteristics in Figs.4 and 5 were not enough for ones of a sensitive gyro-sensor, yet.

(Proto-type 2) Another ultrasonic carbon-fiber gyro-sensor was constructed as in Fig.6(a) and its characteristics were measured as in Fig.6(b), where the diameter of carbon-fiber ring was changed from 40.0(mm$^{\phi}$) to 100(mm$^{\phi}$) and numbers of turn was 3, using the fiber of total length 1190(mm). It was proved experimentally that the ultrasonic carbon-fiber dealt with could also be applied as a gyro-sensor and the proto-type 2 yielded more stable characteristics than the proto-type 1.

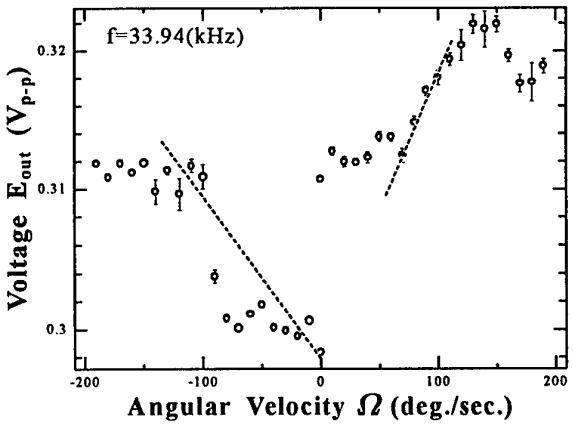
4.CONCLUSION

We proposed an ultrasonic carbon-fiber and measured its basic characteristics on ultrasound propagation at relatively low frequencies. Moreover, we constructed a gyro-sensor using the fiber and made clear experimentally that it was surely operate as a gyro-sensor.

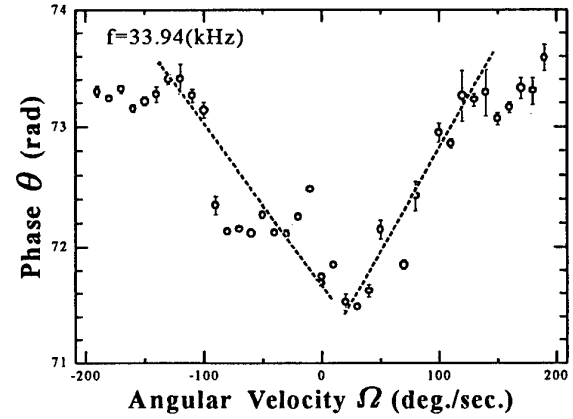
Hereafter characteristics of the gyro-sensor dealt with must be further investigated.

5.REFERENCE

1. C.K.Jen: "Similarities and Difference between Fiber Acoustics and Fiber Optics", Proc. of 1986 IEEE Ultrasonic Symp. pp. 1128-1133 (1986).
2. S.Ueha, T.Sugimoto, Y,Imaide and M,Akiho: "A Flexible Ultrasonic Lithotriptor", 1989 Ultrasonics International 89 Conf. Proc. (1989).
3. A.L.Matthews, K.A.Murphy, R.E.Rogers and R.O.Claus : "Acoustic Fiber Waveguide Coupler" , IEEE Ultrasonic Symposium p.629-631 (1987).
4. K.Kimura, Y.Tomikawa and S.Sugawara : "Characteristics of Ultrasonic Carbon-Fiber and their Application to Gyro-Sensor" , Technical Report of IEICE, Japan US. 95-39 pp. 33-40 (1995-09).



(a) E_{out} vs. Ω characteristics



(b) θ vs. Ω characteristics

Fig.4 Measured gyro-sensor characteristics

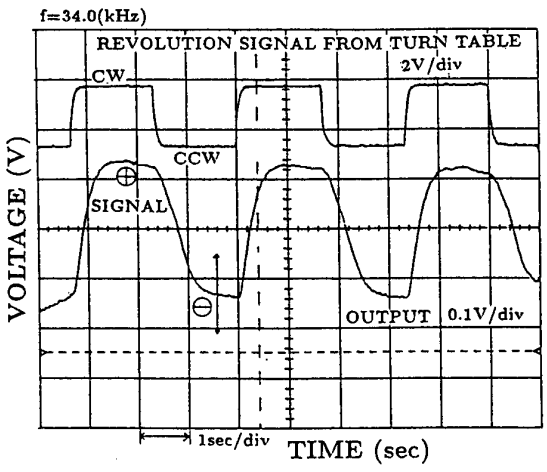


Fig.5 Judgement of revolution direction by synchronous detection

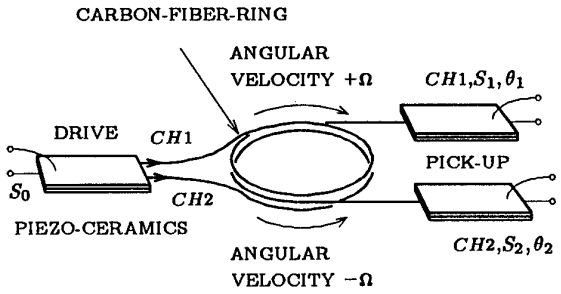


Fig.3 Basic construction of an ultrasonic carbon-fiber gyro-sensor

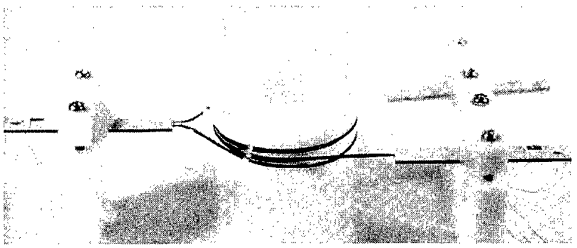
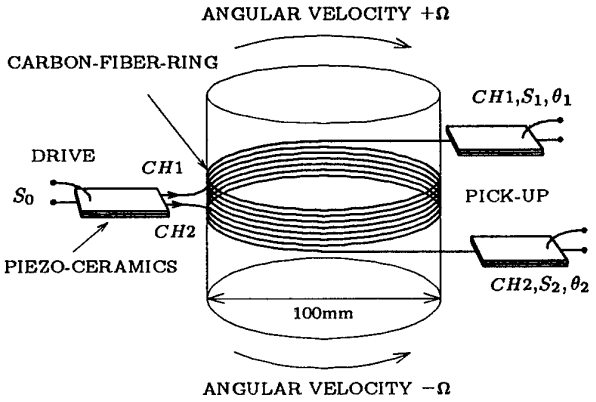
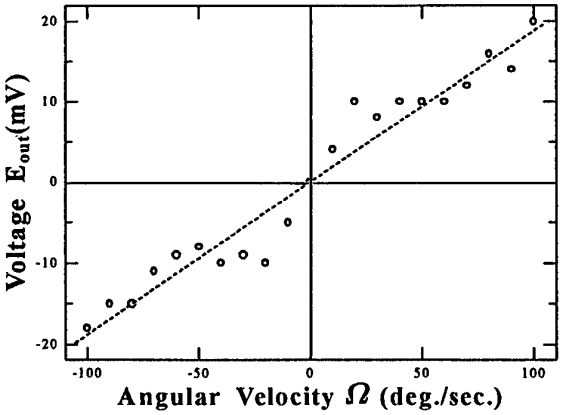


Photo.1 Prototype ultrasonic carbon fiber gyro-sensor



(a) Ultrasonic carbon-fiber gyro 2



(b) E_{out} vs. Ω characteristic

Fig.6 Measured gyro-sensor characteristics

Optoelectronic logical system with thin film photoconducting and electroluminescent devices

Zbigniew Porada
Kraków Polytechnic, Inctitute of Electrical Engineering,
Warszawska 24, PL-31-155 Kraków, Poland

1 INTRODUCTION

The increased utilization of various optoelectronic systems has generated interests in optoelectronic logical circuits with photoconducting (PC) and electroluminescent (EL) thin film devices. They are frequently applied as logical gates, amplifiers of weak light signals, and because of the optical feedback in such system, they can work as memory cells.

A diagram of an optoelectronic memory cell is presented in Figure 1.

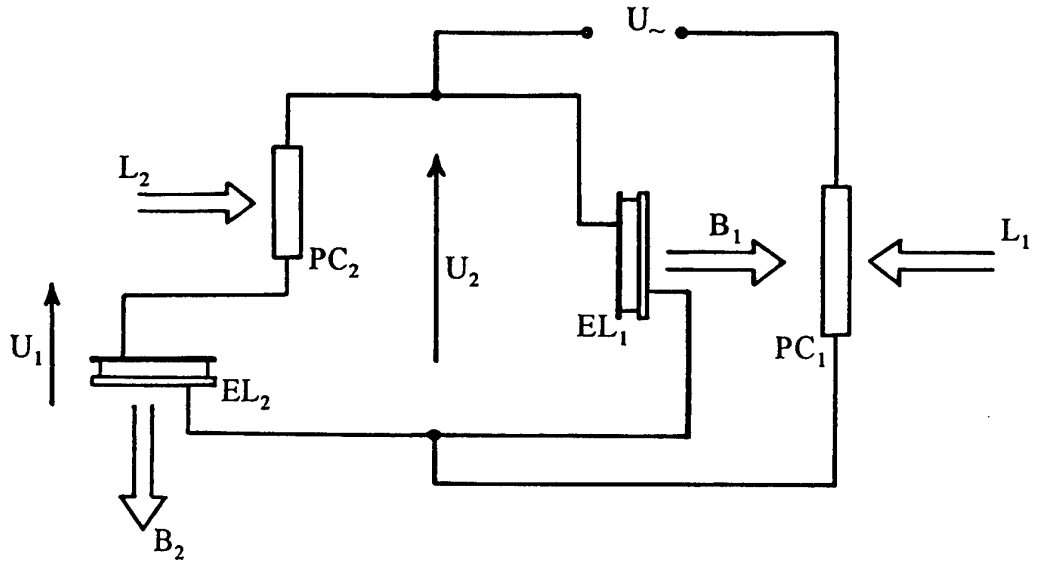


Fig.1. Schematic diagram of an optoelectronic memory cell.

A thin film PC-EL optoelectronic memory element was made by vacuum evaporating photoconductive and electroluminescent layers.

This optoelectronic memory element was supplied with a sinusoidal voltage. The input signal was in the shape of rectangular light pulses illuminating the PC device. The output signal was in the form of the light emitted from the electroluminescent device.

The theoretical analysis shows that a PC_1-EL_1 system with optical feedback may be a bi-stable system on condition that the feedback coefficient β will have a value higher than β_{lim}. As demonstrated in carried out investigation, the limiting value β_{lim} depends on the amplitude of the voltage supplying the PC_1-EL_1 system as well as on its frequency.[1]

If a PC_1 device is illuminated with an input signal L_1, then at the output of the bi-stable PC_1-EL_1 system a signal B_1 appears as the light emitted from the electroluminescent device EL_1 which additionally illuminates the PC_1 device. When the output signal B_1 does not fall to zero, in spite of "switching off" the input signal L_1, then the PC_1-EL_1 system is in the on-state, that is to say it remembers that previously it had been illuminated with the input signal L_1.

Assuming the PC_1-EL_1 system to be in the on-state, the application of the second input signal L_2, illuminating the PC_2 device, causes the appearance of the output signal B_2 in the form of light emitted from the electroluminescent device EL_2.

As the PC_2-EL_2 system is one without optical feedback, the removal of the input signal L_2 results every time in the decay of the output signal B_2 to a value not far from zero.

2. MANUFACTURING TECHNIQUE

A thin film PC-EL optoelectronic memory cell was made by vacuum evaporating photoconductive and electroluminescent layers.

The PC devices (Figure 2) can be prepared as a sandwich-type and gate-type system on a glass substrate. The first layer was a transparent electrode of tin-doped In_2O_3, obtained by the reactive cathode sputtering of a 90% In and 10% Sn alloy.

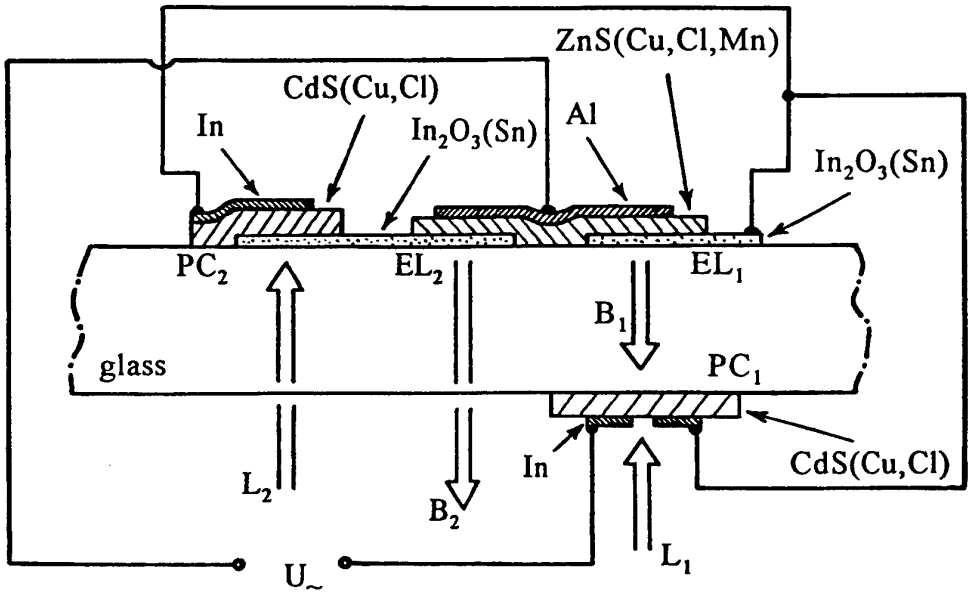


Fig.2. An arrangement of the thin film PC-EL system of an optoelectronic memory cell

The second layer was a photoconductive CdS film[2] doped with copper and chlorine and evaporated under vaccum at a presure of 0.007 Pa. Special purity cadmium sulphide undoped was used evaporated from an alundum crucible heated by a tungsten wire resistor. The temperature of the source was in the range of 900 C to 950 C. The distance of the substrate was held constant at 150 C. CdS films were simultaneously doped, with Cu and Cl, and recrystallized by heating the films whilst embedded in a CdS powder that had previously been doped with Cu and Cl. The recrystallization was carried out at 550 C in air for 30 min. The thickness of CdS(Cu,Cl) films was in the range 6-14 μm.

A metallic indium layer, deposited by vaccum evaporation, formed the upper electrode.

The electroluminescent device (Figure 2) was a thin film capacitor produced by the vaccum evaporation of copper-, chlorine- and manganese-doped ZnS[3,4]. The evaporation was carried out under the pressure of 0.01Pa from an alundum crucible heated to about 1100 C onto the substrate, which was placed 8 cm apart from the source and heated to 200 C. The obtained ZnS(Cu,Cl,Mn) films were recrystallized by heating in a vacuum for 30 min at 300 C. The thickness of ZnS(Cu,Cl,Mn) films was in the range 0,6 - 1,3 μm.

The lower transparent conducting electrode was tin-doped In_2O_3 on a glass substrate, while the upper electrode was a vaccum evaporated thin aluminium film.

3. THEORETICAL CONSIDERATIONS

A mathematical model suitable for analysing the properties of a PC-EL optoelectronic memory cell is proposed using the circuit shown in Figure 1.

The instantaneous value of the current i_1^{PC} through a PC_1 element is given by the formula[5] :

$$i_1^{PC} = C_1^{PC} \frac{d}{dt} u_1^{PC} + u_1^{PC} (G_{01} + G_1^{PC}), \tag{1}$$

where: u_1^{PC} is the instantaneous value of the voltage on the PC_1 element; G_{01} is the dark conductance of the PC_1 element; C_1^{PC} is the capacitance of the PC_1 element; G_1^{PC} is the instantaneous value of conductance of PC_1 element illuminated with a light of illumination L. The illumination L is given by the expression:

$$L + L_1 + \beta B_1, \tag{2}$$

where L_1 is the instantaneous value of illumination of PC_1 element by an external light source, B_1 is the instantaneous value of luminance of the light emitted by electroluminescent cell EL_1, and β is the optical feedback coefficient of PC_1 element with EL_1 element.

The instantaneous value of conductance G_1^{PC} may be calculated by solving the equation[6]:

$$\frac{d}{dt} G_1^{PC} = a_1 (L_1 + \beta B_1) - \frac{G_1^{PC}}{\tau_1}, \tag{3}$$

where a_1 is a constant for the PC_1 element, and τ_1 is the photoconductivity growth time for this element.

The instantaneous value of luminance B_1 can be given by the formula [7]:

$$B_1 = B_{01} \exp(-\gamma_1 t) \exp(-b_1 / \sqrt{|u_1|}), \tag{4}$$

where B_{01}, γ_1 and b_1 are constant values for EL_1 element, and u_1 is the instantaneous value of the voltage across this element.

The instantaneous value of the current i_1^{EL} through an EL_1 element is given by

$$i_1^{EL} = C_1^{EL} \frac{d}{dt} u_1 + G_1^{EL} u_1, \tag{5}$$

where G_1^{EL} and C_1^{EL} are the leakage conductance and the capacitance for EL_1 element, respectively.

Since $i_1^{PC} = i_1^{EL}$ and $u_1^{PC} = u - u_1$, where u is the instantaneous value of the exciting voltage of the optoelectronic memory cell, the equation

$$(C_1^{EL} + C_1^{PC}) \frac{d}{dt} u_1 + u_1 (G_1^{EL} + G_{01} + G_1^{PC}) = C_1^{PC} \frac{d}{dt} u + (G_{01} + G_1^{PC}) u \tag{6}$$

is obtained.

The instantaneous value of the current i_2^{PC} through a PC_2 element is given by the formula:

$$i_2^{PC} = C_2^{PC} \frac{d}{dt} u_2^{PC} + u_2^{PC} (G_{02} + G_2^{PC}), \tag{7}$$

where u_2^{PC} is the instantaneous value of the voltage on the PC_2 element, G_1^{PC} is the instantaneous value of conductance of PC_2 element illuminated with a light of illumination L_2, C_2^{PC} and G_{02} are capacitance and dark conductance of PC_2 element, respectively.

The instantaneous value of conductance G_2^{PC} may be calculated by solving the equation:

$$\frac{d}{dt}G_2^{PC} = a_2 L_2 - \frac{G_2^{PC}}{\tau_2} \tag{8}$$

where a_2 is a constant for the PC_2 element, and τ_2 is the photoconductivity growth time for this element.

The instantaneous value of luminance B_2 of the light emitted by electroluminescent element EL_2, can be given by the formula:

$$B_2 = B_{02} \exp(-\gamma_2 t) \exp(-b_2 / \sqrt{|u_2|}), \tag{9}$$

where B_{02}, γ_2 and b_2 are constant values for EL_2 element, and u_2 is the instantaneous value of the voltage across this element.

The instantaneous value of the current i_2^{EL} through an EL_2 element is given by

$$i_2^{EL} = C_2^{EL} \frac{d}{dt} u_2 + G_2^{EL} u_2, \tag{10}$$

where G_2^{EL} and C_2^{EL} are the leakage conductance and the capacitance for EL_2 element, respectively.

Since $i_2^{PC} = i_2^{EL}$ and $u_2^{PC} = u_1 - u_2$, the equation

$$(C_2^{EL} + C_2^{PC}) \frac{d}{dt} u_2 + u_2 (G_2^{EL} + G_{02} + G_2^{PC}) = C_2^{PC} \frac{d}{dt} u_1 + (G_{02} + G_2^{PC}) u_1 \tag{11}$$

is obtained.

Solving the set of equations (3), (4), (6), (8), (9) and (11), the time dependence of the luminances B_1 and B_2 of the light emitted by the electroluminescent elements EL_1 and EL_2 were computed. The computations were carried out for the case, when the PC_1-EL_1 system was in the state, "switched on", and when this system was in the state "switched off".

4. EXPERIMENTAL RESULTS

An optoelectronic logical circuit, composed of PC and EL thin film devices, were investigated as a memory cell.

A sinusoidal voltage of fixed amplitude and frequency was applied to the PC-EL system. The luminance B_2 of the electroluminescent device EL_2 was measured for various intensities L_1 and L_2 of illuminations of the photoconductive elements PC_1 and PC_2 and for values of β less than β_{lim}. The results were compared with values computed using the above theoretical model. The experimental values of the parameters of the PC and EL elements were found to be as follows: $G_1^{EL} = G_2^{EL} = 7.4 \times 10^{-8}\,\Omega^{-1}$; $C_1^{EL} = C_2^{EL} = 3 \times 10^{-9}$ F; $\gamma_1 = \gamma_2 = 620\ s^{-1}$; $b_1 = b_2 = 17.1\ V^{1/2}$; $B_{01} = B_{02} = 190\ cd/m^2$; $C_1^{PC} = 8 \times 10^{-12}$ F; $C_2^{PC} = 7 \times 10^{-11}$ F; $G_{01} = 7 \times 10^{-9}\,\Omega^{-1}$; $G_{02} = 1{,}2 \times 10^{-8}\,\Omega^{-1}$; $\tau_1 = \tau_2 = 0{,}6$ ms; $a_1 = 8.3 \times 10^{-4}\,\Omega^{-1}\,lx^{-1}\,s^{-1}$; $a_2 = 1.1 \times 10^{-3}\,\Omega^{-1} lx^{-1} s^{-1}$; $\beta = 0.6\ lx\,m^2/cd$.

Rectangular pulses of the light illuminating the photoconductive elements (PC_1 and PC_2) were applied to the input of the PC-EL system and the output signal was the luminance B_2 of the light emitted from the EL_2 element.

Figure 3 shows the time-dependence of luminance B_1 for an applied voltage of amplitude 420V at a frequencies 100, 200, 500 and 1000 Hz, at illuminations of the PC_1 and PC_2 elements with light pulses of L_1 = L_2 =20 lx.

In Fig.4 the dependences of luminance B_2 on the time for supplying voltage of amplitude 420 V and frequencies 200, 500 and 1000 Hz are presented.

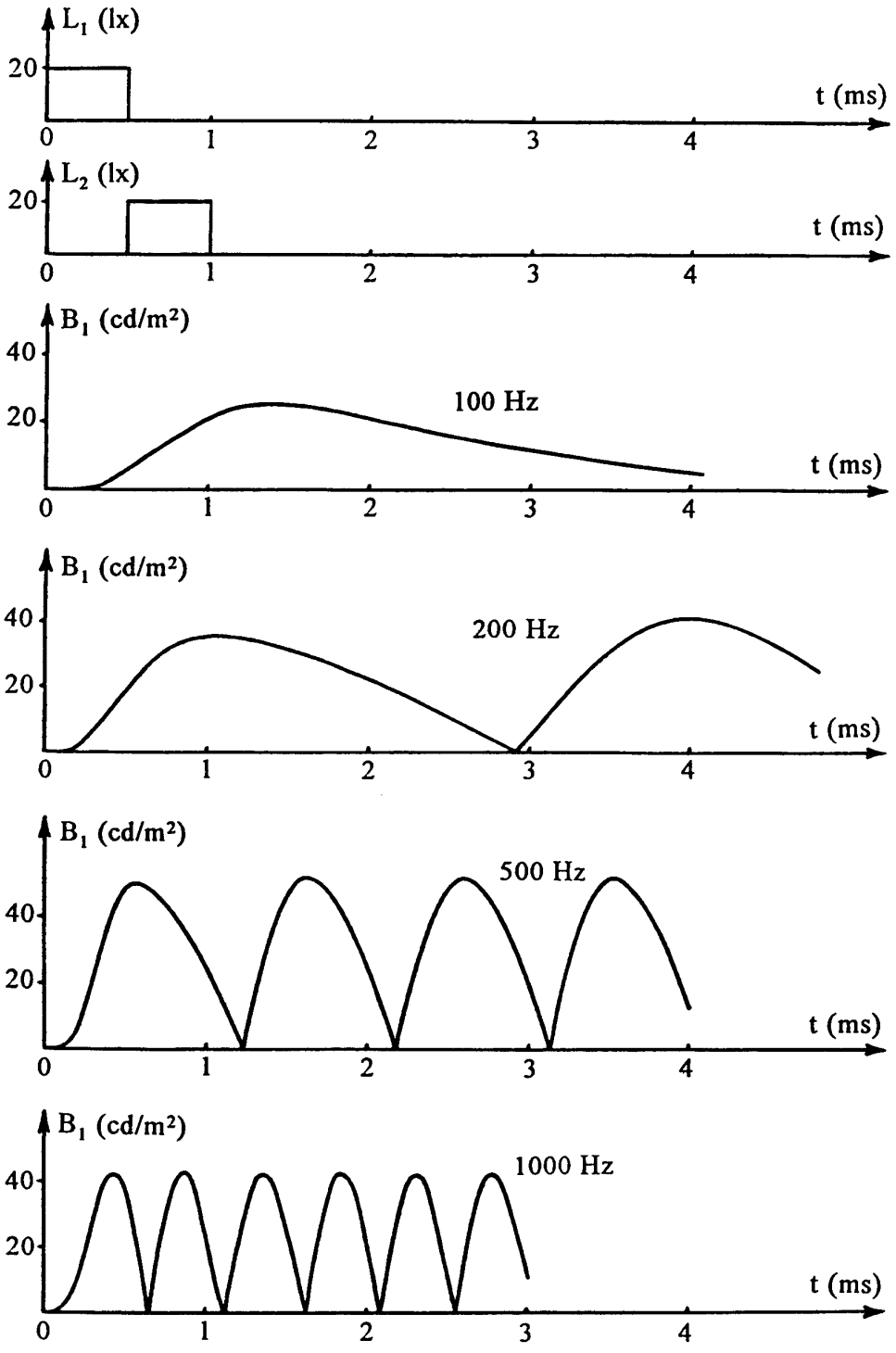


Fig.3. Dependences of luminance B_1 on time for U_0 420 V and frequencies 100, 200, 500 and 1000 Hz

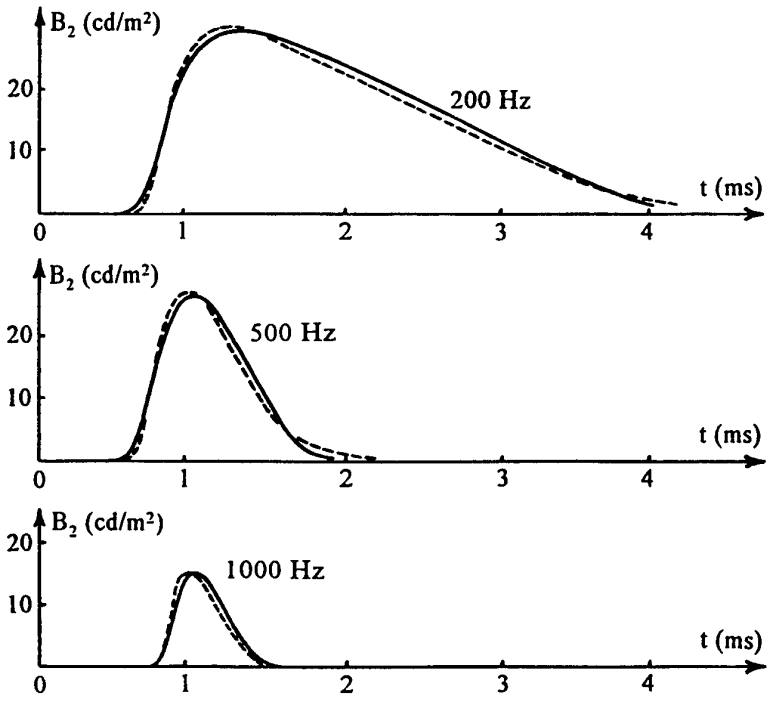


Fig.4. Dependences of luminance B_2 on time for U_0 420 V and frequencies 200, 500 and 1000 Hz (- - - measured values, —— calculated values)

5. CONCLUSIONS

Both the analysis of the proposed theoretical model and the measurements have shown that the maximum values of luminances B_1 and B_2 depend on the amplitude as well as on the frequency of voltage supplying the investigated memory system. As can be seen from Figs.3 and 4, maximum values of luminances B_1 and B_2 for frequencies 200 and 500 Hz are higher than for frequencies 100 and 1000 Hz. from this fact it follows that the limiting value of the optical feedback coefficient β_{lim} depends on the frequency and amplitude of supplying voltage and reaches a minimum for the frequency of about 300 Hz[1]. Thereby the conditions of optical feedback for frequencies 200 and 500 Hz in investigated system are more advantageous than for frequencies 100 and 1000 Hz.

The increase of the amplitude of supplying voltage results also in a increase of the maximum luminances B_1 and B_2. Moreover one observes an earlier appearance of the maximum for higher amplitudes of supplying voltage. It results also from the dependence of β_{lim} coefficient on the amplitude of supplying voltage.

All measured dynamic characteristics for the thin film optoelectronic memory system showed a good conformity with the characteristics calculated on the base of proposed theoretical model.

6. REFERENCES

1 Z.Porada, "Thin Film Light Amplifier with Optical Feedback". *Thin Solid Films*, vol.109, p.213-217, 1983.
2. Z.Porada, E.Schabowska, "Surface and Bulk Photoconductivity of CdS(Cu,Cl) Thin Films", *Thin Solid Films*, vol.69, p.165-169, 1980.
3. Z.Porada, E.Schabowska and T.Piech, "AC Electroluminescence in ZnS(MN,Cu,Cl) Thin Films", *Acta Physica Polonica*, vol.A57, p.267-272, 1980.
4. D.Theis, "Applications of Thin Films Electroluminescent Devices", *J.Luminescence*, vol.23,p.191-198, 1981.
5. Z.Porada, "Dynamic Characteristics of a Thin Film Light Amplifier", *Thin Solid Films*, vol.125, p.341-345, 1985.
6. A.van der Ziel, "Solid State Physical Electronics", Prentice Hall, Inc., New Jersey, 1976.
7. G.F.Alfrey and J.B.Taylor, *Br.J.Appl.Phys.*, vol.4, p.44S-49S, 1995 (supplement).

Electro- and Magnetorheologic Fluids

Invited Paper

Adaptative fluids: rheology and light transmission control

G.Bossis, S.Cutillas, E.Lemaire, A.Meunier, O.Volkova,
Laboratoire de Physique de la Matière Condensée, Université de Nice, Parc Valrose, 06108 Nice, France .

Abstract

We present two new effects related to intelligent fluids. The first one is the control of the transmission of a laser beam by using the change of turbidity of an electrorheological fluid in the presence of an electric field. The second one is the control of the aggregation of non magnetic particles by a magnetic field in order to change the viscosity of the fluid. This fluid is made of non magnetic particles in suspension in a high magnetization ferrofluid.

Introduction

Suspensions of solid dielectric particles can aggregate in the presence of an electric field.This aggregation is due to the electrostatic interactions between the solid particles which have been polarized by the electric field. The same kind of phenomena occurs with suspensions of solid magnetic particles placed in a magnetic field. In both cases the internal structure of the fluid can be controlled by the application of an external field. The control parameter λ is the ratio of the electrostatic(or magnetostatic) energy to the thermal energy. The dipolar energy of two dipoles aligned on the direction of the field is given by :

$$W=\frac{1}{4\pi\varepsilon_0\varepsilon_F}\frac{m^2}{r^3}(1-3\cos^2\theta) \qquad [1]$$

with θ the angle between the field and the line joining the centers of the particles. In the linear domain the dipolar moment of the particle is :

$$m = 4\pi\varepsilon_o\ \varepsilon_f\ \beta\ a^3\ E \qquad [2]$$

The field E in Eq. 2 is the average field inside the sample between by the two plates . . The quantity $\beta = (\varepsilon_p - \varepsilon_f)/(\varepsilon_p + 2\ \varepsilon_f)$ is usually not very different from the unity if the dielctric permittivity ε_p of the particles is much higher than the one, ε_f , of the suspending fluid. Finally, taking β =1 as an order of magnitude and with r = 2a and $\theta = \pi/2$ in Eq. (1) we have:

$$\lambda = \frac{4\ \pi\ \mu_0\ \mu_f\ a^3E^2}{8\ kT} \qquad [3]$$

If the value of λ is much larger than one, the suspension undergoes a phase separation and we obtain a gel-like structure. In that case the rheology of the fluid is tremendously changed by the application of the field since now we have a solid behavior with the presence of a yield stress τ_d which is necessary to break the structure and start the flow. Such fluids called electro or magnetorheological fluids are well known for their potential applications in dampers , robotics and many other devices. If we assume, as it is often the case, that these fluids behave as Bingham fluids with a rheological law given by: $\tau=\tau_d+\eta\gamma$ we understand that it is the ratio $\tau_d/(\eta\gamma)$which will represent the relative change of viscosity due to the application of the field. In practice the yield stresses obtained with MR fluids are much larger than the one obtained with ER fluids. Maximum values obtained till now are 10^5 N/m^2 for a MR fluid in a field H=3000 Oersted and 10^4 N/m^2 for ER fluids in an electric field of 4KV/mm [1],[2]. The values of these fields represent more or less an optimum value: the price to pay in order to obtain higher magnetic fields becomes prohibitive for most of the applications and furthermore the increase in yield stress becomes linear in the field instead of quadratic, due to the magnetic saturation of the fluid. On the other hand for electric fields, the breakdown field is close to 4KV/mm for most of the isolating fluids. Even if M.R. fluids seem more interesting than E.R. fluids for the change in rheology, they are handicapped by the sedimentation with a density which is always larger than 5g/cm^3 . A way to overcome this problem is to suspend them in a gel of low yield stress but it usually contributes a lot to the increase of the zero field viscosity, and the ratio $\tau_d/(\eta\gamma)$ can become quite low if high shear rates are used.

0-8194-2165-0/96/$6.00

In this paper we are going to present two phenomena which can open new domains of applications for these fluids.The first one is related to the transmission of light by E.R. fluids and the second one to the rheology of special magnetic fluids based on magnetic holes.

Control of the light transmission by an ER fluid

When an electric field is applied to an ER fluid we usually observe a phase separation with the formation of large aggregates of solid particles. Between these aggregates we have domains of fluid without particles which are transparent and do not absorb the light. So the transmission of light by an ER fluid usually increases in the presence of a field. But if the value of the parameter λ is only slightly larger than unity, then we do not have a complete phase separation but only the formation of small chains of particles and in this case we observe a strong decrease of the transmitted light.

The suspension used was made of silica particles synthetised by the Stober method and dispersed in a silicone oil of viscosity η = 20 mPa.s . The particles are monodisperse with a radius a = 0.47±0.05 μm. The suspension is placed between two glass disks covered with transparent electrodes. A laser beam is directed perpendicularly to the plane of the disks (and so parallel to the electric field) and the light transmitted through the sample is recorded on a photodetector. In Fig. 1 we present the result of an experiment where we apply a voltage step and we record the change of transmission of the suspension versus the time. The different curves correspond to different voltage steps. What we first notice is a very strong decrease of the transmission after the application of the field.

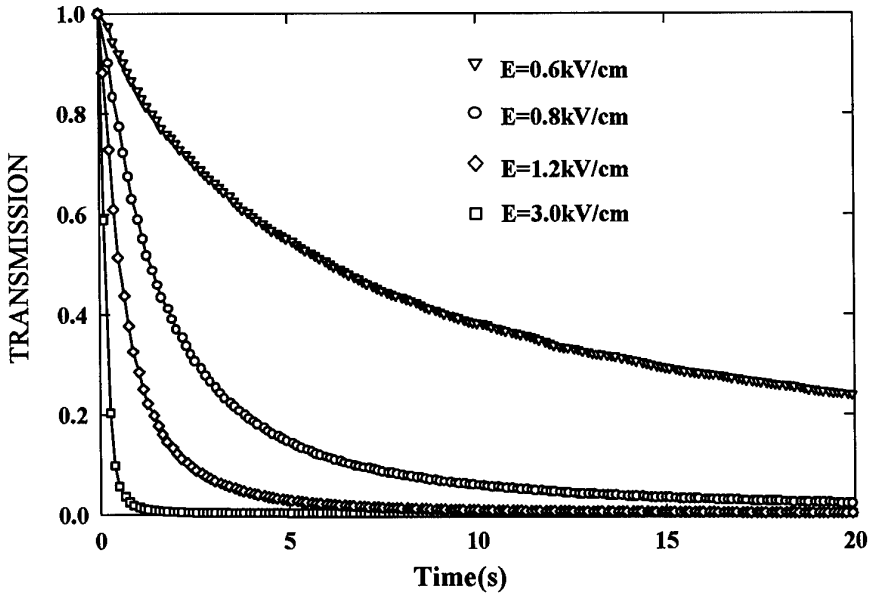


Fig 1. Transmission versus time after the application of different voltage steps

For a cell of thickness of 100 μm the transmission decreases by more than two orders of magnitude and , as expected, the higher the applied voltage the faster the decrease of the transmission. In this experiment we have applied an alternative field at a frequency of 1 kHz. In order to explain this increase in turbidity with the field we can use a simple model based on the Rayleigh - Gans - Debye approximation. In this model we assume single scattering and also that the local electromagnetic field is identical to the incident field. In the frame of this theory the turbidity which is the ratio of the scattered intensity to the incident intensity per unit length, is given for a polarized beam by :

$$\tau = \frac{1}{3}\Phi(m-1)^2 k^4 a^3 \int_0^{\pi} (1 + \cos^2\theta) F(\theta)^2 \sin\theta \, d\theta \qquad [4]$$

with

$$F(\theta)=\frac{3}{(qa)^3}(\sin qa - qa\cos qa);\quad q=\frac{4\pi n}{\lambda}\sin\frac{\theta}{2} \qquad [5]$$

In Eq [4] $k = 2\pi n/\lambda$ with n the refractive index of the suspension, Φ is the volume fraction of the suspension, m the ratio of the refractive index of the particles to the one of the suspension, and a the radius of the particles. $F(\theta)$ is the so-called form factor, which is given by Eq. [5] for a sphere. The intensity transmitted by a cell of thickness h will be given by :

$$I_t(h)=I_0 e^{-\tau h} \qquad [6]$$

We have measured the transmitted intensity in the absence of a field for different thickness of the cell. Taking the slope of the logarithm of the transmission relatively to the thickness we get $\tau_{exp} = 21500$ $m^{-1}$and from Eq. [4] with a = 0.47 μm , m=1.444/1.4023 and Φ = 14.5% we obtain $\tau_{th} = 16500\ m^{-1}$. The agreement is correct, especially taking into account the uncertainty on the radius of the particles. We conclude that we can trust the R.G.D. theory to calculate the turbidity. We have also verified that the value of the turbidity was proportional to the volume fraction at lower densities.

When an electric field is imposed to the suspension, the effect of the dipolar interactions between the particles induces the formation of chains of particles and we can no longer neglect the correlation between the positions of the particles in the calculus of the scattered intensity. In order to obtain the turbidity of a given state of aggregation we can apply the R.G.D. model to cylinders of diameter d = 2a and length L = 2Na with N the number of spheres in the chain. Assuming that all the cylinders have the same length and are aligned on the direction of the field we obtain for a polarized beam[3] :

$$\tau = \Phi\,(m^2-1)^2\,k^4\,a^3\,N\left[I_1 - \frac{I_2}{2}\right] \qquad [7]$$

I_1 and I_2 are two integrals of Bessel functions . In practice they are rather insensitive to the length of the chain and we can see by comparing Eqs (4) and (7) that the turbidity is now proportional to N, the number of spheres which is contained in the cylinder of length L. This factor N expresses the fact that for N particles which would scatter in phase, the scattered field would grow like N and so the intensity like N^2 or ΦN. Using Eq. 5 we obtain (1, 1.81, 2.41, 2.86, 3.20) for the ratios of turbidity of chains of spheres with the number of spheres increasing from 1 to 5. The increase in turbidity is not exactly linear with N due to a weak dependence of the integrals I_1 and I_2 on the length of the chain. An other model where we assume that the field scattered by each sphere comes from its centre (so the phase shifts are only considered between the centres of the spheres) gives very similar results . These models well represent the decrease of the transmited intensity[4].

Since the transmitted intensity decreases exponentially with τ, it is readily seen that the transmitted intensity can be a very sensitive probe of the beginning of aggregation. On the other hand this device can work with small voltages (a few Volts) but the applications are limited by the poor reversibility of the effect:: whereas a full extinction of the beam can be obtained in a few milliseconds the initial state is not recovered so quickly when we turn off the field,because the structure will only disaggregate by Brownian motion which can take a few seconds depending on the viscosity of the suspension.

Ferrofluids with magnetic holes

Ferrofluids are suspensions of very small grains of ferromagnetic materials. The size of these grains (about 10nm) is such that they are monodomain and behave as small magnets with a constant magnetic moment. The advantage of the small size of the grains is the absence of sedimentation and for this reason it would be interesting to use them as a magnetorheological fluid. Unfortunately ,for small particles, the Brownian motion always dominate the magnetic forces ($\lambda<1$) so we cannot create a gel-like structure by applying a magnetic field and indeed the change of viscosity due to the application of a magnetic field is usually quite small. One way to overcome this problem is to suspend large non magnetic particles in a ferrofluid. In this case the application of the field gives to a magnetic hole a magnetic moment which is proportional to its volume but in the opposite direction. The magnetic energy depends on the square of the magnetic moment so the force between the magnetic holes will be of the same order of magnitude as the force between magnetic particles. What we gain is the possibility to find non magnetic particles with a density adjusted to the one of the

ferrofluid. We have synthetized such a fluid by suspending silica particles of average diameter 40μm in an oil based ferrofluid. The equivalent magnetic moment,m, of the particle is just given by the magnetisation of the ferrofluid, M, multiplied by the volume of the particle. In order to have large effects we have used a ferrofluid with a large magnetisation (M=80000A/m). The change of rheology of the suspension with the applied magnetic field is shown in Fig.2 for a volume fraction of 24% of silica particles. In the absence of field (curve1) there is no yield stress and the dynamic viscosity obtained by a Casson fit is 1.4 Pa.s. For a field H=608 Oersted (curve 4) the stress is still three times higher than the zero field stress for a shear rate of $20s^{-1}$. This is not at all a negligible performance taking into account the low external field which is applied by the coil (Ho=315 Oersted). The difference between external and internal field comes from the use of iron plates which increases the magnetic flux. Furthermore we have previously shown[6] that it is important to use iron plates in order to prevent the slipping of the magnetic fluid on the wall. In this study the fluid was placed betwwen two disks located at the centre of Helmotz coils. A more compact device based on two concentric cylinders which could be used either for rheological measurements or in for viscocoupling applications is being realized.

It is possible to predict the field dependence of the yield stress by using a macrocopic model where the aggregates of particles are represented by cylinders[5]. The input of the model is only the magnetisation curve of the ferrofluid. This model shows that there is an optimum volume fraction of non magnetic particles which is about 30%. Some experiments are planned in order to verify this point.

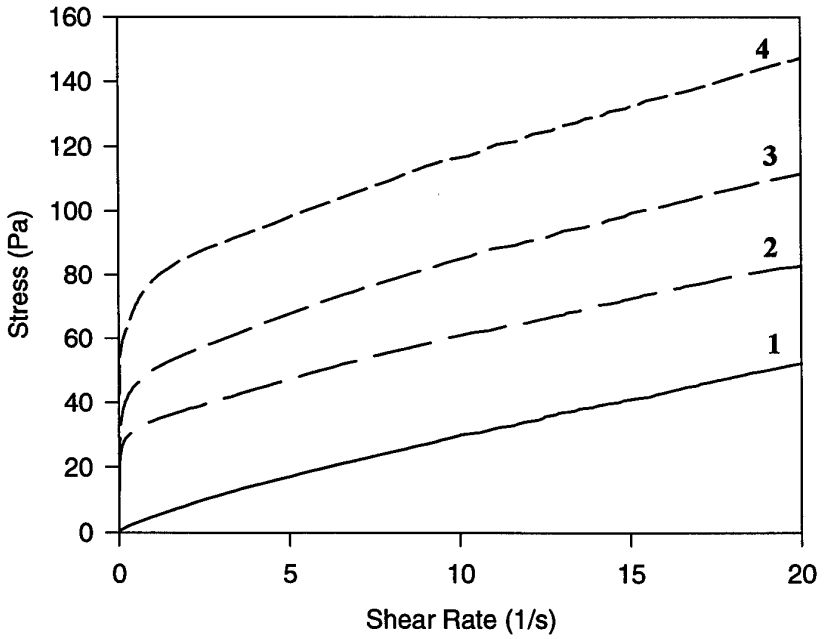


Fig 2: Rheograms of a ferrofluid with 24% in volume of silica particles for different magnetic fields (1:H=0, 2:H=156, 3: H=275 , 4:H=608 Oersted)

Acknowledgments This work was supported in part by a Nato grant 921196 .

References

[1] Weiss K.D.and Duclos T.G., in "Electrorheological fluids" edited by R.Tao and G.D. Roy World Scientific, Singapore, 1994 pp 43-59.

[2] Havelka,K. , Polymer Preprints "Novel Material for Electrorheological Fluids" **35**,315-316(1994)

[3] A.R.Jones, H. Savaloni, Part. Part. Syst. Charact. **6** (1989) 110

[4]S.Cutillas,A.Meunier,E.Lemaire,G.Bossis Int.J.Mod. Phys.B à paraitre

[5] O.Volkova,G.Bossis,E.Lemaire,V.Bashtovoi,N.Matoussevitch,A.Reks Magnitnaya Gidrodinamika, submitted.

[6]E. Lemaire, G.Bossis, J.Phys. D., **24**, 1413_(1991)

Paper presented at the Third ICIM/ECSSM '96, Lyon '96

Engineering with ER Fluids : A Design Methodology Based Upon Generalised Fluid Data

D. J. Peel
R. Stanway
W. A. Bullough

Department of Mechanical and Process Engineering
University of Sheffield, Mappin Street, Sheffield S1 3JD, UK.

ABSTRACT

An effective design methodology for ER devices requires reliable data to characterise the behaviour of the ER fluid as distinct from the test device. In this paper the authors describe a technique they have used for generalising ER fluid data so that it can be used to predict the performance of different types and sizes of device operating with the test fluid. The application of the technique is then illustrated using a problem of current industrial interest : namely the dynamic modelling of a controllable vibration damper for vehicle suspension applications.

1. INTRODUCTION

Electro-rheological (ER) fluids exhibit a rapid (and reversible) increase in their resistance to flow when subjected to an electric field of sufficient intensity. There are many ways in which the properties of ER fluids can be exploited in engineering devices,[1] but vibration control and torque transmission have received most attention to date. Recent developments[2] in the formulation of ER fluids have overcome many of the engineering problems (toxicity, abrasiveness, physical/chemical instability) associated with previous generations of ER fluids and opened the way to wider commercial exploitation. Consequently it is now timely to re-appraise some key applications and, in particular, to consider design methodology for practical devices which employ ER fluid as the working medium.

A substantial body of work relating to the design of engineering devices using ER fluids has accumulated over the years[3]. Attention has been focused mainly on the steady and quasi-steady behaviour of fluids, typically in clutches and dampers. A major difficulty in the development of a design methodology arises because the specification of ER fluid performance has traditionally been specific to a particular type and size of device. Device-specific fluid data is of little value in two common situations: where the results from a laboratory scale device are to be extrapolated to design an industrial scale device; and where results from one type of device are to be applied to another.

To overcome this difficulty, a procedure has recently been developed whereby ER fluid data from laboratory tests on a specific device can be generalised so as to provide reliable design data for different types and sizes of device, operating with the test fluid but on an industrial scale.

In what follows here, the authors will summarise the main features of the generalisation of ER fluid data. They will then proceed to describe its application to a problem of current industrial interest : dynamic modelling of a controllable vibration damper for vehicle suspension applications.

0-8194-2165-0/96/$6.00

2. STATEMENT OF PROBLEM

Traditionally, ER test data has been obtained from steady flow tests involving clutch-type devices (shear mode) or flow-control valves (flow mode). Results from clutches were typically presented as (torque) versus (angular velocity) versus (electric field strength). Valve data was invariably plotted as (pressure drop) versus (flow rate) versus (electric field strength). Early attempts to generalise the data involved reducing experimental results to the form of (shear stress) versus (shear rate) for different values of field strength. Unfortunately, it was found[4] that the shear stress data from the two arrangements did not truly correspond with one another. Moreover the data proved to be inconsistent with results from static shear tests.

It has been found that an effective way of generalising ER fluid data to obtain consistent characterisation of performance is to adopt a non-dimensional formulation for analysis of the fluid data. This technique will now be summarised and reference made to those aspects of validation which have been successfully accomplished.

3. GENERALISATION OF ER FLUID DATA

3.1 Friction Coefficient and Reynolds Number

Consider , for example, a fully developed flow of a Newtonian fluid through any plane valve. Assume that the flow can be characterised in terms of a wall shear stress τ_w, electrode separation h and average velocity $\bar{u}$. The fluid has a density ρ and Newtonian viscosity coefficient μ. The fluid might be a typical ER fluid under conditions of zero applied electric field. We can define a friction coefficient $Cf = \tau / \rho\bar{u}^2$ and a Reynolds number $Re = \rho\bar{u}h / \mu$ whose relationship can be visualised by plotting one variable against the other, the so-called Stanton diagram. For all such laminar flows between smooth, flat plates it can readily be shown[5] that $Re.Cf = 6$, i.e. the relationship is between Cf and Re is linear. For more conventional fluids, the Stanton diagram is used to visualise the departure from ideal behaviour caused, for example, by surface roughness at high Re. For ER fluids we can use the same diagram to visualise the effect of applying an electric field, at different levels of excitation. The same variables and the same non-dimensional parameters can be taken in this way to present test data for a concentric cylinder clutch, using the same form of diagram. The influence of the applied electric field can be illustrated directly from experiments performed on our arbitrary valve device. For example, given measurements of wall shear stress τ_w (from pressure drop/torque) and mean flow velocity $\bar{u}$ (from volume flow rate/rotational speed), the dimensionless quantities Cf and Re can readily be calculated and plotted on the Stanton diagram. To illustrate the kind of result which might be expected, Fig. 1 shows Cf versus Re for an ER flow-control valve. Referring to Fig. 1, the effect of increasing the applied electric field is to increase the friction coefficient Cf at a given value of Reynolds Number Re., consistent with the concept of an applied electric field tending to increase the resistance to flow of an ER fluid.

The problem remains : how to model this effect in terms of generalised fluid data?

3.2 The Hedström Number

In order to quantify the influence of the applied electric field, we introduce a third dimensionless group, $He = \tau_b \rho h^2 / \mu^2$, which is called the Hedström number.[5] The term τ_b represents the yield stress in a Bingham plastic constitutive relationship which we shall assume is capable of accounting for the observed behaviour of the ER fluid. If a value of τ_b were available then He could be calculated for a given fluid. Lines representing constant values of He could then be generated by solving the Bingham plastic equation which for the valve flow is:

$$Cf^3 - [3/2 + 6Re/He]\left(He/Re^2\right)Cf^2 + \left(He/Re^2\right)/2 = 0 \qquad (1)$$

to obtain Cf over a range of values of Re. By assuming a range of values of He from 0 to 10^3 and solving equation (1), constant He lines were generated and are superimposed onto Fig. 1. Note that the constant field strength experimental data lie in a similar fashion to the constant He characteristics.

3.3 Validation of Generalised Model

As a first step towards validating the generalised model, fluid property data derived from flow mode tests was shown to be consistent for different sizes of a valve type over a range of flow rates and applied electric field strengths.[4] The approach was consolidated when static shear test data was used to determine a value for the Hedström number in the absence of flow and a subsequent correction made to account for flow in terms of the Reynolds Number . Thus, the Hedström number is expressed as a function of Reynolds number at constant excitation. This approach provided a model which uses the Bingham plastic constitutive relationship and which is capable of accounting for observed behaviour over a range of valve sizes and operating conditions.[5] More recently the technique has been extended to directly relate concentric clutch and plane valve data, with more than one ER fluid type, and with different test equipment.[6,7]

4. CASE STUDY : A CONTROLLABLE VIBRATION DAMPER

4.1 Previous Work

With the growing confidence which could be placed in the generalised approach as a result of the validation exercise it was decided to examine the feasibility of constructing and modelling an ER controllable vibration damper for application in vehicle suspension systems. A preliminary modelling study of this problem has recently been submitted for publication.[8] In this study the fluid data was taken from a well-established formulation of ER fluid (a dielectric oil with a dispersion of lithium polymethacrylate solids, designated LP30/W, and represented in Fig. 1). The same fluid data has been used as the basis of the controlled ER damper study which follows.

4.2 Description of Controllable Damper

When an ER fluid is subjected to a suitable electric field the result is an increase in the shear stress developed within the fluid. For the control of mechanical vibrations the capability of an ER fluid is considerably enhanced when the available shear stress is transformed into a force through a

combination of an ER flow control valve and a translating actuator or piston. A cross-sectional view of a typical ER valve and piston assembly is shown in Fig. 2. Referring to Fig. 2, the ER valve has electrodes of length ℓ with inter-electrode gap h. The shear stress τ_w at the electrode surface, which is governed principally by the field controlled yield stress developed by the ER fluid, is transformed into a normal stress ΔP which can act at a piston face. It can readily be shown that $\Delta P = (2\ell / h)\tau_w$ and that the transformation ratio can typically be within the range from 200 to 400. By means of this transformation the yield stress and flow capabilities of modern ER fluids can be applied to the specific force and displacement requirements typical of road or rail vehicle suspension damping systems. Also shown in Fig. 2 is the piston which translates inside a cylinder of uniform cross-section. The cylinder is filled with ER fluid. Attainment of a controllable damping force implies the need for a relatively high stiffness of the fluid volume and also of the cylinder and mount. In addition the (uncontrolled) fluid inertia forces should ideally be small in relation to the required damping force. These aspects of ER fluid behaviour (compressibility, inertia) were accounted for in the methodology developed to predict the performance of a controllable damper.

4.3 Summary of Damper Performance Prediction

The methodology for characterising the behaviour of the damper - predicting force vs. velocity vs. displacement - is depicted in the flow chart of Fig. 3. The straightforward steady/quasi-steady flow solution[6,9] cannot be applied when fluid inertia and compressibility are significant, these being represented respectively by mass m and stiffness k. Where x and $\dot{x}$ are known piston displacement and velocity, a displacement x_1 associated with spring constant k gives rise to a velocity defect $\dot{x}_1$ of fluid flow at the valve relative to that at the piston. However x_1, $\dot{x}_1$ and valve pressure drop ΔP are mutually dependent, and thus an iterative solution to the problem is required.

For given valve (ℓ, h and electrode width b) and piston (area A) dimensions , and the given ER fluid generalised characteristic and physical properties, an operating (constant) electric field strength E and piston displacement amplitude X and frequency ω are specified. The iterative procedure is effected by defining a window across which are points n = 1 ... 11 evenly spaced in time at interval δt. At each point, piston displacements and velocities $x_n, \dot{x}_n$ are given when motion is initiated at time t = 0. An initial value of zero is assigned to the corresponding spring displacements $\dot{x}_{1n}$. The volume flow rate of fluid in the valve being given by $Q_n = A(\dot{x}_n - \dot{x}_n)$ at point n, for each time point in the window Re and He for the instantaneous valve flow are known and by solution of equation (1), Cf at the valve can be found, and hence the piston force F_n at each point in the window when the fluid inertial load is added. The spring displacements $x_{1n} = F_n/k$ can now be calculated, and by means of a least-squares polynomial fit, the velocities $\dot{x}_{1n}$ can be deduced by differentiation. The iteration now proceeds by advancing the window by a single time interval δt to take in one new (n = 11) while discarding one old (n = 1) time point, after which the cycle is repeated as far as is required. A single data point is taken as $F_n(x_n, \dot{x}_n)$ at n = 6, while the first and second iterations for a value of x_1 (i.e. n = 10, 11) are not included in the determination of $\dot{x}_1$. By keeping ω and E constant, and repeating the procedure for different amplitudes X, the force vs. velocity vs. displacement surface can be constructed.

5. RESULTS AND DISCUSSION

Figs. 4a and 4b show the results of two calculations, for the same damper model operating at two different frequencies. The valve size is h x ℓ x b = 1 x 100 x 1000 mm, and the piston diameter is 100 mm. The ER fluid has density 1450 kg/m^3 and viscosity 103.7 mPa.s at the assumed constant operating temperature of 30°C - the fluid is the LP30/W fluid whose test characteristic is shown in Fig. 1 - and the constant electric field strength is E = 3kV/mm. The inertial mass is m = 11.2 kg and the spring constant is k = 2.68 x 10^7 N/m. In Fig. 4a, the frequency is 1 Hz and the amplitude range shown is ±30 mm; in Fig. 4b the frequency is 25 Hz and the amplitude range whose is ±3 mm. The direction of motion is anticlockwise on the phase plane.

The results shown highlight several points of interest, expected to be borne out by experiment.
(i) At low piston velocities, a piston force of ≈6 kN is available, offering a high value of equivalent viscous damping coefficient for small amplitude motions.
(ii) The available piston force (approaching 1 tonne) and damping capability will be commensurate with the suspension damping requirement of a vehicle having appreciably greater than 1 tonne weight.
(iii) By far the greater part of the piston force is field-controllable over the operating range shown, resulting from the yield effect which is prominent at the reversal of the valve flow/piston motion at zero velocity.
(iv) In operation at 25 Hz, fluid inertia gives rise to a significant increase in piston force, seen in Fig. 4b as an increase of piston force as displacement diminishes along a constant velocity line.
(v) In operation at 25 Hz, fluid compressibility gives rise to large changes of piston velocity occurring while flow reverses in the valve. These become very prominent at a high frequency in the force vs. velocity characteristic : however the associated piston displacement will maintain a small value, independent of frequency, determined by the spring constant k and the field controlled fluid yield stress.

ACKNOWLEDGEMENTS - The authors wish to thank the Advanced Rail Research Centre (UK) for their financial support of damper modelling work described in this paper.

REFERENCES

1. R. Stanway and J. L. Sproston, "Electro-rheological fluids : a systematic approach to classifying modes of operation", ASME Trans. J. Dyn. Syst. Meas. Contr., vol. 116, pp. 498-504, 1994.
2. H. Block, "Electro-rheological Fluids", Chemtech (Am. Chem. Soc.), pp. 368-373, June 1992.
3. J. E. Bares and J. D. Carlson, "Electro-rheological fluid design : an overview", Proc. 2nd Int. Conf. on ER Fluids, Technomic Publishing, Lancaster, PA, pp. 93-123.
4. D. J. Peel and W. A. Bullough, "Bingham plastic analysis of ER valve flow", Int. J. Mod. Phys. B., vol. 8, pp. 2967-2985, 1994.
5. D. J. Peel and W. A. Bullough, "Prediction of ER valve performance in steady flow". Proc. I.Mech.E. Part C, vol. 208, pp. 253-266, 1994.
6. D. J. Peel and W. A. Bullough, "Comparative behaviour of ER fluids in rotary shear and linear flow modes of steady operation", submitted for publication.
7. D. J. Peel, R. Stanway and W. A. Bullough, "A generalised presentation of valve and clutch data for an ER fluid and practical performance prediction methodology". Int.J.Mod.Phys.B., at press.
8. D. J. Peel, R. Stanway and W. A. Bullough, "Dynamic modelling of an ER damper for vehicle suspension applications", Proc. I.Mech.E., submitted for publication.

9. D. J. Peel, R. Stanway, J. L. Sproston and W. A. Bullough, "An ER long stroke damper : performance modelling under quasi-steady conditions", Proc. 15th Biennial Conf. on Mech. Vib., ASME, Boston, 1995.

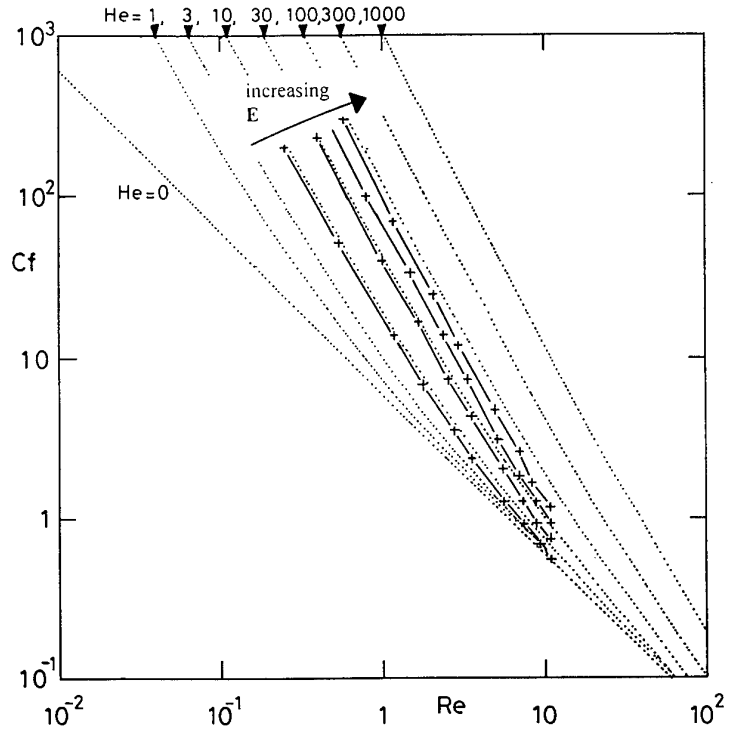


Fig. 1. Dimensionless characteristic of plane valve ER fluid flow

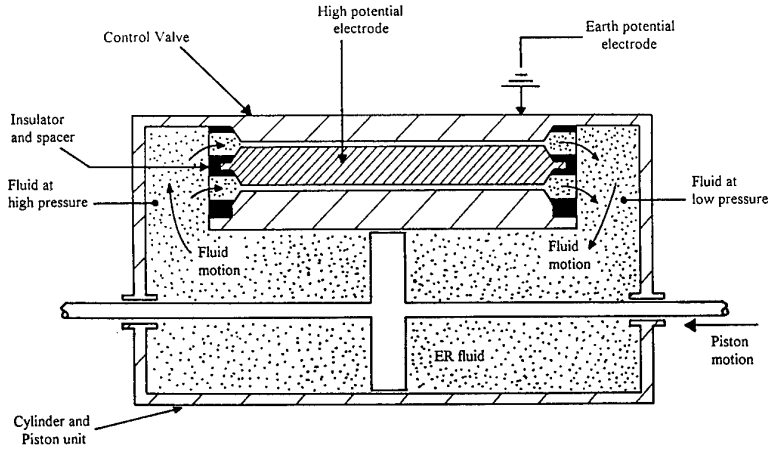


Fig. 2. Schematic diagram of ER valve and piston assembly

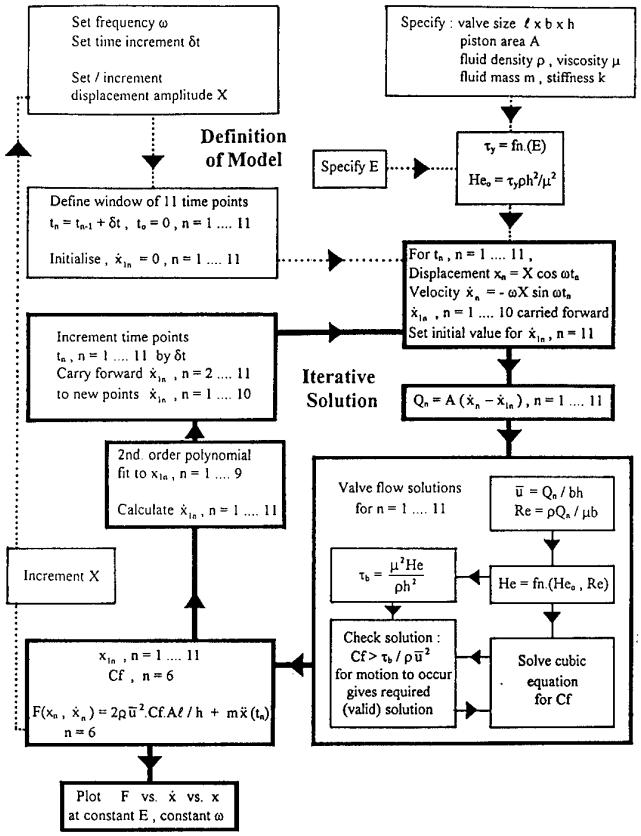


Fig. 3 Flow chart for calculation of damper model characteristic

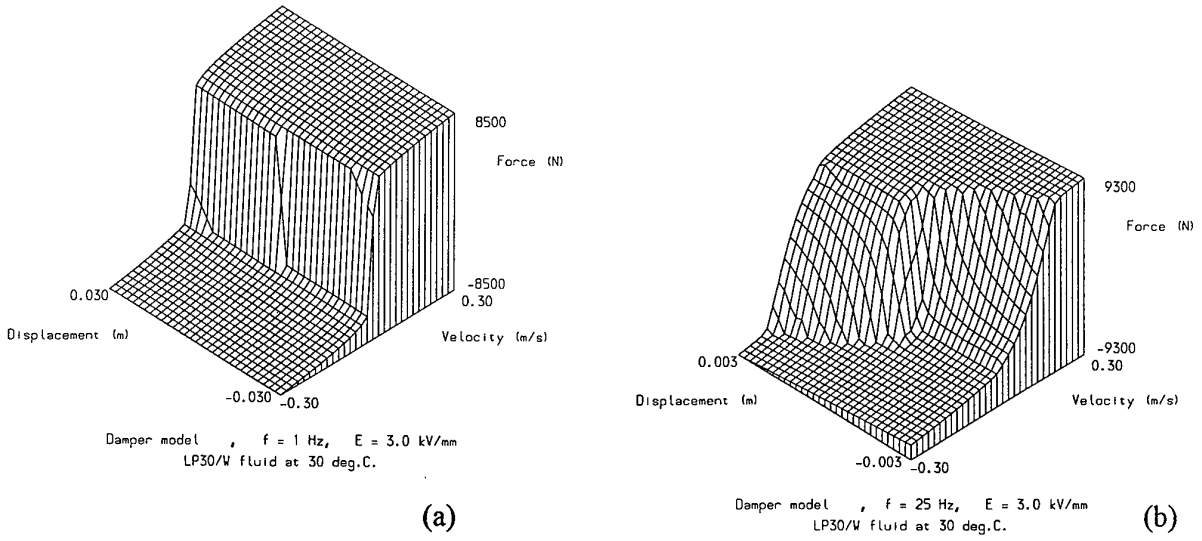


Fig. 4a,b Damper model characteristics for constant electric field excitation

Chemical preparation of new magnetic fluids based on spinnel ferrite nanoparticles

F.A. Tourinho[‡], P.C. Morais[†], M.H. Sousa[‡] and L.G. Macedo[‡]

[‡]Universidade de Brasília, Departamento de Química
70910-900 Brasília (DF) - Brazil
[†]Universidade de Brasília, Departamento de Física
70910-900 Brasília (DF) - Brazil

ABSTRACT

Three new magnetic fluids, that haven't been previously reported, were chemically synthesized by improving the hydrothermal techniques. The fine particle ferrites were produced by coprecipitation and treated further in order to obtain stable ionic sols. Highly concentrated magnetic magnetic fluids (25% volume fraction) can be prepared by following the procedure described here. Characterization was performed using X-ray diffraction techniques.

1. INTRODUCTION

Magnetic fluids are nano-sized ferrite particles suspended in a carrier liquid in order to form very stable colloidal dispersions.[1] Besides numerous interesting industrial applications new research interests have appear as for instance in the biomedical field.[2] Since the first preparation (and application) of magnetic fluids in the 60's, there has been enormous progress that provides a clear account of the magnetic fluid's fundamental physical understanding. The synthesis, however, of very stable magnetic fluids is still a refinement of empirical methods. The magnetic colloidal preparation science was born in the field of physics, and as a result even in these days participation of chemists in international conferences hasn't been expressive. However, some progresses have been obtained concerning the methods of preparation of good magnetic colloidal sols.[3] The magnetic ferrite particles are very interesting for manufacturing magnetic fluids as compared to metallic particles for they present large saturation magnetization values. In addition, magnetic ferrite particles do not be oxidize as metallic particles do, a detail that could endanger the stability of the magnetic fluids. Therefore, all the spinnel ferrite series (MFe_2O_4 with M = Fe, Co, Mn, Cu, Ni and Zn) are able to be used to produce ferrimagnetic particles, and this variety can be applied to a particular application of the magnetic fluid. In this direction, chemical preparation of ionic aqueous magnetic fluids was proposed for magnetite[4], maghemite[5] and cobalt and manganese spinnel ferrites.[6]

In this work, will be reported for the first time, the synthesis of a series of magnetic fluid samples based on spinnel ferrite nanoparticles of copper, nickel and zinc. The new members complete the series of the ferrimagnetic spinnel ferrites. All of them represents new ionic water-based magnetic fluids obtained by the method of condensation, where the ferrite fine particles are obtained by coprecipitation, in alkaline medium, of a mixture of solutions of aqueous metallic ions. These nano-sized particles have a very reactive surface allowing the stabilization of a large spectrum of media, including both polar and non polar solvents. The first efforts to produce magnetic fluids were done in 1779 by Knight[7], followed by Bitter[8] and Elmore[9] who obtained a suspension of large magnetic particles. Though not fully stables those colloids were similar to the present day "magnetic fluids". However, to reach the present day synthesis it was necessary to develop both a method to produce stable suspensions and a technique to remove the big particles through an efficient centrifugation process. The stable magnetic liquid was first obtained by Papell[10], working at NASA. They were magnetic fluids similar to the nowadays commercially available and were designed to control the flux of combustible (fuel) in the absence of gravity in outer space. Between 1965 and 1969, Rosensweig[11] managed to produce magnetic fluids in kerosene and others solvents like water, fluorocarbons and esters. It is interesting to note that until the first quarter of the 70's magnetic fluids were produced through the suspension of magnetite particles obtained from grinding processes. It became necessary to obtain magnetic fluids through faster processes. In 1973 Kalafalla and Riners[12] first proposed a chemical method for the production of surfacted magnetic fluids based on magnetite. In 1979, Massart[13] proposed a chemical synthesis based

0-8194-2165-0/96/$6.00

on the fact that magnetite nanoparticles were dispersed in polar solvents (ionic magnetic fluids), without necessity of surfactants. However, there was a stability problem due to oxidation, i.e., the magnetite transformed into maghemite. It is interesting to observe that this kind of transformation had not happened before because natural magnetite is stable. In 1987, Cabuil[14] forced the oxidation of magnetite in maghemite. In 1989, changing the process of the initial synthesis, Tourinho[15] was able to obtain ultra stable and concentrated magnetic fluids with different magnetic particles (Mn and Co ferrites).

2. EXPERIMENTAL DETAILS

In this work fine particles of Ni, Cu and Zn ferrites are synthesized by condensation method from the chemical reaction among aqueous solutions of metal mixtures in alkaline medium. Since the composition of the initial mixture can vary the magnetic properties of the product, exact concentration of the reactants must be known. Nevertheless, the composition of the particles must be well known during its characterization, even when M(II) and Fe^{+3} are together. So, very specific chemical analysis (gravimetry or volumetry) has to be used to determine the metal concentration for iron is a strong interfering agent for divalent cation determinations (iron concentration is typically twice the concentration of divalent metal ion). The specific methods used here involve gravimetric homogeneous precipitation by dimethylglioxime[16] for Ni^{2+}, a variation of the tritation method using iodine for Cu^{2+} using fluorine as masking agent[17], gravimetric precipitation using 8-hydroxyquinaldinate[18] for Zn^{2+} and ordinary tritation using potassium dicromate[19] for Fe^{3+}. More details about chemical composition determination in magnetic fluids (based on MFe_2O_4, with M(II) = Fe, Co, Mn, Cu, Ni and Zn) are discussed elsewhere.[20] The only products in the chemical reaction that can yield magnetic material are the spinnel type ferrites. So, in order to characterize the crystal structure of the particles, X-ray diffraction measurements were carried out using a Rigaku/Geigerflex X-ray diffractometer system and Fe K_α radiation. As far as particle dimension is concerned the optimum particle diameter of the spinnel ferrite to produce a stable magnetic fluid is in the range of 4nm to 15nm. In order to control the particle diameter, the average particle size is determined by Scherrer's formula using the halfwidth of the (311) X-ray diffraction line.

Preparation process of magnetic fluids needs mainly two principal steps: first, the production of fine magnetic particles and secondly, their stabilization in a desired carrier fluid. Very fine particles (diameter around 100Å), having greater density when compared with the liquid carrier, can be suspended in solution due to Brownian process. The technological process to produce fine magnetic particles can be divided in two mainly categories: dispersion and condensation methods. In the dispersion methods, a sample of magnetic bulk material is broken down into colloidal dimension by a laborious mechanical process. More recently, condensation methods were proposed and involve condensation from a chemical reaction. The condensation methods are faster, cheaper and more flexible. In the present work fine particles of $NiFe_2O_4$, $CuFe_2O_4$ and $ZnFe_2O_4$ was prepared by the condensation method by coprecipitating aqueous solutions of $NiCl_2$-$FeCl_3$, $CuCl_2$-$FeCl_3$ or $ZnCl_2$-$FeCl_3$ mixtures in alkaline medium. In a second step of the fine particles ferrite synthesis, i.e., their stabilization, is performed by addition of a barrier to protect from aggregation because of Van der Walls and magnetic dipole-dipole interactions. The protected particle can be surfacted or ionic. In the surfacted type, a physical barrier is introduced using a suitable dispersing agent (surfactant). Surfactants are molecules that consist of two well defined regions: one which is oil-soluble (hydropholic) and one that is water soluble (hydrophilic). The hydropholic part is non-polar and usually consists of an aliphalic or hydrocarbon residues. The hydrophilic part is polar and usually consists of polar groups which can interact strongly with water (specially hydroxyl, carboxyl and ionic groups). So, for stabilization of the ferrite particles in the non-polar medium, a simple surfactation is required; the hydrophilic part is adsorbed in the particle surface and the hydrophobic part will be therefore compatible with solvent. For polar medium, like water, two layers of surfactant are needed to form an exterior hydrophilic layer. In the ionic magnetic fluids there is a repulsive electrostatic force that allows the particles to stay in solution without agglomeration. This can be obtained due to the fact that a specific adsorption of amphoteric (pH dependence) hydroxyl groups creates an adjustable surface charge density (electric double layer). Therefore, the ionic method is more advantageous than the double surfactation method for solubilization in water. In this work, the new magnetic fluids, based on $NiFe_2O_4$, $CuFe_2O_4$ and $ZnFe_2O_4$ ferrites were prepared using the ionic model, i.e., by peptizing the fine particles obtained in water.

3. RESULTS AND DISCUSSION

Particle nature and size are fixed by the coprecipitation step. It is therefore necessary to make very precise the experimental conditions in order to obtain reproducible results. Parameters acting to a certain extent on this step are the composition of initial mixtures, the composition of the alkaline medium, the operating mode, the temperature and the ionic strength of the initial mixture. All of them have been tested for the success of the new synthesis. As far as the molar ratio is concerned the best initial condition (X_o) for all the three samples prepared corresponds just to the ferrite stoichiometry, i.e., $X_o = 0.33$. The molar ratio is expressed by $X = [M(II)]/[M(II) + Fe(III)]$, with M(II) = Ni(II), Cu(II) and Zn(II). In addition the particular base used, the pH and temperature are extremely important in the synthesis. The best temperature range for the synthesis of $NiFe_2O_4$, $CuFe_2O_4$ and $ZnFe_2O_4$ ferrites is around 100 °C. Usually a base excess is needed due to the acidity of the initial mixture. The reagent addition procedure, including the way and speed of mixing, acts directly to determine the average value of the particle size. The fine particles are obtained by pouring the M(II)-Fe(III) mixture as quickly as possible into the base medium under vigorous stirring. Very high ionic strength as well as base excess are very important in the synthesis of $NiFe_2O_4$ based magnetic particles. Figures 1(a), 1(b) and 1(c) show partial powder diffractograms obtained from fine particles of $ZnFe_2O_4$, $NiFe_2O_4$ and $CuFe_2O_4$, respectively. These diffractograms represent samples that have been used to produce very good magnetic fluids. The more intense X-ray peaks related to the spinnel structure, namely, the ones corresponding to the interplanar spacing (220), (311) and (400) are presented in Figure 1, for each sample. The obtained X-ray relative intensities agree very well with the powder ASTM values as shown in Table 1. The average particle size was calculated from the broadening of the dominant (311) X-ray peak according to the classical relation $D = K\lambda/\beta\cos\theta$, where D is the average crystallite size, K is a proportionality constant ($K = 0.9$), λ is the X-ray wavelength, β is the full width at half maximum of the X-ray peak and θ is the Bragg angle. The obtained D values are given in Table 2.

Finally, after the magnetic particles be synthesized they are washed in acid medium using a ferric nitrate solution at the boiling temperature in order to promote the chemical surface stabilization. The chemical stabilization mechanism is not well know to the best of our knowledge. Very stable and concentrated magnetic fluids are obtained, after the chemical surface stabilization step, by dispersion in acid (alkaline) medium with suitable counterions like NO_3^- or ClO_4^- (TMA^+).

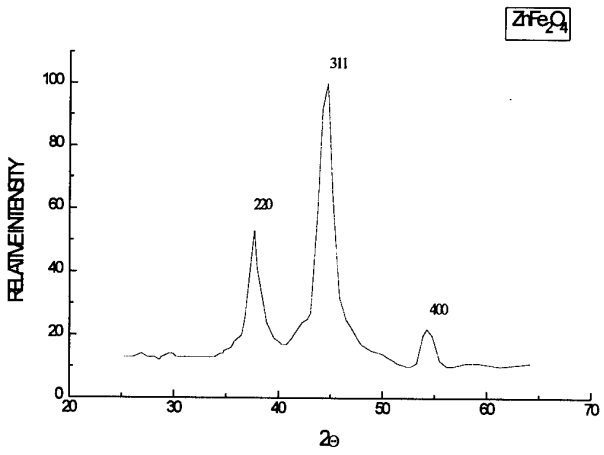


Fig. 1(a). X-ray diffractogram of $ZnFe_2O_4$ fine particles.

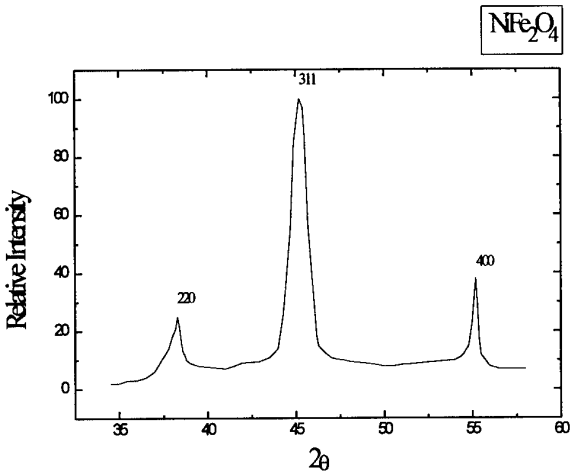


Fig. 1(b). X-ray diffractogram of $NiFe_2O_4$ fine particles.

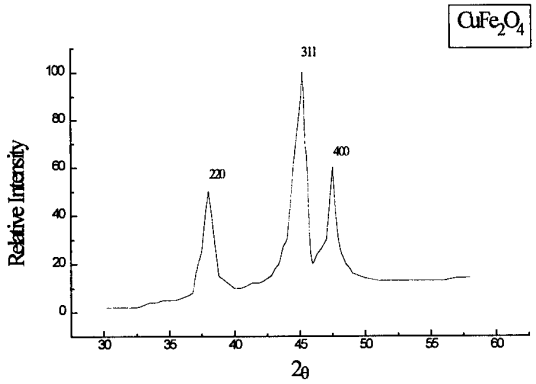


Fig. 1(c). X-ray diffractogram of $CuFe_2O_4$ fine particles.

cubic assignment	$CuFe_2O_4$	$CuFe_2O_4$	$ZnFe_2O_4$	$ZnFe_2O_4$	$NiFe_2O_4$	$NiFe_2O_4$
	this work	ASTM	this work	ASTM	this work	ASTM
111	23	30	11	7	18	20
220	45	50	53	35	25	30
311	100	100	100	100	100	100
400	59	60	22	17	38	25
511	31	40	25	30	25	30

Table 1. Intensities of diffraction peaks for samples in powder form compared with the ASTM standard values.

spinnel ferrite	$CuFe_2O_4$	$ZnFe_2O_4$	$NiFe_2O_4$
particle diameter (nm)	9.8	14.3	10.3

Table 2. Average values for particle diameter calculated from the (311) X-ray line.

4. CONCLUSIONS

In conclusion, we are reporting in this paper the synthesis of three new ionic magnetic fluids based on $ZnFe_2O_4$, $NiFe_2O_4$ and $CuFe_2O_4$ ferrites. X-ray diffractograms are presented as a first characterization technique. The average particle diameter are then obtained from the X-ray analysis as described above. The fine control of parameters like temperature, ionic strength, initial molar fraction, nature of the reaction medium and the steps to be followed is very important as far as the success of the preparation is concerned. We found that the close control of these parameters determines the average particle size, magnetic nature of the particles and surface reactivity. As a final comment, several attempts have been made in the past years, for different research groups around the world, to synthesize Zn, Ni and Cu-ferrite based magnetic fluids with no success.

5. ACKNOWLEDGMENTS

This work was supported by the Brazilian Agencies FAPDF, PADCT and CNPq.

6. REFERENCES

1. F. A. Tourinho, *Thesis*, Université Pierre et Marie Curie, Paris, 1988

2. See S.P. Bhatnagar and R.E. Rosensweig, *J. Magn. Magn. Mat.* **149**, pp. 198-232, 1995.

3. R. Massart, J. Roger and V. Cabuil, *Braz. J. of Phys.* **25**, pp. 135-141, 1995.

4. R.Massart, *US Patent* 4 329 241, 1982.

5. V. Cabuil, *Thesis*, Université Pierre et Marie Curie, Paris, 1987.

6. F.A. Tourinho, R. Franck, R. Massart, *J. of Mat. Sci.* **25**, pp 3249-3254, 1990.

7. See E.P. Wohlfarth, *Ferromagnetic materials* Vol. 2, pp. 512, North-Holland Publishing Co., Amsterdam, 1982.

8. F. Bitter, *Phys. Rev.* **41**, pp. 507-515, 1932.

9. W.C. Elmore, *Phys. Rev.* **54**, pp. 309-310, 1938.

10. S.S. Papell, *US Patent* 3215572, 1965.

11. See E.P. Wohlfarth, *Ferromagnetic materials* Vol. 2, pp. 518, North-Holland Publishing Co., Amsterdam, 1982.

12. S.E. Khalafalla, G.W. Reimers, *US Patent* 3 764 540, 1973.

13. R.Massart, *French Patent* 79 18842, 1979.

14. V. Cabuil, R. Massart, *J. Chim. Phys.* **84**, pp. 967-972, 1987.

15. F.A. Tourinho, R. Franck, R. Massart, R. Perzynski, *Prog. Colloid Polym. Sci.* **79**, pp. 128-134, 1989.

16. E.D. Salesin and L. Gordon, *Talanta* **5**, pp. 81-85, 1960.

17. B. Park, *Industrial and engineering chemistry, Anal. Ed.* **3**, pp. 77-82, 1931.

18. A.I. Vogel, *Textbook of quantitative chem. analysis*, pp. 472-473, Longman Sci. and Techn., Essex, 1989.

19. G. Charlot, *Les Méthodes de la chimie analytique*, Masson et Cie, pp. 737, Paris, 1966.

20. F.A.Tourinho, P.C. Morais, M.H. Sousa and L.G. Macedo (*to be published*)

Paper presented at the Third ICIM/ECSSM '96, Lyon '96

Magnetic particle-particle interaction in single particle systems and agglomerates

M.C.F.L. Lara[†], P.C. Morais[†] and F.A. Tourinho[‡]

[†]Universidade de Brasília, Departamento de Física
70910-900 Brasília (DF) - Brazil
[‡]Universidade de Brasília, Departamento de Química
70910-900 Brasília (DF) - Brazil

ABSTRACT

Magnetic resonance is used to investigate magnetic interaction in magnetic fluids and magnetic agglomerates. Magnetic dipole-dipole interaction between monodomain particles accounts for the magnetic resonance data in magnetic fluids. In magnetic agglomerates however an anisotropic interaction between spins in the agglomerate and spins in the magnetic monodomain dominates the magnetic resonance behavior.

1. INTRODUCTION

A magnetic single particle system is performed by magnetic fluids where monodomain nanoscaled magnetic particles are dispersed in a carrier fluid. Magnetic agglomerates, meaning clusters of magnetic particles, are obtained after removal of the carrier fluid out from a magnetic fluid sample. For decades intensive investigations have been performed in both magnetic fluids and magnetic agglomerates (fine particle systems). However, little effort has been done to understand the relationship between the magnetic properties of single particle systems (magnetic fluids) and their parents magnetic agglomerates. Frozen magnetic fluids have recently attracted some attention particularly because magnetic glass-like behavior has been associated with magnetic dipole-dipole interaction.[1] Magnetic dipole-dipole interaction can be varied by orders of magnitude through dilution of an initially concentrated magnetic fluid sample. Although magnetic particles do not touch one another they are brought very close together in a highly concentrated magnetic fluid. However, after removing the carrier fluid of a magnetic fluid sample the monodomain magnetic particles are brought into close contact in such a way that they collapses into agglomerates, usually as chain-like structures.[2] Magnetic phase transition from a magnetically ordered state to a glass-like state at the freezing temperature has been reported in agglomerates composed by fine particle systems.[3] In the present work we focus our attention at the temperature dependence of the magnetic resonance linewidth in both frozen magnetic fluid and its powder parent. In the next two sections it will be presented a brief review of the theories used to explain the resonance data in both magnetic single particle systems and magnetic agglomerates. Evidences of a close connection between the two parent systems will be presented in the fourth section of this paper.

2. SINGLE PARTICLE SYSTEM

In magnetic fluids magnetic particles are dispersed as single entities in a carrier fluid though they may interact to one another. As far as magnetic resonance linewidth is concerned an approximative calculation based on Van Vleck's method of moments[4] is reviewed here. The method of moments[4] takes into account the amount of diffusion of the magnetic resonance line due to Zeeman, exchange and dipolar interactions. Calculation of the resonance linewidth broadening starts with a Hamiltonian (**H**) that describes a magnetic system composed of identical and regularly arranged magnetic centers in an external magnetic field (H_e)

0-8194-2165-0/96/$6.00

$$\mathbf{H} = g\beta H_e \sum_j S_{zj} + \sum_{k>j} J_{jk}\, S_j\, S_k + \sum_{k>j} B_{jk}\, S_{zj}\, S_{zk}\,, \quad (1)$$

where $A_{jk}=-2J_{jk}+[g^2\beta^2/2(r_{jk})^3][3(\gamma_{jk})^2-1]$ and $B_{jk}=[3g^2\beta^2/2(r_{jk})^3][3(\gamma_{jk})^2-1]$. The Zeeman interaction appears in the first term of Eq. (1). The dipolar interaction appears in the second and third terms of Eq. (1) through coefficients A_{jk} and B_{jk} as described above. The usual exchange integral is described here by J_{jk}. S_{zj} is the z-component of the spin operator related to the magnetic center j, g is the g-factor, β is the Bohr magneton, r_{jk} is the vector from the j^{th} to k^{th} magnetic center and γ_{jk} is the direction cosine of r_{jk} relative to the z-axis. Magnetic resonance linewidth broadening is calculated as the mean square deviation of the resonance frequency from the Larmor value $\langle\Delta\upsilon^2\rangle=\langle\upsilon^2\rangle-(g\beta H_e/2\pi\hbar)^2$. The mean square absorption frequency, i.e., the resonance frequency computed by weighting each fine-structure due to the existing interaction is calculated according to Van Vleck.[4] In terms of magnetic field derivative peak-to-peak full linewidth broadening (ΔH_d) is related to the mean square frequency deviation $<\Delta\upsilon^2>$ by $\Delta H_d=2[(2\pi\hbar/g\beta)<\Delta\upsilon^2>]^{1/2}$. We start by considering a magnetic fluid as a system composed of randomly oriented magnetic centers and thus we can replace the powers of the direction cosines in A_{jk} and B_{jk} by their averages over a sphere. Considering the Hamiltonian as described in Eq. (1) and the expressions for $\langle\Delta\upsilon^2\rangle$, $\langle\upsilon^2\rangle$ and ΔH_d one obtains

$$\Delta H_d = g\beta\left[(12/5)S(S+1)\sum_{k>j}(r_{jk})^{-6}\right]^{1/2}. \quad (2)$$

In a second step we look at the suspended magnetic particles as magnetic centers arranged in a cubic structure. We assume only nearest-neighbor interaction among magnetic centers. Therefore the summation in Eq. (2) is calculated as $[\sum_{k>j}(1/r_{jk})^6]^{1/2}\cong 3.18/D^3$, being D the particle-particle distance, i.e., the nearest-neighbor distance between magnetic centers in the host matrix. Equation (2) then becomes $\Delta H_d=(5g\beta/D^3)[S(S+1)]^{1/2}$. In a third step we consider our system as composed of a suspension of magnetic particles each one having an effective spin $S'>>1$ associated with it. We thus rewrite the derivative peak-to-peak full linewidth broadening (ΔH_d) as $\Delta H_d=5g\beta S'/D^3$. At this point we look at our sample as being composed of uniaxial single-domain superparamagnetic particles in which case the effective spin is written as $S'=\Delta n\times S$, where S is the spin of the magnetic center inside the particle and $\Delta n=(n_- - n_+)$ represents the net population of spins aligned in one of the two distinct orientations parallel to the easy axis of magnetization. The spin population associated with each of the two distinct orientations is n_- and n_+. Thermal fluctuation induces spin transitions between the two available states against an energy barrier ΔE. Classical statistics was used to calculate the net population of spins as $\Delta n=n\times\tanh(\Delta E/2kT)$, being $n=(n_- + n_+)$. Considering these points into $\Delta H_d=5g\beta S'/D^3$ one obtains[5]

$$\Delta H_d = (A/D^3)\times\tanh(\Delta E/2kT), \quad (3)$$

where $A=5g\beta Sn$. According to the pre-factor of Eq. (3) magnetic resonance linewidth broadening depends upon the third power of the mean distance between adjacent particles and thus on the magnetic fluid concentration. Magnetic resonance linewidth broadening depends as well upon the temperature by the Boltzman factor (2kT). Finally ΔH_d depends upon the energy barrier (ΔE) through which the magnetic moment of the monodomain particle relaxes. The energy barrier may includes several contributions depending first on the particular magnetic fluid under study and second on the experimental condition. From the relaxation point of view the system is dominated by a Néel type relaxation mechanism. The Néel relaxation mechanism[6] is a thermal assisted relaxation of the magnetic moment inside a magnetic particle, which is primarily related to the magnetocrystalline anisotropy energy. The Néel relaxation mechanism is characterized by its relaxation time described by

$$\tau_d = \tau_o\times\exp(\Delta E/kT), \quad (4)$$

where τ_0 is typically of the order of a few nanoseconds, $\Delta E=KV$ is the magnetocrystalline anisotropy energy barrier the magnetic moment of the particle has to overcome to flip from one orientation parallel to the easy axis of magnetization to another. However, in the presence of an external magnetic field and considering concentrated samples the energy barrier must includes, in addition to the magnetocrystalline anisotropy term (KV), both interaction between the magnetic moment of the particle and the external field (μH_e) and the magnetic dipole-dipole interaction between adjacent particles (μ^2/D^3).[7] The magnetocrystalline anisotropy constant, particle volume and magnetic moment of the particle are respectively described by K, V and μ.

3. AGGLOMERATES

As the carrier fluid is removed out from a magnetic fluid sample the monodomain magnetic particles are brought into close contact and they stick together into agglomerates which in general have a chain-like structure.[2] The close contact of the individual particles in a chain-like structure gives rise to a system which is, from the magnetic point of view, very similar to a system of a finite cluster of spins coupled to an infinite magnetically ordered cluster of spins. Here the finite cluster of spins is represented by the magnetic monodomain particle while the infinite cluster of spins is represented by the agglomerate. With this geometric picture we look at the low-energy excitations of the infinite magnetically ordered cluster as spin waves. We then treat the coupling of these low-energy modes to the finite clusters as a relaxation channel for the infinite cluster driven by the applied microwave field of frequency ω. We assume that the relaxation process occurs via an anisotropic Dzyaloshinskii-Moryia (DM) interaction between spins in the infinite cluster and the spins in the finite clusters. The Hamiltonian that describes spin waves in a magnetically ordered infinite cluster interacting with finite clusters is[8]

$$\mathbf{H} = \sum_k \varepsilon_k a_k^+ a_k + \mathbf{M} \bullet \sigma \times \mathbf{S}, \quad (5)$$

where $\varepsilon_\kappa = \Delta + M_o\kappa^2$, being κ the wavevector of the spin waves, Δ a spin wave gap and M_o a stiffness constant. The Holstein-Primakoff (HP) boson operators are a_κ^+, a_κ . The coupling constant **M** describes the anisotropic DM interaction between the spin **S** in the infinite cluster and the spins of the finite clusters here represented by the Pauli matrix σ. The damping of the spin waves due to the spin wave-cluster interaction is described by

$$\Omega(\omega) = (8S/n)M^2 I_m \chi(\omega), \quad (6)$$

where $\chi(\omega)=[4kT(1-i\omega\tau_s)]^{-1}\times\mathrm{sech}(E/2kT)$ is the dynamical longitudinal susceptibility component associated to an asymmetric double-well potential with barrier height ΔE and asymmetry parameter E, as shown in Fig. 1.

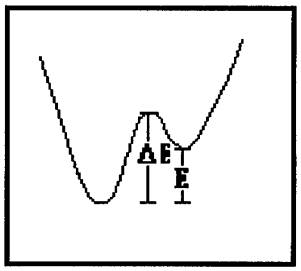


Fig.1. Asymmetric double-well potential of barrier height ΔE and asymmetry parameter E.

The characteristic relaxation time of this process is

$$\tau_s = \tau_o \times \exp(\Delta E/kT) \times \mathrm{sech}(E/2kT). \quad (7)$$

We assume that the asymmetry parameter E follows a constant distribution function given by $f(E)=N_o$ for $0<E<E_{max}$ and $f(E)=0$, otherwise. N_o describes the total number of spins in the magnetic agglomerate. To account for the reduction in the number of clusters with high energy barrier ΔE, due to the polidispersity of the sample, we use an exponential distribution function given by $g(\Delta E)=(1/\Delta E_o)\times\exp(-\Delta E/\Delta E_o)$, where ΔE_o is an activation energy related to the characteristic freezing temperature by $kT_f=\Delta E_o/|\ln\omega\tau_o|$.[9] The broadening of the magnetic resonance line (ΔH_s) is calculated taking into account the polidispersity of the monodomains in the agglomerate through the functions f(E) and $g(\Delta E)$ as[3]

$$\Delta H_s = (\pi S M^2/g\beta n\Delta E)\times\exp(-T/T_f). \quad (8)$$

4. EXPERIMENTAL RESULTS AND DISCUSSION

The starting sample used in our experiment is an ionic water-based $MnFe_2O_4$ magnetic fluid prepared by chemical synthesis.[10] The average values for particle concentration, magnetic moment per particle and particle diameter are of the order of 6.3×10^{16} particles/cm^3, 1×10^{-19} A×m^2 and 10.7 nm, respectively. To obtain the powder sample composed of magnetic agglomerates the starting sample was dried in air. Magnetic resonance spectra were taken from both samples using a 9 GHz spectrometer in the temperature range from 100K up to 250K, thus keeping the magnetic fluid sample frozen. Values for the g factor and resonance field are of the order of 2.1 and 3 Kgauss, respectively. Magnetic resonance linewidth corresponding to each sample was studied as a function of temperature. Resonance linewidth values obtained from the magnetic fluid sample (6.3×10^{16} particles/cm^3) were normalized to unit and the relative linewidth, i.e., the normalized linewidth broadening were plotted (full circles) in Fig. 2 (b). The solid line going through the full circles in Fig. 2 (b) represent the best fit of the experimental data according to Eq. (3). As recently discussed[11] the energy barrier ΔE for this particular magnetic fluid sample depends upon the particle concentration, i.e., it goes with the particle-particle distance according to $\Delta E=7.87\times10^{-15} + 1.29\times10^{-15}/D^6$, where ΔE is given in units of ergs and $1/D^3$ is given in units of 10^{16} particles/cm^3. According to Eq. (3) the solid line in Fig. 2 (a) represents the expected normalized linewidth broadening of the same magnetic fluid sample at a particle concentration of 14.6×10^{16} particles/cm^3. At 14.6×10^{16} particles/cm^3 the particle-particle distance (center-to-center) is equals to D=10.7 nm. At D=10.7 nm, the average distance we would expect in a magnetic agglomerate, the magnetic particles are touching one another inside the magnetic fluid, being the energy barrier of the order of $\Delta E=2.8\times10^{-13}$ ergs. Using the same experimental setup magnetic resonance linewidth values obtained from the parent magnetic powder sample were normalized to unit and the relative linewidth, i.e., the normalized linewidth broadening (full squares) were plotted in Fig. 2 (c). The solid line going through the full squares in Fig. 2 (c) represents the best fit of the experimental data according to Eq. (8) at the freezing temperature of the order of T_f=154K. The normalization procedure described above plays only with the pre-factors of both Eqs. (3) and (8) and therefore does not affect neither ΔE or T_f. The experimental data obtained from the magnetic fluid sample and from its powder parent sample show remarkable differences, indicating that they might follow very different physical pictures as proposed in the previous sections. A basic difference in temperature dependence of the magnetic resonance line broadening results from differences in relaxation mechanisms. In the magnetic fluid sample the magnetic relaxation mechanism has its characteristic relaxation time as described by Eq. (4). In an agglomerate however, there exist another relaxation mechanism which is related to the damping of the magnon modes excited in the agglomerate as they interact with the spins of each one of the individual clusters. Typical relaxation time for the late process is given by Eq. (7).

Comparison of Eqs. (4) and (7) indicates that the magnon assisted process has a relaxation time of two orders of magnitude faster than the dipolar assisted process, i.e., $\tau_s \approx \tau_d/100$.

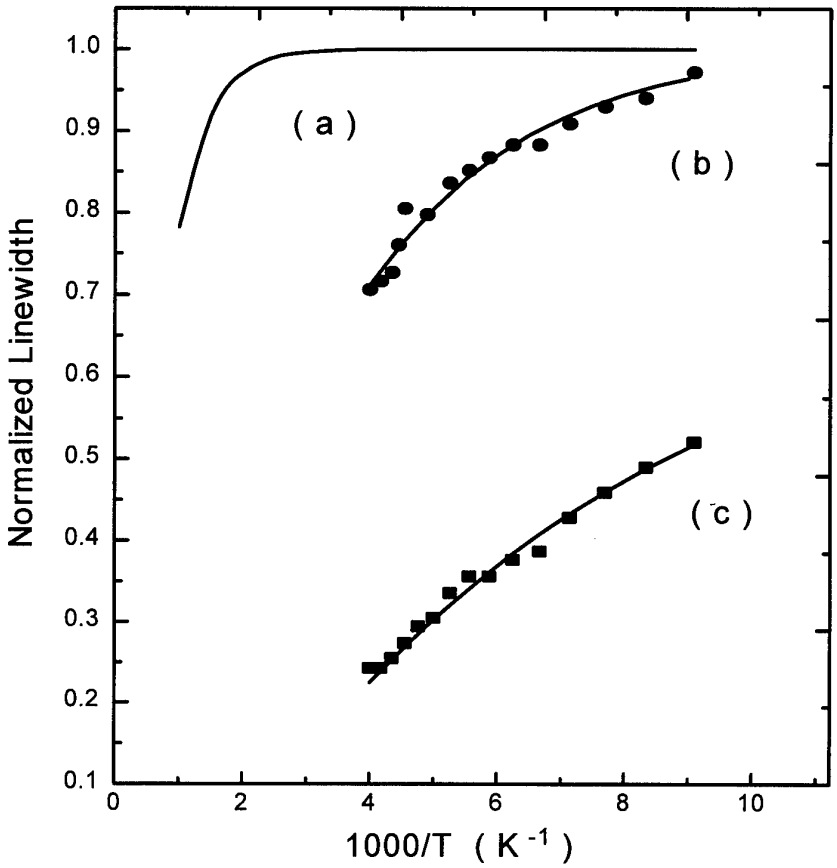


Fig.2. Magnetic ressonance normalized linewidth versus temperature (1000/T).

5. CONCLUSION

In summary, magnetic resonance is used here to study the temperature dependence of the resonance linewidth broadening in two different but closely related systems - the magnetic fluid and its parent powder composed of magnetic agglomerates. The temperature dependence of the magnetic resonance linewidth is very different from one sample (single particle system) as compared to the other (magnetic agglomerate). In fact as the magnetic particles are stuck together in a magnetic agglomerate a quenching of the resonance linewidth broadening is observed. Such a quenching effect is claimed to be due to the onset of a new relaxation channel, via spin waves, which is about two orders of magnitude faster than the channel (dipole-dipole interaction) observed in magnetic fluid samples.

6. ACKNOWLEDGMENTS

This work was supported by the Brazilian Agencies FAPDF, PADCT and CNPq.

7. REFERENCES

1. W. Luo, S.R. Nagel, T.F. Rosenbaum and R.E. Rosensweig, *Phys. Rev. Lett.* **67**, pp. 2721-2724, 1991.
2. P.C. Morais and K. Skeff Neto, *Polyhedron* **2**, pp. 875-880, 1983.
3. P.C. Morais, A.L. Tronconi and K. Skeff Neto, *J. Appl. Phys.* **55**, pp. 3744-3746, 1984.
4. J.H. Van Vleck, *Phys. Rev.* **74**, pp. 1168-1183, 1948.
5. P.C. Morais, M.C.F.L. Lara and K. Skeff Neto, *Phil. Mag. Lett.* **55**, pp. 181-183, 1987.
6. W.F. Brown, *J. Appl. Phys.* **34**, pp. 1319-1320, 1963.
7. A.P. Amulyavichus and I.P. Suzdalev, *Sov. Phys. JETP* **37**, pp. 859-863, 1973.
8. A. Fert and P.M. Levy, *Phys. Rev. Lett.* **44**, pp. 1538-1541, 1980.
9. K.S. Gilroy and W.A. Phillips, *Phil. Mag. B* **43**, pp. 735-746, 1981.
10. F.A. Tourinho, *Thesis*, Université Pierre et Marie Curie, Paris, 1988.
11. P.C. Morais, M.C.F.L. Lara, A.L. Tronconi, F.A. Tourinho, A.R. Pereira and F. Pelegrini *(to be published).*

Investigation of magnetic anisotropy in frozen magnetic fluids

P.C. Morais[†], A.F. Bakuzis[†] and F.A. Tourinho[‡]

[†]Universidade de Brasília, Departamento de Física
70910-900 Brasília (DF) - Brazil
[‡]Universidade de Brasília, Departamento de Química
70910-900 Brasília (DF) - Brazil

ABSTRACT

The magnetic anisotropy constant of magnetic fluids is obtained from the angular dependence of the magnetic resonance field. The sample was frozen below room temperature under the action of a steady magnetic field of 1.45 Tesla. Magnetic anisotropy of the order of -5.4×10^4 erg/cm^3 at 150K and -5.1×10^4 erg/cm^3 at 200K was obtained for a water-based $MnFe_2O_4$ magnetic fluid sample with average particle diameter of 10.7nm

1. INTRODUCTION

Magnetic fluids consist of monodomain nanoscaled magnetic particles dispersed in a carrier fluid. The magnetic anisotropy constant of fine particle systems is traditionally obtained either from relaxation time measurements[1] or from magnetization curves.[2] Despite the similarities between the two systems, i.e., the magnetic fluid and its parent magnetic powder, very important differences in magnetic properties may arise due to differences in particle-particle interactions. Instead of a single magnetic particle system, as observed in magnetic fluids, magnetic agglomerates, meaning clusters of magnetic particles, are obtained upon removal of the carrier fluid from a magnetic fluid sample. In a parent magnetic powder sample the monodomain magnetic particles are brought into close contact in such a way that they collapse into agglomerates. In fact magnetic nanoparticles do not touch one another though they might be brought very close together in highly concentrated magnetic fluids. Therefore, it is very important to establish an experimental routine to measure the magnetic anisotropy in magnetic fluid samples. This paper is addressed to this matter, namely, the use of magnetic resonance to obtain the magnetic anisotropy of a magnetic fluid sample. In recent years magnetic resonance has been succesfully used to investigate other interesting aspects of magnetic fluids such as concentration effects[3], temperature effects[4,5] and ionic strength effects.[6]

2. THEORY

In order to use magnetic resonance to measure magnetic anisotropy in a straightford way we must prepare our magnetic fluid sample to be as close as possible to an ideal system composed of non-interacting uniaxial magnetic nanoparticles dispersed in a solid non-magnetic matrix with the easy axis of magnetization oriented parallel to the horizontal external field. Such a condition can be reached with a magnetic fluid sample having particle concentration up to 3×10^{16} particles/cm^3 cooled in an external magnetic field above 1 Tesla.[5] The sample holder is allowed to rotate around the vertical axis, θ being the angle between the easy axis of the sample and the external magnetic field H_e. The resonance frequency ω_r, i.e., the Larmor precession frequency of the magnetic moment μ of the nanoparticle in the presence of an effective magnetic field H_{eff} is given by

$$\omega_r = \gamma H_{eff}, \quad (1)$$

where γ is the gyromagnetic ratio.

0-8194-2165-0/96/$6.00

In our experimental setup we scanned the magnetic field strength instead of scan the microwave frequency, which is fixed around 10 GHz. In general, the effective field is a result of three components, namely, the external sweeping field (H_e), the anisotropy field (H_a) and the fluctuation field (H_f). In case of superparamagnetic particles the fluctuation field plays a very important role in the effective field and has to be evaluated taking into account a statistical ensemble where the value of the magnetic moment of the sample is a result of the statistical average of the microscopic magnetic moment of each particle under an adequate orientational distribution function. A complete mathematical treatment of the contribution due to the fluctuation field has been recently reviewed.[7] In our case however, the ratio $\mu H_e/kT$ was kept above 15 and therefore the fluctuation field is considered only a small correction for $H_{eff} = (H_e + H_a)$. The anisotropy field is given by $H_a = (2V/\mu)K$, where V is the average volume of the particles and K is the effective anisotropy of the sample. According to Callen and Callen [8] the effective anisotropy of the sample can be expanded in terms of spherical harmonics as

$$K = \sum_{\ell} \sum_{m} K_{\ell} P_{\ell}^{m}(\cos\theta)\, e^{im\phi}, \quad (2)$$

where $P_\ell^m(\cos\theta)$ are Legendre polynomials and K_ℓ are anisotropy coefficients. For uniaxial particles one retains only the $\ell = 2$ term. In addition, considering spherical magnetic particles one retains only the $m = 0$ term. Therefore, the effective anisotropy is writen as $K = K_2 P_2^0(\cos\theta)$ and the anisotropy field approximated to $H_a = (2V/\mu)K_2 P_2^0(\cos\theta)$. Returning the anisotropy field expression as described before back to Eq. (1) we obtain the description of the resonance field H_r as a function of the angle θ

$$H_r = \omega_r/\gamma - (K/I_s)\,[3\cos^2(\theta) - 1], \quad (3)$$

where $I_s = \mu/V$ is the saturation magnetization. Equation (3) above describes the angular variation measurements and will be used to fit the experimental data in order to obtain the effective anisotropy constant $K = K_2$.

3. EXPERIMENTAL RESULTS AND DISCUSSION

The sample used in our experiment was an ionic water-based $MnFe_2O_4$ magnetic fluid prepared by chemical synthesis.[9] The average values for particle concentration, saturation magnetization, magnetic moment per particle and particle diameter are of the order of 2.4×10^{16} particles/cm^3, 260 gauss, 1×10^{-19} A×m^2 and 10.7 nm, respectively. The sample was cooled down to 150K under the action of an external horizontal magnetic field of 1.45 Tesla. The sample holder was attached to a goniometer mounted vertically to allow rotation around the axis perpendicular to the horizontal plane. Magnetic resonance spectra were taken using a X-band spectrometer at 150K (9.447 GHz) and at 200K (9.445 GHz), thus keeping the magnetic fluid sample frozen.Values for the resonance field as a function of the angle between the original orientation (easy axis) and the external field are plotted in Fig. 1.

The solid lines going through the points in Fig. 1 represent the best fit of the experimental data according to Eq. (3). Values for the effective anisotropy constant obtained at 150K and 200K were -5.4×10^4 erg/cm^3 and -5.1×10^4 erg/cm^3, respectively. The values we found in our sample for the effective magnetic anisotropy are smaller than the values reported in the literature for the bulk sample at 150K (-13.9×10^4 erg/cm^3) and 200K (-9.2×10^4 erg/cm^3).[10] Reduction of the magnetic anisotropy in fine particles as compared to the bulk value is not expected. In fact, what is reported in the litterature is an increasing of the magnetic anisotropy with reduction of the particle size.[11,12] The enhancement of the surface to volume ratio has been associated with size-dependence of the magnetic anisotropy. [11,12] The difference here is that we have measured the anisotropy of non-interacting particles while the results reported up to date refer to powder samples where very strong particle-particle interaction may occur.

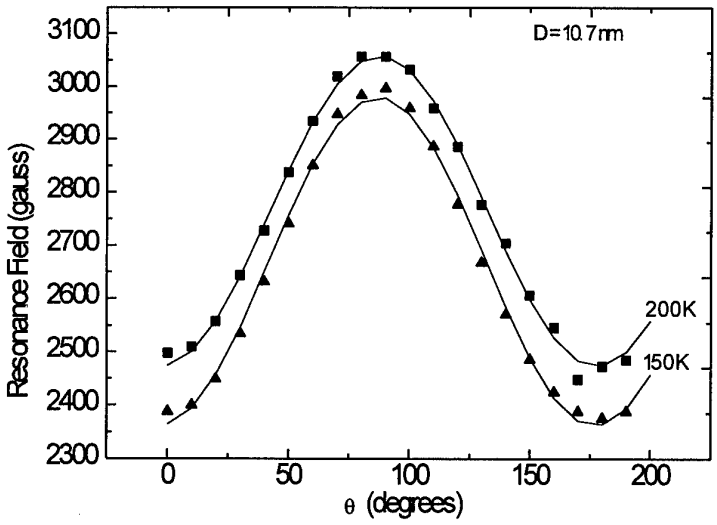


Fig. 1. Angular variation of the resonance field at different temperatures.

4. CONCLUSION

In summary, magnetic resonance is used here to measure effective magnetic anisotropy in magnetic fluids. Magnetic anisotropy is obtained from the angular dependence of the resonance field, as described by Eq. 3, using a field-cooled magnetic fluid sample. The magnetic anisotropy of our sample is smaller than the value reported for bulk samples, in contrast to the behavior observed for powder samples composed of magnetic fine particles. The discrepancy between our results and the results reported for powder samples may be due to the effect of particle-particle interactions. To avoid particle-particle interaction our sample was intensionally prepared with 2.4×10^{16} magnetic particles per cubic centimeter. However, as far as temperature dependence is concerned our data is in accordance with the literature, i.e., the anisotropy decreases with increasing temperature.

5. ACKNOWLEDGMENTS

This work was supported by the Brazilian Agencies FAPDF, PADCT, CAPES and CNPq.

6. REFERENCES

1. R.V. Upadhyay, K.J. Davis, S. Wells and S.W. Charles, *J. Magn. Magn. Mater.* **132**, pp. 249-257, 1994.
2. S. Chickazumi, "*Physics of Magnetism*", John Wiley & Sons, New York, pp. 128-160 (1964).
3. A.L. Tronconi, P.C. Morais, F. Pelegrini and F.A. Tourinho, *J. Magn. Magn. Mater.* **122**, pp. 90-92, 1993.
4. Yu.L. Raikher and V.I. Stepanov, *J. Magn. Magn. Mater.* **149**, pp. 34-37, 1995
5. P.C. Morais, M.C.F.L. Lara, A.L. Tronconi, F.A. Tourinho, A.R. Pereira and F. Pelegrini *(to be published).*
6. P.C. Morais, F.A. Tourinho, G.R.R. Gonçalves and A.L. Tronconi, *J. Magn. Magn. Mater.* **149**, pp. 19-21, 1995.
7. Yu.L. Raikher and M.I. Shliomis, *Adv. Chem. Phys.* **87**, pp. 595-751, 1994.
8. H.B. Callen and E.R. Callen, , *J. Phys. Chem. Solids.* **27**, pp. 1271-1285, 1966.
9. F.A. Tourinho, *Thesis*, Université Pierre et Marie Curie, Paris, 1988.
10. K. Yosida and M. Tachiki, *Prog. Theor. Phys.* **17**, pp. 331-359, 1957.
11. S. Gangopadhyay, G.C. Hadjipanayis, B. Dale, C.M. Sorensen, K.J. Klabunde, V. Papaefthymiou and A. Kostikas, *Phys. Rev. B* **45**, pp. 9778-9787, 1992.
12. F. Bødker, S. Mørup and S. Linderoth, *Phys. Rev. Lett.* **72**, pp. 282-285, 1994.

Damping Control of a CFRP Cantilevered Beam with Electro-Rheological Fluids Actuator

Takehito Fukuda
Faculty of Engineering, Osaka City University
Sugimoto 3, Sumiyoshi, Osaka 558, Japan
Nobuo Oshima
Graduate School of Engineering, Osaka City University

ABSTRACT

Effects of waveform and frequency of electric fields applied to electro-rheological (ER) fluids are investigated on structural damping of a CFRP composite beam containing ER fluids. As the experimental results, the rectangular waveform is more effective for control of ER effects than the sinusoidal one. In vibration analysis, a simplified mass-spring-damper system is adopted to feature the first flexural mode of the cantilevered composite beam, where the damping factor is changed in time as a function of waveform which is applied to electric fields.

1. INTRODUCTION

In smart structures, actuator materials play an important role in the structural control. One of candidates for actuator materials is ER fluids. The apparent viscosity and rheological properties of ER fluids can be varied in a wide range by applied electric field, where the response time is very short, as short as several milliseconds and this change is reversible. Recently, ER fluids have been utilized being sandwiched between Al plates or CFRP laminates with electrical conductivity to suppress structural vibration [1-3]. However, few studies have been reported on effects of waveforms or frequencies of electric fields applied to ER fluids on structural damping of the composite beam.

In the present paper, a CFRP composite beam containing ER fluids is oscillatorily tested by using sinusoidal and rectangular waves with various frequencies of electric fields applied to ER fluids. As the experimental results, the rectangular wave is more effective for control of ER effects than the sinusoidal one. This fact is also analytically explained by using a simplified vibration model of the composite beam having ER fluids actuator.

2. EXPERIMENTS

A specimen is schematically shown in Fig. 1, where the experimental set-up is also briefly illustrated including a non-contacting laser displacement pick-up, an A/D converter, a D/A converter, a personal computer. Electric fields $E_r(t)$ are produced by a high speed power supply unit. The specimen consists of two CFRP laminated plates (Toray T300/#2500) and an ER fluids layer (Nippon Shokubai TX-ER2072). The fiber orientation of CFRP laminates is [+45°/-45°]s. The specimen is 200mm in length and 20mm in width. The thickness of CFRP laminate

0-8194-2165-0/96/$6.00

is 0.5mm and that of ER fluids layer is 0.2mm. In the specimen, ER fluids are filled between two CFRP laminated plates and sealed by a silicone rubber in the same manner as proposed by Choi et al.[1]. CFRP laminated plates are used for electrodes to apply electric fields to ER fluids, since the CFRP laminate is a conductive material.

In the experiments, the specimen was supported on the shaker under the clamped-free condition and ER fluids were applied by the electric field of sinusoidal or rectangular waves with various frequencies. These excitation waves were produced by use of a high speed power supply unit. The deflection response at the free end of the specimen were observed not only in steady state, but also in transient time by using a non-contacting laser displacement pick-up.

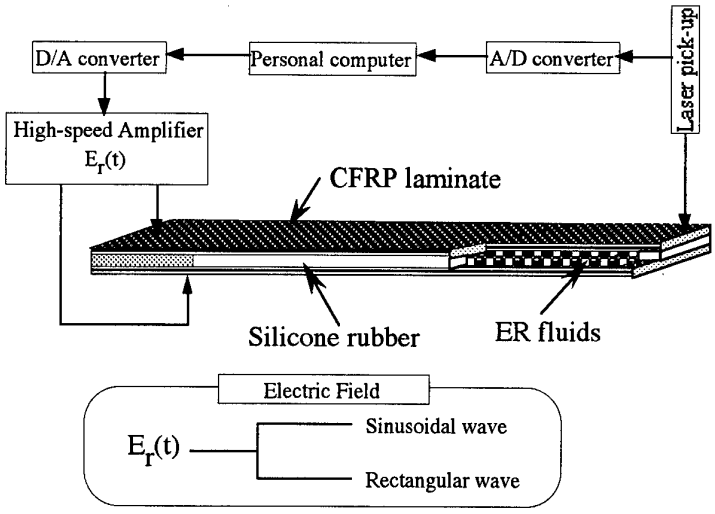


Fig.1 A schematic view of specimen including an experimental setup.

Table 1 Material properties.

Properties of CFRP		Properties of ER Fluids		Propertiees of Silicone Rubber	
Specific gravity	1.4	Specific gravity	1.1	Specific gravity	1.5
Storage Modules	48 GPa	Storage Modules	100 Pa	Storage Modules	1.5MPa
Loss Modulus	1.2 GPa	Loss Modulus	100 Pa	Loss Modulus	0.15MPa

Table 2 Comparison of predicted values of natural frequency and equivalent damping ratio.

	Natural Frequency (Hz)	Equivalent damping ratio
Rayleigh	12.0	0.039
RKU	6.3	0.014

3. EXPERIMENTAL RESULTS

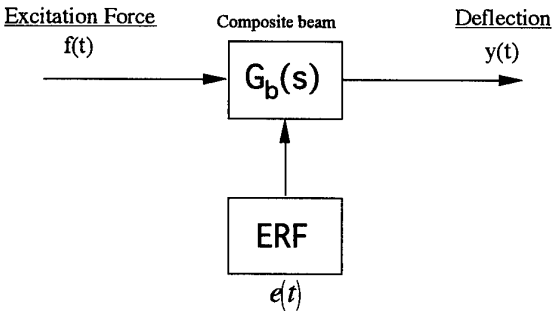
3.1. Waveform effects

First, the natural frequency of the cantilevered specimen was examined by the vibration test. It was 12.3Hz, while its predicted value obtained by using Rayleigh's method was 12.0Hz. The material properties used in calculation are listed in Table 1. In Table 2, values of natural frequency and equivalent damping by Rayleigh's method are compared with those calculated by RKU method. Secondly, in order to investigate the effects of waveform of electric fields applied to ER fluids, the deflection responses in resonant state where the frequency of the excitation force, ω_f was tuned to the natural frequency of the composite beam, ω_n were observed with changing the frequencies, ω_e of electric fields applied to ER fluids. Fig.2 illustrates the relation among the excitation force, f(t),

the electric field, e(t) applied to ER fluids and the deflection at the free end of the composite beam, y(t). As the experimental results, it was found that the rectangular wave is more effective for control of ER effects than the sinusoidal wave when the amplitude and the frequency of both waves are the same. An example of comparison between steady-state responses subjected to rectangular and sinusoidal waveforms is given in Fig.3, where the response under no electric field is also illustrated.

3.2. Frequency effects

The beat phenomena in response of the composite beam have been observed when the frequencies of electric fields close to the natural frequency of the composite beam were applied to ER fluids. An example of beat phenomenon is shown in Fig.4. The frequency range was also found which can suppress the vibration of the composite beam. That is, it is shown that less vibration suppression takes place under the electric fields with the frequencies higher than about 10Hz as shown in Fig.5.



Sinusoidal

$e(t) = e_r \cdot \sin(\omega_e t + \psi)$, ψ : initial phase

Rectanguler

$$e(t) = \begin{cases} e_r & \text{,for } 0 \le t \le \dfrac{(2n+1)\pi}{\omega_e} \\ -e_r & \text{,for } \dfrac{(2n+1)\pi}{\omega_e} \le t \le \dfrac{2n\pi}{\omega_e} \end{cases} \quad (n=0,1,2,\cdots)$$

Fig.2 Relation among the excitation force, f(t), electric field, e(t) applied to ER fluids and deflection at the free end, y(t).

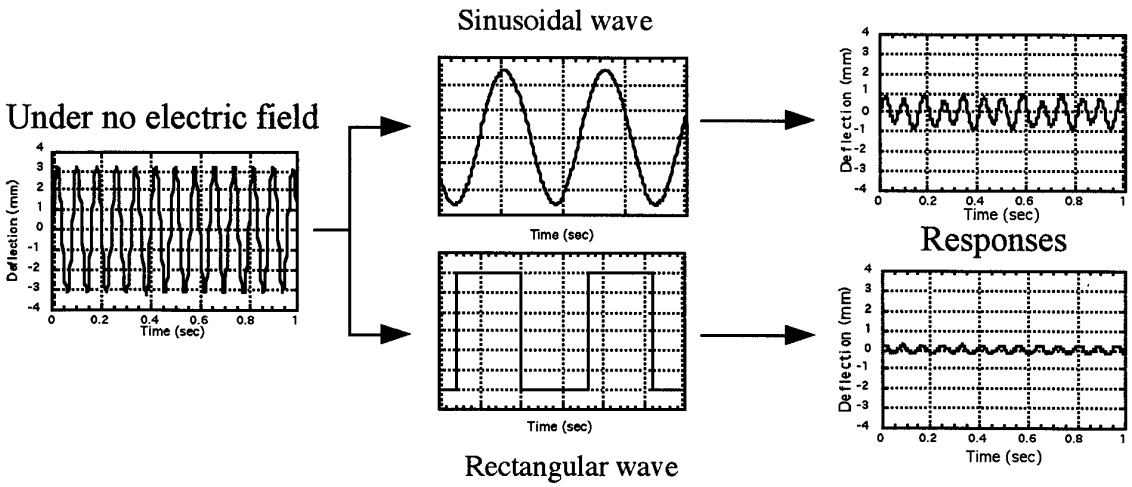


Fig.3 An example of comparison between steady-state responses subjected to rectangular and sinusoidal waves.

3.3. Feedback control

In order to examine the control effects of ER fluids actuator, the impulse response tests were conducted according to the following experimental procedures; (1) the top of the specimen was hit with an impulse hammer, (2) the electric field applied to ER fluids was charged when the deflection at the free end of the composite beam exceeded a limited magnitude. Tested results of impulse responses are shown in Fig. 6. It can be found that the ER fluids actuator can be used as feedback control element.

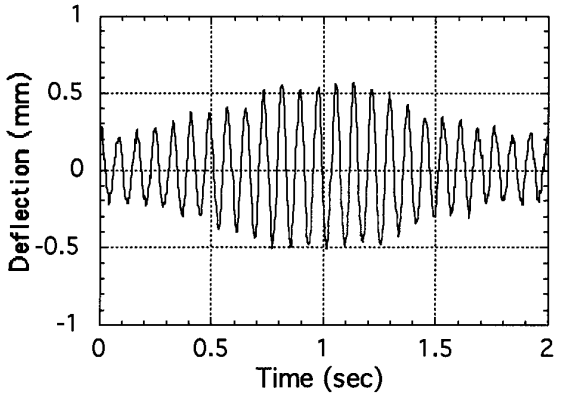


Fig.4 Beat phenomenon of the composite beam under rectangular wave with frequency close to its natural frequency.

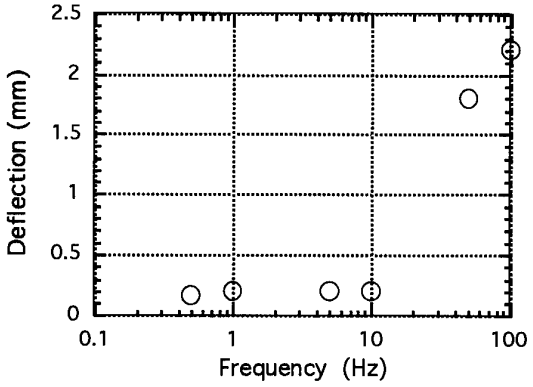
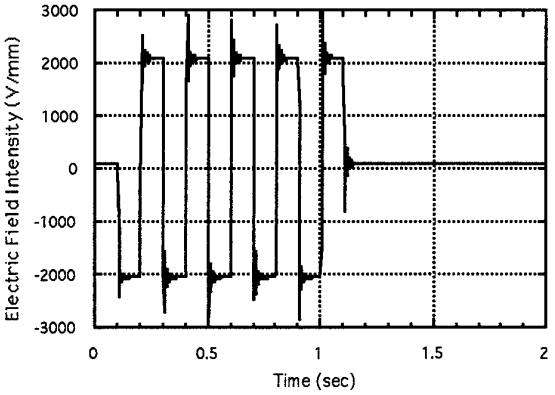
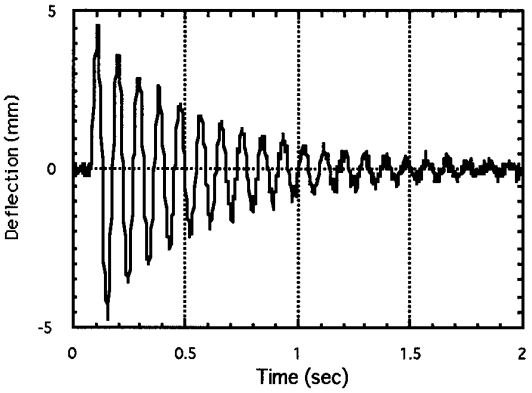


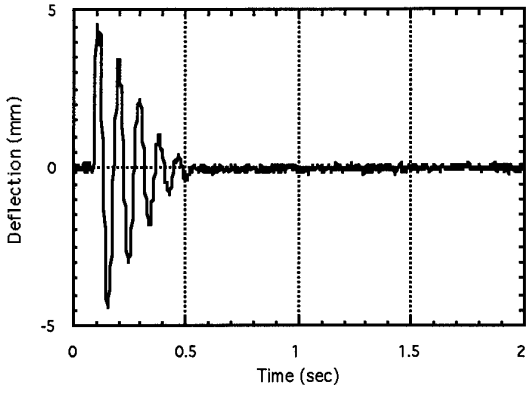
Fig.5 Effect of frequency of electric fields applied to ER fluids on vibration suppression.



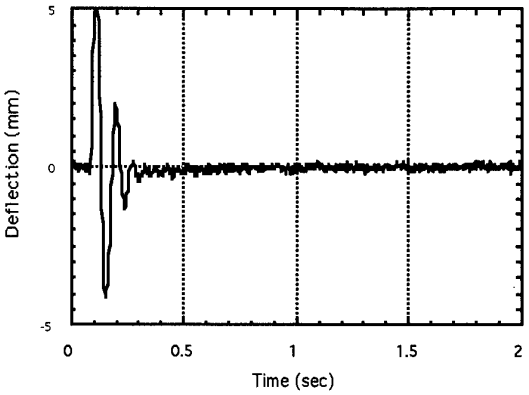
(a)Electric field applied to ER fields.



(b)Impulse response for electric field intensity of 500V/mm.



(c)Impulse response for electric field intensity of 1000V/mm.



(d)Impulse response for electric field intensity of 2000V/mm.

Fig.6 Impulse responses of the composite beam with various electric field intensities.

4. ANALYSIS AND DISCUSSIONS

Recently, Yalcintas, M. et al. (1995) have given a series of reports on analytical studies of ER material based adaptive model [4,5]. In their papers, they use a basic model for multi-layered damped composite beam, where structural adaptability is incorporated by assuming that the complex shear modulus of the ER material is a function of electric field. However, a simplified mass-spring-damper system is available to feature the first flexural mode of the cantilevered composite beam which is used here in the vibration tests. That is, the lumped mass system of the composite beam can be decomposed to the concentrated mass system where the damping factor is changed in time as a function of the waveform which is utilized for electric fields.

Then, the equation of motion of the composite beam is given by

$$\ddot{y} + 2\cdot\zeta(t)\cdot\omega_n\cdot\dot{y} + \omega_n{}^2\cdot y = \frac{1}{m}\cdot f(t) \tag{1}$$

where

$$m = 12.2\times10^{-3}\ \text{kg} \quad \text{and} \quad \omega_n = 77.3\ \text{rad/sec}$$

$$\zeta(t) = \zeta_0 + |e(t)| \qquad (\zeta_0 = 0.030)$$

and in calculation by use of rectangular waveform ,the following equation is utilized.

$$e(t) = \begin{cases} e_r\left\{1 - e^{-\frac{t}{T}}\right\} & \text{,for} \quad 0 \le t < \dfrac{(2n+1)\pi}{\omega_e} \\ 0 & \text{,for} \quad t = \dfrac{(2n+1)\pi}{\omega_e} \end{cases} \tag{2}$$

The schematic waveforms are also illustrated in Fig.7 As an example of simulation by using above-mentioned waveform , the beat phenomenon of the composite beam under sinusoidal wave with frequency of 12.3Hz is illustrated in Fig.8.

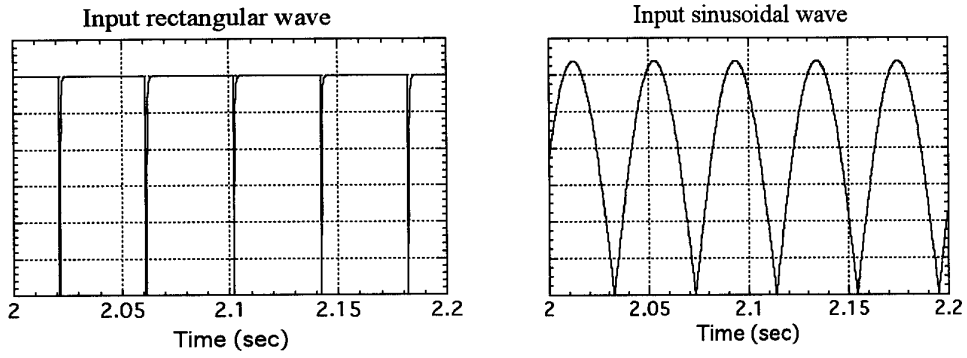


Fig.7 Waveforms of electric fields applied to ER fluids used in simulation.

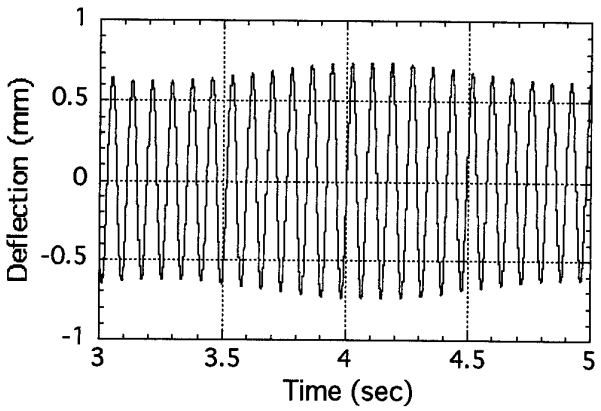


Fig.8 An analytical example of steady-state response of the composite beam (beat phenomenon) , for $\omega_f = \omega_n$ and ω_e=75.4 rad/sec.

5. CONCLUSION

A CFRP composite beam with ER fluids actuator was tested subjected to electric fields of two types of waveform with various frequencies. Experimental and analytical results are summarized as follows;

(1) The rectangular waveform is more effective for control of ER effects than the sinusoidal wave.

(2) The beat phenomena in response of the composite beam have been observed subjected to the electric fields with frequency close to the natural frequency of the composite beam.

(3) These experimental results can be explained by using a simplified vibration model having the time-dependent damping factor.

6. ACKNOWLEDGMENTS

The authors would like to thank Toray Co. Ltd. for providing CFRP laminated plates and Nippon Shokubai Co. for ER fluids. They also appreciate Mr. Yasuyuki Matsusaka, Senior Student of Osaka City University for his helps in vibration test and analysis.

7. REFERENCES

1)Y. Choi, A.F. Sprecher and H. Conrad, "Vibration Characteristics of a Composite Beam Containing an Electrorheological Fluid," J. Intelligent Materials, Systems and Structures, Vol.1, pp.91-104, 1990.

2)Y. Chen, F-G. Yuan and H. Conrad, Proc. the 2nd ICIM, "Damping Characteristics of Laminate Composites Containing Electrorheological (ER) Fluids," pp.328-339, 1994.

3)T. Fukuda and N. Oshima, Proc. the ICCM-10, "Use of ER Fluids for Damping Control of Composite Beams," pp.V/299-V/308, 1995.

4)M. Yalcintas and J.P. Coulter, "Analytical Modeling of Electrorheological Material Based Adaptive Beams", J. Intelligent Materials, Systems and Structures, Vol.6-July, pp.488-497, 1995.

5)M. Yalcintas and J.P. Coulter, "An Adaptive Beam Model with Electrorheological Material Based Application," J. Intelligent Materials, Systems and Structures, Vol.6-July, pp.498-507, 1995.

NONTRADITIONAL APPLICATION OF ELECTRORHEOLOGICAL EFFECT

E.V.KOROBKO
A.V.Luikov Heat and Mass Transfer Institute
Belarussian Academy of Sciences 15 p.Brovka St.
Minsk 220072,Belarus

ABSTRACT

The unique properties of electrorheological fluids (ERF) offer much promise both for the improvement of existing processes and for the development of a new generation of "smart" technologies and devices.

INTRODUCTION

The electrorheological effect (ERE) [1] is based on the structure formation phenomenon caused by the polarization of solid particles and accumulation of a substantial electric charge on their surface. Electrical interactions between the particles bring about the observed changes in mechanical,electrophysical, optical,acoustic and heat transfer properties of ERF. Existing and prospective applications of ERE are connected with its advantages, namely fast response, the possibility of immediate transfer of an electric signal to the fluid without any intermediate mechanical devices, low energy losses in the circuit "electronic control unit-actuating mechanism".

This paper presents the results of extended rheological studies of this effect.

MAIN PART

Purposeful and systematic researches of electrorheological suspensions (ERS) based on dispersed natural and polymer fillers have been carried out at Heat and Mass Transfer Institute of the Belarus Academy of Sciences (Belarus). It has been revealed [1] that as a dispersed medium use is made of any low-viscosity hydrocarbon liquid with high resistivity (10^{16} to 10^{20} ohm^{-1} m^{-1} , e =2 to 5), paraffin and aromatic hydrocarbons, polymer solutions, silicon fluids, hydrocarbon fractions of oil, mixtures of organic fluids and oils. A dispersed phase must possess high adsorptivity, have highly hydroxylated developed surface (desirable 200 to 400 m^2 /g). These are silica (diatomite, aerosyl). alumosilicates (clays, talc, mica), metal (titanium, aluminium, zinc) oxides, starch, polymers. Particles used have sizes from 1 to 10 μm.The third substance, i.e. an activator, is laid onto a surface of a solid phase. As an activator, use may be made, firstly, of organic compounds capable of forming hydrogen bonds (water, ethyl, butyl, propyl alcohols, ethylene glucol, diethylene glucol, etc.) and, secondly, amines (aliphatic, aromatic, primary, secondary). Their amount, as a rule, is chosen experimentally with respect to a maximum of changing an effective viscosity at electric field.Surfactants may serve as the fourth component of a suspension. They are introduced into high-concentration suspensions for the purpose of their liquation and attaining as high as possible, content of particles while in case of diluted suspensions for increasing the sedimentation stability. More often little-soluble non-ionic type surfactants are used, e.g., fat acids and their ethers with alcohols (glycerine, monoomate, oleates, sorbite stearate, etc.). The amount of surfactants is 1-3 molecules per 2 μm^2 area of particles. All physical properties of electrorheological suspensions are astipulated factor. High-speed filming, direct observation of the behaviour of particles in a condenser gap, as well as specklometry have revealed that when an electric field is applied to, the solid

0-8194-2165-0/96/$6.00

phase particles being uniformly distributed up to this moment in a liquid medium and randomly moving, cease immediately their motion due to the field [2],[3] and being to oscillate from electrode to electrode, collide and form associates, clusters and bridges, while in high-concentration suspensions a structural skeleton is formed. The ERS composition, as well as electric intensity exerts a decisive influence on an extent of suspension structurization.

We now dwell in more detail on the rheological behaviour of ERSs subject to simultaneous action of oppose-force fields, i.e., electrical and mechanical. Consider a typical ERS, namely, the suspension of fine-particle oxides and polimer particles in a silicon or a transformer oil with water taken as an activator, and oleic acid as a stabilize. In measurement an electric intensity has been widely varied at room temperature.

The following regimes have been examined: rotational shear at a constant rate [4],viscoelastic deformation and creep behavior [5], periodical reversible elastic deformation [6], and forced flow [7]. When an electric field is applied, an ERF acquires pseudoplastic properties. In the absence of an electric field, the dependence f(y) is linear and passes through the origin of the coordinates. With the applied field, the yield strength develops. Its magnitude increases with raising the electric field strength, E. This testifies to an increase in the interaction forces between solid particles, which results in strengthening of the spatial skeleton. Non-linear behavior of a ERF in an electric field is described by a rheological equation of state:

$$f^{1/n} = f' + my^{1/n} \qquad (1)$$

For moderate concentration suspensions, a dependence of rheological parameters on the electric intensity is described by the relationships:

$$n = n' + n''E,\ f' = a' + a''E^2\ ,\ m = W' + W''E^2 \qquad (2)$$

where the coefficients n',n",a',a",b' and b" depend on concen- trations of the particles and activator,and on temperature.

A change in the electric field strength brings about pronounced manifestation of thyxotropic properties. They reveal themselves as the irreversibility of the curves f(y) for low- and moderate- concentration ERFs with increasing/decreasing the E value. If after the completion of each cycle (deenergizing)the ERF is still strained at a constant shear rate, then its structure returns to the initial state,i.e.to that before the application of an electric field. This occurs the quicker, the smaller was the maximal E value.

In the nonlinear region within the of small shear rates, the slope of the curves f(y) for low- and moderate-concentration ERFs increases with the electric field strength. This is equivalent to an increase in the effective viscosity. For high-concentration ERFs strained at high shear rates, the picture is the opposite. It seems that this behavior is determined by a greater contribution of the first term in Eq.(1).

It is found that for strong electric fields (E>3 kV/mm) and small deformations ERFs manifest viscoelastic properties. The ERE magnitude depends on the kind of an electric signal (constant, alternating of pulse regime) and other external factors, e.g. temperature and vibration. The main factors influencing ERE are connected with the features of an electrorheological fluid, namely dielectric and absorption properties of solid particles, which are determined by their chemical nature (for example,silica, ion-exchange resins, polyelectrolytes, polymers, etc.),their concentration,the presence of various additives(activators and surfactants), type of the dispersion medium, and the ratio of dielectric constants of main components.

All the known ERFs may be divided into three structural-rheological groups according to their main features which determine the application area of the fluids. The mechanical behavior of low concentration ERFs (C<5%) with movable (with respect to the dispersion medium)bridges loosely bound together is similar to that of pure liquids. The viscosity of ERF is unambiguously determined by the electric field strength and abnormal effects are not observed. Such fluids can be used as a heat-transfer agent and in controlled optical devices. A spatial skeleton formed in medium-concentration ERFs

(C=5-30%) is movable. Non- Newtonial behavior under shear and by an increase of effective viscosity by orders of magnitude in an electric field are intrinsic in such fluids. They may be used in robotics,hydraulic automation units, hydroelectric power units, and controlled dampers. High-concentration ERFs (C>30%) in electric fields have the highest increase of effective viscosity; the plastic, elastic and viscoelastic properties manifest themselves most substantially. The properties of such fluids in strong fields resemble the peculiarities of mechanical behavior of solids, e.g. they retain their shape and do not flow by gravity. such fluids may be used as fixing pastes, liquid seals and interlayers with controlled acoustic properties.

The researches performed have revealed that a rheological response of ERFs to external forces is rather complicated; it is characterized by nonlinearity, manifestation of elastic properties typical of solids, and relaxation features. The main rheological dependencies have been obtained under different conditions of straining in wide ranges of the electric field frequency and strength. This makes it possible to determine the scope of the ERF application in chemical technology:

- fragmentation of dispersed material by increasing ERF viscosity in a gap between colloid mill surfaces under friction;

- metering out different suspensions by discrete de-energization electrodes and ejecting a portion of the suspension to a production line;

- filtration using controlled vibroelectric filters;

- precipitation by coagulation of an electrorheological filler in the presence of the electric field with material particles in sump;

- control of mixing and separation processes;

- control of flow rate vs. delivery head characteristics of hydraulic systems;

- in robotics systems, i.e., manipulator grabs, positioning systems, etc.;

- in laboratory research methods, e.g., determination of suspension moisture content ,solid phase concentration, and a degree of purification of liquid dielectrics, measuring viscosity and thermal conductivity of filled media; - voltage control during gas cleaning inelectric filters;

- control of casting of polymeric films with electrosensitive fillers;

- control of a thermal boundary layer in order to affect temperature fields and heat exchange parameters in tubes, channels and chemical reactors.

Special devices have been designed; mechanical load levels and laws of control of electrical regimes of their operation have been determined.

Thus, for instance, in colloid mills designed for wet grinding current-insulated bed and rotor (disc) are connected to a d.c. or a.c. voltagesource. A suspension to be ground, in which a low-conductivity liquid serves as a dispersion medium and solid particles are activated, is subjected to the electric field in a working gap.The ground material is retarded by the field, the stay time of particles in the gap (an impact zone) increases that may be additionally regulated by changing the applied voltage.

One of the typical examples of electrorheological effect action on a process is its use for coagulation of the filtrated suspension particles (suspensions on the base of low-conductivity liquids).

Prior to its delivery to a filter, the suspension is directed to a channel-condenser whose geometry may be changed within wide limits in dependence on the given

conditions . When an electric field (d.c. or a.c.) is applied to the working liquid, there occur structurization and formation of solid particle aggregates. At a certain combination of electric intensity and efflux velocity of the supplied suspension the coarse aggregates formed due to structurization will be blocked by a filtering grid.

The above arrangement may be also used as a remote-control blocking unit.

The coagulation of solid particles of suspensions at an electric field may be employed in some cases for enhancement of a sedimentation process. With this aim in view, the suspension, as in case of filtering, is allowed to pass preliminarily via a channel-condenser. It is most reasonable to use this method in two- and multistage sumps since their design is sugiciently fit for this .

The advantages o f the given method for a certain class of suspensions are obvious since usual addition of a flocculation agent does not avoid the contamination of an end product as well as chemical action on it.

The electrorheological actuator based on the valves consists of hydraulic cylinder 1 with piston 2 and stem 3, ER valves 4 switched in a bridge circuit. The hydraulic cylinder is incorporated,into one diagonal of the bridge while the other incorporates the pump. An electric field in a pulse regime is applied to valves positioned in opposite arms of the bridge. In dependence on the signal form, the cylinder operates in analog, step and oscillatory regimes. ER valves may be also used for designing different damping and antishock devices [8]-[13].

Clutchers, gear boxes, clumping devices for fixture of pieceworks under machining, arrangements for position fixation employ the transition of ERF, subjected to an electrical field from fluid-to -quasisolidstate at amagnitude of specific loads F/S being less than the initial shear stress . They are described at length in [12]-[14] and may find application, for instance, in the textile industry to provide the required tension of threads or in robotics in grips used for transfer of non-magnetic loads and so on. The variation of elastic properties of the ERF layer between electrodes is proposed to apply for creating composite elements [15]-[16] with controlable, in dependence on external load, rigidity, e.g., of air pressure on aeroplane air covering.

ERF may be used not only in actuators as converters of an electrical energy into mechanical but also may serve as indicators, sensors in different technological processes. Thus variation of the parameters of an external medium, e.g. a a vibration level, T or voltage may be judged from a change of conduction .Rheological characteristics in the presence of an electric field may indicate an ERF composition, i.e. the moisture content [17] and percentage of a solid phase [18]. A comparative method permits a design of laboratory devices, such as viscosimeters, for varying characteristics of a wide range of unknown materials [19]. In the nearest future ERFs may turn to be promising for liquid generators, current converters electrokinetic balance, seals, separators.

Convinncing advantages of ERF, their low cost, available technologies must not, however, conceal drawbacks which are important when designing ERF-base commercial devices. Those cover the insufficient stability of properties, a relatively narrow temperature range of activity, a rather low level of mechanical response. All this reduces the multipurpose character of the effect and requires for engineers and scientists to choose selectively the possible objects and technologies of utilization connected, in the first turn, with the latest technology.

CONCLUDING REMARKS

Further trends of electrorheology development are concenrned with creating the complete kinetic ERE theory and use of more perfect and refined experiemntal methods of investigation of ERF physical properties, diagnostics of its microstructure. The problems dealing with ERF physicochemistry and creation of highly stable compositions, particularly, based on polymer disperse materials, are still far from completion. Also, the application of ERF possessing the unique capability of changing reversibly and

purposefully its structure and physical properties in the presence of electric fields has not yet been exhausted.

REFERENCES

1. A.V. Luikov, Z.P.Shulman, Yu.F.Dainega, R.G.Gorodkin, and A.D.Matsepooro, Elecrorheological effect, Nauka i Tekhnika, Minsk , 1972 (in Russian).

2. Z.P.Shulman, A.D.Matsepuro and B.M.Smolsky "A study of ERF 5 structural characteristics in non-aqueus disperse systems", Vesti AN BSSR (Russian), Ser.Phiz.-Energ. Nauk, # 1, pp.60 -65, 1974.

3. G.N.Blinkov, N.A.Fomin, E.V.Korobko, V.K.Gleb and Z.P.Shulman, "Diagnostics of field induced structural change in disperse electrorheosensitive systems", Book of Abstracts of the 5th Int. Symp.on Flow Visualization, Prague, pp 748-747, 1989.

4. A.A.Mokeev , E.V.Korobko and L.G.Vedernikova " Structural viscosity of electrorheological fluids",Journal of Non-Newtonian Fluid Mechanics, Vol.42, pp.213-230, 1990.

5. E.V.Korobko, V.E.Dreval, Z.P.Zhulman and V.G.Kulichikhin "Peculia features in the rheological behavior of ERS", Rheological Acta, Vol.33, pp.117-124, 1994.

6. J.D.Ferry, Viscoelastic properties of polymers, Moskow,1961 (in Russian).

7. V.G.Vasiliev, O.A.Koslov and A.A.Konstantinov , "The eHperimental set-up to study viscoelastic properties of gels and consentrated polymer solutions at small constants of shear stresses", Colloidny Journal, Vol.39, # 5, pp.938 -942, 1977.

8. N.G.Stevens, J.L.Sproston and R.Stanway, "Experimental evaluation of a simple electroviscous damper",Journal of Electrostatics, Vol.15, pp.275- 286, 1984.

9. A.Gerrish, Improvements in or relating to dampers, UK Patent # 1282568,1968.

10. D.K.Bradra and C.A. Harder, "Electroviscous damping for landing aircraft", Electrorheological Fluids. Proceedings of the 2-nd International Conference on ER Fluids, J.D.Carlson, A.F.Sprecher, and H.Conrad, ed. Raleigh, NC: Technomic Publishing Company, Inc.,P.402, 1989.

11. Z.P.Shulman, B.M.Khusid and E.V. Korobko, " Vibroprotection systems on the basis of dempers of viscous friction with ERF, Dokl. AN BSSR, Vol.31, #8, pp.777-782, 1987.

12. Z.P.Shulman, E.V.Korobko and R.G. Gorodkin "Electrorheological fixture arangements", Preprint N8, Minsk: ITMO AN BSSR Press, P.52, 1991.

13. J.L.Sproston, N.G.Stevens and I.M.Page, "An investigation of torque transmission using electrically-stressed dielectric fluids. Proceedings of Electrostatics-83, University of Oxford, UK, pp.53-58, 1989.

14. D.K.Bhadra, W.B.Thompson, and C.A.Harder," Distributed elastodynamic system using ERF", Electrorheological Fluids Conference, Abstracts, R.Tao, ed. Carbondale, ILL., October 15-16, p.43. 1991.

15. J.P.Coulter, and T.G.Duclos, " Applications of electrorheological materials in vibration control, Electrorheological Fluids". Proceedings of the 2-nd International Conference on ERF". J.D.Carlson, Sprecher, A.F.& Conrad,H., ed. Raleigh, NC: Technomic Publishing Company, Inc.,pp.300, 1998.

16. D.L.Margolis and N. Vahdati, "The control of damping in distributed systems using ER-fluids", Proceedings of the 2-nd International Conference on ERF. " " 326, 1989

17. V.M .Nosov, " On the possibility of measuring some technological characteristics of materials with the aid of the dielectric rotation effect", Rheology of Polymer and Disperse Systems and Rheophysics, Z.P.Shulman, ed. Minsk: ITMO AN BSSR Press, Vol.2, pp.73- 76, 1975.

18. Z.P.Shulman and V.M.Nosov, "Rheoelectric converters", Electrorheology: Studies and Applications, Edd. Z.P.Shulman and E.V.Korobko, Minsk: ITMO AN BSSR Press, pp.3-17, 1981.

19. V.K.Gleb , Rotary viscosimeter. USSR Author's Certificate # 976349, 1982.

20. Korobko E.V. Rheodynamics and heat transfer of dielectric suspensions in constant electric fields. Third European Rheology Conference. Ed.D.R.Oliver: Elsevier Pub.1990,277-280

Polymers and Polymeric Gels for Smart Systems

Invited Paper

Polymer Gel- Soft and Wet Intelligent Material

Y. Osada, Y. Ueoka and J. P. Gong

Division of Biological Sciences, Graduate School of Science,
Hokkaido University, Sapporo 060, Japan

ABSTRACT

We have developed an electrically-driven chemomechanical system which shows quick responses with fish-like motility. Behaviors and principle of electrically-driven motion of the polymer gel have been studied. The principle of motility of this system is based upon an electrokinetic molecular assembly reaction of surfactant molecules on the hydrogel caused by both electrostatic and hydrophobic interactions. The cooperative binding of a linear as well as a cross-linked polyelectrolyte with surfactants has been theoretically analyzed. The general formulas derived on the basis of the free energy minimum principle predicted that the cross-linkage enhances the initiation process but strongly suppresses the cooperativity due to the osmotic pressure in the network domain. The theoretical results showed fairly good agreement with the experimental data, confirming the essential features of the theory.

1. INTRODUCTION

Biological materials are usually composed of soft and wet materials in the body. This is in contrast with most of industrial materials such as metal, ceramics and plastics that are dry and hard. Thus, arises the problem of how to design a mobile machine using soft and wet materials, or how to afford the soft material to make shape changes or to generate tensile stresses that can lead to motility without the requirement of a rigid structure. One should notice that there are suitable materials which largely satisfy these requirement. They are wet and soft and look like a solid material but are capable of undergoing large deformation. That is the ***polymer gel***.

The system which undergoes shape change and produce contractile force in response to environmental stimuli is called a "chemomechanical system". This system can transform chemical free energy directly into mechanical work to give isothermal energy conversion and this can be seen in living organisms, for example, in muscle, flagella and in ciliary movement. Synthetic polymer network, "gel", is the only artificial system able to convert chemical energy directly into mechanical work. Gels are ***soft*** with respect to their environments. Machines made of metal or silicon operates as closed systems. They do not adapt to changes in their operating conditions unless a separate sensor system or a human operator is at the controls. Gels, in contrast, are thermodynamically "***open***": they exchange chemicals with the solvent surrounding them and alter their molecular state in the process of accomplishing work. Such materials could be used wherever power for more conventional devices is limited or difficult to obtain: underwater, in space or in the human body.

0-8194-2165-0/96/$6.00

We have developed an electrically-driven chemomechanical system which shows quick responses with worm-like motility. The principle of motility of this system is based upon an electrokinetic molecular assembly reaction of surfactant molecules on the hydrogel caused by both electrostatic and hydrophobic interactions. Behaviors and principle of electrically-driven motion of the polymer gel have been studied.

2. CHEMOMECHANICAL ACTUATOR

Poly(2-acrylamido-2-methylpropanesulfonic acid) (PAMPS) gel was prepared by radical polymerization of 1 mol/l of corresponding monomer in the presence of 5 mol% of crosslinking agent (N,N'-methylenebisacrylamide; MBAA) in the manner described previously[1,2].

When the sheet of PAMPS gel is hung down in the surfactant solution leaving its bottom end free and apply the electric field through an pair of carbon electrodes(Fig.1), the gel showed significant and quick bending toward anode within a second. When the polarity of electric field is altered, the gel starts swinging like a pendulum in the surfactant solution as shown in figure 2. N-dodecylpyridinium chloride ($C_{12}PyCl$) and N-hexadecylpyridinium chloride ($C_{16}PyCl$) showed intensive and steady swinging. On the other hand, the swing motion is weak in the solution of sodium sulfate and N-butylpyridinium chloride (C_4PyCl) and the direction of bending was just opposite, indicating that the hydrophobic nature is necessary to make effective bending.

This kind of moving devices of polymer gel can serve as a new type of "soft-actuator" or "molecular machine". Unlike in motors and hydrodynamic pumps, the motility of this system is produced by the chemical free energy of molecular assembly reaction at the polymer network, with the electrical energy being used to drive direction and control the state of equilibrium. Therefore, the chemomechanical muscle reminisces "gentle" and "flexible" action and its movement is far from the metallic machine systems.

3. PRINCIPLE

The principle of the gel's motion is based on the molecular assembly reaction of cationic surfactant molecules with negatively charged hydrogel caused by both electrostatic and hydrophobic interactions to give the effective contraction.

Generally, the swelling of ionic gel is attributed to the difference of osmotic pressure concerned with the freely mobile ions between inside and outside the gel. and their distribution is well described by Donnan equilibrium. The contraction of the gel in the surfactant solution is connected with the neutralization of negative charges in the gel by forming complex with cationic surfactant molecules. Since the surfactant-gel complex formation has a cooperative nature derived from hydrophobic interaction of surfactant molecules, a marked contraction of the gel is observed only above a certain critical concentration of the surfactant.

Thus, the mechanism of electro-activated quick bending of the gel is connected with the electrokinetic molecular assembly reaction: the positively charged surfactant molecules undergo electrophoretic movement toward cathode and form the complex with negatively charged gel, mainly on a side facing to anode of PAMPS gel and causes anisotropic contraction to give bending toward

anode. When the electric field is reversed, the surfactant admolecules on the surface of the gel leave off and electrically travel away toward anode. Instead, new surfactant molecules approach from the opposite side of the gel, and form the complex preferentially on that side of the gel and stretch the gel. Here, the amount of $C_{12}PyCl$ molecules adsorbed within a second is easily calculated to give the complex formation ratio β less than $1x10^{-3}$, explained that the quick and significant bending under electric field is dominated only by the surface complexation and shrinkage of the gel.

4. THEORETICAL CONSIDERATION OF COMPLEX FORMATION

The stoichiometric binding of surfactant molecules with the charged polymer network is characterized by two processes. One is the electrostatic interaction between the surfactant ion and the oppositely charged network to form salt-like bridging, thus initiating the binding. The other is the hydrophobic interaction between bound surfactants, which stabilizes the aggregation in such a way as to settle the adjacent to the already occupied site along the polymer chain. The former is called "initiation process" and the latter is called "cooperative process"[3,4].

We have made a comparative study on the binding behavior of charged molecules with the linear polyelectrolyte as well as with the charged network. We have treated the hydrophobic interaction between amphoteric molecules using the nearest neighbor interaction model and denoted ΔF_h as the energy gain through the hydrophobic interaction[5]. General formulas of binding isotherms have been derived[6] for a linear polymer as well as a polymer network at difference ionic strenth. When no simple salt is present, the binding curve is

$$\ln C_s v_c = \frac{\Delta F_e + \Delta F_h}{kT} - 1 + \ln \frac{\sqrt{4\beta(1-\beta)[\exp(-\frac{\Delta F_h}{kT})-1]+1} + 2\beta - 1}{\sqrt{4\beta(1-\beta)[\exp(-\frac{\Delta F_h}{kT})-1]+1} + 1 - 2\beta} \qquad (1)$$

for a linear polymer and

$$\ln C_s v_c = \frac{\Delta F_e + \Delta F_h}{kT} - 1 + \ln \frac{\sqrt{4\beta(1-\beta)[\exp(-\frac{\Delta F_h}{kT})-1]+1} + 2\beta - 1}{\sqrt{4\beta(1-\beta)[\exp(-\frac{\Delta F_h}{kT})-1]+1} + 1 - 2\beta} + \ln \frac{(\alpha+\beta-\gamma)V_g}{[1-(\alpha+\beta-\gamma)](V-V_g)} \qquad (2)$$

for a polymer network. Where C_s is surfactant concentrations at equilibrium state, ΔF_e the free energy change due to the electrostatic interaction, β the degree of binding that is the ratio of the molar number of bound surfactants to the polymer. α and γ are numbers of free surfactant ion and its counter ion in the gel in units of unit number of the polymer, respectively.

It is seen that the presence of the cross-linkage introduces an extra ionic osmotic pressure difference inside and outside the network. When β is small, the network always tends to swell which is balanced by the elastic force. This swelling ionic osmotic pressure enhances the initial binding process but suppresses the surfactant aggregation compared with those of the linear polyelectrolyte. If we regard the polymer network as a cross-linked three-dimensional polymer chain in water, the presence of the locally concentrated counter ions, which originate the swelling osmotic pressure, makes the network expand in competition with the conformational shrinkage on binding and thus strongly reduces the cooperativity.

On the other hand, an addition of salt makes the third term in eq. 2 becomes

$$\ln\frac{(P+\alpha+\beta-\gamma)V_g}{[1-(\alpha+\beta-\gamma)](V-V_g)} \qquad (3)$$

here P is the molar ratio between the salt and the network monomer. In the presence of a large amount of salt (P>>1), the above term is no longer sensitive to the change of β. This indicates that a high ionic strength suppresses the network expansion and enables the polymer chain to become flexible, thus promotes the cooperativity. The presence of salt strongly shields the electrostatic repulsion between macroions, thus lowering the electrostatic potential energy. This leads to a shift of the isotherms curve toward a higher equilibrium concentration.

Fig.3 shows the theoretical binding isotherms(solid lines) calculated from eq. 1 and 2, and the observed data (dotted symbols) obtained for $C_{12}PyCl$ bound with a linear as well as a crosslinked PAMPS. The theoretical isotherms showed fairly good agreement with the experimental data, which confirms the essential feature of the theory.

5. REFERENCES

(1) Y. Osada, H. Okuzaki, H. Hori, H. *Nature* **355**, 242(1992).
(2) Osada, Y.; Ross-Murphy, S. B. *Sci. Am.* **268(5)**, 82(1993).
(3) H. Okuzaki, Y. Osada, Y. *Macromolecules* **28**, 4554(1995).
(4) H. Okuzaki, Y. Osada, *Macromolecules* **27**, 502(1994).
(5) R. A. Marcus, *J. Phys. Chem.* **58**, 621(1954).
(6) J. P. Gong, Y. Osada, *J. Phys. Chem.* **99**, 10971(1995).

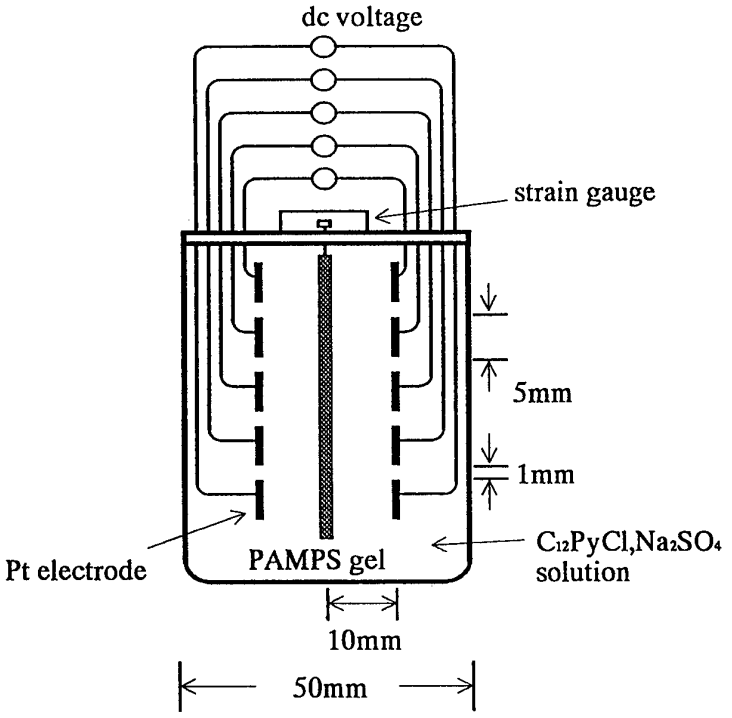


Fig.1 Apparatus for the measurement of bending of the gel under electric field.

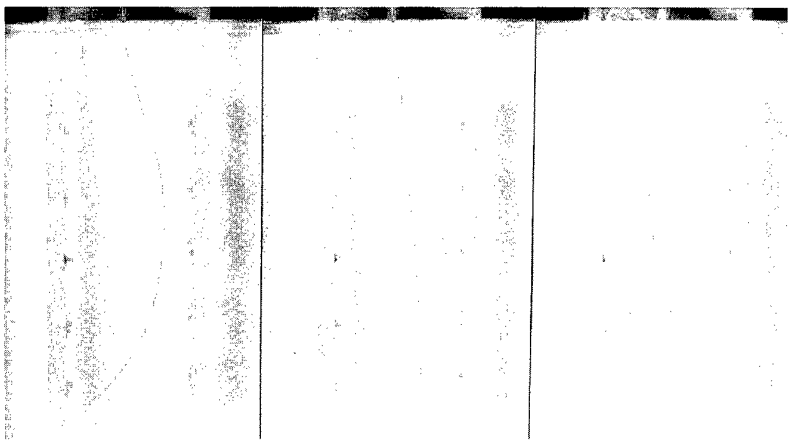


Fig.2 Electro-driven chemomechanical responses of polymer gel in the presence of $C_{12}PyCl$ under alternative change of electric field. The polarity was changed every 2s.

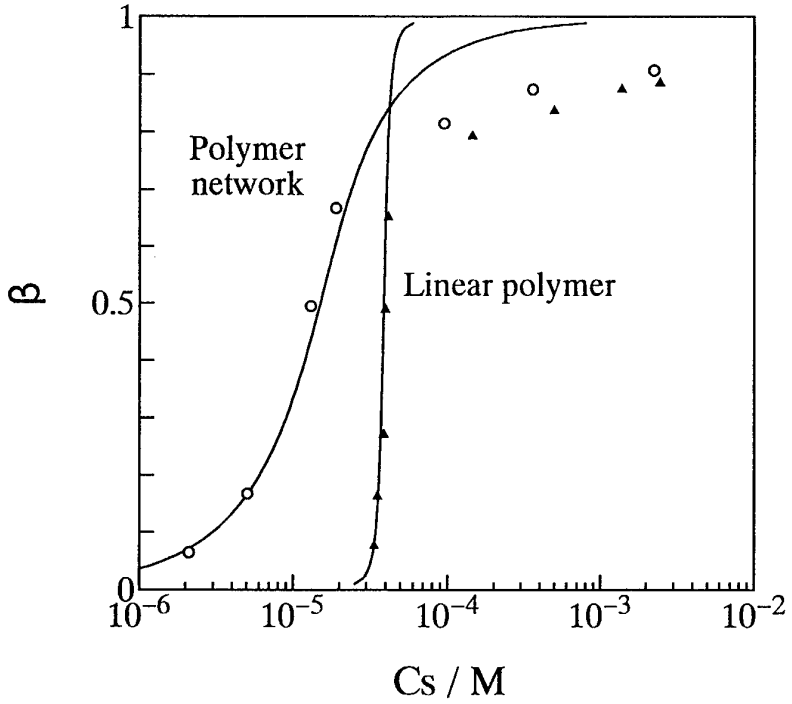


Fig.3 Theoretical binding isotherms(solid lines) and the observed data (dotted symbols) obtained for $C_{12}PyCl$ bound with a linear as well as a crosslinked PAMPS.

Spontaneous Motion of Polymer Gels on Water

S. Matsumoto, J. P. Gong and Y. Osada

Division of Biological Sciences, Graduate School of Science,
Hokkaido University, Sapporo 060, Japan

ABSTRACT

We have discovered that cross-linked polymer gels with hydrophobicity swollen in organic solvent undergo spontaneous motion when immersed in water. The mode of motion largely depends on the shape of the gel: a disc-shaped gel exhibits translational motion while a triangular or a square-shaped one exhibits rotation. The velocity and duration of gel motion are strongly associated with its size and chemical structure. The larger the gel, the longer the gel can keep motion. The mechanism of the gel motion on water has been investigated and we have found that the driven force of motion is from the surface spreading of organic solvent on water surface.

1. INTRODUCTION

A variety of motive power systems have been harnessed to provide machines which move continuously, obtaining their energy from electrical, mechanical, combustive, or hydrostatic sources. The isothermal transformation from chemical to mechanical power is called "chemomechanical" and is involved in inducing motility in many living systems. We have previously reported on a polymer gel with electrically driven motility.[1,2] The motion of the gel is based on the molecular assembly reaction of surfactant molecules with the polymer gel, whereupon an electric field controls the direction and equilibrium of the surfactant binding[3]. However, there should be an inherent economical system in utilizing purely chemical forces and van't Hoff showed the possibility of conversion of a certain amount of chemical "free energy" into mechanical work and suggested a system of osmotic cells with pistons which converts free energy directly to work, as a model of the biological "muscle".[4]

The dynamic properties on a surface due to differeces in surface tension bring about many spectacle phenomena, such as the "dancing" of a piece of camphor on the pure water surface. Such a kind of motion due to the surface tension might be one of the important mechanism of the mass transportation in living system. In this paper, we report our discovery that when a polymer gel swollen in organic solvent was put in water, it exhibited prolonged motion. The mechanism of the gel motion on water has been investigated and we have found that the driven force of motion is from the surface spreading of organic solvent on water surface[5].

0-8194-2165-0/96/$6.00

2. EXPERIMENTAL

Amphoteric polymer gels capable of exhibiting motion are made of crosslinked copolymers of acrylic acid (AA) and hydrophobic acrylates such as stearyl acrylate (SA),[6] 12-acryloyl dodecanoic acid (ADA) and 16-acryloyl hexadecanoic acid (AHA).[7] These polymer gels swell in water-soluble organic solvents such as ethanol by as much as 5~20 times their original volume but shrink in water to form partially crystalline layered structures of ordered long alkyl chains.[6, 7]

3. RESULTS AND DISCUSSION

When the gel swollen upon immersion in ethanol, for example, is immersed in water, it immediately undergoes spontaneous translational and rotational motions with about two-thirds of its volume being immersed in water at the beginning. In the course its motion, the gel gradually sinks and finally settles at the bottom of the container due to contraction and termination of its motion.

The velocity, duration and mode of gel motion are associated with its size, shape and chemical nature. Fig. 1 shows examples of motion photographed by multi-exposures with a programmed stroboscope flasher (10 Hz) for 1 s. A disc-shaped gel exhibits translational motion with occasional abrupt turns(Figs.1(a) and (c)). Velocity of gel motion is dependent on its size: the smaller the gel, the faster it moves. For example, a 100mg ethanol-swollen cylindrical poly (AA-ADA) gel (7mm diameter, 4mm thick, AA 75mol%, ADA 25mol%) undergoes translational motion with a maximum velocity of 5cm/s.

When the gel is triangular or square, it exhibits rapid rotation rather than translational motion(Figs.1(b) and 1(d)). A triangular gel 10mm on its sides and 4mm in thickness exhibits 6~8 rotations per s for the first 20~30 s and then slows down to 4~5 rotations per s over the subsequent 20-min.. The gel often showed translational motion accompanied with extensive rotation (Fig.1(d)). The duration of gel motion is exactly proportional to its size: the larger the gel size, the longer the time of gel motion.

Motion has been achieved by using gels with a variety of combinations of hydrophilic and hydrophobic monomers, such as acrylamide, methacrylic acid, sodium styrenesulfonate with stearyl acrylamide and octadecyl acrylamide.

The fact that the motion can only be observed when a fraction of the gel is floating on the water surface indicates that the gel got a driving force at the water-air interface.

The process of making a gel to perform a prolonged motion in water is considered to be composed of two steps: the first step is the releasing of organic solvent from the gel by the osmotic pressure together with the hydrostatic pressure; the second step is the spreading of the organic solvent on the surface of water and impart motion to the gel.

When the gel swollen upon immersion in ethanol is immersed in water, an osmotic pressure difference is produced between the inside and outside of the gel. Simultaneously, crystallization of

the gel is initiated through hydrophobic interaction of the long n-alkyl side groups and it undergoes volume contraction from the outer surface to give a hydrophobic and dense surface skin layer.[6,7] Contraction of the surface layer leads to a large hydrostatic pressure inside the gel. By virtue of these two pressures, ethanol is ejected from the gel through the skin layer.

Onece the organic solvent is ejected out of the gel, it rises up in the water due to its lower density. On the water surface, the solvent rapidly spreads on it due to the the large difference in their surface tension, and this gives the gel a motion[8-10]. This possible mechanism for the spontaneous motion of the gel is schematically illustrated in Fig.2.

The mode of motion is associated with whether or not the net reaction due to ethanol ejection reaches the center of mass of the gel. Since a counteracting force on the gel is perpendicular to its surface, a disc-shaped gel always receives a force which passes through the center of mass, thus causing a translational motion. In contrast, gels of other shapes may receive a force which does not pass through the center of mass. In such cases, a moment is generated and rotation results.

4. CONCLUSION

The prolonged gel motion obtained by the surface spreading of the organic solvent has several advantages and unique characteristics. Such as no noise and no unnecessary exhaust products like combustion or other chemical reactions. The motion is obtained only by the dilution of organic fluid which can be recovered by using separation technologies such as distillation or membranes. Such a kind of motion is expected to be applicable to soft-touch manipulators, targeting drug-delivery devices, micro-agitators and other biomedical actuators.

5. REFERENCES

1) Y. Osada, H. Okuzaki and H. Hori: *Nature* **355**(1992) 242.

2) Y. Osada and S. B. Ross-Murphy: *Sci. Am.* **268(2)**(1993) 82.

3) H. Okuzaki and Y. Osada: *Macromolecules* **27**(1994) 502.

4) H. Okuzaki, Y. Eguchi, and Y. Osada, *Chemistry of Materials, communications* (1994)

5) Y. Osada, J. P. Gong, M. Uchida, and N. Isogai, *Jpn. J. Appl. Phys.* **34** (1995)L511.

6) A. Matsuda, J. Sato, H. Yasunaga and Y. Osada: *Macromolecules* **27**(1994) 7695.

7) M. Uchida, M. Kurozawa, and Y. Osada, *Macromolecules* **28**(1995)4583.

8) A. W. Adamson, Physical Chemistry of Surfaces, 5th Edition, chapter 4, p116, John Wiley & Sons, Inc., 1990, New York.

9) R. N. O'Brien, A. I. Feher, and J. Leja, *J. Colloid Interface Sci.*, **56**(1976) 474.

10) J. E. Saylor, G. T. Barnes, *J. Colloid Interface Sci.*, **35**(1971)143.

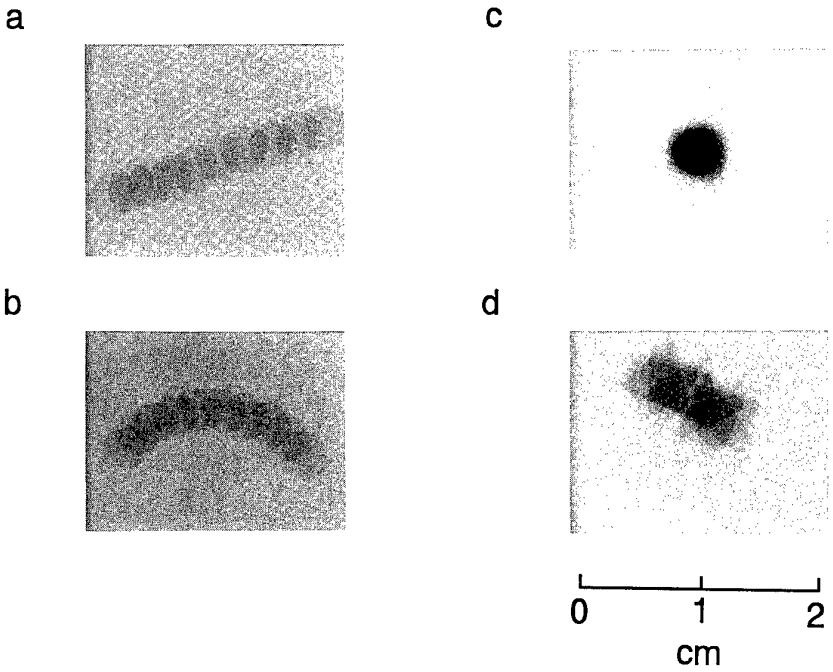


Fig.1. Gels of various shapes in motion. Photographs were taken by multi-exposures with a stroboscope flashing at 10 Hz for 1 s. a) Translational motion of a disc-shaped gel; b) rotational motion of a square gel; c) and d) motions composed of translation and rotation by a disc (c) and a triangular (d).

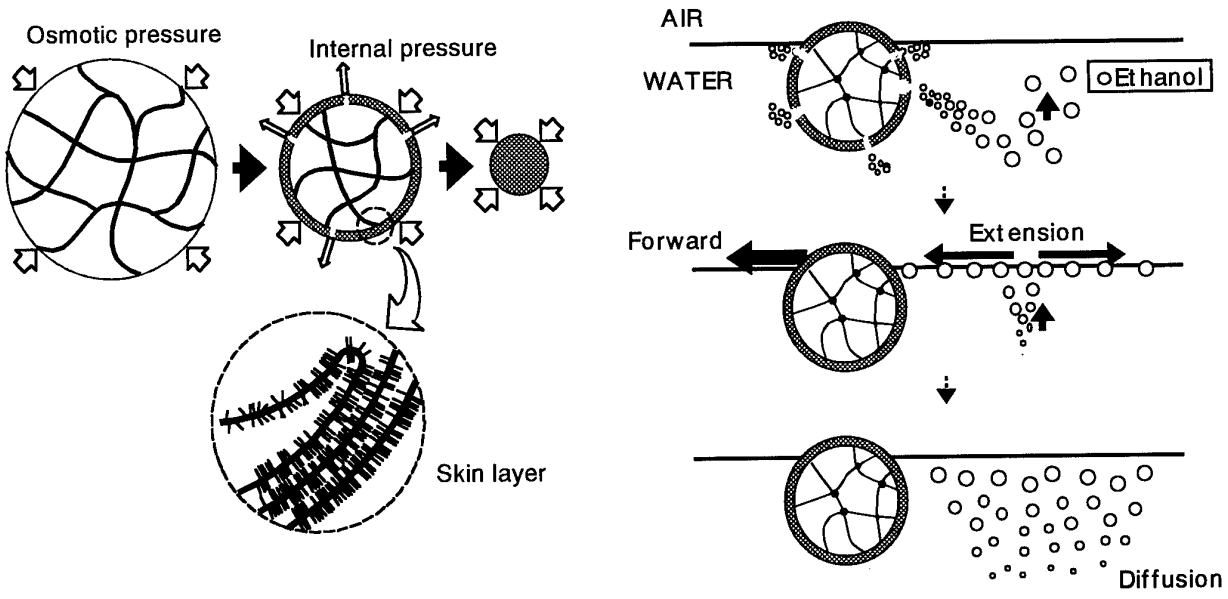


Fig.2. Mechanism for the spontaneous motion of amphoteric polymer gels on water.

Lumped parameter modeling of polymer gel for real time control

Woojin Lee, David Brock

Massachusetts Institute of Technology, Department of Mechanical Engineering
77 Massachusetts Ave., Cambridge, Massachusetts 02139

ABSTRACT

Lumped parameter models of non-electrolyte and electrolyte polymer gel based on the energy method are presented. Emphasis is placed on developing model that is simple enough for real time control implementation, yet able to capture essential inter-domain energy coupling effect. The dynamics of quasistatic polymer gel system are translated to bond graph representation.

1. PREVIOUS WORK

In this section, we briefly describe our previous work on the polymer gel based actuation system.[1] Poly(acrylonitrile) (PAN) gel fibers, which shrink and swell reversibly under acidic and alkaline conditions, were selected because they possess good mechanical properties, rapid contraction rates, well documented fabrication process and commercial availablity.

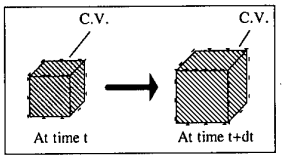
1.1 Material testing

Initially, we evaluated the effect of mechanical properties of PAN gel fiber with respect to the annealing temperature and duration. To determine the effect of thermal crosslinking temperature and the curing time on the tensile force and stiffness, we conducted a series of mechanical measurements on material cured for 2, 3, 4 and 5 hours at 175°, 180°, 190°, 200° and 210° C, and we have found the strength and the stiffness improved with both time and temperature.

1.2 Actuator design

Two linear actuators based on the regulation of pH through PAN gel fiber arrays using an integral fluid irrigation system were designed. The first system used a cylindrical design with gel fiber bundles evenly distributed among an array of irrigating Teflon tubes. Acid and base were alternatively delivered to the gel fiber bundles through the perforated Teflon tubes. Using a simple bang-bang control scheme, the actuator rotated a single linkage arm from zero to 170 degrees and back in approximately 45 seconds, generating a maximum tendon tension of 0.35 N. The second, based on the results from the first system, used a planar array of gel fibers between two fluid reservoirs containing acid and base respectively. The goal was to maximize the surface area of the gel fibers which are exposed to the surrounding fluid and to allow simultaneous infusion of the fluid. The actuator speed roughly doubled that of the cylindrical actuator. For both systems, the PAN fibers annealed at 210° C in air for five hours.

2. LUMPED PARAMETER DYNAMIC MODEL: NON-ELECTROLYTE GEL



Consider the polymer gel network and solvent system inside a control volume (c.v.). The control volume changes as the gel network absorbs the surrounding solvent fluid. The modeling assumptions were: (1) relatively slow process, (2) solvent diffusion-limited, (3) inertial and convection effects negligible, (4) quasistatic (i.e., the properties inside the c.v. is uniform at any instant of time), (5) isothermal, (6) isobaric, (6) two sub-processes (mixing/diffusion and elastic expansion of the polymer-solvent), and (7) polymer and solvent incompressible. The c.v. is surrounded by the solvent fluid at constant temperature, T_O, and constant pressure, P_O. As the solvent fluid enters the c.v., the c.v. expands, and the state of the system inside the control volume at an instant of time can be thermodynamically described by

$$dU_{cv} = T_O dS_{cv} - P_O dV_{cv} + FdL + \mu_P dn_P + \mu_S dn_S$$

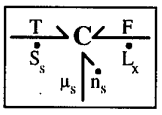
where U_{cv} is the internal energy, S_{cv} is the entropy, V_{cv} is the volume, T_O is the temperature, P_O is the pressure, F is the tensile force (in single axis only), L is the elongation, μ_p is the chemical potential of polymer, μ_s is the chemical potential of solvent, n_p is the number of mole of polymer and n_s is the number of mole of solvent inside the c.v. Since the amount of polymer inside the c.v. is fixed, $\mu_p dn_p = 0$. In addition, $P_O dV_{cv}$ represents the differential expansion work done by the c.v.. Assuming both the polymer and the solvent to be incompressible, $P_O dV_{cv} = 0$ since the expansion of c.v. alone is

0-8194-2165-0/96/$6.00

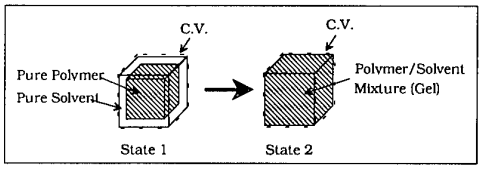
exactly canceled by the flow work done by the solvent flowing into the c.v. Above expression then simplifies to $dU_{cv} = T_o dS_{cv} + \mu_S dn_S + FdL$. With the assumption of a quasistatic process, the system inside the c.v. may be treated as the lumped parameter multiport capacitance field with the relation

$$\frac{dU_{cv}}{dt} = T_o \frac{dS_{cv}}{dt} + \mu_S \frac{dn_S}{dt} + F\frac{dL}{dt} .$$

The first term on the right hand side (RHS) represents the effects of heat transfer, entropy transfer due to convection and entropy generation due to irreversibility. The second term on RHS represents chemical energy brought in by the incoming surrounding solvent, and the last term represents the effect of mechanical work on the gel. The bond graph representation of the system is shown on right. Constitutive relations describing the polymer-solvent gel network system has been derived by Flory [2], and was the base of our multiport capacitance model.



2.1 Mixing/diffusion process: Flory's model

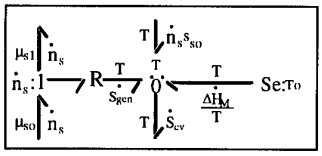


In state 1, pure polymer network and pure solvent inside the control volume (c.v.) are completely separated whereas in state 2, polymer network and solvent inside the control volume mix and form homogeneous polymer solution, while maintaining constant volume of c.v. The process from state 1 to state 2 is therefore entropy generating run-down mixing process, and changes in thermodynamic properties of c.v. due to such mixing process are described by Flory. According to Flory, changes in enthalpy, ΔH_M, entropy, ΔS_M, and Gibbs free energy change, ΔG_M of the control volume due to mixing are

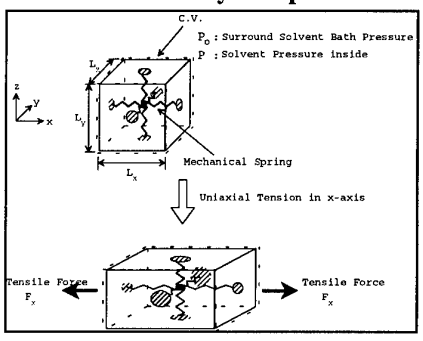
$$\Delta H_M = Rn_s\phi_p b\,;\quad \Delta S_M = -R\left(n_s \ln\phi_s + n_p \ln\phi_p + n_s\phi_p a\right);\quad \Delta G_M = \Delta H_M - T\Delta S_M = RT\left(n_s \ln\phi_s + n_p \ln\phi_p + n_s\phi_p\chi\right),$$

where R is the universal gas constant, n_S is molar quantity of solvent, n_p is molar quantity of polymer, ϕ_s, ϕ_p are volume fractions of solvent and polymer, and χ is the Flory-Huggins polymer-solvent interaction parameter. χ is a temperature dependent dimensionless quantity which characterizes polymer-solvent interactions, and can be expressed in form $\chi=a+b/T$ where a and b are temperature independent quantities. For isothermal, isobaric conditions, quasistatic mixing/diffusion process can be modeled as $\Delta\mu_{s,M}\dot{n}_s = -T\dot{S}_{gen} = \Delta\dot{H}_M - T\dot{S}_{cv} + T\dot{n}_s s_s^o$

in terms of the rate of changes of control volume's entropy and Gibbs free energy, S_{cv} and G_{cv}. This process can be graphically represented by a simple bond graph structure as shown on the right. The entropy generating mixing/diffusion process is modeled by a resistance field driven by solvent's chemical potential difference across the gel's control volume boundary, and the total entropy change of c.v. is sum of the entropy generated and the entropy transferred by the heat/mass transfer processes.



2.2 Rubber elasticity: simple mechanical model



Theory on rubber elasticity of swelling gel has been developed by Flory[2] based on complex statistical theory which remarkably relates how the molecular structure of elastomer responds to an applied strain to the macroscopic deformation behavior. However, this theory still offers only a qualitative approximation to the actual behavior of elastomer, mainly due to the assumption that end-to-end distances of the chains can be described by the Gaussian distribution,[3] and parameters such as effective number of polymer chains gel are difficult to obtain. Given the complexity of the statistical model, the purpose of this section is to approximate the gel's elastic behavior with a simpler mechanical analog. Consider a dry, stress-free gel of linear dimensions L_{xdo}, L_{ydo}, L_{zdo}, isotropically swollen and stretched to dimensions L_x, L_y, L_z. Elastomer volume is assumed to be constant; $A_{xdo}L_{xdo}=A_{xd}L_x$, $A_{ydo}L_{ydo}=A_{yd}L_y$, $A_{zdo}L_{zdo}=A_{zd}L_z$ where A_{ido} is cross-sectional area of dry gel in i-axis (i= x, y, z), A_{id} is cross-sectional area of deformed elastomer unit aligned in i-axis, and L_i is length of deformed elastomer in i-axis. Total volume is the sum of the solvent volume and the elastomer volume; $V = L_xL_yL_z = V_s + V_p = V_s + L_{xdo}L_{ydo}L_{zdo}$. In addition, define the elongation factors α_x, α_y and α_z such that $\alpha_x = L_x/L_{xdo}$, $\alpha_y = L_y/L_{ydo}$, $\alpha_z = L_z/L_{zdo}$. The normal stresses and strains of the elastomer units in x, y and z directions due to swelling and uniaxial tension in x-axis are then

$$\sigma_x = \frac{(P-P_o)(A_x - A_{xd}) + T_x}{A_{xd}};\ \sigma_y = \sigma_z = \frac{(P-P_o)(A_y - A_{yd})}{A_{yd}};\ \varepsilon_x = \frac{L_x}{L_{xdo}} - 1 = \alpha_x - 1;\ \varepsilon_y = \varepsilon_z = \frac{L_y}{L_{ydo}} - 1 = \alpha_y - 1.$$

Applying these results to the general elasticity equations where ν is Poisson's ratio, we arrive at

$$(P-P_o) = \frac{\left(E_d(\alpha_x - 1) - \frac{T_x}{A_{xd}}\right)}{(1-2\nu)\left(\frac{V_{gel}}{V_p} - 1\right)} = \frac{\left(E_d(\alpha_y - 1) + \nu\frac{T_x}{A_{xd}}\right)}{(1-2\nu)\left(\frac{V_{gel}}{V_p} - 1\right)} = \frac{\left(E_d(\alpha_z - 1) + \nu\frac{T_x}{A_{xd}}\right)}{(1-2\nu)\left(\frac{V_{gel}}{V_p} - 1\right)}.$$

Treating the effect of rubber elasticity as purely mechanical, the change in chemical potential of solvent due to the rubber elasticity is then $\Delta\mu_{s,el} = \mu^o(T_o, P) - \mu^o(T_o, P_o)$. In addition, $\Delta\mu^o = \mathrm{v_s}^o \Delta P$ where $\mathrm{v_s}^o$ is molar volume of pure solvent. Combining above results, we have

$$\Delta\mu_{s,el} \approx \frac{\mathrm{v}_s^o\left(E_d(\alpha_x - 1) - \frac{T_x}{A_{xd}}\right)}{(1-2\nu)\left(\frac{V_{gel}}{V_p} - 1\right)} \approx \frac{\mathrm{v}_s^o\left(E_d(\alpha_y - 1) + \nu\frac{T_x}{A_{xd}}\right)}{(1-2\nu)\left(\frac{V_{gel}}{V_p} - 1\right)} \approx \frac{\mathrm{v}_s^o\left(E_d(\alpha_z - 1) + \nu\frac{T_x}{A_{xd}}\right)}{(1-2\nu)\left(\frac{V_{gel}}{V_p} - 1\right)}.$$

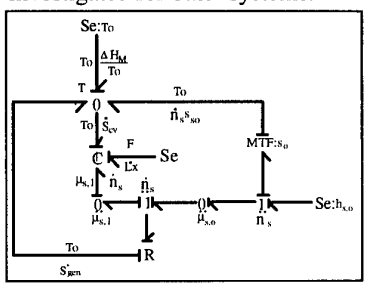
It should be noted that if we approximate A_{id} as A_{ido} (i = x, y, z) neglecting the elastomer's constant volume assumption, neglect Poisson effect and apply above result to the case of highly swollen gel where the volume of the gel is mostly occupied by the solvent, then above result simplifies to

$$\Delta\mu_{s,el} \approx \frac{\mathrm{v}_s^o}{\alpha_y^2}\left[E_d\alpha_x - \frac{T_x}{L_{ydo}L_{zdo}}\right] \approx \mathrm{v}_s^o\frac{E_d}{\alpha_x}.$$

This result is consistent with the results by Flory and Treloar despite the lack of elastomer's Poisson effect representation. Most likely the statistical thermodynamics based model itself did not take into account the Poisson effect as well. Zrinyi and Horkay have shown that the theoretical prediction based on such results were compatible with the experimental results,[4] especially for highly swollen gel. The magnitude of Poisson effect in general needs to be investigated further. In addition, one should note the limitations of this simple mechanical model, namely the lack of thermo-mechanical coupling --- the entropy spring effect. With the real elastomer, there is thermal-mechanical energy conversion, as Flory's model describes in terms of entropy change due to deformation. This energy coupling behavior is expected to be unimportant in our isothermal, isobaric system. However, the importance of this coupling effect needs to be investigated for other systems.

2.3 Overall process: mixing/diffusion and deformation

Combining the results on mixing/diffusion process and elastic deformation process, i.e., $\Delta\mu_s = (\Delta\mu_{s,M} + \Delta\mu_{s,el})$, the bond graph representation of overall process is shown on the right. Note that for the surrounding solvent, $h_s^o = \mu_s^o + Ts_s^o$.



2.4 Elastic modulus and Poisson's ratio estimation

Based on the derived model presented above, we can estimate elastic modulus of the elastomer, E_d, and its Poisson's ratio, ν, by employing free swelling and swelling under uniaxial tension experiments of which governing equations are

$$\Delta\mu_{s,el} = -\Delta\mu_{s,M} \approx \frac{\mathrm{v}_s^o E_d(\alpha_i - 1)}{(1-2\nu)\left(\frac{V_{gel}}{V_p} - 1\right)},\ i = x, y, z;\ \alpha_x - \alpha_y \approx \frac{1}{E_d}\left[(1+\nu)\frac{T_x}{A_{xd}}\right]$$

respectively. (The polymer-solvent interaction parameter χ for our test gel poly(vinyl alcohol) (PVA) in H_2O with respect to the swelling degree has been well studied by various researchers,[5] and therefore, given the swelling degree, the value of $\Delta\mu_{s,M}$ can be calculated.)

2.5 Polymer gel swelling kinetics

Simple phenomenological description of solvent flow rate in terms of solvent chemical potential difference is employed to describe the macroscopic swelling kinetic of the polymer gel; $\dot{n}_s = P_m(\mu_s^o - \mu_s)$, where P_m represents the permeability of

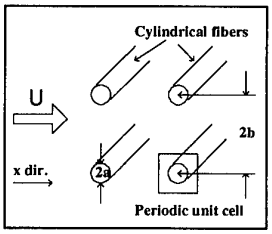
the solvent in polymer gel network. Recognizing that it may also be expressed in terms of the osmotic pressure difference as $\dot{n}_s = P_m v_s^o (P_s^o - P_s)$, dependencies of P_m on critical parameters such as gel thickness, cross-sectional area, and swelling degree can be explicitly defined by comparing with Darcy's law for flow through porous media,

$$U = -\frac{K_m}{\mu_{vis}} \nabla P,$$

where U is the macro-scale "superficial velocity", defined as the flow rate Q divided by the total (solid plus fluid) cross-sectional area, P is the macro-scale pressure, K_m is the permeability, and μ_{vis} is the solvent's fluid dynamic viscosity. For simplified case where the pressure is function of x-axis only, we have

$$P_m \approx \frac{K_m A}{\mu_{vis} v_s^{o2} \Delta x},$$

where Δx is the gel's characteristic thickness solvent travels during swelling. Furthermore, treating the gel as a matrix of essentially cylindrical polymer fibers with zero Reynolds number solvent flowing through a fiber matrix as shown on the right, an approximate analytic expression is obtained for the permeability of a periodic porous matrix[6]



$$K_m = \frac{a^2}{4}\left(\frac{b}{a}\right)^2 \left[\ln\left(\frac{b}{a}\right) - \frac{\left(\left(\frac{b}{a}\right)^4 - 1\right)}{2\left(\left(\frac{b}{a}\right)^4 + 1\right)} \right], \quad \text{where} \left(\frac{b}{a}\right) \approx \left(\frac{V}{V_p}\right)^{\frac{1}{3}}$$

Thus, the dependence of permeability coefficient K_m on swelling degree can easily be defined.

3. LUMPED PARAMETER DYNAMIC MODEL: ELECTROLYTE GEL

In addition to the modeling assumptions for the nonelectrolyte gel model, let us also assume: (1) the characteristic length of gel element is much greater than the Debye length, (2) ionic concentrations inside the gel are uniform at any instant of time, and (3) ions behave as in ideal dilute solution; $\mu_{i,e} = \mu_i^o + RT \ln(x_{i,g}) + z_i F \phi_{i,g}$ where $\mu_{i,e}$ is the electrochemical potential, $x_{i,g}$ is the mole fraction, z_i is the valence and $\phi_{i,g}$ is the electrical potential of the ion i inside the gel.

3.1 Equilibrium conditions

Given the valence z_m and mole fraction x_m of fixed charge groups of polymer gel network, ion concentrations inside the gel at equilibrium are defined by the macroscopic electroneutrality and Donnan equilibrium partitioning law along with charge conservation relations:

$$\Sigma z_i x_{i,g} + z_m x_m = 0 \text{ bulk electroneutrality in gel}, \quad \left(\frac{x_{i,g}}{x_{i,b}}\right)^{\frac{1}{z_i}} = \left(\frac{x_{j,g}}{x_{j,b}}\right)^{\frac{1}{z_j}} \text{ Donnan partition law},$$

where $x_{i,b}$, $x_{j,b}$, $x_{i,g}$, $x_{j,g}$ are mole fractions of i and j ions in the bath and the gel. Strictly speaking, this relations applies to true equilibrium case only. However, in general, it can also be applied to the non-equilibrium case as long as the net transport is much slower than the diffusion or the drift components of the transport process.[7]

3.2 Chemical capacitance

With the assumption of dilute solution, chemical potential of ion in the gel may be described as

$$\mu_{c,i} = \mu_i^o + RT \ln x_i \cong \mu_i^o + RT \ln\left(\frac{n_i}{n_s + s n_p}\right) \text{ where } x_i \cong \frac{n_i}{n_s + s n_p + \sum n_j} \cong \frac{n_i}{n_s + s n_p}$$

by treating the polymer molecule as solvent/ion size molecule with equivalent scaling factor, s. The rate of change of ion's chemical potential may then be approximated by

$$\frac{d\mu_{c,i}}{dt} \cong RT \frac{d}{dt}\left[\ln\left(\frac{n_i}{n_s + s n_p}\right)\right] = RT\left[\frac{1}{n_i}\frac{dn_i}{dt} - \frac{1}{(n_s + s n_p)}\frac{dn_s}{dt}\right].$$

3.3 Electric potential coupling: bulk electroneutrality

In macroscopic scale, the electroneutrality prevails, and the bulk electroneutrality coupling among ions is modeled by a simple ideal parallel plate capacitor [8]

$$\Delta\phi_e = \frac{1}{C_E}\sum_i q_i\,,\quad C_E = \frac{\varepsilon A}{d}\,,$$

where $\Delta\phi_e$ is the induced electric potential, ε is the dielectric constant of the electrolyte, A is the cross-sectional area of the ion transport, d is the typical maximum separation of charges in a volume element, ~ 10^{-10} m, and q_i is the charge of the ion. Note that the induced electric potential disappears as the bulk electroneutrality is reached.

3.4 Electric potential coupling: Donnan potential

In addition to the bulk electroneutrality coupling, there also exists a Donnan potential gradient between two regions of unequal ion concentrations at equilibrium. Although the system of interest is not at true equilibrium during the process, we assumed that the condition is near equilibrium (quasistatic), and we modeled the electric potential difference between two uniform media regions as the average of the individual ion specie's contribution to the electric potential buildup. Defining the reference potential to be at the electrically neutral surrounding bath, the individual ion contribution to the electric potential, ϕ_i and the average electric potential ϕ_{avg} at a region are modeled as

$$\phi_i \cong \frac{RT}{z_i F}\ln\left(\frac{x_{io}}{\bar{x}_i}\right);\quad \phi_{avg} \cong \frac{1}{n}\sum_i^n \frac{RT}{z_i F}\ln\left(\frac{x_{io}}{\bar{x}_i}\right),$$

where n is the number of ion species. The total electric potential and its rate of change at a region then may be expressed as

$$\phi \cong \phi_{avg} + \Delta\phi_e \cong \frac{1}{n}\sum_i^n \frac{RT}{z_i F}\ln\left(\frac{x_{io}}{\bar{x}_i}\right) + \frac{F}{C_E}\left(\sum_i z_i n_i + z_m n_m\right),$$

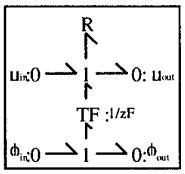
$$\frac{d\phi}{dt} \cong -\frac{1}{n}\sum_i^n \frac{RT}{z_i F}\left[\frac{1}{n_i}\frac{dn_i}{dt} - \frac{1}{(n_s + sn_p)}\frac{dn_s}{dt}\right] + \frac{F}{C_E}\left(\sum_i z_i \dot{n}_i + z_m \dot{n}_m\right).$$

3.5 Ion transport

Modeling both the concentration and electrical potential gradients as linear and considering only one dimensional case for simplification, the average ion transport relation of ions in the gel can be expressed as

$$\Gamma_{i,avg} = -D_{i,avg}\frac{\Delta c_i}{\Delta x} - \frac{z_i}{|z_i|}u_{i,avg}c_{i,avg}\frac{\Delta\phi}{\Delta x},$$

where $\Gamma_{i,avg}$ is the average molar flux of the ith species ion, $D_{i,avg}$ is the average diffusion coefficient, $c_{i,avg}$ is the average concentration, $u_{i,avg}$ is the average mobility, Δc_i, $\Delta\phi$ are ion concentration and electrical potential net differences between two regions, and Δx is the separating characteristic distance. The bond graph structure representing the ion transport process is shown on the right. Although it suggests a entropy generation port at the resistance field, we assumed it was negligible for simplicity. The ion transport kinetics of the resistive element suggested by the bond graph structure is



$$\frac{dn_i}{dt} = K_i\left[\left(\mu_{i,in} - \mu_{i,out}\right) + z_i F\left(\phi_{in} - \phi_{out}\right)\right].$$

Comparing this expression to the previous ion transport equation, we have

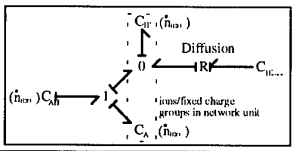
$$K_i \cong \frac{\bar{D}\Delta\bar{c}_i A}{\left(\mu_{i,out} - \mu_{c,in}\right)\Delta x} \cong \frac{\bar{u}_i\bar{c}_{i,avg}A}{|z_i|F\Delta x}.$$

3.6 Ion diffusion/reaction

Diffusing H^+/OH^- in the solvent can react with corresponding conjugate basic/acidic structures on the network; $AH \Leftrightarrow A^- + H^+$ (for the case of negatively charged gel with fixed charge groups -A^-). It was shown that such diffusion-reaction can significantly slow down the overall ion transport process.[9] Not only the overall kinetic of the ion's transport is affected, the concentrations of both mobile ions and fixed charge groups are changed as well --- subsequently changing the overall equilibrium behavior. In many cases, simplifications can be made with the assumption that the reaction occurs at a much faster rate than the diffusion. Thus, the reaction can be considered as "instantaneous" and "always" at equilibrium (quasi-equilibrium), where the overall process is limited by the diffusion of the hydrogen ion into the gel/membrane unit. Under the assumption of dilute solution, the quasi-equilibrium model says $\mu_{AH} = \mu_{H+} + \mu_{A-}$. With fixed total possible number of the binding sites, A_{total}, concentration of fixed charges depends on the H^+ concentration only;

$$c_{A-} = \frac{c_{Atotal} K_{eq}}{c_{H+} + K_{eq}}, \quad \frac{dc_{A-}}{dt} = -\frac{c_{Atotal} K_{eq}}{\left(c_{H+} + K_{eq}\right)^2} \frac{dc_{H+}}{dt}.$$

For this quasi-equilibrium reaction, the bond graph representation is



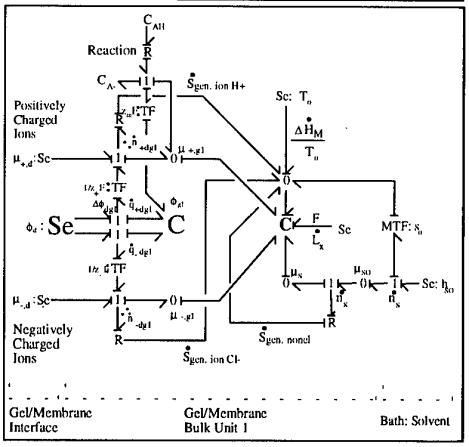
3.7 Overall process: ion transport and polymer gel swelling

Assuming the ionic contribution to the chemical potential change of the solvent to be additive,[2] previous results on nonelectrolyte gel is combined with ion transport model to arrive at the electrolyte gel model;

$$\mu_s - \mu_s^o = (\Delta\mu_s)_{nonel} + (\Delta\mu_s)_{ion}$$

where $(\Delta\mu_s)_{ion} \cong -\nu_1 RT \sum c_{ion}$ (van't Hoff equation)

Furthermore, the region situated just inside of the gel's surface by a few Debye lengths reaches the equilibrium states almost instantaneously when compared to the rest bulk of the gel, and its equilibrium states may be treated as the boundary conditions for the bulk unit. The bond graph representation of single bulk unit electrolyte gel model for binary ions case is shown on the right.



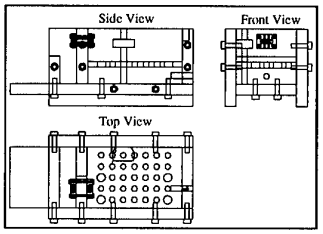
3.8 Limiting process

Even with the simple binary ion case, we have three coupled independent dynamic equations describing the overall dynamic process: two for each ion species, and one for the solvent. However, Grimshaw et. al. has shown that for some gels, swelling rate is limited by diffusion-limited reaction of H^+ ions with gel's charge,[9] and according to De Rossi,[10] such is the case for the gel of our interest, poly(vinyl Alcohol)-poly(acrylic acid) (PVA-PAA), when the pH of the solution in equilibrium with the gel is higher than 2.9. In this case, overall dynamics of the gel can be described by a first order coupled differential equation with time constant,

$$\tau_{H+} = \frac{\Delta x_{d1}^2}{\overline{D}_{H+}} \left[1 + \frac{c_{Atotal} K_{eq}}{\left(c_{H+} + K_{eq}\right)^2} \right]$$

4. CONCLUSION AND FUTURE WORK

In order to adequately model the inter-energy domain coupling effects, lumped parameter models of polymer gel were developed based on energy method, and corresponding bond graphs were presented. Emphasis was placed on developing a model simple enough for real time control while capturing the essential dynamics. Experiments to verify the model are currently under way (schematic of experimental device is shown on right). Once verified, the model will be implemented in a real time control system of polymer gel based actuator.



5. ACKNOWLEDGMENTS

This work was funded in part by ONR grant number N00014-95-1-0986 and in part by Sandia contract number AI-3367.

6. REFERENCES

1. Brock, D., Lee, W., Segalman, D., Witkowski, W., "A Dynamic Model of a Linear Actuator Based on Polymer Hydrogel," Journal of Intelligent Material Systems and Structures, Vol. 5, No. 6, 764-771, 1994.

2. Flory, P. J., Principles of Polymer Chemistry, Cornell University Press, Ithaca, New York, 1990.

3. Young, R. J., Lovell, P. A., Introduction to Polymers, 2nd. Edition, pg. 353, Chapman & Hall, London, 1991.

4. Zrinyi, M., Horkay, F., "On the Thermodynamics of Chemomechanical Energy Conversion Realised by Neutral Gels," Journal of Intelligent Material Systems and Structures, Vol. 4, 190-201, 1993.

5. Sakurada, I., et. al., "Vapor Pressures of Polymer Solutions. II. Vapor Pressure of the Poly(vinyl Alcohol)-Water System," Vol. 35, 497-505, 1959.

6. Happel, J. and Brenner, Low Reynolds Number Hydrodynamics, p. 393, Prentice Hall Publisher, Englewood Cliffs, NJ., 1973.

7. Grodzinsky, A. J., Fields, Forces and Flows in Biological Tissues and Membranes, lecture notes.

8. Oster, G., Auslander, D., "Topological Representations of Thermodynamic System-II. Some Elemental Subunits for Irreversible Thermodynamics," Journal of Franklin Institute, 77-92, 1971.

9. Grimshaw, P. E., Nussbaum, J. H., Grodzinsky, A. J., Yarmush, M. L., "Kinetics of electrically and chemically induced swelling in polyelectrolyte gels," Journal of Chemical Physics, Vol. 93, No. 6, 4462-4472, 1990.

10. De Rossi, D. and Chiarelli, P., "Determination of mechanical parameters related to the kinetics of swelling in an electially activated contractile gel," Progress in Colloid & Polymer Science, 78, 1-6, 1988.

ION-EXCHANGE POLYMER ARTIFICIAL MUSCLE AND ACTUATING SYSTEM

Dominique Vial, Bertrand Tondu, Pierre Lopez
Groupe d'Automatique et de Robotique Industrielle - L.E.S.I.A.
Département de Génie Electrique, Institut National des Sciences Appliquées
Complexe Scientifique de Rangueil, 31077 Toulouse - France

Yves Aurelle
Laboratoire d'Ingénierie du Traitement et de l'Epuration des Eaux
Département de Génie des Procédés Industriels, Institut National des Sciences Appliquées
Complexe Scientifique de Rangueil, 31077 Toulouse - France

Alain Ricard
Laboratoire de Physicochimie des Matériaux Organiques
Ecole Nationale Supérieure d'Ingénieurs de Génie Chimique
18, Chemin de la loge, 31078 Toulouse - France

Keywords : ion-exchange polymer, chemomechanical transformation, artificial muscle, actuator, robotics.

Abstract : Chemomechanical transformations are used to produce a mechanical force from a reversible chemical reaction in order to generate artificial muscular contraction, on the model of the biological muscle. The design and experimentation of an original artificial muscle using an ion-exchange polymer which reacts inside a soft envelope, derived from research on pneumatic artificial McKibben muscle, is presented. Then a chemomechanical actuator constituted of two artificial muscles has been conceived: first results are shown on position control in open-loop mode.

INTRODUCTION

By analogy with the functioning of a biological muscle, the production of a contraction force can be seeked to be artificially generated by using chemomechanical transformations. The objective of this kind of research is then to create actuators paradoxically combining properties of classic actuators such as power, response speed and compactness, and of the human skeletal muscle i.e. softness [SUZ-91] [CAL-93] [RIC-95].
The purpose of this article is to introduce the original work we are presently developing in the GARI laboratory of DGE-INSAT in co-operation with chemists from GPI-INSAT and ENSIGC in Toulouse. This work on chemomechanical artificial muscles is following the studies developed in our laboratory for designing and experimenting naturally compliant robot-arms actuated by pneumatic McKibben artificial muscles [TON-94]. The first part of this paper introduces chemomechanical transformations of "soft gels" (hydrogels and organogels) and "hard gels" (ion-exchange polymers). In the case of ion exchangers with weak basic groups, chemomechanical transformations result from an effect of the solvation in aqueous phase. For such polymers which have a granular morphology, the addition of acidic or alkaline solutions provokes a swelling-deswelling cycle which can be controlled by the reaction stoechiometry. The second part is devoted to our chemomechanical artificial muscle built up from a soft rubber and braid envelope on the McKibben muscle model. Results for isotonic contraction and isometric contraction are reproduced. The third part is devoted to an actuator constituted of two muscles set in antagonism, by analogy with the biceps/triceps system of the human skeleton. Results for a motion cycle in open-loop control of a two-chemomechanical muscle actuator are reported.

0-8194-2165-0/96/$6.00

CHEMOMECHANICAL TRANSFORMATION OF SOFT POLYMERIC GELS AND ION-EXCHANGE POLYMERS (RESINS)

Covalent gels are formed either by irreversible reactions between pre-existing linear chains (cross linking) or by polymerisation of monomers, some of which have more than two reacting groups. Polymeric chains build a tridimensional network which is generally nonhomogeneous and swollen by a solvent. The physical properties of a gel depend on the interaction between the network and the solvent. Gel swelling and deswelling are generally caused by the modulation of the polymer affinity for the solvent by changing pH, temperature, nature of solvent or electric field. Changing these factors induces a volume change which may be as large as 10^3.The polymer/liquid system is in equilibrium under the influence of three strengths contributing to the total osmotic pressure [TAN-82]. Chemomechanical transformations can also be carried out with ion exchangers from a solvation effect in the aqueous phase. In this case, we investigate weak cation exchangers with R-COOH functional sites. According to their ionic form H^+ or Na^+, these groups in aqueous phase induce a large swelling or deswelling of the network which can give a picture of the human muscle cycles. This phenomenon is due to the weak ionisation degree of the organic acid function (COOH) which causes a weak solvation effect and conversely a very high ionisation degree for the associated salt function (COO^-Na^+ for example) which induces a very large solvation effect of Na^+ ions. So it is easy to provoke alternate swelling and deswelling cycles that can be totally controlled from the acid-base reaction stoechiometry resulting from a reaction due to either an acid solution (HCl, H_2SO_4,...) or an alkaline solution (NaOH,...) with a granular cationic weak exchanger.

CHEMOMECHANICAL ARTIFICIAL MUSCLES

The idea of an artificial muscle is based on the reversible contractility principle specific to the biological muscle. This contractility designates a shortening property of the muscle. In the case of the skeletal muscle, it is possible to define a privileged axis of shortening, but in the case of smooth muscles, the contractility exists independently of a privileged length reduction axis. The artificial muscle keeps this very large definition of contractility. Within the framework of this paper, our definition of the artificial muscle will be limited to the skeletal muscle model: the contractility property is restricted to muscle symmetry axis. With this contraction principle are associated a set of specific properties expected from the artificial muscle by analogy with the biological muscle. The combination of these properties must solve a paradox which is rarely considered with classic actuators: on the one hand, the artificial muscle must be powerful, compact and fast enough to move some mechanical structure, on the other, the artificial muscle must be soft enough to make possible a non destructive contact between the mechanical structure and its environment. This experience acquired about pneumatic artificial muscles have led us to bring to light the so called McKibben artificial muscle as a typically artificial muscle by taking into account previous criteria [TON-95] [TON-94]. The McKibben muscle, invented at the end of the fifties, and used as an arm orthics [NIC-65], consists of an inner rubber tube covered by a double helix cordage braid. Metal or PVC plastic fittings affixed to both ends form the termination connectors. When inflated, it produces a real axis contraction force reducing its length and increasing its radius. The originality of the McKibben muscle consists in the production of a contraction force similar to the one produced by the natural muscle: at constant input pressure, the force decreases from the zero contraction state where it is maximum to a maximum contraction state where it is zero [TON-95]. The McKibben muscle follows the artificial muscle criteria defined before: it develops a maximum contraction force greater than 100 kgf under a 5 bar pressure, for an own weight of 50 g and an external diameter varying from 1,5 to 3,5 cm. Furthermore, the force reduction with the contraction ratio gives to the McKibben muscle a spring nature which explains its « softness ». The chemomechanical artificial muscle is closer to the biological one than pneumatic muscle because in that case the contraction force is produced by a transformation of chemical energy into mechanical energy. We presented in [RIC-95] a brief review of current achievements: as it appears, the notion of contractility take various forms in the mentioned examples. The difficulty in designing such a muscle appears in the envelope definition inside which the chemomechanical transformation is produced. Ideally, a material sufficiently rigid to be freed from any envelope would be necessary to simulate the contraction of muscular fibres. No such material seems presently to exist, and current solutions consist in confining the chemical reaction in a chamber. D.G. Caldwell has developed this idea to define "one muscle cell consisting of a water-tight chamber containing 10 strips of 'standard' (0,1 mm thick, 30 mm wide and 45 mm long, giving an effective cross-sectional area of 30 mm^2) polymer muscle in parallel"

[CAL-93]. The polymer muscle is composed of PVA-PAA gel fibres, and the acetone/water stimulation technique is used to obtain contraction and dilation.
We have designed an original artificial chemomechanical muscle having the McKibben muscle envelope as a chamber, which compared to classic cylinder chambers, has the advantage of generating a force response more similar to the one produced by the skeletal muscle as it has been shown. The muscle contraction and dilation are due to the granular ion-exchange polymer confined in the rubber tube. The circulation of NaOH in the rubber tube provokes the swelling (there is Na^+ absorption by substituting to H^+ ions) and the muscle contraction: it is equivalent to the inflation of the tube at a given pressure. The muscle relaxation results from the deswelling of the ion exchanger (Na^+ ions are relaxed: they are rejected and replaced by H^+) due to the circulation of HCl solution in the rubber tube. In the pneumatic muscle it is necessary to maintain the gas pressure for keeping a given contraction state. In the ion-exchange polymer muscle, a given contraction state is maintained even if no more solution circulates: the contraction state has been memorised due to the pressure exerted by materials confined inside the rubber tube. A contraction state change is induced by NaOH or HCl injection. Figure 1 shows the experimental site designed to study the artificial muscle [VIA-94].

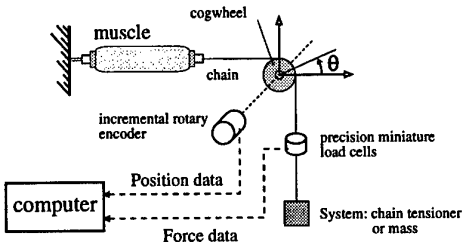
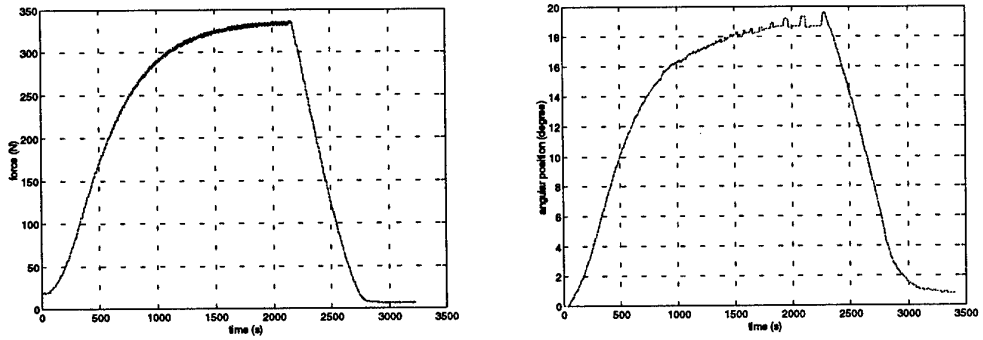


Fig. 1 : Experimental site for study of chemomechanical muscles.

The experimental site gives the possibility of isometric contractions by using a chain tensioner, then the static contraction force is measured. Isotonic contraction is generated by chaining a mass to the free extremity of muscle and then the dynamic angular position of the pulley can be measured. Figure 2 presents the result obtained in isometric and isotonic modes for a working material with a 100% swelling percentage: the muscle considered has a length of 140 mm, a diameter of about 15 mm, a weight of 67 g , 9 g of which taken by the ion-exchange polymer.



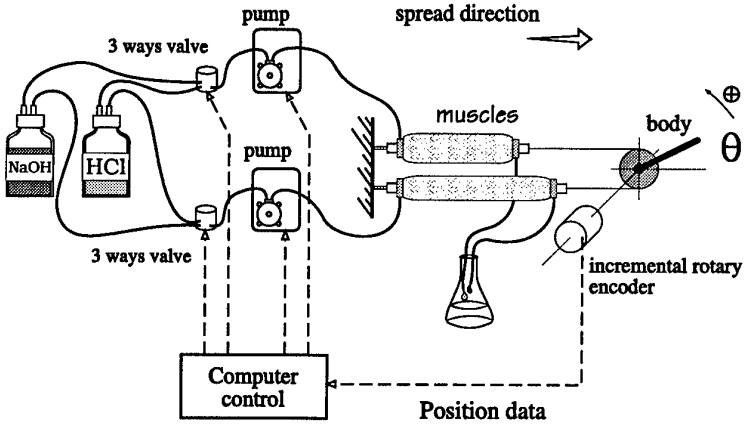
a) b)

Fig. 2 : Muscle response, a) isometric contraction (at a zero contraction rate).
b) isotonic contraction (with a 2 kg mass).

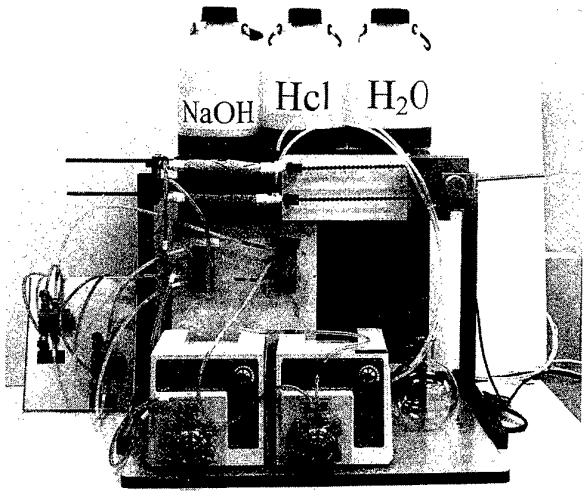
The isometric contraction, performed at a zero contraction rate, generates a force of 332 N with a response time (measured at 95% of the final steady state) of 1313 s for contraction and 505 s for relaxation. The isotonic contraction, performed with a 2 kg mass, leads to a maximum contraction rate of about 20% with a response time of 1430 s in contraction and 638 s in relaxation. It is interesting to note that in the case of our muscle the 332 N force value is equivalent to a force per section unit of 105 $N.cm^{-2}$, much higher than the value of 30 $N.cm^{-2}$ given by Caldwell for his muscle [CAL-93]. This force value is however the maximum one and it decreases until zero for a maximum contraction rate of about 20%.

CHEMOMECHANICAL ACTUATOR

The artificial muscle as previously designed can be completed by considering the notion of degree of freedom associated to a mechanical device driven by the actuator to obtain the principle of the artificial actuator. By putting two artificial muscles in antagonism, an original actuator is designed on the biceps-triceps model. Figure 3 presents the scheme of this association creating one degree of freedom to drive in rotation a body (a shaft in our experiment) around the cogwheel axle perpendicular to muscles plane. The shaft rotation is obtained by the contraction of the agonistic muscle and simultaneously by the relaxation of the antagonistic muscle. The chemomechanical actuator is composed of two muscles having the same characteristics: about 135 mm in initial length, 15 mm in initial radius, a 100% swelling percentage working material, a mass of about 69 g (17g of which being for the ion exchange polymer). These characteristics are close to those of the muscle used to test the isometric and the isotonic contractions previously presented except for the mass of the ion-exchange polymer confined in the rubber tube, which we have increased to generate a higher force. The maximum contraction force obtained is around 480 N to be compared with the 332 N reached with the previous muscle. A cogwheel of 62 mm diameter has been used to create the motor torque. The circulation of the stimulants is regulated under computer control by one peristaltic pump and one valve for each muscle. Each valve with three inputs permits the selection of the solution in the muscle.



a)



b)

Fig. 3 : Chemomechanical actuator experimental site, a) Principle scheme
b) Photography of the experimental site.

The actuator obtained can be controlled both in open-loop and closed-loop. The open-loop control feature is due to the McKibben muscle specificity [TON-94]. In this paper, we will only consider this open-loop approach. To bring to light the open-loop controllability of our chemomechanical actuator, we have performed several cycles of contraction/relaxation. First, one muscle is put in maximum relaxation state and the other one is put in maximum contraction state. By simultaneously making a NaOH solution circulate in the relaxed muscle to generate contraction, and HCl solution in the contracted muscle to generate relaxation, an arm rotation is obtained: the muscle in the contraction phase is the agonistic muscle, the one in the relaxation phase is the antagonistic one. When a predefined « high » angular position has been reached (6 degrees in this case), the valve positions shift, and the activating solutions sent into each muscle are inverted: the agonistic muscle becomes the antagonistic muscle (circulation of HCl), and the antagonistic becomes the agonistic muscle (circulation of NaOH). The arm rotates in the opposite direction. We can note that the delay between the control operation and the effective angular position change is about 320 s: this is due to the transportation time of the solution from the valve input to the muscle input, and also to the chemical reaction kinetics. The maximum angular position measured is inferior to 8 degrees. This value can be increased by choosing longer muscles or a smaller cogwheel diameter. When a predefined « low » angular position has been reached (3 degrees in this experience), the solutions circulating into each muscle are inverted again. This contraction/relaxation cycle is repeated 3 times on figure 4.

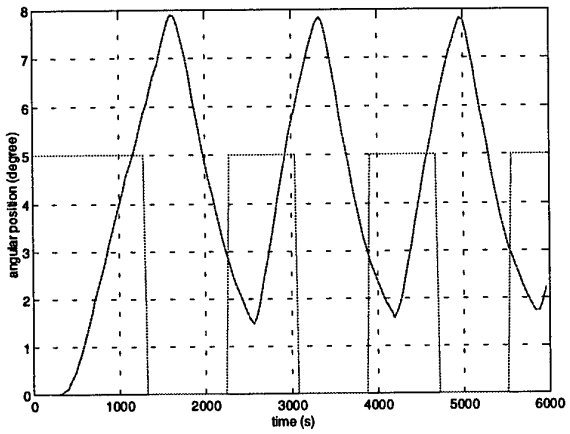


Fig. 4 : Actuator motion cycle in open-loop mode.

CONCLUSION

Classic actuators (electric, pneumatic, hydraulic) are generally rigid devices characterised by a low power/weight as well as power/size ratio. On the contrary, biological muscles present specific properties of softness, a relatively high power/weight and power/size ratio. The question is then to know if chemomechanical transformations allow artificial actuators on the model of biological actuators to be designed. In this paper we have reported works developed by the authors on a chemomechanical muscle using ion-exchange polymer placed inside an envelope of McKibben muscle type. Unlike a rigid cylindrical chamber, the considered McKibben envelope allows the generating of an axial contraction force that decrease with the contraction rate as done by the skeletal muscle, which gives spring-like softness, high maximum force/weight ratio and compactness. A pair of such muscles set in antagonism defines a compliant rotating actuator on the model of a biceps/triceps system. The generated maximum muscle force per section unit of about 100 Ncm^{-2} is satisfying however the contraction response time of about 1000 s remains excessive. Further research will examine possible improvements in response time by using polymeric gels activated by electric field.

REFERENCES

[CAL-93] **CALDWELL D.G.,** « *Natural and Artificial Muscle Element as Robot Actuators* », Mechatronics, Vol. 3, n°3, (1993)

[NIC-65] **NICKEL V.L., SAVILL D.L., KARCHAK A., JUN., ALLEN J.R.,** « *Synthetically Powered Orthotic Systems* », the Journal of Bone and Joint Surgery, Vol. 47-B, n°3, (1965)

[RIC-95] **RICARD A., AURELLE Y., LOPEZ P., TONDU B., VIAL D.,** « Chemomechanical Transformations of Gels - Artificial Muscles and Chemomechanical Actuators », Matériaux et Techniques, Dunod Editeur, to appear, (1995)

[SUZ-91] **SUZUKI M.,** « *Polymer Gels as a New Driving Source for Robotics, Micromachines and Biomedical Applications* », Int. J. Japan. Soc. Prec. Eng., Vol. 25, n°3, pp 169-174, (1991)

[TAN-82] **TANAKA T., NISHIO I., SUN S.T., UENO-NISHIO S.,** "*Collapse of Gels in an Electric Field*", Science, vol. 218, pp 467-469, (1982)

[TON-94] **TONDU B., BOITIER V., LOPEZ P.,** « *Naturally Compliant Robot-Arms Actuated by McKibben Artificial Muscles* », IEEE Int. Conf. on Systems, Man & Cybernetics, SMC 94, San Antonio, USA, (1994)

[TON-95] **TONDU B., LOPEZ P.,** « *Theory of an artificial pneumatic muscle and application to the modelling of McKibben artificial muscle* », C.R. Acad. Sci. Paris, t. 320, Série II*b*, p. 105-114 (1995)

[VIA-94] **VIAL D.,** « *Etude de la faisabilité d'un actionneur à muscles artificiels mécanochimiques* », Mémoire d'ingénieur-DEA, DGE, INSA de Toulouse, France, (1994)

Artificial muscles: Influence of electrolyte concentration on bilayer movement.

T.F. Otero, J.M. Sansiñena

Lab. de Electroquímica, Facultad de Química, Univ. del País Vasco. P.O. Box 1072. 20080 San Sebastián. Spain.

ABSTRACT

An electrochemomechanical device formed by a bilayer polypyrrole-non conducting polymer one side tape was studied in different concentrations of $LiClO_4$ aqueous solution. The artificial muscle was submited to a constant anodic current of 15mA or constant potential of 1000mV vs. SCE. Chronoamperograms and chronopotentiograms were recorded meanswhile the free end of the bilayer crossed over an angle of 90 degrees. The consumed charge was constant whatever the electrical or chemical conditions were. The electrical energy consumed by the device movement decreased, at increasing concentrations of electrolyte, under galvanostatic control. The consumed energy remains constant under potentiostatic control but times required to cross over the 90 degrees decrease from 20 seconds to 6 seconds.

1. INTRODUCTION

The transport of charge-compensating ions that accompanies electrochemical switching of polypyrrole between the conductive (oxidized) and semiconducting (reduced) states has elicited much attention in recent years[1]. A variation of volume between reduced and oxidized states of polymer has been observed during electrochemical oxidation/reduction processes. This variation of volume promote molecular strains into the polymer[2].

These facts have been known since the beginning of eighties and such polymers were applied as actuators able to change in a few micrometers its length to close or open an electrical circuit[3].

A bilayer structure polypyrrole-flexible and inactive polymer has been constructed to transform molecular strain in macroscopic movements[4-8]. Electrical currents trigger oxidation or reduction (chemical) processes developing a mechanical movement: the free end of the bilayer bends arround the fixed end more than 180 degrees in both senses during anodic or cathodic current flows. An electrochemomechanical device has been constructed.There are many similarities between this device and a muscle: an electrical pulse comes from the brain through the nervous system and triggers a chemical process in a muscle. The chemical energy stored in organic molecules is transformed by chemical reactions into mechanical energy; during this transformation a change of volume takes place, ionic and water fluxes are involved.

In this work bilayer movement for a same described angle (90º) from $LiClO_4$ aqueous solutions at different concentrations has been compared under both constant electrical current and constant electrical potential. Both consumed electrical charge (mC) and energy (mJ) by bilayer device has been calculated.

0-8194-2165-0/96/$6.00

2. EXPERIMENTAL

The polypyrrole electrogeneration, the construction of the bilayer and the bilayer test were described in previous papers[4-8]. The bilayer was put in $LiClO_4$ aqueous solutions at different concentrations to study electrolyte concentration influence on this electrochemomechanical device movement.

3. RESULTS

The movement through 90º of the free end of an electrochemomechanical device based on a bilayer constructed with polypyrrole and flexible-inactive polymer films has been studied. Electrochemomechanical properties were followed in different concentrations of $LiClO_4$ aqueous solution: 0.1, 0.25, 0.5, and 0.75M under galvanostatic (constant anodic current, I=15mA) and potentiostatic (constant anodic potential, E=1000mV) conditions.

3.1 Movement under a constant electrical current

The bilayer movement under a constant electrical current flow (15mA) shows an electrical potential decreasing at increasing electrolyte concentration (Fig.1).

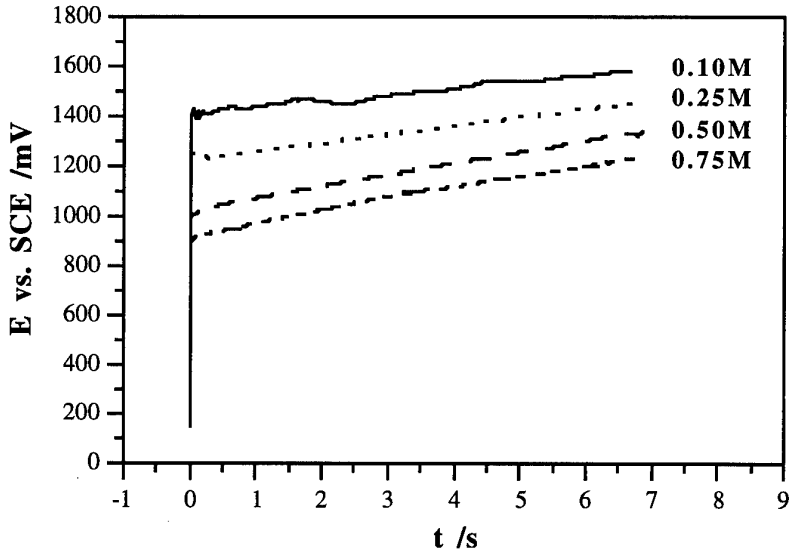


Fig.1: *Chronopotentiograms recorded along galvanostatic control (15mA) of a polypyrrole-non conducting polymer bilayer in different concentrations of LiClO4 aqueous solutions (see figure) The free end of the bilayer moves, along this time, through 9) degrees pushed by expansion in the conducting layer during its oxidation (anodic current).*

However required time to complete the movement is the same for every concentrations. Also taking into account that:

$$Q = \int I \, . \, dt \qquad (1)$$

Q = Electrical charge (C)
I = Electrical current (A)
t = Time (s)

consumed electrical charge by de bilayer has been calculated. The results obtained show a constant value of consumed electrical charge (100 mC) not depending on electrolyte concentration.

3.2 Movement under a constant electrical potential

The bilayer movement under a constant electrical potential (1000mV) shows that rising electrical current flow through the device at increasing electrolyte concentration (Fig.2). Also the device require longer polarizations to complete the movement at decreasing electrolyte concentrations. However the consumed electrical charge remains constant (100 mC) and independent of the electrolyte concentration.

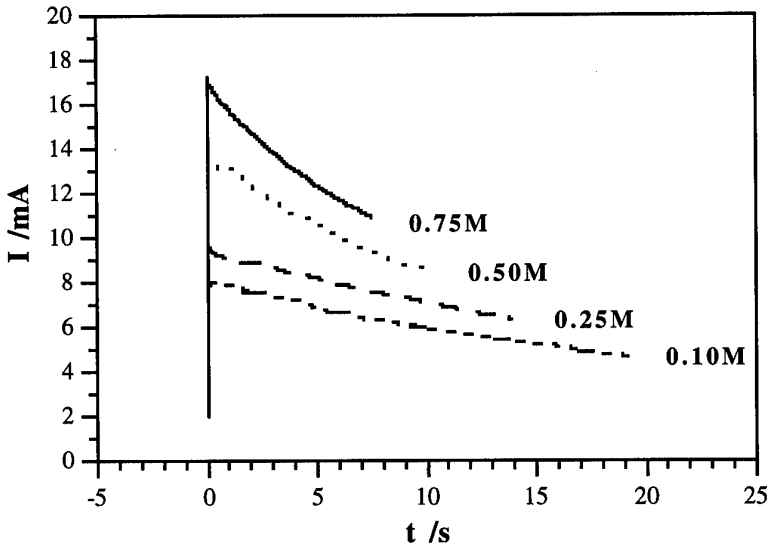


Fig.2: *Cronoamperograms obtained when a bilayer device was submited in different concentrations of $LiClO_4$ aqueous solutions: 0.1, 0.25, 0.5, and 0.75M to a potential steo from 0mV (vs. SCE) to 1000mV. Polarization was stoped when the free end of the bilayer described 90 degrees related to the starting position..*

Galvanostatic and potentiostatic results point to a proportionality between described angle and consumed charge. This proportionality remains independent on the electrolyte concentration, or the electrical variables, being those variables not limiting of the process. Under our experimental conditions not side reactions are detected and all the consumed charge is involved to oxidize polypyrrole film and on the subsequent bilayer movement. The macroscopic movement is related with microscopic volume change into polymer structure promoted by entrance of anions and water molecules from electrolyte solution. Entrance of a fixed amount of anions determines the volume change wich promotes a constant described angle.

On the other hand the rate of anions entrance is directly related to electrical current flow. Therefore electrical current flow is directly related to volume change rate into polymer structure and determine movement rate of bilayer device. This conclusion has been corroborated from obtained results on figures 1 and 2. Under a fixed electrical current flow bilayer device require a constant time to describe a constant angle (Fig.1). However this time decreases at higher electrical current flow (Fig.2).

3.3 Electrical energy consumed in the movement

Electrical energy consumed by the bilayer device (Fig.3) has been calculated from figures 1 and 2 taking into account that:

$$\mathbf{Ø = \int (I \,.\, E) \,.\, dt} \qquad (2)$$

Ø = Electrical energy (J)
I = Electrical current (A)
E = Electrical potential (V) vs. SCE
t = Time (s)

The obtained results show a linear decreasing of electrical energy consumed by the bilayer to cross over 90 degrees at increasing electrolyte concentrations when the movement was promoted by the flow of a constant current (15mA):

$$Ø = 133.22 - 63.735\ [LiClO4] \qquad r = 0.989 \qquad (3)$$

Therefore, at higher electrolyte concentrations, electrochemomechanical bilayer consumes lower amount of electrical energy (Fig.3) for a same developed kinetic energy (same required time to cross a same angle) (Fig.2).

On the other hand, consumed electrical energy remains constant (100mJ) when the movement was promoted by a constant electrical potential (1000mV vs. SCE). However the developed kinetic energy decreases at decreasing electrolyte concentration (larger required time to cross a same angle) (Fig.2).

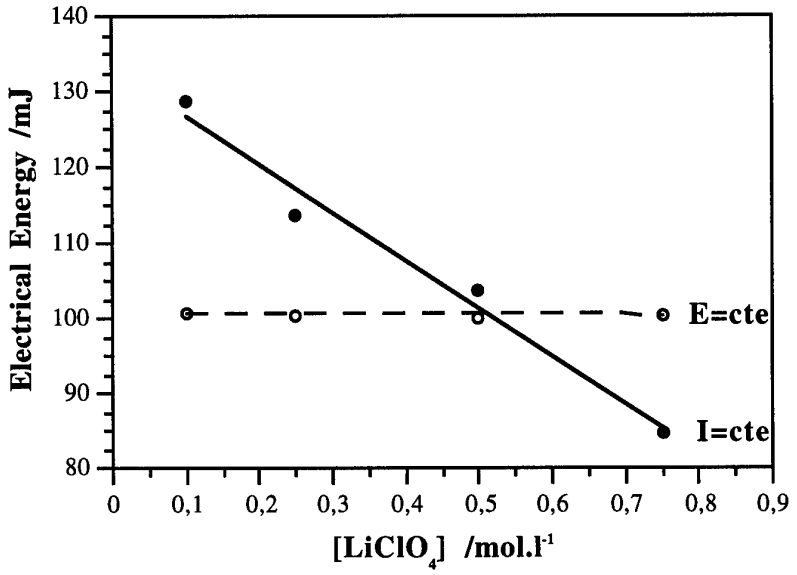


Fig.3: *Electrical energy consumed by a bilayer device during its movement from different $LiClO_4$ aqueous solutions concentrations for a same described angle (90 º) under different electrical conditions: (•) I= cte (15mA), (o) E= cte (1000mV).*

Under a constant current flow the electrical potential necessary to support a same rate of anions entrance decreases at higher electrolyte concentrations (Fig.2) being lower the consumed electrical energy (Fig.3). Also at a constant electrical potential the obtained results show that when electrolyte concentration increases electrical current flow rises increasing bilayer movement rate and decreasing required time to cross over a same angle (Fig.2). However the consumed electrical energy remains constant (Fig.3). Therefore an increase on the electrolyte concentration promotes an easier entrance of anions into polymer structure. The process of electrical energy tranformation into mechanical movement (kinetic energy) has a higher eficiency at increasing electrolyte concentration.

4. CONCLUSIONS

From experimental results it can be concluded that there is a direct dependence between bilayer described angle and consumed electrical charge not depending either on electrolyte concentration or on electrical conditions. The rate of anions entrance is directly related to electrical current flow. Also an electrolyte concentration increasing makes easy entrance of anions into polymer structure. The anions entrance rate rises for a same electrical potential but consumed electrical energy remains constant. Therefore an increase on the electrolyte concentration promotes an easier entrance of anions into polymer structure. The process of electrical energy tranformation into mechanical movement (kinetic energy) has a higher eficiency at increasing electrolyte concentration.

5. ACKNOWLEDGMENTS

This work has been supported by the Basque Government .

6. REFERENCES

1. Y-J. Qiu, J.R. Reynolds, "Dopant anion controlled ion transport behavior of polypyrrole", Polym. Eng. an Science, Vol. 31, pp. 417-421, 1991.
2. P. Marque and J. Roncali, "Structural effect on the redox thermodynamics of poly(tiophenes)", J. Phys. Chem., Vol. 94, pp. 8614-8617, 1990.
3. R.H. Baughman and L.W. Shaklette, Science. and Applications of Conducting Polymers, IOP Publishers Ltd., pp. 47-61, 1990.
4. T.F. Otero, E. Angulo, J. Rodriguez and C. Santamaría, Patents EP-9200095 and EP-9202628, 1992.
5. T.F. Otero, J. Rodriguez, Intrinsically Conducting Polymers: An Emerging Technology, Kluwer Ac. Publishers, 1993.
6. T.F. Otero, E. Angulo, J. Rodriguez and C.Santamaría, "Electrochemomechanical properties from a bilayer: polypyrrole/non-conducting and flexible material- artificial muscle", J. Electroanal. Chemical, Vol. 341, pp. 369-375, 1992.
7. T.F. Otero, J. Rodriguez, and C. Santamaría, "Artificial muscles from bilayer structures", Synth. Met., Vol. 57, pp. 3713-3717, 1993.
8. T.F. Otero, J. Rodriguez and C. Santamaría, "Smart muscle under electrochemical control of molecular movement in polypyrrole films", Mat.Res.Soc.Symp., Vol. 330, pp. 333-338, 1994.

CONDUCTING POLYMER ELECTROMECHANICS: A CONTINUUM MODEL OF PASSIVE MECHANICAL PROPERTIES

A. Della Santa, A. Mazzoldi, C. Tonci, D. De Rossi

°Centro "E.Piaggio", Faculty of Engineering, University of Pisa, Via Diotisalvi 2, 56126 Pisa, Italy.

ABSTRACT

Several porous material systems (e.g.. hydrogels, conducting polymers, electrorheologic fluids) make possible a control of their properties in response to an appropriate stimulus (and viceversa) and therefore. they belong to the class of intelligent materials.
In the present paper we propose a first classification of intelligent porous systems dividing them in three main classes: porous material as semi-permeable media, as reservoir and delivery systems and as biphasic composites with large interfacial area between solid and fluid phases.
Then we present a continuos model to describe the passive mechanical behaviour of a generic porous conducting polymer saturated by a fluid. The model is solved for a stress-relaxation test and it is verified in the specific case of a doped polypyrrole porous matrix saturated by an electrolytic solution. The goodness of fit between experimental date and theoretical data confirms the validity of the model.

INTRODUCTION

Several material systems present a porous morphology. Many of them are three-dimensional solid systems, in which the porosity maximises the contact surface with the external environment, as well as the rouhness in two-dimensional systems. The extension of exchange surface gains importance whenever chemical reactions have to be promoted; for instance, this need is present in the field of battery electrodes and chemical sensors. However, such devices are passive and they do not possess any apparent connotation of intelligent behaviour. If we focus our attention on porous intelligent materials, we usually find that pores host a fundamental component of the system and that they play an important role in the device functioning.
In Table I, we propose a tentative classification of intelligent porous systems by subdividing them in three main classes.
The first two classes fall within the field of intelligent chemical systems. These systems aim to control chemical reactions by stimulating and regulating transport of chemical species across dynamic membranes, whose chemical and/or physical properties vary in response to an appropriate stimulus (temperature, pH changes, UV light, electric signal). Dynamic control of membrane characteristics can regard gas permeability, ion permeability, molecular size selectivity, etc. [1, 2, 3, 4].
The third class is very wide if we wish to consider all porous material systems, in which the pores host the fluid phase and represent the interface between the two phases For instance porous electrodes and porous surfaces also could fall within this class; however, in this case the function of pores is mainly morphological, i.e. to maximise the surface for chemical reactions, without any connotation of active behaviour. Viceversa, whenever a transducing effect is associated to at least one of the two constituent phases, this class of porous materials can be viewed as a subset of the wide class of electrochemo-mechanical intelligent systems. These systems should be able to mechanical act on themselves and/or on the external environment in response to an appropriate electrical or chemical stimulus, transducing electrical or chemical energy in mechanical energy. Many of them are porous polymeric solids or gels, saturated by an appropriate fluid phase. A single or both the phases can present transducing properties. The driving signal can be pH changes in the fluid phase, an electrochemical reaction between the two phases, an appropriate electric signal imposed to the solid or fluid phase [5, 6, 7, 8].
Physical modelling of this class of materials is quite complicate. The main goal of a continuum model should be to find relationships among material characteristics (i.e. porosity, elastic moduli, friction coefficients, etc.) and device characteristics and performances (i.e. actuation strain and force, mechanical response time, etc.).
The complexity of the problem can be split into two steps:

- modelling of the mechanical behaviour of the material system in passive conditions; analysis of standard tests can be useful (i.e. creep test, stress-relaxation test, stress-strain test, etc.);
- modelling of the active behaviour by describing the transducing phenomena; the difficulty of this second step resides in the coupling between mechanical and electrochemical phenomena.

The present paper presents a continuos model of the passive mechanical behaviour of a generic porous conducting polymer saturated by a fluid. Then, the model is solved for a stress-relaxation test and it is tested with regard to the experimental data for the specific case of doped polypyrrole porous matrix saturated by an

0-8194-2165-0/96/$6.00

electrolytic solution. This material system has been already studied; electromechanical charaterisation of its actuating properties has been carried out [9] and a discrete lumped parameter model has been identified. The goodness of fit between experimental date and theoretical data confirms the validity of the model.

TABLE 1: *Classification of intelligent porous material systems*

	Pores Function	Intelligence	Material	Applications
Porous materials as semi-permeable media	Pores are channel for fluid or gas flux through the solid matrix	Tuneable permeability by controlling the size and electrical properties of pores	Hydrogels Conducting polymers	Selective membrane for chemical sensors and valves[1,2,3]
Porous material as reservoir and delivery systems	Pores are reservoirs for trapped molecules which can be delivered in a controlled way	Tuneable delivery by controlling the size of pores	Hydrogels	Drug delivery systems[4]
Porous materials as biphasic composites with large interfacing area between solid and fluid phases	Pores host the fluid phase and control with their size and morphology the mechanical and chemical interactions between the two phases	Control of volume and stiffness changes. Control of fluid-solid friction coefficients	Hydrogels Conducting polymers Electro-rheologic fluids	Muscle-like actuators Adaptive structures for noise suppression Transducers for force-feedback[5,6,7,8]

1. A CONTINUOUS MODEL FOR POROELASTIC SYSTEM

In order to describe the mechanical behaviour of a generic porous system we will utilise the poroelastic theory of Biot [10] successfully modified and applied to charged polyelectrolyte gels [11] and extended here to fluid-saturated conducting polymers.

The following hypotheses are used: small deformations (as in the classical theory of elasticity); porous elastic and isotropic solid matrix; newtonian fluid saturating the pores; viscous friction between solid and fluid phases; constant density of the solid and fluid constituents; negligible thermoelastic effects.

1.1. General equations

The stress tensor in the porous material is the sum of the fluid and solid tensor. The stress tensors of solid phase, σ_{ij}^{s} ,and fluid phase, σ_{ij}^{f}, are defined as follows: if we consider a cube of unit size of the bulk porous material, o_{ij}^{s} represents the tension applied to the solid portion of the cube faces while σ_{ij}^{f} represents the pressure applied to the fluid portion of the cube faces. The previous definition together with the hypothesis of newtonian fluid imply that $\sigma_{ij}^{f} = - \beta P \delta_{ij}$, where β is the porosity of the material, P is the fluid hydrostatic pressure in the pores and δ_{ij} is the delta of Kronecker. The total stress tensor σ_{ij}^{tot} becomes:

$$\sigma_{ij}^{tot} = \sigma_{ij}^{s} + \sigma_{ij}^{f} = \sigma_{ij}^{s} - \beta P \delta_{ij} \tag{1}$$

The strain tensors of solid, ε_{ij}^{s} , and of fluid, ε_{ij}^{f} , are defined as in the classical elasticity theory; we will make use of two other quantities (ε^{s}, ε^{f}) corresponding to the traces of the solid and fluid strain tensors. The quantity ε^{s} is usually referred as the *dilatation field* of the material.

In the hypothesis of conservative system, the constitutive equations of the porous material are:

$$\sigma_{ij}^{s} = 2N\varepsilon_{ij}^{s} + A\varepsilon^{s}\delta_{ij} + Q\varepsilon^{f}\delta_{ij} \tag{2}$$

$$\sigma_{ij}^{f} = Q\varepsilon^{s}\delta_{ij} + R\varepsilon^{f}\delta_{ij} \tag{3}$$

where N, A, Q, R are the characteristic parameters of the poroelastic theory [10].

In order to solve the dynamic problem, the three following equation are provided:

i. the equilibrium equation of the total stress field (in which we neglect the body force, $\rho \ddot{x}$):

$$\mathrm{div}\,\sigma_{ij}^{tot} = 0 \tag{4}$$

ii. the flux equation (Darcy law):

$$\nabla P = -f\frac{\partial}{\partial t}\left(\underline{u}^f - \underline{u}^s\right) \tag{5}$$

where f is the solid-fluid friction coefficient and $\underline{u}^f$ and $\underline{u}^s$ are the fluid and solid displacement vectors; if we take the divergence of equations (5) we can express $\underline{u}^f$ and $\underline{u}^s$ in terms of the strain tensors:

$$\nabla^2 P = -f\frac{\partial}{\partial t}\left(\varepsilon^f - \varepsilon^s\right) \tag{6}$$

iii. the continuity equation of the porous material:

$$\frac{\partial}{\partial t}\left[(1-\beta)\varepsilon^s + \beta\varepsilon^f\right] = 0 \tag{7}$$

From the previous equations, the motion law can be obtained:

$$\frac{\partial \varepsilon^s}{\partial t} = \frac{1}{f}\frac{2N-(A-Q^2/R)}{1+Q/R}\nabla^2\varepsilon^s \tag{8}$$

1.2. Case of incompressible composite material

The case of incompressible porous material corresponds to the condition [10]:

$$\varepsilon^f = -\frac{1-\beta}{\beta}\varepsilon^s \tag{9}$$

By means of relation (9), equations (2), (6) and (8) simplify to:

$$\sigma_{ij}^s = 2N\varepsilon_{ij}^s + \left(A - Q\frac{1-\beta}{\beta}\right)\varepsilon^s\delta_{ij} \tag{10}$$

$$\nabla^2 P = \frac{f}{\beta}\frac{\partial \varepsilon^s}{\partial t} \tag{11}$$

$$\frac{\partial \varepsilon^s}{\partial t} = \frac{1}{f}\left(2N + A - Q\frac{1-\beta}{\beta}\right)\nabla^2\varepsilon^s \tag{12}$$

In this form we can easily recognise that the coefficients N and $(A\text{-}Q(1\text{-}\beta)/\beta)$ play the same mathematical role of the well-known λ and μ Lamè coefficients. Moreover we can make use of the relation between the Lamè coefficients and the Young elastic modulus E and the Poisson ratio ν and we can rewrite the equations (10) and (12) in terms of these coefficients, easier to measure. The new forms of constitutive equations and motion law are:

$$\sigma_{ij}^s = \frac{E}{1+\nu}\varepsilon_{ij}^s + \frac{\nu E}{(1+\nu)(1-2\nu)}\varepsilon^s\delta_{ij} \tag{13}$$

$$\frac{\partial \varepsilon^s}{\partial t} = \frac{1}{f}\frac{(1-\nu)E}{(1+\nu)(1-2\nu)}\nabla^2\varepsilon^s \tag{14}$$

1.3. Case of stress-relaxation of a thin strip sample

The mechanical model is applied to a stress-relaxation experiment carried out in the case of simplified geometry. The sample is a thin strip (length l, width b, thickness a); a cartesian system of coordinates is fixed with the x, y, z axis parallel to sample length, width and thickness respectively. We suppose that the sample length is elongated by a strain ε_0 (along the x-direction) and we calculate the tensile force $F(t)$ along the same direction, as a function of time during stress-relaxation. The thickness of the thin, planar strip is assumed to be negligible in respect to the other dimensions; the system is also assumed to be invariant in respect to translations along the planar coordinates x and y during the experiment. Under these assumptions, the strain components do not depend on the x and y coordinates, and equation (14) reduces to:

$$\frac{\partial \varepsilon^s}{\partial t} = \frac{1}{f}\frac{(1-\nu)E}{(1+\nu)(1-2\nu)}\frac{\partial^2\varepsilon^s}{\partial z^2} \tag{15}$$

The previous equation can be solved, once the initial and boundary conditions on the dilatation field ε^s have been fixed. At the stretching initial time $t=0^+$, the sample behaviour is assumed to be isovolumic: $\varepsilon^s(z,t=0^+)=0$; it means that the rise-time of the displacement step can be considered much smaller than the measured time-constant of swelling or relaxation of the polymer matrix and the hypothesis will be verified a-posteriori. At the final relaxed state ($t\to\infty$), the dilatation field ε^s will be the same of a standard elastic body: $\varepsilon^s(z,\ t\to\infty)=(1-2\nu)\varepsilon_0$. As far as boundary conditions are concerned, we hypothesise that an infinitesimally thin superficial layer of the sample ($z=\pm a/2$) instantaneously swells to its steady state: $\varepsilon^s(z=\pm a/2,\ t)=(1-2\nu)\varepsilon_0$.
The analytical solution of equation (15), under the previous conditions, is [12]:

$$\varepsilon^s=\varepsilon_0(1-2\nu)\left[1-\sum_{n=0}^{\infty}w_n(t,\tau)\cos\left(\frac{(2n+1)\pi z}{a}\right)\right]$$
$$\text{where: } w_n(t,\tau)=\frac{4(-1)^n}{(2n+1)\pi}\exp\left(-\frac{(2n+1)^2 t}{\tau}\right) \text{ and } \tau=\frac{a^2 f}{\pi^2}\frac{(1+\nu)(1-2\nu)}{E(1-\nu)} \tag{16}$$

The characteristic time τ represents the decay time of the first exponential term of the sum in previous equation. From the expression (16), it can be verified that the dilatation field ε^s is zero both prior to and immediately following the imposed stretch, so that the stretch is effectively isovolumic (note that the sum of the series $w_n(t,\tau)$ approximates 1); as t/τ increases, the sample swells towards the final steady state in which it is uniformly dilated. A discontinuity is present at the superficial layer ($z=\pm a/2$), where the dilatation field immediately reaches its steady-state.
The total tensile stress along the stretching x-direction, $\sigma_{xx}^{tot}(z,t)$, is the sum of two terms, as equation (1) shows: the internal elastic stress of the polymeric solid phase, $\sigma_{xx}^{s}(z,t)$ and a term which takes into account the interstitial fluid pressure. The first term can be easily obtained by substituting the expression (16) of $\varepsilon^s(z,t)$, together with the condition $\varepsilon_{xx}=\varepsilon_0$, in the constitutive equation (13):

$$\sigma_{xx}^{s}=\frac{E}{1+\nu}\varepsilon_0+\frac{\nu E}{(1+\nu)(1-2\nu)}\varepsilon^s=E\varepsilon_0-\frac{\nu E}{(1+\nu)}\varepsilon_0\sum_{n=0}^{N}w_n(t,\tau)\cos\left(\frac{(2n+1)\pi z}{a}\right) \tag{17}$$

The second term can be computed by solving equation (11); again the state variable, i.e. the fluid pressure P, is assumed to be variant only in the z-direction. The imposed boundary condition is zero pressure on the superficial layer of the sample: $P(z=\pm a/2,\ t)=0$. We obtain:

$$P(z,t)=\frac{1}{\beta}\frac{(1-\nu)E}{(1+\nu)(1-2\nu)}\left[\varepsilon^s-\varepsilon_0(1-2\nu)\right]=-\frac{1}{\beta}\frac{(1-\nu)E}{(1+\nu)}\varepsilon_0\sum_{n=0}^{N}w_n(t,\tau)\cos\left(\frac{(2n+1)\pi z}{a}\right) \tag{18}$$

Hence, the total stress is:

$$\sigma_{xx}^{tot}=\sigma_{xx}^{s}-\beta P=E\varepsilon_0+\frac{(1-2\nu)E}{(1+\nu)}\varepsilon_0\sum_{n=0}^{N}w_n(t,\tau)\cos\left(\frac{(2n+1)\pi z}{a}\right) \tag{19}$$

Let us discuss the results of previous expressions on the longitudinal median axis of the sample ($z=0$). After the stretch, the elastic stress jumps from 0 to $[E/(1+\nu)]\varepsilon_0$ and then it increases exponentially to its final value, $E\varepsilon_0$. The interstitial fluid pressure jumps from 0 to $-[(1-\nu)E]/[(1+\nu)\beta]\varepsilon_0$ (a negative pressure indicates suction of fluid from the external bath); then it asymptotically approaches the reference external bath pressure, equal to 0. Finally, the total stress decays in a monotonic, multi-exponential fashion, from its initial value, $[(2-\nu)E/(1+\nu)]\varepsilon_0$ to the final value, $E\varepsilon_0$.
In order to calculate the total force, we integrate the total stress over sample cross-sectional area. This integration is quite heavy and it can be found in literature [11]. The expression of the force is again complicate, but it can be widely simplified if a constant cross-sectional area during the stress-relaxation is supposed. In this case, we obtain:

$$F(t)=abE\varepsilon_0\left[1+\frac{(1-2\nu)}{(1+\nu)}\sum_{n=0}^{N}\frac{8}{\pi^2}\frac{1}{(2n+1)^2}\exp\left(-\frac{(2n+1)^2 t}{\tau}\right)\right] \tag{20}$$

At $t=0^+$ the force jumps to $abE(2-\nu)/(1+\nu)\varepsilon_0$ and then relaxes to its final, lower value, $abE\varepsilon_0$, coincident with the internal elastic force exerted by the polymeric solid phase.

2. MODEL TESTING

In this paragraph we test the stress relaxation experiment model with regard to the experimental data for the specific case of a porous conducting polymer matrix saturated by an electrolytic solution. The polymer is polypyrrole (PPy) doped with benzensulfonate anions provided by BASF AG (Germany) and the solution is sodiumbenzensulfonate (10^{-2} M) in a mixture of acetonitrile (95% in volume) and distilled water (5% in volume).

As equation (20) shows, the theoretical force relaxation curve depends on the values of 3 mechanical parameters (the Young modulus E, the Poisson ratio ν, the friction coefficient f) and 3 geometrical parameters (the porosity β, the thickness a, the width b). In order to verify the model, first of all it is necessary to measure the value of all these parameters by means of indipendent experiments. The Young modulus has been measured through stress-strain tests performed by means of a servo-controlled actuator (Model 300H Cambridge Technology Inc., USA); the Poisson ratio has been estimated by measuring the transversal deformation of wet portion of polymer sample during longitudinal stress-strain test; such deformation is detected by a photonic displacement transducer (Model KD-100, MTI Instruments, USA); the friction factor has been deduced from the characterist time of free-swelling tests performed by means of an isotonic displacement transducer (Model 7006 Basile, Italy); finally the porosity has been measured with a porosimeter (Sorptomatic 1900, Carlo Erba, Italy), while the width and the thickness have been evaluated with an optical microscope. The results of these experiments are reported in Table 2, where the average values and the variability range of the 4 parameters are shown.

The second step in model identification consist of an "*a posteriori* estimation" of the same parameters. The model has been solved for a suitable and meaningful case, that is a stress-relaxation test, and the results have been compared with the experimental data coming from the same test. The error between theoretical and experimental data can be minimised by varying the model parameters; if these values of the parameters fall in the variability range estimated by the previous indipendent direct experiments, the model works.

Stress-relaxation tests have been carried out on a polymer thin strip 90 mm long; the lower extremity of the strip is mechanically fixed by a clamp at the bottom of the cell, while the upper extremity is attached to the lever of the servo-controlled actuator; an automatic data acquisition and control system senses the displacement of the lever, sets it at the prescribed position and records the force during the measurement time. A small pre-stretching is imposed to the strip in order to work in elastic field, then, at the time $t=0^+$ the strip is elongated along the x-direction and the isometric tensile force $F(t)$ along the same direction is measured during the stress-relaxation.

The fitting of the theoretical expression of force $F(t)$ to the experimental data $F^*(t)$ has been carried out by means of a chi-square estimation of the error:

$$\aleph^2 = \sum_{i=1}^{N} \left[\frac{F(t_i, \mathbf{a}) - F^*(t_i)}{\sigma^2(t_i)} \right]^2 \qquad (21)$$

where $\mathbf{a}$ is the vector of parameters to be determined in order to minimise the error; in our case: $\mathbf{a}=[E\ \nu\ f\ \beta\ a\ b]$. The algorithm for the minimisation of error function is the Nelder-Meads simplex method; it is an iterative, direct search method. The values of parameters are showed in Table 3; note that they fall in (or close to) the variability range which have been *a-priori* estimated. The characteristic time τ is equal to 5.12 sec.

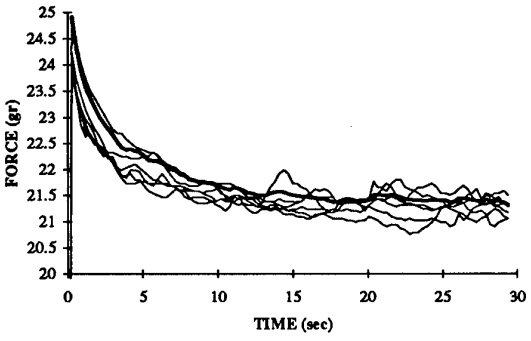


***Figure 1**: Force-relaxation experimental curve (the bold line is the average curve)*

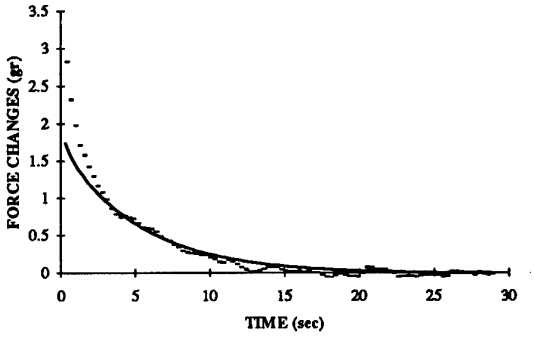


***Figure 2**. Theoretical and experimental (-) stress-relaxation curves*

TABLE 2: *Experimental values.*

E	1200 ± 73 MPa
ν	0.426 ± 0.029
f	$(1.25 \pm 0.1)\ 10^{20}$ Nsm^{-4}
β	0.108 ± 0.01
a	32 ± 3 μm
b	1 ± 0.1 mm

TABLE 3: *Estimated values*

E	1290 MPa
ν	0.412
f	$1.29\ 10^{20}$ Nsm^{-4}
β	0.1
a	35 ± 3 μm
b	1.1 mm

However the theoretical force-relaxation curve doesn't fit the first 4-5 seconds of the experimental one which shows a faster decay (Fig.2); this error could be explained by supposing that the polymeric matrix is viscoleastic by itself. This fact was not included among the theoretical hypotheses, altough it was experimentally noticed in stress-relaxation tests of the dry sample, in which a characteristic time of about 1 sec was evidenced.

CONCLUSIONS

We have proposed a first classification of intelligent porous systems by dividing them in three main classes: porous material as semi-permeable media, as reservoir and delivery systems and as biphasic composites with large interfacial area between solid and fluid phases.

The mechanical behaviour of a porous conducting polymer saturated by an electrolyte fluid has been modelled both in static and dynamic conditions with a continuum poroelastic model. The model has been applied to a specific material system, wet PPy doped with benzensulfonate and it demonstrates to fit quite well.

The fitting between theoretical and experimental curves of a stress-relaxation test has allowed to estimate the values of the 3 material parameters (E, ν, f) and of the 3 geometrical parameters (β, a, b); these values fall in the variability range deduced by the previous indipendent measurements of the same parameters.

The model shows that the characteristic time the materials system is proportional to the friction between the two phases while it is inversely proportional to the stiffness of the polymer. What is more, the response time depends on the square of polymer strip thickness. This last issue indicates that the material configuration needs to be scaled down. Acting on these terms a material with suitable dynamic behaviour could be designed.

REFERENCES

[1] P.E. Grimishaw, A.J. Grodzinsky, M.L. Yarmush and D.M. Yarmush, "Dynamic membranes for protein transport: chemical and electrical control", *Chem. Eng. Sc.*, vol.44, n.4, pp.827-840, 1989.

[2] P.J. Riley and G.G. Wallace, "Intelligent chemical system based on conductive electroactive polymer", *J. of Int. Mat. Sys. & Str.*, vol.2, n.2, pp.228-238, 1991.

[3] P. Burgmayer and R. W. Murray, "Ion gate electrodes", *J. Phys. Chem.*, vol.88, pp.2515-2521, 1984.

[4] W. Xue Shen, A.S. Hoffman and P. Yager, "Synthesis of and insulin release from erodible, poly(N-isopropylacrylamide)-phospholipid composites", *J. of Int. Mat. Sys. & Str.*, vol. 4 n 2, pp. 202-209, Apr. 1993.

[5] R.P. Hamlen, C.E. Kent, S.N. Shafer, "Electrolytically activated contractile polymer", *Nature*, vol.206, pp.1149-1150, 1965.

[6] D. De Rossi, P. Chiarelli, G. Buzzigoli, C. Domenici and L. Lazzeri, "Contractile behaviour of electrically activated mechanochemical polymer actuators", *Trans. Am. Artif. Int. Organs*, vol.22, pp.157-162, 1986.

[7] R.H. Baughman, L.W. Shacklette, "Application of dopant-induced structure-property changes of conducting polymers", *Science and Application of Conducting Polymer,* W.R. Saleneck, D.T. Clark, E.J. Samuelsen, ed.Adam Hilger, pp.47-61, New York, 1990.

[8] C.A. Rogers, "Intelligent material systems: the dawn of a new materials age", *J. of Int. Mat. Sys. & Str.*, vol.4, n.1, pp.4-12, 1993.

[9] P. Chiarelli, A. Della Santa, D. De Rossi, A. Mazzoldi, "Actuation properties of electrochemical driven polypyrrole free standing films", *J. of Int. Mat. Sys. & Str.*, vol.6, n.1, pp.32-37, 1995

[10] M. Biot, "Theory of elasticity and consolidation for a porous anisotropic solid", *J. of Appl. Phys.*, vol.26, n.1, pp182-185, 1955.

[11] P. Chiarelli, P.J. Basser, D. De Rossi, S. Goldstein, "The dynamic of a hydrogel strip", *Biorheology*, vol 29, pp. 383-398, 1992.

[12] G. Carrier, C. Pearson, *Partial differential equations: theory and tecnique*, Academic Press, p.320, 1976.

Polymer composites for temperature and current sensors

Ralf Strümpler

ABB Corporate Research, CH-5405 Baden-Dättwil, Switzerland

ABSTRACT

The electrical resistivity of polymer composites is studied as a function of temperature. The initial resistivity ρ of thermoplastic or thermoset containing a metallic filler is in the range of $1 - 10 \cdot 10^{-2}$ Ω·cm. Around curing temperature of epoxies, the resistivity increases by *eight to twelve orders of magnitude*. For thermoplastic polymers, however, the transition temperature is related to the melting temperature at which a strong volume increase occurs. Hence, the choice of polymer and its processing determine the transition temperature from a conducting state to an insulating state. For a variety of polymers we have observed transitions between 80 °C and 200 °C. Due to a sharp and strong transition at a predetermined temperature, such materials can be used as temperature sensors. Since the resistivity of the cold state is low, they can also carry rather high currents. The balance between heating and cooling determines then a critical value for the current. Thus, the materials can also serve as a current sensors.

1. INTRODUCTION

Intelligent materials are designed to perform both sensing and actuating functions. They are capable to detect a change in the environment and to respond to it in a technical useful way. Among the stimuli, which are interesting to sense in electrotechnical applications, are temperature, pressure, electrical current, electric field, and vibration. Among the useful responses are cooling, heating, change of electrical resistance, mechanical damping, or acoustic damping. A number of intelligent or smart materials with such response have already been proposed[1 - 4].

Sensing of temperature and current is the main objective of this work. Temperature sensors can be prepared from semiconductors with relative large negative temperature coefficient (NTC) of resistance. The dominant effect is the thermal activation of charge carriers over the bandgap. As the temperature increases, additional charge carriers are available and the resistivity drops. The magnitude of this effect is limited to several percent change in resistance value per degree[5].

Positive temperature coefficient of resistance (PTC) thermistors, on the other hand, can display a stronger increase in electrical resistance with increasing temperature. Donor-doped $BaTiO_3$ ceramic is widely used, which exhibits a change in resistivity of four to six orders of magnitude around the ferroelectric Curie temperature[5]. The disadvantages of relatively large room temperature (RT) resistivity ($\approx$100 Ωcm) and high manufacturing cost have been overcome by the development of polymer composite thermistors. Besides their ease of processing, they exhibit resistivity changes of six to eight orders of magnitude within several degrees of temperature and RT resistivities down to 0.5 Ω·cm [6-9]. This has led to the development of commercial current sensors and limiters by Raychem[10] and for high power ratings by ABB Control (PROLIM®)[11].

In the case of thermistors based on a semi-crystalline polymer matrix, the PTC effect occurs around the melting temperature of the polymer. It is generally attributed to the step-like change in specific volume of the polymer caused by the phase transition[6,7,10]. For epoxy composites, on the other hand, it was shown recently, that the origin of the PTC effect is also related to the expansion of the polymer. But in this case the expansion is determined by relaxation of stresses which were built-up during the curing process[12].

For the application as a temperature sensor, an essential aspect is the ability to vary the transition (critical) temperature T_c. Due to the melting temperature of the commonly used polyethylene and the sort of epoxies, which were studied so far, the reported T_c values are confined to the range of 50 - 135 °C.

An increase of T_c is also of special interest in overcurrent protection devices as the maximum operating current rating is increased. During normal operation an equilibrium is established between Joule heating of the PTC device and its cooling. Since cooling by convection is proportional to the temperature difference ΔT between the PTC and the

0-8194-2165-0/96/$6.00

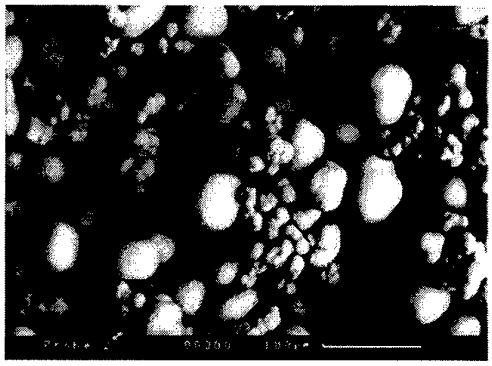


Fig. 1 Scanning electron micro-graph of Ni powder. The white bar indicates a length of 100 μm.

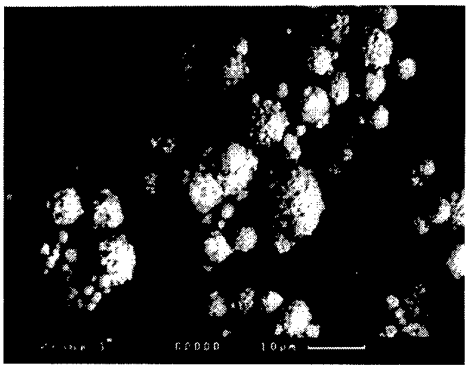


Fig. 2 Scanning electron micro-graph of Ni/Ag powder. The white bar indicates a length of 10 μm.

environment and cooling by radiation is even proportional to $(\Delta T)^4$, a higher T_c means that a higher power loss becomes possible. Hence, the current rating can be extended.

In the present work, the influence of different filler materials and polymers on the RT resistivity, the resistivity increase and the transition temperature are studied. New PTC materials are described, which offer transitions at temperatures >> 135 °C and also exhibit very low RT resistivities. Therefore, they are highly suitable for the use as temperature sensors, current sensors and current limiters.

2. EXPERIMENTAL

Low electrical resistivities can be achieved by mixing metallic powders into the polymer matrix. In order to study the influence of the filler hardness and morphology on the electrical properties, three different materials were used. Ni powder with particle sizes ranging from 40 to 80 μm and Ag-coated Ni powder (20 - 80 μm) was supplied byNovametInc. Scanning electron micro-graphs of some typical Ni and Ni/Ag particles are shown in Figs. 1 and 2, respectively.

Both powders have nearly spherical shape, but the pure Ni particles have a smoother surface than the Ag-coated particles. A further filler material is TiB_2 powder from Cerac Inc., which has a broad particle size distribution between 40 – 200 μm. It was sieved to fractions of 63 - 100 μm and 100 - 200 μm. A further filler material is TiB_2 powder from Cerac Inc., which has a broad particle size distribution between 40 – 200 μm. It was sieved to fractions of 63 - 100 μm and 100 - 200 μm.

Fig. 3 shows the irregular shaped TiB_2 particles embedded in an epoxy matrix. Polycrystalline TiB_2 has an electrical resistivity of about 15 μΩ·cm at room temperature[13]. With a Vickers hardness of 15-36 GPa[14], it is a very hard material compared to Ni (0.69 GPa) and Ag (0.26 GPa)[15].

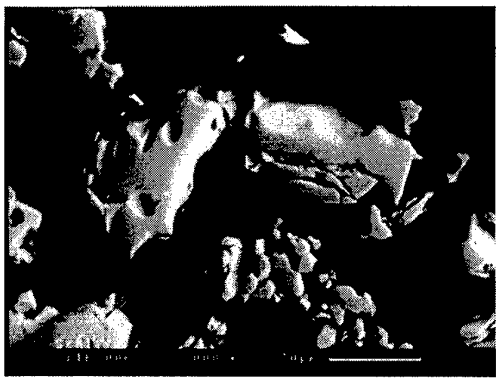


Fig. 3 Scanning electron micro-graph of Spurr B / 43 vol.% TiB_2 (60-100 μm). The white bar indicates a length of 30 μm.

Thermoset and thermoplastic materials were used to form composites. The thermoset systems were Spurr B supplied by Polysciences Inc., Araldit F / HY 905 (1:1) by Ciba Geigy, and Epikote 828 / Epicure MNA / HY 960 (100:90:1) by Shell. In order to avoid inhomogeneities due to settling of the filler particles, the preparation of epoxy composites was restricted to high filler fractions close to the tap density of the powder. The metal powder was tapped into a silicone mold, degassed in slight vacuum at 50 mbar for 30 min. and infiltrated in situ with the epoxy. Spurr B epoxy was cured for 20 - 24 h at 80 °C or 120 °C. Araldit F was heated for 20 h to 140 °C, followed by an optional curing at 180 °C for 2 h. A sequence of 160°C for 2 h, 140 °C for 16 h and 200 °C for 2h was used to cure the Epikote epoxy. The filler content was determined by measuring the mass density of the cured composite. With a Perkin Elmer DSC 7 Differential Scanning Calorimeter the glass transition temperature was measured.

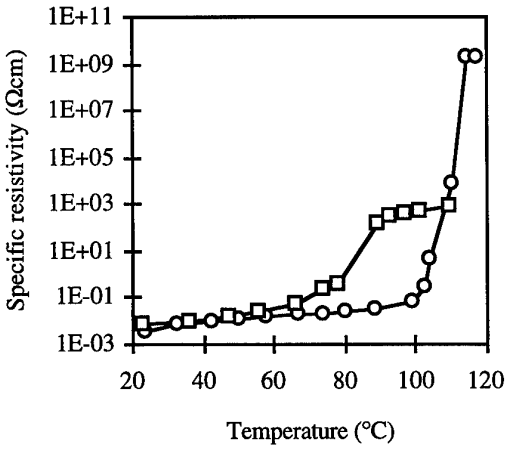


Fig. 4 Specific resistivity as a function of temperature of Spurr B / 66 vol.% Ni (O)and Spurr / 30 vol.% Ni/Ag (□)cured for 20 h at 80 °C.

Thermoplastic composites were compounded using a shear-mixer (Brabender Plasticorder). High-density polyethylene (HDPE, Lupolen 5231 X, BASF) was mixed with the pre-heated filler powder for 10 min. at a temperature of 180 °C. Several mm thick plates were then formed in a hot-press within 3 min. at 145 °C and 139 MPa. Polyphenylene sulfide (PPS, Ryton V1, Philips Petrol) composites were compounded for 10 min. at 290 °C and pressed to plates at 300 °C (3 min.) and 139 MPa .

The dependence of the resistivity on temperature was tested using a Novocontrol Broadband Dielectric Spectrometer (incl. HP 4247 A Impedance Analyzer and Temperature Control). The composites were cut into pieces of (2 - 5) mm x (2 - 5) mm x 30 mm and contacted by four stripes of air-dried silver paint. For the four-probe measurements, spring tips were pressed onto the stripes of silver. In order to determine the current rating of PTC elements, plates of 30 mm^2

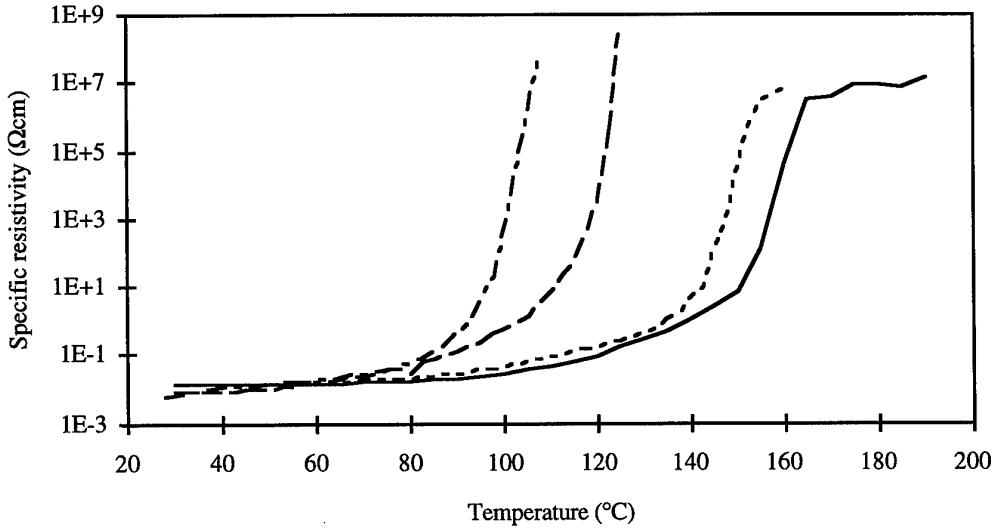


Fig. 5 Specific resistivity as a function of temperature: Spurr B /43 vol.% TiB_2 cured for 20 h at 80 °C (- — -) and 120 °C (— —); Araldit F / 43 vol.% TiB_2 cured for 20 h at 140°C (- - -) and 20 h at 140 °C plus 2 h at 180°C(——).

cross-section and 20 mm length were heated for 6 min. by a constant current. If no tripping was observed within this time frame, the current was slightly increased. This procedure was repeated until the first switching of the PTC occurred.

3. RESULTS AND DISCUSSION

Fig. 4 shows the specific resistivities ρ of Spurr B / 66 vol.% Ni and Spurr B / 30 vol.% Ni/Ag cured for 20 h at 80 °C as a function of temperature. The filler fractions reflect the different tap densities of the two powders. Although the filler content of the Ni/Ag composite is much lower, its RT resistivity is only two times higher (0.006 Ω·cm) than the ρ of the Ni composite (0.0029 Ω·cm). The soft Ag surface allows larger contact areas between touching particles and serves by this for a better conductivity. This agrees with results by Ruschau et al.[16]. As a second consequence, the resistivity increases with increasing temperature "only" by four orders of magnitude ($T_c \approx 80$ °C) compared to *twelve* orders of magnitude in the case of Ni filler ($T_c \approx 110$ °C). The soft Ag-covered particles stick together and can not be fully separated during the expansion of the polymer. For some applications a high resistance level is necessary. Hence, a hard filler material is preferred in these cases.

The influence of the matrix upon the PTC transition is shown in Fig. 5 for Spurr B and Araldit F epoxy. The composites contain 43 vol.% of TiB_2 powder with a particle size of 63-100 µm. One Spurr composite was cured at 80 °C, another one at 120°C (20 h). From the Araldit samples one was cured for 20 h at 140°C, the other one at 140°C (20 h) followed by 2 h at 180°C. All composites exhibit a PTC effect of eight to nine orders of magnitude. Depending on the curing temperature T_{cure}, different transition temperatures are observed. The Spurr composites cured at 80 °C and 120 °C produce transitions at 100 °C and 120 °C, respectively. Curing of Araldit at 140 °C results in a PTC transition around 150 °C. By post-curing at 180 °C, T_c is increased to 160 °C. For high temperatures ($T > T_{cure}$), the Spurr samples achieved resistance values above the detection limit of the test equipment. Therefore, the stable high-resistive state, as observed for Araldit, could not be measured.

The behavior of Epikote composites is similar as shown in Fig.6. After 2 h at 160 °C the epoxy is not yet fully cured. DSC measurements show a glass transition temperature T_g of only 80 °C. Nonetheless a PTC transition is observed around 140 °C. But, after an increase by a factor of 10^5, the resistivity decreases again for T > 150 °C. Further curing at 140 °C (16 h) shifts the PTC transition to 160 °C (T_g = 120 °C). A final heating to 200 °C for 2 h yields a less steep increase of the ρ, but also to a shift to even higher temperatures around 200 °C. In addition, the T_g increases to 144 °C. An overview of the specific resistivities at RT, the PTC transition temperatures T_c and the glass transition

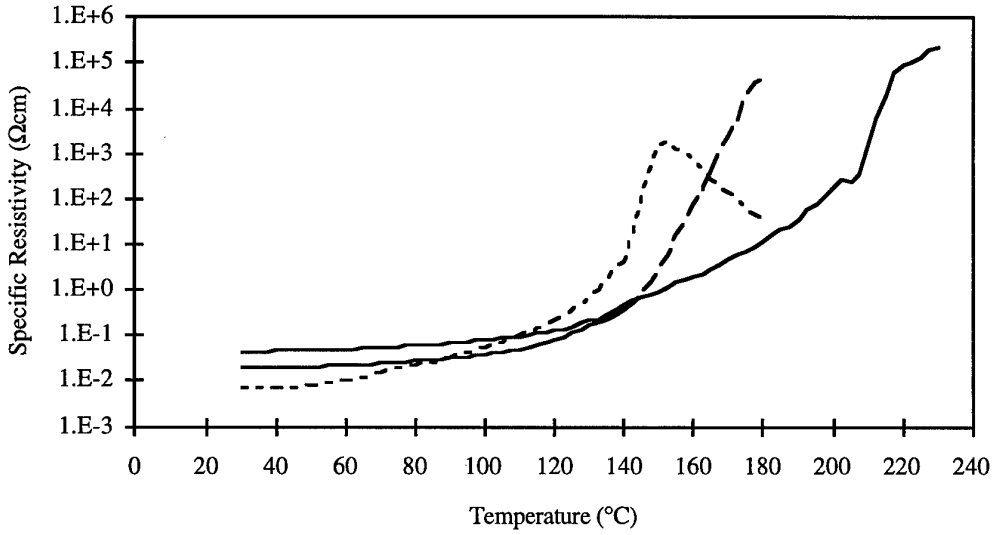


Fig. 6 Specific resistivity as a function of temperature of Epikote 828 epoxy / 43 vol.% TiB_2 (100-200 µm) cured for 2 h at 160 °C (- - -), 2 h at 160 °C plus 20 h at 140 °C (— —), 2 h at 160 °C plus 20 h at 140 °C plus 2 h at 200 °C (——).

Table 1. Glass transition temperature T_g, PTC transition temperature T_c and specific resistivity ρ at RT for different epoxy composite systems and curing cycles.

Material	T_{cure} (°C)	T_g (°C)	T_c (°C)	ρ (Ω·cm)
Spurr/30%Ni/Ag	80	80	80	0.006
Spurr/66%Ni	80	80	110	0.0029
Spurr/43%TiB_2	80	80	100	0.006
Spurr/43%TiB_2	120	90	120	0.008
Araldit/43%TiB_2	140	104	150	0.014
Araldit/43%TiB_2	140, 180	105	160	0.0135
Epik./43%TiB_2	160	80	140	0.007
Epik./43%TiB_2	160, 140	120	160	0.019
Epik./43%TiB_2	160,140, 200	144	200	0.045

temperatures T_g compared to the curing temperatures T_{cure} is given in Table 1. The RT resistivities of the epoxy composites are measured in the range from 0.006 - 0.045 Ω·cm. A comparison of the T_g and T_c values shows that the PTC transition is not determined by the glass transition temperature. But the curing has a strong influence on T_c. In fact, the transition temperature is found quite often close to the curing temperature. During the transition the matrix expands until the contacts between the particles are opened and the composite reaches a high-ohmic state[12]. The expansion depends on internal stresses, which are built-up in the epoxy during the curing process. For materials cured at higher temperatures, a slightly larger expansion is necessary in order to achieve the same increase in resistivity.

Fig. 7 shows two examples of thermoplastic composites. HDPE / 50 vol.% TiB_2 has a resistivity of 0.029 Ωcm at RT which increases to ≈10^7 Ωcm at 125 °C. The main increase by seven orders of magnitude occurs within only 20 °C, which means that the temperature sensitivity is very high. PPS / 43 vol.% TiB_2 has a RT resistivity of only 0.004 Ωcm. The resistivity increase is not as sharp as for HDPE. It starts at about 200 °C and the maximum resistance is achieved at 290 °C. For both polymers, the temperature of the peak resistivity is close to the melting temperature T_m. Polyethylene has a T_m of 134 °C, PPS melts at 290 °C. In both cases the step-like volume increase at T_m is one reason for the PTC effect. But in the case of PPS, the thermal expansion of the material must contribute to the resistivity increase already far below the melting temperature. This causes the relative broad transition. When used as current sensor or limiter, a PTC element with a higher T_c allows higher working temperatures. At 215 °C the resistivity of the PPS composite is still below 1 Ω·cm. If enough cooling is provided, a strong increase of the current rating compared

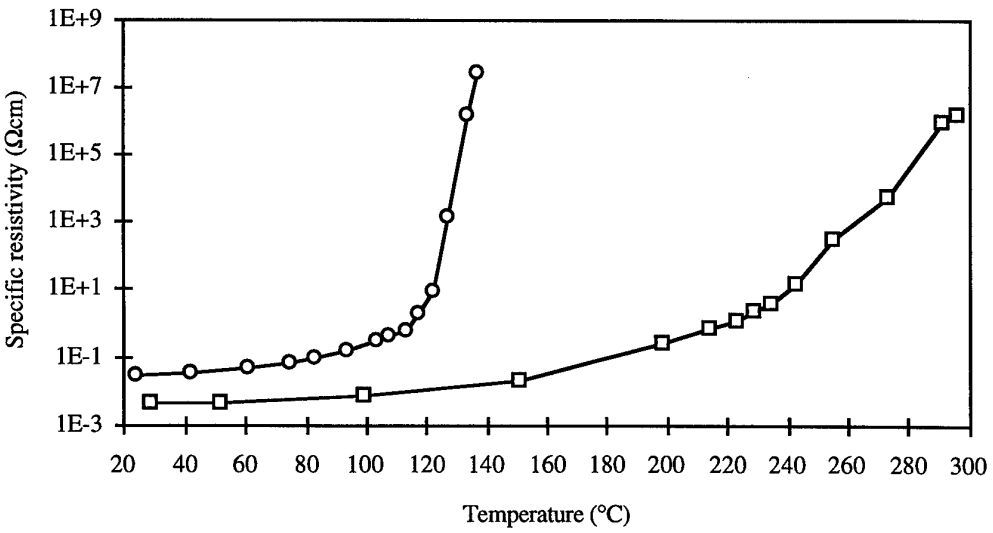


Fig. 7 Specific resistivity of HDPE / 50 vol.% TiB_2 (O) and PPS/ 43 vol.% TiB_2 (□) as a function of temperature.

to HDPE can be expected. In order to enforce the cooling during the tests of the critical current, the samples were placed in a water filled thermostat (T=65 °C) and a strong water beam of 20 l/min. with the same temperature was directed onto the PTC surface. For a HDPE/ 50 vol.% TiB_2 sample of 30 mm^2 cross-section, no tripping was observed within 6 min. for currents of up to 15 A. That means a critical current density of 50 A/cm^2. A PPS / 43 vol.% TiB_2 sample of the same geometry did not switch into the high resistive state for currents up to 36 A (current density 120 A/cm^2). Using PPS the maximum power can be increased by a factor of about six.

4. CONCLUSION

New polymer composites have been prepared, which have high potential for applications as temperature or current sensors. They exhibit a strong increase in resistivity around a critical temperature caused by the thermal expansion of the polymer. For temperature sensors a strong increase of ρ within a small and well defined range of T is desired. A broad spectrum of transition temperatures between 80 and 250 °C is possible if a proper high-temperature polymers is used. While for epoxies the transition temperature can be influenced by the curing, T_c is pre-determined for thermoplastics by the melting temperature. For current sensors and limiters, on the other hand, a low cold resistance and a high temperature of the peak resistance are favorable. Very low RT resistivities can be achieved using hard metallic filler materials. In combination with enforced cooling, rated current densities of 120 A/cm^2 are feasible. Hence, such systems are highly attractive for current sensors and limiters.

5. ACKNOWLEDGEMENTS

The author wishes to thank Felix Greuter, Claus Schüler, Joachim Glatz-Reichenbach, Jørgen Skindhøj and Tudor Baiatu for many helpful discussions and Ruzica Loitzl, Leopold Ritzer, Zdenka Posedel and Andreas Garbin for their technical support.

6. REFERENCES

1. R.E. Newnham and G.R. Ruschau, "Smart Electroceramics", *J. Am. Ceram. Soc.* 74, pp. 436-480 (1991)

2. R.E. Newnham, G.R: Ruschau, "Electromechanical properties of smart materials", *J. Intelligent Material Systems and Structures* 4, pp. 289-294 (1993)

3. R. Strümpler, P. Kluge-Weiss, F. Greuter, "Smart varistor composites", *Advances in Science and Technology* 10, Intelligent Materials and Systems, P. Vincenzi (ed.), Techna S.r.I., pp. 15 - 22 (1995)

4. R. Strümpler, J. Rhyner, F. Greuter and P. Kluge-Weiss, "Nonlinear dielectric composites", *Journal of Smart Materials and Structures* 4, pp. 215-222 (1995)

5. R.C. Buchanan, *Ceramic materials for electronics* (Marcel Dekker, New York), pp. 291-354 (1986)

6. J. Meyer, "Stability of polymer composites as positive-temperature-coefficient resistors", *Polymer Eng. and Sci.* 14, pp. 706 - 716 (1974)

7. D. Moffatt, J.P. Runt, A. Halliyal and R.E. Newnham, "Metal oxide-polymer thermistors", *J. Mat. Sci.* 24, pp. 609 - 614 (1989)

8. K.A. Hu, J. Runt, A. Safari and R.E. Newnham, "TiO-epoxy composite thermistors", *Phase Transitions* 7, pp. 1-4 (1986)

9. T.R. Shrout, D. Moffatt and W. Huebner, "Composite PTCR thermistors utilizing borides, silicides and carbide powders", *J. Mat. Sci.* 26, pp. 145 - 154 (1991)

10. F.A. Doljack, "PolySwitch PTC devices – a new low-resistance conductive polymer-based PTC device for overcurrent protection", *IEEE Trans. on Comp., Hybrids and Manufact. Techn.* Vol. CHMT-4, No.4, pp. 372 (1981)

11. T. Hansson, "Polyethylene current limiters for short-circuit protection", *ABB Review* No. 4/92, pp. 35 - 38 (1992)

12. R. Strümpler, G. Maidorn, A. Garbin, L. Ritzer, F. Greuter, "Electro-mechanical properties of conductive epoxy composites", Proc. of 10th Int. Conf. on Composite Materials (ICCM-10), Whistler, Aug.14 - 18, 1995, eds.: A. Poursartip, K.N. Street, Vol. IV, pp. 473-480, Woodhead Publ. Ltd., Cambridge, UK (1995)

13. A.D. McLeod, J.S. Haggerty and D.R. Sadoway, "Electrical resistivities of monocrystalline and polycrystalline TiB_2", *J. Am. Ceram. Soc.* 67, pp. 705 - 708 (1984)

14. W. J. Lackey, D.P. Stinton, G.A. Cerny, A.C. Schaffhauser, and L.L. Fehrenbacher, *Adv. Ceram. Mat.* 2, pp. 24-30 (1987)

15. H. Wagar, "Principles of conduction through electrical contacts", in *Physical Design of Electronic Systems*, Vol.3, Prentice Hall, Englewood Cliffs, N.J. (1971)

16. G.R. Ruschau, S. Yoshikawa and R.E. Newnham, "Resistivities of conductive composites", *J. Appl. Phys.* 72, pp. 953 - 959 (1992)

Interpolyelectrolyte complexes as smart binders with controllable stability in water-salt solutions.

Dmitry V. Pergushov*, Vladimir A. Izumrudov, Alexander B. Zezin, and Victor A. Kabanov

Department of Polymer Sciences, Faculty of Chemistry, Moscow State University
Moscow 119899, Russia.

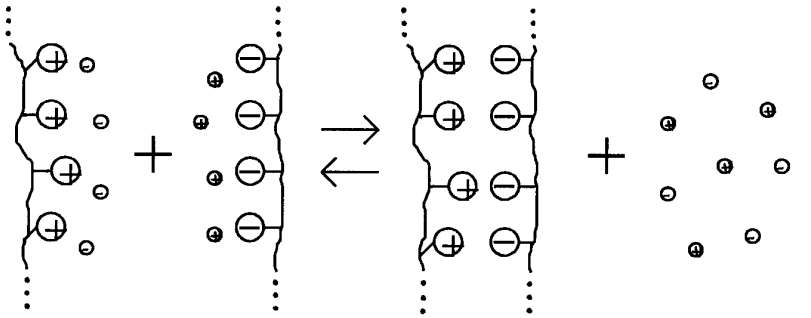
ABSTRACT

The stability of non-stoichiometric interpolyelectrolyte complexes (IPECs), which contain relatively long poly(methacrylate anion)s and relatively short poly(N-ethyl-4-vinylpyridinium cation)s, with respect to their dissociation into constituent polyelectrolytes in water-salt media was studied by fluorescence quenching and velocity sedimentation techniques. The dissociation of IPECs was found to begin at a certain critical salt concentration and to proceed by a gradual release of polycations from IPECs. The effects of polyion chain length and polyion charge density on the stability of IPECs were examined.

1. INTRODUCTION

Interpolyelectrolyte complexes (IPECs) are the products of interactions between oppositely charged macromolecules. These ionic interactions are of a distinct cooperative nature that is responsible for the relatively high stability of IPECs with respect to their dissociation into constituent polyelectrolytes.

The stability of IPECs is known to drastically depend on the concentration of low-molecular-weight salts in the system. Coupling of oppositely charged macromolecules leads to the concomitant release of small ions that were previously associated with polyions. Consequently the equilibrium (1) shifts to the favor IPEC dissociation at high salt concentrations but to the favor IPEC formation at low salt concentrations.



(1)

IPECs are amphiphilic macromolecular compounds, i.e., contain both hydrophobic and hydrophilic sites (Fig.1). Sites formed by coupling polyionic counterparts are sufficiently hydrophobic because of mutual screening by polyions of their charges. Hydrophilic sites include polyelectrolyte units that are not involved in the ionic interactions between oppositely charged macromolecules. Because of the reversibility of the IPEC formation, hydrophobic and hydrophilic sites are able to spontaneously exchange their location within IPECs. These peculiarities of IPEC structure provide a unique oportunity for interactions of IPECs with colloidal particles and surfaces of different natures. Introduced into disperse systems IPECs can adjust themselves for the hydrophilic-hydrophobic balance of microenvironment by the "trial and error" method. Due to such properties, IPECs have been successfully applied as binders for prevention of soils from water and wind erosions, which is one of the important ecological problems [1].

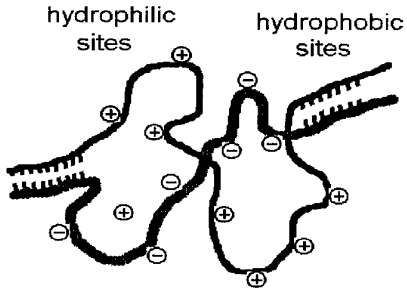


Fig.1. Schematic structure of IPEC.

0-8194-2165-0/96/$6.00

Thus, IPECs can be considered as intelligent (smart) materials because of their ability to adapt themselves to the complex structure of disperse systems via rapid exchange processes and to realize the optimal set of bonds with different colloidal particles and surfaces.

The technological procedure of the preparation and utilization of IPEC binders is quite simple. It includes (i) the preparation of dilute aqueous polyelectrolyte mixtures at high concentations of low-molecular-weight salts (for instanse, mineral fertilizers) when ionic interactions between oppositely charged polyions are completely surpressed, (ii) the introduction of these mixtures into disperse systems usually by splashing of polyelectrolyte mixtures on soil or ground surfaces, and (iii) washing of disperse systems by water in order to remove salts. The decrease in salt concentrations leads to the shift of the equilibrium (1) to the IPEC formation.

Formed by this technological procedure IPECs are repeatedly able to get dry and wet without the deterioration of their adhesive properties. Such a treatment of soils results in mutual binding of soil particles via thin IPEC layers (Fig.2). Different both organic and inorganic low-molecular-weight compounds present in the original mixtures can be immobilized into IPECs. Under the certain conditions, the immobilized substances release from IPECs with a controllable speed. Therefore binding of soil particles by IPECs can be combined with an increase in the soil fertility due to the introduction of fertilizers, herbicides, stimulators of plant growth, etc., into soils.

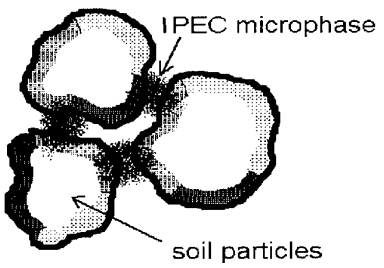


Fig.2. Schematic representation of soil particles bound each other via IPEC layers.

Thus, the technology of preparation and application of IPECs as binders of disperse systems deals with solutions of oppositely charged polyelectrolytes in the presence of sufficiently high quantities of low-molecular-weight salts. Obviously, the search and analysis of factors that affect the stability of IPECs in water-salt media are necessary for the further devolopment and improving of the considered above technological procedure of IPEC utilization. In this work, we investigated the peculiarities of the IPEC dissociation and found that the stability of IPECs drastically changes with the variation in polyion chain length and polyion charge density.

2. EXPERIMENTAL SECTION

2.1. Materials

The syntheses and subsequent fractionation by dropwise precipitation of poly(methacrylic acid) (PMAA) and poly(4-vinylpyridine) (PVP) samples were carried out according to [2,3].

The fractions of PMAA with weight average polymerization degrees P_w=3900, 2100, 1000 (measured by light scattering) were used for the synthesis of fluorescently tagged PMAA* samples via an interaction with pyrenyldiazomethane [4]. From UV spectra of PMAA* water solutions, we evaluated the contents of pyrenyl tags in PMAA* fractions (a characteristic molar absorption coefficient for pyrenyl groups was assumed to be $\varepsilon=5*10^4$ L $mol^{-1}cm^{-1}$ at wavelength 343 nm). On the average, PMAA* samples with P_w=3900, 2100, and 1000 contained one tag per 350, 500, and 600 repeating units, respectively.

The samples of poly(N-ethyl-4-vinylpyridinium bromide) (PEVP) with variable charge density were the products of alkylation of corresponding PVP fractions by ethyl bromide. The degrees of alkylation $\beta=m/(m+n)*100\%$ (where m and n are molar contents of N-ethyl-4-vinylpyridinium and 4-vinylpyridine units in PEVP, respectively) for PEVP samples were measured by IR spectroscopy [6]. PEVP fractions with P_w=1350, 650, 300, 100 and $\beta>90\%$, P_w=100 with β=40, 60%, and number average polymerization degrees P_n=10, 20, 30 (measured by ebulioscopy) and $\beta>90\%$ were used in our study.

2.2. IPEC solutions

In our research, we used water-soluble non-stoichiometric IPECs [5] formed by relatively long PMA* anions and relatively short PEVP cations. Solutions of IPEC of the composition φ=[PEVP]/[PMAA*] (here and further below brackets refer to molar concentrations of repeating units of polyelectrolytes) were prepared by mixing of the proper amounts of PEVP and PMAA* water solutions with subsequent addition of equivalent amount (as calculated for carboxyl groups of polyacid) of tetramethylammonium hydroxide solution. IPEC

solutions were diluted with 0.01 M Tris buffer for 12 h prior to measurements. After dilution, pH of all IPEC solutions was close to 9.5. Under this condition, virtually all carboxyl groups of polyacid are in the ionized state.

2.3. Fluorescence measurements

The utilization of fluorescence technique for studying of IPECs in water-salt solutions is based on the known fact that PEVP cations are quite effectively able to quench the fluorescence of pyrenyl groups of PMA* anions [6]. The fluorescense intensity I of continuously stirred IPEC solutions titrated with solutions of low-molecular-weight salts was measured at 395 nm with a Jobin Yvon-3CS fluorescence spectrometer at room temperature with excitation at 343 nm. The time interval between the addition of a portion of the salt solution and measurement of I was 1 min. The initial concentration of polyanion units in IPEC solutions was held constant at $2.0*10^{-3}$ M.

2.4. Sedimentation measurements

Sedimentation measurements of IPEC solutions were performed in the scan mode using a Beckman-E analytical ultracentrifuge at 48 000 rpm and 20°C. Sedimentation patterns were detected by changes in the optical absorption of IPEC solutions at 276 nm Abs_{276} and at 343 nm Abs_{343}. The concentrations of polyanion and polycation units were held constant at $5.0*10^{-3}$ M and at $1.5*10^{-3}$ M, respectively.

3. RESULTS

3.1. Peculiarities of IPEC dissociation

A typical fluorimetric titration curve that reflects the change in fluorescence of IPEC solution titrated with a NaCl solution is presented in Fig.3 (curve 1). As the salt concentration reaches the certain critical value $[NaCl]^*_{cr.}$ (marked in Fig.3 with an arrow), a sharp increase in the relative fluorescence intensity of the IPEC solution I/I_0 (where I_0 is the fluorescence intensity of neutralized with tetramethylammonium hydroxide PMAA* solutions measured at the same conditions as I) is observed. This result evidences that the number of contacts between pyrenyl tags and polymeric quenchers decreases. The fraction of quenched pyrenyl tags Q was calculated according to the formula: $Q=(I_0-I)/(I_0-I_{min.})$ where $I_{min.}$ is the minimum fluorescence intensity of the IPEC solution for a titration. The dependence Q on the NaCl concentration is also given in Fig.3 (curve 2). A decrease in Q that observed with the increasing salt concentration is associated with the dissociation of IPEC into constituent polyelectrolytes. The fact that Q virtually reaches to zero at relatively high NaCl concentrations indicates that ionic interactions between oppositely charged macromolecules are completely suppressed. The obvious reason for that is binding of low-molecular-weight ions with corresponding polyions incorporated into IPEC.

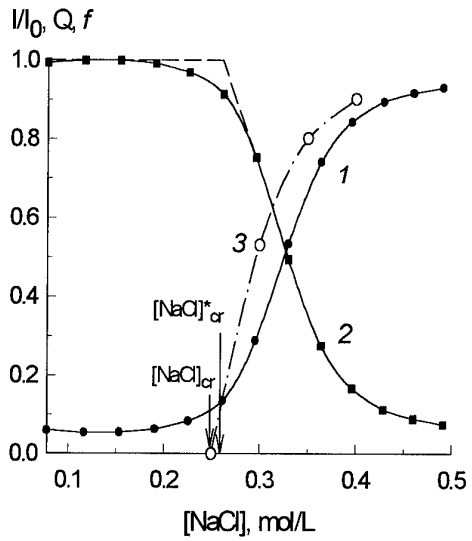


Fig.3. Relative fluorescence intensity I/I_0 (*1*), fraction of quenched pyrenyl tags Q (*2*), and fraction of non-associated with PMA* anions PEVP cations *f* (*3*) versus NaCl concentration for solution of IPEC (φ=0.3) contained PMA* anion with P_w=3900 and PEVP cations with P_n=20.

However the fluorescence quenching technique does not provide the information on the peculiarities of the IPEC dissociation in water-salt solutions. In order to investigate this process in detail, we applied the velocity sedimentation technique.

Fig.4 shows scan sedimentation patterns of IPEC solutions at NaCl concentrations before (a and e) and corresponding (b-d and f-h) the fluorescence increase. Scan sedimentation patterns (a-d) were obtained at 276 nm, i.e., in the spectral region where both pyridinium groups of PEVP cations and pyrenyl groups of PMA*

anions absorb light. In contrast to the pattern (a), patterns (b-d) reveal two distinctly pronounced steps. The sedimentation coefficient of the "slow" step coincides with that for PEVP under the same conditions. As the NaCl concentration increases, the optical absorption of this step Abs_{276}, gradually increases and finally reaches the optical absorption $(Abs_{276})_0$ of the reference PEVP solution prepared at the same conditions as IPEC solutions. Thus, the ratio $f \equiv Abs_{276}/(Abs_{276})_0$ is the fraction of PEVP cations non-associated with PMA* anions. The dependence of f on the NaCl concentration is also given in Fig.3 (curve 3).

Scan sedimentation patterns (e-h) were obtained at 343 nm, i.e., in the spectral region where only pyrenyl groups of PMA* anions absorb light. They reveal one step. The sedimentation coefficient of this step coincides with that for "fast" step detected at 276 nm at the same conditions. Therefore it is attributed to the IPEC particles.

Thus, the data of the sedimentation analysis provide the clear evidence of the IPEC dissociation in water-salt solutions. This process proceeds as a gradual release of relatively short PEVP cations from IPEC and begins at a certain critical, sufficiently high salt concentration $[NaCl]_{cr.}$ (marked in Fig.3 with an arrow). At NaCl concentrations less than $[NaCl]_{cr.}$, IPEC does not dissociate into constituent polyelectrolytes (Fig.4, a,e). At NaCl concentrations higher than $[NaCl]_{cr.}$, PEVP cations ("slow" step) coexist with IPEC particles ("fast" step) that are poor in PEVP cations, as compared with the initial IPEC.

The fact that the content of PEVP cations in IPEC, i.e., IPEC composition φ, decreases with the increasing NaCl concentration in the range $[NaCl]>[NaCl]_{cr.}$ is also demonstrated by a decrease in sedimentation coefficients of IPEC particles (Fig.4, for example, compare scan sedimentation patterns (a,b) with (e,f)). This result is in a good agreement with known data on the effect of φ on the sedimentation coefficients of IPEC particles [7].

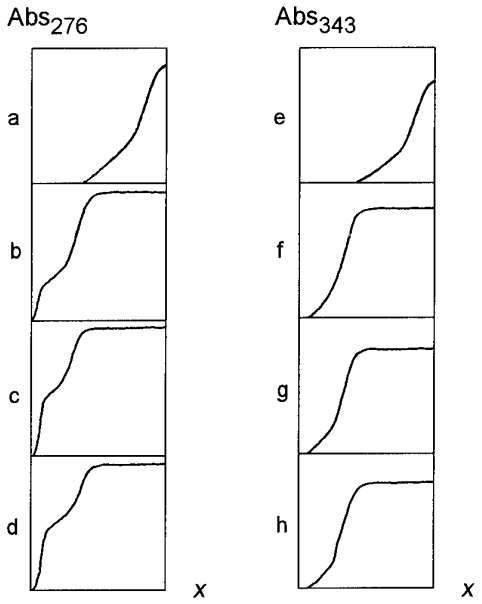


Fig.4. Sedimentation patterns for solutions of IPEC contained PMA* anion with P_w=3900 and PEVP cations with P_n=20. Concentration of NaCl: 0.25 (a,e), 0.30 (b,f), 0.35 (e,g), and 0.40 M (d,h).

Fig.3 indicates that concentrations $[NaCl]_{cr.}$ and $[NaCl]^*_{cr.}$ virtually coincide. Thus, the data of fluorescence quenching and sedimentation techniques are in a good accordance. On the basis of this fact, we used the fluorescence quenching technique when examining the effect of different factors (polyion chain length and polyion charge density) on the stability of IPECs in water-salt media.

3.2. Effect of polyion chain length on IPEC stability

Fig.5 presents the dependence of the fraction of quenched pyrenyl tags Q on the NaCl concentration for IPECs formed by the same PMA* anions (P_w=3900) and series of PEVP cations (β>90%) with different polymerization degrees P_{PEVP}. As P_{PEVP} increases, curves shift to higher salt concentrations. This result means the monotone increase in the stability of IPECs with the increasing PEVP chain length. Fig.5 shows critical NaCl concentration $[NaCl]^*_{cr.}$ obtained from data given in Fig.6 as a function of P_{PEVP}. As can be seen, $[NaCl]^*_{cr.}$ drastically increases with increasing PEVP polymerization degree only at relatively low P_{PEVP} ($P_{PEVP} \leq 100$). With a further increase in P_{PEVP}, $[NaCl]^*_{cr.}$ approaches an asymptote.

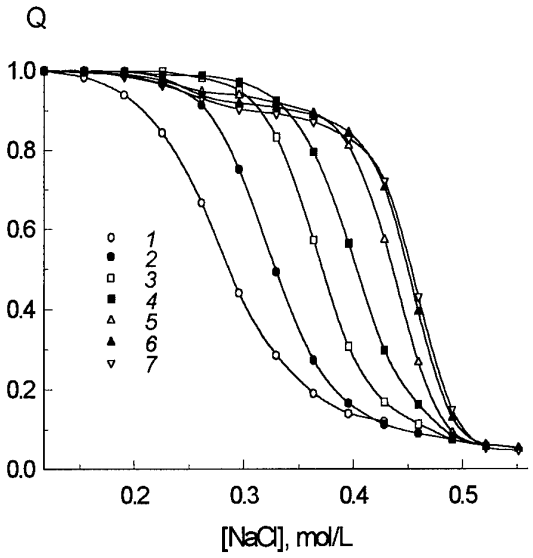


Fig.5. Fraction of quenched pyrene tags Q versus NaCl concentration for solutions of IPECs (φ =0.3) contained PMA* anions with P_w=3900 and PEVP cations with P_n=10 (1), 20 (2), 30 (3), and P_w=100 (4), 300 (5), 650 (6), 1350 (7).

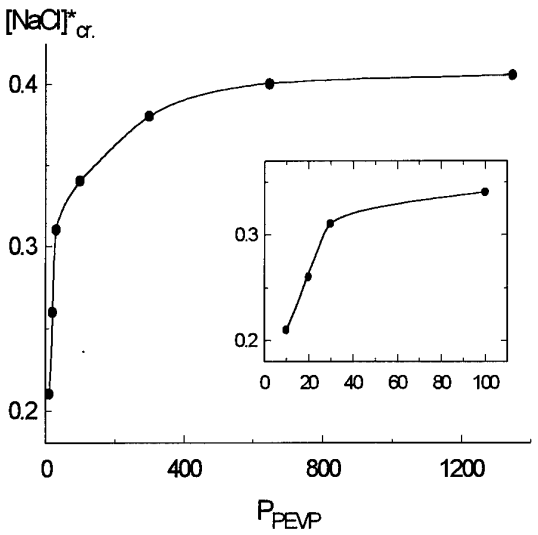


Fig.6. Critical NaCl concentration $[NaCl]^*_{cr.}$ of IPEC solutions versus polymerization degree of PEVP cations.

As for the dissociation of IPECs contained PEVP fractions with different P_{PEVP}, we expected the gradual release of PEVP cations according to their chain length. Fig.7 gives the fluorimetric titration curves for IPECs that contain PEVP fractions with P_n=20 (curve 1), P_w=300 (curve 2), and equal weight amounts of both these PEVP fractions (curve 3). Indeed, the dissociation of IPEC that contains PEVP cations with significantly different P_{PEVP} proceeds in two distinctly pronounced steps. As is evident from the comparison of curve 3 with curves 1 and 2, first and second steps correspond to the release of PEVP cations with P_n=20 and P_w=300, respectively.

Thus, these data clearly demonstrate that the stability of IPECs in water-salt solutions can change when polymerization degree of PEVP cations varies. On the other hand, the IPEC stability appears to be nearly independent of the chain length of PMA* anions P_{PMA*} if condition $P_{PMA*} >> P_{PEVP}$ is maintained (Table).

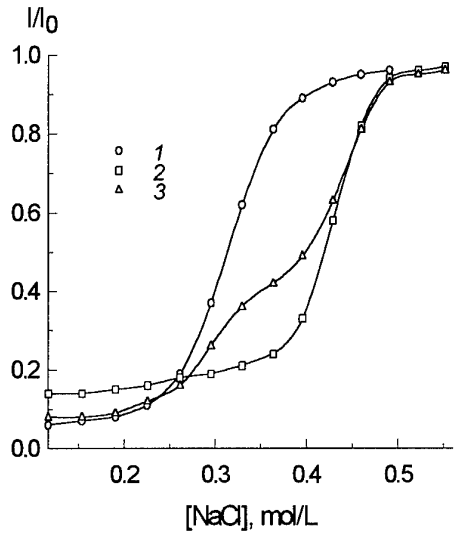


Fig.7. Relative fluorescence intensity I/I_0 versus NaCl concentration for solutions of IPECs (φ=0.3) contained PMA* anions with P_w=3900 and PEVP cations with P_n=20 (1), 300 (2), 20 and 300 taken in the equivalent weight ratio (3).

Table. Effect of polymerization degree of PMA* anion on the stability of IPECs in water-salt media.

P_{PMA*}	3900	3900	3900	3900	3900	1000	1000	1000	1000	1000
P_{PEVP}	10	20	30	100	300	10	20	30	100	300
$[NaCl]^*_{cr}$	0.21	0.26	0.31	0.34	0.38	0.20	0.25	0.29	0.36	0.41

3.3 Effect of polyion charge density on IPEC stability

Fig.8 shows the fluorimetric titration curves obtained for solutions of IPECs formed by the same PMA anions (P_W=3900) and series of PEVP cations (P_W=100) with different alkylation degrees β, i.e., with different charge densities. As can be seen, the decrease in β results in the decrease in $[NaCl]^*_{cr.}$. It is noteworthy that this effect is strongly pronounced at sufficiently low PEVP charges densities. Thus, the effects of polyion charge density and polyion polymerization degree on the IPEC stability appear to be similar.

The comparison of curve 2 in Fig.8 and curve 1 in Fig.7 shows that the stability of IPEC contained PEVP cations with P_W=100 and β =60% is virtually equal to that of the IPEC contained PEVP cations with P_n=20 and β>90%. This interesting fact indicates that the stability of IPECs in water-salt media is significantly affected by the distribution of charged groups along the polyion chain.

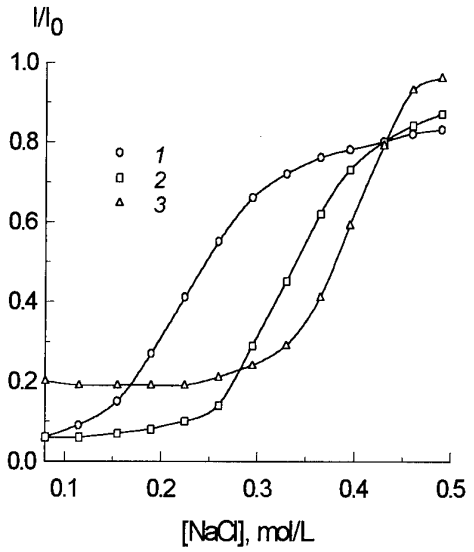


Fig.8. Relative fluorescence intensity I/I_0 versus NaCl concentration for solutions of IPECs (φ=0.2) contained PMA* anions with P_W=2100 and PEVP cations with β=40% (1), 60% (2), and >90% (3).

4. CONCLUDING REMARKS

Thus, experimental data presented in this paper confirm that polyion polymerization degree and polyion charge density are the powerful factors that control the stability of IPECs in water-salt media. It is remarkable that the effects of these factors are especially pronounced at relatively low polyion chain lengths and polyion alkylation degrees. The results of this research demonstrate the possibility for the preparation of IPECs with a desired stability.

Experimental data obtained in this work may be also useful when the practical problem of soil salting that results from the treatment of soils by the IPEC binders arises. Indeed, the results given above show that the concentration of low-molecular-weight salts in original mixtures of oppositely charged IPEC constituents can be significantly reduced if polyelectrolytes with sufficiently low polymerization degrees or charge densities are used.

5. REFERENCES

1. V.A. Kabanov, A.B. Zezin, V.A. Kasaikin, A.A. Yaroslavov, and D.A. Topchiev, Polyelectrolytes for ecology, *Usp. Khim.*, Vol. 60, No. 2, pp. 595-601, 1991.

2. Yu.S. Lipatov, and P.I. Zubov, The effect of temperature on the viscosity of concentrated solutions of poly(methacrylic acid) and its salts, *Vysokomol. Soedin.*, Vol. 1, No. 1, pp. 88-93, 1959.

3. Yu.E. Kirsh, S.K. Pluzhnov, T.S. Shomina, V.A. Kabanov, and V.A. Kargin, Synthetic polymeric analogs of enzymes with esterase activity, *Vysokomol. Soedin., Ser. A*, Vol. 12, No. 1, pp. 186-204, 1970.

4. M.G. Krakovyak, E.V. Anufrieva, and S.S. Skorokhodov, Preparation of polymers with luminescent marks, *Vysokomol. Soedin., Ser. A*, Vol. 11, No. 11, pp. 2499-2504, 1969.

5. V.A. Kabanov and A.B. Zezin, Soluble interpolymeric complexes as a new class of synthetic polyelectrolytes, *Pure Appl. Chem.*, Vol. 56, No. 3, pp. 343-354, 1984.

6. N.R. Pavlova, Yu.E. Kirsh, and V.A. Kabanov, The study of molecular dinamics in solutions of polyelectrolytes and their cooperative complexes by the method of quenching fluorescence, *Vysokomol. Soedin., Ser. A*, Vol. 21, No. 9, pp. 2062-2070, 1979.

7. V.B. Rogacheva, S.V. Ryzhikov, T.V. Shchors, A.B. Zezin, and V.A. Kabanov, Structural-chemical transformations of non-stoichiometric polyelectrolyte complexes in water-salt solutions, *Vysokomol. Soedin., Ser. A*, Vol. 26, No. 11, pp. 2417-2424, 1984.

Superparamagnetic composite material based on polyaniline and magnetite

V.D. Pokhodenko and O.Yu. Posudievsky

L.V.Pisarzhevsky Institute of Physical Chemistry, National Academy of Sciences of Ukraine, Prospect Nauki 31, Kiev 252039, Ukraine

ABSTRACT

The composite material based on polyaniline and magnetite with magnetite loading up to 50 wt. % has been obtained. Nanometric size of magnetite particles leads to superparamagnetism of the composite. Analysis of the spectral characteristics indicates the existence of interaction between composite components.

1. INTRODUCTION

Superparamagnetism often takes place when monodomain ferromagnetic particles are allocated in nonferromagnetic matrix. Then, in the absence of external magnetic field due to magnetic anisotropy the vector of magnitization of an arbitrary particle at sufficiently high temperature may have any allowed direction, so that magnitization of an assembly of such particles is equal zero. External magnetic field leads to partial alignment of individual particle magnetization vector and nonzero magnetization of the whole sample emerges. At strong fields, magnetization vectors of all particles are aligned along the field direction and saturation is observed, so that magnetization curve of a superparamagnet obeys the Langevin equation with a value of saturation magnetization characteristic for ferromagnets.

Due to this peculiarity, superparamagnets have attracted attention of specialists in refrigeration machinery[1], they may be used in immunodiagnostics assays[2], and composites based on conducting polymers are probably able for intense microwave absorption as they include components which generate dielectric and/or magnetic loses depending on the choice of magnetic nucleous nature, particle size, form and so on. Generally, composites based on conducting polymers and inorgenic compounds are now the object of advanced scientific elaboration of functional materials for modern technology[3] as materials of such type usually possess the properties of both components and very often display unaccessible for each individual component properties as in the case of superparamagnetism of polypyrrole/γ-Fe_2O_3 composites[2,4,5].

Superparamagnetism depends on temperature as its criterion has the form:

$$kT > VK_{eff}, \tag{1}$$

where V — ferromagnetic particle volume, K_{eff} — coefficient of magnetic anisotropy. Relation (1) is valid at room temperature when (at typical values of K_{eff} ~ 10^4-10^5 erg/cm^3) the ferromagnetic particles have nanometric size. This implies the use of nanotechnology for preparation of superparamagnets, especially when optimization of magnetic properties is desired.

In present work, magnetic and spectral characteristics of superparamagnetic composite material based on polyaniline (PAni) and magnetite (Fe_3O_4) are investigated.The existence of interaction between composite components is established. Magnetite is used due to its greater, in comparison with γ-Fe_2O_3, saturation magnetization, while polyaniline — owing to high stability of its physico-chemical properties.

2. EXPERIMENTAL

Sol of Fe_3O_4 was prepared according to[6]. Elemental analysis of the composite material was carried out on «Elemental Analyzer, 1106» («Karlo Erba») facility. X-ray study was done on DRON-3M diffractometer with filtrated Cu(K_α) radiation. IR-spectra were recorded on IRS-29 spectrometer on the tabletted with KBr samples with accuracy not worse than 2 cm^{-1}. EPR spectra were registered on «Varian E-9» spectrometer using the spectrum of Mn^{2+} isomorphly substituted in MgO crystal lattice as a standard. Magnetization curve was obtained by means of home-built magnetostatic magnetometer with accuracy not worse than 5%. The saturation magnetization of nickel was used to calibrate the magnetometer.

0-8194-2165-0/96/$6.00

3. RESULTS AND DISCUSSION

PAni/Fe_3O_4 composites were prepared via oxidative polymerization of 0,2M aqueous solution of anilinium chloride in the presence of Fe_3O_4 sol. Ammonium persulphate was added to reaction mixture at constant stirring in small lack relatively to anilinium. The solution, at first, became green and then the dark-green product precipitated. The material was filtered out, washed with distilled water and acetonitrile, dried under air and then under vacuum (10^{-2} torr) for 8 h at 70°C. X-ray diffraction study of composite samples showed that interplane distances, *d*, are in good agreement (table) with ones known for small-crystalline Fe_3O_4 from literature[7]. Elemental analysis confirmed that the magnetite loading is up to 51 wt. %.

Table. X-ray diffraction in magnetite particles of PAni/Fe_3O_4 composite

No.	2Θ, dg	*d*, Å	*d*, Å [7]	Δ, 10^{-2} radn	*D*, nm
1	21.8	4.19	4.19	1.11	12.7
2	35.5	2.53	2.53	1.10	13.0
3	43.0	2.10	2.10	1.10	13.7
4	53.5	1.71	1.71	1.15	12.7
5	57.0	1.61	1.61	1.15	13.3
6	62.8	1.48	1.483	1.10	14.2

At such high magnetite loading agglomeration of its particles during preparation of the composite was quite probable. To clear the matter up, the X-ray line broadening study was performed. As is known, the peak width, *B*, permits to determine the particle size because the angle broadening, Δ, of fine particle peaks relatively to monocrystalline standard peaks, with the width B_s, (monocrystal of silicon with B_s = 0.25 dg has been used as a standard) is equal to $\Delta = (B^2 - B_s^2)^{1/2}$ and is connected with average particle diameter, D, by means of Sherrer equation:

$$D = \frac{0.9\lambda}{\Delta \cos \Theta} \qquad (2)$$

The values of *D* calculated in accordance with eq.(2) agree with the known particle size[6] of Fe_3O_4 sol (12-14 nm) that testifies about the absence of Fe_3O_4 particles agglomeration during procedure of PAni/Fe_3O_4 nanocomposite preparation.

As follows from fig.1, IR-spectrum of the composite is a superposition of magnetite and PAni doped with HCl spectra. The bands at 580, 795 and 890 cm^{-1}, which correspond to vibrations of oxide lattice and deformation vibrations of hydroxyl groups bind with the oxide[8], do not change during composite synthesis. At the same time, the bands which correspond to valence vibrations of C=C bonds in quinoid (Q) (1589 cm^{-1})[9] and benzoid (B) (1496 cm^{-1})[9] rings and C—N bond (1306 cm^{-1})[9] are essetially shifted to lower wavenumbers. Analogous, but less, shift has been observed while doping of PAni base — emeraldine — by inorgenic acids[9]. That's why, for elucidation of the shift nature, the composite was exposed to the action of ammonium hydroxide. As a result, accordingly to fig.1, the bands corresponding to vibrations of the two last bonds return to positions characteristic for emeraldine while the band corresponding to the vibrations of quinoid rings remains appreciably shifted. Besides, the prolonged processing of thoroghly grinded composite by excess of 0.1M NH_4OH do not cause dissapearance of 1145 cm^{-1} band, corresponding to vibrations of bonds in B—$\overset{+}{N}$H=Q or B—$\overset{+}{N}H_2$—B fragments of PAni chains. In this respect, the studied composite differs from the pure PAni for which, as a result of such processing, deprotonation of nitrogen atoms in quinoid fragments and, as a concequence, dissapearance of 1145 cm^{-1} band occur. Apparently, Fe_3O_4 particles are partially reduced during anilinium polymerization and act as

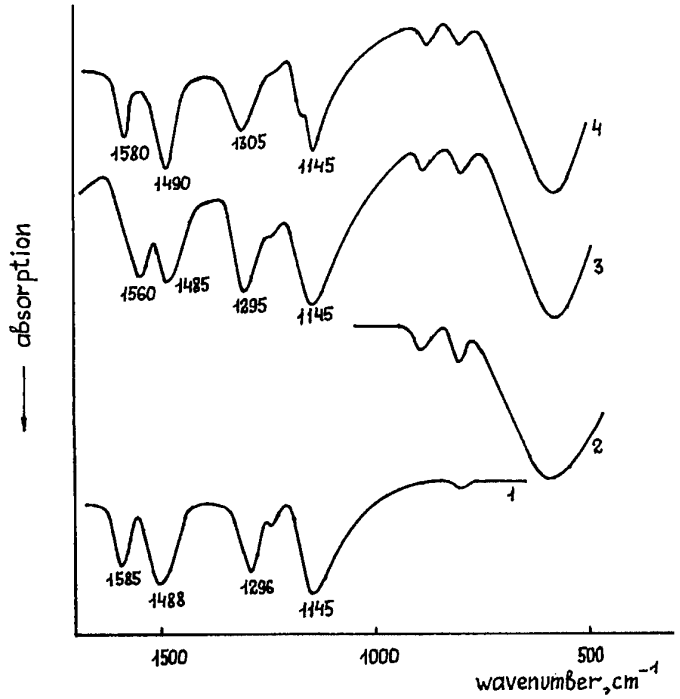


Fig.1. IR-spectra of PAni doped with HCl (*1*), Fe_3O_4 xerogel (*2*), doped (*3*) and undoped (*4*) PAni/Fe_3O_4 nanocomposite.

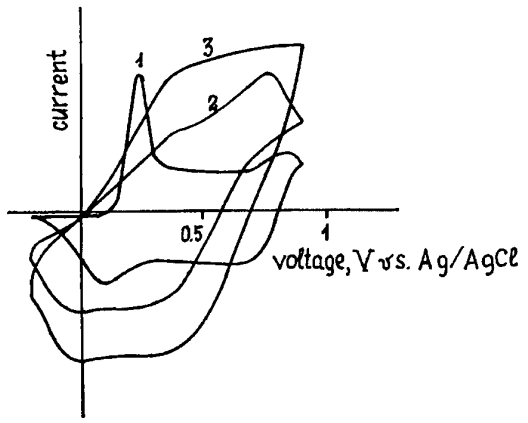


Fig.2. Cyclic voltammograms of PAni (*1*) and PAni/Fe_3O_4 nanocomposites with magnetite loading equal to 7 (*2*) and 51 (*3*) wt. %.

compensators of the doped PAni charge together with chloride anions. Then, under the influence of the base those polymer fragments which interact with the oxide don't return into neutral state that leads to preservation of 1145 cm^{-1} band. However, its intensity decreases and 1165 cm^{-1} band, which corresponds to valence vibrations of C—N bond in B—NH—B polymer fragments[9] and which was not seen earlier on the background of very wide and intense 1145 cm^{-1} band, manifests in the spectrum.

From cyclic voltammograms (CVA) shown on fig.2, it follows that, the first, the studing composite material is electrochemically active. The second, CVA of the composite radically differs from CVA of both PAni and Fe_3O_4 which has in the considered potential interval one redox-potential at 0.55 V *vs* Ag/AgCl corresponding to electrochemical process $Fe^{2+} = Fe^{3+} + e$. One may conclude that PAni/Fe_3O_4 nanocomposite possesses individual properties, characteristic redox-potential being among their number.

EPR spectrum of PAni/Fe_3O_4 nanocomposite at room temperature is a very intense singlet with the line width ΔH_{pp} = 1180 G and g = 2.23 ± 0.01. The value of g-factor coinsides with that received earlier for ferromagnetic resonance in pure magnetite[10]. The form of the resonance line in our case is close to Lorentzian curve in the center and Gaussian curve at the wings that reflects composite nature and, connected with it, heterogeneity of the material. The great width of the line is probably due to high inhomogoneity of effective magnetic field acting on individual Fe_3O_4 particle.

It should be underlined that thorogh measurements showed absence of absorption corresponding to paramagnetic centers on PAni chains. For nanocomposite based on V_2O_5 oxide this effect is connected with antiferromagnetic exchange between polymer and oxide paramagnetic centers[11]. In our case, the effect may be caused by high heterogeneity of internal magnetic field which in such extent widens the absorption signal that it is impossible to register it.

The dependence of PAni/Fe_3O_4 nanocomposite magnetization from applied magnetic field is shown on fig.3. Absence of residual magnetization and high value of saturation magnetization testifies about the superparamagnetism that can be expected on the base of presented data about Fe_3O_4 particles size. Magnetization, M, as a fraction of saturation magnetization, M_0, obeys the Langevin equation:

$$M/M_0 = \coth x - 1/x, \qquad (3)$$

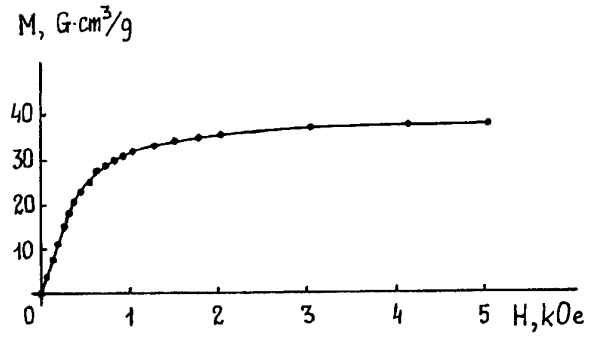


Fig.3 Magnetization curve of PAni/Fe_3O_4 nanocomposite: dots — experimental data, solid line — the best-fit Langevin curve

where x is given by $x = aH$, $a = m/kT$, m is an average magnetic moment of a separate magnetite particle. M_0 and a, determined by fitting eq.(3) to experimental data, are equal to 38 $G \cdot cm^3/g$ and $5.2 \cdot 10^{-3}$ G^{-1} (with correlation coefficient equal to 0.999). The number of Fe_3O_4 particles per 1g of the composite is determined by relation[12] $n = M_0/m$ that allows to calculate the average volume of the particle according to $V = (n\rho)^{-1}$, where ρ is magnetite density. Therefore, the Fe_3O_4 particle diameter is obtained to be equal to 13 nm that correlates well with X-ray diffraction data.

At such size of magnetite particles the superparamagnetism criterion (1) is valid at room temperature if $K_{eff} < 3.5 \cdot 10^5$ erg/cm^3. It can be concluded that in the studing material the coefficient of magnetic anisotropy is at any rate three times less than that of volumetric magnetite. This may be connected with interaction between Fe_3O_4 particle surface and PAni chains mentioned above.

4. CONCLUSIONS

It follows from the data descibed here that the novel composite material based on polyaniline and magnetite with magnetite loading up to 50 wt. % has been obtained. The magnetite particles have nanometric size that leads to superparamagnetism of the material. The nanocomposite possesses individual physico-chemical properties which differs from that of separate components.

5. REFERENCES

1. R.F.Service, «Structure meets function at materials gathering», Science, Vol.264, N 5158, pp.510-511, 1994.

2. M.D.Butterworth, S.P.Armes and A.W.Simpson, «Synthesis of poly(pyrrole)-silica-magnetite nanocomposite particles», Chem. Commun., N 18, pp.2129-2130, 1994.

3. E.Ruiz-Hitzky, «Conducting polymers intercalated in layered solids», Adv. Mater., Vol.5, N 5, pp.334-340, 1993.

4. G.Bidan, O. Jarjayes, J.M.Fruchart and E.Hannecart, «New nanocomposites based on «tailor-dressed» magnetic particles in a polypyrrole matrix», Adv. Mater., Vol.6, N 2, pp.152-155, 1994.

5. M.T.Nguen and A.F.Diaz, «A novel method for the preparation of magnetic nanoparticles in a polypyrrole powder», Adv. Mater., Vol.6, N 11, pp.858-860, 1994.

6. V.I.Baranov and E.E.Bibik, *Practical work on colloid chemistry*., p.147, Vysshaya Shkola, Moscow, 1983 (in Russian).

7. A.I.Kitaygorodsky, *X-ray structure analysis of small-crystalline and amorphous solids*., Moscow, 1952 (in Russian).

8. V.S.Oleynik, L.K.Vysotskaya, V.D.Danchuk, V.P.Dotsenko and Yu.P.Tsyaschenko, «Spectral study of ferro-oxide luminescent magnetopowder compositions», J. Appl. Spectroscopy, Vol.54, N 1, pp.146-149, 1991 (in Russian).

9. S.-A.Chen and L.-C. Lin, «Doping of polyaniline via pseudoprotonation by an ionic salt», Adv. Mater., Vol.7, N 5, pp.473-475, 1995.

10.S.S.Borovik, A.S.Milner and V.V.Eremenko, *Lectures on magnetism*., Kharkov University, Kharkov, p.122, 1972 (in Russian).

11.M.G.Kanatzidis, C.-G.Wu and N.O.Marcy, «Conductive polymer/oxide bronze nanocomposites. Intercalated polythiophene in V_2O_5 xerogels», Chem. Mater., Vol.2, N 3, pp.222-224, 1990.

12. A.U.v.d.Giessen, «Magnetic properties of ultra-fine iron (III) oxide-hydrate particles prepared from iron (III) oxide-hydrate gels», J. Phys. Chem. Solids, Vol.28, N 2, pp.343-346, 1967.

Supramolecular Polymers for Optical Resolution

Naoya Ogata

Department of Chemistry, Sophia University
7-1 Kioi-Cho, Chiyoda-Ku, Tokyo 102, Japan

ABSTRACT

Optical resolution of α-amino acids such as Tryptophan (Try) were carried out either by membranes or temperatutre-responsive polymeric adsorbents. Higher ordered supramolecular structures of polymers were recognized to be quite important for optical resolution by membranes. Optically active and temperature-responsive polymers derived from N-isopyropylacrylamide could be applied for optical resolutions of racemic Try by using dessolution-precipitation behaviors of the temperature-responsive polymeric adsorbents.

1. INTRODUCTION

Optical resolutions of racemic mixtures of optically active sustrates are very important especially in the areas of biomedical and pharmaceutical applications. Optical isomers have normally almost the same chemical and physical properties so that separations of these optical isomers are very difficult by conventional separation methods such as distillation or recrystallization. Recently, optical resolutions by polymeric membranes have been extensivley attracting many interests because of wide industrial applications. However, optical resolution by membranes requires precise molecular recognitions of optical isomers because it is expected that only one side of the isomers permeates through the membranes, while the other isomers should be rejected to permeate through the membranes. Thus, intelligent membranes to recognize optical isomers have to be designed.

Polymers having sharp temperature responces such as poly(N-isopropylacrylamide) PNIPAAm have been widely studied for biomedical applications. PNIPAAm has a sharp phase transition temperaure at 32°C which is called as a lower critical solution temperature (LCST). In other words, PNIPAAm dissolves in water below the LCST, while it becomes insoluble in water above the LCST and this dissolution-precipitation behavior is derived from balance between hydrophilic and hydrophobic characters of amide and isopropyl units within the PNPAAm. When a chiral group is incorporated into the PNPAAm, the chiral group would recognize optical isomers in aqueous solutions and one side of optical isomers would be strongly adsorbed onto the PNIPAAm, thus resulting in phase separations from the aqueous solutions by simply rising temperatures above the LCST. This expectation would led to large scale optical resolutions of optical isomers as the PNIPAAm can be recovered by separating the adsorbed optical isomers with increasing the temperature again above the LCST. Thus, a novel optical resolution would be attained by the intelligent systems by using the temperature-responsive polymeric adsorbent.

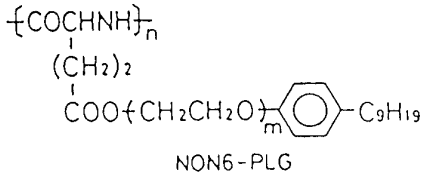
This paper deals with optical resolutons either by intelligent membranes or temperaure-responsive polymeric adssorbents.

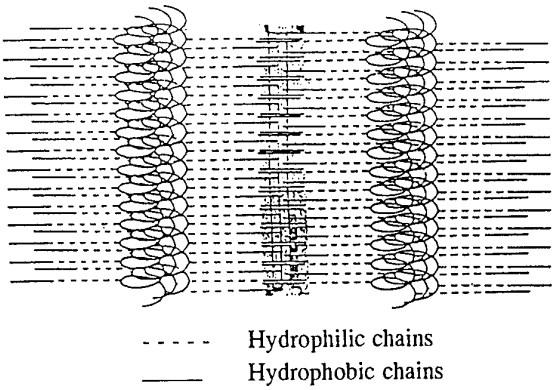
2. OPTICAL RESOLUTIONS BY MEMBRANES

It was previously reported[1]that poly(L-glutamate) having amphiphilic side chain (NON6-PLG) as shown below had a self-organized supramolecular structures by solvent casting, which led to complete optical resolution of racemic Triptophan (Try) through the membrane, as shown in Fig. 1. The complete optical resolution through the PLG

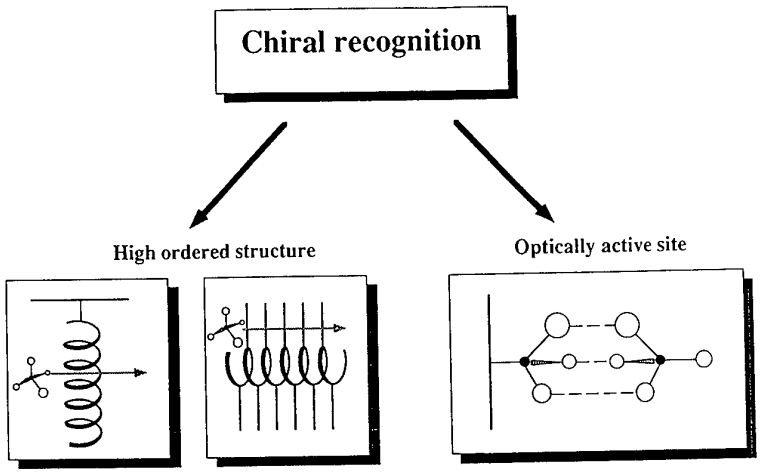
0-8194-2165-0/96/$6.00

by permeating through the hydrophilic domains of the PLG membrane, leading to molecular recognitions of Try

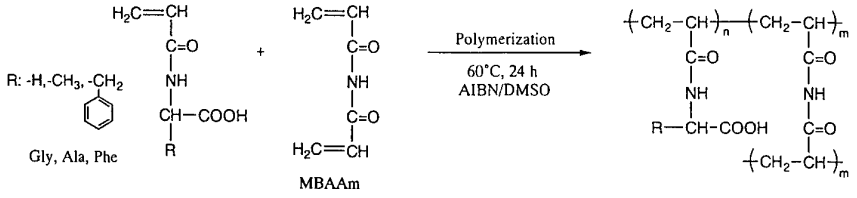


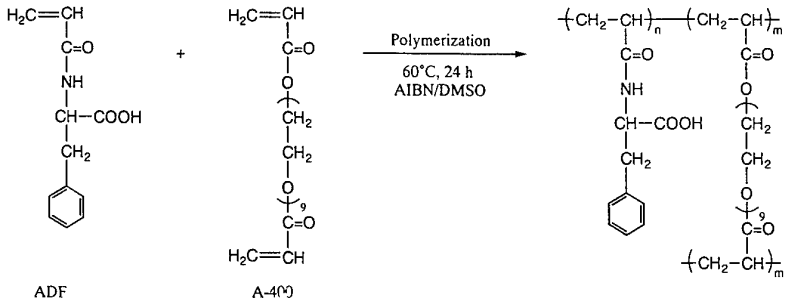


Chiral interactions of substrate with membranes might take place for optical resolution when chiral α-amino acid moieties are incorporated into membranes. It is interesting to compare abilities of optical resolution through membranes having α-amino acids with the NON6-PLG membrane in order to clarify whether high-ordered structures of membranes would be more important for optical resolution than the incorporation of simple chiral groups into the membranes, as schematically shown below:



Thus, hydrogel membranes having various α-amino acids moieties were synthesized as follows:





Permeation experiments of Try by using the hydrogel membranes were carried out at room temperatures and results of the permeation are shown in Figs. 2. The hydrogel membrane having L-alanine permeated D-Try at the intial stage of the permeation, while after certain times L-Try started to permeat through the membrane with almost similar permeation speed. Similar results were obtained when L-phenylalanine was incorporated into the hydrogel membrane, as shown in Fig. 3. These results suggested that molecular recognitions of the hydrogel membranes were not satisfactory and saturation of chiral recoginition points with substrates took place so that the permeation speeds of both L- and D-Tro through the membrane became similar after the saturation, as schematically shown below. These results strongly support that higher-ordered structures of the membares would be much more important for molecular recognitions than single chiral groups incorporated into membranes.

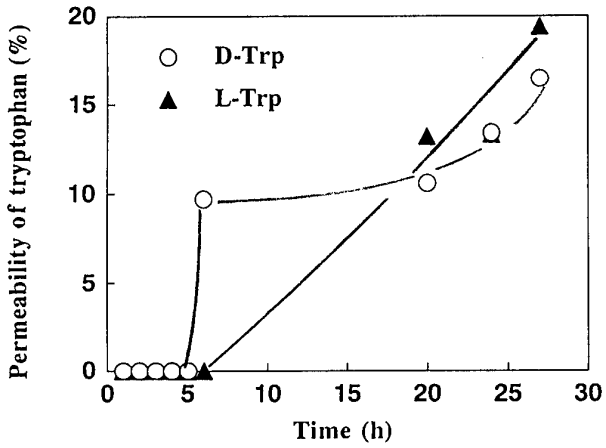


Fig. 1 Permeation of Try through hydrogel membrane having L-alanine moieties at room temperature. Initial Concn. of D, L-Try on donor side=0.05M

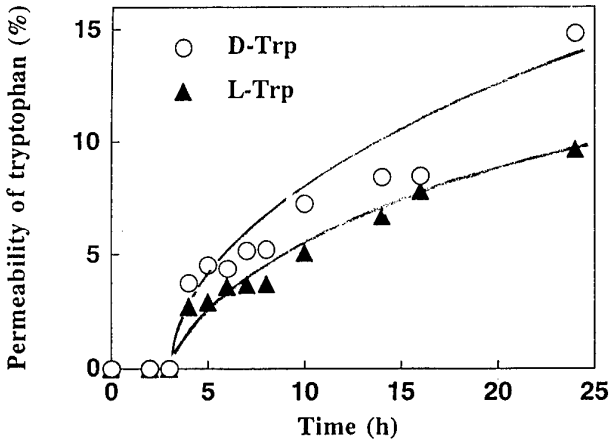
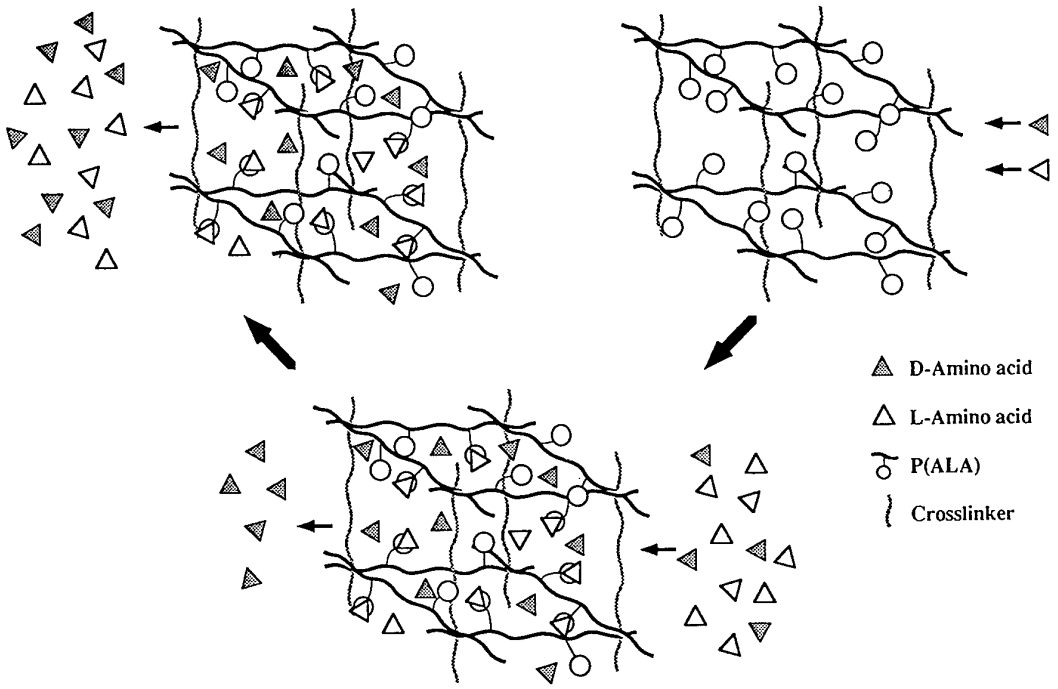
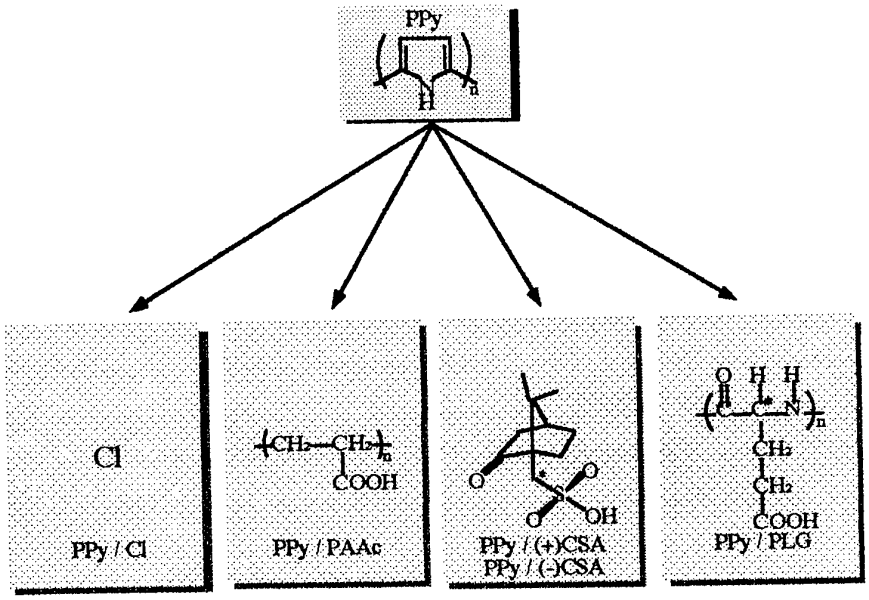


Fig. 2 Permeation of Try through hydrogel membrane having L-phenylalanine units at room temp[erature. Initial concn. of D,L-Try on donor side=0.05M.



Schme of permeation of Try through hydrogel membranes having α-amino acids

Pyrrole is well known to electrically polymerize in aquous solutions containing supporting electrolytes and poly(pyrrole) (PPy) membranes containing anodic dopants are obtained on cathod.
It is expected that electrical polymerization of pyrrole in the presence of anionic chiral compounds as a supporting electrolye might lead to yield membranes doped with these chiral compounds. Base on this expectation, electrical polymerization of pyrrole was carried out in the presence of various anionic dopants, as schematically shown below:



No optical resolution was attained when L- or D-camphere sulfonate, chloride or poly(acrylat anions were doped into the Py membranes. However, when poly(L-glutamic acid) was electrically doped within PPy membranes, L-Try permeated more prefernecially than D-Try, as indicated in Fig. 3.

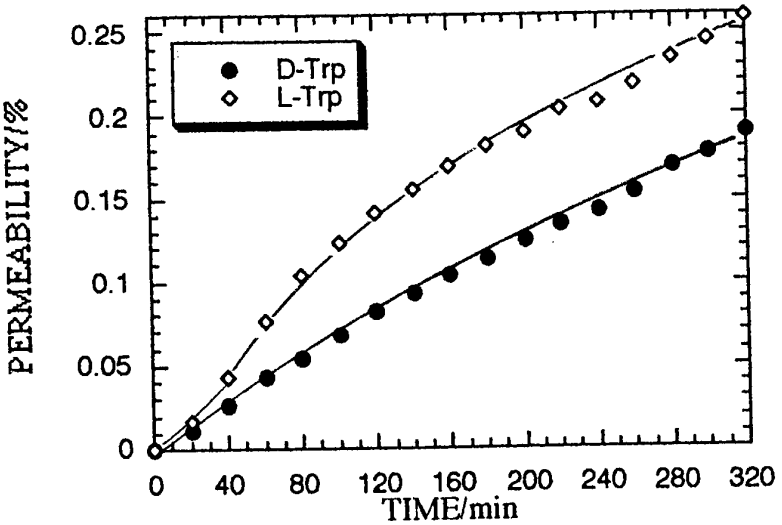


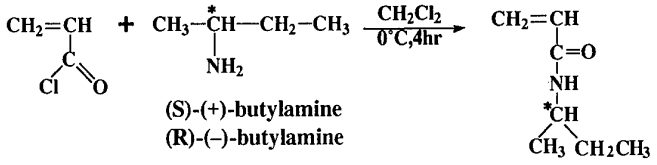
Fig. 3 Permeation of Try through PPy membrane having PLG as a dopoant at room temperature. Initial concn. of D, L-Try on donor side=0.0M5M.

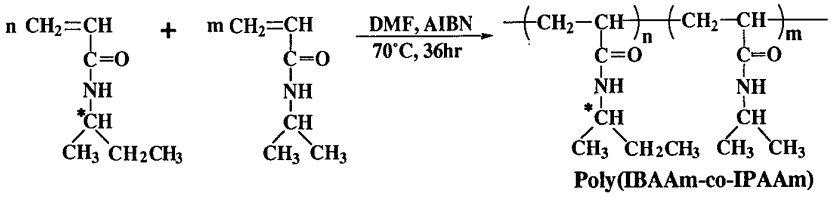
These results again support that higher-ordered structure of the membranes are quite important for molecular recoginition to attain optical resolutions through membranes.

These results again support that higher-ordered structure of the membranes are quite important for molecular recoginition to attain optical resolutions through membranes.

3. Optical Resolution by Temperature-sensitice Polymeric Adsorbents

As mentioned before, PNIPAAm shows a sharp transition temperature at 32°C in terms of dissolution-precipitation behaviors. When opticall active comonomers such as N-isobutylacrylamide (NIBAAm) is copolymerized with NIPAAm, obtained copolymers might have strong chiral interactions with one side of optically active substrate to adsorb onto the copolymers in aqueous solutions. Then, temperature increases above LCST might result in phase separations of the adsorbed copolymers from the solutions. NIBAAm was synthesized and copolymerized with NIPAAm by a conventional radical polymerization, as schematically shown below:





Homopolymer of IBAAm did not dissolve in water and copolymers containing 50/50 molar ratios of IPAAm and IBAAm dissolved in water. The LCST behaviors of the copolymer in aquous solutions were investigated in the presence of Try as a substrate, by measuring transmittance of the aquous solutions with increasing solution temperatures. Table I indicates results of the copolymerization, which show clearly the increase of optical activities with increasing the contents of IBAAm .

Table I. Synthesis of poly(IPAAm-co-IBAAm) at various molar ratios of IBAAm

IBAAm unit	Yield / %	IBAAm : IPAAm[1] / mol%	Mw[2]	$[\alpha]_{20}^{589}$[3]
30mol%				
S-type	34.1	30:70	6000	+1.19
R-type	21.4	26:74	33000	-0.90
Racemic type	36.6	26:74	7600	0.00
50mol%				
S-type	37.1	50:50	8000	+5.98
R-type	38.5	48:52	8600	-7.47
Racemic type	40.6	50:50	7800	0.00

1) Determined by ^{1}H-NMR.

2) GPC in DMF.

3) Measured by polarimeter at 20°C (c = 1.18×10^{-5} mol l^{-1} in water).

Fig. 4 indicates results of the LCST behaviors of the copolymers having 50 mo% of racemic IBAAm in the presence or absence of Try. The LCST of the copolymer was 27°C, while it shifted toward slightly higher temperatures in the presence of L- or D-Try, owing to adsorption of hydrophilic Try onto the copolymer. However, no LSCT changes were observed between L- or D-Try, as seen in Fig. 4. When optically active

S-IBAAm was used, its LCST was the same 27°C as the racemic IBAAm copolymer without Try in the aquous solution. On the other hand, LCSTs of the S-copolymer in the presence of Try shifted toward much higher temperatures than that in the absence of Try and the LCST in the presence of D-Try was lower than that in the presence of L-Try. These results strongly suggested that D-Try was more preferencially adsorbed onto the S-copolymer than L-Try. Reverse result should be obtained when R-type copolymer is used. Fig. 5 indicates results of the LCSTs of the R-type copolymer in the presence of Trp. The LCST of the R-type copolymer was almost the same as that of the S-type copolymer. When Try was present in the aqueous solution, LCSts were shifted toward higher temperatures and the LCST in the presence of D-Try was much higher than that in the presence of L-Try. Therefore, it was clear that L-Try was much strongly adsorbed onto the R-type copolymer than D-Try. The reverse adsorption behaviors of the R-type copolymer strongly support the concept that the optically active temperature-sensitive polymer might lead to a novel optical resolution method.

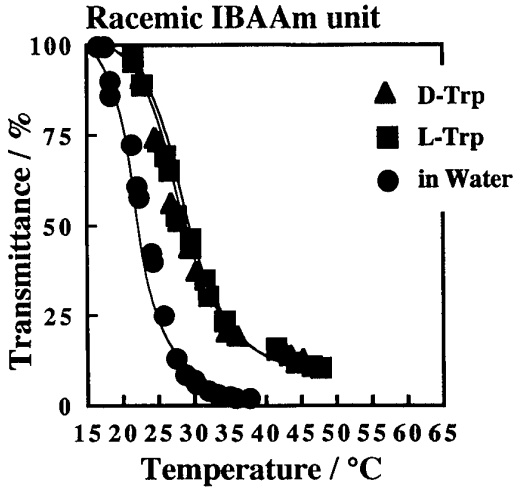


Fig. 4 LCST behaviors of racemic copolymer (50mol% of IBAAm)
Try concn.=0.1wt%

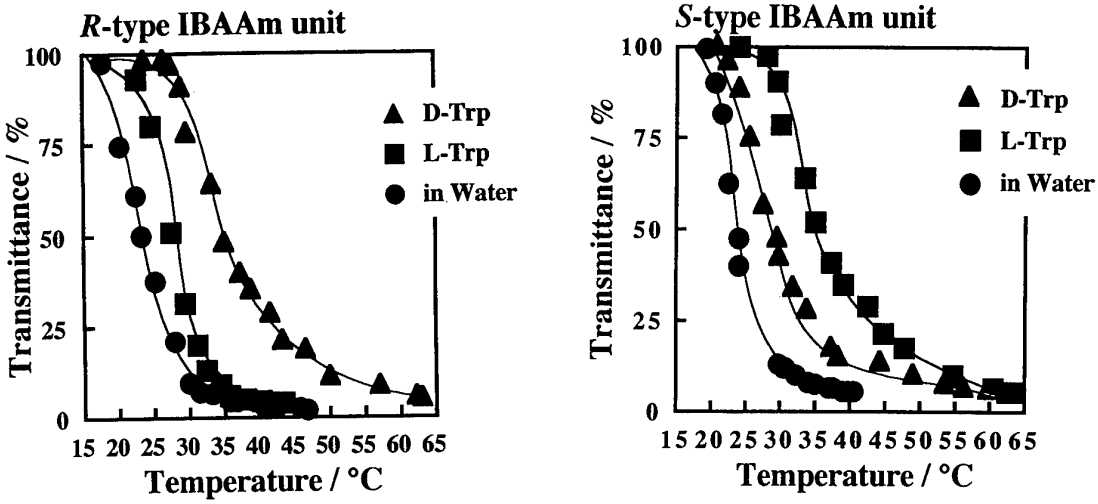


Fig. 5 LSCT behaiors of optically active copolymers (50mol% of IBAAm) in the presence of L- or D-Try (0.1wt%).

Racemic Trys were dissolved in aqueous solutions of racemic, S- or R-types copolymers derived from 50/50 molar ratios of IPAAm and IBAAm and temperatures of the solutions were increased gradually just above the LCSTs of the copolymers. Results of the optical resolution of racemic Try by using the temperature-sensitive poly(IPAAm-co-IBAAm) are summarized in Table II. The racemic copolymer did not have any differences in adsorption behaviors of both L- and D-Try. On the other hand, L-Try was strongly adsorbed onto the S-type copolymer and most amount of D-Try remained in the solution, when the S-type copolymer was used as an adsorbent. Reversibly, D-Try was strongly adsorbed onto the R-type copolymer and most amount of L-Try remained in the solution, when R-type copolymer was used as an adsorbent. Thus, a novel ioptical resoltion was established by the temperature sensitive intelligent polymeric adsorbent.

Table II Optical resolution of racemic Try by temperature-sensitive poly(IPAAm-co-IBAAm) adsorbents

Code	$10^{-2}\times C_{D\text{-}Trp}$ / mmol l-1 (%)		$10^{-2}\times C_{L\text{-}Trp}$ / mmol l-1 (%)	
S-type	**2.3**	**(15.7)**	**5.0**	**(34.0)**
R-type	**6.7**	**(45.0)**	**4.0**	**(27.0)**
Racemic	**2.3**	**(18.0)**	**2.7**	**(15.7)**

Initial concentration of Trp is 1.47×10^{-1}mmol l-1

REFERENCES

1) N.Ogata, *Reactive & Functional Polymers*, **26**,201-208(1995)
2) M.Heskins, E.Guillet, and E.James, *J.Macromnol.Sci.*, **A2**,1441-1455(1981).
3) M.Matsukata, Y.Takei, T.Aoki, K.Sanui, N.Ogata, Y.Sakurai, and T.Okano, *J.Biochem.*,**116**,682-686(1994)

Opaque-transparent transition in polymeric hydrogel systems

Harald Goering, Hans-Rainer Holzbauer, Andreas Schönhals, Hans-Eckart Carius, Arno Seeboth

Institut für Angewandte Chemie Berlin-Adlershof e.V.
D-12484 Berlin, Germany

In consideration of the development of large area displays with improved electro-optical properties new functional materials were prepared based on polymeric supramolecular hydrogel networks. The highly ordered aqueous gel system is provided with particular properties for carrier material of electrically switchable polymer-dispersed liquid crystals as well as for optical valve without assistance.[1]

The high water content gel systems were prepared from mixtures of aqueous poly(vinyl alcohol) [PVA] and poly(ethylene glycol) [PEG] solutions by adding of borax as physical crosslinking agent. The PVA was modified by different degree of ethoxylation. The obtained gels show reversible changing of optical transparency in dependence on temperature. In a certain temperature region it is observable a opaque-clear transition without complete loss of mechanical stability of the gel network. The temperature position as well as the steepness of this transition can be influenced by the concentration and concentration ratio of the basic polymer solutions and also by the molecular mass and molecular mass distribution of the polymeric components. So it is possible to manufacture mechanically stable sheets which reversibly change their optical transparency extremly up to contrast ratio of 85 : 1 within a temperature region of a few Kelvin. These properties are similar to electro-optical addressed polymer dispersed liquid crystal displays with a phase transition from thermotropic nematic to isotropic.[2]

To optimize the behaviour of this hydrogel system for special application in the field of new functional matierials the experimental investigations deals with the structure-properties relationship using polarisation microscopy, UV/VIS spectroscopy, rotational viscosimetry, dynamic mechanical analysis and dielectric relaxation spectroscopy.

Mechanical relaxation studies show, that although this behaviour is caused by a phase transition but it is not connected with the total break down of the continuous polymeric network structure. Even in the clear state at hightened temperature the gel system is provided with a remarkable portion of entropic elasticity. The properties are explainable by the complex structure as supramolecular interpenetrating polymer network [IPN] with a combination of liquid-liquid and liquid-crystalline separation in aqueous media. For smaller molecular mass of PEG in the range < 10.000 a colloidal separation is found , which leads up to a vitrifying of the matrix at higher concentration. By selecting the molecular mass high enough in the range of 20.000 to 50.000 it takes place phase penetration with the aimed quasi-IPN formation at supramolecular level. The PVA chains preferentially with extended conformation form under strong influence of borax fibrillar crystallites, which are the structural basis of the supramolecular network. The PEG component aggregates to radial symmetric droplets in the μm-scale based on helical structures.[3]

Dielectric relaxation spectroscopy in the frequency range from 10^{-2} Hz to 10^{9} Hz was employed to study both relaxational processes and conductivity in a broad temperature range.[4] The data are discussed in terms of the dielectric permittivity and in electric modulus formalism. Because the water molecules are highly polar the opaque-clear transition is masked by other effects like electrode polarization. Therefore no direct correlation between the electrical and optical data are found. But information is provided about the molecular mobility. So the dielectric relaxation spectroscopy can discriminate between different states of water molecules like free or bonded water and gives indirect information about the complex supramolecular structure of these high water content hydrogel systems.

1. A. Seeboth, Thin Solid Films, 223 (1993) 140
2. A. Seeboth and H.-R. Holzbauer, Adv. Mat. (1995) submitted
3. M.J. Schick, Nonionic Surfactants - Physical Chemistry, Marcel Dekker Inc., New York (1987) 949
4. A. Schönhals, F. Kremer and E. Schlosser, Phys. Rev. Lett. 67 (1991) 999

0-8194-2165-0/96/$6.00

Paper presented at the Third ICIM/ECSSM '96, Lyon '96

ADAPTABLE AND ADAPTIVE MATERIALS FOR LIGHT FLUX CONTROL

P.Sixou, A.Magnaldo, J.Nourry, C Laye

CNRS - UA 190 - Physique de la Matière Condensée
Parc Valrose - 06108 Nice CEDEX 02

The purpose of this paper is to describe and examine properties of light flux control materials. Indeed, intelligent light flux control is necessary not only to improve everyday visual convenience but also in an economical point of view in order to reduce global home energetic cost.

Several types of materials are good potential candidates for such functions (1)

- The most well-known investigations concern inorganic materials such as tungsten or molybdenum oxides in which an electrochrom layer darkens when enriched in ions, and looses its colour when impoverished. Unfortunately, at the moment, there is no convenient way to realise correct ions suppliers. Moreover, other drawbacks arise, such as poor reversibility, reactive interferences or a sensitivity of the material to its environment. These systems only need a low voltage level to work. But, their dynamic response, which is correlated to the component surface, is quite long.
- At the present time, another attractive issue seems promising. More and more studies concern micro-composite liquid crystal films.

For first, we shall remind their principles as well as their way of preparation. After having talked about their main advantages as intelligent materials, we shall discuss their control, their light flux adaptability, or their memory capabilities.

The way of preparing micro-composites films :

It is a well-known fact that an electric field perturbs molecular arrangement of liquid crystals and modifies their optical response. These electro-optical effects are used for electronic displays. These materials can be orientated under an electric field. In order to apply this field, mixtures are customarily brought between two conductive substrate plates. The liquid crystal layer is quite thin (usually from 2µm width for chiral smectic films up to about ten microns or so in the other cases), arising big technological difficulties in order to realise large surface samples. Moreover, because of the liquid crystal fluidity, these systems need to be tight.

In contrast, as micro-composite films are solid, such drawbacks never have been experienced. In this case, liquid crystal mixtures are embedded in a polymeric medium in micro-droplets. They also have the same electro-optical effects as the pure liquid crystal films.

Micro-composite materials are usually obtained either by using a micro-emulsion or by phase separation. A great part of today's materials are based on this last method. It consists in inducing firstly, a thermodynamic phase separation among a liquid crystal polymeric mixture, secondly, in quenching the polymer in order to obtain a solid film.

Depending on the mass content of the liquid crystal mixture in the system, one can obtain a closed porosity (formation of liquid crystal micro-droplets in a poor liquid crystal mixture material) or an opened porosity (formation of a polymeric network in a rich liquid crystal mixture material).

There are three different phase separation processes :

- a temperature induced phase separation;
- a solvent induced phase separation;
- and a photo-chemical induced phase separation.

Mechanisms involved (nucleation, growth and spinodal decomposition) are well described elsewhere (2, 3, 4).

Whatever the preparation method is, the electro-optic properties of liquid crystal polymer composite materials deeply depend on their morphology.

In a very simplified manner, two aspects have to be considered:

- Firstly, the liquid crystal molecules may, if they are confined in a very small cavity, have different properties than they should have in a large volume.
- Secondly, the surface interactions of the cavity greatly modify the electro-optical behaviour of the liquid crystal mixture.

Numerous polymer (acrylic, urethane, epoxy resin, ...) and different kinds of liquid crystal (cyanobiphenyl, ...) could be chosen. The right polymer liquid crystal blend depends on their reciprocal compatibility.

Useful properties :

1 - Adaptable materials :

0-8194-2165-0/96/$6.00

The modification of the light flux can be controlled by different parameters as a mechanical or an optical stress, an electric or magnetic field.
The electric field induced modification is a very common way to control the light flux.

The following paragraph will be restricted to this method.
Different types of electro-controlled films can be obtained depending on the nature of the liquid crystal molecules, of the polymer and also, of the micro-composite processing.

1.1 - Light occlusion films :

- From opacity to clearness under an electric field :

These films are strongly diffusive in the off-state and become clear under an electric field (typically beyond the 10 to 100 Volts range).
The opacity comes from light diffusion by the nematic liquid crystal droplets. The materials and the preparation process set the scattering level and the way the system becomes transparent.

- From clearness to opacity under an electric field :

Though an opaque off-state film is interesting as a light flux occlusion, it exhibits two main disadvantages:

- When an electrical breakdown occurs the film remains opaque.
- For systems, like car glasses, which need to be transparent most of the time, a voltage has to be maintained. This is disadvantageous because of high power consumption and a reduced lifetime of the system.

Fig.1 illustrates the way to obtain and control films which are clear in the off-state and opaque under an electric field.
A dual frequency liquid crystal is encapsulated inside a polymer matrix. Such liquid crystal mixtures present a positive dielectric anisotropy when at low frequencies and reveal a negative dielectric anisotropy beyond a cut-off frequency. This threshold frequency is generally situated in the 1kHz range and depends obviously on the liquid crystal nature.

An heterogeneous film may be realised in such a way that the liquid crystal mixture separates from the processor of the polymeric medium. So, that the impinging light is strongly scattered due to the refractive indexes difference between the components. On applying a low frequency voltage, the liquid crystal molecules are aligned parallel to the field and perpendicular to the electrodes. The system appears transparent. The liquid crystal can be aligned while curing. The film remains clear. When the electric field is cut-off, the transparency is still kept.
When applying again a high frequency voltage, the system can be switched from a clear to an opaque state.

1.2 - Selective reflective films :

A cholesteric or a chiral nematic liquid crystal, whose helix is perpendicular to the film level, selectively reflects impinging light according to the Bragg' law, if the light wavelength is equal to the product of the helix pitch p and the mean index of the medium <n>.
Moreover, only 50% of the incident light could effectively be reflected. The optical sense of the light has to match the liquid crystal helix sense.

An easy way to obtain a cholesteric helix perpendicular to the film level is to choose a negative dielectric anisotropy liquid crystal . So, when an high enough electric field is applied the cholesteric selectively reflecting texture is obtained.
For a reflection chosen in the visible range, one may obtain low diffusive thin films. They will be transparent in the off-state and will become reflective under an electric field (Fig. 2).

- Setting the selective reflection :

The wavelength of the selective reflection is easily changed by modifying the chiral concentration in the nematic solvent. Fig. 3 illustrates this aspect.

1.3 - Films possessing numerous states: transparent, scattering, selectively reflecting:

Polymer networks inside a bulk liquid crystal can be used to stabilise more than one state. In this last case, the weight percentage of liquid crystal is very much inferior to that of the liquid crystal (typically around 3%), and depending on the way the cross-linking and growth of the network is done, (i.e. with or without electric field, with a particular surface treatment etc...) very different behaviours are seen. It is thus possible to switch a film from scattering to transparent or vice-versa under a certain field, or even to induce a selectively reflecting texture with no field (see fig. 4) which becomes scattering at another field and eventually transparent for a higher field. One of the most exceptional characteristics of this film concerns it's behaviour as the field is

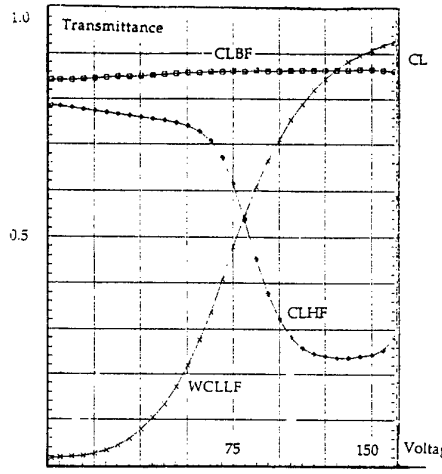


Figure 1: Transparent film at rest, scattering film with high frequency (10KHz) voltage.
WCLLF = Without Crosslinked - Low frequency
CL = Crosslinked
CLBF = Crosslinked Low frequency (500 Hz)
CL HF = Crosslinked High frequency (10KHz)

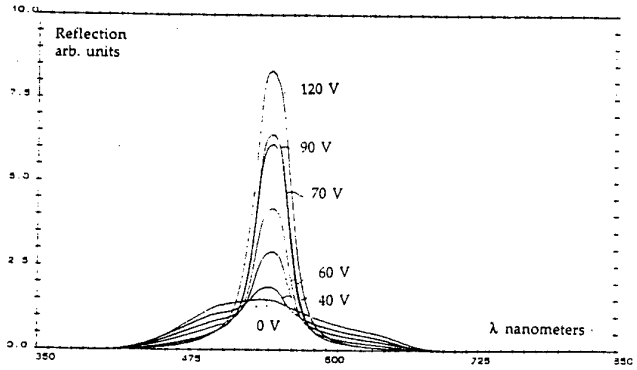


figure 2 - Selective reflection as a function of voltage (indicated in the figure : volts).

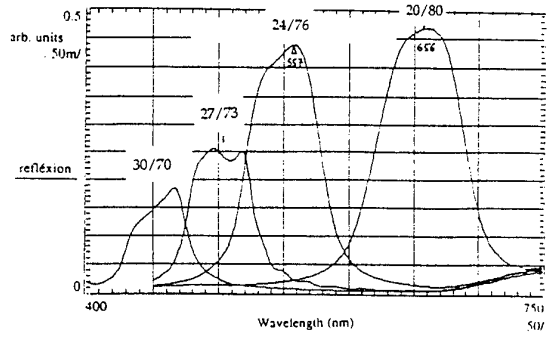


figure 3 - Modification of the selective reflection wavelength by chiral/nematic ratio.

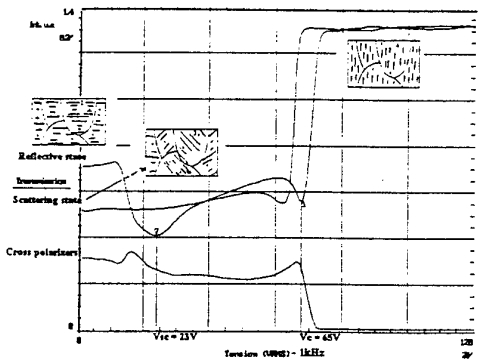
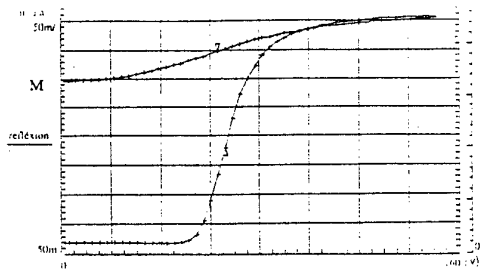


figure 4 - Network realized with cholesteric polymer associated to a cholesteric liquid crystal.



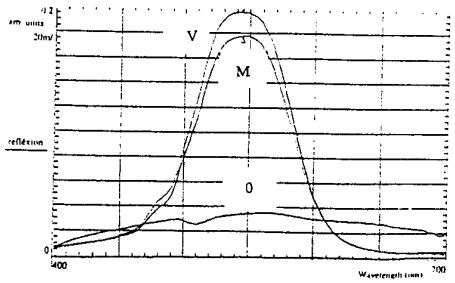


figure 5 - Memory effect : selective reflection band
(0 = without voltage, V = with voltage,
M = without voltage memory state) and magnitude
of memory effect at the top of the selective reflective band.

removed. If the field is removed brutally, the reflecting texture is expected. If the field is removed progressively, a scattering meta-stable texture is found.

2 - Adaptive materials:

Optical characteristics modifications of a material under infringing light has been studied and used in many products (photochromic sun glasses are an example). The photochromic materials used in the above sample can be either of organic or inorganic origin. We will limit ourselves to organic materials (5, 6). The photochromic properties of such substances have been studied when embedded in a matrix, when grafted onto polymer chains or incorporated inside films like Langmuir-Blodgett films... Here we are interested in the case where photochromic substances are included inside liquid crystal micro-inclusions, themselves dispersed inside a polymer matrix. One of the most interesting characteristics of such films is that a flexible, solid film is obtained, which can have a variable optical transmission depending on the incoming light intensity. The host liquid crystal medium could be a low molar mass liquid crystal, a liquid crystal polymer or a blend of both; it therefore becomes possible to adjust the film characteristics such as the thermal reversal kinetics...

3 - Self adaptive and commendable materials

One of the great advantages of a micro-composite polymer/ liquid crystal, in which the liquid crystal contains a photochromic substance, resides in its capability to orientated, by applying an electric field, the liquid crystal and therefore the photochromic substance. Such a film is transparent and darkens with incoming light, but can be instantly switched back to its transparent state even without having removed the incoming light. It is therefore adaptive and commendable. Therefore by adjusting the electric field, it is possible, for a given light intensity, to predetermine a wished grey level amplitude.

4 - Memorising materials

Various types of memory are possible, and different procedures using these materials have been proposed. In addition, various aspects should be considered:

- Re-writing possibilities
- Duration of the memorisation (infinite or not)
- Amplitude of the memorising capability

These aspects characterise the " memory quality ", and will illustrated by the following.

4.1 - Obtaining a memorising material.

The present example concerns a selectively reflective film, obtained with a cholesteric liquid crystal. The thickness of the film is such that in its initial state, the light scattering is strongly reduced, and the film seems transparent. Usually, the composition and the manufacturing of the film is chosen in order to obtain a reversible film, from selectively reflecting under a correct field, back to the transparency of the initial state. It is however possible to manufacture films which maintain the selectively reflecting state after having removed the voltage (7). This interesting property is illustrated fig. 5. The reflection spectra are shown before, during and after having applied a sufficient voltage. The reflection amplitude at the maximal reflection wavelength is also shown. One can see that the reflection level hardly decays after having removed the field, and remains stable for months. The film has memorising capabilities. In order to return the film to its initial state, one needs to heat the film above the nematic the isotropic transition temperature. The film has re-writing possibilities.

4.2 - Controlling the memorisation.

One can show that this memory effect is directly linked to the characteristics of the polymer/ liquid crystal interface zone of the micro-inclusions, and that it is possible to modify these characteristics by various annealing treatments. The annealing effect is proportionally linked to the annealing temperature and annealing time (8). Fig. 6 compares two different annealing treatments with different annealing times. Although the curves concerning the reflection, under electric field, are identical, the characteristics without field are completely different: in one case the reflection is conserved, in the last case, it disappears. All memorisation amplitudes can be obtained by varying the annealing time.

Routes for more elaborated materials

Many possibilities are available, by combining several techniques, to obtain elaborated systems. For example :

- association inside the same layer of various types of micro-inclusions with different properties.
- stacking together different layers allowing, for example heating, scattering, selective reflection, ...

An example is shown (Fig.7) where two layers with cholesteric negative dielectric anisotropy liquid crystal micro-inclusions, each having an opposite twist sense, are stacked. The selective reflection is thus doubled and can approach total reflection at the reflection wavelength maxima.

Coupling with electronic components :

The light flux control can be undertaken by the material or by the same material couple with a micro-system such as a sun-light detector (9), or any other electronic control or command.

Application to " Intelligent windows " :

Once the electrochromic or photochromic material allowing light flux control has been obtained, and the thin film manufacturing problems resolved, questions concerning the energetic gain should be answered. Also, knowledge on the changes of natural lighting is essential.
For a standard room, it is possible to compare the energy efficiency when uses double-glazed or an active electro-commanded reflective film (10). It is shown that the efficiency is enhanced between 6 to 15% with a non-optimised film. The energy gain is far from being insignificant and can still be greatly improved with proper material optimisation.

Conclusion :

Micro-composite liquid crystal /polymer materials seem to be interesting for light flux control applications. In the simplest cases, they can be adaptable, adaptive or both; they can have memory effects predetermined by the manufacturing method and in their most advanced forms, can associate various functions (reflections, scattering, transparency).

References :

1 - C.M.Lampert, C.G. Granqvist, Large-area chromogenics : materials and devices for transmittance control SPIE Vol. IS4, 1989
2 - J.W. Doane Dans Liquid Crystals Applications and uses Ch. 14- Ed B. Bahadur - World Scientific
3 - P.Sixou M. Radian - La Recherche 22, 237, 1354-56, 1991
4 - B. Anina, P. Maissa, P. Sixou Polymer 32, 8, 1510- 15, 1991
5 - C.B. Mac Ardle - Applied photochromic polymer systems - Blackie 1992
6 - R. Guglielmetti - Actualité Photochimique - 1994, 90/94
7 - A. Magnaldo, J. Nourry, P.Sixou J. appl. Phys. (sous presse)
8 - A. Magnaldo, J. Nourry, P.Sixou J. appl. Phys. (soumis)
9 - Microsystèmes et microtechnique - journéées d'études - Paris novembre1995
10 - M. Chantant , J.Gaillard, Contrat JOULE 2 - 1995

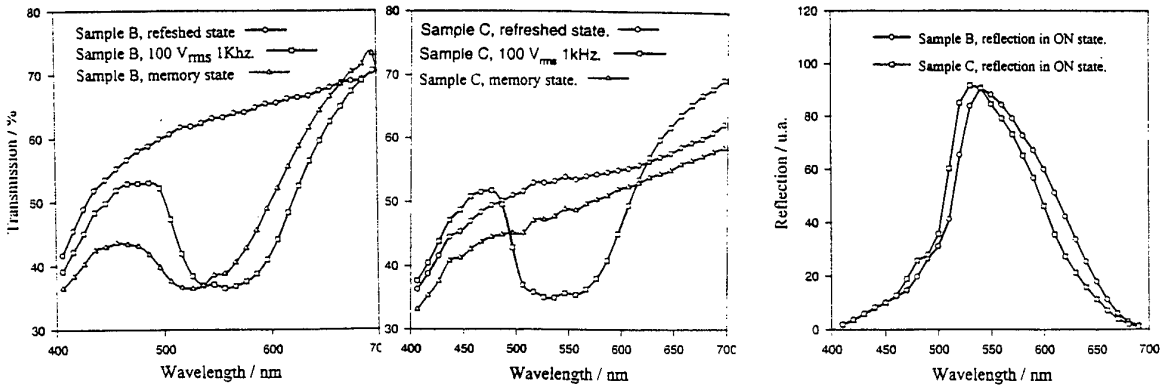


figure 6 - Memory effect : spectral characteristics of two different annealed samples.

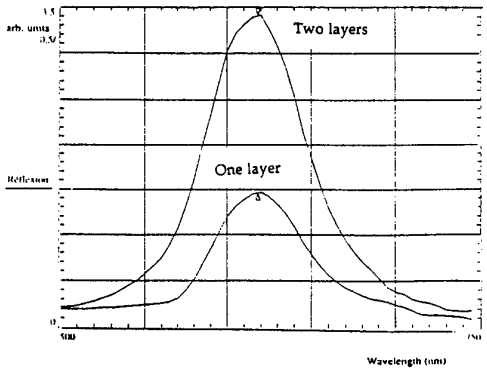


Figure 7 - selective réflexion of one or two layers staked materials (cholesteric with opposit twist).

Some functional macromolecules as exciton converters

Vladimir Syromyatnikov, Valeriy Yashchuk, Tymish Ogul'chanski, Alexey Kolendo,
Irina Savchenko, Vladislav Kudrya

Kiev Taras Shevchenko University, 64, Volodymyrska St., 252033 Kiev, Ukraine

ABSTRACT

The hypothetical structures of macromolecules with direct one-way excitonic conductivity have been examined. The dependence of excitonic current value on number of polymer's cell has been obtained for macromolecules of optimal energetical structure. Some compounds with direct exciton conductivity were designed and synthesized. Such compounds may be used as exciton convectors in nanoelectronics.

The intelligent or "smart" materials and structures attract a world-wide interest and find an application in various areas, such as: modern microelectronics, aerospace, biotechnology and medicine etc. [1]. For design of modern components in nanoelectronics and technics can be used, particularly, polymers and molecular systems with intramolecular energy transfer. To our opinion, as exciton converters or rectifiers may be used macromolecules in which the excitons spread only in determined one-way directions. There are three possibilities of such energy transfer in polymers: in the main chain, in back-bond groups and in macromolecule's fragments.

It is known, that energy transfer in polymer macromolecules is realized by incoherent excitons randomly hopping to nearest neighboring units along the macromolecule [2,3]. The direct exciton current in the macromolecule is possible when there is the decreasing of levels energy values unit to unit along the macromolecular chain. In general case there are three variants of the suitable displacement of energy levels: a) Energy values of singlet levels decrease along the chain; b) Energy values of triplet levels decrease along the chain; c) Both energy values of singlet and triplet sites decrease from unit to unit.

The simplest examples of intramolecular energy transfer in the main chain of macromolecules are observed in binary copolymers with alternated monomer units. Each of them consists of aromatic circle and some covalent carbon atoms as chain spacers. We have synthesized such copolymers using as monomers 1-naphthylacrylate(NAPHA) and 4-acetylphenylmethacrylate(APHMA) [4,5]. The absorption, rapid and delayed fluorescence spectra of monomers and copolymer were obtained at the 293 and 77 K. From APHMA and NAPHA absorption and fluorescence spectra we have obtained data for first excited singlet levels: S_1=27500 cm^{-1} and S_1=31500 cm^{-1} accordingly. Such position of singlet levels excludes the singlet-singlet energy transfer of the electron excitation $S_{1APHMA} \rightarrow S_{1NAPHA}$ under selective excitation of S_{1APHMA} level. The triplet-triplet energy transfer possibility may be shown by phosphorescence spectra:

$$T_{1APHMA}=24100\ cm^{-1},\ T_{1NAPHA}=19700\ cm^{-1}$$

Therefore, under selective excitation of APHMA singlet levels sections only NAPHA-sections phosphorescence is observed and we can conclude that one-way energy transfer is realizable by the scheme being proposed.

From our point of view[6,7] the most interesting situation is that when the position of the first singlet excited state of the initial unit is lower than for the other units in the macromolecule but gradually lowering of triplet levels takes place along the chain. Only in this case the selective exciting of first unit

0-8194-2165-0/96/$6.00

of macromolecule leads to direct one-way propagation from initial to end unit along the macromolecule (Fig.1).

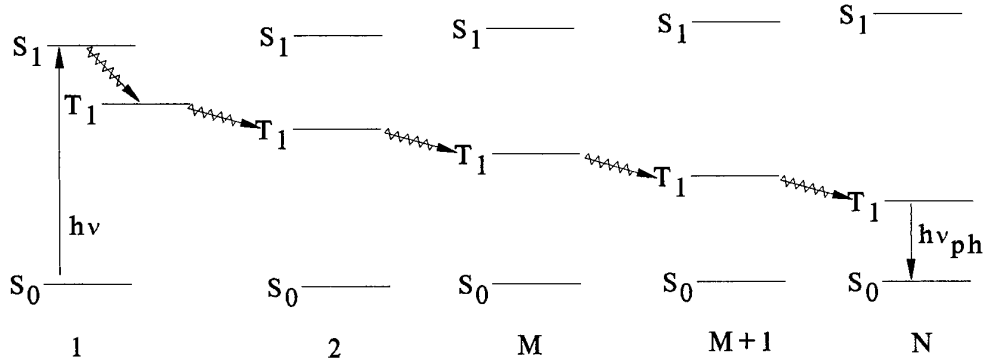


Fig. 1 Scheme of energy transfer from unit to unit in macromolecule.

If in the first unit the I_0 excitons are generating per unit time, it can be shown that the value of the exciton current (this value we introduce as the quantity (N) of excitons which are passing through macromolecular cross-section per unit time) between unit m and unit m+1:

$$I_m \equiv \frac{dN_m}{dt} = I_0 \beta^m \left(1 - \beta e^{-\frac{\Delta E}{kT}}\right)^m$$

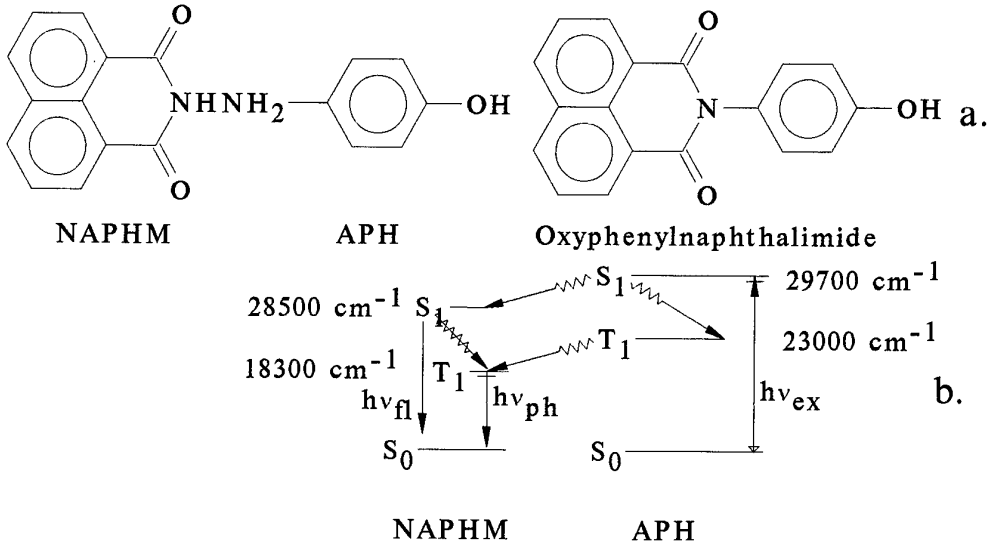
where ΔE - difference between energy values of neighboring units sites, β - the probability of energy transfer between neighboring units without considering of the back transfer. The considering of the possibility of spontaneous deactivation (α) in every unit of macromolecule and processes of back transfer gives such dependence of the total exciton current on number of macromolecule's unit.

$$I = I_0 \left(\frac{1-\alpha}{1 - e^{\frac{\Delta E}{kT}}}\right)^n$$

For triplet excitons[8] in aromatic-containing polymers $\alpha \sim 10^{-5}$. Then for n=10000 and ΔE>>kT $I_n/I_0 \approx$ 0,9. So, the losses of excitons in such model macromolecule are negligible. The initial steps in designing of the compounds with such properties are described below.

As a part of this macromolecule it is proposed the compound which consists of independent several π-electrons systems with determined position of their energy levels. Two possible variants have been examined. 1) In the first of them the decreasing singlet as well as triplet energy levels values takes place from unit to unit and therefore the direct one-way S,T-energy transfer exists. Two compounds possessing such properties have been synthesized: a) oxyphenylnaphthalimide [based on naphthalimide (NAPHM) and aminophenol (APH)]; b) naphthalimidodiphenylbenzoate based on the NAPHM, aminooxydiphenyl (AODP) and benzoic acid (BA). The investigation of absorption, fluorescence and phosphorescence at 293 and 77 K indicates that T- and S-excitons do spread directly in these compounds (Fig.2,3).

Structure formulae of these compounds as well as the scheme of energy levels and some obtained spectra are shown at fig.2,3,4(a,b,c).



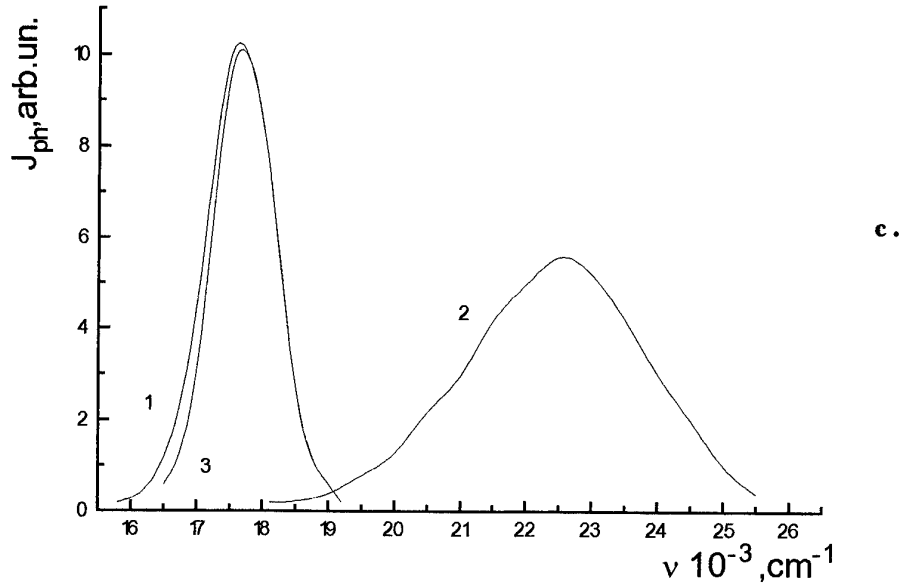
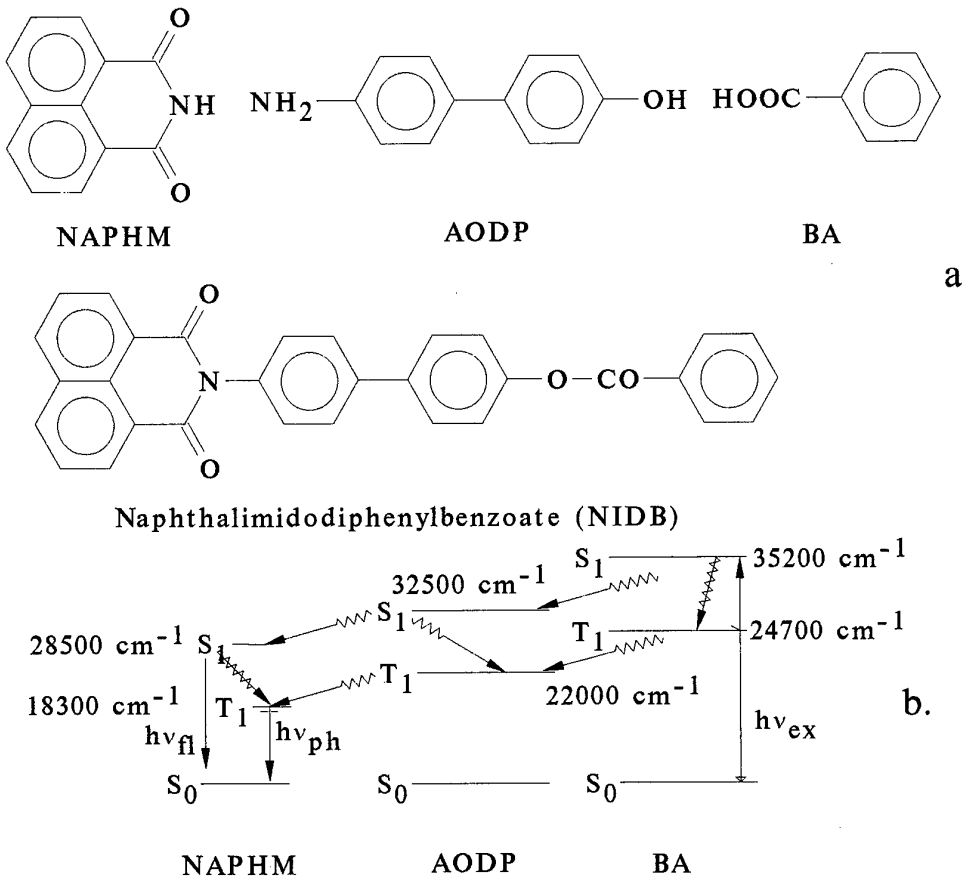


Fig. 2 Energy transfer in oxyphenylnaphthalimide: a - formula and fragments; b - scheme of energy levels; c - phosphorescence spectra: 1 - NAPHM, 2 - APH, 3 - oxyphenylnaphthalimide (dioxane solutions, $C=10^{-4}$ mol/l, T=77K, λ_{ex}=337 nm).



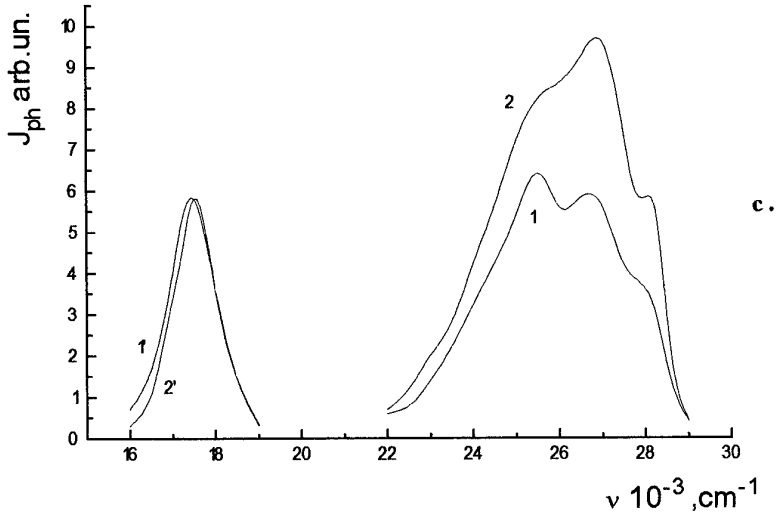
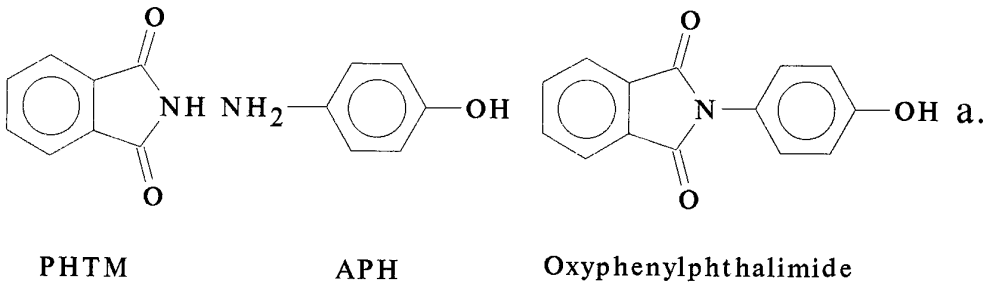
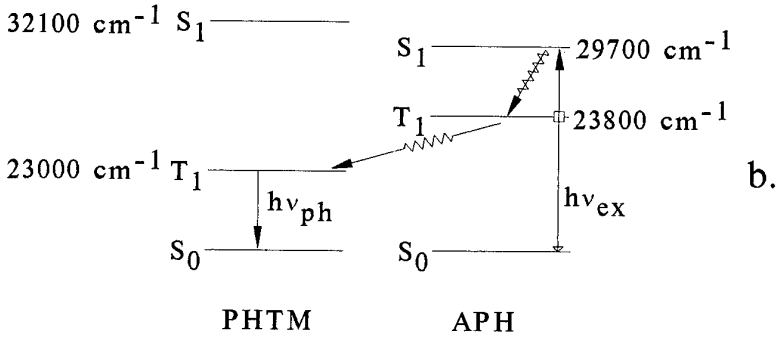


Fig. 3 Energy transfer in naphthalimidodiphenylbenzoate (NIDB): a - formula and fragments; b - scheme of energy levels; c - spectra: 1',2' -phosphorescence of NAPHM and NIDB, 1,2 - fluorescence NAPHM and NIDB.





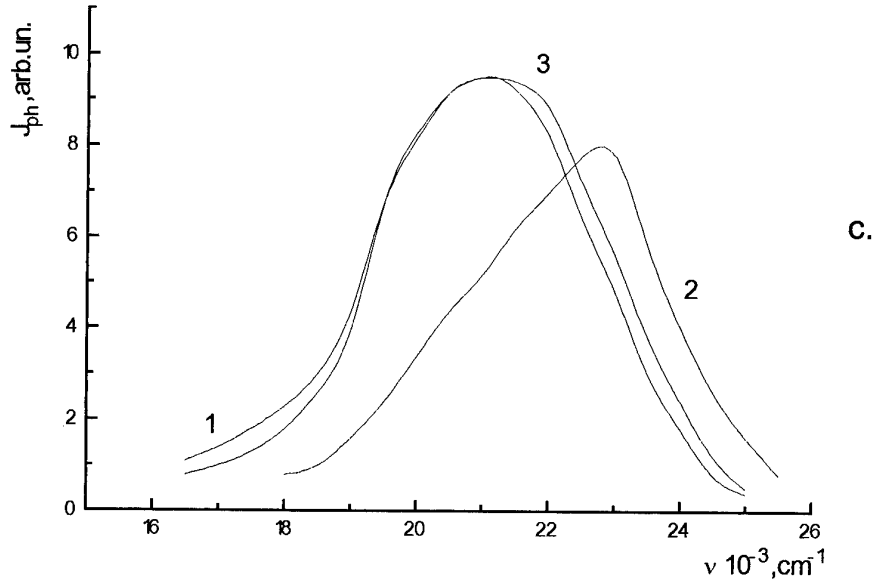


Fig. 4 Energy transfer in oxyphenylphthalimide: a - formula and fragments; b - scheme of energy levels; c - phosphorescence spectra: 1 - PHTM, 2 - APH, 3 - oxyphenylphthalimide (dioxane, $C=10^{-4}$ mol/l, T=77K, λ_{ex}=337 nm).

2) Another variant of the unit's energy level positions has been realized in oxyphenylphthalimide (the compound which consists of APH and phthalimide (PHTM)) (Fig.4). The analysis of absorption and luminescence spectra gives for APH and PHTM's S,T-energy levels S_{1APH}=29700cm^{-1}, S_{1PHTM}=32100cm^{-1}, T_{1APH}=23800cm^{-1}, T_{1PHTM} = 23000cm^{-1}. Such positions of levels except intramolecular S-S energy transfer in compound when S_1-level of APH-unit is excited. However only phosphorescence of PHTM-unit was observed, as a result of selective S_1-level exciting of APH-unit. The last proves that only T-T transfer energy takes place in this compound on scheme:

$$S_{0APH} + h\nu_{ex} \Rightarrow S_{1APH} \Rightarrow T_{1APH} \Rightarrow T_{1PHTM} \Rightarrow S_{0PHTM} + h\nu_{ph}$$

The macromolecules with great number of units may be design on this principle.

The research described in this publication was made possible in part by Grant N K2Q100 from the Joint Fund of the Government of Ukraine and International Science Foundation.

REFERENCES

1. I.Yu.Galaev. "Smart" Polymers in Biotechnology and Medicine" *Russian Chemical Reviews*, 1995, v.64, N 5, pp.505-524.

2. V.V.Slobodyanik., V.N.Yashchuk, V.P.Naidyonov. et al. "Fluorescence and Host-Guest Energy Transfer in Polymeric Chains", *J.Luminescence*, 29, pp.309-320 (1984)

3. W.Klopffer. "Aromatic Polymers in Dilute Solid Solutions. Electronic Energy Transfer and Trapping", in Photophysics of Polymers, edited by Charles E.Hoyle and J.M.Torkelson (Amer.Chem.Soc., Washington, DC 1987), pp.284-285.

4. I.A.Savchenko, A.Yu.Kolendo, T.Yu.Ogul'chanski, V.N.Yashchuk, V.G.Syromyatnikov. "The Direct Intramolecular Transfer of Electronic Triplet Excitations in the 1-naphtylacrylate-4-acetylmetacrylate Copolymer", *Ukr.Chem.J.*, 1995, v.61, N1-2, pp.53-55.

5. V.G.Syromyatnikov, V.N.Yashchuk, I.A.Savchenko, A.Yu.Kolendo, T.Yu.Ogul'chanski. "Some Macromolecules as Basic Elements of Molecular Electronics", *Ukr.Phys.J.*, 1995, v.40, N4, pp.286-288.

6. V.G.Syromyatnikov, V.N.Yashchuk. "The Peculiarities of Electronic Excitations Transport in Polymers", *Proceedings of Internat. school-conference "Electronic processes in organic materials - ISEPOM'95"*, Kiev, 1995, pp.31-32.

7. V.G.Syromyatnikov, V.N.Yashchuk, T.Yu.Ogul'chanski, I.A.Savchenko, A.Yu.Kolendo. "Some Light-Sensitive Molecular Systems With the Determined Functional Properties", *Molecular Crystals and Liquid Crystals* (in press).

8. I.S.Gorban', V.N.Yashchuk et al. "Peculiarities of Elementary Acts of Energy Transfer of Electronic Excitation in Macromolecules", *Zh. Prikl. Spektr.*, 47, pp.96-102 (1987).

Memory elements on the basis of inducted strain in polycarbonate

Janez Golobič and Darko Vasiljević

VTI-VJ, Department of Optics and Optoelectronics, Kataničeva 15, 11000 Beograd, Yugoslavia

ABSTRACT

Theoretical approach to the fundamentals of write-read memory elements based on strain induction in optical materials and the basis of fotoelasticimetry is given. Manufacturing concept of the memory element with inducted strain on polycarbonate and its realization is presented. We presented some earliest result in this domain. Applicability of the strain inducted memoryIt is discussed .

1. INTRODUCTION

For long period of years photoelasticity was used for stress analyses. Our idea is not to detect unknown stress but to induct given strain shape. Next steps are their identification and reading which are based on known principles of photoelasticity. Chosen material is polycarbonate because we think that is useful for production of commercial memory elements on the basis of inducted strain and has good physical properties.

2. BASIC THEORY

Maxwell and Neumann formulated dependence of the index of refraction from strain on the basis that optical materials in nonstrained condition are refractoisotropic and that it become refratcoanisotropic when they are strained[1] :

$$\begin{aligned} n_1 &= n_0 + C_{1\sigma} + C_{2\sigma}(\sigma_2 + \sigma_3) \\ n_2 &= n_0 + C_{1\sigma} + C_{2\sigma}(\sigma_3 + \sigma_1) \\ n_3 &= n_0 + C_{1\sigma} + C_{2\sigma}(\sigma_1 + \sigma_2) \end{aligned} \tag{1}$$

where are: n_0 - refraction index of the material without strain
$C_{1\sigma}$ and $C_{2\sigma}$ - photoelactic coefficients
σ_1, σ_2 and σ_3 - principal stress components
n_1, n_2 and n_3 - principal refraction indices

Refractoanisotropical materials cause birefrigence. Incident ray passing through material, separates on two rays, ordinary and extraordinary which propagate through material with different velocities i.e. material acts as it has two different indices of refraction. Retardation between those two rays on the exit of the material with thickness h is:

$$R = h\left(\frac{c}{v_1} - \frac{c}{v_2}\right) = h(n_1 - n_2) \tag{2}$$

where are: R - linear retardation of transmitted rays
h - thickness of specimen
c - speed of light in vacuum
v_1 and v_2 - principal normal speeds
Substituting (1) in (2) it becomes:

$$R = C_{2\sigma}\, h(\sigma_2 - \sigma_1) \tag{3}$$

Polarized light is used for detecting birefrigence[2]. Isocline or isochrome picture is produced if optical material with inducted strain is placed in polarized light (see fig. 1). If direction of the stress is parallel with axis of the polarizer through analyzer we get thin line i.e. isocline (line along which principal

0-8194-2165-0/96/$6.00

stress have constant direction) or isochrome (line along principal stress have constant value).

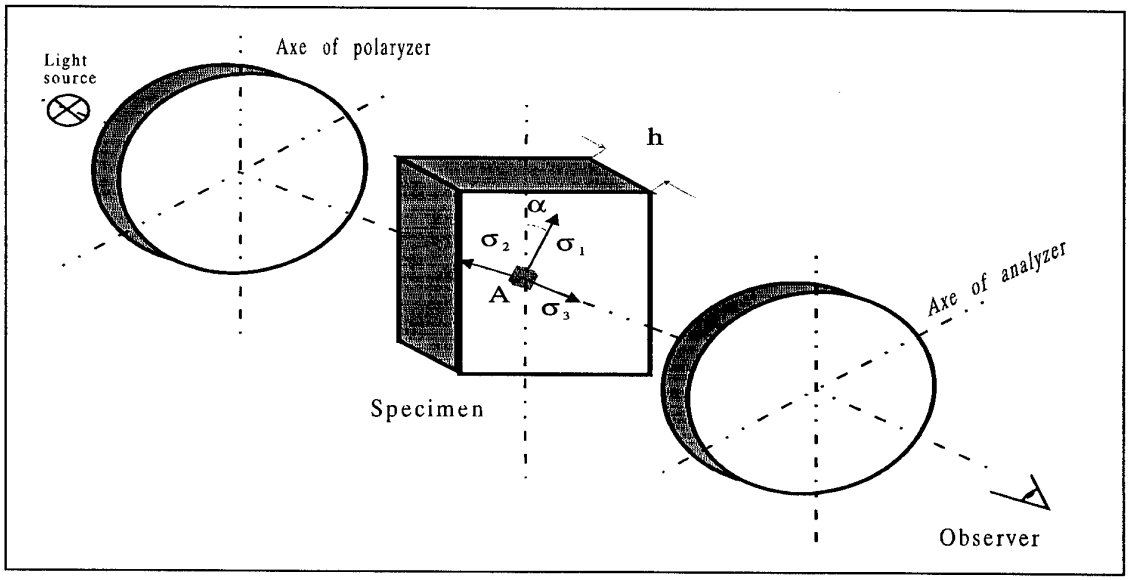


Figure 1 Specimen in linear polarizer

Light intensity I, which pass through specimen and analyzer, in the point A of specimen is:

$$I = k \sin^2(2\alpha) \sin^2\left(\frac{\Delta}{2}\right) \cos^2(\omega t) \qquad (4)$$

where are: k - proportionality coefficient
α - angle between the axis of the polarizer and direction of principal stress
Δ - phase retardation
ω - angular frequency of light

Light intensity I can be zero i.e. dark interference spot can be produced on the analyzer, only in three conditions:

$$1 \qquad 2\alpha = n\pi \qquad n = 1, 2, 3,...$$

$$2 \qquad \frac{\Delta}{2} = n\pi \qquad n = 1, 2, 3,...$$

$$3 \qquad \omega t = \frac{2n+1}{2}\pi \qquad n = 1, 2, 3,...$$

For the first case one of the directions of stress ought to be parallel with axis of polarizer. Second case requires that difference between principal stresses be constant. Third case is connected with the angular frequency of light and is not discussed in photoelasticity. Illustration of the picture of isoclines and isochromes from the model in polariscope is given on fig. 2.

3 MEMORY ELEMENT CONCEPT

Idea is to permanently impress by inducted strain on the polycarbonate plate given picture or bar code and to read it with optoelectronical system[4] is presented.

On the basis of the prior theoretical discussion and our experience, it is impossible to introduce stress in the direction of σ_1 or σ_2 with external force F and to neglect interaction in the balk of the material. As a result of interaction of the external force F and forces in balk of the material interference

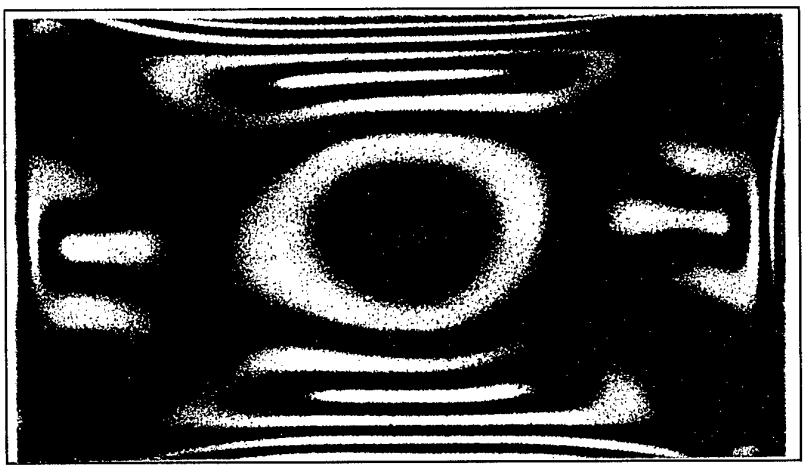


Figure 2 Isoclines and isochromes in strained specimen[3]

picture is produced (see fig. 3).

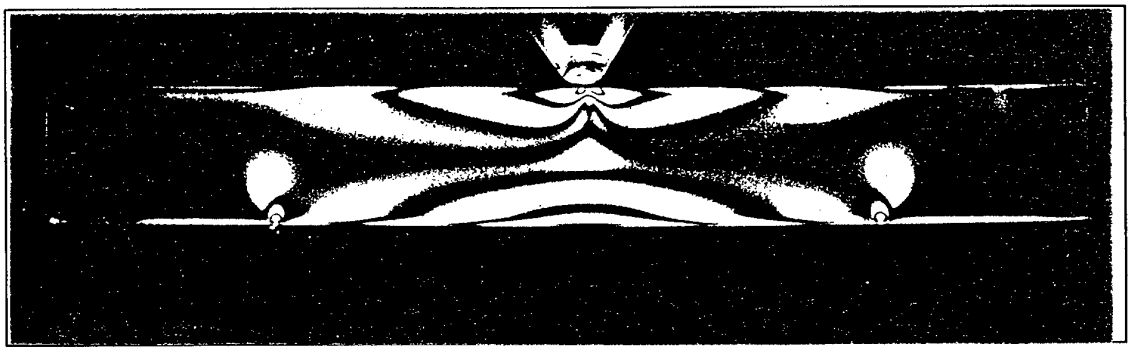


Figure 3 Interference of the external force with material[3]

We impressed given shape in the direction of the stress σ_3 with external force F on the defined surface S. This enabled producing desirable shapes in the direction given in fig. 1. This is possible to produce with force $F < F_k$ (critical force) which don't introduce interference in plain normal on view direction and from equation (1) is seen that $n_1 - n_2$ don't depend on σ_3.

Polycarbonate is chosen because steep change of the module of elasticity in narrow temperature interval[5] . This temperature interval is located in the temperature area which is convenient for use without great or special requirements. Also polycarbonate has the greatest temperature usage from all termoplastical materials. Other advantages of polycarbonate are:

- acceptable transmission
- highly developed surface treatment and protection technology.

Concept of the production of memory element is given in following steps:

- polycarbonate specimen ancaling"
- induction of given shape
- freezing of the picture

Every step requires complete acquaintance and control of properties of materials in a function of temperature, because process is conducted in strictly controlled temperature regimes. One of the earliest work is presented on fig. 4.



Figure 4 Frozen inducted picture on polycarbonate

4. CONCLUSIONS

Memory elements on the basis of inducted strain are interesting for use in systems and documents for which is important copy right law. It is interesting for:

- military applications,
- insurance agencies,
- various copy right agencies, etc. .

For example only you and insurance agent know where you put small piece folia on your car with recognizable code. There is no visible surface deformation and it can be read in reflected and transmitted light. Surely time needed for production of memory element is the subject of further adjustment and research of the parameters of freezing picture and selection of other materials can be shortened. Surely there are systems even now for which protection is more important then the price of induction of the shape.

5. REFERENCES

1. I. Alfirević and S. Jecić, "Fotoelasticimetrija", page 25, University in Zagreb, Zagreb, 1982
2. W. Shurcliff, "Polarized Light", Harvard University Press, page 67, Cambridge, Massachusetts, 1962
3. M. Cagnet, M. Françon and J. C. Thrierr, "Atlas of optical phenomena", Springer-Verlag, Berlin, 1960
4. D. Vasiljević and J. Golobič, "Optical system for reading memories which are based on photoelasticity, Proceedings of the Optics and Information - 6th Topical Meeting of the European Optical Society, 15.5 -15.6 Mulhouse, France, 1995
5. I. Čatić, "Toplo i hladno oblikovanje plastomera", Polimeri, vol. 5, pp 105-112, 1984
6. J. Golobič, "Polycarbonate - optical material of future ", Tehnika, No. 1, NM15-NM20, 1994

Paper presented at the Third ICIM/ECSSM '96, Lyon '96

Thermomechanical properties of shape memory polymer of polyurethane series and their applications

Hisaaki Tobushi, Hisashi Hara and Etsuko Yamada

Aichi Institute of Technology, Department of Mechanical Engineering,
1247 Yachigusa, Yagusa - cho, Toyota 470-03, Japan

Shunichi Hayashi

Mitsubishi Heavy Industries, Ltd., Nagoya Research & Development Center,
High Polymer & Chemical Laboratory,
1 Takamichi, Iwatsuka - cho, Nakamura - ku, Nagoya 453, Japan

ABSTRACT

The thermomechanical properties of a thin film of shape memory polymer of polyurethane series were investigated experimentally. The results are summarized as follows. (1) Modulus of elasticity and yield stress are high below glass transition temperature T_g and low above T_g. The value of loss tangent is large in the vicinity of T_g. (2) The stress-strain curves vary significantly in the early cycles but slightly thereafter under cyclic deformation above T_g. (3) During the heating process after loading above T_g followed by unloading below T_g, strain recovers in the vicinity of T_g. (4) Shape fixity with loading above T_g followed by unloading below T_g does not vary under thermomechanical cycling. Several applications of the polymer are introduced.

1. INTRODUCTION

The development of applications of shape memory polymer(SMP) is drawing attention [1-3]. Because SMP is light, high in shape recoverability, easy to manipulate and economical as compared with shape memory alloy, its development is being actively promoted. In many SMPs, the phase transition temperature is around room temperature. Characteristics such as shape recoverability and shape fixity exist due to the difference between mechanical properties of materials above and below the phase transition temperature [4-5]. SMPs utilizing these characteristics are being used as temperature sensors and actuators.

The SMP of polyurethane series has the features that (1) it can be molded by such methods as injection, extrusion and blowing, similar to conventional plastics, (2) it can be colored to any color as it is transparent and (3) the shape recovery temperature can be set anywhere between room temperature $\pm$50K, marking a wide range of application possible. In the polyurethane series of SMP, not only mechanical properties but also optical properties are different above and below the glass transition temperature T_g. With respect to thin film, moisture permeability varies significantly above and below T_g and the application of the property to clothes is drawing attention.

In the present study, the thermomechanical properties of thin film of SMP of polyurethane series are examined, and the cyclic properties of shape fixity and shape recoverability are investigated. Several applications of the material are introduced.

2. EXPERIMENTAL METHOD

The material used in the experiment was a thin film of SMP of polyurethane of the polyester polyole series. The glass transition temperature T_g of the material was about 328K. The casting film was made from solution(Diary MS5510; produced by Mitsubishi Heavy Industries, Ltd.) under drying condition.

The specimen was a thin film of uniform shape. The dimensions of the testing area were 25mm long, 50 μ m thick and 5mm wide.

0-8194-2165-0/96/$6.00

Four kinds of tests were carried out.
(1) Dynamic mechanical test
(2) Uniaxial tensile test

Uniaxial tensile load was given at a constant strain rate 50%/min under constant temperatures T_g-20K, T_g and T_g+20K.

(3) Cyclic tensile test at high temperature
(4) Thermomechanical cycling test

The three - dimensional stress-strain - temperature relationship during the thermomechanical cycling test is schematically shown in Fig.1. First, at the temperature T_h, the maximum strain ε_m is applied at a constant strain rate of 50%/min ①, and then, maintaining ε_m, the temperature is cooled to T_l ②. After holding at T_l for 5 minutes, it is unload ③. Under the no-load condition, it is heated from T_l to T_h ④ and held for 5 minutes at T_h. This thermomechanical cycle was repeated 10 times. The heating and cooling rate was about 8K/min.

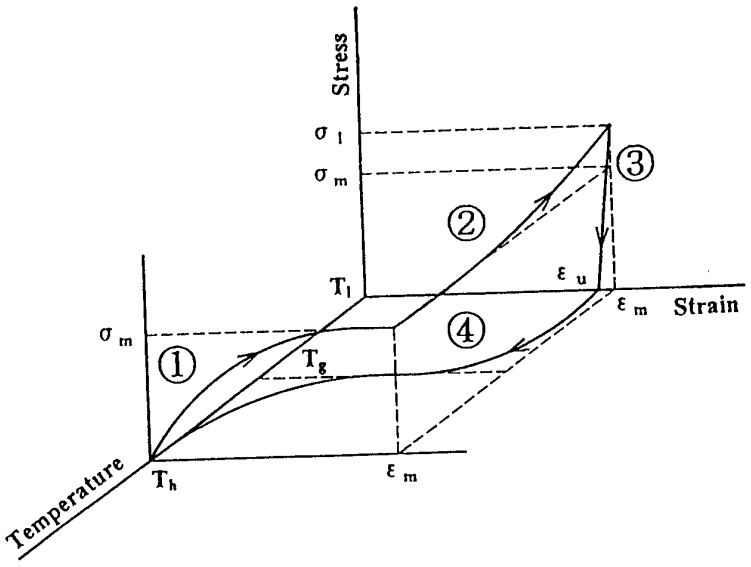


Fig.1 Three-dimensional stress-strain-temperature relationship in the thermomechanical cycling test

3. EXPERIMENTAL RESULTS AND DISCUSSION

3.1 Dynamic mechanical property

The relationships of storage modulus of elasticity E' and loss tangent tan δ with temperature obtained from the heating process in the dynamic mechanical test are shown in Fig.2. As seen in Fig.2, E' and tan δ vary markedly in the vicinity of T_g= 328K. The ratio of E' at temperature above and below T_g is very large, being about 100. This means that the material is easily deformed at high temperature and also deformation resistance is large at low temperature. On the other hand, tan δ becomes very large at temperatures in the vicinity of T_g and the tan δ is about 0.6 at T_g. This means that the function as a high damping material is superior at temperatures in the vicinity of T_g.

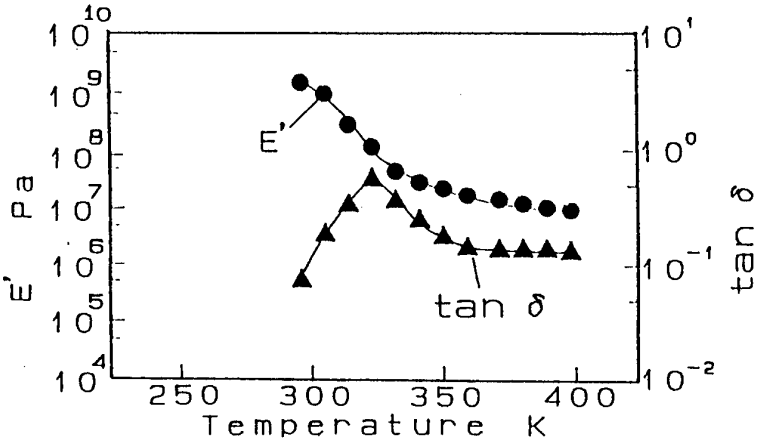


Fig.2 Dependence of storage modulus of elasticity and loss tangent on temperature

3.2 Uniaxial tensile property at constant temperature

The stress-strain curves obtained by tensile tests with maximum strain of 200% at various temperatures are shown in Fig.3. As seen in Fig.3, modulus of elasticity, yield stress and 100% modulus are large when temperature is low. Deformation resistance in the elastic and inelastic regions is large at low temperature.

In the case of 308K, overshoot of stress showing a clear upper yield point appears, and stress increases gradually in proportion to strain at strains above 50%. In the case of T_g and 348K, gradual yielding appears at low stress, and stress increases in proportion to strain at strains above 20%. The lower the temperature, the larger the rate of increase in stress.

In the unloading process, for each temperature, the slope of the stress - strain curves is steep just after the start of unloading and becomes gentle in the range of small stress.

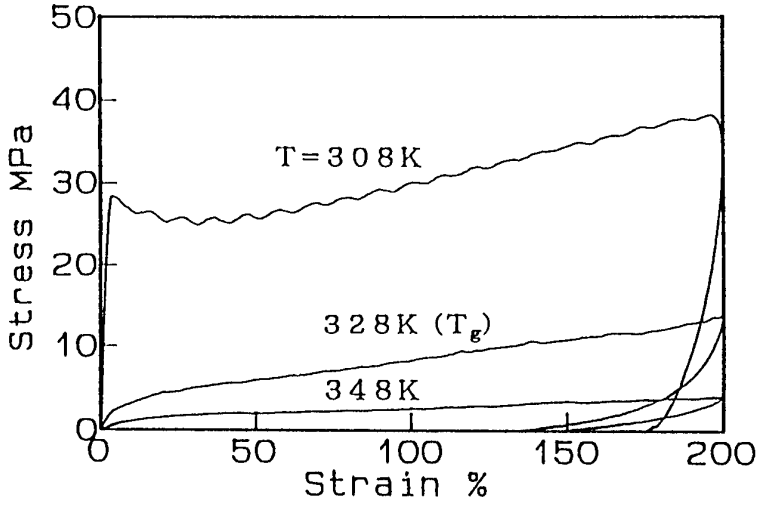
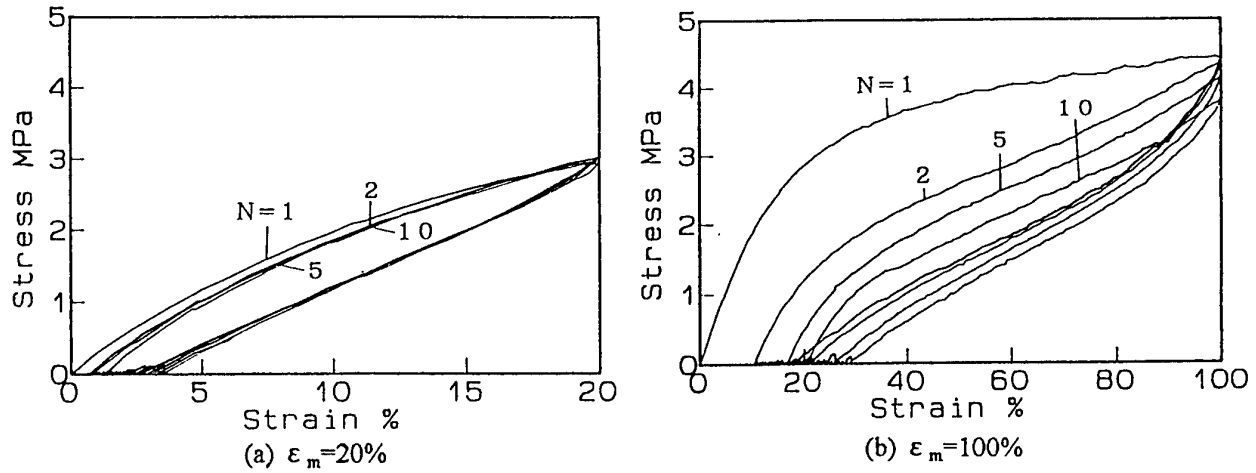


Fig.3 Stress-strain curves in tensile test at constant temperature

These deformation properties may be considered as follows. The SMP used is segmented polyurethane and is composed of a certain ratio of soft segments and hard segments. The above-mentioned phenomena may be caused due to the fact that the micro-Brownian motion of the soft segments is active at temperatures above T_g and is frozen at temperatures below T_g [6].

3.3 Cyclic deformation properties at high temperature

The stress - strain curves, obtained by the cyclic tensile test at constant temperature of T_g+20K under cyclic loading-unloading of ten times for maximum strain ε_m=20% and 100%, are shown in Fig.4. As seen in Fig.4, in the case of ε_m=20%, stress - strain curves does not change under cyclic deformation. In the case of ε_m=100%, yield stress decreases with increase in number of cycles N. The yield stress decreases markedly in the early cycles but decreases gradually thereafter. The coefficient of work hardening shown by a slope of the curves beyond the yield point is gentle in the first cycle but steep after the second cycle. These phenomenon may be caused due to the reason as follows. Because entanglement decoupling of molecular chains in the imperfect crystalline part occurs due



(a) ε_m=20% (b) ε_m=100%

Fig.4 Stress-strain curves in cyclic test at high temperature

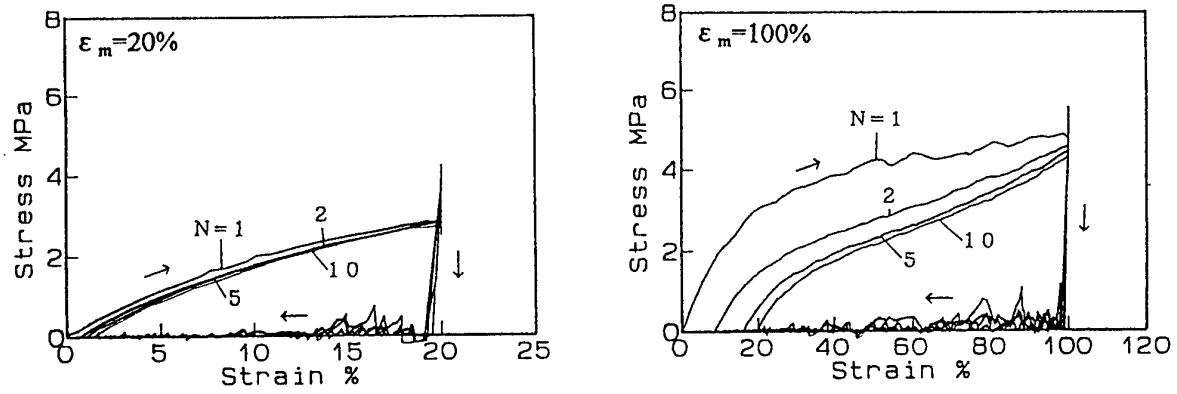
to the first loading, yield stress decreases significantly in the second cycle. Because orientation of molecular chains due to loading with strain of 100% and hardening due to crystallization occur, deformation resistance in the region beyond the yield point increases after the second cycle. The overall stress-strain curves are almost the same form after the second cycle and shift to the right and downward gradually. The amount of shift of the curves decreases with increasing cycles.

3.4 Shape fixity and shape recoverability

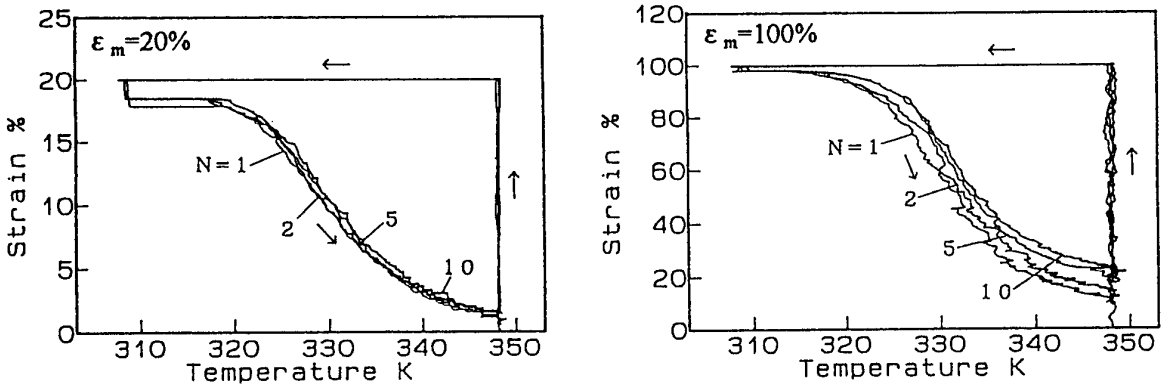
The stress - strain curves and strain-temperature curves obtained by the thermomechanical cycling test for maximum strain ε_m=20% and 100% are shown in Fig.5(a) and Fig.5(b), respectively.

As seen in Fig.5, in the case of ε_m=20%, the stress - strain curves and strain - temperature curves does not change under thermomechanical cycling. Therefore, in the case of small maximum strain, thermomechanical properties of the material is almost constant under cyclic loading.

As seen in Fig.5(a), in the case of ε_m=20% and 100%, the cyclic loading curves at temperature T_h almost coincide with the stress - strain curves during the loading process in Fig.4. This means that, with respect to hysteresis effect of thermomechanical path on cyclic deformation properties, the influence of loading process is most significant among thermomechanical paths. The stress which increases when the specimen is cooled to temperature T_l under constant ε_m is thermal stress due to thermal contraction. Because modulus of elasticity at



(a) Stress-strain curves



(b) Strain-temperature curves

Fig.5 Results in thermomechanical cycling test

temperature T_l is large, strain recovers elastically with a steep slope in the unloading process at T_l. The strain ε_u at the termination point of unloading is nearly equal to ε_m and does not vary with cycling. This means that excellent shape fixity of the material can be obtained in the applications.

As seen in Fig.5(b) in the case of ε_m=100%, in the first cycle, strain starts to recovery at temperature near T_g-5K, recovers markedly in the vicinity of T_g and recovers gradually at temperatures above T_g. This phenomenon may be caused as follows. At low temperature, strain is constant at ε_u under no stress because the micro-Brownian motion of soft segments is frozen. If it is heated to high temperatures above T_g without restraint, the original shape recovers because the micro-Brownian motion becomes active.

The strain-temperature curves shift to the right with an increase in N. This means that recovery temperature rises with cycling. This phenomenon may be caused as follows. Because hardening due to orientation of molecular chains and crystallization progresses with cycling, it needs large thermal energy for strain to recovery, resulting in rise in the recovery temperature. This trend is the same as rise in the transformation temperature with an increase in N for shape memory alloy subjected to cyclic deformation[7].

4. APPLICATIONS

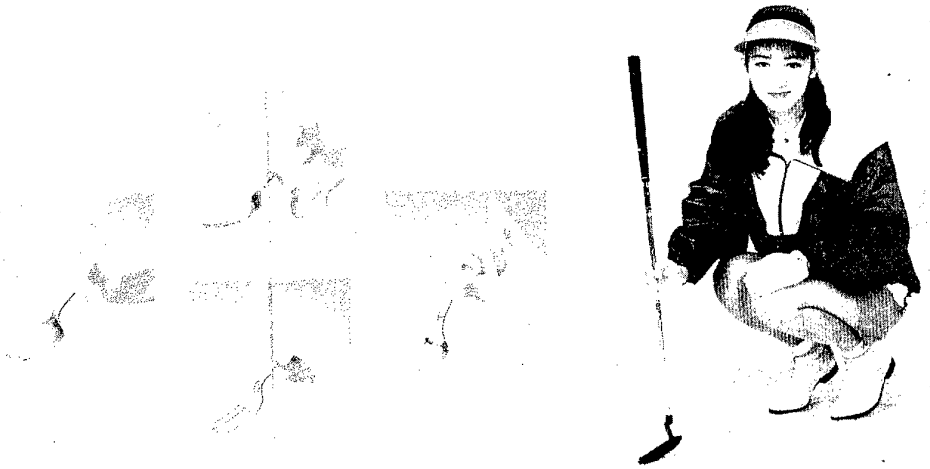
SMPs of the polyurethane series have been used in several fields of practical applications. The applications according to the function of the materials are divided into the following classes.

(1) Use of variation in modulus of elasticity

One of applications to use the large amount of variation in modulus of elasticity depending on temperature is a temperature sensor, in the application, the external bias force is combined. A typical example of the application is an autochoke for engine. Another example of application using the same function is a medical catheter. Because SMP of the polyurethane series has a favorable biological adaptability owing to its flexibility and antithrombotic nature, development of the catheter is expected.

(2) Use of shape fixity and shape recoverability

One of typical applications of these properties is a spoon or fork handle for a handicapped person as shown in Fig.6(a). With respect to the spoon or fork handle, it is deformed by fitting the form of a hand of each person at high temperature and is fixed as its shape at low temperature. The person without grasping power can use the spoon or fork. Another applications are the shape memory straws and films.



(a) Spoon and fork handles for handicapped (b) Sportswear

Fig.6 Applications

(3) Use of variation in moisture permeability, volume expansion and refractive index and damping property

Moisture permeability, volume expansion and refractive index vary significantly above and below T_g according to difference of the kinetic property of molecular chains between temperatures above and below T_g. Damping property is superior at temperatures in the vicinity of T_g. Applications using these properties are under development.

One of applications of moisture permeability of a thin film is a sportswear as shown Fig.6(b). Moisture permeability is high above Tg and low below Tg. For the wear, the heat retaining property at low temperature and gas permeability at high temperature are excellent, yielding high quality for the sportswear.

5. CONCLUSIONS

The thermomechanical properties of a thin film of shape memory polymer of polyurethane series were investigated experimentally. The results are summarized as follows.

(1) Modulus of elasticity and yield stress are high below glass transition temperature T_g and low above T_g. The value of loss tangent is large in the vicinity of T_g.

(2) The stress-strain curves vary significantly in the early cycles but slightly thereafter under cyclic deformation above T_g.

(3) During the heating process after loading above T_g followed by unloading below T_g, strain recovers in the vicinity of T_g.

(4) Shape fixity with loading above T_g followed by unloading below T_g does not vary under thermomechanical cycling.

(5) If the maximum strain is smaller than 20%, the thermomechanical properties does not change under cyclic deformation. Several applications of the polymers were introduced.

6. REFERENCES

1. S. Hayashi, H. Fujimura and Y. Tamura, "Development of Polymeric Shape Memory Material, " Proc. 2nd Japan Int. SAMPE, p. 76, 1991.

2. C. Liang, C. A. Rogers and E. Malafeew, "Preliminary Investigation of Shape Memory Polymers and their Hybrid Composites, " AD-24/AMD-123, Smart Structures and Materials, ASME, pp. 97 - 105,1991.

3. S. Hayashi, N. Ishikawa and C. Jiordano, "High Moisture Permeability Polyurethane for Textile Application " J. Coated Fabrics, 23 , pp. 74 - 83, 1993.

4. H. Tobushi, S. Hayashi and S. Kojima, "Mechanical Properties of Shape Memory Polymer of Polyurethane Series, " JSME Int. J., I, 35 - 3, pp. 296 - 302, 1992.

5. H. Tobushi, S. Hayashi and S. Kojima, "Mechanical Properties of Shape Memory Polymer of Polyurethane Series , " Proc. SEM Spring Conf. Exp. Mech., pp.520 - 527, 1993.

6. J. R. Quay, J. Blackwell and C. D. Lee, "Prediction of Polyurethane Hard Segment Structures Based on Diphenylmethane - Urethane Model Compounds, "J. Macromol Sci. - Phys., B, pp. 61 - 85, 1986.

7. H. Tobushi, H. Iwanaga, K. Tanaka, T. Hori and T. Sawada, "Deformation Behavior of TiNi Shape Memory Alloy Subjected to Variable Stress and Temperature, " Continuum Mech. Thermodyn., 3, pp. 79 - 93, 1991.

Dependence of the molecular dynamics of comb-like polyacrylates and polymethacrylates on the mesophase structure studied by dielectric spectroscopy

Andreas Schönhals[1], Dietmar Wolff[2], Jürgen Springer[2]
[1]Institut für Angewandte Chemie Berlin-Adlershof e.V., Rudower Chaussee 5, D-12489 Berlin, Germany
[2]Technische Universität Berlin, Straße des 17. Juni 135, D-10623 Berlin, Germany

ABSTRACT

Dielectric spectroscopy is employed to study the dependence of the molecular dynamics of liquid-crystalline polyacrylates on the mesophase structure. The temperature dependence of the rate of the β-relaxation which was assigned to rotational fluctuations of the mesogenic unit around its long axis can be described by an Arrhenius equation. Both the preexponential factor and the activation energy increase with the order of the mesophase which is discussed in the frame of the cooperativity of the β-relaxation. It is shown that the activation parameters of this process correlate to lateral distance of mesogenic groups. The α-relaxation is related to the dynamic glass transition. Its dependence on the mesophase structure is interpreted in terms of microphase separation. The rate of the δ-relaxation caused by rotational fluctuations of the mesogenic unit around its short axis is reduced by that of the α-process. The temperature dependence of this ratio is related to that of a molecular order parameter.

1. INTRODUCTION

Polymers having calamitic mesogens in the side chain are smart materials from several points of view. So these systems can be used as materials for optical data storage, holographic applications and electrooptical devices. From the point of basic research these polymers are quite interesting because they combine liquid-crystalline and polymeric properties. For an understanding of its behavior a knowledge about the molecular dynamics is important. It has been proven that dielectric spectroscopy is powerfull to study the relaxational properties[1] and due to the different possibilities of dipole reorientation several dielectric active relaxation processes can be observed[2]. Besides of γ -relaxation processes assigned to reorientations of the tail- and spacer groups with increasing temperature a β-, an α-, and a δ-relaxation have been observed. The β-process was related to rotational fluctuations of the mesogenic group around its long axis and its relaxation rate shows an Arrhenius-like dependence on temperature. The relaxation rate of the α-relaxation was found to be curved in an Arrhenius diagram and this process was assigned to the glass transition which is strongly connected with the segmental motions of chain backbones. The exact molecular mechanism of the δ-relaxation process is unclear up to now but there is strong evidence that the δ-relaxation should be related to rotational fluctuations of the mesogenic groups around their short axis[2,3]. In this paper we discuss the influence of the chemical and of the mesophase structure on the β-,α-, and δ-relaxation of comb-like polyacrylates and polymethacrylates.

2. EXPERIMENTAL

Fig. 1 and Table 1 give the chemical structure of the studied polyacrylates and polymethacrylates. As mesogenic units derivatives of (p-alkoxy-phenyl)-benzoate were used. These polymers are used as model compounds for intelligent materials having for instance photocromic groups in the side chain. Different mesophases ranging from the isotropic up to highly ordered smectic B phases were obtained by small chemical variation (Table 1).

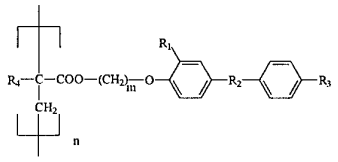


Fig. 1 Structure of the repeating unit of the polymers studied.

0-8194-2165-0/96/$6.00

Some details about the synthesis and the characterization can be found in ref.[4]. The experimental technique to measure the complex dielectric function $\epsilon^*(f) = \epsilon'(f) - i\epsilon''(f)$ (f-frequency, ϵ'-real part, ϵ''-imaginary part, $i=\sqrt{-1}$) in a frequency range from 10^{-2} Hz to 10^6 Hz and the sample preparation have been described elsewhere[4]. As an example Fig. 2 shows the dielectric loss versus temperature at a fixed frequency for the samples P4 and P6. The method for the data evaluation especially to extract the relaxation rate at maximal loss f_p for the different relaxation regions was presented earlier[5,4].

Table 1. Chemical structure, transition temperatures and activation parameters of the β-relaxation of the studied polymers: I, N, S means the isotropic, the nematic and the different smectic states. The at the glass transition temperature frozen in low temperature phase is indicated in bold.

	R_1	R_2	R_3	R_4	m	T_g [K]	Phases	log($f_{\beta\infty}$ [Hz])	$E_{A\beta}$ [kJ/mol]
P1	OCH_3	CO.O	OCH_3	CH_3	6	322	**I**	12.8 ± 0.2	45.7 ± 1.6
P2	H	CO.O	OCH_3	CH_3	4	318	**N**/I 377 K	13.8 ± 0.2	46.5 ± 1
P3	H	CO.O	OCH_3	H	2	343	**N**/I 343 K	14.8 ± 0.2	53.3 ± 1
P4	H	CO.O	OCH_3	CH_3	6	314	**S_A**/N 345 K N/I 383 K	16.5 ± 0.2	57.5 ± 1.4
P5	H	O.OC	OCH_3	CH_3	6	311	**S_A**/I 370 K	16.4 ± 0.2	56.4 ± 1
P6	H	CO.O	OC_4H_9	CH_3	6	315	**S_A**/N 380 K N/I 384 K	17.1 ± 0.2	61.0 ± 1
P7	H	CO.O	OCH_3	H	6	297	**S_A**/N 367 K N/I 394 K	17.5 ± 0.2	62.8 ± 3.2
P8	H	O.OC	OC_4H_9	CH_3	10	304	**S_B**/S_A 318 K S_A/I 394 K	18.2 ± 0.2	63.2 ± 2.1
P9	H	O.OC	OC_6H_{13}	CH_3	6	295	**S_B**/S_C 349 K S_C/S_A 358 K S_A/I 401 K	18.5 ± 0.7	64.9± 3.2
P10	H	O.OC	OC_6H_{13}	CH_3	10	296	**S_B**/S_C 320 K S_C/S_A 330 K S_A/I 399 K	19.4 ± 0.5	68.9± 2.1
P11	Br	CO.O	OCH_3	CH_3	6	323	**I**	----------	----------
P12	H	CO.O	OCH_3	CH_3	8	313	**S_A**/N 383 K N/I 390 K	----------	----------

3. RESULTS AND DISCUSSION

3.1 β-Relaxation

The β-relaxation of liquid-crystalline side chain polymers was assigned to rotational fluctuations of the mesogenic unit around its long axis[2]. Fig. 3 shows the temperature dependence of its relaxation rate $f_{p\beta}$ which can be described by an Arrhenius equation $f_{p\beta} = f_{\beta\infty} \exp[-E_{A\beta}/kT]$. $f_{\beta\infty}$ is the preexponential factor and $E_{A\beta}$ is the corresponding activation energy. The estimated parameter values are given in Table 1. Only for the polymer P1 (no mesophase) $f_{\beta\infty}$ is in the order of magnitude that is characteristic for local motional processes. For all other polymers the $f_{\beta\infty}$-values are much higher and have no direct physical meaning. The data analysis shows that they increase

systematically with the order of the low temperature phase which is frozen in at the glass transition. So we have to conclude that the order of the mesophase determines this relaxation process to a great extent. Details of the chemical structure seem to play an insignificant role (compare the values for P4 and P5). Because the β-relaxation is caused by rotational fluctuations of the mesogenic units around their long axis for a liquid-crystalline material, this relaxational process can only take place if the liquid-crystalline structure is maintained and the actual state allows this motional process. This seems more complicated for a higher ordered phase than for a mesomorphic state which is not so well organized. The higher values of $f_{\beta\infty}$ and $E_{A\beta}$ found for better ordered phases are an expression of this fact and indicate that the mesogenic units in a higher ordered phase act more cooperatively together than in a less ordered one.

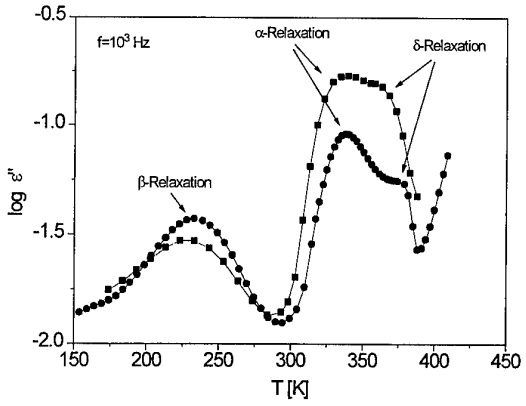


Fig. 2 log ε'' vs. T for the samples P4 (■) and P6(●)

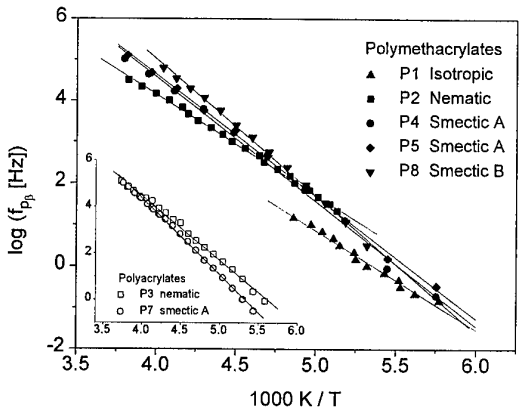


Fig. 3 log $f_{p\beta}$ versus 1000 K / T for different samples Lines are fits of the Arrhenius-equation.

In addition X-ray experiments were carried out on samples oriented in a magnetic field (2.4 T). Using the Bragg-equation the mean lateral mesogenic distance is calculated from the X-ray patterns and plotted versus log $f_{\beta\infty}$ in Fig. 4. For the first time it is shown that both parameters correlate linearly and this correlation supports strongly the developed model of the β-relaxation.

3.2 α-Relaxation

Fig. 5 displays the temperature dependence of the relaxation rate of the α-relaxation $f_{p\alpha}$ for the samples P1, P4 and P11. Remember that only the sample P4 forms mesophases. At high temperatures the different plots of log $f_{p\alpha}$ for polymers discussed here collapse nearly into one chart. Assuming that the α-relaxation is related to the glass transition, this says that at high temperatures all samples have the same dynamic glass transition temperature. Somewhat below the phase transition temperature $T_{N/I}$ the temperature dependence of log $f_{p\alpha}$ of the sample P4 separates from the other ones. Obviously the change in structure leads to a change in the dynamic glass transition temperature. Fig. 5 delivers that at the same temperature log $f_{p\alpha}$ is higher for P4 than for the other polymers and so this sample has also a lower thermal T_g-value than the two other polymers (see Fig. 5, Table 1). In the first moment that is surprising because in general a structure formation raises T_g. So the glass transition temperature of the liquid-crystalline polymer P4 must be due to the competition of two contrary effects. Above $T_{N/I}$ in the isotropic state the mesogenic units are distributed in the melt nearly random. At the phase transition the mesogenic groups will be arranged in liquid-crystalline structures. The polymer backbones are not included in the mesophases. In other words at the phase transition also a microphase separation occurs and at least two microphases are formed, ordered liquid-crystalline and amorphous backbone-rich regions. The glass transition should be related to the later

one. Because the mesogens are stiff and polar (properties which enhance T_g) this reduction of the mesogen concentration in the backbone-rich phase can be regarded as a kind of internal plasticizition which reduces T_g. So the glass transition temperature of the liquid-crystalline polymethacrylates can be understood as a competition of internal plasticizition and molecular ordering, meaning the formation of nematic local layer-like structures.
Because the spacer decouples the main chain from the mesogenic unit, the discussed microphase separation process must be dependent on the spacer length. For a longer spacer the phase separation should be more perfect than for a shorter one. Fig. 6 compares the temperature dependence of the relaxation rate of the α-relaxation as a function of spacer length for several polymethacrylates. For n=6 and n=8 in the isotropic melt again nearly the same dynamic glass transition temperature is obtained. At the phase transition both temperature dependencies separate from each other whereas the polymer with n=8 has the lower T_g value in agreement with the discussed picture.
For the sample with n=4 the dynamic glass transition temperature is higher than for the other two polymers also in the isotropic melt. Obviously for this spacer length the decoupling of the mesogenic unit from the main chain is not strong enough leading to that higher value of the dynamic glass transition temperature in the isotropic state. Clearly for the liquid-crystalline state the Tg value is much higher than for the samples with spacer lengths 6 and 8. This indicates that the microphases are not so well segregated and that the liquid-crystalline structures are not so perfectly ordered. Again these experimental findings support the supposed demixing model to explain the glass transition temperature of liquid-crystalline polymethacrylates.

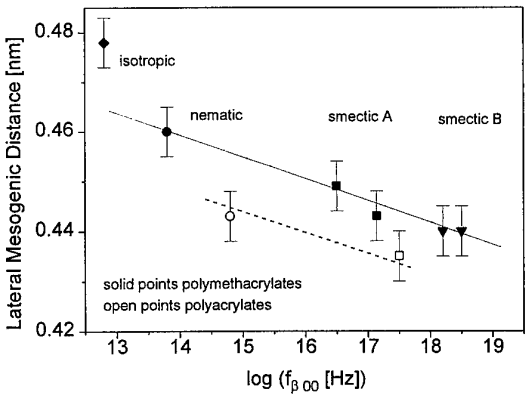


Fig. 4 Lateral mesogenic distance versus log $f_{\beta_{00}}$.

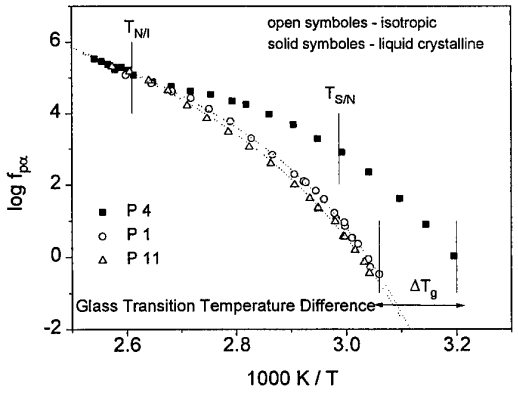


Fig. 5 Activation plot for the α-relaxation of isotropic and liquid-crystalline samples

3. 3 δ-Relaxation

The δ-process is connected with the dipole moment which is parallel to the long axis of the mesogenic unit. The accepted motional mechanism for that relaxation process is a rotational fluctuation of the whole side group around its short axis[2, 3] probably in a complicated multistep process. If this mechanism is true the relaxation rate of the δ-process $f_{p\delta}$ should be proportional to the local friction coefficient of the melt which is known to be proportional to $f_{p\alpha}^{6}$. This says that the relaxation rate of the δ-relaxation $f_{p\delta}$ should be proportional to $f_{p\alpha}$ the rate of the α-process. Therefore in Fig. 7 the logarithm of the ratio of the relaxation rates of the α- and of the δ-relaxation log ($f_{p\alpha}/f_{p\delta}$) is plotted versus temperature. Within the frame of uncertainty of the fit procedure for the polymers which have no mesophase P 1 and P 11 this ratio is nearly a constant which is expected for isotropic melts. For the polymer P4 which forms liquid-crystalline mesophases a quite different behavior is observed. Above the clearing point in the isotropic state this ratio is again nearly independent of temperature but at $T_{N/I}$ it jumps to a higher value and increases further with decreasing temperature. As discussed for liquid-crystalline polymeric side chain samples, the molecular mechanism of the δ-relaxation is assumed as a complicated flip-flop motion of the mesogenic groups

between ordered structures. If this is true the relaxation rate of δ-process should be dependent on the degree of order in these local structures because during this process a mesogenic group will leave a particular local layer and will be incorporated in another (or in the same) one. Of course the rate of incorporation of mesogenic groups depends on the degree of order. For a higher degree of order the incorporation should be more difficult (lower relaxation rate) than for a lower one (higher relaxation rate). Using this picture the jump-like change of $\log (f_{p\alpha}/f_{p\delta})$ at $T_{N/I}$ is due to the developing of local order at the phase transition. With this consideration from Fig. 7 it is further concluded that the local order increases substantially with decreasing temperature for the liquid-crystalline polymer P4.

For low molecular nematics the influence of order on the δ-relaxation is described in the mean-field theory of Meier and Saupe[7] by a nematic potential depending on the local order parameter S. Using this concept one can derive[6] $\log(f_{p\alpha}/f_{p\delta})\sim g(S)$ where g(S) is a reduction factor with g(S=0)=1 (isotropic melt) and $g(S=1)\to\infty$ (completely ordered structure). Using a numerical representation for g(S)[6] and taking $\log(f_{p\alpha}/f_{p\delta})=1$ for $T>T_{N/I}$ from Fig. 7 the order parameter S can be estimated. Fig. 8 gives the result of this calculation where S is plotted versus temperature. At the phase transition $T_{N/I}$ jumps from 0 to 0.167 and increases further to a value of S=0.668 which seems reasonable for polymeric liquid crystals. Near the phase transition the temperature dependence of S can be described by a power law (see inset of Fig. 8). Moreover Fig. 8 compares also the order parameter estimated from our dielectric experiments with that obtained from the quadrupole splitting of the NMR spectra[8]. Although the absolute values are slightly different, the dielectric data are in the same range and moreover they display the same temperature dependence of the order parameter obtained from the NMR data. So we have to conclude that both methods measure the same quantity.

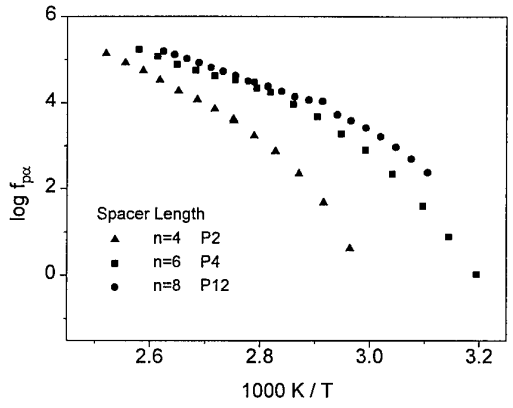


Fig. 6 Activation plot for the α-relaxation. Variation of the spacer length.

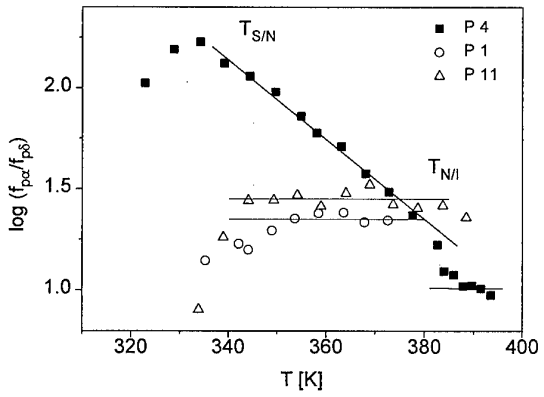


Fig. 7 $\log (f_{p\alpha} / f_{p\delta})$ versus temperature.

If T_g is approached from high temperatures $\log (f_{p\alpha} / f_{p\delta})$ decreases with decreasing temperature for both the isotropic and the liquid-crystalline samples (P1, P4, P11) on Fig. 7. The reason for this behavior also found in ref[9] is not quite clear. One can speculate in a similar way as it was done in ref[10] that this dependence is strongly related to the cooperative nature of the dynamic glass transition.

Fig. 9 compares the temperature dependence of the ratio $\log (f_{p\alpha} / f_{p\delta})$ for different chain architectures including a variation of the spacer length (n=4,6,8) and of the tail group (methoxy and butoxy group). To compare the different samples irrespective of their glass transition temperature the data were plotted versus $T-T_g$. In principle the same behavior, as it has been discussed before, is found for all studied polymers. In the isotropic state $\log (f_{p\alpha} / f_{p\delta})$ is more or less independent of temperature where the absolute value depends on molecular details. As it was expected $\log (f_{p\alpha} / f_{p\delta})$ increases with decreasing spacer length and increasing length of the tail group. At the phase transition, the ratio of the relaxation rates of both processes shows a jump-like behavior and increases linearly with decreasing temperature for $T<T_{N/I}$. Close to the glass transition temperature, $\log (f_{p\alpha} / f_{p\delta})$ displays a maximum and

decreases after that.

For the polymers having the same tail group but different spacer lengths, the log ($f_{p\alpha}$ / $f_{p\delta}$) values collapses into one chart (samples P2, P4 and P12). Relating log ($f_{p\alpha}$ / $f_{p\delta}$) again to the local order parameter, this means that for these samples the local liquid-crystalline order is more or less the same. Because log ($f_{p\alpha}$ / $f_{p\delta}$) is larger for shorter spacer lengths the order is somewhat reduced for smaller n.

For the sample with the butoxy tail group (sample P8) the ratio of the relaxation rates of the α- and the δ-relaxations is much larger than for the corresponding sample with the methoxy tail group (sample P4) . There are two ways to discuss this experimental result. On the one hand side, in the framework of the presented concept that relates log ($f_{p\alpha}/f_{p\delta}$) to the order parameter, this means that the molecular order is much better for the sample P8 than for the sample P4. This interpretation is supported by the fact that the sum of the transition enthalpies is also greater for P8 than P4. On the other hand, it may be that the butoxy group hinders the rotational fluctuations of the mesogenic unit around its short axis more than the methoxy group. Additional investigations including samples with longer tail groups like hexoxy groups are in preparation.

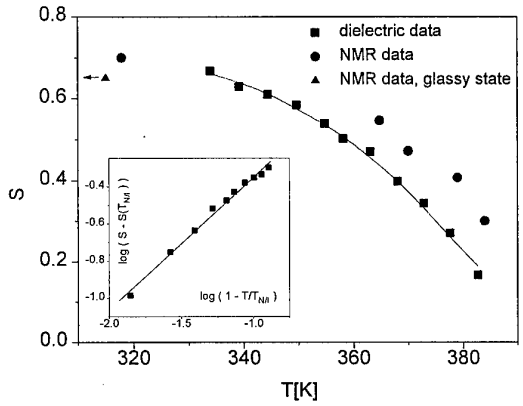


Fig. 8 Temperature dependence of the order prameter S for the sample P4.

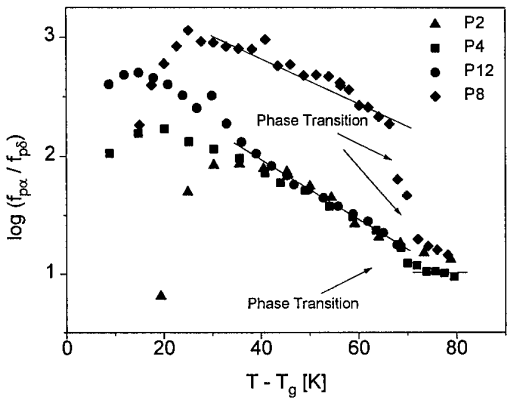


Fig. 9 log ($f_{p\alpha}$ / $f_{p\delta}$) versus temperature for different samples.

4. REFERENCES

1. J. K. Mosciki, in "Liquid crystal polymers: from structures to applications", A. A. Collyer (Ed.) Elsvier Applied Sci., London, 1992, Chapter 4

2. R. Zentel, G. Strobel, H. Ringsdorf , Macromolecules **18**, 960, 1985

3. G. S. Attard, G. Williams, Polymer Commun. **27**, 2, 1985

4. A. Schönhals, D. Wolff, and J. Springer, Macromolecules **28**, 6254-6257, 1995

5. E. Schlosser and A. Schönhals, Colloid Polym. Sci. **267**, 963, 1989; A. Schönhals, U. Geßner and J. Rübner, Macromol. Chem. Phys. **196**, 1671, 1995

6. H. Seiberle, W. Stille, G. Strobl, **23**, Macromolecules **23**, 2008, 1990

7. A. Martin, G. Meier, A. Saupe, Symp. Faraday Soc. **5**, 119, 1971

8. C. Böffel, H.-W. Spiess, in "Side Chain Liquid Crystal Polymers", C.B. Mc Ardle (Ed.) Blackie Glasgow / London 1989 p. 224

9. G. S. Attard, J. J. Moura-Ramos, G. Williams, *J. Polym. Sci. Polym. Phys. Ed.* **25**, 1099, 1987

10. A. Schönhals, F. Kremer, J. Non.-Cryst. Solids **172-174**, 336,1994

Gel dispersed liquid crystals - a new material for displays

Arno Seeboth

Institut für Angewandte Chemie, Rudower Chaussee 5, D-12489 Berlin, Germany

ABSTRACT

An aqueous polymer water gel as well as a microemulsion based gel (MBG) can be used as carrier material for dispersed thermotropic liquid crystals (LC). The LC droplet size in an aqueous water gel was dependent upon the emulsifying power. In a MBG the LC droplet size depends on the nature of the surfactant and the co-surfactant. Gel dispersed LC samples between two electrodes with a cell gap of 25 μm or 100 μm showed a scattering effect dependent upon application of an electric field.

1. Introduction

LC can be classified as thermotropic and lyotropic systems. In this work we discuss only about thermotropic gel dispersed LC.

Low molecular weight LC dispersed in a polymeric carrier material have been widely investigated in recent years. Several polymers, such as epoxies, polycarbonates, polyvinylbutyral or peptides are used as a polymer matrix for dispersed LC (PDLC).
Two types of PDLC systems have been described. In some systems the LC molecules in the separate LC bulk have no preferred orientation[1-3] and in others the LC molecules have a preferred orientation in the LC bulk in absence of an electric field. That means the LC molecules have the same tilt angle and azimuth angle[4].

PDLC systems can be used as windows or Large Area Displays. In dependence on the presence or absence of an electric field a transparent or an opaque mode is to see. What is the background of this effect?
The background of this effect is a random orientation of the LC molecules in the droplet without an electric field. Therefore the system is opaque/milky white. In the presence of an electric field the LC molecules have a preferred orientation and the system is transparent. However this is well known[3].

The aim of this work was to examine the possibility of using a gel as carrier material for dispersed thermotropic LC. Therefore we address the issue of whether it is possible to embed LC as a separate phase in an aqueous gel[5] or in a microemulsion based gel[6], respectively.

Structural investigations of the systems were carried out using a polarization microscope and a scanning electron microscope.
The electrooptical behaviour of the embedded LC in the gel was investigated by mounting the sample between two transparent electrodes and applying an electric field.

2. Results and Discussion

Figure 1 shows thermotropic liquid crystal droplets (E 5, Fa. Merck - five component mixture on the basis of p-substituted cyanobiphenyls) in 5 wt% aqueous pva solution under the polarization microscope (T = 25°C, magnification 25 x). Droplets of embedded LC can be seen clearly in the micrograph. Vigorous manual shaking produced droplets of diameter 40 -300 μm, and homogenisation using 5000 r.p.m. produced droplets in the size range of 3 - 20 μm.
Furthermore, the polarisation optics shows that orientation of the LC in the droplets was random. The aqueous pva / LC emulsion can be gelled by addition of aqueous borax solution. The gelation was very rapid[7].

0-8194-2165-0/96/$6.00

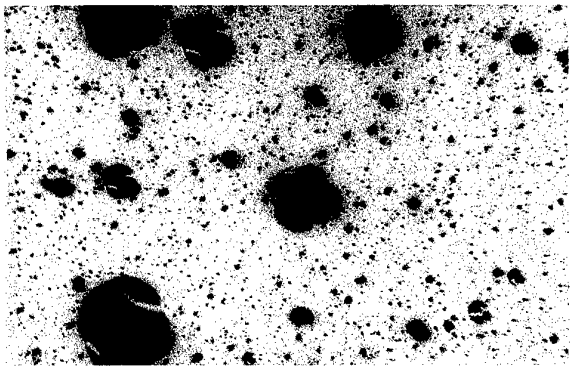


Figure 1. Thermotropic LC droplets (20 wt%) in a 5 wt% aqueous polyvinylalcohol solution

Scanning electron microscopy was used to investigate the structure of the liquid crystal / gel system. Figure 2 show clearly that the LC is embedded in droplet form in the gel.



Figure 2. Scanning electron micrograph of LC droplets embedded in a polyvinylalcohol-water/borax gel

The following question is of interest. What is the reason for the formation of the stable LC emulsion in aqueous pva solution ?
We discuss two models. In the first model, the pva does not adsorbed on the interfacial layer of the LC droplets but merely acts as a stabiliser in connection with the increasing viscosity of the aqueous continuous phase. In the second model, the pva acts as a surfactant and is adsorbed onto the droplet surface.
Electron microscopy provides evidence for the second model. It is evident that there is a shell-like structure that covers the surface of the droplet.

It is interesting clarify the role of the pva molecules within process of the gel formation.

The following experiment was made to investigate this question. Two samples containing 1g of pure 5 wt% aqueous pva solution were prepared. One of which contained 0.2g of embedded LC. Both solutions were titrated with borax solution.
In both samples a gelation occurred after addition of the same amount of borax solution. This indicated that a similar number of hydroxyl groups - which form the complex with borax - was present in the sample irrespective of the presence or absence of LC. This supports a model where the aliphatic chains of the pva project towards the LC droplet surface and the hydroxyl groups are in contact with the aqueous phase[5].
Figure 3 shows the pure pva - water - borax - gel and confirms that the observed inclusions in the gel are LC containing droplets and not other components, so for example embedded air bubbles.

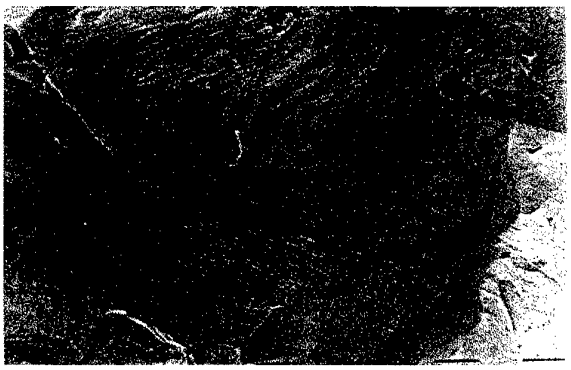


Figure 3. Scanning electron micrograph of a polyvinylalcohol-water/borax gel (5 wt%)

Investigations of the electrooptical properties of the LC molecules embedded as a separate phase in the gel were also made using a polarization microscope. Samples between two transparent electrodes showed a scattering effect dependent upon application an electric field. The threshold voltage was nearly 40 V for a sample with a cell gap of 25 μm and 95 V with a cell gap of 100 μm[5].
It was notable that the droplet structure of the separate LC phase in the gel sample between the transparent electrode was destroyed by the pressure exerted on the gel when the sample was mounted between the transparent electrodes. The droplet structure was lost and replaced by the formation of a LC network.

However, it is an unsolved question if LC molecules can be principally involved in systems of high amounts of organic components, e.g. a microemulsion based gel with water : oil ≈ 1 : 1.

We use gelatin as the gel forming component and AOT (odium salt of bis 2 - ethylhexyl - sulfosuccinate) as a microemulsion forming surfactant. Both components are often use to prepare MBG[6].
In a first step a dispersion of gelatin in water was prepared. To this dispersion we added an optical clear surfactant solution of AOT in heptane. The mixture was strongly shaken and a microemulsion was produced. In a last step the LC was added and the mixture cooled slowly to room temperature.

The main question is to prove the existence of a separate LC - phase in the system prepared.

Using the polarisation microscope the following Figures 4a-d were obtained. The figures show the existence of separate droplets. These droplets are formed by optical anisotropic material. The pattern observed show the characteristic LC radial structure.

The hydrophobic LC obviously does not solve in the hydrophobic phase (in heptane) of MBG. For better understanding it should be mentioned, that even small contents of oil in LC would lead to complete loss of the anisotropy.
The LC bulk exists in form of droplets. This is comparable to the case of embedded LC in an aqueous pva - borax gel. In contrast to the pva - borax system the LC droplets in the MBG show a radial structure. Each droplet has the characteristic cross.

The reason of forming stable droplets in the system and their characteristic configuration is obviously an ordered shell - like AOT surfactant cover. That means the AOT molecules have the same function as the pva molecules in the pva - water -borax - system.

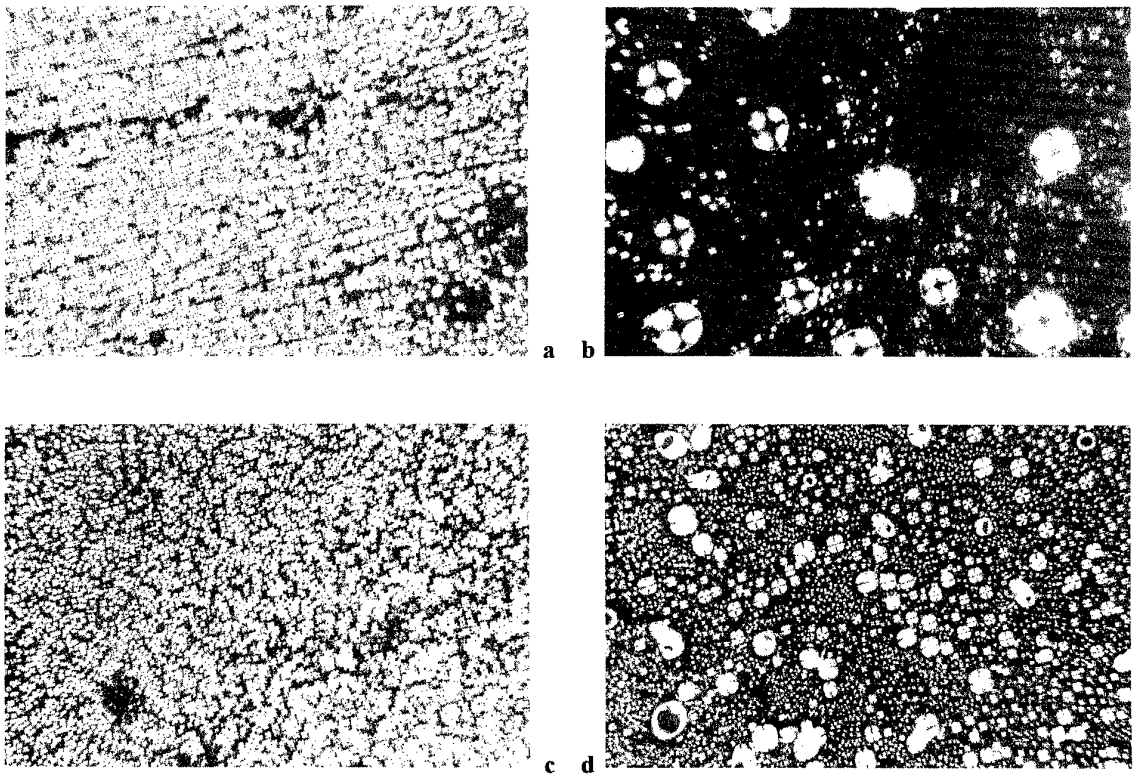


Figure 4. Dispersion of thermotropic LC droplets in a microemulsion based gel (MBG) between crossed polarizer of an optical microscope. a) 0.5 M AOT : 0.5 M butanol = 2:1, b) 0.5 M AOT : 0.5 M butanol = 1 : 2, c) 0.5 M AOT : 0.15 M dodecanol = 2 : 1, d) 0.5 M AOT : 0.5 M dodecanol = 2 : 1

By adding the co-surfactant butanol or dodecanol to the MBG system it is possible to influence LC droplet size and their distribution. Two effects can be observed.

In presence of the co-surfactant the droplet size and their distribution increases. On the other hand this effect depends also on the nature of the co-surfactant.
Figure 4a shows a MBG-LC system with a concentration ratio AOT / butanol of 2:1. The droplet size (25 -30 μm) and their distribution is nearly constant, this is comparable to a system without co-surfactant.

By overwhelming the surfactant concentration, so for example a ratio AOT / butanol of 1:2 the systems are characteristically changed. There are different droplet sizes, and the distribution of the droplets is not constant.

Of course, the hydrophobic and hydrophilic behaviour of the MBG is influenced by adding a co-surfactant. The hydrophilic effect increases with increasing carbon atoms in the carbon hydrogen chain of the co-surfactant. Therefore hydrophilic of an AOT - dodecanol system is higher than an AOT - butanol system.
The change of the hydrophilic - hydrophobic balance in the MBG-LC system is the reason for the change of size and distribution of embedded LC droplets.

Finally it can be concluded that gels can be used as a matrix for dispersed LC on the basis of water as well as of a microemulsion.
However, the gels have no optically properties themselves. In the future we are interested in preparing carrier materials for dispersed thermotropic LC with optically active properties.

3. References

1. S. Zumer and J.W. Doane, Phys. Rev. A, 34, 3373 (1986)
2. G.P. Montgomery, Jr. and N.A. Vaz, Appl. Opt., 26, 738 (1987)
3. G.P. Crawford and J.W. Doane, Condensed Mater News, 6, 5 (1992)
4. A. Seeboth and H. Hermel, Thin Solid Films, 173, L119, (1989), A. Seeboth, H. Hermel and G. Kretzschnar Thin Solid Films, 201, 197 (1991), A. Seeboth, Thin Solid Films, 223, 140 (1993)
5. A. Seeboth, A.R. Mackie, D.C. Clark and S.A. Clark, Colloid and Polym Science, 272, 348 (1994)
6. A. Seeboth, R. Wüstneck and J. Krägel, Colloid and Polym Science, 272, 1151 (1994)
7. R. Audebert et al, Polymer, 36, 49 (1995), M. Shibayama et al, Macromolecules, 27, 1738 (1994)

POLYMER DISPERSED LIQUID CRYSTALS : LIQUID CRYSTAL / POLYMER COMPOSITES AS ELECTRO ACTIVE MATERIALS

Humaira Masood Siddiqi, Michel Dumon*, Jean Pierre Pascault

Laboratoire des Matériaux Macromoléculaires-URA CNRS n°507
Institut National des Sciences Appliquées de Lyon
20, Avenue A.Einstein, F-69621 Villeurbanne France

INTRODUCTION

Polymer Dispersed Liquid Crystals (PDLC) are materials formed by dispersions of liquid crystal (LC) droplets in a polymer matrix [1]. These materials are electro-optical active films which can be switched from a light scattering state (off state) to a transparent state (on state) by the application of a voltage [2]. The embedded mesophase within the droplets can be nematic (N), cholesteric (N*), chiral smectic C (S_C*), or antiferroelectric (S_{CA}*) [2].

Some of the applications include privacy windows for buildings (room dividers) or vehicles (sunroofs), projection displays, light valves [2, 3]. Unlike other types of LC electro-optical devices, PDLC are flexible and require no polarizers. They operate at low power levels and have relatively fast response times.

PDLC systems are at the moment mostly studied from their physical properties (response time of the liquid crystal under electric field, threshold voltage, optical contrast, switching mechanisms, ...). However, these properties, that are related to the use of PDLCs, depend on the morphology of the PDLC system. In turn, the morphology depends on the formation process. PDLC result from the microphase separation of the LC in an initially homogeneous LC / monomer or polymer solution. Depending on the type of polymer used, PDLC are obtained by thermal induced phase separation (TIPS), solvent induced phase separation (SIPS), polymerization induced phase separation (PIPS). In the latter case, the morphology results from the competition between the reaction kinetics and the phase separation kinetics.

We present here epoxy-amine-thermosets containing a commercial nematic liquid crystal. The kinetics of the epoxy-amine reaction is studied in relation to the LC mass fraction, the isothermal reaction temperature and the resulting phase separation. Structural transformation such as gelation and vitrification are also mentioned.

0-8194-2165-0/96/$6.00

EXPERIMENTAL

Preparation of PDLC systems

Diglycidylether of bisphenol A, DGEBA $\overline{n}$=0.03 (DER 332 from Dow) and polypropylene oxide diamine, Jeffamine (D-400 from Texaco) were used as the reactive monomers (stoichiometric amounts of epoxy and amino-hydrogen were used).
The LC additive is the nematic mixture E7 from Merck Ltd at different mass concentrations (0, 10, 30, 50% b/w). The nematic-isotropic transition temperature (T_{N-I}) of this N compound is 61 °C.
The epoxy-amine-LC systems were reacted isothermally at different temperatures (30, 50, 100°C) both in DSC pans and between glass plates.

Analytical techniques

The monitoring of the reaction kinetics and the phase separation kinetics were performed simultaneously by differential scanning calorimetry (DSC, Mettler TA 3000 scanned from -100°C to 320°C at 10°C/min), polarized optical microscopy (POM, Leica 12 POLS with a hot stage Mettler FP 82).

RESULTS AND DISCUSSION

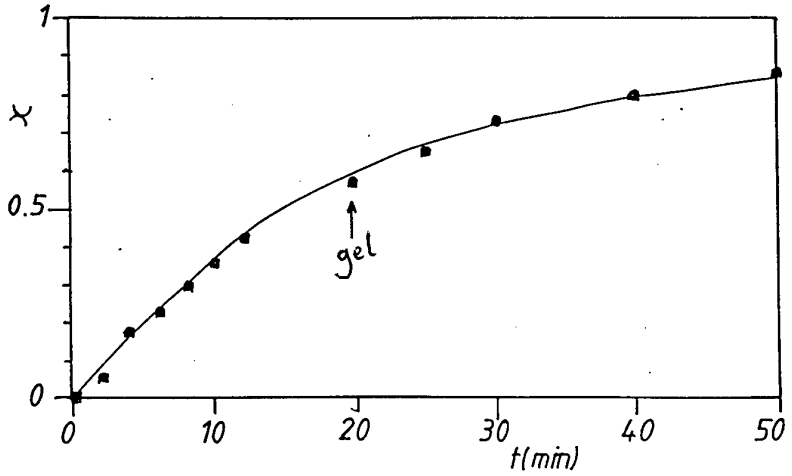
We will investigate successively important parameters that affect the formation process : the reaction rate constants, the structural transformations (gelation, vitrification), the isotropic (I) to nematic (N) transition, the phase separation process.

I- Modelling of the reaction kinetics and gelation

First, the crosslinking of the neat matrix is studied. The epoxy-amine reaction, carried out at either 30°C or 100°C, is found to obey a second order kinetic model as often reported in the literature [4-6]. This model implies two mechanisms : a non catalytic mechanism and a catalytic mechanism which is in fact an autocatalytic process thanks to the OH groups initially present in the reaction medium and those formed by the epoxy-amine reaction. Fig.1 shows the good agreement between experimental conversion values and predicted values. The predicted values are obtained by a Runge-Kutta type resolution [6] for solving the differential equations of the kinetic model.

If k_1, k_2 are defined as the rate constants of autocatalytic reactions for primary and secondary amines and k_1', k_2' the rate constants of non catalytic reactions for primary

Figure 1



and secondary amines, the reactivity ratio,n ,i.e. the ratio of the rate constants for primary to secondary amine is defined by $n = \frac{k_2}{k_1} = \frac{k_2'}{k_1'}$.

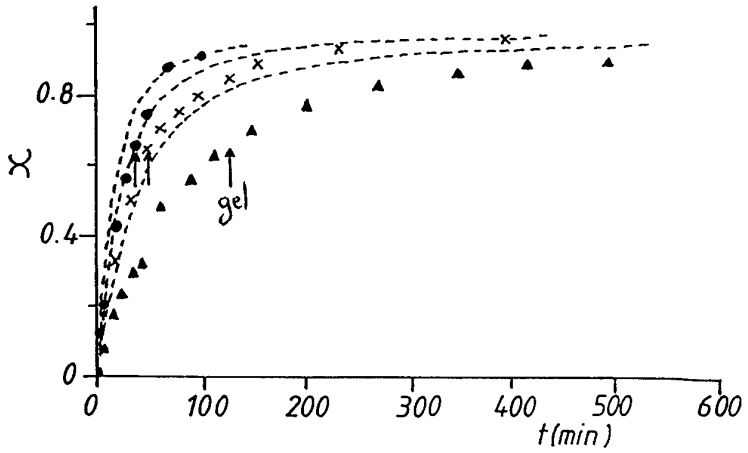
The criterion to calculate n is the minimization of the square error between experimental and calculated values. Our calculation provides a value of n equal to 1 indicating no substitution effect in the epoxy-amine reaction.

Consequently, we measured a conversion at the gel point $x_{gel} = 0.57 \pm 0.015$ consistent with the theoretical value of 0.577 (4) for such a system (diepoxide of functionality 2 and diamine of functionality 4).

Second, the crosslinking of the matrix containing 10, 30, 50 % b/w of LC is studied. When the system is cured at 100°C, it remains homogeneous through out the reaction ; no phase separation occurs. At this temperature, the LC is miscible with the polymer network even in the rubbery state.

Fig.2 shows the evolution of the reaction conversion with time : the epoxy-amine reaction rate slows down with the added concentration of liquid crystal. This retarding effect is not only due to dilution effects : the dashed lines in Fig.2 represent simulated values of conversion taking into account the dilution of the epoxy groups by the LC and n=1. But even, the experimental values are not modelled by the second order model used previously.

Figure 2



Other effects must be considered. One possibility is the occurence of intramolecular reactions favoured by the flexibility of the polypropylene oxide chains and strong hydrogen bonding within the system (7). This hypothesis is supported by the measurement of a conversion at gel $x_{gel} = 0.61 \pm 0.015$ whatever the LC content.
According to the statistics of network formation, this means that the reactivity ratio n approaches 0. Thus, we tried to calculate n; we found 0.87, 0.60, 0.45 for the PDLC containing respectively 10, 30 and 50 % b/w LC.
Table I gives the calculated values of rate constants for the different systems.

Table I

SYSTEMS	DGEBA/D400	DGEBA/D400	DGEBA/D400/ 10% E7	DGEBA/D400/ 30% E7	DGEBA/D400/ 50% E7
Temperature (°C)	30	100	100	100	100
n	1 ± 0.05	1 ± 0.02	0.87±0.1	0.6 ± 0.1	0.45 ± 0.1
K_1 $(min)^{-1}$	$2.63\ 10^{-3}$	$1.14\ 10^{-1}$	$8.5\ 10^{-2}$ ± 0.005	$5.25\ 10^{-2}$ ± 0.0075	$2\ 10^{-2}$ ± 0.0015
K_0 $(min)^{-1}$	$3.18\ 10^{-4}$	$3.57\ 10^{-2}$	$1.8\ 10^{-2}$ ± 0.002	$2\ 10^{-2}$ ± 0.005	$1.6\ 10^{-2}$ ± 0.002
k_1 $(mol^{-2}\ l^2\ s^{-1})$	$0.33\ 10^{-5}$	$1.43\ 10^{-4}$	$1.32\ 10^{-4}$	$1.34\ 10^{-4}$	$1\ 10^{-4}$
k_1' $(mol^{-1}\ l\ s^{-1})$	$0.127\ 10^{-5}$	$1.55\ 10^{-4}$	$8.51\ 10^{-5}$	$1.26\ 10^{-4}$	$1.43\ 10^{-4}$
k_2 $(mol^{-2}\ l^2\ s^{-1})$	$0.315\ 10^{-5}$	$1.40\ 10^{-4}$	$1.15\ 10^{-4}$	$8.04\ 10^{-5}$	$4.5\ 10^{-5}$
k_2' $(mol^{-1}\ l\ s^{-1})$	$0.121\ 10^{-5}$	$1.52\ 10^{-4}$	$7.4\ 10^{-5}$	$7.5\ 10^{-5}$	$6.46\ 10^{-5}$

n = reactivity ratio ; K_1, K_0 = apparent rate constants including ϵ_0. OH_0
k_1, k_2 = absolute rate constants for autocatalytic reactions
k_1', k_2' = absolute rate constants for noncatalytic reactions
1, 2 = for primary and secondary amines respectively

II - Phase separation, I-N transitions and glass transitions

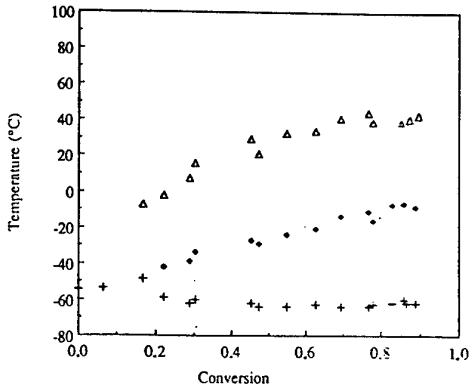
Out of the three systems containing 10, 30, 50 % b/w of LC only the 50 % b/w showed phase separation on cooling to room temperature. Therefore we studied this system cured isothermally at three different reaction temperatures Ti = 30, 50, 100°C chosen according to their proximity of the N-I temperature of the neat LC (61°C).

II-1. System cured at Ti = 100°C >> T_{N-I} (neat LC)

The reactive system remains homogeneous at the cure temperature through out the reaction and phase separation occurs only on quenching to lower temperatures. In the case of DSC quench (runs from -100°C to 320°C), the thermograms show two glass transition remperatures ($Tg\alpha$, $Tg\beta$) and one N-I transition temperature for conversions higher than 0.2 . Fig.3 represents the evolution with conversion of the different transition temperatures. Thus, on quenching the samples, phase separation occurs above a conversion of 0.2. The low temperature glass transition ($Tg\beta$) is attributed to a LC rich phase and remains constant through out the reaction. The high temperature glass transition ($Tg\alpha$) is attributed to a polymer rich phase and increases with conversion until a value $Tg\infty = 5$°C (measured after a second heating scan). This value is much lower than $Tg\infty$ of the neat matrix ($Tg\infty$(neat matrix) = 49°C) : the LC additive acts as a strong plasticizer.

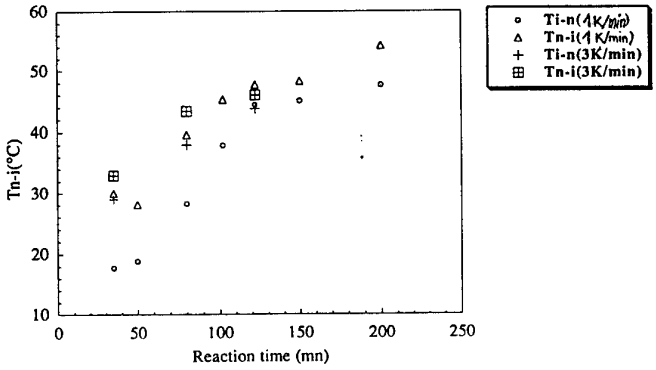
The N-I endothermic transition is characterized by T_{N-I}; T_{N-I} increases with conversion thus showing a purification of the LC rich phase. One can note that T_{N-I} still increases slightly after gelation. Therefore gelation is not always a sufficient criterion to freeze in a system (for example to fix a morphology).

Figure 3



Furthermore, the cooling rates affect the value of T_{I-N} . Fig.4 represents the time evolution of T_{I-N} and T_{N-I} measured by optical microscopy on samples after different cooling rates. The fact that the I-N transition depends on both the cooling rate and the quench depth is in favour of a thermal induced phase separation process occuring in a more and more viscous epoxy network depending on conversion. Phase separation is here rather comparable to crystallization processes in thermoplastic polymers where the size of spherulites depends upon the thermal treatment.

Figure 4



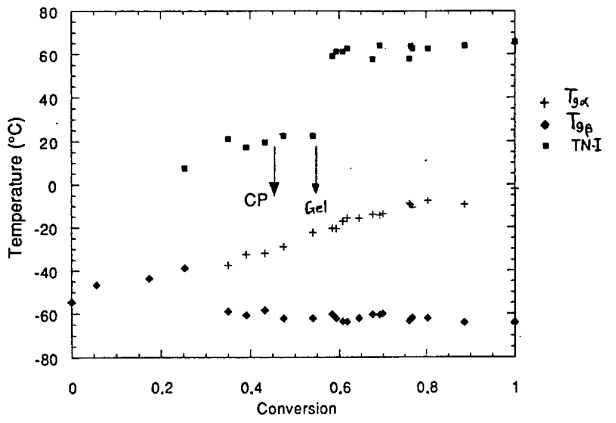
II-2. System cured at Ti = 30°C << T_{N-I} (neat LC).

Now, the reactive system exhibits a phase separation during cure at 30°C above a conversion $x_{CP} = 0.45$. Therefore, for cure at 30°C, the phase separation is due to the molar mass increase at constant temperature.

The evolution with conversion of the different transition temperatures are represented in Fig.5. The glass transition temperatures follow the same trend as in the system cured at 100°C; however the evolution of T_{N-I} is quite different. Indeed T_{N-I} undergoes a step increase at a conversion of 0.55.

This conversion coincides with the conversion at gel measured at $x_{gel} = 0.56$. Therefore, in this system, gelation has a marked influence on the purification of the LC rich phase and therefore on the morphology of the PDLC.

Figure 5



CONCLUSION

In spite of the role of gelation on the phase separation, our experiments highlight the effect of the N-I transition compared to the cure temperature.

For cure temperatures higher than T_{N-I} (neat LC), phase separation proceeds by a thermal process. For cure temperatures quite lower than T_{N-I} (neat LC), phase separation may proceed by a chemical quench. In the former case, morphology depends on the cooling rates ; in the latter case, morphology may be fixed by gelation.

REFERENCES

(1) J.L. West, Mol. Cryst. Liq. Cryst., **157**, 427 (1988)

(2) H.S. Kitzerow, Liquid Crystals, **16,** 1 (1994)

(3) G.P. Montgomery Jr., G.W. Smith, N.A. Vaz in "Liquid Crystalline and Mesomorphic Polymers" Springer Verlag Ed. 1994

(4) K. Dusek, M. Ilavsky, S. Lunak, J. Polym. Sci. Symp., **53**, 29 (1975)

(5) B.A. Rozenberg, Adv. Polym. Sci., **75,** 115 (1986)

(6) C. Titier, J.P. Pascault, M. Taha, B.A. Rozenberg, J. Polym. Sci., **33**, 175 (1994)

(7) K. Dusek, M. Ilavsky, S. Stokrova, L. Matejka, S. Lunak, in "Crosslinked epoxies" Walter de Guyter and co Berlin 1987

Shape Memory Alloys and Adaptive Materials

Invited Paper

On the adaptivity of shape memory alloys for use in adaptive materials

Jan Van Humbeeck

Dept. MTM - K.U.Leuven, de Croylaan 2, B-3001 Heverlee

ABSTRACT

This paper would like to draw the attention to the possibilities of tuning shape memory alloys for optimal use in smart materials. The importance of processing, transformation temperatures, hysteresis, texture is discussed. Finally, it is explained how the microstructure, by means of the presence of precipitates, can lead to dramatic but interesting changes in the E-modulus behaviour during the martensitic transformation.

1. INTRODUCTION

Shape memory alloys may perform several unique macroscopic functional properties: one-way shape memory effect, two way shape memory effect, constraint recovery thereby creating a high (recovery) force, actuator properties, pseudoelasticity and high damping capacity. All those functional properties, already many times explained in detail[1], are related to a (thermoelastic) martensitic transformation. This transformation, generally defined by its transformation temperatures M_s and M_f, respectively the start and finish temperature of the forward transformation, and A_s and A_f, respectively the start and finish temperature of the reverse transformation, occurs in a rather limited temperature range (20 to 60 K), while the transformation temperatures can be selected between absolute zero and about 500 K.

Based on those unique properties, shape memory alloys are considered as interesting adaptive materials, forming one of the constituting elements of a more complex composite material generally defined as smart or even intelligent.

In this environment shape memory alloys can act as well as sensor as actuator but only by adapting itself to the external parameters of strain, stress and temperature. Therefore, calling a SMA smart on itself is too generous and unfair.

2. POTENTIAL USE OF SMA IN SMART MATERIALS

Indeed, regarding the potential applications of SMA in smart composites one has to distinguish two different approaches.

2.1 The use of the functional properties, as defined above.

In this case the material performance is completely defined by its (σ,ε,T) relationship. This relationship can be rather easily established and there are many models attempting to describe this relation phenomenologically[2] or physically. Moreover, because the martensitic transformation is a first order transition, the reverse transformation occurs at higher temperatures than the forward transformation, this way creating a hysteretic effect. This hysteresis is then also reflected in the (σ,ε,T) space. As a consequence the choice of two out of the three variables might lead to two possible solutions of the third variable if one has not defined the path when moving from one point on the (σ,ε,T)-surface to the other.

0-8194-2165-0/96/$6.00

Another difficulty in quantifying the (σ,ε,T) relationship is the fact that the chemical (transformation temperatures), physical (E-modulus, texture, electrical resistance) and mechanical (strength, fatigue, function) properties are very much influenced by the thermomechanical history of the material and can vary significantly.

One should know that SMA-producing companies have concentrated their research in optimising the processing and thermal treatments towards the specific needs of every new application. For example, starting from the same composition of a SMA, the thermo-mechanical processing will be different in case one needs a high number of shape memory cycles than in the case one needs a high recovery force. As a consequence, in the case of application of SMA in smart materials, one has also to adapt the material by the appropriate thermomechanical processing towards the specific function required in the composite.

2.2 The use of changes of physical properties related to the martensitic transformation

Physical properties of materials are related to the crystal structure and microstructure of the involved phases. In spite of the diffusionless character of the martensitic transformation, the lattice parameter, crystal structure and microstructure of the parent phase and the martensite phase, differ significantly. As a consequence, during transformation, values of E-modulus, internal friction, electrical resistance, hardness might change.
For example one of the interesting features of SMA for application in smart materials is the difference between the E-modulus of the martensite phase and the one of the parent phase.

Also in this respect, one has to indicate that the E-modulus as well measured dynamically as well as statically might be largely influenced by the thermomechanical processing. Indeed the modulus is measured based on pure elastic and anelastic behaviour of the materials. Especially the anelastic behaviour is dependent on the presence, interactions and mobility of point-, line- and even "surface"-defects, such as parent-martensite and martensite-martensite interfaces and can largely influence the "apparent" E-modulus. Due to the high anisotropy of the martensite, also texture might have a significant influence on the relative changes of the E-modulus and other physical properties during transformation.

3. LIMITS AND POSSIBILITIES OF THE APPLICATION OF SMA-ALLOYS

Beside or along the above mentioned classification of shape memory based smart materials, several other aspects of this particular material should be taken into account, first of all, the particular advantages and disadvantages of shape memory alloys, especially, when used as actuators. Table 1 and 2 summarise these particular properties[1,3].

Table 1: Advantages of shape memory alloys as actuator

- Reliability
- Simplicity of mechanism
- Large strokes
- Creation of clean, silent and spark-free conditions
- Operational near zero-gravity
- High power/weight ratio

Table 2: Drawbacks of shape memory alloys as actuator

- Low energy efficiency
- Limited bandwidth due to heating and cooling restrictions
- Appropriate processing required to limit degradation and fatigue

Next to those particular aspects one should also take special attention to the matrix-SMA interface. Debounding of the SMA-wire (fibre) should be studied in detail during mechanical and thermal cycling. Especially the latter is important[4].

Shape memory alloys change their properties during heating and cooling. The metallic wires have a good conductivity, which is less the case for the polymer environment. The polymer at the surface of the SMA-wire will be heated and might therefore soften. One should also take into account that the forward martensitic transformation is exothermic, while the reverse transformation is endothermic (order of 10-20 J/gr). Heating and cooling cycles may thus lead to important heat fluxes at the interface, strongly influencing the adhesion of the SMA-element into the matrix. In case a strain-recovery (shape memory) is added to the SMA element, mechanical shearing is superimposed on the above mentioned heat fluxes, detoriating faster the interface bounding. A systematic study of those interface effects has not been performed yet to our knowledge.

4. POSSIBILITIES OF ADAPTING A PARTICULAR SMA-ALLOY TOWARDS THE REQUIREMENTS OF A SMART STRUCTURE. A CASE STUDY: Cu-Al-Ni ALLOYS

4.1 Introduction

In this part we will draw the attention on the fact that shape memory alloys, even at a particular composition can be readily tuned towards special requirements, based on microstructural aspects as a consequence of thermomechanical processing. Several of the further discussed items can be applied to other well-known systems such as Cu-Zn-Al and Ni-Ti.

These possibilities mark the versability of those alloys and contain at the same time a special warning to potential users: applying a non-adapted SMA might lead to desillusion. Success might be obtained when the proper selection is made in order to optimise the envisaged SMA toward the real needs and purpose of the smart material and related smart structure.

4.2 On the adaptivity of Cu-Al-Ni-Ti-Mn alloys

Cu-Al-Ni alloys have a special interest since they can exhibit a martensitic transformation far above 100°C, whereas Cu-Zn-Al and Ni-Ti alloys are so far limited to above 100°C maximum. Moreover, relative to Cu-Zn-Al, they are much less prone to martensite stabilisation even at high temperatures.

For industrial use Ti is added, generally not more than 1 wt%, for grain refining purposes. The addition of Ti form (Cu,Ni)TiAl precipitates which, limits the interdendritic growth during solidification[5]. This way an average grain size of 50 μm or less can be obtained, leading to improved mechanical properties. Mn (2 to 5 wt%) is added in some cases to improve the machinibility and processing and to a lesser extent the ductility[6].

4.2.1 Tuning the transformation temperatures (TT)

a. by alloying:

the transformation temperatures (TT) are very sensitive to the composition. An increase of 0.1 wt% Al, replacing Cu decreases the TT by about 20°C, 0.1 wt% Ni only about 2 to 4°C, 0.1 wt% Mn about 7 to 10°C. Adding Ti, and thus forming (Cu,Ni)TiAl precipitates will influence the nominal composition of the matrix and thus also exhibit an influence on the TT.
Moreover, some Ti can remain in solution, even after heat-treatment. The presence of Ti will lead then to solution hardening of the beta-phase, stabilising the β-phase and so decreasing the TT, calculated from the ternary composition.

b. by changing the order:

Cu-based alloys are generally heat-treated in a temperature region of the β-phase where the lattice forms an A_2 structure, this is a random distribution of all atoms over the bcc lattice.
During cooling, a B2 structure, followed by a DO_3 (or $L2_1$) superstructure will form. Especially the latter can influence significantly the TT. Since this latter order transition is of first order, quenching the alloy from a high temperature will freeze in a significant deviation of the maximal possible order.
Disordered DO_3 ($L2_1$) will depress the transformation temperatures by an order of 60 to 80°C (!) relative to a fully ordered structure.
The extreme slow diffusion in Cu-Al-Ni alloys can retain the disordered structure, keeping the TT low. The TT can be increased to the value of interest by ordering the lattice structure. This is obtained when the material is aged up to one hour in a temperature interval 250-350°C.
The higher the ageing temperature, the faster ordering will occur and thus the faster the TT will increase.
Care should be given during ageing since ageing might lead to the formation of the stable phase: α and or γ. These phases have to be avoided since they will hamper the required functional and physical properties.

4.2.2 Tuning the hysteresis

As mentioned before, the reverse transformation occurs at higher temperatures than the forward transformation forming a hysteretic loop on a temperature-axis. Also pseudoelastic loading and unloading occurs hysteretically. The size of the hysteresis is related to the frictional energy[7] occurring during transformation and to a lesser extent to the elastic stored energy. It is also related to the degree of self-accommodation of the type of martensite. Depending on the system, the size of the hysteresis can be of the order of a few degrees (R-phase transition in NiTi), up to 40-50°C (martensite in Ni-Ti). In Cu-Al-Ni alloys two different types of martensite can occur, β' and γ'-martensite. β'-martensite shows a hysteresis of the order of 10 to 20°C while γ'-martensite hysteresis is of the order of 20 to 40°C. Both types of martensite can also coexist, depending on composition[8] and ageing treatment, showing in this case stepwise hysteresis, as well as during thermal cycling as during thermoelastic loading[9]. The consequence of the hysteresis is that there is no unique relationship between a property that is related to the volume transformed, and the temperature. Within a complete hysteresis loop, subloops can be described. This means that the path to return to the same point might be complicate, i.e. it might happen that one has to heat first before cooling can be started to revert to an identical position at a lower temperature, or vice verca. This hampers the speed of action significantly, especially because cooling is the slowest part of the path.

4.2.3 Tuning the E-modulus

One has to distinguish between the E-modulus of the beta-phase and the E-modulus of the martensite.
As mentioned earlier, the "real" E-modulus is a consequence of a pure elastic and anelastic strain during loading. Tuning of the E-modulus can be especially done by influencing the mechanisms that contribute to the anelastic

strain. However, due to the high anisotropy of Cu-based shape memory alloys, even the elastic part can change significantly, depending on the lattice orientation and consequently the texture.

Fig. 1[10] shows how the E-modulus changes of a CuZnAl alloy with the orientation factor γ, where $\gamma = l^2m^2 + m^2m^2 + n^2l^2$, m, n, l being the direction cosinus of the loading axis. It can be shown that $0 \leq \gamma \leq 1/3$. The modulus has been calculated from measured elastic constants. The dashed line shows the error, due to the error on the elastic constants. For an at random orientation of grains in a polycrystaline material γ is of the order of 0.2.

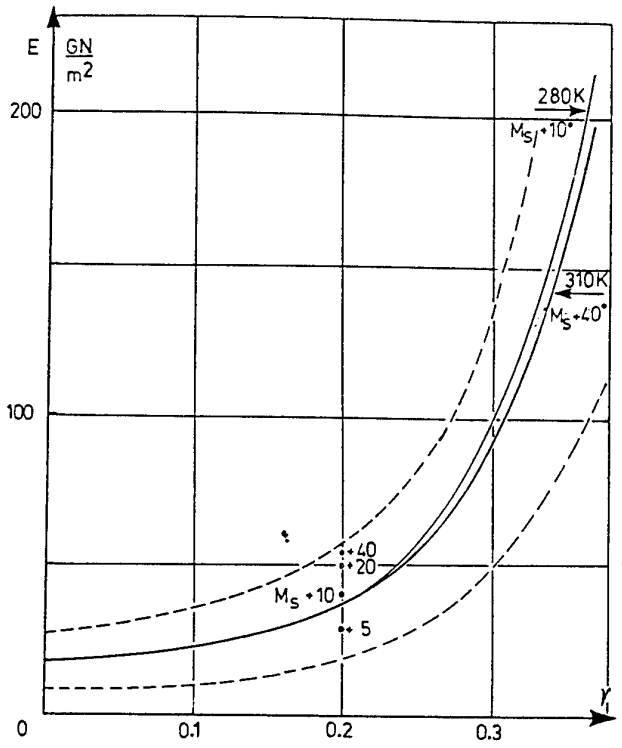


Fig. 1. Elastic modulus of single crystals tested under uniaxial tensile load as a function of crystal orientation. Dashed lines: calculated scatter due to measurements of C_{ij}[10].

The anelastic strain leads to lower E-modulus than the one measured if only pure elastic strain would be measured. It has been shown that this anelastic strain is very sensitive to the presence of defects in the lattice. This will now be treated for Cu-Al-Ni-Ti-Mn alloys. More detailed information can be found in[11,12].

The mechanical properties of Cu-Al-Ni shape memory alloys are improved by the addition of elements such as Titanium, as grain refiner, and Manganese, replacing part of the Al. Ti forms precipitates, designated as χ phase, which have a cubic Heusler type structure ($L2_1$) and a composition close to $(Cu,Ni)_2AlTi$[13,14]. Based on its size and shape, two types of χ-phase precipitates have been distinguished in the Cu-Al-Ni-Ti alloys. The larger ones, few μm in size, are referred to as χ_L and do not have any defined shape. Others, with a size of several tenths of nm (≈45 nm), are the cuboidal χ_S precipitates. No strain contrast effect is reported around the χ_L precipitates, but a coffee bean contrast due to coherency strain has been verified around χ_S precipitates[13].

When Mn is added to the Cu-Al-Ni-Ti alloy, Ratchev *et al*[15,16] denote the presence of particles smaller than 5 nm, χ_{SS},which are not present in the Cu-Al-Ni-Ti material. In their work Ratchev *et al* assume that all the precipitates present in the alloy are χ-phase, $(Cu,Ni)_2AlTi$, with a misfit parameter of +2.14% with respect to the b-phase.

Nakaniwa *et al*[17] and Sugimoto *et al*[18] have investigated the effect of the χ-phase precipitates on the internal friction and Young' modulus of several Cu-Al-Ni-Ti-(Mn) alloys water quenched from high temperature. The behaviour of the Young's modulus is characterised by the following observations:

(a) The height of the internal friction peak associated with the martensitic transformation, measured at a frequency of 600 to 800 Hz with a heating/cooling rate of 2°/min, decreases sharply with increasing volume fraction of χ-phase. In contrast, the magnitude of the corresponding minimum in Young's modulus increases as the volume fraction of χ-phase increases. This result is explained by the decreasing mobility of interfaces between martensite and parent phase due to grain boundaries as well as to the interaction of the martensite interfaces with the finely dispersed χ-phase particles.
(b) The Young's modulus of the martensite phase is reported to increase by the presence of χ-phase according to "a law of mixture". The interfaces between martensite and the χ-phase particles are not considered to contribute appreciably to the Young's modulus because the particles are incoherent.
(c) The Young's modulus of the parent phase is reported to be larger than the Young's modulus of the martensite. This behaviour is attributed to coherency, which causes "an elastically harder state at interfaces between parent phase and χ-phase".

We have recently analysed the effect of the three different χ-phase sizes on the elastic modulus of both β and martensite. Attention will be focused on the Cu-Al-Ni-Ti-Mn alloy (CANTiM), which shows a wider distribution in χ-phase size. The Cu-Al-Ni-Ti alloy (CANTi), in which the small coherent precipitates are not present, will be used for comparison. Also a Cu-Al-Ni alloy without Ti, and consequently without χ-precipitates, will be used as reference and is denoted as CAN.

Three Cu-Al-Ni-(Ti)-(Mn) alloys have been chosen for the present investigation, Table 3. Their compositions correspond to martensitic transformation temperatures above 373 K. The grain refining effect of the Ti addition has been enhanced by extruding and hot rolling the material.

Table 3: Overall composition of the alloys used in this work in wt.%.

composition wt.%	Cu	Al	Ni	Ti	Mn	A_S^*/K
CANTiM	80.1	11.9	5.0	1.0	2.0	398
CANTi	82.6	13.4	3.0	1.0	-	473
CAN	83.0	13.0	4.0	-	-	393

* The initial retransformation temperature, A_S, has been measured after a heat treatment at 1173 K during 1.2 ks followed by a water quenching to room temperature

Samples, 13*7*1 mm^3, were cut from the as rolled material for Differential Mechanical Analysis (DMA) experiments and two kinds of basic heat treatment were performed for each of the CAN, CANTi and CANTiM alloys: The samples were β-tised at 1173 K for 1.8 ks and subsequently either air cooled or water quenched to room temperature.

Their elastic modulus was recorded using the bending resonant method. In the bending mode, the sample, in the form of a rectangular bar, is clamped rigidly at both ends and its central point vibrates sinusoidally by the drive clamp. The angular frequency, f, remains in the order of 10 to 50 Hz. The temperature is measured and controlled

by a Chromel-Alumel thermocouple positioned immediately behind the sample. The scanned temperature range was between 223 to 493 K for the CAN and CANTiM alloys and 223 to 533 K for the CANTi, due to its higher transformation temperatures. The scanning rate was $5*10^{-2}$ K/s and the fixed amplitude 0.10 mm, which corresponds to a sample deformation of approximately $\varepsilon \approx 2*10^{-4}$.

Classification of the χ-phase precipitates.

The χ-phase precipitates have been classified based on their size and shape, as well as on their calculated degree of coherence with the β-phase[19]; this last criterion will become apparent when discussing the internal friction and elastic modulus measurements. Four types of precipitates could be distinguished in the CANTiM alloy. Their characteristics are reflected in Table 4.

Table 4: Classification of all the possible χ-phase precipitates in the CANTiM alloy.

CANTiM alloy	χ_L	χ_S	χ_S'	χ_{SS}
diameter size	several μm	50-150 nm	10 nm	3-5 nm
shape	ovoid	cuboid	cuboid	ellipsoids
coherence degree with the β-phase	incoherent	semi-coherent	coherent ?	coherent

The χ_L precipitates are present after any heat treatment and their shape and amount does not appreciably change. Thus, their presence will not be further explicitly mentioned in the tables. All the χ-phase precipitates, but the χ_{SS} due to their small size, have been identified as an intermetallic of approximate composition (EDAX) $Cu_{.25}Ni_{.25}Al_{.25}Ti_{.25}$ and Heusler type structure. Their distribution strongly depends on the specific heat treatments[20], Table 5.

Table 5: Effect of the quenching temperature and cooling rate on the χ-phase precipitates distribution, CANTiM alloy

heat treatment: heat treatment: 1173 K 1.8 ks and	χ_S	χ_S'	χ_{SS}	remarks†
(1) 5% NaCl-5% KOH WQ (RT)	no	no	no	
(2) water quenched (RT)	no	few, 10 nm	no	coffee bean contrast
(3) air cooled to 873 K & WQ (RT)	>120 nm	10 nm	no	coffee bean contrast
(4) air cooled to RT	150 nm	no	yes	mottled matrix contrast

In contrast to the results from the CANTiM alloy, only three types of precipitates are observed in the CANTi alloy. Their characteristics are reflected in Tables 6 and 7. Another feature observed in this alloy, and not in the CANTiM, is that as the size of the χ_S precipitates increases from 50 to 150 nm, their shape changes from cuboidal towards a shape with protruded corners.

† Mottled matrix and coffee bean contrast refer to the type of contrast observed by TEM[15, 16].

Table 6: Classification of all the possible χ-phase precipitates in the CANTi alloy

CANTi 1617A	χ_L	χ_S	χ_S'	χ_{SS}
size	several μm	50-150 nm	10-20 nm	*3-5 nm*
shape	ovoid	cuboid to octahedral	cuboid	*not present*
coherence degree with the β-phase	incoherent	semi-coherent	semi-coherent ?	*not present*

Table 7: Effect of the cooling rate on the χ-phase precipitates distribution, CANTi alloy

heat treatment: 1173 K 1.8 ks and	χ_S	χ_S'	χ_{SS}	remarks
air cooled	120 nm	yes	no	coffee bean contrast
or water quenched	30-50 nm	no	no	distorted matrix β" (lamellar mixture of 18R and 2H)

Elastic modulus measurements

The elastic modulus curves measured for the three alloys after either air cooling or water quenching from 1173 K are presented in Figure 2.

The *CAN alloy* behaves as a typical shape memory alloy. The level of the elastic modulus for the martensite and β-phase decreases as the temperature increases; during the martensitic transformation a clear minimum is observed, which is more pronounced for the water quenched sample. The elastic modulus in β-phase for the air cooled sample is higher than the one of the water quenched sample.

In the *CANTi alloy* there is a sudden increase of the β-phase elastic modulus after the transformation both for the water quenched and air cooled samples, and there is not a deep minimum during the transformation. Comparing both curves it can be observed that the main difference in elastic modulus among both treatments is not related to the β-phase region but to the martensite. The modulus level of the water quenched sample is lower than that of the air cooled one, especially for the first reverse transformation.

In the *CANTiM alloy* there is not a clear minimum during the transformation, but a continuous decrease of the modulus of the martensite. In the air cooled sample, a significant increment of the elastic modulus is observed just after the direct transformation, in β phase; it nearly doubles its value with respect to the martensite phase just before the transformation. As in the CANTi alloy, the evolution of the elastic modulus is similar in both phases. In the martensite region, the level of the modulus during the first reverse transformation for the water cooled sample is much higher than that in the subsequent cycles.

Thus, the size and distribution of the χ precipitates play an important role in the level of the elastic modulus, both in martensite and β phase and during the transformation, i.e., there is no minimum during the transformation and an important increment in the β-phase elastic modulus with respect to the martensite. It is also worth noticing that the elastic modulus of the martensite measured directly after quenching from 1173 K, is higher than the one obtained in the same sample after the second cooling from β phase.

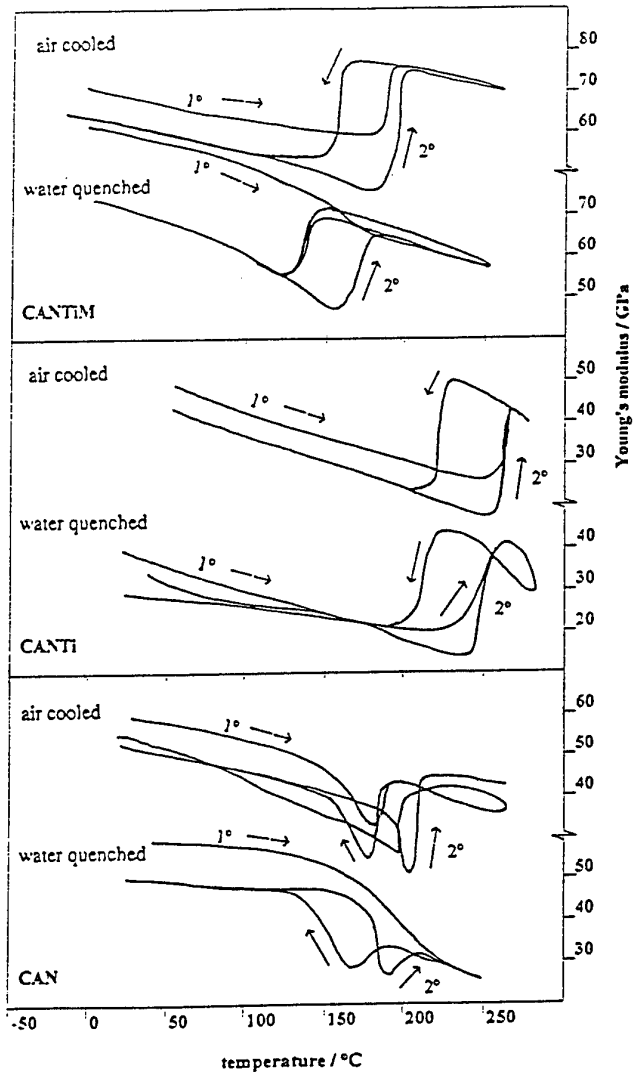


Fig. 2. Elastic modulus curves for the CAN, CANTi and CANTiM alloys. The samples were heat treated at 1173 K and subsequently water quenched or air cooled to room temperature.
1° and 2° denote the first and second heating cycle, respectively. The heating rate is $5*10^{-2}$ K/s, and the strain amplitude $\approx 2*10^{-4}$, with an angular frequency in the range of 10 to 50 Hz.

5. DISCUSSION

The semicoherent cuboidal-like χ-phase precipitates are the main contributors to the measured increase in elastic modulus in the β-phase. Their effect may be qualitatively understood with a dislocation string model in which the semicoherent precipitates act as pinning points. The small precipitates, coherent with the β-phase, would have the effect of opposing the dislocation movements, increasing the elastic modulus.

In the martensite phase, the contribution to the increase in martensite modulus is attributed to the new variant arrangement around the precipitates.

Applying the appropriate heat treatments to this kind of alloys, allows the production of "custom made" fibres with the required properties for use in smart materials.

What has been studied here in detail is probably also applicable to other shape memory alloys. Indeed also the properties of NiTi alloys are many times tuned by precipitates. A detailed investigation on their influence on the E-modulus is performed at present.

6. CONCLUSION

The properties, physical and functional, of shape memory alloys are very sensitive to the microstructure (grain size, precipitates, size of the martensite variant, texture, ...) and to the lattice structure (atomic ordering, paint-, line- and surface defects). As a consequence properties of SMA can be changed and controlled by the thermomechanical processing of the material so that the desired properties are obtained. Therefore, it is a prerequisite to define the expected role of SMA-constituent in adaptive, smart or intelligent materials on forehand in order to use the most appropriate material. Modelling of this kind of behaviour is certainly not completed but adaptive or smart modelling can definitively overcome those difficulties.

7. REFERENCES

1. J. Van Humbeeck, D. Reynaerts, R. Stalmans, Proc. Actuator-94, Bremen, Ed. AXON Tech. GmbH, Bremen, p. 312-316.
2. "Mechanics of phase transformations and shape memory alloys", ASME-1994, AMD-Vol. 189, Ed. C Brinson, ASME, New York, 1994.
3. K. Ikuta, Proc. IEEE Workshop, p. 2156-2161, 1990.
4. C.M. Friend, N. Morgan, Journ. de Physique IV, Colloque C2, Vol. 5, Proc. ESOMAT-94. p. C2-415-420, 1995.
5. R. Elst, J. Van Humbeeck, L. Delaey, Acta Met. **36**, p. 1723-1729, 1988.
6. United States Patent 4.634.477, January 6, 1987 (Sugimoto et al.).
7. J. Ortin, A. Planes, Acta Met. **36**, Overview 68, p. 1873, 1988.
8. Z. Nishiyama, "Martensitic Transformations",Acad. Press, New York, p. 79, 1987.
9. C. Segui, E. Cesari, J. Van Humbeeck, Mat. Trans. JIM **32**, 898-904, 1991.
10. J. Van Humbeeck, L. Delaey, A. Deruyttere, Zeitschrift für Metallkunde **69**, p. 575-580, 1978.
11. I. Hurtado, J. Van Humbeeck, Moo Chi-Mei, SPIE, Vol. 2441, "Smart materials", Ed. P. Jardine, p. 131-138, 1995.
12. I. Hurtado, P. Ratchev, J. Van Humbeeck, L. Delaey, "A fundamental study of the λ-phase precipitation in Cu-Al-Ni-Ti-(Mn) Shape Memory Alloys", Accepted by Acta Met. et Mat.
13. K. Adachi, Y. Hamada. and Y. Tagawa., "Crystal structure of the c-phase in grain refined Cu-Al-Ni-Ti shape memory alloys", Scripta Met. 21, p. 453, (1987).
14. K. Adachi, K. Shoji, Y. Hamada, "Formation of c phases and origin of grain refinement effect in Cu-Al-Ni shape memory alloys added with titanium", ISIJ Inter. 29, p. 378, (1989).
15. P. Ratchev, J. Van Humbeeck, L. Delaey., "Changes in stacking sequence of b_1'-martensite plates in a CANTiM alloy", 14th European Crystallographic Meeting, Enschede, The Netherlands, 2-7 Aug. 1992.
16. P. Ratchev, J. Van Humbeeck, L. Delaey, "On the formation of 2H stacking sequence in 18R martensite plates in a precipitate containing Cu-Al-Ni-Ti-Mn alloy", Acta Metall. et Mater. 41, p. 2441 (1993).
17. M. Nakaniwa, K. Sugimoto, K. Kamei, Y. Nakamura, T. Sugimoto, "Effect of second phase on internal friction and Young's modulus in Cu-Al-Ni shape memory alloys", J. Japan Inst. Metals. 56, p. 30, (1992).
18. K. Sugimoto, "The effect of second phase particles on internal friction and Young's modulus in Cu-Al-Ni-Ti shape memory alloys", Seminar in the Dept. MTM, K.U. Leuven, 15 October 1990.
19. I. Hurtado, P. Ratchev, J. Van Humbeeck, L. Delaey, "Characterisation of the c-phase precipitation in Cu-Al-Ni-Ti-(Mn) shape memory alloys", submitted for publication.
20. I. Hurtado, J. Van Humbeeck, P. Ratchev, L. Delaey L, "Effect of the χ-phase precipitation on the elastic modulus in Cu-Al-Ni-Ti-(Mn) shape memory alloys", submitted for publication to Trans JIM.

Cyclic deformation properties of TiNi shape memory alloy under thermomechanical loading

Hissaki Tobushi, Shinya Yamada and Takashi Hachisuka

Aichi Institute of Technology, Department of Mechanical Engineering
1247 Yachigusa, Yagusa-cho, Toyota 470-03, Japan

Kikuaki Tanaka

Tokyo Metropolitan Institute of Technology,
Department of Aerospace Engineering
6-6 Asahigaoka, Hino, Tokyo 191, Japan

ABSTRACT

The thermomechanical properties of shape memory effect and superelasticity due to the martensitic transformation and the R-phase transformation of TiNi shape memory alloy were investigated experimentally. The transformation stress, transformation line and fatigue property due to both transformations were discussed for cyclic deformation. The thermomechanical properties due to the R-phase transformation were excellent for deformation with high cycles.

1. INTRODUCTION

In shape memory alloy (SMA), shape memory effect (SME) and superelasticity (SE) or transformation pseudoelasticity appear depending on stress and temperature. In TiNi SMA, SME and SE appear due to the martensitic transformation (MT) and the rhombohedral phase transformation (RPT) [1-3].

In the applications to an actuator, a robot and a solid-state heat engine, SMA is used as a working element which performs cyclic motions. The working characteristics of the SMA element are specified by the beginning and completion temperatures of the motion, the working stroke and the working force. These characteristic values are determined by the transformation temperature, the transformation strain and the transformation stress. The characteristic values associated with the transformation vary through cyclic deformation [4], and fatigue occurs under deformation with high cycles [5, 6]. Thus to design the SMA element, the behavior of the above-mentioned characteristic values subjected to thermomechanical cycles becomes crucial.

In the current study, the thermomechanical properties of TiNi SMA associated with MT and RPT, such as SME, SE, transformation line and fatigue, are discussed on a wire.

2. EXPERIMENTAL METHOD

2.1. Materials and specimen

The material was a Ti-55.3wt%Ni SMA wire, 0.75mm in diameter. The specimens were given shape memory of a straight line through shape memory processing. This was done by holding the wire in the desired shape at 673K for 60min and cooling in the furnace. The reverse transformation completion temperature A_f was about 323K.

2.2. Experimental apparatus

The experimental apparatus used for testing SME and SE of the wire was a shape memory property testing machine [7]. The testing machine was composed of a tensile machine and a heating-cooling device. The specimen was heated by hot air or cooled by liquefied carbon dioxide. The gauge length of an extensometer was 20mm.

The experimental apparatus used for testing fatigue of the wire was a rotating-bending fatigue testing device. The

0-8194-2165-0/96/$6.00

specimen bent in a certain curvature was rotated in a chamber at a constant temperature in air.

2.3. Experimental procedure

To investigate the thermomechanical properties, the following three experiments were carried out.

(1) Test for SME

In the experiment, the cyclic properties of SME were examined for the wire [8]. At first, the loading and unloading processes with maximum strain ε_m were performed at the low temperature T_l below A_s. Maintaining load zero, the process of heating was performed to the high temperature T_h above A_f followed by cooling to T_l. These loading-unloading and heating-cooling processes were repeated.

(2) Test for SE

In the experiment, the cyclic properties of SE were examined for the wire [9]. The loading and unloading processes were repeated at temperature T above A_f for the maximum strain ε_m.

(3) Test for fatigue

The rotating-bending test was performed with no load at the constant temperature and the rotational speed was 500rpm [10]. The number of cycles to failure was measured for each strain amplitude ε_a which was the maximum bending strain on the surface of the wire.

3. EXPERIMENTAL RESULTS AND DISCUSSION

3.1. Shape memory effect

3.1.1 SME due to RPT

The stress-strain curves obtained by the experiments for maximum strain ε_m of 1% are shown in Fig.1 and the corresponding strain-temperature curves are shown in Fig.2. The curves are parametrized by the number of cycles N. As seen in Fig.1, yielding due to RPT occurs under stress of 60MPa in the loading process and residual strain of 0.6% appears after unloading. As seen in Fig.2, strain recovers due to the reverse transformation in the heating process, showing SME. Strain is almost zero in the cooling process. The stress-strain curves and the strain-temperature curves vary little in N=1～10. Thus it is ascertained that the property of SME associated with RPT is stable for cyclic deformation.

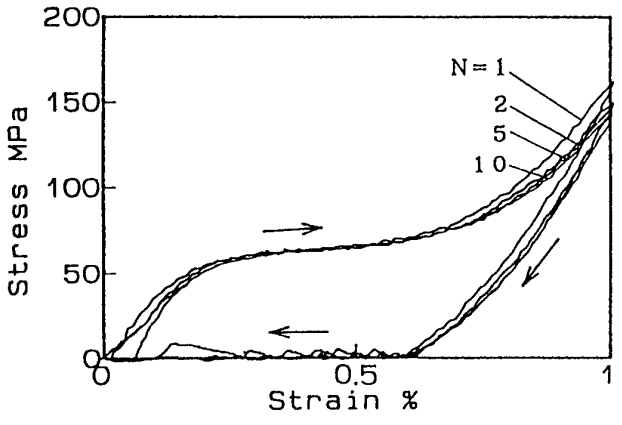


Fig.1 Stress-strain curves for SME due to RPT under thermomechanical cycles

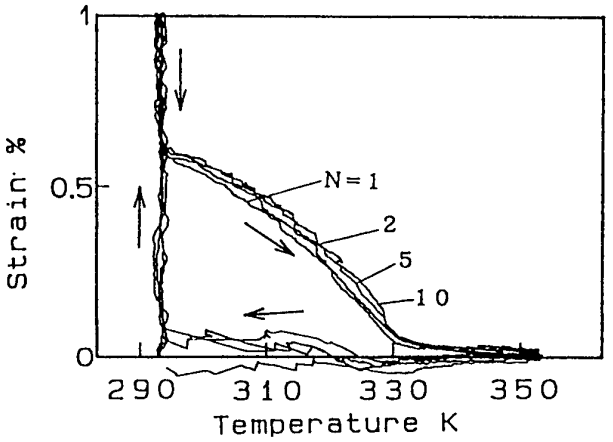


Fig.2 Strain-temperature curves for SME due to RPT under thermomechanical cycles

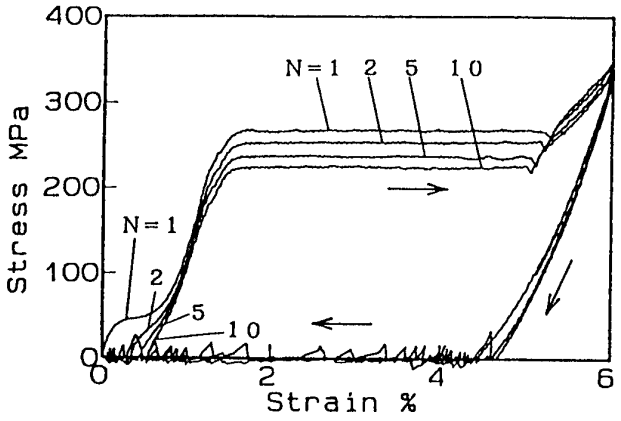


Fig.3 Stress-strain curves for SME due to MT under thermomechanical cycles

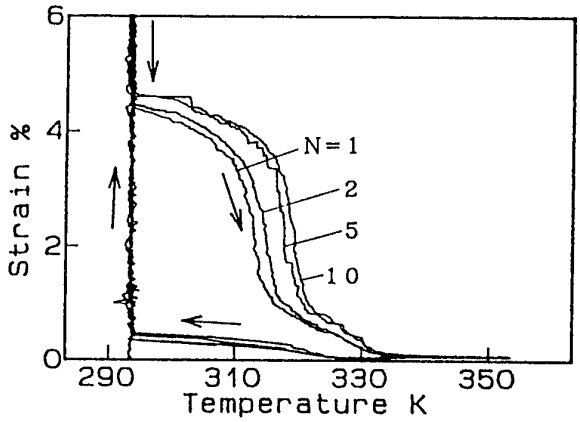


Fig.4 Strain-temperature curves for SME due to MT under thermomechanical cycles

3.1.2 SME due to MT

The stress-strain curves and the strain-temperature curves in the case of maximum strain ε_m=6% are shown in Fig.3 and Fig.4, respectively. The curves are parametrized by the number of cycles N. As seen in Fig.3, yielding due to RPT occurs under stress of 60MPa in N=1, and yielding due to MT appears under stress of 280MPa in N=1. The MT stress decreases with an increase in N. The transformation strain induced in the loading process appears as residual strain after unloading and diminishes by heating under no stress, showing SME. As seen in Fig.4, strain recovers due to the MT reverse transformation at 315K in N=1 and recovers due to RPT thereafter in the heating process. The MT reverse transformation temperature increases with increasing N. In the cooling process under no stress, strain increases at the same temperature as the RPT reverse transformation temperature. The strain induced in the cooling process is called two-way strain which occurs due to the reversible SME. The two-way strain increases with increasing N and is 0.6% in N=10. Therefore the two-way strain is caused due to RPT. The reason why these cyclic properties appear may be considered as follows. During the cyclic deformation, the interface between the parent phase and the R-phase or between the R-phase and the martensitic phase shifts repeatedly [11]. With cyclic movement of the interface, dislocations accumulate around the infinitesimal defects in the interface. Based on the increase in the dislocation density, internal stress increases [12]. Due to action of the internal stress, the MT stress decreases, the MT reverse transformation temperature increases and the two-way strain due to RPT increases with increasing N.

3.2. Superelasticity

3.2.1 SE due to RPT

The stress-strain curves with the loading-unloading cycles under ε_m=1% at temperature T=333K are shown in Fig.5. The curves are parametrized by the number of cycles N. As seen in Fig.5, the nonlinear strain induced due to RPT in the loading process diminishes due to its reverse transformation in the unloading process, resulting in the hysteresis loop of SE. The width of the hysteresis loop is very narrow and the difference in stress between the loading curve and the unloading curve is smaller than 20MPa. The stress-strain curves vary little in N=1～20. Thus it is ascertained that the property of SE associated with RPT is stable for cyclic deformation.

3.2.2 SE due to MT

The stress-strain curves in the case of cyclic loading-unloading under constant maximum strain ε_m=8% at constant temperature T=353K are shown in Fig.6. The curves are parametrized by the number of cycles N. As seen

in Fig.6, the MT stress σ_M and the reverse transformation stress σ_A decrease with the increase in N. Both transformation stresses decrease significantly in the early cycles and only slightly afterwards. The amount of decrease in σ_M with cycling is larger than that in σ_A. The residual strain which appears after unloading increases significantly in the early cycles and only slightly after these cycles. Therefore in order to obtain cyclic stability of SE in applications, the mechanical training before the practical use is necessary.

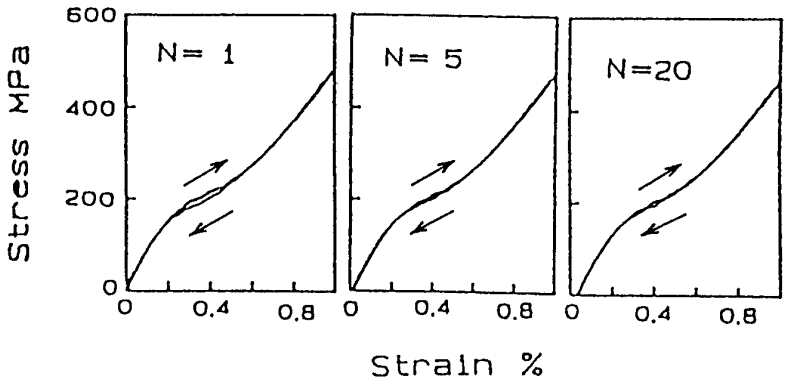


Fig.5 Stress-strain curves for SE due to RPT under loading-unloading cycles at constant temperature

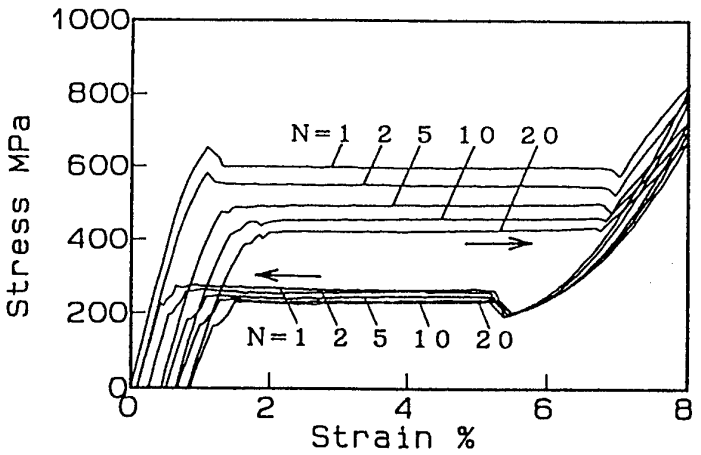


Fig.6 Stress-strain curves for SE due to MT under loading-unloading cycles at constant temperature

At the start point of MT, an overshoot of stress appears in the early cycles. This may occur due to the following reason. Because the externally applied load is removed completely in each cycle, all of the martensitic phase disappears in the unloading process. In order to induce MT in the reloading process, the creation of a nucleus of the martensitic phase is therefore necessary, leading to the observed overshoot of stress. The peak stress of overshooting is proportional to the magnitude of σ_M. The amount of overshooting decreases with increasing N.

On the other hand, an undershoot of stress occurs just before the reverse transformation sets in under constant stress σ_A in the unloading process. This is similar to the overshoot at the start point of MT in the loading process. At the point of ε_m =8% in the completion region of MT, the whole volume of the material consists of the martensitic phase. For the creation of a nucleus of the parent phase, it is necessary for the stress to decrease lower than the constant stress σ_A under which the reverse transformation progresses. Undershooting of stress therefore appears at the start point of the reverse transformation.

3.3. Transformation line

The progress of the transformation is governed by the transformation kinetics. The starting and completing conditions of MT [13,14] and of RPT [15,16] are expressed by the linear functions of stress and temperature, respectively. These functions represent the boundaries between two phases in the stress-temperature phase diagram, which are called the transformation lines.

The cyclic behavior of the transformation lines of MT and RPT is schematically shown in Fig.7. In Fig.7, σ_{Ms}, σ_{Mf}, σ_{As} and σ_{Af} denote the starting lines and the completing lines of MT and its reverse transformation and σ_{Ms}', σ_{Mf}', σ_{As}' and σ_{Af}' the corresponding lines of RPT and its reverse transformation, respectively. Transformation lines in the first cycle and N-th cycle are represented by a solid line and a dashed line, respectively.

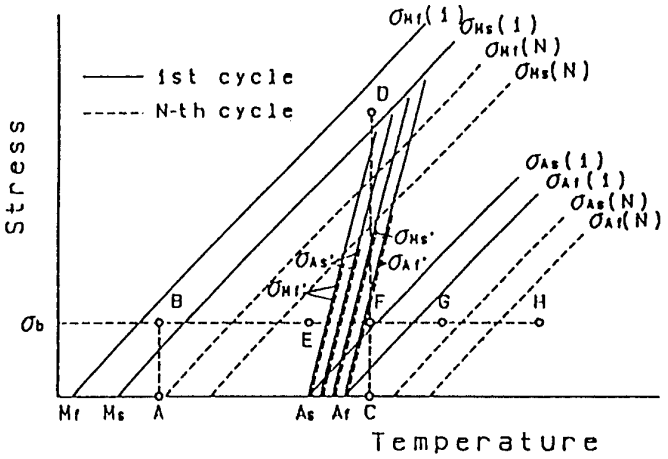


Fig.7 Schematic starting lines and completing lines of MT and RPT in first cycle and N-th cycle

Let us first consider the cyclic properties concerning MT. In the case that, after loading to the stress σ_b at the point B at T_A in which MT appears, a SMA element is heated with σ_b constant, if the temperature is raised above $\sigma_{Af}(1)$, for example, heated at the point G, the transformation strain recovers by the reverse transformation. If $\sigma_{Mf}(N)$ and $\sigma_{Af}(N)$ shift to the right during the cyclic heating-cooling process with constant σ_b, the transformed strain does not recover upon heating at the point G. Then, to recover the transformed strain, it is necessary to raise the temperature at point H. MT is completed at T_A in the cooling process.

On the other hand, as shown in Fig.7, the RPT lines shift little with thermomechanical cycles. In the case that a SMA element is operated under constant σ_b, although it is necessary for MT to heat and cool the element between points B and G, it is sufficient, for achieving RPT, to operate the element between points E and F. From this finding, it is ascertained that, because the difference in temperature to cause deformation associated with RPT is small, the response of the element with heating-cooling is fast. Thus it may be concluded that, for the element in which excellent cyclic property and fast response are important, RPT should be used. In this case, it should be taken into account that the RPT strain is smaller than 1%, which is smaller than onetenth of the MT strain.

3.4. Fatigue property

The relationship between the strain amplitude ε_a and the number of cycles to failure N_f obtained by the rotating-bending test at constant temperature T is shown in Fig.8. The strain amplitude ε_a is the maximum bending strain on the surface of a wire. When the wire is bent, RPT and MT expand from the surface area into the central part with increasing ε_a. Temperature increased by several degrees Kelvin during the rotating-bending cycles. The increase in temperature is proportional to ε_a.

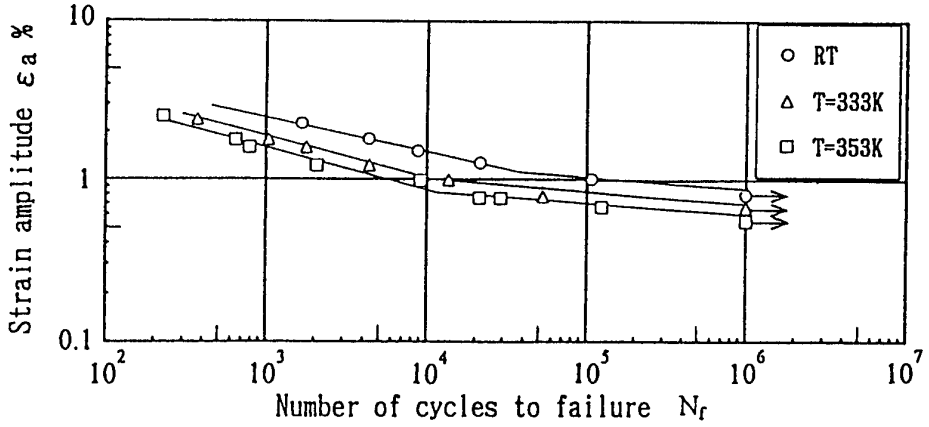


Fig.8 Strain-life curves for rotating-bending test at constant temperature T

As seen in Fig.8, in the region of $\varepsilon_a \geqq 0.8\%$, N_f is small and decreases with increasing ε_a. Corresponding to Manson-Coffin relationship which is valid for normal metal in low-cycle fatigue, the relation between ε_a and N_f is expressed by a equation $\varepsilon_a = \alpha N_f^{-\beta}$. The value of β is 0.24 which is smaller than 0.5 which is valid for normal metal. If ε_a is large, temperature rise is high and therefore the transformation stresses increase, resulting in small value of N_f and consequently leading to small value of β.

In the region of $\varepsilon_a = 0.8 \sim 1\%$ or $N_f = 10^4 \sim 10^5$, the strain-life curve has a knee. That is, if ε_a is in the RPT region of $\varepsilon_a \leqq 0.8\%$, N_f increases largely with decreasing ε_a and the curves approach the horizontal lines.

If the temperature T is high, the strain-life curves shift to the left and downward with increasing T. That is, with respect to same ε_a, N_f decreases with increasing T. This phenomenon occurs due to the fact that the RPT stress and the MT stress increase with increasing T.

4. CONCLUSIONS

The thermomechanical properties of SME and SE due to MT and RPT of TiNi SMA were investigated experimentally by various loading-unloading and heating-cooling tests. The main results obtained are summarized as follows.

1. The MT stress decreases, the MT reverse transformation temperature increases and the MT line shifts with increasing N. These characteristic properties due to MT vary significantly in the early cycles and only slightly afterwards.

2. The thermomechanical properties due to RPT vary little with cyclic deformation.

3. In order to design SMA elements, it is important to take account of the behavior of transformation lines under cyclic deformation.

4. The rotating-bending fatigue life of the wire is quite long in the RPT strain region.

5. REFERENCES

1. S. Miyazaki and K. Ostuka, *Phil. Mag.* A, **50**, p.393, 1984.
2. S. Miyazaki and K. Ostuka, *Metall. Trans.* A, 17A, pp.53-63, 1986.
3. K. Ostuka, Engineering Aspects of Shape Memory Alloys ed. by T. W. Duerig, K. N. Melton, D. Stockel and C. M. Wayman, pp.36-45, Butterworth-Heinemann, 1990.
4. H. Tobushi, H. Iwanaga, K. Tanaka, T. Hori and T. Sawada, *Continuum Mech. Thermodyn.*, **3**, p.79, 1991.
5. J. L. McNichols, Jr. and P. C. Brookes, *J. Appl. Phys.*, **52**, p.7442, 1981.
6. S. Miyazaki, Page 394 in Ref.3.
7. H. Tobushi, K. Tanaka, K. Kimura, T. Hori and T. Sawada, *JSME Inter. J.*, I, **35**-3, pp.278-284, 1992.
8. H. Tobushi, Y. Ohashi, A. Inaba, M. Kawaguchi and H. Sawada, *JSME Inter. J.*, I, **33**, p.256, 1990.
9. H. Tobushi, K. Tanaka, T. Hori, T. Sawada and T. Hattori, *JSME Inter. J.*, A, **36**-3, pp.314-318, 1993.
10. H. Tobushi, P. H. Lin, A. Ikai and S. Yamada, *Trans. of Jpn. Soc. Mech. Eng.*, A, **61**-591, pp.2355-2361, 1995.
11. H. Funakubo ed., Shape Memory Alloys, pp.39-60, Gordon and Breach Science Pub, 1987.
12. S. Miyazaki, T. Imai, Y. Igo and K. Otuka, *Metall. Trans.* A, 17A, pp.115-120, 1986.
13. K. Tanaka, S. Kobayashi and Y. Sato, *Inter. J. Plasticity*, **2**, p.59, 1986.
14. K. Tanaka, T. Hayashi, Y. Itoh and H. Tobushi, *Mechanics of Materials*, **13**, p.207, 1992.
15. T. Sawada, H. Tobushi, K. Kimura, T. Hattori, K. Tanaka and P. H. Lin, *JSME Inter. J.*, A, **36**-4, pp.395-401, 1993.
16. H. Tobushi, P. H. Lin, K. Tanaka, C. Lexcellent and A. Ikai, *J. Physique IV*, C2, 5, pp.409-413, 1995.

Hysteretic behaviour of NiTi shape memory alloy as a function of deformation, temperature and rate of deformation

Piedboeuf M.C., Gauvin R., Trochu F.

Centre de recherche appliquée sur les polymères, Ecole Polytechnique de Montréal
CP 6079, Succ. "Centre-ville", Montréal, Québec, H3C 3A7

ABSTRACT

An extensive study of the effect of deformation, temperature and rate of deformation on the superelastic behaviour of NiTi shape memory alloys wires was undertaken. This paper presents the first results. The temperature effect is to shift the stress-stain curve upward. It is generally believed that the strain rate sensivitivity, sometime observed, is more a temperature effect due to the exo-endothermic transformations. In this research, the strain rate sensitivity of the transformation is demonstrated. Some interactions between the different variables are also shown.

1. INTRODUCTION

Since the last fifteen years, several studies on the use of Shape Memory Alloys (SMA) in smart structures were published[1,2] . Most of these researches concentrated on the use of SMA as actuators to exert some active control on damping. More recently, there has been some interest in the passive control capacities of the SMA[3].

Shape memory alloys are a class of material known for their very interesting damping characteristics. The highest energy absorption occurs during the transition between the austenitic and martensitic phases. This transformation can be stress induced in an austenitic alloy. As the induced martensite is unstable in these conditions, the alloy will revert to the austenitic phase upon removal of the stress. There will be no permanent deformation, but the hysteresis, and the energy absorption, is quite large. This is known as the superelastic effect.

In our laboratory, a research project on the use of SMA reinforcement to add passive damping to a polymer matrix composites is underway. Generally, in a polymer matrix composite, the introduction of the fibre reinforcement reduces the energy absorption capacity of the matrix. The use of a certain amount of SMA reinforcement, with a damping coefficient similar to some of the polymers, should give better damping capacities while maintaining a high strength, this being the long term goal of this research.

The first part of this project is to study the superelastic behaviour of NiTi SMA. Recently, a few papers on this subject were published, with an increasing interest on using those alloys for passive damping[4,5]. In this paper, results are presented to evaluate the combined effect of deformation, temperature and strain rate on the stress induced martensitic transformation of NiTi SMA in a wire form.

2. EXPERIMENTAL PROCEDURE

2.1 Samples

In order to be used as a fibre reinforcement, 100 μm NiTi wires are studied. They were obtained from SMA Inc., in California. These wires are straight annealed and chrome doped (0.2%) for better superelastic effect. Their transition temperature for austenitic start (As) is around - 25°C. The samples were mounted in a way similar to the ASTM D3379 standard. Cardboard was used as tabs. To obtain a good grip, the wires had to be glued up to the end of the tab, through the gripping area. The gage length was 100 mm. Each sample was precycled at a frequency of 5 Hz and a deformation of 4.5 % for 100 cycles before testing in order to stabilize the superelastic effect.

0-8194-2165-0/96/$6.00

2.2 Equipment

The tests were made on a MTS 810 equipped with a 50 N load cell. The data acquisition was done through the use of ASYST software and a DT 2850 card which allowed for 1000 sampling on each test. A controlled temperature chamber insured a well controlled temperature.

2.3 Testing Procedure

The samples were loaded and unloaded at a constant strain rate in a deformation controlled mode. Five strain rates were used (**0.00017, 0.0017, 0.017, 0.086 and 0.17** s^{-1}), for each of the maximum deformations tested (**2, 3, 4 %**). Four samples were tested for each set of testing parameters, for a total of 60 samples tested. All those samples were tested first at **25 °C** and then at **35 °C**. Since there were no significant variations between the samples, the graphical results presented here are for one sample and not average values. However, all the results are used for the statistical analysis reported in table 1 and in figure 3.

The parameters studied were: the modulus E, the upper plateau stress on loading σ_L, and the stresses to start and to finish the austenitic transformation σ_{As} and σ_{Af} respectively. The results were analyzed with STATGRAPHICS, a statistical analysis software.

3. RESULTS

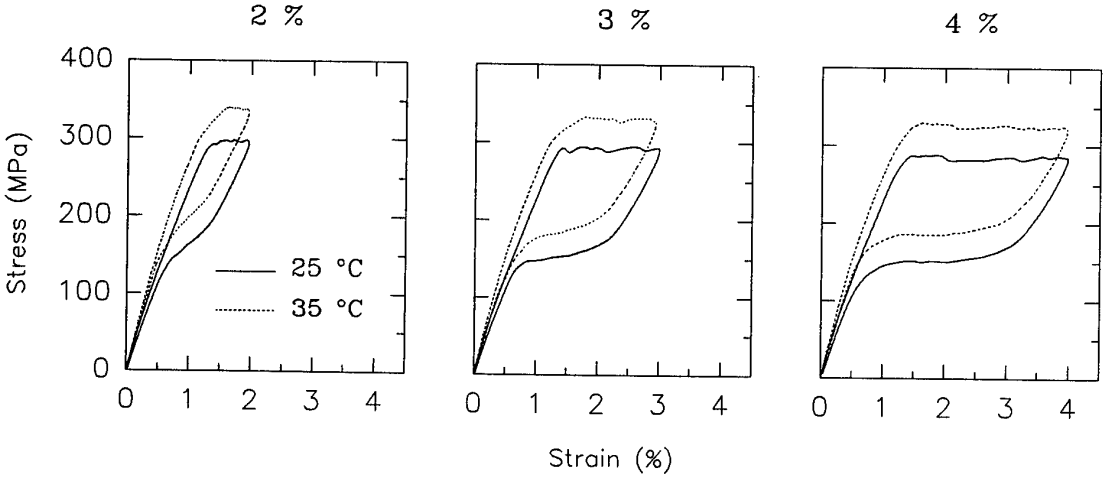


FIGURE 1: Stress-strain curves at a strain rate of 0.017 s^{-1} for the three maximum deformations and two temperatures tested

3.1 Tests results

To illustrate the effect of temperature and maximum deformation, the stress-strain curves obtained for the various deformations and temperatures at a strain rate of 0.017 s^{-1} are shown in figure 1. A similar shift of stress strain curves with an increase of 10 °C in temperature is observed for all the maximum deformations tested.

To illustrate the effect of strain rate, figure 2 shows the results of samples tested at 25 °C with 4 % of maximum deformation for four different strain rates. On each of the curves, the upper plateau stress on loading σ_L, and the beginning and end of the austenitic transformation σ_{AS} and σ_{Af} are shown. σ_L is the mean value of the upper plateau on loading evaluated at $\epsilon = 2\%$. The martensitic-austenitic transformations start at the end of the linear elastic behaviour on the first part of the unloading, and is complete at the beginning of the final elastic unloading. The σ_{As} and σ_{Af} points were then determine as the points were the slope was about 95 % of the value in the linear elastic regions. The value of σ_{As} was the more difficult to determine since the change in slope is very gradual.

	↑ T (°C)	↑ ϵ (%)	↑ $d\epsilon/dt$ (s^{-1})
E (GPa)	↑ 0.4 GPa/°C	No effect	↑ 1 GPa max
σ_L (MPa)	↑ 4.2 MPa/°C	No effect	↑ 35 MPa max (not linear)
σ_{As} (MPa)	↑ 4.2 MPa/°C	↑ 10 MPa max	↑ 56 MPa max (not linear)
σ_{Af} (MPa)	↑ 2 MPa/°C	↓ depend of T	↓ up to 0.017 s^{-1} then increase

TABLE 1: Effect of an increase in temperature (25→35°C); in deformation (2→4%) and strain rate (0.00017→0.17s^{-1}) on the parameters studied.

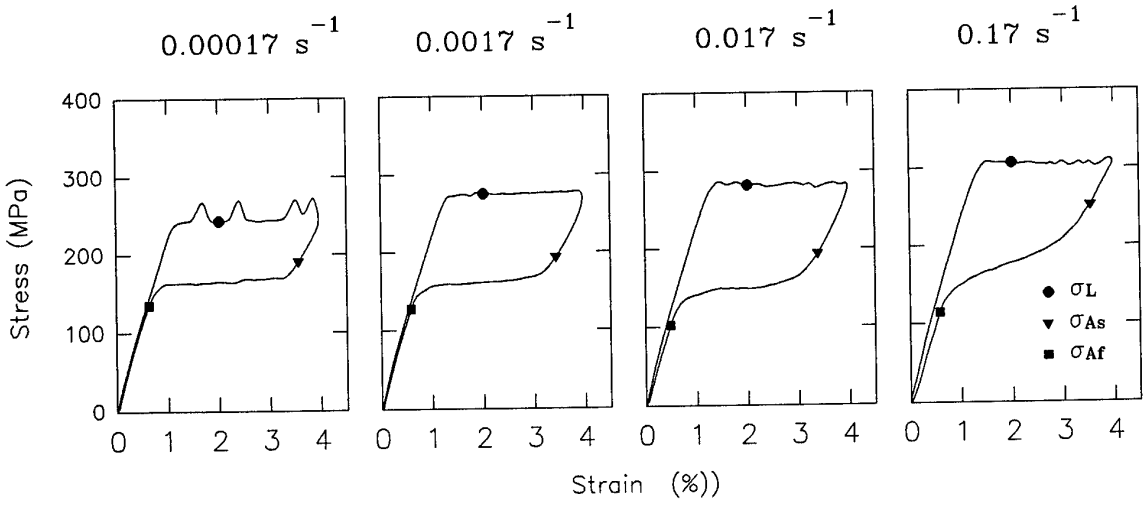


FIGURE 2: Stress-strain curves at 25 °C with a maximum deformation of 4% for four different strain rates (0.00017, 0.0017, 0.017, 0.17 s^{-1}). σ_L: upper plateau stress on loading, σ_{As} and σ_{Af} : stresses to begin and end the austenitic transformation respectively.

3.2 Analysis

Table 1 shows the effects of the various testing parameters on the material properties as determine by the statistical analysis. In the range of temperature tested, the modulus increase with temperature and is slightly affected by the strain rate. The temperature effect is to shifts the stress-strain curves upward as can best be seen in figure 1. It is interesting to note that the temperature effect is different for σ_{Af}.

The maximum deformation has an effect on the unloading parts of the curves. Since there is more martensite formed as the deformation gets higher, there is a σ_{As} increase with the maximum deformation. For the same reason, with higher deformations, there is more transformation of martensite needed and σ_{Af} decreases slightly. With a temperature increase, the variation of σ_{Af} with the maximum deformation is less pronounced.

In literature, it was generally observed that the increase speed produces an increase of temperature in the sample due to the exothermic transformation. A variation of slope of the plateau regions is a manifestation of this effect. The effect of an increase in strain rate can best be seen in figure 2. During loading, it can be seen that there is no slope variation in the loading plateau. During unloading though, there is an evident temperature effect for the higher strain rates (0.17 s^{-1}). The small diameter of the samples used here allowed for a better heat transfer and minimized the temperature effect during loading. Even with this small specimen, the temperature effect during unloading is significant for the high strain rate but reasons are not clear and further investigation is needed.

The effect of the strain rate is complex and figure 3 shows the variation of σ_L, σ_{As} and σ_{Af} with the strain rate. The increase of the upper plateau stress on loading σ_L with the strain rate increase is similar to the increase of yield stress with strain rate observed in metals. On the unloading part of the curves, the response is much more complex, as can best be seen in figure 2. There is a combination of a strain rate effect and a temperature effect since the slope increases with a spreading between the beginning and end of the transformation as the strain rate increase.

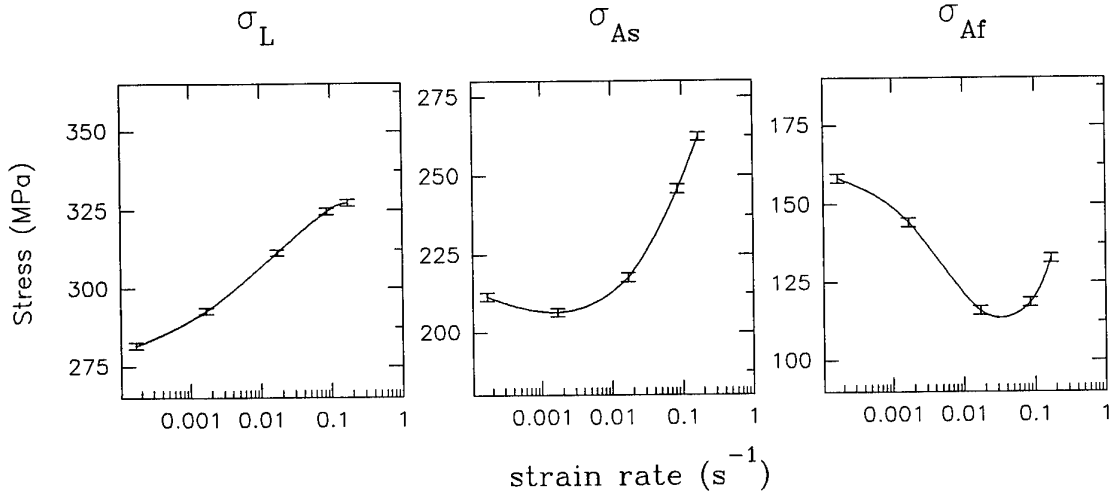


FIGURE 3: Variation of the upper plateau stress on loading σ_L and the stresses to begin and end the austenitic transformation σ_{As} and σ_{Af} with the strain rate.

The increase of σ_{As} with the strain rate is more important than the one observed for σ_L . On the other hand, σ_{Af} decreases with an increase in strain rate up to 0.017 s^{-1} since it is harder to complete the martensite to austenite transformation at higher speeds. For this range, there is no temperature effect since the unloading plateau remains quite flat. For higher strain rates, a temperature effect is obvious and a slight increase of the stress to end the austenitic transformation is observed.

CONCLUSIONS

This work shows an important strain rate effect on the measured SMA wires properties. As the strain rate increases, the transformation is more difficult. There is also a complex temperature effect due to the exo-endothermic transformations that take place at higher speeds during the transformation. Since these wires will eventually be used in a polymer matrix composites, the temperature effect should be studied further.

It should also be noted that in all the tests made, the hysteresis always stayed quite important. This is very promising for use of these SMA wires for damping purposes in composites.

ACKNOWLEDGEMENTS

This work is financially supported by the Natural Science and Engineering Research Council (NSERC) of Canada and the Québec government program FCAR (Formation de Chercheurs et Aide à la Recherche).

REFERENCES

1. Rogers C.A., Liang C., Barker D.K., 1988, "Dynamic Control Concepts Using Shape Memory Alloy Reinforced Plates", *Smart Materials, Structures and Mathematical Issues,* Sept. 15-16, Virginia, pp. 39-62.

2. Venkatesh A., Hilborn J., Bidaux J.E., Gotthardt R., 1992, "Active Vibration Control of Flexible Mechanisms Using Shape Memory Alloy Fibre-Reinforced Composites", *1st European Conf. on Smart Structures and Materials,* Glasgow, session 5, pp. 185-188.

3. Misra M.S., Carpenter B., Maclean B., 1992, "Adaptive Structure Design Employing Shape Memory Actuators", *Smart Structures for Aircrafts*, AGARD conf. proc., pp. 15-1 - 15-6.

4. Graesser E.J., Cozzarelli F.A., 1991, "Shape-Memory Alloys as New Materials for Aseismic Isolation", *Journal of Engineering Mechanics*, Vol. 117, No. 11, pp. 2590-2608.

5. Thomson P., Balas G.J., Leo P.H., 199 , "Pseudoelastic Hysteresis of Shape Memory Wires for Passive Structural Damping:Theory and Experiments", *Smart Structures and Materials 1994: Passive Damping* , SPIE Vol. 2193 , pp. 316-324.

THE INVESTIGATION OF DEFORMATION AND DAMPING MECHANISMS in Ti-50.6%Ni ALLOY.

Alexander A. Ilyin, Igor S. Golovin, Mikhail U. Kollerov and Andrei A. Shinaev.

Metals Science Department of Moscow State Aircraft Technology University, Petrovka 27, Moscow 103767 Russia.

ABSTRACT

Shape memory effect and intrinsic damping capacity (amplitude dependent internal friction ADIF) of Ti-50.6 wt.%Ni alloy have been investigated in different structural states (cold-worked, polygonizing and recrystallization, quenching). Relationship between "normal" plastic deformation due to the dislocation motion and deformation due to martensite transformation are discussed.

2. INTRODUCTION

The development of modern machine-building industry is closely connected with new metallic materials of special properties: superelasticity (**SE**), shape memory effect (**SME**) and high damping (**HD**). SE is the ability of deformed metals to return the initial shape immediately after unloading. From usual elastic behaviour SE is pointed out due to 1) its returned deformation, which might be 10% or more and 2) non-linear type of "$\sigma - \varepsilon$" curves. SME is the ability of deformed materials to return to the initial shape due to heating. SE and SME are based on elastic martensite transformation which are realized without unreversible increasing of imperfection density [1, 2]. One of the most well known metallic materials with the afore mentioned properties are TiNi alloys. The wide use of such alloys helps to create the unique and high-economic mechanisms and devices [3].

3. EXPERIMENTAL PROCEDURA

The commercial Ti-50.6%Ni alloy (TH1) has been investigated. The examined wire samples (l = 80 mm, d = 1.3 mm) were cold worked with ε = 17%. Then samples were vacuum heat treated at different annealing temperatures. X-rays analysis has been carried out on standard DRON 4 equipment with high temperature camera and with the use of Cu K_α rays. Measurements of amplitudes dependent internal friction (ADIF) were made on the inverted torsion pendulum in the amplitude range from 1 to 140 10^{-5} and the temperature range -196...700°C, average frequency of free decayed oscillations ~ 2 Hz.

Parameters of SE and SME were determined with the help of universal torsion equipment on the same samples as on torsion pendulum. Deformation has been applied at the ambient temperature, deformation degree γ was between 0 and 26%. The following parameters were registrated as:

- γ_e - elastic or superelastic deformation,
- γ_r - residual deformation,
- γ_r^r - residual deformation, which can be returned due to heating,
- γ_r^n - residual deformation, which can not be returned by heating.

The heating was carried out from room temperature up to 150°C, $v \approx 5$ K/min. Temperatures of start (A_s^r) and finish (A_f^r) of shape returning were determined with the help of γ_r^r vs. T, C curves.

0-8194-2165-0/96/$6.00

4. Results and Discussion

In the initial cold worked state the structure of samples at ambient temperature consists of R-phase and small volume part of B19' martensite. The width of diffraction maxima evidences the high imperfections density. Annealing at 300-450°C does not change phase equilibrium but mainly leads to the decrease of imperfection density due to polygonizing. There is B2-phase at the room temperature only after annealing at 500-650°C. After annealing at 700-900°C two phases structure R + B19' are present. The appearance of the above mentioned structures is connected with polygonization annealing and dissolution Ti_3Ni_4 type intermetallic compounds.

The NiTi samples were torsion deformed (ε=5%) and γ_e , γ_r , γ_r^r , γ_r^n , A_s^r , A_f^r values were determined after different annealing treatments. In the initial cold worked state and after annealing the applied deformation (5%) was fully returned after unloading and heating. In cold worked state and after annealing at T < 250° C samples demonstrated SE: the main part of applied deformation was returned just after unloading (Fig.1a). Small part of applied deformation was returned after heating in A_s^r - A_f^r range: 30 - 70°C (Fig.1b).

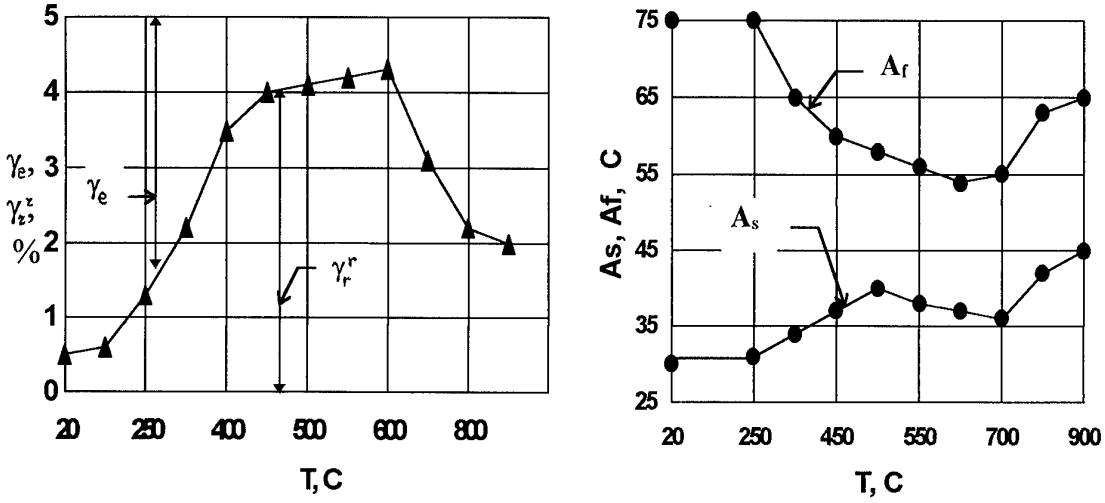


Fig. 1. The influence of annealing temperature (T, °C) on γ_e - elastic deformation, γ_r^r - residual deformation, which can be returned due to heating after total torsion deformation 5% (a), and temperature of start (A_s^r) and finish (A_f^r) of shape returning (b).

The increasing of the annealing temperature (T>250°C) leads to the increase of γ_r^r deformation value, to the decrease of SE and to the decreasing of A_s^r - A_f^r range due to decreasing of imperfections density in structure. After annealing at 575-600°C the SE is absent, the reversible deformation takes place due to SME mainly in the temperature range 40-60°C. The increase of annealing temperature leads to the decrease of SME and increase of SE. The range between A_s^r and A_f^r is stable, but temperature location of A_s^r and A_f^r shifts and after annealing at 900°C A_s^r =45°C, A_f^r =65°C. Internal friction (Q^{-1}) in B2 phase is less than 10^{-3}, in martensite > 10^{-2} (Q^{-1}). ADIF curves for the cold-worked Ti - 50.6%Ni samples show (Fig.2) the weak amplitude dependence of IF. The annealing leads to the increase of $tg\alpha_{ADIF}$ and value of ADIF. The $tg\alpha_{ADIF}$ and level of ADIF are maxima after 900°C annealing. Energies of dislocation impurities interaction have been found out to be 0.9-1.0 eV for well annealed state and $\approx$0.7 eV for the cold worked state. As a result of alloys structural changes due to heat treatment its elastic behaviour changes, too. After cold working the density of imperfections of crystalline lattice increases, the martensite appeared under applied stress has extra free energy and undergoes the initial phase transformation due to unloading. It leads to SE and relatively low ADIF curves level. The annealing at T > 300°C leads to imperfection density decreasing and the easier possibility for martensite appearance due to loading. SE decreasing, SME increasing and damping capacity increasing are observed. Parameters of SE and SME at different applied deformations are generalized in Fig.3. Let's observe the behaviour of alloy after 575°C annealing. If the applied deformation (γ) is less than 8-9% it can be fully returned due to SME mainly. When γ> 8-9% the γ_r^n deformation appears. The value of γ_r^n increases due to the increasing of applied deformation and reaches maximum (γ_r^n ~ 17%) at γ= 26%. Simultaneously γ_e reaches maximum

(~3%). With the increase of applied deformation γ, the γ_r^r value increases and at γ = 20% it has been founded γ_r^r =11%. The following increase of γ leads to γ_r^r decrease.

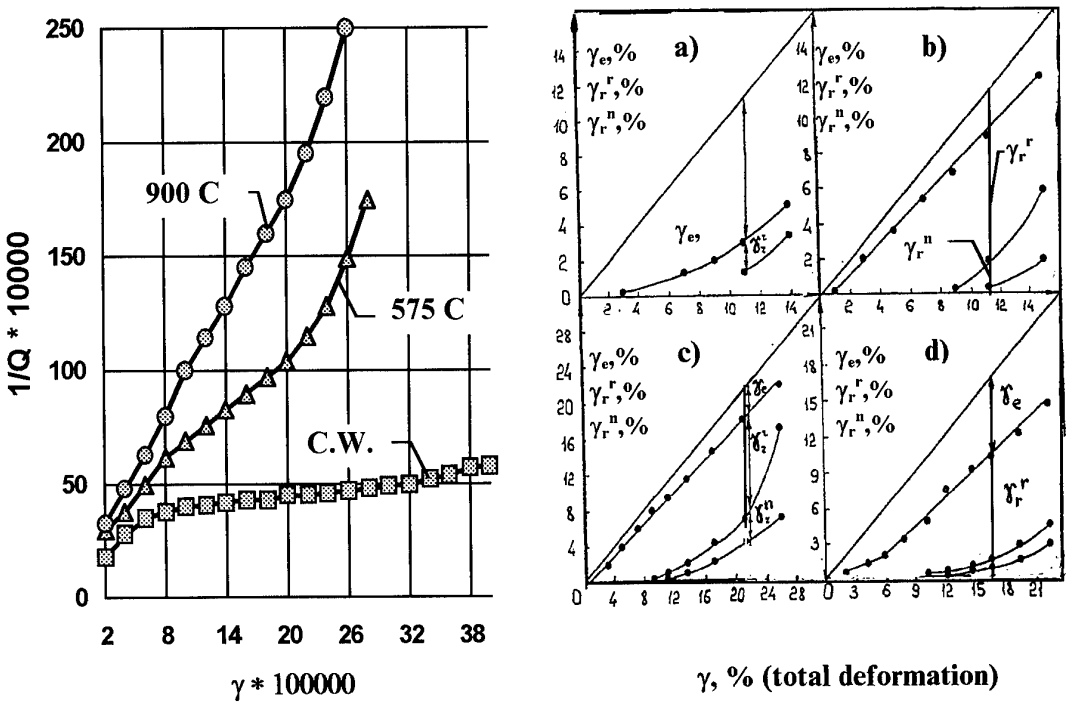


Fig.2. ADIF curves (T=20°C) of Ti-50.6%Ni sample in cold worked state and after annealing at 575 and 900°C.

Fig.3. The influence of applied deformation on SME parameters in cold worked state (a) and after annealing at 450 (b), 575 (c) and 900°C (d).

The X-rays analysis has been carried out for the mechanisms of deformation study. After 575°C annealing the sharp peak of (110) B2 phase has been observed. Diffraction maxima from B19' martensite phase appearance and simultaneous decrease of (110) B2 phase peak height take place due to the increase of γ_r deformation (Fig.4). Complex analysis of intensity of (110) B2 phase, (020) martensite B19' peaks and width of (110) B2 phase peak after different deformations and heating allows to point out three stages of deformation mechanisms:

1) the sharp decrease of B2 volume part due to the martensite transformation (γ_r < 5-6%). There is no increasing of imperfection density in structure, width of B2 phase peak is stable;
2) the suppressing of elastic martensite transformation (6 < γ_r <12%) due to appearance of "normal" plastic deformation;
3) the end of elastic martensite transformation (γ_r > 12%); plastic deformation takes place only.

ADIF curves were measured after different applied deformations. IF level in cold-worked state (ε=17%) samples vs. applied deformation (γ) is stable enough (Fig. 5a) with relatively small background. At the annealed state (b - 575°C, c - 900°C) IF level depends on applied deformation strongly. IF reaches maximum after torsion deformation 6-8%, i.e. in case of thermoelastic martensite transformation without increasing of imperfections density. At deformation range γ > 7-8% the IF level decreases due to the increasing of imperfections density. The influence of applied deformation on SE and SME parameters is generelized in Table 1. Additionally critical deformations γ_{cr1} and γ_{cr2} are pointed out as:

γ_{cr1} - minimum of applied deformation, leads to the appearance of γ_r^n deformation,

γ_{cr2} - applied deformation corresponds to the maximum of $\gamma_e + \gamma_r^r$ deformations sum.

Table 1. **SE and SME parameters for torsion tests of Ti-50,6%Ni alloy**

Treatment	Limit deformation, %	Maximum values of SE and SME parameters				
		γ_{cr1}, %	γ_r, %	$(\gamma_e + \gamma_r)$, %	γ_{cr2}, %	γ_r^n, %
Initial state: ε=17%	14.5	9.6	1.8	11.5	14.5	3.0
Annealing 450 C	14.9	8.6	7.2	9.2	14.9	5.8
Annealing 575 C	25.8	8.6	11.0	14.8	21.4	17.0
Annealing 900 C	22.6	9.0	10.0	18.0	22.6	4.6

The value of γ_{cr1} is maximum after cold worked state. The γ_{cr1} is connected with mechanism of shape changes. At $\gamma < \gamma_{cr1}$ the deformation is due to the appearance and/or martensite reorientation. During unloading or heating B19' martensite is transformed to B2 phase and it induces the shape change of sample. If applied $\gamma > \gamma_{cr1}$, the "normal" plastic deformation starts to develop, i.e. γ_{cr1} is determined by stress value which is necessary for plastic deformation beginning. That is why in the cold worked state (B2 phase is hardened) γ_{cr1} is maximum, and γ_{cr1} decreases after annealing due to decrease of imperfection density.

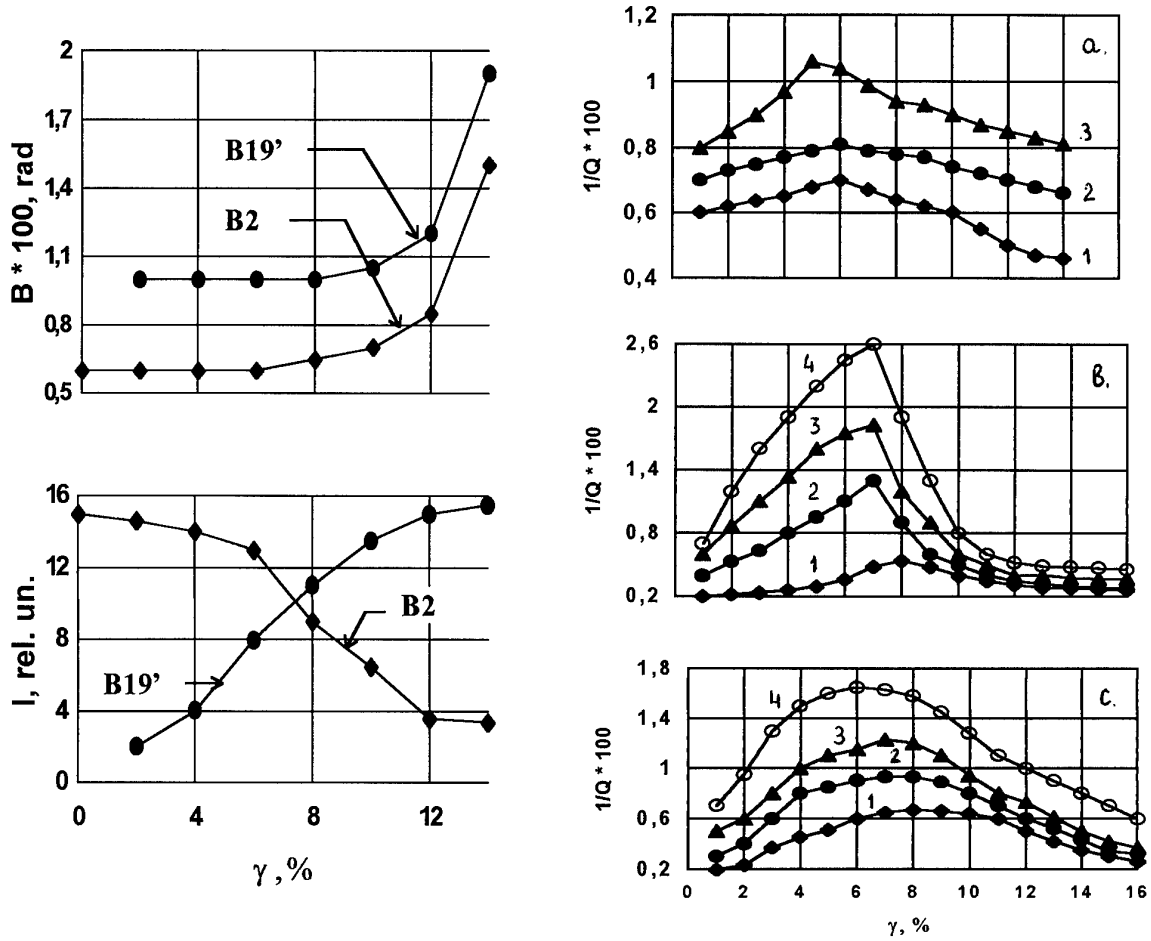


Fig. 4. The influence of applied deformation in width (B) and integral intensity (I) of difraction (110) B2-phase and (020) B19' peaks.

Fig.5. The influence of applied deformation on IF level at different amplitudes of Ti-50.6%Ni sample in cold worked state (a) and after annealing at 575 (b) and 900°C: 1) 1.5, 2) 10, 3) 18 and 4) $27 \cdot 10^{-5}$.

At the deformation range in between γ_{cr1} and γ_{cr2} shape changes mechanisms are mixed and are connected both with appearing and/or reorientation of martensite and "normal" plastic deformation. Plastic deformation leads to B2 phase hardening and increasing of γ_r deformation. At $\gamma > \gamma_r$ the high density of crystalline lattice imperfections leads to suppressing of thermoelastic martensite transformation. The minimum γ_{cr2} value was observed in cold worked state, maximum of γ_{cr2} value - after 575 and 900°C annealing, at the same states the maximum of γ_r^r values are observed.

The ADIF curves of TiNi samples in different structural states are presented in Fig.6 for annealing at T_a = 575°C and measurements of ADIF at T_m =20°C (B2 → B19' transformation); T_a=575°C, T_m =-100°C (100% of B19'); T_a=575°C, T_m=30-70°C (B2 → B19'); T_a=575°C+cooling to-196°C, T_m=20°C (≈ 50%B19'+50%B2 → (B2+B19')). The information of structure is received with X-rays phase analysis. NiTi samples after annealing at 575°C at T_m =100°C show weak $tg\alpha_{ADIF}$ of B2 phase ($tg\alpha_{B2}$)and relatively low IF level. In case T_m = -100°C the $tg\alpha_{ADIF}$ is higher and IF level is 10 times higher due to ≈ 100% martensite structure ($tg\alpha_{B19'}$) (Fig.6). The $tg\alpha_{ADIF}$ at room temperature is higher due to stress induced martensite transformation ($tg\alpha_{B2\text{-}B19'}$) according to Dejonghe equations [4]: $(\partial n / \partial \tau) = (\partial n/\partial T)(\partial T/\partial \tau) + (\partial n/\partial \sigma)(\partial \sigma/\partial \tau)$, where τ is time, T is temperature, σ is stress. With the increasing of T_m the $tg\alpha_{B2\text{-}B19'}$ decreases according to Clausius-Clapeyron law that predicts a linear relationship between the transformation temperature T_{tr} and the critical stress necessary to induce the transformation (σ_c) as: $(d\sigma_c / dT_{tr}) = \Delta S/v\varepsilon^t$, where v is the molar volume, ΔS is the entropy difference between the two phases and ε^t is the strain deformation. And at ≈ 100°C the $tg\alpha_{B2\text{-}B19'}$ value reaches the ADIF level of B2 phase.

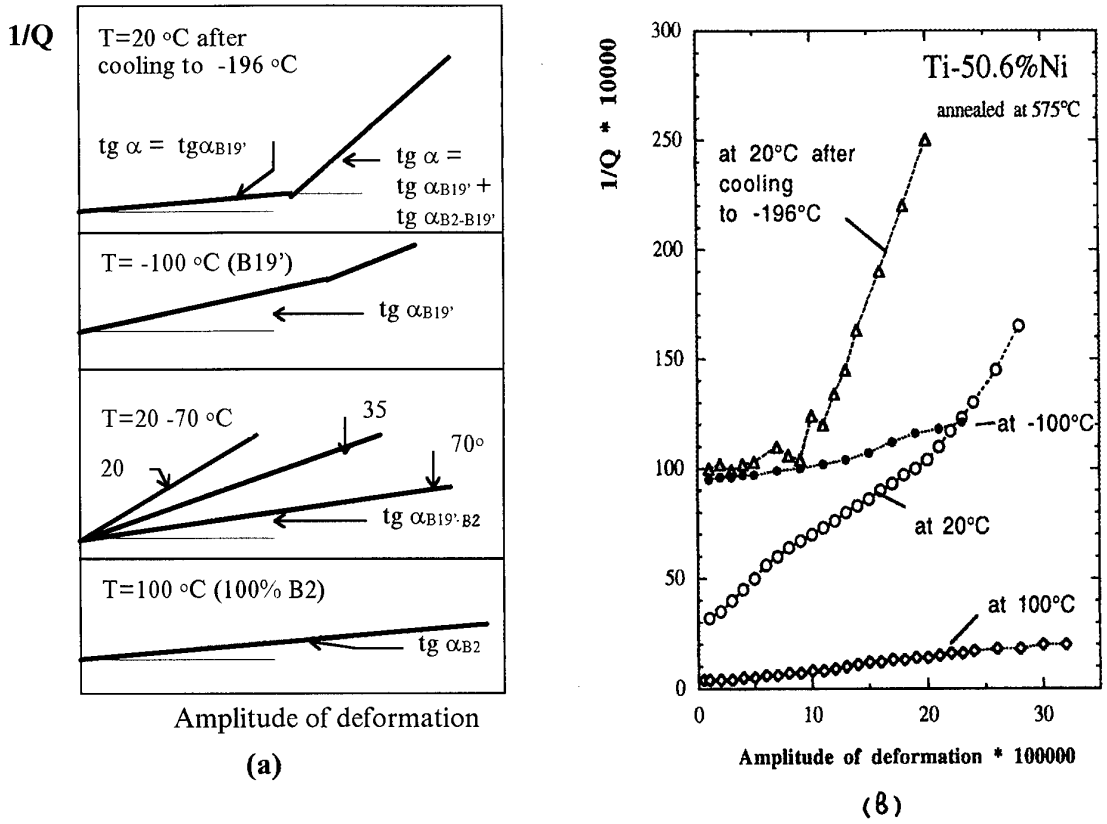


Fig. 6. Scheme (a) and experimental results (b) of formation of ADIF in different structural states.

Two stages on ADIF curves for the samples annealed at 575°C and cooled to -196°C are presented at T_m =20-70°C. At the low range of amplitudes of deformation ($\gamma^* < 10^{-4}$) the $tg\alpha_{ADIF}$ is the same as $tg\alpha_{B19'}$, at condition $\tau > \tau^*$ (where $\tau^* = G\gamma^*$) the $tg\alpha_{ADIF} >> tg\alpha_{B19'}$ and $tg\alpha_{ADIF} \approx tg\alpha_{B2\text{-}B19'}$. The stress range $\tau < \tau^*$ the redistribution in already existent athermal martensite domains takes place ($tg\alpha_{ADIF} \approx tg\alpha_{B19'}$) under the applied stress. With the increase of stress up to $\tau > \tau^*$ the thermoelastic martensite transformation (B2 $\rightarrow$ B19') takes place and the ADIF curve has its typical form. In the $\tau > \tau^*$ the $tg\alpha_{ADIF} \approx tg\alpha_{B19'} + tg\alpha_{B2\text{-}B19'}$. The increase of temperature of measurements T_m leads to the decrease of IF level due to the decrease of volume part of athermal martensite. The $tg\alpha_{ADIF}$ ($\tau > \tau^*$) decreases due to the increase of B2 phase stability for martensite transformation [5].

References

1. Ilyin A.A. Shape memory alloys. In Proc. Итоги науки и техники. Металловедение и термическая обработка. ВИНИТИ. - 1991, v.25. p.3-59.
2. Ilyin A.A. Mechanism and kinetics of phase and sactural transformation in Ti-based alloys. Moscow, Nauka, 1994, 301 p.
3. Khachin V.N., Pushin V.G., Kondratiev V.V. Nickelid of titanium: structure and properties. Moscow, Nauka, 1992. 160 p.
4. Dejonghe J.F., Gobin P.F. Metaux, 573 (1973), 185 and 574 (1973), 209.
5. Golovin I.S., Bataillard L., Schinaeva E.V. Reports of Russian Academy of Science. Metalls (in print: N6 (1996))

THERMOMECHANICAL PROPERTIES IN Cu-Al-Ni SHAPE MEMORY ALLOYS PROCESSED BY POWDER METALLURGY.

J. San Juan (1), R. B. Pérez-Sáez (1), V. Recarte (1), I. Sáez-Ocáriz (1), M.L. Nó (2), O. Ruano (3)

(1) Dpto. Física Mat. Condensada, Fac. Ciencias, Univ. Pais Vasco. Apdo. 644, 48080 Bilbao, Spain
(2) Dpto. Física Aplicada II, Fac. Ciencias, Univ. Pais Vasco, Apdo. 644 - 48080 Bilbao, Spain
(3) Centro Nacional de Investigaciones Metalúrgicas, Gregorio del Amo 8, 28040 Madrid, Spain

1. INTRODUCTION

Among the different kinds of Smart Materials one of the more promising materials are the Shape Memory Alloys (SMA) because of their ability to perform two different tasks: "sensing and actuating" [1,2]. The thermomechanical properties of SMA with view of their use as smart materials have been recently reviewed [2,3]. Nowadays, three kinds of applications (active shape control, active modal modification and active strain energy tuning) based specifically on shape memory alloys are being developed [4,5].

Besides, in order to fulfil the increasing demand of smart materials with a large range of working temperature, several systems of SMA with higher transformation temperatures (until 240°C) are being explored, such as Ni-Al, Cu-Ni-Al, Fe-Mn-Si-X, Ti-Ni-Pd (see [6] for a review). Among them, Cu-Al-Ni shape memory alloys are firm candidates for applications between 100°C and 240°C because of their low cost, relatively easy processing and good shape memory properties. Nevertheless, due to their high elastic anisotropy (A≈13) and large grain size, the Cu-Al-Ni alloys are brittle, and in general show poor mechanical properties that should be improved in order to fulfil the requirements for practical applications.

This improvement is usually accomplished through the addition of grain refiners such as Zr, Ti, B [7] to obtain a grain size lesser than 100μm in diameter.

Nevertheless, in the last years, alternative methods to obtain a fine grain has been developed, such as rapid solidification [8-13] and powder metallurgy (PM) [14-16]. The advantage of PM method over the melt spinning method is that the first allows to obtain bulk material that afterwards can be transformed by traditional methods like extrusion and/or rolling.

In this work we report a new processing route of Cu-Al-Ni SMA by powder metallurgy and we study the thermomechanical properties of the obtained alloys.

2. EXPERIMENTAL METHOD

The alloy of nominal composition Cu-13Al-3Ni (%wt) was melted from 99,99% Cu 99,99% Al and 99,97% Ni in an induction furnace under Argon atmosphere. Fig.1 shows the scheme followed during the samples elaboration. The melt was atomized by Ar gas at a pressure of 2,3 MPa (See [17] for a description of the method). The powder composition was analyzed by an ICP spectrometer (83.6 Cu, 13.06 Al, 3.1 Ni (%wt)). The particle size analysis shows a median particle size about 90 μm. The powder with a particle size between 50μm and 25μm was compacted by HIP at 850°C and a compaction pressure of 150MPa.

After this stage, we have developed two alternative processing routes: The first hiped ingot was directly treated (annealed 30 min at 900°C and quenched in water at 90°C) to obtain the final product 1 (FP1). The second hiped ingot was hot rolled before the thermal treatment to obtain the final product 2 (FP2).

The powders and the final products microstructures were characterized by scanning electron microscopy, (see fig1).

The martensitic transformation (MT) undergone by the final products was studied by internal friction (IF) technique in an inverted torsion pendulum at about 1Hz, with an oscillating amplitude of $\varepsilon=2\times10^{-5}$ and a heating rate of 1K/min.

The thermomechanical properties were studied in a tensile-compression machine using an inverted assembly to introduce the sample in a thermal bath.

0-8194-2165-0/96/$6.00

3. RESULTS AND DISCUSSION

3.1 Microstructure

The morphology of the powders between 25 and 50 μm used for the elaboration of the samples is shown in the upper-left corner micrograph in fig.1. The powder particles are mainly spherical and polycrystalline with a grain size between 5 and 10 μm such as it is shown in the upper-right corner micrograph (fig.1).

The down-left corner micrograph shows the FP1 microstructure. Notice that the grain size and shape is like the powder ones. The presence of a very thin film of superficial oxide in the spherical particle limit inhibits the grain growth during the H.I.P. process. Furthermore the hot-rolling deforms the grains and breaks the intergranular oxide film. The FP2 microstructure is shown in the last micrograph. The grain size is more or less the same that the powder particle size (≈50μm) but its shape does not remember anymore the spherical shape of the powder particles.

It can be concluded that grain growth process is stopped by the thin superficial oxide film of the powder particles, and then the final product grain size is like the powder particles one. Besides it should be remarked that this microstructure has been obtained starting from pure metals without any addition of grain refiners.

3.2 Martensitic Transformation

The MT of the alloy obtained by the two powder metallurgy processing route (atomization+HIP+thermal treatment) and (atomization+HIP+hot rolling+thermal treatment) have been studied by IF and modulus measurements. Fig.2 shows the results obtained for the FP1 sample (left column) and the FP2 sample (right column). The IF spectra in fig 2-a1 and 2-a2 show the characteristic peaks of the direct and reverse MT. Hysteresis of the hiped final product (FP1) (≈13K) is slightly bigger than the hot rolled one (FP2) (≈8K) from these small hysteresis values we conclude that the MT is the β' to β_1' .

In a perfect correlation with the IF peaks, the curves of modulus ($\propto f^2$), fig.2-b1 and fig.2-b2 show the sharp minima due to the shoftening of the lattice during the MT (see [6] for a general overview). Nevertheless we would like remark the anomalous and opposed behaviour of the modulus for both final products, just in the high temperature side of the shoftening peak. This pretransitional shoftening (FP1) and hardening (FP2) could be linked to the different microstructure of both products, that modifies the nucleation conditions of the martensite.

The cumulative integral of the IF spectra shown in fig.2-c1 and fig.2-c2 is proportional to the transformed fraction [18] and allows us to obtain the transformation temperatures for the 5% and 95% of the MT: Ms=353K, Mf=294K, As=309K, Af=369K for the FP1 sample and Ms=367K, Mf=322K, As=330K and Af=377K for the FP2 sample.

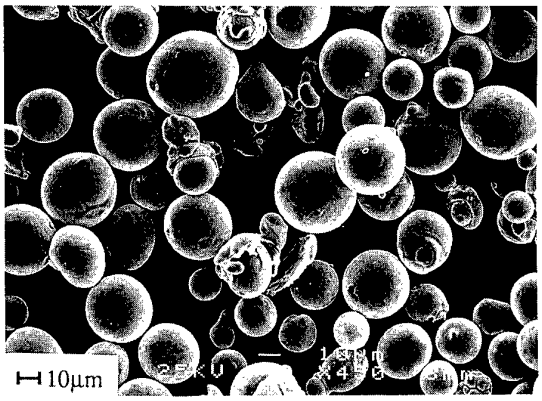
The transformation temperatures of the FP2 sample are slightly higher than the FP1 one. This effect could be due to the restriction imposed by the hard intergranular oxide film on the macroscopic shear produced by the martensite growing.

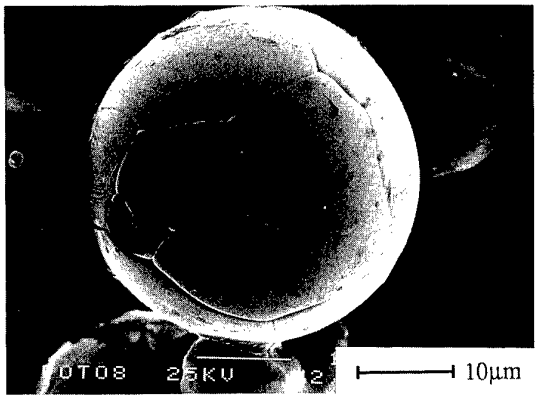
3.3 Thermomechanical Properties

In order to study the thermomechanical properties of the final products obtained by the described elaboration processes, different tensile tests have been carried out at several temperatures.

The tests carried out at higher temperatures than Af show the superelastic behaviour of the alloy measured until 1% of total deformation. As the temperature is increased, more stress is required to induce the martensitic transformation. Plotting this stress versus testing temperature a straight line is obtained for both FP1 and FP2 as it can be expected from the Clausius-Clapeyron equation, (fig.3). The FP1 slope is higher than the FP2 one. The intergranular oxide film in the FP1 sample absorbs the external stress applied on the specimen. The external stress must be increased until the stress inside the grain is able to induce the transformation.

The extrapolation of these straight line to zero stress give a transformation temperature slightly lower than the Ms temperature obtained from the thermally induced transformation by IF measurements. This behaviour has been found previously in polycrystalline Cu-Al-Ni alloys, and can be understood if it is taken into account that although martensite forms





INITIAL PRODUCT
99.99% Cu, 99.99% Al, 99.97% Ni

POWDER COMPOSITION
83.6%Cu-13.1%Al-3.1%Ni

ATOMIZATION
by Ar gas at 2.3MPa

HOT ISOSTATIC PRESSING

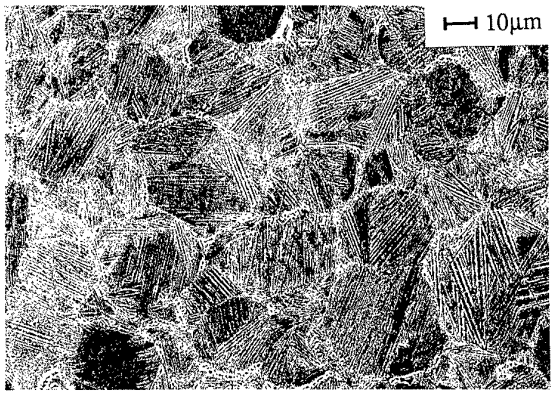
HOT-ROLLED
5mm → 0.8mm

THERMAL TREATEMENT
ANNEALED 30min at 900°C +
QUENCHED in water at 90°C

FINAL PRODUCT 1

THERMAL TREATEMENT
ANNEALED 30min at 900°C +
QUENCHED in water at 90°C

FINAL PRODUCT 2



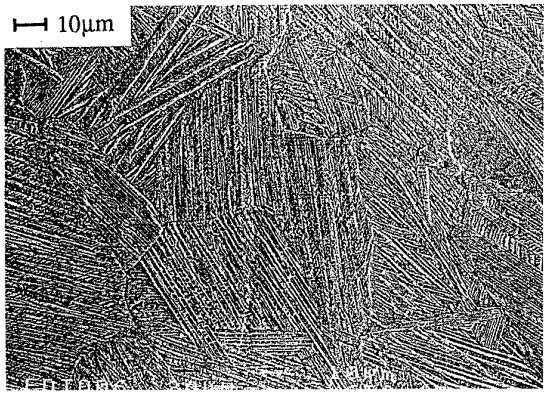


Fig1 General scheme of the elaboration process and micrograph showing powders and final products microstructure.

spontaneously on cooling below Ms, a finite stress is needed to overcome the frictional force due to the martensite-austenite interface movement, thus during the thermally induced transformation the stress does not become zero [19].

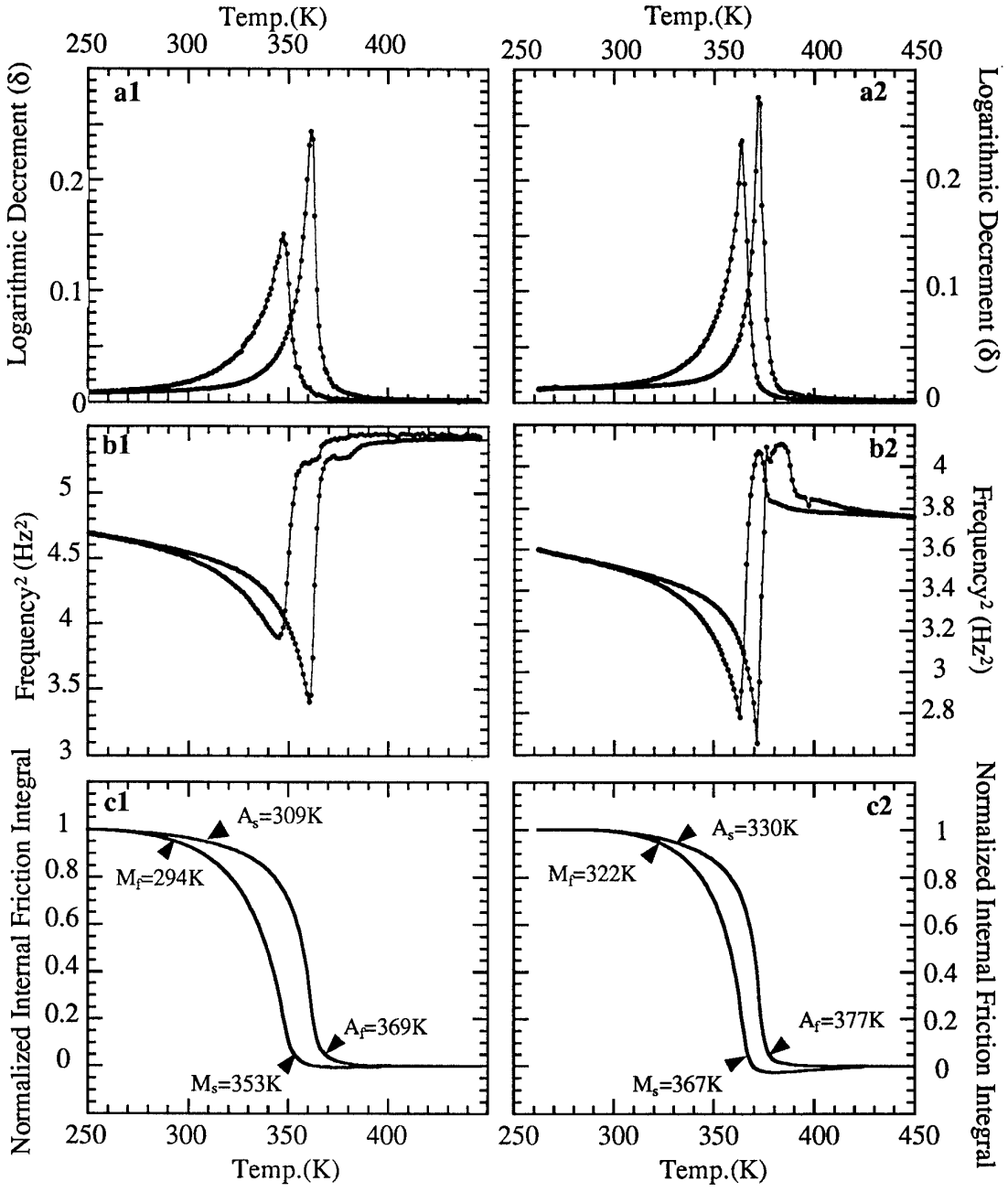


Fig2 **a)** Internal friction spectra during the martensitic transformation (fifth run): (1) FP1 sample (At.+HIP+T.T.), (2) FP2 sample (At.+HIP+H.R.+T.T.).
b) Square of frequency curves: (1) FP1, (2) FP2.
c) Normalized internal friction integral. Martensitic transformation temperatures at 5% and 95%: (1) FP1, (2) FP2.

It should be noted that superelastic tests at 393K until 4,5% of deformation have been performed on the FP2 sample with very good behaviour. During similar tests at 368K, FP1 sample undergone intergranular fracture after a 2% deformation.

Tensile tests below Mf have been also carried out on the FP2 sample, in order to deform the sample in martensitic phase by pseudoelastic effect and to evaluate the simple memory effect by a further heating above Af without applied stress.

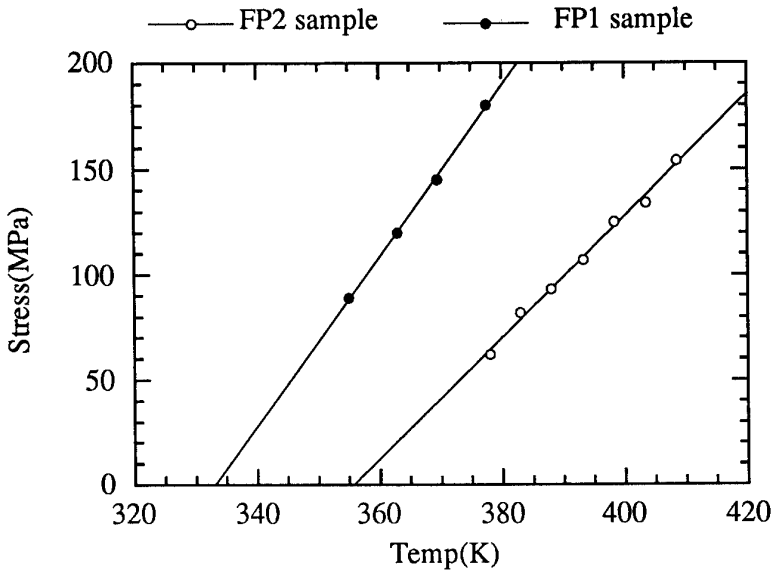


Fig3 Linear relationship between critical stress to induce martensite and test temperature.

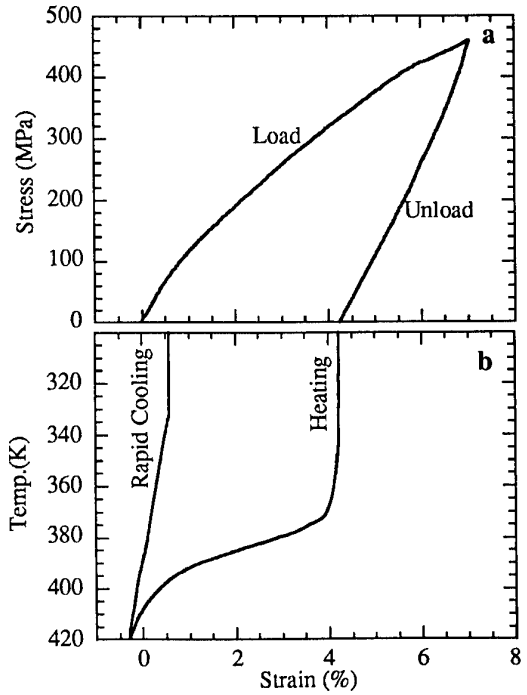


Fig4 **a)** Tensile stress-strain curve until 7% deformation for the hot rolled sample.
b) Shape memory recovery curve after unloading in fig4 a).

Fig 4a shows a tensile test at 277K until a 7% of total deformation. During unloading, a pseudoelastic deformation of 2.75% is recovered, remaining a residual deformation of 4.25%. The shape recovery during heating at zero stress is plotted in fig 4b. At high temperature (420K) the negative deformation of -0.25% is linked to the fact that the origin of the tensile machine was adjusted in martensitic phase in which the sample is longer than in β phase. A further cooling of the sample allows to recover the shape in martensitic phase remaining a final deformation of 0.5%, and therefore the sample has undergone a recovery by simple memory effect of 88% during the first cycle.

4.CONCLUSIONS

It can be concluded that the proposed powder metallurgy processing route is a very good method to produce fine grain shape memory alloys. Besides, the produced alloys show a very reproducible cycle of thermal transformation. The hot-rolled (FP2) alloy shows a better mechanical behaviour than the un-rolled one (FP1). This last route could be a good method to obtain "preformed" actuators, but an improvement of properties is necessary.

5. ACKNOWLEDGEMENT

This work has been carried out with the financial support of the Spanish "Comisión Interministerial de Ciencia y Tecnología (CICyT)" (project nº MAT92-0353).

6. REFERENCES

[1] M.V. Ghandhi and B.S. Thompson, Smart Materials and Structures. Chapman and Hall, 1992

[2] J. Van Humbeck, D. Reynaerts and R. Stalmans, Proc. Actuator-94, Bremen (Germany), 15-17 June 1994, Ed. Axon Techn Consult.-Bremen, pp 312-316.

[3] J. Van Humbeck, IV C.N. Propiedades Mecánicas de Sólidos, Vitoria (Spain), 29June-1July 1994, Ed. J. San Juan, S. Gutierrez, M.L. Nó, ISBN 84-605-3566-5, pp 153-164

[4] L. McD. Schetky, Proc. Met. Res. Soc. Symp. vol 246 (1992) pp 299-307.

[5] C.A. Rogers, C. Liang and D.K. Barker, in Smart Materials, Structures and Mathematical issues. Ed C.A. Rogers, Technomic Publ. 6 Inc. (1989), pp 39-62.

[6] L. Delaey, "Diffusionless Transformation" in Phase Transformation in Materials, P. Haasen Ed., (VCH, Weinheim, Germany, 1991) pp 339-404.

[7] J. San Juan, V. Recarte, J. Herreros, I. Hurtado and M.L. Nó, Proc of Nat. Conf. on Metallurgical Science and Technology, CENIN, Madrid (Spain) 3-5 October 1990, vol.II, pp71-80.

[8] W.M. Stobbs and J.V. Wood, *Acta Metall.* **27** (1979) 575-584.

[9] J.V. Wood, Proc. of the Int. Conf. on Martensitic Transformations, Leuven (Belgium) 8-12 August 1982, L. Delaey and M. Chandrasekaran Eds. *J. Physique C4* **43** (1982) pp 755-760.

[10] R. Oshima, M. Tanimoto, T. Oka, F.E. Fujita, Y. Hanadate, T. Hamada and M. Miyagi, Proc. of the Int. Conf. on Martensitic Transformations, Leuven (Belgium) 8-12 August 1982, L. Delaey and M. Chandrasekaran Eds. *J. Physique C4* **43** (1982) pp 749-754.

[11] J. V. Wood and P.H. Shingu, *Metall. Trans. A* **15** (1984) 471-480.

[12] M. Ahmed, S.W. Husain, Z. Iqbal, F.H. Hashmi and A.Q. Khan, *Stripta Metall* **22** (1988) 803-808.

[13] J.H. Zhu, D.P. Dunne, G.W. Delamore and N.F. Kennon, Proc. of the Int. Conf. on Martensitic Transformations, Monterey, Ca, USA 20-24 July 1992, C.M. Wayman and J. Perkins Eds. (Inst. for Advanced Studies, Monterey, 1993), pp 1083-1088.

[14] T.W. Duering, J. Albrecht and G.H. Gessinger, *Journal of Metals* **43** (1982) 14-20.

[15] J. Jassen, F. Willems, B. Verelst, J. Maertens and L. Delaey, Proc. of the Int. Conf. on Martensitic Transformations, Leuven (Belgium) 8-12 August 1982, L. Delaey and M. Chandrasekaran Eds., *J. Physique C4* **34** (1982) pp 809-812.

[16] R.D. Jean, T.Y.Wu and S.S. Leu, *Scripta Metall.* **25** (1991) 883-888.

[17] M. Lieblich, G. Caruana, M. Torralba and H. Jones, *Mater. Sci. Techn*, (1995) in press.

[18] R.B. Pérez-Sáez, Master Thesis, Univ. País Vasco (1993).

[19] J. San Juan, R.B. Pérez-Sáez, V. Recarte, M.L. Nó, G. Caruana, M. Lieblich and O. Ruano, Proc. of the Int. Conf. on Martensitic Transformations 95, Lausanne (Switzerland), 20-25 August 1995 , *J. Physique C4 (to be published)*

Solder paste / shape memory alloy composite for adaptive solder joint

S. Trombert*, J. Chazelas*, P. Bonniau*, W. Van Moorleghem**, M. Chandrasekaran**, J.F. Silvain***

* Thomson-CSF, division RCM, La clef de st Pierre, F-78852 Elancourt
** AMT.n.v, Industrieweg, 43, B-3540 Herk-de-stad
*** ICMCB-CNRS, Av. du Dr Schweitzer, F-33608 Pessac

ABSTRACT

This paper analyses briefly the different approaches to solve the problem of stresses generated by different thermal expansion coefficients, in brasing joints used to assemble high density electronic devices to printed circuit boards. While retaining certain ideas from some of the promising approaches, a novel approach to solve this problem is proposed in this report which involves developing a new composite solder paste containing superelastic alloy particles. Preliminary results obtained on Ni-coated NiTi wires embedded in a standard SnPb paste are reported which indicate that while the coated wires are wetted by the matrix, the adhesion between the coating and NiTi is poor. The behaviour under tensile stresses have been simulated for NiTi particles incorporated composite pastes, each having a different particle volume fraction. Low strain value results show the decrease of the mean equivalent stress value when the volume fraction is increased.

1. INTRODUCTION

Solder joints used in the surface mounting technique serve three primary purposes: electrical interconnection, heat transfer and mechanical attachement of components. As a consequence, a « good » solder paste must possess at least the following properties:

- Metallurgical and rheological compatibility between packaged component and printed circuit board (PCB),
- High electric conductivity ($Resistivity_{SnPb}=0,15.10^{-6}\Omega.m$),
- Adapted wettability and
- Viscosity.

However, during thermal cycling, failures can appear inside the solder paste leading to an irreversible degradation of the joint. This thermal like failure is linked with the large coefficient of thermal expansion (CTE) difference between the ceramic substrate ($CTE=6.10^{-6}/°C$) and the PCB ($CTE=16.10^{-6}/°C$). These thermally induced stresses minimize considerably the life time of boards as soon as the packages length exceeds one centimeter. On the other hand, the constant evolution of packaging technology in microelectronic industry tends to increase the package size, to optimise the number of operations per component, to reduce the interconnection spaces on PCB by a diminution of tracks and metallic holes diameter, and to increase the electrical performances by a reduction of interconnections length.

The increase of package length, in conjunction with the decrease of connection size, will not favorise the diminution of fissuration in solder joints. In order to solve this problem of crack formation during thermal cycling, it is possible to modify:

- The packaged components,
- The PCB,
- The solder paste.

Some earlier attempts in these respects are reported and analysed in this work. Then the concept for a new solution is outlined, and preliminary studies conducted to evaluate its feasability are reported.

2. PREVIOUS APPROACHES

2.1. Packaged components

The packaging used for surface mounting are mainly made of ceramic. No improvements in its CTE or replacement of this material have been considered because ceramic is indispensable to abide by the rigorous properties such as hermeticity, thermal and electrical conductivity, which are specifically demanded in airborne components. Plastic can be investigated for package components ($CTE=30.10^{-6}/°C$, but lower stiffness), nevertheless, as the CTE problem increases with the package length, the approach of changing the packaging material would not provide a meaningful solution.

0-8194-2165-0/96/$6.00

2.2. Printed circuit board

Several ideas are studied by THOMSON-CSF to adapt the PCB's CTE to the ceramic's one, by modifying the PCB material.

One of the most promising approach consisted in replacing the last copper sheet on PCB by a CuZnAl shape memory alloy (SMA) [1]. The superelasticity properties of a SMA continuous film has been used as an intermediate layer between the PCB and the solder joint. The layer allowed the thermally induced stresses to be relaxed. Consistent with requirements, the SMA also presented a low electrical resistivity (CuZnAl=0,1.10^{-6} Ω.m) and a good wettability in SnPb and Cu.

The following technical problems were encountered with this approach:

- It was difficult to find a compromising thickness for the SMA sheets: on one hand, large and thick enough to ensure a good electrical and mechanical contact, and on the other hand, thin enough to be etched without interfering with the solder pads pitch,
- The austenitic phase of the SMA tends to decompose in more stable products during thermal cycling.

Nevertheless, this study indicates that SMA, provided that they have the requisite properties, are capable of compensating for the difference in CTE.

2.3. Solder joint

Modifying the solder joint is easier and the following attempts were made in this respect:

- The metallic solder was replaced by a conductive adhesive [2]. The mechanical behaviour problems during thermal cycling could be solved in this manner, but the electric resistivity proved to be excessively high (0,05Ω.m),
- Since the crack propagation is aided by the presence of oxyde layers, a mineral coating (Si_3N_4 or SiO_x) was deposited on the entire board to stop the oxygen migration [3]. But in spite of the coating, the phenomenon could not be minimised.
- A more common approach was the incorporation of Ni particles (10% in weight) in solder paste, in order to make it more ductile [4]. This gives rise to an increase in Young's Modulus E (+20%) and the coefficient of elastic limit σ^e (+30/40%), and a small decrease in the solder joint CTE (3ppm/°C at 50°C). Some technical problems have to be eliminated in this approach, such as solder viscosity change and inhomogeneous distribution of Ni particles. Nonetheless, the idea of particle inclusion is worth pursuing.

3. ADAPTIVE SOLDER JOINT

It is seen from the results of the previous attempts and their analysis reported above that:

- It is easier to improve the solder joint rather than package or PCB, and the particle technique seems highly promising in this respect though it does not serve as an adaptive solution;
- The superelastic properties of SMA used in modifying the PCB are worth pursuing towards an adaptive solution, but it is not an easy task to fabricate the SMA material to the dimensions needed in the PCB.

In concept, therefore, a SMA particle incorporated solder paste can be developped. This will require a SMA with transformation and utilisation temperatures compatible with the functionnal specifications of the solder joint. It is presumed that incorporation of SMA particles in SnPb solder paste will lead to an adaptive solder joint, giving it not only the beneficial effects of particle addition to the matrix (increase in E and σ^e) but also the positive effects of SMA superelasticity (strain absorption to relieve local stress build up).

The SMA choosen for the present application must fulfill the following criteria:

- It must have a CTE value between that of the packaging , PCB and solder joint (CTE=24.10^{-6}/°C),
- It must have a melting temperature higher than that of the solder,
- Its addition must not modify the metallurgical and rheological properties of the classical solder paste,
- Its adhesion to the matrix must be strong enough but without formation of fragile interphases at the SMA/solder paste interface,
- In spite of its adhesion the electrical conductivity of the composite must remain acceptable,
- The nature and extent of its chemical interaction with the matrix through interdiffusion should not deteriorate the SMA properties.

4. PRELIMINARY STUDIES

4.1.NiTi tests

As a first step in testing the feasability of the concept outlined above, the capacity of NiTi to be used as a reinforcement in the composite solder paste has been evaluated. NiTi SMA was choosen instead of copper based SMA for the following reasons:

- Higher superelastic strains are obtainable in NiTi,
- The corrosion resistance of NiTi is superior,
- NiTi is readily available not only in particle form, but also as thin wires which can be more conveniently characterized.

Polycristalline NiTi wires (Diameter 220μm, CTE=6,6-10.10^{-6}/°C, resistivity=0,5-1,1.10^{-6}Ωm) are characterized by tensile tests, to confirm their superelastic properties.

Wetting experiments showed that SnPb did not wet the SMA unless a very active flux (« AS1 ») was added. However, because of its highly corrosive behaviour this flux cannot be used in microelectronic applications. Due to the fairly low wetting angle of Ni with NiTi ($\theta<90°$), Ni has been applied on NiTi wires (thickness 1,5μm) by an electrochemical method, in order to make possible the wetting of the SMA with SnPb. With the use of a less corrosive flux (« Z.100.57 »), Ni tends to increase the wettability of the solder paste with respect to NiTi. However, the tensile test measurements of such a micro-composite shows the drastic decrease of the Ni/NiTi mechanical properties (uncoated NiTi: rupture stress σ^R=939MPa, ε^R=7.8%; coated NiTi: σ^R=608MPa, ε^R=5.8%).

The above results indicate that NiTi, based on its properties, is an appropriate material for use in an adaptive solder paste. But it has to be coated with a thin metal layer for reasons of wettability, and Ni doesn't seem to be ideal as a coating. A Scanning Electron Microscopy (SEM) observation show a very poor adhesion between Ni and NiTi, and it is difficult to apply a coating with both thickness less than 1,5 μm and good adhesion with the wire.

4.2. Simulation

Simulation with the ANSYS software [5] was conducted to optimise the mechanical, thermal and electrical properties of the composite material. The equivalent stresses in the composite with changing volume fraction of the particles (Vf) was investigated. The model was based on a two-dimensional unit cell (Fig. 1), and a step by step displacement was imposed along the Y axis, in order to obtain strains varying from 0,5% to 5% at 0,5%. increments. Vf was varying from 5% to 30% at 5% increments.

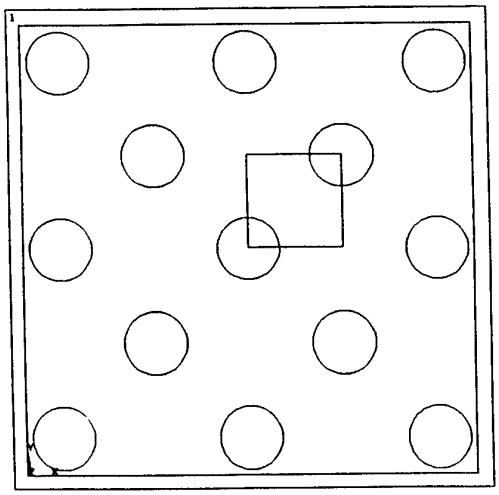


Fig. 1. Cross section of a particle reinforced composite, and the studied unit cell.

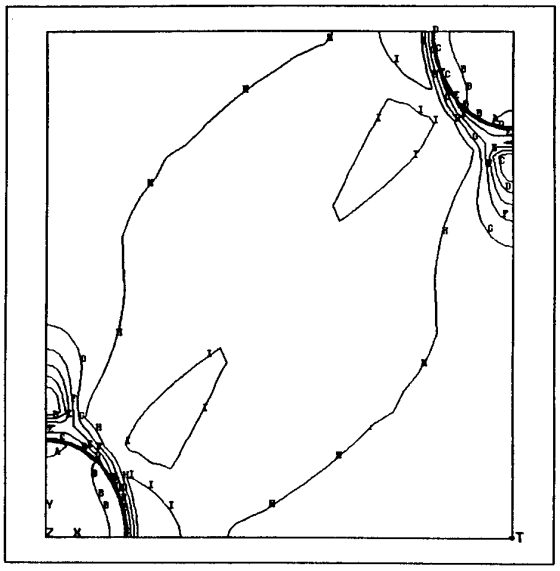


Fig. 2. Iso-line plot of equivalent stresses (Pa) (Vf=5%, ε=2%)

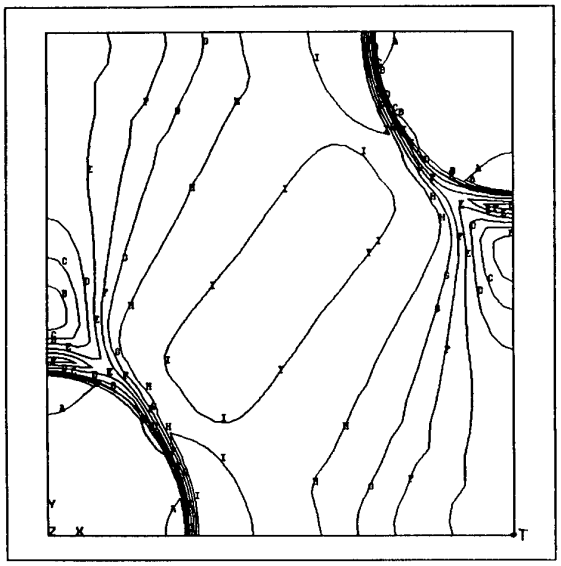


Fig. 3. Iso-line plot of equivalent stresses (Pa) (Vf=15%, ε=2%)

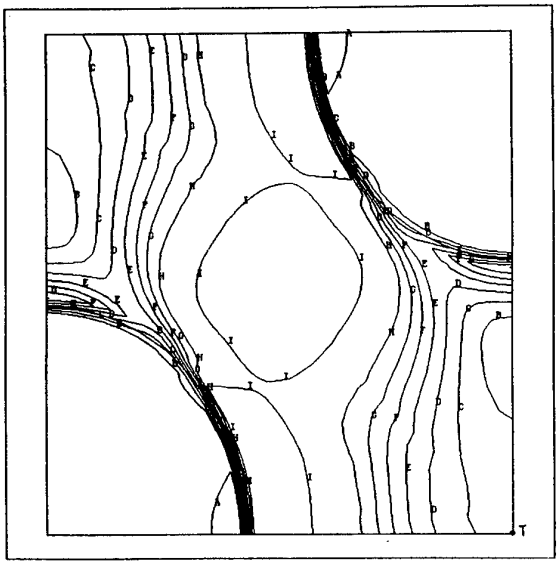


Fig. 4. Iso-line plot of equivalent stresses (Pa) (Vf=30%, ε=2%)

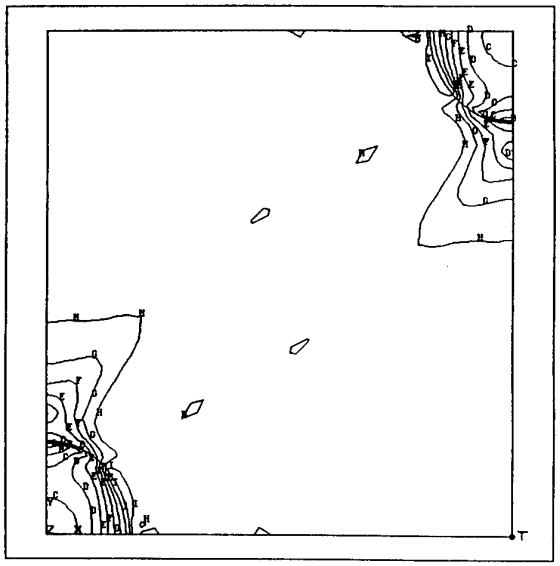


Fig. 5. Iso-line plot of equivalent stresses (Pa)
(Vf=5%, ε=5%)

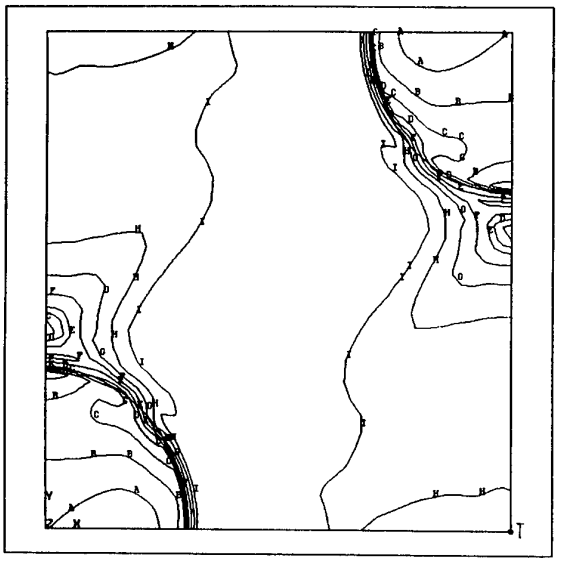


Fig. 6. Iso-line plot of equivalent stresses (Pa)
(Vf=15%, ε=5%)

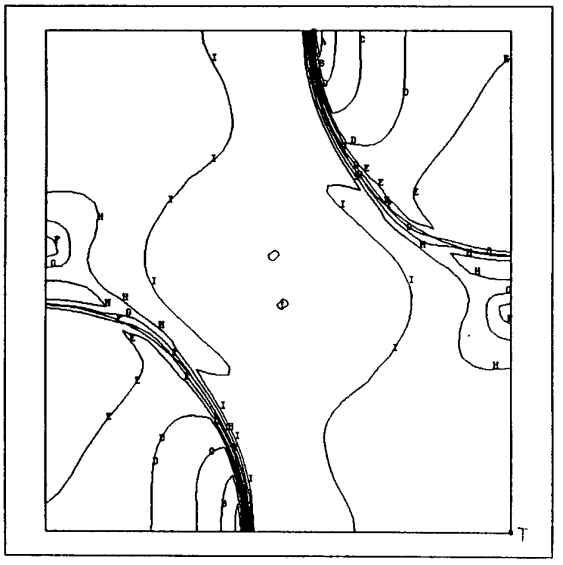


Fig. 7. Iso-line plot of equivalent stresses (Pa)
(Vf=30%, ε=5%)

The equivalent stress variations in the composite are shown in figs. 2-4 for ε=2% and in figs. 5-7 for ε=5%. In the case of SnPb, the equivalent stress is uniform with values of 41,8MPa and 43,5MPa at ε=2% and ε=5% respectively. In the case of composite, the mean equivalent stress tends to decrease with increasing Vf.
Figure 8 shows the variation in the equivalent stress with Vf for different strain values, at a specific point of the unit cell (indicated as T on fig. 2-7). The real equivalent stress value would be given by the integration of the values over the entire unit cell. Between ε=2% and ε=5%, the stress value decreases by a factor of 1,08 for Vf=5%, by a factor of 1,34 forVf=15% and by a factor of 1,86 for Vf=30%. This is interpreted in comparison with pure SnPb by an increase of elastic limit σ^e value when NiTi particle volume fraction increases.
While simulation shows the benefits of increasing Vf, in practice problems of wettability and essentially process compatibility are likely to set a limit to Vf.

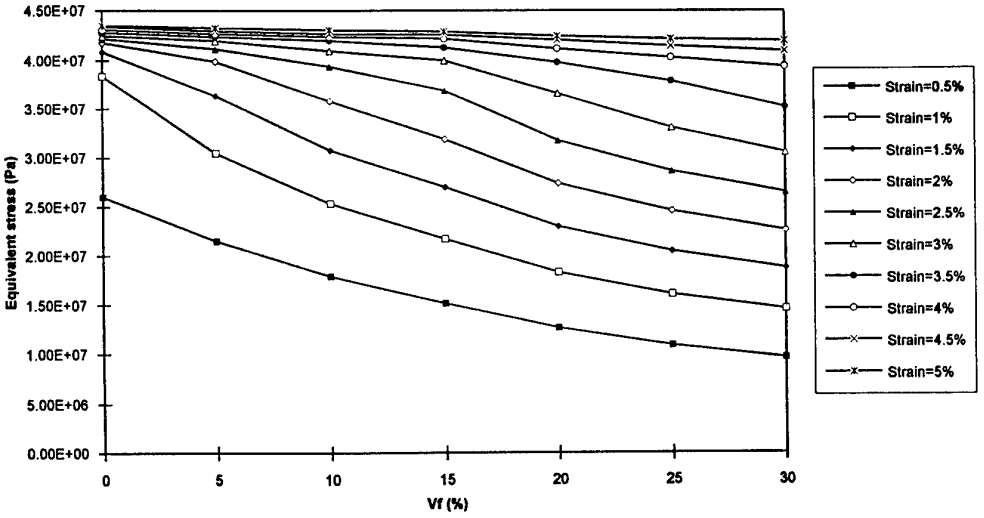


Fig. 8.Variation of the equivalent stress with Vf for different strain values.

5. CONCLUSION

The proposed approach of incorporating NiTi SMA particles in a SnPb solder paste to increase the σ^e value and consequently reduce the thermally induced stresses is very promising. Preliminary results obtained by simulation show that the presence of SMA particles decreases the mean equivalent stress in the composite solder joint. The results of experiments with NiTi wires also show that, based on its properties, it is an appropriate material for use in an adaptive solder paste. But it has to be coated with a thin metal layer for reasons of wettability with SnPb. Attempts will be made in future work to optimise through simulation, the NiTi volume fraction and particle size in the presence of tensile and shear stresses generated by thermal cycling.

6. REFERENCES

[1] C. Val, J.P. Lucas, E. Patoor, « A new concept in packaging - A self-adaptive epoxy printed circuit for any type of package », IMC 1990 Proceedings, Tokyo, may 30-june 1 1990, pp 330-338.

[2] P.J. Amick, « Reliability life testing of CTE-compatible surface mount modules », Proceedings of the technical program NEPCON West'93, 7-11 Feb.1993, Anaheim, CA, USA, pp1540-1543 vol.3.

[3] C. Val, M. Leroy, D. Bourret, R. Sempere, « Hermetic plastic packages with applications to ruggedized boards », IEEE/CHMT Proceedings 1991, IEMT Symposium, San Fransisco, sept. 16-18 1991, pp356-360.

[4] C. Val, M. Leroy, H. Boulharts, « Smart solder pastes - Adaptive solder paste composite », ISHM Microelectronic Soc., 6-8 june 1994, Windsor, UK, pp 119-122.

[5] ANSYS V.5.2 (1995), Swanson Analysis Systems Inc.,Houston PA-15342, USA.

Comparison of the fatigue of two shape memory alloys - CuZnAl and TiNiCu - during shape memory effect cycles.

M.J. BIGEON and M. MORIN

GEMPPM, URA 341, INSA LYON, F69621 VILLEURBANNE CEDEX
fax: (33) 72438830 - E-Mail: morin@gpmmail.insa-lyon.fr

ABSTRACT

The fatigue of TiNiCu and CuZnAl thin wires has been investigated during stress assisted two way memory effects thermal cycles. The influences of the number of thermal cycles and of the applied stress have been measured, and Wöhler type curves are plotted. The evolution of the high and low temperatures shapes during the thermal cycling is also compared for the two alloys.

1. INTRODUCTION

Many applications of martensite alloys in shape memory devices require a large number of thermal cycles and also a stable and reliable Shape Memory Effect (SME). However, one problem is to characterise the thermomechanical fatigue of these alloys. Smarts materials using Shape Memory Alloys (SMA) are particularly concerned by these characteristics [1-2].

The SMA are characterised by a thermoelastic martensitic transformation. This transformation is reversible, accompanied by an hysteresis (5- 20 K) and can be induced by variation of either temperature or stress. In the case of a temperature induced martensitic transformation, formation of martensitic phase starts at temperature M_S and ends at a temperature M_f. The reversible transformation occurs between temperatures noted by A_S and A_f.

When a sample is deformed and unload at a temperature below M_f, the apparently plastic strain is restored during heating to a temperature above A_f : it is the one way Shape Memory Effect.

In the present study, the Stress Assisted Two Way Memory Effect (SATWME) is used : the specimens are thermally cycled under a constant load. This effect is similar to the shape memory effect but both the cooling and the heating are performed under a constant stress. During the cooling, the martensite is oriented by the stress and the strain is large. During the heating the sample recovers its original shape by SME (elastic strain of the austenitic phase).

In this paper measurements of SATWME in two commercial wires 0.5 mm diameter are reported and some thermoelastic fatigue results are developed.

2. EXPERIMENTAL PROCEDURES

2.1. The fatigue machine

The fatigue tests are performed by using a tensile machine that has been specially developed[3]. This machine (figure 1) has a pneumatic controlled moving part and is driven by a computer. The movement of the moving axis is realised by an attached plate (a) which in turn can be moved with the help of associated inner tubes(b, b'). When the upper tube is filled up with air, the plate, thus the axis move downward. Similarly an upward movement is obtained using the other set of inner tube. The air distribution between the two air chambers is directed using a computer-controlled electrovalve. To avoid frictions, two sets of three steel wires assure the elastic guiding the moving axis of the machine.

The machine is equipped with, i) a load captor, with a maximum load limit of 500N, ii) a displacement captor that is able to measure a displacement of 5 mm with a resolution of better than 2 μm.

The machine can work in a stress or in a strain controlled regime by using an electronic regulation.

Each test sample is immersed in a regulated silicone bath in order to obtain a stable and homogeneous temperature.

0-8194-2165-0/96/$6.00

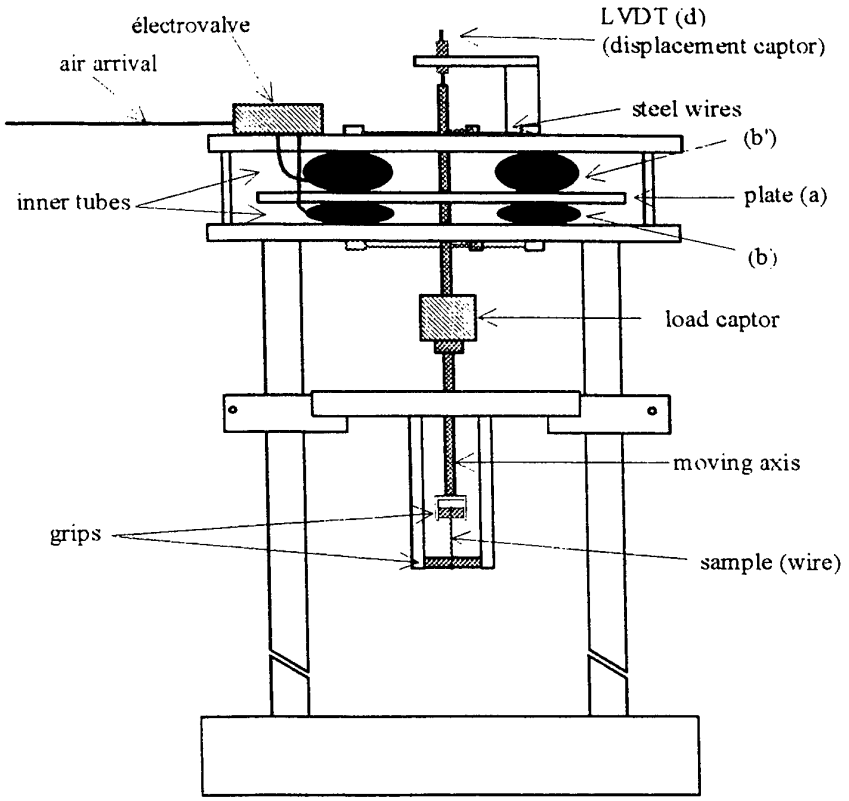


Figure 1 Tensile machine used for fatigue tests.

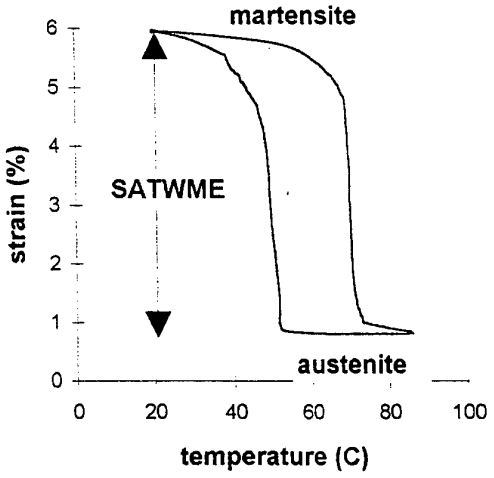


fig 2a. Strain temperature curve.

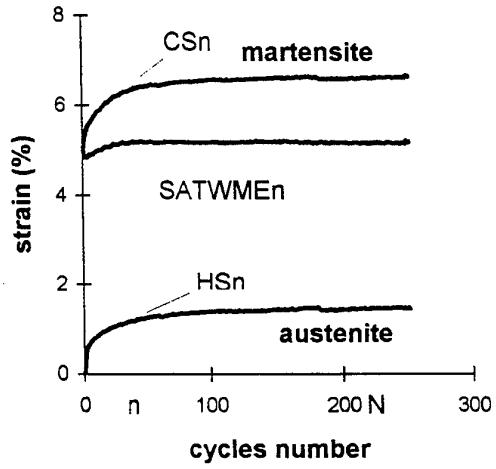


fig 2b. Strains evolution during cycling.

2.2. The thermomechanical fatigue test

With the machine, the wire tensile specimens of 30 mm in length are submitted to a constant load. In the case of the CuZnAl, the load range is 20 to 200 Mpa. Under a higher stress, the CuZnAl wire breaks immediately. The TiNiCu wires are studied under a load varied between 50 and 800 MPa. The lower value is chosen in order to obtain a short test time, and at a load higher than 800 MPa, the plasticity effect is too

important. The wires can be heated-cooled by two means. The first heating-cooling mean (noted slow cycle) is used to low cycles number (no more than 256 cycles); the bath temperature is cycled between 25°C and 80°C. In order to study the fatigue in a larger cycles number, the second heating-cooling mean (noted fast cycle) consists in heating the wire by Joule effect. The temperature of the bath is kept constant about 19°C thanks to a cold water circulation for the cooling. A slow thermic cycle takes about 8 minutes and a fast cycle less than 1 minute. In the both kind of tests[5], the extreme strains of the specimen are recorded versus the cycle number (fig 1b). During a slow cycle, the all strain-temperature curve is recorded (fig 1a). The strain of the martensite phase is noted CS (cold strain), the austenite phase one HS (hot strain), and the strain difference between the cold and the hot phase SATWME (stress assisted two way memory effect). An index specifies when it is necessary the number of the studied cycle. N is the thermal cycle when the specimen breaking occurs.

2.3. The studied alloys.

- **CuZnAl**

Cu - 11% Al - 14% Zn (at. %). The specimens were betatised at 1123K during 30 minutes, quenched in water at room temperature, annealed consecutively at 373K for 30 minutes and at 343K for 30 minutes. After this heat treatment, the vacancies number is minimal and the order degree maximal[6]. The transformation temperatures in this case are: M_S=37°C, M_f=34°C, A_S=43°C, A_f=46°C. The samples had a 'bamboo' structure and the grain size was observed to be on the order of 0.5 mm. Such microscopical observations explain the observed maximal recoverable strain value similar to that often obtained in the case of a single crystal. This structure explains also the large dispersion in the measurements.

- **TiNiCu**

Ti - 45.2% Ni - 6% Cu (at. %). The wires were observed to have a fibrous structure. The final treatments are 35% of cold work and an annealing at 700K for one hour[7,8]). For the TiNiCu specimens, the transformation temperatures are: M_S=38°C, M_f=30°C, A_S=53°C, A_f=62°C.

3. RESULTS

3.1. SATWME (Stress Assisted Two Way Memory Effect)

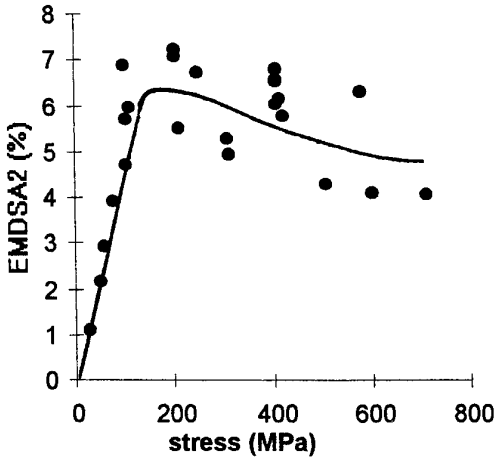


Fig 4a. SATWME2 versus the applied stress in the TiNiCu case.

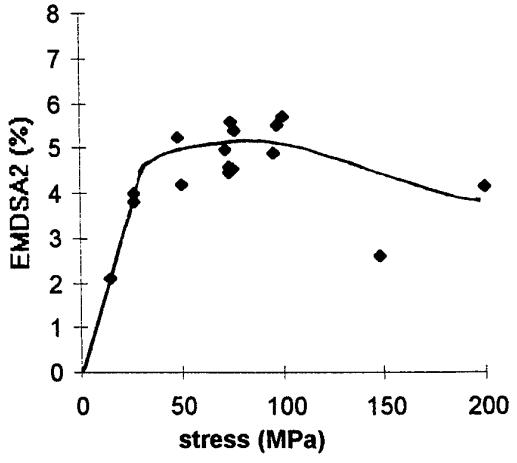


fig 4b. SATWME2 versus the applied stress in the CuZnAl case.

The $SATWME_2$ ($SATWME$ measured at the second cycle)-stress curves are shown in figure 4. For the both alloys, $SATWME_2$ linearly increases at first, and then decreases when the applied stress increases. The

linear increase of the $SATWME_2$ for the low stresses has been described[9] : it is thanks to the increase of the induced martensite fraction that the $SATWME_2$ increases with the applied stress. From a given value of stress (150 MPa in the TiNiCu case and 50 MPa in the CuZnAl one), a saturation phenomenon occurs. The decrease can be explained by the plasticity emergence interfering with the martensite needles development.

3.2. Evolution of the high (HS) and low (CS) temperature shapes during the thermal cycling

It is very important to know the length variation of the sample (SATWME), but the evolution of specimen positions (when the specimen is cold or hot) also presents some interest. In order to describe this evolution, the evolution rates of the both strains during the cycling under a constant stress have been measured. Figure 5 presents this evolution versus the logarithm of cycles number curves. On these curves it is possible to draw two tangent lines. The slopes of these both lines define two strain rates : the evolution rate of the hot or cold strain during the thermal cycling (% per decade of thermal cycles).

These rates are reported in the figures 6 as a stress function.

The strain rates logically increase with the applied stress. For low stresses, (500 MPa in the TiNiCu and 100 MPa in the CuZnAl), the wires length increases slowly with the cycles number. For higher stresses, the length increase rate is more important.

The attention can be brought on the TiNiCu - CuZnAl comparison about the strain evolutions: in the same stress range, the deformation of the two alloys during the thermal cycling are approximately the same, with however a small advantage for the CuZnAl. For example, under 100 Mpa, the strain rates are 1% per decade for the TiNi and only 0.7 % per decade for the CuZnAl alloy.

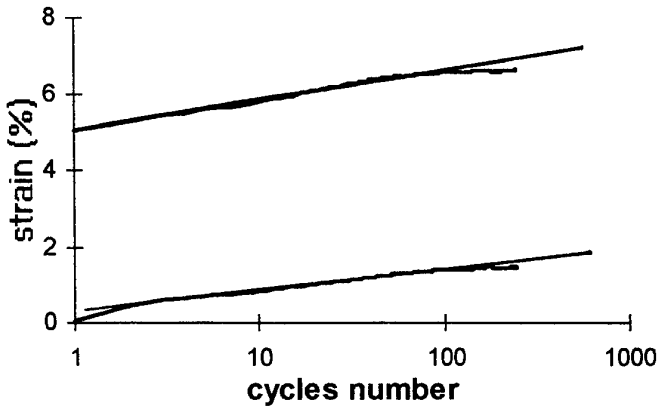


Fig 5. Strains during the cycling. Straight lines have been used to measure the strain rate (fig 6).

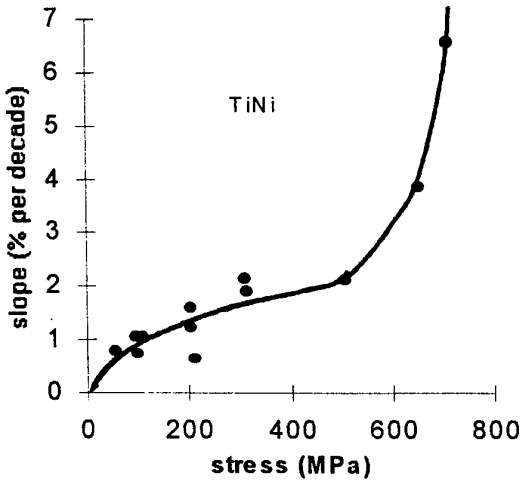


Fig 6a. Strain rates versus the applied stress in the TiNiCu case.

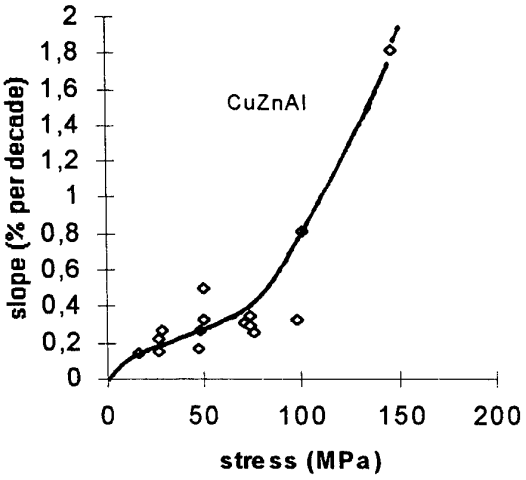


Fig 6b. Strain rates versus the applied stress in the CuZnAl case.

3.3. Applied stress versus the rupture cycle N

In figure 7, the applied stress is plotted as a function of the logarithm of the number of the cycle when the specimen breaks (N). A Wölher type curve is obtained. N varies from 1 to 1000 in a stress range of 20 to 200 MPa in the CuZnAl case, and is 10 times larger at least in the TiNiCu case. It might be noted that under 50 MPa the TiNiCu specimen failure didn't occur after more than 11 000 cycles, and so the test was stopped. From theses curves it appears that if there is a stress under which the rupture doesn't occur, this fatigue limit is low: around 50 MPa in the TiNiCu case and less than 10 MPa in the CuZnAl case. For these fatigue limit, the stress induces a SATWME of 2% in the CuZnAl and 1% in the TiNiCu : these values are low but not negligible and can be enough for many applications.

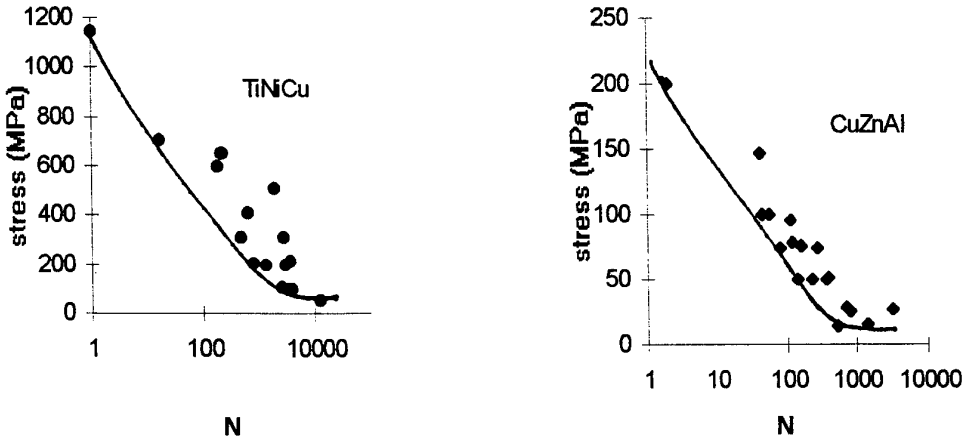


Fig 3. Wölher type curves (N failure cycles number) obtained for TiNiCu and CuZnAl wires.

5. CONCLUSION

To conclude, some interesting results are recalled about the Shape Assisted Two Way Memory Effect measured (SATWME) in two commercial alloys (TiNiCu and CuZnAl) :

-(1) the SATWME is function of the applied stress, it increases to a maximal value and then decreases, but it doesn't change a lot during the thermal cycling. The maximal SME value is about 6-7 % for the both alloys

-(2) the specimen length drift is approximately similar in both alloys. If the plasticity can be left, the strain of the alloy (in austenitic or martensitic phase) at a given cycle number increases with the applied stress at first and then remains almost constant. With regard to the thermal cycling, the drift rate also increases with the applied stress

-(3) the applied stress versus the rupture cycle number curves are typical Woëhler one, and the hypothetical fatigue limit is low.

The two important advantages of TiNiCu are that, firstly, the applied stress can be higher than in CuZnAl, and secondly, this alloy resists to the thermal cycling in a better way.

With regard to some properties, TiNiCu and CuZnAl present identical behaviour, but in two different value ranges.

In an actuator application, it is evident that TiNiCu alloy presents more interest than CuZnAl.

6. REFERENCES

1. Y. Furuya, *Proc. of ISMIMR*, pp. 313-318, Sendai, Japan, sept 1995.
2. J. Van Humbeeck, *Actuator 94*, Axon, Bremen, p.312 (1994).
3. P. Tautzenberg, *IC on martensitic transformation, Wayman CM and Perkings*, Monterey, USA, p. 1295, 1993.
4. M. Morin and M.J. Bigeon, 'Austenitic-martensitic interface damping measurement in SMA by cyclinc tensile machine', *J. of alloys and compounds*, 211/212, pp. 632-635, 1994.
5. M.J. Bigeon, M. Morin, 'Fatigue of the shape memory effect in thin wires- Comparison betxeen TiNi and CuZnAl., *ESOMAT'94*, Journal de Physique, C2-385, 1995.
6. P. Charbonnier - Thesis INSA-LYON, Lyon, France, 1992.
7. D.N. Adujudom, *Materials sciences forum* , vol 56-58, p. 565 1990.
8. S. Miyasaki, *ICOMAT 82*, Journal de Physique, tome 43, C4 , p. 255, 1982.
9. L. Contardo, G. Guenin, *Acta metall. Mater.* , vol.38, no 7, p. 1267 (1990).

Shape-memory-alloy superelastic behavior: 3D finite-element simulations

F. AURICCHIO *
Dipartimento di Ingegneria Civile
Via della Ricerca Scientifica
Università di Roma "Tor Vergata"
Roma, 00133, ITALY

R.L. TAYLOR
Department of Civil Engineering
Davis Hall
University of California at Berkeley
Berkeley, CA, 94720, USA

Abstract

Due to an unusual macroscopic behavior, the *shape-memory alloys* lend themselves to innovative applications. Recently, a 3D constitutive model able to simulate the superelastic behavior has been proposed. The implementation of such a model within a finite-element framework is used here to perform the analysis of two shape-memory-alloy structures: a beam under four-point bending and a microstructure for the treatment of hollow-organ or duct-system occlusions (stent).

1 Introduction

Shape-memory alloys (SMA) are materials which undergo a solid-solid reversible diffusionless transformation, between a crystallographically more-ordered parent phase (*austenite*) and a crystallographically less-ordered product phase (*martensite*).

As a consequence, at sufficiently high temperatures such materials show the so-called *superelastic* behavior (SE): mechanical loading-unloading cycles induce highly-nonlinear large deformations (up to 15%), without producing inelastic deformations. The stress-strain path usually presents a hysteresis loop.

Due to the superelastic behavior, shape-memory alloys lend themselves to innovative applications ranging from medical fields (for examples devices for minimally invasive surgeries) to space field (for examples devices for deployment and control of space structures) [1, 2].

A review of the available literature shows a great effort in performing experimental work and in the study of the involved micromechanics. On the other hand, there is a lack in modeling the structural behavior of SMA elements. In particular, computational aspects are not emphasized.

In the present work we review a three-dimensional (3D) model for the simulation of the superelastic behavior [3]. The implementation of this constitutive model in a finite-element scheme is used here to perform the analysis of two SMA structures: a beam under four point bending and a microstructure for the treatment of the hollow-organ or duct-system occlusions (usually known as a stent).

2 A 3D superelastic model

In the following we briefly review a 3D constitutive model, able to reproduce the shape-memory-alloy superelastic behavior. The model is developed within an internal-variable inelastic theory, well suited for the description of solid-solid phase-transformation processes, such as those occurring in shape-memory materials [3, 4]. A detailed discussion on the 3D model can be found in References [3, 5].

2.1 Control and internal variables

As control variables, we assume the stress, $\boldsymbol{\tau}$, and the temperature, T. To capture the phase transformation effects, we introduce the transformation strain $\boldsymbol{\epsilon}^{tr}$, given by: $\boldsymbol{\epsilon}^{tr} = \epsilon_L \, \xi_S \, \hat{\boldsymbol{N}}$, where ϵ_L is a scalar parameter representing the maximum deformation obtainable only by detwinning of the multiple-variant martensite, ξ_S is the martensite fraction and $\hat{\boldsymbol{N}}$ is a particular direction in the strain space. Thus, the model has one scalar internal variable, ξ_S, and one tensorial internal variable, $\hat{\boldsymbol{N}}$.

2.2 Phase transformations and activation conditions

We consider three phase transformations: (1) the conversion of austenite into single-variant martensite $[A \rightarrow S]$, (2) the conversion of single-variant martensite into austenite $[S \rightarrow A]$, (3) the reorientation of the

*Corresponding author. E-mail: auricchio@tovvx1.ccd.utovrm.it

0-8194-2165-0/96/$6.00

single-variant martensite [$S \rightarrow S$]. The first two phase transformations induce changes in the martensite fraction, while the last one induces changes in the martensite orientation (that is, on $\hat{\boldsymbol{N}}$). Accordingly, we set [1]:

$$\dot{\xi}_S = \dot{\xi}_S^{AS} + \dot{\xi}_S^{SA} \tag{1}$$

Conversion of austenite into single-variant martensite ($A \rightarrow S$). To model the pressure-dependency of some phase transformations, we introduce a Drucker-Prager-type loading function: $F^{AS}(\boldsymbol{\tau}, T) = \|\boldsymbol{t}\| + 3\alpha p - C^{AS}T$, where $\delta = \sqrt{2/3}+\alpha$, $\boldsymbol{t}$ is the deviatoric part of the stress (defined as: $\boldsymbol{t} = \boldsymbol{\tau} - \mathrm{tr}(\boldsymbol{\tau})\mathbf{1}/3$), p is the pressure, C^{AS} and α are material parameters and $\|\cdot\|$ indicates the Euclidean norm. The initial and final transformation function are expressed as:

$$F_s^{AS} = F^{AS} - \left[\sigma_s^{AS}\delta - C^{AS}T_s^{AS}\right] \quad , \quad F_f^{AS} = F^{AS} - \left[\sigma_f^{AS}\delta - C^{AS}T_f^{AS}\right] \tag{2}$$

where σ_s^{AS}, σ_f^{AS}, T_s^{AS} and T_f^{AS} are all material parameters. For the evolution of the single-variant martensite fraction we may assume either a linear or an exponential form:

$$\dot{\xi}_S^{AS} = -H^{AS}(1-\xi_S)\frac{\dot{F}^{AS}}{F_f^{AS}} \quad , \quad \dot{\xi}_S^{AS} = H^{AS}\beta^{AS}(1-\xi_S)\frac{\dot{F}^{AS}}{\left(F_f^{AS}\right)^2} \tag{3}$$

with β^{AS} a material parameter, measuring the speed of the transformation in the latter case. The scalar parameter H^{AS} embeds the conditions for the activation of the phase transformation and it is non zero and equal to one iff: $F_s^{AS} > 0$, $F_f^{AS} < 0$, $\dot{F}^{AS} > 0$.

Conversion of single-variant martensite into austenite ($S \rightarrow A$). Similarly, we introduce a Drucker-Prager-type loading function: $F^{SA}(\boldsymbol{\tau}, T) = \|\boldsymbol{t}\| + 3\alpha\, p - C^{SA}T$, where C^{SA} is a material parameter. The initial and final transformation function can be expressed as:

$$F_s^{SA} = F^{SA} - \left[\sigma_s^{SA}\delta - C^{SA}T_s^{SA}\right] \quad , \quad F_f^{SA} = F^{SA} - \left[\sigma_f^{SA}\delta - C^{SA}T_f^{SA}\right] \tag{4}$$

where σ_s^{SA}, σ_f^{SA}, T_s^{SA}, T_f^{SA} are all material parameters. For the evolution of the single-variant martensite fraction we may assume either a linear or an exponential form:

$$\dot{\xi}_S^{SA} = H^{SA}\xi_S\frac{\dot{F}^{SA}}{F_f^{SA}} \quad , \quad \dot{\xi}_S^{SA} = H^{SA}\beta^{SA}\xi_S\frac{\dot{F}^{SA}}{\left(F_f^{SA}\right)^2} \tag{5}$$

with β^{SA} a material parameter, measuring the speed of the transformation, in the latter case. The scalar parameter H^{SA} embeds the conditions for the phase transformation and it is non zero and equal to one iff: $F_s^{SA} < 0$, $F_f^{SA} > 0$, $\dot{F}^{SA} < 0$.

Single-variant martensite reorientation process ($S \rightarrow S$). To model the single-variant martensite reorientation process for non-proportional changes of stress (changes of direction or rotation), we set:

$$F^{SS} = \|\boldsymbol{t}\| + 3\alpha p - C^{SS}T \quad , \quad F_s^{SS} = F^{SS} - \left[\sigma_s^{SS}\delta - C^{SS}T_s^{SS}\right] \tag{6}$$

where C^{SS}, σ_s^{SS} and T_s^{SS} are material parameters. We assume that the reorientation process is active when: $F_s^{SS} > 0$. Setting: $\boldsymbol{N} = \partial F^{SS}/\partial\boldsymbol{\tau}$, we have that when the reorientation process is active, $\hat{\boldsymbol{N}} = \boldsymbol{N}$, otherwise $\hat{\boldsymbol{N}}$ is equal to the value attained during the last time the reorientation process was active.

2.3 Time-discrete model and finite-element implementation

As carefully addressed in References [3, 5], the described time-continuous model can be integrated using Backward Euler and return map formulas. The corresponding time-discrete model can be implemented within a finite-element scheme either in a small-deformation or in a large-deformation framework.

[1] By convention, the superscripts refer to specific evolution processes; accordingly, the superscript AS refers to the conversion of austenite into single-variant martensite, while the superscript SA refers to the conversion of single-variant martensite into austenite.

3 Finite-element simulations

We now want to assess the ability to perform simulations for typical SMA-based devices exploiting the superelastic behavior through the use of the 3D model previously described. The experimental data and the specimen specifications were provided by Dr. A.R. Pelton and Dr. T.W. Duerig of NDC, Inc. [2]. The material adopted is a standard binary Ni-Ti alloy [6].

3.1 Material-parameter characterization

Two uniaxial tension tests performed on a circular wire of diameter $D = 1.49$ mm are used to identify the material parameters [3, 5]. From the inspection of the experimental stress-strain curves the following material parameters are chosen:

$$E = 60000 \text{ MPa} \quad , \quad T_s^{AS} = T_f^{AS} = 0 \text{ °C} \quad , \quad C^{AS} = 0 \text{ MPa/°C}$$
$$\nu = 0.3 \quad , \quad \tilde{\epsilon}_L = 7.5\% \quad , \quad T_s^{SA} = T_f^{SA} = 0 \text{ °C} \quad , \quad C^{SA} = 0 \text{ MPa/°C}$$

Model	σ_s^{AS}	σ_f^{AS}	β^{AS}	σ_s^{SA}	σ_f^{SA}	β^{SA}
Expon.	520	750	250	550	200	20
Linear	520	600	–	300	200	–

All the quantities in the last table are in MPa. The stress-strain responses simulated using the exponential and the linear model are reported respectively with dash-dot and dash-dash lines in Figure 1; a good match with the experimental data can be observed, especially for the exponential model. From consideration relative to a Ni-Ti-10%Cu alloy [4], the parameter α measuring the different material response between tension and compression is set equal to 0.15.

3.2 Four-point bending test

A four-point bending test was performed on a wire of circular cross section with diameter $D = 1.49$ mm. The test procedure is described in Reference [6]. The setting of the test is idealized in Figure 2-A. The beam is simply supported on rollers, sitting at a fixed distance $L = 20$ mm. The experimental output parameters are the load F and the bottom fiber deflection of the beam middle-span section.

Due to symmetry conditions only half of the half-span beam needs to be studied. For the numerical simulations we use the mesh presented in Figure 2-B. In Figure 3 the plotted load-deflection curves are computed using the exponential and the linear model for the cases $\alpha = 0$ and $\alpha = 0.15$ as well as for the small- and the large-deformation regimes. The experimental load-deflection curve is also reported. From the inspection of the figures it is possible to conclude that:

- For $\alpha = 0$ (the material behaves similarly in tension and compression), the predicted load-deflection curves are lower than the experimental one.
- For $\alpha = 0.15$ (the material behaves differently in tension and compression), the predicted load-deflection curves match quite well the experimental data. However, the part of the curve corresponding to the final unloading portion and the size of the hysteresis loop differ from those found experimentally.
- The large-deformation analysis and the small-deformation analysis give comparable results.
- The exponential and the linear models predict similar results, except in the part of the curve corresponding to the initial unloading portion.

3.3 Analysis of a stent

Stent is the technical word indicating self-expanding micro-structures, which are currently investigated for the treatment of hollow-organ or duct-system occlusions.

An example of a stent with a diamond pattern is given in Figure 4-A. This structural typology can be obtained from a SMA tube using a laser to cut out the diamond patterns. The diamond pattern geometry allows one to easily stretch the stent, which can then be safely and atraumatically inserted due to its small profile. After being released from the delivery system, the stent self-expands to its original diameter and exerts a constant, gentle, radial force on the vessel wall. The radius of the stretched-out stent can be as small as half of the original unstretched radius [7].

[2] Nitinol Device & Components, Inc., 48501 Warm Spring Blvd., Fremont, 94539 CA, USA

The horizontal projection of a diamond pattern spanning an angle γ is presented in Figure 4-B. Due to the symmetry conditions only one quarter of a diamond pattern need to be modeled. The boundary conditions are set to respect all the restrictions imposed by the symmetries and still allow radial displacements.

In the following we focus on a stent with $\gamma = 40^o$, $R_{ext} = 2.25$ mm, $R_{int} = 2.00$ mm; other geometric dimensions are indicated in millimeters in Figure 5-A. These values are estimated from a photograph and may differ from the ones used in actual design. The finite-element mesh is presented in Figure 5-B.

We again use the material parameters estimated through the experimental uniaxial tests. The parameter α is always set equal to 0.15.

We consider two load histories (the first up to 20 N, the second up to 50 N). In Figure 6 we plot respectively the axial load versus the axial displacement and the axial load versus the radial displacement, computed using the linear model within a large-deformation regime.

It is very interesting to observe the unexpected radial displacement pattern, which indicates that, due to the particular geometry under investigation, the stent is unable to undergo radial displacements larger than 0.9 mm (i.e., less than 50% of the initial radius). Thus, from a practical point of view, the stent investigated is not optimal. This highlights the need for a better design for the particular geometry considered here, as well as the value of the proposed method in assessing proposed configurations.

4 Closure

The present work assesses the ability of a proposed computation tool to be used during the design of SMA-based devices.

To assess the viability of the proposed approach we simulate the response of some simple SMA typical structures (uniaxial test and four-point bending test) for which experimental data are available. From the simulations it is possible to evince that the proposed framework:

- produces results which are in good agreement with the experimental data,
- can be used to study devices with different geometry and/or material properties,
- is able to give valuable local information such as displacement and/or stress-strain histories.

The match between the experimental and the predicted data are good, especially considering that the parameters used in the constitutive model have been extrapolated on the basis of only two tension tests.

To validate the previous points, we also simulate the behavior of a SMA stent, which today is an application with possibly very high impact in different medical fields. For the particular geometry considered we are able to investigate the structural response and to find some limiting conditions in terms of maximum reduction of the stent diameter. These limiting conditions can be extremely valuable during a design process.

The overall discussion leads us to conclude that the proposed approach is a plausible initial development of an effective computational tool for the simulation of SMA-based devices.

References

[1] T.W. Duerig, K.N. Melton, D. Stökel, and C.M. Wayman, editors. *Engineering aspects of shape memory alloys.* Butterworth-Heinemann, 1990.

[2] A.R. Pelton, D. Hodgson, and T. Duerig, editors. *Proceedings of the First International Conference on Shape Memory and Superelastic Technologies*, 1994.

[3] F. Auricchio. *Shape memory alloys: applications, micromechanics, macromodeling and numerical simulations.* PhD thesis, University of California at Berkeley, 1995.

[4] J. Lubliner and F. Auricchio. Generalized plasticity and shape memory alloys. *International Journal Solids and Structures*, 1995. to be published.

[5] F. Auricchio, R.L. Taylor, and J. Lubliner. Shape-memory alloys: macromodelling and numerical simulations of the superelastic behavior. 1996. Submitted for publication.

[6] A. Wick. The bending behavior of superelastic NiTi. Master's thesis, Universität Karlsruhe (TH), Institut für Werkstoffkunde I, 1994.

[7] A. Melzer and D. Stökel. Performance improvement of surgical instrumentation through the use of Ni-Ti materials. In A.R. Pelton, D. Hodgson, and T. Duerig, editors, *Proceedings of the First International Conference on Shape Memory and Superelastic Technologies*, pages 401–409, 1994.

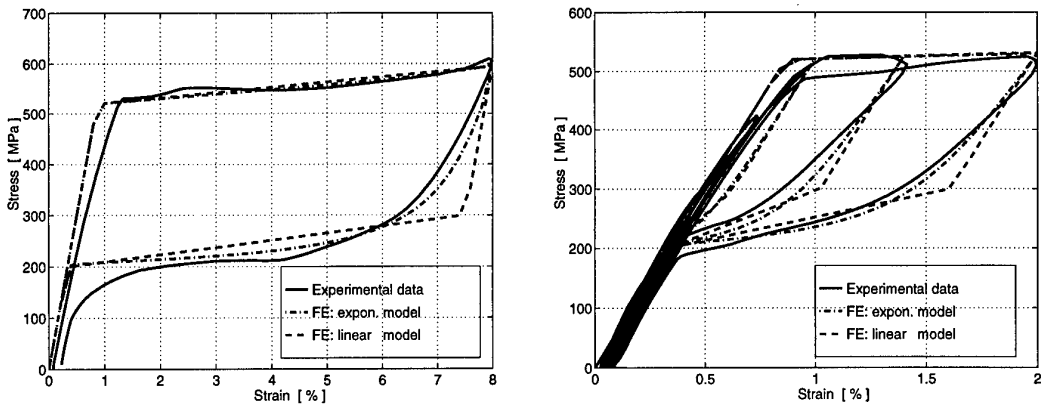


Figure 1: material-parameter characterization. Uniaxial tension stress-strain response for a Ni-Ti alloy: experimental data and numerical simulations using the exponential and the linear model.

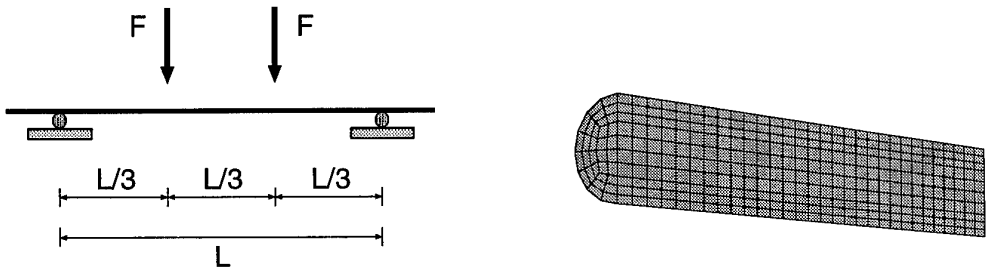


Figure 2: four-point bending test. Test problem and finite-element mesh.

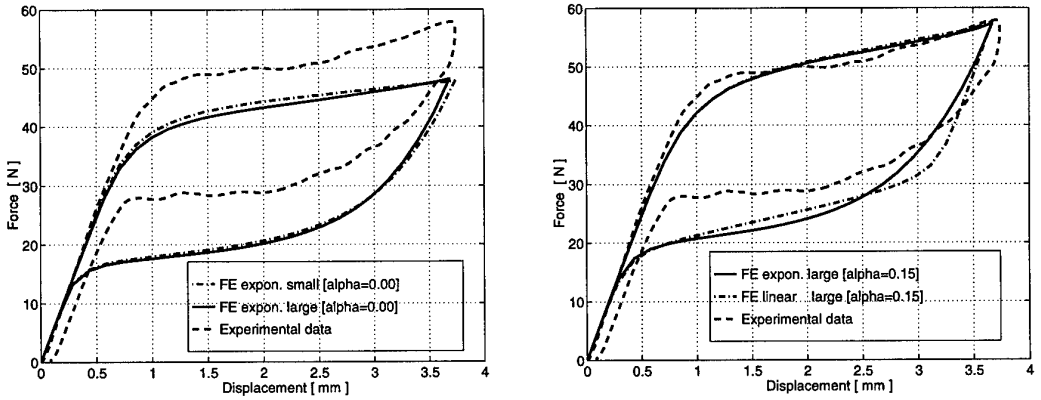


Figure 3: four-point bending test. Load-deflection curves: experimental data and numerical solution using the exponential and the linear model ($\alpha = 0$ and $\alpha = 0.15$).

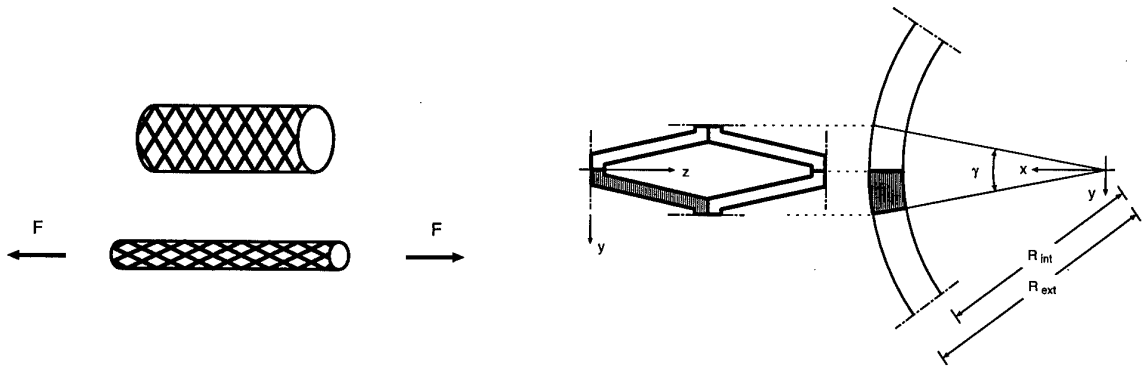


Figure 4: stent. An example of stent with a diamond pattern and horizontal projection of the diamond pattern spanning an angle α.

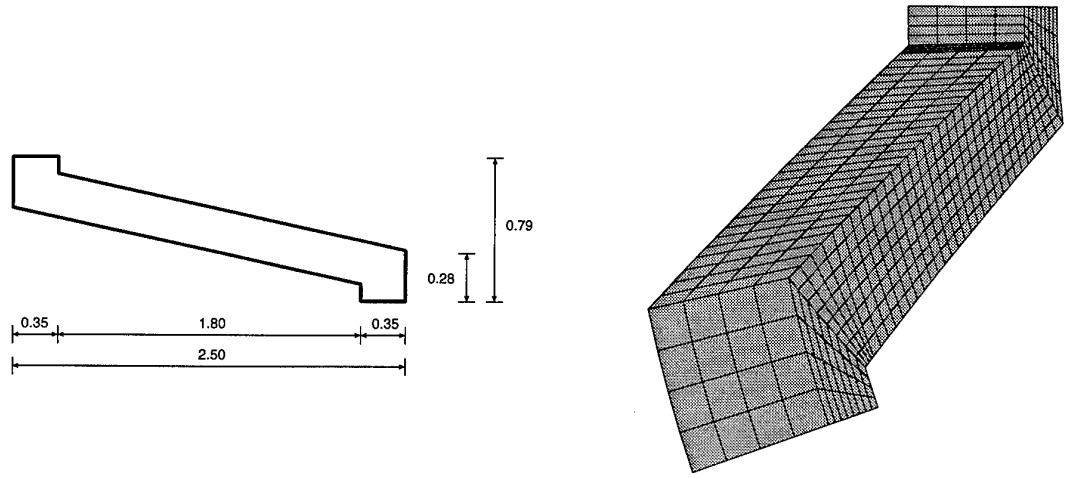


Figure 5: stent. Stent plant and finite-element mesh.

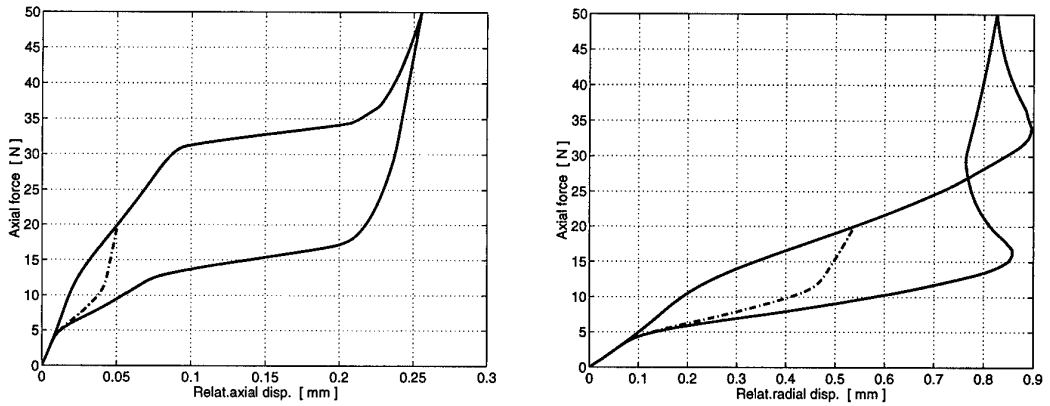


Figure 6: stent. Axial load versus relative axial displacement and versus radial relative displacement. Numerical solutions for two load levels using the linear model in a large-deformation regime ($\alpha = 0.15$).

About the use of shape memory alloys in actuators

G. Guénin and Ph. Gaudez

Institut National des Sciences Appliquées
G.E.M.P.P.M., Bât. 502
69621 Villeurbanne (France)

ABSTRACT

Among the potential materials for embedded actuators in composite smart structures, shape memory alloys are good candidates in many applications. Indeed they are abble to produce large deformations and stresses. However, due to the complex and non linear behaviour of these alloys, their use is often made by empirical way. The present paper gives some general rules for the use of shape memory alloys in actuators.

1. THE BASIC BEHAVIOUR OF SHAPE MEMORY ALLOYS

The thermomechanical behaviour of Shape Memory Alloys (S.M.A.) which is used in actuators is the so called Stress Assisted Two Way Memory Effect (S.A.T.W.M.E.). This effect occurs for every S.M.A. but only Cu-based and Ti-Ni based alloys are presently commercially available. For details concerning the properties and thermomechanical behaviour of these alloys see for example ref. (1) and (2). Basically this effect is represented on figure 1 for a constant stress : there is a reversible exchange between a high temperature strain and a low temperature strain.

Emphasis must be made on the following points :

- Only the high temperature strain (shape) is well fixed, it corresponds to the elastic strain of the S.M.A. sample in the high temperature phase. (often called austenite)
- The low temperature strain (shape) is due to the preferential orientation of martensite variants by the applied stress. It can be pretty high up to 4-6% in traction. This strain depends on many parameters : the applied stress, the microstructure and texture, the grain size, etc ...
- The hysteresis A_f-M_s or A_s- M_f is always present (5 to 30 °C depending on the alloy)
- The speading M_s-M_f or A_f-A_s is always present (5 to 30°C)
- The characteristic temperatures M_s,M_f, A_s, A_f are shifted with the stress amplitude (0.5 °C/MPa for Cu-based alloys, about 0.1 °C/MPa for Ti-Ni alloys)
- The nature of the stresses and strains is not limited : it can be either pure tension or compression, pure shear or a complex combination of these simple sollicitations.
- For each alloy, maximum local stresses and strains can fixed to allow a correct reversible and non destructive use. These values must be lowered when the number of required thermomechanical cycles is increased (see table 1).
- The pertinent variable which drives the stress-strain behaviour of the S.M.A. is the temperature : heat must be provided or released to warm or cool the alloy and to drive the reverse and direct martensitic transformation (enthalpy of transformation). These transfers limit the time response of the movement in spite of the fact that the transformation itself occurs at sound velocity. In best cases this time response is of the order of a tenth of second.

2. THE S.M.A. ABBLE TO PRODUCE MECHANICAL WORK (3)

An activator is a device which provides a mechanical work by transformation of an other kind of energy. In the present case, this last energy is calorific and the associated parameter is the temperature.

Let us for example take a shape memory wire (figure 2) in the high temperature state and apply to this wire a traction force f_m just sufficient to elongate it during cooling in martensite state from y'_e to y_o . The work absorbed by the wire is given by f_m $(y_o-y'_e)$. A thrust is present at y_o and therefore a force F can be applied without changing the elongation. The mechanical work which can be given by heating when the force F is kept constant is given by F. (y_o-y_e) where y_e is the elastic elongation of the wire in the austenitic state under the force F (figure 3a). The thermomechanical cycle can be shut by the decrease of the applied force from F to f_m. The net mechanical work provided by the wire during the cycle is represented by the dark hached part on figure 3b. If F and y_o are chosen to be

0-8194-2165-0/96/$6.00

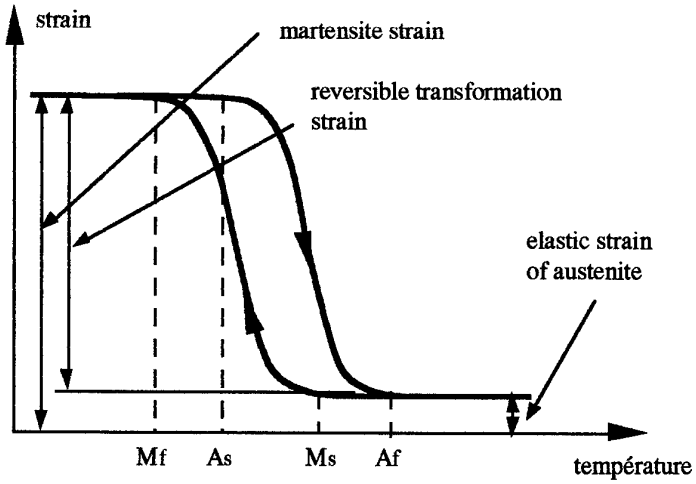


figure 1 : The strain-temperature behaviour of a shape memory sample submitted to a constant stress : this is the Stress Assisted Two Way Memory Effect

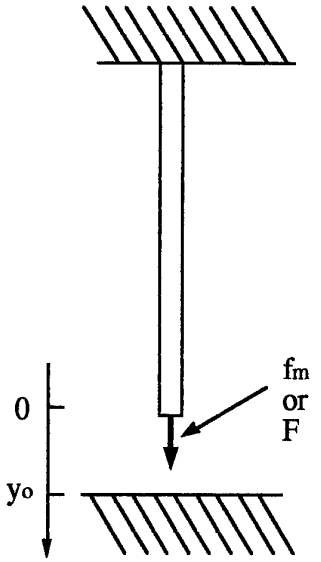


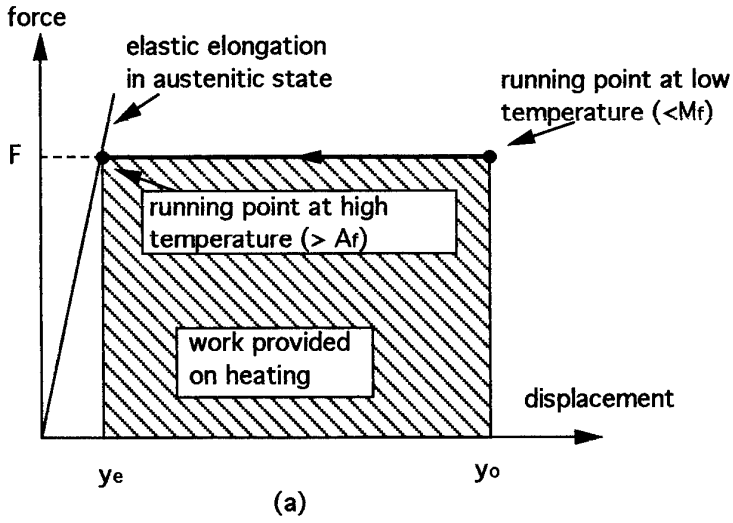
figure 2 : shape memory wire submitted to traction and which elongation is limitted by a thrust

	Ti-Ni		Cu-Al-Ni	
number of cycles	strain	stress	strain	stress
1	8%	400 MPa	5%	200 MPa
10^2	4%	250 MPa	2.5%	100MPa
10^4	2%	140 MPa	1.5%	70 MPa
10^5	1%	100 MPa	0.8%	40 MPa

Table 1 - Indicative values of maximum strains and stresses as a function of number of cycles for Ti-Ni and Cu-Al-Ni shape memory alloys

solicitation mode	Efficiency factor	Ajustable geometrical parameters
Traction, compression	1	Length L, diameter d
Torsion	1/2	L, d
Helical spring	1/2.8 to 1/2.3	wire diameter d, rolling diameter D, number of turns n, thread of the helix
Cantilever	1/9	length L, width b, thickness h
Flexion 3 points	1/9	L, b, h

Table 2 - Efficiency factors and adjustable parameters for different solicitation modes



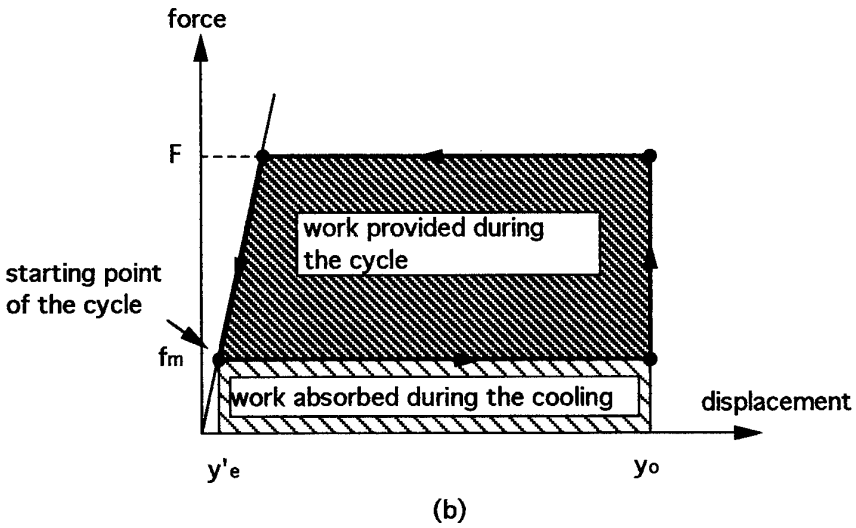


figure 3 : a) work provided on heating by the wire
b) work absorbed during the cooling and
work provided during the cycle

the maximum values that can be used with the given alloy (F_M and y_M), this area defines the maximum work which can be produced by the activator.

3. THE S.M.A. IN AN ACTUATOR

Let us suppose now that the wire is associated to a drawback element which provides a constant tensile force F which amplitude is located between f_m and F_M. The resulting device is an actuator which can provide a mechanical work as well on heating as on cooling as seen on figure 4a. When no additinal force is applied, the representative point of the actuator moves reversibly on an horizontal defined by F and limited by y_M at low temperature and the elastic elongation of austenite at high temperature. On heating the available work which can be provided to exterior by the actuator is shown by the superior hached part on figure 4a : an additional tensile force of (F_M -F) can be applied. On cooling the available work which can be provided to exterior by the actuator is shown by the lower hached part on figure 4a : an additionnal compressive force of (F- f_m) can be applied.

Actually the actuator will not use necessarily all the available work : the figure 4b shows the running point during a thermomechanical cycle. The hached parts correspond the the works really provided on heating and on cooling. The representative point must be included in the hached parts for a good behaviour of the actuator.

It must be emphasized that the whole mechanical work provided by the actuator comes from the S.M.A. wire : during heating with constant force F the S.M.A. gives mechanical energy to the drawback element which store it. It is this energy which is available on cooling.

The drawback force is often produced by a drawback spring : the force therefore depends on the deformation and the situation can be represented by the figure 5.

4. THE PROVIDED WORK DEPENDING ON SOLICITATION MODE

In the previous approach, the work provided by the wire can be reported to its volume and some efficiency can be defined by the ration of the available mechanical energy on the wire volume (or weight). Depending on the solicitation mode, the efficiency can be different as seen now :

4.1 Traction (or compression)

The stresses an strains are homogeneous in all the sample of section S and length L submitted to the force F_M. The maximum work given on heating by the shape memory wire is given by :

$$W_T = F_M \cdot (y_M - y_e) = \sigma_M (\varepsilon_M - \varepsilon_e).S.L = \sigma_M \cdot \varepsilon_t \cdot S \cdot L = \sigma_M \cdot \varepsilon_t \cdot V$$

with V volume of the sample and ε_t the transformation strain.

The efficiency is given by $W_T/V = \sigma_M \cdot \varepsilon_t$

This is the ratio which will be considered for other solicitation modes.

4.2 Torsion of a cylindrical wire

For elastic conditions, the stress and the strain changes linearly with the radius from 0 on the axis to a maximum value on the external fiber. The rough aproximation done is that this remains true also for the shape memory strain.

The work is therefore given by :

$$W_T = \tau_M \cdot \gamma_t \cdot V/2$$

where τ_M is the maximum shear stress on the external fiber and γ_t is the shear strain due to the transformation on the external fiber.

It can be demonstrated that $\tau_M \cdot \gamma_t = \sigma_M \cdot \varepsilon_t$ for a given alloy . The efficiency of the wire in torsion mode is therefore equal $\sigma_M \cdot \varepsilon_t / 2$; that is to say half the value of the one in traction. This is easily understood by the fact that in the case of the torsion, only the external part of the sample "works" on its maximum, the part close to the

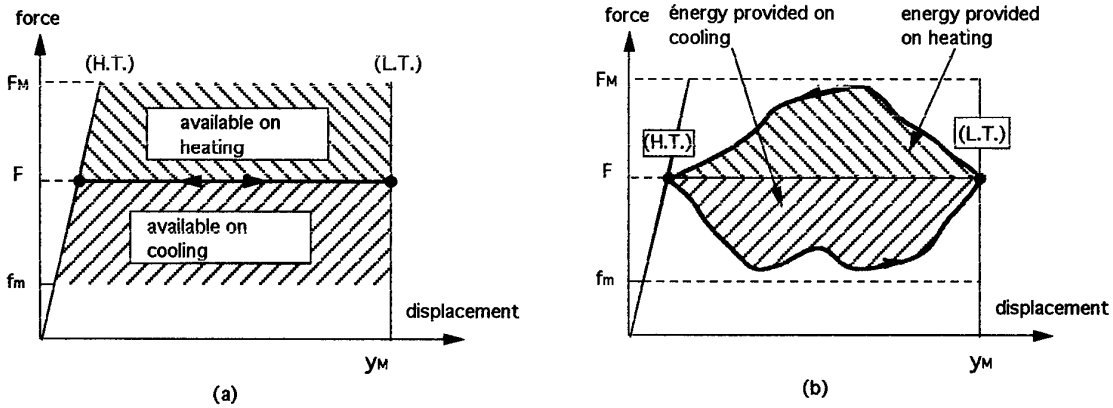


figure 4 : a) available energy on cooling and heating for a drawback force F
b) example of working with drawback force F

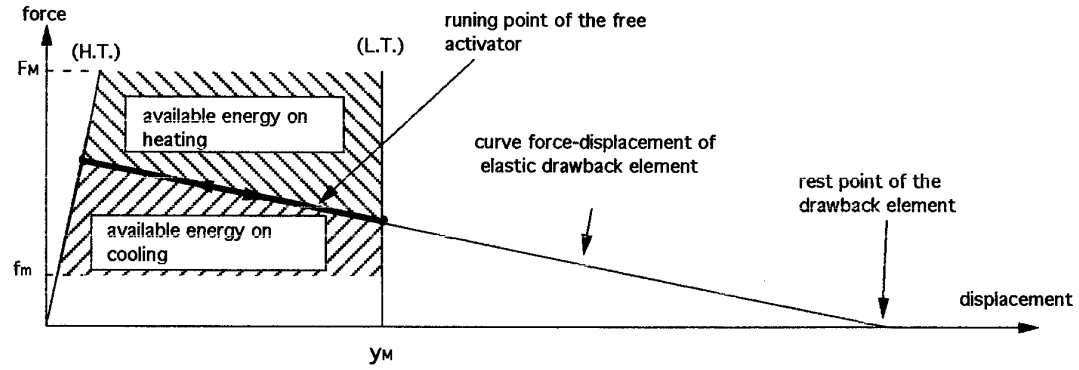


figure 5 : Working scheme of an actuator contituted by the association of a shape memory element and an elastic drawback element

sample axis does not work. In the case of the traction all the elements of the sample work at maximum. Therefore an efficiency factor of 1 / 2 can be defined in relation to the traction.

4.3 Flexion of a cantilever bar

As in the previous case, it will be supposed that the shape of the bar is the same in elastic regime or during the transformation. In these conditions it can be shown that : $W_T = \sigma_M \cdot \varepsilon_t . V/9$

In this expression σ_M and ε_t represent the maximum values of the stress and the strain close to the inbedded part of the bar. It can be seen that the efficiency factor falls to 1 / 9 due to the heterogeneity of the provided work not only on the thickness of the bar but also on its length.

4.4 Other modes

Other solicitation modes have been considered but are not detailed there. The table 2 gives the efficiency factor corresponding to the different modes.

4.5 Comparison of different solicitation modes

The previous results let understand that the traction is the best mode to be used. However this one gives few latitude of sample sizes : the force only depends on the section S and the displacement only depends on the length L (σ_M and ε_t are fixed for a given alloy). For example, a Ti-Ni cylinder with L = 20 mm and diameter 10 mm, which weight of 10 g is able to raise 1000 kg on 1 mm (σ_M = 130MPa, ε_t = 5%). For the torsion the situation is similar : the given torque only depends on the diameter d and the rotation angle of L/d.

The consequence is that a given work W can only be done with limited couples force-displacement. Indeed if the same work as the upper one is needed but with a displacement of 40 mm, the only solution is to use a wire of 800 mm which can give some space problems. The solution is to use other solicitation modes, may be less efficient, but more flexible to define sizes (more degrees of freedom).

For example, an helical spring has 4 degrees of freedom : wire diameter, rolling diameter, thread of the helix, number of turns. The table 2 specifies the adjustable parameters.

5. CONCLUSION

A shape memory element can only* give a mechanical work on heating. However the association of a shape memory element with a drawback element gives an activator which is able to provide a mechanical work on cooling and on heating as well. The work on cooling is produced by the drawback element which has stored elastic energy provided by the shape memory element on previous heating. The table 2 gives the efficiencies of the different solicitation modes but this classification must be modulated in function of use constrains. These use constrains will be more easily solved if many geometrical parameters are involved. Among these use constrains the most important are the available space, the heating and cooling mode, the elaboration mode, the nature of the restoring force element.

*Recent results show that, in the case of copper based alloys some work can be done on cooling for well trained samples (two way memory effect)

6. REFERENCES

1. G. Guénin, "Martensitic transformation and thermomechanical properties" in "Diffusionless phase transitions in oxydes and some reconstructive and martensitic phase transitions" pp.339-392, Trans Tech Publications, ed. C. Boulesteix, Switzerland, 1995.

2. "Technologie des alliages à mémoire de forme", Hermès, ed.E. Patoor and M. Berveiller, Paris, 1994

3. Ph. Gaudez, "Etude et réalisation de dispositifs actionneurs utilisant un élément en alliage à mémoire de forme", Thesis, I.N.S.A. Lyon, 1993.

Stress-Optimised Shape Memory Microactuator

K. D. Skrobanek*, M. Kohl* and S. Miyazaki**
* Forschungszentrum Karlsruhe, IMT, Postfach 3640, 76021 Karlsruhe, Germany
**University of Tsukuba, Institute of Materials Science, Tsukuba, Ibaraki305, Japan

Abstract

A shape memory membrane actuator has been developed, which consists of stress-optimised microfabricated NiTi beam-cantilever devices of 100 μm thickness. For stress-optimisation, the lateral widths of the beams have been designed for homogeneous stress distributions without local stress maxima, allowing a maximum use of active material for bending actuation. As a result, higher work outputs for a given stress level and smaller hystereses are obtained compared to non-optimised actuators with parallel beam-cantilever devices. Thus, improved hysteresis control is possible and better lifetime characteristics are expected. For a strain limit of 2 % the achieved work output is about 24 μNm.

1. Introduction

In microsystems technology the use of Shape Memory Alloys (SMA) for actuator applications is very promising. SMA microdevices provide large displacements and high forces at the same time and can be driven electrically. In particular, the relationship between electrical resistance and displacement may be used for positioning by feedback control [1] and thus SMA microdevices allow actuation as well as sensing functions. Consequently, compact smart SMA devices can be realised, which is an important advantage for the use in microsystems technology. Recent actuator developments concentrated on the integration of thin SMA wires [2,3], or on the fabrication of thin SMA films [4-10], which open up the opportunity for the realisation of integrated actuator systems. Recent developments in this field resulted already in a microvalve product. [11]

The limited height of the sputter deposited thin films of about 20 μm causes restrictions of the available work outputs. Therefore, we started to investigate the realisation of actuator devices based on micromachined SMA sheets with thicknesses in the range of 50-150μm. [8,12] For this purpose, the technologies of laser cutting and electrolytic photoetching have been optimised to manufacture SMA microdevices with lateral dimensions of about 100μm, which allow work outputs at least a factor of 10 higher than thin film actuators of comparable lateral size.

Smart materials need a good stability in lifetime characteristics. This requires a constant stress-strain dependence over a high number of actuation cycles, which is only maintained for SMA devices at low enough stress and strain. [13] On the other hand, high work outputs of SMA devices generally require high stress and strain values. Both contradictory requirements can be taken into account in SMA actuator designs, which reveal homogeneous stress distributions for a given load pattern.

In the present paper, we report on the development of a membrane microactuator driven by microfabricated NiTi devices. For actuation of a polyimide membrane, a stress optimised design of a NiTi device has been developed, which reveals a homogeneous stress distribution and thus allows a maximum use of active material for actuation. Such assemblies may be used e.g. for fluidic applications such as microvalves or microflow regulation systems. In order to demonstrate the advantage of stress optimisation, the mechanical and electrical properties of the actuators are compared with corresponding properties of non-optimised actuators.

2. Physical Properties of the Shape Memory Alloy

The active devices have been fabricated of cold-rolled sheets of an equiatomic NiTi alloy, which have been heat-treated in vacuum at 530°C for 10 minutes to adjust the one-way SMA behaviour. For the characterisation of the design-dependent mechanical and electrical properties, double-beam test devices have been developed and fabricated with a width and height of 100μm and a length of 1200μm. Their mechanical properties have been determined by load-dependent beam-bending experiments using microweights, which have been demonstrated to be a suitable characterisation method for small and sensitive microdevices [8]. The experiments have been performed in quasi-static thermal equilibrium conditions by cycling the temperature between room temperature (23°C) and 95°C for a constant load.

0-8194-2165-0/96/$6.00

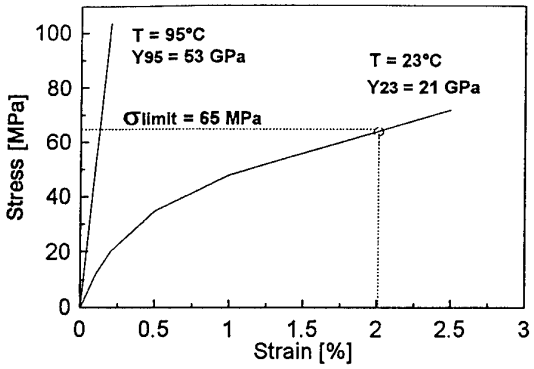


Figure 1: Stress-strain characteristics determined at 23°C and 95°C by FEM simulation of beam-bending experiments. Y_{95} and Y_{23} denote the corresponding Young's Moduli.

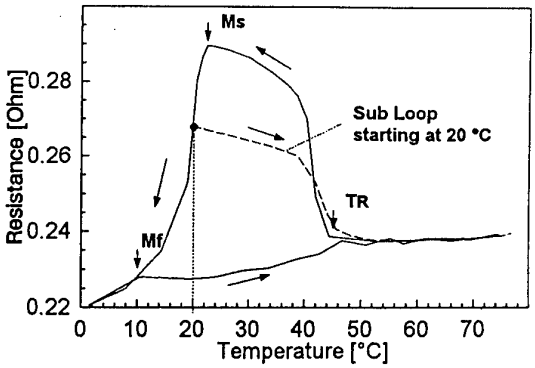


Figure 2: Resistance temperature characteristics determined by the four-point method. The transformation temperatures Ms, Mf and TR are indicated.

By finite element (FEM) simulations of the experimental results, the corresponding stress-strain characteristics have been determined, which are shown in Fig. 1. The linear stress-strain dependence at 95°C is due to the elastic properties of the high-temperature austenitic phase. The corresponding Young's modulus is 53 GPa. At 23°C, large deformations are observed, which are a characteristic feature of martensitic transformations. Such deformations of NiTi devices can be reproduced by cyclic loading and unloading in a reversible manner for a large number of actuation cycles as long as the maximum strain does not exceed about 2% [14]. We therefore design the NiTi devices below a limit of 2%, which corresponds to a stress limit of 65 MPa as determined from Fig. 1.

The electrical resistance of the double-beam devices has been determined as a function of temperature by the four-point method. Fig. 2 shows for zero external load the complete loop of the temperature resistance characteristics between 0°C and 80°C, and a sub loop started at 20°C after cooling down from 80°C. The resistance characteristics reveal the typical features also observed in bulk materials [15,16]. In particular, they allow the determination of phase transformation temperatures, like the rhombohedral transformation temperature (TR) at the increase of the resistance or the martensite start temperature (Ms) at the maximum of the resistance, in the cooling loop. Below the martensite finish temperature (Mf) the cooling and the heating loop coincide. From these measurements and differential scanning calorimetry measurements, we find Ms=23°C, Mf=10°C and TR=44°C. The austenitic transformation temperatures are As=54°C and Af=66°C. It follows from Fig. 2, that at room temperature the phase transformation is incomplete for zero external load.

3. Design and Fabrication of the Membrane Microactuator

The concept of the membrane microactuator is illustrated in Fig. 3. The actuator consists of a micromachined PMMA (**Polymethylmetacrylat**) substrate, a polyimide membrane and the NiTi microdevice, which controls the deflection of the membrane caused by external pressure. Fig. 4 shows one segment of the microactuator. The membrane radius r has been set to 2mm. The height *h* of the different NiTi microdevices is designed for 100μm

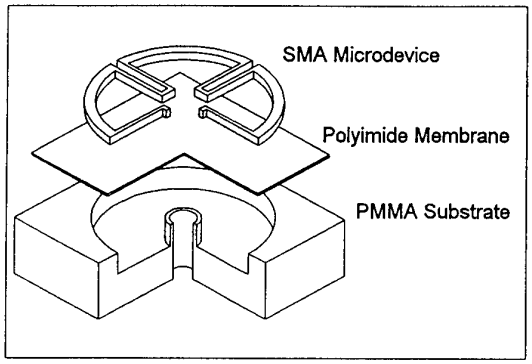


Figure 3: Design concept of the shape memory membrane microactuator.

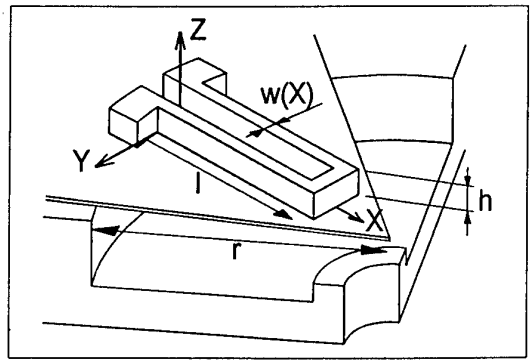


Figure 4: One segment of the actuator. The length, width, height and radius of the actuator is denoted by *l*, *w(x)*, *h* and *r* respectively.

and the length l for 1.5mm. The width of the beam $w(x)$ is kept as a variable dimension, which is optimised according to the relevant load pattern. Since the microdevice in Fig. 4 is deflected by the external pressure below the polyimide membrane, the load pattern in one segment consists of two main contributions. The first is a constant load on the bottom of the double beam, and the second is a constant area load on the free standing area of the membrane. The first contribution can be calculated analytically by

$$q(x) = q_0 \cdot \left(1 - \frac{x}{r}\right) , \tag{1}$$

where qo denotes the line load $qo=(-p\ 2\pi r)/n$, n the number of segments per actuator, and p the external pressure. The constant area load on the free standing area of the membrane may be approximated by a single point load at the beam end x=l as

$$F = -p \cdot \frac{(r-l)^2 \cdot \pi}{n} . \tag{2}$$

The bending-moment can be expressed by the sum of the moments of these two terms:

$$M_y(x) = -\int_0^l q(x) \cdot x \ dx \ - \ F \cdot (l - x) , \tag{3}$$

The stress along the surface $\pm\sigma_s(x)$ on the top and bottom of the SMA microdevice is given by the bending-moment $M_y(x)$, the moment of inertia of the rectangular cross-section $I_y(x)$ and the distance between the surface and the neutral fiber h/2 :

$$\pm\sigma_s(x) = \frac{M_y(x)}{2 \cdot I_y(x)} \cdot \frac{h}{2} \quad . \tag{4}$$

where $I_y(x) = (w(x)\ h^3)/12$ for rectangular cross-sections. For bending actuation, stress-optimised designs should reveal a constant stress profile along the surface, σ_{limit}, which is determined for the used NiTi alloy by a strain limit of 2% in order to guarantee a large number of actuation cycles. From this condition, equation (4) allows the determination of an analytical expression for the corresponding width profile $w(x)$ of the rectangular double beams:

$$w(x) = \frac{3 \cdot M_y(x)}{\sigma_{limit} \cdot h^2} \tag{5}$$

In order to keep the heating current reasonably low, the lateral width of the devices has been designed with a maximum width of 500µm. The minimum width has been designed to 100µm. These values and the given membrane radius of 2mm lead to a design with eight equal stress optimised NiTi double-beams, which is shown in Fig. 5. In order to investigate the influence of stress optimisation we have also designed and realised a device with eight non-optimised parallel double-beams of 100µm width, which is shown in Fig. 6. This has been assembled to a second type of membrane microactuator, which has been used as a reference.

For actuator fabrication, a PMMA substrate has been microstructured by mechanical micromachining to establish a pressure chamber with fluidic connections, shown in Fig. 3. The membrane has been assembled by membrane transfer from a silicon wafer coated by polyimide of 3µm thickness. Finally the NiTi microdevice, micromachined by laser cutting, has been interconnected to the membrane by adhesive bonding. The electrical contacts for resistive heating of the NiTi microdevice have been made by wedge-wedge bonding.

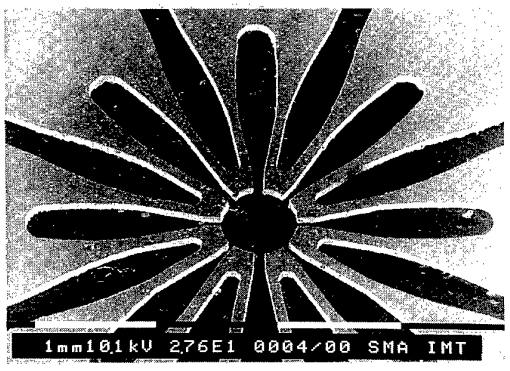


Figure 5: NiTi-microdevice with optimised double-beams.

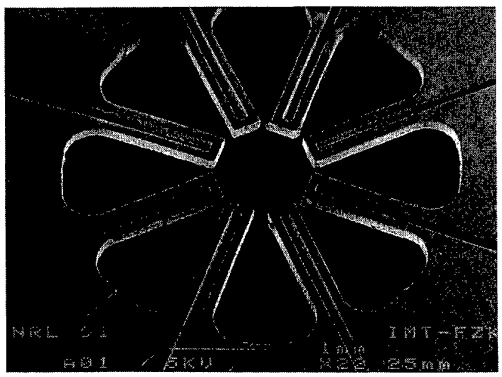


Figure 6: NiTi-microdevice with parallel double-beams, which is used in a reference actuator.

4. Results and Discussion

Figures 7 and 8 show the pressure dependence of the maximum displacement in the center of the actuator for the stress-optimised and the reference actuator, respectively. The measurements have been performed by cycling the device temperature between room temperature and 95°C using resistive heating currents.

In the high temperature regime, linear relationships between pressure and displacement are observed, which are consistent with the elastic mechanical response in the austenitic phase. The displacement offsets at zero pressure of about 25 μm result from the different thermal expansion coefficients of the NiTi device and the polyimide membrane of about 10 and 60 ppm/K, respectively. After subtraction of this thermal influence from the displacement, the experimental results agree with analytical calculations based on elastic beam-bending theory, which neglect the influence of the membrane. We therefore conclude, that the membrane has no other influence on the mechanical behavior of the membrane actuator at high temperatures and small displacements. Even though the displacements observed for both designs at 95°C are quite similar, the maximum stress values differ considerably. In the reference design, the regions of maximum stress and strain only occur close to x=0. Calculations based on our analytical model reveal for 1000 hPa already maximum stress values of 350 MPa. The stress-optimised devices are designed for homogenous stress and strain distributions along the device surfaces and therefore reveal for 1000 hPa only maximum stress values of 65 MPa, which corresponds to a strain of 2 %.

At room temperature, the situation is more complex, since the NiTi material has only partly transformed to martensite and the influence of the polyimide membrane can no longer be neglected. For small external pressures, the displacement-pressure dependence shows a slightly superlinear increase due to the dominant influence of the NiTi microdevices, which already display a large deformation behavior. Above about 1000 hPa, the stress induced by the polyimide membrane on the NiTi beams becomes increasingly important. Therefore, the pressure-displacement dependence becomes more and more sub-linear. Since the interconnection between the membrane and the NiTi devices is fairly stiff, local stress maxima occur close to the interconnection regions, which finally lead to a destruction of the membrane for pressure values higher than about 3300 hPa. Due to the smaller widths of the parallel NiTi beams of the reference actuator compared to the average widths of the stress-optimised actuator, a lower stiffness and thus larger displacements are observed in Fig. 8 compared to Fig. 7. For a given external pressure of 1000 hPa, the displacements are determined to 80 and 95 μm for the optimised and the reference actuator, respectively. Such displacements are very interesting for microactuator applications. In particular, for a strain limit of 2 %, a high work output of about 24 μNm is obtained.

Figures 9 and 10 show resistive heating controlled cycles of the electrical resistance and maximum displacements in the center of the actuators for fixed external pressures. The shape of the resistance curves displays the typical features of the transformation temperature regime between the austenitic phase and the onset of the martensitic phase as also observed for the double-beam test device in Fig. 2. Since the device temperature does not fall below 23°C, only an incomplete transformation occurs causing sub-loops of the resistance. For increasing pressure, a slight shift of the resistance minimum towards higher electrical power values and a slight increase of the hystereses are present. These effects are due to pressure induced local changes of the maximum stresses in the devices, which affect the corresponding transformation temperatures. However, since the electrical resistance displays the average transformation behavior of the whole device, only small changes of the sub-loops are observed.

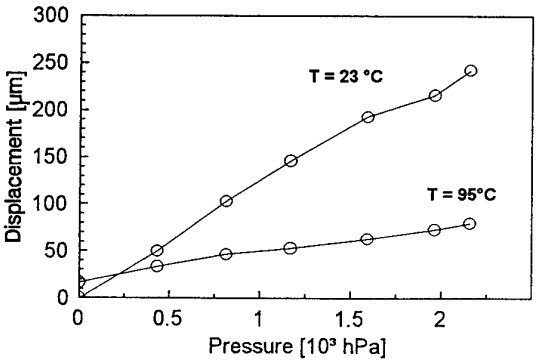


Figure 7: Displacement-pressure characteristics of the stress optimised membrane microactuator.

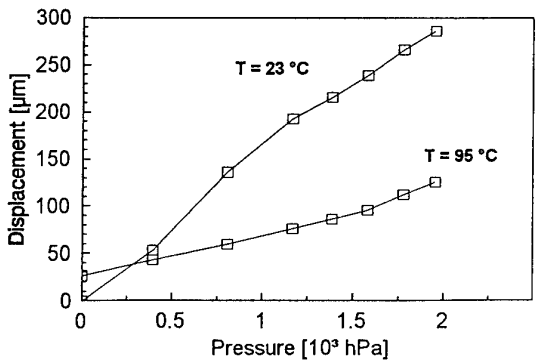


Figure 8: Displacement-pressure characteristics of the reference microactuator

In contrast to the electrical resistance, the displacements are directly determined by the device regions of maximum stress and strain and thus reflect the local phase transformations in these regions. Upon cooling by decreasing the electrical power, the displacements first decrease slightly due to the different thermal expansion coefficients of NiTi and polyimide. At the onset of the rhombohedral phase transformation at TR, the displacements strongly increase. For 1000 hPa in Fig. 9, the stress-optimised actuator displays a one-stage transformation from the austenitic phase to the rhombohedral phase. Such transformations show characteristic narrow hystereses between 1 and 2 K, [17] which corresponds here to a difference in power of about 8 mW. For higher external pressures above about 1500 hPa, a drastic change of the pressure-displacement characteristics is observed. Upon cooling, the onset of the martensitic phase transformation causes a second steep increase of the displacement in the low temperature regime at low power values. For 2000 hPa external pressure, this increase starts below about 30 mW, which corresponds to a device temperature of about 30°C. This temperature shift is caused by the pressure-induced maximum stress in the microdevice occurring along the surface on both sides of the microdevices. Generally, the transformation temperatures increase linearly as a function of stress. In particular, the martensitic transformation temperatures like Ms are much stronger affected by stress than the rhombohedral phase transformation temperature TR due to the larger transformation strain. Therefore, the displacement minimum at TR keeps almost unchanged while the Ms temperature shifts by about 7 K for increasing pressure from 1000 hPa to 2000 hPa. As a result of the two-stage transformation, a rather large hysteresis of about 60mW is observed for 2000 hPa.

Similar large hystereses values are already observed in the reference actuator for much smaller external pressures. In Fig. 10 at 1000 hPa, the hysteresis is about 70 W, at 650 hPa about 65 W. The two-stage rhombehedral and martensitic transformation is not clearly resolved in Fig. 10, since the locations of stress and strain maxima, which are responsible for the observed displacements, are not homogeneously distributed. The difference between the results in Fig. 9 and 10 is caused by the difference in the maximum stress values in both actuator designs of about a factor of 5 for a given external pressure, which has been calculated by elastic beam-bending theory for the austenitic temperature regime. By decreasing external pressure in the non-optimised reference actuator, we consequently expect a reduction of the hysteresis and finally a single-stage rhombohedral transformation below about 200 hPa. This trend is clearly observed in the experiment. However, a single-stage transformation cannot be observed for the reference actuator, since the corresponding displacements are too small, as can be seen from Fig. 8.

These results clearly demonstrate the advantage of stress-optimisation:

- Comparable actuator displacements are obtained for much smaller maximum stress and strain values in the microdevices. For an external pressure of 1000 hPa, net-displacements between 23°C and 95°C of 80 µm are achieved. The maximum stresses induced during an actuation cycle are below about 65 MPa. Such maximum stress values occur in the reference actuator for an external pressure of about 200 hPa.
- The low stress and strain maxima guarantee a much higher lifetime stability and a better fatigue behavior. For strains below 2%, more than 10^5 actuation cycles are expected for the used material.

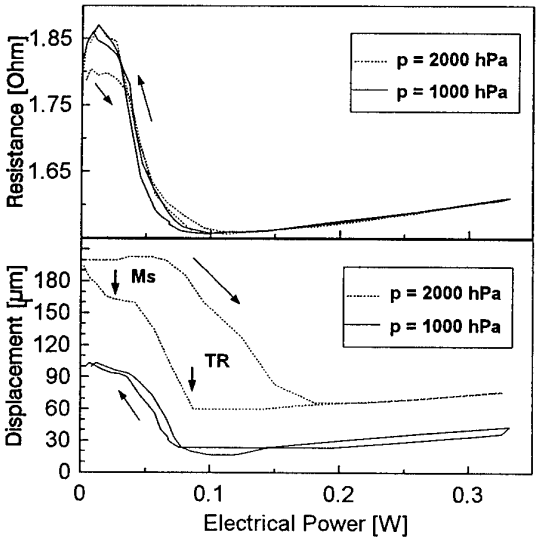


Figure 9: Resistance and displacement characteristics of the stress optimised membrane microactuator for resistive heating. TR and Ms are indicated.

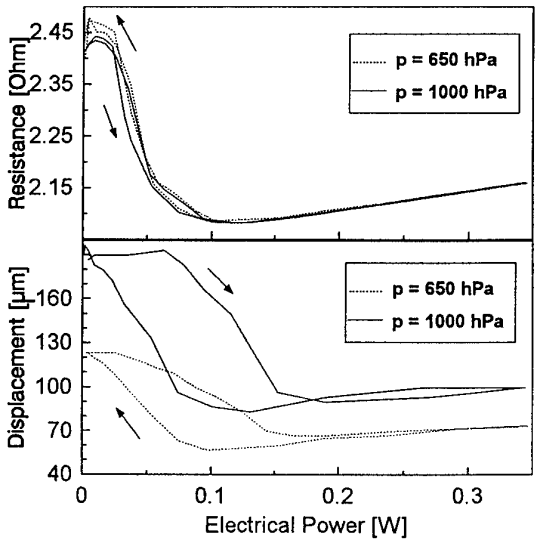


Figure 10: Resistance and displacement characteristics of the reference membrane microactuator for resistive heating.

- The homogeneous stress distributions cause smaller hystereses. In the presented example, this effect is particularly drastic, since the onset of the martensitic transformation at Ms occurs exactly at room temperature causing the observed strong influence of stress-induced transformation temperature changes on the actuator displacements. Narrow hystereses in the order of a few degrees are particularly interesting for positioning applications.
- The actuators can be operated for 1000 hPa external pressure with a low electrical power of about 100 mW, revealing work outputs in the order of 24 µNm.

5. Conclusion

We have designed and realised membrane microactuators, which consist of an active SMA device with a stress-optimised shape. In these devices, the lateral width profile has been designed to obtain homogeneous stress distributions without local stress maxima for a given load pattern. By using microfabricated NiTi sheets with thicknesses of about 100 µm interesting high work outputs of about 24 µNm for a maximum strain of 2% are achieved. The presented stress-optimised microactuators are suitable for applications in the field of microfluidics and can be operated with electrical power below 100 mW in a pressure and displacement range of 500 to 1000 hPa and 30 to 80 µm, respectively. By comparing the mechanical and electrical properties of a stress-optimised membrane actuator with a parallel-beam actuator, we find a factor of 5 lower maximum stress values for similar work outputs, which are promising for a large number of acuation cycles higher than 10^5 and smaller hystereses, which are particularly interesting for positioning applications.

Future projects concentrate on the development of stress-optimised SMA devices for more complicated load patterns and geometries, which require shape optimisation by finite element calculations. Furthermore, the time-dependent features of the devices, which are determined by the efficiency of heating and cooling, have to be taken into account in the shape-optimisation for time-critical applications.

6. Acknowledgement

The authers would like to thank A. Schüßler for laser cutting and S. Pschibl for expert help in microbonding the NiTi microdevices.

7. References

[1] D. Honma, Y. Miwa and N. Iguchi, *Bull. Jpn. Soc. Mech. Eng.* 27, 230 (1989).
[2] D. Honma, Y. Miwa and N. Iguchi, in *Integrated Micro-Motion Systems*, F. Harashima ed. (Amsterdam Elsevier, 1990).
[3] G.Lim, K.Minami, and M.Sugihara, *Proc. MEMS'95*, Holland, Netherlands, (1995), pp.116-121.
[4] J.A.Walker, K.J.Gabriel, and M.Mehregany, *Sensors and Actuators*, A21-A23, (1990), pp.243-246.
[5] A.D.Johnson, *J. Micromech. Microeng.*, 1,(1991), pp. 34-41.
[6] S. Miyazaki and K. Nomura, *Proc. MEMS'94*, Oiso, Japan, (1994), pp. 176-181 .
[7] H.Holleck, S.Kirchner, E.Quandt and P.Schloßmacher, *Proc. Actuator 94*, Bremen, Germany, (1994) , 361-364.
[8] M.Kohl, E.Quandt, A.Schüßler, R.Trapp, and D.M.Allen, *Proc. Actuator 94*, Bremen, Germany, (1994) , pp. 317-320.
[9] T.Kim, Quanmin Su, and M.Wuttig, *Mat. Res. Soc. Symp. Proc.* Vol. 360, (1995), pp. 375-380.
[10] Li Hou, T.J.Pence, and D.S. Grummon, *Mat. Res. Soc. Symp. Proc.* Vol. 360, (1995), pp. 369-374.
[11] U.S. Patend #5,325,880, Jul. 5, (1994).
[12] M.Kohl, K.D.Skrobanek, E.Quandt, P.Schloßmacher, A.Schüßler, and D.Allen, to be published in *Journal de Physique* IV.
[13] S.Miyazaki, in *Engineering aspects of shape memory alloys*, edt. T.W. Duerig et al, Butterworth-Heinemann Ltd, Great Britain, (1990), pp.394-413.
[14] J.Van Humbeeck, D.Reynaerts, and R.Stalmans, *Proc. Actuator'94*, Bremen, Germany, (1994) , pp. 312-316.
[15] S. Miyazaki and K. Otsuka, *Metall. Trans. A*, Vol. 17A, (1986) 53-63.
[16] G.B. Stachowiak, and P.G.McGormick, *Acta metall.* Vol. 36, No. 2,(1988) , pp.291-297.
[17] K.Otsuka, in *Engineering aspects of shape memory allows*, edt. T.W. Duerig et al, Butterworth Heinemann Ltd, Great Britain, (1990), pp.36-45.

Large-stroke and high-strength actuator materials for adaptive structures

Kari Ullakko

Massachusetts Institute of Technology, Cambridge, MA 02139, USA
(on leave from University of Vaasa, 65101, Finland)

ABSTRACT

The most important actuator materials in adaptive structures are shape memory alloys, piezoelectric and magnetostrictive materials and electrorheological fluids. However, no such material is available which would produce rapid and large strokes with high forces. Shape memory alloys exhibit large strokes and forces but their response is slow. Piezoelectric materials and magnetostrictive intermetallics are rapid, but the strokes are small. In the present study, employment of magnetic control of shape memory effect as a principle for rapid large stroke actuator materials is discussed. In such materials, detwinning is controlled by an external magnetic field. Twins in favorable orientation to the magnetic field grow at the expense of other twins and cause a shape change of the actuator. Strokes can be as high as those in shape memory alloys, but response times are short due to magnetic control. Another method which may be applied in actuators is inducing the martensitic transformation and controlling the growth of the martensite plates by magnetostrictive distortions of giant magnetostrictive particles embedded in the shape memory alloy matrix. Magtetostrictive inclusions can also be used as stress sensors in shape memory materials. In pre-stressing and fastening applications, materials which exhibit large strokes and high recovery stresses are required. Nitrogen alloyed shape memory steels, developed for actuators for those applications, is the second topic of this study. In nitrogen alloyed shape memory steels, yield strengths over 1100 MPa and tensile strengths even 1600 MPa were attained. Recoverable strains can be over 4 % and recovery stresses 330 MPa. Stresses over 700 MPa were achieved in fasteners at room temperature. Nitrogen alloyed shape memory steels possess good corrosion properties, machinability and weldability (even the welds exhibit shape memory effect). They are economical to manufacture and use and they are expected to have applications in many fields of engineering.

1. INTRODUCTION

Adaptive structures consist of sensors, actuators and control systems[1,2,3]. In adaptive mechanical systems, actuators change the mechanical characteristics of the structure according to information obtained from sensors. It is obvious that adaptive technologies will cause a revolution in machine design in the nearest future. Employment of adaptive structures in machinery leads to simpler, lighter, faster, more reliable and more economical constructions than by using conventional technology. New actuator and sensory materials have a key role in the deployment of adaptive technologies.

Most important actuator materials are piezoelectric and magnetostrictive materials, electrorheological fluids and shape memory alloys[3,4]. Dimensions of piezolectric (magnetostrictive) materials change when electric (magnetic) field is imposed on them. Electrorheological fluids increase in viscosity, vibration damping capacity and shear strength when exposed to an electric field. Shape memory alloys exhibit an ability to change their shape under thermomechanical control. The response of piezoelectric materials is very rapid and precise but strokes are small. High magnetostrictive Fe-Dy-Tb compounds, *e.g.*, Terfenol[4], exhibit strokes of about 0.15 % and high stresses (tens of MPa), and they operate at frequencies of several kHz. Magnetostrictive materials have been applied in high-force vibrators and pumps, actuators for active vibration control, and in precision tooling.

Shape memory alloys produce large strokes and high forces, but response times are slow due to thermal control. Shape memory materials are employed in couplers, fasteners and valves, and in actuators in robotics and active vibration control. The most widely used shape memory alloys are Ni-Ti, Cu-Zn-Al and Cu-Ni-Al alloys[5]. Processing and application of these alloys are demanding and the alloys are expensive, which have retarded their employment in mass products. Since shape memory effect in Fe-Mn-Si systems was observed[6], increasing attention has been paid to iron based shape memory alloys due to their great technological potential and low price. Properties of Fe-Mn-Si shape memory alloys have been improved by alloying[7] with Cr, Ni, Co and C. A significant improvement on shape memory, mechanical and corrosion properties was attained by introducing nitrogen in the Fe-Mn-Si systems[8,9].

0-8194-2165-0/96/$6.00

2. RESULTS AND DISCUSSION

The present study concerns large stroke and high strength actuator materials. The presentation consists of two parts. In the first part (2.1), principles of new innovative rapid large stroke materials are discussed. Operation of these materials is based on a magnetic control of shape memory effect. Potential applications of these materials are in machine automation, active vibration control and in precision tooling. High-strength actuator materials for fasteners and pre-stressing applications are the topics of part (2.2). Employment of these materials is based mainly on one-way shape memory effect.

2.1 Magnetic control of shape memory effect - principle of rapid large-stroke actuators

A diversity of sensory materials are available for adaptive structures, but actuator materials are only few. At present, no such material exists which could produce rapid and large strokes with high forces. Magnetic control of shape memory effect has been suggested for a principle of new actuator materials with large rapid strokes and high forces[10]. In the following, two different operating principles for such materials are discussed. The first method is based on the control of twinning by external magnetic field. This principle is illustrated in Figure 1b.

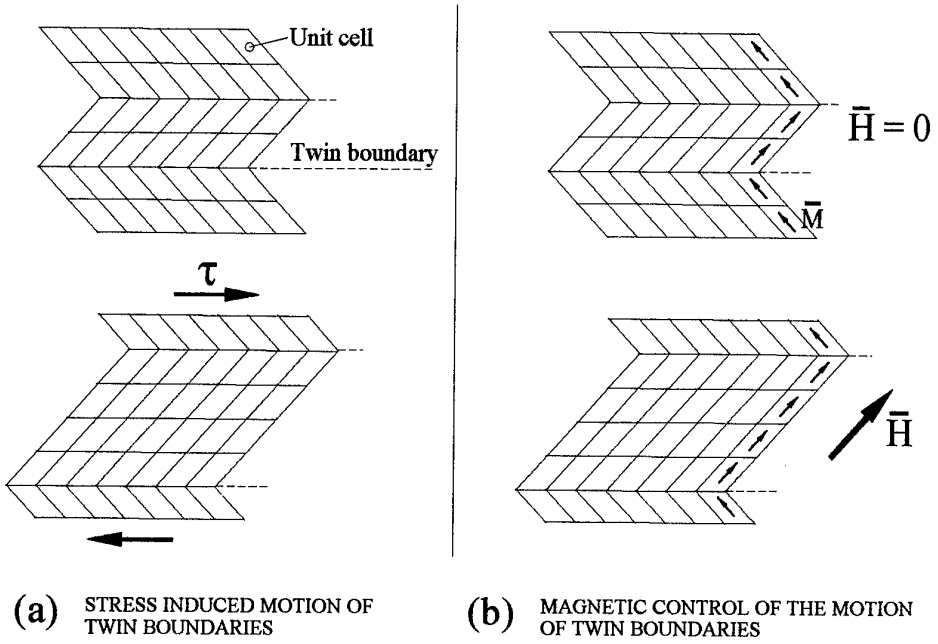


Figure 1. Motion of twin boundaries in martensite by the application of a shear stress τ in conventional shape memory materials (a), and magnetically driven motion of twin boundaries in a new kind of actuator materials (b). The parallel unit cells between two twin boundaries are called a twin variant. Magnetization (denoted by $\underline{M}$) is aligned to the easy magnetization direction in each twin variant (in this simplified illustration it is parallel to the twin axis). In both cases (a) and (b), the motion of twins causes a shape change of the actuator material which produces the stroke of the actuator.

Shape memory effect is based on reversible motion of twins[5]. If a stress is applied to the structure shown in Fig. 1a, the twin boundaries move converting one orientation of twin variant into another. The new structure will accommodate better the applied stress. If the straining is sufficient enough, a single variant of martensite can be produced by straining (this is called detwinning).

Figure 1 b shows the principle of the magnetic control of the motion of twin boundaries. Magnetization vectors of the ferromagnetic actuator material are aligned to the easy magnetization direction in each twin variant. When an external magnetic field (H) is applied, magnetization vectors tend to turn parallel to H. If the magnetocrystalline (anisotropy) energy of the material is high enough and twin boundaries are of low energy and mobile, twin variants whose magnetization is close to H grow at the expense of others variants in the same way as they grow in conventional shape memory alloys by the application of stress. This causes a net shape change of the actuator material which produces the stroke of the actuator. In certain conditions the twin boundaries move back when the external magnetic field is switched off ("magnetosuperelasticity"). Magnetic control of the motion of austenite-martensite interfaces may operate in the same way as the twin boundary motion, if the martensite is completely twinned and ferromagnetic with high magnetic anisotropy energy, and if the strength of austenite phase is high enough and stacking fault energy low to promote the growth of martensite and decrease permanent slip. Some Ni_2MnGa-type Heusler alloys are promising candidates for magnetically driven large-stroke actuator materials, because they exhibit and a suitable magnetic structure and the twin boundaries of their martensite phase move easily[11]. Studies on these materials as well as development of new actuator materials based on the magnetic control of the motion of twin boundaries are in progress.

Growth of the martensitic plates by strains caused by distortions of high-magnetostrictive Terfenol particles embedded in a shape memory alloy matrix was tested. Powders of a Cu-Zn-Al shape memory alloy and Terfenol (15 wt%) were mixed and shock wave compacted. Micrograph of the composite is shown in Figure 2. When a magnetic field is imposed on this composite, Terfenol particles are elongated (about 0.1 %) producing force high enough to induce martensitic transformation in the matrix at appropriate temperatures. Orientation and growth of the martensite plates can be affected by the magnetic field, and by the distribution and properties of the magnetostrictive particles. Dispersing particles whose magnetostriction is negative (*e.g.*, Sm-Fe based compounds) with Terfenol particles in a matrix of the shape memory alloy might lead to more effective control of the shape memory effect. Magnetic control of the shape memory effect through the magnetostrictive inclusions may be used independently, or simultaneously with the thermal control to affect the two-way shape memory characteristics or the dynamics of the actuator. Magnetostrictive particles may also serve as intermaterial stress sensors as suggested by Rogers[12] for adhesives, polymer composites and paints. Changes of the stresses in the shape memory alloy containing magnetostrictive inclusions affect the magnetic charateristics of the inclusions, which can be monitored outside the actuator.

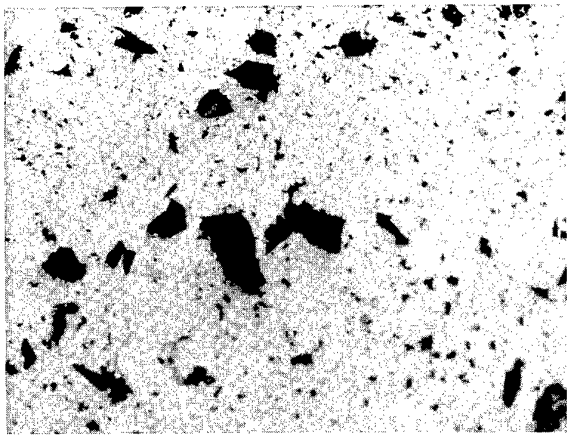


Figure 2. High-magnetostrictive Terfenol inclusions (dark) in a Cu-Zn-Al shape memory alloy matrix (light). Magnification 300 x.

2.2 High-strength actuator materials for fasteners and pre-stressing applications

Nitrogen alloyed shape memory steels were developed for fastening and pre-stressing applications[8,9]. A number of steels containing different amounts of Mn, Si, Cr, Ni, V and N were made for studying the mechanical and shape memory properties. Alloys were induction melted in nitrogen atmosphere. The ingots were drawn to wires in diameter of 3 mm.

The wires were annealed at 800 °C for 2-10 minutes in air atmosphere and water quenched. After quenching the wires were deformed 6 % by drawing. Some wires were annealed at 550 °C for 10 minutes to precipitate Cr and V nitrides.

Nitrogen alloyed shape memory steels exhibits a shape memory effect of few percents with recovery rates 60-100 %[9]. The highest recoverable strains measured were over 4 %. Some alloys exhibited yield strengths $R_{\sigma 02}$ about 1100 MPa and tensile strength over 1600 MPa. The highest recovery stresses were obtained in steels which contained finely dispersed nitrides produced by aging the cold drawn wires at elevated temperatures. Thermomechanical training treatments were demonstrated to improve recoverable strain and recovery rate, and also to decrease A_f temperatures (*i.e.*, temperature at which the reverse transformation is finished). Nitrogen alloyed shape memory steels turned out to exhibit good shape memory and mechanical properties also at cryogenic temperatures.

Figure 3 shows the strain recovered during heating the initially 6 % deformed alloy Fe-13.9Mn-4.68Si-13.1Cr-4.8Ni-0.22 N. During deformation austenite was partially transformed to ε martensite. A strain recovery of 3.5 % occurs at temperatures above 100 °C, which is evidence for the one-way shape memory effect of this alloy. The sample was then cooled to liquid nitrogen temperature -196 °C and heated to 750 °C; and this cycling was repeated several times. The loop (between -160 °C and 150 °C) shown in Fig. 3 was obtained after the third cycle. It is an indication of the two-way shape memory effect (0.4%).

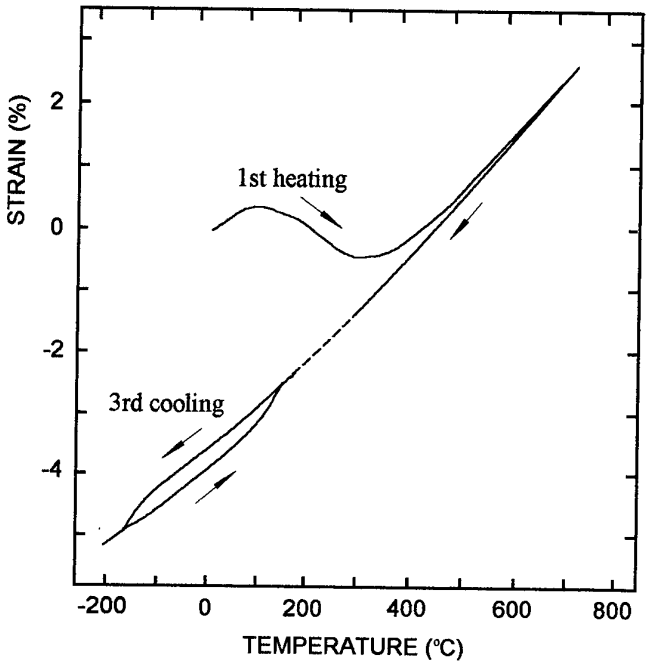


Figure 3. One-way and two-way shape memory effects in alloy Fe-13.9Mn-4.68Si-13.1Cr-4.8Ni-0.22N observed during temperature cycling between 750 °C and -196 °C. The one-way effect of 3.5 % is observed during the first heating, and the two-way effect of 0.4 % after the third cycle between -160 and 150 °C. [9]

A recovery stress measurement of alloy Fe-18.4Mn-5.1Si-9.7Cr-3.7Ni-0.2V-0.2N is shown in Figure 4. The sample was first strained 5.7 % at room temperature (Fig. 4a). When the stress was released, strain of 4.2 % was remained. The positions of the grips in tensile test machine were then fixed, and the heating cycle was performed on a constrained sample. Figure 4b shows the stress monitored during heating and cooling. The stress increased during heating because of the formation of austenite phase. The maximum value of recovery stress 300 MPa was reached at 300 °C. This value is about two times higher than obtained for Fe-Mn-Si-Cr-Ni alloys (*e.g.*, 170 MPa measured for alloy Fe-14Mn-6.2Si-9Cr-5.3Ni[13]). Stress was relaxed during further heating due to thermal expansion of the sample. During cooling, the austenitic sample tends to contract thermally, which increases the stress. The bending of the curve in the temperature region of 300 to 20 °C is attributed to the formation of stress induced ε martensite. Formation of martensite was confirmed by x-ray diffraction measurements. At room temperature the remaining stress was 700 MPa. The high value of recovery stress of this alloy is attributed to the high strength of austenite of this alloy. Austenite is strengthened by finely dispersed Cr and V nitrides in addition to solution strengthening caused by nitrogen atoms in solid solution. The recoverable strain of this alloy is 1.5 %.

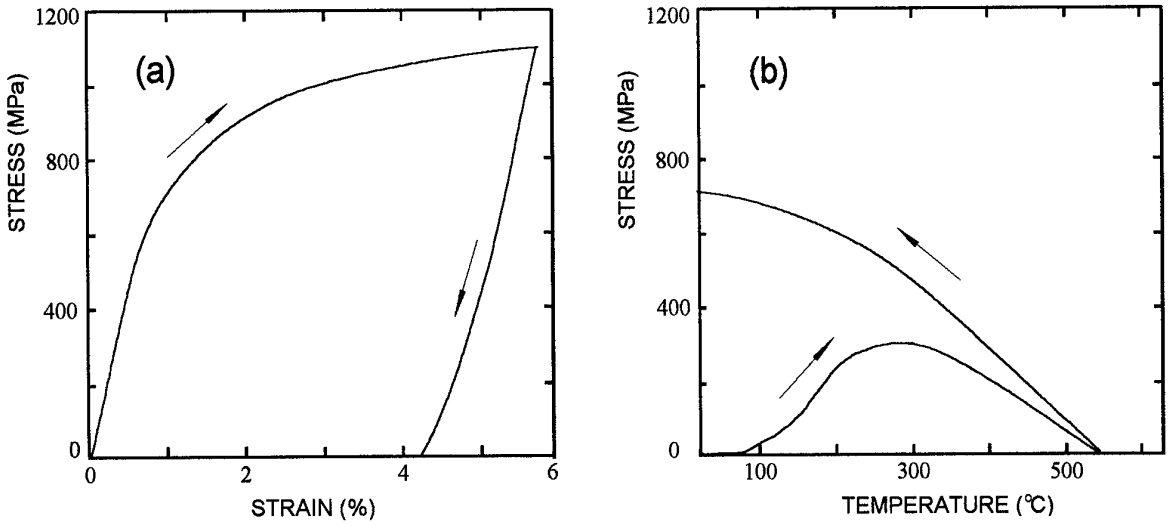


Figure 4. Stress-strain cycle of alloy Fe-18.4Mn-5.1Si-9.7Cr-3.7Ni-0.2V-0.2N (a), and a subsequent stress-temperature cycle which was measured on the constrained sample (b). The cycles were repeated 5 times, and the curves represent the 5th cycle. [9]

Shape memory effect in the present steels is based on the reversible motion of Shockley partial dislocations during the ε martensite transformation[14]. The motion of these dislocations control the martensite and reverse transformations. When an external stress is applied, the completely twinned martensite plates grow and new plates appear. Reverse transformation occurs during heating. A beneficial effect of nitrogen alloying on the shape memory properties of the present steels is based on the facts that nitrogen atoms strengthen austenite phase (more than any other element) and decrease stacking fault energy (in the present concentration range), which promote the formation of martensite during deformation and prevent permanent slip. Nitrogen can strengthen austenite by four hardening mechanisms which can operate simultaneously: solid solution hardening, grain boundary hardening, work hardening and precipitation hardening. These mechanisms were operating also in the present shape memory steels. Nitrogen alloying significantly improves the mechanical properties of the austenitic steels. In stable austenitic high-nitrogen steels, yield strengths over 3000 MPa have been reached. High-nitrogen austenitic steels possess the highest combination of strength and toughness of all materials available presently[15]. Nitrogen alloying improves also corrosion properties, which means that chromium and nickel contents can be reduced if nitrogen content is increased. All of these beneficial effects of nitrogen alloying can be utilized in the further development of high-nitrogen shape memory steels.

Nitrogen alloyed shape memory steels are economical to manufacture and use. Nitrogen alloying of Fe-Mn-Si-Cr based shape memory steels is easy to perform in standard industrial furnaces, because manganese and chromium promote dissolving of high nitrogen contents at a normal pressure. Nitrogen alloyed shape memory steels exhibit an excellent performance, their machinability and weldability are good, and most of them are corrosion resistant. Those steels are expected to be employed in fasteners, couplers and in various pre-stressing applications in engineering.

3. CONCLUSIONS

Operation of the present actuator materials is based on reversible movement of twin boundaries and austenite-martensite interfaces. In the magnetically driven actuator materials, twins are re-oriented by an applied magnetic field, which causes the stroke of the actuator. In the shape memory steels, twinned martensitic structure is controlled by a stress. Mn alloying has a key role in the magnetic and structural characteristics of most of the present actuator materials.

Magnetic control of shape memory effect is a promising method to be utilized in rapid large-stroke actuators. Strokes can be as high as those in shape memory alloys but response is much faster. Potential applications of the magnetically controlled shape memory actuators are in machine automation, robotics, precision tooling, active vibration control and in many applications where mechanical, servohydraulic or electromagnetic drives are used presently.

Nitrogen alloyed shape memory steels exhibit superior shape memory, mechanical and corrosion properties as compared to other Fe-Mn based steels. Their recovery stresses are higher than 300 MPa, recoverable strains over 4 %, and their yield strengths reach 1100 MPa and tensile strengths 1600 MPa with elongation over 30 %. Machinability and weldability of nitrogen alloyed shape memory steels are good, and they are economical to manufacture and apply.

4. ACKNOWLEDGEMENTS

Academy of Finland, The Oskar Öflund Foundation and The Kordelin Foundation are acknowledged for support. Professor V.G. Gavriljuk and Dr. P.T. Jakovenko are thanked for collaboration in developing high-nitrogen shape memory steels, and Mr. M. Korvenkarhu for performing the explosion compacting of the samples.

5. REFERENCES

1. C.A. Rogers, D.K. Barker and C.A. Jaeger, "Introduction to smart materials and structures", in "Smart materials structures, and mathematical issues", ed. C.A. Rogers, Technomic Publishing Co, Inc., 1988, pp. 17-28.
2. B. Culshaw, "Smart structures - a concept or a reality", Proc. Instn. Mech. Engrs., Vol. 206, 1992, pp. 1-8.
3. M.V. Gandhi and B.S. Thompson, "Smart materials and structures", Chapman & Hall, London 1992, 309 p.
4. W. Martin, "Adaptive Materials", Second Short Course on Smart Structures and Materials, 9th - 13th of May 1994, Smart Structures Research Institute, University of Stratchlyde, UK.
5. T.W. Duerig, K.N. Melton, D. Stöcker and C.M. Wayman, "Engineering aspects of shape memory alloys", Butterworth-Heinemann Ltd., Great Britain, 1990.
6. A. Sato, E. Chisima, K. Soma and T. Mori, "Shape memory effect in γ - ε transformation in Fe-30Mn-1Si alloy single crystals", Acta Metall., Vol. 30, 1982, pp. 1177-1183.
7. Q. Gu, J. van Humbeeck and L. Delaey, "A review on the martensitic transformation and shape memory effect in Fe-Mn-Si alloys", Journal de Physique IV, Colloque C3, Suppl au J. de Phys. III, Vol. 4, fevrier 1994, C3-135-143.
8. K. Ullakko, P.T. Jakovenko and V.G. Gavriljuk, "Nitrogen alloyed high-strength shape memory steels", International Conference on Martensitic Transformations ICOMAT-95, Lausanne, Switzerland, August 20-25, 1995 (Abstract).
9. K. Ullakko, P.T. Jakovenko and V.G. Gavriljuk, "High-strength shape memory steels alloyed with nitrogen", submitted to Scripta Metall. *et* Mater., 1995, 6 p.
10. K. Ullakko, "Magnetic control of shape memory effect" , International Conference on Martensitic Transformations ICOMAT-95, Lausanne, Switzerland, August 20-25, 1995 (Abstract).
11. V.V. Martynov and V.V. Kokorin, "The crystal structure of thermally and stress-induced matensites in Ni_2MnGa single crystals", J. Phys. III (France) Vol. 2, 1992, pp. 739-747.
12. C.A. Rogers, Center for Intelligent Material Systems and Structures, Virginia Tech, Blacksburg, Virginia, private comm.
13. H. Ohtsuka, S. Kajiwara and T. Ishikara, "Cyclic γ - ε transformation behavior and its effect on the shape memory characteristics in Fe-Mn-Si-Cr-Ni alloy", Proc. of the Int. Conf. on Martensitic Transformations, 1992, pp. 1169-1174.
14. Y. Hoshino, S. Nakamura, N. Ishikawa, Y. Yamaji, S. Matsumoto, Y. Tanaka and A. Sato, " *In-situ* observation of partial dislocation motion during γ - ε transformation in a Fe-Mn-Si shape memory alloy", Mater. Trans., JIM, Vol. 33, No.3, 1992, pp. 253-262.
15. M.O. Speidel, "Properties of High Nitrogen Steels", Proc. of the 2nd Int. Conf. on High-Nitrogen Steels, Aachen, Germany, Oct. 10-12, 1990, 128-131.

Modelling of the thermomechanical behaviour of shape memory wires embedded in matrix materials

R. Stalmans, J. Van Humbeeck and L. Delaey

Department of Metallurgy and Materials Engineering, K.U.Leuven, De Croylaan 2, B-3001 Heverlee Belgium
rudy.stalmans@mtm.kuleuven.ac.be

ABSTRACT

A fundamental model has been developed which allows to predict the complex thermomechanical behaviour of smart materials composed of matrix materials with embedded shape memory elements. This model is based on a generalised thermodynamic analysis of the thermomechanical behaviour of shape memory alloys. The mathematical approach and the assumptions in this model are selected in such a way that the calculations yield close approximations of the real behaviour and that the final mathematical equations are relatively simple. Therefore, the modelling can be easily incorporated in a computer program. By several illustrations it is shown that this model can be used to calculate the thermomechanical behaviour of complex cases.

INTRODUCTION

Shape memory elements ('smas') can be integrated as actuators or sensors in matrix materials, yielding smart or adaptive materials. In comparison with alternative 'actuating' or 'sensing' materials, smas offer several important advantages and extra possibilities, such as: reversible strains up to 8%, generation of stresses up to 800 MPa, and storage of large amounts of potential energy. Therefore many experts believe that smas offer very promising prospects in the field of smart materials research. An important disadvantage of smas is the complex, non-linear thermomechanical behaviour with hysteresis. Moreover, this complex behaviour is influenced by a large number of parameters. It follows that there are in general no direct and simple relations between the temperature, the position (or strain) and force (or stress). Therefore accurate strain or force control by smas is a difficult task and requires the experimental determination of complex data in combination with advanced control systems. Although many empirical and mathematical models have been developed in recent years by different research groups, those models have not yet been very successful mainly due to the complex nature of shape memory behaviour.

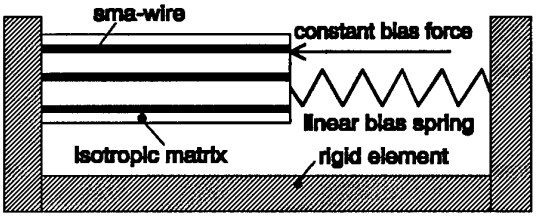
The functional properties of shape memory alloys are closely linked to a temperature or stress induced, crystallographically reversible, martensitic transformation [1, 2]. A generalised thermodynamic model of this transformation has been developed to predict the thermomechanical behaviour of smas. Details of this generalised thermodynamic model can be found elsewhere [3, 4]. The approximations in this model have been selected in such a way that the equations yield close approximations of the real system, and that the final mathematical equations are relatively simple. Additional advantages are the clear physical meaning of the parameters and the large area of application. The use of this thermodynamic model has already resulted in an increased understanding of shape memory behaviour [3, 5]. This thermodynamic model is in this paper further developed to a fundamental model that describes the thermomechanical behaviour during heating of matrix materials with embedded smas-wires.

DERIVATION OF THE THERMOMECHANICAL EQUATIONS

The general procedures are illustrated by the example of the hybrid element depicted in figure 1. This beam shaped element with length L is composed of straight smas-wires uniformly distributed in an isotropic matrix material. The external uniaxial forces acting on this hybrid element are divided into a constant force F_c and a linear bias force with spring constant k[1]. A completely rigid, resp. free element can be modelled by taking the spring constant equal to infinity, resp. zero. The recoverable deformation of the smas-wires at zero stress at the starting temperature T_0, which is below M_f, is given by e_{s0}. The cross section of the matrix is given by Q_m and the total cross section of the smas-wires is is given by Q_s. The reverse martensitic transformation during heating and the connected shape recovery of the smas are hampered by the surrounding matrix material and by the external stresses. The result of these constraining conditions is that during heating so-called 'recovery stresses' are generated by the smas [6]. The task here is to calculate the stresses and strains in the hybrid element and in the composing elements during heating, starting from the temperature T_0.

[1] This configuration allows a uniaxial analysis. Derivations for more complex systems can be performed along the same lines. However, the equations would become more complex, with the result that the analysis becomes less clear.

0-8194-2165-0/96/$6.00



parameters of the system
F_c: constant bias force
k: spring constant of the linear bias spring
L: length of the beam element
Q_m: cross section of the matrix
Q_s: total cross section of the smas-wires

Figure 1: Schematic drawing of the smas-matrix beam. Straight smas-wires are uniformly arranged in the isotropic matrix material. The external bias forces are divided into a constant force and a linear spring.

The total strain of the smas, e_s, can be divided into a recoverable shape memory strain e_{sr}, a thermal dilatation e_{sa} and an elastic strain e_{se}:

$$e_s = e_{sr} + e_{sa} + e_{se} = e_{sr} + a_s*(T-T_0) + \sigma_s/E_s \quad |1|$$

with T the temperature and σ_s, a_s and E_s resp. stress, thermal dilatation coefficient and elasticity modulus of the smas.

The mathematics can be simplified by defining the corrugated shape memory strain e_{sc} as:

$$e_{sc} = e_s - e_{sa} = e_{sr} + e_{se} \quad |2|$$

Similarly, the total strain of the matrix, e_m, can be divided into a thermal dilatation e_{ma} and an elastic strain e_{me}:

$$e_m = e_{ma} + e_{me} = a_m*(T-T_0) + \sigma_m/E_m: \quad |3|$$

with σ_m, a_m and E_m resp. stress, thermal dilatatation coefficient and elasticity modulus of the matrix material.

The matrix material and external conditions hamper the shape change of the smas. This imposes a boundary condition on the thermomechanical action of the smas. A mathematical formulation of this boundary condition follows directly from the equations that express stress and strain equilibrium in the hybrid element:

$$e_s = e_{s0} + a_m*(T - T_0) + \{F_c - k*L*a_m*(T-T_0) - \sigma_s*Q_s\}/(E_m*Q_m + k*L) \quad |4|$$

This boundary condition corresponds to a plane in the thermomechanical $\{e_s\text{-}T\text{-}\sigma_s\}$-space.

Three temperature regions can be distinguished in the thermomechanical behaviour of the smas. The smas are in the martensitic state[2] between T_0 and T_{st}, the temperature at which the reverse martensitic transformation starts. The retransformation continues until a temperature T_{se}, the temperature at which the retransformation ends. Above T_{se}, the smas are in the parent state ('austenite'). The equations in the retransformation region $\{T_{st} \rightarrow T_{se}\}$ are derived first.

In the thermodynamic analysis a generalised Clausius-Clapeyron equation has been derived from the equations that express global thermodynamic equilibrium [3, 4]:

$$\{d\sigma_s/dT\}_{[x]=cst} = -(\rho_0*\Delta s)/\Delta e_{tr\Sigma A}([x]) \quad |5|$$

The material constant Δs is the entropy change during transformation from austenite to martensite. The material constant ρ_0 is the mass density of the smas in stress-free conditions. The volume function [x(r)] represents in any point r the phase and the crystallographic orientation of the phase. Hence, this function also gives the martensite variant arrangement and the martensite mass fraction. The average on all martensite-austenite interfaces ΣA of the transformation strain linked with transformation from austenite to martensite is given by $\Delta e_{tr\Sigma A}([x])$. An important remark is that this transformation strain is not a material constant: $\Delta e_{tr\Sigma A}([x])$ decreases in general with increasing martensite mass fraction and is also influenced by other factors, including the heat treatment and the thermomechanical history [3, 4]. From the derivations follows that this Clausius-Clapeyron equation is only valid for conditions of constant [x]. When [x] is constant, the right-hand part of |5|, $\{-(\rho_0*\Delta s)/\Delta e_{tr\Sigma A}([x])\}$, is also constant. It follows that the stress increases in direct proportion with the temperature.

[2] From a phycical point of view, it would be more correct to state that there is no driving force to a decrease of the shape memory strain e_{sr} in the temperature region between T_0 and T_{st}.

Since the retransformation proceeds during heating of the hybrid element, the conditions for using the Clausius-Clapeyron equation are not fulfilled. Yet, a modified Clausius-Clapeyron that is valid for non-constant [x], can be derived as follows. An infinitesimal temperature increase dT of the smas induces a stress increase $d\sigma_s$ and a strain change de_{sc}. This infinitesimal step from A (T, σ_s, e_{sc}) to C (T+dT, $\sigma_s+d\sigma_s$, $e_{sc}+de_{sc}$) can be also achieved in two intermediate steps, as indicated in figure 2.

The first step is a temperature increase dT *at constant transformation fraction [x]*. This temperature increase yields an increase of the stress by $d\sigma_r$, and an increase of the elastic strain by de_e (A→B). The stress increase $d\sigma_r$ follows directly from the Clausius-Clapeyron equation (15). The elastic strain de_e follows from:

$$de_e = d\sigma_r/E_s \qquad (6)$$

The second step is an unloading by $d\sigma_p$ *at constant temperature* {T+dT}. Since the constrained heating corresponds to retransformation of martensite to austenite, this unloading results in a pseudoelastic decrease of the strain by de_p (B→C). The pseudoelastic strain de_p can be approximated by:

$$de_p = d\sigma_p/P_s \qquad (7)$$

with P_s the pseudoelastic modulus, given by the slope $d\sigma_s/de_s$ during pseudoelastic unloading.

It follows that the stress increase $d\sigma_s$, resp. strain change de_{sc}, are equal to:

$$d\sigma_s = d\sigma_r + d\sigma_p \qquad (8)$$

$$de_{sc} = de_e + de_p \qquad (9)$$

Combination of the boundary condition (14), the Clausius-Clapeyron equation (15) and equations (6-9) results finally in the differential constitutive equation which is valid *during retransformation* in the temperature region $\{T_{st} \rightarrow T_{se}\}$:

$$d\sigma_s/dT = \frac{\{(a_m-a_s) + (P_s-E_s)*\rho_0*\Delta s/(\Delta e_{tr\Sigma A}([x])*P_s*E_s)\} - \{k*L*a_m/(E_m*Q_m + k*L)\}}{1/P_s + Q_s/(E_m*Q_m + k*L)} \qquad (10)$$

The shape memory strain e_{sr} is *before retransformation* equal to the initial value e_{s0}. From equations (1-4) can be deduced that σ_s in the temperature region $\{T_0 \rightarrow T_{st}\}$ is given by:

$$\sigma_s = E_s*\{E_m*Q_m*(a_m-a_s)*(T-T_0) - k*L*a_s*(T-T_0) + F_c\}/(E_s*Q_s + E_m*Q_m + k*L) \qquad (11)$$

By integration of the Clausius-Clapeyron equation (15) it can be deduced that the relationship between the temperature T_{st} and the stress σ_s is given by:

$$T_{st} = T_{tr}(e_{s0}) - \sigma_s*\Delta e_{tr\Sigma A}([x])/(\rho_0*\Delta s) \qquad (12)$$

with $T_{tr}(e_{s0})$ the retransformation temperature corresponding with an initial deformation e_{s0} in stress-free conditions.

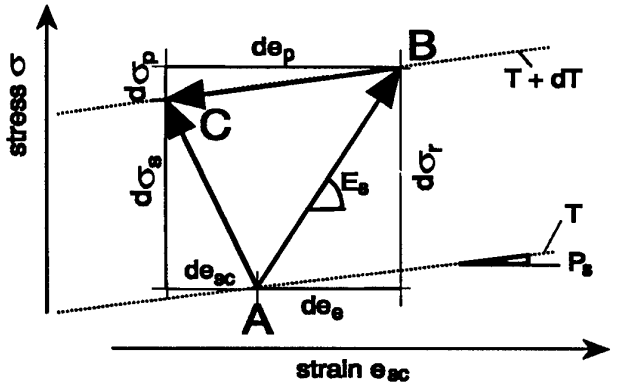


Figure 2: The process of a temperature increase dT at the imposed boundary conditions (A→C) can be replaced by a temperature increase at constant transformation fraction [x] (A→B), followed by an unloading at constant temperature (B→C).

For simplification, a system constant K_1 is introduced:

$$K_1 = E_s/(E_s*Q_s + E_m*Q_m + k*L) \quad |13|$$

Combination of |11|, |12| and |13| results in the following equation, from which T_{st} can be determined:

$$T_{st} = \frac{T_{tr}(e_{s0}) + K_1*[\Delta e_{tr\Sigma A}([x])/(\rho_0*\Delta s)]*\{E_m*Q_m*(a_m-a_s)*T_0 - k*L*a_s*T_0 - F_c\}}{(1 + K_1*[\Delta e_{tr\Sigma A}([x])/(\rho_0*\Delta s)]*\{E_m*Q_m*(a_m-a_s) - k*L*a_s\}} \quad |14|$$

The retransformation ends at the temperature T_{se}. At T_{se}, the shape memory strain e_{sr} becomes equal to zero. From equation |1-4| can be deduced that σ_s *after retransformation* at temperatures above T_{se} is given by:

$$\sigma_s = E_s*\{E_m*Q_m*(a_m-a_s)*(T-T_0) - k*L*a_s(T-T_0) + (E_m*Q_m+k*L)*e_{s0} + F_c\}/(E_s*Q_s+E_m*Q_m+k*L) \quad |15|$$

The solution of the above set of equations requires only a set of simple to determine experimental shape memory data [5]. First, an array of $\{e_{s0}\text{-}T_{tr}\}$ data at zero external stress from which $T_{tr}(e_{s0})$ in |14| can be determined. Secondly, the slopes $d\sigma_s/dT$ for a low and a high value of e_{s0} during heating of the smas-wires in constrained conditions; this allows an accurate estimation of the term $\{\rho_0*\Delta s/(\Delta e_{tr\Sigma A}([x])\}$ in |10| and |14|. Third, the pseudoelastic modulus P_s is calculated from a linear approximation of the slope $d\sigma/de$ during pseudoelastic unloading. Fourth, average values of the thermal dilatation coefficient a_s and the elasticity modulus E_s are also required[3].

The hybrid element is characterised by the following set of input variables. The input variables of the system are: the cross section of the matrix material Q_m, the total cross section of the smas-wires Q_s, the bias force F_c, the bias spring constant k, the length of the hybrid element L, the starting temperature T_0, and the initial deformation e_{s0} of the smas-wires. The input variables for the matrix material are the thermal dilatation coefficient a_m and the elasticity modulus E_m.

For such sets of input variables, the stresses (σ_s and σ_m) and strains (e_s, e_{sc}, e_{sr}, e_{se}, e_{sa}, e_m, e_{me} and e_{ma}) during heating can be computed from the equations above, as follows. When σ_s is known, the different strain components and stress σ_m can always be calculated from |1-4|. In the temperature region $\{T_0 \rightarrow T_{st}\}$, the stress σ_s follows directly from |11|. The transition temperature T_{st} can be calculated from |14|. In the temperature region $\{T_{st} \rightarrow T_{se}\}$, the stress increase $\Delta\sigma_s$ at a small temperature increase ΔT is obtained directly from |10|. The shape memory strain gradually decreases and becomes equal to zero at T_{se}. From that temperature, σ_s can be calculated from |15|. A simple computer program 'sma-hybrid' has been developed that, by use of these equations, calculates the stresses and strains in the hybrid element and in the composing elements during heating. This program can be used to calculate the complex behaviour of smas-matrix beams during heating for different sets of input variables and, more general, also of smas-wires in constrained conditions. Some computed results are shown in figures 3-8. A comparison of the computed results of fig.3 with the experimental results published in [3] shows an excellent *quantitative* agreement.

The differential equation |10| can also be written as:

$$d\sigma_s/dT = P_s*(E_m*Q_m*(a_m-a_s) - k*L*a_s)/(P_s*Q_s + E_m*Q_m + k*L) + K_2*\{\rho_0*\Delta s/\Delta e_{tr\Sigma A}([x])\} \quad |16|$$

in which the system constant K_2 is defined as:

$$K_2 = (E_m*Q_m+k*L)*(P_s-E_s)/\{E_s*(E_m*Q_m + k*L + P_s*Q_s)\} \quad |17|$$

It can be easily shown that in general circumstances K_2 is close to $\{-1\}$.

The first term in equation |16|, $\{P_s*(E_m*Q_m*(a_m-a_s) - k*L*a_s)/(P_s*Q_s + E_m*Q_m + k*L)\}$, is the result of the external stresses and the difference in thermal dilatation between matrix and smas. It can be easily shown that the absolute value of this term is in general smaller than 0.2 MPa/K. Since K_2 is close to $\{-1\}$, the second term $\{K_2*(\rho_0*\Delta s/\Delta e_{tr\Sigma A}([x])\}\}$ closely approximates the right-hand part of the Clausius-Clapeyron equation (|5|). Typical values of this term are 3 to 15 MPa/K. It follows that the first term is relatively small compared to the 'Clausius-Clapeyron' term. This indicates that the stress rate $\{d\sigma_s/dT\}$ *during retransformation* is mainly determined by the 'Clausius-Clapeyron' term, as confirmed in fig.5 and fig.7. Figure 5 and 7 show that the slopes $\{d\sigma_s/dT\}$ in the retransformation region are hardly influenced by changes of the bias spring constant, resp. of the thermal dilatation coefficient of the matrix material. The external stresses and the difference in

[3] Average values of a_s and E_s are used as a first approximation in the present analysis. The dependence of a_s and E_s on the martensite mass fraction will be incorporated in future versions of the computer programs.

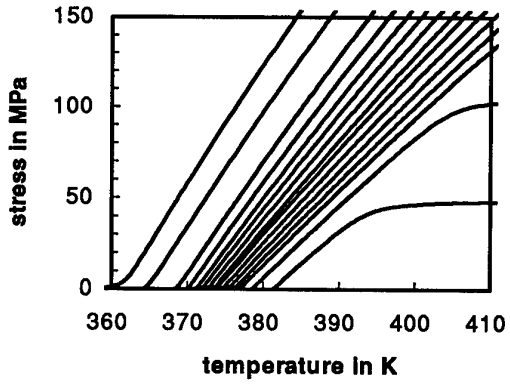


Figure 3: Calculated σ_s-T relations for e_{s0} from 1.04% to 0.06% in steps of 0.07 %. The material data are taken from a trained Cu-base wire [3]. The boundary condition is given by: e_{sc} = constant. Q_m= 0 (no matrix material), T_0=350 K

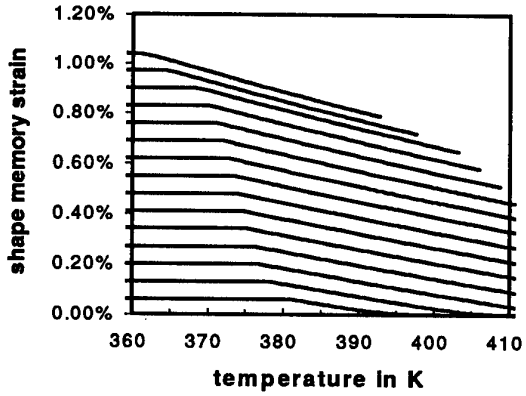


Figure 4: Calculated e_{sr}-T relations for the same conditions as in the figure on the left; e_{sr} equal to zero corresponds to the parent state.

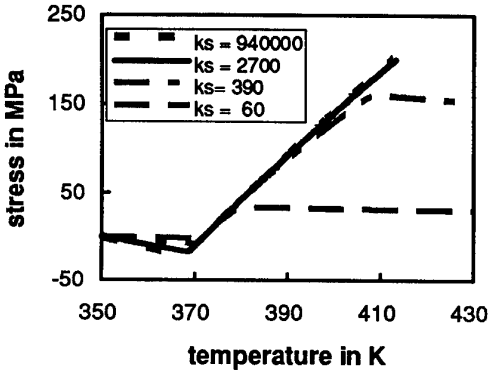


Figure 5: Calculations of σ_s-T relations for different bias spring constants; ks equal to {k/(L*(Q_s+Q_m))} in MPa/% strain; material data as in fig.3; e_{s0} = 0.7%, T_0 = 350K, $Q_s/Q_m = 10^7$

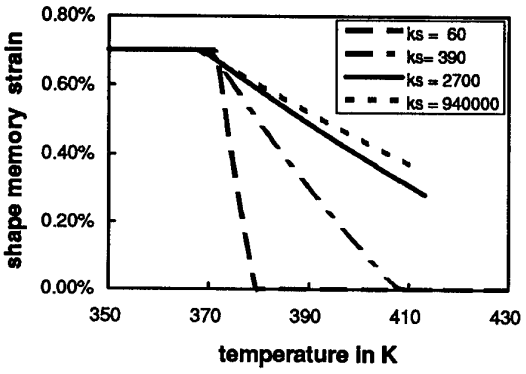


Figure 6: Calculations of e_{sr}-T relations for the same conditions as in the figure on the left.

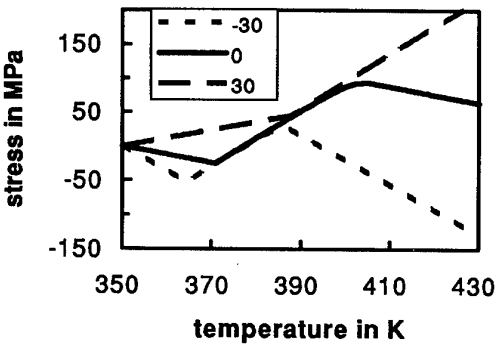


Figure 7: Calculations of σ_s-T relations for different thermal dilatation coefficients a_m of the matrix material; a_m given in 10^6/K; material data as in fig.3; e_{s0}=0.2 %, T_0 = 350K, $Q_s/Q_m = 10^7$

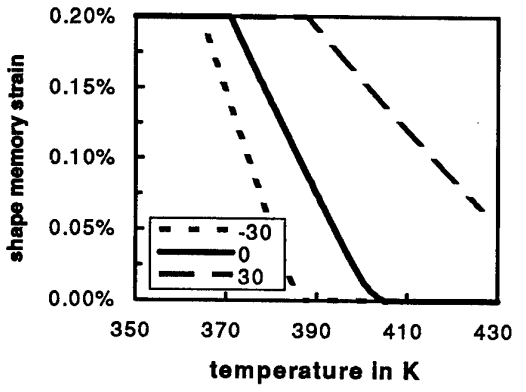


Figure 8: Calculations of e_{sr}-T relations for the same conditions as in the figure on the left.

thermal dilatation between matrix material and smas have however an important influence on the progress of the transformation, expressed by $\{de_{sr}/dT\}$, and on the starting temperature T_{st}, as confirmed in fig.6 and fig.8.

The stress rate $\{d\sigma_s/dT\}$ before and after retransformation can be obtained by derivation of |11| and |15|, which both give the same result:

$$d\sigma_s/dT = E_s*\{E_m*Q_m*(a_m-a_s) - k*L*a_s\}/(E_s*Q_s + E_m*Q_m + k*L) \qquad |18|$$

Since P_s is much smaller than E_s, a comparison of |16| with |18| shows that the input variables (Q_m, Q_s, k, L, a_m and E_m) have a much smaller influence on the stress rate $\{d\sigma_s/dT\}$ during retransformation than before or after retransformation, as illustrated also in fig.7. Recent results obtained on Cu-Al-Ni single crystals have confirmed this important conclusion. This important difference between |16| and |18| is however not taken into account in most models published in recent literature on smart materials (see e.g. [7, 8]).

CONCLUSIONS AND FURTHER DEVELOPMENTS

The modelling in this paper can be used to predict the complex thermomechanical behaviour of smart materials composed of matrix materials with embedded shape memory elements. The main advantages of this modelling are: (i) a very large field of application, (ii) relatively simple mathematical equations and (iii) the calculations only require a limited number of simple to determine shape memory data.

The modelling and computer programs are further developed and improved. Examples of improvements in short term are:

(i) the equations have to be slightly modified when the martensite mass fraction becomes close to zero or one; a subroutine will be added to solve this problem,

(ii) hysteresis and subloops can be formally included in this model and in the computer programs by adding to the equilibrium equation a term $e_{ir}([x])$ which expresses the irreversible contributions [3, 4].

(iii) pseudoelastic unloading is approximated by a constant P_s in the present treatment; the results can be improved by replacing the constant P_s by an array of $\{P_s\text{-}e_s\}$ data.

ACKNOWLEDGEMENTS

R. Stalmans and J. Van Humbeeck acknowledge the N.F.W.O. (National Fund for Scientific Research, Belgium) for a grant as Postdoctoral Researcher, resp. Research Leader.

REFERENCES

1. L. Delaey, "Diffusionless transformations", in: Materials science and technology, Vol.5, Phase transformations in materials, Ed. P. Haasen, VCH Verlagsgesellschaft mbH, Weinheim, Germany, 339-404 (1991).
2. M. Ahlers, "Martensite and equilibrium phases in Cu-Zn and Cu-Zn-Al alloys", Progress in materials science 30, 135-186 (1986).
3. R. Stalmans, "Shape memory behaviour of Cu-base alloys", Doctorate Thesis, Catholic University of Leuven, Department of Metallurgy and Materials Science, Heverlee, Belgium (1993).
4. R. Stalmans, J. Van Humbeeck and L. Delaey, "A generalized thermodynamic model to predict shape memory behaviour", Mechanics of Phase Transformations and Shape Memory Alloys, AMD-VOL.189/PVP-VOL292, ASME, Chicago, USA, 39-44, (1994).
5. R. Stalmans, J. Van Humbeeck and L. Delaey, "Thermodynamic modelling of shape memory behaviour: some examples", to be published in the proceedings of the international conference on martensitic transformations, 6 pages (1996).
6. J. L. Proft and T. W. Duerig, "The mechanical aspects of constrained recovery", Engineering aspects of shape memory alloys, Ed. T. W. Duerig et al., Butterworth-Heinemann Ltd, London, 115-129 (1990).
7. L. C. Brinson, "One-dimensional constitutive behavior of shape memory alloys: thermomechanical derivation with non-constant material functions and redefined martensite internal variable", Journal of intelligent material systems and structures 4, 229-242 (1993).
8. G. Sun and C. T. Sun, "One dimensional constitutive relation for shape-memory alloy-reinforced composite lamina", Journal of materials science 28, 6323-6328 (1993).

Active modification of the vibration frequencies of a polymer beam using shape-memory-alloy fibres

J.-E. Bidaux, J.-A. E. Månson, R. Gotthardt*

Laboratoire de Technologie des Composites et Polymères
Ecole Polytechnique Fédérale de Lausanne, CH-1015 Lausanne, Switzerland
and
*Institut de Génie Atomique
Ecole Polytechnique Fédérale de Lausanne, CH-1015 Lausanne, Switzerland

ABSTRACT

The use of shape memory alloy fibre actuators to modify the natural vibration frequencies of a composite beam is investigated. A model system composed of an epoxy matrix with prestrained shape-memory-alloy fibres is used. The natural frequencies of vibration of the beam are measured in a clamped configuration. When electrically heated, the fibres undergo a reverse martensite-to-austenite transformation. Since the geometry of the fibres during the transformation is restrained by the constraints of both the matrix and the clamping device, a recovery force is generated. This force leads to an increase in the natural vibration frequency of the whole composite beam. The transformation behaviour of the composite is compared to that of the neat fibre.

1. INTRODUCTION

The unique properties of shape memory alloys (SMA), namely shape memory, superelasticity and high damping capacity[1], are related to a displacive, diffusionless and reversible phase transformation from a high temperature austenitic phase to a low temperature martensitic phase. The austenite-to-martensite transformation temperature, M_S, depends on the composition and previous thermomechanical treatments and can be adjusted to the specific need. The martensitic state is characterised by a fine domain structure which can be reoriented under applied stress, the domains which produce a strain in the direction of the stress being favoured compared to the other domains. This results in a macroscopic deformation of the material. The important point is that, unlike normal plastic strain, this deformation can be totally recovered if the alloy is heated above the martensite-to-austenite transformation temperature (A_S). This is due to the fact that all the different domains correspond to the same crystal orientation in the austenitic phase. If the shape recovery is restrained by a bias spring or a clamping device, a stress will appear instead of the normal shape memory. This stress is called recovery stress. Both shape memory and recovery stress effects can be used to build powerful thermally-activated actuators. Advantages of SMA actuators compared to other types of actuators are the very large deformations (>5%) and stresses (>500 MPa) that can be generated.

SMA actuators have recently attracted interest in the field of composite materials. Layers of SMA fibres can be embedded in composites and used to actively control certain important characteristics of the material, e.g. shape, elastic moduli, internal stress level and natural frequencies of vibration.[2-6] Recently, a large body of experiments has been devoted to these new materials. Active strain energy tuning and active modal modification have been successfully used to modify the vibrational characteristics of composite plates containing SMA fibres.[4-9] SMA-silicone rubber composites robot fingers have been developed. In this application, a two-way shape memory effect was obtained without the need of an extra bias spring because of the presence of the silicone rubber matrix.[10] SMA-matrix interaction in composites and the effect of the matrix on the phase transformation of the fibre have been investigated.[11-13] Durability issues related to the use of SMA-composite laminates have been studied.[3]

The purpose of the present work is to investigate certain important properties of SMA-composites on a simple model system in which basic SMA-matrix interaction phenomena can be clearly identified and modelled. Following earlier work by other authors,[4-6] the recovery stresses developed by the reverse martensite-to-austenite transformation of a series of embedded NiTi fibres were used to produce a change of the natural vibration frequency of a simple epoxy beam. The stresses play the same role on the epoxy beam as does an externally applied tension on a guitar string.[4] In an earlier work,[9] the same type of measurements were performed with a maximum thermal cycling temperature close to

0-8194-2165-0/96/$6.00

the glass transition temperature. Large but non-reversible changes of the vibration frequency were obtained. In the present work, measurements were performed at much lower temperatures which allowed reversible changes of the vibrational properties to be observed.

2. EXPERIMENTAL

This work focused on epoxy beams (150 × 10 × 0.7mm) containing five embedded NiTi fibres placed along the neutral plane of the beam at a distance of 2mm from one another, Fig. 1. The fibres were 300μm diameter NiTi fibres (50.17 at% Ni) supplied by SMA INC., USA. The fibres were annealed in an Argon atmosphere and then quenched in water at 20°C. Two annealing treatments were used and compared. The first set of fibres was treated 10min at 477°C and had the following characteristic transformation temperatures: $M_S \cong -3°C$, $M_f \cong -37°C$, $A_S \cong 10°C$, $A_f \cong 63°C$. The second set was annealed 30min at 526°C and had the transformation temperatures: $M_S \cong 23°C$, $M_f \cong 6°C$, $A_S \cong 41°C$, $A_f \cong 69°C$, according to DSC measurements. The fibres were cooled at -30°C to ensure a nearly complete martensitic state, prestrained to 5% at room temperature and embedded into the epoxy resin. The prestrain was maintained during curing, restraining the fibres from their normal shape recovery. The resin, supplied by Ciba Geigy, was composed of LY556 bisphenol A epoxy resin, HY917 anhydride hardener and DY070 amine accelerator, mixed in the proportions 100:90:0.5 by mass. The resin was cured 4h at 80°C and then 8h at 140°C, resulting in a glass transition temperature of $Tg \cong 150°C$.

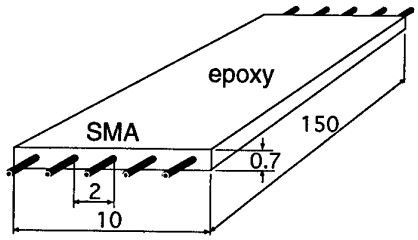


Fig.1. Schematic drawing of the SMA-composite containing five 300μm diameter NiTi fibres embedded in the neutral plane of the beam

A new experimental set-up was developed to study the change of the vibrational response of SMA-composite beams activated by an electrical current heating (Fig. 2). The experimental set-up is composed of a sample holder, an electromagnetic shaker, a Laser Doppler Detector (Brüel & Kjaer) and additional electronic modules to generate, record and treat the measured signals. A description of the electronics can be found in ref. [14]. The U-shaped steel sample holder is fixed on the electromagnetic shaker. Transverse vibrations of the composite beam (displacement perpendicular to the plane of the beam) are excited either by the shaker or manually. Since the changes of the fundamental vibration frequencies were large, manual excitation of the beam was found sufficiently reliable. The fundamental resonance frequency of the beam is extracted by taking the maximum on the Fourier Transform of the measured signal. The sample holder was designed to be sufficiently stiff so as to avoid unwanted resonances in the low frequency range.

The experimental set-up allowed the measurement of the static axial force generated in the beam by the phase transformation of the SMAs. As will be shown later on, the modifications of the frequency response are mainly due to the existence of this static force. The force transducer was made of four strain gauges glued on a machined, 4mm thick, part of the sample holder. Two strain gauges were mounted on each opposite face and connected in full bridge to minimise errors due to changes of temperature. The transducer was calibrated using a series of weights. Despite the finite compliance of the transducer, the sample holder could be considered as rigid: the displacement at the fixtures was calculated to be less than 50μm for a force of 100N. Thus, a maximum unwanted axial strain of less than 0.05% is obtained, which is negligible compared to the NiTi phase transformation strain (5%) and to the thermal expansion in the epoxy resin ($\cong$ 0.7% per 100°C). The composite beam could be pretensioned by means of a screw placed on one of the fixtures of the sample holder.

The NiTi fibres were heated by direct electrical current and cooled both by natural convection at the composite surface and by conduction at the composite ends. The fibres were connected in series to ensure a rigorously constant current in all the fibres. The temperature of the sample was monitored using thin, 100 μm diameter thermocouples. One

thermocouple was introduced and glued in a small hole drilled in the centre of the composite beam close to one of the fibres, another was glued on the surface just above the central fibre. The temperatures measured by the two thermocouples were found to differ by less than 3°C. The cement was composed of talc mixed with sodium silicate. It was used to ensure a good thermal contact between the thermocouples and the sample. It must be kept in mind that the temperature is measured in the matrix and not in the NiTi fibre.

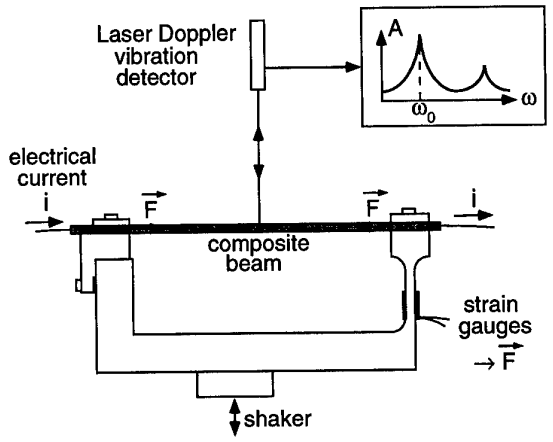


Fig.2 Schematic drawing of the experimental set-up allowing the simultaneous measurement of the axial force and frequency response of SMA-composite beams

3. RESULTS AND DISCUSSION

3.1 The SMA fibre actuator:

The temperature dependence of the axial force (recovery force) developed by SMA fibre actuators is shown in Fig 3. The fibres were initially prestrained by 5% and clamped at both ends.

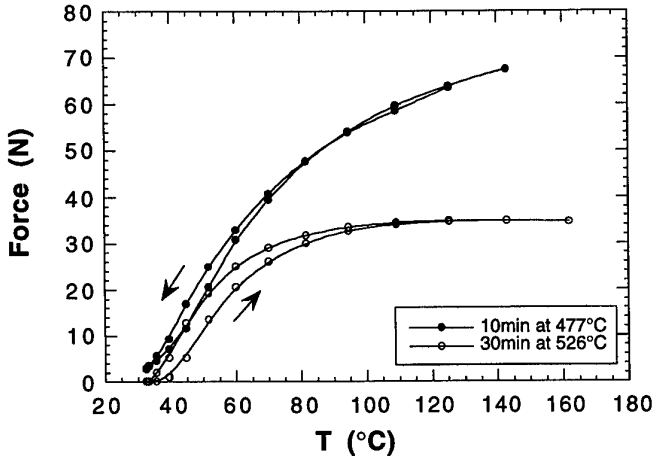


Fig. 3 Axial force versus temperature for 5% prestrained NiTi fibres after two different thermal treatments (a) 10min at 477°C (b) 30min at 526°C

A tensile force develops along the axis of the fibres when heated. At low temperature, the force increases strongly with temperature but tends to level out in the range of about 100°C, especially in the case of the treatment of 30min at 526°C. The initial increase of the force is related to the martensite-to-austenite transformation. The saturation of the

force is probably due to the completion of the transformation process. The force versus temperature behaviour is reversible with a small hysteresis of about 4°C. As seen here, the maximum forces produced by the SMA actuator depend strongly on the previous annealing treatment. To obtain maximum recovery forces, an optimum annealing treatment must be performed. Accordingly, the annealing treatment of 10min at 477°C was chosen for the embedded fibres used throughout this work.

3.2 The SMA-composite:

3.2.1. Force

The total force measured at the extremities of a clamped-clamped composite containing SMA fibres can as a first approximation be written as:

$$F_{tot}(T) = F_0 - F_{th}(T) + F_{rec}(T) \quad (1)$$

where F_0 is the external applied force (if any), $F_{th}(T)$ is the sum of the axial thermal forces and $F_{rec}(T)$ is the recovery force produced by the martensite-to-austenite transformation in the embedded SMA fibres. It can be shown that the forces related to thermal expansion of the fibres are negligible compared to the forces related to matrix thermal expansion. Accordingly, the thermal forces can be written by the following equation:

$$F_{th} = \alpha_m (T - T_0) E_m A_m \quad (2)$$

where E_m, A_m and α_m are the matrix elastic modulus, cross-sectional area and thermal expansion coefficient respectively. T_0 is the room temperature. The recovery force $F_{rec}(T)$ is a complex function which depends mainly on the temperature and on the amount of prestrain but also on the previous thermomechanical treatment. For neat SMA fibres, $F_{rec}(T)$ is given by the curves of Fig. 3. In embedded SMA fibres, the transformation behaviour can be modified by the surrounding matrix and $F_{rec}(T)$ can differ from the behaviour shown in Fig.3.

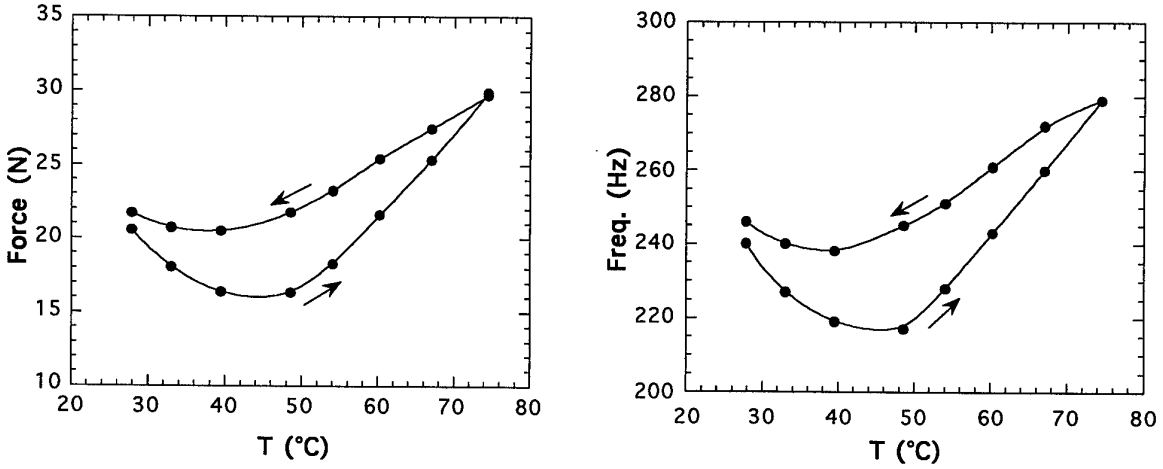


Fig. 4. Axial force (a) and natural frequency of vibration (b) versus matrix temperature with 5% prestrained NiTi fibres and matrix resin with Tg ≅ 140°C.

Fig. 4(a) shows the temperature dependence of the axial force for ab SMA-composite. Starting at an initial tension, F_0, of about 20N, the force initially decreases when the temperature increases. This is due to the thermal expansion of the matrix (see Eqs.1 and 2). Because thermal expansion is prevented by the clamping, an axial compressive force exists in the matrix. As has been shown in a previous paper[9], in the absence of the recovery forces of the NiTi fibres, this compressive force eventually leads to a buckling of the composite beam. At a temperature of about 50°C, an increase of the force (and frequency) is observed. According to Eq. 1, it means that at that temperature, the tensile forces produced by the martensite-to-austenite transformation in the SMA fibres exceed the thermal compressive forces generated by the surrounding matrix. For temperatures above 50°C the slope of the force versus temperature curve is positive, the

behaviour being dominated by the SMA fibres. Upon subsequent cooling, the curve does not follow the same path as during heating. Nevertheless, a nearly closed loop is observed with a hysteresis of the order of 10°C. This is larger than the hysteresis observed in the neat fibres (Fig.3). This kind of loop can be reproduced more that 20 times with minor changes. The most significant difference is the small irreversible increase of the room temperature force observed after each thermal cycle, which is due to a time and temperature dependent phenomenon. The higher the maximum cycling temperature, the higher the irreversible force increase.

Considering the force developed by the neat fibre actuator (Fig.3), i.e. about 40N at 75°C, a total recovery force of about 200N is expected for the composite. Actually, the difference between the maximum and the minimum force measured during the thermal cycle (Fig. 4) is much lower, i.e. about 15N. This may be due to two main reasons: First, the presence of the thermal compressive force which opposes the recovery force. According to Eq. 2 and by taking the room temperature values E_m= 2.9 GPa, A_m= 7mm^2 and α_m= 70×10^{-6}/°C, a considerable thermal force of about -80N is expected. Secondly, as mentioned earlier, the phase transformation behaviour is different in the composite compared to the neat fibre. In particular the hysteresis is considerably higher. All these factors considerably reduce the efficiency of SMA actuators in the composite.

3.2.2. Frequency

Fig. 4(b) shows that, together with the force, the change of the fundamental vibration frequency of the composite beam changes. Both have a similar temperature dependence showing the strong correlation between the two effects. The change in the resonance frequency is directly related to the change in the axial force. The main point to notice is that the force is internally generated by a change of the material state rather than by the application of an external force. The relationship between resonance frequency and the axial force of a beam in a clamped-clamped arrangement is given by the solution of following equation[5]:

$$-2\sqrt{\rho A\lambda} - F_{tot} / \sqrt{EI}\sin(\alpha l)\sinh(\gamma l) + 2\sqrt{\rho A\lambda}\cos(\alpha l)\cosh h(\gamma l) = 0 \qquad (3)$$

where $\lambda=\omega^2$, ρA is the mass per unit length and l is the distance between the clamps. The α and γ coefficients themselves depend on the frequency ω and on the axial force F_{tot}. [5] This equation can be solved numerically. The experimental relationship between the fundamental resonance frequency and the axial force is shown in Fig. 5. These experimental data are compared to the theoretical prediction of Eq.3, using the parameters: l=106mm, E_f=70GPa, E_m=2.9GPa, ρ_f=6.5g/cm^3, ρ_m=1.2g/cm^3. The agreement is fairly good taking into account that the above parameters correspond to room temperature values. This shows clearly that, for the geometry used, the frequency change is dominated by the effect of the axial force and that the temperature dependence of the bending stiffness is negligible.

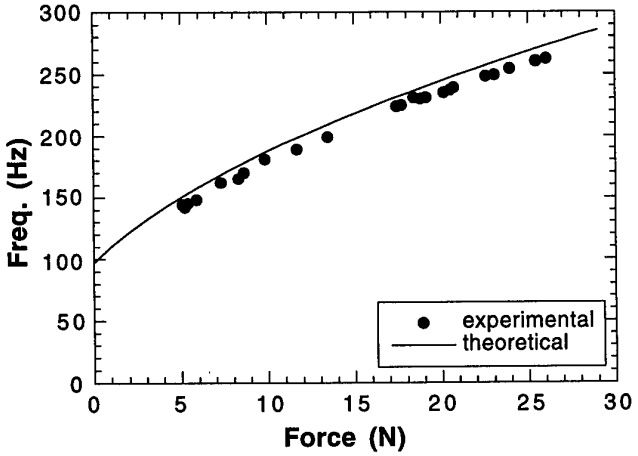


Fig. 5 Vibration frequency versus axial force for an SMA composite measured during a thermal cycle similar to the one shown in Fig. 4

4. CONCLUSIONS

The above results confirm that SMA fibres can be used to control the vibrational behaviour of composites. Reversible increases/decreases of the vibration frequency can be obtained by heating/cooling the fibres using an electrical current. Our results show that the frequency versus temperature characteristic of composites differs from the one of neat SMA fibres. In particular, a higher transformation hysteresis is observed. The fibre volume fraction and the fibre annealing thermal treatment must be optimal to obtain the highest possible recovery force to counterbalance the negative effect of thermal expansion.

5. ACKNOWLEDGEMENTS

The authors would like to thank P. Berguerand, P. Kim and F. Bonjour, from the Laboratoire de Technologie des Composites et Polymères and B. Guisolan from the Institut de Génie Atomique, Ecole Polytechnique Fédérale de Lausanne, Switzerland, for their help in designing and building the sample holder and the composite mould. We also would like to thank Dr A. Karimi and P.-H.Giauque from the Institut de Génie Atomique, for the use of their vibration detector. The financial support of the Swiss Priority Program on Materials Research is acknowledged.

6. REFERENCES

1. T.W. Duerig, K.N. Melton, D. Stöckel, C.M. Wayman, *Engineering aspects of shape memory alloys,* Butterworth-Heinemann, London, 1990
2. M. V. Gandhi, B. S. Thompson, *Smart materials and structures,* Chapman and Hall, London, 1992
3. C.M. Friend, N. Morgan, "The actuation response of model SMA hybrid laminates", *J. de Physique IV,* **5,** C2-pp. 415-420, 1995
4. C. A. Rogers, C. Liang, D.K. Barker, "Dynamic control concepts using shape memory alloy-reinforced plates", U.S. Army Research Office Workshop on Smart Materials, Struct., and Math. Issues, Virginia Polytechnic Inst. and State Univ. Blacksburg, Virginia p. 39, 1988
5. H. G. Mooi, "Active control of structural parameters of a composite strip using embedded shape memory alloy wires", Master Thesis, University of Twente, 1992
6. A. Baz, J. Ro, "Thermodynamic characteristics of Nitinol-reinforced composite beams", *Comp. Engineering,* **2,** Nos 5-7, pp. 527-542, 1992
7. A. Venkatesh, J. Hilborn, J.-E. Bidaux, R. Gotthardt, "Active vibration control of flexible linkage mechanisms using shape memory alloy fibre-reinforced composites", Proc. First European Conf. on Smart Structures and Materials, Glasgow, pp. 185-188, 1992
8. R. Chandra, "Active strain energy tuning of composite beams using shape memory alloy actuators", SPIE vol. 1917, Smart Structures and Intelligent Systems, pp. 267-284, 1993
9. J.-E. Bidaux, N. Bernet, C. Sarwa, J.-A. E. Månson, R. Gotthardt, "Vibration frequency control of a polymer beam using embedded shape-memory-alloy fibres", to be published in Proc. of the Int. Conf. on Mart. Transf., ICOMAT'95, Lausanne, 1995
10. K. Escher, E. Hornbogen, "Aspects of two-way shape memory in NiTi-Silicon composite materials", *J. de Physique,* **1,** C4-pp. 427-432, 1991
11. J.-E. Bidaux, L. Bataillard, J.-A. Månson, R. Gotthardt, "Phase transformation behaviour of thin shape memory alloy wires embedded in a polymer matrix composite", *J. de Physique IV,* **3** , C7-p. 561-564,.1993
12. J.-E. Bidaux, J.-A. Månson, R. Gotthardt, "Dynamic mechanical properties and phase transformation in polymer-based shape memory alloy composites", Proc. of the First Int. Conf. on Shape Memory and Superelastic Technologies, Asilomar, Pacific Grove, 1994, A. R. Pelton, D. Hodgson and T. Duerig Eds., pp. 37-42, 1994
13. J.-E. Bidaux, W.J. Yu, R. Gotthardt, J.-A.E, Månson, "Modelling of the martensitic transformation in shape memory alloy composites", *J. de Physique IV,* **5,** C2-pp. 543-548, 1995
14 A. Karimi, P.H. Giauque, J. L. Martin, A. Salito, G. Barbezat, "Development of high damping alloys using vacuum plasma spraying", Proc. of the Eighth Inter. Conf. on Surface Modif. Technologies, Nice, France, 1994, Surface Modification Technologies VIII, T. S. Sudarshan and M. Jeandin Eds., The Institute of Materials, pp. 759-771, 1995

Paper presented at the Third ICIM/ECSSM '96, Lyon '96

ON THE RESPONSES AND RESPONSIVE SHAPE CONTROL OF ENVIRONMENTALLY RESPONSIVE COMPOSITES WITH EMBEDDED Ti-Ni ALLOY AS EFFECTOR

Hitoshi Yoshida*, Atsuo Funaki** and Shoichiro Yano*
* National Institute of Materials and Chemical Research, 1-1 Higashi , Tsukuba 305, Japan
** Mie Industrial Research Institute , 3485, Ohtsuka, Takachayakomoricho, Tsu, Mie 514, Japan

Abstract

Bi-directional Environmentally Responsive Composites (ERC) composed of Ti-Ni alloy effectors and CFRTP (Carbon Fibre Reinforced Thermoplastic) were created in order to investigate the temperature responses and a methods of responsive shape control of the ERC. Environmental responsiveness was defined as the responsiveness rate and the recovery rate corresponding to the change of environmental temperature. Responsive shape control was done by the controlling for the curvature of ERC, namely, when the mechanical properties and the initial curvature of the effectors were given and the curvatures of ERC at the low and high temperature were set, the equations were derived in order to calculate the initial curvature and flexural rigidity of the matrices. As a result, it was found that a bi-directional responsive ERC has superior performance could be made by appropriately choosing the properties, the geomatries and volume fractions of effectors and matrices. The ratios of experimental and calculating values are very close on 1.0, the numerical results were fairly satisfactory ones.

Introduction

Environmentally responsive materials that respond to the environmental conditions and exhibit various functions are called intelligent or smart materials and research on such materials are actively beginning in various fields. The definitions of intelligent or smart materials are those materials that possess sensor and effector functions within themselves as well as the processing functions to be linked with inside or outside of the materials. In general, environmentally responsive materials are classified into two types, that is, the environmentally responsive materials of microscopically distributed type in type which the three functions are monolithically built-in within the materials, and the environmentally responsive materials of macroscopically distributed type that realize environmental responses by dispersing functional row materials that have the three functions in the matrices and integrating them[1]. Optical fibers, piezoelectric ceramics, shape memory alloy and electro-rheological fluid are being studied as the candidates for the functional raw materials for the environmentally responsive materials of macroscopically distributed type. C.A. Rogers et al.[2] proposed a method to use shape memory alloys (SMA) as effectors (also called actuators) in order to extend material life-span by accelerating closure of fatigue cracks and lowering crack propagation speed using multiple shape memory alloys pasted at the bottom of the notch part where stress concentration took place and by applying electric currents there to raise temperature thus causing contraction forces and lowering the average stress at that part. Y. Furuya[3] showed that stress concentration at notch tips can be reduced by placing Ti-Ni wires that were 1% pre-strained on the surface of tensile test specimens made of photoelastic epoxy resin and by applying electric heating for the Ti-Ni wires to contract with shape memory. In the present research, new environmentally responsive composites that be able to respond in bi-directions depending on the temperature were fabricated and their environmental responses, in particular, their shape responses, were studied by using Ti-Ni alloy wires as effectors which can

0-8194-2165-0/96/$6.00

generate very large forces and by using CFRTP whose absorption energy is large as matrices. As a result, it was found that environmentally responsive composites has bi-directional responsive function be able to be made by appropriately choosing the properties and the volume fractions of the effectors and matrices.

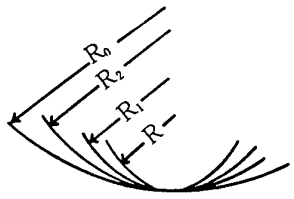


Fig. 1 Flexural responses of environmentally responsive composites

Theory of realizing bi-directional environmental responses

As shown in Figure 1, an effector having an initial curvature of κ_0 ($=1/R_0$) and a matrix having an initial curvature of κ ($=1/R$) are mixed by using RTV(Room Temperature Vulcanization) resin and cured and become to be ERC. The curvature of ERC becomes κ_1 ($=1/R_1$) as releasing of constraint at room temperature. A strain energy per unit length stored in an effector and a matrix is as follows[4]:

$$\bar{U}_{e1} = \frac{E_{e1} I_e}{2} (\kappa_0 - \kappa_1)^2, \qquad \bar{U}_{m1} = \frac{E_{m1} I_m}{2} (\kappa - \kappa_1)^2 \tag{1}$$

where I_e and I_m are the moment of inertia of the effector and the matrix, respectively. The following notations are adopted as

$$\kappa_0 - \kappa_1 = k, \qquad \kappa - \kappa_0 = K \tag{2}$$

Since, following equation is derived from equation (2)

$$\kappa - \kappa_1 = K + k \tag{3}$$

A potential energy of the total system can be expressed by following,

$$\pi = \bar{U}_{e1} + \bar{U}_{m1} = \frac{E_{e1} I_e}{2} k^2 + \frac{E_{m1} I_m}{2} (K + k)^2 \tag{4}$$

The cuvature, , of the composite consisting of the effector and the matrix being in equilibrium is obtained from $\partial \pi / \partial k = 0$, that is

$$\partial \pi / \partial k = E_{e1} I_e k + E_{m1} I_m (K + k) = 0 \tag{5}$$

which results in

$$\kappa_1 = \kappa_0 + \frac{E_{m1} I_m (\kappa - \kappa_0)}{E_{e1} I_e + E_{m1} I_m} \tag{6}$$

The curvature of ERC at high temperature, κ_2, is, similar to equation (6), expressed as

$$\kappa_2 = \kappa_0 + \frac{E_{mh} I_m (\kappa - \kappa_0)}{E_{eh} I_e + E_{mh} I_m} \tag{7}$$

where E_{eh} and E_{mh} are the young's modulus of the effector and matrix at high temperature, respectively. Consequently, this ERC system can repeat bi-directional shape responses within the range between κ_1 and κ_2 for a change in environmental temperatures that accompany with the phase transformation from martensite to austenite.

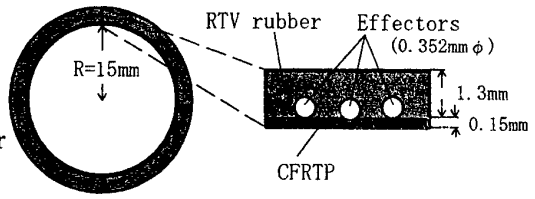


Fig. 2 Dimensions and geometry of ERC specimen

Table 1 Central angle for open part of ERC specimen (designed value, deg.)

Specimen	CA1	CA2	CA3	CA4	CA5
At low temperature	0°	0°	45°	90°	180° (144°)
	$\kappa_1 = 1/15.0$ (1/mm)	$\kappa_1 = 1/15.0$ (1/mm)	$\kappa_1 = 1/17.5$ (1/mm)	$\kappa_1 = 1/20.0$ (1/mm)	$\kappa_1 = 1/25.0$ (1/mm)
At high temperature	90°	45°	90°	180°	270° (230°)
	$\kappa_2 = 1/20.0$ (1/mm)	$\kappa_2 = 1/17.5$ (1/mm)	$\kappa_2 = 1/20.0$ (1/mm)	$\kappa_2 = 1/30.0$ (1/mm)	$\kappa_2 = 1/41.5$ (1/mm)

On the applicable viewpoint, it is important that κ_1 and κ_2 are able to be designed, that is, the responsive shape is able to be controled according to various needs. In the present study, the material properties of matrix were derived from κ_1 and κ_2 when the material properties of effector had been given. After putting to $E_{eh}/E_{el}=p$ and $E_{mh}/E_{ml}=q$ in equations (6) and (7), solving those equations regarding $E_{ml}I_m$ and κ, we can obtain following equations

$$E_{ml}I_m = \frac{qE_{el}I_e(\kappa_0-\kappa_1) - pE_{el}I_e(\kappa_0-\kappa_2)}{q(\kappa_1-\kappa_2)} \quad (8)$$

$$\kappa = \kappa_1 + \frac{q(\kappa_1-\kappa_2)(\kappa_1-\kappa_0)}{q(\kappa_0-\kappa_1) - p(\kappa_0-\kappa_2)} \quad (9)$$

Constituent materials and ERC specimens

Material properties of constituent materials

Ti-Ni alloy wire used in the present study was employed KSM 45 was made by Kanto Special Steel Co., Ltd.. It was 0.352mm in diameter and in initial curvature equal to zero.
The phase transformation temperatures were $A_S = 48$ and $A_f = 61$ degrees centigrade, respectively, where, A_S and A_f express the start and finish temperature for austenite phase. The flexural rigidities at low ($<A_S$) and high ($>A_f$) temperature were $E_{el}I_e = 10.2\,Nmm^2$ and $E_{eh}I_e = 42.6Nmm^2$, hence the ratio of flexural rigidity at low and high temperature is equal to 4.17. As known from equation (6) and (7), the ratio of κ_1 and κ_2 depends on the ratio of flexural rigidity, namely, an effector possess large value of the ratio of flexural rigidity is desirable for constituent material of ERC. CFRTP prepreg used as a matrix was APC-2 was made by ICI Co., Ltd.. These prepreg were formed into the designed curvature by

using electric-furnace prior to fabricating of ERC. CFRTP in after forming was 0.15mm in thickness and 111,000 N/mm^2 in Young's modulus. Young's modulus of RTV resin used as the binder was equal to 1.99 N/mm^2 and this value is negligible small as compared with the one of the CFRTP. Therefore, there are no effects on the flexural rigidity of ERC. Since Young's modulus of CFRTP and RTV resin are approximately constant within the range of experimenntal temperature, it is q=1.0 in equations (8) and (9).

Fabrication of ERC specimens

As shown in Figure 2, canape type specimens were fabricated in the present study. Types of responsive shape were designed five kinds of type for each specimen as shown in Table 1. these types were designed so that the circumferential lengths of each specimen are equal to the circumferential length of the specimen which is 15mm in radious of curvature and closed type one at low temperature, such as specimen CA1 or CA2, and the central angeles for open part of the circumference were designed as shown in Table 1 at low or high temperature, respectively. The values of flexural rigididy, E_mI_m, and initial curvature, κ, of the matrix were calculated from equation (8) and (9) are shown in Table 2.

Table 2 Curvature of ERC specimens were designed and material properties were calculated

Specimen	Curvature of ERC at low temperature, κ_1 (1/mm)	Curvature of ERC at high temperature, κ_2 (1/mm)	Flexural rigidity of CFRTP used as matrix of ERC, E_mI_m (Nmm^2) (kgfmm^2)	Initial curvature of CFRTP used as matrix of ERC, κ (1/mm)	Width of ERC specimen (mm)	Number of embedded efectors
CA1	1/15	1/20	86.8 (8.85)	1/13.5	6.2	2
CA2	1/15	1/17.5	183 (18.7)	1/14.2	6.6	1
CA3	1/17.5	1/20	216 (22.0)	1/16.7	7.8	1
CA4	1/20	1/30	54.4 (5.55)	1/16.9	5.9	3
CA5	1/30 (1/25)	1/60 (1/41.5)	38.3 (3.96)	1/20.6	5.0	4

Experiments

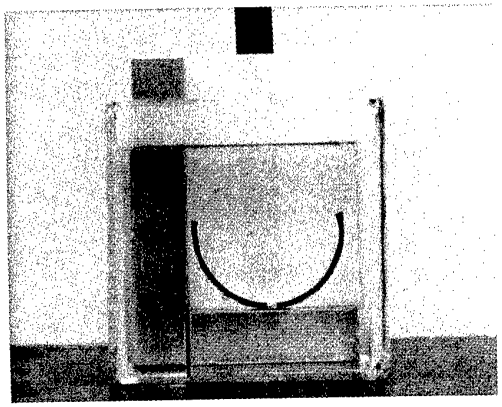


Fig.3 Observing apparatus for the responsive shape of ERC specimen(CA4-5) at high temperature

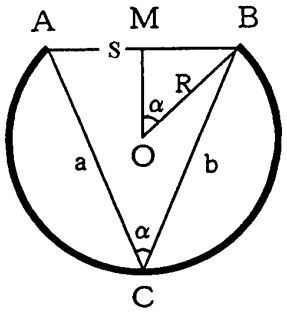


Fig.4 Chimerical model for calculating of responsive shape

Measurement for responsive shape was done by measuring of the shape of specimens on the photograph had been taken at low and high temperature. The shapes of specimens were taken pictures in an air-atmosphere at room temperature and in a high temperature water bath at about 62 degrees centigrade. Figure 3 shows an observing apparatus for the responsive shape of ERC at high temperature. Figure 4 shows the chimerical model for calculating of responsive shape. The radius of curvature at each temperature were derived from fllowing equation according to the notations in Figure 4.

$$R = \frac{s}{2}\sqrt{\frac{1}{1-A^2}} \qquad \text{where,} \qquad A = \frac{a^2+b^2-s^2}{2ab} \tag{10}$$

Figure 5 shows the time dependant process of bi-directional shape response for ERC specimens (specimen No.: CA5-4). In this case , the shape of specimen almost recover to initial state at 90 sec. later of natural cooling.

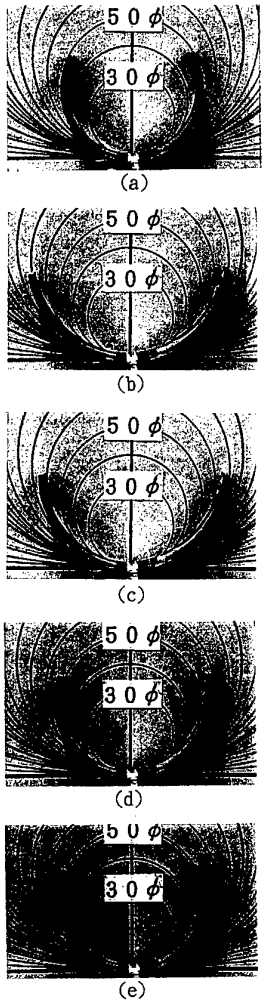


Fig.5 Time dependant process of bi-directional shape response for ERC specimens
(a) initial (at room temperature) state
(b) state at high temperature
(c) 30 sec. later (d) 60 sec. later
(e) 90 sec. later .

Experimental results and discussions

Experimental results for responsive shape control of ERC specimens are shown in Table 3. The ratios of experimental and designed value for the curvature of ERC are from 0.96 to 1.11 at low temperature and from 0.98 to 1.30 at high temperature. The responsiveness rate and recovery rate were defined as κ_1/κ_2 and κ_1/κ_1^* in the present study, where implies the curvature of ERC specimens at 1 hr. later of natural cooling after finishing the experiments at high temperature. Table 4 shows the responsiveness rate and recovery rate of ERC specimens. The ratios of designed and calculated value in the responsiveness rate are entirely below the value of 1.0. This fact means that the shape of ERC specimens did not attain to the shape was previously designed. It is one of the reasons that there were the constraints to fluxural deformation by using an adhesion used for temporary binding for effector and matrix when ERC specimens were fabricated.

Conclusions

In order to realize new types of composites that exhibit bi-directional responses for temperature change, Environmentally Responsive Composites (ERC) using Ti-Ni alloy wires as effectors and CFRTP as matrix were created. Analysis and experiments were conducted on the responsiveness rate as an index to indicate responsive sensitivity and on the recovery rate as index to indicate bi-directional responsiveness. Forthermore, a method of responsive shape control would be importance from the point of view of practical applications was discussed analytically and experimentally. The principle of realizing such a new type of bi-directional responsiveness is to take advantage of the effector's behavior in which the modulus of elasticity above the activation temperature (austenite state) is much larger than that below the activation

Table 3 Experimental results for responsive shape control of ERC specimens

Specimen	Cuvature at low temperature, κ_1 (mm^{-1})			Cuvature at high temperature, κ_2 (mm^{-1})		
	Designed value κ_1	Experimental value, κ_1'	Ratio of κ_1'/κ_1	Designed value κ_2	Experimental value, κ_2'	Ratio of κ_2'/κ_2
CA1-1	1/15.0	1/15.20	0.99	1/20.0	1/17.67	1.13
CA1-2		1/15.43	0.97		1/17.89	1.12
CA1-3		1/15.06	1.00		1/17.43	1.15
CA1-4		1/15.16	0.99		1/17.79	1.12
CA1-5		1/15.36	0.98		1/17.89	1.18
mean		1/15.24	0.99		1/17.73	1.14
CA2-1	1/15.0	1/15.03	1.00	1/17.5	1/16.88	1.04
CA2-2		1/15.03	1.00		1/16.77	1.04
CA2-3		1/15.50	0.97		1/17.05	1.03
CA2-4		1/15.33	0.98		1/16.79	1.04
CA2-5		1/15.04	1.00		1/15.93	1.10
mean		1/15.19	0.99		1/16.68	1.05
CA3-1	1/17.5	1/18.31	0.96	1/20.0	1/20.50	0.98
CA3-2		1/17.81	0.98		1/19.50	1.03
CA3-3		1/17.31	1.01		1/18.89	1.06
CA3-4		1/17.81	0.98		1/19.48	1.03
CA3-5		1/18.24	0.96		1/19.80	1.01
mean		1/17.90	0.98		1/19.63	1.02
CA4-1	1/20.0	1/20.12	0.99	1/30.0	1/27.29	1.10
CA4-2		1/20.18	0.99		1/27.39	1.10
CA4-3		1/19.62	1.02		1/25.74	1.12
CA4-4		1/20.59	0.97		1/27.66	1.08
CA4-5		1/20.36	0.98		1/28.18	1.06
mean		1/20.17	0.99		1/27.25	1.10
CA5-1	1/25.0	1/22.58	1.11	1/41.5	1/34.93	1.19
CA5-2		1/25.38	0.98		1/41.44	1.00
CA5-3		1/22.64	1.10		1/32.03	1.30
CA5-4		1/22.76	1.10		1/33.07	1.25
CA5-5		1/23.52	1.06		1/38.19	1.09
mean		1/23.38	1.07		1/35.93	1.17

temperature (martensite state). Although the values of the responsiveness rate were not necessarily satisfying ones, the overall comparison between the experimental and theoretical values verified the validity of the theoretical analyses.

Acknowledgment

Thanks are due to Mr N. Sekino of Kanto Special Steel Co., Ltd. and Mr S. Kitami of Yokohama Rubber Co., Ltd. for their supports and valuable suggestions in the fabrication of specimens and providing Ti-Ni alloy wires and RTV resin samples.

Reference

1. N. Koshizaki et al., "Intelligent functionalties of composite materials", Bulletin of Industrial Products Research Institute (1992), No.127, 99-128.

2. C.A. Rogers, C. Liang and S. Li, "Active damage control of hybrid material systems using induced strain actuater", Proc. 32nd Structures, Structural Dynamics and Materials Conference

Table 4 Experimental results for responsiveness rate and recovery rate

Specimen	Responsiveness rate, κ_1/κ_2			Initial curvature, κ_1	Curvature after natural cooling, κ_1^*	Recovery rate, $\gamma = \kappa_1^*/\kappa_1$
	Designed value $\lambda = \kappa_1/\kappa_2$	Experimental value, $\lambda' = \kappa_1'/\kappa_2'$	Ratio of λ'/λ			
CA1-1	1.33	1.16	0.87	1/15.20	1/14.97	1.02
CA1-2		1.16	0.87	1/15.43	1/15.17	1.02
CA1-3		1.16	0.87	1/15.06	1/15.29	0.98
CA1-4		1.17	0.88	1/15.16	1/15.47	0.98
CA1-5		1.16	0.87	1/15.36	1/15.66	0.98
mean		1.16	0.87	1/15.24	1/15.31	1.00
CA2-1	1.17	1.12	0.98	1/15.03	1/15.32	0.98
CA2-2		1.12	0.96	1/15.03	1/15.30	0.98
CA2-3		1.10	0.94	1/15.50	1/15.63	0.99
CA2-4		1.10	0.94	1/15.33	1/15.20	1.01
CA2-5		1.06	0.91	1/15.04	1/15.08	1.00
mean		1.10	0.94	1/15.19	1/15.31	0.99
CA3-1	1.14	1.12	0.98	1/18.31	1/18.53	0.99
CA3-2		1.09	0.96	1/17.81	1/17.96	0.99
CA3-3		1.09	0.96	1/17.31	1/17.46	0.99
CA3-4		1.09	0.96	1/17.81	1/17.81	1.00
CA3-5		1.09	0.96	1/18.24	1/17.97	1.02
mean		1.10	0.96	1/17.90	1/17.95	1.00
CA4-1	1.5	1.36	0.91	1/20.12	1/20.29	0.99
CA4-2		1.36	0.91	1/20.18	1/20.14	1.00
CA4-3		1.31	0.87	1/19.62	1/19.25	1.02
CA4-4		1.34	0.89	1/20.59	1/20.67	1.00
CA4-5		1.38	0.92	1/20.36	1/20.60	0.99
mean		1.35	0.90	1/20.17	1/20.19	1.00
CA5-1	1.66	1.55	0.93	1/22.58	1/22.96	0.98
CA5-2		1.63	0.98	1/25.38	1/26.15	0.97
CA5-3		1.41	0.85	1/22.64	1/22.99	0.98
CA5-4		1.45	0.87	1/22.76	1/23.49	0.97
CA5-5		1.62	0.98	1/23.52	1/24.43	0.96
mean		1.55	0.93	1/23.38	1/24.00	0.97

* κ_1^* is the curvature at 1 hr. later of natural cooling after finishing the experiments at high temperature.

(1991), 1190-1203.

3. Y. Furuya, "Materialization of intelligent functions", Proc. of the 2nd Symposium of Intelligent Materials (1993),16-17.

4. H. Yoshida et al., "Two-way temperature responses of intelligent composite structures with embedded Ti-Ni alloy as effectors", Proc. of the 16th International SAMPE Europe Conference of the Society for the Advancement of Material and Process Engineering, Salzburg,Austria, May 30-June 1,1995,31-49.

INFLUENCE OF PROCESSING CONDITIONS ON ACTUATION PROPERTIES OF ADAPTIVE HYBRID COMPOSITES

J. Grando and M. Salvia

Ecole Centrale de Lyon, Département Matériaux Mécanique-Physique, URA CNRS 447, BP 163
69131 Ecully Cedex, France

ABSTRACT

Adaptive hybrid composites are materials in which actuators are embedded into polymer matrix composites. One particular class of these actuators are shape memory alloys (SMA). Thin wires ($\phi = 200$ μm) of Nickel-Titanium-Copper (nitinol) were incorporated into a glass-epoxy unidirectional laminate during lay-up. Then the whole structure was subjected to different curing procedures. The interfacial shear strength between the matrix and the nitinol wires in various structural states was determined by a micromechanical test involving the interface directly - the drop test. Clamped-free (cantilever) beam method was used to evaluate the effect of actuation by heating the nitinol wires embedded into the composite. The comparison between the different composites points out first the leading role of the interfacial shear strength. On the other hand, it can be noted the occurrence of a self-trained two way shape memory effect.

INTRODUCTION

A continuously growing attention has been given in the last years to the development of smart materials and structures. Among them, composite materials have obviously to play a leading role. Due to their processing methods it is relatively easy to embed in the structural material itself, a lot of sensors and actuators at a mesoscopic scale. One particular class of actuators is shape memory alloys (SMA) wires which can be incorporated either in polymeric matrix (Escher & Hornbogen, 1991; Bidaux & al., 1995) or in classical fibre epoxy composites structures (Rogers & al., 1988 ; Hebda & al., 1995).

In metallic alloys the shape memory effect is related to the displacive, diffusionless and reversible transformation between a low temperature martensitic phase and the high temperature austenitic phase. When such an alloy undergoes a permanent deformation in the martensitic state this deformation can be wholly recovered by heating above the martensite to austenite temperature transformation. That is the so-called one way shape memory effect (OWSME). If the shape memory was prevented to occur by means of clamping devices or by embedding into polymer or composite material, an important recovery stress appeared. Actuation applications requires, in principle, the use of SMA exhibiting two way shape memory effect (TWSME). Such effect or training was achieved by suitable temperature cycling between the martensite and austenite phases under constant stress or strain. In these conditions a reversible phase transformation with reversible shape memory or recovery stress can be initiated by heating and cooling.

First attempts to embed SMA wires into fibre reinforced polymer has been unsuccessful, mainly due to manufacturing processes and the related weakness of interfacial bonding. In further studies, SMA wires has been incorporated using either coupling sleeves (Epps & al, 1995) or clamping systems (Doran, 1994). However, in spite of more promising results (Friend & Morgan, 1994 ; Paine & al., 1995) no final conclusions in order to define the best processing conditions and the most suitable structural state of the SMA were given.

In this work four glass-epoxy composites with embedded nitinol wires were made varying either by the structural state of the SMA or by the mechanical characteristics of the surrounding composite in order to relate the activation properties to these different features.

MATERIALS

The SMA wires were Ti-Ni-Cu alloys with 6 at% of Copper produced by Swiss Metal ($\phi = 200\mu m$). Table 1 gives the used nitinol transformation temperatures measured using calorimetric measurements after annealing at 425°C during 1 hour.

A_S (Austenite start)	A_f (Austenite finish)	M_S (Martensite start)	M_f (Martensite finish)
35°C	45°C	18°C	5°C

Table 1 : Phase transformations temperatures of the nitinol wires

The first two systems, referenced A and B, were prepared from E-glass unidirectional fabric (VF211311-100 from Brochier) and Ciba Geigy LY5052 Epoxy with HY5052 hardener. The second two systems (C1 and C2) were made from Vicotex 913 UD prepreg tape (E-glass/Epoxy resin) from Brochier. The manufacture was achieved by wet or prepreg lay up and vacuum bag moulding. Material A was "cold-cured". Other systems were cured during 15 hours at 85°C.

In all the cases the SMA wires were, at first, strained up to 6% in a conditioned room (martensitic state). For the system C_2 the TWSM effect was used : after stretching, the nitinol wires were subjected to cooling and heating within the temperature range : T1 (less than Mf) - T2 (greater than Af). During this training a recovery stress of 100 MPa was measured. The SMA wires were incorporated during lay-up between the first and the second ply, as far as possible of the neutral plan. For the hybrid composites A and B, only a small tensile stress enough to secure the wires alignment was applied during processing. In the other cases, the prestrain was maintained during the different stages of the processing to prevent premature actuation at the cure temperature following the Clausius-Clapeyron relation.

Table 2 defines the five hybrid composites studied and gives the composite characteristics. Figure 1 gives a schematic drawing of the process and of the average geometry of hybrid composite beams.

System ref.	A	B	C1	C2
Epoxy	LY/HY5052	LY/HY5052	913	913
Training	No	No	No	Yes
Strain during curing	No	No	Yes	Yes
Glass content (%)	50	50	55	55
NiTi content (%)	0.7	1.15	0.7	1.45
Tg*	80	118	161	161
E (GPa) at 23°C**	23	23	32	32
Stiffness loss at 65°C (%)**	20	>5	>5	>5

*Table 2 : Definition and mechanical properties for the four systems studied (*Dynamic Spectrometry: Frequency 0.25 Hz ; temperature rate equal to 2 °/min - glass transition temperature defined as the max of the loss factor versus temperature variation ; **measured on composite without nitinol wires)*

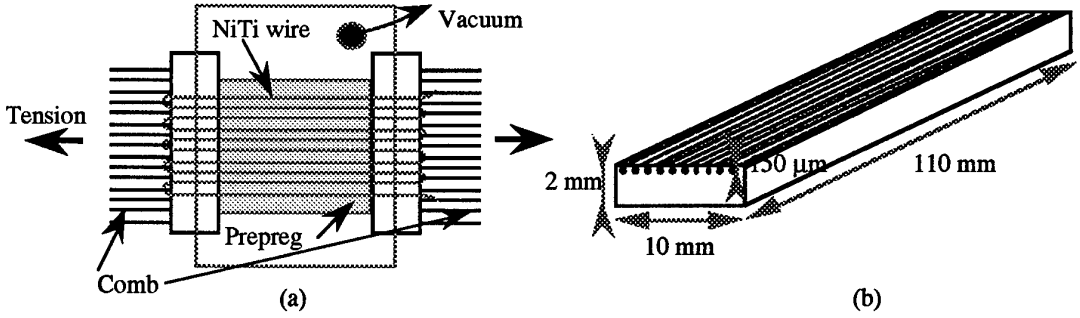


Figure 1 : (a) Schematic drawing of the process ; (b) average geometry of the hybrid composite beams

EXPERIMENTAL RESULTS

Interface characterisation

In order to obtain directly the interface shear strength the drop test was used. This test is a variant of the pull-out test. It consists in performing a tension test on a fibre (or in our case on a SMA wire) fractionally embedded in a matrix droplet. During the test, the droplet is held by means of two blades (Figure 2a).At the other end the wire is subjected to a tension F at a constant strain rate until the fibre is pulled out of the matrix. This test provides the force F_d at which the debonding matrix droplet-fibre occurs.(Figure 2b).

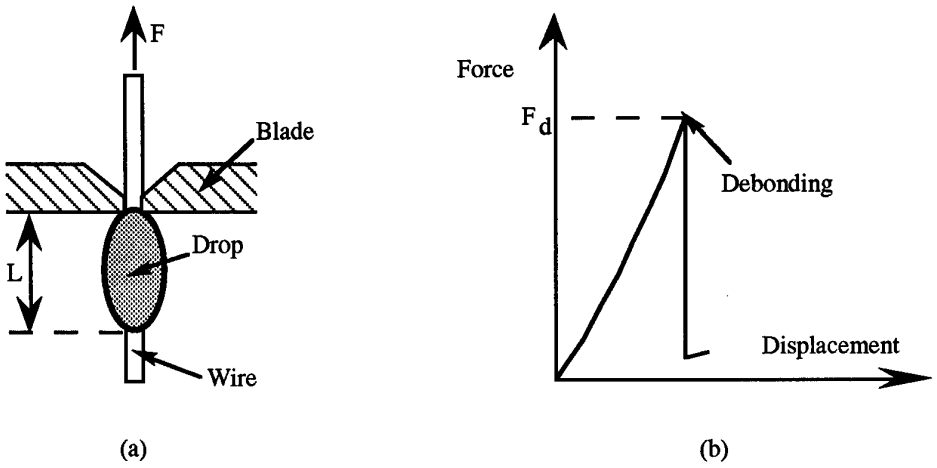


Figure 2 : Drop test : (a) principle of the test ; (b) determination of the debonding force F_d

Tests are performed with an Adamel DY22 tensometer with a force transducer 0-10N. An optical control of the position of the blades is made before the test as well as during the test. After each test the debonded drop length L was measured by SEM. In all cases the failure takes place at the interface and not in the matrix (adhesive failure). From the knowledge of the debonding force F_d, the drop length L and the wire diameter 2r, the interface shear strength is determined in the frame of the "average stress " model :

$$\tau_i = \frac{F_d}{2\pi rL}$$

This test was only performed with the resin LY5052. Indeed, the resin 913 is too viscous to allow application of a drop. In the case of the as-received NiTi wires the mean value of the interface strength, τ_i is equal to 9.1 MPa. If the SMA is prestrained up to 6% before the matrix crosslinking this value becomes 14.6 MPa. This increase of τ_i was associated to a superficial roughness due to the development of well oriented superficial martensitic variants. With a mean value of 10 MPa for the interfacial shear strength the recovery stress of 100 MPa appears without debonding on a critical length of 1 mm.

Actuation evaluation

The hybrid laminate beams were tested in clamped-free conditions (Figure 3a). Since the actuators were off the beam neutral plane, a bending was induced during actuation due to the recovery stress. The tip deflections were used to evaluate actuation effect (Figure 3b). Measurements of the deflection were performed by means of an induction sensor with an accuracy of ±5 µm. The actuators were connected in series and electrically activated by means of resistive heating. The superficial temperature of the beam on the side close to SMA layer was measured by a thin thermocouple.

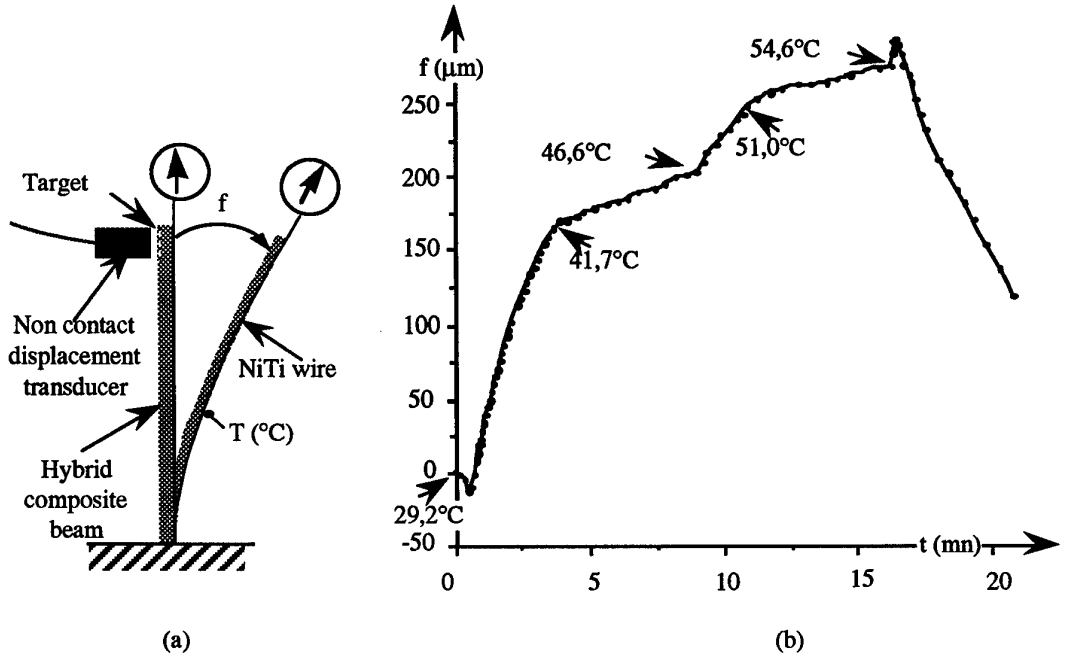


Figure 3 : (a) Principle of the actuation test ; (b) tip deflection of an hybrid beam (C1) versus the superficial temperature

For each kind of material the maximal deflection related to the whole martensite-austenite transformation corresponded to a superficial temperature of 55 ± 5C°. The comparison of the experimental values of the deflection with the theoretical ones determined by an analytical beam buckling modelling is shown in Table 3 by means of experimental to theoretical values of the deflection ratio, R.

System ref.	A	B	C1	C2
R	0,10	0,19	0,87	0,29

Table 3: Experimental to theoretical values of the deflection ratio for the four types of hybrid beams

This Table points out that reversible deflections exist (at different relative levels R), even in cases where the SMA wires were not trained for a TWSME. For the system A the reversible deflection appeared gradually during the successive heating before a stabilisation at a very low relative value. In the case of the material B the reversible effect increased again during a few actuations until a stabilisation at an intermediate relative value. The best behaviour was obtained for the composite C1 for which the shape memory effect was prevented to occur during the curing process after prestraining.

It can be noted that the relative level of maximal actuation is linked to the mechanical properties of the matrix and of the interfacial zones in relation with the difference between the real temperature of the wires and the glass transition temperature of the matrix. The comparison between the behaviour of the samples A and B clearly points out this result. Indeed, in the case of composite A, the local wire temperature is of the order of the glass transition temperature during the heating. So, the shear strength of the zone surrounding the SMA wires became very low (stiffness loss of the order of 20% at 65°C). In these conditions, the recovery stress and the actuation effect associated to the clamping effect of the host composite vanished. The subsequent gradual increase of the tip deflection was due, to some extents, to the growth of the degree of crosslinking in the vicinity of the SMA wires upon successive heating. On the contrary, in the case of the sample B which was post-cured, the shear strength of the interfacial zone kept in a first approximation the value determined by the drop test at room temperature ((stiffness loss less than 5% at 65°C).

In cases of composites A, B and C1 the reversible deflection was due to the occurrence of a self-induced TWSME. Indeed, after the first actuation and deflection each sample returned by cooling to its original shape thanks to the elastic properties of the host laminate composite. This drawback force produced a martensite with preferential orientations involving a shape memory effect during next heating. This induced TWSME grew by cycling during the first cycles. This effect explains the tip deflection increase observed in the cases of materials B and C1 during the very first cycles. The difference between systems C1 and C2 was linked to the training technique. In the case of material C2, the SMA was trained for a TWSME before embedding in the host

laminate. So, it seems that these conditions of training were not so efficient as the self-training due to the drawback force in relation with the elastic properties of the host composite.

CONCLUSIONS

In order to test the influence of the processing conditions on the actuation properties of adaptive hybrid composites, a model system composed of a glass epoxy laminate composite with prestretched shape memory nitinol wires was used. When hybrid composites were electrically heated and cooled the wires underwent a reversible martensite to austenite transformation even if they are not trained for a TWSME before embedding. The real A_f temperature of the SMA wires in embedded conditions has to be much lower than the rubber-glass temperature transition of the matrix in order to keep a significant interfacial shear strength able to bear locally the recovery stress. At last, the most important deflection of the host laminate composite was obtained for the material in which the prestrain of the SMA wires was maintained during the cure in order to prevent premature actuation. A self-training effect occurred in relation with the polarised reverse transformation austenite to martensite during cooling after actuation.

ACKNOWLEDGEMENTS

The authors would like to thank Dr M. Morin from the GEMPPM of the INSA Lyon for valuable suggestions in the fabrication of specimens and Prof. B. Chabert and Dr J.P. Soulier of Université Claude Bernard Lyon I for their assistance and their precious advises concerning the use of the drop test. The authors also wish to thank Dr L.Fiore from Brochier for providing 913 prepreg and UD fabrics.

REFERENCES

K. Escher, E. Hornbogen "Aspects of two-way shape memory in NiTi-Silicon composite materials", J. de Physique 1, C4-pp. 427-432, 1991

J.-E. Bidaux, J.-A. Manson, R. Gotthardt, "Dynamic mechanical properties and phase transformation in polymer-based shape memory alloy composites", Proc. of the First Int. Conf. on Shape Memory and Superelastic Technologies, Asilomar, Pacific Grove, 1994, A. R. Pelton, D.Hodgson and T. Duerig Eds, pp. 37-42, 1994

D.-A. Hebda, M.-E. Whitlock, J.-B. Ditman, S.-R. White "Manufacturing of adaptive graphite epoxy structures with embedded nitinol wires", Journal of Intelligent Material Systems and Structures Vol. 6, n° 2, pp. 220-228, 1995

J.S.N. Paine ,C.A. Rogers, R.A. Smith "Adaptive composites materials with shape memory alloy actuators for cylinder and pressure vessels", Journal of Intelligent Material Systems and Structures Vol. 6, n°2, pp. 210-219, 1995

J. Epps, R. Chandra "Shape memory alloy actuation for active tuning of composites beams", Smart Structures and Materials 1995, San Diego, California, Vol. 2443 Inderjit Chopra Ed., pp. 76-88, 1995

C. M. Friend , N.B. Morgan "The cyclic response of shape memory alloys 'smart' composites", Second European Conference on Smart Structures and Materials, Glasgow, B. Culshaw Ed., pp. 94-97, 1994

C. J. Doran "The effect of prestrain on the actuation performance of embedded shape memory alloy wires", Second European Conference on Smart Structures and Materials, Glasgow, B. Culshaw Ed., pp 98-101,1994

C.A. Rogers, C. Liang, D.K. Barker "Dynamic control concepts using shape memory alloys reinforced plates", U.S. Army Research Office Workshop on Smart Materials, Structures and Mathematical Issues, V. P. I. & State University, Blacksburg Virginia, pp. 39-62 1988

SMART MATERIAL THERMAL CHARACTERIZATION : Ni-Ti shape memory alloy embedded in a resin epoxy matrix

F.THIEBAUD*, B. ZEGHMATI**, J.F. CHARMOILLAUX*, C. LEXCELLENT*

* Laboratoire de Mécanique appliquée R. Chaléat
URA 04 CNRS, UFR Sciences et Techniques
Chemin de l'épitaphe - 25000 Besançon

** Laboratoire de Métrologie des Interfaces Techniques
I.U.T. Belfort - Montbéliard
Rue Engel Gros - 90014 Belfort

ABSTRACT

This paper presents the first results obtained on a smart material element made of a shape memory alloy Ni-Ti fibre (without previous deformation) embedded in a resin epoxy matrix. When an electrical current is applied in the Ni-Ti wire, infrared camera permit to measure the surface temperature lateral faces. The integration of heat equation in a finite element code allows to obtain the local temperature of the resin and so predict its behavior. In the future for technological reasons (change of sample shape or resonance frequencies), the local stress-strain-temperatures fields will be obtained when heating a predeformed Ni-Ti wire embedded in resin produces recovery stress.

1. INTRODUCTION

Smart materials are nowadays one of the most studied fields, because of their ability to change their physical and thermomechanical properties when it is necessary. The non ordinary capacities of such materials lead the researchs naturally toward the high technology fields such like aeronautics, space, car manufacturing...where vibrations, thermic deformations could change or deteriorate certain functions of the system [1,2].

The basic concept of smart materials is that they are their own sensors which are able to change the characteristics of the material. The most used actuators are piezoelectric elements (P.Z.T.) or shape memory alloy (S.M.A.) fibres embedded in a resin. Both actuators work thanks to an electrical current applied. It seems that P.Z.T. actuators are relatively more employed, because of the linearity of their response to the applied current and especially their high response time but also in spite of the low displacement amplitude. At opposite, S.M.A. are characterized by a non linear response linked to the phase transformation (austenite $\leftrightarrow$ martensite or R-phase) with a great transformation amplitude (4 to 8%) but a long response time (5 to 10 seconds). In fact, these actuators P.Z.T. and S.M.A. can be complementary.

Smart materials as composites structures made of a resin reinforced by S.M.A. fibres have more difficulties to spread, for a major reason : the thermomechanical behaviour of S.M.A. is not enough known, particularly when temperature changes during a test heating with the joule's effect, although a lot of important works have been published in this field [3-7].

In this paper, we examine mainly the thermal aspect. The determination of the local temperature field in the hybrid material (S.M.A. fibre embedded in a resin epoxy matrix) when we heat the fibre allows (i) to predict the eventual behaviors of the resin which can be thermoelastic or viscoplastic ones (ii) to establish a link between the advance of the phase transformation and the applied intensity current.

0-8194-2165-0/96/$6.00

2. SAMPLE ELABORATION

Samples are made of an equatomic Ni-Ti wire (furnished by Furakawa society) embedded in a resin epoxy matrix. In order to measure with a good precision the surface temperatures, the chosen section of the sample is a square with the wire at the center. The effect of the proportion fibre-matrix is taken into account by choosing three different aeras (a=10, 15, 30 mm). A length sample L=60 mm is necessary to render negligible the boarder effects. The diameter of the Ni-Ti S.M.A. wire is 0.2 mm without previous deformation.

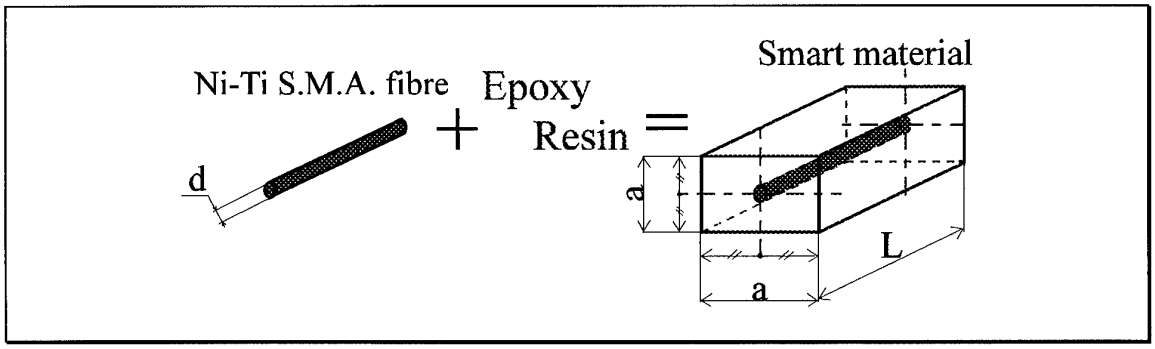


Fig. 1 : Sample elaboration.

In the future, for technical applications, it would be better to investigate the recovery stress induced by heating a predeformed wire embedded in the resin and the resulting effect on the local temperature of the resin [8].

3. EXPERIMENTAL INVESTIGATION

3.1 Experimental process

The figure 2 gives evidence of a classical process.

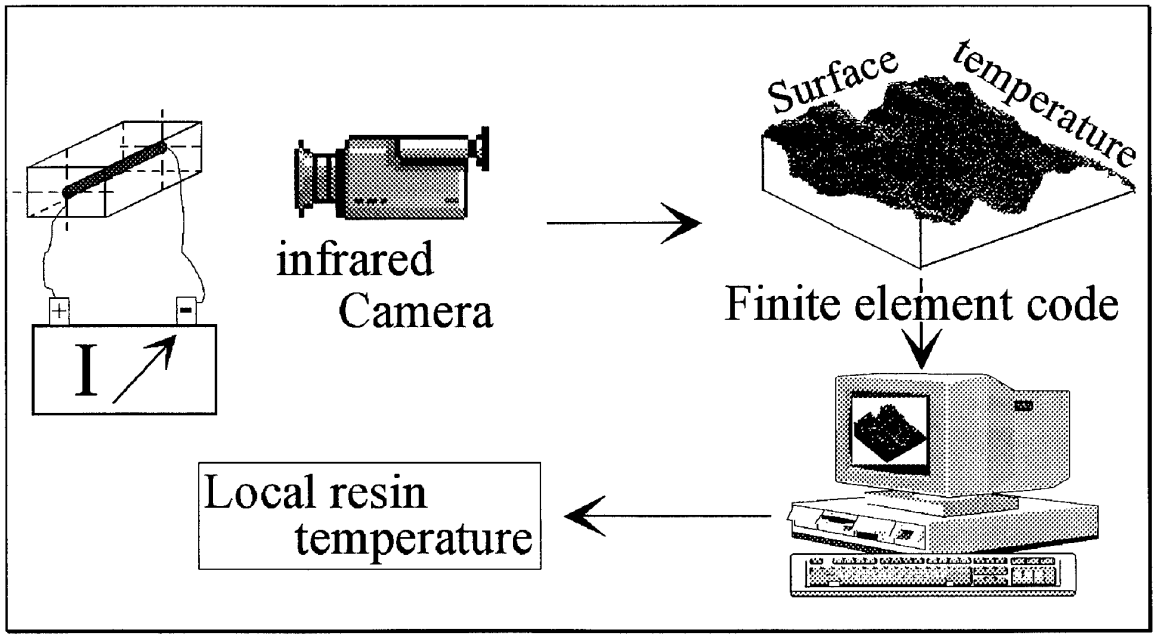


Fig. 2 : Experimental process.

An infrared camera (Agema Thermovision 470) allows the surface temperature measurement. This infrared thermography technic without contact but with a great sensitivity does not disturb the real temperature field and permit to know the surface temperature evolution with time.

3. 2. Experimental results

The intensity of heat flux exchanged by convection and thermal radiation between the resin surface and the external field depend of the size and the shape of the sample. These heat flux are proportional to the resin surface aera. Hence, it is natural that for a given calorific power in the sample, the resin surface temperature is lower as the sample aera is great.

In order to minimize the boarder effects, we measure the surface temperature at the middle of one face of the sample (figure 3).

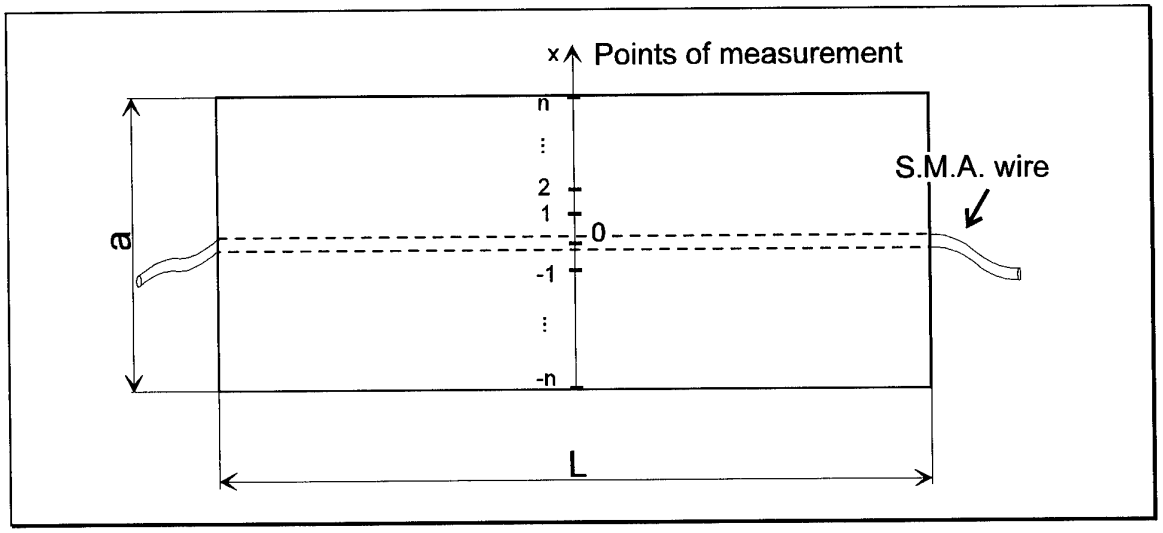
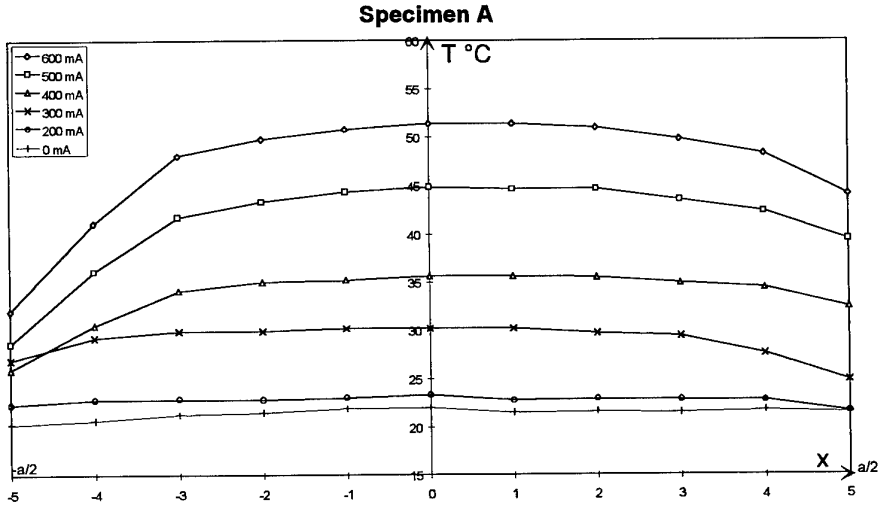


Fig. 3 : Repartition of measurement points on a lateral face of the sample

As it is imposed by the camera resolution, we measure the temperature every each millimeter. Evidently, the thermal situation is the same for the four lateral faces. Moreover, for each imposed intensity, we restrict our analysis to the stationnary state.

The figure 4 show for the three samples the surface temperature evolution with the applied current intensity and the x coordinate position.



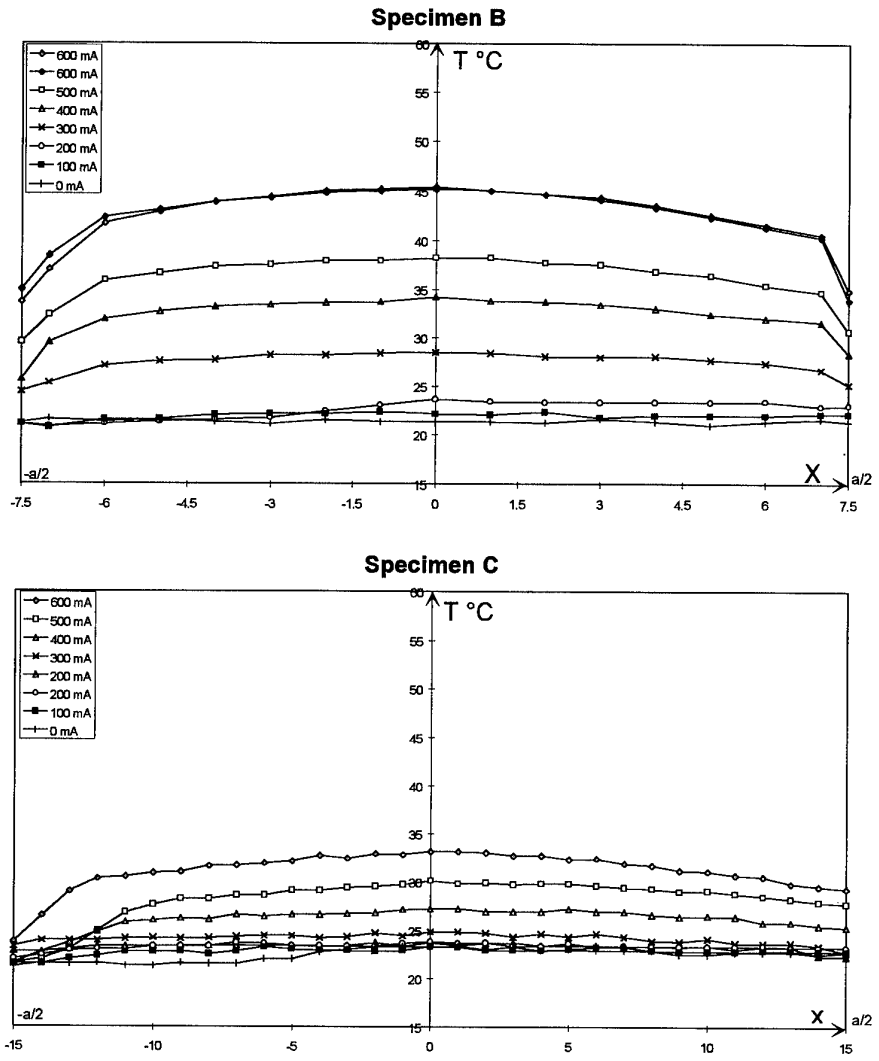


Fig 4 : Surface temperature measurements.
A (a=10 mm), B (a=15 mm), C (a=30 mm)

Hence, it is logical to obtain that the temperature (i) increases with the distance between the wire position and the x point (hence, the experimental results shows that T(x) is a symetric function, if we don't take into account the slight difference of heat flux generated by natural convection between top and bottom of the sample) (ii) also increases with the electrical power delivered by joule's effect in the S.M.A. wire.

Now, the thermal problem is clear, the Ni-Ti fibre constitutes a heat source. This heat is transferred by conduction in the resin epoxy matrix with known boundaries conditions at the surface. For the resin, the integration of the heat equation gives us the local temperature

4. HEAT EQUATION INTEGRATION FOR THE RESIN EPOXY MATRIX

The heat equation is classical

$$\rho C \frac{\partial T}{\partial t} = k \Delta T + Q \qquad (1)$$

with

Q : Heat source density ($Q = 0$)

ρ : body density (kg m^{-3})

C : calorific density (J kg^{-1} K^{-1})

k : Thermal conductivity (W m^{-1} K^{-1})

For the stationnary state, we have to solve the simple equation

$$\Delta T = 0 \tag{2}$$

with the following boundary conditions

(i) T is known on the lateral surfaces

(ii) To take into account the heat power delivered by the Ni-Ti wire, we imposed an heat flux density q at the interface between the matrix and the fibre

$$q = \frac{\rho_f I^2}{2 \pi^2 r^3} \tag{3}$$

with ρ_f : body density of Ni-Ti fibre

I : applied current intensity

r : fibre radius

The calculatus are effectued on a finite element code Ansys. At last, we obtain the temperature distribution in the sample.

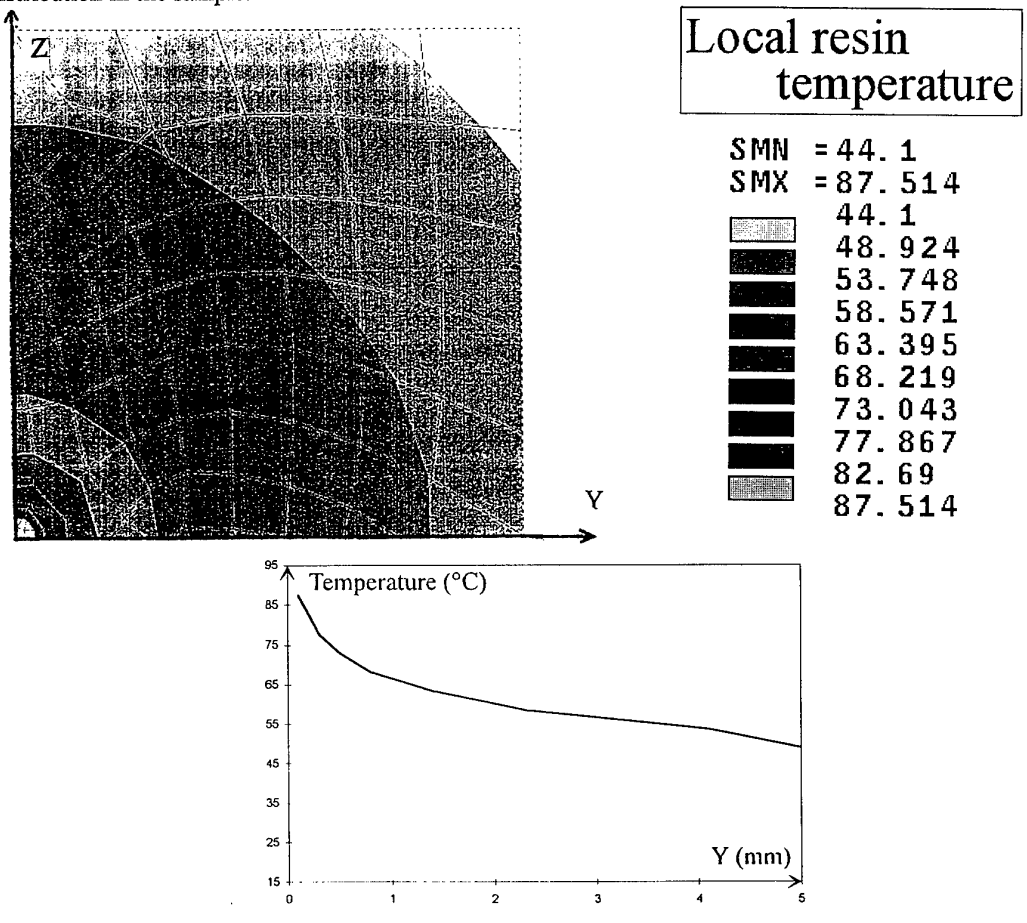


Fig. 5 : The temperature distribution in the sample (a=10 mm and I=600 mA).

5. CONCLUSION

The present paper is mainly devoted to the thermal behavior of the smart material and more particularly the resin ones. The only stresses generated comes from the interface with the different thermoelastic constants between the fibre and the matrix and are not negligible. As the Ni-Ti wire is without deformation in its initial state, the phase transformation during heating (self accomodating martensite platelets → austenite) does not produce any supplementary deformation.

In the future, the real problem to solve is the following : starting with a smart material with a predeformed fibre, heating generates strong recovery stress (on the order of 150 MPa) [9], and we must obtain the local stress, strain and temperature in the resin and the fibre. But, a general modelling of the thermomechanical behavior of shape memory alloys made by Leclercq and Lexcellent [10], and the knowledge of elastoviscoplastic behavior of resin epoxy material [11], will help us in the resolution.

At last, a micromechanic modelling of the multiphase medium (a lot of Ni-Ti fibres embedded in the resin epoxy matrix) is possible with some Mori-Tanaka method [12].

6. ACKNOWLEDGMENTS

The authors wish thank Dr Sylvain Leclercq and Mr Didier Gabory for their help.

7. REFERENCES

1. L. Librescu, C.A Rogers and O. Song, « Static and dynamic behavior of adaptative aircraft wing structures modelled as composite thin-welled beams », 6th Japan-U.S. Conference on Composite Materials, Orlando, Florida, 22-25 June 1992.

2. C.A. Rogers, W.L. Stutzman, T.G. Campbell, J.M. Hedgepeth, « Mission to planet earth technology assesment and development for large deployable antennas », International Astonautical Federation, Dresden, Germany, October 6-12, 1990.

3. C. Liang, C.A. Rogers, « Behavior of shape memory alloy actuators embedded in composites », Proceedings of the 1989 International Composite Conference, Beijing, China, 1-4 August 1989, pp. 475-482.

4. J.S.N. Paine, C.A. Rogers, « The effect of thermoplastic composite processing on the performance of embeded Nitinol actuators », Proceedings, AIAA/ASME/ASCE/AHS/ASC, 32nd Structures, Structural Dynamics and Materials Conference (Baltimore, MD, 8-10 April 1991), AIAA, Inc. Washington, DC, Paper n°AIAA 91-1167, PartI, pp.194-204.

5. C.A. Rogers, C.Liang, J.Jia, « Behavior of shape memory alloy reinforced composite plates, Part I : Model Formulations and Control Concepts », Proceedings of the 30th Structures, Structural Dynamics and Materials Conference (AIAA 89), Mobile, AL, 3-5 April 1989, Vol. 4, pp. 2011-2017.

6. C. Liang, J.Jia and C.A. Rogers, « Behavior of shape memory alloy reinforced plates », Part II : Results, Proceedings of the 30th Structures, Structural Dynamics and Materials Conference (AIAA 89), Mobile, AL, 3-5 April 1989, Vol. 4, pp. 1504-1513.

7. A. Venkatesh, J. Hilborn, J.E. Bidaux, R. Gotthardt, « Active vibration control of flexible linkage mechanisms using shape memory alloy fiber-reinforced composites », 1st European conf. on Smart Structures and Materials, Glasgow 1992, pp. 185-188.

8. S. Leclercq, « De la modélisation thermomécanique et de l'utilisation des alliages à mémoire de forme », Ph D thesis n° 350, Université de Franche-Comté, 1995.

9. S. Leclercq, C. Lexcellent, H. Tobushi and P.H. Lin, « Thermodynamical modelling of recovery stress associated with R phase transformation in Ni-Ti shape memory alloys », Mat Trans JIM 35, 5, pp 325-331, 1995.

10. S. Leclercq, C. Lexcellent, « A general macroscopic descrive of the thermomechanical behavior of shape memory alloys », to appear in Journal of the Mech. and Phys. of solids.

11. P. Le Moal, « Comportement viscoélastique de stratifiés verre-époxy : des propriétés des constituants à celles du matériau composite », Ph D thesis, Université de Franche-Comté, 1993.

12. Q.P. Sun, « A micromechanics analysis for the microstructure design of two phase pseudoelastic composite », Acta Mechanica Sinica 10, 2, 1994, pp 162-168.

ON MATHEMATICAL MODELLING OF THE INCOMPLETE TRANSFORMATIONS IN PSEUDOELASTIC PROCESSES IN BINARY ALLOYS

D. Vokoun and V. Kafka

Institute of Theoretical and Applied Mechanics, Academy of Sciences of the Czech Republic,
Prosecká 74, 190 00 Praha 9, Czech Republic

INTRODUCTION

In his two papers Kafka (1994,1994a) presented a new approach to explanation and to mathematical modelling of shape memory effect and of pseudoelasticity. This approach was based on his general concept of modelling inelastic processes in heterogeneous media (Kafka 1987) and it was shown that this concept can successfully be applied even in the case where the heterogeneity under study is on the atomic scale, i.e. in the case of binary alloys and their shape memory behaviour. In the second quoted paper (Kafka 1994a) quantitative comparisons with experimental data received with samples of NiTi alloy were shown and it was demonstrated that the unified mathematical model is able to quantitatively describe the shape memory effect as well as the pseudoelastic processes under different temperatures.

Another question is the possibility of modelling the process of pseudoelasticity if the transformations are incomplete. This is an important factor since the shape memory devices are often operated under small thermal and/or mechanical loads which are insufficient to complete the transformation. In their recently published paper Tanaka, Nishimura and Tobushi (1995) showed experimental results of this kind and compared them with the so called 'thermodynamic theories'(Müller 1989,Müller and Xu 1991, Raniecki 1992). This comparison led to the conclusion that 'the alloy performance is fully contrary to the prediction of the thermodynamic theory'. We are going to show that our approach is fully consistent with Tanaka's experimental results in the part related to the TiNi alloy. The other investigated material (Fe-based polycrystalline shape memory alloy) cannot be described by our model, as it is not a binary alloy.

MATHEMATICAL MODEL

The general mathematical model applicable to shape memory and pseudoelasticity of binary alloys was presented by Kafka (1994,1994a). Its special form for pseudoelasticity follows from it under the restriction that the temperature is high enough to correspond to the austenitic state if the sample is unloaded and if during the deformation process the temperature does not change. To be concrete we will have in mind the alloy of Nickel and Titanium and the respective indexes of the quantities related to these two elements will be n and t respectively. In this case the form of the constitutive equation with tensorial internal variables and their evolution equations reads:

$$\dot{\bar{\varepsilon}}_{ij} = \dot{\bar{e}}_{ij} + \delta_{ij}\dot{\bar{\varepsilon}}, \qquad \dot{\bar{e}}_{ij} = \mu\dot{\bar{s}}_{ij} + \mathrm{v}_n s_{ijn}\{\dot{\lambda}\}, \qquad \dot{\bar{\varepsilon}} = \rho\dot{\bar{\sigma}}, \tag{1}$$

$$\dot{s}_{ijn} = \dot{\bar{s}}_{ij} + \frac{C}{B}\left(\dot{s}_{ijn}\right)_T + \frac{1}{B\mu}\left[-As_{ijn} + Ds'_{ijn}\right]\{\dot{\lambda}\},$$

$$\dot{s}'_{ijn} = \dot{s}_{ijn} - \dot{\bar{s}}_{ij} + \left(\mathrm{v}_t s_{ijn} - s'_{ijn}\right)\{\dot{\lambda}\}/\mu,$$

with

$$A = \mathrm{v}_t\left(\mathrm{v}_t\eta_t + \mathrm{v}_n\eta_n\right), \tag{2}$$

$$B = \mathrm{v}_t\eta_t + \mathrm{v}_n\eta_n + \eta_n\eta_t,$$

$$C = \eta_n\eta_t,$$

0-8194-2165-0/96/$6.00

$$D = \nu_t \eta_t ,$$

$$\mu = (1+\nu)/E, \quad \rho = (1-2\nu)/E, \tag{3}$$

with ν and E meaning Poisson's ratio and Young's modulus respectively,

$$\left(\dot{s}_{ijn}\right)_T = \hat{q}\tau\dot{s}'_{ijt} = \hat{q}\tau\nu_n\left[\left(\dot{\bar{s}}_{ij} - \dot{s}_{ijn}\right)/\nu_t - s_{ijn}\left\{\dot{\lambda}\right\}/\mu\right], \tag{4}$$

$$\left\{\dot{\lambda}\right\} = 0 \quad for \quad s_{ijn}s_{ijn} < 3c^2/2, \tag{5}$$

$$\left\{\dot{\lambda}\right\} = \tfrac{1}{2}\left(\dot{\lambda} + \left|\dot{\lambda}\right|\right) \quad for \quad s_{ijn}s_{ijn} = 3c^2/2.$$

For the case of a uniaxial tension in the x_1 -direction it holds:

$$\dot{\lambda} = \frac{\hat{B}\dot{\bar{s}}_{11}}{\hat{A}s_{11n} - \hat{D}s'_{11n}}\mu, \tag{6}$$

where $\hat{A}$, $\hat{B}$ and $\hat{D}$ are defined in a way that is quite analogous to the definition of A, B and D , but instead of writing η_t, it is necessary to write Θ that is defined as follows:

$$\Theta = \eta_t/(1+\hat{q}\tau\eta_t/\nu_t),$$

$$\tau = T - T_0, \tag{7}$$

T being current temperature, T_0 equilibrium temperature corresponding to martensite with zero values of $(s_{ijn})_T$ and $(s_{ijt})_T$. (For T_0 the stress-strain diagram has the lowest values of stress, higher or lower temperatures cause internal stresses the result of which are higher macroscopic stresses in the stress-strain diagram that are observed experimentally.)

$$\hat{q} = q(>0) \quad for \quad s'_{ijt}s'_{ijt} < 3\hat{c}^2/2,$$

$$\hat{q} = 0 \quad for \quad s'_{ijt}s'_{ijt} \geq 3\hat{c}^2/2.$$

The remaining quantities that are not explicitely comprised in the constitutive equation are related to the quantities appearing there by the following set of equations:

$$\nu_n\sigma_{ijn} + \nu_t\sigma_{ijt} = \bar{\sigma}_{ij}, \tag{8}$$

$$\nu_n\varepsilon_{ijn} + \nu_t\varepsilon_{ijt} = \bar{\varepsilon}_{ij},$$

$$\varepsilon'_{ijn} = \varepsilon_{ijn} - \bar{\varepsilon}_{ij},$$

$$\varepsilon'_{ijt} = \varepsilon_{ijt} - \bar{\varepsilon}_{ij},$$

$$s_{ijn} - s_{ijt} + s'_{ijn}/\eta_n - s'_{ijt}/\eta_t = 0,$$

$$e_{ijt} = \mu s_{ijt}, \qquad \varepsilon_t = \rho\sigma_t,$$

$$\dot{e}_{ijn} = \mu\dot{s}_{ijn} + s_{ijn}\left\{\dot{\lambda}\right\}, \qquad \varepsilon_n = \rho\sigma_n$$

$$e'_{ijt} = \mu s'_{ijt}, \qquad \varepsilon'_t = \rho\sigma'_t,$$

$$\dot{e}'_{ijn} = \mu\dot{s}'_{ijn} + s'_{ijn}\left\{\dot{\lambda}\right\}, \qquad \varepsilon'_n = \rho\sigma'_n .$$

The symbols with overbars mean macroscopic values; ε_{ij} and σ_{ij} are tensors of strain and stress; v_n and $v_t(=1-v_n)$ are 'volume fractions' of the respective constituents (calculated from the atomic fractions and the atomic weights); σ_{ijn} and σ_{ijt} are average values of the stress tensors in the Ni and Ti infrastructures respectively; η_n and η_t are deviatoric structural parameters; $e_{ijn}/\varepsilon_n(e_{ijt}/\varepsilon_t)[\ s_{ijn}/\sigma_n(s_{ijt}/\sigma_t)]$ mean the deviatoric/isotropic parts of the strain- [stress-] tensors in the Ni and Ti infrastructures; the dots mean time-derivatives; the symbols with primes characterize the heterogeneity of stress- and strain- distribution in the infrastructures (Kafka, 1987).

The constants defining the properties of the material in question are: v_n (=1- v_t), μ, ρ, η_n, η_t, c, $\hat{c}$, q and T_0 . They are determinable from simple macroscopic experiments. The procedure of their determination and a concrete numerical example were shown by Kafka(1992). The example was related to the experimental data found by Miyazaki, Otsuka and Suzuki (1981) for samples of Ti-50.6 at % Ni alloy. The values of the constants of this material were determined as follows:

$v_n\ (=1-v_t) = 0.39$, $\mu = 1.797 \times 10^{-5}$ MPa^{-1} , $\rho = 0.4594 \times 10^{-5}$ MPa^{-1} , $\eta_n = 373.54$, $\eta_t = 139.39$,
$c = 50$ MPa , $\hat{c} = 243.32$ MPa , $q = 1.882 \times 10^{-2}$ K^{-1} , $T_0 = 212$ K .

In the quoted papers by Kafka (1992, 1994a) the experimental and the theoretical pseudoelastic diagrams with complete martensitic transformation were shown to agree very well. Now let us analyse such diagrams in cases of incomplete transforemation, using the material parameters that are given above.

PSEUDOELASTIC INCOMPLETE TRANSFORMATION

In what follows we are going to analyse two different loading paths:

(i) Increasing simple tension up to the level where martensitic transformation begins, further increase of deformation and martensitic transformation up to some degree (but not to complete martensitic transformation) and then complete unloading.

(ii) Increasing simple tension up to the complete martensitic transformation, then incomplete unloading to some degree and a new loading.

The calculation and plotting of the respective diagrams is done for several degrees of loading in the first case and of unloading in the other case.

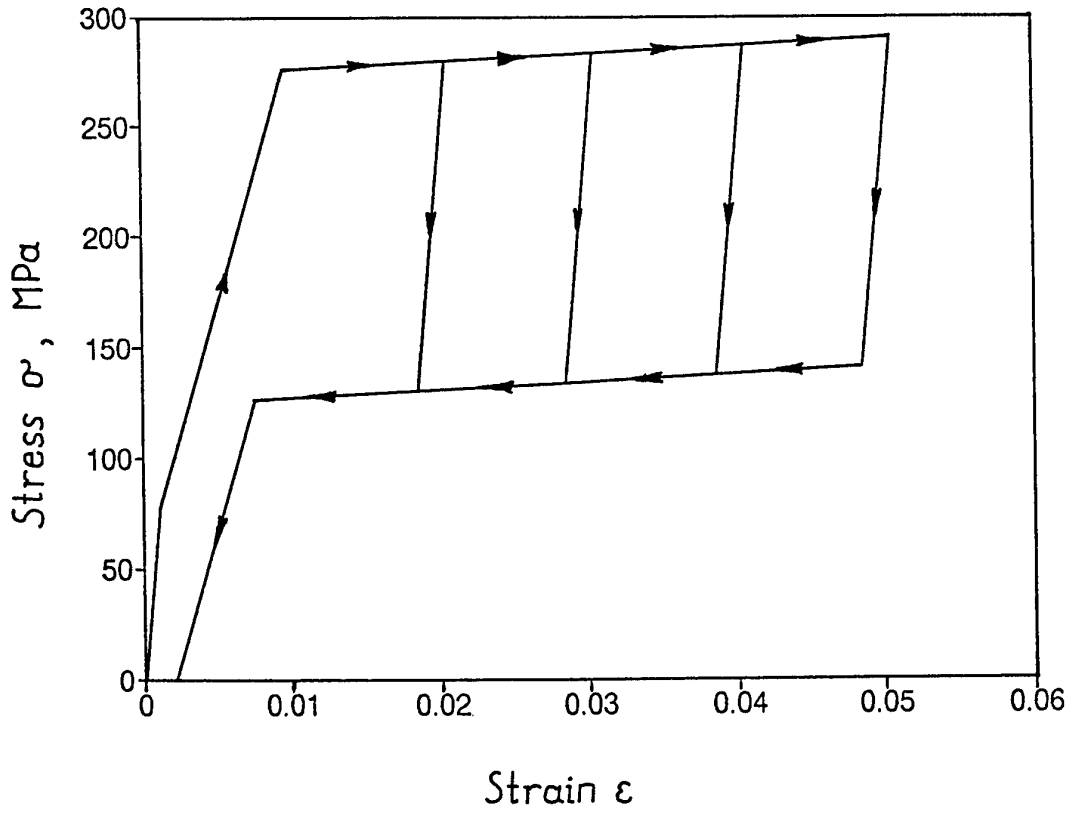


Fig. 1.: Computed stress-strain diagrams with the loading paths of type (i)

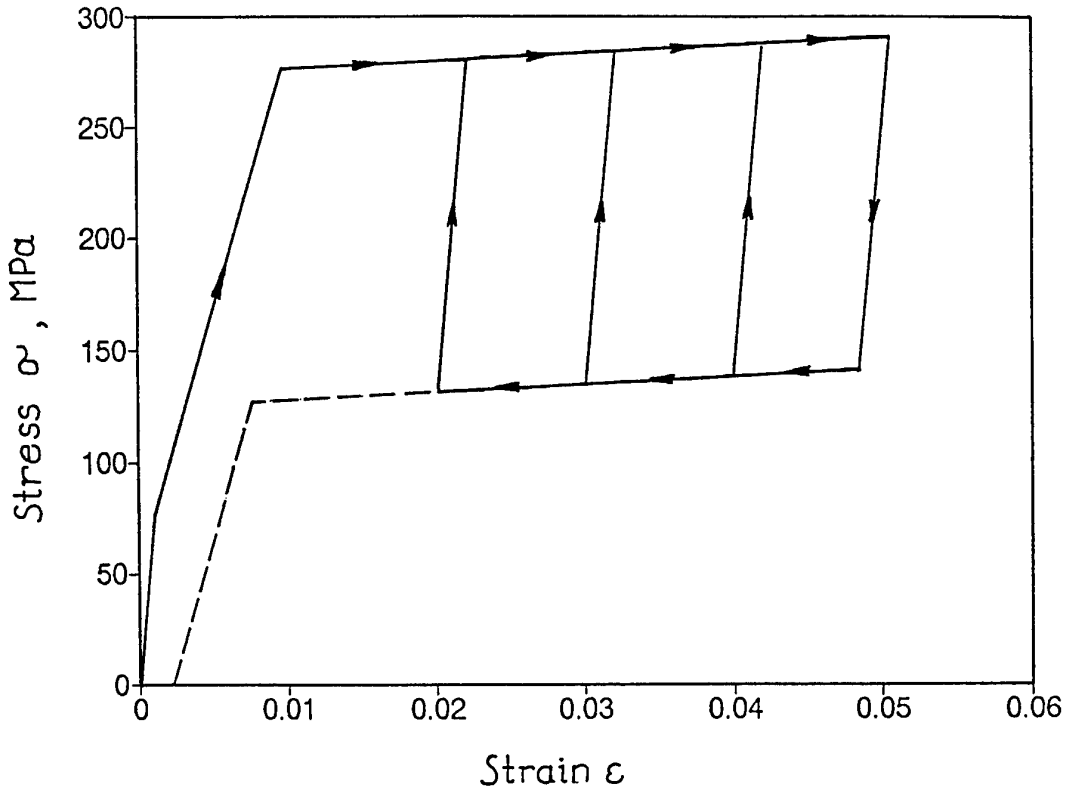


Fig. 2.: Computed stress-strain diagrams with the loading paths of type (ii)

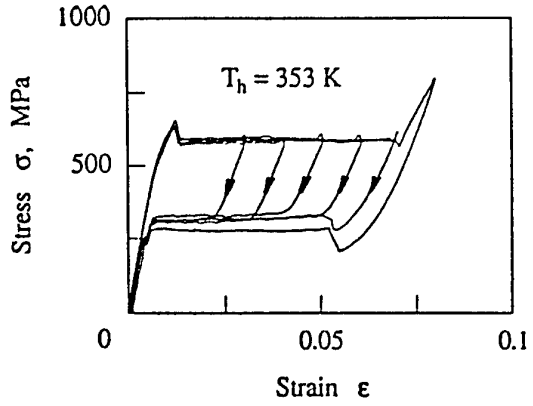


Fig. 3.: Experimentally measured stress-strain diagrams, taken over from (Tanaka 1995), with the loading paths of type (i)

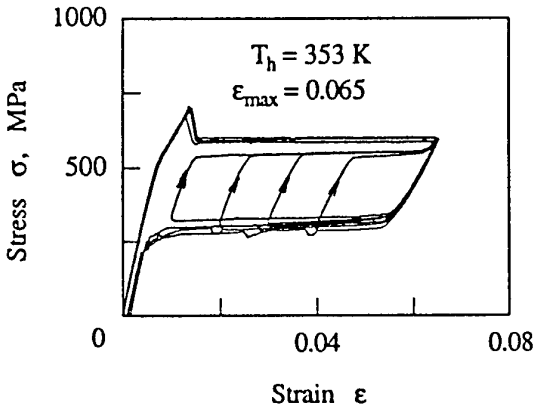


Fig. 4.: Experimentally measured stress-strain diagrams, taken over from (Tanaka 1995), with the loading paths of type (ii)

The constant drop of martensite start stress in Fif. 4 is due to loadcycling (Tanaka 1995).

CONCLUSION

Comparing Fig. 1 with Fig. 3 and Fig. 2 with Fig. 4 we can see good agreement of computed data with Tanaka's experimental results relating to nitinol, as described in (Tanaka 1995). This evidences the merits of Kafka's model in general, and the possibility of describing by it the pseudoelastic incomplete transformation of binary alloys in particular.

REFERENCES

Kafka V. Inelastic Mesomechanics, World Scientific Publ.Co., Singapore, New Jersey, London, Hong Kong, 1987.

Kafka V. The mesomechanical model of pseudoelasticity, Acta Technica CSAV 37(1992)716-740.

Kafka V. Shape memory: A new concept of explanation and of mathematical modelling, Part I: Micromechanical explanation of the causality in the SM processes, Journal of Intelligent Material Systems and Structures 5(1994)809-814.

Kafka V. Shape memory: A new concept of explanation and of mathematical modelling, Part II: Mathematical modelling of the SM effect and of pseudoelasticity, Journal of Intelligent Material Systems and Structures 5(1994)815-824.

Tanaka K., Nishimura F. and Tobushi H. Transformation start lines in the TiNi and Fe-based shape memory alloys after incomplete transformations induced by mechanical and /or thermal loads, Mechanics of Materials 19(1995)271-280.

Miyazaki S., Otsuka K. and Suzuki Y. Transformation pseudoelasticity and deformation behaviour in a Ti-50.6 at % Ni alloy, Scripta Metall. 15(1981)287-292.

Müller I. On the size of the hysteresis in pseudoelasticity, Contin. Mech. Thermodyn. 1(1989)125.

Müller I. and Xu H.B. On the pseudo-elastic hysteresis, Acta Metall. Mater. 36(1991)263.

Raniecki B., Lexcellent C. and Tanaka K. Thermodynamic model of pseudoelastic behaviour of shape memory alloys, Arch. Mech. 44(1992)261.

Smart Systems Using Piezoelectric Sensors and Applications

Invited Paper

SENSOR AND ACTUATOR APPLICATIONS OF PIEZOCOMPOSITE MATERIALS IN LARGE SMART STRUCTURES

Robert Y. Ting

U.S. Naval Undersea Warfare Center
Division Newport
Underwater Sound Reference Detachment
P.O. Box 568337
Orlando, FL 32856-8337 USA

ABSTRACT

Piezoelectric 1-3 composites are being considered for sensor and actuator applications in smart structures. For the coverage of large surfaces, low-cost fabrication techniques for producing these new materials in large size panels were developed. In-air electromechanical characteristics and in-water acoustical properties of these new 1-3 piezocomposite panels were evaluated to assess the effects of temperature, pressure and underwater explosive shock on their acoustical performance.

1. INTRODUCTION

Since the late 1950's, piezoelectric ceramics of lead-zirconate-titanate (PZT) compositions have been used almost exclusively in sonar transducers[1]. Solid solutions of lead zirconate titanate near the tetragonal-rhombohedral phase boundary were shown to exhibit strong piezoelectric effects in terms of planar coupling factor and piezoelectric d constants[2]. These properties were also found to be quite stable with temperature, because the PZT ceramics have relatively higher Curie temperatures than, say barium titanate and Rochelle salt. In recent years, these materials were also used in sensor and actuator applications in smart structures[3,4]. However, these bulk ceramics are dense, heavy and of limited size and shape. When large area coverage is required, they are rather difficult to apply. Furthermore, in some applications involving the coverage of a large surface, the transducers function in a hydrostatic mode. The piezoelectric coefficient in this mode is related to the other coefficients through the following equation:

$$d_h = d_{33} + d_{31} + d_{32}$$

Unfortunately, in PZT ceramics both the coefficients d_{31} and d_{32} have magnitudes nearly equal to half of that of d_{33} but are of a different sign[5]. This results in a very small d_h, or a very poor hydrostatic mode response[6].

This difficulty with bulk PZT ceramics became most evident in the 1970's during the course of the development of large-area hydrophones for use in flank sonar arrays. It was recognized that new materials which are light, flexible or conformal and with improved hydrostatic piezoelectric properties were needed for such an application. New thick-film piezoelectric PVDF polymers seemed to meet the need at that time, and their use was investigated. Recent success of a large flank array for the Royal Australian Navy's Collins class submarine is a good example of such endeavors[7].

It was soon learned, however, that PVDF polymers also have some shortcomings for hydrophone array applications. First, PVDF, like all polymeric materials, has a very low dielectric constant. Second, the material is limited in its temperature range for application and is not stable at high temperatures.

0-8194-2165-0/96/$6.00

Third, the anisotropic nature of the extruded PVDF films makes it difficult to design noise-free hydrophones. The U.S. Office of Naval Research, therefore, initiated work in the development of new materials with improved properties for correcting the problems with PVDF. In addition, it was also stressed that the new materials be processable with low-cost fabrication methods in order to form large sheets for applications demanding the coverage of large surface areas.

This effort promoted research work at the Pennsylvania State University's Materials Research Laboratory, which eventually led to the development of a large variety of piezoelectric composite materials that consist of a ceramic and a polymeric phase with different connectivities[8]. The connectivity in one, two or three dimensions in a composite is designated as 1, 2 or 3. Therefore, a piezocomposite consisting of thin piezoelectric ceramic rods aligned in parallel and embedded in a polymeric resin is called a "1-3" composite. The ceramic rods are connected in only one direction, namely the poled direction of the material, having a connectivity of "1". On the other hand, the polymer phase is connected in all three dimensions, having a connectivity of "3". Figure 1 shows a schematic of the 1-3 piezocomposite concept. In recent years, this type of piezoelectric composite material was investigated for applications in large-area hydrophones and as high-frequency underwater imaging transducers[9,10].

In the past, 1-3 piezocomposite materials were traditionally fabricated by using a dice-and-fill method[11]. This method was adequate for the preparation of small samples required in ultrasonic medical imaging applications. However, it is not only too labor intensive and, therefore, costly to meet the need of large area coverage in Naval applications, but too difficult to maintain material uniformity in large sheets. A number of new initiatives to explore alternative fabrication techniques for low-cost manufacturing of large sheets of 1-3 piezocomposite materials have recently been attempted. One of the more successful approaches was that of the Materials System Inc. (MSI, Littleton, MA), where an injection molding technique was used to make 1-3 composite preforms of manageable size. The individual preform parts were then assembled into large panels of 1-3 piezocomposite by using a polyurethane resin for encapsulation. This work has now been selected for inclusion in the ARPA Smart Materials and Structures Program for further development of the fabrication technique and the piezocomposite. In this paper, the basic configurations of large 1-3 panel structures developed are first described. The in-air electromechanical characteristics of these panels, as well as their in-water acoustical properties, have been determined. The effects of temperature, pressure and underwater explosive shock on the acoustic performance of the panels as large-area sensors and/or actuators in a smart structure are examined. Experimental results of this recent investigation are reported here.

2. FABRICATION AND CONFIGURATION

The basic configuration of the MSI fabrication[12] using an injection molding technique is a ceramic preform 50 mm x 50 mm in size, containing a 19 x 19 array of 361 rods. Each rod is 1.1 mm in diameter and about 6.5 mm in height. The ceramic of present choice is the PZT-5H composition from Morgan Matroc Inc. Ceramic powder was thoroughly mixed with a binder to form a viscous slurry. During the injection molding process, the slurry mixture was forced into a cooled mold to form a net shape green part. This part was subsequently heated in air for the removal of the organic binder. Sintering then took place at 1250°C for one hour with controlled atmosphere to optimize the PZT piezoelectric properties. The preform was then contact-poled under high electric field. Figure 2 shows the preform that was produced by this method. Individual preform parts were assembled to the size of a desirable transducer panel and encapsulated by using castable resins such as polyurethane under applied pressure. The panel assembly was subsequently cured in a vacuum oven, cooled, and finished before permanent electrodes were applied and wires attached. The final 1-3 pizocomposite panel contained approximately 15% volume fraction of PZT with a nominal dielectric constant of 3200 and a density of 1.8 g/cm^3. Presently, the

material is available from MSI under the trade name "SonoPanel 5H".

3. TEST METHODS

Both in-air and in-water impedance measurements of piezocomposite samples were carried out by using a standard Hewlett Packard Impedance Analyzer (HP4194A) to scan the frequency up to 1 MHz. Underwater acoustical properties including the transmitting voltage response (TVR) and the free-field voltage sensitivity (FFVS) were determined in both the USRD Lake Facility and the high pressure Anechoic Tank Facility (ATF) in Orlando, Florida. Generally, the TVR provides information on the behavior of an electroacoustic transducer used in active mode for sound transmission. It is the ratio of the sound pressure apparent at a distance of one meter in a specified direction from the effective acoustic center of the transducer to the signal voltage applied across the electrical input terminals. TVR is reported in decibels referenced to one micropascal per volt. On the other hand, FFVS gives the sensitivity of an electroacoustic transducer used for sound reception. This quantity is the ratio of the output open-circuit voltage to the free-field sound pressure in the undisturbed plane progressive wave, and is reported in decibels referenced to one volt per micropascal. A detailed description of the underwater acoustic calibration methods can be found in the reference by Bobber[13]. Calibration in the ATF enables one to test samples up to an underwater pressure of 7 MPa over the temperature range of 4 to 40°C. For the investigation reported here, only the discrete temperatures of 4 and 22°C were used. The frequency coverage of the measurements was from 100 Hz to 400 kHz. Effects of underwater explosive shock on the performance of the piezocomposite samples were evaluated by using the conical shock tube developed by Poche and Zalesak[14]. Figure 3 is a schematic diagram of this conical shock tube with its slider assembly. A small amount of charge explosive was detonated at the small-diameter breech end of a conical tube. The shock wave from the explosive propagated down the conical tube and the shock front exerted a fast-rising pressure wave on the device under test, which was mounted near the large opening end of the conical tube. Such a pressure front produced both a pressure shock and an inertial shock from the slider arrangement, closely simulating the underwater explosive shock encountered by all transducers on board of a Naval vessel. Figure 4 shows the peak pressure of the shock front as a function of time. It can be seen that a maximum pressure pulse of over 15 MPa was achievable with a rise time of approximately 10 microseconds. The acoustical performance of the transducer before and after the shock exposure was evaluated for comparison in order to assess the effect of such a shock on the device.

4. EXPERIMENTAL RESULTS

The impedance measurement result of a typical 25.4 x 25.4 cm^2 1-3 composite panel, tested both in air and in water, is shown in Fig. 5. The primary thickness mode resonance appeared at about 320 kHz which is as expected from theoretical calculation. The water loading apparently did not change the resonant frequency of this particular mode. In addition, a number of other modes are also evident. The low frequency mode at about 75 kHz is believed to be the length-mode resonance of single ceramic rods in the 1-3 piezocomposite. The other prominent mode at about 180 kHz is related to the elastomer encapsulant, because this mode was absent in unencapsulated panels. Numerical modeling of these different modes is presently being carried out in a separate study. However, it is clear that the origin of these parasitic modes is closely related to the two-phase nature of this composite material. The different acoustic velocities in the ceramic and in the polymer could be the major factor causing this to occur. The geometrical design of the material, such as the rod-to-rod spacing and the aspect ratio of individual rods, is also an important factor.

Figure 6 shows the transmitting voltage response (TVR) of a sample in dB referenced to one

micropascal per volt. In addition to the thickness mode near 300 kHz, one also finds a mode at 100 kHz, which was discussed earlier in Fig. 5. Analysis of the in-air impedance measurement data shows that this is actually a very strong mode, having an effective coupling coefficient of 0.35 or more. Therefore, for actuator applications of the 1-3 piezocomposite panels one may also take advantage of this strong low frequency coupling in addition to the conventional thickness mode of the panel. The increase in TVR with frequency is slightly greater than the normal 12 dB per octave variation. This indicates that the overall panel displacement is somewhat different from that of an idealized point source. If one considers the large size of the piezocomposite panel, this difference is not totally unexpected. In-plane modes of the panel would provide the overall panel with a certain displacement profile. Additional experimental work is being carried out to map this displacement profile in detail. Nevertheless, it is clear that this strong coupling behavior around 100 kHz results in an improved acoustic bandwidth. When increasing the electrical drive level from about 0.16 kV/cm to over 1.1 kV/cm, the source level increases linearly with the drive. This linearity with the electrical drive level is very important for actuator applications, which is certainly a very gratifying result. The effect of an underwater explosive shock on the TVR of the 1-3 composite panel is also shown in Fig. 6, suggesting only a one dB loss in TVR. Furthermore, the panel shows no physical damages due to exposure to two consecutive shocks. However, the shock exposure did alter the directivity pattern of the acoustic response. Figure 7 shows the patterns before and after shock for a panel measured at a frequency of 20 kHz.

The effect of pressure cycling on the TVR of 1-3 composite panels is demonstrated in Fig. 8. When measured at 22°C, the TVR showed a few dB variations due to the change in pressure when pressure was stepped up from the ambient to 3.5 MPa and 6.9 MPa, then reduced to 3.5 MPa before returning the system to the ambient pressure. It seems apparent that the extreme high pressure of 6.9 MPa had a slight effect in degrading the transmitting response. But, the high pressure did not seem to alter the directivity pattern. Figure 9 shows the 50 kHz directivity of a panel measured at 22°C and 3.5 MPa, which maintains the symmetry and is in agreement with the theoretical calculation. The pressure effect on the overall acoustical behavior of the panel is more clearly seen when one examines the receiving response. Figure 10 gives the free-field voltage sensitivity (FFVS) in dB referenced to one volt per micropascal. Nominally a constant FFVS at -185 dB was observed over the frequency band of the measurement. This is not only an adequate sensitivity but also ideal for broadband reception of signals from a few kHz to 100 kHz. When pressure cycling from the ambient pressure to a maximum of 6.9 MPa was carried out at 22°C, the deterioration of the acoustic performance was found to be of the order of 3 dB. However, after the release of this pressure, the material seemed to recover fully with no change from the original FFVS characteristics. Unfortunately, when tested at 4°C, the sensitivity decreased by as much as 10 dB. This strongly suggests that other polymeric resins should be investigated for low-temperature applications in order to develop a panel that has properties stable with hydrostatic pressure at these temperatures. With a variety of available polyurethane resins that show a wide range of glass-to-rubber transition temperature, it is believed that a proper choice of the polymer phase can be identified in the near future to optimize the low-temperature performance of the 1-3 piezocomposites.

5. CONCLUSION

New 1-3 piezocomposite panels have been fabricated by using an injection molding method. Both in-air and in-water measurements show the presence of parasitic modes in addition to the conventional thickness mode of a plate. The present panel configuration appeared to be stable with pressure up to 6.9 MPa and is resistant to underwater explosive shock as determined from tests in a conical shock tube. The underwater acoustic performance of the panels suffers its most severe test when the composite material was exposed to high pressures at 4°C. Alternative polymeric resins should be selected for the polymer phase of the composite in order to produce temperature stable 1-3 piezocomposite for low-temperature

use. In summary, 1-3 piezocomposites appear to be promising candidates for sensor and actuator application in large smart structures, especially when large area coverage is required.

6. REFERENCES

1. D. Berlincourt, "Piezoelectric ceramics: Characteristics and applications," J. Acoust. Soc. Amer. 70, 1586 (1981).
2. B. Jaffe, R.S. Roth and S. Marzullo, "Piezoelectric properties of lead zirconate-lead titanate solid solution ceramics ware," J. Appl. Phys. 25, 809 (1954).
3. R. A. Burdisso and C. R. Fuller, "Design of feedforward ASAC system by eigenfunction assignment," J. Acoust. Soc. Amer. 94, Pt. 2, 1816 (1993)
4. D. Damjanovic and R. E. Newnham, "Electrostrictive and piezoelectric materials for actuator applications," J. Intell. Mater. Syst. Struct. 3, 190 (1992)
5. B. Jaffe, W. R. Cook and H. Jaffe, Piezoelectric Ceramics, Academic Press, New York (1971)
6. R. Y. Ting, "Evaluation of new piezoelectric composite materials for hydrophone applications," Ferroelectrics, 67, 143 (1986)
7. A. Preston, "The Royal Australian Navy's new Collins class submarines," Naval Forces - International Forum for Maritime Power, Vol. 14, No. 5 (1993)
8. R. E. Newnham, L. J. Bowen, K. A. Klicker and L. E. Cross, "Composite transducers," Materials in Eng. 2, 93 (1980)
9. R. Y. Ting, "The hydroacoustic behavior of piezoelectric composite materials," Ferroelectrics, 102, 215 (1990)
10. R. Y. Ting and T. R. Howarth, "Evaluation of 1-3 piezocomposite transducers for underwater applications," J. Acoust. Soc. Amer. 96, Pt. 2, 3299 (1994)
11. W. A. Smith, A. Shaulov and B. M. Singer, "Properties of composite piezoelectric materials for ultrasonic transducers," Proceeding IEEE Ultrasonic Symposium, Vol. 2, 539 (1984)
12. R. L. Gentilman, D. F. Fiore, H. T. Pham, K. W. French and L. J. Bowen, "Fabrication and properties of 1-3 PZT-polymer Composites," Ceramic Transactions, 43, 247 (1994)
13. R. L. Bobber, Underwater Electroacoustic Measurements, Naval Research Laboratory, Washington, DC, July 1970.
14. L. B. Poche and J. F. Zalesak, "Development of a water-filled conical shock tube for shock testing of small sonar transducers by simulation of the test conditions for the heavyweight test MIL S-901D (Navy)," NRL Memo Rept. 7109, Oct. 1992.

7. ACKNOWLEDGEMENT

The author acknowledges the funding support from both the Office of Naval Research and the Advanced Research Projects Agency (ARPA), and the support for the fabrication of piezocomposite panels by the Materials System Inc. under an ARPA contract.

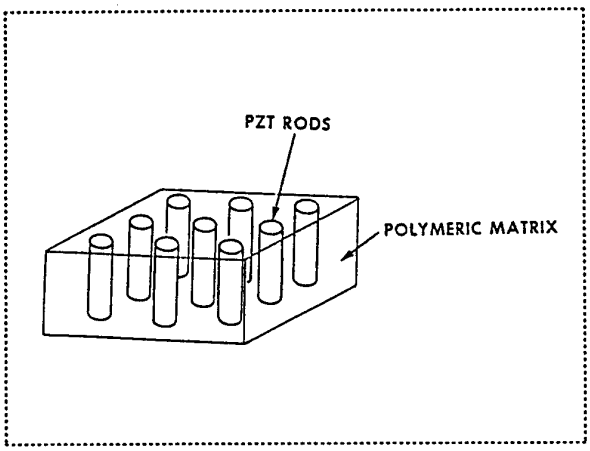


Figure 1: A schematic diagram showing the concept of a 1-3 piezocomposite.

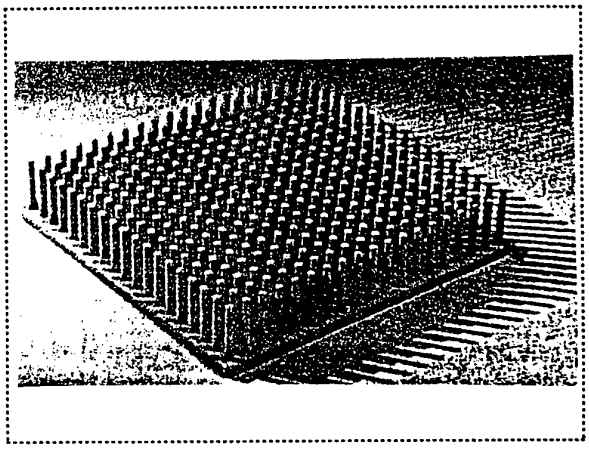


Figure 2: An injection-molded PZT 1-3 preform produced by MSI, Littleton MA.

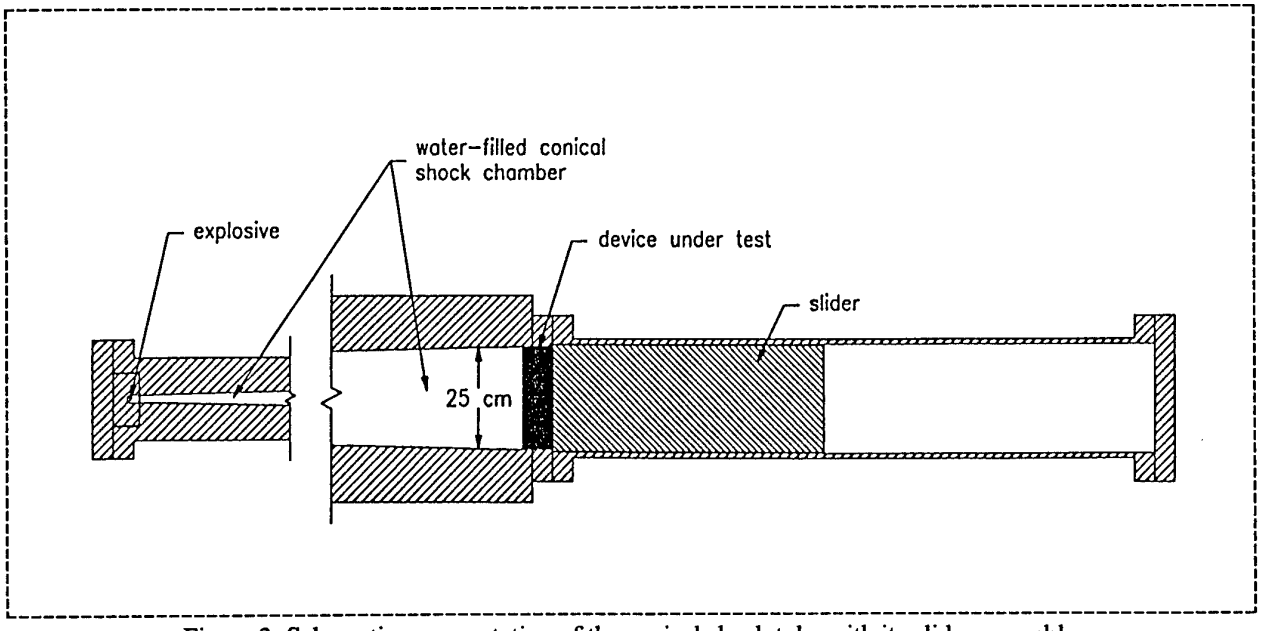


Figure 3: Schematic representation of the conical shock tube with its slider assembly.

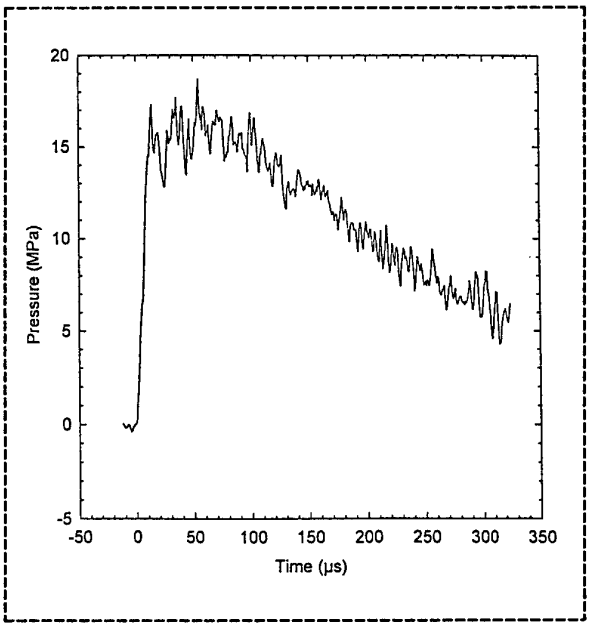


Figure 4: Pressure amplitude of the shock front as a function of propagation time.

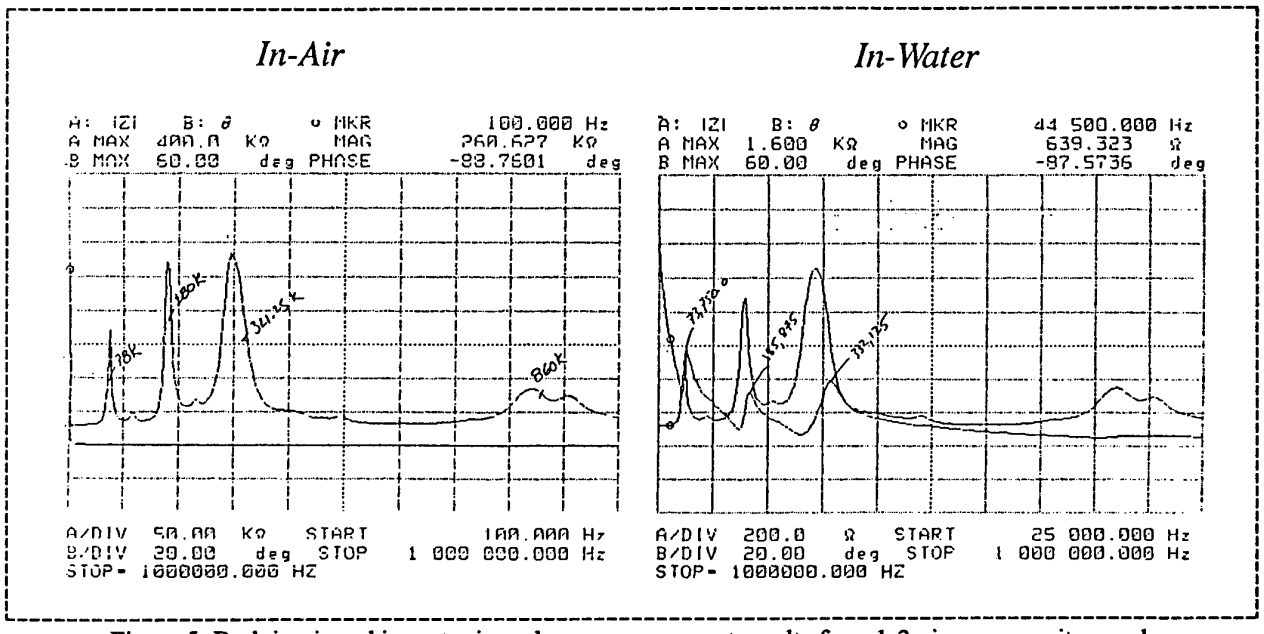


Figure 5: Both in-air and in-water impedance measurement results for a 1-3 piezocomposite panel.

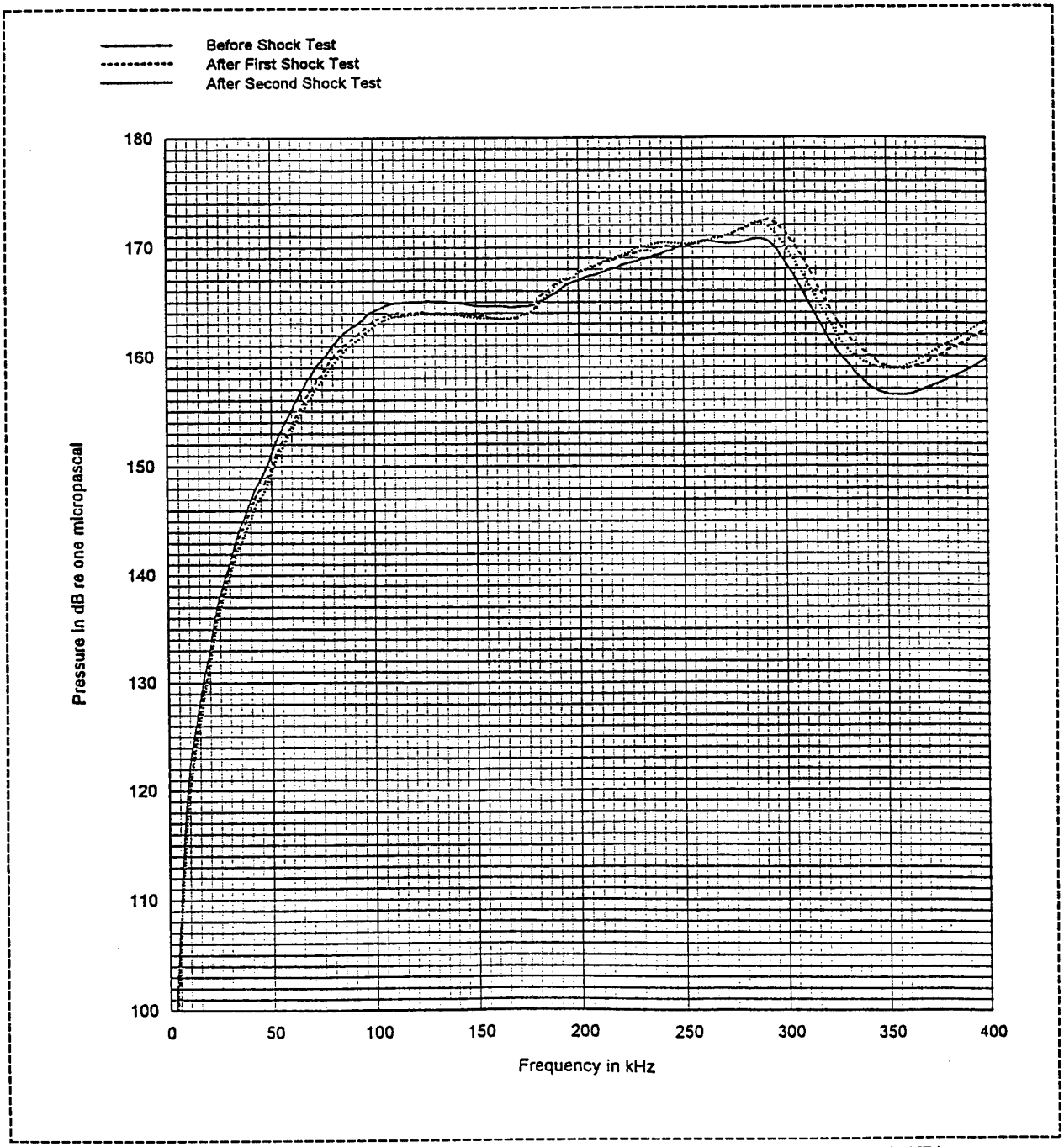


Figure 6: Effect of underwater explosive shock on the transmitting voltage response (TVR) of a 1-3 piezocomposite panel.

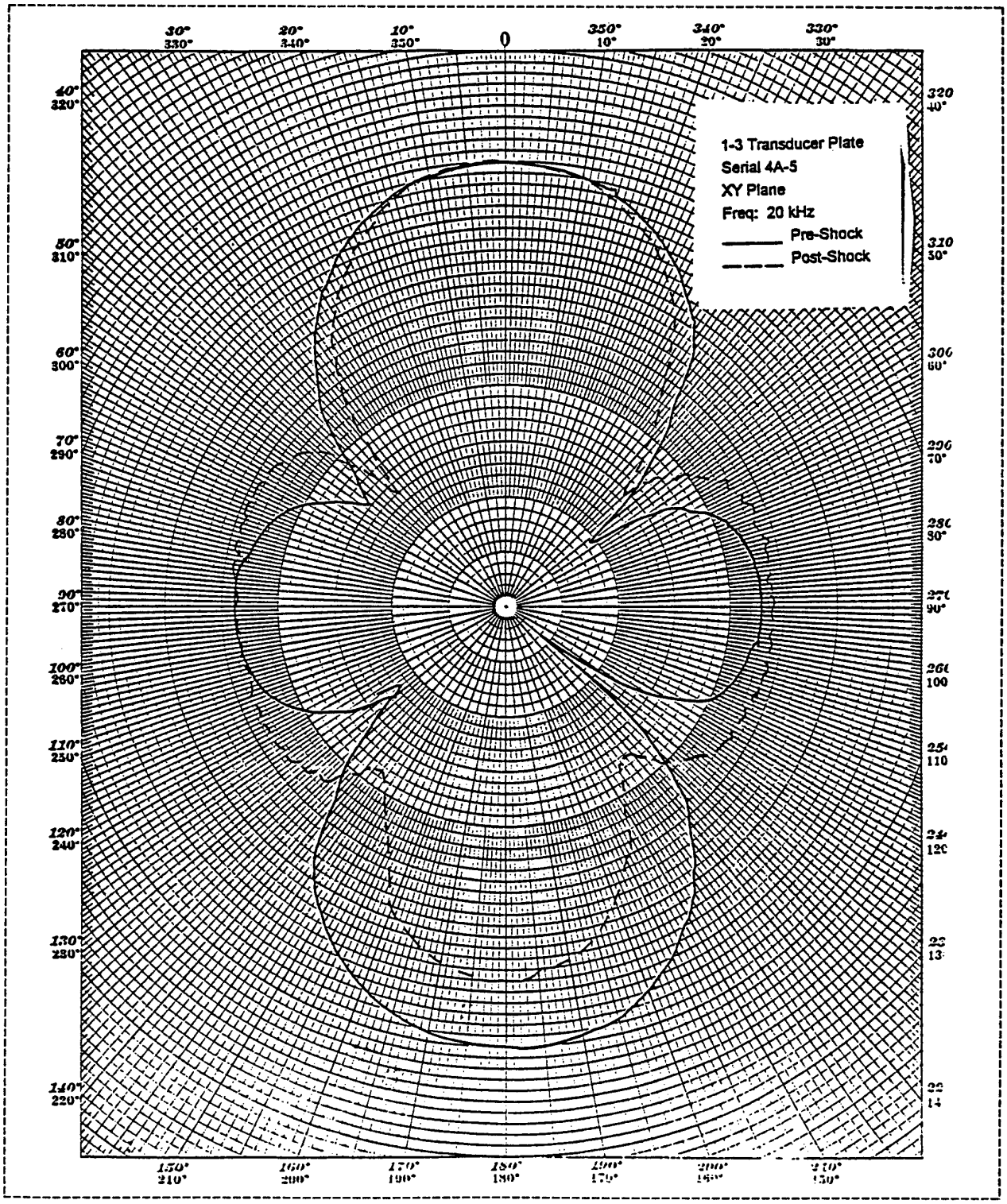


Figure 7: The directivity pattern of a 1-3 piezocomposite panel at 20 kHz showing the effect of an underwater explosive shock.

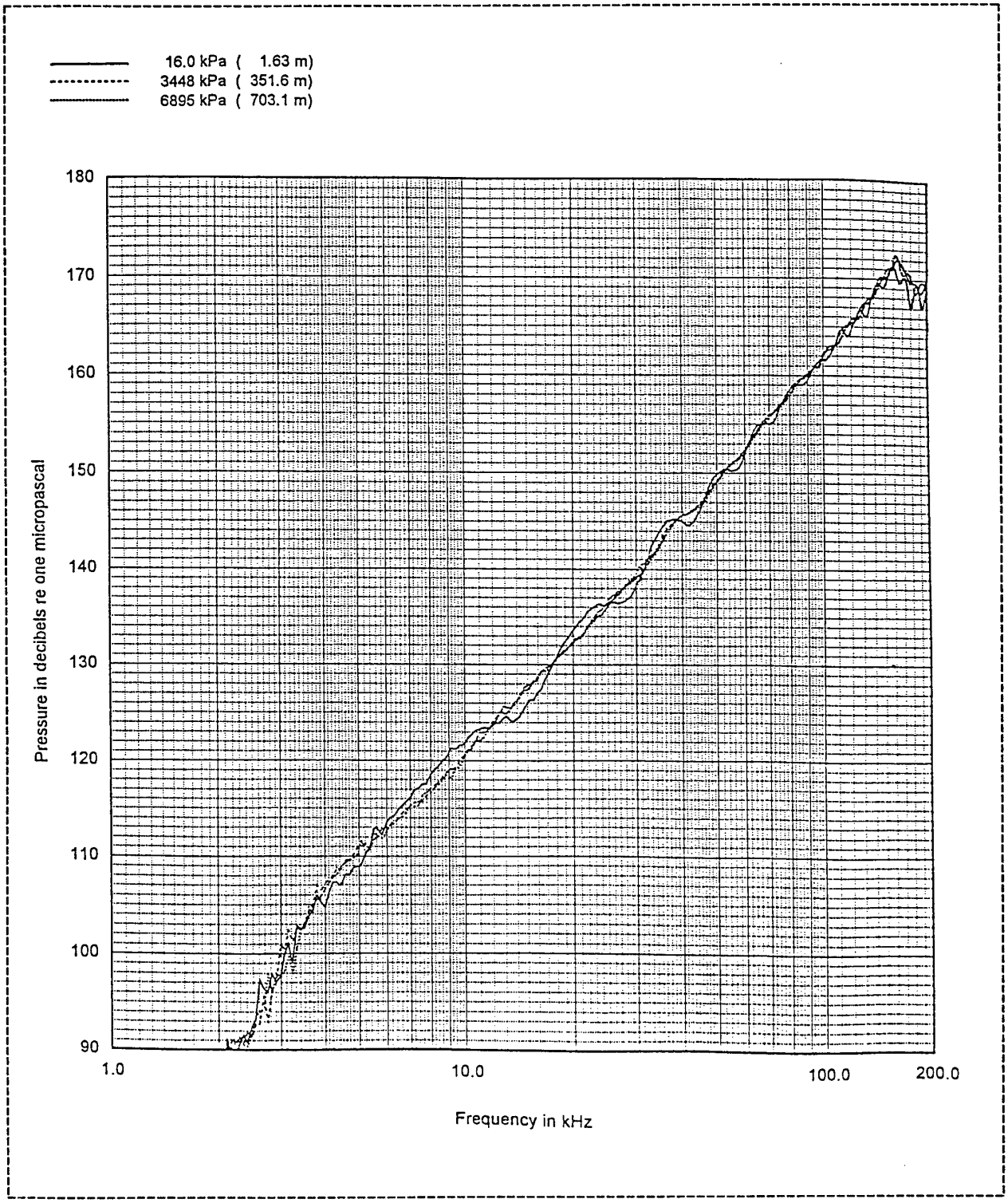


Figure 8: Effect of pressure on the transmitting voltage response (TVR) of a 1-3 piezocomposite panel at 22°C.

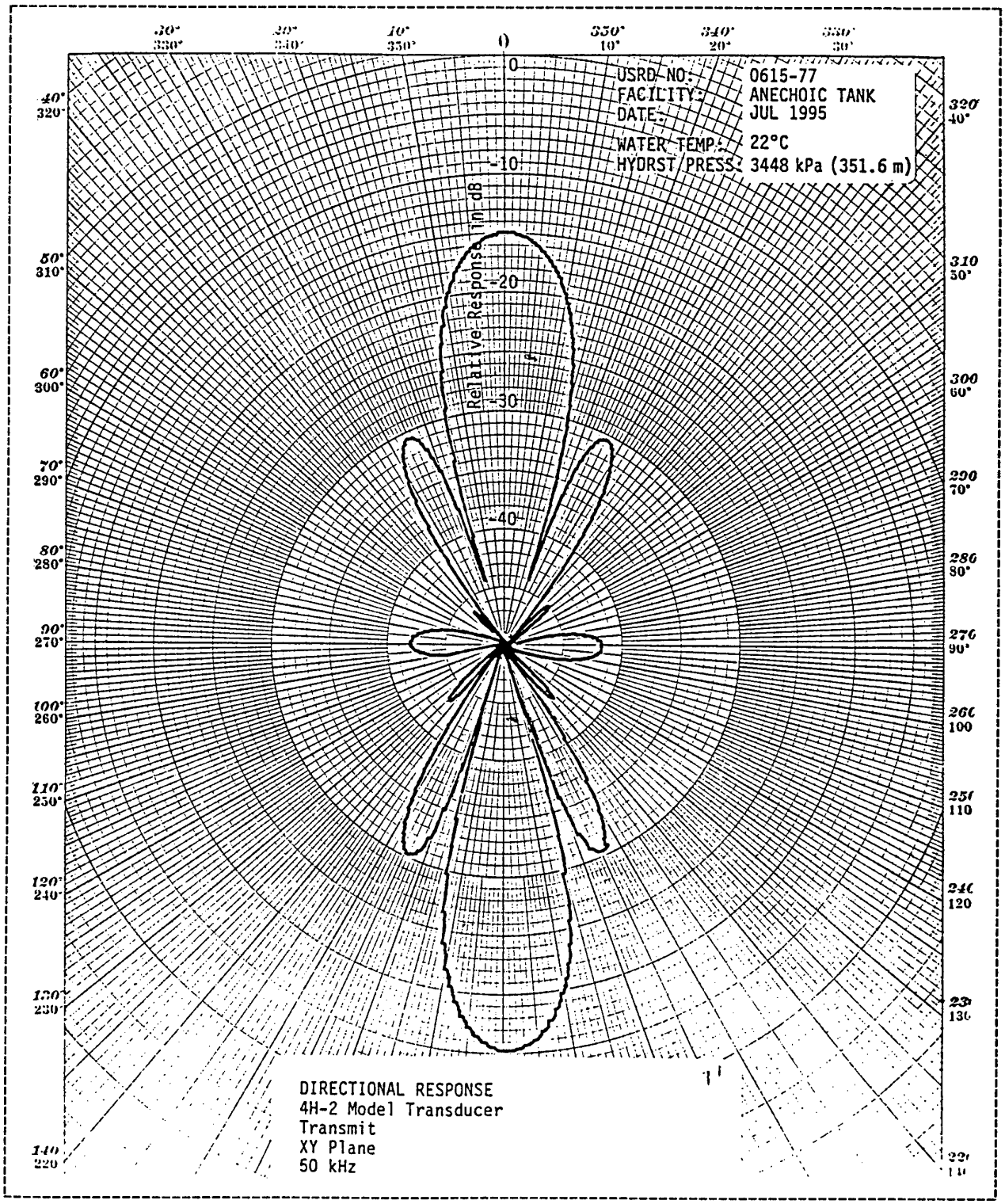


Figure 9: Directivity pattern at 50 kHz of a 1-3 piezocomposite panel measured at 22°C and 3.5 MPa.

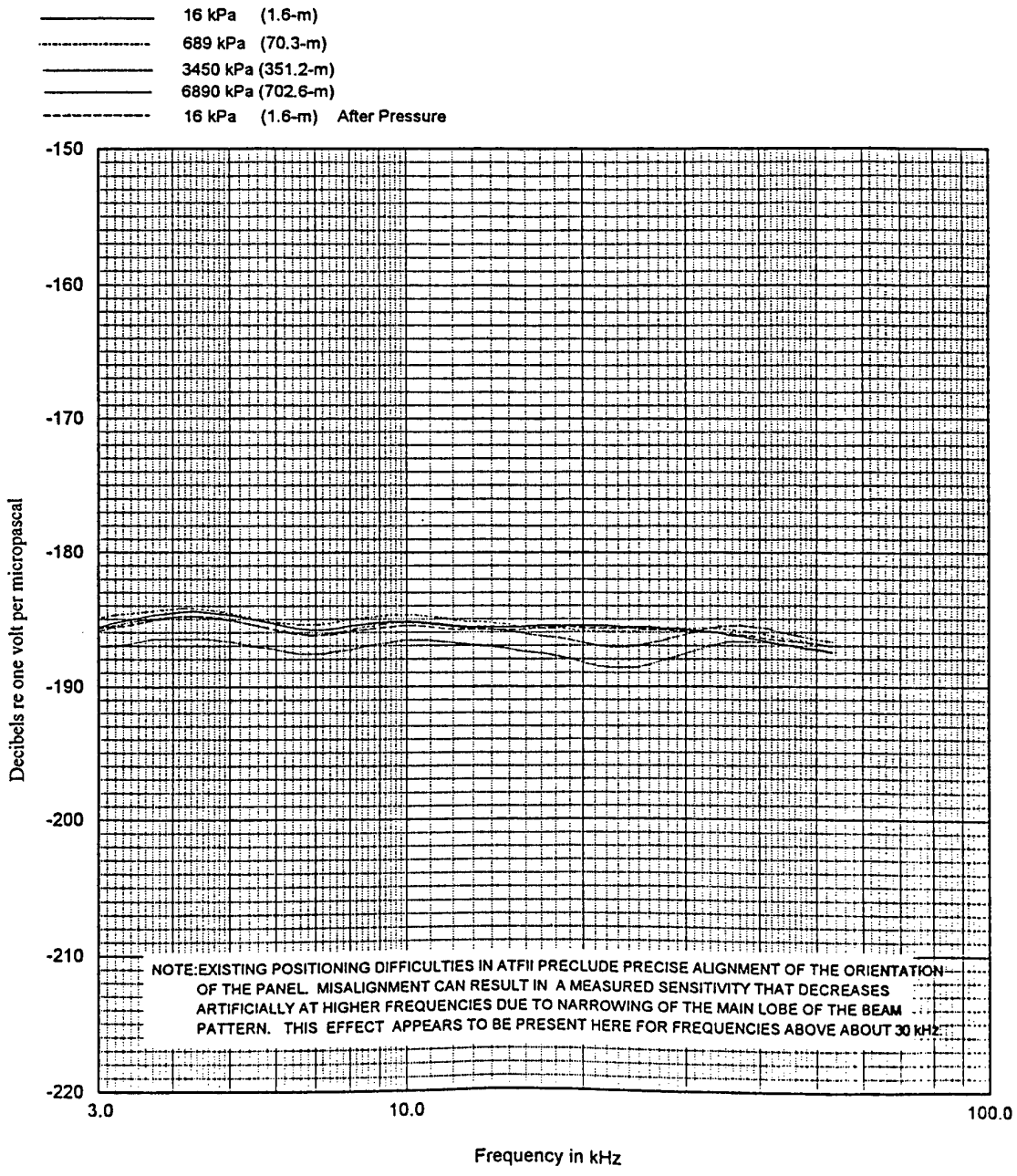


Figure 10: Effect of pressure on the free-field voltage sensitivity (FFVS) of a 1-3 piezocomposite panel at 22°C.

Invited Paper

Fluoridated piezoelectric ceramics for power transducer

Lucien Eyraud, Paul Eyraud, Paul Gonnard, David Audigier
INSA - 20, avenue Albert Einstein - 69621 Villeurbanne Cédex

ABSTRACT

The fluoridation of anionic sites in the perowskite lattice ABO_3 can greatly stabilize the remanent polarization under high stresses level. The dielectric losses are smaller than oxygen deficient materials. The mechanism for stabilization is always allocated to sites which can act either as electron donors or acceptors [1]. The charge transfer induces a polarization which is sufficient to cancel the distribution of bound charge ($\rho = -div\vec{P}$) in the poled phase. The B^{3+} - F^{1-} couples constitute dipoles which have a better stability than the B^{3+} - V_0 couples only present in perowskite ceramics with oxygen vacancies .

1. INTRODUCTION

All "hard" materials, used for power transducers (ultrasonic cleaning systems, nebulizers, sonar,....), are made from ceramics with oxygen vacancies. Many authors [2, 3] investigated this process of stabilization and its origin is the decrease of the domain wall motions, which means an important decrease of the overall losses in dynamic state.

However, this material reveals the following drawbacks :

_ the electrical conductivity is more important than in the no vacancy solid and may provoke difficulties during the sample poling.

_ an important hysteresis appears under high mechanical and electrical levels.

_ the remanent polarization doesn't tolerate very high levels of sollicitations (field ,stress ,strain). On the other hand, the non linearity of polarization often presents troublesome consequences for the user.

This study indicates a new process which allows to obtain "hard" PZT type ceramics with fluoridation of anionic sites. The mechanism of stabilization by fluoridation is described in previous report [4].

A number of published reports [5, 6] deal with the possibility of formation of solid solution with a fluorine substitution in the anionic part of the ABO_3 perowskite structure. These studies concern exclusively the dielectric properties of $BaTiO_3$

2. FLUORIDATED PZT MATERIALS

Owing to the facts that a reaction between solids very often does not proceed to completion, and that a high temperature (900°C) is required, the "dry" process does not always lead to the wanted composition, especially because of the high volatility of PbO.

This is why the "wet" process we use is a coprecipitation in liquid medium followed by a fluoridation (figure 1). The decomposition of intermediate, takes place at 600°C over 10 hours, conditions which ensure the reaction completeness. This is a very reliable process allowing to introduce heterovalent cations and anions in a unique operation at low temperature.

0-8194-2165-0/96/$6.00

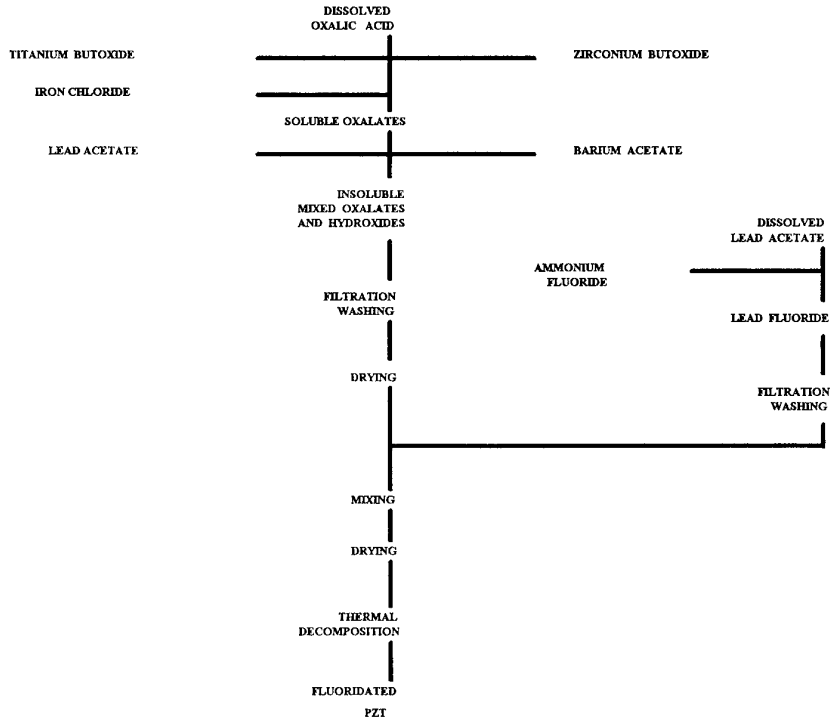


Figure 1 : Fluoridated PZT

3. EXPERIMENTAL STUDY

Figures 2 , 3 , 4 , 5 , show the influence of fluoridation respectively of the d33 coefficient versus the uniaxial stress, dielectric permittivity ε_{33} versus the uniaxial stress, dielectric losses tgδ versus the electric field and electric resistivity at high electric field versus the temperature of a PZT oxygen deficient perowskite :

[Pb,Ba] [Zr,Ti,Fe] [O,F]

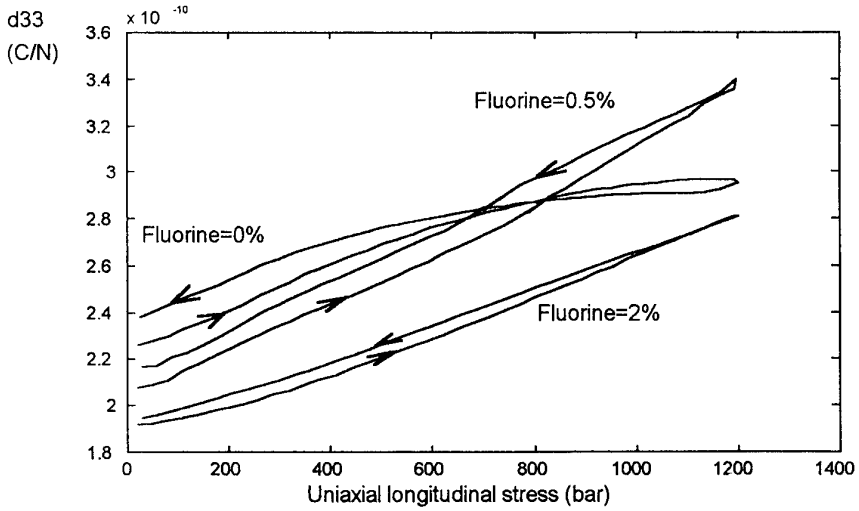


Figure 2 : d33 versus the uniaxial stress for various fluoride concentration

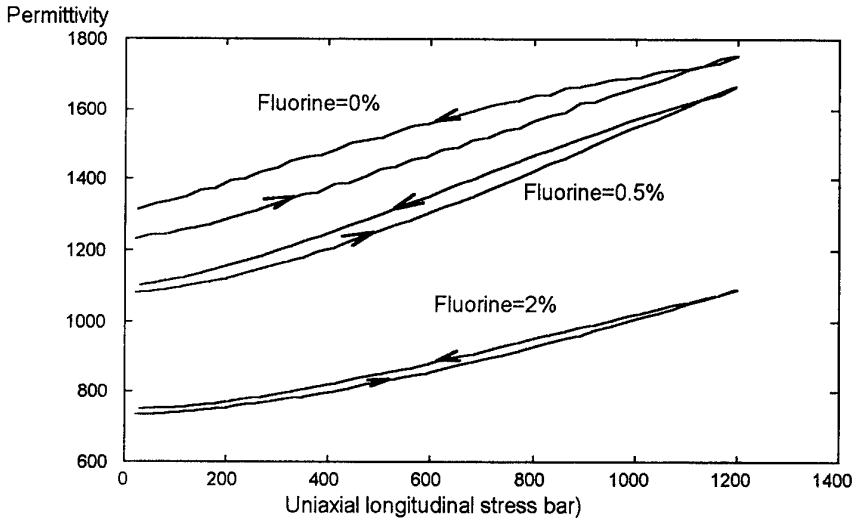


Figure 3 : ε_{33} versus the uniaxial stress for various fluoride concentration

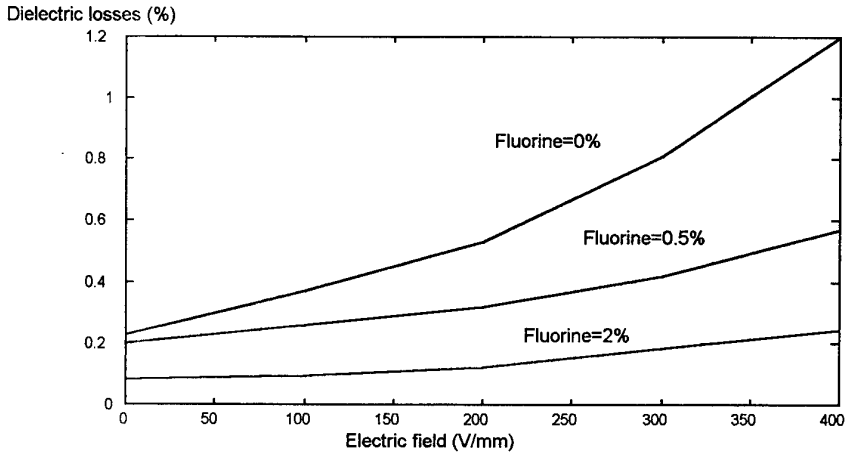


Figure 4 : tgδ versus the electric field for various fluoride concentration

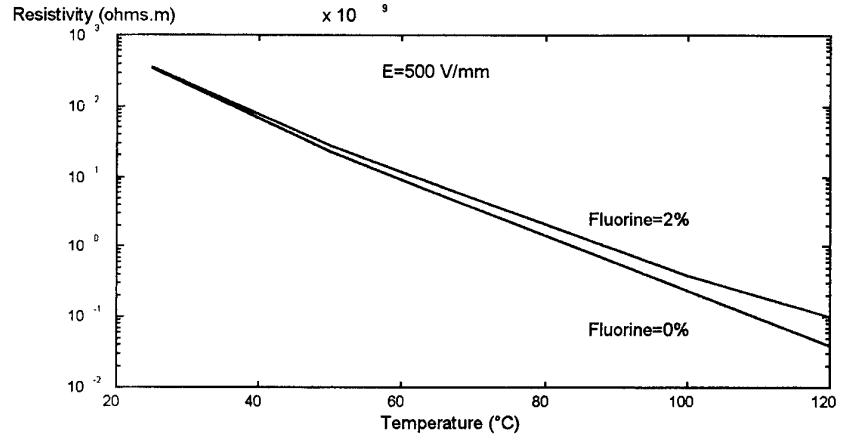


Figure 5 : resistivity versus the temperature for various fluoride concentration

Actually, a new substituted composition, [Pb,Ba,Sr] [Zr,Ti,Fe,Mn] [O,F] allows to obtain very good electro-mechanical properties, greater than Navy III type [7], but with very low dielectric losses and very important stability under high level of sollicitations (Tableau 1).

	Free Rel. Diel. Const.	Diel. Loss Factor (%) at 5V/mm	Diel. Loss Factor (%) at 400V/mm	Piezo. Charge Coefficient (pC/N)	Mech. Qual. Factor
Navy III	1025 ±12.5%	≤0.4	≤1	215 ±15%	≥800
[Pb,Ba,Sr] [Zr,Ti,Fe] [O]	1200	0.2	1	230	1200
[Pb,Ba,Sr] [Zr,Ti,Fe] [O,F]	900	0.06	0.25	190	3000
[Pb,Ba,Sr] [Zr,Ti,Fe,Mn] [O,F]	1100	0.15	0.80	250	1000

Tableau 1

5. DISCUSSION

The previous studies show that the partial or total substitution of F^{1-} ions for O^{2-} vacancies in the anionic sites increases stability of the power ceramics.
In this case, the fluoride ion is an important defect as large as oxygen vacancy and stabilizes the domain walls because it also produces a charge defect in anionic site.
However, this defect is rigidly bound to a site contrary to oxygen vacancy. Indeed, this one moves easily under sollicitation and its electric charge can change.
So, a fluoridated site and this environment of Ti^{4+}, Ti^{3+}, are rigidly bound to lattice and hold these properties of commutation required for stabilization.

6. CONCLUSION

This study shows the interest of the fluorine introduction in power PZT ceramics on the dielectric and piezoelectric properties bound to an important polarization stability under high stresses level and a low aging [8] In this type of materials, the mechanical and electromechanical losses are not optimized and we have to take the design of the piezoelectric power devices into account.

7.REFERENCES

[1] L. Eyraud, P. Gonnard, and B. Claudel, "Causes of Instability and Aging of Piezoelectric Power Ceramics", J. Am. Ceram. Soc., 73 [7] 1854 - 56 (1990).
[2] B. Jaffe, W. R. Cook, and H. Jaffe, Piezoelectric Ceramics; pp. 237 - 69, Academic Press, London and New York, 1971.
[3] K. H. Hardtl, "Electrical and Mechanical Losses in Ferroelectric Ceramics", Ceramics International, 1982, Vol. 8, n° 4, p. 121-127.
[4] L. Eyraud, P. Eyraud, D. Audigier, B. Claudel, "Influence of the Fluoride Ion on the Piezoelectric Properties of a PZT Ceramics", Ferroelectrics (to be published).
[5] I. N. Belyaev and S. A. Shilov, Zh. Neorgan. Khim., 14, 2243 (1969).
[6] M. M. Nekrasov, V. S. Savoshchenko, L. D. Vsevolodskii and A. M. Sych, New Materials and Elements in the Construction of Radio Receiving Sets [in Russian], Znanie, Kiev (1969), p. 15.
[7] IEEE Standart on Piezoelectricity, ANSI / IEEE Std 176, 1987, 54 p.
[8] L. Eyraud, P. Eyraud, F. Eyraud, D. Audigier, M. Boisrayon, "Céramiques Fluorées de Puissance", Pat, n° 95.02744, 9 mars 1995

Paper presented at the Third ICIM/ECSSM '96, Lyon '96

Elaboration of PZT thick films by screen printing

V. Tajan, P. Gonnard, M. Troccaz

INSA, L.G.E.F, Bât. 504 - 20, av. A. Einsteinn 69621 Villeurbanne Cedex, France

ABSTRACT

This study concerns the fabrication of a "soft" lead zirconate titanate (PZT) thick films on a Platinum substrate (5 x 15 mm size, 0.25 mm thickness) by the screen printing method. Various parameters connected with the screen printing (rheological characteristic of the ink, firing conditions of the layer) as well as those concerning the active powder used (grain size, grain distribution) are studied. The screen printed specimens characterized from their dielectric properties and their hysteresis loop show a diminution compared to the bulk ceramic, which may be attributed to the less than completely densified films. A study of the displacement versus an a.c. electrid field of the piezoelectric film on a platinum substrate is also achieved by a laser doppler vibrometry techique. A comparison with a machined down ceramic pasted on this same Pt substrate is carried out.

1. INTRODUCTION

The elaboration of materials in thick films form is in continuous increase since twenty years in the field of hybrid integrated circuits or components useful as micro sensors and actuators for very various applications : medical, military, motor vehicles, telecommunications... In particular a piezoelectric layer excited by an operating voltage of a few volts can produce the vibration of a substrate in a large range of frequencies or inversely detect it. Ferroelectric films, such as PZT, have been extensively investigated in thin film form (thickness less than 1 μm) for their utility as memories. For electro-mechanical applications thick films are required and the screen printing technology has been adopted. Compared with other technologies this method allows the manufacturing of micro components at low cost and provides the possibility of depositing compounds with very different formulae and consequently a wide range of products.

2. PIEZOELECTRICITY AND FERROELECTRICITY

Piezoelectricity is the property of some materials to produce electrical charges when subjected to a mechanical stress (direct effect). Conversely when an electric field is applied a mechanical strain will occur, changing the dimensional shape of the material (inverse effect).

The piezoelectric effect was first observed in naturally single crystal materials as Quartz and Rochelle salt. The unit cells of these compounds do not possess a center of symmetry and consequently distorsion of the unit cells produces electric dipoles. However the most widely used piezoelectric transducer materials are polycrystalline ceramics. Ceramic materials are made up of a vaste number of crystallites with randomly orientated dipoles. Consequently they are isotropic and possess no piezoelectric properties. It is only by the application of a high dc electric field (polarization), causing realignment of the dipoles in the direction of the field, that the ceramics become anisotropic. After this poling treatment the compounds retain a remanent polarization , they are named ferroelectric materials. The graph of polarization versus electric field is a curve analogous to the magnetic hysteresis loop. The remanent polarization of the ferroelectric ceramics is cancelled out by raising its temperature above the Curie Point or by mechanically overstressing.

At the present time the most extensively used ferroelectric materials for electro-mechanical transducers are modified lead zircono-titanates (PZT). Powders of this type were chosen for screen printing, in particular compositions with high values of the dielectric constant ε_r and of the piezoelectric constant d_{33} (ratio of developed strain to the applied field, or charge density to the stress applied).

0-8194-2165-0/96/$6.00

3. SCREEN PRINTING

Thick films technology developed for microelectronic applications has shown the qualities of the screen printing process :

- flexibility : choice of the powders and therefore possibility of deposing compounds with very different formulae, multilayer structures.
- low cost
- mass production adaptation
- possibility of creating integrated systems.

Thick films can be printed on various substrates. The most common are 96% or 99% alumina due to their good electrical, mechanical, thermal conductivity characteristics. However metallic substrates are also employed : buffered silicon, steel, platinum. During this work the substrate will be a platinum sheet, 5 x 15 mm size, 0.25 mm thickness, which is stable at the firing temperatures (about 1050°C) and will constitute at the same time one of the electrodes. This substrate has also a thermal expansion coefficient α compatible with that of the PZT powders at high temperature, as shown in Table 1.

Table 1 : Thermal expansion coefficient for powder and substrates

Temperature °C	$\alpha\ 10^{-6}$ PZT*	$\alpha\ 10^{-6}$ Pt	$\alpha\ 10^{-6}$ Al_2O_3	$\alpha.\ 10^{-6}$ Si
1000	7	10.8	8.9	5
200	2.6	9.2	7.1	3.5

* $Pb\ Zr_{0.55}\ Ti_{0.45}\ O_3$

The screen printing inks are made up by the intimate mixing of the powder of the piezoelectric material to be deposited with an organic phase allowing the flow of the powder through the screen. For this aim the ink contains two main constituents :

* an organic vehicle which determines its printability. The formulation of this organic part is very varied and consists at least of :

- a binder
- a solvent and a plasticiser
- a dispersing agent or deflocculant

* an active material determining the piezoelectric properties of the film ; its amount must be as high as possible, roughly 80% weight of the ink.

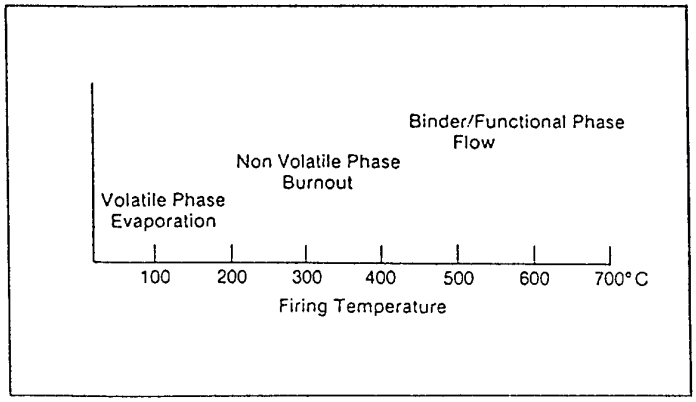
The adjustment of the relative proportions of the various components allows to obtain the necessary rheological characteristics.

4. LAYER SINTERING ON A SUBSTRATE

The different firing stages of the paste deposited on to the substrate are shown in Fig. 1.

The formation process of the thick film is illustrated by Fig.2 : after sintering the thickness of the printing will be reduced to 2/3 or 3/4. The ultimate sintering step has a high importance on the mechanical and piezoelectric characteristics of the printed layer. Contrary to the bulk, this sintering must be made in one dimension and is accompanied by stresses appearance in the layer plane. The model given by Raj and Bordia[1] supplies some main characteristics of the sintering of a powder on a substrate.

- there is an optimal particle size for a given sintering temperature
- the presence of stresses in the layer can be the origin of flaws
- there is a retarded shrinkage in comparison with an unconstrained material.



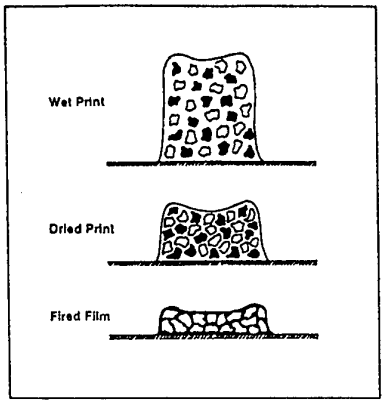


Fig. 1 : Firing temperatures of the organic vehicle

Fig. 2 : Formation process of the thick film

5. EXPERIMENTAL PROCESSING AND RESULTS

The manufacturing of screen printed PZT samples will allow to specify the following points :

4.1 - powders grain size.

The PZT powders are prepared by a coprecipitation process previously described[2]. A "soft" PZT with large values of ε_r and d_{33} coefficients was chosen, the formula of which is $Pb\ Zr_{0.23}\ Ti_{0.37}\ (Nb_{2/3}\ Ni_{1/3})_{0.4}\ O_3$

According to the firing treatment the grain size and the specific area of the powders vary as shown in Table 2.

Table 2 : Characteristics of various PZT powders

Powder	Firing treatment °C	Equivalent diameter at 50% (µm)	Specific area g/m2
BR10	600	0.3	8
BR10	800	0.6	4.6
BR10	900	1.05	2
BR4	900	0.9	2.6

Experimentaly it has been found that a 1 µm average grain diameter is a good size for the preparation of the ink. Previously the naturally occuring agglomerates in the powder were broken by ball-milling or by using an ultrasonic device.

4.2 Ink formulation

As described in paragraph 2 a number of constituents compose the ink. Table 3 lists these materials, as their % weight, for the 1 µm PZT powder.

Table 3 : Constituents of the ink

Materials	Fonction	% weight
PZT powder	active material	77.8
α-terpineol	solvent	11.2
Polyvinyl butyral	binder	2.3
Polyethylene glycol	plasticizer	3.3
Butoxy etoxy ethyl acetate	deflocculant	5.4

The ink prepared in this manner is then homogenized by ultrasonics. The thixotropic paste is allowed to flow through a 250 mesh sieve by a brush at a controlled speed and deposits on to the Pt substrate.

4.3Thermal cycle

The printed layer is allowed to stand at room temperature to remove the mesh marks, dried at 70°C during four hours to remove the solvents and then fired in air according to the conditions shown in Fig. 3 in order to eliminate the organic products and to fix properly the layer to the substrate.

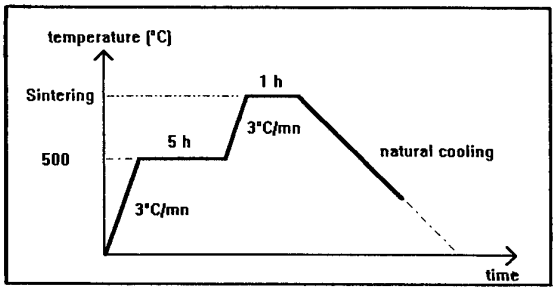


Fig. 3 : Firing conditions for the thick film manufacture

Considering the powders BR10, the best sintering is obtained for a temperature equal to 1050°C with the powder fired at 900°C. The layers prepared from the powders fired at 600 and 800°C are always very porous and cracked, because of a different viscosity of the ink : it will be of primordial importance to adapt a formulation to each kind and characteristic of powders in order to obtain the same rheological behaviour of the ink.

Addition of a glass as binder to improve the cohesion and the adhesion of the sintered layer and at the same time to lower the sintering temperature has been made without success. In order to obtain an homogeneous film without cracks a double layer printing has been carried out, that yields to samples thickness between 50 and 100 μm.

4.4 Electromechanical properties

A top Ag electrode is applied by screen printing (firing 650°C - 15 mm).

The dielectric permittivity ε_r and the dissipation factor tan δ of the film are then measured under the conditions 1 KHz - 0.1 V and the results recorded in Table 4.

Table 4 : Dielectric properties of various PZT films

Powder	Average diameter μm	Specific area m^2/g	Film Thickness μm	ε_r	tanδ %
BR4	0.9	2.6	60	840	3
BR9	1	1.6	80	370	3
BR10	1.05	2	70	730	5

Compared to the ceramic material (ε_r = 2600, tanδ = 0.026) these lower values may be attributed to the much less densified layer. Therefore it has been shown that ε_r can also be much reduced when very thin ferroelectric elements are produced[3]. So the dielectric constant of a machined down ceramic pasted on the same Pt substrate was measured as a function of thickness. It can be seen from Fig.4 that ε_r regularly diminishes up to a value comparable with that of the film.

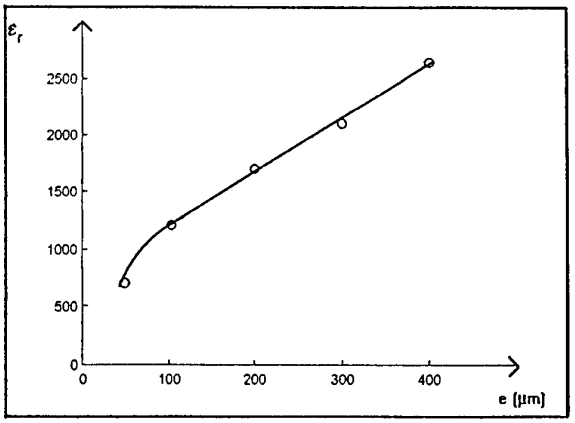


Fig. 4 :Dielectric constant versus thickness for a ceramic pasted on a Pt substrate

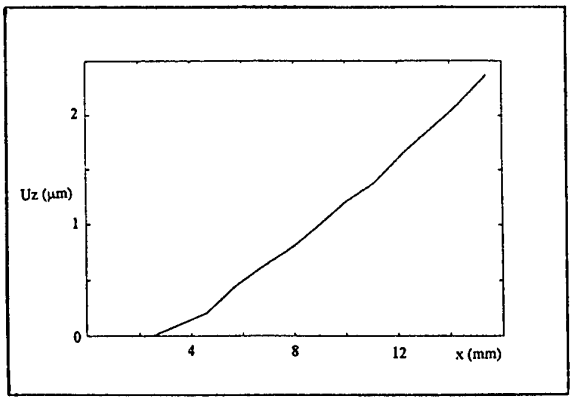
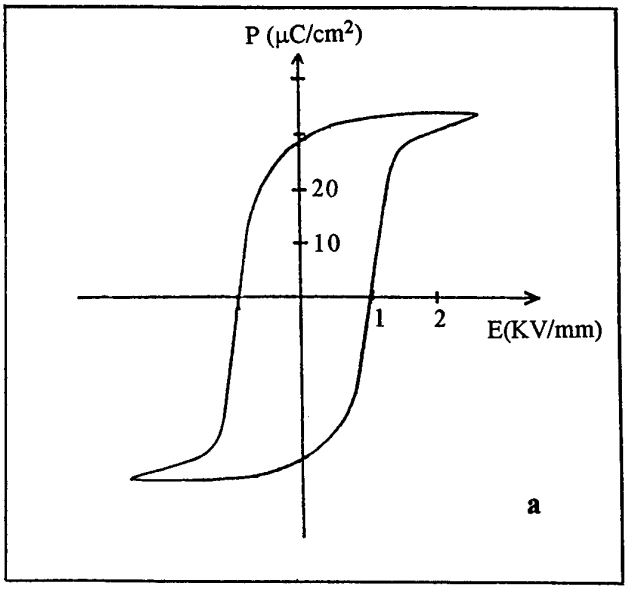


Fig. 6 : Normal strain of a thick film excited by a sinusoidal voltage



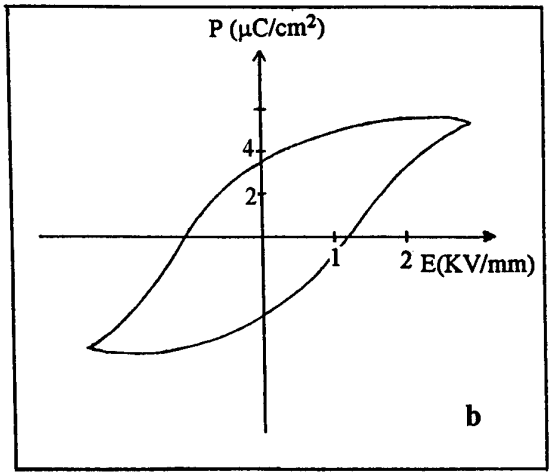


Fig.5 : Hysteresis loops of a bulk ceramic (a) and a thick film (b)

This result seems to confirm the hypothesis of a stressed layer as predicted by the sintering film model. It would remain to be proved that a "hard" PZT material, less sensitive to stress, do not present such a difference. The low frequency hysteresis loops of the bulk ceramic and of the film compared in Fig. 5 show that the coercive fields are comparable whereas the remanent polarization is only 3.5 µC/cm² for the film as found by other authors[4, 5].

If the set poled film-susbtrate clamped by one of its end, whereas the other is free, is excited by a sinusoïdal voltage (7V) it starts vibrating and behaves like a bimorph. Displacement measurement carried out with a double beam laser interferometer on a sample made up of a Pt substrate, 250 µm thick, 2 cm long, and a layer 70 µm thick, is shown in Fig. 6. The normal component of the strain for the first vibration mode of the set at a frequency = 394 Hz reaches 2.5 µm at the end of the plate.

6. CONCLUSION

Crack-free thick films of a solft PZT were fabricated on a Pt substrate. According to the preparation process of the active powder material the screen printing conditions are analysed and an ink formulation is given. Electrical measurements showed an important lowering of the dielectric permittivity and of the remanent polarization which may be due to internal stresses and an incompletely densified film. An interesting strain of the system film-substrate excited by a sinusoidal voltage is obtained.

7. REFERENCES

1 R. Raj and R.K. Bordia, J. Am. Ceram. Soc., 68, 6, 287-292, 1985
2 L. Eyraud, P. Eyraud, P. Gonnard and M. Troccaz, Ferroelectrics, 31, 133-138, 1981
3 R. Lane and K.R. Brown, Trans. J. B2. Ceram. Soc., 73, 3, 65-71, 1974
4 H.D. Chen, K.R. Udayakumar, L.E. Cross, J.J. Bernstein and L.C. Niles, To be published IEEE, 495-498, 1995
5 J. Colhier; I.A. Cornejo and M.J. Haun. Ferroelectrics, 154, 47-52, 1994

Paper presented at the Third ICIM/ECSSM '96, Lyon '96

Co-formed accelerometer - actuator composites using injection molded PZT

Robert D. Corsaro and Joseph D. Klunder

Naval Research Laboratory, Code 7130, Washington, D. C. 20375-5350

Richard Gentilman and Daniel Fiore

Materials Systems, Inc., 521 Great Rd., Littleton MA 01460

ABSTRACT

This paper describes a fabrication approach for producing high-sensitivity low-cost accelerometers. This approach offers the potential for intrinsically combining accelerometers as a dense array within an actuator. Hence sensing and actuation functions can be combined into one co-formed inexpensive transducer array. Results are presented which show that the combined transducer has predictable properties and is well suited for use in sensing, actuation, and active-control applications

1. INTRODUCTION

A general need exists for inexpensive large-area transducer arrays which intrinsically combine various functions such as acoustic or vibration sensing with area actuation. Such combination transducers are particularly needed in active control and smart-materials applications, but additionally could find use in advanced underwater, aerospace or robotic sensing applications. To be practical, however, such a combined transducer must be available as a ready-to-use electro-mechanical component with predictable properties. To be economically attractive it must be relatively simple to manufacture from reasonable cost materials.

Recently MSI began production of a 1-3 composite transducer material using an injection molding approach. The material consists of piezoceramic rods embedded in a soft matrix. It is formed as a flexible shape-conforming actuator material which can be applied over a large surface area, has very high actuator output, provides a uniform surface response and is relatively inexpensive. For these reasons it is well suited for use as the actuator in large surface area active control systems for controlling sound and vibration.

One application of this MSI material was in the smart skin studies at NRL, where NRL was intrigued by the possibility of using this new MSI piezoceramic fabrication approach to combine sensors and actuators into one co-formed transducer array. The associated cost reduction would then permit large or dense arrays of accelerometers to be included within an area actuator or pressure sensor at little added cost.

0-8194-2165-0/96/$6.00

2. INITIAL 1-3 ACCELEROMETER

Conventional piezoelectric accelerometers consist of a mass supported by a piezoelectric element with electrodes. At frequencies much below the spring-mass resonance of this system, the seismic mass exerts a stress on the piezoelectric support which is proportional to the acceleration of the system. Under such a stress, the piezoelectric element delivers a charge or voltage to the electrodes which is proportional to its stress. Hence the output charge or voltage is proportional to the acceleration of the system. Our first proposed approach to forming a dense accelerometer array within the actuator is shown in the figure. Some of the rods in the 1-3 composite actuator were separately wired and support an inertial mass. The electrical output from this region is that of a classical accelerometer..

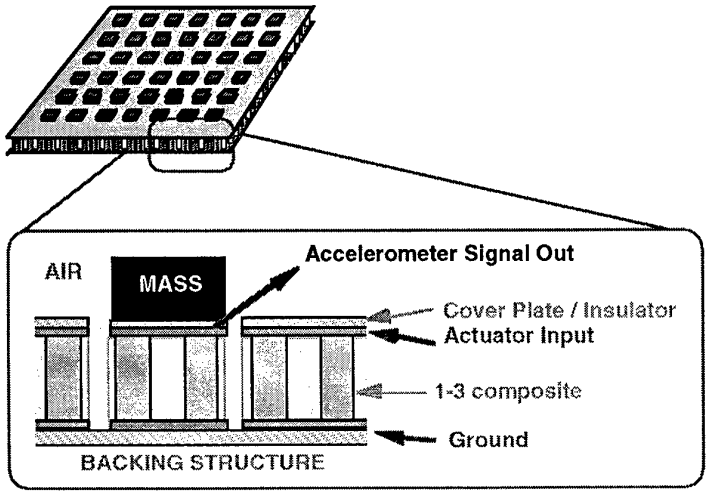


Figure 1. Simplified illustration of an accelerometer array included in a 1-3 composite actuator.

Various versions of this accelerometer were constructed by both MSI and NRL and tested at NRL for sensitivity, noise, resonant frequency, and both electro-magnetic and extraneous-mechanical crosstalk. In all cases, the results agreed with simple mathematical models of the predicted accelerometer performance.

However, two deficiencies in this 1-3 accelerometer design were noted. The most important is that the measured transverse sensitivity was found to be only nominally 10% of the axial sensitivity, with a large transverse resonance in the frequency band of interest. This resonance was identified as the simple lateral mass-loaded transverse resonance of the piezoceramic rods. A second less important issue was the attachment of the mass, which increased the complexity of the design and would introduce thermal strain and noise in some applications.

3 MONOLITHIC ACCELEROMETER

Although not a particularly practical design, Figure 4 illustrates the principles involved in the monolithic accelerometer approach. The fabricated item shown here resembles a disk on a rod, with electrodes placed on top and bottom. The single-unit disk-rod combination can be fabricated of the same piezoelectric ceramic.

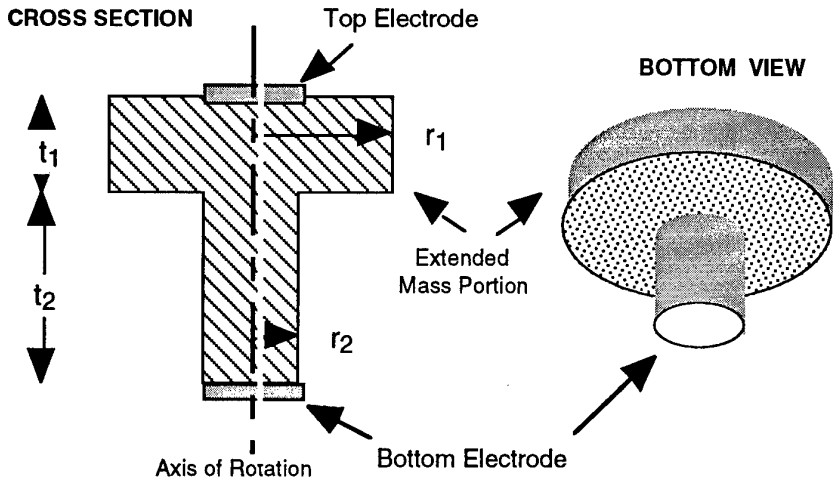


Figure 2. Illustrative drawing of the device.

Consider the top disk-like portion of length t_1 and radius r_1 as serving primarily as a mass. The rod-like portion of length t_2 and radius r_2 can likewise be considered to serve primarily as the sensor. Thus both components of a simple accelerometer are formed as one monolithic unit.

The important feature of such a device is that the mass and sensor elements are formed together from the same material and in the same manufacturing process. Separate construction of the mass is eliminated, as is the process of bonding the mass to the sensor. Reliability is improved since the bond uncertainty is removed. Additionally, the entire accelerometer component can even be injection-molding simultaneously with the 1-3 composite actuator, using just one processing step.

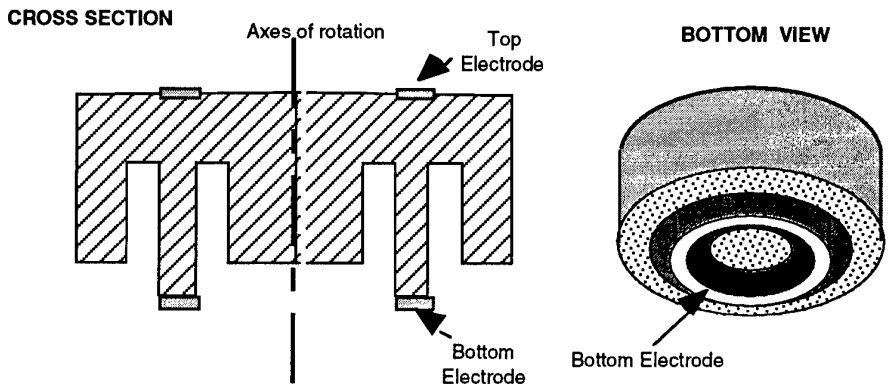


Figure 3. Illustrative drawing of a more practical configuration.

A more practical implementation of this approach is shown in the above figure. Here the principal sensor portion is a cylindrical ring, while much of the remaining volume serves primarily as the mass. For the same cylindrical volume, this new sensor geometry can have better sensitivity, lower noise, and a higher frequency bandwidth due to an increased shear rigidity.

The performance of such devices is highly predictable and competitive with good instrumentation accelerometers. For example, one accelerometer constructed had an outer radius of 6.7 mm and was 7 mm tall. This accelerometer has a measured sensitivity of 0.15 V/g (±1 dB to at least 10 kHz). The minimum detectable acceleration is low (0.2 μg per √Hz). The high frequency limit will be set by the lower of the axial mode or bending mode of support, both of which are higher than 30 kHz. As shown below, the transverse sensitivity of this accelerometer configuration is also quite low with no important resonances in the frequency band of interest.

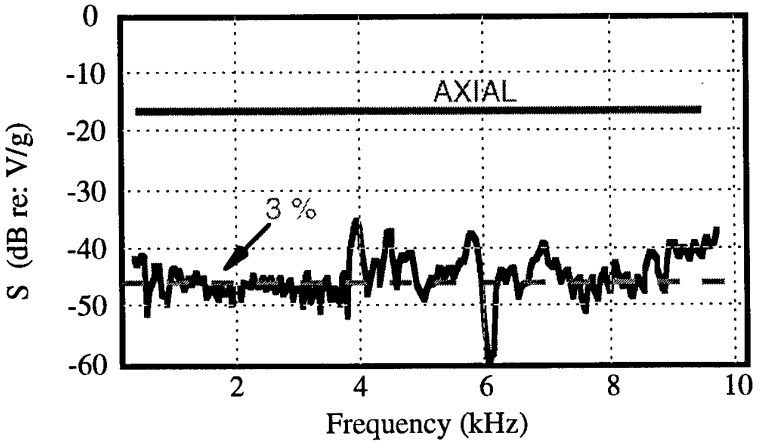


Figure 4. Transverse sensitivity of one Monolithic Accelerometer.

Other configurations and sizes have been evaluated which have higher sensitivity, lower noise figures, and lower transverse sensitivity. The design of an accelerometer for a specific application usually involves tradeoffs in size and performance.

4. ISSUES

When incorporating the accelerometer in the 1-3 composite actuator, two significant issues arose. First, we found that the electrical isolation between the actuator and the accelerometer must be at least 100 dB. This high isolation is needed to avoid instabilities in subsequent active control applications. Prototype sensor-actuator units have confirmed that these electrical coupling requirements can be achieved using conventional shielding and wiring practices.

A second issue is related to the fact that in smart actuator configurations the accelerometer is suspended in a well, attached to the top surface of the actuator. The design must ensure that the top mounting plate is sufficiently stiff that flexural modes will not appear in the frequency band of interest.

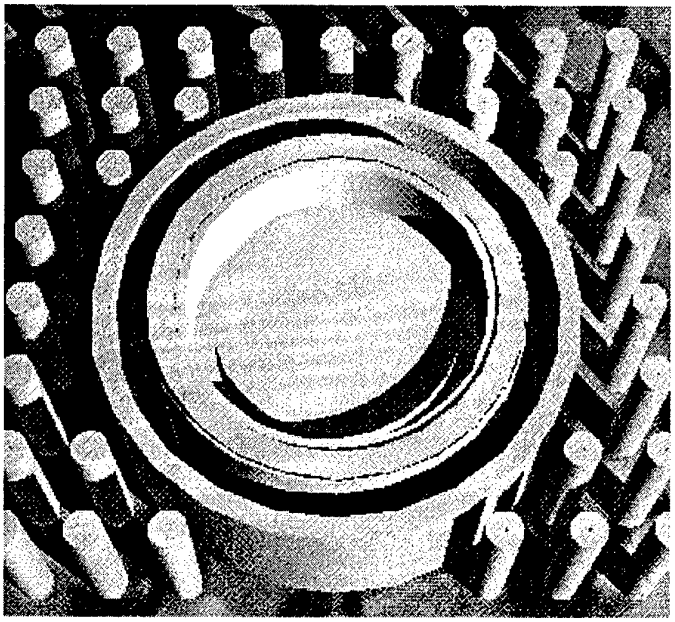


Figure 5. Illustration of the formation of a Monolithic Accelerometer in a 1-3 composite actuator (with mechanical isolation ring)

5. CONCLUSIONS

The important feature of this approach is its ability to form the two key components of the accelerometer as one monolithic structure. Fabrication can be by injection-molding, where multiple units could be formed simultaneously at very low per-unit cost. As illustrated above, the accelerometers can also be simultaneously formed as a component of the 1-3 piezoceramic composite, where the composite serves as either an actuator or pressure sensor. Various design modifications have been produced, and excellent predictability and performance has been demonstrated.

An important feature of this technology is its ability to be used in a large-area device. Structural vibration and acoustic studies have stressed the extraordinarily complex nature of point-excited structures and the severe limitations of single-location monitoring. The use of large-area uniform actuators and sensors significantly reduces this complexity. Such actuators tend to couple primarily to motion in the perpendicular direction, and hence tend not to excite extraneous modes or waves. Likewise sensors which integrate response over a large area tend to extract only perpendicular wave components.

Oxygen Diffusion and Defect Structure in PTCR-Barium Titanate

Hajime HANEDA, Junzo TANAKA,
and Takamasa ISHIGAKI

National Institute for Research in Inorganic Materials,
1-1 Namiki, Tsukuba-shi, Ibaraki 305 JAPAN

ABSTRACT

The diffusivities of oxygen along the grain boundary in the PTCR-samples were greater than those in non-PTCR samples. The grain boundary diffusion characteristics drastically changed at the oxygen partial pressure of appearing the PTCR effect. On the ohter hand, the volume diffusivities of oxygen ions in both samples have the same value. These resuls lead that the structural change at grain boundary in polycrystalline barium titanate occurred at the oxidizing prossece and enhanced oxygen grain boundary diffusion. The origin of the barrier layer of the PTCR effect is considered to be same.

1. INTRODUCTION

It is considered that the PTCR effect is a grain boundary phenomenon and relates to the grain boundary structure.(1, 2, 3 and 4). The grain boundary diffusion is an important parameter clarifying the grain boundary structure. However, experimental study for the grain boundary as a short-circuit path of oxygen ions in barium titanate is qualitative since there are no direct observations of oxygen grain boundary diffusion coefficients. Shirasaki et al.(5) have proposed that the grain boundary of lightly La-doped barium titanate enhances the oxygen diffusion but this method was indirect. The present paper is concerned with the direct observation of the enhanced oxygen diffusion along grain boundary. The PTCR effect is discussed in relation to characteristics of the oxygen grain boundary diffusion.

2. EXPERIMENTAL

A commercial barium titanyl oxalate, $BaTiO(C_2O_4)2.4H_2O$, was used as the precursor material. This oxalate, anatase and lanthanum oxalate , 99.99% purity, as the doping elements to produced semiconducting barium titanate ceramics were wet milled using ethyl alcohol and dried, and the mixture was calcined at 1373K for 4h. The resultant powder was then molded into disks that were sintered at 1623k in Ar atmosphere (O_2, a few ppm) for 24h, annealed in air for 2h, and cooled in the furnace at 100k/h to room temperature in air(oxidized sample, denoted O-BT). The reduced samples (R-BT) were sintered at the same condition as the oxidized samples and cooled in Ar atmosphere. X-ray diffraction pattern showed the sample's structure is tetragonal perovskite one and the relative sintered density was 95%. Before measurement of resistivity temperature characteristics and oxygen diffusion annealing, the insulated skin of polycrystal was removed. Indium gallium electrodes were applied for measuring resistance values as a function of temperature in air by using a two probe method.

The oxygen self-diffusion was investigated by a gas-solid isotopic exchange technique using ^{18}O as the tracer. The polished specimens were diffusion-annealed in O_2 at 5.0×10^4Pa with ^{18}O enrichment of 98% in a high-frequency induction furnace with Pt-Rh susceptor. The ^{18}O concentration of the gaseous phase was measured using a double focusing massspectrometer. The change of ^{18}O content in the gaseous phase could not be detected during diffusion annealing. The normal depth profile and the lateral distribution of oxygen isotopes were measured by a secondary mass-spectrometer(SIMS) with an electron multiplier as the detector. Cesium positive ions were used as the primary ions with the ion currents of 5 to 20nA. A normal induced electron gun was used for relieving the samples of the extra charge. To compare the

0-8194-2165-0/96/$6.00

results to other kind of samples, Y-doped ceramics were used, whose purity was lower than La-doped one(6).

3. RESULTS and DISCUSSION

The results of resistivities are shown in figure 1 and exhibited typical PTCR characteristics in oxidized sample(O-BT), whereas reduced sample(R-BT) has no PTCR effect. Figure 2 shows the normal depth profile of ^{18}O in O-BT, and indicates the surface concentration of ^{18}O was almost same as that of the gaseous phase(98%). The condition of the constant concentration at the surface for a semi-infinite medium can, therefore, be used. The solid line in Fig.2 indicates the fitted value using some date near surface(<100 to 200nm) with a simple error function (7). The profile has a long tail at large depth. It is obvious that the long tail is not due to the lattice diffusion but might be caused by the diffusion along grain boundaries and pores.

As seen in figure 3 of ^{18}O ion image at 1um depth, the grain boundary network could be observed in O-BT samples. In contrast, the ^{18}O concentration at deep position in the sample with no PTCR effect (R-sample) was almost same as natural abundance of ^{18}O, so the grain boundary diffusion does not contribute to the depth profile.

The lattice diffusion coefficients of oxygen ions in two kinds of samples agreed with each other. These values are plotted in figure 4. For lower temperature region volume diffusion coefficient is almost same as the results of Saburi et al(5). In this region, the activation energy of the oxygen lattice diffusion is considered to correspond to that of oxygen migration in oxygen sub lattice. The values increased at higher temperature because of an increasing number of oxygen defects due to the dissociation of oxygen from oxygen sub lattice that clamed by Shirasaki et al.

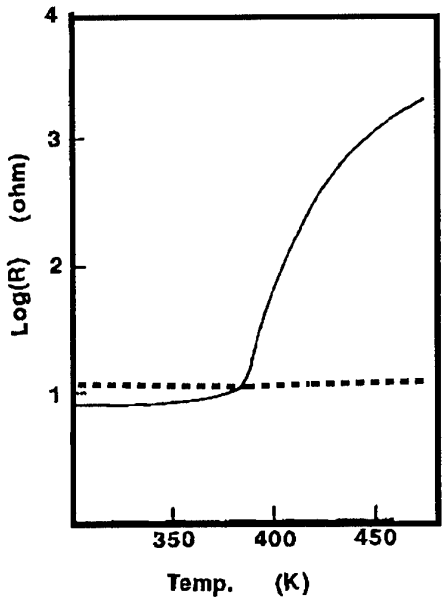


Fig.1. Resistance vs temperature for the lightly La-doped Barium titanate.
Solid line; oxidized sample(O-BT), dashed line; reduced sample(R-BT).

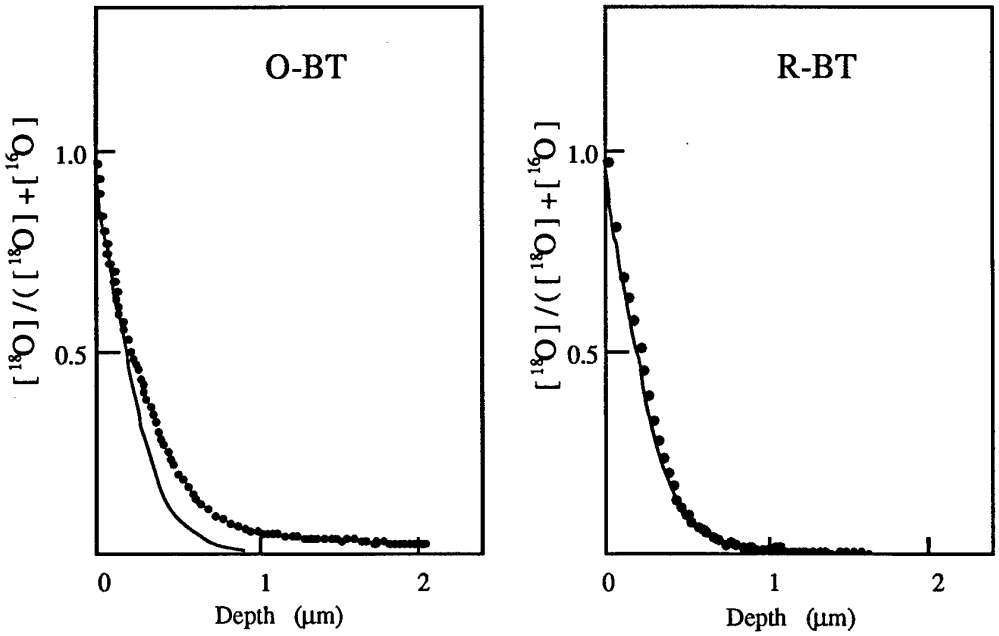


Fig.2. Depth profile of 18O in barium titanate ceramics. Closed circles, the measured values and solid line, calculated valuesby a simple error function.

Le Claire(8) have proposed he relation between the grain boundary diffusion coefficient and concentration at large depth, which is useful in present case. Using his equation, the value of D' is estimated from the slope of Fig.5 Estimated values are listed in Fig.4. A TEM observation shows the typical lattice fringe image about grain boundary, which indicates that no second phase exists at grain boundary, so the result of ^{18}O photo image in figure or long tail at the large depth in the depth profile was caused by grain boundary diffusion, but not by a diffusion in second phase. Atkinson et al.(9) have reported the cation self diffusion along grain boundary in nickel oxide and claimed that the width of the boundary, , is about 1x10-7cm. The grain boundary diffusion coefficient is four orders of magnitude larger than the lattice diffusion coefficient. This degree is in agreement with the results reported by Atkinson et al(9).

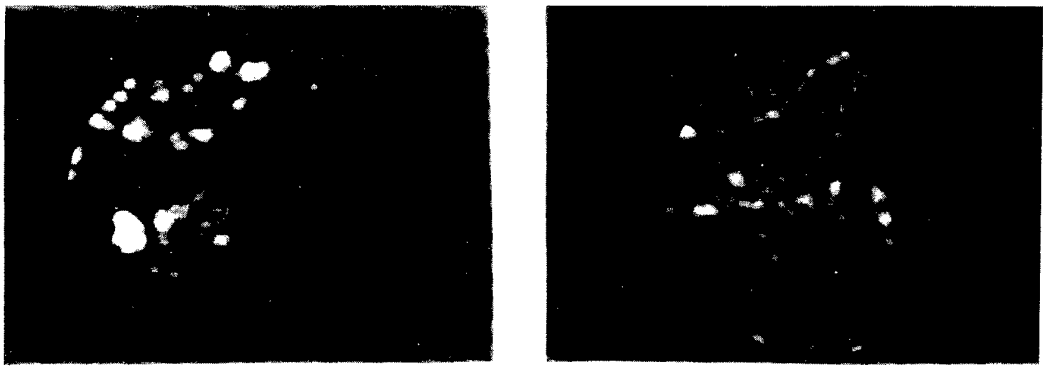


Fig.3. The lateral distribution of oxygen-18 after diffusion-annealing. (a); reduced sample(R-BT), (b); oxidized(O-BT).

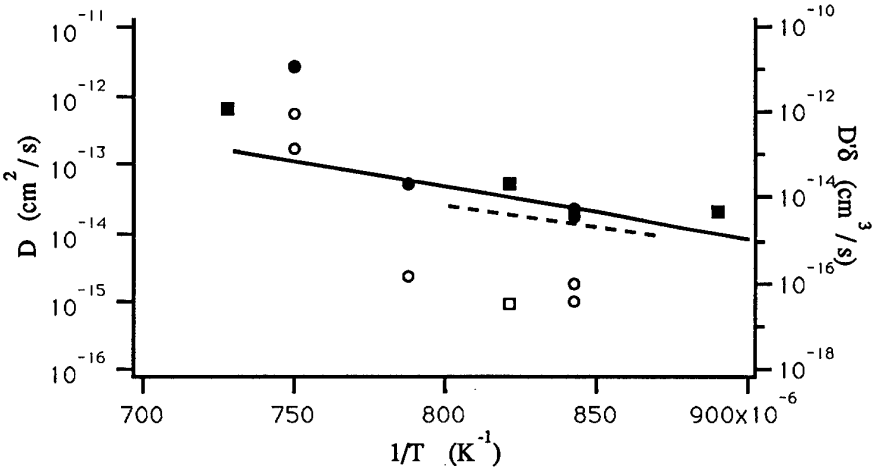


Fig.4. Arrhenius plot of the tracer diffusion coefficient for 18O in the La- and Y-doped barium titanate. Solid line; volume diffusion(present results), dashed line; volume diffusion(Ref.(6)). Closed marks; obsd. volume diffusion coefficients, open marks; products of grain boundary diffusion coefficients and grain boundary width. Circles; La-doped samples, rectangulars; Y-doped samples.

The grain boundary diffusion of oxygen ions could not play the role of a short circuit diffusion in R-sample mentioned above. If the grain boundary diffusion mechanism for oxygen ions should be oxygen vacancy mechanism that occurred in the lattice diffusion, the grain boundary diffusivity of oxygen ions might be larger in R-sample than O-sample, since the possibility of oxygen vacancy formation is larger in reducing atmosphere than in oxidizing atmosphere. In the present results, the characteristic of oxygen grain boundary diffusion tendency is opposite to the normal tendency as above mentioned. Kondo et al. have reported the compositional change near the grain boundary. As their results the behavior of compositional variation was same as each other both in oxidized and reduced samples. We, therefore, believe that the change of grain boundary diffusion mechanism occurred between O- and R-samples.

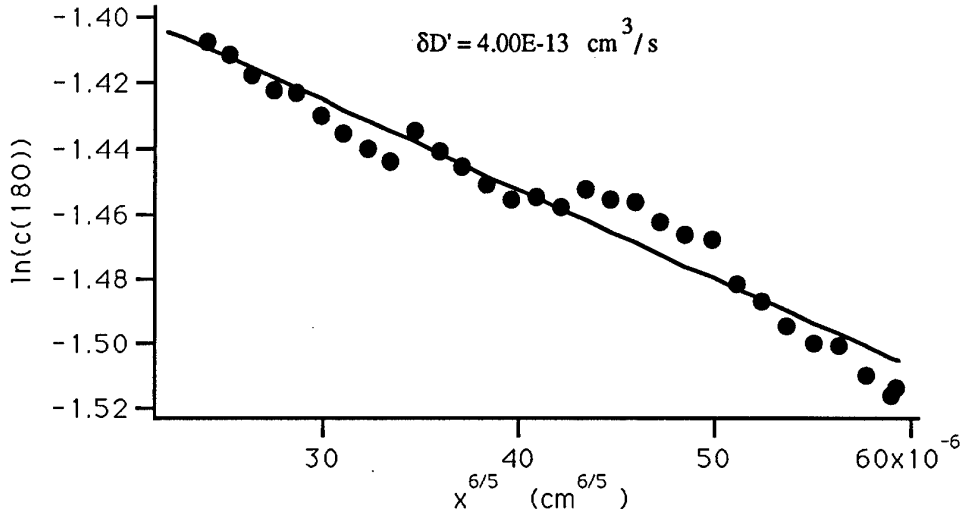


Fig.5. ^{18}O concentration change at the large penetration depth as a function of the value, $x^{6/5}$. Circles; obsd. values, solid line; clcd. value, using Le Claire's analysis for grain boundary diffusion. One can calculate products of garin boundary width, δ, and grain boundary diffusion coefficient, D' , using the slope of this treatment(Ref.(7)).

Saburi et al. have reported the relation between the characteristics of the grain boundary diffusion and the PTCR effect(6). As their results, the diffusivities of oxygen along the grain boundary in the PTCR-samples were greater than those in non-PTCR samples. The grain boundary diffusion characteristics drastically changed at the oxygen partial pressure of appearing the PTCR effect. Our results supported their results.

It is, therefore, concluded that the structural change at grain boundary in polycrystalline barium titanate occurred at the oxidizing prossece and enhanced oxygen grain boundary diffusion. The origin of the barrier layer of the PTCR effect is considered to be same.

REFERENCES

1. W.Heywang and H.Brauer, Solid-state Electron., **8**, 129-35 (1965).
2. C.A.Miller, J. Phys. D, 4, 690-96 (1971).
3. J.Daniels and R.Wernicke, Philips Res. Repts. **31**, 544-59 (1976).
4. I.Ueda and S.Ikegami, J. Phys. Soc. Japan, **20**, 546-52 (1965).
5. S.Shirasaki, H.Haneda, K.Arai and M.Fujimoto, J. Mat. Sci., **22**, 4439-45 (1987).
6. T.Saburi, M.Hori, M.Asano, H.Haneda, J.Tanaka and S.Shirasaki, J.Ceram.Soc.JPN, **98**, 94-98 (1990).
7. J. Crank, in "THE MATHEMATICS OF DIFFUSION,"(Oxford University Press, London, 1957) P.30.
8. A.D.Le Claire, Brit. J. Appl. Phys., **14**, 351-6 (1963).
9. A.Atkinson and R.I.Taylor, Phil. Mag. A, **43**, 999-1015 (1981).

Paper presented at the Third ICIM/ECSSM '96, Lyon '96

Composite transducer for shear stress measurement

Denis Roche, Claude Richard, Lucien Eyraud and Christian Audoly *

Laboratoire de Génie Electrique et Ferroélectricité
Institut National des Sciences Appliquées de Lyon
Bât. 504 - 20, avenue Albert Einstein - 69621 Villeurbanne Cedex - FRANCE

* D.C.N. Ingénierie Sud / LSM, Le Brusc 83800 TOULON NAVAL

ABSTRACT

The measurement of shear stresses in the hydrodynamic boundary layer requires high sensitivity sensors. A floating element type sensor using the piezoelectric effect is proposed. It is constituted of a composite material with high shear stress sensitivity. The evolution of the sensor characteristics with the PZT volume fraction is analysed. The experimental results show a good agreement with the Finite Element Modelling predictions.

1. INTRODUCTION

Fluid flow past a boundary produces shear stresses due to the viscosity of the fluid. The frictional shear stresses in the boundary layer are approximately a few Pa. Knowing the mean shear stress and its fluctuations can lead to a better description of the boundary-layer and to a better understanding of flow noise coupling.

Various measurement techniques have already been used to determine the shear stresses. For example, devices such as the Preston tube or the Stanton tube and hot film anemometers (Figure 1) allow the estimation of aerodynamic shear stresses using indirect techniques, respectively through the measurement of a pressure gradient and a heat transfer. But they strongly depend on empirical laws, with no guarantee of their accuracy in the considered flow[1].

Surface acoustic wave (SAW) devices have also been proposed for this type of measurement. As these surface waves are very sensitive to external perturbation, the shear stresses are responsible for a shift of the SAW oscillator resonance frequency[2].

The floating element sensor, developed for aerodynamic flow, is another device used for shear stress measurements (Figure 1). For example, such a sensor allows the measurement of 1 Pa shear stress by measuring the capacitance variation induced by the motion of a sliding armature facing a fixed one[3].

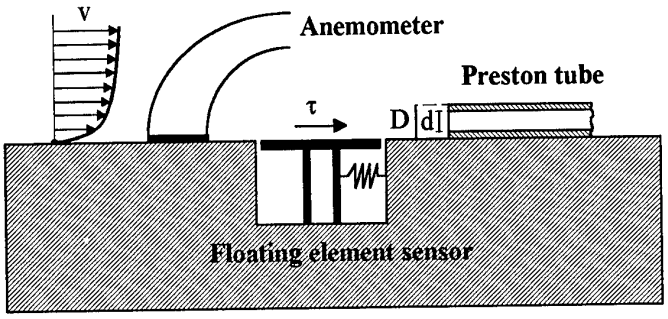


Figure 1 : Shear stress measurement in aerodynamic flow[1]

A shear stress sensor using piezoelectric bimorphs bending is proposed as a new concept of sensors in the boundary-layer research[4]. The principle of this composite sensor, developed for hydrodynamic flow, is exposed

0-8194-2165-0/96/$6.00

first. The transducer optimisation is then discussed with the use of Finite Element Modelling (F.E.M.). In a third part, experimental results for various prototypes are given. They are in good agreement with the theoretical predictions.

2. THE COMPOSITE SENSOR

The proposed device is a floating element type sensor (Figure 2). Its global dimensions are 22 mm × 20 mm × 14 mm. It is composed of a sensing armature ①, in contact with the flow, integrating the applied shear stress on its surface. This floating armature is attached to a fixed one ② by several piezoelectric bimorphs ③ generating an electrical charge proportional to the device drag force counterbalancing the shear effort.

The symmetrical armatures ① and ② are made in a stiff material (epoxy resin) and ensure a suitable clamping of the bimorphs[5].

Each bimorph is constituted of two piezoelectric plates (20 mm × 12 mm × 0.3 mm). These plates are made of P194 PZT ceramics (Quartz et Silice, Saint-Gobain) chosen for their large lateral piezoelectric coefficient d_{31}. They are bonded with an epoxy resin. The adhesive film must be thin enough to allow good mechanical and electrical contacts between the electrodes. Each piezoelectric plate is divided in two parts where the poling vectors **P1** and **P2** are opposite (Figure 3). A thin copper foil 50 µm thick constitutes the central electrode ⑦ while the secondary electrodes ⑥ are connected to each other after poling.

Embedding realised with a soft polymer (Hexcel UR267 polyurethane) ensure the insulation and increases the transducer strength.

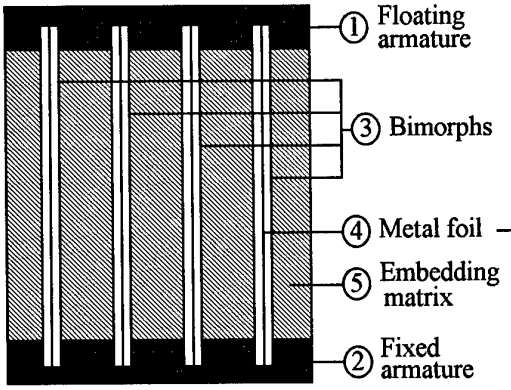


Figure 2 : Composite transducer

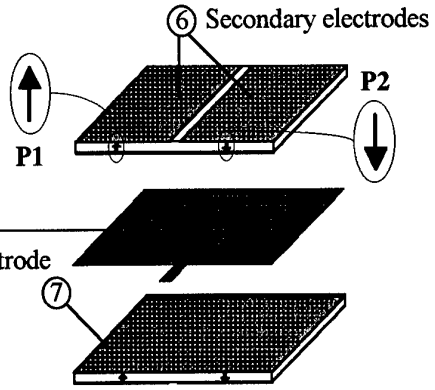


Figure 3 : Bimorph constitution

The optimisation of the composite transducer with the PZT volume fraction depends on a trade-off between, in the one hand, the desired sensor sensitivity and, in the other hand, the complexity of the structure and consequently its cost. It depends also on the working conditions like normal stress, hydrostatic pressure and other environmental data.

3. F.E.M. SIMULATIONS

The use of the Finite Element Modelling program ATILA[6] allows the prediction of the sensor response for various PZT volume fractions.

The evolution of the sensor sensitivity as a function of the PZT volume fraction has first been studied (Figure 4). The plate thickness is 0.3 mm and the sensor size is constant. The sensitivity increases with the ceramic volume fraction. The limit sensitivity is represented by an asymptotic line which corresponds to the sensitivity without

embedding. A sensitivity, approximately equal to 70 % of the full value, can be obtained with a 4 bimorphs transducer, corresponding to a 10% PZT volume fraction.

The evolution of the sensor resonance frequency as a function of the PZT volume fraction has also been analysed (Figure 5). One armature of the transducer is supposed fixed. The sensor resonance frequency is higher than 1 kHz and is constantly increasing with the PZT volume fraction. The polymer embedding allows to get a good mechanical damping of the device. Consequently, the pass-band of the embedded sensor is notably improved compared to the same sensor without embedding.

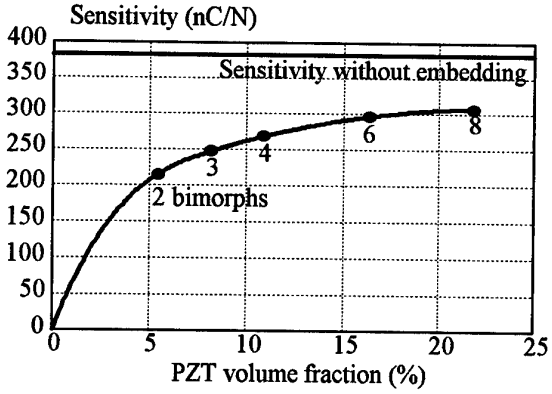


Figure 4 : PZT volume fraction influence on the sensitivity

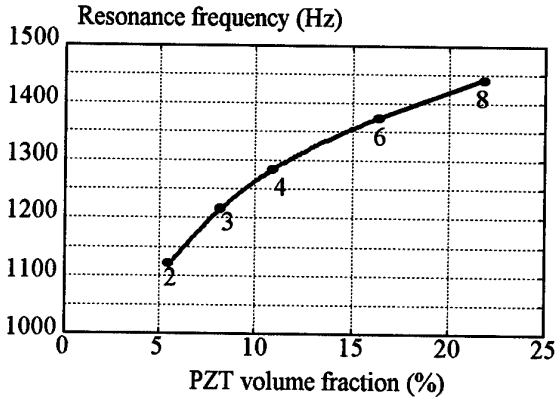


Figure 5 : PZT volume fraction influence on the resonance frequency

4. EXPERIMENTAL RESULTS

4.1 Experimental set-up

The transducer frequency response is measured in the inverse regime using Laser Doppler Vibrometry (L.D.V.) technique. The sensor is mounted on a rigid support in PVC and is driven by a sinusoidal voltage V (Figure 6). The Laser Doppler Vibrometer associated with a lock-in amplifier allows the measurement of the very small vibration speed obtained. The deflection 2δ is derived in the frequency range [10 Hz - 10 kHz].

The inverse sensitivity is defined by $s = {}^{2\delta}/_{V}$ and is in excellent agreement with the direct sensitivity $s = {}^{Q}/_{F}$ obtained under stress excitation where Q is the electrical charge generated under a F force loading [5].

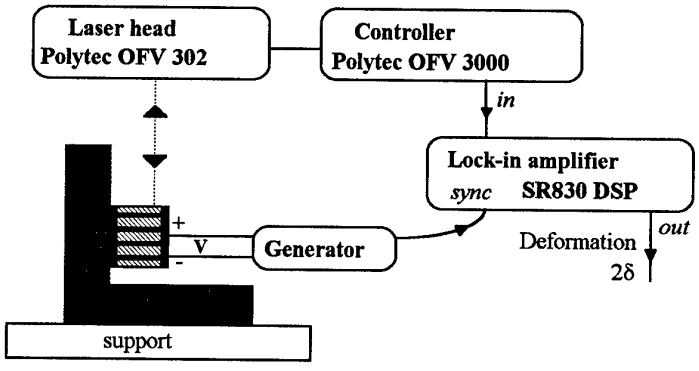


Figure 6 : Laser Doppler Vibrometry experimental set-up

4.2 Transducer deformation

The mapping of the transducer lateral face motion is given on figure 7. The double-flexion strain, induced by the clamping of the bimorphs in the symmetrical rigid epoxy armatures, can be observed. Considering the type of the flexion pattern, appropriate metallisation and poling shown in part 2 were necessary to obtain the optimal displacement.

4.3 Frequency responses

The frequency responses have been plotted in the frequency range [10 Hz - 10 kHz] respectively for transducers made with 2, 4 and 8 bimorphs (Figure 8). Considering the sensor response as a second order system, the sensitivity S0, the resonance frequency and the pass-band are derived.

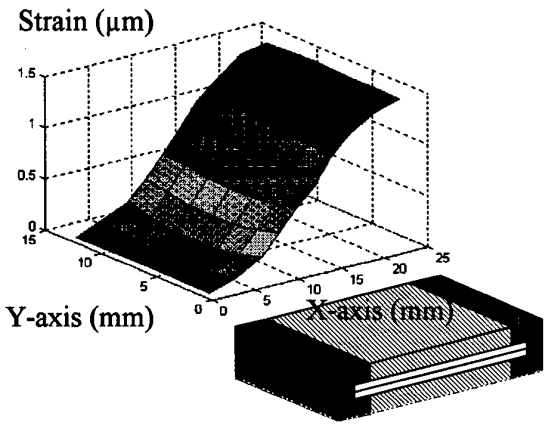


Figure 7 : Transducer deformation

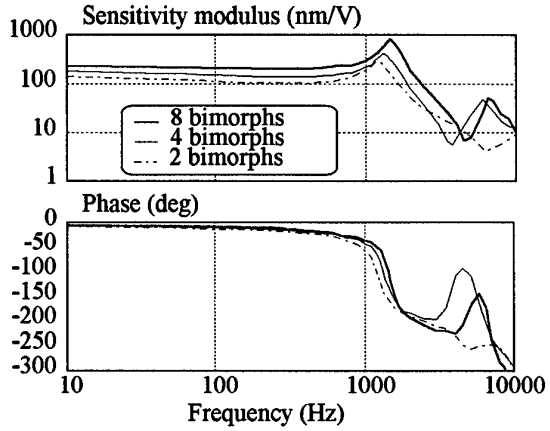


Figure 8 : Frequency responses

Table I presents the experimental results for the three transducers and gives a comparison with Finite Element Modelling simulations.

Sensors		*2 bimorphs*	*4 bimorphs*	*8 bimorphs*
Sensitivity[(1)] S0 (nm/V)	exp.	115	154	212
	F.E.M.	215	268	307
Resonance frequency (Hz)	exp.	1200	1330	1470
	F.E.M.	1121	1283	1440
Quality Factor Q		2.4	2.5	3.75
Pass-band (Hz)[(2)]		900	980	1000

(1) The sensitivity is measured at 100 Hz under a 1 V rms excitation.
(2) The pass-band is derived allowing a 3 dB variation of the frequency response.

Table I : Experimental and theoretical sensor characteristics.

Order of magnitude and general trends of the sensitivity as well as the resonance frequency are in good agreement with the F. E. M. predictions.

However some discrepancies can be observed between experimental and theoretical sensitivities. They are probably due to the imprecision on the mechanical properties data used for the polymer resin.

It is observed that as the PZT volume fraction or bimorphs quantity increases, the mechanical influence of the polyurethane decreases and the agreement between theoretical and experimental data increases.

It is noticeable that, as the poling process of the PZT plate is delicate, some imperfections of the poling can exist at the boundary between both half plates. This can also contribute to the observed discrepancies.

4.4 Influence quantities

As the proposed sensor is supposed to be applied to the characterisation of hydrodynamic flow, its sensitivity to influence quantities such as the hydrostatic pressure or as the normal stresses generated by the vortex lift up has to be quantified.

Normal stress influence

According to the device symmetry, the sensitivity to a normal effort, due to stresses normal to the sensing armature, has to be very weak. However, because of imperfections in the reproducibility of the different parts and in the assembly, a sensitivity is observed.

This sensitivity has been measured as a function of the normal static force (converted in normal static stress according to the sensing armature area) with the device depicted in reference 7. and is plotted on figure 9.

It is shown that the normal stress sensitivity is approximately 2.5 nC/N and is constant with the applied normal stress and with the frequency. This sensitivity represents only 1.5% of the shear stress sensitivity and could be decreased with a more refined fabrication procedure.

Hydrostatic pressure influence

The sensor behaviour under hydrostatic pressure has also been investigated. According to figure 10, the sensor sensitivity to hydrostatic pressure is low (approximately 40 fC/Pa). Moreover, the sensor is resistant and hydrostatic pressure insensitive up to 5 MPa which corresponds to a water depth of 500 m.

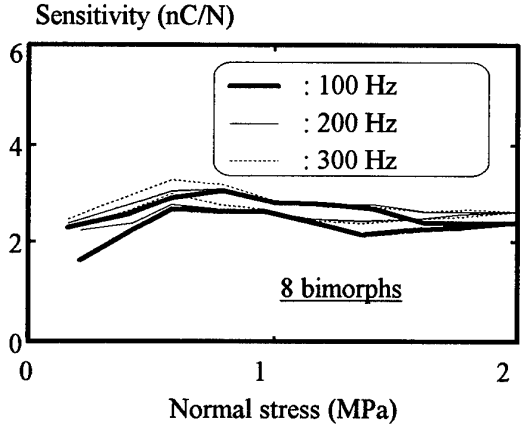


Figure 9 : *Normal stress sensitivity as a function of the normal static stress*

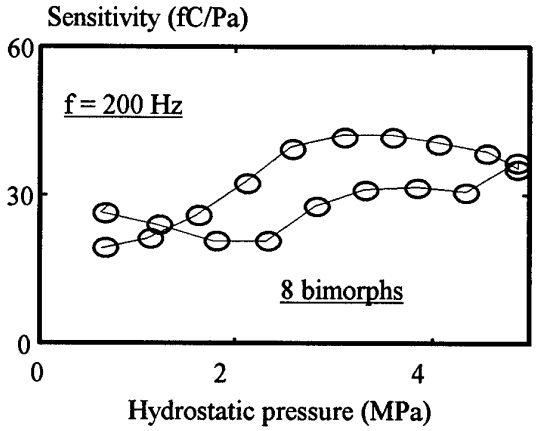


Figure 10 : *Hydrostatic pressure sensitivity as a function of the hydrostatic pressure*

5. CONCLUSION

The floating element sensor principle has been applied in order to perform the direct measurement of shear stress. Using the bending of several piezoelectric bimorphs, the proposed composite sensor, completely embedded and insulated, has a very high sensitivity and the necessary robustness required for the measurement of frictional shear stresses in the boundary-layer of a fluid flow.

The sensitivity and the pass-band of the sensor, predictable using Finite Element Modelling, has been established experimentally. The measured sensitivity is 150 nC/N for a PZT volume fraction of 11% and 200 nC/N for a PZT volume fraction of 22%. This transducer can be used for frequencies lower than 1 kHz. Moreover, for this type of device, the measure is few affected by normal stresses and hydrostatic pressure.

Future prospects will now consist in the sensor calibration in a water tunnel in order to globally validate this new concept of sensor.

6. ACKNOWLEDGEMENTS

The authors are grateful to R. VIGNAT for his assistance in the sample preparation and wish to thank the DCN (CTSN - LSM Toulon) for its support.

7. REFERENCES

1. J.H. Haritonidis, Advances in fluid mechanics measurements, Springer Verlag, New-York, 1989, 229-261.
2. Y.R.Roh, "Development of local/global SAW sensors for measurement of wall shear stress in laminar and turbulent flows", 1991, Thesis, Penn State University.
3. M.A. Schmidt, R.T. Howe, S.D. Senturia and J.H. Haritonidis, IEEE transactions on electron devices, 1988, 15-6, 750-757.
4. D. Roche, C. Richard, L. Eyraud and C. Audoly, "Transducteur à bilames piézoélectriques fonctionnant en double flexion", Pat. n° 9505491, France, 10 mai 1995.
5. D. Roche, "Conception et réalisation d'un capteur piézoélectrique de contraintes de cisaillement pour structure adaptative", Thesis, INSA Lyon, 95 ISAL 0062, 153p.
6. B. Dubus, "ATILA finite element code for piezoelectric and magnetostrictive transducer modelling", Version 5.02, User's manual, 1991, Lille - ISEN.
7. D. Audigier, C. Richard, C. Descamps, M. Troccaz and L. Eyraud, "PZT uniaxial stress dependence : experimental results", Ferroelectrics, 1994, 154, 219-224.

Application of nonlinear dynamics in the study of ferroelectric materials

S. Blochwitz, R. Habel, M. Diestelhorst, H. Beige

Fachbereich Physik der Martin–Luther–Universität Halle–Wittenberg
Friedemann–Bach–Platz 6, D—06108 Halle (Saale), Germany

ABSTRACT

The dielectric nonlinear properties of ferroelectric materials are the main reason for their technical application. There is a wide variety of materials, e.g. liquid crystals, thin layers and even bulk–materials, that have these properties. One problem that must be solved before the technical application is to determine these properties to forecast the dynamical behaviour.

However, so far these parameters were determined in the case of zero excitation. This is a draw–back, because for the application of ferroelectric materials the large signal behaciour is important. We want to show a new way for determining the dynamical nonlinear properties of ferroelectric materials. We present a simple dynamical system, the dielectric nonlinear series resonance circuit, that can be used for studying the large signal behaviour of the mentioned materials. With the help of a macroscopic model which contains the linear and nonlinear material–coefficients and a method that we developed recently, these parameters can be determined from experimentally recorded time–series.

1. INTRODUCTION

The structural phase transitions in ferroelectric materials are connected with strong nonlinear properties.[1,2] This property opens a wide range of technical applications of these materials: Memory–chips, detectors, displays, and even smart compound materials, consisting of one or more different ferroelectric materials and other ones.

For designing a technical application from these materials it is very important to know exactly their properties, especially the linear and nonlinear coefficients that are used for the application. However, so far the determination of the nonlinear coefficients were carried out either in the case that the external field is approximately zero[1] or in the quasistatic case.[2] This is very unrealistic for two reasons:

1. For ferroelectric thin films or thin liquid crystals very small voltages yield high fields. So the statements about the coefficients in the case of zero field may become wrong.
2. For applications the dynamical behaviour of the ferroelectric materials is interesting, not the quasistatic one.

Therefore we want to propose a method, that avoids these draw–backs. In the result we can derive the linear and nonlinear coefficients from the large signal behaviour of the ferroelectric materials.

0-8194-2165-0/96/$6.00

2. THE DYNAMICAL SYSTEM

2.1. Experimental set–up

For studying their dynamical behaviour the ferroelectric materials have to be integrated into a dynamical system. For this purpose we chose a linear series resonance circuit. This circuit is built of a linear air coil and a capacitance filled with the ferroelectric material. The system as a whole is excited by a sinusoidal voltage. Because of the nonlinearities of the capacitance the circuit is an experimental realization of a nonlinear oscillator. The dielectric nonlinear resonance circuit is well suited for both studying the large signal dynamical behaviour of the ferroelectric capacitor and analyzing the ferroelectric material of the capacitor by means of nonlinear dynamics.[3–5] The system has three external parameters to control its properties: Frequency and amplitude of the driving voltage and the temperature that fix the dielectric properties of the capacitor. For reasons of measurement two further components are attached to the resonance circuit introduced above. Using the linear capacitance C_m and the linear resistor R_m makes it is possible to record signals proportional to the dielectric displacement D on the specimen and the current density $j = dD/dt$ with time t through the system respectively (see Fig. 1). In order to be sure that nearly all the applied voltage U_{ext} drops at the dynamical system L (air coil) and C_{nl} (ferroelectric specimen) the unequality $R_m \ll 1/(\omega C_m) \ll 1/(\omega C_{nl})$ holds. The setup shown in Fig. 1 yields a representation of the three–dimensional phase space flow in terms of D (generalized location), j (generalized momentum) and t (time). With the help of a thermostatic or cyrostatic device (omitted in Fig. 1) the temperature of the specimen can be placed to the interesting ferroelectric region.

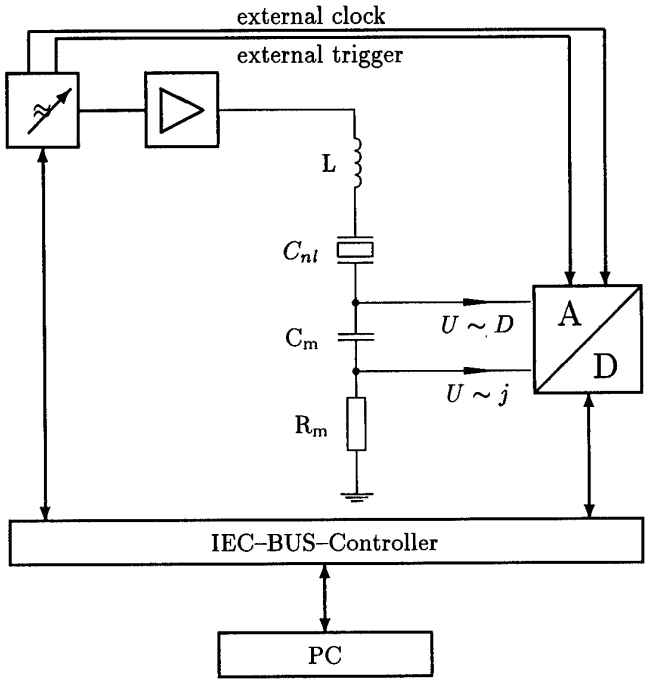


Figure 1: Block diagram of the experimental setup.

2.2. The macroscopic model

The next step we have to do is to model our dynamical system and to connect the model–parameters with the material parameters we are interested in. It has been shown already that the dielectric nonlinear resonance circuit has two main features:

(i) Its behaviour is macroscopic reproducible. That means that the external control parameters mentioned in Sec. 2.1. really control the dynamics of the system.[3,6]

(ii) The dynamics has an underlying symmetrie. If the driving voltage holds $U_{ext}\left(t + \frac{T}{2}\right) = -U_{ext}(t)$ with T as its period the dielectric displacement D either satisfies the same symmetry or there are two attractors A_1 and A_2 and it is valid $D_{A_1}\left(t + \frac{T}{2}\right) = -D_{A_2}(t)$.[4,6]

From feature (i) it can be concluded that the ferroelectric capacitance can be described by a macroscopic model. Therefore the ferroelectric capacitor can be replaced by a substitute–network as it is shown in Fig. 2. There C_{nl} represents the dielectric nonlinear properties of the ferroelectric material, R_p stands for the DC–conductivity of the sample and R_s for losses that are caused by the running current through the capacitor. These losses may be due to motion of domain–walls or polarization reversal. Furthermore, the electric field $E_{C_{nl}}$ along the nonlinear capacity C_{nl} must be homogeneous. Note that $\mathrm{R_L}$ models the linear losses of the inductivity.

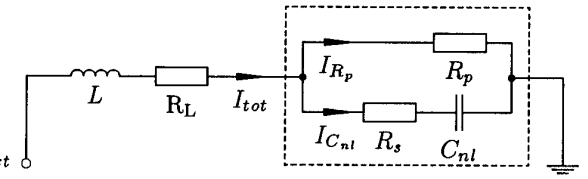


Figure 2: The dielectric nonlinear resonance circuit with a substitute–network (dashed) for the ferroelectric capacitor.

Applying Kirchhoff's laws to the circuit of Fig. 2 yields Eq. (1):

$$U_{ext} = \mathrm{L}\left(\mathrm{F}\ddot{\mathrm{D}} + \dot{\mathrm{I}}_{\mathrm{R_p}}\right) + \mathrm{R_L}\left(\mathrm{F}\dot{\mathrm{D}} + \mathrm{I}_{\mathrm{R_p}}\right) + \mathrm{U}_{\mathrm{R_s}} + \mathrm{U}_{\mathrm{C_{nl}}} \,. \tag{1}$$

It must now be obeyed that feature (ii) has to be valid for Eq. (1). That's why the quantities U_{R_s}, I_{R_p} and $E_{C_{nl}} = U_{C_{nl}}/\mathrm{h}$ can be modelled by the following ansatz:

$$\begin{aligned}
U_{R_s} &= R_s^{(1)}\mathrm{F}\dot{\mathrm{D}} + \mathrm{R}_\mathrm{s}^{(3)}\mathrm{F}^3\dot{\mathrm{D}}^3 + \cdots \\
\frac{dU_{R_s}}{dt} &= R_s^{(1)}\mathrm{F}\ddot{\mathrm{D}} + 3\mathrm{R}_\mathrm{s}^{(1)}\mathrm{F}^3\dot{\mathrm{D}}^2\ddot{\mathrm{D}} + \cdots \\
I_{R_p} &= \frac{1}{R_p^{(1)}}\left(U_{R_s} + \mathrm{hE}_{\mathrm{C_{nl}}}\right) + \frac{1}{R_p^{(3)}}\left(U_{R_s} + \mathrm{hE}_{\mathrm{C_{nl}}}\right)^3 + \cdots \\
\frac{dI_{R_p}}{dt} &= \left[\frac{1}{R_p^{(1)}} + \frac{3}{R_p^{(3)}}\left(U_{R_s} + \mathrm{hE}_{\mathrm{C_{nl}}}\right)^2 + \cdots\right]\left(\frac{dU_{R_s}}{dt} + \mathrm{h}\frac{\mathrm{dE}_{\mathrm{C_{nl}}}}{\mathrm{dt}}\right) \\
E_{C_{nl}} &= \alpha_2 D + \alpha_4 D^3 + \cdots \,.
\end{aligned} \tag{2}$$

Putting this ansatz into Eq. (1) and neglecting all terms of order $\mathcal{O}(D^i\dot{D}^j\ddot{D}^k)$ with $i+j+k=4$ yields

$$\begin{aligned}
&U_{ext} - \mathrm{FL}\ddot{\mathrm{D}} - \mathrm{FR_L}\dot{\mathrm{D}} = \\
&\quad\left[\frac{\mathrm{hL}}{R_p^{(1)}}\left(\alpha_2 + \alpha_4 D^2\right) + \mathrm{FR}_\mathrm{s}^{(1)}\right]\dot{D} + \mathrm{F}^3 R_s^{(3)}\dot{D}^3 + + \mathrm{h}\alpha_2\mathrm{D} + \mathrm{h}\alpha_4\mathrm{D}^3 \,.
\end{aligned} \tag{3}$$

In Eq. (3) it was additionally used that the terms $\frac{1}{R_p^{(3)}}$ and $\frac{\mathrm{R_L}}{R_p^{(1)}}$ can be neglected. Eq. (3) is the equation of motion of a nonlinear oscillator with nonlinear damping and nonlinear effective potential G

$$G(\vartheta, p, D) = G_0(\vartheta, p) + \frac{\alpha_2}{2}D^2 + \frac{\alpha_4}{4}D^4 + \cdots \,. \tag{4}$$

The coefficients α_2 and α_4 of the effective potential may be regarded as the continuation of the *Landau*–expansion of the theory of second order phase transition into the nonequilibrium state of the ferroelectric material.[5,7]

As result of our model we got a differential equation that describes a nonlinear oscillator. This equation has model–paramaters ($R_p^{(1)}$, $R_s^{(1)}$, $R_s^{(3)}$, α_2 and α_4) that are not known in advance, i. e. these parameters depend on the dynamical properties of the ferroelectric sample.

3. RESULTS

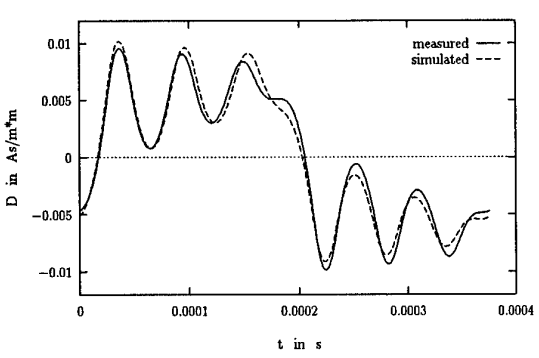
3.1. How to determine the coefficients

There are five model–parameters in Eq. (3): $R_p^{(1)}$, $R_s^{(1)}$ and $R_s^{(3)}$ that model the damping mechanism and α_2 and α_4 for modelling a macroscopic potential. Our aim is to determine these parameters from experimental time–series of the dielectric displacement $D\ (t)$. For that purpose we developed a method that is described in detail in.[8]

The method is based on a transformation of the differential equation (3) into an overdetermined set of linear equations with the model–parameters as unknown quantities. This set of equations can be easily solved by well–known methods, and the goodness of the solution can be stated by comparing the measured time–series with a simulated one from Eq. (3). We want to state that the method we sketched here only briefly can be used for analyzing measured time–series fully automatically. Therefore we can evaluate the behavior of the model–parameters in a wide range of external parameters.

3.2. Ferroelectric bulk materials

Ferroelectric bulk materials are investigated for a long time.[1,2,7,9,5] The advantage of investigating these materials is that the results we got with our method can be compared with other. We investigated TGS and Betainarsenate, which are materials that have well exhibited ferroelectric properties. These materials have at certain temperatures ϑ_C a second order phase transition from the paraelectric into the ferroelectric state.



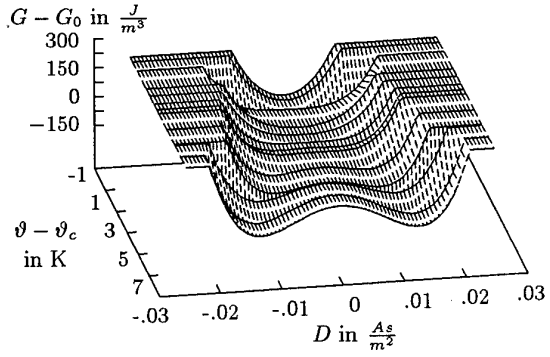


Figure 3: Comparision between measured and simulated time–series (left) and effective potential $G(\vartheta, p, D)$ according to Eq. 4 (right).

The first interesting result is that we do not need the damping-paramters $R_s^{(1)}$ and $R_s^{(3)}$ for describing the behaviour of the circuit. As shown in Fig. 3 there is a good agreement between measured and simulated time–series without these parameters. Secondly, it is interesting that the nonlinear potential $G(\vartheta, p, D)$ of Eq. 4 behaves as predicted by the *Landau*–theory of second order phase transitions. The prediction is, that at the transition temperature ϑ_C the potential changes from single–well type to double–well type. Although the presumptions of

Landau's–theory are not fullfilled (we do not investigate a quasistatic system) even our dynamical system shows the features of a *Landau*–potential.

3.3. Thin ferroelectric liquid crystals

Ferroelectric liquid crystals are substances that will increasingly applied, e. g. as displays. The main difference to ferroelectric bulk–materials is that we need at least one of the damping-paramters $R_s^{(1)}$ or $R_s^{(3)}$ in order to model our system succesfully as shown in Fig. 4. The reason for this is unclear by now. We assume that the influence of domains on the dynamics is in thin liquid crystals bigger than in bulk materials, because the number of domains in the latter is greater than in the former. Therefore the nonlinear damping effects of a single domain in the liquid crystal do not vanish in an overall limit.

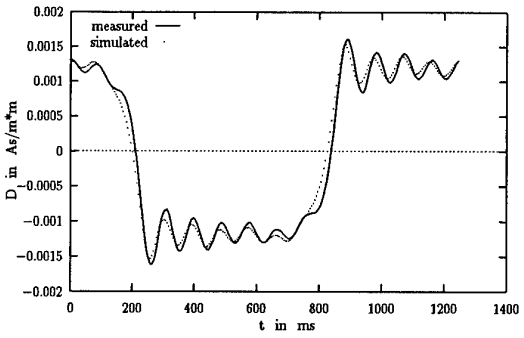


Figure 4: Comparison between measured and simulated time series for a ferroeelectric liquid crystal

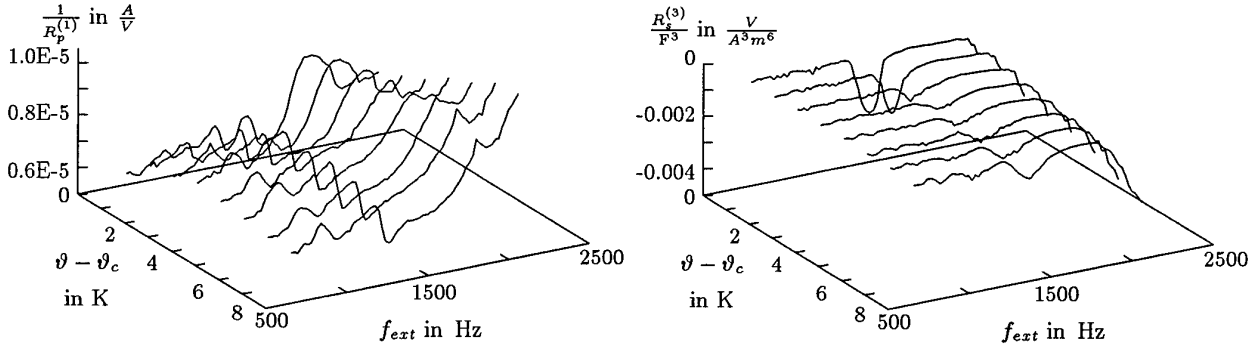


Figure 5: The damping–coefficients $R_p^{(1)}$ and $R_s^{(3)}$ of a ferroelectric liquid crystal. Note the dispersion of these coefficients.

In Fig. 5 the dispersion of the damping–coefficients is shown for a ferroelectric liquid crystal. We think that this dispersion is a feature that has to be carefully paid attention in the case of any application of these materials.

The effective potential $G(\vartheta, p, D)$ behaves as for bulk materials: There is a transition from single–well type to double–well type at the transition temperature.

4. ACKNOWLEDGMENTS

This work has been supported by the Sonderforschungsbereich 185 of the Deutsche Forschungsgemeinschaft and the Kultusministerium des Landes Sachsen–Anhalt. The ferroelectric liquid crystals were prepared by Professor Haase from the TH Darmstadt.

5. REFERENCES

[1] A. S. Sonin and B. A. Strukov: Einführung in die Ferroelektrizität, Akademie–Verlag 1974

[2] M. Diestelhorst, R. Hofmann and H. Beige: Jpn. J. Appl. Phys, **24**, Suppl. 25–2, 1019 (1985)

[3] E. Brauer, H. Beige, L. Flepp and M. Klee: Phase Transitions **42**, 169 (1993)

[4] E. Brauer, S. Blochwitz and H. Beige: International Journal of Chaos and Bifurcation **4**, vol. 4 (1994)

[5] Diestelhorst, M.; Beige, H.; Forster, R.; Albers, J.; Peterson, J.: Chaos Near Structural Phase Transitions, Z. Naturforsch. **45a** (1990), 958

[6] S. Blochwitz: PhD–Thesis (in German), Halle 1994

[7] M. E. Lines and A. M. Glass: Principles and Application of Ferroelectrics and Related Materials, Clarendon Press, Oxford, 1979

[8] S. Blochwitz, H. Beige: How to model from experimental time series, to be published in Phys. Rev. E

[9] Beige, H., Brauer, E., Diestelhorst, M., Blochwitz, S.: The Application of Nonlinear Dynamics in the Study of Ferroelectric Materials, Ferroelectrics **159** (1994), 7

Power limitations in acoustic transducer due to PZT material nonlinearities

Nathalie Aurelle, Daniel Guyomar and Lucien Eyraud

Laboratoire Génie Electrique et Ferroélectricité
Institut National des Sciences Appliquées de Lyon
Bât. 504, 20 Avenue Albert Einstein, 69621 Villeurbanne cedex, France

ABSTRACT

The characterization work is an important step when studying a piezoelectric material, it allows to link the mechanical characteristics to the electrical ones. Nevertheless for high excitation levels, significant changes in piezoelectric properties occur. They result in a performance limitations for high power transducers. A better understanding of this nonlinear behavior is needed to optimize heavy duty transducers. We chose to study a symmetrical Langevin transducer close to its resonance frequency, so under high stress and strain, and we elaborated a transducer model based on nonlinear piezoelectric constitutive equations. Simulation results fit nicely with experimental data. Moreover, introduction of nonlinear terms leads to a new explanation of the dissipated power in heavy duty transducers and correlation between model and experiments gives an estimation of the nonlinear parameters.

1. INTRODUCTION

Nonlinear phenomenon is a fast growing field in physics [1,2,3]. This paper focuses on the ferroelectric ceramics, and particularly on PZT power materials, and their nonlinear behavior observed under high excitation levels (high stress and strain). When such a material enters in a nonlinear working domain, its characteristics fluctuate creating instabilities and ceramic performance limitations [4,5]. After presenting experimental results, a piezoelectric nonlinear model will be mathematically developed. Then, the simulation results will be given and compared with the experimentation in a first part and with an other linear model based on the viscous factor increase in a second part.

2. EXPERIMENTAL OBSERVATIONS

2.1. Practical procedure

Experiments have been performed on hard PZT materials (Navy III type of power ceramics), from Quartz & Silice manufacturer. These ceramics have been tested in a prestressed symmetrical Langevin transducer, working in the air at its resonance frequency. On account of the transducer resonance frequency shift occuring when the excitation level is increased, the driving frequency is always adjusted so as to correspond to the maximum current.
During these experiments the piezoelectric ceramics are forced to work under high dynamical stress and strain, actually working in the air requires low electric fields for the PZT ceramics.

2.2. Measurements

The experimentation permits to record in the time or frequency domain the signals of current, vibration velocity, voltage and stress (Cf fig 1 and 2).

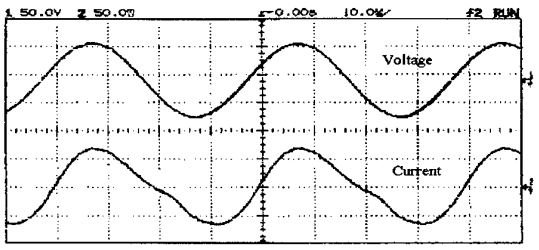


Fig. 1 : Voltage and current signals

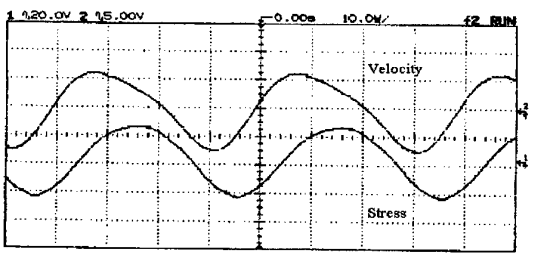


Fig. 2 : Stress and velocity signals

(Transducer : prestress 400 bars / P189 / 65 Vpeak)

0-8194-2165-0/96/$6.00

It is to be noted that the vibration velocity, measured on a tail mass of the transducer, is given by a laser vibrometry device[5]. Moreover the stress signal is issued from a stress sensor, composed of two thin piezoelectric rings, that can be inserted at the middle of the piezostack. The power signal can also be stored (Cf fig 3).

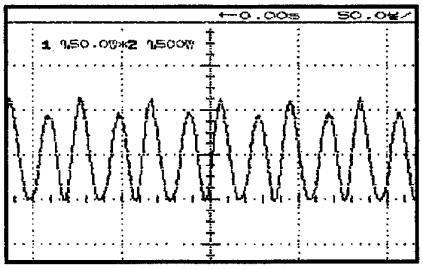


Fig. 3 : Electrical power signal
(Transducer : prestress 400 bars / P189 / 65 Vpeak)

Figures 1, 2 and 3 exhibit that a distinct distortion appears on current, velocity or stress signals when the excitation level of the transducer increases. It results in an harmonics generation in the spectral domain.

3. NONLINEAR PIEZOELECTRIC EQUATIONS

To model these nonlinearities, we chose to extend up to the second order the piezoelectric constitutive equations[5]. In these circumstances, the stress T and the induction D are given by the following equations :

$$\begin{aligned} T &= T_0 + cS - eE + \frac{\alpha S^2}{2} + \frac{\beta E^2}{2} - \gamma SE \\ D &= D_0 + eS + \varepsilon E + \frac{\gamma S^2}{2} + \frac{\delta E^2}{2} - \beta SE \end{aligned} \qquad (1)$$

where : S is the strain, E the electric field, c the elastic stiffness coefficient, e the piezoelectric stress coefficient, ε the dielectric permittivity, α β δ and γ the nonlinear coefficients introduced.

As the transducer radiates in the air, the electric fields applied are low (Emax < 30Vpeak/mm) therefore nonlinear terms in E squared will be neglected in the following calculations. Moreover, to take account for attenuation, a damping coefficient λ_1 has to be introduced in the stress equation. Finally, the considered piezoelectric equations are :

$$\begin{aligned} T &= cS - eE + \frac{\alpha S^2}{2} - \gamma SE + \lambda_1 \frac{\partial S}{\partial t} \\ D &= eS + \varepsilon E + \frac{\gamma S^2}{2} - \beta SE \end{aligned} \qquad (2)$$

To describe the transducer behavior, in the low frequency regime, a lumped system approach is taken :

$$M \frac{\partial^2 u}{\partial t^2} = -T\Sigma \qquad (3)$$

where M is the mass of one tail mass, Σ the ceramic ring surface and u the tail mass displacement.

Substituting in the equation (3) the expression of the stress T given by (2) and writing that S = u / l, with l the half length of the piezostack, leads to the following relation :

$$\frac{\partial^2 u}{\partial t^2} + \frac{c\Sigma}{lM} u + \frac{\alpha\Sigma}{2l^2 M} u^2 - \frac{\gamma\Sigma}{lM} uE + 2\lambda w \frac{\partial u}{\partial t} = \frac{e\Sigma}{M} E \qquad (4)$$

where : $\frac{c\Sigma}{lM} = w^2$, with w the eigenpulsation of the system, $\frac{\alpha\Sigma}{2l^2M} = \alpha_1$ and $\lambda = \frac{\lambda_1\Sigma}{2w\,lM}$

Equation (4) becomes :

$$\frac{\partial^2 u}{\partial t^2} + w^2 u + \alpha_1 u^2 - \frac{\gamma\Sigma}{lM} uE + 2\lambda w \frac{\partial u}{\partial t} = \frac{e\Sigma}{M} E \qquad (5)$$

In the first part, we showed that the experimental velocity signal is distorted but remains periodic; consequently, the displacement u can be mathematically expressed as a Fourier sum :

$$u(t) = \sum_{n=-\infty}^{n=+\infty} C_n e^{j n \Omega t} \qquad (6)$$

where Ω is the driving pulsation. Moreover, the driving electric field is written :

$$E(t) = \frac{E_0}{2}(e^{j\Omega t} + e^{-j\Omega t}) \qquad (E_0 \text{ peak value of the electric field }). \qquad (7)$$

Substitution in equation 5 leads to :

$$-\Omega^2 \sum_{n=-\infty}^{n=+\infty} n^2 C_n e^{j n \Omega t} + w^2 \sum_{n=-\infty}^{n=+\infty} C_n e^{j n \Omega t} + \alpha_1 \sum_{n=-\infty}^{n=+\infty} \sum_{m=-\infty}^{m=+\infty} C_n C_m e^{j (n+m) \Omega t} -$$

$$\frac{\gamma\Sigma E_0}{2lM} \left(\sum_{n=-\infty}^{n=+\infty} C_n e^{j (n+1) \Omega t} + \sum_{n=-\infty}^{n=+\infty} C_n e^{j (n-1) \Omega t} \right) + 2\lambda w j \Omega \sum_{n=-\infty}^{n=+\infty} n C_n e^{j n \Omega t} = \frac{e\Sigma E_0}{2M}(e^{j\Omega t} + e^{-j\Omega t}) \qquad (8)$$

Moreover, the same development can be made for the electric displacement expression, it gives :

$$D(t) = \frac{e}{l} \sum_{n=-\infty}^{n=+\infty} C_n e^{j n \Omega t} + \varepsilon \frac{E_0}{2}(e^{j\Omega t} + e^{-j\Omega t}) +$$

$$\frac{\gamma}{2l^2} \sum_{n=-\infty}^{n=+\infty} \sum_{m=-\infty}^{m=+\infty} C_n C_m e^{j (n+m) \Omega t} - \frac{\beta E_0}{2l} \left(\sum_{n=-\infty}^{n=+\infty} C_n e^{j (n+1) \Omega t} + \sum_{n=-\infty}^{n=+\infty} C_n e^{j (n-1) \Omega t} \right) \qquad (9)$$

Equating equation 8 for each frequencies (0, Ω, 2Ω ...) gives the modulus and phase of the coefficients C_0, C_1, C_2, C_3... versus the value of the driving electric field. From these calculations, we can deduce the displacement u associated with each frequency : the fundamental and its harmonics. Besides, solving equation 9 leads to the current amplitude for each frequency. Thus, simulations of equations 8 and 9 allow to obtain the fundamental or harmonics amplitudes evolutions, for the current or displacement. It also explains the resonance shift. Then, comparisons with experimental data allow first to adjust the nonlinear coefficients and then to determine if the proposed model is suitable or not.
The following parts will give these simulations results.

4. SIMULATIONS RESULTS

In order to simulate the transducer behavior, a good guess for nonlinear coefficients must be known. To get an idea of these nonlinear values, we relied on the curves, plotted in static regime on ceramic rods, representing the stress as a function of the deformation. For strain close to 10^{-3}, close to our experimental conditions, a variation of approximately 10 % has been noticed. Thus, 10 % nonlinearities have been introduced for the first simulations before fitting more precisely.

The simulations results, that will be introduced in the next parts of this paper, have been calculated with the following parameters :

$w = 2\pi\ 27000$ Hz	$\lambda = 0.0015$ Ns^2/m/kg
$\Sigma = 8\ 10^{-5}$ m^2	$\alpha 1 = -\ 1.55\ 10^{15}$ N/m^2/kg
$l = 6.6\ 10^{-3}$ m	$\gamma = -\ 2.8\ 10^4$ N/m/V
$M = 20\ 10^{-3}$ kg	$\beta = 6\ 10^{-5}$ N/V^2

When a low excitation voltage is entered, the model gives a symmetrical curve, centered on the pulsation w (associated with the resonance frequency of the transducer), for the displacement, current or admittance curves function of the driving frequency. While increasing the excitation, the resonance frequency shift and hysteresis phenomena appear on the previous mentioned simulated curves (Cf fig 4).

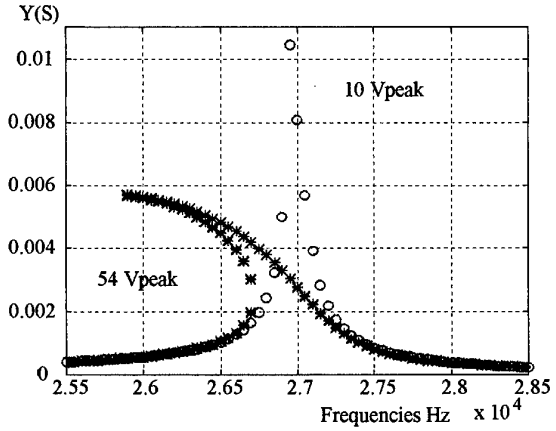


Fig.4 : Simulated admittance curves

If the fundamental and first harmonic evolutions of the current or displacement are plotted for different excitation levels, a saturation effect is observed in both cases. Figures 5 and 6 present these results : the curve plotted in continuous line represents the simulations results whereas the dots symbolize the measurements; they show that a good agreement between numerical approach and experimentation can be found.

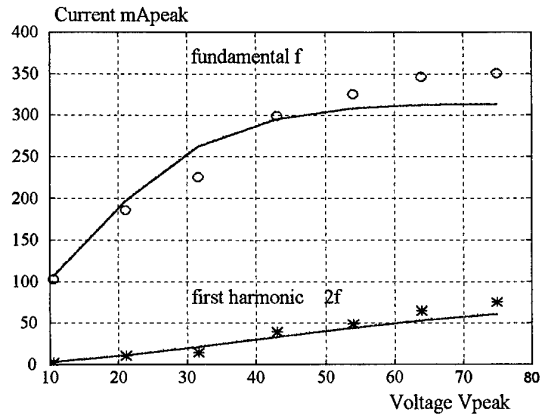


Fig. 5:Experimental and simulated current

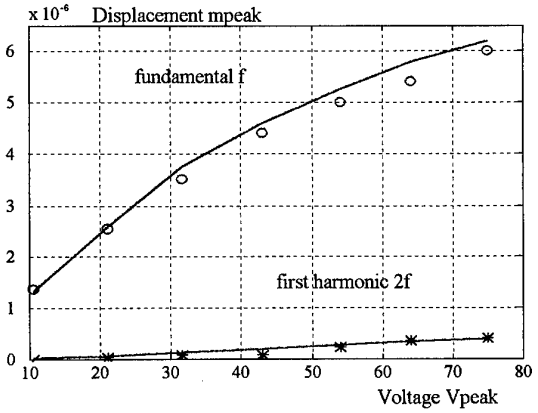
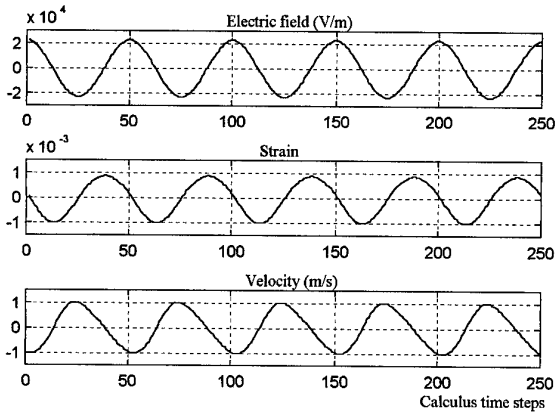


Fig.6:Experimental and simulated displacement

(/ o : measurements continuous line : simulations)*

Besides, by means of simulations, the different signals describing the system can be plotted in the time domain. Figure 7 exhibits the signals obtained for an high excitation level (taking into account the fundamental f and first harmonic 2f) : a distinct distortion can be noticed, especially on signals such as current, vibration velocity or stress. Moreover it is interesting to note that the simulated signals present the same kind of distortion as the one observed experimentally and previously displayed in figures 1 and 2.



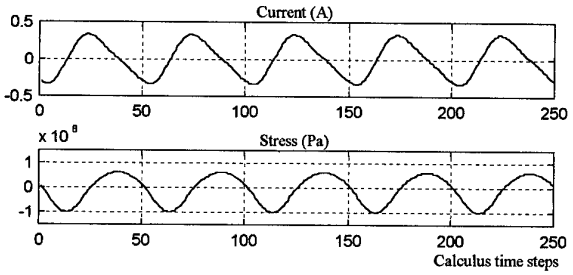


*Fig 7 : Simulated signals in the time domain (75 Vpeak / time step = 1/(50*25000) s)*

5. POWER SIMULATIONS

In this last paragraph, we are going to consider the electrical power. The simulated signal U(t).I(t) (instantaneous power) is plotted in figure 8 for high driving level : distortion effect occurs that nicely fits with experimental data.

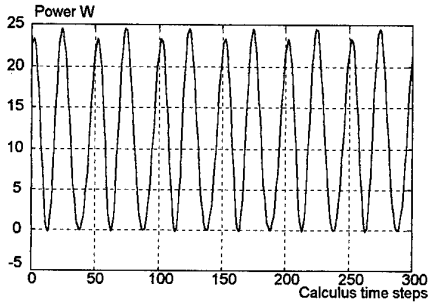


Fig. 8 : Simulated power signal (75 Vpeak)

Now, let us consider the power spectrum : its different components can be obtained by a convolution of the voltage and current spectra. Assuming that the imposed voltage remains linear and taking current terms up to the first harmonic we obtain :

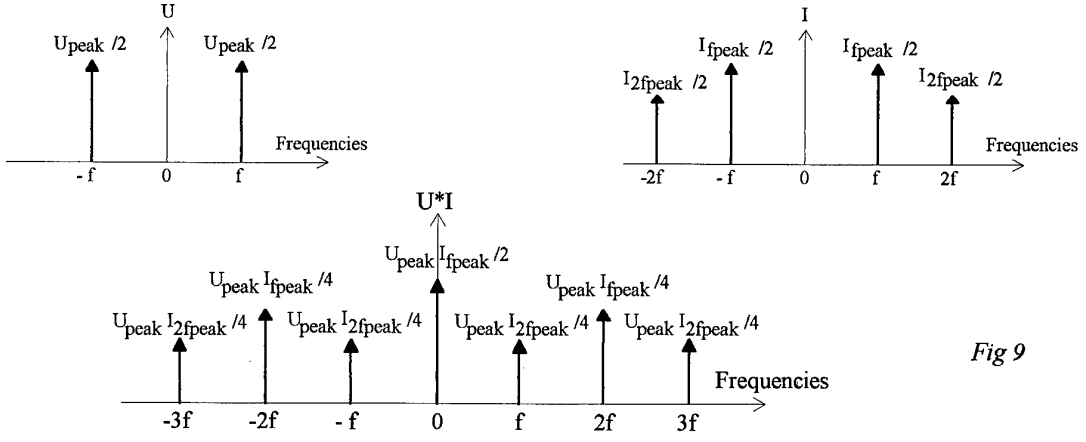


Fig 9

(Upeak : voltage peak value and Ifpeak, I2fpeak : fundamental and first harmonic current peak values)

The continuous components (Upeak Ifpeak/2) corresponds to power dissipated in the transducer. The term at 2f exists in the linear regime. The other terms at f and 3f are nonlinear terms.

Knowing the power expressions associated with each frequency, the power components evolutions can be plotted as a function of the excitation level applied to the transducer.

The simulations results obtained are in good agreement with the power experimental data (Cf fig. 10).

Generally, the amplitude saturation effects were explained as in terms of viscous factor increase with the field E. This paper introduces an alternative explanation using nonlinearities. In order to face these two possible interpretations, the power has been studied in both cases and compared with experimental data. To model the viscous factor increase, the nonlinear coefficients have been suppressed and the damping coefficient λ modified for each driving voltage to fit with the experimental displacement amplitude; then the power components (constant and fluctuating powers) were computed.
Figure 11 displays the different curves obtained for the power :

- by experimental means
- by simulation with a variable damping coefficient (and no nonlinearities)
- by simulation with nonlinearities (and a constant damping coefficient).

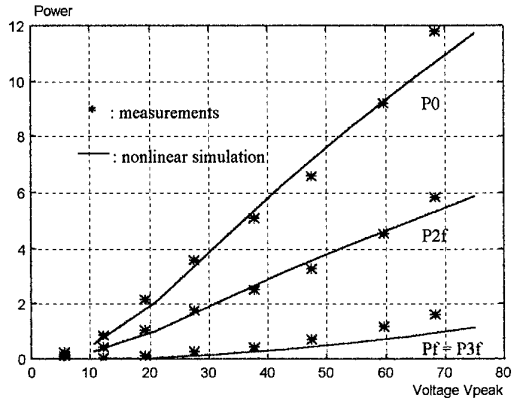


Fig 10

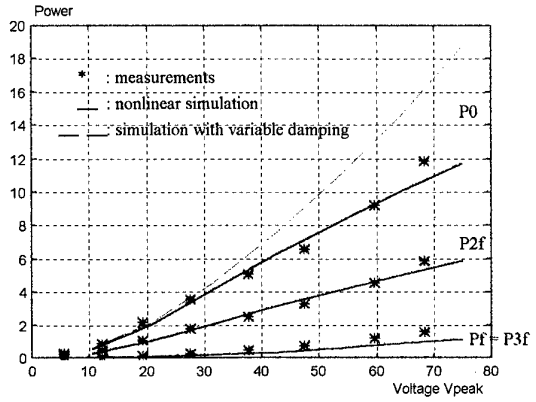


Fig 11

The model introducing nonlinearities is the only one that can explain the powers located at frequencies f and 3f, that are directly due to the current harmonics. Moreover, the nonlinear model gives power values for the frequencies 0 and 2f that are closer to experimental data than the values given by the model based on the viscous factor increase. It clearly shows that the viscous factor evolution overestimates by 40% the power losses.
Consequently, the nonlinear interpretation appears more adapted to describe the piezoelectric ceramics behaviors under high excitation levels.

6. CONCLUSION

The nonlinear constitutive piezoeletric equations permit to describe the phenomena observed on PZT power ceramics under high working levels. Indeed, resonance frequency shift, amplitudes saturation effects, typical signals distortions and power evolutions are found thanks to simulations, and confirm the experimental observations. This new nonlinear interpretation allows to fit more precisely the experimental transducer power evolution. It significates that a better knowledge of the nonlinear piezoelectric coefficients is important to foresee the behavior of devices using ferroelectric ceramics.

7. ACKNOWLEDGMENTS

The authors are grateful to the CERDSM-DCN of Toulon, especially to Dr D.Boucher, for supporting this research.

8. REFERENCES

1. L.D. Landau and E.M. Lifshitz, *Mechanics* , Course of theoretical physics, third edition, Pergamon.
2. L. Meirovitch, Elements of vibration analysis, Mechanical engineering series, 2nd edition, chap.9/10, Mc Graw-Hill International editions.
3. G.A. Maugin, *Nonlinear electromechanical effects and applications*, Series in theoretical and applied mechanics, Vol.1, editor : R.K.T. Hsiek / World Scientific.
4. H. Beige and G. Schmidt, " Electromechanical resonances for investigating linear and nonlinear properties of dielectrics " *Ferroelectrics*, Vol.41, pp 39-49, 1982.
5. D. Guyomar, N. Aurelle, C. Richard, P. Gonnard and L. Eyraud, " Non linearities in Langevin transducers " *IEEE Ultrasonics Symposium*, Vol.2, pp 925-928, 1994.

Sensor - actuator panels for underwater acoustic control

Robert D. Corsaro and Brian Houston

Naval Research Laboratory, Code 7130, Washington, D. C. 20375-5350

ABSTRACT

Local control of an acoustic projector or boundary can, in principal, be accomplished using large area locally-controlled actuators with an imbedded or intimately bonded sensor arrays. However in practice the marriage of an actuator and sensor array is not straightforward. In a basic research study, this paper considers the design and performance of a generic smart actuator for underwater acoustic applications. Both surface pressure and surface velocity sensing are included Models are presented for understanding the importance of some of the mechanisms and construction issues involved, and for predicting the resulting system transfer functions. The predictions are compared with freefield experimental results.

1. INTRODUCTION

A new research platform has been constructed at NRL for underwater structural-acoustics studies of sensor / actuator coupling mechanisms. It consists of a 15 tile array of smart actuators, henceforth referred to as "ABC" tiles. These tiles are arranged in a 5 x 3 array and adhered to a backing structure, which is an air-backed 0.5 inch thick steel plate. Each tile of this array consists of a driver, a pressure sensor layer, and a velocity sensing layer. The overall tile design is illustrated in Figure 1. The actual construction details are more complicated than shown here, and include two important mechanical components: a transverse decoupler between the actuator and pressure sensor, and aluminum conditioning disks under the accelerometer.

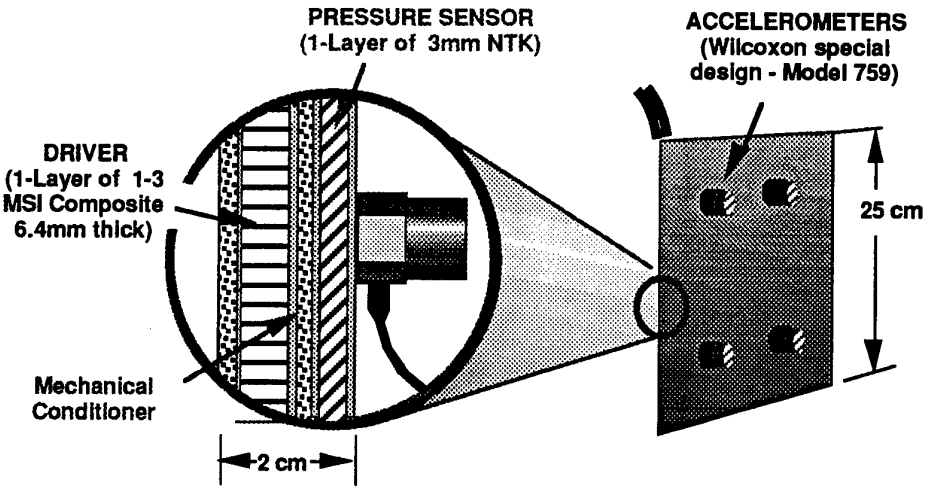


Figure 1. ABC Tile overall approach

0-8194-2165-0/96/$6.00

This present paper presents some details of the tile design and the predictive models used. Acoustic characteristics of the ABC tile were evaluated in the NRL Laboratory for Structural Acoustics (a large highly-instrumented pool facility), and these results are compared with predictions. Implications for local control of the actuator's surface are also discussed, however a detailed consideration of actual control implementation is beyond the scope of this present publication.

2. TRANSDUCER CHARACTERISTICS

2.1 Actuator

The actuator material selected for this final ABC tile is the 1-3 composite, only recently available from Material Systems Inc. (MSI). This actuator material offers some important advantages for this current application including (a) *very high actuator authority* (an effective value of d_h on the order of 400×10^{-12} C/N); (b) *uniform surface velocity* (as determined at NRL using, NRL Laser Doppler Vibrometry); (c) *reasonably low cost.* (in large quantity procurements it's cost is approximately one third that of comparable transducer technologies).

The Transmit Voltage Response TVR can be predicted from the usual expressions, where, TVR is the farfield pressure produced by one volt, projected back to a distance of one meter using the inverse-distance spreading law. The expected performance of this actuator based on an effective piezoelectric (d_{33}) constant of 400 pC/N is found to be in very good agreement with experimental measurements, finding a measured TVR at 2 kHz of 109.5 dB re: µPa/V.

2.2 Pressure sensor

The pressure sensor layer (hydrophone) uses piezorubber (PR-307 from NTK Corp.) as the transducer material. Using the value for g_h given by the manufacturer (0.111V-m/N) and a typical thickness of 2.8 mm, the predicted sensitivity (voltage-pressure transfer function) of this sensor is -190.2 dB re: V/mpa. The measured free field sensitivity of the pressure sensor (as assembled in the final tile) is on approximately -193 dB re: V/µpa. Although this is approximately 3 dB lower than predicted such a reduction was not unexpected; similar reductions have been frequently observed in our previous free-field pool measurements on large-area hydrophones constructed of flexible material (PVDF, Piezorubber, etc.).

The overall noise level for the sensor is found to be dominated by the input noise of the preamplifier selected. The minimum detectable acoustic pressure level is $P_{(min)}$ = 76.3 dB re: µpa.

2.3 Velocimeter

We were unable to locate any suitable large-area velocity sensor. We therefore resorted to using an array of commercially available accelerometers. The output signals of these accelerometers are summed and integrated using a custom NRL-designed on-board module to obtain an output signal proportional to velocity. Wilcoxon Model 759 accelerometers were selected. Their main attributes are high resonance frequency (25 kHz) and very low noise floor (approximately 0.10 µg/√Hz). They are also reasonably insensitive to non-normal acceleration, and are waterproof.

We have elected to use four accelerometers per tile. This is sufficient to adequately sample internally-driven flexural waves on backing structures of interest in our associated studies. It also provides some local averaging, and reduces the noise floor by 6 dB. To increase the stiffness of the underlying rubber composite structure, and increase the rotational stiffness of the accelerometer in the non-normal velocity field, a thin aluminum disk is placed beneath each accelerometer. From a parametric analysis, it was judged that the best aluminum disk dimensions for present purposes are: 0.64 cm (1/4 inch) thick and 9 cm (3.5 inch) diameter.

The measured free field sensitivity of each accelerometer in the velocity sensor (as well as the output from the on-board summing and integration module) was found to be reasonably uniform and in good agreement with predictions.

3. TRANSDUCER COUPLING

For an active control system, an important transfer function is the electrical coupling between the actuator layer and sensor. These coupling factors are of particular importance in the design of a smart actuator, since they are the inverse of the neutralization gain required. Hence smoothly varying functions with high coupling levels are desirable, since they suggest that a stable low-gain control system can be configured. In our case it is also important that this coupling be exclusively via acoustic mechanisms.

3.1 Pressure sensor / actuator coupling

For the pressure sensor, the expected driver coupling can be predicted by computing the pressure at all locations in the plane of the sensor and then integrating this field over the area of the sensor. The area integrated normalized output for any separation distance then becomes a triple integral. The result is shown in the following figure (which includes the infinite-tile case as an array reference).

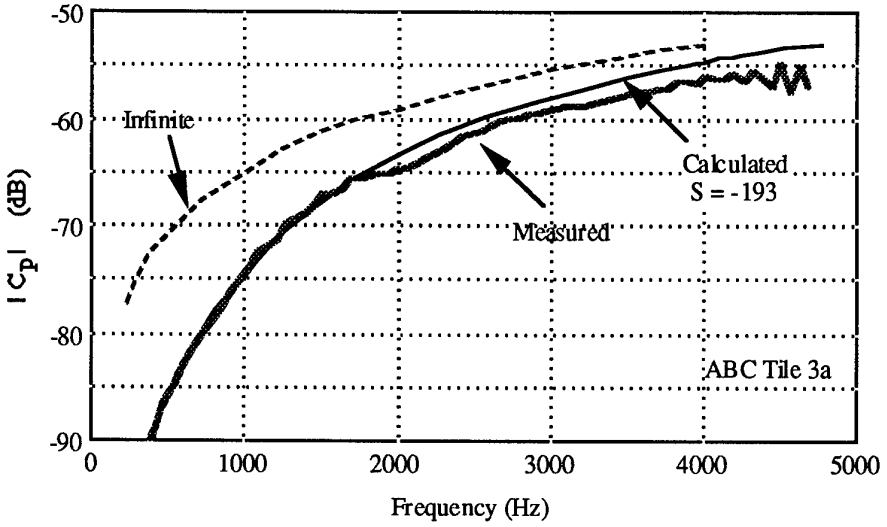


Figure 2. Magnitude of the free-field pressure coupling

The experimental measurement of pressure coupling is straightforward: a known voltage is applied to the actuator, and the voltage obtained from the pressure sensor layer is measured. Hence coupling is a simple ratio of the output to input voltage. The measured result is shown in the above figure, which is in excellent agreement with the predicted result.

3.2 Velocity sensor / actuator coupling

The electrical coupling between the actuator layer and the velocity sensor via acoustic mechanisms can be predicted from the gradient of the above calculated pressure field (using Euler's relation to solve for the axial and radial components of the velocity vector at the accelerometer location).

Velocity coupling is measured by applying a voltage to the actuator, and measuring the voltage obtained from each accelerometer. The predicted and measured performance for each individual accelerometer element is shown in the following figure.

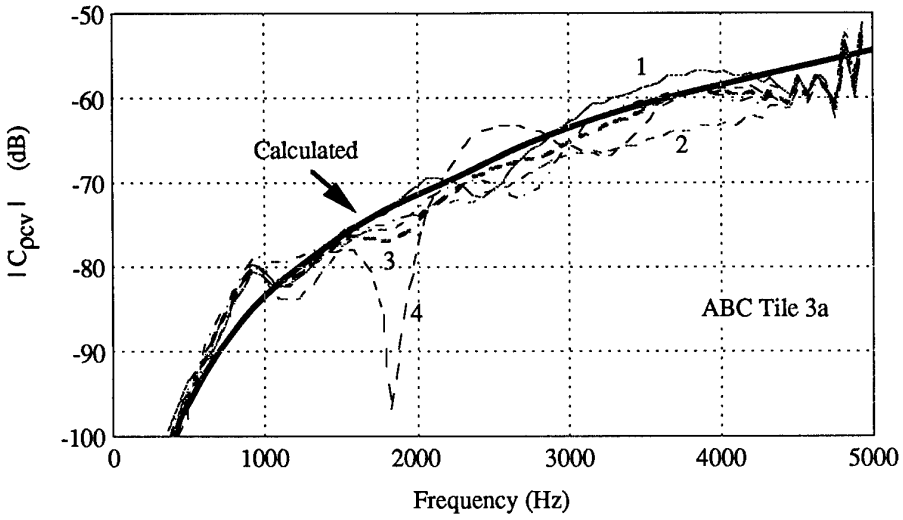


Figure 3. Magnitude of the free-field velocity coupling.

The measured magnitude of the velocity coupling for each of the four accelerometer outputs is seen to be in excellent agreement with that predicted. When these outputs are summed and averaged by the on-board module), the result is a smooth curve (not shown) generally within a few decibels of that predicted.

4. CONCLUSIONS

The overall tile performance is quite satisfactory for use in planed NRL structural acoustics studies. The models used in the design of this ABC tile appear to have been generally successful in describing the measured acoustic transfer functions. The mechanisms responsible for most features of the data have been identified.

Following these evaluations, this tile was mounted on an air filled flat backing structure, where the front surface is a rib-supported 1.25 cm (0.5 inch) thick steel plate. The acoustic response of this tile was evaluated in the NRL Highly Instrumented Pool Facility. The structure evaluated is illustrated below.

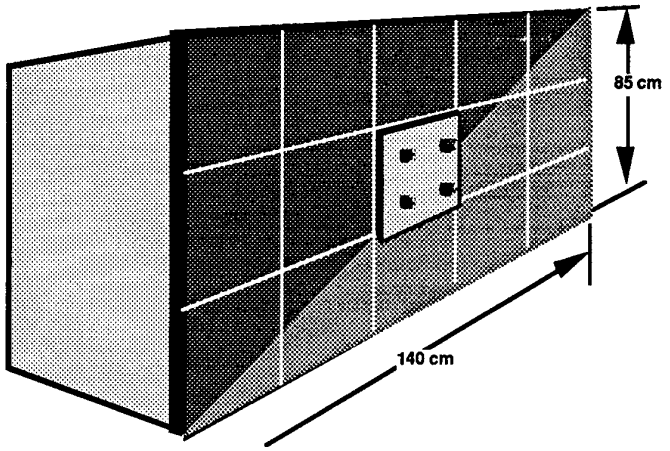


Figure 4. Single ABC Tile on the backing structure

At high frequencies, the mounting surface of the backing structure presents an acoustic input impedance of approximately that of a simple air-backed steel plate (where the effective plate thickness is that corresponding to the combined stiffness of the surface plate and rib supports). The effect of this backing impedance is to introduce a (predictable) correction to the measured transfer functions. However at lower frequencies the backing impedance presented by this structure becomes very complicated due to the presence of flexural modes related to the finite size of the backing, the location of ribs, and the area of the actuator. The transfer functions evaluated for tiles on this backing structure at frequencies below 2.5 kHz are therefore somewhat more complicated.

Following the evaluation of this single tile, 14 additional copies of this tile were constructed and adhered to the above backing structure to form a 3 by 5 tile array. Inter and intra-tile coupling measurements were collected, and experiments in single tile active control were performed, culminating in a control demonstration with all 15 tiles simultaneously and independently operating. While a discussion of these control results is beyond the scope of this paper, we consider this new 15 tile testbed to represent a significant new research platform for underwater studies of sensor-actuator coupling mechanisms.

Smart actuators with piezoelectric materials

Hartmut Janocha, Daniel J. Jendritza, Peter Scheer

Consultant agency new actuators with microsystem and signal concepts (*D*ASS*)
D - 66041 Saarbrücken, University of Saarland, Building 13, Germany

ABSTRACT

Piezoelectric solid-state actuators continue to gain in technical and economic significance for a great variety of applications such as quick fine-positioning tasks, control of structural stability and active noise and vibration control due to the high driving forces, short reaction times and compact construction of these actuators. Microelectronics and signal processing must be combined intelligently to form "smart actuators" in order to do justice to the growing demand for precision, miniaturisation, efficiency and cost.
Energy transducers with piezoelectric PZT ceramics (PZT: lead-zirconate-titanate) simultaneously possess actuator and sensor capacities. An important requirement for the construction of smart actuators is fulfilled by separating the sensor information (charge ~ external force) from the actuator control quantities (elongation ~ electric field strength).
A closed-loop control structure with digital signal processing (DSP) and a voltage controlled power amplifier were developed to enable nearly load-independent linearisation of the actuator's response characteristic (elongation-voltage curve) even under dynamic operating conditions by making use of the "self-sensing" effect and without using extra force or displacement sensors.
The effectiveness of the developed approach for realising smart actuators was verified and specified with the help of a computerized large-signal measurement set-up using a low-voltage piezoelectric ceramic stack as an example.

1. INTRODUCTION

Ideally, a technical system should be capable of optimally adapting its function to external influences of temperature, pressure, moisture or voltage. The availability of smart actuators fulfills an important requirement for realising self-adapting systems. An actuator consists of the series connection of an electronic amplifier and an electromechanical energy transducer, with possible inclusion of housing and gear (e.g. displacement amplifier). Interesting materials for realising smart actuators include piezoelectric ceramics as well as magnetostrictive materials such as Terfenol-D.[1] The energy transducer can be described as a network with two-ports, one electrical and one mechanical (Figure 1). A change in the mechanical output load on piezoelectric ceramics effects the parameters of the electrical input making possible the simultaneous use of the energy transducer as a sensor. Some of the first attempts to realise smart piezoelectric actuators in an appropriate application are presented by Inman et al. [2,3]. With the help of simple electrical bridge circuitry, a single piezoelectric transducer can be used simultaneously as a sensor and an actuator in an analog closed control loop for active vibration damping. Useful results have also been supplied from applications such as fine positioning of laser mirrors with simultaneous force sensing using piezoelectric stacks [4,5,6].

2. THEORETICAL FUNDAMENTALS AND REQUIREMENTS

2.1 Ferroelectricity

The widely known piezoelectric ceramic PZT used in the construction of actuators and sensors of today is a polycrystalline material with ferroelectric properties. Ferroelectric ceramics consist of individual crystallites with randomly oriented axes of polarisation; there exists no net dipole moment. The polycrystalline ceramic is polarised by applying a constant external electric field resulting in a remanent polarisation P_r . The ceramic now exhibits piezoelectric properties. Due to their ferroelectric nature, transducers with PZT ceramics demonstrate material specific nonlinearities, hysteretic phenomena with respect to strain and electric field (between polarisation and electric field) as well as creep and aging. These effects become more significant with increasing field strength (large-signal behaviour).[7] However, the system response behaviour can be remarkably linearised by controlling the electrical charge instead of the voltage.[8]

0-8194-2165-0/96/$6.00

2.2 Fundamental equations of piezoelectricity

The piezoelectric effect can be described as a coupling of Maxwell's equations of electromagnetism with those from elasticity theory. Evaluation of the linearised form of the thermodynamic potentials from Gibbs [9,10] results in the equations of state

$$\begin{aligned} \varepsilon_{ij} &= s_{ijlm}^{E,T}\ \sigma_{lm} + d_{ijn}^{T}\ E_n + \alpha_{ij}^{E}\ \Delta T \\ D_k &= d_{klm}^{T}\ \sigma_{lm} + \varepsilon_{kn}^{\sigma,T}\ E_n + p_k^{\sigma}\ \Delta T \\ \Delta S &= \alpha_{lm}^{E}\ \sigma_{lm} + p_n^{\sigma}\ E_n + \frac{\rho\, c^{\sigma,E}}{T_0}\ \Delta T \end{aligned} \tag{1}$$

with the variables σ_{ij} (components of the mechanical stress tensor), E_k (components of the electric field), T (absolute temperature), S (entropy), D_k (components of the dielectric displacement), ε_{ij} (components of the elastic strain) and the coefficients $s_{ijlm}^{E,T}$ (modulus of elasticity), d_{ijn}^{T} (piezoelectric modulus), α_{ij}^{E} (thermal coefficient of expansion), $\varepsilon_{kn}^{\sigma,T}$ (dielectric permitivity), p_k^{σ} (pyroelectric coefficient), ρ (density), $c^{\sigma,E}$ (specific heat).

By ignoring changes in temperature in (1), the simplified fundamental equations of piezoelectricity, written in tensor form, become

$$\begin{aligned} \{\varepsilon\} &= \left[s^{E}\right]\{\sigma\} + [d]\{E\} \\ \{D\} &= [d]^{T}\ \{\sigma\} + \left[\varepsilon^{\sigma}\right]\{E\} \end{aligned} \tag{2}$$

Under conditions of no load, these equations can be reduced to

$$\begin{aligned} \{\varepsilon\} &= [d]\{E\} \\ \{D\} &= \left[\varepsilon^{\sigma}\right]\{E\} = \varepsilon_0\ \{E\} + \{P\} \end{aligned} \tag{3}$$

for polarisation P. Nonlinearities in the system response behaviour can be considered by including higher order terms in the equations of (1). The piezoelectric transducer's strain-field strength curve which is highly linear in small-signal operation can sufficiently be described with the equations of (2). The ferroelectric properties of the particular PZT transducer material must be taken into consideration for large-signal operation ($E \geq$ 500 V/mm).

2.3 Method of compensating hysteresis

One possible formulation of the ferroelectric polarisation-field strength hysteresis is based on the reversal of domains (regions of uniform dipole orientation) through the influence of an external alternating electric field.[7] The number of dipoles oriented in the direction of the field changes linearly with the external field. The change of polarisation is caused by the motion of ions and is related to the piezoelectric strain. Therefore, no hysteresis is expected between the polarisation and strain (or between dielectric displacement and strain), although the relation is not entirely linear. The domain switching process provides a good means of describing the nonlinear strain-field strength behaviour and the electromechanical hysteresis in ferroelectrics (PZT ceramics), representing a combination of macroscopic aspects with microscopic material properties. The difficulty lies in the experimental determination of the parameters necessary for this model. The hysteretic behaviour has a complex dependency upon the mechanical load and temperature of the piezoelectric transducer.[11,12]
When simplified, a relationship exists between a change in the dielectric displacement ΔD and the polarisation ΔP relative to a starting point under the influence of an electric field E.

$$\Delta D = \varepsilon_0\ E + \Delta P \qquad P = \xi\ \varepsilon_0\ E \qquad \textit{and} \qquad \xi = \varepsilon - 1 \tag{4}$$

ΔP is dependent upon the amplitude, the frequency ν, the electric field E, the temperature T and the history of the ceramic. Since $\xi >> \varepsilon_0$, then $\Delta D \sim \Delta P$ under no load conditions and therefore: $\Delta D \sim \Delta x$.
A measurement of the change in electric charge of the piezoelectric transducer is a measure for the change in the polarisation.[8] A linear relationship between the charge and the strain in the piezoelectric ceramic exists

over a wide range. Charge controlled power amplifiers exhibit some disadvantages with respect to those implementing voltage control concepts. A stable approach to measuring electric charge is only possible with a relatively large investment in the circuitry. This circuitry also exhibits a high output resistance with the result that reactions such as variations of the mechanical output load could have a strong effect at the electrical input.
An additional possibility to linearise the strain-field strength curve is offered by modelling the hysteretic behaviour according to Preisach[1] followed by saving the inverse model in a computer connected between the control signal and the actuator. This approach is disadvantageous due to the greater degree of programming and computer effort, and this mathematical model applies only to a fixed operating point (constant temperature T, constant frequency ν, constant force F) without including the time varying behaviour of piezoelectric transducers.
An alternative concept will be presented next in which a voltage controlled power amplifier and a digital signal processing controller make use of the "self-sensing" effect in an effective way to compensate nonlinearities and hysteresis.

2.4 Feedback and the self-sensing effect

For operating frequencies up to 1% of the natural frequency, piezoelectric transducers can be interpreted as a series connection of a voltage source U_s with a charge, frequency and temperature dependent capacitance $C(q,\nu,T)$ (compare with the *Mason*-Modell, the fundamental equations in (2) and Figure 7).
Written in terms of scalar quantities, the sensor voltage U_s is a function of the control voltage U_0.

$$U_s = \frac{q}{C(q,\nu,T)} - U_0 \qquad \text{and} \qquad q = q_0 + q_s \tag{5}$$

q_0 is the impressed or free electric charge in the transducer; q_s is the piezoelectric polarising charge which is proportional to the force acting on the piezoelectric transducer. Measurement of $U_0(t)$ and $q(t) = \int I(t)\,dt$ makes it possible to determine the change in force at the transducer output based solely upon the electrical input[13,14], assuming that the capacitance $C(q,\nu,T)$ is known.

3. REALISATION OF A SMART ACTUATOR

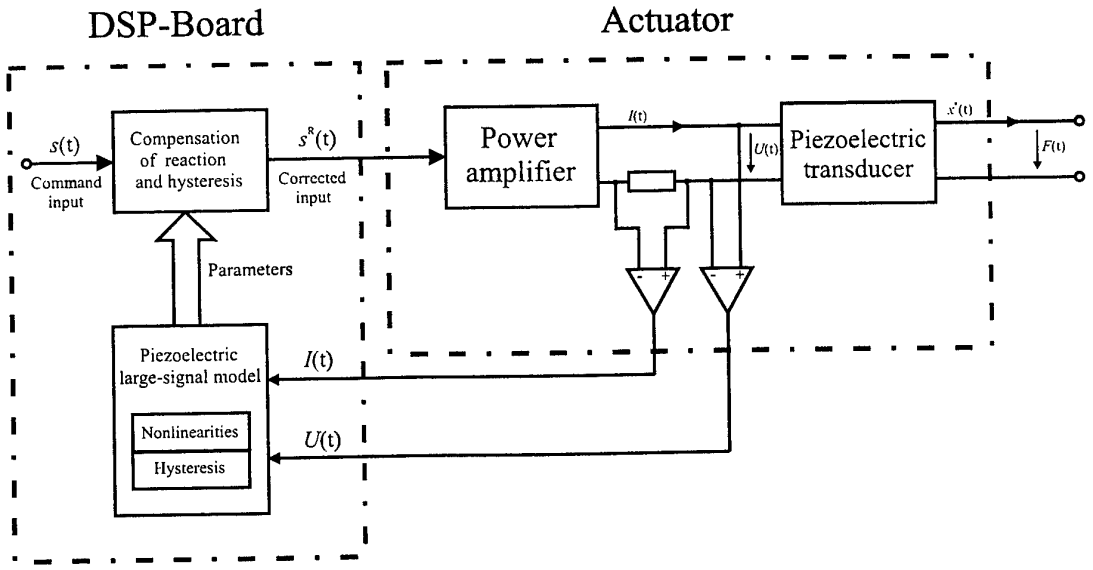


Figure 1: Functional representation of a "smart piezoelectric actuator"

The central component in the closed control loop is a programmable digital signal processor (Figure 1). A corrected control signal $s^R(t)$, which is directed to the actuator through a low-pass filter, is calculated from the control signal $s(t)$ and the quantities current $I(t)$ and voltage $U(t)$ measured at the transducer input. The control algorithm compares the measured current signal $I(t)$ following correction of the offset, integration and scaling

with voltage $U(t)$, adds the difference to the original control signal $s(t)$ and outputs the regulated control signal $s^R(t)$. Sensors and the phase-corrected control signal $s^P(t)$ provide measurement data and enable their display. The digital controller is currently optimised for control signal frequencies from 1 to 100 Hz. The energy transducer implemented was a low-voltage piezoelectric stack consisting of 10 plates (each 40 µm thick) with dimensions 5x5x20 mm^3.

4. COMPENSATION OF HYSTERESIS AND NONLINEARITITES

The superiority of a DSP supported, digital charge controller over an analog concept is apparent in the nearly complete compensation of hysteresis and the so called minor-loops (Figure 2). The displacement resulting in the regulated system remains nearly constant since the maximum displacement minus the thermal expansion of the ceramic material in an unregulated system increases with increasing temperature (up to a Curie temperature dependent limit), and the strain-voltage hysteresis curve becomes narrower[15] (ν = 200 Hz, F = 0 N). Even the width of the hysteresis remains somewhat constant (< 4 % of the maximal displacement) in the measured temperature range (Figure 3a). The effective displacement decreases with increasing frequency and the hysteresis becomes wider for isothermic and no-load conditions (F = 0 N, $T \approx$ 23°C). Reversal of the domains is delayed due to friction forces between the domains resulting in heat generation. Charge control provides the same effect as in the previous example (Figure 3b). The effectiveness of digital control with respect to the mechanical transducer load is apparent for ν = 100 Hz and $T \approx$ 23 °C (Figure 3c). While the width of the hysteresis can be reduced across the entire operating range, the value of the maximum displacement minus the mechanical compression remains only constant up to about 75% of the blocking force. Perhaps the elastic limit of the transducer or electrode material has been reached (effect of the electrical contact and bonding joints). The resulting remainder in hysteresis (right half of Figure 3a, 3b, 3c) can be explained by tolerances in the displacement sensors, errors in the measurement of current and uncompensated mechanical reaction in the measurement system. Microscopic fractures in the piezoelectric ceramic and the formation of additional joints due to thermal and mechanical overload also have negative affect on the resulting control behaviour of the smart actuator. Despite digital control, the elongation of the transducer reduces considerably above a limiting temperature $\approx 0.5\ T_C$ (T_C: Curie temperature) for a constant control signal. This reduction in displacement can be explained by internal losses.

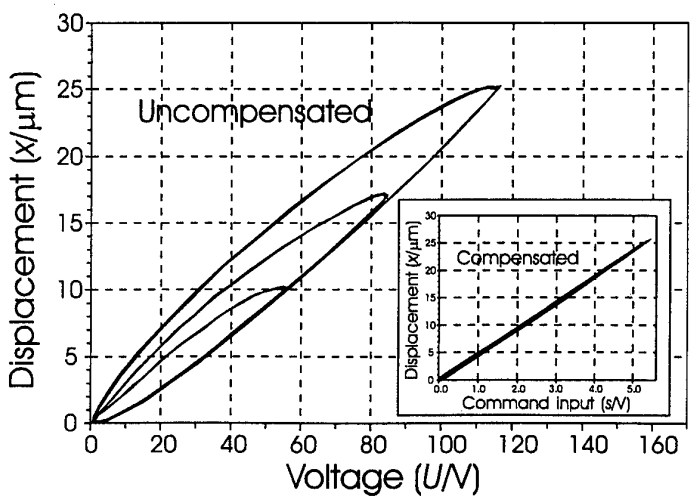


Figure 2: Linearisation of the strain-voltage (field strength) curve using electric charge control methods

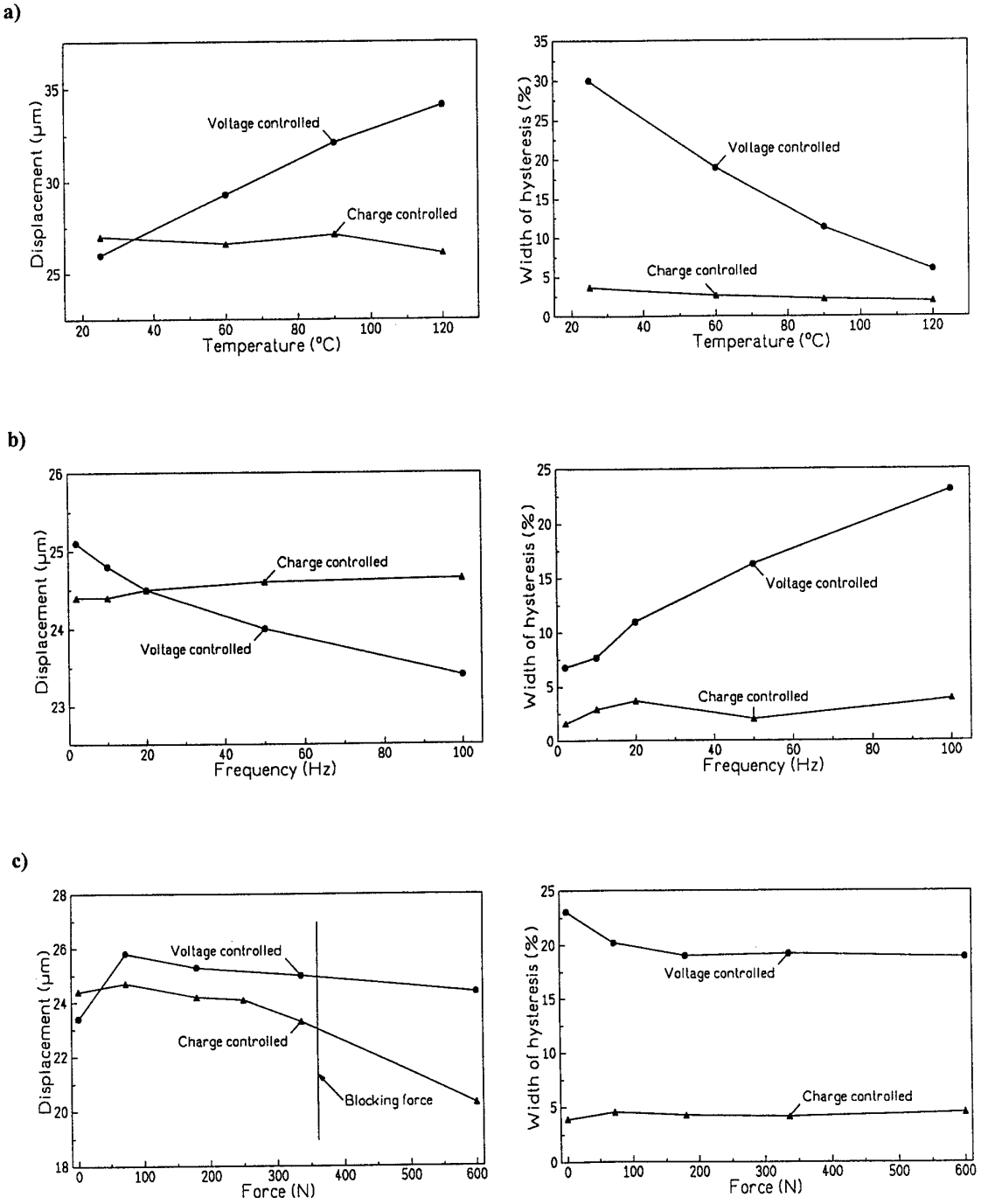


Figure 3: Displacement and hysteresis width for $U = 120$ V. **a)** temperature dependence **b)** dependence upon control signal frequency **c)** dependence upon the mechanical output load of the tranducer

5. THERMAL STRAIN AND ITS MECHANICAL EFFECT

As illustrated in a small-signal measurement of the capacitance and elongation (Figure 4), the electrical input data for the piezoelectric transducer suffices for determining the thermal elongation of the transducer. A mechanical loading cycle at the mechanical transducer output can be detected and evaluated at the electrical transducer input (Figure 5). The transducer voltage does not change but the current signal is superimposed with a disturbance. The direct influence of the applied control circuitry must be taken into consideration here (coupling of the amplier output and transducer input, i.e. interactions). Integration of the disturbance signal

results in the load response q_s sensed by the piezoelectric transducer which must be proportional to the impressed force signal. A sensor signal (Figure 6a) can be determined from the load response using equation (5) with consideration of the current effective capacitance (Figure 7). An approximation of sensor signal was achieved using only the signal amplitude so that small deviations appeared in the identification of the load (Figure 6b).

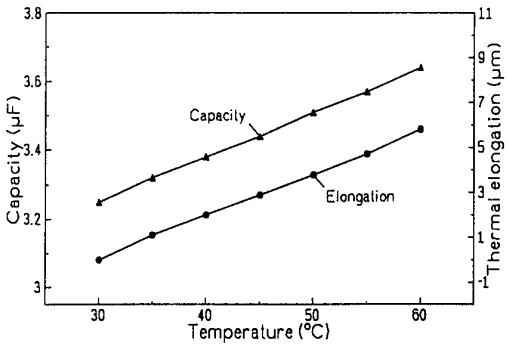


Figure 4: Temperature response of the small-signal capacitance and the tranducer elongation

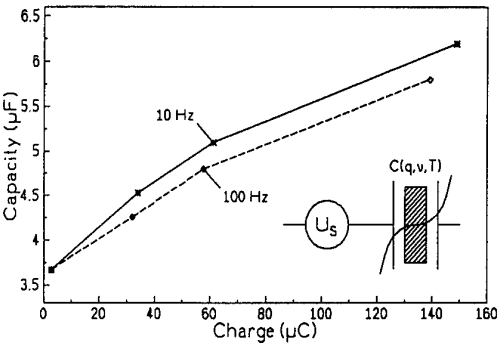


Figure 7: Capacitance as a function of the net generated electric charge

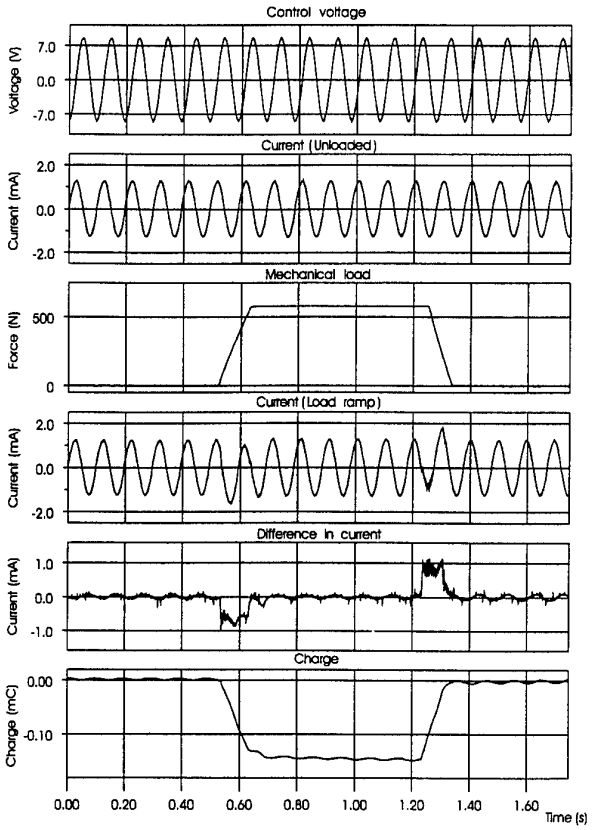


Figure 5: Effect of a change in the mechanical output load on the electrical signal values

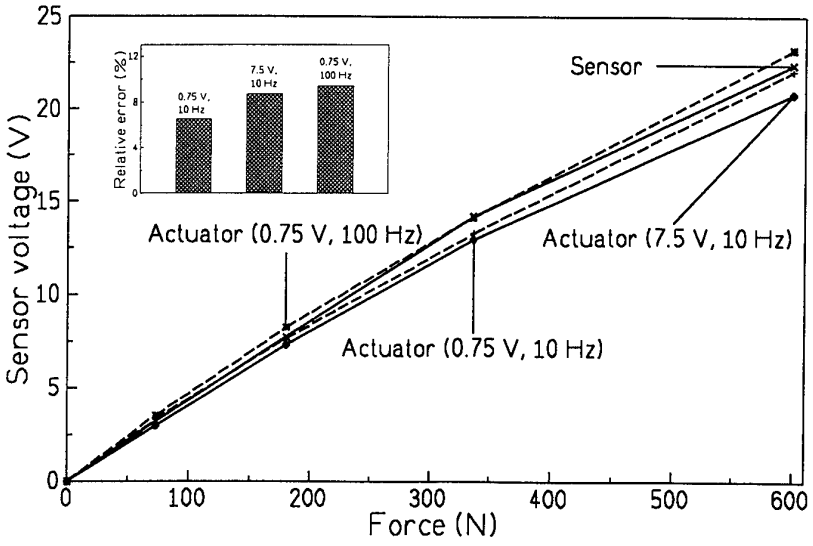


Figure 6: Piezoelectric "sensor" voltage and relative error for various operating conditions

6. SUMMARY AND OUTLOOK

Hysteresis, drift and aging of piezoelectric ceramics are ferroelectric in nature and can be compensated by incorporating an actuator in a closed control loop.
By implementing a DSP-supported control algorithm, a smart piezoelectric actuator was realised with which nearly load-independent and hysteresis free displacements could be generated without additional force and displacement sensors. Only the electrical quantities of voltage and current at the transducer input are necessary. For defined operating conditions, the displacement can be controlled independent of the history of the ceramic, the amplitude, frequency, mechanical loading and surrounding temperature through on-line variation and adaptation of the actuator control voltage with respect to the current and voltage error signals. The result is a relatively simple, stable and well adaptable method without the need for expensive sensors and the disadvantage of additional size and weight.
The effectiveness of digital control could be increased through the implementation of improved piezoelectric ceramics and electrical contact techniques - currently available transducer designs demonstrate definite secondary effects and signs of fatiguing. Control with DSP also enables simple adaptation to various transducer and amplifier types as well as the use of adaptive control algorithms. Optimised fine positioning systems and active vibration damping and noise control can be realised with the help of smart piezoelectric actuators.[16,17] In contrast to distributed sensor/actuator systems, a smart system requires no additional sensors and offers the possibility for self-monitoring and error diagnosis. Continued work on this project should improve the efficiency of the approach and permit higher operating frequencies.

7. LITERATURE

1. H. Janocha, J. Schäfer and D.J. Jendritza, "Smart solid-state actuators", *Proc. 4th Technologie Transfer Congress Actuator 94*, pp. 224 - 228, 1994
2. J.J. Dosch, D.J. Inman and E. Garcia, "A self-sensing piezoelectric actuator for collocated control", *J. of Intell. Mater. Syst. and Struct.*, Vol. 3, pp. 166 - 185, January 1992
3. E.H. Anderson, N.W. Hagood and J.M. Goodliffe, "Self-sensing piezoelectric actuation: Analysis and application to controlled structures", AIAA-92-2465 CP, *Proc. 33rd AIAA SDM*, pp. 2141 - 2155, April 1992
4. D.J. Leo and D.J. Inman, "Modeling and control simulations of a slewing frame containing active members", *Smart Mater. Struct. 2*, pp. 82 - 85, 1993
5. B.J. Hurlbut and M.E. Regelbrugge, "Development of a self-sensing multilayer piezoceramic actuator for structural damping applications", *Fourth Internat. Conf. on Adapt. Struct.*, pp. 29 - 41, Cologne 1993
6. K. Duong, L. Jones, E. Garcia and H. Waites, "Smart actuators for precision control of adaptive reflectors", *Fourth Internat. Conf. on Adapt. Struct.*, pp. 290 - 302, Cologne 1993
7. X.D. Zhang and C.A. Rogers, "A macroscopic phenomenological formulation for coupled electromechanical effects in piezoelectricity", *J. of Intell. Mater. Syst. and Struct.*, Vol. 4, pp. 307 - 316, July 1993
8. C.V. Newcomb and I. Flinn, "Improving the linearity of piezoelectric ceramic actuators", *Electronics Letters*, Vol. 18, No. 11, pp. 442 - 444, May 1982
9. S.P. Joshi, "Nonlinear constitutive relations for piezoceramic materials", *ADPA / AIAA / ASME / SPIE Conf. on Active Materials and Adaptive Structures - Session 12*, pp. 217 - 222, 1992
10. D. Damjanovic and R.E. Newnham, "Electrostrictive and piezoelectric materials for actuator applications", *J. of Intell. Mater. System. and Struct.*, Vol. 3, pp. 190 - 208, April 1992
11. G. Borchardt, E. Wehrsdorfer and P. Pertsch, "Dielectric large signal measurements on piezoelectric stacks", *Proc. 4th Technologie Transfer Congress Actuator 94*, pp. 179 - 182, 1994
12. T. Inoue and S. Takahashi, "Measurements for piezoelectric ceramic properties applied compressive stress parallel to the polar axis", *The Transactions of the IECE of Japan*, Vol. E 69, No. 11, pp. 1180 - 1188, November 1986
13. D.J. Jendritza, P. Scheer and P. Stephan, "Large signal measurements for the characterisation and optimization of piezoelectric high- and low-voltage actuators, (german) *Sensor '95, Procedings*, pp. 667 - 672, 1995
14. D.J. Jendritza, "Piezoelectric actuator for large-signal applications", (german) *Dissertation* , University of the Saarland, January 1995
15. M. Yokusuha, "Electrical and electromechanical properties of hot-pressed $Pb(Fe_{1/2}Nb_{1/2})O_3$ ferroelectric ceramics", *Jpn. J. Appl. Phys.*, Vol. 32, pp. 1142 - 1146, 1993
16. D.J. Jendritza, *Technical application of new actuators.* (german, after Sommer 1996 also in englisch) Expert Verlag GmbH, Renningen, 1995
17. D.J. Jendritza, *Actuation* (in C M Friend: Smart structures and materials), Chapman & Hall, London, 1996

Piezoelectric and electrostrictive bimorph actuators and sensors for smart microsystems

P. Gaucher

Thomson CSF-LCR, Domaine de Corbeville

91404 Orsay Cedex France

1. ABSTRACT

Piezoelectric materials (PZ-PT 50-50, PMN-PT 65-35) and electrostrictive materials (PMN-PT 90-10) are potential candidates for the future integrated micro-systems because of their high dielectric constant and elastic modulus. They can be used in a cantilever laminated structure for active vibration control, smart acoustic sensors and agile transducers.

The first stage of the study has been made with screen printed thick films : modelling of transfer functions of sensor and actuator is made by analytical methods and experimentation of closed loop regulation is shown on a 15 mm long device.

The second stage is the miniaturization of the device on silicon substrate by using sol-gel deposition, microlithography and wet etching. The modelling of a 10 times smaller device is made with data coming from experimental measurements on thin films. Expected deviations and sensitivities are calculated with the same model as above.

2. EXPERIMENTAL SETUP

A cantilever beam (Fig. 1) is clamped in the force head of a Berlincourt piezometer (Channel Products) and is allowed to vibrate under the excitation of the laminated piezoceramic. The displacement at the tip of the beam is measured using a non contact optical probe (MTI Photonic Sensor) and a phase lock amplifier (EGG).

When a perturbation is induced in the force head, an analog feedback between another laminated piezoceramic (sensor) and the actuator enables a closed loop control of the vibration.

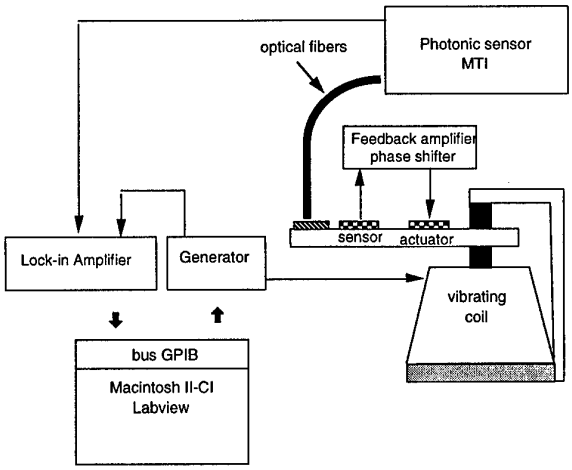


Fig. 1 : experimental setup

0-8194-2165-0/96/$6.00

3. MATERIALS

Well known ceramics in the PZT ($PbZr_xTi_{1-x}O_3$) solid solution system are currently used in most of the transducer and sensor applications. The morphotropic composition ($x \approx 0.5$) has optimized remanent polarization P_r and dielectric constant ε giving the high longitudinal and transverse charge piezoelectric coefficients:

$$d_{33} = 2\varepsilon_0 \varepsilon Q_{11} P_r \quad (1)$$

$$d31 = 2\varepsilon_0 \varepsilon Q_{12} P_r \quad (2)$$

where Q_{11} and Q_{12} are electrostrictive coefficients.

Still better piezoelectric properties can be obtained with materials having high ε, like in the PMN ($PbMg_{1/3}Nb_{2/3}O_3$) - PT ($PbTiO_3$) system. The morphotropic composition $PMN_{1-x}PT_x$ with x=0.35 has been extensively studied in our laboratory[1,2] and allows d_{33} larger than 600 $pC.N^{-1}$ with a mechanical Q factor around 100.

The electrostrictive composition x=0.1 is known in new hysteresis free actuators. Its application in resonant transducers may have a great interest because of the absence of domain walls resulting in improved aging properties and reliability. Another point of interest is the tunability of the electrochemical conversion in this kind of material: in equation (1) or (2), we can replace P_r by the induced polarization $P_i = \chi.E$, where $\chi = \varepsilon_0(\varepsilon - 1) \approx \varepsilon_0\varepsilon$ is the dielectric susceptibility and E the external electric field. This results in a quadratic effect at zero field and a linear effect under a DC bias as shown below:

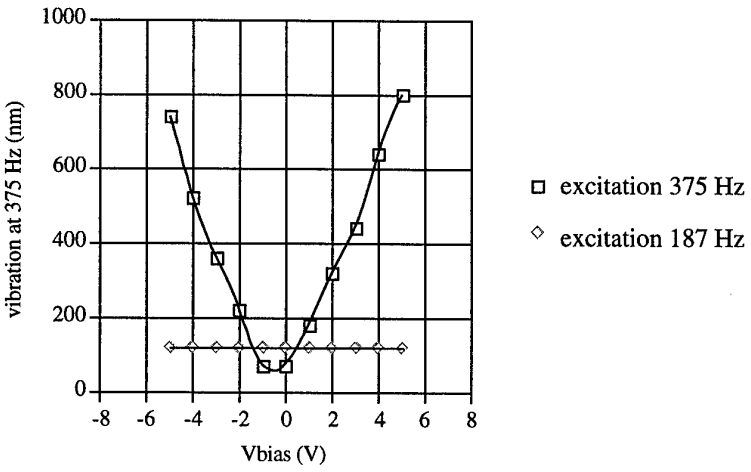


Fig. 2 : frequency doubling and tunability with PMN-PT relaxor material

4. RESULTS WITH THICK FILM TECHNOLOGY

Low sintering temperature PMN-PT powders allow to make laminated piezoelectric bimorphs on metallic substrates[3]. The technology can be used for making acoustic wave motors. Only results concerning cantilever beam actuation are presented here. The figure 3 below shows the transfer function between a piezoelectric sensor and a piezoelectric actuator (PMN-PT 65-35). The first three modes of the beam are clearly visible and in accordance with a simple 2D cantilever model.

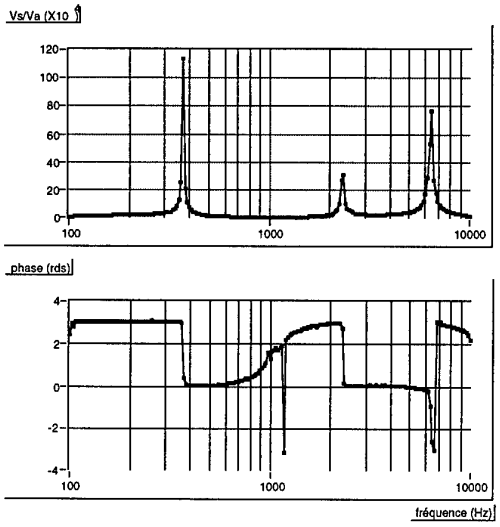


Fig. 3 : Transfer function between sensor and actuator

This function can be expressed as:

$$F^* = \frac{B_a.B_s}{m_i(\omega_i^2-\omega^2)+jD_i\omega}$$

where B_a and B_s are related to the actuator and sensor properties, m_i, D_i and ω_i are respectively the modal mass, damping factor and frequency for the mode i.

An example of active damping with this structure is shown below:

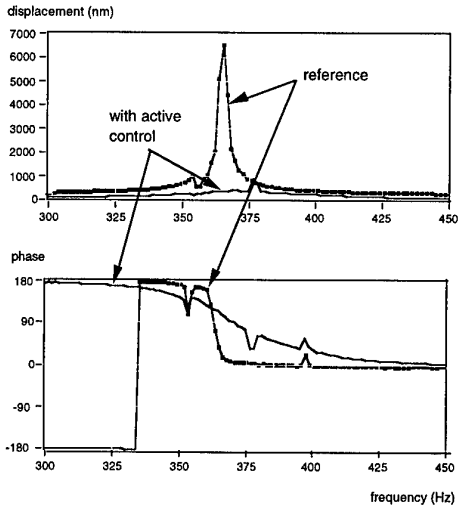


Fig. 4 : Active damping with closed loop regulation

5. THIN FILM TECHNOLOGY

A device ten times smaller is currently being developed within a European Brite project (SEMDEFT). The integration in Silicon needs to use microlithography and sol-gel spin coating[4] instead of screen printing. Silicon bulk micromachining will be used to make the free standing cantilever. The dye is represented below, it will allow in the future the integration of the analog feedback in the Si wafer:

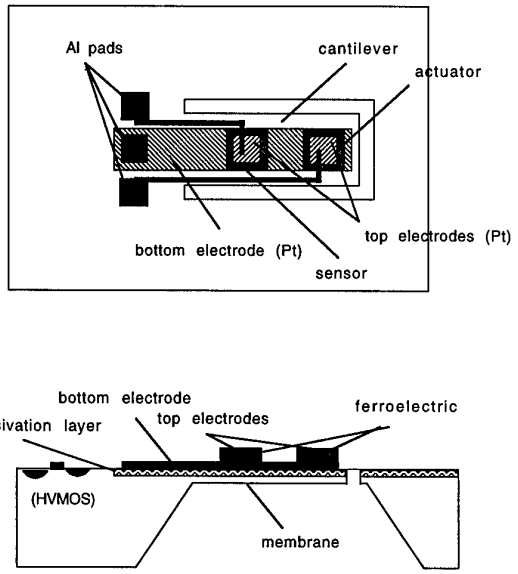


Fig. 5 : Si microsystem obtained

6. MODELLING

The modelling of such a microsystem can be made with purely analytical tools. Thicknesses and stiffnesses of the different layers, and position of the sensor and of the actuator, are the main inputs. The shape function of the beam for the mode i is expressed in the form:

$$\Phi_i(x) = N_i(e^{-a_i x} + \sin a_i x - \cos a_i x)$$

The chart of the modelling is shown in fig. 6.

The result of the modelling of a silicon cantilever having a length of 1.5 mm, a width of 0.5 mm and a thickness of 10 µm, are shown in Fig. 7. The beam is actuated and sensed by a PZT thin film having 1 µm thickness. The gain of the feedback amplifier is set to 100. One can see the influence of the phase shifter on the resonance peak (near 2 kHz) when the phase is varied between $-\pi$ and $+\pi$.

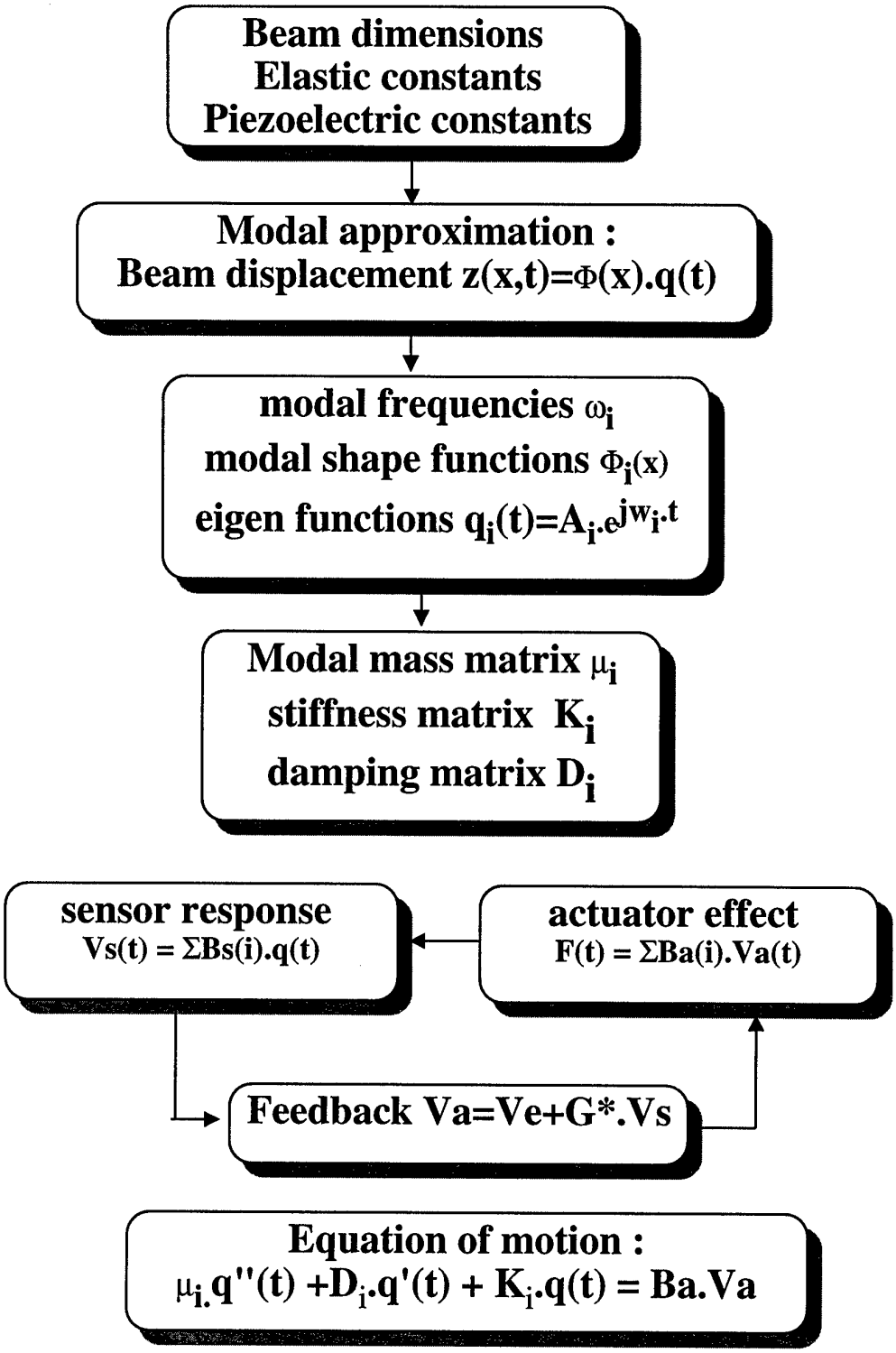


Fig. 6: micro cantilever modelling

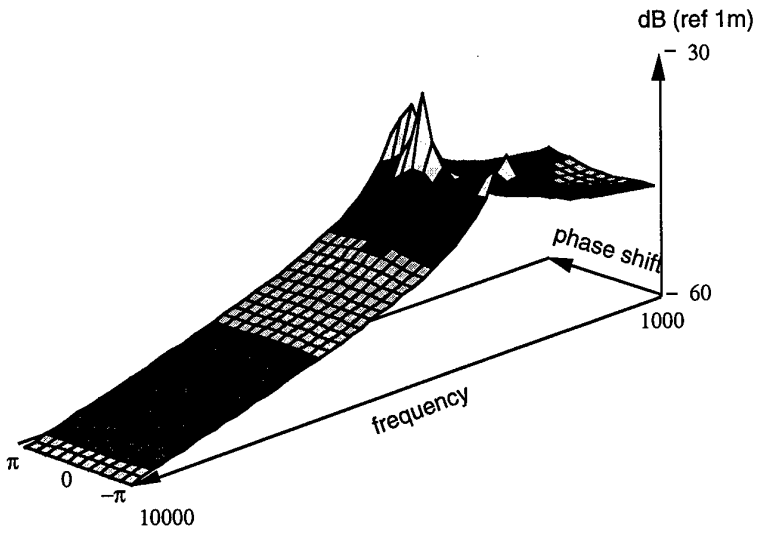


Fig. 7: Modelling of a smart silicon cantilever

7. CONCLUSION

This work shows the possibility of making self-regulated structures using laminated piezoelectrics. A very simple analog amplifier associated with a phase shifter allow a closed loop control that can be used for example for active damping of small devices or for integration within a smart skin. In the centimeter scale, hybrid technologies can be used with thick films. In the milimeter scale or below, microtechnologies can be combined with deposition techniques like sol-gel.

The use of electrostrictive materials in these structures will be of great interest because low bias voltages (a few volts) will be enough to give high piezoelectric induced effects, combined with an additional degree of freedom (tunability).

8. REFERENCES

1. O. Noblanc, P. Gaucher, ""Influence of domain walls on piezoelectric and electrostrictive properties of PMN-PT 65/35 ceramics ", Ferroelectrics, Vol 160, pp. 145-155, 1994.

2. O. Noblanc, P. Gaucher, "PMN-PT ceramics for active vibration control", in UK Transducer material workshop, DRA Malvern (UK), 1995, (to be published in Ferroelectrics).

3. P. Gaucher, C. Deljurie, R. Duffait, F. Bastien, J. F. Manceau, "Procédé de réalisation collective de microactionneurs et de micromoteurs piezoelectriques et electrostrictifs", (1995), French patent 95 01330, 6/02/95

4. P. Gaucher, J. Hector, J. C. Kurfiss, "Organically modified sol-gel precursors for ferroelectric deposition by spin coating", in NATO Advanced research workshop, Villa del Mare (Italy), 1994, Science and technology of electroceramic thin films, 147-156, Kluwer Acad Pub (NL), 1995.

Micromechanical ultrasonic transducer for liquid nebulization

Roumiana Paneva

Chair of Electron Devices, University Erlangen-Nuremberg, Cauerstr. 6, 91058 Erlangen, Germany

ABSTRACT

A piezoelectric ZnO layer is used to set thin silicon membrane into vibrations. The possibility to apply this micromechanical structure as an ultrasonic transducer is studied. High vibration modes are characterized with a considerable ultrasonic radiation. The application of the structure for ultrasonic nebulization is discussed.

1. INTRODUCTION

Piezoelectric ultrasonic transducers (UST) have a lot of application fields - in diagnostics, material processing, nebulization, etc. The commonly used materials - quartz, $LiNbO_3$ or PZT ceramics, possess excellent properties as UST, but have the disadvantage of noncompatibility with silicon microelectronic technology. This fact makes the further miniaturization and integration of UST difficult. Silicon is nonpiezoelectric and cannot be used directly as an UST. The aim of this work was to study the ultrasonic generation produced from ZnO piezoelectrically driven thin silicon membranes and to use them for nebulization of small amounts of liquids. The process of ultrasonic liquid nebulization in thin liquid films is based on the generation and destruction of capillary waves. A lot of devices use this principle of nebulization.[1,2] A micromechanical design using surface acoustic waves in $LiNbO_3$ was already reported.[3]

2. EXPERIMENTAL

5 Ωcm CZ p-type (100) silicon wafers were used in this experiment. For precise membrane thickness control an anisotropic etching with an electrochemical etch-stop was used. It was carried out in a two-electrode-system in a 40 % KOH solution at 65°C at the end of the manufacturing process. A 200 keV energy phosphorus ion implantation with doses of $5 \cdot 10^{14}$ cm^{-2} and $1 \cdot 10^{16}$ cm^{-2} and different annealing steps at 1100°C produced n-layers. A 100 keV phosphorus ion implantation with a dose of $2 \cdot 10^{15}$ cm^{-2} formed the ohmic contact to the substrate and the bottom contact to the ZnO layer. A 550 nm thin ZnO layer was sputtered on a 50 nm thin thermal SiO_2 and annealed. A 100 nm thin Al layer formed the top contact to the ZnO layer.

The final square membrane edge length was 5.35 mm. The thicknesses of the membranes were determined from IR transmission spectra. They were in the range between 5.9 μm and 15 μm. X-ray diffraction spectrum of the annealed ZnO layer showed a well defined preferential [002] orientation. A Michelson interferometer was used for membrane vibration amplitude, frequency and mode determination. The modes were defined as *mxn*, where *m* and *n* are the number of half waves along the membrane edges. The acoustic radiation of the micromechanical UST at a constant AC driving voltage was detected using a *Brüel & Kjaer 4135* condenser microphone with preamplifier 2639. The frequency response characteristic of the microphone was flat within ± 2 dB in the frequency range 4 Hz - 100 kHz with a sensitivity of 3.39 mV/Pa. The measurements were corrected with the free-field correction factor of the microphone. The drop diameter was measured with a phase Doppler anemometer with and without a frequency shift. The experimental set-up with a frequency shift allowed also the determination of the velocity direction. So it was possible to distinguish between flying up drops and

0-8194-2165-0/96/$6.00

the falling down ones.

3. RESULTS AND DISCUSSION

In the studied membrane thickness region the positions of the different vibration modes didn't depend on the membrane thickness. The number of the observed modes depended on the driving voltage. For a sufficiently large bias (typical above 10 V_{pp}), 18 different vibration modes were detected in the vibration frequency region up to 100 kHz. The nodal lines were always parallel to the membrane edges. The behavior of the micromechanical stucture at resonance indicated the existence of a "hard spring" effect, i.e. the membranes were driven into nonlinear vibrations.[4]

3.1 Ultrasonic radiation

The distribution of the axial acoustic radiation pressure normal to the membrane surface for different vibration modes was studied. The pressure field picture of the 1x1 vibration mode was different from that for higher vibration modes (Fig. 1). The measurement points were in a 50 μm distance from each other starting at an initial distance of 0.5 mm from the membrane surface and were omitted in the figure.

For a rectangular piston the position of the last maximum in the pressure fluctuation region, known as near field or Fresnel region z_{FN} is defined as (1)[5]:

$$z_{NF} = \hat{v} \frac{S}{4\lambda_{US}} \qquad (1)$$

Here is S the vibrating membrane surface, λ_{US} - the wave length of the ultrasound in air and the coefficient $\hat{v}$ gives the dependence on the membrane geometry. For a square membrane it is $\hat{v} = 1.37$. In the case under discussion we get $z_{FN} = 0.4$ mm. This result correlates with our measurements for 1x1 vibration mode where no pressure fluctuations were observed. This was an indication that the measurements were taken out of the near field (Fresnel) region. In this approximation for distances much larger than the piston dimensions ($z \gg \sqrt{S}$) the pressure amplitude of the piston $|\vec{p}(z)|$ decreases with the distance from the vibrating surface z as $|\vec{p}(z)| \propto \frac{1}{z}$ in the case of circular waves and as $|\vec{p}(z)| \propto \sqrt{\frac{1}{z}}$ for cylinder waves. For a rectangular piston the pressure amplitude of circular waves in the far field region is (2)[6]:

$$|\vec{p}(z)| = \frac{\omega_m^2 \rho_L l_o S}{2\pi z} \int_S \int \frac{1}{S} \hat{l}(x,y)\, dx\, dy \qquad (2)$$

Here ω_m denotes the circular vibration frequency of the membrane with vibration amplitude l_o and normalized mode shape $\hat{l}(x,y)$, ρ_L is the air density. We denoted the coefficients for the integral in (Eq. 2) as M and for the 1x1 vibration mode M = 0.0195 Nm^{-1}. The measurements were fitted with the functions $|\vec{p}(z)| \propto \frac{1}{z}$ and $|\vec{p}(z)| \propto z^e$ (Fig. 2). In the case of 1x1 vibration mode it was not possible to take measurements at distances larger than 10.5 mm because the sound pressure level was already low and comparable with the noise level. The

best fitting to our measurement points were found for $\varepsilon = -0.69 \simeq -2/3$. It is obvious that the Fraunhofer approximation for circular waves is not valid for distances smaller than two times the membrane edge length.

The radiation pressure of the higher vibration modes was considerably larger than that from the fundamental one because of their larger vibration amplitudes. The higher vibration modes can be divided into two groups depending on the larger structure edge length determined by the nodal lines. The modes 3x*n* (3x3, 3x4 and 3x5) belong to the first one with a structure edge length of 5.35/3 = 1.78 mm. There is only one member of the second group - the 4x5 vibration mode with a structure edge length of 1.34 mm. The observed fluctuations of the radiation pressure outside of the region right after the vibration membrane were periodic (Fig. 1). For the 4x5 mode there was an excellent coincidence between the measurement and the function $|\vec{p}(z)| \propto \frac{1}{z}$ in the whole region. The modes from the 3x*n* group coincided with the function at distances larger than 10 mm. This result indicates that the Fraunhofer approximation of the piston theory can be applied to structures which surfaces don't vibrate with uniform phase and amplitude.

The vibration amplitude of the membrane was correlated to the generated radiation pressure in a distance of 0.5 mm from the membrane (Fig. 3). The correlation between the sound pressure at some point and the displacement of an air particle $|\vec{\xi}|$ is given by[5]:

$$|\vec{p}| = Z\omega_m|\vec{\xi}| \qquad (3)$$

The coefficient Z is the acoustic impedance of air (Z = 411.5 $kgm^{-2}s$ at 20°C). The particle displacement is an indirect function of the membrane vibration amplitude. Because of the interference picture the different modes manifested different radiation efficiency at equal vibration amplitudes.

3.2 Liquid nebulization

The influence of liquid layers on the membrane vibration was studied. Suitable are liquids with low enough surface tension - it allows the formation of a thin layer over the membrane. The nebulization of solutions containing alcohol is of great interest for technical and medical application. Therefor, n-isopropyl alcohol was used as a test liquid ($2.378 \cdot 10^{-2}$ N/m surface tension).

The nebulization processes at a membrane vibration frequency of 86.5 kHz was studied. According to the capillary wave theory the frequency of the induced capillary waves was two times smaller than the membrane frequency and was equal to 43 kHz. The measurements without a frequency shift gave a drop distribution with a second peak al larger diameters. Because the position of the two distribution peaks was symmetrical to the middle point of the measurement cycle it was assumed that the second peak was introduced by falling down drops. The measurements with a frequency shift confirmed this assumption (Fig 4). At a 2 mm distance from the vibrating surface the median diameter of the drop distribution was 17 μm. This value correlates with the predicted one from the capillary wave theory (15.9 μm) if the proportionality constant 0.34 between the median drop diameter and the capillary wave length is used[7,8].

The nebulization process was associated with a specific sound which assumes the existance of "hard" cavitation in the liquid. The onset of "hard" cavitation depends on the liquid properties, ultrasonic frequency and pressure amplitude. In the present case pressure amplitudes above 0.1 MPa should be necessary[9]. The pressure distribution measurements indicated that the pressure in the vicinity of the vibrating membrane was well above

this limit (Fig. 1). The pressure fluctuations resulted in a fluid film thichness dependent nebulization rate. An integral value of 36 µl/min over a liquid film thickness of 140 µm was determined. This value will be larger under optimal film thickness controll, for example with a precise micropump. The power consumption of the UST was about 0.2 W.

4. CONCLUSIONS

A micromechanical ulrtasonic transducer with thin silicon membrane was studied. Thin silicon membranes who are driven in nonlinear vibrations posses a lot of vibration modes with large vibration amplitudes. Higher vibration modes are more efficient in ultrasonic radiation than the fundamental one. In the far field region the radiation pressure amplitude decreases with the distance from the vibrating membrane as $\propto\frac{1}{z}$. The micromechanical ultrasonic transducer was applied for liquid nebulization. The nebulization prosess was associated with "hard" cavitation. The observed drop distribution correlated with the capillary wave theory.

5. ACKNOWLEDGMENTS

The financial support by the German Academic Exchange Service (DAAD) for this work is deeply appreciated. The author wish to thank P. Volkholz for the phase Doppler anemometer measurements and for the helpful discussions.

6. REFERENCES

1. W.-D. Drews, Liquid nebulization with ultrasound, *Elektronik*, 10 (1979) pp. 83-86, (in German).

2. H.-J. Roscher, K. Wolf, "Piezoelectric liquid nebulizer", *Wiss. Zeitschrift der Hochschule K.-M.-Stadt, 26 (1984) pp. 560-563*, (in German).

3. M. Kukosawa, T.Watanabe and T. Higuchi, "Surface acoustic wave atomizer with pumping effect", *Proc. 8th IEEE International Workshop on Micro Electro Mechanical Systems, Amsterdam, The Netherlands, Jan. 30 - Feb. 2, 1995, pp. 25-30.*

4. R. Paneva, G. Temmel and H. Ryssel, "Ultrasonic transducer with silicon - a well known material with new applications", *Sensors and Actuators A*, 50 (1996) pp. 1-4.

5. J. Krautkrämer and H. Krautkrämer, *Werkstoffprüfung mit Ultraschall*, p. 82, Springer-Verlag, Berlin, 1986.

6. O. Brand, *Micromachined Resonators For Ultrasound Based Proximity Sensing*, PhD Thesis, Physical Electronics Laboratory, ETH Zurich, No. 10896, 1994, p. 39.

7. J.A. Rooney and K.S. Suslick (ed.), *Ultrasound*, VCH Publishers, New York, 1988, Ch. 2, pp. 77-78.

8. Y. Mizutani and Y. Uga, "An Investigation on Ultrasonic Atomization", *Bulletin of the JSME*, 15 (1972) pp. 620-627.

9. H. Kuttruff, *Physik und Technik des Ultraschalls*, S. Hirzel Verlag, Stuttgart, 1988, Ch. 12.

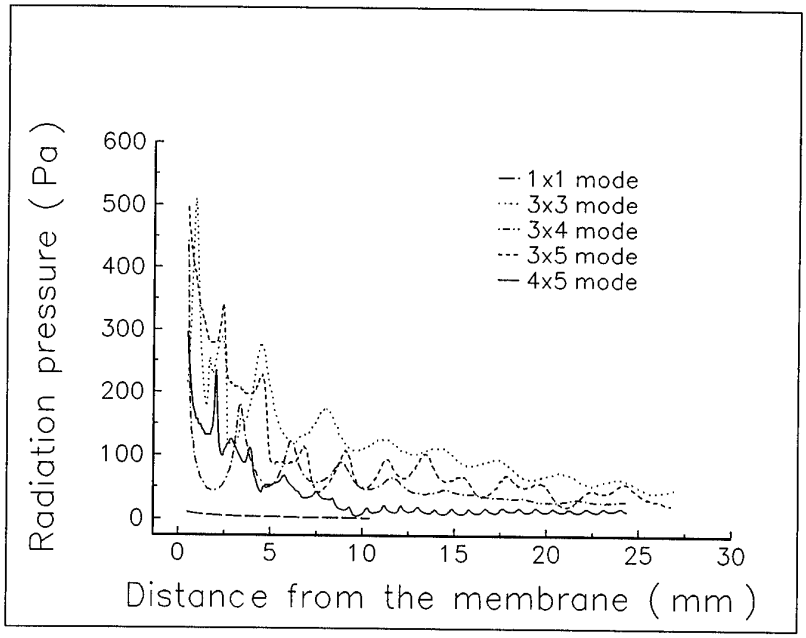


Fig. 1 Radiation pressure amplitude at constant AC driving bias for different vibrations modes.

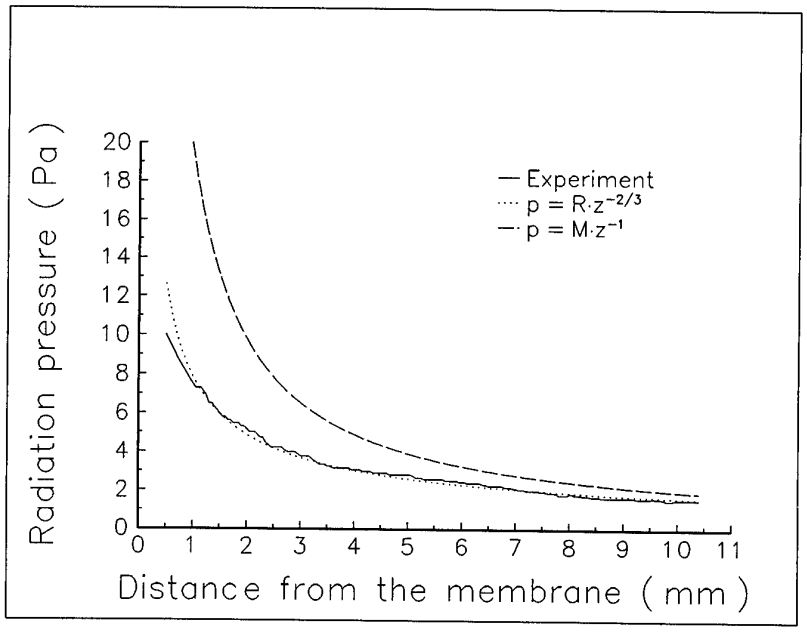


Fig. 2 Radiation pressure distribution of the fundamental vibration mode ($R = 0.0683\ Nm^{-3/4}$, $M = 0.0195\ Nm^{-1}$).

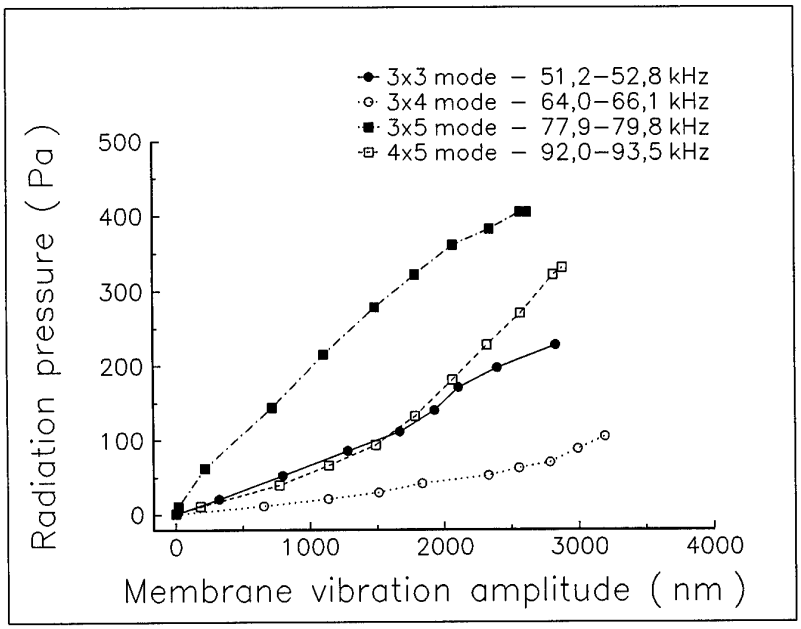


Fig. 3 Correlation between the vibration amplitude and the generated radiation pressure. The measurements were taken in the resonance region at constant AC bias. The resonance vibration frequency region for each mode is indicated.

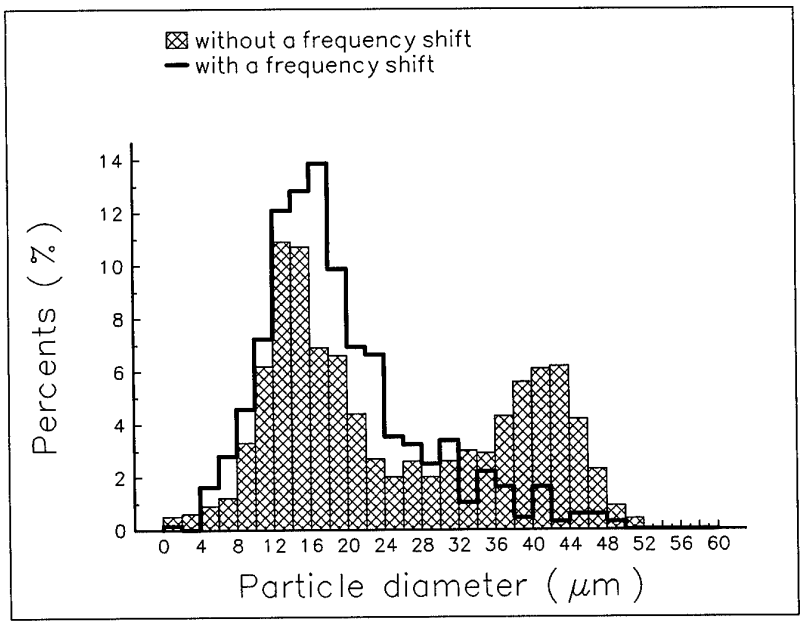


Fig. 4 Phase Doppler anenometer data of a n-isopropyl alcohol nebulization process at 86.5 kHz membrane vibration frequency.

Two-dimensional (x-y) actuator using multimode degeneration of a piezoelectric ring vibrator

Takehiro Takano, [1]Yoshiro Tomikawa, [1]Hidetoshi Hata and [1]Seiji Hirose

Department of Communication Engineering, Tohoku Institute of Technology, Sendai, Miyagi 982 Japan
[1]Department of Electrical and Information Engineering, Faculty of Engineering, Yamagata University, Yonezawa, Yamagata 992 Japan

ABSTRACT

This paper deals with a two-dimensional (x-y) actuator using multrimode degeneration of bending vibrations - B_{21}, B_{21}' modes - and a radial vibration - (R,1) mode - excited in a piezoelectric ring vibrator. This actuator is aimed for not so large movement such as the one of a camera lens. The operating principle and the driving methods for movements of the actuator are presented. Degeneration conditions of the modes are considered by applying F.E.M., and the construction and characteristics of a prototype actuator are shown. It was found that the two dimensional (x-y) actuator can be made possible using the multimode ring vibrator proposed here.

1. INTRODUCTION

Many kinds of ultrasonic motors and piezoelectric actuators have been investigated and the constructions and characteristics have been proposed.[1] Some of them have been put into practical application up to the present.[2,3] However, most of them are rotary and linear type ones moving in one-dimensional direction. This paper deals with a two-dimensional actuator using multimode degeneration of two bending vibrations - B_{21}, B_{21}' modes - and a radial vibration - (R,1) mode - excited in a piezoelectric ring vibrator.[4] First, we present the operating principle of the actuator. The (x-y) movement is given by combinations of linear and rotary movements of the actuator. The linear movement is produced by using two degeneration modes of B_{21}, B_{21}' and (R,1) modes, and the rotary movement is produced by using two orthogonal degeneration B_{21} and B_{21}' modes. The degeneration condition for resonance frequencies of these modes is determined by applying F.E.M. On the basis of the analysis, we made a two-dimensional actuator using a piezoelectric ring vibrator on an experimental basis and measured characteristics of linear and rotary movements of the prototype actuator.

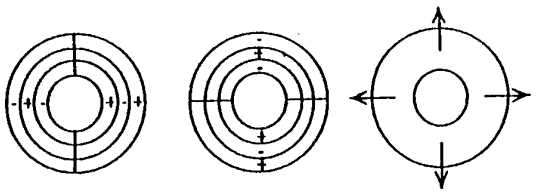
2. OPERATING PRINCIPLE

2.1 Operation of linear movement

Vibration modes used in this study are shown in Fig.1, where B_{21} and B_{21}' modes (in general, B_{nm} mode, where the subscripts n and m denote the number of nodal circle and nodal diameter respectively) are degeneration modes of bending vibration with the same form. (R,1) mode (in general, (R,n) mode, where n denotes harmonic number of the vibration) is a radial vibration with symmetric vibration displacement in radial direction.

It is well-known that a combination of two modes with vibration displacements perpendicular to each other forms elliptical motions of displacement.[1] In the case of the combination of B_{21} mode and (R,1) mode, the elliptical motions are formed on the surface of vibrator as shown in Fig.2. That is, the motions bring linear movement of the vibrator in left and right directions on this paper. On the other hand, the motions formed by the combination of B_{21}' mode and (R,1) mode bring the linear movement in up and down direction.

0-8194-2165-0/96/$6.00



(a) B_{21} mode (b) B_{21}' mode (c) (R,1) mode

Fig.1 Vibration modes used for construction of the actuator.

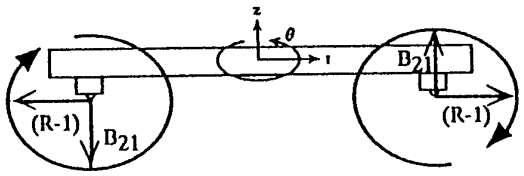


Fig.2 Elliptical motions of displacement formed by B_{21} and (R,1) modes.

2.2 Operation of rotary movement

It is well-known phenomenon that a particle moves elliptically at the surface of a flexural vibrating disk which has two resonance modes of the same form.[2] For degenerate modes as shown in Figs.1(a) and 1(b), each mode can be independently excited by two electrical input signals with a phase different of 90°, i.e. sin ω t and cos ω t. The elliptical motion of displacement occurs on the surface and the motion brings a rotary movement of the vibrator. A movement of the vibrator in circumferential direction is provided by the rotary movement and movements of the vibrator in diameter direction are provided by the linear movement mentioned above. It is expected that the combination of both movements will enable the vibrator to move in arbitrary direction.

2.3 Driving methods and elliptical motion of displacement

Electrode of a piezoceramics used in the experiment are divided in four parts and input signals are applied in each electrode as shown in Fig.3, where Figs.3(a) and (b) show the driving methods for linear movement and Fig.3(c) shows the method for rotary movement. In the case of Fig.3(a), the two vibrations, B_{21} and (R,1) modes, are excited simultaneously by two input signals. The composition of the two displacements due to the two input signals for B_{21} and (R,1) modes are obtained as follows.

1. at point P_1 shown in Fig.4(a),

$$u_z = u_{B21}\sin(\omega t) - u_{B21}\cos(\omega t) = -\sqrt{2}\,u_{B21}\cos\left(\omega t + \frac{\pi}{4}\right) \quad (1)$$

$$u_r = u_{(R\text{-}1)}\sin(\omega t) + u_{(R\text{-}1)}\cos(\omega t) = \sqrt{2}\,u_{(R\text{-}1)}\sin\left(\omega t + \frac{\pi}{4}\right) \quad (2)$$

2. at point P_2,

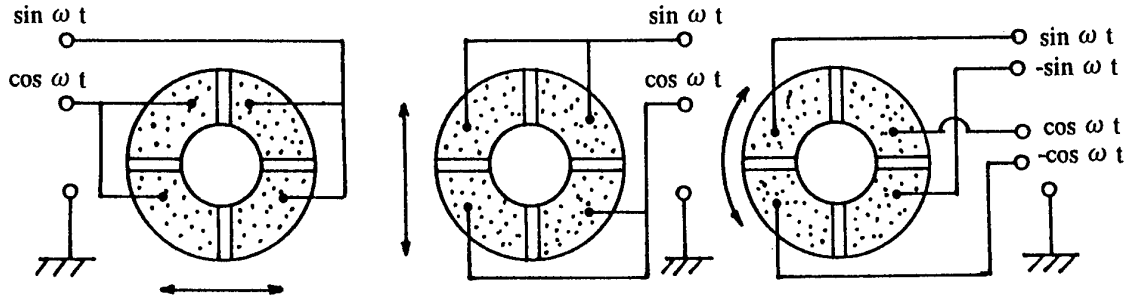
$$u_z = -u_{B21}\{\sin(\omega t) - \cos(\omega t)\} = \sqrt{2}\,u_{B21}\cos\left(\omega t + \frac{\pi}{4}\right) \quad (3)$$

$$u_r = u_{(R\text{-}1)}\{\sin(\omega t) + \cos(\omega t)\} = \sqrt{2}\,u_{(R\text{-}1)}\sin\left(\omega t + \frac{\pi}{4}\right) \quad (4)$$

where u_{B21} and $u_{(R,1)}$ represent the mode function of B_{21} and (R,1) vibrations respectively. Hence, from Eqs.(1)~(4), Eq.(5) is derived at points P_1 and P_2.

$$\left(\frac{u_z}{\sqrt{2}\,u_{B21}}\right)^2 + \left(\frac{u_r}{\sqrt{2}\,u_{R\text{-}1}}\right)^2 = 1 \quad (5)$$

That is, the same elliptic motions are formed at these points and the linear movements in the same direction are obtained.



(a) B_{21} and (R,1) modes (b) B_{21} ' and (R,1) modes (c) B_{21} and B_{21} 'modes

Fig.3 Driving methods for linear movements and rotary movement (⟷ : Moving direction).

3. F.E.M. ANALYSIS

The finite element method (F.E.M.) was used for vibration analysis of a piezoceramics vibrator.[4] Table1 and Table 2 show material constants of piezoceramics and metal disk used in the analysis. The metal disk is made of stainless steel. Figures4(a) and 4(b) show the simulated results of B_{21} and (R,1) mode patterns respectively. B_{21}' vibration mode is an orthogonal one to B_{21} mode with the same form.

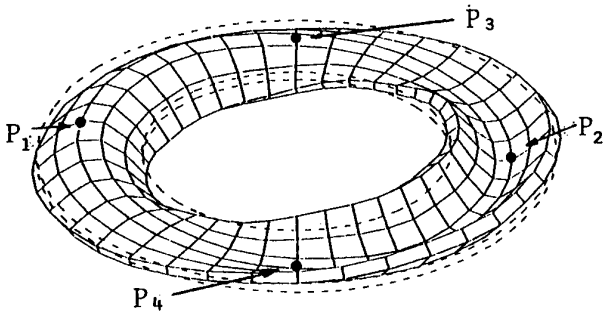
Next, we calculated resonance frequencies of B_{21} and (R,1) modes to realize the degenerate state for these modes. Simulated resonance frequencies are shown in Fig.5, for a ring vibrator of outer diameter 2a=50mm and thickness t=2mm, as a function of diameter ratio b/a (2b:inner diameter). From these results, it is seen that the resonance frequency of B_{21} mode is increased and the one of (R,1) mode is reduced by increasing the diameter ratio b/a. Hence, it is possible to make these modes degenerate easily to each other by changing the ratio b/a. In this simulate, the ratio was b/a=0.45. In Fig.6, simulated frequencies of a ring vibrator with outer diameter 2a=50mm and inner diameter 2b=30mm, are shown , as a function of the thickness. In this case, these modes degenerate to each other when the thickness is t=0.88mm. Then the resonance frequency was about 32 kHz. The ring vibrator used in following experiment was prepared on the basis of the later simulated result.

Table 1 Material constants of piezoceramics.
(Fuji ceramics: C-213)

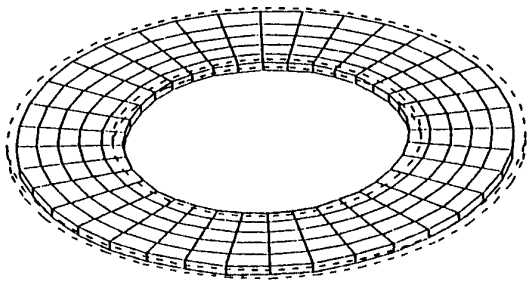
	Symbol	Unit	
C^E constants	C_{11}^E	N/m^2	16.7×10^{10}
	C_{12}^E		10.5×10^{10}
	C_{13}^E		11.0×10^{10}
	C_{33}^E		15.4×10^{10}
	C_{44}^E		2.5×10^{10}
	C_{66}^E		3.1×10^{10}
e constants	e_{31}	C/m^2	-2.2
	e_{33}		19.2
	e_{15}		13.5
ε constants	$\varepsilon_{11}^S/\varepsilon_0$		735
	$\varepsilon_{33}^S/\varepsilon_0$		732
Poisson's ratio	σ^E		0.29
Density	ρ	kg/m^3	7.8×10^3

Table 2 Material constants of metal disk.
(Stainless steel)

	Symbol	Unit	
C constants	$C_{11}\sim C_{33}$	N/m^2	26.5×10^{10}
	$C_{12}=C_{13}$		10.5×10^{10}
	$C_{44}\sim C_{66}$		8.03×10^{10}
Poisson's ratio	σ		0.283
Density	ρ	kg/m^3	7.7×10^3



(a) B_{21} mode.



(b) (R,1) mode.

Fig.4 Vibration modes obtained by F.E.M.

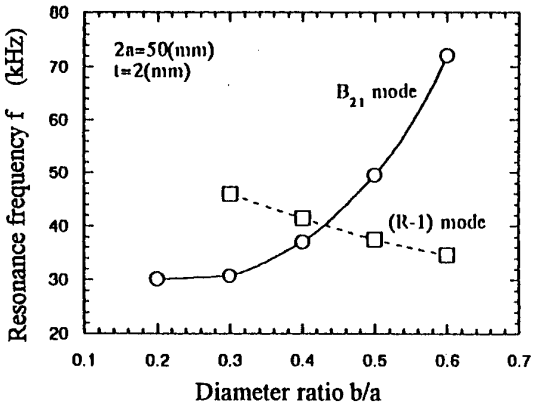


Fig.5 Simulated frequencies as a function of b/a.

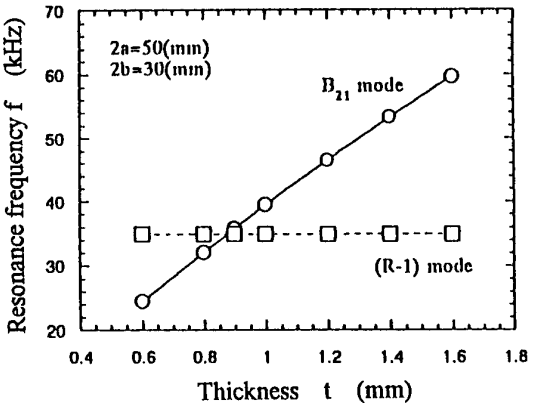


Fig.6 Simulated frequencies as a function of thickness.

4. CONSTRUCTION OF ACTUATOR

Construction of a two dimensional (x-y) actuator is shown in Fig.7. A piezoceramics ring is bonded to a stainless steel ring and the electrode of the piezoceramics ring is deviled into four parts as shown in the Figure. The dimensions of the prototype actuator are 50.0mm in outer diameter, 29.0mm in inner diameter (b/a=0.58) and 0.88mm in thickness. On the back surface of the vibrator, silicon nitride balls(diameter 1.0mm) to take mechanical driving forces are installed at points P_1,P_2,P_3 and P_4 (see Fig.4) where are vibration loop points of B_{21} and B_{21}' modes as shown in Fig.4. The balls are in contact with a base plate made of iron. That is, the vibrator is to move around in arbitrary direction on the plate.

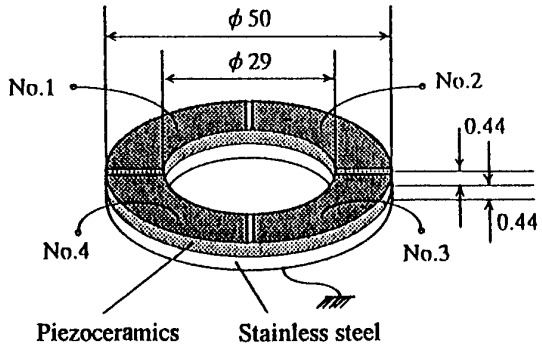


Fig.7 Construction of two dimensional (x-y) actuator.

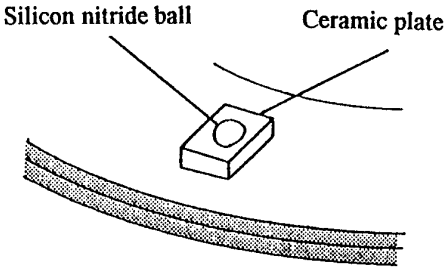


Fig.8 Contact apparatus of the actuator.

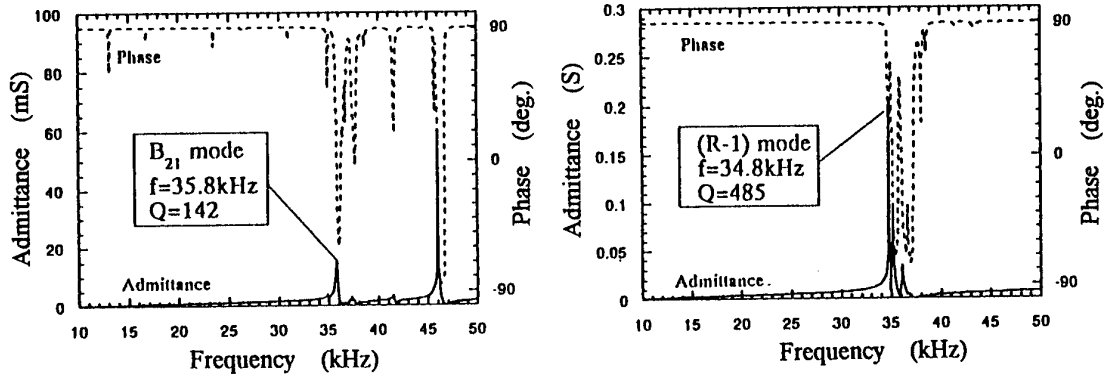
5. EXPERIMENTAL RESULTS

5.1 Admittance characteristics of the vibrator

Figures9(a) and 9(b) show admittance characteristics of B_{21} and (R,1) modes of the vibrator. Resonance frequencies of B_{21} and (R,1) modes are 35.8 kHz and 34.8 kHz, and quality factor Q are 142 and 485 respectively. It is considered that these frequencies are sufficiently close to each other.

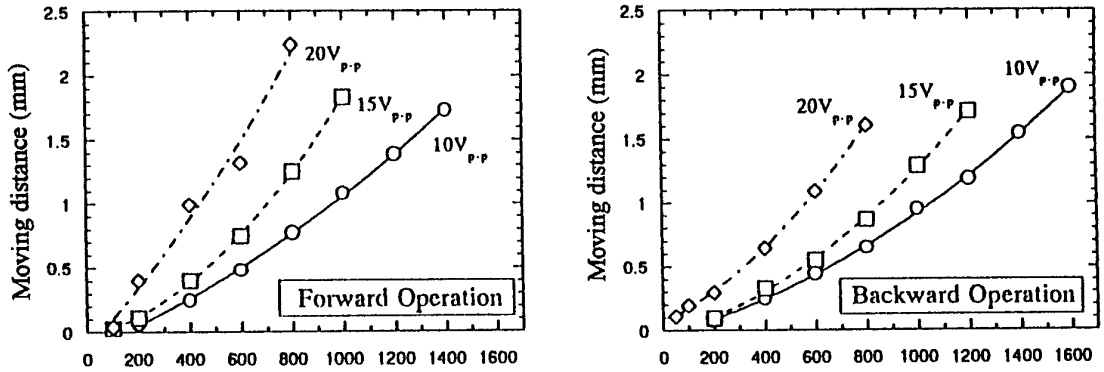
5.2 Moving characteristics of a prototype actuator

Characteristics of linear movements of the prototype actuator are shown in Figs.10(a) and 10(b). The driving method of Fig.3(a) is adopted and driving frequency is 34 kHz. Moving distance is measured as a function of number of input pulse. Almost the same characteristics were obtained in forward and backward operations. However, it was seen that the operations became unstable as the input voltage is higher. Figuere11(a) and 11(b) show characteristics of rotary movement of the prototype actuator. The driving method of Fig.3(c) is adopted and rotating angle was measured as a function of number of input pulse. Driving frequency is 36.5 kHz. It is seen that the rotating angle increases in proportional to the number of input pulse in the region of the angle 0~30 degree.



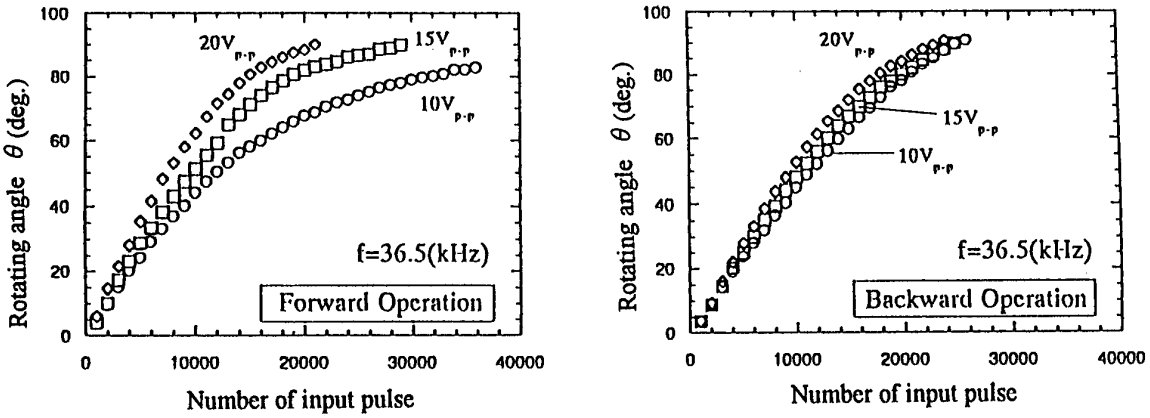
(a) B_{21} mode. (b) (R-1) mode.

Fig.9 Measured admittance characteristics of the prototype actuator shown in Fig.7.



(a) Forward operation (b) Backward operation

Fig.10 Linear movement characteristics of the prototype actuator.



(a) Forward operation
No.1: sin wave, No.2: cos wave
No.3:-sin wave, No.4:-cos wave

(b) Backward operation
No.1: cos wave, No.2: sin wave
No.3: -cos wave, No.4:-cos wave

Fig. 11 Rotating movement characteristics of the prototype actuator.

6. CONCLUSIONS

We have investigated a two dimensional (x-y) actuator using a piezoelectric ring vibrator, and showed the construction and characteristics of linear and rotary movements of a prototype actuator experimentally. It was found the actuator proposed here exhibits satisfactory characteristics as a two dimensional actuator. However, there were such problems as slight scattering of moving distance in linear movement and rotating angle in rotary one. Hereafter, it will be necessary to study further the suitable contact state between the vibrator and the base plate. Also F.E.M. analysis considering supporting apparatus of silicon nitride balls must be tried in order to realize more proper degenerate state of two resonance frequencies.

7. REFERENCES

1. S.Ueha and Y.Tomikawa:"Ultrasonic motors - Theory and Applications", Oxford science publications, Clarendon press, Oxford, pp.8-34 1993.

2. T.Kenjo and T.Sashida:"Ultrasonic Motors - Theory and Design - ", Chapters5-7, Clarendn Press, Oxford 1993.

3. T.Maeno, T.Tsukimoto and A.Miyake:"The Contact mechanism of an Ultrasonic Motor", Proceedings of IEEE International Symposium on Applications of Ferroelectrics, pp.535-538 1990.

4. H.Hata, y.tomikawa, S.Hirose and T.Takano:"A Two Dimensional (x-y) Actuator Using Multi-Mode Degeneration of a Piezoelectric Ring Vibrator", In Technical Report of IEICE Japan, US95-40 Sept. 1995 [in Japanese].

Estimation of available performances of ultrasonic motors

Lionel Petit, Laurent Lebrun, Roland Briot and Paul Gonnard

Laboratoire de Génie Electrique et Ferroélectricité
Institut National des Sciences Appliquées de Lyon
Bât. 504, 20 avenue Albert Einstein, 696621 Villeurbanne Cedex, France

ABSTRACT

Ultrasonic motors have very interesting features as high torque at low speed and low inertia. The principle of such motors is based on a double energy conversion. This paper deals with the measurements required to characterize these conversions. Experimental results on some structures investigated in our laboratory are proposed.

1. INTRODUCTION

Ultrasonic motors which use mechanical vibration have important features with the following advantages: high torque and high power at low speed without gears, quiet operation, high starting torque, low inertia, non electromagnetic noise, and no magnetic field [1]. The principle of such motors is based on a double energy conversion :
(i) Electromechanical conversion :
The piezoelectric material converts electrical energy into mechanical vibrations. These vibrations cause the elliptical displacement motion of the surface particles of the stator.
(ii) Mechanical conversion :
A rotor pressed on this vibrating surface, moves due to the frictional forces at the interface.

Hence, depending on the method of forming elliptical motion, various types of motors can be constructed.
Two examples investigated in our laboratory are simply recalled :
(i) Hybrid Transducer Ultrasonic Motors (HTUM)
Two resonators generate two orthogonal mechanical vibrations which are in phase quadrature.
(ii) Travelling Wave Ultrasonic Motors (TWUM)
Progressive wave is created in the stator and causes elliptic motion.
Two motors of this type are reported in the litterature : One using a progressive flexural wave induces in a circular plate [2] and the other using the non axisymetric vibration of an ceramic ring [3, 4].

In the first paragraph, electromechanical equivalent circuit of a free stator and the parameters needful to characterize the first conversion defined above are reminded. The two following paragraphs deal with the electrical and acoustical measurements of these parameters. Finally, the mechanical conversion is estimated through measurements described in the last paragraph. Experimental results illustrate these different designations along the paper.

2. EQUIVALENT CIRCUIT

The fundamental equations of electromechanical transformation for a piezoelectric transducer are used. They give the relation between the terminal voltage V and current I, the mechanical force F and the vibration velocity $\dot{u}$ (eqs1).

$$I = -N\dot{u} + j\omega C_b V \quad \text{and} \quad F = NV + Z_m \dot{u} \qquad (1)$$

where ω is the angular frequency, Cb the clamped capacitance, N the force factor and Z_m the mechanical impedance under constant electric field conditions.
When two mechanical ends are free a piezoelectric transducer can be approximated near its series resonance frequency by a Mason's equivalent circuit shown in figure 1, in which in the electromechanical conversion is represented by a transformer.

0-8194-2165-0/96/$6.00

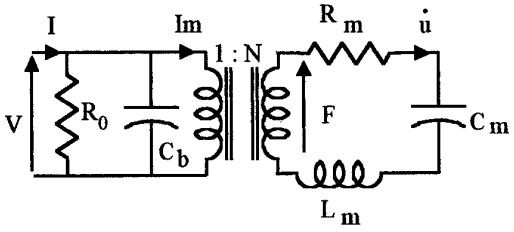


Figure 1.
Mason's electromechanical equivalent circuit
(two mechanical ends free)

In figure 1, I_m is called the motional current and R_m, L_m, C_m represent the mechanical losses, the vibrating mass and the compliance of the system respectively. R_o represents the dielectric losses.
The electromechanical turn ratio or force factor N is given by :

$$N = \frac{I_m}{\dot{u}} = \frac{F}{V} \qquad (2)$$

The circuit of figure 1 can be transformed into the equivalent circuit of figure 2.

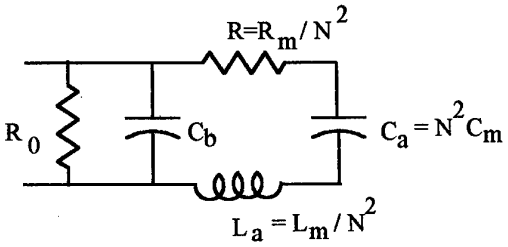


Figure 2.
Electromechanical equivalent circuit
under constant electric field
(two mechanical ends free)

Important parameters can be calculated from this equivalent circuit around series resonance $f_m = \frac{1}{2\pi\sqrt{L_m C_m}}$:

(i) Quality factor $Q_m = \frac{1}{R}\sqrt{\frac{L_a}{C_a}}$ corresponding to the mechanical internal losses at the stator.

(ii) Electromechanical dynamic coupling factor $k = \sqrt{\frac{C_a}{C_a + C_b}}$ which represents the electromechanical conversion ratio i.e. the ratio of energy stored in mechanical form to the total electrical energy provided by the source.
Q_m and k must be higher as possible to obtain low mechanical losses and high electromechanical conversion.
Moreover, the vibrating velocity $\dot{u}$, when the motor is driven near its series resonance can be expressed by :

$$\dot{u} = N\frac{V}{R_m} \quad \text{where} \quad N = k\sqrt{\frac{C_{LF}}{C_m}}$$

with $C_{LF} = C_a + C_b$ and $C_a = k^2 C_{LF}$

and finally : $\dot{u} = kQ_m\sqrt{\frac{C_{LF}}{C_m}}.V \qquad (3)$

From equation (3), it follows that $\dot{u}$ is directly proportional to k.Qm product.

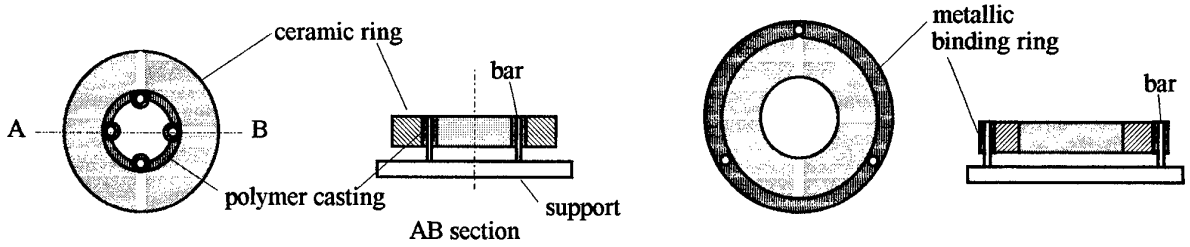
3. ELECTRICAL MEASUREMENTS

In order to determine the values of the electrical equivalent circuit parameters (C_b ,C_a, R et L_a) and consequently calculate k, Qm and ù the admittance is measured in terms of frequencies with the help of a HP network analyser (HP4194A), around a resonance frequency of the stator.
Because the mechanical performances (speed, torque) are directly linked to the value of the vibrating velocity, these measurements are very useful for the design and evaluation of stators. Some examples of different steps in stator design are given below:
(i) influence of the ceramic-to-metal bonding
A stator of a TWUM consists of a piezoelectric ceramic ring bonded on a metal annular plate. The employed adhesive and the bond method must satisfy distinct requirements (strong bond, thin film,...) to obtain high-capacity stator. The results obtained with two stators using different adhesive are reported in table 1. If the characteristics of stator 1 are satisfying, stator 2 is not conforming to the specify requirements.

	f_s (kHz)	R Ω	L_a mH	C_a pF	C_b pF	k (%)	Q_m
Stator 1	49.800	97	240	43.3	4850	9.4	770
Stator 2	49.015	962	506	20.7	5810	5.9	162

Table 1

(ii) influence of the stator support
A stator using non axisymetric vibration mode of a ring ceramic is shown in figure 3. In order to select the better method to hold it, several supports had been tested. The results obtained with a polymer central casting as illustrated in figure 3a are summarized in the third column of Table 2. The increase of mechanical losses (R) due to the polymer damping shows that this support method is not satisfying. Another solution consists of using a metallic binding ring (figure 3b) : The increase of losses is less significant and that support is utilizable.



a) b)

Figure 3. Non axisymetric stator and tested supports

	Ceramic ring without support	Ceramic with polymer casting	Ceramic with binding ring
f_s (kHz)	37,7	37,4	40.03
R (Ω)	59	700	200
k (%)	23.3	19,5	11
Q_m	1030	160	1120

Table 2

4. L.D.V. MEASUREMENTS

A complete automatic measurement unit (figure 4) built around a Laser Doppler Vibrometer (L.D.V.) has been developed in the laboratory [5]. This non contact measurement technique permits to obtain experimental value of the particular velocity (or displacement) of the vibrating surface.

These measurements allow :

(i) Confirmation of the theoretical behaviour of the transducer.

(ii) Identification of vibration mode and detection of parasite vibration mode of the transducer.

(iii) Computation of the force factor N by equation (2).

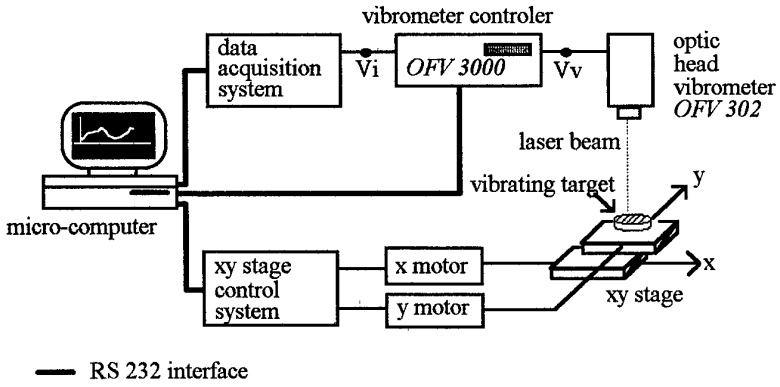


Figure 4.
The principle of the measurement system

Two applications are investigated here : a free stator of a TWUM and a monoelement transducer vibrating along its shearing mode.

The results obtained with the former example are shown in figure 5 where the curves represent the absolute value of the normal displacement $|\dot{u}_z|$.Each standing wave (mode number n = 3) appears when the corresponding electrical port is powered. The simultaneous supply of the two electrical ports induces the progressive wave.

Without going into further detail, here is simply reminded that the sum of 2 standing waves shifted in space of $\lambda/4$ and in time of $\pi/2$ provides a travelling flexural wave which generates a particular elliptic movement on surface of the stator.

Satisfactory stators cannot be made unless the presence of these 2 standing waves, around the same frequency with similar amplitude in order to reduce the standing wave ratio (SWR).

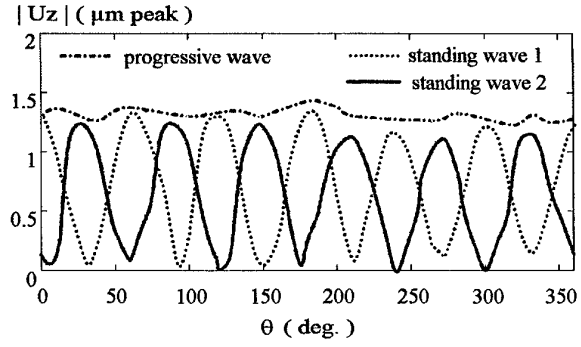


Figure 5.
Standing and travelling waves on a TWUM along the stator periphery.

With the later example, the detection of an unwanted vibration mode is obtained on a monoelement transducer (figure 6). This type of transducer can be used in multimode motors.

For example, a thickness-shearing motor uses 2 transducers-one vibrating along its thickness mode and the other along its shearing mode at the same frequency-coupled mechanically. Before building a complete motor, the shearing monoelement described has been tested and the desired behaviour provides a vibration of the 2 masses in opposite phase, as shown in figure 6 (a). Although the shearing phenomenon is confirmed, we observed a parasite vibration of face 3 (figure 7).

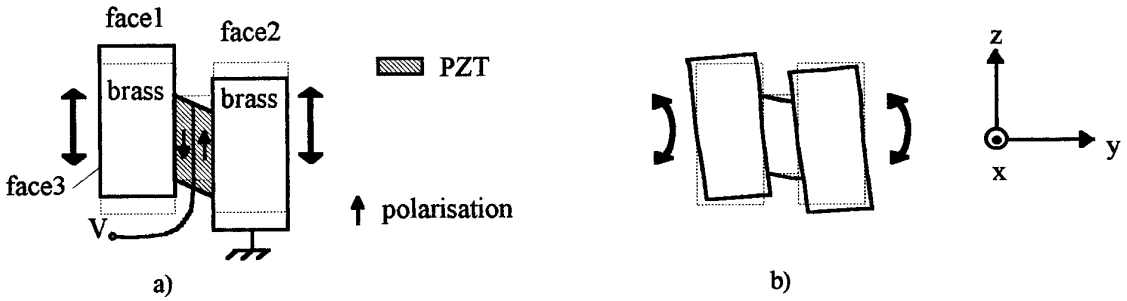


Figure 6 : The shearing transducer. Desired behaviour (a) and real vibrating behaviour (b)

The real vibrating behaviour of the transducer (shown in figure 6b) leading to a decrease of the contact area with the rotor.

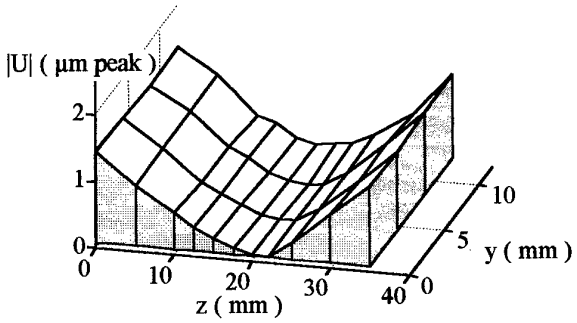


Figure 7.
Normal component of the vibration amplitude of face 3

5. TORQUE/SPEED CHARACTERISTIC AND TEMPERATURE MEASUREMENTS

In order to characterize the whole motor, a speed/torque measurement unit is used. The rotation speed (N) in term of the torque of the motor (Γ) is plotted. The mechanical power (P) and the efficiency (η) are calculated.
An infrared pyrometer is used for temperature measurements.
Here is an example of the motor using a (1,1) non axisymmetric mode depicted in figure 3b. The rotor is made of multi roller rings contacting the external surface of the stator (figure 8) with a total static stress around two hundreds Newtons.

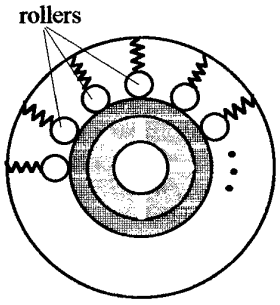


Figure 8
Principle of the multi rollers rings type rotor

The mechanical characteristics are given in figure 9 and the overheating of the rotor at the maximum efficiency point is plotted in figure 10

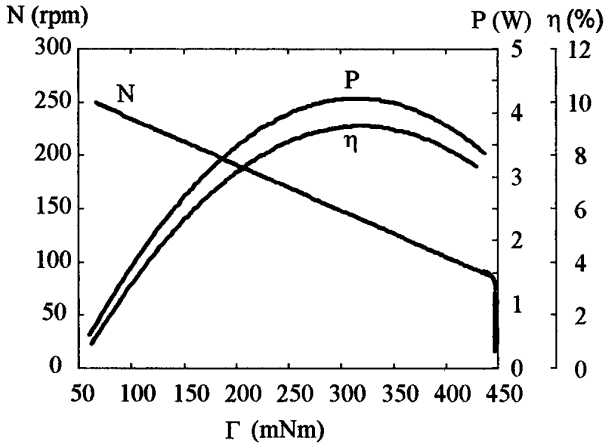


Figure 9: Mechanical characteristics as a function of loading torque

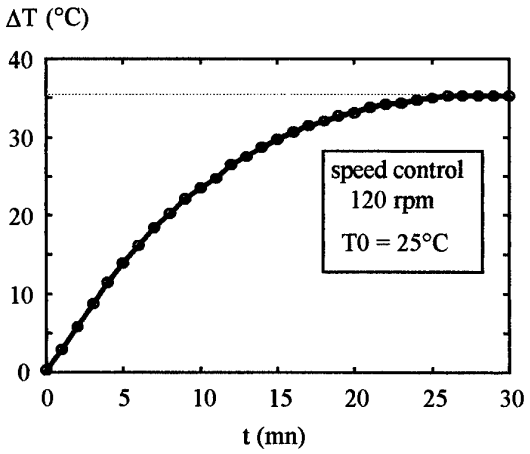


Figure 10: Overheating as a function of time at maximum effective power

6. CONCLUSION

A complete measurement technique based on electrical measurements, Laser Doppler Vibrometry technique, torque/speed characteristics and temperature measurement to characterize ultrasonic motor has been proposed. With the help of experimental results, we have shown that these techniques are very useful to design motors. Electrical measurements permit to confirm the viability of a free stator and provide its mechanical performances. The L.D.V. technique allows the identification of vibration mode and detection of an eventual unwanted vibration. And finally, the on-load properties of the complete motor are obtained with the help of a torque/speed measurement unit.

7.ACKNOWLEDGEMENTS

This work is supported by the French "Ministère de la Recherche et de l' Enseignement Supérieur" and the "Région Rhône-Alpes".

8. REFERENCES

1. VEMA S., TOMIKAWA Y., "Ultrasonic Motors , Theory and applications", Clarendon Press, OXFORD, 1993.
2. SASHIDA T., KENJO T., "An introduction to ultrasonic motors", Clarendon Press, OXFORD, 1993.
3. TAKANO T., TOMIKAWA Y. OGASAWARA T. and KIRATA H., "Japan J. Appl. Phys., 28-2, 202, 1993.
4. LEBRUN L., PETIT L. and GONNARD P., "Piezoelectric motor using a (1,1) non axisymetric mode," Ultrasonics international' 95, Edimbourgh.
5.GUILLEMOT-AMADEI M.M., PETIT L., LEBRUN L., BRIOT R. and GONNARD P.,"A non contact measurement technique for piezoelectric transducers," Meas. Sc. and Tech., 6, 458, 1995.

A new multi-mode piezoelectric motor

F. Claeyssen*, R. LeLetty*, L. Chouteau*, N. Lhermet*, L. Petit**, R. Briot**, P. Gonnard**

* Cedrat Recherche Comp., ZIRST 4301, F38943 Meylan
** Lab.Génie Elec. and Ferroelectrics., I.N.S.A., bat. 504, F69621 Villeurbanne

ABSTRACT

A new structure of a multi-mode piezoelectric motor is proposed and uses two longitudinal actuators and a mechanical coupler. The basic principle is first presented and the corresponding modelling based on numerical tools and electromechanical circuits is performed to design a first prototype. Preliminary measurements indicates the reliability of the principle, a good agreement with predictions and interesting motor performances.

1. INTRODUCTION

Various structures of piezoelectric motors have been studied intensively [1]. Among them, multi-mode motors use a combination of vibration modes to produce elliptic motion of the contact surface that drive the rotor by friction. However, a lot of these structures use flexural modes of the piezoceramics and are thus strongly stress-limited [2]. These motors have been studied to provide linear forwarding devices [3]. The purpose of this paper is to describe a new structure that removes these limitations.

2. BASIC PRINCIPLE

It is based on two longitudinal pre-stressed actuators and a mechanical coupler that amplifies the vibration in the normal direction (figure 1). This structure has two modes : a translation mode of the coupler occurs when the actuators are excited in opposition. Alternatively, since the actuators are both excited, the coupler exhibits a flexural vibration. Thus, if the actuators are excited with 90° difference of phase, the tip of coupler moves elliptically, as shown in the figure 2.

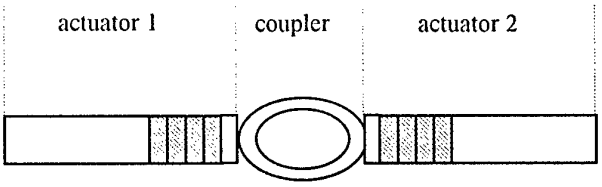


Figure 1 : Basic structure of the stator

3. NUMERICAL MODELLING

The major difficulty in designing such motor is to ensure the same resonance frequency for the two modes. The finite element software ATILA has been used to realize this task [4]. Figure 3 shows the strains of the structure. Since ATILA takes the piezoelectric effect into account, the electrical admittance can be computed (figure 4).

0-8194-2165-0/96/$6.00

Another interesting feature is the capability of the software to calculate the equivalent electromechanical scheme, that is commonly used to deal with performances of ultrasonic motors (figure 5) [5]. In this circuit, the two blocked branches account for capacitive nature of the actuators, while the two motional branches represent the two vibration modes.

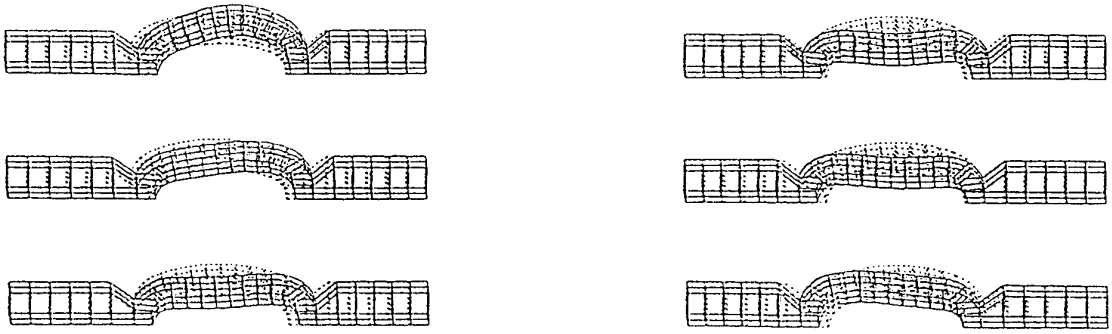


Figure 2 : Working principle of the motor

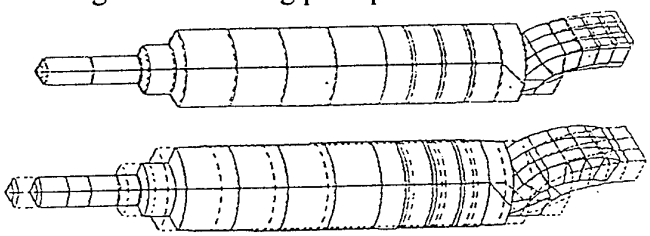


Figure 3 : Computed mode shapes of the stator (dotted line are rest position and only a eight of the structure is shown) : a) flexural mode, b) translation mode.

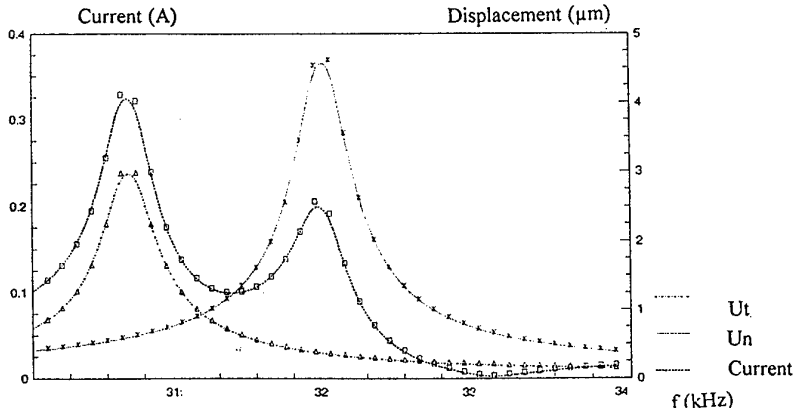


Figure 4 : Computed current of an actuator and displacements in the normal ant tangential directions (a 90° difference of phase being applied to the actuators).

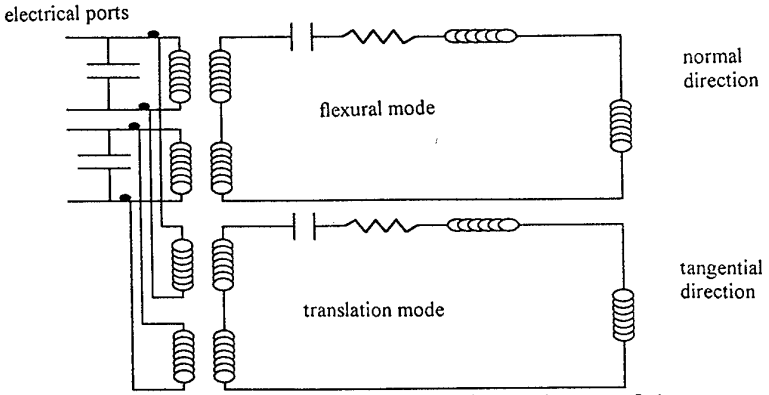


Figure 5 : Equivalent electromechanical scheme of the stator.

4. EXPERIMENTAL RESULTS

The prototype has been measured using current probe and laser interferometry measurement techniques [6]. Their electromechanical characteristics are summarized in table 1 and compared to those obtained in section 3. The figures 6 and 7 display respectively the electrical admittance and vibration velocity at the tip of the coupler. The phase difference of the velocities between the normal and the tangential direction shows that the coupler moves elliptically between the two resonance modes as expected. The stator has been used to rotate a roller. The motor is driven near the resonance frequency of the translation mode with an applied voltage of 60 volts rms and a preload of 3.5 Newton. This configuration leads to a high speed revolution and low torque system. The measured performances are depicted on figure 8.

	Resonance frequency (kHz)	Coupling factor (%)	Quality factor	Force factor (N/V)
Flexural mode	30.1 31.9	32. 27.	200. -	0.2 0.2
Translation mode	29.4 30.6	38. 34.	140. -	0.42 0.48

Table 1 : Electromechanical characteristics of the stator (1st line : measurements, 2nd line : modelling).

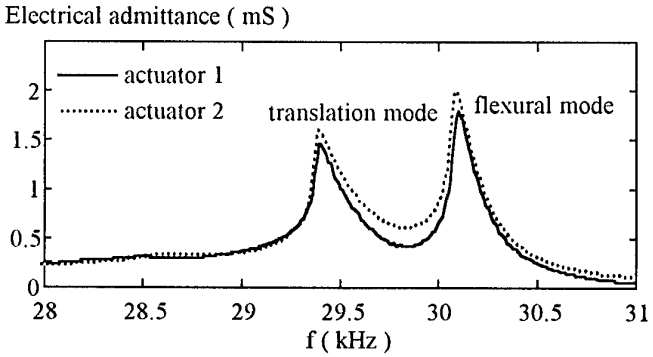


Figure 6 : Measured electrical admittance of the stator

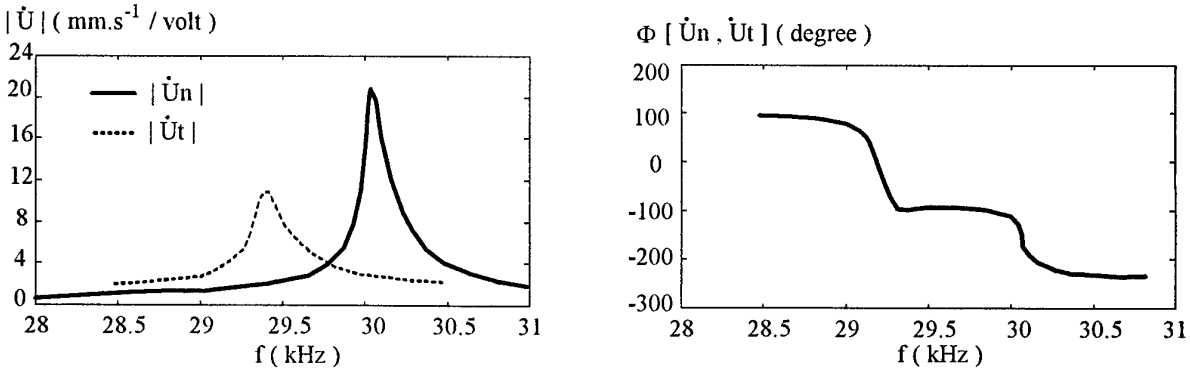
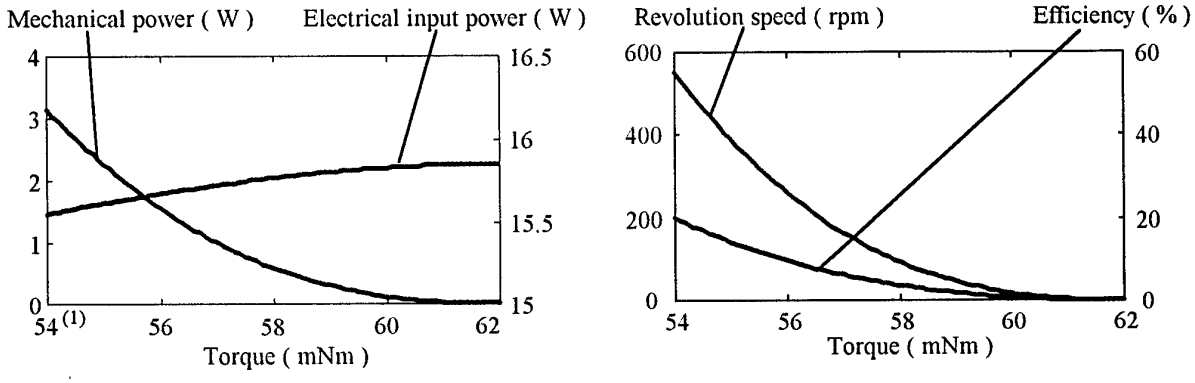


Figure 7 : Measured amplitude at the tip of the coupler and phase difference between the normal (Un) and the tangential (Ut) component of vibrating velocity.



(1) : residual torque of measurement unit

Figure 8 : Measured motor performances.

5. CONCLUSION

A new multi-mode piezoelectric motor has been proposed. The working principle has been explained and assessed experimentally. The numerical modelling tools has been useful to to design the stator, especially in tuning the two resonance frequencies. The pre-stressed actuators and the high measured mechnical Q of the stator are interesting features to provide an efficient motor. Possible applications of such vibrating stator may be in the field of forwarding devices.

ACKNOWLEDGMENT

The authors acknowledge the French Ministry of Research for its financial support and the industrial partners for their help in providing the pieces of the prototype.

REFERENCES

[1] Ueha, S., Tomikawa, Y., Ultrasonic motors - theory and applications, Oxford Sci. Pub., 1993, 297 p.

[2] Tomikawa, Y., Nishitsuka, Ogasawara, T., Takano, T., "A paper of card forwarding device using a flat-type ultrasonic motor", *Sensors and Materials*, 1989, vol. 1(6), p. 359-379.

[3] Yabuki, A., Aoyagi M., Tomikawa, Y., Takano, T., "Piezoelectric linear motors for driving head element of CD-ROM", *Jpn. J. Appl. Phys.*, vol. 33, 1994, p. 5365-5369.

[4] ATILA - 5.03, User's Manual, ISEN Lille (Fr).

[5] Le Letty, R., Claeyssen, F., Gonnard, P., Hamonic B., "Combined finite element - normal mode expansion methods for ultrasonic motor modeling", *I.E.E.E. Ultr. Symp. Proc*, 1994, p. 531-534.

[6] Guillemot-Amadei, M.M., Petit, L., Lebrun, L., Briot, R., Gonnard, P., "A non contact measurement technique for piezoelectric transducers", *Meas. Sc. Tech.*, 1995, p. 458-466.

A model for the nonlinear response of a Terfenol-D-type magnetostrictive actuator

Antonio DeSimone

Dipartimento di Ingegneria Civile
Università di Roma "Tor Vergata"
00133 Roma, Italy

ABSTRACT

A variational model of the nonlinear response of a magnetostrictive actuator to applied magnetic fields and loads, taking into account the complex behavior of the underlying domain patterns, is discussed. Magnetostriction curves for a Terfenol-D-like material in a two-dimensional geometry are calculated exactly, and compared with experimental measurements for Terfenol-D, suggesting an explanation for the observed behavior.

1. INTRODUCTION

Magnetostriction is the reversible deformation that in a magnetic material accompanies a change of its state of magnetization, which can be induced by the application of an external magnetic field. With the recent development of Terfenol-D, an alloy of terbium, iron, and dysprosium that exhibits magnetostrictive strains as large as 2×10^{-3} at room temperature, commercial high-power magnetostrictive actuators have become feasible[1].

Optimization of actuator performance demands some degree of understanding of the mechanisms by which a magnetostrictive solid responds to the action of an applied magnetic field. This is a nontrivial task, for several reasons. First, the geometry of the specimen dramatically affects its response. This is due to the fact that the specimen itself generates a magnetic field (self-field), which strongly depends on the shape of its boundary, and to which the magnetic state of the specimen is sensitive. In particular, since Terfenol-D can only be grown in the shape of rods with axis along a specific crystallographic direction (a [*112*] direction in the cubic basis) and comprising very thin twinned dendritic sheets, a realistic model of the behavior of a commercial actuator can only be based on the complex geometry schematically depicted in Figure 1. Second, the macroscopic response of a magnetostrictive actuator is inherently nonlinear. Indeed, since after a strong magnetic field has oriented the magnetization in the whole specimen parallel to itself, no further change of magnetization can be induced by an increasing the field strength, it follows that all magnetostiction curves saturate for high field strengths. Further "knees" are also recognizable in a typical magnetostriction curve (see Figure 2), corresponding to transitions from one to another microscopic arrangement of atomic magnetic moments. Since large slopes imply that larger strains are achieved with the same field strengh increment, predicting the location of these knees, and how they are affected by applied mechanical loads is of great interest for actuator design.

Micromagnetics[2], a classical variational model, seems to the author the most satisfactory tool at our disposal to capture the subtleties described above - in particular, to pay due attention to the fact that the macroscopic response of a magnetostrictive solid is nothing but an average description of complex microscopic phenomena involving the rearrangement of magnetic domains - and hence improve our understanding of the behavior of a magnetostrictive actuator. In this paper, in order to carry out a quantitative analysis in full mathematical rigor, we are forced to assume that the saturation magnetostrictive strains along the [*111*] and [*100*] directions to be equal, as discussed below. This assumption is not true for Terfenol-D and, for this reason, we call the material we study Terfenol-D-*like,* having taken for all the other material parameters those of Terfenol-D.

0-8194-2165-0/96/$6.00

2. DOMAIN PATTERNS AND EFFECTIVE ENERGIES

We consider a model problem, and we identify the specimen under study with the two-dimensional domain Ω shown in Figure 1. Also, we assume that the magnetization $\mathbf{M}$ always lie in the plane of Ω. The picture shows that Ω consists of thin growth-twinned parallel platelets, with the orientation of the crystallographic axes and of the magnetically easy directions shown in the inset. We consider a specimen subjected to a compressive normal stress σ of 5 MPa along the [*112*] direction, and we study the deformations induced by a spatially uniform magnetic field applied along the same direction.

The magnetization is not constant within the platelets of Figure 1. Rather, each platelet is further subdivided into small regions, called magnetic (elastic) domains, in each of which the magnetization (the state of elastic distortion) is approximately unifirm, as shown in the inset. Contrary to the boundaries between the growth twins, the interfaces separating magnetoelastic domains (domain walls) are extremely mobile in response to changes of magnetic field and applied surface forces. Predicting the average properties of energetically optimal microscopic domain patterns under given fields and loads (Which are the magnetization directions present ? With which volume fractions ? With which domain wall orientations ?) is the goal of our analysis.

Rather than giving the precise mathematical formulation of the problem, and the technical details needed to obtain a solution in closed from - for this, we refer the reader to previous work of ours[3,4,5] -, we focus here on the conceptual outline of our method. We replace the unknown magnetization $\mathbf{M}$ (which exhibits spatial oscillations which are fine as compared to the thickness of the growth twins) with its local average $\langle \mathbf{M} \rangle$, and we associate with the field $\langle \mathbf{M} \rangle$ an effective energy, defined as the smallest energy approachable by a magnetization field (i.e., a domain pattern) with local average magnetization $\langle \mathbf{M} \rangle$. A crucial observation, here, is that the assumption that the saturation magnetostrictive strains λ_{100} and λ_{111} be equal is essential to guarantee the existence of stress-free configurations for an arbitrary field $\langle \mathbf{M} \rangle$*. In this case, roughly speaking, at a point x of Ω where the magnetization is $\mathbf{M}(x)$, the material will be deformed according to its spontaneous, or stress-free strain $\mathbf{E}_0(\mathbf{M}(x))$. Then, we solve the minimization problem in the unkown field $\langle \mathbf{M} \rangle$. In this step, we make the further assumption that $\langle \mathbf{M} \rangle$ is constant in each platelet; provided that the focus of attention is global energy minimization, rather than hysteresis modelling, this seems reasonable, in view of the thinness of the platelets[3]. Finally, for each value of the applied magnetic field, we reason as in Reference 4 to recover the local magnetization orientations $\mathbf{M}_i$, their local volume fractions ϑ_i, and hence the local average magnetostrictive strain $\langle \mathbf{E} \rangle = \Sigma \vartheta_i \mathbf{E}_0(\mathbf{M}_i)$ from the energy minimizing field $\langle \mathbf{M} \rangle$.

3. DISCUSSION

The computations outlined in the previous section enable us to plot the magnetostriction curve of Figure 2. Having chosen an orthogonal reference frame with first axis parallel to the rod axis (a [*112*] direction), second axis parallel to a $[\bar{1}\bar{1}1]$ direction, and third axis parallel to a $[1\bar{1}0]$ direction, as defined by the cubic axes for the parent phase, the curve of Figure 2 is a plot of the average over Ω of the strain along [*112*], i.e., the component $\langle \mathbf{E} \rangle_{11}$ of the tensor field $\langle \mathbf{E} \rangle$, versus the strength of the corresponding magnetic field. In spite of the assumption $\lambda_{100} = \lambda_{111} = 1.2 \times 10^{-3}$, our computed curve is in surprising agreement with the experimental measurements for Terfenol-D[1], for which $\lambda_{100} << \lambda_{111}$.

In fact, computing also the average strains along the $[\bar{1}\bar{1}1]$ and $[1\bar{1}0]$ directions (i.e., the averages over Ω of $\langle \mathbf{E} \rangle_{22}$ and $\langle \mathbf{E} \rangle_{33}$), for which experimental measurements are available[7], we do obtain significant discrepancies. Indeed, contrary to the behavior of Terfenol-D, our ideal material exhibits

* A technical remark is needed at this point: typically, a configuration corresponding to a generic $\langle \mathbf{M} \rangle$ field can only be stress-free in an asymptotic sense, corresponding to very fine domain patterns[6].

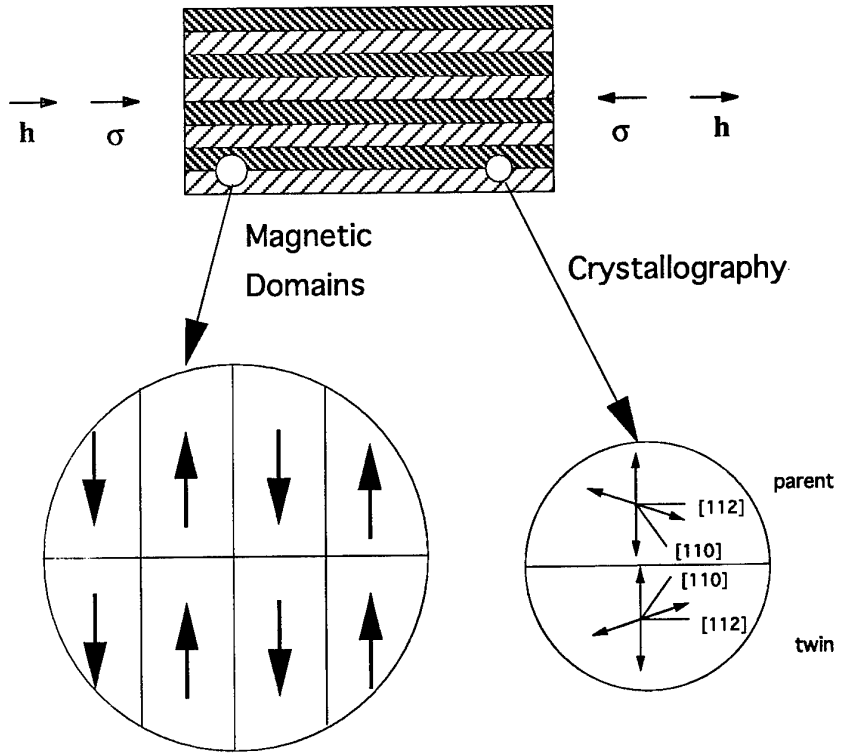


Figure 1. The geometry of our problem.

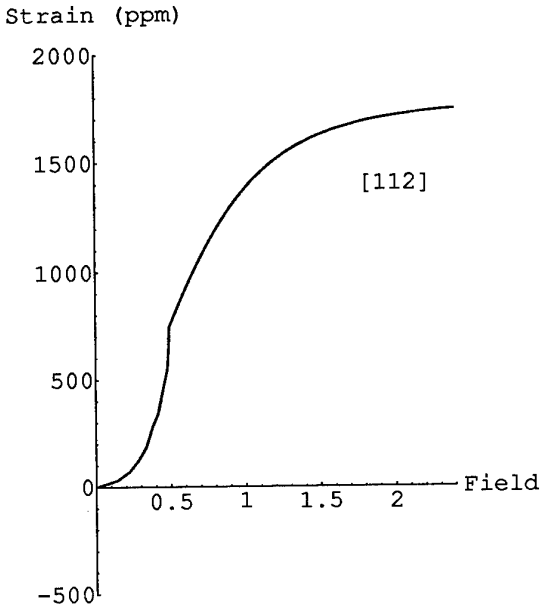


Figure 2. Magnetostriction curve with $\lambda_{100} = \lambda_{111} = 1.2 \times 10^{-3}$.

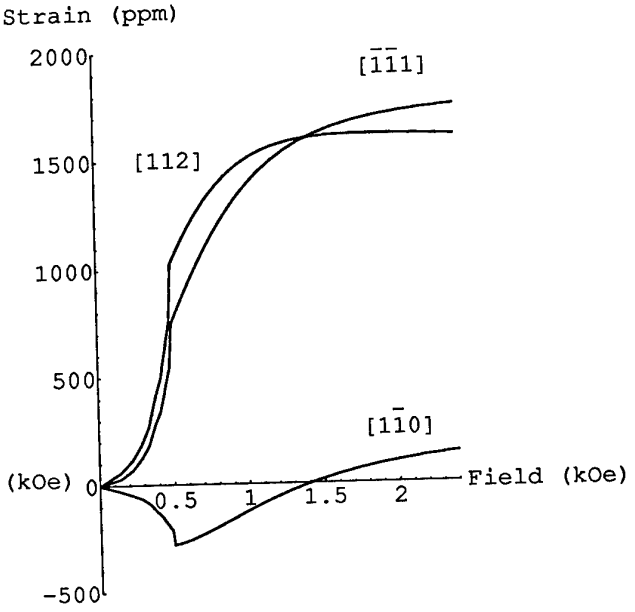


Figure 3. Magnetostriction curves with $\lambda_{100} = 0.06 \times 10^{-3}$ and $\lambda_{111} = 1.2 \times 10^{-3}$.

average strain along $[\bar{1}\bar{1}1]$ equal and opposite to the one along $[112]$ (thus, the average strain along $[1\bar{1}0]$ vanishes, since $\mathbf{E}_0(\mathbf{M})$ is traceless for every $\mathbf{M}$).

To test whether our computed microscopic domain patterns are at all realistic for Terfenol-D, we have constructed the curves of Figure 3, obtained starting from the magnetic domain patterns computed as in Section 2 (i.e., with $\lambda_{100} = \lambda_{111}$), and then formally evaluating the average strains over Ω through the stress-free strains corresponding to $\lambda_{100} = 0.06 \times 10^{-3}$ and $\lambda_{111} = 1.2 \times 10^{-3}$, as it is more realistic for Terfenol-D. Following Teter et al.[7], we have plotted the negative of the strain along $[\bar{1}\bar{1}1]$. The comparison of our plots with the experimentally measured curves shows that the energetically optimal domain patterns for Terfenol-D are not the ones appropriate for our Terfenol-D-like material. Very recent work in progress[8] shows that the fact that the strains along $[\bar{1}\bar{1}1]$ exceed in magnitude those along $[112]$ can be explained by allowing the magnetization vectors to take values out of the plane of Ω.

4. ACKNOWLEDGEMENTS

This research was supported in part by the Italian Consiglio Nazionale delle Ricerche. The author wishes to thank R.D. James for helpful discussions.

5. REFERENCES

1. K.B. Hathaway and A.E. Clark, "Magnetostrictive materials", MRS Bulletin, 18(4): 34-41, 1993.
2. W.F. Brown Jr., Magnetoelastic Interactions, Springer Verlag, Berlin, 1966.
3. A. DeSimone, "The effect of applied loads on the magnetostrictive response of a Terfenol-D-type material", Scripta Met., 33(10-11): 1869-1875, 1995.
4. A. DeSimone, "Energy minimizers for large ferromagnetic bodies", Arch. Rat. Mech. Anal., 125: 99-144, 1993.
5. A. DeSimone, "Characterization of the macroscopic response of magnetostrictive materials via microstructural analysis", to appear in Proceedings of ICIAM 95, Hamburg, 1995.
6. R.D. James and D. Kinderlehrer, "A theory of magnetostriction with application to $TbDyFe_2$", Phil. Mag. B, 68(2): 237-274, 1993.
7. J.P. Teter, M. Wun-Fogle, A.E. Clark, and K. Mahoney "Anisotropic perpendicular axis magnetostriction in twinned $Tb_xDy_{1-x}Fe_{1.95}$", J. Appl. Phys., 67(9): 5004-5006, 1990.
8. A. DeSimone and R.D. James, "A proposed mechanism for anisotropic magnetostriction in Terfenol-D", in preparation.

On the dynamic interaction between piezoelectric bonded actuators and an axial beam

Stefano ACCETTELLA, Paolo GAUDENZI
Universitá di Roma "La Sapienza" , Dipartimento Aerospaziale
Via Eudossiana 16, 00184 Roma, Italy

- Introduction

Aim of the present paper is to analyze and compare two different models used to study the axial vibration problem of a beam structure actuated by piezoelectric layers bonded to it.
Crawley and de Luis [4] have recently set up a distributed dynamic model for both the axial and the flexural dynamic of an actuaded beam structure. Rogers has explored the possibility of describing the dynamic interaction between piezoelectric actuators and a beam structure by means of a lumped model [5]. In the first section of this paper a completely lumped parameters model will be presented and discussed; the results wiil be compared in the second section with the ones obtained for a distributed model.

- Problem geometry

A substrate beam of constant section with perfectly bonded symmetric piezoelectric actuator patches is considered (see fig. 1); the actuators cover all the lenght and the width of the structure; by assuming that the electric field in the piezoelectric material is given, the actuation mechanism is produced by imposing a piezoelectrically induced strain Λ to the perfectly bonded passive structure. (In the following the subscript "a" will denote the actuator properties while the subscript "b" will be relevant to the substrate; e.g. $L = l_b = l_a$ for the lenght, $Y = y_b = y_a$ for the width.)
The Pin-Force and the Euler-Bernoulli models [1], [2], [3] give the following result for the axial strain field ε_0, when applied to a beam structure like the one previously described:

$$\varepsilon_0 = \frac{2}{2+\Psi}\,\Lambda \tag{1}$$

with $\Psi = (E_b\, t_b)/(E_a\, t_a)$. E denotes the Young's modulus, t_b and t_a the thickness respectively of host structure and of the actuators of the considered beam structure. For the axial vibration problem a new parameter is introduced: $R = (\rho_b\, t_b)/(\rho_a\, t_a)$ where ρ_b and ρ_a are respectively the mass density of the beam and the actuators. A lumped parameter describing in a global manner the dynamic stiffness H of a distributed structure is also needed. In this way the axial beam structure will be described by means of the following parameters:

- statical lumped stiffness: $K = (E\, Y\, t)/L$
- lumped mass: $m = \rho\, Y\, t\, L$ {ρ is mass per unit volume}
- dynamic undamped lumped stiffness: $H = K - \omega^2\, m$
- natural frequency of lumped structure: $\omega_n^2 = K/m$

1 Fully Lumped Model

In the static case for a positive induced displacement $\tilde{X}_{in}$ a positive displacement at equilibrium is observed, in this configuration the substrate, pulled by the actuators, is working in a traction condition, while the actuators, are working in compression. In the following a positive actuation force will be

assumed at the static equilibrium corresponding to a positive induced displacement $\tilde{X}_{in}$. In this way the displacement at the equilibrium $\tilde{X}_{eq}$ of a lumped parameters model (as in figure 2) reads:

$$\tilde{X}_{eq} = \frac{2\,K_A}{2\,K_A + K_B}\,\tilde{X}_{in} \tag{2}$$

recalling that $\widetilde{F_a} = -2K_A\,(\tilde{X}_{eq} - \tilde{X}_{in})$, the actuating force will be:

$$\widetilde{F_a} = \frac{2K_AK_B}{2K_A + K_B}\,\tilde{X}_{in} \tag{3}$$

The foregoing equations hold in general for a lumped model, i.e. it will be sufficient to replace the statical stiffness by the dynamical one to obtain the desired lumped dynamic equations. As a lumping technique from a description in terms of continuous variables it is possible to assume that: $\tilde{X} = \tilde{u}(L)$ or better $\tilde{X} = \tilde{\varepsilon}_0\,L$ and $\tilde{X}_{in} = \Lambda_0\,L$; where $u(x)$ is the axial component of the displacement field, and Λ (the free actuator induced strain) is taken as: $\Lambda(t) = \Lambda_0\,e^{j\omega t}$; moreover for the vibration problem the displacement $X(t)$ and the actuation force $F_a(t)$ are assumed to be: $F_a(t) = \tilde{F}_a\,e^{j\,\omega\,t}$ $X(t) = \tilde{X}\,e^{j\,\omega\,t}$. At this point, by characterizing the behaviour of the host structure by its own dynamic stiffness H_B, and the effect of dynamic behaviour of the actuators by means of their dynamic stiffnesses, the free edge displacement at equilibrium $\tilde{U}_1$ and the actuation force $\tilde{F}_{a1}$ will be obtained by replacing the static stiffnesses in the equation (2) and (3) with the dynamic ones. By introducing the adimensional quantities: $U_1 = \tilde{U}_1/\tilde{X}_{in}$, $F_1 = \tilde{F}_{a1}/(K_B\,\tilde{X}_{in})$, $\Omega = \omega/\omega_b$, the following expressions can be written.

$$U_1(\Omega) = \frac{2\left[1 - \frac{\Psi}{R}\,\Omega^2\right]}{2\left[1 - \frac{\Psi}{R}\,\Omega^2\right] + \Psi\,(1 - \Omega^2)} \tag{4}$$

$$F_1(\Omega) = U_1(\Omega)\,(1 - \Omega^2) \tag{5}$$

By observing eqns.(4) and (5) the following natural frequency is recognized:

$$\Omega_1^2 = \frac{2 + \Psi}{\Psi}\,\frac{R}{2 + R}\;\;;\;\;\text{or}\;\;\omega_1{}^2 = \frac{E_a}{\rho_a}\,\frac{2 + \Psi}{2 + R}\,\frac{1}{L^2}\;\;;$$

moreover it is noted that the model seems to have different behaviours for $\Psi/R > 1$ or for $\Psi/R < 1$. It is clear that by defining: $\omega_a^2 = K_A/m_a$ and $\omega_b^2 = K_B/m_b$ the ratio $(\omega_a/\omega_b)^2$ will be: $(\omega_a/\omega_b)^2 = R/\Psi$ In this way, it easy to recognize that the condition $\omega_a < \omega_b$ is the same of $R < \Psi$; that is $\omega_a < \omega_b$ if and only if $\rho_b/E_b < \rho_a/E_a$ and vice versa, i.e. $\omega_a < \omega_b$ is a condition dependent only upon the mechanical characteristics of the substrate material and the piezoelectric material. In the following three cases different dynamic conditions of the considered beam are discussed in terms of the relationship between Ψ and R.

1. $\Psi < R$
   Under this condition: $\omega_b < \omega_1 < \omega_a$. In figure 3 the two functions $\hat{U}_1(\Omega)$ and $\hat{F}_1(\Omega)$ are plotted for the case of $\Psi = 2$ and $R = 5$; it is possible to recognize different working conditions:

   (a) $0 < \Omega < 1$ quasi-static: $(0 < \omega < \omega_b)$
   U_1 and F_{a1} have a value similar to the one of the static case, but more importantly U_1 has the same sign of the induced displacement $(\tilde{X}_{in})$.

   (b) $1 < \Omega < \Omega_1$ dynamic in-phase: $(\omega_b < \omega < \omega_1)$
   in this case U_1 and F_{a1} have opposite signs but U_1 has still the same sign of the induced displacement (this is why this case is denoted as "in-phase").

   (c) $\Omega_1 < \Omega < R/\Psi$ dynamic out-of-phase: $(\omega_1 < \omega < \omega_a)$
   the U_1 has an opposite sign with respect to the induced displacement.

   (d) $R/\Psi < \Omega$ dynamic in-phase: $(\omega_a < \omega)$ the U_1 is reaching an asymptotic value while the F_{a1} is indefinitely growing: no blocking force can be defined.

2. $\Psi = R$
   From equations (4) and (5) the following expressions is obtained as $\Psi/R \rightarrow 1$:

$$U_1(\Omega) = \frac{2}{2+\Psi} \tag{6}$$

$$F_1(\Omega) = \frac{2}{2+\Psi}\,(1-\Omega^2) \tag{7}$$

   from the equation (6) U_1 appears not depending upon the frequency of the applied electric field, holding for every value of the frequency of the applied electric field the same value of the static case. This result is explained by analyzing the condition $\Psi/R \rightarrow 1$ which implies $E_a/\rho_a \rightarrow E_b/\rho_b$ and hence $\omega_a \rightarrow \omega_b$. It is easy now to recognize that for $\Psi/R \rightarrow 1$ $H_B/H_A \equiv K_B/K_A = \Psi$, so the results described in equation (6) appear reasonable.

3. $\Psi > R$
   This condition means: $\omega_a < \omega_b$; from figure 4 plotted for the case $\Psi = 5$ and $R = 2$ different working conditions can be observed:

   (a) $0 < \Omega < R/\Psi$ quasi-static $(0 < \omega < \omega_a)$

   (b) $R/\Psi < \Omega < \Omega_1$ dynamic out-of-phase $(\omega_a < \omega < \omega_1)$

   (c) $\Omega_1 < \Omega$ dynamic in-phase $(\omega_1 < \omega)$

As it will be seen in the next section, it must be pointed out that the response of the lumped model is significantly different from one of the distributed model for high values of ω. However one interesting result of this lumped approach is that for two frequencies, namely ω_b and ω_a no actuating force can be provided. In fact, as expected from the physical point of view, by applying an electric field at $\omega = \omega_b$ the actuators do not feel the presence of the substrate and conversely applying an electric field at $\omega = \omega_a$ the substrate does not see the presence of an actuating piezoelectric layer. The response of the lumped system can be also illustrated in figures 5 and 6 (actuation charts) from which it can be seen that there is a range of U_1 that cannot be obtained no matter what is the value of F_{a1}.
Also if this aspect is not considered in the present paper, it is worth noting that the lumped model could be considered also for the modeling of an axial in which the actuators are not bonded to the upper and lower surface of it but connected just at the edges of the beam in a physically lumped geometry of the system.

2 Euler-Bernoulli model

A dynamic model is now described as done by J. de Luis [4] on the basis of Euler-Bernoulli beam hypothesis, then the results of this approach are compared with the ones of the previous discussed lumped models. As in the previous section the analysis will be restricted to the simple axial problem, the governing equation of which can be written as follows:

$$\frac{\partial}{\partial x}\left[E_a t_a(2+\Psi)\frac{\partial u}{\partial x} - 2E_a t_a \Lambda(x,t)\right] = \rho_a t_a (2+R)\frac{\partial^2 u}{\partial x^2} \tag{8}$$

Boundary and initial conditions are of course necessary to complete the description of the mechanical problem. The simple axial problem of a cantilever rod, with omogeneus initial conditions is considered. The boundary condition at the right side and at the free edge reads:

$$u(0,t) = 0 \quad ; \quad \left[\frac{\partial u}{\partial x}\right]_L = \frac{2}{2+\Psi}\Lambda(L,t)$$

The actuating term $\Lambda(x,t)$ is assumed to be: $\Lambda(x,t) = \Lambda_0\, e^{j\omega t}$ where $\Lambda_0 = d_{31}\, G_0/t_a$. By taking for the axial displacement component:$u(x,t) = (A\ sinkx + B\ coskx)\, e^{j\omega t} = \tilde{u}(x)\, e^{j\omega t}$ with:

$$k^2 = \omega^2\, \frac{\rho_a}{E_a}\, \frac{2+R}{2+\Psi}$$

and by solving the set of boundary conditions equations, it is found for the free edge displacement:

$$\tilde{u}(L) = \frac{2}{2+\Psi} \frac{\tan(kL)}{kL} \Lambda_0 L \tag{9}$$

With this model the natural frequencies of the beam are:

$$\omega_n^2 = \frac{E_a}{\rho_a} \frac{2+\Psi}{2+R} \left(\frac{2n-1}{2}\right)^2 \left(\frac{\pi}{L}\right)^2$$

as a consequence of equation (9) $\tilde{u}(L)$ vanishes if k is assuming one of the following values: $k_n = (n\,\pi)/L$. For the actuation force will be:

$$\widetilde{F_a} = \frac{2\,\Psi}{2+\Psi} \frac{E_a t_a Y}{L} \Lambda_0 L \tag{10}$$

By recalling that $(kL)^2 = \Omega^2\,\Psi/R\,(2+R)/(2+\Psi)$, it is easy to normalize equations (9) and (10):

$$u(L) = \frac{2}{2+\Psi} \frac{\tan(kL)}{kL} \tag{11}$$

the actuation force can also be written as:

$$F = \frac{2}{2+\Psi} \tag{12}$$

where: $F = \tilde{F}_a/(K_B\,\Lambda_0\,L)$. It must be observed that the magnitude of the actuation force does not vary with the frequency of the applied electric field; however the magnitude of dynamic response of the actuated structure grows indefinitely when the applied electric field frequency reaches the structure eigenfrequency. In this way, no infinite magnitude actuation force, but infinite magnitude displacement could be obtained. This prediction is in contrast with the one of the lumped model as described by the actuation charts. Another interesting result is that $u(L)$ vanishes at the frequencies corresponding to the eigenfrequency of a structure clamped on both sides. A similar result has been obtained for the lumped model. The physical meaning of this fact is that the host structure does not feel the presence of the actuators when the electric field is applied at certain frequencies. The expression of ω_n^2 can be also put in the form:

$$\omega_n^2 = \omega_{nb}^2 \frac{R\,(2+\Psi)}{\Psi\,(2+R)}$$

where ω_{nb} are the eigenfrequencies of the host structure alone; in this way it can be seen that in the case of $\Psi \to R$, or vice versa, the dynamic of the complete structure will be the same of the one of the host structure considered alone, with an external load, due to the piezoelectric actuators, of constant magnitude.

References

1. Barboni R. Gaudenzi P. Strambi G. "On the Stress Distribution in a Simple Adaptive Structure Actuated in Bending Mode" Second European Conference on Smart Structure and Materials, Glasgow 1994, SPIE volume 2361, pp.71-74.

2. Chaudry Z. , Rogers C.A. "The Pin-Force Model Revisited" J. of Intelligent Material Systems and Structures. Vol. 5 May 1994.

3. Strambi G., Barboni R. , Gaudenzi P. "Pin-Force and Euler-Bernoulli Models for Analysis of Intelligent Structures."AIAA Journal Vol.33 n.9, pp.1746-1749.

4. de Luis J. "Design and Implementation of Optimal Controllers for Intelligent Structures Using Infinite Order Structural Modes", PhD thesis Massachuttes Institute of Technology, 1989.

5. Rogers C.A. "Static VS. Dynamical Application of Intelligent Material Systems." Seminar held at the University of Rome "La Sapienza", September 14, 1993

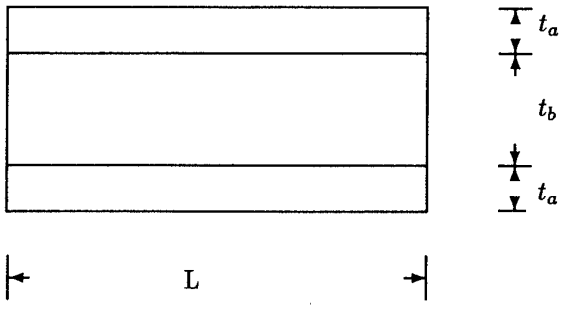


Fig.1

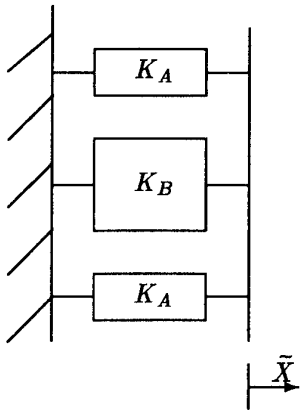


Fig.2

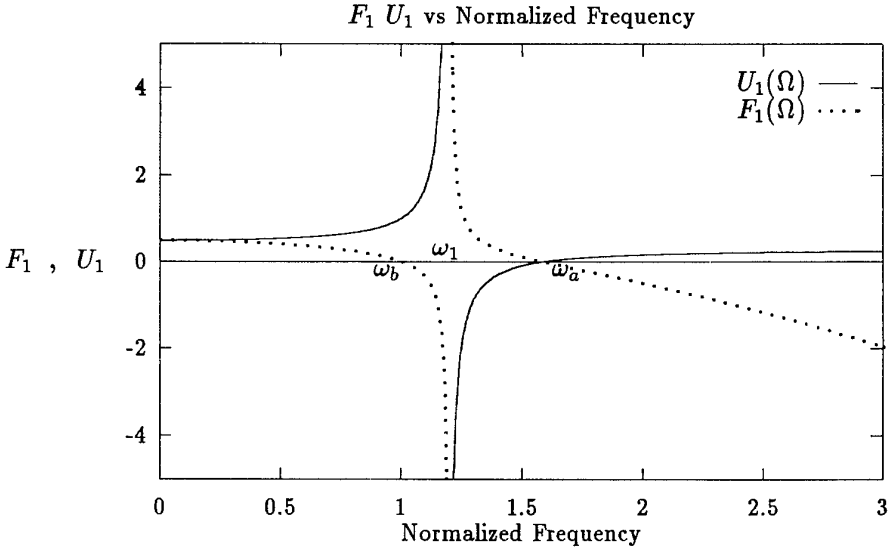


Fig.3

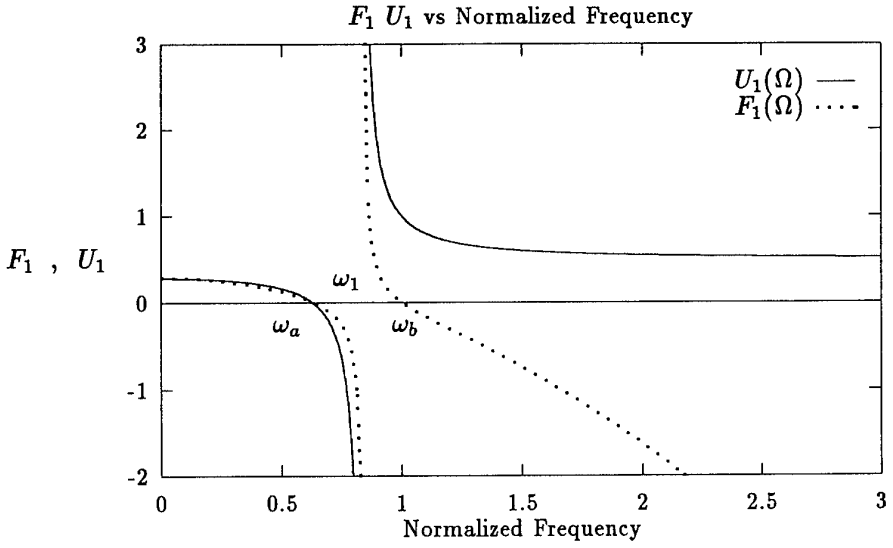


Fig.4

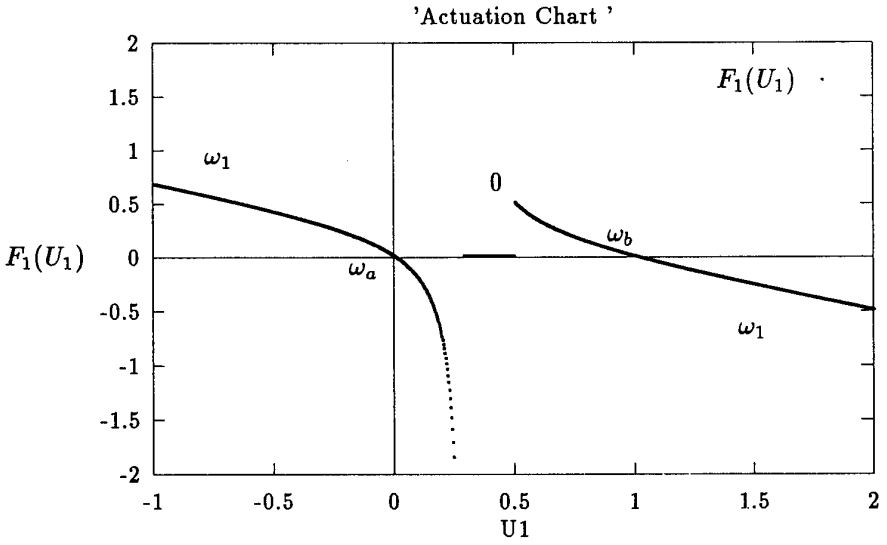


Fig.5

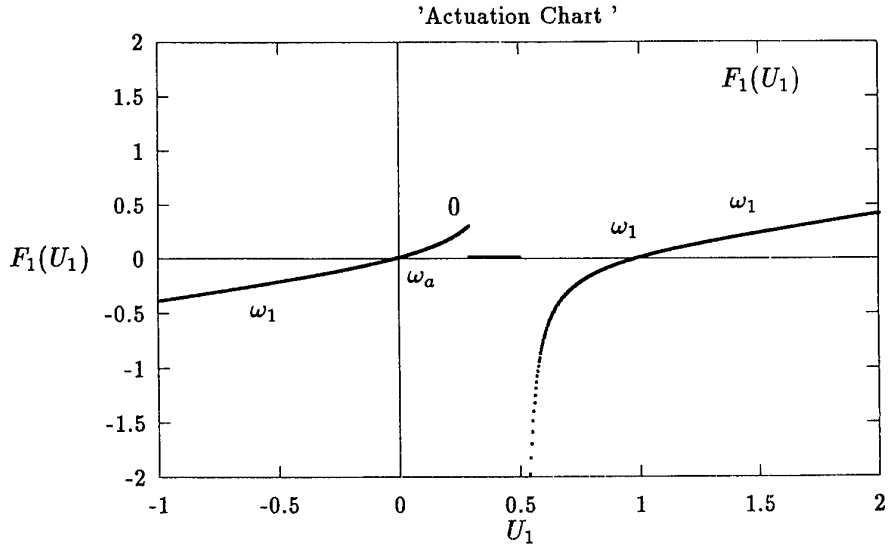


Fig.6

Performance optimisation of active control with piezo-ceramics

Didier LANG, Livier REITHLER, Christophe ROUSSET

Aerospatiale, Centre Commun de Recherches Louis-Blériot
Materials Department, Suresnes, France

ABSTRACT

This paper presents the methodology to design and optimise a feasibility demonstrator for low-frequency active vibration control of a composite plate. An original approach has been achieved and several problems due to the behaviour of the piezoceramic explained and solved.

1. INTRODUCTION

1.1. Fields of work and possible applications

With the point of view of an aerospace manufacturer the field of application of smart materials and structures is very wide, from health monitoring to active geometry and active vibration control. The purpose is a feasibility study of a demonstrator with the following applications : vibrations, decoupling interfaces, integrated structural vibration damping, dynamic shape control for aerodynamic optimisation. This study is the second step of a larger research program : the first step consisted in the development of the active shape and vibration control of a cantilevered beam which was successfully implemented. The controller based on the old principle of the dynamical damper simulated through a simple analog filter gave more than satisfactory performances. The goals of the following study are to generate pre-design data and to draw up mass and energy balances on a more representative structure.
Following the global aims and the precise goals of the study, we adopted a methodology widely used in the industry.

1.2. Methodology

Considering the specifications of the problem the idea was to list all the function to be achieved, find all the possible solutions for each one, choose the best achievable one and optimise it. We feel that there is no universal solution as there is no unique problem and as we have to deal with external constraints some choices have to be made which strongly depend on the objectives of the study.

2. SPECIFICATION OF THE PROBLEM

The goal of the study is to prove the feasibility of the active vibration control of a composite structure dynamically loaded with various mechanical excitations :

- impacts,
- excited vibrations,
- white noise,
- structure variations (modification of the geometry, mass, stiffness or boundary conditions)...

The frequency range to be controlled has been arbitrary fixed up to 500 Hz. The structure has to be representative of the structures usually found in the aeronautical industry with rich but not too complex mode shape distribution : a cantilevered beam is all but representative, a bidimensional orthotropic structure seems to be more adequate.
The major constraints we have to face are apparatus availability and time and cost limitations. As a consequence only on-the-shelf technologies are to be used in such a study. The essential difficulties arise in the integration and the gathering of different sciences and techniques such as material science, mechanics, modelling, data processing, control science...
In our study four major functions can be listed :

- the mechanical function,
- the actuation,
- the sensing
- the control.

0-8194-2165-0/96/$6.00

3. REVIEW OF ACTIVE CONTROL STRATEGIES

The key issue of the selection of the most suitable solution is to choose the control strategy. On purpose the theoretical implications of control are disregarded. Because of the above listed limitations only on-the-shelf technologies which are well known and quite easy implement have to be used. As a consequence the strategies are listed regarding the physical means.

3.1. Analog techniques

There are a lot of different type of filters more or less complex to implement.
The main advantage of analog filters is their fast and easy implementation. However there is no analog technique for adaptativity.

3.2. Digital strategies

Two functions are necessary for digital strategies :

- analog-to-digital and digital-to-analog conversion : 20 kHz is a sufficient sample rate,
- computing.

The main advantage of digital strategies is adaptativity : different algorithms could be tested with little trouble. However the development costs and hardware investment raise quickly and could be incompatible with time and cost limitations in an industrial development.

3.3. Dual analog-digital strategies

An interesting way of control is to profit from the speed and relative simplicity of analog techniques and from the adaptativity of digital techniques. There seems to be two different ways to mix analog and digital techniques :

- very-low frequency vibration control via digital techniques, higher frequency via analog techniques : as the very-low frequency vibrations are more energetic a digital control with adaptation capability would be appropriate to have the greatest efficiency, and a great profit could be taken from the analog control techniques for higher frequencies,
- digitally commandable analog filters :that technique takes the advantages of both analog and digital technologies : it's fast, easy to implement, can be adaptive without requiring a very fast and efficient computer.

3.4. Computing performance requirement considerations

For the evaluation of the performance we assumed that the adaptation for dual analog-digital control strategies is performed less than once a second. For digital or analog-digital control strategies the computing performance requirement depends on the algorithm. For simple or non-adaptive real-time algorithms (for which the main advantage of digital techniques disappears...) the required performance can be provided by a simple personal computer. More complex algorithms require a workstation and even a mainframe. However considering that the adaptation don't need to be performed more than once a second more complex algorithms can be implemented without requiring huge computing performances.

3.5. Conclusion

For generic application demonstrator it appears that the most interesting techniques are the dual analog-digital strategies : they profit from the advantages of both fully analog and fully digital techniques without having their major drawbacks. Moreover their implementation is quite simple and evolutive : they consist in a few analog chips of simple electronics, many different algorithms can be implemented without requiring extensive computing power and expensive acquisition hardware.

4. THE APPROPRIATE SOLUTION

4.1. Structure

The material chosen for the structure is a 16 ply high resistance carbon fibre/epoxy resin composite. the geometry and the boundary conditions are defined as shown on figure 1. A finite element model of the plate gives an evaluation of the resonance frequencies and the associates mode shapes. The first mode at 5.00 Hz is the first bending mode, the second at 21.42 Hz is the first torsion mode and the third at 32.63 Hz is the second bending mode. An optimisation of the location of the piezo-ceramic actuators has been performed : only four actuators located next to the clamped areas are sufficient to control the first six modes as shown on figure 1. The first experiment performed on the structure was the determination of the resonance frequencies and the damping factors : the frequency of the first three modes are 4.13 Hz, 17.77 Hz and 28.50 Hz, giving thus a good confidence level in the location optimisation of the actuators.

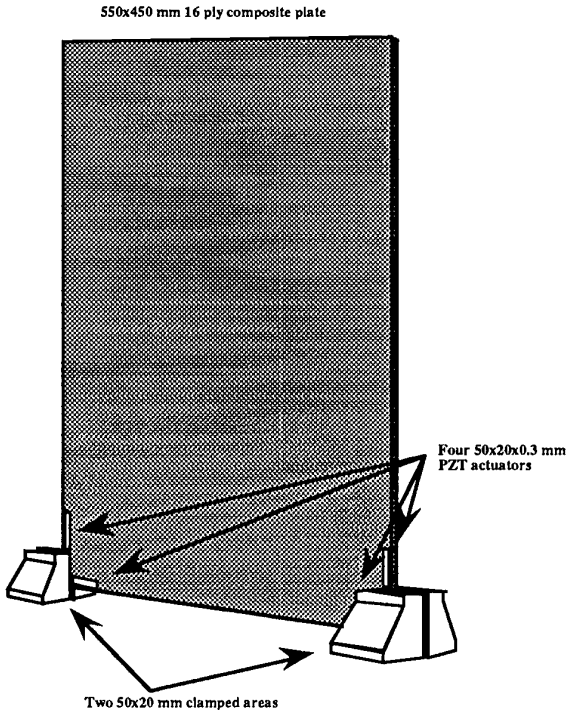


Figure 1 : Geometry and boundary conditions

4.2. Controller

The control strategy which appeared the more interesting is the dual analog-digital technique using digitally commandable second order filters. In fact this method is actually one of the best known and oldest method used in order to eliminate vibration as second order filters are the electronic equivalent of a dynamical damper.
The dynamical dampers are implemented via digitally commandable switch-capacitor second order filters : they need a reference frequency and the parameters which can be programmed are the quality factors and the ratio between the reference frequency and the cut-off frequency. A PC fitted with a Timing/Digital IO board is sufficient to command the whole controller.

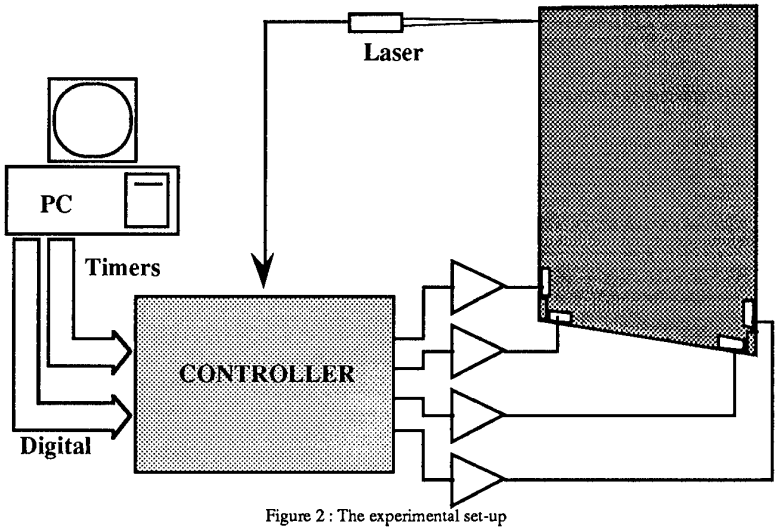


Figure 2 : The experimental set-up

4.3. Actuators and sensors

4.3.1. Description

The sensors we used are laser displacement sensors.
PZT piezo-actuators were chosen due to there high authority and stiffness compatible with the composite structure. Moreover their availability and easy to design make them perfectly suitable for a feasibility study. Nevertheless the highly non-linear behaviour and type of memory effect raise some experimental issues to determine the operating conditions to confer them the expected and constant authority.

4.3.2 Characterisation of the piezo-ceramic actuators

The two major problems we had to face with the behaviour of the piezo-ceramic actuators were an unexplained loss of efficiency and a "strange" dynamical behaviour.

Microscopic aspects :

After the manufacturing there is no piezoelectric effect, the mesh of the crystal is cubic and because of the random orientation of the grains. The ceramic gains piezo-electric properties in a precise direction during the polarisation treatment : the ceramic is placed at high temperature in an intense electric field. After this treatment the dipoles stay in this configuration giving the ceramic a remanent polarisation and a permanent deformation removing its initial isotropy.

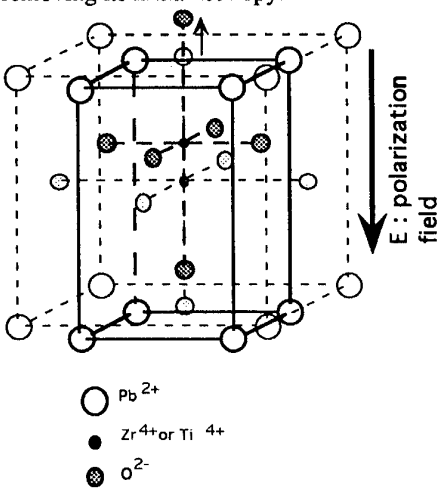


Figure 3 : Polarisation of a PZT

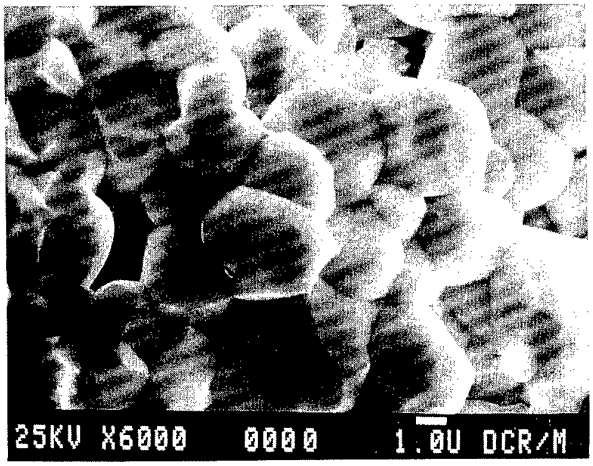


Figure 4 : Picture of a PZT plate

As it can be deduced from the figure 3 there are two different states of polarisation according to whether the oxygen ions are on one or the other side of the plane of the lead atoms. It seems that a too high electric field with a direction inverse from the polarisation field makes the ceramic change to the other state of polarisation. We call the two inversion voltages V_{inv}^{-} and V_{inv}^{+}.

Macroscopic aspects :

As shown on the figure 4 the piezo-ceramic is a set of up to 5 µm grains. Each grain has a polarisation, the polarisation of the whole ceramic is equal to the sum of the polarisation of every grain. When a voltage is applied to the piezo-ceramic each grain undergoes a strain proportional to the voltage and its polarisation. The deformation of the whole ceramic is the algebraic sum of every deformations.

Variations of the polarisation :

When the piezo-ceramic is excited with a voltage which is the range from V_{inv}^{-} to V_{inv}^{+}., the polarisation remains constant. But if the voltage exceeds that range, the polarisation changes.

Electrodynamical behaviour under a sinus wave :

If the amplitude of the sinus wave remains within the range from V_{inv}^{-} to V_{inv}^{+}., the behaviour of the piezo-ceramic is hysteretic. If not, the behaviour is far more complex (as shown on figure 4) and depends on the previous excitations applied to the ceramic. This phenomenon is under investigation.

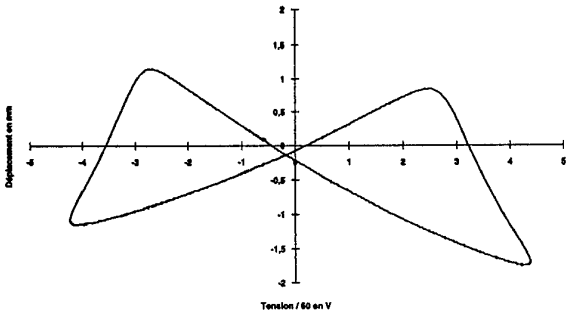


Figure 4 : Behaviour of the piezo-ceramic with high amplitude sine-wave

Conclusion :

All this study has defined a very strict procedure to be followed before using the piezo-ceramic actuators in order to profit from their maximum efficiency or to regenerate their original authority. First a voltage greater than V_{inv}^{+} is applied during a period of 10 minutes, than the polarisation is checked. During the use the maximal voltage must not overstep 80 percents of V_{inv}^{-} and V_{inv}^{+}.

5. PERFORMANCE EVALUATION

The measurements have been made with an external electromagnetic shaker.

5.1. On a single mode

The first part of the performance evaluation is the control of a single mode : the structure is excited at the resonance frequency of the first or the second mode. Attenuations up to 35 dB (division by of a factor of 56 of the amplitude of the vibration) were obtained with two actuators on the first mode. A simple manual optimisation has shown that the cut-off frequency has to be equal to the resonance frequency of the first mode in order to obtain the maximum efficiency. The damping factor is set to 14 % which is an evaluation of the controlled structure damping factor. For the second mode attenuations up to 27 dB (division by of a factor of 22 of the amplitude of the vibration) were obtained with only one actuator.

5.2. On two modes

The structure is simultaneously excited at the resonance frequencies of the first and the second mode. Attenuations up to 21 dB (division by of a factor of 10 of the amplitude of the vibration) were obtained with only two actuators without any optimisation. The principle is therefore validated and can be applied to the control of more than two modes if they are sufficiently separated.

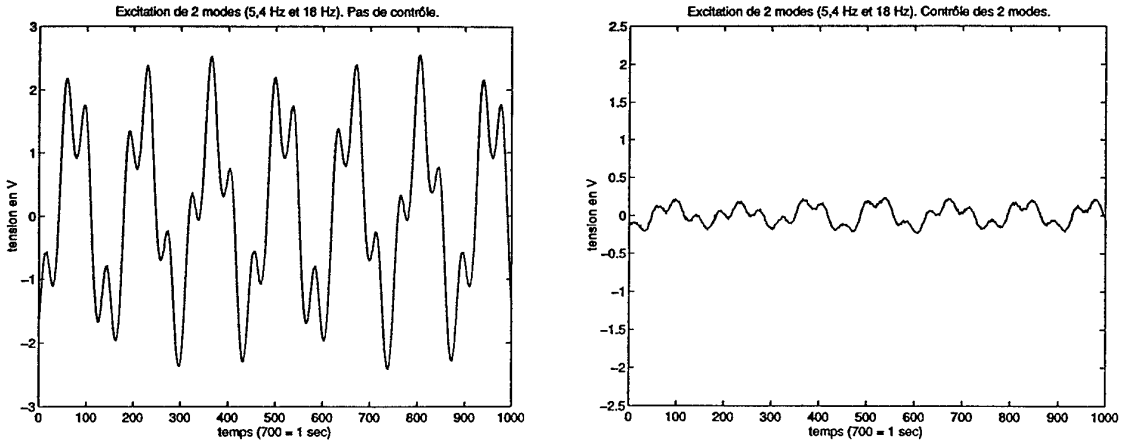


Figure 5 : Control of two modes

6. CONCLUSION AND FUTURE WORKS

The purpose of the present study was to prove the feasibility of the active vibration control of a composite structure. A methodology widely used in the industry has been used in order to develop the right concept which fits the bets with our long term objectives which are the vibration control in aeronautical structures. The concept described here has been successfully implemented on a demonstrator which has shown very high performances. The next steps of the study are the control of a higher number of modes, the adaptativity and the implementation of the concept on real structures.

7. REFERENCES

P. Borne, G. Dauphin-Tanguy, J.-P. Richard, F. Rotella, I. Zambettakis, "Modelisation et identification de processus"
Méthodes et Pratiques de l'Ingénieur, Technip

F. Casciati & Faravelli, "Neural Network Applications for Active Structural Control"
Proceedings of the conference on "Active Control in Mechanical Engineering", Lyon, June 1993

E. Garcia, "The application of smart structures to the vibration suppression problem"
Journal of Intelligent Material Systems and Structures, vol.3 n°4, 10/92

B. Jaffe, H. Cook, "Piezoelectric ceramics"
Academic Press

B. Widrow, S. D. Stearns, "Adaptive signal processing"
Prentice-Hall

W. H. Press, B. P. Flannery, S. A. teukolsky, W.T. Vetterling, "Numerical Recipes in C : The Art of Scientific Computing"
Cambridge Press

D. Lang, L. Reithler, "Active control of a composite plate : from the specific problem to an optimised solution"
Proceedings of the "1995 North American Conference on Smart Materials and Structures", San Diego, February-March 1995

Vibration and Sound Control

Invited Paper

An overview of active/passive damping techniques employing viscoelastic materials

Geoffrey R Tomlinson

Department of Mechanical and Process Engineering
The University of Sheffield
Mappin Street
Sheffield, S1 3JD
UK

ABSTRACT

The use of passive and active damping techniques which employ viscoelastic materials as the damping medium is discussed. The importance of identifying the correct material properties is described and certain problems which can occur at high frequencies are mentioned. A comparison is drawn between active damping (AD) and active constrained layer damping (ACLD) using PZTs as the actuators and it is shown that for the examples studied, ACLD offers advantages. The paper finishes with comments on the future directions for damping studies.

1. INTRODUCTION

There is widespread interest in the use of passive and active damping technologies which is becoming increasingly important as technology drives performance factors higher in terms of noise and vibration control requirements. Much of the work is concerned with the application of high loss factor materials, such as viscoelastic layers designed to operate in their optimum (transition) range. These materials are normally associated with passive damping methods but more recently they have been combined with actuators and sensors eg. PZT, PMN, PVDF patches and have been placed in the category of active damping and "smart" structures [1-4].

Active and passive damping methods embrace a wide technology field encompassing materials, geometry, control theory, sensors and actuators. To increase damping levels, energy has to be dissipated which means that attention must be paid to the dissipation mechanism. In the case of viscoelastic materials this is via strain energy induced cyclically into the material and hence this needs to be optimised, these optimisation studies usually being carried out via FEM, Transfer Matrix or state space formulations [4-6]. This paper begins by looking at the way in which purely passive damping methods can be employed to suppress structure borne vibration and extends this to hybrid active/passive damping methods, the dissipation medium in both cases being a viscoelastic material.

2. SOME IMPORTANT FEATURES OF VISCOELASTIC DAMPING MATERIALS

Effective application of viscoelastic materials for active or passive damping requires accurate knowledge of the material properties since these are strongly dependent on temperature and frequency. The frequency-temperature dependence is well known and forms an essential part of the design process for optimising the performance of a damped structure. Figure 1 shows a typical Master Curve for a viscoelastic material with the three characteristic regions, Rubbery, Transition and Glassy which need to be addressed for effective damping control. It is the transition region which is often the target region for damping applications, whether free layer, constrained layer or active/passive methods are employed.

0-8194-2165-0/96/$6.00

In this region the mobility of the chains of polymer molecules is high. However, when an external deformation is applied there is a time delay in their rearrangement with a corresponding time delay of the internal stress state. For small deformations linear viscoelastic theory can be employed to relate the stress to the strain:

$$\sigma(t) = D\varepsilon(t) - \int_{\infty}^{t} h(t-t')\varepsilon(t')\,dt' \qquad [1]$$

$\sigma(t)$ is the instantaneous stress, ε (t) the strain, D the stress coefficient and h(t) is the viscoelastic relaxation function. Transforming to frequency via Fourier transforming (1) gives,

$$\begin{aligned}\sigma(\omega) &= \left[D - h(\omega)\right]E(\omega)\\ &= E^{*}(\omega)E(\omega)\\ \text{where } E^{*} &= E'(\omega) + jE''(\omega)\\ &= E'(\omega)\left[1 + j\eta(\omega)\right]\end{aligned} \qquad [2]$$

$\eta(\omega)$ = loss factor
$E'(\omega)$ = real or storage modulus
$E''(\omega)$ = imaginary or loss modulus

For damping applications it is important to note that,

$$\eta(\omega)\big|_{\omega\to 0} = \eta(\omega)\big|_{\omega\to\infty} = 0 \qquad [3]$$

This implies that the dynamic modulus becomes a real quantity at very low and very high frequencies,

$E'(\omega)\big|_{\omega\to 0} = E_o$ (the long term or static modulus)
$E'(\omega)\big|_{\omega\to\infty} = E\infty$ (the instantaneous modulus)

and with increasing frequency the modulus always increases, thus

$$E\infty - E_o > 0 \qquad [4]$$

In Figure 1 it can be seen that this range covers two orders of magnitude for a typical viscoelastic material over the frequency range 1 - 10^5 Hz. In some cases, such as bituminous materials which are frequently used for free layer damping treatments on car bodies, the elasticity modulus and loss factor can vary by up to 100 or more at room temperature. Whether steady state or transient vibrations are to be actively or passively controlled, inclusion of the frequency and temperature dependent material properties may prove essential for accurate predictions of the dynamic system characteristics.

3. PASSIVE DAMPING

Passive damping employing viscoelastic materials usually employs either a free layer or a constrained layer mechanism to induce cyclic strain energy losses in the viscoelastic material and thus requires a high elastic modulus and a correspondingly high value for the loss factor. The energy dissipated per cycle (or hysteresis loss) in extension of a "lossy" material is given by the expression, $\pi E'\eta\varepsilon^2$ and for a given strain level the product of the elastic modulus E' and the loss factor η needs to be a maximum. The location of the damping material is also critical in that the best locations are where the strain energy is a maximum, usually obtained from a Finite Element analysis [7]. However, the use of free layer damping treatments in "Smart" applications has not apparently been researched in any detail, although shape optimisation of unconstrained damping layers has received some attention [8].

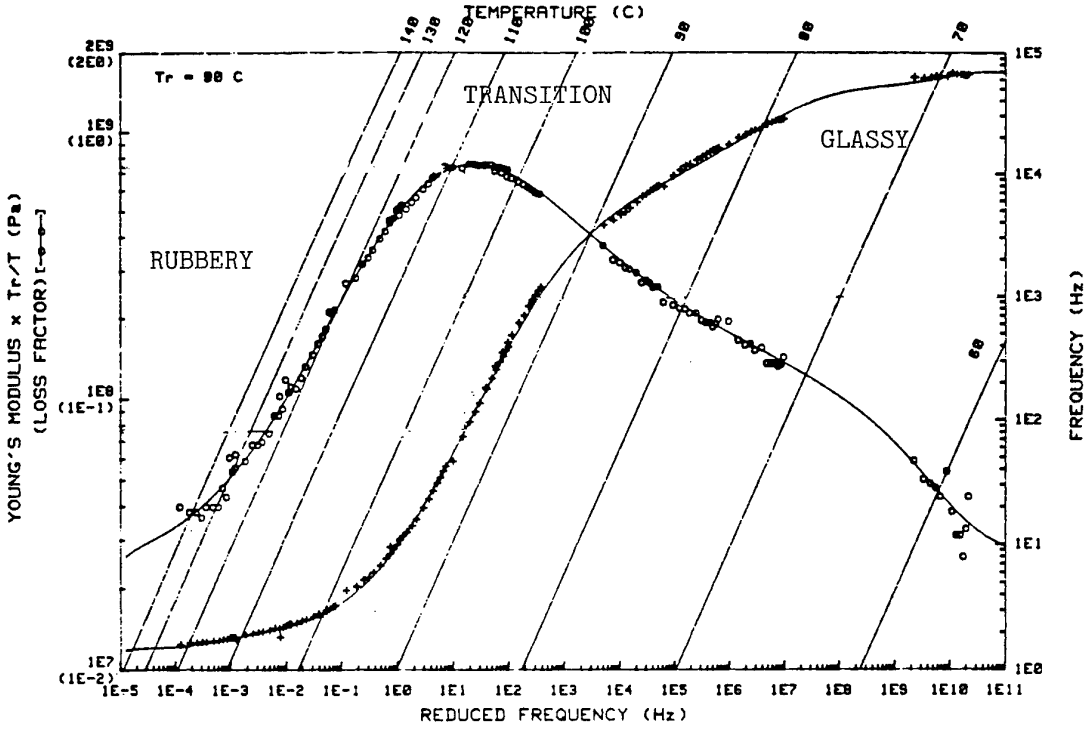


Figure 1: Master curve for a typical viscoelastic material

A tremendous volume of work has been reported on the use of passive, constrained layer damping (CLD) methods. However, the use of CLD methods needs to be treated with some care. An example of this is shown in Figure 2 where the Modal Strain Energy (MSE) ratio is plotted as a function of frequency for both straight and curved beams with CLD [9].

The modal loss factor is proportional to the modal strain energy ratio [7]:

$$\eta \text{ total} = \frac{SE_v}{SE \text{ total}} \eta_v = MSE\, \eta_v \qquad [5]$$

where η_V = loss factor of the viscoelastic material
SE_v = strain energy in the viscoelastic material
SE_{total} = total strain energy of a given mode
MSE = Modal Strain Energy

It can be seen in Figure 2 that the effect of curvature of the beam does not affect the MSE. However, there is a frequency range (3 kHz - 8kHz) where two maxima (at 3.7 kHz and 6.2 kHz) and one minimum (at 5 kHz) occur. The maxima are where both shear and radial effects occur, significantly increasing the MSE ratio. The minimum MSE is due to the mode shape being a longitudinal mode where little relative shear strain energy is induced in the constrained layer. These effects can be clearly seen in Figure 3. Thus it is essential to recognise that the type of relative motion between the constraining layer and the structure can result in significant reduction/increase in the modal damping. Further, if radial effects are significant the design process may need to account for the fact that a low modulus is needed in order to enhance the strain energy inducement.

One approach that could lead to the design of 'quiet' structures is the use of 'damped joints' in which sub-structures are connected via optimised (in the sense of energy dissipation) viscoelastic joints which provide both static structural integrity, eg. static strength, and dynamic energy dissipation. Examples of such concepts are beginning to appear. One such application is the use of 'potted joints' for outlet guide vanes, which are non-rotating vanes on typical aircraft jet engines [10]. A potted joint is simply one in which the two sub-structures

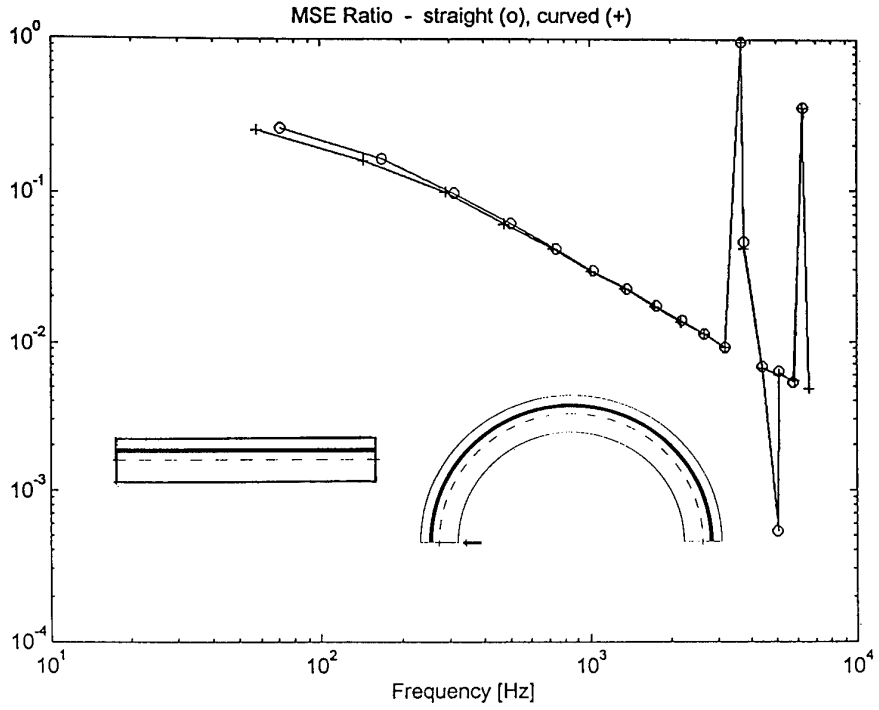


Figure 2: Modal Strain Energy for straight and curved CLD beams

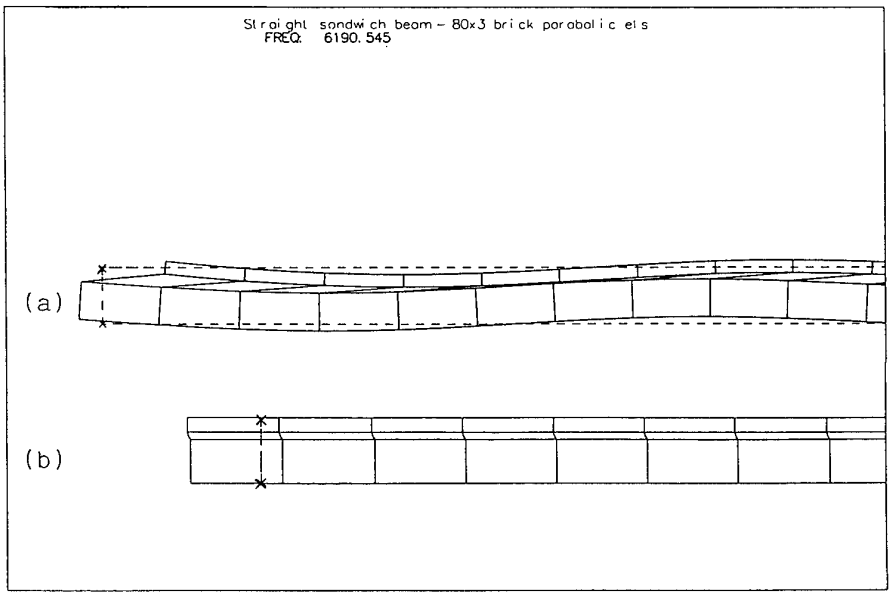


Figure 3: Mode shapes of the straight beam (a) 6.2 kHz and (b) 5 kHz

are joined by embedding one in the other as shown in Figure 4(a) where a carbon composite vane has its ends 'potted' in a viscoelastic material in its location blocks. Figure 4(b) shows the finite element model of the assembly which was used to optimise the material properties and geometry of the joint. Optimisation for vibration suppression requires that the Young's and Shear moduli (which are complex functions depending upon the frequency and the temperature) of the viscoelastic material and the potting aperture geometry result in the maximum strain energy being dissipated in the viscoelastic material for the critical vibration modes of interest.

In Figure 5(a) a comparison is drawn between the experimental vibration transmissibility characteristics (the ratio of the accelerations measured at the centre of the vane to the value measured at the input, ie. the end blocks) for the unpotted and the potted vane, optimised for the material properties at 100°C where the material is in its glass transition region; the unpotted vane means that the ends of the vane were clamped directly into the aluminium end blocks.

It can be seen that the vibration amplitudes of the first flexural mode have been considerably reduced, giving Q values of 15, compared to about 190 for the unpotted case. However, when the temperature is changed to 20°C, the vibration transmissibility results are not as good, as can be seen in Figure 5(b) which compares the potted results at 20°C to those at 100°C. This is readily explained by examining the Master Curves for the viscoelastic material, shown in Figure 1. At 400-500Hz and 20°C the Young's modulus and the loss factor have values of the order of 2 GPa and >0.1 respectively whereas at 100°C these become 0.6 GPa and 0.75 respectively.

This concept of potted joints is easily be applied to a range of structures and, if optimised, could lead to quieter structures.

4. ACTIVE DAMPING USING SMART TECHNOLOGIES

The previous sections have dealt with only passive viscoelastic damping methods. For the past several years there has been a growing interest in the use of active constrained layer damping treatments and combined active/passive, ie. hybrid, methods. Often this is accomplished via "smart" configurations where combined sensing/actuation materials such as PZT, PMN, PVDF or SMA are used [3, 11, 12].

There are several active damping concepts in use which employ viscoelastic materials. Figure 6 shows some of the common configurations and it is not unusual to find all of these being called active constrained layer damping (ACLD), although it is clear that they are quite different. There is little published literature on rigorous mathematical analyses of ACLD, although some recent papers describe a mathematical framework for ACL/ACLD structures which offer a way forward [11-14].

The principal advantages of using ACLD are related to the enhanced shear that can be actively induced in the viscoelastic material, the inherent reduction of spillover effects and the fact that the control gains needed to produce a given controllability are smaller. The maximum feedback gain that can be used is not only limited by instability due to spillover but also by the material non-linearity of the actuation device, eg. the PZT at high feedback voltages.

Referring to the case of Figure 6(a), the variation of actuator (PZT) voltage required to achieve a desired feedback gain when the base excitation has a peak acceleration of 0.5g over the frequency range 0-100Hz is shown in Figure 7 where it can be seen that for the PZT actuator located on the surface of the constraining layer on the beam, the feedback gains are considerably higher than those for the actuator located on the bare beam (no constrained layer damping). This in turn results in an improved reduction in resonant peaks for the same feedback gain, and also allows higher gains.

Another advantage of this configuration is that both longitudinal and flexural motion can be controlled. The analysis for a rectangular section cantilevered beam with symmetrically placed constraining layers and PZT actuators is described in [11]. The experimental arrangement of this configuration is shown in Figure 8. Figure 9(a), (b) shows the frequency response functions over the range 0-10kHz for the beam with the PZTs

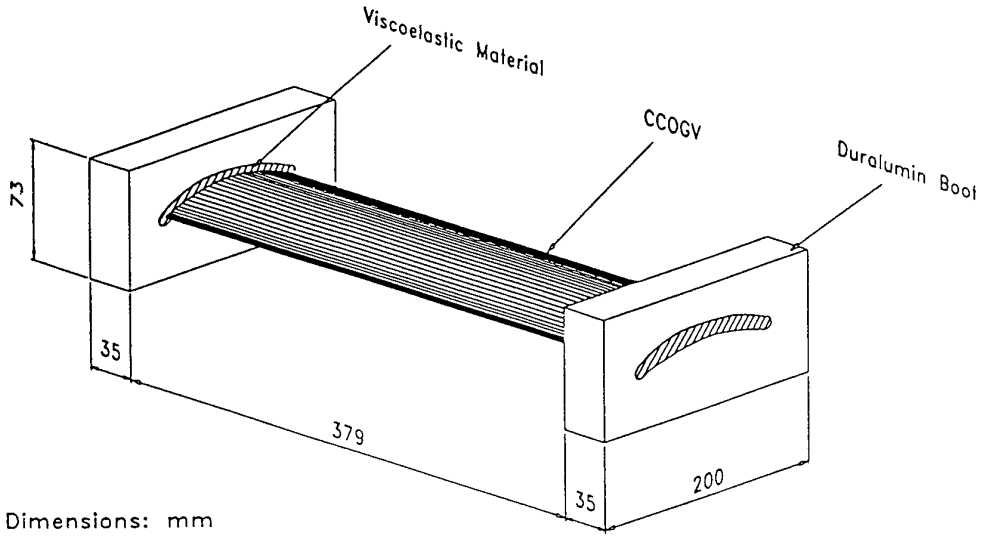


Figure 4(a): Potted joint assembly

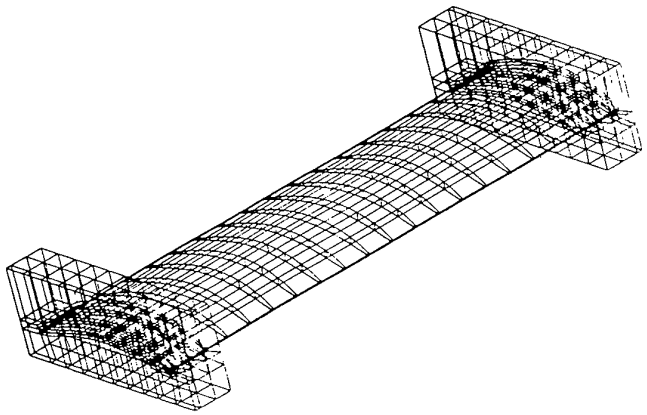


Figure 4(b): FE Model of the assembly shown in Figure 4(a)

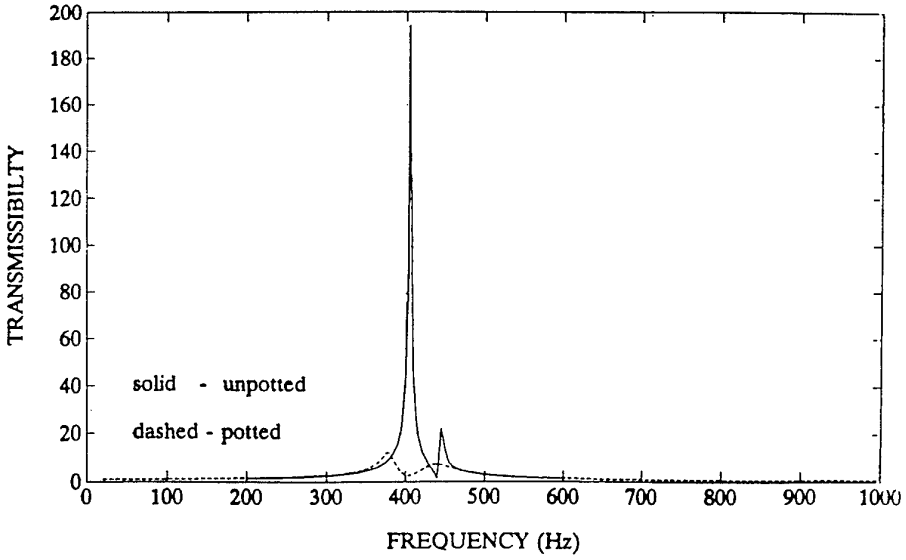


Figure 5(a): Comparison of potted and unpotted vibration transmissibility characteristics at 100°C

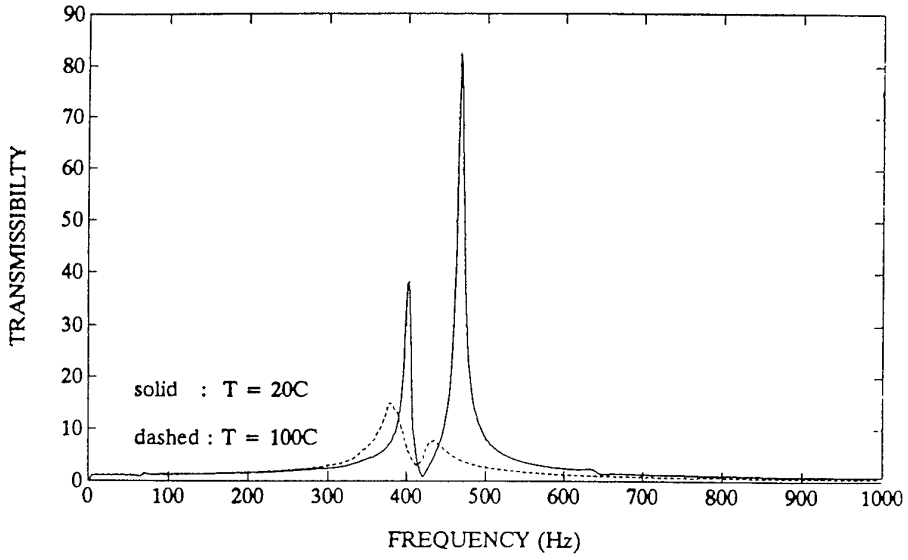


Figure 5(b): Effect of temperature on the potted vane assembly

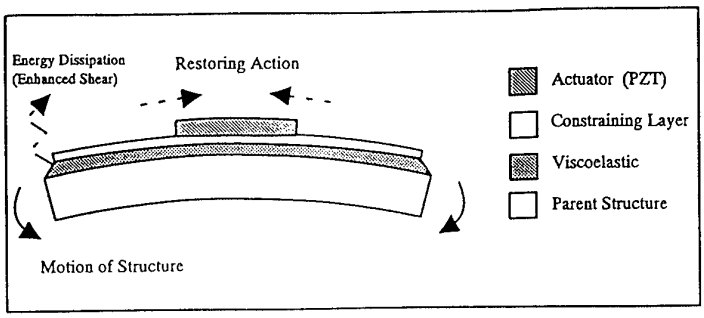


Figure 6(a): Active Constrained Layer Damping (as defined in this paper)

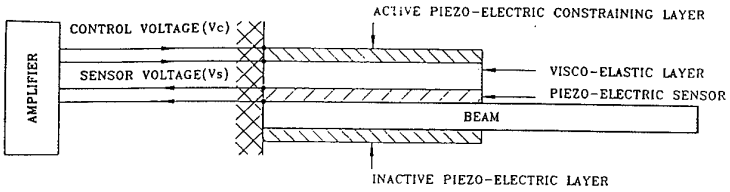


Figure 6(b): Alternative version of ACLD (ref 12)

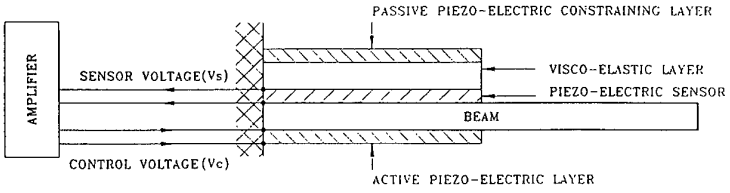


Figure 6(c): Active/Passive CLD (ref 12)

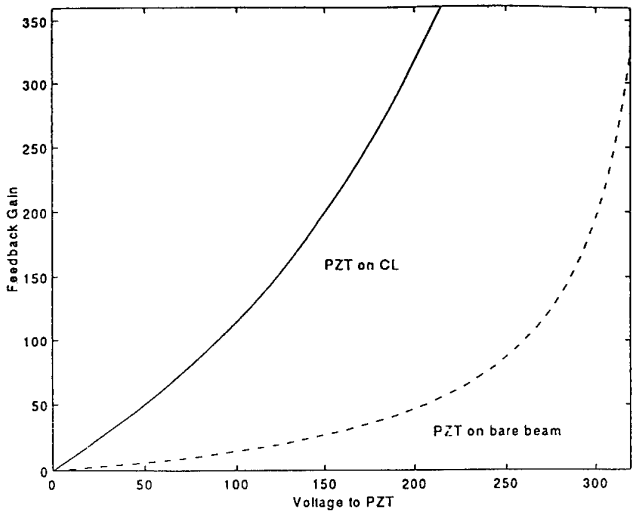


Figure 7: Feedback gain versus PZT excitation voltage for the PZT patch on the constraining layer (CL) and on the beam directly

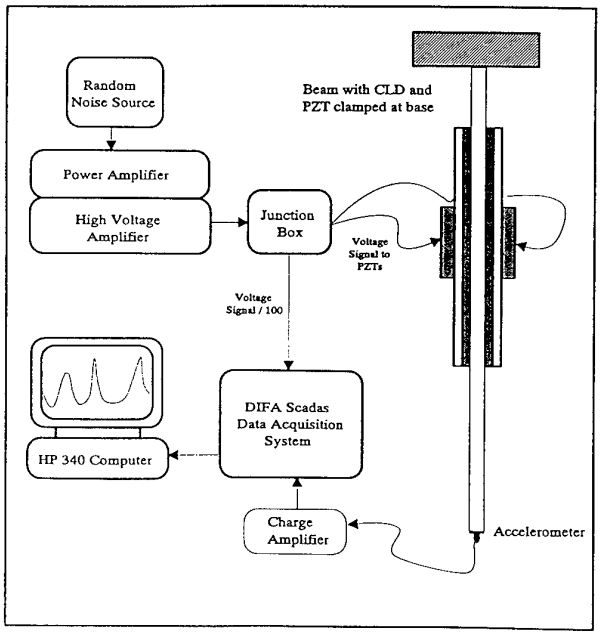


Figure 8: Experimental arrangement used for symmetric (longitudinal) and asymmetric (flexural) ACLD studies

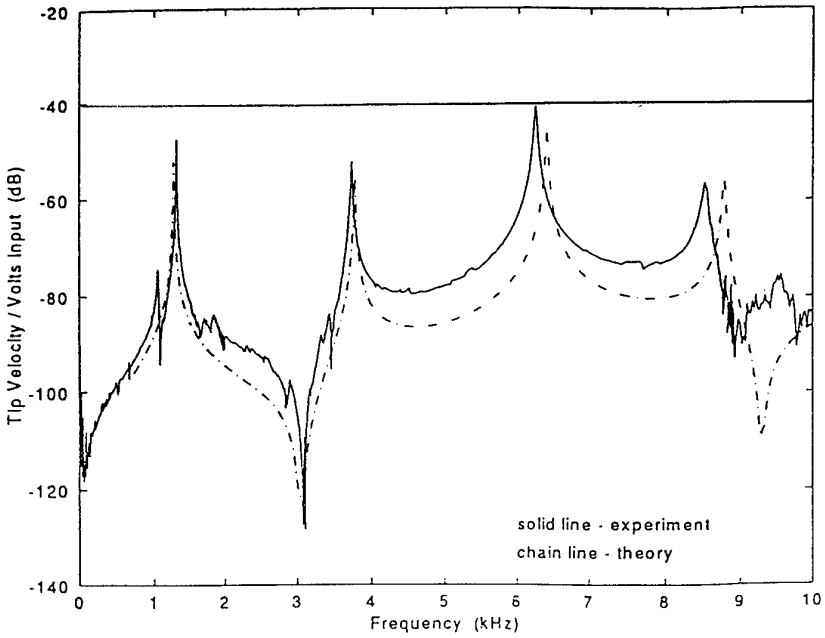


Figure 9(a): PZT patches directly bonded to the beam - longitudinal vibration characteristics

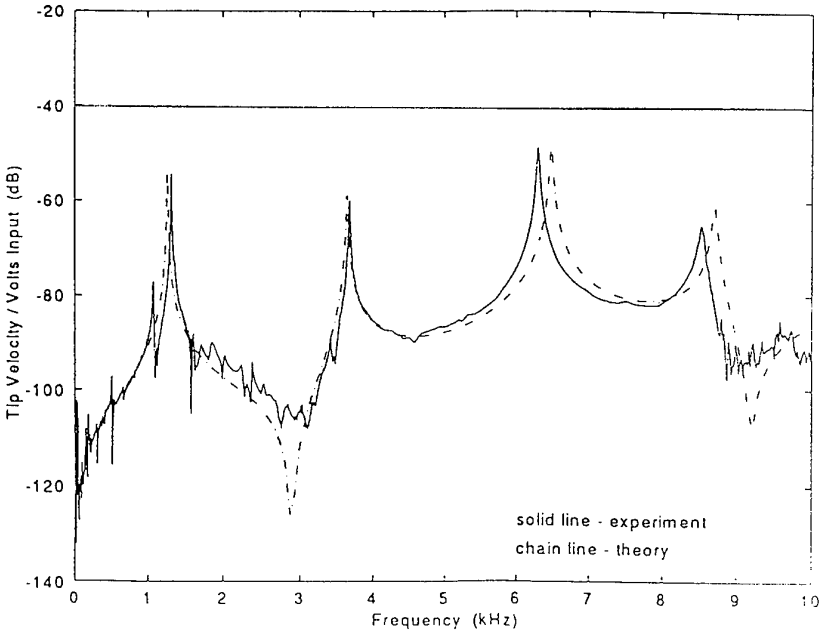


Figure 9(b): As in Figure 9(a) but with the PZT patches bonded to the constraining layer

bonded to the constraining layers and to the bare beam in the case of longitudinal motion. Overall there is a reduction of about 10 dB across the frequency range for the ACLD. Figure 10 shows the results for the flexural case. Significant improvements are found here, where a reduction of almost 20 dB across the 100 Hz frequency has been achieved.

4.1 Comparison of Active Damping (AD) and Active Constrained Layer Damping (ACLD)

In order to compare AD with ACLD the two beam configurations used above were employed. Case A in which the PZT actuators were bonded directly to the beam and Case B with the actuators bonded to the constraining layer. The tip velocity, derived from the integrated accelerometer was used as the feedback signal [11]. The PZTs were located at the optimum position to ensure the most effective actuation for the first four flexural modes. Although co-location of sensors and actuators is known to reduce spillover effect, non-collocation was used to further demonstrate the benefits of ACLD.

Figures 11 and 12 show the tip to base transmissibility as the feedback gain was increased for Cases A and B respectively. In Figure 11 it can be seen that the third mode became unstable at a gain of about 50 (due to the non-collocation of the sensor/actuator). As the gain was increased above this the non-linearity (saturation) of the PZTs resulted in no improvement in the results. In Case B, major improvements are achieved, in particular the fourth mode, which was barely affected by the Case A approach due to the positioning of the actuators, has virtually disappeared and the previously unstable third mode is also barely evident.

A comparison between the configurations of Figure 6(a), (b), (c) has not been carried out. However, it is clear from the work reported here and that reported in [11 - 14] that worthwhile benefits accrue from combining passive and active viscoelastic damping technologies using PZT actuation materials.

5. FUTURE DIRECTIONS

It is considered important to finish this paper by mentioning some possible future developments in damping technology. Recent work has shown that "directional damping" can be obtained via the appropriate orientation of fibres in a resin matrix doped to give good loss properties [15].

Integral damping using embedded viscoelastic layers in composites (damped laminates) and metal matrix composites will probably play important roles in automotive and aerospace applications. Combining these with actuation/sensing and design/prediction methods will lead to increased life cycle performance as damping can be designed-in with confidence.

The increasing developments in MEMs will require an understanding of how to model and introduce damping at the micro and nano levels, leading to new concepts in both passive and active damping methodologies.

Biological and biomimetics should be applied to damping. Examples exist of cellular automata being used to evolve structural topologies where cells die and are re-born depending on the stress state [16]. Extending this to resonant regions in structures could be interesting.

6. CONCLUSIONS

This paper has presented a somewhat brief overview of passive and active damping methods employing viscoelastic materials and smart technologies. Some new concepts in both areas have been indicated and comparisons drawn between passive/active methods. It is clear from the results presented here on a simple beam structure that ACLD using PZT patches with the appropriate feedback control will always outperform active control and provide the added benefit of a fail-safe mechanism from the passive CLD. However, the optimisation of such configurations needs further research, including the extension to much higher frequencies where additional effects need to be considered (radial expansion and shear) and to realistic structures where coupled flexural, torsional and longitudinal vibrations may occur.

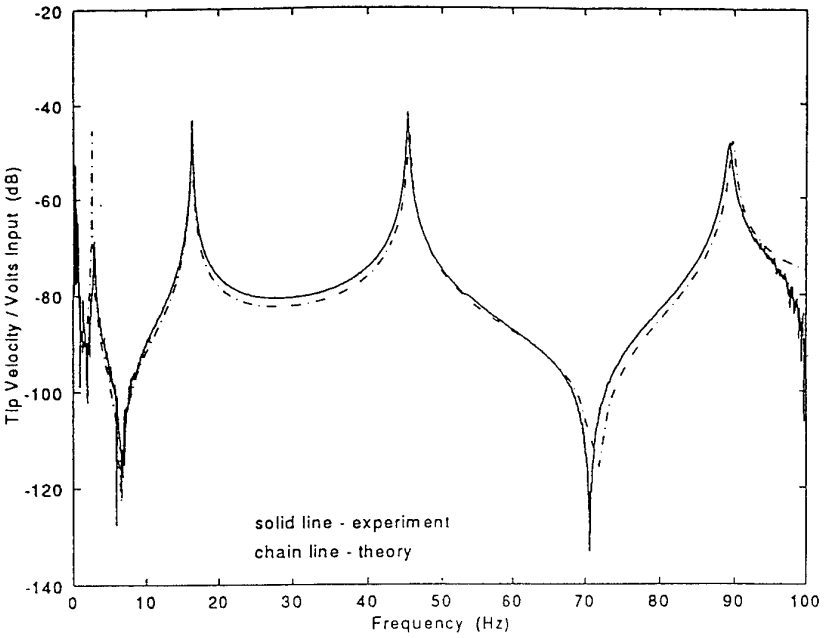


Figure 10(a): PZT patches bonded directly to the beam - flexural vibration characteristics

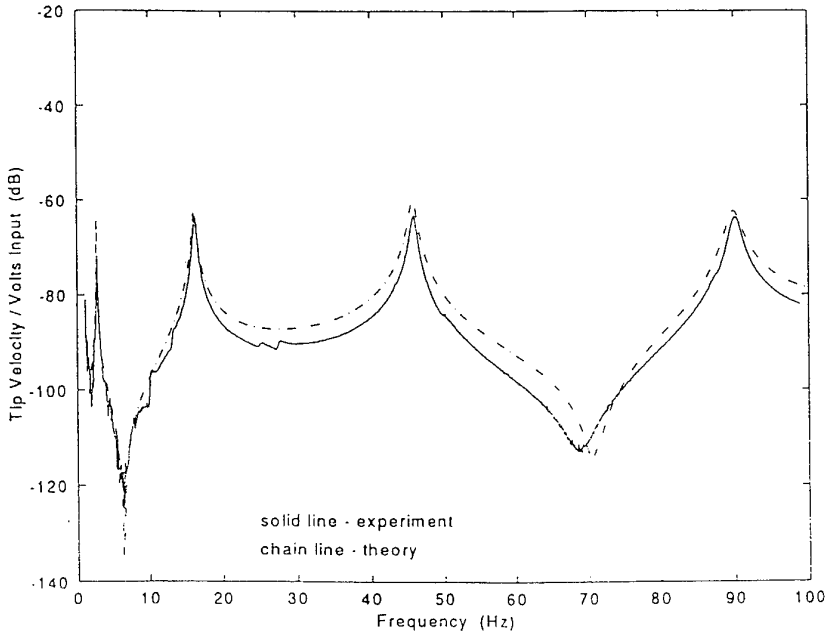


Figure 10(b): PZT patches bonded to the constraining layer

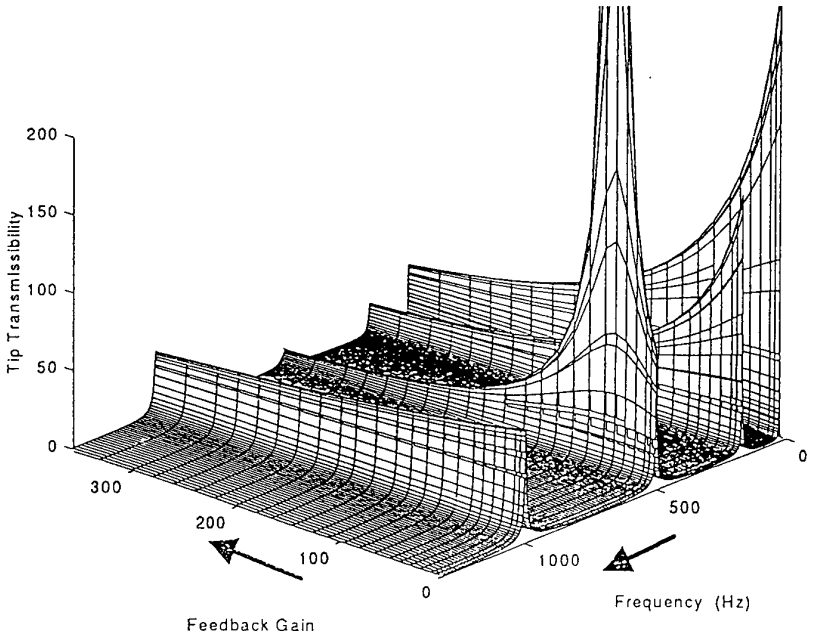


Figure 11: Tip/Base transmissibility characteristics as a function of the feedback gain - PZT patches bonded directly to the beam

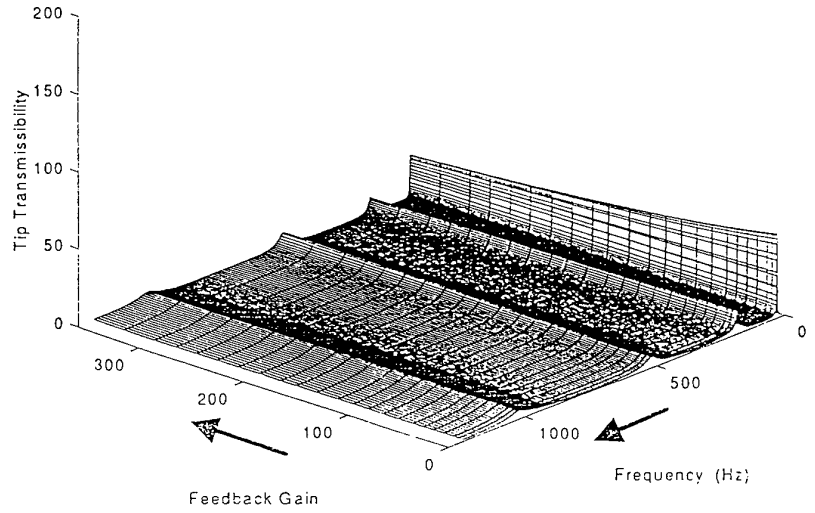


Figure 12: As Figure 11 but with the PZT patches bonded directly to the constraining layer

7. REFERENCES

1 Baz, A and Ro, J, 1993a, "Partial treatment of flexible beams with active constrained layer damping". Recent Developments in Stability and Control of Structural Systems, Proc ASME, AMD-167, pp 61-80.

2 Shen, I Y, 1994b, "Hybrid damping through intelligent constrained layer treatments", ASME Journal of Vibration and Acoustics, Vol 116, pp 341-349.

3 Van Nostrand, W C, 1994. Active constrained layer damping using PZT actuators, PhD Dissertation, State University of New York, Buffalo.

4 Baz, A and Ro, J, 1993b, "Finite element modelling and performance of ACLD", 9th VPI & SU Conference on Dynamics of Large Structures, Blacksburg, VA.

5 Tschudi, H R, 1993, "Transfer matrix theory of damping of multi-layer structures", Unikeller Conference, Rieter Automotive, Switzerland.

6 Anderson, E H, 1995, "Interpretation of active dampers as variable-parameter passive devices", ASME Design Engineering Technical Conference, Vol 84-3, Pt C, pp 727-735

7 Johnson, C D and Kienholz, D A, 1982, "Finite element prediction of damping in structures with constrained viscoelastic layers", AIAA Journal, Vol 20, No 9.

8 Lumsdaine, A and Scott, R A, 1995, "Shape optimisation of unconstrained beam and plate damping layers", ASME Design Engineering Technical Conference, Vol 84-3, Pt C, pp 15-22.

9 Riva, A and Tomlinson, G R, 1995, "Effect curvature on the modal strain energy of beams", MONICA report, Politechnico di Torino.

10 Oyadiji, S O and Tomlinson, G R, 1995, "Controlling the vibration levels of vibrating vanes using viscoelastic materials", ASME Design Engineering Technical Conference, Vol 84-3, Pt C, pp 709-718.

11 Rongong, J A, Wright, J R, Wynne R J and Tomlinson, G R, "Modelling of a hybrid constrained layer/piezoceramic approach to active damping", to be published in the ASME Journal of Vibration and Acoustics (1996).

12 Baz, A and Ro, J, 1995, "Active control and passive CLD versus ACLD", to be published in ASME Journal of Vibration and Acoustics.

13 Liao, W H and Wang, K W, 1995, "On the active-passive hybrid vibration control actions of structures with active constrained layer treatments", ASME Design Engineering Technical Conference, Vo, 84-3, Pt C, pp 125-141.

14 Banks, H T, Medhin, N G and Zhang, Y, "A mathematical framework for curved active constrained layer structures: Well posedness and approximation", submitted to ASME Journal of Vibration and Acoustics.

15 House, J R, Bell, S and Strode, M, 1996, "Optimisation of intrinsic damping by exploitation of fiber orientation with viscoelastic composites, SPIE Conference on Smart Structures and Materials, Paper 2720-34, San Diego.

16 Worden, K and Tomlinson, G R, 1995, "On structures from cellular automata", Proceedings of the International Conference on Microsystems, Intelligent Materials and Robots, IFS, Sendai, Japan.

Invited Paper

Smart composite cylindrical shells without vibration

Junji Tani and Jinhao Qiu

Institute of Fluid Science, Tohoku University
Katahira 2-1-1, Aoba-ku 980, Sendai, Japan
Tel. +81-22-217-5247, Fax: +81-22-217-5311
E-mail tani@ifs.tohoku.ac.jp

ABSTRACT

The forced vibration of a cylindrical shell is controlled using the distributed piezoelectric actuators and hybrid control method. The shell is constructed from a polyester film in the middle surface and two piezoelectric films, one on each side. The electrodes on the surfaces of the piezoelectric films are divided into several parts and two parts of the films are used as actuators. The shell is vertically mounted on a vibration table and excited by the horizontal motion of the table. The hybrid control method which is a combination of μ-synthesis control and disturbance cancellation method is used. Simulation and experiment were carried out and the results show that the hybrid control is more effective than each individual control method.

1. INTRODUCTION

Cylindrical shells are widely used in engineering structures, such as oil tanks, MRI equipment and bodies of aircraft and space shuttles. The vibration control of cylindrical shells was first initiated by cabin noise problem in turbopropeller powered passenger aircraft[1,2] and has become an active area of research in the last few years.[3-9] In the early research, point actuators which produce concentrated force are used in vibration control of cylindrical shell.[3] In the recent work, small patches of PZT actuators[4,5] and distributed PVDF actuators[6,8] were widely used, since spillover due to distributed actuators can be reduced by the optimization of the size, position and output of the actuators.

Several control methods have been used in the past research. These methods can be divided into two categories: disturbance cancellation method and active control method. The disturbance cancellation method(DCM) can only be used in the control of vibration induced by predetermined disturbances or disturbances which can be measured, but is more effective than active control method.[7,9] They are often used in the control of high-frequency vibration, since they can easily be realized by analog circuit. The active control method is suitable for the control of vibration induced by both the predetermined and unknown disturbances.[6,7] Usually they are combined with digital control and used in the control of vibration under 100Hz due to the limit of sampling frequency.

This paper aims at the vibration control of a multi-layered composite piezoelectric shell using the integrated distributed actuators and a hybrid control method which is a combination of the active control method and disturbance cancellation method. It is expected that the combination of the two control methods will give better control effect than each single method. The μ-synthesis control theory is applied in the implementation of active control. Moreover the integration of actuators into the structures to be controlled is an important step in the realization of smart materials and structures.

2. MODEL AND ANALYSIS

Figure 1 shows the configuration of the cylindrical shell used in this study. The cylindrical shell is made of two layers of piezoelectric films and one layer of polyester film, which are pasted together. The electrodes on the surface of the piezoelectric films are divided into several patches so that two of them can be used as actuators as shown in Figure 1.

The lower end of the shell is fixed to a vibration table and the upper end is free. The shell is excited by the horizontal motion of the vibration table. A photonic sensor that is fixed to the vibration table is used to measure the relative displacement of shell. When two piezoelectric films in the same actuator are applied with the in-phase voltages, they generate uniform in-plane resultant forces in the actuator area. When the two films

0-8194-2165-0/96/$6.00

are applied with voltages of opposite phases, they will generate a distributed bending moments in the actuator area. The distributed in-plane forces or bending moments are used as the control force.

The coordinate system is fixed to the vibration table as shown in Figure 6. Based on the assumption that the shell is homogeneous and isotropic, Flügge's equation can be used to describe the motion of the cylindrical shell which contains the piezoelectric film actuator. The displacements in x, y and z directions of point $(x,\ y)$ are denoted by $U(x,y,t)$, $V(x,y,t)$ and $W(x,y,t)$, respectively. For convenience, the coordinates and displacements are non-dimensionalized as follows.

$$\xi = \frac{x}{L},\quad \eta = \frac{y}{L},\quad \bar{\nabla}^2 = \frac{\partial^2}{\partial\xi^2} + \frac{\partial^2}{\partial\eta^2},\quad u = \frac{RU}{Lh},\quad v = \frac{RV}{Lh},\quad w = \frac{W}{h} \tag{1}$$

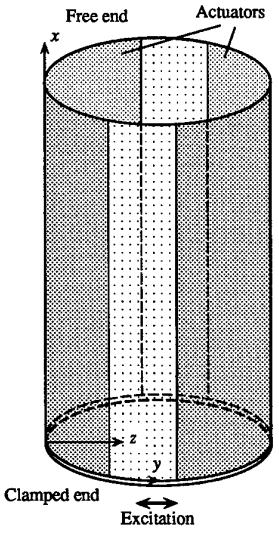
where R, L and h are radius, length and thickness of the shell.

Using the dimensionless coordinates and displacements, the equation of motion can be expressed in the following form:

$$\left.\begin{aligned}
&u_{,\xi\xi} + \nu_1(1+k)u_{,\eta\eta} + (1-\nu_1)v_{,\xi\eta} - \nu w_{,\xi} + k\kappa\cdot(w_{,\xi\xi\xi} - \nu_1 w_{,\xi\eta\eta}) - \frac{1}{\kappa\Omega^2}u_{,tt} = -\frac{RL}{Ch}(f_{cx} + f_{dx})\\
&(1-\nu_1)u_{,\xi\eta} + \nu_1(1+3k)v_{,\xi\xi} + v_{,\eta\eta} - w_{,\eta} - \frac{1}{\kappa\Omega^2}v_{,tt} = -\frac{RL}{Ch}(f_{cy} + f_{dy})\\
&-\nu u_{,\xi} - v_{,\eta} + k\kappa^2\bar{\nabla}^4 w + k\kappa(u_{,\xi\xi\xi} - \nu_1 u_{,\xi\eta\eta}) + (1+\nu_1)k\kappa v_{,\xi\xi\eta} + (1+k)w + 2k\kappa w_{,\eta\eta} + \frac{1}{\Omega^2}w_{,tt}\\
&\quad = \frac{R^2}{Ch}(f_{cz} + f_{dz})
\end{aligned}\right\} \tag{2}$$

where f_{cx}, f_{cy} and f_{cz} are distribution of forces generated by the actuator and f_{dx}, f_{dy} and f_{dz} distribution of forces generated by external disturbances. Moreover, k, κ, C and Ω are given in the following expressions:

$$k = \frac{h^2}{12R^2},\quad C = \frac{Eh}{1-\nu^2},\quad \kappa = \frac{R^2}{L^2},\quad \Omega = \frac{E}{\rho R^2(1-\nu^2)} \tag{3}$$



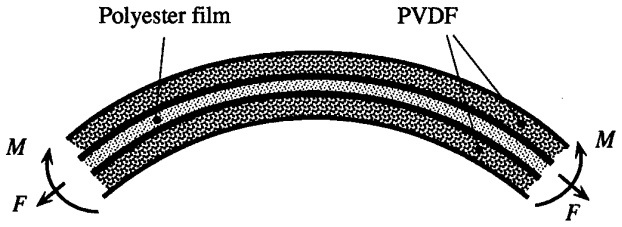


Figure 1. Configuration of the shell

Table 1. Parameter of the model

Length of shell L (mm)	600
Radius of shell R (mm)	50
Young's modulus of shell E (N/m^2)	2.3×10^9
Young's modulus of PVDF E_p (N/m^2)	2.0×10^9
Internal damping coefficient ζ	0.02
Density of shell ρ (kg/m^3)	1.78×10^3
Thickness of PVDF h_p (mm)	0.052
Thickness of shell h (mm)	0.19
Width of actuators (mm)	$2\pi R/3$
Sensing point (x, y) (mm)	(295, 0)

Table 2. Natural frequency

Mode (i, j)	(1, 1)	(1, 2)	(1, 5)
Simulation (Hz)	75.3	27.5	87.9
Experiment (Hz)	73.5	28.6	–

where E, ν and ρ are Young's modulus, Poisson's ration and density of the shell. The values of material properties and geometrical parameters are shown in Table 1.

The distribution of control force can be obtained from the following expression:

$$\left.\begin{aligned} f_{cx} &= \frac{1}{L}\left(\frac{\partial N_x}{\partial \xi} + \frac{\partial N_{xy}}{\partial \eta}\right) \\ f_{cy} &= \frac{1}{L}\left(\frac{\partial N_y}{\partial \eta} + \frac{\partial N_{xy}}{\partial \eta} + \frac{1}{R}\frac{\partial M_{xy}}{\partial \xi} - \frac{1}{R}\frac{\partial M_y}{\partial \eta}\right) \\ f_{cz} &= \frac{1}{L^2}\left(\frac{\partial^2 M_x}{\partial \xi^2} + 2\frac{\partial^2 M_{xy}}{\partial \xi \partial \eta} + \frac{\partial^2 M_y}{\partial \eta^2}\right) + \frac{1}{R}N_y \end{aligned}\right\} \tag{4}$$

where N_x, N_y and N_{xy} are components of the in-plane forces and M_x, M_x and M_{xy} the bending moments generated by the actuators. Since the main modes to be controlled is circumferentially and axially first mode, there are two ways to apply voltages to the films. The first one is to apply voltages of opposite phase to the two films in the same actuator so that each actuator produces bending moments. The other is to apply in-phase voltages the two films in the same actuator but voltages of opposite phase to the two actuators. In this way, each actuator generates in-plane forces, but the pair of x components of the in-plane forces of the two actuators constitutes a bending moment which can be used in the control of the axially 1st mode. The later is proved more effective than the former and is used in this study. The property of voltages lead to the following in-plane forces and bending moments:

$$\begin{aligned} N_x &= 2E_p d_{31} V[H(\eta_1, \eta_2) - H(\eta_3, \eta_4)]H(\xi_1, \xi_2) \\ N_y &= 2E_p d_{32} V[H(\eta_1, \eta_2) - H(\eta_3, \eta_4)]H(\xi_1, \xi_2) \\ N_{xy} &= M_x = M_{xy} = M_y = 0 \end{aligned}$$

The distribution of disturbance forces are as follows:

$$f_{dx} = 0, \quad f_{dy} = \rho h a \sin\frac{L}{R}\eta, \quad f_{dz} = \rho h a \cos\frac{L}{R}\eta \tag{5}$$

where a is the acceleration of the vibration table.

The lower end of the shell is clamped and the upper end is free. The boundary conditions of the clamped

end can be written in the following form:

$$w = w_{,\xi} = u = v = 0 \qquad (\xi = 0)\ . \tag{6}$$

The boundary condition of free end is expressed as follows:

$$S_x = M_x = N_x = T_x = 0 \qquad (\xi = 1). \tag{7}$$

where S_x, M_x, N_x and T_x are lateral force, bending moment, in-plane force and shear force, respectively.

3. STATE EQUATION

The following second-order ordinary differential equation can be obtained for each mode by using the modal analysis method:

$$\ddot{q}_{ij} + 2\zeta\omega_{ij}\dot{q}_{ij} + \omega_{ij}^2 q_{ij} = b_{1ij}u_c + b_{2ij}w_d \qquad (i = 1, \cdots, \infty,\ \ j = 0, \cdots, \infty) \tag{8}$$

where i and j are the axial and circumferential wave number, q_{ij} the modal variable, ω_{ij} the natural frequency of mode (i, j), ζ the damping coefficient of shell, u_c the control input, w_d the external disturbance, and b_{1ij} and b_{2ij} coefficients. In the present case, the external disturbance is the acceleration a of the vibration table. Although there are infinite numbers of modes, most of them have little influence on the total vibration of the shell. By ignoring the unimportant modes and renumbering the remained mode in the ascending order of frequency by a single index, Equation (8) can be expressed in the following form:

$$\ddot{q}_k + 2\zeta\omega_k\dot{q}_k + \omega_k^2 q_k = b_{1k}u_c + b_{2k}w_d \qquad (k = 1, 2, \cdots, n) \tag{9}$$

From equation (9), the following state equation can be obtained.

$$\dot{\mathbf{X}}(t) = \mathbf{A}_c\mathbf{X}(t) + \mathbf{B}_1 u_c(t) + \mathbf{B}_2 w_d(t) \tag{10}$$

where

$$\mathbf{X}(t) = [q_1(t)\ \cdots\ q_n(t)\ \dot{q}_1(t)\ \cdots\ \dot{q}_n(t)]^T \tag{11}$$

$$\mathbf{A}_c = \left[\begin{array}{c|c} \mathbf{O} & \mathbf{I} \\ \hline -\Omega^2 & -c\Omega \end{array}\right],\ \mathbf{B}_1 = \left[\begin{array}{c} \mathbf{O} \\ \hline \Theta_1 \end{array}\right],\ \mathbf{B}_2 = \left[\begin{array}{c} \mathbf{O} \\ \hline \Theta_2 \end{array}\right]$$

$$[\Omega] = \begin{bmatrix} \omega_1 & & 0 \\ & \ddots & \\ 0 & & \omega_n \end{bmatrix},\ [\Theta_1] = \begin{bmatrix} b_{11} \\ \vdots \\ b_{1n} \end{bmatrix},\ [\Theta_2] = \begin{bmatrix} b_{21} \\ \vdots \\ b_{2n} \end{bmatrix}$$

Since the exciting force is a uniform horizontal inertial force, only the mode with wave number (1, 1) is induced and all other modes are not. Hence, only mode (1, 1) is excited and need to be controlled. On the other hand, though the actuators couple strongly with the mode to be controlled, they are also coupled with other modes. This means that they will excite other modes when it controls mode (1, 1). Hence the modes that couple with the actuators should be included in the state equation. In this study, modes (1, 1) and (1, 5) are considered. Mode (1, 5) couples with the actuator and have natural frequency near that of mode (1, 1) as shown in Table 2.

When a sensor is used to measure the displacement of the shell, the output of the sensor can be expressed as a function of the state vector as follows:

$$y_c = \mathbf{C}_c\mathbf{X} \tag{12}$$

where $\mathbf{C}_c$ is a row vector depending upon the coordinate of the measuring point. Equation (12) is the output equation of the shell system.

4. DESIGN OF CONTROLLER

In this study, the feedback control and the disturbance cancellation method are combined in the calculation of the control input, that is, the control input u_c is the sum of the control inputs obtained from the two control methods and can be expressed in the following form:

$$u = u_a + u_p \tag{13}$$

where u_a and u_p are control inputs calculated from feedback controller and disturbance cancellation controller. If the transfer function of the active controller and disturbance cancellation controller are denoted by K_a and K_p, the outputs u_a and u_p can be expressed in the following form:

$$u_a(s) = K_a(s)y_c(s) \tag{14}$$

$$u_p(s) = K_p(s)w_d(s) \tag{15}$$

The input of active control is calculated from the output y_c and the input of disturbance cancellation is calculated from the external disturbance. The controllers K_a and K_p are designed independently as discussed below.

4.1 Design of Active Controller

There are many active control methods such as PID, LGR, $\mathcal{H}_\infty$, μ-synthesis and sliding mode control. In this study, the active controller is designed by using $\mathcal{H}_\infty$ control theory and improved by μ-synthesis method. The $\mathcal{H}_\infty$ control and μ-synthesis methods have good robustness and the model error can be considered in the design of controller. In order to use $\mathcal{H}_\infty$ control theory, an expanded system as shown in Figure 2 is constructed, where G_1 is nominal plant and Δ_G the perturbation of G_1. The signals u_c, y_c, z_c, w_c, d and e are control input, control output, modal error input, modal error output, disturbance input and control error output, respectively. The nominal plant G_1 and disturbance input can be expressed in the following form:

$$G_1 = \mathbf{C}(s\mathbf{I} - \mathbf{A})^{-1}\mathbf{B}_1 \,, \tag{16}$$

$$d(s) = G_2(s)w_d(s) \tag{17}$$

where $w_d(s)$ is the external disturbance and $G_2(s)$ is the transfer function from w_d to d. From the state equation, the following relation can be obtained:

$$G_2 = \mathbf{C}(s\mathbf{I} - \mathbf{A})^{-1}\mathbf{B}_2 \,. \tag{18}$$

Weight function W_{del} is introduced to describe the frequency domain characteristics of the disturbance and weight function W_p to describe the desired performance in the frequency domain. The two weight functions are given in the following form:

$$W_{del} = \frac{10(s+100)}{s+10000} \,, \quad W_p = \frac{0.2(s+8200)}{s+82} \tag{19}$$

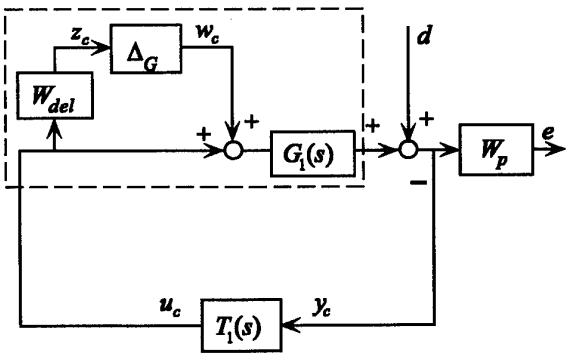


Figure 2. Expanded system

The gain plot of the two weight function are shown in Figure 3. After the plant and weight function are given, the controller $K_a(s)$ can be designed by using the Matlab μ-synthesis toolbox. The performance of the controller is measured with the nominal performance which is evaluated by the transfer function T_{wz} from w_c to z_c and

robust stability which is evaluated by the transfer function T_{de} from d to e in the expanded system. When the two transfer functions satisfies the following two inequality

$$\|T_{wz}\|_\infty = \|W_{del}T_1G_1(I+T_1G_1)^{-1}\|_\infty < 1 \tag{20}$$

$$\|T_{de}\|_\infty = \|W_p(I+G_1T_1)^{-1}\|_\infty < 1 \tag{21}$$

the nominal performance and robust stability are satisfied. The maximum singular values of the two transfer functions are shown in Figure 4. Since the maximum singular values of both the two transfer functions are less than one in the whole frequency range, it can be found that both nominal performance and robust stability are satisfied.

4.2 Design of Disturbance Cancellation Controller

In the problem of structural vibration control, the output response is generated by the excitation force which is considered as the external disturbance. If a control input which will generate the same response as the disturbance is applied simultaneously to actuators, the vibration will be suppressed completely. This method is called disturbance cancellation method and can be applied to the control of vibration induced by predetermined disturbances or disturbances which can be measured, since an adequate control input can be calculated from the disturbance. In this section the design of disturbance cancellation controller is discussed.

The output induced by the external disturbance is the same as the disturbance input in Figure 2 and given out in Equation (17). On the other hand, the output generated by the input of disturbance cancellation control can obtained from Equation (15) and expressed as following form:

$$y_p(s) = G_1(s)u_p(s) = G_1(s)K_p(s)w_d(s) \tag{22}$$

From the definition of disturbance cancellation method, the two output should cancel each other so that the total output is zero. This condition yields

$$G_1(s)K_p(s) + G_2(s) = 0 \tag{23}$$

From Equation (23), the transfer function of the disturbance cancellation controller can easily be calculated.

The external disturbance is needed for the calculation of control input in the disturbance cancellation method. When the external disturbance is known, the output will always be zero in the ideal state. This means that the vibration can suppressed completely. However in most cases the external disturbance is not known and must be measured on line by sensors. The measured value of external disturbance $\bar{w}$ can be expressed in the following

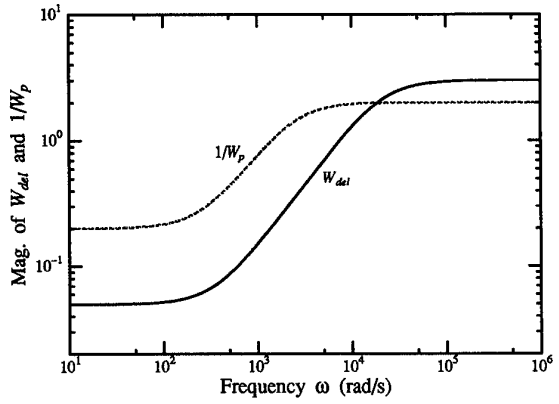


Figure 3. Weight functions W_{del} and W_p

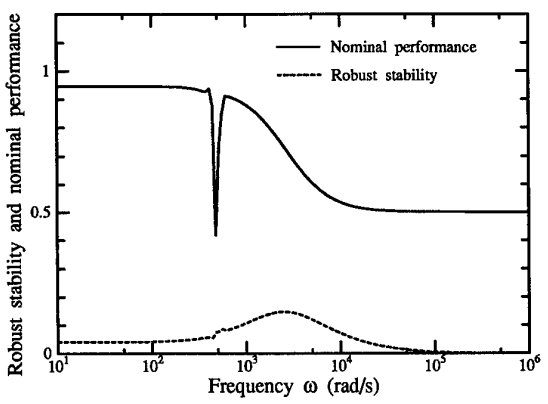


Figure 4. Robust stability and nominal performance

form:

$$\bar{w}_d(s) = T_{s2}(s) w_d(s) \tag{24}$$

where $T_{s2}(s)$ is the transfer function of the sensor used to measure the external disturbance. Since $\bar{w}_d(s)$ is only an approximation of $w_d(s)$, it is impossible to suppress the vibration completely by using the disturbance cancellation method only.

5. EXPERIMENTAL SETUP

The experimental setup is shown in Figure 6. The shell was vertically mounted on a vibration table. The upper end of the shell was free and the lower end clamped. The vibration table was excited horizontally by an electromagnetic exciter and the shell was excited by the base movement. The motion of the table was measured by an acceleration sensor and the vibration of the shell was measured by a photonic sensor which was rigidly fixed to the table and moved together it.

The outputs of the acceleration sensor and photonic sensor were converted to digital signals and sent to the personal computer. The control input were calculated from the two sensor outputs by using the designed active controller and disturbance cancellation controller. The control output was converted to analog signal, amplified and applied the piezoelectric actuators.

The sensitivity of the photonic sensor was 1.37 V/mm. The sampling frequency of the A/D and D/A converters were set to 2 kHz. The control input and sensor output were recorded by both the FFT analyzer and the personal computer. Figure 5(a) and (b) show the time history and its spectrum of the sensor output recorded by the FFT analyzer and the PC when the shell was excited by a harmonic force of 75 Hz. It can be easily found that the signal recorded by PC contains larger random noise components than that recorded by the FFT. The data recorded by FFT is more accurate since the date length of FFT is 16 bits but the data

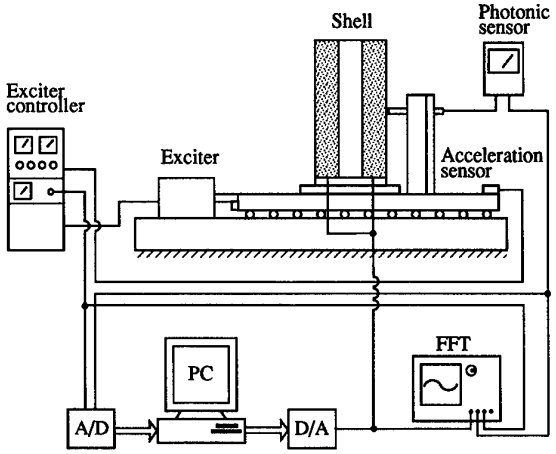
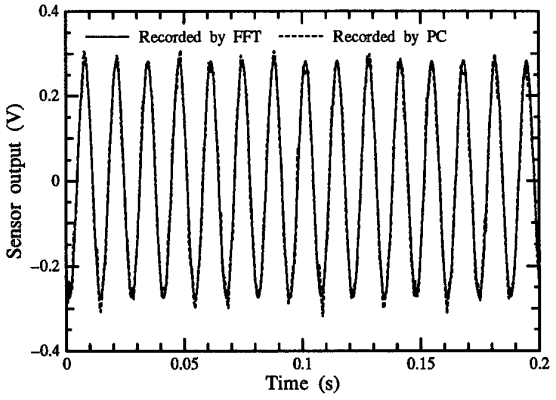
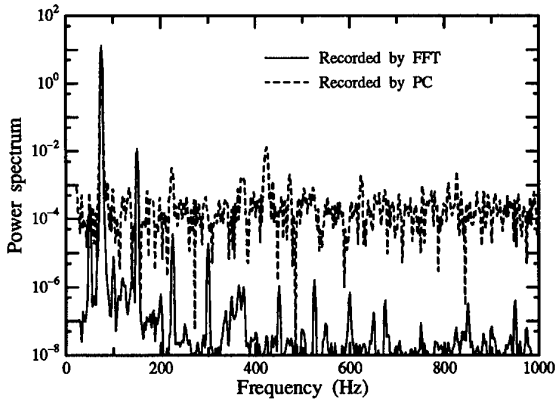


Figure 6. Experimental setup



(a) Time history



(b) Spectrum

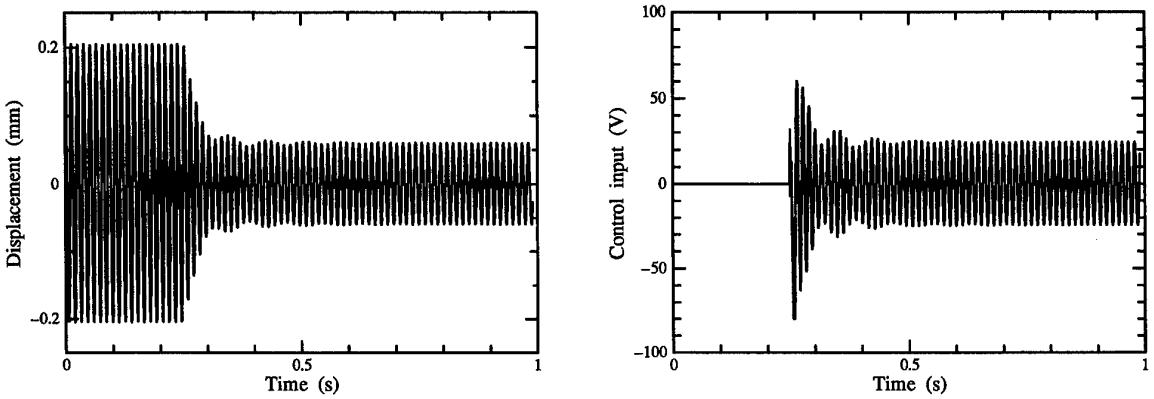
Figure 5. Comparison of signals recorded by PC and FFT

length of A/D converter is only 12 bits. However the transient response at the beginning of control was recorded only by PC due the difficultness of synchronizing of PC and FFT.

6. RESULTS AND DISCUSSION

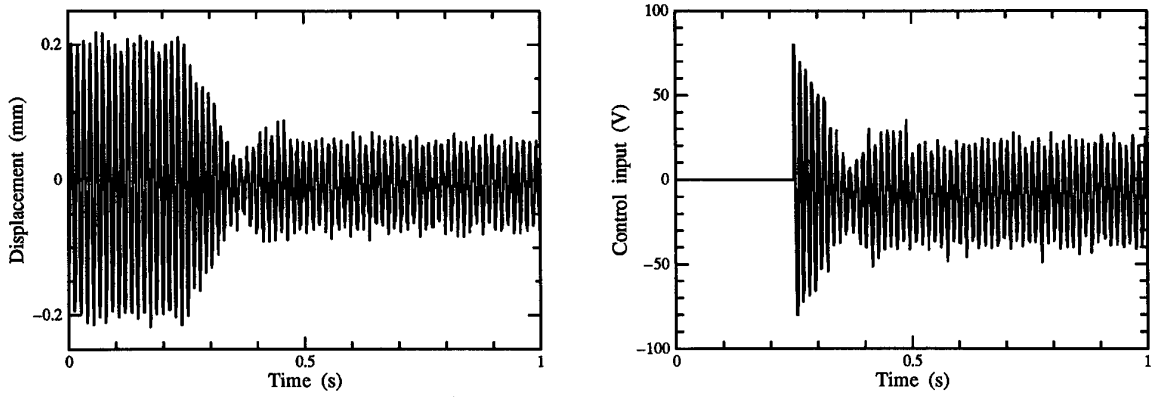
The frequency response of the shell is obtained by measuring the variation of vibration amplitude when excitation frequency is sweeped 10Hz to 120Hz. The experimental value of natural frequencies with modes (1, 1) and (1, 2) are estimated from the frequency response curve and listed in Table 2 to make a comparison with the simulation results. Since the vibration amplitude of mode (1, 5) is very small, its frequency can not be measured experimentally.

In the control experiment, the shell was excited at the frequency of 75 Hz which is approximately equals to the natural frequency of mode (1, 1). The exciting amplitude of the table is set to 20μm, The forced vibration of the shell was controlled by using the μ-synthesis method, disturbance cancellation method and the combination of the two method, respectively and the results are compared.



(a) Displacement of measuring point (b) Control input

Figure 7. Simulation result of response and input: μ-synthesis only



(a) Displacement of measuring point (b) Control input

Figure 8. Experimental result of response and input: μ-synthesis only

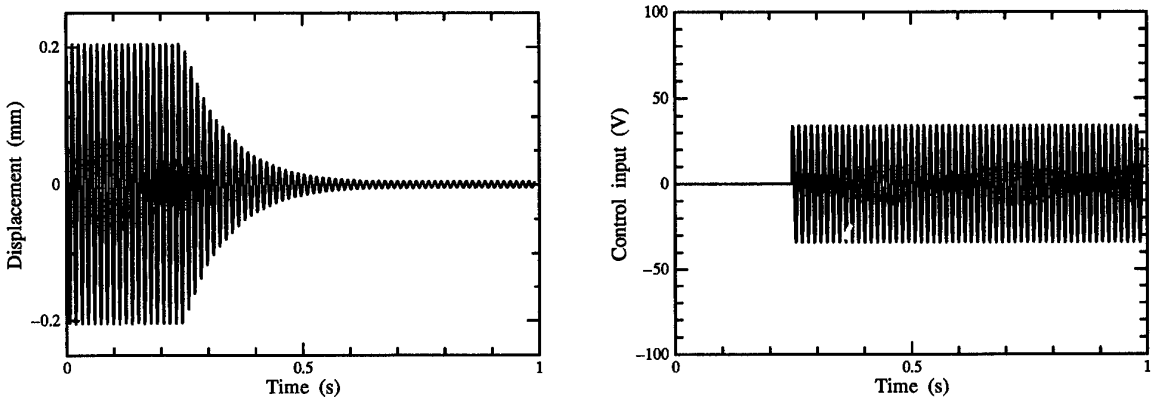
6.1 Results of Active Control

Figure 7 shows the simulation result of the displacement response at the measuring point and the control input when μ-synthesis control method is used. The amplitude of vibration is reduced to about 1/4 in a few cycles after control input is applied. Figure 8 shows the experimental results obtained under the same condition as the simulation. The experimental results is similar to the simulation results except that vibration was over-suppressed at the beginning of control. Large noise can also be found in the experimental results since they were recorded by the PC.

A little better control effect can be achieved by increasing the gain of the controller. But the robustness of the controller will deteriorate when the gain is increased. Furthermore there is a limit for the gain of controller since the controller will become unstable if it is too large. Therefore there is a limit of control performance for feedback control.

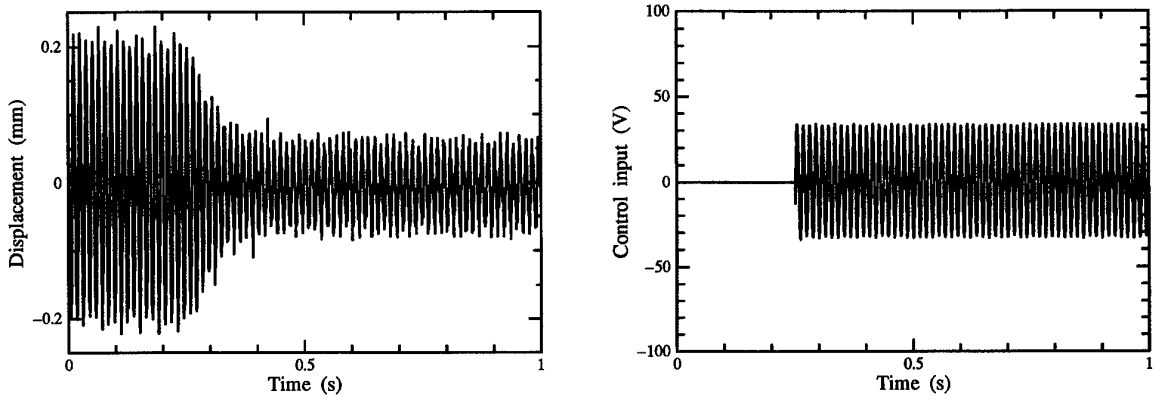
6.2 Results of Disturbance Cancellation

Figure 9 shows the simulation results when disturbance cancellation method is used. The amplitude of the shell vibration decays with time and becomes very small at last. But the decaying process depends on the damping ratio of the system, since the control input and the external disturbance cancels each other so that the process is



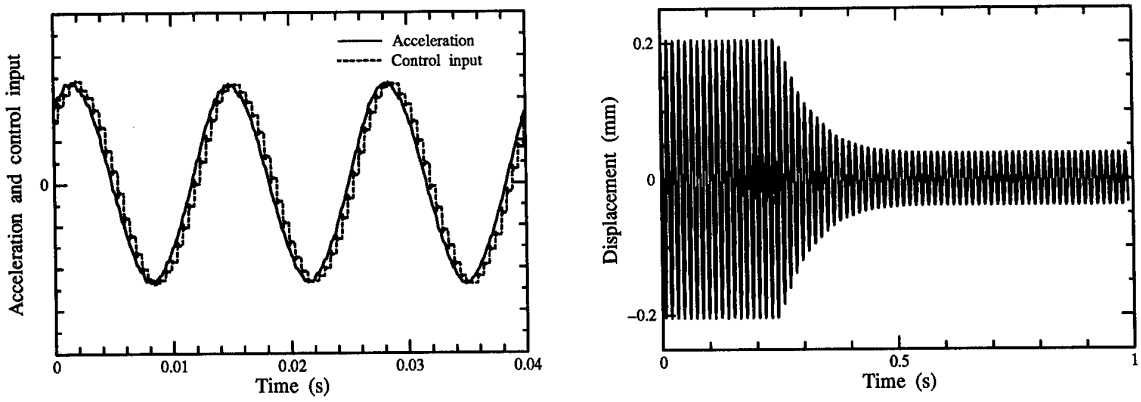
(a) Displacement of measuring point (b) Control input

Figure 9. Simulation result of response and input: DCM only



(a) Displacement of measuring point (b) Control input

Figure 10. Experimental result of response and input: DCM only



(a) Phase delay

(b) Influence of phase delay on control effect

Figure 11. Phase delay of control input and its influence on control effect

close to the free vibration process induced by initial excitation and it takes many cycles in this case due to small internal damping of the shell. The amplitude of control input does not varies with time since the control input is computed from the external disturbance according to Equation (15) and the amplitude of excitation force does not vary with time.

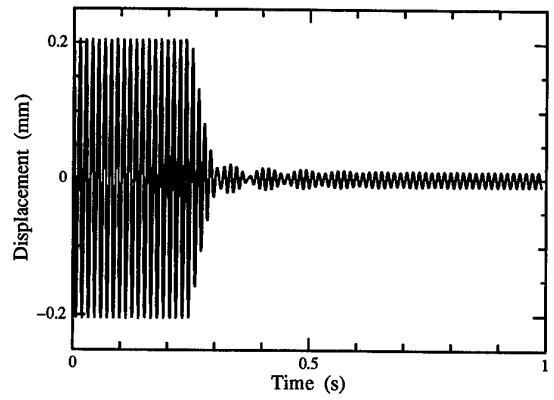
The experimental results is shown in Figure 10. It can be found that the control input is in good agreement with the simulation input, but the amplitude of vibration is reduced only to about one third of the uncontrolled vibration. There are two main factors which lead to the difference. In the simulation the exact disturbance is known and used in the computation of the control input, but in the experiment it is unknown and the measured one is used in the computation of control input. The measurement error is one of the main factors. The second main factor is the phase delay of control input due to calculation time. Figure 11(a) shows the sensor output and the control input after D/A conversion which are recorded by the two channels of FFT. Although these two signals have been rescaled so that their amplitude have no meanings, the phase delay can easily be seen. From the Figure, the phase delay can be estimated to be 12°.

When the phase delay is considered in the simulation, the results as shown in Figure 11(b) are obtained. The amplitude of controlled vibration in simulation is still smaller than that in experiment, but the experimental results and simulation results have become much closer. If the measurement error could be considered in the simulation, they would be in better agreement. But it is impossible to include the measurement error in the simulation since it it unknown.

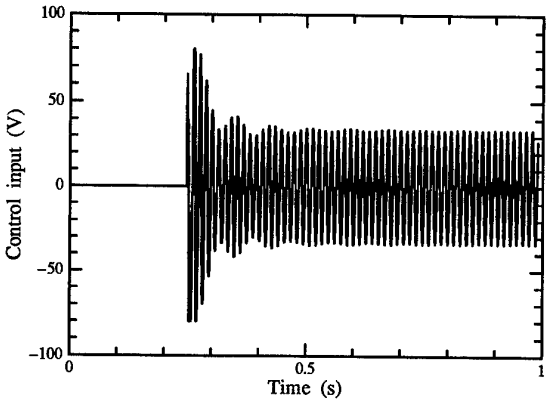
6.3 Results of Hybrid Control

From the above discussion, it can be known that there is a limit of control performance for feedback control but the decaying process is very fast. On the other hand, the disturbance cancellation method has better control effect but the decaying process is slower in the ideal state. The control effect of disturbance cancellation method deteriorate significantly when the phase delay increases due to calculation of control input in the digital control. To achieve better control effect, the two control methods are combined in the calculation of control input as shown in Equation (13).

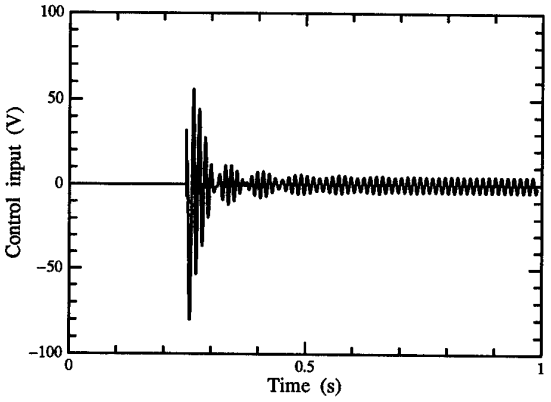
Figures 12 shows the simulation result of the hybrid control when the phase delay of control input is considered. The amplitude of the shell vibration is reduced to very small in a few cycles after the control input is applied. It can easily be found that the decaying process of the hybrid control is much faster than that of disturbance cancellation method, but the amplitude of residual vibration is much smaller than that of μ-synthesis control. The corresponding experimental results is shown in Figure 13. Although the decaying process takes more cycles and the signals contains large noise, they are close to the simulation results. The signals recorded by the FFT contain smaller noise and the steady-state response of the uncontrolled and controlled vibration are shown in Figure 14. From this figure, it can be found that the amplitude of the residual vibration is about one tenth of that of uncontrolled vibration. The effect of hybrid control is better than each individual method.



(a) Displacement of measuring point

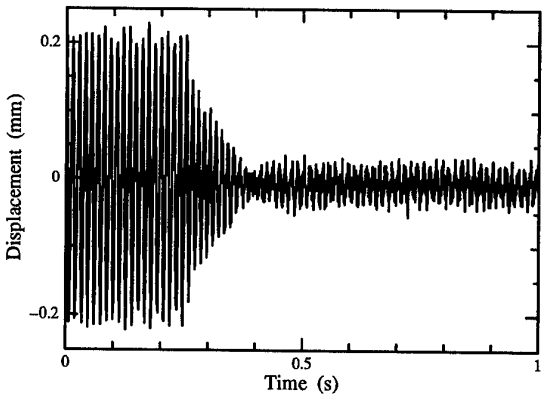


(b) Control input

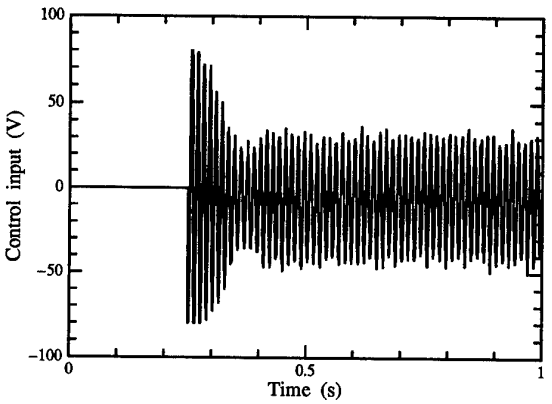


(c) μ-synthesis control input in hybrid control

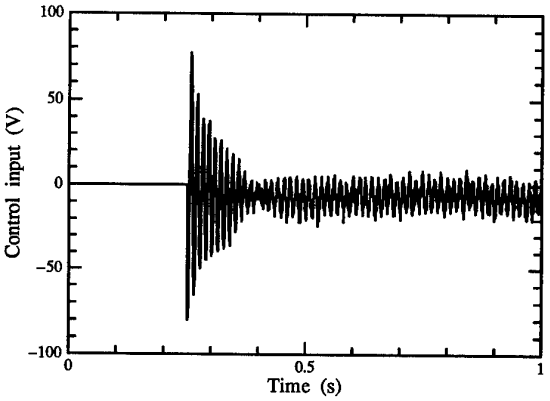
Figure 12. Simulation result of response and input: hybrid control



(a) Displacement of measuring point



(b) Control input



(c) μ-systhesis control input in hybrid control

Figure 13. Experimental result of response and input: hybrid control

Figures 12(c) and 13(c) shows the component of control input generated by the controller of μ-synthesis in the hybrid control. The controller of μ-synthesis generates a large input signal at the beginning of control which leads to faster decaying of vibration amplitude. When vibration amplitude trends to zero, control input generated by μ-synthesis trends to zero, but that by disturbance cancellation remains constant as shown in Figures 9(b) and 10(b).

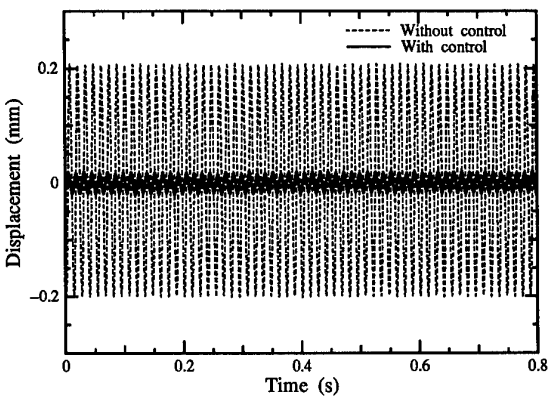


Figure 14. Responses recorded by FFT

7. CONCLUSION

Simulation and experiments were carried out on the control of forced vibration of a cantilever piezoelectric composite cylindrical shell excited by a horizontal base movement. The integrated piezoelectric films are used as distributed actuators. The hybrid control is used and its control effect is compared with the active control method and disturbance cancellation method. From the simulation and experimental results, the following conclusions can be reached.

(1) The integrated piezoelectric actuators are effective in the control of the shell vibration excited by base vibration.

(2) The hybrid control method gives better control effect than the active control method and the disturbance cancellation when they are used individually. It is also expected that hybrid control will have wide application in control of engineering structures since the external disturbance can be measured in many cases.

8. REFERENCES

[1] C. R. Fuller, "Noise Control Characteristics of Synchrophasing, Part 1: Analytical Investigation", *AIAA Journal*, Vol.24, No.7, pp.1063–1068, 1986.

[2] J. D. Jones and C. R. Fuller, "Noise Control Characteristics of Synchrophasing, Part 2: Experimental Investigation", *AIAA Journal*, Vol.24, No.8, pp.1271–1276, 1986.

[3] J. D. Jones and C. R. Fuller, "Reduction of Sound Fields in Flexible Cylinders by Active Vibration Control", *International Journal of Analytical and Experimental Modal Analysis*, Vol.4, No.1, pp.45–50, 1989.

[4] H. C. Lester and S. Lefebvre, "Piezoelectric Actuator Models for Active Sound and Vibration Control of Cylinders", *Journal of Intelligent Material System and Structures*, Vol.4, No.2, pp.295–306, 1993.

[5] J. Pan, C. H. Hansen and S. D. Snyder, "Active Vibration Control of Thin Cylindrical Shell", *Proc. Int. conf. on Recent Advances in Active Control of Sound and Vibration*, Technomic Publishing Company, Inc., Lancaster, Pennsylvania, pp.15-17, April 1991.

[6] J. Tani, J. Qiu and H. Miura, "Vibration Control of Cylindrical Shell System Using Piezoelectric Film", *Trans. of JSME*(C), Vol.60, No.570, pp.443-449, 1994.

[7] J. Qiu and J. Tani, "Vibration Control of a Cylindrical Shell Using Distributed Piezoelectric Sensors and Actuators", *Journal of Intelligent Material Systems and Structures* Vol.6, No.6, pp.474-481, 1995.

[8] J. Qiu and J. Tani, "Vibration Control of a Cylindrical Shell Used in MRI equipment", *Journal of Smart Materials and Structures*, Vol.4, Supplement A, pp.75-81, 1995.

[9] J. Qiu, J. Tani and K. Ohtomo, "Intelligent Coil Drum with Electromagnetic Force Cancellation for MRI Equipment", *Trans. of JSME*(C), Vol.61, No.581, pp.2412-2417, 1994.

HIGH PRECISION FORM MEASUREMENTS THROUGH THE USE OF ADAPTIVE STRUCTURES TECHNOLOGY

L. Flavio Campanile, Rolf Lammering, Jörg Melcher

Deutsche Forschungsanstalt für Luft- und Raumfahrt e.V. (DLR)
Lilienthalplatz 7, 38108 Braunschweig, Germany

ABSTRACT

A smart solution to vibration suppression in form measuring machines is presented in which the machine's vibrations are counteracted actively. For this purpose, the machine was equipped with a sensing system, an active interface, and a special controller. This new concept has been successfully tested on a real form measuring machine.

1. INTRODUCING THE PROBLEM OF VIBRATION-INDUCED MEASUREMENT ERRORS IN FORM MEASURING MACHINES

During the design stage of a mechanical workpiece, not only is its ideal geometry defined, but also the range of allowable deviations of the real geometry from the ideal are set in order to ensure the workpiece's proper operation.

The object's ideal *shape,* which is one geometrical attribute (beside its shape and its surface properties), is defined by means of simple geometrical elements, without supplying any numerical data: a cylinder, a spherical or plane surface and a section composed of two concentric circles are typical examples.

1.1 Shape deviations

Since 1985 an international standard exists[1], which defines the shape deviations for many shape properties. For the purpose of this paper is not necessary to discuss these definitions in detail. The following general, 'fuzzy' definition will suffice: a shape deviation gives the order of magnitude of the differences between the actual shape and the ideal one. Since these differences generally involve length measurements, shape deviations are, as a rule, expressed in a length measurement unit.

1.2 Form measuring machines

The issue of shape deviations and tolerances plays an important role in many branches of industry. It becomes extremely important in mechanical engineering, where shape deviations are often the primary cause of undesired events like vibrations, increased friction, and wear.

The fundamental task of shape deviations measurement is performed by means of special machines, called *form measuring machines.*

A typical form measuring machine consists of a high-precision measuring robot and a processing unit. The measuring robot is responsible for the evaluation of the object's surface along a given line (*profile measurement*). The profile data constitutes the basis for the shape determination, which is performed by the processing unit.

The profile evaluation involves displacement measurements whose precision can range from some tens of nanometers to some microns depending on the size and kind of the machine.

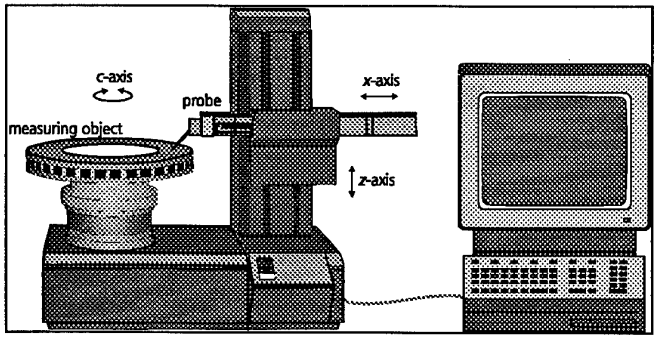


Figure 1: The Mahr MMQ40 form measuring machine

0-8194-2165-0/96/$6.00

Figure 1 represents the form measuring machine which was used in the present work. The machine's measuring robot has a two-carriage system, which allows the probe to move in a vertical plane relative to the machine's base. The object to be measured is placed on a turntable, so that the relative position between probe and object is defined by three coordinates: the vertical coordinate, z, the horizontal coordinate, x and the rotational coordinate, c. The probe hosts a high-sensitive displacement sensor. Depending on the position of the probe arm, the sensor can measure in horizontal (x-axis) or vertical direction (z-axis).

During the profile measurement, the probe moves relative to the measured object parallel to the ideal profile along one of the three available axes. The probe arm remains in contact with the object surface, and as a result, the sensor signal describes the deviation of the real profile from the ideal one.

Depending on the motion and measurement directions, different kinds of profile measurement are possible.

A typical case is the evaluation of a horizontal round section, used in many form measurements like roundness, cylindricity, concentricity and so on. In this case, the relative motion takes place along the c-axis, while the probe measures in x-direction.

Another common case is a vertical straight profile, in which the probe moves along the z-axis and measures in the x-direction. This profile measurement is typically used for evaluation of straightness.

1.3 The problem of internal vibrations and some standard solutions

An exact profile measurement would require that no relative motion between probe and measured object takes place in the measurement direction. In practice, such relative motions do occur, mainly caused by vibrations, and as a result, errors in the shape evaluation arise.

The characteristic 'constraints' on a form measurement makes vibration-induced measurement errors difficult to avoid:

- the task of form measurement requires that the form measuring machine takes a robot-like design, which is typically vibration sensitive;
- a form measuring machine should be directly installed on the factory floor, or in any case not far from production machines; this operating environment is generally rich in vibration sources;
- due to the high precision requirements, even very small relative displacements (some tens of nanometers) cannot be tolerated.

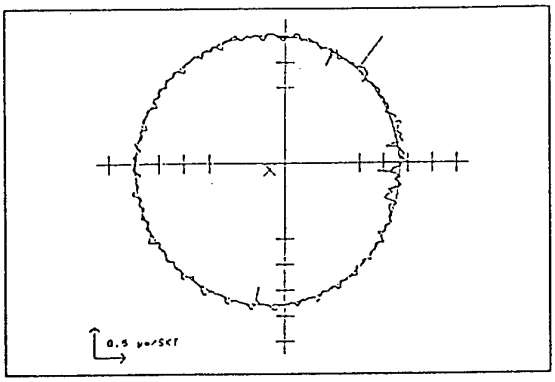


Figure 2: Roundness measurement without external excitation. Roundness deviation 0.65 µm

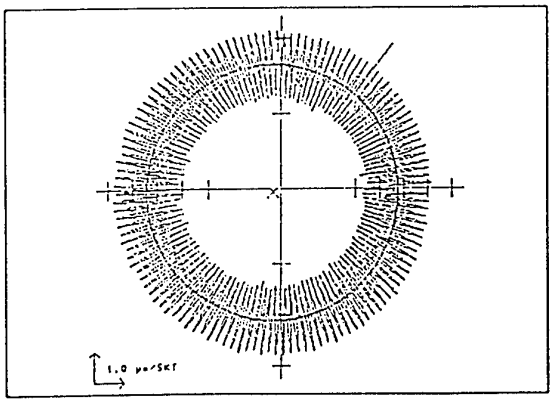


Figure 3: Roundness measurement with external excitation. Excitation frequency 10.85 Hz. Roundness deviation 3.00 µm.

Figures 2 and 3 show the result of a roundness measurement on a high-precision object, with and without a monofrequent disturbance, realized by means of an external shaker. The presence of the relative motion (amplitude about 1.2 micron) definitely compromised the result (form measurement error over 400%).

Presently this problem is addressed in different ways.

First, an extremely solid design is adopted for the measuring robot. High-stiffness materials and high-precision bearings are used, in order to reduce the system's flexibility. This increases the production and maintenance costs.

A reduction of the vibration-induced disturbances can also be achieved through a passive reduction of the excitation source level, e. g. by using a specially isolated table or by shielding the operating place. These countermeasures also involve additional costs, and sometimes reduces the machine's functionality, especially if the machine has to be installed far away from the production area.

Another standard solution consists of low-pass filtering the probe signal prior to processing it. In this way, an effective error reduction can be achieved, at the cost of a measurement speed reduction if a high precision level is to be preserved.

Filtering the signal with a given cut-off frequency eliminates the disturbances due to resonances lying above that frequency. At the same time however, the profile's components under a certain wavelength are also filtered out. The measurement speed defines the relationship between this wavelength and the cut-off frequency for the probe signal. If the measurement speed is kept at a low level, the lost information is not significant, since it belongs to the surface characterization (low wavelength). Higher measurement speeds involve a progressive distortion in the shape evaluation.

2. THE 'SMART' SOLUTION

The 'smart' idea for the reduction of vibration-induced errors in form measurement consist in counteracting the vibrations by means of an *active interface*. The interface is governed by a special *controller*, which receives the information about the machine's vibration from the *error/reference sensing systems*.

2.1 Active interface

The active interface (Fig. 4) is located at the connection between the probe and the horizontal slide. It is realized with four piezoceramic stacks, pre-stressed with four screws.

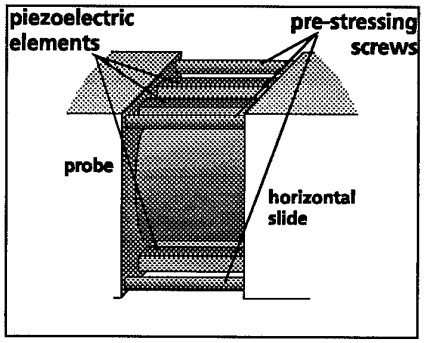


Figure 4: The active interface

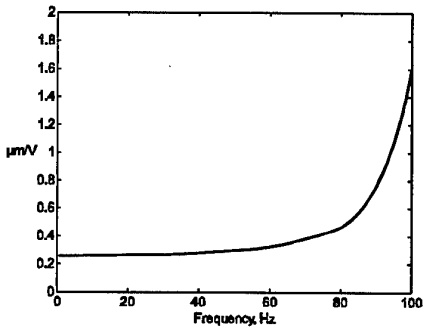


Figure 5: Dynamic performance of the active interface

The interface's construction guarantees its passive load-carrying function besides the active one. In this way, when the interface is switched off, the form measuring machine can operate the standard way.

For this reason, low-voltage piezoceramics were used as active elements, because of their higher stiffness compared to the high-voltage ceramics. Besides this, low-voltage ceramics are to be preferred for safety reasons, particularly in view of the goal of an integration of the interface into series production.

The interface was run in a one-channel mode, in which the upper two elements were wired in parallel and the lower ones as well, with the same voltage amplitude and different signs for the upper and the lower element groups. In this way, the interface response is roughly a pure rotation around the probe arm's rotation axis, which is able to compensate the most part of the vibration-induced disturbances. Different operating modes, generating a more complex motion of the probe (i.e. including a rotation around the z-axis) are possible without any structural changes just through the use of different wiring schemes. This possibility will be useful for further developments.

The interface's static performance shows a displacement range of about ± 15 micron, measured by the probe sensor for a vertical probe arm position. The dynamic performance within the frequency range of interest (0-100Hz) constitutes the basis for very good system controllability (Figure 5).

2.2 Error/reference sensing system

In order to operate properly, the interface's feedforward controller needs two different input signals:

- a *reference* signal providing information about the presence of external disturbances and
- an *error* signal, which should supply information about the vibration-induced form measurement errors.

If the interface is not active, the reference and the error signal should be equal. Activating the interface should decrease the error signal (ideally to zero), while the reference signal should remain unchanged for a given disturbance.

The development of a proper error/reference sensing system was a very challenging phase of the project.

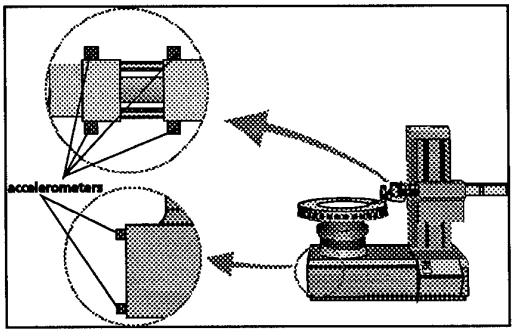


Figure 6: The error/reference system

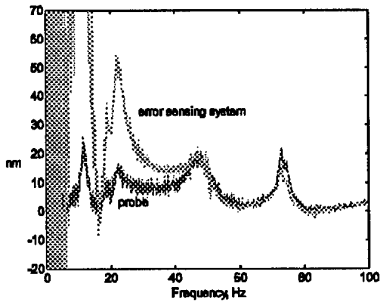


Figure 7: Reliability test of the error sensing system.

In the initial configuration (Figure 6), which was conceived for the case of horizontal probe measurement (x-direction), six accelerometers are used as sensors. The accelerometers' signals are combined linearly and integrated twice to build the error and the reference signal.

Since the linear combination implies subtraction between the sensor signals, which are often very similar to one another, the reference and the error signal are extremely sensitive to noise in the accelerometers' signal. Due to integration, the noise effect is inversely proportional to the square of frequency. This sets a lower limit to the operating range of the error/reference sensing system. This limit can be lowered by increasing the accelerometers' resolution.

Figure 7 shows the comparison between probe and error signal for an external broadband excitation. During the test, the probe arm is kept in contact with the object's surface, without operating the machine's motion axes. In this case, the probe and the error sensing system are expected to give the same signal. The above-mentioned lower frequency limit is clearly detectable around 40Hz.

2.3 Controller

Generally, the structural parts of the form measuring machine that must be isolated from any vibrations may vary with time due to changing nonstationary environments or changing structural geometries. In situations where physical system parameters are indeed variable or not accurately known, a *self-optimizing* or *adaptive* controller must be used. The most promising types of structural dynamic controllers for the actual application seem to be the digital real-time filter systems[2,3].

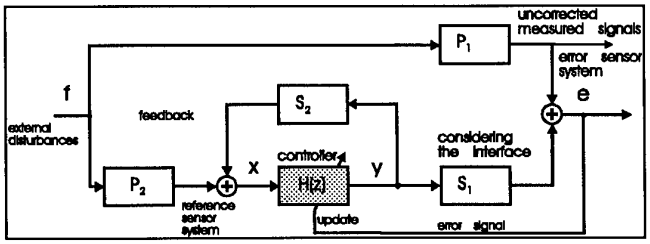


Figure 8: Block diagram of feedforward controllers for actively controlled form measurements

Figure 8 shows the equivalent block diagram of the adaptively controlled interface junction. Different blocks represent the continuous transfer functions $P_1(s)$, $S_1(s)$, $P_2(s)$, and $S_2(s)$ which are defined in the analog s-plane and represent the relationships between the appropriate forces and accelerations. An integration

procedure to obtain the displacement is not necessary. The discrete transfer function H(z) gives the relationship between the measured reference accelerations and the interface driving signal y. To simplify the block diagram, all A/D and D/A converters have been omitted. If y is optimally adjusted, the error e becomes zero with respect to the block diagram

$$H_{opt} = -S_1^{-1}P_1\left[P_2 - S_2S_1^{-1}P_1\right]^{-1}. \tag{1}$$

The effect of y back to the reference x, given by $S_2(s)$, can usually be neglected. Thus, Eq. (1) reduces to

$$H_{opt} = -S_1^{-1}P_1P_2^{-1}. \tag{2}$$

H(z) consists of two digital filter systems, F(z) and G(z). Both components have a linear form, but the use of an adaptation algorithm G(z) makes H(z) non-linear. G(z) itself is then reduced to zero, and no significant error feedback exists.

In situations where only harmonic disturbances reduce the performance of the form measuring machine, a simple realization of the controller is possible: a simplified adaptive linear combiner F(z) with only two weights a_0 and a_m. This is also proposed by Widrow and Stearns[4] in similar form. Its filter equation is

$$y(n) = a_0x(n) + a_mx(n-m) \tag{3}$$

where the integer $m \geq 1$ causes a real time delay of m·T seconds when T is the sampling time. Together with the leaky least-mean-square (LMS) adaptation filter G(z), whose description in the time domain is given by

$$\begin{aligned} a_0(n+1) &= \gamma \cdot a_0(n) + 2 \cdot \mu(n) \cdot x(n) \cdot e(n) \\ a_m(n+1) &= \gamma \cdot a_m(n) + 2 \cdot \mu(n) \cdot x(n) \cdot e(n) \end{aligned} \tag{4}$$

the combiner is able to vary both the amplitude and phase of y as required in order to reduce the error.

As a step-size parameter, $\mu(n)$ defines the compromise between accuracy and the convergence rate. μ may be constant or, in a more sophisticated version, dependent on the error and reference signals. The leakage parameter γ is a real, positive constant chosen in the range $0 < \gamma \leq 1$.

For broadband applications, a transversal controller, consisting of a digital FIR filter F(z) combined with a leaky-LMS algorithm G(z) can be used. F can be described in the time domain as

$$f_i(n) = \sum_{i=0}^{L} h_i v_f(n-i) \tag{5}$$

where the h_i are transversal filter coefficients and G in a filtered version as

$$h_i(n+1) = h_i(n) + 2 \cdot \mu(n) \cdot \delta_i(n) \cdot e(n) \forall i \in [0, L] \tag{6}$$

where $h(n)=[h_0(n)\ h_1(n)\ldots\ h_L(n)]^t$ stands for the coefficient vector and $\delta(n)$ are the corresponding gradient components. These elements are calculated by a filtering of x(n) by $S_1(z)$, i.e. the estimation of the transfer function $S_1(s)$.

A further controller which is useful for broadband applications is the realization of H as an IIR filter with both transversal and recursive filterings.

3. OUTLOOK

The experimental verification of the new concept showed excellent results. Future work will include:

- extending operation frequency range of the sensing system by means of high-resolution accelerometers;
- performing experimental tests in the form measuring machine's real operating environment.
- developing an 'intelligent' compensation algorithm for bias errors in the accelerometers' signal (e.g. calibration and positioning errors);
- completing the error/reference sensing system, with three additional accelerometers, in order to enable operation also for probe measurement in *z*-direction.

4. ACKNOWLEDGMENT

The financial support of the German Ministry of Research and Technology is gratefully acknowledged.

5. REFERENCES

1. International Standard Organization (ISO). „Technical drawings, geometrical tolerancing, tolerances of form, orientation, location and runout; generalities, definitions, symbols on drawings", ISO Regulation No. 1101.
2. Clark, R.L. and Fuller, C.R., 1991. „Control of Sound Radiation with Adaptive Structures", Journal of Intelligent Material Systems and Structures, 2(3), July 1991, 431-452.
3. Melcher, J., 1992. „Active Vibration Isolation Using Multifunctional Interfaces and Adaptive Digital Controllers", Proceedings of the Third International Conference on Adaptive Structures, Nov. 9-11, 1992, San Diego, CA, USA, 388-401.
4. Widrow, B. and Stearns, D., 1985. „Adaptive Signal Processing". Englewood Cliffs, NJ, USA, Prentice Hall Inc., 1985.

Paper presented at the Third ICIM/ECSSM '96, Lyon '96

Multi-modal Vibration Control of Laminated Composite Plates using Piezoceramic Materials

Young Kyu Kang, Moon Hyun Kim, Hyun Chul Park*, Woonbong Hwang and Kyung Seop Han

Department of Mechanical Engineering, POSTECH, Pohang, Kyungbuk, Korea, 790-784

ABSTRACT - Multi-modal vibration control of laminated composite plates using collocated piezoelectric sensor/actuator is analyzed theoretically and verified experimentally for various fiber orientations. The modal damping($2\zeta\omega$) is chosen as a performance index rather than the damping ratio(ζ) for the vibration suppression in the structure. The active modal dampings of the first bending and the first torsional modes are measured experimentally and are in good agreement with those of finite element analysis.

Introduction

Piezoelectric sensor/actuators have been widely used in structural vibration control. In the case of the piezoceramics, depending on the applied voltage to the piezoceramics, electromechanical coupling of the forcing transducer to the structure, and the location of the piezoelectric transducers, a degree of vibration control of flexible structures can be considered. Most of researches using piezoceramics have taken into account only the stiffness of the piezoceramics and did not consider the damping and the stiffness of the adhesive layer and the piezoceramics at the same time (Detwiler and Shen, 1994; Ha, Keilers and Chang, 1992). The damping and the stiffness of the adhesive layer and the piezoceramics must be considered simultaneously in system modeling in order to have a good compatibility between the analytical model and the corresponding experimental system. Structural vibration control using the piezoceramic material has considered only the bending mode and has not taken into account the bending and the torsional modes simultaneously(Prakah-Asante and Craig, 1994; Tani and Miura, 1995).

In this paper, structural vibration control of the laminated composite plates with two pairs of the piezoceramic sensors and actuators bonded on the surface of the plates are investigated numerically and verified experimentally for various fiber orientations. The piezoelectric sensor/actuators are collocated to guarantee the control stability. Two pairs of the piezoceramic sensor/actuator function independently and can control the bending and the torsional mode of the plate at the same time. Damping and stiffness of the adhesive layer and the piezoceramics are taken into account in the finite element formulation, simultaneously. Concept of the modal damping($2\zeta\omega$) is chosen as a performance index of structural vibration, while most other researches have used the damping ratio(ζ) as the index. The damping ratio represents only a measure of amplitude decay during one cycle. But the modal damping takes into account the damping ratio as well as the natural frequency. The active modal dampings of the first bending and the first torsional modes are measured experimentally and then compared with those of finite element analysis.

Method

Laminated composite plates with the piezoceramic sensor/actuator are modeled as 2-D plates. Hamilton's principle is used to derive the equation of motion for the plate. The piezoceramic sensor/actuator layers and the adhesive layers are treated as another layer with different material properties in deriving the kinetic and the potential energy.

When the transverse vibration is considered only, the in-plane displacements can be ignored. So, the displacement vector, **u**, and the strain vector, ε, are expressed as follows :

$$\mathbf{u} = \begin{bmatrix} u_x \\ u_y \\ u_z \end{bmatrix} = \begin{bmatrix} -z\dfrac{\partial w}{\partial x} \\ -z\dfrac{\partial w}{\partial y} \\ w \end{bmatrix} = \begin{bmatrix} z\beta_x \\ z\beta_y \\ w \end{bmatrix} \tag{1}$$

0-8194-2165-0/96/$6.00

$$\varepsilon = \begin{bmatrix} \varepsilon_x \\ \varepsilon_y \\ \gamma_{xy} \end{bmatrix} = \begin{bmatrix} z\dfrac{\partial \beta_x}{\partial x} \\ z\dfrac{\partial \beta_y}{\partial y} \\ z\dfrac{\partial \beta_y}{\partial x} + z\dfrac{\partial \beta_x}{\partial y} \end{bmatrix} = z\kappa \qquad (2)$$

where w is the transverse displacement, β_x and β_y the rotation about the x- and y-axis, and κ the curvature vector.

The displacement $\mathbf{u}$ and the curvature κ are expressed in terms of nodal displacements with shape functions using the 4-node, 12-degree-of-freedom quadrilateral plate bending element, as follows (Batoz and Tahar, 1982)

$$\mathbf{u} = \Psi_u \mathbf{q}^e \qquad (3)$$

$$\kappa = \Psi_\kappa \mathbf{q}^e \qquad (4)$$

where Ψ_u and Ψ_κ are the interpolation functions for $\mathbf{u}$ and κ respectively, and $\mathbf{q}^e$ is the element nodal displacemnet vector. The equations of motion for the system in terms of nodal displacements are expressed as follows:

$$(\mathbf{M}_S + \mathbf{M}_B + \mathbf{M}_P)\ddot{\mathbf{q}} + (\mathbf{K}_S + \mathbf{K}_B + \mathbf{K}_P)\mathbf{q} = \mathbf{F}_{\text{Ext}} \qquad (5)$$

where

$$\mathbf{M}_S = \sum_{elem} \int_{V_S} \Psi_u^T \rho_S \Psi_u dv \qquad (6a)$$

$$\mathbf{M}_B = \sum_{elem} \int_{V_B} \Psi_u^T \rho_B \Psi_u dv \qquad (6b)$$

$$\mathbf{M}_P = \sum_{elem} \int_{V_P} \Psi_u^T \rho_P \Psi_u dv \qquad (6c)$$

$$\mathbf{K}_S = \sum_{elem} \int_{A_S} \Psi_\kappa^T \mathbf{D}_S \Psi_\kappa dA \qquad (6d)$$

$$\mathbf{K}_B = \sum_{elem} \int_{A_B} \Psi_\kappa^T \mathbf{D}_B \Psi_\kappa dA \qquad (6e)$$

$$\mathbf{K}_P = \sum_{elem} \int_{A_P} \Psi_\kappa^T \mathbf{D}_P \Psi_\kappa dA \qquad (6f)$$

$$\mathbf{F}_{Ext} = \sum_{i=1}^{n_f} \Psi_u^T(\mathbf{x}_i)\mathbf{f}(\mathbf{x}_i) \qquad (6g)$$

and the subscripts S, B, and P represent the main structure, the adhesive layer, and the piezoceramic materials, respectively.

Damping in the fiber direction is low and damping in the transverse direction is very high due to the characteristics of polymeric matrix. The damping property of composite materials exhibits anisotropic characteristics and can be controlled by changing the fiber orientations and the stacking sequences. In this paper, the damping analysis of laminated composite plates is carried out using the concept of specific damping capacity(SDC) suggested by Lin, Ni and Adams(1984). Since the damping of the adhesive layer and the piezoceramic sensor/actuator play an important role in the dynamics of the entire system, they must be considered in the system modeling. The specific damping capacity is defined as follows:

$$\varphi = \Delta U/U \qquad (7)$$

where ΔU is the energy dissipated during a stress cycle and U the maximum strain energy during a stress cycle. The dissipated energy, ΔU, is expressed as follows:

$$\Delta U = \tfrac{1}{2}\int_A \kappa^T D^\Delta \kappa dA \qquad (8)$$

where

$$D_{ij}^\Delta = \tfrac{1}{3}\sum_{k=1}^{N_S}(\overline{Q}_{S_{ij}}^\Delta)_k(z_k^3 - z_{k-1}^3) + \tfrac{1}{3}\sum_{k=1}^{N_B}(\overline{Q}_{B_{ij}}^\Delta)_k(z_k^3 - z_{k-1}^3) + \tfrac{1}{3}\sum_{k=1}^{N_P}(\overline{Q}_{P_{ij}}^\Delta)_k(z_k^3 - z_{k-1}^3) \qquad (9)$$

$$\overline{\mathbf{Q}}_S^{\Delta} = \mathbf{S}^{-1} diag\{\varphi_{S1} \quad \varphi_{S2} \quad \varphi_{S12}\}\mathbf{Q}\,\mathbf{S} \tag{10}$$

$$\overline{\mathbf{Q}}_B^{\Delta} = diag\{\varphi_{B1} \quad \varphi_{B2} \quad \varphi_{B12}\}\mathbf{Q}_B \tag{11}$$

$$\overline{\mathbf{Q}}_P^{\Delta} = diag\{\varphi_{P1} \quad \varphi_{P2} \quad \varphi_{P12}\}\mathbf{Q}_P \tag{12}$$

and φ_{S1}, φ_{S2} and φ_{S12} are the damping capacities in the fiber direction, the transverse direction and the shear direction, respectively. The material properties of the adhesive layer can be thought of isotropic and the damping capacities φ_{B1}, φ_{B2} and φ_{B12} are assumed to be the same. The material properties of the piezoceramics exhibit transversely isotropic and the damping capacities φ_{P1} and φ_{P2} are assumed to be the same(Fuji Ceramics, 1994). All the damping capacities in Equations (10), (11) and (12) are measured using the impulse technique. When ΔU is discretized by Equation (4) and expressed in nodal variables, the SDC, φ, can be rewritten as

$$\varphi = \frac{\mathbf{q}^T \mathbf{K}_D \mathbf{q}}{\mathbf{q}^T (\mathbf{K}_S + \mathbf{K}_B + \mathbf{K}_P)\mathbf{q}} \tag{13}$$

where

$$\mathbf{K}_D = \sum_{elem} \int_A \Psi_\kappa^T \mathbf{D}^{\Delta} \Psi_\kappa dA \tag{14}$$

and $\mathbf{K}_D$ is the damped stiffness matrix. The SDC can be derived for each vibration mode, which is called the modal SDC. When the i-th mode shapes $\{\phi\}_i$ are replaced by $\mathbf{q}$ in Equation (13), the i-th modal SDC can be obtained. The modal damping matrix $\overline{C}$ can be derived from the modal SDC as follows:

$$\overline{C} = diag\left(2\zeta_1\omega_1 \quad 2\zeta_2\omega_2 \quad \cdots \quad 2\zeta_n\omega_n\right) \tag{15}$$

where

$$2\zeta_i = \varphi_i / 2\pi \tag{16}$$

In Equation (16), $2\zeta_i$ is the damping factor of the i-th mode and φ_i is the SDC of the i-th mode.

The total charge developed on the piezoceramic sensor in terms of nodal variable is as follows:

$$\Gamma(t) = \overline{z}^s \int_A e\kappa dA = \Theta^T q \tag{17}$$

where $\Theta^T = \sum_{elem} \overline{z}^s \int_{-1}^{1}\int_{-1}^{1} e\Psi_\kappa |J| d\xi d\eta$ and e the piezoelectric coefficient. When the piezoceramics is used as a strain-rate sensor, the sensor voltage is given as follows :

$$V^s = \frac{1}{C_p}\Theta^T \dot{q} \tag{18}$$

where C_p is the capacitance of the piezoceramic sensor. The equivalent actuator moments M^a as a function of actuator voltage are

$$M^a = L\mathrm{u}_c \tag{19}$$

where $L_i = \overline{Q}_{ij} d_{3j} \overline{z}$, $\mathbf{u}_c = -\mathrm{GV}^s$ and G the feedback gain. And the control force is as follows:

$$F_c = \int_{A^a} \Psi_\kappa^T L dA V^a = D_a u_c \tag{20}$$

where $D_a = \sum_{elem} \int_{-1}^{1}\int_{-1}^{1} \Psi_\kappa^T L |J| d\xi d\eta$.

The equation of motion of a adaptive structure with multiple degrees of freedom is expressed in discretized form as follows :

$$\mathbf{M}\ddot{\mathbf{q}} + \mathbf{C}\dot{\mathbf{q}} + \mathbf{K}\mathbf{q} = \mathbf{F}_{Ext} + \mathbf{D}_a \mathbf{u}_c \tag{21}$$

where $\mathbf{q}(t)$ is the n x 1 displacement vector, $\mathbf{M}$ ($=\mathbf{M}_S+\mathbf{M}_B+\mathbf{M}_P$) the mass matrix, $\mathbf{C}$ the structural damping, $\mathbf{K}$ ($=\mathbf{K}_S+\mathbf{K}_B+\mathbf{K}_P$) the stiffness matrix, $\mathbf{F}_{Ext}$ the external force vector, $\mathbf{D}_a$ the actuator influence matrix and $\mathbf{u}_c$ the control input to suppress the structural vibrations. The initial conditions are as follows.

$$\mathbf{q}(0) = \mathbf{q}_0, \quad \dot{\mathbf{q}}(0) = \dot{\mathbf{q}}_0$$

We introduce the modal coordinate transformation as follows:

$$\mathbf{q}(t) = \Phi\eta(t) \tag{22}$$

where Φ is the open-loop modal matrix obtained by solving the eigenvalue problem associated with the nominal mass and the stiffness matrices, and $\eta(t)$ is the n x 1 vector of the modal coordinates.

Then the transformed equation of motion(closed loop) becomes

$$\overline{M}\ddot{\eta} + \overline{C}\dot{\eta} + \overline{K}\eta = \overline{F}_{Ext} + \overline{D}u_c \tag{23}$$

and where the transformed modal space mass, damping, stiffness, external forces and the control influence matrices are, respectively, given by:

$$\overline{M} = \Phi^T M\Phi = I \tag{24a}$$

$$\overline{C} = \Phi^T C\Phi = diag(2\zeta_1\omega_1,\ 2\zeta_2\omega_2,\ldots,\ 2\zeta_n\omega_n) \tag{24b}$$

$$\overline{K} = \Phi^T K\Phi = diag(\omega_1^2,\ \omega_2^2,\ldots,\ \omega_n^2) \tag{24c}$$

$$\overline{F}_{Ext} = \Phi^T F_{Ext} \tag{24d}$$

$$\overline{D} = \Phi^T D_a \tag{24e}$$

Results and Discussions

Vibration control of the carbon/epoxy laminated composite plates using the piezoceramic sensor/actuator actuator is investigated with the stacking sequence of $[\theta_4/0_2/90_2]_S$, where θ = 0, 15, 30, 45, 60 and 90 deg. Specimen is made of the carbon prepreg(CU125NS). Thickness of the carbon prepreg is 0.125mm and size of the specimen is 200 x 200 x 2mm. Table 1 shows the mechanical properties of the carbon/epoxy laminates. The damping properties φ_{S1}, φ_{S2} and φ_{S12} are measured using the impulse technique. The plate with the piezoceramic sensor/actuator is shown in Figure 1. The size of piezoceramics in Figure 1 is 50 x 20 x 0.5mm. The basic mechanical properties of the piezoceramics are summarized in Table 2. The adhesive material to attach the piezoceramic sensor/actuator on the plate is the cyanoacrylate adhesive(Lee and Marcus, 1981). The measured thickness of the adhesive layer is 0.05±0.01mm. Negative velocity feedback is applied for the active control of the plate. Two pairs of sensor/actuator function independently and the control technique is implemented on digital system. Experimental setup is shown in Figure 2.

The damping and the stiffness of the plates are controlled passively by changing fiber orientation in the outer layer. Damping ratio, natural frequency and modal damping of each vibrational mode changes as the piezoceramic sensor/actuator is attached to the plate. Measurements of the damping ratio, the fundamental frequency and the modal damping of the first bending and the first torsional modes are carried out to verify the validity of the finite element formulation using the impulse technique. Figure 3 and Figure 4 show the natural frequency of the plates without and with the piezoceramics, respectively. The measured data are in good agreements with those of finite element analysis. Figure 5 and Figure 6 show the modal damping($2\zeta\omega$) of the first bending and the first torsional modes of the plates, respectively. The measured modal damping agrees very well with the predicted value.

Conclusions

Vibration control of laminated composite plates with the collocated piezoelectric sensor/actuator is investigated numerically and verified experimentally. The finite element method is used to predict the structural characteristics of the laminated composite plates. The following conclusions have been drawn.

A systematic and quantitative method is proposed for the vibration control of laminated composite plates. Analyses of the passive and the active control are both in good agreement with those of experiments.

The attachment of the piezoceramics increases the modal damping of the plate. The dynamic characteristics of the laminated composite plate changes passively as the outer layer fiber orientation changes. Modal damping increases very much through active control. Influence of the active control on the modal damping is different for various fiber orientations and vibrational modes.

References

1. Batoz, J. L. and M. B. Tahar. 1982. "Evaluation of a New Quadrilateral Thin Plate Bending Element," International Journal of Numerical Methods in Engineering, 18 : 1655-1677.
2. Detwiler, D. T. and M. H. Shen. 1994. "Two-dimensional Finite Element Analysis of Laminated Composite Plates containing Distributed Piezoelectric Actuators and Sensors," A Collection of Technical Papers of the AIAA/ASME Adaptive Structures Forum, pp. 451-460.
3. Fuji Ceramics. 1994. Piezoelectric Ceramics. Fuji Ceramics Co., Ltd.
4. Ha, S. K., C. Keilers and F. K. Chang. 1992. "Finite Element Analysis of Composite Structures Containing Distributed Piezoceramic Sensor and Actuators," AIAA Journal, 30(3) : 772-780.
5. Lee, J. K. and M. A. Marcus. 1981. "The Deflection-Bandwidth of Poly(Vinylidense Fluoride) Benders and Related Structures," Ferroelectrics, 32 : 93-101.
6. Lin, D. X., R. G. Ni and R. D. Adams. 1984. "Prediction and Measurement of the Vibrational Damping Parameters of Carbon and Glass Fibre-Reinforced Plastic Plates," Journal of Composite Materials, 18 : 132 - 152.
7. Prakah-Asante, K. O. and L. C. Craig. 1994. "The Application of Multi-channel Design Methods for Vibration Control of an Active Structure," Smart Materials and Structures, 3(2) : 329 - 343.
8. Tani, J., J. Qui and H. Miura. 1995. "Vibration Control of a Cylindrical Shell using Piezoelectric Actuators," Journal of Intelligent Material Systems and Structures, 6 : 380 -388.

Table1 Mechanical Properties of Carbon/Epoxy laminates(CU125NS)

Property	Symbol	Value
Young's modulus in fiber direction	E_1	114.7×10^9 Pa
Young's modulus in transverse direction	E_2	7.589×10^9 Pa
Shear Modulus	G_{12}	4.77×10^9 Pa
Poisson Ratio	ν_{12}	0.28
Volume Density	ρ	1510 kg/m^3
Damping capacity in fiber direction	φ_{S1}	0.013966
Damping capacity in transverse direction	φ_{S2}	0.049120
Damping capacity in shear direction	φ_{S12}	0.074344

Table 2 Mechanical Properties of Piezoelectric Ceramics

Property	Symbol	Value
Piezoelectric charge constants	d_{31}	-260×10^{-12} C/N
Piezoelectric voltage constants	e_{31}	-8.7×10^{-3} m^2/C
Piezoelectric constants	d_{15}	750×10^{-12} C/N
Relative Dielectric Constants	$\varepsilon_{11}/\varepsilon_0$	3100
Relative Dielectric Constants	$\varepsilon_{33}/\varepsilon_0$	3400
Young's modulus	E_{11}	59×10^9 Pa
Young's modulus	E_{33}	52×10^9 Pa
Young's modulus	E_{55}	21×10^9 Pa
Damping capacity	φ_{P1}	0.0748644
Damping capacity	φ_{P2}	0.0748644
Damping capacity in shear direction	φ_{P12}	0.1061625

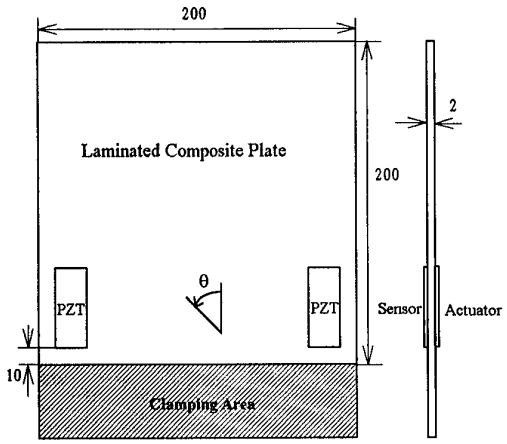


Figure 1 Configuration of Specimen

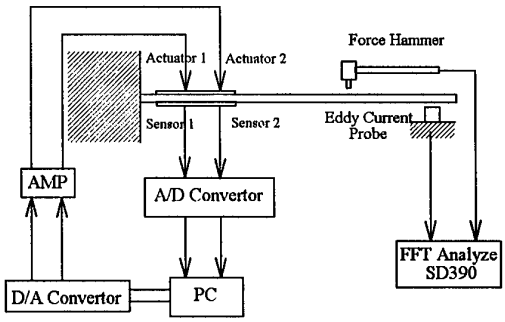


Figure 2 Experimental Setup

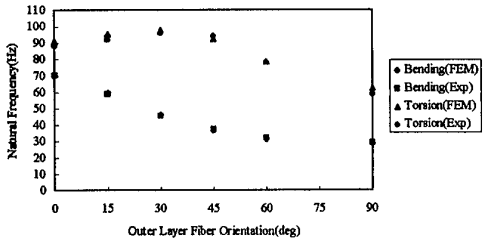


Figure 3 Natural Frequency of Plate without PZT

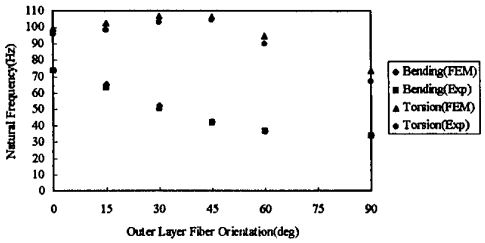


Figure 4 Natural Frequency of Plate with PZT

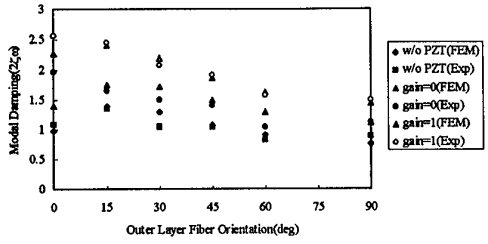


Figure 5 Modal Damping of Bending Mode

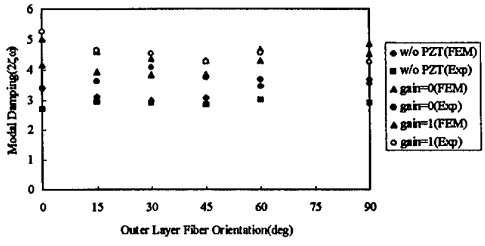


Figure 6 Modal Damping of Torsional Mode

Piezo-Damping : a low power consumption technique for semi-active damping of light structures

Dominique BONDOUX

Metravib R.D.S. Active Control Division
200 chemin des Ormeaux, 69760 Limonest, France

ABSTRACT

By including piezo-materials into a light structure, it is possible to convert a part of its vibrational energy into electrical energy. When this electrical energy is addressed to a dissipative impedance, a damping effect is obtained. The achievable performances for various kinds of dissipative impedances are derived from modelling results. It is shown how the used dissipative impedance acts on the structure (mechanical equivalence) and how the obtained performances are related to a non-dimensional coupling factor. Finally numerical and experimental results from a case study are presented.

1. INTRODUCTION

The simplest form of piezo-damping is achieved by using piezo-materials included in the vibrating structure to be damped and by addressing the corresponding delivered current to a passive electrical resistance. In this case the achievable piezo-damping is strongly limited due to the shunt effect of the electrical capacity of the used piezo-patches versus this resistance.
Then, the efficiency can be strongly improved if the used dissipative impedance also includes either a negative capacity [1] cancelling this shunt effect, or an inductance allowing to achieve an electrical resonant circuit tuned to the mechanical frequency to be damped. The effectiveness of these different kinds of dissipative circuits are presented in the following section.

2. MODELLING OF A PIEZO-DAMPED STRUCTURE WITH DIFFERENT DISSIPATIVE CIRCUITS

2.1 Piezo-damping implementation on a vibrating structure and corresponding modelling:

Let us consider a vibrating structure S with embedded or surface mounted piezo-material patches P wired in parallel and linked to a dissipative electrical impedance Z (see fig. 1)

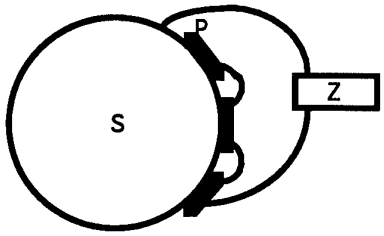


Fig. 1 : piezo-damping of a vibrating structure

The current i_p and the voltage e_p delivered by each patch P are linked to its elongation velocity ΔV_p and delivered force Fp by a transformation coefficient n :

$$e_P = \frac{F_P}{n} \text{ and } i_P = n \Delta V_P \; ; \; n = \frac{d_P S_P E_P}{l_P} \; ; \quad \text{with: (see fig. 2)}$$

d_P:	used piezo-coefficient,
S_P, l_P:	corresponding surface and length,
E_P:	corresponding Young's modulus.

As we use N piezo-ceramics wired in parallel, the delivered current ip is summed up and the voltage ep is common. By considering that these piezo-patches are of identical shape and properties, and by introducing C_p their common electrical capacity the equivalent electrical circuit is defined as shown fig. 3 :

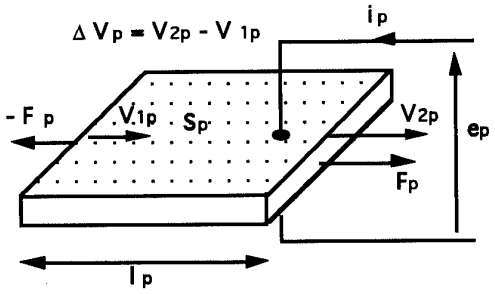


Fig. 2 : definition of useful quantities of the piezo-patches

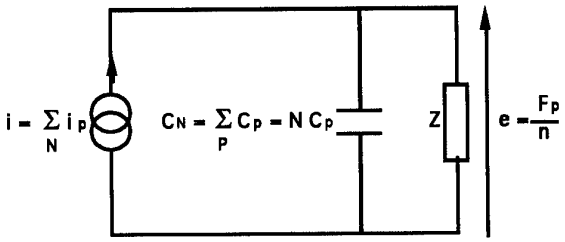


Fig. 3 : electrical circuit for N piezo-patches wired in parallel

Then after some computations the modal response of a structural mode to be damped is described in the frequency domain by :

$$- \omega^2 m_s \alpha + k_s \alpha + \mu_s \alpha + n^2 \left[\sum_N (\phi_{P2} - \phi_{P1}) \right]^2 \frac{Z j \omega}{1 + j \omega C_N Z} \alpha = t\{\phi\} \{F_e\} \qquad (1)$$

where:

m_s, μ_s, k_s are the modal mass, stiffness and damping;

$\{\phi\}$ is the modal amplitude vector,

$\{F_e\}$ is the excitation forces vector;

α is the generalised modal amplitude of the mode to be damped;

(response displacement vector is $\{X\} = t\{\phi\} \alpha$);

$j^2 = -1$;

t denotes transpose;

ω is the pulsation;

ϕ_{P1}, ϕ_{P2} are the modal amplitudes at extremities 1 and 2 of piezo-patch P.

From (1) the shunting effect of the capacity C_N is obvious :

$$\frac{Zj\omega}{1 + j \omega C_N Z} \rightarrow \frac{1}{C_N} \text{ when } \omega C_N Z >> 1$$

2.2 Use of a negative capacity :

Z is equal to a negative capacity - C (achievable with an active circuit) wired in parallel with a resistance R_D (see fig. 4).

Then by introducing the following coefficients for the structural mode to be damped:

$$\Omega_s = \sqrt{\frac{k_s}{m_s}} \text{ resonance pulsation, } \xi_s = \frac{\mu_s}{2 \sqrt{k_s m_s}} \text{ initial damping ratio;}$$

and the following coefficients for the electrical part:

$\beta = \frac{C_N - C}{C_N}$ reduction ratio of the electrical capacity; $\xi_D = R_D C_N \Omega_S$ electrical damping ratio;

a non-dimensional expression of (3) is obtained:

$$\left\{\left[1 - \left(\frac{\omega}{\Omega_S}\right)^2 + 2\,j\,\xi_S\left(\frac{\omega}{\Omega_S}\right)\right] + \frac{n^2 D}{\left(m_S C_N \Omega_S^{\,2}\right)} x\, j\left(\frac{\omega}{\Omega_S}\right)\frac{\xi_D}{1 + j\left(\frac{\omega}{\Omega_S}\right)\beta\,\xi_D}\right\}\alpha = \frac{1}{m_S \Omega_S^{\,2}}\, t\{\phi\}\,\{F_e\} \quad (2)$$

$$\text{where: } V_C = \frac{n^2 D}{\left(m_S C_N \Omega_S^{\,2}\right)} = \frac{n^2\left[\sum_N \left(\phi_{P2} - \phi_{P1}\right)\right]^2}{\left(m_S C_N \Omega_S^{\,2}\right)} \quad (3)$$

is a coupling factor between the ceramics and the structure. The greater this coupling factor is, the greater the potential piezo-damping efficiency.

The mechanical equivalency of expression (2) is shown fig. 4.

2.3 Use of tuned resonant circuits :

Z is equal to an inductance L wired in parallel with a resistance R_D or wired in series with a resistance R_L (see fig.5). Then by introducing the additional following coefficients :

$\Omega_D = \left(\frac{1}{L C_N}\right)^{1/2}$ electrical resonance pulsation of the LC circuit, $Q_D = \left(\frac{L \Omega_D}{R_L}\right)$ quality factor of the self,

$\xi_D = \frac{R_D}{\left(2\sqrt{\frac{L}{C_N}}\right)}$ electrical damping ratio,

a non-dimensional expression of (3) is obtained:

$$\left\{\left[1 - \left(\frac{\omega}{\Omega_S}\right)^2 + 2\,j\,\xi_S\left(\frac{\omega}{\Omega_S}\right)\right] + \left(\frac{n^2 D L}{m_S}\right)\left(\frac{\Omega_D}{\Omega_S}\right)^2 \frac{j + \frac{1}{Q_D}\frac{\Omega_D}{\omega}}{j\left(\frac{\Omega_D}{\Omega_S}\right)^2\left[-1 + \left(\frac{\omega}{\Omega_D}\right)^2 - \frac{1}{(2Q_D\xi_D)}\right] + \left(\frac{\Omega_D}{\omega}\right)\left[\frac{1}{(2\xi_D)} + \frac{1}{Q_D}\right]}\right\}$$

$$x\,\alpha = \frac{1}{m_S \Omega_S^{\,2}}\, t\{\phi\}\,\{F_e\} \quad (4)$$

$$\text{where: } V_L = \left(\frac{n^2 D L}{m_S}\right) = \left(n^2\left[\sum_N \left(\phi_{P2} - \phi_{P1}\right)\right]^2 \frac{L}{m_S}\right) \quad (5)$$

is a coupling factor between the ceramics and the structure, the greater $\left(\frac{n^2 D L}{m_S}\right)$ is, the greater the potential piezo-damping efficiency. If the tuning of the electrical resonance is correct ($\Omega_S = \Omega_D$), then this coupling factor (5) is equal to the coupling factor of the negative capacitance option (3).

The two options for the tuned circuit are obtained with Q_D reaching infinity for the "L//R" option and ξ_D reaching infinity for the "L+R" option.

The mechanical equivalencies of these two options are shown figure 5.

2.4 Performances prediction and discussion :

Fig. 4 and 5 provides values of modal amplitudes α versus non dimensional frequencies. From these figures the improvements in term of maximal structural response, above the use of a dissipative circuit limited to a simple resistance is obvious.

The use of a negative capacity provide a broad band efficiency allowing to damp different modes. The efficiency is nevertheless limited by the use of a negative capacity that can generate electrical unstabilities. That means that for practical applications the capacity reduction ratio β must remain above values around 1/3.

The use of a tuned inductance provides an intrinsically stable circuit. The inductance has generally high values that implies the use of a very simple active electronic circuit in order to simulate it rather than to use a real inductance. The mean limitation arises from the tuned approach that means that only one mode can be damped with such an approach.

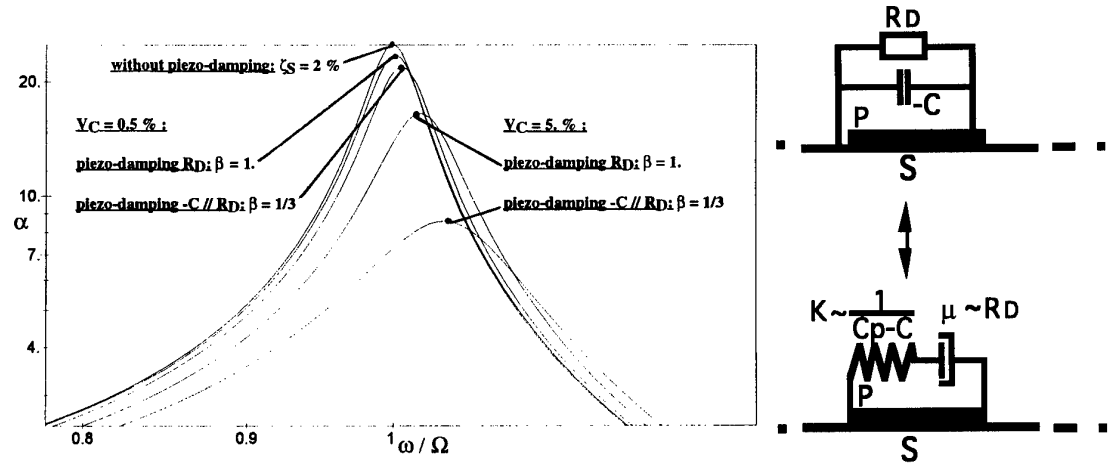


Fig. 4 : performances prediction with a dissipative circuit including a negative capacity

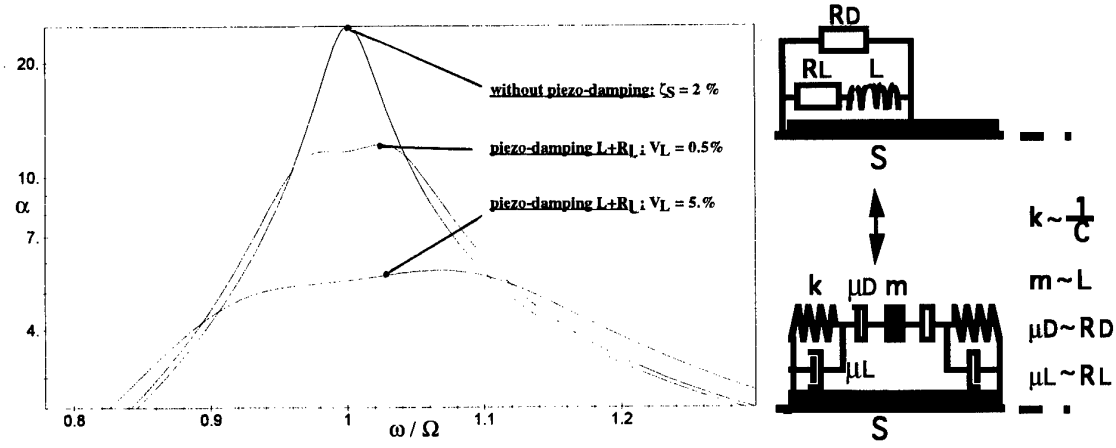


Fig. 5 performances prediction with a dissipative circuit including a tuned inductance

3. EXPERIMENTAL AND NUMERICAL RESULTS FROM A CASE STUDY

3.1 Case study description :

Some satellite equipments are isostatically mounted on their receiving structures by using three so-called V blades (see fig. 6). Then the equipment suspension modes are mainly related to the tensile stiffness of each side of the V-blades. The purpose is to damp these modes by a piezo-damping technique. A proof of concept has been achieved with the arrangement described in fig. 7.

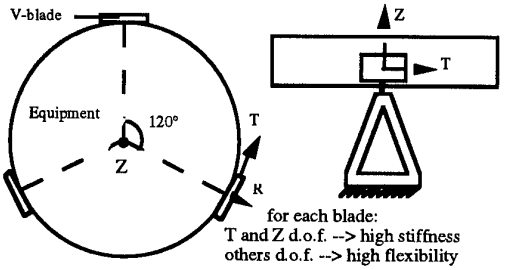


Fig.6 Isostatic mounting of satellite equipment.

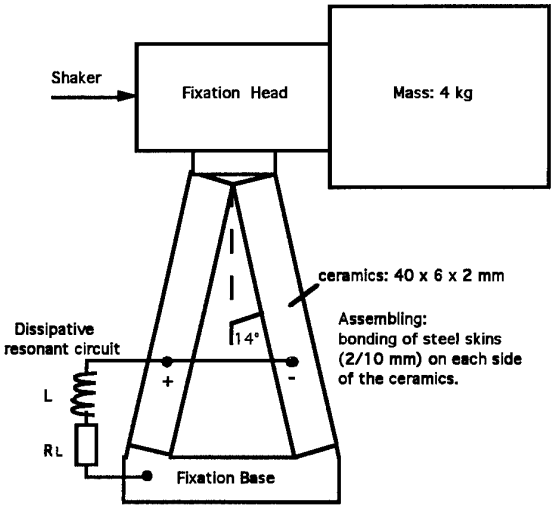


Fig.7 : experimental set-up

3.2 Experimental results :

The effect of the piezo-damping upon the mass acceleration are provided in figure 8 for various tuning frequencies of the inductance L. For all the curves the dissipative resistance R is unchanged.

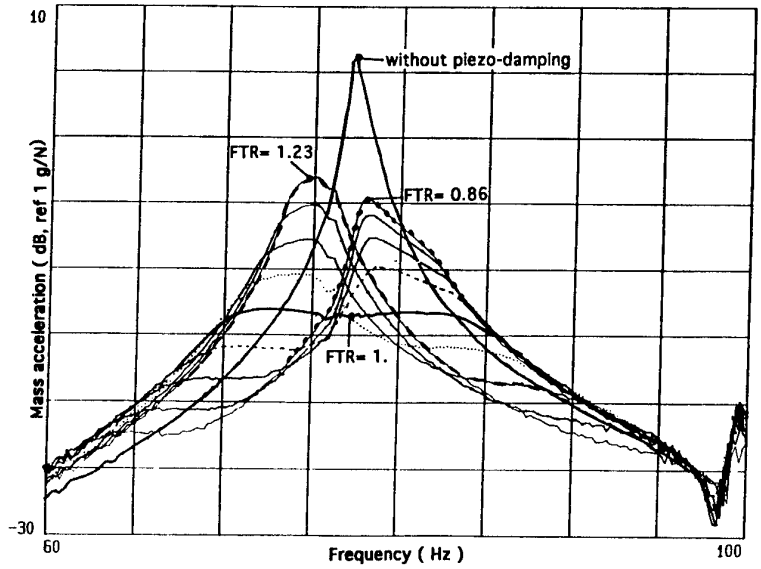


Figure 8: piezo-damping experimental results

3.3 Numerical results

Equation (4) has been used to predict the piezo-damping performances of the tested V-blades. The needed data have been derived from a finite element model (modal amplitudes) and from the used piezo-ceramics properties. The comparison between the predicted results and the experimental ones is very good (see table 1).

Additionally, the relative mechanical resonance frequency variation induced by these two mistunings of the electric circuit are quite equal :

- experimentation = 5 %
- prediction = 4 %

	MAXIMUM AMPLIFICATION FACTOR	
	TESTS	PREDICTION
well tuned circuit	7,5	8
electrical frequency detuned from mechanical frequency by + 23 % (FTR = 1.23)	23	16
electrical frequency detuned from mechanical frequency by - 16 % (FTR = 0.86)	16	22

Table 1 : test and prediction results

3.4 Discussions

This case study illustrates the validity of the used model in particular it perfectly demonstrates the like tuned vibration absorber behaviour.

The computation of the associated current and voltage from the piezoceramics provides very low values of 9,2 mA and 21 V for a vibration velocity at the resonance frequency of 1 mms-1. These values illustrate the very low electrical power needed by the electronic dissipative impedance for applications aiming to control low level vibrations as for satellite applications.

4. CONCLUSIONS

The proposed piezo-damping technique is proven efficient. Its main advantages above passive viscoelastic damping techniques are its best efficiency and its very low thermal sensitivity.

The main limitation arise from the need of a high coupling coefficient for achieving a high damping. That means that the location of the piezo-material into the structure to be damped must be defined carefully and that a large amount of such material must be used.

5. ACKNOLEDGEMENTS

This work has been performed by METRAVIB R.D.S. in complement to ESA contract "Very High Pointing Accuracy AOCS" work order 17 to ESTEC contract 9558/91/NL/JG, the main contractor being MATRA MARCONI SPACE France.

6. REFERENCES

1. Patent n° 88-17046 (19/12/1988)

Control of High-Frequency Smart Structures Through Embedded NiTiNOL Fibers

A. V. Srinivasan
Department of Mechanical Engineering
Worcester Polytechnic Institute
Worcester, MA 01609

D. Michael McFarland
Howard A. Canistraro
Eric K. Begg
Department of Mechanical Engineering
University of Connecticut
Storrs, CT 06269–3139

Abstract

A method to increase the usable bandwidth of shape memory alloy (SMA) actuators for structural control is investigated. Because the change in material properties exploited in SMA components requires significant temperature variation, usually achieved through resistive heating, the response time of SMA actuators is ultimately limited by heat transfer in many applications. Typically, very rapid heating can be achieved but the time needed for cooling is long compared to the vibratory period of a mechanical or civil structure. By using several actuators in parallel and energizing subsets of these during successive cycles of structural motion, an effective bandwidth can be achieved that is greater than the bandwidth possible with a single actuator. This is demonstrated here for an active structural system comprised of SMA wires embedded in the outer laminae of a composite beam specimen. The beam was mounted as a cantilever and its first and second modes of vibration were excited by energizing the embedded wires.

1 Introduction

Shape memory alloys (SMAs), since their discovery in the mid-60s, have moved from laboratory to a mature industry. Nickel-titanium and copper-based alloys are now available and can be used to develop devices that can perform a wide variety of functions: as actuators, components for smart materials, medical and orthodontic devices, safety valves, mechanical and electrical fasteners, eye glass frames, etc. The inherent damping capacity of the material allows its use for damping machinery, buildings and other structures.

The uniqueness of the material arises from the so-called shape memory effect through which an article deformed at a certain temperature can completely recover its original shape at a higher temperature. The behavior is essentially a consequence of a reversible phase transformation from the austenitic phase (parent phase) at a higher temperature to the martensitic phase at a lower temperature (Schetky, 1979; Wayman, 1993). There are four characteristic temperatures that represent the phase changes and are denoted by A_f (completely austenitic), M_s (start of martensite), M_f (completely martensitic), and A_s (start of parent phase) and can be visualized as four corners of a parallelogram in the shape change vs. temperature domain. The range of temperatures between the extreme states (i.e. A_f and M_f) can be 5 °C to 50 °C and is therefore characterized by a hysteresis. The martensites are self-accommodating and therefore represent a stress-free transformation. Up to 10% "permanent strain" can be recovered.

The features discussed above are commonly exploited in the design and development of actuators. In practice, an SMA device is deformed in the martensitic phase and shape recovery is accomplished through a reverse transformation to its parent phase. Clearly, if this recovery is prevented through constraints, then a force is manifested and imparted and can be used to meet a design goal.

The most common SMA devices in use are essentially quasi-static. Most applications and developments have remained in the quasi-static domain because of an important feature inherent in the material, i.e. its response to a thermal input. While the application of heat through, for example, electrical resistance (i^2R) heating raises the temperature almost instantaneously, it takes a far longer time for the material to cool. Thus, any application which requires a continuous on/off mechanism of equal duration suffers from the inherent asymmetry in the thermal response of the material. Therefore the use of the material in actuators for use in a vibratory environment has been limited, until now, because of the poor frequency response of the material. The investigation which

0-8194-2165-0/96/$6.00

forms the subject matter of this paper is based on a unique approach which shows promise as a way of overcoming the inherent limitations discussed above. The approach is based on using several NiTiNOL wires as actuators in parallel and energizing subsets of these during successive cycles of structural motion. Thus an effective bandwidth can be achieved for the array and is demonstrated to be greater than the bandwidth of a single actuator. This serves the eventual goal of controlling vibration at frequencies higher than was thought possible with this material.

2 Concept of Multiplexed Actuation: Theoretical Basis

In order to overcome the bandwidth limitations inherent in SMA actuators, the use of an array of actuators in parallel has been proposed (Srinivasan et al., 1991). The relationship of the signal driving any one actuator, taken to be a rectangular pulse of period T_e, to the desired structural response, of period T_r, is shown in Figure 1.

For concreteness, four actuators in parallel have been assumed, but the method is applicable to any number. The excitation has a short duty cycle (ratio of time "on" to pulse length), with the "on" period equal to approximately $T_r/2$, i.e., the portion of a cycle of the response during which the structure is moving in one direction (shown as the positive-going half-cycle in the figure). The corresponding actuator responds quickly to heating, producing an increasing force during the "on" pulse, then cools and relaxes during the succeeding 3 1/2 cycles of structural response. No actuator is driven during the negative-going half of the first structural response cycle of Fig. 1, but at the end of time T_r an identical pulse is applied to the second of the four actuators. This process is repeated with the remaining two actuators, so that after all four have been switched on

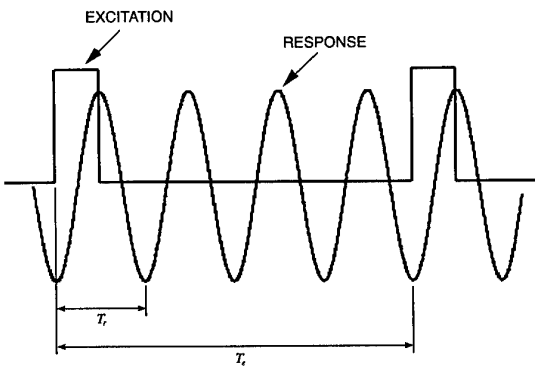


Fig. 1. Theoretical timing of SMA excitation and beam response.

for $T_r/2$ and allowed to cool for $7T_r/2$, the first is again activated. The force experienced by the structure is the superposition of the four actuator outputs, and has period $T_r = T_e/4$, that is, the time-varying force driving the structure has a frequency four times that of the electrical signal driving each actuator. More generally, the force experienced by the structure will be of a frequency equal to the electrical driving frequency multiplied by the number of actuators in parallel.

The specimen discussed in this paper incorporated four actuators, each consisting of several NiTiNOL fibers electrically connected in series. Passing current through the wires of an actuator produced a bending moment which deflected the cantilevered beam specimen toward the actuator, i.e., up or down, depending on the whether the actuator wire was nearer to the top or bottom face of the beam.

The nomenclature of "firing" (driving) an actuator and of a "firing order" for the actuator array was adopted, along with a convention for describing the signals used. Those actuators arranged so as to pull the beam up are denoted by T_i, and those pulling it down by B_i. The composite beam had two independently controlled sets of wires in its top face, comprising actuators T_1 and T_2, and two sets in its bottom face, actuators B_1 and B_2. The firing order for the actuator array is described for one period T_e of the excitation by stating the actuators to be fired during each half-cycle of a structural response period T_r separated by commas, with semicolons used to separate the groups for consecutive periods T_r. Zero is used as a place holder to indicate that no actuator is energized for one half-cycle of structural motion. For example, the excitation shown in Fig. 1 would be denoted $T_1, 0$. Some additional complexity is introduced when actuators oppose one another and can act during successive half-cycles of structural motion. Considering the composite specimen with actuators T_1 and T_2 opposed by actuators B_1 and B_2, we can have, for example, T_1 pulling up for a period $T_r/2$ followed by B_1 pulling down for $T_r/2$, with this pattern then repeated by T_2 and B_2. Such a firing order is denoted $T_1, B_1; T_2, B_2$. Note that this implies $T_e = 2T_r$ rather than $T_e = 4T_r$, i.e., the frequency of structural excitation available from the actuators used this way is twice rather than four times that of the electrical driving signal. For a fixed total number of actuators, less frequency gain can be achieved if the structure is driven during the entirety of each response cycle rather than during only one-half of each cycle.

3 Analytical Basis for the Design of Composite Beams

In order to design a composite specimen with shape memory alloy wires as well as conventional passive

fibers embedded in an epoxy matrix material, it is necessary to account for the effects of the SMA on the mechanical properties of the composite as well as for its role as an actuator. Since the volume fraction of SMA, at least within some laminae, may be large, it is natural to treat the wires as inclusions in a matrix of composite material whose properties are known. This allows the use of existing formulas to estimate the influence of SMA fraction and placement on bending and in-plane stiffnesses and thus on the specimen's natural frequencies of free vibration.

In the case of a one-dimensional structure such as the beam specimen of interest here, significant simplifications are possible. By considering simultaneously the geometry and material properties of the laminae, Gibson and Plunkett (1976) derived an equivalent modulus for a composite beam in bending. This modulus can be used directly in formulas previously derived for homogeneous, isotropic beams. This equivalent modulus aids physical insight as well as computational convenience. For a beam symmetric about its midplane and with an odd number n of laminae, the equivalent modulus is given by

$$E_c = \frac{8}{n^3}\left[\frac{E_0}{8} + \sum_{j=1}^{\frac{n-1}{2}} E_j(3j^2 - 3j + 1)\right]$$

where E_j is the modulus, in the longitudinal direction, of the j th lamina. These properties were readily available for the prepreg materials under consideration at the time the composite specimen was being designed.

Major features of the beam cross section are shown schematically in Fig. 2. The presence of NiTiNOL wires in some of the beam laminae was taken into account by computing an effective modulus for those plies using a rule of mixtures based on the volume fractions of SMA and prepreg material. Because the equivalent modulus equation above assumes all the beam's laminae are of the same thickness, the foam core was modeled as a number of plies each as thick as one prepreg strip but with the isotropic material properties of the much more compliant foam.

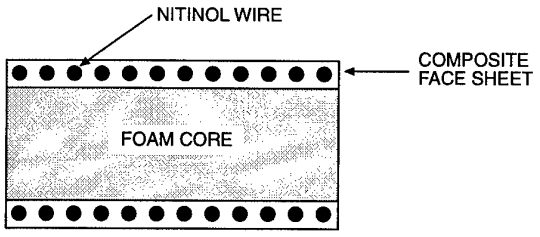


Fig. 2. Cross section of composite beam with embedded NiTiNOL wires.

4 Control Scheme and Test Specimens: Analysis and Design

This section discusses the control software and hardware used to generate and amplify the electrical driving signals, and the design of the composite specimen, which was fabricated by Martin Marietta.

4.1 Electrical Control System

A schematic of the test setup is shown in Fig. 3. Voltage signals were generated using a digital signal processing (DSP) card installed in a PC-compatible computer. Code written in the C language on the PC was cross-compiled, then downloaded to the DSP card and executed there under the control of a user program running on the PC. Input and output (I/O) to and from the DSP was in the form of analog signals in the range ±2.5 V. Four independent signals were available to drive the test apparatus. A signal generator program was written to run on the DSP and an executive program to run on the PC; the latter could be used to update the output levels and frequency on the fly, with pulse shaping and synchronization done automatically.

The DSP output signals drove four voltage-controlled current sources, and each of these in turn powered one set of SMA wires in series (one actuator). The current sources had a sensitivity of 2.0 A/V and could apply up to 5 A or 20 V DC to a resistive load before overheating or saturating.

Although the DSP outputs are extremely stable, the finite rate of analog-to-digital conversion has the effect of discretizing the available output frequency spectrum. Most tests reported here were performed with a conversion frequency in the range of 1 kHz to 10 kHz. While the resulting precision was much better than could be attained with an analog signal generator, the steps in driving frequency are reflected in some of the response plots of Section 6.

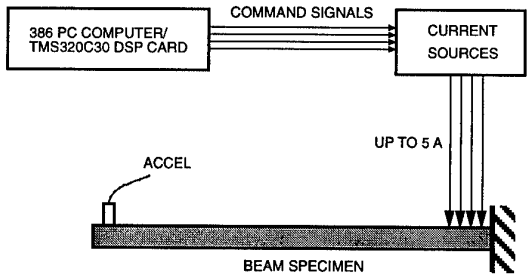


Fig. 3. Block diagram of electrical system.

4.2 Composite Beam with Embedded Fiber Actuation

On the basis of the equivalent modulus equation of Section 3, several sets of design curves were computed. It was desired to design a specimen whose first natural frequency was high enough, greater than approximately 10 Hz, to allow the use of existing dynamic test equipment, but not so high that significant heating and cooling of the embedded SMA could not take place during one cycle of vibration.

The beam consisted of a rectangular foam core, of cross section 13 x 36 mm, to which were bonded two composite face sheets each consisting of 14 plies of glass-epoxy composite in an alternating 0/90° layup. The sprung length of the beam was 559 mm. Embedded in each face sheet were twelve strands of NiTiNOL wire, evenly spaced and parallel to the beam axis. These were connected in a total of four electrical circuits, one to be driven by each channel of the control system. Thus, with the beam mounted as a horizontal cantilever, there were two sets of 6 wires each in the top face sheet and two sets in the bottom, each set of 6 wires acting as a single actuator. The wires of each set were selected to be symmetric about the vertical plane of symmetry of the specimen, so that activating any one set of wires would produce bending but not torsion of the beam. The embedded wires had $A_f = 57°\,C$ and were installed with 3% prestrain. The six wires in series comprising each actuator had a resistance of approximately 18 Ω.

5 Overview of the Test Program and Test Stages

The data reported here were taken in a sequence of tests performed during the summer and fall of 1995. These tests occurred in three blocks of a few days each, separated by longer periods devoted to experimental design, preliminary data reduction and control hardware modification and programming. For reporting purposes, the three periods devoted to testing are identified herein as "stages".

At each stage of testing, the specimen was mounted as a cantilevered beam. The lowest natural frequencies and the corresponding damping ratios of this structure were then identified by modal analysis using data obtained from a standard "hammer test", in which the beam was struck near its tip with a hammer instrumented to measure force and the response to this blow was measured with a miniature accelerometer attached to the specimen with wax, also near the tip. The force and acceleration signals were processed using a Bruel & Kjaer Model 2034 spectrum analyzer, with further data processing being done on an attached PC. The effect of constant heating was examined by producing a constant current in the SMA wires, letting the specimen reach thermal equilibrium, and repeating the hammer tests. At high temperatures, the accelerometer was thermally insulated from the composite specimen by a small mica washer to avoid degradation of its performance due to heating. Natural frequencies and damping ratios were estimated by fitting single-degree-of-freedom models to individual peaks in the frequency response function (FRF) magnitude plots, as displayed on the B & K analyzer. The acceleration response data were converted to equivalent velocity response information (by division by $j\omega$ in the frequency domain) to facilitate the model fitting process, and this velocity-state representation is used in this paper for FRF plots.

Once the resonant frequencies were identified, the SMA actuator wires were driven electrically and the resulting structural response was measured using the same accelerometer as in the hammer tests. This transducer, in conjunction with its power supply, had a sensitivity of 100 mV/g, and it proved convenient to record and process response information directly in these units. Because of the complex nature of the excitation needed for this kind of test, the spectrum analyzer could not be used to obtain, for example, frequency response plots. Rather, a desired electrical input was established using the DSP equipment and programs described in Section 4.1, then the peak-to-peak amplitude of the acceleration signal was read from the screen of a Tektronix storage oscilloscope.

Because equipment to obtain reliable temperature measurements was not available until Stage 3 of the tests, electrical driving currents are referred to throughout the following discussion to indicate the level of excitation applied. Temperature data, including thermocouple readings and infrared images of the composite in operation, were taken at the conclusion of Stage 3 testing and are discussed separately in Section 6.3.

6 Results and Discussion

For each of the three stages of testing, the composite beam was mounted in the test fixture as previously described. Hammer tests were carried out at each stage to identify the first and second natural frequencies and damping ratios at room temperature and with various constant currents flowing in the NiTiNOL wires. Pulsed electrical excitation of the SMA was then employed to drive the structural response, and beam tip acceleration was recorded.

6.1 Modal Testing

In Stage 2, hammer tests were conducted on the composite specimen at room temperature and while constant currents of 0.25 and 0.50 A were supplied to its NiTiNOL actuator wires. The response in the first mode was virtually unaffected by the this heating, but the second mode response amplitude was significantly

increased. Natural frequency and damping ratio estimates obtained from the constant-current FRFs are given in Table 1.

Table 1. Natural frequency and damping ratio estimates from hammer tests of the composite beam with embedded NiTiNOL wires.

	Constant Current, A			
	0.00	0.25	0.50	0.75
Stage 2				
f_1	22.20	22.01	21.96	—
ζ_1	5.1	4.9	5.1	—
f_2	140.30	139.11	139.29	—
ζ_2	1.9	1.6	1.6	—
Stage 3				
f_1	23.47	23.51	23.50	23.49
ζ_1	1.9	1.9	1.6	1.9
f_2	144.01	143.28	142.34	141.58
ζ_2	1.2	1.4	1.4	1.6

Similar results were found from the Stage 3 hammer tests, and are included in Table 1. This time an additional constant current, 0.75 A, was used. The FRFs from this stage of testing for currents of 0.00 and 0.50 A are compared in Fig. 4. Note that the heat dissipation due to the 0.50 A current flowing in all four sets of actuator wires was the same as was produced by the 1.0 A current driving only one wire at a time that was used in the tests of the electrically driven response, discussed below. The effect of constant heating was more pronounced here than it was in Stage 2, but the FRFs of the structure at 0.50 A were quite similar in the two stages.

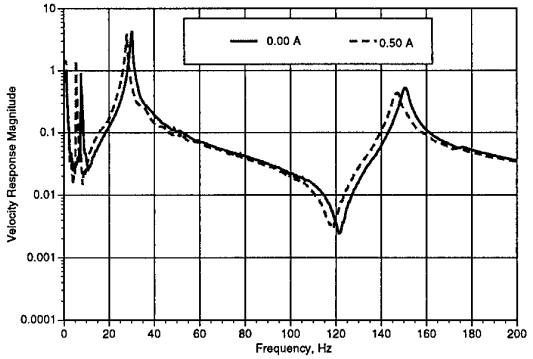


Fig. 4. Comparison of Stage 3 FRFs at constant currents of 0.00 and 0.50 A.

6.2 Excitation of Composite Beam via NiTiNOL Fibers

In these experiments the beam was driven only by electrical heating of the embedded NiTiNOL wires. An actuator firing order of $T_1, B_1; T_2, B_2$ was used, and preliminary experiments led to the selection of 1.0 A as the driving current pulse amplitude.

Stage 2 and 3 testing of the electrically driven response was straightforward. Results obtained with a driving current pulse amplitude of 1.0 A are plotted in Figs. 5 and 6. The signal generator frequency discretization discussed in Section 4.1 is obvious in these plots. Resulting natural frequency and damping ratio estimates are given in Table 2, where they are compared to hammer test data.

No significant response of the composite beam could be produced (even in the first mode) when all four sets of wires were driven during every cycle of structural motion.

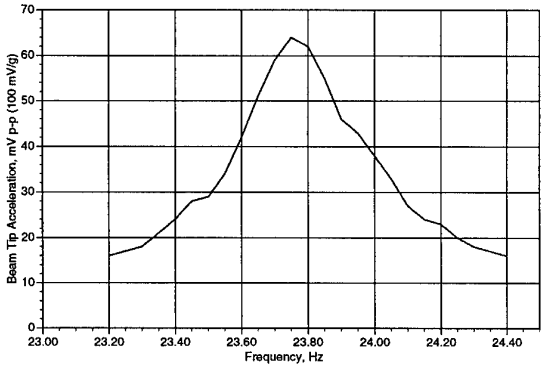


Fig. 5. Composite beam tip acceleration, mode 1, Stage 3 (0.05 Hz step size).

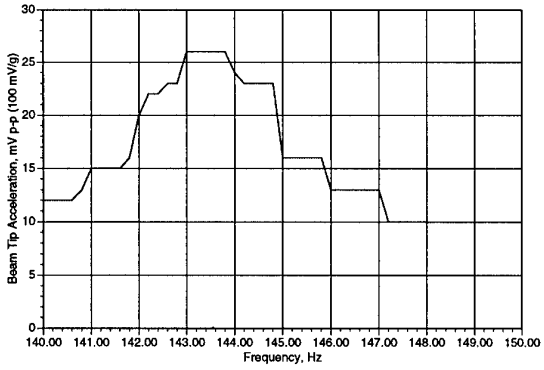


Fig. 6. Composite beam tip acceleration, mode 2, Stage 3 (0.2 Hz step size).

Table 2. Natural frequency and damping ratio estimates from electrically driven tests of the composite beam specimen (partial hammer test results are included for comparison).

		Electrically Driven	Hammer Tests (0.5 A continuous)
Stage 2:	f_1, Hz	23.15	21.96
	ζ_1, %	1.5	5.1
Stage 3:	f_1	23.75	23.50
	ζ_1	0.6	1.6
	f_2	144.70	142.34
	ζ_2	0.9	1.4

6.3 Temperature Measurements

In Stage 3, temperature as well as structural response data were taken. Most of this information was obtained through the use of an Inframetrics Model 600 infrared camera. Because the camera used liquid nitrogen for a temperature reference, there were limits on its orientation. Therefore, all thermal tests were done with the beam and mounting fixture rotated so that the beam axis was vertical. The system was calibrated by mounting a type K thermocouple to the beam and using its output as a reference to correct the raw numbers available from the camera.

The beam temperature profile at a fixed longitudinal position was measured at ten evenly spaced stations across the face of the beam. During these measurements, the beam was driven electrically at mode 1 resonance with a pulse amplitude of 1.0 A. The temperature values recorded are plotted in Fig. 7. Edge effects are evident, as was expected, and the symmetry of the profile about the beam centerline is also apparent.



Fig. 7. Temperature profile of composite beam in operation.

7 Conclusions

The single most important objective of this research effort was to demonstrate the potentials of shape memory alloys for use in structures where the operating frequencies may be in a range never before attempted with this material. Specifically this attempt was oriented to excite the first two modes of a composite cantilevered beam with embedded NiTiNOL wires. Tests showed that both the first and second modes could be excited through sequential excitation of the wires.

It is concluded that the objectives of the research were met and that the unique control scheme adopted variety of smart structures for use in industrial applications.

Acknowledgments

The authors take this opportunity to thank Lockheed Martin Astronautics/Martin Marietta Technologies Inc. for supporting this research effort.

References

Gibson, R. F. and Plunkett, R., "Dynamic Mechanical Behavior of Fiber-Reinforced Composites: Measurement and Analysis," *Journal of Composite Materials*, Vol. 10, October 1976, pp. 325–341.

Schetky, L. M., "Shape-Memory Alloys," *Scientific American*, Vol. 241, No. 5, November 1979, pp. 74-82.

Srinivasan, A. V., Cutts, D. G., and Schetky, L. M., "Thermal and Mechanical Considerations in Using Shape Memory Alloys to Control Vibrations in Flexible Structures," *Metallurgical Transactions A*, Vol. 22A, March 1991, pp. 623–627.

Wayman, C. M., "Shape Memory Alloys," *Materials Research Society Bulletin*, Vol. 18, No. 4, April 1993.

Active Vibration Control by Piezoceramic Actuators on a Jet Aircraft Partial Frame Structure

Leonardo Lecce, Massimo Viscardi, Stefania Cantoni

Department of Aeronautical Engineering , University of Naples " Federico II "
Via Claudio, 21 - 80125 Naples - Italy

Abstract

During the last five years, the Dept. of Aeronautical Engineering of the University of Naples, has carried out a lot of work , especially on the experimental side , focused on assessing the feasibility of an active vibration and noise control approach, based on the use of piezoceramic actuators and sensors bonded to different structural elements. This paper concerns an applications of this technique relative to a partially curved stiff frame of a medium civil transport jet aircraft.
The general procedure, as previously assessed on different test articles, requires as first step, the dynamic characterization of the test article, to best point out the target of control procedure in termd of deformed shapes relative to the frequency of most interest. The use of PZT piezoactuators to be bonded on the structure guarantee at the same time high actuators forces in front of a low weight increment. The hearth of the MIMO (Multi Input Multi Output) feedforward control procedure that is usually applied, is then represented by an ANN (Artificial Neural Network) control alghoritm that use the evaluation of experimental FRF as measured by reference accelerometer, to calculate the optimum control forces to be applied to the actuators to minimize a target cost function.
Experimental results provided over 32 dB of overall vibration level reduction in a single controlled mode shape, without any spillover effect.

1. INTRODUCTION

Noise and Vibrations Control is an important design goal in various modern means of transport (aircraft, car, etc.) . Active Control methods of the acoustic interior field have been developed and tested, but problems remain in terms of cost, space and weight.On the other hand, the potential benefits of the active control, aimed at vibration and noise level reduction, were widely demonstrated, [1].

The most promising way to reach this objective appears to be the one based on the use of " Intelligent Systems and Structures ", [2], as an application of the ASAC (Acoustic Structural Active Control) concept, and advanced actuators like piezoceramics bonded or embedded in the structure, seem to represent the best solution [3] since they can produce a remarkable excitation level, with of a low weight, low cost and easy integration in the structure itself.

A depth theorethical and numerical study, with the support of many experimental tests, began some years ago and is still going on, to assess the feasibility , to evaluate and improve the performance of this new approach.

A MIMO AVC technique, as the one here experienced, requires high performance actuators and sensors, but above all a powerful Control Alghoritm.

With reference to this circumstance, intelligent controllers have to learn the behaviour of the system to be controlled during operations and as a consequence, they should be able to express actions not forecast in the design phase: they must adapt themselves to the external environment. Artificial Neural Networks (ANN's), seem to offer promising applications : they are able to identify the system to be controlled, and the necessary control forces as well as to face non-linear problems, with good results [4-7].

To point out the advantages of such control, different test articles were investigated in the last years and many tests of active control were expecially performed on light and thin walled structures. After many of the related problems were solved, the opportunity to realize this kind of control on structure

0-8194-2165-0/96/$6.00

The input information consists, as said of transfer functions (in amplitude and phase) between each sensor and each singular piezo excitation (for a reference voltage: ad example 100 V) and external disturbance that causes vibrational fields.

As output the ANN furnishes the values of voltage to be applied at each piezo (needed to minimize the level of vibration measured by the sensors) as well as the predicted " controlled " level (expressed in dB) at each frequency considered in the range of interest .

3. ACTIVE VIBRATION CONTROL OF A TYPICAL AIRCRAFT FRAME

3.1 Introduction to aircraft noise and vibration problems

Even if the use of a turboprop propulsion system, permits to obtain a large cut in the direct operative costs, unfortunately it causes inside the passenger's cabin maximum noise levels higher than those in jet airplanes. Furthermore, because the propellers are the most important noise source, these maximum levels are measured at a low frequency (< 200 Hz), where the usual interior noise control systems, based on the use of soundproofing materials, have low efficiency.

Frequency spectra produced by pressure fields generated by turboprop engines, consist infact of a set of pure tones whose foundamental frequency is strictly correlated to the blade passage frequencies (BPF). This BPF frequency lies at around 100 Hz for the different airplanes.

The fuselage wall has been identified, for a long time, as the most important source of noise trasmission for these aircrafts, mostly due to the extremities of the propeller blades being so close to the fuselage itself (this is a typical airborne noise trasmission path) . In particular, the frames, whose modes dominate in the low frequency range, can be regarded as the most significant elements in the noise trasmission paths on these kind of aircraft.

By this way, an Active Vibration Control seems [4] to represent a possible way of reducing interior noise levels and at the same time acting in positively on some structural requirements : less addictional weight, less crew fatigue due to noise and vibration, et cetera.

3.2 Active Vibration Control of a Stiff Curved Frame - Experimental Test Description

As previously said, the test article, represent a partially curved stiff frame of a medium civil transport aircraft .

The frame, made of a typical alluminium alloy , presents a variable I section shape with a lenght of about 1660 mm , as reported in Fig 3; in the lower part of the same figure comes also evident the integrated floor support, with a similar section shape to the frame itself, and the simulated full constrained boundary condition.

Frame's section varies along the curvature, continuously since the border area to the adiacent frame, where a strong discontinuity is evident; the lower stiffness of this part makes evidence of the light torsion of this area associated to all the frame's eigenmodes.

The general procedure, as described before, has been applied and, as a first step, rising from the numerical and experimental modal analysis, the mode at 121.2 Hz, that represents the second bending mode of the frame, was chosen as the target mode to be controlled (the small number of available actuators has permitted to realize a one mode control), see Fig. 4.

The analysis of mode shape permits also to define a simple definition of the piezoelectric actuators positions by calculating the second order derivatives of the mode's shape (Fig. 5).

The reason for this can be searched in the way of working of the piezoactuators, itself. A piezoactuators is a strain actuators and for this reason to maximize the relative modal forces [3], it has to be placed in locations of maximum strain, as to say where is maximum the value of the seconde derivative of the structure displacements. This circumstance remembers the one that force actuators have to be placed in high displacement locations. The evaluation of this data was performed by the use of Mathcad software and two optimal locations were pointed out, while the "strain nodes" were carefully avoided)

Four actuators were placed at these locations on two each opposite sides of the I section flange, while a fifth one was placed in the lower part and was used as excitation source and reference signal (at frequency of 121.1 Hz) (Fig. 6) .

with higher stiffeness and weight was investigated, and a partial frame of a modern jet aircraft was used as test article.
An overall reduction of over 32 dB of the vibration level was experimentally obtained, when only 4 piezoceramic actuators were used , in two opposite flange of a I section.

2. MULTI INPUT MULTI OUTPUT ACTIVE VIBRATION CONTROL BY THE USE OF AN ANN CONTROLLER

2.1 Overview of the procedure

The general procedure of this approach, that involves the use of several sensors and actuators and whose theorethical aspects are well known, can be sinthetized in the flow chart of Fig. 1

The first step of the procedure is the understanding of the dynamic behaviour of the structure and the extraction of modal parameters, as eigenfrequencies, eigenmodes and structural damping. The excitation of these modes during the operative conditions, brings about to the associated phenomena of resonance with all the unpleasent consequences, and so generally represent the target of Active Control Systems.

With this goal, the experimental modal analysis is performed and generally at the same time, a FEM numerical model is built and validated. This latter model could later permit further investigations.

By referring to the excitation frequencies the most significant modes to be controlled can be identified. Consequently the number and position of the actuators and the sensors can be optimized using different tools such as the Genetic Alghoritm (GE) [9] or the Second Derivative Technique, as later described.

After the piezo actuators and sensors have been placed on the structure in the best positions, the recording of experimental FRF between disturbance and sensors, and actuators and sensors fournishs the required functions to the control alghoritm that provides as output, the voltage and phase to be applied to each actuator in order to minimise a fixed cost function (which could be the overall vibration or the noise level).

This MIMO AVC control technology presents all the characteristics of : stability, linearity and robustness, as will later come out.

The physic control system used in the above mentioned tests is a very simple analogic tool. The device that has been built has up to sixteen I/O channels. It permits a signal phase variation , between the input and the output, in the range $\pm$ 180°, to be changed indipendently for each channel. Likewise it is possible to vary the gain of each channel in a such way as to achieve a maximum tension equal to 200 Vcc for the output channel. The input signal must be in the range 0-5 V.

2.2 Control algorhitm by artificial neural network (ANN)

As previously mentioned, the real obstacle to the application of classical active noise and vibration control methods is due to the non-linear nature of the associated phenomena and to the variability of the operative conditions. A good response to all these requirements may be reached by the use of Artificial Neural Networks (ANN) [9].

This new technique of programmation permit to realize a complex structure (the ANN), made up of a lot of elementary operative elements, connected to each other (Fig. 2); the relative importance of each of them is built up on a small number of examples, representative of the problem to be analyzed, the so colled " training set " . The final configuration learns the characteristics of the physical phenomena in the way of being examined and realizes a numerical representation of it, by properly correlating the input (cause) to the output (effect) ; in other words, it simulates a transfer function based on a structural information network.

Usually the basic processing elements are organized in different layers :an input layer, an output layer and one or more hidden layers (intermediate). In this applications a three layer network with one neuron for input and one for the hidden layer, has been used (a greater number of them needs more internal connections and consequently higher computation time).

The FRF of all the actuators as that of the disturbance source, with reference to five acceleration control point along the beam span, were recorded and evaluated as the use of Artificial Neural Network requires, and next furnished to the Control Alghoritm itself.

After a training set of about 18.000 cicles. Corresponding to 3'30" of computational time on a 486/33 Mhz PC, ANN provided an expected reduction of 35.1 dB with the value of amplitude and phase to be applied to each actuators, to reach it. Handly assessed on Analogic Control Unit, an overall reduction of 32 dB came out, in the experimental final test (Fig. 7).

Above all the absolute stability, and the additive properties (superposition of effects) of piezoactuators was verified as shown in Fig. 8 .

4. CONCLUSIONS AND FUTURE DEVELOPMENT

At the end of this work it can be concluded that an Active Vibration and Noise Control by the use MIMO ASAC technologies, based on the use of piezo actuators and sensors, is something that works.

A reduction of over 30 dB was experimentally obtained and the advantages correlated to these kind of actuators and alghorithms in terms of weight, strain, linearity and stability, has been demonstrated.

Aniway further investigations are needed for the development of a stand-alone Control System and therefore these results only represent a first step of an ongoing research that is being carried on at Department of Aeronautical Engineering.

5. REFERENCES

[1] Meirovitch L., " Dynamics and Control of Structures ", John Wiley, 1990

[2] Wada B.K. , Fanson J.L. , Crawley E.F. , " Adaptive Structures " , Journal of Intelligent Materials and Structures, Vol.1, N.2, 1990, pp. 157-174

[3] Crawley E.F. , de Luis J. , " Use of Piezoelectric Actuators as Elements of Structures", AIAA Journal, Vol. 25, Nr. 10, Oct. 1987, p. 1373

[4] Lecce L. , Viscardi M. , Siano D. , Concilio A., " Active Noise Control in a Fuselage Section by Piezocaramic Actuators", Active95 Int. Congr. , Newport Beach (CA -USA), July 1995 , pp. 595-606

[5] Cabel R.H., Lester H.C., " Investigation of Force Distribution for Interior Noise Control Using a Neural Network ", Recent Advances in Active Control of Sound and Vibrations. 2nd Int. Conf., Blacksburg (VA - USA), Apr. 1993

[6] Concilio A., Sorrentino A., Vitiello P., Lecce L., " Interior Noise Active Control by Neural Network and Piezoelectric Actuators ", in italian , Nat. Conf. AIDAA '93 , Como (I) , July 1993

[7] Lecce L., Sorrentino A. , Concilio A., " Active Vibration Control of a Thin Walled Section Beam by Neural Networks and Piezoelectric Actuators" presented at the 1994 International Conference on Intelligent Mterials,Williamsburg (VA - USA) .

[8] L.Lecce, A Concilio,F.S, Del Gatto : Active Control of Noise and Vibrations on Panels with a Simple Self Adaptive System Using Distributed Piezoelectric Devices , Proceedings of the 2nd ATA International Conference on Vehicle Comfort, Bologna 14-16 October 1992, Vol.2 pp 777

[9] L. Lecce, A. Ovallesco, A. Concilio, A Sorrentino, " Optimal Positioning of Sensors by using Genetic Alghoritms in an Active Noise Control System with Piezoelectric Actuators", presentedat the 8th Cimtec Ceramic World Congress, Firenze (I), 28 June - 4 July 1994

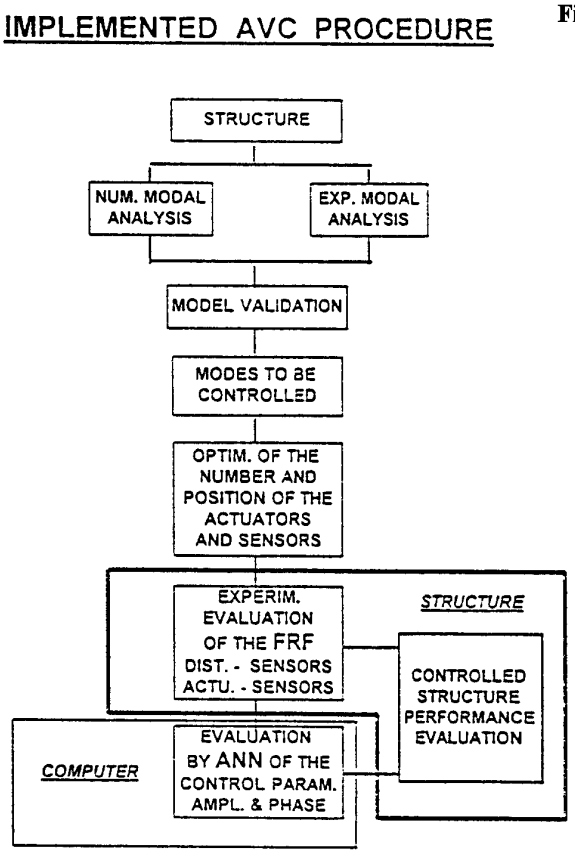


Fig.1 - General MIMO Procedure

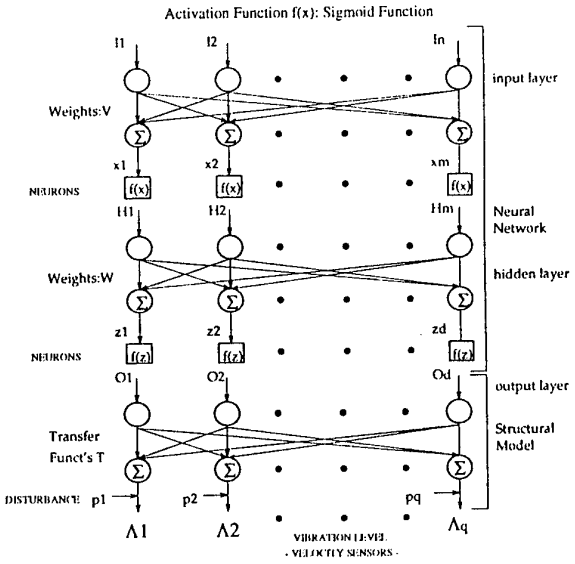
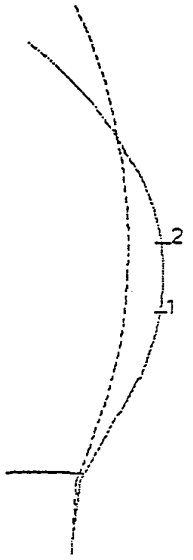


Fig. 2 - ANN's General Architecture



Fig.3 - Partial Curved Beam Test Article



MODE SHAPE AT 121.5 Hz

Fig.4 - Target Mode Shape

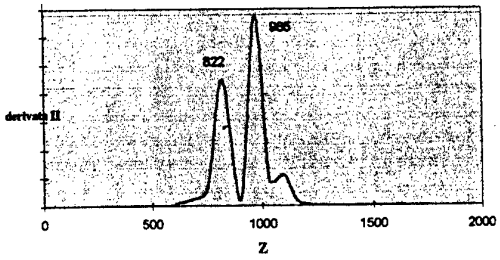
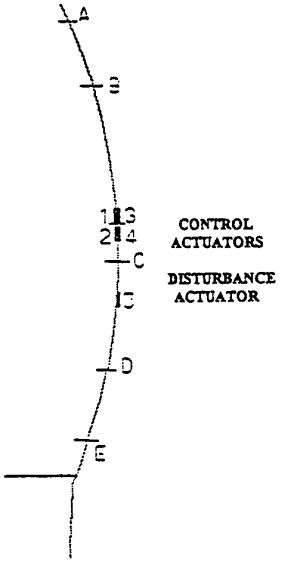


Fig. 5 - Second Derivative Diagram



PIEZO ACTUATOR POSITION

Fig. 6 -Piezo Actuators Positions

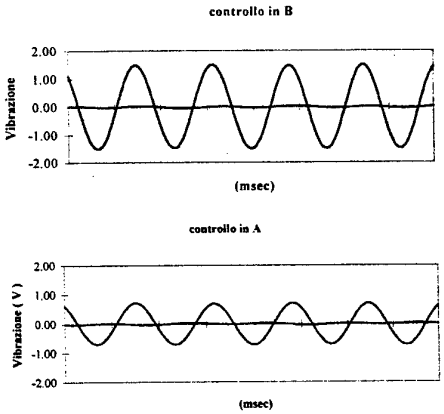
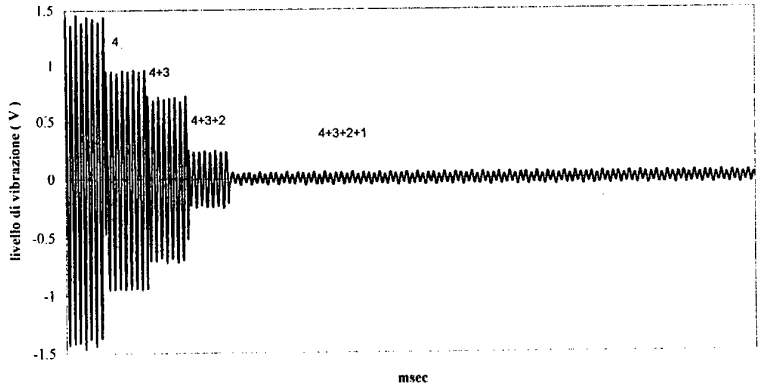


Fig. 7 - Curved Beam Control Results

Fig. 8 - Piezoactuators Superposition Effect



Paper presented at the Third ICIM/ECSSM '96, Lyon '96

Reduction of the Sound Power Radiation of a Typical Helicopter Panel by the use of Piezoceramic Actuators

L. De Vivo, A. Concilio

C.I.R.A. S.C.p.A. (Italian Aerospace Research Center)
Via Maiorise, loc. Silvagni 81043 Capua(Ce) ITALY

1 INTRODUCTION

"Design to Noise" is one of the new aspects considered during the planning phase of new aircraft, for different political, economical and enviromental reasons. In the low frequency range, active control seems to give the right answers to the needs. In propeller aircraft, active systems based on microphones-loudspeakers architectures[5] have overtaken the classical methods based on the use of the Dynamic Vibration Absorbers.[7] The problems of weight, cost and so on, could be solved by the application of "Smart Structures", well summarised in many works and publications (e.g. C. Fuller[6]). Further work is being carried out at CIRA, on the use of piezoceramic devices as vibration actuators inside system architectures based on the approach known as Acousto Structural Active Control (ASAC[9,10]). Recently, the attention of the aeronautical research world has been directed towards helicopters, where the acoustic problems are greater with respect to aeroplanes: extremely low frequencies involved, little noise insulation, etc.. . In addition, the inherent structural demands present some peculiarities, such as the use of large, flexible, composite elements, etc.. .

In this paper, a feasibility study of a control system based on the use of piezoceramic actuators for typical helicopter structural panels is addressed. In particular, the results relative to a FEM numerical simulation of a feed forward active noise control for a very large panel (1.5 x 2.00 m) similar to the roof of the EH101 are reported. This kind of structure presents modes at very low frequencies (< 20 Hz) characterised by very large vertical displacements when compared to the strains: it means that piezo actuators have to work in unfavourable conditions: in fact the energy they introduce into the structure is proportional to the strain itself while it is aimed at suppressing the normal movement. The control is based on a Fortran implementation of classical LMS routines[1,2] aimed at minimising the Sound Power Radiation (SWR) due to a pressure field composed of three acoustic waves inciding at different angles with respect to the plate surface.[4] This kind of load makes each point of the plate subject to a different complex force, and as a consequence the vibrating field is complex and, in principle, difficult to control also at resonance frequencies. The distribution of the actuators has been optimized with reference to the control of the acoustic field emitted in correspondence with the first structural mode. No specific automatic tool was used, but the authors successfully implemented some tools based on Genetic Algorithms in similar applications.[8] The upper loading limit of the piezo was automatically taken into account through a process of constrained optimisation. In detail, taking advantage of a simplified model of the electric impedance related to a piezoceramic, attention was also devoted to the evaluation of the electric power absorbed by the actuators for the mentioned performance but excluding those linked to the necessary annexed electronic circuit.

0-8194-2165-0/96/$6.00

2 FEM MODEL

The "test" plate is an isotropic structure measuring 2x1.5 m and 2 mm thick. It was divided in 20 parts along the x axis and in 15 parts along the y. The mesh consists of a 20x15 grid elements (QUAD8) and 21x16 nodes, up to more than 2000 DOF's. The dimension of each element resulted in 100x100 mm. Actuators were thought to have the same planar extension (Fig. 2). The panel, clamped at the edges, was subjected to a numerical "Airborne" load, obtained by composing 3 pressure waves with different angles of incidence (30° with respect to the xz plane, 60° with respect to the yz plane; normal to the xy plane) for a total intensity load (the square root of the sum of the squared amplitude) of 100 dB (see Fig. 1). A dynamic analysis was carried out by acquiring the transfer function in the range between 0 and 50 Hz. The same analysis with the plate loaded by moments simulating the piezo's action, was executed.[4] In particular, 9 piezo's were applied close to the middle of the plate (see Fig 2). The results of both analyses have been utilised to evaluate the performance of the LMS-feedforward control.

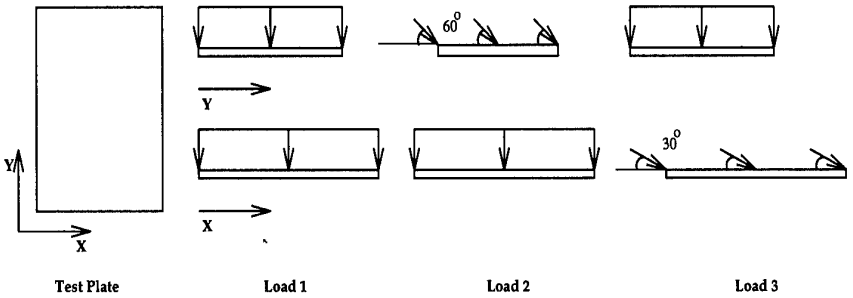


Figure 1: *Load sketch*

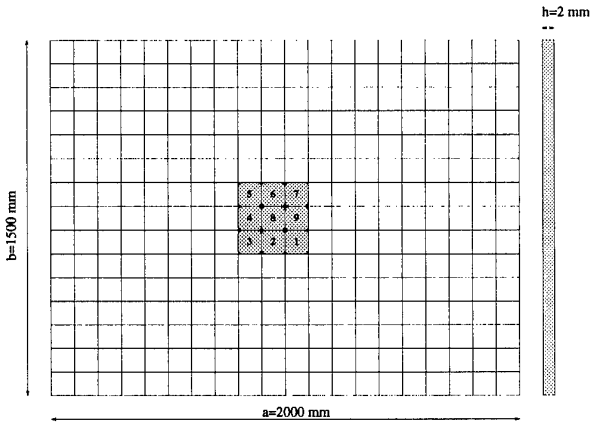


Figure 2: *"test" plate sketch*

3 FEED FORWARD CONTROL

The Feedforward control implemented on the plate made use of an LMS-type algorithm[1,2] referring to the SWR as the cost function. It was calculated by dividing the surface of the plate into a finite number of rectangular

elements. Each of them was supported to act as a single spherical source of sound radiating in a rigid infinite baffle. By assuming that the effect of the pressure of the external fluid on the dynamic response of the plate is negligible and considering that the impedance matrix is symmetrical, SWR can be approximated by,[3,4]:

$$W = \frac{1}{2}\mathbf{v}^H \mathbf{S} Re(\mathbf{Z}) \mathbf{S} \mathbf{v}^H \tag{1}$$

where: $\mathbf{v}$ is the complex vector velocity of the source; $\mathbf{S}$ is the diagonal matrix binding the elementary areas to the single sources; Re($\mathbf{Z}$) is the real part of the impedance matrix. According to the linear hypothesis, $\mathbf{v}$ may be considered as the sum of the contributions due to the primary and secondary (control) loads. This second term may be expanded as $\mathbf{v} = \mathbf{M}\mathbf{f_s}$, where $\mathbf{M}$ is the Mobility Matrix and $\mathbf{f_s}$ are the secondary applied forces. The minimum of the function (1) and the relative expression for the secondary forces can be then found:

$$\mathbf{f_s}_{opt} = -(\mathbf{M}^H Re(\mathbf{Z}) \mathbf{M})^{-1} \mathbf{M}^H Re(\mathbf{Z}) \mathbf{v_p} \tag{2}$$

$$SWR_{min} = \frac{1}{2}(\mathbf{v_p}^H Re(\mathbf{Z}) \mathbf{v_p} + \mathbf{v_p}^H Re(\mathbf{Z}) \mathbf{M} \mathbf{f_s}_{opt}) \tag{3}$$

A Fortran program executing these calculations was prepared. This kind of control may require high control forces, values not suitable for practical applications. In fact the code based on the expressions (2) and (3) does not take into account available actuator physical limits. For this reason, the need for a restraint coefficient is great. To this end a weight factor (β) measuring the control effort was introduced, hence:

$$\mathbf{f_s}_{opt} = -(\mathbf{M}^H Re(\mathbf{Z}) \mathbf{M} + \beta \mathbf{I})^{-1} \mathbf{M}^H Re(\mathbf{Z}) \mathbf{v_p} \tag{4}$$

where, $\mathbf{I}$ is the Identity Matrix. In the case reported, the maximum allowable voltage is 300 Volts. Equation (4) is not able to correlate β to the maximum available load values. This is evident when n actuators are working contemporarily, so that the value of the "cost factor" should consider all feasible "surplus" values with respect to the physical "roof" (one value $\rightarrow n$ limits for n values, that must be computed simultaneously). Therefore, to develop an iterative procedure "ad hoc", it was necessary to calculate the optimal β values, which will result in a frequency function on the strength of the approach given to the problem. This is an advanced reality, carried out in an original way during this activity.

4 PIEZO ABSORBED POWER

Under far from resonance conditions ($\ll$ 10 kHz for the used patches), the piezoceramic equivalent electrical circuit can be considered as a resistance in parallel with a capacity, based on material characteristics in terms of resistivity and dielectricity respectively. For the considered material (Quartz & Silice P1-60), by considering the piezo's dimension ($a_c \times b_c \times t_c = 100 \times 100 \times .5$mm) the following values are obtained for the resistance (R) and the capacity (C):

ρ	$10^{10}\Omega m$	$\Longrightarrow$	R	$5 \times 10^8 \Omega$
$\varepsilon = \varepsilon_{33,r} \cdot \varepsilon_0$	$1.416 \times 10^{-8} F/m$	$\Longrightarrow$	C	$2.832 \times 10^{-7} F$

The circuit, (Fig. 3), can therefore be constructed

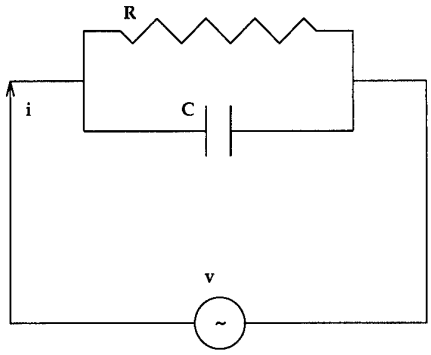


Figure 3: *Equivalent Piezoceramic Circuit*

According to the data, equivalent impedance is given by:

$$Z = 17.5 - j9.37 \times 10^4 \Omega$$

For an imposed voltage of 300 V, the current in the circuit, the expended and the absorbed Powers (W) are respectively:

$$|i| \simeq 3.20\text{mA}$$

$$W_{exp} = 8.64\text{VA}$$

$$W_{abs} = 1.60\text{mW}$$

5 RESULTS

In the present application, control of the first mode was pursued because it represents a very critical situation for the type of actuator used. For this reason, the nine actuators were placed in the middle of the panel according to the principle that a piezo can transmit the highest energy for a given spatial dynamic deformation when placed in the maximum curvature regions: this coincides with the maximum deformation, under the hypothesis of small displacements. The piezo distribution leads to an incremental weight ($\Delta W/W$) of 2 % for a covering factor ($\Delta A/A$) of 3 %. SWR expressed in dB in the range $0 \div 50$ Hz is reported in Fig.4; very clear peaks for each resonance frequency inside the considered band are present, particularly those relative to the first and the fourth harmonic (6 Hz and 27 Hz ca.). Applied to the test plate, the considered control algorithm leads to the results shown in Figs. 4 and 5 in terms of SWR cancellation. The control action can be seen to cut off all resonance peaks (up to a maximum of 25 dB). Poor effectiveness is noted outside the resonance zone; it could be easily improved by increasing the number of piezoes (using 16 piezo's, $\Delta W/W \simeq 3.5\%$ and $\Delta A/A \simeq 5\%$ is arrived at) and optimising actuator placement. This low effectiveness is mainly due to the kind of load that causes multiple mode contributions, resulting in very complex responses (the points do not vibrate "in phase"). This does not decrease the result importance, because by using this system the radiation would be brought into a broadband-type condition with a maximum sound power level emission at least lower than 20 dB with respect to the previous.

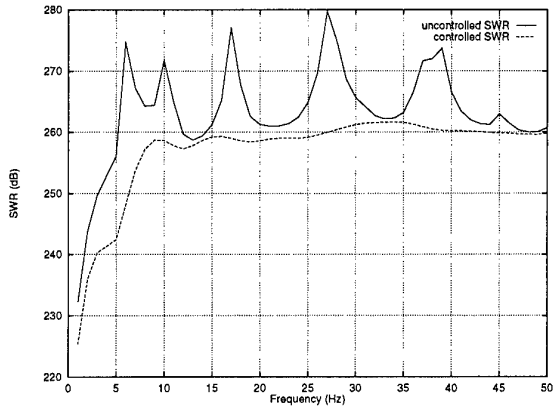


Figure 4: *LMS control applied to the "test" plate subjected to an "Airborne" load*

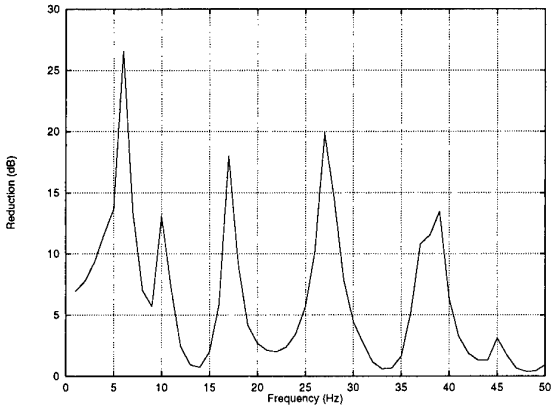


Figure 5: *Sound Power Radiation Reduction of the "test" plate subjected to an "Airborne" load and controlled by 9 Piezo Actuators (FF-LMS)*

In Fig. 6 the required voltage graph for each piezo is shown. By considering the resonance and the antiresonance points, the actuators can be seen to give the maximum effort around the first resonance frequency, while they do not appear to be as effective at the other frequencies. Generally, piezoactuators supply the highest effort close to the resonances, while the opposite is verified at the antiresonances; this indicates (as expected) that the chosen piezo location is ineffective when farthest from the eigenmodes (really, the piezo's are located for a lot of modes close to the nodal lines so that their capabilities are strongly affected in antiresonance where many modes contribute at the same numerical level. Lastly, the diagram of the cost factor β is reported (Fig. 7). Although no physical meaning, it is remarkable that, for the first resonance frequency it is bigger than those at different frequencies by several orders of magnitude. This points out that the piezo's could produce a very relevant reduction if it were possible to improve the input voltage or the transmission effectiveness (in fact, β is a measurement of how much the voltage has to be limited with respect to the ideal solution). Finally, the investigated architecture characteristics are summarised in Table 1.

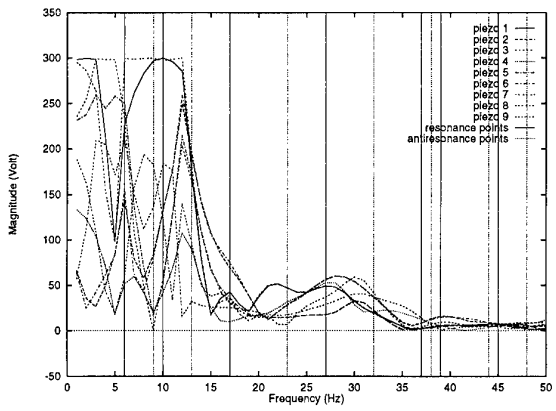


Figure 6: *Required Voltage for each piezo to control the "test" plate subjected to an "Airborne" load*

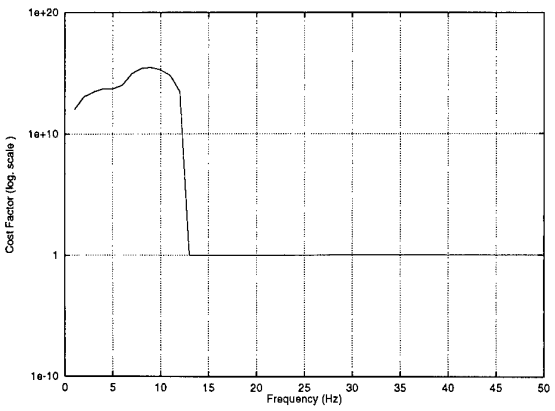


Figure 7: *Cost Factor to limit the required voltage to control the "test" plate subjected to an "Airborne" load*

Frequency 6 Hz	
Reduction (dB)	26
Weight Increment ($\Delta W/W$)	2%
Area Increment ($\Delta A/A$)	3%
Absorbed Power (mW)	1
Expended Power (VA)	8
Current (mA)	3
ΔW (g)	344

Table 1: *Summary Table*

6 ACKNOWLEDGEMENTS

The authors would like to thank Prof. L. Lecce for his useful suggestions and support.

7 REFERENCES

[1] Nelson, P.A., Curtis A.R., Elliott S.J., Bullmore J., "Active Minimisation of Harmonic Enclosed Sound Fields, part I: Theory", Journal of Sound and Vibrati on, 117, pp.1-13.

[2] Nelson, P.A., Curtis A.R., Elliott S.J., Bullmore J., "Active Minimisation of Harmonic Enclosed Sound Fields, part II: Computer Simulation", Journal of Sou nd and Vibration, 117, pp.13-33.

[3] Fahy F., "Sound and Structural Vibration", Academic Press, London (UK), 1985.

[4] De Vivo L., Concilio A., "Riduzione della Potenza Sonora Radiata da un Pannello Tipico di Elicottero", CIRA-TN-95-0121 September 1995 (in italian)

[5] Emborg U., "Application of active Noise Control in Saab 340 and Saab 2000", Nordic Conf. on Vehicle and Machine Vibrations Proceedings, Stockholm (S), September 1994.

[6] Fuller C.R., "Recent Developments in Active Control of Vibration", Proceedings of the Nordic Conference on Vehicle and Machine Vibrations, Stockholm (S), September 1994.

[7] Paonessa A., Sollo A., Lecce L., Marulo F.; "Optimization of a Noise and Vibration Level Reduction System in Turboprop Aircraft", XI AIDAA National Congress, Forlì(I), October 1991.

[8] Concilio A., Lecce L., Ovallesco A., "Position and Number of Actuators and in an Active Noise Control System by using Genetic Algorithms", XVI CEAS/AIAA Aeroacoustics Conference, Munich (D), 12-15 June 1995.

[9] Concilio A., Sorrentino A., Vitiello P., Lecce L.,"A Comparison of Different Methodologies for Aircraft Internal Noise Reduction by Active Vibration Control", 3rd International Congress on Air- and Structure-Borne sound and Vibration, Montreal (CAN), June 1994.

[10] Rogers C.A., Fuller C.R.(editors): "Recent Advances in Active Control of Sound and Vibrations", Proceedings of the Conference, VPI, Blacksburg (Va, USA), April 15th-17th, 1991, Technomic Ph. Co., Lancaster-Basel, 1991.

Piezoceramics/CFRP composites for active vibration control and shape control of aerospace structures

Ursula Herold-Schmidt, Wolfgang Schäfer and Helmut Zaglauer

Daimler-Benz Dornier Research Center, 88039 Friedrichshafen, FRG

ABSTRACT

The application of piezoceramics/CFRP composites for active control of aerospace structures was investigated on a laboratory scale. Exemplary results are presented for active vibration damping of CFRP plates with integrated PZT sensors and actuators as well as for shape control of an antenna reflector shell using piezoelements.

1. INTRODUCTION

Aerospace structures usually have to realize high strength and stiffness at minimum weight. A number of modern components such as helicopter blades, aircraft rudders and tails, spacecraft antennas or various payload carrying components are therefore made of carbon fibre reinforced plastics (CFRP). In the future the amount of CFRP parts in the aerospace industry is expected to increase further.

In several of these applications structures are subjected to vibrations that have to be damped. As passive damping often is limited in its efficiency active methods must additionally be applied. Structures which could benefit from active damping are for example solar arrays of satellites exhibiting very low intrinsic damping rates after e.g. thermal shocks[1], aircraft panels fluttering at supersonic speed operation[2], vertical tail aircraft beeing subjected to unsteady buffet vibrations[3], or sensitive space payloads suffering from high acoustic loads during launch. Other aerospace applications require active shape control of large, high precision structures in order to compensate environmental influences. Examples are support structures for telescopes, reflectors and large antennas.

The use of intelligent materials as actuating and sensing devices in active control systems has been investigated extensively[4]. One of the most promising materials are piezoceramics which offer significant advances for low frequency vibration control and shape control of lightweight aerospace structures[5]. Piezoceramic actuators can be bonded to the surface of a structural element or embedded in a composite laminate. The strain produced by piezoelements can alter the strain in a structure and therefore modify its displacements or damping characteristics. In addition, piezoelements are relatively easy to control. Some laboratory examples of the application of piezoceramics / CFRP composites for active control of aerospace structures are presented below.

2. ACTIVE VIBRATION CONTROL

Different active control mechanisms can be applied in order to reduce vibrational loads in lightweight composite structures. They include the distribution of sensors and actuators in component skins, the positioning of discrete active elements at load bearing sections of structures, or the separation of components from vibration sources by active interfaces. The integration of laterally distributed piezoceramic wafers with sensing and actuating functions is a very promising possibility to establish a smart skin which can react upon vibrational loads by phase-shifted counterforces. For this case some materials and control aspects will be considered.

Fig.1 shows the cross section of a piezoceramics/CFRP composite consisting of a PZT piezoceramic translator which is insulated against the conducting carbon fibres of the laminate by a thin layer of glass fibre reinforced epoxy. In order to induce an optimum combination of force/moment and strain into the CFRP by the piezoelectric effect a careful design and investigation of this interface was performed.

For this purpose a computer code based on laminate plate theory[4] was developed that allows to model the effective stiffness as well as actuator-induced strains, forces and moments of a laminate consisting of an arbitrary number of -possibly orthotropic- CFRP, PZT and insulating layers. It was used to optimize a number of design parameters for the PZT/CFRP composite such as layer thickness, orientation with respect to fibre

0-8194-2165-0/96/$6.00

orientation and actuator location. As an example the dependence of the strain transfer efficiency on the thickness of the CFRP layers is displayed in Fig. 2 for different fibre orientations.

As another materials aspect the temperature compatibility of all composite components during the curing process of laminates as well as within a large range of operating temperatures was investigated. The results showed that CFRP parts with high curing temperatures require subsequent integration of the piezoelements

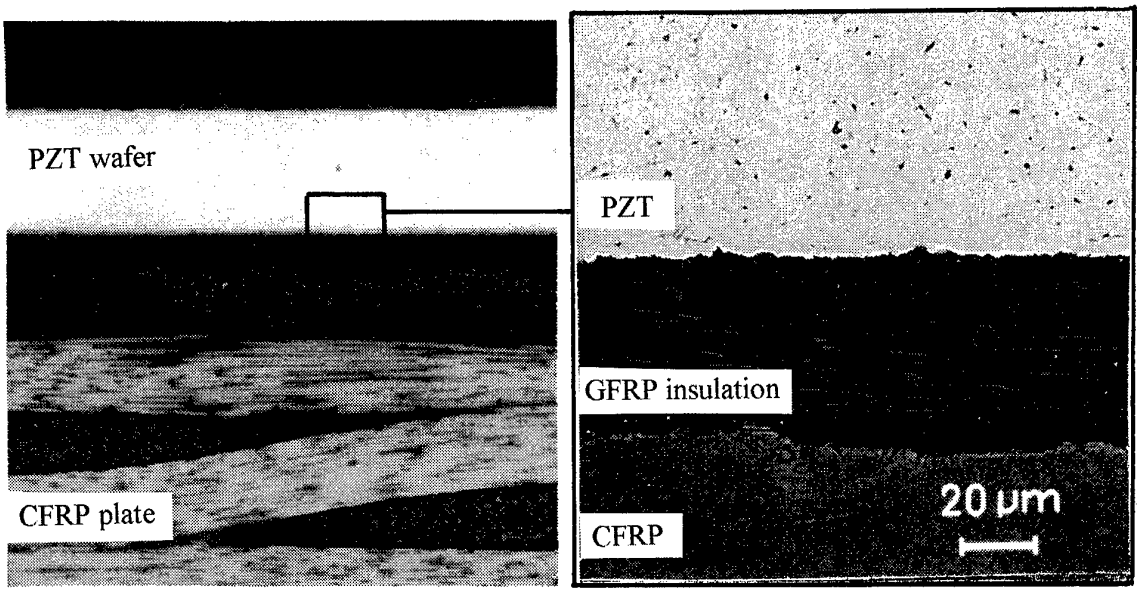


Fig. 1 Cross section of a PZT/CFRP composite with an insulating glass fibre/epoxy layer.

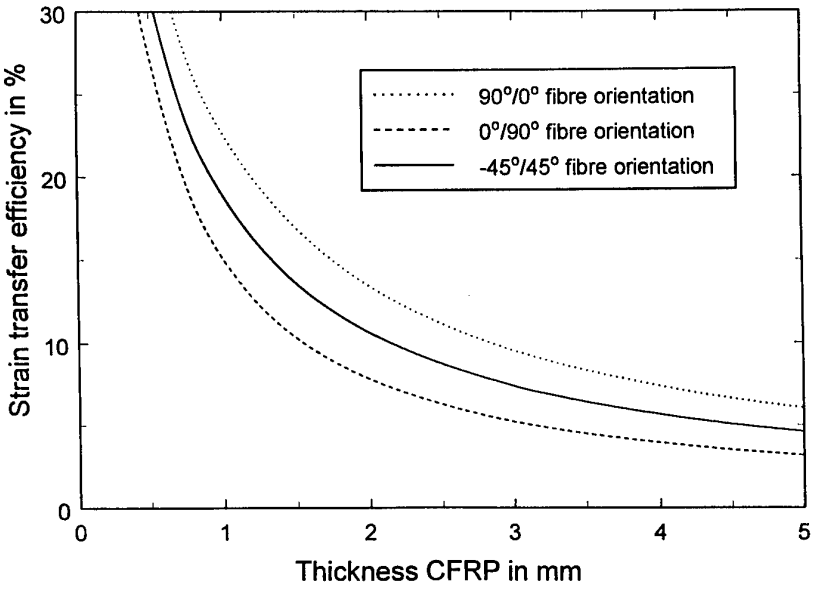


Fig. 2 Modelling for strain transfer efficiency of a PZT actuator mounted on top of a CFRP composite plate as a function of CFRP thickness. Every two CFRP layers have alternating fibre orientations. Three cases were considered: 90°/0° (top/bottom layer), 0°/90° and -45°/45°.

using low temperature curing systems. Functional tests between -50°C and +150°C revealed that a proper selection not only of the ceramic components but also of electrodes and leads is necessary. In addition, degradation effects concerning depolarization of the piezoceramic materials under thermal and mechanical loads as well as fatigue phenomena especially of ceramics and interfaces under cyclic loads are under investigation.

The design of the controlled system with respect to optimized actuator and sensor size and positioning and the choice of the control algorithms under consideration of the nonlinearity of the piezoelectric effect were important issues of the vibration control architecture for piezoceramics/CFRP composites. Fig. 3 shows the

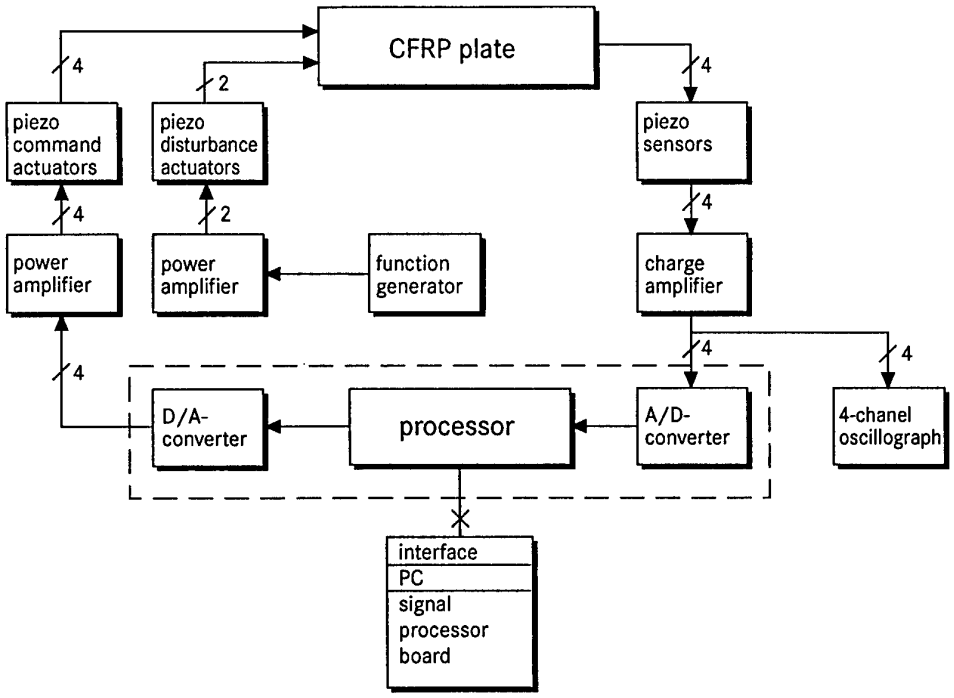


Fig. 3 Experimental set-up for vibration control of a PZT/CFRP composite plate.

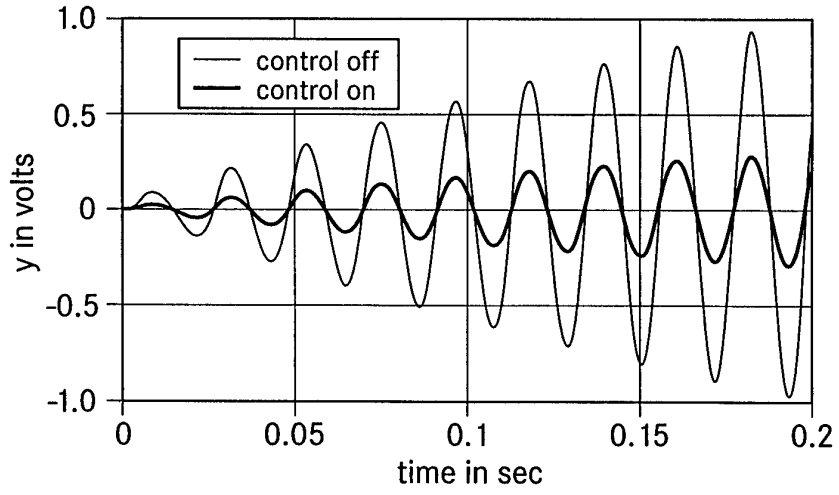


Fig. 4 Damping of a PZT/CFRP composite plate for periodic excitation at 45 Hz (1st eigenfrequency).

experimental set-up for the vibration control of a PZT/CFRP composite plate. The arrangement of disturbance, command and sensor piezoelements took into account the eigenfrequencies of the structure. Considerable damping was achieved for various excitation modes as shown in Figs. 4 and 5.

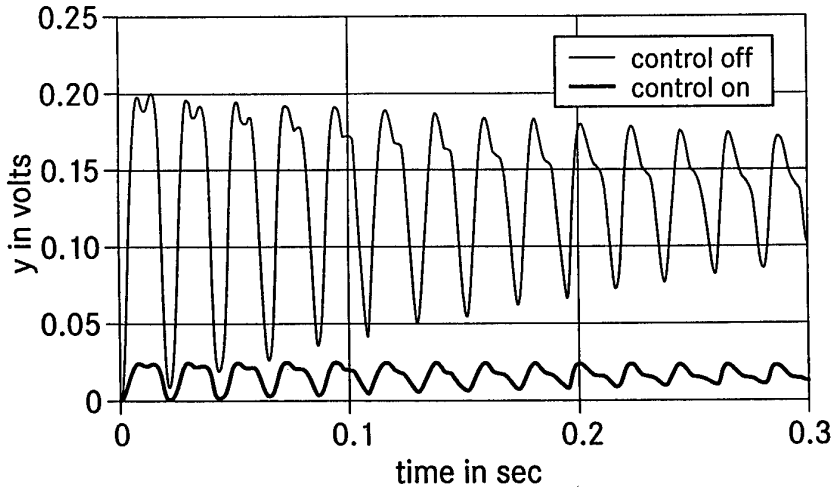


Fig. 5 Damping of a PZT/CFRP composite plate for transient excitation.

3. ACTIVE SHAPE CONTROL

A large application field for active shape control using piezoelements are high-precision space antennas and reflectors. The feasibility was shown for a parabolic antenna reflector shell consisting of an aluminium honeycomb structure of 0.8 m diameter with CFRP face sheets (Fig.6). 132 piezoceramic translator wafers were assembled as 12 groups of 11 elements each and surface bonded to the face sheets. Tests comprised active compensation of small deviations from the ideal geometry in the as-manufactured state as well as the balancing of artificial deformations applied by external forces. The efficiency of the shape control was verified by a precise mechanical 3D measuring unit. Results are presented in Fig. 7 for a central deformation. The test revealed that the system worked for symmetric as well as for non-symmetric loads. Deviations up to ± 20 microns were compensated successfully.

4. CONCLUSION

Piezoceramic actuators can be used for active vibration damping and shape control of aerospace structures made from CFRP. First laboratory demonstrator parts with specially adjusted control units successfully showed the feasibility of this technical approach. On-going work now is focused on tests under application conditions and with respect to long term stability.

5. ACKNOWLEDGEMENT

The authors gratefully acknowledge the cooperation of Mr. Dietmar Scheulen (Dornier Satellitensysteme GmbH, Friedrichshafen, FRG) and Mr. Kay Dittrich (Daimler-Benz Aerospace AG, Ottobrunn, FRG).

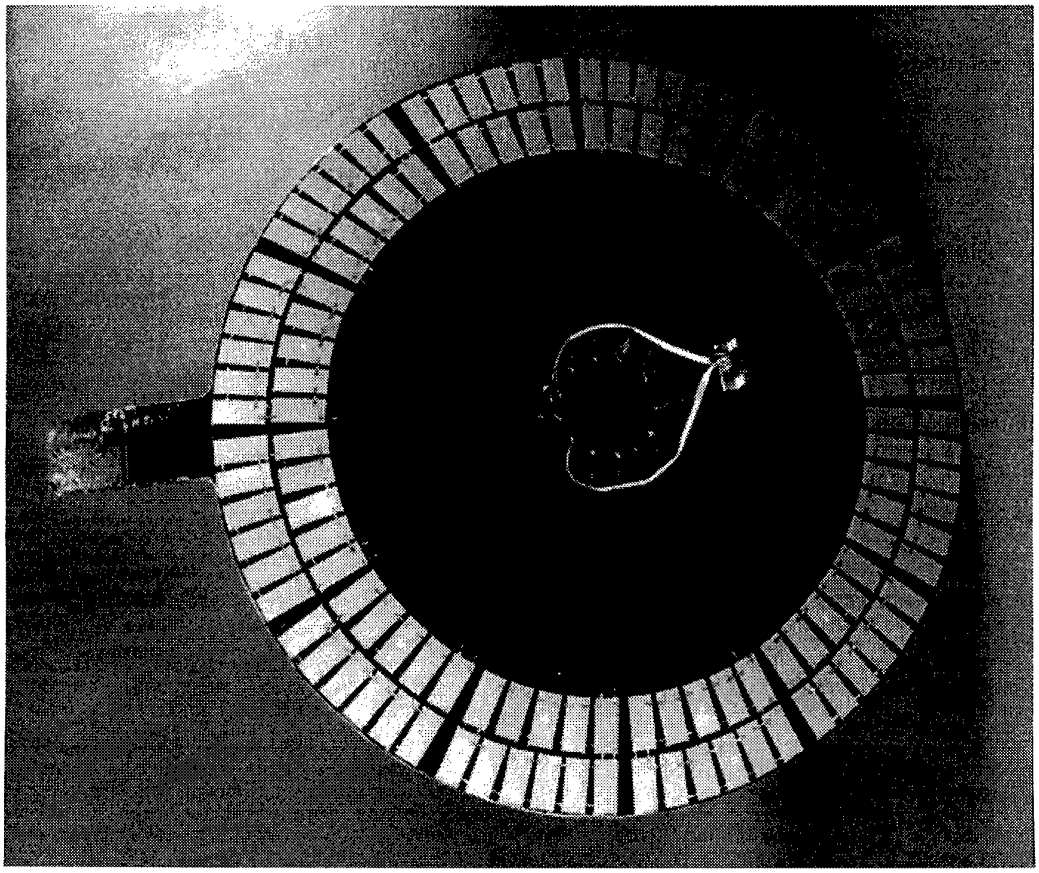


Fig. 6 Antenna reflector shell with 132 piezoactuators mounted on the face sheet for shape control.

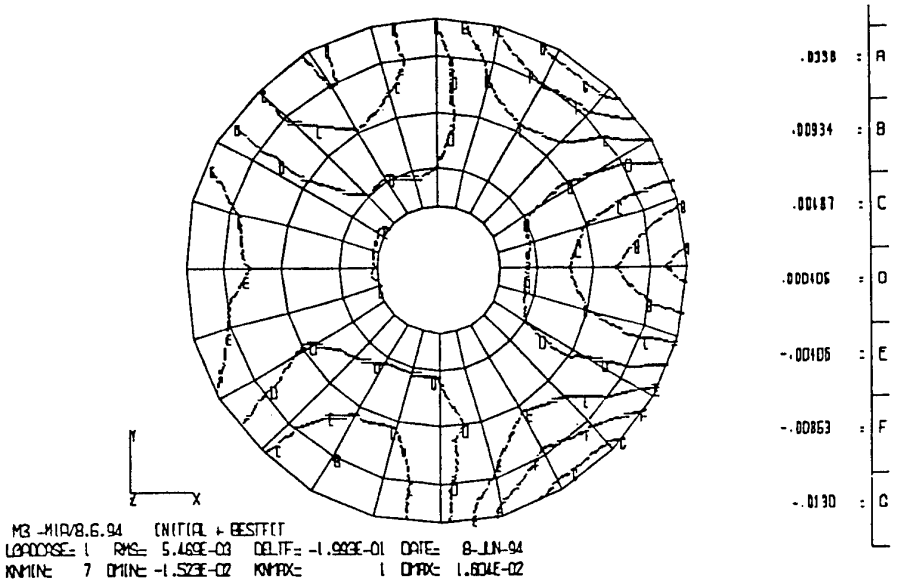


Fig. 7 3D-measurements at the antenna reflector shell demonstrating the shape control using piezoelements (central deformation of 12 N).

a) Deformation difference (min/max) without control = 31.3 microns, RMS = 5.5 microns.

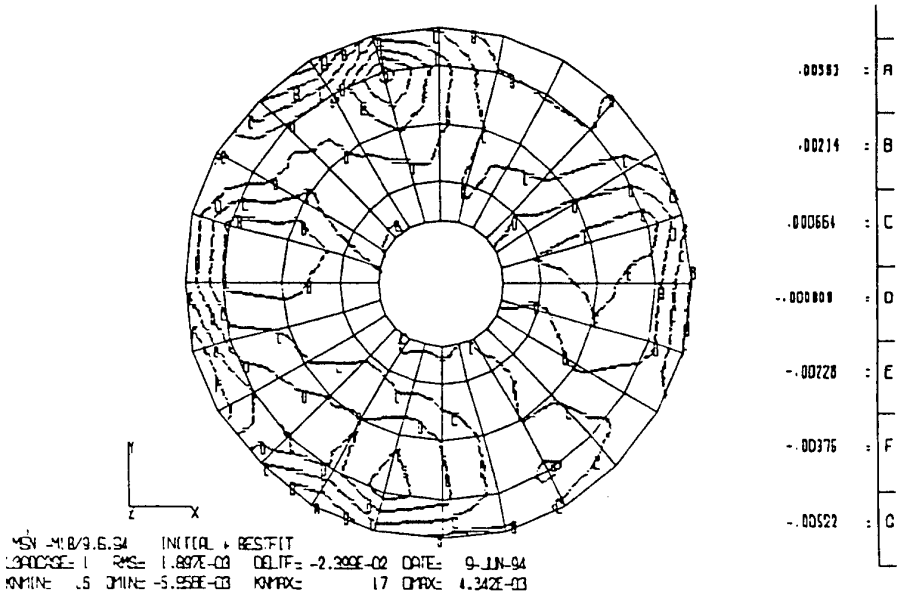


Fig. 7 3D-measurements at the antenna reflector shell demonstrating the shape control using piezoelements (Central deformation of 12 N).

b) Deformation difference (min/max) with control = 10.2 microns, RMS = 1.9 microns.

6. REFERENCES

1. W. Charon and H. Baier, „Active mechanical components as a step towards adaptive structures in space", J. of Intelligent Material Systems and Structures, Vol.6, pp. 396-402, May 1995.

2. Z. Lai, D. Y. Xue, J. K. Huang and C. Mei, idem, Vol.6, pp. 274-281, March 1995.

3. K. B. Lazarus, E. Saarmaa and G. S. Agnes, „An active smart material system for buffet load alleviation," SPIE Proc., Vol. 2447, pp. 179-192, 1995.

4. E. Crawley and J. de Louis, „Use of piezoelectric actuators as elements of intelligent structures", AAIA J., Vol. 25, pp. 1373-1385, 1987.

5. R. E. Newnham and G. R. Ruschau, „Smart electroceramics", J. Am. Ceram. Soc., Vol. 74 (3), pp. 463-480, 1991.

Magnetic Field Requirements for an Active Control Flap on a Rotorcraft

Greg Carman & Milan Mitrovic

UCLA MANE Dept
38-137m Engineering IV
Los Angeles Ca 90095
(310) 825-6030

ABSTRACT

In this paper, we describe a nonlinear constitutive relation for magnetostrictive materials that includes coupling between temperature, applied loads, and magnetic field strengths. The model is used to predict the magnetic field requirements for actuating a control flap to reduce the vibrational loads in a rotorcraft system. This prediction is based on the force/displacement requirements presently available in the literature for a particular flap. Results indicate that reasonable changes in the ambient temperature and centrifugal forces generated by the rotating blade strongly influence magnetic field requirements.

INTRODUCTION

Over the last decade, scientists and engineers have investigated the use of electro-magneto-thermal actuators for controlling and altering the response of structural components. Some of the actuators currently being investigated for accomplishing these tasks include piezoceramics, electrostrictive materials, magnetostrictive materials, and shape memory alloys. Recent research on magnetostrictive materials shows that they provide certain advantages over their electro-mechanical counterparts, including marginally larger strains [1] and the ability to generate larger forces. These advantages have led investigators to explore the benefits of using magnetostrictive material (Terfenol-D) in specific structural systems, such as in an active control flap for reducing the vibrations in a rotorcraft system [2 & 3].

While investigators are exploring applications for Terfenol-D, modeling efforts are still predominantly based on linear behavior. Current modeling approaches for magnetostrictive materials rely on the theoretical developments for linear piezoelectric material systems [4]. While these approaches do provide an analytical framework for approximating the response of the material in specific regimes, they neglect critical coupling terms which must be included to develop accurate predictive capabilities required in structural applications. Some of the necessary coupling terms are the effect of preload, magnetic field intensity, and temperature dependence on the mechanical response as pointed out by Clark [5]. Previous efforts for developing nonlinear constitutive relations are presented in books by Parton and Kudryavtsev [6] and Brown [7], using thermodynamics and energy approaches. In addition to these, Joshi [8] presented a nonlinear constitutive relation for piezoelectric materials including nonlinear coupling terms historically disregarded in piezoelectric materials. In this paper he explicitly defines symmetry relations for the nonlinear terms. In regard to magnetostrictive materials, Clark [9] discuses phenomenological approaches to develop constitutive relations for magnetostrictive materials. DeSimone [10] focuses on predicting the macroscopic response of magnetostrictive materials by taking into account the underlying microstructure and geometry of the specimens. However, current modeling approaches do not provide a reasonable description of the complex constitutive behavior exhibited by Terfenol-D over a broad operating regime.

In this paper, we describe a nonlinear constitutive relation for magnetostrictive material and compare it to experimental results. The model is used to predict the magnetic field requirements for actuating a control

0-8194-2165-0/96/$6.00

flap to reduce the vibrational loads in a four bladed rotorcraft described by Millot [3]. Results indicate that temperature and centrifugal forces will influence the design of a magnetostrictive actuated flap.

CONSTITUTIVE RELATIONS

The development of a constitutive relation is typically based on experimental results. That is, test results provide an indication of the relation existing between constants in the constitutive model. This information is used in the development of the mathematical relations for a given material. For example, experiments indicate that conventional passive materials exhibit linear stress/strain relations which eliminates the need to include quadratic terms when deriving the constitutive relations. On the other hand, experimental observations [5] for Terfenol D (magnetostrictive material) indicate that strain (displacement) versus magnetic field relations are nonlinear and symmetric with respect to magnetic field direction. This suggests that magnetic field terms will appear in the constitutive relations as even powers. Experimental results also indicate that stiffness changes as a function of applied magnetic field, that preloads influence the magnetostrictive response, and that the temperature alters the magneto-mechanical response. Using this experimental information coupled with the methodology outlined in [6], the following constitutive relations were suggested [11].

$$B_m = H_n \mu_{mn}^{T\sigma} + \Delta T P_m^{\sigma} + \sigma_{ij} H_n d_{klnm}^{T} + \Delta T \sigma_{ij} H_n \alpha_{ijnm} + \frac{1}{2}\sigma_{ij}\sigma_{kl} H_n S_{ijklnm}^{T}$$

$$\varepsilon_{kl} = \sigma_{ij} S_{ijkl}^{TH} + \Delta T \alpha_{kl}^{H} + \frac{1}{2} H_n H_m d_{klnm}^{T} + \frac{1}{2} H_n H_p \sigma_{ij} S_{klijnp}^{T} + \frac{1}{2} H_m H_n \Delta T \alpha_{klmn} \qquad (1)$$

where B is magnetic flux, H is magnetic field, T is temperature, ε is strain, and σ is stress. The constants μ is permeability, P is pyromagnetic, d is magnetostrictive, α is coefficient of thermal expansion, and S represents compliance terms. Higher order tensor values of S represent magneto-mechanical effects while higher order α 's represent magneto-thermal interactions. The superscripts on the constants define the physical conditions that each was measured under, i.e. constant stress, temperature, or magnetic field.

ANALYTICAL / EXPERIMENTAL COMPARISON

The mechanical behavior of a magnetostrictive material is characterized by three distinct regions [12]. While the strain/field relationships for each of these regions are distinctly different, magnetostrictive materials are typically designed to operate in the medium field region due to obvious strain advantages. But even in this medium field regime the linear *d'* coefficients [4] are highly dependent upon preload and applied field strength. Thus, a number of experiments must be performed to accurately characterize the magnetostrictive material over a wide range of operating profiles. This item is a critical concern in applications where the load changes as a function of actuation. On the other hand, the constitutive relation presented in this paper provides a tool to predict the response of a magnetostrictive material based on a limited number of experiments and extrapolate to a wide range of operating profiles. A comparison of predicted strain field curves using Equation 1 with experimentally obtained curves [12] are presented in Figure 1. These curves are generated for different prestress levels as depicted in the figure. For the first two regions, low and medium fields, the model accurately predicts the behavior of the magnetostrictive materials. In the high field region, substantial differences appear. Typically transducers and actuators are designed to operate only in the second region, for which the model gives a reasonable prediction of the material behavior. The percent error between the analytical and experimental values varies for different preloads and is dependent upon definition. For the first five bias/preload conditions the error is less than 30%, while for the last three bias/preload conditions the predicted values are all nested within the hysteresis loops. Based on the results presented in Figure 1, the nonlinear constitutive model provides a reasonable means to predict the response over a broader regime than do existing linear approaches.

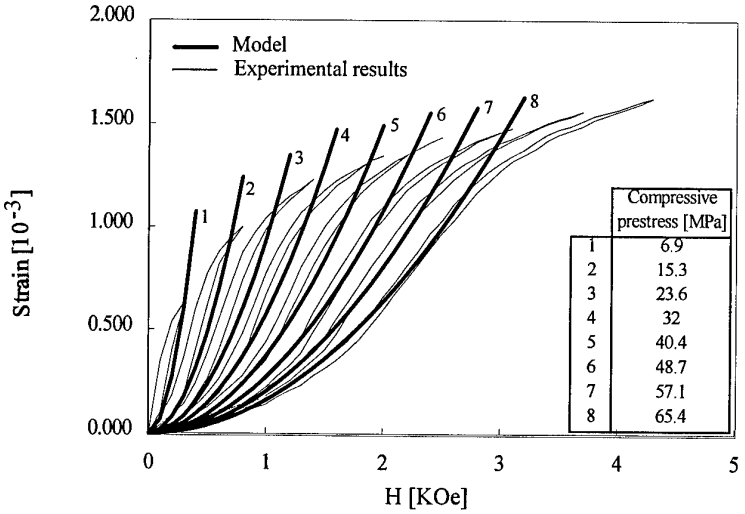


Figure 1. Extensional strain vs. applied magnetic field of $Tb_{0.3}Dy_{0.7}Fe_{1.93}$ for different values of compressive prestess (comparison 1D nonlinear model - experimental results)

To demonstrate a useful application of the model, results generated on a magnetostrictive actuated control flap to reduce the vibrational loads in a rotorcraft is presented. For a physical description of the active control flap as well as force and displacement requirements the reader is referred to Millot [2]. In Figure 2, the azimuth angle represents the position of the blade relative to the cab of the rotorcraft while the vertical axis represents the magnetic field required to achieve a 90% reduction in vibrations when compared to cruise conditions for the rotorcraft.

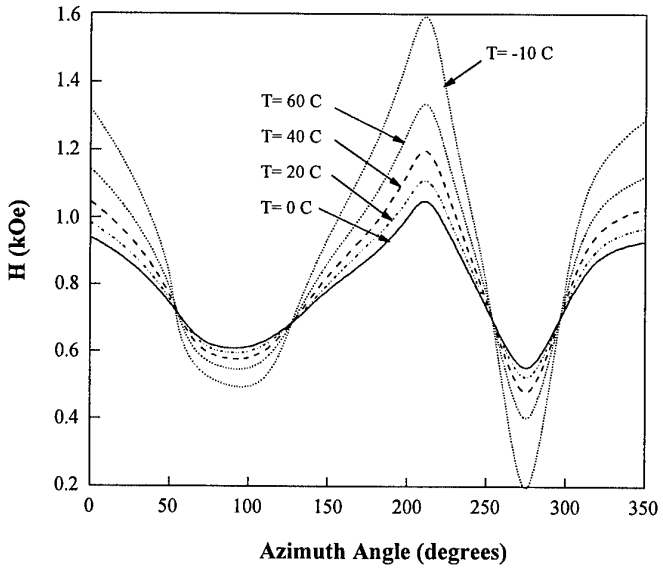


Figure 2. Magnetic field requirements for an active control flap on a rotorcraft.

As the blade turns, the force and displacement requirements for the active control flap change. To achieve a specific displacement profile, the magnetic field controlling the actuator in the flap must change as a function of position. This functional dependence is presented in Figure 2. The five curves presented in the figure are the magnetic field required for a specific actuation calculated at different ambient operating temperatures. As the results in the figure indicate, at 0 degree C the flap requires the smallest magnetic field to cause a reduction in vibration levels. However as the temperature increases or decreases, substantial increases in magnetic field requirements arise.

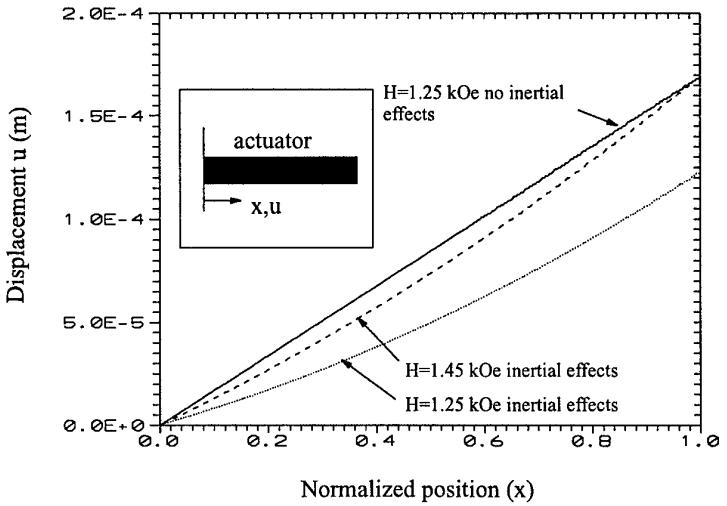


Figure 3. Magnetic field requirements for an active control flap on a rotorcraft including centrifugal forces.

Finally, we consider the influence of centrifugal forces induced by the rotating blade. The analysis was performed using a nonlinear finite element code developed for Terfenol-D [11]. Results presented in Figure 3 are based on the assumption that the actuator is subjected to centrifugal forces associated with its own mass distribution. Furthermore, the deformation of the magnetostrictive rod is neglected and only the influence of centrifugal forces on the magnetostrictive coefficients is considered. These assumption are thought to represent a best case scenario. The solid line in the figure represents the magnetic field required to actuate the control flap in the absence of a centrifugal force at an azimuth angle of 200 degrees. The lower dotted line depicts the reduction in displacement when the magnetic field strength is maintained at H= 1.25 kOe but centrifugal forces are included. Finally, the middle dashed line represents the increase in magnetic field required to adequately actuate the active control flap. This latter line represents an increase of approximately 20% in magnetic field strength when compared to neglecting centrifugal forces.

CONCLUSIONS

In this paper we presented a set of nonlinear constitutive relations for a magnetostrictive material system. Using experimental data, we were able to demonstrate relatively good agreement with the 1-D behavior of a Terfenol-D rod. The model was used to evaluate the magnetic field requirements for a proposed active control flap in a rotorcraft system. This evaluation included the influence of thermal effects and centrifugal forces indicating that these effects are important.

ACKNOWLEDGEMENTS

The authors gratefully acknowledge the support of the University of California Los Angeles academic senate for partial support of this work.

REFERENCES

1. Clark, A.E. 1992. "Giant Magnetostriction Materials From Cryogenic Temperatures to 250°C," Proceedings of SPIE, V. 1543, pp. 374-381.

1. Fenn R., et al. 1993. "Terfenol-D Driven Flaps for Helicopter Vibration Reduction," Smart Structures & Materials Conference, New Mexico, pp. 407-419.

3. Millot, T.A. and P.P. Friedmann. 1994. "Magnetostrictively Actuated Control Flaps for Vibration Reduction in Helicopter Rotors," Proceedings of the Second International Conference on Intelligent Materials, June 1994, Colonial Williamsburg, VA., pp. 900-913.

4. IEEE Standard on Magnetostrictive Materials: Piezomagnetic Nomenclature, no. 319, 1971.

5. Clark, A.E. 1992. "High Power Rare Earth Magnetostrictive Materials," Recent Advances in Adaptive and Sensory Materials and their Applications, Blacksburg, VA., pp. 387-398.

6. Parton, V.Z. and B.A Kudryavtsev. 1988. Electromagnetoelasticity, Gordon and Breach Science Publishers, pp. 1-68.

7. Brown W., 1966. Magnetoelastic Interactions, Springer-Verlag.

8. Joshi, S.P. 1992. "Non-Linear Constitutive Relations for Piezoceramic Materials," Smart Materials and Structures, V.1, pp. 80-83.

9. Clark, A.E. 1980. "Magnetostrictive Rare Earth-Fe_2 Compounds," Ferromagnetic Materials, V.1, pp. 532-589.

10. DeSimone, A. 1994. "Macroscopic Response of Magnetostrictive Materials to Applied Magnetic Fields and Loads", Smart Structures and Materials 94, SPIE Proc., Vol 2192

11. Carman, G.P. and M. Mitrovic. "Nonlinear Constitutive Relations for Magnetostrictive Materials with Applications to 1-D Problems", submitted to *Journal of Intelligent Material Systems and Structures,* August 1994.

12. Moffett, M.B., A.E. Clark, M. Wun-Fogle, J. Linberg, J.P. Teter, E.A. McLaughlin. 1991. "Characterization of Terfenol-D for Magnetostrictive Transducers", J. Acoust. Soc. Am. 89, pp. 1448-1455.

Active Control Headset Protector Using Piezoceramic Material Actuator

M. Brissaud *, P.Gonnard *, J.C. Béra**, M.Sunyach**
*INSA Lab.Génie Electrique et Férroélectricité,20 Ave A Einstein F69621 Villeurbanne cedex.
**Ecole Centrale de Lyon,Lab. d'Acoustique,URA CNRS 263 36 Ave G. de Collongue BP 163.F69131 Ecully cedex.

ABSTRACT

This paper describes the achievement of active control headset protector using piezoceramic actuators leading to a noise attenuation of about 20dB within a 1kHz frequency span located at around 1to2kHz.To this end,several types of piezoceramic transducers or actuators have been designed and tested.They are based on flexural modes of bimorphs constituted by a thin piezoelectric ceramic disk cemented on a metallic plate.The main problems encountered are the spurious frequency regenerations which mask the noise reduction in the expected frequency range.Thus only a few of them meet the above specifications and can be used for reducing the noise inside the headset protector.

1. INTRODUCTION

Many current researches have been developed to determine intelligent structures that can adapt to their environment for reducing noise or radiated pressure inside a limited domain[1-4]. Generally the transducers used for driving into vibration the structures are based on electrodynamic or electromagnetic phenomena.They are very efficient transducers but have many drawbacks.In particular they are heavy ,large and need high AC. voltages The aim of this paper is the design and the building of an active headset protector for reducing noise inside the headset cavity. In this case the actuators have to be small,light,efficient and fed with low amplitude voltages.As it will be shown piezoelectic materials meet these requirements and lead to satisfactory results in a frequency span of about 1kHz around 1-2 kHz.

2. ACTIVE CONTROL PRINCIPLE

Numerous techniques were developed for reducing noise inside a given volume.The method used here is based on a feedback control system.Fig.1 illustrates the structure of such an active control feedback system.The incident pressure ,P_i ,appearing in the headset cavity located in front of the ear will be cancelled using an out of phase pressure ,denoted P_a ,obtained by filtering and amplifying the error pressure $P_\varepsilon=P_i+P_a$.The two transfer functions,denoted H and G in Fig.1,correspond to the transfer functions of the loop filter and the amplifier -piezoceramic actuator set ,respectively .The filter role is to modify of the phase and the gain of the loop in order to insure the loop stability and prevent from spurious oscillations .The chosen filter structure is based on a biquadratic cell,that is,the filter is a rational function of $s=j2\pi f$ having two conjugate poles and zeros.Such an analog filter is currently used in commercial active control headsets[4].It is important to notice that, in this method,neither P_i nor the counter-pressure P_a were measured because the actual pressure inside the headset cavity is equal to the error pressure $P_\varepsilon=P_i+P_a$.So an only one microphone is needed.for measuring the error

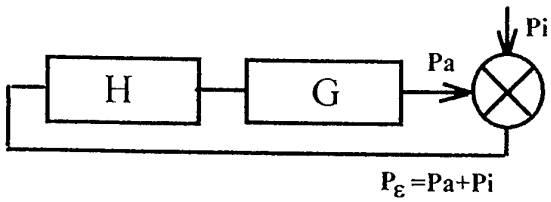


Fig.1 Active Feedback Control System.

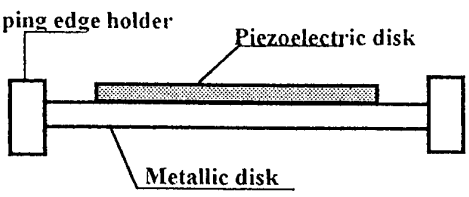


Fig.2 Structure of the bimorph actuator

pressure.It has to be located as close as possible to the actuator radiating face in order to introduce a very small delay inside the control loop which will little modify the control loop stability

0-8194-2165-0/96/$6.00

3. ACTUATOR STRUCTURES

3.1 Introduction

Two approaches can be used for generating the out of phase pressure which cancels the noise pressure inside the headset:either the actuator is vibrating well below its first resonance or its first resonant frequency is located exactly in the frequency range which has to be damped.The former necessitates high voltages for obtaining large displacements of the radiating face.Because the actuator has to be inserted in a headset this approach is not suitable for worker safety.The latter leads to small actuators or transducers having a large sensitivity.Furthermore they can be driven with low electric voltages.Among the different low frequency resonant transducers ,flexural resonators were chosen.Fig.3 shows the experimental configuration of the bimorph consisting of a piezoceramic disk cemented on a metallic disk.The actuator sensitivity depends upon both the piezoelectric material properties and the radius to thickness ratio of the passive disk[5] .The edge clamping conditions govern the actuator resonance frequencies[5].

3.2 Experimental transfer function of the bimorph

In order to determine the best bimorph structure and also the best headset protector configuration ,simulated and experimental studies were carried out.First,finite element method was used for determining the theoretical performances of the simulated structures.The most promising were then tested. To that effect,bimorphs were inserted into a very simple structure formed by a PVC cylindrical tube.This structure is called "modular system".One side is ended by a PVC plate and the the other side is fixed to an artificial head(Brüel & Kjaer 4128).With this set up the bimorph can easily be moved inside the tube which allows to readily modify the front and back volume cavities (Fig.3).The measurement microphone is the loop microphone located near the piezoelectric disk centre .Several kinds of bimorphs have been modelled ,built and tested.They used either different piezoceramic materials or different passive metallic plates.Best results were obtained with P189 PZT piezoceramic disk (Quartz and Silice™)whose the diameter and thickness are 17.5mm and 0.5mm ,respectively.The piezoceramic disk is cemented with an aradite type glue on a brass disk(diameter 22.5mm,thickness 0.5mm).Polyurethane cements leads to very important losses which increase the damping when the frequency increases6,7.Except for these last structures the bimorph resonances are very sharp.In order to widen the resonance bandwidth of the bimorphs ,araldite disks were used instead of metallic disks.As expected the actuator resonances are widen but unfortunately the radiated pressure level is very low and this type of actuators cannot be used in an headset protector.[6]

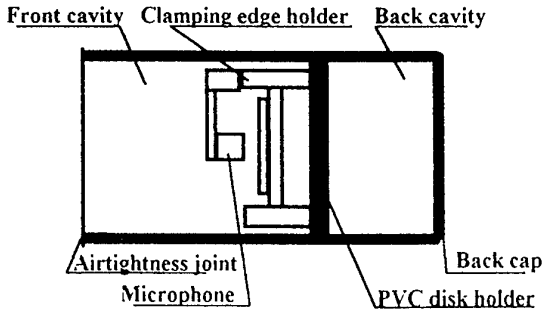


Fig.3.Modular system used for determining the headset performances.

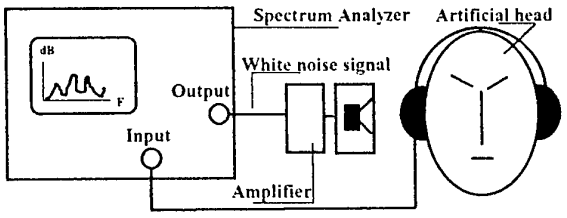


Fig.4.Experimental set up for measuring the bimorph transfer function.

In order to measure the open loop. transfer function the actuator inserted in the cylindrical cavity of the modular system is fed by a white noise voltage proved by a spectrum analyzer (Hewlett Packard 35665A).The signal coming from the measurement microphone is applied to the spectrum analyzer which determines the transfer function of the loop formed by the bimorph -microphone set.Figs.5and 6 shows the transfer functions obtained when the bimorph is located either in front or at the bottom of the tube cavity.From these results one can conclude that the back cavity dimensions do not significantly modify the pressure level delivered in the front cavtiy.When the front cavity is small ,the resonance is sharp which leads to a rapid increase of the loop phase and can create loop instabilities.It should be noted that the experimental curves are plotted with a relative dB scale which will be the same for the set of the experimental tests.The actual level strongly depends upon the microphone sensitivity and its position in front of the radiating bimorph face.Several microphone positions have been tested For example,the microphone were moved to the nodal circle position of the bimorph disk corresponding to the second flexural resonance.It follows that the low frequency response is decreased.of about 20dB and the useful resonance ,around

2kHz has disappeared.Furthermore mechanical coupling between the actuator and microphone has highly increased (40 to 50dB).If now the microphone is located on the metallic disk edge, its sensitivity is about 30dB lower because the edge displacement is very small compared to that obtained at the disk center.In this case,mechanical coupling due to the metallic material is large which can produce very important cross coupling and gives loop instability.[7]

The bimorph sensitivity can be increase using a metallic disk inserted between two piezoceramic disks poled in opposite directions and fed by the same AC. voltage

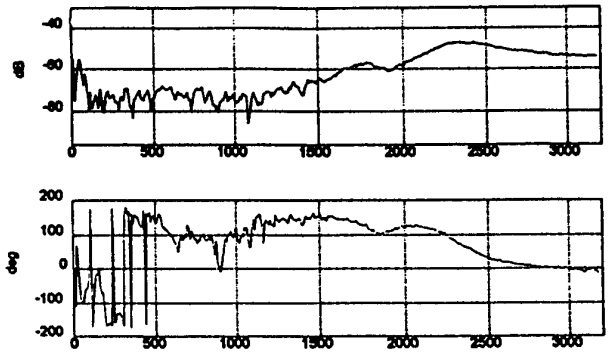


Fig.5.Experimental transfer function :bimorph located in front of the tube.

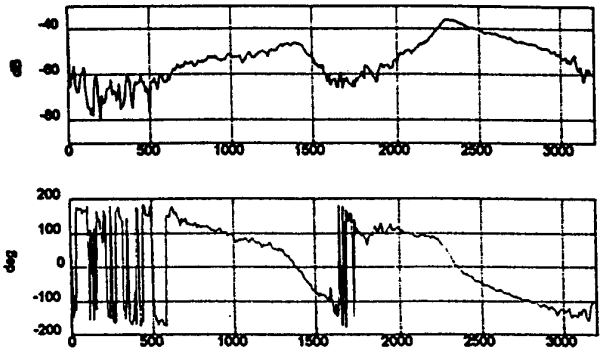


Fig.6.Experimental transfer function:bimorph located at the bottom of the tube.

4.EXPERIMENTAL RESULTS

4.1.Modular system

It is the previous system used for testing the bimorph efficiency.It has been fixed to an B&K artificial head and a one order filter was used (AD11ES94).Beeing based on an ADSP,the parameters of the digital filter can easily be changed using a P.C..The open loop transfer function is given Fig.7.It shows that 1700Hz and 3800Hz spurious oscillations or regenerations will occur because for these two frequencies the open loop phase is equal to -180°. The close loop attenuation obtained with such a configuration is given Fig.8.It is shown that an expected 20dB attenuation occurs between 2000Hz and 3000Hz but,two strong regenerations appear below (1700Hz) and above (3800Hz) this frequency range..It should be noted that at low or high frequency there is no significantly active noise reduction.This property is achieved by choosing cavity dimensions which do not modify passive attenuation of the headset i.e. using a back cavity smaller than the front cavity as it has been shown in section 2.3.

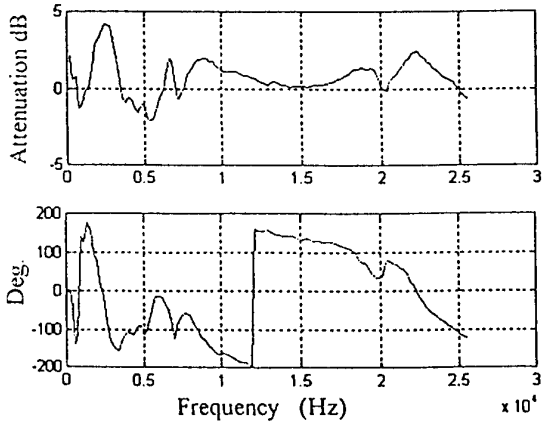


Fig.7.Open loop transfer function obtained with 1st order filter and the bimorph located in front of the tube.

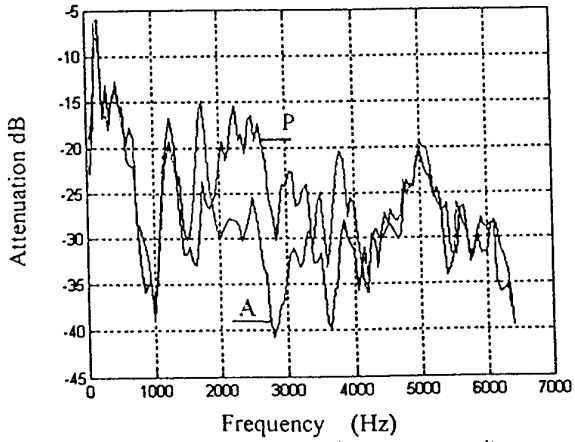


Fig.8.Close loop attenuation cooresponding to the Fig.7:(P) passive and (A) active attenuations.

Moving the bimorph to the middle of the tube ,the two cavities have the same dimensions.Fig.9 shows the experimental active and passive attenuations obtained.In this case the expected attenuation is decreased but the spurious regenerations has been removed.

4.2 Commercial modified head set protector

A commercial passive headset protector was modify for using in an active control system. The bimorph was inserted into the headset protector (SYLEC) and several kinds of filters were used.Fig.10 shows the passive and active attenuations obtained with this headset protector and a one order filter.A 10dB attenuation is obtained.Some spurious regenerations occur for frequencies above 2500Hz.

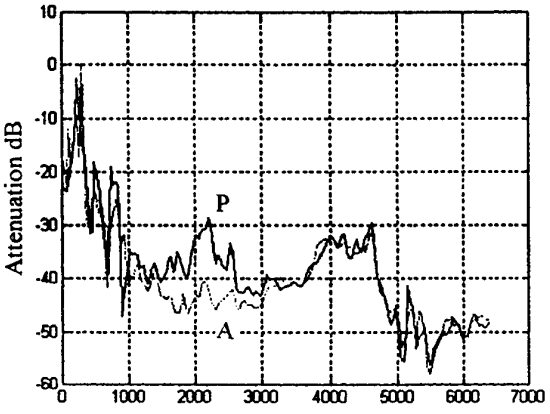


Fig.9. Experimental passive(P) and active (A)attenuations: bimorph located at the middle of the tube

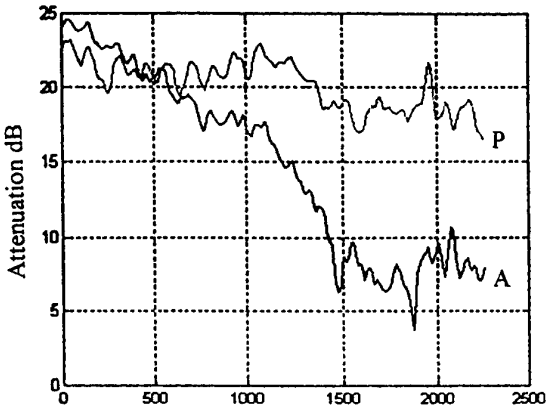


Fig10. Modified commercial passive headset protector:one order filter.

Fig.11 gives the results obtained with a third order filter .The active attenuation is about 10-15dB in a large frequency span (500 to 2000Hz).Unfortunatly,there is a strong spurious resonance for 3500Hz and a sound level about 15dB higher than the passive attenuation.

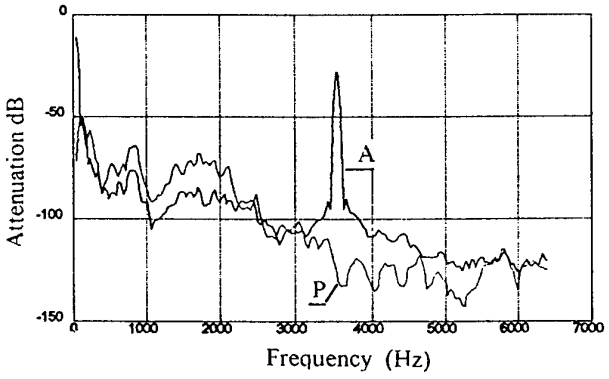


Fig.11. Same active headset as Fig.10. but with a third order filter (P,Passive, A,Active attenuations).

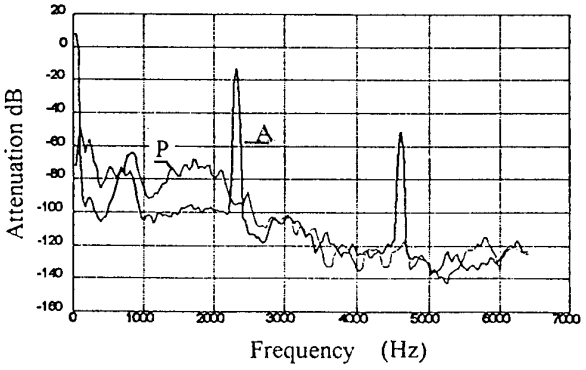


Fig.12.Same active head set as Fig.10. but with a fourth order filter(P,Passive,A, Active attenuations).

Active attenuation with a fourth order filter is better than the one obtained with a third for a frequency range below 2000Hz (Fig12).There are two spurious resonances(2200Hz and 4600Hz).At high frequency active and passive sound levels have the same order of magnitude .

5.CONCLUSIONS

It has been shown that active control noise reduction could be obtained in a headset protector in a frequency span of about 1kHz between 2kHz to 3kHz.The corresponding noise attenuation is about 10 to 20dB within the same range and according to the bimorph structure.However,spurious resonances or regenerations occur above or sometimes below the frequency range.These phenomena strongly limits the use of such a system.If lower attenuations are to be used together with more sophisticated filters ,the spurious oscillations could be cancelled.For improving both active noise attenuation and control loop stability an other approach could be used.For example,a least mean square algorithm (LMSA) which directly the directly minimizes the error pressure[8] would,perhaps,be able to lead to better results than the method using digital filter.

6.ACKNOWLEDGMENTS

The authors would to thank C. CASSIER,J.P. DUMAS,V. MATHEVON,O. POLETTI for their help in obtaining simulated and experimental data.

7.REFERENCES

1.P.A.Nelson and S.S.Elliott,"Active control of sound",Academic Press,London 1992.
2.J.F.Ordona-Bustamente,P.A.Nelson,"An adaptative controller for the active absorption of sound",J.Acoust.Soc.Amer.Vol 91
3.R.Schirmacher and D.Guicking,"Theory and implementation of a broadband active noise control system using fast RLS algorithm",ACTA ACUSTICA,Vol 2 n°4,pp 291-299,August 1994.
4.J.C.Béra,M.Sunyach and K.Buch,"Testing of different types of active hearing protectors",ACTA ACUSTICA,Vol 3 n°2,pp 203-207,April 1995.
5.A.Zoghdani,M.Brissaud,G.Grange,"Capteur piézoélectrique semi-encastré.",ACUSTICA,Vol 80 n°2,pp 352-364,1993.
6.V.Mathevon,"Dispositif antibruit actif à base de céramique piézoélectrique.Mémoire de DEA d'Acoustique,INSA LYON Sept.1995.
7.C.Cassier,"Casque antibruit utilisant des céramiques piezoélectriques,Mémoire de DEA d'Acoustique INSA LYON Sept.1995
8 C.R.Fuller,J.P.Vipperman and R.A. Budiaso,"Active control of broadband structural vibration using the LMS adaptative algorithm",J. of Sound and Vibration,Vol 166,n°2,pp283-299,1993.

Actively enhanced porous layers for free field acoustic absorption

Furstoss Marc

Thenail Denis

Galland Marie-Annick

Laboratoire de Mécanique des Fluides et d'Acoustique
Ecole Centrale de Lyon, BP 163, 69131 ECULLY Cedex

ABSTRACT

An active system which improves the absorbent properties of a porous material sample in free field is presented. The method, which is based on the "$\lambda/4$ resonance absorber" principle, associates active and passive means : a pressure minimization is achieved at the rear face of a porous layer to realize an impedance matching between its surface and the acoustic incident waves. The performances of a system including a single secondary loudspeaker, then a 3×3 array, are presented under normal and oblique incidence, for low frequencies under 1000 Hz.

1 INTRODUCTION

In the active enclosed sound field control domain of research, the emphasis has been for many years on reducing noise with localized control sources and sensors.[1] The alternative strategy, which consists in absorbing sound by attenuating the sound incident on a surface, considered as an acoustic boundary, so that the sound reflection is controlled or minimized, has not been very much considered and remains still an emerging technology. Practical realizations of the impedance control technique concept in both one and three dimensional environments have been initiated and successfully experienced by Guicking and colleagues in the 80's.[234] For some years, the interest for the adaptive control of acoustic impedance has been increasing and the number of papers concerned with this topic of research has been growing.[56]

The Laboratory of Fluid Mechanics and Acoustics at the Ecole Centrale de Lyon has initiated this topic of research in France for some years. Until now, our concern was to realize active systems able to assign a local desired impedance value at a surface. A direct impedance control system, processing the acoustic pressure and velocity signals in the vicinity of a loudspeaker membrane, has been designed and successfully tested in an impedance tube.[7] The modification of the normal impedance presented by the loudspeaker membrane in a desired way, especially to realize a perfectly absorbent surface, has also been recently achieved in free field, under normal and oblique incidence, for frequencies below 1000 Hz. Results will be presented soon in an article. This set-up has been used by the authors in recent studies[8] to actively control the impedance of the rear face of a porous layer, in order to drive the front face impedance to a prescribed value. Beside the possibility to assign a desired

0-8194-2165-0/96/$6.00

normal impedance value on a porous material surface, the system has allowed us to justify both theoretically and experimentally the "active equivalent of the $\lambda/4$ resonance absorber", firstly experienced by Guicking[3] and recently improved by the authors,[8,9] as an optimal system which maximizes the absorption properties of a thin material sample under normal incidence for low frequencies. An hybrid passive/active system which absorbs sound is therefore designed and presented here in details.
The impedance condition which is assigned in this case at the back face of the material sample is 0. The impedance control is therefore reduced to a pressure minimization and is realized by an active control set-up. The influence of this rear face condition on the material absorbent properties is studied, both under normal and oblique incidence, with first one control system (the control microphone, the filter and the control source). In order to increase the material front surface which local absorption coefficient is improved, the control systems are multiplied behind the same material sample to achieve several pressure reduction points. A system including a 3×3 array of secondary loudspeakers is then tested.

2 INFLUENCE OF THE REAR FACE IMPEDANCE OF A POROUS LAYER ON ITS ABSORBENT PROPERTIES

The absorption by a porous layer, such as fiberglass for example, depends not only on the layer, but also on the overall acoustic environment. Especially, how is backed the layer is predominant. Clearly, a relatively thin porous material layer is inefficient in low frequency ranges when it is supported by a motionless and impervious surface. The problem to increase the absorption is to act so that the material acoustic properties, which are "seen" by the incoming plane wave, are significantly different to that of the rigid impervious support. For example, at low frequencies, an important amount of material can be used. Another solution to increase the poor absorption at low frequencies of a weakly sized layer is to change the inadequate boundary conditions at its rear face. An air gap between the material rear face and the impervious rigid surface generally improves the low frequency absorption. The extreme application of this idea is the "$\lambda/4$ resonance absorber" where λ is the incident wavelength. The impervious rigid condition (the acoustic velocity is theoretically zero) at the back face is changed the most since it is replaced by an acoustic short circuit (the acoustic velocity is a maximum).
The maximum benefits of this method are obtained if the material characteristics are also accounted for. At low frequencies, viscous effects are predominant in a porous layer and the acoustic behavior is mostly described by the flow resistance, which definition is now recalled. A static pressure drop ΔP across a porous layer of thickness e induces a steady flow of air which mean value equals V. The flow resistance σe, σ being the flow resistivity, is expressed by :

$$\sigma e = \frac{\Delta P}{V} \tag{1}$$

(It is assumed that V has a low value so that σ is a constant.) The above equation is also an approximation of the material asymptotic low frequency behavior and can be written as :

$$\sigma e = \frac{p_2 - p_1}{v} \tag{2}$$

where p_1, p_2 and v are now acoustic quantities (p_1 is the acoustic pressure at the back face, p_2 at the front face, and v the mean flow velocity). Thus, if the porous layer is arranged at $\lambda/4$ for a rigid impervious surface, the layer input impedance can be approximated by the flow resistance :

$$\frac{p_2}{v} = \sigma e \tag{3}$$

Consequently, if the layer flow resistance is the air impedance, a very good low frequency absorber is designed. However, such a technique raises two major problems: the required air gap for a very low frequency becomes very large (e.g., $\lambda/4 = 86\ cm$ in air at $100\ Hz$) and the system is only effective in frequency bandwidths as narrow as the concerned frequencies are low. These drawbacks are circumvented by the use of active means. The idea is to achieve a sufficiently low impedance at the back face with an active control system. This method

was experimented in an impedance tube by Guicking and Lorentz[3] who improved the absorption coefficient of a glasswool sample up to 0.8 for frequencies below 500 Hz. Since, this design has been improved by the authors with modern electronic and signal processing devices to realize a perfectly absorbing porous termination at the end of an impedance tube, for the frequency range $(200, 1400)$ Hz.[8]

Nevertheless, when frequency as well as incidence are increasing, the previous asymptotic low frequency case under normal incidence is left, and an acoustic short circuit at the rear face of the $\rho_0 c_0$ resistant layer does not theoretically provide the complete cancellation of the reflected wave at the layer front face. Therefore, in order to investigate the withdraw between the zero impedance condition and the optimal one, the frequency and incidence dependencies of the optimal impedance value which is to be assigned at the rear face of a porous material sample, so that no reflection occurs at the front face, have been studied. The material dynamic behavior has been taken into account via a recent modeling.[10] The aim of the present paper being rather to present experimental performances, the theoretical part will not be presented here but it has been detailed in previous papers.[8] Two main conclusions can be underlined. First, on the frequency range $(0, 1000)$ Hz, under normal incidence, the optimal impedance value remains close to zero and can be approximated by a pressure minimization. Second, on such frequency range, the absorbent properties of the material are, in that case, largely improved under oblique incidence and the lack of performances does not require the assignment of a different back condition.
Therefore, in what follows, the impedance matching between plane incident waves and the material sample backed by one or more pressure releases will be studied for both normal and oblique incidence.

3 THE ACTIVE $\lambda/4$ RESONANCE ABSORBER

In all the experiments, performed in an anechoic room, normal or oblique incident plane waves are generated by an unbaffled loudspeaker ("the primary source"), driven with random noise, which is a dipole source set about 1.2 m above the porous panel (Figure 1). The incident waves impinges on the front face of the material sample which is a 1 m^2 square and 2 cm thick fiberglass panel, which flow resistivity equals approximately $\sigma = 20000$ $Rayls/m$. The pressure at its rear face is actively driven to zero at a single microphone location set about 2 cm from the secondary loudspeaker and some millimeters from the material rear face.

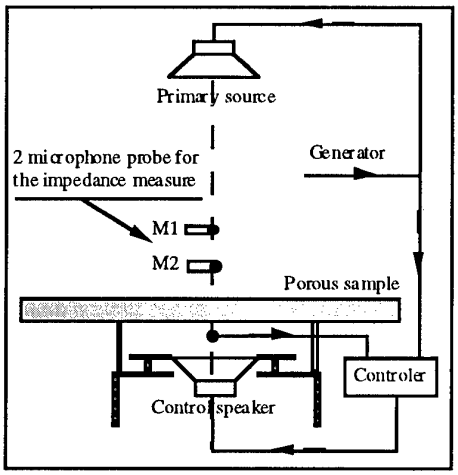


Figure 1: *Experimental set-up.*

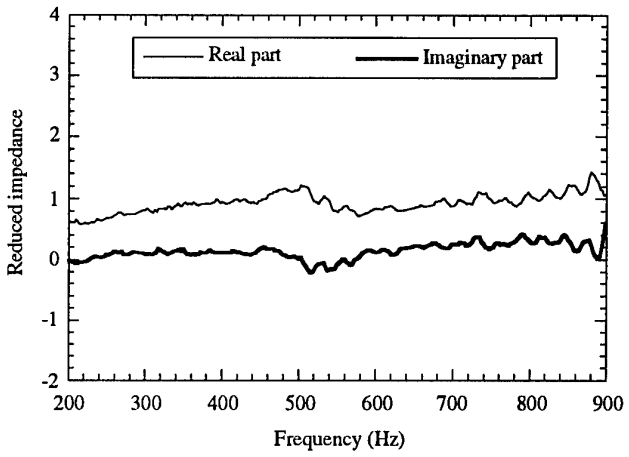


Figure 2: *Measured reduced impedance presented by the material under normal incidence*

The secondary loudspeaker has a circular membrane which diameter is 20 cm. The controller A is a digital

filter and its hardware, which includes an Analog Devices ADSP 2101 digital signal microprocessor, allows a time updating of its coefficients according to the classical "filtered-X" LMS algorithm. In terms of signal processing, the best performances are reached because the controller input signal is the electric signal that serves also as input for the primary noise source. Thus, no closed loop feedback instability is to be taken into account and causality is the least a constraint for the application of a feedforward technique. The panel input impedance is measured via a two microphones probe, according to the method proposed by Allard and colleagues,[1112] when the attenuation at the control microphone is about 25 dB over the whole frequency range $(200, 900)$ Hz.

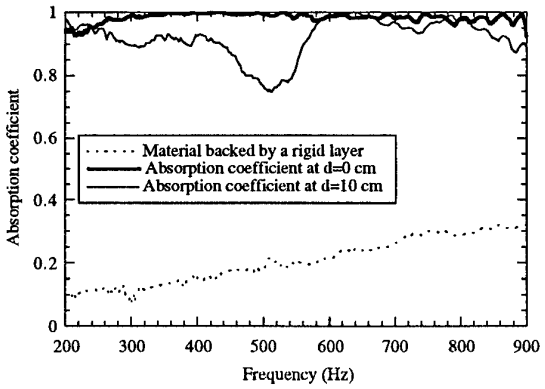


Figure 3: *Measured absorption coefficient under normal incidence*

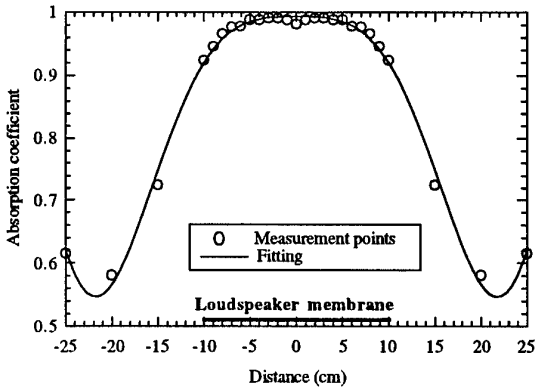


Figure 4: *Controlled surface above the loudspeaker membrane*

The real and imaginary parts of the reduced impedance (related to Z_0) measured at the material surface above the microphone location in the normal incidence case is presented in Figure (2). The impedance at the material front face is seen to be approximately equal to that of air, Z_0. The impedance matching between the incident acoustic waves and the porous material surface is then perfectly realized in practice at the measurement point. The surface can therefore be considered locally as totally absorbent on the whole considered frequency range, which is confirmed by the absorption coefficient curve measured at $d = 0$ (Figure 3). As a comparison, the absorption coefficient of the same material sample when it is backed by an impervious rigid layer is also reported. The benefits in the absorption are also evaluated as a function of the radial distance from the location (at the panel front face) above the center of the membrane, where is also positioned the control microphone. Figure (3) shows the variations of the absorption coefficient with the frequency above the center of the membrane ($d = 0cm$) and at the limit of the membrane ($d = 10cm$). It is seen from the figure that the material is nearly totally absorbent on the whole frequency range when the microphone probe is set at M, just above the control microphone. At $d = 10$ cm, though the acoustic pressure at the panel rear face is less released (8 dB instead of 25 dB at $d = 0$), the absorption coefficient is also very important. Figure (4) shows the variations of the absorption coefficient at $400Hz$ with the radial distance from the location $d = 0$. The benefits in the absorption are very important over the whole surface of the fiberglass above the loudspeaker membrane. The absorption decreases rapidly in the outer region.

The system is also tested for both 45 and 60 degrees incidence acoustic waves, and the measurements are reported in Figure (5). The influence of the pressure minimization at the panel rear face to the front face absorption coefficient remains very positive till 60 degrees incidence and its effect is constant on the frequency range. As in the normal incidence case, measurements are performed a radial axis from the location above the center of the secondary loudspeaker membrane. Again, the effect is quite uniform above the whole membrane, while no influence is practically noted in the outer region.

In order to increase the material controlled surface, the number of active cells (including the error sensor, the controller and the loudspeaker) has to be increased. Indeed, previous results demonstrate that the absorbent properties are not improved outside the region defined by the loudspeaker membrane. A 3 × 3 array has therefore been tested and is presented in the next section.

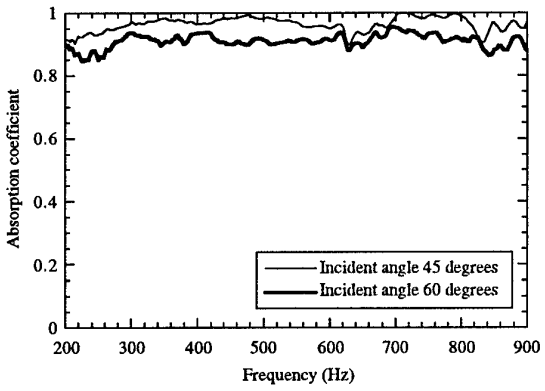


Figure 5: *Absorption coefficient under oblique incidence.*

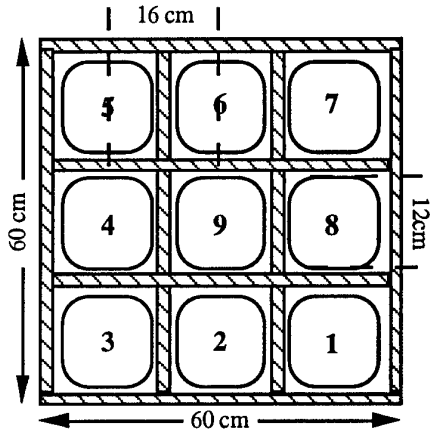


Figure 6: *Array of 3 × 3 loudspeakers in a wooden enclosure*

4 INCREASE OF THE CONTROLED SURFACE BY MULTIPLYING THE PRESSURE RELEASES BEHIND THE POROUS MATERIAL

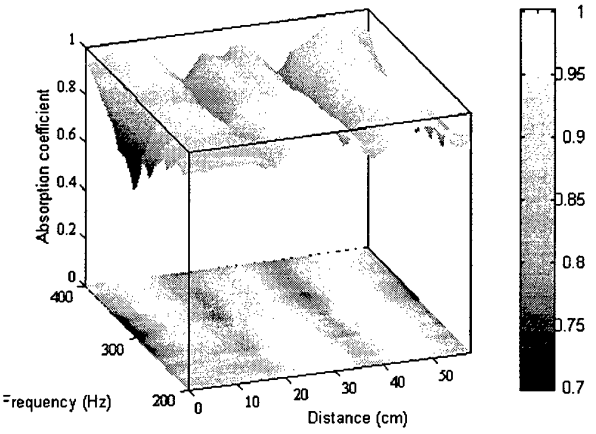


Figure 7: *Absorption coefficient measured at the sample surface along an axis joining loudspeakers 4, 9 and 8 under normal incidence. The 2D curve is the projection of the 3D curve on the plane $z = 0$.*

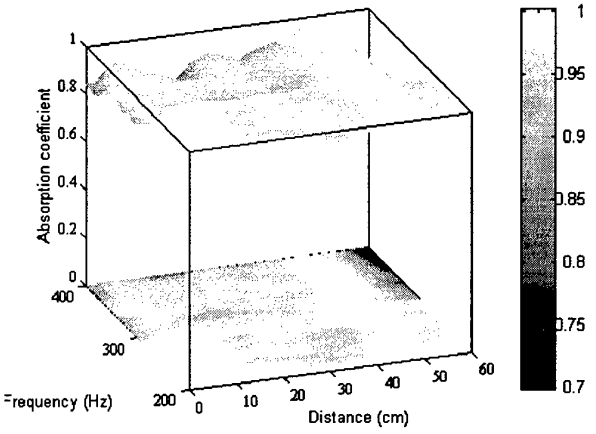


Figure 8: *Absorption coefficient measured at the sample surface along an axis joining loudspeakers 4, 9 and 8 under 45 degrees incidence. The 2D curve is the projection of the 3D curve on the plane $z = 0$.*

The experiments are then performed with the same material sample, backed by an array of 3 × 3 loudspeakers, each with a 12 *cm* square edge flat membrane (Figure 6). A control microphone is set in front of each secondary actuator and a local pressure minimization is achieved at each sensor. Our concern being here to simplify the control set-up, each pressure release is achieved by an analog filter, according to a feedback control method. With a such closed-loop technique, feedback instabilities limit to $(200, 400)$ Hz the frequency bandwidth which leads

to good absorbent performances.
Figure (7) shows the absorption coefficient measured at the material surface along an horizontal axis passing above the loudspeakers 4, 9 and 8 under normal incidence. A pressure reduction of 20 dB is achieved in front of each 9 loudspeakers. These results can therefore be generalized to all horizontal axis. Same measurements have been realized under 45 degrees incidence, and the absorption coefficient is presented on Figure (8). In both cases, the absorption coefficient is largely improved and the 60 $cm \times 60$ cm surface can be considered as nearly totally absorbent.

5 CONCLUSION

An hybrid passive/active system, which changes a material sample surface in an anechoic boundary for wide ranges of low frequencies and incident angles, has been designed. It has been demonstrated that the multiplication of active setups at the porous layer rear face increases the anechoic surface dimensions. Our present investigations are dealing with the influence of such systems on realistic acoustic fields.

6 REFERENCES

[1] P. A. Nelson and S. J. Elliott. *Active Control of Sound.* Academic Press, 1992.

[2] D. Guicking and K. Karcher. Active impedance control for one-dimensional sound. *ASME J. Vib. Acoustics, Stress Reliab. Des.*, 106(3):393–396, 1984.

[3] D. Guicking and E. Lorentz. An active sound absorber with porous plate. *ASME J. Vib. Acoustics, Stress Reliab. Des.*, 106(3):389–404, 1984.

[4] D. Guicking, K. Karcher, and M. Rollwage. Coherent active methods for applications in rooms acoustics. *J.Acoust.Soc.Am.*, 78(4):1426–1434, 1985.

[5] F. Orduña Bustamante and P. A. Nelson. An adaptive controller for the active absorption of sound. *J.Acoust.Soc.Am.*, 91(5):2740–2747, 1992.

[6] G.C. Nicholson and P. Darlington. Active control of acoustic absorption, reflection and transmission. In *Proc. IOA*, volume 15, pages 403–409, 1993.

[7] D. Thenail and M. A. Galland. Development of an active anechoidal boundary. In *Proc. Idee-Force EUR'ACOUSTICS, W4*, Ecole Centrale de Lyon, 1992.

[8] D. Thenail, M. A. Galland, M. Furstoss, and M. Sunyach. Absorption by an actively enhanced material. In *Proc. of the 1994 ASME Winter Annual Meeting*, volume DE-75, pages 441–448, Chicago, Il, 1994. AM-16D.

[9] M. Furstoss, D. Thenail, and M.A. Galland. Active absorbent panels. In *15th International Congress on Acoustics*, volume 4, pages 429–432, Trondheim, 1995.

[10] J. F. Allard and Y. Champoux. New empirical equations for sound propagation in rigid frame fibrous materials. *J.Acoust.Soc.Am.*, 91:3346–3353, 1992.

[11] J. F. Allard and B. Sieben. Measurements of acoustic impedance in a free field with two microphones and a spectrum analyser. *J.Acoust.Soc.Am.*, 77(4):1617–1618, 1985.

[12] J. F. Allard, R. Bourdier, and A. M. Bruneau. The measurement of acoustic impedance at oblique incidence with two microphones. *J.of Sound and Vibration*, 101:130–132, 1985.

Intelligent Processing

Invited Paper

Fabrication of polymers and composites containing embedded sensors.

Hugh Denham, Graeme George*, Llew Rintoul* and Paul Calvert,

Arizona Materials Laboratories, Tucson Arizona, 85712;
*Department of Chemistry, Queensland University of Technology, Brisbane.

ABSTRACT

Freeform fabrication is a family of techniques for preparing solid objects from a three-dimensional computer-based design. The best known method is stereolithography. To date, freeform fabrication has been mainly applied to making prototypes and molds. Similar techniques can be applied to make functional parts of a range materials, including metals and ceramics as well as polymers. In collaboration with Advanced Ceramics Research Corp. of Tucson, Arizona, we have been developing a reactive extrusion method where a part is built up by extrusion of a material stream through a fine needle. A curing reaction at the deposition site allows solid components to be formed. This approach can be readily modified to deposit several materials in the same part and hence to fabricate intelligent materials containing embedded sensors and actuators. This paper describes the application of this method to an epoxy part containing an optical fiber sensor and the response of embedded polyvinylidenefluoride piezoelectric films.

2. INTRODUCTION

Freeform fabrication is a family of techniques for preparing solid objects from a three-dimensional computer-based design. The best known method is stereolithography, where a laser writes a series of layers in a bath of photopolymerizable monomer, progressively building up the solid object in cross-linked resin [1]. Other methods include solid laser sintering and three-dimensional printing in which successive layers of powder are bonded to form the shape, and fused deposition modeling where liquid wax or polymer is extruded to build the part layer-by-layer. The annual symposium on freeform fabrication gives an overall view of these methods [2].

To date, freeform fabrication has been mainly applied to making prototypes but the methods for forming molds are now being developed. In the longer term it is clear that similar techniques can be applied to make functional parts of a range materials, including metals and ceramics as well as polymers. Beyond this the methods have considerable potential for the formation of new types of composites and materials with internal gradients in properties and composition. This suggests that materials could be formed with a similar level of complexity to that found in biological tissues.

In collaboration with Advanced Ceramics Research Corp. of Tucson, Arizona, we have been developing a reactive extrusion method where a part is built up by extrusion of a material stream through a fine needle [3,4]. A curing reaction at the deposition site allows solid components to be formed. Our recent efforts have been directed at making a range of polymers, ceramics, metals and composites to explore the range and limitations of the process. This paper describes the application of this method to an epoxy part containing an optical fiber sensor.

3. EXPERIMENTAL

The reactive extrusion freeforming method has been described elsewhere [3,4].

The apparatus used to form the epoxy samples was a simplified version based on a moving sample stage above which was suspended a 3ml disposable syringe. The syringe was fitted with a 22 gauge needle (0.5 mm ID), cut off short. The x-y stage was

0-8194-2165-0/96/$6.00

an MD2 9"x9" belt drive system from Arrick Robotics (Hurst, TX), controlled via the printer port of a Compaq Aero computer. The piston of the syringe was driven by an Oriel (Stratford CT) "stepper mike" motor and a second Oriel motor controlled the height of the syringe, both motors were addressed via an RS232 interface. The MD2 and syringes were controlled by a program written in Basic. Samples were formed as square plates 20mm x 20mm x 5mm. Each layer was written as a series of up-and-down sweeps with alternate layers written left-and-right. The line spacing was selected to allow neighbors to just touch. Each layer took about 60 seconds to write and had a thickness of about 0.2 mm.

4. FIBER-OPTIC MONITORING OF EPOXY CURE

TGDDM, (N,N,N',N'-tetraglycidyl-4,4'-diaminophenylmethane), as MY721, was obtained from Ciba-Geigy and blended with 27 wt% DDS (Aldrich Chemical Co.) by mixing at 60°C. This mixture was blended with 15 wt% dioxane and 3 wt% of Degussa R202 hydrophobic fumed silica. The resulting mixture had the consistency of toothpaste and would hold its shape when formed into a small cone using a spatula.

Freeforming was carried out onto a hotplate at 100°C such that slow loss of dioxane stiffened the paste progressively. After 10 layers an optical fiber was placed across the surface of the soft resin such one end was a few millimeters from the edge and the other end extended 20 cm from the sample. Successive layers were then deposited to bury the fiber.

Optical fibers were Quartz et Silice PCS plastic-clad silica 600W and a doped (low hydroxyl) silica-clad silica fiber AS200/280. Some early samples were formed containing 600 μm optical fibers but once adequate spectral intensity was attained, 200 μm fibers were used subsequently. In addition to being less mechanically disruptive, these finer fibers had fewer spectral artefacts and a low absorbance at 7000 cm^{-1}, the hydroxyl spectral region. The polymer coating was stripped from the end few millimeters of the fiber prior to embedding.

After forming, the part was precured overnight at 100°C in an air-circulating oven to form a brittle yellow opaque solid. Subsequent full curing at 160°C or 170°C gave a brown partly transparent block. During the full curing cycle the sample was removed at intervals for NIR spectroscopy. Water uptake was monitored also at intervals after exposure to ambient air or after immersion in water at 60°C. Spectra were taken on a Perkin Elmer 2000 FT-Raman/NIR spectrometer using InGaAs and cooled InSb detectors. The laser and NIR sources were shut off. The free end of the optical fiber was carefully positioned at the focus of the Raman compartment with the sample dangling outside the compartment. The sample was placed in the beam of a Schott 150W quartz-halogen microscope illuminator, with the heat filter removed. The radiation passed through about 2mm of resin and was then collected by the embedded end of the optical fiber. Light emerging from the free end of the fiber was collected by the high-aperture optics of the Raman compartment and passed to the N-IR spectrometer (figure 1).

Several features were observed from these spectra when compared with published spectral changes during the curing of bulk resin [5]. Firstly, it was noted that the precuring reaction at 100°C for 16 hours has results in total consumption of primary amine since the strong combination band at 5067 cm^{-1} is absent. However, there is still unreacted epoxide was shown by the clearly defined band at 6057 cm^{-1}. The major cure reaction at 160°C enables this epoxide to react with the secondary amine groups resulting from the earlier epoxide-primary amine reaction. The removal of secondary amine is essential to achievement of a high glass transition temperature and to lower the number of active sites for sorption of water. The curing reaction produces a higher crosslink density through both etherification (epoxy-hydroxyl reaction) and reaction of epoxide with secondary amines to produce tertiary amines. The first reaction produces no net increase in hydroxyl groups while the second produces both an increase in -OH and a decrease in -NH-. In the spectra, there is a growth of the -OH peak at 7000 cm^{-1} and a loss of the -NH- peak at 6600 cm^{-1}.

Figure 2 shows spectra of a dry sample and one soaked in water at 60°C for 53 hours. It can be seen that the water OH

combination band at 5223 cm^{-1} reflects the increasing water content. Some change in the -OH peak at 7000 cm^{-1} would also be expected but the effect of added water is small compared to that of the -OH resulting from opening of the epoxy rings. As there is no contribution from alcoholic -OH groups to the peak at 5223 cm^{-1}, this may be used as a direct monitor of water uptake.

5. EMBEDDED PIEZOELECTRIC FILMS

We have also studied the response of piezoelectric films embedded in cyanate ester composite laminates. Our initial expectation was that the piezoelectric response would disappear above the poling temperature and so would be lost in composites where the film was in place during curing. The PVDF sensors exhibit a hysteresis type behavior for response to load over temperature. We had no doubt that the response would be lost irreversibly at the polymer melting point (170°C).

In fact, the sensors lose their response upon heating at about 190 °C but it returns upon cooling at around 150°C. At the curing temperature for cyanate ester resins, 177 °C, about 10% of the signal remains. This unexpected result was attributed to the constraint on film shrinkage due to the layers of composite. The melting behavior of drawn textile fibers is similarly raised if the fiber is clamped by the ends rather than free.

Polyvinylidenefluoride polymer sheets were supplied by Kureha of Japan in nine micron thicknesses and are metallized on both surfaces with either aluminum or nickel. A sensor size of one square centimeter was chosen. 30 μm copper leads were attached with conducting epoxy. We found that getting a repeatable signal from the sensors during our experiments required the development of some circuitry. The polymer film has a very fast relaxation time and, due to the small amount of charge involved, the signal produced is not easily captured. For this reason a charge amplifier circuit was designed based on the schematic of Campbell *et al* [6]. Our design was very similar but made use of a single polar op amp.

Composite sheets with interlaminar PVDF films were fabricated. Sensor strips were made by placing a single sensor between two prepreg sheets and cured under the pressure of an aluminum block. The response of the film to a series of step loadings was determined. A series of small weights were placed on the cured sensor strips and removed rapidly. This produced a rapid change in strain in the film, and a voltage response. These experiments were performed for a series of curing conditions (Figure 3). As can be seen the response was fairly linear and decreased with temperature exposure. The applied loads, around 1kPa, are very small compared to loads expected in the composite in use.

When the films are heated unconstrained they warp, curl, and shrink predominantly in the direction of the manufacturing stretch. The films cured between the prepreg sheets have little shrinkage during the temperature cycling. Experiments on unconstrained films were performed by placing the films between glass slides and heating them. The glass slides provide a small level of constraint as the film must be kept from curling during the measurements. The signal was seen to decrease with temperature and did not return when cooled (Figure 4). The films exhibited large shrinkage resulting from the temperature cycling. Embedded films (constrained) were tested for their response at temperature using the sensor sheets described before. The input loading in this case was vibrational, provided by an electric engraver. The sensor response was a loop with the signal dropping off with temperature and disappearing around 190 °C, and returning around 150°C when cooled (Figure 5).

6. DISCUSSION

These embedded sensors represents a first steps towards fully integrated intelligent materials. We envisage using the freeforming technique to write sensors, actuators and connections into composites such that the product is cured into a unified structure.

7. ACKNOWLEDGMENTS

PC would like to thank the University of Arizona for sabbatical leave to do this work and Queensland University of Technology for a visiting fellowship. The support of the Lockheed Advanced Development Corp., the US Army Research Office, the Air Force Office of Scientific Research and ARPA is gratefully acknowledged.

8. REFERENCES

1. P.F. Jacobs. *Rapid prototyping and manufacturing* (SME, Dearborn MI, 1992).
2. M.A. Harris, *et al. Solid freeform fabrication symposium proceedings* (Univ. of Texas, Austin, Texas, 1990-1995).
3. K. Stuffle, A. Mulligan, J. Lombardi, P. Calvert and B. Fabes. in *Mater. Res. Soc. Symp. Proc.* 1027-1031 1994).
4. K. Stuffle, A. Mulligan, P. Calvert and J. Lombardi. *Solid freebody forming from polymerizable slurry* pp. 60-63 (Univ. of Texas, Austin, 1993).
5. G.A. George, N.A. StJohn, C.J. deBakker and P.A. Cole-Clarke. *Studies of thermoset cure and performance using near infrared spectroscopy* in 6th Annual International Conference on Cross-linked Polymers pp.61-78 (Noordwijk, Holland, 1992).
6. J.F. Campbell, E.G. Vanderheiden, L.A. Martinez, D.S. Cairns and M.G. Abdallah, *Journal of Composite Materials* Vol. 26, pp. 334-349, 1992.

Figure 1: Geometry of embedded fiber-optic sensor in an epoxy block.

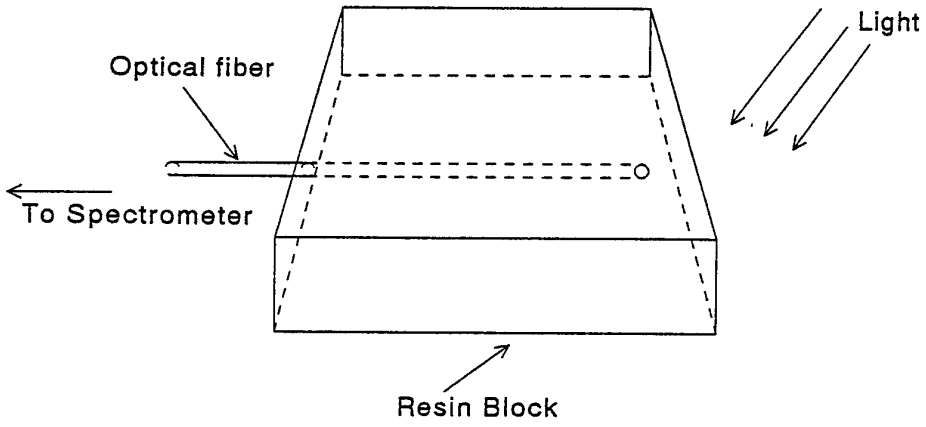


Figure 2: Embedded fiber-optic NIR spectra of TGDDM/DDS cured at 160°C for 100 minutes, dry and after 53 hours in water at 60°C.

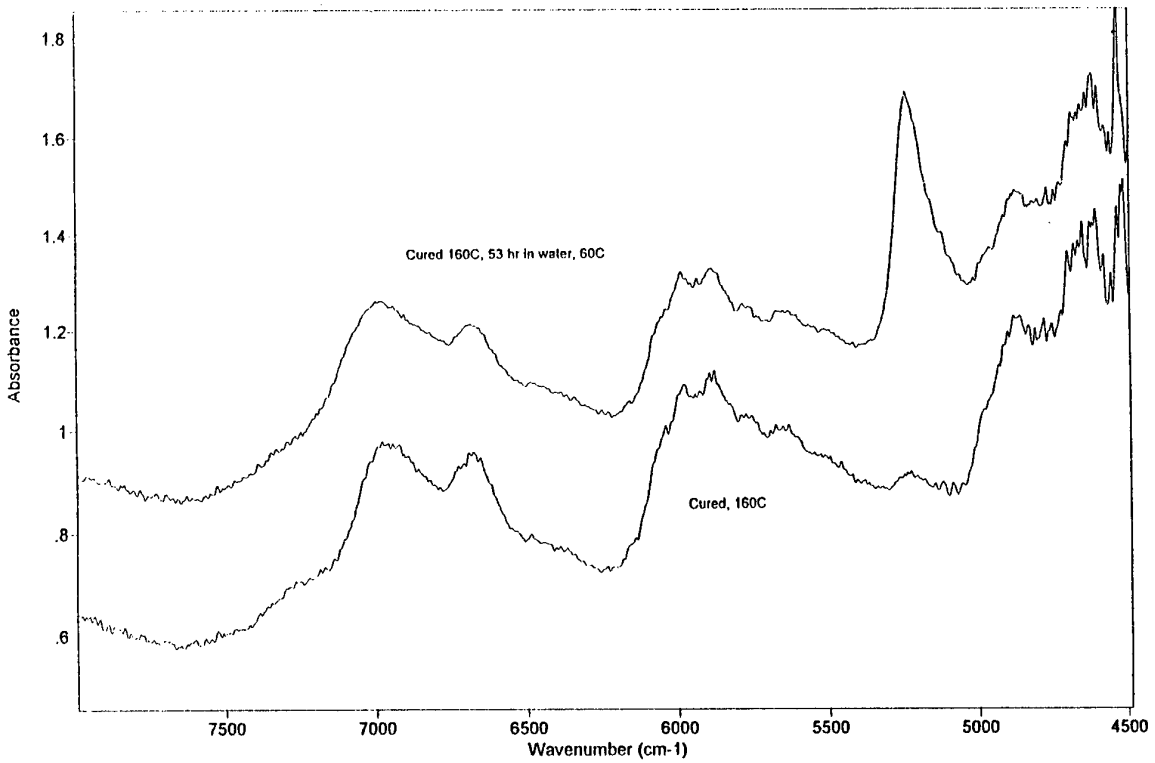


Figure 3: Signal (peak mV) from picking a weight off a cured sandwich of PVDF sensor between cyanate ester prepreg layers.

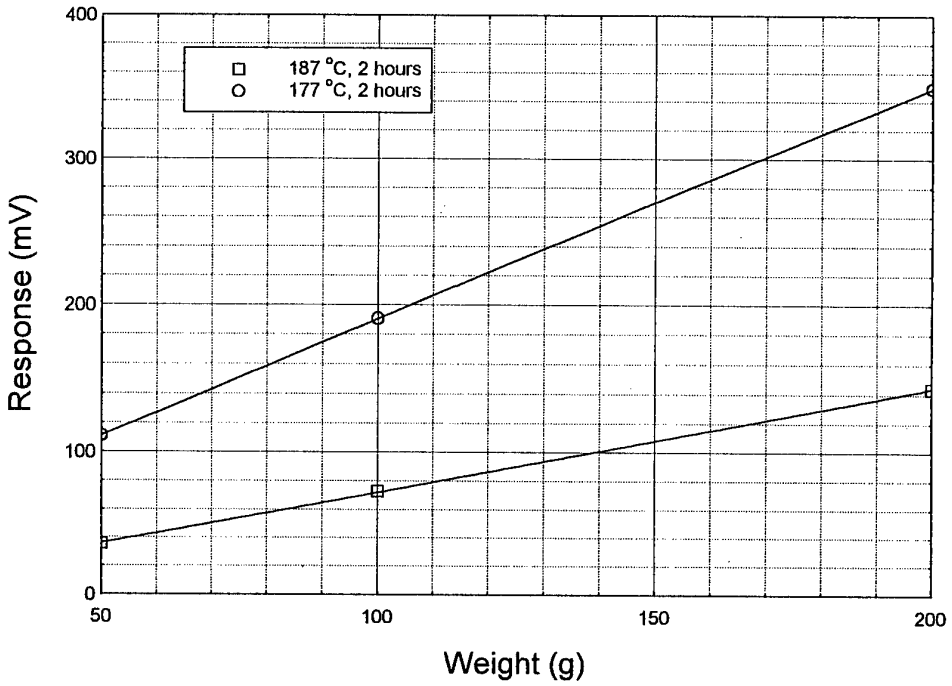


Figure 4: Signal due to unweighting an unconstrained sensor film vs. temperature.

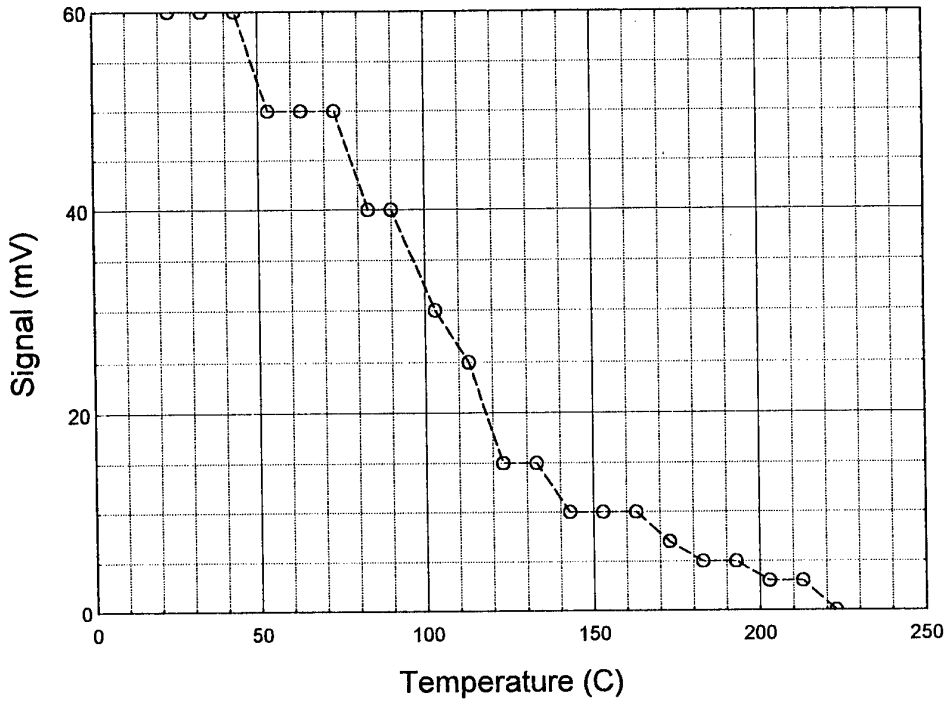
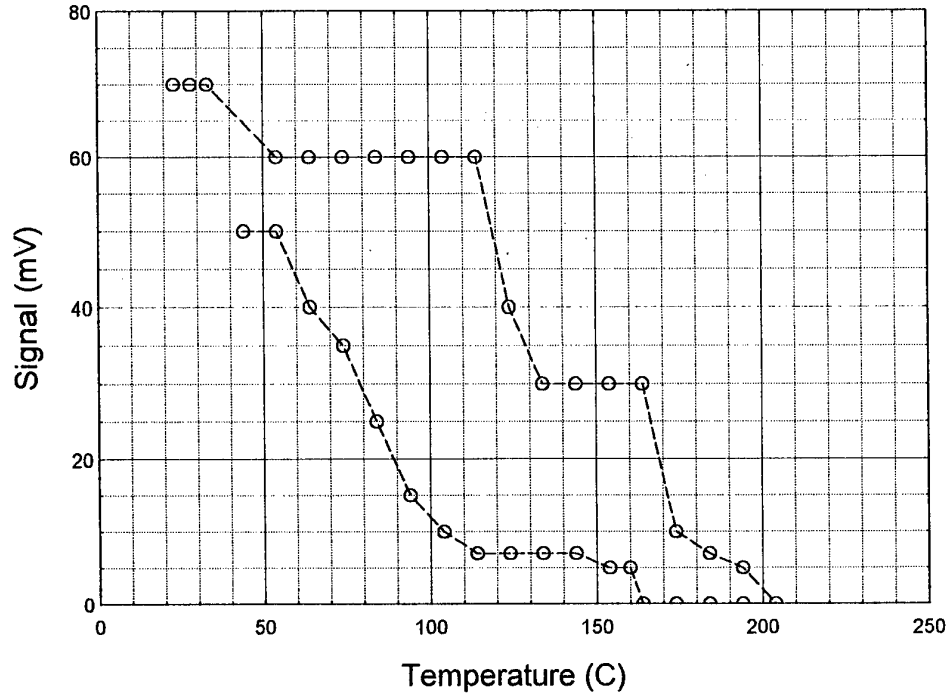


Figure 5: Signal due to vibration by an engraver of a sandwich, as figure 1, during heating (upper curve) and cooling (lower curve).



Invited Paper

Self-Controlled Material Processing

Yoshinobu AOYAGI

The Institute of Physical and Chemical Research (RIKEN)
Wako-shi, Saitama, 351-01, Japan
Tel:+81-48-462-1111, Fax:+81-48-462-4659

1.Introduction

Recently material processing with intlligency has been interested. Self-formation and alignment of quatum dots structure on semiconductor surface are a typical example. In this case no lithgraphic technique which is conventionally used for fabricating such a ultra fine structure is necessary. Another typical intelligent material processing is atomic layer manipulation with self-limiting process in which exact one monolayer layer-by-layer stacking or etching is automatically achieved.
Atomic layer manipulation - layer-by-layer addition (Atomic layer epitaxy) and/or subtraction (Atomic layer etching) of atomic layer of a crystal - is a promising technology for future nano-device fabrication. In atomic layer manipulation, a source gas or an etching gas is alternatively fed into a reactor and self-limiting mechanism is realized. In self-limiting mechanism, source gas or etchant recognizes automatically an one molecular layer addition or subtraction of crystal and the growth or etching is automatically stopped just after one molecular layer addition or subtraction of the crystal.

In this paper the self-limiting process of atomic layer manipulation of GaAs semiconductor is described and characteristics of the atomic layer manipulation, that is, the atomic layer epitaxy and the atomic layer etching are reported. In the conference in addition to this atomic layer manipulation, recent topics on intelligent material processing including self-assembling of quantum dot structure, self ordiering of atomic dot are reported.

2. Atomic layer epitaxy

In a typical laser atomic layer epitaxy (ALE) of GaAs(1), source gases of AsH_3 and $Ga(CH_3)_3$, (TMG) or $Ga(C_2H_5)_3$, (TEG) are fed into reactor alternatively and laser light is introduced at the moment of TMG gas supply as shown in Fig. 1 for realizing the self-limiting mechanism.
Fig. 2 shows a typical crystal growth rate as a function of temperature of reactor with and without laser light irradiation. without laser light irradiation, any saturation of crystal growth rate at one molecular layer/cycle is not observed but with laser light irradiation the growth rate saturates at one molecular layer/cycle. The crystal growth rate also saturates at one molecular layer/cycle as functions of laser light intensity and TMG or TEG gas feeding rate. This self-limiting crystal growth at one molecular layer/cycle can be described by introducing a concept of site selective photo-assisted reaction of TMG or TEG under the laser light

0-8194-2165-0/96/$6.00

irradiation. That is, TEG or TMG can decompose to Ga on As surface but not on Ga surface under the laser irradiation. This model has been confirmed by analyzing the rate equation of the reaction, the wavelength dependence of the crystal growth and dynamic RHEED experiment.

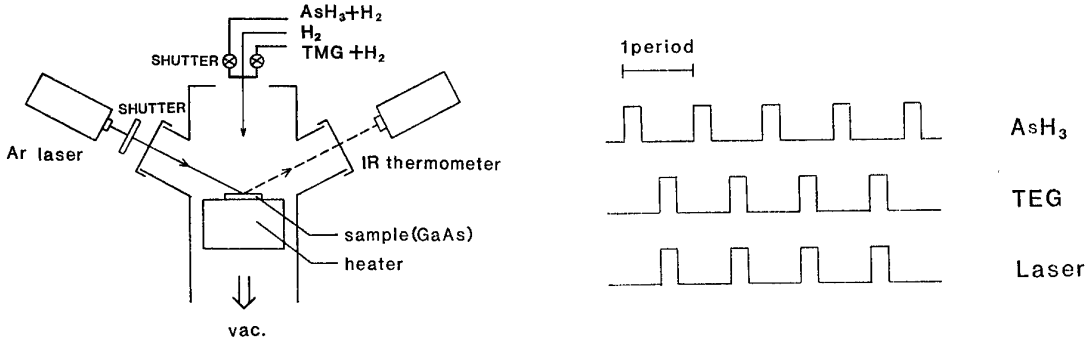


Fig. 1 Schematic diagram of the furnace of the laser ALE and typical time sequences of the source gas flow and the laser irradiation.

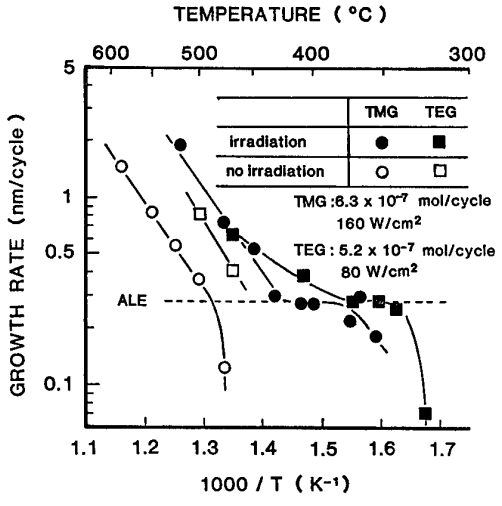


Fig. 2 Temperature dependence of the growth rate with and without the laser irradiation for TMG and TEG.

3. Atomic layer etching

In case of atomic layer etching of GaAs, an energetic beam like electron beam, ion beam or photon beam is introduced onto the sample after feeding of Cl gas into the reactor to realize the self-limiting mechanism at one monolayer etching/cycle as shown in Fig. 3.

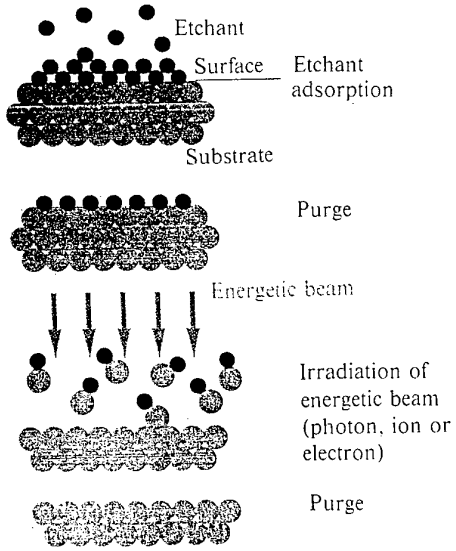


Fig. 3 Time sequences of gas feed, purging, and sample biasing for atomic layer etching.

In this case one monolayer adsorption of etchant on the GaAs substrate and successive introduction of energetic beam to attack the back bond of the surface atom of the crystal which is weakened by the adsorption of etchant on the surface are essential to realize the self-limiting etching. It is found that the etching rate/cycle is independent of the flux of energetic beam and dosing rate of Cl gas as shown in Fig. 4.

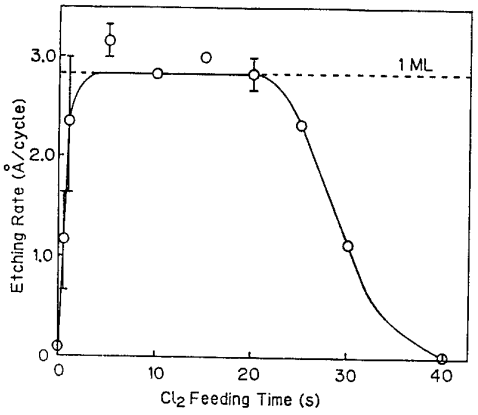


Fig. 4 Etching rate as a function of Cl_2 feeding time.

4. Application

This self-limiting atomic layer manipulation is successfully applied to fabricate a well defined quantum wire structure.

Fig. 5 shows a typical example of the SEM image of the structure. The well defined rectangular quantum wire structure is observed. If we fabricate the structure using conventional crystal growth technique, the uniform thickness of the quantum wire observed can not be obtained due to anomalous crystal growth at the V shape corner. In conventional technique no self-limiting mechanism at one molecular layer/cycle which is independent of the shape of the substrate is realized.

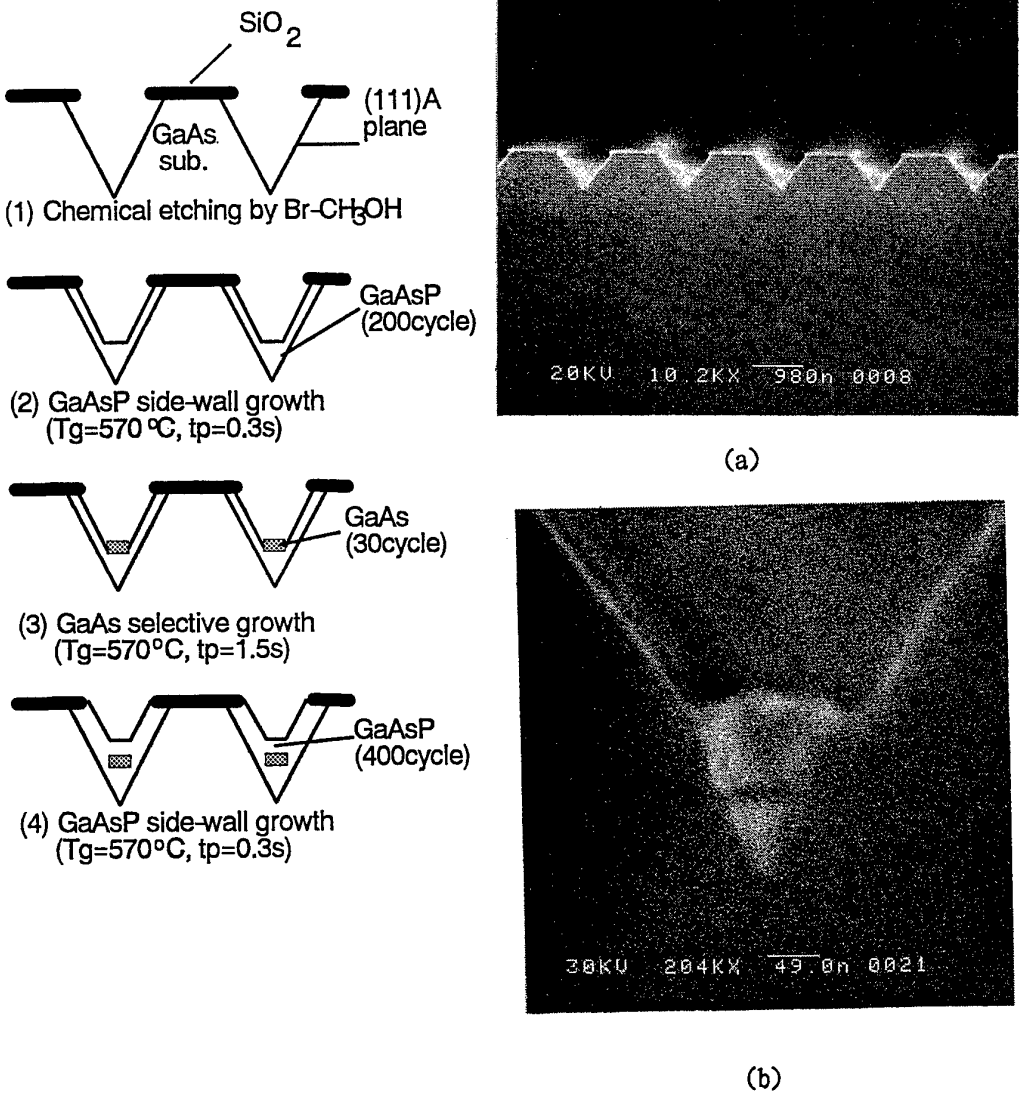


Fig. 5 Quantum wire fabrication process by ALE and the SEM photograph.
(a) Vgroove of substrate before ALE growth,
(b) GaAs/GaAsP quantum wire fabricated by ALE.

5. Conclusion

Self-limiting mechanism in atomic layer manipulation is a kind of automatic feedback of the material processing at one molecular layer addition or subtraction. The self-controlled material processing is quite useful for future nano-device fabrication in which atomic scale control of materials is required.

Invited Paper

RESEARCH PROJECT ON NANO-SPACE LABORATORY AND RELATED TOPICS

Isao YAMADA
Ion Beam Engineering Experimental Laboratory
Kyoto University, Sakyo, Kyoto 606, Japan

Abstract The research project on Nano-Space Laboratory and related topics are reviewed. This project has been funded by the Special Coordination Funds for Promoting Science and Technology since 1994. The project is classified into three major topics: (1) materials development by atom lab, (2) materials development by molecular lab and (3) development of theory and basic technology for nano-space research. The paper describes progress of the research with emphasis placed especially on new process technologies.

INTRODUCTION

The nano-space is defined as an ultimate material volume of manometer dimensions which can exhibit unique material characteristics. The constituent materials of the nano-space may be metals, insulators, ceramics, organic materials, Bo-materials or their combinations. The region where the nano-space is created may be inside, at surfaces, interfaces or grain boundaries of materials. The examples of the nano-spaces are shown in Fig.1. The purposes of the present research are focused upon the creation of such nano-space regions exhibiting new material characteristics. By this definition, the nano-space laboratory might be regarded as an ultimate size beaker. The research project on the "nano-space laboratory and materials development" consists of three major topics: (1) atomic level materials development, (2) molecular level materials development and (3) development of theory and basic technology for nano-space research.

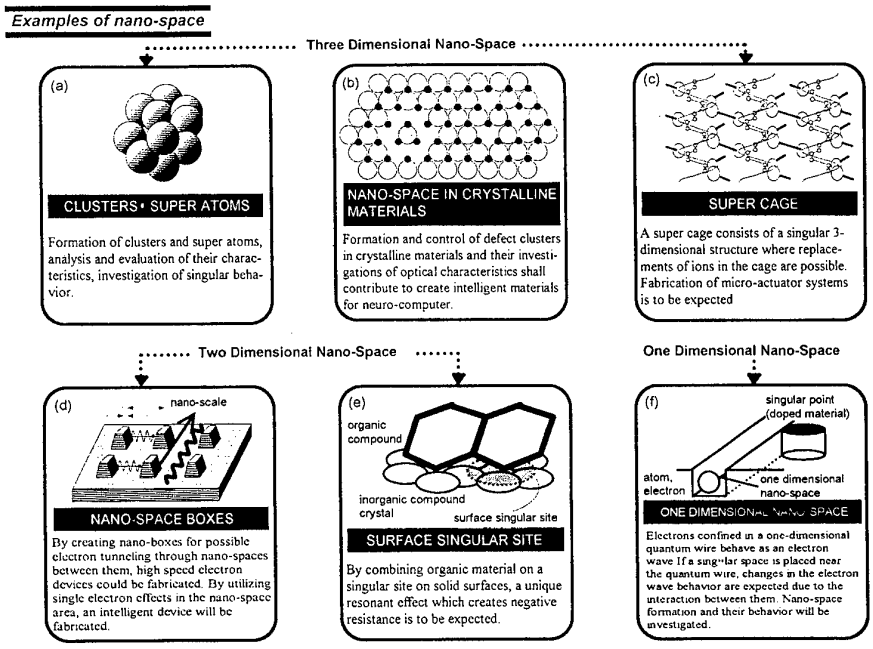


Fig.1 Various types of nano-spaces which create unique material characteristics

0-8194-2165-0/96/$6.00

This project was started as one of the large scale projects funded by the Special Coordination Funds for Promoting Science and Technology in 1994. The project is divided into two research periods. The first stage began in 1994 and will continue for 3 years. This will be followed by a 2-year second stage based upon the first stage accomplishments. Seven government institutions, eight universities and four private companies are joined under the program. The scope of the project was reported in 1995 at the International Symposium on Intelligent Materials in Tokyo [1]. Recent achievements in the various subjects under the three major topics will be described.

RECENT ACHIEVEMENTS OF THE PROJECT

(1) Materials development in the atom lab.

The objectives of research subjects in the atom lab are related to synthesis and control of singular atom assembles, synthesis of new materials, development of techniques to use new phenomena and development of new methods of measurement and evaluation. Four subjects have been defined. In Table 1 titles of these research subjects and their principal investigators are listed .

Table 1 Research Subjects in Atom Lab.

Studies of structural and optical characteristics of defect clusters and their control in formation processes, National Institute for Research in Inorganic Materials (K. Kitamura)
Optical characterization of periodic nano-spaces in crystalline materials and investigation of related quantum phenomena, Tokyo Institute of Technology (F. Minami)
Analysis of electronic structures of interface-nano-space and investigation of their electronic function Hitachi Central Research Laboratories. (K. Takahashi)
Control of long range periodic structures and super-structures of surface-nano-space and investigation of their reaction characteristics Nippon Steel Corp. (M. Sakashita)

A new material containing defect clusters which exhibits a unique photo-refractive effect has been proposed. The phenomenon of changes in the photo-refractive index during illumination by light is called the photo-refractive effect. Control of non-stoichiometric defect structures, for example in $LiNbO_3$, and the arrangement of cluster assembles are important factors in creating high performance photo-refractive materials. In order to create these materials, a fabrication technology to control non-stoichiometric defect-clusters has been established. Investigations of the behavior of electrons and impurities in defect-clusters are on going. High performance materials thus created will be applied to the fabrication of new devices for processing of optical information and for optical computing systems [2,3].

In order to evaluate optical characteristics of the periodic nano-spaces, new Brewster-reflection spectroscopy has been developed and confinement in nano-space in layered materials has been investigated [4].

In the research concerning analysis of electrical structures of interface nano-space, non-linear varistor characteristics in ZnO have been investigated. For this purpose, a special evaluation system equipped with SEM with a temperature controlled sample stage and micro needle electrodes has been developed. Segregation of additive Bi and

Mo ions at the grain boundary nano-space regions of ZnO varistor was revealed by μ-AES and their effect on the chemical bonding state and electronic state at the grain boundary was suggested [5].

Long periodic-structures and super-structures of surface-nano-space have been fabricated using sputtering methods to form TiO_2 islands on sapphire substrates. Measurements of surface charge distributions by multi-mode AFM have been performed [6].

(2) Materials development in the molecular lab.

Four research subjects in the molecular lab have been defined. These are shown in Table 2. Syntheses of new materials including inorganic clusters, semiconductor clusters, organic clusters and other complexes are being performed.

Table 2 Research Subjects in Molecular Lab.

Control and rearrangement of inorganic clusters and investigation of optical function National Research Institute for Metals (N. Koguchi)
Size control of solid clusters and investigation of electrical functions University of Telecommunication (S. Nozaki)
Atomic layer control of coupled clusters and investigation of coulomb blockade phenomena Institute of Physical and Chemical Research (Y. Aoyagi)
Control of periodic structures of organic clusters and investigation of their optical, electrical and combined functions Tokyo University of Agriculture and Technology (S. Miyata)

In the research on the control and rearrangement of inorganic clusters and related optical functions, equipment for nano-space control has been developed. This allows structural evaluations of 10-100 nm size GaAs clusters on GaAs or AlGaAs. Characteristics of absorption layer on single crystal surfaces are being investigated [7].

Technology for controlling solid clusters has been studied by developing equipment for deposition of solid phase Si and Ge clusters by evaporation in gas atmospheres. Nano-particles about 5 nm in diameter have been deposited and blue light emission has been observed [8].

For fabricating coupled clusters like coupled quantum dots and quantum wires, atomic layer manipulation, self organization, and conventional electron beam lithography techniques are being explored. Optical and electrical properties of the coupled clusters are being examined with an emphasis on coulomb blockade phenomena [9].

In the research of control of periodic structures of organic clusters, equipment for automatic synthesis of cage-molecules has been developed. High productivity of 7% for cage molecules could be achieved. The equipment can be operate for 6 hrs continuously [10].

(3) Development of theory and basic technology for nano-space research.

In close cooperation with the atom and molecular lab research, fundamental theoretical research and development of common basic process technologies are being performed for concave (atom lab) and convex (molecular lab) structural formations. The research projects related to the theory and basic technology and their principal investigators are listed in Table 3.

Table 3 Research Subjects in the Group of the Development of Theory and Basic Technology

Basic theoretical investigation and fundamental measurements of nano-space materials science Electrotechnical Laboratory (H. Okushi)
Study of evaluation methods for nano-space structures and functions University of Library and Information Science (J. Isoya)
Establishment of cluster science by ion beam engineering methods and investigation of fundamental s of nano-space lab Ion Engineering Institute Corp. (M.Watanabe)
Fundamental research of generation of cluster beam and their application to creation of new materials Kyoto University (N. Imanishi)
Investigation of new application fields of nano-space materials Kobe University (T. Minemoto)
Study of the application of nano-space in crystalline materials for optical devices Tokyo Woman's Medial College (Y. Sakurai)
Design of nanospace interfaces between biomolecules and inorganic materials for the generation of bioelectronics function Okayama University (H. Shinohara)

In basic theoretical research, new quantum material science will be established by applying a first principle quantum treatment. Simulation of nano-space lab is going on by using the model of defects in a-Si:H. Changes in electronic structure under optical excitation and calculation of g-value electron spin centers formed by dangling bonds will be studied [11].

By using the pulsed ESR technique, both the arrangement of H_2O molecules around hydrogen atoms trapped in the cavity of zeolite network and the size of micropores in a-SiO_2 network have been determined with the accuracy comparable to the X-ray diffraction method [12].

Organic and inorganic hetero-nanostrucures have been formed. Size effects of exitons is investigated. Nano boxes and nano sheets composed of organic molecular crystal of copperphthalociyanyne (CuPc) and amorphous ceramics of titanium oxide (TiOx) and silicon dioxide(SiO_2) were formed. Quite different phenomena of CuPc molecular exciton between structures of CuPc-SiO_2 and CuPc-TiOx have been observed. [13].

A novel ion beam process technique for unique nano-space formation has been developed. This is called gas-cluster ion beam technology. Techniques for generating cluster ion beams from gas phase materials such as Ar, O_2, N_2 and reactive gases have been developed [14]. The gas cluster ion beam processing is expected to be suitable as a material processing technology for nano-space formation because the bombarding effects occur under equivalently low energy and high density due to multiple collisions between the constituent atoms of the cluster and the substrate atoms. Their characteristics are low energy and high lateral sputtering effect (more than 100 times higher than for monomer ions), very low space charge effect and low damage surface treatment. Surface smoothing is an important characteristic which might have effective application to nano-space structure formation. These new basic technologies are expected to be established.

In the study of new application fields of nano-space materials, wavelet transformation of pattern information by optical systems is being studied [15]. In order to produce suitable optical characteristics for this purpose, doping effects of Si in $BaTiO_2$ and $Bi_{12}SiO_{20}$ are being studied and photo-refractive characteristics are being investigated.

Hydrophilic/hydrophobic microdomain structure (domain spacing: 15-20 nm) has been formed by block copolymers composed of 2-hydroxyethylmetancrylate (HEMA) and styrene. This structure has proved to induce platelets functional change and prevent platelets activation. [16].

Nanoscale layers of conducting polymers were prepared around redox enzyme molecules on electrode surfaces and were applied to electric interfaces to perform the smooth electron transfer and to control the enzymatic function [17].

PROSPECTS OF NANO-SPACE LABORATORY

The prospects of nano-space laboratory and materials development are shown in Fig. 2. Emphasis of the research project is put on the creation and evaluation of nano-space lab, the control of electrons and atoms in the nano-space region. The evaluation of related phenomena, the establishment of theoretical treatment of nano-spaces and the development of their applications are also important tasks. New organic and inorganic bio-materials will be studied with respect to the nano-space lab concept.

The fundamental research in this project could contribute new intelligent materials synthesis. It is expected that development of an optical device system for super-parallel information processing, and development of an algorithm for a phase conjugated mirror with non-linear optical characteristics will be accomplished. These advances will be followed by the development of new quantum devices, new optical devices and neuro-computer materials.

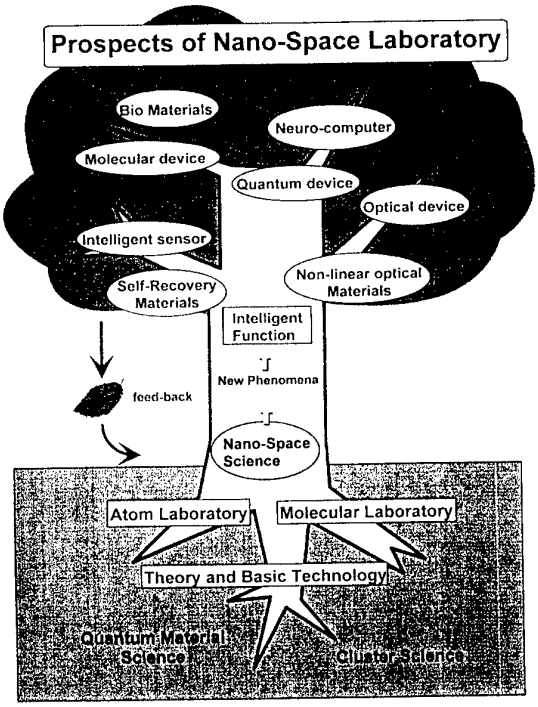


Fig.2 Prospects of nano-space laboratory and the fields of application

REFERENCES

[1] I. Yamada, "Nano-Space Laboratory and Materials Development", Proc. the 3rd Asia-Pacific Workshop on Intelligent Materials & the 4th Symposium on Intelligent Materials, (The Society of Non-Traditional Technology Intelligent Materials Forum, Tokyo, 1995) pp.112-114.

[2] K. Kitamura, "Crystal Growth of Nonstoichiometric Oxide Materials Using Double Crucible CZ Method", Ceramic Transaction Series, (in press).

[3] N. Iyi, K. Kitamura, Y. Yajima, S. Kimura, Y. Furukawa and M. Sato, "Defect Structure Model of MgO-Doped $LiNbO_3$", J. Solid State Chemistry, 18 (1995) 148.

[4] F. Minami, T. Kuroda, M. Hayashi, K. Inoue, K. Yoshida and H. Fujiyasu," Excitonic Structures in II-VI Super Lattice Observed by Brewster-Angle Reflectance", J. Appl. Phys., 76 (1994) 553.

[5] S. Tanaka, K. Takahashi, I. Sakaguchi and J. Tanaka, " Chemical Compositions of Grain Boundaries in ZnO Varistors", Proc. Inter. Conf. on Electronic Components and Materials/Sensors and Actuators (ICECM-ICSA '95), (1995) pp.415-418

[6] M. Sekoguchi, S. Miyajima, T. Sakon, K. Shimanoe and M. Sakashita," Evaluation of Adhesion Forces in Liquid with on Atomic Force Microscope", J. Adhesion Science and Technology (to be published).

[7] S. Tsukamoto and N. Koguchi, "Surface Reconstruction of Sulfur-Terminated GaAs(001) Observed During Annealing Process by Scanning Tunneling Microscopy", J. Crystal Growth, 150 (1955) 33.

[8] S. Nozaki, S. Sto, H. Ono and H. Morisaki, "Blue-Light Emission From Silicon Ultra fine Particles", MRS Symposium Proc., 351 (1994) 399.

[9] H. Isshki, Y. Aoyagi, S. Iwai, T. Meguro and T. Sugano, "Characterization of GaAs/GaAsP Quantum Wire Structures Fabricated by Atomic Layer Epitaxy", J. Appl. Phys., 78(12) (1995) 7277.

[10] Y. Hashimoto and S. Miyata, "Preparation and Characterization of Poly (arylamine sulfornes) and Poly (arylether sulfones) Carrying the C_{61} Fulleroid Pendant Group", Chem. Mater., 6 (1994) 2023.

[11] N. Orita and H. Katayama-Yoshida, "Electronic Structure and Dynamics of Intrinsic Defects in Hydrogenated Amorphous Silicon by Abinitio Molecular Dynamics", Proc. 22nd Inter. Conf. on Physics of Semiconductors, Ed. by D. J. Lockwood (World Scientific, 1995) 2693

[12] J. Isoya, "Structure Determination by Using Pulsed ESR", Proc. Inter. Conf. On Materials and Measurements of Molecular Electronics (to be published).

[13] J. Takada, "Size Effects of Molecular Exitons in Organic-Inorganic Hetero Nanostructures", Jpn. J. Appl. Phys., 34 Suppl.34-1 (1995) 158.

[14] I. Yamada, J. Matsuo, Z. Insepov and M. Akizuki, "Surface Modification by Gas Cluster Ion Beams", Nucl. Instr. and Methods. in Phys. Res. B106 (1995) 165.

[15] J. Joseph, T. Oura and T. Minemoto, "Optical Implementation of a Wavelet Transform by the Use of Dynamic Holographic Recording in a Photorefractive Materials", Appl. Opt., 34, No.20 (1995) 3997.

[16] T. Okano, K. Suzuki, N. Yui, Y. Sakurai and S. Nakahama, " Prevention of changes in platelet cytoplasmic free calcium levels by interaction with 2-hydroxyethyl methacrylate/styrene block copolymer surfaces", J.Biomedical Materials Research, 27 (1993) 1519.

[17] H. Shinohara, "Design of Nanospace Interfaces for the Performance of Electrochemical Communication between Redox Enzymes and Electrode Systems", Proc. the 3rd Asia-Pacific Workshop on Intelligent Materials & the 4th Symposium on Intelligent Materials, (The Society of Non-traditional Technology Intelligent Materials Forum, Tokyo 1995) pp.133-135.

NANOSCALE PROCESSING BY GAS CLUSTER ION BEAMS -NOVEL TECHNIQUE IN ION BEAM PROCESSING-

Isao YAMADA and Jiro MATSUO,
Ion Beam Engineering Experimental Laboratory
Kyoto University, Sakyo, Kyoto 606, Japan,

Abstract Gas cluster ion beam techniques have been developed for nanoscale surface processing. Bombarding process fundamentals are distinctly different than those produced by conventional monomer ion irradiation. The unique characteristics of gas cluster ion bombardment are low energy and high current effects. Multiple collision during the bombardment solid surface produces complicate nonlinear effects. Very shallow ion implantation, low damage and high rate lateral sputtering and low temperature thin film formation are suggested application fields and have been experimentally demonstrated.

I. INTRODUCTION

Recent trends in processing require the control of surface structure at the order of nanometer size. For these processes, necessary ion beam energies are in the range of a few hundreds of eV. These low energy ion beams are very difficult to produce at high intensity because of their space charge effects. One of the possible solutions to obtain low energy and high current ion beams is to use cluster ion beams. We have proposed a gas cluster ion beam technique [1-3]. The principles of this technique are quite different than those of conventional ion beam techniques. In order to investigate fundamental characteristics of the effects of gas cluster ion bombardment on solid surfaces, three different gas cluster ion beam systems with maximum acceleration voltages of 10kV, 30kV and 200kV have been designed and constructed [4]. Unique damage production mechanisms [5], very high yield sputtering [6], low damage surface cleaning [7], atomically smooth surface formation [8] and low temperature surface oxidization [9] have been demonstrated. Molecular dynamics (MD) studies of cluster ion bombardment have also been performed to understand cluster ion beam bombardment phenomena such as strong damage production, high temperature effect, high pressure effect, lateral sputtering effect, etc. [10].

This paper reviews recent results concerning surface processing by gas cluster ion beam bombardment. Design principles of gas cluster ion beam equipment and characteristics of gas cluster bombardment processes will be shown. Experimental studies of atomic level surface processing, shallow ion implantation, high yield sputtering, surface smoothing and low temperature surface oxidization will be discussed.

II. GAS CLUSTER ION BEAM SPUTTER EQUIPMENT

Figure 1 shows a schematic diagram of the 30 kV gas-cluster ion beam sputtering equipment. Cluster ion beams from gaseous materials such as Ar, N_2, O_2, CO_2, N_2O and SF_6 are generated by expanding the corresponding gases through a Laval nozzle with 0.1 mm throat diameter into a high-vacuum chamber and then collimating by a skimmer. Subsequent ionization is performed by electron bombardment. Mass analysis is accomplished by an electrostatic retarding potential method (deceleration) which makes use of fact that clusters of different size possessdifferent kinetic energies. Measurements of cluster sizes and structures have been done using electron

0-8194-2165-0/96/$6.00

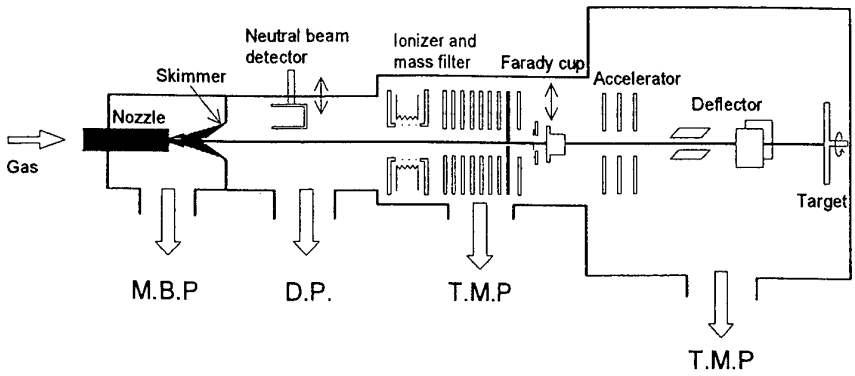


Fig.1 Schematic diagram of 30kV gas-cluster ion beam equipment.

diffraction and retarding electric field methods [2]. Mass selected cluster ion beams are then electrostatically accelerated by potentials of up to 30 keV.

The size of the Ar cluster ions ranges up to several thousand atoms with an average size of about 3000 atoms. Monomer ions are suppressed by applying a low extraction voltage and adjusting the electrostatic lenses. The ion current of mass-separated Ar clusters has been measured as a function of source pressure. Below 1000 Torr, cluster ions are not observed and only monomer ions are found in the ion beam. The cluster ion current increases linearly with the source gas pressure. The threshold pressure for cluster formation is found to be around 1000 Torr [4]. Electrostatic mass filtering by a retarding field method has an advantage because the equipment required can be simple and light compared to a magnetic field based analyzer. In the present equipment, when the retarding potential is set at 200 volts, an Ar cluster beam with more than 3000 atoms/cluster can be extracted from the source and impacted upon the substrate. The highest cluster ion beam current obtained has been about 200 nA. This current corresponds to an Ar atom flux of 1.9×10^{15} molecules/s/cm^2.

III. LOW DAMAGE BOMBARDMENT EFFECTS

Range and damage produced by ion bombardment depend primarily on ion beam energy, ion doses and ion-substrate materials combinations. In the case of cluster ion beam bombardment, they depend also on cluster sizes. In cluster ion bombardment, it has been expected that low energy bombardment and high mass transport effects should be produced. Low energy effects by cluster ion bombardment have been confirmed experimentally by using a 200 keV cluster ion beam system with an E×B mass analyzer. Bombardments on Si(100) surfaces by 150 keV cluster ions and by 50,100,150 keV Ar monomer ions have been compared. The size distribution of the Ar cluster ion beam ranged from 1000 to 5000 atoms. The peak size was approximately 3000 atoms/cluster. Doses of

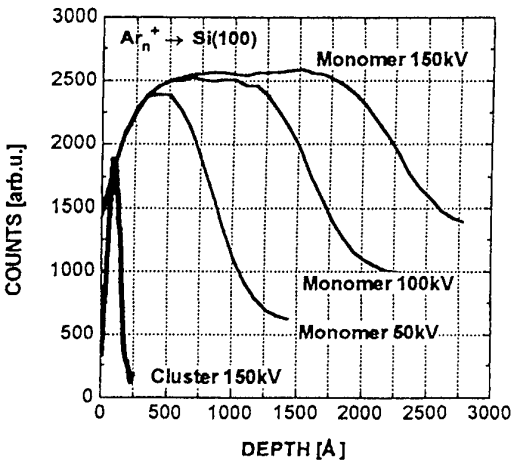


Fig.2 Channeling spectra of Si (100) surfaces bombarded with a 150 keV Ar cluster ion beam and by 150, 100 and 50 keV Ar monomer ion beams.

cluster and monomer ions were 2.5×10^{13} and 1×10^{15} ions/cm^2, respectively. The Ar cluster ion beam current was 5 nA. Figure 2 shows RBS spectrum from Si(100) substrates bombarded by cluster ions and monomer ions. The thickness of the damaged layer due to implantation by the 150 kV cluster ions was less than 25 nm, which was much shallower than in the case of monomer ion bombardment at the same energy.

Acceleration voltage dependence of damage produced in Si substrates by Ar cluster ion bombardment has been measured by RBS and channeling methods [11]. Ar cluster ion beams with mean cluster size of 3000 atoms/cluster were implanted into thermally grown SiO_2 layers of 100 and 200 Å thickness on Si substrates. A Si substrate surface is easily oxidized, especially by cluster ion beam bombardment, even under vacuum of 10^{-7} Torr. In order to prevent measurement error due to oxide formation, substrate surfaces covered by SiO_2 were used. The number of displaced atoms below the 100 Å of grown SiO_2 increased with increasing implantation doses of the cluster ion beam and cluser sizes. For the surface bombarded with the cluster ion beam of the sizes less than 100 atoms/cluster, very little change could be seen. Figure 3 shows the measurement results obtained by RBS. These results indicate that cluster ion bombardment induced damage influences by the cluster sizes evern at the same total energy per cluster. However, cluster ion implantation can be possisble much shallower implantation range than by monomer ion beams accelerated to the same voltage.

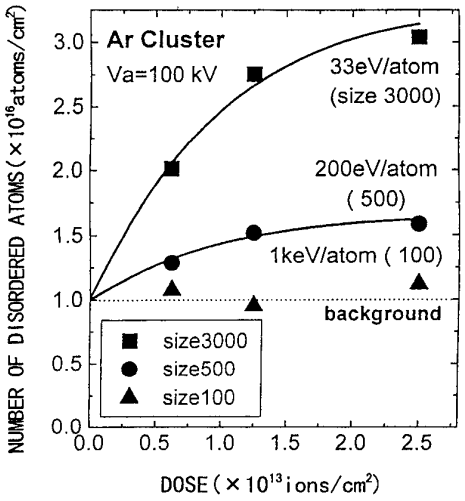


Fig.3 Dose dependences of the number of disordered atoms on Si substrate surface. Bombardments were made by Ar cluster ion beams of 100keV with the three different cluster sizes of 100, 500 and 3000 atoms/cluster through thermally grown SiO_2 layers of 100 Å thickness on Si substrates.

IV. LATERAL SPUTTERING EFFECTS

A lateral sputtering effect has been observed due to bombardment by large size cluster ion beams. This effect produces extremely high sputtering yields more than two orders of magnitude higher than those of monomer ions. The lateral sputtering effect has been confirmed by measuring angular distribution of the sputtered atoms. Figure 4 shows the angular distribution of atoms sputtered from a Cu target by an Ar cluster ion beam and by a monomer ion beam. Sputtered atoms were collected on two different substrates, Si and C, in order to eliminate effects due to different sticking coefficients for different substrate materials. For cluster ion bombardment, considerable amounts of sputtered atoms were collected at the angle close to the direction parallel to the

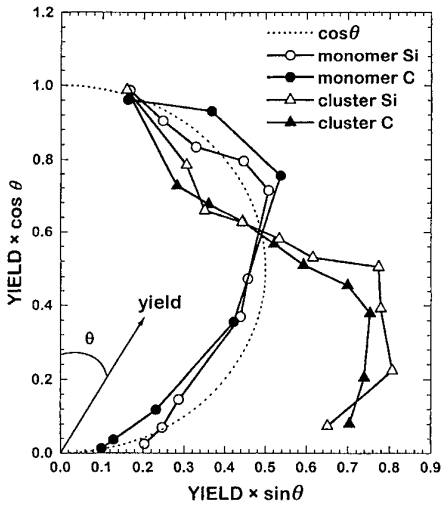


Fig.4 Angular distribution of atoms sputtered from a Cu target by an Ar cluster ion beam and by a monomer ion beam.

MD results [10,14].

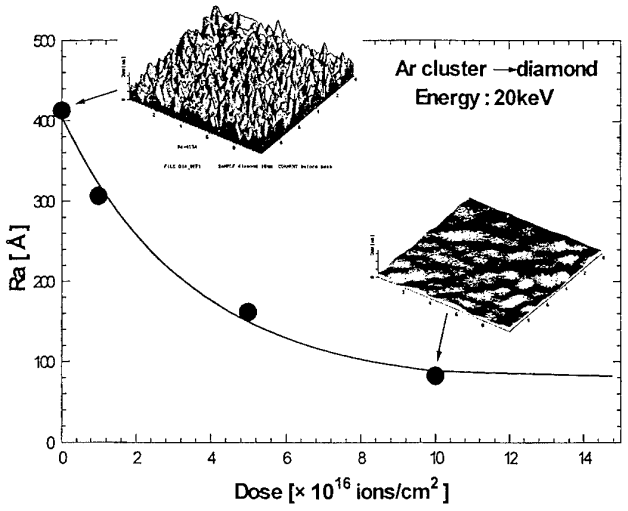


Fig.7 Average surface roughness (Ra) and sputter depth in a Cu coated Si substrate irradiated by 20 kV Ar cluster ion beams.

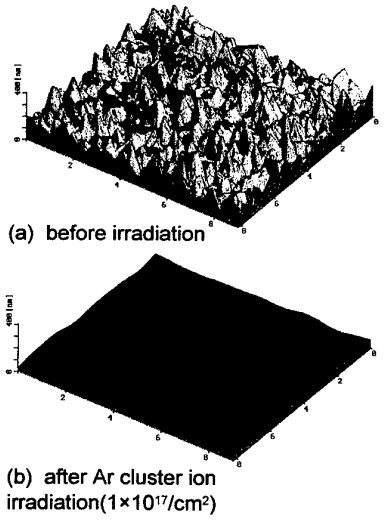


Fig.8 Atomic force image of diamond film surface irradiated by 20 keV Ar cluster ion beam

(c) Surface cleaning

A high removal rate of surface impurities by cluster ion bombardment has been confirmed in connection with low damage effects [15]. Figure 9 shows the dose dependence of normalized impurity concentrations on silicon substrate surfaces irradiated with cluster and monomer ions. Silicon wafers were intentionally contaminated with 1×10^{15} Cu atoms/cm^2 and 6×10^{21} Ni atoms/cm^2 and were irradiated with 20 keV Ar and 10 keV CO_2 ions, respectively. Compared with the smaller reduction of impurity concentration of about 4 % in the case of monomer irradiation, 80 % of the impurity atoms were removed from the surfaces after irradiation with Ar and CO_2 cluster ions at doses of 6×10^{14} and 2×10^{15} ions/cm^2, respectively. The impurity concentration decreased exponentially with increasing doses.

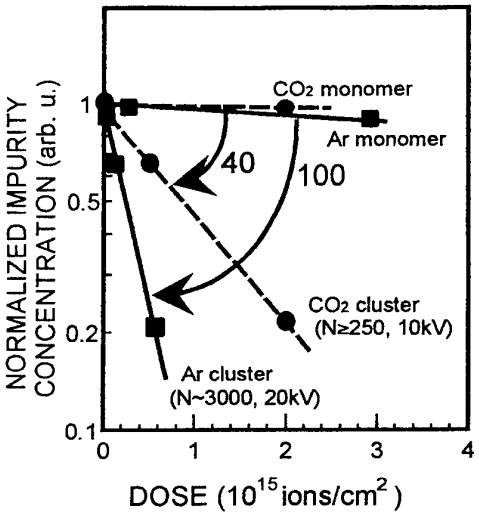


Fig.9 Dose dependence of normalized impurity concentration on Si substrate surfaces.

The removal rates of impurities by Ar and CO_2 cluster ion irradiation were 40 and 100 times higher than by monomer ion irradiation, respectively. The difference corresponds to approximately the difference in sputtering yields. Since the mean sizes of the Ar and CO_2 cluster ions were 3000 and 1500, the average energies per constituent atom were approximately 7 eV and 2 eV for Ar and CO_2 cluster ions, respectively. Thus, low irradiation damage can be expected.

(d) Thin film formation

substrate surface. Atoms sputtered by monomer ion beam exhibit cosine law behavior.

(a) Sputtering yield

The sputtering yield has been observed to have a strong dependence on the target species for Ar clusters with an energy of 20 keV. Figure 5 shows the dependence on the atomic number of sputtering yields for 20 keV Ar cluster ions. With the same equipment, Ar monomer ions have also been produced, and the same targets have been sputtered . These results show a normal tendency of the sputtering yield on the atomic number of the target materials. Figure 5 also indicates reactive sputtering yields of Si and W due to SF_6 beam bombardment shown in comparison with the yields due to Ar cluster beam sputtering. Sputtering yields of Si and W are considerably higher than those by the Ar cluster ion bombardment. Figure 6 shows an example of a sputtered Si(100) substrate irradiated to 3×10^{15} ions/cm^2 by 20 keV SF_6 cluster ions with mean cluster size of 2000 atoms. The etched layer was 600 nm deep. The substrate surface was covered by a patterned SiO_2 layer of thickness 300 nm. In this materials combination between ion and substrate, the sputtering yield is calculated to be 10,000 atoms/cluster ion. The yields of monomer ion beam sputtering agreed well with the predicted and measured values [12].

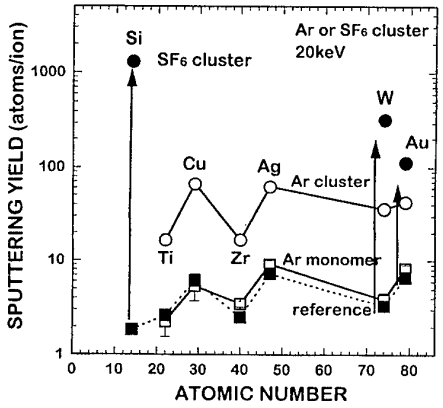


Fig.5 Dependence on the atomic number of sputtering yields due to 20 keV Ar cluster ions and monomer ions. Reactive sputtering yield of Si and W due to SF_6 cluster ion beam bombardment is also shown.

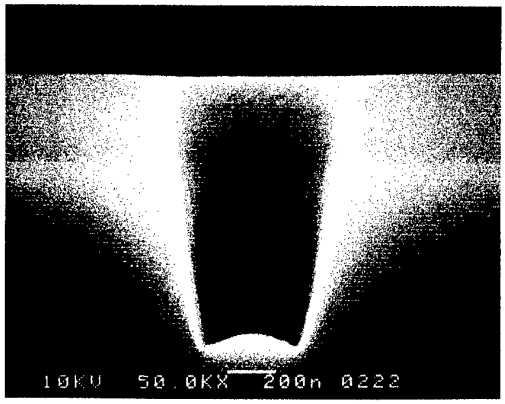


Fig.6 Cross-sectional secondary electron microscope photographs of a Si substrate etched by 20 keV SF_6 cluster ion beams at a dose of 10×10^{15} ions/cm^2.

(b) Surface smoothing

Changes in surface roughness after cluster ion bombardment have been measured by an atomic force microscope. Figure 7 indicates the experimental average surface roughness (Ra) and sputter depth in a Cu coated Si substrate which was irradiated with Ar cluster ions accelerated to 20 kV. The cluster size was approximately 3000 atoms/cluster. The roughness (Ra) decreased from an initial value of 5.8 nm monotonically with sputtering time and saturated at a value of 0.8 nm. In the case of monomer ion bombardment, the minimum value of Ra was 4.9 nm. The roughness decreased initially at low irradiated fluences and then subsequently increased at higher doses.

In order to demonstrate etching of a hard material, CVD grown polycrystalline diamond has been treated. Figure 8 shows the results [13]. Surface roughness before irradiation was 400 nm. After Ar cluster ion bombardment, average roughness was reduced to 1.8 nm. For many other materials such as poly-Si, Cu, Pt, SiO_2, Si_3N_4 films and glass substrates, similar results have been obtained. This smoothing effect can be explained by the lateral sputtering which is suggested by

Very thin oxide layer formation by O_2 cluster ion beam bombardment on Si substrate surface has been studied. O_2 cluster ion beam doses at 10×10^{15} ions/cm^2 at 7 kV acceleration 11nm oxide layer could be formed to on room temperature substrate surface. From C-V characteristic measurement, it has been shown that the damage produced by cluster ion bombardment could not influenced in the characteristics. O_2 cluster assisted deposition has also been tried during Pb deposition. Extremely smooth surface PbO film could be formed [16].

V. CONCLUSIONS

Characteristics of gas cluster bombardment effects have been demonstrated. The results show that beams of clusters of a few hundred atoms with an energy of a few hundred keV create thinner damaged layers on Si substrate surfaces than do monomer ion beams at the same energies. Surface smoothing, surface cleaning and very high yield sputtering by cluster ion bombardment were also observed on various kinds of materials. These effects are believed to be caused by lateral sputtering. In a low energy region, extremely low damage surface cleaning and highly reactive thin film formation have been demonstrated. These results show that cluster beams exhibit unique ion-surface interactions. They can be applied to modify a wide variety of materials and represent promising tools for nanometer scale surface processing.

REFERENCES

[1] I.Yamada, Proc. 14th Symp. on Ion Sources and Ion-Assisted Technology, Tokyo, (The Ion Engineering Society of Japan, Tokyo,1991) pp.227-235.

[2] I.Yamada, W.L.Brown, J.A.Northby and M.Sosnowski, Nucl. Instrum. & Methods, B79 (1993) 223.

[3] G.H.Takaoka, G. Sugahara, R. E. Hummel, J. A. Northby, M. Sosnowski and I. Yamada, in Materials synthesis and processing using ion beams, edited by R.J.Culbertson O.W.Holland K.S.Jones and K.Maex, (Mat. Res. Soc. Symp. Proc. 316 Pittsburgh PA, 1994) pp.1005-1010.

[4] J. Matsuo, H. Abe, G. H. Takaoka and I. Yamada, Nucl. Instr. and Methods, B99 (1995) 244.

[5] J.Matsuo, D.Takeuchi, A.Kita and I.Yamada, E-MRS 1995 Spring Meeting, May 1995, Strasbourg, France, Symposium C and J Paper J-I.5, Nucl. Instr. and Methods, in Press.

[6] I. Yamada, G.H. Takaoka, M. Akizuki, C.E. Ascheron and J. Matsuo, Ion Implantation Technology-94, edited by. S.Coffa, G.Ferla, F.Priolo E.Rimini (Elsevier Science B.V., Amsterdam 1995) pp.1002-1005.

[7] M. Akizuki, J. Matsuo, H. Harada, S. Ogasawara, , A. Doi, K.Yoneda, T.Yamaguchi, G.H. Takaoka, C.E. Ascheron and I. Yamada, Proc. 7th Int. Symp, on Small Particles and Inorganic Clusters, Kobe 1994, Surface Rev. Lett., in Press.

[8] T. Yamaguchi, J. Matsuo, M. Akizuki, C.E. Ascheron G.H. Takaoka and I. Yamada, Nucl. Instr. and Methods, B99 (1995) 237.

[9] M. Akizuki, J. Matsuo, S. Ogasawara, H. Harada, A. Doi, and I. Yamada, Extended abstract of the 1995 International Conference on solid State Devices and Materials, Osaka, (Japan Society of Applied Physics, Japan, 1995) p.31. Jpn. .Appl. Phys., in Press.

[10] Z. Insepov, M. Sosnowski and I. Yamada, in Laser and Ion Beam Modification of Materials, edited by I.Yamada, H.Ishiwara, E.Kamijyo, T.Kawai, C.W.Allen and C.W.White (Elsevier, Amsterdam, 1994) pp. 111-118.

[11] J. Matsuo, D.Takeuchi, A.Kita and I.Yamada, E-MRS 1995 Spring Meeting, May 1995, Strasbourg, France Symposium C and J Paper J-I.5.J, Nucl. Instr. and Methods, in press.

[12] N.Laegreid and G.K.Wehner,J.Appl.phys.,32 (1961) 365.

[13] A.Yoshida, M.Deguchi, M.Kitabatake, T.Hirao, J.Matsuo, N.Toyoda and I.Yamada, E-MRS 1995 Spring Meeting, May 1995, Strasbourg, France Symposium C and J Paper, Nucl. Instr. and Methods, in press.

[14] Z. Insepov and I. Yamada, Proc. 13th Conf. on Appl. of Accelerator, Denton, 1994, Nucl. Instr. and Methods, B99 (1995) 248.

[15] M. Akizuki, J. Matsuo, H. Harada, S. Ogasawara, A. Doi, and I. Yamada, Proc. Int. Conf. on Nano-Cluster and Granulars Materials (NCGM'95), Sendai, 1995, Materials Science and Engineering A (Elsevier Amsterdam 1996), in Press.

[16] Akizuki, H. Harada, S. Ogasawara, A. Doi, J.Matuo and I. Yamada, Proceedings of the JSPS Cnference on Cluster Ion Beam Processing, Kyoto 1996

Clusters assembled materials : a new class of nanostructured materials with original structures and properties

A. Perez, P. Melinon, V. Dupuis, J. Tuaillon, B. Prevel

Département de Physique des Matériaux,
Université Claude Bernard Lyon 1, F-69622-Villeurbanne, France

and M. Pellarin, J.L. Vialle, M. Broyer

Laboratoire de Spectroscopie Ionique et Moléculaire,
Université Claude Bernard Lyon 1, F-69622Villeurbanne, France

ABSTRACT

The low energy cluster beam deposition technique (LECBD) is used to produce nanostructured materials with original structures and properties. In this technique, clusters do not fragment upon impact on the substrate leading to the formation of granular films by nearly random stacking of incident clusters. Both nanostructured films and films of clusters embedded in various matrices are produced using this technique. The production and deposition of controled size distributions of free clusters are briefly described as well as the specific nucleation and growth process characteristic of the LECBD. In the second part of the paper are presented some characteristic examples of novel materials prepared by this technique. The formation and properties of films of covalent materials (C, Si) and metallic materials (Fe, Co, Ni) are presented to emphasize the memory effect of the free cluster structure in the first case and the effect of the nanocrystalline film structure through the magnetic properties in the second case.

1. INTRODUCTION

Cluster assembled materials form a new class of solid materials exhibiting original structures and properties. They can be obtained by random stacking of free clusters using the Low Energy cluster Beam Deposition Technique (LECBD)[1]. This technique consists to deposit neutral clusters having the very low energy gained in the supersonic jet expansion at the source exit (i.e : when using inert gas condensation cluster sources). In this case, clusters do not fragment upon impact on the substrate leading to a nearly random substrate "pavement" when the mean cluster size is high enough to limit their diffusion. Consequently, highly porous nanostructured thin films are systematically obtained by this technique with any kind of materials (metallic, covalent ...). In terms of atomic structure, the cluster assembled materials can be classified in between amorphous and crystalline solids. In fact, depending on the cluster source parameters, the incident free clusters exhibit well defined structures and geometries[1, 2]. Consequently, the characteristic length of the local order in the cluster assembled films will be the grain size, typically, and no long range order will be observed due to the random stacking of nanosize grains. This is different from amorphous materials in which the local order is limited to the first nearest neighbours. Moreover, at a nanoscale the grains are characterized by a non negligible number of atoms at the surface with respect to the number of atoms in the volume, with different local environements. As for the properties of cluster assembled materials, they can be influenced by the intrinsic structure of grains as well as by the interactions between grains. Confinement effects related to the nanosize of grains play also an important role on the electronic properties.

In this context, the LECBD technique is a well suited method to produce controled nanostructures. The structures of the incident free clusters are studied in flight using spectroscopy techniques such as photoionization, photofragmentation ...[3]. In a second stage, well characterized clusters are deposited on substrates in well defined conditions in order to control the nucleation and growth process. The key parameters are in this case : nature and size distribution of incident free clusters, nature and temperature of the substrate, vacuum conditions to control the pollution of clusters which generally are very reactive.

In this paper we report recent results on the specific nucleation and growth process characteristic of the LECBD deposition technique. Also, some significant examples of cluster assembled materials obtained using this technique are presented. In the case of covalent materials (carbon and silicon films) a memory effect of the free cluster structures and properties is evidenced, while in the case of transition metal films (Fe, Co, Ni), the specific effects related with the granular structure are observed via the magnetic properties.

2. EXPERIMENTAL PROCEDURE

Among various types of cluster sources we have chosen the laser vaporization source which allows to produce any kind of clusters even of the most refractory materials or complex systems (bimetallic, oxides ...)[4, 5]. A time of flight mass spectrometer coupled with a tunable laser for neutral cluster photoionization is mounted at the source exit perpendicularly to the

0-8194-2165-0/96/$6.00

cluster jet emited. Using this geometry the mass distributions of both ionized clusters directly produced in the source or photoionized neutral clusters can be continuously analyzed during the deposition of neutral clusters in the UHV-chamber on line with the source. Rather high deposition rates are required for deposition experiments in order to produce thick films (~ 100 nm) in reasonable times. For this purpose, special improvments of the Milani and De Heer type of source[5] allow us to obtain neutral cluster deposition rates measured with a quartz balance close to the substrate in the UHV chamber as large as 1Å/s to 1Å/minute, for any kind of materials, in the cluster size range from few atoms to one thousand of atoms, typically. Depending on the types of characterizations to be performed ex-situ on the cluster assembled films, a UHV transfer system or an amorphous carbon thin layer (5 to 10 nm) coating can be used for sample transfers.

3. NUCLEATION AND FILM GROWTH

The so-called DDA model (Deposition-Diffusion-Aggregation) (6) can be used to describe the formation of cluster assembled films. The three stages are defined as follows :

- Deposition : particles are deposited at randomly chosen positions of the surface at a flux F per lattice site per unit time. Taking into account their very low energy they do not fragment upon impact on the substrate.
- Diffusion : all particles and clusters (sets of connected particles) are chosen at random and attempted to move north, east, south or west by one lattice constant per unit time. The probability that they actually move is proportional to their mobility which is assumed to be given by $D_S = D_1 s^{-\gamma}$, where s is the number of particles in the cluster, D_1 is the diffusion coefficient for a monomer (s = 1), and the parameter γ characterizes the dependence of D_S on cluster size.
- Aggregation : if two particles come to occupy neighboring sites, they (and therefore, the clusters to which they belong) stick irreversibly.

Using this DDA model it was possible to simulate the morphologies of various type of cluster deposits and to test the role of some key parameters such as : the incident free cluster size and flux, the diffusion effects which are influenced by the nature and the size of incident clusters as well as by the nature and temperature of the substrate... Finally, this model generates a wide variety of fractal structures characteristic of different models such as percolation[7, 8], diffusion limited aggregation (DLA)[9, 10], or cluster-cluster aggregation (CCA)[11].

A particularly interesting effect which come out from cluster deposition experiments and simulations is the existence of a critical size N_C (~ few thousands of atoms) of the supported particles above which the coalescence effects become negligible as well as the diffusion of particles. In this particular case, the cluster deposit consists on a nearly random substrate "pavement" by the incident free clusters. The percolation threshold indicating the transition from a discontinuous to a continuous film is reached for a coverage rate of 50 % as predicted by the 2D-percolation model[12]. Above this threshold the thick film growth takes place by random stacking of clusters. Consequently, in this particular regime, nanostructured films are systematically obtained whatever the nature of materials (covalent, metallic). Due to the random stacking process of clusters, these films are nanoporous with densities as low as 50 to 60 % of the densities of the corresponding bulk materials and the grain size can be more or less controled from the deposition parameters : size distribution and flux of incident clusters, vacuum conditions which determine the cluster surface pollution capable to influence the coalescence and sticking effects of clusters, nature, structure, and temperature of the substrate. One has to remember that only neutral clusters are used for the LECBD experiments under consideration in this work, as mentioned in section 2. Thus, charge effects which could influence the nucleation and growth process are not considered contrary to ionized cluster depositions. The nanostructured morphologies of various cluster assembled films obtained by depositions of size controled distributions of rigid clusters (relatively high melting temperature materials) of different materials (covalent : C, Si and metallic : Sb, Fe, Co, Ni) on different substrates (amorphous : a-C, glass and crystalline : Si wafers, sapphire, graphite) at room and liquid nitrogen temperatures, have been recently studied[1]. The observations performed by complementary techniques (Transmission Electron Microscopy (TEM)), Scanning Tunel Microscopy (STM, AFM)[13] are in a rather good agreement with the simulated morphologies deduced using the DDA-model in a coverage rate range up to about 20 %, typically. Additional TEM and X-ray (diffraction (GIS) and absorption (EXAFS)) measurements on thick films (up to several hundreds nm) have confirmed the existence of the granular and highly porous structure characteristic of the LECBD deposits, independently of the deposited thickness. Random stacking of well crystallized grains with rather sharp size distributions are the main nanostructural characteristics of these films. About the above mentioned critical size Nc, it has been roughly estimated around 2500 atoms for Sb-cluster deposited on graphite (HOPG) at room temperature and between 1000 and 2000 atoms for transition metal clusters (Fe, Co, Ni) deposited on a-C substrates at 300 K. In this size range around few thousands atoms corresponding to cluster diameters of the order of few nanometers we know from the gas phase studies that they exhibit well defined atomic structures and geometries (i.e. icosahedral structures for Co or Ni-clusters)[14] depending on the source regime. Consequently, in the case of film growth by random stacking of these elementary bricks, the problem of the memory effect of the free cluster structures and properties in the thick films is seriously posed. The existence of such a memory effect has been clearly observed in the case of carbon fullerene assembled films[15] discussed in more details in the next section. However, no such clear evidence of the memory effect can be reported in the case of metallic cluster

assembled films for some well understandable reasons discussed in section 4.2. concerned with the particular case of transition metal (Fe, Co, Ni) films and related magnetic properties.

Finally, by considering the particular nucleation and growth process characteristic of the LECBD technique with a possible memory effect of the free cluster specific structures and properties, promising results in the production of novel materials are expected as illustrated in the next sections.

4. EXAMPLES OF NOVEL MATERIALS WITH ORIGINAL STRUCTURES AND PROPERTIES PRODUCED BY LECBD

4.1. Carbon and silicon films

The electronic structures of carbon clusters in the form of cage molecules (fullerenes) are strongly size dependent because of the carbon plan curvature[16]. Consequently, hybridizations from purely sp^3 (Diamond like) to sp^2 (graphite like) are predicted. For example, in the first predicted fullerene : C_{20}, having the form of a dodecahedron, each carbon atom is threefold bonded with an interorbital angle ($\Theta_{\sigma\pi}$) of 110° 50' very close to those in diamond (109° 28'), thus leading to an sp^3-hybridization. On the opposite, large carbon cluster C_n (~ n > 300 atoms) exhibit the graphite structure ($\Theta_{\sigma\pi} = 90°$, sp^2). Intermediate hybridizations are calculated for medium size fullerenes such as, for example, $sp^{2.3}$ for the well known C_{60}[16].

Experiments consisting in depositing on various substrates at room temperature three different size distributions of carbon clusters centered around C_{20}, C_{60} and C_{900}, have been performed[15, 17]. These distributions nearly gaussian in shape were sufficiently narrow to exhibit a strong sp^3-character in the case of those centered around C_{20}, a strong sp^2-character for those centered around C_{900}, and an intermediate sp^2-sp^3 character for the C_{60}-centered distribution. The corresponding films (~ 100 nm thick) were systematically analyzed using various complementary techniques such as : Raman spectroscopy, Electron energy loss spectroscopy (EELS) and X-ray absorption near edge structure (XANES). All these measurements converged to confirm the sp^3, sp^2 and intermediate character of the C_{20}, C_{900} and C_{60}-films, respectively. This was the first evidence of a memory effect of the free cluster structures in the films. Moreover, the properties of the films were in agreement with the more or less diamond or graphite character of the films. For example, optical absorption spectra, electrical condivities[18] and hardnesses[19] were coherent with the above mentioned results emphasizing the capability of the LECBD technique to produce materials with adjustable structures and properties. In terms of morphology, AFM-observations of the deposits[19] showed in all cases the granular structure while the nanoporous character was confirmed by density measurements. In fact, density as low as about 1g/cm^3 was determined which can be compared to the value of about 2g/cm^3 generally found for diamond like carbon films obtained by other techniques (i.e. CVD).

Among various carbon films obtained by LECBD, the most fascinating is the C_{20} one because of its sp^3-character. In fact, in the size range around C_{20}, closed cages are probably much less stable that open curve graphitic sheets which minimize the number of adjacent pentagon rings. However, in our laser vaporization cluster source, the high sursaturation ratio involves a great number of cluster-helium gas collisions, allowing to stabilize metastable structures. Finally, we conclude that some metastable particles such as small fullerenes may be produced in our experimental device. This has been verified by changing the regime of the source (laser pulse intensity and pressure of injected He-gas), to control the balance between different isomers, in order to produce from comparable size distributions centered around C_{20}, two completely different materials : one of the sp^3-type and one of the sp^2-type[1]. As previously mentioned, each carbon atom in the C_{20}-fullerene has a dangling bond (threefold bonded). One can easily imagine the stabilization of these molecules on the substrate by associations via the dangling bonds. This assumption seems confirmed by the Raman spectroscopy measurments indicating a shift of the spectra (~ 130 cm^{-1} towards lower wave numbers) compatible with the hybrid misalignements between adjacent C_{20}-cages[17]. Finally, this materials with a well defined short range order in the form of C_{20}-dodecahedron and no long range order is a new sp^3-hybridized carbon form, different of an hypothetic amorphous diamond.

Comparable sets of experiments have been performed more recently with silicon since interesting cluster structures are predicted for this materials (Si_{20}, Si_{33}, Si_{45} ...)[20].

An interesting feature of these structures is the presence of large numbers of pentagonal rings at the origin of a rehybridization of Si and a subsequent change of the electronic structure with respect to the bulk material. As in the case of carbon, the silicon films prepared by LECBD were granular and highly porous. However, the Raman spectra were comparable to those of conventional amorphous silicon (a-Si) as shown in figure 1a, b despite a strong visible luminescence in red (fig. 1.f.) which is not the case of a-Si. This luminescence effect could be the signature of silicon participating to the pentagonal rings in the incident free clusters and the subsequent electronic structure modification. This hypothesis is supported by Raman spectroscopy measurements of a silicon clathrate sample (fig. 1.e.) the structure of which consists on a fcc-arrangement of Si_{20}-dodecahedrons with Si_{24} in between. Also, the comparison of XANES spectra obtained with various silicon forms (a-Si, LECBD-Si, Si-clathrate and crystalline Si) is an additional argument to support the previous hypothesis. Finally, with silicon using the

LECBD technique we obtain a novel metastable form which could be considered for future optoelectronic applications because of its intense red luminescence. In this context it will be interesting to compare this LECBD-Si with the luminescent nanoporous-Si produced by electrochemical method in which confinement effects and/or siloxene formation are involved to explain the red luminescence observed[21].

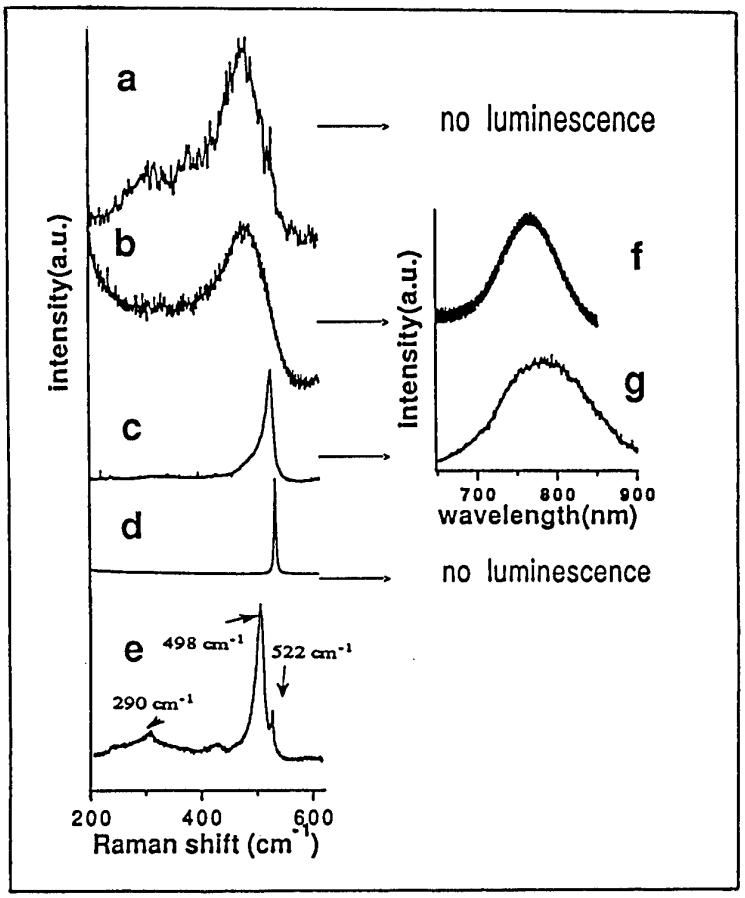


Figure 1 : First order Raman spectra measured at room temperature for various silicon samples : amorphous-Si (a) LECBD-Si (b), porous-Si (c), crystalline-Si (d) and clathrate-Si (e). For these measurements the excitation wavelength was 514.5 nm. (f) and (g) are the luminescence spectra of LECBD-Si and porous-Si, respectively, simultaneously recorded with the Raman spectra.

4.2. Fe, Ni and Co magnetic films

Magnetic nanostructures is a field of growing interest on account of the potential applications for dense memory devices. In this context, the LECBD technique could be by nature an original way to produce such nanostructured magnetic systems. Two different types of cluster assembled films have been produced. In the first case, selected size distributions of Fe, Co or Ni-clusters were deposited on various substrates at 77 and 300 K to produce granular films by random stacking of clusters. In the second case, incident clusters were embedded in coevaporated matrices (insulating : SiO_2 or non magnetic and conducting : Ag). Both types of samples were structurally characterized using TEM, GIS and EXAFS. The magnetic behaviours were studied using SQUID magnetometry (conventional and micro-SQUID techniques), ferromagnetic resonance (FMR), conversion electron Mössbauer spectroscopy (CEMS, in the particular case of Fe-samples) and magnetoresistance (in the particular case of clusters embedded in matrices) measurements.

In the case of films formed by random stacking of clusters, we used a very sensitive microSQUID detection technique to follow the magnetic properties as a function of the coverage rate, from isolated particles up to the thick films. This technique has been described in details elsewhere[22].

Incident free clusters were directly deposited in the window of the detector consisting on a microbridge DC Superconducting Quantum Interference Device (SQUID), fabricated by electron beam lithography. In the deposition conditions used (substrate at 300 K, size distributions of incident free clusters centered around Fe_{150}, Co_{300} and Ni_{300}), the mean supported grain sizes were 5 nm, 3 nm and 4 nm for Fe, Co and Ni, respectively. Moreover, these grains were perfectly crystallized in the bcc system for Fe and fcc for Ni and Co. Note that the bulk Co-phase is hcp but nanoparticles having the form of troncated octahedrons are crystallized in the fcc structure[23]. In figure 2 are shown the characteristic hyteresis loops observed with Co-films as a function of the deposited thickness.

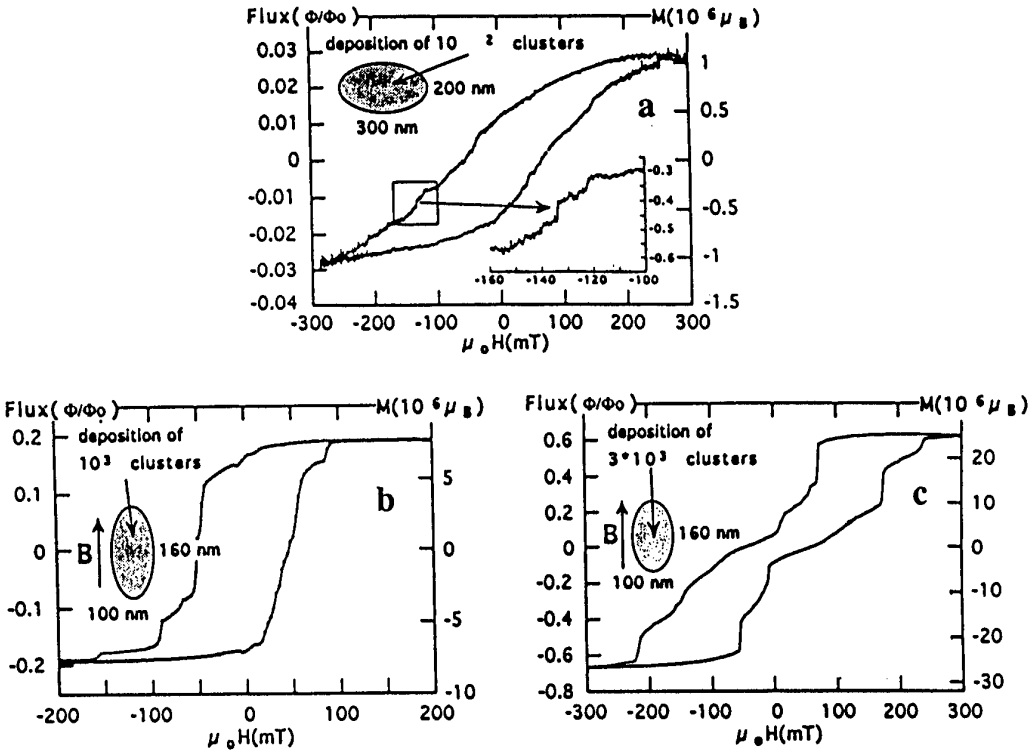


Figure 2 : Hysteresis loops measured at 0.2 K of 0.2 (a), 5 (b) and 15 nm (c) thick Co-cluster films which are deposited in the windows (elliptical shape) of the micro-SQUIDS at 300 K. The measured flux changes are given in units of $\Phi_0 = h/2e = 2.10^{-15}$ Wb and approximately in units of μ_B. The inset in (a) presents a zoom of the hysteresis loop showing small magnetization jumps.

For a low deposited thickness of about 0.2 nm, corresponding to about 10^2 clusters in the microSQUID window, the hysteresis loop (Fig. 2a) reveals small magnetization jumps coming from several clusters which are strongly coupled. For deposited thicknesses larger than the percolation threshold (~ 2 nm) of the films, clusters are strongly coupled by dipole and exchange interactions. The switching field decreases as the thickness increases and the hysteresis loop tends to a rectangular shape (Fig. 2b) as in single-domain particles. For thicker samples (15 nm, Fig. 2c), the hysteresis loop is similar to those of multi-domain particles. Systematic studies of the magnetization behaviours of thick (~ 100 nm) cluster assembled films allowed us to interpret these behaviours in the frame of the random anisotropy model previously proposed by E. Chudnowsky[24] for amorphous materials. However, in our nanostructured films, the characteristic parameter Ra (correlation length of anisotropy axes) corresponds to the mean radius of the grains (~ 1.5 to 2.5 nm), contrary to amorphous materials in which it represents the characteristic length of the local order (~ few Å). The radius of the ferromagnetic domain Rf corresponds to few grains (i.e. Rf ~ 2.4 Ra ~ 14 nm for Fe-films)[25]. Finally, at zero magnetic field the behaviour of the films is comparable to

a correlated spin glass, and under magnetic field two regimes are observed. For applied magnetic fields lower than a cross over field ($H_{CO} = 2$ A/Ms Ra^2, where A and M_S are the exchange constant and the saturation magnetization, respectively) the total grain anisotropy dominates and the magnetization regime ($\Delta M/M_S$) is proportional to $1\sqrt{H}$ while above H_{CO}, particle-particle exchange interaction dominates and $\Delta M/M_S$ is proportional to $1/H^2$. In amorphous materials, since R_a is small, H_{CO} is large (several hundreds kOe), and the high field regime ($H > H_{CO}$) has never been observed. In our nanostructured films, Ra is of the order of the grain size thus Hco becomes attainable (i.e. $H_{CO} \sim 3.5$ kOe for Fe-films)[25], and both regimes have been observed.

As mentioned in section 3 a limited coalescence of supported clusters leads to grain sizes in the films slightly larger than the incident free cluster sizes. In order to limit this effect we have developped a technique which consists to coevaporate a matrix in order to produce samples of isolated clusters embedded in various matrices. This technique is interesting since it allows to produce any type of system (miscible or immiscible) in which the grain size is nearly independent of the concentration, contrary to the systems obtained from a precipitation process[26]. Transport measurements performed recently on Co/Ag (cobalt clusters embedded in a silver matrix, thickness ~ 100 nm) samples have shown a giant magnetoresistance effect (GMR) maximum for a Co-concentration close to the 3D-percolation threshold (~ 20 %) as shown in figure 3. Coupling of embedded Co-clusters via the conduction electrons of the silver matrix could be involved in this case. However, coupling by Tunnel effect could be also considered in the case of magnetic clusters embedded in an insulating matrix as i.e. the system Co/SiO_2 tested at the present time. The results of SQUID magnetization measurements on Co/Ag samples are in good agreement with the GMR results. For a low concentration of Co-clusters (i.e. 10 %), a magnetization regime in 1/T is observed, characteristic of a superpaparamagnetic behaviour, while for concentration above the percolation threshold (i.e. 30 %), a Block regime in $T^{3/2}$ is observed. One has to mention that the samples of magnetic clusters embedded in matrices exhibit some promising magnetic properties for applications in magnetic head or magneto-optic systems, depending on the nature of the matrix.

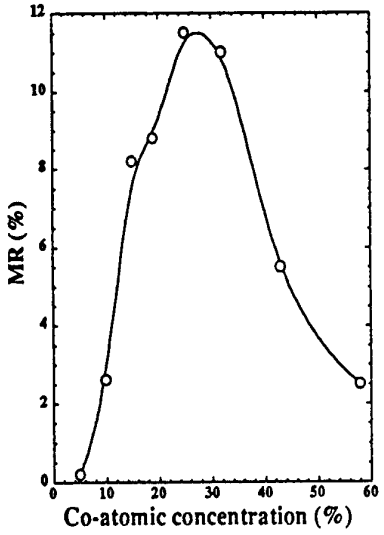


Figure 3 : Magnetoresistance measurements (MR = ρ(H) - ρ(H = 0)/ρ(H = 0), (where ρ is the resistivity and H the magnetic field) of Co/Ag films as a function of the Co-concentration in the form of clusters (diameter ~ 3 nm) embedded in the Ag-matrix.

5. CONCLUSION

The low energy cluster beam deposition is a promising technique to produce nanostructured materials with original structures and properties. Both a memory effect of the incident free clusters and a specific nucleation and growth process can be at the origin of novel materials formation. The memory effect has been clearly observed in the case of covalent clusters (C and Si) allowing the production of original diamond like carbon films and luminescent silicon films. As for the effects of the specific nucleation and growth process, it has been successfully used to produce magnetic nanostructures with interesting magnetic behaviours. Future developments of the LECBD technique using monoatomic clusters but also more complex systems (bimetallic, oxides ...) must be carried out for applications in various fields : optic, electronic, magnetism, catalysis ...

6. ACKNOWLEDGEMENTS

We are indebted to Dr. P. Jensen (Departement de Physique des Matériaux, Univ. Claude Bernard, Lyon, France) for fruitfull discussion and comments on the DDA model. We are grateful to B. Champagnon and Y. Guyot for performing Raman

Spectroscopy measurements on C and Si-films. We are also grateful to Drs. B. Barbara, L. Thomas and W. Wernsdorfer (Laboratoire Louis Neel, CNRS, Grenoble, France) and L. Steren, F. Parent and A. Fert (Laboratoire mixte Thomson-CNRS, Orsay, France) who performed magnetic measurements on granular films and magnetoresistance measurements on films of clusters embedded in matrices, respectively.

7. REFERENCES

1. P. Melinon, V. Paillard, V. Dupuis, A. Perez, P. Jensen, A. Hoareau, J.P. Perez, J. Tuaillon, M. Broyer, J.L. Vialle, M. Pellarin, B. Baguenard, J. Lerme, Int. J. Mod. Phys. B, 9, 339 (1995).
2. T.P. Martin, J. Bergmann, H. Göhlich, T. Lange, J. Phys. Chem., 95, 6421 (1991).
3. W.A. De Heer, Rev. Mod. Phys., 65, 611 (1993).
4. D.L. Michalopoulos, M.E. Gensic, S.G. Hansen, D.E. Powers, R.E. Smalley, J. Phys. Chem., 86, 3914 (1982).
5. P. Milani, W.A. De Heer, Rev. Sci. Instrum., 61,1835 (1990).
6. P. Jensen, A. Laszlo Barabasi, H. Larralde, S. Havlin, H.E. Stanley, Phys. Rev. B, 50, 15316 (1994).
7. D. Stauffer, A. Aharony, *Introduction to percolation theory* (Taylor and Francis, London, 1992).
8. *Fractals and disordered systems*, Ed. A. Bunde and S. Havlin (Springer Verlag, Berlin, 1991).
9. T.A. Witten, L.M. Sander, Phys. Rev. Lett., 47, 1400 (1981).
10. T. Vicsek, *in Fractal growth phenomena*, 2nd ed. (World Scientific, Singapore, 1992).
11. H.J. Herrmann, Phys. Rep. 136, 153 (1986).
12. R. Zallen, *in the Physics of amorphous solids*, (John Wiley and Sons, New York, 1983)
13 C.H. De Villeneuve, L. Porte, L. Bardotti, B. Cabaud, A. Hoareau, M. Treilleux, M.M.M., 4, 471 (1993).
14. M. Pellarin, B. Baguenard, J.L. Vialle, J. Lermé, M. Broyer, J. Miller, A. Perez, Chem. Phys. Lett., 217, 349 (1994).
15. V. Paillard, P. Melinon, V. Dupuis, J.P. Perez, A. Perez, B. Champagnon, Phys. Rev. Lett., 71, 4170 (1993).
16. R.C. Haddon, Le Brus, K. Raghavachari, Chem. Phys. Lett., 131, 16 (1986).
17. V. Paillard, P. Melinon, V. Dupuis, A. Perez, J.P. Perez, G. Guiraud, J. Fornazero, Phys. Rev. B, 49, 11143 (1994).
18. V. Paillard, P. Melinon, J.P. Perez, V. Dupuis, A. Perez, J.L. Loubet, H. Pascal, A. Tonck, M. Fallavier, Nanostruct. Mat., 4, 759 (1994).
19. V. Paillard, M. Meaudre, P. Melinon, V. Dupuis, J.P. Perez, S. Vignoli, A. Perez, R. Meaudre, J. Non Cryst. Sol., in press (1995).
20. E. Kaxiras, Phys. Rev. Lett., 64, 551 (1990).
21. J.C. Vial, J. Derrien, *Porous Silicon Science and Technology*, Editions de Physique, Les Ulis (Springer Verlag, Heidelberg, 1995).
22. W. Wernsdorfer, K. Hasselbach, A. Benoit, B. Barbara, D. Mailly, J. Tuaillon, J.P. Perez, V. Dupuis, J.P. Dupin, G. Guiraud, A. Perez, J. Appl. Phys., in press (1995).
23. J. Tuaillon, V. Dupuis, P. Melinon, B. Prevel, M. Treilleux, A. Perez, Phys. Rev. B, submitted (1995).
24. E.M. Chudnovdky, J. Appl. Phys., 64, 5770 (1988).
25. J.P. Perez, V. Dupuis, J. Tuaillon, A. Perez, V. Paillard, P. Melinon, M. Treilleux, L. Thomas, B. Barbara, B. Bouchet-Fabre, J. Mag., Mag. Mat.,145, 74 (1995).
26. A.E. Berkowitz, J.R. Mitchell, M.J. Carey, A.P. Young, D. Rao, A. Starr, S. Zhang, F.E. Spada, F.T. Parker, A. Hutten, G. Thomas, J. Appl. Phys., 73, 5320 (1993).

Application of ionized cluster beam (ICB) deposition

Alexander S. Zolkin
Novosibirsk State University, Department of Physics
Novosibirsk -·90, 630090, Russia
e-mail: Zolkin@adm.nsu.nsk.su
Fax: 7-(383-2)-355-237

ABSTRACT

The design and testing of a new two-temperature metal vapour source for ionized cluster beam (ICB) method are described. The vaporized material (Ag, atoms and clusters) from a crucible with vapour superheating is partially ionized by electrons at the crucible exit where the vapour has its highest density then accelerated in electric field (5÷10 keV) and deposited on substrate of HTSC Y-Ba-Cu-O films. Very thin (100÷200 nm) metal films with high density and low-resistance contacts Ag/Y-Ba-Cu-O ($10^{-5} \div 10^{-8}$ Ohm·cm^2) were fabricated by ICB. The surface of the films was analyzed by SEM (SE, BSE) with computer analyzer.

The application of two-temperature sources in technologies allows one to produce atomic or cluster beams, control the gas dynamic flow and produce high-quality metal thin films as a result.

1. INTRODUCTION

In 1956 E.W.Becker, K.Bier and W.Henkes[1] have demonstrated for the first time the possibility of cluster beam formation by the method of gas jet expansion into vacuum with subsequent separation. A unique possibility has appeared to conduct the physical experiment with a new material object, i.e. clusters. The experiments on electron ionization and cluster acceleration in the electric field, which were performed by M.Henkes in 1962, have opened the perspective of investigations with clusters of different energies[2]. The cluster ion accelerators[3] for studying plasma physics and solid physics received a large development effort. Starting from 1972 [4] the ionized cluster beams (ICB) have been used for the synthesis of thin films. As far as in the first works T.Takagi, I.Yamada et el.[5], the authors of this method, have especially emphasized the role of ionized clusters of different energies in the process of the growth of high-quality films of different substances including compounds.

Taking into account a great applied importance of this method, its different aspects are studied currently such as the formation of beams with clusters of the given size, the study of their energetic state, ionization degree, movability on the surface, etc.

This paper presents the results on the modified ICB-technology and its application in the formation of low-thin film silver contacts to High-Temperature Superconductor Y-Ba-Cu-O films.

2. PRINCIPLES AND ADVANTAGES OF ICB DEPOSITION

In the ICB technique[5], the deposition material is evaporated in a crucible at an elevated temperature. The vapour is then ejected through a nozzle of 1÷2 mm diameter. The ejected species are then partially ionized by electron bombardment and are accelerated to the substrate by applying a bias potential (0÷10 kV). During the expansion of the vapour, the thermal energy transfers into the kinetic energy of the beam and the temperature of the beam drops rapidly. The beam becomes supersonic. The cooling of the vapour can lead to the formation of clusters through condensation[5].

In principle, the method could have the following advantages:

1. Cluster ions are easily accelerated. Not only the cluster itself, but also the area hit directly will melt locally, if the kinetic energy is high enough. A compact, strongly adhering thin film can be formed.

2. A lower substrate temperature can be used then with the standard method, as the atoms gain lateral mobility upon cluster break up.

3. Due to the high local temperatures involved, the method can be inherenty self cleaning.

4. Space charge problems are reduced as the cluster ions carry one or few charges.

0-8194-2165-0/96/$6.00

5. A better step coverage compared to the standard sputtering technique can be expected from the directed cluster ion beam.

6. The thermal load from the ion beam is negligible.

To the authors opinion, the problem of cluster formation and generation, in particular, of metal clusters, is the major one among the problems encountered in the application of ICB method. The investigators face drastic difficulties in cluster registration under the conditions recommended by the authors[5]. The available methods for the calculation of nucleation rate yield the values differing by several orders of magnitude[6,7] and the lack of experimental data complicates the existing situation. Information on the development of a new phase in expanding vapour-metal flows is insufficient and contradictory[5,8,9], but beautiful thin films have been produced by the ICB method.

3. NEW SOURCE FOR ICB DEPOSITION

Unlike the traditional scheme of the ICB method we used a specially developed source with vapour heating. This gives a possibility to keep the precipitation velocity constant in time. In order to increase the probability of cluster formation in the flow a supersonic conical nozzle was used in the source. A special ionizer with the space charge, which gives a possibility to register clusters in the flow, was developed for ionization of a molecular beam.

A source of Ag vapour (Fig. 1) does not principally differ from that described earliar[10]. It represents a double Knudsen cell used in mass-spectral thermodynamic investigations[11]. Structurally, the source consists of two basic parts: a crucible 1 with metal and vapour superheater 2 connected by a vapour pipe line 3. The crucible has the volume about 30 cm^3. The vapour superheater 2 has a cylindrical body, inside which a barrier is installed which prevents direct passing of the vapour flow. The construction of superheater promoted to heating the metal vapour up to saturation temperature. A nozzle for thermal contact is tightly inserted in its upper part. The point of its connection with a superheater is welded up using an Ar-arc. The vapour pipeline channel 3 in the form of a thin-walled tube is thermal by passing, thermal resistance between a crucible and a superheater and allows one to maintain the temperature of vapour higher than of a crucible with metal by more than 500 K. Heater 4 in the form of double coaxial cylinders, made of tantalum 0,2 mm thick foil, were used for radiative heating of the crucible and the nozzle. The external cylinder served as heated screen that facilitated the control of thermal loading of the source. A crucible and a superheater are protected thoroughly by a screen isolation 5 made of tantalum. To maintain the temperature gradients in the crucible, special attention is paid to thermal insulation of the crucible. Screens in the region of the nozzle were located so as to preserve, if possible, a screen insulation with its small effect on the metal-vapour flow out of the nozzle. Fig. 2 presents the dependence of heater temperature on electric characteristics of the heater. A thermocouple (W-Re) t_1 is mounted at the crucible bottom. Two thermocouples t_2, t_3 for controlling temperature T_0 of vapour expansion from the source are mounted in the nozzle at a distance of 5 mm from its edge. The conic nozzle was used ($2\alpha = 0°$, $d_* = 0.4$ mm, $L = 6$ mm).

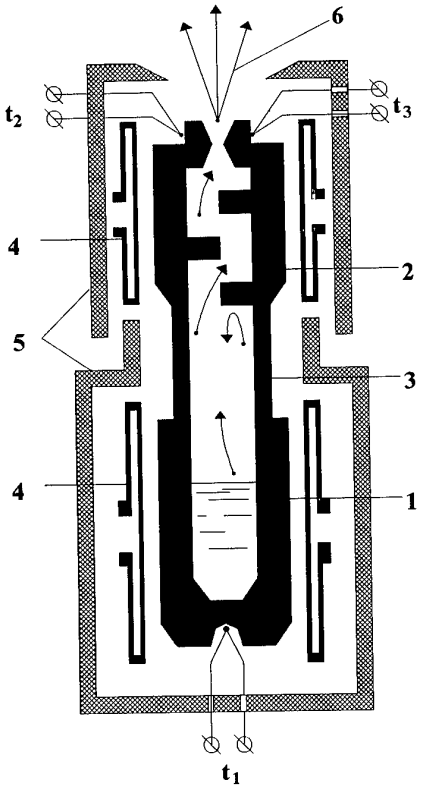


Fig. 1. Metal vapour source.

An ionizer is an electron gun with a radially convergent electron beam (Fig. 3) was developed for ionization of a molecular beam. The ionizer represents a cylindrical diode, the inner space of which comprises the ionization area. Electrons are oscillating in intergrid space, and as this takes place, some distribution of electric potential, connected with the space charge of positive and negative particles, has been set up. The diaphragms of the ionizer entrance and exit have holes in the form of channels in order that the ionization area could be carefully shielded from outer electric fields. Studies of the ionizer show that in the ionization area the depth of the negatively charged potential well is approximately 5 V at the following conditions: electron emission current is

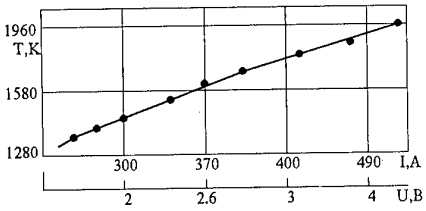


Fig. 2. Heating element temperature (T) versus the current (I) and electric voltage (V).

$J_e \approx 60$ mA, electron energy $E_e \approx 200$ eV, pressure in the vacuum chamber is less or equal to 10^{-3} Pa. The current of ionized atoms of residual atmosphere from ionization area was not registered. This can be attributable to the ion capture in the area of the space charge. Ions can't leave the potential well because their "Thermal" energy is not enough to overcome this potential barrier. The ionizer with the space charge may be applied for the qualitative investigation into cluster beam, i.e. determination of existence of "heavy" particles in a neutral beam, kinetic energy of which is enough to leave the potential well (the ionization area).

Application of such technique permits to answer the main question "Are there clusters in a beam?" and gives a possibility to receive a qualitative result. However, a question on a quantitative result is connected with additional methodical investigations.

We used the given method for the search of formation conditions of high-energetic particles of silver clusters at metal vapour expansion into vacuum. We were interested in vapour pressure in a crucible and temperature of vapour expansion, at which one can register high-energetic ionized particles in a molecular beam. Energetic ion spectrum was measured by electrostatic energy analyzer (Fig. 3). Radius of ion path is R = 5 cm, $\alpha = 127°30'$. The distance between plates is $\Delta R = 1$ cm, the width of entrance and exit slots is 1 mm. On the exit from analyzer an ion collector of Faraday cylinder type is situated.

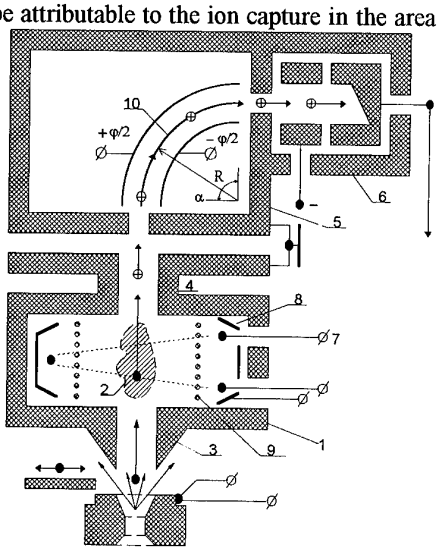


Fig.3. Experiment scheme for energy measurement of silver charged particles. Electron gun – 1; ionization area – 2; entrance diaphragm – 4; electrostatic analyser – 5; ion collector – 6; cathode – 7; reflecting electrode – 8; electron accelerating grid – 9; ionized particles – 10.

Figure 4 presents the distribution of ionized silver particles along the energy at vapour expansion into vacuum ($P \approx 10^{-3}$ Pa). The spectrum has two picks. The first pick (1) is observed in the area of low energies and the second wider pick (2) is observed in the area of high energies.

The first maximum may be regarded to incipient clusters, the second – to the clusters, formed at collisions in the flow. Figure 4 also presents the recording of the "zero" ion signal (1), when the molecular beam is overlapped by the chopper (Fig. 3). Comparison of two spectrum gives the basis to suppose that heavy silver particles-clusters, kinetic energy of which is enough to leave the potential well of the space charge of ionization area, are registered.

4. APPLICATION OF ICB DEPOSITION. LOW-RESISTANCE Ag- CONTACTS APPLIED TO Y-Ba-Cu-O FILMS

Forming low-resistance contacts on high T_c films has become an urgent matter because of the planned use of high T_c superconductors in microelectronics and electrical engineering. The contacts should have a low electrical resistance and a strong mechanical bond with the surface of the superconductors.

4.1. Experimental details

In the previous paper[12] we have reported a study of the specific surface contact resistance as a function of the energy of silver particles deposited on the surface of Y-Ba-Cu-O films by ICB technology.

The ion cluster deposition method which we used was similar to that described in Ref. 5, but with a new metal-vapour source. The particle energy was varied from 0.1 eV to 10 keV[12]. The silver clusters were formed during the expansion of a vapour through a nozzle 0.4 mm in diameter into a vacuum of $P=10^{-4}$ Pa. The vapour pressure was $(2\div2.6)\cdot10^3$ Pa (!), the temperature of vapour was approximately 1900 K. The vapour pressure and the vapour temperature in the source corresponded to such outflow conditions that the flux contained clusters of 100÷200 atoms. The deposition rate under these conditions was near 100 nm/min. The metal vapour was ionized by electrons with energy 200 eV in a current 60÷200 mA. The ionized particles were accelerated in the gap between the ionizer and the substrate holder, whose potential was varied over the range $U_{ac} = 0\div10$ kV. The contacts were applied at a temperature no

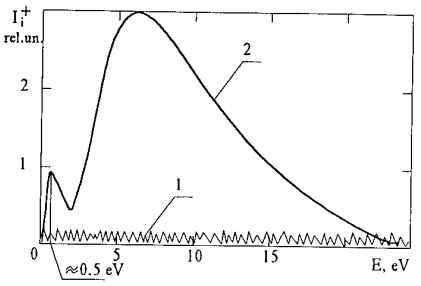


Fig. 4. Energy distribution of silver ionized particles.

more than 370K in order to partially remove adsorbed layers of gas from the surface of the superconducting film. The energy of the ionized particles being deposited was: 0; 2; 4; 7 or 10 keV. The deposition time at any energy was 10 minutes.

The superconducting films were grow by laser deposition on sapphire substrates. Since the films which were synthesized exhibited some scatter in superconducting properties (in the transition temperature and the critical current), some samples with approximately the same superconducting properties were selected for the metal deposition. Since the surface properties of the individual films could vary, the contact areas for the deposition of Ag-particles with different energies were selected on the same film.

The resistance of the contacts was measured by the four-probe method at 78 K. An electrode serving as both a current probe and a potential probe was applied to the contact under study. Current probes and potential probes were clamped to the contact areas. The sensitivity of the method was no more than $\approx 2 \cdot 10^{-9}$ Ohm·cm^2. The films with the contacts were annealed in oxygen at atmospheric pressure at T = 773 ± 5K for 5 minutes in order to reduce the resistance.

5. RESULTS

Analysis of the contact resistance as a function of the energy of the incident particles showed that there is a certain energy interval: $E_i \approx 8.3 \pm 0.5$ keV, in which the contact resistance has only a small scatter in values, and this scatter is essentially independent of the history of the superconducting films.

This result may be important for selecting technological conditions for applying contacts to films with degradation layers of various thicknesses, e.g., tens of nanometers, as in these experiments. When the energy of the incident particles is more than 8÷9 keV, we find a sharp increase in the scatter of the values of the contact resistance. The explanation probably lies in both the properties of the surface layer and the reduced effect of the high-energy particles on the growth of the degradation layer.

During the deposition of contacts by particles at thermal energies, the resistance of the contacts on different films are quite different: $10^{-5} \div 1.0$ Ohm·cm^2. The deposition of contacts at a particles energy $E_i = 8.3 \pm 0.5$ keV makes it possible to lower the upper limit on the resistance to 10^{-3} Ohm·cm^2. This effect may be sufficient for fabricating electronic devices for which technological considerations rule out annealing the superconducting film. Annealing the contacts resulted in a significant decrease in the contact resistance of all the samples, to $10^{-6} \div 10^{-8}$ Ohm·cm^2.

The surface of metal contacts was investigated by the Scanning Electron Microscope Opton-960 in backscatted electrons (BSE) with the computer treatment in order to determine the fulling degree of the development HTSC film surface by silver. An electron beam was scannering the surface under different angles so that there was a possibility to determine: if there exists a silver covering in that places, where it is hard to cover by the direct molecular flow. We were sure that the deposition by accelerated ionized particles helps to receive a surface covering with complex profile.

6. SUMMARY

The design and testing of a new two-temperature metal vapour source for ionized cluster beam (ICB) method are described. The vaporized material (Ag atoms and clusters) from a crucible with vapour superheating is partially ionized by electrons at the crucible exit where the vapour has its highest density and then particles are accelerated in electric field and deposited on the substrate of HTSC Y-Ba-Cu-O films. Very thin metal films with high density and low-resistance contacts Ag/Y-Ba-Cu-O ($10^{-5} \div 10^{-8}$ Ohm·cm^2) were fabricated by ICB. The application of metal-vapour source with superheating in technologies allows one to produce high-quality films.

7. ACKNOLEDGEMENTS

The author is grateful to his colleagues: Yu.G. Shukhov and A.V. Kozhin for their help in measurements carrying out, valuable discussions and to OPTON's (Germany) research workers for providing SEM testing the surface of the thin films.

A part of this work realized in the frame of the State Program on High-Temperature Superconductivity (Russia) and was supported by the International Science Foundation (Soros,USA, JKD-100). The author thanks these organizations with great pleasure.

8. REFERENCES

1. E.W. Becker, K. Bier, W.Henkes: Z. Phys. Bd.146. H.3.(1956), 320

2. E.W. Becker, W.Henkes : D.P.1178252. (1962)
3. E.W. Becker : Laser and Particle Beams. 7. Part.4.(1989),743
4. T.Takagi, I.Yamada, M.Kunori, S.Lobiyama: Proc. 2nd Inter. Conf. on Ion Sourceres. Osterreichische Studiengesellshaft fur Atomenergie, Vienne. (1972),790
5. Ionized - Cluster Beam Deposition and Epitaxy, T.Takagy: Noyes Publications. New Jersey; 1988
6. H.Haberland: Z. Phys. D. Atoms, Moleculars and Clusters, 26. 1-4 (1993) 8;229
7. A.G.Sutugin : Uspekhi khimii (Rus). 38. 1 (1969), 166
8. A.A.Lushnikov, A.G. Sutugin: Uspekhi khimii (Rus). 45. 3 (1976), 385
9. O.F.Hagena : Z. Phys. D. Atoms, Molecules and Clusters.4(1987), 291
10. D.Turner, H. Shanks : J Appl Phys 70. 10.(1991) 5385
11. A.Zolkin, Yu.Shukhov : Preprint 263 (1992). Inst. of Thermophysics Academy of Science, Novosibirsk, Russia, 35 p. (Eng).
12. L.Sidorov, M.Korobov, L.Zhuravleva L.V. Mass-spectrometric thermodynamic investigations.(Rus). MGU(1985).
13. A.Zolkin , A.Kozhin ,Yu. Shukhov : Supercondactivity 5.2 (1992) 337.

Exciton confinement effect in semiconductor quantum wells studied by resonant second harmonic generation

Hiroyuki Ito and Fujio Minami
Department of Applied Physics, Tokyo Institute of Technology, Meguro-ku, Tokyo 152, Japan

Kouji Yoshida and Kuon Inoue
Research Institute for Electronic Science, Hokkaido University, Sapporo 060, Japan

Kenji Watanabe
National Institute for Research in Inorganic Materials, Tsukuba, Ibaraki 305, Japan

ABSTRACT

We have investigated the electronic structures of GaAs/Al(Ga)As and GaAs/AlAs quantum wells by resonance effects of second-harmonic generation. Second-harmonic generation signals manifest themselves in two-photon resonance with the confined 1S and/or 2P excitons in GaAs/Al(Ga)As and ZnSe/ZnS quantum wells. The assignment of the resonance is directly determined from comparison to the results of one-photon and two-photon absorption data. From the energy splitting of the 1S and 2P exciton levels, the exciton binding energies can be determined. There is a significant increase in the binding energy as compared to that in bulk materials. This increase is caused by the exciton confinement effect.

1. INTRODUCTION

Recent advances in crystal growth techniques, such as molecular beam epitaxy (MBE), have made possible to produce a semiconductor quantum well consisting of an ultrathin layer (<10 nm) of a semiconductor sandwiched between thin layers of a wide gap semiconductor. In such a nanostructure, the electron wavefunction is confined within a layer and therefore electrons only have the freedom of two-dimensional interlayer motion. A most important and interesting feature is that the exciton binding energy in quasi-two-dimensional systems is strongly enhanced, as compared to the three-dimensional case.[1] In this paper, we have studied the enhancement of exciton binding energy in semiconductor quantum wells by using resonant second harmonic generation (SHG).

The SHG processes have been investigated so far in a large number of crystals with a view to searching for new nonlinear optical materials. Frequency dispersion of the SHG coefficient has also attracted much interest.[2] This includes a resonant effect of the coefficient, i.e., an enhancement of SHG which occurs when one of the relevant photon energies is resonant with that of a specific energy level.[3-6] However, only a few works on a resonant SHG phenomenon in quantum wells has been reported until now.[7] In this paper, we have investigated SHG processes in the confined energy region for GaAs/Al(Ga)As and ZnSe/ZnS quantum wells. Resonant behavior of SHG signal is found when twice the incident photon energy, $2\hbar\omega$, coincides with excitation energy of the relevant 1S or 2P excitons confined in GaAs and ZnSe layers. Based on the data, we show below that this new phenomenon will provide a promising tool for the study of electronic structures in quantum wells.

0-8194-2165-0/96/$6.00

2. THEORETICAL BACKGROUND

In SHG process, polarization comes about through the admixture of two different states , $|f\rangle$ and $|I\rangle$, to the ground state $|g\rangle$. Thus the SHG tensor d_{jlm} becomes[6]

$$d_{jlm} \propto \sum_{I,f} \frac{\langle g|e^{-i2\mathbf{k}_i\cdot \mathbf{r}}\mathbf{e}_j\cdot \mathbf{p}|f\rangle\langle f|e^{i\mathbf{k}_i\cdot \mathbf{r}}\mathbf{e}_l\cdot \mathbf{p}|I\rangle\langle I|e^{i\mathbf{k}_i\cdot \mathbf{r}}\mathbf{e}_m\cdot \mathbf{p}|g\rangle}{(E_f-2\hbar\omega+i\Gamma)(E_I-\hbar\omega)}, \qquad (1)$$

where $\mathbf{k}_i$ represents the wave vector of the incident light, Γ represents the damping constant of state $|f\rangle$, and $\mathbf{e}_j$ is a unit polarization vector of the light beam $\mathbf{E}_j$, and E_f (E_I) refers to the energy of state $|f\rangle$ ($|I\rangle$). When $2\hbar\omega$ approaches the energy of an appropriate excited state $|f_0\rangle$, resonant SHG comes about. In this case, d_{jlm} becomes much larger than in off-resonance case. In our experiment, the 1S or 2P state of quasi-two-dimensional excitons in quantum wells is chosen for state $|f_0\rangle$.

Next we shall make a short mention of two-photon absorption. The two-photon absorption in semiconductors can be described in a similar way as SHG.[8] Allowed two-photon transitions in semiconductors occur to final P-exciton states via discrete S-exciton states as intermediates. The lowest-energy final state is then the 2P exciton. For the 2P exciton, the two-photon absorption coefficient α_{TPA} becomes[8]

$$\alpha_{TPA} \propto \left| \sum_{I} \frac{\langle 2P|\mathbf{e}_l\cdot \mathbf{p}|I\rangle\langle I|\mathbf{e}_m\cdot \mathbf{p}|g\rangle}{(E_I-\hbar\omega)} \right|^2 \mathrm{Im}(E_{2P}-2\hbar\omega+i\Gamma_{2P})^{-1}, \qquad (2)$$

where $\mathbf{e}_j$ is again a unit polarization vector of the light beam $\mathbf{E}_j$, Γ_{2P} represents the damping constant of the 2P exciton, and I refers to the intermediate state with the energy E_I. It can be seen from this equation that two-photon absorption results are quite similar to those of the resonant SHG around the 2P exciton region. The situation of two-photon absorption in semiconductor quantum wells is not so different from the bulk case, if the polarization vectors of the incident lights are normal to the growth direction z.[9] The lowest-energy state reached is the 2P state of the hh1-c1 excitons. We use hereinafter the notation hhi-cj and lhi-cj for the optical transitions, where hh(lh) refers to the heavy (light) hole, and i (j) is the hole (electron) subband.

3. EXPERIMENTAL

Samples of GaAs/Al(Ga)As and ZnSe/ZnS quantum wells were grown by MBE on (001) GaAs substrates. For the GaAs/Al(Ga)As quantum wells, the experimental data were obtained from two samples: a GaAs/AlGaAs quantum well consisting of 300 periods of 40 Å GaAs and 60 Å $Al_{0.4}Ga_{0.6}As$ layers, and a GaAs/AlAs quantum well composed of 100 periods of 38 Å GaAs and 38 Å AlAs. The ZnSe/ZnS quantum well was composed of 1200 periods of 20 Å ZnSe and 18 Å ZnS layers. The experimental arrangement is shown in Fig. 1. The excitation source for the GaAs/Al(Ga)As quantum wells was a home-made pulsed Cr:YAG laser pumped by a cw Q-switched Nd:YAG laser, and that for the ZnSe/ZnS quantum well was a Ti:sapphire laser pumped by a cw Q-switched intracavity frequency-doubled Nd:YAG laser. The

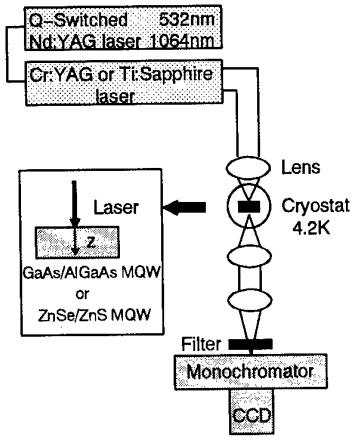


Fig. 1. Experimental setup.

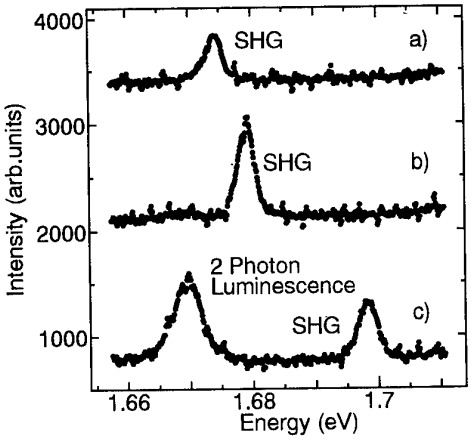


Fig. 2. Example of SHG signal in the GaAs/AlGaAs quantum well for two photon excitation energy of a) 1.675eV, b) 1.680 eV and c)1.689 eV.

Cr:YAG laser has a wavelength tuning range from 1.38 to 1.58 μm, and the Ti:sapphire laser has a range of 700-1000 nm. Both lasers have a pulse duration of 200 ns, a repetition rate of 3 kHz, and an average power of 100 mW. The tuning accuracy was about 0.3 meV. A focused and linearly polarized laser beam was propagated perpendicularly to the epitaxial layer. The SHG signal was detected by a 25cm-single-monochromator equipped with a cooled CCD camera. The spectral resolution of the present measurement is mainly limited by the linewidth of the tunable solid state lasers. All experiments were performed at 4.2 K.

4. RESULTS AND DISCUSSION

Examples of the SHG spectra observed for two-photon excitation in the exciton region of the GaAs/AlGaAs quantum well are shown in Fig. 2. A SHG signal is clearly seen to emerge at the position of $2\hbar\omega$, in addition to a recombination emission (luminescence) from the 1S exciton. It is found that the SHG signal is enhanced as $2\hbar\omega$ approaches the energy of 1.68 eV. Further, under the same detecting conditions, the exciton luminescence intensity was found to be below the noise level when the value of $2\hbar\omega$ was smaller than 1.682 eV.

Variation of the SHG intensity with $2\hbar\omega$, i.e., two-photon excitation spectrum for SHG, is shown in Fig. 3. No correction due to reabsorption of signal was made for simplicity. The widths of the excitation peaks are estimated to be 10 meV, which is much wider than thelinewidth of the resonant SHG signal. The line width seems to reflect inhomogeneities in layer thickness.

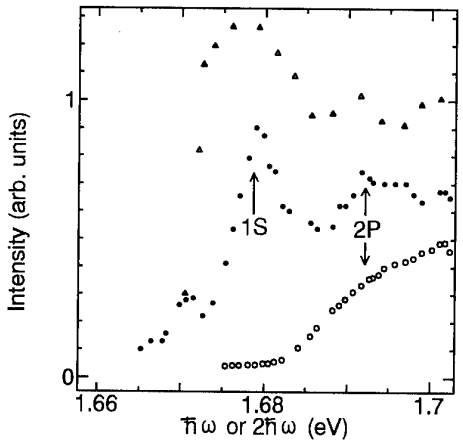


Fig. 3. SHG intensity versus $2\hbar\omega$ (circle), two photon absorption spectrum (dot), and one–photon absorption spectrum (triangle) of the GaAs/AlGaAs quantum well.

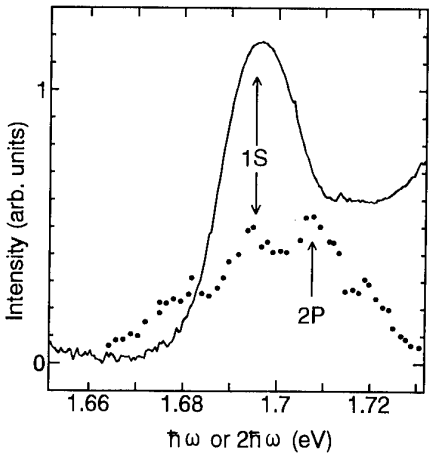


Fig. 4. SHG intensity versus $2\hbar\omega$ (dot), and one–photon absorption spectrum (solid line) of the GaAs/AlAs quantum well.

In order to determine the origins of the peak, we also measured one-photon and two-photon absorption spectra for the same sample. The results are also shown in the figure. In one-photon spectrum, the 1S exciton peak can be observed in the energy region concerned. Comparing the one-photon absorption and resonant SHG data, the peak at 1.679 eV in the SHG excitation spectrum is found to correspond to hh1-c1 1S exciton transition. It is noted that this 1S exciton peak is absent in the two-photon absorption. The onset of the two-photon absorption should occur at the 2P exciton. But the 2P exciton is not seen clearly in the two-photon absorption, i.e., the 2P exciton state cannot be resolved well from the continuum state. On the other hand, in the resonant SHG excitation spectrum, there is a clear peak at 1.692 eV. Thus the shoulder at the same energy should correspond to the 2P exciton state.

Fig. 4 shows one-photon absorption and SHG excitation spectra for the GaAs/AlAs sample. In this sample, two photon luminescence was too weak to measure the two-photon absorption spectra, whereas resonant SHG signals were strong enough to obtain the excitation spectrum. On the analogy of GaAs/AlGaAs sample, two peaks at 1.695 eV and 1.707 eV are assigned to the hh1-c1 1S and 2P exciton states, respectively.

From the obtained energy splitting between the 1S and 2P excitons, we can determine the exciton binding energies. The binding energies of the hh1-c1 excitons are found to be 16 ± 1 meV for 40 Å-GaAs/60 Å-AlGaAs and 15 ± 1 meV for 38 Å-GaAs/38 Å-AlAs. There is a significant increase in the binding energy in our samples, as compared to that in bulk GaAs (~5 meV). This increase will be caused by the exciton confinement effect. The exciton binding energy seems slightly smaller in the thinner well. A variational calculation predicted that the values of binding energies increase as well width is reduced until they reach their maximum value and then begin to decrease.[10] Our results might be explained by

this model.

Now, we consider the reason why the 2P exciton peak can be clearly observed only in the SHG excitation spectrum. It is found from eqs. (1) and (2) that the contribution of homogeneous broadening is different for two-photon absorption and SHG, i.e., $\alpha_{TPA} \sim 1/\Gamma$ and $|d_{jlm}|^2 \sim 1/\Gamma^2$. At higher energy states with large Γ, therefore, the SHG signals are not enhanced sufficiently, leading to decreased intensity. This makes a difference between the two-photon absorption and SHG data.

Next we show the excitation spectrum for SHG in the ZnSe/ZnS quantum well [Fig. 5]. In this case, four peaks exist strikingly in the energy region concerned. In order to check the origins of the peaks, we also measured one-photon absorption spectrum for the same sample [Fig. 5(a)]. Two 1S exciton peaks are observed clearly in the energy region concerned. The splitting of the 1S exciton arises from the heavy and light hole valence band split due to the quantum well potential. The exciton (hh1-c1,1S) composed of the heavy-hole belonging to the first subband (n=1) and the electron belonging to the first subband (n=1) appears at the energy than that (lh1-c1,1S) of the light hole. From a comparison between both spectra, we can identify the lowest and the third lowest peaks in the excitation spectrum for SHG [Fig.5(b)] as originating in two-photon resonance with the respective excitons. Similarly, a comparison to two-photon absorption spectrum allows one to easily identify the second and fourth as appearing as a result of resonance with the corresponding 2P exciton. This phenomenon is considered to be a quantum well version of the one already observed for thin films of ZnSe.[6] We may explain microscopically the present result in a similar way to the bulk case, i.e., by invoking a weakly allowed dipole transition in the $\mathbf{k} \cdot \mathbf{p}$ perturbation for one virtual transition involved between the 2P exciton and the ground states.[6]

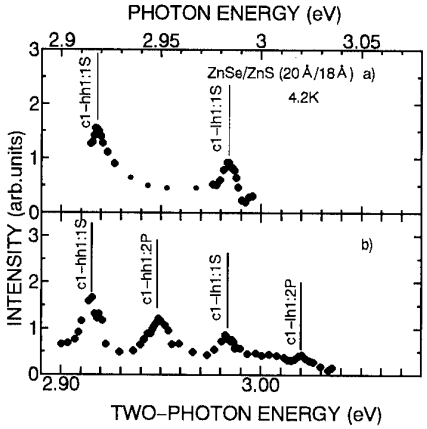


Fig. 5. a):One –photon absorption spectrum
b):The SHG signal intensity from the ZnSe/ZnS quantum well as a function of $2\hbar\omega$

From the resonant SHG data alone, we can estimate the respective binding energies as 38 and 44 meV for heavy-hole and light-hole related excitons in the ZnSe/ZnS quantum well. This indicates that the excitons are confined to a considerable extent in ZnSe layer, since the binding energy for bulk ZnSe is 20 meV. An appreciable difference in the binding energy between the hh and lh excitons can be detected, as the effective mass theory predicted.[10]

5. CONCLUSION

We have studied the 1S and 2P exciton states in semiconductor quantum wells by the resonant SHG spectroscopy. The exciton 2P state in GaAs quantum wells, which is not seen in two-photon absorption, was observed clearly in the resonant SHG excitation spectra. This method has improved the accuracy in determination of exciton binding energy in the quantum wells. It should be interesting to apply this method to other semiconductor quantum wells.

6. ACKNOWLEDGMENTS

This work has been partially supported by Special Coordination Funds for Promoting Science and Technology entitled "Research on New Material Development by Nanospace Lab".

7. REFERENCES

1. See, for example, N. Peyghambarian, S.W. Koch and A. Mysyrowicz, Introduction to Semiconductor Optics, (Prentice Hall, New Jersey, 1993).
2. See, for example, Y.R. Shen, The Principle of Nonlinear Optics, (John-Wiley & Sons, New York, 1984).
3. D.C. Haueisen and H. Mahr, Phys. Rev. Lett. 26 (1971) 838; Phys. Rev. B8 (1972) 734.
4. B.F. Levine, R.C. Miller and W.A. Nordland Jr, Phys. Rev. B12 (1975) 4512.
5. S.H. Stevenson, C.K. Johnson and G.J. Small, J. Chem. Phys. 128 (1988) 157.
6. F. Minami, K. Inoue, Y. Kato, K.Yoshida and K. Era, Phys. Rev. Lett. 67 (1991) 3708.
7. F. Minami, K. Yoshida, K. Inoue and H. Fujiyasu, J. Crystal Growth 138 (1994) 796.
8. H. Mahr, in Quantum Electronics, Vol. I, eds. H. Rabin and C.L. Tang (Academic Press, New York, 1975) p.285.
9. K. Tai, A. Mysyrowictz, R. J. Fisher, R. E. Slusher and A. Y. Cho : Phys. Rev. Lett. 62, (1989) 1784.
10. R.L. Greene, Phys. Rev. B29 (1981) 1807.

Direct formation of GaAs quantum dot structure by droplet epitaxy

Nobuyuki Koguchi and Keiko Ishige
National Research Institute for Metals
1-2-1 Sengen, Tsukuba, Ibaraki 305, Japan

ABSTRACT

Numerous GaAs epitaxial microcrystals were fabricated on a sulfur-terminated GaAs substrate by sequentially supplying Ga and As molecular beams. The process consists of forming Ga droplets on the inert surface and reacting the droplets with As to produce GaAs microcrystals. This method termed droplet epitaxy is thought to be a promising growth method for fabricating the GaAs quantum dot structure, especially coupled quantum dot structure.

1.INTRODUCTION

Predictions of enhanced electron mobility device[1] and advanced semiconductor laser[2] with high-monochromized and low threshold current density have been made for the application of quantum dot structures. It is necessary to fabricate numerous epitaxial semiconductor microcrystals with homogeneous size of around 100 Å and density of near 10^{12} cm^{-2} for a so-called coupled quantum dot structure[1,3]. For the fabrication of these dot structures, usually a pattern is defined by high resolution lithography and transferred to a semiconductor quantum well substrate. The physical properties of structures fabricated in these manner often are determined by surface effect which caused by a process induced damage. Also there is a problem in spatial resolution of lithography. Recently, alternative techniques which form the quantum dot structures directly during growth are proposed. These techniques are based on three-dimensional Volmer-Weber type[4-6] or Stranski-Krastanov type[7-8] island growth modes during initial stage of thin film growth. However, the size of individual dot is larger than 100 Å and the density of the dots is usually low.

We have observed a three-dimensional island growth of GaAs epitaxial microcrystals on a sulfur- or selenium-terminated GaAs surface in MBE system[4-6]. This method, termed droplet epitaxy, is promising for the direct formation of GaAs quantum dot structure, especially coupled quantum dot structure. In this paper, we describe three-dimensional growth of GaAs epitaxial microcrystals on a sulfur-terminated (S-terminated) GaAs substrate by droplet epitaxy.

2.EXPERIMENT

The MBE system used in this work was a conventional system (ANELVA-620) with a sample introduction chamber. Elemental Ga and As were used as molecular-beam source materials. A valved Knudsen cell charged with elemental S was installed in the sample introduction chamber. The background pressure of the sample introduction chamber was 5×10^{-8} Torr.

First, GaAs buffer layer was grown on a GaAs (001) substrate to obtain a well defined (2x4) As-stabilized surface. For the S-termination of the GaAs (001) surface, the substrate temperature was decreased to room temperature. Then the sample was heated again to 520 C to obtain a Ga-stabilized surface without an As molecular beam. Next, the sample was transferred into the sample introduction chamber and exposed to sulfur vapor which generates a chamber pressure of 1×10^{-5} Torr at 300 C for 3 min. The sample was then transferred into the growth chamber again and kept at 400C for 30 min. The Ga droplets were deposited on these substrate surfaces at various temperatures. After the deposition of the Ga droplets, As cell was heated and the As cell shutter was opened.

3.RESULTS AND DISCUSSION

The RHEED patterns observed before and after the Ga deposition and after the As molecular beam supply on the S-terminated GaAs substrates at 200 C are shown in Fig.1 along complementary <110> and <1$\bar{1}$0> azimuths. In this case, the total amount of Ga was equivalent to 2.7 monolayers of GaAs, and the As molecular beam of 3×10^{-6} Torr beam equivalent pressure (BEP) was supplied to the surface. The surface reconstruction of the sample was (2x4) at 580 C and changed to the coexistence of (4x6) and (3x6) which correspond to a Ga-stabilized surface structure at 300 C just before the exposure to the sulfur vapor. After the exposure the sample to the sulfur vapor and annealing at 400 C, clear (2x6) reconstruction appeared. This was presumably originated from making stable Ga-S bonds. This surface structure changed to Ga-stabilized (4x2) at temperatures above about 500 C without As molecular beam. Then the surface structure of (2x6) reconstruction thought to be a sulfur-terminated surface.

0-8194-2165-0/96/$6.00

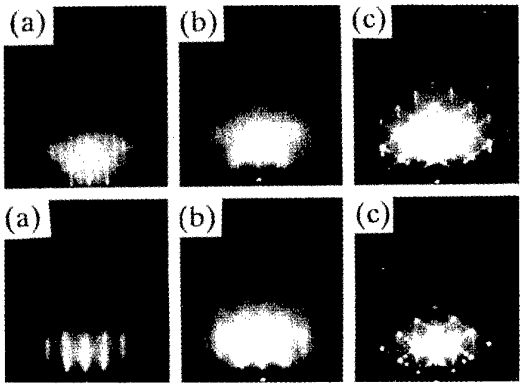


FIG.1. The RHEED patterns observed on each stage of the growth process on the S-terminated GaAs substrate. (a) is a pattern after the S-termination by annealing the sample at 400 C. (b) is a pattern after the Ga deposition at 200 C. (c) is a pattern after the As molecular-beam supply at 200 C. Upper row: electron beam along <110>; lower row: electron beam along <110>.

Recently, the GaAs(2x6)-S surface reconstruction, of which unit cell contains five S-S adatom dimers and one missing dimer, was determined by scanning tunneling microscopy[9]. Simultaneous diffraction patterns of halo and (2x6) reconstruction were observed on the Ga deposited surface. The halo is caused by the diffraction of Ga droplets deposited on the substrate surface. After the As molecular beam irradiation, the RHEED pattern changed to the spotty feature with streaks along <111> and <113> azimuths. The <111> streaks were observed clearly along <110> azimuth rather than those along <1$\bar{1}$0> azimuth. Some twin spots were observed along both azimuths. The (2x6) surface reconstruction remained after the appearance of the transmission spots. This means the substrate surface between Ga droplets and between microcrystals grown by the subsequent As molecular beam supply are original S-terminated surface.

The change of the specular beam, halo, and (004) transmission diffraction intensities during Ga deposition and the subsequent As molecular beam radiation are shown in Fig.2. The halo intensity was measured at the most intensive point of the radial distribution of the diffraction. The intensity of the specular beam decreased monotonously by the Ga deposition and subsequent As molecular-beam supply. The halo intensity increased immediately after the Ga deposition and decreased by the As molecular-beam supply. The halo intensity shows a maximum and decreased slightly during Ga deposition. This phenomena caused by the absorption of the electron beam by the droplets, because the size of the Ga droplets increased with increasing the deposition time. The intensity of (004) transmission diffraction spot increased gradually with vanishing of the halo by the As molecular-beam supply. The halo disappeared after 50 s radiation of As molecular-beam with BEP of 3 x 10^{-6} Torr to the droplets. Since the average diameter of the Ga droplets is 800 Å as mentioned later, the total amount of As atoms impinging directly from the As molecular-beam on a individual droplet for 40 s is estimated as 5 x 10^6 atoms, and is nearly equal to the number of the Ga atom in the droplet. This coincidence suggests that the GaAs microcrystals grow by the direct incorporation of As atoms from the molecular beam.

These changes of the RHEED intensities showed that the impinging Ga atoms condensed and formed droplets without reaction to the surface first and then the three dimensional growth of GaAs epitaxial microcrystals occurred by the subsequent As molecular-beam supply. The almost filled dangling bond nature of the S-terminated surface[9] resulted in the appearance of the inert surface for the adsorption of foreign atoms. Since the surface of the droplets is thought to be effectively random high index or roughened surface with a lot of available site for the adsorption of the

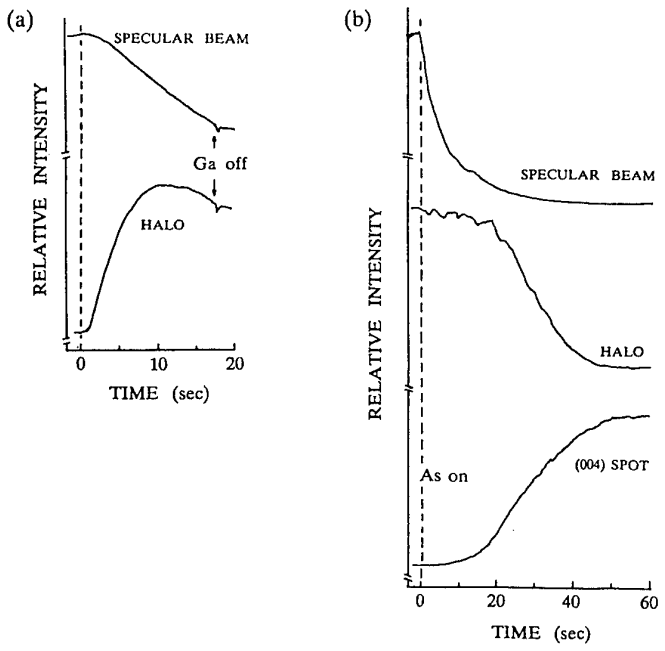


FIG.2. The variation of the RHEED intensities during Ga deposition (a) and the As molecular beam supply (b) on the S-terminated GaAs substrate at 200 C.

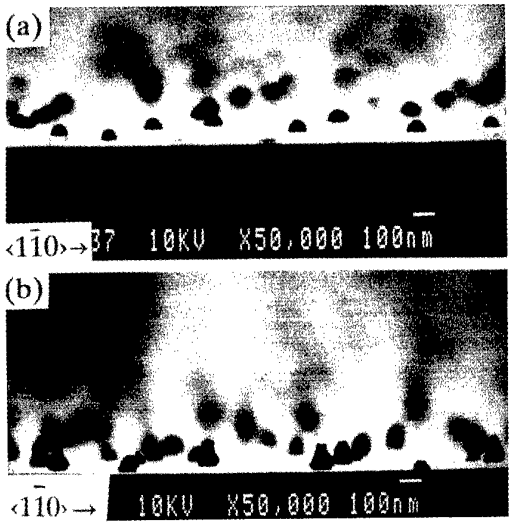


FIG.3. Surface morphology of the samples after Ga deposition(a) and subsequent As molecular beam supply (b) on the S-terminated GaAs (001) at 200 C.

As atom at the liquid-vapor interface, the sticking coefficient of the As atom to the Ga droplets is thought to be nearly unity.

The surface morphology of the samples after Ga deposition and subsequent As supply observed by high-resolution scanning electron microscope(SEM) are shown in Fig.3 for the S-terminated GaAs substrate. Many hemispherical shaped Ga droplets with uniform size formed on the S-terminated surface after the Ga deposition. The average diameter of the Ga droplets is 800 Å and the standard deviation of the size distribution is less than 10 %. The total amount of the Ga atoms in the droplets estimated from the hemispherical shape and the diameter is nearly equal to the total amount of the supplied Ga atoms. This means that the Ga atoms coalesced without reaction to the surface as speculated in the RHEED pattern changes mentioned above. These Ga droplet changed to the microcrystals surrounded mainly by (111) and (110) facets after the As molecular-beam supply. The base size of the microcrystals is about 700 Å x 700 Å which is nearly equal to the diameter of the Ga droplet. The (111) facets along <110> direction are well defined rather than along <1$\bar{1}$0> direction.

On the contrary, two dimensional lateral growth of GaAs occurred by the same procedure on a GaAs (001) surface without S-termination. Figure 4 shows the RHEED intensity variations during Ga deposition and subsequent As molecular-beam irradiation on the c(4x4)

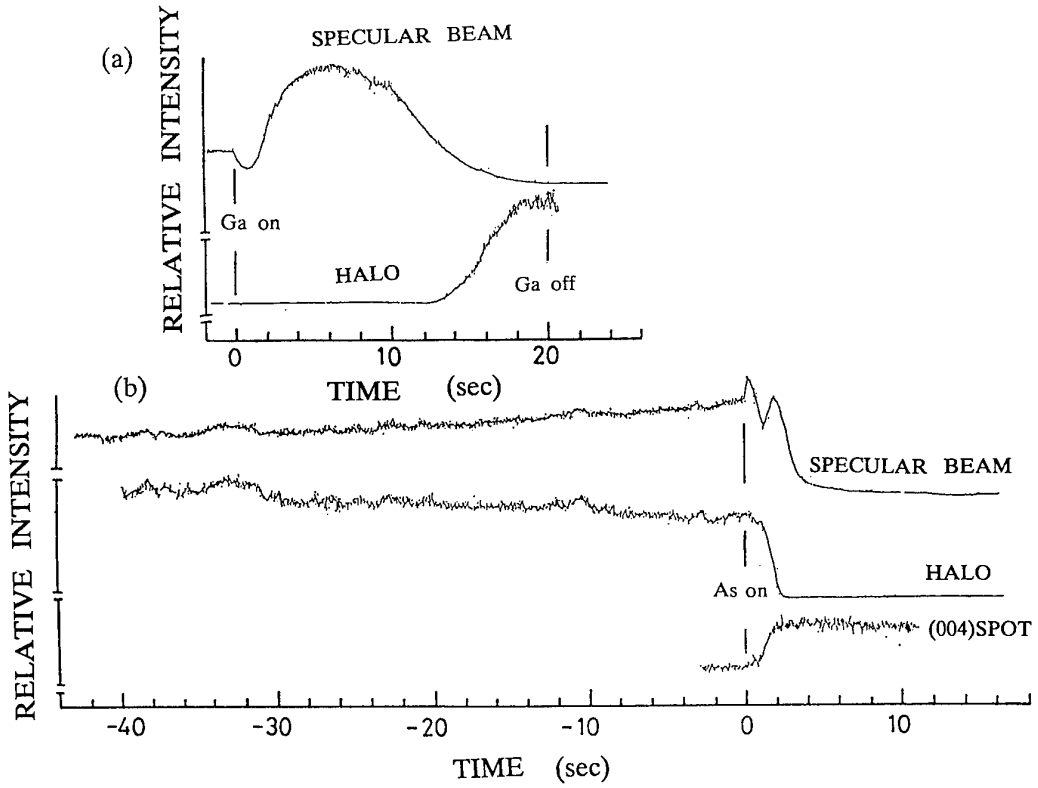


FIG.4. The variation of the RHEED intensities during Ga deposition (a) and the As molecular beam supply (b) on the As-adsorbed GaAs substrate at 200 C.

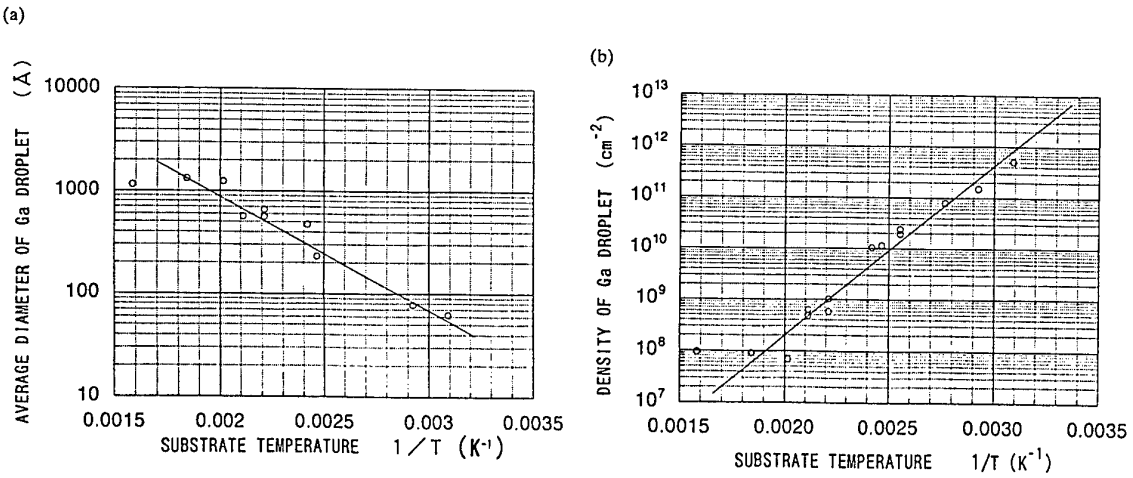


FIG.5. Temperature dependence of average diameter of Ga droplet (a) and density of Ga droplet (b). Solid lines in (a) and (b) show theoretical value calculated from total amount of supplied Ga and density of Ga droplet and activation energy of 0.67 eV, respectively.

As-adsorbed surface at 200 C. In this case, the specular beam intensity decreased first and then increased to a maximum value during Ga deposition and decreased again with appearance of the halo. The specular beam intensity reached a maximum value after the Ga deposition corresponding to an amount required to form about 1.7 equivalent monolayer of GaAs. Similar results were obtained by Deparis and Massies[10] for the Ga deposition on the GaAs surface with c(4x4) reconstruction. Although they have not observed the halo intensity change, the fact that the halo appeared after the deposition of 1.7 equivalent monolayer of Ga indicates that the surface coverage of As atoms is 1.7 for c(4x4) reconstruction, which is equal to the value obtained by Biegelsen et al[11]. The halo indicates the appearance of Ga droplets. The specular beam intensity increased first by the As molecular-beam irradiation to the surface, then decreased, increased again and finally decreased. The intensity change in the specular beam is very similar to the migration enhanced epitaxy (MEE) growth at low substrate temperatures. Deparis and Massies observed the RHEED pattern change during As molecular-beam irradiation to the Ga-stabilized surface. In their results, the As-stabilized (2x4) surface reconstruction appeared at the first and second maxima and the Ga-stabilized (4x2) surface reconstruction appeared at the minimum of the specular beam intensity change during As molecular-beam irradiation. This is due to the difference in the specular beam intensity between the As- and Ga-stabilized surfaces. The surface with (1x3) reconstruction, which was caused by an As-adsorption phase below 300 C, appeared in the final stage. The halo intensity decreased rapidly after the appearance of the minimum in the specular beam intensity change. These results indicate that layer-by-layer two dimensional growth was predominant. This is a striking contrast with three dimensional island growth on the S-terminated substrate mentioned above.

The base size and the density of microcrystals grown on the S-terminated substrate are nearly equal to those of Ga droplets. The size and the density of Ga droplets depend on the Ga molecular-beam flux intensity, the total amount of Ga deposition and the substrate temperature during Ga deposition. Figure 5 shows the results for the substrate temperature dependence of the average diameter and the density of the Ga droplets deposited on the S-terminated GaAs (001) for Ga molecular-beam intensity of 3.3×10^{14} $cm^{-2}s^{-1}$. The total amount of Ga was equivalent to 2.7 monolayers of GaAs. The density of the Ga droplets in this figure means a saturation density of the nuclei. The nucleation mechanism of the Ga droplets will be described in detail elsewhere. The size decreases and the density increases with the substrate temperature. The activation energy in the temperature dependence of the Ga droplet density is 0.67 eV. We can obtain homogeneous size Ga droplets with a diameter below 100 Å and a density near 10^{12} cm^{-2} by maintaining the substrate temperature during Ga deposition around 60 C.

4.CONCLUSIONS

The surface of GaAs was terminated by sulfur atoms in the molecular beam epitaxy system. The epitaxial growth of GaAs microcrystals occurred on this surface by sequentially supplying Ga and As molecular beams. We have already demonstrated that numerous GaAs epitaxial microcrystals having nearly equal size were grown on a S-terminated GaAlAs surface by the droplet epitaxy and the GaAlAs layer growth over the GaAs microcrystals was performed by MEE process for burying GaAs microcrystals[12]. This method, termed Droplet Epitaxy, is promising for the direct formation of GaAs quantum dot structures with size of each microcrystals below 100 Å and the density of dots over $10^{12}cm^{-2}$.

5.ACKNOWLEDGEMENTS

The authors wish to thank Drs. T.Chikyow and S.Tsukamoto for valuable discussions and Mr. S.Takahashi for SEM observations. This work has been partly supported by the project named "NANOSPACE LAB." of Science and Technology Agency , Japan.

6.REFERENCES

1.Y.Arakawa and H.Sakaki, "Multidimensional quantum well laser and temperature dependence of its threshold current," Appl. Phys. Lett., 40, pp939-941, 1982.

2.H.Sakaki, "Quantum wire superlattices and coupled quantum box arrays: a novel method to suppress optical phonon scattering in semiconductor," Jpn. J. Appl. Phys., 28, ppL314-L316. 1989.

3.Y.Arakawa, "Fabrication of quantum wires and dots by MOCVD selective growth," Solid-State Electronics, 37, pp523-528, 1994.

4.N.Koguchi and K.Ishige, "Growth of GaAs epitaxial microcrystals on an S-terminated GaAs substrate by successive irradiation of Ga and As molecular beams," Jpn. J. Appl. Phys., 32, pp2052-2058, 1993.

5.N.Koguchi K.Ishige and S.Takahashi, "New selective molecular-beam epitaxial growth method for direct formation of GaAs quantum dots," J. Vac. Sci. Technol., B11, pp787-790, 1993.

6.T.Chikyow and N.Koguchi, "Microcrystal growth of GaAs on a Se-terminated GaAlAs surface for the quantum-well box structure by sequential supplies of Ga and As molecular beams," Appl. Phys.Lett., 61, pp2431-2433, 1992.

7.J.Aphopelto, A.A. Yamaguchi, K.Nishi, A.Usui and H.Sakaki, "Nanoscale InP islands for quantum box structures by hydride vapor phase epitaxy," Jpn. J. Appl. Phys., 32, ppL32-L35, 1993.

8.R.Noetzel, J.Temmyo and T.Tamamura, "Self-organization of boxlike microstructures on GaAs (311)B surfaces by metalorganic vapor-phase epitaxy," Jpn. J. Appl. Phys., 33, ppL275-L278, 1994.

9.S.Tsukamoto and N.Koguchi, "Observation of sulfur-terminated GaAs (001)-(2x6) reconstruction by scanning tunneling microscopy," Appl. Phys. Lett., 65, pp2199-2201, 1994.

10.C.Deparis and J.Massies, "Surface stoichiometry variation associated with GaAs (001) reconstruction transitions," J. Crystal Growth, 108, pp157-172, 1991.

11.D.K.Biegelsen, R.D.Bringans, J.E.Northrup and L.-E.Swartz, "Surface reconstructions of GaAs (001) observed by scanning tunneling microscopy," Phys. Rev., B41, pp5701-5706, 1990.

12.N.Koguchi, K.Ishige and S.Tsukamoto, "Direct formation of GaAs-GaAlAs quantum dots structure by droplet epitaxy," Mat. Res. Soc. Symp. Proc. Growth, Processing, and Characterization of Semiconductor Heterostructures, G.Gumbs, S.Luryl, B.Weiss and G.W.Wicks, 326, Material Research Society, 1994.

Paper presented at the Third ICIM/ECSSM '96, Lyon '96

Optoelectronic Functions in Organic-Inorganic Hetero Nanosystems

J. Takada, M. Hoshi, T. Yamamoto[1], M. Watanabe[1] and T. Takagi[1]

Research Institute for Radiation Biology and Medicine
Hiroshima University, 2-3 Kasumi 1-chome, Hiroshima 734, Japan
[1]Ion Engineering Research Institute Corporation,
Tsuda, Hirakata, Osaka 573-01, Japan

ABSTRUCT

Formations of organic-inorganic hetero nanostucture consisting copperphthalocyanine, C_{60}, TiO_x and SiO_2, have been reported, and Basic information on the formation of hetero nanostructures by vacuum thin film technology was discussed. Optoelectronic functions in organic-inorganic hetero nanosystems have been demonstrated and discussed from the viewpoints of carrier generation at the interface, size effects, the difference of dielectric constance between organic and inorganic solids, and molecular orientation.

1. INTRODUCTION

The organic-inorganic hetero nanosystem is a heterostructure consisting of nanoscopic size organic and inorganic components with systematic functions. [1)] In organic-inorganic hetero nanosystems, the freedom of design for functional materials or devices becomes extremely high by utilizing not only the individual merits but also the interfacial properties between the components. In this system, an organic molecule is treated as an important unit to fabricate a functional system. This kind of material system has been studied since the first proposal of Takada et al in 1992. [2)]

We expect an effective transfer of information or energy at the interfaces, and fantastic properties originating from the size effects of exciton confinement in hetero nanostructures. This organic-inorganic hetero nanosystem is one strategy for realizing molecular devices or intelligent materials in solid states. In this new material concept, an organic molecule is treated as a structural and functional unit in solids.

Cooperation between the optical sensing or actuating function of organic molecules and the transporting function of electronic signals or energy in inorganic materials is possible through interfaces in organic-inorganic hetero nanosystems. In these systems, high electron mobilities of inorganic solids can be utilized. For examples, electron mobilities in Si and GaAs are 1450 and 8500 cm^2/Vs at room temperature respectively.[3)] In nanosize scale heterostructures, communication between individual molecules and inorganic materials works efficiently since each molecule contacts with or most molecules contact with inorganic materials.

Compared with bulk material synthesis, the thin film vacuum process offers a major advantage in fabricating artificial nanostructures from the viewpoints of material combination and size controllability due to the nonequilibrium process. Recently, various types of organic-inorganic hetero nanostructures were successfully fabricated by evaporation and reactive evaporation techniques.[1, 3, 4)]

In this paper, we report the formation of artificial hetero nano-structures by the thin film vacuum process and discuss optoelectronic and optical functions of these new material system.

2. FORMATION OF HETERO NANOSTRUCTURE

Organic-inorganic hetero layered nanostructures were fabricated by thermal and reactive evaporation techniques using the organic crystal growth multi-ion source type ICB deposition apparatus at Ion Engineering Center Corporation. A tungsten crucible with a nozzle diameter of 2 mm for organic molecules of copperphthalocyanine (CuPc) and C_{60} and graphite crucibles with a nozzle diameter of 8 mm for Ti and Si were heated at 840, 2270 and 1700 K respectively to maintain an evaporation rate of 0.1 nm/s in each case. Alternating layered structures were constructed by using shutters for each crucible, while monitoring the film growth with an oscillating quartz crystal thickness monitor. An O_2 ambient pressure of $2x10^{-4}$ Torr was maintained using a mass flow controller during the TiO_x or SiO_2 film growth. The vacuum level during C_{60} deposition was $2x10^{-6}$ Torr. Hetero structures were formed at a substrate temperature of 420 K. Metal oxides are amorphous due to the low temperature of the substrates. The stoichiometry of the TiO_x films was estimated from X-ray photoelectron spectroscopy to be x~1.5. The silicon oxide is considered to be approximately SiO_2 from the optical properties.

Figure 1 shows a cross-sectional transmission electron microscopy (TEM) image for a superlattice of CuPc/SiO_2 on a Si substrate indicating the successful formation of an organic-inorganic hetero structure in a nano scale. The direct

0-8194-2165-0/96/$6.00

TEM observation confirms that there is no severe mixing at the interfaces of the ceramics layer on a CuPc layer . Surprisingly, a CuPc crystalline form of the layer exists just below the ceramics layer, indicating that the CuPc crystal structure is not always destroyed by the reactive formation of ceramics. A detailed cross sectional TEM image at an interface is shown in Fig. 2. This part indicates an interface of TiO_x layer on CuPc layer whose designed thickness is four mono layers. Four molecular layers of CuPc can be seen under the TiO_x layer. The structure is considered to be CuPc crystal with b-axis parallel to the interface by comparing a cross- sectional TEM image of thick CuPc film which has been characterized by x-ray diffraction. The mixing layer whose thickness is approximately equivalent to a mono layer of CuPc, can be seen just below the TiO_x layer.

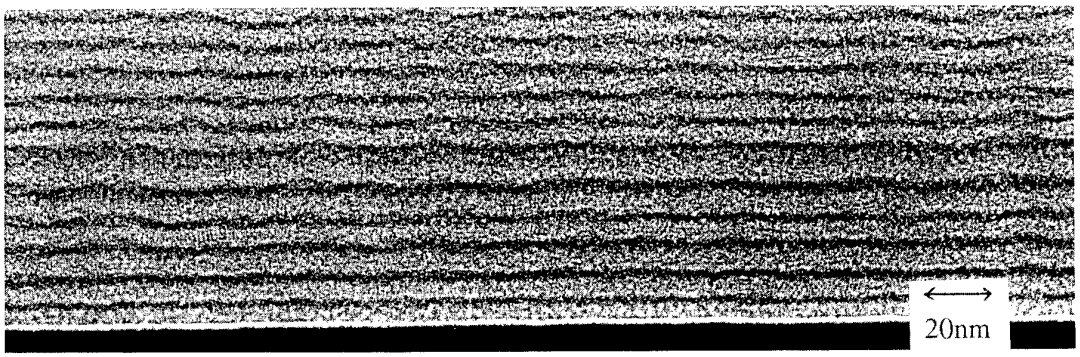


Fig. 1 A cross-sectional TEM image of a CuPc/SiO_2 superlattice. Bright and dark layeres correspond to CuPc and SiO_2 layers respectively.

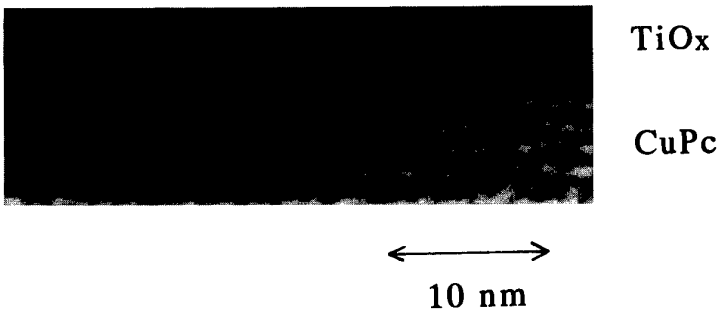


Fig. 2 A cross-sectional TEM image of an interface of TiO_x layer on CuPc layer .

C_{60} films which were deposited without acceleration of the ionized molecules became non-uniform in thickness. A high acceleration voltage made the crystalline quality of the C_{60} films low. Adequate acceleration of the C_{60} molecules seems to be necessary to fabricate a C_{60} layer with good quality for hetero nanosystem formation. A single layer of C_{60} with 50 monolayers (ML) on mica substrate deposited at acceleration voltage (Vacc) of 500 V exhibited a good-quality fcc crystalline structure as shown in the x-ray diffraction of Fig.3. X-ray diffraction corresponding to the fcc(100) plane can not be observed in the film deposited at Vacc =2000 V. High voltage acceleration of C_{60} may destroy the molecular structure itself since the optical absorption spectrum for such a film is very different from those for films deposited at an acceleration voltage lower than 1000V. We notice that C_{60} films on amorphouss substrates are amorphouss. Therefore layers of C_{60} film in suparlattices with amorphous metal oxides is amorphus. This is compleatly different from suparlattices with CuPc layers.[2, 4)]

Double layered structures of a TiO_x layer with 13 nm thickness on 16 ML of C_{60} exhibited x-ray diffraction peaks corresponding to the (111) surface of C_{60} fcc crystal as shown in Fig. 4. This indicates that the reactive formation of ceramics layer onto C_{60} molecular crystal does not destroy at least several of the moleculer layers of crystal under the ceramics.

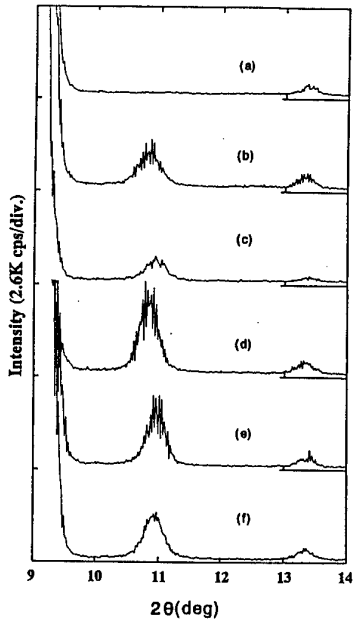


Fig. 3 X-ray diffraction spectra for C_{60} single layers with 50 ML deposited at acceleration voltage of a) 2000 V, b) 1000 V, c) 700 V, d) 500 V, e) 300 V, f) o V.

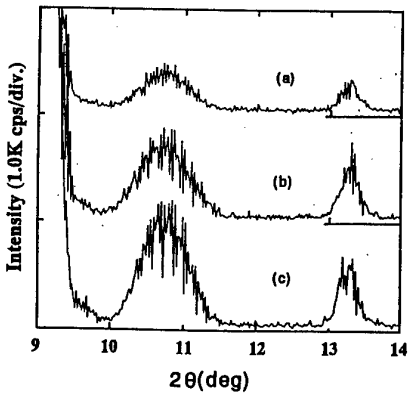


Fig. 4 X-ray diffraction spectra for double layers of a TiO_X layer on a C_{60} layer in which Ti beams were evaporated at the acceleration voltage of a) 1000 V, b) 500 V, c) 0 V.

3. OPTOELECTRONIC FUNCTIONS OF ORGANIC-INORGANIC HETERO NANOSYSTEMS

Optoelectronic functions such as light detector, photovoltaic activity , and light emission are expected in organic-inorganic hetero nanosystems. In these systems, an organic-inorganic heterointerface has the very important roles of carrier generations from molecular excitons (M*), spatial separation of free electrons and holes, and electronic communication between a molecule (M) and an inorganic material.

The quantum efficiency of the charge carrier formation, which is defined as the number of free electrons and holes formed per absorbed light quantum, is very small in most organic solids due to the many ways of deactivating the excited state.

Since the dielectric constant in organic semiconductors is low, the energy needed to separate the initial ion pair may be greater than the energy to excite a molecule. Coulomb interaction between an electron (e^-) and a parent positive ion (M^+) is effective at long range and is magnified by the low dielectric constant of the organic solids. Therefore geminate recombination is dominant in organic semiconductors. [5)]

$$MMMM \xrightarrow{h\nu} M^*MMM \xrightarrow{\text{gem. recomb.}} M^+Me^-MM \longrightarrow MMMM \quad (1)$$

3.1 Charge generation and spatial separation of photocarriers at the hetero-interface

Let's consider the charge generation process after the light absorption of a molecule in an organic-inorganic heterostructure with an inorganic semiconductor (IS) having a relatively large electron affinity and dielectric constant.

Under illumination, photons create molecular excitons in an organic semiconductor where the energy gap of the organic semiconductor is smaller than that of an inorganic semiconductor. A molecular exciton diffuses to the interface between the organic and inorganic layers, and donates its excited electron directly into the conduction band of the inorganic semiconductor to leave a free hole in the valence band of the organic semiconductor.

$$MMMM / IS \xrightarrow{h\nu} M^*MMM / IS \longrightarrow MMMM^* / IS \longrightarrow MMMM^+ / e^- IS \quad (2)$$

In this heterostructure, the efficiency of photocarrier generation at the interface is expected to be extremely high when the thickness of the organic layer is less than the diffusion length of the molecular exciton.

Another process, i. e., the spatial separation of photocarriers generated in the organic region, makes the probability of recombination low. In case of charge generation in the molecular solid, electrons drift or difuse to the inorganic semiconductor with large electron affinity. This leads charge separation at the organic-inorganic hetero-interface.

$$MMMM / IS \xrightarrow{h\nu} M^*MMM / IS \longrightarrow M^+Me^-MM / IS \longrightarrow M^+MMMe^- / IS \longrightarrow M^+MMM / e^- IS \quad (3)$$

This charge separation process is illustrated in Fig.5.

We have demonstrated the optoelectronic properties of $CuPc/TiO_X$ superlattice structures as a model case mentioned above. In this system, only CuPc molecules absorb visible light since the energy gaps of CuPc and TiO_X layers are 2.0 and 3.2 eV respectively. A superlattice with an artificial period of 40nm exhibited a 40 times higher value of in-plane photoconductivity and larger light intensity dependence for red light illumination than a single layer of CuPc as shown in Fig. 6.[2] These phenomena suggest larger photocarrier generation and less recombination probability in superlattices than in organic single layers. Moreover, transverse photoconduction measurements against the interface-plane showed the occurrence of electron transfer from CuPc to TiO_X at the interfaces. [4]

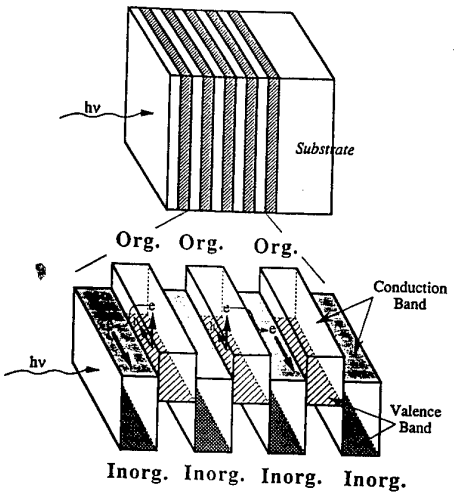


Fig. 5. Schematic illustration of photoconduction in an organic-inorganic hetero-superlattice.

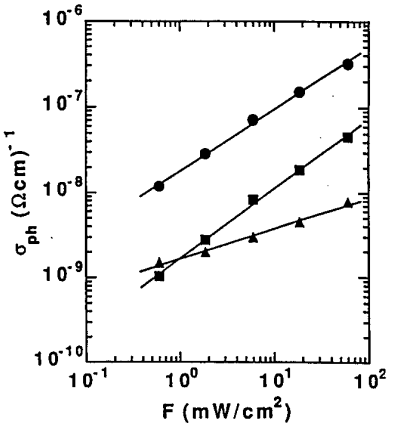


Fig.6. In-plane photoconductivity (σph) as a function of incident light intensity (F) for a CuPc single layer (▲) and for multilayers of CuPc(96Å)/TiO_X(96Å)( ) and CuPc(192Å)/TiO_X(12Å) (●).

3.2 Nanosize optical phenomena

Nanosize optical phenomena of organic solids have recently been attracting attention from both basic and application points of view. [1, 6, 7, 8, 9, 10, 11] Several papers have been reported on low dimensional phenomena of molecular excitons. A question arises. Do molecular excitons behave in the same manner as inorganic nanostructures? A low value of dielectric constance in organic materials may result in an extremely small size of Frenkel type exciton. Namely, does the nano size deform the shape of such a small exciton? Such an effect may be small compared to inorganic semiconductors.

We know that the Bohr radius of the exciton is proportional to the dielectric constance of the media. Therefore, the state of a molecular exciton in an inorganic matrix must be modified by a large dielectric constance of the matrix. This is molecular doping into an inorganic semiconductor.

$$IS/M' / IS \xrightarrow{h\nu} IS/M'^* / IS \quad (4)$$

The energy of the first excited state S_1 is of CuPc molecules which exhibit a red-shift in CuPc-TiO_X alloy. [4]

Electronic states on nano size sheets, lines and boxes of molecular solids may be easily modified by inorganic matrices with a relatively large dielectric constant since most molecules in such small organic solids contact with the matrix. Nanoboxes of CuPc molecular crystals exhibit a red-shift in optical absorption in a TiO_X matrix like a CuPc-TiO_X alloy. [5] Moreover, it is possible to confine the motion of molecular excitons by the inorganic barrier (IB).

$$IB/MMMM / IB \xrightarrow{h\nu} IB/MM^* MM/ IB \quad (5)$$

Hetero layered structures can be well defined by artificially comparing them to the form of the alloy and the nanobox. The thickness dependence of the organic layer on the energy shift of molecular excitons was investigated in the form of heteo layered structures. Optical absorption spectra were measured at room temperature for tri-layered

samples with various thicknesses of CuPc layer and a 2nm thickness of SiO_2 and TiO_x oxide layers. These two heterostructures are type I and type II, respectively, as shown in Fig. 7. The energy (E_{S1}) of an exciton which is formed by excitation of the CuPc molecule into its first excited state S_1 is determined for various samples from the peak of the Q band absorption spectrum. Although the values of E_{S1} for SiO_2/CuPc/SiO_2 samples are almost the same as the value for a CuPc single layer, the values for TiO_x/CuPc/TiO_x decrease drastically when the thickness of the CuPc layer decreases below 2.6 nm as shown in Fig.8.

This thickness value corresponds to two mono layers of CuPc if the b axis of the α-form of CuPc crystal is parallel to the surface. This structure is correct at least for hetero structures with a CuPc layer thicker than six mono layers from TEM data. It is extremely difficult to observe the crystalline structure of heterostructures with two mono layers of CuPc at the present. However, there may not be essential difference of CuPc crystalline structure between TiO_x/CuPc/TiO_x and SiO_2/CuPc/SiO_2 since both the ceramic layers are amorphous. Therefore, a critical condition for this effect may be the necessity of direct contact between all of the molecule and inorganic materials with large dielectric constant. Excited electrons of CuPc molecules can easily penetrate into the TiO_x layer due to the large electron affinity and large dielectric constant of TiO_x, especially when the thickness of the CuPc layer is less than two mono layers.

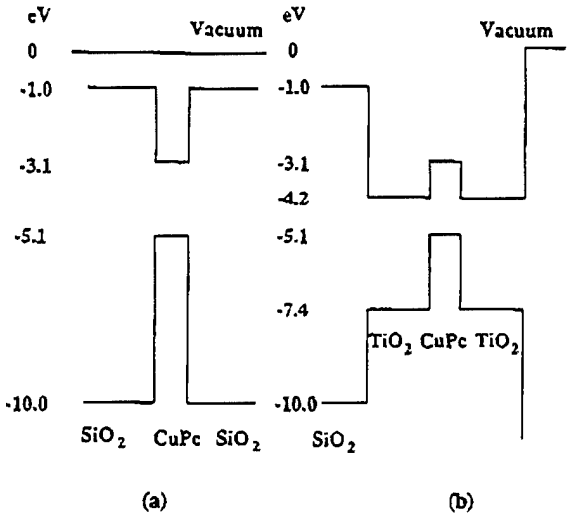


Fig. 7. Models of energy level diagrams for two types of organic-inorganic heterostructures : Type I of SiO_2/CuPc/SiO_2 (a) and Type II of TiO_2/CuPc/TiO_2 (b) deposited on SiO_2 substrate.

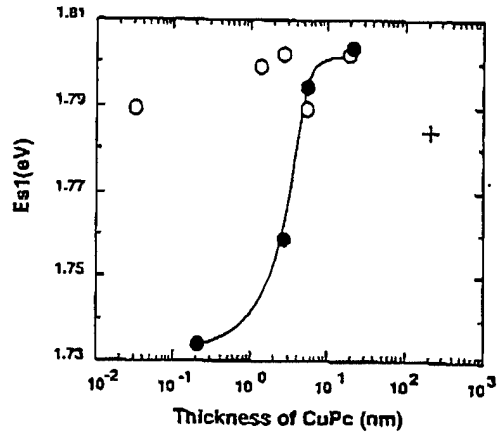


Fig. 8. The energy of an S_1 exciton of CuPc molecule in the two kinds of hetero structures with 2nm thickness of oxide layers, SiO_2/CuPc/SiO_2 (o) and TiO_2/CuPc/TiO_2 (•), and in a CuPc single layer (+).

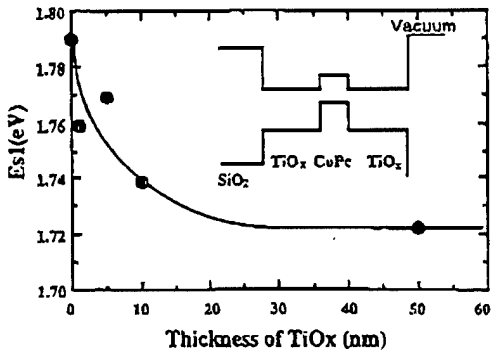


Fig. 9. Thickness dependence of inorganic layer on the energy of an S_1 exciton of CuPc molecule in TiO_x/CuPc/TiO_x hetero structures with 2.6 nm thickness of CuPc layers.

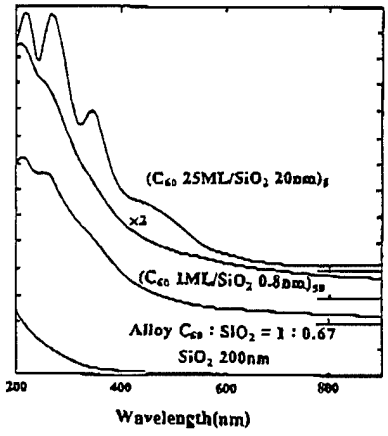


Fig. 10. Absorption spectra for several superlattice structures of C_{60} / SiO_2 a) (C_{60} 25 ML / SiO_2 20nm)$_5$, b) (C_{60} 1 ML / SiO_2 0.8nm)$_{50}$, c) Alloy of C_{60} : SiO_2 = 1 : 0.67 90nm thickness, d) SiO_2 100 nm thickness

The size effect of an inorganic solid on molecular excitons in organic-inorganic hetero nanosystems may be observed when the electron orbital of the molecular exciton expands into the inorganic region. We make an assumption for molecular excitons, in which the size becomes large when contacting with an inorganic layer with large dielectric constance. If this is so, the Bohr radius of a molecular exciton is limited by the nano size inorganic layer with vacuum barriers.

Samples of TiO_x/CuPc/TiO_x on SiO_2 substrates with CuPc of a fixed thickness of 2.6 nm exhibited energy shifts of CuPc excitons by changing the thickness of TiO_x layer (d_{TiOx}) on a nano scale. The exciton energy approaches the original value of CuPc molecules at the limit of d_{TiOx} =0 layer and to a value of a large exciton whose Bohr radius is determined by the dielectric constant of TiO_x layer, at the limit of d_{TiOx} =∞ as shown in Fig.9. [5]

Fig 10 shows the absorption spectra for several superlattice structures of C_{60} / SiO_2 . We note that the spectrum of a superlattice of (C_{60} 1 ML / SiO_2 0.8nm)$_{50}$ is different from both 1ML of C_{60} and a superlattice of (C_{60} 25 ML / SiO_2 20nm)$_5$ but is similar to that of an alloy of C_{60} and SiO_2, indicating a large interaction between C_{60} and SiO_2 in a superlattice with 1 ML of C_{60}. On the contrary, the superlattice with a C_{60} layer of more than 3ML maintains the original molecular state in this heterostructure.

4. SUMMARY

Formations of organic-inorganic hetero nanostucture consisting CuPc, C_{60} , TiO_x and SiO_2, habe been reported, and Basic information on the formation of hetero nanostructures by vacuum thin film technology was discussed. We succeeded in fabricating various types of organic-inorganic hetero nanostructures composed of CuPc molecular crystals and amorphous metal oxides of TiO_x and SiO_2 such as superlattice structure and nanobox by applying vacuum thin film technology. A cross sectional TEM study revealed that the thickness of the mixing layer at the ceramics interface on CuPc molecular crystal is at most a monolayer of CuPc in superlattice structures.

Although the reactive formation of ceramics layer onto C_{60} molecular crystal does not destroy at least several of the moleculer layers of crystal under the ceramics, we never succeed the superlattice structure with C_{60} molecular crystals. We notice that C_{60} molecular crystals are easily destroyed by formation of metalic layer onto it. This dose not occure in the case of the heterostructure with CuPc crystal.

Optoelectronic functions in organic-inorganic hetero nanosystems have been demonstrated and discussed from the viewpoints of carrier generation at the interface, size effects, the difference of dielectric constance between organic and inorganic solids, and molecular orientation. In these systems, an organic-inorganic heterointerface has the very important roles of carrier generations from molecular excitons, spatial separation of free electrons and holes, and electronic communication between a molecule and an inorganic material. As an example, high photoconductivity of CuPc-TiO_x superlattice structures were demonstrated.

Size effects of the molecular exciton in the hetero nano structures were demonstrated for both heterostructures consisting of CuPc or C_{60} molecules. Understanding the mechanisms on the effects will require further investigation both experimentally and theoretically. However, the effects suggest that we can exploit and control the noble properties of molecules combining electronic lone molecules and inorganic materials in which the wave function of the free electron spreads. In the future, intelligent optoelectronic materials which surpass the limits of the traditional paradigm of material classification will be created by this concept of organic-inorganic hetero nano systems.

ACKNOWLEDGMENT

This research work has suported by Science and Technology Aigency of Japan.

REFERENCES

1) J. Takada: Jpn. J. Appl. Phys. 34 (1955) 3864.
2) J. Takada, H. Awaji, M. Koshioka, A. Nakajima, and W. A. Nevin: Appl. Phys. Lett.61 (1992)2184.
3) S. M. Sze, Physics of Semiconductor Devices, (John Wiley & Sons, New York, 1981).
4) J. Takada, H. Awaji, M. Koshioka,W. A. Nevin, M. Imanishi and N. Fukada: J. Appl. Phys. 75 (1994) 4055.
5) J. Simon and J. J. Andre: Molecular Semiconductors (Springer, Berlin, 1985).
6) J. Takada: Jpn. J. Appl. Phys. 34-1 (1995) 158.
7) F. F. So, S. R. Forrest, Y. Q. Shi and W. H. Steier: Appl. Phys. Lett. 56 (1990) 674.
8) Y. Ohmori, A. Fujii, M. Uchida, and K. Yoshino: Appl. Phys. Lett. 62 (1993) 3250.
9) S. Tokito, J. Sakata, and Y. Taga: Appl. Phys. Lett, 64 (1994) 1353.
10) Y. Imanishi, S. Hattori, A. Kakuta, and S. Numata: Phys. Rev. Lett. 71 (1993) 2098.
11) J. Takada, H. Awaji, M. Koshioka, A. Nakajima, W. A. Nevin, M.Imanishi, and N. Fukada: Advanced Materials '93, II / A: Biomaterials, Organic and Intelligent Materials, Elsevier B. V. 15A (1994) 667.

Morphology of Thin Film Growth of Gallium Nitride by Atmospheric Pressure Organometallic Vapor Phase Epitaxy

S.M. Liao*, J.H. Wen*, H.F. Hung**and S.M. Lan**

*Institute of Electronic Engineering, Chung Yuan Christian University,
Chungli 32023, Taiwan, R.O.C.
**Institute of Nuclear Energy Research, P.O. Box 3-11,
Lungtan 32500, Taiwan, R.O.C.

ABSTRACT

Morden approaches to the growth of high quality gallium nitride(GaN) thin films have focused on the use of organometallic vapor phase epitaxy(OMVPE). One of the keys to obtain the high quality thin film was the use of a thin buffer layer between the sapphire substrate and the growth film. Thin films of GaN were successfully prepared by our atmospheric pressure(AP) OMVPE system using GaN buffer layer over basal plane (0001) sapphire substrates. The present study will discuss the role of buffer and the influence of the temperature and ammonia/trimethylgallium(NH3/TMG) mass flow ratio in controlling morphology of GaN thin films. Normarski differential interference contrast optical microscopy and scanning electron microscopy(SEM) reveal the surface and cross-section morphologies of different growth conditions. To the best of our knowledge the "volcanic cone-like" hillock structure describe here is the first reported the morphology for single crystal GaN thin films.

1. Introduction

The semiconductors in the III-V materials systems have received much attention since their discovery because they are weak suited for a wide range of applications in electronics and optoelectronics. GaN is a wide band gap semiconductor material with potential applications for green to ultraviolet light emitting diodes(LEDs) and InGaN for yellow to blue LEDs.[1]

Epitaxy films of GaN have been grown by several growth techniques, such as organometallic vapor phase epitaxy(OMVPE) and molecular beam epitaxy(MBE) using sapphire(Al_2O_3) as the most common substrate. As-grown GaN films are known to contain a high density of defects(mainly threading dislocations), due to the large lattice mismatch(~14%) and thermal expansion coefficient difference between the epilayer and the substrate. A low temperature AlN[2] or GaN[3] buffer layer considerably improves the crystal quality of the GaN epilayers. In addition to searching for better lattice and thermally matched substrates, such as SiC and ZnO, recent efforts have more concentrated on the growth mechanism of GaN on sapphire using an GaN buffer layer grown at low temperature. This suggests that the low temperature buffer layer might play a critical role for good quality GaN epitaxy.

0-8194-2165-0/96/$6.00

Besides, the temperature and ammonia/trimethylgallium (NH_3/TMG) mass flow ratio effects to surface morphology are also important to grow high quality thin films but have no sufficient disccusion utill recent. This issue focuses how these two conditions affect GaN morphology and also introduces the thin film surfaces with "volcanic cone-like" morphology which never reported and disccussed elsewhere.

2. Experimental and Growth

GaN single crystals were grown on (0001) sapphire substrates. The sapphire substrates were from the cutted sapphire wafer into 1 × 1 cm^2 pieces in order to reduce the substrate cost of epilayer growth experiments. The epilayer growth were carried out in a conventional OMVPE system with a simple horizontal quartz chamber at atmospheric pressure. The substrates were heated by a radio-frequency heated SiC-coated graphite susceptor which held by a quartz carrier. Before loading into the deposition chamber, sapphire were sequentially cleaned with hot trichloroethylene, hot aceton, and hot methanol. Then, the substrates were etched in a hot H_2SO_4:H_3PO_4=3:1 solution(~160 ℃) for 12mins, rinsed in de-ionzed water and blown dry with filtered nitrogen. Trimethylgallium(TMG) and ammonia(NH_3) were used as the sources of Ga and N respectively to grow GaN buffer and epitaxial layers. Organometallic sources(OM) diluted with H_2 and a large amount of NH_3 with H_2 were mixed and fed through a delivery tube to a slanted substrate(45 degrees).

During etching the ambient gas H_2 flow was 5SLM(standard liter per minute) and during growth was 1.5 SLM. Prior to growth, the substrates were subjected to NH_3 etch(with 5SLM H_2) at temperatures 80 ℃ higher than those of thin films growth as heat treatment for 10 minutes to remove unintentional contamination and to reduce the surface damage caused by the wafer cutting and polishing processes. In order to study the effects of growth conditions on thin film growth, GaN buffer layer was grown of TMG flow rate 24umol/min, NH_3 2SLM and ambient gas H_2 1.5SLM. By feeding TMG and NH_3 gases into chamber, a thin GaN amorphous layer was deposited. The substrate was then raised to a growth temperature for 30 minutes, so that a GaN epitaxial film of 1~2um thick was observed. The growth rates of epilayers were about 3~4um/hr. The two-step growth process is draw in Fig. 1. In this process, a thin GaN buffer layer(about 500 anstroms, measured by ellipsometry) is grown at relatively low temperature(about 550 ℃, measured by thermal couple) followed by a higher temperature growth at temperature of 960~1120 ℃, and NH_3 flow rate 0.5~9SLM of the rest of the film. Using this method, we could easily obtain wurtzite structure of GaN on sapphire substrates.

The temperature given in this paper is of the susceptor surface, the substrate temperature was determined to be 40 ℃ lower than the suceptor surface. The temperature was measured with an optical pyrometer which was calibrated by observing the melting point of a small amount of previously melted copper(Cu) on the susceptor surface. The surface morphologies of the epitaxial layers were characterized by Normarski differential interference contrast optical microscopy and scanning electron microscopy(SEM) using a JOEL company's JXA6400P 25kV electronicprobe micro analyzer and JSM6400 scanning microscope.

3. Results and Discussion

Fig. 2(a) and 2(b) show the buffer layers with and without thermal annealing effect caused by ramping to the growth temperature before their postgrowth of GaN thin film layer. See from Fig. 2(a), amorphous layer of GaN clusters were obserbed from low temperature growth. Since buffer layer also acts as nucleation layer and offers sources for over-layer thin film growth, thus the uniformness is important. Fig. 2(b) shows a high density grains of GaN with smoother surface than that Fig. 2(a) which was caused by thermal annealing and these nuclei were believed that they came from solid phase epitaxy process and reduced its roughness from recrystallizing of amorphous nuclei with some facet-like islands[4]. Suggesting that they may affect thin film layer over grown on it, result in "volcanic cone-like" hillock structure describe later. With buffer layer growth, we will not observed GaN films with hexagonal characteristics and effectively eliminate pyramid hillock island structure[1,2] which were easily observed in early papers.

GaN grown on sapphire with predeposition buffer layer shows a variety of surface morphologies that depend on temperatures and NH_3/TMG flow ratios. After choosing the GaN buffer layer thickness to be 500 anstrom, the growth temperature was varied between 960 and 1080 ℃ for the GaN thin film. From Fig. 3(a)~3(d), we see that the thin films change from polycrystalline(Fig. 3(a)) to single crystal films with holes(Fig. 3(b)) and then fairly smooth featureless mirrorlike(Fig. 3(c) and 3(d)). In our experiment, the range of temperature to grow GaN single crystal thin film is between 1000 and 1080 ℃. Outside this range GaN films will become polycrystalline or even without growth. The holes of Fig. 3(b) were caused by islands grew together but not coalescenced well that showed 3-dimensional island growth. And smooth films of Fig. 3(c) and 3(d) show no obvious trend observed by SEM graph as strong dependence of temperature and seems of its best range to observe high quality morphology with mirrorlike surface.

In an attempt to investigate the effect of the V/III mass flow ratio on the GaN film morphology, the NH_3 flow was varied for growth still using a GaN buffer layer and keep the same temperature. We see the cross-section of SEM photos in the first place. Fig. 4(a)~4(d) show that cross-section of GaN thin film change from polycrystalline to smooth film surfaces. From Fig. 5(a)~5(e) we see that thin film morphologies change from smooth surface, with some pinholes, higher density pinholes, then larger holes and holes with channel structures. For these films, we observed trend in various of NH_3 flow rate which shows worse surface morphology as the NH_3 flow was increased. Our possible explanation for the films grown at higher NH_3 flow is that total folw rate of H_2 and NH_3 was increased and caused cooler surface where reactions happen, it may decreasing the amount of prereaction between the TMG and NH_3 because of decreasing reaction temperature.

Shown in Fig.6(a) and 6(b) are the typical surface morphology and cross-sectional view of a GaN thin film on a sapphire substrate studied by SEM. It can be seen that the film has a relatively flat surface. The cross-sectional view shows no evidence of columnar morphology, another indication that the film is single crystallize. The surface is smooth with steps less than tens anstrom hight, which resulted from a layer-by-layer growth. These results suggest that addition optimization of the growth process could lead to near-atomically smooth surfaces.

sample No.	temperature	H2(SLM)	NH3(SLM)	TMG(SLM)
3(a)	960	1.5	4	24
3(b)	1000	1.5	4	24
3(c)	1040	1.5	4	24
3(d)	1080	1.5	4	24
4(a)	1040	1.5	0.5	24
4(b)	1040	1.5	1	24
4(c)	1040	1.5	2	24
4(d)	1040	1.5	5	24
5(a)	1040	1.5	4	24
5(b)	1040	1.5	6	24
5(c)	1040	1.5	7	24
5(d)	1040	1.5	8	24
5(e)	1040	1.5	9	24

Table. 1 Growth conditions

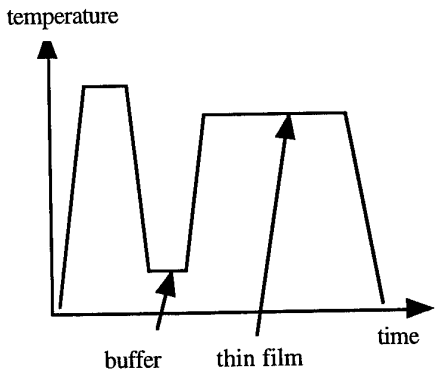


Fig.1 growth condition

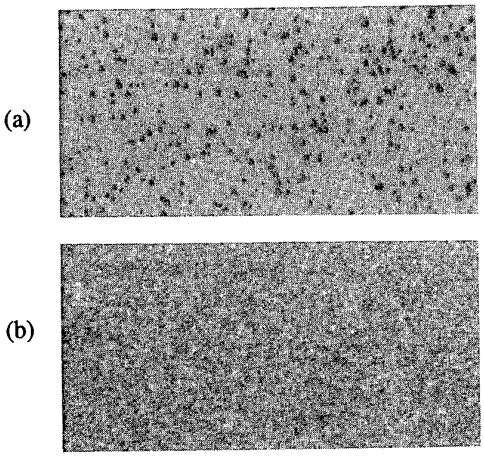


Fig.2(a) Buffer layer without annealing (b) with annealing

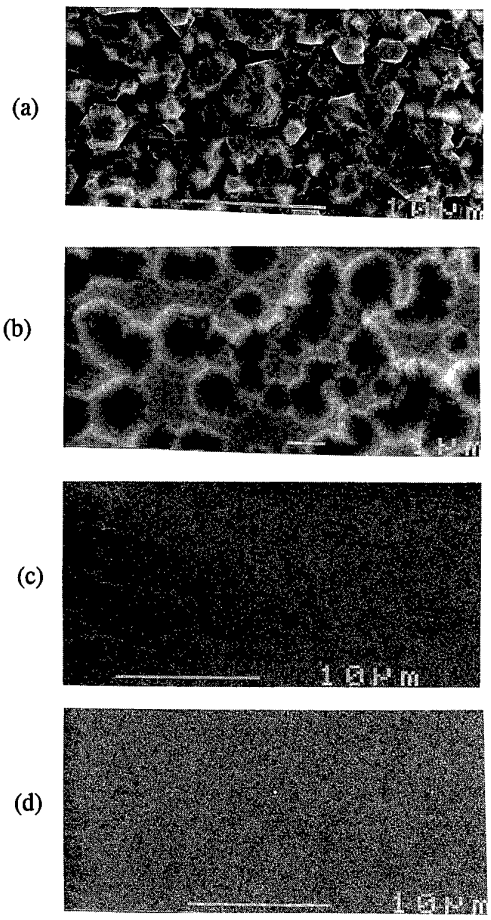


Fig.3(a)~(d) SEM of morphologies with various temperature

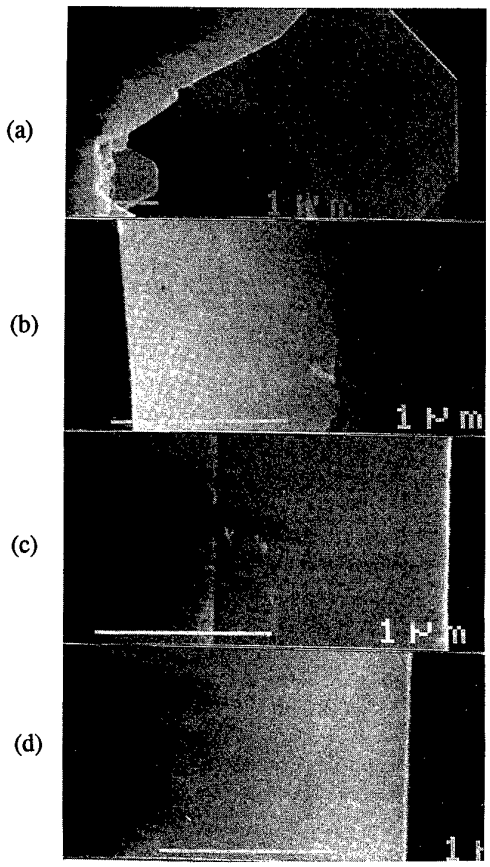


Fig. 4(a)~(d) SEM of cross-section morphologies with various NH3 flow rate

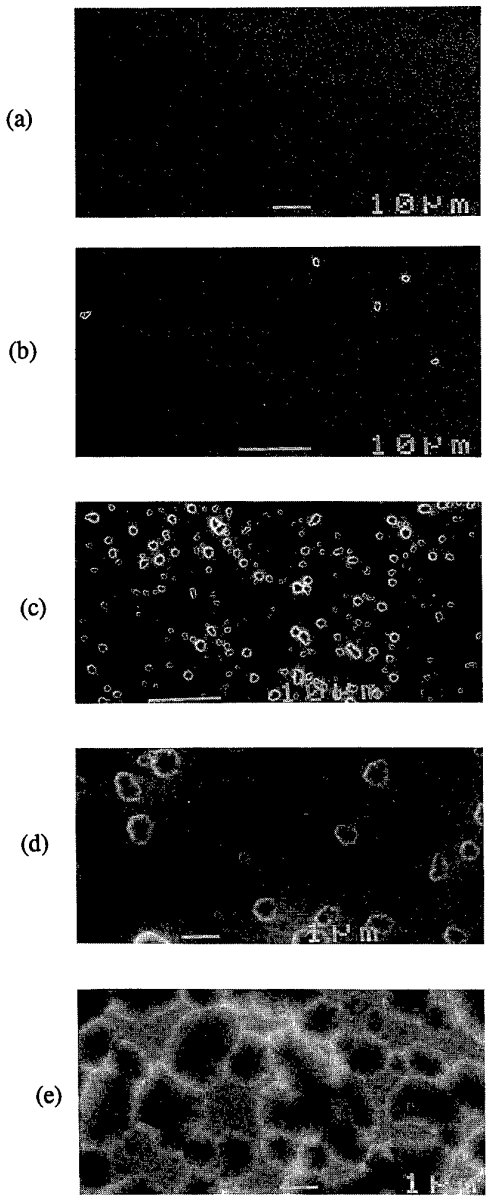


Fig. 5(a)~(e) SEM of morphologies with various NH3 flow rate

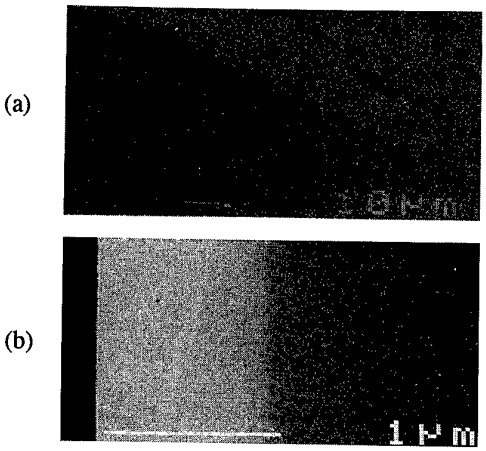
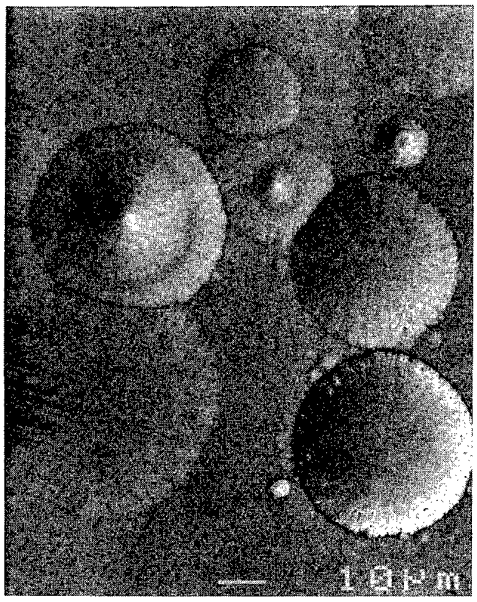


Fig.6(a) Typical surface morphology (b) typical cross-section morphology

(a)



(b)

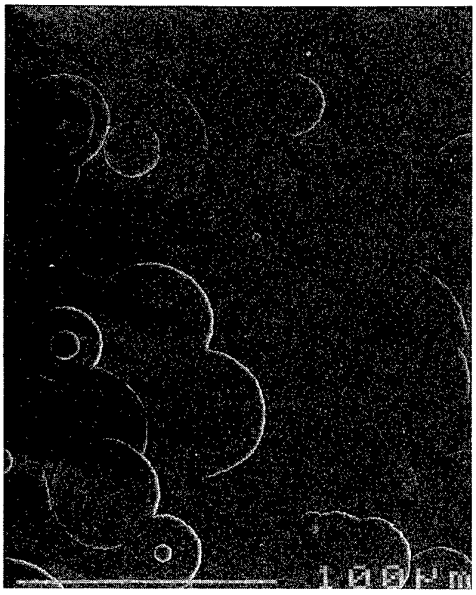


Fig. 7(a) volcanic cone-like structure (b) trucated volcanic cone-like structure

Fig. 7(a) and 7(b) show that thin films with "volcanic cone-like" structure and truncated volcanic cone-like hillock under growth conditions of growth temperature at 1120 ℃ with the same other conditions and growth temperature at 1120 ℃ with NH_3 flow rate up to 4SLM respectively. We strongly suggest that the volcanic cone-like hillock came from the random island structure of annealed smooth uniform buffer layer, and treated with different growth conditions of thin films of them may cause different growth mechanisms, resulting in various density of volcanic cone-like hillock of thin film and possibly eliminating it. When the growth temperature goes up, the film tends to become 3-dimensional growth and traces vividly the surface morphology of buffer layer predeposited. By adding higher NH_3 flow rate, the volcanic cone-like structure seems become truncated and smoother the surface with tendency of become featureless smooth surface. We suggesting that the NH_3 flow rate play an important role as enhance the liquid-like growth mechanism. This kind of hillock is the first report of GaN thin film growth, and also the first description that it may affect by temperature and NH_3 flow rate. The enhance growth mechanism of NH_3 flow rate is the first report here.

4. Summary and Conclusions

The buffer layer we have grown in the two-step process is used to relieved the strain stress which may cause from lattice mismatch between sapphire and GaN thin film. After annealing which acts as solid phase exitaxy process, the subsequent epitaxy of GaN at higher temperature is like homoepitaxy on a defective substrate. For the conditions investigated in the present study, it appears that GaN grown on a GaN buffer layer has different surface morphology depend on temperature and NH_3/TMG mass flow ratio.

Although the buffer layer can act as a seed layer and form smoother surface on sapphire for GaN thin film growth after annealing, there may be some island structure show up and may cause volcanic cone-like hillock. For growth at temperature up to 1120 ℃, the volcanic cone-like hillock was appeared. And for growth at temperature of 1120 ℃ with NH_3 flow rate up to 4SLM, we also observed that volcanic cone-like structure show up but was truncated. The volcanic cone-like structure may smooth by adding NH_3 flow rate as enhancement of liquid-like growth mechanism and effecitively achieve featureless mirror-like surface of GaN thin film.

5. References

1. S. Nakamure, M. Senoh, N. Iwasa and S. Nagahama, "High-Brightness InGaN Blue, Green and Yellow Light-Emitting Diodes with Quantum Well Structures", Jpn. J. Appl. Phys. Vol. 34, pp. L797-799, July 1995.

2. H. Amano, N. Sawaki and I. Akasaki, "Metalorganic vapor phase epitaxial growth of a high quality GaN film using an AlN buffer layer", Appl. Phys. Lett. 48(5), pp. 353-355, February 1986.

3. S. Nakamura, "GaN growth Using GaN buffer Layer", Jpn. J. Appl. Phys. Vol. 30, pp. L1705-1707, October 1991.

4. A. E. Wickenden, D. K. Wickenden and T.J. Kistenmacher, " The effect of thermal annealing on GaN nucleation layer deposited on (0001) sapphire by metalorganic chemical vapor deposition", J. Appl. Phys. 75(10), pp. 5367-5371, May 1994.

Paper presented at the Third ICIM/ECSSM '96, Lyon '96

Pinning-Controlled Metal/Semiconductor Interfaces

S.Hara, T.Teraji*, H.Okushi, and K.Kajimura*

Electrotechnical Laboratory
1-1-4, Umezono, Tsukuba, Ibaraki 305, Japan
* Also with Faculty of Materials Science, University of Tsukuba,
1-1-1, Tennodai, Tsukuba, Ibaraki 305, Japan

ABSTRACT

We propose a new systematical method to control Schottky barrier heights of metal/semiconductor interfaces by controlling the density of interface electronic states and the number of charges in the states. The density of interface states is controlled by changing the density of surface electronic states, which is controlled by hydrogenation. We apply an establishing hydrogen termination technique for the hydrogenation using a chemical solution, *p*H controlled buffered HF or hot water. The density of interface charges is changeable by controlling a metal work function. When the density of interface states is completely hydrogenated, the barrier height is determined simply by the difference between a work function of a metal ϕ_m and an electron affinity of a semiconductor χ_s . In such an interface with zero density of interface states, an Ohmic contact with a zero barrier height is formed when we select a metal with $\phi_m < \chi_s$. We have already demonstrated controlling Schottky and Ohmic properties by changing the hydrogenation on silicon carbide (0001) surfaces.

1. INTRODUCTION

The Schottky barrier heights of metal/semiconductor interfaces have historically been a passive physical function in terms of artificial controlling. This is mainly due to an interfacial Fermi level pinning which automatically determines the barrier height, resulting in the difficulty in controlling the barrier height. This low controllability has needed much efforts on Ohmic formation because the interfaces always have pinned Schottky barriers. The history of Ohmic formation was that of leaking currents through the barrier instead of lowering the barrier heights. A leaky Schottky barrier has complex mechanisms on current transports because of complex interface atomic and electronic structures caused by an interfacial reaction depending on an experimental condition. This difficulty in Ohmic formation will be basically solved if we can reduce the barrier height down to zero.

In our concept, Schottky and Ohmic formations are dealt with in the same category, where we control the density of interface electronic states to provide us controllable barrier heights as an intelligent function. Also, these intelligent Schottky and Ohmic interfaces have a simple current transport mechanism of thermionic emission with a minor effect of tunneling current.

In this report, we propose a new concept to unify the Schottky and Ohmic

0-8194-2165-0/96/$6.00

formations as mentioned above and we demonstrate barrier height controls from a pinned Schottky barrier down to an Ohmic with a zero barrier height by changing the pinning rate.

2. CONVENTIONAL SCHOTTKY AND OHMIC FORMATIONS

A Schottky barrier height ϕ_{bn} between a metal and an n-type semiconductor is classically expressed using Schottky-Mott rule,

$$\phi_{bn} = \phi_m - \chi_s . \qquad (1)$$

A practical system, however, has interface states which tend to pin the Fermi level within a band gap. When a pinning phenomenon is observed, ϕ_{bn} is expressed as,

$$\phi_{bn} = \frac{\partial \phi_{bn}}{\partial \phi_m}(\phi_m - \chi_s) + C , \qquad (2)$$

where, $0 \le \frac{\partial \phi_{bn}}{\partial \phi_m} \le 1$. We define the pinning rate p as $1 - \frac{\partial \phi_{bn}}{\partial \phi_m}$. Therefore, the pinning rate is $0 \le p \le 1$. When p is 0, ϕ_{bn} satisfies eq.1 in principle. The situation with $p = 0$ is called the Schottky limit, where the Fermi level is free from pinning. When p is 1, ϕ_{bn} in eq.2 becomes constant, and is independent from the metal work function ϕ_m. This situation of the strongest pinning is the Bardeen limit. Since practical interfaces are present within the Schottky limit and Bardeen limit, we can control the barrier height to some extent by changing a metal. For instance, the maximum and minimum barrier heights for silicide/Si interfaces are around 0.5eV to 0.9eV and the width of controlling the barrier height is around 0.4eV [1], where no Ohmic interface is formed. So far, there existed no technique to control the pinning rates, the Schottky barriers were out of control. As a result, the pinning rates have been belonging to their semiconductors themselves.

Ohmic contacts had a more practical aspects. The most certain way to obtain the Ohmic property is a heavy impurity doping to thin the Schottky barrier so as to increase a tunneling current. This is inefficient in a new material because of the difficulty of high doping. Also, a minimum contact resistivity by this way is limited by the doping concentration. The second way is to grow epitaxially another semiconductor with a narrower band gap which restricts the maximum barrier height within the band gap width. This is applicable to only systems where a heteroepixial technique is available. The most convenient way is to anneal the system. This, however, is ambiguous in terms of Schottky or Ohmic formation. Actually, annealing is a good way to form a stable Schottky barrier with a low leakage current in some cases, while annealing is the best way to form an Ohmic contact in other cases. The last one is to use a contact metal with a low work function for n-type semiconductor to reduce Schottky barrier height. For p-type, a high work function is needed. This way also often forms Schottky barriers with bad ideal factors because of no anneal resulting in contaminated interfaces formed by initial surfaces with contaminations and oxides.

As a general trend, a Schottky barrier has been formed for an ideal abrupt interface, whereas an Ohmic contact has been formed by losing the interface abruptness or by lowering the crystallinity of the semiconductor.

3. UNIFYING SCHOTTKY AND OHMIC FORMATIONS BY CONTROLLING THE FERMI LEVEL PINNING

It is known that the pinning rate is dominated by the density of interface states D_{it} [2] as follows,

$$p = 1 - \frac{\varepsilon_i}{\varepsilon_i + q\delta D_{it}}, \qquad (3)$$

where ε_i is the permitivity of the interfacial layer and δ its thickness [2]. Therefore, we can control the degree of the Fermi level pinning by changing D_{it}. Recent techniques using chemical solutions to terminate semiconductor surfaces progress to reduce the density of surface states and make their surfaces flat atomically. Such an ideal surface should result in forming an interface with a low D_{it}. We utilize two chemical solutions, *p*H modified buffered HF or hot water to suppress D_{it}. *p*H modified buffered HF has been found to terminate the Si(111) surface only by monohydrides [3]. Hot water also has the same effect[4]. In a semiconductor surface layer with a low crystallinity which becomes the origin of high D_{it}, removing the surface layer by an oxidation followed by a chemical etching is effective before the chemical termination.

Further, An actual barrier height is determined by the number of interface charges Q_{it} in D_{it}. Q_{it} is changeable if the metal work function ϕ_m is changed because the change in Fermi levels between the metal and the semiconductor yields a charge transfer. When D_{it} -> 0, the interface is in the Schottky limit. In the limit with zero D_{it}, the Ohmic property is obtained when ϕ_m is smaller than χ_s because C in eq.2 is generally small. Since this Ohmic interface has no Schottky barrier, the contact resistivity ρ_c is zero, independent on the donor concentration N_D. In contrast, in a common Ohmic contact, there exists a large D_{it} resulting in a Schottky barrier formation restricting the current conductivity. In such a contact, the minimum of ρ_c is limited by the Schottky barrier width determined by N_D because the current flows through the Schottky barrier by tunneling.

4. DEMONSTRATION OF CONTROLLING BARRIER HEIGHTS IN METAL/6H-SiC(001) INTERFACES

Unintentionally doped *n*-type 6H-SiC (0001) bulk substrates grown by modified Lely method and nitrogen doped *n*-type 6H-SiC (0001) epitaxial layers were used. Si-faces of the SiC samples were used for all depositions and characterizations. The carrier concentrations N_D determined by capacitance vs. voltage (C-V) measurements were ~ 2×10^{17} cm^{-3} for the bulk substrates and ~ 5×10^{17} cm^{-3} for the epitaxial layers. Some of the samples were oxidized in a quartz tube furnace. The thickness of oxidized layers was about 30 Å. The oxidized layers were etched by dipping in 5 % HF solution. We refer to this oxidation and the successive HF etching as O/E treatment hereafter. Some of the samples with O/E treatment were dipped in boiling water or in *p*H-modified buffered HF for 10 min. Finally, the samples were rinsed in deionized water. Titanium and nickel were deposited with an electron beam evaporator to form contact electrodes. During the depositions, the sample temperatures were kept below 100 °C. No annealing was

carried out for the Ti electrodes. Some of the Ni contacts were annealed at 1000 °C for 60 min in pure Ar to form Ohmic contacts.

Typical current vs. voltage (*I-V*) characteristics between two Ti contacts on the bulk substrates are shown in figure 1(a). The contacts without O/E treatment show rectification properties as depicted by dashed line. The contacts are found to have Schottky properties with a bad ideal factor of around 1.45 as indicated in fig.1(b). The

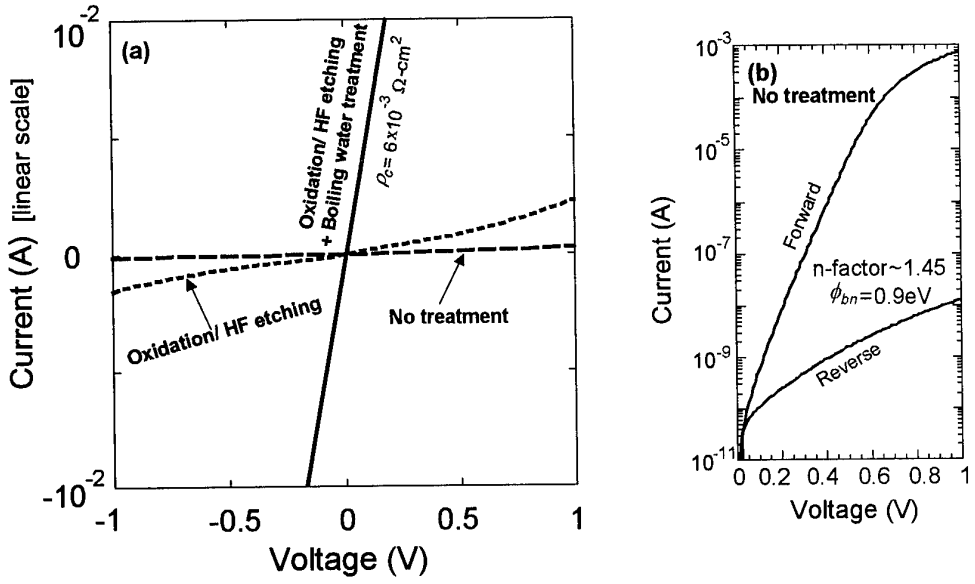


Figure 1. *I-V* characteristics between two Ti electrodes on 6H-SiC(0001) crystals (N_D ~2×10^{17}cm^{-3}). (a) linear *I-V* characteristics of no treatment, oxidation/HF etching treatment, and boiling water treatment. (b) a logarithmic *I-V* characteristic of no treatment.

barrier height is 0.9eV. After O/E treatment, the properties of Ti contacts on the bulk substrates change from rectification to Ohmic, showing good linearity (dotted line). However, ρ_C varies widely depending on electrodes. After dipping of bulk substrates in boiling water, the average ρ_C of Ti contacts decreases to $6\times10^{-3}\pm1\times10^{-3}$ Ω-cm^2 (solid line) and shows good uniformity.

Fig.2 shows the ϕ_{bn} as a function of ϕ_m in each treatment. Ni contacts in all treatments show Schottky properties and the heights are almost constant. Whereas in the Ti contacts ϕ_{bn} depends largely on the treatments. p obtained from the slopes of three straight lines connecting Ti and Ni in each treatment are 0.6 for no treatment, 0.3 for the O/E treatment and 0 for the boiling water treatment. It is found that the Fermi level is being released from pinning in order with proceeding the treatments. The cross point of the three lines in the figure, around 1.2eV of ϕ_{bn}, indicates the pinning position of the Fermi level because it is independent on the surface treatments. The corresponding ϕ_m in the pinning position is around 5.2eV in the figure. Since Ni has a work function of 5.35eV[5] which is almost the same as the pinning position, Ni shows the independency on the surface treatments. In the Ti contacts, they depend largely on the treatments because the work function of Ti is 4.33eV [5] which is much lower than the pinning position.

Ohmic contacts in the present experiments are formed on the lightly doped substrates (N_D~10^{17} cm^{-3}). In such an interface with a wide depletion layer, a tunneling current is negligible. Therefore, the Ohmic currents in the present experiments are generated by current flows over barriers with very low heights. Further, it should be noted that the Ohmic contacts are formed without post-annealing.

As a result, fig.2 demonstrates the pinning control between the Schottky barriers and the Ohmic conductivity by changing the degree of hydrogen termination.

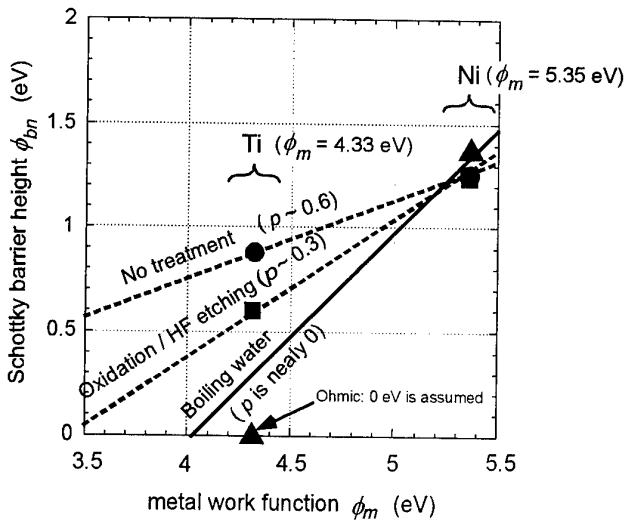


Figure 2. Schottky barrier heights as a function of metal work functions. No treatment (short dashed line), oxidation followed by HF etching treatment (long dashed line), and dipping treatment in boiling water (straight line) are indicated.

4. CONCLUSION

We proposed a new method to control electric potential barriers by changing the Fermi level pinning and by changing the metal work function. This method unifies Schottky barriers and Ohmic conductivities in terms of their artificial control. It has a simple current transport mechanism with a minor effect of tunneling current. The pinning control was achieved by dipping silicon carbide crystals into *p*H modified buffered HF or boiling water before metallizations. These treatments have an effect to reduce the density of the surface states and the resultant density of the interface states. Ohmic interfaces were formed by selecting Ti with a low work function as a contact metal for the pinning suppressed surfaces.

REFERENCES

1. S.M.Sze, *Physics of Semiconductor Devices, 2nd ed.* chap.5 (John Wiley & Sons, NY, 1981) 292.

2. E.H.Rhoderick and R.H.Williams, *Metal-Semiconductor Contacts, 2nd ed.* (Oxford University Press, Oxford, 1988) 20.

3. G.S.Higashi, Y.J.Chabal, G.W.Trucks, and K. Raghavachari, Appl.Phys.Lett. **56** (1990) 656.

4. S.Watanabe, M.Shigeno, N.Nakayama, and T.Ito, Jpn.J.Appl.Phys. **12B** (1991) 3575.

5. H.B.Michaelson, J. Appl. Phys. **48** (1977) 4729

Two dimensional design of Intelligent Materials, - Introduction of Froc-Project -

Hiroaki YANAGIDA
Department of Industrial Chemistry, Faculty of Engineering
Unversity of Tokyo
7-3-1 Hongou, Bunkyo-ku, Tokyo JAPAN

ABSTRACT

A new concept "Frontier Ceramics" is proposed to proceed a new research project on advanced ceramics. The key lies in understanding of two dimensional structure such as boundaries or interfaces. The research project is to tailor the ceramic interface through controlling the structure and composition at interface with novel processing techniques to achieve the desired properties. Establishing an advanced model for the interface is certainly the fundamental step in this research.

1. Needs for Frontier Ceramics.

The objective of any ceramic materials R & D is always either to improve the manufacturing processes and or to achieved improvements in either manufacture or performance of the existing ceramics, or to introduce novel functions. Materials with excellent performance and novel functions are particularly ideal candidates for future technology[1]. "Frontier ceramics" proposed here(as seen in table 1) are one such special class of materials . Various functional ceramics have already been developed and are still being developed. The frontier ceramics is considered to be one of the "post-advanced ceramics."

It may not be an exaggeration that no electronic device can be constructed without ceramic components. Due to this reason ceramics are also being developed in parallel with electronic devices for various applications. One of the major concerns of the device R & D is to reduce or even miniaturization of the device size. A typical example is a ceramic capacitor as can be seen from Fig. 1. In general capacitor consists of a sintered body as a dielectric. It is well known that in a sintered body is a network of grains with a large grain boundary area . Reducing the grain boundary area may be one of the probable ways to attack the down sizing objective. In presently available ceramic capacitors a ceramic with few hundred grains is the dielectric body. The goal of the future capacitor is to construct it with a ceramic of few grains if not a single grain. In such a case an averaging effect can not determine the stability of the

0-8194-2165-0/96/$6.00

properties as in regular ceramics and one has to consider property of each grain boundary or interface rather precisely. Due to this stringent reason, the main themes of the " Frontier Ceramics" research are to design the structure and composition of ceramic interfaces and to establish the relation between the designed interface and the function of the ceramic as a whole. Unifying all the existing models of grain boundary behavior explanation and to come up with a unique and single model will be carried as a phase two of this research. Similar needs are widely seen in the R & D of electrode, catalysis, engineering ceramics, and so on.

Table 1 Comparison of "Frontier Ceramics" with the usual ceramics.

	Raw materials	Processing	Phases	Interfacial chemical composition	Interfacial structure	Origin of properties
Traditional Ceramics	Natural products	(Liquid-phase) Sintering	Many and complicated phases, uncontrollable.	uncontrollable.	uncontrollable.	Bulk characteristics.
Advanced Ceramics	Artificial materials	(Liquid-phase and solid-phase) Sintering	Relatively small number of phases, partially controllable.	Partially controllable.	Statistical variation, partially controllable.	Mainly bulk characteristics.
Frontier Ceramics	Artificial materials	Sintering + Advanced Processing (Sputtering, MBE, etc.)	A few and simple phases, precisely controllable.	Design and precise control.	Design and precise control.	Mainly interfacial characteristics.

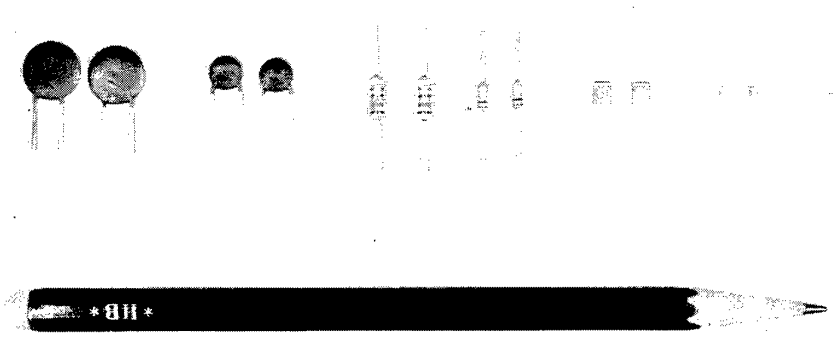


Fig.1. Recent down-sizing of case -size of condenser.

2. Grain boundary research to the fundamental study of the frontier ceramics.

Surface of solids can be touched and seen. The surface science is progressed by STM(touching), AES or ESCA(seeing), some techniques of ion scattering(touching and seeing) and so on. On the contrary, the material interface can not be generally touched and seen. This handicap about the interface observation has arrested its the growth of that particular science for a long time. However, the veil of interface is being stripped. A typical improvement on interface science has been presented in a study of structural analysis using a high resolution transmission electron microscopy, seen in Figure 2[2]. Although it is a destructive analysis, we have been able to understand the structure of interface in atomic scale. An example in Fig.2. shows an interface between alumina ceramics and a metal, where these materials have different bonding nature but directly connect with each other.

Development of structural analysis gives a possibility to observe some unique phenomenon as seen in Figure 3[3]. which is concerned with a specified structure. Since we are in a position to discuss phenomena on the basis of understanding of interfacial structure in atomic scale, now we can forecast a function corresponding with a modeled structure of interface. All models can not be made at present, as ceramics processing is constituted mainly with sintering. However, the designing of structure will be possible using advanced material processing techniques such as sol-gel process, plasma process, MBE and CVD, etc. A purpose of the frontier ceramic research is that a combination of utilizing or developing both advanced processes advanced process and modern evaluation techniques along with the construction of an advanced interface model. The basis and justification of the model are in the scope of the theoretical aspects of the research.

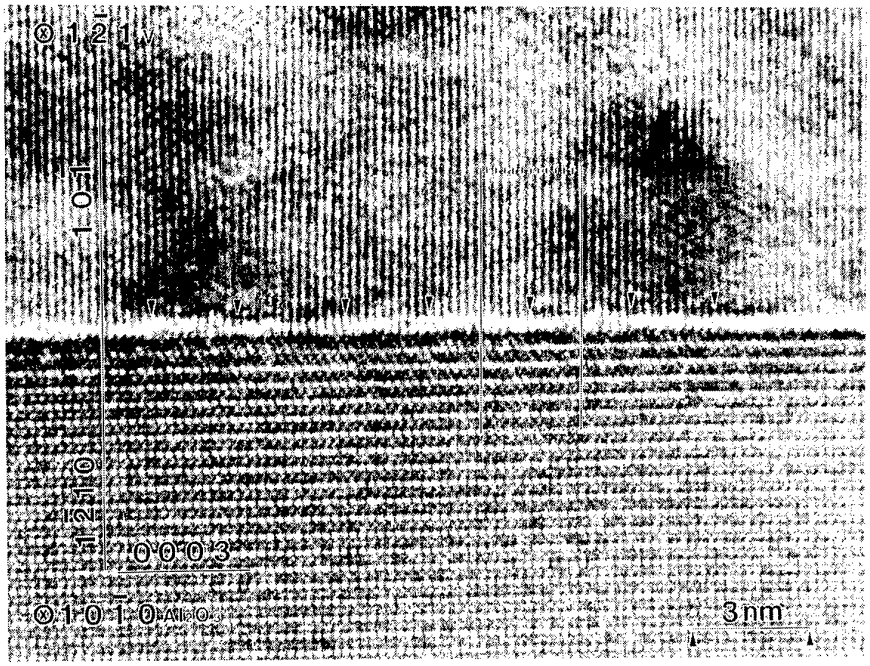


Fig.2. TEM observation of interface between alumina and vanadium[2].

3. Fundamental concepts for modeling interface.

Science of ceramics deals with various kinds of interfaces including surface[4]. To have better control over the field one has to consider constructing materials(Homo or hetero interface), and understanding the anisotropy of phenomenon(across or along interface), the macro-structure(closed or opened interface), and so on in detail. To characterize the various interfaces, we focused three kinds of interface models. One is "singular point model," second, "ordering interface model," and the last, "continuous interface model." In the singular point model, the point defects, impurities or clusters at interfaces are studied using a molecular orbital theory.

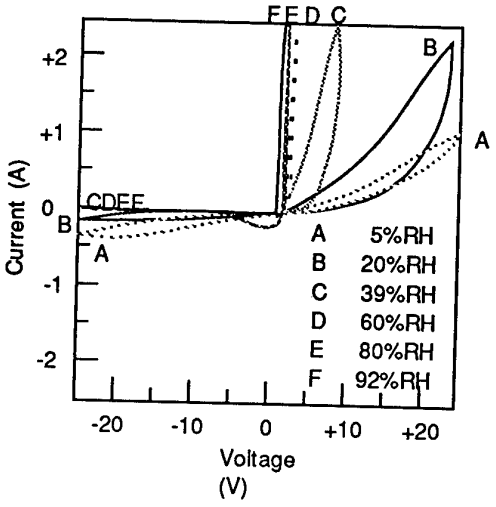


Fig. 3. Humidity dependent voltage-current characteristics of an intelligent humidity sensor made of hetero-contacts between copper oxide and zinc oxide . RH=relative humidity.

The second one "ordering interface model" will reveal the periodical properties at periodic interface such as "CLS," where the band theory and the molecular dynamics will be the basis. Finally in the continuous interface model, the compositional distribution near interface will be mainly studied, and non-equilibrium thermo dynamics will be applied as a principle[5]. This fundamental concept is shown in Figure 4.

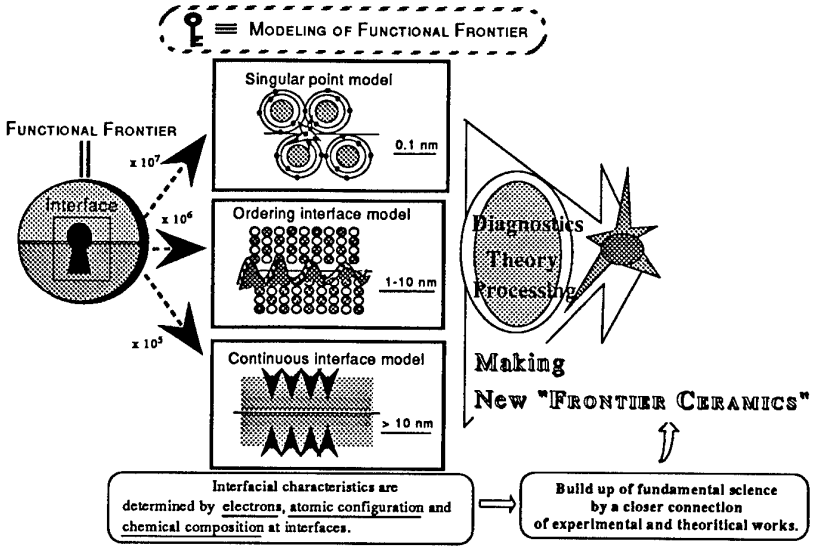


Fig.4. Concepts for making the new "Frontier Ceramics" and three kinds of interface-models. Interfacial phenomenon understood in atomistic order to mezoscopic order.

Physical properties have been mainly studied at ceramic interface. However, the characteristics of ceramic interface are not simply physical in nature aspect but also bound by chemical aspects strongly. Chemical reactions are more important in the interfaces of catalysis, sensor and electrode materials. The chemical reactions are considered to be reflex of a role as interaction field at interfaces(here, called "functional frontier"). Therefore, the two kinds of aspects, chemical reaction and chemical interaction, will be installed in basic axis for construction of models, which are dynamic aspects and depend on the statistical aspects such as structure or chemical composition. Unification of these models will help in processing the "Frontier Ceramics"

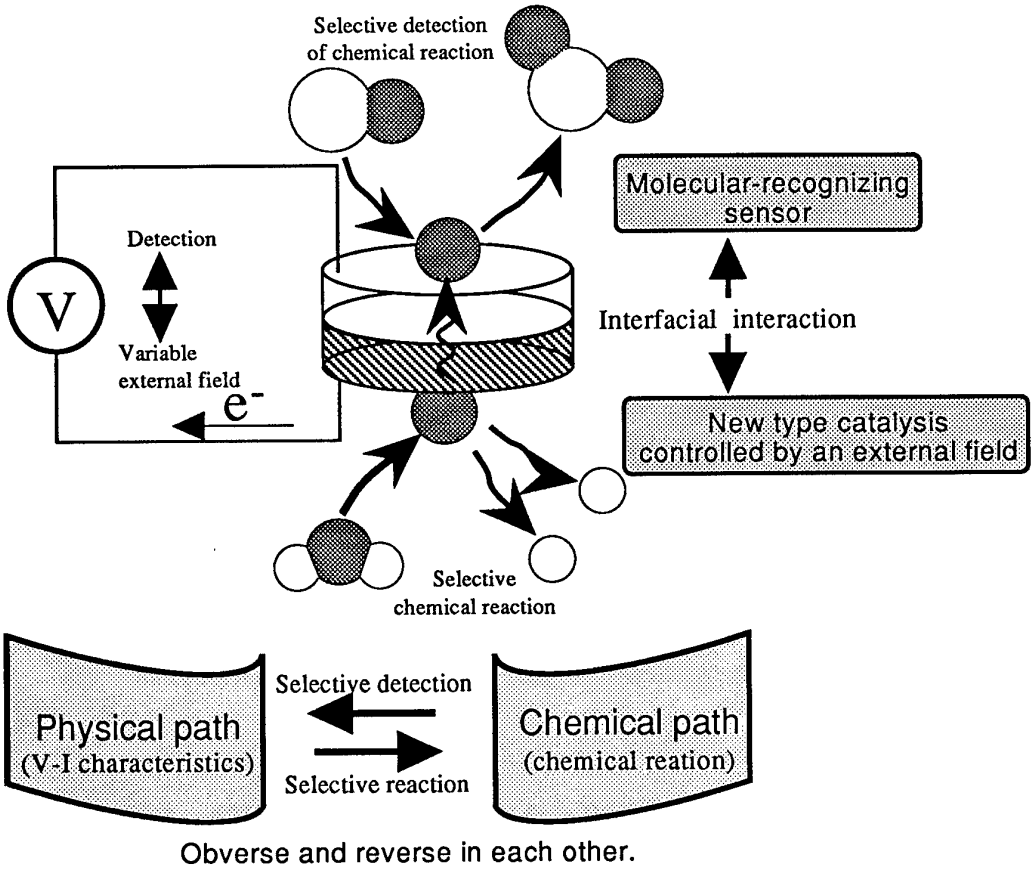


Fig.5. Expected materials upon frontier ceramics concept. Two materials, in relation of obverse and reverse with interfacial interaction between " Chemical Path" and "Physical Path."

Molecular-recognizing sensor" and a new type catalysis controlled by an external field are illustrated as expected-materials in Figure 5. These materials are obverse and reverse in each other. As the former will use the physical signal such as electric field or current as the result of chemical reaction at interfaces while the latter will use the chemical reaction at interface controlled by a physical field. In these materials, a conversion between "chemical path" and "physical path" at interface will be used.

REFERENCES

1). H.Yanagida, Angeb.Chem. **100**, 1443 (1988).
2). Y.Ikuhara and P.Pirouz, Ultramicroscopy, **52**, 421 (1993).
3). H.Yanagida, Y.Toyoshima, M.Miyayama and K.Koumoto, Jpn.J.Appl.Phys., **22**, 1933 (1983).
4). H.Yanagida, KagakuToKogyo, **39**, 831 (1986).
5). M.Fujimoto, proc. JP-US Workshop Func. Fronts in Adv. Ceram. pp.59-62, (1994).

Paper presented at the Third ICIM/ECSSM '96, Lyon '96

Sol-Gel Route to Functional and Hierarchical Ceramic Matrix Composites

Ph. Colomban

ONERA, Direction des Matériaux, BP 72, 92322 Chatillon Cedex (France)
and CNRS, LASIR, 2 rue Henri Dunant, 94320 Thiais (France)

ABSTRACT

The use of sol-gel technique to fabricate functionally graded ceramic matrix composites reinforced with woven fibres is illustrated with composites made by alternating dielectric and conducting layers (microwave absorbent) or by alternating materials that have high hardness and good corrosion resistance. Emphasis on the preparation of multiscale reinforced composites is given according to the idea of biomimetic materials.

1. INTRODUCTION

Many advanced systems require or would benefit from new chemically, thermally stable, low density materials. A range of separate and often conflicting material properties are demanded in the same material. For example, the replacement of metals and alloys in air cooled aircraft engine parts by thermally stable materials would help to decrease NO_x pollution. On the other hand, in the case of high velocity missiles, the part shape and composition may need to satisfy stringent thermomechanical requirements which implies the use of ceramics. Furthermore, stealthiness is now a required specification for modern weapons and parts made of specific materials may be used to absorb the emitted electromagnetic energy and to minimize the wave reflected in the direction of the radar receiver.[1] Similar materials can be used in kitchen microwave ovens. Thus, new ceramic materials could be made by combining materials that have high hardness with those that have good corrosion resistance, with those that have high microwave absorption or low permittivity, with those that have high electronic or ionic conductivity, low or high thermal conductivity, low or high thermal expansion, etc. Materials selection is limited since the thermal expansion coefficients, the sintering temperature, the atmosphere used for the preparation, ..., must be compatible. The composition can be changed continuously or stepwise according to the target properties.

The great weakness of monolithic ceramics is their intrinsic inability to tolerate mechanical damage without brittle rupture because of their polycrystalline state and the nature of the chemical bonds existing in these compounds. The use of long, woven ceramic fibres embedded in a refractory ceramic matrix results in a composite material exhibiting greater toughness through a specific micromechanism at the fibre-matrix interface : the cracks are deflected, dissociated and then stopped at the interfaces and thus the composite exhibits a fibrous, pseudo-plastic fracture. The knowledge of the ultimate strength allows the choice of acceptable load and calculations with safety coefficients could thus be made for the part design. The electrical properties of a composite should depend on the fibres, the matrix, the interfaces (or interphases) and on other parameters such as the microstructure, the topology, etc.

The problem arising in the preparation of refractory matrix composites lead to the difficulty of achieving an open porosity below 10%. The fibres must be thoroughly embedded in the matrix and the matrix must be incorporated through the voids between fibres (a few microns or less, in size). This is only possible by infiltration of liquid or gaseous precursors for which the ceramic yield is necessarily low. The latter method is used for the synthesis of covalent bonded ceramics having a simple composition (e.g. SiC, BN, ...)[2] whereas the former is more versatile[3] (SiC, Si_3N_4, oxide, ...). In both cases, it results in considerable shrinkage after pyrolysis which generates new voids ; the presence of the woven fabrics inhibits the coherent shrinkage of the matrix. The liquid ceramic precursor can infiltrate the yarns easily reducing the porosity but the shrinkage associated with the pyrolysis creates new voids. In the case of one or two dimensional reinforcements (1/2D composites), this dilemma is solved by the use of a very reactive sol-gel matrix precursor in association with a liquid interface precursor which polycondenses, *in situ*, within the fibre yarns into a gel.[4]

2. SOL-GEL ROUTES TO OXIDES (OXINITRIDES, OXICARBIDES)

For many years, ceramists have been interested in sintering at "low temperature" to manufacture devices that incorporate different materials sintering together. Within a few decades, evolution towards increasingly pure raw materials, especially prepared by chemists, brought significant progress in quality, despite an increase in sintering temperatures. Sol-gel routes have been widely used for many centuries in earthenware and china

0-8194-2165-0/96/$6.00

production : the sol-gel technology allows the lowering of the densification temperature and furthermore the control of manufacturing process at micro and macroscopic scales, the synthesis of homogeneous microstructure and the control of chemical purity and crystallinity. Conversely to single crystals, glasses, polymers and some metal products, ceramics are constituted by a set of grains, bounded by interfaces : it is a population of often similar, but sometimes different individuals and a few abnormalities can adversely affect the resulting properties. Thus, it is essential to obtain reproducibly a homogeneous micro (nano) structure. This is obtained in traditional ceramics by the use of a liquid precursor, a slurry of colloidal particles of clays, which is converted into gel before firing.

A gel is a network which is swollen by solvent. The solvent is trapped in the particle network. The network prevents the liquid from flowing while the liquid prevents the solid from collapsing into a compact mass. Gels generally look dry. Partial dehydration produces an elastic solid called xerogel. Colloidal solutions or "sols" contain either large molecules or small particles (at least one dimension within the range 1-100nm) and occupy an intermediate position between true solutions and coarse dispersions. A gel can be created when the concentration of the dispersed phase increases (and the viscosity increases much faster) -e.g. the well-known case of clays, or the case of silicic acid, vanadic acid, ...[5]- or when the size of the polymeric species issued from the hydrolysis-polycondensation of metallic (non-metallic) alkoxides or related metal-organic reagents is sufficiently large.[5,6] A sol-gel method is a method where one or many elements (the "gel formers") are used in the form of sol and/or gel in order to obtain a homogeneous, mainly amorphous solid. As a first approximation, the surface is only active for the gel formation in the first case (called physical gel) whereas the latter case (chemical gel) involves a more complex process.[5,6] The first ceramics obtained by using sol-gel routes were nuclear reactor fuels and zirconia. A few years later PLZT ceramics were manufactured in the form of large optically-clear ceramics using the alkoxide route.[5] Synthesis of multicomponent films, of oxide fibres and of oxynitride glasses were demonstrated in the seventies.[5,6] Review papers on sol-gel routes are as numerous as the potentialities of this process.[5-7] However, the approaches are different : glass scientists focus their attention on the homogeneity of silica-rich compositions whereas ceramists try to control micro (nano) heterogeneity of the final ceramics, both after high temperature treatments. On the other hand, chemists preparing gels with tailored optical properties keep the gel in its initial state. However, the route leading directly from a liquid state via a viscous one to a monolithic piece offers some effective or potential advantages, previously developped in whiteware and enamel technology : the manufacture of pieces of special form without machining, deposit film using the viscous properties... The following difficulties are still present, e.g. the difference in the kinetics of alkoxides hydrolysis-polycondensation, the carbon traces which remain in the thermally treated material.

The easy synthesis of optically-clear, large monoliths by atmospheric moisture hydrolysis is an important indicator for the quality of a composition to act as a gel former. Such compositions are based on $SiO_2(GeO_2)$-$Al_2O_3(ZrO_2, TiO_2, SnO_2)$-$P_2O_5(Nb_2O_3)$ phase diagrams.[5] Two routes are possible : i) the powder route is based on the rapid hydrolysis of a gel former, the other elements, if necessary, are added by other reagents or powder ; ii) the monolithic route is based on a very slow hydrolysis. Gel shrinkage is first rapid below 300°C with the departure of water soaked within the mesopores and its rate decrease up to ~800-1000°C (depending on the oxide composition), where a drastic shrinkage results from the departure of the last OH^- groups, which enhances a catastrophic densification of the amorphous inorganic polymeric network.[8] Generally nucleation takes place with densification.[5]

3. COMPOSITE PREPARATION

The composite preparation takes place in three stages and combines slow and rapid hydrolysis polycondensation processes :

i) Impregnation of the fibre yarns of the fabric with a liquid alkoxide mixture which slowly hydrolyses and polycondenses into a gel, *in situ*, by reaction with air moisture. This gel would be converted by heating into a glass-ceramic or a ceramic according to the composition. The mixture composition is chosen to give a temporary liquid second phase (e.g. B_2O_3 or GeO_2) during the hot-pressing cycle. The liquid phase contributes to the densification by liquid assisted sintering but also helps to lubricate the matrix powder/gel embedded yarns under pressure and to maximize the amount of contact between ceramic grains of pyrolysed matrix and interface, despite the presence of the fibre network (fibre volume 35-40%).

ii) Deposition of a fine amorphous and reactive matrix precursor : a gel powder which has been prepared by rapid hydrolysis and heated at ~700°C, in air, in order to evacuate most of the protonic species and hence to reduce the shrinkage. This powder is deposited onto the polymerized interface precursor-impregnated fabric.

iii) Hot-pressing of the impregnated, coated and stacked fabrics in a graphite mould. Details of the manufacturing technology are given in references 4 and 9.

This preparation route allows one to manufacture composites combining various matrices, various fibres and fabrics, various interphases embedding the fibres in the same composite. The composition can be changed continuously, if necessary, from the fibre to the matrix (e.g. changing the alcali content to prevent fibre degradation).[9]

4. HIERARCHICAL REINFORCED COMPOSITES

Nature gives illustration of the exciting properties of materials with gradient structure at its different microscopic levels : typical examples are bamboo,[7] woods[8], bone and nacre.[9] The sol-gel process allows the tailoring of ceramic heterogeneity at the micro and nanostructure level. The mixing of liquid alkoxides allows the "molecular" mixing of the different elements. This homogeneous dispersion is frozen by the gelification and is kept on heating. Homogeneous nucleation is achieved with the densification which occurs at relatively low temperature (1000°C, typically). At this temperature the diffusion coefficients are low for refractory materials and hence the precipitates remain the same size (20-50nm), at least up to ~1400°C.[10]

An example of hierarchical reinforcement is given in figure 1 with an SiC fibre/zirconia-containing-mullite matrix composite made with a zirconia containing aluminosilicate interphase. A homogeneous dispersion of ZrO_2 nanoprecipitate (20-50nm) is obtained in the interfabric layer matrix. The size of the precipitate is larger within the fibre interphase (~0.5µm) due to an increase in the diffusion coefficient related to the presence of a temporary liquid sintering aid.[14]

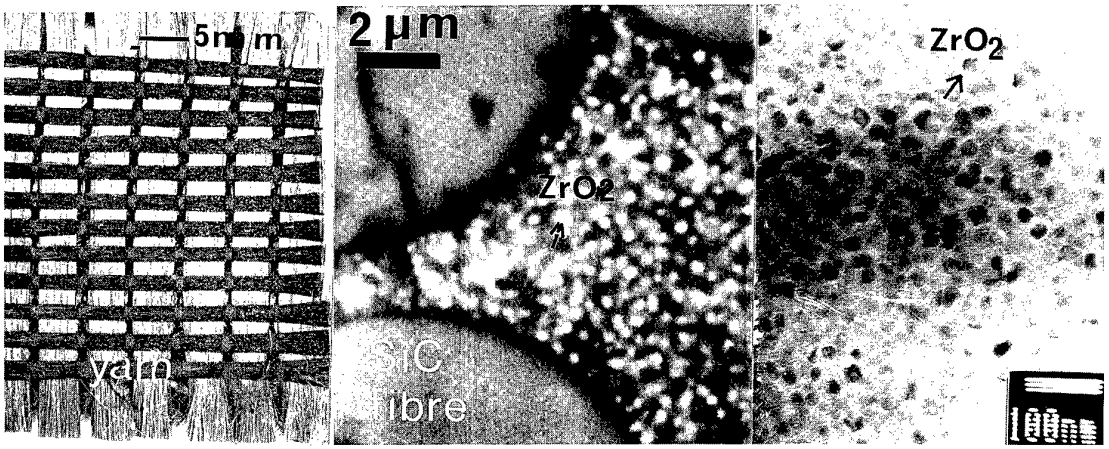


Fig. 1. Hierarchical reinforcement in multiscale ceramic matrix composites at the millimeter scale by the woven yarn network (left, interlacing 3-6mm), at the micrometer scale by the fibre-matrix interphase interface (center), at the nanometric scale by the precipitate (e.g. zirconia)/matrix (e.g. mullite) interface. (The cracks within the center of SiC Nicalon NLM202™ (Nippon Carbon) fibre result from an indentation test).

5. COMPOSITES WITH TAILORED PROPERTIES

Until now, both the matrices and the ceramic fibres have been selected on the basis of thermomechanical criteria for very short life time applications. More recently, the requirement for special physical properties (e.g. electromagnetism, see below) has led to the need for new composites for medium life time applications. For aeronautical applications involving operating times exceeding a hundred or even several thousands of hours the criteria of chemical thermostability, corrosion or abrasion resistance become preponderant. Composites can be made by combining or alternating materials that have high hardness (e.g. zirconia) with those that have good corrosion resistance, e.g. mullite (or celsian) ; an example is shown on figure 2. By selecting the appropriate

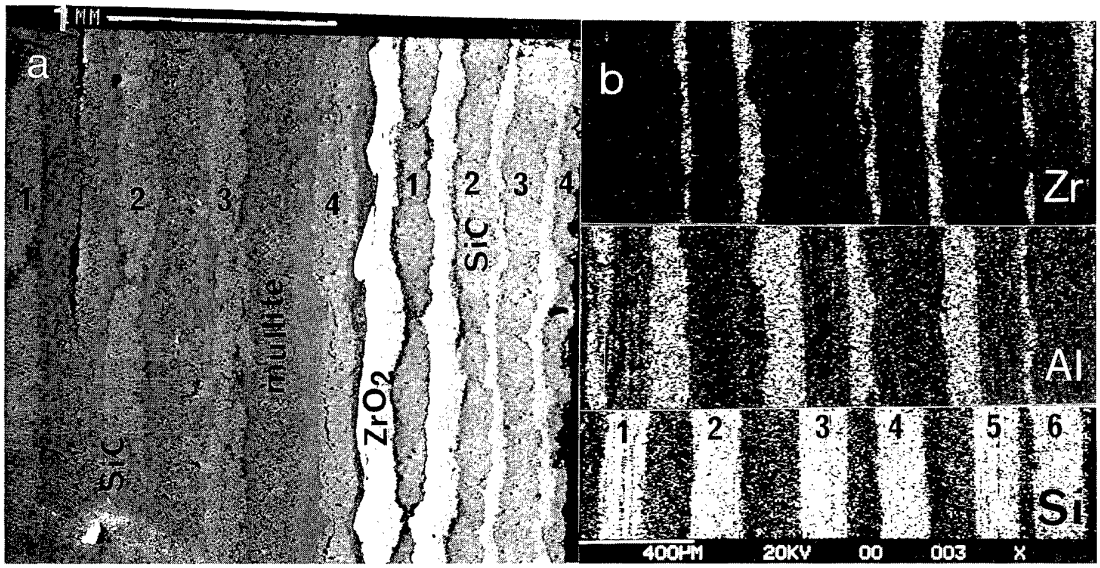


Fig. 2. Combination of several matrices in the same composite : scanning electron micrograph (a) and X-ray line scan maps (b) of the polished section of two different one-dimensional composites (a : transversal section, b : longitudinal section). The composite shown in (a) is composed of four layers of SiC Nicalon NLM202^{TM} fibres embedded in a mullite-like matrix (left part) plus four SiC fibre layers embedded in zirconia matrix (appears white), an aluminosilicate interphase is used. The composite shown in (b) is composed of six SiC fibre layers embedded in aluminosilicate interphase with alternating mullite and zirconia matrices. Si (bottom), Al (center) and Zr (top) X-ray maps are shown.

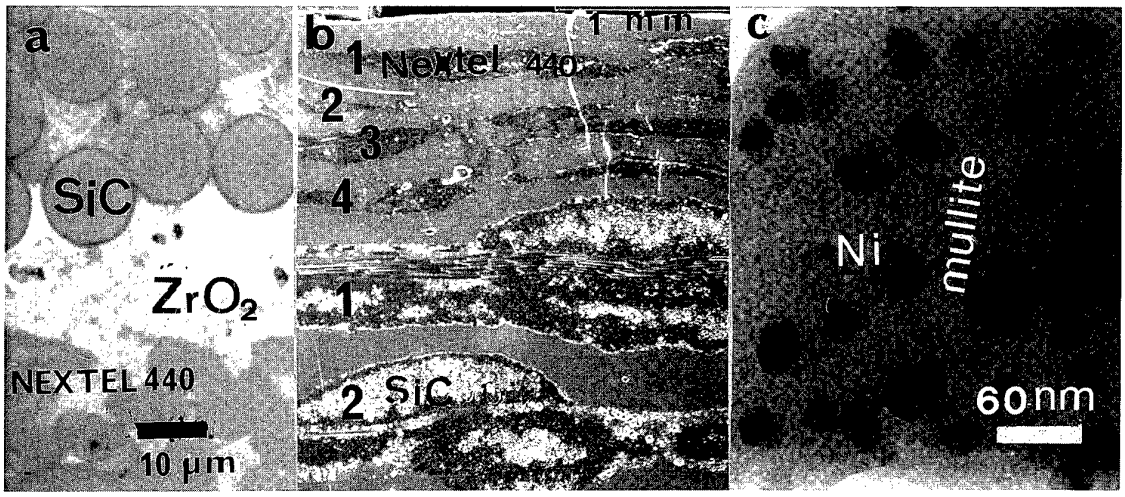


Fig. 3. Combination of several different kinds of fibres (a) and of impregnated fibre/interphase matrix layers (b) in the same composite. Scaning electron micrographs of the polished sections of two composites are shown : the composite shown in (a) is composed of a ZrO_2 matrix reinforced with Nicalon NLM202^{TM} fibres and Nextel 440^{TM} fibres (3M Co). An aluminosilicate interphase is added for SiC fibres. The composite shown in (b) is composed of a NASICON matrix reinforced with four layers of woven Nextel 440^{TM} fibres plus two layers of woven SiC NLM202^{TM} fibres. A boron doped silicozirconophosphate interphase is used. Electromagnetic properties can be additionally tailored by dispersion of (Ni) metallic nanoprecipitates, e.g. in a nanocrystalline mullite-like matrix (c).

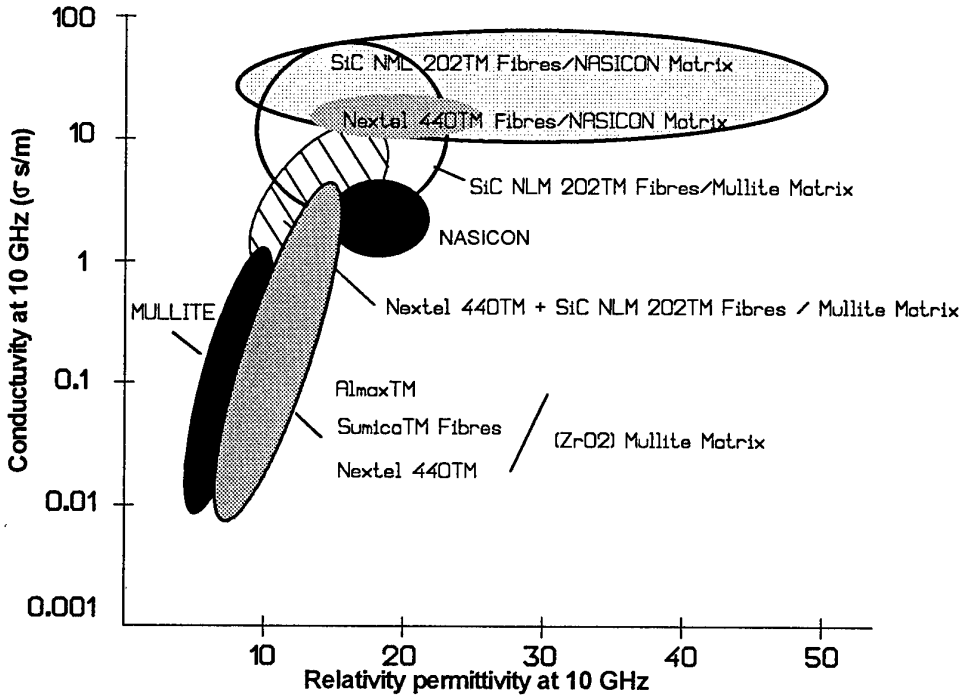


Fig. 4. Semi lorgarithmic plots of the microwave conductivity/permittivity values achieved in ceramic-matrix composites made by associating dielectric aluminosilicate fibres (Almax^{TM} (Mitsui), Sumica^{TM} (Sumitomo), Nextel 440^{TM}) and mullite matrix and/or semi-conducting fibres (Nicalon NLM202^{TM}) and a superionic NASICON ($Na_{2.9}Zr_2Si_{1.9}P_{1.1}O_{12}$) matrix. The domains achieved for sol-gel prepared mullite and NASICON matrices are shown.

interface precursors, the dwell temperature required to prepare the composite can be lowered (e.g. addition of tributylborate, tributylphosphate[9] or tetraethoxy(propoxy)germane)[14] or raised (addition of zirconium propoxide, increase in the Al/Si ratio).[3] This makes it possible to combine several different kinds of fibre/matrix in the same composite. Examples are given in figure 2 (with the combination of four sheets of SiC fibres/aluminosilicate interphase/mullite composite unit with four sheets of SiC fibres/aluminosilicate interphase/zirconia matrix and of six alternate layers of SiC fibre/aluminosilicate interphase/zirconia matrix) and in figure 3 (combination of fabrics of SiC NLM202 fibre and Nextel 440 fibre with zirconia matrix and with Nasicon matrix (a superionic conductor with the composition $Na_{2.9}Zr_2Si_{1.1}P_{1.9}O_{12}$)).

6. COMPOSITES WITH FUNCTIONALLY GRADED MICROWAVE ABSORPTION

As indicated above, some advanced aerospace systems require materials combining several functions in a single entity, e.g. mechanical strength, thermal protection and reduction of the radar cross-section. This requires a good knowledge of the problems associated with the preparation of ceramic matrix composites with tailored microwave properties. Sol-gel prepared mullite ($3Al_2O_32SiO_2$) and NASICON ($Na_{2.9}Zr_2Si_{1.9}P_{1.1}O_{12}$) matrices sinter at temperatures of 1000-1300°C-sufficiently low to avoid degradation of the fibre. Mullite is a pure dielectric ($\varepsilon'_{10Ghz} \leq 5$). On the other hand, the permittivity of NASICON superionic conductor is high ($\varepsilon'_{10Ghz} \sim 16$, $\sigma_{10GHz} \sim 10^{-1}$S/m at room temperature). The absorption of an electromagnetic wave requires a good penetration of the wave (the permittivity of the surface materials must be very low, similar to that of the external medium, i.e. air) and a strong dissipation within the materials (i.e. a large conductivity which generates high dielectric losses). The combination of dielectric mullite, conducting NASICON or semi-conducting SiC satisfies these requirements. Furthermore, we have demonstrated that the reaction with alkali or earth alkali ions occuring at the fibre-matrix interface (e.g. carbon precipitation at the SiC Nicalon NLM202 fibre) increases the conductivity of the composite.[9] Figure 4 illustrates the set of conductivity/permittivity values which can be tailored using various matrices, interphases and fibres. As shown in figure 3, the combination of several fibre/interphase/matrix layers allows us to prepare a composite with graded electrical properties. A dispersion of metallic nanoprecipitates (Ni, Co) can be included in the matrix to tailor the magnetic losses as well.[15]

The electrical properties of the composite are functions of the relative volume of matrix and reacted fibres and of the fibre properties. The real permittivity of a phase mixture can be described using the Looyenga model in which the average permittivity is a polynomial function of the phase concentrations. However, the microwave properties of SiC fibre-NASICON matrix composites are dominated by the electrical properties of the reacted fibre periphery containing carbon precipitates. Electromagnetic properties may be adjusted by adaptation of the permittivity and permeability. To date investigation performed on scattering by magnetic loss are fews. Absorption by magnetic materials may be considered as occuring via domain wall relaxation or by a natural spin resonance mechanism. This last phenomenon takes place in microwave range for Fe, Co ; Ni and their alloys and gyromagnetic microwave absorption of Co-aluminoborosilicate nanocomposites prepared using the sol-gel method have been demonstrated[15,16].

The examples reported in this paper show that the sol-gel route offers many tools for the tailoring of the macro-micro-nanostructure of multiphase and composite materials and hence for the development of new advanced systems.

7. ACKNOWLEDGEMENTS

The author wishes to thank Drs. M. Parlier and D. Abbé for helpful discussions and Drs. E. Mouchon and V. Vendange for their contributions.

8. REFERENCES

1. Mazé-Merceur, N. Bardy, A. Verdier and V. Saavedra, "Microwave characterization of materials", *Chocs*, Vol. 8, pp. 55-64, 1993.

2. R. Naslain and F. Langlais, "CVD processing of ceramic-ceramic composite materials", *Tailoring Multiphase and Composite Ceramics, Mat. Sci. Res., Plenum Press, New* York, Vol. 20, pp. 145-164, 1985.

3. M. Parlier, T. Grenier, S. Renevey, B. Passilly, E. Mouchon, E. Bruneton and Ph. Colomban, "Mullite and SiC matrix-SiC fibre composites for high temperature applications", *Proc. 4th Int. Symposium on Ceramic Materials and & Components for Engines*, R. Carlson, T. Johanson and L. Khalman eds., Elsevier Appl. Sci., Barking, 1992. Patents : FR 2672283, EP 92 400 235.5, US 7930804.

4. Ph. Colomban, "Process for fabricating a ceramic matrix composite incorporating woven fibres and materials with different compositions and properties in the same composite", *Materials Technology*, Vol. 10(5/6), pp. 93-96, 1995.

5. Ph. Colomban, "Gel technology in ceramics, glass-ceramics and ceramic-ceramic composites", *Ceramics International*, Vol. 15, pp. 23-50, 1989.

6. L.C. Klein (editor), "Sol-gel technology", *Noyes Publications, Park Ridge*, N.J., 1988.

7. D. Segal, "Chemical synthesis of advanced ceramic materials", *Cambridge University Press*, pp. 33-88, 1989.

8. V. Vendange and Ph. Colomban, "Densification mechanisms of alumina, aluminosilicates and alumino-borosilicates gels, glasses and ceramics", *J. Sol-Gel Science and Technology*, Vol. 2, pp. 407-411, 1994.

9. E. Mouchon and Ph. Colomban, "Microwave absorbent : preparation, mechanical properties and rf-microwave conductivity of SiC (mullite) fibre reinforced NASICON matrix composites", *J. Materials Science*, Vol. 30, 1995.

10. S. Amada, T. Munekata, Y. Nagase and N. Shimizu, "Hierarchical gradient structures of bamboo", *Proc. FGM'94*, Oct. 10-12, 1994, Lausanne, B. Ilschner and N. Cherradi eds., pp. 689-694, 1995.

11. N. Parviz, "Wood multilevel gradient structure", *Proc. FGM'94*, Oct. 10-12, 1994, Lausanne, B. Ilschner and N. Cherradi eds., pp. 695-701, 1995.

12. J. Vincent, "Materials technology from nature", *Metals and Materials*, January, pp. 7-11, 1990.

13. Ph. Colomban and L. Mazerolles, "Nanocomposites in mullite-ZrO_2 and mullite-TiO_2 systems synthesized through alkoxide hydrolysis gel routes : microstructure and fractography", *J. Materials Science*, Vol. 26, pp. 3503-3510, 1991.

14. Ph. Colomban, E. Bruneton, J.L. Lagrange and E. Mouchon, "Sol-gel mullite matrix-SiC and mullite 2D woven fabrics composites with or without zirconia containing interphase", *Mullite'94, J. Eur. Ceramic Soc.*, 1996.

15. V. Vendange, E. Flavin and Ph. Colomban, "Gyromagnetic microwave resonance of cobalt-alumino borosilicate nanocomposites", *J. Material Science Letts.*, in press, 1995.

16. V. Vendange and Ph. Colomban, "Elaboration and thermal stability of alumina, aluminosilicate-Fe, Co, Ni magnetic nanocomposites prepared through a sol-gel route", *Materials Science and Engineering*, Vol. A168, pp. 199-203, 1993.

Thermodynamic Considerations on Mass Transfer along/across Grain Boundaries in Ceramic Materials

Harumi Yokokawa, Natsuko Sakai, Teruhisa Horita and Masayuki Dokiya
National Institute of Materials and Chemical Research
1-1, Higashi, Tsukuba, Ibaraki 305, Japan

abstract

The chemical potentials of electrons(holes), oxide ions and cations have been analyzed to clarify the mass transfer across/along grain boundaries. We have adopted two ways of 1) examining the mass transfer in grain boundaries in an analogous way to bulk phenomena and of 2) examining the chemical potential properties intrinsic to grain boundaries. For the first purpose, interesting bulk phenomena have been examined and analogous phenomena in grain boundaries are discussed in terms of a similar diffusion mechanism. For the second purpose, the non-equilibrium nature in grain boundaries are focused.

1. Introduction

To facilitate the investigation of Intelligent Materials, it is highly desired to systematize the mass transfer in a materials fabrication process and under an operation as intelligent materials. The theoretical and experimental investigations on the mass transfer of single carrier have been extensively made in past. Even so, when more than two carriers are concerned, many interesting phenomena may occur and could provide fruitful functions for intelligent materials. Unfortunately, these have not yet examined in the ceramic materials in a systematized and extensive manner, although the fundamental theoretical framework has been already given by the irreversible thermodynamics. Possible reasons for this situation seem to be the followings;

1) Ceramic materials have surface and grain boundaries; this makes things quite complicated.
2) Diffusion and chemical reactions occur frequently at the same time. Diffusion in ceramics have been discussed in defect chemistry, while chemical reactions have been examined in terms of the Gibbs energy change for plausible reactions. There has been a gap between two approaches.
3) Phenomena caused by multi carriers consist of processes with different time constants which are functions of temperature and oxygen potential.

In recent years, we have made thermodynamic considerations on materials problems by constructing thermodynamic database and using associated advanced software to make thermodynamic calculations[1]. Particularly, we have proposed that the chemical potentials are the key property for simultaneously considering the mass transfer and chemical reactions in the interface vicinity between dissimilar materials[2].

Actually, we have made attempts to analysis on chemical reaction at the interfaces between materials in different categories with success[2]. Nevertheless, the mass transfer in ceramic materials takes place through the diffusion of mainly charged species(cations, anions, electron, hole). Sometimes, this gives rise to phenomena which cannot be interpreted in terms of the elemental chemical potentials. The present investigation is aimed to include the effect of charged particles on diffusion and chemical reactions in the interface or grain boundaries.

2. Characteristic features of chemical potentials in Ceramic Materials

The chemical potential is the key thermodynamic properties to give a basis of understanding the mass transfer in grain boundaries particularly in elements. In ceramic materials, however, the situation of chemical potentials becomes more complicated. The driving force of mass transfer should be given in the chemical potential gradient. The thermodynamic factor, which is needed to derive the flux of species, is not a large value in alloy systems. However, the thermodynamic factor in ceramic materials may be enormously large. This means that the chemical potentials depend quite sensibly on composition. This is particularly true for the nearly stoichiometric compounds.

Since ceramic materials consist of several elements, changes in one elemental chemical potential should be accompanied with corresponding changes in other elemental chemical potentials according to the Gibbs Duhem relation;

$$x_1 d\mu_1 + x_2 d\mu_2 + x_3 d\mu_3 = 0 \qquad (1)$$

Furthermore, the mass transfer in ceramic materials is taken place through diffusion of charged particles. The charge neutrality is another requirement; correspondingly, the chemical potentials of elements, ions and electrons should be related as follows;

0-8194-2165-0/96/$6.00

$$M = M^{n+} + n\,e^- \quad (2)$$

$$\mu(M) = \phi(M^{n+}) + n\phi(e^-) \quad (3)$$

where $\phi(M^{n+})$ is the electrochemical potential of M^{n+} including the effect of the electrical potential, V.

3. Basic idea of applying chemical potential approach to grain boundaries

In surfaces, interfaces, or grain boundaries, segregation of particular elements are often observed. Explanation for such segregation can be given from either the equilibrium or the non-equilibrium points of view. The equilibrium approach is based on the fact that even when the chemical potentials are constant across the interface or grain boundaries (this is the requirement for the equilibrium), concentration can be changed. Sometimes, a concept of "interface phase" is introduced to make an explicit treatment of segregation. On the other hand, the non-equilibrium approach is focused on the driving force for segregation. We think that the latter approach is quite important in ceramic materials, although little efforts have been paid for this approach.

Here. chemical potentials in the grain boundary vicinity are discussed by considering that they can be deviated from those in bulk.

1) Features to be intrinsic to grain boundaries

When ceramic materials are fabricated at high temperatures, the chemical potentials at grain boundaries should be equal to those in bulk. Usually, the ionic configuration in the grain boundaries are loser and therefore the entropy term in the chemical potential can be larger than those in bulk; correspondingly, the entropy term should be also larger. When temperature is lowered, this structure is no longer stable since the larger entropy term in the grain boundaries makes their chemical potentials higher than those in bulk. When the bulk diffusion is faster than that through grain boundaries, a new structure with lower energy and with lower entropy can be reconstructed along the grain boundaries.

At low temperatures where the bulk diffusion is lower than the grain boundary diffusion, the reconstruction of the structure is no longer made and the ionic configuration should be frozen. In a such a case, the chemical potentials in grain boundaries are no longer equal to those in bulk. This tendency becomes more significant when some species are diffused through grain boundaries.

2) Features to be compared with bulk properties.

In ceramic materials, diffusion rates are different among species. Since many diffusion species are charged, diffusion should be taken place under a condition of charge neutrality. This means that the fastest and the second fast species should be diffused as a pair, namely anbipolar diffusion. When there are more than two diffusion species, interesting phenomena may happen even in bulk. Therefore, examination of such phenomena in bulk should help us to understand the mass transfer along/across the grain boundaries.

4. Some Examples

Here, interesting phenomena in bulk substances are examined and, if possible, the analogous phenomena related to grain boundaries are considered.

1) Kinetic demixing and segregation in grain boundaries

When the grain boundary diffusion is slightly higher than the bulk diffusion, a steep chemical potential gradient can be formed across the grain boundaries after some species is diffused along the grain boundaries. Under the local equilibrium approximation, the steep gradient of one particular species should be accompanies the corresponding gradients of other species as shown in Fig. 1; this may therefore cause diffusion of other species. This is an analogous phenomenon to so-called kinetic demixing or kinetic decomposition[3] which have been well examined in bulk substances. In some cases, this can be observed as grain boundary segregation due to the non-equilibrium origin. In other cases, there are some possibility that

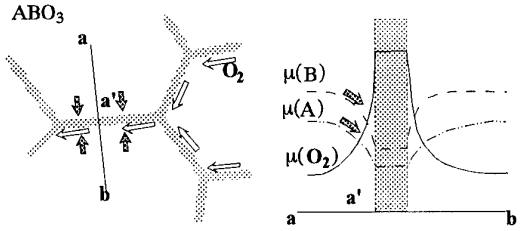


Fig. 1 Fast grain boundary diffusion of oxygen in ABO_3 and predicted chemical potential gradient across grain boundaries. The chemical potentials of metallic elements A and B should have similar but reverse gradients across the same grain boundaries, leading a driving force for grain boundary segregation of A or B and/or for changes in defect concentration or in defect structure between **a** and **a'**.

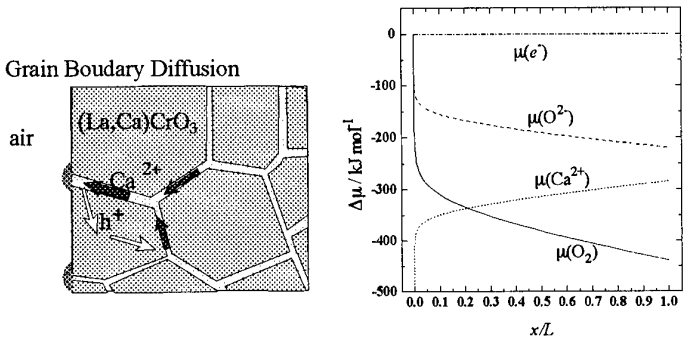


Fig. 2 Enhanced grain boundary diffusion of calcium ions under an oxygen potential gradient in $(La,Ca)CrO_3$ in CaO excess. The steep chemical potential of oxide ions gives rise to the corresponding gradient of chemical potential of Ca^{2+} in CaO which exists in grain boundaries.

defect concentration or defect structure will be changed across the grain boundaries; in the nearly stoichiometric compounds, the concentration of defects or the defect structure sensitively depends on the associated chemical potentials.

2) Migration to surface

Along the interface between two different materials, coupled diffusion can occur to satisfy the charge neutrality by charged species having the different diffusion path. For example, the sophisticated Ni/YSZ(yttria stabilized zirconia) anode for solid oxide fuel cells can be fabricated by the electrochemical vapor deposition technique, in which the oxide ions diffuse through YSZ, while electrons diffuse through nickel. Note that diffusion of oxide ions in nickel and of electrons in YSZ are both quite slow. Therefore, the diffusion of oxygen is fast only in the interface between two materials.

Similar phenomena can be taken place through grain boundaries of the calcium lanthanum chromite, $(La,Ca)CrO_3$, to be used as interconnect in solid oxide fuel cells. This materials is placed between air and fuel and therefore an oxygen potential gradient is developed inside materials[4]. This profile is determined by the anbipolar diffusion of oxide ions and holes. Since the electron conductivity is much faster than the ionic conductivity, the electron chemical potential is almost flat, while the chemical potential of oxygen and the electrochemical potential of oxide ions exhibit steep gradients in the air side. This material is adopted as calcium excess in composition to accelerate sintering. Such excess CaO exists in grain boundaries. This implies that the activity of CaO inside this material is nearly equal to unity. In such a case, the chemical potential of Ca^{2+} can be derived from the following relations;

$$\Delta_f G°(CaO) = \mu(Ca^{2+}) + \mu(O^{2-}) \qquad (4)$$

The bulk diffusion rate of Ca^{2+} is slow so that no migration in bulk can be expected. However, the grain boundary diffusion may take place with aid of the hole conduction in bulk substance. This was actually observed in our experiment on oxygen permeation through this material[5].

3) Moving hot spot in super conductive copper oxide wire

Recently, Okamoto et al.[6] have found an hot spot in a wire made of super conductive copper oxides which starts to light above 400 °C and slowly moves towards the same direction of the electrical current[ ]. This can be also interpreted in terms of the gradient in the electrochemical potential of oxide ions which can be determined by the electron electrochemical potential and the chemical potential of oxygen gas.

This suggests that the movement of charged ions might be important when a resistivity of grain boundaries is high and a high voltage is applied across the grain boundaries. At present, we do not know analogous phenomena related with the grain boundaries and interfaces.

4) Reduction induced by oxidation

Recently, Fukatsu et al.[7] have analyzed the hydrogen enrichment in aluminum melt which is caused by the introduction of air on the melt. This reaction proceeds via the diffusion of aluminum ions through alumina. Since the electronic conductivity is extremely low, proton instead of electrons (or holes) can be diffused to satisfy the charge neutrality. As shown in Fig. 3, the electrochemical potential of H^+ have a down-hill type gradient in the layer where the chemical potential of hydrogen gas shows a up-hill type gradient. This is due to the following equation;

$$d\mu(H_2,gas) = 2d\phi(H^+) + 2d\phi(e^-) \qquad (5)$$

This explains why the enrichment of hydrogen in aluminum melt occurs. This is accompanied with the oxidation of aluminum which is the true driving force for this phenomena.

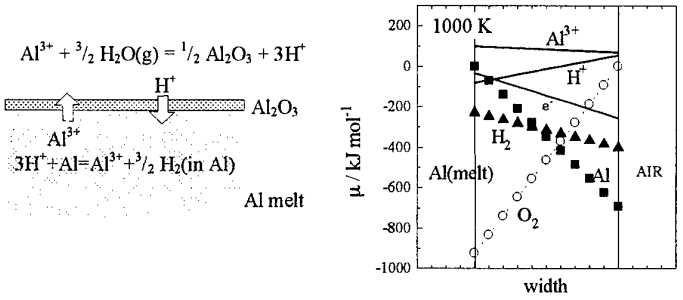


Fig. 3 Reduction induced by oxidation. When aluminum is oxidized by water, water can be reduced to hydrogen. For the case where this reaction takes place through an alumina thin layer, proton diffuses through the layer resulting in the highly concentrated dissolved hydrogen in aluminum.

If the electron diffusivity would be relatively high, the gradient of its electrochemical potential become more flat in Fig. 3 and therefore the electrochemical potential of proton and the chemical potential of hydrogen may have the gradient in the same direction. In such a case, no transportation of hydrogen occurs and just the oxidation of aluminum alone takes place.

Similar phenomena can be taken place in grain boundaries in ferrite. Recently, Fujimoto[8] has found an interesting phenomenon related with the precipitation of copper metal in CuO, ZnO, NiO doped ferrite. Copper was found along the grain boundaries after rapid cooling. During rapid cooling, the followings can be expected to occur. Since the atmosphere is the same during a cooling process, the equilibrium between solid and gas is broken and gas becomes more oxidative. Thus, solid should be oxidized from surface. This oxidation process depends on the relative magnitude of diffusion rates among cations, oxide ions and electrons. When cation diffusion is dominant and the proton conductivity is higher than the electron conductivity, a reduction process may occur inside the materials along grain boundaries. Fujimoto suggested that the metal copper was partly oxidized after its formation. This implies that the cooling process is not steady state but transient so that the driving force for reduction induced by oxidation may cease in the late stage of the cooling and the normal oxidation process may take place instead of the reduction.

5. Summary

The present investigation has clarified that the chemical potentials of charged species are closely related with each other, and therefore the difference in diffusion rate among charged species gives rise to interesting phenomena of the mass transfer in grain boundaries as well as in bulk. Since the diffusion properties of such species are sensibly dependent on temperature and oxygen potential, an appropriate model of representing the thermodynamic and transportation properties of charged systems as functions of temperature and oxygen potential is highly desired to make it possible to analyze mass transfer. Such a model may help us to investigate an appropriate way of fabricating intelligent materials or of setting up new functions indispensable for intelligent materials.

References

1) H. Yokokawa, S. Yamauchi, T. Matsumoto, *Thermochimica Acta* **245**, 45-55 (1994).
2) H. Yokokawa, N. Sakai, T. Kawada, M. Dokiya, "Chemical Thermodynamic Stability of the Interface," pp. 752-763, in Science and Technology of Zirconia V, ed. by S. P. S. Badwal et al, the Australasian Ceramic Society, 1993; H. Yokokawa, N. Sakai, T. Kawada, M. Dokiya, *J. Electrochem. Soc.* 138, 2719 (1991).
3) H. Schmalzried, *J. \chem. Soc. Faraday Trans.* **86,** 1273 (1990).
4) B. A van Hassel, T. Kawada, N. Sakai, H. Yokokawa and M. Dokiya, *Solid State Ionics* 66, 41-47 (1993).
5) N. Sakai, T. Horita, H. Yokokawa, M. Dokiya, "Oxygen Permeation Measurement of $La_{1-x}Ca_xCrO_{3-d}$ by Using an Electrochemical Method," to be published in *Solid State Ionics*
6) T. Okamoto et al., *Jpn. J. Appl. Phys.* **33**, L1212 (1994).
7) N. Fukatsu, Y. Tsukeshiba, N. Kurita and T. Ohashi, "Role of oxide layer formed on the surface of molten aluminum in the hydrogen absorption of the melt." pro. 20th commemorative international symposium on solid state ionics in Japan, Nov. 1-2, Tokyo, 1994, pp.129-130.
8) M. Fujimoto, "Inner Stress Induced by Cu Metal Precipitation at Grain Boundaries," Proc. Japan-US Workshop on Functional Fronts in Advanced Ceramics (Boundaries and Defects), Dec. 6-8, 1994 Tsukuba, Japan, STA, NIRIM, 1994, pp. 59-62.

DEFECT CONTROL IN CRYSTAL GROWTH OF PHOTOREFRACTIVE MATERIALS

Kenji Kitamura, Nobuo Iyi and Junzo Tanaka

National Institute for Research in Inorganic Materials (NIRIM)
1-1 Namiki, Tsukuba, Ibaraki 305 Japan

ABSTRACT

Some multi-component photorefractive crystals exhibit wide variations in their properties associated with the nonstoichiometry of the constituent cations. In order to grow single crystals with high quality and high homogeneity under nonstoichiometry control, a double crucible Czochralski method has been developed. In this method, the melt was dividedinto two parts by a double structure (two chamber system) crucible. The crystal was grown from the inner melt, and a powder with the same composition as the growing crystal was supplied to the outer melt. The powder was supplied continuously and smoothly at the rate of weight increase of the growing crystal. This rate was automatically controlled to match the weight increase of the growing crystals as monitored by a load cell. As an example, $LiNbO_3$ single crystals with a composition close to stoichiometric were grown, and their photorefrative properties were compared with those of Nb-rich congruent $LiNbO_3$ crystal. As the result, it turned out that the stoichiometric LN crytal exhibited higher efficiency and faster responsitivity than the congruent crystal.

1. INTRODUCTION

In recent years, the photorefractive materials are attracting attentions for their intelligent functions since the photorefractive effect can be easily applied to optical information processing and optical computing. The photorefractive effect is generally explained by the complex microscopic mechanisms in the following; When light of a suitable wavelength is incident on a crystal, photoelectrons are geneated in the irradiatedregion, migrate in the lattice and are trapped at new site in the dark region. The resulting space charges give rise to an elctric field stregth distribution in the crystal which chagnes the refractive index via the eletro-optic effect. In these mechanisms, intrinsic (nonstoichiometric) defects in photorefractive crystal play an essential role. Besides the photorefractive applications, a wide variety of oxide single crystals are of interest for use in optical applications. Most of these materials are multi-component oxides (intermediate oxide compounds) and, in a strict sense, are nonstoichiometric in the ratio of constituent cations due to defects in the crystals [1,2]. Since structures and densities of these intrinsic defects substantially influence on the optical properties, the relationship between the defects and properties is a significant subject to be studied. In this paper, nonstoichiometric nature of LiNbO3 (LN in abbreviation), which is one of typical photorefractive materials, and the intrinsic (nonstoichiometric) defectmodel are first describedbreifly.

In order to control the defectdensity, crystal growth with high crystal quality from the off-congruentmelt is required. The main oxide crystals commercially produced for optical applications have been grown by the Czochralski (CZ) method. In the ordinary CZ method, however, the composition of the growing crystal varies according to the progress of the crystallization when the crystals are grown from melts of off-congruent compositions or from a melt dopedwith a particular component. In order to overcome this problem in the conventional CZ method, we have developeda double crucible CZ method. The idea of using a double crucible was first proposed in the fifties in order to realize homogeneous doping of particular components in Ge and Si crystals [3,4]. Such technology was not commercially utilized until recently. Now, the double crucible method is once again attracting attention as some companies are applying it to the commercial production of doped Si crystals [5]. Although a similar method has been applied to single crystal growth of some oxides such as Nd-dopedYAG and LN, this technology has not yet been sufficiently developed[6]. In this paper, some essential techniques of our double crucible CZ method and its application to single crystal growth of LN under nonstoichiometric control are demonstrated.

If high quality single crystals can be grown from melts of off-congruent compositions, the optimum property relationship could be determined.In the last section, the photorefractive parameters dependingon the nonstoichiometry of LiNbO3 will be discussed.

2. NONSTOICHIOMETRICNATURE OF LN

$LiNbO_3$ is one of the hopeful photorefractive materials, commercially producedby the Czochralski method, that exhibits considerably wide nonstoichiometric solid solution. In this case, the solid solution range expands only toward the Nb component side [7,8] as schematically illustrated in Fig. 1. Therefore, the congruent melting composition shifts toward the excess component side of the stoichiometric composition. The compositional deviation from

0-8194-2165-0/96/$6.00

stoichiometry is directly caused by the density of defects. A crystal of congruent composition consequently contains a certain amount of defects. Generally, such defectdensities of nonstoichiometry are larger by 2 or 3 orders than ordinary impurity concentration levels.

From the conmpositional relationship between the melts and the crystals grown from them, the crystal composition, that is,nonstoichio-metric defect density, can be controlled by the melt composition. The phase diagram previously reported [8] suggests that stoichiometric LN is grown from a Li-rich melt, about 58 Li_2O mol %. The congruent composition has been reported as being 47.5 ~ 47.6 Li_2O mol %.

The nonstoichiometry of LN is caused by excess Nb ions occupying the Li ion site generating cation vacancies necessary for electric charge balance. Two possible defect structure models have been proposed to describe the cation vacancies. They are the Nb-site vacancy model [9] and the Li-site vacancy model [10]. In both models, LN crystals of the congruent composition contain large amount of such defects. In the first model, about 5% of Li-ion sites are occupied by Nb ions and 4 % of Nb-ion sites are vacant. In the latter, about 1 % and 4 % of Li-ion sites are occupied by Nb ions and vacancies, respectively. They are indicated as follow;

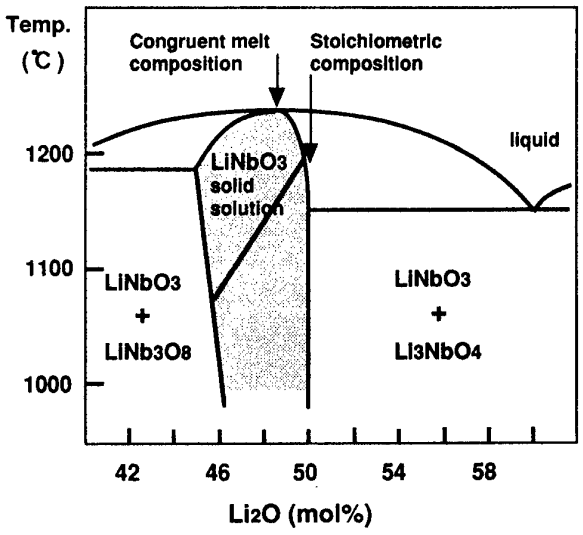


Fig. 1:Schematic phase diagram of $LiNbO_3$ in the Li_2O-Nb_2O_5 system[8].

Nb-site vacancy model: $[Li_{0.95}, Nb_{0.05}][Nb_{0.96}, V_{0.04}]O_3$

Li-site vacancy model : $[Li_{0.95}, Nb_{0.01}, V_{0.04}]NbO_3$,

where V stands for vacancy. It is still being argued which model is more likely for the LN nonstoichiomery [11]. In the former model, the Nb ion occupancy at the Nb ion site is decreased by an increase of the excess Nb ion concentration. However, Iyi et al. analyzed that occupancy in the LN single crystals grown from melts of different compositions. The occupancy was almost constant independentlyof the crystal compositions [10]. In the latter model, the excess Nb ionconcentration at the Li ion site is only 1%. According to this model, when 5 mol % MgO is doped to the congrunet melt in order to suppress the optical damage, the vacancy concentration in the MgO doped crystal becomes heigher than that in the congruent crystal. Iyi et al. suggested this increase of vacancy concentration by highly doping of MgO from the chemical analysis of LN crystals with different compositions [12]. These defect densities strongly influence the optical properties as mentioned later.

3. CRYSTAL GROWTH BY DOUBLE CRUCIBLE CZ METHOD

As mentioned above, some photorefractive materials exhibit considerably wide variations in their properties by changing the melt compositions from which the crystals are grown. In the conventional CZ growth, however, there are two main disadvantages; one is that if crystals are grown from melts of off-congruent compo- sitions or from a melt doped with a particular component, the composition of the growing crystal varies according to the progress of the crystallization. The other disadvantage is that the melt depth changes (decreases)as the crystallization progress. This causes some significant changes in thermal conditions and melt convections during the growth, and consequently makes growth of single crystals with high homogeneity difficult. We have developeda double crucible Czochralski method equipped with an automatic powder supply system in order to realize the growth of high quality single crystals from the off-congruent melt.

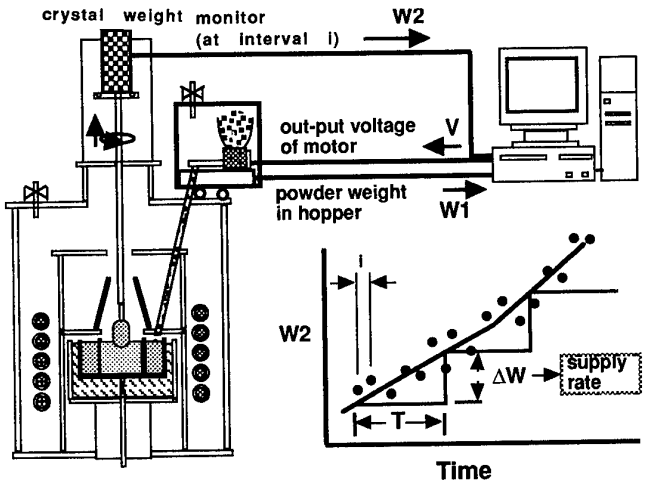


Fig.2: Diagram of double crycible CZ method with full automatic powder supply system.

This method has been applied to growth of stoichiometric LN crystals. Stoichiometric LN can be grown from the Li-rich (about 58 Li2O mol %) melt as shown in Fig. 1. A schematic diagram of the double crucible CZ method is shown in Fig. 2. In this method, an ordinary CZ furnace equipped with a radio frequency generator was used. The Pt crucible had a double structure which divided the melt into two parts. The inner crucible was a platinum cylinder (100 mm diameter) placed on the bottom of the outer crucible (140 mm diameter, 70 mm height). The outer melt could enter the inner crucible through the small gap between the bottom of the outer crucible and the inner cylinder. In order to grow stoichiometric LN crystals, the compositions of the inner melt and outer one should be kept Li-rich and stoichiometric, respectively. The weight of the growing crystal was monitored by a load cell. LN stoichiometric powder was supplied to the outer melt at the same rate as the weight increase of the growing crystal by an automatic powder supply system attached on the chamber of the CZ furnace (see Fig. 2). In this supply system, calcined stoichiometric LN powder was placed in a holding container (hopper). The powder was delivered from the bottom of this container by a cork-screw-like mechanism. The weight of the holding container including the powder was monitored every second by an electronic balance. The weight decrease of the powder in the hopper per certain period was calculated and adjusted to the supply rate by automatically modifying the rotation rate of the cork-screw mechanism. The supply rate was also automatically set from the calculation of the weight increase of growing crystal during a certain period (for example, 10 minutes). Fig. 3 shows an example of LN single crystal grown by this method. The maximum size of stoichiometric LN grown so far, using this system, was 5.5 mm diameter, 140 mm long and about 850 g weight. The difference in the Curie temperatures through the crystal (from neck to tail) was about 1 °C.

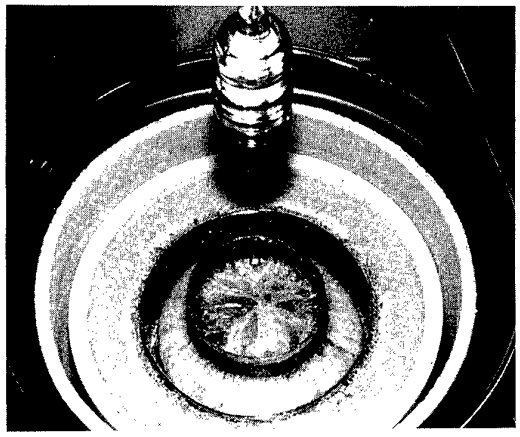


Fig.3: LN single crystal pulled from double crucible under nonstoichiometry control

4. OPTICAL PROPERTIES OF LN DEPENDING ON NONSTOICNIOMETRY

From the defect structure models, it has turned out that the defect densities increase proportionally to the excess Nb concentration and in turn strongly influence the optical properties. Fig. 4 shows optical absorption spectra of LN crystals grown from different melt compositions. The spectra were measured by using a spectrophotometer, on c-plate samples. The Curie temperatures of the crystals, measured by DTA analysis, are indicated in the figure. Crystal composition can be estimated from the Curie temperature using the equation proposed by O'Bryan et al. [13].

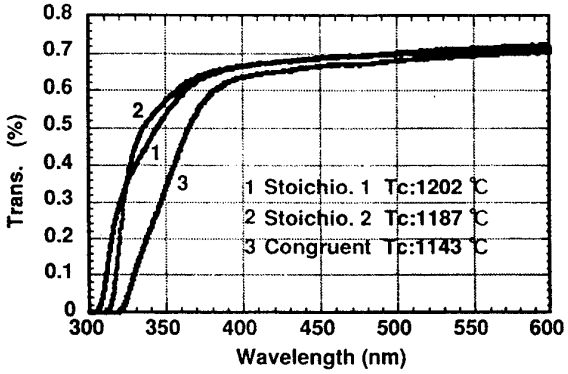


Fig.4: Transmissibility of LN crystals grown from different melt compsition

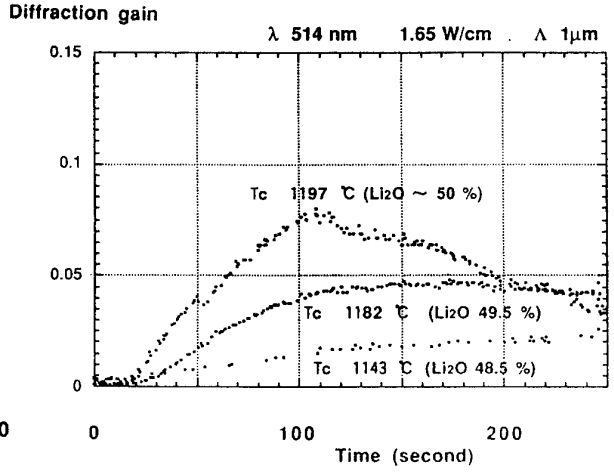


Fig.5: Diffraction gain time dependence of LN measured by two beam coupling method.

According to ref.[13], Sample 3 with the Curie temperature of 1143 °C was grown from the congruent melt composition of 48.5 Li_2O mol %. The other samples were grown from Li-rich melts. The Curie temperature of 1187 °C on Sample 2, grown from a melt of 57.0 Li_2O mol %, corresponds to a crystal composition of 49.7 Li_2O mol %. This figure clearly indicates that the absorption decreases in crystals grown from Li-rich melts. Sample 1 was grown from a melt composition of 59.5 Li_2O mol %. From the compositional relationship between the melts and grown crystals, its crystal composition can be regardedto be very close to stoichiometric or, there is a possibility that the composition is Li-rich. Although the wavelength of the absorption edge of Sample 1 is shorter than that of Sample 2, some absorption can be observedas a shoulder between 320 and 370 nm. This absorption has also been observed in stoichiometric LN grown from a K_2O dopedmelt [14], however, it has not yet been explained.

In addition to the absorption behavior, some photorefractive parameters also strongly depend on the [Li]/[Nb] ratio in the crystal. According to Furukawa et al. [15], the optical damage, a kind of photorefractive effects, was enhancedin LN crystals with composition close to stoichiometric. Fig. 5 indicates a irradiation time dependenceof diffractionefficiency of non-dopedLN grown from the melts of differentcompositions. The diffraction efficiencywas measured by the 2 beam coupling method using an Ar-laser (514 nm wavelength) at a power of 1.65 W/cm with a grading period of 1 micron. The crystal compositions were estimated from thier Curie temperature as illustraten in the figure. The crystal of the composition close to stoichiometry exhibited high diffraction gain and high sensitivity. This tendency is supporting the result previously reported[15].

It has been reportedthat the optical damage can be suppressed by doping with Mg, Zn and Sc [16-18]. A blue shift of the absorption edge was also observed for crystals doped with these components. It is noteworthy that the stoichiometry control and doping of particular components exhibit different effects on their optical properties. In order to interpret these phenomena, changes in the defect structures depending on the concentration of dopant in the crystal must be clarified[12]. This is one of the main future objectives in this field.

5. SUMMARY

The photorefractive materials which are attracting attentions for their intelligent funcitons exhibit a strong dependenceof properties on structure and density of nonstoichiometric defects. In order to develop new photorefractive mateirals, much understandingon the relationship between the properties and intrinsic defectsin the crystals is required. For such understanding, single crystals with high quality and homogeneity grown under nonstoichiometry control are necessary. However, the materials commercially producedare extremely limited, and most are grown by the ordinary CZ method from the congruent melts. If high quality single crystals can be grown from the melts of off-congruent compositions, the optimum properties for particular applications would be able to be chosen from the wide variation in properties. However, some difficulties still exist in growth of high quality single crystals from off-congruent composition melts

Some breakthroughs to grow single crystals with high quality and high homogeneity from off-congruent composition melts are still required. We have developeda double crucible Czochralski method as one possibility. In this method, the melt was dividedinto two parts by a double structure crucible. The crystal was grown from the inner melt, and a powder with the same composition of the growing crystal was supplied to the outer melt continuously and smoothly at the rate of weight increase of the growing crystal. This rate was automatically controlled to match the weight increase monitored by a load cell. As an example, LN single crystals with composition close to stoichiometric were successfully grown from a Li-rich melt using this method.

ACKNOWLEDGEMENTS

This work has been carried out as project titled "New Mateiral Developement by Nanospece Lab" which has been supported by Special Coordination Funds for Promoting Science and Technology.

REFERENCES

[1] J. R. Carruthers: "Treatise on Solid State Chemistry" Vol. 5, ed. by N. B. Hannay, (Plenum Press New York, (1975) p.383.
[2] K. Kitamura, T. Sawadaand S. Kimura: J.Japn.Assoc.Crystal Growth, 14 (1987) 163.
[3] W .F. Leverton: J. Appl. Phys. 29 (1958) 1241.
[4] J.C. Brice: "The Growth of Crystals from the Melt" (North-Holland, Amsterdam, 1965) p.153.
[5] M. Kojima, Y. Yamashita and H. Hirano:Toshiba Review, 43 (1988) 829.
[6] K. Kitamura,J.K.Yamamoto, N.Iyi, S.KImura and T.Hayashi: J. Crystal Growth,116 (1992) 327.
[7] P. Lerner, C. Legras and J.P. Dumas: J. Crystal Growth 3/4 (1968) 231-235.

[8] J.R. Carruthers, G.E. Peterson, M.Grasso and P.M.Bridenbaugh: J. Appl. Phys. 42 (1971) 184.
[9] S.C. Abrahams and P. Marsh: Acta Cryst. B42 (1986) 61.
[10] N. Iyi, K. Kitamura, F.Izumi, J.K. Yamamoto, T. Hayashi, H. Asano and S. Kimura: J. Solid State Chemistry, 101 (1992) 340.
[11] H.J.Donnerberg, S.M.Tomlinson, C.R.A. Catlow and O.F. Schirmer: Phys. Rev. B40, 11 (1989) 909.
[12]N. Iyi, K. Kitamura, Y.Yajima, S.Kimura, Y.Furukawa and M.Sato: J. Solid State Chemistry 118 (1995) 148.
[13] H.M.O'Bryan, P.K.Gallagher and C.D.Brandle: J. Am. Ceram. Soc. 68 (1985) 493-496.
[14] G.I. Malovichko, V.G.Grachev, E.P. Kokanyan, O.F.Schirmer, K.Betzler, F. Jermann, S. Klauer, U.Schlarb and M. Wohlecke: Appl. Phys. A 56, (1993) 103.
[15] Y. Furukawa, M. Sato, K. Kitamura, Y. Yajima and M. Minakata: J. Appl. Phys,72 (1992) 3250.
[16] Y. Furukawa, M. Sato, F. Nitanda and K. Ito: J. Crystal Growth, 99 (1990) 832.
[17] T.R. Volk, V.I. Pryalkin and N. M. Rubinina: Opt. Lett.,15 (1990) 996.
[18]J.K. Yamamoto, K. Kitamura, N. Iyi, S.Kimura, Y. Furukawa and M. Sato: J. Crystal Growth 128 (1993) 920.

Self-organization of phthalocyanine molecules along the atomic step arrays on sapphire

Takayoshi Hayashi, Akira Yamashita, Tohru Maruno, Stefan Fölsch* and Shiro Matsumoto

NTT Interdisciplinary Research Laboratories
Musashino-shi, Tokyo, 180 Japan
*Present Address: Institut für Experimentalphysik (WE1), Freie Universität Berlin
Arnimallee 14, 14195 Berlin, Germany

Hideo Konami and Masahiro Hatano

Institute for Chemical Reaction Science, Tohoku University
Katahira, Aoba-ku, Sendai 980, Japan

ABSTRACT

An example of structural control of organic thin film by self-organization is described. Equally spaced parallel atomic step arrays exist on polished sapphire (1012) surface. Dibenzo [b, t] phthalocyaninato-Zn (II) (ZnDBPc) molecules deposited by UHV molecular-beam deposition on this surface stack themselves to form columnar crystal grains. Since the direction of these columns is parallel to the atomic step direction, thin films of ZnDBPc grown on the sapphire (1012) surfaces show unidirectional in-plane ordering over the entire substrate. The direction and spacing of the parallel atomic step arrays are directly related to the misorientation direction and angle of the polished surface from the exact (1012) surface. Therefore the ordering direction of the ZnDBPc thin film has no relation to the crystallographic axes of the sapphire, which is totally unlike ordinary epitaxial growth. Since the step spacings can be controlled over a wide range, we can expect to be able to improve the ordering by adjusting the step spacings to the lattice spacing of organic crystals.

1. INTRODUCTION

Metallo-phthalocyanine (MPc) thin films have remarkable properties such as photo-conductivity and third-order optical nonlinearity.[1,2] Since these properties of MPc thin films are closely related to molecular stacking, it is important to control the ordering of molecules on the substrate during thin film growth. However, ordinary epitaxial growth technique is not adequate to obtain highly ordered thin film due mainly to the large difference in lattice parameters between organic crystals and inorganic substrate crystals.

At the 2nd international conference on intelligent materials, we reported that a unidirectionally ordered structure in as-deposited thin film had been successfully formed over the entire surface of a polished sapphire (1012) substrate by using a less-symmetrical MPc, dibenzo[b,t] phthalocyaninato-Zn(II) (ZnDBPc).[3] However, we could not explain the ordering mechanism of ZnDBPc with the ordinary epitaxial growth mechanizm since there was no relationship between the crystallographic orientations of the sapphire substrate and that of the ZnDBPc film. Since thin films of ordinary four-fold symmetrical MPc's (ZnPc, CuPc, TiOPc and so on) formed by the same deposition condition did not show any ordering, this unidirectional ordering was considered to be attributed to the self-organizing properties of the less-symmetrical MPc molecule.

In this study, to investigate the ordering mechanism of ZnDBPc on polished (1012) surfaces of sapphire, we examined the atomic-scale surface morphologies of the sapphire substrates and of the ZnDBPc films grown on them.[4]

2. EXPERIMENTAL PROCEDURE

The polished sapphire crystals, nominally having (1012) faces, were commercially obtained from Kyocera Corp. Misorientation angles (off-angles) from the exact (1012) surface were specified to be within 2 degrees. The actual misorientation directions and angles of the polished surfaces were measured by X-ray diffraction (XD). The ZnDBPc molecules were synthesized and purified according to the method described by Ikeda et al.[5] Organic molecular-beam deposition

0-8194-2165-0/96/$6.00

of ZnDBPc was performed in an ultra-high vacuum chamber, which was diffusion-pumped to a base pressure of less than 3 x 10^{-10} Torr. The sapphire substrate was first chemically cleaned with aqueous hydrofluoric acid and a mixture of sulfuric acid (H_2SO_4) and hydrogen peroxide (H_2O_2), and then heated in vacuum at 300 °C for 30 min before deposition. In-situ RHEED observations confirmed that atomically flat and clean surfaces could be obtained by this surface-cleaning procedure. The substrate temperature was set to about 200 °C.

We observed the surface morphology in air with an Olympus OMPM-AFM-100 atomic force microscope (AFM) with a standard diamond tip. To observe the ZnDBPc film surfaces, the contact force was set as low as possible (around 1 nN) to minimize scratching of the surfaces by the AFM tip. The in-plane molecular orientation of the ZnDBPc was evaluated by polarization absorption spectroscopy using a 5-mm diameter normally incident polarized light beam.

3. RESULTS AND DISCUSSION

Figure 1 shows typical AFM images of polished sapphire $(\bar{1}012)$ surfaces from two different samples. The magnifications and the crystallographic directions are the same in the two images. Equally spaced parallel lines can clearly be seen in both specimens. The directions of these lines vary among the samples and have no relationship to the crystallographic directions. The line spacings also vary among the samples. Equally spaced parallel lines exist everywhere over every sample, and the direction and spacing of the lines are fairly uniform on a given sample. We confirmed that these parallel lines are atomic steps corresponding to the misorientation of the polished surface and that the step height is equal to a $(\bar{1}012)$ lattice spacing of 0.37 nm by using XD to measure the misorientation directions and angles of the polished surface from the exact (1012) surface. No special sample preparations were needed to observe the atomic step arrays on the sapphire surface, which suggests that the atomic step arrays are formed in the polishing process and are chemically and thermally stable within the present experimental conditions.

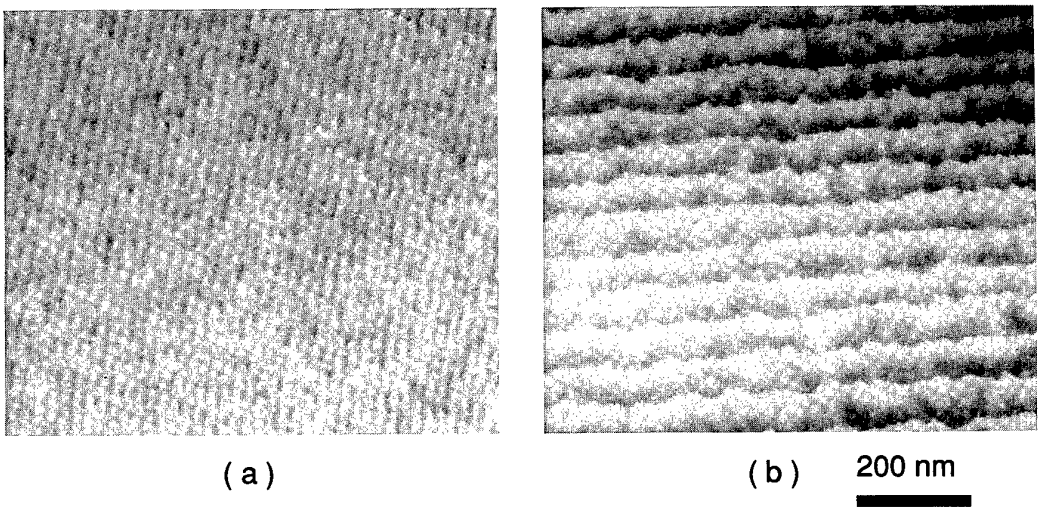


Fig. 1. AFM images of polished sapphire $(\bar{1}012)$ surfaces from two different samples.

Figure 2 (a) is an AFM image of the ZnDBPc film at the early stage of the growth at 200 °C. Columnar shaped crystal islands with unidirectional ordering can be clearly seen. The sapphire surface is not completely covered by ZnDBPc film, namely the dark regions are the uncovered sapphire surface. A higher magnification image of the center region of Fig. 2 (a) is shown in Fig. 2 (b). Atomic step arrays can be seen in the dark regions of Fig. 2 (b), and their direction is parallel to the average direction of the long axes of columnar shaped ZnDBPc islands.

From the results of our previous paper[6], we expected the crystal structure of ZnDBPc films on sapphire to be triclinic: $|\boldsymbol{a}|$ = 1.56 nm, $|\boldsymbol{b}|$ = 0.38 nm, $|\boldsymbol{c}|$ = 1.32 nm, a = 113°, b = 86°, and g = 109°. The unit cell contains one molecule, and the ZnDBPc molecules stack themselves along the $\boldsymbol{b}$-axis to form molecular columns. Since an interplanar spacing d_{001} of 1.21nm has been observed for ZnDBPc films grown on sapphire at 200°C[7], the $\boldsymbol{a}$-$\boldsymbol{b}$ planes must be parallel to the sapphire

surface. Combining these results with the present results, we conclude that the possible arrangements of ZnDBPc unit cells at the step edge are as shown in Fig. 3. Due to the triclinic symmetry, there are four different unit-cell arrangements whose ***b***-axes are parallel to the step direction and whose ***a-b*** planes are parallel to the surface.

The in-plane molecular orientation was evaluated by absorption spectroscopy using a normally incident polarized light beam. The azimuthal angle dependence of the Q-band intensities at 660 nm for the ZnDBPc film showed a clear dichroism. The direction of maximum Q-band intensity was perpendicular to the step direction. If arrangements (a) and (c) in Fig. 3 grew predominantly, or if (b) and (d) grew predominantly, the direction of maximum Q-band intensity would not be perpendicular to the step direction. Therefore, the results of the polarization spectroscopy indicate the co-existence of these four arrangements in actual ZnDBPc films. Figure 4 schematically shows how the ZnDBPc molecules may stack themselves to form a column along the step direction for arrangement (a) in Fig. 3.

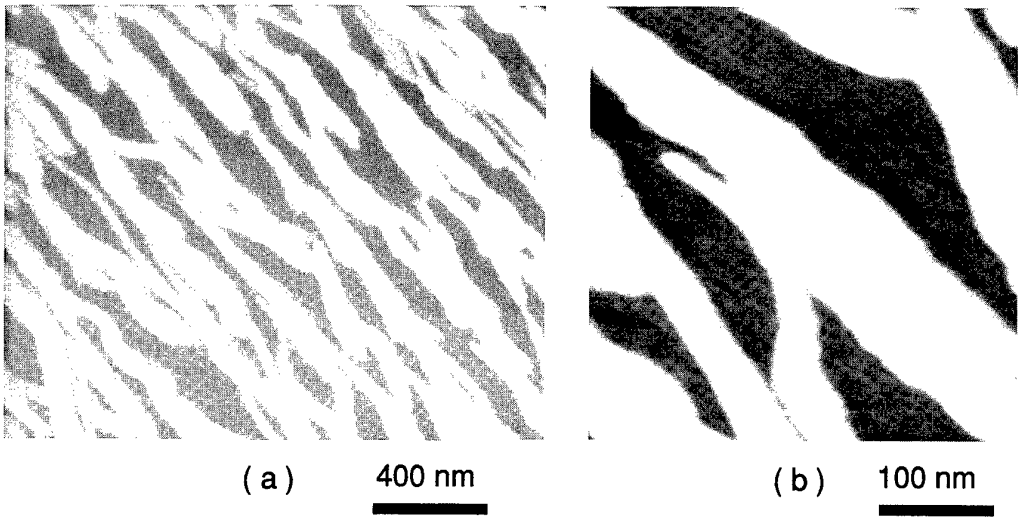


Fig. 2. (a) low-magnification and (b) high-magnification AFM images of 10-nm-thick ZnDBPc film on a sapphire substrate.

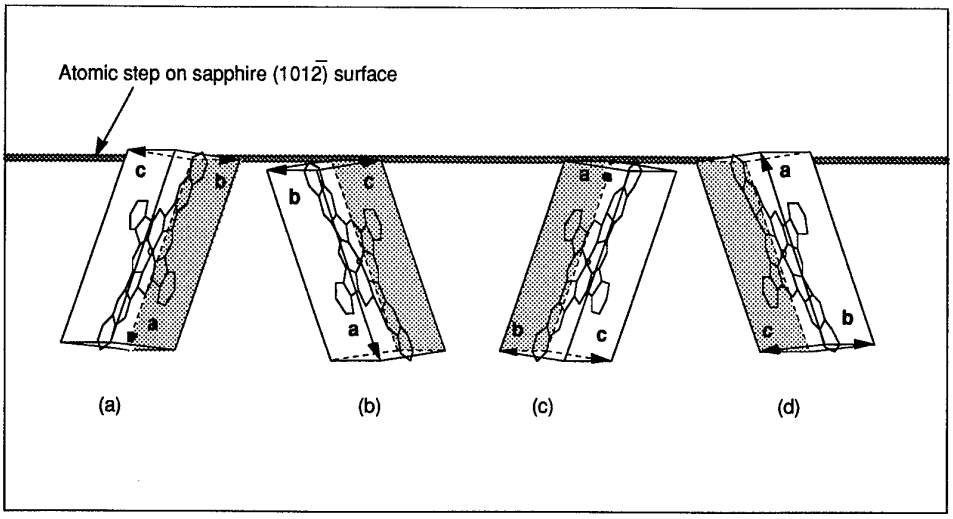


Fig. 3. Top view of four unit-cell arrangements whose ***b***-axes are parallel to the atomic step direction and whose ***a-b*** planes are parallel to the surface of the sapphire substrate. Possible arrangements of the ZnDBPc molecules in the unit cells are also drawn, although we need further study to determine the exact position and direction of the ZnDBPc molecule in the unit cell.

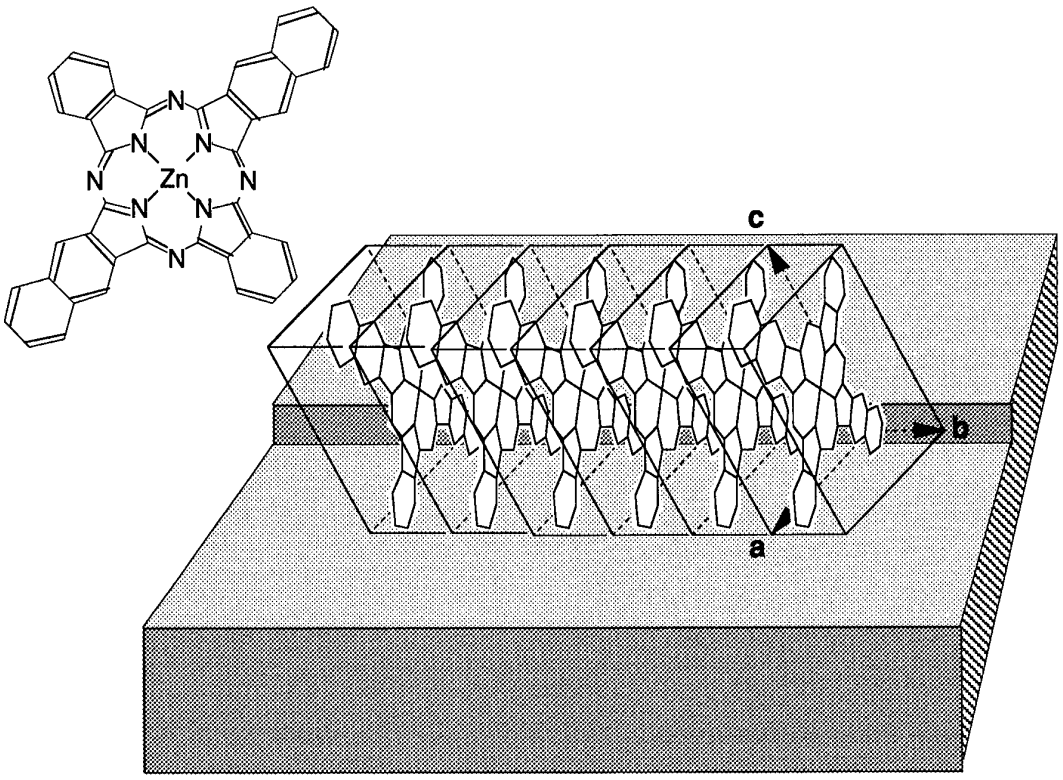


Fig. 4. Perspective view of the columnar stacking of ZnDBPc molecules along the step direction for arrangement (a) in Fig. 3. The molecular structure of ZnDBPc is also shown on the left.

As shown in Figs. 3 and 4, the ***b***-axis of the ZnDBPc film is parallel to the atomic step direction, which is determined by the misorientation direction of the polished surface and therefore has no relationship to the crystallographic direction of the sapphire substrate. One possible explanation for the ordering mechanism of ZnDBPc due to the atomic steps on the polished sapphire is as follows, although further study is needed to clarify the details. If we assume that a substrate temperature of 200 °C is high enough for ZnDBPc molecules to move around on the terraces and along the step edges to find stable nucleation sites, then since the interaction between ZnDBPc molecules and steps is stronger than that between molecules and terraces, the density of ZnDBPc molecules is enhanced at the step edges. Therefore, the nucleation and growth is initiated by the ZnDBPc molecules that are constrained along the step edges. When the ZnDBPc molecules stack themselves to form stable columnar nuclei, while keeping themselves in contact with the step edges, the column axes (***b***-axes) of the nuclei are necessarily aligned parallel to the step direction, as shown in Fig. 4.

The ordering direction is not governed by the crystallographic orientation of the sapphire substrate, which is totally unlike ordinary epitaxial growth. The step-induced ordering can be enhanced by applying a larger misorientation angle, which increases the density of the parallel steps. Furthermore, we can expect a new possibility of resonantly enhanced ordering by matching the step spacings to the lattice spacing of the organic crystals. Since the step spacings can be controlled over a wide range by changing the misorientation angles, this idea is applicable to a variety of organic crystals.

4. ACKNOWLEDGMENTS

We thank Dr. M. Igarashi of NTT Interdisciplinary Research Laboratories for his AFM observations and helpful discussions. We also thank Dr. Y. Shiratori and K. Ohhira of the Mitsumaru Pharmaceutical Co. Ltd. for synthesizing the ZnDBPc. This work was partly supported by Grant-in-Aid for Scientific Research No.05555181 from the Japanese Ministry of Education, Science and Culture.

5. REFERENCES

1. C.C. Lenznoff and A.B.P. Lever, Phthalocyanines: Properties and Applications, VCH Publishers Inc., New York, 1989.
2. M. Hosoda, T. Wada, A. Yamada, A.F. Garito, and H. Sasabe, "Phases and third-order optical nonlinearities in tetravalent metallophthalocyanine thin films", Jpn. J. Appl. Phys. 30, L1486, 1991.
3. T. Hayashi, T. Maruno, and Y. Ishii, "Nano-structure fabrication by using self-organizing properties of materials", Proc. 2nd ICIM 617, 1994.
4. T. Hayashi, A. Yamashita, T. Maruno, S. Fölsch, H. Konami and M. Hatano,"In-plane ordering of dibenzo [b, t] phthalocyaninato-Zn(II) thin film due to the atomic step arrays on sapphire (1012) surface", J. Cryst. growth 156, 245, 1995.
5. Y. Ikeda, H. Konami, M. Hatano, and K. Mochizuki, "Synthesis of non-symmetrically benzo-substituted phthalocyanines and their electronic spectra", Chem. Lett. 763, 1992.
6. S. Fölsch, T. Maruno, A. Yamashita, T. Hayashi, M. Tomita, H. Konami, and M. Hatano, "Crystallographic structure of the novel metallophthalocyanine derivative 2,3:12,13-dibenzophthalocyaninato-Zn(II)", J. Crystal Growth 141, 256, 1994.
7. T. Maruno, A. Yamashita, T. Hayashi, H. Konami, M. Hatano, Y. Shiratori, and K. Ohhira, "Highly ordered thin films of a novel less-symmetrical metallophthalocyanine formed by organic molecular beam deposition", Jpn. J. Appl. Phys. 32, L628, 1993.

Paper presented at the Third ICIM/ECSSM '96, Lyon '96

Growth and tubule formation of boron filament by electron beam heating in an electron microscope

Masato Tomita, Takayoshi Hayashi, Satoru Suzuki, and Junzo Tanaka*

NTT Interdisciplinary Research Laboratories

9-11, 3-Chome, Midori-cho, Musashino, Tokyo 180, Japan

* National Institute for Research in Inorganic Materials

Tsukuba, Ibaraki, 305, Japan

ABSTRACT

In a transmission electron microscope (TEM), we have shown that an amorphous boron filament can be obtained by Vapour-Liquid-Solid (VLS) growth under intense electron irradiation (current density > 100 A / cm^2) on an amorphous Boron Nitride (BN) film deposited a few-nm gold as agent. The grown filaments have gold particles on the tops and the diameter were from 10 to 100 nm. Detailed analysis of Electron Energy-Loss Spectrum (EELS) of the amorphous boron was carried out. We also dynamically observed shrinking of filaments by evaporation of boron through gold particles. As a special case, boron-rich tubules of several hundreds nm diameters were also formed.

1. INTRODUCTION

Fabrication of nano-structured materials by self-organization is a promising approach for developing new advanced materials. Inorganic materials can be grown in a variety of shapes, such as whiskers and particles, in a suitable growth environment. Because the conditions required for such growth are limited to a certain range, reaction-controllability is an important factor. From this point of view, an electron microscope is not only a powerful tool to analyze the materials but can also be used as a "nano-space lab.", in which we can fabricate nano-structured materials observing the self-organization dynamics in realtime.

In this report, we show that an amorphous boron filament can be obtained by the VLS mechanism[1] under intense electron irradiation on a-BN film in a conventional transmission electron microscope.[2] Usually, boron filaments are grown by CVD using diborane or boron-halides. However, in our experiment, we used a-BN film as a boron source. Dynamical observation of filament shrinkage and tubule formation in a filament is also described.

2. EXPERIMENTAL

A 300-nm-thick amorphous BN film with 5 nm thick Au on the surface was prepared by ion beam deposition. The chemical composition was determined by Auger electron spectroscopy to be B:N:C:O:Ca=50:40:7:2:1 inside the film. The sample for the TEM was supported on a holey carbon film. The electron irradiation and high resolution observations were carried out in a H9000 TEM (Hitachi) operated at 250 kV. A UHV-HF2000(Hitachi) was used for micro-diffraction and electron energy-loss spectroscopy (EELS) with a Gatan model 666 EELS system. 100 kV electrons were used for the EELS measurement to reduce radiation damage. An electron current almost ten times as high as for ordinary operation can be obtained at the sample position by removing the condenser aperture of the H9000. The current density is 200 - 300 A/cm^2, so an insulator sample can be heated to over the melting temperature of gold (1063 C°).

3. RESULTS and DISCUSSION

3.1 Filament growth and EELS analysis

Using intense electron irradiation on the a-BN film (Fig. 1 (a)) with gold particles (dark dots), we obtained filaments in a TEM (Fig. 1 (b)). Immediately after intense irradiation, the film started to evaporate and gold particles began to move and grow. Most of the gold particles seemed to melt. When the particle sizes reached about 10 nm or larger, filaments began to grow with gold droplet on their tops. The grown filaments had gold particles on their tops and their diameters were from 10 to 100 nm. From the diffuse ring patterns of the electron diffraction (Fig. 2) and the EELS[3] (Fig. 3), we identified the filaments as amorphous

0-8194-2165-0/96/$6.00

boron. The gold droplet plays a very important role in this VLS mechanism (Fig. 4). It acts as filtering collector that select only boron among the other components, and it acts as something like a pump that transports the collected boron to the other side of the droplet without any reactions.

B-K energy -loss spectra of a-B(boron filament), β-rhom. boron and boron carbide are shown in Fig. 5(a). The orbital population of B2p and H1s orbitals in the unoccupied orbitals derived from DV-Xα MO calculation of a $B_{12}H_{12}$ molecule are also shown in the figure. Each experimental spectrum shows a small peak at the threshold of about 192 eV. The orbital population analysis shows that the LUMO corresponding to the peaks around 192 eV mainly consist of orbitals of boron and there is almost no contribution of hydrogen orbitals. This suggest that the electronic states just above the Fermi level of boron-rich solids are strongly localized on B_{12} icosahedra.

Both B-K and C-K energy-loss spectra of boron carbide are shown in Fig. 5(b) (the energy values are shifted for comparison). Although the overall features are quite similar with each other due to hybridization between boron and carbon orbitals, no peaks corresponding to the small peak at the B-K threshold is observed in the C-K spectrum. This indicates that the electronic states just above the Fermi level of boron carbide are strongly localized on B_{12} icosahedra and supports the calculated figure discussed above.

3.2 Shrinkage of filaments

When the grown filaments were re-irradiated by intense electrons, some of the filaments began to shrink or evaporate from the tips with the melted gold particles. Figure 6 shows the initial stage of evaporation. Figure 7 shows sequential video images of the evaporation of a 800-nm-thick filament. The gold particle on the filament, which initially had a polyhedral shape, was irradiated by intense electrons (Fig. 7(a)). After 5 seconds, the gold particle melted and the droplet dug into the filament. The interface between the droplet and the filament became concave during the evaporation, as shown in Fig. 7(c). Wagner proposed a mechanism for his process called Solid-Liquid-Vapor etching.[4] In this process, liquid alloy can act as a catalyst for etching. This seems to be the same process as we observed in filament evaporation.

3.3 Tubule formation in filaments

Under some conditions, a filament-wall was left after the digging droplet had passed down the filament. Figure 8 shows a typical example of this process. The 500-nm-thick filament in Fig. 8(a) was irradiated by intense electrons. After the droplet reached the bottleneck in the filament (Fig. 8(b)), a tubule-like structure was formed without the filament wall collapsing (Fig. 8(c)). The wall thickness was less than 10 nm. The chemical composition of tubules is found to be B:O:C:Ca=10:6:2:1 by EELS. The tubules had amorphous structures. Although the chemical composition of a tubule can be estimated roughly, it is difficult to identify the main wall-material because the composition is non-uniform and there is contamination.

As far as we know, there have been no previous reports on the tubule formation. Although the mechanism is still under investigation, this phenomena has potential to be used as a new technique for microfabrication, since many materials can be grown in filaments and whiskers. For example, a Si filament covered with siliconcarbide or siliconnitride could be drilled by this mechanism and a tube could be obtained.

4. ACKNOWLEDGEMENTS

The authors would like to thank Dr. F. Shimokawa, Mr. S. Mizuno and Mr. H. Okamoto for preparing the a-BN film and making the AES measurements.

5. REFERENCES

1. R.S. Wagner, "VLS Mechanism of Crystal Growth",*Whisker Technology*, ed. A.P. Levitt, pp. 47-119, Wiley, New York, 1970.
2. M. Tomita, T. Hayashi, and F. Shimokawa, "In-situ Observation of Boron-Whisker growth and its Analysis", eds. B. Jouffrey and C. Colliex, Proc. 13th Int. Cong. on Electron Microscopy Vol.2B, pp. 777-778, July 1994
3. S. Suzuki, M. Tomita, and T. Hayashi, "Electron Energy Loss Spectroscopy of Amorphous Boron Filaments", Jpn. J. of Appl. Phys., Vol. 34, pp. L191-L194, February 1995.
4. R.S. Wagner, "A Solid-Liquid-Vapor etching process", J. Crystal Growth Vol. 3/4, pp.159-161, 1968.

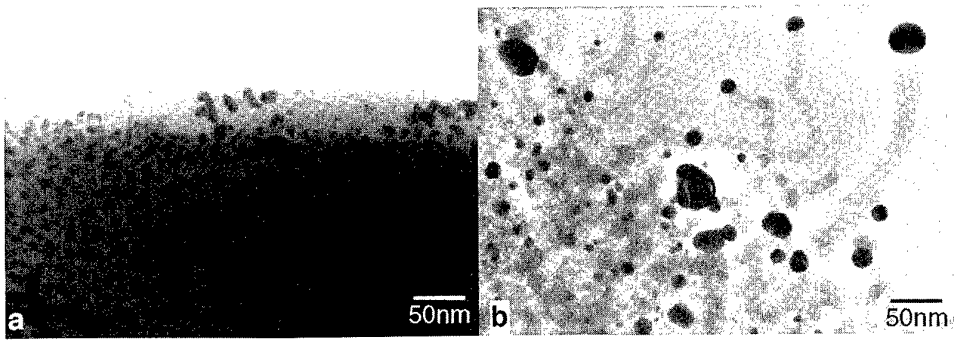


Figure 1:Typical views of a-BNO film (a) before and (b) after intense 250-kV electron irradiation in TEM with the condenser aperture removed. Filaments with Au particles on the top have grown around the irradiated area.

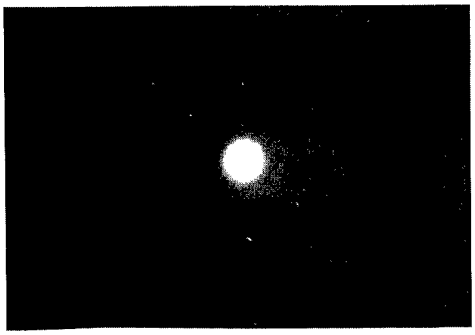


Figure 2 : micro electron diffraction for a particle with Au ; spots are from Au particle

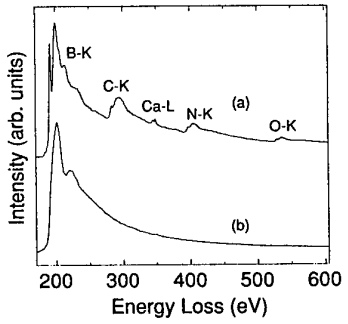


Figure 3 : EELS from (a) a-BN film & (b) filament

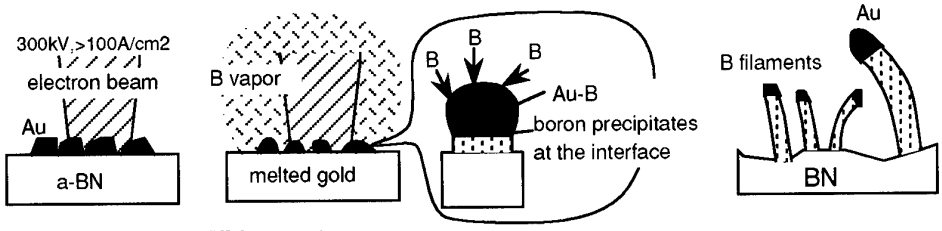


Figure 4 : Schema of VLS mechanism

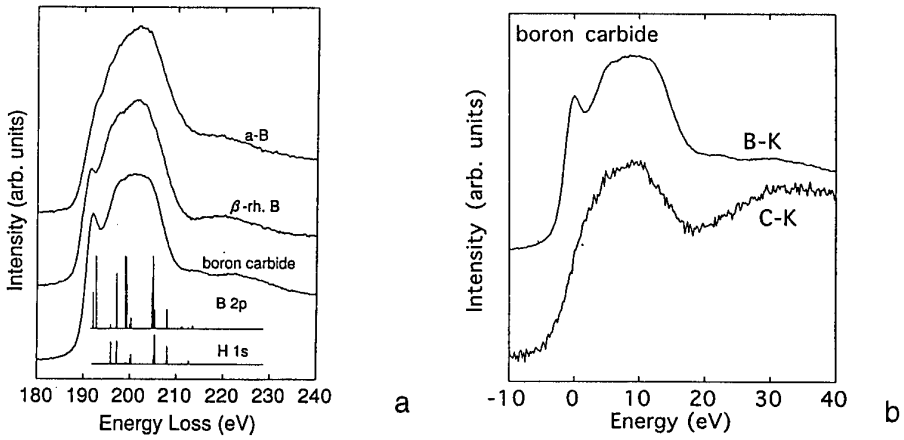


Figure 5 : (a)B-K EELS of a-B (filament). b-rhom. boron and boron carbide with calculated B2p and H1s unoccupied orbitals of $B_{12}H_{12}$. (b) B-K and C-K EELS of boron carbide (shifted for comparison).

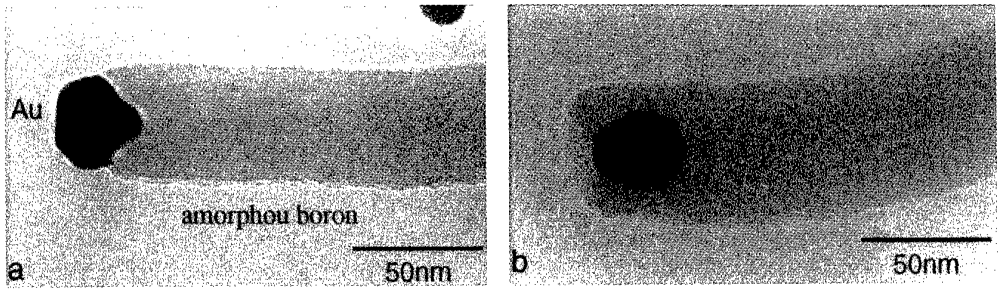


Figure 6 : Examples of the initial stage of evaporation

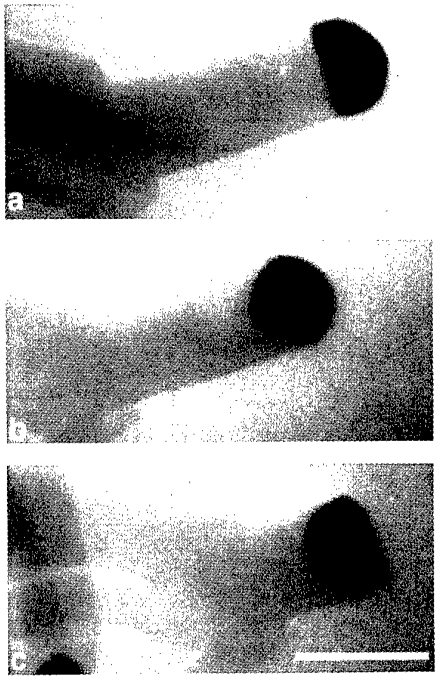


Fig. 7 Sequential images of filament evaporation (Bar 100nm)

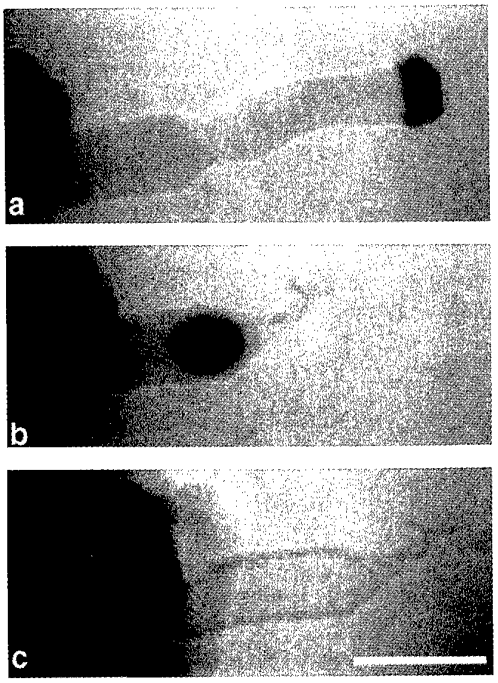


Fig. 8 Sequential images of tubule formation (Bar 100nm)

The modified aerosol pyrolysis as a preparation route of hexaferrite particles for magnetic media.

V.Pankov, A.Henis, D.Dubanevich, A.Malashevich, A.Shablovski

Institute of Solid State Physics & Semiconductors, P.Brovki 17, Minsk 220072 Belarus

ABSTRACT

A survey is given of the modification in aerosol pyrolysis procedure for decreasing the particles size up to 10 nm adding the inert component (NaCl, NaCl + BaB_2O_4) to of the starting precursor of barium, iron nitrate and citrate solutions and demonstrate the facility of this technique in the synthesis of $MeFe_{2y-2x}Co_xTi_xO_{19}$ (x = 0 - 0.8; y = 5.6 - 6.0; Me = Ba, Sr) small particles.

1. INTRODUCTION

Hexagonal-ferrite small particles are being widely considered as interesting material for high density magnetic recording media. Therefore a great effort is being made to prepare materials with proper size, crystal size homogeneity and controlled magnetic properties[1] . Various techniques have been developed to prepare ultra fine hexaferrites for these purposes. Meanwhile all the methods mentioned above permit to obtain particles with the least sizes of 30 nm at the best.

In this paper we report modifications in procedures of the aerosol synthesis technique and coprecipitation method for decreasing the particles size up to 10 nm, adding the inert components to the starting precursor solutions.

For the fine hexaferrite particles, possessing the high value of anisotropy constant, there are few investigations on the behaviour of the particles in superparamagnetic state. This is explained by difficulties in synthesis of powder with particles of up to 10 nm in size.

2. EXPERIMENTAL

Finely divided particles $MeFe_{2y-2x}Co_xTi_xO_{19}$ (x = 0 - 0.8; y = 5.6 - 6.0; Me = Ba, Sr) have been produced by using pyrolisis of an aerosol, generated by ultra high-frequency spraying of a solution, containing together with starting reagents, inert component.

The solution was dispersed in an ultrasonic room humidifier with the formation of fine liquid droplets estimated to be less than 1 mm in diameter. A 0.8 MHz beam emanating from the transducer is focused closed to the liquid surface producing a fountain with a fog. This aerosol is conveyed by air with a flow rate of 3 l/min, afterwards it goes through a tube furnace (D = 5 cm) with different heating sections. The residence time at maximum temperature (950°C) was about 1 s. Thus the solvent evaporates, leading to the formation of precursor particles in a matrix of inert component. These particles are collected outside the furnace with an electrostatic filter.

The $Ba(NO_3)_2$,$Fe(NO_3)_3 \cdot 9H_2O$ (series 2); $BaCO_3$, iron citrate, citric acid (series 3); $BaCl_2 \cdot 2H_2O$, H_3BO_3, $Fe(NO_3)_3 \cdot 9H_2O$, Na_2CO_3 (series 4); were weighted and mixed with distilled water to form a homogeneous aqueous solution. The hexaferrite particles were synthesized from 0.03M aqueous solutions with addition of 30-50 wt % of NaCl. Once the particles were obtained further heat treatment was made at 500-900°C in order to study the evolution of the microstructure and to identify the reaction path. After that the powders were washed in distilled water (series 2,3) and in weak acetic acid (series 4) to remove the inert components (NaCl, BaB_2O_4). Afterwards particles were dried at 120° C.

During modified coprecipitation technique[2] $FeCl_3 \cdot 6H_2O$ and $Ba(Sr)Cl_2 \cdot 2H_2O$ were mixed together and added to the required quantity of Na_2CO_3 (series 1). For hexaferrite particles with Co, Ti-substitution $CoCl_2 \cdot 6H_2O$ and $TiCl_3$ are used. Then the NaCl containing coprecipitates were spray-dried at 250°C using a nozzle-type atomiser and heated at 500-900°C. After NaCl has been dissolved in water, finely divided, loose powder is obtained.

Magnetic and morphological properties of the powders have been investigated by Mossbauer spectroscopy, DTA,

0-8194-2165-0/96/$6.00

EMPA, SEM, TEM and X-ray analysis. A vibrating sample magnetometer was used to measure the magnetic properties at the room temperature in maximum field of 80 kOe.

3. RESULTS AND DISCUSSION

To decrease the droplet size up to 1 mm and less during spray drying we have started using the method of aerosol pyrolisys. This gave the opportunity to minimise the amount of segregation during the solidification of the salt solution. In addition, the introduction of the inert component (NaCl, BaB_2O_4) to the precursors allows one to prevent aggregation during crystal growth and to synthesise particles with the size closed to 10 nm.

As it turned out to be, the particles with the least sizes are formed when citrate solutions are used (series 3). For the samples of series 4 extremely high degree of homogeneity in particle size is typical. On photomicrograph the particles look like almost monodispersed (Fig.1). Among the differences of the samples of series 4 from the other series samples one is that inert component (in this case it is BaB_2O_4) doesn't melt at the temperature of pyrolysis (900°C) unlike NaCl (T_{melt} - 800°C). Obviously, almost solid inert component matrix doesn't ensure the conditions for discontinuous particles growth, which is partly observed in the liquid matrix of NaCl (series 1,2).

Table I. Morphological and hysteresis properties of the sample obtained with different precursors

series	Precursor	d, nm	Annealing temper.,°C	H_C, kOe	M_S, emu/g
1	$SrCl_2$, $FeCl_3$, Na_2CO_3	70	900	6.80	71.8
2	$Ba(NO_3)_2$, $Fe(NO_3)_3$, NaCl	30	400	3.15	67.3
3	$BaCO_3$, Fe-citrat, ciric acid, NaCl	10	as received	2.19	57.7
4	$BaCl_2$, $Fe(NO_3)_3$, H_3BO_3, Na_2CO_3	40	790	3.49	70.7

Coercivity has been found to increase with particle size increasing in single domain interval (up to 500 nm). In our case regardless precursor for the non substituted particles H_C sharply begins to decrease below 30 nm particle size. Such a behaviour indicates on the correspondence of the experimental data to the superparamagnetism theory for randomly oriented uniaxial particles and it could be interpreted in terms of the spins thermal activation. Coercivity decreases due to the spins thermal activation below the particle volume of about 100 V_o. Where V_o is the superparamagnetic critical volume.

As in many other papers we observed the decreasing of the saturation magnetisation with particle size decreasing. It could be supposed, that the specific magnetisation is influenced by the fraction of superparamagnetic particles, by the occupation of the fife magnet sublattices and by the thickness of effective nonmagnetic surface layer. On the Mossbauer spectra taken at room temperature the paramagnetic centre line, corresponding to the superparamagnetic fraction begins to appear for the powders in which particles of 30 nm in diameter and less are

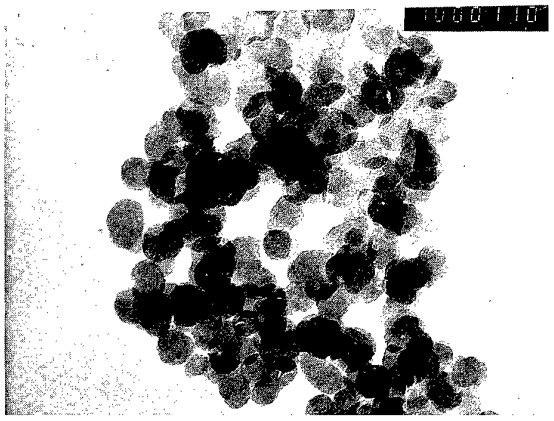


Fig.1. TEM micrograph of hexaferrite powder obtained by pyrolysis of aerosol of $BaCl_2$, $Fe(NO_3)_3$, Na_2CO_3, H_3PO_3 precursor (series 4). ×100.000

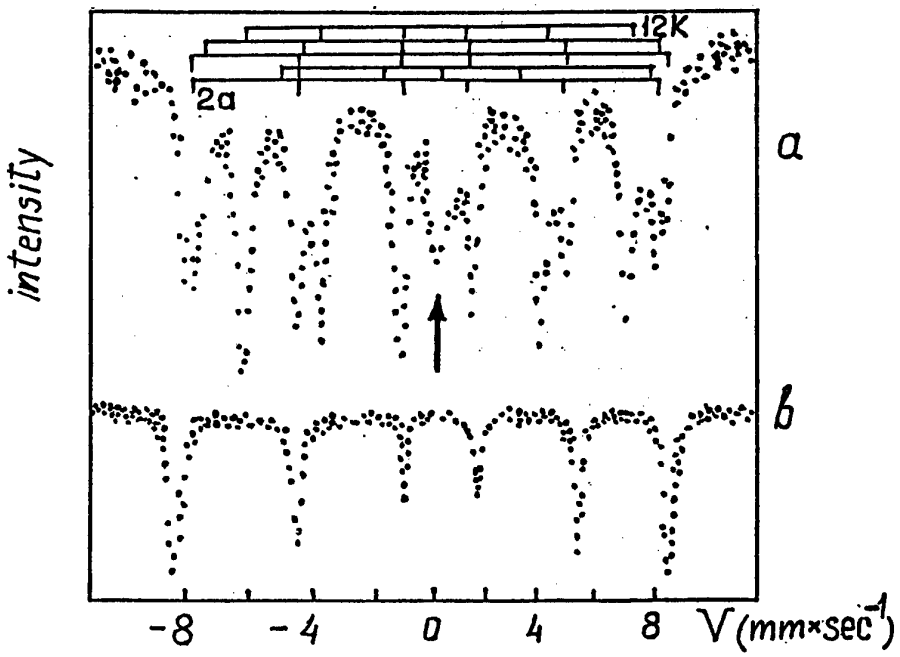


Fig.2. Room-temperature Mossbauere spectra of the Ba hexaferrite powder (series 3) with the overage particle size 20 nm (a) and Fe_2O_3 (b).

spectrum components indicates that not more than 10 % of substance is in a superparamagnetic state under these conditions. In this work the Mossbauer spectra were obtained at different temperatures which are lower than hexaferrite Curie point. The absence of a hyperfine splitting on Mossbauer spectra obtained at 350°C indicates on the presence of the superparamagnetic particles in the powders of lager than 20 nm particle sizes and on the presence of the nonmagnetic layer in the particles. For fine particles there is a dependence of Curie point from the particle size, which allows to distinguish the particles in superparamagnetic state by registration of paramagnetic line in Mossbauer spectra.

4. CONCLUSIONS

The modified aerosol synthesis technique has been successfully applied to preparation of fine hexaferrite powder with sizes up to 10 nm.

The smallest particle size has been obtained with citrate precursor in the presence of NaCl.

Due to high magnetic anisotropy constant of hexaferrites the critical size of particles transition to superparamagnetic state is below 10 nm.

5. REFERENCE

1. T. Fujiwara, M. Isshiki, Y. Koike, T. Oguchi, "Recording performance Ba-ferrite coated perpendicular magnetic tapes", *IEEE Trans. on Magnetics*, Vol. MAG-18, ' 6, pp. 1200-1202, November 1982.

2. V.V.Pankov, S.M.Pernet, P.Germi, P.Mollard, "Fine hexaferrite particles for perpendicular recording prepared by the coprecipitation method in the presence of an inert component", J. Magn. Magn. Mater. 120, pp. 69-72, 1993.

Paper presented at the Third ICIM/ECSSM '96, Lyon '96

Formation method of particles arrangement on substrate and its analysis

Kobayashi Mikihiko, Fudoji Hiroshi, Egashira Mitsuru and Shinya Norio

National Research Institute for Metals, 5th Research Group
1-2-1, SENGEN, TSUKUBA-SHI, IBARAKI 305, JAPAN

ABSTRACT

We proposed a particles assembling method to create intelligent and multi-functional materials. The arrangement of particles on substrates was studied as one of the important techniques for this approach.

The arranging process is as follows. Electrified patterns were drawn on dielectric calcium titanate($CaTiO_3$) substrates with electron beam scanning. The substrates were dipped in a solvent where silica (SiO_2) particles of 5.1$\mu m\phi$ were dispersed. The particles were attracted to the electrified patterns by the electrostatic force, and were arranged along the electrified patterns.

In this paper, undrawn substrates were used to know how many particles adhered on the unelectrified part, and then, arranging experiments using drawn substrates were carried out under various conditions to confirm the above process. We also discussed on the basic aspects of the arrangement, such as attraction force, motion of particles in the solvent, etc.

1.INTRODUCTION

Multi-functional materials and intelligent materials are both new concepts in material science, and many efforts have been done in these areas. We proposed a particles assembling method to create such materials[1]. The method is to build up an intelligent material from various kind of particles. The material fabricated by assembling particles is expected to display the intelligent functions by integrating the primitive functions which is possessed by each particle.

Key technologies of the method are new techniques to assemble fine particles more precisely. One of the important techniques is to arrange particles on substrates. We proposed the following process of the arrangement in the previous paper[1,2]. A pattern is drawn with the electron beam on an insulating substrate, i.e., the pattern is electrified with the negative charges. Particles placed near the pattern are attracted with the electrostatic force and adhered on the pattern.

The aim of this paper is to confirm the above arranging process and to discuss the basic matters such as the attraction force on the particles. Preliminary experiments using undrawn substrates are also described.

2.PROCEDURE

Electrified patterns are drawn on insulating substrates in the SEM chamber using electron beam scanning. The scanning for pattern drawing is controlled by a programmable beam controller. The scanned region is electrified positively or

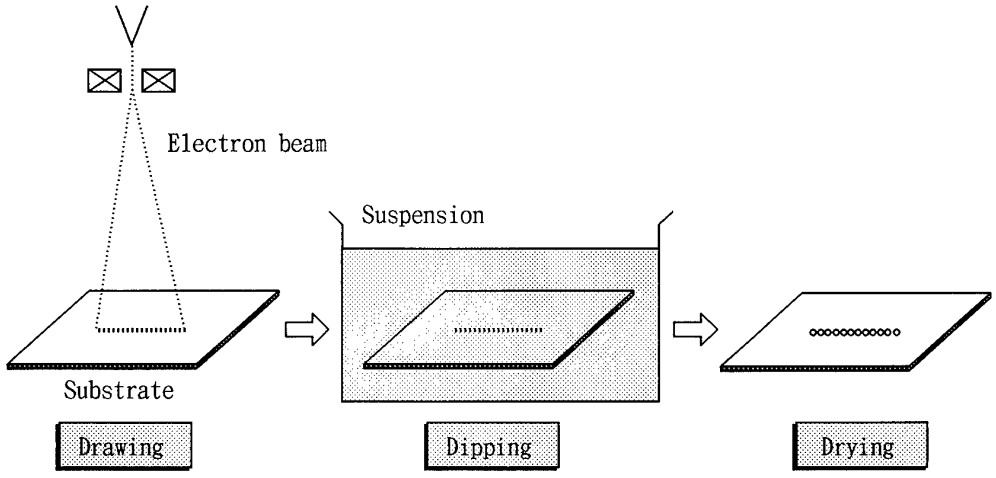


Fig. 1 Schematic process flow of particles arrangement on substrate.

0-8194-2165-0/96/$6.00

negatively according to the scanning condition. We can, therefore, draw any electrified pattern on the substrates.

The next step is to adhere particles on the electrified pattern. When a particle is placed near the pattern, the particle will be attracted and adhered on the pattern by the electrostatic force. As the electrostatic force is generally weakened steeply with distance, we must bring particles sufficiently close to the pattern. Otherwise the gravitation will be stronger than the attraction force.

Particles are dispersed in a proper solvent, and the substrate is immersed in the suspension to bring particles close to the pattern. We call it as a wet method. The wet method has a merit to diminish the influence of the gravitation.

Once the particles adhered, the gravitation can be negligible for fine particles comparing with the adherent force. The substrate is drawn up from the suspension after immersing it for a proper period of time, and is dried. Then, we get the substrate on which particles are arranged. The process flow is shown in Fig. 1.

3.EXPERIMENTS

3.1 Adhesion of particles on undrawn substrate

Polished calcium titanate($CaTiO_3$) plates cut to 8 x 8mm were used as insulating substrates. The substrates were dipped in the suspension where spherical silica(SiO_2) particles of 5.1μmϕ were dispersed. The dispersion medium was a non-polar and inert solvent(Fluorinert FC-40, Sumitomo 3M). The substrates were dried in air after dipping in the volatile solvent for several seconds. Then, the number of adhered particles were counted. Properties and characteristic of the particle, the substrate, and the solvent were shown in Table I.

Table I Properties and characteristics of spherical SiO_2 particle, $CaTiO_3$ substrate, and Fluorinert FC-40.

SiO_2	Crystal	Glassy
	Relative dielectric constant	4.5
	Diameter	5.1μm
$CaTiO_3$	Crystal	Polycrystal
	Relative dielectric constant	100
	Resistivity	$10^{14}\Omega$cm
	Surface flatness	$\pm$0.02μm
Fluorinert FC-40	Relative dielectric constant	1.89
	Resistivity	$4.0\times10^{15}\Omega$cm

3.2 Arrangement of particles on electrified pattern

Electrified patterns of lines or circles were drawn with different doses of 0.2 to 2.0pC/μm^2 on $CaTiO_3$ substrates. The preset width of drawing line is 1μm, and the acceleration voltage of primary electron beam was 15kV. The drawing pattern can not be observed by the optical method. Thus, the charge distribution on the surface of the substrates was observed by taking a SEM image at a low of 2kV called as the voltage contrast method. Following the drawing, the substrates were dipped in the suspension and dried as the same way with the undrawn substrates. Particles adhered on the pattern were counted.

4.RESULTS

4.1 Adhesion of particles on undrawn substrate

Figure 2 shows the relationship between the number of adhered particles and the dipping time. When the suspension concentration was 1.1 $x10^6$/ml, particles adhered rapidly on the substrate in the first several seconds. Adhered particles were 5.2/mm^2 for 5 seconds. The increasing rate was gradually down up to 100 seconds, and then after 100 seconds adhered particles increased almost linearly. When the suspension concentration was $1.1x10^7$/ml, increasing rate of the initial 50 seconds is 6 times larger than that for $1.1x10^6$/ml. Adhered particles were too many to count after 100 seconds. On the other hand, adhered particles were negligible for the $1.1x10^5$/ml; only 2.6 particles in 1 mm^2 adhered for 100 seconds.

The number of adhered particles at a constant dipping time were plotted against the suspension concentration on the full-log paper in Fig. 3. Experimental points scattered around the dotted line with unit slope as shown in Fig. 3. Adhered particles, therefore, increased proportionally to the time.

The relations shown in Figs. 2 and 3 were used to evaluate the number of particles adhered in undesired part (noisy particles) in analysys of particles arrangement on electrified patterns. Considering the noisy particles and the rate of adhesion on the electrified pattern, dipping time was changed from 5 to 100 seconds, and suspension concentration was fixed to about $1x10^6$/ml.

4.2 Arrangement of particles on electrified pattern

4.2.1 Charge distribution

Figure 4 shows the SEM image of the electrified substrate obtained by the voltage contrast method. Negative electrification is expressed by the white, positive electrification by the black, and unelectrification by the medium value.

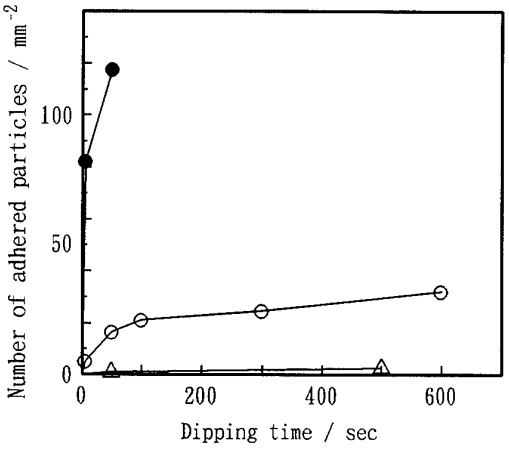


Fig. 2 Relationship between the number of adhered particles and the dipping time for undrawn substrates. Suspension concentration are $1.1x10^7$(black circle), $1.1x10^6$(white circle), and $1.1x10^5$/ml(white triangle), respectively.

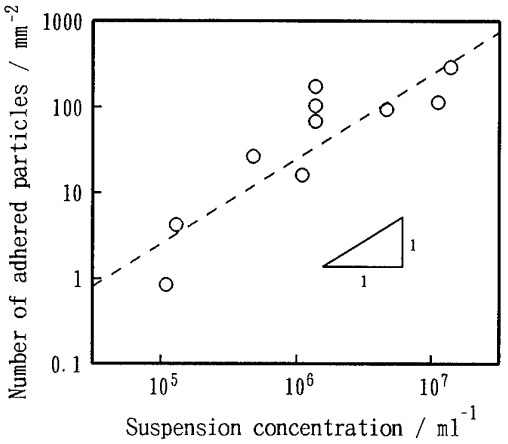


Fig. 3 Relationship between the number of adhered particles and the suspension concentration for undrawn substrates. Dipping time is 50 seconds.

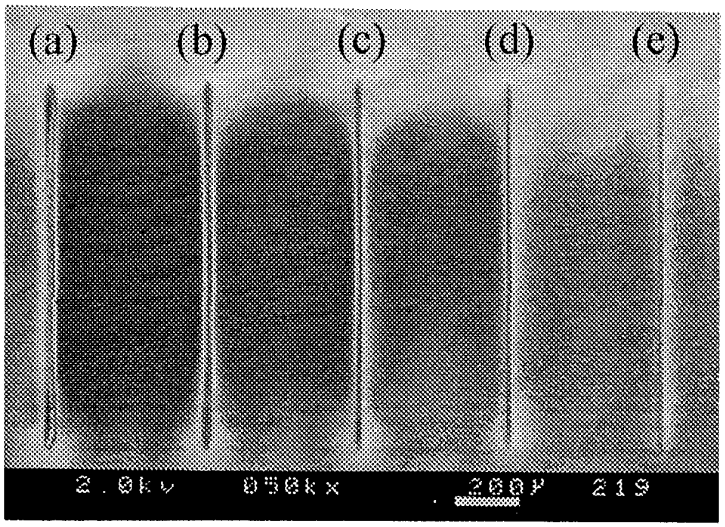


Fig. 4 SEM image of the electrified pattern observed by the voltage contrast method. Doses are (a): 2.0, (b): 1.5, (c): 1.0, (d): 0.5, and (e): 0.2pC/μm^2, respectively.

We can see the black lines where the electrified lines were drawn. White region exists around the black lines. Width of the black lines are 10 to 20μm.

4.2.2 Effect of dipping time

A circle was drawn at a dose of 1pC/μm^2 on the substrate and the substrates were dipped in the suspension of $1.4x10^6$/ml for 5 to 100 seconds. The results are shown in Fig. 5. The circle images can be seen in all photographs in Fig. 5. This proved that the particles can be arranged by the proposed method, though various modifications are necessary to the process.

Number of adhered particles on the circle pattern was increased and also the resulting circle image was more clear with an increase in dipping time. A part of the increasing particles scattered to the radius direction. Therefore, the line width of the particles image also became broad with the dipping time.

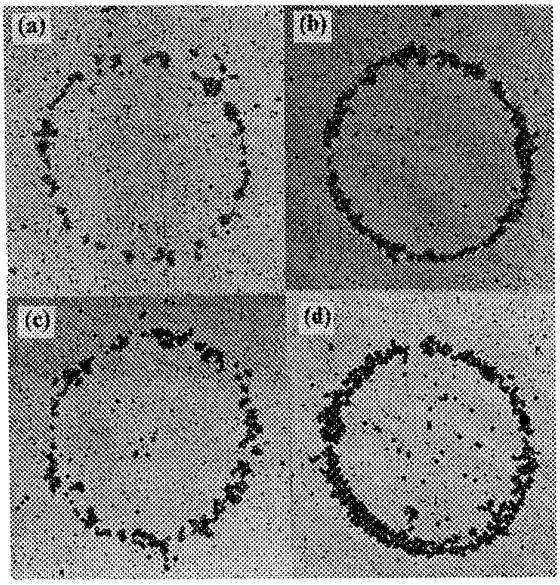


Fig. 5 Particles arrangement on the electrified circle. Dose of the circle is 0.5pC/μm^2 and the suspension concentration is 1.4x10^6/ml. Dipping time are (a): 5, (b): 20, (c): 50, and (d): 100 seconds, respectively.

4.2.3 Effect of dose

Figure 6 shows the result carried out at dipping time: 10 seconds and suspension concentration: 3x10^6/ml. The electrified pattern was five parallel lines with different doses. It was confirmed that the adhered particles increased with an increase in dose, and that the particles concentrated at the end of the line. When the dose is 2.0pC/μm^2, the adhered particles formed two parallel lines as shown by (a) in Fig. 6. This was generally observed when the dose is higher than 1.5pC/μm^2.

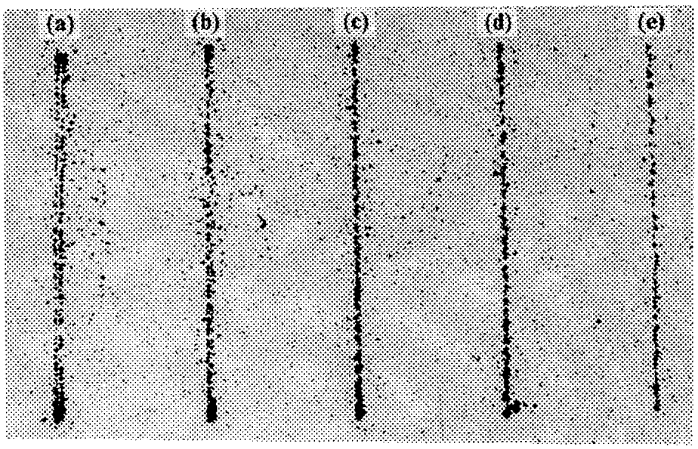


Fig. 6 Particles arrangement on the electrified line. Dipping time and suspension concentration are 10 seconds and 3x10^6/ml, respectively. Doses of the line are (a): 2.0, (b): 1.5, (c): 1.0, (d): 0.5, (e): 0.2pC/μm^2, respectively

5.DISCUSSION

5.1 Attraction force

Charge on the substrate will form a non-uniform electric field. Thus, the gradient force will act on the SiO_2 particles in the solvent. The gradient force, F_g, can be expressed by,

$$F_g = 2\pi a^3 \frac{(\varepsilon_s - 1)}{(\varepsilon_s + 2)} \varepsilon_0 \varepsilon_m \, grad \, E^2 \qquad (1)$$

where a is the radius of the particles, ε_s and ε_m are relative dielectric constants of SiO_2 and the solvent, respectively, ε_0 is a free space dielectric constant, and E is intensity of the field. We assume that the charge on the substrate can be substituted to the line charge, i.e., the charge is uniformly distributed on an infinite line. For simplifying the calculation, we, furthermore, assume that the substrate can be replaced by the solvent, i.e., only the line charge is in a solvent. Then, E is expressed as a function of r, distance from the line charge, as shown by Eq. (2).

$$E = \frac{q}{2\pi\varepsilon_m r} \tag{2}$$

where q is charge density.

A dose of 1pC/μm^2 corresponds to 10^{-6}C/m of charge density. Substituting this value and other characteristic values shown in Table I into Eqs. (1) and (2), we have,

$$F_g = \frac{1.2\times10^{-42}}{r^3}[N] \tag{3}$$

Acceleration at the point of r=5μm is estimated as 8.6x10^{-9}μm/s^2 from Eq. (3). Microscopic observation shows that the particles are attracted to the electrified pattern at a distance of about 20μm from the substrate. Calculated value of the attraction force is extremely small considering the observation. The difference is too large to rid the discrepancy by modification of the gradient force model.

Coulomb's force may act in arranging process. Electrification of the particles may occur by the friction with the solvent. When a point charge, q_0, is placed in an electric field, E, the Coulomb's force, F_c, at the point is expressed by,

$$F_c = q_0 E \tag{4}$$

Assuming that the acceleration of the SiO_2 particle for r=20μm is 1μm/s^2, the charge of the particle is calculated as q_0=10^{-27}C from Eqs. (2) and (4).

5.2 Adherent force

Once a particle adhered on the pattern, the particle does not move or miss during the drying step. This is also true for the noisy particles. The adherent force is, therefore, not the electrostatic force but the intermolecular force. The intermolecular force becomes strong for a small substance. Measurement by a centrifuge shows that the adherent force is greater than 15000G for a SiO_2 particle of 5.1μm.

5.3 Voltage contrast method

In Fig. 4, white region exists around the black lines. The width of the black line is 10 to 20 μm and the white region extend to more than 50μm from the center axis of the black line. Electrified lines are considered to be drawn where the black lines are observed, and the electron beam is controlled to draw lines of 1μm in width. Thus, following two unpredicted problems are caused.

(1)The black line, which means unelectrification, appears where the electron is doped.

(2)The white region, which means negative electrification, extends from the drawing line.

The second is explained by the diffusion of charge through the surface. The first problem leads us to the next question, i.e., whether Fig. 4 represents the true charge distribution or not. Since the electron beam is low of 2kV for the observation, the electron may be scattered by the electric field formed by the doped charges. If so, the black line will be observed just on the drawing line. Another explanation is that polarization of the substrate cancels the charge of the doped electron.

As shown (a) in Fig. 6, particles image is almost same with the pattern formed by the white region, when the dose is greater than 1.5pC/μm^2. It is an indirect evidence to support the former hypothesis. However, we consider that the evidence is insufficient to reject the latter.

5.4 Particles movement in suspension

Some arranging experiments were carried out under the microscopic observation to know the motion of the particles. Flow pattern of the solvent can be known from the motion of the particles. The solvent above the substrate moves along the surface of the substrate, which is called the laminar film flow. The flow rate is about 10 to 50 μm/s. The laminar film is divided into small region, and the flow direction in each region is random.

Particles moving with the laminar film flow drift to random direction above the surface. When the particles pass through the effective region of the attraction force, about 20μm, they are adhered on the pattern. Most of adhered particles are

considered to be supplied from the laminar film flow.

5.5 Accuracy of arrangement

The number of particles within 20μm from the drawing line is counted. It is referred to as N_{20}. The values of N_{20} increase for dose of 0.2 to 1.0pC/μm^2 and decrease or reach top for dose of 1.0 to 2.0pC/μm^2.

The ratio of N_{20} to the total particles in the photograph (referred to as N_T) will be a rough measure of the accuracy of arrangement. The relationship between the ratio, N_{20}/N_T, and dose is shown in Fig. 7. The values, N_{20}/N_T, decrease with the amount of dose. The effects of dipping time and dose on N_{20}/N_T is relatively small in comparing with those on N_{20}. It means that when the adhered particles are increased by increasing the dose, the noisy particles also increase. Thus, factors other than dose and dipping time should be considered to modify the particles arrangement such as positive electrification of particles, effective supply of the particles, etc.

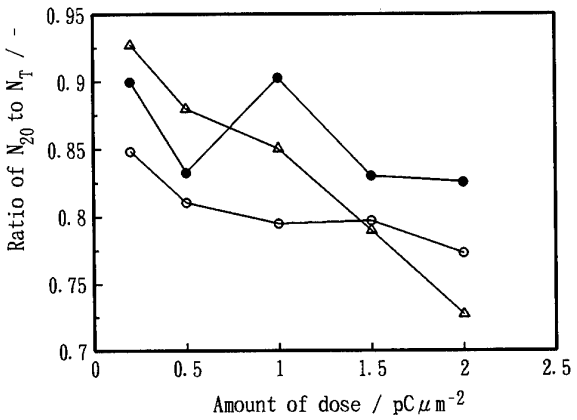


Fig. 7 Relationship between the ratio of N_{20} to N_T and the amount of dose. Letter N_{20} is defined as the number of particles adhered within 20mm from the drawing line, and letter N_T as the total number of particles adhered in the view of the photograph. Suspension concentration is 3.0x10^6/ml and dipping time are 2(white circle), 10(black circle), and 50 seconds(white triangle), respectively.

6.CONCLUSION

Arrangement of spherical SiO_2 particles on the dielectric $CaTiO_3$ substrates was tried by dipping the electrified substrate into a solvent in which the particles were dispersed. Experiments were carried out under the following conditions.

Acceleration voltage of the primary electron beam for drawing the electrified pattern: 15kV
Dose current density in the electrified pattern: 0.2 to 2pC/μm^2
Suspension concentration: about 1x10^6/ml
Dipping time: 5 to 100 seconds

Particles were observed to adhere on the electrified pattern in all experiments, and validity of the arranging process was ensured. Adhered particles on the pattern were increased with an increase in dose and dipping time. The noisy particles, however, also increased, when the particles on the pattern were increased.

Particles in the solvent were considered to be attracted to the pattern by the gradient force. However, the calculated value of the gradient force was very small and it was inconsistent with the observation. The possibility of the electrification of particles was suggested.

Charge distribution was observed by the voltage contrast method. It was shown that the drawing line of 1μm wide was extended to that of about 50μm wide by diffusion. Charge image was not detected at the center axis of the electrified line. Two explanations were possible for this phenomenum. One was that the charge was canceled by polarization. The other was that the voltage contrast method missed to express the real charge distribution due to the influence of the electric field formed by the doped electron.

REFERENCES

1. N. Shinya, M. Egashira and H. Fudoji, "Powder Particle Assembly Using Electron Beam for Creation of Multi-Functional Materials," *Proc. of 2nd Int. Conf. on Intelligent Materials*, pp.1741-1745, Technomic Publishing Co. Inc., Virginia, 1994.

2. M. Kobayashi, H. Fudoji, M. Egashira and N. Shinya, "Particles Arrangement on Dielectric Substrates Using Electron Beam," *Proc. of Int. Symposium on Microsystems, Intelligent Materials and Robots*, pp.205-208, Sendai, 1995.

Effects of double Schottky barrier on the electric properties of ceramic semiconductors

Kazuo Mukae, Koichi Tsuda, and Akinori Tanaka

Fuji Electric Corporate Research and Development Ltd.
2-2-1, Nagasaka, Yokosuka, 240-01 Japan

ABSTRACT

Effects of the interface states at the grain boundaries on the applied voltage dependence of the double Schottky barrier(DSB) are theoretically discussed. Based on the simplified models of rectangular density distributions for the interface states, effects of the energy level, density of states, and the distribution width of the interface states are quantitatively calculated. The I-V characteristics of DSB's are also calculated and the nonlinear I-V relations are discussed. The nonlinear exponent α of the I-V relation was found to be determined mainly by the barrier height and the total charge of the interface states. The observed ICTS spectra and other electric properties of ZnO varistors and PTC thermistors are discussed on the basis of the above DSB model.

1. INTRODUCTION

Recent investigations have indicated that the electric properties of the grain boundaries are related mainly to the double Schottky barrier(DSB) formed at the grain boundary.[1,2] Therefore it is important to understand the precise role of the grain boundaries for creation and design of new intelligent ceramic materials. Although Heywang already explained the characteristics of PTC thermistors by the DSB model in 1964[3], there are still some quantitative discrepancies between theoretical calculations and the observed results. The most important reason for the discrepancies is the negligence of the precise consideration for the interface states at the grain boundaries. Therefore the precise analysis of DSB is important to understand the characteristics of grain boundaries of ceramic semiconductors. In this paper the quantitative analysis of the applied voltage dependence of the interface states in a DSB is carried out by simplifying the density distribution of the interface states and this treatment is extended to interpret the electric properties of ZnO varistors and PTC thermistors.

2. DOUBLE SCHOTTKY BARRIER AND INTERFACE STATES

2.1 Formation of double Schottky barrier

Imperfections and inclusions at grain boundaries often form acceptor states which capture electrons from each grain of both sides resulting in formation of an electric potential barrier. The typical shape of DSB is shown in Fig. 1. When we denote $-Q_o$, N_d, l_o and q as the charge density of the grain boundary, the donor concentration of the semiconductor grains, the width of the depletion layer of a grain and elementary charge, respectively, the following equation can be obtained because the grain boundary charge should be compensated by that of depletion layers of both sides.

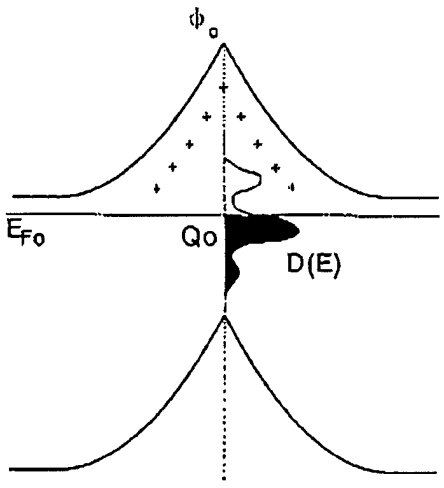


Fig. 1 Band structure of double Schottky barrier.

$$Q_o = 2qN_d l_o \qquad (1)$$

The potential barrier can be expressed by the following equation if x is the position from the grain boundary and $|x| \le l_o$.

$$\phi = \frac{q^2 N_d}{2\varepsilon_s}\left(|x| - l_o\right)^2 \qquad (2)$$

Since this electric potential barrier is composed of two Schottky barriers symmetrically connected with each other, we call this double Schottky barrier(DSB). The barrier height at no applied voltage, ϕ_o, is expressed by the following equation.

$$\phi_o = \frac{q^2 N_d}{2\varepsilon_s} l_o^2 = \frac{Q_o^2}{8\varepsilon_r N_d} \qquad (3)$$

0-8194-2165-0/96/$6.00

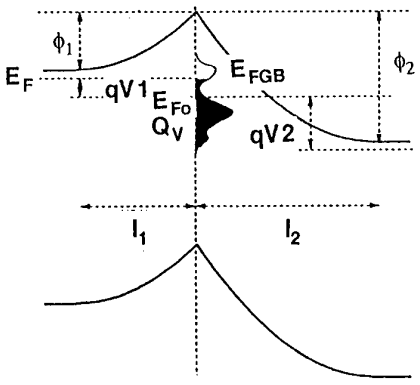


Fig. 2 Band structure of DSB with an applied voltage.

If D(E) is the distribution function of the density of the interface states, f(E) is Fermi-Dirac distribution function, and E_{FGB} and E_{FGBo} are the Fermi level of the interface states and that when interface states are neutral, the interface charge density, Q_o, is obtained by the integration of the following equation.

$$Q_o = q\int_{E_{FGBo}}^{E_{FGB}} D(E)f(E)dE \qquad (4)$$

where

$$f(E) = \frac{1}{1+\exp\{(E-E_F)/kT\}} \qquad (5)$$

Therefore the actual DSB is determined by equations (2), (3), (4) and (5).

2.2 Applied voltage dependence of DSB

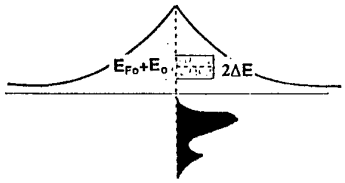
When a finite voltage is applied to a DSB, the shape of the barrier is deformed as shown in Fig. 2. If we define S as the interface charge ratio to the initial value(Q_o), ϕ_1 which is the height of the forward biased barrier is expressed by the following equation.

$$\phi_1 = S^2\left(1-\frac{qV}{4S^2\phi_o}\right)^2\phi_o \qquad (6)$$

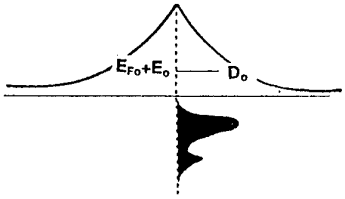
Therefore if we know S as a function of V, ϕ_1 can be obtained as a function of V. However in the actual case, dependence of S on V is rarely known because experimental measurement of D(E) is difficult. Therefore we will simplify the D(E) and numerically simulate the applied voltage dependence of ϕ_1 in the following discussion.

2.2.1 $D(E) = 0, \quad (E > E_{Fo})$ **(Heywang Model)**

In this case, there are no interface states above E_{Fo}, interface charge remains constant. Then eq.(6) can be easily transformed to the next equation.



(a) Rectangular D(E)



(b) Monoenergetic D(E)

Fig.3 Model of distribution function of interface states.

$$\phi_1 = (1-\frac{qV}{4\phi_o})^2\phi_o \qquad (7)$$

This equation shows well known parabolic decrease in barrier height and disappearance of ϕ_1 at $V = 4\phi_o$. Although ϕ_1 changes as V, it should be noted that the total depletion length remains constant because of the constant interface charge. Consequently the capacitance of the DSB should be kept constant.

2.2.2 Rectangular D(E)[4]

When D(E) has a rectangular density distribution with a center at $E_o + E_{Fo}$ and $2\Delta E$ width as shown in Fig. 3 and the following equations, S can be also calculated as a function of V.

$$D(E) = D_o, \quad (E_{Fo}+E_o-\Delta E < E < E_{Fo}+E_o+\Delta E) \qquad (8)$$
$$D(E) = 0, \quad (E < E_{Fo}+E_o-\Delta E, \ E > E_{Fo}+E_o+\Delta E \qquad (9)$$

Until the Fermi level meets the bottom of the rectangle, the interface charge does not

increase similar to Heywang Model, but at $V = V_o$ where $E_F = E_{Fo} + E_o - \Delta E$, electron injection into the interface states begins. In this case, V_o can be obtained as the following equation.

$$qV = 4\left[\phi_o - \sqrt{\phi_o\{\phi_o - (E_o - \Delta E)\}}\right] \tag{10}$$

When the Fermi level reaches the top of rectangle where $V = V_F$, the interface states are completely filled. Therefore, while $V_o < V < V_F$, the following equation can be obtained.

$$qV = 4\phi_o\left[1 + \{qV_1 - (E_o - \Delta E)\}\frac{qD_o}{Q_o}\right]^2 - 4\sqrt{\phi_o(\phi_o - qV_1)}\left[1 + \{qV_1 - (E_o - \Delta E)\}\frac{qD_o}{Q_o}\right] \tag{11}$$

Although solution of eq.(11) for V_1 as a function of V cannot easily be obtained, one can obtain V_1-V relation numerically. This numerical relation and eq.(7) enable simulation of ϕ_1-V relation. Since the interface states are completely filled at $V = V_o$, the interface charge is kept constant above $V > V_F$. Therefore V_F and ϕ_1 are expressed by the following equations.

$$qV_F = 4\phi_o(1 + 2\Delta E\frac{qD_o}{Q_o})^2 - 4\sqrt{\phi_o\{\phi_o - (E_o + \Delta E)\}}(1 + 2\Delta E\frac{qD_o}{Q_o}) \tag{12}$$

$$\phi_1 = S_F{}^2(1 - \frac{qV}{4S_F{}^2\phi_o})^2\phi_o \tag{13}$$

$$S_F = 1 + \frac{2qD_o\Delta E}{Q_o} \tag{14}$$

Figure 4 shows 4 cases of this simulation where total quantity of the interface states is fixed as $1.2\text{x}10^{12}/\text{cm}^2$ and the D_o and ΔE are changed. Figure 4 shows that decrease in ϕ_1 is retarded at V_o and recover the decreasing rate at V_F. The degree of retardation was larger as D_o increases. If D_o is extremely large, ϕ is kept constant as $\phi_o - (E_o - \Delta E)$. This phenomenon is so called pinning of the Fermi level.

3. APPLICATION TO CERAMIC SEMICONDUCTORS

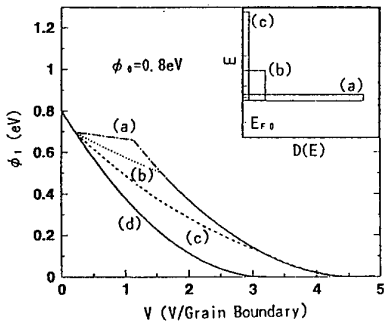


Fig. 4 Calculated ϕ_1-V relation for rectangular D(E).
Q_o=6X10^{12}q/cm^2.
(a) ΔE=0.02eV, D_o=30X10^{12}/eV/cm^2
(b) 0.1 6
(c) 0.3 2
(d) 0

3.1 ZnO varistors

Zinc oxide varistor is one of the most typical ceramic semiconductor devices. When the conduction mechanism of ZnO varistors is assumed to be based on thermoionic process of DSB, the current-voltage characteristics is theoretically calculated by the following equation where A is Richardson constant and T is absolute temperature.

$$I = AT^2\exp(-\frac{\phi_1}{kT}) \tag{15}$$

$$\alpha_{max} = \frac{\phi_o S_F{}^2}{2kT} \tag{16}$$

Equation (15) gives I-V curves for three typical cases discussed above as shown in Fig 5 in which an observed I-V curve of a ZnO:Pr varistor is also indicated. The maximum theoretical nonlinear exponent, α_{max}, is obtained from eq. (16). Equation (16) indicates that large ϕ_o and large total charge at the interface states will result in higher nonlinearity. All curves in Fig.5 exhibit nonlinear characteristics. Calculated curves for rectangular and monoenergetic D(E) have

larger α of 22 than that for Heywang Model. However that of the observed curve for a ZnO:Pr varistor was more than 80. Therefore the non-linearity in ZnO varistors should be attributed to the different mechanism from fulfill of the interface states. The observed curve of ZnO varistor in Fig. 5 also shows the low nonlinearity at low voltage area. This phenomena suggests pinning of Fermi level.

3. 2 PTC thermistors

The basic conduction mechanism of PTC thermistors has already been established by the early workers, such as Heywang and Jonker[3,5]. However, the theories of these workers neglected the change in Q at DSB's because of difficulties to estimate Q. In this section we describe the PTC effect in view of change in ϕ and Q where pinning phenomenon of E_F is occurred.

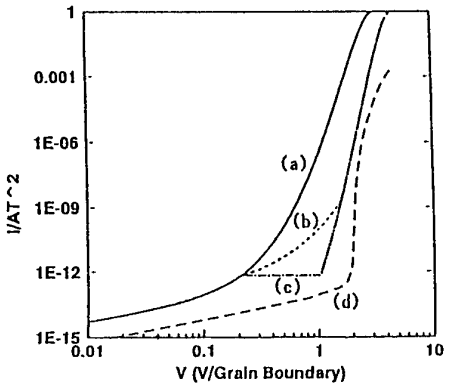


Fig. 5 Calculated I-V characteristics of DSB.
(a) Heywang model.
(b) Rectangular D(E)
$D=6X10^{12}/eV/cm^2$.
$\Delta E=0.1eV$.
(c) Monoenergetic D(E).
$D=1.2X10^{12}/eV/cm^2$
(d) Observed curve of ZnO:Pr varistor.

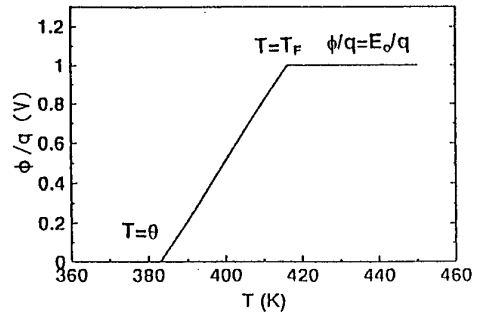


Fig. 6 Schematic temperature dependence of ϕ of PTC thermistor.

As mentioned before, when D_o of D(E) is extremely high or D(E) is monoenergetic, E_F is pinned by the interface states. Therefore, ϕ change near the Curie temperature (θ) can be divided into three regions. At low temperature, ϕ is very small as explained by Jonker, therefore the resistivity is very small. This region is denoted as "Low resistive region". Since dielectric constant decrease in accordance with Curie-Weis law above Curie temperature, ϕ can be expressed by the following equation.

$$\phi = \frac{Q_o^{\,2}(T-\theta)}{8\varepsilon_o N_d C}, \qquad (17)$$

This area is denoted as "Curie-Weis region". In this region PTC effect is obtained , because ϕ of DSB linearly increases as the temperature becomes high as shown in eq. (17). When the temperature becomes higher than T_F where E_F meets the top of the interface states, pinning of E_F occurs. In this area ϕ is kept constant at the depth of the interface states(E_o). This area is denoted as "Pinning region". These three regions are illustrated in Fig. 6. At the pinning region, temperature dependence of resistivity shows similar characteristics to usual semiconductors. Therefore $\ln R - 1/T$ relation can be also indicated by the following relations. In Fig. 7 these relations are illustrated.

$$\ln R = \ln R_o \qquad \text{Low resistive region} \qquad (18)$$

$$\ln R = \ln R_o + \frac{(qD_o)^2}{8k\varepsilon_o N_d C}\left(1-\frac{\theta}{T}\right)$$

$$\text{Curie-Weis region} \qquad (19)$$

$$\ln R = \frac{E_o}{kT} + Const. \qquad \text{Pinning region} \qquad (20)$$

From eq. (19), one can understand that magnitude of PTC effect depends on D_o, N_d, and θ. Large density of interface states gives high PTC effect. T_F where resistivity becomes maximum is obtained by substituting ϕ as E_o in eq. (17). If we know θ and E_o, we can calculate $\ln R - 1/T$ characteristics numerically. Since Fig. 5 and Fig. 6 show quantitative change in barrier height, one can describe PTC phenomenon quantitatively by these illustrations. For example, the calculated $\ln R - 1/T$ relation is shown in Fig.7 when we assume $N_d=1X10^{18}/cm^3$, $\theta=383K$ and $C=1.5X10^5K$. These values are typical for $BaTiO_3$. The slope of resistivity change is steeper as D_o increases and T_F is lowered by the increase of D_o.

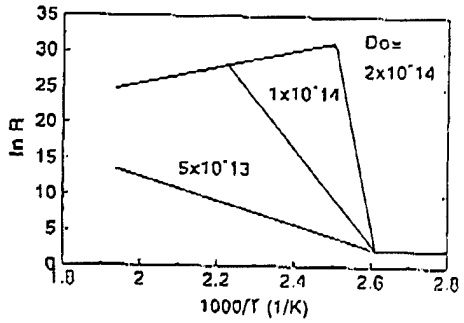


Fig. 7 Calculated ln R-1/T relation of PTC thermistor.

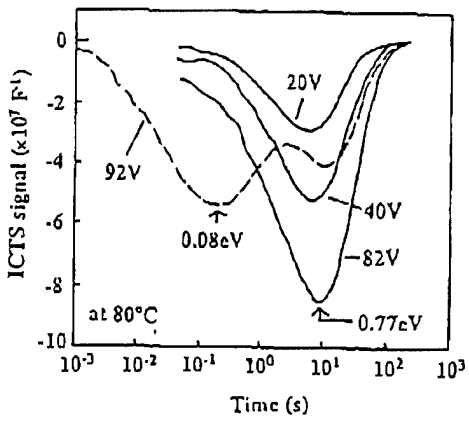


Fig. 8 Observed ICTS spectrum of ZnO:Pr varistor

4. Characterization of electronic interface states at grain boundaries by ICTS measurement

4.1 ZnO varistors

ICTS(Isothermal Capacitance Transient Spectroscopy) is an intensive method to investigate the interface states in ceramic semiconductors[6,7]. This method gives peaks not only for the bulk traps in the grains but also for the interface states at the grain boundaries. Figure 8 shows the observed ICTS peaks of a ZnO:Pr varistor generated by various height of the applied pulses. When applied pulses are lower than the varistor voltage, ICTS peaks were observed at the same position. This result indicates that E_F is pinned by the interface states. In addition, the calculated shape of the ICTS peak for monoenergetic interface states coincided with the observed peak. On the other hand when the applied pulses are higher than the varistor voltage, a new ICTS peak appeared at shallower position. This phenomena indicates that E_F is released from pinning through some mechanism which is not yet clear. Therefore high nonlinear I-V characteristics should be strongly related this release of pinning.

4.2 PTC thermistors

When ICTS method is applied to PTC thermistors, similar information about interface states can also be obtained. Figure 9 shows the observed ICTS result of a PTC thermistor. Since the temperature of the sample is 175°C which is 25°C below the temperature where resistivity becomes maximum, this spectrum indicates that for the Curie-Weis region. As mentioned before, Heywang model of PTC thermistors

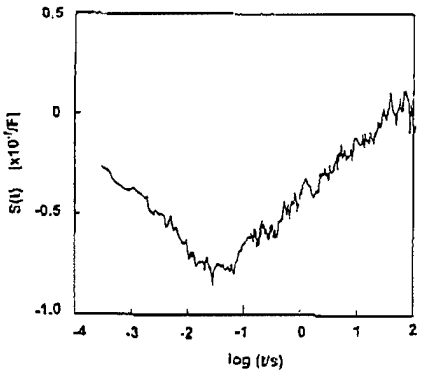


Fig.9 ICTS spectrum for PTC thermistor at Curie-Weis Region. T=175°C

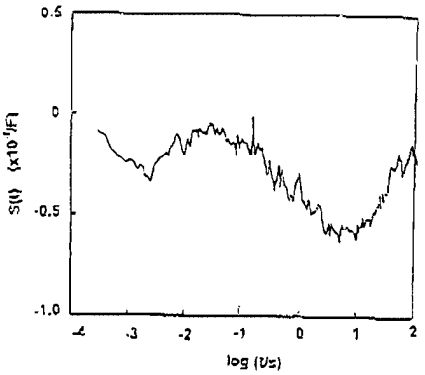


Fig. 10 ICTS spectrum forPTC thermistor at pinning region. T=210°C.

contains no interface states above E_o. Therefore, ICTS measurement should not give no peak. However one can find a peak at $\log t \approx -1.5$ in Fig. 9. This result shows there exist some interface states above E_o. Figure 10 shows the similar ICTS result at 210°C where the pinning region has already started. Two new peaks appeared at $\log t \approx -2.5$ and $\log t \approx 1$. The quicker peak can be interpreted to have the same origin as that in Fig. 9 because the higher temperature reduced the life time of the interface states. The slower peak in Fig. 10 can be interpreted to correspond with the deep traps at E_o which pin the Fermi level.

5. Conclusions

The applied voltage dependence of DSB was quantitatively simulated by simplifying the density distribution of the interface states. It was pointed out that interface states play important role on the electrical properties of ceramic semiconductors. The calculated results are compared with the observed results of I-V and ICTS measurement to obtain the following conclusions.

(1) The interface states retard the decrease in ϕ_1 and extremely high density interface states will fix the Fermi energy and ϕ_1.

(2) I-V characteristics are influenced not only by energy levels but also by their density and width of the energy distribution.

(3) Although saturation of electron charge into the interface states will produce steep rise in current, its nonlinear exponent, α, is confined to 22 and other mechanism is needed for explanation of high nonlinearity in ZnO varistors.

(4) PTC effect can be quantitatively understood by taking into account of interface states based on DSB model.

(5) ICTS measurement of the ZnO:Pr varistor showed that the Fermi level of the ZnO grains is fixed by the interface states and that the interface states are distributed monoenergetically. These results agreed with the calculated results of the DSB structure. Moreover, the applied voltage higher than the varistor voltage release pinning of E_F and bring about a different conduction mechanism which should be the origin of high nonlinear I-V characteristics.

(6) ICTS results of the PTC thermistor showed the existence of interface states above the deep traps at E_o. The peak corresponding to deep traps appeared at $\log t \approx 1$ at higher temperature.

6. References

[1] K.Mukae and I.Nagasawa, "Effect of Praseodymium Oxide and Donor Concentration in the Grain Boundary Region of ZnO Varistors", 331, "Advances in Ceramics, Vol.1", Ed., L. M. Levinson, Am. Ceram. Soc., (1981).

[2] H. Ihrig, "Physics and Technology of PTC-type $BaTiO_3$ Ceramics", 117, "Advances in Ceramics, Vol.7", Ed., M. F. Yan and A. H. Heuer, Am. Ceram. Soc., (1983).

[3] W. Heywang, "Resistivity Anomaly in Doped Barium Titanate", J.Am.Ceram.Soc., Vol.47, 484,1964.

[4] K.Mukae and K.Tsuda, "Effects of Interface States on Applied Voltage Dependence of Double Schottky Barrier(Part 1)", J.Ceram.Soc.Jpn., Vol.101, 1125, 1993.

[5] G. H. Jonker, Solid State Electron., Vol. 7, 895,1964.

[6] T. Maeda and M. Takata, "Detection and Characterization of Trap Centers in ZnO Varistor by ICTS", J. Ceram. Soc. Jpn, Vol.97, 1219, 1989.

[7] K.Tsuda and K.Mukae, "Characterization of Interface States in ZnO Varistors using Isothermal Capacitance Transient Spectroscopy", J.Ceram.Soc.Jpn, Vol. 100, 1239, 1992.

Mathematics for Smart Materials and Structures

Invited Paper

Design and manufacturing of material microstructures and micromechanisms

Ole Sigmund

Department of Solid Mechanics
Technical University of Denmark
DK-2800 Lyngby, Denmark

ABSTRACT

This paper suggests how two inverse problems can be solved using topology optimization methods. The first problem consists of designing materials with optimal or special properties such as maximum stiffness to weight ratios or negative Poisson's ratio materials. The second problem consists of designing optimal compliant micromechanisms for use in MicroElectroMechanical Systems (MEMS). The proposed material microstructures and compliant micromechanisms have been manufactured using micromachining techniques and they show the expected behavior in tests.

1 Introduction

Being able to design materials with optimal or special elastic properties opens many interesting perspectives.[1] The basic engineering goal, to designing light and stiff structures, makes it rewarding to design materials with maximum stiffness to weight ratios. Another example is the recent interest in producing materials with negative Poisson's ratio, i.e. materials that expand transversely, subject to an applied tensile load. Such materials have been produced by Lakes,[2] who expects that they can be used, among other applications, as shock absorbers and fasteners. Avellanada and Swart[3] report that negative Poisson's ratio materials play a crucial role in the enhancement of hydrophone performance.

Compliant mechanisms are flexible structures that convert an input motion or force to a desired output motion or force by undergoing elastic deformation, as opposed to the rigid body motions of conventional mechanisms. By using compliant mechanisms instead of rigid body mechanisms, production costs are lowered due to simplification or elimination of assembly procedures. An interesting application of compliant mechanisms is in MicroElectroMechanical Systems, MEMS, where the small scale (below 1 millimeter) excludes the use of rigid body mechanisms and conventional assembly procedures. MEMS are used for micromanipulation purposes and it is expected that they can be used for (in-body) surgery and health monitoring.

Approaches to design of materials with optimal or special elastic properties has been done by Milton and Cherkaev,[4] who prove that materials with elastic properties ranging over the entire set compatible with thermodynamics can be built by layerings of infinitely soft and infinitely weak material and Sigmund,[5] who suggests a numerically based design method that produces truss-like material microstructures with extreme elastic proper-

0-8194-2165-0/96/$6.00

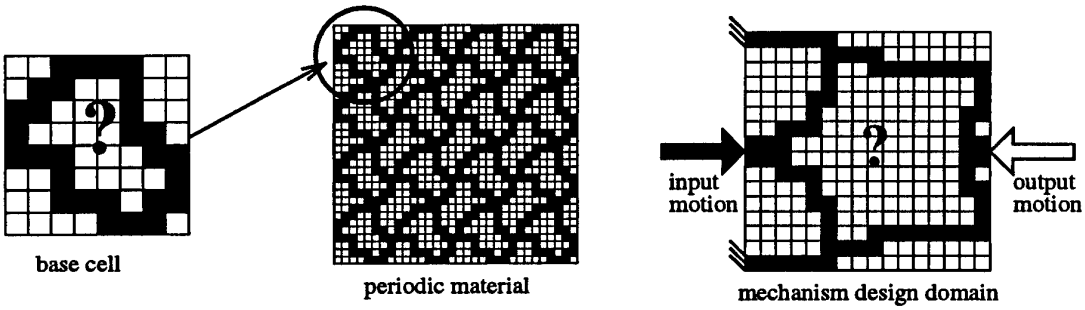


Figure 1: Two inverse problems: The material design problem is sketched left and the compliant mechanism design problem is sketched right. Both design domains are discretized by finite elements and the density of material in each of the elements is the design variable.

ties. Both approaches, however, suffer from the fact that the proposed materials are difficult if not impossible to manufacture. The former because of the assumption of microstructure at several different length scales and the latter because of the assumption of an idealized truss structure with microscopic hinges and sliding surfaces. In this paper, we develop a numerical method similar to the one proposed in Sigmund,[5] but assuming a continuum like discretization of the microstructure that does not allow hinges and sliding surfaces, thereby ensuring manufacturability of the proposed materials.

Design of compliant mechanisms has been done by Howell and Midha[6] by modifying existing rigid body mechanisms. Specifying complicated or multiple input and output motions, may lead to difficulties in coming up with rigid body mechanisms that perform the desired output. To overcome this problem, Sigmund[7] proposed a numerical method for the design of optimal rigid body mechanism topologies. The mechanisms obtained in Sigmund[7] cannot directly be converted to compliant mechanisms because of crossing bodies, which are difficult to manufacture. Therefore, this paper suggests a method to design compliant mechanisms using topology optimization techniques and ideas from Sigmund[7] and Ananthasuresh *et al.*.[8]

The material design problem and the compliant mechanism design problem are very similar in nature and can be defined as

The material design problem

- *How do we distribute material and void in a periodic base cell such that optimal or desired effective material properties are obtained?*

The compliant mechanism design problem

- *How do we distribute material and void in a design domain such that a given input motion is converted into a desired output motion with minimum loss of energy?*

The two design problems are sketched in Fig. 1. The material design problem consists in finding the (porous) microstructural topology (base cell topology, Fig. 1, left) which, periodically repeated (Fig. 1, center), results in a material with the optimal or desired effective elastic properties. The compliant mechanism design problem can be exemplified with the simple problem in Fig. 1, right: Which mechanism topology will, with a minimum loss of energy, convert an input motion (black arrow) to an output motion in the opposite direction (white arrow) given the design domain (squared region) and the supports (slanted lines)?

Both the material design and the compliant mechanism design problems can be solved using topology optimization techniques as founded in Bendsøe and Kikuchi.[9] The standard topology optimization method consists of discretizing the design domain by finite elements and letting the material density in each of the elements be a design variable. By means of an iterative procedure, the optimal density distribution, and thereby the topology optimizing the given performance criteria, is found. The topology optimization method has been used primarily for problems with simple objective functions, such as minimization of compliance or maximization of eigenfrequencies. In this paper the topology optimization method is applied to material and compliant mechanism design by defining multiple non-self-adjoint load cases, which makes it possible to obtain specific elastic material properties and to optimize the input/output relations defined as geometrical and mechanical advantages for compliant mechanisms.

2 Topology optimization

This section will outline the general topology optimization problem applicable to both material and mechanism design and discuss how it can be solved using sequential linear programming. In subsections 2.1 and 2.2, objective functions and constraints specific for the two design problem will be discussed in detail.

The design domain is discretized by N finite elements. Letting the density of material in each element be a design variable, we can define the design vector $\mathbf{x}$ of length N. The design variables are allowed to vary between $x_{min} = 10^{-4}$ (void) and 1 (solid). Because of potential singularity problems in the finite element problem, the design variables are not allowed to take the value zero. However, choosing a low value of x_{min} eliminate the structural significance of the regions with minimum densities such that they can be interpreted as being void. The general topology optimization problem can be written as

$$\begin{aligned}
&\textit{Minimize} && : \text{Objective function,} \quad \Phi(\mathbf{x}) \\
&\textit{Variables} && : \text{Distribution of material in basecell/designdomain,} \quad \mathbf{x} \\
&\textit{Subject to} && : \text{Constraints on material volume,} \quad V(\mathbf{x}) \leq V^* \\
& && : \text{Isotropy constraint (only material design),} \quad I(\mathbf{x}) = 0 \\
& && : \text{Minimum constraints on stiffness (only material design),} \quad S_{i(min)} \leq S_i(\mathbf{x}), \quad i = 1, \ldots, m \\
& && : \text{Side constraints on design variables,} \quad \mathbf{0} < \mathbf{x}_{min} \leq \mathbf{x} \leq \mathbf{1}
\end{aligned} \tag{1}$$

Conventional topology optimization problems can be solved very efficiently using optimality criteria methods, but due to the more complex objective functions and constraints in this paper, it was chosen to solve the optimization problem Eq.(1) by a sequential linear programming method (SLP) (see f.ex. Pedersen[10]). The SLP method consists of the sequential solving of an approximate sub-problem, obtained by writing linear Taylor series expansions of the objective and constraint functions. With a good movelimit strategy for the allowed changes of the design variables, the SLP method is a very robust and efficient tool for structural optimization. The movelimit strategy applied here, consists of increasing the movelimit for a design variable with a factor of 1.2, if two preceding steps have the same direction and decreasing the movelimit with a factor of 0.7, if two preceding steps have opposite directions. The optimization problem solved by the SLP method is the following formalization of the one in Eq.(1)

$$\begin{aligned}
&\textit{Minimize} && : \Phi(\mathbf{x}) + rI(\mathbf{x}) \\
&\textit{Subject to} && : V(\mathbf{x}) - V^* \leq 0 \\
& && : S_{i(min)} - S_i(\mathbf{x}) \leq 0, \quad i = 1, \ldots, m \\
& && : \mathbf{0} < \mathbf{x}_{min} \leq \mathbf{x} \leq \mathbf{1}
\end{aligned}$$

Because equality constraints are difficult to impose as normal constraints in the SLP method, it was chosen to add the isotropy constraint as a penalty term to the cost function. The sensitivity analysis necessary for each iteration step is performed analytically, based on the preceding finite element analysis step. A flowchart of the

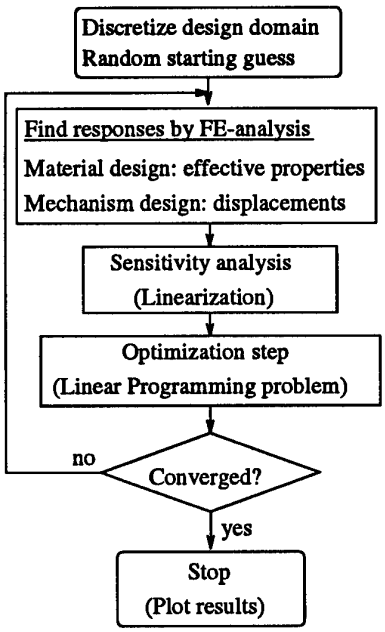


Figure 2: Flowchart of the design algorithm.

overall design algorithm is shown in Fig. 2. For more details on the computational algorithms and procedures to overcome certain finite element related difficulties, the reader is referred to Sigmund.[11]

2.1 Design of material microstructures

The effective properties of a periodic materialstructure, assuming linear elasticity, can be found using the standard numerical homogenization method.[12] The homogenization is performed by solving three (six in three dimensions) finite element problems corresponding to a horizontal, a vertical and a shear test case of the base cell. The homogenization procedure returns the effective elasticity matrix E_{ij}^H. In this paper we will only discuss isotropic materials and thus the plane stress elasticity matrix in two dimensions can be written as

$$E_{ij} = \frac{E}{1-\nu^2}\begin{bmatrix} 1 & \nu & 0 \\ \nu & 1 & 0 \\ 0 & 0 & (1-\nu)/2 \end{bmatrix} \tag{2}$$

where E is Young's modulus and ν is Poisson's ratio.

The cost function for material design can be any combination of the constitutive matrix but here we will consider the two objective functions: Maximization of the bulk modulus $k = E/2(1-\nu)$ and minimization of Poisson's ratio ν. The condition for isotropy of the effective elasticity matrix is

$$I(\mathbf{x}) = \frac{(E_{11}^H - E_{22}^H)^2 + (E_{33}^H - (E_{11}^H - E_{12}^H)/2)^2}{\frac{1}{4}(E_{11}^H + E_{22}^H)^2} = 0 \tag{3}$$

The minimum constraints on stiffness are written as ($m = 2$ for 2-d and $m = 3$ in 3-d)

$$S_i(\mathbf{x}) = E_{ii}^H \geq pE_{ii}^0, \quad i = 1, \ldots, m \tag{4}$$

where E^0_{ii} are the stiffness components of a solid basecell and p is the desired stiffness percentage. In three dimensions, the stiffness matrix Eq.(2) has dimension 6 by 6 and the expression for isotropy Eq.(3) is somewhat more complicated.

2.2 Design of compliant mechanisms

The main goal of complaint mechanism design is to find the mechanism topology that converts an input displacement into a desired output displacement. For compliant mechanisms, the geometrical advantage GA, defined as output displacement divided by input displacement, is not equal to the inverse of the mechanical advantage MA, defined as output force divided by input force, as opposed to rigid body mechanisms. A secondary goal of compliant mechanism design is therefore to get the product $GA\ MA$ as close to one as possible - this ensures a high mechanical efficiency of the compliant device.

To calculate GA and MA, we need to define two load cases for the finite element problem. Let $\mathbf{f}_1$ denote the first load case consisting of the input force p_1 (e.g. black arrow in Fig. 1) and let $\mathbf{f}_2$ denote the second load case consisting of the unit dummy load p_2 applied at the output point (e.g. white arrow in Fig. 1). The displacement vectors $\mathbf{d}_1$ and $\mathbf{d}_2$ are the solutions to the standard finite element problems

$$\mathbf{S}\mathbf{d}_1 = \mathbf{f}_1 \text{ and } \mathbf{S}\mathbf{d}_2 = \mathbf{f}_2 \tag{5}$$

where $\mathbf{S}$ is the global stiffness matrix.

Having solved the finite element problems in Eq.(5), the geometrical advantage can be calculated as the displacement at the output point u_{21} divided by the displacement at the input point u_{11} and the mechanical advantage can be calculated as the reaction force at the output point R divided by the input force p_1

$$\begin{aligned} GA &= \frac{u_{21}}{u_{11}} = \frac{p_1 \mathbf{d}_1^T \mathbf{S}\mathbf{d}_2}{p_2 \mathbf{d}_1^T \mathbf{S}\mathbf{d}_1} \\ MA &= \frac{R}{p_1} = \frac{p_2 u_{21}}{p_1 u_{22}} = \frac{\mathbf{d}_1^T \mathbf{S}\mathbf{d}_2}{\mathbf{d}_2^T \mathbf{S}\mathbf{d}_2} \end{aligned} \tag{6}$$

Typically, the user wants a mechanism with some specific geometrical or mechanical advantage GA^* or MA^*. To allow the user to specify GA^* or MA^*, and at the same time ensure an efficient mechanism by getting the product $GA\ MA$ close to one, the following cost function is proposed

$$\Phi(\mathbf{x}) = \frac{(GA - GA^*)^2}{(GA^*)^2} + \frac{(MA - MA^*)^2}{(MA^*)^2} \tag{7}$$

where $MA^* = 1/GA^*$ when the user has specified GA^* and vice versa. If the optimization algorithm manages to get the cost function Eq.(7) close to zero, an efficient mechanism with the specified geometrical or mechanical advantage has been obtained.

3 Examples

In this section the performances of the material and compliant mechanism design procedures are demonstrated by several examples. For more examples on material design the reader is referred to Sigmund[11] and for more examples on compliant mechanism design, the reader is referred to Larsen.[13]

3.1 Design of material microstructures

As discussed in the introduction, it is rewarding to design materials with maximum stiffness to weight ratios and materials with negative Poisson's ratio. The selected design examples for this paper are therefore the maximization of bulk modulus for a given volume fraction and the minimization of Poisson's ratio. Both design problem will be addressed in two and three dimensions.

The material design problems are non-dimensionalized, that is, we use a base material with Young's modulus $E = (1 - \nu^2)$ and Poisson's ratio 0.3 in two dimensions, and Young's modulus $E = (1 - \nu)/((1 + \nu)(1 - 2\nu))$ and Poisson's ratio 0.3 in three dimensions. This implies, that a solid base cell has stiffness matrix components $E_{ii} = 1$. If we want to use a real material, say a polymer or a metal, as base material, the effective values can simply be multiplied with the actual Young's modulus. It is not expected that actual Poisson's ratios of base materials differing from 0.3 will result in radically different designs.

For the two dimensional examples, the results are represented as pictures of a single base cell discretized by 30 by 30 four-node finite elements. Black elements denote regions with structure and white denote void regions. To visualize the repeated material structures, the base cells are also shown repeated in blocks of three by three cells. For the three dimensional examples, only one base cell is shown with small cubes (individual finite elements) denoting regions with material. The three dimensional base cells are discretized by 20 by 20 by 20 elements. In both cases several thousand iterations are required to reach the optimal solutions, but due to the difference in number of finite elements (900 in 2-d and 8000 in 3-d) it may take 5 hours of computing time on an Indigo 2 workstation to reach a solution in two dimensions whereas, it might take a week to reach a solution for the three dimensional case.

First example: maximization of bulk modulus in 2-d

Volume fraction of material in the base cell is constrained to 50 % and the effective material is required to be isotropic. The design problem is solved for two different base cell geometries. Optimal topology for a square base cell is seen in Fig. 3(top), which has the values: $k = 0.161$ and Poisson's ratio $\nu = 0.567$. Optimal topology for a rectangular base cell is seen in Fig. 3(bottom), which has the values: $k = 0.160$ and Poisson's ratio $\nu = 0.454$.

Second example: minimization of Poisson's ratio in 2-d

Some readers might object that there already exists a simple material microstructure with negative Poisson's ratio, namely the inverted honeycomb shown in Fig. 4(top). However, this microstructure is not isotropic, or in other words it responds differently to loads in different directions. The inverted honeycomb is very soft when loaded in the diagonal direction. To design an isotropic material with negative Poisson's ratio, the following microstructure design problem was solved: Minimize Poisson's ratio subject to minimum constraint on the stiffness (5 % of a solid base cell), isotropy constraint and 40 % volume fraction. The result is seen in Fig. 4(bottom), which shows the isotropic material microstructure with Poisson's ratio equal to -0.63. When compressed horizontally the triangles "close" and result in a vertical contraction of the material structure.

Third example: maximization of bulk modulus in 3-d

Volume fraction of material in the base cell is constrained to 50% and the effective material is required to be isotropic. The optimal base cell is shown in Fig. 5(left), the obtained bulk modulus is $k = 0.144$ and the Poisson's

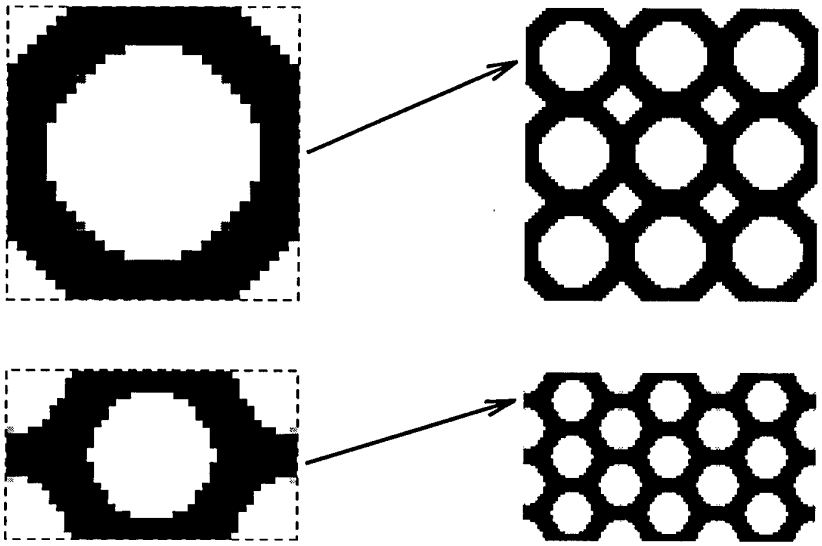


Figure 3: Resulting 2-dimensional quadratic (top) and rectangular (bottom) base cell obtained by maximization of the bulk modulus. Obtained bulk moduli are $k = 0.161$ and $k = 0.160$ respectively. One base cell (left) and arrays of nine base cells(right).

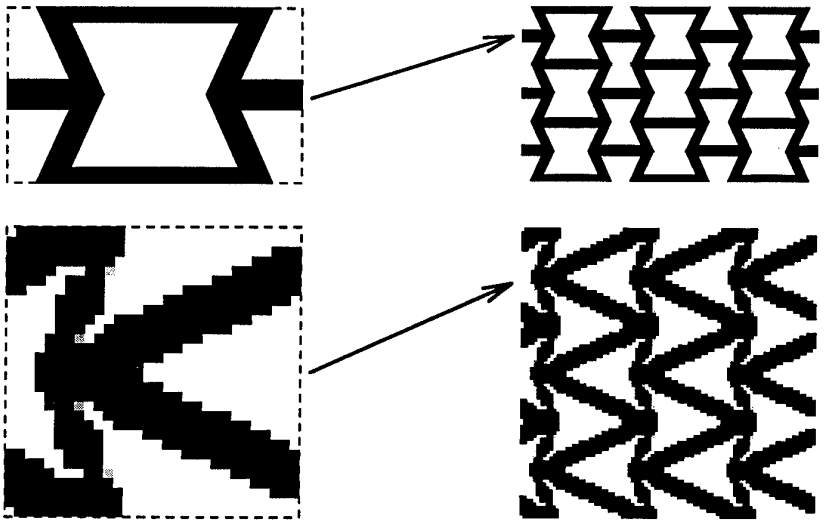


Figure 4: Two material structures with negative Poisson's ratio. Top: the well known inverted honeycomb - note that this material is not isotropic. Bottom: an isotropic negative Poisson's ratio material microstructure designed with the suggested procedure (Poisson's ratio is -0.63).

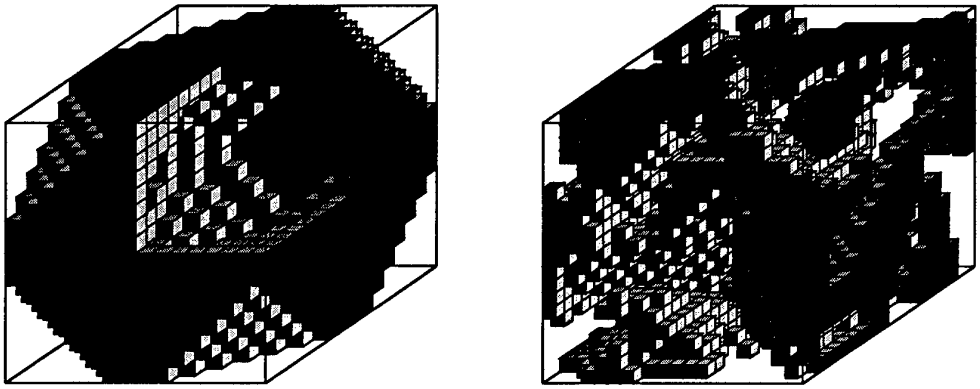


Figure 5: Left: Resulting isotropic 3-dimensional base cell obtained by maximizing bulk modulus (front quarter of cell is cut away to show that the cell is hollow). Right: Resulting isotropic 3-dimensional base cell obtained by minimizing Poisson's ratio.

ratio is $\nu = 0.275$. Note that the microstructure is hollow, which means that the repeated microstructure will be like a "closed-wall foam" structure.

Fourth example: minimization of Poisson's ratio in 3-d

Again we consider the minimization of Poisson's ratio with volume fraction 40%, isotropy constraint and minimum stiffness constraints of 5%. The optimal topology is shown in Fig. 5(right). At the deadline for the submission of the paper, the program had not converged fully so the obtained Poisson's ratio is "only" $\nu = -0.25$. It is expected that a lower value will be obtained when the program converges. It is difficult to imagine the deformation mechanism leading to the negative Poisson's ratio by looking at the figure. Therefore, it is planned to build a model of the cell using stereolithography processes in the near future.

3.2 Design of compliant mechanisms

To demonstrate the performance of the compliant mechanism design procedure, three examples are discussed. In Fig. 6(top) the three design domains are sketched. Grey areas define the design areas, black areas are fixed to be solid and white areas are fixed to be void. The design domains are discretized by 4000 elements. Example *a* is a force inverter mechanism, the input force (black arrow) should be converted to a force in the opposite direction (white arrow). Example *b* is a gripping mechanism, an input displacement (black) arrow should result in closing of the jaws (in the direction of the white arrows). Example *c* corresponds to example *b*, except that the jaws of the gripper should move in parallel. To solve example *c* an extra set of geometrical and mechanical advantages are added to the cost function in Eq.(7). The resulting mechanism topologies are shown in Fig 6(bottom).

4 Manufacturing using micromachining techniques

In cooperation with Ulrik Darling Larsen and Siebe Bouwstra at Mikroelektronik Centret (MIC), Technical University of Denmark, the mechanisms and the two-dimensional negative Poisson's ratio structure were built in

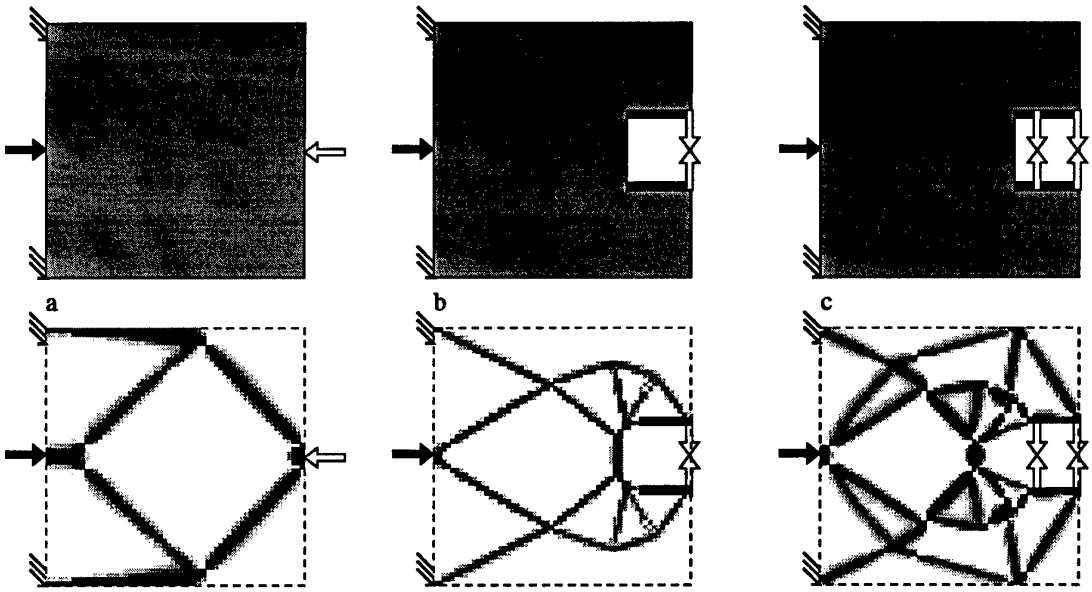


Figure 6: Example of micromanipulators. Top: design domains, bottom: optimal designs. a) force inverter, b) gripping mechanism, c) gripping mechanism with parallel moving jaws.

microscale using laser micromachining and surfaceetching techniques known from the semi-conductor industry. For details on the processing techniques, the reader is referred to Larsen.[13] Fig. 7 shows two of the micromachined devices. A negative Poisson's ratio test beam, composed of 20 by 8 repeated base cells taken from Fig. 4(bottom), is shown in Fig. 7(left). The beam is one millimeter long, 6 microns thick and each cell has dimension 50 by 50 microns. The beam was tested using an external probe and the measured Poisson's ratio was $-0.92 \pm 13\%$. Fig. 4(right) shows the manufactured microgripper from Fig. 6*b*. The jaws of the gripper span approximately 50 micron and, actuated by an external probe, this device showed the expected behavior as well.

5 Discussion

The examples in this paper have shown that topology optimization techniques can be successfully applied to complex problems such as the design of material microstructures with exotic properties in two and three dimensions and to the design of compliant mechanisms. The theoretically designed negative Poisson's ratio materials and the compliant devices have been built using micromachining techniques and show the expected behavior. The three dimensional material microstructures cannot be built using existing micromachining techniques, however, the author hopes to produce them, in a larger scale, using stereolithography processing in the near future. Current theoretical work is devoted to extensions of the topology optimization method to include two base materials. Early results show that it is possible to design bimaterial structures with negative thermal expansion coefficients and optimal piezoelectric composites, which can be used as actuators and as smart materials. These results will be reported elsewhere.

Acknowledgements

The work presented in this paper received support from Denmarks Technical Research Council (Programme of Research on Computer-Aided Design). The author also gratefully acknowledges the work of Ulrik Darling Larsen and Siebe Bouwstra at Mikrolektronik Centret (MIC), Technical University of Denmark, who produced and tested the micromachined devices.

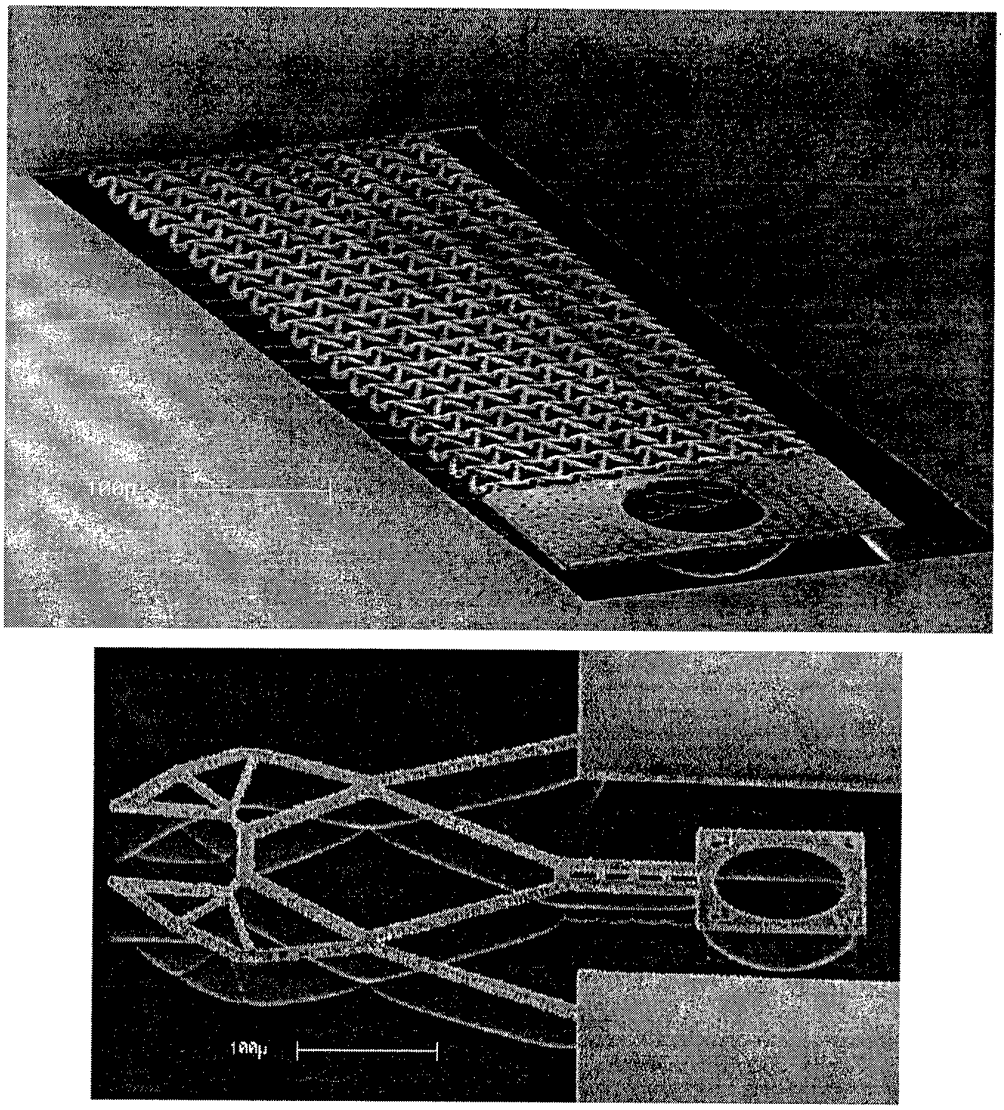


Figure 7: Top: micromachined negative Poisson's ratio testbeam composed of 20 by 8 base cells. The length of the testbeam is 1.2 millimeters and the measured Poisson's ratio was $-0.92 \pm 13\%$. Bottom: micromachined microgripping mechanism, the span of the jaws is approximately 50 microns.

6 REFERENCES

[1] R. Lakes. Materials with structural hierarchy, review article. *Nature*, 361:511–515, 1993.

[2] R. Lakes. Foam structures with negative Poisson's ratio. *Science*, 235:1038, 1987.

[3] M. Avellanada and P.J. Swart. Calculating the performance of 1-3 piezocomposites for hydrophone applications: an effective medium approach. *Submitted*, 1995.

[4] G.W. Milton and A.V. Cherkaev. Which elasticity tensors are realizable? *Submitted*, 1995.

[5] O. Sigmund. Tailoring materials for specific needs. *Journal of Intelligent Materials, Systems and Structures*, 5:736–742, 1994.

[6] L.L. Howell and A. Midha. A method for design of compliant mechanisms with small length flexural pivots. *Transactions of the ASME*, 116:280–290, 1994.

[7] O. Sigmund. Some inverse problems in topology design of materials and mechanisms. In W. Shielen, editor, *IUTAM Symposium on Optimization of Mechanical Systems, Stuttgart, Germany, March 26-31.* Kluwer (to appear), 1995. Also appeared as DCAMM Report No. 499, Technical University of Denmark.

[8] G.K. Ananthasuresh, S. Kota, and Y. Gianchandani. A methodical approach to the design of compliant micromechanisms. In *Solid-state sensor and actuator workshop*, pages 189–192, 1994.

[9] M.P. Bendsøe and N. Kikuchi. Generating optimal topologies in optimal design using a homogenization method. *Computational Methods in Applied Mechanics and Engineering*, 71:197–224, 1988.

[10] P. Pedersen. On the minimum mass layout of trusses. In *AGARD conference proceedings No. 36, Symposium on structural optimization*, volume AGARD-CP-36-70, pages 189–192, 1970.

[11] O. Sigmund. *Design of material structures using topology optimization.* PhD thesis, Technical University of Denmark, Department of Solid Mechanics, December 1994.

[12] J.F. Bourgat. Numerical experiments of the homogenization method for operators with periodic coefficients. In *Lecture notes in mathematics*, volume 704, pages 330–356. Springer Verlag, Berlin, 1977.

[13] U.D. Larsen, O. Sigmund, and S. Bouwstra. Design and fabrication of compliant mechanisms and material structures with negative Poisson's ratio. *Submitted*, 1995.

A dynamical controller which insure a given exponential decay rate, Application to the stabilization of plate vibrations with piezoelectric actuators.

Michel Lenczner
Groupe Matériaux intelligents,
Laboratoire de Calcul Scientifique,
Université de Franche Comté,
16, Route de Gray,
25000 Besançon,
France.

Abstract : *For given operational differential equations of first or second order, we find dynamical controllers such that the resulting coupled system is exponentially stable with a prescribed exponential decay rate. An application to the stabilization of plate vibrations with distributed piezoelectric actuators is described.*

I. Introduction.

We are interested on the stabilization of the equation

$$u' = Au + Bv \text{ and } u(0) \in H \tag{1}$$

where u is the state variable, v is the control variable, H an Hilbert space, A an operator whose domain $D(A)$ is dense in H and B an operator defined on an Hilbert space V such that $B(V) \subset H$. The stabilization of (1) can be achieved with a static control $v = Ku$ where K is an operator defined on V or with a dynamic controller (see [1], [2] and the bibliography of [1] for example) which leads to the coupled system

$$u' = Au + Bv,\ v' = Cu + Dv \text{ and } u(0) \in H,\ v(0) \in V. \tag{2}$$

In this work, the dynamical controller characterized by the operators C and D that we find insure a given exponential decay rate of the coupled system. This is achieved for the particular case where B is an isomorphism from U to H. A similar result is obtained for a second order equation and an application of this second result is described for the stabilization of plate vibrations by a distribution of piezoelectric actuators. The interest of the resulting controllers is that they are simple functions of A.

II. Stabilization of a first order problem.

1. Case where A is a bounded operator.

The operator $\mathcal{A}$ is assumed to be a bounded operator defined on H. Let us consider two differents complex numbers λ_1, λ_2 with negative real parts such that λ_1 does'nt vanish. Let us assume that $B = \lambda_1 Id$. Let us denote $\overline{A} = \frac{A}{\lambda_1}$, $\widetilde{A} = A - \lambda_1 Id - \lambda_2 Id$, $C = -\widetilde{A}\overline{A} - \lambda_2 Id$ and $D = -\widetilde{A}$. The matrix of the coupled system is then $\mathcal{A} = \begin{pmatrix} \lambda_1\overline{A} & \lambda_1 Id \\ -\widetilde{A}\overline{A} - \lambda_2 Id & -\widetilde{A} \end{pmatrix}$. The couple $U = (u, v)$ is solution of the system $U' = \mathcal{A}U$.

Theorem. *For every initial conditions $U \in H \times H$, the preceding equation admit an unique solution $U \in C^0(0, T; H)$. The operator $\mathcal{A}$ has exactly two eigenvalues λ_1 and λ_2. Then the solution U is exponentially stable with the exponential decay rate equal to* $\max(Re\lambda_1, Re\lambda_2)$.

0-8194-2165-0/96/$6.00

Proof : Let us introduce two operators

$$P = \begin{pmatrix} Id & \lambda_1 Id \\ Id - \overline{A} & \lambda_2 Id - \lambda_1 \overline{A} \end{pmatrix} \text{and } Q = \frac{1}{\lambda_1 - \lambda_2} \begin{pmatrix} \lambda_2 Id - \lambda_1 \overline{A} & -\lambda_1 Id \\ \overline{A} - Id & Id \end{pmatrix}$$

Lemma. *P is an isomorphism from H^2 to H^2 and $Q = P^{-1}$.*

Proof of the lemma : Because A is a bounded operator then P and Q are bounded operators. The equality $PQ = QP = Id$ leads to the conclusion. □

Let us consider the matrix of operators $D = \begin{pmatrix} \lambda_1 Id & 0 \\ 0 & \lambda_2 Id \end{pmatrix}$. A simple calculation shows that $\mathcal{A}P = PD$, it is equivalent to $\mathcal{A} = PDQ$. It follows that the eigenvalues of $\mathcal{A}$ are λ_1 and λ_2 and that $\mathcal{A}$ is also an isomorphism from H to H. The conclusions of the theorem follows. □

2. Case when A is an unbounded operator.

Now, the operator A is assumed to be an unbounded operator of domain $D(A)$ dense in the Banach space H. Let us consider two complex numbers λ_1 and λ_2 defined as in the first paragraph. First, let us assume that $B = \lambda_1 Id$. The operator Q is defined as in the preceding section, but here its domain is $D(Q) = D(A) \times H$. The operator P is defined as follows $P(u,v) = (u+\lambda_1 v, u+\lambda_2 v - \overline{A}(u+\lambda_1 v))$ for functions $U = (u,v) \in V_P = \{(u,v) \in H \times H / u+\lambda_1 v \in D(A)\}$, the norm on V_P is $||U||_{V_P} = ||u||_H^2 + ||v||_H^2 + ||u + \lambda_1 v||_H^2$. The operator $\mathcal{A}$ can be defined as in the first paragraph but on a more restricted set $D(\mathcal{A})$ of functions U then the differential equation $U' = \mathcal{A}U$ can be solved for initial conditions in $D(\mathcal{A})$. In order to obtain a larger class of initial conditions, we consider a weak formulation of this equation : $QU' = DQU$ with initial conditions $U(0) = U^0 \in P(D(A)^2)$.

Theorem. *The above differential equation has an unique solution. This solution decay exponentially, its exponential decay rate is $\omega = \sup(Re\lambda_1, Re\lambda_2)$.*

Proof : Let us consider the differential equation $F' = DF$ with initial conditions $F(0) = F^0 \in D(A)^2$. The operator D is bounded on $D(A)^2$, then there is a unique solution $F \in L^2(O,T; D(A)^2)$ for every $T > 0$ of this equation. This solution is such that $||F||_{D(A)^2} \leq ||F^0||_{D(A)^2} e^{\omega t}$. Let us remark that

Lemma. *The operator Q is an isomorphism (algebraic and topologic) from $D(A) \times H$ to V_P.*

The function $U = PF$ is solution of the equation $QU' = DU$ with initial conditions $U(0) = PF^0$ and is such that $||U||_{D(A)\times H} \leq ||P||\ ||Q||\ ||U^0||_{D(A)\times H} e^{\omega t}$. This achieves the proof of the theorem.□

Remarks : (i) Because $D(A)$ is dense in H, $P(D(A)^2)$ is dense in $D(A) \times H$.
(ii) For numerical or experimental considerations, the weak formulation $QU' = DQU$ is more convenient than the formulation $U' = \mathcal{A}U$ because the order of the operators applied to U are smaller.
(iii) From the equation $QU' = DU$ and the nominal equation the controller equation is obtained : $-\widetilde{A}u' - \lambda_1 v' - \lambda_1 \lambda_2 u = 0$.

For B not equal to $\lambda_1 Id$, B is assumed to be equal to $\lambda_1 \overline{B}$ where $\overline{B}$ is an isomorphism from a Banach space V_B to H. Let us denotes $w = \overline{B}v$, then the vector (u,w) is solution of the system

$\begin{pmatrix} u \\ w \end{pmatrix}' = \begin{pmatrix} \lambda_1\overline{A} & \lambda_1 Id \\ \overline{B}C & \overline{B}D\overline{B}^{-1} \end{pmatrix}\begin{pmatrix} u \\ w \end{pmatrix}$. The above method can then be applied to this equation.

3. Example.

We consider the heat equation with internal control

$$u' = -\lambda_1\Delta u + \lambda_1 v \text{ in } \Omega \text{ and } u = 0 \text{ on } \Gamma$$

where Ω is a domain of $\mathbb{R}^n$ and Γ is its boundary. Here, $A = -\lambda_1\Delta$, $\overline{A} = -\Delta$, $\widetilde{A} = -\lambda_1\Delta - \lambda_1 Id - \lambda_2 Id$, $D(A) = H^2(\Omega)\cap H_0^1(\Omega)$. The resulting controller is $(\lambda_1\Delta + \lambda_1 + \lambda_2)u' - \lambda_1\lambda_2 u - \lambda_1 v' = 0$ for the initial conditions $(u^0, v^0) \in H^2(\Omega)\cap H_0^1(\Omega) \times L^2(\Omega)$.

III. The case of second order operator.

We consider the stabilization of the second order equation

$$u'' = Au + Bv \tag{1}$$

where A is an operator defined on his domain $D(A) \subset H$.

1. Case where A is a bounded operator.

If A is a bounded operator, then $D(A) = H$. We are interested on finding a controller which have the form

$$v'' = C_1u' + C_0u + D_1v' + D_0v. \tag{2}$$

Let us consider four real numbers $a_0, ..., a_3$ such that the four roots $\lambda_1, ..., \lambda_4$ of the algebraic equation $\lambda^4 + a_3\lambda^3 + a_2\lambda^2 + a_1\lambda^1 + a_0 = 0$ are distincts and have a negative real part. Let us choose

$$C_0 = A^2 + a_2A - a_0Id,\ D_0 = A + a_2Id,\ C_1 = -Aa_3 + a_1Id \text{ and } D_1 = -a_3Id.$$

Theorem. *The solution (u, v) of the system (1),(2) exists and is unique for every $U^0 = (u^0, v^0) \in H \times H$. In addition, $||u, v|| \leq ce^{\omega t}$ where $\omega = \sup(Re\lambda_1, .., Re\lambda_4)$.*

Proof : The system (1),(2) formulated as a first order system is $U' = \mathcal{A}U$ with the initial conditions $U(0) = U^0 \in H^4$ where $\mathcal{A}$ is the given by $\mathcal{A} = \begin{pmatrix} 0 & Id & 0 & 0 \\ A & 0 & Id & 0 \\ 0 & 0 & 0 & Id \\ C_0 & C_1 & D_0 & D_1 \end{pmatrix}$. Let us consider the matrix $M = \begin{pmatrix} 1 & 1 & 1 & 1 \\ \lambda_1 & \lambda_2 & \lambda_3 & \lambda_4 \\ \lambda_1^2 & \lambda_2^2 & \lambda_3^2 & \lambda_4^2 \\ \lambda_1^3 & \lambda_2^3 & \lambda_3^3 & \lambda_4^3 \end{pmatrix}$, $N = \begin{pmatrix} Id & 0 & 0 & 0 \\ 0 & Id & 0 & 0 \\ -A & 0 & Id & 0 \\ 0 & -A & 0 & Id \end{pmatrix}$, $L = \begin{pmatrix} Id & 0 & 0 & 0 \\ 0 & Id & 0 & 0 \\ A & 0 & Id & 0 \\ 0 & A & 0 & Id \end{pmatrix}$ and $D = \begin{pmatrix} \lambda_1 Id & 0 & 0 & 0 \\ 0 & \lambda_2 Id & 0 & 0 \\ 0 & 0 & \lambda_3 Id & 0 \\ 0 & 0 & 0 & \lambda_4 Id \end{pmatrix}$. The matrix M is invertible, then we define $\widetilde{D} = MDM^{-1}$.

Lemma. *(i) The operator L is an isomorphism from H^4 to H^4 and $L^{-1} = N$.*

(ii) $\mathcal{A} = (NM)D(NM)^{-1} = N(MDM^{-1})L$.

From this lemma, it is immediat that the solution of the equation $U' = \mathcal{A}U$ admit an unique solution for every initial conditions in H^4. In addition, the eigenvalues of $\mathcal{A}$ are $\lambda_1, ..., \lambda_4$ then the proof of the theorem is done.□

2. Case where A is an unbounded operator.

Here, $\mathcal{A}$ is assumed to be unbounded with domain $D(A)$ dense in H. The domainsof the operators N and L are denoted $D(N)$ and $D(L)$. They are both equal to $D(A)^2 \times H^2$. We consider a weak formulation of the equation $U' = \mathcal{A}U$ on the form $LU' = \tilde{D}LU$ with the initial conditions $U \in L(D(A)^4)$.

Theorem. *The above differential equation admit an unique solution U. This solution is such that* $||U||_{D(A)^4} \leq ||L||\ ||N||\ |||U^0||_{D(A)^2 \times H^2} e^{\omega t}$.

Proof : Let us consider the problem $F' = \tilde{D}F$ with the initial conditions $F(0) = F^0 \in D(A)^4$. The operator $\tilde{D}$ is bounded on $D(A)^4$, then this equation has an unique solution $F \in C^0(0, T; D(A)^4)$ for every $T > 0$.

Lemma. *The operator L is an isomorphism from $D(A)^2 \times H^2$ in $D(A)^2 \times H^2$ and $L^{-1} = N$.*

The above lemma implies that $U = NF \in L^2(0, T; D(A)^2 \times H^2)$ and that reciprocally $F = LU$. With this definition of U it follows that U is the unique solution of the equation $LU' = \tilde{D}LU$. In addition, $||F||_{D(A)^4} \leq ||F^0||_{D(A)^4} e^{\omega t}$ then $||U||_{D(A)^4} \leq ||L||\ ||N||\ |||U^0||_{D(A)^2 \times H^2} e^{\omega t}$.

Remarks : (i) In order to obtain the controller equation we consider the last equation of the system :

$$Au'' + v'' = \sum_{j=1}^{4} \tilde{D}_{4j} \begin{pmatrix} u \\ u' \\ Au + v \\ Au' + v' \end{pmatrix}_j .$$

(ii) In the case where $B \neq Id$, we assume that B is an isomorphism from V_B to H and we pose $w = Bv$. The contolled system is then equivalent to $u'' = Au + w$, $w'' = \overline{C}_1 u' + \overline{C}_0 u + \overline{D}_1 w' + \overline{D}_0 w$. Then the preceding method can be applied to this system.

IV. Application to the stabilization of the vibrations of a plate with a distribution of piezoelectric actuators.

Let us consider a vibrating plate composed with three layers : an elastic layer covered in both faces by piezoelectric layers. The two piezoelectric layers are supposed to be of the same thickness and to cover the total surface of the elastic plate. The electrical field in the upper layer is supposed to be constrained to be in phase opposition with respect to the electrical field in the lower layer. Then the mechanical in plane displacements are discoupled with the out plane displacements. The resulting model has the following form

$$u'' = -\Delta\Delta u - \Delta E \text{ in } \Omega,\ \delta = -\Delta u + cE \text{ in } \Omega \text{ and } u = \frac{\partial u}{\partial n} = 0 \text{ on } \partial\Omega.$$

In the realistic models, the operators Δ and $\Delta\Delta$ have to be replaced by more general second and fourth order operators. The present analysis hold also for the realistic model. Here no Dirac forces are generated by such coupling because the piezoelectric layers are not supposed to be covered by conductors films. In the above equations, the domain occupied by the section of the plate is denoted Ω and the boundary of the plate is supposed to be clamped. The field u represents the mechanical displacement of the plate in the normal direction, E represents the electrical field in the normal direction. The result of paragraph III is applied with $B = -\Delta$ defined on $V_B = H^2(\Omega) \cap H_0^1(\Omega)$, $A = -\Delta\Delta$, $D(A) = H^4(\Omega) \cap H_0^2(\Omega)$. Let us defined $F = -\Delta E$, the controller is on the form $v'' = C_1 u' + C_0 u + D_1 F' + D_0 F$. The resulting controller is

$$-\Delta\Delta u'' - \Delta E'' = \Sigma_{j=1}^{4} \widetilde{D}_{4j} \begin{pmatrix} u \\ u' \\ -\Delta\Delta u - \Delta E \\ -\Delta\Delta u' - \Delta E' \end{pmatrix}_j$$

expressed in term of δ and F :

$$-\Delta\Delta B^{-1}(\delta - cE)'' + E'' = \Sigma_{j=1}^{4} \widetilde{D}_{4j} \begin{pmatrix} B^{-1}(\delta - cE) \\ B^{-1}(\delta - cE)' \\ -\Delta\Delta B^{-1}(\delta - cE) - \Delta E \\ -\Delta\Delta B^{-1}(\delta - cE)' - \Delta E' \end{pmatrix}_j$$

Bibliography.

[1] R. Curtain and G. Weiss, *Preprint of the Laboratory of Mathematics, University of Groningen, Netherland (1995).*

[2] A. Benabdallah and F. Ammar Khodja, Stabilisation de l'équation des ondes par un contrôleur dynamique. *C.R.A.S. Paris 321, Série I, pp 195-198 (1995).*

Optimal Placement of Piezoelectric Actuators in Intelligent Structures Using Genetic Algorithms

I. Lee and J.- H. Han

ABSTRACT

Many piezo actuators can be used without increasing costs and weights of corresponding control system with common control command. Piezo actuator configurations which maximizes degrees of controllability are obtained using genetic algorithms(GAs), general optimizers. Optimal placement of piezo actuators is determined for a cantilevered plate, and it is observed that actuator pattern is closely related to the phase of modal control force of each actuator.

INTRODUCTION

In recent years composite materials have been used in several areas of industries including aerospace industries to reduce structural weight and to increase performances. However, these light structures are prone to vibrate more severely than conventional structures. These excess of vibration cause malfunction of structures, sometimes yield disastrous structural failure. So many researchers have studied various ways to reduce vibration levels and to make structures more reliable. Especially in space structure applications an effective vibration control is highly desirable because no air damping is expected. Among the active devices, piezoelectric materials have been drawn attention recently because of their light weight, high force and low power consumption. Also actuator structures are so simple that it is possible to place piezo-actuators with more design freedom. Actuator placement problems have been treated importantly, because misplaced actuators sometimes cannot control certain modes (lack of controllability), or sometimes excite residual modes unnecessarily (control spillover). A number of papers on placement of actuators have been published. Hamdan and Nayfeh [1] proposed a measure of controllability that can be easily calculated and has strong correlation with other proposed measures of controllability. Lammering, Jia, and Rogers [2] treated an optimal placement of piezoelectric actuators in adaptive structures. Lee et al.[3] proposed an electrode shaping method to actuate a particular mode.

Fully-distributed or widely-distributed piezo actuators sometimes suffer from lack of controllability. Therefore segmentations of piezo actuators or a number of small actuators can be used to control more effectively or to control several modes simultaneously. However, lots of electronic components are needed to use a lot of measurements and control commands. So it is not appropriate to increase the number of independent control commands. In this paper a problem of shaping electrodes or placements of piezoelectric actuators has been investigated to enhance their control performances. While maintaining control commands to a limited number, lots of piezo actuators can be used with common control commands. An actuator can be constructed by independent piezo-patches or just by dividing their electrodes properly. So the main purpose of this study is to find an optimal combinations of piezo actuators which has good control performances.

However this problem is a kind of optimal combination problem and the problem size are generally very large. Also the problem itself is a discrete problem and no gradient information exists. Therefore conventional optimization algorithms are not appropriate to solve this problem. In this study a problem of optimal placements has been investigated using Genetic Algorithms which have good characteristics in combinatorial problems.

PROBLEM DEFINITION

An example problem considered here is a cantilevered composite plate with symmetrically bonded piezoelectric materials at its root. The governing equation of this system can be obtained using the finite element method based on the piezo-laminated composite plate theory[3] and the first-order shear deformation

In Lee, and Jae-Hung Han, Dept. of Aerospace Engineering, KAIST, Yusong-gu, Taejon, Korea.

0-8194-2165-0/96/$6.00

plate theory. The material properties are given in Table 1, and the stacking sequence is $[0/\pm 30/90]_S$. The piezoelectric materials are divided into 20 actuators as shown in Figure 1, and each actuator is assigned an indication number(1, 2, ...,20). Notice that dividing actuators does not mean physical dividing of piezo materials. The effective independent actuators can be obtained by dividing electrodes. The governing equations in modal domain are as follows:

$$\ddot{\eta}_r(t) + 2\zeta_r \omega_r \dot{\eta}_r(t) + \omega_r^2 \eta_r(t) = \sum_{i=1}^{m} \overline{B}_{ri} u_i(t) \quad (r = 1,2,\cdots) \tag{1}$$

where η_r is the modal coordinate, ω_r is the natural frequency, ζ_r is the damping ratio, u_i is the control voltage, and $\overline{B}_{ri}$ is an element of modal participation matrix. Actually $\overline{B}_{ri}$ is the rth modal control force caused by the ith unit control command. The first five natural frequencies are 57.78, 95.91, 203.62, 350.67, 392.94 Hz. Let B_{rk} as the rth modal control force caused by the unit control command at the kth actuator, and let a set of actuators which is governed by ith control voltage as U^i. Then $\overline{B}_{ri}$ can be Written as follows:

$$\overline{B}_{ri} = \sum_{k=1}^{n} B_{rk} f(i,k) \tag{2}$$

where

$$f(i,k) = 1 \text{ if } k \in U^i,$$
$$f(i,k) = 0 \text{ if } k \notin U^i \tag{3}$$

The governing equation can be written as the first order space state form as follows.

$$\dot{x} = Ax + Bu \tag{4}$$

As Hamdan and Nayfeh[1] proposed ith mode's gross measures of controllability, ρ_i can be obtained as follows:

$$\rho_i = \|f_i\|_2 \tag{5}$$

where

$$f_i^T = q_i^T B / \|q_i\| \tag{6}$$

where q_i is the ith left eigen vector of system matrix A. The least controllable mode is considered to be critical in many cases, so we define the smallest value of ρ_i as the controllability index for the system. Notice that Kim and Junkins[4] proposed an output measure of controllability with the idea of cost analysis. However, in this study the modal contributions of some of lower modes are equally weighted. The parameters selected in this paper are as follows:

Number of actuators (n) = 20
Number of control input (m) = 2
Inherent damping ζ_r = 0.5%

GENETIC ALGORITHMS

Genetic algorithms (GAs) are search procedures based on the mechanics of natural selection and natural genetics[5]. GAs are particularly powerful in combinatorial problems, and GAs use a domain independent representation, bit-strings. The main idea of GAs is briefly outlined here. After initialization of the first generation, parents are selected according to their relative fitness(objective) values via tournament selection method. In other words those individuals with higher relative fitness are more likely to be selected as parents. The child generation are produced with recombination of selected parents. Some bits of chromosome (bit string structures) of child generation are changed randomly via mutation processes. GAs are considered as general optimizers. Recombination is considered as primary operator which make GAs converge to an extremum very fast, while mutation is a complementary operator which prohibit converging to a local extremum. In order to apply GAs to our actuator placement problem, a bit-structure can be defined as follows:

$$l = a_1 a_2 \cdots a_{20} \tag{7}$$

where

$$a_i = 0 \quad \text{when } i \in U^1,$$
$$a_i = 1 \quad \text{when } i \in U^2 \tag{8}$$

In this analysis 4 objective functions are selected as equation (9). The first three objective functions mean the corresponding mode's controllability measure and the 4th one means system controllability measure.

$$J_1 = \rho_1, \quad J_2 = \rho_2, \quad J_3 = \rho_3, \quad J_4 = \min_{i=1,\ldots,5} \rho_i \tag{9}$$

RESULTS

With the procedures explained in the above, an optimization for configurations of piezoelectric actuators has been conducted using genetic algorithms. The parameters needed in the calculation are as follows:

Population size = 30	Length of chromosome = 20
Maximum number of generation = 30	Crossover probability = 0.8
Mutation probability = 0.05	Select winner of randomly selected 5 individuals.

Best chromosome obtained for each objective is shown in Table 2, and convergence processes are shown in Figure 2. The actuator pattern obtained are plotted in Figure 3, where white areas mean U^1, and hatched areas mean U^2. As shown in Figure 3 (a), using one actuator command is effective in controlling the first mode because there is no cancel out effect. One noticeable fact is that the actuator pattern we obtained is exactly the same as that of the phase of modal control force of each actuator area. As actuator pattern becomes complex, more generations are required to get converged results. The solution obtained in Figure 3 (d) is considered as optimal or near-optimal solution which maximizes performance index J_4, which means controlling the first five modes effectively. With the obtained actuator configuration, closed loop performances are studied using simple control algorithms. Using the direct negative velocity feedback with some predetermined control gains, we find that the degree of damping enhancements is closely correlated with the measure of controllability.

CONCLUSIONS

From this investigations, the following conclusions can be obtained.

1) With the idea of common control commands, lots of piezo electric actuators can be used without increasing costs and weights associated with electronic components.

2) Genetic Algorithms can be used effectively to find optimal patterns of actuators, and it is observed that actuator pattern for controlling a particular mode is determined by the phase of modal control forces.

3) Genetic Algorithms can be applied to maximize observability because there exists a duality between controllability and observability.

REFERENCES

1. Hamdan, A. M. A., and Nayfeh, A. H., "Measures of Modal Controllability and Observability for First- and Second-Order Linear Systems," *Journal of Guidance, Control, and Dynamics,* Vol. 12, No. 3, 1989, pp. 421-428. and Vol. 12, No. 5, 1989, pp. 768.
2. Lammering, R., Jia, J., and Rogers, C. A., "Optimal Placement of Piezoelectric Actuators in Adaptive Truss Structures," *Journal of Sound and Vibration,* Vol. 171, No. 1, 1994, pp. 67-85.
3. Lee, C.- K., and Moon, F. C., "Modal Sensors/Actuators," *Journal of Applied Mechanics,* Vol. 57, 1990, pp. 434-441.
4 Kim, Y., and Junkins, J. L., "Measure of Controllability for Actuator Placement," *Journal of Guidance, Control, and Dynamics,* Vol. 14, No. 5, 1991, pp. 895-902.
5. Goldberg, D. E., *Genetic Algorithms in Search , Optimization & Machine Learning,* Addison-Wesley Publishing Company, Inc., 1989.

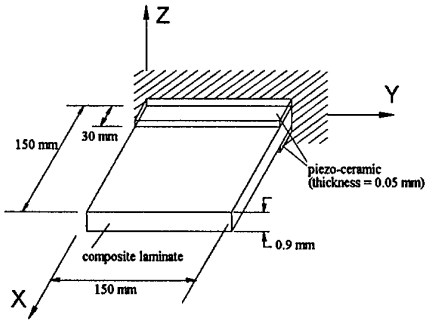
Table 1. Material properties.

	Graphite/Epoxy	Fuji C-82
E_1	1300 GPa	59.0 GPa
E_2	10.0 GPa	59.0 GPa
G_{12}	4.85 GPa	22 GPa
G_{23}	3.29 GPa	21 GPa
ν_{12}	0.31	0.34
t	0.1125 mm	0.05 mm
ρ	1480 Kg / m^3	7400 Kg / m^3
$d_{31} = d_{32}$		−260 pC / N

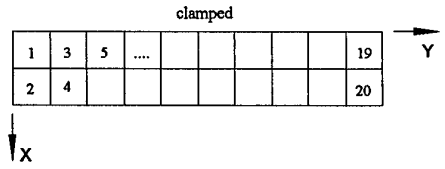
Table 2. Result of Actuator Placement Optimization.

	Best final chromosome	Objective function	*
J_1	0000000000000000000	0.0699	7
J_2	00000000101111111111	0.0516	9
J_3	11110100000000111111	0.0616	15
J_4	10000000000011111111	0.0365	6

* : Generation when best chromosome obtained.



(a) Configuration of overall system.



(b) Piezo actuator numbering.

Figure 1. Configuration and actuator distribution.

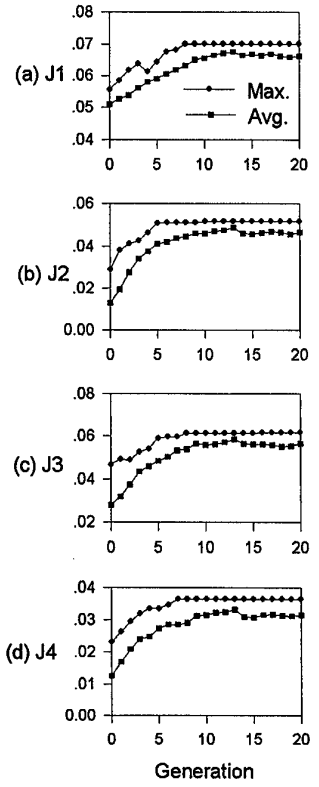


Figure. 2 Convergence process of Genetic Algorithms.

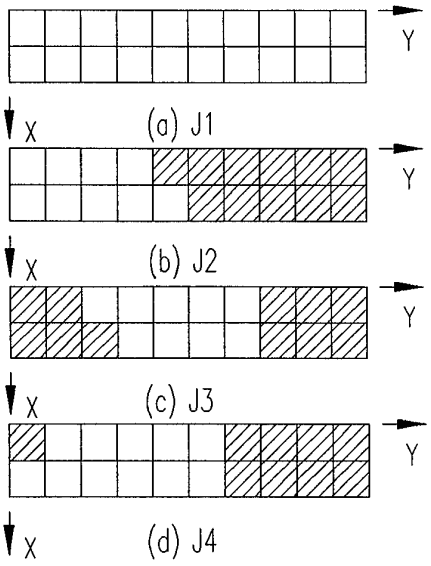


Figure. 3 Actuator patterns for maximizing perfomance indices.

Smart system Model : thin plate with distributed sensors and actiators

M. RAHMOUNE (1), D.OSMONT (2)

(1)CNAM Méchanics (2)ONERA Structure epartement

Abstract :
We propose to adapt the asymptotic model of plate developed by CIARLET[1] to take account specific effects had to the behavior of a piezoelectric device . Then we show how distribute them in the thickness of a stratified composite structure, so as to detect or activate its strains optimal manner.

These last years, devices piezoelectric have revolutionized the art of the engineer. to their specific properties that give them the particularity to transform mechanical energy in electrical energy and conversely. The inclusion of these devices in stratified structures allows to produce or to identify strains of the structure. If these devices piezoelectric are thick, they modify its mass and its stiffness important manner. What disturbs its behavior during its service. This is why one has generally resorted to devices piezoelectric thins. Our study limits therefore to this framework. It consists in make the analysis of the behavior of these devices when it are isolated, manner to better surround their action on the rest of the structure.
Asymptotic techniques show us that one ends naturally to the Kirchhoff-Love displatement and that, on the one hand, the potential is necessarily linear in the thickness of the thin homogeneous device piezoelectric, and that on the other hand, the transverse polarization of this device produces only the stretching strain. By taking account values of coefficients piezoelectric correlated to the electrical field, one has noticed that the electrical field has to be raised if one wants to obtain from significant mechanical effects.
The electrical equation allows us to express the electrical field according to the strain. After substitution of the electrical field in the equilibrium equation, one returns to a linear elasticity problem .
One shows that the polarization thin device transverse product also of the flexion., if values of coefficients piezoelectric are more large.

On justifies the utilization of thin piezoelectric devices in the manufacture of smart structures. One shows that the extension strain of the piezoelectric device pasted on an elastic structure entails its flexion. It is necessary therefore at least two active devices (actuators) to produce the bending independently of the extension strains.The two devices induce therefore a couple of forces that bending the structure. It is important to power act separately on each device, therefore the discontinuity of the electrical field is essential to act on each layer independently. The action of a uniform transverse polarization on the smart system bending is null.
One show also that an alone device suffices to detect all strains, but without no precision on their natures (bending or stretching strain). to have an completes information on the two types of strains, one has two passive devices (sensors) symmetrically by report to the average plan of the structure. This allows to establish two independent relationships that separates the bending and stretching strain detection. Here also, the electrical equation allows to express the electrical field as function to the strain. The substitution of the electrical field by its expression in equilibrium equations returns us to a linear elasticity problem where the bending and stretching strains are ins uncoupled. One multilayer supplied four devices piezoelectricly had symmetrically whose two are passive (sensors) and two assets (actuators), is a smart system. Indeed, the amplified sensor signal then used to excite the actuators, generates an feedback effect that allows an autonomous control of the structure.
In general, bending modes and membrane modes are naturally separated. This explains the choice of the smart system is threelayers in the dynamic case. This threelayers is constituted with a actuator and a sensors disposed symmetrically on the two faces of a composite structure.
On has developed a finite element to undertake the calculation of the displacement in return for a

0-8194-2165-0/96/$6.00

modification of the piezoelectric constitutive law in a linear elastic onstitutive law. One has restrained to the numerical resolution of a three layers where one has separated the study of the sensor of that the actuator. In the study of the actuator, the electrical field is introduced as a force to knew. In the study of the sensor, one begins by calculating the displacement then one calculates the electrical field in post - processing from values of the diplacement.
In the practice, one knows to impose (or to detect) only the potential uniforms on faces of devices piezoelectric. It is therefore difficult to detect (or to act) all strains at the same time. This is why one proposes a study of a distribution of these devices in the form of pasted pastilles symmetrically on the two faces of the main structure. This distribution designates here is a distribution of devices of small carve,or a distribution of electrodes soldered on a device piezoelectric. These distributions allow to detect (or to generate) separately the various components of the strain. For distributions of an important number of pastilles piezoelectric, one proposes a technique of homogenization.

I - Thin homogeneous piezoelectric device model :
One considers Ω_ε a open domain busy by a homogeneous piezoelectric material characterized by elastic coefficients a^ε_{ijkl}, piezoelectric coefficients $e^\varepsilon_{k,ij}$ and dielectric coefficients c^ε_{ij} One notes $\Sigma^{+\varepsilon}$ its face superior, $\Sigma^{-\varepsilon}$ its inferior face and Γ^ε its lateral face.More precisely, ω is opened an R^2 of enough regular frontier. $\partial\omega$ One defines:
$\Omega_\varepsilon = \omega\times]-\varepsilon,\varepsilon[$ and $\Sigma^{+\varepsilon} = \omega\times\{\varepsilon\}$, $\Sigma^{-\varepsilon} = \omega\times\{-\varepsilon\}$ and $\Gamma^\varepsilon = \gamma\times]-\varepsilon,\varepsilon[$ where $\gamma = \partial\omega$.
One supposes that it is armoured on $\Gamma^\varepsilon_0 = \gamma_0\times]-\varepsilon,\varepsilon[$ and free on $\Gamma^\varepsilon_1 = \gamma_1\times]-\varepsilon,\varepsilon[$, where $\gamma^\varepsilon_1 \cup \gamma^\varepsilon_0 = \partial\omega$.
where ε is a real positive that tends to zero. i, j, k and l are indices that vary from 1 to 3.
one will designate by σ and ε stress and strain tensors, and by D, E displacement vectors and electrical field. One notes u the displacement, and φ the potential electric.
The problem consists in find (u, φ) : $\Omega_\varepsilon \rightarrow \mathbf{R}^3\mathrm{x}\mathbf{R}$ satisfying next equations:
Equation of the movement:

$$\begin{cases} \mathrm{div}\sigma^\varepsilon = f^\varepsilon \\ \mathrm{div}D^\varepsilon = 0 \end{cases} \quad \text{dans } \Omega_\varepsilon \qquad (1)$$

The bondary condition :
In a first time, one imposed a potential on the two faces of the device (actuator) such that:

$$\begin{cases} \varphi^\varepsilon = V^\varepsilon & \text{sur } \Sigma^{+\varepsilon} \\ \varphi^\varepsilon = 0 & \text{sur } \Sigma^{-\varepsilon} \end{cases} \qquad (3)$$

$$D^\varepsilon_\alpha n_\alpha = q^\varepsilon \quad \text{sur } \Gamma^\varepsilon \qquad (4)$$

In a second time, the potential is not know, where the device (sensor) is submissive to mechanical constraints only.
The constituyive law :

$$\begin{cases} \sigma^\varepsilon = a\varepsilon(u^\varepsilon) - e^t E(\varphi^\varepsilon) \\ D^\varepsilon = e\varepsilon(u^\varepsilon) + cE(\varphi^\varepsilon) \end{cases} \qquad (5)$$

$$\begin{cases} \varepsilon(u^\varepsilon) = \frac{1}{2}(\nabla u^\varepsilon + \nabla^t u^\varepsilon) \\ E(\varphi^\varepsilon) = -\nabla\varphi^\varepsilon \end{cases} \qquad (6)$$

The variational problem associate to the problem descib above is the next form

$$\begin{cases} \text{Find } (u^\varepsilon, \varphi^\varepsilon) \text{ in } \mathbf{V} \\ B((u^\varepsilon, \varphi^\varepsilon),(v^\varepsilon, \psi^\varepsilon)) = L(v^\varepsilon, \psi^\varepsilon) \quad \forall (v^\varepsilon, \psi^\varepsilon) \in \mathbf{V} \end{cases} \qquad (7)$$

where V is the admissible solution space defines by:

$$\mathbf{V}=\left\{v^{\varepsilon},\psi^{\varepsilon}\in H^1(\Omega_\varepsilon)^3\times H^1(\Omega_\varepsilon)/\ v^{\varepsilon}_{/\Gamma_0^{\varepsilon}}=0,\ \psi^{\varepsilon}_{/\Sigma^{+\varepsilon}}=V^{+\varepsilon}\ \text{et}\ \psi^{\varepsilon}_{/\Sigma^{-\varepsilon}}=0\right\} \tag{8}$$

and

$$\begin{cases} B((u^{\varepsilon},\varphi^{\varepsilon}),(v^{\varepsilon},\psi^{\varepsilon}))=\displaystyle\int_{\Omega_\varepsilon}\sigma(u^{\varepsilon},\varphi^{\varepsilon})\varepsilon(v^{\varepsilon})+D(u^{\varepsilon},\varphi^{\varepsilon})E(\psi^{\varepsilon}) \\ L(v^{\varepsilon},\psi^{\varepsilon})=\displaystyle\int_{\Gamma_\varepsilon}D^{\varepsilon}_{\alpha}n_{\alpha}\psi^{\varepsilon} \end{cases} \tag{9}$$

One supposes that $q^{\varepsilon}\in L^2(\Gamma_\varepsilon)$, a^{ε}_{ijkl} and, $c^{\varepsilon}_{ij}.\in L^{\infty}(\Omega^{\varepsilon})$ (10)

$$B((u^{\varepsilon},\varphi^{\varepsilon}),(u^{\varepsilon},\varphi^{\varepsilon}))=\int_{\Omega_\varepsilon}[a]\varepsilon(u)\varepsilon^{t}(u)+[c]E(\varphi)E^{t}(\varphi) \tag{11}$$

As wombs, elasticity and dielectricity are defined positive it comes that:

$\exists\alpha_1\rangle 0$ et $\alpha_2\rangle 0$ such that :

$$\forall\ \tau_{ij}(\tau_{ij}=\tau_{ji})\in L^2(\Omega_\varepsilon)\ \text{et}\ \forall\ E_i\in L^2(\Omega_\varepsilon)\ \text{on a :} \tag{12}$$

$$B((u^{\varepsilon},\varphi^{\varepsilon}),(u^{\varepsilon},\varphi^{\varepsilon}))=\alpha_1\left\|u^{\varepsilon}\right\|^2_{H^1(\Omega_\varepsilon)}+\alpha_2\left\|\varphi^{\varepsilon}\right\|^2_{H^1(\Omega_\varepsilon)}$$

B(.,.) is therefore V - elliptic, multilenear and continuous. L is a continuous linear form. Under these hypothesis Lax-Milgram allows us to assert the existence and uniquesses of a solution .

I-1 Aspect actuator of a thin homogeneous device:

One is interested in this paragraph, to the indirect effect of the piezoelectricity, by imposing a potential V^{ε} on the surface superier.of the device and a null potential on the inferior surface.

I - 1.1 Drawn toscale Placement of the potential and the electrical density :

By supposing that $V+^{\varepsilon}\ \in H^{\frac{1}{2}}(\Sigma^{+\varepsilon})$, there exists therefore a continuous recovery in. $H^1(\Omega_\varepsilon)$ to $H^{\frac{1}{2}}(\Sigma^{+\varepsilon})$. One builds now a recovery of V that one notes $\varphi^{0\varepsilon}$ it defines by:

$$\varphi^{0\varepsilon}=\frac{v^{+\varepsilon}}{2\varepsilon}x_3+\frac{v^{+\varepsilon}}{2} \tag{13}$$

One writes therefore a unique manner under the next form:

$$\varphi^{\varepsilon}=\varphi^{0\varepsilon}+\phi^{\varepsilon}\ \text{où}\ \phi^{\varepsilon}\in H^1_0(\Omega_\varepsilon) \tag{14}$$

Remark:

This restriction to a null potential on one of faces allows to establish the inequality of Poincaré. One could have follow the same step for potentials non nulls on the two faces by noticing that the inequality of the Poincaré remains valid in the space $H^1(\Omega_\varepsilon)$ /**R** since potentials are determined to a constant near.

By resuming the asymptotic technique used by CIARLET [1] to establish the Kirchhoff-Love.model For the elastic part resumes some exactly the same step. For piezoelectric and dielectric parts one adopts the same technique. One plans especially, to establish the suitable order of the drawn to scale placement of the value of the electrical potential on the face superior of the device and the electrical density on its lateral face. The linear recovery builds above is completely determined by it giving on the face superior. One shows therefore that in order that the posed problem above admits a limit, it is necessary to take at least $V^{+\varepsilon}$ and q^{ε} in the order ε^3 for ϕ^{ε} order ε^2

I -1.2 Thin actuator thin Model:

One returns to a geometry fixes Ω independently ε , by making the change of variable proposed in [1] on the displacement and one considers that the material coefficients are independent ε. And one puts a priori the

change of variable following:

$$\varphi^{\varepsilon}\left(x^{\varepsilon}\right)=\varepsilon^{2}\phi(\varepsilon)(x)+\varepsilon^{3}\varphi^{0}(\varepsilon)(x) \quad \text{and} \quad \psi^{\varepsilon}\left(x^{\varepsilon}\right)=\varepsilon^{2}\chi(\varepsilon)(x)+\varepsilon^{3}\psi^{0}(\varepsilon)(x) \quad (15)$$

After substitution of the various functions, indiced by ε, by their defined expressions above, and by taking into account the ellepticity and the continuity of the form bilineair B and the continuity and the linearity of the operator L. One shows that the potential (resp. the displacement) is staked in $H^{1}\left(\Omega\right)$ (resp. in $H^{1}(\Omega)^{3}$). There exists therefore one under-noted $\left(u(\varepsilon),\varphi^{0}(\varepsilon)+\phi(\varepsilon)\right)$ $H^{1}(\Omega)\times H^{1}(\Omega)^{3}$. continuation that converges feebly in. $H^{1}(\Omega)\times H^{1}(\Omega)^{3}$.

This allows us to establish the Kirchhoff-Love displacement for the elasticity part, and the expression of the asymptotic electrical potential following:

$$\varphi=\frac{v^{+}}{2}x_{3}+\frac{v^{+}}{2}-\int_{-1}^{x_{3}}E_{3}\left(\phi^{*}\right)dy_{3} \qquad (16)$$

where ϕ^{*} is the weak limit of $\varepsilon^{-1}\phi(\varepsilon)$; $\phi^{*}=\int_{-1}^{x_{3}}E_{3}\left(\phi^{*}\right)dy_{3}$ belong to $H_{0}^{1}\left(\Omega\right)$.

The electrical equation allows us to show that $E_{3}\left(\phi^{*}\right)$ is independent of x_{3}. Consequently the potential is null. The potential induced ϕ^{*} by the strain of the actuator is negligible ahead the potential imposed on its edge. The electrical potential is therefore completely determined by its values to the edge.

The asymptotic constitutive law is therefore the next form:

$$\begin{cases}\sigma_{\alpha\beta}(0)=a_{\alpha\beta\gamma\delta}\varepsilon_{\gamma\delta}-e_{3\alpha\beta}E_{3}\\ D_{3}(0)=e_{3\gamma\delta}\varepsilon_{\gamma\delta}-c_{33}E_{3}\end{cases} \qquad (17)$$

This justifies the hypothesis considers only stress plan and that normal vector components of the field and electrical displacement in thin piezoelectrc devices.

The displacement is linear in the thickness, one introduces notations of the effort stretching $N_{\alpha\beta}$ and the moment $M_{\alpha\beta}$. The constitutive law becomes therefore:

$$\begin{cases}N_{\alpha\beta}=2a_{\alpha\beta\gamma\delta}\gamma_{\gamma\delta}-2e_{3\alpha\beta}E_{3}\\ M_{\alpha\beta}=\frac{2}{3}a_{\alpha\beta\gamma\delta}\partial_{\gamma\delta}\omega\end{cases} \qquad (18)$$

The electrical field is coupled only to the stretching strain. This implies that the transverse electrical polarization of a thin piezoelectrc device produces only the stretching strain.

I - 2 . Aspect sensor of thin homogeneous piezoelectrc device:

One uses in this paragraph the direct effect of piezoelectricity to describe the sensor role of the piezoelectric device .

The domain Ω_{ε} busy by the piezoelectric device sudden maintain a force of body density f_{i}^{ε} and a force of surfacique density g_{i}^{ε} on these two faces superior and inferior. $\Sigma^{\pm\varepsilon}$ One maintains the null potential on the inferior face by the dispositif. En posing the same change of variable proposed in the case actuator and the same change of variable on forces them that in [1]. By following the same step, one ends to the same result. The potential is linear, it suffices then to know the values of the potential on the face superior to determine completely the potential. The electrical equation allows us to express the electrical field as funcion of the stretching strain:

$$E_{3}=\frac{e_{3\gamma\delta}}{c_{33}}\gamma_{\gamma\delta} \quad . \qquad (19)$$

Alone the stretching strain is detected. On able determine the displacement by modifying the constitutive law . One returns therefore to a elasticity problem whose constitutive law is the following:

$$\begin{cases} N_{\alpha\beta} = \left[2a_{\alpha\beta\gamma\delta} - \dfrac{2e_{3\alpha\beta}e_{3\gamma\delta}}{c_{33}} \right] \gamma_{\gamma\delta} \\ M_{\alpha\beta} = \dfrac{2}{3} a_{\alpha\beta\gamma\delta} \partial_{\gamma\delta}\omega \end{cases} \qquad (20)$$

The electrical field will be determined in post - processing from values of he displacement.
Remark:

By supposing that one terms $e^{\varepsilon}_{\alpha\gamma\delta}$ is $\dfrac{1}{\varepsilon}$ time more large that the largest $e^{\varepsilon}_{3\gamma\delta}$, one shows that the transverse polarization of the device produces also the flexion.

II Multilayer plate whose some are piezoelectric layers :

One distinguishes two natural aspect devices piezoelectric. An aspect actuator that active the straints of the plate. And a aspect sensor that detects its strains.
By leaving from a multilayer, one proposes a rigorous strategy of the position of devices in its thiknes so as to activate or detect its movement a multilayer of an optimal manner.

II - 1 Aspect actuator:

the transverse polarization of a device actuator piezoelectric produces only the stretching The diplacement in service of a actuator, pasted on an elastic structure, entails its flexion. It is therefore reasonable to have the actuator symmetrically by report to the mid structure, to act independently on the two type of strains.The effect of the obtained bending will be as much more important than devices will be distanced the mid surface of the global plate. This justifies to paste device actuator on the faces of plate.

II - 2 Aspect sensor:

An alone sensor device can detect all the strains without no precision on its nature. To detect separately the bending and the stretching strain, one has sensors symmetrically by report the mid surface of the multilayers.
This allows us to establish the two next relationships:

$$\begin{cases} E_3^{+p} + E_3^{-p} = -\dfrac{2e_{3\gamma\delta}}{c_{33}} \gamma_{\gamma\delta} \\ E_3^{+p} - E_3^{-p} = -\dfrac{2e_{3\gamma\delta}z_p}{c_{33}} \partial_{\gamma\delta}\omega \end{cases} \qquad (21)$$

where p designates the busy layer by the sensor p and -pits conjugated. zp.et -zp. are respectively quotations of the two sensors conjugated.
On can therefore return to a problem of elasticity by modifying the law of behavior, by substituting the electrical field by its expression according to the strains. The electrical field and potential will be calculated in post-traitement.
Le electrical signals induced by the bending is all the more important that sensors will be distanced the midsurface of the global plate. To have a good electrical output it's important to place sensors on faces of the structure stratified.

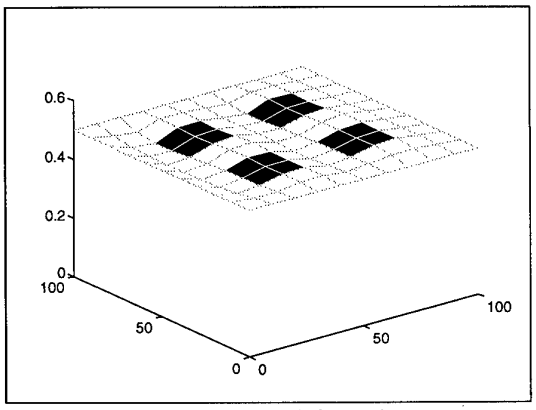
III The piezoelectric devices distribution on the two faces of a composite structure:

In practice, one knows imposed only the potential uniform and to detect only the average of the potential on the section of measure. It is therefore very difficult to detect (or to generate) all strains at the same time. This is why one uses a distribution of devices that to allow to detect (or to generate) separately the various components of the strains. For a distribution of a large number of piezoelectric devices , one proposes to develop a homogenization technique . On considers therefore that devices are distributed periodically and

that the each device size is very large ahead the thickness of the global plate. The non homogeneo problem us in the cell of basis is a linear elasticity problem. One returns therefore to a homogenization problem of a structure to elastic inclusion . For more details the reader return to G. ALLAIRE [2] and especially to the thesis of H.DUMONTET [3] The definition of homogenization proposed in G.ALLAIRE allows us concentrated our study on the homogeneous coefficient determination, taking into account the local equation defines on a cell of basis.By following the same technique to use by H.DUMONTET, one ends to the same type of equation described in.[3] This study shows the influence of the geometry of devices on the global behavior of the structure.
The optimization of the geometry can be foreseeable for a good output of these devices. The homogenization hypothesis imposes that the devices distribution is periodic or quasi-periodic. For the optimized the position of the device, one envisages others methods that to allow to put in obviousness the role impotant of the position of device in the detection and the actuation of the different strains.

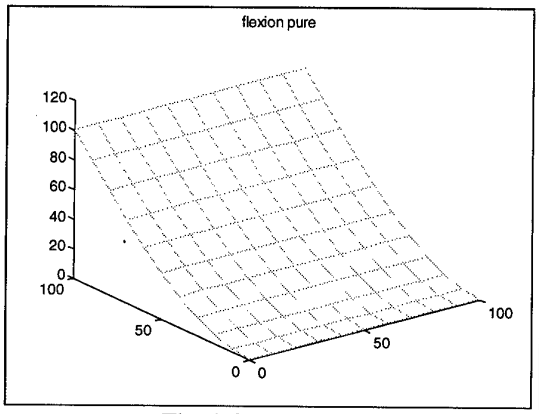
VI Numerical example:
One has undertaken the development of a rectangular finished element switchboard, so as to caculated the displacement then one has evaluated the field and the electrical potential from values of the diplacement.

VI-1 Aspect actuator:
One supposes therefore to study the behaviour of a squared side plate 10 cm and thickness 1 mm, characterized by a Young moduleE = 23 GPA and a Poisson coefficient υ =0.3. One covers respectively the two faces of this plate by four actuators identical of thickness 0.5 mm. and similarly elastic characteristic that the plate, and coefficient piezoelectrics $e_{311} = e_{322}$=0,14 C/m^2 et c_{33}=11.e^9. On imposes a null potential on the two face of the plate, and 50 V on faces superior of devices of the over, and -50 V on inferior device faces of dessous.On obtains the deformed following:

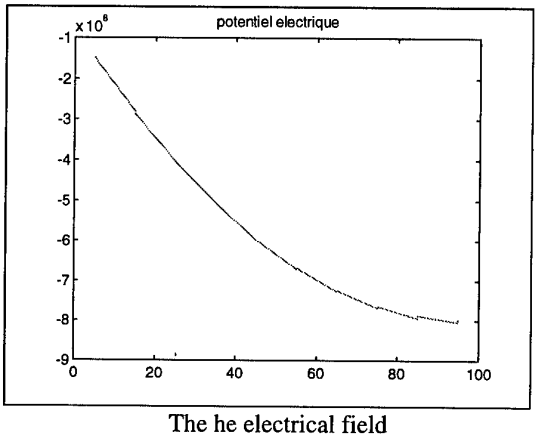


The structure deformed

VI - 1 sensor Aspect:
Taking into account the even plates that one covers it now completely these two faces by the same devices. One armours this three layer on an edge and one imposes a displacement on the edge oppsite one has therefore the deformed and the electrical field following:



The deformed (view of profile)



The he electrical field

Conclusion:

The purpose of this study was to examine how to take counts the influence of devices piezoelectric in the structural models of plates, and to show that handling piezoelectric effects could be made, in general, by modifying the elastic constitutive law and by compting a posteriori the potential once the displacement determined.

As an extension of this work we are using this thecnique to detect the material deffects.

References

[1] P-G. CIARLET,Plate and junction in elastic multi-structures an asymptotic analysis, Série RMA 14, Masson (1990).

[2] D. CAILLERIE, Thin elastic and periodic plates. Math. Meth. in Applied Sciences, Vol 6 (1984), p.159.

[3] H. DUMONTET:Thèse de Doctorat d'Etat : Homogénéisation et effets de bords dans les matériaux composites (juillet 1990).

Dynamic Analysis of Piezoelectric Actuator Bonded on Beam

Xiaoming Wang*

State Key Laboratory of Mechanical Structural Strength and Vibration
Xian Jiaotong University
Xian, Shaanxi, 710049, China

Claus Ehlers and Manfred Neitzel

Institut für Verbundwerkstoffe GmbH,
University of Kaiserslautern
67663, Kaiserslautern,Germany

ABSTRACT

The dynamic behavior of piezoelectric actuators bonded on structures are completely different from its static behavior. The strong interaction between actuators and host structures delivers the response of actuators and associated power supply to be closely dependent on the dynamic state as well as the configuration of the host structures. The paper presents a new electro-mechanical dynamic model of a pair of actuators featuring the combination of an in-plane longitudinal wave induced by the piezoelectricity and transverse vibration concordant with the bending vibrating of the actuator-bonded beam. The analytical results display that both kinds of movement of piezoelectric actuator are coupled with each other and deeply involved into the bending vibrating of the beam. Moreover, its in-plane displacement and velocity reponse to the exciting voltage imposed across the actuators are affected not only by the resonant frequency of a bending vibrating of the beam, but also by the resonant frequency of a longitudinal wave of the piezoelectric actuator and the virtual eigen frequency of longitudinal wave of the actuator which is imaged to have the same length as the beam.The final results show that the electrical admittance of the actuator is contributed by a static, dynamic capacity of the actuator and also has the dedication of both longitudinal wave and transverse vibration coupled with the bending vibrating of the beam.

Key words : Piezoelectric, actuator, dynamic response, admittance, smart structures, beam

1. INTRODUCTION

The wide use of the piezoelectric elements as actuators in the smart structures make many people devote themself to investigate the interaction between the actuators and the host structures. The starting point of an analytical model to reveal the actuation mechanism of piezoelectric elements bonded on or embedded in beams was suggested by Crawley and Luis[1]. Under the assumption of pure one-dimensional shear in the bonding layer and pure extensional strain in the piezoelectric element bonded on or the linear strain distribution of the actuator embedded in a Bernoulli-Euler beam, the actuating force and moment generated by the actuator subjected to exciting voltage were estimated by using static analysis. Based on the strain energy conservation Wang and Rogers [2] considered that the effective moment induced by actuator was equal to one associated with assumed strain distribution on the beam cross section. As a result, the pure tension, pure bending or combined deformation of the beam was realized by applying different phases of the exciting voltage imposed across the upper and the lower piezoelectric

* Present address: Institut für Verbundwerkstoffe GmbH (see above)

0-8194-2165-0/96/$6.00

actuators. They[3] also presented the model based upon CLPT theory to predict the deformation of laminated plates with embedded finite-length, multiple-layer induced strain actuator patches. The Heaviside function was introduced to describe the size and location of actuators to facilitate the analysis.

It is true that the attached actuators on structures are able to control the deformation and movement of the host structures, but it is inevitable that some features of the host structures will be changed due to the integration of actuators. Kirby etc.[4] found that the local stiffening and additional mass of surface bonded piezoelectric actuator change both the resonant frequency of the structures as evidence of pole shift from original frequency and zero shift related to distortion of mode shape. Yang and Lee[5] also pointed out the effect of the actuators on the natural frequency of beam. These effects should be even taken into account in the optimal design of the placement of piezoelectric actuators in beams and plates[6].

By contrast, the behaviors of actuators are also greatly impacted by host structures. As known, it is very significant to know the power supply and consumption of the actuators in the pratical application. Particularly, the electric energy consumption is related to the heat rise which probably could generate high temperture to exceed the Curie temperature and result in the loss of piezoelectric characteristic of actuators[7]. In this regard, Liang etc.[8] applied the impedance method to analyse the electric admittance of the actuators, which turned out to be deeply effected by the resonant frequency of host structures. This method is widely used to investigate the several dynamic behavior of smart structures with piezoelectric actuators[9,10,11,12,13]. It is neccessary to point out that the model of the impedance method is based on the implicate assumption which the dynamic equations of piezoelectric actuator are independent of the dynamics of host structures, and the relation between them is on the basis of the deformation compatibility and force equilibrium on their contact or connection region which is only a point, meanwhile the piezoelectric actuator has only the movement resulting from in-plane wave. Evidently, the movement of the piezoelectric actuator is at least composed of the in-plane wave induced by exciting voltage and another form of the vibration concordant with vibrating of host structures unless the induced movement of actuation has the same kind as the host structures, such as the longitudinal wave in the piezoelectric stack and bar.

This paper presents a new electro-mechanical dynamic model of piezoelectric actuators bonded on beams by considering the coupling between the in-plane longitudinal wave excited by imposed voltage and the out-of-plane vibration compatible with the beam, and derives the related dynamic equations in detail. The velocity distribution and the electrical admittance of actuators will be given. The effects of the host structures and the coupling characteristic movement on the dynamic behavior of actuators will be explicitly expressed.

2. DYNAMICS OF PIEZOELECTRIC ACTUATOR BONDED ON BEAMS

The Bernoulli-Euler beam rather than other complicated beam model is now applied because the paper just aims to clarify the dynamics of actuators. As shown in Fig.1, when a pair of piezoelectric actuators are bonded on the lower and upper surface of the beam and imposed by the out-of-phase electric voltage, the in-plane displacement u_a of the piezoelectric actuator should be composed of the extension deformation u_t and displacement u_t which conforms to the bending of the beam which displacement distribution u_s is also changed, that is

$$u_a = u_t - z\frac{\partial w}{\partial x} \quad , \quad u_s = z(\frac{u_t}{h_s} - \frac{\partial w}{\partial x}) \tag{1}$$

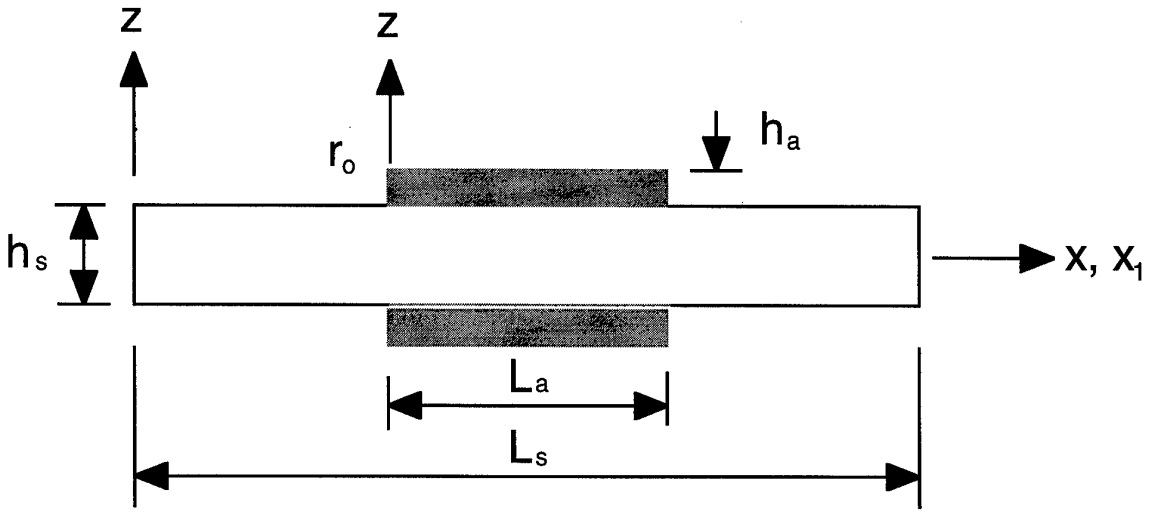


Fig.1 Configuration of actuator-bonded beam

where w is the transverse displacement at the neutral plane of the beam.The associated strain distribution on the cross section of the actuator and beam is then described by

$$\varepsilon_a = \frac{\partial u_t}{\partial x} + z\kappa \quad , \quad \varepsilon_s = \frac{z}{h_s}\frac{\partial u_t}{\partial x} + z\kappa \tag{2}$$

where κ is the curvature of the beam and equal to $-\frac{\partial^2 w}{\partial x^2}$ for the Bernoulli-Euler beam. With the use of constitutive relation of the piezoelectric materials

$$\varepsilon_a = \frac{1}{Y_a}\sigma_a + d_{31}E \tag{3}$$

it is not difficult to get the normal force P on the actuator cross section and the moment M on the combined cross section of the actuator and the beam, they are

$$P = Y_a h_a(\frac{\partial u_t}{\partial x} - d_{31}E) + \frac{1}{2}Y_a Q_a \kappa$$

$$M = (Y_a I_a + Y_s I_s)\kappa + (Y_a Q_a + \frac{Y_s I_s}{h_s})\frac{\partial u_t}{\partial x} - Y_a Q_a d_{31} E \tag{4}$$

where σ is the normal stress on the cross section, E is the exciting electric field imposed across both actuators, d_{31} is the piezoelectric constant, and Y, I represent the Young's modulus and the moment of inertia of the cross section area, the subscript 'a' and 's' denote the actuator and beam repectively. $Q_a = bh_a(2h_s + h_a)$, here b is the width of beam and actuator, 2h is the thickness. When the actuator-bonded beam is excited by piezoelectric actuator and vibrating transversly, the dynamic equilibrium for the actuator and actuator-bonded beam requires

$$\frac{\partial P}{\partial x} = \rho_a A_a \frac{\partial^2 u_t}{\partial t^2} - \frac{1}{2}\rho_a Q_a \frac{\partial^3 w}{\partial x \partial t^2}$$

$$\frac{\partial^2 M}{\partial x^2} = (\rho_a A_a + \rho_s A_s)\frac{\partial^2 w}{\partial x^2} - (\rho_a I_a + \rho_s I_s)\frac{\partial^4 w}{\partial x^2 \partial t^2} \tag{5}$$

Substituting equation (4) into (5), we have the dynamic governing equations for the extension of the piezoelectric actuator and transverse displacement of the actuator bonded beam as following

$$\frac{\partial^2 u_t}{\partial x^2} - \frac{\rho_a}{Y_a}\frac{\partial^2 u_t}{\partial t^2} = \frac{Q_a}{2h_a}\frac{\partial}{\partial x}\left(\frac{\partial^2 w}{\partial x^2} - \frac{\rho_a}{Y_a}\frac{\partial^2 w}{\partial t^2}\right)$$

$$(Y_a I_a + Y_s I_s)\frac{\partial^4 w}{\partial x^4} + (\rho_a A_a + \rho_s A_s)\frac{\partial^2 w}{\partial t^2} - (\rho_a I_a + \rho_s I_s)\frac{\partial^4 w}{\partial x^2 \partial t^2} = (Y_a Q_a + \frac{Y_s I_s}{h_s})\frac{\partial^3 u_t}{\partial x^3} \tag{6}$$

It is necessary noting that although the piezoelectric term in equations (4a, b) are not included into the dynamic governing equation, two terms are equivalent to the situation that both ends of the actuator at $x = r_0$, $r_0 + l_a$, shown as in Fig 1, are subjected to the traction $Y_a h_a d_{31} E$, and the actuator-bonded beam suffers from the moment $Y_a Q_a d_{31} E$ at the same place. With the combination of above additional conditions due to the actuation and the boundary conditions of the beam, the equations (6) could be solved in principle. Then the velocity and strain distribution on the actuator are obtained without any difficulty. By using the constitutive relation of piezoelectric materials

$$D = Y_a d_{31} E + (\in - d_{31}{}^2 Y_a) E \tag{7}$$

we are able to have the the electric current

$$I = \int_A \dot{D} dA \tag{8}$$

where D is the electric displacement and $\in$ is the dielectric constant.

3. DYNAMIC ANALYSIS OF A SIMPLE SUPPORTED BEAM WITH BONDED ACTUATORS

As known in equation (6), the coupling between the longitudinal wave in the actuator and the bending of actuator-bonded beam make the solution of dynamic problem to be very difficult. However, if the piezoelectric actuator is small enough compared to the beam, and has ignorable effect on the global dynamic behavior of the beam, the equation (6b) is simplified into

$$Y_s I_s \frac{\partial^4 w}{\partial x^4} + \rho_s A_s \frac{\partial^2 w}{\partial t^2} - \rho_s I_s \frac{\partial^4 w}{\partial x^2 \partial t^2} = 0 \tag{9}$$

Considering the moment induced by actuation to impose the simple supported beam at both ends of the actuator, we can obtain transverse displacement of the vibrating beam [14,

$$w = \sum_{n=1}^{\infty} \frac{W(n) Y_a d_{31} E}{(\omega^2 - \omega_s^2(n))} \sin\frac{n\pi x}{l_s} e^{i\omega t} \tag{10}$$

since the electric field generated by exciting voltage V imposed on the actuator is

$$E = \frac{V}{h_a} e^{i\omega t} \tag{11}$$

where $i = \sqrt{-1}$, $W(n)$ and $\omega_s(n)$ describe the mass density dependent geometrical parameter and resonant frequency of the actuator-bonded beam, they are

$$W(n) = \frac{2n\pi Q_a}{\rho_s A_s + \rho_s I_s (\frac{n\pi}{l_s})^2} (\cos\frac{n\pi r_0}{l_s} - \cos\frac{n\pi (r_0 + l_a)}{l_s})$$

$$\omega_s^2(n) = \frac{Y_s I_s (\frac{n\pi}{l_s})^4}{\rho_s A_s + \rho_s I_s (\frac{n\pi}{l_s})^2} \qquad (n = 1,2,3,\ldots) \tag{12}$$

The in-plane longitudinal displacement of the actuator is then obtained with the superposition of two parts where one is the solution of the actuator subjected to the traction $Y_a h_a d_{31} E$ at the boundary of the actuator, another is one resulting from the forced vibration as consequence of the coupling term at the equation (6a), that is

$$u_t = \left\{ (A\sin kx_1 + B\cos kx_1) + \sum_{m=1}^{\infty} \frac{Y_a d_{31} E}{(\omega^2 - \omega_a^2(m))} \left[\sum_{n=1}^{\infty} \frac{G(m,n)(\omega^2 - \omega_{as}^2(n))}{(\omega^2 - \omega_s^2(n))} \right] \cos\frac{m\pi x_1}{l_a} \right\} e^{i\omega t} \tag{13}$$

where $x_1 = x - r_0$, and

$$A = \frac{P}{kh_a} \quad , \quad B = \frac{P(\cos kl_a - 1)}{h_a k \sin kl_a} \tag{14}$$

the mass density dependent parameter $G(m,n)$ is

$$G(m,n) = \frac{Q_a}{2h_a} W(n) (\frac{n\pi}{l_s}) \left[\frac{2}{l_a} \int_0^{l_a} \cos\frac{n\pi(x + r_0)}{l_s} \cos\frac{m\pi x}{l_a} dx \right] \tag{15}$$

the wave number k and longitudinal resonant frequency $\omega_a(m)$, $\omega_{as}(n)$ are

$$k^2 = \frac{Y_a}{\rho_a}\omega$$

$$\omega_a^2(m) = \frac{Y_a}{\rho_a}(\frac{m\pi}{l_a})^2 \qquad (m = 1,2,3,\ldots) \tag{16}$$

$$\omega_{as}^2(n) = \frac{Y_a}{\rho_a}(\frac{n\pi}{l_s})^2 \qquad (n = 1,2,3,\ldots)$$

It is interesting that the existance of the frequency $\omega_{as}(n)$ which is now named virtual eigen frequency of longitudinal wave because it is equal to the resonant frequency of the longitudinal wave of the actuator which has the imaginary length l_s and is the same as of the beam. Moreover, the influence of the bending resonant frequency $\omega_s(n)$ of the beam on u_t is undeterminable when $\omega = \omega_s(m) = \omega_{as}(n)$, namely

$$\frac{c_a}{c_s} = \frac{n\pi}{l_s} \tag{17}$$

where c_a are the velocity of the longitudinal wave in the piezoelectric actuator, and c_s is the velocity of the bending wave of the beam, i.e.

$$c_a = \sqrt{\frac{Y_a}{\rho_a}} \quad , \quad c_s = \sqrt{\frac{Y_s I_s}{\rho_s A_s + \rho_s I_s (\frac{n\pi}{l_s})^2}} \tag{18}$$

Substituting equations (10), (13) into equation (1), we can easily get the velocity distribution on the actuator as following

$$\dot{u}_a = i\omega(u_t - z\frac{\partial w}{\partial x}) \tag{19}$$

By combining equations (2), (10), (13), and substituting them into equations (7) , (8), we can have the electric admittance of the actuator, that is

$$Admi = \frac{I}{V} = i\omega(C_{st} + C_d + C_c + C_b) \tag{20}$$

where C_{st} , C_d are the static and dynamic capacity of the actuator. C_c is the capacity pertinent to the coupling feature between the longitudinal wave in actuator and bending vibrating of the beam. C_b is the capacity induced by the transverse vibration of the actuator to conform to the bending vibration of the beam. They are described by

$$C_{st} = (\epsilon - d_{31}^2 Y_a)\frac{bl_a}{h_a}$$

$$C_d = \frac{2bd_{31}^2 Y_a^2}{h_a k \sin kl_a}(1-\cos kl_a)$$

$$C_c = -\frac{2bd_{31}^2 Y_a^2}{h_a}\sum_{m=1}^{\infty}\left[\frac{1}{(\omega^2-\omega_a^2(2m-1))}\sum_{n=1}^{\infty}G(2m-1,n)\left(\frac{\omega^2-\omega_{as}^2(n)}{\omega^2-\omega_s^2(n)}\right)\right] \qquad (21)$$

$$C_b = \frac{bd_{31}^2 Y_a^2(2h_s+h_a)}{h_a}\sum_{n=1}^{\infty}\left[\frac{W_n}{\omega^2-\omega_s^2(n)}\left(\frac{n\pi}{l_s}\right)\sin\frac{n\pi(r_0+\frac{1}{2}l_a)}{l_s}\sin\frac{n\pi l_a}{2l_s}\right]$$

It is clear that besides the electric admittance is affected by the placement and geometrical dimension of the actuator, and certainly by the boundary condition and configuration of the beam, it is also strongly distorted when the exciting frequency reaches $\omega_s(n)$ or $\omega_a(m)$ and also disturbed by the virtual eigen frequency $\omega_{as}(n)$. However, it is found, from equation (21), that even the resonant frequency of longitudinal wave in piezoelectric actuators have no impact on the electric admittance.

4. CONCLUSION

The new electro-mechanical model of dynamic actuation of piezoelectric actuator bonded on beams has been presented. It is pointed out that the bending vibration concordant with the bending beam should be taken into account in the dynamic analysis of the actuation of the actuator. As a consequence, the coupling between the longitudinal wave in actuator and bending vibration of actuator bonded beam is found, and it leads to the electric admittance to be affected not only by the resonant frequency of transversly vibrating of the beam, but also influenced by the resonant frequency of the longitudinal wave in the actuator and virtual eigen frequency of the actuator, which is not reflected in the previous impedance method.

5. ACKNOWLEDGEMENT

The authors are very grateful to the Alexander von Humboldt Foundation for its support. The first author is also supported by Chinese NSF Foundation.

6.REFERENCES

1. Crawley,E.F. and Luis,J., 1987, ' Use of Piezoelectric Actuators as Elements of Intelligent Structures', AIAA J, Vol.25, No.5, pp.1373-1385.
2 Wang,B.-T. and Rogers,C.A., 1991, 'Modeling of Finite-Length Spatially Distributed Induced Strain Actuators for Laminate Beams and Plates', J. Intell. Mater. Syst. and Struct., Vol.2, No.1, pp.38-58.
3. Wang,B.-T. and Rogers,C.A., 1991, ' Laminated Plate Theory for Spatially Distributed Induced Strain Actuators', J.Composite Mater., Vol.25, pp.433-452.
4. Kirby,G.C., Linder, D.K., Matic,P. and Mirmak,M., 1994, 'Mode Shape Distortions due to Piezoelectric Actuators and Implications for Control', Proceedings, Smart Structures and Intelligent Systems, SPIE Vol.2190, Orlando, February, 1994, pp.647-657.

5. Yang,S.M. and Lee,Y.J., 1994, ' Interaction of Structure Vibration and Piezoelectric Actuation', Smart Mater. Struct., Vol.3, pp.494-500.
6. Main,J.A., Garcia,E. and Howard,D., 1994, ' Optimal placement and sizing of paired Piezoactuators in Beams and Plates', Smart Mater. Struct., Vol.3, pp.373-381.
7. Flint,E.M., Liang,C. and Rogers,C.A., 1995, ' Self induced temperature rise of stack actuators due to dynamic excitation', Proceedings, Smart Structures and Integrated Systems, SPIE Vol.2443, San Diego, February, 1995, pp.422-443.
8. Liang,C., Sun, F.P., and Rogers,C.A., 1994, ' Electro-Mechanical Impedance Modeling of Active Material Systems', Proceedings, Mathematics and Control in Smart Structures, SPIE Vol.2192, Orlando, February, 1994, pp.232-253..
9. Sun,F.P., Liang,C. and Rogers,C.A., 1994, ' Structural Modal Analysis Using Collocated Piezoelectric Actuator/Sensors - An Electromechanical Approach', Proceedings, Smart Structures and Intelligent Systems, SPIE Vol.2190, Orlando, February, 1994, pp.238-249.
10. Liang,C., Sun,F.P. and Rogers,C.A., 1994, ' Development of an Actuator Power Factor Meter for Experiental Determination of an Optimal Actuator Location', Proceedings, Smart Structures and Intelligent Systems, SPIE Vol.2190, Orlando, February, 1994, pp.262-273.
11. Zhou,S., Liang,C and Rogers,C.A. , 1995, ' Integration and Design of Piezoelectric Patch Actuators', J. Intell. Mater. Syst. and Struct., Vol.6, pp.125-132.
12. Lalande,F., Chaudhry Z. and Rogers,C.A., 1995, 'Impedance-based modeling of actuators bonded to shell structures', Proceedings, Smart Structures and Integrated Systems, SPIE Vol.2443, San Diego, February, 1995, pp.396-408.
13. Sermoneta,A., Liang C., Sun, F. and Rogers,C.A., 1995, 'Dynamic Analysis of Active Structures under Multiple Actuators Excitations Using an Impedance Approach', Proceedings, Smart Structures and Integrated Systems, SPIE Vol.2443, San Diego, February, 1995, pp.448-457.
14. Timoshenko,S., Young,D.H. and Weaver,W.Jr., 1974, 'Vibration Problems in Engineering', John Wiley & Sons, New York.

Bodies with controllable constitutive laws — some mathematical issues for active optimisation

Maurizio Brocato

Università di Genova, Facoltà di Architettura, Istituto di Costruzioni
Stradone di Sant'Agostino, 37 - 16123 Genova, Italia

ABSTRACT

The response of some bodies to strain can be modified by external fields; it thence appears that some of their mechanical processes can be controlled through an appropriate insertion of sensors-processors-actuators. Thus, we imagine a body where the stress response function depends also on a set of control fields, as would happen in a linear elastic body for which the Young's modulus E could be altered, within limits, by a fitting choice of an external field κ: $E=E(\kappa(x,t))$. The changes are set to achieve a goal: an assigned functional must reach its extreme value.

Consequently problems must be tackled of the type considered in the theory of distributed controls, but a basic issue is to be pointed out: here the controls may influence the terms under partial derivative in the equations of motion rather than those expressing external actions, thus possibly changing the kind of solution of the system (e.g. acting on the elastic coefficients of a vibrating rod all its fundamental modes do change both in frequency and shape). We refer to some tools already available in the literature and adapt some to a feasible circumstance.

1. INTRODUCTION

We consider a body with controllable constitutive properties and analyse it with the control theory.

The starting point is a natural extension of the continuum with microstructure [2]. Such a continuum is a set of material elements X each occupying an exclusive place x in the Euclidean space (with all the usual continuity requirements defining the class of such placements), but endowed also with a micro state that has to be further defined assigning m order parameters ν^α. Those parameters can be seen as coordinates, in some local chart, of an element ν of M, manifold of finite dimension m. Therefore the material element X is a lagrangian system with 3+m degrees of freedom, constrained to its neighbours by the internal power begot locally by the velocities related to such freedom, up to their first gradient. Such a body's evolutions (as those of a classical continuum) could be controlled from the exterior, quite in general acting through its boundary, but all its internal degrees of freedom obey eagerly to the thermo-mechanical balance laws through a fitting set of constitutive laws.

Controllable material properties may then be introduced by means of k internal order parameters κ^β, also understood as coordinates of an element κ of a manifold K, that, not contributing with their virtual velocities to the balance of powers, can be assigned at will, possibly within given limits. Hence material elements have k additional degrees of freedom, the evolution of the which, unlike that of ν^α, is not governed by dynamic balance equations, even though it may be (and generally is) bounded into a closed subset K of the manifold K. Thus some of the material properties are available to an external operator that can assign them according to some optimality requirement.

Optimality will be understood, like in classical control theory, as the minimum of a given functional J, evaluating the cost of the process or, however, its performance.

A first example is that of electro-rheological materials: by means of an electric field the visco-elastic properties of those bodies can be directly altered; note that, unlike in piezo-elasticity, there is no coupling between the actual motion and the applied electric field. Therefore a smart system can be conceived achieving an active control through ruled sequences of corrections of the stress response of an electro-rheological material.

Passive control of processes can be obtained laying the initial conditions in to get optimal results; then it is natural to search for optimal initial micro states. In metal forming, for instance, the elastic energy stored in lattice misfits and the anisotropy due to the distribution of crystals orientations are usually adjusted by metallurgists before the final process by convenient treatments. In this case the controllable parameters κ aren't but the initial conditions that must be assigned to (some of) the uncontrollable microstructure ν; the question of contriving the optimal set κ^*, once mathematically determined, may then be tackled studing the preparing treatments and thus by different models and tools.

It has to be pointed out that problems we look at are basically different from those prevalently stressed in the literature about controls of continuous systems (mainly after the work of Lions [4]): there actions are performed from outside the body (like boundary tractions or displacements or electric charges) that even though modify the solution of

0-8194-2165-0/96/$6.00

the equations of motion leave unchanged its characteristics. The main feature of controllable materials is that, as the stress response function is under control, the term under the divergence operator in the equilibrium equation changes, in some extents, at will. Thus not all alternative processes are of the same kind and, at least in some cases, the optimal path may consist of portions of solutions of different nature.

For instance we may think of an electro-elastic free-vibrating rod: altering its Young's modulus one acts on all the eigen values of the settled system and investigations for optimality involves solutions represented through different eigen functions.

The introduction of uncontrollable microstructures does not change the fundamental steps of the present analysis; therefore we will deal in the following about an ideal material the microstructure of the which can be entirely controlled.

A first study of the control of integro-differential continuous systems was performed by Wang [6] on the basis of the optimality principle of Bellman; Wang's result, as the author itself pointed out, gives also a generalisation to continuous systems of Pontryagin's principle of maximality [5]. It is understood that, as Pontryagin's and Bellman's principles do not correspond to each other, Wang's generalisation of the former is restricted to the cases where the performance of the process is expressed by a continuously differentiable functional of the system's generalised coordinates.

A similar optimality requirement ensues actually by a straightforward procedure of calculus of variations that we present here in a form suitable to the case of continua with non holonomic behaviour.

First we set the problem of the control of a body's motion through its constitutive equations, then we get an optimality condition that may give a solution of the given problem. (We will not argue about the existence of such solutions, nor, as customarily done in searching optimal controls, will we deal about unicity). Next we apply this procedure to the propagation of elastic waves into a body with controllable constitutive relations and show some of the optimal control characteristics discussing few issues of such problem.

2. GENERAL PROBLEM

Let V_0 be the domain occupied by the body in the Euclidean space at time t_0 and V_t that occupied at the current instant t (next to t_0); let $\mathbf{u}$ the displacement between V_t and some next configuration and $\mathbf{v}$ the velocity on V_t; let $\mathbf{b}$ and $\mathbf{f}$ the forces acting per unit mass and per unit surface on the body and $\mathbf{T}\in$Sym the Cauchy stress tensor. Motion follows the system:

$$\begin{aligned}
&\mathbf{u}(x,t_0) = \mathbf{u}_0(x)\ ;\ \mathbf{v}(x,t_0) = \mathbf{v}_0(x) && \text{in } V_0\\
&\mathrm{div}\mathbf{T} + \rho\mathbf{b} = \rho\dot{\mathbf{v}} && \text{in } V_t\times[t_0,t_f]\\
&\mathbf{T}\mathbf{n} = \mathbf{f} && \text{on } \partial V_{ft}\times[t_0,t_f]\\
&\mathbf{v} = \hat{\mathbf{v}} && \text{on } \partial V_{vt}\times[t_0,t_f]
\end{aligned} \tag{1}$$

with assigned $\mathbf{u}_0$, $\mathbf{v}_0$, $\mathbf{b}$, $\mathbf{f}$, $\hat{\mathbf{v}}$ (according to mixed boundary conditions) and a controlled constitutive equation, within the limits that phenomenology states for the control field:

$$\forall(x,t)\in V_t\times[t_0,t_f]:\ \mathbf{T}(x,t)=\int_{-\infty}^{t}\int_{V_\tau}\mathbf{S}\left(\mathbf{u}(y,\tau),\mathbf{v}(y,\tau),\kappa(y,\tau)\right)\,dV_\tau(y)d\tau\quad \kappa\in K \tag{2}$$

The process' performance is, by statement, determined by the cost functional:

$$J\left\{\mathbf{u},\mathbf{v},\kappa\ ;\ [t_0,t_f]\right\}=\int_{t_0}^{t_f}\int_{V_t} f(x,t\ ;\ \mathbf{u}(x,t),\mathbf{v}(x,t),\kappa(x,t),\ldots)\,dV_t(x)dt \tag{3}$$

The problem is to find functions $\mathbf{u}$, $\mathbf{v}$ and $\kappa \in K$ according to (1) and (2), such that the functional (3) is minimum.

We assume that the boundary conditions can be expressed in terms of $\mathbf{u}$ and $\mathbf{v}$ only. This happens in particular if tractions are not prescribed anywhere on the boundary, or if the body is elastic.

The given problem is equivalent to that of finding four functions $\mathbf{u}$, $\mathbf{v}$, $\mathbf{p}_u$ and $\mathbf{p}_v$, which are admissible in a sense we are going to precise, and a function κ admissible as a control, such that the functional:

$$I\{\mathbf{u},\mathbf{v},\mathbf{p}_u,\mathbf{p}_v,\kappa\ ;\ [t_0,t_f]\} = \int_{t_0}^{t_f} \int_{V_t} \left[\left(\mathbf{v} - \dot{\mathbf{u}}\right)\cdot\mathbf{p}_u + \left(\frac{\mathrm{div}\mathbf{T}}{\rho} + \mathbf{b} - \dot{\mathbf{v}}\right)\cdot\mathbf{p}_v + \mathbf{f} \right] dV_t dt \tag{4}$$

achieves its minimum. The fields $\mathbf{u}$ and $\mathbf{v}$ have to satisfy initial and boundary conditions to be admissible; $\mathbf{p}_u$ and $\mathbf{p}_v$, being the Lagrangian multiplier of the equation of motions, are for the time being arbitrary functions defined almost everywhere on $V_t \times [t_0,t_f]$.

Let us define the augmented Hamiltonian:

$$H\{\mathbf{u},\mathbf{v},\mathbf{p}_u,\mathbf{p}_v,\kappa\} = \int_{V_t} \left[\mathbf{v}\cdot\mathbf{p}_u + \left(\frac{\mathrm{div}\mathbf{T}}{\rho} + \mathbf{b}\right)\cdot\mathbf{p}_v + \mathbf{f} \right] dV_t \tag{5}$$

The minimisation can than be tackled by calculus of variation recalling that the control κ belongs to a closed region the optimal solution may hit the boundary of the which. Hence Fourier's inequality applies for all admissible variation of the solution $(\mathbf{u},\mathbf{v},\mathbf{p}_u,\mathbf{p}_v,\kappa)$. In particular no variation $\delta\mathbf{u}$ and $\delta\mathbf{v}$ are allowed where kinematical conditions are imposed, i.e. on the whole boundary ∂V_t as well as at the initial state and, possibly, at the final one. All variations, but those of κ, may be taken with arbitrary sign.

Thus, for $\delta\kappa=0$, we get Hamilton's canonical equations with the orthogonality conditions between $\mathbf{u}$ and $\mathbf{p}_u$ and $\mathbf{v}$ and $\mathbf{p}_v$ at the final instant (note that this system gives the solution for fixed control):

$$\frac{\delta H}{\delta \mathbf{p}_u} = \dot{\mathbf{u}}\ ;\ \frac{\delta H}{\delta \mathbf{p}_v} = \dot{\mathbf{v}}\ ;\ \frac{\delta H}{\delta \mathbf{u}} = -\dot{\mathbf{p}}_u\ ;\ \frac{\delta H}{\delta \mathbf{v}} = -\dot{\mathbf{p}}_v \tag{6}$$

$$\int_{V_t} \delta\mathbf{u}\cdot\mathbf{p}_u dV_t\Big|_{t=t_f} = \int_{V_t} \delta\mathbf{u}\cdot\mathbf{p}_u dV_t\Big|_{t=t_0} = 0 \quad \forall \delta\mathbf{u} \text{ adm.}\ ;\ \int_{V_t} \delta\mathbf{v}\cdot\mathbf{p}_v dV_t\Big|_{t=t_f} = \int_{V_t} \delta\mathbf{v}\cdot\mathbf{p}_v dV_t\Big|_{t=t_0} = 0 \quad \forall \delta\mathbf{v} \text{ adm.}$$

and the global minimum condition for H that makes the optimality of a solution $(\mathbf{u},\mathbf{v},\mathbf{p}_u,\mathbf{p}_v,\kappa)$ sure:

$$\int_{t_0}^{t_f} \left[H\{\mathbf{u},\mathbf{v},\mathbf{p}_u,\mathbf{p}_v,\kappa+\delta\kappa\} - H\{\mathbf{u},\mathbf{v},\mathbf{p}_u,\mathbf{p}_v,\kappa\} \right] dt \geq 0 \tag{7}$$

The functional H obeys the principle of causality (as system (1)+(2) does), therefore if we take a $\delta\kappa(x,t)=k(x,t)h_\tau(t)$ with $h_\tau(t)$ step function at time $t_f-\tau$, with arbitrary τ and arbitrary $k(x,t)$, the following minimum condition for H results:

$$\int_{t_f-\tau}^{t_f} \left[H\{\mathbf{u},\mathbf{v},\mathbf{p}_u,\mathbf{p}_v,\kappa+\delta\kappa\} - H\{\mathbf{u},\mathbf{v},\mathbf{p}_u,\mathbf{p}_v,\kappa\} \right] dt \geq 0 \quad \forall \tau \in [0,t_f-t_0] \tag{8}$$

$\forall\delta\kappa$ admissible within closed limits and for $(\mathbf{u},\mathbf{v},\mathbf{p}_u,\mathbf{p}_v,\kappa)$ optimal solution.

This minimum condition can be further exploited as it entails that the functional:

$$\int_{t_f-\tau}^{t_f} H(t)dt - \min_{\kappa\in K}\left\{\int_{t_f-\tau}^{t_f} H(t)dt\right\} \tag{9}$$

has almost everywhere a stationary minimum (with value zero) as a function of the time left τ. By derivation, recalling the orthogonality conditions at the end point, it ensues for $\tau=0$ that [6,5]:

$$H(t_f) = \lim_{\tau\to 0}\frac{\partial}{\partial\tau}\min_{\kappa\in K}\left\{\int_{t_0}^{t_f-\tau}\int_{V_t} f\, dV_t dt\right\} \tag{10}$$

and then, in particular, the end-point condition $H(t_f)=0$ for the optimal path whenever the minimum of J is stationary in time.

We conclude this section resuming Pontryagin's sufficient condition [5]. In the cases studied by Pontryagin not only the causality of the problem is considered to reduce the variations of H ensuing control's variations, but causality itself is invoked with reversed time. Consequently any part of the optimal path must be optimal as (7) insures that H is minimum at any time, but both H and f have to have no memory of the past, a hint worth recalling later. Thus for continuous systems too the condition reads: if for a given control κ^* there exist a solution $(\mathbf{u}^*,\dot{\mathbf{u}}^*,\mathbf{p}^*_u,\mathbf{p}^*_v)$ of Hamilton's canonical equations (with given initial conditions on the kinematical state $(\mathbf{u},\dot{\mathbf{u}})$ and final conditions on whether $(\mathbf{u},\dot{\mathbf{u}})$ or $(\mathbf{p}_u,\mathbf{p}_v)$) such that:

$$H\{\mathbf{u}^*,\dot{\mathbf{u}}^*,\mathbf{p}^*_u,\mathbf{p}^*_v,\kappa^* ; t\} = \min_{\kappa\in K} H\{\mathbf{u},\mathbf{v},\mathbf{p}_u,\mathbf{p}_v,\kappa ; t\} \quad \forall t\in[t_0,t_f] \tag{11}$$

then κ^* is an optimal control.

For such theorem to hold we stress the important condition that all parts of the optimal path are optimal, in the sense of (10). As, generally speaking, the state of a given material depends on its history, this condition is not true even if the function f depends only on the actual state; therefore, equations (10) and (11) to apply, we have to handle a non hysteretic process with a local instantaneous cost that depends only on some reversible part of the material element's state.

3. RHEOLOGIC CONTROL OF ELASTIC WAVES

Let us study the case of an isotropic linearly elastic body, the equilibrium of the which is slightly perturbed by waves propagating in its bulk, with imposed kinematic on the body's surface and no body forces acting. Lame's coefficients $\mu(\kappa)$ and $\lambda(\kappa)$ are controllable, as for an electro-rheological material, within the limits $[\mu_{min}, \mu_{max}]$ and $[\lambda_{min}, \lambda_{max}]$; actually we will take account of a single control field $\kappa(x,t)$ taking values in the closed real interval [-1,1] by means of:

$$\mu(\kappa)=\mu_0+\Delta\mu\kappa \; ; \; 2\mu_0 = \mu_{max} + \mu_{min} \; ; \; 2\Delta\mu = \mu_{max} - \mu_{min} \; ; \; \kappa\in[-1,1] \tag{12}$$

and similar definitions for λ.

We aim to dump the waves in the most proficient way by suitable changes of the elastic response. Therefore the problem reads:

$$\begin{aligned}
&\mathbf{u}(x,t_0)=\mathbf{u}_0(x) \; ; \; \dot{\mathbf{u}}(x,t_0)=\mathbf{v}_0(x) && \text{in } V\\
&\mu(\kappa)\Delta\mathbf{u} + (\lambda(\kappa)+\mu(\kappa))\,\mathrm{graddiv}\mathbf{u} = \rho\ddot{\mathbf{u}} && \text{in } V\times[t_0,t_f]\\
&\mathbf{u} = \hat{\mathbf{u}} && \text{on } \partial V\times[t_0,t_f]
\end{aligned} \tag{13}$$

with $\kappa\in[-1,1]$, minimising the work of internal forces:

$$J\{\mathbf{u},\dot{\mathbf{u}},\kappa\ ;\ [t_0,t_f]\}=\int_{t_0}^{t_f}\left[-\int_V\left[2\mu(\kappa)\text{symgradu}:\text{grad}\dot{\mathbf{u}}\ +\ \lambda(\kappa)\text{divu}\,\text{divv}\right]\,dV\right]dt \tag{14}$$

Let us look only at isochoric waves for shortness. The problem being anyway linear, condition (11) applies to the Hamiltonian:

$$H\{\mathbf{u},\mathbf{v},\kappa\}=\int_V\left\{\mathbf{p}_u\cdot\mathbf{v}\ +\ \frac{1}{\rho}\,\mathbf{p}_v\cdot\text{div}[2\mu(\kappa)\text{symgradu}]\ -\ 2\mu(\kappa)\text{symgradu}:\text{gradv}\right\}dV \tag{15}$$

the minimum of the which occurs for a bang-bang control:

$$\kappa=\text{sgn}\left\{\text{symgradu}:\text{grad}\left(\frac{\mathbf{p}_v}{\rho}\ +\ \mathbf{v}\right)\right\}\ \text{in}\ V\times[t_0,t_f]\ \text{and}\ \kappa=-\text{sgn}\left\{\frac{\mathbf{p}_v}{\rho}\cdot\text{symgradu}\cdot\mathbf{n}\right\}\ \text{on}\ \partial V\times[t_0,t_f] \tag{16}$$

a one parameter family of solutions of Hamilton's canonical equations, defined whenever $\dot{\mu}=0$, is:

$$\mathbf{p}_u\overset{a.e.}{=}-C\text{div}[2\mu(\kappa)\text{symgradu}]\ ;\ \mathbf{p}_v\overset{a.e.}{=}(C-1)\rho\mathbf{v}\quad\forall C\in\mathbb{R} \tag{17}$$

$$H\{\mathbf{u},\mathbf{v},\kappa\}=-\int_V\text{div}[2\mu(\kappa)\text{symgradu}\cdot\mathbf{v}]\,dV\ \ ;\ \ \kappa=\text{sgn}(C)\text{sgn}\{\text{symgradu}:\text{gradv}\}$$

The end-point orthogonality conditions does not reduce the indeterminacy as the kinematic state must be constrained to rest when the final time goes to infinity. Nevertheless we may choose the solution leading, as required, to a decrease of the internal work:

$$\underset{\text{sgn}(C)}{\text{Max}}\left\{\int_{t_0}^{t^*}\left[-\int_V 2\mu(\kappa)\text{symgradu}:\text{grad}\dot{\mathbf{u}}\,dV\right]dt\ -\ \int_{t_0}^{t^*+\Delta t}\left[-\int_V 2\mu(\kappa)\text{symgradu}:\text{grad}\dot{\mathbf{u}}\,dV\right]dt\right\}\rightarrow\text{sgn}(C)=1$$

$$\kappa=\text{sgn}\left\{\text{symgradu}:\text{grad}\dot{\mathbf{u}}\right\} \tag{18}$$

Therefore the minimum of H is achieved if $\mu(\kappa)$ is piece wise constant and jumps with discontinuity from one end to the other of its admissible interval $[\mu_{min}\ ,\ \mu_{max}]$ on a set of surfaces instantaneously defined by the equation:

$$\text{symgradu}:\text{grad}\dot{\mathbf{u}}=\text{tr}(\text{symgradu}\cdot\text{grad}\dot{\mathbf{u}})=0 \tag{19}$$

i.e. on the loci of null internal power's density for the solution.

The case of plane waves allows for an useful illustration of such result. Denoting with ξ a coordinate along the direction of propagation of the waves, with ϕ the corresponding displacement and with a prime the derivative with respect to the ξ direction, the optimal dumping control of the waves is:

$$\kappa(\xi,t)=\text{sgn}\left[\phi'(\xi,t)\dot{\phi}'(\xi,t)\right]=\text{sgn}\left\{\left[\phi'(\xi,t)^2\right]^{\bullet}\right\}=\text{sgn}\left\{\left|\phi'(\xi,t)\right|^{\bullet}\right\} \tag{20}$$

Therefore the optimal control is $\kappa=1$ whenever the absolute value of the deformation ϕ' increases with time and switches to $\kappa=-1$ where this value decreases; the switch happens on two families of travelling planes, where either $\phi'=0$ or $\dot{\phi}'=0$, i.e. on extrema of displacement and of velocity with respect to ξ. Furthermore ϕ is solution of:

$$\rho\ddot{\phi} - 2\mu\phi'' - 2\Delta\mu\left[\mathrm{sgn}\left(\phi'\dot{\phi}'\right)\phi'\right]' = 0 \tag{21}$$

and, away from discontinuities due to the sgn operator, i.e. for a given constant and uniform control κ^*, it takes the usual form in terms of forward and backward waves, with velocity of propagation depending on the control:

$$\phi^*(\xi,t) = w_{\rightarrow}(\xi - c(\kappa^*)t) + w_{\leftarrow}(\xi + c(\kappa^*)t) \;\; ; \;\; c^2(\kappa) = 2\mu(\kappa)/\rho \tag{22}$$

As quoted above this solution holds only in a region, where $\kappa^* = \mathrm{sgn}(\phi^{*\prime}\,\dot{\phi}^{*\prime})$, delimited by the planes:

$$\xi = \chi(t) : w'_{\rightarrow}(\chi(t) - c(\kappa^*)t) + w'_{\leftarrow}(\chi(t) + c(\kappa^*)t) = 0$$

$$\xi = \zeta(t) : w''_{\rightarrow}(\zeta(t) - c(\kappa^*)t) - w''_{\leftarrow}(\zeta(t) + c(\kappa^*)t) = 0 \tag{23}$$

crossing the which, as the control's sign switches, in general not only the velocity of propagation changes, but also the wave functions, according to the usual jump conditions at discontinuities of the elastic properties.

If the body vibrates with no energy's drain or supply, κ being fixed at any constant value κ^*, the corresponding solution ϕ^* of (21) describes at given ξ an ellipse in the $(\phi', \dot{\phi})$ plane with radii's rate given by $c(\kappa^*)$:

$$\phi^{*\prime}(\xi,t)^2 + \left[\frac{\dot{\phi}^*(\xi,t)}{c(\kappa^*)}\right]^2 = g(\xi)^2 \tag{24}$$

The third of (20) shows that along solutions of that kind $\kappa = \mathrm{sgn}(\phi'\dot{\phi})$. Thence we have two sets of ellipses, each occuping two opposite quarters of the $(\phi'\dot{\phi})$ plane: any optimal solution will jump from one to the other set, according to κ, moving toward the origin. It is then possible to identify the optimal path starting from any given initial condition (fig.1).

Observing this result we see that the optimal control must slow the waves down, taking the lowest stiffness, wherever in the body the kinetic energy increases and the internal energy decreases, and fasten the waves, stiffening the material, where the energetic exchange has opposite direction.

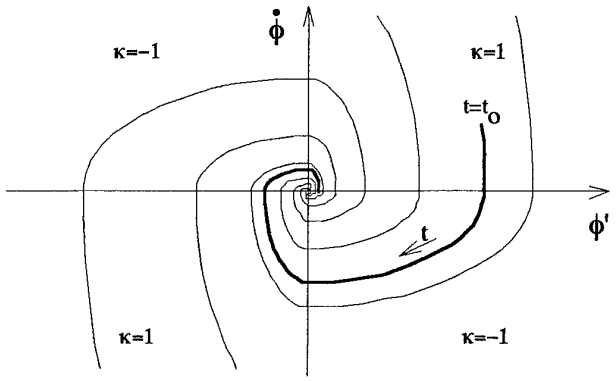


Fig.1: Optimal paths to dump elastic waves

4. ACKNOWLEDGEMENTS

This work was funded by a scholarship granted by the "Gruppo Nazionale per la Fisica Matematica" of the Italian "Consiglio Nazionale per le Ricerche". The author is grateful to professor Gianfranco Capriz for his direction.

5. REFERENCES

1. M. Brocato and G. Capriz, "Sui continui controllati," Proc. XII AIMETA Conf., Napoli, pp. 81-86, Oct. 1995.
2. G. Capriz, *Continua with Microstructure*, Springer Verlag, New York, 1989.
3. C. Lanczos, *The variational Principles of Mechanics*, 4th ed., University of Toronto Press, Toronto, 1970.
4. J.L. Lions, *Contrôle optimal de systèmes gouverneés par des équations aux dérivées partielles*, Dunod, Paris, 1968.
5. L.S. Pontryagin et al., *The mathematical theory of optimal processes*, John Wiley & Sons, New York, 1962.
6. P.K.C. Wang, *Control of Distributed Parameter Systems*, J. Mech. Control, pp. 75-172, 1964.

Use of Artificial Neural Networks as Estimators and Controllers

A. Concilio, A. Sorrentino
C.I.R.A. S.C.p.A., Italian Aerospace Research Center
via Maiorise, loc. Silvagni, 81043 Capua-CE, ITALY

1 INTRODUCTION

Active noise control is one among the most promising applications of the so-called Smart Structures, because it ensures, or promises, lower weight, lower cost, more effectiveness and all what is desirable in a vehicle design process, with respect to the current solutions. More and more attention in the research world has been devoting to this argument, pushed by both political, economical and environmental reasons, the one connected to the others. Piezoceramic actuators, integrated into the structure, seem to offer the most fashionable and practical solutions among all the proposed architectures, [1-2]. As sensors, microphones demonstrated to be the most performing, above all because they give the most suitable representation of the field that has to be cancelled, [3-4]. This approach is known as Acousto-Structural Active Control, ASAC, [5].
However, according to Fuller's definition, [6], an intelligent controller is needed to ensure the development of an "Intelligent Structure". Its main characteristic should be represented by the capability of learning by examples, of following the structure during its evolution, of being the system "brain". This peculiarity may be offered by Artificial Neural Networks (ANN's), [7-8]. They present other important features, like the capability, in principle, of treating non-linear as well as linear problems, [9], of identifying dynamic systems, [10], of properly acting as a controller. Then, such a net could integrate in itself the function of "system estimator" or "observer", and of interpolator - extrapolator and controller, contemporarily. The authors have been working on such subjects for a long time, proposing for instance ANN's as time-domain structural parameters estimators on a simple 2D element (a framed plate), [11], as noise and vibration controllers in a FF system, [12-13], as materials damping parameters extractors from experimental data, [14]. All these applications were aimed at noise reduction problems. The results were very encouraging.
The current application concerns the use of ANN's as both estimator of a system transfer function and controller of vibrations, on a very simple 1D element (a rectangular section cantilever beam). The objective of this very preliminary study was in fact related to test the ANN's capabilities in identifying the structure, in following its evolution during the history, and its own "robustness" in terms of control performance vs. structural variations. Basically, two different ANN's were built, both in the frequency domain: an estimator and a controller. Two aspects were investigated: at a certain point of the life of the structure, it is supposed to break at its extremity. The speed according which the controller is able to follow this variation, is evaluated. To reduce the number of sensors placed on the structure, an estimator is then called to simulate the structural dynamic response by information acquired through a reduced set of devices only.

2 FEM MODELS

A scheme of the FEM models, is reported in Fig.1. The structure under investigation is a simple cantilever beam, 1000 mm span, with a rectangular section, 100 × 10 mm. A white-noise vertical point force (1N), acts in the range between 0 and 1000 Hz. A number of 5 piezoceramic actuators, 60 mm long, 5 mm thick, t_c, and 10

0-8194-2165-0/96/$6.00

mm wide, b_c, are used to control the vibration induced by the external disturbance, Fig.1. Then, the structure breaks into a smaller one, 800 mm long. The models are idealized through a mesh made by 51 and 41 Grids, and 50 and 40 Beams up to a total of 306 and 246 DOF's, respectively. The piezoactuators are simulated through the moment M_t they transmit to the structure, computed through the classical expression, [15]:

$$M_t = \frac{\psi}{\psi + 4} E_c b_c t_c \Lambda \tag{1}$$

where, ψ is a strain reduction factor, and E_c is the Young's module. The actuators center of gravity are located at 130 mm and following, step 200 mm. In the second configuration, the fifth actuator is missing. Ten velocity sensors are originally placed at 50 mm and following, step 50 mm. When the beam breaks, only 8 sensors remain active. Numerical and analytical eigenvalues were compared, finding an almost perfect agreement, as expected for such simple structural elements. The structures were supposed to have only in-plane displacements. The percentage difference between the eigenfrequencies, is constant and equal to 56.2 %. FRF's were acquired in the range between 0 and 1000 Hz, for both the structural elements.

3 ANN ARCHITECTURES

Two different ANN's were used: a controller and an estimator.
A scheme of the controller is reported in Fig.2, [7]; it consists of 4 layers: input, hidden, output and structural. A variable number of neurons is associated to each level; particularly, in this application the input, containing a reference number usually put equal to 1, and the hidden layers are made of 1 neuron. The number of the actuators is associated to the output neurons (in this case 5 and 4, respectively), while the number of sensors corresponds to the structural layer neurons (10 and 8). Each neuron is linked to the others, in the sense that the input information is a linear combination of all the data coming from the previous layer. The coefficients multiplying the data are called "weights", and are modified according to an "error" function, in this case evaluated as the difference between the former and the current values (complex back-propagation, [13]).
The ANN used as estimator is a classical three-layered Neural Network. Its scheme is similar to the former, with the exception that the "structural layer" is missing. The input processing elements (neurons) number is twice the sensors number, because for each of them both real and imaginary part of the FRF's are considered. In the same way, the output neurons number is twice the actuators number. Standard back-propagation algorithm was used. The ANN learns the behaviour of the system through the examples that are presented. In a second step, the net is able to reproduce the desired FRF starting from a limited set of information, [11]. The obtained FRF's, are then used by the ANN controller to obtain the control forces able to reduce the vibration field.

4 TESTS & RESULTS

The objective function to be minimized is represented by the vibrational energy, defined as:

$$E_v = \sum_{i=1}^{n} v_i^2 \tag{2}$$

n being the number of sensors and v_i is the velocity, as recorded at the i-th sensor. According to the linearity hypothesis, they can be considered as the combination of the contributions due to the primary (v_p) and the secondary forces ($v_{s,j}$):

$$v_i = v_{s,i} + \sum_j v_{s,ij} \tag{3}$$

The equation (1) represents an operation among complex numbers. An ANN controller aims at minimizing this cost function, [12-13]. Suddenly, the beam loses the final segment, 200 mm long. The structure, that could simulate a satellite antenna hit by a meteorite, changes its dynamic behaviour. The variation from the initial state may be measured in many ways, for instance:

Lenght variation	$= 20\ \%$
Tip displacement to a point force	$\simeq 50\ \%$
First eigenfrequency	$\simeq 60\ \%$

Apart from these, two sensors and one actuator are cut out. The ANN controller capability of following the structural variations, can be measured by the speed (number of cycles) it is able to define the new control forces. Practically, it consists of preserving the old ANN "weights", as computed on the original configuration, and making the learning phase start from this background knowledge (experience). The considered variations are "statics" (no investigation was carried out in the transient period). Some results are reported in Fig.3-4. In resonance conditions, the net is able of approximating the optimal parameters after a few number of cycles, it can be seen; far away, more time is needed. Fig.3 regards a frequency near the broken beam 5^{th} resonance. Both the nets are able in providing good reduction values soon, and the difference is limited even though the best performance of the "trained" net is evident. However, when a non-resonant frequency is investigated the behaviour of the nets changes a lot: Fig.4 is relative to the original beam 2^{th} mode (no longer coincident with a broken beam autosolution); the "experienced" net practically gives the maximum reduction starting from the first cycle (really, the line has a little slope), while the "unexperienced" net provides acceptable reduction values only after more than 800 cycles. Truely, this last is an extreme case; at other frequencies, the behaviour lays in between these extremal attitudes. Such nets can be considered easily appliable to adaptive control problems.
A second application, is referred to the use of an ANN as a structural simulator. The net is called at reproducing the dynamic response of the structure under the disturbance action, in the range between 0 and 1000 Hz. The aim is to reduce the sensors number, by extrapolating the responses in other points. The information from 6 sensors (1,2,3,5,7,9) was used; 10 outputs were given, corresponding to the previous acquisition points. A typical result in a learning sensor is reported in Fig.5, representing the net capability of reproducing what learns (100,000 cycles; FEM data). The strongest differences are at low frequencies and at the anti-resonances. In the same way, what happens in a simulated sensor is reported in Fig.6. The vibration level of the simulated and the real article is reported in Fig.7. The difference between these global values may be considered as an absolute measure of the ANN capability in identifying the structural system. A comparison between the controlled levels, as predicted by the neural net operating on simulated information, and as verified by inserting the net-computed control forces inside the FEM code (MSC/Nastran), is reported in Fig.8. Again, some important differences can be noted at low frequencies. This gives a first response about the feasibility of using integrated ANN's as both estimators and controllers. The used architecture was not optimized, it has to be stressed; several changes need, for instance by building a parameters-adaptive net (learning coefficients, normalization factors, and so on); currently, the computed weights result from an iterative learning process at different frequencies, but their value minimizes the difference by referring only to the last one and extrapolating the FRF at the others: this limit shall be overcome. Neural net controllers were proved to give absolutely coherent results with FEM simulation in previous works, [12-13]: then, the evidenced differences are due to the simulation process only.

5 CONCLUSIONS

Starting from well-assessed results on the use of ANN as controllers, a preliminary validation of the feasibility of using them in a feedforward adaptive control system, was carried out. In the same way, a first evaluation in using these tools as transfer functions identifiers was tried, from some experiences in the use of ANN as structural parameters estimators. The results obtained by this application, were used as input to the former ANN, so to realize an integrated ANN "observer-controller". The triviality of the investigated structural element could be considered as a strong limitation: but the aim of this first step of the work, was simply voted to verify the capabilities of entities ANN-based in identifying the system and following the structural variations.
Further steps should be addressed to assess the different ANN's integration; to improve the identification algorithm

so to significatively reduce the sensors number and to improve the output quality; to verify the capability of the controller-observer in following the system evolution; finally, to apply these results and experiences to more complex structures and to realize the hardware to experimentally verify such an approach.

6 BIBLIOGRAPHY

1 Wada B.K., Fanson J.L., Crawley E.F., "Adaptive Structures", Journal of Intelligent Materials and Structures, Vol.1, N.2, 1990, pp. 157-174.

2 Liang C., Sun F., Rogers C.A., "An Investogation of the Energy Consumption and Conversion of Piezoelectric Actuators Integrated in Active Structures", ICIM '94, Williamsburg (VA - USA), June 1994.

3 Banks H.T., Smith R.C., "Noise Control in a 3D Structural-Acoustic System: Numerical Simulations", ICIM '94, Williamsburg (VA - USA), June 1994.

4 Mathur G.P., Tran B.N., Simpson M.A., "Active Structural Acoustic Control of Aircraft Cabin Noise using Optimized Actuator Arrays - Laboratory Tests", I CEAS/AIAA Aeroacoustic Conference, Munich (D), June 1995.

5 Clark R.L., Fuller C.R., "Active Structural Acoustic Control with Adaptive Structures using Wavenumber Considerations", Recent Advances on Smart Materials System and Structures Conf., Williamsburg (VA - USA), April 1993.

6 Fuller C.R., "Recent Developments in Active Control of Vibration", Nordic Conference on Vehicle and Machine Vibrations, Stockholm (S), September 1994.

7 Cabell R.H., Lester H.C., "Investigation of Force Distribution for Interior Noise Control Using a Neural Network", Recent Advances on Smart Materials System and Structures Conf., Williamsburg (VA - USA), April 1993.

8 Dovstam K., Sorrentino A., Dalenbring M., "AHL/ANN Approach for Material Damping Parameter Estimation", to be submitted for publication, November 1995.

9 Cook A.B., Fuller C.R., O'Brien W.F., Labell R.W., "The Prediction of Nonlinear Dynamic Loads on helicopters from Flight Variables Using ANN", 14th DGLR/AIAA Aeroacoustic Conference, Aachen (D), May 1992.

10 Napolitano M.R., Chen C.I., Nutter R., "Application of a Neural Obeserver as State Estimation in Active Vibration Control of a Cantilever Beam", Int. Journal of Smart Materials & Structures, N.1, 1992, pp.69-75.

11 Lecce L., Sorrentino A. et al., "Estimation of the Dynamic Behaviour of Complex Structures by Neural Networks", Recent Advances on Smart Materials System and Structures Conf., Williamsburg (VA - USA), April 1993.

12 Lecce L., Sorrentino A., Concilio A., "Interior Noise Active Control By ANN and Piezoelectric Actuators" (in Italian), AIDAA '93, Como (I), July 1993.

13 Lecce L., Sorrentino A., Concilio A., "Active Vibration Control of a Thin-Walled Section Beam by Neural Networks and PiezoActuators", ICIM '94, Williamsburg (VA-USA), June 1994.

14 Bianchini E., Marulo F., Sorrentino A., "MSC/Nastran Solution of Structural Dynamics Problems using Anelastic Displacement Fields", 36th Structures, Strutural Dynamics and materials Conference, New Orleans (LA-USA), April 1995.

15 Concilio A., Del Gatto F.S., Lecce L., Vitiello P., "Active Noise Control on Plates and Double Partitions Using Discrete Piezoelectric Devices", 14th DGLR/AIAA Aeroacoustic Conference, Aachen (D), May 1992.

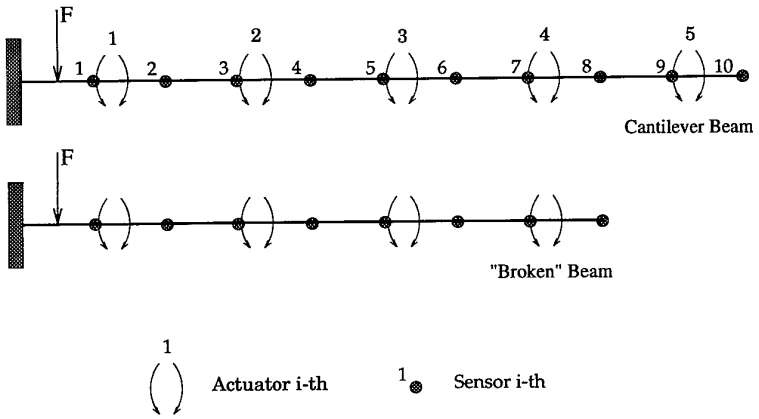
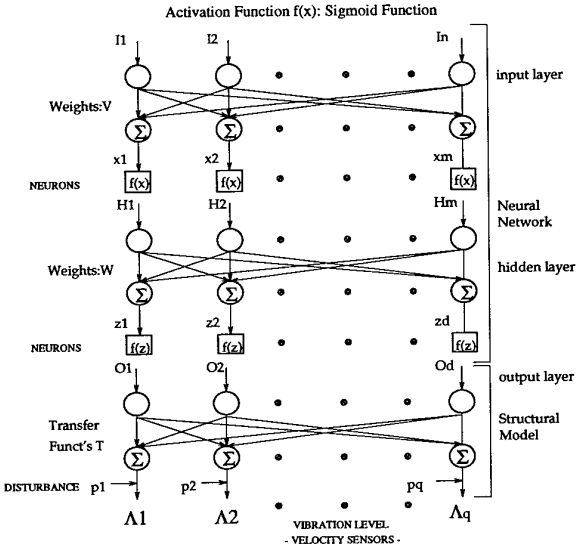
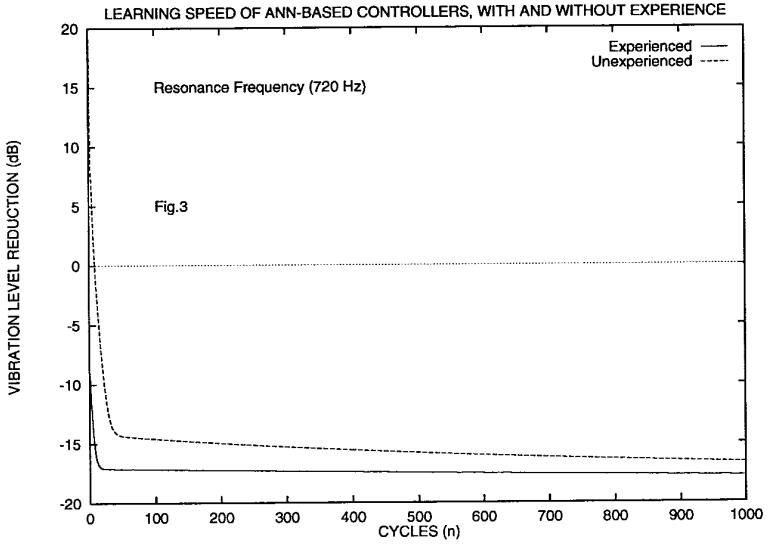
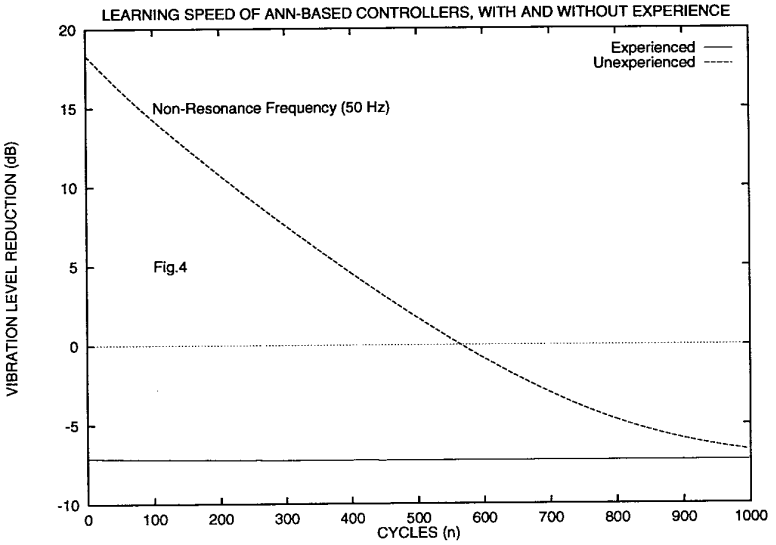


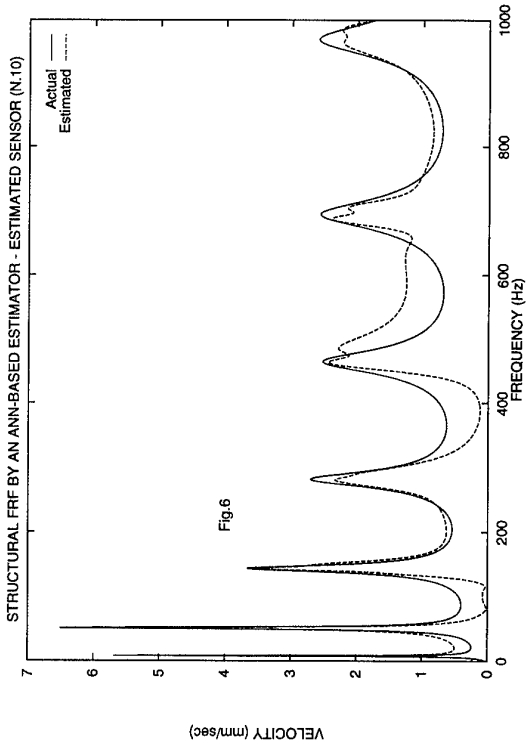
Fig.1 Test articles configuration

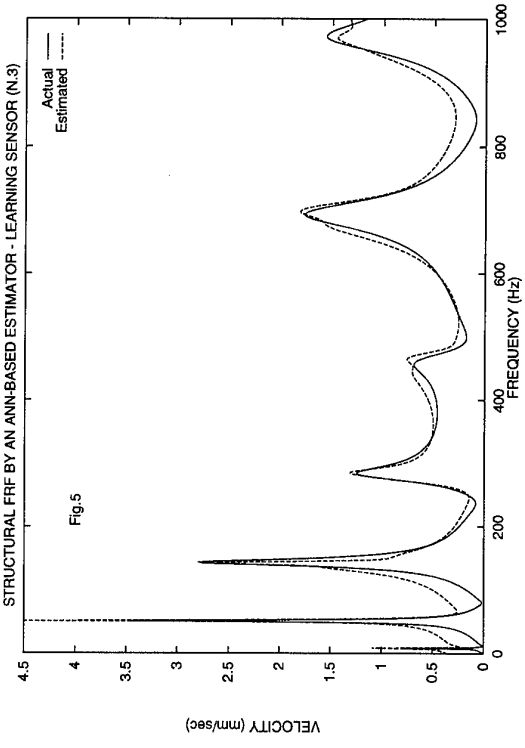
Fig.2 ANN CONTROLLER (ESTIMATOR) ARCHITECTURE

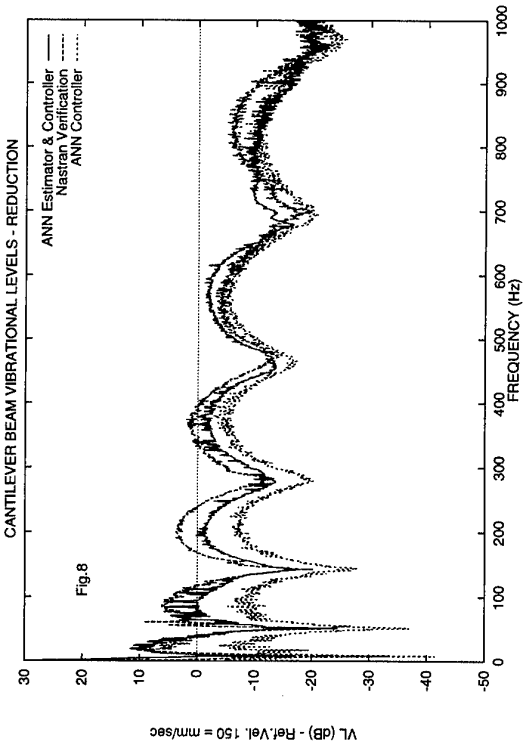







STRUCTURAL FRF BY AN ANN-BASED ESTIMATOR - ESTIMATED SENSOR (N.10)
Actual
Estimated
Fig.6
VELOCITY (mm/sec)
FREQUENCY (Hz)


STRUCTURAL FRF BY AN ANN-BASED ESTIMATOR - LEARNING SENSOR (N.3)
Actual
Estimated
Fig.5
VELOCITY (mm/sec)
FREQUENCY (Hz)


CANTILEVER BEAM VIBRATIONAL LEVELS - REDUCTION
ANN Estimator & Controller
Nastran Verification
ANN Controller
Fig.8
VL (dB) - Ref.Vel. 150 = mm/sec
FREQUENCY (Hz)

CANTILEVER BEAM VIBRATIONAL LEVELS
Estimated Level
Broken Beam
Cantilever Beam
Fig.7
VL (dB) - Ref.Vel. = 150 mm/sec
FREQUENCY (Hz)

Paper presented at the Third ICIM/ECSSM '96, Lyon '96

Active control of blade-vortex interactions using a neuro-fuzzy controller

Ramesh Swaminathan, J.V.R. Prasad, and L.N. Sankar,
School of Aerospace Engineering, Georgia Institute of Technology,
Atlanta, GA 30332-0150, U. S. A.

ABSTRACT

Rotorcraft blade-vortex interactions(BVI) result in large pressure fluctuations over rotor blades leading to increased unsteady blade loads, noise, and vibration. Previous studies have indicated that an effective method for reducing BVI is through the use of active control schemes. As a workable dynamic model of the process for controller design is difficult to develop a rule-based fuzzy controller is used in this study. As the choice of the fuzzy controller parameters for acceptable performance depend on flight condition, a neural network is trained to adaptively modify the fuzzy controller parameters as a function of flight condition. The resulting neuro-fuzzy control scheme is evaluated using a numerical simulation model of BVI in order to demonstrate the effectiveness of the proposed scheme.

1. INTRODUCTION

During flight a helicopter rotor blade passes close to vortices shed by itself and by preceding blades. These blade-vortex interactions (BVI) give rise to pressure fluctuations on each blade resulting in significant increase in unsteady blade loads, noise and vibration. There has been considerable research over the last decade on the subject of blade vortex interactions which included both analytical and experimental investigations. For instance, a series of wind tunnel test results were obtained wherein blade load variations during blade-vortex interactions were included[1] and a viscous flow model was used to investigate the interaction of airfoil sections with vortices[2]. An important conclusion from these and various other research efforts is that the blade vortex interaction can be characterized by a pressure pulse which appears at the leading edge portion of the blade as the vortex passes by. The study conducted using a scaled rotor identifies four nondimensional parameters that are very important for BVI noise; hover tip Mach number, advance ratio, local inflow and thrust coefficient[3]. Out of these, the local inflow can be significantly altered through active control means.

A few of the studies conducted in the past included ways and means of reducing the undesirable effects of BVI. For instance, a passive scheme was investigated wherein winglets were placed on the rotor blade in order to reduce noise[4]. However, all the passive schemes considered to date have met with limited success. An active control scheme using higher harmonic control was tested in windtunnel to minimize blade-vortex interaction noise[5]. However, the scheme was found to be effective only at the design flight condition. The effects of leading and trailing edge flaps on the aerodynamics of airfoil/vortex interactions were investigated using computational fluid dynamics analysis[6]. It was shown that a trailing edge flap was effective for subcritical interactions while a leading edge flap was needed for supercritical interactions. Reduction of the characteristic BVI pressure pulse with the aid of a trailing edge flap was also investigated[7] and it was shown that with a pressure sensor on the leading edge and a flap at the trailing edge, a feedback control scheme could be formulated to reduce the vortex induced pressure pulse.

Because of the complex nature of BVI analytical models, a majority of the studies in the past have used ad-hoc strategies for developing control laws. A dynamic model of BVI that is tractable to control design techniques is difficult to develop and it would involve many approximations. On the other hand, a controller based on fuzzy logic is rule-based and does not require a dynamic model in its synthesis and design. The present study considers a fuzzy rule-based controller and a trailing edge flap control scheme for active control of BVI. Rules for the fuzzy controller are formulated using simulation studies and a genetic algorithm is used to optimize for input membership functions, and fuzzification and defuzzification weights. In order for the controller to be effective over a range of flight conditions, adaptation of fuzzification and defuzzification weights with flight condition using a neural network is considered. The paper is organized as follows: First, a general scheme involving a neuro-fuzzy controller for active control of BVI is proposed. Next, an application of the proposed neuro-fuzzy control scheme using a numerical simultion model of BVI is presented followed by simulation results, conclusions and recommendations.

0-8194-2165-0/96/$6.00

2. THE NEURO-FUZZY CONTROLLER

The measurements required for control of the pressure pulse amplitude are chosen to be pressure coefficient C_p, and pressure coefficient rate $\dot{C}_p$. The fuzzy controller output "u" feeds into the flap actuator which in turn deflects the trailing edge flap. Both the measurements and fuzzy controller outputs are classified into desired number of fuzzy partitionings. Although the choice of membership functions for fuzzification of measurements is not unique, previous studies indicate that triangular membership functions are effective for similar fuzzy control problems[8,9]. The defuzzification is carried out using the center of gravity method[10]. Usually, the shape of these membership functions and weighting parameters used in a fuzzy controller are tuned using a trial and error approach. However, in a Multiple Input Multiple Output (MIMO) setting such an approach would prove to be tedious and nonoptimal. Hence, a genetic algorithm is used to optimize for the membership function shapes, fuzzification and defuzzification weighting parameters.

Genetic Algorithms(GA) are different from conventional search methods in the following ways[11]:

i) GA works with a coding of the parameter set, not the parameters themselves.

ii) GA searches from a population of points, not a single point.

iii) GA uses probabilistic transition rules, not deterministic transition rules to guide the search process.

GA requires the natural parameter set of the optimization problem to be coded as a finite-length string. These strings then pass through the GA operations of selection, crossover and mutation over several GA generations[11] to evolve into an optimal solution. An advantage of a genetic algorithm is the problem-independent characteristic of its search process. Hence, GA could be considered as a block to evolve the required parameter set to optimize a given cost function. The performance index used in GA optimization is formulated to achieve a reduction in the pressure pulse amplitude at a selected point or at several points on the blade. For the control of blade-vortex interactions the GA performance index (PI) is expressed as

$$J(\bar{p}) = \int_0^T (w_1 C_p^2 + w_2 \dot{C}_p^2 + w_3 \delta^2 + w_4 \dot{\delta}^2) dt, \qquad (1)$$

where w_1, w_2, w_3, and w_4 are preselected relative weights, δ and $\dot{\delta}$ are flap angle and flap deflection rate, respectively. The linguistic rules for the control problem are fixed based on the available knowledge base. The effectiveness of the optimized fuzzy controller in suppressing the pressure pulse amplitude was found to be dependent on the helicopter flight condition. Hence, the fuzzy controller parameter vector $\bar{p}$ is adapted as a function of the given flight condition using a Neural Network (NN). The data for training the NN is GA optimized parameter vectors $\bar{p}_i$ at several flight conditions.

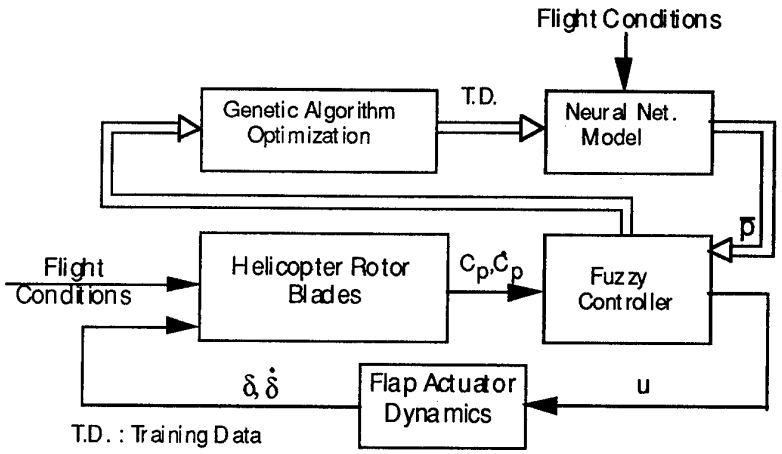


Figure 1. Schematic of the Controller Design Process

In the past several researchers have shown the approximating capabilities of a multilayered feedforward NN[12]. Hence, such a network is used to model the fuzzy controller parameter vector function. An appropriate activation function for the neurons is chosen and the network is trained using the back propagation algorithm[12]. The NN is trained to ensure a good generalization capability of the network

while maintaining accuracy of the approximation to within acceptable levels. A schematic of the proposed controller design process is presented in Figure 1.

3. CONTROLLER DESIGN AND RESULTS

The neuro-fuzzy controller scheme proposed in the previous section is evaluated using a two dimensional unsteady, inviscid, incompressible subsonic potential flow solution[7]. According to this solution the blade airfoil section is divided into several panels as shown in Figure 2. The pressure coefficient C_p, and pressure coefficient rate $\dot{C}_p$ at a point in close proximity to the airfoil leading edge, are used as measurements for controller evaluation studies. At different angles of attack, the closed-loop C_p, and $\dot{C}_p$

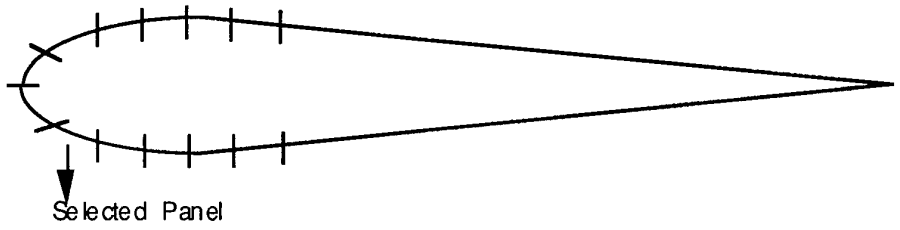


Figure 2. An Airfoil Section with Sample Panels

responses are simulated for a passing vortex disturbance over the blade airfoil section. In this study the measurements, and control "u" are classified into three fuzzy partitionings. Triangular membership functions are used for fuzzificztion of the measurement variables and the control was defuzzified using the center of gravity method[10]. Sigmoidal activation functions are used for neurons in the NN model. The control penalty terms are not included in the GA cost function of equation (1). The parameter vector used for NN training consist of fuzzification and defuzzification weighting parameters and the training is carried out for 12 epochs. Simulation results are obtained for a flight condition angle of attack different from those used for NN training. The variation of pressure coefficient(C_p), and pressure coefficient rate($\dot{C}_p$) are shown in figures 3a, and 3b, respectively, for both open-loop and closed-loop simulations. From these results, it is seen that the proposed neuro-fuzzy control scheme is effective in reducing the BVI induced pressure pulse amplitude. Further investigations are required to study the possibility of adaptively modifying the membership functions shapes in addition to the weighting parameters. Furthermore, a control penalty along with any other control constraints need to be included.

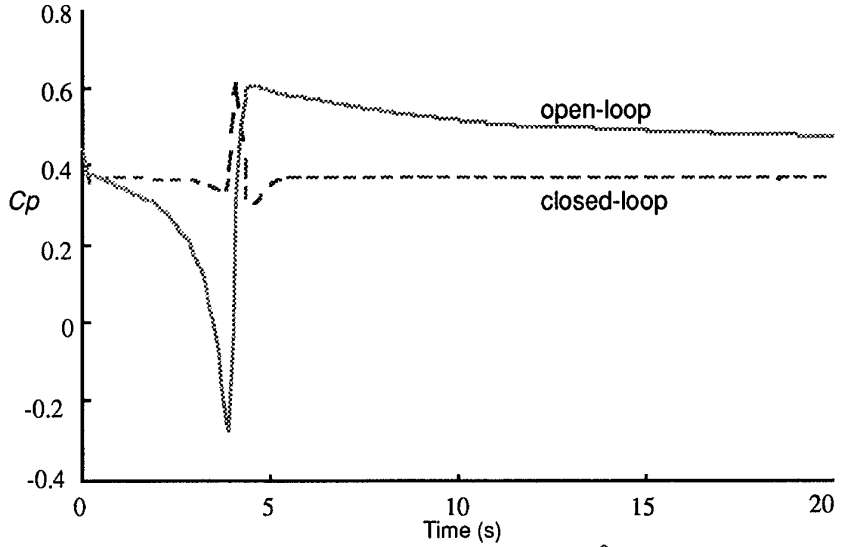


Figure 3a. Response Plot for $\alpha=9^0$

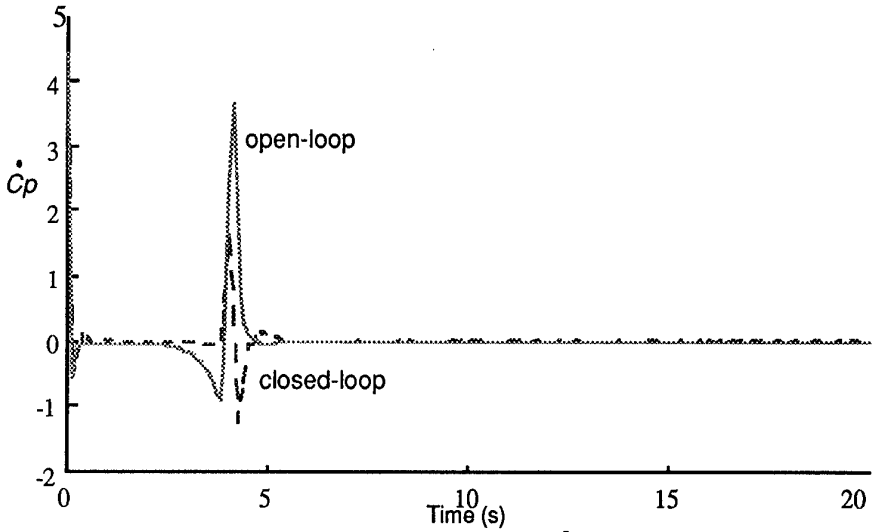


Figure 3b. Response Plot for $\alpha=9^0$.

4. CONCLUSIONS AND RECOMMENDATIONS

An optimal neuro-fuzzy control acheme for active control of blade-vortex interaction is proposed in this study. The scheme is evaluated using a numerical simulation model of BVI. Preliminary results indicate that the proposed acheme is effective in reducing the BVI induced pressure pulse amplitude. Further investigation is required to study the possibility of adaptively modifying the membership function shapes in addition to weighting parameters.

5. REFERENCES

1. Kokkalis, A., and Galbraith, R.A. McD., "Results from the Glasgow University BVI Facility," *13th European Rotorcraft Forum, Arles, France*, Sep. 8-11, 1987.

2. Tang, W., and Sankar, N.L., "Strong Blade-Vortex Interactions Including Collision," *American Society of Mechanical Engineers, Fluid Engineering Division (Publication) FED, Vol.52, ASME, New York, NY*, 1987.

3. Boxwell, D.A., Schmitz, F.H., Splettstoesser, W.R. and Schultz, K.J., " Helicopter Model Rotor Blade-Vortex Interaction Impulsive Noise: Scalability and Parametric Variations," *Journal of the American Helicopter Society, Vol. 32, No. 1*, January 1987.

4. Mueller, M., "Influence of Winglets on Rotor Aerodynamics," *Proceeding of the 43rd Annual Forum of the American Helicopter Society*, 1987.

5. Pressier, J.S., Brooks, T.F., and Martin, R.M., "Rotorcraft Blade/Vortex Interaction Noise: Its generation, Radiation, and Control," Presented to the *International Council of the Aeronautical Sciences, 17th Congress, Stockholm, Sweden,* Sep. 9-14, 1990, ICAS-90-5.2.2 .

6. Hassan, A.A., Sankar, L.N. and Tadghighi, H., "Effects of Leading and Trailing Edge Flaps on the Aerodynamics of Air Foil/Vortex Interactions," *Journal of the American Helicopter Society, Vol. 39, No. 2*, April 1994.

7. Prasad, J.V.R., Bowles, T. and Vandekerchove, D., "Active Control of Blade Vortex Interaction," Paper presented at the *specialists' meeting on rotorcraft basic research, Atlanta, GA*, March 1991.

8. Phillips, C., Karr,C., and Walker, G., "A Genetic Algorithm for Discovering Fuzzy Logic Rules," *Proc of the International Fuzzy Systems and Intelligent Control Conference, Louisville, KY*, Mar. 1994.

9. Jiang, T.Y., Prasad, J.V.R., and Swaminathan, R., "Synthesis of an integrated Fuzzy/Nonlinear Controller for Rotorcraft," *American Helicopter Society, 51st Annual forum, Fort Worth, TX*, May 9-11, 1995.

10. Takagi, T., and Sugeno, M., "Fuzzy Identification of Systems and its Applications to Modeling and Control," *IEEE Trans., on Systems, Man, and Cyber., vol.151* , 1985.

11. Goldberg, D.E., "Genetic Algorithms in Search, Optimization, and Machine Learning," *Addison-Wesley Publishing Company, Inc*, 1989.

12. Krishnakumar, K., "Optimization of the Neural Net Connectivity Pattern using a Back Propagation Algorithm," *Journal of Neurocomputing, No.5, pp. 273-286*, 1993.

Controlling a chaotic response

M. Battaini and F. Casciati

Department of Structural Mechanics, University of Pavia,
Via Abbiategrasso 211, 27100 Pavia, Italy

1 Abstract

Attention is focused on low-damping-rubber base-isolators. Instead of thinking in terms of intelligent materials, this paper pursues the definition of conditions of behaviour which result intelligent in view of a coupling with an active control device (hybrid control). In particular, situations which show a chaotic behaviour of the dynamic response to external excitations are promising in terms of control efficiency. The regions of chaotic behaviour are identified by evaluation of the corresponding Lyapunov exponents.

2 Introduction

Since chaotic motion [1],[5],[8] is neither predictable nor controllable, it was initially regarded as something to avoid. Further studies emphasized how a suitable selection of driving terms can lead a chaotic system to behave in a desired manner. In a recent report [10] the presence of chaos is regarded as a desired feature for an actively controlled system; tiny perturbations on a chaotic state can be used to stabilize a regular dynamic behaviour and to rapidly direct chaotic trajectories toward a desired state.
The aim of this paper is to investigate the possible chaotic behaviour of a low-damping hysteretic oscillator and the final goal is the development of a control device operative on chaotic conditions. To identify the chaotic regions into the parameter space, the Lyapunov exponents are evaluated [11]. On the other side, the hysteretic behaviour is represented by a suitable endochronic model [4],[6] The influence of the model parameters on the dynamical behaviour of the oscillator is numerically investigated.

3 Governing Equations

3.1 Equation of motion

The system to be investigated is a hysteretic single-degree-of-freedom system (Figure 1). Its equation of motion can be expressed as:

$$m\ddot{x} + c\dot{x} + \Phi(x,t) = f(t) \tag{1}$$

where m and c represent the mass and the viscous damping coefficient, respectively, of the oscillator; $f(t)$ is the external action, assumed to be periodic of amplitude α and frequency ω, respectively, and Φ is the hysteretic restoring force. In general, the term Φ can be regarded as the sum of a linear part rx and a hysteretic contribution z:

$$\Phi = rx + z \tag{2}$$

In Eq. (2) r represents the linear stiffness term and z is an auxiliary variable. Its first derivative with respect to time t is:

$$\dot{z} = \gamma \mid \dot{x} \mid z + \beta\dot{x} \mid z \mid + A\dot{x} \tag{3}$$

It expresses the so called Bouc-Wen model.

3.2 The endochronic model

Figure 2 shows a shape of the Bouc-Wen model which is consistent with the constitutive law of a low-damping rubber. For this purpose, if one assumes $A = 0.4$ in Eq. (3), the parameters β and γ must

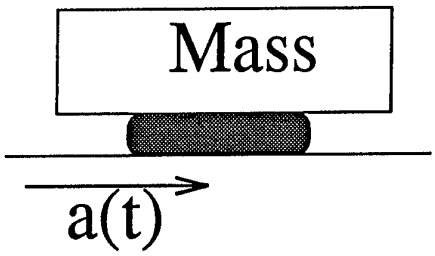


Figure 1: Base isolator device

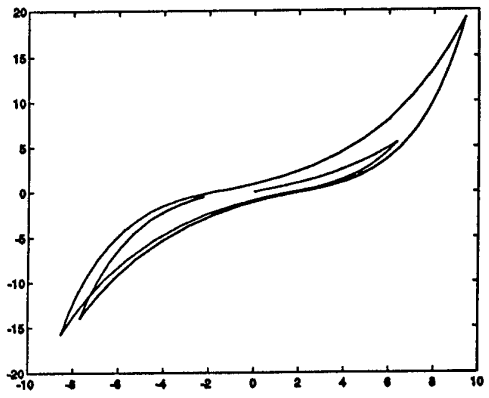


Figure 2: Bouc-Wen model

satisfy the following constraints:

$$\begin{aligned} 0.01 < \gamma < 0.5 \\ -1.2 < \beta < 0.3 \end{aligned} \tag{4}$$

In particular, since the chaotic behaviour of the Duffing oscillator

$$m\ddot{x} + c\dot{x} + x + x^3 = f(t) \tag{5}$$

was deeply investigated in the literature, attention is initially focused on those values of β and γ which make the Bouc-Wen model identical to the constitutive law which characterizes Eq. (5) (see Figure 3) They are:

$$\begin{aligned} \gamma = 0.01 \\ \beta = -1.2 \end{aligned} \tag{6}$$

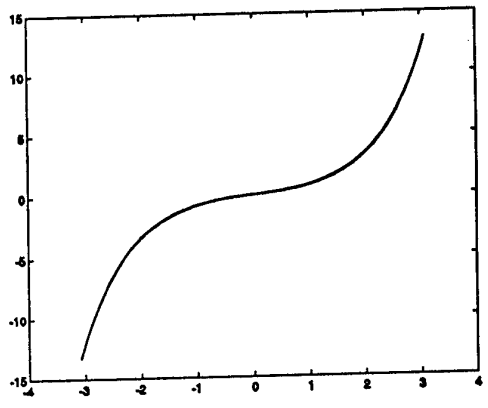


Figure 3: Adopted Bouc-Wen model

3.3 Lyapunov exponents

A system showing at least one positive Lyapunov exponent is chaotic, with the magnitude of the exponent reflecting the time scale on which the system dynamics becomes unpredictable.
Consider a continuous dynamical system in an n dimensional phase space and monitor the long-term evolution of an n dimensional infinitesimal hypersphere of initial conditions. The hypersphere will become an n dimensional hyperellipsoid due to the locally deforming nature of the flow. The i-th dimensional Lyapunov exponent is defined in term of the length $l_i(t)$ of the ellipsoid principal axis:

$$\lambda_i = \lim_{n\to\infty} \frac{1}{t} log_2 \frac{l_i(t)}{l_i(0)} \tag{7}$$

Let the exponents λ_i be ordered from the largest to the smallest one.
Each positive exponent reflects a "direction" in which the system experiences the repeated stretching and folding that correlates states on the attactor. Therefore the long term behaviour of initial condition cannot be predicted. The algorithm used in this paper for the Lyapunov exponent calculation is the one developed in [11]

4 Controlling a chaotic system

Chaotic systems are characterized by extreme sensitivity to tiny perturbations. This characteristic can be used both to stabilize dynamic behaviour and to direct chaotic trajectories toward a desired state. Thus small, carefully chosen perturbations are able to effect a large beneficial change in the long term system behaviour.
Indeed, a possible technique to control a chaotic system could be through the stabilization of the unstable orbits by applying small parameter adjustments as discussed in [10] put Eq. (1,3) in the general form of a system of autonomous ordinary differential equations $d\psi/dt = G(\psi)$, where $d\psi(t)$ is a vector of length M and t is the continous time variable. By an integration of $d\psi/dt = G(\psi)$ over (t_n, t_{n+1}), the response ψ_{n+1} at time $n+1$ is calcutaed from the one at time t_n and the map $\psi_{n+1} = F_\psi(\psi_n)$ is defined. Let p be the system parameter vector that could be modified to control the response. One writes the map in the form:

$$\psi_{n+1} = F_\psi(\psi_n, p) \tag{8}$$

It is possible to reduce the size M of the map ψ_n by introducing a $M-1$ Poincaré map. Let Z_n be the associated vector. As a consequence the map (8) becomes:

$$Z_{n+1} = F(Z_n, p) \tag{9}$$

Let p_0 be any nominal value of p and $Z^*_{n+1} = F(Z^*_n, p_0)$ be the associated trajectory. For values of p close to p_0 the following linear map can be introduced:

$$(Z_{n+1} - Z^*_{n+1}) = \Theta(Z_n - Z^*_n) + \Gamma(p - p_0) \tag{10}$$

where Θ is $N \times N$ Jacobian matrix $\Theta = \partial F/\partial Z$ and Γ is the column vector of size N, $\Gamma = \partial F/\partial p$. These partial derivatives calculated at $Z = Z^*_n$ and $p = p_0$. If one adopts the policy of changing p at each iteration, the last value of the sequence Z_n is found on the basis of small changes of p from p_0 to p_n. Introduce now the linear control law:

$$(p_n - p_0) = -K^T(Z_n - Z^*_n) \tag{11}$$

which for given K (a constant column vector of size N) specifies p_n on each iteration. Introducing Eq. (11) into Eq. (10), one obtains:

$$\delta Z_{n+1} = (\Theta - \Gamma K^T)\delta Z_n \tag{12}$$

where $\delta Z_n = Z_n - Z^*_n$.
The trajectory Z^*_n will be stable if one can take K so that the matrix $(\Theta - \Gamma K^T)$ has all the eigenvalues with modulus smaller than one. In this case $\delta Z_n \to 0$ as $n \to \infty$. This procedure gives the time dependent parameter value p_n required to stabilize an unstable trajectory in a chaotic system. This strategy has the advantage that the explicit form of F is not required. It however is only effective in stabilizing trajectory near existing periodic orbits.

5 Model parameters

Two groups of parameters are considered:

1. the parameters of the external force (represented as a periodic function): $p_1 = \{\alpha, \nu\}^T$
2. the parameters of the hysteretic oscillator defined by Eq. (3): $p_2 = \{\beta, \gamma\}^T$

To investigate the possibilty of chaotic behaviour two parametric analyses were therefore carried out. The Bouc-Wen parameters are initially selected $p_2 = \bar{p_2}$ in order to obtain a restoring force similar to the cubic term of the Duffing oscillator for $c = 0.1$. For this example $r = 0.4$ is used. The aim is to reproduce the response of the Duffing oscillator.
The vector p_1 has entries ranging between 0.4 and 4 for α and 0.2 and 0.8 for ν. Integrating the system of linear and nonlinear equations, the Lyapunov map is calculated. The chaotic region defined by $\bar{p_1} = \{0.055, 1.5\}$ was adopted for the second parametric analysis which studies the effect of the parameters in $p_2 = \{\beta, \gamma\}$. The parameter γ varies from 0.01 to 0.5 and β ranges between -1.2 to 0.3. The new map of the Lyapunov exponents is shown into the figures 4 and 5. It is worth noting that the chaotic behavior is possible only where the dissipation is very low (from figures 4 and 5 the Lyapunov exponents are positive only when the parameters β and γ values are close to the ones of $p_2 = \bar{p_2}$), while increasing the dissipation term the system, after an inital transient phase, becomes stable.
All the results are obtained integrating the system over 50 times the external force period and using a time step of $\frac{1}{200}$ of the force frequency.
For a point where a chaotic response was discovered, three section of the Poincarè map are computed over a time range of 20000 force period and neglecting the initial transient part of 500 period. The sections are in the phase spaces: displacement - velocity. (Figure 6).

6 Conclusions

This paper moves within the framework of a new approach to the design of hybrid structural control devices which uses the extreme sensitivity of chaotic systems to tiny perturbations to stabilize the dynamic behaviour.
This specific contribution investigates the regions of chaotic response for hysteretic oscillators which closely idealize the behaviour of low-damping-rubber base isolator.

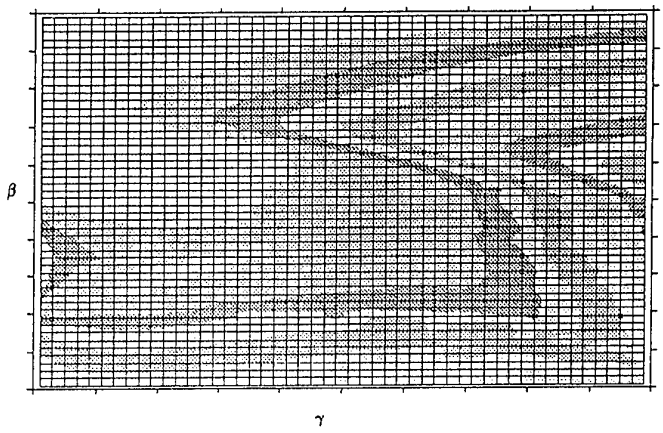


Figure 4: Lyapunov exponents map in the plane $_{I}$, ρ: blanck areas means negative exponents; dark areas positive exponents. The different dark shade reflects the exponents values (darker means greater value)

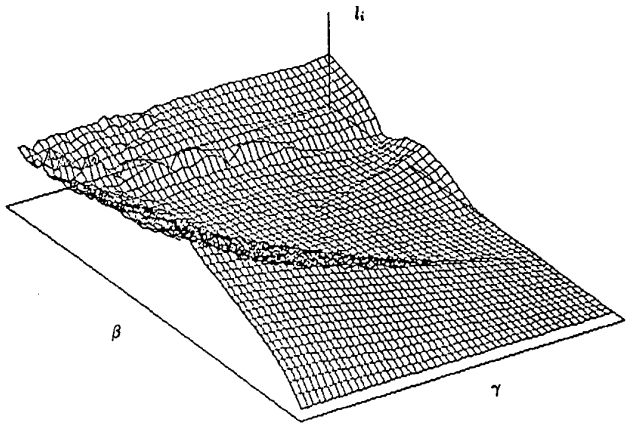


Figure 5: Lyapunov exponents three dimensional map in the plane γ, β; l_i represents the exponent value

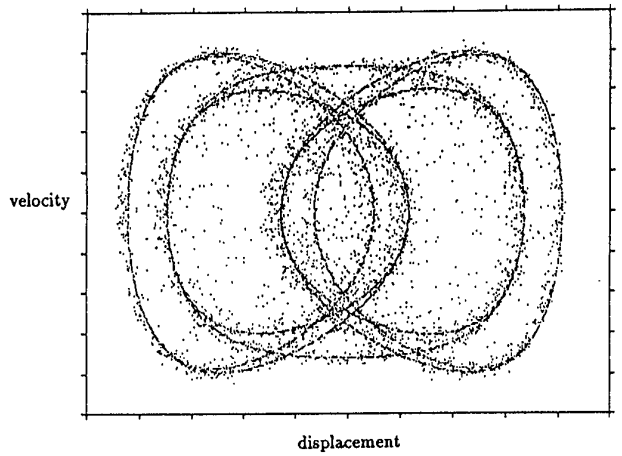


Figure 6: Poincarè map in the plane displacement - velocity

[1] G. L. Baker and J. P. Gollub, 1990, *Chaotic Dynamics*, Cambridge University Press, Cambridge

[2] F. Bontempi, 1993, Computational Aspects in Chaotic and Stochastic Dynamics, *Dynamic motion chaotic and stochastic behaviour*, CISM Courses and Lectures No. 340, International Centre for Mechanical Sciences, Springer-Verlag Wien New York

[3] F. Bontempi and F. Casciati, 1994, Chaotic Motion and Stochastic Excitation, *Nonlinear Dynamics* 6: 179-191

[4] F. Casciati, 1989, Stochastic Dynamics of Hysterestic Media, *Structural Safety*, 6 259-269

[5] F. Casciati, 1993, *Dynamic motion chaotic and stochastic behaviour*, CISM Courses and Lectures No. 340, International Centre for Mechanical Sciences, Springer-Verlag Wien New York

[6] F. Casciati and L. Faravelli, 1991a, *Fragility Analysis of Complex Structural Systems*, Research Studies Press, Tauton

[7] G. Rega, F. Benedettini and A. Salvatori, 1991, Periodic and Chotic Motions of an unsymmetrical oscillator in nonlinear structural dynamics, *Chaos, Solitons and Fractals* 1(1), 39-54

[8] M. Tabor, 1989, *Chaos and Integrability in Nonlinear Dynamics*, John Wiley, Chichester, UK

[9] H. Troger and A. Steindl, 1994, *Nonlinear stability and Bifurcation Theory, An Introduction for Engineers and Applied Scientists*, Springer- Verlag Wien New York

[10] T. Shinbrot, C. Grebogy, E. Ott and J.A. Yorke, 1993, Using small perturbations to control chaos, em Nature, Vol 363, 411-417

[11] A. Wolf and J.B. Swift, H.L. Swinney and J.A. Vastano, 1985, Determining Lyapunov Exponents from a Time Series, *Physica 16 D, 285-317*, North-Holland, Amsterdam

Finite element modeling of PMN electrostrictive materials

J.C. Debus, B. Dubus,

IEMN Département ISEN, 41 Bd Vauban, 59046 Lille Cedex,France.

M. McCollum, S. Black,

NUWC/USRD, P.O. Box 568337, Orlando FL 32856-8337, USA.

ABSTRACT

New electrostrictive lead magnesium niobate ceramics (PMN) are promising materials for applications in the field of actuators, transducers and motors. These materials have strains roughly an order of magnitude larger than those of the lead zirconate-titanate (PZT) ceramics. This is due to PMN dielectric permittivity which is also a factor of ten or more larger than dielectric permitttivity of PZT materials. However, the use of these electrostrictive materials for practical applications presents some difficulties: highly non-linear properties, temperature dependence of dielectric permittivity near the dielectric maximum, DC bias field needed. To improve the use of these electrostrictive materials, a better knowledge of the physical tensors of PMN and the developement of a numerical tool are necessary. The scope of this paper is to present the development of a two-dimensional electrostrictive element in the ATILA code for non-linear static analysis. The electrostrictive finite element is based on the assumption that the induced strain is proportional to the square of the applied electric field. The validity to the new capability is demonstrated by comparing computed strain and charge density with analytical solution and measured results for a PMN bar at various electric DC fields and mechanical prestresses.

1. THE ELECTROSTRICTIVE EFFECT

PMN electrostrictive materials are relatively new and complicated in behaviour[1]. Non-linear constitutive models for electrostrictors are not as mature as models for piezoelectrics[2]. As shown in Fig. 1, the electric field in an electrostrictor exhibits a quadratic dependence with the electric field when $E<E_0$ (E_0 = 1 MV/m). At high electric field ($E>E_0$), the polarization begins to saturate and higher-order terms must be added to the model. In this work, it is considered that the induced strain is proportional to the square of the applied electric field. Therefore, the model is valid as long as the electric field is lower than E_0. As the electromechanical coupling is determined by the electric displacement rather than the electric field[3], the stress and the electric displacement are chosen as independant variables. The constitutive equations can be written:

$$\begin{cases} \underset{\sim}{S} = \left[s^D\right] \underset{\sim}{T} + \left[g\,(Q, \underset{\sim}{D})\right] \underset{\sim}{D} \\ \underset{\sim}{E} = -2\left[g\,(Q, \underset{\sim}{D})\right] \underset{\sim}{T} + \left[\beta^T\right] \underset{\sim}{D} \end{cases} \tag{1}$$

where $\underset{\sim}{S}$ and $\underset{\sim}{T}$ are the strain and stress condensed tensors, $\underset{\sim}{E}$ and $\underset{\sim}{D}$ are the electric field and electric displacement vectors, $\left[s^D\right]$ is the elastic compliance tensor at constant excitation and $\left[\beta^T\right]$ is the dielectric impermeability matrix at constant stress. The non-linear behaviour is described by the "piezoelectric" strain constant tensor $[g]$ defined as:

$$[g] = \begin{bmatrix} Q_{11}D_1 & Q_{12}D_1 & Q_{12}D_1 & 0 & (Q_{11} - Q_{12})D_3 & (Q_{11} - Q_{12})D_2 \\ Q_{12}D_2 & Q_{11}D_2 & Q_{12}D_2 & (Q_{11} - Q_{12})D_3 & 0 & (Q_{11} - Q_{12})D_1 \\ Q_{12}D_3 & Q_{12}D_3 & Q_{11}D_3 & (Q_{11} - Q_{12})D_2 & (Q_{11} - Q_{12})D_1 & 0 \end{bmatrix} \tag{2}$$

0-8194-2165-0/96/$6.00

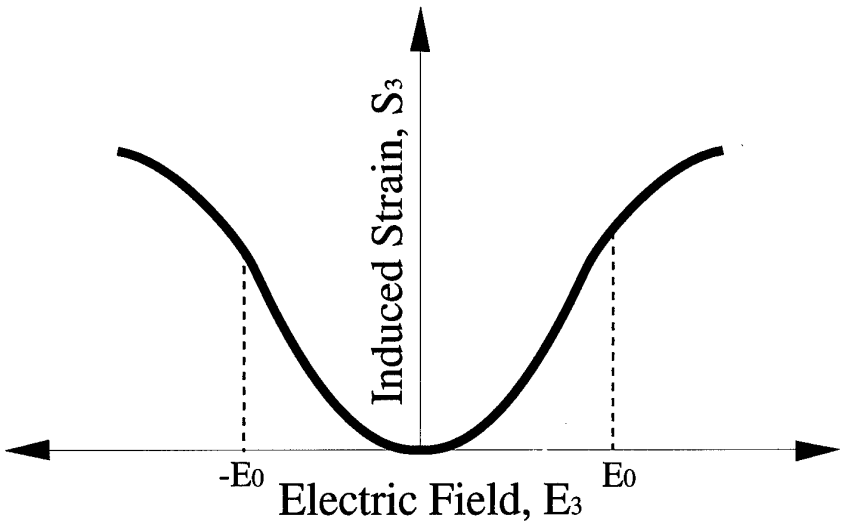


Figure 1: typical electrostrictive response (induced strain versus applied electric field) for a relaxor ferroelectric.

where $[Q]$ is the reduced tensor of the electrostrictive constants[2-4].

2. FINITE ELEMENT FORMULATION

The electrostrictive finite element is developped in the ATILA Code[5] as a piezoelectric finite element with a non-linear [g] tensor. The complete set of equations for the electrostrictive structure can be written:

$$\begin{bmatrix} [K_{uu}] & [K_{u\Phi}] \\ 2[K_{u\Phi}]^T & [K_{\Phi\Phi}] \end{bmatrix} \begin{Bmatrix} \underset{\sim}{U} \\ \underset{\sim}{\Phi} \end{Bmatrix} = \begin{Bmatrix} \underset{\sim}{F} \\ -\underset{\sim}{Q} \end{Bmatrix} \tag{3}$$

where $\underset{\sim}{U}$, $\underset{\sim}{\Phi}$, $\underset{\sim}{F}$ and $\underset{\sim}{Q}$ are the vectors of the nodal values of the displacement, the electric potential, the external force and the electric charge respectively. $[K_{uu}]$, $[K_{u\Phi}]$ and $[K_{\Phi\Phi}]$ are the classical stiffness, piezoelectric and dielectric matrices of a piezoelectric finite element model. They result from the assembling of the elementary matrices:

$$[K_{uu}] = \sum_e \int_{\Omega^{(e)}} [B_u^{(e)}]^T [c^{E(e)}] [B_u^{(e)}] \, d\Omega^{(e)} \tag{4}$$

$$[K_{u\Phi}] = \sum_e \int_{\Omega^{(e)}} [B_u^{(e)}]^T [e^{(e)}] [B_\Phi^{(e)}] \, d\Omega^{(e)} \tag{5}$$

$$[K_{\Phi\Phi}] = -\sum_e \int_{\Omega^{(e)}} [B_\Phi^{(e)}]^T [\varepsilon^{S(e)}] [B_\Phi^{(e)}] \, d\Omega^{(e)} \tag{6}$$

The matrices $[B_u^{(e)}]$ and $[B_\Phi^{(e)}]$ contain respectively information related to the derivatives of the shape function for the element displacement and electric potential fields. $[c^{E(e)}]$ is the stiffness tensor at constant electric field, $[e^{(e)}]$ is the piezoelectric stress tensor and $[\varepsilon^{S(e)}]$ is the dielectric permittivity matrix at constant strain. Using physical constant tensor relations, it can be easily shown that these tensors depend on the [g] tensor and therefore on the electric displacement. In element e, the electric displacement is expressed as:

$$\underset{\sim}{D}^{(e)} = 2[e^{(e)}][B_u^{(e)}]\underset{\sim}{U}^{(e)} - [\varepsilon^{S(e)}]^T[B_\Phi^{(e)}]\underset{\sim}{\Phi}^{(e)} \tag{7}$$

It appears clearly that equation (3) is non-linear because $[K_{uu}]$, $[K_{u\Phi}]$ and $[K_{\Phi\Phi}]$ are fonctions of $\underset{\sim}{U}$, and $\underset{\sim}{\Phi}$.

The problem is solved using an iterative procedure. Element data are the matrices $[s^D]$, [Q] and $[\varepsilon^T]$ which are considered as having constant values. The five steps are:

i) initialization of $\underset{\sim}{D}$,

ii) assembling of equation (3),

iii) solving of equation (3),

iv) computation of the new $\underset{\sim}{D}$ using equation (7),

v) comparison of old and new $\underset{\sim}{D}$, and iteration from ii) to v) until convergence.

Initialization and computation of electric displacement are made at each Gauss point used in the numerical integration of equations (4) to (6).

3. ANALYSIS OF AN ELECTROSTRICTIVE BAR

To validate the previous developements, a long electrostrictive bar (2x2x10mm) with electrodes located at both ends is analyzed (Fig. 2). A static mechanical force F is applied at both ends and a quasi-static (10 Hz) electric voltage Φ_0 is prescribed between the electrodes. The corresponding analytical and numerical models are described in sections 3.1 and 3.2 respectively. Numerical and analytical results are compared to measurements made at NUWC New London[6] in section 3.3.

3.1. Analytical model

It is assumed that the width w and the thickness t of the bar are small compared to its length *l*. Mechanical and electrical boundary conditions on lateral faces give:

$$T_1 = T_2 = T_4 = T_5 = T_6 = 0 \tag{8}$$

$$D_1 = D_2 = 0 \tag{9}$$

$\underset{\sim}{D}$ and $\underset{\sim}{T}$ are chosen as independant variables. The electrostrictive set of equations is:

$$\begin{cases} S_3 = s_{33}^D T_3 + Q_{11} D_3^2 \\ E_3 = -2 Q_{11} T_3 D_3 + \beta_{33}^T D_3 \end{cases} \tag{10}$$

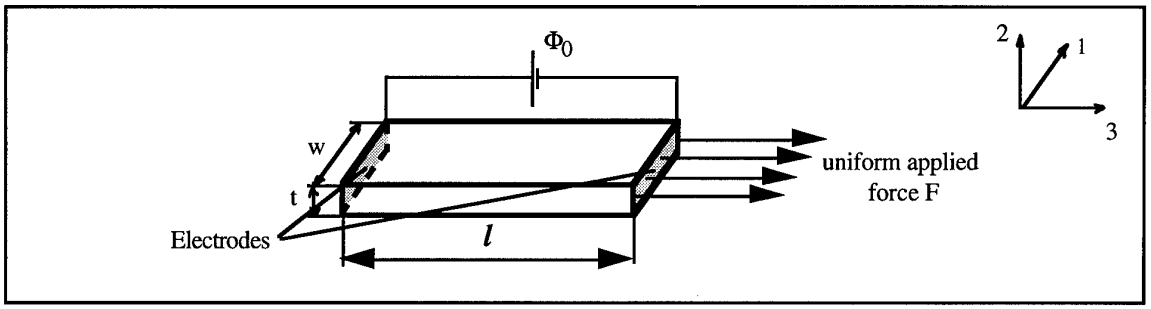


Figure 2 : geometry of the electrostrictive bar

Using Newton's law:

$$\frac{\partial T_3}{\partial z} = 0 \tag{11}$$

it is found that T_3 is constant along the bar:

$$T_3 = \frac{F}{wt} \tag{12}$$

Using Gaussian theorem:

$$\frac{\partial D_3}{\partial z} = 0 \tag{13}$$

it is found that D_3 is constant along the bar. From the second line of equation (10), E_3 is constant and is equal to:

$$E_3 = -\frac{\Phi_0}{l} \tag{14}$$

After combining equations (10), (12) and (14), we obtain:

$$D_3 = -\frac{\Phi_0}{l\left(\beta_{33}^T - \frac{2\,Q_{11}\,F}{wt}\right)} \tag{15}$$

$$S_3 = s_{33}^D \frac{F}{wt} + \frac{Q_{11}\,\Phi_0^2}{l^2\left(\beta_{33}^T - \frac{2\,Q_{11}\,F}{wt}\right)^2} \tag{16}$$

3.2. Numerical model

The bar is modelled assuming axisymmetry. Half of the bar is described using 4 elements (Fig. 3) with a symmetry condition at one end. The material properties are obtained from reference 6:

$$s_{11}^D = s_{22}^D = s_{33}^D = 0.3703\ 10^{-11}\ m^2/N \tag{17}$$

$$s_{12}^D = s_{13}^D = s_{23}^D = -0.1296\ 10^{-11}\ m^2/N \tag{18}$$

$$s_{44}^D = s_{55}^D = s_{66}^D = 1.0\ 10^{-11}\ m^2/N \tag{19}$$

$$\varepsilon_{11}^T = \varepsilon_{22}^T = \varepsilon_{33}^T = 2.1928\ 10^{-7}\ C/Vm \tag{20}$$

and the electrostrictive constants from reference 4:

$$Q_{11} = 0.133\ 10^{-1}\ m^4/C^2 \qquad Q_{12} = -0.606\ 10^{-2}\ m^4/C^2 \tag{21}$$

3.3. Comparaison of numerical, analytical and experimental results

Figure 3 presents the quasistatic electric displacement (or charge density) versus the quasi-static applied electric field for various static prestresses. The analytical and numerical models agree very well. Measurements are slightly different from theoretical results due to a small non-linearity of the dielectric permittivity. A remanent electric displacement is measured a zero-electric field.

Figure 4 presents the quasi-static strain versus the quasistatic applied electric field for various prestresses. The static strain (first term of equation (16)) is not measured. The quadratic behaviour is perfectly described by both numerical and analytical models. The deviation observed on measurements is due to the non-linearity on the dielectric permittivity which is not taken into account in the model.

From a numerical point of view, the convergence of the results is obtained with 2, 4, 5, 7, 8, 9 and 12 iterations for prestresses of 0, 2, 4, 6, 8, 10 and 12 kpsi respectively. The number of iterations is independant of the applied electric field excepted for a zero-field. At zero-field, the problem is linear and the result is obtained with 1 iteration for any prestress.

4. CONCLUSION

The electrostrictive finite element model described in this paper is based on the assumption that the induced strain is proportional to the square of the applied electric field. The analysis of a PMN bar submitted to a static prestress and a quasi-static voltage display results in very good agreement with analytical results and experiments at low electric field (E<1 MV/m). Developments concerning the adding of higher order terms in the strain-electric field law in order to describe the polarization saturation and the transient analysis are under progress.

5. REFERENCES.

1. K. M. Rittenmeyer, "Electrostrictive ceramics for underwater transducer applications", *J. Acoust. Soc. Am.*, vol 95-2, pp 849-856, Feb. 1994.

2. C. L. Hom and N. Shankar, "A fully coupled constitutive model for electrostrictive ceramic materials", *J. of Intell. Mater. Syst. and Struc.*, Vol. 5 pp 795-801, November 1994.

3. W. P. Mason, "Piezoelectric crystals and their application to ultrasonics", D. Van Nostrand Company, Princeton, 1964.

4. C. L. Hom, S. M. Pilgrim, N. Shankar, K. Bridger, M. Massuda, and S. Winzer, "Calculation of quasi-static electromechanical coupling coefficients for electrostrictive ceramic materials", *IEEE Trans. on UFFC*, Vol. 41-4, pp 542-551, July 1994.

5. "ATILA Finite-Element code for Piezoelectric and Magnetostrictive Transducer Modeling, Version 5.03", *User's Manual*, Institut Supérieur d'Electronique du Nord, Acoustics Laboratory, September 1993.

6. J. Powers, E. A. McLaughlin and M. Moffet, "PMN measurements at NUWC", *NUWC Report*, July 1995.

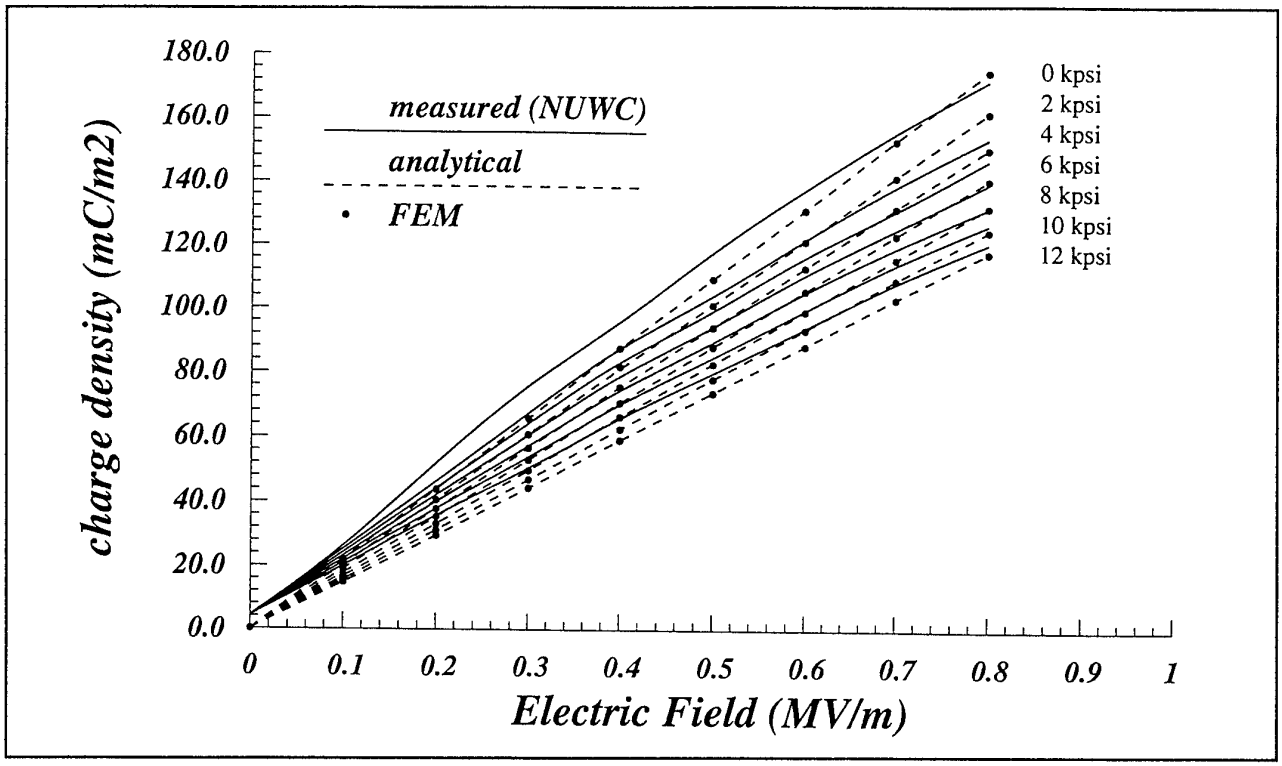


Figure 3: charge density versus electric field for a PMN bar under various prestresses

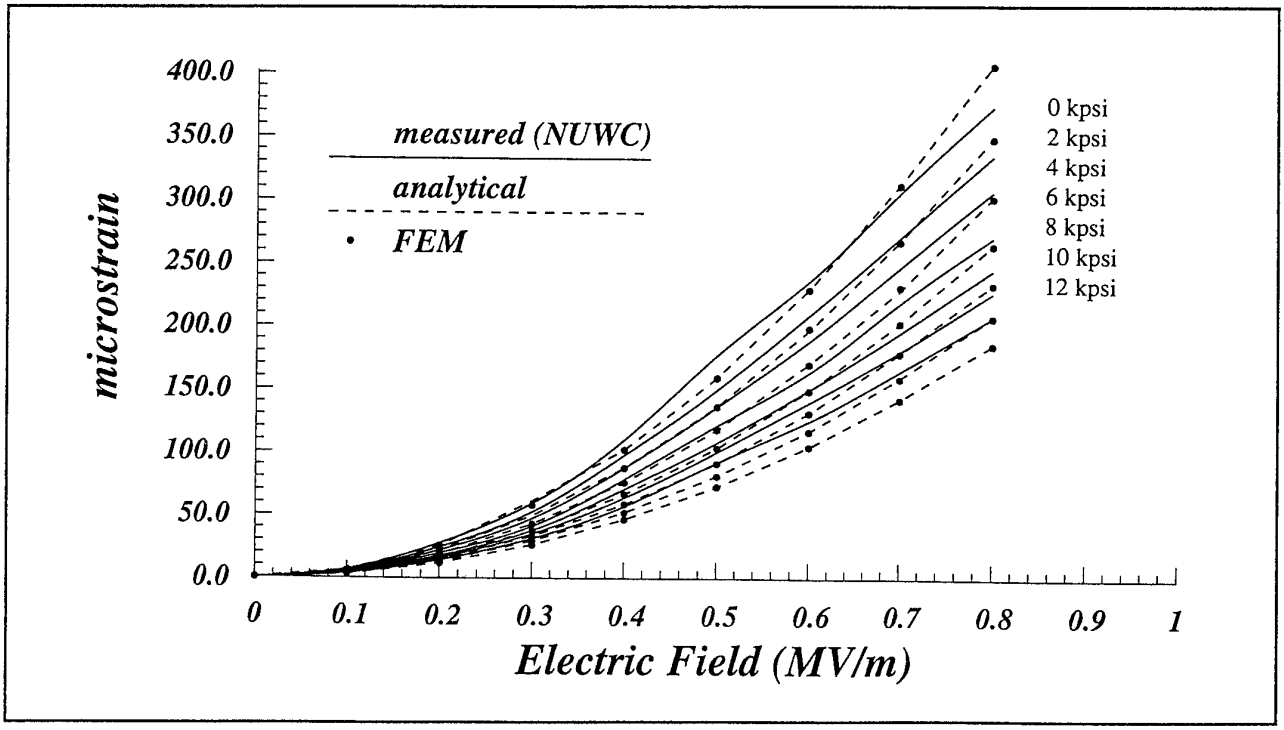


Figure 4: strain versus electric field for a PMN bar under various prestresses

Bifurcation diagrams and dissipative structures formation in noncrystalline materials

Alexei Shatalov, Michael Maryan, Alexander Kikineshy

Uzhgorod State University, Department of Solid State Electronics,
Uzhgorod, Ukraine

ABSTRACT

A model is proposed to describe crystal-liquid (liquid-crystal) equilibrium phase transition, emergence of bifurcations in non-equilibrium systems and dissipative structures formation in noncrystalline materials. We have investigated temperature dependencies of the share of atoms in liquid-like states and mean-square atomic displacements, in which regions corresponding to stable (crystal, liquid), metastable (superheated crystal, supercooled liquid) and virtual states are present. It is shown that system transits into non-equilibrium state when the melt freezing rate increases. Bifurcation diagrams, which define parameters deviations from their equilibrium values, when freezing rate is different are plotted. Process of dissipative structures formation in noncrystalline materials is described and their characteristics: life time and spatial sizes are defined.

1. INTRODUCTION

Noncrystalline state of matter represents peculiar self-organizing system with certain degree of ordering and life time, which are determined by external control parameters (temperature, pressure, electromagnetic radiation), and includes sufficiently wide range of materials from glassy matters with organic and non-organic origin to bioobjects[1,2,3]. It provides broad range of their properties and character of interaction with external fields. Self-organizing system formation requires execution of following conditions:

1. System must be open and exchange energy or matter with surroundings.
2. Feedback has to be present in system, that conditions system non-linearity; such processes are described by nonlinear differential equations.
3. When value of external influence exceeds certain critical magnitude homogeneous stationary state must become unstable and as a result transition into new stationary non-equilibrium state with some degree of spatial-temporal ordering occurs.

Example of self-organizing systems is dissipative structures formation, when freezing the melt, for which all above enumerated requirements are fulfilled (technology of freezing process causes presence of open system; feedback is provided by interaction of field of dynamic displacements, viscosity and force constants; transition realizes under certain rate of external conditions change). Solution of this problem is connected with investigation of structure and properties of equilibrium (crystalline, quasicrystalline, liquid) and strongly non-equilibrium (noncrystalline) materials in the vicinity of phase transition.

2. EQUILIBRIUM PHASE TRANSITION

Crystallization of the melt takes place during equilibrium liquid-crystal phase transition, as temperature lowers under thermodynamic equilibrium. Transition model must take into account anharmonicity of atomic oscillations, what is provided by use of self-consistent phonon theory (SCPT)[4] so long as classic harmonic and quasiharmonic approximations for system in transforming temperature region are not applicable. When heating, as amplitude of heat oscillations increases, quantity of defects goes up, what leads to their uniting. In phase transition vicinity concentration of such heterophase fluctuation essentially rises and as homogeneous atomic heat oscillations has considerable influence on the physical properties of the system[5].

First of all, we consider system containing N atoms which have two stationary states:

- liquid-like states, characterized by high dynamic displacements amplitude and low value of shear modulus;
- solid-like states.

So, Hamiltonian of the system in pair interaction approximation is as follows:

$$H = \sum_{l=1}^{N} \sum_{f} T_f(l)\, \sigma_f(l) + \frac{1}{2} \sum_{l \neq l'} \sum_{f,f'} \Phi_{ff'}(\vec{r}_{ll'})\, \sigma_f(l)\, \sigma_f(l'), \qquad (1)$$

0-8194-2165-0/96/$6.00

where $T_f(l) = \dfrac{\vec{P}^2(l)}{2M}$ is a kinetic energy of atom l, $\Phi_{ff'}(\vec{r}_{ll'})$ is a potential energy of atomic interaction, $\sigma_f(l)$ characterizes observed state of atom l: $\sigma_f(l) = 0$, if the atom l is in f state, $\sigma_f(l) = 1$, if the atom l is not in f state ($f = 1$ corresponds to solid-like state, $f = 2$ corresponds to liquid-like state).

The effective Hamiltonian of the system is

$$H_0 = \sum_f H_{0f} + (1-\sigma_2)^2 \sum_{l,l',\alpha} I_\alpha(l,l') v_\alpha(l), \quad v_\alpha(l) = \sum_m v_\alpha\left(\tfrac{l}{m}\right)\sigma_2(m), \tag{2.1}$$

$$H_{0f} = \sigma_f \sum_l T_f(l) + \frac{\sigma_f^2}{2} \sum_{l,l'} \sum_{\alpha,\beta} \left[\Phi(\vec{R}_{ll'}) + \frac{1}{2} u^\alpha(l,l') \tilde{\Phi}_f^{\alpha\beta}(l,l') u^\beta(l,l') \right], \tag{2.2}$$

model parameters of which are share of atoms in liquid-like states σ_2, force constants $\tilde{\Phi}_f^{\alpha\beta}(l,l')$ and atomic mean-square atomic displacements $y_{\alpha\beta}(l,l') = \langle u^\alpha(l,l')\, u^\beta(l,l') \rangle$ being determined by free energy variation principle

$$F \le F_0 + \langle H - H_0 \rangle_0, \quad F_0 = \sum_f F_{0f} - TS, \quad F_{0f} = -\Theta \ln\left\{ SPe^{\frac{-H_{0f}}{\Theta}} \right\}, \tag{3}$$

where $S = -k_b \ln\left[\prod_f \left\{ \dfrac{g_f!}{N_f!\,(g_f - N_f)!} \right\} \right]$ is entropy, g_f is statistic weight of f state, $\vec{r}_l = \vec{R}_l + \vec{u}_l + \vec{v}_l$, $\vec{u}_l$ and $\vec{v}_l$ are dynamic and static displacements of atom l, when the atom m is in liquid-like state, $\Theta = k_b T$, k_b is Boltzmann constant. Variation of F in parameters σ ($\sigma \equiv \sigma_2$), $\tilde{\Phi}_f^{\alpha\beta}(l,l')$, $y_{\alpha\beta}(l,l')$ when temperature T and pressure P are fixed

$$\delta F = \left[\frac{\partial F}{\partial \sigma}\right]_{y_{\alpha\beta},\tilde{\Phi}_f^{\alpha\beta}} \cdot \delta\sigma + \left[\frac{\partial F}{\partial \tilde{\Phi}_f^{\alpha\beta}}\right]_{\sigma,y_{\alpha\beta}} \cdot \delta\tilde{\Phi}_f^{\alpha\beta} + \left[\frac{\partial F}{\partial y_{\alpha\beta}}\right]_{\sigma,\tilde{\Phi}_f^{\alpha\beta}} \cdot \delta y_{\alpha\beta} \tag{4}$$

allows to define their temperature dependencies for equilibrium ($\delta F = 0$) and non-equilibrium ($\delta F \neq 0$) transformations. Functional equation which determines probability of liquid-like states formation can be obtained from (2), (3) as:

$$\frac{\partial F}{\partial \sigma} = \frac{\partial F}{\partial \sigma} + \frac{\partial}{\partial \sigma}\langle H - H_0 \rangle_0 = \tilde{T}_2 - \tilde{T}_1 + 2\sigma(\tilde{\Phi}_2 - \tilde{\Phi}_1) - 2\tilde{\Phi}_1 - 4\tilde{I}(1-\sigma)\sigma - 2\Theta N \ln \frac{\frac{g_2}{\sigma} - 1}{\frac{g_1}{1-\sigma} - 1}, \tag{5}$$

where $\tilde{T}_f = \sum_l \left\langle \dfrac{\vec{P}_f^2(l)}{2M} \right\rangle$, $\tilde{\Phi}_f = \dfrac{1}{2}\sum_{l,l'} \langle \Phi_f(l,l') \rangle$, $\tilde{I} = \left\langle \sum_{l,l'} \sum_{\alpha,m} I_\alpha(\vec{r}_{ll'}) v_\alpha\left(\tfrac{l}{m}\right) \right\rangle$.

Analogous functional equations for mean-square atomic displacements $y_{\alpha\beta}(l,l')$ and force constants $\tilde{\Phi}_f^{\alpha\beta}(l,l')$ are got:

$$\frac{\partial F}{\partial y_{\alpha\beta}(l,l')} = \frac{\partial}{\partial y_{\alpha\beta}(l,l')}\langle H - H_0 \rangle_0 = \frac{1}{4}\left(\left\langle \nabla_{ll'}^\alpha \nabla_{ll'}^\beta \Phi_f(\vec{r}_{ll'}) \right\rangle \sigma_f^2 - \tilde{\Phi}_f^{\alpha\beta}(l,l') \right), \tag{6}$$

$$\frac{\partial F}{\partial \tilde{\Phi}_f^{\alpha\beta}(l,l')} = \frac{\partial F_0}{\partial \tilde{\Phi}_f^{\alpha\beta}(l,l')} + \frac{\partial}{\partial \tilde{\Phi}_f^{\alpha\beta}(l,l')}\langle H - H_0 \rangle_0 = \frac{\hbar}{2MN} \sum_{\vec{k}} \frac{\sin^2 \frac{\vec{k}\vec{r}_{ll'}}{2}}{\omega(\vec{k})} \coth \frac{\hbar\omega}{2\Theta} - \frac{y_{\alpha\beta}(l,l')}{4}, \tag{7}$$

where $\vec{k}$ is wavevector, ω is vibrational frequency.

Mutual atomic interaction may be presented as $\Phi(r)=\Phi_1(r)+\Phi_2(r)$, where its short-acting part $\Phi_2(r)$ is approximated by hard sphere-type potential and long-acting part $\Phi_1(r)$ is given by sum of Morse-type potential $\Psi(r)=V_0\left(e^{-12\frac{r-a}{r}}-2e^{-6\frac{r-a}{r}}\right)$ and non-central potential $G(\delta)=-G_0e^{-4\left(\frac{\delta}{a}\right)^2}$ (δ is the displacement of atom in the plane which is perpendicular to the bond direction, G_0 and V_0 are potentials parameters). Calculating solid equilibrium under external pressure we finally derive self-consistent system of equations :

$$F_1(\sigma)=\sigma\xi+(1-\sigma)z\left\{\frac{e^{-y_l}}{2}\left[B(y_l)-\frac{P^*e^{y_l}}{12(1-\sigma)^2}\left(\frac{r}{a}\right)^2\right]+\frac{G_0}{V_0\left(1+2y_l\right)}\right\}-$$

$$-z(1-\sigma)\sigma\left(1+\frac{y_l}{4}-\frac{1}{6}ln\frac{B(y_l)}{2}\right)A(y_l)-\tau\,ln\frac{\frac{g_2}{\sigma}-1}{\frac{g_1}{1-\sigma}-1}=0,$$

$$F_2(y_l)=\frac{3e^{-y_l}\tau}{8\sqrt{2}(1-\sigma)}\left[B(y_l)+\frac{P^*e^{y_l}}{6(1-\sigma)^2}\left(\frac{r}{a}\right)^2\right]^{-1}\left(1+\frac{0.022(1+2y_t)^{-2}}{e^{y_l}\left[B(y_l)+\frac{P^*e^{y_l}}{6(1-\sigma)^2}\left(\frac{r}{a}\right)^2\right]}\right)-y_l=0, \tag{8}$$

$$F_3(y_t)=\frac{3\left(1+y_t\right)\tau}{8(1-\sigma)e^{\frac{y_l}{2}}}\left[B(y_l)+\frac{P^*e^{y_l}}{6(1-\sigma)^2}\left(\frac{r}{a}\right)^2\right]^{-\frac{1}{2}}-y_t=0,$$

where y_l , y_t are mean-square atomic displacements along the bonding and transversal direction, $\tau=\frac{\Theta}{V_0}$ is the reduced temperature, $A(y_l)=0.62\left[e^{\left\{0.36-0.91y_l+1.94ln\frac{B(y_l)}{2}\right\}}-e^{\left\{0.18-0.955y_l+0.97ln\frac{B(y_l)}{2}\right\}}\right]$, $\xi=\frac{\varphi}{V_0}$,

$P^*=\frac{PV}{6zNV_0}$ is the reduced pressure, $B(y_l)=1+\left[\frac{P^*r^2e^{y_l}}{6(1-\sigma)^2a^2}\right]^{\frac{1}{2}}$.

Solutions results of self-consistent system (8) are shown in Fig. 1,2. In temperature dependencies of share of atoms in liquid-like states we can mark out five distinctive parts which correspond to different system states:

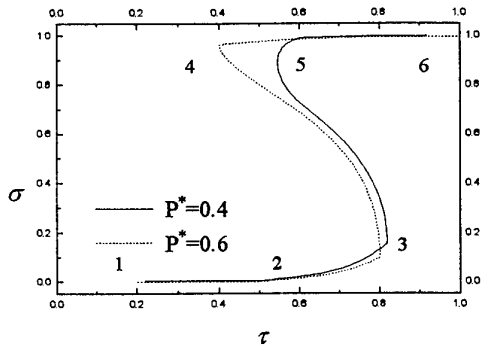


Figure 1. Temperature dependence of the share of atoms in liquid-like states.

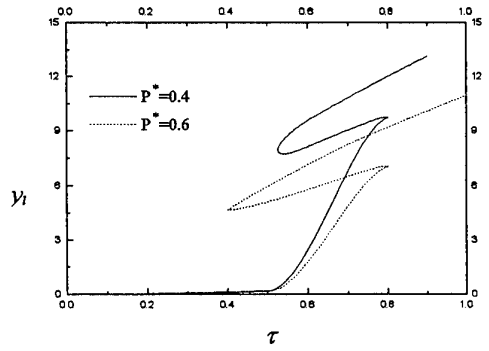


Figure 2. Temperature dependence of mean-square atomic displacements.

- stable: part 1-2 - crystalline ordered state, part 6-5 - liquid disordered state;
- metastable: part 2-3 - superheated crystal, part 5-4 - supercooled liquid;
- virtual system state: part 3-4 - state is thermodynamically unstable, when $\frac{\partial\sigma}{\partial\tau}<0$, $\frac{\partial y_l}{\partial\tau}<0$ and hence $C_p<0$.

As external pressure lowers we can observe displacement of phase transition point to lower temperatures region and increasing of dynamic oscillations amplitude for which solid state disorders. Increasing of the anisotropy of potentials in liquid and crystalline phases and decreasing of static spread of equilibrium sites leads to the same influence on system behavior: leads to the growing of regions where metastable states exist.

3. NON-EQUILIBRIUM PHASE TRANSITION

In non-equilibrium state $\delta F\neq 0$. In terms of the deviations η_i of the system variation parameters from their equilibrium values, the total free energy F of the system can be expressed in the form

$$F = F_0 + \frac{1}{2}\sum_{i,j} a_{ij}\eta_i\eta_j + \frac{1}{3}\sum_{i,j,k} c_{ijk}\eta_i\eta_j\eta_k + \frac{1}{4}\sum_{i,j,k,l} b_{ijkl}\eta_i\eta_j\eta_k\eta_l, \tag{9}$$

where $a_{ij}=\left(\frac{\partial^2 F}{\partial\eta_i\partial\eta_j}\right)_e$, $c_{ijk}=\frac{1}{2}\left(\frac{\partial^3 F}{\partial\eta_i\partial\eta_j\partial\eta_k}\right)_e$, $b_{ijk}=\frac{1}{6}\left(\frac{\partial^4 F}{\partial\eta_i\partial\eta_j\partial\eta_k\partial\eta_l}\right)_e$, $\eta_1\equiv\eta=\sigma-\sigma_e$, $\eta_2\equiv\eta_y=\{\eta_y^\alpha\}$, $\eta_y^\alpha=y_\alpha(l,l')-y_\alpha(l,l')_e$, $\eta_3\equiv\eta_{y\Phi}=\{\eta_\Phi^\alpha\}$, $\eta_\Phi^\alpha=\tilde{\Phi}^{\alpha\alpha}(l,l')-\tilde{\Phi}^{\alpha\alpha}(l,l')_e$ and is taken into account that $\left(\frac{\partial F}{\partial\eta_i}\right)_e=0$ ("e" corresponds to the equilibrium state).

With the aid of Landau-Khalatnikov equation[6], according to which $\frac{\partial\eta_i}{\partial t}=-\gamma_i\left(\frac{\partial F}{\partial\eta_i}\right)$, using (9) we obtain system of nonlinear kinetic equations for order parameters

$$-\gamma_i^{-1}\frac{\partial\eta_i}{\partial t}=\sum_j a_{ij}\eta_j+\sum_{j,k} c_{ijk}\eta_j\eta_k+\sum_{j,k,l} b_{ijkl}\eta_j\eta_k\eta_l .$$

Linear items coefficients in these equations describes energy dissipation process with relaxation time $\tau_{ij}=a_{ij}^{-1}$, nonlinear item coefficients - modes interaction process. Taking into account that quadratic and higher order in η_y and η_Φ items are apriori low, we get

$$\begin{aligned} -\gamma_1^{-1}\frac{\partial\eta}{\partial t}&=a_{11}\eta+a_{12}\eta_y+a_{13}\eta_\Phi+c\eta^2+b\eta^3,\\ -\gamma_2^{-1}\frac{\partial\eta_2}{\partial t}&=\sum_{j=1}^{3}a_{2j}\eta_2\eta_j\ ,\ -\gamma_3^{-1}\frac{\partial\eta_3}{\partial t}=\sum_{j=1}^{3}a_{3j}\eta_3\eta_j\ . \end{aligned} \tag{10}$$

Let us use Prigogine subordination principle[7,8] which allows, when analyzing non-equilibrium transition to reduce order parameters quantity during consideration of adiabatic submission of stable mode alteration as unstable ones change. Asymptotically stable stationary solutions of the system (10) are defined by the system of characteristic equations as follows:

$$\begin{aligned} &a_{11}\eta+a_{12}\eta_y+a_{13}\eta_\Phi+c\eta^2+b\eta^3=0,\\ &a_{22}\eta_y+a_{23}\eta_\Phi=0,\ a_{31}\eta+a_{32}\eta_y+a_{33}\eta_\Phi=0. \end{aligned} \tag{11}$$

From second and third equations we get $\eta_y=\chi_1\eta$, $\eta_\Phi=\chi_2\eta$, where $\chi_1=\frac{a_{31}a_{23}-a_{21}a_{33}}{a_{22}a_{33}-a_{23}^2}$, $\chi_2=\frac{a_{32}a_{21}-a_{31}a_{22}}{a_{22}a_{33}-a_{23}^2}$, substitution of which into equation (11) allows to transform it to:

$$a\eta + c\eta^2 + b\eta^3 = 0. \qquad (12)$$

Coefficients a, b, c are functions of temperature, pressure and control parameter - temperature change rate $q = \frac{dT}{dt}$. So long as in equilibrium state $\delta F = 0$, $\delta^2 F > 0$, then quadratic form $\sum_{i,j} a_{ij}\eta_i\eta_j$ must be positively determined, what provides that coefficient $a(T,P,q)>0$. In this case asymptotically stable solution of equation (12) is $\eta = 0$. In non-equilibrium state $\eta \neq 0$. Stationary states with order parameter $\eta = \frac{-c \pm \sqrt{c^2 - 4ab}}{2b}$ different from zero are asymptotically stable when $a(T,P,q)<0$ (solution $\eta = 0$ becomes asymptotically unstable when $a(T,P,q)<0$). So, during the transition into non-equilibrium state with order parameter different from zero coefficient $a(T,P,q)$ changes sign and can be approximated by $a = -a_0 \cdot a\tan\left(ln\{1+\tilde{q}\}\right)$, where $\tilde{q} = \frac{q - q_c}{q_c}$ (q_c is critic freezing rate). Equation (12) defines bifurcation diagram of noncrystalline matter formation process from the melt. In adiabatic approximation of subordination principle for $\frac{\partial F}{\partial \eta_i}$ we can obtain:

$$\frac{\partial F}{\partial \eta} = -a_0 \cdot a\tan\left(ln\{1+\tilde{q}\}\right)\eta + c\,\eta^2 + b\,\eta^3, \quad \frac{\partial F}{\partial \eta_y} = \frac{\eta_y}{\tau_y}, \quad \frac{\partial F}{\partial \eta_\Phi} = \frac{\eta_\Phi}{\tau_\Phi}.$$

Thus, for non-equilibrium phase transition model we finally derive following self-consistent equations system:

$$F_1(\sigma) = -a_0 \cdot a\tan\left(ln\{1+\tilde{q}\}\right)\eta + c\eta^2 + b\eta^3,$$

$$F_2(y_1) = \frac{\eta_{y_1}}{\tau_{y_1}}, \qquad (13)$$

$$F_2(y_t) = \frac{\eta_{y_t}}{\tau_{y_t}}.$$

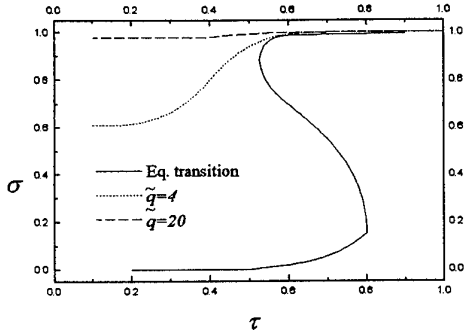


Figure 3. Temperature dependence of the share of atoms in liquid-like states.

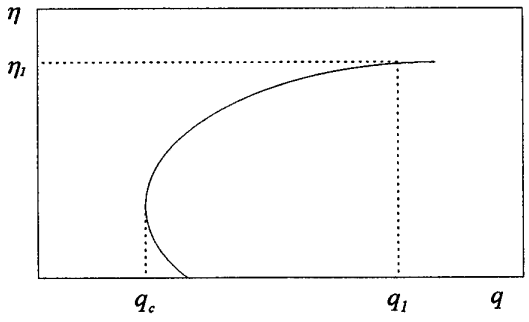


Figure 4. Bifurcation diagram.

During increase of the melt freezing rate, the narrowing of temperature range of metastable regions existence and phase transition point shift to lower temperatures area are observed. When q reaches certain critic value metastable regions completely vanish and system transits into non-equilibrium state. The degree of the system deviation from equilibrium is defined by deviation of order parameter from its equilibrium value. Corresponding results of self-consistent system solution are shown in Fig. 3.

Noncrystalline matter formation needs considerable system deviation from equilibrium state when phase transition takes place. Deviation value is defined by external control parameter - freezing rate. As freezing rate is higher than critic to represent transition character we must take into account occurred in the system bifurcations,

which lead to dissipative structures formation. The convenient way of investigation of bifurcations origin and their influences on the system state is exploring the bifurcation diagrams (Fig. 4), which characterize changes of system parameters deviation from equilibrium under different values of external control parameter. For example, in region $q<q_c$ system is in equilibrium ($\eta = 0$). When $q \geq q_c$ the melt does not transform to crystal completely and partially transits to noncrystalline solid. Namely these two cases are represented by diagram: when $q=q_1$, $\eta = 0$ corresponds to crystallization, $\eta=\eta_1\neq 0$ corresponds to the transformation into noncrystalline solid - dissipative structures formation.

4. DISSIPATIVE STRUCTURES FORMATION

During the melt cooling under strongly non-equilibrium conditions the part of system energy, which is in the atoms and molecules heat motion, transits in macroscopic organized motion by spatial-temporal correlations. This motion stipulates formation of complex spatial system organization (dissipative structure), when the largest dissipation of the energy is observed. In stationary case, formed dissipative structures are stable formations with distinctive shape and volume, and as shape so volume is stable to low disturbances.

To investigate stability of forming dissipative structures and determine their characteristics (sizes, shape, arrangement, spatial distribution of η parameter) we take into account diffusion in the system and rewrite equation (12) as

$$a\eta + c\eta^2 + b\eta^2 + D\nabla^2\eta = 0, \tag{14}$$

where D is diffusion coefficient. In the vicinity of stationary solution η_s, which is defined by equation $a\eta_s + c\eta_s^2 + b\eta_s^3 + D\nabla^2\eta_s = 0$, we decompose η into the series of low disturbances $\eta = \eta_s + \delta\eta$, $\delta\eta = e^{\lambda t + i\vec{k}\vec{r}}$. As a result we obtain characteristic equation $\lambda = a + 2c\eta_s + 3b\eta_s^2 - Dk^2$. According to this equation we get $k_c^2 = \dfrac{a + 2c\eta_s + 3b\eta_s^2}{D}$. Under condition $k^2 \leq k_c^2$ homogeneous distribution becomes unstable. Characteristic spatial size of ordered region is as $L_s = \dfrac{2\pi}{k_c}$ and life time of dissipative structure is equal to $\tau = \lambda^{-1}$, $\tau \xrightarrow[q\to q_c]{} 0$.

5. REFERENCES

1. Amorphous semiconductors. Edited by M.H.Brodsky. - Berlin, Heldelberg, New York. Springer - Verlag. 1979.

2. Babloyantz A. Molecules, dynamics and life. - New York, Chichester, Brisbane, Toronto, Singapore. Wiley. 1986.

3. Maryan M.I., Kikineshy A.A., Mishak A.A. Photoinduced instabilities in chalcogenide glasses for optical recording media. - Phil. Mag. B: 1993. V. 68. N5. P. 688-695.

4. Plakida N. M. Double-time Green's function method in the theory of anharmonic crystals./ Stat. physics and quantum field theory. - Moscow. Nauka. 1973. P. 205 - 240.

5. Yukalov V.I. Spaces of states for heterophase systems. - Physica. 1982. V. A 110. N. 1 - 2. P. 247 - 256.

6. Keizer J. Statistical thermodynamics of non-equilibrium processes. - New York. Springer - Verlag. 1987.

7. Prigogine I. From being to becoming. - San Francisco. Freeman. 1980.

8. Haken H. Self-organization and information. - Phys. Script. 1987. V. 35. N. 3. P. 247 - 254.

On Thermal Protection Memory Capacity

A. K. Alekseev

RSC Energia, Kaliningrad, Moscow Region, Russia, 141070

Abstract

The problems of Heat Memory capacity of some smart material of thermal protection are addressed by the analysis of Fisher informational matrix eigenvalues spectra and by numerical experiments.

2. Thermal protection smart matherials

A thermal protection that contains some thermosensitive substances can be considered in the frame of Intelligent materials[1,2]. We can treat the thermal protection as a processor performing processing and retaining of external signal. The following functional elements can be marked:

1. Processor: External signal $Q_w(t)$ is transformed by material into temperature field $T(t,x,y)$.
2. Memory (dynamic): the temperature field $T(t,x,y)$ is some analog of RAM.
3. Memory (static): Irreversible processes in end-point state retain information on the history $Q_w(t)$.
4. Actuator: the temperature field $T(t,x,y)$ starts the set of processes such as thermal decomposition, gas injection, ablation etc.

2.1 Processor

Thermal protection coating is subjected to unsteady-state action $Q_w(t)$. External heat flux (signal) $Q_w(t)$ by means of boundary condition

$$\lambda \left.\frac{\partial T}{\partial x}\right|_{x=L} = Q_w(t); \qquad (1)$$

transforms into temperature field $T(t,x,y)$ within the material

0-8194-2165-0/96/$6.00

$$\rho(t,x,y)\cdot C(T)\,\frac{\partial T(t,x,y)}{\partial t} - \frac{\partial(\lambda(T)\,\partial T(t,x,y)/\partial x)}{\partial x} -$$

$$- \frac{\partial(\lambda(T)\,\partial T(t,x,y)/\partial y)}{\partial y} = 0; \qquad (2)$$

$$y\in(0,Y_{max});\ x\in(0,L(y));t\in(0,t_f);T(0,x,y)=T_0;$$

On other boundaries:

$$\partial T/\partial y\Big|_{y=0}=0;\ \partial T/\partial y\Big|_{y=Y_{max}}=0;\qquad \frac{\partial T}{\partial x}\Big|_{x=0}=0; \qquad (3)$$

The set of N irreversible processes (thermal indicators) is considered. Their characteristic values $C_i(x_k,y_k)$ variation in point k (x_k,y_k) is described by equations of type that follows:

$$C_i(x_k,y_k,t)=\int_0^t F_i(T(\tau,x_k,y_k))\cdot d\tau;\ i=1...N;\ k=1...NX; \qquad (4)$$

The uniqueness and stability of direct heat conduction problem provides serviceability of processor discussed. Inverse Heat Conduction Problem[3,4] demonstrates the features of given processor, connected with damping of heat flux high frequencies in the depth of material while Inverse Retrospective Problem shows the information die out in time. Inverse Problems of Heat Memory[1,2,5] permit to use information related to irreversible processes for thermal history restoration.

2.2 The Actuator

The set of processes being brought into operation by annealing occur in thermal protection materials and can be considered as actuators. They are the phase transition processes (occurring with heat sinks), vaporing, thermal decomposition, filtration. These processes as a rule should provide a negative backfeed loop: to decrease a temperature if

it is higher some admissible level.

2.3 The Dynamical Memory

The temperature field T(t,x,y) is an analog of random access memory of distributed type. The significant part of Inverse Heat Transfer Problems[3,4] is based on this memory using for boundary conditions determination.

The utilization of temperature measurement in separate points $T(t,x_j)$ is specific for Inverse Boundary Problems. The memory capacity can be estimated either by heat flux recoveration quality or by Fisher information matrix properties (determinant and condition number).

The utilization of $T(x) = \int F(T(t,x))\cdot dt;\ \left(F=\delta(t-t_f)\cdot T(t,x)\right)$ is specific for Inverse Retrospective problems. As this take place, the memory capacity can be estimated by time interval Δt of feasible restoration.

2.4 Static Memory

The irreversible processes within thermal protection materials are usually described with nucleus of the following types:

$$F_i=\delta(T(t,x)-T_i) \qquad (5)$$

that describes phase transition processes (fusible thermal indicators),

$$F_i=\exp(-E_i/T(t,x)) \qquad (5.1)$$

that describes process of kinetic or diffusion type (crystals exposed to radiations, kryptonates etc)

$$F(x_j)=\sum^{N} C_i(x_j)\exp(-E_i/T(t,x)) \qquad (5.2)$$

that describes a thermal decomposing material density variation.

The Heat Memory Problem statement follows: the values $C_i(x_k,y_k,t_f)$ determined by Equations (1-5) are known for final moment, the heat flux $Q_w(t)$ should be determined.

3. The Heat Memory Capacity

As the quantitative criterion determining the problem degeneracy and the amount of information that is inherent in

input data the Fisher informational matrix was used (determinant, condition number and the number of eigenvalues exceeding some critical magnitude):

$$I_{ij} = S_{ki} \cdot S_{kj}; \qquad (6)$$

where S_{ki} is the sensitivity coefficients matrix:

$$S_{ki} = \frac{\partial C(x_k, y_k)}{\partial Q_i}; \qquad (7)$$

$$Q_i = Q(t_i), \quad C(x_k, y_k) = C_1(x_k, y_k);$$

These matrix allow easily detect the nonuniqueness, related to "shadowing" of some signal parts[1] and other problem degeneration events. In nonuniqueness event the number of matrix eigenvalues close to computer zero shows the degeneracy degree, that is the deficiency of mapping of control parameters Q_i space into the space of measured parameters $C(x_k, y_k)$. The global structure of problem solvability in control parameters space Q_i can be investigated too.

The number of informational matrix eigenvalues μ_i exceeding the measured data dispersion σ^2 is often considered as a maximum number of decidable control parameters Q_i. In present paper this approach is considered for Heat Memory Problems. The informational matrix is computed for Inverse Boundary Problem and Inverse Heat Memory Problem (Eq. 1-4.5.1).

Inverse Boundary Problem includes the heat flux determination using inner point temperature measurements. Both heat flux and temperature were considered as piecewise linear functions. The measured and control parameters were their (heat flux and temperature) values in time knots. This problem was considered as standard one because of being well studied[3,4]. The problem is ill-posed, that is why the different condition number and consequently different result accuracy are present on different solutions. The matrix condition number is small (10-50) and eigenvalues deviations is small also ($\mu_{min} \sim 0.2$) on the smooth solution with one

maximum. The condition number is of the order of 10^3 on the solution with two maximums. The final in time values of heat flux have small impact on the temperature and so highly increase the condition number. Nevertheless, the good results in heat flow reconstructions are obtained.

Inverse Heat Memory Problem was considered in the statement of paper[1] as the heat flux reconstruction using maximum temperature distribution in final state. It is feasible to recover from 2-3 up 5-6 parameters in space one-dimensional event with input data accuracy about 0.01 (depending on the $Q_w(t)$ shape) that corresponds the number of eigenvalues exceeding 10^{-4}. The global solvability of problem (1-4,5.1) was researched. The "shadow" regions are found with solution nonuniqueness of deficiency Nd>1. Above this, the degeneracy was determined connected with the relative duration of signal in comparison with specific time of specimen thermal relaxation (temperature gradient in depth decreases with temperature relaxation time reduction, and input data informativity falls.

4. The Heat Memory Capacity for Two-Dimensional Problem

The Heat Memory of material with thermal indicator stripes located depthwise is considered in the paper[1]. In paper[2] the Heat Memory of thermal protection material based on the fiberglass with insulating sublayer is discussed. The density profile in thermal decomposing material and the maximum temperature distribution were considered as the input data. The one-dimensional in space statement was used in both papers.

In present work the problems of Heat Memory for the structure with thermosensitive elements of phase transition type are considered in two dimensional in space statement. The numerical experiments were performed for heating history reconstruction and for informational matrix computation in the vicinity of exact solution. The HeatMem code was used that was described in papers[1,5].

The spatially two dimensional statement permit to reduce the condition number by some orders (2-3) because of using an

additional information along the second variable. In one-dimensional event up to 5-6 parameters can be reconstructed using data with the reasonable accuracy. In two-dimensional case (at special geometry option) this number can achieve 10. It depends both on the recovered signal shape and the measurement points location. The presence of nonuniformities in Y direction in thermophysical properties, thickness, the presence of other materials affect the number of eigenvalues exceeding the error level. Relatively small rank of control parameters space indicates the successful solution to be feasible only in the case of $Q_w(t)$ precise parameterization by small number of basic functions.

5. Conclusion

The thermal protection coating can be considered as an intelligent material processing, remembering and responding to the external signal. Inverse Heat Transfer Problems are the natural statement for smart thermal protection design. The Fisher informational matrix own value set can serve as a quantitative criterion of Heat Memory capacity. It can be enlarged by transition to two-dimensional statement and by the choice of optimum measurement points position.

6. References

1. Alekseev A.K., "Heat memory of Structures with Phase Transitions", *Journal of Intelligent Material Systems & Structures*, 1994, v.5, N 1, pp. 90-94

2. Alekseev A.K., Molotilin Y.A. & Shuvalov M.P., "Indirect Determination of Heat Flux to a Lander Heat Protection System", *J. of Thermoph. and Heat Transfer*, v. 9, N 2, 1995.

3. Alifanov O.M., *Inverse Heat Transfer Problems*, Springer-Verlag, Berlin, 1994

4. Beck J.V., Blackwell B., St.Clair C., *Inverse Heat Conduction. Ill-Posed Problems*, John Wiley & Sons, Inc., N.Y., 1985

5. Alekseev A.K. "On the Determination of Paleoheat-Flux Using Data on End-Point State of Thermal Indicators", *Mathematical Geology*, V. 27, N 5, p. 633-639, 1995.

Smart Technology Applications

Paper presented at the Third ICIM/ECSSM '96, Lyon '96

Invited Paper

DISTRIBUTED SENSING FOR INTELLIGENT CIVIL ENGINEERING STRUCTURES.

W Craig Michie, University of Strathclyde, 204 George St., Glasgow, G1 1XW.

ABSTRACT

Over the past twenty years considerable advances have been made in new optical fibre sensor technology able to measure physical parameters as a function of linear position. Such advances are of interest to the civil engineering community who have the problem of implementing measurement systems which can provide data on the structural state of health of large constructions such as bridges. This paper reviews the background to the measurement problem and outlines the relevant optical fibre techniques which have been considered in this context. The potential and the limitations of these measurement approaches is discussed.

1. INTRODUCTION.

The need to monitor civil engineering structures, particularly bridges, has become widely recognised in recent years as structural weaknesses are identified on an increasing scale. A recent survey of bridges in the United States of America[1] has revealed that of the 500 000 highway bridges in service approximately 200 000 have been declared as being structurally deficient. More than 130 000 bridges have imposed load restrictions and approximately 5 000 are closed in any one year. To redress this situation, it is estimated that a programme of remedial works costing around $90 billion would be required. Furthermore, the situation in the United States is by no means unique. Surveys carried out within Europe provide statistics which indicate that structural problems exist on a similar scale[2].

The nature of the problem is complex and includes a combination of both defects and deficiencies. ***Defects*** are inadequacies which have arisen due to faults or flaws in the original designs, materials and construction processes. On the other hand, bridges which are not ***defective*** may be considered to be ***deficient*** with respect to present day operational requirements due to the fact that the performance standards have been raised to keep pace with the ever increasing traffic loading. Given the scale of things as summarised above, the remediation issue will clearly be a long term consideration and in the meantime structures which are not in full accordance with design codes will continue to be used. The need to implement effective structural monitoring systems, in order to ensure the safety of existing structures and to derive data for the design of new and remedial works, is becoming increasingly apparent[3].

There is no simple package of instrumentation which can be purchased and installed to address the monitoring requirements of a large structure such as a bridge. Each system has to be designed to meet individual needs. The general principle which can be applied is that the measurement is broken down into three constituent components:

- **macro** level measurements are used to describe the overall movements of the structure relative to fixed positions. These should be taken over an extended time period to quantify movements such as sway, creep, tidal, load and thermally induced changes.
- **meso** level measurements are required to determine the relative movements of components within the structure over extended time periods.
- **micro** level measurements establish the stresses/loads within and the chemical stability of the materials which comprises the structure.

In addition to all of these, the environmental conditions surrounding the structure should be monitored in order to calibrate the sensor data and to correlate the structural movements to seasonal loadings. A wide range of measurement instruments are commercially available and are used to perform the tasks outlined above. However these sensors have to be integrated into complex measurement arrays. The need for distributed measurement devices which can alleviate much of the sensor integration and data capture burden can be illustrated with the following case study.

2. CASE STUDY.

The Kingston Bridge in Glasgow is the busiest motorway bridge in Europe carrying 154 000 vehicles per day. A variety of defects and deficiencies in the bridge were identified in the late 1980's and an extensive health

0-8194-2165-0/96/$6.00

monitoring programme was embarked upon in 1990[4]. A monitoring system was devised for the bridge and over the period of several years this has been revised and developed. The instrumentation used can be summarised as follows.

On the **macro-level** of investigation, a continuous structural survey was commissioned to identify global movements within the bridge as a function of time. Twenty four reflective targets, eight on each outer edge of the bridge and eight on the north side of the bridge were installed and measurements were made between these and four reference stations on the corners of the pier foundations using electronic distance measurement apparatus. Measurements were taken once a month and the three dimensional position of each of the reference points was recorded to an accuracy of +/- 2mm[4].

Meso-level information was derived from the following. Fifty-six LVDT's were used to measure the relative movements of the north and south expansion joints and the top and bottom of the north pier. Sixteen hydraulic flat jacks were used to measure horizontal loads transmitted from the bridge onto the north approach structure. One hundred and eight temperature sensors were located on top, bottom and lateral structural elements of the bridge and readings were updated every fifteen seconds. Air temperature, humidity and wind speed were recorded together with wind speed and ultra violet radiation above the bridge. Four inclinometers were used to measure movements in the sub soil behind the quay walls adjacent to the bridge foundations.

On the **micro-scale** bridge components were inspected by close visual survey and all cracks mapped and the widths recorded. Electro-potential mapping of the concrete was carried out using copper sulphide half cells and the chloride content at various depths of within the concrete was measured in a laboratory using swept samples of concrete dust. Surface strains were measured using an array of strain gauges and inspection of the steel reinforcement was carried out using endoscopic investigation techniques.

All data recorded was used to calibrate and verify finite element analysis of the structure which was used to predict the bridge behaviour during the course of remedial works and subsequent settling. The bridge continues to be instrumented for the foreseeable future in order to assess the success of the repair work.

Clearly the instrumentation of large structures poses considerable technical challenges. As demonstrated above the measurements can be effectively carried out using a range of proven and widely available instruments. The difficulty lies in networking these instruments into an effective measurement system. In particular the problem of data retrieval represents one of the most demanding challenges. Distributed measurement methods which would eliminate the bulk of the wiring harness associated with an instrumentation project as that described above would represent a considerable step forward. This capability is often seen as a key advantage that fibre optic sensors have over other technologies and is the subject of this paper. Generally the fibre optic sensor types which are most conveniently integrated into large arrays are those which transducer the measurement parameter to one of the following:

- scattering (usually causing signal loss),
- time of flight (distance),
- wavelength.

These measurement processes will be examined in the context of civil engineering applications requirements.

3. DISTRIBUTED MEASUREMENTS SYSTEMS.

3.1 OPTICAL TIME DOMAIN REFLECTOMETRY (OTDR).

Two distinct measurement process are associated with OTDR: direct length measurement and distributed loss measurement, these are depicted schematically in Figure 1. The loss measurement, normally referred to as Rayleigh OTDR, measures the evolution of the Rayleigh back scatter signal as a function of time from the launch of the interrogating pulse. Cabling structures have been devised to translate measurement parameters into loss by introducing microbends into the fibre. Direct length measurements, Fresnel OTDR, record the time of flight for a pulse to travel between the interrogating laser source and discrete Fresnel reflections used to delineate the fibre into multiple sensing segments.

The Rayleigh back scatter signal strength from a pulse of light travelling along a fibre, measured using a

receiver positioned adjacent to the launch laser is given by[5]

$$P_b = \frac{P_O S \alpha_S W v}{2 e^{-2\alpha(l)}} \quad (1)$$

where S is the capture ratio of the scattered light and α_S is the scattering coefficient of the fibre (equivalent to the attenuation due only to Rayleigh scattering). W is the pulse width and $\alpha_S l$ is the cumulative attenuation at the time of measurement, t, experienced by a pulse positioned $l = vt/2$ from the detector, where v is the speed of light in a fibre.

The back scatter capture fraction S, defined as the ratio between the instantaneous coupled reverse power and the total scattered power at the scattering point is given by

$$S = 0.25\left[\frac{NA}{n_1}\right]^2 \quad (2)$$

where NA is the numerical aperture of the fibre and n_1 is the core index.

Typically S varies from 0.001 for a single mode fibre to 0.005 for a graded index fibre illustrating the sensitivity needs for a receiver measuring OTDR back scatter signals.

The linear spatial resolution of an OTDR instrument improves as the pulse width, W, is reduced. However this further restricts the available signal to noise ratio available at the receiver. To obtain a spatial resolution of 100 mm requires that $W < 1$ nsec. A single mode fibre can have an attenuation of 0.1 dB/km (or 23.10^{-6} N/m) attributed to scatter. For such a fibre the collected power from a 100 mm length of fibre would be in the region of 2.10^{-9} if the launch power. Thus the signal strength at the receiver is very small and to obtain the necessary SNR measurements are integrated over several minutes. OTDR measurements are therefore slow.

3.1.1 Microbend Strain Measurement Devices.

It is well known that mechanical perturbations or bends can alter locally the level of back scatter, particularly if the disturbance is periodic and equal to the modal separation between guided and radiative modes. In graded index fibres a maximum in mode coupling under a periodic perturbation if the period of the microbend Δ_m is

$$\Delta_m = \frac{2\pi a}{\sqrt{2\delta}} \quad (3)$$

where **a** is the core radius and δ is the maximum refractive index difference between the core and the cladding[6]. For graded index type fibres with a 25 μm core radius Δ_m is typically of the order of 1 mm.

Strain measurement devices which make use of periodic mechanical stresses to deliberately introduce microbend losses have been under development for several years[7,8]. Examples include the Stranded Optical Fibre Sensor (SOFS), manufactured by SICOM, (see Figure 2) which has been widely used in measurement applications throughout Europe. For example a network of microbend transducers was installed in the Berlin -Marienfelde bridge to monitor crack growth and dynamic loading. Similar systems have also been installed within the UK[9]. G2 systems in the United States have had several field application trials monitoring pipelines using a similar type of sensor cable[10].

Sensitivity: Microbend sensors can be made to be highly sensitive to strain (changes in length of 1 micron can be detected) but at the expense of dynamic range. A good quality OTDR unit has a dynamic range of around 20 dB, a spatial resolution of less than one metre and can resolve changes in the OTDR back scatter signature of around 0.01 dB. To make an analogue measurement with a resolution of 8 bits (256 resolvable strain increments), requires that each sensor would require 2.56 dB of dynamic range. Thus around 7 sensors with

the above specification could be monitored along a single fibre length. In this case the distributed measurement potential becomes questionable. For high resolution measurements it is generally accepted that the sensor performs most efficiently under dynamic loads. In this situation the OTDR unit will not have an adequate response time and the distributed measurement capability is lost.

Linearity: An additional difficulty with analogue loss measurements is that of non-linearity. The attenuation process relies on the fact that guided modes are coupled to radiative modes and as the high order modes become de-populated, the sensor loses sensitivity[11]. This implies that sensors which are further away from the launch source can have their characteristics modified, usually reduced by events which take place closer to the cable launch. This can be compensated for by introducing dead zones or mode scrambling zones in order to maximise the mode fill at all sensing locations.

Distributed measurement systems based upon microbend loss have therefore many intrinsic problems which have thus far restricted their use. In contrast, microbend sensors which operate as alarms, to detect the presence or absence can make more effective use of the distributed nature of the measurement process[12]. An example of this will be given later.

3.1.2 FRESNEL BASED LENGTH MEASUREMENTS.

In Fresnel based measurements the dynamic range considerations are less important since abrupt reflective interfaces are used to identify locations along a fibre length and the relative distances between these reflectors are measured. These measurements can be directly related to structural movements and such systems can in principle be used to compliment the structural surveying procedures outlined earlier. The measurement principle relies on the ability to detect small changes, typically 1 psec, in the arrival time of a pulse. This implies a high degree of stability in the clock recovery circuitry and a wide receiver bandwidth. Commercially available instruments are available which specify a measurement resolution for incremental changes in the fibre length of 250 μm[13]. Recent work[14] suggests that this resolution can be improved through the use of analogue correlation techniques to a mich higher precision of around 1 μm although the long term stability of the system and operation in field environments has not been reported.

SICOM[8] have used Fresnel based systems for strain distribution mapping in ground anchors and stressing tendons in underground environments where the temperature is relatively constant. The Kammerick Massif, a rock fall prone area in the vicinity of important traffic routes, is one. The sensors were installed in permanent ground anchors which were stressed up to 2 MN to monitor the loading profile along the grouted length of the anchor. Length changes of up to 3 mm were noted over the first 50 cm of the grouted section as the load applied was raised up to the 2 MN level. The Fresnel based system allows around 30 sensors to be simultaneously integrated into a single sensing length. However despite this, the minimum resolvable distance increment of around 200-250 μm does not meet the broad range of requirements for these applications and the acceptance of these systems has been limited.

3.2 BRILLOUIN SCATTERING.

Perhaps the most technically advanced of all the fibre optic distributed strain sensing techniques is that of Brillouin scattering. These systems have recently been developed as a means of mapping the strain profile of underground and sub sea fibre optic cable systems for communications applications. The sensor uses the scattering which takes place as an optical probe beam interacts with an acoustic wave generated from high intensity pump pulse. The distribution of the acoustic frequency (the Brillouin gain peak) shifts by approximately 60kHz/$\mu\epsilon$ (and 1 MHz/°C). The advantage that this measurement method offers over Rayleigh systems is that the measurement parameter is detected as a shift in optical frequency, the energy is not lost. Consequently a strain map (an example of which is shown in Figure 3) can be generated over long fibre lengths[15]. At present only one commercial system capable of performing such measurements exists[15,16] and provides a truly distributed strain map with a strain resolution of 0.01%ϵ of strain, and a spatial resolution of around 5 m over a measurement length of between 200 to 300 km. The measurement takes approximately 15 minutes to interrogate the entire fibre length. To date no application trials using Brillouin systems as a means of structural monitoring have been reported, however the potential capability in applications such as pipeline monitoring are obvious.

3.3 WAVELENGTH MEASUREMENT SYSTEMS: BRAGG GRATINGS.

The construction of arrays of discrete point sensors of Bragg gratings is receiving a considerable degree of attention world wide. Strain, or temperature, fields modify the period of the Bragg grating such that the resonance condition is modified and the peak reflection wavelength changes according to[17]

$$\frac{\delta\lambda_B}{\delta\lambda_O} \approx 8.885.10^{-6}\,\delta T + 8.7\,\delta\epsilon \qquad (4)$$

Measurement of the exact wavelength of the peak of the Bragg reflection allows the strain or temperature to be determined at that location. For precise quasi-static strain measurements, determining the wavelength with sufficient accuracy and compensating for temperature changes represents a considerable technical challenge. However for dynamic measurements, extremely high strain resolutions of better than 100nε/Hz can be achieved relatively easily.

Bragg gratings offer the potential for a low cost solution to the fabrication of large scale measurement arrays (the current projected cost of a unit Bragg grating is around $50)[18]. The bulk of the online fabrication issues have been resolved and 3M appear to be close to bringing Bragg gratings to the market.

The large scale multiplexing of Bragg grating arrays remains to be demonstrated but several recent publications of combined time and frequency multiplexed systems generating strain distribution maps on composite laminates[19] have given confidence that the technical issues are resolvable. Preliminary investigations using arrays of Bragg gratings in field trials on the Beddington Trail Bridge, Calgary, indicate that the gratings are detecting the relaxation of the strain levels experienced by reinforcing tendons during the months following the initial construction[20].

3.4 WHITE LIGHT INTERFEROMETRY.

Recently a white light interferometric measurement system has been developed for measuring length changes with very high precision[21] (of micron dimensions). The measurement principle is shown schematically in Figure 4. Two single mode fibres are placed in a structure to be monitored. One of the fibres is firmly attached to the structure while the other is free to move within a loose tube. All deformations which take place within the structure cause length changes between these two fibres and a low coherence Michelson interferometer is used to make precise measurements of this path imbalance. Since the measurement recovers the absolute optical path difference between the two fibres, deformations within the structure can be monitored with out the need for a continuous monitoring system.

The operation of the system has been tested over a period of one year on a 20 m by 5 m by 0.5 m concrete test sample. The sensing scheme was shown to able to track the shrinkage in the concrete which takes places following the casting process as the concrete cures. Shrinkage dominated the measurement over the first six months after which length changes due to changes in seasonal (thermal) conditions were tracked. Observation of creep in the sensor over the course of the trials was not evident.

Several sensor sections (up to around 10) can be multiplexed onto a single optical fibre and can be made to be sufficiently robust to withstand the harsh mechanical environment of a civil engineering construction site. Extremely promising results have come from early field trials. A first attempt to monitor foundation piles using this sensor was carried out in Morges (Switzerland) which served to highlight some of the engineering issues (particularly fiber protection) associated with using fibre optic measurement equipment in civil engineering applications.

4. STRAIN MEASUREMENTS: PRACTICAL ISSUES.

Many promising research ideas have been demonstrated within the laboratory but to date relatively few have reached the stage of in service use or even full scale field evaluation. Transferring measurement systems from

the laboratory into the field requires that a number of basic technical issues be addressed.

Compensating for thermal drift is essential but even more fundamental issue is that of establishing the process by which the optical sensor is attached to or embedded in the structure under test, of which a central consideration is measuring compressive loads. For optical fibres this typically entails introducing a tensile bias to avoid compressive loads. Not only does this introduce problems of slippage and creep, it compromises the strength of the fibre itself. While optical fibres can exhibit extremely large failure strains up to 7%, pre-tensioning the fibre dramatically reduces the fibre lifetime. Suppliers of fibre optic cable generally recommend that a static strain of no more than 25% of the proof failure strain is applied to the fibre over extended periods[22]. Typically the proof tests carried out are in the range of 1 to 2% strain although fibre tested to 3% strain can be obtained. This means that the static tensioning of a fibre should not exceed 0.5-0.7% strain if the fibre is to be guaranteed over a 50 year lifetime. The above estimates of strained lifetime may be conservative since they are calculated with kilometre lengths of fibre in mind. Shorter gauge lengths have a longer life expectancy or can be strained to higher levels. Nonetheless this problems represents a considerable technical barrier for fibre optic technology.

The principal cause of failure in optical fibre is the propagation of micro-cracks along the fibre surface, generally the result of a weakening of the chemical bonds due to water ingress. Hermetically sealed fibres (carbon coated) have been estimated to offer improvements in life cycle duration of several orders of magnitude[23]. However such coatings are not widely available at the present time but they will have an increasingly important role to play in future fibre systems.

Temperature compensation is a critical issue for all fibre optic measurement schemes. Typically a 1 °C temperature change produces a change in sensor output equivalent to a 10 $\mu\epsilon$ loading. It is possible to reference out this temperature effect using an unstressed sensing length but ensuring that the fibre is contained within a friction free enclosure is difficult, particularly for long sensor gauge lengths.

Much has been said of measurement schemes whereby two or more measurements are performed simultaneously on the same sensing fibre in order to separate temperature and strain fields but none of these have been effectively demonstrated for distributed measurements[24,25]. Combinations of polarimetry and modal interference, in conjunction with white light interferometry, have been examined but no obvious solution to a range of practical problems has emerged[26]. Dispersion measurements have been proposed and some interesting laboratory experiments have been reported[25], however no distributed measurements have been demonstrated using this approach. Processing schemes for Bragg gratings using two overlapping gratings of different centre frequency have been proposed as means of extracting both strain and temperature[27] information but these require extremely precise wavelength measurements (1 pm)[26]. The Rayleigh scatter measurements are not in themselves strongly influenced by temperature fluctuations but the microbend transducers generally are. Weaknesses can be found in all of the measurement schemes proposed to date. Significantly more effort will be required in all areas associated with the practical implementation of optical sensing schemes before the transfer from the laboratory to the field can be made.

5. DISTRIBUTED CHEMICAL MEASUREMENTS.

Although the bulk of research activity has concentrated of physical parameters, in many instances these measurements simply reflect underlying problems which have progressed to the extent that structural weakness can be identified. Detection of the chemical conditions, prior to the event of the structural damage is a more effective monitoring method. One particular example of this is a distributed measurement system which uses a water swellable to modulate the loss in an optical fibre thus enabling chemical species to be detected and located.

5.1 HYDROGEL DISTRIBUTED SENSOR.

Hydrogel polymers are materials which are able to absorb water to produce a significant volumetric expansion without dissolving[28]. Furthermore they can be tuned to respond such that the water uptake process is inhibited unless the appropriate stimulus is present[29] (for example that the water has a specific pH value). This swelling behaviour can be harnessed to produce work on the form of exerting a mechanical force. Acting through a periodic cabling geometry which enables the optical fibre to be mechanically stressed, the swelling of the hydrogel is used to introduce loss into the optical signal. This can be detected an localised using OTDR

instruments thus allowing the location of the swelling hydrogel (the point of chemical activity of interest) to be identified and the chemical parameter measured.

The sensor construction is depicted schematically in Figure 5. Hydrogel polymer is dissolved in an alcohol solvent and deposited onto a central supporting former which is then held in intimate contact with an optical fibre by a helically wound thread with a 2 mm winding pitch. In the presence of water (or the target parameter) the hydrogel swells and pushes the fibre against the thread to create local deformations or microbends. These microbends cause a loss of power in the vicinity of the water enabling it to be detected. With the present fibre (standard graded index fibre with a 62.5/125 μm core/cladding diameter and a 250 μm acrylate buffer layer) a hydrogel layer of around 12 μm thick produces a signal loss around 100 dB/km when the gel is in the swollen condition.

5.1 Distributed Water Ingress Alarm.

The cable as designed can be directly used as a water ingress alarm when interrogated with an OTDR unit[30]. An example of this is shown in Figure 6 where two wet sections are identified over a 30 metre length of sensing fibre. The wetted lengths in this figure were several metres long in order to provide a clear visual image of the sensor operation but in practice they can be made much shorter limited by the resolution of the measurement apparatus. OTDR units are able to measure changes in signal strength with a sensitivity of 0.01 dB. To minimise the probability of falsely identifying a low loss region as a high loss region it is normal practice to use 0.05 dB as a minimum measurement threshold to give an adequate signal to noise ratio. With the present sensor cable, which shows a wet attenuation of over 100 dB/km, such instruments could be used to detect water ingress locations of less than 50 centimetres length.

5.2 Determination of Grout Fill in a Reinforcing Tendon Duct.

In many cases where locating leaks is the primary concern, a minimum detectable wet length of 1 m would be adequate. However, with improved spatial resolution, the sensor can be applied to a greater range of applications. Determining the grout distribution profile of a reinforcing tendon duct is one[31].

Steel tendons in post tensioned reinforced structures are used to maintain a compressive load on the concrete throughout the structures lifetime. Chemical attack on the tendons, particularly pitting due to chloride ion ingress, can significantly reduce the tendon strength and have dramatic consequences on the overall structural integrity. To protect the tendons, the ducts where they are routed are usually filled with a cement based grout to form a seal. This has found to be effective provided that the duct is completely filled with grout along its length. Voids or poorly grouted areas leave sections of tendons which are exposed to chemical ingress. One difficulty in the use of this construction process is that it is not easy to determine whether or not the tendon ducts have been adequately grouted since the entire duct length is contained within the concrete structure. The distributed measurement properties of the hydrogel sensor provides a potential solution to this problem.

To investigate this potential, a length of hydrogel sensor was made into a cable with a mechanically supporting inner surrounded by a porous braid. This cable was inserted into a tendon duct and the grouting process carried out as normal but with voided areas introduced at selected positions. Areas of high loss, the wet areas, correspond to positions where the grouting had been effectively carried out. Figure 7 shows a comparison of the areas of sensor identified as being low loss, ie dry regions, with the voided zones and confirms that the sensor was effective in performing this task. The dry regions, voids, were located with a spatial precision of around 0.5 m and with a success rate of greater than 85%. This preliminary work was extremely encouraging due to the fact that the voided areas were identified using a sensor which was not optimised for the measurement purpose (the wet loss gradient limited the spatial resolution to around 0.5 m) and minimal signal process used to identify the areas of low loss.

5.3 SOIL WATER POTENTIAL MEASUREMENTS.

The moisture content of soils has a significant influence on their load bearing capacity. A measurement probe buried beneath a large structure reporting information on the water content over extended distances could therefore provide valuable information to structural engineers. The hydrogel probe should in principle be capable of providing this information since the signal attenuation within the sensor is directly related to the amount of water that the hydrogel absorbs. This in turn depends upon the availability of water to diffuse into the gel

material. Under conditions where the gel is not fully saturated, the sensor will show a lower degree of loss.

The amount of water that the sensor is able to absorb depends upon the relative differences in water potential between the surrounding environment and the gel itself. If the sensor is in a wet environment, water will readily diffuse into the gel and cause the signal attenuation to increase. In drier environments less water penetrates and the sensor displays a lower loss. It is not simply the volume of water in the surrounding environment which influences the sensor behaviour (although for many applications this will be the case). Water potential can be modified by the presence of dissolved ions. Soil scientists studying plant water uptake behaviour, simulate dry environments by adding controlled amount of salt to aqueous solutions to reduce the water potential and hence inhibit the water uptake in the plant[32]. This approach was used to make a preliminary evaluation of the sensor operation in humid, but not fully saturated, environments.

The sensor attenuation was measured following immersion in a variety of salt solutions of different concentrations. An example of this (for the case of NaCl) is shown in Figure 8. As the solution concentration is increased towards the 6 molar level, the signal attenuation approaches that of the dry sensor.

The full implications have not been evaluated to date but there are some promising indications. The response curve of Figure 8 follows the range of soil moisture conditions from the fully saturated case to almost completely dry. Clearly the sensor experiences significantly different variation over this range and should therefore be capable of resolving moisture content differences. The exact sensitivity of the sensor remains to be determined however the following experiment which represents the beginning of a complimentary study shows some promising features.

A 34 m length of coiled sensor was placed in fine sand in a sintered plate funnel and water was added until saturation. At equilibrium the attenuation was measured using an OTDR and estimated to be 113 dB/km. The funnel was hermetically sealed and a hydrostatic pressure of -45 kPa (suction) was applied and found to reduce the attenuation to 110.7 dB/km. While a more detailed and refined set of experiments are necessary to fully analyze and validate the sensor performance the immediate conclusion that can be drawn is that the sensor is able to discriminate soil water potentials over the range applied during this test, implying that the minimum resolution is 45 kPa. The measurements made in NaCl solutions enable the operational range of the sensor to be estimated to lie in the region of 0 to -1500 kPa.

6. CONCLUSIONS.

A substantial amount of research effort has been expended in developing optical fibre measurement methods for distributed sensing. This paper has presented an overview of the sensing methods which are of relevant to civil engineering/structural monitoring. The sheer size of civil engineering structures makes them difficult to monitor effectively for changes in stress concentrations or movements simply because of the number of sensors which are required. As a consequence of this, the civil engineering community has been quick to realise the potential benefits which optical fibre sensors can offer and interest in these measurement techniques is increasing worldwide.

Despite the obvious interest in this area, the penetration of fibre optic systems has been limited to date. Microbend loss sensors have been installed in a number of structures in Europe and measurements have been made using Bragg gratings in Canada. However these systems are really representations of field trials and fibre optics have yet to make any real impact. One of the main features which has thus far restricted the growth of optical fibre sensors is the lack of confidence in their field reliability. The bulk of activity that has been reported within the fibre sensing domain has been restricted to laboratory demonstrations. A significant effort in the process of technology transfer, moving optics from the laboratory into the field and demonstrating that problems such as durability, reliability, creep and temperature compensation can be overcome, is required before the systems will gain widescale acceptance.

Given the scale of the measurement problem as higlighted in the introduction, the need for advanced measurement systems can be expected to continue to grow for some time. Optical fibre measurement systems will undoubtedly feature prominantly in this area. The distributed measurement capability places optical fibres in a unique position with respect to other measurement technologies. This capability, coupled with the physical scale of the measurements required for civil structures will ensure that a promising future lies ahead.

REFERENCES

1. Dunker K, Rabbat B G, Scientific American March 1993, pp66-70.

2. Caussignac J M 'Civil engineering applications for Smart Structures', presented at the Inaugural European Seminar of the 'Smart Structures Research Institute', Arch de la Defense, Paris September 1991.

3. A McGown, H Wright, C Michie, P Gardiner'Fibre Optic Monitoring for Civil Engineering Structures' 2nd Conference on Civil Engineering, Cairo 1994.

4. P. Milne, A. McGown "Integrated System of Deformation Measurement on Kingston Bridge, Glasgow", Engineering Survey 94, Leeds University.

5. S.D. Personick "Photon Probe - An Optical Time Domain Reflectometer", The Bell System Technical Journal Vol.56 No.3, March 1977.

6. Attenuation of a parabolic index fibre with periodic bends, J.N. Fields, Applied Physics Letters, **36**, 779-801, 1979.

7. Abe T, Mitsanuga Y, Koga H.' Strain sensor using twisted optical fibres' Optics Letters Vol.9, No.8, 1984 pp373-374.

8. Wolf R 'Civil Engineering Applications: Monitoring of bridges and ground engineering structures' Short Course on Smart Structures and Materials, University of Strathclyde 1993.

9. Dill M J, Curtis I 'Monitoring of concrete structures using optical fibre sensors' Concrete September/October 1993, pp31-35.

10. Griffiths R, Nelson G W 'Recent and current developments in distributed fibre optic sensing for structural monitoring' Proc SPIE 985, pp12 1988.

11. K Wanser 'Distributed Fibre Optic Sensors for Civil Structures using OTDR' in 'Applications of Fibre Optic Sensors in Engineering Mechanics' American Society of Civil Engineers, New York 1993.

12. Bergqvist, E.A.'An optical fibre cable for detecting a change in temperature.' European Patent Application 91850294.9.

13. B. Zimmermann, R. Claus, D. Kapp, K. Murphy "Fibre Optics Sensors using high resolution OTDR systems", Journal of Lightwave Technology, Vol.8, No.9, pp.1273-1277, 1990.

14. H Gieger, J P dakin, N C Eaton, P J Chivers, 'New OTDR Technique for Monitoring the Range of Reflective Markers' Optical Fibre Sensors 10, pp 150-154, Glasgow 1994.

15. Horiguchi T, Kurashima T, Koyamda Y, 'Measurement of temperature and strain distribution by Brillouin frequency shift in silica optical fibres' SPIE vol 1797 Distributed and Multpilexed Sensors II 1992.

16. ANDO Instruments, AQ-807 product data sheet 1994.

17. A.D. Kersey, T. Berkoff, W. Morey "High Resolution Fibre Grating Strain Sensor with Interferometric Wavelength Shift Detection", Electronic Lett. 28(3], pp.226-228, 1992.

18. W W Morey, G Meltz, J M Weiss'Recent Advances in Bragg Gratings for Utility Industry Applications' SPIE 2594, 'Self Calibrated Intelligent Optical Sensors and Systems' October 1995 pp2594-08

19. M A Davis, D G Bellemore, A D Kersey 'Structural Strain Mapping using a Wavelength/Time Division Addressed Fiber Bragg grating Array' 2nd European Conference on 'Smart Structures and Materials' pp 342-346.

20. T. Alavie, R. Maaskant, M. Ohn, R. Lee, S. Karr, S. Huang, R.M. Measures "Fibre Optic Sensing System Integrated into Highway Bridge", ICAPT 94, Toronto, Canada, June 1994

21. D Inaudi, L Vulliet, L Pfung, S Vurpillot, A Wyser 'Low Coherence Sensors for Monitoring Underground Works' SPIEE 244 pp170-178, Smart Sensing Processing and Instrumentation, San Diego 1995.

22. Optical Fibres 'The Strength of Optical Fibres', product information sheet supplied by Optical Fibres, Deeside Industrial Park, Deeside, Clwyd CH5 2NX, UK.

23. Biswas D R 'Coatings make optical fibres stronger and more reliable' Laser Focus World April 1993.

24. W. C Michie, G Thursby, D Walsh, B Culshaw, M Konstantaki 'Simultaneous recovery of Temperature and Strain Fields Using Two Moded Polarimetry' Optics Letters, October 1995.

25. Gusmeroli V. Gusmeroli and M. Martinelli, Optics Letters, Vol.19, No.24, 1994, 2164-2166

26. W Jin, W C Michie, G Thursby, M Konstantaki, B Culshaw 'Simultaneous Strain and Temperature Recovery: Error Analysis' submitted to OFS 11, 1996.

27. M.G. Xu, J.-L. Archambault, L. Reekie and J.P. Dakin, 'title ' Tenth International Conference on Optical Fibre Sensors, B. Culshaw and J.D.C. Jones, Editors, Proc. SPIE 2360, 1994, 191-194.

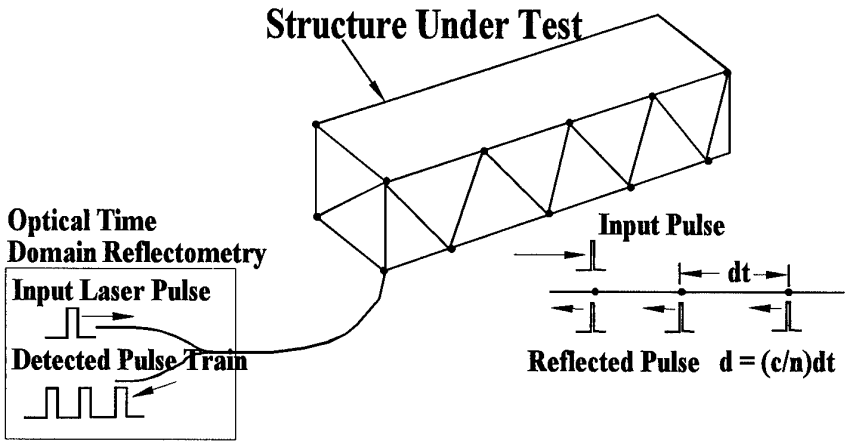
28. Swelling of Ionic Gels:Quantitative Performance of the Donnan Theory, J Ricka and T. Tanaka, Macromolecules, **17(2)**, 2916-2921, 1984.

29. Moran C, Graham, N B 'Random block co-polymers' UK Patent Application N0. 9306887.2 1993.

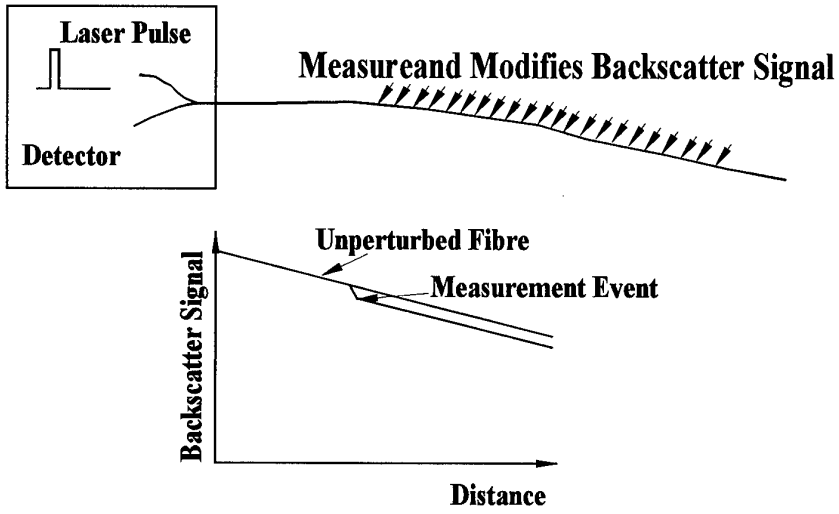
30. S Hadjiloucas, W C Michie, B Culshaw, M Konstantaki, D A Keating, M J Usher, NB Graham, C Moran 'Hydrogel based distributed fiber-optic sensor for measuring soil salinity and soil water potentials' IEE Colloquium, 'Progress in Optical Fibre Sensors and their Applications' 7 Nov., 1995.

31. Michie W C, McKenzie I, Culshaw B, Gardiner P 'Optical Fibre Grout Flow Monitor for Post Tensioned Reinforced Tendon Ducts' 2nd European Conference on Smart Structures and Materials October 1994.

32. A R G Lang 'Osmotic Coefficients and Water Potentials of Sodium Chloride Solutions from 0 to 40 C', Aust. Journ. Chem., 1967, vol. 20, pp2017-23.



a: Fresnel OTDR Measurement



b: Rayleigh OTDR Measurement.

Figure 1: Schematic of OTDR Measurement.

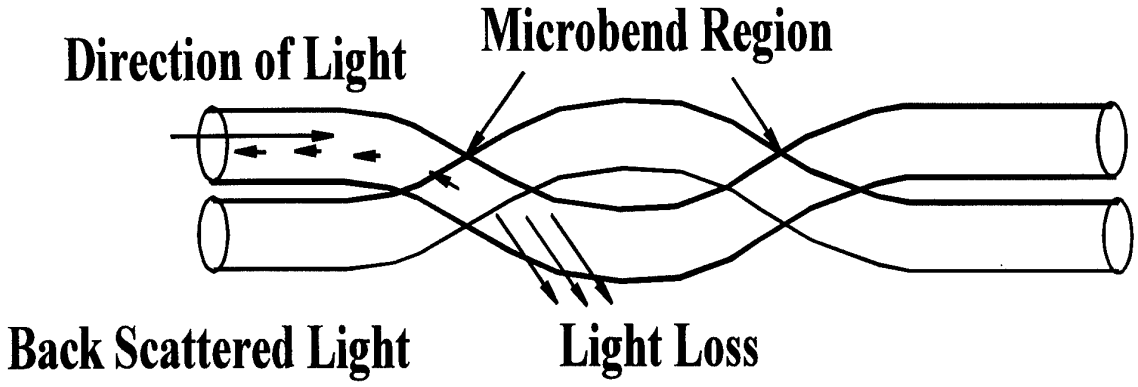


Figure 2: Microbend Loss Strain Sensor (Dill, 1993)

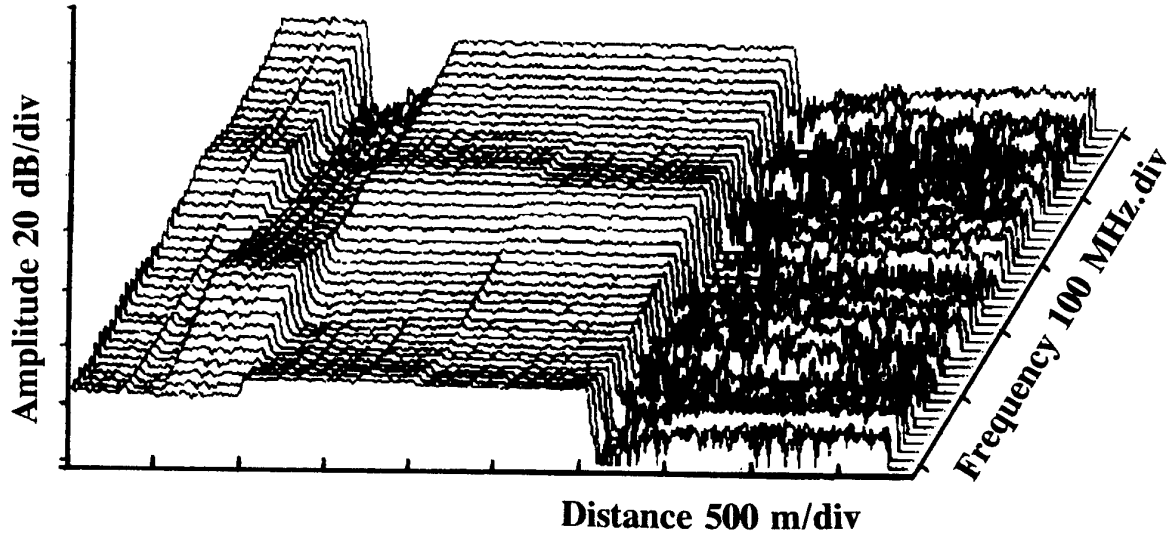


Figure 3: Brillouin Scattering Measurement, 3 km Fibre Length (Ando Instruments, 1994)

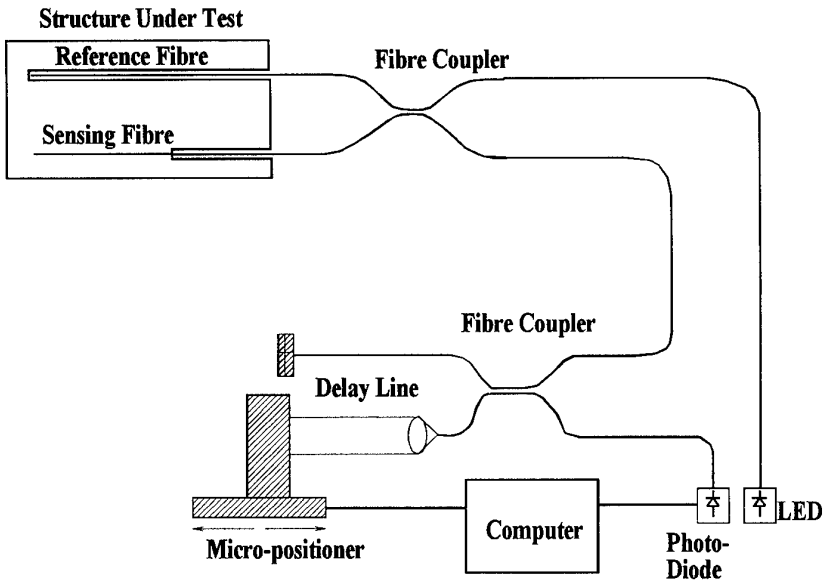


Figure 4: White Light Interferometer (Inaudi, 1995).

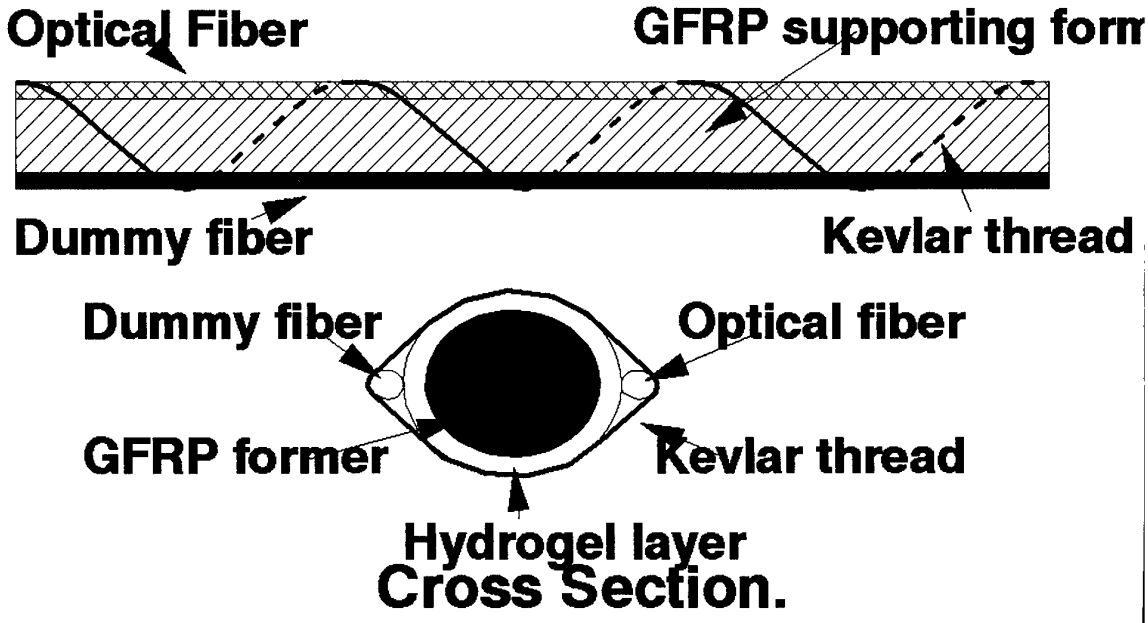


Figure 5: Schematic of Hydrogel Sensor

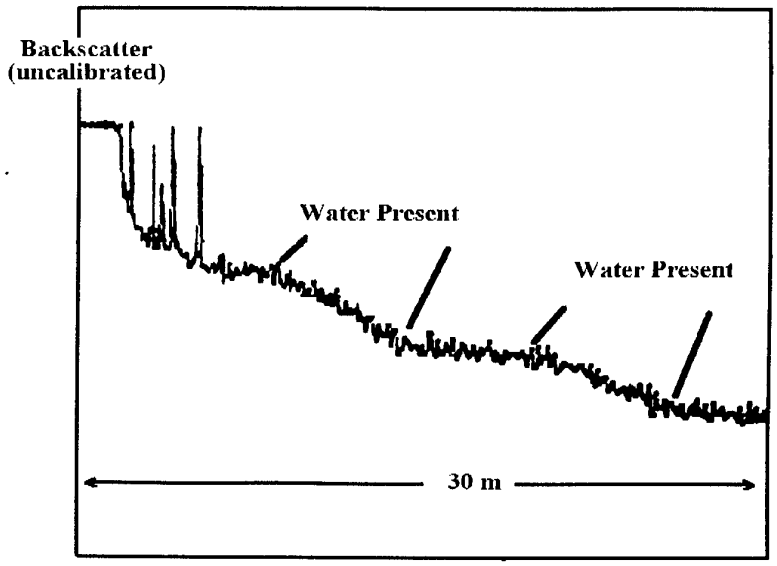


Figure 6: Distributed Water Ingress Measurement.

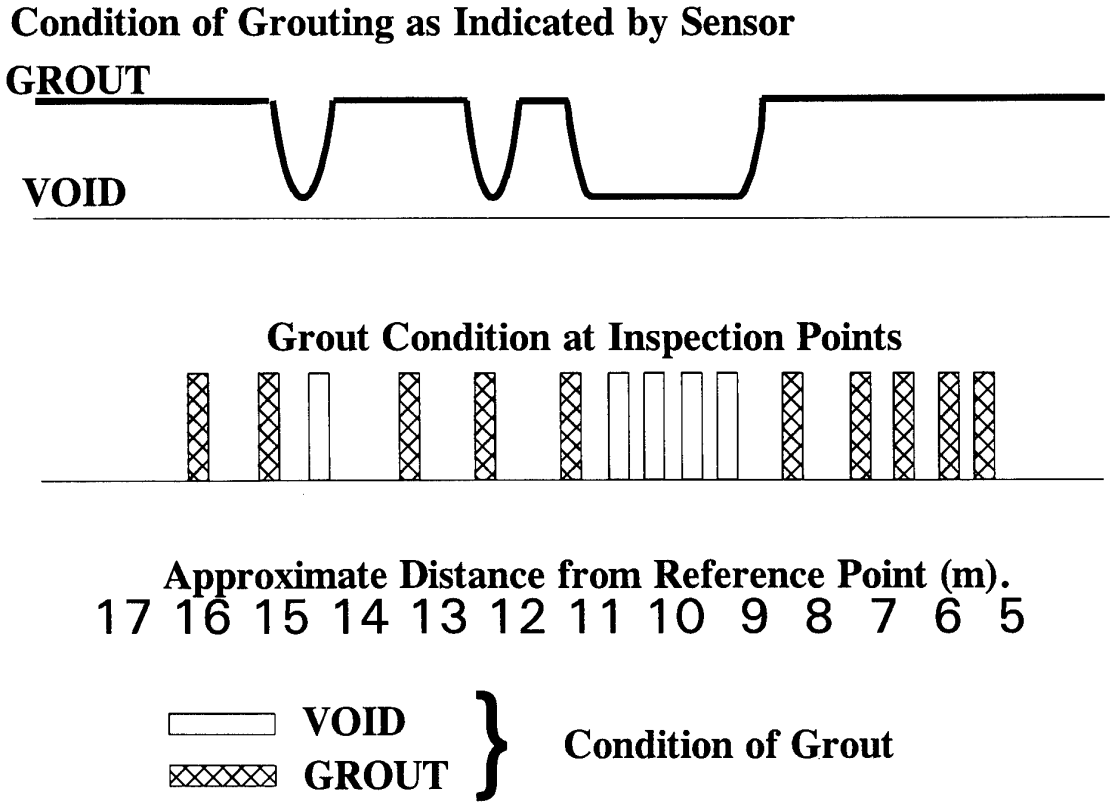


Figure 7: Sensor Indication of Grout Fill

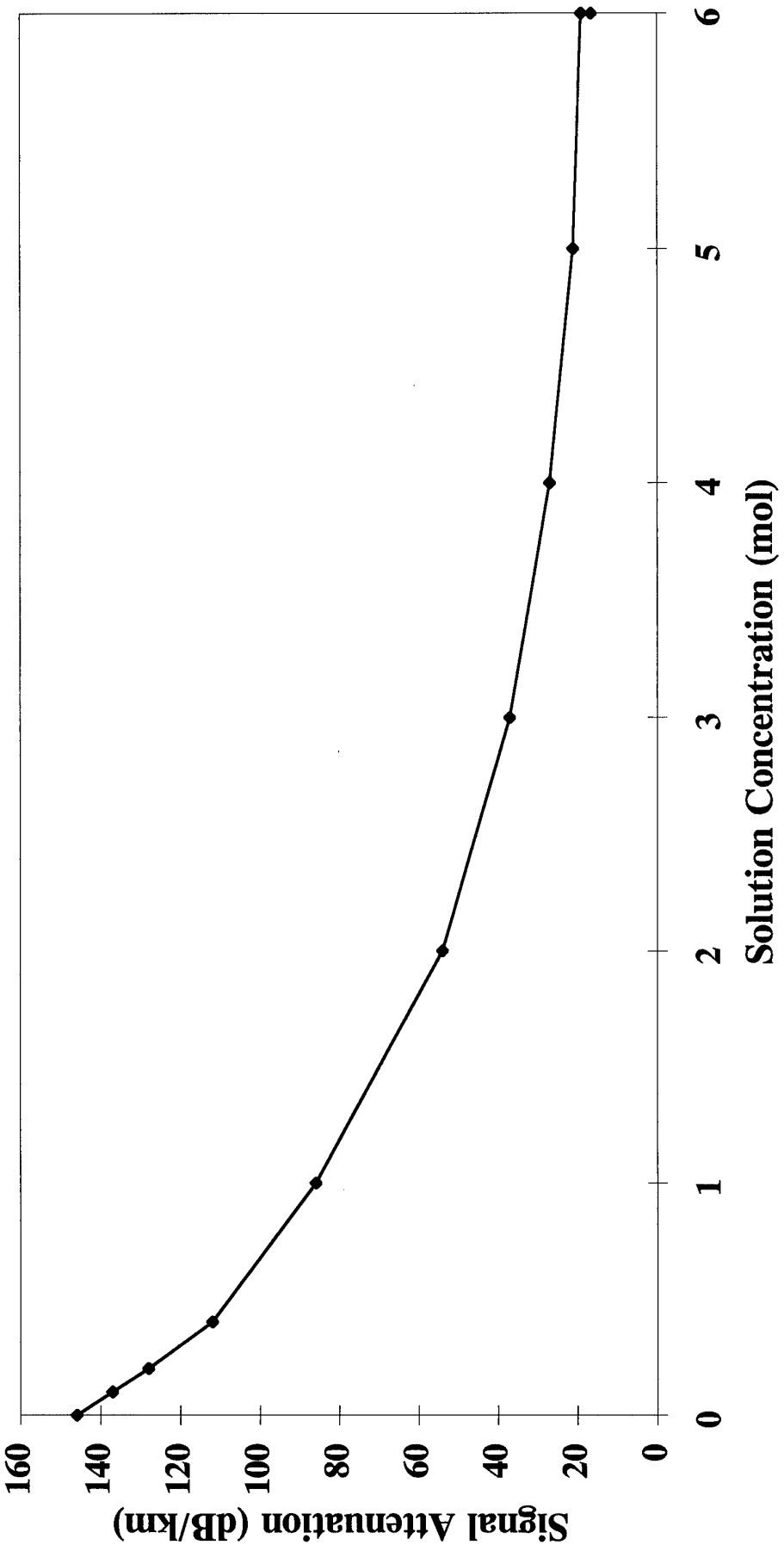


Figure 8: Sensor Attenuation Versus NaCl Concentration

A synthesis of science and art; creating a new domestic world of sensual products

Chris Thorpe and Cliff Friend

Smart Materials Group, Cranfield University
Shrivenham Campus, Swindon, SN6 8LA, England

ABSTRACT

The creation of intelligent objects with sensual capabilities and caring personalities; objects which will share our domestic environments and our public spaces, is a vision at once both unnerving and inviting. As research into smart materials, intelligent material systems and the whole spectrum of related areas such as biomimetics, nano-technology and neural systems converge, we are now in a situation where in ten years intelligent objects could realise this lucid projection.

The problem comes when we begin to look at the implications of such future object-environments. Our eagerness to solve the complex technical problems associated with the processing and manufacture of smart materials must be placed in the broader context of human considerations.

If we are to realise their potential, and optimise the benefits which smart materials and intelligent material systems could bring to our quality of life, we must develop a new approach that is both technologically advanced and sympathetic towards human needs. An approach that is a synthesis of the objective reality sought through science and the irrational, emotional subjectivity embraced in the arts. This paper looks at the design of intelligent objects for the home, examining the role of design, the product interface and the relationship between objects and ourselves within the home environment.

1. INTRODUCTION

We know from history that materials have been essential to the development of our culture. From stone age to the current electronic age, we have applied and processed materials with increasing sophistication. This apparently natural ability to embrace new materials technology which was initially vital to our survival, has increasingly been driven by economic forces. Products spawned from the recent advances in micro-chip technology have spread inexorably, creating a host of related product areas and saturated life style trends.

As the new infant 'age of intelligent materials' matures, our understanding and vision of the future must adopt a different model to the past. This is necessary because 'intelligent materials' are *fundamentally* different to so called 'monolithic' materials and this difference must be understood and used to effect a human, user centred approach in the design of new 'intelligent' products.

1.1 Intelligent and monolithic materials

The attempts to classify and define material 'intelligence' are already well documented.[1] Characteristically these have placed such materials within a hierarchy in which structural materials form the simplest and intelligent materials the most advanced stages of materials technology.[2] The fundamental difference, however, between 'intelligent' and 'monolithic' materials is that monolithic materials like metal, wood and stone are unable to change in response to stimuli. Intelligent materials are both animate and responsive to stimuli and at an optimum level capable of performing complex 'life' functions.

The intelligence in a material can come from linking sensor, actuator and processor within a *dumb* material, or as a result of chemical/molecular level changes within the material itself. Whichever the case the *concept* of material intelligence is the same, the essential feature of which is the ability to sense, process and act upon stimuli.

0-8194-2165-0/96/$6.00

In this way intelligent materials have a strong analogy to life forms, a concept which is clearly seen if we apply *intelligence* to an object such as a cup.

An 'intelligent' cup, unlike a normal one, would be able to change its shape and colour in accordance with its contents. It would also be able to change its texture and firmness according to its user and ultimately learn to identify the person using it from their touch. In other words the 'intelligence' enables it to adapt to its environment and develop behavioural patterns in accordance with its surroundings.

This analogy between intelligent materials and nature has proved vital in the development of intelligent materials technology for a number of reasons:

- First, it allows the *concept* of intelligent materials to be clearly understood and communicated.
- Second, the realisation that we are attempting to develop objects with 'life functions' similar to our own has elucidated the complex issues involved.
- Finally, the imagination of scientists, engineers and designers has been stimulated to consider new applications. These have arisen directly from the potential within materials to generate dynamic sensory 'life-like' responses.

This last point particularly has been central to a change in perception by the scientific profession. This has happened quite naturally from the growing realisation that intelligent materials are concerned more with subjective human considerations than with the so-called traditions of science.

2. SCIENCE OR ART ?

" The popular perception is that the scientist's work is concerned with logical enquiry. The objective of science is knowledge through empiricism, theory and deduction."[3]

This stiff generalisation, it could be argued, holds some truth but places science a long way from the expressive world of the arts. The human, biological focus inherent in intelligent materials has, however, augmented a change in the way scientists work. This is evident in a number of areas each of which has affected the perception of scientists and engineers, taking them ultimately much closer towards the human, subjective considerations embraced in the arts.

2.1 Isolation to interaction

The development of intelligent materials has catalysed the process of interaction between relevant disciplines. The need for enabling technologies to be developed in parallel has meant it is vital for those in different but related fields to work together. Intelligent materials technology is reliant on the work of engineers, chemists, materials scientists and designers. The notion of any one area working in isolation would be ineffective, to say the least, because the foundations for the technology are built across different fields.

2.2 Optimum to intelligent

The preoccupation with developing 'optimum' materials, making them increasingly lighter and stronger has been replaced by the move toward increasing material *functionality*. This has in turn led to a different approach in the manufacture and design of buildings and artefacts. An 'intelligent' structure which can compensate and relate information about its well-being back to us, can be built without the need for excess bulk and strengthening; consequently the approach to designing intelligent structures and artefacts has been reappraised.

The so-called 'Frankenstein' approach has clearly illuminated the inadequacy of a traditional bolt together approach and we are now witnessing a focus toward integrated design and manufacturing *strategies* based on nature's design patterns. Yanagida has already outlined the superior benefits of adopting such a *natural* design philosophy.[4]

2.3 Surface to interface

With the shift in focus toward holistic design strategies, the understanding of materials and surfaces has also changed. As we begin to consider the prospect of internal or molecular level intelligence in objects, our whole notion of what an object surface is, where it begins and ends will be different. Our perception of intelligent objects will be as integrated harmonious *systems* not separate component parts serving different functions. Intelligent products will be perceived as living connecting human *interfaces*. This will be especially apparent in objects of a human scale designed for use in a human environment - at a level where there is a high degree of intimacy between the person and object.

Such intimacy is most evident in what appears to be a largely unrealised area for the potential of intelligent materials; the domestic environment.

3. THE DOMESTIC ENVIRONMENT

Essentially the home is a dwelling place for families. It is a place rich in symbols of both cultural and individual identity, expressing the daily actions of people including:

- Relaxation and entertainment
- Ablutions and defecation
- Working
- Preparing and eating food
- Sleeping

Each of these different actions creates a corresponding interplay between ourselves, the environment and the objects we use. These interactions stimulate different and ever changing emotions and perceptions each directed through our sensory responses.

3.1 Relaxation and entertainment

In order to relax we may listen to music or watch television. In either case our relationship to the objects is largely through visual and auditory senses; we see the images on television and we hear the music. The television and hi-fi are synthetic technological *'vehicles of experience'* which create the possibility for reflection, imagination and escapism via our eyes and ears.

3.2 Ablutions and defecation

In taking a bath or shower we directly expose our body to soap and water. Cleansing the body involves changes in temperature and humidity, the interface of which is both soft, smooth and fluid. Our bodies warm and relax in a process that is highly tactile throughout. Washing, rinsing and drying ourselves is a kinaesthetic process of 'self-preparation'. Shower and bath are both object and environment while toilets and sinks are shiny pillars of cleansing ritual.

3.3 Preparing and eating food

The preparation of food is an expressive process of manufacture, its consumption a vivid stimulation of all senses. Using different tools; a whisk, a bowl and a stove, we process a range of edible materials; milk, eggs and salt, to create food,- in this case an omlette! Cooking and eating is one of the most ritualistic and sensual parts of daily life. The process employs all our senses and the object interface varies unlike any other area in the home. Microwaves are used alongside bowls and wooden spoons; elemental substances like water and salt with synthetic compounds.

It is apparent even from these brief descriptions that we employ a combination of sensory responses continually in our daily actions. Our sensory interaction with objects in the home is almost mirrored by the close relationship we have with one another. What is most important is that in all cases the interaction happens at the interface between us and the objects. That is to say at the exact point of contact between our senses and the opposing *surface*. We will now look more closely at the way this interface works.

4. THE INTERFACE

4.1 Emotion

We have already seen how emotions are stimulated via the senses in the brief analysis of food preparation. The process of cooking and eating excites our feelings of hunger and also our expectations by the twofold process of touching ingredients as we prepare the food and through the olfactory sensations we have in the cooking of food.

Emotions are direct instinctual reactions, they are in many ways animalistic and free of moral or ethical considerations. They are neither rational nor intellectual and while we may stop to describe food or analyse it with language on an *intellectual* level, our emotions come prior to the generation of our perceptions and their communication as abstract thought.

4.2 Perception

Our ability to see, taste, touch, smell and hear enables us to form complex sophisticated sensory perceptions. The senses we use, largely out of our conscious control, work at the *interface* of the material world. This is at the exact point of contact between our own sense receptors, eyes, ears, etc. and the opposing surface.

The perceptions we have may use any combination or hierarchy of the senses. Our perception of an orange may be 'bi-sensory' if we primarily consider it round and smooth, or 'mono-sensory' if we are overwhelmed by its citrus smell. In this way our first reaction to an object comes from what we might term its 'sensory-profile', a short hand sensory version of what that object *is*.

4.3 Abstraction

Our ability to abstract the perceptions which arise directly from our senses is central to the concept of intelligence. In this context, the difference in sensory interaction between objects and people is very important. The sensory interface between ourselves and objects enables us to modify and change our behaviour, the objects themselves having no such autonomy. However when we meet another person, we respond to their body language long before linguistic communication. This situation is quite different when we encounter an object; the difference is that an object cannot respond while another person can. The creation of a 'person to person', responsive interface, is the essence of creating 'intelligent' objects.

If an object could generate an internal dialogue starting from the feedback of our touch and if it could then modify its behaviour, we would say that the object was intelligent. Being able to sense and then interpret those sensations would, like us, enable it to perform the key functions necessary for intelligence; the ability to communicate by forming abstract concepts. The implications of an object exhibiting such functions are however quite another thing.

5. THE QUESTION OF DESIGN

The prospect of using intelligent materials to enhance the function of domestic products is very exciting. Having examined the nature of intelligence, the domestic environment and the interface, we will now look at the important role which design plays in the future of intelligent products.

5.1 A material revolution

When plastics first became available for general use in the early 1930's designers and manufacturers were able to use their properties to make objects with colours, forms and shapes that were previously impossible. Products were enhanced by the specific characteristics which plastics exhibited. Surfaces could be made smoother and more durable, objects made more quickly and cheaply. As a result peoples attitudes toward hygiene and cleanliness changed along with their basic set of values.

Intelligent materials will have an impact even more radical than the plastics age. Adding functionality to materials will change the fundamental principles of design and manufacture. With plastics the enhanced

qualities of objects came via new aesthetic, engineering and processing possibilities. Intelligent materials will also affect aesthetics and manufacture, but unlike plastics they will bring a new dimension to objects as a result of their functional characteristics. So not only will we be able to manufacture objects in different ways and with a new aesthetic, we will also design the way it responds to stimuli. It is this aspect above all which will necessitate a revolution in the design and manufacturing process.

5.2 The designer

The various processes of design and the many types of designer are now so widespread that the term design could be applied to almost any creative act. Designers are often described as 'problem-solvers', sometimes as 'synthesists'.[6] So with regard to the area of product or industrial design, how should we describe what they do? We would like to offer the following definition:

The product designer's role is to change or adjust the interface between people and their actions so that their needs are better satisfied.

This is quite a broad definition which attempts to describe the most important part of the product designer's work; to link peoples needs - be they for security, comfort or expression - with a means of achieving them. In this case the product designer is very much a synthesist, acting as a connection between people on one side and the manufacturer on the other. Their job is to understand the needs of people within their environment and then give shape to the interface, be it a shoe or a toaster.

5.3 Human needs

The designer, placed somewhere between user needs and manufacturing technology, will face an even greater responsibility with the arrival of intelligent materials.

Undoubtedly the basic human needs; for food, shelter, clothing and so on, are still the core elements for survival. Beyond these we have a system of social, personal and emotional needs which are just as important for the individual or family within the home. The strain of modern life has placed a greater emphasis on the home as a stable sanctuary; a place where we can lock out the tensions of work and be with our families - comforted and loved.

Technology already plays a key role in the home. Our knowledge has been extended by television, and the ability to communicate globally has transformed the way we now perceive the world. On a mundane level we can also clean our houses, cook and wash with utmost efficiency. But technology has also left us cold and confused. It is often manifest in a soulless black box with a myriad of wires and buttons, appearing to offer us control.

Our needs are not so much for control, but for understanding and harmony. We have a deep need for 'soft' not 'hard' values in the home and for an environment that is friendly and flexible not austere and rigid. Our daily actions should be enhanced by a communicating, human interface; one which respects and provides for our needs of warmth, comfort, humour and interaction.

5.4 Enhanced function

With the availability of intelligent materials, the product designer will be ideally placed to reconcile our deeper human needs. Designers will be able to *enhance* the functions of objects beyond their ordinary tasks; the kettle will still be an implement to boil water but it will connect dynamically to the user, changing its form, colour and texture in response to our touch.

As these intelligent materials develop beyond a simple one-stimuli one-response stage, designers will be able to imbue objects with ever more complex functional characteristics. The term 'pet-value' is already used to describe the tactile, warm and living qualities which designers are attempting to give their appliances. Intelligent materials will make real this notion of objects with pet features. Objects will also have an innate ability to 'self-monitor'; a *function* which will enable objects not only to repair themselves by sensing when they are broken but to eventually re-cycle or self-decompose at their natural lifes end.

5.4 Semantics and product language

The way objects communicate and what objects mean has been the concern of designers since the birth of design culture. 'Semantics' and 'product language' are both terms used to describe this concept. By adding functionality to materials we will be able to design objects that really do communicate. This will not only alter the way we understand aesthetics and object function but will change the fundamental basis of a product's 'semantic' value.

We will certainly no longer be able to describe an object by its static formal qualities, if it can change its shape and colour. It may look geometric and ordered one minute,- random and asymmetric the next,- it's surface may look like wood and then change to become metallic, and it may feel like rubber, then seconds later, feel more like hard plastic.

The 'functional' qualities of objects will mean that our understanding should be similarly dynamic. The new semantic values will be based on behavioural patterns, as opposed to formal qualities. In this way we might describe the next generation of home appliances as sympathetic, which will in turn give us a greater respect for the objects in our homes and may reverse the questionable values of a consumer society.

6. CONCLUSION

Many working with the technology of intelligent materials have focused wholly on the technical problems associated with making intelligent structures. However, what we must remember is that this new technology must be developed for the benefit of people. Forgetting to add our token human to the full equation will therefore not only restrict the vision behind the development, but will place the emphasis upon standard of living when what we should really be considering is quality of life.

If we are to optimise the human benefits which smart materials could bring to our lives, we will need to form an understanding which is both technological and humane. In other words we must adopt an approach to the design of a sensual world generated from a synthesis of science and art. This is the the only way to deal effectively with a technology which at its most advanced, has a potential (which we should hope to realise) to generate enhanced, sensual, object-environments,- and with such environments, benefits and implications that are both technologically and culturally inter-dependant.

7. REFERENCES

1. T. Takagi, 'A Concept of Intelligent Materials', US Japan Conference on Smart/Intelligent Materials and Structures, p 3-10, I. Ahmed, A. Crowson, C. A. Rogers, M. Aizawa, Technomic, Lancaster 1992
2. M.V. Ghandi and B. S. Thompson, Smart Materials and Structures, Chapter 2, Chapman and Hall 1992
3. R. S. Root-Bernstein 'Sensual Education, The Sciences, p 13, Sept 1990
4. H. Yanagida, Technology's New Horizons, Chapter 7, Oxford university Press 1995
5. S. A. Gregory, The Design Method, Chapter 2, London Butterworth 1966
6. P. Gorb, Design Talks, Part 4, The Design Mind, Design Council 1988

Smart Materials in Construction

Tony Sheehan

Ove Arup & Partners, 13 Fitzroy Street,
London W1P 6BQ

ABSTRACT

The aim of this paper is to provide an assessment of the potential for smart materials in construction. Significant material developments from the smart research field are outlined, and possible applications identified.

1. BACKGROUND

The selection of structural construction materials is generally made by considering a number of criteria. These may include:

- Safety
- Strength and strength to weight ratio
- Stiffness
- Expected life/chemical resistance/durability
- Environmental Impact
- Fire Performance
- Ease of manufacture (on/off site)
- Context (site and environment)
- Appearance (texture, colour, etc)

In recent years, a large number of new and improved materials have arisen from research into smart materials and systems. The aims of smart materials and systems are the same; to both sense a change in their environment and to automatically respond to that change. Whilst a smart material is inherently capable of carrying out such an activity, a smart system will comprise

- Sensors - devices to sense a change in local conditions.
- Actuators - devices to take action to allow for local conditions
- Control technologies - the 'smart' technology that allows a 'decision to act' to be made.

Promising material developments can be identified both in areas of sensor and actuator technology from smart systems research, as well as those from smart materials research. Each of these fields, and their potential for construction are now considered in turn.

2. SENSORS

Two developments in the smart sensors field are particularly noteworthy; optical fibres and TRIP steels.

Conventional strain gauges have a number of weaknesses when applied to large structures; their sampling area is limited, as is their ability to 'multiplex' a large number of sensors together to provide real time data on a structure's condition. Optical fibre sensors have now been developed to monitor factors as diverse as strain, corrosion, temperature and so on. Concepts such as 'optical domain time reflectometry' have been applied such that the time delay between sending out a light pulse and receiving a reflection can successfully predict

0-8194-2165-0/96/$6.00

the location along a fibre where any change occurs.

Major developments in optical fibre technology in communications currently allow vast quantities of data to be transported across extended distances with negligible signal loss. Optical fibres can thus allow both

- Measurement along extended lengths (through use of fibre sensors) and
- Remote monitoring (through use of fibres as communication devices)

Optical fibre sensors have been used to monitor bridge and other civil structures worldwide. Significant potential has been shown in such fields as

- Corrosion monitoring[1]
- Structural monitoring of structures[2,3]

The ability to then access such information remotely has been used to good effect on the Winooski One Hydroelectric Dam where a network of fibre optic sensors have been cast into the structure[4]. The ability to monitor the structure on the internet allows potentially great cost savings in inspection to be obtained. By combining such technology with, for example, a network of embedded sensors to track the rate of carbonation or chloride ion ingress into a concrete structure (following the concept of 'corrosion ladders' used on several structures) a reasonably smart structure could be obtained.

TRIP steels offer similar potential. As these materials are strained, they undergo a progressive, irreversible phase change from a non magnetic face centred cubic to a ferromagnetic body centred cubic phase. TRIP steels are so called due to this TRansformation Induced Plasticity. By direct measurement of the state of magnetism of TRIP steels, it is possible to assess the peak strains experienced by the material (and any structure it is attached to) over a period of time. This technology could be applied to peak strain measurement of large structures such as bridges[5] (and has been applied to several bridges in Georgia, USA) and could also be exploited for structures subject to earthquakes. Localised measurement of key elements (e.g. peak strain sensing of rock bolts used in tunnels) could also be considered.

The key exploitation of sensor technology for construction will be twofold ;

- Monitoring existing structures
- Monitoring new materials of uncertain properties

Much has been written about the ability of sensor materials such as optical fibres and TRIP steels to provide monitoring capability on existing structures. Often, however, clients are reluctant to incorporate such monitoring systems either on new structures (since they should be designed and built properly in the first place) or on existing structures unless clear signs of degradation are present.

New materials, however, offer considerably more potential. Much of the use of materials in construction is dependent on long established rules and Codes of practice that are only readily available for traditional construction materials (e.g. steel, concrete, brick, etc). By combining newer materials such as polymer composites with sensors[6], newer materials could be used in construction with increased confidence, and existing barriers to innovation could be reduced.

3. ACTUATORS

Actuators act in order to convert one form of potentially harmful energy into another which must then be dissipated. Key actuator technologies of relevance to the construction sector include shape memory alloys and viscoelastic materials. Considerable effort has also been directed towards piezoelectric (charge generation in

response to stress or strain generation in response to an electric field) electrostrictive and magnetostrictive materials, but their energy requirements and loads generated do not generally lend themselves to Civil Engineering structures at present.

Shape memory alloys are a family of materials that exhibit a transformation between high temperature stable austenitic phase to a low temperature stable martensitic phase as the temperature is raised or lowered[7]. The concept has been applied to, for example, automatic window openers (forcing the window to open as the temperature is raised) and to pipe couplers (providing a 'shrink fit' joint between adjacent sections).

Shape memory alloys can also be forced to transform between phases by straining the material. This conversion, in response to applied strain, from austenite to martensite to stress induced martensite and back to austenite can generate considerable 'hysteresis' losses (i.e. converting strain energy to transformation energy). Provided such losses can be dissipated, shape memory alloys offer considerable potential as a means of vibration/earthquake suppression.

Viscoelastic materials (VEM) also offer considerable potential as a means of passive (or partially active) vibration suppression in structures. Viscoelastic materials are already widely used for vibration control in aerospace applications, where vibrations in the structure are converted to a combination of recoverable energy and heat. Similar principles could be applied to civil structures, although the prediction of detailed material behaviour is complex[8] and aspects such as frequency dependence of these materials and problems concerning ease of energy dissipation have yet to be fully resolved.

Clear needs for effective means of vibration control have existed in civil structures for many years. The potential development of effective devices incorporating shape memory alloys, VEMs and other materials are likely to materialise into real applications in the short term[9,10].

4. SMART MATERIALS

Truly smart materials will be able to both sense a change in their environment and respond to that change without the need for further input. Intumescent materials provide an example of a reasonably smart material already widely used in construction; such materials offer a decorative paint coating to structural steelwork, but in the event of a fire are capable of both sensing the fire and, at an appropriate temperature, foaming up to provide an insulative char to separate the structural element from the fire.

Products of similar potential include hydrogels; materials that swell up when activated by either moisture or some other species. Such materials are now available commercially as waterstops (i.e. to present water seepage through gaps formed during construction). They have been used successfully in onerous applications such as swimming pools and offshore platforms where they act as a 'smart seal' between concrete elements. They have also been used within smart sensors to good effect (e.g. to detect grout within prestressing ducts[11]).

Looking further to the future, new materials such as self healing materials could see increased application. These materials would be capable of both sensing damage and effecting self-repair automatically. This concept is far closer to reality than one may think; researchers at the University of Illinois[12] have developed a range of hollow fibres which can be filled with resin, then cast within other matrices (e.g. of concrete or polymer). Significant cracking of the matrix leads to cracking of the fibre, release of the resin, and some form of repair to be carried out. Such concepts are at an early stage, but worthy of note, nonetheless.

Overall, new, smarter materials will only find application in construction if they

- Are sufficiently durable (civil structures often require 60-100 year life with little or no maintenance)

- Provide real technical advantages over tried and tested alternatives
- Are cost effective (most construction materials are high volume for minimal cost)

The idealised goal of the totally automated building should not always be the ultimate target. For many years, photochromic glazing (where the glass darkens automatically in response to incident radiation) was thought to be the ideal for controlling light/heat ingress in office buildings. In fact, recent research has concentrated more on electrochromic glazing (where the glass is controlled by an electrical switch) since office workers tend to prefer to control their own environment rather than experience a fully automated one. Technology for technology's sake will never find applications in the construction industry; real needs will develop required solutions.

5. CONCLUSIONS

Several of the promising developments within the smart materials field and their potential for construction have been addressed. It is clear that potential applications could comprise (for example)

- Sensors (e.g. optical fibres and TRIP steels on civil structures)
- Actuators (e.g. shape memory alloys and VEM's for vibration suppression)
- Truly smart materials (e.g. self healing materials in structural applications)

Examples of smart materials in construction do exist; intumescent materials for fire protection and hydrogels for waterproofing provide good examples. Smart technology is currently the subject of considerable research across many disciplines. The levels and quality of research in progress will, however, lead to increasing applications in construction in the coming years.

6. REFERENCES

1. K.D. Bennett and L.R. McLaughlin "Monitoring of corrosion in steel structures using optical fiber sensors", Proceedings, Smart Structures and Materials 1995, Smart System for Bridges, Structures and Highways, Ed. Larryl K. Matthews Volume 2446, Page 48-59, SPIE, Washington, 1995

2. Wolfgang R. Habel and Bernd Hillemeier, "Results in monitoring and assessment of damages in large steel and concrete structures by means of fiber optic sensors". Proceedings, Smart Systems for Bridges, Structures and Highways, Ed. Larryl K. Matthews, Volume 2446 Page 25-36, SPIE, Washington 1995.

3. Richard W Griffiths, "Structural integrity monitoring of bridges using fiber optics" Proceedings, Smart Structures and Materials 1995, Smart System for Bridges, Structures and Highways, Ed. Larryl K. Matthews Volume 2446, Page 127-138, SPIE, Washington, 1995.

4. P.L. Fuhr, D.R. Huston, T.P. Ambrose and E.F. Mowat, "An Internet observatory : remote monitoring of instrumented civil structures using the information superhighway" Smart Materials and Structures, Volume 4 Number 1, March 1995 page 14-19, March 1995.

5. Bruce D. Westermo and Larry D. Thompson "Design and evaluation of passive and active structural health monitoring systems for bridges and buildings" Proceedings, Smart Structures and Materials 1995, Smart System for Bridges, Structures and Highways, Ed. Larryl K. Matthews Volume 2446, Page 37-46, SPIE, Washington, 1995.

6. J.A. Green et al, "Optical fiber sensing technique for impact detection and location in composites and metal specimens", Smart Materials and Structures, Volume 4, Number 2, June 1995 page 93-99.

7. Robert Krumme, Jack Hayes and Steve Sweeney, "Structural damping with shape memory alloys: one class

of device" Proceedings, Smart Structures and Materials 1995, Passive Damping, Ed. Conor D. Johnson, Volume 2445, Page 225-240, SPIE, Washington 1995.

8. Y.W. Chan, J.R. Wright and G.R. Tomlinson, "Dynamic Scaling of Viscoelastic elements" Proceedings, Smart Structures and Materials 1995, Passive Damping, Ed. Conor D. Johnson, Volume 2445, Page 324-335, SPIE, Washington 1995.

9. Simon Kim, "Passive Control Techniques in Earthquake Engineering", Proceedings, Smart Structures and Materials 1995, Passive Damping, Ed. Conor D. Johnson, Volume 2445, Page 214-224, SPIE, Washington 1995.

10. Christian A. Smith and Eric H. Anderson "Passive Damping by Smart Materials : analysis and practical limitations", Proceedings, Smart Structures and Materials 1995, Passive Damping, Ed. Conor D. Johnson, Volume 2445, Page 136-148, SPIE, Washington 1995.

11. W. Craig Michie et al, "Optical Fibre Grout Flow Monitor for Post Tensioned Reinforced Tendon Ducts" Proceedings, Second European Conference on Smart Structures and Materials, Ed. A McDonach, PT Gardiner, RS McEwen, B Culshaw, SPIE Volume 2361,Page 186-189, SPIE, Washington 1994.

12. C.M. Dry "Adhesive liquid core optical fibers for crack detection and repairs in polymer and concrete matrices". Smart Structures and Materials, 1995, Smart Sensing, Processing and Instrumentation, Ed William B Spillman Jr. Volume 2444, page 410-413, SPIE, Washington 1995.

SMART EARTHQUAKE RESISTANT MATERIALS (USING TIME RELEASED ADHESIVES FOR DAMPING, STIFFENING, AND DEFLECTION CONTROL)

Associate Professor Carolyn Dry

School of Architecture - University of Illinois at Urbana-Champaign
Champaign, Illinois USA

ABSTRACT

Preventing buildings and bridges from damage from severe dynamic loading events is a primary goal of civil infrastructure. Present designs attempt to control structural response by making the structures more massive, by increasing lateral stiffness through bracing, and by damping technology such as mass damping and base-isolation. These attempts affect portions of the governing equation: for an idealized building frame or bridge, the free vibrational behavior is described by

$$Mu + cu + ku = -mug(t)$$

where m = mass, c=damping coefficient, k=lateral stiffness, u=deflection, and ug(t)=ground acceleration.[1]

The use of adhesive released internally in a material based way of addressing the problem. The time release of low modulus adhesive chemicals would assist the damping characteristics of the structure, use of a stiffer adhesive would allow the damaged structure to regain some lateral stiffness (k) and adjustment of the set times of the adhesives would act to control the deflection. These can be thought of as potential new method of controlling vibration of behavior in case of a dynamic loading event. In past experiments, self-healing concrete matrices were shown to increase post-yield deflection and load carrying capability by the release and setting of adhesives[2]. The results were promising in resisiting damage of dynamic loads applied to frames. This indicates that self-healing concrete would be extremely valuable in civil engineering structures that were subjected to failure-inducing loads such as earthquakes.

INTRODUCTION

Self-healing concretes have embedded adhesives which are released inside the concrete when and where cracking occurs. It has been shown to improve the strength of cracked portions of the cement and increase ability to deflect in a ductile manner under load. This results in a self-repair mechanism for the concrete, and it has many potential applications to structures. Buildings, for instance, could benefit from self-healing concretes, since a substantial amount of cracking occurs after construction especially if subjected to dynamic loads. Embedding adhesives in the concrete

0-8194-2165-0/96/$6.00

will repair cracking, which would result in less maintenance and prolonged life of the structure.

The object of this research is to assess the feasibility of using this new concept of self-healing concretes for structural elements. Our research has concentrated on the material behavior of self-healing cements. The focus of this research is on the use of self-healing concretes in structural members that may be damaged by dynamic events such as earthquakes, impacts. A follow on study will investigate the influence of different types of adhesives and release mechanisms in the concrete elements under several load histories, for self-healing of the structural element.

In the experimental program, the first set of specimens used typical elements, such as frames containing adhesive loaded fibers. The results were positive. We will next study joints containing several types of adhesives and release mechanisms. These will be tested on a small shake table in which actuators, load sensors, and a deflection monitor are mounted on a base. The adhesives will have different set times, strength of bond with the matrix, and elastic moduli. The specimens will be tested for the effect of adhesive type on deflection, stiffness, and damping of the members.

There is no other competing system for automatic internal repair of cracking in concrete. This innovative technology releases repair chemicals upon demand in response to cracking. It is designed to enhance service life and reduce maintenance and ensure continued use throughout the occurrence of natural disasters. The potential impact is enormous in the enhancement of life safety and cost effectiveness. It is estimated that the cost of hollow fibers/release mechanisms and adhesives will pay for themselves within the first expected repair cycle even through the initial cost of the concrete may be half again to nearly double the concrete without these fibers.

PAST RESEARCH ON SELF-REPAIR OF MATERIALS

In our past research[3], experiments were performed on specimens containing small-diameter reinforcing bars and adhesive-filled brittle fibers. The adhesive-filled fibers were evenly distributed along the longitudinal axis below the neutral axis of the samples. A control set of specimens were also tested in which the specimens were identical to the first group but without the embedded adhesive. Each sample was loaded in 3-point bending applied with a static deformation rate. Specimens were loaded with enough strain to cause the fibers to fracture and release the adhesives into the cement matrix. They were allowed to rest for one week and then tested. A comparison of the records (see figures 1 and 2) of the first loading in flexure (before release of the chemical) and the second bend test loading (after release of the adhesive into the matrix) revealed several important facts. Most of the adhesive-loaded samples carried more of the load on the second bend than on the first bend, while in general, that was not the case for the controls. The inference made from this is that the crack opening displacement curve for the controls follows the normal reduction in load resistance, while the adhesive-filled samples reverse it, in that crack-opening displacement is reduced with the next loading and the samples carry more load in the second test. Also ductility as measured by deflection was improved for the samples containing released adhesive.

BENDING TESTS				
Sample	1st Test (kN)	2nd Test (kN)	Increase (kN)	% Increase
A	0.7484	0.8845	0.1361	18.2
B	0.7711	0.9526	0.1814	23.5
C	0.8051	1.0297	0.2245	27.9
D	0.8959	0.9888	0.0930	10.4
E	0.7893	0.7666	-0.0227	-2.9
Control 1	0.7802	0.6713	-0.1089	-14.0
Control 2	0.7938	0.6985	-0.0953	-12.0
Control 3	0.7666	1.0660	0.2994	39.1

Figure 1. Capacity of samples to carry a load at first bend and second. [3]

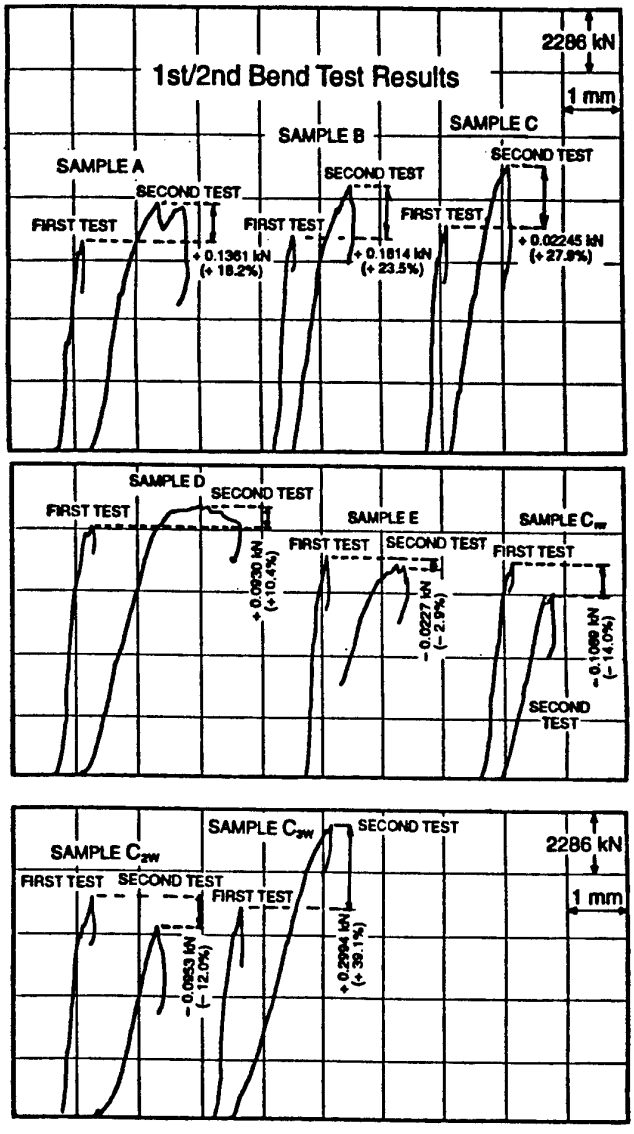


Figure 2. Load displacement diagram for each sample for first and second 3-point bending test. [3]

CONVENTIONAL TREATMENTS FOR CRACKING AND DYNAMIC LOADING

Micro-cracks are generally the source of larger crack growth, particularly when the member is subjected to inelastic deformations or fatigue loading or dynamic loading. Conventional treatments for concrete cracking include: 1) surface application of paints and coatings, 2) application of epoxy resins, asphalts or polymers which penetrate into the surface to block the pores, 3) injection of asphalt or polymers which penetrate into the surface and block the pores, 4) injection of epoxies and polymers into the body of the concrete, and 5) very rapid setting cements applied as overlays. Surface treatments tend to concentrate future crack development into areas not treated, and moisture may get trapped inside the concrete with these type of treatments, resulting in further damage. A repair strategy which is automatic, timely, safe and applied directly to cracking internally is clearly desirable because it would reduce loss of in-service time and reduce maintenance costs. Self-healing concretes, with the ability to repair concrete cracking, satisfy these requirements and there is no other system that does so.

Present design strategies which attempt to control structural response to dynamic events such as earthquakes are to make the structure more massive, increase lateral stiffness through bracing, or add damping technology such as mass damping or base-isolation. They rely on redesign of the structure to resist earthquake damage. No system resists the effect of dynamic loads by material properties alone. These attempts to modify the structure affect the portions of the equation governing bridge's free vibrational behavior as described by

$$Mu + cy + ku + -mug(t)$$

where m=mass, c=damping coefficient, k- lateral stiffness, u = deflection, and ug(t) = ground acceleration. y is a constant.

MATERIAL APPROACH TO TIME RELEASED ADHESIVES

The choice of the adhesive attributes in our system of altering material properties could supplant these massive structural remedies for resistance to dynamic loads. The release of a low modulus adhesive would assist the damping characteristics (c) of the structure, use of a stiffer adhesive which would allow the damaged structure to regain lateral stiffness (k) and adjustment of the set times of the adhesives would act to control the deflection (u). These are the different adhesive attributes in our system. Rubber-like epoxies which can absorb the deformations of crack opening/closing will be used.

A large volume of fibers can be added without balling by a bundling procedure. It also prevents brittle fiber breakage. Water soluble glue between fibers or a tape holds the bundle together. During mixing, these are dispersed and water in the concrete dissolves the glue releasing the individual fibers.

Questions Most Asked

1) How can large enough hollow brittle fibers be put in and mixed without breaking especially against the aggregates? We have had success in inserting bundled fibers during the mixing process with aggregates and cement. The fibers are bound with a water soluble tape. 3M first developed this method for their polyolefin fibers. They found they could add 4-8% volume fibers.

2) Can large cracks as occur in dynamically loaded structures be repaired? The system has two methods for repair of large cracks. One is the use of a viscous adhesives suitable for large cracks, the other method is the use of very quick setting adhesives which instantly repair smaller cracks thus preventing their growth into large cracks.

3) Why does one not mix adhesive in the wet concrete; why not add fibers to retard cracking? The system is designed to repair micro-cracks where and when they form and so retard further crack growth. Adhesives mixed in the concrete will not only change its chemical properties but will not be available later to flow into the cracks which form in a hardened concrete. They system constitutes a method of having liquid repair chemicals available inside the concrete for use at the cracks location for use just in time (as they form).

The brittle fibers retard cracking similarly to other fibers. Their cracking further absorbs crack energy.

4) In most structures subjected to loads and thermal fluctuation, and especially in dynamically loaded ones, cracks open and close, thus loosening any repair material in the cracks. The problem of conventional resin injection into cracks with varying, changeable width is usually ignored so that repairs of unstable cracks are reopened. One of our adhesive, the damping enhancing epoxy rubber-like one can absorb deformations of up to 50%. Its volume can be compressed because of gas filled microballoons which it contains. (This material was developed by researchers at the Technical University in Munich for this purpose.)

RESEARCH APPROACH TAKEN IN FIRST EXPERIMENTS

As shown in figures 3 and 4, a concrete beam and supporting columns as a frame were the specimens. Glass fibers (pipettes) were situated throughout the beam and into the moment connections at the columns. A series of cyclical loads acting as parallel to the beam was applied at the center-line of the beam. The device applying these loads was a hydraulically actuated testing machine. This machine is capable of exerting specific predetermined loads on the structure, while at the same time recording the deflection of the test specimen. A computer within the machine tracked and plotted the results in real time.

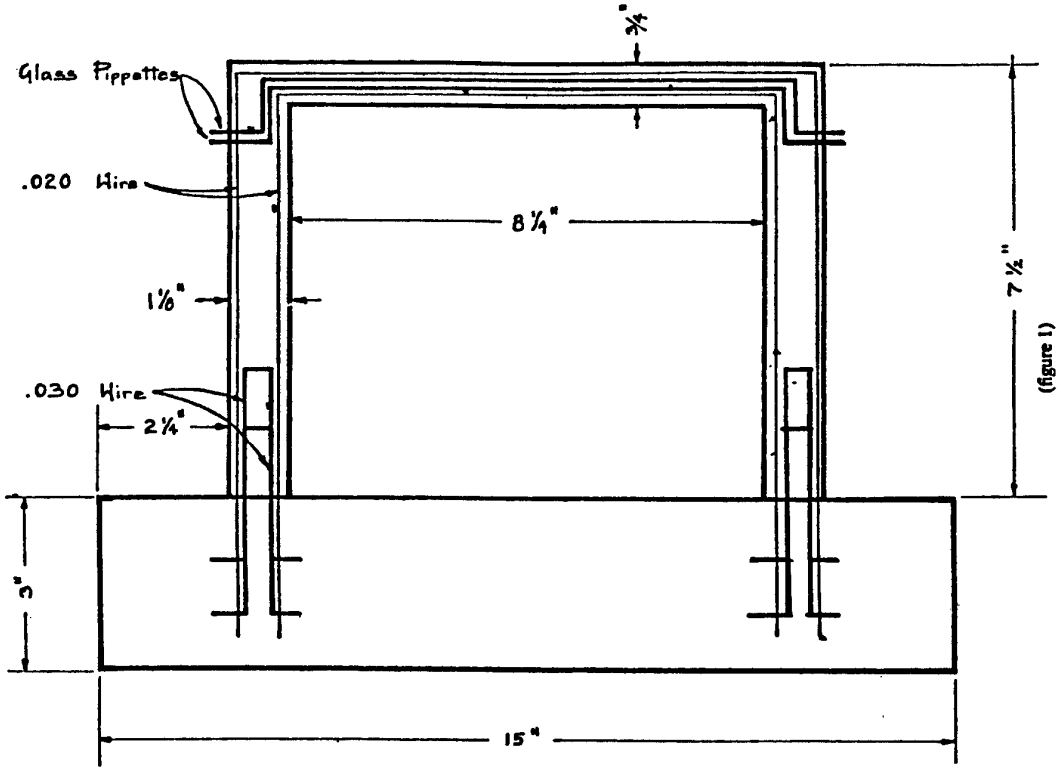


Figure 3. Concrete test beam, front view

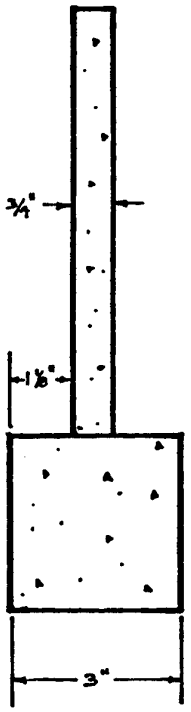


Figure 4. Concrete test beam, side view

The specimens were tested with an increasing load until cracking is evident. There, the test stopped to allow time for the agent to release from the fibers and set-up. One week was allotted between the first and second tests, and the second and third tests. During this period of time, the adhesive was released from the fibers (pipettes) and allowed time to set-up. After the pre-determined time, testing resumed on the specimens, and all information was recorded as it was earlier.

Four concrete samples were formed in accordance with the design drawings. One of the four samples acted as the control. The control sample contained the same reinforcing as the other three, however, it did not contain the glass pipettes that the other three samples have. After the standard 28 days had passed for the concrete to reach its full strength, testing began. The samples were tested with a hydraulically actuated testing machine. This machine is capable of applying differing forces in a cyclical manner, as in an earthquake. The force was applied on a single axis for ease of calculations, and acted on the structure in a direction parallel to the main beam. The specimens were clamped onto the testing device in a vertical position. The hydraulically actuated arm contacted the specimen on the center line of the beam and applied the load. Three separate tests were done, with a week between each, allowing time for the adhesive to set-up. During each test, photographs and video were taken to aid in locating where the cracks occur and in what order. The numbers were gathered from the tests (load kN versus displacement mm) and reviewed to compare strength and deflection of the samples with control.

Test Results

The first results were graphed showing the load required (kN) to displace the structure 3 mm. The numbers involved between test 1 and test 2 showed an increase in the strength retained in the adhesive loaded samples as compared to the control without adhesive (figure 5). This increase was shown as the percentage increase test 1 - 2 column. The same favorable increase in adhesive repaired samples was also evident when comparing test 1 and test 3.

Between test 2 and test 3, there was an even larger increase in strength for the samples with the adhesive. The strength of the control was again decreased, while the strengths of the samples with adhesive increased dramatically. During this increase between test 2 and test 3, the strengths of the samples with adhesive regained the majority of their strength values. In fact, the strengths of these samples were nearly equal to their strengths during test one.

	BENDING TESTS at 3 mm								
Sample	1st Test	2nd Test	3rd Test	Increase	Increase	Increase	% Increase	% Increase	% Increase
	(kN)	(kN)	(kN)	test 1 & 2	test 2 & 3	test 1 & 3	test 1 & 2	test 2 & 3	test 1 & 3
control	0.42	0.2	0.17	-0.22	-0.03	-0.25	-52.40%	-15.00%	-59.50%
101b	0.55	0.3	0.47	-0.25	0.17	-0.08	-45.45%	56.70%	-14.50%
101c	0.55	0.5	0.52	-0.05	0.02	-0.03	-9.10%	4.00%	-5.00%
101d	0.3	0.25	0.33	-0.05	0.08	0.03	-16.6	32%	10%
	BENDING TESTS at .6 kN								
	1st Test	2nd Test	3rd Test	Increase	Increase	Increase	% Increase	% Increase	% Increase
Sample	(mm)	(mm)	(mm)	test 1 & 2	test 2 & 3	test 1 & 3	test 1 & 2	test 2 & 3	test 1 & 3
control	6	7.2	9	1.2	1.8	3	20%	25.00%	50%
101b	3.5	6	4	2.5	-2	0.5	71.40%	-33.30%	14.30%
101c	3.1	4	2.5	0.9	-1.5	-0.6	29.00%	-37.50%	-19.40%
101d	------	4.8	6	------	1.2	------	------	25%	----

Figure 5 . Bending tests data

CONCLUSIONS

Conclusions for these tests show that while the strengths of the samples with adhesive dropped initially, they again rose after the adhesive had time to permeate the cracks and set up (10 days time). The results produced from the testing indicate that when adhesives are released after initial concrete cracking, the strength of the concrete increases (relative to the strength of controls with no adhesives).

DISCUSSION

Because there is a large difference in the amount of resistance exerted between test 1 and test 2 when compared to the control, but a small difference between test 2 and test 3, it may be assumed that the concrete had completely failed after test 2. If this were the case, the amount of resistance exerted during test 3 could be attributed solely to the steel reinforcement and not to the failed concrete. By realizing that the were 52.4% decrease in the among of resistance exerted between test 1 and test 2 when compared to the control, and only a 15% decrease between test 2 and test 3, it can be safely assumed that the concrete had reached its yield point at the end of test 2.

Because the samples tested were in the form of a structural system and not a prismatic form,

displacement values could differ, depending on the location of cracks on the "columns". The farther the cracks are from the location of the applied force, the less resistance exerted by the structure. Therefore, control joints must be used to allow cracks to form in the same location on each specimen.

PROPOSED FUTURE WORK

Stage One

The set of specimens will be typical elements in a frame tested on a small shake table to which actuators, load sensors, and a deflection monitor are mounted on a base. These samples will be tested for deflection, stiffness, and damping. Hollow fibers containing the three types of adhesives, one to increase stiffness, one to increase damping and one to control deflection, will be placed at critical regions, especially joints, where loading will be applied. These specimens will be used to study the effectiveness of the adhesives and release mechanisms on the parameters of vibration effect equation; namely on damping, deflection, stiffness. A forced vibration test of each sample was conducted so that the increased damping, stiffening capacity, and deflection reduction can be calculated from observed and recorded dynamic behavior. In order to calculate the damping and restoring force characteristics of a viscously damped structure, it is necessary to obtain base acceleration, mass acceleration, and mass deflection throughout the test. This will be accomplished through the use of servo accelerometers to measure base and mass acceleration and linear voltage differential transformers (LVDT) to measure displacement. From the data collected from these devices, quantities such as fundamental period and damping ratio will be calculated. Between dynamic tests static load tests will be performed to gage the lateral stiffness of the recovering joints. These results will form the basis of our choice of adhesive type(s) and release method to use in stage two when we will vary the dynamic load history.

Stage Two

The second set of specimens will consist of specimens representing typical members at joints subjected to dynamic loading histories. Two of the specimens will act as controls, the remaining 6 will include adhesive releasing elements. The adhesive will be released via vibration-induced tensile stresses generated in brittle fibers placed in theoretically critical regions of the frame. Reinforced concrete will be modeled with a cement and sand mortar with aggregate and wire reinforcing.

REFERENCES

1. Englekick, Robert E., Gary C. Hart. Earthquake Design of Concrete Masonry Buildings: Vol. 1, Prentice-Hall, Englewood Cliffs, NJ. 1936

2. Dry, Carolyn M., "Timed Release of Chemicals into Cementitious Material After the Material has Hardened to Repair Cracks, Rebond Fibers, and Increase Flexural Toughening," Fracture Mechanics: 25th Volume, ASTM STP 1220, F. Erdogan and Ronald J Hartranft, eds., American Society of Testing and Materials, Philadelphia, 1994.

3. Dry, Carolyn M., Ibid.

Active Materials for Application in Room Acoustics

Xavier Meynial

Centre Scientifique et Technique du Bâtiment
24 rue Joseph Fourier, 38400 Saint Martin d'Hères, France

ABSTRACT

This paper presents a preliminary study on the application of the principle of motional feedback (MFB) to active acoustic materials. The ultimate goal is the application of these materials -having an adjustable reflection coefficient which may exceed unity- for the control of reverberation in rooms. The present study focuses on the functionning of a cell which comprises a transducer -acting both as a sensor and actuator- placed in an impedance bridge, a filter, and an amplifier. Varying the gain of the amplifier allows control on the reflection coefficient. A model is presented which predicts the functionning of a cell. This model is validated by an experiment in a tube using a traditionnal moving coil loudspeaker. In this experiment, modulus of the reflection coefficient ranging from 0.5 to 2.3 have been obtained around the resonance frequency of the loudspeaker as predicted by the model. Running the model enables us to define the characteristics of a tranducer tailored for our application, specially regarding its moving mass which must be very low.

0. INTRODUCTION

One can see an active material as a material having an acoustic impedance which can be controlled using as external source of energy and a (usually electronic) control circuit. Thus, this topic is also refered to as active impedance control.

Controlling the acoustic impedance means controlling the transmission, reflection and absorption properties of the material. The idea is very pleasant, and its application numerous.

This principle is fundamentally different from one underlying traditionnal active noise control, whch aims at minimising the sound level in a given space by interfering the undesired acoustic wave with a secondary wave.

Active acoustic materials can be found in underwater acoustics. The aim is to wrap submarines which active materials which absorbs sound waves inpinging on it, making the submarine undetectable by sonars. Piezoelectric transducers are generally used [1,2].

The problem is a lot more difficult in air because of the impedance mismatch between transducers and the medium. Recently, interesting results obtained with « smart foams » have been reported [3]. Following Olson [4] and Guicking [5], Thenail reports about an almost total sound absorption in a tube above 200Hz using a hybrid passive/active technique [6].

For active control of reverberation, Guicking et al. [7] and Ren [8] have proposed « active walls » consisting in an array of cells each comprising a microphone, a filter, an amplifier, and a loudspeaker. Sophisticated digital signal processing based on adaptive filters is used to cancel the direct acoustic feedback from loudspeaker to microphone. Results were reported for one cell only.

Actual impedance control in three dimensional field require sensor and actuator to be placed close to each other (at a distance much smaller than the smallest wavelength of interest) so that the material is locally reacting. This problem is solved when sensor and actuator are only one. This can be done by using a reversible transducer acting both as a sensor and an actuator, as in the motional feedback (MFB) principle. Okda et al used this principle for active noise control in ducts with limited success [9]. This principle is also used for reduction of loudspeaker nonlinear distortion [10] or dynamic impedance matching between an amplifier and a loudspeaker [11].

In the following, we shall investigate the possibility of using MFB for active reverberation control in rooms. An active material having an a reflection coefficient R adjustable over a large range and in a large frequency bandwidth (!) would reduce the reverberation when it would be absorbant ($|R|\approx 0$) or raise it when it would be « super-reflecting » ($|R|>1$). Swarte [12] had the same idea, but the circuit he proposed (which was not MFB) was not likely to acheive this goal.

As always in active control, problems due to limitations and imperfections of transducers play a major rôle in the above mentionned works. They are also central in the approach presented in this paper.

0-8194-2165-0/96/$6.00

1. PRINCIPLE

1.1 Active pannels

Let us consider a system consisting in a planar array of cells as depicted in figure 1. Each cell may capture and re-emit an incoming acoustic wave, as in [13,8].

Such a system can reflect specularly a plane wave arriving under the incidence θ if

$$d < (\lambda/2).\sin(\theta)\,, \qquad (1)$$

where d is the distance between adjacent cells, and λ the wavelength.Thus considering all angles of incidence and a maximum frequency of 5kHz leads to very small cells : d < 34 mm (i.e. 865 cells per square metre).

In the frequency domain corresponding to eq (1), the material may be characterised by its acoustic impedance Z_a, ratio of the complex amplitude P of the pressure at a given point to the complex amplitude V_n of the normal velocity at the same point :

$$Z_a = P / V_n\,. \qquad (2)$$

Then, the plane wave reflection coefficient is

$$R = (Z_a - Z_c) / (Z_a + Z_c)\,, \qquad (3)$$

where Z_c is the characteristic impedance of the medium (air). The absorption coefficient of the material is

$$\alpha = 1 - |R|^2$$

If the real part of Z_a is positive, the material is absorbing ($1 \geq \alpha > 0$). If Z_a is purely resistive and matches Z_c, then the absorption is total ($\alpha=1$). If the real part of Z_a is negative, then $|R|>1$ and $\alpha<0$. The material reflects more energy than it receives. We shall talk about « super-reflection ».

The present study focuses not on the active pannels which will be future step, but on the functionning of a cell.

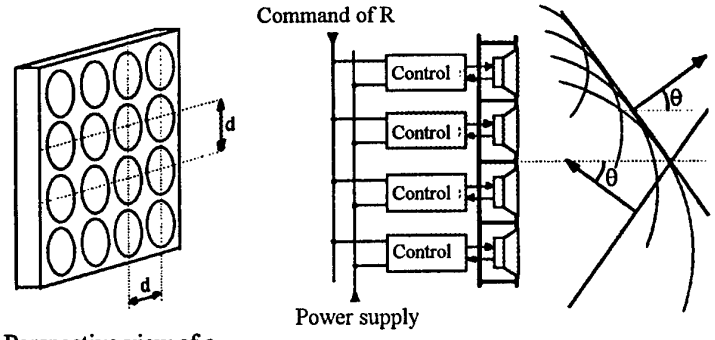


Figure 1 : Arrangement of cells in an active pannel

Perspective view of a 4x4 cells pannel

Section view and principle

1.2 MFB-cells

Each cell comprises a transducer and an electronic control circuit (figure 1). It is expected that integration of the transducer and the (simple) electronic circuit will lead to low cost manufacturing.

There are two types of MFB-cells. The one shown in figure 2a is based on a « double transducer » such as a double coil loudspeaker. This is the situation one tends to when tightly bonding together a sensor and an actuator (e.g. an accelerometer sticked onto a louspeaker membrane).

The other circuit shown in figure 2b is more original. A transducer is placed in an impedance bridge which delivers the sensor signal. When the bridge is at equilibrium ($Z_0.Z'_1 = Z_1.Z'_0$, where Z_1 is the electrical impedance of the transducer), the differential voltage V_d is solely dependent upon the sensor behavior of the transducer, not upon the output voltage of the amplifier.

If the bridge balances the electrical part of the transducer impedance only (not the motional part), then V_d is proportional to the velocity of the transducer membrane, and can be used in a feedback for reducing the

loudspeaker nonlinear distortion [9].
Z_0 and Z'_0 are generally chosen much greater than Z_1 and Z'_1 in order to minimise the current in this branch.

In the following, we shall present our work using the bridge circuit. Results obtained with a double coil loudspeaker were less promising.

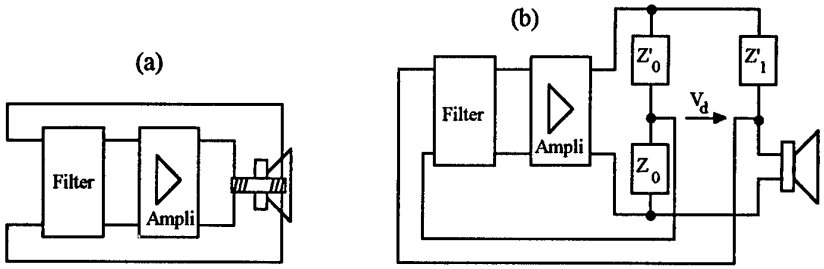


Figure 2 : Two circuits using MFB. (a) double transducer circuit ; (b) impedance bridge circuit.

2. MODELLING

Figure 3 shows a model of the circuit described in figure 2b. In this model, the amplifier and the filter are represented by a Thevenin source, the transducer by a two-port network, and the acoustic part by another Thevenin source. The functionning of the system -in particular the transducer- is supposed to be linear.

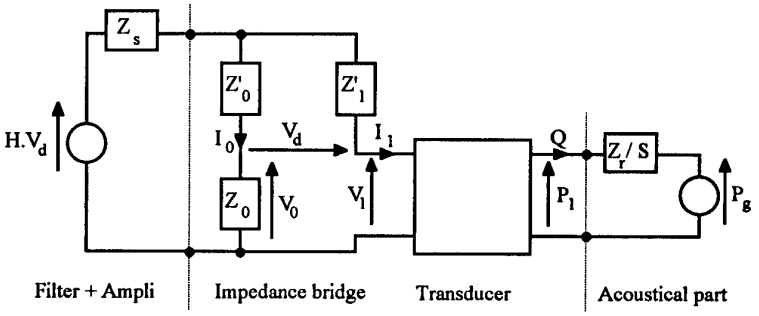


Figure 3 :

Electrical network equivalent to circuit of figure 2b.

Z_r is the radiation impedance which approximately equals $\rho.c$ in case of plane waves, where ρ is the mass per unit volume for air, and c the speed of sound in air.

The acoustical impedance of the transducer (loaded with the electronic circuit) is $Z_a = - S.P_1/Q$, where P_1 is the pressure on the membrane, Q is the volume flow of the membrane, and S the surface of the membrane.
One can show that

$$Z_a = S.\frac{B - D.(V_1 / I_1)}{A - C.(V_1 / I_1)} \tag{4}$$

where A, B, C, and D are the parameters of the two-port network representing the transducer :

$$V_1 = A.P_1 + B.Q \tag{5a}$$
$$I_1 = C.P_1 + D.Q \tag{5b}$$

The open loop gain can be found to be

$$T = H\frac{Z_1Z'_0 - Z_0Z'_1}{Z_s(Z_0 + Z'_0 + Z_1 + Z'_1) + (Z_0 + Z'_0)(Z_1 + Z'_1)} \tag{6}$$

This expression clearly shows that the system is stabe when the bridge is at equilibrium ($Z'_0Z_1 = Z_0Z'_1$).
This model was programmed using the Mapple software.

3. VALIDATION OF THE MODEL

In this paragraph, we shall present the results obtained experimentally with an electrodynamic moving coil loudspeaker (dome medium diameter 40 mm) placed in a tube. The parameters A, B, C, and D were issued from the Thiele-Small model of the loudspeaker.

In figure 4, one can see the impedance of the transducer measured and obtained with the Thiele-Small model. The resonance frequency f_s of the loudspeaker is 710 Hz. On figure 4 is also shown the impedance Z_0 we have used in the bridge.

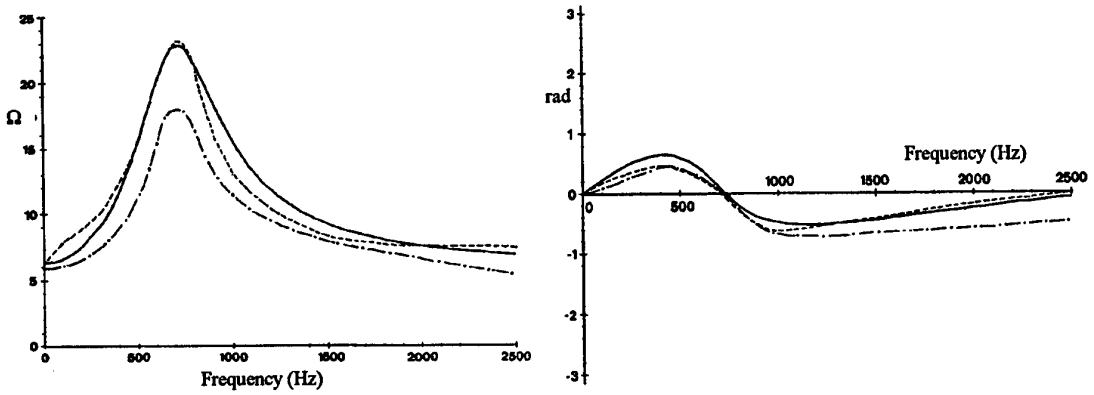


Figure 4 : Loudspeaker impedance measured (- - - -) and modelled (------), and impedance Z_0 measured (-- . -- . --). Left : modulus ; right : argument.

We have then used the experimental setup descibed in figure 5. In this setp, an acoustic wave is sent in the tube by the loudspeaker on the right, and is reflected on the transducer at the left end of the tube. The latter loudspeaker, loaded with its electronic circuit, is the active material. A microphone placed in the middle of the tube captures the pressure waves travelling in the tube. Maximum length sequences were used to measure the impulse response. The absorbant material on the right of the tube prevents the system from being unstable in case of high reflection coefficient (|R|>1) at the other end. Sound waves are assumed to be plane in the tube.

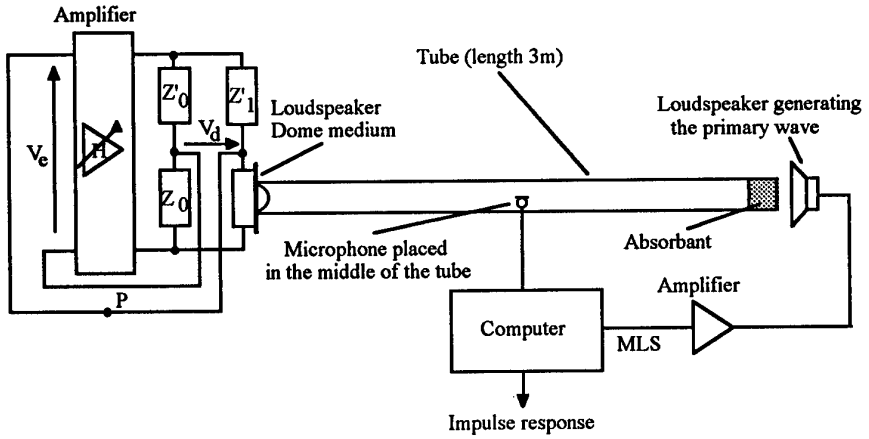


Figure 5 : Experimental setup used for validation of the model.

The impedances of the bridge were chosen as follows :

Z_0 : parallel resonant circuit (resonance freq. 710Hz, quality factor 2.84) in series with 4.7Ω (see fig 4).
$Z'_0 = 7.9\ \Omega$ $Z'_1 = 10\ \Omega$.

The measured open loop gain is similar to the one predicted with our model, although the fit could be better with a more accurate modelling of the tansducer (see figure 4). Analysis of the open loop gain shows that values of gain H within [-32 ; 26] are allowed without instability.

Figure 6 shows the modulus of the reflection coefficient as predicted by the model as a function of frequency and amplifier gain H for this set of parameters. It can be seen that |R| may vary from nearly zero to very high values around f_s. For H=+20, the argument of R is close to π. For H=-20, it is close to 0. We shall come back later on this figure.

Figure 7 shows results obtained as compared with those predicted by the model. It is clear that trends are well respected. Differences are due to the hypothesis underlying the model, to the approximations in the input parameters, and to the uncertainties associated with the measurement technique (in particular the low frequency resolution of 125Hz).

One can see on figure 7 that |R| varies with H from 0.5 to 2.3 around f_s, which corresponds to $\alpha \in [-4.3 ; 0.75]$.

These results show that obtaining reflection coefficients variable over a large range is possible with MFB, and that our model, although perfectible (specially regarding the transducer) predicts reasonably well the results.

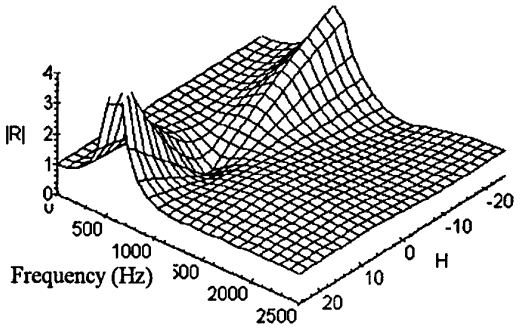


Figure 6 : Modulus of the reflection coefficient predicted with our model for the experimental setup configuration as a function of frequency and ampifier gain H.

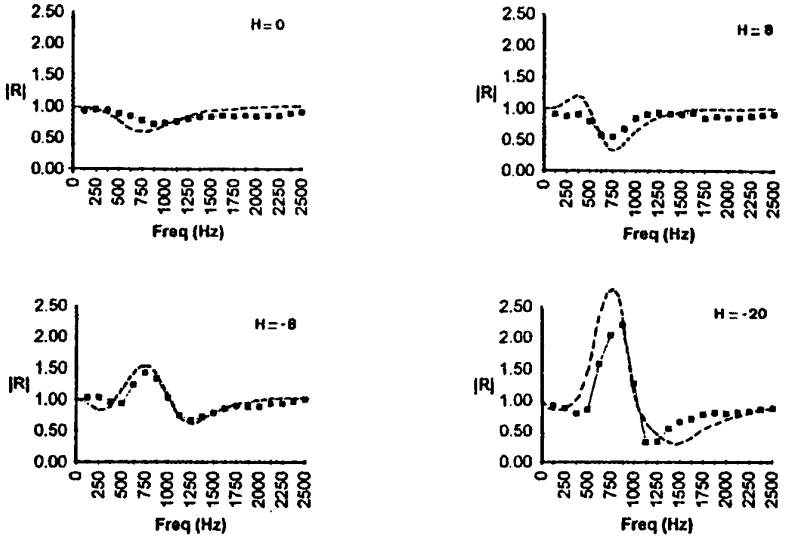


Figure 7 : Modulus of the reflection coefficient obtained as a function of frequency and amplifier gain H.

▮▮ : measured ;

- - - - : model

4. ANALYSIS OF THE RESULTS. DISCUSSION

Let's go back to figure 6. The efficiency of the system is optimal around f_s because the impedance match between the transducer and the medium is fair there. Below f_s the compliance of the loudspeaker imposes the mechanical impedance to be much greater than $S.Z_r$, and above f_s the moving mass imposes the same.

It is clear that an interesting result can be acheived over a given frequency band only if the mechanical imedance of the transducer is sufficiently small -i.e. not much greater than S. Z_r- in this frequency band.

Traditional moving coil loudspeaker are not favorable in this regard as their moving mass is high. Electrostatic loudspeakers are better because their soft membrane can be extremely light. The same applies to PVDF transducers. In addition to that, a low moving mass enables reducing significantly the weight of the transducer, which can be very interesting for some applications, particularly in transports. But the above transducers suffer from severe limitations : their low efficiency implies high amplifier gain resulting in high risk of instability ; special amplifiers are required that deliver high output voltages and cope with their capacitive impedance ; the aging of these transducers often poses problems ; industrial techniques for manufacturing them is not as developped as it is for traditional moving coil loudspeakers.

These observations lead us to consider the isodynamic transducers [14] which can combine low moving mass, high efficiency, and resistive impedance.

Figure 8 shows what could be obtained with an ideal transducer of this type, having a surface $S=20cm^2$, a moving mass $m=0.02g$, a compliance $C_{ms}=0.01m/N$, and a force factor $Bl=1N/A$.

It is clear that the key of the present problem is the realisation of such a transducer.

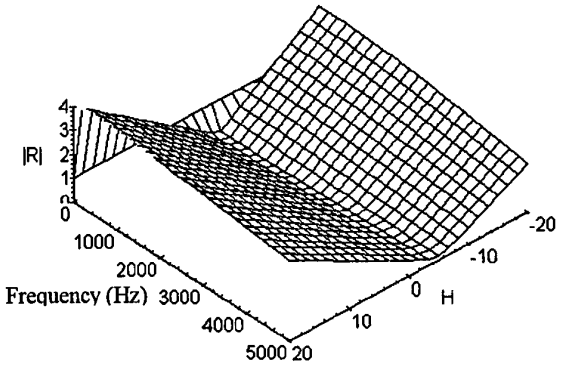


Figure 8 : Modulus of the reflection coefficient predicted with our model for an ideal isodynamic transducer as a function of frequency and amplifier gain H. (Argument of R tends towards 0 when H tends towards $-\infty$, and tends towards π when H tends towards $+\infty$).

5. CONCLUSION

This preliminary study shows that reflection coefficients variable over a large range can be obtained using MFB and a very simple control circuit. Reflection coefficient ranging from 0.5 to 2.3 have been obtained experimentally around the resonance frequency of a moving coil loudspeaker as predicted by our model. Running our model, we have been able to define the main characeristics of a tranducer tailored for our application, particularly concerning its very low moving mass. We are now looking for a technology that is likely to satisfy these requirements.

We are also looking at possible interfaces between the transducer and the radiation that would enhance the impedance matching. Our first invesigations with small horns were disappointing.

Numerous points remain to be explored, like the acoustic interaction beween cells, the behaviour of a pannel in a reverberant environment, etc...

REFERENCES

1. T. Howarth, V.K. Varadan, X. Bao, V.V. Varadan, "Piezocomposite coating for active underwater sound reduction", J. Acoust. Soc. Am. **91** (2), Feb 1992, 823-831.
2. L. Dwynn, F. Shields, J. Hendrix, "Acoustically active surfaces using piezorubber", J. Acoust. Soc. Am. **90** (3), Sept 1991, 1230-1237.
3. C. Fuller, M. Bronzel, C. Gentry, D. Whittington, "Control of sound radiation/reflection with adaptive foams", Noise-Con 94, Florida, May 1994, 429436.
4. H. Olson, E. May, "Electronic sound absorber", J. Acoust. Soc. Am. **25** (6), Nov 1953, 1130-1136.
5. D. Guicking, E. Lorenz, "An active sound absorber with porous plate", Journal of Vibration, Acoustics, Stress, and Reliability in Design, vol **106**, July 1984, 389-392.
6. D. Thenail, "Contrôle actif d'impédance et optimisation des performances d'un matériau poreux", Thèse de l'Ecole Centrale de Lyon, Soutenue le 4-04-95, N° d'ordre 95-11.
7. D. Guicking, K. Karcher, M. Rollage, "Coherent active methods for applications in room acoustics", J. Acoust. Soc. Am., Vol **78**, No 4, October 1985, 1426-1434.
8. Z. Ren, "Application de filtres adaptatifs en acoustique des salles pour la synthèse de réflexions", T. S. **12** (1), 1995, 93-101.
9. J. Okda, T. Nishimura, Y. Nishimura, T. Usagawa, M. Ebata, "Active noise control system using motional feedback loudspeaker", J. Acoust. Soc Jpn. (E) **12**, 6 (1991), 291-296.
10. E. De Boer, "Theory of Motional Feedback", IRE Trans. on Audio, Jan-Feb 1961.
11. D. Birt, "Loudspeaker power amplifiers with load-adaptive impedance", J. Audio Eng. Soc. Vol 36 No 7/8, July/Aug 1988, 552-561.
12. P. Swarte, "Electro-acoustic system having a variable reflection/absorption characteristic", U.S. Patent No 4,712,247 , Dec 1987.
13. D. Guicking, K. Karcher, "Active impedance control for one-dimensional sound", Journal of Vibration, Acoustics, Stress, and Reliability in Design, vol **106**, July 1984, 393-396.
14. M. Colloms, "High performance loudspeakers", 4th edition, Pentech Press, 1991.

Paper presented at the Third ICIM/ECSSM '96, Lyon '96

CONCEPT OF FUNCTIONAL MATERIALS USE IN UNCONVENTIONAL MEANS FOR NUCLEAR PLANTS

Prof. R.R.Ionaitis
Russia, Moskow, 101000, POB 788,
Research and Development Institute of Power Engineering
and Moscow State Technical University of Bauman

Certain conventional safety means (SM), which can confine harmful impact on public and environment have been developed in each engineering branch as well as traditions of their use.
Safety and reliability of any power plant (PP) can be estimated, provided and enhanced by successive and complex application of PRINCIPLES AND TECHNICAL CRITERIA OF RELIABLITY AND SAFETY:

* Internal Safety	of power plants and safety means
* Provided Equipment	safety means
* Provided functions:	shut down, cooling, localization
* Structural division:	control, actuation, monitoring
* Constancy of functions	under operation and under shut down
* Automatization	of SM actuation
* Provided fast-action:	short delays, high velo city
* Safe failure	freedom from failure
* Redundancy	* structural, * termal, * functional, * informational
* Independence	on function and size
* Diversity	different types, unsimilarity
* Defence in-depth	deep esheloning by meen of SM
* Checkability	of readiness and the fact of actuation
* Tested	in natural conditions
* Passivity	of PP
* Dedication	to a single aim
* Low power	(spare conditions at PP and SM)
* Protection	from external influences
* Modular design	ampular design
* Simplicity	of design decisions and maintenance
* Harmless action	for environment
* Friendliness	to operational Staff
* Complete action	unceased action

UNCONVENTIONAL SAFETY MEANS:

- NOT WIDELY SPREAD
- DIVERSIFIED ACTUATION PRINCIPLE
- NEW DESIGN SOLUTION
- ADDITIONAL TO CONVENTIONAL MEANS
- ARE APPLIED DURING DEVELOPMENT OF NEW REACTORS
- ARE APPLIED TO MODIFY EXISTING POWER PLANTS
- ARE APPLIED TO ALL HIGH POWER-RATED OBJECTS

USM PURPOSE AND FUNCTIONS:

- ASSURANCE OF NORMAL OPERATION (CONNECTION, SEALING, STRENGTHENING, DIAGNOSTICS, INSTRUMENTARION, ETC.)
- SHUT-DOWN
- CEASING OF MAIN PROCESS (INFLUENCE (IMPACT) ON REACTIVITY OF REACTOR)
- EMERGENCY CORE COOLING (INFLUENCE ON HEAT-CARRIER)
- ASSURANCE OF SAFETY FROM FIRE AND EXPLOSION (NEUTRALIZATION OF DANGEROUS GASES)
- LOCALIZATION OF ACCIDENT CONSEQUENCES

0-8194-2165-0/96/$6.00

STRUCTURAL PARTS OF SAFETY MEANS:

- EXECUTIVE (IMPLEMENTS PROTECTION)
- CONTROLLING (CONTROLS NP AND FORMS EMERGENCY SIGNAL)
- MONITORING-DIAGNOSTIC (OF READINESS TO ACTUATE AND THE FACT OF ACTUATION; SM SELF-CHECKING)
- SUPPLYING (WITH POWER, COOLING, VENTILATION)

Some of the specified parts of USM can be joined in one device, especially in case of functional materials use: with shape memory and others.

USM OPERATION CONDITIONS AT PP ARE VERY SEVERE:

- ENVIRONMENT DIVERSITY (GAS, DISTILLATE, LIQUID METAL)
- CORROSION AND EROSION COOLANT ATTACK
- HIGH WORKING TEMPERATURES (20-350°C) IN CAVITIES OF USM LOCATION
- HIGH TEMPERATURES OUTSIDE THE LOCATION CAVITIES (500-700°C)
- NARROW TEMPERATURE DROP RANGE UNDER ACTUATION (10-15°C)
- NEUTRON IRRADIATION (FLUENCE UP TO 10^{20}-10^{22} N/SM^2)
- SMALL DIAMETERS OF THE PLANT CAVITIES (2-100 MM)
- VERTICAL DIMENSIONS (0.1-20 M)
- SMALL NUMBER OF MODE PARAMETERS IN THE CORE (NEUTRON FLUX, -COOLANT FLOW RATE)
- REQUIRED MULTIPLE ACTUATION -THE CHANGE OF SPACE POSITION

GENERAL REQUIRED PROPERTIES OF USM TO WORK IN PP:

- SMALL SIZES
- THE REQUIRED ACTUATION TEMPERATURE
- THE POSSIBILITY TO AFFECT ON THE ACTUATION TEMPERATURE (BY ALLOYING (DOPING) OR BY OTHER MEANS)
- TO ACTUATE WITHIN NARROW TEMPERATURE RANGE (RELAY PRINCIPLE OF ACTUATION: DEFORMATION-TEMPERATURE)
- CONSERVATION OF THE PROPERTIES DURING LONG STORAGE AND DURING SPECIFIED CYCLES
- CORROSION AND EROSION RESISTIVITY
- SUFFICIENT FORCE TO PROVIDE EXECUTION OF THEIR FUNCTIONS
- THE PERMISSIBLE NOISE LEVEL
- NON-SENSITIVITY TO OVERHEATING (WITHIN SPECIFIED TEMPERATURE RANGE, OVER ACTUATION TEMPERATURE)
- ADAPTABILITY TO MANUFACTURE
- DIVERSITY OF GEOMETRIC SHAPES (ROD, SPRING, PLATE, RING, CRAMP, STRIP, WIRE, ETC)
- HIGH FAST-ACTING
- VIBRO-SHOCK RESISTIVITY PROPERTIES
- ACCEPTABLE COST

REQUIRED PROPERTIES OF USM IN RESPONSE TO IRRADIATION:

- ABSOLUTE CONSERVATION OF PROPERTIES (AS MUCH AS POSSIBLE)
- PARTIAL CONSERVATION OF PROPERTIES (SUFFICIENT FOR EXECUTION OF THEIR FUNCTIONS)
- POSSIBILITY TO USE OUTSIDE IRRADIATION ZONE
- DISTANT SIGNAL TRANSFER (DEPARATION OF SENSITIVE AND
- EXECUTIVE COMPONENTS)
- EASY REPLACEMENT

Now USM are developed on base of **FUNCTIONAL MATERIALS (WITH UNIQUE PROPERTIES):**
-WITH SHAPE MEMORY EFFECT-METAL GLASSES-MELTS WITH CHANGEABLE CONDUCTANCE-CAPPILARY (HEAT PIPES) ONES-DETONATIONAL CORD-GAS GENERATING ONES-GAS-LIQUID METAL-CERAMIC ONES-CHANGEABLE COLOR COVERINGS.

REACHABLE FEATURES OF FIXING ELEMENTS (ON THE BASIS OF SHAPE MEMORY MATERIALS):

- HIGH QUALITY-SAFETY-SIGNIFICANT, FORCE
- CONNECTION OF VARIOUS (NON-WELDED) MATERIALS
- HIGH DEFORMATION
- ABSENCE OF SPECIAL POWER SOURCES (ACTUATION PASSIVITY)
- ABSENCE OF OPEN FLAME (DURING INSTALLATION)
- ACTUATION IN A WIDE RANGE OF TEMPERATURES
- COMPACT SIZE, ASSEMBLYING IN LIMITED ROOM TIMELY MOUNTING
- INDEPEDANCE TO LOCATION
- OPERATIVENESS OF MONTAGE
- CORROSION AND EROSION, IMPACTS AND VIBRATION RESISTIVITY
- ECOLOGICALLY FRIENDLY -LOW IRRADIATION OF THE PERSONNEL

BARS OF SHAPE MEMORY MATERIAL:

- RODS 8-230 MM
- WIRE 0,2-7 MM
- PIPES 14-60 MM
- LEAVES 0,5-10 MM
- SHIELDS -0,04-3 MM

RANGE OF TRANSFORMATION TEMPERATURES OF SHAPE MEMORY MATERIALS:

- UNDER 100°C: Ti-Ni, Au-Cd;
- 100-200°C: Ti-Ni, Ti Nb, Cu-Al-Zn, Cu-Al-Ni, Mn-Cu(Cr);
- 200-300°C: Fe-Mn-Si, Cu-Ni, Ni-Al, Ni-Mn;
- 300-400°C: Cu-Al;
- 400-500°C: Fe-Ni, Ti-Ta, Cu-Al-Mn;
- over 500°C: Ti-Ni-X (X= Pd, Pt, Ag, Hf, Nb, Zr)

A rather wide range of **MOTIONLESS CONSTRUCTIONAL ELEMENTS** for joining, canning, etc. can be created (and it has already been created) (fig.1):

- CAPS, BODIES (IN THE TOP AND IN THE WALLS)
- SEALINGS (OF FLANGE SPACERS, FOR FITTINGS SADDLES REPAIR AND OTHERS)
- THERMO-COUPLING, FLANGE GASKETS, FIXERS (EXTERNAL AND INTERNAL)
- WELDED JOINTS FITTINGS (LEAKAGE REMPTERS, STEAM-GENERATOR TULES, CONSTRUCTING DEVICES)
- ELECTRICAL CORDS JOINERS (PLUGS)

REQUIRED FEATURES OF MEMBERS TO AFFECT ON REACTIVITY:

- SMALL DIAMETRAL SIZES (2 TO 100 MM), LARGE AXIAL LENGTH (UP TO 20 M)
- SHORT ACTUATION DELAY
- SMOOTH INSERTION (INTO THE CORE)
- HIGH INSERTION SPEED (INTO THE CORE)
- HIGH EFFICIENCY OF NEUTRON ABSORPTION
- SUFFICIENT RETARDATION (AT THE END OF RUN)
- ACCEPTABLE EFFORTS FOR COCK (FOR RECONSTRUCTION)

SPECIAL FEATURES OF COOLANT USE IN PP:

- COOLANT (OF FUEL AND STRUCTURE MATERIALS)
- ABSORBER AND MODERATER (OF NEUTRONS)
- CONTRACTIOIN AND ACCELERATION (OF MOVEMENT)
- PROTECTION AGAINST IRRADIATION
- SOURCE OF RADIOLITICAL GASES (OXYGEN, ETC.)
- TRANSPORT MEAN (FOR GASES AND CONTROLLING BODIES)

EXECUTIVE UNCONVENTIONAL SHUT DOWN MEANS:

- PROFILIED (IN THE FLOW-THROUGH PART)(FIG.2)
- DYNAMIC (FOR THE COOLANT FLOW RATE)(FIG.3)
- FLOAT-TYPE (ABSORBERS AND DISPLACERS)(FIG.3A)
- ACCUMULATOR (BUILT-IN)(FIG.4)
- MEMBRANE-TYPE (CAPTURE AND ACCEPTANCE)(FIG.4)
- LIQUID-TYPE (IN SEPARATE CHANNELS)(FIG.3Â)
- GRANULAR (WITH SMALL-BALL SUBSTANCE)(FIG.4)
- TWO-PHASE (GAS-LIQUID)(FIG.2B)
- GAS-TYPE (WITH GAS AS THE WORKING BODY OR ABSORBER)(FIG.4)
- LIQUID-METAL (WITH ABSORBING METAL)(FIG.4)

TYPICAL ELEMENTS OF EXECUTIVE USM:

- FOR HOLDING (TORNED, RIBBON-LIKE MEMBRANES; WITH SM ELEMENTS)
- FOR INSERTION (PYROCHUCKS, EXPLOSIVE PRESSURE ACCUMULATORS, WITH SME)
- FOR BREAKING (DEVICE WITH SME)
- FOR SIGNAL TRANSFER (DETONATIONAL CORDS, WITH SME)

Automatical self-actuating devices learn of the nessesity to actuate themselves (in response to neutron flow increasing, to heatcarrier temperature and to other parameters). They can themselves execute emergency actions useing unique smart materials properties.

EMERGENCY (SELF-ACTUATING) DEVICES (CONTROL-EXECUTION):

- FROM REGIME PARAMETER (POWER INCREASE; REACTOR POWER EXCURSION; DETERIORATION OF HEAT REMOVAL; PRESSURE INCREASE)
- WITH FORMATION OF ELECTRIC SIGNAL (TRANSFORMING NEUTRON FLUX; THERMAL-EMISSION)
- PASSIVE (FUSIBLE; WITH SHAPE MEMORY; MEMBRANE; THERMAL NEUTRONIC)

Table 1

SELF-STARTING EMERGENCY DEVICES

Nos	Description	Purpose	Status of development
1	Leakage flow rate limiter	Reduction of coolant loss under piping rupture as compared to its analogs	In operation at NPP
2	Reactor shut- down reactivity control system	Control over reactor shut down reactivity under nuclear hazard activities	Under testing at NPP
3	Self-contained hydrogen-proof device	Hydrogen neutralization in gaseous mixtures without forced blow-down and power supply	Tested at the special test rig
4	Generation of electric signal	Generation of AZ electric signal due to conductivity change in the gap between emitter and collector	Tested at test rigs
5	Gamma-detector with threshold electron transducer	Prompt signal under emergency power surge	Tested at the research reactor IR-50
6	Fuse	Provision of system self- start (passive-system)	Tested at prereactor rigs
7	Devices with application of shape memory metals	AZ passive actuation	Testing was carried out at the research reactor IVV-2M

Neutron Electric Breaker (see fig.5a):
Purpose: emergency protection;
Mounting: above the reactor core;
Testing date: Oktober 1990;
Core height: 500 mm;
Distance from the center of the core: 340-390 mm;
Fluence: 2×10^{18} 1/sm^2 0(E>1MeV);
Working body: Mn-Cu spring;
Long term irradiation at 75°C;
Contact closure at 80,5 ± 2,5°C;
Contact disclosure at 83,5 ± 4°C;

Neutron flows relations and contact closure and disclosure:
- factial 1,27; 1,27; 1,24; 1,23; 1,23; 1,25; 1,23;
- everage 1,25+1,7%

The SE self starting devices are effective in case of their direct insertion into the core which influences the reactivity of the substance in liquid (fluid, gas, liquid metal) or in granular (fig.5b-h).
Such devices would be perfect directly acting defence means in case of irradiation resistant metals selection or their irradiation resitance ensuring defence measures development (fig.6).
The problem of irradiation influence is very important in case of use of any functional materials which as a rule lose their intelligence under irradiation. It is especially important for directly acting devices. That is why a substantional study of this question has been held on. 11 shape memory materials have been irradiated and the results were very diverse: from complete loss of their properties to sufficient integrity.

FLOW RATE CONTROL DEVICES HAVE THEIR OWN PECULIARITIES:
- MAINTENANCE, REGULATION, SWITCHING OFF (OF LIQUID FLOWS)
- HIGH THROTTLE DEGREE (PRESSURE DROP/"FLOW SQUARE")
- WIDE FLOW RANGE OF FLOW CHANGE
- INTENSIFICATION OF THE FLOW-THROUGH PART (WIDENING, CONSTRICTION; ROUGHNESS; CURLS; TURNS)
- THROTTLE GROOVES (RING-TYPE; INTERESTING)
- LOWFLUX VELOCITY (ABSENCE OF VIBRATION, CAVITATION, EROSION)
- ABSENCE OF NOISE
- LONG LIFE-TIME
- LOW COST

FLOW LIMITING DEVICES:
- GAS-LIQUID MEMBRANES (GAZ-YES, LIQUID-NO)
- FLOATS -SELF-LOCKING DEVICES WITH SME -NARROWING INSERTS.

SELF-LOCKING DEVICES WITH SME:
- TO PREVENT OUTFLOW
- WHEN TUBE CLEAVAGE
- WHEN THE ENVIROMENT TEMPERATURE CHANGES -FOR FIXING AND DEFIXING OF WORKING BODY
- AS CONTROL DEVICES (WITH DIFFERENT TEMPERATURE OF ACTUATION)

UNCONVENTIONAL MEANS TO DETERMINE SM CONDITION HAVE BEEN DEVELOPED:
- THERMAL-ELECTRIC (WITH MEASUREMENT OF MEDIUM TEMPERATURE AND THE WALL TEMPERATURE AT THE BOUNDARY WITH THE WORKING BODY)
- PNEUMATIC (WITH GAS SUPPLY, STATIC AND DYNAMIC)
- HYDRAULIC (STATIC WITH PRESSURE AND MEDIUM FLOW CHANGES; DYNAMIC WITH PERTUBATION INSERTION INTO MEDIUM FLOW)
- RECOMBINATIONAL (DANGEROUS GAS CONCENTRATION INFORMATORS).

UNCONVENTIONAL PROVIDING SYSTEMS INCLUDE RATHER DIFFERENT FUNCTIONS:

- MONTAGE (SME DEVICES, MANUAL PRESSES)
- COOLING BY THIN LIQUID LAYERS (FILM COOLING)
- PRESSORE ACCUMULATION (BY PYROTECHNICAL AND DETONATIONAL DEVICES)
- VENTILATION OF GAS CAVITIS FROM DANGEROUS GASAS (BY EJECTION-GAS GRIPPING BY FLOWING LIQUID)
- OF INDEPENDENT (PASSIVE) HYDROGEN NEUTRALIZATION
- FIRE SHUTTING (OF TUBES, ROOMS)

THERE SOME PROPOSALS CONCERNING UNCONVENTIONAL LOCALIZATION MEANS:

- RUPTURE MEMBRANES (BETWEEN THE DEFENDED AND LOCALIZATING VOLUMES)
- SEPARATORS WITH SME
- ABSORBERS MEETING COREUM (CORE FUEL)

ARE AVAILABLE:

- THE USE STRATEGY
- THE SET OF PRINCIPAL AND DESIGN SOLUTIONS (INCLUDING INVENTIONS) ON USM
- THEORETICAL BASIS
- EXPERIMENTAL RESEARCH FACILITIES
- EXPERIMENTAL CHARACTERISTICS
- TESTS AND EXPERIENCE IN OPERATION IN REACTOR CONDITIONS
- USM ENHANSMENT PROGRAMM TO INCREASE THE IRRADIATIN RESISTANCE, SPEED OF ACTION, CORROSION RESISTANCE.

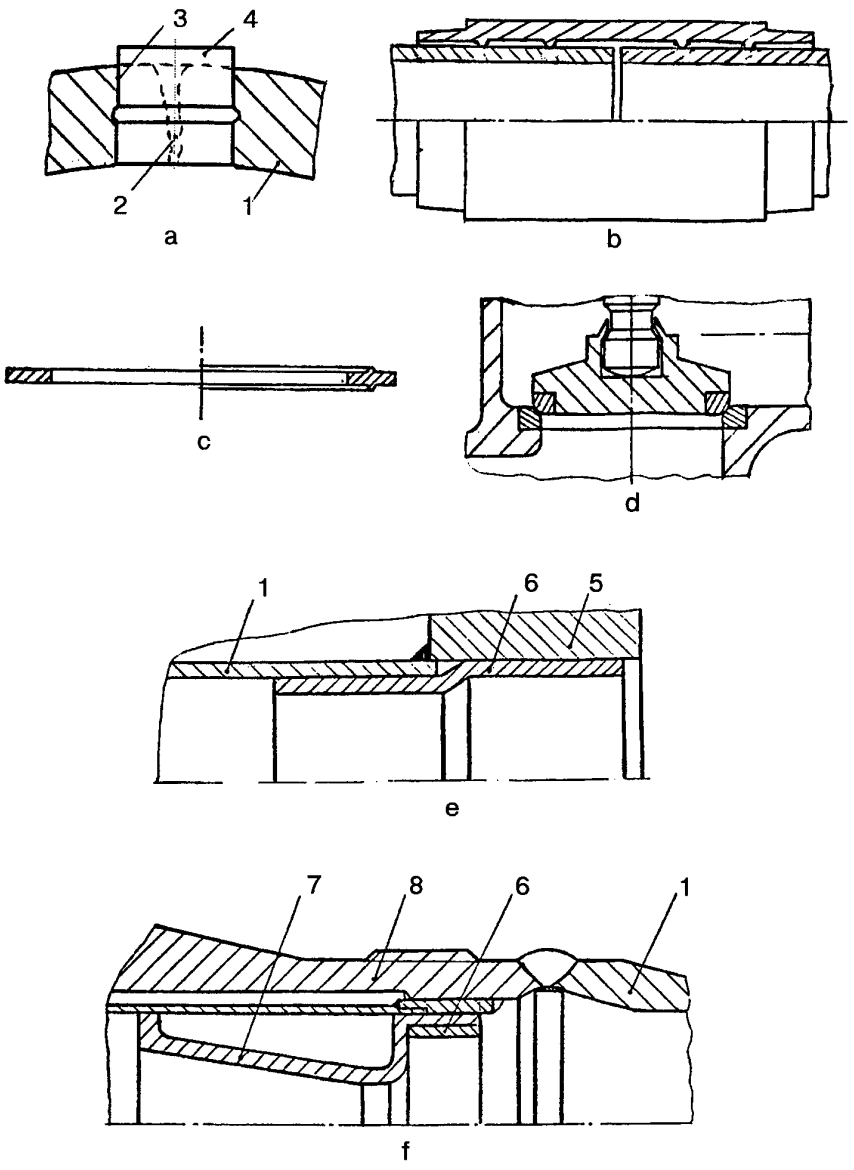
RECOMENDED WORKS ON NUCLEAR REACTOR USM:

- SCIENTISTIC AND TEHNICAL INVESTIGATION
- THE USE CONCEPTS CREATION
- THE OBJECT EXAMINATION
- RECOMENDATIONS ON THE OBJECT'S EQUIPMENT WITH KNOWN USM
- CREATION OF SCIENTISTIC AND TEHNICAL INFORMATION BLOCKS
- NEW SAFETY MEANS DEVELOPMENT, ESPECIALLY ON THE BASIS OF FUNCTIONAL MATERIALS
- CALCULATIONS
- PROCESS STUDY OF EMERGENCY SIGNALS RECEIVING, CREATION
- TRANSFER (TRANSPORTATION), EXECUTION, REFLECTION
- A SET OF STATIC AND DYNAMIC CHARACTERISTICS RECEIVING
- IRRADIATION INFLUENCE STUDY
- EXPERIMENTIAL IMPROVEMENT
- DEMONSTRATION ON MODELS AND FULL-SCALE PROTOTYPES
- RECOMENDATIONS (PRINCIPLES, METHODS AND REQUIREMENTS) ON NPP EQUIPMENT WITH NEW USM
- ORGANIZATION OF PRODUCTION
- SERTIFICATION
- MONTAGE AND PUTTING RIGHT AT OBJECT
- AUTHOR SURVEYLANCE OF EXPERIMENTAL OPERATION
- PRODUCTION

References

1. R.R.Ionaitis. Implemented Unconventional Means for Nuclear Reactor Control. In Proceeding of Int. Symp. on Nuclear Power Plant Instrumentation and Control. Tokyo, 1992, 10p.
2. R.R.Ionaitis. Unconventional Control Means for Nuclear Reactor. Moscow, MSTU of Bauman, 1992, 230p.
3. V.I.Abramov, R.R.Ionaitis a.o. Irradiation Effect on the Alloys with the Shape Memory. In Proceedings of Int. Seminar "Functional and Mechanical Properties of New Materials". Pskov, 1993, p.206-207.
4. R.R.Ionaitis, V.V.Kotov. Shape Memory Alloys in the Russian Nuclear Power Industry. In Proceedings of Int. Workshop. EPRI-TR-105072, Palo-Alto, 1995, p.10.1-10.5.

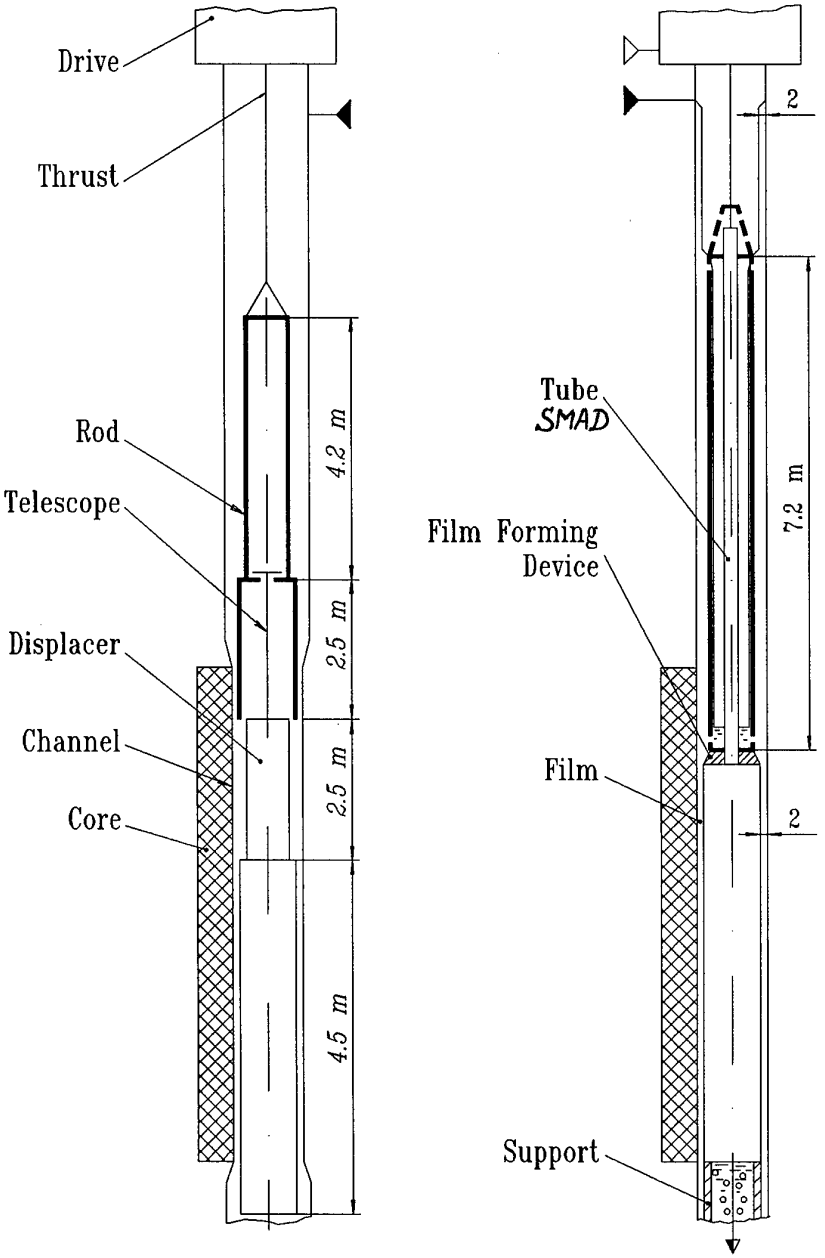
SHAPE MEMORY LOCKS AND SEALINGS



a-plug; b-external thermomuft; c-flange gasket; d-armature seat sealing; e,f-internal termomuft; e-of heat exchanger; f-of restricting device. 1-pipe wall; 2-grub; 3-drilling; 4-plug; 5-board; 6-isolator; 7-limitation nozzle;8-branch pipe.

Fig.1

ACTUATORS WITH PROFILE FLOWING PART



With mechanical water displacement, hollow rod, stepped cooling channel and overlapping absorber

With gas displacer, film cooling and ejecting ventilation

Fig.2

DYNAMIC CONTROL SYSTEMS

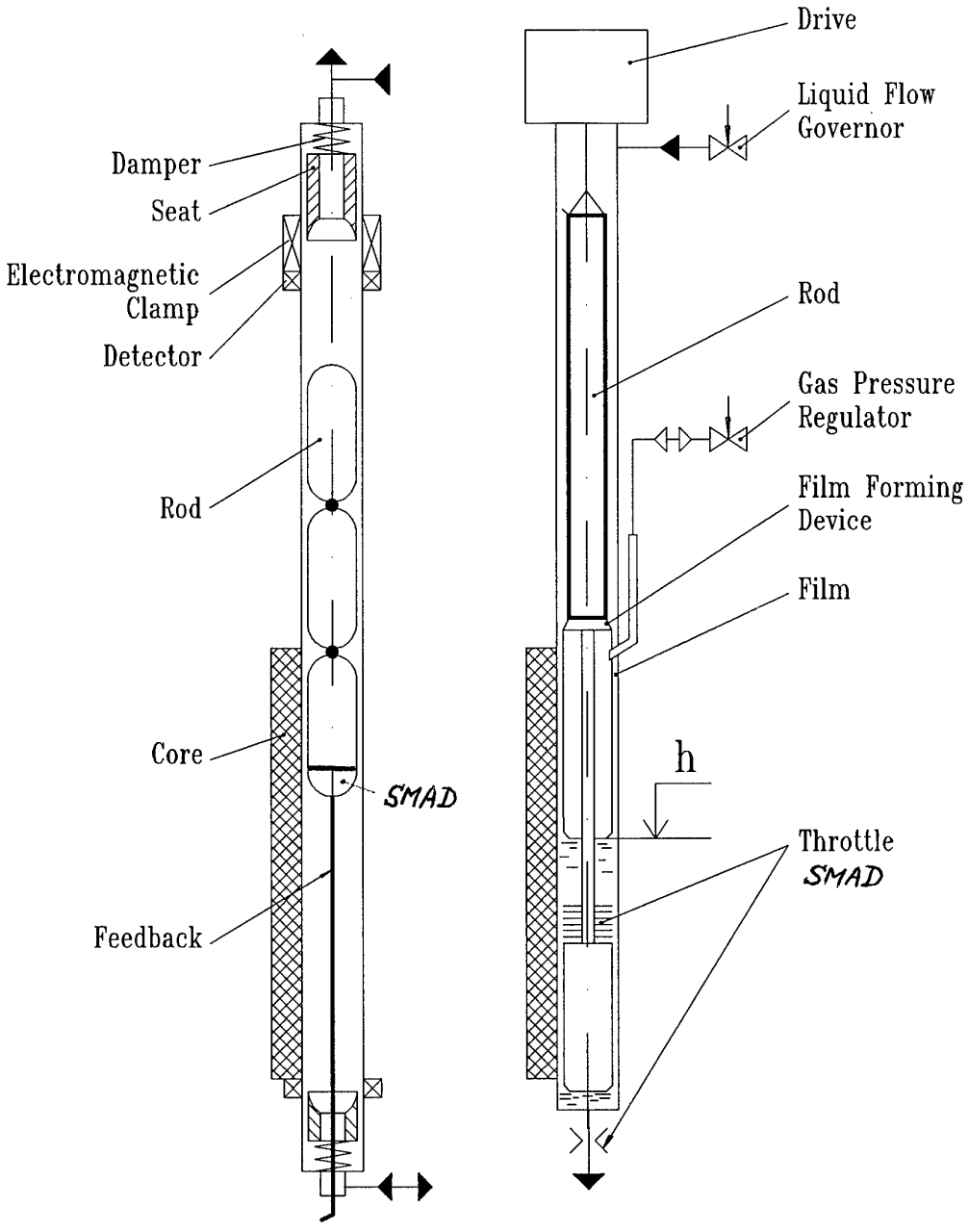


Fig.3

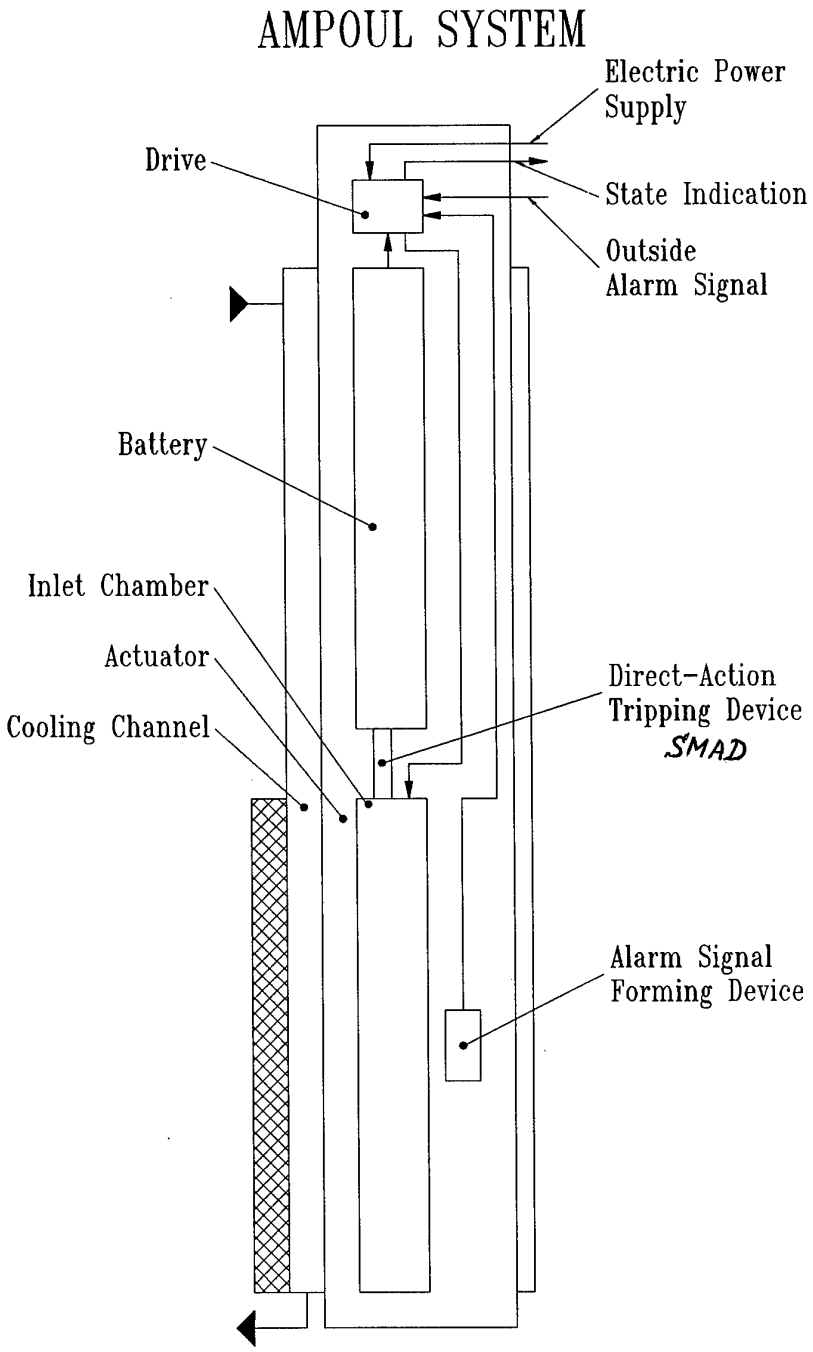
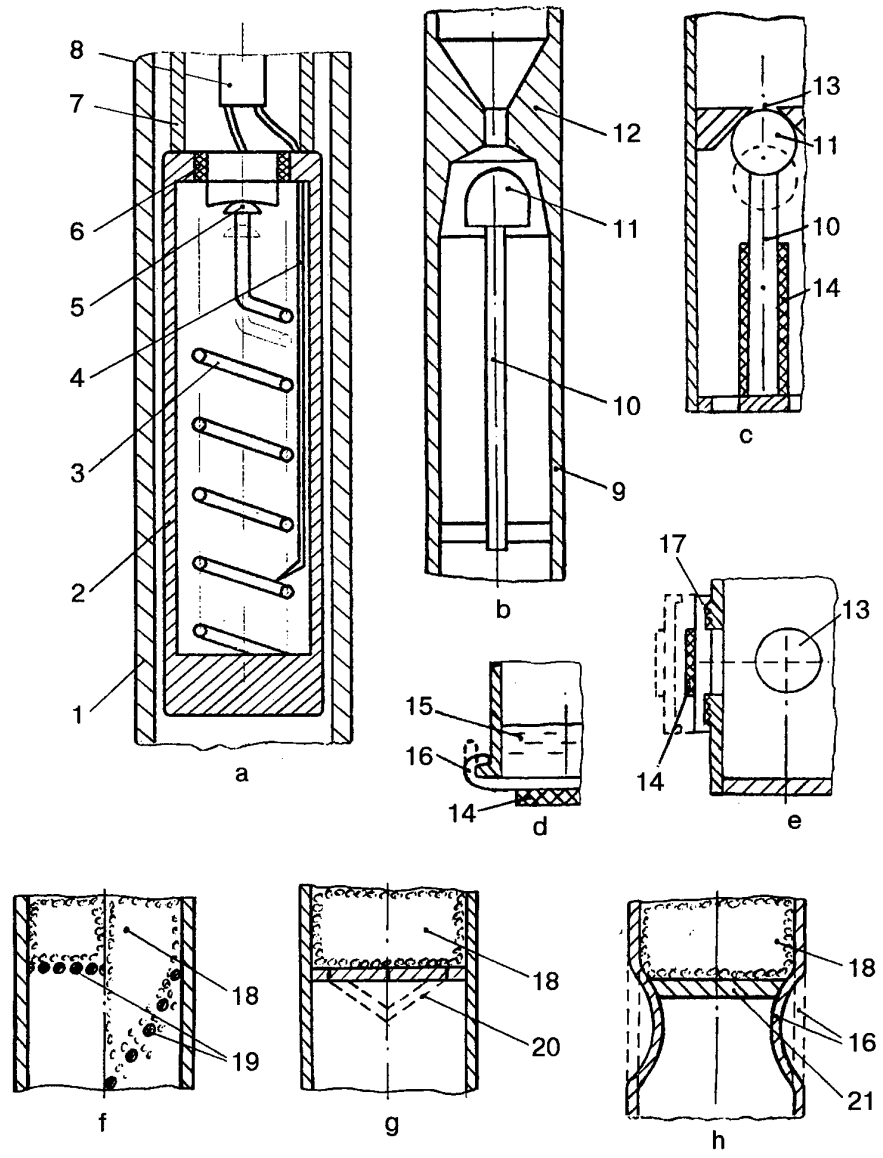

AMPOUL SYSTEM
Electric Power Supply
Drive
State Indication
Outside Alarm Signal
Battery
Inlet Chamber
Actuator
Cooling Channel
Direct-Action Tripping Device
SMAD
Alarm Signal Forming Device

Fig.4

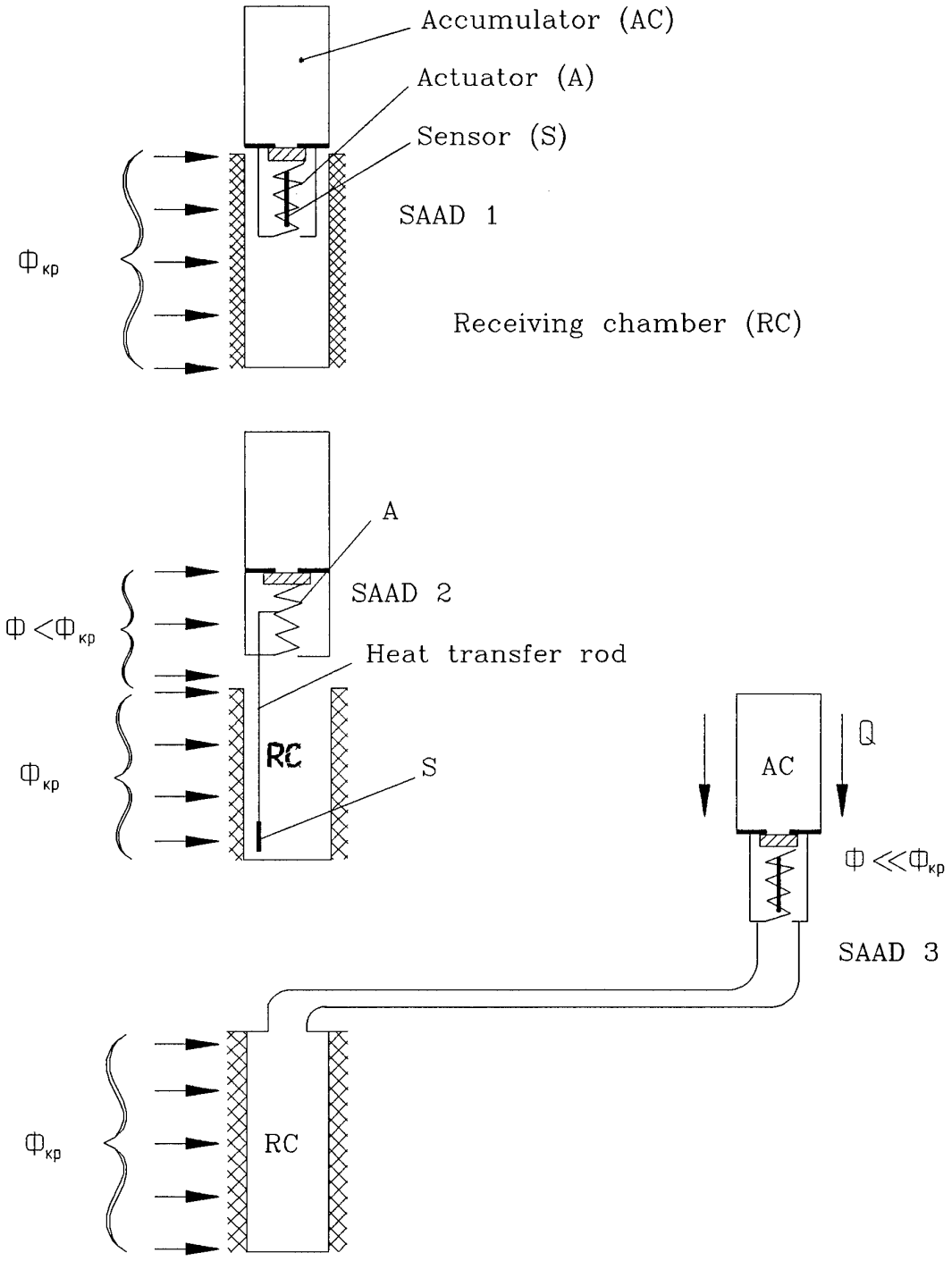
DIRECT-ACTING EMERGENCY SHAPE MEMORY DEVICES



a-by chain break; b-by medium flow stoppage; c-h-by control substance release.
1-socket or channel; 2-body; 3-shape memory spring; 4-temperature state detector; 5-contact; 6-isolator; 7-drive; 8-cable; 9-pipe; 10-rod; 11-valve;12-seat; 13-release window; 14-heater; 15-control fluid; 16-SM clamp; 17-SM plug; 18-granular mean; 19-SM spiral; 20-SM lope; 21-bottom

Fig.5

STRAIGHT–ACTION ACTUATION DEVICES (SAAD)



SAAD 1 – radiation durability SME – alloys
SAAD 2,– SME – alloys, with full or particular
SAAD 3 degradation of the features under the irradiation

Fig. 6.

Elaboration and the first experience of application of nitinol extravessel corrector with the shape memory effect

S.D.Prokoshkin, A.C. Butckevitch, A.P.Chadaev, E.P.Ryklina, I.Yu. Khmelevskaya

Moscow Steel and Alloys Institute, Department of Plastic Deformation of Special Alloys, Leninsky pr., 4, Moscow, 117936
Russian State Medical University, Department of General Surgery, Ul.Ostrovitjanova, 1, Moscow, 117437

ABSTRACT

The original method for restoring of the function of relatively incompetent valves and the design of the corrector for realisation of the methods are elaborated.

The principle of the corrector functioning is based on the shape memory effect, which permits to subject the design to significant plastic deformation at the temperature below zero. Being brought up to the place of implantation the corrector restores its initial ellipse-like form, surrounding the vein and changing its section in the necessary place.

The method and the device were applied in the surgical treatment of 13 patients, aged from 20 to 72. The simplicity of the correction reduces the trauma possibility and allows to achieve adequate correction of the vein while reducing the obstacle of the venous blood flow makes this method favourable for wide application in clinical practice.

1. RESULTS AND DISCUSSION

Varicose disease of the lower extremities is widely spread. More than 80 million people in the USA suffer from this disease.[1] According to P.C.Smith et al [2] in the United Kingdom up to 500 thousand and up to 800 thousand people in the USA suffer from chronic venous insufficiency complicated with leg ulcers. Almost in 80% cases varicose disease is accompanied with ectasia of deep vein and relative valvular incompetence.[3]

During last decades there were elaborated methods of extravessel_correction of the function relatively incompetent valves which reduce the degree of venous hypertention and possibility of the development of further pathological changes of venous system. The method is based on extravessel constriction of the vein in the valvular area which leads to the closing of valvular leafs and corrects the function of the valve. This method favourably differs from valvuloplasty,[4-6] requiring the section of vein with its minor trauma and technical accessibility. For constricting the vein different materials are applicated: muff from autovein,[7,8] fascial sleeve [9] or dacrone [10]. However, the most popular method of correction of the function of relatively incompetent valves of deep vein is constricting of the vein in the valvular area with the help of lavsan or polyurethane spiral of the round section [11].

In 1993-1994 in the Clinic of General Surgery of paediatric faculty of Russian State Medical University 110 patients with varicose disease were operated on. In 18,2% (20 patients) the disease was complicated with leg ulcers. Phlebography and Doppler US before operation showed valvular incompetence of the femoral vein of different grade in 51,8% cases (57 patients). In these last cases there was carried out the phlebectomy with the correction of the valves function with the lavsan spiral. Test phlebography in post-operation period confirmed the adequacy of the correction of the valve function in 86,4% cases. In 15,5 cases there was noted the moderate edema of the rear of the foot and of the shin.

0-8194-2165-0/96/$6.00

Under the known method of correction with the spiral of the round section the vein is restricted in the valvular area for 1/4-1/3 of the initial diameter. If the adequate correction is not achieved, this is usually connected with anatomical insufficiency of valves. However while analysing the method some deficiencies are brought to light.

Under normally functioning valves the relation of the length of the free edge of valvular leaf to the diameter of the vein (L/D) is sufficiently constant. Constriction of the vein causes the decrease in its diameter (D), while the length of the free edge of the leaf (L) remains as initial, which leads to its relative lengthening. So, under constriction of the vein for 1/4 of its initial diameter (25%) there takes place the relative lengthening of the free edge of the leaves fo 33%.

$$\frac{L}{D_1} = \frac{L}{0{,}75D} = 1{,}33\frac{L}{D}, \tag{1}$$

where D - the initial diameter of the vein, D_1 -the diameter of the vein after its constriction by 1/4 of initial diameter, L - the length of the free edge of the valvular leaves. Under constriction of the vein in the valvular area for 1/3 of its initial diameter the relative lengthening of the valvular leaves reaches 50%.

The square of section of the vein (S_0) is $S_0 = \pi R_0^2$, where S_0 - the initial square of the section, $\pi = 3{,}14$, R_0 - the initial radius of the vein. Square section of the vein (S_1) after its constriction with the round spiral is

$$S_1 = \pi R^2 = \pi\frac{9}{16}R_0^2, \tag{2}$$

where R - the radius of the vein after its constriction.

The decrease of square section of the vein (δ_1) under its even constriction with the round spiral amounts 43%:

$$\delta_1 = \frac{S_0 - S_1}{S_0} = 1 - \frac{S_1}{S_0} = 1 - \frac{R^2}{R_0^2} = 1 - \frac{9}{16} = \frac{7}{16} = 0{,}43, \tag{3}$$

where S_0 - the initial square section, S_1 - square section of the vein after its constriction with the round spiral.

Square section of the vein (S_2) under its constriction with the elliptic spiral amounts $S_2 = \pi R_0 R_1$, , where R_0 - the initial radius of the vein, R_1 - the short radius of the section (Fig. 1).

The decrease of the common square section (δ_2) amounts 25%:

$$\delta_2 = \frac{S_0 - S_2}{S_0} = 1 - \frac{S_2}{S_0} = 1 - \frac{R_1}{R_0} = 1 - \frac{3}{4} = \frac{1}{4} = 0{,}25 \tag{4}$$

The gain in square section of the vein (δ_3) under vein constriction with the ellipse spiral amounts 33%:

$$\delta_2 = \frac{S_2 - S_1}{S_1} = \frac{S_2}{S_1} - 1 = \frac{R_0}{R_1} - 1 = \frac{4}{3} - 1 = 0{,}33 \qquad (5)$$

Thus, under vein constriction in the valvular area for 1/4 of initial diameter in the direction perpendicular to the free edge of the leaves the former are coming together, and their correction is achieved. In this case the constriction of the leaves along their free edge doesn't take place. It doesn't lead to the relative elongation of the valvular leaves and reduces the square of general section of the vein by 33%. In its turn this reduces the obstacle to the venous blood flow.

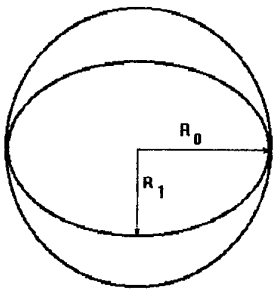


Fig. 1. The scheme of the section of the vein with round and elliptic spiral

Under vein constriction with the round spiral for 1/3 of the initial diameter the reduction of the general square of the section achieves 50% and in the case of using elliptic spiral only 33%. These simple mathematic counts show the necessity of using of modified elliptic spiral. However, the production of such spirals is faced with great difficulties, connected with screw-like deformation of articles based on the retained plasticity of the material.

As a result for elliptic spiral production we have used the alloy with the shape memory effect - NiTi, applicated formerly in endosurgery for stenting blood vessels and tubular structures. The relation of axis lengths of the elliptic section amounts 0,8, which is proved by accounts given above. The distance between the twists is small enough not to prevent quick revascularization of vein walls, preventing its ingrowth between twists. The quantity of the pitch is based on theory and experiments. The material for the design was subjected to thermomechanical treatment to obtain superelasticity under specially elaborated regimes. The superelasticity effect is necessary for providing of the design form restoration after possible significant deformation when implanting.

The suggested model of nitinol elliptic spiral was applicated in surgical treatment of three patients suffering from varicose disease from 4 to 30 old. The patients were operated on at the department of General Surgery of Russian State Medical University (Clinical Hospital No 4, Moscow). In preoperative period all patients demonstrated pathologic venous reflux of femoral vein of II-III stage. Test retrograde phlebography in postoperative period showed adequate correction of the valves function.

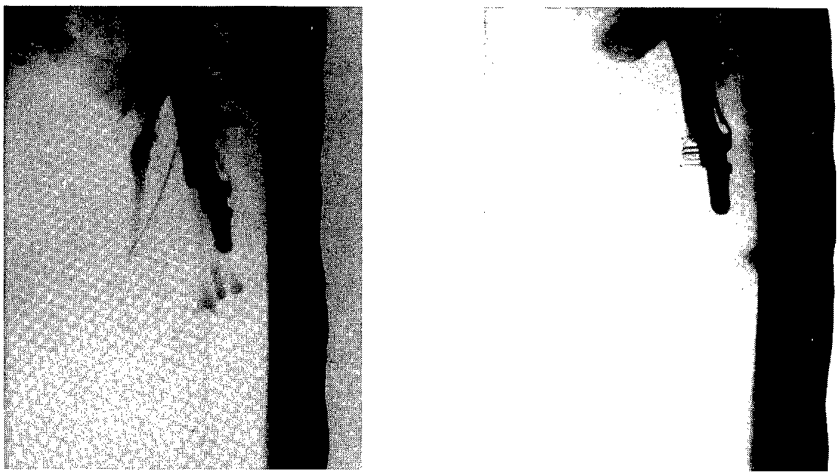
Further experimental work on the corrector perfection lead to the creation of principally new original design. The elaborated corrector is performed of nitinol wire in sine-shaped form, rolled up along its axis as an elliptic tube with non-traumatic tips.

The corrector is placed so, that vein diameter reduction takes place in the direction perpendicular to the line of closing of valvular leaves.

The principle of the corrector functioning is based on the shape memory effect, which permits to subject the design to significant plastic deformation (in our case unfolding the apexes of sine-shaped corrector in the ice bath with the temperature below zero). Being brought up to the

place of implantation the corrector restores its initial ellipse-like form, surrounding the vein and changing its section in the necessary place.

The elaborated model of the extra-vessel corrector was applied in the surgical treatment of 10 patients, aged from 20 to 72, suffering from varicose disease of low extremities with the femoral vein incompetence of II-III stage. Under test phlebography in post-operating period 9 patients showed adequate correction (Fig.2)., one patient showed the significantly reduced pathologic venous reflux Edema in postoperative period was not noted.



a b

Fig.2. Descending phlebography

a) Relatively incompetent valves of the femoral vein; b) After operation. The valvular function is restored.

The simplicity of the correction of the function of relative incompetent valves reduces the trauma possibility (there is no necessity in the circular mobilisation of the vein for the long distance) and allows to achieve adequate correction while reducing the general section of the vein and reducing the obstacle of the venous blood flow makes this method favourable for wide application in clinical practice.

REFERENCES

1. M.P.Goldman, P.J.Mitchel, "Scleroteraphy treatment for varicouse & telangiostatic veins in the United States: past, present & future", *Dermatol Surg. Oncol.*, Vol.16(7), p.p. 606-607, 1990.

2. P.C.Smith, S.Sarin., J.Hasty, J.Sourr, "Sequential gradian pneumatic compression enhances venous ulcer healing: a randomixed trial", *Surgery,* Vol.108(5), p.p. 871-875, 1990.

3. G.D. Konstantinova, A.E.Bogdanov, "Contemporary aspects of treatment of the venous chronical diseases", *Ther. Arkhiv*, Vol.10, p.p. 125-128, 1990.

4. R.L.Kistner "Surgical repair of the incompetent femoral vein valve", *Arch. Surg.,* Vol.110, p.p. 1336-1342, 1975.

5. S.Raju, "Venous insufficiency of the lower limb & stasis ulceration", *Ann. Surgery,* Vol.197, p.p. 688-697, 1983.

6. D.J.Moor, P.D.Himmel, D.S.Sumner, "Distribution of venous valvular incompetence in patients with the postphlebitic syndrome", *J. Vasc. Surg.,* Vol. 3, p. 49, 1986.

7. R.P.Zelenin, N.P.Kurakov. "To the question of surgical correction of the valvular incompetence", *Khirurgiya,* Vol. 9, p.p. 27-29, 1979.

8. Kuo-hua Zhang, Fa-qi Liang, " Autovenous sleeve around superficial femoral venous valve to trat primary deep venous incompetence", *International Surgical Week, 35th World Congress of International Society of Surgery,* 1993, Hong Kong, Abstract 439.

9. R.G.Askerhanov, "Choice of treatment of the initial varicouse disease of low extrimeties", *Vestnik Khirurgii,* Vol. 6, p.p. 40-43, 1984.ju S., Jackson. Vasa Supplement, 1991; 33; 42-43.

10 A.N.Vedensky. "Valvuloplasty in chronic venous insufficiency. A worthwhile procedure" *Varicouse disease,* Leningrad, Medicina, 1986.

Paper presented at the Third ICIM/ECSSM '96, Lyon '96

Biomedical engineering in designing and application of nitinol stents with the shape memory effect

E.P.Ryklina, I.Yu. Khmelevskaya, T.V.Morozova, S.D.Prokoshkin

Moscow Steel and Alloys Institute, Department of Plastic Deformation of Special Alloys, Leninsky pr., 4, Moscow, 117936

ABSTRACT

Our studies in the field of endosurgery in collaboration with the physicians of the National Research Centre of Surgery of the Academy of Medical Sciences are carried out beginning in 1983. These studies laid the foundation for the new direction of X-ray surgery - X-ray Nitinol stenting of vessels and tubular structures.

X-ray nitinol stents are unique self-fixing shells based on the shape memory effect and superelasticity of nickel-titanium alloys self-reconstructed under human body temperature. Ap[plied for stenting of arteries in cases of stenosis etc., bile ducts in cases of benign and malignant stenoses, digestive tract in cases of oesophsgeal cancer and cervical canal uterus in cases of postsurgical atresiss and strictures of uterine. The purpose of stenting is restoration of the shape of artery or tubular structure by a cylinder frame formation.

The especially elaborated original method of srenting allows to avoid the traditional surgical operation, i.e. the stenting is performed without blood, narcosis and surgical knife. The stent to be implanted is transporyed into the affected zone through the puncture under the X-ray control.

Clinical applications of X-ray endovascular stenting has been started in March 1984. During this period nearly 400 operations on stenting have been performed on femoral, iliac, brachio-cephalic, subclavian arteries, bile ducts, traheas, digestive tract and cervical canal uterus.

1. RESULTS AND DISSCUSSION

There is a lot of reports on successful application of shape memory and superelastic alloys, which proved themselves to be excellent implants in these fields of application in traumatology and orthopaedy.

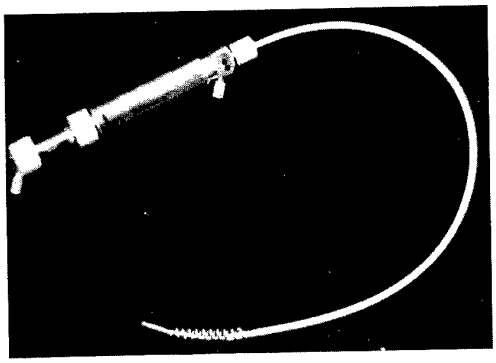
First in the world practice beginning in 1983 the specialists of the Moscow Steel and Alloys Institute and the National Research Centre of Surgery of the Academy of Medical Sciences put the foundation of the new direction of X-ray surgery - X-ray Nitinol stenting of vessels and tubular structures. Endovascular nitinol spiral stent (diameter 3-12 mm) is transported in a compact form to a necessary place by means of original delivering device which provides quick and precise implantation. The operation is performed through a punction hole in femoral artery under fluoroscopic guidance without a traditional surgery. Nitinol stent corrects all the defects of a vessel wall appearing after dilatation due to tearing of intima and media. Being a supporting shell stent prevents constriction of a vessel caused by perivascular sclerosis. Endostenting operation takes less than 45 minutes and is 10 times cheaper than the traditional surgical intervention.

The new method is applied for stenting of arterial vessels in cases of stenosis and perivascular sclerosis. Biliar stent can be used for restoration of bile ducts patency for the purpose of preserving bill flow in cases of benign and malignant stenosis. Endoesophageal stenting is a bloodless method of restoration of digestive tract permeability. Endocervical stenting can be applied

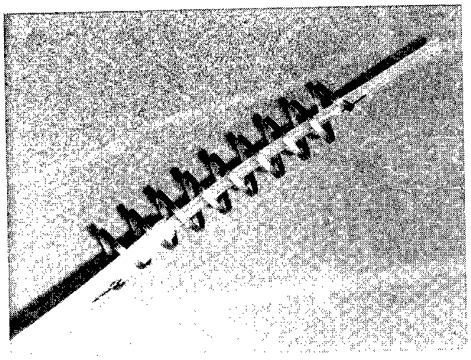
0-8194-2165-0/96/$6.00

in cases of postsurgical atresias and strictures of uterine cervical canal and allows to form a scaffold for providing a functionally effective cervical canal. Stent design is unique for each case of surgical intervention.

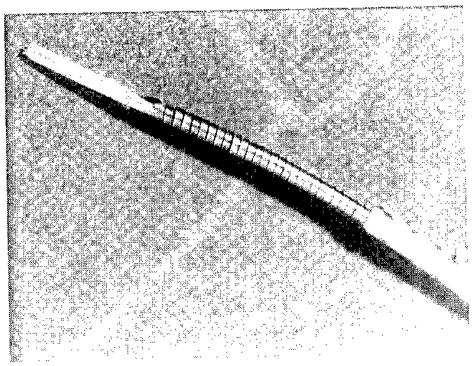
Before operation the stents were exposed to the gas sterilisation (or to any method of sterilisation at the temperature not above 70^0C). Stenting is carried out in the following way: stent in its compact form (Fig.1a) is transported to an insertion site with the help of an delivering device which provides quick and precise implantation exactly to a necessary place. Being transported to the necessary place the stent recovers ("reminds") its cylinder shape given at the body temperature. Stent is firmly fixed in the insertion site due to the precisely chosen diameter and additional fixing elements. The tips of implantated stent are consecutively detached from the delivering device and the latter is removed.



a



b



c

Fig.1. X-ray endovascular stent for the femoral artery in its initial shape just before implantation (a,b) and in its compact shape (c) on the distal tip of the delivering device.

The delivering device may be used repeatedly, but the constructive elements contacting with the patient's blood must be substituted.

The dimensions of the designed stents are listed in table 1.

Table 1. The dimensions of Stents applied in X-ray endosurgery

Stents, used for	Stent diameter mm	Stent length mm	Delivering device* length, mm
Brachio-cephalic and subclavian artery	5 6 7 8	25-30	1200
Iliac artery	7 8 9 10	25-30	350
Femoral artery	4 5 6 7	25-30	600
Popliteal artery	4 5 6	25-30	500
Bile ducts	4 5 6 7 8	40-80	350

*The handle of the delivering device is manufactured in two variants: for endovascular and for endobiliar stents..

Nearly 400 stents produced in our laboratory in a number of hospitals in CIS have been implanted. Patients who had not any complications in the early post-operation period (96,2%) recovered in 15 hours. The results of implantation just after stenting and then every year were evaluated by the angiographic control on by means of other methods of evaluation of the blood flow. Unsatisfactory, such as re-stenosis and re-occlusion have been observed in 1,5% cases.

During the whole period the implanted stent had not been dislocated and thereby maintained the patency of the reconstructed place. In all cases of implantation of nitinol stents there have been revealed doubtless positive results.

The great economical effect of the application of the new method to medical practice is composed of the decrease of patient's hospital days before operation and of the shortening of the followed up recovery period (7-10 days).

As a result of the last two years investigations in addition to endostenting systems we can suggest basically new devices designed for dilatation of various tubular structures, cava-filters, multi-extravessel correctors, purpose clamps and superelastic guides of various modifications. According to the evaluation of the specialists these articles are in high demand and their design and functional properties are unique.

Temperature measurement of human body

B. Stadnyk, M. Stepanyak, E. Dziuban

State University "Lviv Polytechnic", Chair of Data Measuring Technique,
Lviv13, 290646 Ukraine

ABSTRACT

The information about physiological bases of warmth-radiation of a person is given and the opportunity of microwav application of dielectrics aerials and dielectrics of resonators at measurements of temperature in the clinical diagnostics considered.

1. INTRODUCTION

Thermography is a method of diagnostic radiology, having absolute harmlessness and total absence of contra-indicatio to its use.

The thermographic method of diagnostics is based on non-contact remote registration of spontaneous infra-red radiati of skin covers of a person with the help of special instruments. The result of registration is a thermogram, which represen two dimentional card of distribution of temperature on the surface of a body. The analysis of the card permits to give t qualitative evaluation of the character of display and quantitative criteria of temperature gradients

2. THEORETICAL BACKGROUND

Thermography is based on two main laws of radiation, formulated for the so called black body, absorbing all the bea falling on it.

1. The Stephàn -Boltsmann's law . The radiation ability of the absolutely black body W is proportional to the four power of absolute temperature T:

$$W = \delta T^4$$

Where δ –Stephan-Boltzmann's constant, equal to 5,78 10^{-8} $W \cdot m^{-2} \cdot K^{-4}$.
And under radial ability is understood the quantity of energy, radiated as radiation from unit surface of a body in 1 sec. A all kinds radiation are thus taken into account: the visible light, infra-red, ultra-violet beams. The change of temperatu radiant of body whole on 20 % results in change of capacity radiation in 2 times.

2. The Vien law. The length of wave λm, to which the maximum radiation corresponds is back proportional to absolu temperature T:

$$\lambda_m = \frac{B}{T}$$

Where B - Vien constant, equal to 2900 $\mu m \cdot K$.

3. EXPERIMENTAL STUDY

Many substances , transparent for the visible area of light, absorb infra-red the beams partially or completely. Wat strongly absorbs the radiation with length of wave more 1,5 μm.

0-8194-2165-0/96/$6.00

On the contrary, some substances, not transparent for visible light, pass infra-red beams. For example, ebonite, germanium some kinds of special glass. Tissues of human organism, in skin in particular, strongly absorb infra-red radiation with length of wave of 1.4 - 1.6 μ m.

The infra-red radiation scatters in a less degree, than visible light, penetrates foggy media. This important property causes a lot of features of application of infra-red beams in thermography practice, for example, in investigating eye media in the ophthalmology.

The body is practically always warmer than the environment and also human is source infra-red rays. According to the Vien low, maximum radiation of a human body assuming the temperature of skin covers to be + 30 °C occurs at length of wave of 9,6 μm. The distribution of energy in the radiation spectrum of a body can be characterised by parameters (tab. 1).

Tab.1

λ, μm	0,8 -5	5 - 9	9-16	16-th more
E , %	1	20	38	41

In area of lengths of waves from 5.6 to 25μm the human skin radiates as the absolutely black body independent on the race and other individual features . According to the Stephan-Boltzmann's low the increase of temperature on 1 ° C results in increase of the total radiation by 1.4 %.

Because all areas of the body concave relative to the adjacent zones, are sites of absorption of certain quantity of the infra-red radiation, emitted from the opposite side, and weak circulation of air, there arises a so called strip effect. This effect hinders the reading of thermograms.

The human organism in the power-generating aspect may to be considered as an opened thermodynamic system, absorbing energy from the environment and emitting heat on its part . And inside of the system, various kinds of transformations of energy are made, final stage of which is heat formation . The primary source of energy in the organism for production of all works is the chemical energy of food products released at their oxidation.

As a result of irreversible biochemical reactions and biophysical processes in the organism, the thermal energy is released.

The human organism functions in quasi-isothermal conditions. The thermal energy formed in the organism is used for maintenance of constant temperature of body as one of major conditions of maintenance homeostasis - constancy of all parameters the organism . The thermoregulation centers of the organism are located in hypothalamus . On the skin cover are located thermal receptors. If the temperature of organism deflects from the norm, information about it goes from thermal receptors in the regulation center, which, based on its analysis, sends directive signals along the moving and vegetative nerves to the tissues responsible for heat release or for its exit from organism.

The maintenance of constant temperature of organism in quantitatively is determined by thermal balance between its heating efficiency and conventive heat exchange, in to the environment[1]. The equation of thermal balance of the organism may be recorded as a one-zoned model :

$$Q\_ = 7{,}4^{0{,}73}\ \text{W (for male)} = 4.31\ \text{W},$$

$$Q\_ = 6^{0{,}73}\ \text{W (for female)} = 3.70\ \text{W}.$$

Besides, not only in a sick organism, but also in a healthful organism the temperature of different bodies and systems is different. For example, the head brain has a temperature of 37-37,5° C and arms muscles - 34-35 °C. Therefore the main task at remote measurement of temperature to increase accuracy. The allowadble error should not exceed ±0,1 K.

And thermal radiation of centimetric and decimeter ranges comes from rather deep layers . Measuring the intensity of such radiation, and it is strictly connected with temperature of its sources, that is, some internal organs, it is possible to

define their temperatures.

The development of aerials is one of serious tasks of radiothermometry. Such aerials should be characterized by high efficiency. It is necessary that they set tune up well have small sizes, closely adjoin to the surface of surveyed site.

The study of various human tissues on superhigh frequencies, conducted for recently in a number of countries, has shown, that by their electromagnetic properties the tissues are divided in two groups. One group muscles, brain, blood - by its properties and characteristics (the value of dielectric permeability of 60-80 strong attenuation of electromagnetic waves) is similar to physiological solution. The other group, to it belong fat tissues or bones, wave length their dielectric permeability being only 5-6, attenuation of wave occurs considerably weaker, properties reminding the distillatory water.

The attenuation of wave is characterized by a so called permeation depth,with which the radiation passes to surface of skin becoming , about 2,73 times weaker. Has appeared, that in muscle tissue for waves shorter than 30cm it is equal about 1/20 lengths of wave, in fat tissue - 1/4.

Receiving radiowaves radiatedly internal organs, is possible by applying to the skin a dielectric with the same value of dielectric permeability as that of body's, the aerial being put in side the dielectric.

Since the acrial is in the dielectric and should react time wave, sometimes shorter than in the air, its detensions decrease as many time. The minimum linear size of the area (it is called resolution force on surface), the aerial can occupy and under which the temperature is measured, for closen λ=30 cm is 4 cm wave length. The radiothermometer measures average temperature of body in the volume of a cylinder with a base , equal to the area of aerial, and hight equal to the depth.

For determination of temperature at a greater depth is necessary to be used radio waves of greater length.

At present miniuarization of wave and oscillation microwave systems is based, mainly, on the use as distribution medium of elecromagnetic fluctuations of dielectrics with large dielectric permeability (ε_d >10). Increasing the dielectric permeability of dielectric resonators (DR) material , it is possible to reduce them 10-100 times without increase in losses of power and reductions of eigen quality.

The dielectric resonators as the simplest ones, are close to elementary ones, emitters can successfully be used in antenna arrays (AA) . At restriction of frequency band, in which the radio electronic system, is to operate of DR in AA is preferable in comparison with other known emitters.

Based on DR one can the construct effective AA , which are very urgent at present . Linear AA , is Yagi aerial on cylindrical DR. In order to get maximum amplification of such an AA, distances dn each passive DR to the active resonator in the diagram are to be taken equal to

$$Dn = (2 n-1) \lambda o /4,$$

Where n - the number of passive DR; λo - resonant length wave. Wave length DR on the main type of fluctuations. It is explained as follows. Using DR and filters on their bases (multiplexers, dividers of power) in combination with semiconductor devices, it is possible to create multifunctional solid-state devices, in addition to frequency selectance of signal, stabilization of frequency, management of level, phase, radiation or reception [2].

One should remember to have in view of, that the use of conventional element base does not permit to solve this problem, since the sizes of main microwaves of elements (waveguide, filters on their bases, aerials of device etc .) depend on the working frequency and cannot be reduced with preservation of electrical characteristics . Therefore the use of new non-traditional approaches to constructions of the superhigh -frequency(SHF) tracts on their bases should be based on the following principles: 1)the path is made as a set of cartridges (lines) according to the number fixed microwaves of the SHF range; 2) each cartridge (line) of the represents monolithic narrow-band on frequency non -reconstruction module , performing functions of reception, frequency and polarization of section, amplification and transformations of frequencies

of signals; 3) to reconstruct (to set up) path on fixed waves is possible by supplying power to an appropriate of line.

Such a module can bet made as a uniform block, consisting of aerial and case, in which several units are combined.

4. CONCLUSIONS

Recently at treatments of oncological diseases, hyperthermy the methods are applied. One of them consists in heating the affected tissue to 42-43 °C by means of SHF electromagnetic radiation. The cells of cancer tumour die, and the healthy ones survive such a regime. Overheating is not allowable , and underhealting does not give effect. Therefore it is necessary to support the temperature at a strict level, controlling the power of SHF radiation, and, of course to measure the temperature of tumour very accurately. Radiothermometry using microwaves of dielectrics aerials and dielectric resonators in combinations with semiconductor devices permits to solve the problem of control of temperature at hypothermia and diagnostics.

5. REFERENCES

1. Под ред . Л.Г.Розельфельда ,"Основы клинической дистанционной термодиагностики",Киев,1988. - 224 с.

2. М.Е. Ильченко, В.Ф. Взятышев, Л.Г.Гасанов и др. , "Диэлектрические резонаторы", Киев,1989.- 328с.

Additional Papers

MULTI-FINGERED GRABBERS AS SMART STRUCTURES FOR ROBOTIC APPLICATIONS

MOHSEN SHAHINPOOR
INTELLIGENT MATERIALS, STRUCTURES AND SYSTEMS LABORATORY
SCHOOL OF ENGINEERING, UNIVERSITY OF NEW MEXICO
ALBUQUERQUE, NEW MEXICO 87131, EMAIL : SHAH@UNM.EDU

Abstract. Presented first is a novel design for a class of multi-fingered robotic grabbers capable of rapidly deploying their robotic fingers to grab moving objects within their workspace. A simple mathematical model is then presented for computer-graphic simulation of such multi-fingered robotic grabbers. Finally, some experimental results pertaining to dynamic perfomance and control of a number of robotic grabbers fabricated in our laboratory are presented. The dynamic performance of these types of rapidly deployable multi-fingered robotic grabbers have been observed to be quite remarkable and consistent with the proposed computer simulation model.

1. Introduction. Multi-fingered robotic grippers kinematics, dynamics and control have been under extensive theoretical and experimental investigation by robotics researchers for over a decade now. The reader is referred to Hanafusa and Asada (1977), Kato and Sadamoto (1977, 1987), Roveta (1981), Salisbury and Craig (1982), Caporali and Shahinpoor (1984), Kerr (1984), Mason and Salisbury (1985), Jameson (1985), Cutkosky (1985), Lee and Derby (1986), Cutkosky and Wright (1986), Kerr and Roth (1986), Jameson and Leifer (1986), Jacobson, Iverson, Knutti, Johnson and Biggers (1986), Dario and Buttazzo (1987), Shahinpoor (1987, 1994), Shahinpoor and Tootoonchi (1988, 1989, 1992), Imamura, Kaneko, Yokoi and Tanie (1990), Venkataraman and Iberall (1990), Maekawa (1992), Maekawa, Yokoi, Tanie, Kaneko, Kimura and Imamura (1992), Deno, Murray, Pister and Sastry (1992) and Meghdari, Mahmoodian and Arefi (1992).

In this paper, a novel design for a class of multi-fingered robotic grabbers is presented first in the following section. The proposed design is capable of rapidly deploying the grabbers robotic fingers to grab moving objects within their workspace. A simple mathematical model is then presented in section 3 for computer-graphic simulation of such multi-fingered robotic grabbers. Finally, some experimental results pertaining to dynamic performance and control of a number of robotic grabbers fabricated in our laboratory are presented in section 4. The dynamic performance of these types of rapidly deployable multi-fingered robotic grabbers have been observed to be quite remarkable and consistent with the proposed computer simulation model.

In the following section some design details are presented for such structures in various forms.

2. Design Details. The present section describes a novel design for multi-fingered mechanical grabbers that may be easily robotized or automated. The automation means comprise pneumatic, hydraulic, solenoid-type, lead or ball screw-driven, cable-type, electromagnetic or artificial muscle-type (see Shahinpoor,1992 ,1995, Shahinpoor, Wang and Mojarrad, 1994 and Shahinpoor and Mojarrad, 1994).

Mechanically, the design is comprised of an arbitrary number of mechanical fingers or deployable structures that can be opened and closed in a curvilinear fashion in their workspace in the three-dimensional space. This section first describes the design characteristics of a double-finger robotic grabber or structure. This is followed by the description of the design characteristics of a multi-fingered electro-mechanical grabber. Finally, this section concludes with the description of specific design of such structures which may be used as multi-pronged or multi-winged spatially curvilinearly deployable structures for either robotic grabbing or structural applications situations of practical interest .

Referring to Figures 1(a) and 1(b), the schematics of a double finger or structure is shown. As is seen, the structure of a double grabber finger is composed of a pair of lazy tong-like linkage system such that the central pivot point is located off-center as compared to a normal lazy tong. This off-set causes the structure to move curvilinearly throughout the three-dimensional space if expanded or contracted through mechanical, chemical, electrical, magnetic, pneumatic, hydraulic or a combination of these means. The

0-8194-2165-0/96/$6.00

pair of lazy tongs are attached and connected to each other by means of stand-offs and end pivot points as shown in Figure 2(a).

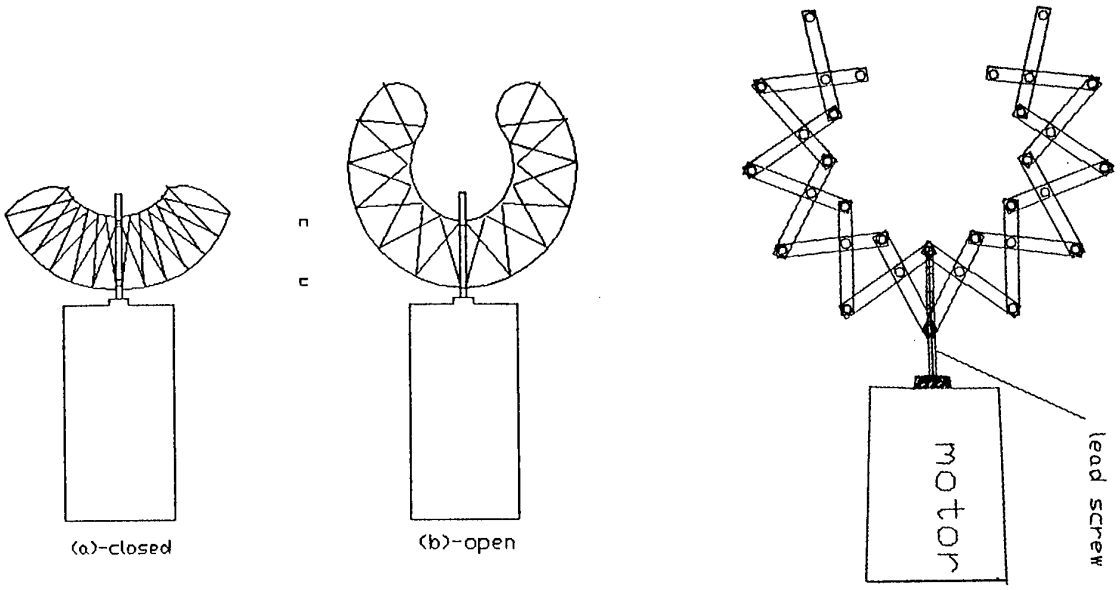


Figure 1- Plane view of a two-fingered robotic grabber in closed and deployed configurations

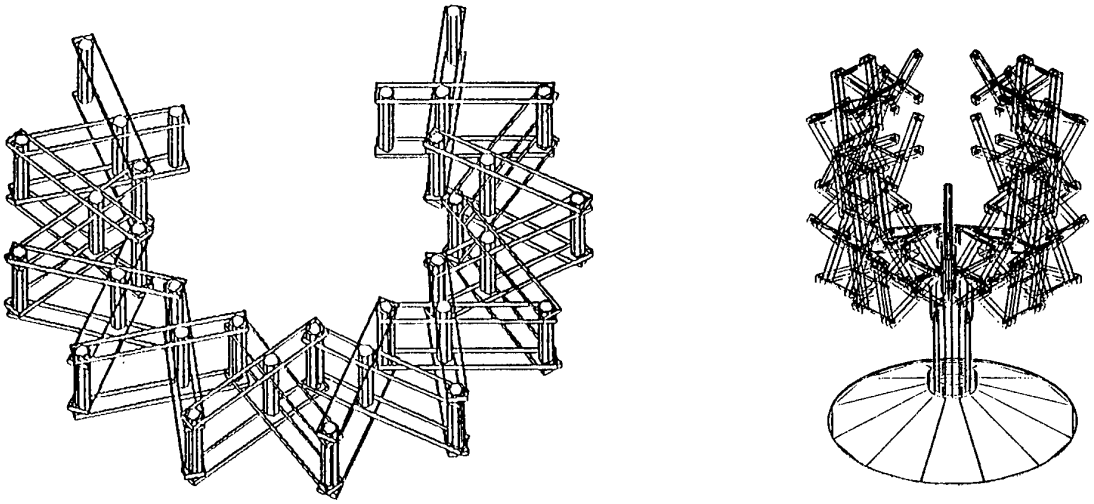


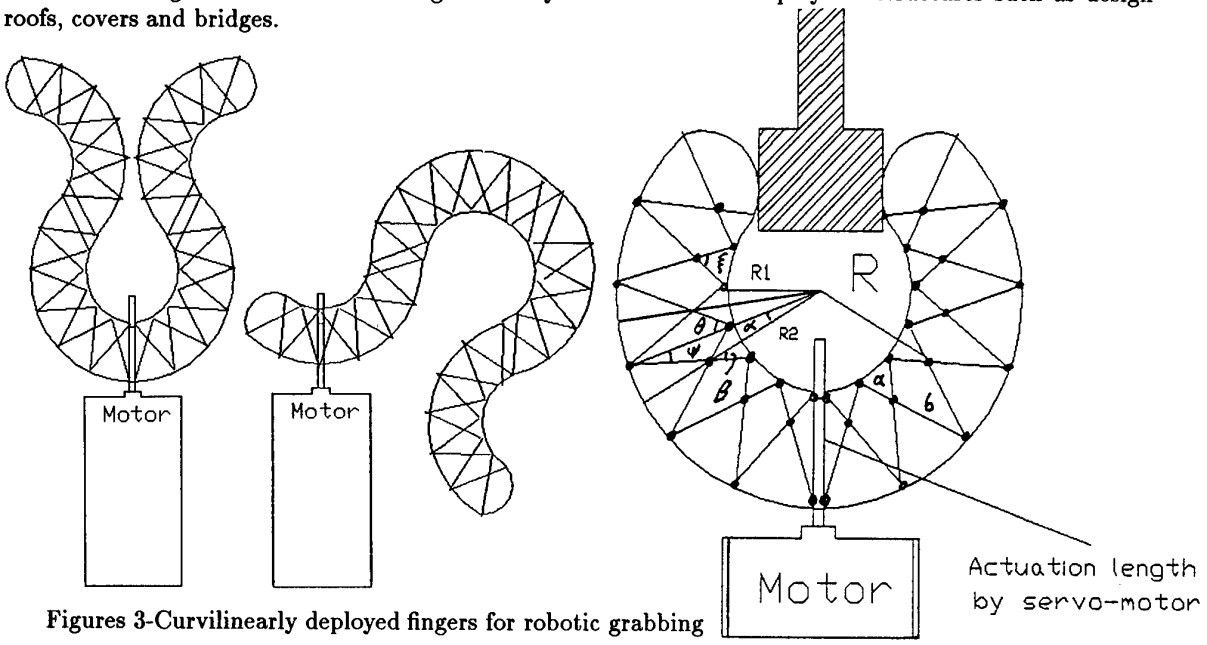
Figure 2- A 3-D view of two curvilinearly deployed multi-fingered robotic grabbers

The mechanical actuation to move and expand the finger in a curvilinear fashion from a closed or contracted state (Figure 1(a)) to an open or expanded state (Figure 1(b)) in the three-dimensional space is provided by means of changing the off-set distance.

Referring to Figure 2(a), an arrangement for a two-fingered grabber attached to an actuator system 1 is shown. Figure 2(b) depicts an arrangements for a four-fingered grabber attached to an actuator system.

Referring to Figure 3(a) and 3(b), an arrangement for a deployable finger is depicted such that the distance of pivot points from one end of the strips have been varied so as to produce a curvilinear deployable finger or structure in the three-dimensional space.

Such arrangements as shown in Figure 3 may also be used for deployable structures such as design roofs, covers and bridges.



Figures 3-Curvilinearly deployed fingers for robotic grabbing

3. Mathematical Model. Consider a semi-circular two-fingered robotic grabber shown in Figure 3(c) below. Note that the fingers are composed of a serially connected lazy-tong structures with an off-setted central pivoting point such that the length of each link $\ell = a + b$. The off-setted central pivoting points play the key function in curving the deployable fingers in the three-dimensional robotic workspace of such grabbers.

Referring to Figure 3(c), let R_1, R_2 and R be the inner, the outer and the mean or pitch radius of the curving fingers, respectively. Note that

$$RSin\alpha = aSin\theta = bSin\psi \tag{1}$$

$$R_1 = R - aCos\theta, \; R_2 = R + bCos\psi \tag{2}$$

$$\ell_\alpha = aCos\theta + bCos\psi \tag{3}$$

$$Cos\psi = [1 - Sin^2\psi]^{1/2} = [1 - ((a^2/b^2)Sin^2\theta)]^{1/2} \tag{4}$$

$$\ell_\alpha = aCos\theta + b[1 - ((a^2/b^2)Sin^2\theta)]^{1/2} = f_1(a, b, \theta) \tag{5}$$

where ℓ_α is the motor actuation length for computer control. Note that every θ defines an ℓ_α and vice-versa, i.e., $\theta = \widehat{\theta}(a, b, \ell_\alpha)$. Note that α is a function of a,b, and θ as shown below ;

$$\alpha = \theta - \beta,\ \xi = \psi + \theta = 2\beta \rightarrow\ \beta = (1/2)(\theta + \psi) \tag{6}$$

Thus ,

$$\alpha = (1/2)(\theta - \psi) = \alpha(\widehat{a, b}, \theta) \tag{7}$$

Note further that the mean radius or the pitch radius R of the curving finger is also a function of θ such that, based on equations 1 and 7 :

$$R = (aSin\theta/Sin\alpha) = f_2(a, b.\theta) \tag{8}$$

Thus, the local radius of curvature of a grabber finger or a curvilinearly deployable structure is a function of the deployability angle θ, the off-set ratio (a/b) and the actuation distance ℓ_α as derived in equation 5 and the following equation :

$$R = \{aSin\theta/Sin(1/2)[\theta - Sin^{-1}[(a/b)Sin\theta]]\} \tag{9}$$

Thus, computer control of such robotic grabbers can be accomplished in such simple cases by controlling a single motor. These equations can also be used for computer simulations of the kinematics of multi-fingered grabbers as shown in Figure 2 . Note that by adjusting the off-set distance of the pivoting points of the curvilinearly deployable fingers any curvilinear structure may be robotically deployed throughout the 3-D space.

In the next section, discussed are the performance of a number of prototype multi-fingered grabbers fabricated and tested in our laboratory.

4. Experimental Performance Evaluation. Discussed in this section are a number of experimental prototype design of the multi-fingered grabber. Photo 1 depicts a sequence of configurations for a two-fingered grabber. Photo 2, on the other hand depicts a number of consecutive structural configurations of a four-fingered motorized robotic grabber. The grabbing speed of such grabbers are quite large. This is due to the fact that as the motor travels a distance of $\delta\ell_\alpha$ in time δt,the robotic fingers travel a much larger distance about πR, thus creating phenomenal speeds.

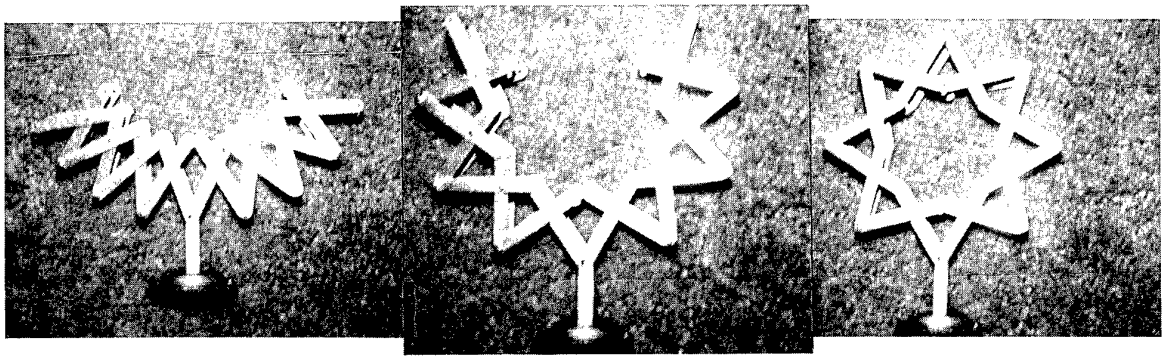


Photo 1-A sequence of deployable configurations for a planar two-fingered mechanical grabber

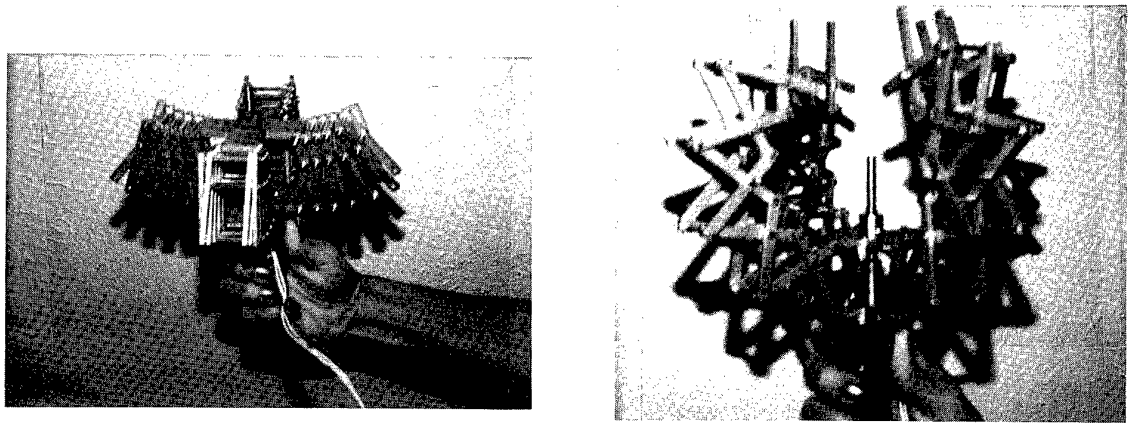


Photo 2-A sequence of deployable configurations for a motorized 4-fingered robotic grabber

The experimental performance of these robotic grabbers indicate that a single motor motion and tip force control is quite feasible and can be easily achieved. Furthermore, by magnetically adjusting the pivoting points of consecutive eccentric lazy-tong elements a variety of deployable curvilinear space structures can be constructed. The dynamic modeling of such deployable robotic grabbers are presently under considerations and will be reported later. These types of robotic grabbers may find niche applications in manufacturing, hunting and grabbing flying objects such as satellites and meteors and articulated dynamic spatial structures.

5. Conclusions. Presented first was a novel design for a class of multi-fingered robotic grabbers capable of rapidly deploying their robotic fingers to grab moving objects within their workspace. A simple mathematical model was then presented for computer-graphic simulation of such multi-fingered robotic grabbers. Finally, some experimental results pertaining to dynamic performance and control of a number of robotic grabbers fabricated in our laboratory were presented. The dynamic performance of these types of rapidly deployable multi-fingered robotic grabbers have been observed to be quite remarkable and consistent with the proposed computer simulation model. These types of robotic grabbers may find applications in automated assembly and manufacturing, capturing and grabbing flying or moving objects such as machine parts in an automated flow line or space assets such as satellites and meteors in outer space as well as articulated dynamic spatial structures.

6. Acknowledgement. This work is partially supported by the Environmental Robots Incorporated.

7. References.

1-H. Hanafusa and H. Asada, "A Robot Hand with Elastic Fingers and Its Application to Assembly Process," Proc. of IFAC Symposium, pp. 127-134, (1977)

2-J.K. Salisbury and J.J. Craig,"Articulated Hands : Force Control and Kinematic Issues," The Int. J. Robotic research, vol. 1, pp. 4-17, (1982)

3-S.C. Jacobson, E.K. Iverson, D.F. Knutti, R.T. Johnson and K.B. Biggers, "Design of UTAH/MIT Dexterous Hand," Proc. 1986 IEEE Robotics & Automation Conf., pp. 1520-1532, (1986)

4-P. Dario and G. Buttazzo, "An Anthropomorphic Robot Finger For Investigating Artificial Tactile Perception," Int. J. of Robotics Research, vol. 6, pp. 25-48, (1987)

5-N. Imamura, M. Kaneko, K. Yokoi and K. Tanie, "Development of A Two-Fingered Robot Hand With Compliance Adjustment Capability," Proc. US-Japan 1990 Symposium on Flexible Automation, Iscie, Kyoto, Japan pp. 997-1004, (1990)

6-A. Roveta," On Functionality of A New Mechanical Hand," Transactions of ASME J. of Mech. Design, vol. 103, pp. 277-280, April (1981)

7-A. Meghdari, M. Mahmoudian and M. Arefi," Kinematics and Dynamics Modeling of the Sharif Artificial Hand,", J. of Engi eering, vol.4, no. 2, pp. 23-33, (1992)

8-H. Maekawa," Stable Grasp and Manipulation of 3D Objects by Multi-Fingered Hands,", Proc. Second International Symposium on Measurement and Control in Robotics (ISMCR'92), November 1992, Tsukuba, Japan, pp. 335-342, (1992)

9-H. Maekawa, K. Yokoi, K. Tanie, M. Kaneko, N. Kimura and N. Imamura," Development f A Three-Fingered Robot Hand with Stiffness Control Capability," Mechatronics, vol. 2, no. 5, pp. 483-494, (1992)

10-M.T. Mason and J. Kenneth Salisbury," Robot hands and the Mechanics of Manipulation," The MIT Press, Cambridge, Massachusetts, London, England, (1985)

11-I. Kato and K. Sadamoto," Mechanical Hands Illustrated," in Japanese, Kogyo Chosakai Publishing Company, Tokyo, Japan, (1977)

12–I. Kato and K. Sadamoto," Mechanical Hands Illustrated," Hemisphere Publishing Company, Washington, New York, London, (1987)

13-S.T. Venkataraman and T. Iberall, "Dexterous Robot Hands," Springer-Verlag Publishing Company, New York, Berlin, Heidelberg, London, Paris, Tokyo, Honk Kong,(1990)

14-M. Shahinpoor and A. Tootoonchi, "Analysis of A Two-Fingered Manufacturing Robotic hand For Fine Automation Processes," Proc. 1988 IEEE Robotics & Automation Conf., pp. 402-407, (1988)

15-D. Kurtis Deno, R.M. Murray, K.S.J. Pister, and S. Shankar Sastry,"Finger-Like Biomechanical Robots," Proc. 1992 IEEE Robotics & Automation Conf., pp. (1992)

16-Choong Sang Lee and S. Derby,"A Robot Gripper Program," Proc. 1986 ASME Design Engn. Technical Conference, ASME Publication 86-DET-38, pp. 1-5, (1986)

17-M. Shahinpoor,"A Robot Engineering Textbook," Harper and Row Publishing Company, New York, London and Paris, (1987)

18-M. Shahinpoor,"Intelligent Robotic Systems : Modeling & Simulation," ERI Press, Albuquerque, New Mexico, (1994)

19-M.R. Cutkosky,"Robotic Grasping and Fine Manipulation," Kluwer Academic Publishing Company, Boston, (1985)

20-J.R. Kerr,"An Analysis of Multi-Fingered Hands," Ph.D. Dissertation, Department of Mechanical Engineering, Stanford University, (1984)

21-J.R. Kerr and B. Roth,"Analysis of Multi-Fingered Hands," Int. J. Robotics Research, vol. 4, no. 4, pp. 3-17, (1986)

22-M.R. Cutkosky and P.K. Wright, "Modeling Manufacturing Grips and Correlations with the Design of Robotic Hands," Proc. 1986 IEEE Robotics & Automation Conf., San Francisco, pp. 13-20, March (1986)

23-J.W. Jameson,"Analytic Techniques for Automated Grasp,"Ph.D. Dissertation, Mechanical Engineering Department, Stanford University, (1985)

24-J.W. Jameson and L.J. Leifer,"Quasi-Static Analysis : A Method for Predicting Grasp Stability," Proc. 1986 IEEE Robotics & Automation Conf., San Francisco, pp. 24-29, March (1986)

25-M. Shahinpoor, "Micro-Electro-Mechanics of Ionic Polymeric Gels As Electrically Controllable Artificial Muscles," Int. J. Intelligent Material Systems and Structures, vol.6, no.3, pp.307-314, (1995)

26-M. Shahinpoor,"Electro-Mechanics of Ionic Polymeric Gels As Artificial Muscles for Robotic Applications," Proc. 1993 IEEE Robotics & Automation, Conf.,vol. 2, pp.380-385 , (1993)

27-M. Shahinpoor, G. Wang and M. Mojarrad, "Electro-Thermo-Mechanics of Spring-Loaded Contractile Fiber Bundles with Applications to Ionic Polymeric Gel and SMA Actuators," Proc. Int. Conf. Intelligent materials, ICIM'94, edited by : C.A. Rogers and G.G. Wallace, Technomic Publication Comp.,Lancaster-Basel, pp. 1105-1116, (1994)

28-M. Shahinpoor and M. Mojarrad,"Active Musculoskeletal Structures Equipped with A Circulatory System and A Network of Ionic Polymeric Muscles,'Proc. Int. Conf. Intelligent materials, ICIM'94, edited by : C.A. Rogers and G.G. Wallace, Technomic Publication Comp.,Lancaster-Basel, pp. 11079-1085, (1994)

The Ionic Flexogelectric Effect In Polymeric Gels

Mohsen Shahinpoor, shah@unm.edu
Intelligent Materials, Structures and Systems Laboratory
School of Engineering, University of New Mexico
Albuquerque, New Mexico 87131

Abstract

Reported are a number of quantitative observations and analytical modeling of a new effect in ionic polymeric gels such as poly(2-acrylamido-2-methylpropanesulfonic acid) or PAMPS, polyacrylic acid plus sodium acrylate cross-linked with bisacrylamide (PAAM) or various chemically-doped combinations of polyacrylic acid plus polyvinyl alcohol (PAA-PVA). This new effect, hereafter, referred to as "Flexogelectric Effect" is basically the inverse of the effect originally reported in 1965 by three GE researchers, namely, Hamlen, Kent and Shafer in which the imposition of an electric field on an ionic polymeric gel fiber produced extension or contraction. Here, it is shown , both theoretically and experimentally, that mechanically induced nonhomogeneous deformations, and in particular bending of strips of such ionic gels can produce an electric field and the associated voltage. For typical samples of such gels (4x4x40mm) with copper or platinum foil electrodes snugly contacting a pair of opposite sides (4x40mm) of the strip, the difference in voltage measured between the electrodes for extreme bending configurations of the gel is typically in the 10's of milivolts range. This voltage difference which is quite significant for many engineering applications, such as large strain and deformation sensing, is still an order of magnitude smaller than the voltage necessary to induce similar deformations in the gel itself. A plausible explanation is also presented for such discrepancies.

Introduction

Ionic polymeric gels are three-dimensional networks of cross-linked macromolecular polyelectrolytes that swell or shrink in aqueous solutions on addition of alkali or acids, respectively. It has been experimentally observed that swelling and shrinking of ionic gels can also be induced electrically. Thus, direct computer control of large expansions and contractions of ionic polymeric gels by means of a voltage gradient appears to be possible.

Katchalsky [1], and Kuhn [2] originally reported on the possibility that certain copolymers can be chemically contracted or swollen like a synthetic muscle (pH muscle) by changing the pH of the solution containing them. Chemically stimulated pseudo-muscular actuation has also been discussed recently by Li and Tanaka [3], De Rossi, Chiarelli, Buzzigoli, Domenici, and Lazzeri [4], Caldwell and Taylor [5], De Rossi, Kajiwara, Osada, and Yamauchi [6], Segalman, Witkowski, Adolf, and Shahinpoor [7], [8].Hamlen, Kent, and Shafer [9] were the first to report that contraction and swelling of these gels can also be obtained electrically by placing fibrous samples of PAA-PVA in an electric field. One of the earlier mathematical modeling of deformation of ionic gels in an electric field was presented by Tanaka, Nishio, Sun and Ueno-Nishio [10] proposing a phase transformation phenomenon responsible for such electrically-induced contraction. Other experimental and theoretical investigations addressing the electrically-induced contractile behavior of ionic polymeric gels are Osada and Hasebe [11], Grimshaw, Nussbaum and Grodzinski [12], Shiga and Kurauchi [13], Kishi, Hasebe, Hara and Osada [14], Doi, Matsumoto and Hirose [15], Osada, Okuzaki and Hori [16], Shahinpoor [17], [18], [19], Segalman, Witkowski, Adolf and Shahinpoor [20] , Gong, Nitta and Osada [21], [22] and Shahinpoor and Osada [23]. These findings clearly indicate that the short-time response of the gel to the electric field is due to electrophoretic migration of unbound counter ions in the gel, and to impingement of solvent ions on the surfaces of the gel samples. It is the surplus or deficiency of such ions which determines the osmotic pressure, free volume and therefore deformation of such gels. Recently, Shahinpoor and Osada [23] and [24], have presented a dynamic model of the contraction of polyelectrolyte gels with satisfactory agreements with experimental results on PAMPS samples by Gong, Nitta and Osada [21] and [22]. In the next section, the case of either electrically-induced bending or mechanically-induced voltage generation of strips of ionic polymeric gels is considered. Exact expressions are given relating the deformation characteristics of the gel to the electric field strength or voltage gradient,

0-8194-2165-0/96/$6.00

gel dimensions and other physical parameters such as the resistance and the capacitance of the gel strip. It is concluded that the model is symmetric enough to predict both the mechanically-induced electric field and the electrically-induced mechanical deformation in ionic polymeric gels.

Theoretical Model

In order to describe either the electrically-induced deformation or mechanically-induced voltage generation of ionic polymeric gels we consider the process of bending of strips of ionic polymeric gels in a transverse electric field.

Suppose a long thin straight strip of an ionic gel of length ℓ^*, thickness $t^* = 2C$, and width w^*, is bent into a curve-strip by an imposed voltage gradient across its thickness t^*. It is assumed that initially the gel is in a natural bending-stress free state equilibrated with a $pH = 7$. Now, referring to Figure 2, note that the strain ϵ (defined as the ratio of the actual incremental deformation (δl) to the initial length (l_0) is given by $\epsilon = \epsilon_c + \kappa_E \eta = \lambda - 1$, where ϵ_c is the strain along the neutral central line (line going through the centers of areas of all cross-sections), κ_E is the curvature of the strip due to presence of a voltage gradient, λ is the stretch and η is a cross-section variable, such that $-C \leq \eta \leq C$, $t^* = 2C$, where t^* is the thickness of the gel strip. Due to the presence of an electrical voltage gradient across the thickness t^* of the gel the gel strip is bent into a curved strip by a non-uniform distribution of fixed as well as mobile ions in the gel. Note that an electric field gradient may be imposed across the thickness of the gel by charged surfactant molecules. Thus, it is clear that $\lambda_+ - \lambda_- = 2\kappa_E C$. If the gel possesses a specific capacitance C_g and a specific resistance R_g, the Kirchhoff's law can be written in the following form:

$$\text{(1)} \qquad \text{v} = C_g^{-1} Q + R_g \dot{Q}, \longleftrightarrow \dot{Q} = i,$$

where v is the voltage across the thickness of the gel, and Q is the specific charge (charge per unit mass) accumulated in the gel, $\dot{Q}$ being the current density i through the gel strip across its thickness. Equation (1) can be readily solved to yield

$$\text{(2)} \qquad Q = C_g \text{v}[1 - \exp.((-t/R_g C_g))],$$

assuming at $t = 0$, $Q = 0$. Equation (2) relates the voltage drop across the thickness of the gel to the charge accumulated which eventually causes the gel to deform. Thus, equation (2) will serve as a basis for the electrical control of gel deformations. The imposed voltage gradient across the thickness of the gel forces the internal fixed and mobile ions to redistribute within the polymeric network.

In order to mathematically model the nonhomogeneous deformation or bending forces at work in an ionic polyelectrolyte gel strip, a number of simplifying assumptions are made. The first assumption is that the polymer segments carrying fixed charges are cylindrically distributed along a given polymer chain

This assumption is not essential but greatly simplifies the analysis. Consider the field of attraction and repulsion amongst neighboring rows of fixed or mobile charges in an ionic gel. Let r_i, Z_i be the cylindrical polar coordinates with the ith. row as an axis such that the origin is at a given polymer segment. Let the spacing in the ith. row be b_i, and let the forces exerted by the atoms be central and of the form cr^{-s}such that the particular cases of $s = 2$, $s = 7$ and $s = 10$, represent, respectively, the Coulomb, van der Waals and short range repulsive forces. Then it can be shown that the component of the electric potential field per unit charge at the point (r_i, Z_i) perpendicular to the row is represented in a series such that

$$\text{(3)} \qquad R(r_i, Z_i) = \sum_{n=-\infty}^{\infty} \{ \frac{r_i}{[(Z_i - nb_i)^2 + r_i^2]^{(1/2)(s+1)}} \},$$

This function is periodic in Z_i, of period b_i, is symmetrical about the origin. It may therefore be represented in a Fourier series such that the total field due to the presence of N strands per unit length of the strip is then given by

$$R(\eta, Z) = \sum_{i=1}^{N} 16\pi b_i^{-2}[\sum_{m=1,3,5,..}^{\infty} mK_1(\frac{2\pi m r_i}{b_i})Cos(2\pi m Z_i/b_i)], \tag{4}$$

where η is the cross-section variable defined before. For simplicity, let us assume that all $b_i's$, $Z_i's$ and $r_i's$ are equal to b, Z and η respectively, where b is defined as the mean interior ionic distance in the gel so that on the average $N = 2/b$. With this assumption equation (3) reduces to

$$R(\eta, Z) = 32\pi b^{-3}[\sum_{m=1,3,5,..}^{\infty} mK_1(\frac{2\pi m\eta}{b})Cos(2\pi m Z/b)], \tag{5}$$

The mean Coulomb's attraction or repulsion force associated with the mean field $R(\eta, Z)$ is then given by $F(\eta, Z)$ such that

$$F(\eta, Z) = kq^2\ell^* R(\eta, Z), \tag{6}$$

where k is a constant of proportionality, ℓ^* is the length of the gel strip and q corresponds to total charge between a pair of adjacent ionic surfaces in the gel strip. Note that, thus $q = b^{-1}\rho C w \ell^* Q$ where ρ is the average density of the gel strip and w is its average width. This force is repulsive (positive) or attractive (negative) according to whether like or unlike charges lie in the adjacent rows of charges. Figure 1 displays a simple solution configuration for bending of strips of ionic polymeric gels.

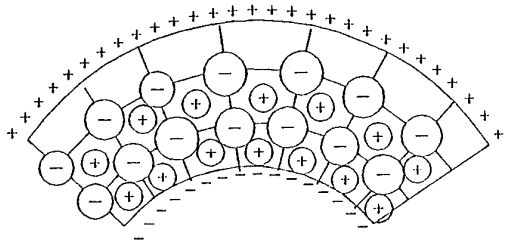


Figure 1- A possible solution configuration for the flexogelectric effect

Clearly the simple solution shown in Figure 1 can be generalized to produce local bending towards, say, the anode or the cathode electrodes.Thus, the solution for the force field given be equation (5) is quite capable of creating a bending or a series of bending in the gel in the presence of an electric field gradient. Note that from equation (5) an average stress over the cross section of the gel strip (width= w,thickness= $2C$) may be defined as

$$\sigma(\eta, Z) = [-16\pi k\ell^* q^2 b^{-3}/wC][K_1(\frac{2\pi\eta}{b})\ Cos(2\pi Z/b)], \tag{7}$$

where the negative sign ensures that the stress is negative when the gel is in a contracted state. Now in order to find the curvature κ_E, the difference $\lambda_+ - \lambda_-$ should be calculated.

Assuming a Neo-Hookean type constitutive equation for polymer elasticity it is concluded that

$$\sigma_+ = -(E_+/3)(\lambda_+ - \lambda_+^{-2}), \tag{8}$$

$$\sigma_- = -(E_-/3)(\lambda_- - \lambda_-^{-2}), \tag{9}$$

where E_+ and E_- are elastic moduli and are functions of the pH or local ionic concentration and temperature and λ_+ and λ_- refer to the stretches in the most remote fibers in the gel under bending. From equation (9) it is calculated that

$$\sigma_+ = \sigma(C,Z) = [-16\pi k\ell^* q^2 b^{-3}/wC]\, K_1(\frac{2\pi C}{b})\, Cos(2\pi Z/b)], \tag{10}$$

$$\sigma_- = \sigma(-C,Z) = [-16\pi k\ell^* q^2 b^{-3}/wC][K_1(\frac{-2\pi C}{b})\, Cos(2\pi Z/b)], \tag{11}$$

Thus, the above equations give rise to the following set of cubic equations for λ_+ and λ_- :

$$\lambda_+^3 + ((3\sigma_+/E_+))\lambda_+^2 - 1 = 0, \tag{12}$$

$$\lambda_-^3 + ((3\sigma_-/E_-))\lambda_-^2 - 1 = 0. \tag{13}$$

The possible curvatures with a real value is then calculated as

$$\kappa_E = ((\lambda_+ - \lambda_-)/2C), \tag{14}$$

From these equations it is clear that the nonhomogeneous force field and the curvature in bending of ionic gels can give rise to an electric field which can be changed with mechanically-induced deformations. Conversely, the imposition of an electric field can give rise to deformation and bending. In this context, the difference $\lambda_+ - \lambda_-$ is related through equations (12) and (13) to the stresses σ_+ and σ_-. These stresses are in turn related to the charges q and Q and other physical parameters by equations (10) and (11). The total charge Q is then related to the voltage v and other electrical parameters C_g and R_g by equation (2) as described before. This then allows the designer to robotically control such deformations in ionic gels by means of a voltage controller or conversely measure the mechanical deformation of gels by the voltage produced due to such deformations. In this sense the gel body becomes a large strain or deformation sensor. In the next section the results of a series of experimental measurements on PAAM and PAMPS gels are reported.

4-Experimental Observation on Ionic Flexogelectric Effect

In order to measure the voltage generated by the deformation, and in particular bending, of strips of ionic polymeric gels, a series of styrofoam annular molds were fabricated. A pair of either copper or platinum foil electrodes were glued snugly to the inner walls of the annular slots of the styrofoam molds.

Essentially, circular annular strips of various mean diameters, and curvatures (inverse diameter), of thickness t^* and width w^* were cut out of soft styrofoam sheets of thickness w^* to create appropriate annular slots for the placement of rectangular ionic polymeric gel strips. These cutouts were snugly fitted with either copper or platinum ribbon electrodes as shown in Figure 2. Identical strips of gels were prepared from PAAM and PAMPS ionic polymeric gels with dimensions of 4x4x40mm and were placed snugly between the inserted electrodes. The voltage and current through the gel strips were then measured with high accuracy. A number of typical responses for both the PAAM and the PAMPS samples are shown in Figure 2.

The typical voltages generated by bending of polymeric gel strips appears to be an order of magnitude smaller than typical voltages necessary to induce such bending deformations in similar gel samples. This discrepancy is presently under investigation. However, it appears to be partially due to the need for additional energy to bend a strip of ionic gel in an aqueous viscous solution and partially due to geometrical complexities of the experimental arrangement to induce bending in ionic polymeric gel strips suspended in an aqueous viscous solution and in the presence of an electric field. While the reverse experiment is performed in absence of any viscous solution and is purely the voltage created by bending of such strips in air. Attempts are presently underway in our laboratory to deposit soft porous copper or platinum electrodes on the surfaces of these gel samples to enable dynamic vibrations and bending/flexing experiments. These strips of PAAM and PAMPS gels will be latex membrane-encapsulated for a variety of engineering applications..

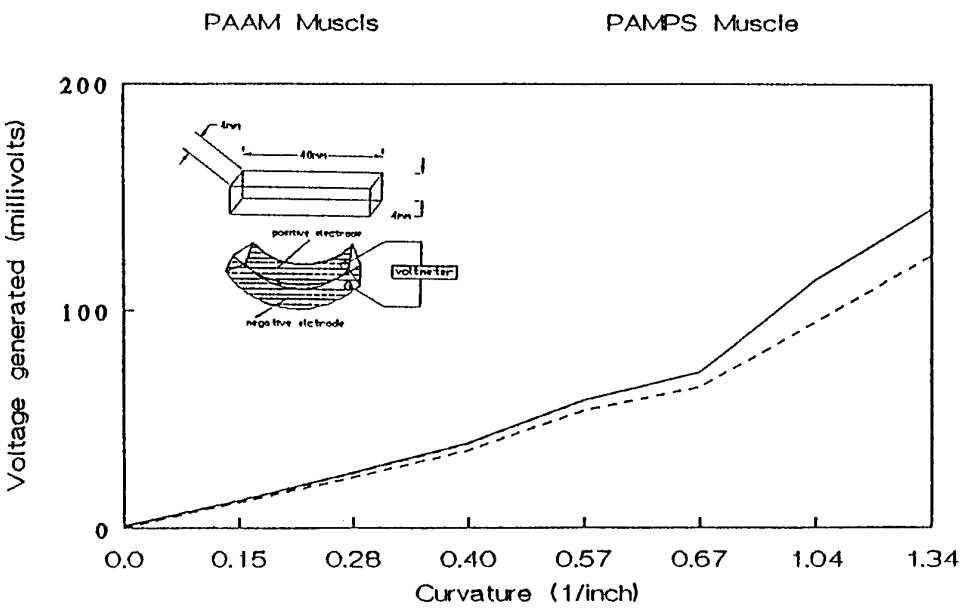


Figure 2- Experimental observation of deformation-induced voltage in ionic polymeric gels

5-Conclusions

A number of quantitative observations and analytical modeling of a new effect in ionic polymeric gels such as poly(2-acrylamido-2-methylpropanesulfonic acid) or PAMPS, polyacrylic acid plus sodium acrylate cross-linked with bisacrylamide (PAAM) or various chemically-doped combinations of polyacrylic acid plus polyvinyl alcohol (PAA-PVA) were described. The newly observed effect,were referred to as "Ionogelectric Effect" and was shown to be basically the inverse of the effect originally reported in 1965 by three GE researchers, namely, Hamlen, Kent and Shafer in which the imposition of an electric field on an ionic polymeric gel fiber produced extension or contraction. Here, it was shown , both theoretically and experimentally, that mechanically induced nonhomogeneous deformations, and in particular bending

of strips of such ionic gels can produce an electric field and the associated voltage. For typical samples of such gels (4x4x40mm) with copper or platinum foil electrodes snugly contacting a pair of opposite sides (4x40mm) of the strip, the difference in voltage measured between the electrodes for extreme bending configurations of the gel is typically in the 10's of milivolts range. This voltage difference, which is quite significant for many engineering applications, can be employed, for example, in applications involving large strain and deformation sensing or direct conversion of mechanical motion to electricity.This voltage is still an order of magnitude smaller than the voltage necessary to induce similar deformations in the gel itself. This discrepancy is attributed to the geometrical complexities of the latter experimental arrangement. Further investigation on this effect is presently being conducted to gain more understanding on this ionic "flexogelectric" effect.

6-Acknowledgment

This research is partially supported by Sandia National Laboratories. Thanks are extended to our electronic technician Ron Kay and my research assistants Hengameh Keshavarzi, Mehran Mojarrad, Karim Salehipoor and Mathew Thompson, for experimental support.

7-References

1.Katchalsky, Experientia, vol. 5, pp.319-320, (1949).

2.Kuhn, W., Experientia, vol. 5 pp 318-319, (1949).

3. Li, Y., and Tanaka, T., J. Chem. Phys., vol. 92, pp 1365-1371, (1990).

4. De Rossi, D.E., Chiarelli, P., Buzzigoli, G., Domenici, and Lazzeri, L., Trans, Am. Soc. Artif. Intern. Organs, XXXII, pp. 157-162, (1986).

5.Caldwell, D.G., and Taylor, P.M., Int. J. Engr. Sci., vol. 6, pp.797-808, (1990).

6.De Rossi, D.E., Kajiwara, K., Osada, Y., and Yamauchi, A., Proc.Int. Symp. Polymer Gels, Tsukuba, Japan, 18-21 September, Plenum Press, New York, (1991).

7.Segalman, D., Witkowski, W., Adolf, D., and Shahinpoor, M., Proc. *ADPA/AIAA/ASME* SPIE/Conf. on Active Materials and Adaptive Structures, edited by G.J. Knowles, Nov. 1991, Alexandria, Va., IAP Press, pp. 335-345. (1992).

8.Segalman, D., Witkowski, W., Adolf, D. and Shahinpoor, M., Smart Materials and Structures Int. J., vol. 1, Nov. 1, pp. 95-100, (1992).

9. Hamlen, R.R., Kent, C.E., and Shafer, S.N., Nature, vol. 206, pp. 1148-49, (1965).

10.Tanaka, T., Nishio, I., Sun, S.U., and Ueno-Nishio, S., Science, vol.218, pp.467-469, (1982)

11- Osada, Y. and M. Hasebe, 1985, Chem. Lett., 1285-1288.

12-Grimshaw, P.E., Nussbaum, J.H., and Grodzinski, A.J., J. Chem. Phys., vol. 93, no. 6, pp.4462-4472, (1990)

13- Shiga, T. and Kurauchi, T., J. Appl. Polymer Science, vol. 39, pp. 2305-2320, (1990).

14- Kishi, R., M. Hasebe, M. Hara, and Y. Osada, 1990, Polymers for Advanced Technologies 1:19-25.

15- Doi, M., M. Matsumoto, and Y. Hirose, 1992, Macromolecules 25: 5504-5511.

16- Osada, Y., H. Okuzaki, and H. Hori, 1992, Nature, 355: 242-244.

17- Shahinpoor, M., Proc. SPIE 1993 Conference on Smart Structures and Materials, Feb. 1-4, (1993), Albuquerque, New Mexico.

18-Shahinpoor, M., Int. J. Smart Materials & Structures, vol.1, no. 1, pp. 91-94, (1992)

19-Shahinpoor, M.,Proc. ICIM'94, June 5-8, Williamsburg, Va., (1994)

20-Segalman, D.J., Witkowski, W.R., Adolf, D.B., and Shahinpoor,M., Int. J. Smart Materials & Structures, vol.1, no. 1, pp. 95-100, (1992)

21-Gong, J.P., Nitta, T., Osada, Y., Proc. ICIM'94, June 5-8, Williamsburg, Va, (1994)

22-Gong, J.P., Nitta, T., Osada, Y., J. Phys. Chemistry, vol. 98, September 22, (1994)

23-Shahinpoor, M., and Osada, Y., Proc. Sapporo Symposium on Intelligent Polymer Gels, October 6-8, Hokaido University, Sapporo, Japan, (1994)

24-Shahinpoor, M. and Osada, Y., Proc. SPIE 1995 Smart Structures and Materials Conference, February 28-March 3, 1995, SanDiego, Calif., volume 2441, no. 46, (1995)

Paper presented at the Third ICIM/ECSSM '96, Lyon '9

Ion Exchange Membrane-Platinum Composites As Electrically Controllable Artificial Muscles

M. Mojarrad and M. Shahinpoor
Intelligent Materials, Structures and Systems Laboratory
School of Engineering, University of New Mexico
Albuquerque, New Mexico 87131, USA

1 Abstract

Ion exchange membranes (IEM) chemically treated with platinum salt solutions gives rise to IEM-platinum composites that undergo large deformations in an electric field of a few volts (2-4 volts/mm). They also show remarkable vibrational characteristics of about 80 Hz bandwidth. A simple theoretical treatment as well as some experimental evidence on the dependence of deformation amplitude on the imposed voltages and frequencies are presented.

2 Introduction

Grodzinsky [1], Grodzinsky and Melcher [2], [3] were the first to present a plausible continuum model for electrochemistry of deformation of charged polyelectrolyte membranes such as collagen or fibrous protein. Kuhn [4] and Katchalsky [5] however should be credited to have been the first investigators to report the ionic chemomechanical deformation of polyelectrolytes such as polyacrylic acid (PAA), polyvynil chloride (PVA) systems. Kent, Hamlen and Shafer [6] were also the first to report the electrochemical transduction of PVA-PAA polyelectrolyte system. Recently revived interest in these area with concentration on artificial muscles can be traced to Shahinpoor [7]- [11], and [15], Shahinpoor and Mojarrad [12], [13], Shahinpoor, Wang and Mojarrad [14], Osada [16], Oguro, Asaka and Takenaka [17], Asaka, Oguro, Nishimura, Mizuhata and Takenaka [18], Guo, Fukuda, Kosuge, Arai, Oguro and Negoro [19]. Essentially polyelectrolytes posses many ionizable groups on their molecular chain. These ionizable groups have the property of dissociating and attaining a net charge in a variety of solvent medium. These net charge groups which are attached to network of macromolecules are called polyions and give rise to intense electric fields of the order of 10^{10} V/m. Shahinpoor [11], [15] has recently presented a number of plausible models for microelectromechanics of ionic polymeric gels as electrically controllable artificial muscles. Furthermore by placing two electrodes in close proximity of the membrane walls and applying a voltage (Fig. 1), the forced transport of ions within a solution through membrane becomes possible at microscopic level. For a solvent such as water then local swelling and deswelling of membrane can be controlled depending on polarity of the electrode nearby more like the behavior of the bimorphic materials. This can be achieved by chemical or other possible means of plating of conductive materials on membrane surfaces. Platinum is one such conductor that can be deposited on the IEM. Also being ionic in microscopic structure, IEM has the ability to shift its mobile ions of the same charge polarity within itself when it is placed in an electric field which results in ionic attraction or repulsion between the fixed charges of opposite polarity contained in the side groups within the polymer molecular chain. This leads to local collapse or expansion of the polymer membrane

0-8194-2165-0/96/$6.00

macroscopically. Physically this causes a stress gradient on opposite sides of the membrane causing it to bend. A simple model for microelectrmechanics of polyelectrolyte IEM-platinum composite membrane is presented in the next section. For additional references on this subject see [20]-[29].

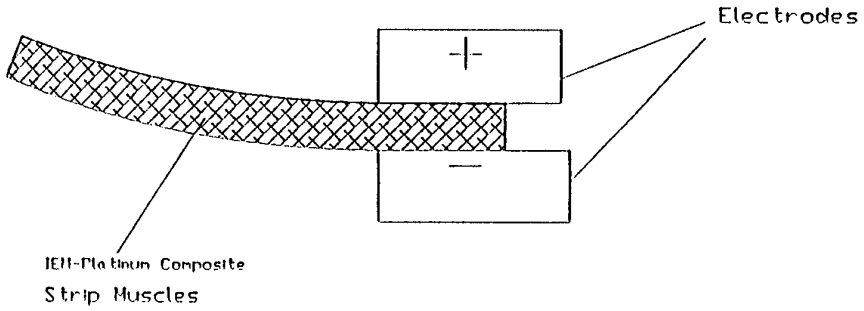


Figure 1. Bending of an ionic gel strip due to an imposed voltage gradient.

3 Theoretical Model

When a strip of such ionic polymeric gels undergoes bending in the presence of a transverse electric field with hardly any water exudation there are generally three competing forces acting on the gel polymer network. These are the rubber elasticity, the polymer-polymer affinity and the ion pressure. These forces, collectively create the osmotic pressure which determines the equilibrium state of the gel. The competition between these forces changes the osmotic pressure and produces the volume change or deformation. Rubber elasticity tends to shrink the gel under tension and expand it under compression. Polymer-polymer affinity depends on the electrical attraction between the polymer and the solvent. Ion pressure is the force exerted by the motion of the cations or anions within the gel network. Ions enter the gel attracted by the opposite charges on the polymer chain while their random motions tend to expand the gel like an ionic (Fermionic) gas. In order to describe either the electrically-induced deformation or mechanically-induced voltage generation of ionic polymeric gels we consider the process of bending of strips of ionic polymeric gels in a transverse electric field. Suppose a long thin straight strip of an ionic gel of length ℓ^*, thickness $t^* = 2C$, and width w^*, is bent into a curve-strip (Fig. 2) by an imposed voltage gradient across its thickness t^*. It is assumed that initially the gel is in a natural bending-stress free state equilibrated with a $pH = 7$. Note that the strain ϵ (defined as the ratio of the actual incremental deformation (δl) to the initial length (l_0) is given by:

$$\epsilon = \epsilon_c + \kappa_E \eta = \lambda - 1, \tag{1}$$

where ϵ_c is the strain along the neutral central line (line going through the centers of areas of all cross-sections), κ_E is the curvature of the strip due to presence of a voltage gradient, λ is the stretch and η is a cross-section variable (Fig. 2), such that $-C \leq \eta \leq C$, $t^* = 2C$, where t^* is the thickness of the gel strip. Due to the presence of an electrical voltage gradient across the thickness t^* of the gel the gel strip is bent into a curved strip by a non-uniform distribution of fixed as well as mobile ions in the gel. Note that an electric field gradient may be imposed across the thickness of the gel by charged surfactant molecules or surface contacting electrodes. Thus, it is clear that:

$$\lambda_+ - \lambda_- = 2\kappa_E C, \tag{2}$$

If the gel possesses a specific capacitance C_g and a specific resistance R_g, the Kirchhoff's law can be written in the following form:

$$v = C_g^{-1}Q + R_g\,\dot{Q}, \longleftrightarrow \dot{Q} = i, \tag{3}$$

where v is the voltage across the thickness of the gel, and Q is the specific charge (charge per unit mass) accumulated in the gel, $\dot{Q}$ being the current density i through the gel strip across its thickness. Equation (3) can be readily solved to yield:

$$Q = C_g v[1 - \exp.(-t/R_g C_g)], \tag{4}$$

assuming at $t = 0$, $Q = 0$. Equation (4) relates the voltage drop across the thickness of the gel to the charge accumulated which eventually causes the gel to deform. Thus, equation (4) will serve as a basis for the electrical control of gel deformations.

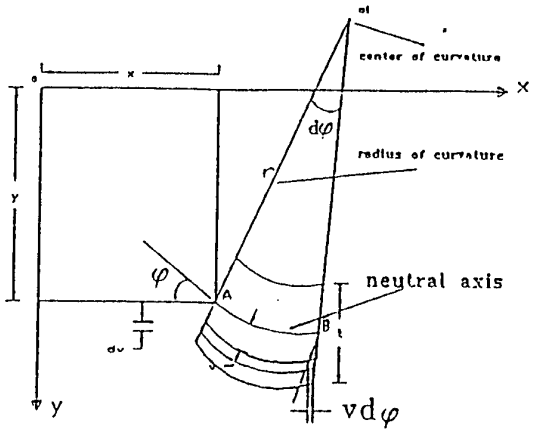


Figure 2- Geometry of micro bending for an elastic strip of ionic gels.

For a cylindrical polar coordinate configuration, the component of mean force field per unit charge $F(\eta, Z)$, in radial direction across the thickness of the gel can be shown to be:

$$F(\eta, Z) = 32\pi k\ell^* q^2 b^{-3}[\sum_{m=1,3,5,..}^{\infty} mK_1(\frac{2\pi m\eta}{b})Cos(2\pi mZ/b)], \tag{5}$$

Thus, the solution for the force field given by above equation is quite capable of creating a bending or a series of bending in the gel in the presence of an electric field gradient. It can further be shown that the stresses at outer fibers are given by:

$$\sigma_+ = \sigma(C, Z) = [-16\pi k\ell^* q^2 b^{-3}/wC]K_1(\frac{2\pi C}{b})Cos(2\pi Z/b)], \tag{6}$$

$$\sigma_- = \sigma(-C, Z) = [-16\pi k\ell^* q^2 b^{-3}/wC][K_1(\frac{-2\pi C}{b})Cos(2\pi Z/b)], \tag{7}$$

Now in order to find the curvature κ_E in equation (2) the difference $\lambda_+ - \lambda_-$ should be calculated. Assuming a Neo-Hookean type constitutive equation for polymer elasticity it is concluded that:

$$\sigma_+ = -(E_+/3)(\lambda_+ - \lambda_+^{-2}), \tag{8}$$

$$\sigma_- = -(E_-/3)(\lambda_- - \lambda_-^{-2}), \tag{9}$$

where E_+ and E_- are elastic moduli and are functions of the pH or local ionic concentration and temperature and λ_+ and λ_- refer to the stretches in the most remote fibers in the gel under bending. Thus σ_+ and σ_- gives rise to the following set of cubic equations for λ_+ and λ_- :

$$\lambda_+^3 + (3\sigma_+/E_+)\lambda_+^2 - 1 = 0, \tag{10}$$

$$\lambda_-^3 + (3\sigma_-/E_-)\lambda_-^2 - 1 = 0, \tag{11}$$

The possible curvatures with a real value is then calculated as; $\kappa_E = (\lambda_+ - \lambda_-)/2C$. Now from the above equations it is clear that the nonhomogeneous force field and the curvature in bending of ionic gels can give rise to an electric field which can be changed with mechanically-induced deformations. Conversely, the imposition of an electric field can give rise to deformation and bending. In this context, the difference $\lambda_+ - \lambda_-$ is related to the stresses σ_+ and σ_-. These stresses are in turn related to the charges q and Q and other physical parameter as shown earlier. The total charge Q is then related to the voltage v and other electrical parameters C_g and R_g by equation (4) as described before. This then allows the designer to robotically control such deformations in ionic gels by means of a voltage controller or conversely measure the mechanical deformation of gels by the voltage produced due to such deformations. In this sense the gel body becomes a large strain or deformation sensor. In the next section the results of a series of experimental measurements on IEM-Platinum composites are described.

4 Experimental Results

A 1.5in×3in piece of IEM (Nafion 117, Du Pont Company) was chemically deposited with platinum to produce the IEM-platinum composite artificial muscle. Then a strip of 1in×1/16in (25.4mm×1.6mm) of membrane composite was cut and completely swollen in water. The composite weighed 0.05 grams and its thickness was about 0.0072in after platinum was deposited on its two surfaces. The strip was then held by a clamping setup between two platinum plate terminals which were wired to a signal amplifier and generator apparatus driven by Labview software through an IBM compatible PC containing an analog output data acquisition board. An amplifier (Crown model D-150A) was used to amplify the signal output of a National Instrument data acquisition card (AT-AO-10). A software was written to produce various waveforms such as sinusoid, square, triangular and sawtooth signals at desired frequencies up to 100 Hz and amplitudes up to 10 volts. When a low voltage was applied, the membrane composite bent toward the anode side each time. So by applying an alternating signal we were able to observe alternating bending of the actuator that followed the input signal very closely up to 35 Hz frequency. At voltages higher than 2.0 volts, the hydrolysis of water in the composite was observed which led to degradation of displacement output of the actuator. Also due to excessive heat generation at higher voltages the membrane composite degraded leading to oxidation and eventually melting. Another factor affecting membrane composite performance was the dehydration. Water act as single most important element for the composite bending by sequentially leaving and entering the composite. The side facing the anode dehydrates faster then the side facing the cathode leading to a differential stresses which ultimately leads to bending of the composite. So, prior to each experiment, the composite was completely swollen in water. The displacement of the free end of the composite membrane was then measured for frequency range of $0.1 - 35$ Hz for sinusoid input voltage at 2.0 volts amplitude (Fig. 3a). Resonance was observed at 20 Hz frequency where the displacement was maximum of 7.5 mm. It should be noted that as the actuator dehydrates the resonant frequency and maximum displacement varies accordingly. For our sample actuator the resonance occurred in the frequency range$12 - 28$ Hz. Another measurement of the displacement of the free end was done by varying the amplitude of the sinusoid input voltage from $0.5 - 2.0$ volts range at constant frequency of 0.5 Hz (Fig. 3b).

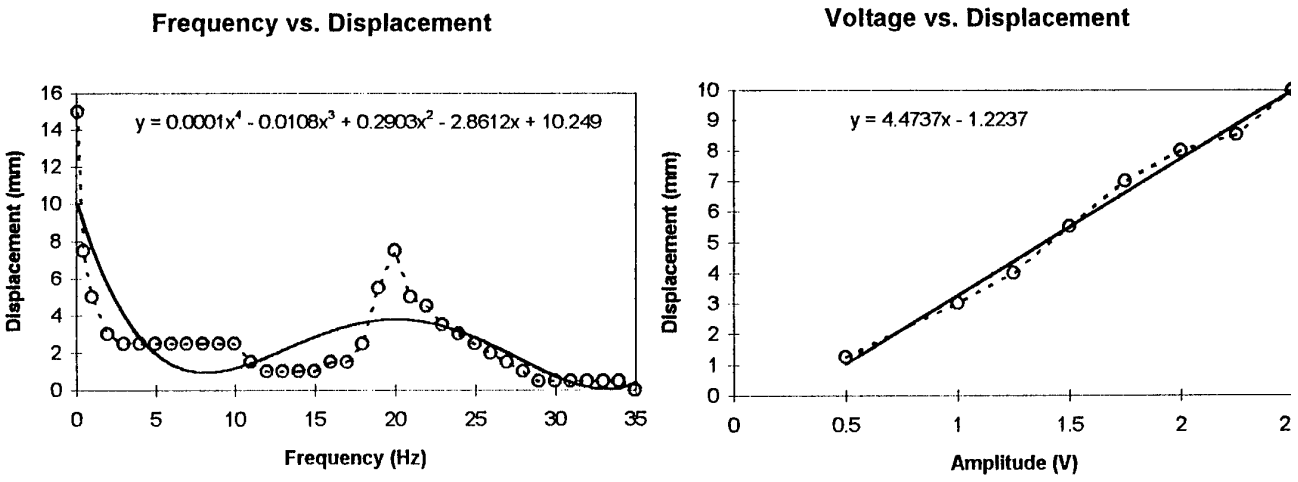


Figure 3- Displacement versus a) the imposed frequency for a fixed voltage of 2 volts, b) the imposed voltage for a fixed frequency of 0.5 Hz.

5 ACKNOWLEDGEMENT

This research is partially supported by Artificial Muscles Research and Development Inc., in Albuquerque, New Mexico.

6 References

1. Grodzinsky, A. J., Electromechanics of Deformable Polyelectrolyte Membranes, Sc.D. dissertation, Dept. of Elec. Eng., MIT, Cambridge, June 1974.

2. Grodzinsky, A. J., Melcher, J. R., Electromechanics of Deformable, Charged Polyelectrolyte Membranes, Proc. 27th Annu. Conf. Engineering in Medicine and Biology, Vol. 16, 1974, paper 53.2.

3. Grodzinsky, A. J., Melcher, J. R., Electromechanical Transduction with Charged Polyelectrolyte Membranes, IEEE Transactions on Biomedical Engineering, Vol. BME-23, No. 6, pp421-433, November 1976.

4. Kuhn, W., Reversible Dehnung und Kontraktion bei Anderung der Ionisation eines Netzwerks Polyvalenter Fadenmolekulionen, Experientia, Vol. V, pp318-319, 1949.

5. Katchalsky, A., Rapid Swelling and Deswelling of Reversible Gels of Polymeric Acids by Ionization, Experientia, Vol. V, pp319-320, 1949.

6. Hamlen, R. P., Kent, C. E., Shafer, S. N., Electrolytically Activated Contractile Polymer, Nature, Vol. 206, pp1149-1150, 1965.

7. Shahinpoor, M., Conceptual Design, Kinematics and Dynamics of Swimming Robotic Structures Using Ionic Polymeric Gel Muscles, Smart Materials and Structures, Vol. 1, pp91-94, 1992.

8.Shahinpoor, M., Microelectro-Mechanics of Ionic Polymeric Gels as Artificial Muscles for Robotic Applications, Proceeding of the 1993 IEEE Robotics and Automation Conference, vol. 2, pp.375-384, 1993.

9.Shahinpoor, M., Nonhomogeneous Large Deformation Theory of Ionic Polymeric Gels in Electric and pH Fields, Proceedings of the SPIE Conference on Smart Structures and Materials, Feb. 1-4, Albuquerque, Vol. 1916, pp40-50,.1993.

10.Shahinpoor, M., Micro-Electro-Mechanics of Ionic Polymeric Gels as Electrically Controllable Artificial Muscles, Proceedings of the Second International Conference on Intelligent Materials, ICIM'94, pp. 1095-1104, (1994).

11.Shahinpoor, M., Continuum Electro-Mechanics of Ionic Polymeric Gels as Artificial Muscles For Robotic Applications, Smart Materials and Structures Int. Journal, vol. 3, pp. 367-372, (1994)

12.Shahinpoor, M. and Mojarrad, M., unpublished report, Smart Materials, Structures and Systems Laboratory, College of Engineering, Univ. of New Mexico, December (1992).

13.Shahinpoor, M., Mojarrad, M., Active Musculoskeletal Structures Equipped with a Circulatory System and a Network of Ionic Polymeric Gel Muscles, Proceedings of the Second International Conference on Intelligent Materials, ICIM'94, pp1079-1085, 1994.

14.Shahinpoor, M., Wang, G., Mojarrad, M., Elctro-Thermo-Mechanics of Spring-Loaded Contractile Fiber Bundles with Applications to Ionic Polymeric Gel and SMA Actuators, Proceedings of the International Conference on Intelligent Materials, pp1105-1116, 1994.

15.Shahinpoor, M., Micro-Electro-Mechanics of Ionic Polymeric Gels as Electrically Controllable Artificial Muscles, Journal of Intelligent Material Systems and Structures, vol. 6, No. 3, pp. 307-314, (1995)

16.Osada, Y., Electro-Stimulated Chemomechanical System Using Polymer Gels (An Approach to Intelligent Artificial Muscle System), Proceeding of the International Conference on Intelligent Materials, pp155-161, 1992.

17.Oguro, K., Asaka, K., Takenaka, H., Polymer Film Actuator Driven by Low Voltage, Proceedings of 4th International Symposium on Micro Machine and Human Science at Nagoya, pp39-40, 1993.

18.Asaka, K., Oguro, K., Nishimura, Y., Mizuhata, M., Takenaka, H., Bending of Polyelectrolyte Membrane-Platinum Composites by Electric Stimuli, I. Response Characteristics to Various Waveforms, Polymer Journal, Vol. 27, No. 4, pp436-440, 1995.

19.Guo, S., Fukuda, T., Kosuge, K., Arai, F., Oguro, K., Negoro, M., Micro Catheter System with Active Guide Wire Structure, Experimental Results and Characteristic Evaluation of Active Guide wire Using ICPF Actuator, Osaka National Research Institute, Japan, pp191-197, 1994.

20.Segalman, D., Witkowski, W., Adolf, D., and Shahinpoor, M., Proc. *ADPA/AIAA/ASME* SPIE/Conf. on Active Materials and Adaptive Structures, edited by G.J. Knowles, Nov. 1991, Alexandria, Va., IAP Press, pp. 335-345. (1992).

21.Segalman, D., Witkowski, W., Adolf, D. and Shahinpoor, M., Smart Materials and Structures Int. J., vol. 1, Nov. 1, pp. 95-100, (1992).

22- Shahinpoor, M., Proc. SPIE 1993 Conference on Smart Structures and Materials, Feb. 1-4, (1993), Albuquerque, New Mexico.

23-Shahinpoor, M., Int. J. Smart Materials & Structures, vol.1, no. 1, pp. 91-94, (1992)

24-Shahinpoor, M.,Proc. ICIM'94, June 5-8, Williamsburg, Va., (1994)

25-Segalman, D.J., Witkowski, W.R., Adolf, D.B., and Shahinpoor,M., Int. J. Smart Materials & Structures, vol.1, no. 1, pp. 95-100, (1992)

26-Shahinpoor, M., and Osada, Y., Proc. Sapporo Symposium on Intelligent Polymer Gels, October 6-8, Hokaido University, Sapporo, Japan, (1994)

27-Shahinpoor, M. and Osada, Y., Proc. SPIE 1995 Smart Structures and Materials Conference, February 28-March 3, 1995, San Diego, Calif., volume 2441, no. 46, (1995)

28-Mojarrad, M., and Shahinpoor, M., Noiseless Propulsion for Swimming Robotic Structures Using Polyelectrolyte Ion-Exchange Membrane, Proc. SPIE Conference on Smart Structures and Materials, Feb 26-March 2, San Diego, California, Vol. 2716, pp183-192, 1996.

29-Mojarrad, M., Shahinpoor, M., Methods of Manufacturing and Applications of Electrically Controllable Artificial Muscles from Polymeric Ion-Exchange Membranes, International patent pending, ref. UNM-429, 1995.

Author Index

Aandahl, H., 112
Accettella, Stefano, 642
Aizawa, Masuo, 50
Alekseev, A. K., 925
Andre, Jean-Claude, 240
Aoyagi, Yoshinobu, 748
Arjyal, Bish, 142
Audigier, David, 560
Audoly, Christian D., 580
Aurelle, Nathalie, 592
Aurelle, Yves, 359
Auricchio, F., 487
Baboux, J. C., 152
Bakuzis, A. F., 328
Baran, Markijan, 198
Battaini, M., 907
Begg, Eric K., 700
Beige, H., 586
Benyattou, Taha, 289
Bera, J. C., 729
Bidaux, J.-E., 517
Bigeon, M. J., 481
Black, S., 913
Blanquet, P., 146, 180
Blochwitz, S., 586
Boiteux, G., 112
Boller, Christian, 16
Bondoux, Dominique, 694
Bonniau, P., 475
Bossis, G., 306
Bourasseau, S., 180
Bradt, Jens-Hilmar, 78
Briot, Roland, 628, 634
Brissaud, M., 729
Brocato, Maurizio, 891
Brock, David, 353
Broyer, M., 765
Bullough, W. A., 310
Butckevitch, A. C., 986
Calvert, Paul, 742
Campanile, L. Flavio, 682
Canistraro, Howard A., 700
Cantoni, Stefania, 706
Carius, Hans-Eckart, 401
Carman, Gregory P., 724
Casciati, F., 907
Ceysson, Olivier, 136
Chadaev, A. P., 986
Chailan, J. F., 112
Chandrasekaran, M., 475
Chang, Fu-Kuo, 118
Charmoillaux, J. F., 535
Chazelas, Jean, 475
Chen, S., 192
Chiarelli, P., 371
Chiu, W. K., 124
Chouteau, L., 634
Chovet, A., 289
Christophorov, Leonid N., 58
Claeyssen, F., 634
Colomban, Ph., 813
Concilio, A., 712, 897
Corsaro, Robert D., 570, 598
Coutellier, D., 180
Crott, M., 275
Culshaw, Brian, 174
Cutillas, S., 306
Damrongchai, N., 50
Darvish, S., 209
De Rossi, Danilo, 28, 371
De Vivo, L., 712
DeSimone, Antonio, 638
Debus, J. C., 913
Del Medico, S., 289
Delaey, L., 511
Delebarre, C., 130, 146, 180
Della Santa, A., 371
Demol, T., 146, 180
Denham, Hugh, 742
Diestelhorst, M., 586
Dokiya, Masayuki, 819
Dry, Carolyn M., 164, 958
Dubanevich, D., 838
Dubus, B., 913
Dumon, Michel, 435
Dupont, M., 180
Dupuis, V., 765
Dziuban, E., 994
Egashira, Mitsuru, 842
Egawa, Koichi, 100
Ehlers, Claus, 883
El-Sherif, Mahmoud A., 203
Emmerson, Gordon T., 235
Engelhardt, Harald, 72
Eremeev, Nicolay L., 66
Eyraud, Lucien, 560, 580, 592
Eyraud, Paul, 560
Fernandes, Luís, 269
Fiore, Daniel, 570
Fitzgerald, Edwin R., 83
Fitzgerald, James W., 83
Fölsch, Stefan, 828
Fortunato, Elvira, 269
Friend, Clifford M., 947
Fudoji, Hiroshi, 842
Fukuda, Takehito, 331
Funaki, Atsuo, 523
Furstoss, Marc, 734

Gachagan, Anthony, 174
Gafsi, Rachid, 230
Galiotis, Costas, 142
Galland, Marie-Annick, 734
Gaucher, P., 610
Gaudenzi, Paolo, 642
Gaudez, Ph., 493
Gauvin, R., 458
Gendry, M., 289
Gentilman, Richard, 570
George, Graeme, 742
Gerard, J. F., 112
Goering, Harald, 401
Golobič, Janez, 414
Golovin, Igor S., 463
Gong, J. P., 344, 349
Gonnard, Paul, 560, 564, 628, 634, 729
Gorbunov, Andre A., 72
Gotthardt, Rolf, 517
Grando, J., 530
Green, A. K., 209
Gümes, Alfredo, 217
Guénin, G., 493
Guillot, Gerard, 289
Guyomar, Daniel, 592
Habel, R., 586
Hachisuka, Takashi, 452
Han, Jae-Hung, 872
Han, Kyung Seop, 688
Haneda, Hajime, 575
Hara, Hisashi, 418
Hara, S., 802
Haralampus, N., 112
Haruyama, T., 50
Hata, Hidetoshi, 622
Hatano, Masahiro, 828
Hayashi, Shunichi, 418
Hayashi, Takayoshi, 828, 833
Hayward, Gordon, 174
Henis, A., 838
Herold-Schmidt, Ursula, 718
Hirose, Seiji, 622
Holzbauer, Hans-Rainer, 401
Hong, Chang Sun, 213
Hood, David, 112
Horita, Teruhisa, 819
Hoshi, M., 788
Houston, Brian H., 598
Hu, Yigun, 192
Hung, H. F., 794
Hwang, Woonbong, 688
Ilyin, Alexander A., 463
Inoue, Kuon, 777
Ionaitis, R. R., 974
Ishigaki, Takamasa, 575
Ishige, Keiko, 783
Ito, Hiroyuki, 777
Iwase, Mitsuo, 260
Iyi, Nobuo, 823
Izumrudov, Vladimir A., 383
Janocha, Hartmut, 603
Jayet, Y., 152, 158
Jendritza, Daniel J., 603
Jones, R., 124
Kabanov, Victor A., 383
Kaczmarek, H., 130, 146
Kafka, V., 541
Kajimura, Koji, 802
Kang, Young Kyu, 688
Kasherininov, Peter G., 266
Kazanskaya, Novella F., 66
Khmelevskaya, I. Yu., 986, 991
Kichaev, Andrei V., 266
Kikineshy, Alexander A., 919
Kikuchi, Akihiko, 34
Kim, Chun Gon, 213
Kim, Moon Hyun, 688
Kimura, Kazuhiro, 294
Kirsch, Remo, 72
Kitamura, Kenji, 823
Klunder, Joseph D., 570
Kobatake, E., 50
Kobayashi, Mikihiko, 842
Koguchi, Nobuyuki, 783
Kohl, M., 499
Kolendo, Alexey, 408
Kollerov, Mikhail U., 463
Konami, Hideo, 828
Kordos, P., 275
Korobko, Evgenija V., 337
Kranbuehl, D., 112
Kudrya, Vladislav, 408
Kuvshinnikov, S. V., 255
Kwon, Il Bum, 213
Labarrère, M., 230
Lalande, Frederic, 106
Lammering, Rolf, 682
Lan, S. M., 794
Lang, Didier, 648
Lara, M. C. F. L., 322
Lavareda, Guilherme, 269
Laye, C., 402
LeLetty, R., 634
Lebrun, Laurent, 628
Lecce, Leonardo, 706
Lecoy, Pierre, 230
Lee, In, 872
Lee, Woojin, 353
Lemaire, E., 306
Lenczner, Michel, 867
Levin, Klas, 222
Lexcellent, C., 535
Lhermet, N., 634
Liao, S. M., 794
Loos, A. C., 112
Lopez, Pierre, 359
Lüth, Hans, 275
Maazouz, A., 112

MacRae, J. D., 112
Macedo, L. G., 317
Magnaldo, A., 402
Malashevich, A., 838
Malki, Abdel R., 230
Månson, J.-A. E., 517
Mantegazza, P., 186
Martins, Rodrigo, 269
Maruno, Tohru, 828
Maryan, Michael, 919
Matsumoto, S., 349
Matsumoto, Shiro, 828
Matsuo, Jiro, 759
Mazzoldi, A., 371
McCollum, Michele D., 913
McFarland, D. Michael, 700
McNab, Alistair, 174
Melcher, Jörg, 682
Melinon, P., 765
Menéndez, José M., 217
Mensch, Axel, 72
Mertig, Michael, 72, 78
Meunier, A., 306
Meynial, Xavier, 968
Michel, Le Du, 230
Michie, W. Craig, 932
Minami, Fujio, 777
Mitrovic, Milan, 724
Miyazaki, Shuichi, 499
Mojarrad, M., 1012
Morais, P. C., 317, 322, 328
Morin, M., 481
Morisaki, Hiroshi, 260
Morozova, Tamara V., 991
Mukae, Kazuo, 848
Neitzel, Manfred, 883
Newby, W., 112
Nilsson, Soren, 222
Nó, M. L., 469
Nourry, J., 402
Nozaki, Shinji, 260
Ogata, Naoya, 393
Ogul'chanski, Tymish, 408
Okano, Teruo, 34
Okushi, H., 802
Ono, Hiroshi, 260
Osada, Yoshihito, 344, 349
Oshima, Nobuo, 331
Osmont, D., 876
Otero, T. F., 365
Paneva, Roumiana, 616
Pankov, V., 838
Park, Hyun Chul, 688
Pascault, Jean Pierre, 112, 435
Peel, D. J., 310
Pellarin, M., 765
Perez, A., 765
Pérez-Sáez, R. B., 469
Pergushov, Dmitry V., 383
Pernice, M., 180
Petit, Lionel, 628, 634
Philp, Wayne R., 174
Piedboeuf, M. C., 458
Pierce, S. G., 174
Pitt, S., 124
Pokhodenko, V. D., 389
Pompe, Wolfgang, 72, 78
Porada, Zbigniew W., 298
Posudievsky, O. Yu., 389
Prasad, J. V. R., 903
Prevel, B., 765
Prokoshkin, S. D., 986, 991
Qiu, Jinhao, 670
Radhakrishnan, Jayakumar, 203
Rahmoune, M., 876
Recarte, V., 469
Reithler, Livier, 648
Ricard, Alain, 359
Richard, Claude, 580
Richard, Pierre, 42
Rintoul, Llew, 742
Risson, Tania, 136
Roche, Denis, 580
Rogers, Craig A., 48, 106
Roh, Youn-Seo, 118
Ronkel, F., 275
Rousset, Christophe, 648
Ruano, O., 469
Ryklina, E. P., 986, 991
Sáez-Ocáriz, I., 469
Saint-Pierre, N., 152, 158
Sakai, Natsuko, 819
Sala, G., 186
Salvia, Michelle, 136, 530
San Juan, J., 469
Sankar, L. N., 903
Sansiñena, J. M., 365
Sato, Seiichi, 260
Sautereau, H., 112
Savchenko, Irina, 408
Schäfer, Wolfgang, 718
Scheer, Peter, 603
Schönhals, Andreas, 401, 424
Schöning, M. J., 275
Schulte, Karl, 90
Schultze, J. W., 275
Seeboth, Arno, 401, 430
Sewing, Andreas, 72
Seytre, G., 112
Shablovski, A., 838
Shafir, Ehud, 209
Shahinpoor, Mohsen, 1000, 1006, 1012
Shatalov, Alexei, 919
Sheehan, Anthony, 953
Shinaev, Andrei A., 463
Shinohara, Hiroaki, 53
Shinya, Norio, 842
Siddiqi, Humaira Masood, 435

Sigmund, Ole, 856
Sigolaéva, Larisa V., 66
Silvain, J. F., 475
Simon, C., 130
Sisido, Masahiko, 53
Sixou, Pierre, 402
Skrobanek, K. D., 499
Soares, Fernando, 269
Sorrentino, A., 897
Sousa, M. H., 317
Springer, Jürgen, 424
Srinivasan, A. V., 700
Stadnyk, B., 994
Stalmans, R., 511
Stanway, Roger, 310
Stepanyak, M., 994
Strümpler, Ralf G., 377
Sugawara, Sumio, 294
Sunyach, M., 729
Suzuki, Satoru, 833
Swaminathan, Ramesh, 903
Syromyatnikov, Vladimir G., 408
Tajan, V., 564
Takada, Jun, 788
Takagi, Toshinori, 2, 788
Takahashi, Kiyoshi, 260
Takano, Takehiro, 622
Tanaka, Akinori, 848
Tanaka, Junzo, 575, 823, 833
Tanaka, Kikuaki, 452
Tani, Junji, 670
Tardy, J., 289
Tatibouët, Jacques, 158
Tatti, Marco, 186
Taylor, R. L., 487
Teraji, T., 802
Thenail, Denis, 734
Thiebaud, F., 535
Thiele, Uwe, 78
Thiriot, Alain, 180
Thorpe, Chris, 947
Thust, M., 275
Ting, Robert Y., 548
Tobushi, Hisaaki, 418, 452
Tomikawa, Yoshiro, 294, 622
Tomita, Masato, 833
Tomlinson, Geoffrey R., 656
Tonci, C., 371
Tondu, Bertrand, 359
Tourinho, F. A., 317, 322, 328
Tracy, Michael, 118
Traversa, Enrico, 281
Troccaz, M., 564
Trochu, F., 458
Trombert, S., 475
Tsuda, Koichi, 848
Tuaillon, J., 765
Ueoka, Y., 344
Ullakko, Kari, 505
Van Humbeeck, Jan, 442, 511
Van Moorleghem, W., 475
Vasil'ev, A. N., 255
Vasiljević, Darko M., 414
Venet, T., 289
Vial, Dominique, 359
Vialle, J. L., 765
Viscardi, Massimo, 706
Vokoun, D., 541
Volkova, O., 306
Voloshok, T. N., 255
Wang, Xiaoming, 883
Watanabe, Kenji, 777
Watanabe, M., 788
Wen, Jung Hung, 794
Winzer, Bettina, 78
Wolff, Dietmar, 424
Yamada, Etsuko, 418
Yamada, Isao, 753, 759
Yamada, Shinya, 452
Yamamoto, T., 788
Yamashita, Akira, 828
Yanagida, Hiroaki, 807
Yano, Shoichiro, 523
Yashchuk, Valeriy, 408
Yokokawa, Harumi, 819
Yoshida, Hitoshi, 523
Yoshida, Kouji, 777
Yuan, Jianming, 203
Zaglauer, Helmut W., 718
Zahlan, Nabil, 235
Zeghmati, B., 535
Zellouf, D., 158
Zezin, Alexander B., 383
Zolkin, Alexander S., 772